Cover Picture

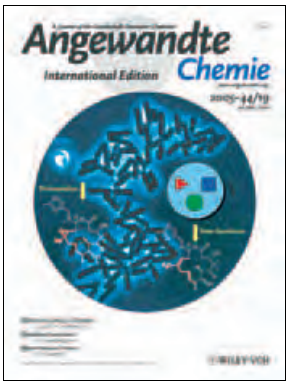

Alexey Rivkin, Ting-Chao Chou, and Samuel J. Danishefsky*

Synthetic and biological studies of epothilone B (isolated from a myxobacterium) led to the discovery of a 26-trifluoro analogue that is remarkably active in treating xenograft tumors in nude mice. These findings underscore the potential of using natural products as leads, in conjunction with directed total synthesis, in the quest for new drugs. S. J. Danishefsky and co-workers present their synthetic strategy along with biological data in their Minireview on page 2838 ff.

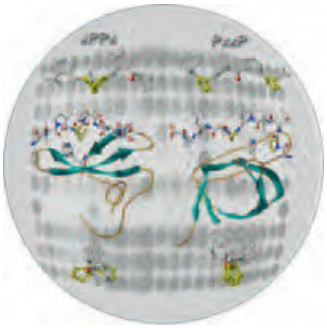

Protein Recognition
Many cellular processes involve proline-mediated protein–protein interactions. In their Review on page 2852 ff. L. J. Ball, H. Oschkinat, et al. describe the structural characteristics of the binding domains concerned and the complexes formed.

Magnetic Nanoparticles
T. Hyeon et al. obtain 6 to 13 nm monodispered magnetic iron oxide nanoparticles by a technique that they report in their Communication on page 2872 ff. The method is a variation of a seed-mediated growth approach.

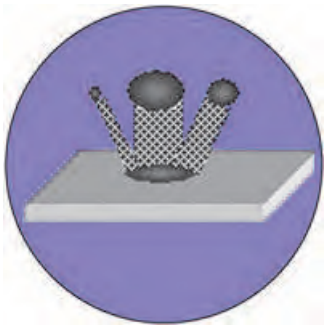

Nanowires
Quasi-parallel nanowires that originate from well-controlled single particle sites are formed in the low-temperature chemical vapor deposition process described by H. Dai and co-workers in their Communication on page 2925 ff.

VIP *The following Communications have been judged by at least two referees to be "very important papers" and will be published online at www.angewandte.org soon:*

Meeting Reviews

Books

Highlights

V for victory? Theory has suggested that V-shaped molecules may provide a route to biaxial nematic liquid crystals (see picture). The identification of a biaxial nematic phase is, however, a challenging task. Even if it is yet to be agreed that the hunt is over, it appears that this path is well worth pursuing.

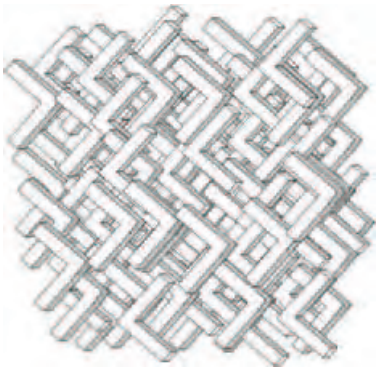

Liquid Crystals

Minireviews

A retrospective account of the discovery through chemical synthesis of the second-generation epothilone drug candidates the 9,10-dehydroepothilones (e.g. fludelone (**1**)) is presented. The importance of natural products as leads in drug development is highlighted, as well as the use of molecular editing through chemical synthesis to fine-tune the biological and pharmacodynamic properties of the natural product to develop a viable drug.

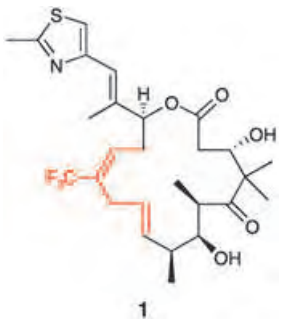

1

Epothilone Derivatives

The best in chemistry –

for more than a hundred years

A Journal of the Gesellschaft Deutscher Chemiker

Angewandte
International Edition **Chemie**

www.angewandte.org

1888: ***The beginning of a success story***

Constant Innovations

1962: *First issue of the International Edition*
1976: *Graphical abstracts*
1979: *Cover pictures*
1988: *Centenary of Angewandte*
1989: *Routine use of color*
1991: *New section: Highlights*
1992: *Computerized editorial tracking system*
1995: *Internet service for readers*
1998: *Regular press service; full-text online*
2000: *New section: Essays; EarlyView: Communications available online ahead of the printed version*
2001: *New section: Minireviews*
2002: *Online submission of manuscripts*
2003: *Weekly publication; new section: News; new layout*
2004: *Backfiles (1962-1997); ManuscriptXpress: Online system for authors and referees*

Angewandte's advisors...

Martin Jansen
Max-Planck-Institut für Festkörperforschung, Stuttgart

»Professional presentation of the latest research in all fields of chemistry is the distinguishing characteristic that makes ***Angewandte Chemie*** *indispensable. This journal leads students to the cutting edge of chemical knowledge.«*

Angewandte Chemie International Edition *is a journal of the German Chemical Society (GDCh)*

GDCh

WILEY InterScience® DISCOVER SOMETHING GREAT

WILEY-VCH

1894504_gu

Reviews

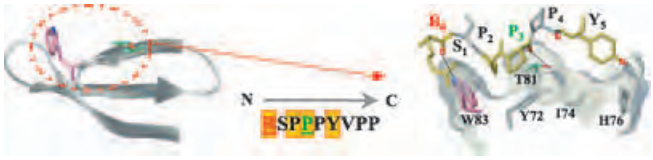

Solving the mystery of mutual attraction: Proline-mediated protein–protein interactions are involved in the regulation of numerous essential cellular processes. Analysis of the structures of complexes formed between proline-rich peptides and their respective binding domains (see figure) reveals fundamental features of this mechanism of recognition, which is highly specific, yet only requires low binding affinities.

Communications

Accurate to size: Monodisperse magnetic iron oxide nanoparticles with a continuous size spectrum of 6–13 nm have been synthesized by a procedure similar to seed-mediated growth and characterized by transmission electron microscopy (see picture) and magnetic measurements. This method yields monodisperse nanoparticles directly without a size-selection process.

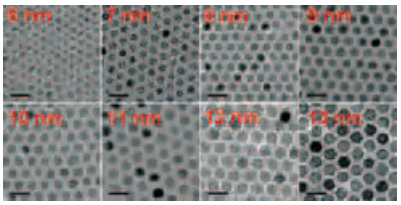

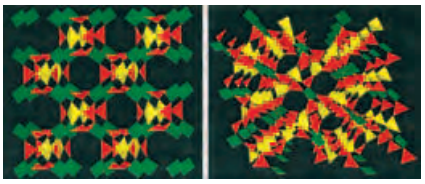

Three not of a kind: Two metal–organic nets sustained by three different molecular building blocks, triangles, squares, and tetrahedra, are prepared and characterized. The shapes (see picture red triangles, green squares, yellow tetrahedra) reveal how appropriate combinations of vertex-linked polygons or polyhedra afford novel topologies that could be prototypal of an even wider range of organic and metal–organic compounds.

For the USA and Canada:
ANGEWANDTE CHEMIE International Edition (ISSN 1433-7851) is published weekly by Wiley-VCH PO Box 191161, D 69451 Weinheim, Germany. Air freight and mailing in the USA by Publications Expediting Inc. 200 Meacham Ave., Elmont, NY 11003. Periodicals postage paid at Jamaica NY 11431. US POSTMASTER: send address changes to *Angewandte Chemie*, Wiley-VCH, 111 River Street, Hoboken, NJ 07030. Annual subscription price for institutions: US$ 4948.00/4498.00 (valid for print and electronic / print or electronic delivery); for individuals who are personal members of a national chemical society, or whose institution already subscribes, or who are retired or self-employed consultants, print only: US$ 394.00. Postage and handling charges included. All Wiley-VCH prices are exclusive VAT.

Contents

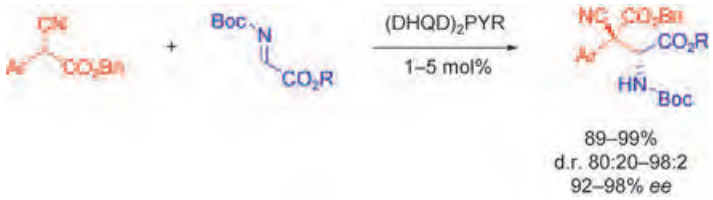

Metal-free catalysis: Highly functionalized molecules with two contiguous stereocenters are easily accessed in high yield with high enantio- and diastereoselectivity by using a commercially available organocatalyst ($(DHQD)_2PYR$, see scheme). The easily removed Boc protecting group in the product is an added value to this method as an important tool in asymmetric synthesis.

Asymmetric Synthesis

An effective macrocyclic ionophore for F^- ions that contains an array of positively charged imidazolium units has been prepared. The calix[4]imidazolium[2]pyridine cation formed a complex with F^- ions in a 1:1 stoichiometry, as shown by binding studies using ^1H NMR spectroscopic analysis, X-ray crystallographic determination (see structure), and density functional calculations.

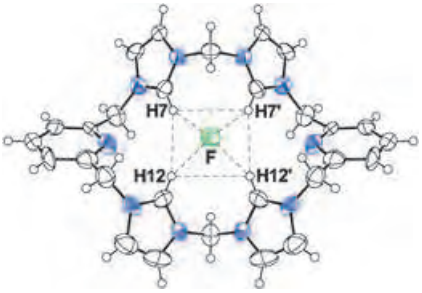

Supramolecular Chemistry

Inhibitors of the interaction between protein VLA-4 and its natural ligand VCAM-1 have been designed, even though the structure of the protein remains unresolved. The rational design relied on the simulation of the steric and electronic properties of the active loop of VCAM-1, whose structure is known (see picture), and the inhibitors were readily prepared by stereoselective stepwise [3+2] cycloadditions.

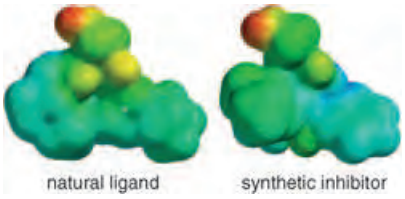

Synthetic Inhibitors

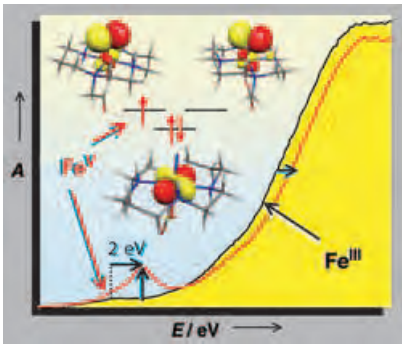

Low-spin, high-valent iron centers: A high-valent iron–nitrido species containing a Fe^V center is accessible by the photolysis of $[(cyclam\text{-}ac)Fe^{III}N_3]^+$. The identity of the resulting $[(cyclam\text{-}ac)Fe^{V}(N)]^+$ species was verified by spectroscopic methods, magnetic susceptibility data, and DFT calculations (see picture). Unexpectedly, the analysis provides strong evidence for a low-spin d^3 ($S = 1/2$) ground-state electron configuration at the Fe^V center.

Bioinorganic Chemistry

Contents

Several breakthroughs in nanowire synthesis are reported for germanium nanowires grown from gold nanoparticle seeds by a low-temperature chemical vapor deposition process. Conditions were optimized to observe the formation of nanowires in near-quantitative yields, and post-growth flow-alignment was used to obtain quasi-parallel nanowires that originate from well-controlled singleparticle sites (see images).

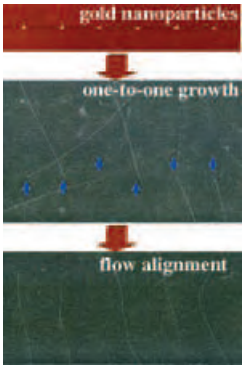

Nanostructures

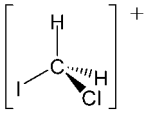

The vibrational spectrum of $[CH_2{}^{35}ClI]^+$ (see formula) was recorded by mass-analyzed threshold ionization (MATI) spectrometry. Spin–orbit effects were used in density functional calculations to determine the structure of the ground state of the cation. The results suggest that spin–orbit terms should be treated the same as other relativistic effects in some cases.

Dihalomethane Structures

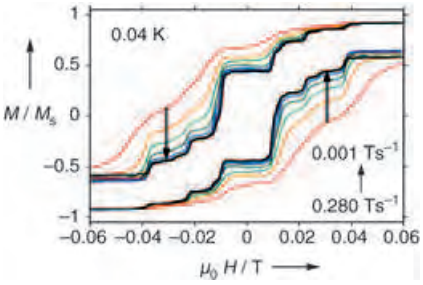

Staircase-like structures in the hysteresis loops at 0.04 K (see picture) are shown by doped single crystals of $TBA[(Pc)_2Tb^{III}_{0.02}Y^{III}_{0.98}]^-$ (Pc = phthalocyaninato, TBA = tetrabutylammonium), the first lanthanide single-molecule magnet. They are assigned to resonant quantum tunneling of magnetization between entangled states of the electron and nuclear spin systems. The Dy complex was also studied.

Single-Molecule Magnets

Right angles: In solid-state magic-angle spinning (MAS) NMR spectra, the line widths of carbonyl carbon atoms in polycrystalline cholesteryl acetate are found to be as narrow as 0.039 ppm if the magic angle is adjusted very accurately, that is, within $\pm 0.004°$ (see picture). The line broadening observed for slightly miss-set angles is mostly due to residual chemical shift anisotropy (CSA) interactions. Long spin-echo life times up to $T_2' = 3.6$ s open the way to sophisticated NMR methods.

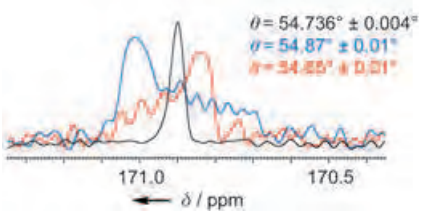

NMR spectroscopy

Contents

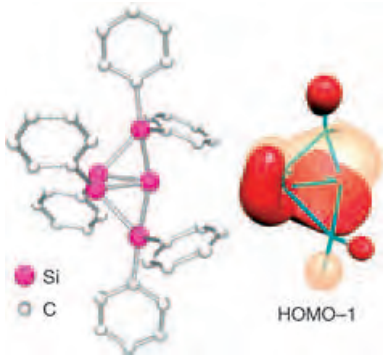

Reaction of a disilenide with $SiCl_4$ produces a silicon cluster with π-bonding topology reminiscent of a Möbius array, as determined by structural data and DFT calculations (see picture). Partially hydrogenated silicon clusters are important for the optical properties of many silicon materials. The availability of a derivative that is stable in the absence of surrounding Si^0 yields insight into the structure of such compounds.

Cluster Compounds

It can come as a surprise to plant lovers to find the fruit bodies of *Leucocoprinus birnbaumii* (see picture) in their flower pots. This fragile fungus, which is harmless to plants, owes its yellow color to the unusual alkaloids birnbaumin A and B, in which a 1-hydroxyindole-3-glyoxylic acid amide is attached through a tetramethylene unit to *N*-hydroxyoxamidine. *N*-Hydroxyoxamidines have not been described previously.

Structure Elucidation

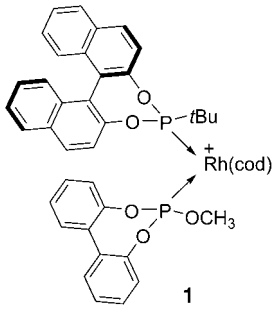

1

Mixed (pre)catalysts such as **1** arise when $[Rh(cod)_2]BF_4$ is combined with a 1:1 mixture of a BINOL-derived monodentate phosphonite or phosphite ligand and a configurationally fluxional atropisomeric phosphite with a biphenol backbone. These systems provide excellent results for the Rh-catalyzed asymmetric hydrogenation of β-acylamino acrylates. BINOL = 2,2′-dihydroxy-1,1′-binaphthyl; cod = cycloocta-1,5-diene.

Combinatorial Catalysis

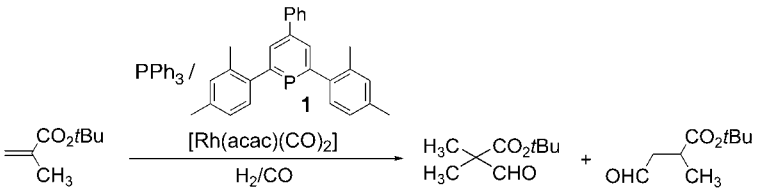

1 + 1 ≠ 2: The mixture of triphenylphosphine and phosphinine **1** with $[Rh(acac)(CO)_2]$ forms a hydroformylation catalyst that effects the preferential formation of the branched product, even though each ligand alone mediates the opposite regioselectivity. Similar effects were observed for a series of other ligand combinations.

Combinatorial Catalysis

Contents

Service

Dendrimers: Platforms for Chemical Functionality**

Jean-François Nierengarten*

Since the pioneering work of F. Vögtle in the late 1970s, the synthetic concept based on repetitive growth with branching units has been extensively investigated leading to a wide range of core–shell macromolecular structures now recognized as dendrimers.[1] In recent years, the rapid advances in dendrimer synthesis have moved toward the creation of functional dendrimers with increased attention to potential applications. Because of their intrinsic branched structure, dendrimers are original scaffolds for the preparation of high molecular weight compounds. One of the most appealing features is the possibility of tuning their properties by changing the number, chemical nature, and relative position of functional units within the branched structure. In this way, dendritic architectures are capable of generating specific properties. The exploitation of this new type of macromolecule in a variety of applications ranging from materials science to biology were the focus of the recent Leopoldina Meeting in Heidelberg, Germany organized by L. H. Gade and H. Werner with the support of the Deutsche Akademie der Naturforscher "Leopoldina" and the Sonderforschungsbereich 623.

The first session immediately revealed the large diversity of structures in the field of dendrimers. The opening lecture of K. Müllen (Mainz, Germany) focused on polyphenylene-based dendrimers[2] which have a rigid framework in contrast to most types of dendrimers. As a result, these compounds are shape-persistent and can therefore define the positioning of active functions in the core, the dendritic scaffold, or on the surface. The latter structural peculiarity, for example, was used to produce multichromophoric systems in which the intramolecular energy transfer events between multiple dyes can be controlled through their relative distance and orientation within the dendritic framework. These studies are not only important for the fundamental understanding of photoinduced processes, but appears to be of great interest for the design of single-photon emitters. A. D. Schlüter (Zürich, Switzerland) presented the preparation and characterization of dendritic monomers as well as their polymerization to give functionalized dendronized polymers. The thickness of these polymers is in the range of several nanometers and they can be visualized by AFM as elongated wormlike structures;[3] they are amongst the largest molecules ever synthesized.

Dendritic-based materials are widely used as soluble supports in homogeneous catalysis,[4] enabling easy recycling of the catalyst through nanofiltration. This concept was the main focus of the communications of J. N. H. Reek (Amsterdam, The Netherlands), R. J. M. Klein Gebbink (Utrecht, The Netherlands) and D. Astruc (Bordeaux, France). The dendritic framework can be functionalized with the catalyst either at the core or at the periphery, which determines catalytic performance to a great extent. Of particular interest is the use of noncovalent interactions to attach the catalytic entities to a dendritic scaffold. The research group from Utrecht, for example, has developed a new type of cationic core–shell dendrimer architecture derived from oligoamine core molecules, in which permanent cationic charges are located at the cores of the resulting dendrimers. With ionic exchange reactions, a predefined number of anionic guest molecules with catalytic properties can be affiliated with these dendrimers. The reversible nature of this type of anchoring allows controlled de- and re-functionalization of the support, which enables facile reuse of the support. An example is depicted in Figure 1.

R. M. Crooks (College Station, Texas, USA) is also focused on applications in the field of catalysis,[5] but his approach is completely different. The materials he described were synthesized by a template method in which metal

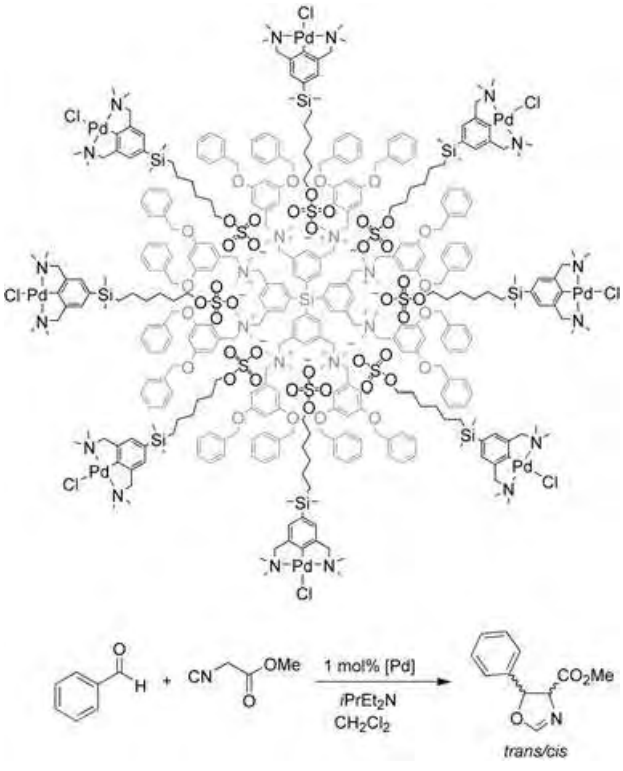

Figure 1. Dendrimers with a polycationic core surrounded by poly(aryl ether) dendrons applied as host molecules for the noncovalent binding of catalytically active palladium(II) complexes, and an example of a catalyzed reaction (kindly provided by R. J. M. Klein Gebbink, Utrecht, The Netherlands).

[*] Dr. J.-F. Nierengarten
Groupe de Chimie des Fullerènes et des Systèmes Conjugués
Université Louis Pasteur et CNRS, Ecole Européenne de Chimie, Polymères et Matériaux (ECPM)
25 rue Becquerel
67087 Strasbourg Cedex 2 (Frankreich)
Fax (+33) 390-24-27-06
E-mail:
jfnierengarten@chimie.u-strasbg.fr

[**] Leopoldina Meeting "Dendrimers: Platforms for Chemical Functionality", organized by the Deutsche Akademie der Naturforscher Leopoldina and the Sonderforschungsbereich "Molekulare Katalysatoren" (Sfb 623), Heidelberg (Germany), March 18–19, 2005.

  DOI: 10.1002/anie.200501226

ions are sorbed into the dendrimer interior and subsequently subject to chemical reduction to yield nearly monodisperse metal particles of oxidation state 0 and diameters of less than 4 nm. The dendrimer component of these composites serves not only as a template for nanoparticle preparation, but also to stabilize the nanoparticle, making it possible to tune solubility and to enhance catalytic selectivity. These materials have been used for a broad range of catalytic reactions, including hydrogenations, Heck coupling, and Suzuki reactions.

In the field of materials science, the nanometer scale of dendrimers is believed to allow the elaboration of complex nanoarchitectures and devices. J.-P. Majoral (Toulouse, France) highlighted the role played by phosphorus dendrimers developed in Toulouse for the development of organic–inorganic hybrid materials and for the controlled modification of inorganic surfaces.[6] Particularly appealing is the work involving the application in DNA chips. A 5'-amino-modified 35mer oligonucleotide (probe) was spotted onto slides modified with dendrimers bearing peripheral aldehyde units (Figure 2). The resulting imine bonds as well as the remaining aldehydes were reduced. Hybridization was then carried out with a fluorescent 15mer Cy5-labeled complementary strand (target). These "dendri-chips" are very stable and reusable. Indeed, repeated hybridization/stripping cycles were possible without any loss of signal. In addition, the detection limit of such chips was found to be better than most of the commercially available activated slides. This high sensitivity is particularly interesting and probably results from the three-dimensional form of the dendrimers which keeps the oligonucleotides away from the solid surface of the chip.

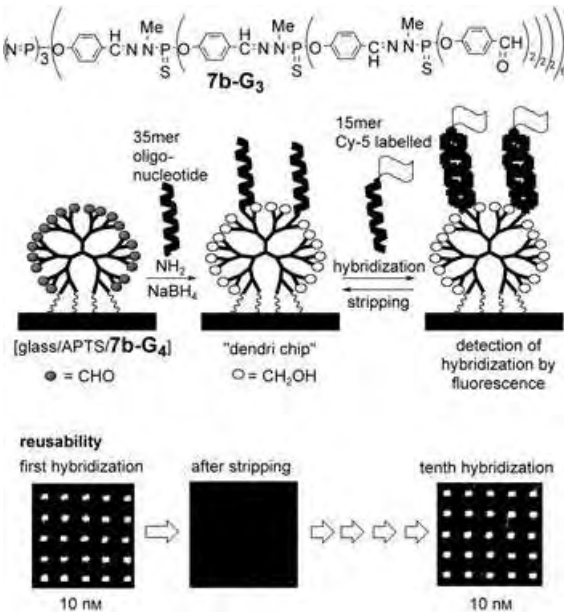

Figure 2. Top: elaboration of a "dendri-chip" with dendrimers as spacers. Bottom: fluorescence detection of hybridization of the 15mer Cy-5 labeled oligonucleotide on the "dendri-chip". Results after 10 hybridization/stripping sequences with a target concentration of 10 nM. (kindly provided by J.-P. Majoral and A.-M. Caminade, Toulouse, France).

Core–shell-structured nanotransporters have gained great attention over the last year for the transport of active substances.[7] R. Haag (Berlin, Germany) presented the latest advances of his research group in the use of dendritic architectures for the delivery of DNA and drugs. He introduced a new molecular nanotransport system suitable for the encapsulation of both polar and nonpolar molecules. The architecture of this universal type of nanocarrier consists of two shells with different polarity arranged around a dendritic core. Linkers between the shells or between the shell and core can be either chemically stable or chemically labile. In this manner the liberation of encapsulated molecules can be induced by external signals, such as a change in pH.

The final lecture given by F. Vögtle (Bonn, Germany) was an overview of the field. He clearly demonstrated that dendrimers have already shown a wide range of unique physical and chemical properties that make them attractive for medicinal chemistry and the preparation of new advanced materials. Dendrimer applications encompass a wide range of technologies. One of the most important conclusions is that many developments rely on new materials and our ability to obtain an intimate understanding of their properties. Modern organic synthesis is the starting point of this research, as compounds must first be made and studied, and then modified to improve their properties towards projected applications. In the long run, there will be a move toward the design and creation of an increasing number of new materials for direct industrial application.

[1] a) E. Buhleier, W. Wehner, F. Vögtle, *Synthesis* **1978**, 155–158; b) G. R. Newkome, C. N. Moorefield, F. Vögtle, *Dendrimers and Dendrons: Concepts, Syntheses, Applications*, Wiley-VCH, Weinheim, **2001**.

[2] A. J. Berresheim, M. Müller, K. Müllen, *Chem. Rev.* **1999**, *99*, 1747–1785.

[3] A. D. Schlüter, *C. R. Chim.* **2003**, *6*, 843–851.

[4] D. Astruc, F. Chardac, *Chem. Rev.* **2001**, *101*, 2991–3024.

[5] Y. Niu, R. M. Crooks, *C. R. Chim.* **2003**, *6*, 1049–1059.

[6] J.-P. Majoral, A.-M. Caminade, V. Maraval, *Chem. Commun.* **2002**, 2929–2942.

[7] R. Haag, *Chem. Eur. J.* **2001**, *7*, 327–335.

Liquid Crystals

V-Shaped Molecules: New Contenders for the Biaxial Nematic Phase

*Geoffrey R. Luckhurst**

Keywords:
bent-core molecules · biaxial nematic · liquid crystals · mesophases · phase transitions

Since their discovery in the 1880s, the number of different thermotropic liquid-crystal phases has grown, with an increasingly complex molecular organization observed within the phases. The discovery of new phases has often been accidental, although in recent years theoretical predictions have stimulated such discoveries; the twist grain boundary phase formed on introducing molecular chirality into smectic phases is an excellent example.[1] Another example of the prediction of a liquid-crystal phase is the biaxial nematic phase. The simplest and commercially most important liquid crystal is the uniaxial nematic phase, N_U, which is taken to have $D_{\infty h}$ symmetry. The term uniaxial is borrowed from the field of optics and indicates that plane-polarized light can travel along just one axis without a change in its state of polarization. This axis is the optic axis, and on a molecular level it corresponds to the axis also known as the director and denoted by the apolar unit vector, ***n***, along which the constituent rodlike molecules tend to be orientationally ordered.

Although the molecules that form the majority of thermotropic liquid crystals are certainly elongated,[2] they do not have the infinite rotation axis often assumed for them. From the molecular structure of a typical calamitic mesogen, such as 4,4′-dimethoxyazoxybenzene shown in Figure 1a, it is clear that its shape is boardlike and that its symmetry is closer to D_{2h} than $D_{\infty h}$. In 1970 Freiser[3] suggested that this reduction in molecular symmetry should result in the formation not only of the uniaxial nematic but also of a new nematic phase. He termed the new phase as biaxial, N_B, to indicate that there are now two axes along which plane-polarized light can travel without a change in the state of polarization, consistent with the D_{2h} symmetry of the phase. The molecular organization within the new phase is sketched in Figure 1b; the three directors, ***l***, ***m***, and ***n***, are associated with the preferred orientation of the three symmetry axes of the orthorhombic molecular blocks. It was also predicted that as the molecular biaxiality increased, so the stability of the biaxial with respect to the uniaxial nematic phase increased until at a unique value of the biaxiality the isotropic phase underwent a second-order transition directly to the biaxial nematic phase.[3,4] This unique value is known as a Landau point. This behavior is in clear contrast to the first-order uniaxial-nematic–isotropic transition, although the biaxial-nematic–uniaxial-nematic transition is second order. These predictions concerning the transitions have proved to be of value in attempting to characterize the nature of the phases for real nematogens.

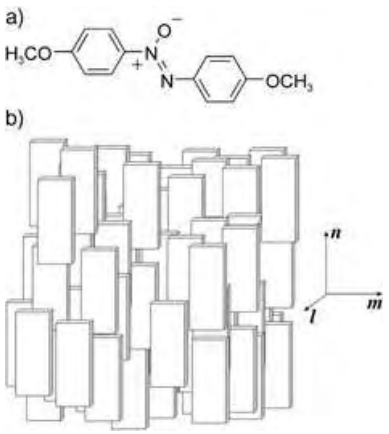

Figure 1. a) The biaxial structure of a typical mesogenic molecule, and b) the organization of the molecular blocks in a biaxial nematic phase.

The design and synthesis of biaxial molecules with sufficient anisotropy to form liquid-crystal phases is relatively straightforward in principle, but it was not until 16 years after Freiser's seminal prediction that the first claim to have found the biaxial nematic phase appeared.[5] There then followed a number of such claims for materials in which the molecular biaxiality resulted from a mixture of rodlike and disklike structural elements in the molecule.[6] In view of the manifest molecular biaxiality, it was perhaps to be expected that they would exhibit the biaxial nematic phase. A variety of techniques were employed to identify the phase,[7] and one such method was based on the observation of the optical texture under the polarizing microscope, which is so powerful in assigning other liquid-crystal phases. More significantly, the biaxiality in tensorial properties such as the refractive index or dielectric permittivity should provide the most convincing demonstration of the phase symmetry. However, the determination of this biaxiality is not trivial as it is usually necessary to apply constraints to the system to align two of the directors uniformly throughout the sample, while the third will follow the other two. In the case of the refractive

[*] Prof. G. R. Luckhurst
School of Chemistry and
Southampton Liquid Crystal Institute
University of Southampton
Southampton SO171BJ (UK)
Fax: (+44) 23-8059-3781
E-mail: gl@soton.ac.uk

  DOI: 10.1002/anie.200500709

index, conoscopy provides an extremely sensitive method with which to determine the biaxiality.[7] However, this is also its weakness because the surfaces used to align the thin film may induce a phase biaxiality that could be responsible for any small optical biaxiality that is observed.[7]

In principle, ^{2}H NMR spectroscopy provides a more powerful approach as the bulk phase is studied and the directors are not required to be uniformly aligned.[8,9] This method has been applied to at least three compounds that were claimed to form a biaxial nematic phase, and it was found that the nematic phase is, in fact, uniaxial.[10–12] It would seem that although the molecules are certainly biaxial, the uniaxial nematic phase crystallizes or is interrupted by a smectic phase before the anticipated biaxial nematic phase can be formed.

This failure to find a compound capable of exhibiting the biaxial nematic phase suggests that the molecular design needs to be guided more quantitatively by theory and that possibly other strategies should be explored. One new approach that has been suggested is to use a bent molecule, which we refer to as V-shaped, although the terms bent-core, banana-like, or boomerang-like are also employed. In V-shaped molecules, two rodlike mesogenic groups are linked together through a central unit, as shown in Figure 2a. Such a molecule is clearly biaxial and displays near-C_{2v} symmetry. What is needed, however, is the value of the inter-arm angle (θ_V) that will maximize the stability of the biaxial nematic. This parameter has been studied theoretically with a model based purely on repulsive molecular interactions[13] and subsequently with another model using, implicitly, both attractive and repulsive anisotropic interactions.[12]

For a symmetric V-shaped molecule, the dependence of the transition temperatures on the inter-arm angle predicted by the latter model[12] is shown in Figure 2b. For the linear conformation, the system can only form a uniaxial nematic, but as the molecule is bent a biaxial nematic is introduced and the uniaxial-nematic–isotropic transition temperature falls. The Landau point is found when the angle adopts the tetrahedral value of 109.47°, which is identical to that predicted by the model based on repulsive interactions.[13] The phase diagram in Figure 2b also shows a conservative estimate of the lowest temperature at which the system is expected to crystallize, and it is immediately apparent that the range of angles for which the biaxial nematic phase should be observed is extremely small, at approximately $\pm 2°$. Such a narrow range is consistent with the limited concentration and temperature range over which lyotropic biaxial nematics are found to exist.[14] Of course, the fundamental units in thermotropic and lyotropic liquid crystals are quite different, however, the macroscopic order parameters that characterize the two nematic phases are the same.

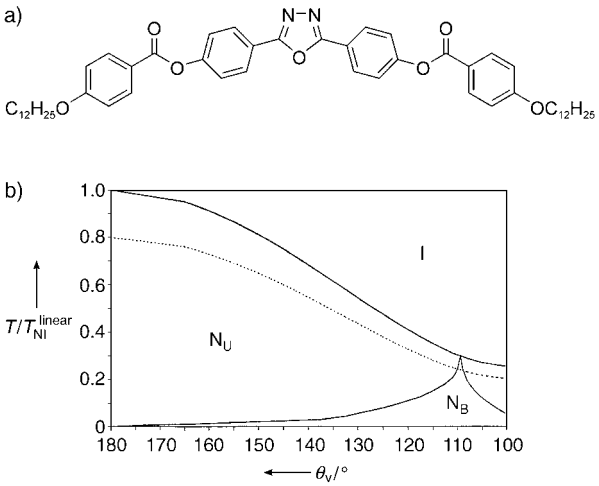

Figure 2. a) The structure of a V-shaped mesogenic molecule, and b) the predicted dependence of the transition temperatures on the inter-arm angle (θ_V). T_{NI}^{linear} is the nematic–isotropic transition temperature for the linear conformation.

One of the first V-shaped molecules for which a biaxial nematic phase was claimed is that shown in Figure 2a. The compound displays the phase sequence isotropic and nematic followed by two unidentified smectic phases.[15] The angle between the two mesogenic arms is about 140° and this is far outside the range for which a biaxial nematic has been predicted. However, the large transverse electrical dipole may stabilize the biaxial phase, although such interactions might be expected to result in a polar biaxial nematic.[16] It is important that the evidence supporting the phase assignment is strong. This evidence involves the optical texture, which is consistent with a biaxial nematic but is not unequivocal. Conoscopy shows that the refractive index is biaxial, but this biaxiality is small and its temperature variation is weak. This observation contrasts with theoretical predictions and the behavior found for a lyotropic biaxial nematic.[14]

The bulk system has been studied by ^{2}H NMR spectroscopy, which is a challenging experiment given the very high temperatures (173–222 °C) over which the biaxial nematic exists. Detailed simulations of the spectra suggest that the phase is biaxial, although the phase biaxiality is relatively small and not as sensitive to changes in temperature as theory predicts. The other significant piece of evidence in support of the phase biaxiality is provided by X-ray scattering studies.[17] Alignment of the ***n*** director by a magnetic field results in an unusual small-angle scattering pattern which seems to indicate that the ***m*** director is also aligned, although the origin of the torque responsible for this is not clear. The directors for a biaxial nematic formed from V-shaped molecules are shown in Figure 3a.

In a second experiment, surfaces were used to align the ***n*** director in the plane of the surface and surprisingly the small-angle scattering pattern again suggests that the ***m*** director is also aligned in the plane but orthogonal to ***n***. Application of an electric field orthogonal to the surface causes the ***m*** director to align parallel to the electric field and so orthogonal to the surface to result in a significant change in the scattering pattern. This does suggest that the nematic phase is indeed biaxial as the wide-angle scattering shows that the orientation of the ***n*** director is unchanged. However, there is always the possibility that the electric field ($E = 6\,\mathrm{MV\,m^{-1}}$) polarizes the phase and so induces the phase biaxiality, although the field may be somewhat small to achieve this.

The evidence presented concerning the phase symmetry of compounds formed from V-shaped molecules certainly suggests that the synthesis of

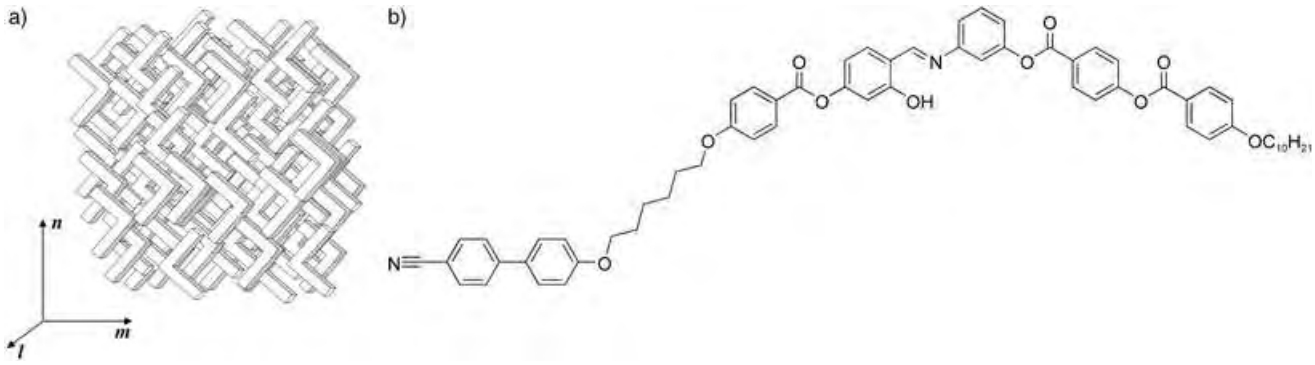

Figure 3. a) The molecular organization in a biaxial nematic phase formed from V-shaped molecules, and b) the structure of an elaborated nonsymmetric V-shaped mesogenic molecule.

analogous structures preferably with lower transition temperatures would be of merit. Such compounds would facilitate the experiments to determine the phase symmetry and would remove any concerns over the thermal stability of the compounds. Another design strategy, in addition to changing the interarm angle, would be to make the anisotropy of the two arms different, as theory shows that this effect should also change the stability of the phase. Indeed a more elaborate, nonsymmetric V-shaped molecule, shown in Figure 3b, has been reported in which a rodlike unit is attached by means of a flexible spacer to the V-shaped unit.[18] In its all-*trans* conformation this extra group would remove the equivalence of the two mesogenic arms. However, the flexibility of the spacer, the terminal decyloxy chain, and the links to the central unit means that the molecule will adopt a range of conformations, often not V-shaped, and have a lower biaxiality. In consequence, the overall molecular biaxiality is difficult to judge. Nonetheless, evidence from the studies of optical texture and conoscopy suggest that the nematic phase is biaxial. However, experience has shown that this evidence is not sufficient and that definitive confirmation of the biaxial symmetry of the nematic phase requires NMR spectroscopy and possibly X-ray scattering experiments.

Published online: April 21, 2005

[1] P. G. de Gennes, *Solid State Commun.* **1972**, *10*, 753–756; S. R. Renn, T. C. Lubenski, *Phys. Rev. A* **1988**, *38*, 2132–2147; J. W. Goodby, M. A. Waugh, S. M. Stein, E. Chin, R. Pindak, J. S. Patel, *J. Am. Chem. Soc.* **1989**, *111*, 8119–8125.

[2] M. Hird in *The Physical Properties of Liquid Crystals: Nematics* (Eds.: D. A. Dunmur, A. Fukuda, G. R. Luckhurst), IEE INSPEC, London, **2001**, chap. 1.1.

[3] M. J. Freiser, *Phys. Rev. Lett.* **1970**, *24*, 1041–1043.

[4] N. Boccara, R. Mejdani, L. de Seze, *J. Phys.* **1977**, *38*, 149–151.

[5] J. Malthête, H. T. Nguyen, A. M. Levelut, *J. Chem. Soc. Chem. Commun.* **1986**, 1548–1549.

[6] S. Chandrasekhar, B. K. Sadashiva, B. R. Ratna, V. J. Raja, *Pramana* **1988**, *30*, L491–L494; K. Praefcke, B. Kohne, D. Singer, D. Demus, G. Pelzl, S. Diele, *Liq. Cryst.* **1990**, *7*, 589–594; S. Chandrasekhar, G. G. Nair, D. S. S. Rao, S. K. Prasad, K. Praefcke, D. Singer, *Mol. Cryst. Liq. Cryst.* **1996**, *288*, 7–14.

[7] Y. Galerne, *Mol. Cryst. Liq. Cryst.* **1998**, *323*, 211–229.

[8] P. J. Collings, D. J. Photinos, P. J. Bos, P. Ukleja, J. W. Doane, *Phys. Rev. Lett.* **1979**, *42*, 996–999.

[9] F. P. Nicoletta, G. Chidichimo, A. Golemme, N. Picci, *Liq. Cryst.* **1991**, *10*, 665–674.

[10] S. M. Fan, I. D. Fletcher, B. Gundogan, N. J. Heaton, G. Kothe, G. R. Luckhurst, K. Praefcke, *Chem. Phys. Lett.* **1993**, *204*, 517–523.

[11] J. R. Hughes, G. Kothe, G. R. Luckhurst, J. Malthête, M. E. Neubert, I. Shenouda, B. A. Timimi, M. Tittlebach, *J. Chem. Phys.* **1997**, *107*, 9252–9263.

[12] G. R. Luckhurst, *Thin Solid Films* **2001**, *393*, 40–52.

[13] P. I. C. Teixeira, A. J. Masters, B. M. Mulder, *Mol. Cryst. Liq. Cryst.* **1998**, *323*, 167–189.

[14] L. J. Yu, A. Saupe, *Phys. Rev. Lett.* **1980**, *45*, 1000–1003.

[15] L. A. Madsen, T. J. Dingemans, M. Nakata, E. T. Samulski, *Phys. Rev. Lett.* **2004**, *92*, 145505.

[16] B. Mettout, P. Toledano, H. Takezoe, J. Watanabe, *Phys. Rev. E* **2002**, *66*, 01701.

[17] B. R. Acharya, A. Primak, T. J. Dingemans, E. T. Samulski, S. Kumar, *Pramana* **2003**, *61*, 231–237; B. R. Acharya, A. Primak, S. Kumar, *Phys. Rev. Lett.* **2004**, *92*, 145506.

[18] C. V. Yelamaggad, S. K. Prasad, G. G. Nair, I. S. Shashikala, D. S. S. Rao, C. V. Lobo, S. Chandrasekhar, *Angew. Chem.* **2004**, *116*, 3511–3514; *Angew. Chem. Int. Ed.* **2004**, *43*, 3429–3432.

Epothilone Derivatives

On the Remarkable Antitumor Properties of Fludelone: How We Got There**

*Alexey Rivkin, Ting-Chao Chou, and Samuel J. Danishefsky**

Keywords:
anticancer drugs · drug development · epothilones · natural products · total synthesis

Dedicated to Professor George Olah

Small-molecule natural products are presumably often biosynthesized with a view to optimizing their ability to bind to strategic proteins or other biomolecular targets. Although the ultimate setting in which a drug must function may be very different, the use of such natural products as lead compounds can serve as a significant head start in the hunt for new agents of clinical value. Herein we reveal the synergistic relationship between chemical synthesis and drug optimization in the context of our research program around the epothilones: how synthesis led to the discovery of more-potent epothilone derivatives, and discovery inspired the development of new synthetic routes, thus demonstrating the value of target-directed total synthesis in the quest for new substances of material clinical benefit.

1. Introduction

Nature, during the course of evolution, has provided prospectors with a diverse and formidable collection of structurally complex, small-molecule natural products. Indeed, it is likely that the many structures that have been discovered to date represent only a miniscule fraction of what nature, in principle, has to offer.[1]

Although the field of natural products is certainly cluttered with uninspiring "me too" entries, from time to time those busily engaged in the isolation, biological screening, purification, and structure determination of collections of natural products are rewarded. They may well discover architecturally truly novel compounds, whose properties prompt the launching of new directions in biological and even clinical research.[2]

To bring forth a new drug capable of providing real patient benefit while meeting the appropriately discerning standards of regulatory agencies is a daunting task characterized by high failure rates. Those committed to drug discovery can't help but be sensitive to the staggering set of risk factors that bestride the complex path from concept to approved, valuable drug. The discovery and study of small-molecule natural products has been a productive setting in the discovery of drugs.[3] Clearly we are far from understanding the evolutionary forces and developmental advantages in the biosynthesis of small molecules in plants, corals, bacteria, fungi, and higher organisms. At least for the present, it can be said that leads from small molecule natural product structures (for example, steroids, prostaglandins, β-lactams, polyketides, aminoglycosides, and statins) allow one to enter the intimidating arena of drug discovery at a later stage in the development progression than other modalities, including the mass screening of pharmaceutical sample collections and commercially available combinatorial libraries.

Why do such small-molecule natural product structures present such an advantage? Presumably they are often biosynthesized with a view to optimizing their ability to bind to strategic proteins or, in some instances, other biomolecular targets. Binding to strategic proteins is a key feature of virtually all drugs. Aside from their often exquisitely novel structural motifs, honed and fine-tuned by evolution for their interactivity with pertinent biomolecules, small-molecule natural products come with the built-in advantage that, by definition, they have been maintained in some biologically

[*] Dr. A. Rivkin, Prof. S. J. Danishefsky
Laboratory for Bioorganic Chemistry
Sloan-Kettering Institute for Cancer Research
1275 York Avenue, New York, NY 10021 (USA)
Fax: (+1) 212-772-8691
E-mail: s-danishefsky@ski.mskcc.org
Prof. S. J. Danishefsky
Department of Chemistry
Columbia University, Havemeyer Hall
3000 Broadway, New York, NY 10027 (USA)
Dr. T.-C. Chou
Preclinical Pharmacology Core Facility
Sloan-Kettering Institute for Cancer Research
1275 York Avenue, New York, NY 10021 (USA)

[**] This Minireview is dedicated to Professor George Olah for his pioneering contributions to organofluorine chemistry.

  DOI: 10.1002/anie.200461751

viable entity. This genealogy, however different in context from the ultimate setting in which a drug must function, and however imperfect a marker it is for predicting pharmacodynamics and safety profiles, can already be seen as a significant head start in the hunt for new agents of clinical value.

2. Natural Product Anticancer Agents: From Taxol to the Epothilones

2.1. Total Synthesis

Natural products have made a huge impact on drug discovery, particularly in the quest for new antitumor agents.[4] A well-known example of a clinically important agent, initially discovered through the screening of plant natural products, is taxol (**5**).[5] The value of taxol (subsequently renamed paclitaxel) in the treatment of several types of early-stage cancers and even some metastatic tumors is well established.[6] Also of established usefulness is a semisynthetic variant of taxol termed taxotere.[7] Both compounds inhibit microtubule depolymerization, which is an essential phase in mitosis. Other semisynthetic taxoids are at various stages of development.

The involvement of our research group in the study of taxol was initially inspired largely by chemical interests.[8] It has been our custom to make use of the rich structural diversity of small, biologically generated natural products to organize and focus our thoughts about the strategy and methodology of chemical synthesis. In the case of taxol, we sought to take advantage of smooth access to either enantiomer of the Wieland–Miescher ketone (**1**; Scheme 1). Moreover, we hoped to integrate the various stereochemical biases within the Wieland–Miescher ketone with a suitable degradative strategy to facilitate access to baccatin III (**4**), a precursor to taxol. In the event, a key transformation (**2**→**3**), masterminded by Dr. John Masters, did occur. However, the confidence and optimism occasioned by the stunning utilization of an intramolecular Heck reaction by Masters soon gave way to near desperation, as the route from **3** to **4** proved exceptionally troublesome as a result of difficulties associated with selectively excising the external methylene group. It was only the imaginative persistence of Dr. Wendy Young and Dr. J. T. Link, along with that of Masters, that allowed us to chart and realize a path to reach the natural

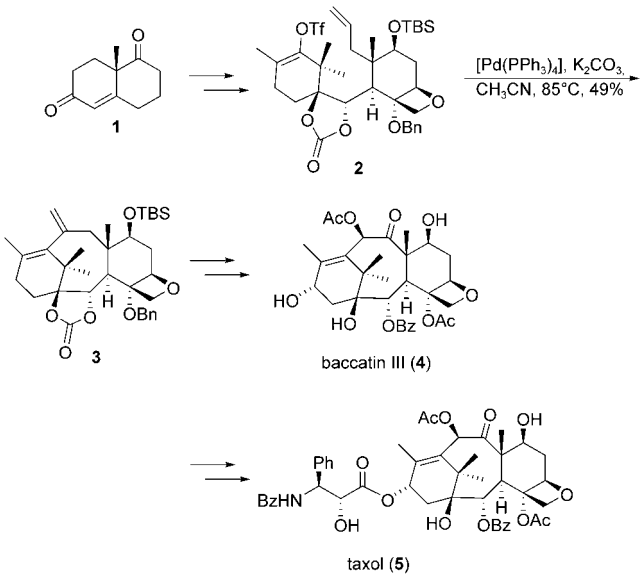

Scheme 1. Synthesis of taxol. Bn = benzyl, Bz = benzoyl, Tf = trifluoromethanesulfonyl, TBS = *tert*-butyldimethylsilyl.

product. We note, parenthetically, that for all of the frustrations and disappointments of the total synthesis, we were able to deliver the appropriate enantiomer of taxol (**5**) without the need for resolution and without recourse to relay synthesis (in which a fragment of the natural product is used as a starting material). These particular conditions had not been met in the two total syntheses of taxol completed previous to our own.[9,10]

Accomplishments on a chemistry level notwithstanding, our taxol effort did not deliver on one of its central purposes. Initially, we had hoped to synthesize late-stage intermediates containing the requisite side chain and housing the pharmacophores critical for the bioactivity of taxol. The complications of the final steps of the total synthesis left us with precious little material (and energy!) for structure–activity investigations.

This failing at the discovery level was particularly unfortunate since taxol is far from an ideal drug.[11] Although cytotoxic side effects are not unexpected in a tubulin-targeting agent, taxol carries two additional liabilities. The first arises from difficulties associated with its formulation. These problems are overcome by recourse to various delivery

Alexey Rivkin received his BS in chemistry and biochemistry from the University of California, San Diego in 1996. He completed his PhD in 2001 at the University of Pittsburgh, where he focused on synthetic studies of the structurally intriguing natural product penitrem D under the guidance of Dennis P. Curran. He then worked as an NIH postdoctoral fellow with Samuel Danishefsky at the Memorial Sloan-Kettering Cancer Center, where his synthetic studies of epothilones led to the discovery and development of the (E)-9,10-dehydroepothilones. He is currently a medicinal chemist at Merck.

Ting-Chao Chou completed his PhD at Yale University and is currently director of the Preclinical Pharmacology Core Laboratory at the Memorial Sloan-Kettering Cancer Center in New York. He was Professor of Pharmacology at Cornell University from 1988 to 2000, and has been honorary professor at the Chinese Academy of Medical Sciences since 1993. The median-effect equation he created and the combination-index equation he created with P. Talalay, along with the computer software Biosoft, UK, have received over 2000 citations in over 250 biomedical journals.

vehicles, which create their own safety and tolerance issues in real treatment settings. Perhaps even more serious is the vulnerability of paclitaxel to disablement at the clinical level by innate or acquired multidrug resistance (MDR). All too often it proves impossible to overcome MDR by increasing the dosage of the toxic drug. These complications in the aggregate often lead to "taxol failure" in the clinic with reemergence of the disease in metastatic form.

It was in this setting of seeking "life after taxol" that we heard a report about a new anticancer agent, which functioned by the taxol mechanism. The epothilone family of natural products had been discovered at the Gesellschaft für Biotechnologische Forschung mbH (GBF) by Höfle and associates, following an extremely well-executed pharmacognosy program. The Höfle group had postulated possible applications of epothilones in various agricultural contexts.[12] Broad multidisciplinary interest in the epothilones was aroused following a milestone publication by a natural products discovery group led by Bollag at Merck.[13] The features of the Merck disclosure that were most provocative were that the new family of natural products, known as epothilones (Scheme 2), seemed to owe their cytotoxic

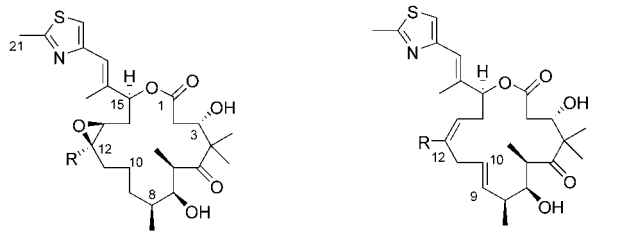

6: epothilone A (EpoA), R = H
7: epothilone B (EpoB), R = CH_3

8: (*E*)-9,10-dehydro-dEpoB, R = CH_3
9: 26-trifluoro-(*E*)-9,10-dehydro-dEpoB, R = CF_3 (fludelone)

Scheme 2. Structures of epothilones.

properties against various cancer cell lines to the same tubulin-interference mechanism exhibited by taxol. However, importantly, unlike taxol, epothilones A (**6**) and B (**7**) seemed to be remarkably effective against apparent MDR cell lines.[14] As discussed above, taxol failure is often attributable to the onset of MDR. Although the absolute configuration of the epothilones was not known at that time, their overall structures suggested that they would constitute a more manageable challenge from the point of view of chemical synthesis than taxol derivatives. Accordingly, we hoped that total synthesis as a means of drug discovery would be more productive with the epothilones than had been the case with the taxol program.

A focused effort directed towards the synthesis of the epothilones by chemical means could not be launched until their configurations were defined. The Merck group was apparently not pursuing the full definition of configuration.[13] As noted above,[12] the actual discovery of the epothilones went back to pioneering studies by Höfle et al. However, it was not until a key publication, again from the research group of Höfle, that the configurations of epothilones A and B were revealed.[15] This information led to a disciplined effort towards total synthesis with an ultimate view to biological investigation. Indeed, since we had no access to epothilones in any quantity for independent investigations, total synthesis would be our only recourse. We identified epothilones A (**6**) and B (**7**) as our targets for total synthesis. We started by targeting epothilone A, which lacks the methyl group at C12, in the hope that lessons learned in that foray would serve us well in the synthesis of epothilone B, which was reported to be the more potent compound.[16]

Herein we relate, in a retrospective way, the interactive relationship between chemical synthesis and drug optimization in our research program around the epothilones. It was this synergism that led to the discovery of the remarkable (*E*)-9,10-dehydro-12,13-desoxyepothilones **8** and **9**, particularly the congener **9** bearing a trifluoromethyl group rather than a methyl group at C12.[17] We describe how this discovery flowed from a unique synergy between chemistry and preclinical experimental pharmacology. We have reason to believe that this type of interdisciplinary interaction offers excellent prospects in a variety of projects.

It is important to emphasize a matter of policy that influenced the design of our syntheses to a considerable extent. From the outset, our orienting goal was to produce adequate quantities of preclinical lead compounds to carry out in vivo evaluations in xenograft mouse models. We assigned to this goal a far higher degree of urgency than to the mass screening of individual compounds in vitro. Since our resources were clearly finite, the decision to place emphasis on evaluations of in vivo efficacy implicitly meant that we would make fewer compounds, albeit in larger quantities than are generally prepared in total syntheses in an academic environment. This decision in turn placed a very high premium on the attainment of high levels of stereoselectivity in the individual steps.

Accordingly, we could ill afford to deal with complex mixtures of stereoisomers. It seemed probable to us from the outset that ring-closing metathesis (RCM), by then a very popular method for forming cyclic olefins,[18] would, in the case of the epothilones, lead to an *E*/*Z* mixture of stereoisomers at the C12–C13 double bond if a precursor such as **10** or **11** was used (Scheme 3).[19] This expectation proved accurate. We thus came to favor cross-coupling strategies in which the eventual C12–C13 double-bond geometry was already defined in the olefinic precursors. Incidentally, we were aware that in placing emphasis on quality syntheses to

Samuel Danishefsky completed his BS at Yeshiva University in 1956 and his PhD at Harvard University with Peter Yates. After postdoctoral studies at Columbia University with Gilbert Stork he began his independent academic career in 1963 at the University of Pittsburgh, where he became professor in 1971. In 1980, he moved to Yale University, but returned to New York in 1993 as Professor of Chemistry at Columbia University and Kettering Professor at the Memorial Sloan-Kettering Cancer Center. His research interests include synthetic strategy, reagent development, cytotoxic natural products, and fully synthetic carbohydrate-based tumor antigens.

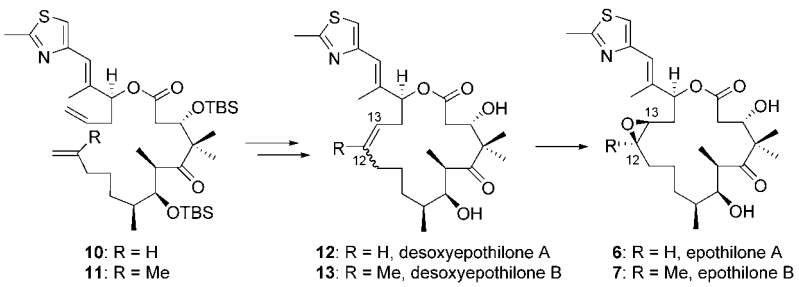

Scheme 3. Synthesis of epothilones by ring-closing metathesis.

produce carefully thought-out structures, we were deviating from the prevailing trends—based on stochastic approaches—of those times. We return to this issue toward the end of this Minireview.

We were attracted to the palladium-mediated B–alkyl Suzuki cross-coupling, a reaction that was underappreciated at the time, to establish the C12(sp^2)–C11(sp^3) bond.[20] The synthesis of EpoA commenced with compound **16**, prepared by taking advantage of chemistry developed to a large extent by our research group.[20] Thus, the Lewis acid catalyzed diene–aldehyde cyclocondensation reaction[21] of **14** and **15** afforded dihydropyrone **16** in high yield and with high relative and absolute stereoselectivity (Scheme 4). This compound was converted into intermediate **18**, which underwent the key B–alkyl Suzuki reaction with **19** to afford **21**. A virtually unprecedented ester enolate–aldehyde macrocyclization[22] followed by appropriate functional-group manipulations led us to desoxyepothilone A (dEpoA, **12**). Epoxidation of the 12,13-alkene with dimethyldioxirane proceeded with very high regio- and stereoselectivity (15–20:1 in favor of the β epoxide[23]) to complete the first total synthesis of epothilone A (EpoA, **6**).[24] Happily, the logic of the synthetic route was readily adapted to the first synthesis of EpoB (**7**).[16b] The key features of the pioneering effort are adumbrated in Scheme 4. Experimental protocols have been described in detail in the literature.

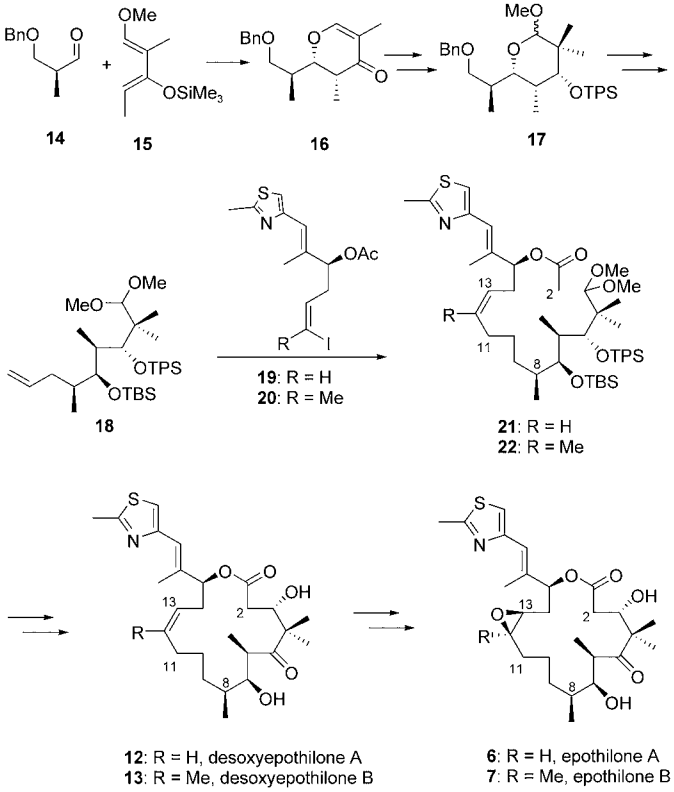

Scheme 4. First reported total synthesis of EpoA and EpoB.

2.2. Biological Activity

With synthetically derived material in hand, we soon confirmed the various claims in the literature concerning inhibition of microtubule disassociation and the cytotoxicity of epothilones A and B.[25] Remarkably, in vitro experiments revealed that the 12,13-desoxy precursor of EpoB (i.e. dEpoB) also exhibited tubulin-stabilization properties within the range of those of EpoB, though the cytotoxicity was diminished.[12] By permuting the total synthesis described above in various ways, we built a family of epothilone congeners, which served to define the first in vitro SAR (structure–activity relationship) map of the epothilones.[20] We were able to determine which structural elements of the epothilones could be modified without loss of cytotoxicity or tubulin-binding characteristics.

Although our initial syntheses of EpoA and EpoB were quite long, our newly launched drug-discovery program benefited greatly from their high stereoselectivity. With considerable diligence, we were able to accumulate adequate quantities of totally synthetic probe structures for meaningful in vivo determinations. The experiments involved implanting human tumor cells into immunodeficient mice and assessing the effects of the drugs on the growth profiles of the tumors. We also conducted parallel investigations on tumors that had become insensitive to various known anticancer drugs as a consequence of MDR. Hence, these fully synthetic drug samples could be used to determine whether the claims of Bollag and co-workers about MDR insensitivity (for example, in the case of epothilone B)[12] were also true in an in vivo setting. We conducted the first in vivo investigations with epothilone B. Our findings were highly worrisome. Although the potency of EpoB was certainly indicated, its toxicity profile was quite serious: deaths and troubling weight losses resulted even at doses as low as 0.6 mg kg^{-1} (Table 1).

With appropriate changes in dosing, it might well have been possible to learn to administer EpoB in such a way as to achieve useful therapeutic indices that would justify its

Table 1: Toxicity of EpoB and dEpoB in normal nude mice.

Group	Dose [mg kg^{-1}][a]	Deaths
control	–	0/4
EpoB (**7**)	0.6	8/8[b]
dEpoB (**13**)	25	0/6

[a] QDx4 (administered every day, 4 doses in total), intraperitoneal (i.p.). [b] Mice died of toxicity on day 5,6,6,7,7,7,7,7.

potential development as a drug. In fact, Novartis did enter this drug into phase I clinical trials.[26] However, we were concerned that toxicity issues would, in the end, prevent EpoB from maturing into the sort of breakthrough drug we sought to discover.

We hypothesized that perhaps the serious toxicity of EpoB was partly the consequence of nonspecific toxicity superimposed on tubulin-directed antimitotic properties. It seemed that the 12,13-epoxide of EpoB could well be a source of nonselective toxicity.[16] Thus, we wondered whether "molecular editing" of the epoxide in favor of a *cis*-12,13-alkene would give rise to agents with reduced toxicity and therefore broader and more exploitable therapeutic indices.

3. Second-Generation Epothilones

3.1. Desoxyepothilone B: Synthesis and Activity

As dEpoB had demonstrated cytotoxicity and tubulin-binding characteristics comparable to those of taxol in vitro, but with activity in MDR cell lines reminiscent of that of EpoB, we decided to evaluate this compound in vivo. Multigram quantities of synthetic dEpoB (**13**) were required for this task and delivered by later-generation syntheses (see below).

Comprehensive in vivo studies showed dEpoB to be much more promising than EpoB itself with respect to the usefulness of its therapeutic index (Table 1).[25e] Subsequently, we expanded our efforts by examining the effects of various formulations, routes, and schedules of intravenous (i.v.) administration. We discovered that dEpoB performed similarly to paclitaxel in tumor xenografts such as MX-1, in which each demonstrated a complete tumor remission. Similar results were seen in the treatment of HT-29 colon tumor and SK-OV-3 ovarian tumor with dEpoB and taxol. However, strikingly superior effects of dEpoB relative to taxol were observed against multiple-drug-resistant (MDR) tumors in our own models. For example, dEpoB (30 mg kg^{-1}, 6-h i.v. infusion, Q2Dx5 = administered every other day, 5 doses in total) demonstrated a full curative effect when administered to nude mice bearing the resistant human lymphoblastic T-cell leukemia CCRF-CEM/paclitaxel, which was 57-fold resistant to paclitaxel (Figure 1 a).

Additionally, the superior effects of dEpoB relative to other commonly used anticancer agents were clearly shown in the treatment of adriamycin-resistant MCF-7/Adr tumor xenografts with frontline chemotherapeutic agents, such as paclitaxel (24 mg kg^{-1}), adriamycin (3 mg kg^{-1}), vinblastine (0.8 mg kg^{-1}), and etoposide (VP-16, 30 mg kg^{-1}), each at the maximal tolerated doses. In these evaluations, adriamycin demonstrated a lack of therapeutic effect even at the nearly lethal dose, and vinblastine, etoposide, and paclitaxel showed little therapeutic effect. Upon treatment with dEpoB, a significant decrease in tumor size was observed (Figure 1 b).

As a consequence of these promising preclinical successes with dEpoB, it became important for us to develop a more concise route for its synthesis. Some of the drawbacks of the first-generation synthesis[20] included the awkwardness of the introduction of the C4 *gem*-dimethyl group, the multistep chain extension of the C9 benzyl ether, and the nonstraightforward opening of the pyran system to expose the C3 aldehyde. We sought to overcome these issues while still making use of the stereoselective B–alkyl Suzuki route.

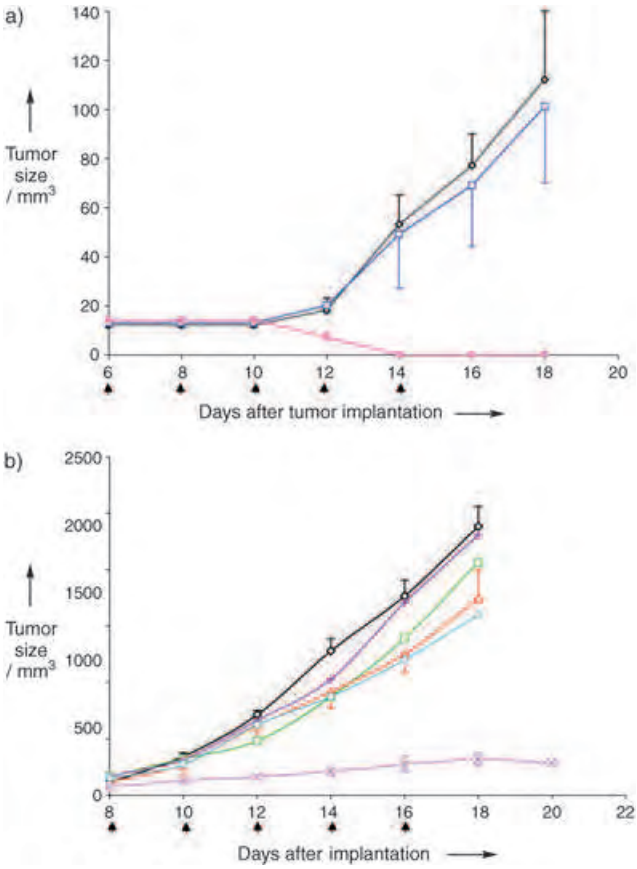

Figure 1. Activity of dEpoB against a) paclitaxel-resistant tumors and b) an adriamycin-resistant mammary adenocarcinoma: a) ◇ control; □ paclitaxel, 20 mg kg^{-1}; × dEpoB, 30 mg kg^{-1}; b) ◇ control; □ vinblastine, 0.8 mg kg^{-1}; △ paclitaxel, 24 mg kg^{-1}; × dEpoB, 30 mg kg^{-1}; + adriamycin, 3 mg kg^{-1}; ○ etoposide (VP-16), 30 mg kg^{-1}.

We were able to achieve these objectives in our second-generation synthesis of dEpoB (Scheme 5).[27] This route commenced with the readily available β-ketoester **23**. Following the conversion of **23** into enol ether **24**, an aldol reaction with aldehyde **25** and subsequent manipulations eventually gave β-ketoester **26**. The opposite enantiomer of aldehyde **25** had already been prepared by Overman and co-workers[28] through recourse to Evans oxazolidinone methodology,[29] which makes use of a suitable auxiliary to direct the diastereofacial sense of C2–C3 bond formation. Suzuki coupling of **26** and **27** afforded **28**. The stereocenter at C3 was installed by a Ru–binap-catalyzed reduction developed by Noyori et al.[30] Ultimately, macrolactonization of **29**, followed by deprotection, led to dEpoB (**13**). A total of about 60 g of fully synthetic dEpoB was prepared by this route.

We were now able to evaluate dEpoB relative to taxol, epothilone B, and a semisynthetic 15-desoxy-15-aza congener, which had also been entered into clinical trials.[31] We also

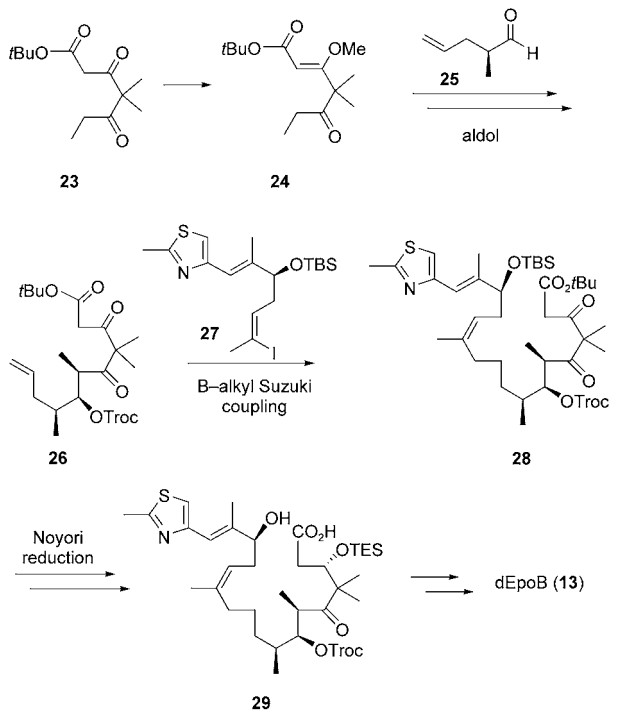

Scheme 5. A more streamlined synthesis of dEpoB. Troc = trichloroethoxycarbonyl.

looked into questions such as the stability of dEpoB to lactone-ring opening in various in vivo models and the performance of dEpoB in vivo against sensitive or resistant tumors. In our judgment, based on xenograft models, dEpoB demonstrated major advantages over potential competitors in the range of its likely therapeutic index and in its robustness with respect to MDR disablement. These results have been documented extensively.[25c–e]

Another important event in the progression of desoxyepothilone B to clinical evaluation was the entry of the Kosan Biosciences Company as a licensee of Sloan-Kettering for further development of the compound. Brilliantly, and with great diligence, our commercial collaborators solved the problem of obtaining desoxyepothilone B by fermentation methods.[32] Their success in doing so was much facilitated by their highly advanced technology, which promoted the expression of **13** through the modification of particular polyketide metabolites by controlling the biosynthesis of such polyketides.[32] Our collaborators were able to prepare the compound for phase I clinical trials. The human clinical evaluations, which commenced at the end of 2001, have advanced to a phase II stage in a much expanded effort, which now includes the participation of the company Hoffmann-La Roche.[33]

3.2. (E)-9,10-Dehydroepothilone Derivatives

The very effective and timely involvement of Kosan in the project also provided another important step in our progression to the (*E*)-9,10-dehydro compounds, including fludelone. In the course of their pivotal fermentation work, Kosan scientists detected and isolated, albeit in small amounts, a desoxy and dehydro derivative of epothilone B, which they named epothilone 490 (Epo 490).[34] The Kosan investigators recognized Epo 490 as the derivative of EpoB without the 12,13-epoxide and with an additional *E* double bond at C10–C11. We looked upon Epo 490 as a dehydro version of dEpoB (**13**). However, the chemical transformation of dEpoB into this new Kosan metabolite was far from a straightforward matter. We were anxious to take advantage of our previous extensive efforts in total synthesis to gain access to meaningful amounts of Epo 490. In other words, we would try to adapt the total synthesis we had developed for dEpoB to target Epo 490 directly.

To understand the steps taken in the development of the new synthesis, it is important to be familiar with the then state-of-the-art synthesis of the vinyl iodide component (compound **35**) for the Suzuki coupling process. Since we have described previously the many methods that were explored during the course of our investigations, we can quickly turn to the optimal method for preparing this alcohol. The route is summarized in Scheme 6.[35]

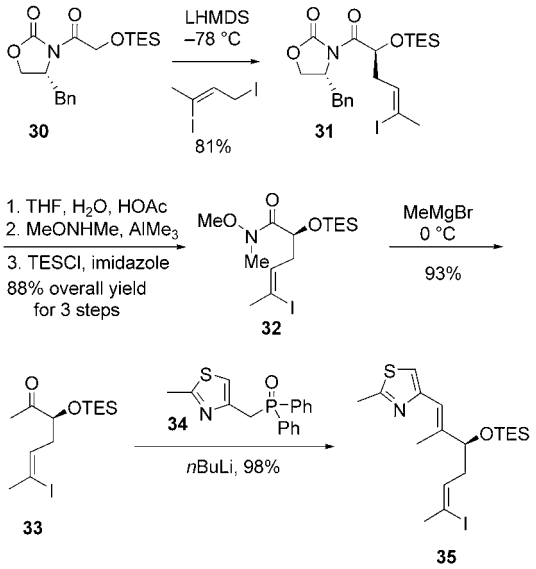

Scheme 6. Synthesis of the left-hand fragment **35**. TES = triethylsilyl, LHMDS = lithium hexamethyldisilazide.

A postdoctoral colleague, Dr. Jon Njardarson, offered an interesting proposal for the synthesis of epothilone 490. His idea brought us back to a more careful consideration of the RCM method, which had been left on the sidelines for the reasons discussed above. The coupling of the iodoalkene **35** with a suitable vinyl derivative should give substrate **36**. Following esterification with **37**, ring-closing metathesis could well lead to the desired (*E*)-10,11-(*Z*)-12,13-diene, which, upon appropriate functional-group transformations, should allow access to epothilone 490 (**40**). Indeed, this synthesis was soon completed (Scheme 7).[36] The exact method for introducing the vinyl group involved a Stille cross-coupling reaction of **35** with tri-*n*-butylvinylstannane. Since Epo 490 could be smoothly converted into **13** by a selective imide

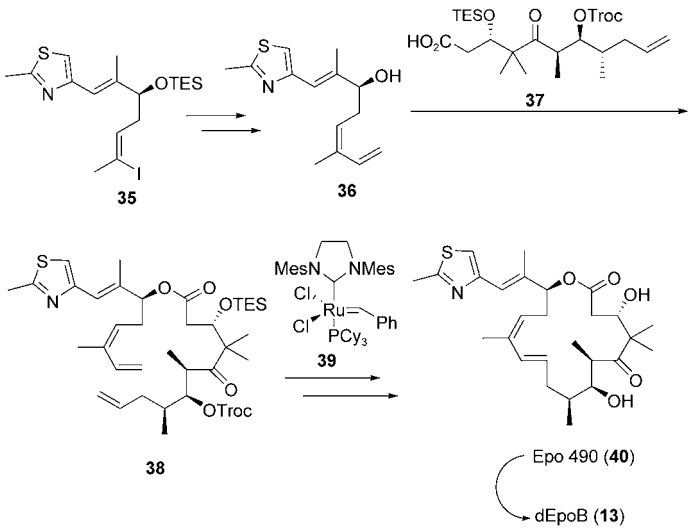

Scheme 7. Total synthesis of epothilone 490 by ring-closing metathesis. Mes = 2,4,6-trimethylphenyl.

reduction, the chemistry described in Scheme 7 constitutes an independent total synthesis of dEpoB.

Unfortunately, the excellent in vitro results observed with epothilone 490 did not translate to in vivo experiments conducted with mouse xenografts on our fully synthetic material. Although clear evidence for the suppression of tumor growth could be found, tumor shrinkage, let alone disappearance, was not observed.[21] On the basis of biostability studies, we believed that this lack of translation to an in vivo setting might be specific to the mouse tumor host.

Thus, pharmacostability studies suggested that Epo 490 is particularly unstable with respect to esterase action in mouse sera. Remarkably, the compound was actually quite stable in human sera of cell homogenates. However, in the real world of advancing oncostatic agents for development, progress depends rather critically on the promising performance of the agent in the mouse models. Although the Epo 490 project continues to provide a forum for testing interesting chemistry, efforts to utilize Epo 490 as a drug have been discontinued in our laboratory.

Concurrently with the Epo 490 project, we undertook the synthesis and evaluation of a 26-trifluoro epothilone derivative. In this connection, we were not unmindful of many instances in which the strategic incorporation of fluorine atoms can lead to major effects on drug activity, including altered lipophilicity, incremental stabilization to metabolism, and modified binding affinities.[37] Even in the absence of a clear-cut rationale for doing so, we set out to synthesize dEpoB derivatives with a trifluoromethyl group at C12.

Naively, we assumed that the hard-won lessons from the synthesis of dEpoB could be readily transferred to the problem at hand. Thus, at the outset we set as our targets 26-trifluoro compounds in both the Epo 490 family (see compound **42**) and the dEpoB series (see **43**).[38] Surprisingly, the strategies that had worked well in the syntheses of the nonfluorinated congeners failed in the presence of the trifluoromethyl group. Thus, with the trifluoromethyl group installed, ring-closing metathesis (**41**→**42**), nucleophilic methylation of the Weinreb amide (**44**→**45**), and B–alkyl Suzuki coupling (**44**+**26**→**46**) were all unsuccessful (Scheme 8).[39]

Clearly, we had significantly underestimated the consequences of the inclusion of the trifluoromethyl group for our synthesis. Since a Stille cross-coupling reaction had allowed us to construct the precursor **41**, we investigated the possibility of introducing an allyl group at the future C12 vinylic carbon atom en route to a 26-trifluoro epothilone derivative. We hoped that the inclusion of even a single methylene spacer would attenuate the effects of the trifluoromethyl group, thus enabling the realization of a RCM reaction. Happily, with the

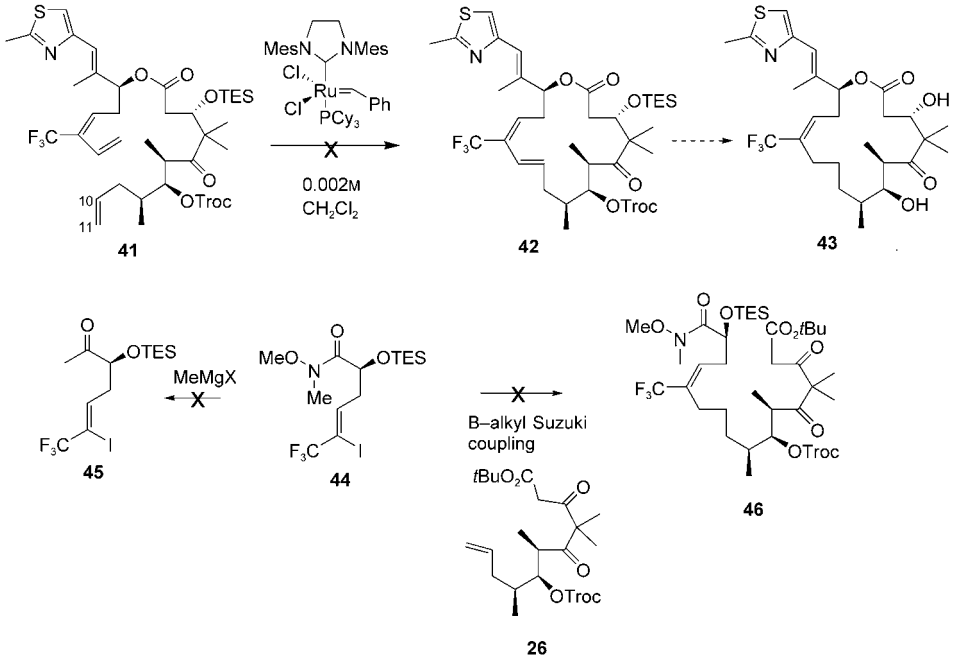

Scheme 8. Failed strategies for the synthesis of 26-trifluoro-dEpoB.

one carbon spacer in place, RCM of **47** did produce compound **48** in a respectable yield (Scheme 9). Now, of course, the epothilone functions were displayed in the context of a 17- rather than a 16-membered ring. Not surprisingly, the

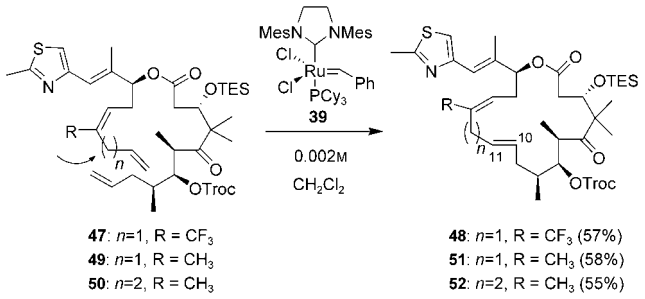

Scheme 9. Successful ring-closing metathesis.

same sequence could be carried out to give the analogue **51** containing a dehydrohomodesoxyepothilone B scaffold and a methyl group at C12.[40] To broaden our SAR base, we also introduced a butenyl function on the C12 vinylic carbon atom. RCM of this compound led to the epothilone macrolide **52**. Remarkably, in all cases the double bonds formed in the RCM reactions were exclusively of the *E* configuration.

In a fateful set of experiments, we examined the in vitro activity of these ring-expanded epothilones. As it turned out, the 18-membered-ring congener **52** was totally inactive. By contrast, the 17-membered-ring compound **51** exhibited substantial in vitro activity. This result at first seemed puzzling, as Nicolaou and co-workers had reported that the monodihydro congener of **51**, in which the C10–C11 bond was saturated, was devoid of useful epothilone activity.[41] This observation led us to speculate that perhaps this second double bond of our synthetic construct could also impart exploitable incremental biological function to epothilones with the usual 16-membered macrocycle.

The limitations imposed on our operative synthetic schemes by the trifluoromethyl group really left us with only one option if we were to stay within the broad parameters of our route. We would take advantage of the fact that the trifluoromethyl group does not interfere with Stille-like allylation. Furthermore, with the single methylene spacer in place, olefin metathesis in the ring-closing mode was indeed a viable reaction. To get back to the 16-membered ring, we would now have to delete one carbon atom from the component containing the carboxylic acid functionality in the esterification reaction. A key reaction in the assembly of this component would now be a chelation-controlled aldol reaction of **53** and **54** (Scheme 10). The aldehyde **54** was obtained smoothly from readily available 2-hydroxybutyric acid—a charter member of the chiral pool. Hence, a fringe benefit of targeting the dehydro-dEpoB system was that we could now dispense with the need for recourse to a chiral

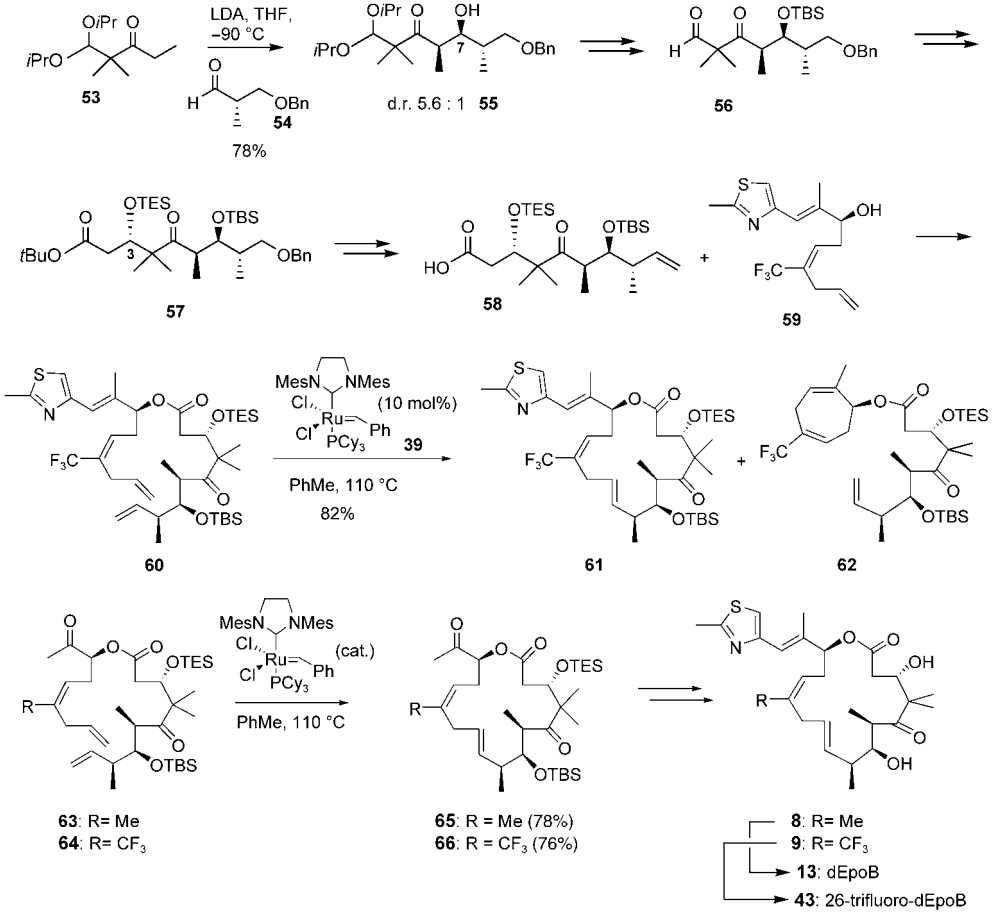

Scheme 10. Synthesis of 9,10-dehydroepothilones through ring-closing metathesis.

auxiliary to reach the previously used aldehyde **25**.[28] Ring-closing metathesis of **60** in the presence of the recently developed catalyst **39** provided exclusively the *E* isomer **61** along with the corresponding 7-membered-ring side product **62** in a 1:3 ratio and 82% combined yield.

At last, we had succeeded in preparing a 12,13-desoxy compound with a 16-membered ring and the desired trifluoromethyl group. However, the major RCM product was the unwanted cycloheptadienyloxy compound **62** arising from extrusion of the thiazole side chain. Clearly, this result did not meet our goal of a viable total synthesis for drug discovery and, hopefully, development.

We postulated that this problem might be resolved by resequencing the steps of the synthesis and conducting the RCM with the ketone precursor to the thiazole side chain still in place. We tested this proposal on the 12-methyl substrate **63** and were pleased to discover that the desired RCM adduct was obtained in 78% yield. Olefination of the ketone with emplacement of the thiazole unit occurred in high yield to give, after deprotection, the desired compound **8**.[42]

When we carried out this synthesis, **8** was believed to have been previously synthesized. Indeed, the compound claimed to be **8** was reported to be only marginally cytotoxic.[43] We were therefore surprised to find that the spectroscopic properties of our synthesized **8** were not consistent with those reported for the compound previously thought to be **8**. The actual structure of the compound originally assigned as **8** has been reevaluated and shown to be an isomer in which the C12–C13 double bond is in the *E* configuration.[44] The real compound **8** had, in fact, never before been prepared and, accordingly, never been evaluated as a potential antitumor agent.

Having established the feasibility of the modified RCM–olefination strategy with the methyl substrate **63**, we refocused our attention on the ultimate goal of synthesizing 26-trifluoro-9,10-dehydro-dEpoB (**9**). Happily, we were able to utilize the same set of transformations to obtain the desired compound **9**, which we named fludelone, from ketone **64** in high yield (Scheme 10).[17b,42]

In the title of this retrospective, we posed the question as to "How We Got There". We had fashioned a special and highly selective sequence of reactions for the total synthesis of the epothilones. As matters transpired, the chemistry needed for the incorporation of the 12-CF_3 group required us to access the 9,10-dehydro series, in which we found a new family of epothilone drugs with extremely promising biological activity. We conclude with a summary of the rather remarkable and promising findings from evaluations of these 9,10-dehydro compounds.

4. Biological Activity of Fludelone

Having synthesized the 12-proteo analogue **8** as a chemical model, we set out to examine its biological activity, in part to set a baseline for comparison with fludelone (**9**). Indeed, compound **8** seems to be a promising second-generation drug candidate. As described elsewhere,[17] it is significantly more potent than dEpoB (**13**) and is much more stable in a variety of biological contexts than **13**. The treatment of various xenograft tumor models with compound **8** led to dramatic tumor shrinkage in these model in vivo contexts (Figure 2). However, although the drug completely suppressed tumor growth, there were obstacles to full tumor eradication with **8**. The problem was that the greater toxicity of **8** (maximum tolerated dose in xenografts is about 4 mg kg^{-1}) made it difficult to dose with sufficient amounts of the drug to remove the last traces of tumor. The exploitable therapeutic index of **8**, particularly in clinical settings, awaits fuller exploration.

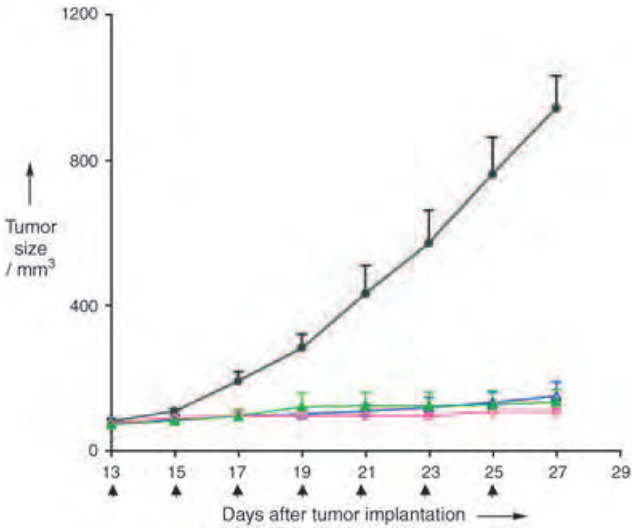

Figure 2. Therapeutic effect of 9,10-dehydro-dEpoB (**8**) in nude mice bearing the HCT-116 xenograft (6-h i.v. infusion (except 5-mg kg^{-1} dosage: i.v. injection), Q2Dx7 = administered every other day, 7 doses in total, $n = 3$; arrows indicate drug administrations): ● control; △ 3 mg kg^{-1}; ◇ 4 mg kg^{-1}, ($n = 4$); ▲ 5 mg kg^{-1}.

By contrast, the 26-trifluoro derivative fludelone (**9**) exhibits a remarkably broad therapeutic index in vivo in xenografts. Dramatic results are observed for a range of tumors. Indeed, fludelone has emerged as our star compound in the epothilone series. The data given below form the basis of our preclinical case.

All chemotherapeutic experiments in vivo were carried out with human-tumor xenografts in immunodeficient nude mice. For all its imperfections, this model is the one most widely used in evaluating antitumor lead compounds prior to clinical trials. Remarkably, the treatment of MX-1 xenografts with 25-mg kg^{-1} dosages of fludelone resulted in complete tumor disappearance and the absence of any relapse for over two months after the suspension of treatment (see Figure 3). Most importantly, these therapeutic successes can be achieved either by 6-h i.v. infusion (Figure 3) or by oral administration (Figure 4). In contrast, the treatment of the MX-1 xenografts by oral administration of taxol did not appreciably affect the tumor, which highlights another significant advantage of fludelone (see Figure 4). The treatment of taxol-resistant tumor xenografts with fludelone administered by 6-h i.v. infusion can lead to complete tumor remission (Figure 5),

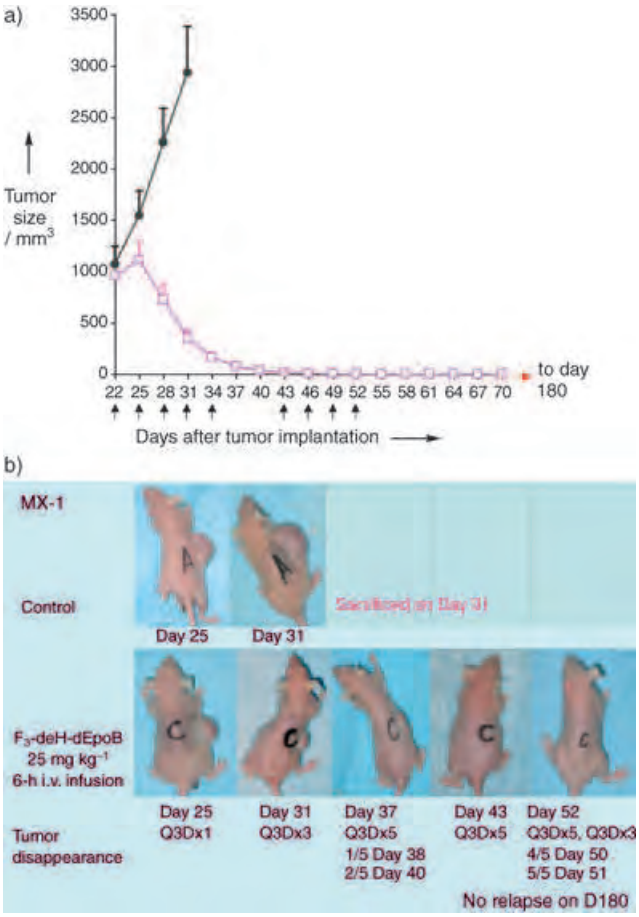

Figure 3. Therapy of an extra-large MX-1 tumor xenograft: a) MX-1 tumor tissue (50 mg) was implanted subcutaneously (s.c.) on day 0. Tumor-size changes in the vehicle-treated control (●) and fludelone-treated group (25 mg kg^{-1}, □; $n=5$ in each group) were observed. On day 22 (D22), when the size of the tumor had reached 960 ± 132 mg (about 3.4% of body weight), fludelone treatment was commenced. Fludelone (25 mg kg^{-1}, 6-h i.v. infusion, Q3Dx5) was given on D22, D25, D28, D31, and D34, as indicated by the arrows. The second cycle of treatment, following a 9-day rest, was given on D43, D46, D49, and D52. For the fludelone-treated group, 5/5 tumors disappeared (on D38, D40, D50, D50, D51). Observation was continued Q3D for up to 180 days, and no relapse was observed 128 days after cessation of treatment on D52. b) Photographs of the nude mice (one mouse each selected from the control group and the treated group) taken on D25, D31, D37, D43, and D52.

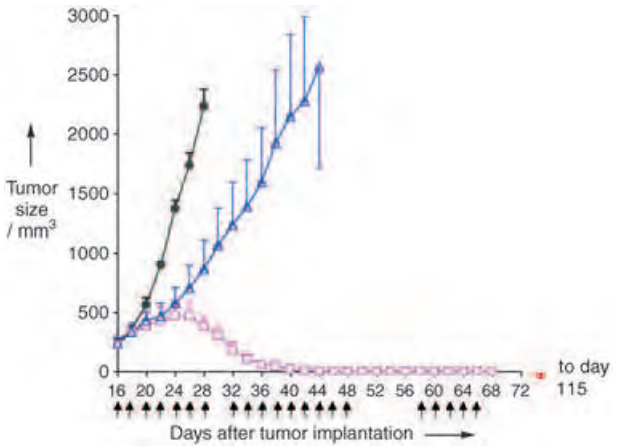

Figure 4. Therapeutic effects against the human mammary carcinoma MX-1 xenograft by orally administered fludelone or paclitaxel (taxol). Female nude mice were used. Fludelone (30 mg kg^{-1}, □, $n=3$) was given orally Q2Dx7 beginning D16 after tumor implantation and then Q2Dx9 on D32 to D48, as indicated by arrows. The tumors of all three mice disappeared (on D40, D45, and D48). As consolidation therapy, a third cycle of treatment was given Q2Dx5 from D58 to D66 when all mice were tumor free on D48. There was no relapse observed on D115 (49 days after stopping treatment). Control (●, $n=2$) received the vehicle only. A comparative experiment was carried out in parallel with taxol (30 mg kg^{-1}, △, $n=3$) with oral dosing beginning D16, Q2Dx3; the dose was then increased to 40 mg kg^{-1}, Q2Dx3 (D22–D26) and then 60 mg kg^{-1}, Q2Dx3 (D28–D40).

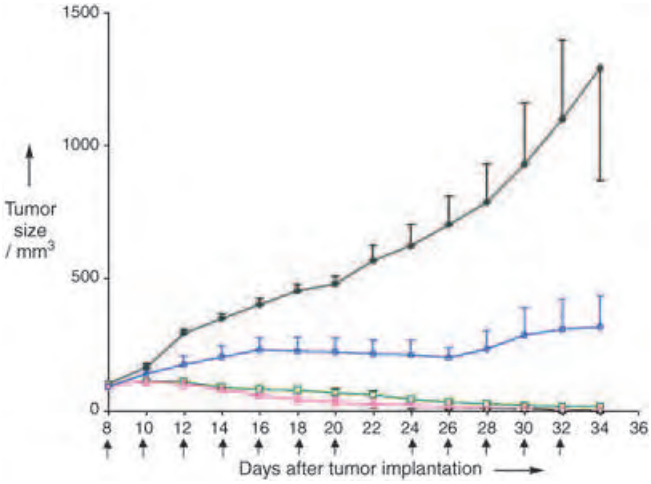

Figure 5. Therapeutic effects against the taxol-resistant human T-cell lymphoblastic leukemia CCRF-CEM/taxol xenograft by fludelone and taxol. Tumor tissue of CCRF-CEM/taxol (44-fold resistant in vitro), 50 mg/mouse was implanted s.c. into nude mice on day 0. Treatment (6-h i.v. infusion) started on D8 with fludelone (15 mg kg^{-1}, □, $n=3$ and 30 mg kg^{-1}, △, $n=4$) or taxol (20 mg kg^{-1}, ○, $n=4$), Q2Dx7 (D8 to D20), D22 dose was skipped, and then treatment was resumed Q2Dx5 on D24, D26, D28, D30, and D32, as indicated by arrows. The control group (●, $n=4$) received the vehicle only. With fludelone at a dose of 15 mg kg^{-1}, the tumor of 1/3 mice disappeared on D37, and at a dose of 30 mg kg^{-1} the tumors of 3/4 mice disappeared on D22, D22, and D32.

whereas the treatment of human colon carcinoma (HCT-116, Figure 6) with fludelone by 6-h i.v. infusion can lead to a complete "cure". The experiments with human-mammary-carcinoma (MX-1) and human-colon-carcinoma (HCT-116) xenografts in nude mice lasted 6.0 and 6.6 months, respectively. There was no tumor relapse in either experiment during 4.3 and 5.3 months, respectively, following the cessation of treatment. For the HCT-116 experiment, taxol and fludelone were used at 20 mg kg^{-1} and both caused tumor disappearance. However, the taxol-treated group relapsed 1.1 months after treatment was discontinued, whereas the animals treated with fludelone were tumor free for over 5.3 months.

These results are based on a particularly long and thorough therapeutic study with xenografts and demonstrate the longest periods of complete remission that have been

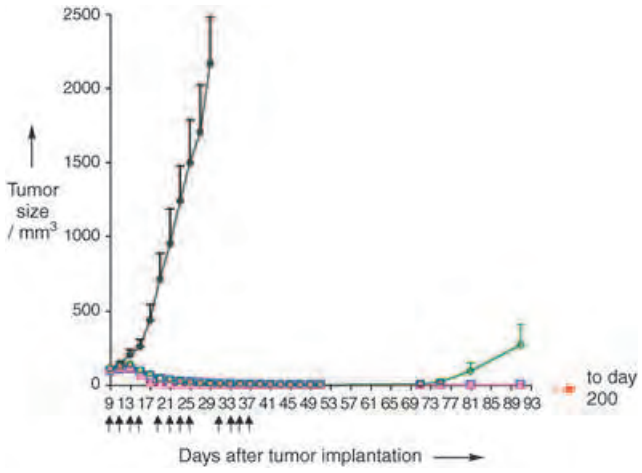

Figure 6. Therapeutic effects against the human colon carcinoma HCT-116 xenograft by fludelone and taxol. HCT-116 tumor tissue (50 mg/mouse) was implanted s.c. into nude mice on day 0. Treatment (Q2Dx4, 6-h i.v. infusion) was carried out for three cycles on D9, D11, D13, D15; D19, D21, D23, D25; and D31, D34, D35, D37 with fludelone (20 mg kg^{-1}, □ and 30 mg kg^{-1}, △), and taxol (20 mg kg^{-1}, ○); control: ●; $n = 4$ in each group. Complete tumor disappearance in all mice occurred (on D33, D35, D41, D45 for fludelone (20 mg kg^{-1}), on D21, D23, D33, D41 for fludelone (30 mg kg^{-1}), and on D33, D33, D41, D45 for taxol (20 mg kg^{-1})). There was no tumor relapse observed in either fludelone-treated group on D200. However, the group treated with taxol (○) suffered relapses on D71, D75, D81, and D81, which correspond to the 34th, 38th, 41st, and 41st day after stopping treatment.

reported either with parenteral or oral administration of a single antitumor agent. It is relatively common to find compounds that suppress tumor growth. It is rarer to find a drug candidate that causes tumor shrinkage, and particularly rare for a compound to shrink the tumor to the point of nondetectability. The dramatic finding regarding fludelone is that tumors did not relapse during observation for 4.3 months or longer (i.e. $>20\%$ of a typical mouse lifespan). This type of result has very few counterparts in the literature.[45] The achievement of complete tumor disappearance and long-term remission by oral treatment could well be of particular significance, as it could lead to outpatient home usage. Furthermore, the use for drug delivery of cremophor vehicles, which can themselves lead to severe allergic reactions, could be avoided.

It is important to keep in mind that the ultimate purpose of chemotherapeutic research is to provide clinically valuable treatment for cancer patients. Although the results of the xenograft studies discussed herein are certainly very encouraging, it remains to be seen whether these dramatic findings will translate to human patients. Thus, only progression to clinical trials will fully establish the value of these novel, later-generation epothilones as effective anticancer agents. However, we are prepared to predict that the dramatic preclinical performance of the 9,10-dehydro-dEpoB epothilones will spur much research in synthesis, compound optimization, and biotarget identification.

5. Concluding Remarks

We conclude our documentary of retrospection with some thoughts of a more general nature. With continuing advances in the technology of isolation, purification, and characterization, the number of natural products available in the future for screening could increase dramatically. This expansion in the reservoir could certainly lead to a substantial increase in lead structures for drug discovery. The ongoing study of the epothilones serves to underscore the value of target-directed total synthesis in the quest for new substances of material clinical benefit.

This point is well worth making in the current research environment, which favors recourse to massive numbers of compounds for screening in preference to smaller numbers of hypothesis-driven candidate structures based on natural product leads. Although we readily concur that it is not inconceivable that purely chance-driven diversity collections may give rise to successful drug candidates, we would assert that the wisdom inherent in natural products, now augmented by the growing field of chemical synthesis, represents a valuable resource that has been little appreciated of late.[46] In essence, we are suggesting that in the drug discovery process there are two directions that can be taken. One possibility is to hurl a mind-boggling number of compounds at a problem. There is certainly merit in this approach. For reasons of personal taste, we prefer to make fewer compounds by tapping the generous hints provided by nature and exploiting the resources of human creativity and improvisation. This lesson may in itself prove to be a valuable fringe benefit of the journey which led us to fludelone.

Received: August 20, 2004

[1] S. F. Brady, C. J. Chao, J. Clardy, *J. Am. Chem. Soc.* **2002**, *124*, 9968.
[2] a) V. Knight, J. J. Sanglier, D. DiTullio, S. Braccili, P. Bonner, J. Waters, D. Hughes, L. Zhang, *Appl. Microbiol. Biotechnol.* **2003**, *62*, 446; b) D. J. Newman, G. M. Cragg, K. M. Snader, *Nat. Prod. Rep.* **2000**, *17*, 215.
[3] a) D. C. Myles, *Curr. Opin. Biotechnol.* **2003**, *14*, 627; b) Y.-Z. Shu, *J. Nat. Prod.* **1998**, *61*, 1053; c) L. A. Wessjohann, *Curr. Opin. Chem. Biol.* **2000**, *4*, 303; d) D. J. Newman, G. M. Cragg, K. M. Snader, *J. Nat. Prod.* **2003**, *66*, 1022.
[4] A. G. Ravelo, A. Estevez-Braun, H. Chavez-Orellana, E. Perez-Sacau, D. Mesa-Siverio, *Curr. Top. Med. Chem.* **2004**, *2*, 241, and references therein.
[5] M. C. Wani, H. L. Taylor, M. E. Wall, P. Coggan, A. T. McPhail, *J. Am. Chem. Soc.* **1971**, *93*, 2325.
[6] a) P. B. Schiff, S. B. Horwitz, *Proc. Natl. Acad. Sci. USA* **1980**, *77*, 1561; b) P. B. Schiff, S. B. Horwitz, *Nature* **1979**, *277*, 665; c) J. Parness, S. B. Horwitz, *J. Cell Biol.* **1981**, *91*, 479; d) K. C. Nicolaou, W.-M. Dai, R. K. Guy, *Angew. Chem.* **1994**, *106*, 38; *Angew. Chem. Int. Ed. Engl.* **1994**, *33*, 15; e) E. K. Rowinsky, *Annu. Rev. Med.* **1997**, *48*, 353.
[7] D. Guenard, F. Gueritte-Vogelein, P. Potier, *Acc. Chem. Res.* **1993**, *26*, 160.
[8] S. J. Danishefsky, J. J. Masters, W. B. Young, J. T. Link, L. B. Snyder, T. V. Magee, D. K. Jung, R. C. A. Isaacs, W. G. Bornmann, C. A. Alaimo, C. A. Coburn, M. J. DiGrandi, *J. Am. Chem. Soc.* **1996**, *118*, 2843.

[9] a) K. C. Nicolaou, Z. Yang, J. J. Liu, H. Ueno, P. G. Nantermet, R. K. Guy, C. F. Claiborne, J. Renaud, E. A. Couladouros, K. Paulvannan, E. J. Sorenson, *Nature* **1994**, *367*, 630; b) K. C. Nicolaou, P. G. Nantermet, H. Ueno, R. K. Guy, E. A. Couladouros, E. J. Sorenson, *J. Am. Chem. Soc.* **1995**, *117*, 624; c) K. C. Nicolaou, J. J. Liu, Z. Yang, H. Ueno, E. J. Sorenson, C. F. Claiborne, R. K. Guy, C. K. Hwang, M. Nakada, P. G. Nantermet, *J. Am. Chem. Soc.* **1995**, *117*, 634; d) K. C. Nicolaou, Z. Yang, J. J. Liu, P. G. Nantermet, C. F. Claiborne, J. Renaud, R. K. Guy, K. Shibayama, *J. Am. Chem. Soc.* **1995**, *117*, 645; e) K. C. Nicolaou, H. Ueno, J. J. Liu, P. G. Nantermet, Z. Yang, J. Renaud, K. Paulvannan, R. Chadha, *J. Am. Chem. Soc.* **1995**, *117*, 653.

[10] a) R. A. Holton, C. Somoza, H. B. Kim, F. Liang, R. J. Biediger, P. D. Boatman, M. Shindo, C. C. Smith, S. C. Kim, H. Nadizadeh, Y. Suzuki, C. L. Tao, P. Vu, S. H. Tang, P. S. Zhang, K. K. Murthi, L. N. Gentile, J. H. Liu, *J. Am. Chem. Soc.* **1994**, *116*, 1597; b) R. A. Holton, H. B. Kim, C. Somoza, F. Liang, R. J. Biediger, P. D. Boatman, M. Shindo, C. C. Smith, S. C. Kim, H. Nadizadeh, Y. Suzuki, C. L. Tao, P. Vu, S. H. Tang, P. S. Zhang, K. K. Murthi, L. N. Gentile, J. H. Liu, *J. Am. Chem. Soc.* **1994**, *116*, 1599.

[11] a) E. K. Rowinsky, E. A. Eisenhauer, V. Chaudhry, S. G. Arbuck, R. C. Donehawer, *Semin. Oncol.* **1993**, *20*, 1; b) B. S. Fletcher, D. A. Kujubadu, D. M. Perrin, H. R. Herschman, *J. Biol. Chem.* **1992**, *267*, 4338; c) M. Tsuji, R. N. Dubois, *Cell*, **1995**, *3*, 493; d) D. M. Essayan, A. Kagey-Sobotka, P. J. Colarusso, L. M. Lichtenstein, R. F. Ozols, E. D. King, *J. Allergy Clin. Immunol.* ***1996***, 97, 42; e) P. Giannakakou, D. L. Sackett, Y.-K. Kang, Z. Zhan, J. T. Buters, T. Fojo, M. S. Poruchynsky, *J. Biol. Chem.* **1997**, *272*, 17118, and references therein.

[12] G. Höfle, N. Bedorf, K. Gerth, H. Reichenbach (GBF), DE-B 4138042, **1993**; *Chem. Abstr.* **1993**, *120*, 52841.

[13] D. M. Bollag, P. A. McQueney, J. Zhu, O. Hensens, L. Koupal, J. Liesch, M. Goetz, E. Lazarides, C. M. Woods, *Cancer Res.* **1995**, *55*, 2325. We thank Professor Gunda Georg of the University of Kansas for calling this publication to our attention, and Dr. D. M. Bollag of Merck Sharp and Dohme for providing us with about 1 mg of epothilone A to commence studies (ultimately unsuccessful) towards the determination of its configuration.

[14] a) See reference [12]; b) R. J. Kowalski, E. Terhaar, R. E. Longley, S. P. Gunasekera, C. M. Lin, B. V. Day, E. Hamel, *Mol. Biol. Cell* **1995**, *6*, 2137; c) E. K. Rowinsky, E. A. Eisenhauer, V. Chaudhry, S. G. Arbuck, R. C. Donehawer, *Semin. Oncol.* **1993**, *20*, 1; d) B. S. Fletcher, D. A. Kujubadu, D. M. Perrin, H. R. Herschman, *J. Biol. Chem.* **1992**, *267*, 4338; e) M. Tsuji, R. N. Dubois, *Cell* **1995**, *3*, 493; f) D. M. Essayan, A. Kagey-Sobotka, P. J. Colarusso, L. M. Lichtenstein, R. F. Ozols, E. D. King, *J. Allergy Clin. Immunol.* **1996**, *97*, 42; g) P. Giannakakou, D. L. Sackett, Y.-K. Kang, Z. Zhan, J. T. Buters, T. Fojo, M. S. Poruchynsky, *J. Biol. Chem.* **1997**, *272*, 17118, and references therein.

[15] G. H. Höfle, N. Bedorf, H. Steinmetz, D. Schomburg, K. Gerth, H. Reichenbach, *Angew. Chem.* **1996**, *108*, 1671; *Angew. Chem. Int. Ed. Engl.* **1996**, *35*, 1567.

[16] a) A. Balog, D. F. Meng, T. Kamenecka, P. Bertinato, D.-S. Su, E. J. Sorensen, S. J. Danishefsky, *Angew. Chem.* **1996**, *108*, 2976; *Angew. Chem. Int. Ed. Engl.* **1996**, *35*, 2801; b) D.-S. Su, D. F. Meng, P. Bertinato, A. Balog, E. J. Sorensen, S. J. Danishefsky, Y. H. Zheng, T.-C. Chou, L. F. He, S. B. Horwitz, *Angew. Chem.* **1997**, *109*, 775; *Angew. Chem. Int. Ed. Engl.* **1997**, *36*, 757; c) D. F. Meng, P. Bertinato, A. Balog, D.-S. Su, T. Kamenecka, E. J. Sorensen, S. J. Danishefsky, *J. Am. Chem. Soc.* **1997**, *119*, 10073.

[17] a) A. Rivkin, F. Yoshimura, A. E. Gabarda, T.-C. Chou, H. Dong, W. P. Tong, S. J. Danishefsky, *J. Am. Chem. Soc.* **2003**, *125*, 2899; b) T.-C. Chou, H. Dong, A. Rivkin, F. Yoshimura, A. E. Gabarda, Y. S. Cho, W. P. Tong, S. J. Danishefsky, *Angew. Chem.* **2003**, *115*, 4910; *Angew. Chem. Int. Ed.* **2003**, *42*, 4761; c) F. Yoshimura, A. Rivkin, A. E. Gabarda, T.-C. Chou, H. Dong, G. Sukenick, S. J. Danishefsky, *Angew. Chem.* **2003**, *115*, 2622; *Angew. Chem. Int. Ed.* **2003**, *42*, 2518.

[18] In an early RCM-based approach studied in our laboratory, the 12,13-epoxide was already in place. We also investigated RCM to reach the 12,13-alkene, but only in the context of surveying various possibilities. For reviews of RCM, see: a) R. H. Grubbs, S. J. Miller, G. C. Fu, *Acc. Chem. Res.* **1995**, *28*, 446; b) T. M. Trinka, R. H. Grubbs, *Acc. Chem. Res.* **2001**, *34*, 18; c) A. Fürstner, *Alkene Metathesis in Organic Chemistry*, Springer, Berlin, **1998**; d) A. Fürstner, *Angew. Chem.* **2000**, *112*, 3140; *Angew. Chem. Int. Ed.* **2000**, *39*, 3012; e) R. R. Schrock, *Top. Organomet. Chem.* **1998**, *1*, 1.

[19] See reference [16c] and A. Rivkin, Y. S. Cho, A. E. Gabarda, Y. Fumihiko, S. J. Danishefsky, *J. Nat. Prod.* **2004**, *67*, 139.

[20] C. R. Harris, S. J. Danishefsky, *J. Org. Chem.* **1999**, *64*, 8434, and references therein.

[21] a) S. J. Danishefsky, *Aldrichimica Acta* **1986**, *19*, 59; b) S. J. Danishefsky, *Chemtracts* **1989**, *2*, 273.

[22] Naturally, when we conceived this remarkable aldolization we were aware of the non-enolizability of the "C3" aldehyde in the C2–C3 seco structure.

[23] S. J. Stachel, S. J. Danishefsky, *Tetrahedron Lett.* **2001**, *42*, 6785.

[24] See reference [16a]. Shortly after our synthesis, two other efforts, each exploiting olefin metathesis, were described: a) Z. Yang, Y. He, D. Vourloumis, H. Vallberg, K. C. Nicolaou, *Angew. Chem.* **1997**, *109*, 170; *Angew. Chem. Int. Ed. Engl.* **1997**, *36*, 166; b) D. Schinzer, A. Limberg, A. Bauer, O. Böhm, M. Cordes, *Angew. Chem.* **1997**, *109*, 543; *Angew. Chem. Int. Ed. Engl.* **1997**, *36*, 523.

[25] For the first SAR (structure–activity relationship) map, see: a) D.-S. Su, A. Balog, D. Meng, P. Bertinato, S. J. Danishefsky, Y.-H. Zheng, T.-C. Chou, L. He, S. B. Horwitz, *Angew. Chem.* **1997**, *109*, 2178; *Angew. Chem. Int. Ed. Engl.* **1997**, *36*, 2093; see also: b) K. C. Nicolaou, D. Vourloumis, T. Li. , J. Pastor, N. Winssinger, Y. He, S. Ninkovic, F. Sarabia, H. Vallberg, F. Roschanger, N. P. King, M. Ray, V. Finlay, P. Giannakakou, P. Verdier-Pinard, E. Hamel, *Angew. Chem.* **1997**, *109*, 2181; *Angew. Chem. Int. Ed. Engl.* **1997**, *36*, 2097; for the earliest in vivo assays of dEpoB, see: c) T.-C. Chou, X. G. Zhang, C. R. Harris, S. D. Kuduk, A. Balog, K. A. Savin, J. R. Bertino, S. J. Danishefsky, *Proc. Natl. Acad. Sci. USA* **1998**, *95*, 15798; d) T.-C. Chou, X. G. Zhang, A. Balog, D. Su, D. F. Meng, K. Savin, J. R. Bertino, S. J. Danishefsky, *Proc. Natl. Acad. Sci. USA* **1998**, *95*, 9642; e) T.-C. Chou, O. A. O'Connor, W. P. Tong, Y. Guan, Z.-G. Zhang, S. J. Stachel, C. Lee, S. J. Danishefsky, *Proc. Natl. Acad. Sci. USA* **2001**, *98*, 8113.

[26] Novartis is the sponsor of the clinical trials with EpoB. For EpoB preclinical data reported by Novartis, see: a) K.-H. Altmann, M. Wartmann, T. O'Reilly, *Biochim. Biophys. Acta* **2000**, *1470*, M79; b) J. Rothermel, M. Wartmann, T. Chen, J. Hohneker, *Semin. Oncol.* **2003**, *6*(Suppl.30), 51.

[27] C. R. Harris, S. D. Kuduk, A. Balog, K. Savin, P. W. Glunz, S. J. Danishefsky, *J. Am. Chem. Soc.* **1999**, *121*, 7051.

[28] N.-H. Lin, L. E. Overman, M. H. Rabinowitz, L. A. Robinson, M. J. Sharp, J. Zablocki, *J. Am. Chem. Soc.* **1996**, *118*, 9062.

[29] D. A. Evans, J. V. Nelson, T. R. Taber, *Top. Stereochem.* **1982**, *13*, 1.

[30] R. Noyori, T. Ohkuma, M. Kitamura, H. Takaya, N. Sayo, H. Kumobayahshi, S. Akutagawa, *J. Am. Chem. Soc.* **1987**, *109*, 5856.

[31] Bristol-Myers Squibb (BMS) is sponsoring clinical trials of the 15-desoxy-15-aza congener: a) R. M. Borzilleri, X. Zheng, R. J. Schmidt, J. A. Johnson, S.-H. Kim, J. D. DiMarco, C. R. Fairchild, J. Z. Gougoutas, F. Y. F. Lee, B. H. Long, G. D. Vite, *J. Am. Chem. Soc.* **2000**, *122*, 8890; b) F. Y. F. Lee, R. Borzilleri, C. R.

Fairchild, S.-H Kim, B. H. Long, C. Reventos-Suarez, G. D. Vite, W. C. Rose, R. A. Kramer, *Clin. Cancer Res.* **2001**, *7*, 1429; BMS is also sponsoring clinical trials of another epothilone derivative (BMS310705): c) R. M. Borzilleri, G. D. Vite, *Drugs Future* **2002**, *27*, 1149.

[32] L. Tang, S. Shah, L. Chung, J. Carney, L. Katz, C. Khosla, B. Julien, *Science* **2000**, *287*, 640.

[33] For more information about the clinical trials of dEpoB, visit: www.kosan.com.

[34] R. L. Arslanian, L. Tang, S. Blough, W. Ma, R. G. Qiu, L. Katz, J. R. Carn, *J. Nat. Prod.* **2002**, *65*, 570.

[35] M. D. Chappell, S. J. Stachel, C. B. Lee, S. J. Danishefsky, *Org. Lett.* **2000**, *2*, 1633.

[36] K. Biswas, H. Lin, J. T. Njardarson, M. D. Chappell, T.-C. Chou, Y. Guan, W. P. Tong, L. He, S. B. Horwitz, S. J. Danishefsky, *J. Am. Chem. Soc.* **2002**, *124*, 9825.

[37] a) B. E. Smart, *J. Fluorine Chem.* **2001**, *109*, 3; b) I. Ojima, T. Inoue, S. Chakravarty, *J. Fluorine Chem.* **1999**, 97; c) R. A. Newman, J. Yang, M. R. V. Finlay, F. Cabral, D. Vourloumis, L. C. Stephens, P. Troncoso, X. Wu, C. J. Logothetis, K. C. Nicolaou, N. M. Navone, *Cancer Chemother. Pharmacol.* **2001**, *48*, 319; d) Special issue on "Fluorine in the Life Sciences", *ChemBioChem* **2004**, *5*, 557 – 726.

[38] A. Rivkin, K. Biswas, T.-C. Chou, S. J. Danishefsky, *Org. Lett.* **2002**, *4*, 4081.

[39] Unpublished results.

[40] A. Rivkin, J. T. Njardarson, K. Biswas, T.-C. Chou, S. J. Danishefsky, *J. Org. Chem.* **2002**, *67*, 7737.

[41] K. C. Nicolaou, F. Sarabia, S. Ninkovic, M. Ray, V. Finlay, C. N. C. Boddy, *Angew. Chem.* **1998**, *110*, 85; *Angew. Chem. Int. Ed. Engl.* **1998**, *37*, 81.

[42] A. Rivkin, F. Yoshimura, A. E. Gabarda, Y. S. Cho, T.-C. Chou, H. Dong, S. J. Danishefsky, *J. Am. Chem. Soc.* **2004**, *126*, 10913.

[43] J. D. White, R. G. Carter, K. F. Sundermann, M. Wartmann, *J. Am. Chem. Soc.* **2001**, *123*, 5407.

[44] J. D. White, R. G. Carter, K. F. Sundermann, M. Wartmann, *J. Am. Chem. Soc.* **2003**, *125*, 3190.

[45] For a recent and impressive case of long-term cure, see: M. J. Towle, K. A. Salvato, J. Budrow, B. F. Wels, G. Kuznetsov, K. K. Aalfs, S. Welsh, W. Zheng, B. M. Seletsky, M. H. Palme, G. J. Habgood, L. A. Singer, L. V. DiPietro, Y. Wang, J. J. Chen, D. A. Quincy, A. Davis, K. Yoshimatsu, Y. Kishi, M. J. Yu, B. A. Littlefield, *Cancer Res.* **2001**, *61*, 1013. Our case is particularly noteworthy in that the cures were established consistently. Furthermore, they were established on high tumor burdens, and the drug shows oral-administration efficacy.

[46] R. Breinbauer, I. R. Vetter, H. Waldmann, *Angew. Chem.* **2002**, *114*, 3002; *Angew. Chem. Int. Ed.* **2002**, *41*, 2878.

Protein Recognition

Recognition of Proline-Rich Motifs by Protein–Protein-Interaction Domains

Linda J. Ball, Ronald Kühne, Jens Schneider-Mergener, and Hartmut Oschkinat**

Keywords:
binding domains · molecular recognition · proline · protein folding · proteins

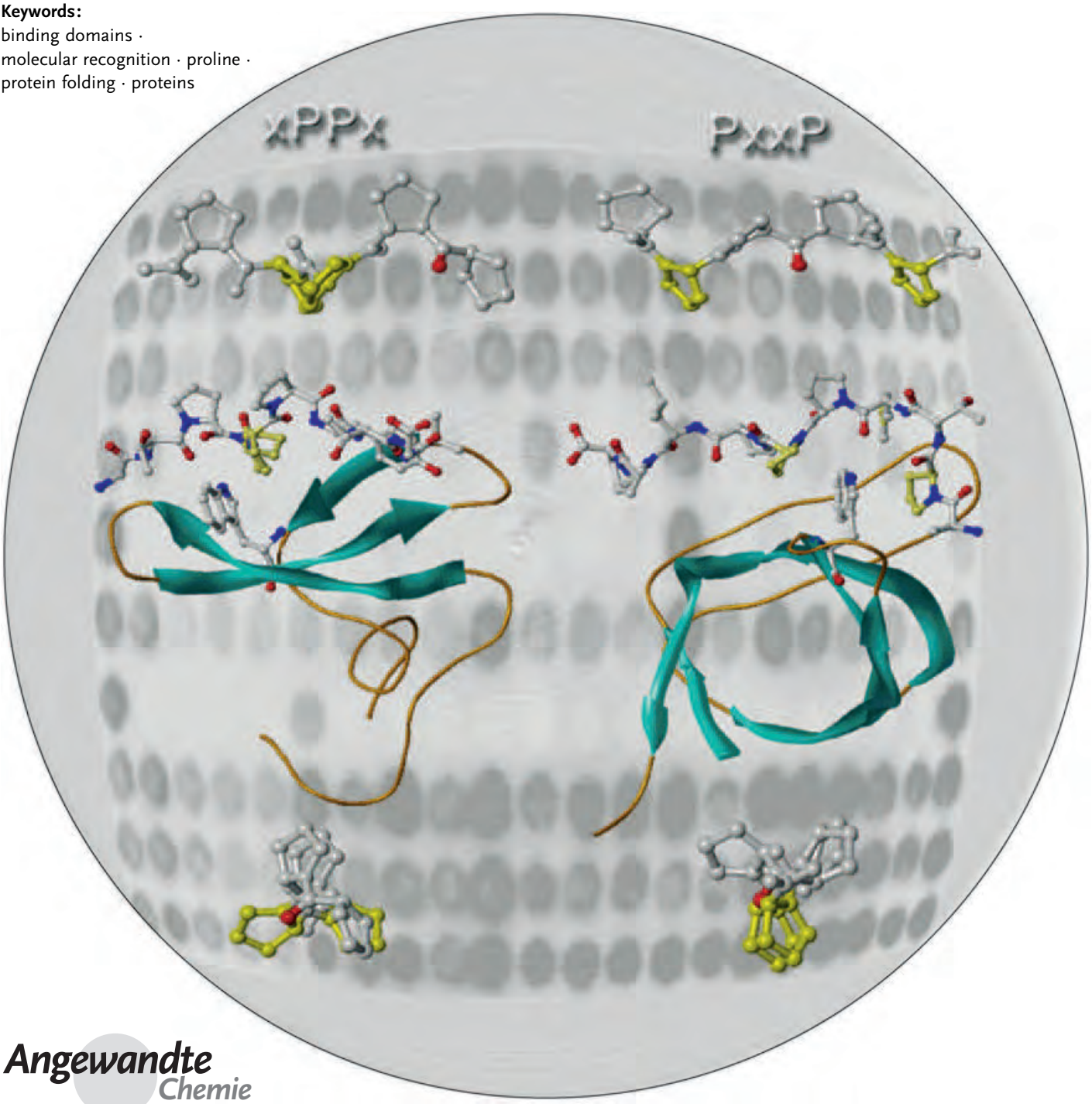

DOI: 10.1002/anie.200400618

Protein–protein interactions are essential in every aspect of cellular activity. Multiprotein complexes form and dissociate constantly in a specifically tuned manner, often by conserved mechanisms. Protein domains that bind proline-rich motifs (PRMs) are frequently involved in signaling events. The unique properties of proline provide a mechanism for highly discriminatory recognition without requiring high affinities. We present herein a detailed, quantitative assessment of the structural features that define the interfaces between PRM-binding domains and their target PRMs, and investigate the specificity of PRM recognition. Together with the analysis of peptide-library screens, this approach has allowed the identification of several highly conserved key interactions found in all complexes of PRM-binding domains. The inhibition of protein–protein interactions by using small-molecule agents is very challenging. Therefore, it is important to first pinpoint the critical interactions that must be considered in the design of inhibitors of PRM-binding domains.

From the Contents

1. Introduction

Modular proteins involved in signal transduction utilize highly conserved noncatalytic adaptor domains to mediate protein–protein interactions during the formation of multiprotein signaling complexes. These interactions must fulfill certain requirements: First, accurate recognition of the binding partner is required to guarantee a highly specific interaction. Second, the interaction must be readily reversible to allow complexes to dissociate again as soon as a stimulus is removed, thus requiring affinities in the micromolar to nanomolar range.

A number of different families of protein–protein-interaction domains have been described to date (for reviews, see references [1–6]). In many cases, the domains recognize target core motifs containing phosphorylated residues. Well-known examples are the Src-homology 2 (SH2) domains and the phosphotyrosine-binding (PTB) domains, which bind core sequence motifs containing phosphorylated tyrosine residues.[7–9] The Forkhead-associated (FHA) domains found in a variety of signaling proteins bind phosphoserine- and phosphothreonine-containing peptides. It was suggested that FHA domains may act as SH2 equivalents in phosphoserine- and phosphothreonine-dependent signaling pathways.[10] Members of the 14-3-3 family of proteins and class IV WW domains also bind phosphoserine and phosphothreonine, thus revealing interesting and unexpected similarities between these families.[10–12] Another well-known family of protein-interaction domains is the postsynaptic density/disc large/ZO1 (PDZ) family, which recognize and bind the extreme C-terminal sequences of their binding partners.[7] Furthermore, several domain families are known that recognize peptides containing proline-rich motifs (PRMs). These PRM-binding domains, which form the focus of this Review, are highly abundant and particularly interesting in the context of multicomponent signaling events.

1.1. Recognition of Proline-Rich Motifs by PRM-Binding Modules

Six distinct families of PRM-binding modules are currently known: the Src-homology 3 (SH3) domains,[13,14] the WW domains,[15,16] the EVH1 domains,[17–19] the GYF domains (also known as CD2-binding domains),[20,21] the UEV domains,[22,23] and the single-domain profilin proteins.[24,25] All interact with their target PRMs with K_d values typically in the range of 1 to 500 μM and rely on interactions with core-flanking epitopes to achieve the necessary specificities. The high-resolution structures of representative members from each family of PRM-binding domains known to date are shown in Figure 1. The N and C termini of the domains are generally located relatively close together, thus allowing the domains to slot into their respective host proteins with minimal disruption of the overall protein structure, while the domains themselves are exposed and accessible to recruit target proteins. Highly conserved clusters of exposed aromatic residues, sometimes referred to as "aromatic cradles",[26] are a characteristic of all PRM-binding domains and are necessary for the recognition of specific PRMs (see Figure 1). The relative orientation of the aromatic side chains of these clusters and the distances between the side chains determine the specificity of PRM recognition.

[*] Dr. L. J. Ball, Dr. R. Kühne, Prof. Dr. H. Oschkinat
Forschungsinstitut für Molekulare Pharmakologie (FMP)
Robert-Rössle-Strasse 10, 13125 Berlin (Germany)
Fax.: (+49) 30-94793-169
E-mail: linda@fmp-berlin.de
oschkinat@fmp-berlin.de
Prof. Dr. J. Schneider-Mergener
Institut für Medizinische Immunologie
Charité, Humboldt Universität
Hessische Strasse 3–4, 10115 Berlin (Germany)

 DOI: 10.1002/anie.200400618

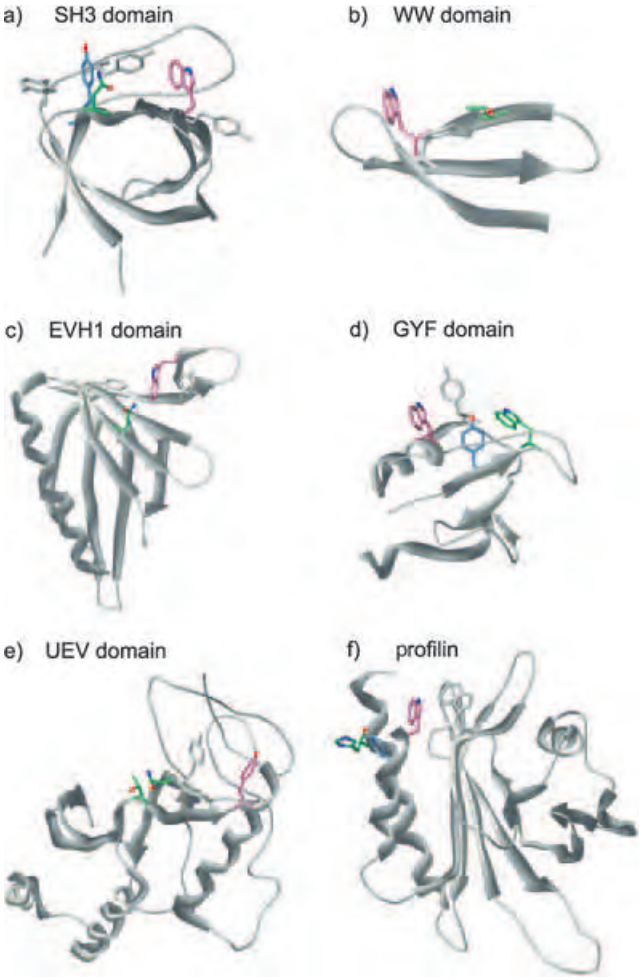

Figure 1. Three-dimensional structures of representative examples of each of the known families of PRM-binding domains in complexes with PRM-containing peptides: a) SH3 domain of human Fyn tyrosine kinase (1fyn); b) WW domain of human dystrophin (1eg4); c) EVH1 domain of mouse Evl (1qc6); d) GYF domain of human CD2BP2 (1l2z); (e) UEV domain of human Tsg101 (1m4p); f) profilin from human platelets (1cjf). The figure shows the overall folds of the domains and the location of the peptide-binding site comprising the exposed, aromatic clusters. The peptide ligand docks onto this site by packing proline rings into the hydrophobic cavities surrounding the Trp (pink) and Tyr (blue) side chains. Residues of the binding site indicated in green form additional hydrogen bonds to the peptide.

PRM-binding domains recognize specific 3–6-residue proline-containing sequences comprising so-called "core motifs" within accessible target peptides of 5–10 amino acids in length in the binding partner. These core motifs are often recognized by several members of a family of domains. Within a domain family, the affinity and specificity of a particular domain for a given target peptide is further modulated by additional, highly localized interactions between the core-flanking epitopes of the peptide and exposed side chains on the domain surface (known as epsilon determinants[27]). The core-flanking epitopes can consist of single amino acid residues, small groups of residues, post-translationally modified residues, or combinations of those residue types, and can be located either N or C terminally to the core motif (Fn and Fc, respectively[27]). Depending on the binding energies contributed by these additional interactions, domains of a given family will show different preferences for a certain core motif. Conversely, a single domain can recognize a number of different peptides with binding affinities within a certain range. This ligand degeneracy enables many signaling proteins to perform multiple or overlapping functions.

This Review examines in detail the specific structural requirements for PRM recognition by each of the six different families of PRM-binding domains. The preferences of these families for distinct core motifs are discussed in the light of the high-resolution NMR spectroscopic and X-ray crystal structures now available for a large number of these domains and their complexes with peptide ligands. The derivation of consensus binding motifs within target peptides by peptide-library screening, in particular by using the SPOTs synthesis technique,[28–32] is also discussed. By combining the available structural and binding data, we have identified a number of general features common to all known PRM-binding domains and their complexes. The presence of these structural features in other proteins could be a useful indicator of PRM-binding activity and may aid the search for possible binding partners. Furthermore, this information could provide new clues about the function of these proteins.

1.2. Proline Conservation in PRMs and the PPII Helix

The proline-rich target peptides recognized in signaling events generally contain several consecutive proline residues,

Linda J. Ball studied chemistry at the University of Oxford (UK) and graduated with a PhD in biochemistry and structural biology from the University of Cambridge (UK) in 1997. She then carried out postdoctoral research as an EMBO Fellow on protein-structure determination in the research group of Prof. Oschkinat in the Department of NMR-Supported Structural Biology at the FMP Berlin (Germany). She now pursues independent research at this institute on the use of NMR spectroscopy to probe the structures and interactions of signaling domains and cytoskeletal regulatory proteins.

Ronald Kuehne studied biochemistry at the Martin-Luther-Universität Halle-Wittenberg (Germany), where he completed his PhD in biochemistry in 1980. Following a period in the research group for molecular modeling at the Institute of Drug Research, he is now head of the research group for molecular modeling/ligand design at the FMP. His research is focused on modeling protein–ligand interactions by using molecular-dynamics simulations and automated docking procedures.

some of which are absolutely necessary for binding, while others appear to be less important. The patterns of proline conservation observed can be largely explained in terms of the secondary structure adopted by poly-L-proline in aqueous solution. The conformational restriction of the torsion angles of the peptide backbone, $\Phi = -78°$ and $\Psi = +146°$, results in an extended structure known as the left-handed polyproline II (PPII) helix.[33–36] This structure, shown in Figure 2a, has pseudo C_3 rotational symmetry about the helical axis with exactly three residues per turn. It is therefore not surprising that the majority of proline-rich target sequences found in nature repeat with a periodicity of three (e.g. PxxPxxP or PPxPPxPP). The PPII structure thus forms a unique recognition motif with the proline side chains and carbonyl groups of the peptide backbone exposed to the solvent at regular intervals. The absence of intramolecular hydrogen bonding in the PPII helix (as a result of the absence of a backbone amide functionality in proline) leaves the backbone carbonyl groups freely available to undergo intermolecular hydrogen-bond formation with the PRM domains. Furthermore, the carbonyl group of proline is more electron-rich than those of all other natural amino acids,[33,37,38] thus making proline a very good hydrogen-bond acceptor. The PPII structure also possesses a second, C_2 rotational pseudosymmetry axis perpendicular to the long axis of the helix. A rotation of 180° about this axis leaves the peptide backbone and the side chains in approximately the same position (see Figure 2b). This property leads to the possibility of binding in two orientations (often termed forward and reverse), in which the same recognition elements of the peptide are used, as well as the same hydrogen-bond donors of the side chains and hydrophobic clefts of the domain. For SH3 domains, WW domains, and profilins, both forward and reverse ligand binding have been reported. Nevertheless, different classes of domains within a given PRM-binding family generally show distinct preferences for either N–C- or C–N-oriented peptides.

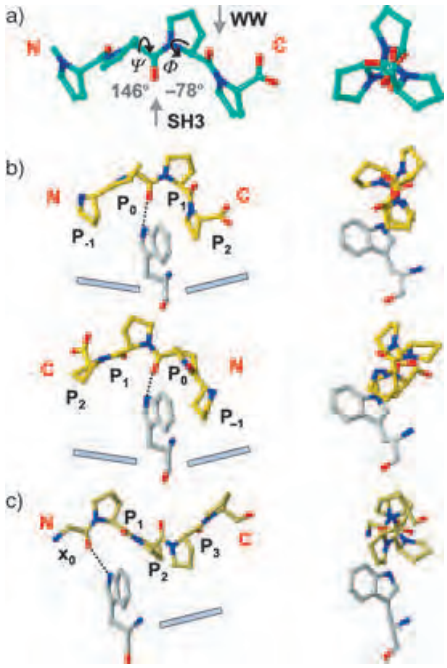

Figure 2. a) Left-handed polyproline II (PPII) helix, side on and in cross section to show the perpendicular C_2 and C_3 rotational pseudosymmetries. b) Binding mode 1 (SH3 and EVH1 domains, and profilin). The peptide forms an umbrella-like structure around the exposed hydrogen-bond-donating aromatic side chain (Trp or Tyr) of the domain. The same hydrogen-bond donors are utilized regardless of peptide orientation. c) Binding mode 2 (WW, GYF, and UEV domains). The domain binds to the opposite side of the PPII peptide. Gray bars give an idea of the rough shape of the binding pocket formed by aromatic side chains surrounding the PRM-recognition cluster of the domain.

The PRM-binding domains may approach the peptides from opposite sides, as indicated by the arrows in Figure 2a. In the case of profilin, the first and fourth proline residues in the peptide sequence (P_{-1} and P_2 in Figure 2b) are oriented toward the domain as a result of the C_3 pseudosymmetry of the PPII structure. The Cβ, Cγ, and Cδ atoms are in close contact with the domain, thus leading to the general conservation pattern PxxP in the profilin ligands. In the second binding mode, observed, for example, with the WW domains, two adjacent proline residues pack into a hydrophobic groove (Figure 2c). In this case, the Cβ atom of P_1 and the Cδ atom of P_2 are the most critical recognition elements within the peptide and make the closest contact with the domain. Some variation is possible in the first position of the dipeptide unit (as all amino acids except glycine have a Cβ atom), but the second position must be occupied exclusively by a proline residue, as only proline has Cδ substitution at the amide nitrogen atom. Thus, the conservation pattern xP

Jens Schneider-Mergener studied chemistry in Bielefeld and München (Germany) and completed his PhD in biochemistry at the Ludwig-Maximilians-Universität München in 1986. After postdoctoral research from 1987 to 1990 at the California Institute of Technology (USA), he became a group leader at the medical faculty Charité of the Humboldt-Universität zu Berlin in 1991, and was appointed associate professor there in 1999. His research focuses on the role of peptides in biomedical research. He also founded the company Jerini AG, which pioneers peptide-based drug discovery and development.

Hartmut Oschkinat studied chemistry at the University of Frankfurt (Germany), where he completed his PhD in 1986. After postdoctoral research with Prof. Bodenhausen at the University of Lausanne (Switzerland), he was an NMR spectroscopist at the Max-Planck-Institut für Biochemie in Martinsried (Germany). In 1992, he completed his habilitation in biophysical chemistry at the Technische Universität München and moved to the EMBL in Heidelberg. Since 1998 he has been Head of the Department of NMR-Supported Structural Biology at the FMP and Professor of Structural Chemistry at the Freie Universität Berlin.

results for the dipeptide unit, and this conserved motif packs into the so-called "xP"-binding groove of the domain.[39]

The favored mode of binding clearly determines the pattern of proline conservation in the ligand motif: either PxxP (mode 1) or xPPx (mode 2). Amino acids other than proline then complete the core motif to provide specificity for a given family and class of domain. With longer interfaces, that is, when the proline-rich sequences of the ligand are long enough (e.g. in the case of SH3 and profilin complexes), combinations of both binding modes described above are observed (see Figure 3).

A further advantage of interactions with peptides that have proline-rich segments is the low entropic cost of binding. As two well-defined, preformed surfaces come into contact when a PRM docks onto its binding site, the decrease in entropy upon binding is minimized. One of the main reasons for this effect is the low number of degrees of rotational freedom in proline residues along the peptide backbone relative to other amino acids. It has been estimated that each degree of rotational freedom in a dipeptide is equivalent to 3.5 kJ mol^{-1} at 300 K,[40] and since the dipeptide xP has only two, rather than the usual four degrees of rotational freedom about the backbone bonds, each occurrence of the motif xP leads to an increase in the ΔG value for complex formation by 7 kJ mol^{-1}.[40] The smaller drop in entropy on binding therefore affords complexes with PRM peptides a greater overall binding energy than complexes with more flexible peptides. The affinities of PRM interactions may also be increased by the occurrence of several PRMs in close multiple tandem repeats, for example in the proteins zyxin and ActA, which bind Ena/VASP EVH1 domains,[41,42] and for the cytoplasmic tail region of CD2, which is bound by GYF domains.[20]

Although proline usually dominates the composition of PPII helices, a number of other amino acids are often found flanking or interleaved with the proline residues. The presence of the amino acid Glu in and around PPII helices is very common, as the hydrogen-bonding pattern in polyglutamic acid promotes the formation of the PPII structure. Other amino acids often found in proline-rich peptides of four residues or more in length are Gln, Arg, Ala, Leu, Ser, Asp, and His.[43]

2. SH3 Domains

The Src-homology 3 (SH3) domains are small protein-interaction modules of about 60 residues (Figure 1a) found in a large number of eukaryotic cytoskeletal and signaling proteins.[44–46] The various functions of proteins that contain SH3 domains include the control of cell compartmentalization, the localization of proteins to cytoskeletal microfilaments and membrane ruffles, and the regulation of enzymatic activities.[1]

2.1. Classification of SH3 Domains and Target-Sequence Preference

SH3 domains generally bind proline-rich sequences containing the characteristic PxxP motif (a more accurate description of the consensus sequence is PpϕP, in which p is usually a proline residue and ϕ is a hydrophobic residue (usually Leu, Pro, or Val)[27]). To date, SH3-domain classification has been based solely on whether a peptide ligand binds in a forward (N-to-C-terminal) or reverse (C-to-N-terminal) orientation. (The former is also referred to in the following as orientation 1, the latter as orientation 2.) SH3 domains of class 1 recognize sequences with a positive charge at their N terminus (consensus (R/K)xxPxxP), whereas SH3 domains of class II bind in the reverse orientation peptides containing a positively charged residue at their C terminus (consensus PxxPx(R/K); Table 1).[14,35,47] This broad classification scheme seems insufficient for such a large family of domains, and a more detailed classification is needed. To this end, comprehensive studies of peptide recognition by different SH3 domains, chosen from specificity classes identified by phage-display experiments, are currently underway to determine more-detailed ligand specificities of these domains.[112] The results of such studies will not only enable a more thorough classification of SH3 domains, but will also help to identify binding partners in the cell.

Table 1: Different binding domains for PRM-containing peptides.[a]

	Domain family and class	Example host protein	Consensus PRM
1.	SH3 domains		
	class I	Src, Yes, Abl, Grb2-A, Lyn, PI3K, Fyn,	(R/K)pϕPxϕP
	class II	Src, cortactin, p53BP2, PLCγ, Crk-A, Nck SH3-B, CAP SH3-C, amphiphysin	ψPpϕPϕ(R/K)
2.	WW domains		
	class I	BAG3, YAP65, Nedd-4, dystrophin	(L/P)Pp(Y/*po*Y)
	class II	FBP-11	PPLP p
	class III(a)	FE65	(p/ϕ)P(p/g)PPpR
	class III(b)	FBP21	(p/ϕ)PP(R/K)gPp
	class IV	Ess1, PIN1, Nedd-4	(*po*S/*po*T)P
	class V	PRP40-2	(p/ϕ)PPPPP
3.	EVH1 domains		
	class I	Ena, Mena, VASP, Evl	(D/E)FPxϕP
	class II	Homer-1a, Vesl-2	PPxx(F/Y)
4.	GYF domains	cytoplasmic tail of CD2	(R)xxPPgxR
5.	UEV domains	viral Gag protein	P(T/S)AP
6.	profilin	profilin (single-domain protein)	poly-L-proline

[a] ψ, ϕ, and x represent aliphatic, hydrophobic, and any amino acid residue, respectively; *po*S = phosphoserine, *po*T = phosphothreonine. Lower-case letters represent favored but not highly conserved residues. When more than two copies of a domain occur in a host protein, the one closest to the N terminus is labeled A.

2.2. The SH3/PRM Interface and Rationalization of Consensus SH3 Target Sequences

The high-resolution NMR spectroscopic and X-ray crystal structures now available for many different SH3 domains in complexes with proline-rich peptides[13,48–58] enable us to identify important, recurring features and to rationalize the consensus peptide sequences. Figure 3a,b shows detailed SH3/PRM interfaces for representative examples of ligand binding in the forward and reverse orientations. Two exposed aromatic side chains (Trp and Tyr) of the domain form hydrogen bonds to the carbonyl oxygen atoms of the peptide. The PPII conformation of the peptide ensures that the first and fourth proline residues of a PxxP target sequence pack efficiently into the hydrophobic pockets around the exposed Tyr residue of the domain. The most closely packed peptide residues are highlighted in yellow in Figure 3.

The PPII helix extends only over the peptide fragment from positions (0) to (6) in orientation 1 ($_0$MPPPLPP$_6$ in Figure 3a) and contains both of the two binding sites shown in Figure 2b,c. The exposed Trp residue is surrounded by a PxxxP motif that does not adopt a PPII helix structure. In this binding mode the ligand adopts a conformation that resembles a double umbrella, with the PPII-helix umbrella (PxxP) located around the central hydrogen-bonded Tyr residue (see Figure 2b). An alternatively shaped (PxxxP) umbrella surrounds the exposed, hydrogen-bonded Trp side chain. In orientation 2, the Trp

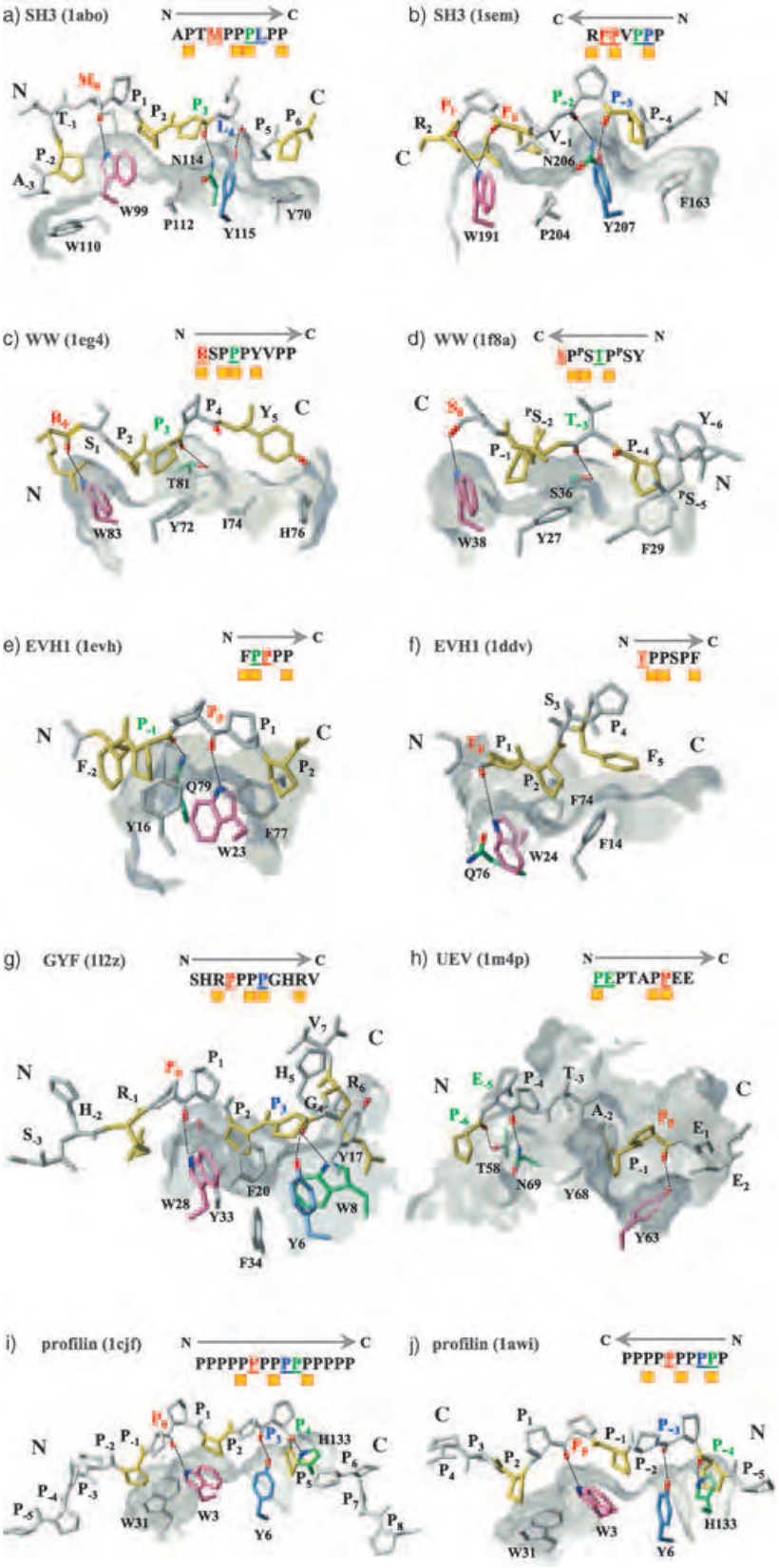

Figure 3. Detailed intermolecular interactions of representative members of each of the known PRM-binding families with their peptide ligands. Examples of both orientations of peptide binding: a), b) SH3 domain; c), d) WW domain; i) j) profilin. No reverse peptide orientation has yet been reported for the EVH1 domains, but two significantly different binding modes are known in which the peptide binds in the same orientation (e,f). g) ,h) Single binding modes known to date for the GYF and UEV domains. Pink: aromatic residue (hydrogen-bond donor) which forms the base of the primary stem of the "umbrella structure" (usually Trp, but Tyr in the UEV domain); blue: aromatic residue (hydrogen-bond donor) which forms the base of the second stem in the "double umbrella" (Tyr); green: more variable hydrogen-bond donor (Asn, Thr, Ser, Gln, or His); yellow: ligand side chains which make close hydrophobic contacts with the domain. The ligand sequence is shown above each complex with hydrogen-bond-acceptor residues underlined (red: hydrogen bond to Trp/Tyr, primary stem; blue: hydrogen bond to Tyr, second stem; green: hydrogen bond to more variable residue). Color coding of ligands corresponds to that in Tables 2–7. Yellow boxes: positions in close contact with the domain. The primary hydrogen-bond-acceptor residue in the ligand is assigned the number zero. Only those peptide residues that were detected in the three-dimensional X-ray crystal or NMR spectroscopic structures are shown. The full-length peptides in all of the complexes analyzed are given in the PDB codes (in brackets).

residue is instead surrounded by an RxP motif (Figure 3b). In both orientations, the Tyr and Trp hydrogen bonds are supported by a further hydrogen bond from an Asn side chain. The preference for a hydrophobic amino acid, not necessarily proline, at the less conserved, central position indicated by ϕ in the PpϕP motif, is explained by the side-on contacts this residue makes with the domain surface (see Figures 2 and 3). Substitution of one of the two most highly conserved proline residues by any other natural amino acid generally results in loss of binding. However, the replacement of one of these "essential" residues by an *N*-substituted amino acid can actually lead to increased binding affinities.[59] This observation could have important implications for the design of selective SH3 inhibitors.

2.3. Influence of "Core-Flanking" Ligand Residues

The two orientations of peptide binding are made possible by the symmetry of the PRMs, which allow the formation of very similar hydrogen-bonding networks in both orientations (Figure 2b). The hydrogen-bond acceptors are the carbonyl oxygen atoms of the peptide residues labeled in red, blue, or green in the sequence fragments in Figure 3. The corresponding hydrogen-bond-donating residues of the domain are colored similarly. Ligand orientation is determined by core-flanking interactions which do not involve proline residues and which can be either N terminal or C terminal to the core PRM. A positively charged residue next to the PRM usually forms a salt bridge with an appropriately positioned, oppositely charged residue on the domain surface. In cases of near-palindromic forward and reverse peptide sequences, binding is often observed in both orientations. The SH3 domain of Src, for example, binds both the peptide RPLPPLP and the "reverse" peptide PPVPPR (conserved proline residues are underlined).

2.4. Alternative Modes of Ligand Binding in SH3 Domains

In addition to the two orientations described above, several alternative SH3/PRM binding modes have also been described. For example, the peptide-binding groove of the SH3 domain recognizes a discontinuous epitope comprising nonsequential amino acid residues brought together by the tertiary structure of the binding partner. The SH3 domain of the p53-binding protein, p53BP2, interacts in this way with two segments of the L3 loop of p53.[60] The positions of the residues in the discontinuous binding epitope are determined by the overall structure of p53 and do not form a linear PRM core motif of the type discussed above.

A further discontinuous binding surface was identified for the SH3 domain of Csk. This domain binds a 25-residue peptide from the Pro/Glu/Ser/Thr-rich region (PEST region) of the PEP protein. To bind this peptide, the SH3 domain of Csk requires two separate interactions with the ligand: both the conventional PPII-helix recognition and additional interactions with two sequential hydrophobic residues (Ile and Val) located closer to the C terminus of the peptide.[58] NMR spectroscopic studies of the two interaction sites on the Csk SH3 domain showed them to have independent dynamics.[58]

In another unusual class of SH3–ligand binding interaction, the specificity for a particular target sequence can be modified by the dimerization of SH3 domains. The SH3 domain of Eps8, the receptor substrate of epidermal growth factor, forms intertwined dimers.[61] The dimer interface partially overlaps with the PxxP-binding site, so that in the dimeric form a new face is presented with altered ligand specificity. The intertwined SH3 dimer does not recognize the usual PxxP motif, but instead binds the new motif PxxDY.[62] SH3 domains may thus use multimerization as a mechanism to alter their binding specificity for particular partners in response to cellular requirements.

A number of intramolecular SH3-domain interactions have also been observed. The Src, Hck, and Abl proteins all contain multiple SH3 domains as well as SH2 and catalytic kinase domains. The SH3 domains interact with a linker region between the SH2 and catalytic kinase domains to hold them in a catalytically inactive conformation.[63–68] In another example, an SH3 domain of Itk, the cellular oncogene product, binds to an intramolecular KPLPPTP sequence.[69] Such interactions with intramolecular PRMs clearly play important roles in the regulation of eukaryotic signal transduction and cytoskeletal events.

Several SH3 interactions with sequences that are not proline-rich have also been reported. The C-terminal SH3 domain of the Gads T-cell adaptor protein binds a peptide from SLP-76 that contains an RxxK consensus sequence.[70] In this complex, the peptide adopts a right-handed helical conformation very different to the left-handed PPII helices observed for proline-rich peptides. Further examples include the recognition of a RKxxYxxY consensus by a number of class I SH3 domains.[47] Unlike for the majority of class I interactions, for which either an Arg or a Lys residue is required, in this case both positively charged residues are required for SH3 binding.

3. WW Domains

The WW domain is a protein module composed of 34–40 amino acids found in a number of signaling and regulatory proteins (Figure 1b).[71–73] Two highly conserved tryptophan residues give the domain its name. One of these residues is essential for folding, and the other is exposed on the protein surface. The latter forms part of an exposed hydrophobic cluster in which the side chains of a Trp/Tyr combination form an angle of approximately 90° which defines the shape of the proline-binding cavity.[16,26] In the WW domain of YAP65, the human Yes-kinase-associated protein, the whole cluster comprises Trp39, Tyr28, and Leu30.

3.1. Classification of WW Domains and Target-Sequence Preference

The results of many peptide-binding studies and substitution screens have allowed the identification of consensus

binding sequences for a large number of WW domains. The five known classes of WW domains are categorized according to ligand preference[74–76] and summarized in Table 1. Class I WW domains, such as that of YAP65, recognize an (L/P)Pp(Y/*po*Y) motif[77,78] (in which *po* represents a phosphorylated residue[27]). It has been proposed that tyrosine phosphorylation regulates the activity of these domains, although many domains have been observed to bind phosphorylated sequences with only slightly reduced affinities.[79] The second class of WW domains binds specifically to a PPLPp motif. An example of this class is the WW domain of the formin-binding protein FBP-11. The third class binds Pro-Arg-rich motifs. These domains can be further separated into two independent subclasses that recognize sequences of the type (p/ϕ)P(p/g)PPpR and (P/ϕ)PP(R/K)gpPp,[76,80] which are bound, for example, by the WW domains of FE65 and FBP21, respectively. Members of the fourth class of WW domains, such as the PIN1 WW domain, bind motifs (*po*S/*po*T)P in which proline residues are preceded by phosphorylated serine or threonine residues.[11,12,76] Finally, a fifth class, which includes the two tandemly repeated N-terminal WW domains of the yeast PRP40 protein, binds uninterrupted polyproline sequences of the type (p/ϕ)PPPPP, in which the first residue of the sequence must be hydrophobic.[76] Interestingly, both PRP40 WW domains also recognize class 1 and class 2 binding motifs.[81] It has been suggested that these tandemly repeated domains could participate in bridging interactions by binding simultaneously to PRMs in separate binding partners, thereby holding together complex interaction networks.[81]

Although different classes of WW domains show preferences for specific ligand PRMs, a considerable degree of ligand degeneracy is observed, as is illustrated by the results of peptide-library screening by the SPOTs technique and peptide-binding studies. Figure 4a shows the preferred amino acid sequences of the class I human YAP65 WW domain when screened for binding against six doubly substituted variants of the known PPPY binding motif.[113] In this experiment, residues at each of the variable positions within the PPPY motif were substituted simultaneously for all other 19 amino acids in two-dimensional grids. It was found that the YAP65 WW domain binds strongly only to motifs containing Tyr in the last position and either Pro or Leu in the first position of the sequence, thus confirming the consensus motif (L/P)PxY. Significantly weaker interactions were detected with motif sequences containing Arg or Tyr in the first position (e.g. YRPY, RRPY, RPRY, YPRY). If the first (Pro) and last (Tyr) positions are retained, Lys or Ala can also occur in position (3), thus confirming the PPxY consensus (see also Figure 3c). Figure 4b shows the effect of the substitution of a single amino acid within a longer, PPPY-containing YAP65 ligand of the sequence GTPPPPYTVG by all natural amino acids.[16,82] The minimal binding motif PPPY was obtained by shortening the peptide systematically from the N and C termini (Figure 4c).[82] Interestingly, very little tolerance toward the exchange of individual amino acids in the peptide

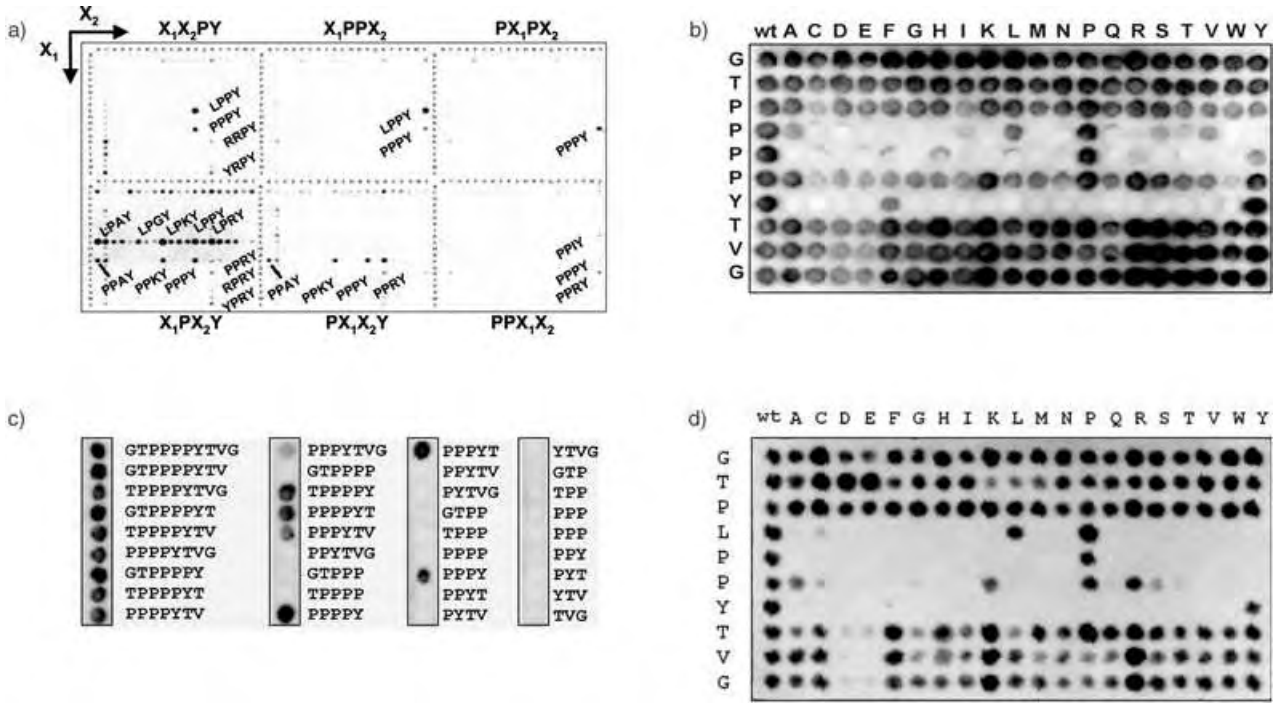

Figure 4. a) Double amino acid substitution analysis of the PPPY binding motif of class 1 WW domains (shown for the WW domain of human YAP65). All possible combinations of doubly substituted variants of this motif were synthesized on six two-dimensional grids. The different pairs of simultaneously substituted amino acids X_1 and X_2 are shown on the vertical and horizontal axes of each grid. b) Single amino acid substitution analysis of GTPPPPYTVG showing the most-conserved residues; wt = wild type. c) Minimization of the binding epitope; the minimal binding motif is PPPY. d) Single-substitution analysis of GTPLPPYTVG; similar overall conservation as in (b), with generally weaker overall binding to the WW domain.

core sequence was observed for GTPLPPYTVG (Figure 4d), probably as a result of the weaker interaction of the peptide with the domain when L replaces P in the (L/P)PxY motif. The absolute requirement for the second proline residue in the (L/P)PxY motif is clear from Figure 4. This residue appears to be a prerequisite for the correct docking of the PPII helix onto the hydrophobic peptide-binding groove of the class I WW domain.

In a "reverse substitution" experiment,[83] each of the 47 residues of the entire human YAP65 WW domain were substituted in turn (Figure 5). This experiment allowed the identification of the critical residues of the WW domain that are needed for both fold stabilization and ligand-binding activity (in this case to the 13-mer EYPPYPPPPYPSG[84]). High levels of conservation in residues of the protein core most likely indicate the involvement of those residues in folding, but high conservation in known surface-exposed residues suggests strongly that these residues are important for ligand interactions and hence protein function. In a more recent study, which combined the SPOTs synthesis technique with native-peptide ligation, many thousands of variants of the human YAP65 WW domain were created on cellulose membranes for the systematic study of three simultaneous substitutions (at positions L30, H32, and Q35).[31] Although GTPPPPYTVG and EYPPYPPPPYPSG peptides are known to bind the human YAP65 WW domain in vitro, the biological relevance of these complexes within the cell is still unclear.

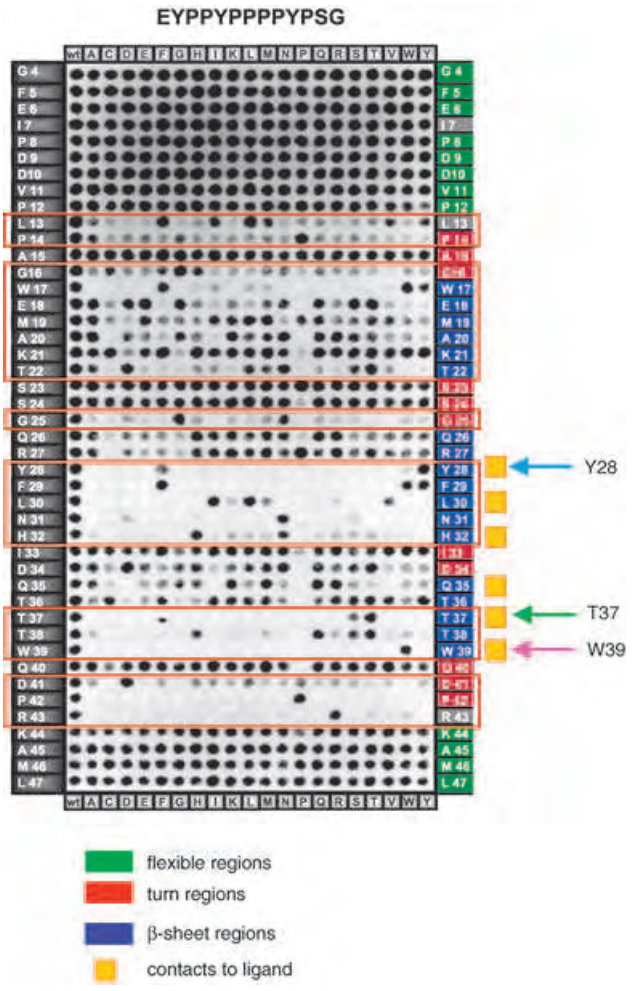

Figure 5. "Reverse" SPOTs scan in which all 42 amino acids of the WW domain of YAP65 were substituted while keeping the peptide sequence of the ligand constant (EYPPYPPPPYPSG; reprinted with the permission of Toepert et al.[83]). Red boxes: important regions of the WW domain for peptide binding. These include regions of secondary structure necessary for maintaining the WW fold and surface-exposed residues required specifically for ligand binding. The amino acid residues of the aromatic cluster are very highly conserved. In contrast, the flexible regions (green) are unimportant for peptide binding.

3.2. The WW/PRM Interface and Structural Rationalization of Consensus Target Sequences of the WW Domain

Inspection of the high-resolution structures of complexes of WW domains with proline-rich peptides[12,26,82,85] allows rationalization of the preferred core motifs of the ligand. The peptide is approached by the WW domain from the opposite side—compared to SH3–peptide complexes—of the PPII helix (see Figure 2), thus resulting in the close packing of two consecutive proline rings (highlighted in yellow) into the hydrophobic groove of the WW domain (Figure 3c,d). For example, the class I WW domain of dystrophin[26] binds a PPPY motif (Figure 3c), whereby the two underlined proline residues pack into the hydrophobic groove between Tyr72 and Trp83. Furthermore, the close packing of the peptide Tyr residue (PPPY) into another hydrophobic groove, on the other side of the Tyr72 side chain, explains the conservation of this peptide core residue. The substitution of this Tyr residue for Phe (PPPF) attenuated binding to the YAP65 WW domain by a factor of three.[16] This result implies the loss of a hydrogen bond and/or less-efficient packing of the aryl residue in the second hydrophobic groove.

The ligand in the WW complex shows only one half of the umbrella-like structure observed in SH3/PRM interactions (see Figure 2c). Again, the exposed Trp side chain forms a central hydrogen bond to a carbonyl oxygen atom of the ligand (position (0)) at the stem of this structure. A further hydrogen bond from the side chain of either a Thr or a Ser residue of the domain to the carbonyl oxygen atom at position (3) of the ligand depends on the orientation of the ligand (Thr in orientation 1, Ser in orientation 2; see Figure 3c,d and Tables 2–7). The same hydrogen-bond-donating side chains of the domain are used for each of the two possible peptide orientations. The hydrogen-bond-acceptor residues of the ligand (shown in red, green, and blue in Figure 3c,d) are also arranged similarly in both orientations.

3.3. The Significance of Non-proline Residues in the PRM

The orientation of ligand binding by WW domains is determined by non-proline residues within the core PRM, such as the Tyr residue at the C-terminal end of PRMs that bind specifically to WW domains of class I. In contrast to the ligands of SH3 and EVH1 domains, the PRM core residues of WW ligands are alone important for binding affinity and specificity determination; thus, these ligands contain a very

Table 2: SH3 domains with peptides in orientations 1 and 2.[a],[b]

Protein domain	Ligand (2 orientations)	PDB code (method)	Plane angles $Trp_{(domain)}$ and $P_{(ligand)}$	Plane angles $Tyr_{(domain)}$ and $P_{(ligand)}$	Potential H bonds $Trp\text{-}NH\varepsilon$ to $CO_{(ligand)}$	Potential H bonds $Tyr\text{-}OH$ to $CO_{(ligand)}$	Potential H bonds $Asn\text{-}NH\delta_{1,2}$ to $CO_{(ligand)}$
Ligand N to C:							
SH3 Fyn tyrosine kinase (human)	PPVPLPVAPGSKT 2101234567---	1a0n (NMR)	W_{129}-P_{-2}: badly defined L at +2	Y_{147}-P_{+3} = 31 Y_{147}-P_{+6} = 39	W_{129}-$R_{\delta(CO)}$ = 4.1 Å	Y_{147}-$V_{4(CO)}$ = 2.4 Å	N_{146}-$P_{3(CO)}$ = 2.7 Å
SH3 Fyn tyrosine kinase (human)	PPAYPPPPVP 3210123456	1fyn (X-ray)	W_{120}-P_{-2} = 37 W_{119}-P_{-2} = 29	Y_{137}-P_{+3} = 45 Y_{137}-P_{+6} = 40	W_{119}-$Y_{\alpha(CO)}$ = 2.7 Å	Y_{137}-$P_{4(CO)}$ = 3.6 Å	N_{136}-$P_{3(CO)}$ = 2.2 Å
SH3 Abl tyrosine kinase (human)	APSYSPPPPP 3210123456	1bbz (X-ray)	W_{36}-P_{-2} = 34 W_{36}-P_{2} = 31	Y_{52}-P_{+3} = 40 Y_{52}-P_{+6} = 19	W_{36}-$Y_{\alpha(CO)}$ = 2.0 Å	Y_{52}-$P_{4(CO)}$ = 2.7 Å	N_{51}-$P_{3(CO)}$ = 4.3 Å
SH3 Abl tyrosine kinase (mouse)	APTYPPPLPP 3210123456	1abo (X-ray)	W_{99}-P_{-2} = 42 W_{99}-P_{2} = 37	Y_{115}-P_{+3} = 43 Y_{115}-P_{+6} = 28	W_{99}-$M_{\alpha(CO)}$ = 2.1 Å	Y_{115}-$L_{4(CO)}$ = 2.7 Å	N_{114}-$P_{3(CO)}$ = 2.4 Å
SH3 c-Src (avian sarcoma virus)	VSLARPLPPLP --3210123456	1qwf (NMR)	A at −2 L at +2	Y_{90}-P_{+3} = 2 Y_{90}-P_{+6} = 24	W_{42}-$R_{\delta(CO)}$ = 2.3 Å W_{42}-$P_{1(CO)}$ = 3.2 Å	Y_{90}-$P_{4(CO)}$ = 2.6 Å	N_{59}-$P_{3(CO)}$ = 2.1 Å
SH3 domain of c-Src (chicken)	RALPPLPRY 01234567-	1rlp (NMR)	no residue at −2 L at +2	Y_{90}-P_{+3} = 48 Y_{90}-P_{+6} = 69	W_{42}-$R_{\delta(CO)}$ = 2.5 Å W_{42}-$A_{1(CO)}$ = 3.2 Å	Y_{90}-$P_{4(CO)}$ = 2.7 Å	N_{59}-$P_{3(CO)}$ = 7.9 Å
SH3 domain of c-Src (chicken)	xPLPPLP 0123456	1nlo (NMR)	no residue at −2 L at +2	Y_{90}-P_{+3} = 4 Y_{90}-P_{+6} = 24	W_{42}-$X^1_{\alpha(CO)}$ = 2.3 Å	Y_{90}-$P_{4(CO)}$ = 2.8 Å	N_{59}-$P_{3(CO)}$ = 2.5 Å
SH3 domain of c-Src (chicken)	APLPPLP 0123456	1nlp (NMR)	no residue at −2 L at +2	Y_{90}-P_{+3} = 9 Y_{90}-P_{+6} = 25	W_{42}-$X^2_{\alpha(CO)}$ = 2.3 Å	Y_{90}-$P_{4(CO)}$ = 2.6 Å	N_{59}-$P_{3(CO)}$ = 2.4 Å
Ligand C to N:							
N-terminal SH3 mutant Grb2 (human)	RRRPPVPPPV 4321012345	1aze (NMR)	W_{36}-P_{0} = 43	Y_{52}-P_{+3} = 32 Y_{52}-P_{0} = 39	W_{36}-$P_{0(CO)}$ = 2.2 Å W_{36}-$P_{1(CO)}$ = 2.4 Å	Y_{52}-$P_{-3(CO)}$ = 3.4 Å	N_{51}-$P_{-2(CO)}$ = 4.9 Å
N-terminal SH3 Grb2 (mouse)	RRRPPVPPPV 4321012345	4gbq (NMR)	W_{36}-P_{0} = 40	Y_{207}-P_{+3} = 23 Y_{207}-P_{0} = 28	W_{36}-$P_{0(CO)}$ = 3.2 Å W_{36}-$P_{1(CO)}$ = 2.9 Å	Y_{207}-$P_{-3(CO)}$ = 2.7 Å	N_{51}-$P_{-2(CO)}$ = 2.6 Å
N-terminal SH3 c-Crk (mouse)	RKKPPLAPPP 4321012345	1cka (X-ray)	W_{169}-P_{0} = 14	Y_{188}-P_{+3} = 11 Y_{188}-P_{0} = 27	W_{169}-$P_{0(CO)}$ = 2.0 Å W_{169}-$P_{1(CO)}$ = 2.8 Å	Y_{188}-$P_{-3(CO)}$ = 3.4 Å	no H-bond donor
N-terminal SH3 c-Crk (mouse)	RRRPPVPPP 432101234	1ckb (X-ray)	W_{169}-P_{0} = 16	Y_{188}-P_{+3} = 6 Y_{188}-P_{0} = 14	W_{169}-$P_{0(CO)}$ = 2.0 Å W_{169}-$P_{1(CO)}$ = 2.4 Å	Y_{188}-$P_{-3(CO)}$ = 2.8 Å	no H-bond donor
SH3 c-Src (avian sarcoma virus)	LRPRNRPPLPPA --543210 1234	1qwe (NMR)	W_{42}-P_{0} = 44	Y_{90}-P_{+3} = 48 Y_{90}-P_{0} = 44	W_{42}-$P_{0(CO)}$ = 2.3 Å W_{42}-$P_{1(CO)}$ = 3.1 Å	Y_{90}-$P_{-3(CO)}$ = 2.3 Å	N_{59}-$P_{-2(CO)}$ = 3.0 Å
C-terminal SH3 Src (C. elegans)	RRRPPVPPP 432101234	1sem (X-ray)	W_{191}-P_{0} = 19	Y_{60}-P_{+3} = 8 Y_{60}-P_{0} = 18	W_{191}-$P_{0(CO)}$ = 2.5 Å W_{191}-$P_{1(CO)}$ = 2.5 Å	Y_{60}-$P_{-3(CO)}$ = 2.7 Å	N_{206}-$P_{-2(CO)}$ = 2.0 Å
SH3 domain of c-Src (chicken)	RRPLPPAFA 210123 45-	1prl (NMR)	W_{42}-P_{0} = 42	Y_{60}-P_{+3} = 75 Y_{60}-P_{0} = 65	W_{42}-$P_{0(CO)}$ = 4.1 Å W_{42}-$R_{1(CO)}$ = 4.9 Å	Y_{60}-$P_{-3(CO)}$ = 2.3 Å	N_{59}-$P_{-2(CO)}$ = 7.9 Å
SH3 domain of c-Src (mouse)	--EPTREPLPPPI-- --543210 12345--	1jeg (NMR)	W_{42}-P_{0} = 24	Y_{64}-P_{+3} = 31 Y_{64}-P_{0} = 16	W_{42}-$P_{0(CO)}$ = 1.7 Å W_{42}-$E_{1(CO)}$ = 2.8 Å	Y_{64}-$P_{-3(CO)}$ = 5.5 Å	N_{63}-$P_{-2(CO)}$ = 3.7 Å

[a] Quantitative comparison of important conserved hydrogen bonds and important conserved angles between planar residues on the domain and in the ligand found in interactions with PRMs. Yellow boxes: Ligand side chains which pack closely into the domain surface. Potential hydrogen-bond donors are underlined and colored red for Trp, blue for Tyr, and green for other hydrogen-bond donors. Ligand-residue numbering begins with (0) for the first hydrogen-bond to Trp/Tyr (see Figure 3). Residues N terminal to (0): gray background, negative number; residues C terminal to (0): white background, positive number. Only the peptide residues detected in the experimental structures are numbered. In cases in which forward and reverse peptide orientation is known, the complexes are divided into two groups. The corresponding peptide sequences are then written from left to right either from N to C terminus or C to N terminus, respectively, to highlight patterns of conserved prolines. ψ, ϕ, and x represent aliphatic, hydrophobic, and any residue, respectively. Lower-case letters: favored residues which are not 100% conserved. [b] SH3 complexes with both forward and reverse ligand orientations; consensus binding sequences: (N)-$\underline{\psi}$p$\phi\underline{\text{Pp}}\phi$P-(C) (forward) and (C)-(R/K)$\underline{\text{pP}}\phi\underline{\text{pP}}$p-(N) reversed. ($\kappa$ and λ are nonpeptide elements described in the PDB files: 1nlo, 1nlp).

Table 3: WW domains with peptides in orientations 1 and 2.[a],[b]

Protein domain	Ligand (2 orientations)	PDB code (method)	Plane angles $Trp_{(domain)}$ and $P_{(ligand)}$	Plane angles $Tyr_{(domain)}$ and $P_{(ligand)}$	Potential H bonds $Trp\text{-}NH\varepsilon$ to $CO_{(ligand)}$	Potential H bonds $Tyr\text{-}OH$ to $CO_{(ligand)}$	Potential H bonds $Tyr\text{-}OH$ to $CO_{(ligand)}$
Ligand N to C:							
WW dystrophin (human)	--PYPSPPPYVPP --2101234567-	1eg4 (X-ray)	W_{83}-P_{2} = 27	Y_{72}-P_{3} = 41	W_{83}-$R_{\delta(CO)}$ = 1.7 Å	Y_{72}-$P_{3(CO)}$ = 4.9 Å Y_{72}-$P_{4(CO)}$ = 5.3 Å	T_{81}-$P_{3(CO)}$ = 3.3 Å
WW YAP (human) L30K mutant	GTPPPPYTV 101234567	1jmq (NMR)	W_{39}-P_{2} = 49	Y_{28}-P_{3} = 82	W_{39}-$T_{\alpha(CO)}$ = 2.1 Å	Y_{28}-$P_{3(CO)}$ = 6.7 Å Y_{28}-$P_{4(CO)}$ = 7.7 Å	T_{37}-$P_{3(CO)}$ = 2.5 Å
WW III Rnedd4 (rat)	--PGTPPPNYDSL --2101234567-	1i5h (NMR)	W_{487}-P_{2} = 29	Y_{476}-P_{3} = 34	W_{487}-T_{0} = 3.3 Å	no H-bond donor	T_{485}-$P_{3(CO)}$ = 4.9 Å
Ligand C to N:							
WW *Pin1* (human)	pPpoSTPpoSY 01 234 5 6	1f8a (X-ray)	W_{34}-P_{1} = 40	Y_{23}-P_{-1} = 65 Y_{23}-P_{+4} = 81	W_{34}-$S_{\alpha(CO)}$ = 1.7 Å	Y_{23}-$P_{-4(CO)}$ = 3.7 Å Y_{23}-$T_{+3(CO)}$ = 4.1 Å	S_{36}-$T_{-3(CO)}$ = 2.8 Å

[a] See Table 2. [b] WW complexes with ligands in forward and reverse orientations; consensus binding sequences: (N)-p$\underline{\text{PPx}}$Y-(C) and (C)-P*poS*$\underline{\text{x}}$P*poS*Y-(N), respectively; *poS* = phosphoserine.

small recognition epitope. Even short peptides of the type Ac-PPPPY-NH_2 bind to WW domains with full affinity.[82] The singular importance of the PRM core residues is also clear from the high degree of tolerance toward the substitution of amino acids at all positions outside the core PRM (Figure 4). Structurally, these observations can be rationalized by the small size of the WW domain and the small surface available for ligand interactions. All affinity, specificity, and orientation determinants must therefore be encoded in a very short core amino acid sequence.

Table 4: EVH1 binding modes 1 and 2 with the same peptide orientation.[a],[b]

Protein domain	Ligand (2 classes, same orientation)	PDB code (method)	Plane angles $Trp_{(domain)}$ and $P_{(ligand)}$	Plane angles $Tyr_{(domain)}$ and $P_{(ligand)}$	Potential H bonds Trp-NH to $CO_{(ligand)}$	Potential H bonds Tyr-OH to ligand	Potential H bonds Gln-$NH_{\varepsilon 2}$ to $CO_{(ligand)}$
Class 1 ligand N to C							
EVH1 Mena (mouse)	FPPPPT 21012-	1evh (X-ray)	W_{23}-P_{-1} = 19 W_{23}-P_2 = 18	not applicable	W_{23}-$P_{0(CO)}$ = 1.7 Å	none	Q_{79}-$P_{-1(CO)}$ = 2.2 Å
EVH1 Evl (mouse)	FEFPPPPTDEE --210123---	1qc6 (X-ray)	W_{23}-P_{-1} = 17 W_{23}-P_2 = 12	not applicable	W_{23}-$P_{0(CO)}$ = 1.9 Å	none	Q_{80}-$P_{-1(CO)}$ = 3.2 Å
EVH1 VASP (human)	SFEFPPPTEDEL -432101234567	1jng (NMR)	W_{23}-P_{-1} = 11 W_{23}-P_2 = 15	not applicable	W_{23}-$P_{0(CO)}$ = 1.8 Å	none	Q_{81}-$P_{-1(CO)}$ = 1.8 Å
Class 2 ligand N to C							
EVH1 Homer (rat)	PPSPF 012345	1ddv (NMR)	W_{24}-P_2 = 18	not applicable	W_{24}-$T_{0(CO)}$ = 3.1 Å	none	no peptide residue at position (−1)

[a] See Table 2. [b] EVH1 complexes. To date, only one ligand orientation is known. The two classes of EVH1 domain recognize distinct consensus binding sequences: class I (Ena/VASP family) binds (N)-FPxϕP-(C) and class II (Homer/Vesl family) binds (N)-xPPxxF-(C).

Table 5: GYF domain.[a],[b]

Protein	Ligand (N to C orientation only)	PDB code (method)	Plane angles $Trp_{28(domain)}$ and $P_{(ligand)}$	Plane angles $Tyr_{(domain)}$ and $P_{(ligand)}$	Potential H bonds Trp_{28}-NH to $CO_{(ligand)}$	Potential H bonds Tyr-OH to NH$_{(ligand)}$	Potential H bonds Trp_{8}-$NH_{\varepsilon 1}$ to $CO_{(ligand)}$
GYF CD2BP2 (human)	SHRPPPGHRV 321012 4567	1l2z (NMR)	W_{28}-P_2 = 14	Y_{6}-P_2 = 64 Y_{6}-P_3 = 78	W_{28}-$P_{8(CO)}$ = 2.1 Å	Y_{6}-$P_{3(CO)}$ = 2.3 Å	W_{8}-$P_{8(CO)}$ = 2.5 Å

[a] See Table 2. [b] GYF domain in a complex with the RPPPPGHR-containing peptide of the cytoplasmic tail of CD2.

Table 6: UEV domain.[a],[b]

Protein	Ligand (N to C orientation only)	PDB code (method)	Plane angles $Tyr_{63(domain)}$ and $P_{(ligand)}$	Plane angles $Tyr\ 68_{(domain)}$ and $P_{(ligand)}$	Potential H bonds Tyr_{63}-OH to $CO_{(ligand)}$	Potential H bonds Thr-OH to $CO_{(ligand)}$	Potential H bonds Asn-$NH_{\delta 2}$ to $CO_{(ligand)}$
UEV domain of Tsg101 (human)	PPTAPPEE 654321012	1m4p (NMR)	Y_{63}-P_0 = 45 Y_{63}-P_1 = 59	Y_{68}-P_0 = 74 Y_{68}-P_1 = 9	Y_{63}-$P_{0(CO)}$ = 2.7	T_{58}-$P_{8(CO)}$ = 2.7	N_{66}-$E_{5(CO)}$ = 1.7

[a] See Table 2. [b] UEV domain in a complex with the PTAP-containing peptide of the HIV-1 viral Gag protein.

Table 7: Profilin with poly-L-proline in orientations 1 and 2.[a],[b]

Protein domain	Ligand (2 orientations)	PDB code (method)	Plane angles between $Trp_{(domain)}$ and $P_{(ligand)}$	Plane angles between $Tyr_{(domain)}$ and $P_{(ligand)}$	Potential H bonds Trp-NH to $CO_{(ligand)}$	Potential H bonds Tyr-OH to $CO_{(ligand)}$	Potential H bonds His-$NH_{\varepsilon 2}$ to $CO_{(ligand)}$
Class 1 ligand N to C							
platelet profilin (human)	PPPPPPPPPPPPPPP 543210123456789	1cjf (X-ray)	W_3-P_{-1} = 11 W_3-P_2 = 12	Y_6-P_2 = 29 Y_6-P_5 = 18.98	W_3-$P_{8(CO)}$ = 1.7 Å	Y_6-$P_{3(CO)}$ = 2.6 Å	H_{133}-$P_{4(CO)}$ = 1.9 Å
Ligand C to N :							
platelet profilin (human)	PPPPPPPPPP 4321012345	1awi (X-ray)	W_3-P_{-1} = 18 W_3-P_2 = 55	Y_6-P_{-4} = 22 Y_6-P_{-1} = 15	W_3-$P_{8(CO)}$ = 1.9 Å	Y_6-$P_{-3(CO)}$ = 3.1 Å	H_{133}-$P_{-4(CO)}$ = 1.9 Å
platelet profilin (human)	PPPPPPPPP 21012345	1cf0 (X-ray)	W_3-P_{-1} = 37 W_3-P_2 = 77	Y_6-P_{-4} = 11 Y_6-P_{-1} = 19	W_3-$P_{8(CO)}$ = 2.0 Å	Y_6-$P_{-3(CO)}$ = 2.8 Å	H_{133}-$P_{-4(CO)}$ = 1.9 Å

[a] See Table 2. [b] Profilin complexes with poly-L-proline in both forward and reverse orientations.

4. EVH1 Domains

The Ena/VASP homology 1 (EVH1) domains[86–89] are protein-interaction modules of about 115 residues in length (Figure 1c) found in a large number of multidomain signaling proteins. This group includes the Ena/VASP family of proteins, which modulate actin cytoskeleton dynamics, the Wiscott–Aldrich syndrome proteins (WASP), which regulates actin assembly downstream of Cdc42 and phosphatidylinositol-4,5-bisphosphate (PIP_2) signaling pathways, and the synaptic terminal protein families Homer and Vesl, which are thought to play a role in long-term potentiation in excitatory synapses.[90] The structures of the EVH1 domains of the VASP, Mena, Evl, Homer, and N-WASP proteins[42,91–94] show a high similarity to the structures of the pleckstrin homology (PH) and phosphotyrosine-binding (PTB) domains[95] despite a low degree of sequence similarity with these families.

4.1. Classification of EVH1 Domains on the Basis of PRM Consensus Sequences

Three classes of EVH1 domains have been identified so far on the basis of ligand preference[86] (Table 1). The first class comprises the Ena/VASP proteins, which recognize specifically the FPPPP sequences found in focal adhesion proteins, such as zyxin and vinculin. Closely spaced FPPPP repeats also occur in the ActA protein of the intracellular pathogen *Listeria monocytogenes*.[87,96] The EVH1 domains of

the Homer/Vesl family of postsynaptic-receptor-associated proteins form the second class. These proteins recognize the consensus target sequence PPxxF found in the metabotropic glutamate receptors (mGluRs), inisitol-1,4,5-triphosphate receptors (IP3Rs), ryanodine receptors (RyRs), and Shank proteins.[97,98] The third class comprises the WASP/N-WASP EVH1 domains. The N-WASP EVH1 domain is not known to bind any independent, short peptides, but does bind intramolecularly to a 25-residue peptide from the WASP-interacting protein (WIP) when this peptide is expressed together with the domain, fused to its N terminus by a linker five amino acids in length.[94]

Single-residue peptide-substitution experiments (SPOTs analyses) have identified the consensus PRM recognized by class I EVH1 domains as FPxϕP (in which ϕ is a hydrophobic residue[27]). Figure 6 shows the data for the substitution

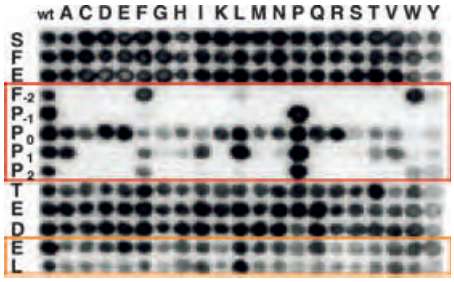

Figure 6. Single amino acid substitution analysis of the EVH1-domain-binding peptide SFEFPPPPTEDEL from the ActA protein of *Listeria monocytogenes*. The figure shows the class 1 EVH1 domain from the human VASP protein.[42] Red box: conserved target PRM; orange box: additional ActA-affinity-increasing epitope.

analysis with a ligand of the EVH1 domain of the human VASP protein.[42] The peptide residue which participates in hydrogen-bond formation with the conserved Trp residue on the domain surface (corresponding to Trp 23 in VASP and Mena proteins) is defined as position (0). Proline residues in positions (-1) and (2) (FPPPP) are essential for binding to EVH1, whereas the proline residues in positions (0) and (1) (FPPPP) need not be conserved. Position (0) is largely nonspecific and can accommodate almost any other amino acid without loss of EVH1-binding ability, whereas position (1) must be occupied by a hydrophobic residue (Pro, Leu, Ala, Ile, or Val) for EVH1 binding to be maintained.[86] Proline residues are nonetheless often found at these central positions, probably because of the excellent hydrogen-bond-acceptor properties of this amino acid and because proline is ideally suited to induce a PPII helical structure in the ligand.

4.2. The EVH1/PRM Interface and Structural Rationalization of Consensus PRM Sequences for EVH1 Binding

The structures of the class I EVH1/PRM complexes[42,92,93] show that PRMs are recognized by clusters of three highly conserved aromatic residues on the surface of the domain (Figure 1c). In the Mena protein (see Figure 3e), this recognition triad comprises the residues Tyr 16, Trp 23, and Phe 77. In class I EVH1/PRM complexes the P_{-1} and P_2 residues of the FPPPP ligand pack into the hydrophobic binding pockets created by the side chains of Tyr 16 and Trp 23, and Trp 23 and Phe 77 (Mena numbering) of the EVH1 domain to form an umbrella-like structure (see Figure 2b), which is stabilized by a hydrogen bond from Trp 23 to P_0 (see Figure 3e).[42,92,93] The close hydrophobic contacts of P_{-1} and P_2 with the domain, and especially the coplanar contacts of the proline rings with the side chain of Trp 23, explain the conservation of these proline residues in the PRM consensus sequence. In contrast, P_0 makes no contact with the domain surface and P_1 makes only side-on contacts, thus resulting in the tolerance of many amino acid types in position (0) and the requirement for a hydrophobic residue at position (1) (Figure 6).

In the class II Homer proteins, Tyr 16 is replaced by Ile 16, thus altering the shape of the hydrophobic pocket which binds P_{-1} in the Mena complex. Additionally, Met 14 (Mena) is replaced by the aromatic residue Phe 14 (Homer). This substitution provides a new binding pocket for the side chains of P_1 and P_2 in the Homer peptide TPPxxF between the side chains of Phe 14, Trp 24, and Phe 74. The F_5 residue of the ligand forms a further close contact with the domain (Figure 3f). Thus, the ligand preferences of these different classes of EVH1 domains are determined by just a small number of amino acid substitutions in the PRM-recognition triad.[86]

A second hydrogen bond between Gln 79 (Mena numbering) of the domain and the carbonyl oxygen atom of P_{-1} is also present in class I EVH1 interactions. On the basis of the structural information gathered so far on EVH1–ligand complexes, it is tempting to predict that this second hydrogen bond should also be present in class II interactions. However, the peptide studied in the Homer 1a complex terminated at position (0) (Figure 3f) and therefore lacked a correctly positioned hydrogen-bond acceptor. This peptide would therefore need to be extended by at least one additional N-terminal amino acid to test this hypothesis.[86]

4.3. Peptide Orientation, Specificity, and the Role of PRM-Flanking Residues

To date, the binding of independent peptides to EVH1 domains has only been detected in one orientation. In class I (Ena/VASP) EVH1/PRM complexes, the PRM consists of a Phe residue followed by a short PPII helix (i.e. FPPPP). The Phe side chain packs into a specific groove in the domain,[42,93] thus determining the orientation of the ligand. The location of the Phe residue in the TPPSPF ligand of the class II (Homer 1a) EVH1 domain at the opposite (C-terminal) end of the PRM would seem to suggest a reverse binding mode for this peptide. However, the crystal structure of the complex showed that TPPSPF binds the Homer 1a EVH1 domain in the same orientation as FPPPP binds the Ena/VASP EVH1 domains.[91] The Phe residues are therefore in contact with different sites in the respective domains. In each case, this Phe residue determines the positioning or "register" of PRM binding to the EVH1 domain. Interestingly, the intramolec-

ular interaction of the N-WASP EVH1 domain with its N terminally fused WIP peptide occurs in the opposite orientation.[94] However, as this is not an intermolecular EVH1/PRM interaction, it is not discussed in detail herein.

The binding affinities of isolated core motifs for EVH1 domains range from very weak to undetectable.[42] Therefore, further interactions are needed to increase these affinities to biologically useful levels. Epitopes more distant from the PRM form additional hydrophobic, hydrogen-bonding, or electrostatic interactions. The affinity-increasing epitope of the ActA surface protein of *Listeria monocytogene*s comprises just two amino acids, EL, which are located C terminally to the FPPPP motif. This epitope interacts with a hydrophobic patch located in close proximity to the main peptide-binding groove on the surface of the EVH1 domain.

5. GYF Domains

The GYF domains, named after the conserved GYF motif in their primary sequences (also known as CD2-binding domains), are 86-residue protein modules (Figure 1d) which bind proline-rich sequences of the type PPPPGHR (Table 1). The GYF domain of the CD2-binding protein 2 (CD2BP2) binds the PPPPGHR-SQAPSHR-PPPPGHR tandem repeat[20] found in the cytoplasmic tail of the CD2 cell-surface receptor protein responsible for T-cell activation.[99] The three-dimensional solution structure of the unbound GYF domain from CD2BP2 revealed a novel fold for this family of domains, and residues important for binding to the CD2-tail peptide were identified by the analysis of the ^{1}H,^{15}N chemical shifts at increasing peptide concentration.[21] As seen in all other families of PRM-binding domains, a conserved, exposed aromatic cluster was found to be crucial for peptide binding.

5.1. The GYF/PRM Interface

The solution structure of the GYF domain in a complex with the peptide SHRPPPPGHRV shows this binding mode in more detail (Figure 3g).[100] The exposed cluster of aromatic residues that comprise the peptide binding site in the GYF domain extends over a larger area than the aromatic clusters of other PRM-binding domains. The three aromatic residues Phe20, Trp28, and Tyr33 form one half of the cluster (a subcluster) with a hydrogen bond between the ε-NH group of Trp28 and P_0 of the ligand as observed in WW domain interactions (Figure 2c). The side chains of R_{-1} and P_2 of the peptide pack into the hydrophobic grooves on either side of the Trp28 ring. Tyr6, Trp8, and Tyr17 form a second subcluster, in which Trp8 and Tyr6 both form hydrogen bonds to the carbonyl oxygen atom of the closely packed ligand residue P_3. Residues G_4 and R_6 make further close contacts with the surface of the domain. On the basis of the structure of the complex, we predict that the residues that make the closest contacts with the domain (highlighted in yellow in Figure 3g) should be the most highly conserved in the PRM and the most crucial for GYF recognition,[100] whereas the substitution of residues whose side chains are exposed to the solution with other amino acids should have a smaller effect on binding affinity. This reasoning leads to a predicted consensus PRM of (R)xxPPgxR for GYF domains.

6. UEV Domains

The UEV (ubiquitin E2 variant) domain is a 145-residue module (Figure 1e) found in the human Tsg101 protein (tumor susceptibility gene 101). The domain is recruited by the major structural proteins of the HIV and Ebola viruses to facilitate viral budding. In nonlytic viruses this interaction is essential for replication. The UEV domain binds specifically to P(T/S)AP peptide motifs in these binding partners with typical K_d values for PRM interactions[22,23] (Table 1).

6.1 The UEV/PRM Interface

The solution structure of the Tsg101 UEV domain in a complex with the peptide PEPTAPEE from the HIV-1_{NL4-3} $p6^{Gag}$ protein ($K_d = 3\ \mu M$)[22] is shown in Figure 3h. The exposed aromatic cluster of the UEV domain is generally quite similar to those of the other PRM-binding domains, but with the main difference that it lacks the Trp side chain present in all the other families. In the UEV domain, Tyr63 (colored pink in Figure 3h) forms the primary hydrogen bond to the peptide. The interface is most similar to that seen in WW interactions (see Figure 2c), and one would expect the two consecutive ligand residues P_{-1} and P_0, which are buried in a hydrophobic pocket on one side of Tyr63 of the domain, to be the most conserved residues of the UEV ligands. However, to date there are no data available for peptide substitution of UEV-binding peptides. The UEV–peptide interface is also characterized by further hydrogen bonds between the exposed Asn69 and Thr58 side chains (shown in green) and the carbonyl oxygen atoms of the peptide residues E_{-5} and P_{-6}, respectively. A potential bifurcated hydrogen bond involving the carbonyl oxygen atom of the peptide residue T_{-3} and side chains Ser143 and Arg144 of the UEV domain has also been proposed (not shown in Figure 3h).[22] No hydrogen bond is formed between Tyr68 (blue) and the ligand because of the orientation of the Tyr ring.

7. Profilins

Profilins are a family of small (12–15 kDa), ubiquitous proteins involved in the regulation of actin-filament assembly and actin polymerization. They differ from the other modules discussed herein in that they are independent, single-domain proteins rather than modules that are part of larger host proteins. Profilins are known to bind simultaneously to monomeric G-actin[101] and poly-L-proline (pLP)[25,102] (Table 1). They also bind phosphatidylinositol-4,5-bisphosphate (PIP_2), a component of the phosphatidylinositol cycle involved in cell signaling events. This interaction causes dissociation of the profilin/actin complex. The crystal structures of isoforms I and II of the profilin of *Acantha-*

moeba,[92,103,104] the plant profilin of *Arabidopsis thaliana* (a major human allergen),[105] and bovine profilin, both isolated[106] and in a complex with bovine actin,[25] have all been solved and were found to be highly similar.[105]

7.1 The Profilin/pLP Interface

The pLP-recognition site of profilin involves residues Trp3, Tyr6, Ile21, Gly23, Trp31, Ala33, Tyr133, (His133 in bovine profilin), and Leu134, as shown by X-ray and NMR spectroscopy,[107,108] mutagenesis,[109] and fluorescence-quenching experiments.[107,110]

Like SH3 and WW domains, profilins are known to bind their proline-rich ligands in either of two possible orientations (Figure 3i,j). In all crystal structures of profilin obtained to date, four aromatic side chains (Trp3, Tyr6, His133, and Trp31) are exposed in a cluster on the protein surface. In a similar manner to the cluster residues in SH3 domains, the side chains of the profilin cluster are ideally arranged to accommodate two turns of a PPII helix. The pLP ligand docks onto the profilin surface with every third proline residue packed closely into the pockets between the side chains of Trp3 and Tyr6, and Tyr6 and His133, to form a double-umbrella-like structure (Figure 3i,j). Conserved hydrogen bonds in profilin complexes are formed between the hydrogen-bond donors in Trp3 and Tyr6 and the carbonyl oxygen atoms of P_0 and P_3. These two hydrogen bonds form the stems of the "umbrellas". A further hydrogen bond exists between His133 and the carbonyl oxygen atom of P_4.

7.2. Peptide Orientation, Specificity, and Affinity in the Absence of PRM-Flanking Residues

As the ligands of profilins consist of long chains of consecutive proline residues (usually six or more in succession), the possibility of aromatic or hydrophobic side chains being used as anchors for defining the register of ligand binding is excluded. Hence, multiple profilin/pLP complexes may form, with "frame-shifted" binding of the pLP ligand in the peptide-binding groove, as observed in the X-ray crystal structure of the complex formed between human-platelet profilin (HPP) and a pLP decamer. In this case two distinct structures, HPP-A and HPP-B, were reported.[24] Additionally, since all side chains in pLP ligands are pyrrolidine rings, there can be no polar or electrostatic stabilizing interactions with the protein. Therefore, the complexes can only be stabilized and their binding affinity controlled by hydrogen bonds, hydrophobic interactions, and steric restrictions. The lack of non-proline, core-flanking residues, which in other PRMs modify specificity and binding affinity, explains the observation that all cellular profilins bind pLP with similar affinities,[24] and that profilins can bind the same ligand in both orientations.[111]

8. General Features of Protein Interactions with PRMs

Comparison of the different classes of PRM-binding interfaces reveals a number of general features that recur in PRM recognition:

1) All domains bind the PRMs of their respective ligands through a cluster of surface-exposed aromatic side chains, sometimes referred to as an "aromatic cradle". The distances and angles between the aromatic side chains define the shape of the proline-binding cavity.[16,26]
2) Binding of the ligand involves a conserved network of hydrogen bonds, and coplanar arrangements of proline residues and aromatic rings.
3) The register and orientation of the ligand are determined by non-proline residues located at one end of the core motif. These residues usually have a large side chain that acts as an "anchor". Typical examples are the Arg, Tyr, and Phe residues of certain classes of ligands of the SH3, WW, and EVH1 domains, respectively.
4) Additional epitopes which flank the core PRM serve to fine-tune the ligand-binding affinities.

8.1. Key Structural Characteristics of PRM-Recognition Sites

Recognition of PRMs is determined by the precise three-dimensional arrangement of the exposed aromatic side chains. The most important feature of the binding sites is the presence of hydrogen-bond-donor aromatic residues (Trp, Tyr) whose side chains are oriented perpendicular to the protein surface to allow for efficient hydrogen-bond formation with the oxygen atom of a carbonyl group in the peptide backbone of the ligand. These amino acid residues are directly flanked by other aromatic residues, whereby an angle of approximately 90° to the hydrogen-bond donor is formed (see Figure 1). The flanking aromatic side chains may be oriented either parallel or perpendicular to the protein surface, but in each case they form a hydrophobic, approximately right-angled cavity into which the proline side chains of the ligand pack efficiently.

8.2. Conserved Hydrogen-Bonding Networks and Recognition of Proline Rings

The PRM-containing peptides are recognized by their respective domains as PPII helices, and the domains may approach the peptides from either of two sides (see arrows in Figure 2a). In the binding mode observed for SH3, EVH1, and profilin (Figure 2b), the key hydrogen bond is formed between the aromatic side chain of Trp and a carbonyl oxygen atom of the ligand. This hydrogen bond forms the stem of an umbrella-like structure, and the proline residues pack against the aromatic ring of the hydrogen-bond donor (see Tables 2, 4, and 7). In the ideal case of a ligand with a true PPII helical structure (e.g. FPPPP), the hydrogen-bonded carbonyl group (in the underlined residue) is at the center of the four-proline-

residue motif. The two central proline residues do not interact with the protein surface and may be substituted for other residues, whereas the two outer proline residues are packed into the domain and are highly conserved. The proline rings are approximately coplanar with the aromatic ring of the key hydrogen-bond donor (see columns 4 and 5 in Tables 2, 4, and 7) and form head- or side-on hydrophobic contacts with the flanking aromatic side chains in the binding site (see Figure 3). The hydrogen bond is thus in a hydrophobic environment in which hydrophobic interactions and hydrogen bonding occur cooperatively. These interactions occur in both binding orientations, as highlighted in Figure 2b. In each case, P_{-1} and P_2 are approximately coplanar to the aromatic ring of the hydrogen-bond donor and make contacts with the other aromatic rings of the ligand-binding site through their Cβ, Cγ, and Cδ atoms. This binding mode recognizes sequences of the type PxxP, which form the umbrella around the aromatic residue of the domain; this aromatic residue forms the hydrogen bond to the carbonyl oxygen atom of x_0.

The second binding mode, observed in WW, GYF, and UEV domains, involves the binding of the PPII helix from the opposite side (Figure 2a,c) but relies essentially on the same structural features. An aromatic hydrogen-bond donor (usually Trp) is oriented perpendicular to the surface and forms a hydrogen bond to a carbonyl group in the peptide backbone. One proline residue of the ligand lies roughly coplanar to the aromatic ring (for angles and hydrogen bonds, see Tables 3, 5, and 6). This situation corresponds to one of the two halves (right or left) of the complexes shown in Figure 2b. However, in this binding mode, the peptide continues with another proline residue, which forms coplanar contacts with a second aromatic residue of the domain (Figure 3c). This aromatic side chain, which is approximately parallel to the protein surface and perpendicular to the critical Trp residue, does not form a hydrogen bond to the ligand. In this binding mode, contact is made between peptides with two sequential proline residues and a single hydrophobic binding pocket on one side of the hydrogen bond (the "xP" pocket) through the Cβ and Cδ atoms, respectively, of the peptide.[39] Examples are the PPxY and PPLP motifs of WW domains.

These general principles are illustrated for selected complexes of PRM-binding domains in Figure 3. In SH3 and profilin complexes, double-umbrella structures are generally observed in which two hydrogen bonds (from the Trp and Tyr side chains of the domain) form the stems of two individual umbrella-like structures. The exception is SH3 complexes in orientation 2, in which the Trp involved in hydrogen bonding is surrounded by a much shorter RxP sequence. The interfaces contain a further hydrogen bond from either an Asn or a His side chain of the domain. The essential difference between these complexes is that in complexes with SH3 domains (orientation 1) the ligand umbrellas are separate and only one is of the typical PPII helix geometry, whereas in profilin complexes, the pLP ligand forms two turns of an idealized PPII helix, with the proline residue being shared between the two umbrella stems. EVH1 domains bind PRMs in a similar way but use just a single hydrogen bond as the stem of the umbrella structure (Figure 3c). The PRM-binding mode of WW, GYF, and UEV domains (Figure 3c,d,g,h) differs from those described above in that the main hydrogen-bond-donating side chain (pink) is not surrounded by two coplanar proline rings, but instead one proline from the ligand packs in a coplanar manner on one side of the aromatic ring. Both PRM-binding modes recognize ligands in both forward and reverse orientations.

The importance of the coplanar interactions of the proline rings with the aromatic side chains that they surround can be substantiated in several ways. First, in peptide-substitution analyses (Figures 4 and 5), the coplanar proline residues (yellow in Figure 3) are shown consistently to be those that are essential for binding and confer specificity to the ligand. Second, these proline residues are highly conserved in the PRMs recognized by the respective domains. Tables 2–7 summarize the angles made between the most closely packed proline side chains of the ligands and the Trp and Tyr residues of the aromatic clusters in the different PRM-binding domains. Within any given family of PRM-binding domains, these angles are generally similar.

A key characteristic of PRM complexes is the conserved network of hydrogen bonds involving the exposed aromatic residues (see Figure 3). In most cases, further hydrogen bonds are formed from additional surface-exposed Asn, Thr, Ser, His, or Gln side chains (Tables 2–7; green residues in Figure 3) to the oxygen atoms of carbonyl groups in the peptide backbone. These additional interactions vary according to the class of PRM-binding domain and provide scope for ligand specificity within domain families (see Figure 3). The lengths of the hydrogen bonds from these residues are given in Tables 2–7 for all structures of PRM complexes deposited in the Protein Data Bank (PDB).

8.3. Position and Orientation of the Ligand: The Role of the Proline and "Anchoring" Residues in the Core Motif

As a result of its highly symmetrical structure, the PPII helix is able to bind a protein domain in either of two opposite orientations through contacts with the same hydrogen-bond donors and orthogonal aromatic rings, regardless of the peptide orientation. Furthermore, the repetitive nature of this structure allows the possibility of docking at a number of positions along a peptide-binding groove. The phenomenon of multiple binding orientations and multiple "frame-shifted" ligand positioning have been described for SH3 domains, WW domains, and profilins.[24,57] The correct positioning and orientation of a particular peptide must therefore be determined by interactions with non-proline residues of the core PRM: These may be any combination of electrostatic, polar, hydrophobic, or hydrogen-bonding interactions.

A number of charged or hydrophobic residues generally form part of the core PRMs and act as "anchors" to specify ligand orientation. Good examples are the Phe residue in the FPPPP motif targeted by the Ena/VASP family of EVH1 domains; the Phe residue of the PPxxF motif recognized by Homer EVH1 domains; the tyrosine residue of the PPxY motif targeted by the human YAP65 WW domain;[16] and the Arg, Lys, and His residues of the PPxPx(R/K/H) peptides

targeted by class II SH3 domains.[14,35,57] As the substitution of these anchoring residues often results in loss of binding, they are considered an integral part of the core binding motif.

8.4. Control of Specificity and Binding Affinity by More-Distant Residues

Core-flanking epitopes and anchoring residues outside of the PRM can greatly enhance binding affinities and thus play a crucial role in determining specificity. They can increase the degree of specificity of the ligand to allow discrimination between PRM-binding domains within the same family. For example, a lysine residue in the peptide PPPALPPKKR from the C3G protein makes the ligand highly specific for the c-Crk SH3 domain, whereas the same peptide does not bind the SH3 domains of Nck, Src, Abl, phospholipase Cγ, and spectrin.[56] Similarly, a Glu–Leu epitope found in the peptide sequence SFEFPPPPTEDEL of the ActA surface protein of *Listeria monocytogenes* provides ActA with a high specificity for class I EVH1 domains.[42,96] The presence of this epitope increases the EVH1-binding affinity of ActA strongly enough that it successfully outcompetes natural, cellular EVH1-domain-binding proteins, such as zyxin and vinculin, which lack this affinity-increasing epitope. Such affinity-determining epitopes are highly specific to the proteins that contain them, making them interesting templates for the rational design of novel specific inhibitory drugs.

9. Conclusions and Outlook

The binding of low-molecular-weight ligands to proteins requires the synergy of a number of well-balanced interactions. Prior to the synthesis of nonpeptidic competitors of natural PRM ligands, it is necessary to understand how these interactions contribute to the formation and stability of the interfaces between proline-rich peptide motifs and their respective binding domains. In the ideal case, the oxygen atom of a carbonyl group in the peptide backbone interacts with a hydrogen-bond-donating aromatic residue (Trp or Tyr) oriented perpendicular to the domain surface to form a hydrogen bond. The two peptide side chains immediately flanking the peptide carbonyl group involved in the hydrogen bond are exposed to the solvent. The subsequent two side chains on either side (usually proline rings) are positioned in a near-coplanar arrangement with the hydrogen-bonded aromatic side chain they surround, so that they pack into hydrophobic cavities in the protein surface. In the majority of high-resolution structures analyzed, the angles between the planes of the aromatic ring of the domain and the surrounding proline rings were less than 30° (see Tables 2–7). To optimize the hydrophobic contacts with the proline rings of the peptide, the domain surface contains rigid, hydrophobic "boxes" formed by additional aromatic residues arranged at roughly 90° to the hydrogen-bond-donating side chain (i.e. parallel to the domain surface). These aromatic residues make head-on contacts with the γ and δ carbon atoms of the proline rings of the ligand. As a result of the conformational restriction of the PPII helix structure of the peptides, binding occurs between two well-defined, preformed surfaces, thus minimizing the entropic costs of binding and conformational strain in the complex.

How can the survey presented herein help us in planning synthetic efforts to mimic PRM-containing peptides? First, the considerable data now available on WW, EVH1, and SH3 interactions should facilitate the design of inhibitors of these domains. Very short peptides comprising as few as five residues can bind with considerable affinity. We therefore assume that compounds in the range of 500 to 700 Da could be designed that may be able to bind with high affinity and selectivity to a PRM-binding domain. Second, suitable ligands must be able to participate in hydrogen-bonding interactions with the exposed aromatic side chain of the domain, as well as hydrophobic interactions with the specific hydrophobic cavities next to this exposed aromatic residue. A "hydrophobic chelator" around this exposed aromatic residue would allow an optimal interaction.

The detailed analysis presented herein incorporates and expands upon previous studies of PRM complexes, which have highlighted the importance of hydrophobic ridges between aromatic side chains as cavities for *N*-substituted amino acids.[26,39] In nature, of course, these cavities accept proline residues, but they can also be occupied by other hydrophobic residues, such as leucine and methionine, as shown by substitution analyses with peptide libraries. This interaction alone is likely to be very weak, but in combination with the conserved hydrogen bond in this hydrophobic environment considerable affinities can be reached. The models for binding presented herein also explain the strict conservation of tryptophan and tyrosine residues as exposed hydrogen-bond donors present in all PRM-binding domains. Phenylalanine is thus not observed in these positions, but is often found as part of the supporting "aromatic cradles"[26] or "boxes", which optimize the hydrophobic interaction. The aromatic rings of most of the PRM-binding sites are arranged nearly perpendicular to the domain surface, as can be appreciated from Figure 1. The observations presented herein should form a basis for the establishment of fundamental rules for the identification of further PRM-binding domains, and should also be useful for the rational design of PRM mimics.

The authors thank J. Zimmermann for proofreading.

Received: July 11, 2003
Revised: November 10, 2004

[1] G. B. Cohen, R. Ren, D. Baltimore, *Cell* **1995**, *80*, 237.
[2] G. W. Reuther, A. M. Pendergast, *Vitam. Horm.* **1996**, *52*, 149.
[3] M. Sudol, *Prog. Biophys. Mol. Biol.* **1996**, *65*, 113.
[4] S. E. Shoelson, *Curr. Opin. Chem. Biol.* **1997**, *1*, 227.
[5] T. Pawson, J. D. Scott, *Science* **1997**, *278*, 2075.
[6] M. Sudol, *Trends Biochem. Sci.* **1996**, *21*, 161.
[7] J. Kuriyan, D. Cowburn, *Annu. Biophys. Biomol. Struct.* **1997**, *26*, 259.
[8] G. Waksman, D. Kominos, S. C. Robertson, N. Pant, D. Baltimore, R. B. Birge, D. Cowburn, H. Hanafusa, B. J.

Mayer, M. Overduin, M. D. Resh, C. B. Rios, L. Silverman, J. Kuriyan, *Nature* **1992**, *358*, 646.
[9] Z. Songyang, S. E. Shoelson, M. Chaudhuri, G. Gish, T. Pawson, W. G. Haser, F. King, T. Roberts, S. Ratnofsky, R. J. Lechleider, *Cell* **1993**, *72*, 767.
[10] M. B. Yaffe, L. C. Cantley, *Nature* **1999**, *401*, 30.
[11] P.-J. Lu, X. Z. Zhou, M. Shen, K. P. Lu, *Science* **1999**, *283*, 1325.
[12] M. A. Verdecia, M. E. Bowman, K. P. Lu, T. Hunter, J. P. Noel, *Nat. Struct. Biol.* **2000**, *7*, 639.
[13] H. Yu, J. K. Chen, S. Feng, D. C. Dalgarno, A. W. Brauer, S. Schreiber, *Cell* **1994**, *76*, 933.
[14] A. B. Sparks, J. E. Rider, N. G. Hoffman, D. M. Fowlkes, L. A. Quillam, B. K. Kay, *Proc. Natl. Acad. Sci. USA* **1996**, *93*, 1540.
[15] H. I. Chen, M. Sudol, *Proc. Natl. Acad. Sci. USA* **1995**, *92*, 7819.
[16] M. I. Macias, M. Hyvönen, E. Baraldi, J. Schultz, M. Sudol, M. Saraste, H. Oschkinat, *Nature* **1996**, *382*, 646.
[17] M. Reinhard, K. Jouvenal, D. Tripier, U. Walter, *Proc. Natl. Acad. Sci. USA* **1995**, *92*, 7956.
[18] M. Reinhard, K. Giehl, K. Abel, C. Haffner, T. Jarchau, V. Hoppe, B. M. Jockusch, U. Walter, *EMBO J.* **1995**, *14*, 1583.
[19] M. Reinhard, M. Rüdiger, B. M. Jockusch, U. Walter, *FEBS Lett.* **1996**, *399*, 103.
[20] K. Nishizawa, C. Freund, J. Li, G. Wagner, E. L. Reinhertz, *Proc. Natl. Acad. Sci. USA* **1998**, *95*, 14897.
[21] C. Freund, V. Dötsch, N. Kazuhisa, E. L. Reinhertz, G. Wagner, *Nat. Struct. Biol.* **1999**, *6*, 656.
[22] O. Pornillos, S. L. Alam, D. R. Davis, W. I. Sundquist, *Nat. Struct. Biol.* **2002**, *9*, 812.
[23] O. Pornillos, S. L. Alam, R. L. Rich, D. G. Myszka, D. R. Davis, W. I. Sundquist, *EMBO J.* **2002**, *21*, 2397.
[24] N. M. Mahoney, P. A. Janmey, S. C. Almo, *Nat. Struct. Biol.* **1997**, *4*, 953.
[25] C. E. Schutt, J. C. Myslik, M. D. Rozycki, N. C. W. Goonesekere, U. Lindberg, *Nature* **1993**, *365*, 819.
[26] X. Huang, F. Pey, R. Zhang, A. Joachimiak, M. Sudol, M. J. Eck, *Nat. Struct. Biol.* **2000**, *7*, 634.
[27] R. Aasland, C. Abrams, C. Ampe, L. J. Ball, M. T. Bedford, G. Cesarini, M. Gimona, J. H. Hurley, T. Jarchau, L. Veli-Pekka, M. A. Lemmon, R. Linding, B. J. Mayer, M. Nagai, M. Sudol, U. Walter, S. J. Winder, *FEBS Lett.* **2002**, *513*, 141.
[28] R. Frank, *Tetrahedron* **1992**, *48*, 9217.
[29] A. Kramer, J. Schneider-Mergener, *Methods Mol. Biol.* **1998**, *87*, 25.
[30] R. Frank, *J. Immunol. Methods* **2002**, *267*, 13.
[31] F. Toepert, T. Knaute, S. Guffler, J. R. Pires, T. Matzdorf, H. Oschkinat, J. Schneider-Mergener, *Angew. Chem.* **2003**, *115*, 1168; *Angew. Chem. Int. Ed.* **2003**, *42*, 1136.
[32] K. Bialek, A. Swistowski, R. Frank, *Anal. Bioanal. Chem.* **2003**, *376*, 1006.
[33] P. M. Cowan, S. McGavin, *Nature* **1955**, *176*, 501.
[34] P. J. Flory, *Statistical Mechanics of Chain Molecules*, Hanser, **1988**.
[35] B. K. Kay, M. P. Williamson, M. Sudol, *FASEB J.* **2000**, *14*, 231.
[36] M. P. Williamson, *Biochem. J.* **1994**, *297*, 249.
[37] A. E. Hagerman, L. G. Butler, *J. Biol. Chem.* **1981**, *256*, 4494.
[38] A. Veis, C. F. Nawrot, *J. Am. Chem. Soc.* **1970**, *92*, 3910.
[39] A. Zarrinpar, R. P. Bhattacharyya, W. A. Lim, *Sci. STKE* **2003**, *2003*, RE8.
[40] D. H. Williams, M. S. Searle, J. P. Mackay, U. Gerhard, R. A. Maplestone, *Proc. Natl. Acad. Sci. USA* **1993**, *90*, 1172.
[41] C. Bachmann, L. Fischer, U. Walter, M. Reinhard, *J. Biol. Chem.* **1999**, *274*, 23549.
[42] L. J. Ball, R. Kuhne, B. Hoffmann, A. Hafner, P. Schmieder, R. Volkmer-Engert, M. Hof, M. Wahl, J. Schneider-Mergener, U. Walter, H. Oschkinat, T. Jarchau, *EMBO J.* **2000**, *19*, 4903.
[43] A. A. Adzhubei, M. J. Sternberg, *J. Mol. Biol.* **1993**, *229*, 472.
[44] B. J. Mayer, M. Hamaguchi, H. Hanafusa, *Nature* **1988**, *332*, 272.
[45] M. L. Stahl, C. R. Ferenz, K. L. Kelleher, R. W. Kriz, J. L. Knopf, *Nature* **1988**, *332*, 269.
[46] V. P. Lehto, V. M. Wasenius, P. Salven, M. Saraste, *Nature* **1988**, *334*, 388.
[47] H. Kang, C. Freund, J. S. Duke-Cohan, A. Musacchio, G. Wagner, C. E. Rudd, *EMBO J.* **2000**, *19*, 2889.
[48] D. A. Renzoni, D. J. Pugh, G. Siligardi, P. Das, C. J. Morton, C. Rossi, M. D. Waterfield, I. D. Campbell, J. E. Ladbury, *Biochemistry* **1996**, *35*, 15646.
[49] A. Musacchio, M. Saraste, M. Wilmanns, *Nat. Struct. Biol.* **1994**, *1*, 546.
[50] M. T. Pisabarro, L. Serrano, M. Williams, *J. Mol. Biol.* **1998**, *281*, 513.
[51] S. Feng, C. Kasahara, R. J. Rickles, S. L. Schreiber, *Proc. Natl. Acad. Sci. USA* **1995**, *92*, 12408.
[52] S. Feng, J. K. Chen, H. Yu, J. A. Simon, S. L. Schreiber, *Science* **1994**, *266*, 1241.
[53] S. Feng, T. M. Kapoor, F. Shirai, A. P. Combs, S. L. Schreiber, *Chem. Biol.* **1996**, *3*, 661.
[54] M. Vidal, N. Goudreau, F. Cornille, D. Cussac, E. Gincel, C. Garbay, *J. Mol. Biol.* **1999**, *290*, 717.
[55] M. Wittekind, C. Mapelli, V. Lee, V. Goldfarb, M. S. Friedrichs, C. A. Meyers, L. Mueller, *J. Mol. Biol.* **1997**, *267*, 933.
[56] X. Wu, B. Knudsen, S. M. Feller, J. Zheng, A. Sali, D. Cowburn, H. Hanafusa, J. Kuriyan, *Structure* **1995**, *3*, 215.
[57] W. A. Lim, F. M. Richards, R. O. Fox, *Nature* **1994**, *372*, 375.
[58] R. Ghose, A. Shekhtman, M. J. Goger, H. Ji, D. Cowburn, *Nat. Struct. Biol.* **2001**, *8*, 998.
[59] J. T. Nguyen, C. W. Turck, F. E. Cohen, R. N. Zuckermann, W. A. Lim, *Science* **1998**, *282*, 2088.
[60] S. Gorina, N. P. Pavletich, *Science* **1996**, *274*, 1001.
[61] K. V. Kishan, G. Scita, W. T. Wong, P. P. Di Fiore, M. E. Newcomer, *Nat. Struct. Biol.* **1997**, *4*, 739.
[62] A. M. Mongioví, P. R. Romana, S. Panni, M. Mendoza, W. T. Wong, A. Musacchio, G. Cesareni, P. P. Di Fiore, *EMBO J.* **1999**, *18*, 5300.
[63] J. C. Williams, A. Weijland, S. Gonfloni, A. Thompson, S. A. Courtneidge, G. Superti-Furga, R. K. Wierenga, *J. Mol. Biol.* **1997**, *274*, 757.
[64] W. Xu, S. C. Harrison, M. J. Eck, *Nature* **1997**, *385*, 595.
[65] I. Moarefi, M. LaFevre-Bernt, F. Sicheri, M. Huse, C. H. Lee, J. Kuriyan, W. T. Miller, *Nature* **1997**, *385*, 650.
[66] F. Sicheri, I. Moarefi, J. Kuriyan, *Nature* **1997**, *385*, 602.
[67] D. Barila, G. Superti-Furga, *Nat. Genet.* **1998**, *18*, 280.
[68] J. C. Williams, R. K. Wierenga, M. Saraste, *Trends Biochem. Sci.* **1998**, *23*, 179.
[69] A. H. Andreotti, S. C. Bunnell, S. Feng, L. J. Berg, S. L. Schreiber, *Nature* **1997**, *385*, 93.
[70] Q. Liu, D. Berry, P. Nash, T. Pawson, C. J. McGlade, S. S. Li, *Mol. Cell* **2003**, *11*, 471.
[71] P. Bork, M. Sudol, *Trends Biochem. Sci.* **1994**, *19*, 531.
[72] B. Andre, J. Y. Springael, *Biochem. Biophys. Res. Commun.* **1994**, *205*, 1201.
[73] K. Hofmann, P. Bucher, *FEBS Lett.* **1995**, *358*, 153.
[74] M. Sudol, T. Hunter, *Cell* **2000**, *103*, 1001.
[75] M. J. Macias, S. Wiesner, M. Sudol, *FEBS Lett.* **2002**, *513*, 30.
[76] L. Otte, U. Wiedemann, B. Schlegel, J. R. Pires, M. Beyermann, P. Schmieder, G. Krause, R. Volkmer-Engert, J. Schneider-Mergener, H. Oschkinat, *Protein Sci.* **2003**, *12*, 491.
[77] H. I. Chen, A. Einbond, S. J. Kwak, H. Linn, E. Koepf, S. Peterson, J. W. Kelly, M. Sudol, *J. Biol. Chem.* **1997**, *272*, 17070.
[78] H. Linn, K. S. Ermekova, S. Rentschler, A. B. Sparks, B. K. Kay, M. Sudol, *Biol. Chem.* **1997**, *378*, 531.
[79] J. L. Isley, M. Sudol, X. Espanel, S. J. Winder, *Cell Signal.* **2001**, *13*, 625.

[80] M. T. Bedford, D. Sabassova, J. Xu, P. Leder, M. B. Yaffe, *J. Biol. Chem.* **2000**, *275*, 10359.
[81] S. Wiesner, G. Stier, M. Sattler, M. J. Macias, *J. Mol. Biol.* **2002**, *324*, 807.
[82] J. R. Pires, F. Taha-Nejad, F. Toepert, T. Ast, U. Hoffmüller, J. Schneider-Mergener, R. Kühne, M. J. Macias, H. Oschkinat, *J. Mol. Biol.* **2001**, *314*, 1147.
[83] F. Toepert, J. R. Pires, C. Landgraf, H. Oschkinat, J. Schneider-Mergener, *Angew. Chem.* **2001**, *113*, 922; *Angew. Chem. Int. Ed.* **2001**, *40*, 897.
[84] X. Espanel, M. Sudol, *J. Biol. Chem.* **2001**, *276*, 14514.
[85] V. Kanelis, D. Rotin, J. D. Forman-Kay, *Nat. Struct. Biol.* **2001**, *8*, 407.
[86] L. J. Ball, T. Jarchau, H. Oschkinat, U. Walter, *FEBS Lett.* **2002**, *513*, 45.
[87] F. B. Gertler, K. Niebuhr, M. Reinhard, J. Wehland, P. Soriano, *Cell* **1996**, *87*, 227.
[88] C. Haffner, T. Jarchau, M. Reinhard, J. Hoppe, S. M. Lohmann, U. Walter, *EMBO J.* **1995**, *14*, 19.
[89] M. Reinhard, M. Halbrugge, U. Scheer, C. Wiegand, B. M. Jockusch, U. Walter, *EMBO J.* **1992**, *11*, 2063.
[90] A. Kato, F. Ozawa, Y. Saitoh, K. Hirai, K. Inokuchi, *FEBS Lett.* **1997**, *412*, 183.
[91] J. Beneken, J. C. Tu, B. Xiao, M. Nuriya, J. P. Yuan, P. F. Worley, D. J. Leahy, *Neuron* **2000**, *26*, 143.
[92] A. A. Fedorov, K. A. Magnus, M. H. Graupe, E. E. Lattman, T. D. Pollard, S. C. Almo, *Proc. Natl. Acad. Sci. USA* **1994**, *91*, 8636.
[93] K. E. Prehoda, D. J. Lee, W. A. Lim, *Cell* **1999**, *97*, 471.
[94] B. F. Volkman, K. E. Prehoda, J. A. Scott, F. C. Peterson, W. A. Lim, *Cell* **2002**, *111*, 565.
[95] M. Saraste, M. Hyvönen, *Curr. Opin. Struct. Biol.* **1995**, *5*, 403.
[96] K. Niebuhr, F. Ebel, R. Frank, M. Reinhard, E. Domann, U. D. Carl, U. Walter, F. Gertler, J. Wehland, T. Chakraborty, *EMBO J.* **1997**, *16*, 5433.
[97] S. Naisbitt, E. Kim, J. C. Tu, B. Xiao, C. Sala, J. Valthschanoff, R. Weinberg, P. Worley, M. Sheng, *Neuron* **1999**, *23*, 569.
[98] J. C. Tu, B. Xiao, J. P. Yuan, A. A. Lanahan, K. Leoffert, M. Li, D. J. Linden, P. F. Worley, *Neuron* **1988**, *21*, 717.
[99] M. L. Dustin, M. W. Olszowy, A. D. Holdorf, J. Li, S. Bromley, N. Desai, P. Widder, F. Rosenberger, P. A. van der Merwe, P. M. Allen, A. S. Shaw, *Cell* **1998**, *94*, 667.
[100] C. Freund, R. Kuehne, H. Yang, S. Park, E. L. Reinhertz, G. Wagner, *EMBO J.* **2002**, *21*, 5985.
[101] T. D. Pollard, *Annu. Rev. Cell Biol.* **1994**, *10*, 207.
[102] M. Tanaka, H. Shibata, *Eur. J. Biochem.* **1985**, *151*, 291.
[103] W. J. Metzler, K. L. Constantine, M. S. Friedrichs, A. J. Bell, E. G. Ernst, T. B. Lavoie, L. Mueller, *Biochemistry* **1993**, *32*, 13818.
[104] V. K. Vinson, S. J. Archer, E. E. Lattman, T. D. Pollard, D. A. Torchia, *J. Cell Biol.* **1993**, *122*, 1277.
[105] K. S. Thorn, H. E. Christensen, R. Shigeta, D. Huddler, L. Shalaby, U. Lindberg, N. H. Chua, C. E. Schutt, *Structure* **1997**, *5*, 19.
[106] E. S. Cedergren-Zeppezauer, N. C. Goonesekere, M. D. Rozycki, J. C. Myslik, Z. Dauter, U. Lindberg, C. E. Schutt, *J. Mol. Biol.* **1994**, *240*, 459.
[107] W. J. Metzler, A. K. Bell, E. Ernst, T. B. Lavoie, L. Mueller, *J. Biol. Chem.* **1994**, *269*, 4620.
[108] S. J. Archer, V. K. Vinson, T. D. Pollard, D. A. Torchia, *FEBS Lett.* **1994**, *337*, 145.
[109] C. Bjorkegren, M. Rozycki, C. E. Schutt, U. Lindberg, R. Karlsson, *FEBS Lett.* **1993**, *333*, 123.
[110] I. Perelroizen, J.-B. Marchand, L. Blancchoin, D. Didry, M.-F. Carlier, *Biochemistry* **1994**, *33*, 8472.
[111] N. Mahoney, D. A. Rozwarski, E. Fedorov, A. A. Fedorov, S. C. Almo, *Nat. Struct. Biol.* **1999**, *6*, 666.
[112] J. Schneider-Mergener, G. Cesareni, personal communication.
[113] J. Schneider-Mergener, H. Oschkinat, unpublished results.

Communications

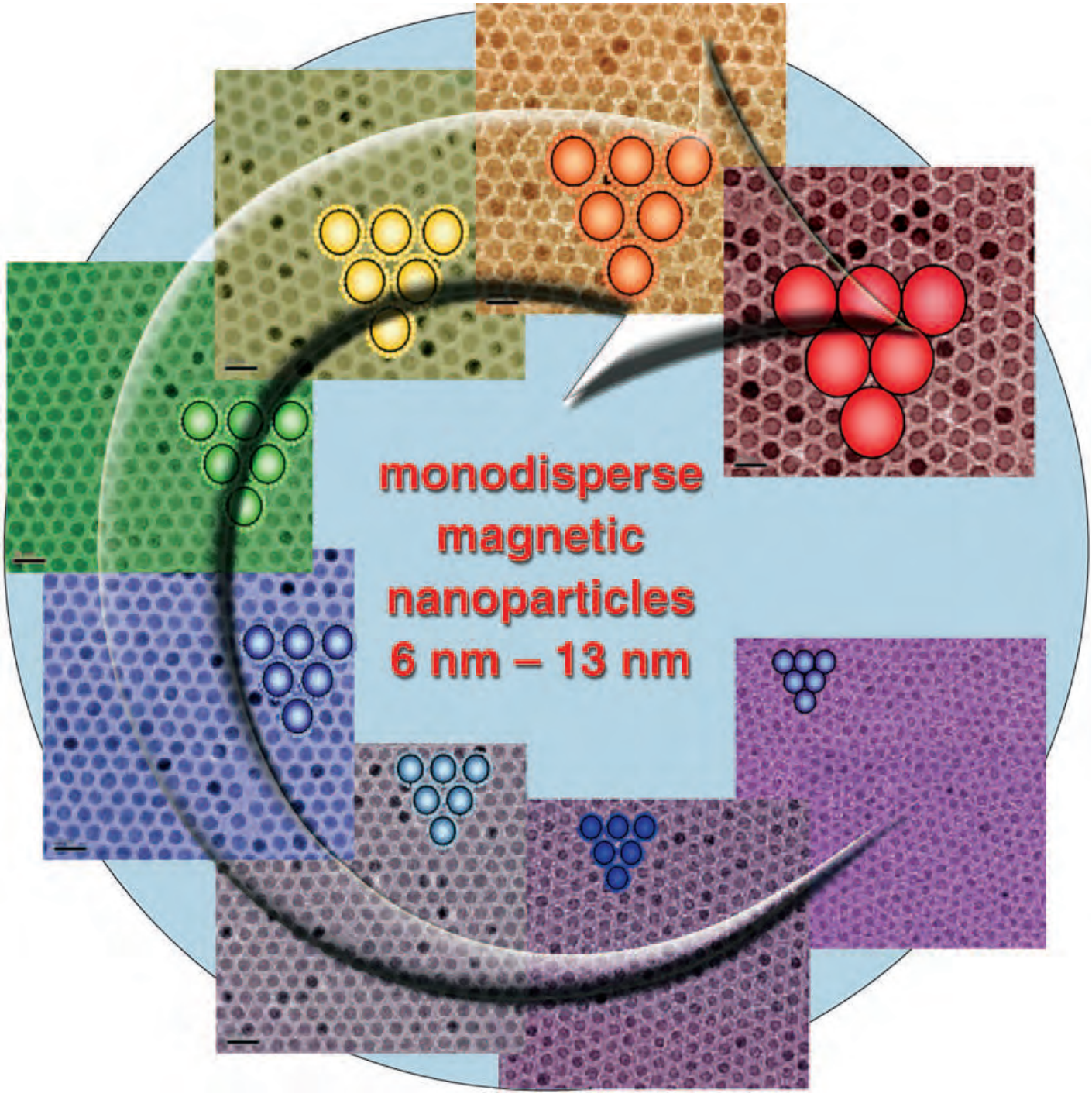

Monodisperse magnetic iron oxide nanoparticles with a continuous size spectrum of 6–13 nm were produced by controlled growth on previously synthetisized monodisperse nanoparticle seeds. The detailed synthetic procedure and characterization is described in the communication by T. Hyeon et al. on the following pages.

  DOI: 10.1002/anie.200461665

Nanoparticle Synthesis

One-Nanometer-Scale Size-Controlled Synthesis of Monodisperse Magnetic Iron Oxide Nanoparticles**

*Jongnam Park, Eunwoong Lee, Nong-Moon Hwang, Misun Kang, Sung Chul Kim, Yosun Hwang, Je-Geun Park, Han-Jin Noh, Jae-Young Kim, Jae-Hoon Park, and Taeghwan Hyeon**

The synthesis of nanoparticles has been intensively pursued not only for their fundamental scientific interest but also for many technological applications,[1] monodisperse nanoparticles (standard deviations $\sigma \leq 5\%$) with controlled particle sizes are of key importance because the electrical, optical, and magnetic properties of these nanoparticles depend strongly on their size.[2,3]

Recently, several colloidal chemical synthetic procedures have been developed to produce monodisperse nanoparticles of various materials. In the classical LaMer mechanism, a short burst of nucleation from a supersaturated solution is followed by the slow growth of particles without any significant additional nucleation, thereby achieving a complete separation of nucleation and growth.[4] Various similar procedures have been employed to synthesize almost monodisperse nanoparticles of CdSe,[5] related II–VI semiconductors,[5] and magnetic materials.[6] Watzky and Finke introduced a novel synthetic procedure that combines slow, continuous nucleation and fast, autocatalytic surface growth.[7] More recently, seed-mediated growth has been employed for the synthesis of larger metallic nanoparticles on smaller seeds. For example, Buhro and co-workers reported the synthesis of monodisperse nanoparticles of Bi, Sn, and In using Au nanoclusters as seeds.[8] In addition, monodisperse nanoparticles of Au,[9] Fe,[10] and Fe_3O_4[11] have been synthesized following similar procedures. Many monodisperse gold nanoparticles have been synthesized by a digestive ripening process or by surfactant exchange reactions.[12] The ultimate goal in the synthesis of nanoparticles is atomic-level size-controlled synthesis, similar to atomic layer deposition in thin-film processing,[13] of monodisperse nanoparticles without a size-selection process (Scheme 1), which has yet to be achieved.

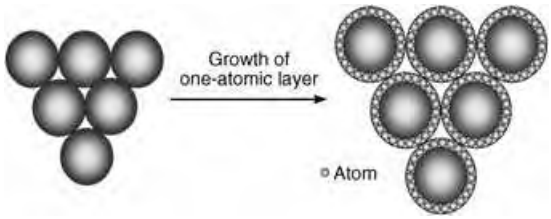

Scheme 1. Direct and atomic-scale controlled synthesis of monodisperse nanoparticles.

Our research group has developed new procedures for the synthesis of monodisperse nanocrystals of metals,[1e,4] metal oxides,[15] and metal sulfides[16] without going through a laborious size-sorting process. In these syntheses, metal–surfactant complexes generated in situ are thermally decomposed to form monodisperse nanoparticles. We report herein the synthesis of monodisperse iron oxide nanoparticles with a continuous size spectrum of 6–13 nm.

The process conditions required for the synthesis of monodisperse particles of micrometer size are relatively well established,[17] and a similar principle is expected to apply to the synthesis of monodisperse nanoparticles. It would be ideal if a certain species contributes exclusively to growth, instead of participating in both nucleation and growth processes, which means that the growth process is separated from additional nucleation. Such a separation between nucleation and growth is necessary for the direct synthesis of monodisperse nanoparticles, and this condition must have been satisfied in our previous direct synthesis of monodisperse iron nanoparticles.[1e,15a] On analyzing these procedures,[1e,15a] we tried to distinguish the species that contributes to nucleation from that which contributes to growth and reached a conclusion that pentacarbonyliron mainly contributes to nucleation, whereas the iron oleate complex generated in situ contributes exclusively to growth. We also found that the nucleation resulting from the thermal decomposition of pentacarbonyliron takes place at relatively low temperature, whereas the growth derived from the decomposition of the iron oleate complex occurs at a higher temperature. In other

[*] J. Park, E. Lee, S. C. Kim, Prof. Dr. T. Hyeon
National Creative Research Initiative Center for Oxide Nanocrystalline Materials and
School of Chemical and Biological Engineering
Seoul National University
Seoul 151-744 (Korea)
Fax: (+82) 2-886-8457
E-mail: thyeon@plaza.snu.ac.kr
Prof. Dr. N.-M. Hwang
School of Materials Science and Engineering and
Nano-Systems Institute (NSI-NCRC)
Seoul National University
Seoul 151-744 (Korea)
M. Kang, Y. Hwang, Prof. Dr. J.-G. Park
Department of Physics and Institute of Basic Science
Sungkyunkwan University, Suwon 440-746 (Korea)
Dr. H.-J. Noh, Dr. J.-Y. Kim, Prof. Dr. J.-H. Park
Department of Physics and
Pohang Light Source
Pohang University of Science and Technology
Pohang 790-784 (Korea)

[**] T.H. thanks the National Creative Research Initiative Program of the Korean Ministry of Science and Technology for financial support. N.M.H. thanks the National Core Research Center program of the Korea Science and Engineering Foundation (KOSEF) through the NANO systems Institute at Seoul National University for support. The work at POSTECH was supported by KISTEP through the X-ray/particle-beam Nanocharacterization Program. The work at Sungkyunkwan University was supported by the CSCMR and the Proton Accelerator User Program (No. M102KS010001-02K1901-01810) of the Proton Engineering R&D Project.

Supporting information for this article is available on the WWW under http://www.angewandte.org or from the author.

words, nucleation and growth seem to be ideally separated in our procedure. Consequently, we reasoned that if we prepare the iron oleate complex separately and use the complex as a growth source, we might synthesize monodisperse iron nanoparticles with controlled size by the additional incremental growth of the previously synthesized monodisperse iron nanoparticles. The overall process is similar to seed-mediated growth.[8–11]

As we described previously, we were able to synthesize monodisperse iron nanoparticles with sizes of 4, 8, and 11 nm from reaction mixtures containing 1:1, 1:2, and 1:3 molar ratios of pentacarbonyliron and oleic acid, respectively. Solutions containing 1.5, 3.0, and 4.5 mmol of the iron oleate complex were prepared by heating appropriate amounts of pentacarbonyliron and oleic acid in dioctyl ether at 403 K for 12 h. After refluxing the mixtures generated from the various combinations of the iron nanoparticles and the iron oleate solutions, we were able to synthesize monodisperse iron nanoparticles with particle sizes of 6, 7, 9, 10, 12, 13, and 15 nm (Table 1).

Table 1: Size of final iron nanoparticles produced from combinations of initial monodisperse iron nanoparticles and iron oleate solutions.

Final iron nanoparticles [nm]	Initial iron nanoparticles [nm]	Iron oleate solution [mmol]
6	4	1.5
7	4	3.0
9	8	1.5
10	8	3.0
12	11	1.5
13	11	3.0
15	11	4.5

These iron nanoparticles were readily oxidized to iron oxide on exposure to air.[18] The transmission electron microscopy (TEM) images of the air-oxidized iron oxide nanoparticles are shown in Figure 1. All of the nanoparticles, except the 6-nm-sized particles ($\sigma = 8.5\,\%$), exhibit particle-size distributions with standard deviations (σ) of less than 5%. These monodisperse nanoparticles were obtained directly without a size-selection process, and the synthetic procedure is highly reproducible. We expect that this concept of continuous growth without additional nucleation should be applicable to the incremental 1-nm size-controlled synthesis of monodisperse nanoparticles of many other materials. Subsequent further oxidation of these nanoparticles with trimethylamine *N*-oxide produced monodisperse and highly crystalline iron oxide nanocrystals. The TEM images of the resulting chemically oxidized nanocrystals are very similar to those obtained before the chemical oxidation in terms of particle sizes and their distributions, and the high-resolution transmission electron microscopy (HRTEM) images reveal their highly crystalline nature (see the Supporting Information).

The iron oxide nanocrystals were characterized by X-ray powder diffraction (XRD), X-ray absorption spectroscopy (XAS), and X-ray magnetic circular dichroism (XMCD). The XAS and XMCD measurements were performed at Pohang Light Source 2A1 beamline. The XRD patterns of the nanocrystals (Figure 2a) were assigned to the (111), (220), (311), (400), (422), (511), and (440) reflections of the inverse spinel structure of maghemite (γ-Fe_2O_3; JCPDS no. 39–1346). It should be noted that the standard XRD patterns of magnetite (Fe_3O_4) and maghemite are nearly identical. As the particle sizes get larger, the XRD peaks become narrower (Figure 2b), and the particle sizes calculated from the Scherrer formula match well with those obtained from the TEM data (see the Supporting Information).

X-ray absorption spectroscopy (XAS) and X-ray magnetic circular dichroism (XMCD) measurements at the Fe $L_{2,3}$ edges were carried out for the quantitative identification of the compositions of the iron oxide nanocrystals. Figure 3a, b show the XAS spectra and XMCD results, respectively, of the iron oxide nanocrystals with diameters of 4, 6, 8, 9, 11, and 13 nm, in comparison with those of two reference materials, bulk γ-Fe_2O_3 (maghemite) and bulk Fe_3O_4 (magnetite), which have nearly the same spinel crystal structure with only about 1% difference in the cubic lattice constant. Both the XAS and MCD spectra of the 4-nm-sized nanocrystals are very similar to those of γ-Fe_2O_3, which contains only a Fe^{3+} ion. As the particle size increases, the line shapes gradually change and both spectra for the iron oxide nanocrystals with a large particle size became similar to those of Fe_3O_4, which contains Fe^{3+} and Fe^{2+} ions. From the XAS and XMCD results, we were able to make a quantitative estimation of the compositions of the iron oxide nanocrystals in the form of $(\gamma\text{-}Fe_2O_3)_{1-x}(Fe_3O_4)_x$. The estimations are $x = 0.20 \pm 0.05$, 0.35 ± 0.05, 0.44 ± 0.05, 0.52 ± 0.05, 0.62 ± 0.05, 0.64 ± 0.05, and 0.65 ± 0.05 for the 4-, 6-, 8-, 9-, 11-, 12-, and 13-nm-sized nanocrystals, respectively. Therefore, γ-Fe_2O_3 is the dominant phase of the small 4-nm-sized iron oxide nanocrystals, whereas the fraction of the Fe_3O_4 component gradually increases with increasing particle size.

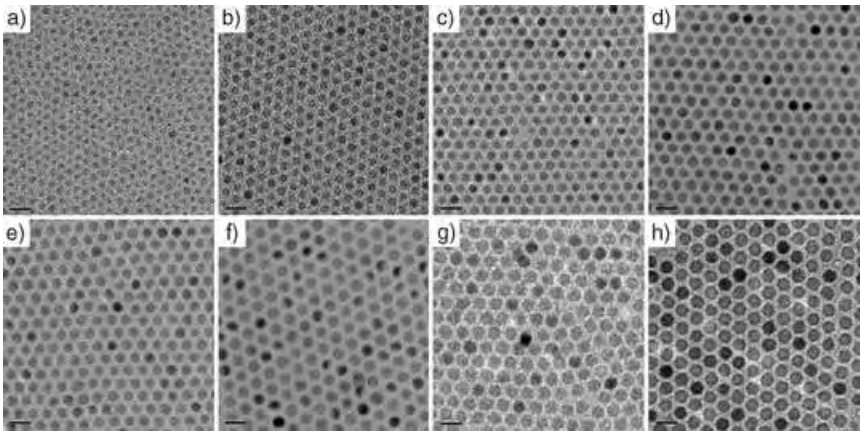

Figure 1. TEM images of a) 6-, b) 7-, c) 8-, d) 9-, e) 10-, f) 11-, g) 12-, and h) 13-nm-sized air-oxidized iron oxide nanoparticles showing the one nanometer level increments in diameter. (The enlarged TEM images and particle-size distribution histograms are supplied in the Supporting Information.)

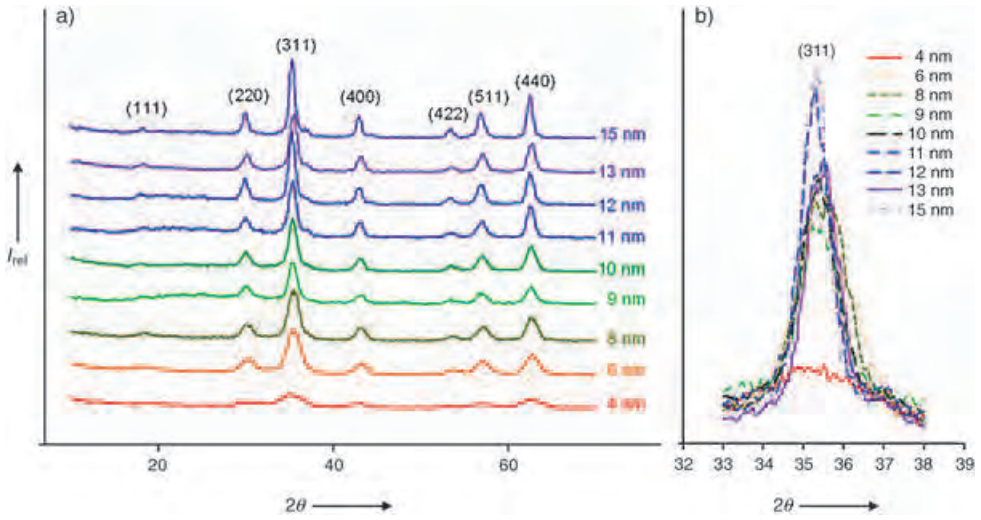

Figure 2. a) XRD patterns of iron oxide nanocrystals of 4, 6, 8, 9, 10, 11, 12, 13, and 15 nm, and b) the change of the (311) peak intensity of each nanocrystal.

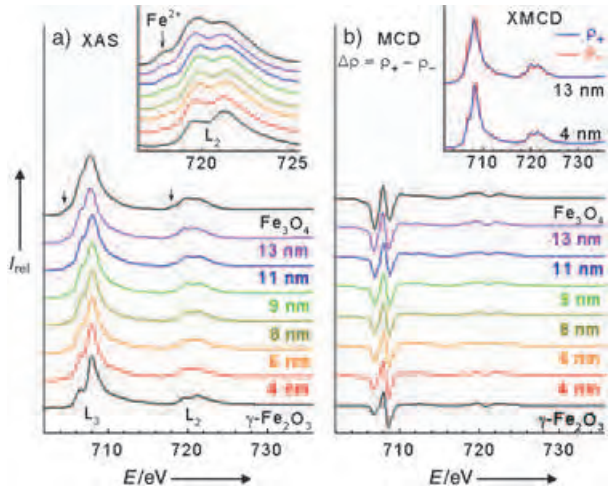

Figure 3. Fe $L_{2,3}$ edge a) XAS and b) XMCD spectra of 4, 6, 8, 9, 11, and 13 nm iron oxide nanocrystals compared with those of bulk reference materials (γ-Fe_2O_3 and Fe_3O_4). The magnified L_2 region XAS spectra of the nanocrystals and XMCD spectra of the 4 and 13 nm nanocrystals are shown in the insets of (a) and (b), respectively.

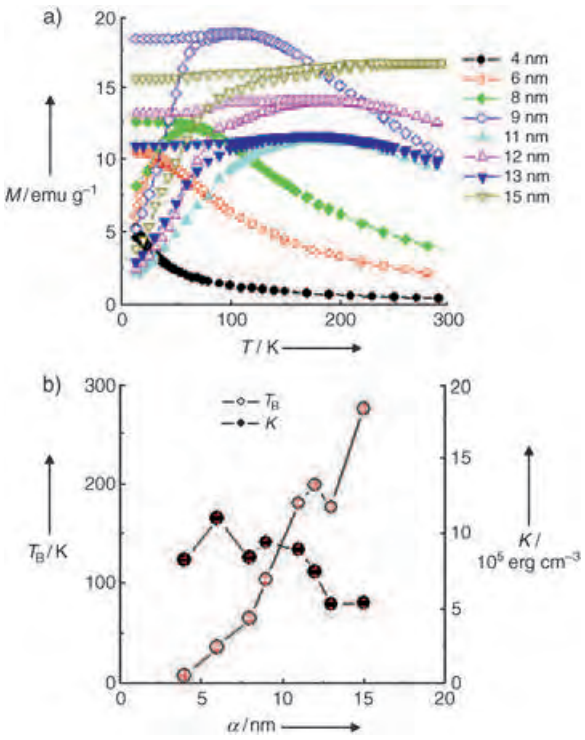

Figure 4. a) Temperature dependence of magnetization measured after zero-field cooling (ZFC) and field cooling (FC) at 100 Oe for 4, 6, 8, 9, 11, 12, 13, and 15 nm particles. b) Size dependence of the blocking temperature, T_B, obtained from M(T) in Figure 4a. The magnetic anisotropy constant, K, was obtained as described in the text.

The magnetic properties of these iron oxide nanocrystals were studied using a vibrating sample magnetometer (Lake Shore, 9300). Figure 4a shows the temperature dependence of magnetization measured at 100 Oe from 300 to 14 K. All our samples show superparamagnetic behavior at high temperatures. However, on cooling, the zero-field-cooled magnetization begins to drop and deviate from the field-cooled magnetization at the blocking temperature T_B. For the 4 nm sample, the blocking temperature seems to be close to the lowest temperature measured (14 K). For further measurements of the magnetization down to 2 K, we used a SQUID magnetometer and found that the blocking temperature is 8 K. With increasing particle size, the blocking temperature increases continuously (Figure 4b); for example, the blocking temperature increases to 275 K for the 15-nm-sized nanocrystals. We then used the measured blocking temperature to calculate the magnetic anisotropy constant K by using the formula: $K = 25 k_B T_B V^{-1}$,[19] where k_B is the Boltzman constant, T_B is the measured blocking temperature, and V is the total volume of a particle whose diameter was determined from TEM measurements. Considering that all our samples are spherical and, consequently, there is no shape anisotropy involved for the nanocrystals, the dominant anisotropy should be because of magnetocrystalline anisotropy. It is noticeable

that, unlike other nanocrystals, the magnetic anisotropy constant does not increase significantly with a reduction in particle size. For comparison, the magnetic anisotropy constant[20] of bulk Fe_3O_4 is 4×10^5 erg cm^{-3}, which is slightly higher than that of our 15-nm-sized sample. This unusual result seems to be because of the strong dipolar interactions between the nanoparticles, which might mask the size dependence of the magnetic anisotropy. In fact, the peaks in the magnetic susceptibility appear to be much broader than would be expected for monodisperse nanoparticles, thus demonstrating the strong dipolar interaction in our samples.

In conclusion, we have synthesized monodisperse iron oxide nanoparticles with a continuous size spectrum of 6–13 nm. The synthesis of iron nanoparticles with particle sizes of 6, 7, 9, 10, 12, 13, and 15 nm was achieved by the controlled additional growth of the previously synthesized monodisperse iron nanoparticles; the overall synthetic procedure is similar to seed-mediated growth. These monodisperse nanoparticles were obtained directly without a size-selection process, and the synthetic procedure is highly reproducible. Subsequent chemical oxidation produced monodisperse and highly crystalline iron oxide nanocrystals. This concept of continuous growth without additional nucleation could be applicable to other materials for the incremental, 1-nm size-controlled synthesis of monodisperse nanoparticles.

Experimental Section

Monodisperse 4-, 8-, and 11-nm-sized iron oxide nanoparticles were prepared as described previously.[15a] For example, to prepare 11-nm-sized monodisperse iron nanoparticles, $[Fe(CO)_5]$ (0.2 mL, 1.52 mmol; Aldrich, 99.999%) was added to a mixture containing dioctyl ether (10 mL; Aldrich, 90%), and oleic acid (1.28 g, 4.56 mmol; Aldrich, 99%) at 373 K. The resulting mixture was heated to reflux and kept at that temperature for 1 h. During this process, the initial orange solution gradually became black. It was then cooled to room temperature and anhydrous trimethylamine *N*-oxide (0.34 g, 4.56 mmol, prepared from $(CH_3)_3NO{\cdot}2H_2O$: Aldrich, 98%) was added. The mixture was then heated to 403 K in an argon atmosphere and maintained at this temperature for 2 h, whereupon the solution became brown. The reaction temperature was slowly increased to reflux and the reflux continued for 1 h; the color of the solution gradually turned from brown to black. The solution was then cooled to room temperature, and ethanol was added to yield a black precipitate, which was then separated by centrifugation. Starting mixtures containing $[Fe(CO)_5]$ and oleic acid in 1:1 and 1:2 molar ratios yielded iron oxide nanoparticles of 4 and 8 nm, respectively.

Iron oleate complex solutions with three different concentrations were prepared by mixing $[Fe(CO)_5]$ (0.2 mL, 1.52 mmol), dioctyl ether (10 mL), and oleic acid (0.43 g, 1.52 mmol; 0.85 g, 3.04 mmol; or 1.28 g, 4.56 mmol; respectively) which were heated at 403 K for 12 h to form the iron oleate complex solutions designated as 1.5, 3.0, and 4.5 mmol, respectively. For the synthesis of iron nanoparticles of the desired sizes, various combinations of the iron oleate solutions and the iron nanoparticle suspensions (before the chemical oxidation with trimethylamine *N*-oxide) were mixed (Table 1). The resulting solution was heated to reflux for 1 h to produce iron nanoparticles that were further oxidized with anhydrous trimethylamine *N*-oxide to produce highly crystalline iron oxide nanocrystals.

Received: August 16, 2004
Revised: February 2, 2005
Published online: March 30, 2005

Keywords: iron · magnetic properties · materials science · nanoparticles

[1] a) G. Schmid, *Nanoparticles: From Theory to Application*, Wiley-VCH, Weinheim, **2004**; b) K. J. Klabunde, *Nanoscale Materials in Chemistry*, Wiley-Interscience, New York, **2001**; c) A. P. Alivisatos, *Science* **1996**, *271*, 933; d) C. Pacholski, A. Kornowsli, H. Weller, *Angew. Chem.* **2002**, *114*, 1234; *Angew. Chem. Int. Ed.* **2002**, *41*, 1188; e) T. Hyeon, *Chem. Commun.* **2003**, 927; f) M. P. Pileni, *Nat. Mater.* **2003**, *2*, 145.

[2] a) M. Nirmal, L. Brus, *Acc. Chem. Res.* **1999**, *32*, 407; b) C. B. Murray, C. R. Kagan, M. G. Bawendi, *Annu. Rev. Mater. Sci.* **2000**, *30*, 545; c) A. L. Rogach, D. V. Talapin, E. V. Shevchenko, A. Kornowski, M. Haase, H. Weller, *Adv. Funct. Mater.* **2002**, *12*, 653.

[3] a) S. Sun, C. B. Murray, D. Weller, L. Folks, A. Moser, *Science* **2000**, *287*, 1989; b) D. E. Speliotis, *J. Magn. Magn. Mater.* **1999**, *193*, 29; c) R. C. O'Handley, *Modern Magnetic Materials*, Wiley, New York, **1999**.

[4] V. K. LaMer, R. H. Dinegar, *J. Am. Chem. Soc.* **1950**, *72*, 4847.

[5] a) C. B. Murray, D. J. Norris, M. G. Bawendi, *J. Am. Chem. Soc.* **1993**, *115*, 8706; b) X. Peng, J. Wickham, A. P. Alivisatos, *J. Am. Chem. Soc.* **1998**, *120*, 5343; c) D. V. Talapin, A. L. Rogach, E. V. Shevchenko, A. Kornowski, M. Haase, H. Weller, *J. Am. Chem. Soc.* **2002**, *124*, 5782; d) Z. A. Peng, X. Peng, *J. Am. Chem. Soc.* **2001**, *123*, 183; e) W. W. Yu, X. Peng, *Angew. Chem.* **2002**, *114*, 2474; *Angew. Chem. Int. Ed.* **2002**, *41*, 2368.

[6] a) S. Sun, C. B. Murray, *J. Appl. Phys.* **1999**, *85*, 4325; b) F. Dumestre, B. Chaudret, C. Amiens, P. Renaud, P. Fejes, *Science* **2004**, *303*, 821; c) E. V. Shevchenko, D. V. Talapin, A. L. Rogach, A. Kornowski, M. Haase, H. Weller, *J. Am. Chem. Soc.* **2002**, *124*, 11480; d) F. Dumestre, B. Chaudret, C. Amiens, M. Respaud, P. Fejes, P. Renaud, P. Zurcher, *Angew. Chem.* **2003**, *115*, 5371; *Angew. Chem. Int. Ed.* **2003**, *42*, 5213; e) F. Dumestre, B. Chaudret, C. Amiens, M.-C. Fromen, M.-J. Casanove, M. Respaud, P. Zurcher, *Angew. Chem.* **2002**, *114*, 4462; *Angew. Chem. Int. Ed.* **2002**, *41*, 4286; f) J. Park, B. Koo, Y. Hwang, C. Bae, K. An, J.-G. Park, H. M. Park, T. Hyeon, *Angew. Chem.* **2004**, *116*, 2332; *Angew. Chem. Int. Ed.* **2004**, *43*, 2282; g) V. F. Puntes, K. M. Krishnan, A. P. Alivisatos, *Science* **2001**, *291*, 2115; h) V. F. Puntes, D. Zanchet, C. K. Erdonmez, A. P. Alivisatos, *J. Am. Chem. Soc.* **2002**, *124*, 12874; i) S.-J. Park, S. Kim, S. Lee, Z. G. Khim, K. Char, T. Hyeon, *J. Am. Chem. Soc.* **2000**, *122*, 8581.

[7] a) M. A. Watzky, R. G. Finke, *J. Am. Chem. Soc.* **1997**, *119*, 10382; b) K. R. Brown, M. J. Natan, *Langmuir* **1998**, *14*, 726.

[8] H. Yu, P. C. Gibbons, K. F. Kelton, W. E. Buhro, *J. Am. Chem. Soc.* **2001**, *123*, 9198.

[9] a) N. R. Jana, X. Peng, *J. Am. Chem. Soc.* **2003**, *125*, 14280; b) J. P. Wilcoxon, P. P. Provencio, *J. Am. Chem. Soc.* **2004**, *126*, 6402.

[10] D. Farrell, S. A. Majetich, J. P. Wilcoxon, *J. Phys. Chem. B* **2003**, *107*, 11022.

[11] a) S. Sun, H. J. Zeng, *J. Am. Chem. Soc.* **2002**, *124*, 8204; b) S. Sun, H. Zeng, D. B. Robinson, S. Raoux, P. M. Rice, S. X. Wang, G. Li, *J. Am. Chem. Soc.* **2004**, *126*, 273.

[12] a) X. M. Lin, H. M. Jaeger, C. M. Sorensen, K. J. Klabunde, *J. Phys. Chem. B* **2001**, *105*, 3353; b) S. Stoeva, K. J. Klabunde, C. M. Sorensen, I. Dragieva, *J. Am. Chem. Soc.* **2002**, *124*, 2305; c) B. L. V. Prasad, S. I. Stoeva, C. M. Sorensen, K. J. Klabunde, *Chem. Mater.* **2003**, *15*, 935; d) S. I. Stoeva, B. L. V. Prasad, S. Uma, P. K. Stoimenov, V. Zaikovski, C. M. Sorensen, K. J. Klabunde, *J. Phys. Chem. B* **2003**, *107*, 7441; e) T. Shimizu, T. Teranishi, S. Hasegawa, M. Miyake, *J. Phys. Chem. B* **2003**, *107*, 2719; f) T. Teranishi, S. Hasegawa, T. Shimizu, M. Miyake, *Adv. Mater.* **2001**, *13*, 1699; g) L. O. Brown, J. E. Hutchison, *J. Phys.*

Chem. B **2001**, *105*, 8911; h) L. O. Brown, J. E. Hutchison, *J. Am. Chem. Soc.* **1999**, *121*, 882; i) J. E. Martin, J. P. Wilcoxon, J. Odinek, P. Provencio, *J. Phys. Chem. B* **2000**, *104*, 9475.

[13] M. Leskela, M. Ritala, *Angew. Chem.* **2003**, *115*, 5706; *Angew. Chem. Int. Ed.* **2003**, *42*, 5548.

[14] a) S.-W. Kim, J. Park, Y. Jang, Y. Chung, S. Hwang, T. Hyeon, Y. W. Kim, *Nano Lett.* **2003**, *3*, 1289; b) S. U. Son, Y. Jang, J. Park, H. B. Na, H. M. Park, H. J. Yun, J. Lee, T. Hyeon, *J. Am. Chem. Soc.* **2004**, *126*, 5026; c) S. U. Son, I. K. Park, J. Park, T. Hyeon, *Chem. Commun.* **2004**, 778.

[15] a) T. Hyeon, S. S. Lee, J. Park, Y. Chung, H. B. Na, *J. Am. Chem. Soc.* **2001**, *123*, 12798; b) T. Hyeon, Y. Chung, J. Park, S. S. Lee, Y.-W. Kim, B. H. Park, *J. Phys. Chem. B* **2002**, *106*, 6831; c) J. Park, K. An, Y. Hwang, J.-G. Park, H.-J. Noh, J.-Y. Kim, J.-H. Park, N.-M. Hwang, T. Hyeon, *Nat. Mater.* **2004**, *3*, 891; d) J. Joo, T. Yu, Y.-W. Kim, H. M. Park, F. Wu, J. Z. Zhang, T. Hyeon, *J. Am. Chem. Soc.* **2003**, *125*, 6553.

[16] J. Joo, H. B. Na, T. Yu, J. H. Yu, Y.-W. Kim, F. Wu, J. Z. Zhang, T. Hyeon, *J. Am. Chem. Soc.* **2003**, *125*, 11100.

[17] a) T. Sugimoto, *Monodispersed Particles*, Elsevier, Amsterdam, **2001**; b) T. Sugimoto, *Adv. Colloid Interface Sci.* **1987**, *28*, 65.

[18] K. Woo, J. Hong, S. Choi, H.-W. Lee, J.-P. Ahn, C. S. Kim, S. W. Lee, *Chem. Mater.* **2004**, *16*, 2814.

[19] B. D. Cullity, *Introduction to Magnetic Materials*, Addison-Wiley, Reading, **1972**.

[20] S. Chikazumi, *Physics of Ferromagnetism*, 2nd ed., Clarendon, Oxford, **1997**.

Coordination Polymers

Ternary Nets formed by Self-Assembly of Triangles, Squares, and Tetrahedra**

*Zhenqiang Wang, Victor Ch. Kravtsov, and Michael J. Zaworotko**

It has now been almost thirty years since Wells catalogued network structures in crystals[1] in a manner that has facilitated the crystal engineering[2] of a wide range of infinite 2D and 3D nets. That crystal engineered nets invoke geometric design principles means that a chemically diverse range of molecular building blocks (MBBs) are available for study as exemplified by coordination polymers (i.e. metal–organic networks),[3] polymers sustained by organometallic linkages[4] and hydrogen-bonded organic networks.[5] Coordination polymers are particularly attractive targets for study: metal coordination and cluster geometries are diverse but they are controllable in a manner that facilitates the design of nets with predictable topology and dimensions; metal moieties can be pre-selected so as to impart functional properties, such as magnetism,[6] luminescence[7] or, in the case of open-framework nets, permanent porosity;[3c,e,8] multifunctional organic ligands can also be selected for their geometric attributes. Coordination polymers can be rationalized and designed using the "node-and-spacer" approach,[3a,b] which simplifies molecular building blocks into topological points and lines. Aesthetically pleasing and potentially functional coordination polymers that have been isolated in recent years are exemplified by (10,3)-a,[9] NbO,[10] diamondoid,[11] and primitive cubic nets.[12] An alternative strategy for the interpretation and design of nets takes into account the shape of the MBBs and represents nets as being sustained by vertex-linked polygons or polyhedra (VLPP).[6a,13] As revealed by Scheme 1, the aforementioned four net types

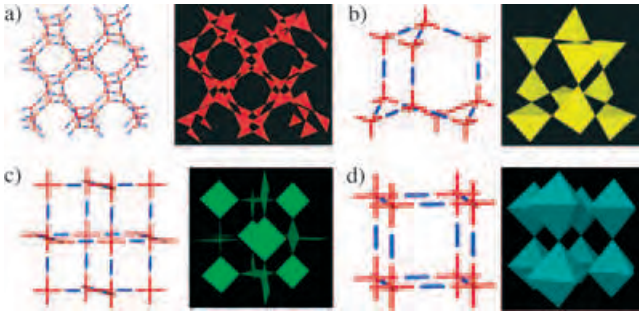

Scheme 1. Four unitary nets represented in both node-and-spacer and VLPP format: a) (10,3)-a net, b) diamondoid net, c) NbO net, d) primitive cubic net.

can be visualized as being either "node-and-spacer" or VLPP networks. From the VLPP perspective, the four nets shown in Scheme 1 are all examples of unitary nets in that they are built entirely from one type of polygon or polyhedron. The VLPP approach comes into its own for binary nets, that is, nets sustained by pairs of polygonal or polyhedral MBBs. The structural diversity possible from even the simplest of MBBs is exemplified by (3,4)-connected nets. If squares are connected exclusively to triangles and vice versa, two distinct (3,4)-connected binary nets have been isolated: the Pt_3O_4[14] and twisted boracite nets.[13a,15] Likewise, if tetrahedra are linked exclusively to triangles and vice versa, two additional (3,4)-connected binary nets are accessible, the boracite[16] and cubic C_3N_4 nets[17] (Scheme 2). Herein we address how the VLPP approach can be extended to ternary nets, that is, those sustained by a combination of three polygons or polyhedra.

We report the synthesis and crystal structures of two compounds that represent prototypal examples of ternary VLPP nets sustained by three distinct MBBs: $[\{[Zn_6(btc)_4(isoquinoline)_6(MeOH)]H_2O(benzene)_2\}_n]$ (USF-3; btc = 1,3,5-benzenetricarboxylate), and $[\{[Zn_6(btc)_4(isoquinoline)_4(MeOH)_2](MeOH)_8(chlorobenzene)\}_n]$ (USF-4). USF-3 and USF-4 are sustained by vertex linkage of triangular, square, and tetrahedral MBBs and represent to our knowledge the first reported examples of ternary nets. The

[*] Z. Wang, Dr. V. Ch. Kravtsov, Prof. Dr. M. J. Zaworotko
Department of Chemistry
University of South Florida
4202 E Fowler Ave (SCA 400), Tampa, FL 33620 (USA)
Fax: (+1) 813-974-3203
E-mail: xtal@usf.edu

[**] We gratefully acknowledge the financial support of the National Science Foundation (DMR 0101641).

Supporting information for this article is available on the WWW under http://www.angewandte.org or from the author.

 DOI: 10.1002/anie.200500156

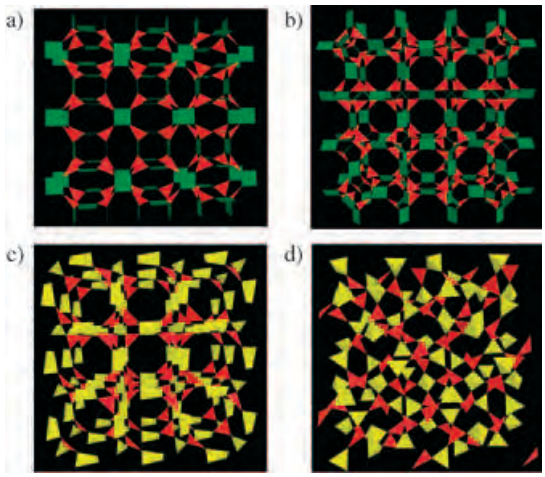

Scheme 2. Four (3,4)-connected binary nets represented in VLPP format: a) Pt_3O_4 net, b) twisted boracite net, c) boracite net, and d) cubic C_3N_4 net.

triangular MBB utilized in this study is the 1,3,5-benzenetricarboxylate anion (**A**). The square MBB is the previously reported $Zn_2(RCO_2)_4$ (**B**) and the tetrahedral MBBs are $Zn_2(RCO_2)_2(RCO_2)_2$ (**C**) or $Zn_2(RCO_2)_3(RCO_2)$ (**C′**), for USF-3 and USF-4, respectively, Scheme 3. Zinc(II)-based MBBs were selected because such a wide variety of zinc(II) carboxylate chromophores have been documented.[3d] The formation of the two new ternary nets and the relative ratio of **B** and **C** (2:1) in USF-3 or **B** and **C′** (1:2) in USF-4 appear to be controlled by template molecules and reaction conditions. It is of note that the Zn^{II} and btc can generate other supramolecular isomers[3a] in the presence of other solvents or templates.[9b,13a] Zinc nitrate, 1,3,5-benzenetricarboxylic acid, and isoquinoline in methanol templated by benzene affords USF-3 whereas similar reaction conditions give rise to USF-4 if chlorobenzene is employed as a template. This difference in products obtained is presumably a reflection of the relative size of the template molecules.

The structures of USF-3 and USF-4 were determined by X-ray single-crystal diffraction[18] and they are depicted in Figure 1 and Figure 2, respectively. There are two different Zn^{II} chromophores present in USF-3: square "paddle-wheel"

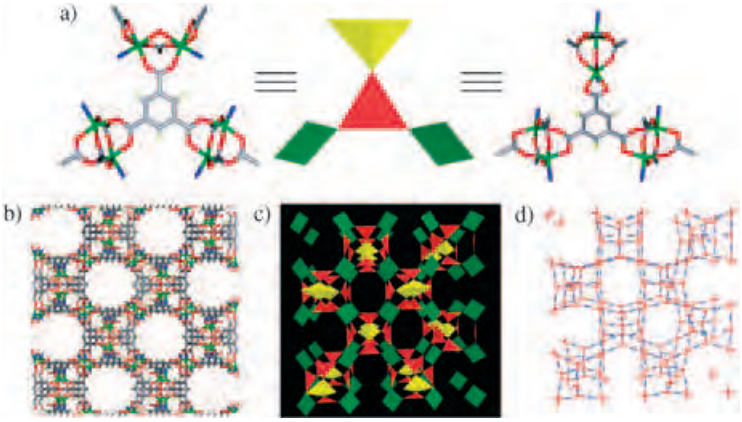

Figure 1. a) Representation of btc units linked to two square MBBs and one pseudo-tetrahedral MBB (two different orientations of the MBBs are shown). b) Crystal structure of USF-3 in stick representation (isoquinoline, benzene, and water are deleted for clarity). Selected bond lengths [Å]: Zn-O 1.985(5)–2.295(5), average 2.082; Zn-N 2.003(7)–2.104(3), average 2.063. c) Schematic representation of USF-3 in VLPP format. d) Schematic representation of USF-3 in node-and-spacer format.

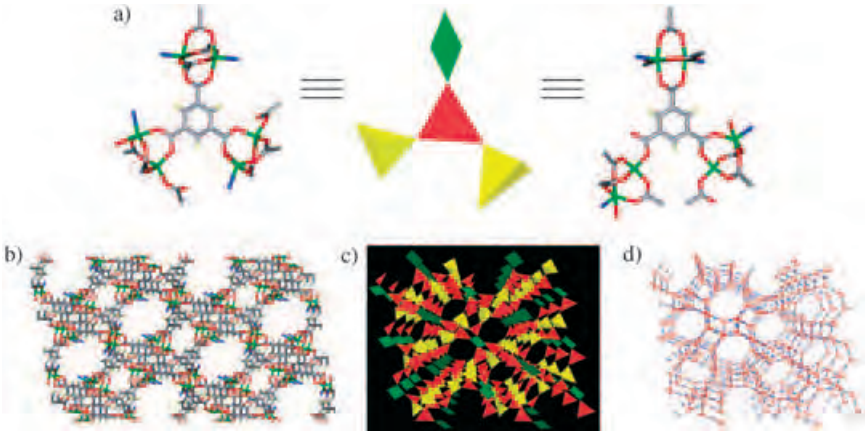

Figure 2. a) Representation of btc units linked to one square MBB and two pseudo-tetrahedral MBBs (two different orientations of the MBBs are shown). b) Crystal structure of USF-4 in stick representation (isoquinoline, methanol, and chlorobenzene are deleted for clarity). Selected bond lengths [Å]: Zn-O 1.912(3)–2.166(4), average 2.005, Zn-N 2.028(5)–2.031(4), average 2.030. c) Schematic representation of USF-4 in VLPP format. d) Schematic representation of USF-4 in node-and-spacer format.

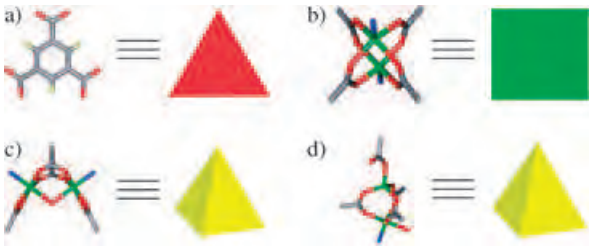

Scheme 3. Molecular building blocks (MBBs) employed in the ternary nets USF-3 and USF-4: a) **A**, b) **B**, c) **C**, d) **C′**.

MBBs, **B**, and pseudo-tetrahedral **C**, in a ratio of 2:1. **B** is perhaps the most frequently used MBB and is present in over 1200 crystal structures that have been deposited in the Cambridge Structural Database (CSD).[19] MBB **C** is far less common than **B** and comprises a binuclear Zn^{II} unit, two bridging carboxylate groups, one bridging oxygen atom, and two chelating carboxylate groups. Methanol and/or isoquinoline serve as axial ligands. As revealed by Figure 1, USF-3 is generated from vertex linking of **A**, **B**, and **C** in the ratio 4:2:1, thereby retaining the 4:3 ratio necessary for sustaining a (3,4)-

connected net in which 3-connected nodes are exclusively linked to 4-connected nodes and vice versa. Ideally, these three types of MBBs would generate a net structure with large open channels; however, no such channels are observed in USF-3 because isoquinoline, a bulky molecule, is protruding and blocking the possible channels. As a result, there are two different types of cavities within which disordered benzene molecules are trapped (see Supporting Information). One water molecule per asymmetric unit is also present, which engages in hydrogen bonding with the bridging methanol molecules. Thermal gravimetric analysis (TGA) and X-ray powder diffraction data suggest that USF-3 is stable up to at least 130 °C whereas further heating above 180 °C leads to collapse of the framework (see Supporting Information). USF-4 also has two Zn^{II} MBBs: a mixture of **B** and a different pseudo-tetrahedral MBB **C**′. The overall ratio of **A**: **B**: **C**′ is 4:1:2. MBB **C**′ features a binuclear Zn^{II} unit, three bridging carboxylate groups, and one monodentate carboxylate. USF-4 also has cavities but open channels are precluded by the presence of coordinated isoquinoline molecules. However, USF-4 possesses a higher free volume[20] than USF-3, 32.2% versus 19.3%, in which methanol and disordered chlorobenzene molecules are located. Thus, USF-3 and USF-4 are the first reported examples of (3,4)-connected ternary nets: triangular, square, and tetrahedral MBBs in the ratios 4:2:1 and 4:1:2, respectively.

That USF-3 and USF-4 might have general implications in the context of designing coordination polymers can be justified by the following considerations. First, although it is established that knowledge of molecular symmetry facilitates the design and synthesis of nets in a systematic manner, until now this has been limited to unitary or binary nets. USF-3 and USF-4 suggest that the use of three or perhaps even more MBBs could represent a facile approach to the construction of VLPP nets with unprecedented topologies. Second, the recently discovered porous metal–organic structures that are capable of guest-induced shape-responsive fitting represent a class of materials that resemble the degree of induced-fit behavior of bioenzymes, such as metalloproteins.[21] That the formation of USF-3 and USF-4 is so dependent upon the presence of guest/template illuminates a possible mechanism for translating structural information from an external medium into the formation of a novel framework. Third, although considerable effort in the field of coordination polymers has been devoted to the pursuit of new structures with unprecedented topologies,[3] discovery and recognition of novel three-periodic nets remains a nontrivial experience. USF-3 and USF-4 are based upon unique connectivity and they represent two examples of hitherto undocumented (3,4)-connected nets.[1] The Schläfli symbols for USF-3 and USF-4 are $(6{\cdot}6{\cdot}6)_4(6_2{\cdot}6_2{\cdot}8_2{\cdot}8_2{\cdot}12_2{\cdot}12_2)_2(6_2{\cdot}6_2{\cdot}8{\cdot}8{\cdot}8{\cdot}8)$ and $(4{\cdot}6{\cdot}8)_2(6{\cdot}6{\cdot}8_2)_2(6{\cdot}6{\cdot}8{\cdot}8{\cdot}10_4{\cdot}*)$ $(4{\cdot}6{\cdot}6{\cdot}8{\cdot}8{\cdot}10_4)_2$, respectively.[22] Therefore, USF-3 can be regarded as an "intermediate" structure between boracite and twisted boracite, as implied by their vertex symbols. USF-4 represents a more complicated and less symmetric (3,4)-connected net.[1,22] Nevertheless, the new structures are inherently modular and they are sustained by MBBs with shapes that are found throughout molecular chemistry. Therefore, there is every reason to assert that nets with the same topologies as USF-3 and USF-4 will be accessible from a much wider range of MBBs. However, it must be noted that the existence of USF-3 and USF-4 is at least partly a reflection of the tendency for Zn^{II} to exhibit multiple coordination geometries and the one-pot synthetic process employed herein is unlikely to be successful for other metals. In our opinion, as the number of MBBs increases, synthetic strategies will likely have to focus upon preformed MBBs rather than those generated in situ.

In summary, we have demonstrated that molecular triangles, squares, and tetrahedra are capable of self-assembling at their vertices to generate VLPP ternary nets. Such a ternary approach to generation of VLPPs is inherently modular in nature and consequently we anticipate it to be a strategy that will prove to be feasible for other combinations of molecular polygons and polyhedra.

Experimental Section

USF-3: A solution of 1,3,5-benzenetricarboxylic acid (140 mg, 0.667 mmol) and isoquinoline (0.350 mL, 3.00 mmol) in methanol (20 mL) was heated gently for about 10 min and then carefully layered onto a solution of $Zn(NO_3)_2{\cdot}6H_2O$ (297 mg, 1.00 mmol) in methanol/benzene (3:1, 20 mL). Colorless single crystals formed within 12 h under ambient conditions (217 mg, 59.6% yield).

USF-4: A solution of 1,3,5-benzenetricarboxylic acid (70 mg, 0.33 mmol) and isoquinoline (0.177 mL, 1.50 mmol) in methanol (20 mL) was carefully layered onto a solution of $Zn(NO_3)_2{\cdot}6H_2O$ (149 mg, 0.500 mmol) in methanol/chlorobenzene (2:1, 20 mL). Colorless single crystals formed within 12 h under ambient conditions (56 mg, 30.9% yield).

Received: January 14, 2005
Published online: April 8, 2005

Keywords: coordination polymers · crystal engineering · self-assembly · zinc

[1] a) A. F. Wells, *Three-Dimensional Nets and Polyhedra*, Wiley, New York, **1977**; b) A. F. Wells, *Further Studies of Three-dimensional Nets*, ACA Monograph, Washington, DC, **1979**.

[2] G. R. Desiraju, *Crystal Engineering: the Design of Organic Solids*, Elsevier, Amsterdam, **1989**.

[3] a) B. Moulton, M. J. Zaworotko, *Chem. Rev.* **2001**, *101*, 1629–1658; b) S. R. Batten, R. Robson, *Angew. Chem.* **1998**, *110*, 1558–1595; *Angew. Chem. Int. Ed.* **1998**, *37*, 1460–1494; c) M. Eddaoudi, D. B. Moler, H. Li, B. Chen, T. M. Reineke, M. O'Keeffe, O. M. Yaghi, *Acc. Chem. Res.* **2001**, *34*, 319–330; d) A. Erxleben, *Coord. Chem. Rev.* **2003**, *246*, 203–228; e) S. Kitagawa, R. Kitaura, S. Noro, *Angew. Chem.* **2004**, *116*, 2388–2430; *Angew. Chem. Int. Ed.* **2004**, *43*, 2334–2375; f) C. Janiak, *Dalton Trans.* **2003**, 2781–2804.

[4] M. Oh, G. B. Carpenter, D. A. Sweigart, *Acc. Chem. Res.* **2004**, *37*, 1–11.

[5] K. T. Holman, A. M. Pivovar, M. D. Ward, *Science* **2001**, *294*, 1907–1911.

[6] a) B. Moulton, J. Lu, R. Hajndl, S. Hariharan, M. J. Zaworotko, *Angew. Chem.* **2002**, *114*, 2945–2948; *Angew. Chem. Int. Ed.* **2002**, *41*, 2821–2824; b) S. R. Batten, K. S. Murray, *Coord. Chem. Rev.* **2003**, *246*, 103–130; c) H. Imai, K. Inoue, K. Kikuchi, Y. Yoshida, M. Ito, T. Sunahara, S. Onaka, *Angew. Chem.* **2004**, *116*, 5736–5739; *Angew. Chem. Int. Ed.* **2004**, *43*, 5618–5621.

[7] a) M. L. Tong, X. M. Chen, B. H. Ye, L. N. Ji, *Angew. Chem.* **1999**, *111*, 2376–2379; *Angew. Chem. Int. Ed.* **1999**, *38*, 2237–2240; b) M. C. Brandys, R. J. Puddephatt, *J. Am. Chem. Soc.* **2001**, *123*, 4839–4840; c) B. Zhao, X. Y. Chen, P. Cheng, D. Z. Liao, S. P. Yan, Z. H. Jiang, *J. Am. Chem. Soc.* **2004**, *126*, 15394–15395.

[8] a) D. N. Dybtsev, H. Chun, S. H. Yoon, D. Kim, K. Kim, *J. Am. Chem. Soc.* **2004**, *126*, 32–33; b) L. Pan, M. B. Sander, X. Huang, J. Li, M. Smith, E. Bittner, B. Bockrath, J. K. Johnson, *J. Am. Chem. Soc.* **2004**, *126*, 1308–1309; c) X. Zhao, B. Xiao, A. J. Fletcher, K. M. Thomas, D. Bradshaw, M. J. Rosseinsky, *Science* **2004**, *306*, 1012–1015.

[9] Representative examples: a) B. F. Abrahams, S. R. Batten, H. Hamit, B. F. Hoskins, R. Robson, *Chem. Commun.* **1996**, 1313–1314; b) O. M. Yaghi, C. E. Davis, G. M. Li, H. L. Li, *J. Am. Chem. Soc.* **1997**, *119*, 2861–2868; c) B. F. Abrahams, P. A. Jackson, R. Robson, *Angew. Chem.* **1998**, *110*, 2801–2804; *Angew. Chem. Int. Ed.* **1998**, *37*, 2656–2659; d) C. J. Kepert, M. J. Rosseinsky, *Chem. Commun.* **1998**, 31–32; e) C. J. Kepert, T. J. Prior, M. J. Rosseinsky, *J. Am. Chem. Soc.* **2000**, *122*, 5158–5168; f) T. J. Prior, M. J. Rosseinsky, *Inorg. Chem.* **2003**, *42*, 1564–1575; g) D. Bradshaw, T. J. Prior, E. J. Cussen, J. B. Claridge, M. J. Rosseinsky, *J. Am. Chem. Soc.* **2004**, *126*, 6106–6114.

[10] Representative examples: a) S. S. Turner, D. Collison, F. E. Mabbs, M. Halliwell, *J. Chem. Soc. Dalton Trans.* **1997**, 1117–1118; b) M. Eddaoudi, J. Kim, M. O'Keeffe, O. M. Yaghi, *J. Am. Chem. Soc.* **2002**, *124*, 376–377; c) A. B. Burdukov, G. I. Roschupkina, Y. V. Gatilov, S. A. Gromilov, V. A. Reznikov, *J. Supramol. Chem.* **2002**, *2*, 359–363; d) B. L. Chen, F. R. Fronczek, A. W. Maverick, *Chem. Commun.* **2003**, 2166–2167; e) X. H. Bu, M. L. Tong, H. C. Chang, S. Kitagawa, S. R. Batten, *Angew. Chem.* **2004**, *116*,194–197; *Angew. Chem. Int. Ed.* **2004**, *43*, 192–195.

[11] Recent representative examples: a) M. Sasa, K. Tanaka, X. H. Bu, M. Shiro, M. Shionoya, *J. Am. Chem. Soc.* **2001**, *123*, 10750–10751; b) O. R. Evans, R. G. Xiong, Z. Wang, G. K. Wong, W. Lin, *Angew. Chem.* **1999**, *111*, 557–559; *Angew. Chem. Int. Ed.* **1999**, *38*, 536–538; c) Y. H. Liu, H. C. Wu, H. M. Lin, W. H. Hou, K. L. Lu, *Chem. Commun.* **2003**, 60–61; d) M. Oh, G. B. Carpenter, D. A. Sweigart. *Angew. Chem.* **2001**, *113*, 3291–3294; *Angew. Chem. Int. Ed.* **2001**, *40*, 3191–3194; e) B. F. Abrahams, M. G. Haywood, R. Robson, D. A. Slizys, *Angew. Chem.* **2003**, *115*, 1144–1147; *Angew. Chem. Int. Ed.* **2003**, *42*, 1112–1115; f) K. Liang, H. Zheng, Y. Song, M. F. Lappert, Y. Li, X. Xin, Z. Huang, J. Chen, S. Lu, *Angew. Chem.* **2004**, *116*, 5900–5903; *Angew. Chem. Int. Ed.* **2004**, *43*, 5776–5779.

[12] Recent representative examples: a) H. L. Li, M. Eddaoudi, M. O'Keeffe, O. M. Yaghi, *Nature* **1999**, *402*, 276–279; b) M. Eddaoudi, J. Kim, N. Rosi, D. Vodak, J. Wachter, M. O'Keefe, O. M. Yaghi, *Science* **2002**, *295*, 469–472; c) J. X. Chen, Z. C. Liu, T. Yu, Z. X. Chen, J. Y. Sun, L. H. Weng, B. Tu, D. Y. Zhao, *Chem. Lett.* **2003**, *32*, 474–475.

[13] a) J. Lu, A. Mondal, B. Moulton, M. Zaworotko, *Angew. Chem.* **2001**, *113*, 2171–2174; *Angew. Chem. Int. Ed.* **2001**, *40*, 2113–2116; b) S. A. Bourne, J. Lu, A. Mondal, B. Moulton, M. J. Zaworotko, *Angew. Chem.* **2001**, *113*, 2169–2171; *Angew. Chem. Int. Ed.* **2001**, *40*, 2111–2113; c) G. J. McManus, Z. Wang, M. J. Zaworotko, *Cryst. Growth Des.* **2004**, *4*, 11–13; d) M. O'Keeffe, M. Eddaoudi, H. Li, T. M. Reineke, O. M. Yaghi, *J. Solid State Chem.* **2000**, *152*, 3–20; e) M. Eddaoudi, J. Kim, D. Vodak, A. Sudik, J. Wachter, M. O'Keeffe, O. M. Yaghi, *Proc. Natl. Acad. Sci. USA* **2002**, *99*, 4900–4904; f) H. Chun, D. Kim, D. N. Dybtsev, K. Kim, *Angew. Chem.* **2004**, *116*, 989–992; *Angew. Chem. Int. Ed.* **2004**, *43*, 971–974.

[14] B. Chen, M. Eddaoudi, S. T. Hyde, M. O'Keeffe, O. M. Yaghi, *Science* **2001**, *291*, 1021–1023.

[15] S. S. Y. Chui, S. M. F. Lo, J. P. H. Charmant, A. G. Orpen, I. D. Williams, *Science* **1999**, *283*, 1148–1150.

[16] B. F. Abrahams, S. R. Batten, H. Hamit, B. F. Hoskins, R. Robson, *Angew. Chem.* **1996**, *108*, 1794–1796; *Angew. Chem. Int. Ed. Engl.* **1996**, *35*, 1690–1692.

[17] D. N. Dybtsev, H. Chun, K. Kim, *Chem. Commun.* **2004**, 1594–1595.

[18] Crystal data for USF-3: $M_r = 2201.89$, orthorhombic, *Pmmn*, $a = 19.2471(17)$, $b = 19.9798(18)$, $c = 12.6644(11)$ Å, $V = 4870.1(7)$ Å^3, $Z = 2$, $\rho_{calcd} = 1.502\ g\,cm^{-3}$, $2\theta_{max} = 50.08°$ ($-22 \le h \le 22$, $-23 \le k \le 20$, $-15 \le l \le 10$), $T = 100$ K, 25527 measured reflections, $R1 = 0.0796$ and $wR2 = 0.2388$ for 2959 reflections ($I > 2\sigma(I)$), and $R1 = 0.1225$, $wR2 = 0.2669$ for 4570 independent reflections (all data) and 350 parameters, GOF = 1.013. Crystal data for USF-4: $M_r = 2170.27$, monoclinic, $P2_1/n$, $a = 14.5949(14)$, $b = 12.5583(12)$, $c = 25.741(3)$ Å, $\beta = 100.093(2)°$, $V = 4644.9(8)$ Å^3, $Z = 2$, $\rho_{calcd} = 1.552\ g\,cm^{-3}$, $2\theta_{max} = 54.00°$ ($-18 \le h \le 13$, $-14 \le k \le 16$, $-29 \le l \le 32$), $T = 100$ K, 21791 measured reflections, $R1 = 0.0644$ and $wR2 = 0.1296$ for 6924 reflections ($I > 2\sigma(I)$), and $R1 = 0.1007$, $wR2 = 0.1418$ for 10044 independent reflections (all data) and 649 parameters, GOF = 1.003. Data were collected on a Bruker SMART-APEX CCD diffractometer using $Mo_{K\alpha}$ radiation ($\lambda = 0.71073$ Å), operating in the Ω and ϕ scan mode. All crystal data were corrected for Lorentz and polarization effects, and the SADABS program was used for absorption correction. The structures were solved by direct methods and the structure solutions and refinements were based on $|F^2|$. All non-hydrogen atoms were refined with anisotropic displacement parameters, whereas hydrogen atoms were placed in calculated positions and given isotropic U values 20% higher than the atom to which they are bonded. All crystallographic calculations were conducted with the SHELXTL software suite. CCDC-260729 (USF-3) and CCDC-260730 (USF-4) contains the supplementary crystallographic data for this paper. These data can be obtained free of charge from the Cambridge Crystallographic Data Centre via www.ccdc.cam.ac.uk/data_request/cif.

[19] F. H. Allen, *Acta Crystallogr. Sect. B* **2002**, *58*, 380–388.

[20] A. L. Spek, *J. Appl. Crystallogr.* **2003**, *36*, 7–13.

[21] R. Matsuda, R. Kitaura, S. Kitagawa, Y. Kubota, T. C. Kobayashi, S. Horike, M. Takata, *J. Am. Chem. Soc.* **2004**, *126*, 14063–14070.

[22] Vertex symbols for the four (3,4)-connected binary nets discussed herein: Pt_3O_4 net $(8_5{\cdot}8_5{\cdot}8_5)_4(8_2{\cdot}8_2{\cdot}8_4{\cdot}8_4{\cdot}8_4{\cdot}8_4)_3$; twisted boracite net $(6{\cdot}6{\cdot}6)_4(6_2{\cdot}6_2{\cdot}8_2{\cdot}8_2{\cdot}12_2{\cdot}12_2)_3$; boracite net $(6{\cdot}6{\cdot}6)_4(6_2{\cdot}6_2{\cdot}8{\cdot}8{\cdot}8{\cdot}8)_3$; cubic C_3N_4 net $(8_5{\cdot}8_5{\cdot}8_5)_4(8_3{\cdot}8_3{\cdot}8_3{\cdot}8_3{\cdot}8_4{\cdot}8_4)_3$.

Microarray Immobilization

Fabrication of Chemical Microarrays by Efficient Immobilization of Hydrazide-Linked Substances on Epoxide-Coated Glass Surfaces**

*Myung-ryul Lee and Injae Shin**

Small molecules that regulate biological processes serve as valuable tools in studies of the functions of biomolecules, especially proteins, as well as in the development of drugs.[1] An important component of efforts that target the discovery of bioactive molecules is high-throughput screening. Technologies that rely on the use of DNA, protein, and carbohydrate microarrays have been widely employed to accelerate the selection of lead compounds and as high-throughput analytical tools in genomic, transcriptomic, proteomic, and glycomic research.[2–4] Microarray platforms enable the simultaneous assessment of a large number of samples that are available in limited quantities.

Similarly, small-molecule microarrays have been used as high-throughput methods to identify substances that selectively bind to proteins.[5] Most of the small molecules of interest in these efforts possess a number of different functional groups, such as hydroxy (OH), amino (NH_2), carboxy (CO_2H), and sulfanyl groups (SH). The major requirement of techniques used to fabricate small-molecule microarrays is that immobilization of the diversely functionalized compounds to the modified surfaces must be highly selective. Strategies that employ efficient and chemoselective ligation processes would be generally applicable to the fabrication of microarrays that possess covalently linked, biologically interesting molecules. Herein we describe a novel chemoselective immobilization process in which hydrazide-containing compounds react with epoxides coated on glass slides. This new technique has been applied to the efficient construction of chemical microarrays, which have been used to evaluate protein binding to peptides and small molecules.

Several criteria must be met in designing a general method to prepare diverse chemical microarrays. Firstly, the diverse substances containing the specific functional groups used for selective reactions with the modified solid surfaces must be easily prepared by solid-phase synthesis. Also, functional groups that will selectively react with the small molecules must be readily incorporated onto the solid surfaces. Lastly, following their release from a solid support, the diversely structured and functionalized small molecules must undergo site-specific covalent attachment to the modified surfaces. Strategies employing highly chemoselective ligation reactions fit these criteria. We have investigated a novel technique for immobilization, which relies on the use of reactions between hydrazide-containing small molecules and epoxide-coated glass slides (Scheme 1). The hydrazide groups are incorporated into the small molecules while they are attached to a solid support and are used as a handle in their solid-phase synthesis.[6] The epoxide-derivatized glass slides are easily created by immersing amine-coated glass slides into a solution of poly(ethylene glycol) diglycidyl ether (3% solution in 10 mM $NaHCO_3$, pH 8.3).[7]

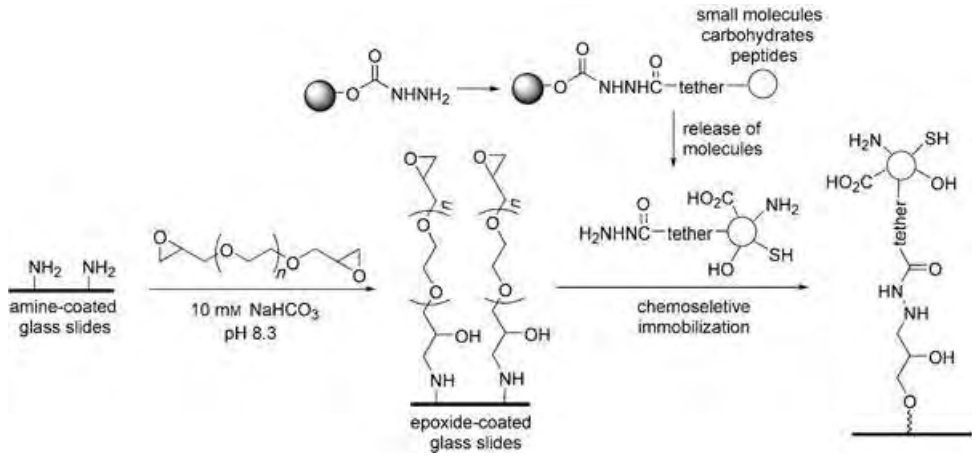

Scheme 1. Strategy for the fabrication of a chemical microarray based on the immobilization of hydrazide-containing compounds on epoxide-derivatized glass slides.

[*] M.-r. Lee, Prof. Dr. I. Shin
Department of Chemistry, Yonsei University
Seoul 120-749 (Korea)
Fax: (+82) 2-364-7050
E-mail: injae@yonsei.ac.kr

[**] This work was supported by a grant of the Center for Integrated Molecular Systems (KOSEF) and the Ministry of Science and Technology.

Supporting Information for this article is available on the WWW under http://www.angewandte.org or from the author.

A hydrazide-linked fucose probe (**S**- or **L**-Fuc-$NHNH_2$, **S**: short, **L**: long; Scheme 2) was used to probe optimal conditions (pH, time, and concentration) for the immobilization process. Preparation of **S**- or **L**-Fuc-$NHNH_2$ was initiated by transforming alcohol groups on a Wang resin into *p*-nitrophenyl carbonates.[8] The resulting resin was then treated with hydrazine to yield the hydrazide-containing resin, which was coupled with the Fmoc-protected **L** or **S** tether in the presence of NEM, BOP, and HOBt. The amino groups

 DOI: 10.1002/anie.200462720

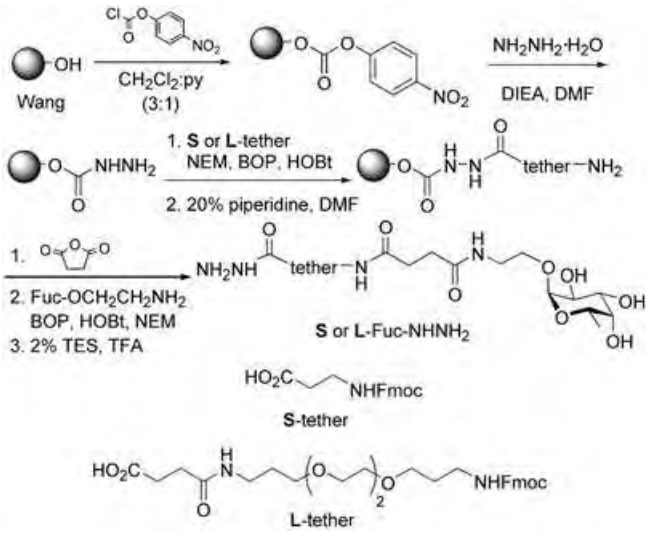

Scheme 2. Synthesis of the hydrazide-linked fucose probes **S**- and **L**-Fuc-$NHNH_2$. Py: pyridine, DIEA: ethyldiisopropylamine, DMF = *N*,*N*-dimethylformamide, NEM = *N*-ethylmorpholine, BOP = 1-benzotriazolyloxytris(dimethylamino)phosphonium hexafluorophosphate, HOBt = 1-hydroxybenzotriazole, TES = triethylsilane, TFA = trifluoroacetic acid, Fmoc = 9-fluorenylmethoxycarbonyl.

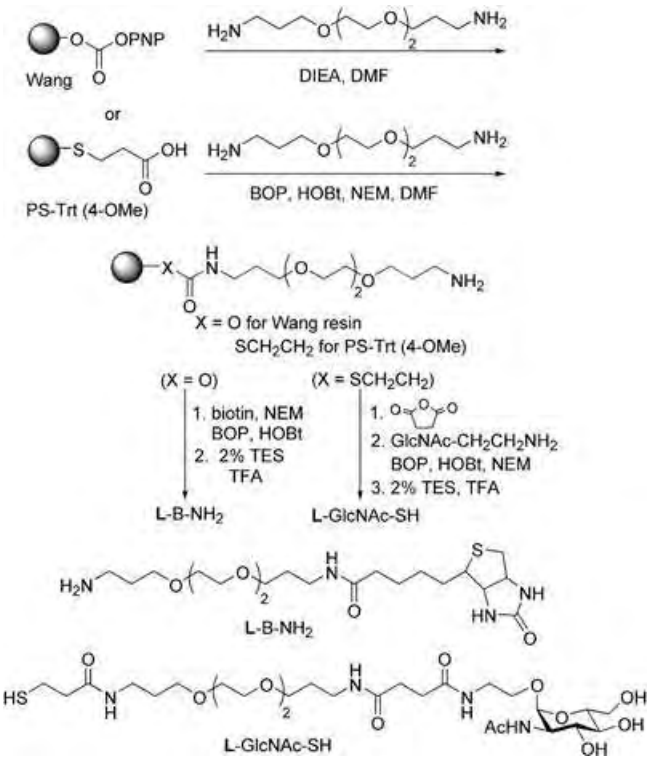

Scheme 3. Synthesis of amine-linked biotin (**L**-B-NH_2) and thiol-linked GlcNAc (**L**-GlcNAc-SH) probes. PNP = *p*-nitrophenyl.

produced by treatment of the resin with piperidine were treated with succinic anhydride to generate carboxylic acids, which underwent an amide-bond-forming reaction with aminoethyl α-fucopyranoside. Finally, the desired compounds were released from the resin by treatment with 2% TES in TFA.

In order to find the proper immobilization conditions, a solution of **L**-Fuc-$NHNH_2$ was printed onto the epoxide-derivatized glass slides and then the resulting slides were probed with Cy5-labeled *Aleuria aurantia* lectin (Cy5-AA) for 1 h (Cy5: indodicarbocyanine).[9] It was found that substrate concentrations of 0.5–1 mM and times of 3–4 h at pH 3–5 were appropriate for efficient immobilization reactions.[8]

An important feature of the method we have developed for constructing small-molecule microarrays is chemoselectivity. This was demonstrated in studies of selective attachment of hydrazides onto the epoxide-coated surfaces in the presence of other potent nucleophilic groups, such as amines and thiols. For these studies, amine-linked biotin (**L**-B-NH_2) and thiol-linked *N*-acetylglucosamine (**L**-GlcNAc-SH) probes were synthesized on solid supports by using *p*-nitrophenol-activated Wang and 2-carboxyethanethiol 4-methoxytrityl polystyrene (PS-Trt-(4-OMe)) resins, respectively (Scheme 3).[8]

A 1:1 mixture of **L**-Fuc-$NHNH_2$ and **L**-GlcNAc-SH (1 mM in 30% glycerol in 100 mM sodium phosphate, pH 3–10) was applied to the epoxide-functionalized slides, which were then treated with Cy5-AA and Cy3-labeled *Triticum vulgaris* lectin (wheat germ agglutinin; Cy3-TV; Cy3: indocarbocyanine).[9] Fluorescence analysis showed that the hydrazide substrate (**L**-Fuc-$NHNH_2$) was selectively immobilized in reactions conducted at low pH values, while the thiol substrate (**L**-GlcNAc-SH) underwent a more efficient reaction with the epoxide residues at a higher pH value, when the thiol moiety is deprotonated (Figure 1a).

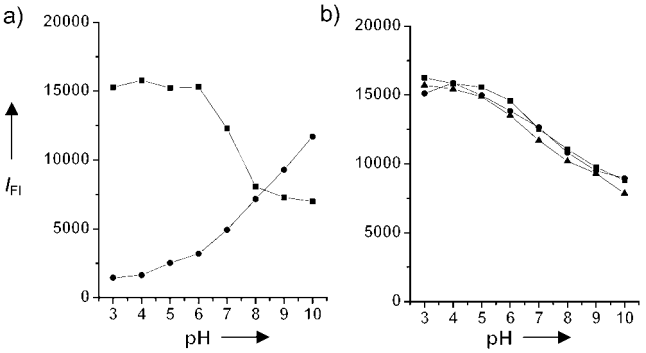

Figure 1. a) Immobilization of **L**-Fuc-$NHNH_2$ in the presence of one equivalent of **L**-GlcNAc-SH (■ probed with Cy5-AA, ● probed with Cy3-TV). b) Immobilization of **L**-Fuc-$NHNH_2$ in the presence of **L**-B-NH_2 (■ **L**-Fuc-$NHNH_2$ only, ● **L**-Fuc-$NHNH_2$:**L**-B-NH_2 (1:1), ▲ **L**-Fuc-$NHNH_2$:**L**-B-NH_2 (1:4); all probed with Cy5-AA).

Next, selective attachment of hydrazides to the epoxide-coated slides in the presence of amines was examined. Mixtures of **L**-Fuc-$NHNH_2$ and **L**-B-NH_2 (1:1 and 1:4 in 30% glycerol in 100 mM sodium phosphate, pH 3–10) were applied to the epoxide-derivatized slides and then probed with Cy5-AA. Since in some biologically interesting substrates (especially peptides) several amino groups are present, these immobilization reactions were run with mixtures

containing an excess of **L**-B-NH_2 of up to four molar equivalents. As shown in Figure 1 b, the fluorescence intensity of spots containing **L**-Fuc-$NHNH_2$ was barely changed when **L**-B-NH_2 was present, a result indicating that hydrazide-linked fucose (**L**-Fuc-$NHNH_2$) was selectively attached to the surface over the range of pH 3–10 even when a large excess of amine-containing biotin was used. The results of these competition experiments demonstrate that hydrazides are immobilized on the epoxide-coated surface more rapidly than substrates with both amine and thiol functional groups.

As part of a practical application of this technique to the fabrication of chemical microarrays, we synthesized hydrazide-linked substrates containing biotin (**S**- or **L**-B-$NHNH_2$), peptides (**S**- or **L**-GSH-$NHNH_2$, **S**- or **L**-strep-tag-$NHNH_2$ and its analogues), and phenanthridinium derivatives (Schemes 4 and 5).[8] The strep-tag peptide sequence and its

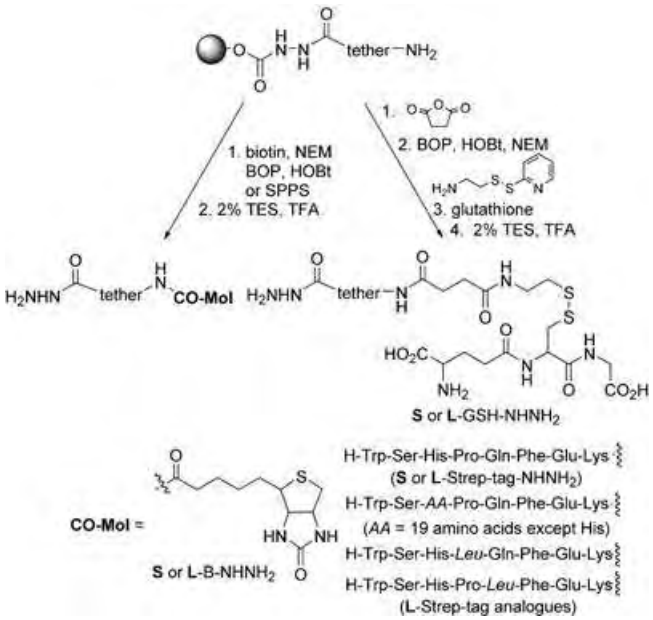

Scheme 4. Synthesis of hydrazide-linked probes containing biotin, glutathione (GSH), or the streptavidin tag (strep tag) and its analogues.

analogues were directly assembled on solid supports by using the conventional Fmoc strategy. Strep-tag analogues were prepared by replacing the histidine residue with 1 of the other 19 amino acids or by replacing the proline and glutamine residues with leucine. GSH was coupled to the resin by using a disulfide exchange reaction. Four phenanthridinium derivatives for acetylcholinesterase (AChE) inhibitors were prepared by solution-phase synthesis and subsequently coupled to the carboxylic acid derivatized resin.

Eight **S**/**L**-tethered fucose-, glutathione-, biotin-, and strep-tag-containing hydrazides (1 mM in 30% glycerol in 100 mM sodium phosphate, pH 5) were microspotted onto the epoxide-derivatized glass slides and then incubated with Cy5-AA, Cy3-streptavidin, Cy3-avidin, or glutathione S transferase (GST). GST incubation was followed by treatment with fluorescein isothiocyanate (FITC) labeled anti-GST antibody. As shown in Figure 2 a–d, fucose, glutathione, and the strep

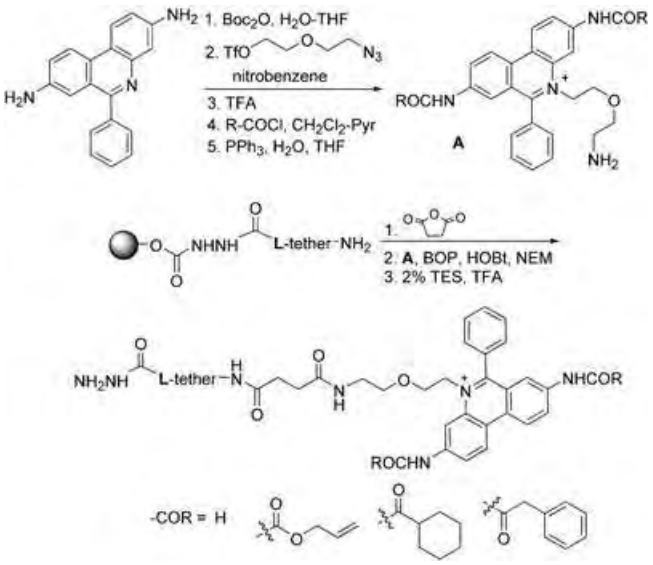

Scheme 5. Synthesis of probes containing phenanthridinium derivatives. Boc: *tert*-butoxycarbonyl, Tf: trifluoromethanesulfonyl.

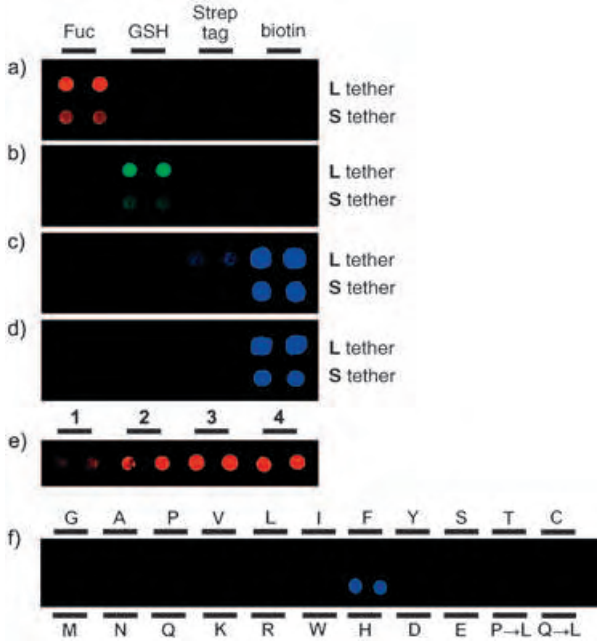

Figure 2. Fluorescence images of chemical microarrays containing fucose, GSH, the strep tag, and biotin, when probed with a) Cy5-AA, b) GST followed by FITC-labeled anti-GST antibody, c) Cy3-streptavidin, and d) Cy3-avidin. Fluorescence images of chemical microarrays containing e) phenanthridinium derivatives probed with Cy5-AChE (**1** COR = H, **2** COR = cyclohexylcarbonyl, **3** COR = allyloxycarbonyl, **4** COR = phenylacetyl) and f) strep tag and its analogues probed with Cy3-strepavidin (single letter amino acid codes given for the residue that replaced histidine in the strep tag, P→L: replacement of proline with leucine in the strep tag, Q→L: replacement of glutamine with leucine in the strep tag). Spot size: ≈100 μm, distance between centers of spots: ≈250 μm.

tag were selectively recognized by AA, GST, and streptavidin, respectively. The strep tag is known to bind to streptavidin rather than avidin and, as expected, microspots containing

this substance were recognized only by streptavidin.[10] Microspots containing biotin display much stronger fluorescence than strep-tag microspots because the binding affinity of streptavidin to biotin is much greater than that of streptavidin to the strep tag.[11] Interestingly, microspots produced by reaction of **L**-tethered substrates bound to the corresponding proteins more tightly than those with **S**-tethered substrates. The fluorescence intensities of microspots containing **L**-tethered compounds are more than twice as strong as those of microspots containing **S**-tethered ones.

Small-molecule microarrays with four phenanthridinium derivatives were also fabricated by following the method described above. Fluorescence analysis of slides treated with Cy5-AChE showed that substituted phenanthridinium derivatives bound to the proteins more strongly than their unsubstituted derivatives (Figure 2e).[12] Finally, we constructed peptide microarrays with the **L**-tethered strep tag and 21 of its analogues. The peptide microarrays, after probing with Cy3-streptavidin, showed that streptavidin only bound to the strep tag (Figure 2f). This is consistent with previous results showing that the amino acid sequence His-Pro-Gln is critical for streptavidin binding.[13]

In conclusion, a new, efficient, and simple method for fabricating chemical microarrays has been developed. The technique employs selective immobilization reactions of hydrazide-linked small molecules with epoxides on the solid surfaces. The length of the tether between the hydrazide groups and the active ligands governs protein binding; slides containing longer tethers exhibit stronger binding of proteins than those with shorter tethers. The immobilization technique is suitable for covalently attaching diverse compounds, including small molecules, carbohydrates, and peptides, to glass surfaces. The utility of this method is shown by its application to the fabrication of peptide and small-molecule microarrays, which have been used to screen for selective protein binding. We believe that the chemoselective ligation reaction developed in this effort will find many applications in the preparation of bioconjugates, such as neoglycopeptides, peptide–nucleic acid conjugates, and tagged peptides.

Received: November 25, 2004
Published online: April 12, 2005

Keywords: chemoselectivity · high-throughput screening · immobilization · microarrays · protein binding

[1] For recent reviews, see: a) R. S. Lokey, *Curr. Opin. Chem. Biol.* **2003**, *7*, 91; b) C. A. MacRae, R. T. Peterson, *Chem. Biol.* **2003**, *10*, 901; c) A. C. Bishop, O. Buzko, K. M. Shokat, *Trends Cell Biol.* **2001**, *11*, 167; d) B. R. Stockwell, *Trends Biotechnol.* **2000**, *18*, 449.

[2] For recent reviews of DNA microarrays, see: a) S. V. Chittur, *Comb. Chem. High Throughput Screening* **2004**, *7*, 531; b) D. J. Villeneuve, A. M. Parissenti, *Curr. Top. Med. Chem.* **2004**, *4*, 1329; c) W. H. Koch, *Nat. Rev. Drug Discovery* **2004**, *3*, 749.

[3] For recent reviews of protein microarrays, see: a) F. X. Zhou, J. Bonin, P. F. Predki, *Comb. Chem. High Throughput Screening* **2004**, *7*, 539; b) H. Zhu, M. Snyder, *Curr. Opin. Chem. Biol.* **2003**, *7*, 55; c) D. S. Wilson, S. Nock, *Angew. Chem.* **2003**, *115*, 510; *Angew. Chem. Int. Ed.* **2003**, *42*, 494; d) T. Kodadek, *Chem. Biol.* **2001**, *8*, 105; e) S. R. Weinberger, E. A. Dalmasso, E. T. Fung, *Curr. Opin. Chem. Biol.* **2001**, *5*, 86.

[4] For reviews of carbohydrate microarrays, see: a) I. Shin, J. W. Cho, D. W. Boo, *Comb. Chem. High Throughput Screening* **2004**, *7*, 565; b) I. Shin, S. Park, M.-R. Lee, *Chem. Eur. J.* **2005**, in press; c) T. Feizi, W. Chai, *Nat. Rev. Mol. Cell Biol.* **2004**, *5*, 582; d) T. Feizi, F. Fazio, W. Chai, C.-H. Wong, *Curr. Opin. Struct. Biol.* **2003**, *13*, 637.

[5] a) D. P. Walsh, Y. T. Chang, *Comb. Chem. High Throughput Screening* **2004**, *7*, 565; b) A. N. Koehler, A. F. Shamji, S. L. Schreiber, *J. Am. Chem. Soc.* **2003**, *125*, 8420; c) M. Köhn, R. Wacker, C. Peters, H. Schröder, L. Soulère, R. Breinbauer, C. M. Niemeyer, H. Waldmann, *Angew. Chem.* **2003**, *115*, 6010; *Angew. Chem. Int. Ed.* **2003**, *42*, 5830, and references therein; d) F. G. Kuruvilla, A. F. Shamji, S. M. Sternson, P. J. Hergenrother, S. L. Schreiber, *Nature* **2002**, *416*, 653; e) K. S. Lam, M. Renil, *Curr. Opin. Chem. Biol.* **2002**, *6*, 353.

[6] a) F. Stieber, U. Grether, H. Waldmann, *Chem. Eur. J.* **2003**, *9*, 3270; b) F. Stieber, R. Mazitschek, N. Soric, A. Giannis, H. Waldmann, *Angew. Chem.* **2002**, *114*, 4951; *Angew. Chem. Int. Ed.* **2002**, *41*, 4757; c) C. Rosenbaum, H. Waldmann, *Tetrahedron Lett.* **2001**, *42*, 5677.

[7] M. L. Lesaicherre, R. Y. Lue, G. Y. Chen, Q. Zhu, S. Q. Yao, *J. Am. Chem. Soc.* **2002**, *124*, 8768.

[8] See the Supporting Information for experimental details.

[9] I. E. Liener, N. Sharon, I. J. Goldstein, *The Lectins: Properties, Functions, and Applications in Biology and Medicine*, Academic Press, New York, **1986**.

[10] T. G. M. Schmidt, A. Skerra, *Protein Eng.* **1993**, *6*, 109.

[11] T. G. M. Schmidt, J. Koepke, R. Frank, A. Skerra, *J. Mol. Biol.* **1996**, *255*, 753.

[12] a) W. G. Lewis, L. G. Green, F. Grynszpan, Z. Radić, P. R. Carlier, P. Taylor, M. G. Finn, K. B. Sharpless, *Angew. Chem.* **2002**, *114*, 1095; *Angew. Chem. Int. Ed.* **2002**, *41*, 1053; b) Z. Radić, P. Taylor, *J. Biol. Chem.* **2001**, *276*, 4622.

[13] a) J. J. Devlin, L. C. Panganiban, P. E. Devlin, *Science* **1990**, *249*, 404; b) K. S. Lam, S. E. Salmon, E. M. Hersh, V. J. Hruby, W. M. Kazmierski, R. J. Knapp, *Nature* **1991**, *354*, 82.

Anticancer Agents

Structure and Unique Interactions with DNA of a Cationic *Trans*-Platinum Complex with the Nonplanar Bicyclic Piperidinopiperidine Ligand**

*Yousef Najajreh, Dmitri Prilutski, Yael Ardeli-Tzaraf, Jose Manuel Perez, Elena Khazanov, Yechezkel Barenholz, Jana Kasparkova, Viktor Brabec, and Dan Gibson**

The ability of square-planar platinum(II) complexes to covalently bind to cellular DNA and distort its structure has had an overwhelming impact on the lives of many cancer patients worldwide. The anticancer drug cisplatin (Figure 1a), exerts its cytotoxic effect by binding covalently to two adjacent guanine residues on the same DNA strand (1,2-GpG cross-link), and the ensuing distortion of the DNA, triggers cellular processes that lead to the death of the cancer cell.[1,2] The two crucial properties of cisplatin that make it an efficient anticancer agent are its inertness that enables it to survive the onslaught of the plethora of platinophiles in the extra- and intracellular fluids on the way to the DNA, and its ability to distort the DNA.[3,4] Cisplatin is an extremely effective anticancer agent, whose clinical success is marred by the ability of tumors to acquire resistance to the drug. One approach to try and overcome the acquired resistance to cisplatin was to prepare platinum(II) complexes having *trans* geometry that are incapable of binding two adjacent guanines on the same strand, so they end up forming other lesions with the DNA and distort it differently than cisplatin. Transplatin itself (Figure 1b) is not cytotoxic, yet, several classes of *trans*-platinum complexes with planar heterocyclic amine ligands, bulky aliphatic amine ligands or iminoether ligands, or nonplanar heterocyclic amine ligands have displayed a variety of DNA binding properties as well as impressive cytotoxic properties.[5–11]

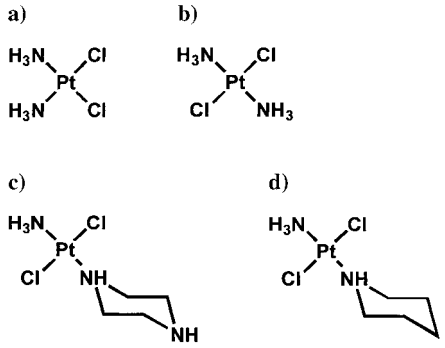

Figure 1. The structures of platinum complexes. a) cisplatin; b) transplatin; c) *trans*-$[PtCl_2(NH_3)(pz)]^+$; d) *trans*-$[PtCl_2(NH_3)(pip)]$.

We have recently reported on the preparation, cytotoxicity and the DNA-binding properties of *trans*-platinum complexes with piperazine (pz) and piperidine (pip) ligands (Figure 1c and d), which circumvent cisplatin resistance in human ovarian cancer cell lines.[12,13]

Piperazine was selected as a ligand because we wanted a soluble, cationic, *trans*-platinum complex that will not only covalently modify the DNA, but in addition, the ligand itself will interact with the DNA at a second site which is removed from the Pt^{II} modification site.

As a natural extension of this rationale, we have recently prepared the complex *trans*-$[PtCl_2(NH_3)(pip\text{-}pip)]\cdot HCl$ (**1**),[14] and now we report its X-ray crystal structure and some of its DNA-binding and pharmacological properties. X-ray quality crystals were obtained by slow evaporation from aqueous solution (Figure 2a).[15] The conformation of the two piperidine rings together with the molecular dimensions are depicted in Figure 2b. Structurally, we can divide the molecule into three parts: 1) the platinum(II) coordination sphere, 2) the first piperidine ring, and 3) the second piperidine ring. The platinum forms the usual square-planar coordination geometry with the Pt–Cl bond lengths around 2.30 Å and the Pt–N bonds around 2.06 Å.

In the solid state structure both piperidine rings adopt the chair conformation (Figure 2b). While the platinum can in

[*] Dr. Y. Najajreh,[+] Y. Ardeli-Tzaraf, Dr. D. Gibson[#]
Department of Medicinal Chemistry and Natural Products
School of Pharmacy
The Hebrew University of Jerusalem
Jerusalem 91120 (Israel)
Fax: (+972) 2-675-7076
E-mail: gibson@md.huji.ac.il
D. Prilutski
Interdepartmental Equipment Unit
The Hebrew University-Hadassah Medical School
Jerusalem 91120 (Israel)
Dr. J. M. Perez
Departamento de Química Inorgánica
Facultad de Ciencias, Universidad Autónoma de Madrid
28049-Madrid (Spain)
E. Khazanov, Prof. Y. Barenholz
Laboratory of Membrane and Liposome Research
Department of Biochemistry
The Hebrew University-Hadassah Medical School
Jerusalem 91120 (Israel)
Dr. J. Kasparkova, Prof. V. Brabec
Institute of Biophysics
Academy of Sciences of the Czech Republic
61265 Brno (Czech Republic)
[+] Current address:
Department of Medicinal Chemistry and Natural Products
Faculty of Pharmacy/Al-Quds University, Jerusalem
P.O.Box 20002 (Palestine)
[#] Affiliated with the David R. Bloom, Center for Pharmacy at The Hebrew University of Jerusalem, Israel.

[**] D.G. acknowledges the partial support of the Israel Science Foundation and of the Alex Grass Center For Drug Design and Synthesis. This work was partially supported by Spanish CICYT (grant SAF2004-03111). The research of J.K. and V.B. was supported by the Grant Agency of the Academy of Sciences of the Czech Republic (Grants 5004101, B5004301) Support and sponsorship by European COSTD20/0003/00 action is gratefully acknowledged. Y.B. thanks the Belfer Foundation and the Barenholz Fund.

Supporting information for this article (NMR spectra of **1**) is available on the WWW under http://www.angewandte.org or from the author.

 DOI: 10.1002/anie.200462389

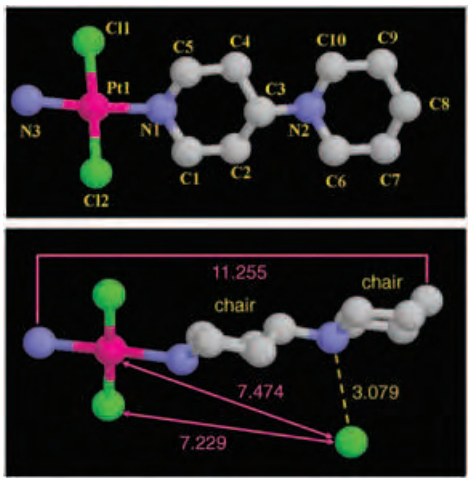

Figure 2. a) The X-ray crystal structure of **1**. b) A side view of the same structure showing that both piperidine rings are in the chair conformation and that N2 is hydrogen bonded to the chloride counterion (yellow dotted line). Depicted in pink are the distances between both ends of the complex (top) and between the platinum region and the hydrogen-bond acceptor (bottom).

principle, bind to either the equatorial or axial lone pair of N1, in this case the platinum is bound to the equatorial position, probably to minimize steric repulsions. N2 is protonated, conferring one positive charge to the complex, making it water soluble, and causing it to crystallize as a salt, with a Cl^- counterion (Figure 2b) that is hydrogen bonded to N2 (N···Cl distance of 3.079 Å). The positive charge is 6.44 Å from the metal center allowing the ligand to interact with hydrogen-bond acceptors at a distance of approximately 7 Å.

We performed an NMR spectroscopic analysis of this complex, and assigned the ^1H and ^{13}C resonance signals (see Supporting Information). The most interesting feature was the NOESY that appears in Figure 3. In phase sensitive NOESY, cross peaks that have the same phase as the diagonal peaks are not NOE[14] peaks but exchange peaks. In the spectrum of **1**, the phases of all the cross peaks of the first piperidine ring (protons 1–3) are opposite to those of the

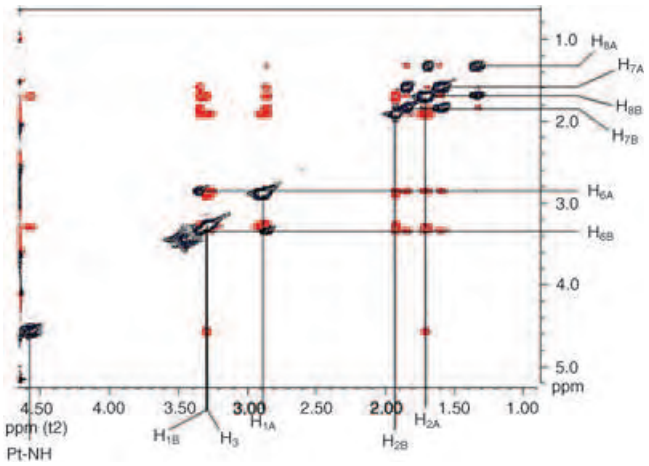

Figure 3. The NOESY spectrum of **1** showing negative contours in black and positive contours in red. For details see text.

diagonal peaks, while all the cross peaks originating from the second piperidine ring (protons 6–8) have the same phase as the diagonal peaks. This result indicates that the cross peaks generated by the protons of the second piperidine ring are exchange peaks and that the second ring is fluxional and its conformation is rapidly changing on the NMR time scale.

The $t_{1/2}$ of the covalent binding of cisplatin and transplatin to DNA is 120 min, and the rate-determining step is the aquation of the first chloride ligand to form the cationic $[PtCl(H_2O)(NH_3)_2]^+$.[16] The classic kinetic studies with square-planar Pt^{II} complexes teach that substitution reactions proceed by an associative mechanism involving a trigonal-bipyramidal intermediate, and that a dramatic decrease of substitution rate occurs for complexes with sterically hindered ligands.[17] Thus, it seems reasonable to expect that the steric hindrance of the bulky bicyclic pip-pip ligand will cause compound **1** to bind to DNA significantly slower than cisplatin or transplatin. The $t_{1/2}$ of the covalent binding of **1** to calf thymus DNA (CT-DNA) is 11 min,[18] indicating extremely rapid binding to DNA.

We studied the rate of conversion of *trans*-$[PtCl_2(NH_3)$-(pip-pip)$]^+$ into *trans*-$[PtCl(H_2O)(NH_3)$(pip-pip)$]^{2+}$ by UV spectroscopy and by ^{195}Pt NMR spectroscopy. The UV spectra of 0.1 mM of **1** (Figure 4) and of *trans*-$[PtCl(H_2O)(NH_3)$(pip-pip)$]^{2+}$ (Figure 4) were recorded and the value of A_{275}/A_{250} was determined (2.3 for **1** and 1.0 for *trans*-$[PtCl(H_2O)$-(NH_3)(pip-pip)$]^{2+}$). Over two hours at 37 °C, no change in the

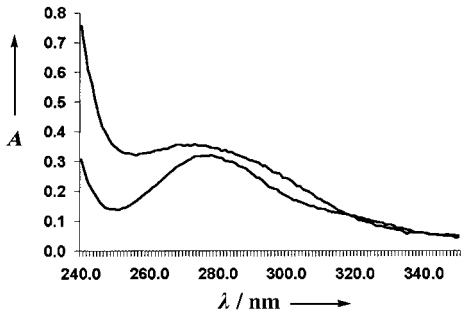

Figure 4. The UV spectra of **1** (lower trace) and *trans*-$[PtCl(H_2O)(NH_3)$-(pip-pip)$]^{2+}$ (upper trace).

UV spectrum of **1** could be detected indicating that no significant aquation occurred during this time. As an additional check, 5 mM aqueous solution of **1** was warmed to 37 °C in a 10-mm NMR tube and a spectrum was acquired every 5 min for 2 h. Over the two hour period the spectrum remained unchanged having a single resonance signal at $\delta = -2177$ ppm and no traces of *trans*-$[PtCl(H_2O)(NH_3)$(pip-pip)$]^{2+}$ at $\delta = -1895$ ppm. Thus, we think that the binding of **1** to the DNA occurs by an initial, rapid, electrostatically driven, "pre-association" of the complex with the double-stranded DNA (dsDNA) that positions the platinum center in the correct orientation for direct substitution of the Cl by the N7 of the purines. The $t_{1/2}$ values for the neutral *trans*-$[PtCl_2(NH_3)$(pip)$]$ (**2**) (113 min), and the cationic *trans*-$[PtCl_2(NH_3)$(pz)$]^+$ (**3**) (20 min), and *trans*-$[PtCl_2$(pz)(pip)$]^+$ (**4**) (22 min), coupled with the fact that no hydrolysis was observed in a 2 hour period for compounds **3** and **4**, support

the claim that electrostatics are the most important factor in determining the platination rate.

The *trans*-$[PtCl_2(pip)(pz)]^+$ ion can be considered the symmetric analogue of the *trans*-$[PtCl_2(NH_3)(pip\text{-}pip)]^+$ ion in the sense that they both have two nonplanar six membered rings and both have a cationic charge that is removed from the metal center. The nonsymmetric **1** binds DNA twice as fast as its symmetric analogue, *trans*-$[PtCl_2(pz)(pip)]^+$, and twice as fast as the less bulky cationic complex *trans*-$[PtCl_2(NH_3)(pz)]^+$. This situation may be due to either the location of the charge relative to the platinum center or to the flexibility of the second pip ring of **1**. Also, the binding of **1** stabilizes CT-DNA more than the symmetric analogue (raising the Tm by 14 °C for **1** and 7.9 °C for *trans*-$[PtCl_2(pz)(pip)]^+$ for $r_b = 0.05$; Tm is the melting temperature at which 50 % of the DNA double helix is denatured, r_b is the number of molecules of the platinum compound bound per nucleotide). Another feature of the unique interaction of **1** with the DNA is the 30° unwinding angle of dsDNA compared with 13° for cisplatin and 17° for the symmetric compound. The additional unwinding may be associated with the interaction of the pip-pip ligand with the duplex upon covalent binding of platinum.

The cytotoxicity of **1** was measured against three pairs of cisplatin sensitive and resistant cancer cell lines (A2780/A2780cisR, 41M/41McisR, and CH1/CH1cisR) that encompass all known resistance mechanisms to cisplatin.[19–22] Compound **1** is twice as potent as cisplatin in all three cisplatin-resistant cell lines (IC_{50} (compound concentration which induces 50 % cell death) values against A2780cisR, CH1cisR, and 41McisR are 24, 15, and 48 μM, respectively, for **1**, versus 38, 23, 107 μM for cisplatin) demonstrating the ability of this complex to circumvent all of the three known resistance mechanism to cisplatin. It is of note that the nonsymmetric 1 is 2–5 times more potent against the resistant cell lines than the symmetric analogue.

In summary, we described a new type of platinum complex that has a *trans* configuration, is asymmetric, has a singly charged nonplanar semifluxional bicyclic ligand, that binds extremely rapidly to DNA by direct substitution (not requiring initial aquation as does cisplatin), distorts DNA in a unique manner and circumvents all of the known cisplatin-resistance mechanism in human ovarian cancer cell lines.

Experimental Section

The compound **1** was prepared in a similar way to that described in ref. [11].

All NMR spectroscopy experiments were performed on an INOVA 500 MHz spectrometer using standard pulse sequences. The data were processed with VNMR or MestRe-C using cosine-squared apodization in both dimensions for the phase-sensitive experiment and unshifted sinbell for in both dimensions for the AV experiments.

The DNA binding studies have been performed as described.[12,13]

The cytotoxicities studies have been performed as previously described.[11]

Received: October 21, 2004
Revised: December 26, 2004
Published online: April 8, 2005

Keywords: antitumor agents · bioinorganic chemistry · DNA binding · piperidinopiperidine · platinum

[1] G. Giaccone, *Drugs* **2000**, *59 Suppl 4*, 9–17; discussion 37–18.
[2] Z. H. Siddik, *Oncogene* **2003**, *22*, 7265–7279.
[3] J. Reedijk, *Chem. Rev.* **1999**, *99*, 2499–2510.
[4] S. M. Cohen, S. J. Lippard, *Prog. Nucleic Acid Res. Mol. Biol.* **2001**, *67*, 93–130.
[5] J. M. Perez, M. A. Fuertes, C. Alonso, C. Navarro-Ranninger, *Crit. Rev. Oncol. Hematol.* **2000**, *35*, 109–120.
[6] G. Natile, M. Coluccia, *Coord. Chem. Rev.* **2001**, *216*, 383–410.
[7] N. Farrell, T. T. Ha, J. P. Souchard, F. L. Wimmer, S. Cros, N. P. Johnson, *J. Med. Chem.* **1989**, *32*, 2240–2241.
[8] E. I. Montero, S. Diaz, A. M. Gonzalez-Vadillo, J. M. Perez, C. Alonso, C. Navarro-Ranninger, *J. Med. Chem.* **1999**, *42*, 4264–4268.
[9] M. Coluccia, A. Boccarelli, M. A. Mariggio, N. Cardellicchio, P. Caputo, F. P. Intini, G. Giovanni, *Chem.-Biol. Interact.* **1995**, *98*, 251–266.
[10] E. Khazanov, Y. Barenholz, D. Gibson, Y. Najajreh, *J. Med. Chem.* **2002**, *45*, 5196–5204.
[11] Y. Najajreh, J. M. Perez, C. Navarro-Ranninger, D. Gibson, *J. Med. Chem.* **2002**, *45*, 5189–5195.
[12] J. Kasparkova, O. Novakova, V. Marini, Y. Najajreh, D. Gibson, J. M. Perez, V. Brabec, *J. Biol. Chem.* **2003**, *278*, 47516–47525.
[13] J. Kasparkova, V. Marini, Y. Najajreh, D. Gibson, V. Brabec, *Biochemistry* **2003**, *42*, 6321–6332.
[14] Abbreviations: piperidinopiperidine (pip-pip), nuclear Overhauser effect (NOE).
[15] TEXSAN: Single Crystal Structure Analysis Software, Version 5.0, Molecular Structure Corp. The Woodlands, TX, **1989**. All crystallographic computing was done on a VAX 9000 computer at The Hebrew University of Jerusalem. CCDC-266822 contains the supplementary crystallographic data for this paper. These data can be obtained free of charge from the Cambridge Crystallographic Data Centre via www.ccdc.cam.ac.uk/data_request/cif.
[16] D. P. Bancroft, C. A. Lepre, S. J. Lippard, *J. Am. Chem. Soc.* **1990**, *112*, 6860–6871.
[17] C. H. Langford, H. B. Gray, *Ligand Substitution Process*, Benjamin, New York, **1965**.
[18] Y. Ardeli-Tzaraf, J. Kasparkova, Y. Najajreh, L. Balter, D. Prilutski, J. M. Perez, E. Khazanov, Y. Barenholz, D. Gibson, unpublished results..
[19] L. R. Kelland, G. Abel, M. J. McKeage, M. Jones, P. M. Goddard, M. Valenti, B. A. Murrer, K. R. Harrap, *Cancer Res.* **1993**, *53*, 2581–2586.
[20] S. Y. Loh, P. Mistry, L. R. Kelland, G. Abel, K. R. Harrap, *Br. J. Cancer* **1992**, *66*, 1109–1115.
[21] P. M. Goddard, R. M. Orr, M. R. Valenti, C. F. Barnard, B. A. Murrer, L. R. Kelland, K. R. Harrap, *Anticancer Res.* **1996**, *16*, 33–38.
[22] B. C. Behrens, T. C. Hamilton, H. Masuda, K. R. Grotzinger, J. Whang-Peng, K. G. Louie, T. Knutsen, W. M. McKoy, R. C. Young, R. F. Ozols, *Cancer Res.* **1987**, *47*, 414.

Nanoporous Materials

Nanoporous Polyelectrolyte Spheres Prepared by Sequentially Coating Sacrificial Mesoporous Silica Spheres**

*Yajun Wang, Aimin Yu, and Frank Caruso**

Mesoporous silicas (MS), porous materials with extremely high surface areas and pore sizes in the range of 2 to 50 nm, have attracted significant interest since being reported in the early 1990s.[1,2] Owing to their unique pore structures, these materials have been utilized as hosts for the template synthesis of various materials, including metal,[3] metal oxide,[4] carbon,[5] and polymer[6] replicas. In a typical synthesis strategy, the constituent materials (e.g., metal precursors, sucrose, organic monomers) are infiltrated into the mesopores. Reduction, carbonization, or cross-linking reactions are then performed to obtain an interconnected network, and the silica template is removed by dissolution. Despite these studies, there has been no report on the sequential infiltration and coating of MS materials with preformed polymers for the fabrication of controlled porous polymer structures. Porous polymer materials, especially in particulate form, are of interest in a diverse range of applications, including drug delivery, molecular separation technology, and as hosts for chemical synthesis.[7]

A facile approach for coating MS is to exploit electrostatic interactions between the MS support and charged polymers (polyelectrolytes, PEs) through solution self-assembly. Sequentially depositing PEs of opposite charge by the layer-by-layer (LbL) technique would potentially permit the formation of PE multilayers inside the MS pores. Since its introduction in 1991,[8,9] the LbL method has been widely used to deposit multilayers of various materials (such as, polymers, enzymes, nanoparticles, dyes) on both planar[10] and colloidal[11] supports. More recent studies have focused on the use of porous substrates, such as macroporous titania,[12] polycarbonate membranes,[13] alumina membranes,[14] and porous calcium carbonate microparticles.[15] However, there has been no report of the LbL assembly of PEs in MS structures and, more specifically, of the LbL MS-templated formation of porous materials with interconnected polymer networks.

[*] Dr. Y. Wang, Dr. A. Yu, Prof. F. Caruso
Centre for Nanoscience and Nanotechnology
Department of Chemical and Biomolecular Engineering
The University of Melbourne
Victoria, 3010 (Australia)
Fax: (+61) 3-8344-4153
E-mail: fcaruso@unimelb.edu.au

[**] This work was supported by the Australian Research Council (Discovery Project and Federation Fellowship Schemes) and the Victorian State Government, Department of Innovation, Industry and Regional Development, Science, Technology and Innovation initiative. The Particulate Fluids Processing Centre is acknowledged for support. J. Quinn, Q. Li and B. Radt are thanked for assistance with SEM, FTIR, and CLSM experiments, respectively.

Herein, we report the LbL coating of MS spheres with PEs and the subsequent removal of the silica templates to obtain micrometer-sized nanoporous PE spheres (NPS). The procedure for the preparation of the NPS involves two main steps, as depicted in Scheme 1. The first entails the LbL deposition of oppositely charged PEs (poly(acrylic acid) (PAA) and poly(allylamine hydrochloride) (PAH)) within the MS spheres, with subsequent cross-linking of each PE layer by heating. In the second step, the MS template is removed by exposure to hydrofluoric acid (HF). A main advantage of this approach is that it offers a general and versatile route to the preparation of nanoporous PE materials of diverse and tailored composition, as it is based on sequential self-assembly. Hence, it is applicable to a broad range of PEs. Further, the LbL method is largely independent of substrate morphology, making it amenable to MS of different shapes and sizes to generate porous PE networks. Herein we focus on the use of spherical MS particles in the micrometer size range, as these systems represent an interesting class of materials as supports for immobilization and encapsulation of various species (e.g., biomacromolecules). In this study, we also demonstrate the high capacity of the prepared NPS for enzyme entrapment.

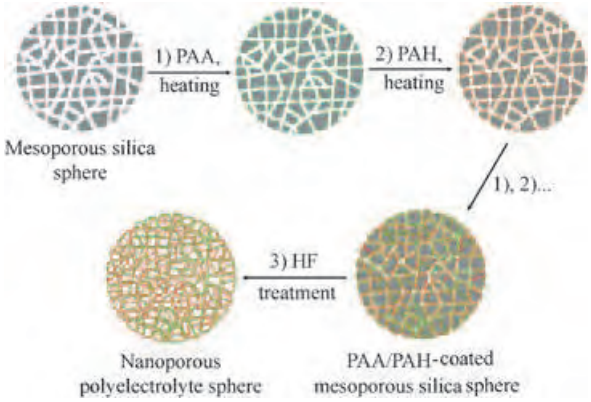

Scheme 1. Schematic illustration showing the preparation of nanoporous polyelectrolyte spheres (NPS). 3-aminopropyltriethoxysilane (APTS)-modified bimodal MS (BMS) spheres were layer-by-layer coated with PEs of opposite charge (PAA and PAH; multiple repetition of steps 1 and 2), with the samples heated (160 °C for 2 h) after deposition of each PE to partially cross-link the layers. The BMS template was then dissolved by exposure to HF (step 3), yielding intact NPS.

The MS spheres, prepared according to an established method,[16] possess a bimodal pore structure; that is, smaller pores in the 2–3 nm range and larger pores between 10–40 nm.[16] The particles, herein denoted as BMS (bimodal MS) spheres, have a diameter of 2–4 μm, a surface area of 630 $m^2 g^{-1}$ and a pore volume of 1.72 $mL g^{-1}$. We chose to employ BMS spheres for several reasons: 1) BMS possesses a high pore volume (1.2 $mL g^{-1}$) for the 10–40 nm pores, making it suitable for infiltration and adsorption of PEs; 2) the three-dimensional disordered pore structure and thin pore walls (ca. 3 nm) facilitates the formation of interconnected nanoporous PE networks after removal of the BMS templates; and 3) the spherical morphology aids in monitoring shape and size

  DOI: 10.1002/anie.200462135

variations as a result of LbL PE coating. The BMS surface was first functionalized by grafting a layer of 3-aminopropyltriethoxysilane (APTS) onto the BMS skeleton.[17] This process introduces amine (NH_2-) surface functional groups to the BMS, which promotes specific adsorption of the subsequently deposited PAA through interaction of the $-NH_2$ and $-COOH$ groups. The APTS-grafted BMS (APTS–BMS) spheres have a surface area of 465 $m^2 g^{-1}$ and a pore volume of 1.32 $mL g^{-1}$. The large mesopores (10–40 nm) have a volume of approximately 1.0 $mL g^{-1}$.

Polyelectrolyte solutions were prepared by dissolving PAA or PAH in deionized water containing sodium chloride (NaCl), without adjusting the pH value. PAA ($M_w = 2000$) was deposited onto the APTS–BMS spheres from an aqueous 5 $mg mL^{-1}$ PAA solution of pH 2.9 containing 0.7 M NaCl. Adsorption was conducted at 20 °C for 15 min with sonication (to aid the transport of the PEs into the mesopores[13]), and subsequent shaking for 6 h. Excess PAA was removed by four cycles of centrifugation (500 *g* for 3 min) and washing with 0.1 M NaCl. PAH ($M_w = 15000$) was deposited from an aqueous 5 $mg mL^{-1}$ PAH solution of pH 4.3 with 0.7 M NaCl. To facilitate infiltration into the pores of the APTS–BMS spheres, low molecular weight PEs were used,[13] and NaCl was added to the adsorption solution to promote coiling of the PE molecules.[18] Cross-linking of each PE layer was performed by heating the dried sample at 160 °C for 2 h.[19,20] Under this treatment, amide bonds are formed by the $-COOH$ groups (in PAA) and the $-NH_2$ moieties (in PAH or on the APTS–BMS template), enhancing the structural stability of the layers.[19,20] It was found that without the cross-linking process, the PE layers partially desorbed from the mesopores during subsequent PE adsorption steps, forming aggregates on the particle surface and in solution.[21]

Evidence for the successive deposition of PAA and PAH within the pores of the APTS–BMS spheres was obtained by Fourier transform infrared (FTIR) experiments. FTIR spectra of the APTS–BMS particles as a function of PAA and PAH deposition steps are shown in Figure 1 a. For the APTS–BMS spheres, the absorption band at 1635 cm^{-1} (A) is assigned to the Si–OH vibrations[22] and the N–H bending (scissoring) vibrations of APTS. The peaks at 1720 (B), 1570 (C), and 1400 (D) cm^{-1} are attributed to the $-COOH$ carbonyl and $-COO^-$ asymmetric and symmetric stretches, respectively, of PAA.[19,23] The large fraction of non-ionized acid groups in the PAA chains is caused by the low assembly pH value in our experiments.[24] The intensities of the peaks at 1635 cm^{-1} (assigned to the N–H bending (scissoring) vibration of PAH for layer number = 2) and at 1720 cm^{-1} increase with PAH and PAA layer number, respectively, confirming the sequential deposition of PAA/PAH multilayers. The following observations can be made from the spectra: a) The presence of $-COOH$ (from PAA) after heating at 160 °C indicates that only partial cross-linking of the layers occurs, which is in agreement with earlier work.[19] Only about 10–15 % reduction in intensity of this peak was observed after heating the films. b) The amide bonds formed as a result of cross-linking (peak at $\nu \approx 1670$ cm^{-1}) are not discernible, largely because of the relatively low degree of cross-linking and masking from the peak at 1635 cm^{-1} (arising from the APTS-BMS substrate and PAH).[19,22] c) The total amount of PAA deposited per APTS–BMS particle increases with PAA layer number, although the amount adsorbed per layer decreases with increasing PAA layer number (Figure 1 b).[25] This trend is attributed to increased blockage of the larger mesopores in the APTS–BMS templates with increasing PE layer number.

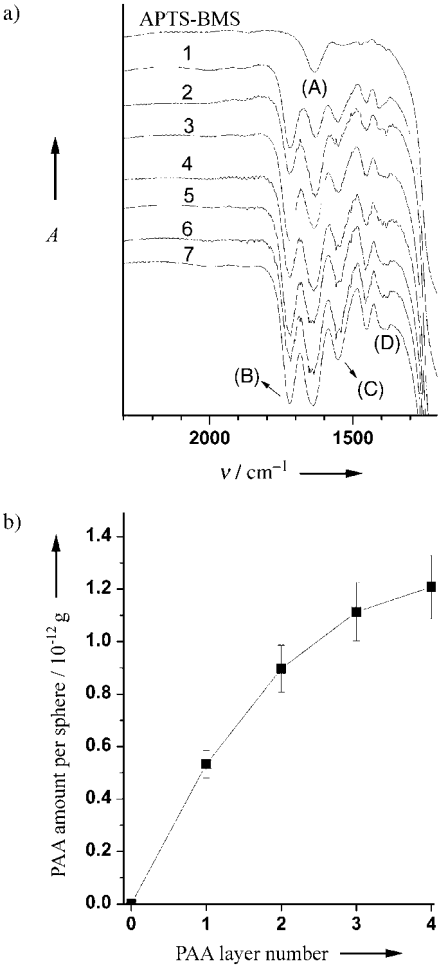

Figure 1. a) FTIR spectra of the APTS–BMS spheres before and after the alternate deposition of PAA and PAH layers. The deposited layers were partially cross-linked by heating at 160 °C for 2 h prior to recording each spectrum. The numbers correspond to the number of PE layers deposited, commencing with PAA. APTS–BMS spheres were used as the internal reference for measuring each spectrum. The spectra are shifted vertically for clarity. b) The amount of PAA deposited on the APTS–BMS particle as a function of layer number was determined from the ratio of the peak at 1720 cm^{-1} (PAA) with the peak at 800 cm^{-1} (APTS–BMS).[25] The relative strength of the PAA signal compared to the APTS–BMS signal was determined to be 2.4 by measuring the IR spectrum of a 1:1 (weight) mixture of PAA and APTS–BMS powders. The APTS–BMS has an average weight of 4.3×10^{-12} g, assuming the particle has a size of 2.5 μm and a density of 0.53 $g mL^{-1}$.

To examine the influence of sphere porosity, we used MS spheres with only 2–3 nm pores and nonporous silica spheres for comparison. No distinguishable peaks arising from PAA and PAH in the FTIR spectra of either of the PAA/PAH-coated silica spheres were observed, even after deposition of seven layers (i.e., 3.5 PAA/PAH bilayers). This result indicates that PE deposition predominantly occurs in the

larger mesopores of the APTS–BMS particles, and that the contribution to the FTIR intensities from PE adsorption on the outer surface of the particles is negligible.

Nitrogen adsorption measurements were also conducted to follow the changes in the surface area of the APTS–BMS spheres after PE deposition. The first layer of adsorbed PAA dramatically decreased the surface area from 465 $m^2 g^{-1}$ (APTS–BMS template) to 284 $m^2 g^{-1}$. This decrease is caused by the high PAA loading and blocking of some of the mesopores. Deposition of subsequent PAH and PAA layers resulted in a surface area decrease of approximately 20 $m^2 g^{-1}$per PE adsorption step. After deposition of seven layers, the surface area of the coated spheres was approximately 160 $m^2 g^{-1}$. These data further confirm the stepwise deposition of PEs within the APTS–BMS spheres.

NPS were prepared by exposing the PAA/PAH-coated APTS–BMS spheres to an aqueous 10 wt% HF solution for 12 h. Silica particles readily decompose in HF to form $[SiF_6]^{2-}$ ions, which can readily diffuse through PE multilayers.[26] Effective removal of the BMS template was demonstrated by energy-dispersive X-ray (EDX) analysis and FTIR experiments. EDX data showed that only a small amount of silicon (0.8%) was detected after removal of the BMS template (not shown). The small residual amount of silicon probably arises from silicon-alkyl groups ($\equiv$Si-$(CH_2)_3$-NH_2), which are stable in the presence of HF.[27] These groups are introduced into the sample through the APTS modification of the BMS particles.

Spherical NPS were obtained for samples that comprise two or more PAA and PAH layers. Figure 2 shows TEM and

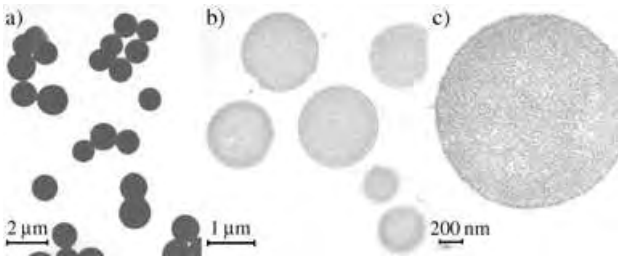

Figure 2. TEM images of the NPS that comprises a) $(PAA/PAH)_2/PAA$ (5-NPS) and ultramicrotomed thin sections of the same spheres at b) low and c) higher magnification. The 5-NPS were partially cross-linked by heating at 160°C for 2 h after deposition of each PE layer. Images (b) and (c) show the porosity of the PE spheres. The large difference in the diameters seen is a result of the ultramicrotoming process.

Figure 3 SEM images of 5-layer $[(PAA/PAH)_2/PAA]$ NPS (5-NPS). These NPS retain the original shape of the BMS templates, and do not show signs of collapse, as is typically observed for PE capsules.[9] The diameters of the resulting NPS were found to depend on the number of PE layers deposited on the template APTS–BMS particles. APTS–BMS spheres coated with more PE layers underwent less shrinkage. For example, the PAA/PAH NPS (2-NPS) had diameters ranging from 0.8–1.3 μm, representing shrinkage of around 55–60%, compared with the original APTS–BMS templates, in which over 90% of APTS–BMS particles are within 2–3 μm. The 7-NPS were between 1.4–2.1 μm, 25–30% smaller than the template particles. No aggregation of the NPS was observed from TEM (Figure 2a). The inner structure of the NPS was examined by TEM of ultramicrotomed (approximately 90 nm thin slices) spheres. Figure 2b confirms that the PEs infiltrated into the BMS spheres, as PE can be seen in the interior of the NPS. At higher magnification (Figure 2c), a homogeneous porous structure with a pore size distribution of around 5–50 nm is clearly seen, confirming the nanoporosity of the spheres. SEM images of broken spheres (not shown) confirmed the interconnected PE network of the spherical particles. SEM also revealed the NPS to be individual particles, with no obvious aggregation of the particles observed (Figure 3a). At higher magnification, the roughness

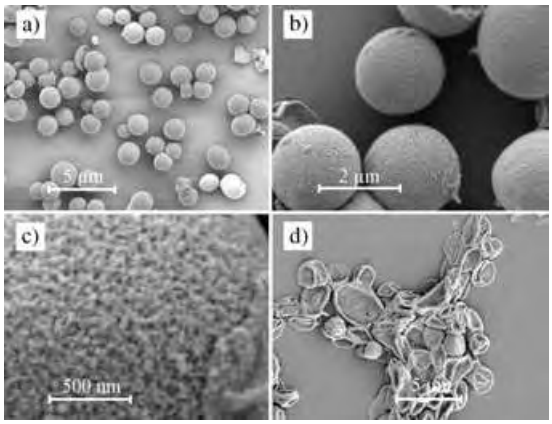

Figure 3. SEM images of 5-NPS $[(PAA/PAH)_2/PAA]$ at different magnifications (a, b, c), and $(PAA/PAH)_2/PAA$ capsules prepared when PAA and PAH are deposited in the absence of added salt in the adsorption solution (d). The 5-NPS and capsules were partially cross-linked by heating at 160°C for 2 h after deposition of each PE layer.

and porosity of the spheres is apparent (Figure 3b), with homogeneous pores in the range of approximately 10–50 nm seen (Figure 3c). Figure 3d shows the collapsed capsule structure of the product prepared by the same procedure when the PE layers were deposited in the absence of salt. This indicates that, as mentioned above, the salt facilitates PE coiling and penetration into the mesopores of the BMS templates. In the absence of salt, the PEs assume a more linear conformation[18] and therefore will be mainly restricted to the surface. We note that the highly efficient role of the APTS–BMS spheres as templates for the preparation of interconnected porous particles is attributed to the abundant and disordered pore structure of the larger mesopores and high surface area (465 $m^2 g^{-1}$) of the APTS–BMS particles. For example, a recent study employing porous (radial channel-like) $CaCO_3$ microparticle templates (surface area ca. 8.8 $m^2 g^{-1}$) resulted in PE microcapsules that collapse when dried,[15] which is in stark contrast to the free-standing NPS reported herein.

The capacity of the NPS as hosts for the immobilization of biomacromolecules was investigated through lysozyme adsorption studies. Approximately 10 mg of the NPS were dispersed in 15 mL of a 1 mg mL^{-1} lysozyme ($M_w = 14.6$ kDa) solution containing 50 mM phosphate buffer (pH 7.0). The

immobilization and distribution of enzyme in the NPS were examined by confocal laser scanning microscopy (CLSM). Figure 4 shows the CLSM images of the 5-NPS after incubation in fluorescein isothiocyanate-labeled lysozyme

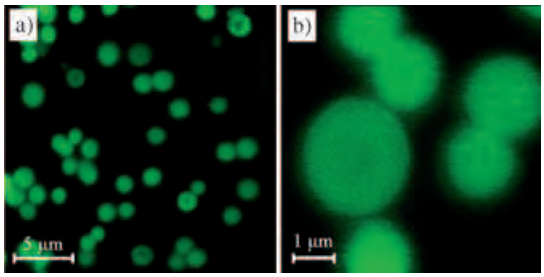

Figure 4. CLSM images of FITC-labeled lysozyme immobilized in the 5-NPS at a) low and b) higher magnification. The 5-NPS were partially cross-linked by heating at 160 °C for 2 h after deposition of each PE layer.

(FITC-lysozyme) for 1 h, and subsequent washing with water. The images show that FITC-lysozyme is distributed homogeneously throughout the NPS. The amount of enzyme immobilized by the NPS was determined spectrophotometrically by measuring the difference in lysozyme absorbance at 280 nm before and after adsorption. For the 5-NPS, the weight of the NPS increased by approximately 90 % after lysozyme immobilization, corresponding to 6.7×10^{-17} mol of lysozyme per sphere. This value corresponds to a concentration of about 470 mg mL^{-1} of lysozyme in 5-NPS, which is approximately a factor of two times larger than that obtained for the direct immobilization of lysozyme onto BMS spheres under the same conditions (220 mg mL^{-1}), and for that reported for bovine serum albumin in poly(styrene sulfonate)/PAH capsules with a "matrix-type interior" (250 mg mL^{-1}).[15] The high enzyme immobilization capacity of the NPS is attributed to the nanoporous PE framework in the NPS.

In conclusion, intact NPS with an interconnected PE network have been prepared by the LbL assembly of PEs onto APTS–BMS spheres and subsequent removal of the template. Electron microscopy data show that the NPS have pores ranging from 5–50 nm. The NPS show excellent capacity for immobilization of enzymes (lysozyme). Since the LbL method is amenable to the deposition of diverse PEs, the preparation of NPS of controlled composition and functionality can be achieved by the reported approach. This feature will facilitate designing NPS for the uptake of various species, such as macromolecules, low-molecular-weight drugs, pesticides and fragrances, and nanoparticles through, for example, electrostatic association or hydrogen bonding with the NPS host. The broad range of MS materials available with tunable size, morphology and porosity will enable the preparation of tailored porous PE materials that are envisaged to find application in biocatalysis, separation technology, and controlled drug delivery systems.

Received: September 28, 2004
Revised: December 1, 2004
Published online: April 7, 2005

Keywords: layer-by-layer technique · mesoporous materials · nanoporous spheres · polyelectrolytes · silica

[1] T. Yanagisawa, T. Shimizu, K. Kuroda, C. Kato, *Bull. Chem. Soc. Jpn.* **1990**, *63*, 988.
[2] T. Kresge, M. E. Leonowicz, W. J. Roth, J. C. Vartuli, J. S. Beck, *Nature* **1992**, *359*, 710.
[3] a) Z. Liu, Y. Sakamoto, T. Ohsuna, K. Hiraga, O. Terasaki, C. H. Ko, H. J. Shin, R. Ryoo, *Angew. Chem.* **2000**, *112*, 3237; *Angew. Chem. Int. Ed.* **2000**, *39*, 3107; b) Y. J. Han, J. M. Kim, G. D. Stucky, *Chem. Mater.* **2000**, *12*, 2068; c) K.-B. Lee, S.-M. Lee, J. Cheon, *Adv. Mater.* **2001**, *13*, 517; d) T. A. Crowley, K. J. Ziegler, D. M. Lyons, D. Erts, H. Olin, M. A. Morris, J. D. Holmes, *Chem. Mater.* **2003**, *15*, 3518.
[4] a) B. Tian, X. Liu, H. Yang, S. Xie, C. Yu, B. Tu, D. Zhao, *Adv. Mater.* **2003**, *15*, 1370; b) K. Zhu, B. Yue, W. Zhou, H. He, *Chem. Commun.* **2003**, 98; c) A. Dong, N. Ren, Y. Tang, Y. Wang, Y. Zhang, W. Hua, Z. Gao, *J. Am. Chem. Soc.* **2003**, *125*, 4976.
[5] a) R. Ryoo, S. H. Joo, S. Jun, *J. Phys. Chem. B* **1999**, *103*, 7743; b) R. Ryoo, S. H. Joo, M. Kruk, M. Jaroniec, *Adv. Mater.* **2001**, *13*, 677; c) C. Yu, J. Fan, B. Tian, D. Zhao, G. D. Stucky, *Adv. Mater.* **2002**, *14*, 1742.
[6] a) C. G. Goltner, S. Henke, M. C. Weissenberger, M. Antonietti, *Angew. Chem.* **1998**, *110*, 633; *Angew. Chem. Int. Ed. Engl.* **1998**, *37*, 613; b) K. Kageyama, J.-I. Tamazawa, A. Aida, *Science* **1999**, *285*, 2113; c) J. Y. Kim, S. B. Yoon, F. Kooli, J. Yu, *J. Mater. Chem.* **2001**, *11*, 2912; d) E. Yilmaz, O. Ramsrtöm, P. Möller, D. Sanchez, K. Mosbach, *J. Mater. Chem.* **2002**, *12*, 1577.
[7] a) U. Meyer, A. Larsson, H. P. Hentze, R. A. Caruso, *Adv. Mater.* **2002**, *14*, 1768; b) D. G. Shchukin, R. A. Caruso, *Chem. Commun.* **2003**, 1478; c) O. Norrlöw, M. Glad, K. Mosbach, *J. Chromatogr.* **1984**, *299*, 29; d) A. G. Mayes, K. Mosbach, *Anal. Chem.* **1996**, *68*, 3769.
[8] a) G. Decher, J. D. Hong, *Ber. Bunsen-Ges.* **1991**, *95*, 1430; b) G. Decher, *Science* **1997**, *277*, 1232.
[9] For reviews, see: a) F. Caruso, *Adv. Mater.* **2001**, *13*, 11; b) F. Caruso, *Chem. Eur. J.* **2000**, *6*, 413; c) C. S. Peyratout, L. Dähne, *Angew. Chem.* **2004**, *116*, 3850; *Angew. Chem. Int. Ed.* **2004**, *43*, 3762.
[10] a) C. Tedeschi, F. Caruso, H. Möhwald, S. Kirstein, *J. Am. Chem. Soc.* **2000**, *122*, 5841; b) A. A. Mamedov, A. Belov, M. Giersig, N. N. Mamedova, N. A. Kotov, *J. Am. Chem. Soc.* **2001**, *123*, 7738; c) W. Jin, X. Shi, F. Caruso, *J. Am. Chem. Soc.* **2001**, *123*, 8121.
[11] a) F. Caruso, R. A. Caruso, H. Möhwald, *Science* **1998**, *282*, 1111; b) E. Donath, G. B. Sukhorukov, F. Caruso, S. A. Davis, H. Möhwald, *Angew. Chem.* **1998**, *110*, 2323; *Angew. Chem. Int. Ed. Engl.* **1998**, *37*, 2201; c) F. Caruso, H. Lichtenfeld, E. Donath, H. Möhwald, *Macromolecules* **1999**, *32*, 2317.
[12] D. Wang, F. Caruso, *Chem. Commun.* **2001**, 489.
[13] Z. Liang, A. S. Susha, A. Yu, F. Caruso, *Adv. Mater.* **2003**, *15*, 1849.
[14] a) S. Ai, G. Lu, Q. He, J. Li, *J. Am. Chem. Soc.* **2003**, *125*, 11140; b) S. Hou, C. Harrell, L. Trofin, P. Kohli, C. R. Martin, *J. Am. Chem. Soc.* **2004**, *126*, 5674.
[15] a) D. V. Volodkin, A. I. Petrov, M. Prevot, G. B. Sukhorukov, *Langmuir* **2004**, *20*, 3398; b) G. B. Sukhorukov, D. V. Volodkin, A. M. Günther, A. I. Petrov, D. B. Shenoy, H. Möhwald, *J. Mater. Chem.* **2004**, *14*, 2073.
[16] G. Schulz-Ekloff, J. Rathouský, A. Zukal, *Int. J. Inorg. Mater.* **1999**, *1*, 97.
[17] In this process, the dried BMS powder was dispersed in toluene by sonication for 20 min before APTS was added to the suspension. The molar ratio of the BMS particles (calculated as SiO_2:APTS:toluene) was fixed at 5:1:500, and the suspension was heated under reflux for 24 h. The APTS-grafted BMS

particles were separated from the solution by centrifugation, and washed in toluene and methanol twice, respectively. Finally, the pellet was dried at 80 °C for 12 h.
[18] G. Decher, J. Schmitt, *Prog. Colloid Polym. Sci.* **1992**, *89*, 160.
[19] J. J. Harris, P. M. DeRose, M. L. Bruening, *J. Am. Chem. Soc.* **1999**, *121*, 1978.
[20] P. Schuetz, F. Caruso, *Adv. Funct. Mater.* **2002**, *13*, 929.
[21] Under the conditions used (low M_w PEs and relatively high NaCl concentrations), partial desorption of the adsorbed PE layer by the incoming PE from solution occurs. Such effects ("PE stripping") have been been observed before (Z. Sui, D. Salloum, J. B. Schlenoff, *Langmuir* **2003**, *19*, 2491). Sonication may also cause some removal of adsorbed PE.
[22] R. Takahashi, S. Sato, T. Sodesawa, M. Kawakita, K. Ogura, *J. Phys. Chem. B* **2000**, *104*, 12184.
[23] J. L. Stair, J. J. Harris, M. L. Bruening, *Chem. Mater.* **2001**, *13*, 2641.
[24] D. Yoo, S. S. Shiratori, M. F. Rubner, *Macromolecules* **1998**, *31*, 4309.
[25] Since the peak around 1635 cm^{-1} is a combination of the Si–OH vibration of the APTS–BMS spheres and the N–H bending (scissoring) vibrations of the APTS and PAH, and overlaps with the amide band owing to film cross-linking, calculation of the adsorbed amount of PAH is complicated. Therefore, we chose to analyze the peak at 1720 cm^{-1} originating from PAA.
[26] L. Dähne, B. Baude, A. Voigt, Patent WO 2004/014540A1, **2003**.
[27] a) J. Choi, J. Harcup, A. F. Yee, Q. Zhu, R. M. Laine, *J. Am. Chem. Soc.* **2001**, *123*, 11420; b) R. O. R. Costa, W. L. Vasconcelos, *Macromolecules* **2001**, *34*, 5398.

Virus-Decorated Biocomposites

Engineering Virus Functionalities on Colloidal Polyelectrolyte Lipid Composites**

*Martin Fischlechner, Olaf Zschörnig, Jörg Hofmann, and Edwin Donath**

The fabrication of functional supramolecular assemblies of nanometer dimensions consisting of both biological and artificial constituents is an exciting and rapidly developing new field at the intersection of biology, chemistry, and physics.

[*] M. Fischlechner, Dr. O. Zschörnig, Prof. Dr. E. Donath
Institute of Medical Physics and Biophysics
Leipzig University
Liebigstrasse 27, 04103 Leipzig (Germany)
Fax: (+49) 341-971-5709
E-mail: done@medizin.uni-leipzig.de
Dr. J. Hofmann
Institute of Virology
Leipzig University, Leipzig (Germany)

[**] This research was supported by a grant from Volkswagenstiftung within the framework of the program "Complex Materials". We thank D. Enderlein and C. Götte for support in RLP preparation and analysis, I. Estrela-Lopis for an introduction to the fabrication of polyelectrolyte–lipid composites, and B. Benke for the design of Figure 1.

From the standpoint of pure research it is challenging to study the structure and function of these "bionanocomposites". In addition, smart biocomposite systems for drug delivery and artificial vectors for gene therapy should have exciting applications in medicine.

In the course of evolution nature designed viruses, small particles that defy categorization as actual living entities or just small assemblies of biomolecules. Viruses actually are nanocomposites consisting of only a few polymeric species and often equipped with a lipid membrane. They carry genetic information for their replication but need a host cell to accomplish reproduction. The virus envelope, composed of less than a handful of macromolecular species, nevertheless, bears all the functions needed to recognize and enter a host cell. This is exploited in various biotechnological applications such as protein production, vaccine design, development of genetic libraries, and gene therapy.

If it would be possible to engineer colloidal particles with surfaces bearing the functionality of viruses, this would be a novel means for the delivery of a variety of materials into cells and tissues. A possible strategy would be to fabricate composite particles or capsules equipped on their surface with all the necessary virus functions for cell-membrane passage. This approach could be used, for example, to deliver a cocktail of material packed into a small colloidal entity into cells; this is not easy to do with the existing delivery devices. In this communication we describe how such virus-modified particles have been fabricated by the Layer-by-Layer (LbL) approach originally introduced for macroscopic surfaces,[1] and how their functionality has been proved.

Through the consecutive adsorption of oppositely charged polyions on colloidal particles, multilayers can be fabricated.[2] Their thickness and composition can be tuned on the nanometer scale. When this synthetic method is applied to colloids with soluble cores, capsules can be fabricated.[3] Various functions can be added by either employing functional species for adsorption or by subsequent modification.[4] Capsules can be loaded with different materials,[5] and lipid bilayers can be added.[6]

At the same time molecular biology, in particular, virology, provides a variety of tools for genetic engineering. Techniques for the manipulation of viruses are well established. Various proteins and peptides can be expressed at the virus surface.[7] These modified viruses thus provide great flexibility in the choice of biologically engineered surfaces. Combining the assembly of virus-like LbL colloids and capsules with genetic engineering thus would open novel pathways for fabricating functional bionanocomposites of complex but fully controlled interfacial composition. They may be useful as combinatorial entities in a variety of biomedical and biotechnological applications such as diagnostics, vaccination, and delivery.

In this work, Rubella-Like Particles (RLPs)[8] were employed as the virus-like material. These particles are identical copies of the lipid-enveloped rubella virus (RV) except without the virus RNA. The RLPs can be harvested from CHO cells transfected with an expression plasmid containing a cDNA of the RV subgenomic RNA. RV binds to its host cell surface, and induces endocytosis and fusion with

  DOI: 10.1002/anie.200460763

the late endosomal membrane. Binding and fusion are mediated by the rubella virus membrane protein E1 present in a complex with E2, the only other membrane protein of the rubella virus. The E1 protein function is triggered by pH, a feature displayed by many lipid-enveloped viruses. Cell-membrane binding occurs at physiological pH, while fusion with the late endosomal membrane takes place under the acidic conditions inside the endosome. The fusion competence of the E1 protein[9] is activated at low pH.

The protocol for the fabrication of RLP-decorated LbL colloids is illustrated in Figure 1. Initially a polyelectrolyte multilayer consisting of poly(allylamine hydrochloride) (PAH) and poly(sodium 4-styrenesulfonate) (PSS) was assembled onto a colloidal core. A variety of cores may be used, which can be removed afterwards, resulting in hollow polymeric capsules. The next step consisted in adding a phosphatidylserine (PS) bilayer onto this polyelectrolyte multilayer cushion. Small unilamellar PS vesicles[10] were incubated with the LbL-coated colloids having as the top layer the positively charged PAH. A bilayer was formed spontaneously by vesicle adsorption and spreading. The existence and stability of this PS bilayer was proved by means of confocal laser scanning microscopy (CLSM).[11]

On incubation of PS-coated LbL colloids with RLPs at low pH (pH 4), the particles attached to the lipid layer by electrostatic forces and subsequently fused with the membrane, presenting RV envelope proteins E1 and E2 on the surface. Tryptophane fluorescence spectroscopy was used to detect the presence of the RLPs. When the RLP-coated colloids were transferred into a buffer with pH 7.4, those RLPs which did not fuse at pH 4 desorbed, as revealed by the tryptophane fluorescence in the supernatant (see Figure 2). The amino termini of the RV E1 and E2 proteins as well as the amino groups of the virus lipids, mostly sphingomyelin, were labeled with tetramethylrhodamine. Their localization was then studied by means of CLSM (see Figure 3). The presence of the virus components was demonstrated by the homogeneous fluorescent coat on the colloids. Furthermore, SDS polyacrylamide gel electrophoresis revealed the presence of the complete set of structural RV proteins on the colloids (data not shown).

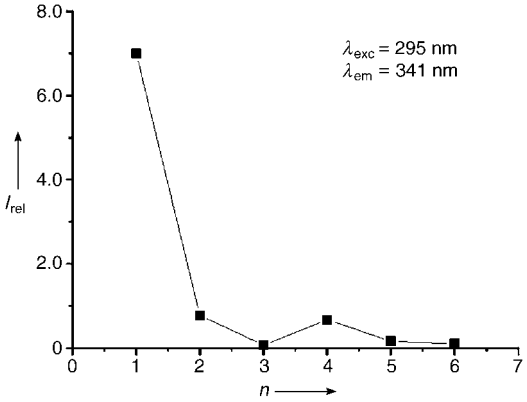

Figure 2. Tryptophane fluorescence intensity (I_{rel} in arbitrary units) in supernatants of washing cycles (n) following incubation of lipid polyelectrolyte composite particles with RLPs. Washings 1–3 were performed in 0.2 M phosphate/0.1 M citrate buffer at pH 4, washings 4–6 in 0.2 M phosphate/0.1 M citrate buffer at pH 7.4. RLPs that did not fuse with the lipid layer were desorbed and were detected by the small jump of fluorescence in the supernatant from washing cycle 4.

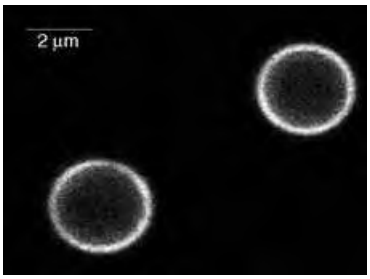

Figure 3. Fluorescence of rhodamine-labeled RLPs engineered on PS polyelectrolyte-coated silica particles.

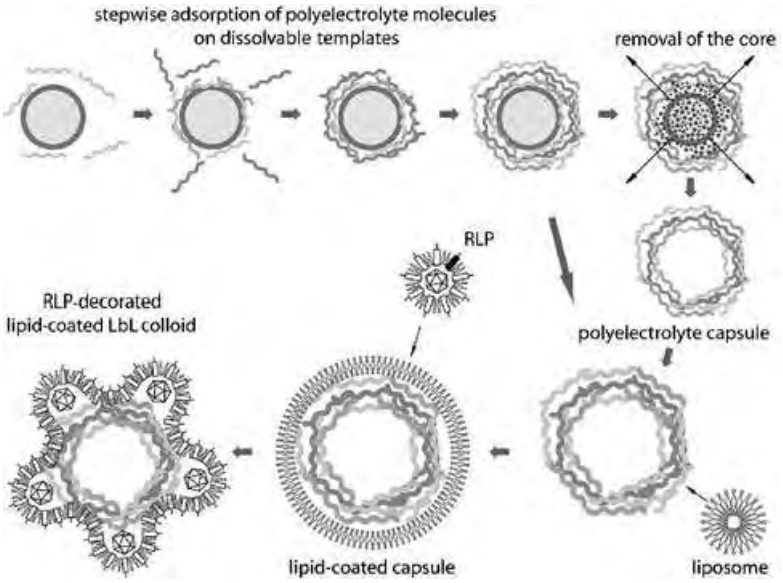

Figure 1. Protocol for engineering virus functionality on polyelectrolyte lipid composite colloids and capsules. Removal of the core is optional.

The octadecylrhodamine (R18) dequenching assay[12] was used to demonstrate the mixing of the virus membrane with the PS layer present on the colloids. The probe was added to RLPs in such a concentration that its fluorescence was partly quenched. Upon fusion it should mix with the bilayer of the target, resulting in dilution of the probe and partial dequenching of fluorescence. At pH 4 it was found that at least one-fourth of the applied RLPs had fused with the PS layer, whereas at neutral pH the observed small dequenching indicated fusion of not more than a few percent. In addition, Foerster energy transfer was demonstrated between the top polyelectrolyte layer containing FITC-labeled PAH and the R18 probe, which proves that the distance between the two labels is on the order of only a few nanometers. Because of the size of the capsid structure of the RLPs, significant energy transfer is possible only if the R18 probe

present in the RLP envelope is able to dilute laterally in the phosphatidylserine bilayer of the capsules.

Figure 4 reveals that E1 epitopes are indeed presented on the surface of the fabricated composite colloids. Here a monoclonal antibody raised against the major immunodominant epitope of E1 was applied. To reduce unspecific binding of the primary as well as secondary antibody to the particle surface, several blocking reagents were tested. Satisfying results were obtained with protamine sulphate, while the use of bovine serum albumine lead to considerable background signals.[13]

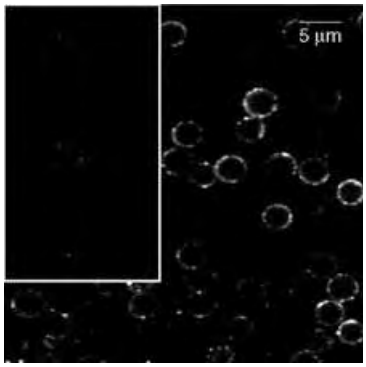

Figure 4. Confocal image of immunofluorescence against rubella virus E1 epitope on engineered silica particles. The presence of E1 is revealed by the fluorescence of the secondary antibody bound to the primary antibody against E1. The inset shows the control under identical fluorescence conditions.

The key function of the virus surface is the binding to a host cell surface, induction of endocytosis, and subsequent fusion with the late endosome membrane. In order to demonstrate the retained biological activity and functionality of E1, these engineered constructs were presented to living cells. As shown in Figure 5, LbL-coated colloids and capsules were taken up by endocytosis into Vero cells.[14] The endocytosed particles form clusters of fluorescence near the nucleus. The degree of uptake depends strongly on the nature of the top layer. While coated particles with PS as the top layer were rarely found inside the cells, those colloids which had been fused with the RLPs were effectively incorporated. The difference in uptake between the RLP-decorated PS and only PS as the top layer of the colloids can be clearly attributed to the presence of viral envelope proteins.

It is worth mentioning that particles with the polycation PAH on their surface were also found in large amounts inside the Vero cells. In this case, cell damage was observed. The uptake of particles with PAH as the top layer is probably initiated by their strong binding. This nonspecific binding was avoided when various negatively charged biopolyelectrolytes were utilized as the top layer. It is not known yet if they got stuck in the endosome or had gained access to the cytosol. This remains an exciting unresolved question for further experiments involving selective targeting and delivery of incorporated substances such as DNA[15] and proteins. Defoliation of the multilayer and improved biodegradability of the composite constituents are other issues for future research.

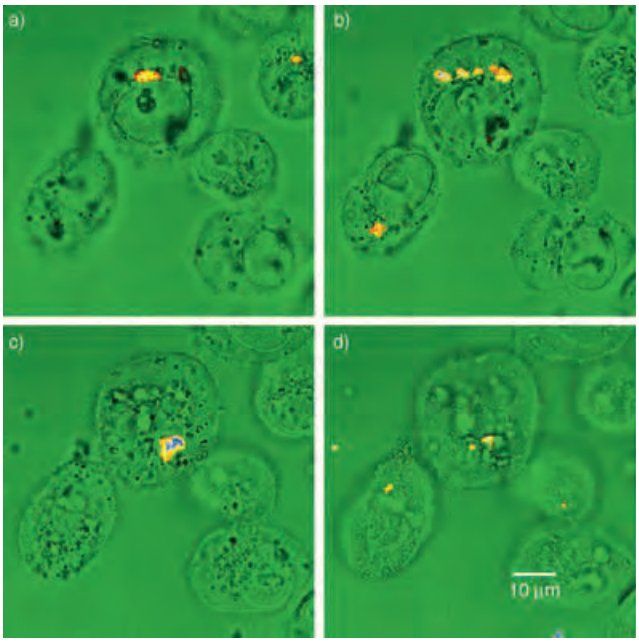

Figure 5. Uptake of 1-µm RLP-coated fluorescent LbL colloids (the fifth layer contained FITC-labeled PAH) into Vero cells. The images in a)–d) represent four consecutive confocal scans from top to bottom through the cultured Vero cells. Fluorescent colloids forming clusters near the nucleus can be identified by their red to bright yellow color. The blue color in the fluorescent spots indicates the overflow of intensity.

We conclude that the surface of lipid and polyelectrolyte multilayer coated colloids and capsules can be modified with rubella-like particles. It is very likely that this can be also achieved with other viruses or virus-like particles that infect cells by endosomal uptake.[16] This could be utilized potentially for the development of particle or capsule systems with targeting properties utilizing the specific binding properties of certain viral proteins. Moreover, with the well-developed techniques in genetic engineering, it should be possible to add membrane proteins of nonviral origin to the surface of viruses or virus-like particles. Hence, it may be possible to fabricate particles with virus functions at their surfaces along with other desired biological properties in designed arrangements on the nanometer scale. Considering all these features together, this technique could be a general approach for the transfer of biological functionalities of various kinds onto colloids, capsules, and flat surfaces.

Experimental Section

Materials: Silica particles with diameters of 3 µm and 1 µm were purchased from microparticles GmbH (Berlin, Germany). Poly(allylamine hydrochloride) ($M_w \approx 70000$) and poly(sodium 4-styrenesulfonate) ($M_w \approx 70000$) were purchased from Aldrich. L-α-Phosphatidylserine (brain, porcine; sodium salt; 20 mg mL^{-1} in chloroform) (PS) was purchased from Avanti Polar Lipids, Inc.

RLP preparation: RLPs were isolated according to the method of Hobman et al.[8] Briefly, permanent transformed CHO cells were grown on triple flasks (Nunc) at 37 °C in 5% CO_2 atmosphere. The RLPs were secreted into the supernatant of transfected cells. The

culture medium was concentrated initially using an Amicon hollow fiber equipment (H1-100) and subsequently with an Amicon stirring cell. The concentrated solution was processed on a Sepharose 4B-Cl chromatography column. Protein content was determined using the bichinonic acid assay from Sigma.

Addition of the lipid layer: The lipid bilayer was formed by adsorption of unilamellar vesicles to multilayer-coated colloids or capsules with PAH as the top layer. Vesicles and the substrates were stirred for 30 min at 37 °C on an Eppendorf Thermomixer Comfort in 0.1 M NaCl. After incubation, tween 80 (Serva, Heidelberg/New York) was added to a final concentration of 0.05 % (v/v), and the vesicles were incubated for another 5 min and subsequently washed four times with 0.1 M NaCl or PBS.

Fusion procedure: Fusion of rubella-like particles onto the lipid-coated colloids was conducted in 0.2 M phosphate/0.1 M citrate buffer at pH 4 by incubation with RLPs for 30 min at 37 °C followed by four washings with a 0.2 M phosphate/0.1 M citrate buffer, pH 7.4. For a total particle surface of 0.01 m^2, 200 μL RLPs in 0.2 M phosphate/0.1 M citrate buffer pH 4 (1 mg mL^{-1} protein) were used.

Octadecylrhodamine dequenching assay: The phospholipid content of the RLPs was estimated according to the method of Bardeletti et al.[17] The protocol for labelling RLPs with R18 (octadecyl rhodamine B, chloride salt; Molecular Probes, Inc.) was as follows: A 2-mM solution of R18 in methanol was added to RLPs in PBS corresponding to a final concentration of 4 % (mol/mol) R18 per lipid. The labeling reaction was performed at room temperature for 1 h in the dark. Subsequently, the RLPs were purified over a Sephadex G75 column. Fractions were analyzed by fluorescence spectroscopy for simultaneous occurrence of label and protein. Triton-X-100 (Merck, Darmstadt/Germany) was used at a final concentration of 0.1 % (v/v).

Immunofluorescence: Coating the particles with protamine sulfate (from herring, Sigma) prior to fixation with paraformaldehyde prevented unspecific binding of the primary antibody. Lipid polyelectrolyte particles as the negative control and particles coated with RLPs were incubated with 1 mL protamine sulfate (1 mg mL^{-1} in 0.1 M NaCl) for 10 min at room temperature. Three washings in PBS followed. The samples were spotted on a glass slide and incubated for 30 min with paraformaldehyde (2 % w/v). Subsequently, the primary antibody (Mab < Rubella > M-1B9-IgG, kindly provided by Roche Diagnostics, Germany) diluted 1:200 in PBS/1 % BSA, centrifuged for 10 min/14 krpm) was added, and the particles were incubated for another 2 h. The samples were washed five times in PBS for 10 min. Then the secondary antibody (Anti-mouse-IgG Cy3, Sigma #C 2181) diluted 1:75 in 1 % BSA in PBS, centrifuged at 10 min/14 krpm) was added. An incubation for 1 h and three washings in PBS each for 5 min followed.

Uptake in Vero cells: Vero cells were grown in Dulbecco's modified eagle medium alpha with Glutamax (Gibco BRL) on LAB-Tek slides (Nunc) to confluency. Coated particles 1 μm in diameter were pipetted to the cells in a ratio of 3:1, and the cells were incubated overnight at 37 °C in 5 % CO_2 atmosphere. Prior to examination the samples were washed three times with PBS.

Received: May 24, 2004
Revised: September 13, 2004
Published online: April 13, 2005

Keywords: colloids · membranes · polyelectrolytes · viruses

[1] a) G. Decher, J. D. Hong, J. Schmitt, *Thin Solid Films* **1992**, 210/211, 831; b) G. Decher, *Science* **1997**, *277*, 1232.
[2] a) E. Donath, D. Walther, V. N. Shilov, E. Knippel, A. Budde, K. Lowack, C. A. Helm, H. Möhwald, *Langmuir* **1997**, *13*, 5294; b) G. B. Sukhorukov, E. Donath, H. Lichtenfeld, E. Knippel, M. Knippel, A. Budde, H. Möhwald, *Colloids Surf. A* **1998**, *137*, 253; c) F. Caruso, E. Donath, H. Möhwald, *J. Phys. Chem. B* **1998**, *102*, 2011.
[3] a) E. Donath, G. B. Sukhorukov, F. Caruso, S. A. Davis, H. Möhwald, *Angew. Chem.* **1998**, *110*, 16; *Angew. Chem. Int. Ed.* **1998**, *37*, 2202; b) F. Caruso, R. A. Caruso, H. Möhwald, *Science* **1998**, *281*, 1111; c) E. Donath, G. B. Sukhorukov, H. Möhwald, *Nachr. Chem. Tech. Lab.* **1999**, *47*, 401; d) A. Voigt, H. Lichtenfeld, G. B. Sukhorukov, H. Zastrow, E. Donath, H. Bäumler, H. Möhwald, *Ind. Eng. Chem. Res.* **1999**, *38*, 4037; e) A. Voigt, E. Donath, H. Möhwald, *Macromol. Mater. Eng.* **2000**, *282*, 13; f) F. Caruso, D. Trau, H. Möhwald, R. Renneberg, *Langmuir* **2000**, *16*, 1485; g) B. Neu, A. Voigt, R. Mitlöhner, S. Leporatti, C. Y. Gao, E. Donath, H. Kiesewetter, H. Möhwald, H. J. Meiselmann, H. Bäumler, *J. Microencapsulation* **2001**, *18*, 385.
[4] a) Z. Dai, A. Voigt, S. Leporatti, E. Donath, *Adv. Mater.* **2001**, *13*, 1339; b) A. S. Susha, F. Caruso, A. L. Rogach, G. B. Sukhorukov, A. Kornowski, H. Möhwald, A. Eychmüller, H. Weller, *Colloids Surf. A* **2000**, *163*, 39; c) A. Voigt, N. Buske, G. B. Sukhorukov, A. A. Antipov, S. Leporatti, H. Lichtenfeld, H. Bäumler, E. Donath, H. Möhwald, *J. Magn. Magn. Mater.* **2001**, *225*, 59; d) G. Berth, A. Voigt, H. Dautzenberg, E. Donath, H. Möhwald, *Biomacromolecules* **2002**, *3*, 579; e) Z. Dai, L. Dähne, E. Donath, H. Möhwald, *Langmuir* **2002**, *18*, 4553; f) B. D. Jung, J. D. Hong, A. Voigt, S. Leporatti, L. Dähne, E. Donath, H. Möhwald, *Colloids Surf. A* **2002**, *198*–200, 483.
[5] a) S. Moya, G. B. Sukhorukov, M. Auch, E. Donath, H. Möhwald, *J. Colloid Interface Sci.* **1999**, *216*, 297; b) G. B. Sukhorukov, A. A. Antipov, A. Voigt, E. Donath, H. Möhwald, *Macromol. Rapid Commun.* **2001**, *22*, 44; c) X. Qiu, S. Leporatti, E. Donath, H. Möhwald, *Langmuir* **2001**, *17*, 5375; d) N. G. Balabushevitch, G. B. Sukhorukov, N. A. Moroz, D. V. Volodkin, N. I. Larionova, E. Donath, H. Möhwald, *Biotechnol. Bioeng.* **2001**, *76*, 207; e) L. Dähne, S. Leporatti, E. Donath, H. Möhwald, *J. Am. Chem. Soc.* **2001**, *123*, 5431; f) G. B. Sukhorukov, A. S. Susha, S. Davis, S. Leporatti, E. Donath, J. Hartmann, H. Möhwald, *J. Colloid Interface Sci.* **2002**, *247*, 251.
[6] a) S. Moya, E. Donath, G. B. Sukhorukov, M. Auch, H. Bäumler, H. Lichtenfeld, H. Mohwald, *Macromolecules* **2000**, *33*, 4538; b) R. Georgieva, S. Moya, S. Leporatti, B. Neu, H. Bäumler, C. Reichle, E. Donath, H. Möhwald, *Langmuir* **2000**, *16*, 7075; c) S. Moya, W. Richter, S. Leporatti, H. Bäumler, E. Donath, *Biomacromolecules* **2003**, *4*, 808.
[7] a) M. J. Schnell, L. Buonocore, E. Kretzschmar, E. Johnson, J. K. Rose, *Proc. Natl. Acad. Sci. USA* **1996**, *93*, 11359; b) D. Mottershead, I. van der Linden, C. H. von Bonsdorff, K. Keinanen, C. Oker Blom, *Biochem. Biophys. Res. Commun.* **1997**, *238*, 717.
[8] T. C. Hobman, M. L. Lundstrom, C. A. Mauracher, L. Woodward, S. Gillam, M. G. Farquhar, *Virology* **1994**, *202*, 574.
[9] C. Y. Wang, G. Dominguez, T. K. Frey, *Virology* **1994**, 68, 3550.
[10] Vesicles were prepared by freeze-thawing followed by extrusion.
[11] Rhodamine-labeled phosphatidylethanolamine (1 % m/m) was used as the fluorescent marker.
[12] D. Hoekstra, T. Deboer, K. Klappe, J. Wilschut, *Biochemistry* **1984**, *23*, 5675.
[13] Blocking with bovine serum albumin was inefficient, probably because it did not fully cover the likewise charged PS surface.
[14] Vero cells are sensitive toward infection with rubella virus.
[15] a) V. S. Trubetskoi, A. Loomis, J. E. Hagstrom, V. G. Budker, J. A. Wolff, *Nucleic Acids Res.* **1999**, *27*, 3090; b) D. Shchukin, A. A. Patel, G. B. Sukhorukov, Y. M. Lvov, *J. Am. Chem. Soc.* **2004**, *126*, 3374.
[16] T. S. Jardetzky, R. A. Lamb, *Nature* **2004**, *427*, 307.
[17] G. Bardeletti, D. C. Gautheron, *Arch. Virol.* **1976**, *52*, 19.

Asymmetric Synthesis

Direct Organocatalytic and Highly Enantio- and Diastereoselective Mannich Reactions of α-Substituted α-Cyanoacetates**

*Thomas B. Poulsen, Carlos Alemparte, Steen Saaby, Marco Bella, and Karl Anker Jørgensen**

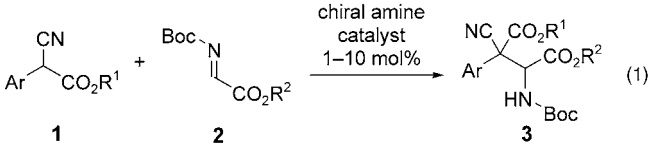

The Mannich reaction is a fundamental C–C bond-forming reaction in synthetic organic chemistry.[1] The development of an asymmetric version of this reaction is of great importance, and would allow chemists to control the configuration of the new stereocenters formed. Several catalytic enantioselective versions of the Mannich reaction have emerged that are based on chiral metal complexes.[2] Recently, metal-free (organocatalytic) systems have complemented and occasionally challenged established metal-based systems.[3] In particular, the use of chiral secondary amines as organocatalysts has been successful for a range of transformations, including the asymmetric Mannich reaction.[4] The latter takes place via a chiral enamine intermediate which undergoes nucleophilic addition to the imine in an enantioselective manner.

Alternatively, chiral tertiary amines have also been successfully applied in various organocatalytic transformations,[3,5] acting as nucleophilic,[6] phase-transfer,[7] and chiral-base catalysts.[8] However, this concept has not yet been applied to the Mannich reaction, despite the potential for the straightforward formation of highly functionalized products that contain attractive structural features.[9]

Recently, we described a highly enantioselective procedure for the direct amination of α-aryl-substituted cyanoacetates and β-dicarbonyl compounds with the chiral tertiary amine catalyst β-isocupreidine, derived in one step from inexpensive and commercially available quinidine.[8d] As the use of α-substituted cyanoacetates as nucleophiles in catalytic asymmetric reactions has been limited so far,[10] we were interested in expanding the methodology to encompass C–C bond-forming reactions. Herein we report the development of a new organocatalytic approach to the direct Mannich reaction, which affords highly functionalized products with two consecutive stereogenic carbon atoms, one of which is quaternary by all-carbon substitution [Eq. (1)].[11] Furthermore, this approach employs an α-imino ester with the readily removable *tert*-butoxycarbonyl (Boc) protecting group on the nitrogen atom.

Owing to the structural similarity of *N*-Boc-protected α-imino esters and dialkyl azodicarboxylates, we first attempted the conditions previously developed for the amination reaction.[8d] The Mannich reaction of a *tert*-butyl cyanoester with β-isocupreidine as the catalyst in toluene gave a high product yield, but with an unexpectedly poor enantioselectivity (< 20 % *ee*) and a negligible diastereoselectivity as well.

Therefore, an extensive screen of reaction conditions was undertaken, and some of the results are listed in Table 1. Variation of the catalyst (entries 1–6) showed the commercially available $(DHQD)_2PYR$ to be the most effective in both enantio- and diastereoselectivity. The nature of the cyanoacetate ester group is critical for the stereochemical outcome of the reaction. A decrease in size from *n*-propyl to methyl caused a slight decrease in the enantioselectivity of the major diastereomer (entries 6 and 7). The bulkier isopropyl group had a beneficial effect (entry 8) but a larger group was less effective (entry 9). Finally, the benzyl group gave optimal results, and the Mannich product was obtained with considerable preference for one of the two possible diastereomers, and with excellent enantioselectivity (96 % *ee*, entry 10). The influence of the structure of the α-imino ester **2** was also evaluated, but was found to be less significant when benzyl cyanoacetates were applied.[12] An increase in temperature caused a decrease in reaction selectivity (entries 11 and 12).

A further optimization of the reaction conditions (entries 13 and 14) showed that CH_2Cl_2 is a better solvent than Et_2O and surprisingly, better than toluene as well. The latter observation differs from what is intuitively expected in asymmetric reactions involving ion pair intermediates—namely that the highest selectivities are obtained in nonpolar, noncoordinating media.[13]

A decrease in catalyst loading is clearly desirable for a catalytic reaction. Although organocatalysis has proven successful in many respects, most of these processes require 10 mol % or more of the catalyst for sufficient product formation and maintenance of stereoselectivity. The reaction reported herein can be performed without notable loss of selectivity even with a catalyst loading of 1 mol % (entries 15 and 16). Finally, a controlled slow addition of the imine electrophile was found to be beneficial (entry 17).

An important advantage of this catalytic stereoselective Mannich reaction is the use of *N*-Boc-protected imines, generated in situ by dehydrobromination of Boc-protected α-bromoglycine esters.[14] A drawback for many reactions of α-imino esters with an electron-withdrawing group (commonly tosyl) on the nitrogen atom has been the subsequent deprotection step.[15] This synthetic problem has been overcome with the present methodology, however, as the Boc protecting group is easily removed.

[*] T. B. Poulsen, Dr. C. Alemparte, Dr. S. Saaby, Dr. M. Bella, Prof. Dr. K. A. Jørgensen
The Danish National Research Foundation
Center for Catalysis
Department of Chemistry, Aarhus University
8000 Aarhus C (Denmark)
Fax: (+45) 8919-6199
E-mail: kaj@chem.au.dk

[**] This work was made possible by a grant from The Danish National Research Foundation. We are grateful to Dr. Jacob Overgaard for X-ray crystallographic analysis.

Supporting information for this article is available on the WWW under http://www.angewandte.org or from the author.

  DOI: 10.1002/anie.200500144

Table 1: Some screening results for the organocatalytic direct Mannich reaction.

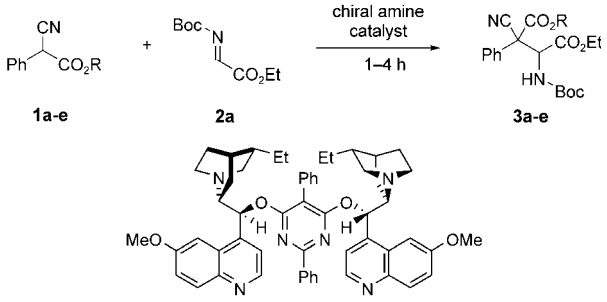

Entry	R	Cat.[a] ([mol%])	*T* [°C]	Solvent	Prod.	d.r.[b]	*ee*[c] [%]
1	*n*Pr (**1a**)	quinine (10)	−78	CH_2Cl_2	**3a**	55:45	29/46
2	*n*Pr (**1a**)	$(DHQD)_2PHAL$ (10)	−78	CH_2Cl_2	**3a**	58:42	40/18
3	*n*Pr (**1a**)	DHQ-MEQ (10)	−78	CH_2Cl_2	**3a**	58:42	41/41[d]
4	*n*Pr (**1a**)	$(DHQD)_2AQN$ (10)	−78	CH_2Cl_2	**3a**	57:43	42/13
5	*n*Pr (**1a**)	DHQD-PHN (10)	−78	CH_2Cl_2	**3a**	58:42	68/58
6	*n*Pr (**1a**)	$(DHQD)_2PYR$ (10)	−78	CH_2Cl_2	**3a**	72:28	85/41
7	Me (**1b**)	$(DHQD)_2PYR$ (10)	−78	CH_2Cl_2	**3b**	69:31	82/67
8	*i*Pr (**1c**)	$(DHQD)_2PYR$ (10)	−78	CH_2Cl_2	**3c**	74:26	90/5
9	*t*Bu (**1d**)	$(DHQD)_2PYR$ (10)	−78	CH_2Cl_2	**3d**	60:40	69/21
10	Bn (**1e**)	$(DHQD)_2PYR$ (10)	−78	CH_2Cl_2	**3e**	87:13	96/38
11	Bn (**1e**)	$(DHQD)_2PYR$ (10)	−40	CH_2Cl_2	**3e**	79:21	91/47
12	Bn (**1e**)	$(DHQD)_2PYR$ (10)	0	CH_2Cl_2	**3e**	67:33	72/29
13	Bn (**1e**)	$(DHQD)_2PYR$ (10)	−50	toluene	**3e**	66:24	90/58
14	Bn (**1e**)	$(DHQD)_2PYR$ (10)	−78	Et_2O	**3e**	73:27	93/28
15	Bn (**1e**)	$(DHQD)_2PYR$ (5)	−78	CH_2Cl_2	**3e**	85:15	93/32
16	Bn (**1e**)	$(DHQD)_2PYR$ (1)	−78	CH_2Cl_2	**3e**	84:16	94/39
17[e]	Bn (**1e**)	$(DHQD)_2PYR$ (5)	−78	CH_2Cl_2	**3e**	89:11	97/32

[a] Catalyst structures available in Supporting Information. [b] Determined by ^1H NMR spectroscopy of the crude product mixture. [c] Determined by CSP-HPLC analysis; values for both diastereomers given (CSP = chiral stationary phase). [d] The opposite enantiomers were obtained in this case. [e] Slow addition of the imine over a period of 30 min.

The optimized conditions were used to evaluate the scope of the Mannich reaction.[16] A series of benzyl α-aryl-α-cyanoacetates **1e–l** were combined with *N*-Boc-protected imines **2a–c** in reactions catalyzed by $(DHQD)_2PYR$ (5 mol%) (Table 2). Substituents present in the *meta* and *para* positions were well-tolerated (entries 2–5), providing the *N*-Boc-protected products in high yields with excellent enantioselectivities of the major diastereomer. Likewise, the polyaromatic 2-naphtyl derivative **1i** is a useful substrate (entry 6), which gave Mannich product **3i** in essentially quantitative yield with 96% *ee* in the major *u*-diastereomer, which was favored by a factor of 88:12 over the minor *l*-diastereomer.[17]

Heteroaromatic and disubstituted aromatic substrates **1j** and **1k** also afforded the Mannich products with satisfactory selectivities (entries 7, 8). Interestingly, the *ortho*-substituted bromocyanoester **1l** displayed anomalous behavior relative to the other substrates. The reaction was still very clean, but favored formation of the *l*-diastereomer instead, and the *u*-diastereomer was obtained with a disappointing 11% *ee* (entry 9). Further developments revealed that a mere change of the reaction solvent from CH_2Cl_2 to toluene drastically changed the stereochemical outcome of the reaction. With toluene as the solvent, the *u*-diastereomer was favored once more, although with low selectivity. Importantly, however, the enantiomeric excess increased to 90%. The different behavior of substrate **1l** was substantiated by the fact that the structure of the α-imino ester electrophile **2** had a significant influence on the diastereoselectivity of the reaction. A change in the ester substituent from an ethyl group in **2a** to an isopropyl group in **2b** improved the reaction selectivity to a value similar to those observed with the other substrates (entry 10). A further increase in the bulk of the ester substituent (to *t*Bu) provided the Mannich product **3n** in quantitative yield and with almost perfect stereoselectivity (entry 11). Importantly, the opposite enantiomer of the Mannich products can also be

Table 2: Direct catalytic Mannich reaction of different benzyl α-aryl cyanoacetates (**1e–l**) with α-imino esters **2a–c**[a].

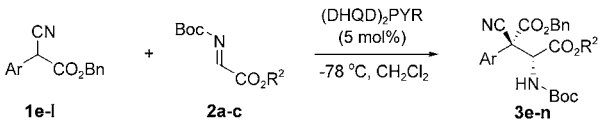

Entry	Ar	R^2	Prod.	Yield[b] [%]	d.r.[c] (*u*/*l*)	*ee*[d] [%]
1[e]	C_6H_5 (**1e**)	Et (**2a**)	**3e**	98(96)	89:11(79:21)	97(89)
2	4-Cl-C_6H_4 (**1f**)	Et (**2a**)	**3f**	99	80:20	91
3[f]	4-Cl-C_6H_4 (**1f**)	Et (**2a**)	**3f**	99	83:17	94
4	3-Me-C_6H_4 (**1g**)	Et (**2a**)	**3g**	97	86:14	97
5	4-MeO-C_6H_4 (**1h**)	Et (**2a**)	**3h**	97	85:15	96
6	2-naphthyl (**1i**)	Et (**2a**)	**3i**	99	88:12	96
7	2-thienyl (**1j**)	Et (**2a**)	**3j**	89[g]	82:18	92
8	3,4-$(MeO)_2C_6H_3$ (**1k**)	Et (**2a**)	**3k**	97	85:15	97
9	2-Br-C_6H_4 (**1l**)	Et (**2a**)	**3l**	95	18:82	11
10[h]	2-Br-C_6H_4 (**1l**)	*i*Pr (**2b**)	**3m**	98	85:15	98
11[e,i]	2-Br-C_6H_4 (**1l**)	*t*Bu (**2c**)	**3n**	99(99)	98:2(95:5)	98(92)

[a] Reactions performed in CH_2Cl_2 (0.05 M) with **1** (0.1 mmol) and **2** (0.12–0.15 mmol) added by syringe pump (1 h). [b] Yield of the isolated diastereomeric mixture. [c] Determined by ^1H NMR spectroscopy. [d] Determined by CSP-HPLC for the *u*-diastereomer (Supporting Information). [e] Yield, d.r., and *ee* values in parentheses correspond to reactions catalyzed with $(DHQ)_2PYR$ (5 mol%; see text). [f] Reaction performed by slow addition of the imine over 3 h. [g] Slight decomposition of the starting cyanoester was observed. [h] Reaction carried out in toluene. [i] Reaction carried out in toluene with $(DHQ)_2PYR$ at 10 mol%.

efficiently accessed with commercially available pseudoenantiomeric $(DHQ)_2PYR$ as the catalyst (entries 1 and 11). Alkyl-substituted cyanoacetates also underwent the Mannich reaction to afford high yields of the corresponding products. However, lower enantio- and diastereoselectivities were observed.[18]

The absolute and relative configurations of the Mannich reaction products were assigned by X-ray crystallographic analysis.[19] Compound **3o** was prepared under the standard reaction conditions discussed above. Recrystallization from a mixture of TBME and hexane precipitated the minor diastereomer (TBME = *tert*-butyl methyl ether). The mother liquor was evaporated, and the compound was slowly crystallized from a mixture of EtOAc/hexane to give **3o** as a single stereoisomer (fine colorless needles, mp = 110–111 °C) with the configuration as shown in Figure 1. Through comparison of HPLC traces and NMR spectra, the same configuration for the Mannich products **3e–n** could be inferred.

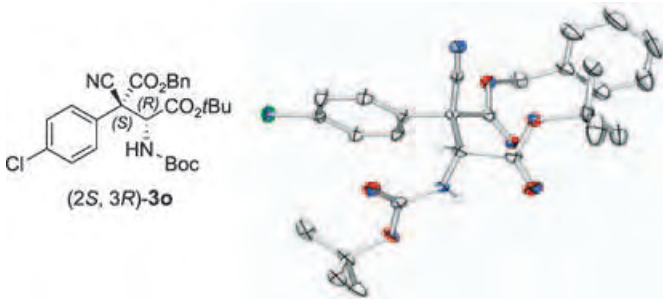

Figure 1. X-ray crystallographic structure of (2*S*,3*R*)-**3o**.

The use of *N*-Boc-protected imines **2** as electrophilic partners in the Mannich reaction allows straightforward deprotection of the products. Under standard conditions, compound **3h** was deprotected to afford the hydrochloride salt **4** in 97% yield, without affecting the diastereomeric or enantiomeric excess values (Scheme 1).

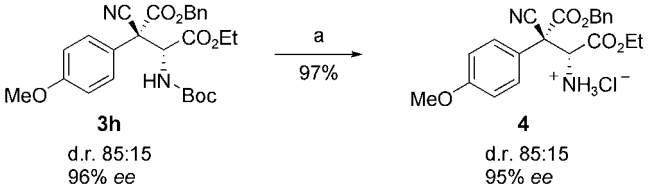

Scheme 1. Removal of the Boc protecting group: a) HCl (4 M) in 1,4-dioxane, room temperature, 5 h.

The substrate tolerance of the catalytic system was further demonstrated by the use of the β-ketoester **5** derived from 1-indanone as the nucleophilic partner in the Mannich reaction (Scheme 2). The reaction smoothly afforded the *N*-Boc-protected Mannich product **6** in high yield and essentially as a single diastereomer. We were pleased to find that the major diastereomer was obtained in 96% *ee*.

In summary, we have reported the first highly enantioselective and diastereoselective Mannich reaction of α-substituted cyanoacetates and a β-ketoester with commercially available $(DHQD)_2PYR$ as the metal-free organic chiral catalyst. An interesting solvent effect was demonstrated in reactions of an *ortho*-bromo-substituted substrate which gave dramatic changes in stereoselectivity. Work is currently underway toward a mechanistic understanding of this system and its use as a synthetic tool in asymmetric synthesis.

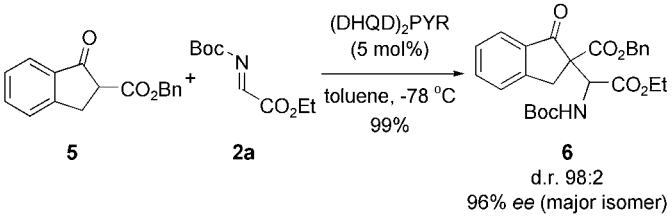

Scheme 2. Catalytic enantioselective Mannich reaction of β-ketoester **5** with imine **2a**.

Received: January 14, 2005
Published online: April 13, 2005

Keywords: asymmetric catalysis · diastereoselectivity · enantioselectivity · Mannich bases · organocatalysis

[1] a) M. Arend, B. Westermann, N. Risch, *Angew. Chem.* **1998**, *110*, 1096–1122; *Angew. Chem. Int. Ed.* **1998**, *37*, 1044–1070; b) E. F. Kleinmann in *Comprehensive Organic Synthesis*, *Vol. 2* (Eds.: B. M. Trost, I. Fleming), Pergamon, New York, **1991**, Chap. 4.1.

[2] For reviews on Mannich reactions with preformed enolates see: a) S. Kobayashi, M. Ueno in *Comprehensive Asymmetric Catalysis*, *Supplement*, *Vol. 1* (Eds.: E. N. Jacobsen, A. Pfaltz, H. Yamamoto), Springer, Berlin, **2004**, pp. 143–150; b) S. Kobayashi, H. Ishitani, *Chem. Rev.* **1999**, *99*, 1069–1094; c) S. E. Denmark, O. J.-C. Nicaise in *Comprehensive Asymmetric Catalysis*, *Vol. 2* (Eds.: E. N. Jacobsen, A. Pfaltz, H. Yamamoto), Springer, Berlin, **1999**, pp. 923–961; for direct Mannich reactions, see: d) A. Córdova, *Acc. Chem. Res.* **2004**, *37*, 102–112; e) S. Matsunaga, T. Yoshida, H. Morimoto, N. Kumagai, M. Shibasaki, *J. Am. Chem. Soc.* **2004**, *126*, 8777–8785; f) M. Marigo, A. Kjærsgaard, K. Juhl, N. Gathergood, K. A. Jørgensen, *Chem. Eur. J.* **2003**, *9*, 2359–2367; g) B. M. Trost, L. Terrell, *J. Am. Chem. Soc.* **2003**, *125*, 338–339; h) K. Juhl, N. Gathergood, K. A. Jørgensen, *Angew. Chem.* **2001**, *113*, 3083–3085; *Angew. Chem. Int. Ed.* **2001**, *40*, 2995–2997.

[3] For general reviews on organocatalysis, see: a) P. I. Dalko, L. Moisan, *Angew. Chem.* **2004**, *116*, 5248–5286; *Angew. Chem. Int. Ed.* **2004**, *43*, 5138–5175; b) *Acc. Chem. Res.* **2004**, *37*(8) special issue (Eds.: K. N. Houk, B. List); c) E. R. Jarvo, S. J. Miller, *Tetrahedron* **2002**, *58*, 2481–2495; d) P. I. Dalko, L. Moisan, *Angew. Chem.* **2001**, *113*, 3840–3864; *Angew. Chem. Int. Ed.* **2001**, *40*, 3726–3748.

[4] a) W. Notz, S.-I. Watanabe, N. S. Chowdari, G. Zhong, J. M. Betancort, F. Tanaka, C. F. Barbas III, *Adv. Synth. Catal.* **2004**, *346*, 1131–1140; b) W. Zhuang, S. Saaby, K. A. Jørgensen, *Angew. Chem.* **2004**, *116*, 4576–4578; *Angew. Chem. Int. Ed.* **2004**, *43*, 4476–4478; c) N. S. Chowdari, J. T. Suri, C. F. Barbas III, *Org. Lett.* **2004**, *6*, 2507–2510; d) A. Córdova, *Chem. Eur. J.* **2004**, *10*, 1987–1997; e) W. Notz, F. Tanaka, S. Watanabe, N. S. Chowdari, J. M. Turner, R. Thayumanavan, C. F. Barbas III, *J. Org. Chem.* **2003**, *68*, 9624–9634; f) Y. Hayashi, W. Tsuboi, I. Ashimine, T. Urushima, M. Shoji, K. Sakai, *Angew. Chem.* **2003**, *115*, 3805–3808; *Angew. Chem. Int. Ed.* **2003**, *42*, 3677–3680;

g) A. Córdova, W. Notz, G. Zhong, J. M. Betancort, C. F. Barbas III, *J. Am. Chem. Soc.* **2002**, *124*, 1866; h) A. Córdova, F. Watanabe; S. Tanaka, W. Notz, C. F. Barbas III, *J. Am. Chem. Soc.* **2002**, *124*, 1842 – 1843; i) B. List, P. Porjarliev, W. T. Biller, H. J. Martin, *J. Am. Chem. Soc.* **2002**, *124*, 827 – 833; j) B. List, *J. Am. Chem. Soc.* **2000**, *122*, 9336 – 9337.

[5] General reviews: a) S.-K. Tian, Y. Chen, J. Hang, L. Tang, P. McDaid, L. Deng, *Acc. Chem. Res.* **2004**, *37*, 621 – 631; b) K. Kacprzak, J. Gawroński, *Synthesis* **2001**, 961 – 998.

[6] S. France, D. J. Guerin, S. J. Miller, T. Lectka, *Chem. Rev.* **2003**, *103*, 2985 – 3012.

[7] a) T. Ooi, K. Maruoka, *Acc. Chem. Res.* **2004**, *37*, 526 – 533; b) B. Lygo, B. I. Andrews, *Acc. Chem. Res.* **2004**, *37*, 518 – 525; c) M. J. O'Donnell, *Acc. Chem. Res.* **2004**, *37*, 506 – 517; d) C. Carter, A. Nelson in *Organic Synthesis Highlights V* (Eds.: H.-G. Schmalz, T. Wirth), Wiley-VCH, Weinheim, **2003**, pp. 125 – 133; e) K. Maruoka, T. Ooi, *Chem. Rev.* **2003**, *103*, 3013 – 3028.

[8] For recent examples, see: a) H. Li, Y. Wang, L. Tang, F. Wu, X. Liu, C. Guo, B. M. Foxman, L. Deng, *Angew. Chem.* **2005**, *117*, 107 – 110; *Angew. Chem. Int. Ed.* **2005**, *44*, 105 – 108; b) X. Liu, H. Li, L. Deng, *Org. Lett.* **2005**, *7*, 167 – 169; c) M. R. Acocella; O. García Mancheño, M. Bella, K. A. Jørgensen, *J. Org. Chem.* **2004**, *69*, 8165 – 8167; d) S. Saaby, M. Bella, K. A. Jørgensen, *J. Am. Chem. Soc.* **2004**, *126*, 8120 – 8121; e) M. Bella, K. A. Jørgensen, *J. Am. Chem. Soc.* **2004**, *126*, 5672 – 5673; f) H. Li, Y. Wang, L. Tang, L. Deng, *J. Am. Chem. Soc.* **2004**, *126*, 9906 – 9907; g) P. McDaid, Y. Cheng, L. Deng, *Angew. Chem.* **2002**, *114*, 348 – 350; *Angew. Chem. Int. Ed.* **2002**, *41*, 338 – 340; h) H. Brunner, P. Schmidt, *Eur. J. Org. Chem.* **2000**, 2119 – 2133; i) R. Alvarez, M.-A. Hourdin, C. Cavé, J. d'Angelo, P. Chaminade, *Tetrahedron Lett.* **1999**, *40*, 7091 – 7094.

[9] a) J. R. Dimmock, P. Kumar, *Curr. Med. Chem.* **1997**, *4*, 1 – 22; b) *Enantioselective Synthesis of* β*-Amino Acids* (Ed.: E. Juaristi), Wiley-VCH, Weinheim, **1997**.

[10] For examples, see: a) R. B. Grossman, S. Comesse, R. M. Rasne, K. Hattori, M. N. Delong, *J. Org. Chem.* **2003**, *68*, 871 – 874, and references therein. For successful examples, see: b) M. S. Taylor, E. N. Jacobsen, *J. Am. Chem. Soc.* **2003**, *125*, 11204 – 11205; refs. [8a,b,d]; see also: c) N. Shibata, E. Suzuki, T. Asahi, M. Shiro, *J. Am. Chem. Soc.* **2001**, *123*, 7001 – 7009.

[11] For recent reviews on asymmetric construction of quaternary carbon atoms, see: a) C. J. Douglas, L. E. Overman, *Proc. Natl. Acad. Sci. USA* **2004**, *101*, 5363 – 5367; b) J. Christoffers, A. Baro, *Angew. Chem.* **2003**, *115*, 1726 – 1728; *Angew. Chem. Int. Ed.* **2003**, *42*, 1688 – 1690; c) E. J. Corey, A. Guzman-Perez, *Angew. Chem.* **1998**, *110*, 402 – 415; *Angew. Chem. Int. Ed.* **1998**, *37*, 388 – 401.

[12] Changing the imine ester group (Me, Et, *n*Pr, *i*Pr, *t*Bu) gave enantioselectivities for the preferred diastereomer above 90% *ee*. The d.r. ranged between 80:20–89:11, the highest value having been observed for ethyl.

[13] a) H. Hiemstra, H. Wynberg, *J. Am. Chem. Soc.* **1981**, *103*, 417 – 430; b) K. Hermann, H. Wynberg, *J. Org. Chem.* **1979**, *44*, 2238 – 2244.

[14] The carbamate-protected imine was prepared in situ following the procedure developed by Kobayashi and co-workers; see: a) Y. Nakamura, R. Matsubara, H. Kiyohara, S. Kobayashi, *Org. Lett.* **2003**, *5*, 2481 – 2484; b) S. Kobayashi, H. Kitagawa, R. Matsubara, *J. Comb. Chem.* **2001**, *3*, 401 – 403. The synthesis and use of α-bromo glycine derivatives in the preparation of acyl α-imino esters was initially developed by Steglich and co-workers; see: c) R. Kober, W. Steglich, *Liebigs Ann. Chem.* **1983**, 599 – 609; d) P. Münster, W. Steglich, *Synthesis* **1987**, 223 – 225.

[15] For a discussion of the difficulties in the deprotection of tosyl amines, see: R. R. Milburn, V. Snieckus, *Angew. Chem.* **2004**, *116*, 910 – 912; *Angew. Chem. Int. Ed.* **2004**, *43*, 892 – 894.

[16] As noted (Table 2) the reactions were performed on a 0.1-mmol scale. Compound **3h** was also prepared on a 0.5-mmol scale under the optimized conditions with similar results [95% yield, 85:15 (*u*/*l*), and 95% *ee*].

[17] The terms *u* (unlike) and *l* (like) were introduced by Seebach and Prelog as a general way of designating relative configurations in molecules with several chiral centers, particularly those in which terms like *syn*/*anti* or *erythro*/*threo* are not easily adopted; see: D. Seebach, V. Prelog, *Angew. Chem.* **1982**, *94*, 696; *Angew. Chem. Int. Ed. Engl.* **1982**, *21*, 654 – 660.

[18] Up to 61:39 (d.r.) and up to 51% *ee*. This fact has also been observed in other cinchona alkaloid-catalyzed reactions of α-substituted cyanoacetates; see refs. [8b,d].

[19] CCDC 260994 contains the supplementary crystallographic data for this paper. These data can be obtained free of charge from the Cambridge Crystallographic Data Centre via www.ccdc.cam.ac.uk/data_request/cif.

Supramolecular Chemistry

A Calix[4]imidazolium[2]pyridine as an Anion Receptor**

Kavitha Chellappan, N. Jiten Singh, In-Chul Hwang, Jung Woo Lee, and Kwang S. Kim**

The design and synthesis of efficient receptors capable of binding biologically and environmentally important anionic species is an emerging field in supramolecular chemistry.[1] Anion receptors with amide, pyrrole, urea, ammonium, and guanidinium groups as binding sites form N–H···A^- hydrogen bonds.[2] In contrast, we have studied several benzene- and anthracene-based receptors with two or three imidazolium units which bind effectively with anionic species through (C–H)$^+$···A^- hydrogen-bonding interactions.[3] The discovery of calix[4]pyrroles as anion receptors has led to detailed studies and further synthetic modifications being carried out for use in a range of applications, including anion sensing and transport.[4] Synthesis of these receptors to selectively sense

[*] Dr. K. Chellappan,[+] N. J. Singh,[+] Prof. I.-C. Hwang, J. W. Lee, Prof. K. S. Kim
National Creative Research Initiative Center for Superfunctional Materials
Department of Chemistry
Division of Molecular and Life Sciences
Pohang University of Science and Technology
Pohang 790-784 (Korea)
Fax: (+82) 54-279-8137
E-mail: kim@postech.ac.kr

[+] contributed equally to this work.

[**] This work was supported by CRI (KOSEF/MOST) and BK21. We thank Prof. F. P. Schmidtchen for his help with the data analysis and Prof. C. S. Wilcox for allowing us access to the HOSTEST program.

Supporting information for this article is available on the WWW under http://www.angewandte.org or from the author.

 DOI: 10.1002/anie.200500119

fluoride ions is of special importance because of the unique properties and hygienic importance of the fluoride ion.[5] The ionic hydrogen-bonding interactions formed by the imidazolium moieties, which are stronger than the hydrogen-bonding interactions formed by the pyrrole and urea moieties (see the Supporting Information), could be used to improve the binding affinity of the receptor for the anion. In particular, a receptor designed so that it possessed an array of positively charged imidazolium moieties in a calix form should have an enhanced binding affinity towards anions. The selectivity order of the anions could also be varied by adjusting the cavity size of the receptor. Herein, we report the first example based on this design, calix compound calix[4]imidazolium[2]-pyridine (**1**), and discuss its synthesis, characterization, and recognition abilities.

The reaction of equal quantities of 1-(1*H*-imidazol-1-ylmethyl)-1*H*-imidazole and 2,5-bis(bromomethyl)pyridine in acetonitrile followed by anion exchange with NH_4PF_6 afforded **1**-$(PF_6)_4$ as colorless microcrystals after recrystallization from acetone (Scheme 1). Single crystals of **1**-Br_4 and

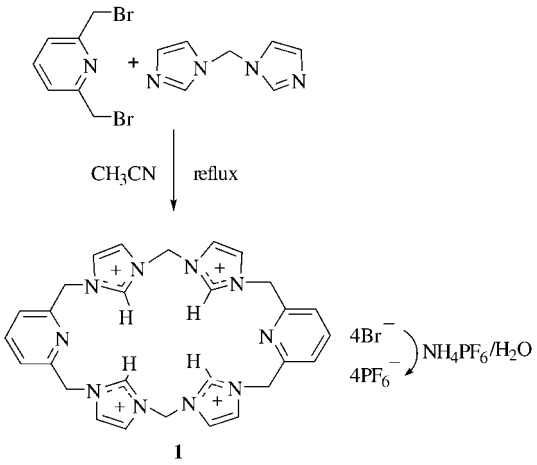

Scheme 1. Synthesis of **1**.

1-$(PF_6)_4$ were obtained from water/ethanol and acetonitrile/acetone solutions, respectively. Macrocycle **1** was characterized on the basis of the spectroscopic data of these salts (see the Supporting Information) and X-ray diffraction analysis.

Single-crystal structures of **1**-$Br_4{\cdot}6H_2O$ and **1**-$(PF_6)_4{\cdot}2$MeCN are shown in Figure 1. Macrocycle **1** adopts a chairlike conformation with all four imidazolium $(C{-}H)^+$ groups pointing towards the center of the macrocyclic core. Two of the four counteranions are "sandwiched" between two adjacent macrocycles and the other two are located outside the cage with no apparent interaction with the macrocycle. Compound **1** has many potential hydrogen-bond donor sites and a relatively large cavity; consequently, it is expected to be an interesting complexing agent for various anions.

Binding studies of **1**-$(PF_6)_4$ with various anions (F^-, Cl^-, Br^-, I^-, CH_3COO^-, and HSO_4^-) were carried out in dry CD_3CN and [D_6]DMSO by monitoring the changes in the chemical shift of the $(C{-}H)^+$ hydrogen atom in the imidazo-

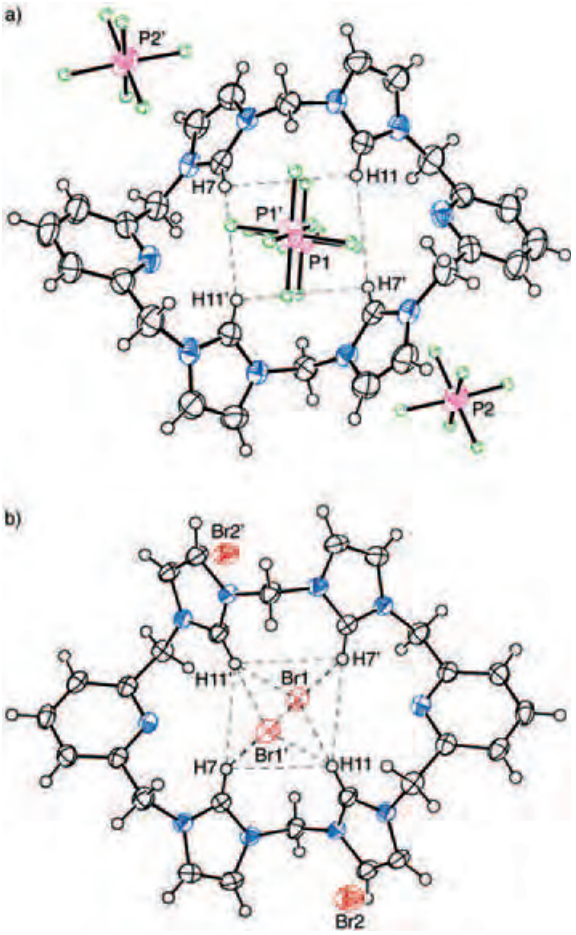

Figure 1. Crystal structures of a) **1**-$(PF_6)_4{\cdot}2CH_3CN$ and b) **1**-$Br_4{\cdot}6H_2O$. The displacement ellipsoids are given with 50% probability, except for the F atoms in the PF_6^- ion. The CH_3CN and H_2O molecules are omitted for clarity. All the anions (PF_6^- and Br^-) are located outside the cage with no direct interactions with the imidazolium moieties.

lium moiety during ^{1}H NMR spectroscopic titrations. The addition of an equimolar amount of fluoride anions as the tetrabutylammonium salt (tetrabutylammonium fluoride (TBAF)) to **1**-$(PF_6)_4$ induced a large downfield chemical shift $\Delta\delta$ of the positively charged imidazolium $(C{-}H)^+$ hydrogen atom to $\Delta\delta = 3.14$ ppm in CD_3CN, whereas the shift was $\Delta\delta = 1.77$ ppm in [D_6]DMSO; further addition caused no other significant changes in the chemical shift. Job-plot analysis showed a maximum change in chemical shift at a mole fraction of 0.5, thus indicating a 1:1 binding stoichiometry (see the Supporting Information). The bridging CH_2 group between the two imidazolium groups also showed $\Delta\delta = 0.87$ and 0.30 ppm in CD_3CN and [D_6]DMSO, respectively. The addition of one equivalent of tetrabutylammonium chloride (TBACl) moves the resonance of the $(C{-}H)^+$ hydrogen atom of **1** from $\delta = 9.42$ to 10.02 ppm and up to $\delta = 10.49$ ppm after addition of two molar equivalents in [D_6]DMSO, thus inferring a more complicated binding pattern. The association constant K_a, calculated with the HOSTEST program,[6] revealed evidence of strong binding with the fluoride anions in a 1:1 stoichiometry. The titration

curves for all the other anions tested were best fit to 1:2 receptor/anion stoichiometries. The association constant for **1**-$(PF_6)_4$ with F^-, Cl^-, Br^-, and I^- ions exceeded $K_a \approx 10^5$ by ^{1}H NMR spectroscopic titrations in CD_3CN, so the highly polar solvent [D_6]DMSO was employed for the quantitative analysis of anion binding with **1**-$(PF_6)_4$. The binding constants (M^{-1}) were found to be $K_1 = 28\,900$ for F^- ions, $K_1 = 2030$ and $K_2 = 2790$ for Cl^- ions, and $K_2 \gg K_1$ for Br^-, I^-, and HSO_4^- ions. It should be noted that the binding constant for the F^- ions was obtained in the presence of a trace amount of water which arose from the use of the trihydrate salt. The binding constants for $H_2PO_4^-$ ions were not determined because of the disappearance of the imidazolium $(C-H)^+$ hydrogen atom signal after the addition of one equivalent of the anions during ^{1}H NMR spectroscopic titration.

Crystals of the **1**-F$(PF_6)_3$ complex of sufficient quality for X-ray diffraction studies[7] were obtained by the addition of TBAF·3H_2O to a solution of **1**-$(PF_6)_4$ in acetonitrile (Figure 2). This structure determination further supported the idea that host **1** binds a single fluoride anion. Orientation of all the four $(C-H)^+$ groups of **1** towards the cavity anchors the fluoride anion in the center of the macrocyclic core through strong H–F interactions (with distances of 1.991 and 2.082 Å for H7···F and H12···F, respectively; CH_2···F = 2.576 Å).

Interestingly, crystallization of the host complex **1**-$(PF_6)_4$ with TBACl (molar ratio = 1:1) from acetonitrile solution afforded crystals of **1**-$Cl_2(PF_6)_2$ of sufficient quality for X-ray diffraction studies, which showed that the receptor/anion ratio was 1:2 (Figure 3a).[7] It is of note that the addition of one equivalent of tetrabutylammonium bromide (TBABr) to **1**-$(PF_6)_4$ results in a crystal in which the unit cell contains two layers: one composed of **1**-$Br_2(PF_6)_2$ and the other composed of the free receptor **1**-$(PF_6)_4$ (Figure 3c). The structure of the **1**-$Br_2(PF_6)_2$ layer is analogous to the structure of **1**-$Cl_2(PF_6)_2$ (Figure 3b). The chloride and bromide anions, as they are larger and favor nonspherical or surface conformations[8] in order to keep the extra electron in a large empty space, do not fit in the center of the cavity of **1**, unlike the fluoride anion, and the two chloride anions reside 2.194 Å above and below the plane, slightly offset from the center of the macrocyclic core. One chloride anion forms strong interactions with the

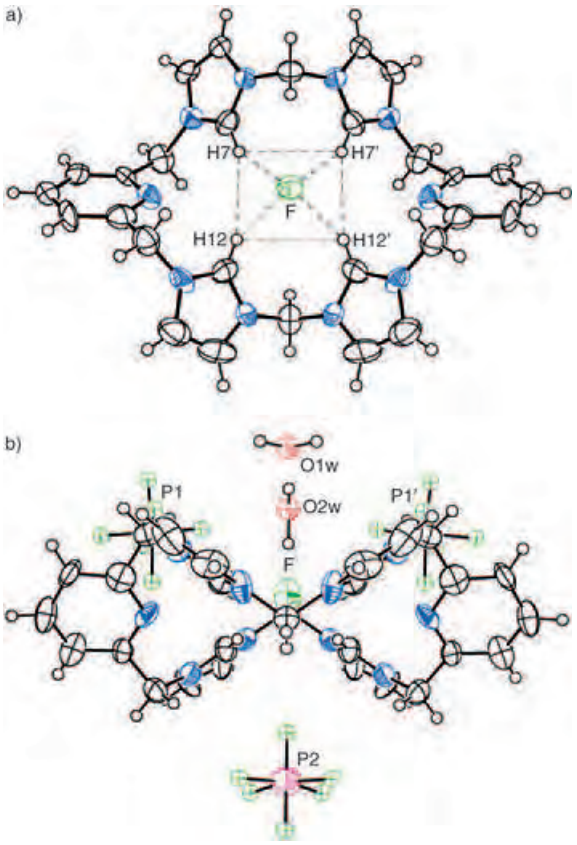

Figure 2. View of the molecular structure of **1**-F$(PF_6)_3$·2H_2O. a) Top view of the **1**-F unit and b) side view of **1**-F$(PF_6)_3$·2H_2O, with displacement ellipsoids at 50% probability.

H(11) and H(7) protons of the imidazolium rings at distances of 2.610 and 2.759 Å, respectively, whereas the other chloride anion is closer to the H(7′) and H(11′) protons and forms interactions with them at distances of 3.075 and 3.498 Å, respectively.

We further investigated the conformations of the free receptor and the receptor/anion complexes using B3LYP/6-31G(+)* density functional calculations (see the Supporting Information). The binding energy of **1** with F^- ions in the gas

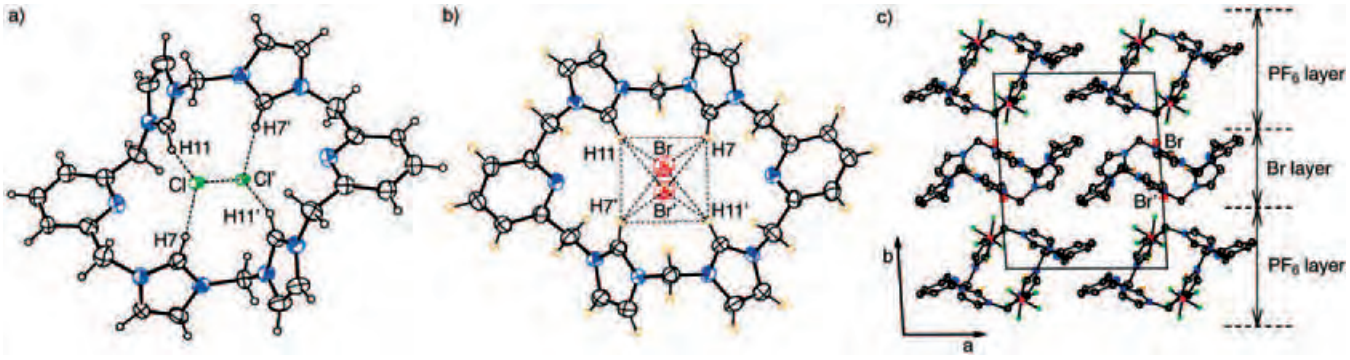

Figure 3. a) Crystal structure of the {**1**-Cl_2} unit from **1**-$Cl_2(PF_6)_2$·2CH_3CN, with displacement ellipsoids at 50% probability. The PF_6^- ions and CH_3CN molecules are omitted for clarity. b) Single-crystal structure of the {**1**-Br_2} unit from $\mathbf{1}_2$-$Br_2(PF_6)_6$, with displacement ellipsoids at 50% probability. c) Unit cell structure of [**1**-Br_2][**1**-$(PF_6)_2$][PF_6]$_4$·2CH_3CN, with displacement ellipsoids at 30% probability except for the F atoms in the PF_6^- ion.

phase is 315.9 kcal mol^{-1}, which is larger than those of the Cl^- and Br^- ions (279.2 and 273.3 kcal mol^{-1}, respectively) but is less stable than the **1**:2 F complex (537.2 kcal mol^{-1}; Table 1). However, the gain in free energy in DMSO favors the formation of the **1**:F complex over the **1**:2 F complex by 1.3 kcal mol^{-1} and the 1:1 complexes of **1** with Cl^- and Br^- ions by approximately 2 and 3 kcal mol^{-1}, respectively.

Table 1: Experimental free energies and calculated interaction energies for **1**/anion complexes (kcal mol^{-1}).[a]

Anion	K_a [M^{-1}] ([D$_6$]DMSO)		$-\Delta G_{NMR}$	$-\Delta E^{gas}_{calcd}$	$-\Delta E^{sol}_{calcd}$	$-\Delta G_{scaled}$
	K_1	K_2				
F^-	28900	–	6.08	315.9 (537.2) [304.9]	20.29 (16.14) [19.96]	6.09 (4.84) [5.99]
Cl^-	2030	2790	4.51/4.70	279.2(477.9)	13.80(19.52)	4.14(5.86)
Br^-	100	10700	2.73/5.49	273.3(469.7)	10.13(14.97)	3.04(4.49)
I^-	130	3330	2.88/4.80	–	–	–
CH_3COO^-	5040	1940	5.05/4.48	–	–	–
HSO_4^-	40	1120	2.18/4.16	–	–	–

[a] The association constants K_a (M^{-1}) were measured using ^{1}H NMR spectroscopic titrations (25 °C). Errors estimated to be $<10\%$. The anions were used as their tetrabutylammonium salts. ΔE^{gas}_{calcd} is the interaction energy in the gas phase at the B3LYP/6-31(+)G* level of theory. $\Delta E^{sol}_{calcd} = \Delta E^{sol}_{1/anion} - \Delta E^{sol}_{sol/anion} - \Delta E^{sol}_{TBA\ anion}$, where $\Delta E^{sol}_{1/anion}$ is the interaction energy of the **1**/anion complex in DMSO based on the isodensity surface polarized continuum model (IPCM), $\Delta EE^{sol}_{sol/anion}$ is the interaction energy of the anion with the solvent molecules in the first solvation shell of an anion. $\Delta EE^{sol}_{TBA\ anion}$ (sol = DMSO) is the interaction energy of the tetrabutylammonium ion with the anion in solution. The countercation correction was applied only to the F^- ions as this effect is not significant for the other anions.[9] The free energy change (ΔG_{scaled}) was obtained approximately by scaling the internal energy change, on the basis of the results of the internal versus the free solvation energy of the halide anions in the first solvation shell.[8] Values in parentheses are for 1:2 complexes, values in square brackets are for a 1:1 complex in which the F^- ions interact with one extra water molecule.

This result is in agreement with the experimental K_a values and the formation of the 1:1 complex from the host **1** and the F^- ions as observed in the crystal structure. The presence of one water molecule associated with the F^- ions lowers the free energy by 0.1 kcal mol^{-1} in DMSO, thus suggesting that the presence of a trace amount of water in DMSO slightly weakens the interactions between the receptor and the fluoride anion, which is in agreement with the experimental results.[2h] However, the 1:2 complexes of **1** with the Cl^- and Br^- ions in DMSO are more stable than the corresponding 1:1 complexes, respectively. The method used for these calculations described herein, although not accurate, helps us to predict the selectivity order of the receptor for the anions and determine whether a 1:1 or 1:2 complex will be formed.

In summary, we have synthesized novel macrocyclic anion receptor **1** that has an array of positively charged imidazolium units and has proved to be an effective receptor for F^- ions. Modification of this system would allow the development of a new class of calix containing many positively charged moieties that would be suitable for anion recognition by ionic hydrogen-bonding interactions and as precursors for N-heterocyclic carbenes for application in metal-coordination chemistry.[10]

Received: January 12, 2005

Keywords: anions · calix compounds · halides · ionophores · supramolecular chemistry

[1] a) P. de Hoog, P. Gamez, I. Mutikainen, U. Turpeinen, J. Reedijik, *Angew. Chem.* **2004**, *116*, 5939 – 5941; *Angew. Chem. Int. Ed.* **2004**, *43*, 5815 – 5817; b) J. L. Sessler, D. Seidel, *Angew. Chem.* **2003**, *115*, 5292 – 5333; *Angew. Chem. Int. Ed.* **2003**, *42*, 5134 – 5175; c) P. D. Beer, P. A. Gale, *Angew. Chem.* **2001**, *113*, 502 – 532; *Angew. Chem. Int. Ed.* **2001**, *40*, 486 – 516; d) *Supramolecular chemistry of anions* (Eds.: A. Bianchi, K. Bowman-James, E. García-España), Wiley-VCH, New York, **1997**; e) J. Y. Kwon, N. J. Singh, H. N. Kim, S. K. Kim, K. S. Kim, J. Yoon, *J. Am. Chem. Soc.* **2004**, *126*, 8892 – 8893; f) F. P. Schmidtchen, M. Berger, *Chem. Rev.* **1997**, *97*, 1609 – 1646.

[2] a) C. R. Bondy, P. A. Gale, S. J. Loeb, *J. Am. Chem. Soc.* **2004**, *126*, 5030 – 5031; b) M. J. Chmielewski, M. Charon, J. Jurczak, *Org lett.* **2004**, *6*, 3501 – 3504; c) K. A. Nielsen, J. O. Jeppesen, E. Levillain, J. Becher, *Angew. Chem.* **2003**, *115*, 197 – 201; *Angew. Chem. Int. Ed.* **2003**, *42*, 187 – 191; d) E. J. Cho, J. W. Moon, S. W. Ko, J. Y. Lee, S. K. Kim, J. Yoon, K. C. Nam, *J. Am. Chem. Soc.* **2003**, *125*, 12376 – 12377; e) K. J. Wallace, W. J. Belcher, K. F. Syed, J. W. Seed, *J. Am. Chem. Soc.* **2003**, *125*, 9699 – 9715; f) T. Mizuno, W.-H. Wei, L. R. Eller, J. L. Sessler, *J. Am. Chem. Soc.* **2002**, *124*, 1134 – 1135; g) M. Haj-Zaroubi, N. W. Mitzel, F. P. Schmidtchen, *Angew. Chem.* **2002**, *114*, 111 – 114; *Angew. Chem. Int. Ed.* **2002**, *41*, 104 – 107; h) F. P. Schmidtchen, *Org. Lett.* **2002**, *4*, 431 – 434; i) G. Cafeo, F. H. Kohnke, G. L. La Torre, A. J. P. White, D. J. Williams, *Angew. Chem.* **2000**, *112*, 1556 – 1558; *Angew. Chem. Int. Ed.* **2000**, *39*, 1496 – 1498; j) M. , Sirish, H.-J. Schneider, *J. Am. Chem. Soc.* **2000**, *122*, 5881 – 5882; k) K. Niikura, A. P. Bisson, E. V. Anslyn, *J. Chem. Soc. Perkin Trans. 2* **1999**, 1111 – 1114.

[3] a) S. K. Kim, N. J. Singh, S. J. Kim, H. G. Kim, J. K. Kim, J. W. Lee, K. S. Kim, J. Yoon, *Org. Lett.* **2003**, *5*, 2083 – 2086; b) S. Yun, H. Ihm, H. G. Kim, C. W. Lee, B. Indrajit, K. S. Oh, Y. J. Gong, J. W. Lee, J. Yoon, H. C. Lee, K. S. Kim, *J. Org. Chem.* **2003**, *68*, 2467 – 2470; c) H. Ihm, S. Yun, H. G. Kim, J. K. Kim, K. S. Kim, *Org. Lett.* **2002**, *4*, 2897 – 2900; d) K. Sato, S. Arai, T. Yamagishi, *Tetrahedron Lett.* **1999**, *40*, 5219 – 5222.

[4] a) K. A. Nielsen, W.-S. Cho, J. O. Jeppensen, V. M. Lynch, J. Becher, J. Sessler, *J. Am. Chem. Soc.* **2004**, *126*, 16296 – 16297; b) P. Piatek, V. M. Lynch, J. L. Sessler, *J. Am. Chem. Soc.* **2004**, *126*, 16073 – 16076; c) J. L. Sessler, V. Krol, T. V. Shishkanova, P. A. Gale, *Proc. Natl. Acad. Sci. USA* **2002**, *99*, 4848 – 4853; d) C. Bucher, R. S. Zimmerman, V. Lynch, J. L. Sessler, *J. Am. Chem. Soc.* **2001**, *123*, 9716 – 9717; e) P. A. Gale, J. L. Sessler, V. Král, V. Lynch, *J. Am. Chem. Soc.* **1996**, *118*, 5140 – 5141.

[5] a) S. O. Kang, J. M. Llinares, D. VanderVelde, K. Bowman-James, *J. Am. Chem. Soc.* **2003**, *125*, 10152 – 10153; b) C. J. Woods, S. Camiola, M. E. Light, S. J. Coles, M. B. Hursthouse, M. A. King, P. A. Gale, J. W. Essex, *J. Am. Chem. Soc.* **2002**, *124*, 8644 – 8652; c) M. Takeuchi, T. Shioya, T. M. Swager, *Angew. Chem.* **2001**, *113*, 3372 – 3376; *Angew. Chem. Int. Ed.* **2001**, *40*, 3372 – 3376; d) P. Anzenbacher, K. Jursikova, J. L. Sessler, *J. Am. Chem. Soc.* **2000**, *122*, 9350 – 9351.

[6] C. S. Wilcox in *Frontiers in Supramolecular Organic Chemistry and Photochemistry* (Eds.: H.-J. Schneider, H. Durr), VCH, Weinheim, **1991**, pp. 123 – 143.

[7] Crystallographic data for **1**-Br_4·6H_2O: triclinic, space group $P\bar{1}$, $a = 7.281(7)$, $b = 10.693(1)$, $c = 12.749(1)$ Å, $\alpha = 71.270(2)$, $\beta = 80.668(2)$, $\gamma = 83.539(2)°$, $V = 925.6(1)$ Å^3, $Z = 1$, GOF = 1.001, $R1 = 0.030$, $wR2 = 0.0765$. **1**-$(PF_6)_4$·CH_3CN: triclinic, space group $P\bar{1}$, $a = 7.905(1)$, $b = 11.993(1)$, $c = 12.597(1)$ Å, $\alpha = 108.540(2)$, $\beta = 99.468(2)$, $\gamma = 98.131(2)°$, $V = 1092.6(2)$ Å^3, $Z = 1$, GOF = 1.067, $R1(I>2\sigma(I)) = 0.0664$, $wR2 = 0.1838$. **1**-Cl_4·5H_2O: triclinic, space group $P\bar{1}$, $a = 7.219(1)$, $b = 10.55(1)$, $c = 11.805(1)$ Å, $\alpha = 100.637(2)$, $\beta = 93.709(2)$, $\gamma = 101.095(2)°$, $V = 862.3(1)$ Å^3, $Z = 1$, GOF = 1.100, $R_1(I>2\sigma(I)) = 0.0282$, $wR_2 = 0.0782$. **1**-F$(PF_6)_3$·2H_2O: monoclinic, space group Cm, $a = 13.901(2)$, $b = 20.921(3)$, $c = 8.504(1)$ Å, $\beta = 93.709(2)°$, $V = 2085.8(5)$ Å^3, $Z = 2$, GOF = 1.058, $R_1(I>2\sigma(I)) = 0.0835$, $wR_2 = 0.2208$. **1**-$Cl_2(PF_6)_2$·2MeCN: triclinic, space group $P\bar{1}$, $a = 8.496(1)$, $b = 11.494(2)$, $c = 12.072(2)$ Å, $\alpha = 80.212(3)$, $\beta = 71.576(3)$, $\gamma = 69.760(3)°$, $V = 1047.0(3)$ Å^3, $Z = 1$, GOF = 0.996, $R_1(I>2\sigma(I)) = 0.0933$, $wR_2 = 0.1187$. {**1**-$Br_2(PF_6)_2$}{**1**-$(PF_6)_4$}: triclinic, space group $P\bar{1}$, $a = 12.201(1)$, $b = 14.143(1)$, $c = 14.204(1)$ Å, $\alpha = 96.825(2)$, $\beta = 109.519(1)$, $\gamma = 90.931(2)°$, $V = 2291.3(3)$ Å^3, $Z = 2$, GOF = 0.951, $R_1(I>2\sigma(I)) = 0.0657$, $wR_2 = 0.0963$. CCDC-234170–234172 and -259317–259319 contain the supplementary crystallographic data for this paper. These data can be obtained free of charge from the Cambridge Crystallographic Data Centre via www.ccdc.cam.ac.uk/data_request/cif.

[8] a) J. Kim, H. M. Lee, S. B. Suh, D. Majumdar, K. S. Kim, *J. Chem. Phys.* **2000**, *113*, 5259 – 5272; b) H. M. Lee, D. Kim, K. S. Kim, *J. Chem. Phys.* **2002**, *116*, 5509 – 5520; c) K. S. Kim, P. Tarakeshwar, J. Y. Lee, *Chem. Rev.* **2000**, *100*, 4145 – 4186.

[9] J. R. Blas, M. Marquez, J. L. Sessler, F. J. Luque, M. Orozco, *J. Am. Chem. Soc.* **2002**, *124*, 12796 – 12805.

[10] a) J. Ruiz, M. E. G. Mosquera, G. García, F. Marquinez, V. Riera, *Angew. Chem.* **2005**, *117*, 104 – 107; *Angew. Chem. Int. Ed.* **2005**, *44*, 102 – 105; b) X. Hu, I. Castro-Rodriguez, K. Meyer, *Organometallics*, **2003**, 22, 3016 – 3018; c) W. A. Herrmann, *Angew. Chem.* **2002**, *114*, 1326 – 1341; *Angew. Chem. Int. Ed.* **2002**, *41*, 1290 – 1309.

Synthetic Inhibitors

Application of Stereocontrolled Stepwise [3+2] Cycloadditions to the Preparation of Inhibitors of $\alpha_4\beta_1$-Integrin-Mediated Hepatic Melanoma Metastasis**

*Aizpea Zubia, Lorea Mendoza, Silvia Vivanco, Eneko Aldaba, Teresa Carrascal, Begoña Lecea, Ana Arrieta, Tahl Zimmerman, Fernando Vidal-Vanaclocha, and Fernando P. Cossío**

Dedicated to Professor Cecilia Sarasola

Intravascular circulation of cancer cells represents a frequent event along neoplasic progression that seriously increases the probability of occurrence of metastasis. However, the adhesion of blood-borne cancer cells to the microvascular wall is a prerequisite for metastatic cell implantation at target organs. Similar to capillary homing of leukocytes, this process is proinflammatory cytokine-inducible and the mechanism involves specific binding between cancer and endothelial cell adhesion molecules.[1] Previously, we and others reported that integrin "very late antigen 4" (VLA-4, $\alpha_4\beta_1$) accounts for melanoma cell adhesion to endothelium in metastasized organs.[2] As vascular adhesion cell molecule 1 (VCAM-1) is the natural ligand of VLA-4, the VLA-4–VCAM-1 interac-

[*] Dr. A. Zubia, Dr. S. Vivanco, E. Aldaba, Prof. B. Lecea, Prof. A. Arrieta, Prof. F. P. Cossío
Facultad de Química-Kimika Fakultatea
Universidad del País Vasco-Euskal Herriko Unibertsitatea
P. O. Box 1072, 20080 San Sebastián-Donostia (Spain)
Fax: (+34) 943-212-236
E-mail: fpcossio@sq.ehu.es

Dr. L. Mendoza, Dr. T. Carrascal
Dominion Pharmakine, Ltd.
Zamudio Technology Park
48170 Zamudio (Spain)

Prof. F. Vidal-Vanaclocha
Facultad de Medicina y Odontología-Medikuntza eta Odontologia Fakultatea
Universidad del País Vasco-Euskal Herriko Unibertsitatea
48940 Lejona-Leioa (Spain)

T. Zimmerman
Centro Nacional de Investigaciones Oncológicas (CNIO)
Structural and Computational Biology Programme
Melchor Fernández Almagro 3, 28029 Madrid (Spain)

[**] This work was supported by the Universidad del País Vasco-Euskal Herriko Unibertsitatea, Gobierno Vasco-Eusko Jaurlaritza (grants 9/UPV00170.215-13548/2001 and -13641/2001), Dominion Pharmakine Ltd., and by the Spanish Ministerio de Educación y Ciencia (grants BQU2001-0904, BIO2003-02246, and SAF99-0042). A.Z. and E.A. are recipients of fellowships from the GV-EJ. We thank Dr. Francisco J. Blanco and Dr. Pascal García (CNIO, Spain) for their advice on the ^{15}N–^{1}H HSQC experiments. We also thank Dr. Antonio Llamas (Unidade de Raios X, Universidade de Santiago de Compostela, Spain) for the X-ray diffraction analysis of compound **11d**.

Supporting information for this article is available on the WWW under http://www.angewandte.org or from the author.

 DOI: 10.1002/anie.200462497

tion may, therefore, constitute an interesting molecular target for innovative therapy against melanoma dissemination. However, no results on the antimetastatic effects of synthetic VLA-4/VCAM-1 inhibitors have been reported to date, although interesting studies on synthetic inhibitors of the VLA-4/VCAM-1 interaction have been recently reported.[3] Herein, we demonstrate that small synthetic molecules which are designed to mimic the minimal requirements for binding between the natural macromolecules completely abrogate 1) melanoma cell adhesion to cytokine-activated endothelial cells and 2) melanoma cell responses to soluble and immobilized VCAM-1, and 3) efficiently inhibit metastatic development in vivo, without significantly affecting their cell viability, proliferation rate, or major metabolic activities.

Structural and electronic features of VCAM-1 were first examined in order to reproduce these features in the synthetic inhibitors.[4] The crystal structure of domains 1 and 2 of VCAM-1 has been resolved by X-ray diffraction analysis.[5] Additionally, directed mutagenesis studies have determined that the CD loop in domain 1 of VCAM-1 is crucial for binding to VLA-4[5] (Figure 1 a). In the solvated molecule, the carboxymethyl group of Asp_{40} has considerable conformational freedom and is surrounded by a relatively hydrophobic environment (Figure 1 b). We reasoned that the compounds shown in Table 1 could mimic the structural and electronic features of the Ile39-Asp40-Ser41-Pro42 sequence of domain 1 of VCAM-1 (Figure 1 c). Thus, the carboxymethylamido chain of these novel compounds reproduces the binding ability of Asp40, whereas the remaining groups provide the environment required for simulating the structural and electrostatic features of the remaining residues. Furthermore, the pyrrolidine ring confers the necessary restriction of conformational freedom to the molecule to mimic the energetically available conformations of the CD loop in the β barrel of domain 1 of VCAM-1 (Figure 1 b and c). Therefore, these unnatural highly substituted pyrrolidine rings should bind to VLA-4 to disrupt VLA-4/VCAM-1-interaction-dependent mechanisms.

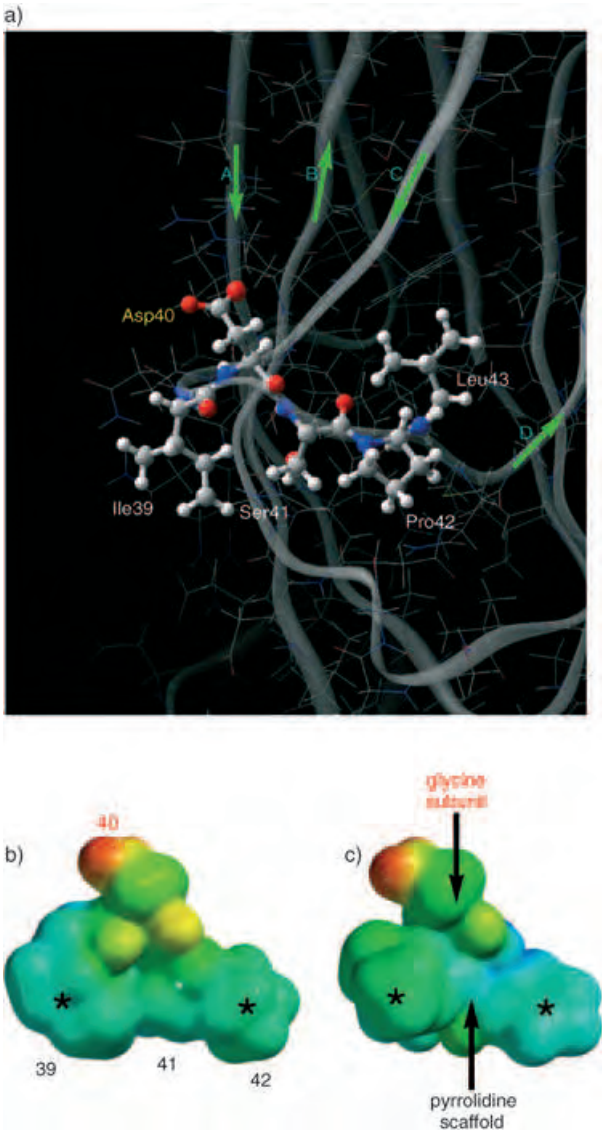

Figure 1. a) X-ray crystal structure (taken from ref. [5]) of the active loop of VCAM-1 which is involved in binding with integrin VLA-4. b), c) Electrostatic potential projected onto the electron density of the Ile39-Asp40-Ser41-Pro42 tetramer (b) and inhibitor **11d** (c); energies range from −138.2 (red) to +100.2 kcal mol^{-1} (blue); asterisks (*) indicate the hydrophobic regions in both structures.

Table 1: General structure and retrosynthetic analysis of the novel inhibitors of the VLA-4/VCAM-1 interaction.

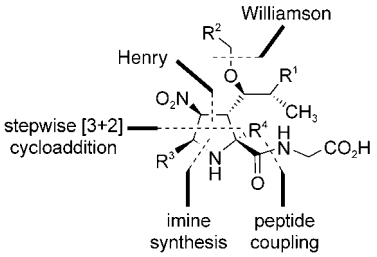

11	R^1	R^2	$R^{3[a]}$	R^4
a	Me	Ph	Ph	H
b	Me	Ph	*t*Bu	H
c	Me	2-FC_6H_4	Ph	H
d	Et	Ph	Ph	H
e	Me	2,6-$F_2C_6H_3$	Ph	H
f	Et	Ph	*c*Hex	H
g	Et	3,5-$F_2C_6H_3$	Ph	H
h	Et	Ph	*c*Pr	H
i	Et	2,3-$F_2C_6H_3$	Ph	H
j	Et	Ph	Ph	Me
k	Et	Ph		H

[a] *c*Hex = cyclohexyl, *c*Pr = cyclopropyl, Bn = benzyl.

The new compounds **11** were synthesized in 12 preparative steps according to the design depicted in Table 1 and Scheme 1 (for more details, see Supporting Information). The starting materials were readily accessible and inexpensive chemicals such as L-α-amino acids (glycine, alanine, valine, and leucine), halides **3**, and aldehydes **7**. The key step in the synthetic route shown in Scheme 1 is the formal [3+2] cycloaddition between *E*-nitroalkenes **6** and imines **9** to yield pyrrolidines **10**. This reaction takes place with complete

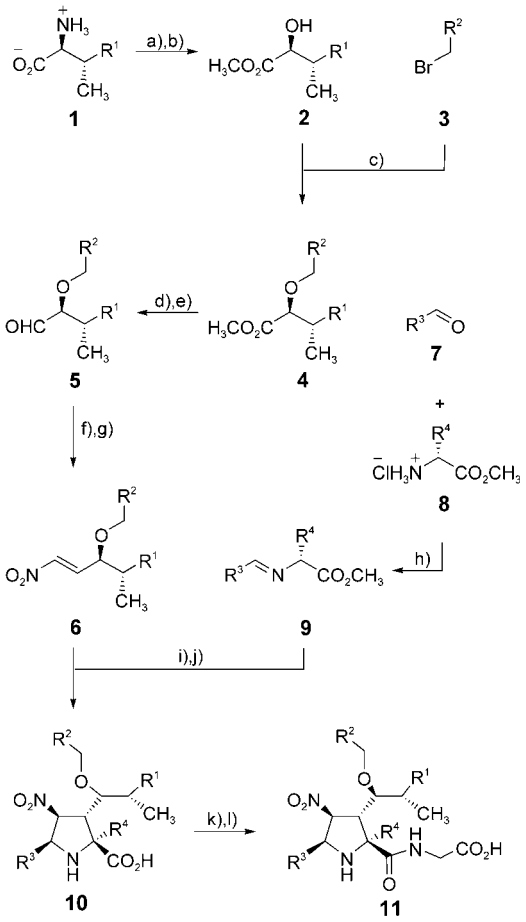

Scheme 1. Synthesis of compounds **11**. a) **1** (1.0 equiv in 1 N H_2SO_4), $NaNO_2$ (1.5 equiv in H_2O), 0 °C, 24 h, 83–90%; b) DMP (1.0 equiv), TsOH·H_2O (0.007 equiv), MeOH, 45 °C, 24 h, 88–96%; c) **2** (1.0 equiv), NaH (1.0 equiv), anhydrous THF/DMF (2:0.6), 0 °C, 10 min, then **3** (1.2 equiv), RT, 24 h, 45–64%; d) $LiAlH_4$ (1.0 equiv), Et_2O, 0 °C, then **4** (1.0 equiv), Et_2O, RT, 3 h, 80–90%; e) ClCOCOCl (1.5 equiv), DMSO (2.0 equiv), TEA (4.0 equiv), CH_2Cl_2, −67 °C, 5 h, 79–90%; f) **5** (1.0 equiv), CH_3NO_2 (5.0 equiv), TEA (0.14 equiv), RT, overnight, 87–96%; g) MsCl (1.2 equiv), DIPEA (2.5 equiv), CH_2Cl_2, −78 °C, 2 h, 85–95%; h) **8** (1.15 equiv), TEA (1.25 equiv), $MgSO_4$, CH_2Cl_2, RT, 1 h, then **7** (1.0 equiv), RT, overnight, 75–95%; i) **6** (1.0 equiv), **9** (1.0 equiv), AgOAc (0.1 equiv), TEA (1 equiv), CH_3CN, RT, 5 h, 60–92%; j) 1 N DME/LiOH (5:3, aq), 0 °C, 1–4 h, 82–95%; k) **10** (1.0 equiv), MeGly·HCl (1 equiv), DECP (1.2 equiv), DMF, 0 °C, then TEA (2.0 equiv), RT, overnight, 64–95%; l) 1 N DME/LiOH (5:3, aq), 0 °C, 1–4 h, 85–97%. DMP = 2,2-dimethoxypropane, Ts = *p*-toluenesulfonyl, DMF = *N*,*N*-dimethylformamide, DMSO = dimethylsulfoxide, DMP = 2,2-dimethoxypropane, TEA = triethylamine, DIPEA = diisopropylethylamine, DME = 1,2-dimethoxyethane, MeGly = glycine methyl ester, DECP = diethylcyanophosphonate.

stereocontrol when R^3 is a phenyl group, and R^1 = Me or Et (compounds **10a,c–e,g,i,j**). When R^3 is an alkyl group, the stereocontrol is variable and ranges from greater than 99:1 when R^3 = *t*Bu (**10b**) to 91:9 when R^3 = *c*Hex (**10f**) or *c*Pr (**10h**). In the case of pyrrolidine **10k**, which has a chiral group at R^3, three stereoisomers were obtained in a ratio of 77:15:8.

Previous studies[6] have shown that the reaction between π-deficient alkenes and metalated azomethine ylides takes place through a stepwise mechanism, not a concerted mechanism, to give the [3+2] cycloadduct. The first step comprises a Michael-type nucleophilic attack of the α carbon atom of the azomethine ylide **A**, which forms in situ, on the β carbon atom of the nitroalkene (Scheme 2). The cyclization step takes place by means of an intramolecular Henry-type reaction between the intermediate nitronate moiety and the iminic fragment of the zwitterionic intermediate denoted as **B** in Scheme 2.

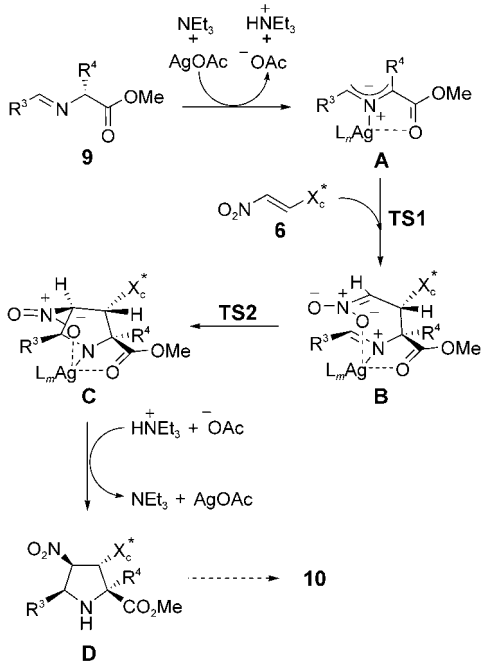

Scheme 2. Mechanism of formation of cycloadducts **10** from the reaction between imines **9** and nitroalkenes **6**. X_c^* = chiral group.

To understand the origins of the stereocontrol of the reaction, we computed the two possible diastereomeric transition-state structures **TS1** and **TS1′** for the model system depicted in Figure 2.[7] As shown in Figure 2 and Scheme 2, part of the stereocontrol of the reaction stems from the retention of configuration of the *E*-nitroalkene and the

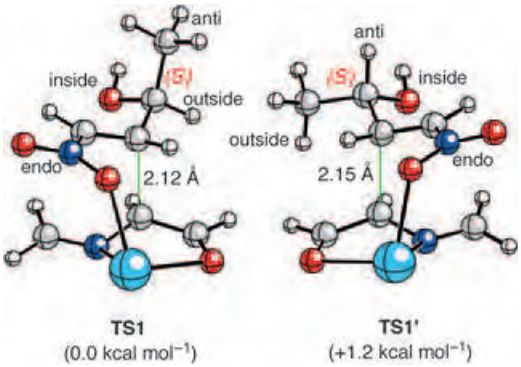

Figure 2. Ball-and-stick representations of the fully optimized structures of transition-state structures **TS1** and **TS1′** (C gray, O red, N dark blue, Ag light blue); green lines represent the new sigma bonds that form; see ref. [7] for further details.

chelated nature of the metalated azomethine ylide. The diastereoselectivity can be explained in terms of a two-electron interaction between the localized σ* orbital of the C–C bond that forms and the localized σ orbital of the antiperiplanar C–CH_3 bond, with the alkoxy group occupying the inside position with respect to the pyrrolidine ring that forms, as seen in Figure 2. The alternative diastereomeric transition-state structure **TS1′**, in which the C–H bond is *anti* with respect to the new C–C bond that forms, is more than 1 kcal mol^{-1} higher in energy than **TS1** and corresponds to high stereocontrol in favor of the (2*S*,3*R*,4*S*,5*S*) cycloadduct, provided that groups which are bulkier than methyl are used. The absolute configuration of the new stereogenic centers was verified by X-ray diffraction analysis on compound **11d** and confirmed the validity of our computational results.[8]

Next, the potential VLA-4 antagonism of compounds **11** was tested through a previously established model[2b] on VLA-4/VCAM-1-interaction-dependent B16M cell adhesion to primary cultured hepatic sinusoidal endothelial (HSE) cells in vitro. As shown in Figure 3, both B16M cell adhesion to TNF-α (tumor necrosis factor alpha)-treated HSE—which increases VCAM-1 expression on endothelial cells—and H_2O_2-treated B16M cell adhesion to unstimulated HSE cells—which increases VLA-4 activation in cancer cells—significantly increased relative to their respective untreated control cells ($P < 0.01$, where P is the statistical probability value).[2b] Preincubation of B16M cells with compounds **11** and measurement of adhesion to HSE resulted in variable responses as shown in Figure 3. Interestingly, compounds **11b** and **11h** with *t*Bu and *c*Pr groups at R^3, respectively, did not show any significant antiadhesive activity. Similarly, compound **11e**, with a 2,6-difluorophenyl group at R^2 and a methyl group at R^1 was also almost inactive. In contrast, the presence of a quaternary atom at the α-position of the pyrrolidine ring (R^4 = Me), such as in **11j**, did not result in a significant loss of activity.

To assess if interactions other than VLA-4/VCAM-1 were involved in the inhibitory activity of compounds **11**, we used the chemical shift perturbation method[9] on the I domain of the α_2-subunit of $\alpha_2\beta_1$-VLA-2 integrin which is also relevant in melanoma metastasis and binds different ligands such as collagen or laminin.[10] ^{15}N–^{1}H heteronuclear single-quantum coherence (HSQC) NMR spectra[9] of uniformly ^{15}N-labeled I domain were recorded in the presence and the absence of inhibitors **11a–j**. In these spectra each amino acid of the I domain appeared as a cross-peak that corresponds to the NH group of its amide backbone. Analysis of the spectra at different pH values (pH 6.5 and 7.4) and at different temperatures (T = 283 and 298 K, see Supporting Information) did not lead to any significant shift of the cross-signals upon addition of the inhibitors, which indicates the lack of binding and, therefore, the high selectivity of these compounds with respect to integrin VLA-2.

Although the best activity in vitro was shown by compound **11f**, which has a cyclohexyl group at R^3, preliminary assays in vivo were carried out with **11d** (R^3 = Ph) because of its higher solubility in water. Additionally, **11d** displayed comparable antiadhesive activity to monoclonal antibodies against murine VLA-4 (Figure 3b). Furthermore,

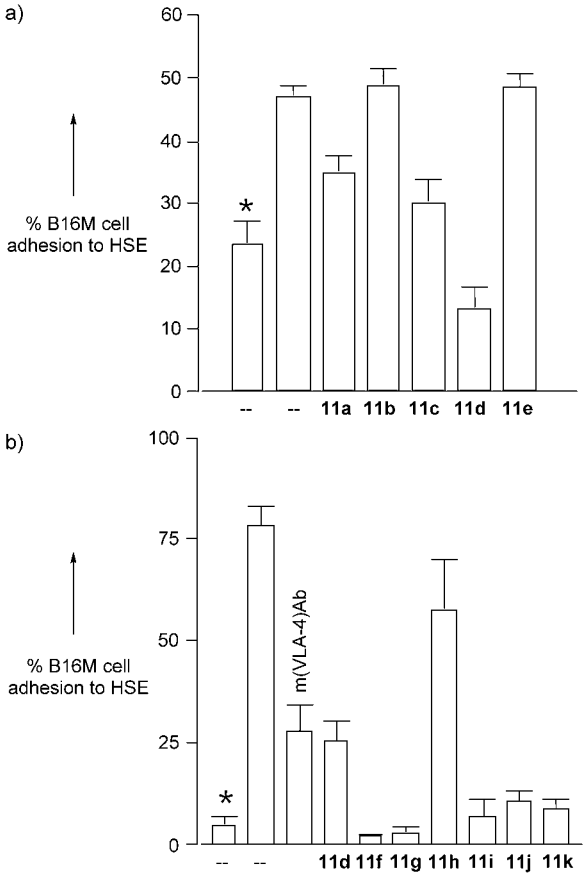

Figure 3. Inhibition of adhesion between HSE and B16M cells by compounds **11**. The degree of inhibition was measured on a) TNF-α-activated cultured HSE cells and b) H_2O_2-pretreated melanoma B16M cells. Asterisks (*) indicate the inhibition measured on unstimulated HSE. The concentration of compounds **11** was 50 μg per 1×10^6 B16M cells. The lyophilized compounds were dissolved in DMSO and diluted to a final working stock solution of 5 mg mL^{-1} in serum-free medium. 1×10^6 B16M cells resuspended in 300 μL of serum-free medium were preincubated with **11** (10 μL of stock solution, 50 μg) for 15 min at 37 °C before the adhesion assay. m(VLA-4)Ab denotes rat anti-mouse CD49d monoclonal antibody (Serotec Ltd, Oxford, UK) against VLA-4. In this case, B16M cells were incubated with 10 μg mL^{-1} of m(VLA-4)Ab before the adhesion assay. The results are the mean standard deviation of three independent experiments, each performed in sextuplicate (n = 18).

addition of **11d** compound to IL-1β (interleukin-1β)-treated melanoma cells completely abrogated their adhesion to immobilized VCAM-1 and prevented vascular endothelial growth factor (VEGF) production induced by soluble-VCAM-1-stimulated cells (see Supporting Information), which confirms the potent VLA-4 antagonism of compound **11d**. Finally, metastasis density and volume significantly decreased ($P < 0.01$) by 60% and 95%, respectively, in mice that were intrasplenically injected with **11d**-pretreated B16M cells relative to those that received untreated cells (Figure 4). Parallel measurements on cell viability and cytotoxicity, intracellular oxidative metabolism, and cell-proliferation rates of **11d**-treated melanoma cells excluded that antimetastatic effects of **11d** compound may have been caused by

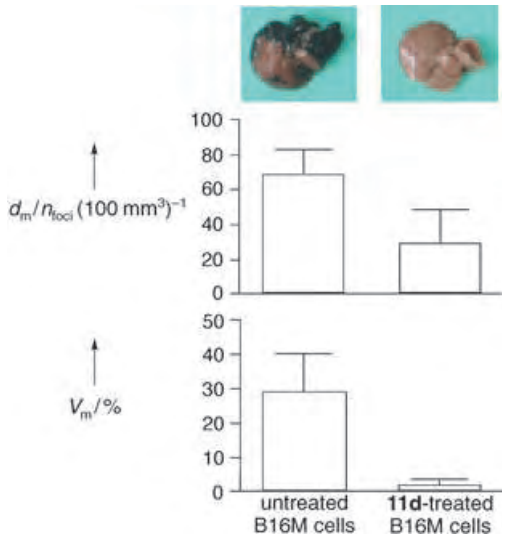

Figure 4. Antimetastatic activity of compound **11d** on male C57BL/6J mice (6 to 8 weeks old). At least 30 mice were used per experiment, and each experiment was carried out 3 times. The bars on the left correspond to the control group. The test group was treated with **11d**-preincubated B16M viable cells (50 μg per 1×10^6 B16M cells). Livers were removed on day 12 after intrasplenical injection of B16M cells and photographed. Photographs on the left and on the right correspond to livers obtained from the control and test groups, respectively. Metastases can be identified as black melanotic nodules. Metastasis density (d_m) was measured as the number of foci per 100 mm^3 of liver, and metastasis volume (V_m) was measured as the percentage fraction of liver volume occupied by metastases.

indirect effects on cell functions other than those specifically operated through a VLA-4-dependent mechanism.[11]

In summary, we have described a new family of inhibitors of the VLA-4/VCAM-1 interaction that 1) block the in vitro adhesion of melanoma cells to microvascular endothelium induced by proinflammatory cytokines and oxidative stress, 2) prevent melanoma cell production of VEGF induced by VCAM-1 in vitro, and 3) exhibit a potent antimetastatic activity in vivo. These small synthetic molecules fulfill the bioavailability requirements proposed by Lipinski et al.[12] Finally, the synthetic route developed for these inhibitors was convergent, completely regio- and stereoselective, versatile, and did not require sophisticated experimental devices or purifications. Therefore, it is well-suited to extensive studies of structural variation to refine the biological properties of the most promising lead compounds.

Received: November 2, 2004
Revised: February 14, 2005
Published online: April 13, 2005

Keywords: cell adhesion · cycloaddition · drug design · inhibitors · proteins

[1] a) I. J. Fidler, *Nat. Rev. Cancer* **2003**, *3*, 1; b) J. D. Hood, D. A. Cheresh, *Nat. Rev. Cancer* **2002**, *2*, 91.
[2] a) G. E. Rice, M. P. Bevilacqua, *Science* **1989**, *246*, 1303; b) F. Vidal-Vanaclocha, G. Fantuzzi, L. Mendoza, A. M. Fuentes, M. J. Anasagasti, J. Martín, T. Carrascal, P. Walsh, L. L. Reznikov, S.-H. Kim, Novick, M. Rubinstein, C. A. Dinarello, *Proc. Natl. Acad. Sci. USA* **2000**, *97*, 734.
[3] For example, see: a) J. Boer, D. Gottschling, A. Schuster, B. Holzmann, H. Kessler, *Angew. Chem.* **2001**, *113*, 3988; *Angew. Chem. Int. Ed.* **2001**, *40*, 3870; b) S. Wattanasin, B. Weidmann, D. Roche, S. Myers, A. Xing, Q. Guo, M. Sabio, P. v. Matt, R. Hugo, S. Maida, P. Lake, M. Weetall, *Bioorg. Med. Chem. Lett.* **2001**, *11*, 2955; c) L. Chen, J. Tilley, R. v. Trilles, W. Yun, D. Fry, C. Cook, K. Rowan, V. Schwinge, R. Campbell, *Bioorg. Med. Chem. Lett.* **2002**, *12*, 137; d) G. A. Doherty. T. Kamenecka, E. McCauley, G. V. Riper, R. A. Mumford, S. Tong, W. K. Hagmann, *Bioorg. Med. Chem. Lett.* **2002**, *12*, 729; e) I. E. Kopka, D. N. Young, L. S. Lin, R. A. Mumford, P. A. Magriotis, M. MacCoss, S. G. Mills, G. V. Riper, E. McCauley, L. E. Egger, U. Kidambi, J. A. Schmidt, K. Lyons, R. Stearns, S. Vincent, A. Coletti, Z. Wang, S. Tong, J. Wang, S. Zheng, K. Owens, D. Levorse, W. K. Hagmann, *Bioorg. Med. Chem. Lett.* **2002**, *12*, 637; f) D. R. Leone, K. Giza, A. Gill, B. M. Dolinski, W. Yang, S. Perper, D. M. Scott, W.-C. Lee, M. Cornebise, K. Wortham, C. Nickerson-Nutter, L. L. Chen, D. Lepage, J. C. Spell, E. T. Whalley, R. C. Petter, S. P. Adams, R. R. Lobb, R. B. Pepinski, *J. Pharmacol. Exp. Ther.* **2003**, *305*, 1150.
[4] For a related computational analysis of VCAM-1, see: A. Macchiarulo, G. Constantino, M. Meniconi, K. Pleban, G. Ecker, D. Bellocchi, R. Pellicciari, *J. Chem. Inf. Comput. Sci.* **2004**, *44*, 1829.
[5] E. Y. Jones, K. Harlos, M. J. Bottomley, R. C. Robinson, P. C. Driscoll, R. M. Edwards, J. M. Clements, T. J. Dudgeon, D. I. Stuart, *Nature* **1995**, *373*, 539.
[6] S. Vivanco, B. Lecea, A. Arrieta, P. Prieto, I. Morao, A. Linden, F. P. Cossío, *J. Am. Chem. Soc.* **2000**, *122*, 6078.
[7] These calculations were performed at the B3LYP level of theory; see: a) A. D. Becke, *J. Chem. Phys.* **1993**, *98*, 5648; b) A. D. Becke, *Phys. Rev. A* **1988**, *38*, 3098; c) C. Lee, W. Yang, R. G. Parr, *Phys. Rev. B* **1980**, *37*, 785; d) S. H. Vosko, L. Wilk, M. Nusair, *Can. J. Phys.* **1980**, *58*, 1200. Carbon, nitrogen, oxygen, and hydrogen atoms were described by means of the 6-31G(d) basis set, whereas silver atoms were described by the Hay – Wadt effective core potential; see: P. J. Hay, W. R. Wadt, *J. Chem. Phys.* **1985**, *82*, 299. Harmonic analyses on **TS1** and **TS1′** showed that both saddle points have only one imaginary frequency associated with nuclear motion along the reaction coordinate associated with formation of a new C–C bond. Differences in energy include zero-point vibration energy corrections.
[8] CCDC 252339 contains the supplementary crystallographic data for this paper. These data can be obtained free of charge from the Cambridge Crystallographic Data Centre via www.ccdc.cam.ac.uk/data_request/cif.
[9] a) A. Bax, M. Ikura, L. E. Kay, D. A. Tochia, R. Tschudin, *J. Magn. Reson.* **1990**, *86*, 304; b) G. Bodenhausen, D. J. Buben, *Chem. Phys. Lett.* **1980**, *69*, 185.
[10] a) R. Mortarini, A. Anichini, G. Parmiani, *Int. J. Cancer* **1991**, *47*, 551; b) D. Baronas-Lovell, J. L. Lauer-Fields, J. A. Borgia, G. F. Sferrazza, M. Al-Ghoul, D. Minond, G. B. Fields, *J. Biol. Chem.* **2004**, *279*, 43503.
[11] F. Vidal-Vanaclocha, L. Mendoza, N. Gallot, N. Telleria, F. P. Cossio, A. Zubia, E. Aldaba, unpublished results.
[12] C. A. Lipinski, F. Lombardo, B. W. Dominy, P. J. Freeney, *Adv. Drug Delivery Rev.* **1997**, *23*, 3.

Bioinorganic Chemistry

The Geometric and Electronic Structure of [(cyclam-acetato)Fe(N)]$^+$: A Genuine Iron(V) Species with a Ground-State Spin $S = 1/2$**

Núria Aliaga-Alcalde, Serena DeBeer George, Bernd Mienert, Eckhard Bill, Karl Wieghardt, and Frank Neese**

High-valent transition-metal complexes play a crucial role as intermediates in the reaction cycles of metalloenzymes[1,2] and, consequently, the synthesis of low-molecular-weight compounds that model the active sites is a major challenge in synthetic inorganic chemistry. Many of these observed heme- and non-heme enzyme intermediates contain terminal oxo ligands.[2] While in recent years a number of heme- and non-heme Fe^{IV}=O complexes have been prepared and spectroscopically characterized,[3] much less is known about the corresponding high-valent iron–nitrido species despite their possible involvement in enzymes from the biogeochemical nitrogen cycle. However, over the course of the last few years a number of high-valent non-heme metal–nitrido species containing V^V, Cr^V, Mn^V, and Fe^V ions have been prepared by atom and/or group-transfer reactions or by photolysis.[4,5] We note that Wagner and Nakamoto[5c,d] have previously reported the photochemical generation of $[Fe^V(N)(TPP)$ (TPP^{2-} = tetraphenylporphinate(2−)) and measured its resonance Raman spectrum. Most recently, Betley and Peters synthesized and characterized the distorted tetrahedrally coordinated terminal Fe^{IV}–nitrido species $[PhBP^iPr_3]Fe^{IV}N$ ($[PhBP^iPr_3] = [PhB(CH_2P^iPr_2)_3]^-$).[6] This compound was shown to be diamagnetic at room temperature and exhibit ^{15}N NMR resonances near $\delta = 952$ ppm and a ν(FeN) stretching frequency of 1034 cm^{-1}. Furthermore, density functional theory (DFT) calculations at the B3LYP level of theory predicted a very short Fe≡N bond of 1.49 Å.

Efforts in our group to characterize high-valent iron–nitrido species started with the synthesis of two non-heme azidoiron(III) precursors, *cis*- (**1**) and *trans*-$[(cyclam)Fe^{III}(N_3)_2](ClO_4)$ (**2**), by using the spectroscopically innocent ligand cyclam (1,4,8,11-tetrazacyclotetradecane).[5a] Photolysis of **2** in a frozen matrix yielded products that were assigned to Fe^{II} (ca. 29%) and Fe^V (ca. 54%) species on the basis of zero-field Mössbauer spectroscopy.[5a] It was concluded that homolytic Fe–N_3 cleavage (to give Fe^{II} and $N_3^{\bullet}$; photoreduction) and heterolytic N–N cleavage (to give Fe^VN and N_2; photooxidation) both occur.[5a] Subsequently, the synthesis and photolysis of $[(cyclam\text{-}ac)Fe(N_3)]^+$ (cyclam-ac^- = 1,4,8,11-tetraazacyclotetradecane-1-acetate) (**3**) was reported.[5b] It was shown that photolysis at $\lambda > 420$ nm, that is, irradiation into the $N_3^- \rightarrow Fe$ ligand-to-metal charge transfer band at 80 K, resulted in >80% conversion to the desired $[(cyclam\text{-}ac)Fe(N)]^+$ species (**3ox**) and dinitrogen. A spin state of $S = 3/2$ was initially proposed for complex **3ox** by comparing the field-dependent Mössbauer spectra (>1 T) with previous data for complex **2**.[5b]

We have now undertaken an in depth spectroscopic and computational study of **3** and **3ox** to elucidate the electronic structure of this fascinating high-valent system. Herein, we present our initial results of X-ray absorption spectroscopy (XAS)/extended X-ray absorption fine structure (EXAFS) spectroscopy together with Mössbauer spectroscopy, magnetic susceptibility data, and electronic structure calculations at the density functional theory (DFT) level. The results reveal that, unexpectedly, the ground-state total spin of the $(FeN)^{2+}$ core is $S = 1/2$ and not $S = 3/2$ as has been previously assumed based on the results of EPR and Mössbauer spectroscopy.[5]

The fitting of the zero-field Mössbauer spectra[5b] of a solid sample of **3**, which was irradiated at 80 K, shows the superposition of two subspectra (not shown): a minor quadrupole doublet (ca. 16% relative intensity) with parameters corresponding to the starting material (**3**), with a chemical shift $\delta = 0.27(2)$ mm s^{-1} and a quadrupole splitting of $|\Delta E_q| = 2.30(2)$ mm s^{-1}, and second, an intense symmetric quadrupole doublet at $\delta = -0.02(2)$ mm s^{-1} with a quadrupole splitting of $|\Delta E_q| = 1.60(2)$ mm s^{-1} (**3ox**, ca. 84% relative intensity). Other side products were not observed in the solid sample of **3ox**. The values of the isomer shift and quadrupole splitting of the main solid beige species were very similar to those found in the past for $[(cyclam\text{-}ac)Fe(N)]^+$ in acetonitrile solution ($\delta = -0.04(2)$ mm s^{-1} and $|\Delta E_q| = 1.67(2)$ mm s^{-1}).[5b] It is therefore concluded that photolysis in the solid state is an efficient method to obtain high yields of solid **3ox** without the presence of the photoreduced Fe^{II} species. Moreover, the photooxidized species produced by photolysis in frozen solution and in the solid state are spectroscopically indistinguishable.

The Mössbauer results, in particular, the low isomer shift of **3ox**, are consistent with a high-valent species and have previously led to the formulation of **3ox** as an Fe^V species.[5] Independent experimental data to corroborate this conclusion and to obtain further information about the electronic and geometric structure of **3ox** are highly desirable. An ideal local probe of the geometric and electronic structure of the central iron is XAS. The XAS edge is sensitive to the electronic structure and may be used as an indicator of the oxidation state.[7,8] The pre-edge region is particularly diag-

[*] Dr. N. Aliaga-Alcalde, B. Mienert, Dr. E. Bill, Prof. Dr. K. Wieghardt, Priv.-Doz. Dr. F. Neese
Max Planck Institut für Bioanorganische Chemie
Stiftstrasse 34–36, 45470 Mülheim an der Ruhr (Germany)
Fax: (+49) 208-306-3951
E-mail: wieghardt@mpi-muelheim.mpg.de
neese@mpi-muelheim.mpg.de
Dr. S. DeBeer George
Stanford Synchrotron Radiation Laboratory
SLAC, Stanford University, Stanford, CA 94309 (USA)

[**] N.A.A. thanks the Max Planck society for a postdoctoral fellowship. SSRL operations are funded by DOE, BES. The SMB program is supported by NIH, NCRR, BMTP and by DOE, BER. S.D.G. thanks Prof. J. I. Brauman and Dr. D. Walthall for use of their xenon arc lamp. Cyclam-acetato = 1,4,8,11-tetraazacyclotetradecane-1-acetato.

Supporting information for this article is available on the WWW under http://www.angewandte.org or from the author.

  DOI: 10.1002/anie.200462368

nostic and an increase of about 1 eV per oxidation state is typical for first-row transition metals. In addition, the pre-edge region provides a measure of 3d–4p mixing and thus increased intensity may be induced by exceptionally short metal–ligand bonds. EXAFS data give complimentary metrical information, providing very accurate metal–ligand bond lengths.

A comparison of the Fe K-edge spectra of **3** and **3ox**, which, for technical reasons, were recorded in frozen butyronitrile solution, is shown in Figure 1. It is observed that the

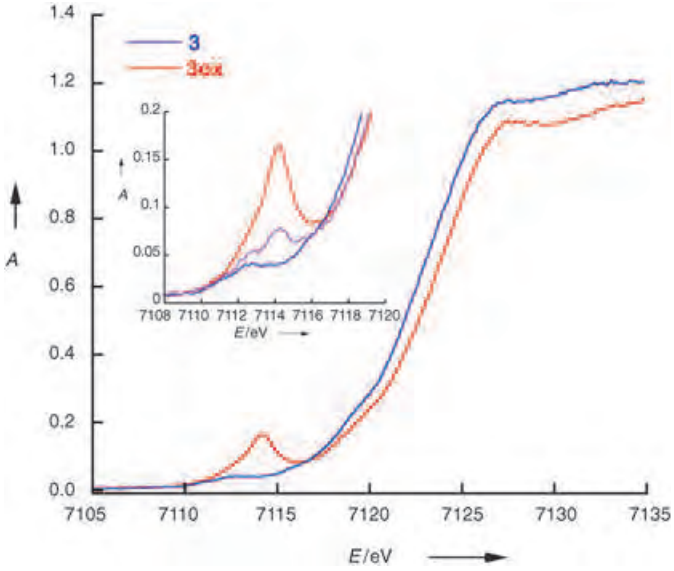

Figure 1. Iron K-edge X-ray absorption spectra of **3** (blue) and **3ox** (red). The inset is an expansion of the pre-edge region. The spectrum shown in purple was taken at an intermediate stage of illumination. *A* = normalized absorption.

pre-edge of **3ox** (at 7114.2 eV) is shifted to higher energy than **3** by about 2 eV (Fe^{III}; 7112.4 eV), consistent with a two-electron oxidation. To our knowledge, the pre-edge position of **3ox** is at the highest yet observed energy for any iron complex ($Fe^{IV}O$ edges are typically observed at about 7113.2 eV,[9] when using a reference calibration point of 7111.2 eV for the first inflection point of an Fe foil). The position of the rising edge (7123.0 eV for **3** versus 7124.1 eV for **3ox**) is also consistent with an increase in oxidation state; however, an exact assignment may be complicated by the presence of shake-up or shake-down transitions superimposed on the rising edge. Furthermore, a very intense pre-edge feature develops in **3ox** (with an area of 27 ± 2 units) at about 7114.2 eV, which is consistent with grossly increased 4p mixing into the 3d manifold and consequently with a short metal–ligand bond being formed in **3ox**. Similar features have previously been observed in high-valent $Fe^{IV}O$ species[9] and appear to be characteristic of high-valent sites with a short metal–ligand bond.

Figure 2 shows a comparison of the non-phase shift corrected Fourier transforms and EXAFS data, together with the best fits (Table 1), for complexes **3** and **3ox**. The best fit of complex **3** was obtained by including two Fe–N/O

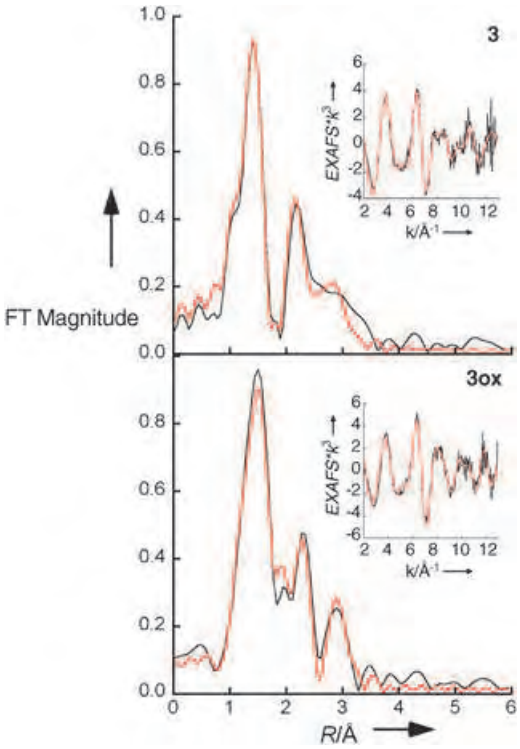

Figure 2. Comparison of non-phase shift corrected Fourier transforms for **3** and **3ox**. Experimental data are shown in black and fits in red. The insets show the respective EXAFS data.

Table 1: EXAFS fit results for **3** and **3ox**.

	R [Å]	σ^2 [Å^2]	ΔE_0	Error[a]
		3		
2 Fe–N/O	1.94	0.0018	−9.25	0.353
4 Fe–N/O	2.07	0.0064		
6 Fe–C	2.83	0.0063		
4 Fe–C	3.00	0.0032		
2 Fe–C	3.39	0.0026		
		3ox		
1 Fe–N	1.61	0.0144	−8.59	0.292
5 Fe–N/O	2.02	0.0079		
6 Fe–C	2.85	0.0047		
4 Fe–C	3.02	0.0033		
2 Fe–C	3.36	0.0026		

[a] Error is given by $\Sigma[(\chi_{obsd}-\chi_{calcd})^2 k^6]/\Sigma[(\chi_{obsd}{}^2 k^6]$.

contributions at a distance of 1.94 Å and four Fe–N/O at 2.07 Å, with outer-shell Fe–C contributions from the cyclam ligand (Figure 2, top). It should be noted that separation of these two contributions is just beyond the resolution limit of the data (ca. 0.14 Å). Fits were also attempted with a single Fe–N/O shell at 1.98 Å, giving excellent agreement with the crystallographic values,[5b] but a significantly larger residual. In either case an average Fe–N/O coordination sphere of 1.98–2.03 Å is obtained, in reasonable agreement with the crystallography.

The best fit to **3ox** (Figure 2, bottom) was obtained by including five Fe–N/O contributions at 2.02 Å and one short Fe–N distance at 1.61 Å, with additional outershell Fe–C contributions from the cyclam ligand. However, the Debye–

Waller value (σ^2) for the short Fe–N component is quite large. This value becomes much more reasonable[10] (0.006 Å^2) by decreasing the coordination number associated with the short Fe=N interaction to 0.5. The necessity of this decrease is consistent with incomplete conversion of **3ox**, as discussed above. Fits which did not include the short 1.61 Å Fe–N interaction had a significantly higher error (normalized error = 0.403) and a long frequency beat pattern, consistent with a short Fe–N vector, in the fit residual (see Supporting Information) which is clearly not observed for in the residual of **3** (see Supporting Information).[11] In addition, fits were also attempted starting with the short Fe–N distance at 1.73 Å, however, allowing this value to float resulted in a value of 1.60 Å for the shortest Fe–N distance. Finally, any attempt to modify the background subtraction always led back to the conclusion that the longest feasible Fe=N distance is $\leq$1.65 Å. We conclude from this data that there indeed is a short Fe=N bond of about 1.60 Å in **3ox**.

In our DFT calculations, we have considered two possible reaction products that differ in their spin multiplicities: a doublet (^{2}**3ox**) and a quartet (^{4}**3ox**) ground state were taken into consideration. Previously, the reaction was assumed to lead to a quartet species ^{4}**3ox** despite this being a spin-forbidden process. At the time this appeared to be reasonable because Fe^V species (d^3) are isoelectronic with the analogous Cr^{III} and Mn^{IV} species which invariably have $S = 3/2$ ground states. Quite surprisingly, the B3LYP DFT calculations on **3ox** even after inclusion of zero-point energies and solvent effects predict a doublet ground state ^{2}**3ox** (Figure 3).

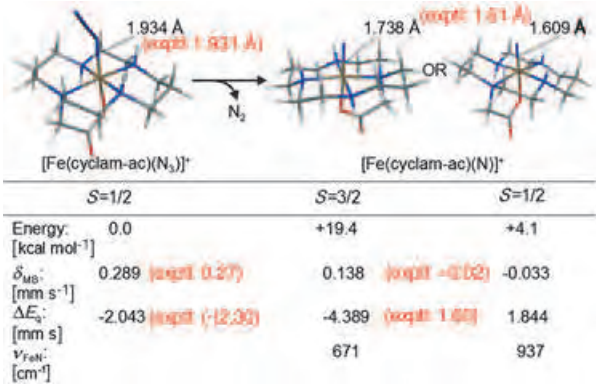

Figure 3. Computed structures, energies, and properties of **3ox**, ^{4}**3ox**, and ^{2}**3ox** (experimental values in red).

However, it is known that DFT methods are biased in favor of low-spin states.[12] Thus, despite the considerable energy difference of about 15 kcal mol^{-1} (ca. 14 kcal mol^{-1} in MeCN) between ^{2}**3ox** and ^{4}**3ox**, which is outside the accepted error bars of the B3LYP method, one is well advised in seeking more evidence in favor of such an unusual spin-state assignment. As will be elaborated in detail elsewhere, the magnetic properties of **3ox** are not straightforwardly interpreted, owing to the presence of other doublet and quartet terms lying close to the ground state. Thus, EPR, MCD, and magnetic Mössbauer analyses require a more elaborate spin Hamiltonian model than is usual for $S = 1/2$. However, the presence of a doublet ^{2}**3ox** species could be experimentally corroborated from a magnetic susceptibility measurement (Figure 4). Since the macroscopic susceptibility data are much less sensitive to details of the electronic structure, we could

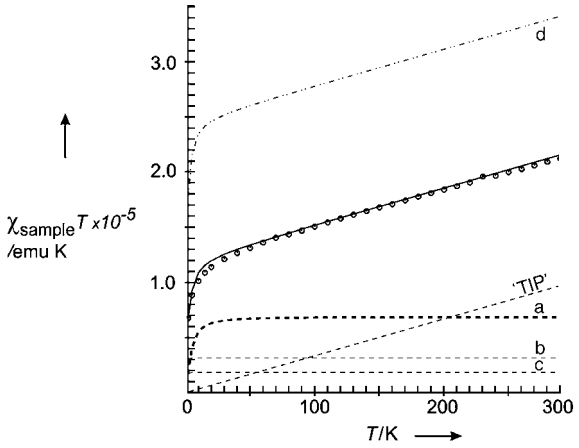

Figure 4. Temperature dependence of the magnetic susceptibility times temperature of a powder sample of photolyzed **3** (open circles) and deconvolution into three major paramagnetic components (traces a–c) and a TIP-like contribution ('TIP', temperature-independent paramagnetism). The 'TIP' arises most probably from minor contamination of small magnetic (oxide) particles (2%). The weights of the different paramagnetic contributions are given in molar percentages that were calculated with molecular weights of $M_r = 472.1$ g mol^{-1} (**3ox**, $S = 1/2$, 57%, trace a), $M_r = 500.1$ g mol^{-1} (**3**, 26%, $S = 1/2$, trace b), $M_r = 458.1$ g mol^{-1} ([(cyclam-ac)Fe^{II})], $S = 2$, 15%, trace c). Diamagnetic contributions were not taken into account since their signal is hidden under the 'TIP' contribution. The dashed lines for the contributions from ^{2}**3ox**, **3**, and the Fe^{II} component are simulations with the usual spin-Hamiltonian.[5a] The upper line in the graph (d) corresponds to the fitting of the data when the spin ground state of **3ox** is taken to be $S = 3/2$.

apply the usual spin Hamiltonian approach for a simulation of the temperature-dependence of χT for a powder sample. The data are perfectly deconvoluted into three paramagnetic contributions, namely from the remaining starting complex **3** (26%, $S = 1/2$) and an Fe^{II} contamination from some photoreduction (15%, $S = 2$), and from the target material ^{2}**3ox** which is the major component (57%, $S = 1/2$). Since the relative amounts of the different constituents correspond within a narrow error margin of $\pm$1.4% of an 80 K Mössbauer spectrum of an aliquot of the SQUID sample (see Supporting Information), we trust that **3ox** in fact has indeed the postulated doublet ground state. By contrast, the trace (d) in Figure 4 demonstrates that there it is not possible to fit the data under the assumption of a $S = 3/2$ ground state for **3ox**.

Rather interestingly, the optimized structures of ^{2}**3ox** and ^{4}**3ox** show a large difference in the computed Fe=N bond lengths, which are 1.609 Å for ^{2}**3ox** and 1.738 Å for ^{4}**3ox**. We note that the Fe^{III}–N_3 distance in low-spin **3** is accurately predicted by the calculations (1.934 Å calculated versus 1.931 Å (X-ray) and 1.94 Å (EXAFS)). Since DFT is typically accurate within 0.01–0.03 Å for short and strong metal–ligand bonds such as the ones formed with oxo ligands in complexes

analogous to **3** and **3ox**,[5b,10] this provides strong evidence that the short Fe=N bond observed by EXAFS spectroscopy indeed corresponds to ^{2}**3ox** and not to ^{4}**3ox**.

Further strong evidence for the doublet ground state of **3ox** is obtained from the calculated Mössbauer parameters of ^{2}**3ox** and ^{4}**3ox**: the calculated isomer shifts are $-0.033\ mm\,s^{-1}$ and $0.138\ mm\,s^{-1}$, respectively. Thus, the experimental value of $-0.02\ mm\,s^{-1}$ agrees only with the computed isomer shift of ^{2}**3ox**. Based on previous isomer shift calculations, the error in the predicted value is expected to be less than $0.1\ mm\,s^{-1}$.[10,13,14] Consequently, the calculations provide strong evidence for ^{2}**3ox** and not ^{4}**3ox** being the observed species. The calculation of the quadrupole splitting is in line with this result, giving values of $-4.39\ mm\,s^{-1}$ for ^{4}**3ox** and $+1.84\ mm\,s^{-1}$ for ^{2}**3ox** compared with the experimental value of $|\Delta E_q| = 1.60\ mm\,s^{-1}$. The large value calculated for ^{4}**3ox** is far from that derived from the experiment and outside the error bar of the calculations which usually give results within about $0.3\ mm\,s^{-1}$ of those from the experiment even in complicated bonding situations.[14,10] As an independent check we note that the Mössbauer parameters calculated for **3** are in excellent agreement with the experimental values ($\delta_{calcd} = 0.289\ mm\,s^{-1}$, $\delta_{exptl} = 0.27\ mm\,s^{-1}$; $|\Delta E_q^{calcd}| = 2.04\ mm\,s^{-1}$, $|\Delta E_q^{exptl}| = 2.30\ mm\,s^{-1}$).

Having fairly rigorously established that ^{2}**3ox** is the species produced in the photolysis experiments, we want to briefly comment on the nature of the iron–nitrido bond in this unprecedented bonding situation (Figure 5). It is well known

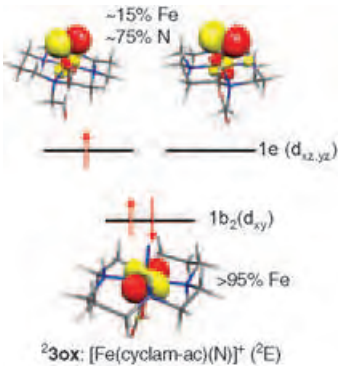

Figure 5. Ground-state electronic configuration of ^{2}**3ox**. The quartet state configuration is obtained by occupying all three MOs with one spin-up electron.

that in distorted octahedral environments the metal d orbitals split into an (almost) degenerate π-(anti)bonding t_{2g} and an (almost) degenerate σ-(anti)bonding set. However, if there is a dominant short metal–ligand bond, as in the present case of high-valent species, the splittings in both sets may become very large and often exceed 1 eV.[4h] In this case, the general rules about relative spin-state energetics as contained in the Tanabe–Sugano diagrams for octahedral symmetry may fail to hold, and in addition, there will be a very large anisotropic covalency induced by the strongly covalent metal–ligand bonds to the terminal oxo or nitride ligand. For the d^3 system examined here, the splitting between the almost pure metal d_{xy} orbital and the metal-derived $d_{xz,yz}$ orbitals apparently becomes so large that it is energetically more favorable to assume the (orbitally degenerate) configuration $^2E((d_{xy})^2\text{-}(d_{xz,yz})^1)$ (in approximate C_{4v} symmetry) as compared to the "canonical" configuration $^4A_2((d_{xy})^1(d_{xz})^1(d_{yz})^1)$. This will be further elaborated by high-level multireference ab initio calculations together with the results from MCD spectroscopy in a forthcoming paper. We indeed observe in the DFT calculations a very large anisotropic covalency of the iron–nitrido bond with the two metal-derived $d_{xz,yz}$ orbitals having only about 15% metal and as much as 75% N character according to a Löwdin population analysis. Moreover, the 4p character in the unoccupied metal-d derived MOs increases from 0.2% in **3** to 5.8% in ^{4}**3ox** and 7.3% in ^{2}**3ox.** The dramatic increase in 4p character explains the very intense XAS pre-edge feature of **3ox** (despite the decrease in 3d character). The very low metal character in the formally metal $d_{xz,yz}$ orbitals is, to a certain extent, underestimated by DFT calculations. Highly correlated ab initio methods provide somewhat larger values. However, a very large amount of charge transfer from N^{3-} to Fe^V is already expected on electrostatic grounds. Thus, a possible formulation of the electronic structure as a resonance between $Fe^V(S_{Fe}=3/2)N^{3-}(S_N=0) \leftrightarrow Fe^{III}(S_{Fe}=1/2)N^-(S_N=1)$ seems plausible for ^{4}**3ox**, whereas ^{2}**3ox** may best be represented by the resonance structures of the type $Fe^V(S_{Fe}=1/2)N^{3-} \leftrightarrow Fe^{II}(S_{Fe}=0)N^{\cdot}(S_N=1/2)$. The system will nevertheless behave to a certain extent like a d^3 system and we prefer to formulate the species as an Fe^V species. It is noted that the amount of charge transfer from N^{3-} to Fe^V is much larger than from O^{2-} to Fe^{IV} in $(FeO)^{2+}$ where the metal-derived $d_{xz,yz}$ orbitals are more equally shared between Fe and O.[3b,15]

The large calculated increase in Fe–N distance of about 0.13 Å in ^{4}**3ox** compared to ^{2}**3ox** is nicely explained by the strongly antibonding character of the $1e(d_{xz,yz})$ set, which is doubly occupied in ^{4}**3ox** but only singly occupied in ^{2}**3ox**. Likewise, we have calculated an increase in the harmonic vibrational Fe=N stretching frequency from $671\ cm^{-1}$ in ^{4}**3ox** to $937\ cm^{-1}$ in ^{2}**3ox** corresponding to an increase in force constant from about $0.19\ mdyn\,Å^{-1}$ to about $0.42\ mdyn\,Å^{-1}$. These numbers tend to be reliable from DFT but an independent experimental confirmation is, unfortunately, missing. In terms of formal bond order, one has to view the $(FeN)^{2+}$ core as a highly covalent unit with a double bond in ^{4}**3ox** and a bond of order 2.5 in ^{2}**3ox**. It is most intriguing that the ground state of ^{2}**3ox** is (almost) orbitally degenerate and will thus feature two low-lying Kramers doublets. As will be elaborated in detail elsewhere, this situation is experimentally difficult to distinguish from a zero-field split spin quartet state and leads to fascinatingly complicated magnetic behavior.

In summary, we have shown in this work through a combination of theory and experiment that photolysis of the non-heme Fe^{III}–N_3^- complex **3** in the solid state nearly quantitatively affords the desired genuine Fe^V–nitrido complex **3ox**. This complex features a highly unusual, almost orbitally degenerate, spin doublet ground state with a short (1.60 Å) Fe=N distance corresponding to a Fe=N bond of order 2.5. While in terms of the formal oxidation state, there is no doubt that **3ox** is to be formulated as an iron(v) species, the spectroscopic oxidation state[16] in this system is much harder

to determine unambiguously. In particular, the XAS and Mössbauer parameters are in full agreement with a highly oxidized iron center, whereas the DFT calculations, which lead to agreement with the spectroscopic experiments, show an excessive transfer of negative charge from the nitride ligand to the central iron.

Experimental Section

The irradiation process of **3** was performed on a suspension of powder samples in liquid N_2 over 4 h with a Rayonet Photochemical Reactor (RPR-100) equipped with 419 nm tubes. The photolysis process was followed optically by changes in the color of the species, from red-brown to pale beige, and monitored by IR spectroscopy. Mössbauer and magnetic susceptibility data were collected and analyzed as reported previously.[5] For SQUID measurements (radiation for about 10 h), the sample powder was not in direct contact with liquid N_2, but sealed in a flask to avoid condensation of water and subsequent deterioration during sample transfer to the SQUID magnetometer at ambient temperature.

XAS data for complexes **3** and **3ox** were recorded at the Stanford Synchrotron Radiation Laboratory (SSRL) on focused beam line 9–3, as previously described.[17] Internal energy calibration was performed by assigning the first inflection point of the Fe foil spectrum to 7111.2 eV. XAS samples of **3** (ca. 2 mM) were dissolved in degassed PrCN, loaded into 2 mm Lucite XAS cells with polypropylene windows and then frozen immediately in liquid nitrogen prior to XAS measurements. The photooxidation of **3** to **3ox** was performed in liquid N_2 by exposure for about 1.5 h to a 1000 W Xenon arc lamp equipped with a monochromator and a long pass filter for energy selection at 420 nm. During XAS measurements, samples were maintained at a constant temperature of 10 K by an Oxford Instruments CF1208 continuous-flow liquid-helium cryostat. Data were processed and analyzed as described in reference [17]. Samples were monitored for photoreduction throughout the course of data collection. Only those scans, which showed no evidence of photoreduction were included in the final averages.

Electronic structure calculations were performed with the program package ORCA developed in our laboratory. Structures were optimized at the BP86 level of DFT with polarized triple-ζ basis sets.[18] Calculation of the harmonic force fields of all species at the same level proved all structures to be local minima on the potential energy surface and provided vibrational frequencies used to calculate zero-point energies and thermal corrections. Total electronic energies were calculated with the TZVPP basis set and the B3LYP functional. The same functional was used together with special basis sets for the prediction of Mössbauer parameters.[14] Environmental effects were modeled with the conductor like screening model (COSMO) as implemented in ORCA and using acetonitrile ($\varepsilon = 36.6$) as solvent.

Received: October 20, 2004
Published online: April 21, 2005

Please note: Minor changes have been made to this manuscript since its publication in *Angewandte Chemie* EarlyView. The Editor.

Keywords: electronic structure · EXAFS spectroscopy · iron · Mössbauer spectroscopy · nitrido ligands

[1] L. D. Slep, F. Neese, *Angew. Chem.* **2003**, *115*, 3048; *Angew. Chem. Int. Ed.* **2003**, *42*, 2942, and references therein.
[2] a) M. Costas, M. P. Mehn, M. P. Jensen, L. Que, Jr., *Chem. Rev.* **2004**, *104*, 939; b) D. L. Harris, *Curr. Opin. Chem. Biol.* **2001**, *5*, 724.
[3] a) J.-U. Rohde, J.-H. In, M. H. Lim, W. W. Brennessel, M. R. Bukowski, A. Stubna, E. Münck, W. Nam, L. Que, Jr., *Science* **2003**, *299*, 1037; b) A. Decker, J.-U. Rhode, L. Que, Jr., E. I. Solomon, *J. Am. Chem. Soc.* **2004**, *126*, 5378.
[4] a) T. Jüstel, J. Bendix, N. Metzler-Nolte, T. Weyhermüller, B. Nuber, K. Wieghardt, *Inorg. Chem.* **1998**, *37*, 35; b) J. Bendix, K. Meyer, T. Weyhermüller, E. Bill, N. Metzler-Nolte, K. Wieghardt, *Inorg. Chem.* **1998**, *37*, 1767; c) T. Jüstel, M. Müller, T. Weyhermüller, C. Kressl, E. Bill, P. Hildebrandt, M. Lengen, M. Grodzicki, A. X. Trautwein, B. Nuber, K. Wieghardt, *Chem. Eur. J.* **1999**, *5*, 793; d) K. Meyer, J. Bendix, N. Metzler-Nolte, T. Weyhermüller, K. Wieghardt, *J. Am. Chem. Soc.* **1998**, *120*, 7260; e) K. Meyer, J. Bendix, E. Bill, T. Weyhermüller, K. Wieghardt, *Inorg. Chem.* **1998**, *37*, 5180; f) J. Bendix, T. Weyhermüller, E. Bill, K. Wieghardt, *Angew. Chem.* **1999**, *111*, 2932; *Angew. Chem. Int. Ed.* **1999**, *38*, 2766; g) J. Bendix, R. J. Deeth, T. Weyhermüller, E. Bill, K. Wieghardt, *Inorg. Chem.* **2000**, *39*, 930; h) C. A. Grapperhaus, E. Bill, T. Weyhermüller, F. Neese, K. Wieghardt, *Inorg. Chem.* **2001**, *40*, 4191, and references therein; i) J. Bendix, *J. Am. Chem. Soc.* **2003**, *125*, 13348; j) T. Birk, J. Bendix, *Inorg. Chem.* **2003**, *42*, 7608; k) M. H. Huynh, T. J. Meyer, M. A. Hiskey, D. L. Jameson, *J. Am. Chem. Soc.* **2004**, *126*, 3608; l) W.-L. -Man, T.-M. Tang, T.-W. Wong, T.-C. Lau, S.-M. Peng, W.-T. Wong, *J. Am. Chem. Soc.* **2004**, *126*, 478.
[5] a) K. Meyer, E. Bill, T. Weyhermüller, K. Wieghardt, *J. Am. Chem. Soc.* **1999**, *121*, 4859; b) C. A. Grapperhaus, B. Mienert, E. Bill, T. Weyhermüller, K. Wieghardt, *Inorg. Chem.* **2000**, *39*, 5306; c) W.-D. Wagner, J. Nakamoto, *J. Am. Chem. Soc.* **1988**, *110*, 4044; d) W.-D. Wagner, J. Nakamoto, *J. Am. Chem. Soc.* **1989**, *111*, 1590.
[6] T. A. Betley, J. C. Peters, *J. Am. Chem. Soc.* **2004**, *126*, 6252.
[7] J. L. DuBois, P. Mukherjee, T. D. P. Stack, B. Hedman, E. I. Solomon, K. O. Hodgson, *J. Am. Chem. Soc.* **2000**, *122*, 5775.
[8] T. E. Westre, P. Kennepohl, J. G. DeWitt, B. Hedman, K. O. Hodgson, E. I. Solomon, *J. Am. Chem. Soc.* **1997**, *119*, 6297.
[9] a) M. H. Lim, J.-U. Rohde, A. Stubna, M. R. Bukowski, M. Costas, R. Y. N. Ho, E. Münck, W. Nam, L. Que, Jr., *Proc. Natl. Acad. Sci. USA* **2003**, *100*, 3665; b) J.-U. Rohde, S. Torelli, X. Shan, M. H. Li, J. Kaizer, K. Chen, W. Nam, L. Que, Jr., *J. Am. Chem. Soc.* **2004**, *126*, 16750.
[10] L. D. Slep, A. Mijovilovich, W. Meyer-Klaucke, T. Weyhermüller, E. Bill, E. Bothe, F. Neese, K. Wieghardt, *J. Am. Chem. Soc.* **2003**, *125*, 15554.
[11] It should be noted that EXAFS fits were also performed on the sample at an intermediate stage of illumination, shown in Figure 1. These data clearly required a short Fe–N distance (1.61 Å) in the fit (see Figure S4–S6 in the Supporting Information), supporting the fact that the change in electronic structure is coupled to the formation of a short Fe–N bond (1.6 Å).
[12] a) M. Reiher, *Inorg. Chem.* **2002**, *41*, 6928; b) A. Fouqueau, S. Mer, M. E. Casida, L. M. L. Daku, A. Hauser, T. Mieva, F. Neese, *J. Chem. Phys.* **2004**, *120*, 9473.
[13] R. Garcia Serres, C. A. Grapperhaus, E. Bothe, E. Bill, T. Weyhermüller, F. Neese, K. Wieghardt, *J. Am. Chem. Soc.* **2004**, *126*, 5138.
[14] F. Neese, *Inorg. Chim. Acta* **2002**, *337C*, 181.
[15] F. Neese, J. M. Zaleski, K. E. Loeb, E. I. Solomon, *J. Am. Chem. Soc.* **2000**, *122*, 11703.
[16] C. K. Jörgensen in *Oxidation Numbers and Oxidation States*, Springer, Heidelberg, **1969**.
[17] E. C. Wasinger, N. Mitić, B. Hedman, J. Caradonna, E. I. Solomon, K. O. Hodgson, *Biochemistry* **2002**, *41*, 6211.
[18] TZVP: A. Schäfer, C. Huber, R. Ahlrichs, *J. Chem. Phys.* **1994**, *100*, 5829.

Nanoparticles

Molecular Recognition by Calix[4]arene-Modified Gold Nanoparticles in Aqueous Solution**

T. Robert Tshikhudo, Domenico Demuru, Zhenxin Wang, Mathias Brust, Andrea Secchi, Arturo Arduini, and Andrea Pochini**

The concept of exploiting metal clusters for nanotechnology applications dates back to the development of the original Au_{55} cluster by Schmid et al. in 1981.[1] Over the past decade, so-called monolayer protected clusters (MPCs) of gold and, to a lesser extent, silver have been studied extensively owing to their extreme stability and the plethora of tunable properties that are controlled by the particle size and by the ligand chemistry.[2–8] The stability is usually achieved by the use of thiolate ligands, which form a protective shell around the particles to which they are attached by the strong Au–S interaction. Typical sizes of MPCs range from 1 to approximately 40 nm depending on the preparation method used. Since most preparations lead to materials that are insoluble in water a comparatively small number of studies have been carried out in aqueous systems.[9–18] In particular, in view of future bioanalytical applications it is, however, desirable to develop new MPC systems that are not only stable and soluble in water, but also capable of molecular recognition in aqueous systems. Very stable, yet chemically versatile water-soluble MPCs are obtained when a sulfanylalkyl oligo(ethylene glycol) is used as a stabilizing ligand.[16] Herein we report the preparation and chemical properties of 14-nm gold MPCs, which are stabilized in this way and, in addition, carry in their ligand shell calix[4]arene moieties, which confer their specific molecular recognition properties to the particles. Calixarenes are host molecules which can bind cationic guests strongly and with high specificity depending on the size of the calixarene cavity.[19,20] Some of us have recently shown that, in non-aqueous systems, the incorporation of calixarenes in 1.5–4-nm MPCs can enhance their affinity to guest molecules.[20] By themselves, calixarenes are completely insoluble in water, which significantly limits their potential applications as molecular recognition units. The sulfanylalkyl oligo(ethylene glycol) ligands in the system described herein act therefore not only as stabilizers for the MPCs but also as solubilizers for the attached calix[4]arene units. It is thus now possible to demonstrate molecular recognition by an unmodified calixarene cavity in water. The particles prepared have been characterized by transmission electron microscopy (TEM) and by UV/Vis, and NMR spectroscopy. Specific recognition of immobilized cationic pyridinium moieties by the calixarene-modified MPCs in aqueous solution has been demonstrated by a simple color test and by atomic force microscopy (AFM).

The preparation of the calixarene-modified nanoparticles is schematically illustrated in Figure 1. Citrate-stabilized gold

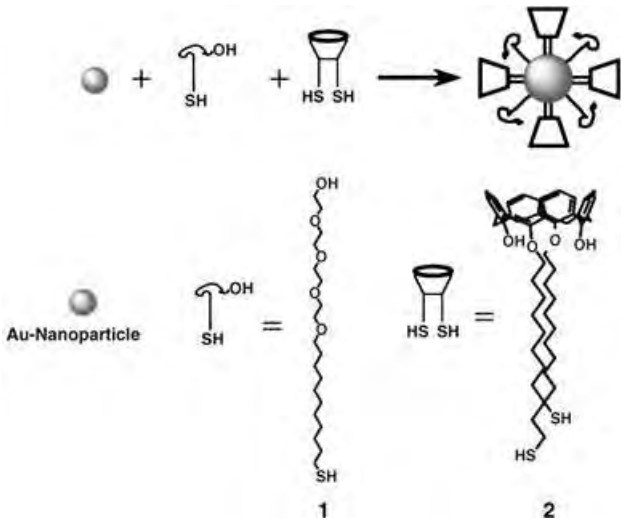

Figure 1. Reaction scheme illustrating the one-step stabilization and functionalization of gold nanoparticles with **1** and **2** carried out in a THF/water mixture.

hydrosols were treated with a 2:1 mixture of the stabilizing ligand (1-sulfanylundec-11-yl) tetraethylene glycol (**1**) and 25,27-bis(11-thio-1-oxyundecan)-26,28-dihydroxycalix[4]arene (**2**) in a water/THF solvent system to directly give the modified particles **3**, which were isolated from excess ligand material by centrifugation. Given the conformation of the relatively rigid **2** it is reasonable to assume that both thiol functionalities of **2** bind to the surface of the same gold particle. Otherwise, cross-linking of particles by bisthiol bridges and precipitation of aggregates could be expected,[21] but this has not been observed in this case. On the contrary, the particles are extremely stable and can be centrifuged, dried, and re-suspended in aqueous solution several times without loss of material. The ruby red suspensions are very robust against non-specific aggregation. For example, unlike most other hydrosols, the particles do not aggregate even in a 2 M sodium chloride solution. They exhibit a characteristic plasmon absorption band in the UV/Vis spectrum at 526 nm and their size is that of the original citrate-stabilized particles (14 ± 1 nm) as confirmed by TEM (Figure 2).

[*] T. R. Tshikhudo, Dr. Z. Wang, Dr. M. Brust
Centre for Nanoscale Science
Department of Chemistry
University of Liverpool
Liverpool L69 7ZD (UK)
Fax: (+44) 151-794-3588
E-mail: m.brust@liv.ac.uk
D. Demuru, Dr. A. Secchi, Prof. A. Arduini, Prof. A. Pochini
Dipartimento di Chimica Organica ed Industriale
dell'Università
Parco Area delle Scienze 17/a, 43100 Parma (Italy)
Fax: (+39) 521-905472
E-mail: andrea.pochini@unipr.it

[**] The Authors thank Mintek, South Africa (Project AuTEK), the BBSRC (Centre for BioArray Innovation) and the Italian FIRB (Manipolazione Molecolare per Macchine Nanometriche) for financial support.

Supporting information for this article is available on the WWW under http://www.angewandte.org or from the author.

 DOI: 10.1002/anie.200462909

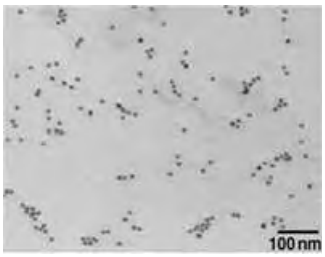

Figure 2. TEM image of the 14-nm gold nanoparticles **3**, that are stabilized and functionalized with **1** and **2**.

The molecular composition of the ligand shell has been studied by ^{1}H NMR spectroscopy (Figure 3). As expected, the spectrum of the particles shows significant peak broadening, in particular of the methylene protons adjacent or close to the sulfur atom that binds to the surface of the particle. This effect is chiefly due to the lack of mobility of the closely packed molecules in the ligand shell, which on the nanometer scale resembles a solid-state material. Several other factors contributing to line broadening in NMR spectra of MPCs have also been suggested, and the phenomenon is still subject to some debate.[5,6,14] Although the broadening of the features impedes a more detailed interpretation, it is apparent that all the main characteristic features of the two different ligands are present in the spectrum of the particles. Importantly, slightly broadened signals between $\delta = 6.6$ and 7.2 ppm, which are characteristic of the aromatic protons in the calixarene cavity are clearly present in the spectrum of the particles. This result indicates the inclusion of **2** in the ligand shell. It can be inferred from previous studies of peptide-stabilized MPCs of the same size that the number of thiol ligands is typically between 800 and 1000 molecules per gold particle.[18] Under the assumption of similar adsorption kinetics for both **1** and **2** it can thus be estimated that each gold particle carries on the order of 300 molecules of **2**. A quantitative analysis of the binding properties of the material will be required to confirm this estimate. Such experiments are underway. The binding properties of a solution-free, water-soluble model calix[4]arene derivative towards *N*-alkyl pyridinium salts in D_2O are given quantitatively in the Supporting Information. The molecular recognition properties of the particle-bound calixarene in water are qualitatively demonstrated by specific binding studies using two different chemically modified substrates (Figure 4). In the simplest case the substrate

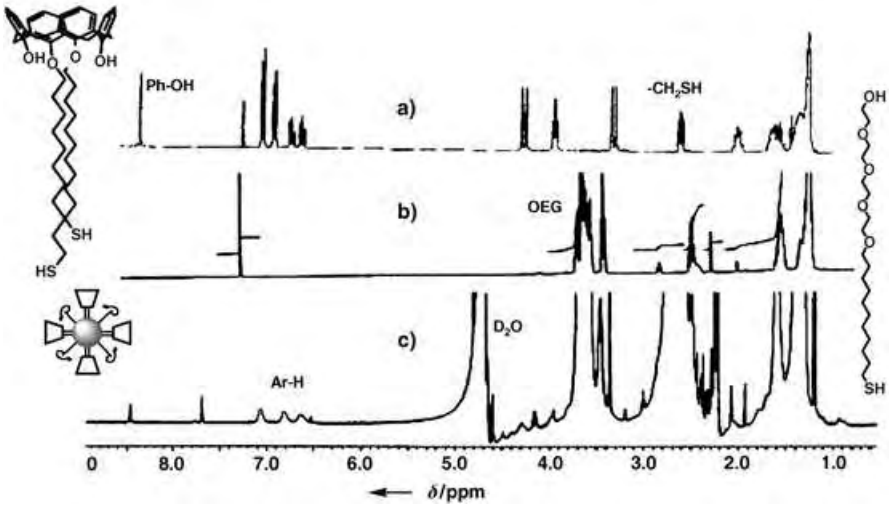

Figure 3. ^{1}H NMR spectra of **2** (a) and **1** (b) in $CDCl_3$, and of **3** (c) in D_2O showing that **1** and **2** have been attached to the gold nanoparticles (the signals of the methylene protons adjacent to the thiol and oligoethylene glycol (OEG) protons are marked). In particular, the signals of the aromatic protons (Ar-H) in spectrum (c) indicate the presence of the calixarene cavity in the ligand shell of the particles.

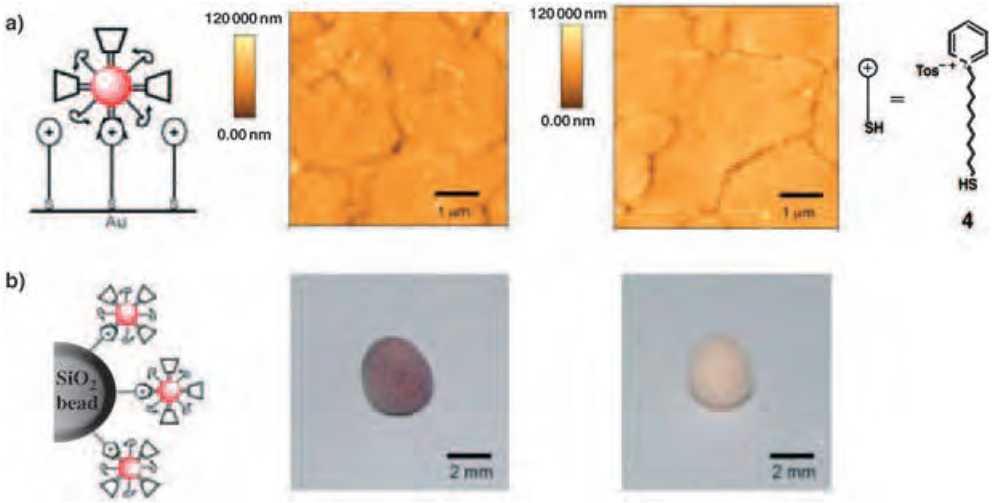

Figure 4. Specific binding of the calixarene-modified gold nanoparticles **3**, from aqueous solution to a self-assembled monolayer (SAM) of the pyridinium ions of **4** (Tos = (4-methylphenyl)sulfonyl) on a gold surface shown by AFM (a) and to a molecular sieve bead primed with **4** (b). The control experiments (right) show the nonspecific attachment of only very few particles to the SAMs (a) and no visible attachment of particles to the molecular sieve beads (b).

was prepared by the nonspecific adsorption of **4** (Figure 4) to white molecular sieve beads. For non-aqueous media it is known that the cationic pyridinium moiety is specifically recognized by calix[4]arenes.[20] The nanoparticles **3** bind specifically from aqueous solution to the molecular sieve beads primed with **4** indicating that the calixarene cavity of **2** exhibits its characteristic cation binding properties also in aqueous media and when immobilized in the ligand shell of the MPCs. This binding interaction is easily observed with the naked eye owing to the intense red color of the gold nanoparticles. A number of control experiments clearly confirmed that both the pyridinium and the calixarene moieties have to be present to achieve any attachment of MPCs to the molecular sieve beads. Further binding studies were carried out by AFM using a self-assembled monolayer (SAM) of **4** on a flat gold surface as the substrate. As demonstrated in the AFM images in Figure 4 a the calixarene-modified nanoparticles **3** were found to bind selectively to this SAM from aqueous solution, while binding to clean gold surfaces occurred only as a non-specific minority event. MPCs without calixarene in their ligand shell did not show any significant binding to the SAMs or to clean gold surfaces.

In conclusion, we have introduced a very simple route for the preparation of water-soluble calixarene-functionalized MPCs of gold. Importantly, it has been demonstrated that in an aqueous environment the calixarene retains its molecular recognition properties, which have been utilized herein to bind the MPCs selectively to chemically modified substrates. The MPCs also act as readily detectable markers of the specific recognition events demonstrating a high potential for simple, color-based diagnostic tests, for example, those required for many routine bioanalytical applications. The preparative method is very general and can readily be adapted to other artificial molecular recognition systems. Particularly attractive is the opportunity demonstrated, to make totally water insoluble recognition systems amenable to aqueous solutions, which again is of interest in the context of bioanalytical applications of MPCs.

Experimental Section

Citrate-stabilized gold nanoparticles of 14 nm diameter were prepared following the classical Turkevich Frens procedure.[22,23] Briefly, an aqueous solution of sodium citrate (10 mL, 17 mM) was added to a boiling aqueous solution of $HAuCl_4$ (180 mL, 0.3 mM), and the reaction mixture was heated under reflux for 30 min. It was then allowed to cool to room temperature, stirred overnight, and filtered before use (0.45 μm millipore filter). **1** was synthesized as described in [24]. **2** was synthesized as described in [20].

3: THF (12.5 mL) was added to an aqueous solution of citrate-stabilized gold nanoparticles (12.5 mL, 2.9 nM). To this mixture, solutions of **1** (10 mg, 0.025 mmol, 0.5 mL) and **2** (10 mg, 0.012 mmol, 0.5 mL) in THF were added simultaneously under stirring. It was stirred for 3 h and filtered (0.45 μm millipore filter). The particles were purified by repeated centrifugation (3 times) at 11000 rpm (Sigma 1-13 model) and re-dispersion in water. A molar absorption coefficient of $4.2 \times 10^8\,M^{-1}cm^{-1}$ (at 526 nm) based on gold nanoparticles of 15 ± 1.2 nm diameter was used to calculate a final concentration of 1.5 nM (12.5 mL).[25] For ^1H NMR spectroscopy pellets of centrifuged particles were dried under vacuum overnight and re-dissolved in D_2O.

4: Thioacetic acid S-[11-(toluene-4-sulfonyloxy)-undecyl] ester (**a**) was prepared by refluxing a mixture of toluene-4-sulfonic acid undec-10-enyl ester (5 g, 15.4 mmol) and thioacetic acid (2.3 g, 31 mmol) in toluene (200 mL) for 3 h under exclusion of oxygen and in the presence of a catalytic amount of 2,2′-azobis[(2-methyl)-propanenitrile] (AIBN) and subsequent removal of the solvent by rotary evaporation. The solid crude product was dissolved in CH_2Cl_2, washed with water and sodium hydrogen carbonate, and purified by column chromatography (silica gel, hexane 90%/ ethyl acetate 10%) to give a yellowish viscous solid (90% yield). Pyridine (0.5 g, 5 mmol) was added to a solution of **a** in acetonitrile (2 g, 5 mmol, 100 mL) and heated under reflux for 24 h. The solvent was removed by rotary evaporation and the pure white solid product was obtained by precipitation in ethyl acetate/acetone in good yield (80%). This white solid (2 g, 4 mmol) and *para*-toluene sulfonic acid (1 g, 7 mmol) were dissolved in methanol (20 mL) and heated under reflux overnight then the solvent was removed by rotary evaporation. Precipitation of the resulting mixture in CH_2Cl_2 yielded a pure white sticky solid product **4** (75% yield). SAMs of **4** on gold (gold films of approximately 250-nm thickness on quartz glass, Arrandee) were prepared by overnight immersion of the cleaned and flame-annealed substrates in a solution of **4** in $CHCl_3$ (5 mL, 1.2×10^{-4} M) and subsequent thorough rinsing with $CHCl_3$ and drying in a stream of nitrogen. Single molecular-sieve beads (4 Å type, Aldrich) were modified by overnight immersion in solutions of **4** (2.5 mL, 1.2×10^{-4} M) in chloroform. After removal from the solution, the beads were washed thoroughly with chloroform and allowed to dry at room temperature. Specific recognition experiments were carried out by overnight immersion of the substrates (SAMs and beads) in a solution of **3** (0.034 nM, 2.5 mL for SAMs and 1.2 nM, 1.5 mL for beads). Adequate control experiments were performed to exclude the possibility of nonspecific binding.

For spectroscopic data and elemental analyses see the Supporting Information.

Received: December 11, 2004
Published online: April 7, 2005

Keywords: calixarenes · gold · molecular recognition · nanoparticles · water solubility

[1] G. Schmid, R. Pfeil, R. Boese, F. Bandermann, S. Meyers, G. H. M. Calis, W. A. Vandervelden, *Chem. Ber.* **1981**, *114*, 3634.
[2] M. Brust, M. Walker, D. Bethell, D. J. Schiffrin, R. Whyman, *J. Chem. Soc. Chem. Commun.* **1994**, 801.
[3] R. L. Whetten, M. N. Shafigullin, J. T. Khoury, T. G. Schaaff, I. Vezmar, M. M. Alvarez, A. Wilkinson, *Acc. Chem. Res.* **1999**, *32*, 397.
[4] G. Markovich, C. P. Collier, S. E. Henrichs, F. Remacle, R. D. Levine, J. R. Heath, *Acc. Chem. Res.* **1999**, *32*, 415.
[5] A. C. Templeton, W. P. Wuelfing, R. W. Murray, *Acc. Chem. Res.* **2000**, *33*, 27.
[6] A. Badia, R. B. Lennox, L. Reven, *Acc. Chem. Res.* **2000**, *33*, 475.
[7] M. Brust, C. J. Kiely, *Colloids Surf. A* **2002**, *202*, 175.
[8] M. C. Daniel, D. Astruc, *Chem. Rev.* **2004**, *104*, 293.
[9] W. P. Wuelfing, S. M. Gross, D. T. Miles, R. W. Murray, *J. Am. Chem. Soc.* **1998**, *120*, 12696.
[10] T. G. Schaaff, G. Knight, M. N. Shafigullin, R. F. Borkman, R. L. Whetten, *J. Phys. Chem. B* **1998**, *102*, 10643.
[11] M. Bartz, J. Kuther, G. Nelles, N. Weber, R. Seshadri, W. Tremel, *J. Mater. Chem.* **1999**, *9*, 1121.
[12] J. Liu, S. Mendoza, E. Roman, M. J. Lynn, R. Xu, A. E. Kaifer, *J. Am. Chem. Soc.* **1999**, *121*, 4304.
[13] A. C. Templeton, S. W. Chen, S. M. Gross, R. W. Murray, *Langmuir* **1999**, *15*,66.

[14] O. K. Kohlmann, W. E. Steinmetz, X. Mao, W. P. Wuelfing, A. C. Templeton, R. W. Murray, C. S. Johnson, Jr., *J. Phys. Chem. B* **2001**, *105*, 8801.
[15] E. E. Foos, A. W. Snow, M. E. Twigg, M. G. Ancona, *Chem. Mater.* **2002**, *14*, 2401.
[16] A. G. Kanaras, F. S. Kamounah, K. Schaumburg, C. J. Kiely, M. Brust, *Chem. Commun.* **2002**, 2294.
[17] P. Pengo, S. Polizzi, M. Battagliarin, L. Pasquato, P. Scrimin, *J. Mater. Chem.* **2003**, *13*, 2471.
[18] R. Levy, N. T. K. Thanh, R. C. Doty, I. Hussain, R. J. Nichols, D. J. Schiffrin, M. Brust and D. G. Fernig, *J. Am. Chem. Soc.* **2004**, *126*, 10076.
[19] a) W. Abraham, *J. Inclusion Phenom. Macrocyclic Chem.* **2002**, *43*, 159; b) A. Arduni, E. Brindani, G. Giorgi, A. Pochini, A. Secchi, *J. Org. Chem.* **2002**, *67*, 6188.
[20] A. Arduini, D. Demuru, A. Pochini, A. Secchi, *Chem. Commun.* **2005**, 645.
[21] M. Brust, D. Bethell, D. J. Schiffrin, C. J. Kiely, *Adv. Mater.* **1995**, *7*, 795.
[22] J. Turkevich, P. C. Stevenson, J. Hillier, *Discuss. Faraday Soc.* **1951**, *11*, 55.
[23] G. Frens, *Nature Phys. Sci.* **1973**, *241*, 20.
[24] C. Pale-Grosdemange, E. S. Simon, K. L. Prime, G. M. Whitesides, *J. Am. Chem. Soc.* **1991**, *113*, 12.
[25] L. M. Demers, C. A. Mirkin, R. C. Mucic, R. A. Reynolds, R. L. Letsinger, R. Elghanian, G. Viswanadham, *Anal. Chem.* **2000**, *72*, 5535.

Metallaboranes

Synthesis and Characterization of [*exo*-$BH_2(Cp^*M)_2B_9H_{14}$] (M = Ru, Re), and the Conversion of the Ruthenaborane into [$(Cp^*Ru)_2B_{10}H_{16}$] with an Open Cluster Framework Based on a Capped Truncated Tetrahedron**

*Sundargopal Ghosh, Bruce C. Noll, and Thomas P. Fehlner**

The evolution of main-group and transition-metal cluster structural chemistry since the development of the electron-counting rules in the 1970s is an important achievement of modern inorganic chemistry.[1,2] The useful connection between cluster geometry and electronic structure defined by the electron counting rules provides a solid foundation for the rational approach to larger clusters and nanoparticle systems that lie between small clusters and bulk crystalline materials with extended structures.[3]

Given the firm connection between the cluster-electron count and the cluster geometry for subicosahedral main-group clusters, it could be assumed that the structures of clusters based on supraicosahedral frameworks will provide similar unambiguous information. Not so. For example, 14 skeletal electron pair (sep), 12-fragment heteroatomic clusters with carbon or carbon plus a transition metal exhibit at least five different open cluster shapes depending on heteroatom content.[4–6] Even the structure of the 13-vertex closed carborane cluster, 1,2-μ-$C_6H_4(CH_2)_2$-3-Ph-1,2-$C_2B_{11}H_{10}$, is a variant of the docosahedral structure found by calculations most stable for the 13-vertex homonuclear borane (Scheme 1).[7] In this case, the additional stabilization achieved by generating vertices of connectivity four for the carbon centers more than compensates for that lost in converting a diamond into a rhombus arrangement. Thus for supraicosahedral clusters, the energy differences between possible geometries are much smaller than for subicosahedral clusters and the stabilization achieved by accommodating the properties of hetero atoms determines the observed cluster shape.

Herein novel boron-rich metallaboranes with geometries based on supraicosahedral frameworks provide a carbon-free comparison and demonstrate further structural types. These observations do not define the basic supraicosahedral framework structures for homonuclear boranes even though more of the structures accessible can be mapped out empirically. In addition, provided barriers for interconversion are large relative to room-temperature, intermediates in the cluster-building process are also likely to be isolated. As shown below, this characteristic of supraicosahedral cluster frameworks has allowed us to isolate and characterize a metallaborane with an unusual structure and to demonstrate that it is an intermediate in the boron cluster framework expansion reaction.

In terms of systematic cluster expansion, the most versatile metal is rhenium where known Re_2B_n frameworks run from $n = 4$ to 10.[8] Ruthenium offers fewer compounds[9,10] but revisiting both systems utilizing large BH_3 excess and forcing conditions permits the isolation of three different compounds with the molecular formula [$Cp^*_2M_2B_{10}H_{16}$], M = Ru or Re, $Cp^* = C_5Me_5$. With formal electron counts of 14 and 13 sep they offer an interesting case study for electron counting/supraicosahedral cluster relationships.

The structure of [$Cp^*_2Ru_2B_{10}H_{16}$] (**1**) is shown in Figure 1.[11] The presence of an exopolyhedral boron atom (B11) is clear from the structure solution and the assigned positions of the associated hydrogen atoms (not all found) are completed by two dimensional ^1H–^{11}B NMR spectroscopy experiments. The principal cluster framework of **1** contains one vertex of connectivity six occupied by a ruthenium atom; hence, it can be derived from a 13-vertex docosahedron that is missing two vertices of connectivity five and six. This is the geometry adopted by many 14 sep, 12 fragment metallacarboranes (one vertex of connectivity six unoccupied); however, the formal electron count of **1** is only 13 sep (the

[*] S. Ghosh, B. C. Noll, Prof. T. P. Fehlner
Department of Chemistry
University of Notre Dame
Notre Dame, IN 46556 (USA)
Fax: (+1) 504-631-7234
E-mail: fehlner.1@nd.edu

[**] This work was supported by the National Science Foundation (CHE-0304008); $Cp^* = \eta^5$-C_5Me_5.

  DOI: 10.1002/anie.200500343

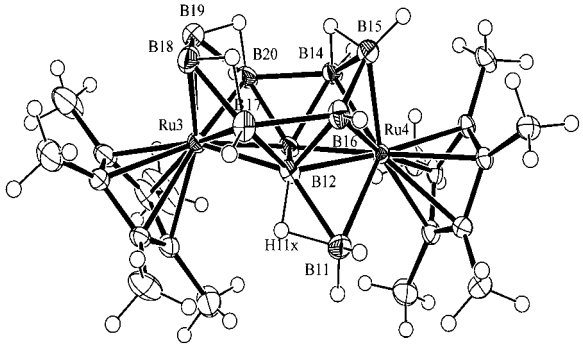

Figure 1. Molecular structure of **1**. Selected bond lengths [Å] and angles [°]: Ru3-B18 2.121(7), Ru4-B15 2.103(7), B14-B20 1.948(9), B16-B17 1.976(9), B12-B16 1.811(9); B18-Ru3-B19 49.4(3), B15-Ru4-B14 51.5(3), B11-Ru4-B12 48.2(2), Ru3-B12-B11 142.0(4), B19-B20-B14 120.5(5).

bridging BH_2 unit adds one electron). Some ways by which transition metals can stabilize framework geometries with vertices of high connectivity have been discussed and the susceptibility of these large clusters to secondary factors, such as heteroatom effects, has been pointed out above.[8]

The external BH_2 fragment of **1** bridges a B–Ru edge and is bonded to the boron atom B12 by a B-H-B bridge, that is, the boron atom B12 has no terminal hydrogen atom. On heating, **1** slowly converts exclusively into $[Cp^*_2Ru_2B_{10}H_{16}]$ (**2**). The ^{11}B NMR spectrum of **2** exhibits three rather than 10 resonance signals (found for **1**) and none of these signals corresponds to an exopolyhedral borane. Reinsertion of the borane and formation of a cluster framework with higher symmetry is implied and the solid-state structure in Figure 2

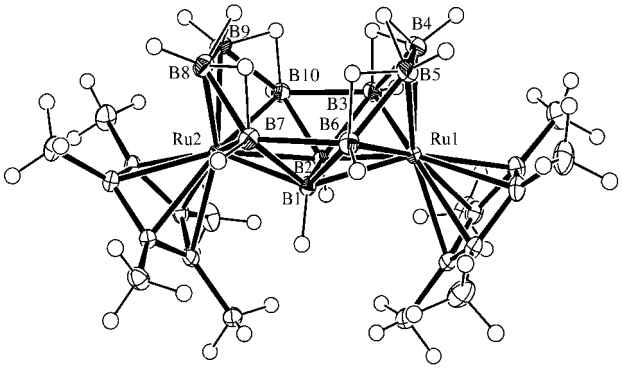

Figure 2. Molecular structure of **2**. Selected bond lengths [Å] and angles [°]: Ru1-B4 2.129(2), Ru1-B6 2.193(2), B1-B7 1.751(3), B1-B2 1.772(3), B3-B10 1.966(3), B6-B7 1.978(3); B5-Ru1-B3 91.81(8), B3-Ru1-B6 107.82(8), B4-Ru1-B2 89.77(8), B9-Ru2-B10 49.09(8), B8-Ru2-B10 90.69(8), B7-B1-B2 119.03(14).

shows a 12-atom open framework for **2** of C_{2v} symmetry with 6 B-H-B bridges on the open face.[11] The framework can be derived from a capped truncated tetrahedron of a type observed for naked tin clusters in the solid state.[12] As shown in Scheme 1, the two metal atoms occupy two of the four hexagonal faces; the other two hexagonal faces plus the two adjacent three-connect vertices are unoccupied. Like the

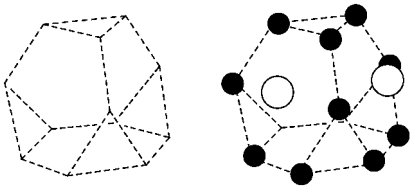

Scheme 1. Left: a truncated tetrahedron. Right: representation of a 12-vertex $[Cp^*_2Ru_2B_{10}H_{16}]$ framework where two ruthenium atoms cap two of the four hexagonal faces of a truncated tetrahedron and two adjacent 3-connect vertices are missing; ● B, ○ Ru.

tetrahedron, this cluster shape requires $n+4$ sep; hence, **2** requires 18 sep whereas formally only 14 sep are available.

$[Cp^*_2Re_2B_{10}H_{16}]$ (**3**) was isolated from a reaction mixture that also contains the closed series of compounds $[Cp^*_2Re_2B_nH_n]$, the structure of **3** is shown in Figure 3. The

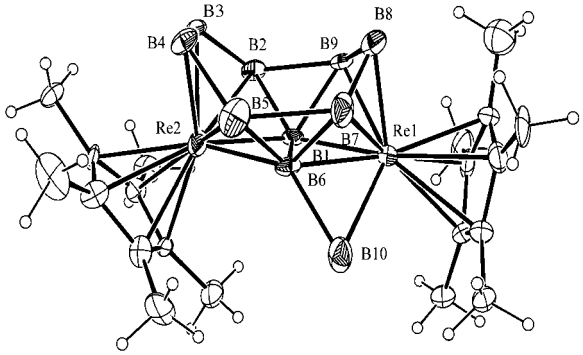

Figure 3. Molecular structure of **3**. Selected bond lengths [Å] and angles [°]: Re1-B1 2.15(3), Re1-B7 2.20(4), Re2-B5 2.11(4), B1-B6 1.71(4), B5-B7 2.13(6), B6-B10 1.91(5), B2-B9 1.96(5); B1-Re1-B8 79.9(13), B8-Re1-B6 81.0(15), B8-Re1-B9 48.5(17), B9-B1-Re2 129.7(19), B9-B1-Re1 69.9(14), B6-B5-B4 118(3).

heavy-atom framework corresponds to $[exo\text{-}BH_2\text{-}(Cp^*Re)_2B_9H_{14}]$, and is the same as **1** despite the fact that two rhenium atoms provide two fewer valence electrons than two ruthenium atoms![11] The X-ray structure did not provide the positions of any hydrogen atoms but the NMR spectroscopy results suggest, in contrast to **1**, that the boron atom (B6) of the borane bridged B–Re edge forms a B-H-Re bridge to the other rhenium center rather than a B-H-B bridge to the B atom of the exo-BH_2 fragment. Heating **3** under the same conditions as **1** results in the degradation of **3** but no evidence for either rearrangement to a single cage or hydrogen loss to produce $[Cp^*_2Re_2B_{10}H_{10}]$ was forthcoming.

First observed in metallacarborane chemistry,[13] the exopolyhedral BH_2 group now found in both **1** and **3** is likely to be of mechanistic importance in boron fragment growth of metallaboranes. A smaller ruthenacarborane cluster containing a exopolyhedral BH_2 group was shown earlier to be a versatile intermediate. Depending on substituents and conditions, it can undergo reinsertion of the BH_2 bridge, loss of the bridge, or participation of the bridge in external cluster hydroboration to give unusual organoborane cage substituents.[14,15] In principle, then, the same possibilities

exist for **1** and **3**. Reversible metal-cluster fragment extrusion is known in metallacarborane chemistry[16] and this mechanistic feature is now shown to apply to main-group-cluster fragments as well. Evidence for its role in other cluster systems can now be sought.

Experimental Section

1: Colorless **1** was isolated by silica gel thin layer chromatography (TLC) with hexane in 12% yield (20 mg) from the products of the reaction of $[(Cp^*Ru)_2B_4H_8]$ (0.15 g, 0.28 mmol) in toluene (30 mL) with BH_3·THF (10 equiv) at 105 °C for 28 h. MS (FAB) P^+(max) 597 (isotopic pattern for 2 Ru and 10 B atoms), $^{12}C_{20}{}^{1}H_{46}{}^{11}B_{10}{}^{101}Ru_2$ calcd: 600.2617; obsd: 600.2642. ^{11}B NMR (C_6D_6, 128 MHz, 22 °C): $\delta = 24.9$ (s, br, $J_{B\text{-}H} = 50$ Hz, 1 B-H-B), 18.1 (d, $J_{B\text{-}H} = 126$ Hz, 1 B), 14.7 (br, 1 B), 14.9 (br, 1 B), 11.5 (d, $J_{B\text{-}H} = 140$ Hz, 1 B), 6.5 (d, $J_{B\text{-}H} = 144$ Hz, 1 B), 4.6 (d, $J_{B\text{-}H} = 142$ Hz, 1 B), −0.8 (d, $J_{B\text{-}H} = 128$ Hz, 1 B), −4.9 (br, 1 BH_2), −6.1 ppm (d, $J_{B\text{-}H} = 152$ Hz, 1 B), ^{1}H NMR (C_6D_6, 400 MHz, 22 °C): $\delta = 4.18$ (partially collapsed quartet (pcq), 1 BH_t (H_t = terminal)), 3.24 (pcq, 1 BH_t), 3.18 (pcq, 2 BH_t), 2.79 (pcq, 1 BH_t), 2.73 (pcq, 1 BH_t), 2.59 (pcq, 1 H of BH_2), 2.44 (pcq, 2 BH_t and 1 H of BH_2), 1.76 (s, 15 H, 1 Cp*), 1.52 (s, 15 H, 1 Cp*), −0.81 (br, 1 B-H-B); −2.34 (br, 1 B-H-B); −2.97 (br, 1 B-H-B); −3.28 (br, 1 B-H-B); −5.10 (br, 1 B-H-B); −5.24 ppm (br, 1 B-H-B); IR (hexane): $\tilde{\nu} = 2498$w, 2464w cm^{-1} (B-H_t). Elemental analysis (%) calcd for $^{12}C_{20}{}^{1}H_{46}{}^{11}B_{10}{}^{101}Ru_2$: C 40.25, H 7.77; found: C40.50, H 7.69.

2: Compound **1** (0.05 g, 0.08 mmol) in [D_6]benzene (0.7 mL) heated for 12 days at 80 °C gave colorless **2** (20 mg, 40%) after TLC hexane. MS (FAB) P^+(max) 597 (isotopic pattern for 2 Ru and 10 B atoms), $^{12}C_{20}{}^{1}H_{46}{}^{11}B_{10}{}^{101}Ru_2$ calcd: 600.2617; obsd: 600.2616. ^{11}B NMR (C_6D_6, 128 MHz, 22 °C): $\delta = 24.8$ (d, $J_{B\text{-}H} = 120$ Hz, 2 B), 14.2 (d, $J_{B\text{-}H} = 122$ Hz, 4 B), 11.2 ppm (d, $J_{B\text{-}H} = 115$ Hz, 4 B); ^{1}H NMR (C_6D_6, 400 MHz, 22 °C): $\delta = 3.96$ (pcq, 2 BH_t), 3.49 (pcq, 4 BH_t), 2.88 (pcq, 4 BH_t), 1.62 (s, 30 H, 2 Cp*), −2.77 (br, 4 B-H-B); −3.53 ppm (br, 2 B-H-B); IR (hexane): $\tilde{\nu} = 2504$w, 2476w cm^{-1} (B-H_t).

3: Brown **3** (0.004 g, 4%) was isolated by TLC with hexane from the products of the reaction of $[(Cp^*Re)_2B_4H_8]$ (0.1 g, 0.14 mmol) in toluene (30 mL) with BH_3·THF (10 equiv) at 95 °C for 18 h. MS (FAB) P^+(max) 765.45 (isotopic pattern for 2 Re and 10 B atoms), $^{12}C_{20}{}^{1}H_{46}{}^{11}B_{10}{}^{186}Re_2$ calcd: 765.3544; obsd: 765.3568 (Exact mass calculated for $[M^+-2]$; ^{11}B NMR (C_6D_6, 128 MHz, 22 °C): $\delta = 68.6$ (br, $J_{B\text{-}H} = 50$ Hz, 1 ReHB), 13.2 (d, $J_{B\text{-}H} = 122$ Hz, 1 B), 4.1 (br, 2 B); 2.9 (br, 1 B), 0.25 (br, $J_{B\text{-}H} = 60$ Hz, 1 B), −5.7 (d, $J_{B\text{-}H} = 140$ Hz, 1 B), −8.9 (d, $J_{B\text{-}H} = 142$ Hz, 1 B), −15.3 (d, $J_{B\text{-}H} = 136$ Hz, 1 B), −19.8 ppm (br, 1 BH_2); ^{1}H NMR (C_6D_6, 400 MHz, 22 °C): $\delta = 4.88$ (pcq, 1 BH_t), 3.84 (pcq, 1 BH_t), 3.66 (pcq, 1 BH_t), 3.41 (pcq, 1 BH_t), 3.11 (pcq, 1 H of BH_2), 3.00 (pcq, 1 H of BH_2), 2.89 (pcq, 1 BH_t), 2.73 (pcq, 1 BH_t), 1.30 (pcq, 1 BH_t), −0.07 (pcq, 1 BH_t), 1.79 (s, 15 H, 1 Cp*), 1.68 (s, 15 H, 1 Cp*), −1.41 (br, 1 B-H-B), −2.22 (br, 1 B-H-B), −3.67 (br, 1 B-H-B), −5.43 (br, 1 B-H-B), −7.06 (br, 1 B-H-B), −15.09 ppm (br, 1 Re-H-B). IR (hexane): $\tilde{\nu} = 2496$w, 2472w cm^{-1} (B-H_t).

Received: January 28, 2005
Published online: April 13, 2005

Keywords: boron · metallaboranes · rhenium · ruthenium

[1] K. Wade, *Inorg. Nucl. Chem. Lett.* **1972**, *8*, 559.
[2] D. M. P. Mingos, *Nature Phys. Sci.* **1972**, *236*, 99.
[3] D. M. P. Mingos, D. J. Wales, *Introduction to Cluster Chemistry*, Prentice Hall, New York, **1990**.
[4] J. R. Pipal, R. N. Grimes, *J. Am. Chem. Soc.* **1978**, *100*, 3083.
[5] J. R. Pipal, R. N. Grimes, *Inorg. Chem.* **1979**, *18*, 1936.
[6] K. J. Donaghy, P. J. Carroll, L. G. Sneddon, *J. Organomet. Chem.* **1998**, *550*, 77.
[7] A. Burke, C. Ellis, B. T. Giles, B. E. Hodson, S. A. Macgregor, G. M. Rosair, A. J. Welch, *Angew. Chem.* **2003**, *115*, 235; *Angew. Chem. Int. Ed.* **2003**, *42*, 225.
[8] L. Guennic, H. Jiao, S. Kahal, J.-Y. Saillard, J.-F. Halet, S. Ghosh, M. Shang, A. M. Beatty, A. L. Rheingold, T. P. Fehlner, *J. Am. Chem. Soc.* **2004**, *126*, 3203.
[9] X. Lei, M. Shang, T. P. Fehlner, *J. Am. Chem. Soc.* **1999**, *121*, 1275.
[10] S. Ghosh, A. M. Beatty, T. P. Fehlner, *Angew. Chem.* **2003**, *115*, 4826; *Angew. Chem. Int. Ed.* **2003**, *42*, 4678.
[11] CCDC-234012, CCDC-234011, and CCDC-251474 (the structures of **1**–**3**) contain the supplementary crystallographic data for this paper. These data can be obtained free of charge from the Cambridge Crystallographic Data Centre via www.ccdc.cam.ac.uk/data_request/cif.
[12] S. Bobev, S. C. Sevov, *J. Am. Chem. Soc.* **2002**, *124*, 3359.
[13] H. Yan, A. M. Beatty, T. P. Fehlner, *Angew. Chem.* **2002**, *114*, 2690; *Angew. Chem. Int. Ed.* **2002**, *41*, 2578.
[14] H. Yan, A. M. Beatty, T. P. Fehlner, *J. Organomet. Chem.* **2003**, *680*, 66.
[15] H. Yan, A. M. Beatty, T. P. Fehlner, *J. Am. Chem. Soc.* **2003**, *125*, 16367.
[16] J. A. Belmont, J. Soto, R. E. King III, A. J. Donaldson, J. D. Hewes, M. F. Hawthorne, *J. Am. Chem. Soc.* **1989**, *111*, 7475.

Anion Sensors

Host Solids Containing Nanoscale Anion-Binding Pockets and Their Use in Selective Sensing Displacement Assays**

María Comes, Gertrudis Rodríguez-López, M. Dolores Marcos, Ramón Martínez-Máñez, Félix Sancenón, Juan Soto, Luis A. Villaescusa, Pedro Amorós, and Daniel Beltrán*

The development of chromogenic and fluorogenic chemosensors for molecular sensing is an area of current interest.[1,2] The most widely used protocol in this field has been the

[*] M. Comes, G. Rodríguez-López, Dr. M. D. Marcos, Prof. R. Martínez-Máñez, Dr. F. Sancenón, Dr. J. Soto, Dr. L. A. Villaescusa
Universidad Politécnica de València, Departamento de Química
Camino de Vera s/n, 46022 València (Spain)
Fax: (+34) 96-387-9349
E-mail: rmaez@qim.upv.es
Dr. P. Amorós, Prof. D. Beltrán
Institut de Ciència dels Materials (ICMUV)
Universitat de València
P.O. Box 22085, 46071 València (Spain)

[**] We thank the Ministerio de Ciencia y Tecnología (MAT2003-08568-C03 and REN2002-04237-C02-01), Generalitat Valenciana (GRUPOS03/035, GRUPOS03/099, and GV04B-420), and Universidad Politécnica de Valencia (PPI-06-03) for support. L.A.V. and F.S. thank the Ministerio de Ciencia y Tecnología for a Ramón y Cajal contract. M.C. also thanks the Conselleria de Educación y Ciencia for her grant.

  DOI: 10.1002/anie.200461511

binding site/signaling subunit approach, in which molecular coordination sites are covalently attached to chromogenic/fluorogenic reporters which transduce guest coordination into optical signals. Recently, two additional methodologies have been developed. One is the chemodosimeter approach, which is related to the use of guest-induced irreversible reactions,[2] and the other is the displacement protocol, which also involves the use of a binding site and a signaling reporter, although here the two subunits are not covalently attached but form a molecular ensemble.[3–5] In the latter systems addition of a certain guest to solutions of the sensing ensemble results in a displacement reaction: the binding site coordinates to the guest, and the signaling subunit is released. This method, inspired by displacement reactions in immunoassay protocols,[6] has been recently reported for the sensing of small anions with very good results.[7,8] This approach has several advantages. For instance, the noncovalent anchoring of binding sites and indicator groups allows a large number of combinations to be tested with minimum effort in order to obtain tuned sensing systems. Furthermore, these sensing ensembles usually operate in pure water or water/organic solvent mixtures. However, the displacement approach also has several limitations. One restriction is that the spectroscopic characteristics of the indicator in the molecular ensemble must be different to those in its noncoordinated form.[3] Another disadvantage is that sometimes it requires extensive and time-consuming synthetic efforts to finally obtain somewhat complex receptors.

All of these systems are based on the use of molecular anion hosts[2] having in common the presence of binding sites placed in suitable cavities that fit in size and charge with the guest to be coordinated and sensed. These binding pockets have typically been obtained by the use of 1,3,5-trisubstituted 2,4,6-triethylbenzene scaffolds[7i,8a,8e–8h] or cages incorporating metal complexes.[7b–h,8c,8d,8i] Following a different approach, we and others recently reported that adequately functionalized nanosized cavities in mesoporous solids can somehow mimic active-site cavities found in biological systems.[9–13] Our aim was to demonstrate that functionalized pores in mesoporous solids could act as binding pockets and be used as anion hosts in chromogenic displacement assays. The protocol is schematically shown in Figure 1. Suitable nanosized pores are functionalized with appropriate binding sites. The functionalized solid is then loaded with a dye capable of coordinative interaction with the anchored coordination sites. In the presence of a target anion displacement of the dye into the solution is achieved and results in colorimetric detection of the guest.

To check this idea, host solids **S2** and **S3** containing nanoscale cavities with anion-binding sites were prepared and loaded with suitable dyes. The mesoporous starting material UVM-7[14] was first treated with an excess of 3-aminopropyltriethoxysilane to yield solid **S1** (Scheme 1). Solid **S2** was obtained by reaction of **S1** with an excess of 2-methylthio-2-imidazoline hydroiodide in refluxing methanol for 16 h.[15] Solid **S3** was synthesized by reaction of **S1** with mannose in the presence of sodium cyanoborohydride.[16] Both solids were exhaustively washed and dried (40% yield). Solid **S2** was then converted to solid **S2**-**1** by loading with the dye

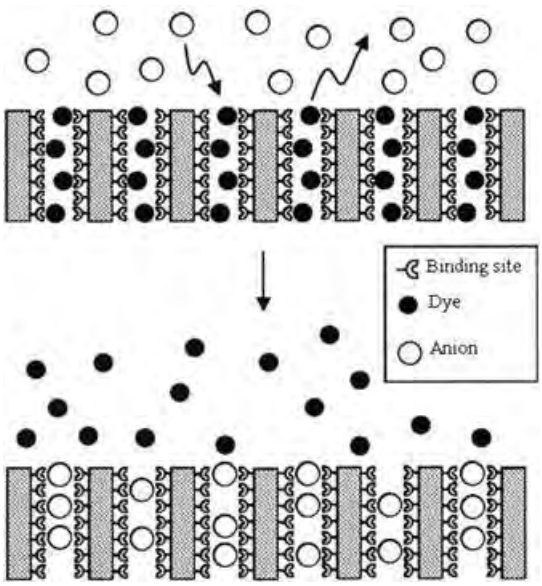

Figure 1. Idealized representation of the use of functionalized mesoporous materials in colorimetric displacement assays.

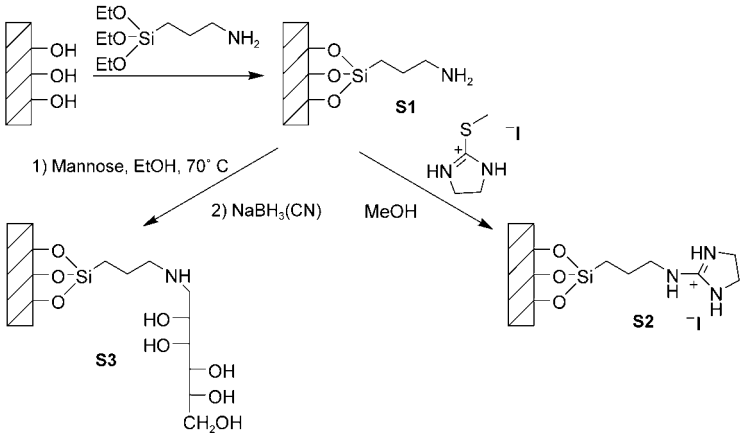

Scheme 1. Synthesis of solids **S1**, **S2**, and **S3**.

Methylthymol blue (**1**), which contains four carboxy groups and is expected to form strong complexes with guanidinium groups.[17] In a similar manner, solid **S3** was loaded with azoic dye **2** to give solid **S3**-**2**.[18] This dye was selected because of

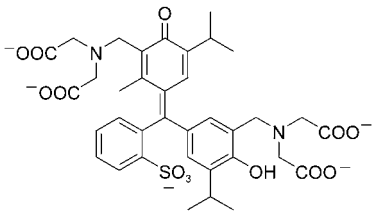

1

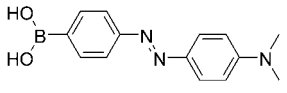

2

the well-known affinity of boronic fragments towards carbohydrate residues. Solids were washed until no elimination of dye was observed. Table 1 lists the chemical composition of the active solids, calculated from thermogravimetric and

Table 1: Functionalization of **S2** and **S3**.

Solid	Binding molecules[a]/SiO_2	Solid	Dye/SiO_2[a]
S2	6.4×10^{-2}	**S2-1**	1.5×10^{-2}
S3	8.4×10^{-2}	**S3-2**	3.7×10^{-2}

[a] Molar ratios.

elemental analysis. The guanidine content of **S2** was determined by analysis of the iodide counterion after dissolution in 34 wt% aqueous HF. The dye content of **S2-1** was calculated by colorimetric analysis after dissolution as for **S2**.

Figure 2b (inset) shows the ^{29}Si MAS-NMR spectrum of **S1**, in which the presence of two peak groups, assigned to the Q ($\delta = -105, -97, -87$ ppm) and T silicon centers ($\delta = -61, -53$ ppm), clearly indicates anchoring of the silane derivative

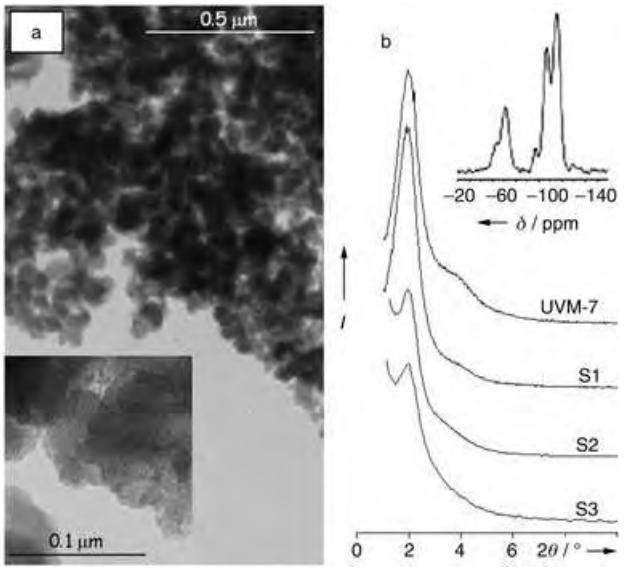

Figure 2. a) TEM micrograph of the guanidinium-functionalized solid after loading with methylthymol blue (**S2-1**). b) Powder XRD pattern of **S2** and **S3** compared with those of their precursors UVM-7 and **S1**. Inset: ^{29}Si MAS-NMR spectrum of functionalized **S1**.

to the silanol groups of the silica surface. Peak deconvolution gave a ratio of Q and T centers of 3:1, in good accordance with the chemical analysis. The successive functionalization process is displayed in Figure 3 which shows the IR spectra of the solids. In **S1**, bands due to OH vibrations have disappeared, and others related to the presence of NH_2 and CH_2 groups can be seen. In **S2**, bands assigned to the guanidinium groups are clearly observed (e.g., 1670 and 1600 cm^{-1}, assignable to the NH δ vibration). In the spectrum of **S2-1** bands due to dye vibrations (e.g., 1625 and 1404 cm^{-1}, assignable to the carboxylate groups) are observed. For solids **S3** and **S3-2**

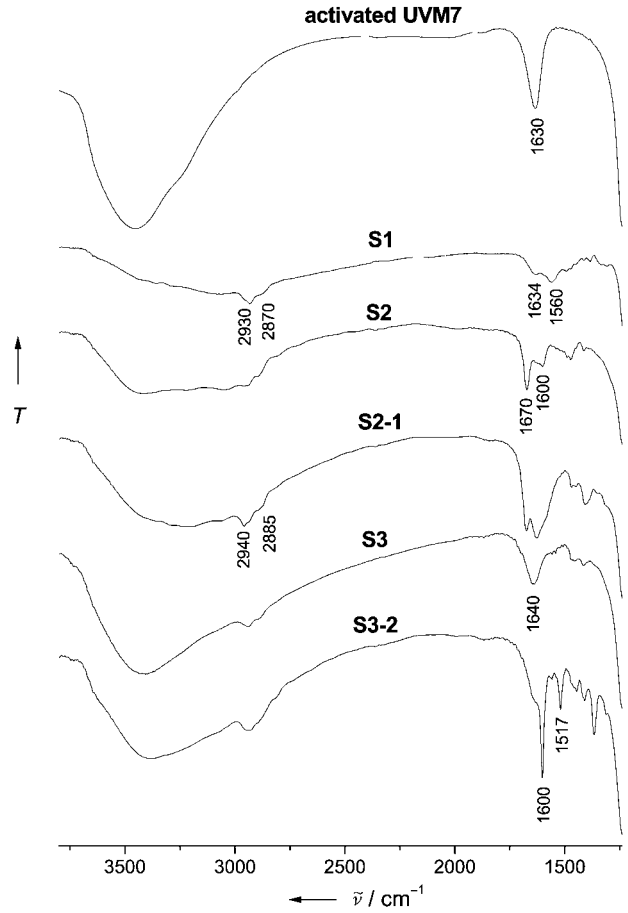

Figure 3. IR spectra of UVM-7, **S1**, **S2**, **S2-1**, **S3**, and **S3-2**. *T* = transmittance.

the bands due to the mannose residue and the azoic dye were also observed in the corresponding spectra.

Structural characterization of the solids was carried out by TEM, powder XRD, and isothermal adsorption/desorption of N_2. Figure 2a shows a representative TEM micrograph of solid **S2-1** with the characteristic texture of UVM-7-type materials. Additionally, the inset clearly shows that the wormholelike MCM-41-type mesoporosity of the inorganic matrix is still present. Similar TEM images were obtained for the other materials. Figure 2b shows the variation of the powder XRD pattern of the UVM-7 matrix as it is functionalized to obtain **S2** and **S3**. The gradual intensity decrease is related to the loss of contrast as the amount of organic material anchored to the matrix increases. This increase in the organic fraction also influences the porosity of the obtained material. Table 2 summarizes the values obtained from the N_2 adsorption/desorption isotherms. A gradual decrease in specific surface area is associated with a concomitant decrease in pore size and volume. The changes are more pronounced for the small mesopores than for the large textural pores.

Guanidinium groups are known to undergo hydrogen-bonding interactions with carboxy groups, and therefore the **S2-1** ensemble was tested in displacement assays in water in the presence of the carboxylates citrate, succinate, lactate, malate, acetate, oxalate, propionate, formate, oxalacetate,

Table 2: Specific surface area and porosimetric data of **S1** and **S2**.

Solid	Specific surface area [$m^2 g^{-1}$]	Pore size[a] [nm]	Pore size[b] [nm]	Pore volume[a] [$cm^3 g^{-1}$]	Pore volume[b] [$cm^3 g^{-1}$]
S1	870	2.67	41.1	0.72	0.68
S2	377	2.1	35.4	0.24	0.58
S2-1	156	<1.7	18.2	0.08	0.21

[a] MCM-41-type pores. [b] Textural pores.

tartrate, maleate, malonate, glutarate, adipate, pimelate, and phthalate. The ensemble was suspended in water at pH 7.5 (HEPES 0.01 M) in the presence of a certain carboxylate, and after 10 min the mixture was filtered and the absorbance at 604 nm (visible band of dye **1**) measured. The results are summarized in Figure 4. A citrate-selective response was found that indicates that the binding pockets in **S2** are capable of recognizing this anion due to favorable coordination with respect to other carboxylates. Figure 4 also shows the calibration curve with citrate. No changes were observed in the presence of inorganic anions such as phosphate, sulfate, nitrate, carbonate, chloride, iodide, or bromide.

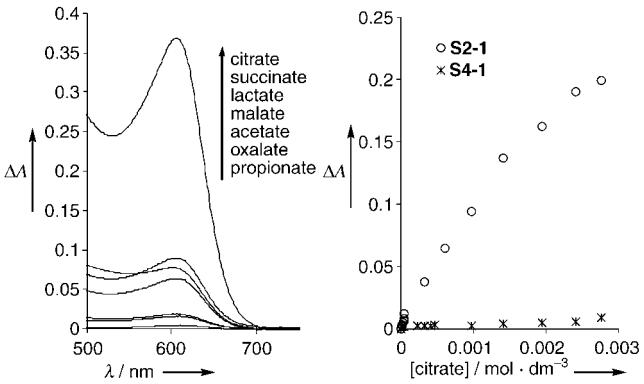

Figure 4. Left: Vis spectra (after filtering) of **S2-1** ensembles in the presence of different carboxylates. As examples, the responses to citrate, succinate, lactate, malate, acetate, oxalate, and propionate are shown. No significant response was found for other carboxylates. Right: citrate calibration curves for **S2-1** and **S4-1**. A detection limit for citrate of about 2×10^{-5} mol dm^{-3} was found for **S2-1**.

To test the effect of the nanoscale pores, we prepared **S4**, a similar material to **S2** but obtained from fumed silica (200 $m^2 g^{-1}$), which lacks the homogeneous porosity characteristic of mesoporous solids (**S4**: 1.5×10^{-2} guanidinium molecules per SiO_2, **S4-1**: 3.6×10^{-3} dye molecules per SiO_2; both values as molar ratios). Studies with citrate and **S4-1** (see Figure 4) showed a very poor response compared to that of **S2-1**. Despite the similar functionalization of **S2** and **S4**, their responses are remarkably different. This suggests that the presence of cylindrical-shaped pores in **S2** could favor spatial proximity between guanidinium subunits and thus enhance the coordinating ability of the binding groups in the nanoscale pockets towards citrate. This enhanced response was not observed for the nonporous surface of **S4**.

To further study the utility of the concept shown in Scheme 1, colorimetric sensing of borate in water/acetonitrile (80/20 v/v) was developed by using the **S3-2** ensemble. The ensemble was suspended at neutral pH in the presence of borate, and after 5 min the mixture was filtered and the band at 455 nm (due to release of **2** into the solution) measured. Dye displacement was observed in the presence of borate due to selective borate coordination with the diol groups in the surface of **S3**. Dye displacement is selective for borate (see Figure 5) and it is, as far as we know, the first chromogenic system based on supramolecular concepts for sensing the environmentally relevant borate anion.

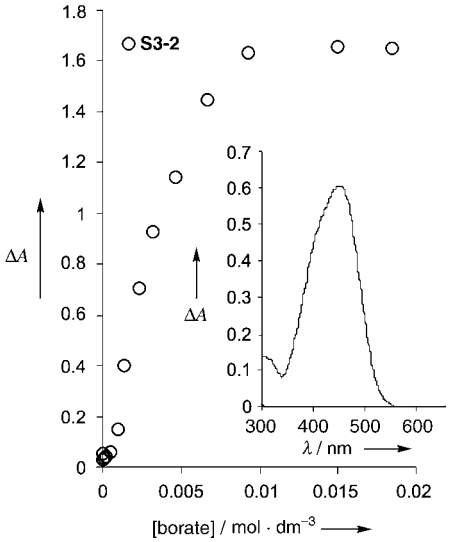

Figure 5. Borate calibration curve for **S3-2** (detection limit ca. 6×10^{-5} mol dm^{-3}). Inset: Vis spectrum (after filtering) of **S3-2** in the presence of borate and a mixture of different anions typically present in water (chloride, phosphate, sulfate, carbonate, etc.).

In summary, we have shown that functionalized mesoporous solids can act as binding pockets in anion-recognition processes. In particular, we have developed solids for displacement colorimetric assays in water for the selective detection of citrate and borate. We believe these findings can open new perspectives in the use of solids as hosts in solid-state/supramolecular chemistry concepts. The possibility of using a large number of mesoporous materials functionalized with different binding sites makes the approach suitable for the design of new chromo/fluorogenic probes for target guests.

Received: August 2, 2004
Revised: December 4, 2004
Published online: April 13, 2005

Keywords: anions · mesoporous materials · molecular recognition · sensors

[1] P. D. Beer, P. A. Gale, *Angew. Chem.* **2001**, *113*, 502 – 532; *Angew. Chem. Int. Ed.* **2001**, *40*, 486 – 516.

[2] R. Martínez-Máñez, F. Sancenón, *Chem. Rev.* **2003**, *103*, 4419 – 4476.

[3] S. L. Wiskur, H. Aït-Haddou, J. J. Lavigne, E. V. Anslyn, *Acc. Chem. Res.* **2001**, *34*, 963 – 972.

[4] T. S. Snowden, E. V. Anslyn, *Curr. Opin. Chem. Biol.* **1999**, *3*, 740 – 746.

[5] L. Fabbrizzi, M. Licchelli, A. Taglietti, *Dalton Trans.* **2003**, 3471 – 3479.

[6] M. J. Perry in *Monoclonal Antibodies: Principles and Applications* (Eds.: J. R. Birch, E. S. Lennox), Wiley-Liss, New York, **1995**, pp. 107 – 120.

[7] a) M. Montalti, L. Prodi, *Chem. Commun.* **1998**, 1461 – 1462; b) L. Fabbrizzi, N. Marcotte, F. Stomeo, A. Taglietti, *Angew. Chem.* **2002**, *114*, 3965 – 3968; *Angew. Chem. Int. Ed.* **2002**, *41*, 3811 – 3814; c) M. A. Hortalá, L. Fabbrizzi, N. Marcotte, F. Stomeo, A. Taglietti, *J. Am. Chem. Soc.* **2003**, *125*, 20 – 21; d) Y. Takahashi, D. A. P. Tanaka, H. Matsunaga, T. M. Suzuki, *J. Chem. Soc. Perkin Trans. 2*, **2002**, 759 – 762; e) R. Prohens, G. Martorell, P. Ballester, A. Costa, *Chem. Commun.* **2001**, 1456 – 1457; f) L. Fabbrizzi, A. Leone, A. Taglietti, *Angew. Chem.* **2001**, *113*, 3039 – 3042; *Angew. Chem. Int. Ed.* **2001**, *40*, 3066 – 3069; g) C.-F. Chow, B. K. W. Chiu, M. H. W. Lam, W.-Y. Wong, *J. Am. Chem. Soc.* **2003**, *125*, 7802 – 7803; h) M. Boiocchi, M. Bonizzoni, L. Fabbrizzi, G. Piovani, A. Taglietti, *Angew. Chem.* **2004**, *116*, 3935 – 3940; *Angew. Chem. Int. Ed.* **2004**, *43*, 3847 – 3852; i) K. Niikura, E. V. Anslyn, *J. Org. Chem.* **2003**, *68*, 10156 – 10157.

[8] a) A. Metzger, E. W. Anslyn, *Angew. Chem.* **1998**, *110*, 682 – 684; *Angew. Chem. Int. Ed.* **1998**, *37*, 649 – 652; b) K. Niikura, A. Metzger, E. V. Anslyn, *J. Am. Chem. Soc.* **1998**, *120*, 8533 – 8534; c) H. Aït-Haddou, S. L. Wiskur, V. M. Lynch, E. V. Anslyn, *J. Am. Chem. Soc.* **2001**, *123*, 11296 – 11297; d) M. S. Han, D. H. Kim, *Angew. Chem.* **2002**, *114*, 3963 – 3965; *Angew. Chem. Int. Ed.* **2002**, *41*, 3809 – 3811; e) S. L. Wiskur, E. V. Anslyn, *J. Am. Chem. Soc.* **2001**, *123*, 10109 – 10110; f) Z. Zhong, E. V. Anslyn, *J. Am. Chem. Soc.* **2002**, *124*, 9014 – 9015; g) J. J. Lavigne, E. V. Anslyn, *Angew. Chem.* **1999**, *111*, 3903 – 3906; *Angew. Chem. Int. Ed.* **1999**, *38*, 3666 – 3669; h) S. L. Wiskur, P. N. Floriano, E. V. Anslyn, J. T. McDevitt, *Angew. Chem.* **2003**, *115*, 2116 – 2118; *Angew. Chem. Int. Ed.* **2003**, *42*, 2070 – 2072; i) Z. Zhong, E. V. Anslyn, *Angew. Chem.* **2003**, *115*, 3113 – 3116; *Angew. Chem. Int. Ed.* **2003**, *42*, 3005 – 3008; j) B. T. Nguyen, S. L. Wiskur, E. V. Anslyn, *Org. Lett.* **2004**, *6*, 2499 – 2501; k) M. N. Piña, M. C. Rotger, A. Costa, P. Ballester, P. M. Deyà, *Tetrahedron Lett.* **2004**, *45*, 3749 – 3752.

[9] a) A. B. Descalzo, D. Jiménez, M. D. Marcos, R. Martínez-Máñez, J. Soto, J. El Haskouri, C. Guillém, D. Beltrán, P. Amorós, *Adv. Mater.* **2002**, *14*, 966 – 969; b) M. Comes, M. D. Marcos, R. Martínez-Máñez, F. Sancenón, J. Soto, L. A. Villaescusa, P. Amorós, D. Beltrán, *Adv. Mater.* **2004**, *16*, 1783 – 1786; c) A. B. Descalzo, K. Rurack, H. Weisshoff, R. Martínez-Máñez, M. D. Marcos, P. Amorós, K. Hoffmann, J. Soto, *J. Am. Chem. Soc.*, **2005**, *127*, 184 – 200.

[10] R. Casasús, M. D. Marcos, R. Martínez-Máñez, J. V. Ros-Lis, J. Soto, L. A. Villaescusa, P. Amorós, D. Beltrán, C. Guillem, J. Latorre, *J. Am. Chem. Soc.* **2004**, *126*, 8612 – 8613.

[11] D. R. Radu, C.-Y. Lai, J. W. Wiench, M. Pruski, V. S.-Y. Lin, *J. Am. Chem. Soc.* **2004**, *126*, 1640 – 1641.

[12] R. Hernandez, H.-R. Tseng, J. W. Wong, J. F. Stoddart, J. I. Zink, *J. Am. Chem. Soc.* **2004**, *126*, 3370 – 3371.

[13] L. Basabe-Desmonts, J. Beld, R. S. Zimmerman, J. Hernando, P. Mela, M. F. García Parajó, N. F. van Hulst, A. van den Berg, D. N. Reinhoudt, M. Crego-Calama, *J. Am. Chem. Soc.* **2004**, *126*, 7293 – 7299.

[14] J. El Haskouri, D. Ortiz, C. Guillem, J. Latorre, M. Caldés, A. Beltrán, D. Beltrán, A. B. Descalzo, G. Rodríguez-López, R. Martínez-Máñez, M. D. Marcos, P. Amorós, *Chem. Commun.* **2002**, 330 – 331.

[15] The reaction was carried out using similar conditions to those described in the synthesis of guanidinium derivatives: see for instance S. R. Mundla, L. J. Wilson, S. R. Klopfenstein, W. L. Seibel, N. N. Nikolaides, *Tetraedron Lett.* **2000**, *41*, 6563 – 6566.

[16] The reaction was carried out using similar conditions to those described in the synthesis of amino sugars: see for instance R. E. Huisden, J. C. Kraak, H. Poppe, *J. Chromatogr.* **1990**, *508*, 289 – 299.

[17] S. C. McCleskey, A. Metzger, C. S. Simmons, E. V. Anslyn, *Tetrahedron* **2002**, *58*, 621 – 628.

[18] N. Di Cesare, J. R. Lakowicz, *Org. Lett.* **2001**, *3*, 3891 – 3893.

Fluorescent Probes

2,4-Dinitrobenzenesulfonyl Fluoresceins as Fluorescent Alternatives to Ellman's Reagent in Thiol-Quantification Enzyme Assays**

Hatsuo Maeda, Hiromi Matsuno, Mai Ushida, Kohei Katayama, Kanako Saeki, and Norio Itoh*

Since its first description in 1959,[1] 5,5′-dithio-bis(2-nitrobenzoic acid) (DTNB or Ellman's reagent) has been used widely for the quantification of thiols, especially for assays of various enzymes including acetyl- and butyrylcholinesterase (AChE and BChE, respectively)[2] in which substrates release thiols through enzymatic reactions.[3] 4,4′-Bipyridyl disulfide[4] and 5-(2-aminoethyl)dithio-2-nitrobenzoic acid[3] were also shown to be useful for colorimetric analyses of thiols. However, fluorescent or chemiluminescent thiol probes would be more practical than these chromogenic probes for enzyme assays, especially for high-throughput programs to screen enzyme inhibitors as new drugs. Recently, the use of a dioxetane-disulfide derivative as a chemiluminescent probe in place of DTNB led to an improved sensitivity of the AChE assay with acetylthiocholine (ASCh) by a factor of ten.[5] However, the assay required a rather tedious procedure in

[*] Prof. H. Maeda, H. Matsuno, M. Ushida, K. Katayama, K. Saeki, N. Itoh
Division of Analytical Chemistry
Graduate School of Pharmaceutical Sciences
Osaka University
1–6 Yamada-oka, Suita, Osaka 565-0871 (Japan)
Fax: (+81) 6-6879-8206
E-mail: h-maeda@phs.osaka-u.ac.jp

[**] The authors thank Eisai Co., Ltd. (Tokyo, Japan) for the generous gift of donepezil. This work was supported in part by a Grant-in-Aid for Scientific Research (B 15390012) from the Ministry of Education, Culture, Sports, Science, and Technology of Japan.

Supporting information for this article, including experimental procedures and spectral data for **5**, is available on the WWW under http://www.angewandte.org or from the author.

  DOI: 10.1002/anie.200500114

which the enzyme reaction and detection steps were performed independently owing to the limited solubility of the chemiluminescent probe in aqueous media.

At present, a wide variety of fluorescent probes for thiols are available.[6] Among them, maleimide-type probes CPM[6] and ThioGlo_3,[7] and a haloalkyl-type probe monobromobimane[6] may be utilized for thiol-determination enzyme assays. However, these probes have disadvantages that attenuate their utility in enzyme assays. CPM and ThioGlo_3 suffer from limited solubility in aqueous media, similar to the dioxetane-disulfide chemiluminescent derivative mentioned earlier, as well as inevitable side reactions of their maleimide groups to form fluorescent byproducts. Also, under mild conditions, reactions of monobromobimane with thiols are relatively slow.[8] Thus, these fluorescent probes have found applications in the labeling of biopolymers and derivatization of thiols for separation analysis rather than in enzyme assays.

Recently it was found that **2** (Scheme 1) works as a highly specific probe for superoxide ($O_2^{-\bullet}$) based on deprotection of 2,4-dinitrobenzenesulfonyl (DBS) groups by $O_2^{-\bullet}$, whereas **1**

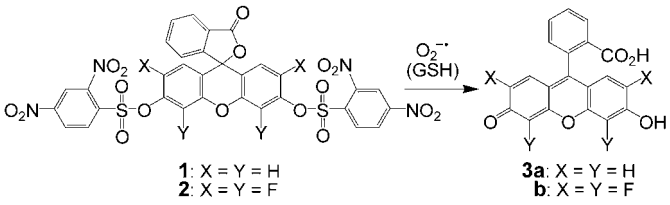

Scheme 1. A previously reported fluorescent probe for superoxide.

is transformed to **3a** much more effectively upon reaction with glutathione (GSH) through nucleophilic aromatic substitution[9,10] than with $O_2^{-\bullet}$.[11] The latter observation provided us with a clue for the design of novel fluorescent probes for thiols. So far, nucleophilic aromatic substitution has been capitalized only as a derivatizing reaction for the separation analysis of thiols with halogenated benzofurazans.[12] This fact also encouraged us to develop thiol probes based on nucleophilic aromatic substitution. Compound **1** is unlikely to work as a thiol probe as the observed fluorescence response of **1** toward GSH was relatively small. However, changing the protection mode with DBS groups from bis to mono was expected to enhance not only the reactivity toward thiols but also its solubility in aqueous media. Furthermore, it is well known that nucleophilic aromatic substitution proceeds more effectively as the acidity of leaving groups decreases.[10] These considerations led us to design **5b** as well as **5a** (Scheme 2) as fluorescent alternatives to DTNB for thiol-quantification enzyme assays. Herein we describe the characteristics of **5** as thiol probes and their utility in screening assays for ChE inhibitors.

As expected, monoprotection with a DBS group imparted to **5** a high degree of solubility in aqueous media. Working solutions of these probes were prepared by 200-fold dilution of ethanolic solutions of **5** with aqueous HEPES buffer (pH 7.4, HEPES = *N*-(2-hydroxyethyl)piperazine-*N*′-2-ethanesulfonic acid). Relative quantum efficiencies (Φ_{fl}) of **5a** and **5b** in HEPES buffer (pH 7.4) were 0.0007 and 0.0003,

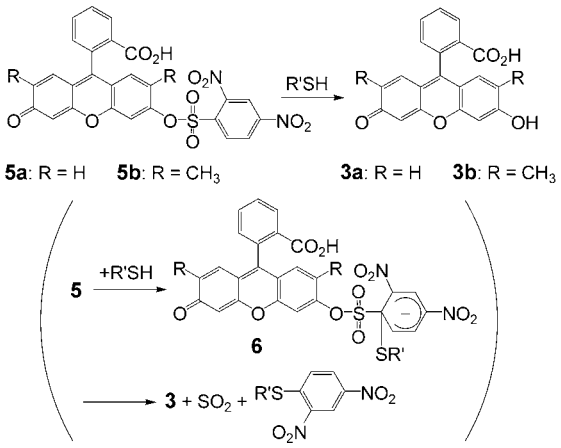

Scheme 2. Probes **5** for thiols, and the reactions that give rise to their fluorescent products **3**, as used in this study.

respectively, relative to **3a** in 0.1 M NaOH ($\Phi_{fl} = 0.85$) as standard.[13] Similar estimates of Φ_{fl} for **3a** and **3b**[14,15] in the same buffer were 0.75 and 0.58, respectively. Compound **5a** was treated at room temperature with PhSH (1.1 equiv) in HEPES buffer (pH 7.4) containing 5% EtOH. After 10 minutes, **5a** was almost completely consumed and (2,4-dinitrophenyl)phenylsulfide was isolated in 96% yield [Eq. (1)]. No byproducts other than PhSSPh (4%) were

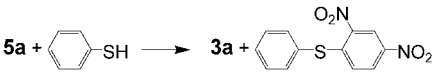

(1)

observed. Additionally, only 0.7 and 1.1% of **5a** and **5b**, respectively, decomposed to the corresponding compound **3** after 1 hour of incubation in buffer solution at 37 °C. These results demonstrate that conversion of **5** into **3** is a useful reaction for the determination of thiols in aqueous media, through the switching "on" of fluorescence. Also, its hydrolysis at a negligible level is the only expected side reaction in aqueous solution.

Excitation and emission spectra were recorded at several intervals during the reaction of **5** with GSH at 37 °C in HEPES buffer (pH 7.4, see Figure 1). As soon as GSH was added, excitation and emission peaks for **3** appeared in the spectra as a result of its generation from **5**, with rapidly increasing intensity that stabilized 10 minutes after the initial incubation. The rate constants k_{obsd}[16] for reaction of **5a** or **5b** with GSH at pH 7.4 and 37 °C were 1.7×10^2 and $1.4 \times 10^2\ M^{-1}\ s^{-1}$, respectively. Compounds **5** reacted with cysteine (Cys) and $H_2NCH_2CH_2SH$ (AET) with rate constants that were similar to those for GSH, while deprotection of **5** by $HSCH_2CH_2CO_2H$ (MPA) was about ten times slower than that by GSH (Table 1). The rate constant k for the reaction of DTNB with GSH at 25 °C is $3.5 \times 10^4\ M^{-1} s^{-1}$.[17] For comparison the k values of the present probes are included in Table 1 and indicate that compounds **5** react with GSH approximately ten times slower than DTNB. However, this fact was not a disadvantage for determining thiols with **5**. When an assay

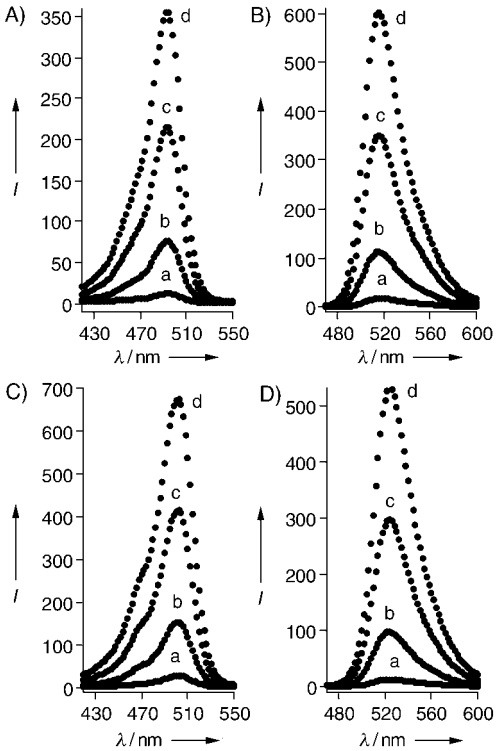

Figure 1. Excitation and emission spectra of **5a** (A, B) and **5b** (C, D) measured at 37 °C at a) $t = 0$, b) $t = 1$, c) $t = 4$, and d) $t = 10$ minutes after addition of GSH (final concentration: 50 μM; $\lambda_{em} = 560$ nm, $\lambda_{ex} = 460$ nm). Final concentrations of solutions of **5** were 25 μM in HEPES buffer (10 mM, pH 7.4, 3 mL) containing 0.5% EtOH.

with **5** was performed for the thiols described in Table 1 in a 96-well microtitre plate, detection limits of less than 2.0 pmol/well were noted for GSH, Cys, and AET, and a linear calibration curve was obtained for each of these thiols up to 1000 pmol/well. Sensitivity, as expressed by the slope of the calibration curves, suggested that **5b** was slightly more sensitive than **5a**.

Dependency of the present fluorometric assay on pH was also examined for the reaction of **5b** with GSH, and **5b** was found to act as a probe down to pH 7.0, although the slope of the calibration curve obtained at pH 7.0 was about one-quarter of that determined at pH 7.4. The fluorescence intensities of **3b** at pH 7.0 and 6.6 (HEPES buffer) were 88 and 74%, respectively, of that measured at pH 7.4. Thus, the lower increase in fluorescence on reaction of **5b** with GSH at pH values lower than 7.4 is ascribed to a decrease in the reactivity of GSH at lower pH values. The observed pH dependency would not militate against application of the present fluorometric assay to thiol-quantification enzyme assays, as assays of various enzymes with DTNB are generally carried out at pH 7.5–8.0.

The results of fluorometric assays using **5** of human erythrocyte AChE and serum BChE with ASCh and butyrylthiocholine (BSCh) as substrates, respectively, are shown in Figure 2. Each of the enzyme reactions was performed in HEPES buffer (pH 7.4) at 37 °C for 10 minutes. Fluorometry with **5b** enabled the determination of AChE and BChE, even at 0.05 and 0.001 mU/well (1 mU of AChE (or BChE) is defined to hydrolyze 1 nmol of ASCh (or BSCh) per minute at pH 7.4 and 37 °C), respectively. The detection limits for these analytes with **5a** were 0.05 and 0.01 mU/well, respectively. Compound **5b** also performed better than **5a** for the ChE assay. Thus, the fluorometric assay with **5b** was applied to determine inhibitory constants (IC_{50}) of some ChE inhibitors. After a mixture of **5b**, ChE, its substrate, and a ChE inhibitor was incubated at 37 °C for 10 minutes, an increase in fluorescence intensity was observed. Inhibition curves were analyzed by a four-parameter logistic regression to afford IC_{50} values. The results are summarized in Table 2, which also includes the constants determined with DTNB. A good correlation was obtained

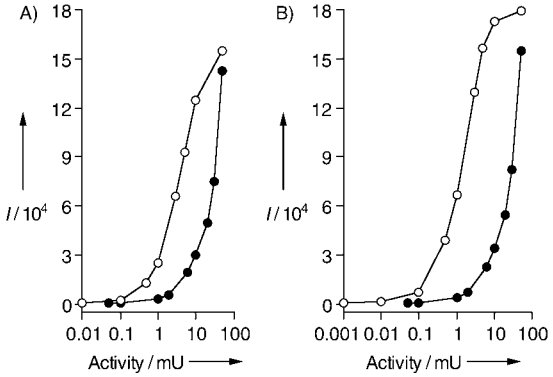

Figure 2. Assays of human erythrocyte AChE (●) and serum BChE (○) in the presence of **5**. Assays were performed after incubating a mixture of the analyte ChE (10 μL), its substrate (ASCh for AChE and BSCh for BChE, respectively; 1.0 mM, 10 μL in H_2O), and either A) **5a** or B) **5b** (25 μM, 170 μL in HEPES (10 mM, pH 7.4) containing 0.5% EtOH) in a 96-well microtitre plate at 37 °C for 10 minutes. The final volume of the reaction mixture was adjusted to 200 μL by addition of H_2O (10 μL). See main text for definition of mU (activity).

Table 1: Characteristics of **5a** and **5b** as fluorescent probes for GSH, Cys, MPA, and AET.[a]

	Thiol	k_{obsd} [$M^{-1}s^{-1}$] for reaction with thiols[b]	Assay	
			Detection limit [pmol]	Sensitivity [au $pmol^{-1}$][c]
5a	GSH	1.7×10^2 (3.9×10^3)	2.0	22.0
	Cys	2.7×10^2 (4.0×10^3)	2.0	27.5
	MPA	1.8×10 (5.0×10^4)	10	2.6
	AET	6.4×10^2 (5.0×10^3)	2.0	27.3
5b	GSH	1.4×10^2 (3.3×10^3)	0.7	31.9
	Cys	2.5×10^2 (3.6×10^3)	2.0	36.3
	MPA	1.5×10 (4.0×10^4)	5.0	3.5
	AET	5.3×10^2 (4.1×10^3)	1.0	31.6

[a] All data were obtained with **5** (final concentration: 25 μM) in HEPES buffer (10 mM, pH 7.4) containing 0.5% EtOH at 37 °C. GSH = glutathione, Cys = cysteine, MPA = 3-mercaptopropanoic acid, AET = 2-aminoethanethiol. [b] The numbers in parentheses are the rate constants k for the reaction of **5** with the corresponding thiolate anion estimated with $k = k_{obsd}(1+10^{pK_a-pH})$, with 8.75, 8.54, 10.84, and 8.23 used as the microscopic pK_a values of sulfhydryl groups in GSH, Cys, MPA, and AET, respectively.[18] [c] au = arbitrary units.

Table 2: Comparison of IC_{50} of ChE inhibitors on human erythrocyte AChE and serum BChE obtained with **5b** and DTNB

Inhibitor	Probe	IC_{50} [nM]		Selectivity for AChE[a]
		AChE	BChE	
donepazil	**5b**	11.8 ± 1.5	5260 ± 290	446
	DTNB[b]	19 ± 7	4100 ± 1800	216
BW284C51	**5b**	58.0 ± 5.4	19800 ± 750	341
	DTNB[c]	18.8	48000	2550
physostigmine	**5b**	142.0 ± 3.9	2090 ± 42	14.7
	DTNB[d]	27.9 ± 2.4	16.0 ± 2.9	0.57
tacrine	**5b**	111.0 ± 5.3	11.5 ± 1.2	0.10
	DTNB[b]	108 ± 7	29 ± 2	0.27

[a] Expressed as IC_{50} for BChE divided by IC_{50} for AChE. [b] See Ref. [2b]. [c] See Ref. [2c]. [d] See Ref. [2d].

between the IC_{50} values afforded by the present method and the DTNB method, except for physostigmine. This is likely a result of not preincubating ChE and each inhibitor before commencing the enzymatic reaction in the present method (all values cited using Ellman's method were estimated after a preincubation step). In fact, physostigmine is known to exhibit strong inhibitory activity against ChE only after preincubation for rather long periods of time.[19]

In conclusion, almost-nonfluorescent compounds **5** are transformed effectively to highly fluorescent **3** through reaction with thiols in aqueous buffer, with significantly shorter reaction times under mild conditions and without any side reactions, except for a low level of their hydrolysis. Thus, compounds **5** may be used as fluorescent probes for thiols and allow a simple and reliable fluorometric system for measuring ChE inhibitory activities to be developed. It is believed that fluorometry with **5** facilitates thiol-quantification assays of various types of enzymes as a high-throughput technique for screening enzyme inhibitors as new drugs. Further studies along these lines are currently underway in our laboratory.

Received: January 12, 2005
Published online: April 8, 2005

Keywords: enzymes · fluorescence · high-throughput screening · inhibitors · sensors

[1] G. L. Ellman, *Arch. Biochem. Biophys.* **1959**, *82*, 70 – 77.
[2] a) G. L. Ellman, K. D. Courtney, V. Andres, Jr., R. M. Featherstone, *Biochem. Pharmacol.* **1961**, *7*, 88 – 95; b) D. R. Liston, J. A. Nielsen, A. Villalobos, D. Chapin, S. B. Jones, S. T. Hubbard, I. A. Shalaby, A. Ramirez, D. Nason, W. F. White, *Eur. J. Pharmacol*, **2004**, *486*, 9 – 17; c) E. Giacobini, *Pharmacol. Res.* **2004**, *50*, 433 – 440; d) Q.-S. Yu, N. H. Greig, H. W. Hollway, *J. Med. Chem.* **1998**, *41*, 2371 – 2379.
[3] J. Zhu, I. Dhimitruka, D. Pei, *Org. Lett.* **2004**, *6*, 3809 – 3812.
[4] D. R. Grassetti, J. F. Murray, Jr., *Arch. Biochem. Biophys.* **1967**, *119*, 41 – 49.
[5] S. Sabelle, P.-Y. Renard, K. Pecorella, S. de Suzoni-Dézard, C. Créminon, J. Grassi, C. Mioskowski, *J. Am. Chem. Soc.* **2002**, *124*, 4874 – 4880.
[6] R. P. Haugland, *Handbook of Fluorescent Probes and Research Products*, *9th ed.*, Molecular Probes, Eugene, **2002**, pp. 79 – 98.
[7] M. E. Langmuir, J.-R. Yang, A. M. Moussa, R. Laura, K. A. LeCompte, *Tetrahedron Lett.* **1995**, *36*, 3989 – 3992.
[8] A. E. Radkowsky, E. M. Kosower, *J. Am. Chem. Soc.* **1986**, *108*, 4527 – 4531.
[9] G. Bartoli, P. E. Todesco, *Acc. Chem. Res.* **1977**, *10*, 125 – 132.
[10] T. Fukuyama, M. Cheung, C.-K. Jow, Y. Hidai, T. Kan, *Tetrahedron Lett.* **1997**, *38*, 5831 – 5834.H.
[11] H. Maeda, K. Yamamoto, Y. Nomura, I. Kohno, L. Hafsi, N. Ueda, S. Yoshida, M. Fukuda, Y. Fukuyasu, Y. Yamauchi, N Itoh, *J. Am. Chem. Soc.* **2005**, *127*, 68 – 69.
[12] K. Shimada, K. Mitamura, *J. Chromatogr. B* **1994**, *659*, 227 – 241.
[13] H. Kojima, Y. Urano, K. Kikuchi, T. Higuchi, Y. Hirata, T. Nagano, *Angew. Chem.* **1999**, *111*, 3419 – 3422; *Angew. Chem. Int. Ed.* **1999**, *38*, 3209 – 3212.
[14] C. A. Elliger, *Synth. Commun.* **1985**, *15*, 1315 – 1324.
[15] W.-C. Sun, K. R. Gee, D. H. Klaubert, R. P. Haugland, *J. Org. Chem.* **1997**, *62*, 6469 – 6475.
[16] G. M. Whitesides, J. E. Lilburn, R. P. Szajewski, *J. Org. Chem.* **1977**, *42*, 332 – 338.
[17] P. Eyer, D. Podhradsky, *Anal. Biochem.* **1986**, *153*, 57 – 66.
[18] J. M. Wilson, D. Wu, R. Motiu-Degrood, D. J. Hupe, *J. Am. Chem. Soc.* **1980**, *102*, 359 – 363.
[19] H. Ogura, T. Kosasa, Y. Kuriya, Y. Yamanishi, *Methods Find. Exp. Clin. Pharmacol.* **2000**, *22*, 609 – 613.

Nanostructures

Deterministic One-to-One Synthesis of Germanium Nanowires and Individual Gold Nanoseed Patterning for Aligned Nanowire Arrays**

*Dunwei Wang, Ryan Tu, Li Zhang, and Hongjie Dai**

Germanium nanowires (GeNWs) have attracted much attention in recent years[1–9] owing to the advanced electrical properties of germanium, such as high carrier mobilities,[10] and the facile chemical synthesis of single-crystal GeNWs at relatively low temperatures (well below 400 °C).[5] Various synthetic methods for crystalline GeNWs that use gold nanoparticles as seeds have been reported and include chemical vapor deposition (CVD),[5,8,9,11] physical vapor deposition (PVD),[2,3] and solvothermal reactions.[1,4] Never-

[*] D. Wang, R. Tu, L. Zhang, Prof. Dr. H. Dai
Department of Chemistry
Stanford University
Stanford, CA 94305 (USA)
Fax: (+1) 650-725-0259
E-mail: hdai@stanford.edu

[**] This work was supported by a DARPA 3D Electronics Program, the Stanford INMP, and SRC/AMD. R.T. acknowledges the NSF for a graduate fellowship.

 DOI: 10.1002/anie.200500291

theless, one-to-one growth (1-1 growth) in which each gold particle seed produces one nanowire[12] and the chemistry needed for such growth is not well-established for GeNWs. To achieve this goal is important for the deterministic synthesis of nanowires with controlled yield, size, growth locations, and orientations.

Here, we demonstrate excellent control over the synthesis of GeNWs by low-temperature CVD. GeNWs have been obtained in 100% yield relative to the gold nanoparticle seeds, and by understanding and optimizing the growth chemistry, we report 1-1 correspondence of GeNWs with gold seeds and that the optimum growth temperature for GeNWs is dependent on the size of the gold nanoparticle. We have also developed a method of patterning individual gold nanoparticles and growing GeNWs in 100% yield from the well-defined nanoparticle arrays. Furthermore, we show that the orientation of the GeNWs grown from the patterned sites can be manipulated by a post-growth flow-aligning treatment to afford quasi-parallel arrays of GeNWs with well-defined spacing.

The synthesis of GeNWs reported herein is based on a previous CVD method[5] with the slight modification that a low-pressure CVD (LPCVD) system (Figure 1a) is used instead of the atmosphere-pressure CVD (APCVD) system used previously. GeNWs were grown at various temperatures in the range of 270–400 °C on substrates decorated with preformed gold nanoparticles (diameter, $d = 5$–50 nm) by using GeH_4 as the precursor for germanium. As shown previously, the growth mechanism is well-described by the vapor–liquid–solid (VLS) model.[5,13,14] A main advantage of synthesis by LPCVD over APCVD is that the concentration of GeH_4 in the CVD system is better controlled by varying the pressure in the system than by diluting GeH_4 with carrier gases. The partial pressure of GeH_4 for optimum growth of GeNWs is between 4–8 Torr, below which the yield of nanowires is low as a result of insufficient feedstock and above which undesirable pyrolysis of GeH_4 is observed. Another important advantage of the LPCVD approach is the rapid removal by vacuum pumping of O_2 and H_2O trapped in the system which efficiently reduces the contaminants in the system and leads to highly reproducible growth results between experiments.

The main outcome of the current work is that the optimum growth condition of GeNWs is size-dependent; that is, the temperature at which optimum 1-1 growth of GeNWs is observed varies with the size of the gold seeds. Under a fixed partial pressure of GeH_4 (p_{GeH4}) of 5 Torr, the optimum growth temperature for gold seeds of diameter $d = 20 \pm 2$ nm is around 295 °C, under which temperature every gold seed can produce a GeNW (Figure 1b and c). The total number of nanowires grown matches the number of starting gold nanoparticle seeds, and the nanowires originate from the positions of the starting particles (Figure 1b). The quantitative yield and 1-1 growth at 295 °C for the 20-nm particles are robust and have been reproduced with ten batches of samples. For larger gold seeds ($d = 50 \pm 3$ nm), the optimum growth temperature for the GeNWs is approximately 310 °C and 1-1 growth was observed (Figure 2b). At a lower temperature of

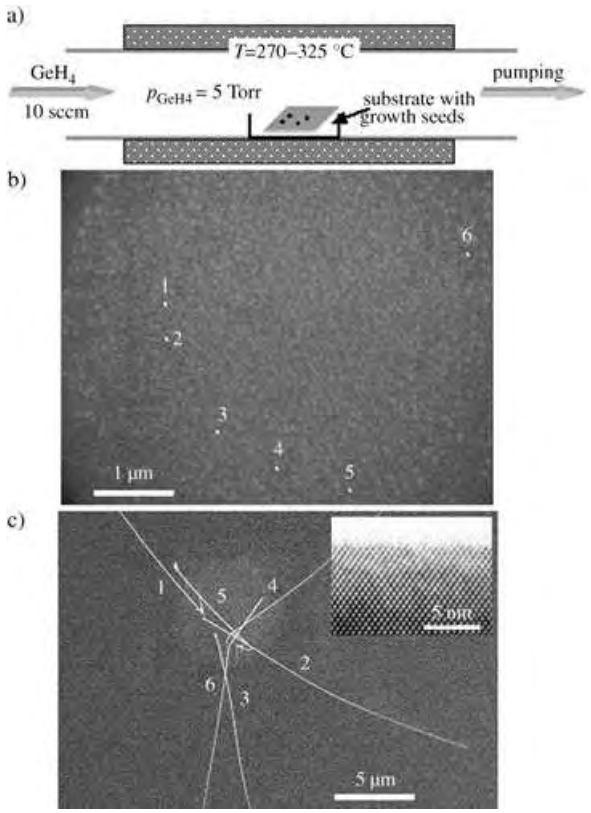

Figure 1. One-to-one growth of 20-nm GeNWs. a) Schematic of the LPCVD setup (sccm = standard cubic centimeters per minute), b) SEM image of six gold nanoparticles ($d \approx 20$ nm) as growth seeds, and c) SEM image of the six GeNWs grown from the gold seeds labeled in (b). (The inset shows a high-resolution transmission electron microscopy image of a single-crystalline GeNW grown under the same conditions as those shown in the main panel).

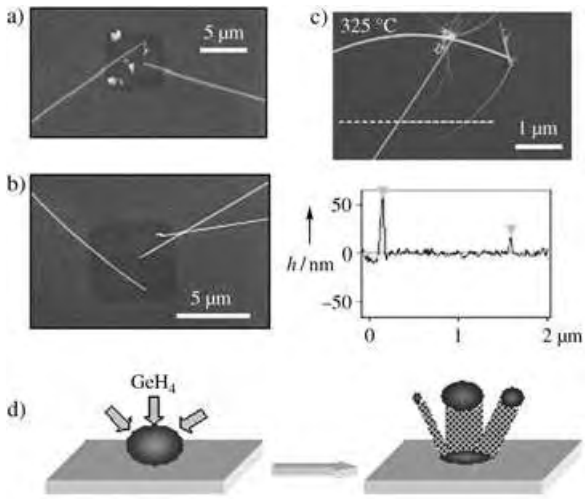

Figure 2. Growth results from 50-nm gold seeds at a) 295, b) 310, and c) 325 °C. Several blotches in (a) correspond to gold particles that have failed to produce nanowires. 1-1 growth is observed in (b) which suggests that the optimum growth of nanowires occurs at 310 °C for 50-nm seeds. The lower panel in (c) is a height (h) profile measured by atomic force microscopy (AFM) of GeNWs grown at 325 °C which shows that smaller ($d \approx 20$ nm) nanowires grow alongside 50-nm GeNWs. d) A schematic of multiple nanowires grown from one large parent particle.

295 °C, not all of the 50-nm gold seeds were capable of producing GeNWs (Figure 2a). On the other hand, if the growth temperature was high (e.g. at 325 °C), the 50-nm gold seeds produced more GeNWs than the number of starting seed particles and, interestingly, nanowires with diameters that are much smaller than the starting particles ($d \approx 50$ nm) were observed (Figure 2c). This observation suggests that splitting of the gold seeds with $d \approx 50$ nm into smaller particles occurred to produce smaller nanowires at the higher growth temperature (Figure 2d).

The optimum growth temperatures of GeNWs by CVD for gold seed particles with diameters in the range of 5 to 50 nm are summarized in Figure 3. A general trend is that

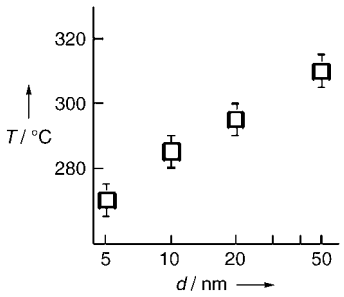

Figure 3. Size-dependent conditions for the growth of nanowires. A plot of the optimum temperature (T) for growth of the GeNW as a function of the size of the gold particle seeds, and hence the size of the nanowire, by CVD under a fixed partial pressure of 5 Torr of germane. For each particle size, the optimum growth temperature is denoted by a hollow square and the error bars span less than 10 °C.

smaller gold seeds can nucleate and grow nanowires at lower temperatures. For large particles ($d \approx 50$ nm) a low growth temperature produces GeNWs in low yields, and too high a temperature tends to overproduce wires as a result of splitting of gold seeds. These results can be explained by considering several key factors involved in the VLS growth process. The first factor is that the eutectic melting temperature of Ge–Au is size-dependent and higher for larger particles. Such size-dependence of the melting temperature has been documented for single- and binary-element particles.[15,16] It is therefore reasonable that larger particles require a higher temperature for efficient supersaturation and growth to occur. Second, diffusion of germanium in the gold particle is an important kinetic factor of the VLS growth process. The size of the gold seeds determines the length over which germanium must diffuse to saturate the Ge/Au solution for nucleation and growth of one nanowire from the seed particle. Higher temperatures will facilitate diffusion of germanium and thus the growth of nanowires from larger particles. The third factor is the feedstock supply of germanium. Higher temperatures will lead to more-efficient decomposition of the GeH_4 precursor and provide an efficient supply of germanium needed for larger gold particles.

The VLS growth of nanowires from large gold seed particles appears to be diffusion-limited. At high temperatures, the feeding of germanium precursor could be rapid while the diffusion of the feedstock atoms in gold may not be sufficiently high to supersaturate a large particle. Rather, smaller regions of the gold cluster are supersaturated rapidly, which leads to nucleation and growth of smaller nanowires from the parent gold particle (Figure 2d). In a control experiment, we attempted to grow germanium and silicon nanowires from GeH_4 and SiH_4, respectively, by using ultra-large gold particles with $d \approx 250$ nm. At all of the temperatures tested, we were unable to observe 1-1 growth from these large particles and always observed the growth of only small wires as a result of splitting of the gold particles. We believe that the diffusion limitation for the growth of large nanowires and the size-dependent growth of nanowires is general to the synthesis of various nanowire materials by the VLS mechanism.

With the 1-1 growth understood, we next pursued patterning of individual gold nanoparticles to achieve 1-1 growth of GeNWs at controlled locations and with monodispersed sizes by first using electron-beam lithography to pattern arrays of small gold islands on a substrate (Figure 4a).

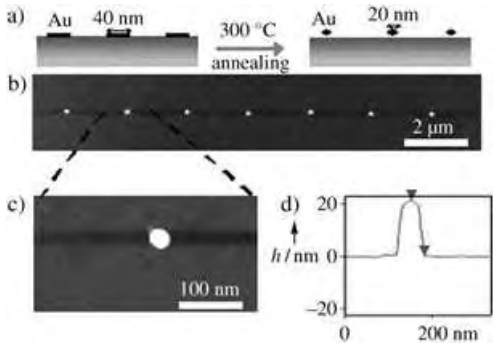

Figure 4. Patterning of individual gold nanoparticles. a) Schematic of the patterning process, b) AFM image of an array of Au dots regularly spaced at 2 μm, c) magnified AFM image of one gold nanoparticle, and d) height profile that shows the size of the gold nanoparticle ($h \approx 20$ nm) in (c).

The islands were 40-nm wide with various thicknesses (1–10 nm) and were formed by an evaporation and lift-off technique. Upon annealing at 300 °C, Au atoms in each island aggregated to form well-defined gold dots with controllable diameters in the range of 5–50 nm (the size of the dot is dependent on the thickness of the metal in the 40-nm-wide islands). Figure 4b shows an array of regularly spaced gold particles with $d \approx 20 \pm 3$ nm formed by this method. CVD growth using the optimum conditions identified in Figure 3 for 20-nm gold seeds led to successful 1-1 growth of GeNWs from the nanoparticle arrays (Figure 5). This result demonstrates that the synthesis of nanowires can be well-controlled at the single-particle level by making use of the understanding of the growth of nanowires as well as the state-of-the-art lithographic patterning technique.

We also explored the possibility to control the orientations of the GeNWs in an approach that utilized fluid flow[17,18] to manipulate and reorient the GeNWs grown from the patterned gold particle arrays, as shown schematically in Figure 5a. In the VLS tip-growth process, one of the ends of an as-grown GeNW is anchored onto the substrate at the point from which it grows, as highlighted by arrows in

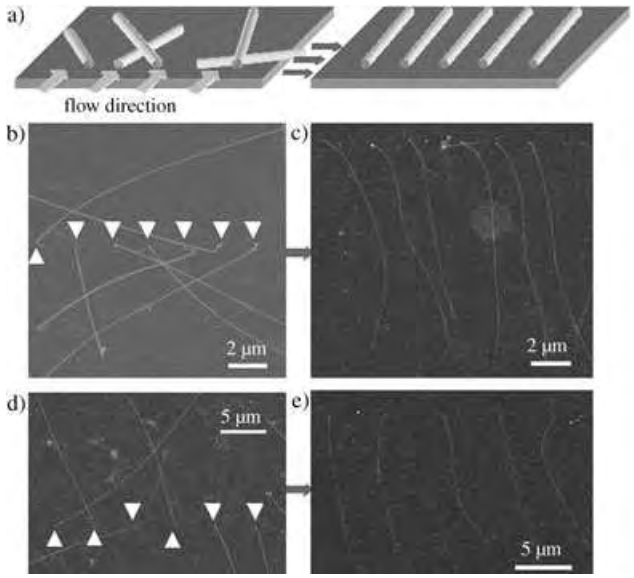

Figure 5. Post-growth reorientation of nanowires. a) Schematic of the process to flow-align GeNWs grown from an array of patterned gold seeds, b) SEM image of GeNWs grown from an array of 20-nm Au dots similar to those in Figure 4b (the arrows indicate the original positions of the Au dots and the fixed ends of the as-grown GeNWs), c) SEM image of quasi-aligned GeNWs (2-μm pitch) after flow treatment of the sample in (b), and d) and e) SEM images of GeNWs grown in a one-to-one manner from patterned Au dots (5-μm pitch) before (d) and after (e) flow-alignment.

Figure 5b and d, and acts as a pivotal point for the wire. After a stream of deionized water is flowed across the substrate surface, the nanowires are reoriented towards the flow direction and become quasi-aligned while maintaining the same spacing between their pivoted ends (Figure 5c and e).

In summary, we have demonstrated controlled one-to-one synthesis of GeNWs in near-quantitative yields from gold seed particles. Size-dependent optimum growth conditions for the GeNW have been identified. For gold seeds with diameters of less than 50 nm, underproduction, 1-1 growth, and overproduction can occur depending on the conditions. Growth of large GeNWs appears to be diffusion-limited. These results have generic implications in the synthesis of other types of nanowires through the VLS mechanism. Patterning and positioning of individual gold nanoparticles was observed by lithographic patterning and used for successful one-to-one nanowire growth. Finally, post-growth flow-alignment was used to obtain quasi-parallel nanowires that originate from well-controlled locations. These results are important to the fundamental synthesis of nanomaterials and may find important applications in various fields including high-performance nanoelectronics.

Experimental Section

Deposition of preformed gold nanoparticles: A silicon substrate was soaked in an aqueous solution of 3-aminopropyltriethylsilane (APTES; 12 μL APTES in 20 mL H_2O) for 2 minutes. After thorough rinsing with deionized H_2O and blow-drying with N_2, the substrate was then soaked in a solution of Au colloids (5–50 nm) for 5 minutes. The resulting density of Au particles on the substrate was determined by the concentration of the colloidal solution. For instance, a prepared solution of 20-nm Au colloids (Ted Pella, Inc., CA, USA) contains 10^{11} nanoparticles mL^{-1}. Dilution by 1000 was performed to obtain a concentration of 10^8 cm^{-3}. When deposited on a silicon substrate, a density of approximately 1 particle/3 μm^2 could be reliably obtained with such a concentration. After deposition of Au nanoparticles, calcination in air at 300 °C for 15 minutes was carried out to remove organic residues. The as-prepared substrate was imaged by scanning electron microscopy (SEM, FEI XL30 Sirion) to record the locations of individual nanoparticles in certain regions. Then, the substrate was subjected to CVD growth followed by SEM imaging of the same regions to correlate the synthesized nanowires with their parent nanoparticle seeds.

CVD synthesis of GeNWs: In a typical experiment, the CVD quartz tube chamber (2.54 cm) was first evacuated to its base pressure of 150 mTorr and then heated up to a growth temperature in the range of 270–325 °C. The chamber was then filled with precursor species of GeH_4 (germane, 10% in He, Voltaix Inc. NJ, USA) to the desired growth pressure (total pressure $\approx$ 50 Torr, $p_{GeH4} \approx 5$ Torr) and maintained at that pressure throughout the growth. During this process, GeH_4 was flowed at a rate of 10 sccm (standard cubic centimeters per minute). At the end of the reaction, the feeding of GeH_4 was stopped and the chamber was pumped to its base pressure again and cooled down to room temperature. (One of the criteria of optimum growth is that the quartz growth chamber after CVD should be free of pyrolytic deposits of GeH_4).

Patterning of individual gold nanoparticles: A 100-nm-thick film of polymethylmethacrylate (PMMA) was formed by spin-coating onto a Si substrate. Electron beam lithography (Raith 150) was used to create wells in the PMMA film with dimensions of 40×40 nm^2. A Au film of 1–10 nm thickness was then deposited onto the PMMA-patterned substrate in an electron-beam evaporator, followed by lift-off of the PMMA to afford 40-nm-wide Au islands. The substrate was then annealed in Ar at 300 °C for 15 minutes during which time the small Au islands aggregated to form single Au nanoparticles.

Manipulating the orientations of nanowires after one-to-one growth: After CVD growth of GeNWs on a substrate with patterned Au dots, a droplet of H_2O was placed onto the substrate to cover the as-grown GeNWs. N_2 was then flowed to blow-dry the surface along a desired direction. After this simple process, the nanowires were quasi-aligned with the flow direction.

Received: January 25, 2005
Published online: April 7, 2005

Keywords: chemical vapor deposition · germanium · gold · nanostructures

[1] J. R. Heath, F. K. LeGoues, *Chem. Phys. Lett.* **1993**, *208*, 263.
[2] Y. Wu, P. Yang, *Chem. Mater.* **2000**, *12*, 605.
[3] G. Gu, M. Burghard, G. T. Kim, S. Dusberg, P. W. Chiu, V. Krstic, S. Roth, W. Q. Han, *J. Appl. Phys.* **2001**, *90*, 5747.
[4] T. Hanrath, B. K. Korgel, *J. Am. Chem. Soc.* **2001**, *123*, 1424.
[5] D. Wang, H. Dai, *Angew. Chem.* **2002**, *114*, 4977; D. Wang, H. Dai, *Angew. Chem. Int. Ed.* **2002**, *41*, 4783.
[6] D. W. Wang, Q. Wang, A. Javey, R. Tu, H. J. Dai, H. Kim, P. C. McIntyre, T. Krishnamohan, K. C. Saraswat, *Appl. Phys. Lett.* **2003**, *83*, 2432.
[7] D. Wang, Y. L. Chang, Q. Wang, J. Cao, D. B. Farmer, R. G. Gordon, H. Dai, *J. Am. Chem. Soc.* **2004**, *126*, 11602.
[8] A. B. Greytak, L. J. Lauhon, M. S. Gudiksen, C. M. Lieber, *Appl. Phys. Lett.* **2004**, *84*, 4176.
[9] J. W. Dailey, J. Taraci, T. Clement, D. J. Smith, J. Drucker, S. T. Picraux, *J. Appl. Phys.* **2004**, *96*, 7556.

[10] S. M. Sze, *Physics of Semiconductor Devices*, Wiley, New York, **1981**.
[11] T. I. Kamins, X. Li, R. S. Williams, *Nano Lett.* **2004**, *4*, 503.
[12] T. Martensson, P. Carlberg, M. Borgstrom, L. Montelius, W. Seitert, L. Samuelson, *Nano Lett.* **2004**, *4*, 699.
[13] R. S. Wagner, W. C. Ellis, *Appl Phys Lett.* **1964**, *4*, 89.
[14] Y. Wu, P. Yang, *J. Am. Chem. Soc.* **2001**, *123*, 3165.
[15] P. Baffat, J. P. Borel, *Phys. Rev. A* **1976**, *13*, 2287.
[16] M. Wautelet, J. P. Dauchot, M. Hecq, *Nanotechnology* **2000**, *11*, 6.
[17] B. Messer, J. H. Song, P. Yang, *J. Am. Chem. Soc.* **2000**, *122*, 10232 – 10233.
[18] Y. Huang, X. F. Duan, Q. Wei, C. M. Lieber, *Science* **2001**, *291*, 630.

Dihalomethane Structures

A Dramatic Spin–Orbit Effect Observed in the Vibrational Frequencies of the Chloroiodomethane Cation**

*Mina Lee, Hyoseok Kim, Yoon Sup Lee, and Myung Soo Kim**

Several theoretical studies have suggested that a spin–orbit-induced isomer may be found for a molecule of the as-yet-unknow superheavy element 118, that is, $(118)F_4$,[1] but there have been no reports of an experimentally observed molecule for which the inclusion of spin–orbit effects is essential for the correct identification of the ground state structure. We report here a molecular ion, $[CH_2ClI]^+$, for which spin–orbit interactions are crucial for the identification of the structure and vibrational frequencies of the correct ground state. Theoretically, the spin–orbit interaction is part of the relativistic effect. The importance of relativity for the description of heavy atoms is well recognized.[2] Scalar relativistic effects are routinely included in electronic-structure calculations of molecules containing heavy elements through the use of relativistic effective core potentials (RECP), but spin–orbit interactions are usually omitted when deriving optimized structures partly because of the assumption that their influence on the molecular structures is negligible and partly due to computational difficulties. Even when spin–orbit terms are available in RECPs, the usual treatment involves perturbational inclusion of these terms after the variational determination of orbitals and structures. Quantum chemical calculations employing RECPs and spin–orbit operators from the start have been available for some time.[3] The spin–orbit density functional theory (DFT) method available in NWChem is particularly useful for the present purpose of demonstrating spin–orbit effects on geometries since the geometry can be optimized with both electron correlations and spin–orbit interactions included.[4]

We have been investigating the reactivity of mixed dihalomethane cations for some time. Hence, we have recorded the vibrational spectra of the cations by mass-analyzed threshold ionization (MATI) spectrometry.[5] Figure 1 shows the MATI spectrum of CH_2ClI recorded by monitoring $[CH_2{}^{35}ClI]^+$ in the electronic ground state. The most intense peak at around 78644 cm^{-1} corresponds to the 0–0 band. The distance of each peak from the 0–0 band in this spectrum corresponds to the vibrational frequency of the cation. CH_2ClI has nine nondegenerate normal modes: modes 1–6, with a' symmetry, and modes 7–9, with a'' symmetry. All the fundamentals and overtones of the totally symmetric modes, a', are dipole-allowed, while only the even-numbered overtones of the a'' modes are allowed. Utilizing the selection rule and the frequencies in the neutral species,[6] plausible assignments can be made for the prominent peaks; these are listed in Table 1. Modes 2 and 3 are due to CH_2 motion, modes 4 and 5 are C–Cl and C–I stretchings, respectively, and mode 6 is I–C–Cl bending. Other peaks in the spectrum are due to overtones and combinations.

Our normal routine is to perform quantum chemical calculations for the vibrational frequencies, isotope shifts, and Franck–Condon factors to confirm, improve, or revise the phenomenological assignments. In particular, results from the DFT/B3LYP calculations have been found to be adequate in most cases.[5] When we performed DFT/B3LYP calculations for $[CH_2ClI]^+$ with Gaussian 98, using a well-known RECP for iodine such as LanL2DZ,[7] we always obtained two distinct stationary states, $^2A'$ and $^2A''$, formed by removal of an electron from in-plane and out-of-plane iodine nonbonding orbitals, respectively. Even though their energies are nearly the same, their geometries are noticeably different because of the partial antibonding characteristics contained in essentially iodine nonbonding orbitals. The vibrational frequencies in the two states are also noticeably different, suggesting that the observed spectrum would be a superposition of two spectra.

The fact that a rather straightforward phenomenological assignment of the MATI spectrum was possible is not compatible with the calculated results. Moreover, the experimental frequencies could not be correlated with the calculated results with the accuracy expected for the DFT/B3LYP results (± 15 cm^{-1}). We thought that neglecting the spin–orbit effect could be one possible cause of this discrepancy, and we therefore performed the spin–orbit DFT calculations implemented in NWChem for neutral and cationic CH_2ClI in the electronic ground states using RECPs with the effective spin–

[*] M. Lee, Prof. M. S. Kim
National Creative Research Center for Control of Reaction Dynamics and School of Chemistry, Seoul National University
Seoul 151-742 (Korea)
Fax: (+82) 2-889-1568
E-mail: myungsoo@plaza.snu.ac.kr
H. Kim, Prof. Y. S. Lee
Department of Chemistry and
School of Molecular Science (BK21), KAIST
Daejeon 305-701 (Korea)

[**] This work was financially supported by CRI, the Korea Research Foundation (KRF-2004-041-C00161), the Ministry of Science and Technology, the Brain Korea 21 Projects awarded to Seoul National University and KAIST, the Ministry of Education, and CNMM of KIMM, Republic of Korea. M.L. thanks the Ministry of Education for a Brain Korea 21 fellowship.

 DOI: 10.1002/anie.200463090

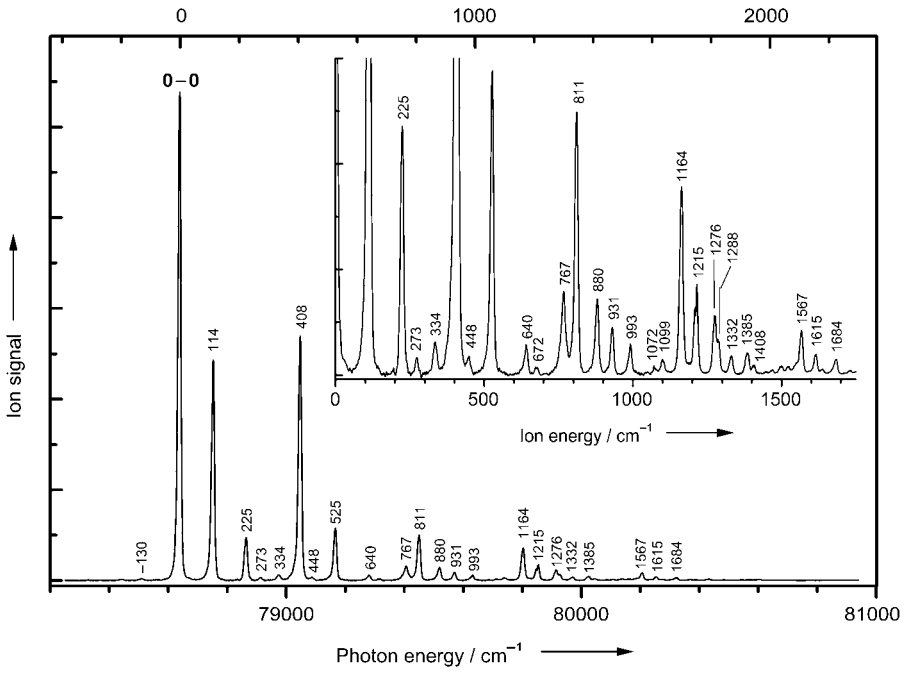

Figure 1. One-photon MATI spectrum of CH_2ClI recorded by monitoring $[CH_2{}^{35}ClI]^+$ in the electronic ground state. The *x* scale at the top corresponds to the vibrational frequency scale for the cation. Its origin is at the 0–0 band position. The spectrum in the 0–1700 cm^{-1} region magnified by 10 along the *y* axis is shown as an inset.

Table 1: Experimental vibrational frequencies [cm^{-1}] of CH_2ClI and $[CH_2ClI]^+$ in the electronic ground state and calculated data without (w/o) and with (w) the spin–orbit effect.[a]

Mode[b]	CH_2ClI			$[CH_2ClI]^+$			
		w/o S.O.	w S.O.		w/o S.O.		w S.O.
	exp.[c]	$^1A'$	^1A	MATI	$^2A'$	$^2A''$	^2A
1	3001	3126	3126	–	3132	3044	3106
2	1412	1439	1439	1385	1434	1382	1420
3	1188	1202	1202	1164	1169	1168	1175
4	740	707	709	767	726	726	747
5	536	523	518	408	507	359	419
6	192	188	186	114	163	180	112
7	3066	3207	3207	–	3216	3103	3206
8	–	1128	1127	1072	1073	1098	1089
9	–	782	780	–	847	789	791

[a] Calculated at the B3LYP level using the RECP of ref. [8] for halogen atoms and aug-cc-pVTZ for other atoms. The spin–orbit term in the same reference was used when needed. [b] Mulliken notation. [c] Raman spectroscopic data taken from ref. [6].

orbit potentials reported in ref. [8] for the halogen atoms. The size of the basis set was increased until the basis-set dependence of the vibrational frequencies became less than 15 cm^{-1}. To determine the importance of the spin–orbit terms, all the calculations were done with and without the spin–orbit potential but with the same RECP. The calculated equilibrium geometries of the neutral species and the cation have C_s symmetry. The optimized geometry of the neutral species is hardly affected by the spin–orbit terms (Table 2). For the cation, however, only one equilibrium geometry was obtained with the spin–orbit terms, instead of the two found in their absence. For the double group symmetry of the fine structure state in the presence of spin–orbit terms, both the ground and lowest excited states of the cation have the same symmetry. Unlike the DFT calculations without the spin–orbit terms, the spin–orbit DFT calculations did not locate the second state as the lowest fine-structure state. The second state is well separated, by about 4000 cm^{-1}, from the ground state.[9]

The most striking influence of the spin–orbit terms on the cation geometry (Table 2) is observed for the I–C–Cl bond angle. With the aug-cc-pVTZ basis set, these are 96.1° and 116.1° for $^2A'$ and $^2A''$, respectively, in the absence of the spin–orbit terms, and 106.0° in their presence. The trend observed in the vibrational frequencies (Table 1) is similar. The influence of the spin–orbit terms on the vibrational frequencies of the neutral is not significant, and the results are compatible with the experimental data. In the case of the cation, however, the two sets of frequencies calculated without the spin–orbit terms could not be correlated with the experimental data. The single set of vibrational frequencies obtained with the spin-obit terms, however, agrees well with the experimental data. For example, the I–C–Cl bending, mode 6, has the frequencies 163 and 180 cm^{-1} in $^2A'$ and $^2A''$, respectively, in the absence of the spin–orbit terms and 112 cm^{-1} in their presence; the experimental frequency is 114 cm^{-1}.

To the best of our knowledge, this is the first time that a dramatic spin–orbit effect has been observed for the vibrational frequencies and the shape of the ground state of a polyatomic molecule. The presence of an iodine atom is certainly a factor responsible for the above observation. Also important is the fact that two nearly degenerate electronic states with different geometries are present for the radical

Table 2: Bond length [Å] and angles [°] of CH_2ClI and $[CH_2ClI]^+$ in the electronic ground state without (w/o) and with (w) the spin–orbit effect.[a]

C_s	CH_2ClI			$[CH_2ClI]^+$		
		w/o S.O.	w S.O.	w/o S.O.[c]		w S.O.[d]
	exp.[b]	$^1A'$	^1A	$^2A'$	$^2A''$	^2A
C–I	2.137	2.181	2.187	2.187	2.243	2.242
C–Cl	1.774	1.778	1.777	1.767	1.716	1.738
C–H	1.062	1.081	1.081	1.082	1.090	1.084
I-C-Cl	112.5	114.4	114.4	96.1	116.1	106.0
H-C-I	108.3	106.6	106.6	109.6	101.0	104.9
H-C-Cl	108.4	108.6	108.7	111.9	112.9	112.7
H-C-H	111.0	112.1	112.0	115.8	111.8	114.5

[a] Calculated under the same conditions as in Table 1. [b] Microwave spectroscopic data taken from ref. [10]. [c] Two distinct stationary geometries with nearly the same energy appear in the absence of the spin–orbit term. [d] Only one stationary geometry is obtained in the presence of the spin–orbit term.

cation in the absence of the spin–orbit effect. The spin–orbit interactions lift this accidental orbital degeneracy by mixing two states strongly in the region connecting two minima.

The lack of experimental data displaying noticeable spin–orbit effects has been one of the justifications for ignoring its computational treatment even for molecules with quite heavy elements. The present results suggest that spin–orbit terms should be treated the same as other relativistic effects in some cases, and demonstrate unequivocally that accounting for the relativistic effect can be critical for the studies of radicals with heavy atoms. Also to be noted is that the calculated frequencies do not match the experimental results as well as in other systems reported previously,[3b] even when the spin–orbit terms are included, which implies that further refinement and improvement are desirable for the treatment of relativistic effects in open-shell systems. The present data provide a useful benchmark in the computational treatment of the relativistic effect. Preliminary studies indicate that the spin–orbit effect is important for other cations with an iodine atom.

Experimental Section

The vacuum ultraviolet (VUV) radiation generated by four-wave mixing in Kr was overlapped with the CH_2ClI molecular beam to excite the neutral species to their Rydberg states. These were ionized by an electric field pulse applied after a time delay. Measuring the molecular ion current as a function of the VUV wavelength gives the MATI spectrum, which is essentially a vibrational spectrum of the molecular cation.

Received: December 29, 2004
Published online: April 13, 2005

Keywords: density functional calculations · dihalomethanes · spin–orbit coupling · structure elucidation · vibrational spectroscopy

[1] a) C. S. Nash, B. E. Bursten, *Angew. Chem.* **1999**, *111*, 115; *Angew. Chem. Int. Ed.* **1999**, *38*, 151; b) Y.-K Han, Y. S. Lee, *J. Phys. Chem. A* **1999**, *103*, 1104.

[2] a) P. A. Christiansen, W. C. Ermler, K. S. Pitzer, *Annu. Rev. Phys. Chem.* **1985**, *36*, 407; b) P. Pyykko, *Adv. Quantum Chem.* **1978**, *11*, 353; c) Y. S. Lee, A. D. McLean, *J. Chem. Phys.* **1982**, *76*, 735.

[3] a) Y.-K. Han, C. Bae, S.-K. Son, Y. S. Lee, *J. Chem. Phys.* **2000**, *112*, 2684; b) Y. J. Choi, Y. S. Lee, *J. Chem. Phys.* **2003**, *119*, 2014.

[4] High Performance Computational Chemistry Group, *NWChem, A Computational Chemistry Package for Parallel Computers*, Version 4.1, Pacific Northwest National Laboratory, Richland, Washington, USA, **2003**..

[5] a) S. T. Park, S. K. Kim, M. S. Kim, *Nature* **2002**, *415*, 306; b) M. Lee, M. S. Kim, *J. Chem. Phys.* **2003**, *119*, 5085; c) M. Lee, M. S. Kim, *J. Phys. Chem. A* **2003**, *107*, 11401.

[6] V. Sablinskas, P. Klaeboe, C. J. Nielsen, D. Sülzle, *Analyst* **1992**, *117*, 365.

[7] Gaussian 98 (Revision A.6), M. J. Frisch, G. W. Trucks, H. B. Schlegel, G. E. Scuseria, M. A. Robb, J. R. Cheeseman, V. G. Zakrzewski, J. A. Montgomery, R. E. Stratmann, J. C. Burant, S. Dapprich, J. M. Millam, A. D. Daniels, K. N. Kudin, M. C. Strain, O. Farkas, J. Tomasi, V. Barone, M. Cossi, R. Cammi, B. Mennucci, C. Pomelli, C. Adamo, S. Clifford, J. Ochterski, G. A. Petersson, P. Y. Ayala, Q. Cui, K. Morokuma, D. K. Malick, A. D. Rabuck, K. Raghavachari, J. B. Foresman, J. Cioslowski, J. V. Ortiz, B. B. Stefanov, G. Liu, A. Liashenko, P. Piskorz, I. Komaromi, R. Gomperts, R. L. Martin, D. J. Fox, T. Keith, M. A. Al-Laham, C. Y. Peng, A. Nanayakkara, C. Gonzalez, M. Challacombe, P. M. W. Gill, B. G. Johnson, W. Chen, M. W. Wong, J. L. Andres, M. Head-Gordon, E. S. Replogle, J. A. Pople, Gaussian, Inc., Pittsburgh, PA, **1998**..

[8] a) L. F. Pacios, P. A. Christiansen, *J. Chem. Phys.* **1985**, *82*, 2664; b) L. A. LaJohn, P. A. Christiansen, R. B. Ross, T. Atashroo, W. C. Ermer, *J. Chem. Phys.* **1987**, *87*, 2812.

[9] I. Novak, J. M. Benson, A. W. Potts, *Chem. Phys.* **1986**, *107*, 129.

[10] I. Ohkoshi, Y. Niide, M. Takano, *J. Mol. Spectrosc.* **1987**, *124*, 118.

Single-Molecule Magnets

Quantum Tunneling of Magnetization in Lanthanide Single-Molecule Magnets: Bis(phthalocyaninato)terbium and Bis(phthalocyaninato)dysprosium Anions**

Naoto Ishikawa, Miki Sugita, and Wolfgang Wernsdorfer**

Single-molecule magnets (SMMs) are the class of high-spin molecules that exhibit magnetization hysteresis at low temperature, that is, the property of macroscopic magnets.[1–5] Most SMMs are composed of several transition-metal ions, whose spins are coupled by strong exchange interactions to give a large effective spin with a predominant uniaxial anisotropy. The quantum nature of SMMs is manifested by staircase hysteresis loops,[5,6] temperature-independent relaxation,[7–12] and quantum phase interference.[13] The discovery of these phenomena led to potential applications in quantum computing.[14]

The finding of slow magnetization relaxation in lanthanide complexes has opened the possibility of constructing

[*] Prof. Dr. N. Ishikawa
Department of Applied Chemistry
Faculty of Science and Engineering, Chuo University
1-13-27 Kasuga, Bunkyo-ku, Tokyo 112-8551 (Japan)
Fax: (+81) 338-171-910
E-mail: ishikawa@chem.titech.ac.jp

Dr. W. Wernsdorfer
Laboratoire Louis Néel, CNRS
BP 166, 25 Avenue des Martyrs, 38042 Grenoble Cedex 9 (France)
Fax: (+33) 4-7688-1191
E-mail: wernsdor@grenoble.cnrs.fr

M. Sugita
Department of Chemistry, Tokyo Institute of Technology
O-okayama, Meguro-ku, Tokyo 152-8551 (Japan)

[**] This work was partly supported by the EC-TMR Network "QuE-MolNa" (MRTN-CT-2003-504880) and by a Grant-in-Aid for Science Research No. 15550046 from the Ministry of Education, Science, Sports, and Culture of Japan.

 DOI: 10.1002/anie.200462638

SMMs containing only a single metal ion as a magnetic center.[15] Alternating current (ac) magnetic susceptibility measurements have been reported for the bis(phthalocyaninato)terbium anion $[Pc_2Tb]^-$ (Pc = dianion of phthalocyanine) and an isostructural dysprosium complex $[Pc_2Dy]^-$ above 2 K.[15,16] One of the important results was that slow

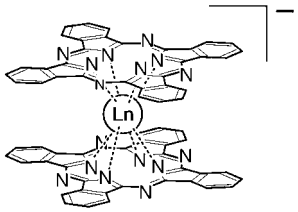

magnetization relaxation was observed in temperature ranges that were significantly higher than those of previously known transition-metal SMMs. For example, the peak positions in the χ'' versus T plot (χ_M'' refers to the out-of-phase component of ac susceptibility) of the Tb and Dy complexes are at 40 and 10 K, respectively, for a 1-kHz ac frequency.[15,16] The Arrhenius analysis showed that the dominant relaxation path in the high-temperature range, above 25 K for $[Pc_2Tb]^-$ and 3 K for $[Pc_2Dy]^-$, is a thermally activated Orbach process that involves excited substates in the ground multiplet.[16] Hysteresis loops were measured at 1.7 K; however, no clear evidence of quantum tunneling was observed because of instrumental limitations.[16]

Herein, we report magnetic hysteresis measurements for these lanthanide single-ion SMMs in the subkelvin temperature range. Clear evidence of quantum tunneling of magnetization (QTM) is presented for the first time. We found that the quantum process in these single-ion SMMs is a result of the resonant quantum tunneling between entangled states of electron and nuclear spin systems, which was first reported for the scheelite-structured compound $LiYF_4$ doped with trivalent Ho ions.[17]

The compounds were prepared as reported in the literature[18,19] with certain modifications.[20] The doped single-crystalline samples were prepared by recrystallization from a mixed solution of TBA[Pc_2Ln] (TBA = tetrabutylammonium) and TBA[Pc_2Y] with a [Ln]/[Y] ratio of 1:49 in acetone. All measurements were performed using the micro-SQUID technique (SQUID is a superconducting quantum interference device).[21] The field was aligned parallel to the easy axis of magnetization by the transverse field method.[22]

Figure 1 shows magnetization versus field measurements for the diluted sample of the $[Pc_2Tb]^-$ ions at 0.04 K and several field scan rates. These hysteresis loops present a clear staircase-like structure, which indicates the occurrence of QTM. Such measurements were also performed on less-diluted and undiluted TBA[Pc_2Tb] samples, and revealed similar features that were, however, significantly broadened because of magnetic dipolar interactions among adjacent molecules. Notably, the figure shows no clear step at $\mu_0 H = 0$ T.

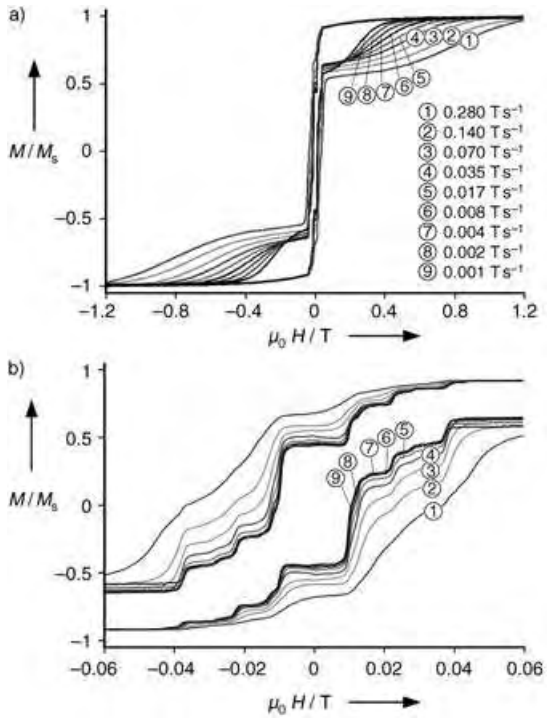

Figure 1. a) Hysteresis loops at 0.04 K for a single crystal of TBA[$(Pc)_2Tb_{0.02}Y_{0.98}$] measured at several field scan rates. The applied magnetic field was aligned along the easy axis of magnetization. b) Enlargement of the hysteresis loops in (a).

In known transition-metal-cluster SMMs, where energy separations between substates with different $|S_z|$ values are of the order of 1–10 cm^{-1}, QTM occurs when energy levels of two substates coincide under an appropriate magnetic field and the states are brought to resonance. In the lanthanide single-ion SMM $[Pc_2Tb]^-$, such level crossings occur only at very high fields because the substates are separated by a few hundred cm^{-1}.[20,23,24] This situation is illustrated in Figure 2a, which shows a Zeeman diagram for the $J = 6$ ground multiplet

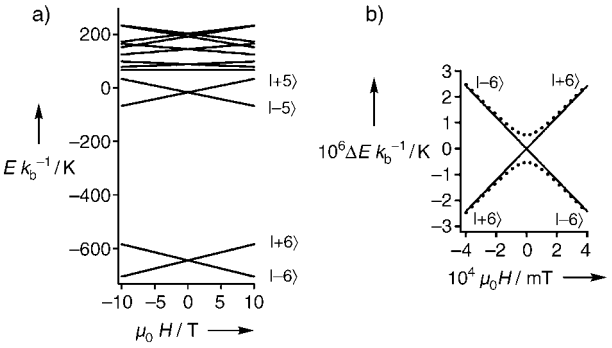

Figure 2. a) Zeeman energy diagrams as a function of longitudinal magnetic field for the $J = 6$ ground multiplet with the ligand-field parameters determined for TBA[Pc_2Tb] in a previous work:[20] $A_2^0\langle r^2\rangle = 414\ cm^{-1}$, $A_4^0\langle r^4\rangle = -228\ cm^{-1}$, and $A_6^0\langle r^6\rangle = 33\ cm^{-1}$. b) Enlargement of the region around the intersection between the lowest substates. The dotted lines are obtained with an additional $A_4^4\langle r^4\rangle O_4^4$ ligand-field term with $A_4^4\langle r^4\rangle = 10\ cm^{-1}$. The plot shows a tunnel splitting of 1.05×10^{-6} K.

of TBA[Pc_2Tb] obtained by using the ligand-field (LF) parameters previously determined.[20]

Figure 2b shows the enlargement of the area around zero field for the lowest $J_z = \pm 6$ substates. Under the assumption that all off-diagonal matrix elements of the LF Hamiltonian are negligible,[20] no mixing occurs among the two sublevels at $\mu_0 H = 0$ T (solid lines). In the case of C_4 symmetry, the LF terms $A_4^4\langle r^4\rangle O_4^4$ and $A_6^4\langle r^6\rangle O_6^4$, which comprise the off-diagonal elements that couple $|J_z\rangle$ and $|J_z-4\rangle$ states, can take nonzero values.[25] The plots with dotted lines in the Zeeman diagram are calculated with a small nonzero $A_4^4\langle r^4\rangle$ value. This result illustrates that the $J_z = \pm 6$ substates are brought to resonance at $\mu_0 H = 0$ T, thus giving rise to an "avoided level crossing" which allows QTM to occur.

This picture itself, however, provides only an insufficient explanation for the step structures observed at nonzero magnetic fields. Terbium has a nucleus with $I = 3/2$ spin in a natural abundance of 100%. It is therefore necessary to take into account the interaction between the $(4f)^8$ system and the nucleus. Exact numerical diagonalization of a $[(2J+1)(2I+1) \times (2J+1)(2I+1)]$ matrix, which includes the above ligand-field parameters, the hyperfine interaction $A_{hf}\boldsymbol{JI}$, and the nuclear quadrupole interaction term $P\{I_z^2 - 1/3\, I(I+1)\}$, was performed. Figure 3 shows the Zeeman diagram for the eight $|J_z\rangle\,|I_z\rangle$ states created from the combinations of the $J_z = \pm 6$ doublets and $I = 3/2$ quartets. The level intersections are seen at 13 magnetic-field positions. All step positions observed in Figure 1 are reproduced by using $A_{hf} = 0.0173\ cm^{-1}$ and $P = 0.010\ cm^{-1}$. The four largest avoided level crossings are indicated. An important conclusion drawn from this numerical study is that the inclusion of the nuclear quadrupole term is mandatory to explain the seemingly irregularly arranged staircase structures in the hysteresis loops of $[Pc_2Tb]^-$. The hyperfine interaction term alone cannot account for all the steps observed. This finding is in sharp contrast to the situation for Ho ions in a $LiYF_4$ matrix where equidistantly positioned steps were observed which have been fully explained by the hyperfine interaction alone.[17]

Figure 4 shows hysteresis loops for the $[Pc_2Dy]^-$ complex at 0.04 K with varied field scan rates. A steep drop in magnetization is observed near zero field, unlike the in the Tb case. Apart from this zero-field step, only slight indications of steps can be seen at about $\mu_0 H = 7$ and 14 mT. Small remanent magnetization is present at low sweep rates.

The situation for the Dy complex is more complicated than that for the Tb complex. There are seven naturally occurring isotopes of Dy, namely, ^{156}Dy, ^{158}Dy, ^{160}Dy, ^{161}Dy, ^{162}Dy, ^{163}Dy, and ^{164}Dy, with a natural abundance of 0.06, 0.01, 2.34, 18.91, 25.51, 24.90, and 28.18%, respectively. ^{161}Dy and ^{163}Dy have a nuclear spin of $I = 5/2$ while other nuclear species have $I = 0$.

In the cases of $I = 0$, there is only one level crossing at $\mu_0 H = 0$ T. However, no tunneling should occur because of the Kramers theorem of spin parity. This theorem asserts that no matter how unsymmetric the crystal field, an ion possessing an odd number of electrons (that is, a half-integer spin system) must have a ground state that is at least doubly degenerate (that is, no tunnel splitting), even in the presence

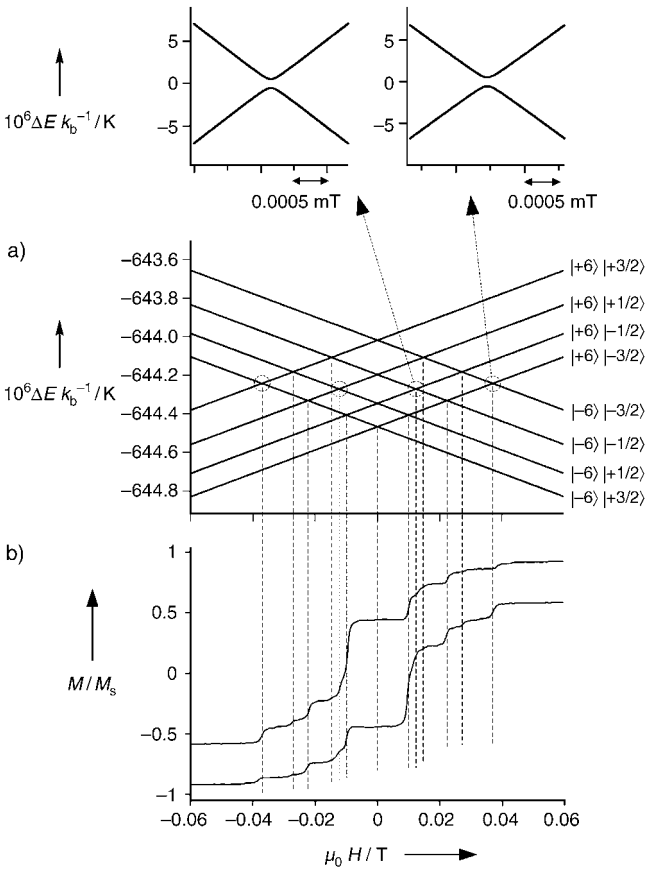

Figure 3. a) Zeeman diagrams for the lowest $J_z = \pm 6$ substates combined with the $I = 3/2$ nucleus state calculated with the LF parameters used in Figure 2b, $A_{hf} = 0.0173\ cm^{-1}$ for the hyperfine interaction term, and $P = 0.010\ cm^{-1}$ for the nuclear quadrupole interaction term. The circles indicate the positions where avoided level crossing occurs. b) Hysteresis loop at 0.04 K for a single crystal of TBA[$(Pc)_2Tb_{0.02}Y_{0.98}$] measured at 0.001 Ts^{-1}.

of crystal fields and spin–orbit interactions.[26] Hence, the Dy complexes with $I = 0$ should not contribute to the step structure. However, the Dy complexes with a nuclear spin $I = 5/2$ have avoided level crossings because two coupled half-integer spins ($J = 13/2$ and $I = 5/2$) lead to an integer total spin. Figure 5 shows the Zeeman diagram for the lowest sublevels calculated for the $I = 5/2$ case, with the same value for $A_4^4\langle r^4\rangle$ as in the above Tb case and the LF parameters determined previously.[20] Five avoided level crossings are seen. The hyperfine constant A_{hf} was assumed to be $0.0042\ cm^{-1}$, so that the avoided level crossings coincide with the positions indicated by the broken lines in Figure 4. A major difference from the Tb case concerns the tunnel splitting: the gaps are smaller by two orders of magnitude. This may be the reason why in the Dy case no clear step structures are observed at $\mu_0 H \neq 0$ T. Generally, a greatly reduced gap leads to significantly smaller tunneling probability according to the Landau–Zener model.[27]

In conclusion, we have shown the occurrence of QTM in the first lanthanide SMMs, $[Pc_2Tb]^-$ and $[Pc_2Dy]^-$ ions, by hysteresis loop measurements of doped single crystals in the subkelvin temperature range. There is a fundamental differ-

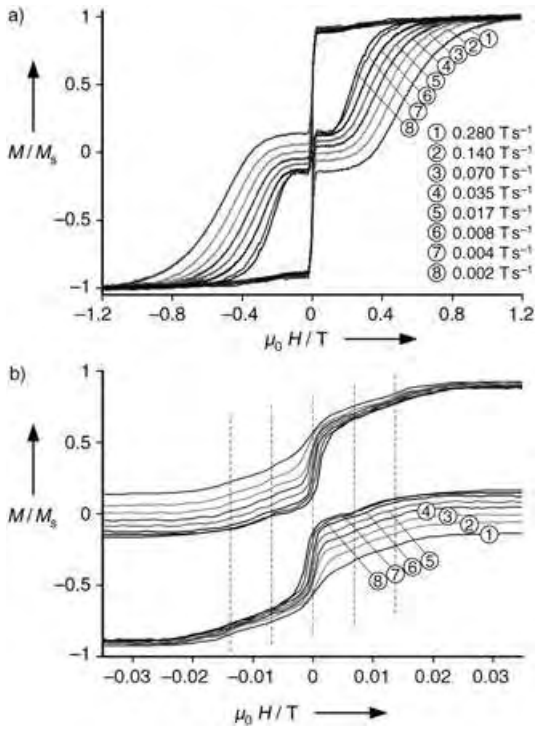

Figure 4. a) Hysteresis loops at 0.04 K for a single-crystalline sample of TBA[$(Pc)_2Dy_{0.02}Y_{0.98}$] measured at several field scan rates. The applied magnetic field was aligned along the easy axis of magnetization. b) Enlargement of the hysteresis loops in (a). The broken lines indicate the expected quantum resonances.

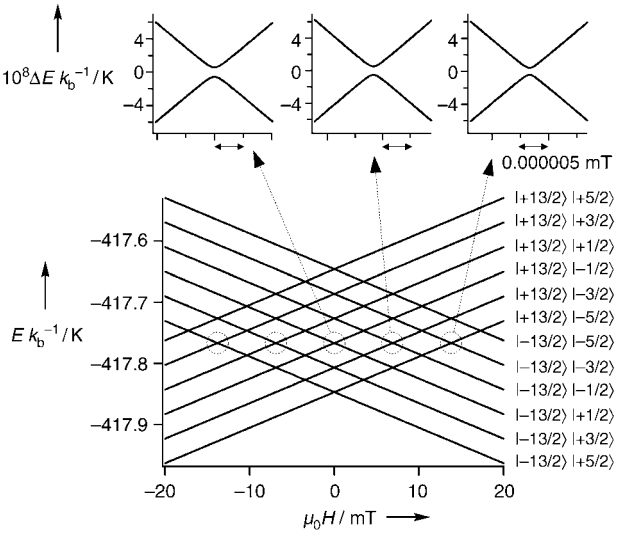

Figure 5. Energy as a function of the longitudinal magnetic field for the lowest $J_z = \pm 13/2$ substates combined with the $I = 5/2$ nucleus state calculated with the LF parameters previously determined[20] and $A_4^4\langle r^4\rangle = 10\ cm^{-1}$. The hyperfine constant is assumed to be $A_{hf} = 0.0042\ cm^{-1}$. The circles indicate the positions where avoided level crossing occurs.

ence in the mechanism of QTM between the lanthanide SMMs and the previously known transition-metal-cluster SMMs. The latter mechanism exhibits QTM between different substates $|S_z|$, whereas the former manifests QTM between the entangled states $|J_z\rangle|I_z\rangle$ of the electron and nuclear spin system.[17] The Tb complex with $J_z = \pm 6$ ground doublet and $I = 3/2$ nuclear spin gives avoided level crossings at the intersection of $|6\rangle|I_z'\rangle$ and $|-6\rangle|I_z\rangle$. In the Dy case, only ^{161}Dy and ^{163}Dy complexes, with a nonzero nuclear spin of $I = 5/2$, can exhibit avoided level crossings at the intersection of $|13/2\rangle|I_z\rangle$ and $|-13/2\rangle|I_z'\rangle$.

Received: November 17, 2004
Revised: February 15, 2005
Published online: April 11, 2005

Keywords: lanthanides · magnetic properties · phthalocyanines · quantum tunneling · single-molecule studies

[1] R. Sessoli, H.-L. Tsai, A. R. Schake, S. Wang, J. B. Vincent, K. Folting, D. Gatteschi, G. Christou, D. N. Hendrickson, *J. Am. Chem. Soc.* **1993**, *115*, 1804.
[2] R. Sessoli, D. Gatteschi, A. Caneschi, M. A. Novak, *Nature* **1993**, *365*, 141.
[3] G. Christou, D. Gatteschi, D. N. Hendrickson, R. Sessoli, *MRS Bull.* **2000**, *25*, 66.
[4] S. M. J. Aubin, M. W. Wemple, D. M. Adams, H.-L. Tsai, G. Christou, D. H. Hendrickson, *J. Am. Chem. Soc.* **1996**, *118*, 7746.
[5] J. R. Friedman, M. P. Sarachik, J. Tejada, R. Ziolo, *Phys. Rev. Lett.* **1996**, *76*, 3830.
[6] L. Thomas, F. Lionti, R. Ballou, D. Gatteschi, R. Sessoli, B. Barbara, *Nature* **1996**, *383*, 145.
[7] S. M. J. Aubin, N. R. Dilley, M. W. Wemple, M. B. Maple, G. Christou, D. N. Hendrickson, *J. Am. Chem. Soc.* **1998**, *120*, 839.
[8] S. M. J. Aubin, N. R. Dilley, L. Pardi, J. Krzystek, M. W. Wemple, L.-C. Brunel, M. B. Maple, G. Christou, D. N. Hendrickson, *J. Am. Chem. Soc.* **1998**, *120*, 4991.
[9] C. Sangregorio, T. Ohm, C. Paulsen, R. Sessoli, D. Gatteschi, *Phys. Rev. Lett.* **1997**, *78*, 4645.
[10] E. K. Brechin, C. Boskovic, W. Wernsdorfer, J. Yoo, A. Yamaguchi, E. C. SaVudo, T. R. Concolino, A. L. Rheingold, H. Ishimoto, D. N. Hendrickson, G. Christou, *J. Am. Chem. Soc.* **2002**, *124*, 9710.
[11] a) M. Soler, W. Wernsdorfer, K. Folting, M. Pink, G. Christou, *J. Am. Chem. Soc.*, **2004**, *126*, 2156; b) M. Soler, E. Rumberger, K. Folting, D. N. Hendrickson, G. Christou, *Polyhedron* **2001**, *20*, 1365.
[12] H. Andres, R. Basler, A. J. Blake, C. Cadiou, G. Chaboussant, C. M. Grant, H.-U. Güdel, M. Murrie, S. Parsons, C. Paulsen, F. Semadini, V. Villar, W. Wernsdorfer, R. E. P. Winpenny, *Chem. Eur. J.* **2002**, *8*, 4867.
[13] W. Wernsdorfer, R. Sessoli, *Science* **1999**, *284*, 133.
[14] M. N. Leuenberger, D. Loss, *Nature* **2001**, *410*, 789.
[15] N. Ishikawa, M. Sugita, T. Ishikawa, S. Koshihara, Y. Kaizu, *J. Am. Chem. Soc.* **2003**, *125*, 8694.
[16] N. Ishikawa, M. Sugita, T. Ishikawa, S. Koshihara, Y. Kaizu, *J. Phys. Chem. B* **2004**, *108*, 11265.
[17] R. Giraud, W. Wernsdorfer, A. M. Tkachuk, D. Mailly, B. Barbara, *Phys. Rev. Lett.* **2001**, *87*, 057203.
[18] A. De Cian, M. Moussavi, J. Fischer, R. Weiss, *Inorg. Chem.* **1985**, *24*, 3162.
[19] H. Konami, M. Hatano, A. Tajiri, *Chem. Phys. Lett.* **1989**, *160*, 163.
[20] N. Ishikawa, M. Sugita, T. Okubo, N. Tanaka, T. Iino, Y. Kaizu, *Inorg. Chem.* **2003**, *42*, 2440.
[21] W. Wernsdorfer, *Adv. Chem. Phys.* **2001**, *118*, 99.
[22] W. Wernsdorfer, N. E. Chakov, G. Christou, *Phys. Rev. B* **2004**, *70*, 132413.
[23] N. Ishikawa, *J. Phys. Chem. A* **2003**, *107*, 9543.

[24] N. Ishikawa, T. Iino, Y. Kaizu, *J. Phys. Chem. A* **2002**, *106*, 9543.
[25] A. Abragam, B. Bleaney, *Electron Paramagnetic Resonance*, Clarendon, Oxford, **1970**, chap. 18.
[26] H. A. Kramers, *Proc. K. Ned. Akad. Wet.* **1930**, *33*, 959.
[27] a) L. Landau, *Phys. Z. Sowjetunion* **1932**, *2*, 46; b) C. Zener, *Proc. R. Soc. London Ser. A* **1932**, *137*, 696; c) S. Miyashita, *J. Phys. Soc. Jpn.* **1995**, *64*, 3207.

NMR spectroscopy

High-Resolution NMR Spectroscopy in Solids by Truly Magic-Angle Spinning**

*Sasa Antonijevic and Geoffrey Bodenhausen**

There is an ever increasing interest in obtaining high-resolution NMR spectra of $S = 1/2$ nuclei, such as ^{13}C, in solids. Solid-state NMR spectroscopy is important for material science, for (bio)organic chemistry, for protein structure determination,[1–3] and for the characterization of pharmaceutical products (e.g., crystalline polymorphism).[4] The combination of magic-angle spinning (MAS) with heteronuclear dipolar decoupling leads to line narrowing, and hence to an improvement of both resolution and sensitivity (peak-height-to-noise ratio). Herein, we show that the line width of ^{13}C resonances can be narrowed to 0.039 ppm (3.9 Hz for ^{13}C at 100.6 MHz or 9.4 T). Such a narrow resonance is observed for carbonyl carbon atoms of polycrystalline cholesteryl acetate if the magic angle ($\theta_m = \arccos 3^{-1/2} \approx 54.736°$) is adjusted very accurately, that is, within $|\Delta\theta| = |\theta - \theta_m| = 0.004°$, as commonly done for satellite-transition magic-angle spinning (STMAS) NMR spectroscopy of quadrupolar nuclei.[5,6] The lower limit of the line width (which is inversely proportional to the effective spin-echo decay time constant T_2') can be as little as 0.09 Hz for carbonyl carbon atoms in choresteryl acetate. We also demonstrate by ^{207}Pb NMR spectroscopy that temperature gradients across the sample (which lead to a distribution of isotropic chemical shifts) can provide an important contribution to the line width, in addition to imperfect decoupling,[7] structural disorder,[8] and magnetic susceptibility effects.[8–10]

[*] Dr. S. Antonijevic, Prof. Dr. G. Bodenhausen
Laboratoire de Résonance Magnétique Biomoléculaire (LRMB)
Institut des Sciences et Ingénierie Chimiques (ISIC)
Ecole Polytechnique Fédérale de Lausanne (EPFL)
BCH, 1015 Lausanne (Switzerland)
Fax: (+41) 21-693-9435
E-mail: geoffrey.bodenhausen@epfl.ch
Prof. Dr. G. Bodenhausen
Département de Chimie
associé au CNRS, Ecole Normale Supérieure
24 rue Lhomond 75231, Paris Cedex 05 (France)

[**] This work was supported by the Fonds National de la Recherche Scientifique (FNRS) and the Commission pour la Technologie et l'Innovation (CTI), Switzerland.

A common way to adjust the magic angle is to optimize the envelope of ^{79}Br rotational echoes in KBr. Herein we suggest a procedure that is more sensitive, and involves two steps: First, the angle can be adjusted to an accuracy of $|\Delta\theta| < 0.01°$ ($\Delta\theta$ = deviation from the magic angle) by minimizing the residual ^2H quadrupolar splitting in a rotor-synchronized MAS spectrum of a deuterated sample, such as $[D_6]\alpha$-oxalic acid dihydrate. The residual splitting (Figure 1) allows the angle θ to be determined if it is miss-set by more than $|\Delta\theta| = 0.01°$. A fine adjustment to an accuracy $|\Delta\theta| < 0.004°$ can be achieved by maximizing the height of the $ST_1 \rightarrow CT$ shifted-echo signal in a one-dimensional ^{87}Rb STMAS spectrum of $RbNO_3$.[6]

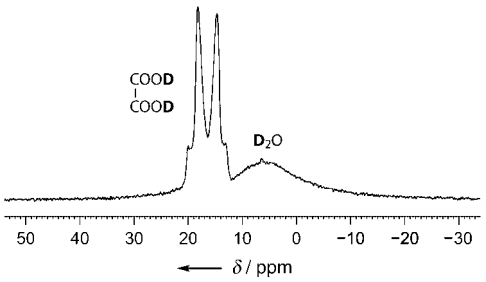

Figure 1. Rotor-synchronized ^2H MAS spectrum (spinning speed $\nu_R = 20$ kHz) of $[D_6]\alpha$-oxalic acid dihydrate. The broad hump to the right stems from motionally averaged water deuterons.[11] The residual quadrupolar powder pattern to the left, which stems from the carboxyl deuterons, allows the deviation from the magic angle to be estimate as $\Delta\theta = -0.036$.

Samples packed in 2.5 mm outer diameter ZrO_2 rotors were spun at 30 kHz (unless otherwise stated) in a standard Bruker triple resonance CPMAS probe in a 9.4 T widebore magnet of an Avance 400 spectrometer. The static field homogeneity was shimmed for ^{13}C line widths in adamantane $\Delta\nu = 3$ Hz (full width at half-height). Cross-polarization (CP) was used with a proton radio-frequency (RF) amplitude of 85 kHz. Two-pulse phase modulation (TPPM) proton decoupling was used during signal acquisition with 100 kHz RF amplitude, pulse-widths of 3.9 μs, and a phase difference between two successive pulses of 35°. Amino acids (Cambridge Isotope Laboratories), and cholesteryl acetate (Fluka) were used without further purification or recrystallization.

Figure 2a shows the ^{13}C CPMAS spectrum of cholesteryl acetate recorded at the magic angle. The line widths $\Delta\nu = 1/(\pi T_2^*)$ (full width at half-height) of the ^{13}C resonances range from 3.9 Hz for the carbonyl carbon to 12.6 Hz for some protonated carbons atoms (Table 1), and are even narrower than previously reported.[12] The width $\Delta\nu = 3.9$ Hz (only 0.9 Hz more than the line width of the plastic crystalline adamantane) is, to our knowledge, the narrowest ^{13}C resonance reported for polycrystalline solids. Intentional deviations from the magic angle $\Delta\theta = 0.134°$ and 0.234° (Figure 2b, c) lead to an increase in the line widths. Not all resonances are broadened to the same extent. The carbonyl signals enlarged in Figure 3 feature residual chemical shift anisotropy (CSA) powder line shapes that are scaled by $(3\cos^2\theta - 1)/2 = -0.00333$, $+0.00211$, and 0 for Figure 3a, b, and c, respec-

 DOI: 10.1002/anie.200463049

Table 1: Twelve ^{13}C resonances in cholesteryl acetate.[a]

δ_{iso} [ppm]	170.90	141.47	121.78	73.49	52.71	41.57	37.48	34.27	32.84	28.48	21.32	13.89
$1/(\pi T_2^*)$ [Hz]	3.9	5.2	7.3	6.0	9.4	9.1	4.1	12.6	6.6	6.9	4.8	10.1
T_2' [ms]	3600	2300	130	160	150	60	420	70	150	90	370	280
$1/(\pi T_2')$ [Hz]	0.09	0.14	2.4	2.0	2.1	5.3	0.75	4.5	2.1	3.5	0.86	1.1

[a] Apparent line widths $\Delta\nu = 1/(\pi T_2^*)$, time constants T_2' of echo decays, and corresponding homogeneous (best possible) line widths $1/(\pi T_2')$. Partial assignments can be found in the work of De Paëpe et al.[12]

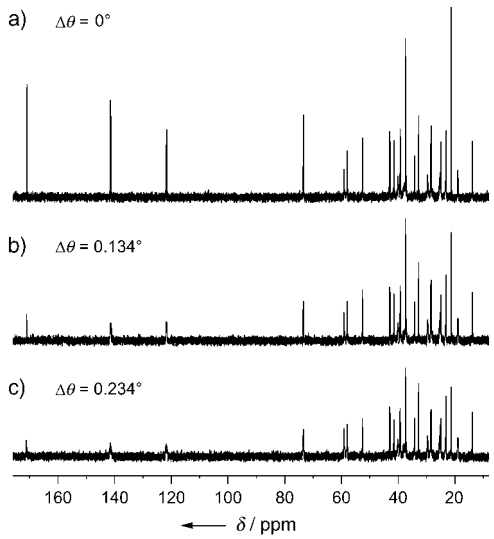

Figure 2. ^{13}C CPMAS spectra of cholesteryl acetate recorded at 9.4 T (100.6 MHz) as a function of the angle θ a) at the magic angle, that is, $\Delta\theta = 0$, b) and c) at deviations from the magic angle. The CP contact time was 1 ms, the recycle interval 4 s, the acquisition time 0.273 s for each of 1280 transients. No line broadening was applied.

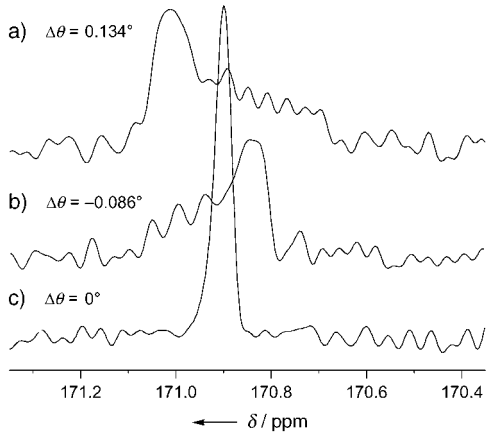

Figure 3. ^{13}C CPMAS resonances of the carbonyl carbon in cholesteryl acetate recorded as a function of the angle θ (spectrum c) at the magic angle, that is, $\Delta\theta = 0$. b) and a) at deviations from the magic angle, featuring scaled powder patterns characteristic of a symmetrical CSA tensor. With scaling factors $(3\cos^2\theta - 1)/2 = -0.00333$ (a) and $+0.00211$ (b) predicted from residual observed quadrupolar splittings in ^2H MAS spectra, powder patterns can be simulated that closely match the two spectra observed with $\Delta\theta \neq 0$ if the CSA principal components are assumed to be $\delta_{xx} = \delta_{yy} = 138.9$ ppm and $\delta_{zz} = 234.9$ ppm. The widths of the scaled powder patterns are directly proportional to the static magnetic field ($B_0 = 9.4$ T in this case).

tively, corresponding to $\Delta\theta = 0.134°$, $-0.086°$, and $0°$. It is remarkable that the residual scaled CSA effects are not masked by broadening owing to imperfect decoupling, structural disorder, temperature gradients, and magnetic susceptibility effects.

In comparison to cholesteryl acetate, amino acids often exhibit greater line widths, usually ascribed to magnetic susceptibility and structural disorder. The accurate adjustment of the magic angle also plays a significant role as demonstrated in ^{13}C CPMAS spectra of L-alanine (Figure 4).

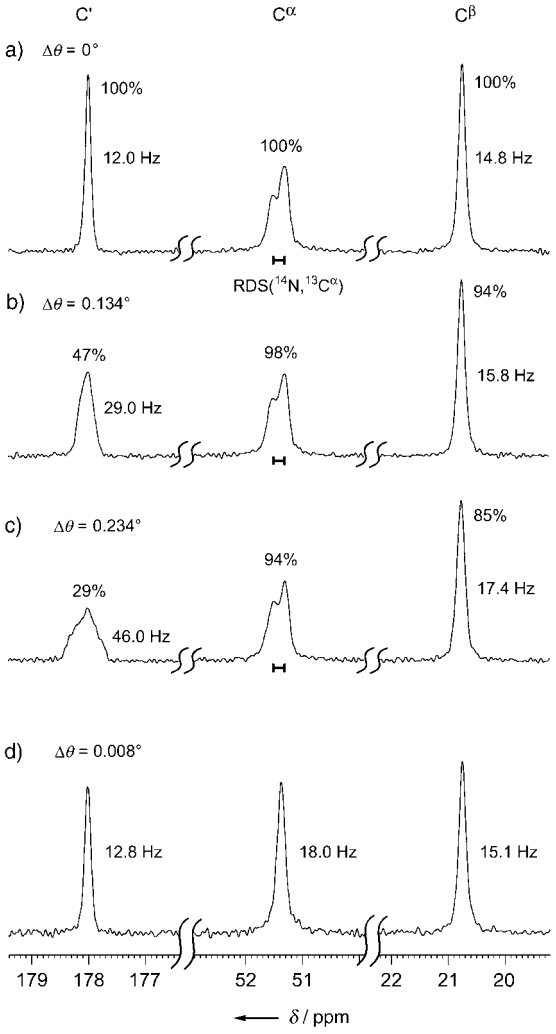

Figure 4. ^{13}C CPMAS spectra of a)–c) [^{14}N]L-alanine at different $\Delta\theta$ values and d) [^{15}N]L-alanine. The spectra result from averaging 640 transients with a recycle interval of 2 s. The CP contact time was 500 μs. The acquisition time was 0.136 s. No line broadening was applied.

For $\Delta\theta \neq 0$, the main contributions to the line widths again originate from residual CSA effects. The CSA tensors in L-alanine, determined independently by Ye et al.,[13] give $\delta_{CSA} = -70, -20, -12$ ppm and $\eta_{SA} = 0.79, 0.35$ and 1 for C′, C^{α} and C^{β}, respectively, using the definitions $\delta_{CSA} = \delta_{zz} - \delta_{iso}$, $\eta_{SA} = (\delta_{yy} - \delta_{xx})/\delta_{CSA}$, and re-ordering the principal components so that $|\delta_{zz} - \delta_{iso}| \geq |\delta_{xx} - \delta_{iso}| \geq |\delta_{yy} - \delta_{iso}|$. The line widths of the C′ and C^{β} resonances of L-alanine in Figure 4a are only 12 and 15 Hz, significantly narrower than previously reported under slightly different experimental conditions.[7] The C^{α} line widths are so narrow that a 1:2 doublet of approximately 20 Hz can be clearly observed. The doublet arises from the residual dipolar splitting (RDS) (^{14}N,^{13}C), also known as second-order quadrupole-dipole cross term.[14–18] This dipolar splitting is not completely eliminated by MAS because the large quadrupular interaction of the ^{14}N nucleus tilts the axis of quantization of the ^{14}N spin away from the direction of the static magnetic field, so that the angular dependence of the interaction cannot be averaged out by spinning at the magic angle.[14–16] In ^{15}N enriched L-alanine by contrast (Figure 4d), the dipolar ^{15}N-^{13}C coupling is averaged to zero, and the C^{α} line collapses to a singlet.

The C^{α} resonance of natural-abundance glycine in Figure 5a has a slightly asymmetric peak (full width at half-height 48.6 Hz) tailing towards high frequency which can be ascribed to an ill-resolved RDS(^{14}N,^{13}C). The C′ carbon shows a symmetric resonance with a line width of 30.5 Hz. Selective enrichment of the C^{α} atom (Figure 5b) results in a splitting of the C′ resonance into a doublet of 53 Hz arising from the scalar coupling $^{1}J(C',C^{\alpha})$. The ability to resolve this doublet strongly depends on the accurate setting of the magic angle, since $\Delta\theta \neq 0$ leads to a residual CSA interaction (it was determined by Ye et al. that $\delta_{CSA} = -71$ ppm[13]). The line widths of the C′ and C^{α} resonances in glycine are not significantly affected by ^{13}C enrichment of the C^{α} site.

The observed line widths $\Delta\nu = 1/(\pi T_2^*)$ can be compared with the limiting homogeneous line widths $\Delta\nu' = 1/(\pi T_2')$.[7,19,20] The limiting homogeneous line widths provide a good criterion to evaluate the performance of proton decoupling.[7] The T_2' values reported in Table 1 were determined from the mono-exponential decays of spin echoes. The defocusing and refocusing intervals τ were chosen to be multiples of the rotor period, while the longest delay was $2\tau = 150$ ms. For cholesteryl acetate, the T_2' time constants and corresponding line widths $\Delta\nu' = 1/(\pi T_2')$ are listed in Table 1. The longest $T_2' = 3.6$ s was found for the carbonyl carbon, corresponding to $\Delta\nu' = 0.09$ Hz. Such long T_2' time constants make it possible to design very complex pulse sequences, well beyond those currently used in liquid-state NMR spectroscopy. The width of 3 Hz observed under similar conditions for adamantane ($\nu_r = 10$ kHz) is believed to be mostly due to B_0 inhomogeneity. The experimental width for the carbonyl carbon signal being 3.9 Hz, the difference of 3.9–0.09–3 = 0.81 Hz must therefore be due to magnetic susceptibility effects, to a chemical shift dispersion arising from structural disorder, and to temperature gradients.[19] For the protonated carbon atoms in cholesteryl acetate, T_2' is much shorter, which indicates that the observed width is due in part to incomplete proton decoupling. In $^{13}C^{\alpha}$-enriched glycine, $T_2'(C^{\alpha}) = 52$ ms, while in natural abundance L-alanine $T_2' = 403$ for C′, 73 for C^{α}, and 69 ms for C^{β}. To evaluate the performance of decoupling with a slight miss-set of the angle, spin-echo decay curves were recorded for $\Delta\theta = 0.134°$. The resulting T_2' values in L-alanine were found to be 466 for C′, 75 for C^{α}, and 69 ms for C^{β}, that is, there is a slight increase for the C′ resonance, and little effect for C^{α} and C^{β}.

Friction results in sample heating and temperature gradients across the sample, which leads to line broadening.[21–24] Nuclei such as ^{207}Pb have isotropic shifts with a pronounced temperature dependence.[24] The ^{207}Pb MAS spectra of $Pb(NO_3)_2$ (Figure 6) show that different spinning

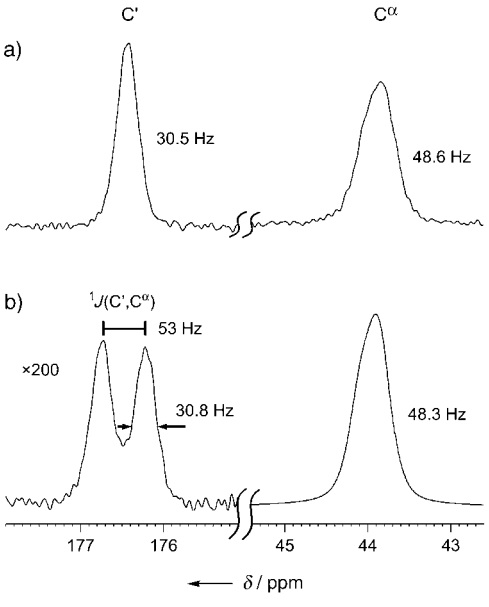

Figure 5. ^{13}C CPMAS spectra of a) natural-abundance glycine and b) glycine enriched in ^{13}C at the C^{α} position, recorded at the magic angle. The $^{1}J(C',C^{\alpha})$ coupling in (b) can be read directly from the spectrum. The spectra result from averaging 640 transients with a recycle interval of 2 s and a CP contact time of 1 ms. The acquisition time was 0.136 s. No line broadening was applied.

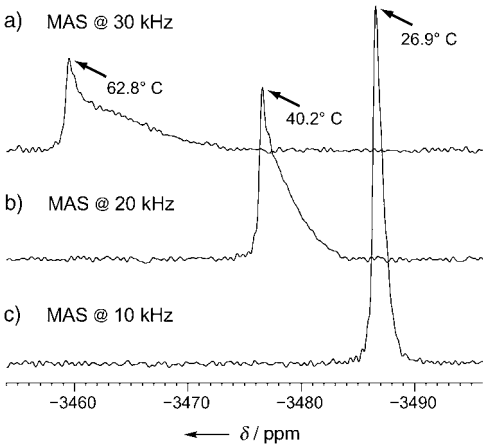

Figure 6. ^{207}Pb MAS spectra of $Pb(NO_3)_2$ recorded at different spinning rates, which lead to different temperature gradients across the sample. The spectra result from averaging of 320 transients with a recycle interval of 5 s.

Table 2: Differences ($\Delta\delta_{iso}$) between isotropic chemical shifts of ^{13}C of cholesteryl acetate observed at temperatures of 39 °C ($\delta_{iso}(39°)$) and 17 °C ($\delta_{iso}(17°)$).[a]

δ_{iso} [ppm][b]	170.90	141.47	121.78	73.49	52.71	41.57	37.48	34.27	32.84	28.48	21.32	13.89
$\Delta\delta_{iso}$ [Hz][c]	22	31	21	34	29	33	28	19	31	27	28	30
$\Delta\delta_{iso}/\Delta T$ [ppm/°][d]	0.010	0.014	0.010	0.015	0.013	0.015	0.013	0.009	0.014	0.012	0.013	0.014

[a] Nominal temperatures measured by a thermocouple in the air flow near the rotor. [b] The isotropic shifts in the first row correspond to 39 °C. [c] $\Delta\delta_{iso} = \delta_{iso}(39°) - \delta_{iso}(17°)$. [d] Derivatives $\Delta\delta_{iso}/\Delta T$ in ppm/degree. Partial assignments can be found in the work of De Paëpe et al.[12]

rates affect the temperature gradients. The absolute temperature is calibrated from the chemical shift difference of the two proton resonances in liquid methanol, which can be spun up to 30 kHz.[25] The temperature distribution across the sample is asymmetric, and its range increases from about 3° at 10 kHz to as much as 17° at 30 kHz. To estimate contributions from temperature gradients to line widths of ^{13}C spectra obtained under similar conditions, we recorded spectra of cholesteryl acetate and L-alanine in natural abundance at two different nominal temperatures. All line widths remain the same, but various downfield shifts are observed. The differences in chemical shifts $\Delta\delta = \delta_{iso}[39°] - \delta_{iso}[17°]$ for cholesteryl acetate are given in Table 2. For L-alanine $\Delta\delta = 20$ for C′, 30 for C^{α}, and 25 Hz for C^{β}. Clearly, the temperature gradient in the samples of cholesteryl acetate and L-alanine are much smaller than in $Pb(NO_3)_2$, otherwise the lines would be much broader and feature an asymmetry like that in Figure 6. Materials have different densities, heat capacities, electric and thermal conductivities, and dielectric properties, all of which can affect heating under sample rotation and RF irradiation. It is conceivable that the combined effects of mechanical friction and RF heating lead to a (fortuitous) reduction of the temperature gradients across our samples. The deliberate reduction of temperature gradients should lead to further improvements in resolution.

To summarize, we have shown that the accuracy of the adjustment of the magic angle is critical to obtain high-resolution MAS NMR spectra. The main contribution to the line widths in ^{13}C spectra recorded with a slight miss-set of the angle is due to residual CSA interactions. For quaternary carbon atoms, the increase in line widths is therefore greater than for proton-carrying carbon atoms. For the latter, the performance of heteronuclear proton decoupling is more critical, although it is not significantly affected by a small miss-set of the angle. Nevertheless, the observed line widths are still larger than the homogeneous limit given by the time-constant T_2' of spin echo decays. The remaining line widths are believed to be mainly due to magnetic susceptibility effects and to chemical shift dispersion arising from structural disorder or temperature gradients. Such effects can limit resolution at higher fields.

Received: December 23, 2004
Published online: April 7, 2005

[1] F. Castellani, B. van Rossum, A. Diehl, M. Schubert, K. Rehbein, H. Oschkinat, *Nature* **2002**, *420*, 98.
[2] M. Etzkorn, A. Böckmann, A. Lange, M. Baldus, *J. Am. Chem. Soc.* **2004**, *126*, 14746.
[3] M. Ernst, A. Detken, A. Bockmann, B. H. Meier, *J. Am. Chem. Soc.* **2003**, *125*, 15807.
[4] P. A. Tishmack, D. E. Bugay, S. R. Byrn, *J. Pharm. Sci.* **2003**, *92*, 441.
[5] Z. Gan, *J. Am. Chem. Soc.* **2000**, *122*, 3242.
[6] S. E. Ashbrook, S. Wimperis, *J. Magn. Reson.* **2002**, *156*, 269.
[7] G. De Paëpe, A. Lesage, L. Emsley, *J. Chem. Phys.* **2003**, *119*, 4833.
[8] D. Sakellariou, S. P. Brown, A. Lesage, S. Hediger, M. Bardet, C. A. Meriles, A. Pines, L. Emsley, *J. Am. Chem. Soc.* **2003**, *125*, 4376.
[9] M. Alla, E. Lippmaa, *Chem. Phys. Lett.* **1982**, *87*, 30.
[10] A. Samoson, T. Tuherm, Z. Gan, *Solid State Nucl. Magn. Reson.* **2001**, *20*, 130.
[11] S. E. Ashbrook, S. Antonijevic, A. J. Berry, S. Wimperis, *Chem. Phys. Lett.* **2002**, *364*, 634.
[12] G. De Paëpe, A. Lesage, S. Steuernagel, L. Emsley, *ChemPhysChem* **2004**, *5*, 869.
[13] C. Ye, R. Fu, J. Hu, L. Hou, S. Ding, *Magn. Reson. Chem.* **1993**, *31*, 699.
[14] J. G. Hexem, M. H. Frey, S. J. Opella, *J. Am. Chem. Soc.* **1981**, *103*, 224.
[15] A. Naito, S. Ganapathy, C. A. McDowell, *J. Chem. Phys.* **1981**, *74*, 5393.
[16] K. Takegoshi, T. Yano, K. Takeda, T. Terao, *J. Am. Chem. Soc.* **2001**, *123*, 10786.
[17] R. K. Harris, A. C. Olivieri, *Prog. Nucl. Magn. Reson. Spectrosc.* **1992**, *24*, 435.
[18] C. A. McDowell in *Encyclopedia of Nuclear Magnetic Resonance*, *Vol. 5* (Ed.: D. M. Grant, R. K. Harris), Wiley, Chichester, **1996**, p. 2901.
[19] G. De Paëpe, N. Giraud, A. Lesage, P. Hodgkinson, A. Böckmann, L. Emsley, *J. Am. Chem. Soc.* **2003**, *125*, 13938.
[20] A. Medek, L. Frydman, *J. Am. Chem. Soc.* **2000**, *122*, 684.
[21] F. Aguilar-Parrilla, B. Wehrle, H. Braunling, H. H. Limbach, *J. Magn. Reson.* **1990**, *87*, 592.
[22] L. C. M. van Gorkom, J. M. Hook, M. B. Logan, J. V. Hanna, R. E. Wasylishen, *Magn. Reson. Chem.* **1995**, *33*, 791.
[23] B. Langer, I. Schnell, H. W. Spiess, A.-R. Grimmer, *J. Magn. Reson.* **1999**, *138*, 182.
[24] P. A. Beckmann, C. Dybowski, *J. Magn. Reson.* **2000**, *146*, 379.
[25] A. L. van Geet, *Anal. Chem.* **1970**, *42*, 679.

Keywords: line widths · NMR spectroscopy · solid-state NMR spectroscopy · temperature gradients

Density Functional Calculations

Two Faces of a Biomimetic Non-Heme HO–Fe^{V}=O Oxidant: Olefin Epoxidation versus *cis*-Dihydroxylation**

Arianna Bassan, Margareta R. A. Blomberg, Per E. M. Siegbahn, and Lawrence Que, Jr.**

The family of non-heme iron complexes—exemplified by $[Fe^{II}(tpa)(CH_3CN)_2]^{2+}$, where tpa is the tetradentate tripodal tris(2-pyridylmethyl)amine ligand—efficiently utilizes H_2O_2 to carry out stereospecific olefin epoxidation and *cis*-dihydroxylation.[1–4] The latter reaction was not previously known to be catalyzed by a synthetic iron complex and is precedented only in the chemistry of Rieske dioxygenases,[5] non-heme iron enzymes responsible for *cis*-dihydroxylation in the biodegradation of arenes by soil bacteria. Isotope-labeling experiments on the biomimetic reaction show the involvement of a highly selective metal-based oxidant capable of introducing water into the product.[1,2] This oxidant is proposed to result from the low-spin complex $[Fe^{III}(tpa)(H_2●)(OOH)]^{2+}$ (**1**) and be a formally H●–Fe^{V}=O species (**2**; ● indicates an oxygen atom with isotope labeling), both shown in Figure 1.

Previous DFT calculations have demonstrated the feasibility of an O–O bond heterolysis mechanism that leads to an $S = 3/2$ *cis*-HO–Fe^{V}=O species with a short Fe–O bond (1.66 Å) and a longer Fe–OH bond (1.77 Å).[6] The three unpaired electrons are mainly distributed on the iron atom (1.58), the oxo oxygen atom (1.0), and the hydroxo oxygen atom (0.44): a spin distribution not unlike that found for compounds I of heme peroxidases and cytochrome P450 and related model complexes.[7,8] The corresponding sextet and doublet states of HO–Fe^{V}=O lie more than 10 kcal mol^{-1} higher in energy than the quartet ground state.[9]

Further DFT calculations presented herein provide new insight into how this unique oxidant can carry out both olefin epoxidation and *cis*-dihydroxylation. Hence, the present study focuses on the subsequent reaction of **2** with olefins (see the Supporting Information) to reveal that olefin epoxidation and *cis*-dihydroxylation in fact represent different faces of the same oxidant.

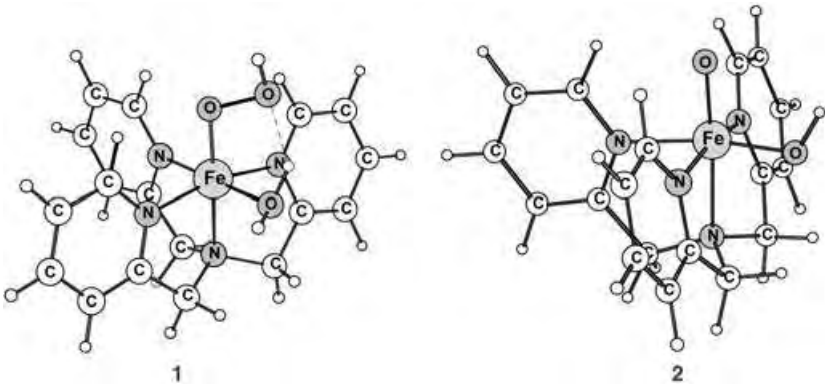

Figure 1. Structures of the $[Fe^{III}(tpa)(H_2O)(OOH)]^{2+}$ precursor (**1**) and the proposed metal-based *cis*-HO–Fe^{V}=O oxidant (**2**).

The key results of our DFT study are illustrated by the energy profiles in Figure 2, showing that **2** can react with olefins (namely, 2-butene) through two different channels. As shown on the left, the oxo group attacks the olefin to form the C1–O1 bond and intermediate **A**-Fe^{IV} (path A). On the right, the hydroxo ligand attacks the olefin to form the C2–O2 bond and intermediate **B**-Fe^{IV} (path B). Both intermediates have an iron(IV) center and a radical on the partially oxidized substrate.

Intermediate **A**-Fe^{IV} is an iron(IV) complex with a hydroxide ($r_{Fe-O2} = 1.79$ Å) and the partially oxidized olefin as ligands. The formation of the new C1–O1 bond is exergonic by 2.5 kcal mol^{-1} and involves an activation energy of 7.8 kcal mol^{-1}; solvent effects (+3.1 kcal mol^{-1}), entropy effects (+0.6 kcal mol^{-1}), and big-basis effects (+2.1 kcal mol^{-1}) contribute to increase the barrier by 5.6 kcal mol^{-1}. Unpaired spin density can be found on the metal center (1.53), the partially oxidized olefin (0.97), and the remaining ligands (0.50). Antiferromagnetic coupling of the unpaired electron on the partially oxidized olefin with those of the metal center affords an $S = 1/2$ state that is more stable by about 1–2 kcal mol^{-1} than the corresponding $S = 3/2$ state. Thus, a spin crossing between the quartet and the doublet surfaces may occur in the vicinity of this intermediate during the course of epoxidation. Intermediate **A**-Fe^{IV} in the $S = 1/2$ state decays spontaneously and without any significant barrier to the epoxide in the first coordination sphere of iron. No low-energy pathway producing the *cis*-diol from **A**-Fe^{IV} can be found. Almost identical barriers were obtained when epoxidation of propene was investigated.

In contrast, *cis*-dihydroxylation of the olefin occurs when the hydroxo ligand of **2** attacks the substrate, thus leading to

[*] Dr. A. Bassan, Prof. M. R. A. Blomberg, Prof. P. E. M. Siegbahn
Department of Physics
Stockholm University
SE 106 91, Stockholm (Sweden)
Fax: (+46) 8-5537-8601
E-mail: arianna@physto.se
Prof. L. Que, Jr.
Department of Chemistry and
Center for Metals in Biocatalysis
University of Minnesota
Minneapolis, MN 55455 (USA)
Fax: (+1) 612-624-7029
E-mail: que@chem.umn.edu

[**] The bio-inspired catalysis work at the University of Minnesota is supported by the US Department of Energy (grant no. DE-FG02-03ER15455 to L.Q.). We gratefully acknowledge the National Supercomputer Center (Sweden) for generous grants of computer time. We thank Dr. Megumi Fujita for useful discussions.

Supporting information for this article is available on the WWW under http://www.angewandte.org or from the author.

 DOI: 10.1002/anie.200463072

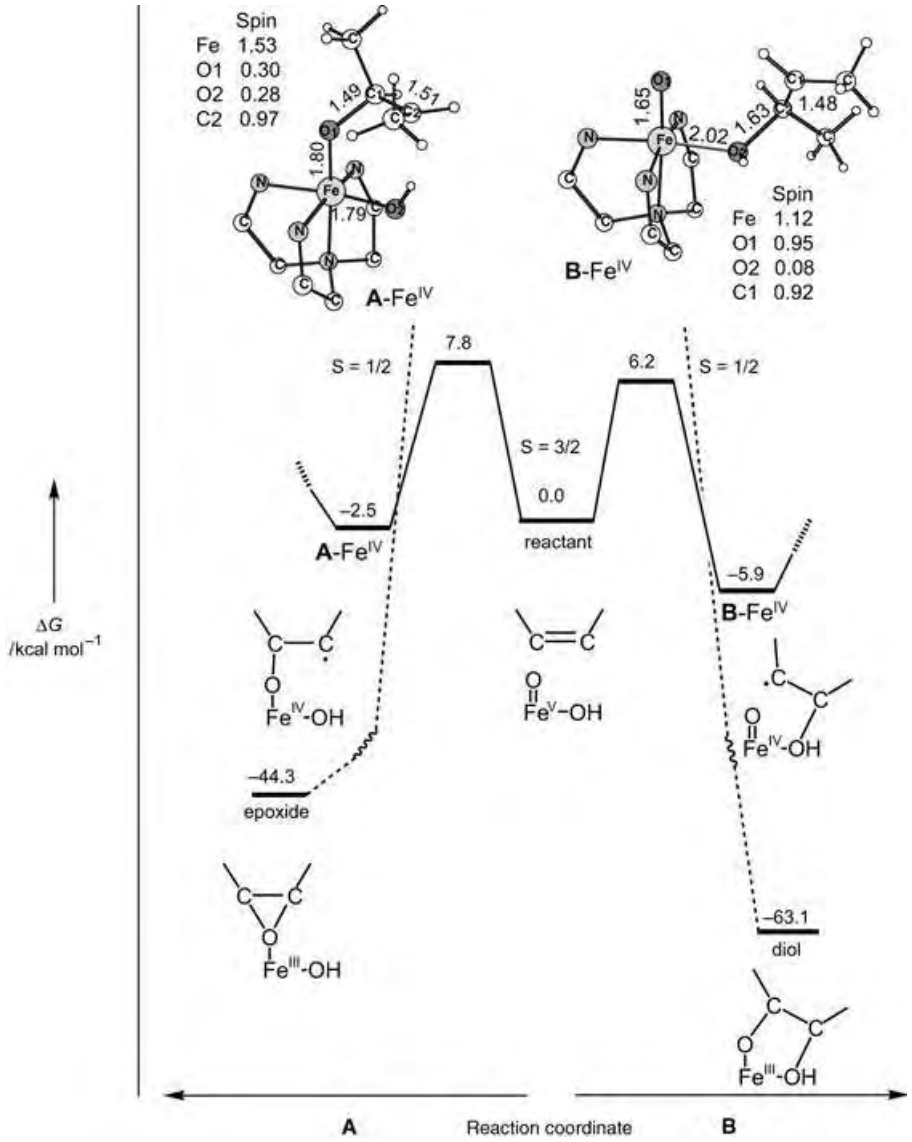

Figure 2. Energy profiles for olefin epoxidation (path A) and olefin *cis*-dihydroxylation (path B).

the formation of intermediate **B**-Fe^{IV}. The Fe=O double bond is maintained ($r_{Fe\text{-}O1} = 1.65$ Å) in this species and a weak C2–O2 bond ($r_{C2\text{-}O2} = 1.63$ Å) is formed. For the $S = 3/2$ state of **B**-Fe^{IV}, unpaired spin density can be found on the metal center (1.12), the oxo oxygen atom (0.95), and the partially oxidized olefin (0.97). The transition state for C2–O2 bond formation in propene was found to have an energy barrier of 6.2 kcal mol^{-1}, a value which includes solvent effects (2.2 kcal mol^{-1}), big-basis effects (1.5 kcal mol^{-1}), and thermal and zero-point corrections (0.6 kcal mol^{-1}). In the case of butene, the corresponding transition-state structure could not be optimized but is approximated to have a relative energy similar to that of the propene complex. As with the epoxidation pathway, a spin crossing from the quartet to the doublet state of **B**-Fe^{IV} results in the formation of the product, because the $S = 1/2$ state readily leads to the diol without any significant energy barrier. In line with the chemistry of other transition metal oxides, for example, osmium tetroxide,[10] the concerted [3+2] addition of HO–Fe=O across the olefin C=C bond was also probed, but all attempts to optimize the corresponding structure led to a transition state where only one C–O bond was initially formed.

We also considered the possibility that *cis*-diol is produced from the initially formed epoxide. Figure 3 shows the calculated energy profile for this conversion for the $S = 5/2$ state, which is the ground state for both products (see the Supporting Information). Figure 3 also reports the energy required for epoxide dissociation from the metal center. Interestingly the epoxide-to-diol conversion is disfavored relative to epoxide release from the metal center by approximately 7 kcal mol^{-1}. Thus, diol formation most likely occurs by the direct reaction of olefin with the HO–Fe^{V}=O species, rather than via the epoxide.

The Fe(tpa) family of complexes are unique oxidation catalysts that are capable of both olefin epoxidation and *cis*-dihydroxylation.[4] As previously suggested,[1,2,6] it is likely that a high-valent iron–oxo species is formed along the reaction pathway, and our DFT calculations have provided insight into the mechanism of olefin oxidation by the exceptional HO–Fe^{V}=O oxidant. It is possible that epoxidation may also occur by direct attack of the precursor Fe–OOH on the olefin, and a preliminary study in this direction has suggested that such a pathway is slightly disfavored over the competing O–O bond cleavage to generate the HO–Fe^{V}=O oxidant.

If the Fe(tpa) catalysts carry out olefin oxidation via the high-valent iro–oxo species, then epoxidation occurs by attack of the oxo oxygen atom on the olefin, and *cis*-dihydroxylation is initiated by attack of the hydroxo oxygen atom, followed by rebound of the incipient carbon radical with the oxo oxygen atom. This scheme provides a rationale for the observed incorporation of one oxygen atom from H_2O_2 and one oxygen atom from solvent into the diol product.[2] Such a mechanism may also explain why the oxygen atom of the epoxide derives principally, but not exclusively, from H_2O_2. Previous DFT calculations have determined that oxo–hydroxo tautomerization of the H●–Fe^{V}=O species leading to label scrambling has an energy barrier of about 10 kcal mol^{-1},[9] a value that is somewhat higher than that computed here for olefin epoxidation, so oxo attack on the olefin would be expected to occur before significant label scrambling occurs, in agreement with experimental observations.

Lastly, the calculations reveal that olefin epoxidation and *cis*-dihydroxylation have comparable activation barriers, with the latter being favored by about 1 kcal mol^{-1} (Figure 2). On the basis of transition-state theory, this difference predicts a diol-to-epoxide ratio of about 5:1. Experimentally, the *cis*-diol

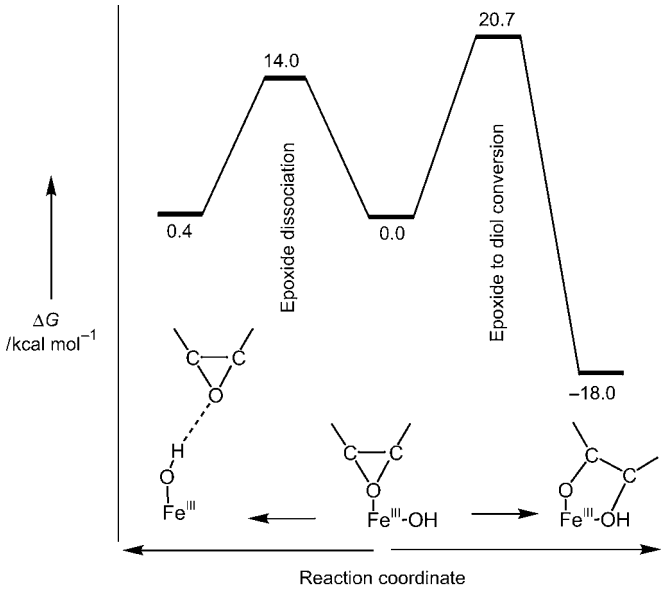

Figure 3. Energy profiles for epoxide dissociation and epoxide-to-diol conversion for the $S = 5/2$ state.

product is indeed favored over the epoxide, but only by factors of 1.2–3, depending on the olefin, results well within the accuracy of the present computational approach.

These new insights, only obtainable from DFT calculations thus far, provide a solid foundation for understanding the reaction mechanisms of a new family of bio-inspired non-heme iron catalysts for olefin oxidation. The stage has thus been set for future work aimed at rationalizing the strong preference for epoxide products by related Fe(bpmen) and α-Fe(bpmcn) catalysts[11] as well as the exclusive production of *cis*-diol product in the oxidation of electron-deficient olefins like acrylate and fumarate by the Fe(tpa) catalyst.[12]

Methods

The energy profiles and the structures included in the present study were obtained employing the B3LYP functional and using the quantum chemical programs Jaguar 4.2[13] and Gaussian 98.[14] Fully optimized transition states were obtained through the evaluation of the second derivatives with respect to the nuclear coordinates of approximate structures. Hessians for reactants, intermediates, and transition states were used to derive the zero-point effects and the thermal corrections necessary for determining Gibbs free energies. Free energies are reported including zero point and thermal effects, evaluated for 298.15 K. Relative free energies for epoxidation and *cis*-dihydroxylation were calculated with a supermolecular approach including both the metal complex and the olefin (see, for example, Figure S1 in the Supporting Information). This is likely to underestimate the energy barriers but does not affect the conclusions of this study.

An effective core potential was used to describe the iron atom. In the geometry optimizations and in the Hessian evaluations all the other atoms were described by a standard double zeta basis set, labeled lacvp in Jaguar. The final B3LYP energies for the fully optimized structures were computed using a basis set that includes polarization functions on all atoms (labeled lacv3p** in Jaguar). Spin populations obtained with the lacvp basis set are reported. Solvent effects were evaluated employing the self-consistent reaction field as implemented in Jaguar[13] together with a dielectric constant of 36.64 and a probe radius of 2.155 Å.

On the basis of previous benchmarks, an accuracy of about 3–5 kcal mol^{-1} could affect the energy profiles reported in the present investigation.[15,16] However, such an accuracy should be enough to discriminate among different reaction mechanisms.

Received: December 27, 2004

Keywords: density functional calculations · dihydroxylation · enzyme models · epoxidation · iron

[1] K. Chen, L. Que, Jr., *J. Am. Chem. Soc.* **2001**, *123*, 6327–6337.
[2] K. Chen, M. Costas, J. Kim, A. K. Tipton, L. Que, Jr., *J. Am. Chem. Soc.* **2002**, *124*, 3026–3035.
[3] K. Chen, M. Costas, L. Que, Jr., *J. Chem. Soc. Dalton Trans.* **2002**, *5*, 672–679.
[4] M. Costas, M. P. Mehn, M. P. Jensen, L. Que, Jr., *Chem. Rev.* **2004**, *104*, 159–172.
[5] D. T. Gibson, R. E. Parales, *Curr. Opin. Biotechnol.* **2002**, *13*, 235–243.
[6] A. Bassan, M. R. A. Blomberg, P. E. M. Siegbahn, L. Que, Jr., *J. Am. Chem. Soc.* **2002**, *124*, 11056–11063.
[7] G. H. Loew, D. Harris, *Chem. Rev.* **2000**, *100*, 407–419.
[8] S. Shaik, S. P. de Visser, F. Ogliaro, H. Schwarz, D. Schröder, *Curr. Opin. Chem. Biol.* **2002**, *6*, 556–557.
[9] A. Bassan, M. R. A. Blomberg, P. E. M. Siegbahn, L. Que, Jr., *Chem. Eur. J.* **2004**, *11*, 692–705.
[10] D. V. Deubel, G. Frenking, *Acc. Chem. Res.* **2003**, *36*, 645–651.
[11] M. Costas, L. Que, Jr., *Angew. Chem. Int. Ed.* **2002**, *41*, 2179–2181 (bpmen = *N*,*N*′-bis(2-pyridylmethyl)-*N*,*N*′-dimethyl-1,2-diaminoethane, bpmcn = *N*,*N*′-bis(2-pyridylmethyl)-*N*,*N*′-dimethyl-*trans*-1,2-diaminocyclohexane.
[12] M. Fujita, M. Costas, L. Que, Jr., *J. Am. Chem. Soc.* **2003**, *125*, 9912–9913.
[13] JAGUAR 4.2, Schrödinger, Inc., Portland, Oregon, **2000**; see: G. Vacek, J. K. Perry, J.-M. Langlois, *Chem. Phys. Lett.* **1999**, *310*, 189–194.
[14] Gaussian 98 (Revision A.7), M. J. Frisch, G. W. Trucks, H. B. Schlegel, G. E. Scuseria, M. A. Robb, J. R. Cheeseman, V. G. Zakrzewski, J. A. Montgomery, R. E. Stratmann, J. C. Burant, S. Dapprich, J. M. Millam, A. D. Daniels, K. N. Kudin, M. C. Strain, O. Farkas, J. Tomasi, V. Barone, M. Cossi, R. Cammi, B. Mennucci, C. Pomelli, C. Adamo, S. Clifford, J. Ochterski, G. A. Petersson, P. Y. Ayala, Q. Cui, K. Morokuma, D. K. Malick, A. D. Rabuck, K. Raghavachari, J. B. Foresman, J. Cioslowski, J. V. Ortiz, B. B. Stefanov, G. Liu, A. Liashenko, P. Piskorz, I. Komaromi, R. Gomperts, R. L. Martin, D. J. Fox, T. Keith, M. A. Al-Laham, C. Y. Peng, A. Nanayakkara, C. Gonzalez, M. Challacombe, P. M. W. Gill, B. G. Johnson, W. Chen, M. W. Wong, J. L. Andres, M. Head-Gordon, E. S. Replogle, J. A. Pople, Gaussian, Inc., Pittsburgh, PA, **1998**.
[15] M. R. A. Blomberg, P. E. M. Siegbahn in *Transition State Modeling for Catalysis* (Eds: D. G. Truhlar, K. Morokuma), American Chemical Society, Washington DC, **1999**, pp. 49–60.
[16] P. E. M. Siegbahn, *J. Comput. Chem.* **2001**, *22*, 1634–1645.

Organometallic Chemistry

C–H Activated Isomers of [M(AlCp*)$_5$] (M=Fe, Ru)**

*Tobias Steinke, Mirza Cokoja, Christian Gemel, Andreas Kempter, Andreas Krapp, Gernot Frenking, Ulrich Zenneck, and Roland A. Fischer**

Quantum mechanical calculations on the model compounds [Fe(ECH$_3$)$_5$] (E = Al, Ga, In) suggest the existence of the homoleptic, trigonal-bipyramidal d^8 metal complexes of the exotic ligands E^{I}R (R = C(SiMe$_3$)$_3$, Cp*; Cp* = C$_5$Me$_5$).[1] The M–E bonds are strong and determined by coulomb interactions, whereas the π-acceptor properties are weak for E^{I}R if R = Cp*, but considerably stronger for alkyl substituents R.[2] However, only the d^{10} complexes [M(E^{I}R)$_4$] (M = Ni, Pd, Pt) are known, which can be considered as analogues of [Ni(CO)$_4$] or [M(PR$_3$)$_4$], highlighting the similarity of the ligands E^{I}R to CO or phosphines.[3] Furthermore, clusters [M$_a$(ECp*)$_b$] have been reported, which also contain tetrahedrally coordinated Pd or Pt centers.[4] While numerous reports on [(CO)$_4$Fe(AlCp*)] and other related, CO-substituted complexes exist,[5,6] the question as to what is the limit for the coordination number n in the homoleptic compound [M(E^{I}R)$_n$], is still unanswered: is $n = 5$ possible, perhaps also $n = 6$, or even more? Does the steric demand of ECp* (Tolman angle of 112° for E = Ga[7]) hinder the stability of [M(ECp*)$_n$] with $n > 4$? Recently we could show by the structural characterization of [(CO)$_3$M(ECp*)$_3$] (M = Mo, W; E = Al, Ga), that the coordination of three ECp* ligands is possible in a facial geometry.[8] Thus we concentrated our attention on complexes of the type [Fe(AlCp*)$_n$] and chose [Fe(η^6-toluene)(η^4-1,3-butadiene)] as the Fe^0 source for the introduction of AlCp*.[9]

If a red suspension of [Fe(η^6-toluene)(η^4-1,3-butadiene)] and six equivalents of AlCp* in toluene is heated to 80 °C (Scheme 1), an orange solution is rapidly formed. The ^{1}H NMR spectroscopic data point to a mixture of two products in the ratio of 3:1, neither of which has the structure [Fe(AlCp*)$_5$]! Characteristic highfield resonance signals (δ = −18 to −20 ppm) and the complexity of the Cp* signals in the aliphatic region suggest a C–H activation of the methyl groups. Compound **1a** can be isolated from a toluene solution of the product mixture by crystallization at −30 °C for a few minutes (yield 35 %). The yellow, prismatic crystals do not contain any **1b** (by ^{1}H NMR spectroscopy). Recrystallization of this sample gave single crystals of **1a**. Crystallization of the mother liquor over a longer period of time increases the amount of **1b** in the solid. Pure **1b** could not be isolated. Repeated fractional crystallization leads to defined yellow

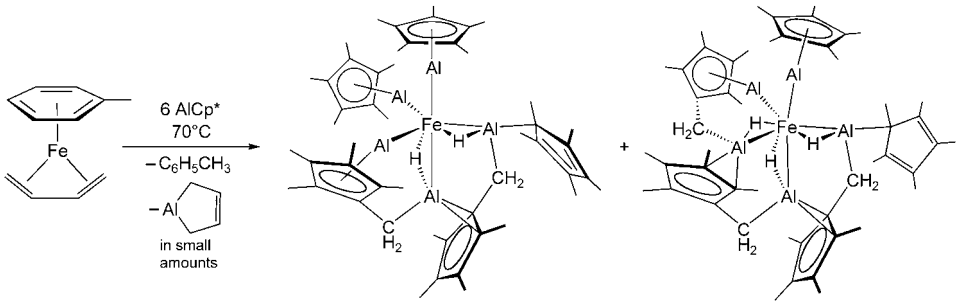

Scheme 1. Preparation of **1a** and **1b**, isomers of the hypothetical compound [Fe(AlCp*)$_5$] (relative amounts in percent according to ^{1}H NMR spectroscopy data).

single crystals (isolated yield ca. 5 %) containing **1a** (50 %) and **1b** (50 %) (NMR spectroscopy). Pure **1a** does not give **1b** on heating in toluene to 110 °C for several hours.

X-Ray analysis of **1a** confirms the composition suggested by NMR spectroscopy and elemental analysis (Figure 1). Two CH_3 groups of two different Cp* rings (on Al3 and Al4) are C–H activated. The methylene moieties (C30 und C39) are slightly bent out of the ring plane (ca. 15°) and bound two the adjacent Al atoms Al4 and Al5. Thus, a tridentate chelate ring {(η^1-Cp*Al)-CH$_2$-(η^2-C$_5$Me$_4$Al)-CH$_2$-(η^5-C$_5$Me$_4$)Al} is formed. The coordination environment of the Fe center can be described as either distorted trigonal-bipyramidal or distorted square pyramidal. The atoms Fe, Al1, Al2, and Al4 are almost coplanar (angular sum 359.03°), whereas the "axial" positions Al3 and Al5 (Al3-Fe-Al5 160.09(5)°) are bent towards Al2 and Al4 owing to the bridge Fe1-H2-Al5. The bridging atoms H1 and H2 could be localized and were

[*] Dr. T. Steinke, Dipl.-Chem. M. Cokoja, Dr. C. Gemel, Dipl.-Chem. A. Kempter, Prof. Dr. R. A. Fischer
Lehrstuhl für Anorganische Chemie II – Organometallics & Materials
Ruhr-Universität Bochum
44780 Bochum (Germany)
Fax: (+49) 234-321-4174
E-mail: roland.fischer@ruhr-uni-bochum.de
Dipl.-Chem. A. Krapp, Prof. Dr. G. Frenking
Fachbereich Chemie, Philipps-Universität Marburg
Hans-Meerwein-Strasse, 35032 Marburg (Germany)
Prof. Dr. U. Zenneck
Institut für Anorganische Chemie
Universität Erlangen-Nürnberg, 91058 Erlangen (Germany)

[**] Organo earth-metal complexes of d-block elements, Part XXXVII. for Part XXXVI see Ref. [16]. Cp* = C$_5$Me$_5$.

Supporting information for this article is available on the WWW under http://www.angewandte.org or from the author.

 DOI: 10.1002/anie.200462834

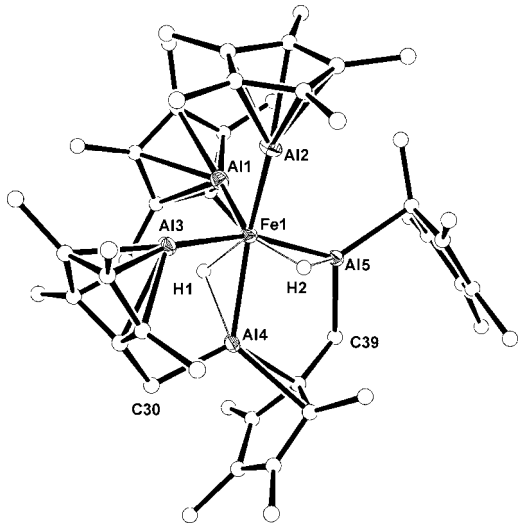

Figure 1. Molecular structure of **1a** (ORTEP plot, thermal ellipsoids set at 50% probability for Fe and Al. The C atoms were depicted isotropcally for clarity. Hydrogen atoms are omitted for clarity except H1 and H2). Selected bond lengths [Å] and angles [°]: Fe1-Al1 2.2124(15), Fe1-Al2 2.2419(15), Fe1-Al3 2.2404(15), Fe1-Al4 2.3686(15), Fe1-Al5 2.3272(14), Fe1-H1 1.59(8), Al4-H1 1.88(8), Fe1-H2 1.46(7), Al5-H2 1.89(7), Al4-C30 2.030(5), Al5-C39 1.990(4), $Cp^*_{centroid}$-Al1 1.914, $Cp^*_{centroid}$-Al3 1.891; Al1-Fe1-Al2 90.44(6), Al1-Fe1-Al3 108.83(6), Al1-Fe1-Al4 118.07(6), Al1-Fe1-Al5 88.02(5), Al2-Fe1-Al3 84.78(6), Al2-Fe1-Al4 150.52(6), Al2-Fe1-Al5 106.21(6), Al3-Fe1-Al4 79.19(5), Al3-Fe1-Al5 160.09(5), Al4-Fe1-Al5 83.55(5), $Cp^*_{centroid}$-Al1-Fe1 161.00, $Cp^*_{centroid}$-Al2-Fe1 172.22, $Cp^*_{centroid}$-Al3-Fe1 149.43, Al1-Fe1-Al2-Al4 165.9(5).

freely refined: Fe1–H1 1.59(8), Fe1–H2 1.46(7), Al4–H1 1.88(8), Al5–H2 1.89(7) Å. No other complexes with Fe-H-Al motifs are known for comparison. However, typical Fe-H-Fe bond lengths are 1.5–1.8 Å[10] and the Al–H bond in **1a** is very similar to that in [Ni(AlCp*)$_3$(HAlCp*Ph)] (Al–H 1.76(3) Å).[11] The Fe–Al bond lengths correlate to the formal oxidation states of the aluminum centers, Al^I for AlCp* and Al^{III} for the fragments [HAl(Cp*)(CH$_2$C$_5$Me$_4$)]. The Fe–Al^I distances (Al1, Al2, and Al3) are in between 2.2124(15) and 2.2419(15) Å, whereas the Fe–Al^{III} distances (Al4 and Al5) are elongated by about 10 pm owing to the higher coordination number and the different electronic situation (2.3272(14) and 2.3686(15) Å).

The ^{1}H NMR spectrum of **1a** in C$_6$D$_6$ (298 K) shows two intense singlets at $\delta = 2.20$ (15H) and 1.82 ppm (30H) representing the fluxional C$_5$Me$_5$ groups at Al5 (η^1-Cp*) and Al1 and Al2 (η^5-Cp*), respectively. The methyl groups of both activated Cp* rings give rise to four weaker signals of equal intensity at $\delta = 2.23$ (6H), 2.09 (6H), 1.88 (6H), and 1.63 ppm (6H). For the bridging CH$_2$ groups, two singlets at $\delta = 1.04$ (2H, CH$_2$) and 0.76 ppm (2H, CH$_2$) were detected. Only one signal at $\delta = -19.00$ ppm (s, 2H) was found for the two hydrogen atoms H1 and H2. However, based on the asymmetric structure of **1a** in the solid state, two resonances would be expected. Clearly a fluxional process is present. No broadening of the signals was observed in the temperature range between 25 °C and 80 °C in C$_6$D$_6$. Thus, it is unlikely that a reversible C–H bond activation is responsible for the fluxionality of the hydrides in solution. Presumably H1 and H2 rapidly exchange their position, which is also consistent with the quantum mechanical calculations. The ^{27}Al NMR spectrum has only one very broad signal at $\delta = -2.5$ ppm ([(CO)$_4$Fe(AlCp*)]: $\delta = 0.4$ ppm[5]). The other, presumably also very broad ^{27}Al resonance signals (for the Al^{III} centers), are masked by the signal of the probe head ($\delta = +66.8$ ppm).

Quantum mechanical calculations[12] show a very good agreement between the structural parameters of the optimized structure, **1aM**, and the experimentally determined structure **1a** (see Supporting Information), with one exception: The atom H1 in **1aM** is better specified as a terminal hydride according to the calculations and is even located somewhat closer to Al1 (2.103 Å) than to Al4 (2.156 Å). This result may be an indication for a very flat energy surface for the hydrogen migration, and a distinction between terminal hydrides (classical) and bridging hydrides is no longer appropriate, particularly because the structures investigated are dynamic in nature.[13]

Surprisingly, a hypothetic structure [Fe(AlCp*)$_5$] with five Fe–Al bonds and intact Cp* ligands without bridging hydrogen atoms does not represent an energetic minimum. A geometry optimization starting from a structure with local D_{3h} symmetry at Fe without symmetry restrictions leads to **1aM**, which shows no imaginary frequencies. A calculation with restricted C_s-symmetry leads to a structure with intact CH$_3$ groups but with η^1-Cp* rings, which is 22.0 kcal mol^{-1} higher in energy than the minimum. Thus, the driving force for the C–H activation is significant. An analysis of the charge distribution by the natural bond orbital (NBO) method[14] shows significant differences between terminal and bridging atoms. The methylene carbon atoms C39 (−1.06) and C30 (−1.04) bear a higher negative charge than the methyl carbons (−0.64 to −0.67). The aluminum atoms bound to C39 and C30, Al5 (+1.16) and Al4 (+1.24) therefore bear a higher positive charge than Al3 (+0.92), Al2 (+0.75), Al1 (+0.94). As expected, the atoms H1 (−0.17) and H2 (−0.16) are negatively charged and are thus definitely hydridic, whereas all other hydrogen atoms are weakly positively charged.

The molecular structure of **1b** (Scheme 1), already suggested by NMR spectroscopy, was confirmed by X-ray analysis of a mixed crystal of **1a** and **1b** (see Supporting Information). The structural solution and refinement was performed under the assumption of a disorder of both isomers over the positions in the unit cell. No superlattice reflections were observed. The molecular structures of **1a** and **1b** are very similar, but **1b** has three C–H activated Cp* rings (Al3, Al4, and Al5). Thereby the tilting angle of the Cp* ring on Al4 to the axis Al4–$Cp^*_{centroid}$ is distinctly different. Whereas in **1a** this Cp* ring coordinates in an η^5 mode to Al4, this unit can be described as η^3-Cp*Al in **1b**. Also in **1b**, the Cp*unit of the adjacent Al5 is shifted closer towards Al4 than in **1a**, leading to a short Al4–C46 distance of 2.146 Å. The structural parameters of the heavy atoms of **1a** and **1b** in the mixed crystal were not distinguishable owing to the disorder, but are very different from those of pure **1a**. For a deeper analysis of **1b**, quantum mechanical calculations (RI-BP86/SVP) were performed. Model compound **1bM** (Figure 2) represents an

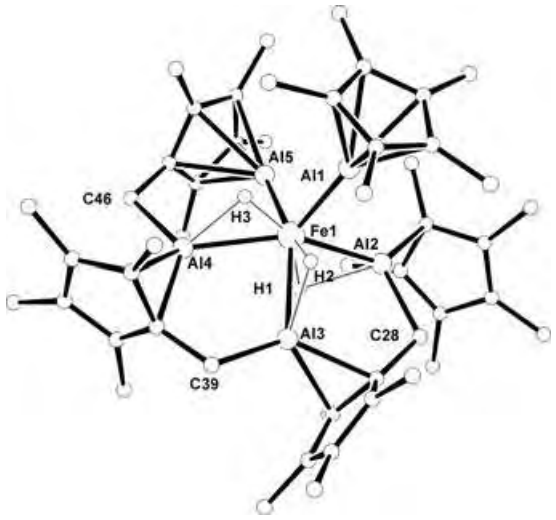

Figure 2. Calculated molecular structure **1bM**. Selected bond lengths [Å] and angles [°]: Fe1-Al1 2.223, Fe1-Al2 2.378, Fe1-Al3 2.405, Fe1-Al4 2.444, Fe1-Al5 2.263, $Cp^*_{centroid}$-Al1 1.923, $Cp^*_{centroid}$-Al5 1.893; Al1-Fe1-Al2 82.96, Al1-Fe1-Al3 119.42, Al1-Fe1-Al4 127.59, Al1-Fe1-Al5 95.10, Al2-Fe1-Al3 85.23, Al2-Fe1-Al4 149.41, Al2-Fe1-Al5 95.75, Al3-Fe1-Al4 80.41, Al3-Fe1-Al5 145.24, Al4-Fe1-Al5 81.17, $Cp^*_{centroid}$-Al1-Fe1 163.55, $Cp^*_{centroid}$-Al5- Fe1 148.97, Al1-Fe1-Al3-Al5 172.5.

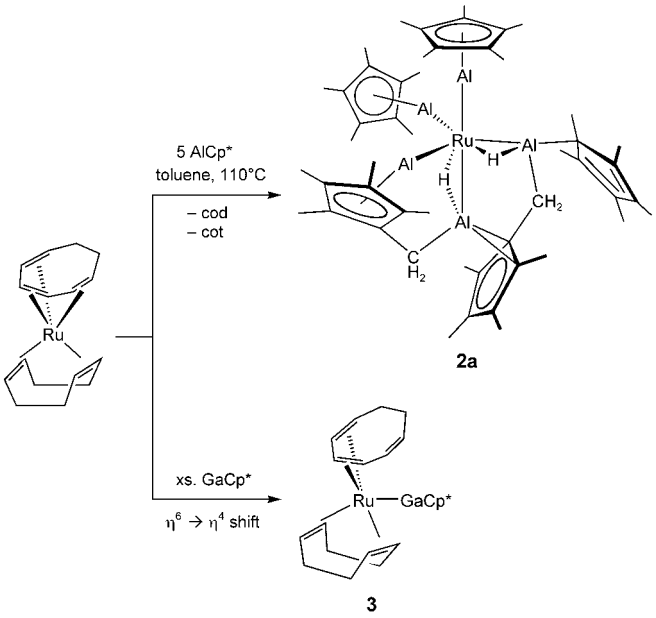

Scheme 2. Preparation of **2a** and **3**; cod = 1,5-cyclooctadiene, cot = 1,3,5-cyclooctatriene.

energetic minimum and is almost identical in energy to the doubly activated structure **1aM** (+0.16 kcal mol^{-1}).

The atoms H1, H2, and H3 bridge the bonds Fe–Al(2,3,4). The bridging CH_2 groups lead to small Al-Fe-Al angles of 80–85°, whereas the angle Al5-Fe1-Al2 (95.75°) is considerably larger. Compared to **1aM** (or **1a**), the structure of **1bM** is more distorted towards a square-pyramidal structure with Al1 in the axial position, a consequence of the three Fe-H-Al bridges. The axial ligand Al1 moves towards the open site between Al2 and Al5, leading to smaller angles Al1-Fe1-Al(2,5) (82.96 and 95.10°) in comparison to the larger angles Al1-Fe1-Al(3,4) (119.42 and 127.59°). Clearly, a fourfold activated product is unfavorable because of steric reasons. Whether a similar situation is possible in the octahedral complexes [M(AlCp*)$_6$] remains to be investigated.

The activation of AlCp* is not only restricted to [Fe(AlCp*)$_5$] (Supporting Information). [Ru(η^4-cod)(η^6-cot)][15] reacts with AlCp* (toluene, 110 °C) to give the $RuAl_5$ complex **2a** (isostructural to **1a**) in 60 % yield (Scheme 2). A complex **2b** which is analogous to **1b** could not be identified or isolated. Whereas [Fe(η^6-toluene)(η^4-1,3-butadiene)] is inert towards GaCp*, [Ru(η^4-cod)(η^6-cot)] reacts with GaCp* to give quantitatively the addition product [(η^4-cod)(η^4-cot)Ru(GaCp*)] (**3**).

The formation of [Ru(GaCp*)$_5$] or its C–H activated isomers could not be observed even with a great excess of GaCp*. InCp* is inert towards the Fe^0 and Ru^0 sources. We assume that low-coordinate intermediates [Fe(AlCp*)$_n$] ($n <$ 5) on the pathway leading to **1a** or **1b**, respectively, are responsible for the intramolecular C–H activation reactions. Thus, on reaction of [Cp*Rh(Me)$_2$(L)] (L = dmso, py; py = pyridine) and ECp* (E = Al, Ga), the zwitterionic species [Cp*Rh($C_5Me_4EMe_3$)] are formed and the complex [Cp*RhMe$_2$(ECp*)] has been isolated as an intermediate.[16a]

The intramolecular C–C bond activation proceeds at the Group 13 metal E and not at the rhodium center.[16b] Clearly, the electrophilicity of the aluminum is considerably increased on coordination of the Cp*Al unit,[1,2] which favors C–H activation and limits the availability of the compounds [M(AlCp*)$_n$]. The reaction of [$(Ph_3P)_3RuCl_2$] with six equivalents GaCp* quantitatively gives [Ru(GaCp*)$_6Cl_2$], the Cl ligands each bridging two of the Ga centers that surround the Ru^{II} center and thus blocking C–H activation reactions (see Supporting Information). This example suggests a route to[M(ECp*)$_n$] with $n \geq 6$.[17,18]

Experimental Section

1a: [Fe(η^6-toluene)(η^4-1,3-butadiene)] (0.100 g, 0.495 mmol) and [(AlCp*)$_4$] (0.478 g, 0.742 mmol) were suspended in toluene and heated to 80 °C for 2 h. After filtration of the orange solution and removal of the solvent in vacuo (25 °C, 10^{-2} Torr) from the filtrate, the yellow, microcrystalline residue was dissolved in warm toluene (6 mL) and the product crystallized at −30 °C over 2 h. Yield: 0.274 g (64 %). Pure **1a** can be isolated after a few minutes (Yield: 0.145 g, 35 %). M.p. 265 °C (decomp); ^{1}H NMR (C_6D_6, 250 MHz, 25 °C): δ = 2.23 (s, 6H, CH_3), 2.20 (s, 15H, CH_3), 2.09 (s, 6H, CH_3), 1.88 (s, 6H, CH_3), 1.82 (s, 30H, CH_3), 1.63 (s, 6H, CH_3), 1.04 (s, 2H, CH_2), 0.76 (s, 2H, CH_2), −19.00 ppm (s, 2H); ^{13}C{^{1}H} NMR (C_6D_6, 62.9 MHz, 25 °C): δ = 126.9 (C_5Me_5), 123.9 (C_5Me_5), 118.9 (C_5Me_5), 118.2 (C_5Me_5), 114.8 (C_5Me_5), 112.7 (C_5Me_5), 112.6 (C_5Me_5), 110.5 (C_5Me_5), 17.3 (CH_2), 15.1 (CH_2), 14.3 (C_5Me_5), 12.3 (C_5Me_5), 12.2 (C_5Me_5), 11.2 (C_5Me_5), 11.1 (C_5Me_5) 11.0 ppm (C_5Me_5); ^{27}Al NMR (C_6D_6, 65.2 MHz, 25 °C): δ = −2.5 ppm; elemental analysis: calcd (%) for $C_{50}H_{75}Al_5Fe$: C 69.28, H 8.72; found: C 69.43, H 8.84.

1b: Compound **1b** could not be obtained in pure form, but only as a mixed crystal together with **1a**. The volume of the mother liquor of the synthesis of **1a** described above was decreased and the concentrated solution kept at −30 °C for some time. Repeated fractional crystallization of the material obtained increased the amount of **1b** in the crystals. ^{1}H NMR (C_6D_6, 250 MHz, 25 °C): δ = 2.02 (s, 15H, CH_3), 1.77 (s, 15H, CH_3), 1.03–0.75 (m, 6H, CH_2),

−18.17 ppm (only the characteristic signals are listed, see Supporting Information).

Crystal Structure analyses (Oxford Excalibur 2 diffractometer): The structural solution and refinement was performed using the programs SHELXS-86 and SHELXL-97.[19] **1a**: $C_{50}H_{75}Al_5Fe$, M_r = 866.88, 0.30 × 0.25 × 0.15 mm, monoclinic, $P2(1)/n$, a = 10.930(3), b = 20.473(5), c = 21.400(6) Å, α = 90, β = 94.71(2), γ = 90°, V = 4772(2) Å^3, Z = 4, ρ_{calcd} = 1.206 g cm^{-3}, $\lambda(Mo_{K\alpha})$ = 0.71073 Å, T = 103(2) K, 34170 reflections measured (8437 unique), R(int) = 0.0846, $R1$ = 0.0986, $wR2(F^2)$ = 0.1752. The atoms H1 and H2 could be localized; they were taken into account for the subsequent structural refinement. **1b**: Mixed crystals of **1a**/**1b** $C_{50}H_{75}Al_5Fe$, M_r = 866.88, 0.20 × 0.15 × 0.10 mm, monoclinic, $C2/c$, a = 17.539(6), b = 16.314(5), c = 33.601(17) Å, α = 90, β = 98.61(4), γ = 90°, V = 9506(7) Å^3, Z = 8, ρ_{calcd} = 1.211 g cm^{-3}, $\lambda(Mo_{K\alpha})$ = 0.71073 Å, T = 105(2) K. 29009 reflections measured (8391 unique), R(int) = 0.0859, $R1$ = 0.1396, $wR2(F^2)$ = 0.1798. The structural solution and refinement was done under the assumption of a disorder of both isomers on the positions in the unit cell. Both parts of the disordered structure could not be freely refined (AFIX 109) and their relative amounts were determined to be: **1a** (0.51796) and **1b** (0.48204). No bridging H atoms could be localized because of the disorder. **2a**: $C_{50}H_{75}Al_5Ru$, M_r = 912.11 0.20 × 0.15 × 0.20 mm, monoclinic, $P2(1)/n$, a = 11.932(2), b = 24.352(5), c = 16.903(3) Å, α = 90, β = 96.84(3), γ = 90°, V = 4876.2(17) Å^3, Z = 4, ρ_{calcd} = 1.242 g cm^{-3}, $\lambda(Mo_{K\alpha})$ = 0.71073 Å, T = 103(2) K. 17067 reflections measured (8286 unique), R(int) = 0.0767, $R1$ = 0.1256 und $wR2(F^2)$ = 0.1157. CCDC-257541 (**1a**), CCDC-257542 (**1b**), and CCDC-257543 (**2a**) contain the supplementary crystallographic data for this paper. These data can be obtained free of charge from the Cambridge Crystallographic Data Centre via www.ccdc.cam.ac.uk/data_request/cif.

Received: December 6, 2004
Revised: January 10, 2005
Published online: April 12, 2005

Keywords: aluminum · carbenoids · C-H activation · iron · ruthenium

[1] J. Uddin, G. Frenking, *J. Am. Chem. Soc.* **2001**, *123*, 1683 – 1693.
[2] a) J. Uddin, C. Boehme, G. Frenking, *Organometallics* **2000**, *19*, 571 – 582; b) W. Uhl, M. Benter, S. Melle, W. Saak, G. Frenking, J. Uddin, *Organometallics* **1999**, *18*, 3778 – 3780.
[3] a) W. Uhl, M. Pohlmann, R. Wartchow, *Angew. Chem.* **1998**, *110*, 1007 – 1009; *Angew. Chem. Int. Ed.* **1998**, *37*, 961 – 963; b) P. Jutzi, B. Neumann, L. O. Schebaum, A. Stammler, H.-G. Stammler, *Organometallics* **1999**, *18*, 4462 – 4464; c) W. Uhl, S. Melle, *Z. Anorg. Allg. Chem.* **2000**, *626*, 2043 – 2045; d) C. Gemel, T. Steinke, D. Weiss, M. Cokoja, M. Winter, R. A. Fischer, *Organometallics* **2003**, *22*, 2705 – 2710.
[4] a) D. Weiss, M. Winter, R. A. Fischer, C. Yu, K. Wichmann, G. Frenking, *Chem. Commun.* **2000**, 2495 – 2496; b) T. Steinke, C. Gemel, M. Winter, R. A. Fischer, *Chem. Eur J.* **2005**, *11*, 1636 – 1646.
[5] J. Weiss, D. Stetzkamp, B. Nuber, R. A. Fischer, C. Boehme, G. Frenking, G. *Angew. Chem.* **1997**, *109*, 95 – 97; *Angew. Chem. Int. Ed. Engl.* **1997**, *36*, 70 – 72.
[6] a) P. Jutzi, B. Neumann, O. Schebaum, A. Stammler, H. G. Stammler, *Organometallics* **1999**, *18*, 4462 – 4464; b) Q. Yu, H. Purath, A. Donchev, H. Schnöckel, *J. Organomet. Chem.* **1999**, *584*, 94 – 97.
[7] P. Jutzi, B. Neumann, G. Reumann, H.-G. Stammler, *Organometallics* **1998**, *17*, 1305 – 1314.
[8] M. Cokoja, T. Steinke, C. Gemel, T. Welzel, M. Winter, K. Merz, R. A. Fischer, *J. Organomet. Chem.* **2003**, *684*, 277 – 286.
[9] a) U. Zenneck, *Angew. Chem.* **1990**, *102*, 171 – 182; *Angew. Chem. Int. Ed. Engl.* **1990**, *29*, 126 – 137; b) S. D. Ittel, C. A. Tolman, *Organometallics* **1982**, *1*, 1432 – 1436; c) D. L. Williams-Smith, L. R. Wolf, P. S. Skell, *J. Am. Chem. Soc.* **1972**, *94*, 4042 – 4043.
[10] a) M. A. Andrews, G. van Buskirk, H. D. Kaesz, *J. Am. Chem. Soc.* **1979**, *101*, 7245 – 7254; b) H.-C. Böttcher, K. Merzweiler, C. Wagner, *Z. Anorg. Allg. Chem.* **1999**, *625*, 857 – 865; c) A. Winter, L. Zsolnai, G. Huttner, *Chem. Ber.* **1982**, *115*, 1286 – 1304; d) V. D. Patel, N. J. Taylor, A. J. Carty, *Chem. Commun.* **1984**, 99 – 100.
[11] T. Steinke, C. Gemel, M. Cokoja, M. Winter, R. A. Fischer, *Angew. Chem.* **2004**, *116*, 2349 – 2352; *Angew. Chem. Int. Ed.* **2004**, *43*, 2299 – 2302.
[12] The calculations for **1a** and **1b** were performed using the software package TURBOMOLE: a) R. Ahlrichs, M. Bär, M. Häser, H. Horn, C. Kölmel, *Chem. Phys. Lett.* **1989**, *162*, 165 – 169; b) O. Treutler, R. Ahlrichs, *J. Chem. Phys.* **1995**, *102*, 346 – 354; Becke–Perdew(BP86) exchange corellation functional and "Resolution of the Identity" approximation (RI): c) D. Becke, *Phys. Rev. A* **1988**, *38*, 3098 – 3100; d) S. H. Vosko, L. Wilk, M. Nusair, *Can. J. Phys.* **1980**, *58*, 1200 – 1211; e) J. P. Perdew, *Phys. Rev. B* **1986**, *33*, 8822 – 8824; Erratum: J. P. Perdew, *Phys. Rev. B* **1986**, *34*, 7406; f) K. Eichkorn, O. Treutler, H. Öhm, M. Häser, R. Ahlrichs, *Chem. Phys. Lett.* **1995**, *242*, 652 – 660; For the density functional theory (DFT) calculations SVP basis sets were used: g) A. Schäfer, H. Horn, R. Ahlrichs, *J. Chem. Phys.* **1992**, *97*, 2571 – 2577; h) A. Schäfer, C. Huber, R. Ahlrichs, *J. Chem. Phys.* **1994**, *100*, 5829 – 5835; i) K. Eichkorn, F. Weigend, O. Treutler, R. Ahlrichs, *Theor. Chem. Acc.* **1997**, *97*, 119 – 124.
[13] K. K. Pandey, M. Lein, G. Frenking, *Organometallics* **2004**, *23*, 2944 – 2948.
[14] A. E. Reed, L. A. Curtiss, F. Weinhold, *Chem. Rev.* **1988**, *88*, 899 – 926.
[15] K. Itoh, H. Nagashima, T. Ohshima, N. Ohshima, N. Nishiyama, *J. Organomet. Chem.* **1984**, *272*, 179 – 188. The synthesis of [Ru(η^4-cod)(η^6-cot)] was prepared according to literature. Instead of an ultrasonic bath, a magnetic stirrer was used: M. Hirano, R. Asakawa, C. Nagata, T. Miyasaka, N. Komine, S. Komiya, *Organometallics* **2003**, *22*, 2378 – 2386.
[16] a) T. Cadenbach, C. Gemel, R. Schmid, S. Block, R. A. Fischer, *Dalton Trans.* **2004**, 3171 – 3172; b) T. Cadenbach, diploma thesis **2005**, Ruhr-Universität Bochum.
[17] a) M. Cokoja, C. Gemel, T. Steinke, F. Schröder, R. A. Fischer, *Dalton Trans.* **2005**, 44 – 54; b) T. Steinke, C. Gemel, M. Cokoja, M. Winter, R. A. Fischer, *Chem. Commun.* **2003**, 1066 – 1067; c) T. Steinke, C. Gemel, M. Cokoja, M. Winter, R. A. Fischer, *Dalton Trans.* **2005**, 55 – 62.
[18] C. Gemel, T. Steinke, M. Cokoja, A. Kempter, R. A. Fischer, *Eur. J. Inorg. Chem.* **2004**, 4161 – 4176.
[19] G. M. Sheldrick, SHELXS-86, Program for solution of crystal structures, University of Göttingen, Germany, 1986; G. M. Sheldrick, SHELXL-97, Program for refinement of crystal structures, University of Göttingen, Germany, 1997.

Cross-Coupling Reactions

Cobalt(II)-Catalyzed Cross-Coupling of Polyfunctional Aryl Copper Reagents with Aryl Bromides and Chlorides**

*Tobias J. Korn and Paul Knochel**

There are now a number of efficient experimental procedures available for palladium- and nickel-catalyzed cross-coupling reactions of aromatic organometallic reagents with aryl halides.[1,2] However, the high cost of palladium and the required phosphine ligands, as well as the high toxicity of nickel catalysts, led us to explore the use of alternative metals for such coupling reactions. Following the pioneering work of Kochi and co-workers and others,[3] we found recently that functionalized aryl copper reagents smoothly undergo cross-coupling with aryl iodides in the presence of $[Fe(acac)_3]$ as the catalyst.[4] In contrast to the elegant method of Fürstner and co-workers,[5] in our case only aryl iodides could be used; aryl bromides and chlorides did not react.

To extend the scope of this cross-coupling reaction, we examined other metal salts as catalysts. We reported recently the cobalt(II)-catalyzed cross-coupling of allylic chlorides with dialkyl zinc reagents[6] and of heteroaromatic chlorides with aromatic and heteroaromatic Grignard reagents.[7] Other cobalt-catalyzed reactions have also been discovered recently by the research groups of Cahiez,[8] Oshima,[9] and Gosmini.[10] Preliminary experiments showed that $[Co(acac)_2]$ catalyzes efficiently the cross-coupling of aryl copper derivatives with aryl bromides and chlorides; the reaction is therefore complementary to the recently reported iron-catalyzed process.[4] As a test reaction, we examined the coupling of ethyl 2-bromobenzoate (**1a**; 1 equiv) with the phenylcopper reagent **2a** (3 equiv),[11] which was prepared by the reaction of PhMgCl with CuCN·2 LiCl[12] in a 2:1 mixture of DME/THF at 80 °C. In the absence of the catalyst, no reaction was observed after 4 h; the desired product **3a** was only detected after 24 h.[13] When $[Co(acac)_2]$ (10 mol %) was added, a conversion of 46 % was observed after 15 min; however, the conversion increased to just 49 % within the next 4 h of reaction time. A significant improvement was observed upon the addition of Bu_4NI (3 equiv),[14] which led to a conversion of 81 % after 21 h. The addition of 4-fluorostyrene (**4**; 20 mol %), which was known to promote cross-coupling reactions,[15] was not effective alone,[16] but in combination with Bu_4NI a conversion of 100 % was reached within 21 h. The use of DMPU[17] as a cosolvent also led to a considerable rate improvement. A conversion of 100 % was now observed after 15 min at 80 °C, with the desired product **3a** formed as the sole product. Under optimized reaction conditions (**1a** (1 equiv), **2a** (1.7 equiv), $[Co(acac)_2]$ (7.5 mol %), Bu_4NI (1 equiv), **4** (20 mol %)), the ester **3a** was isolated in 77 % yield (Scheme 1).

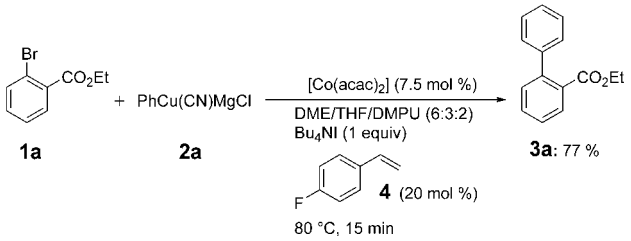

Scheme 1. The Co^{II}-catalyzed cross-coupling reaction of **2a** with ethyl 2-bromobenzoate (**1a**) under optimized conditions. acac = acetylacetonate, DME = 1,2-dimethoxyethane, DMPU = 1,3-dimethyl-3,4,5,6-tetrahydro-2(1*H*)-pyrimidinone.

The additives Bu_4NI and styrene **4** were still required in the polar solvent mixture containing DMPU, as only partial conversion was observed in their absence. We studied the scope of the reaction and found that a broad range of aryl copper reagents of type **2** reacted with a variety of aryl bromides with electron-withdrawing substituents. Thus, the 4-methoxyphenylcopper reagent **2b** underwent a smooth cross-coupling reaction with **1a** at 80 °C to afford the desired biphenyl derivative **3b** in 79 % yield (Table 1, entry 2). Aryl copper species with electron-withdrawing substituents displayed lower reactivity. However, **2c** underwent the coupling with the reactive compound **1b** at 80 °C to give ketone **3c** in 62 % yield (Table 1, entry 3). Similarly, the bromo diester **1c** reacted with various aryl copper derivatives of low reactivity, such as **2d** or **2e**; in these cases the cross-coupling products **3d** and **3e** were isolated in 65 and 54 % yield, respectively (Table 1, entries 4 and 5). The heterocyclic copper reagent **2f** reacted rapidly with **1b** at 80 °C to give the substituted pyridine **3f** in 62 % yield (Table 1, entry 6). As mentioned above, aryl copper compounds with an electron-donating substituent displayed high reactivity in these cross-coupling reactions. Thus, **2b** reacted with **1b** within 1 h at room temperature (89 % yield; Table 1, entry 7). 4-Bromobenzophenone (**1d**) also underwent complete conversion at 25 °C within 7.5 h (73 % yield; Table 1, entry 8). However, 3-bromobenzophenone (**1e**) reacted only slowly in the desired cross-coupling; the expected product **3i** was obtained in 25 % yield after 24 h at room temperature (Table 1, entry 9). Interestingly, the corresponding cyano-substituted aryl copper derivatives **2g–i** reacted smoothly with **1b** to provide ketones **3j–l** in 74–90 % yield (Table 1, entries 10–12). A methyl ketone is an especially sensitive functionality, which can be readily deprotonated by numerous organometallic species. Remarkably, we found that 2-bromoacetophenone (**1f**) reacted smoothly with various aryl copper reagents to

[*] Dipl.-Chem. T. J. Korn, Prof. Dr. P. Knochel
Department Chemie
Ludwig-Maximilians-Universität München
Butenandtstrasse 5–13, Haus F, 81377 München (Germany)
Fax: (+49) 89-2180-77680
E-mail: paul.knochel@cup.uni-muenchen.de

[**] We thank the Fonds der Chemischen Industrie, the Deutsche Forschungsgemeinschaft (DFG), and Merck Research Laboratories (MSD) for financial support. T.J.K. thanks the DFG and the CNRS for a fellowship. We also thank Chemetall and BASF for generous gifts of chemicals.

Supporting information for this article is available on the WWW under http://www.angewandte.org or from the author.

 DOI: 10.1002/anie.200500099

Table 1: [Co(acac)$_2$]-catalyzed reaction of aryl copper derivatives **2** with aryl bromides **1** to give products **3**.

Entry	Aryl bromide **1**	Aryl copper reagent **2**[a]	Product **3**	Conditions [°C, h]	Yield [%][b]
	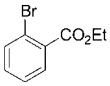	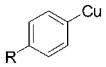	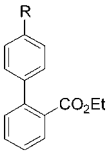		
1	**1a**	**2a:** R = H	**3a:** R = H	80, 0.25	77
2	**1a**	**2b:** R = OMe	**3b:** R = OMe	80, 0.25	79
	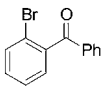		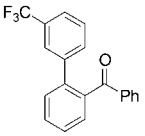		
3	**1b**	**2c**	**3c**	80,3	62
	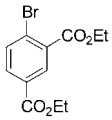		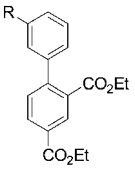		
4	**1c**	**2d:** R = F	**3d:** R = F	80, 0.5	65
5	**1c**	**2e:** R = CO_2Et	**3e:** R = CO_2Et	80, 18	54
	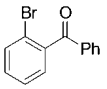	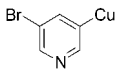	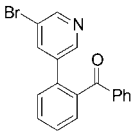		
6	**1b**	**2f**	**3f**	80, 16	62
	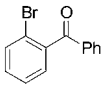	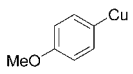	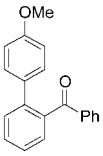		
7	**1b**	**2b**	**3g**	RT, 1	89
	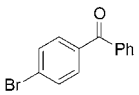	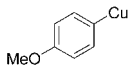	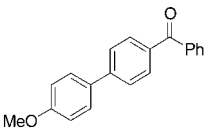		
8	**1d**	**2b**	**3h**	RT, 7.5	73
	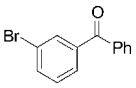	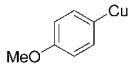	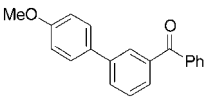		
9	**1e**	**2b**	**3i**	RT, 24	25
	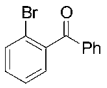	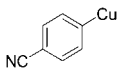	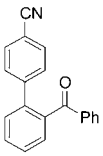		
10	**1b**	**2g**	**3j**	RT, 0.5	90

Table 1: (Continued)

Entry	Aryl bromide **1**	Aryl copper reagent **2**[a]	Product **3**	Conditions [°C, h]	Yield [%][b]
	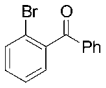	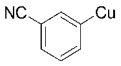	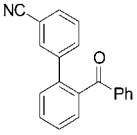		
11	**1b**	**2h**	**3k**	RT, 0.5	80
	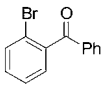		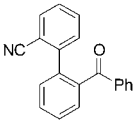		
12	**1b**	**2i**	**3l**	RT, 2.5	74
	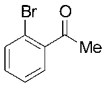	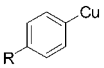	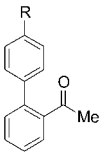		
13	**1f**	**2b:** R = OMe	**3m:** R = OMe	RT, 0.5	90
14	**1f**	**2g:** R = CN	**3n:** R = CN	RT, 1	77
	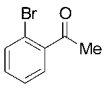		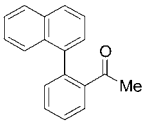		
15	**1f**	**2j**	**3o**	RT, 15	83
	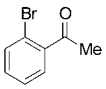	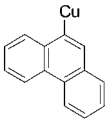	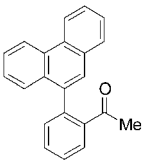		
16	**1f**	**2k**	**3p**	RT, 0.25	70
	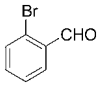	PhCu	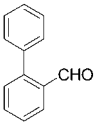		
17	**1g**	**2a**	**3q**	RT, 0.25	42

[a] The copper reagent is better represented as ArCu(CN)MgCl. [b] Yield of analytically pure product. RT = room temperature.

give the polyfunctional ketones **3m–p** in 70–90% yield (Table 1, entries 13–16). An unexpected reactivity difference was observed between the 9-phenanthrylcopper reagent **2k** and the 1-naphthylcopper reagent **2j**. Whereas **2k** reacted with **1f** within 15 min at room temperature, **2j** required a reaction time of 15 h at the same temperature (Table 1, entries 15 and 16). Finally, we found a remarkable compatibility of the reaction conditions with an aldehyde functionality. Thus, 2-bromobenzaldehyde (**1g**) reacted readily with **2a** to provide 2-phenylbenzaldehyde (**3q**) in 42% yield (Table 1, entry 17).

The excellent reactivity of aryl bromides with electron-withdrawing substituents led us to examine cross-coupling reactions with aryl chlorides. The reaction of 2-chlorobenzophenone (**5**) with the aryl copper compounds **2a**, **2b**, and **2h** proceeded smoothly at 25 °C within 15 min to 1.5 h under our typical reaction conditions and furnished the expected ketones **3r**, **3g**, and **3k** in almost quantitative yield (Scheme 2).

In further experiments to establish the scope of this method, we investigated the cross-coupling of bromoketones **6a**,**b** with heterocyclic substituents. An efficient cross-coupling reaction took place with **2h**, as well as with the heteroaromatic copper reagents **2f** and **2l**; the products **7a–c** were formed in 74–88% yield (Scheme 3).

In summary, we have shown that $[Co(acac)_2]$ catalyzes the cross-coupling of functionalized aryl copper reagents with a variety of chloro- and bromoaryl ketones and bromoaryl

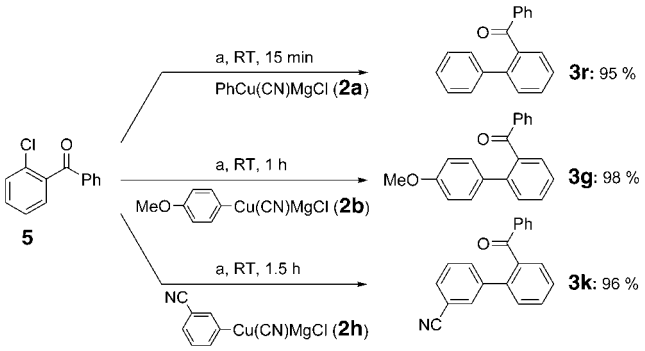

Scheme 2. Cobalt-catalyzed cross-coupling reactions of 2-chlorobenzophenone (**5**) with aryl copper compounds: a) **5** (1 equiv), **2** (1.7 equiv), $[Co(acac)_2]$ (7.5 mol%), DME/THF/DMPU (3:2:1), **4** (20 mol%), Bu_4NI (1 equiv).

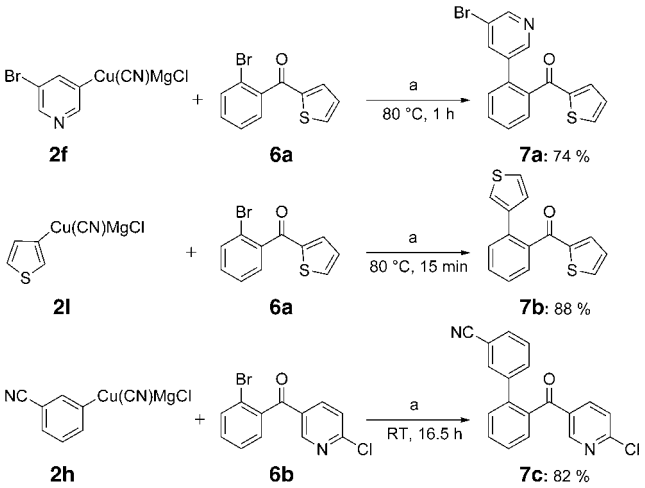

Scheme 3. Cobalt-catalyzed cross-coupling reactions of heterocycle-substituted bromoaryl ketones **6** with heteroaryl and aryl copper compounds: a) **6** (1 equiv), **2** (1.7 equiv), $[Co(acac)_2]$ (7.5 mol%), DME/THF/DMPU (3:2:1), **4** (20 mol%), Bu_4NI (1 equiv).

esters in a DME/THF/DMPU solvent mixture in the presence of the promoters 4-fluorostyrene and Bu_4NI. The reaction leads to polyfunctional biphenyl derivatives and heterocyclic analogues. The remarkable functional-group compatibility of organocopper reagents with esters, ketones, and even aldehydes should make this cross-coupling method especially attractive for multistep syntheses, as it should be possible to avoid the extensive use of protecting groups.

Experimental Section

Typical procedure: **3j**: 4-Bromobenzonitrile (309 mg, 1.70 mmol) was added to *i*PrMgCl·LiCl (1.73 mL, 1.70 mmol, 0.98 M in THF) at −20 °C in a 25-mL Schlenk tube equipped with a magnetic stirring bar and a septum. The reaction mixture was warmed to 0 °C and stirred at this temperature for 2 h. A solution of CuCN·2 LiCl (1.9 mL, 1.9 mmol, 1 M in THF) was then added, and the mixture was stirred for an additional 10 min. DME (6.0 mL), DMPU (2.0 mL), Bu_4NI (370 mg, 1.00 mmol), 4-fluorostyrene (25 mg, 0.20 mmol), $[Co(acac)_2]$ (19.3 mg, 0.075 mmol), and 2-bromobenzophenone (261 mg, 1.00 mmol) were then added, and the reaction mixture was stirred for 0.5 h at room temperature, then quenched with a saturated, aqueous solution of NH_4Cl/NH_3 (9:1; 50 mL). The organic phase was washed a second time with a saturated, aqueous solution of NH_4Cl/NH_3 (9:1; 50 mL), and the combined aqueous phases were extracted with EtOAc (3 × 40 mL). The combined organic phases were washed with brine (50 mL), dried over $MgSO_4$, and filtered, and the solvent was evaporated in vacuo. Purification by flash chromatography on silica gel (pentane/diethyl ether 4:1) furnished **3j** as a light-yellow solid (256 mg, 0.90 mmol, 90%; m.p.: 91.4–92.3 °C).

Received: January 11, 2005
Published online: April 12, 2005

Keywords: cobalt · cross-coupling · Grignard reagents · heterocycles · organocopper compounds

[1] a) *Metal-catalyzed Cross-coupling Reactions* (Eds.: A. de Meijere, F. Diederich), 2nd. ed., Wiley-VCH, Weinheim, **2004**; b) J. Tsuji, *Transition Metal Reagents and Catalysts: Innovations in Organic Synthesis*, Wiley, Chichester, **1995**; c) "Cross-Coupling Reactions: A Practical Guide": *Top. Curr. Chem.* **2002**, *219*; d) *Handbook of Organopalladium Chemistry for Organic Synthesis* (Ed.: E. Negishi), Wiley-Interscience, New York, **2002**; e) *Transition Metals for Organic Synthesis* (Eds.: M. Beller, C. Bolm), Wiley-VCH, Weinheim, **1998**.

[2] a) C. Dai, G. C. Fu, *J. Am. Chem. Soc.* **2001**, *123*, 2719; b) A. F. Littke, G. C. Fu, *J. Am. Chem. Soc.* **2001**, *123*, 6989; c) A. F. Littke, L. Schwarz, G. C. Fu, *J. Am. Chem. Soc.* **2002**, *124*, 6343; d) A. F. Littke, G. C. Fu, *Angew. Chem.* **2002**, *114*, 4350; *Angew. Chem. Int. Ed.* **2002**, *41*, 4176; e) I. D. Hills, M. R. Netherton, G. C. Fu, *Angew. Chem.* **2003**, *115*, 5927; *Angew. Chem. Int. Ed.* **2003**, *42*, 5749; f) A. C. Frisch, A. Zapf, O. Briel, B. Kayser, N. Shaikh, M. Beller, *J. Mol. Catal. A* **2004**, *214*, 231; g) A. Tewari, M. Hein, A. Zapf, M. Beller, *Synthesis* **2004**, 935; h) F. Rataboul, A. Zapf, R. Jackstell, S. Harkal, T. Riermeier, A. Monsees, U. Dingerdissen, M. Beller, *Chem. Eur. J.* **2004**, *10*, 2983; i) M. Kumada, *Pure Appl. Chem.* **1980**, *52*, 669; j) T.-Y. Luh, *Acc. Chem. Res.* **1991**, *24*, 257; k) S. Sengupta, M. Leite, D. S. Raslan, C. Quesnelle, V. Snieckus, *J. Org. Chem.* **1992**, *57*, 4066; l) A. F. Indolese, *Tetrahedron Lett.* **1997**, *38*, 3513; m) E. Shirakawa, K. Yamasaki, T. Hiyama, *Synthesis* **1998**, 1544; n) A. Sophia, E. Karlström, K. Itami, J.-E. Bäckvall, *J. Am. Chem. Soc.* **2000**, *122*, 6950; o) J. Montgomery, *Acc. Chem. Res.* **2000**, *33*, 467; p) R. Giovaninni, P. Knochel, *J. Am. Chem. Soc.* **1998**, *120*, 11186; q) B. H. Lipshutz, *Adv. Synth. Catal.* **2001**, *343*, 313; r) B. H. Lipshutz, G. Bulwo, F. Fernandez-Lazaro, S.-K. Kim, R. Lowe, P. Mollard, K. L. Stevens, *J. Am. Chem. Soc.* **1999**, *121*, 11664.

[3] a) M. Tamura, J. K. Kochi, *J. Am. Chem. Soc.* **1971**, *93*, 1487; b) M. Tamura, J. K. Kochi, *Synthesis* **1971**, *93*, 303; c) M. Tamura, J. K. Kochi, *J. Organomet. Chem.* **1971**, *31*, 289; d) M. Tamura, J. K. Kochi, *Bull. Chem. Soc. Jpn.* **1971**, *44*, 3063; e) M. Tamura, J. K. Kochi, *Synthesis* **1971**, 303; f) J. K. Kochi, *Acc. Chem. Res.* **1974**, *7*, 351; g) S. Neumann, J. K. Kochi, *J. Org. Chem.* **1975**, *40*, 599; h) R. S. Smith, J. K. Kochi, *J. Org. Chem.* **1976**, *41*, 502; i) see also: G. Molander, B. Rahn, D. C. Shubert, S. E. Bonde, *Tetrahedron Lett.* **1983**, *24*, 5449; j) G. Cahiez, S. Marquais, *Pure Appl. Chem.* **1996**, *68*, 669; k) G. Cahiez, S. Marquais, *Tetrahedron Lett.* **1996**, *37*, 1773; l) G. Cahiez, H. Avedissian, *Synthesis* **1998**, 1199; m) H. Shinokubo, K. Oshima, *Eur. J. Org. Chem.* **2004**, 2081; n) M. A. Fakhfakh, X. Franck, R. Hocquemiller, B. Figadère, *J. Organomet. Chem.* **2001**, *624*, 131; o) M. Hocek, H. Dvoráková, *J. Org. Chem.* **2003**, *68*, 5773; p) B. Hölzer, R. W. Hoffmann, *Chem. Commun.* **2003**, 732; q) W. Dohle, F. Kopp, G. Cahiez, P. Knochel, *Synlett* **2001**, 1901; r) M. Hojo, Y. Murakami, H. Aihara, R. Sakuragi, Y. Baba, A. Hosomi, *Angew. Chem.* **2001**, *113*, 641; *Angew. Chem. Int. Ed.* **2001**, *40*, 621; s) M.

Nakamura, A. Hirai, E. Nakamura, *J. Am. Chem. Soc.* **2001**, *123*, 978; t) E. Alvarez, T. Cuvigny, C. H. du Penhoat, M. Julia, *Tetrahedron* **1998**, *54*, 119; u) V. Finandanese, G. Marchese, V. Martina, L. Ronzini, *Tetrahedron Lett.* **1984**, *25*, 4805.

[4] I. Sapountzis, W. Lin, C. C. Kofink, C. Despotopoulou, P. Knochel, *Angew. Chem.* **2005**, *117*, 1682; *Angew. Chem. Int. Ed.* **2005**, *44*, 1654.

[5] a) For an excellent review on iron-catalyzed reactions, see: C. Bolm, J. Legros, J. Le Paih, L. Zani, *Chem. Rev.* **2004**, *104*, 6217; b) A. Fürstner, A. Leitner, M. Méndez, H. Krause, *J. Am. Chem. Soc.* **2002**, *124*, 13856; c) A. Fürstner, A. Leitner, *Angew. Chem.* **2002**, *114*, 632; *Angew. Chem. Int. Ed.* **2002**, *41*, 609; d) A. Fürstner, A. Leitner, *Angew. Chem.* **2003**, *115*, 320; *Angew. Chem. Int. Ed.* **2003**, *42*, 308; e) G. Seidel, D. Laurich, A. Fürstner, *J. Org. Chem.* **2004**, *69*, 3950; f) B. Scheiper, M. Bonnekessel, H. Krause, A. Fürstner, *J. Org. Chem.* **2004**, *69*, 3943; g) A. Fürstner, D. De Souza, L. Parra-Rapado, J. T. Jensen, *Angew. Chem.* **2003**, *115*, 5516; *Angew. Chem. Int. Ed.* **2003**, *42*, 5355; h) M. Nakamura, K. Matsuo, S. Ito, E. Nakamura, *J. Am. Chem. Soc.* **2004**, *126*, 3686; i) T. Nagano, T. Hayashi, *Org. Lett.* **2004**, *6*, 1297; j) R. Martin, A. Fürstner, *Angew. Chem.* **2004**, *116*, 4045; *Angew. Chem. Int. Ed.* **2004**, *43*, 3955; k) R. B. Bedford, D. W. Bruce, R. M. Frost, J. W. Goodby, M. Hird, *Chem. Commun.* **2004**, 2822.

[6] C. K. Reddy, P. Knochel, *Angew. Chem.* **1996**, *108*, 1812; *Angew. Chem. Int. Ed. Engl.* **1996**, *35*, 1700.

[7] T. J. Korn, G. Cahiez, P. Knochel, *Synlett* **2003**, 1892.

[8] a) H. Avedissian, L. Bérillon, G. Cahiez, P. Knochel, *Tetrahedron Lett.* **1998**, *39*, 6163; b) G. Cahiez, H. Avedissian, *Tetrahedron Lett.* **1998**, *39*, 6159.

[9] a) For an excellent review, see: H. Shinokubo, K. Oshima, *Eur. J. Org. Chem.* **2004**, 2081; b) T. Fujioka, T. Nakamura, H. Yorimitsu, K. Oshima, *Org. Lett.* **2002**, *4*, 2257; c) T. Tsuji, H. Yorimitsu, K. Oshima, *Angew. Chem.* **2002**, *114*, 4311; *Angew. Chem. Int. Ed.* **2002**, *41*, 4137; d) K. Wakabayashi, H. Yorimitsu, K. Oshima, *J. Am. Chem. Soc.* **2001**, *123*, 5374; e) H. Ohmiya, T. Tsuji, H. Yorimitsu, K. Oshima, *Chem. Eur. J.* **2004**, *10*, 5640; f) Y. Ikeda, T. Nakamura, H. Yorimitsu, K. Oshima, *J. Am. Chem. Soc.* **2002**, *124*, 6514; g) K. Mizutani, H. Shinokubo, K. Oshima, *Org. Lett.* **2003**, *5*, 3959.

[10] a) P. Gomes, C. Gosmini, J. Périchon, *Org. Lett.* **2003**, *5*, 1043; b) P. Gomes, C. Gosmini, J. Périchon, *Synthesis* **2003**, 1909.

[11] a) B. H. Lipshutz, S. Sengupta, *Org. React.* **1992**, *41*, 135; b) R. J. K. Taylor, *Organocopper Reagents*, Oxford University Press, Oxford, **1994**; c) N. Krause, *Modern Organocopper Chemistry*, Wiley-VCH, Weinheim, **2002**.

[12] P. Knochel, M. C. P. Yeh, S. C. Berk, J. Talbert, *J. Org. Chem.* **1988**, *53*, 2390.

[13] After a reaction time of 24 h only 47% conversion was observed.

[14] a) M. Piber, A. E. Jensen, M. Rottländer, P. Knochel, *Org. Lett.* **1999**, *1*, 1323; b) S. W. Wright, D. L. Hageman, L. D. McClure, *J. Org. Chem.* **1994**, *59*, 6095; c) J.-F. Nguefack, V. Bollit, D. Sinou, *Tetrahedron Lett.* **1996**, *37*, 5527; d) N. A. Powell, S. D. Rychnovsky, *Tetrahedron Lett.* **1996**, *37*, 7901; e) K. Nakamura, H. Okubo, M. Yamaguchi, *Synlett* **1999**, 549; f) W. A. Herrmann, C. Brossmer, C.-P. Reisinger, T. H. Riermeier, K. Öfele, M. Beller, *Chem. Eur. J.* **1997**, *3*, 1357.

[15] A. E. Jensen, P. Knochel, *J. Org. Chem.* **2002**, *67*, 79.

[16] After a reaction time of 4 h at 80°C, 29% conversion was observed, and after 21 h, 42% conversion was observed.

[17] Besides DMPU, 1-methyl-2-pyrrolidinone (NMP) and *N*,*N*-dimethylacetamide (DMAC) also led to a rate acceleration when used as cosolvents, but DMPU showed the strongest effect.

Homogeneous Catalysis

Hydroamination/Hydrosilylation Sequence Catalyzed by Titanium Complexes**

*Andreas Heutling, Frauke Pohlki, Igor Bytschkov, and Sven Doye**

Over the past few years, strategies for the one-pot synthesis of interesting target molecules that require more than one chemical transformation have gained increasing attention. In this context, the use of a single catalyst for a combination of different catalytic reactions (multifunctional catalysis) is one of the most promising approaches.[1] One way to realize a corresponding strategy is the combination of different transitions-metal-catalyzed reactions into a sequence. In this case, a single catalyst that mediates several consecutive reactions is used for the one-pot process. Each individual reaction is initiated by a change of the reaction conditions or the addition of a new reagent.[2]

During the last few years, we have been intensively involved in the development of the Ti-catalyzed hydroamination of alkynes, which converts alkynes and primary amines into imines in the presence of Ti^{IV} catalysts.[3] The corresponding imine products were usually reduced with stoichiometric amounts of $NaBH_3CN$ to give secondary amines. Herein, for the first time, we describe a sequential combination of the Ti-catalyzed hydroamination of alkynes with the Ti-catalyzed reduction of imines.[4] By this new reaction sequence, alkynes and primary amines can be converted into secondary amines in a fully catalytic one-pot protocol employing a single Ti-precatalyst (Scheme 1).[5]

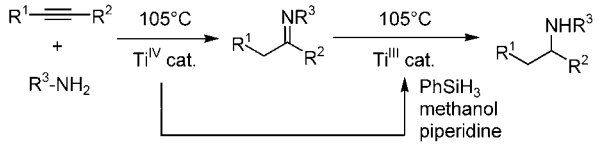

Scheme 1. Ti-catalyzed hydroamination/hydrosilylation sequence.

The catalytically active species involved in the Ti-catalyzed reduction (hydrogenation, hydrosilylation) of imines is presumed to be a Ti^{III} hydride.[4b] This species is generated in situ immediately prior to the reaction from a Ti^{IV} precursor

[*] Dr. A. Heutling, Dr. F. Pohlki, Dr. I. Bytschkov, Prof. Dr. S. Doye
Organisch-Chemisches Institut
Ruprecht-Karls-Universität Heidelberg
Im Neuenheimer Feld 270, 69120 Heidelberg (Germany)
Fax: (+49) 6221-54-4205
E-mail: sven.doye@urz.uni-heidelberg.de

[**] This work was supported by the Deutsche Forschungsgemeinschaft, the Fonds der Chemischen Industrie, and the Dr. Otto Röhm Gedächtnisstiftung, Darmstadt. We thank Professor E. Winterfeldt for his generous support of our research.

Supporting information for this article is available on the WWW under http://www.angewandte.org or from the author.

 DOI: 10.1002/anie.200462250

and a reducing agent. Since a Ti^{IV} species remains in the reaction mixture obtained after a successful hydroamination of an alkyne, we assumed that this Ti^{IV} compound can also be converted into a Ti^{III}-species, which then catalyzes the reduction of the generated imine. To verify this assumption, a mixture of 1-phenylpropyne (**1**) and aniline (**2**) in toluene was heated to 105 °C for 24 h in the presence of 10 mol % $[Cp_2TiMe_2]$.[6] Subsequently, phenylsilane (3 equiv), piperidine (40 mol %), and MeOH (40 mol %)[4d] were added, and the resulting mixture was heated to 105 °C for additional 24 h.[6] After aqueous workup (decomposition of NSi compounds), the corresponding secondary amine **12a** was isolated in 85 % yield [Eq. (1), Table 1, entry 1].

With this promising result in hand, we performed a number of hydroamination/hydrosilylation sequences under identical reaction conditions employing 1-phenylpropyne (**1**) and various amines [Eq. (1), Table 1]. We found that aromatic amines (entries 1–8) gave comparable good results as long as they do not possess an *ortho* substituent. While the hydrosilylation reaction still proceeded slowly in the case of 2-methylaniline (**7**; 57 % yield after a hydrosilylation reaction time of 48 h), no successful reduction was observed when the sterically very demanding 2,6-dimethylaniline (**8**) was used. However, worse results were obtained with alkyl amines (entries 9–12). In these cases, under the employed reaction conditions, the desired secondary amines could be isolated in only modest to poor yields, even when the reaction time for the hydrosilylation was extended to 48 h.[7] Since the regioselectivity of the reaction sequence is generally determined during the hydroamination step, the ratios of the regioisomeric secondary amines are very good to excellent, as expected.[3] Additionally, two reaction sequences were performed with the *ansa* complex **22**[8] as the precatalyst (entries 5, 11). Both reactions also led to the formation of the desired secondary amines.

We also investigated the performance of various alkynes in Ti-catalyzed hydroamination/hydrosilylation sequences. For that purpose, we compared several reaction sequences employing 4-methylaniline (**5**) and the alkynes **1** and **23**–**29** [Eq. (2), Table 2]. We found that 1-phenylpropyne derivatives (**1**, **23**, **24**) and terminal alkynes (**25**–**27**) were very good substrates, while sterically more demanding alkynes such as diphenylacetylene (**28**) and 3-hexyne (**29**) gave worse results. In the case of highly reactive terminal alkynes, very good results were obtained in the presence of only 5 mol % of the catalyst. Furthermore, only short reaction times (3 h) were necessary for the hydroamination step. The observed regioselectivities were again in the expected ranges for the various substrates.[3]

Finally, we focused on intramolecular reaction sequences of aminoalkynes **37** and **38** [Eq. (3), Table 3]. In addition to $[Cp_2TiMe_2]$ and **22** we also employed the chiral catalysts [(*S*,*S*)-(ebthi)$TiMe_2$] (**41**)[4] and (*R*,*R*)-**42**[9] (ebthi = ethylene-1,2-bis(η^2-4,5,6,7-tetrahydro-1-indenyl). The expected cyclic secondary amines **39** and **40** were obtained in modest to good yields in all cases, and the products were generated in enantiomerically enriched form (up to 66 % *ee*) when [(*S*,*S*)-(ebthi)$TiMe_2$] (**41**) and (*R*,*R*)-**42** were used as precatalysts.[10,11]

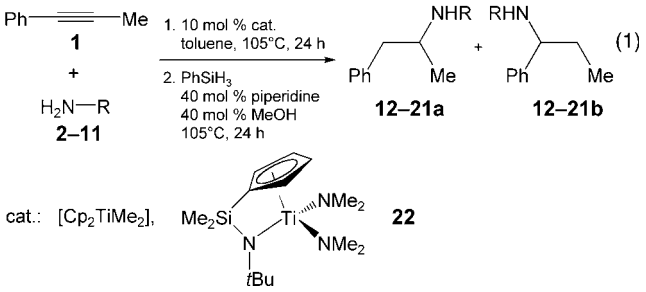

Table 1: Intermolecular Ti-catalyzed hydroamination/hydrosilylation sequence employing various amines [Eq. (1)].

Entry	Amine	Cat.	Yield [%][a]	Sel. **a**/**b**[b]
1	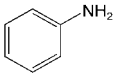 **2**	$[Cp_2TiMe_2]$	85 (**12a**)	99:1
2	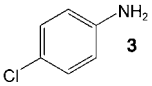 **3**	$[Cp_2TiMe_2]$	83 (**13a**)	99:1
3	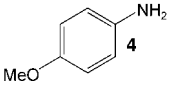 **4**	$[Cp_2TiMe_2]$	86 (**14a**)	99:1
4	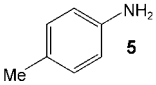 **5**	$[Cp_2TiMe_2]$	85 (**15a**)	99:1
5	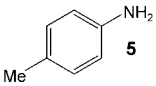 **5**	**22**	99[c] (**15a**)	99:1
6	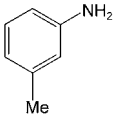 **6**	$[Cp_2TiMe_2]$	71 (**16a**)	99:1
7	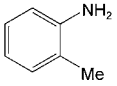 **7**	$[Cp_2TiMe_2]$	35 (**17a**), 57[d] (**17a**)	99:1
8	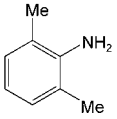 **8**	$[Cp_2TiMe_2]$	–[d] (**18a**)	
9	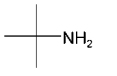 **9**	$[Cp_2TiMe_2]$	6[d] (**19a**)	99:1
10	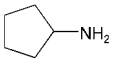 **10**	$[Cp_2TiMe_2]$	39[d] (**20a**/**b**)	95:5
11	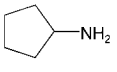 **10**	**22**	44[c,d] (**20a**/**b**)	95:5
12	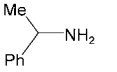 **11**	$[Cp_2TiMe_2]$	11[d] (**21a**/**b**)	92:8

[a] Reaction conditions: 1) alkyne **1** (2.40 mmol), amine (2.64 mmol), $[Cp_2TiMe_2]$ (0.33 mol L^{-1} in toluene, 0.24 mmol, 10 mol %), toluene (0.28 mL), 105 °C, 24 h; 2) $PhSiH_3$ (7.20 mmol), piperidine (0.96 mmol, 40 mol %), MeOH (0.96 mmol, 40 mol %), 105 °C, 24 h. Yields refer to isolated compounds. Reaction times have not been minimized. All hydroamination reactions reached 100 % conversion. [b] GC–MS analysis prior to chromatography. [c] **22** (0.24 mmol, 10 mol %), toluene (1.0 mL). [d] The reaction time of the hydrosilylation step was 48 h.

We have shown that a sequential combination of the Ti-catalyzed hydroamination of alkynes with the Ti-catalyzed hydrosilylation of imines, which employs simple precatalysts, is an efficient and fully catalytic one-pot process for the conversion of alkynes and primary amines into secondary amines. The application of related Ti precatalysts is presently under investigation in our laboratories.

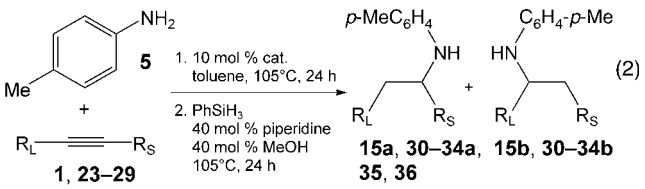

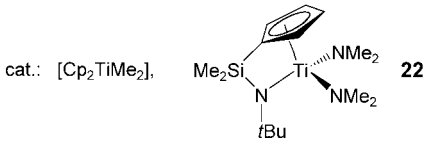

Table 2: Intermolecular Ti-catalyzed hydroamination/hydrosilylation sequence employing various alkynes [Eq. (2)].

Entry	Alkyne	Cat.	Yield [%][a]	Sel. **a**/**b**[b]
1	Ph—≡—Me **1**	$[Cp_2TiMe_2]$	85 (**15a**)	99:1
2	4-MeOC$_6$H$_4$—≡—Me **23**	$[Cp_2TiMe_2]$	83 (**30a**)	98:2
3	4-ClC$_6$H$_4$—≡—Me **24**	$[Cp_2TiMe_2]$	86 (**31a**)	98:2
4	*n*C$_6$H$_{13}$—≡—H **25**	$[Cp_2TiMe_2]$	88[c,d,e] (**32a**/**b**)	31:69
5	Ph—≡—H **26**	$[Cp_2TiMe_2]$	65[c,d] (**33a**/**b**)	57:43
6	Ph—≡—H **26**	**22**	50[c,f] (**33a**/**b**)	76:24[g]
7	Ph, H **27**	$[Cp_2TiMe_2]$	76[c,d,e] (**34a**/**b**)	39:61
8	Ph—≡—Ph **28**	$[Cp_2TiMe_2]$	31 (**35**)	
9	Et—≡—Et **29**	$[Cp_2TiMe_2]$	33 (**36**)	

[a] Reaction conditions: 1) alkyne (2.40 mmol), amine **5** (2.64 mmol), $[Cp_2TiMe_2]$ (0.33 mol L^{-1} in toluene, 0.24 mmol, 10 mol%), toluene (0.28 mL), 105 °C, 24 h; 2) $PhSiH_3$ (7.20 mmol), piperidine (0.96 mmol, 40 mol%), MeOH (0.96 mmol, 40 mol%), 105 °C, 24 h. Yields refer to isolated compounds. Reaction times have not been minimized. All hydroamination reactions reached 100% conversion. [b] GC—MS analysis prior to chromatography. [c] The reaction time of the hydroamination step was 3 h. [d] Prior to the addition of alkyne, $[Cp_2TiMe_2]$, amine **5**, and toluene were heated to 105 °C for 90 min. [e] Reaction conducted with 5 mol% $[Cp_2TiMe_2]$, 20 mol% piperidine, and 20 mol% MeOH. [f] Reaction conducted with **22** (0.24 mmol, 10 mol%) and toluene (1.0 mL). [g] Small amounts of the imine that corresponds to amine **33b** were observed, **a**/**b** (including imine) 69:31.

Experimental Section

A Schlenk tube equipped with a Teflon stopcock and a magnetic stirring bar was charged with 1-phenylpropyne (**1**, 279 mg, 2.40 mmol), 4-methylaniline (**5**, 283 mg, 2.64 mmol), $[Cp_2TiMe_2]$ (0.72 mL, 0.33 M in toluene, 0.24 mmol, 10.0 mol%), and toluene (0.28 mL). The resulting mixture was heated to 105 °C for 24 h. The brown mixture was then cooled to room temperature, and phenylsilane (0.89 mL, 7.20 mmol), piperidine (95 μL, 96 mmol), and methanol (39 μL, 0.96 mmol) were added. The mixture was heated to 105 °C for further 24 h, cooled to room temperature, diluted with Et_2O (25 mL), and poured into 1N aqueous NaOH (25 mL). After this mixture had been stirred at 25 °C for 20 h, the organic layer was separated. The aqueous layer was extracted with Et_2O (4 × 30 mL), and the combined organic layers were dried with $MgSO_4$. After concentration under vacuum, the residue was purified by flash chromatography (SiO_2).

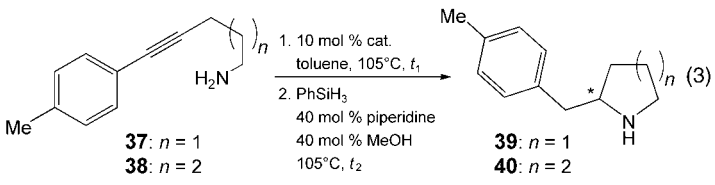

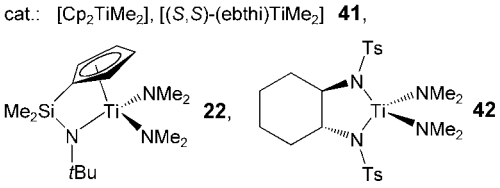

Table 3: Intramolecular Ti-catalyzed hydroamination/hydrosilylation sequence employing various aminoalkynes [Eq. (3)].

Entry	*n*	Cat.	t_1 [h]	t_2 [h]	Yield [%][a]	*ee* [%][b]
1	1	$[Cp_2TiMe_2]$	6	22	62 (**39**)	–
2	1	**22**	6	22	82 (**39**)	–
3	1	**41**	15	36	46 (**39**)	66
4	1	**42**	6	36	68 (**39**)	25
5	2	**22**	6	22	68 (**40**)	–
6	2	**41**	15	36	50 (**40**)	60
7	2	**42**	6	36	68 (**40**)	55

[a] Reaction conditions: 1) aminoalkyne (1.0 mmol), cat. (0.1 mmol, 10 mol%), toluene (0.42 mL), 105 °C; 2) $PhSiH_3$ (3.0 mmol), piperidine (0.4 mmol, 40 mol%), MeOH (0.4 mmol, 40 mol%), 105 °C. Yields refer to isolated compounds. Reaction times have not been minimized. All hydroamination reactions reached >95% conversion (TLC). [b] GC–MS analysis of the corresponding (*S*)-(−)-*N*-(trifluoroacetyl)-prolyl amides.

Received: October 8, 2004
Publication delayed on authors' request.
Published online: April 8, 2005

Keywords: alkynes · amines · hydroamination · hydrosilylation · titanium

[1] For a review, see: A. Ajamian, J. L. Gleason, *Angew. Chem.* **2004**, *116*, 3842–3848; *Angew. Chem. Int. Ed.* **2004**, *43*, 3754–3760.

[2] a) J. Louie, C. W. Bielawski, R. H. Grubbs, *J. Am. Chem. Soc.* **2001**, *123*, 11312–11313; b) A. Fürstner, A. Leitner, *Angew. Chem.* **2003**, *115*, 320–323; *Angew. Chem. Int. Ed.* **2003**, *42*, 308–311; c) B. Schmidt, *Eur. J. Org. Chem.* **2003**, 816–819; d) B. Schmidt, *Chem. Commun.* **2004**, 742–743; e) A. N. Thadani, V. H. Rawal, *Org. Lett.* **2002**, *4*, 4317–4320; f) A. N. Thadani,

V. H. Rawal, *Org. Lett.* **2002**, *4*, 4321 – 4323; g) P. A. Evans, J. E. Robinson, *J. Am. Chem. Soc.* **2001**, *123*, 4609 – 4610; h) E. Teoh, E. M. Campi, W. R. Jackson, A. J. Robinson, *Chem. Commun.* **2002**, 978 – 979; i) J. Tian, N. Yamagiwa, S. Matsunaga, M. Shibasaki, *Angew. Chem.* **2002**, *114*, 3788 – 3790; *Angew. Chem. Int. Ed.* **2002**, *41*, 3636 – 3638; j) H. Du, K. Ding, *Org. Lett.* **2003**, *5*, 1091 – 1093.

[3] For reviews, see: a) I. Bytschkov, S. Doye, *Eur. J. Org. Chem.* **2003**, 935 – 946; b) S. Doye, *Synlett* **2004**, 1653 – 1672.

[4] a) C. A. Willoughby, S. L. Buchwald, *J. Am. Chem. Soc.* **1992**, *114*, 7562 – 7564; b) C. A. Willoughby, S. L. Buchwald, *J. Am. Chem. Soc.* **1994**, *116*, 8952 – 8965; c) C. A. Willoughby, S. L. Buchwald, *J. Am. Chem. Soc.* **1994**, *116*, 11703 – 11714; d) X. Verdaguer, U. E. W. Lange, M. T. Reding, S. L. Buchwald, *J. Am. Chem. Soc.* **1996**, *118*, 6784 – 6785; e) X. Verdaguer, U. E. W. Lange, S. L. Buchwald, *Angew. Chem.* **1998**, *110*, 1174 – 1178; *Angew. Chem. Int. Ed.* **1998**, *37*, 1103 – 1107; f) M. C. Hansen, S. L. Buchwald, *Org. Lett.* **2000**, *2*, 713 – 715; g) J. Okuda, S. Verch, T. P. Spaniol, R. Stürmer, *Chem. Ber.* **1996**, *129*, 1429 – 1431; h) A. Tillack, C. Lefeber, N. Peulecke, D. Thomas, U. Rosenthal, *Tetrahedron Lett.* **1997**, *38*, 1533 – 1534.

[5] Recently, a hydroamination/hydrosilylation sequence catalyzed by cationic Ir^{I} complexes was reported: L. D. Field, B. A. Messerle, S. L. Wren, *Organometallics* **2003**, *22*, 4393 – 4395.

[6] In order to compare the various experiments, reaction times were kept constant and were not minimized.

[7] For comparison: The $[Cp_2TiMe_2]$-catalyzed hydroamination between **1** and **10** followed by reduction with $NaBH_3CN/ZnCl_2$ gave **20a/b** in 89% yield.

[8] a) W. A. Herrmann, M. J. A. Morawietz, *J. Organomet. Chem.* **1994**, *482*, 169 – 181; b) D. W. Carpenetti, L. Kloppenburg, J. T. Kupec, J. L. Petersen, *Organometallics* **1996**, *15*, 1572 – 1581; c) J. Okuda, *Chem. Ber.* **1990**, *123*, 1649 – 1651.

[9] a) S. Pritchett, P. Gantzel, P. J. Walsh, *Organometallics* **1999**, *18*, 823 – 831; b) L. Ackermann, R. G. Bergman, *Org. Lett.* **2002**, *4*, 1475 – 1478; c) L. Ackermann, R. G. Bergman, R. N. Loy, *J. Am. Chem. Soc.* **2003**, *125*, 11956 – 11963.

[10] Chiral catalysts (*S*,*S*)-**41** and (*R*,*R*)-**42** both favor formation of the same enantiomers of **39** and **40**. We are currently investigating which enantiomer is the main product.

[11] For recent examples of enantioselective hydroaminations of alkenes, see: a) P. W. Roesky, T. E. Müller, *Angew. Chem.* **2003**, *115*, 2812 – 2814; *Angew. Chem. Int. Ed.* **2003**, *42*, 2708 – 2710; b) P. D. Knight, I. Munslow, P. N. O'Shaughnessy, P. Scott, *Chem. Commun.* **2004**, 894 – 895.

Cluster Compounds

A Molecular Silicon Cluster with a "Naked" Vertex Atom**

*David Scheschkewitz**

Silicon clusters have been the subject of intense research efforts[1] owing to the ubiquitous role of elemental silicon in a variety of electronic and optical applications, such as integrated circuits, photovoltaic cells, and optical sensors.[2] In fact, the optical properties of many silicon-based materials depend to a large extent on the presence of small- to medium-sized, partially hydrogenated clusters within the surrounding matrix of bulk silicon. Luminescence phenomena in porous silicon, for instance, have been attributed to the photoexcitation of such clusters.[3,4]

The difficulties in the structural characterization of these compounds could be circumvented by the synthesis of discrete molecular derivatives. Advances in the preparation of molecular germanium and tin clusters with "naked" (unsubstituted) vertices have been recently summarized.[5] Indeed, in the case of silicon's higher homologues a few examples have been prepared.[6] Whereas a variety of alkyl-terminated, medium-sized silicon clusters have been characterized by electron microscopic techniques,[7] small discrete molecular clusters are known only as either totally unsubstituted Zintl-type anions[8] or fully substituted deltahedral derivatives of the type Si_nR_n.[9] Theoretical studies predict interesting structural motifs for their elusive partially substituted congeners.[10]

Reductive dehalogenation of a divalent species in the presence of $GeCl_2$ had proven successful for the preparation of the germanium cluster Ge_6R_2 as reported by Power and coworkers.[6c] Unfortunately, the instability of divalent silicon compounds renders such an approach unsuitable.[11] On the other hand, the recently reported disilenides, analogues of vinyl anions, should be good precursors for multiply unsaturated silicon π systems, which could subsequently rearrange to yield the desired partially substituted clusters owing to the low stability of Si=Si double bonds. The pentadiene **2** was chosen as the initial target compound, produced by treatment of $SiCl_4$ with 2 equivalents of the lithium salt of disilenide **1** (Scheme 1).[12a] Crystallization of the complex reaction mixture yielded uniform red crystals in marginal yield (< 1%).

[*] Dr. D. Scheschkewitz
Institut für Anorganische Chemie
Bayerische Julius-Maximilians Universität
Am Hubland, 97074 Würzburg (Germany)
Fax: (+49) 931-888-4623
E-mail: scheschkewitz@mail.uni-wuerzburg.de

[**] The author thanks Prof. H. Braunschweig for continuous support, Dr. R. Bertermann for NMR spectra, Dr. M. Büchner for mass spectra, R. Schedl for combustion analysis and differential scanning calorimetry, and Prof. M. Kaupp and Prof. A. Berndt for fruitful discussions.

Supporting information for this article is available on the WWW under http://www.angewandte.org or from the author.

  DOI: 10.1002/anie.200462730

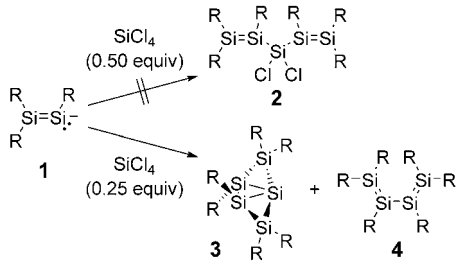

Scheme 1. Synthesis of the partially substituted silicon cluster **3** (R = Tip = 2,4,6-triisopropylphenyl).

However, a preliminary X-ray diffraction study on the crystals of mediocre quality revealed the connectivity of the partially substituted, five-vertex cluster **3** with one "naked" endohedral silicon atom.

Formation of **3** from **1** and $SiCl_4$ requires a further 2 equivalents of the disilenide **1** for reduction of the putative intermediate **2**. Indeed, the use of 4 equivalents of disilenide **1** essentially led to a 1:1 mixture of **3** and **4**, the formal oxidation product of **1** (Scheme 1). The tetrasilabutadiene **4** was identified by comparison of the ^1H and ^{29}Si NMR spectroscopic shift values with those reported in the literature.[13] Separation of the reaction mixture proved tedious, affording yields of **3** that varied between 22 and 37% of theoretical prediction.[14]

The ^{29}Si NMR spectrum shows three signals in a ratio of 2:2:1 at $\delta = 7.4$, -108.4, and -124.8 ppm. In the ^{29}Si–^1H-correlated 2D NMR spectrum only the signals at $\delta = 7.4$ and -108.4 ppm show cross-peaks to two and one aryl substituents, respectively. These findings, together with an apparent C_2 symmetry deduced from ^{13}C and ^1H NMR spectra, confirm the structural integrity of the cluster **3** in solution. Two distinct UV/Vis spectroscopic absorptions are observed at $\lambda = 365$ and 540 nm, the latter being significantly less intense.

An especially notable analytical feature of **3** was found in the EI MS data: a peak at $m/z = 1415.9$ can be assigned to Si_7Tip_6 by comparison with the calculated isotopic distribution pattern. This cluster expansion apparently takes place upon heating of the sample in the condensed phase (required for evaporation of the compound under high vacuum preceding ionization), given that no such peak was observed with milder ionization techniques. The highest mass detected by FAB MS is the molecular ion peak at $m/z = 1359.9$. This interpretation is supported by the detection of an exothermic process at 144 °C by differential scanning calorimetry of **3**. It should be noted that the hydrogenated congeners of **3** have been implied as intermediates in the chemical vapor deposition of silanes for the preparation of thin elemental silicon films.[10]

With a reproducible synthetic protocol in hand, good quality single crystals of **3** were finally obtained. X-ray crystallographic analysis (Figure 1) confirmed the structure of the partially substituted silicon cluster.[15] The distance between Si2 and Si3 (2.306(1) Å) is significantly shorter than a conventional Si–Si single bond (2.34 Å).[16] Surprisingly, the transannular distances Si2–Si5 (2.343(1) Å) and Si3–Si5 (2.337(1) Å) precisely reflect the typical Si–Si single bond length. Nevertheless, if one ignores these transannular

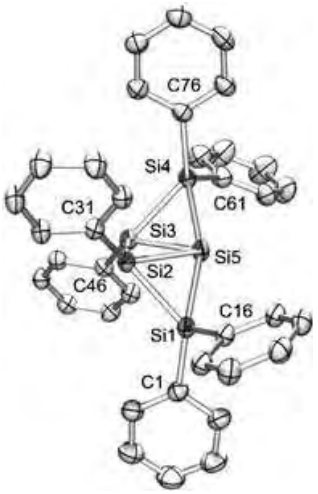

Figure 1. Molecular structure of **3** in the solid state (thermal ellipsoids at 50% probability). Isopropyl groups and protons are omitted for clarity. Selected bond lengths [Å]: Si1–Si2 2.3651(9), Si1–Si5 2.3456(9), Si2–Si3 2.3061(9), Si2–Si5 2.3430(9), Si3–Si5 2.3373(8), Si3–Si4 2.3596(9), Si4–Si5 2.3445(9), Si1–C1 1.929(2), Si1–C16 1.916(2), Si2–C31 1.917(2), Si3–C46 1.913(2), Si4–C61 1.915(2), Si4–C76 1.925(2); selected bond angles [°]: Si5-Si1-Si2 59.65(2), Si3-Si2-Si5 60.36(2), Si5-Si2-Si1 59.76(3), Si2-Si3-Si5 60.60(2), Si5-Si3-Si4 59.89(3), Si4-Si5-Si1 161.02(3).

interactions, Si2 and Si3 are only slightly pyramidal (bond-angle sums: Si2, 358.9°; Si3, 359.0°). The planes defined by Si1-Si2-C31 and Si3-Si4-C46 are almost perpendicular (torsion angle = 88.7°). The corresponding angle was determined to be 54.4° for the highly twisted disilene $(tBu_2MeSi)_2Si{=}Si(SiMetBu_2)_2$.[17]

DFT calculations at the B3LYP/6-31G(d,p) level of theory on the H-substituted parent compound **3u** were carried out to clarify the nature of the interactions that lead to the extreme distortions of **3**.[18] Interestingly, **3u** was only found to be a transition state of the ring inversion of the potential bis-homoaromatic isomer in which both silicon bridges are present on the same side of the central three-membered ring moiety.[19] The bulky substituents apparently favor **3** to an extent that the transition state becomes an energy minimum. Nonetheless, the experimental structure is reasonably well-reproduced by the calculations. Whereas the transannular distances Si5–Si2 and Si5–Si3 in **3u** are slightly longer (2.42 Å; **3**: 2.34 Å), the Si2–Si3 bond is a bit shorter (2.26 Å; **3**: 2.30 Å) than the corresponding distances in **3**. The dihedral angle H-Si2-Si3-H of 138.2° is significantly wider (**3**: C31-Si2-Si3-C46 = 112.8°) and thus is even closer to an ideal *trans* arrangement of the somewhat more pyramidal, formal sp^2-hybridized silicon centers (bond-angles sum: 354.3°).

To provide more insight into this curious bonding situation, the molecular orbitals of **3u** were calculated (Figure 2). Whereas HOMO and HOMO−1 are only separated by 0.14 eV, the difference to the next highest orbital HOMO−2 (1.34 eV) is almost ten times as large. The Heilbronner criterion for Möbius aromaticity, namely that $4n$ mobile electrons must be available, is therefore formally fulfilled.[20] Indeed, the appearance of the HOMO−1 does resemble a Möbius array, such as that calculated for *trans*-

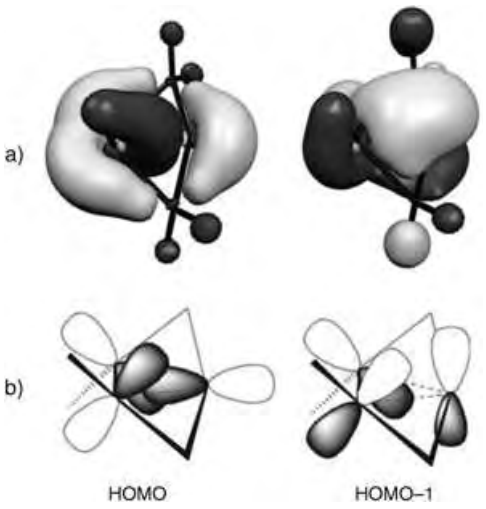

Figure 2. Molecular orbitals of **3u** as calculated at the B3LYP/6-31G-(d,p) level of theory: a) HOMO and HOMO−1, b) schematic representation of the atomic orbitals involved.

benzene.[21] The unsuccessful search for corresponding 3c-2e bonds in **3u** by NBO analysis, however, draws a picture that seemingly contradicts this interpretation of the canonical MOs. The analysis yields two degenerate orbitals with high p-character (95.26%) which are each strictly localized between two silicon atoms: Si5 and Si2, and Si5 and Si3. Therefore, an alternative description of **3** as a classical Lewis structure exclusively with 2c-2e bonds must be considered as well.

In conclusion, the first discrete partially substituted silicon cluster has been isolated and structurally characterized. Its chemical and physical features suggest that it might serve as a model for its partially hydrogenated congeners in bulk silicon materials.

Received: November 26, 2004
Revised: January 14, 2005
Published online: April 13, 2005

Keywords: cluster compounds · density functional calculations · silicon · structure elucidation · subvalent compounds

[1] K.-M. Ho, A. A. Shvartsburg, B. Pan, Z.-Y. Lu, C.-Z. Wang, J. G. Wacker, J. L. Fye, M. F. Jarrold, *Nature* **1998**, *392*, 582, and references therein.
[2] Review: A. Shah, P. Torres, R. Tscharner, N. Wyrsch, H. Keppner, *Science* **1999**, *285*, 692.
[3] L. Kronik, R. Fromherz, E. Ko, G. Ganteför, J. R. Chelikowsky, *Eur. Phys. J. D* **2003**, *24*, 33.
[4] M. P. Stewart, J. M. Buriak, *Comments Inorg. Chem.* **2002**, *23*, 179.
[5] A. Schnepf, *Angew. Chem.* **2004**, *116*, 680; *Angew. Chem. Int. Ed.* **2004**, *43*, 664.
[6] a) A. Sekiguchi, Y. Ishida, Y. Kabe, M. Ichinohe, *J. Am. Chem. Soc.* **2002**, *124*, 8776; b) A. Schnepf, R. Köppe, *Angew. Chem.* **2003**, *115*, 940; *Angew. Chem. Int. Ed.* **2003**, *42*, 911; c) A. F. Richards, H. Hope, P. P. Power, *Angew. Chem.* **2003**, *115*, 4205; *Angew. Chem. Int. Ed.* **2003**, *42*, 4071; d) A. Schnepf, *Angew. Chem.* **2003**, *115*, 2728; *Angew. Chem. Int. Ed.* **2003**, *42*, 2624; e) A. F. Richards, M. Brynda, M. M. Olmstead, P. P. Power, *Organometallics* **2004**, *23*, 2841.
[7] R. K. Baldwin, K. A. Pettigrew, J. C. Garno, P. P. Power, G.-Y. Liu, S. M. Kauzlarich, *J. Am. Chem. Soc.* **2002**, *124*, 1150, and references therein.
[8] J. M. Goicoechea, S. C. Sevov, *J. Am. Chem. Soc.* **2004**, *126*, 6860.
[9] a) N. Wiberg, *Coord. Chem. Rev.* **1997**, *163*, 217; b) H. Matsumoto, K. Higuchi, S. Kyushin, M. Goto, *Angew. Chem.* **1992**, *104*, 1410; *Angew. Chem. Int. Ed. Engl.* **1992**, *31*, 1354; c) A. Sekiguchi, T. Yatabe, C. Kabuto, H. Sakurai, *J. Am. Chem. Soc.* **1993**, *115*, 5853.
[10] S. D. Chambreau, L. Wang, J. Zhang, *J. Phys. Chem. A* **2002**, *106*, 5081.
[11] M. Kira, *Pure Appl. Chem.* **2000**, *72*, 2333.
[12] a) D. Scheschkewitz, *Angew. Chem.* **2004**, *116*, 3025; *Angew. Chem. Int. Ed.* **2004**, *43*, 2965; b) M. Ichinohe, K. Sanuki, S. Inoue, A. Sekiguchi, *Organometallics* **2004**, *23*, 3088.
[13] M. Weidenbruch, S. Willms, W. Saak, G. Henkel, *Angew. Chem.* **1997**, *109*, 2612; *Angew. Chem. Int. Ed. Engl.* **1997**, *36*, 2503.
[14] Experimental details are given in the Supporting Information.
[15] Crystal structure determination of **3**: red blocks from hexane; $C_{90}H_{138}Si_5$, monoclinic, space group $P2_1/c$; $a=1426.8(3)$, $b=1361.4(3)$, $c=4453.1(10)$ pm, $\alpha=90°$, $\beta=95.296(4)°$, $\gamma=90°$, $V=8613(3)\times10^{-30}$ m^3; $Z=4$, $\rho_{calc}=1.049$ g cm^{-3}; crystal dimensions: $0.28\times0.25\times0.12$ mm^3; diffractometer: Bruker SMART APEX CCD; $Mo_{K\alpha}$ radiation, 173 K; $2\theta_{max}=52.74$; 68217 reflections, 17602 independent ($R_{int}=0.0408$), direct methods; absorption correction SADABS ($\mu=1.24$ cm^{-1}); refinement (against F_o^2) with SHELXTL (version 5.1) and SHELXL-97, 971 parameters, 0 restraints, $R_1=0.0562$ ($I>2\sigma$) and wR_2 (all data) $=0.1429$, GooF $=1.038$, max/min residual electron density: $0.426/-0.184\times10^{30}$ e m^{-3}. CCDC-256745 contains the supplementary crystallographic data for this paper. These data can be obtained free of charge from the Cambridge Crystallographic Data Centre via www.ccdc.cam.ac.uk/data_request/cif.
[16] M. Weidenbruch, *The Chemistry of Organic Silicon Compounds*, *Vol. 3* (Eds.: Z. Rappoport, Y. Apeloig), Wiley, Chichester, UK, **2001**, chap. 5.
[17] A. Sekiguchi, S. Inoue, M. Ichinohe, Y. Arai, *J. Am. Chem. Soc.* **2004**, *126*, 9626.
[18] Gaussian 03 (Revision B.04), M. J. Frisch, G. W. Trucks, H. B. Schlegel, G. E. Scuseria, M. A. Robb, J. R. Cheeseman, J. A. Montgomery, Jr., T. Vreven, K. N. Kudin, J. C. Burant, J. M. Millam, S. S. Iyengar, J. Tomasi, V. Barone, B. Mennucci, M. Cossi, G. Scalmani, N. Rega, G. A. Petersson, H. Nakatsuji, M. Hada, M. Ehara, K. Toyota, R. Fukuda, J. Hasegawa, M. Ishida, T. Nakajima, Y. Honda, O. Kitao, H. Nakai, M. Klene, X. Li, J. E. Knox, H. P. Hratchian, J. B. Cross, C. Adamo, J. Jaramillo, R. Gomperts, R. E. Stratmann, O. Yazyev, A. J. Austin, R. Cammi, C. Pomelli, J. W. Ochterski, P. Y. Ayala, K. Morokuma, G. A. Voth, P. Salvador, J. J. Dannenberg, V. G. Zakrzewski, S. Dapprich, A. D. Daniels, M. C. Strain, O. Farkas, D. K. Malick, A. D. Rabuck, K. Raghavachari, J. B. Foresman, J. V. Ortiz, Q. Cui, A. G. Baboul, S. Clifford, J. Cioslowski, B. B. Stefanov, G. Liu, A. Liashenko, P. Piskorz, I. Komaromi, R. L. Martin, D. J. Fox, T. Keith, M. A. Al-Laham, C. Y. Peng, A. Nanayakkara, M. Challacombe, P. M. W. Gill, B. Johnson, W. Chen, M. W. Wong, C. Gonzalez, J. A. Pople, Gaussian, Inc., Pittsburgh, PA, **2003**.
[19] The C_s symmetric isomer with both sp^3-hybridized silicon atoms on the same side of the ring is a minimum at the B3LYP/6-31G(d,p) level of theory, 14.8 kcal mol^{-1} lower in energy than **3u**. The internal reaction coordinate that connects it to **3u** features an intermediate local minimum, 9.0 kcal mol^{-1} lower than **3u**. It shows one significantly elongated (2.80 Å) and one slightly shortened (2.31 Å) transannular interaction. Details on all stationary points are given in the Supporting Information.
[20] E. Heilbronner, *Tetrahedron Lett.* **1964**, 1923.
[21] R. P. Johnson, K. J. Daoust, *J. Am. Chem. Soc.* **1996**, *118*, 7381.

Structure Elucidation

Birnbaumin A and B: Two Unusual 1-Hydroxyindole Pigments from the "Flower Pot Parasol" *Leucocoprinus birnbaumii***

*Andrea Bartsch, Monika Bross, Peter Spiteller, Michael Spiteller, and Wolfgang Steglich**

Dedicated to Professor Timm Anke on the occasion of his 60th birthday

Occasionally the Yellow Parasol or Flower Pot Parasol (*Leucocoprinus birnbaumii* (Corda) Singer) appears in flowerpots and greenhouses, where it attracts attention because of its intense yellow color and delicate shape. It originated in the tropics and was distributed worldwide with plants and potting soil.[1] Until now, the chemical constituents of the fungus have remained unknown. Herein, we report the unusual structures of its yellow pigments, which we have named birnbaumin A and B.

To isolate the pigments, the fruit bodies were extracted carefully with methanol. Subsequent separation of the extract by preparative reversed-phase HPLC yielded birnbaumins A and B, together with L-tryptophan. Although the two pigments have similar UV/Vis spectra, the major compound, birnbaumin B, exhibits a bathochromic shift of the absorption maximum from 322 (for birnbaumin A) to 356 nm (both in MeOH). Birnbaumin A shows a $[M+H]^+$ peak in the ESI mass spectrum at m/z 361. High-resolution measurements revealed the molecular formula $C_{16}H_{20}N_6O_4$. According to ESI MS, birnbaumin B differs from birnbaumin A by an additional oxygen atom.[2] ESI MS/MS spectra of the pigments display a fragmentation of the molecules into two characteristic parts. A fragment with a peak at m/z 200 ($C_7H_{14}N_5O_2$) is common to both compounds, whereas the other fragment shows a peak at m/z 160 ($C_9H_6NO_2$) in the spectrum of birnbaumin A and at m/z 176 ($C_9H_6NO_3$) in that of birnbaumin B. The high content of Na^+ and K^+ ions detected by atom absorption spectroscopy of the samples suggests that the birnbaumins have the ability to complex metal ions.

Further insight into the structure of the birnbaumins was provided by their NMR spectra. The ^{1}H NMR spectrum ([D$_6$]DMSO; DMSO = dimethyl sulfoxide) of birnbaumin A shows signals corresponding to a 1,2-substituted benzene ring, a single hydrogen atom on an aromatic ring (at δ_H = 7.98 ppm), and a $-NHCH_2CH_2CH_2CH_2NH-$ unit. Additionally, at low field there is a sharp singlet at $\delta_H = 11.95$ ppm and a broad signal at $\delta_H = 12.32$ ppm, which we assign to OH protons. The ^{13}C NMR spectrum contains 16 signals, which correspond to four methylene and five aromatic methine groups, as well as seven quaternary carbon atoms (signals at $\delta_C = 109.8$, 121.4, 134.1, 151.4, 156.7, 161.6, and 183.8 ppm). The HMBC spectra of birnbaumin A enabled the deduction of the partial structure shown in Scheme 1, whereby an

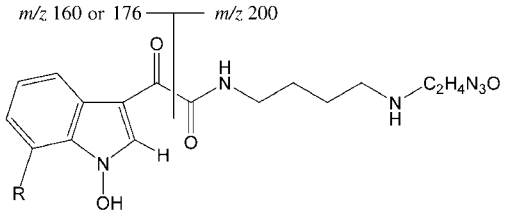

Scheme 1. Partial structures of birnbaumins A (R = H) and B (R = OH) with the key ions observed in the ESI MS/MS spectra.

α fragmentation between the two carbonyl groups would explain the generation of the key ions with m/z 160 and 200 in the mass spectra. According to the NMR spectra and HMBC experiments, birnbaumin B contains an additional hydroxy group on the indole ring system at the 7-position, which is in agreement with the production of the fragment ions with m/z 176 and 200.

To confirm the substitution pattern, birnbaumin B was reduced with zinc in glacial acetic acid. The reductive loss of the *N*-hydroxy group causes a large shift of the 2-H signal in the ^{1}H NMR spectrum ([D$_6$]DMSO) from $\delta_H = 7.73$ to 8.59 ppm; a coupling of 2.9 Hz with the adjacent NH hydrogen atom of the indole ($\delta_H = 12.40$ ppm) also appears. Moreover, the unknown end group, $-C_2H_4N_3O$, loses its oxygen atom in the course of the reduction and is transformed by addition of two hydrogen atoms into $-C_2H_6N_3$. This transformation excludes the possibility of an amidinourea[3] or carbamoylguanidine end group. The excellent agreement of the aromatic signals of the reduction product with those of the synthetic comparison compound **1** confirms the location of the hydroxy group at the 7-position in birnbaumin B (Scheme 2).[4]

To elucidate the structure of the end group, the birnbaumins A and B were permethylated at 0 °C with diazomethane/ether in methanol to yield a dimethyl ether and a trimethyl ether, respectively. The reaction involved methylation of the hydroxy group on the nitrogen atom of the indole ($\delta_H = 12.32$ and 12.06 ppm, respectively) and the hydrogen-bonded OH group ($\delta_H = 11.95$ and 11.89 ppm, respectively), as well as of the phenol functionality in birnbaumin B. The *O*-methyl groups could be assigned by analysis of the NOESY spectra;

[*] Dr. A. Bartsch, Dr. M. Bross, Dr. P. Spiteller, Prof. Dr. W. Steglich
Department Chemie
Ludwig-Maximilians-Universität München
Butenandtstrasse 5–13, Haus F, 81377 München (Germany)
Fax: (+49) 89-2180-77756
E-mail: wos@cup.uni-muenchen.de
Prof. Dr. M. Spiteller
Institut für Umweltforschung
Universität Dortmund
Otto-Hahn-Strasse 6, 44227 Dortmund (Germany)

[**] This work was supported financially by the Deutsche Forschungsgemeinschaft (SFB 369). We are indebted to Till Hägele (Botanischer Garten München), Claudia Dubler, Tina Hübscher, Dr. Franz von Nussbaum, and many others for helping to collect the fungi and to Dr. Andrew J. Hall for linguistic help.

Supporting information for this article is available on the WWW under http://www.angewandte.org or from the author.

 DOI: 10.1002/anie.200500082

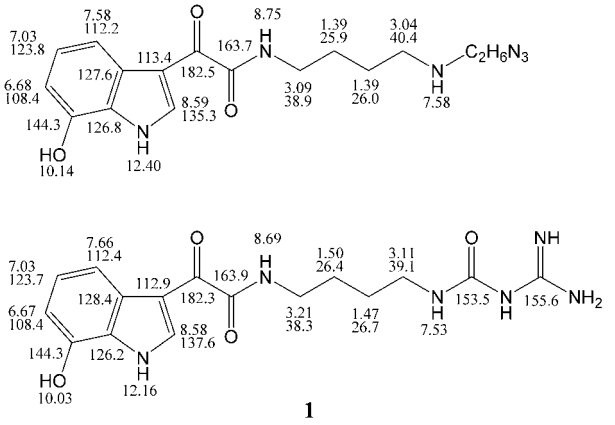

Scheme 2. Comparison of the NMR spectroscopic data (δ_H (above) and δ_C values (below, when two values are given) of reduced birnbaumin B (top) with those of the synthetic reference compound **1** (spectra recorded in [D_6]DMSO).[4]

this analysis also confirms the substitution pattern of the birnbaumins (Scheme 3). The correlation in the HMBC spectrum of the signal at $\delta_H = 3.88$ ppm for the methoxy

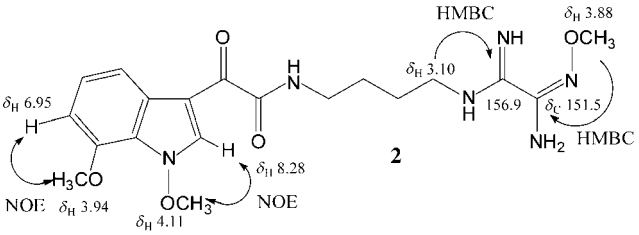

Scheme 3. Important NOE and HMBC correlations for birnbaumin B trimethyl ether (**2**; spectra recorded in [D_6]DMSO).

group positioned at the end of the side chain with the signal for an unsaturated carbon atom at $\delta_C = 151.5$ ppm is especially important, since it is consistent only with structure **2** (Scheme 3). In accordance with this deduction, the signal at $\delta_H = 3.10$ ppm for one of the terminal methylene groups shows a correlation with the carbon-atom signal at $\delta_C =$ 156.9 ppm. Analogous correlations are also observed in the spectra of birnbaumin A dimethyl ether, thus allowing the assignment of structures **3** and **4** to birnbaumins A and B. The

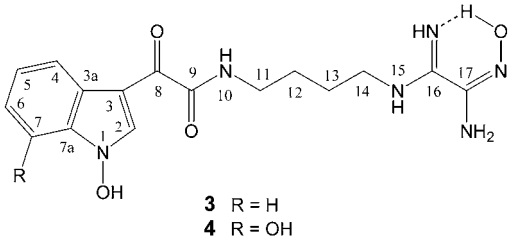

hydrogen bond in the terminal *N*-hydroxyamidine residue explains unambiguously the characteristic sharp singlet in the ^{1}H NMR spectra of the birnbaumins and the HMBC correlation of the OH hydrogen atom to the amidoxime carbon atom. Furthermore, the ^{1}H,^{15}N HMBC correlations for birnbaumin B are in agreement with the proposed structures (see Supporting Information).

We propose the aminal structure **5** for the reduction product, which was obtained in the form of its trifluoroacetate salt. Signals in its NMR spectra at $\delta_H = 5.27$ and $\delta_C = 58.0$ ppm indicate the presence of a methine group. The aminal group is apparently stabilized by a hydrogen bond to the adjacent amidinium functionality.

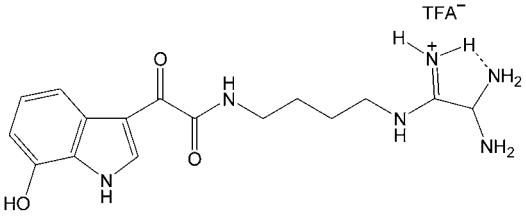

The birnbaumins are characterized by several unusual structural features. For example, to the best of our knowledge, simple *N*-hydroxyoxamidines were unknown until now, and 1-hydroxyindoles,[5] in contrast to their more stable *O*-methyl derivatives,[6] occur only rarely in nature. Similarly, only a few natural 7-hydroxyindoles have been described to date, including the coscinamides, isolated from marine sponges.[7] These indolylglyoxylic acid amides are structurally similar to birnbaumins A and B. We propose a pathway for the biosynthesis of the birnbaumins which starts from L-tryptophan, citrulline, glycine, and nitrite (see Supporting Information). Experiments to verify this hypothesis are underway.

Experimental Section

Isolation of the pigments: The fresh, deep-frozen, or lyophilized fungi were extracted on a shaker with nitrogen-saturated MeOH under the exclusion of light until complete decolorization was observed. The solvent was then evaporated under vacuum. The residue was dissolved in MeOH (HPLC-grade), prepurified on an RP-18 cartridge, and then separated by preparative HPLC (column: nucleosil 100 C-18, 7 μm, 16 × 250 mm (Macherey & Nagel); solvent A: CH_3CN/H_2O (1:9)+0.25% trifluoroacetic acid (TFA), solvent B: CH_3CN; gradient: 100% A linear in 35 min to 50% A/50% B; flow rate: 5.00 mL min^{-1}; detection: UV). The purity of the compounds was checked by analytical HPLC (column: nucleosil 100 C-18, 5 μm, 4 × 250 mm (Knauer); solvent: as above; gradient: 100% A linear in 25 min to 50% A/50% B; flow rate: 1.0 mL min^{-1}). Retention times: t_R(**4**) = 11.2 min; t_R(L-tryptophan) = 12.3 min; t_R(**3**) = 15.5 min. The pigments were stored under a nitrogen atmosphere at −20 °C. From a 42-g batch of fresh fruit bodies, 59 mg of birnbaumin A (0.14%), 228 mg of birnbaumin B (0.54%), and 58 mg of L-tryptophan (0.14%) were isolated. Yields can differ depending on the age and the condition of the fungi.

3: yellow pigment; TLC: $R_f = 0.84$ (RP-18, MeOH+2 drops of TFA); UV/Vis (MeOH): λ_{max} (lg ε) = 212 (4.42), 250 (4.03), 322 nm (3.96); IR (KBr): $\tilde{\nu}$ = 3403 s, 3205 m, 2945 m, 2863 m, 1665 s, 1625 m, 1575 m, 1537 m, 1508 m, 1483 m, 1452 m, 1438 m, 1371 m, 1340 m, 1324 m, 1250 m, 1203 s, 1139 m, 1066 m, 1009 m, 890 m, 842 m, 801 m, 751 m, 722 m, 674 m, 600 m, 426 cm^{-1} m; ^{1}H NMR (600 MHz, CD_3OD, reference: $\delta = 3.35$ ppm, 25 °C): $\delta = 1.68$ (br m, 4H, 12-H,

13-H), 3.26 (t, $J = 6.1$ Hz, 2H, 11-H), 3.39 (t, $J = 6.1$ Hz, 14-H, partially hidden by MeOH signal), 7.34 (dd, $J = 7.8$, 7.5 Hz, 1H, 5-H), 7.40 (dd, $J = 8.0$, 7.5 Hz, 1H, 6-H), 7.56 (d, $J = 8.0$ Hz, 1H, 7-H), 7.92 (s, 1H, 2-H), 8.25 ppm (d, $J = 7.8$ Hz, 1H, 4-H); ^{1}H NMR (600 MHz, [D$_6$]DMSO, reference: $\delta = 2.49$ ppm, 25 °C): $\delta = 1.48$ (br m, 4H, 12-H, 13-H), 3.10 (pseudo q, $J = 5.6$ Hz, 2H, 14-H), 3.17 (pseudo q, $J = 5.6$ Hz, 2H, 11-H), 7.27 (dd, $J = 7.5$, 7.4 Hz, 1H, 5-H), 7.33 (dd, $J = 7.8$, 7.4 Hz, 1H, 6-H), 7.52 (d, $J = 7.8$ Hz, 1H, 7-H), 7.57 (br s, 1H, N15-H), 7.99 (s, 1H, 2-H), 8.10 (d, $J = 7.5$ Hz, 1H, 4-H), 8.28 (br t, $J = 5.6$ Hz, 1H, N10-H), 11.95 (s, 1H, 17-NOH), 12.32 ppm (br s, 1H, 1-OH); ^{13}C NMR (151 MHz, CD$_3$OD, reference: $\delta = 49.0$ ppm, 25 °C): $\delta = 27.1$ (C12), 27.7 (C13), 39.5 (C11), 42.1 (C14), 110.4 (C7), 111.8 (C3), 122.5 (C4), 123.5 (C3a), 124.5 (C5), 125.1 (C6), 135.6 (C2), 136.2 (C7a), 152.2 (C17), 158.6 (C16), 164.3 (C9), 185.9 ppm (C8); ^{13}C NMR (151 MHz, [D$_6$]DMSO, reference: $\delta = 39.5$ ppm, 25 °C): $\delta = 26.0$ (C12), 26.2 (C13), 38.1 (C11), 40.4 (C14), 109.6 (C7), 109.8 (C3), 120.8 (C4), 121.4 (C3a), 122.9 (C5), 123.6 (C6), 133.6 (C2), 134.1 (C7a), 151.4 (C17), 156.7 (C16), 161.6 (C9), 183.8 ppm (C8); MS (FAB+): m/z (%): 361 (100) $[M+H]^+$; HRMS (FAB+): m/z: 361.1576 $[M+H]^+$, calcd for $C_{16}H_{21}N_6O_4$: 361.1624; HR MS/MS (ESI+, −30 eV): m/z: 361, 200 $[C_7H_{14}N_5O_2]^+$, 184 $[C_7H_{14}N_5O]^+$, 160 $[C_9H_6NO_2]^+$, 157 $[C_6H_{13}N_4O]^+$.

4: yellow pigment; TLC: $R_f = 0.88$ (RP-18, MeOH+2 drops of TFA), $R_f = 0.25$ (silica gel 60 F_{254}, *n*BuOH/H$_2$O/EtOH/AcOH 4:1:1:1); UV/Vis (MeOH): λ_{max} (lg ε) = 214 (4.74), 248 (4.34), 267 (sh, 4.19), 356 nm (4.16); IR (KBr): $\tilde{\nu} = 3415$ m, 3210 m, 2930 m, 2856 m, 1666 s, 1628 m, 1538 m, 1493 m, 1436 m, 1374 m, 1332 m, 1279 m, 1144 m, 1086 w, 1045 w, 986 w, 865 m, 837 m, 799 m, 723 m, 673 cm^{-1} m; ^{1}H NMR (600 MHz, CD$_3$OD, reference: $\delta = 3.35$ ppm, 25 °C): $\delta = 1.66$ (br m, 4H, 12-H, 13-H), 3.23 (br t, $J = 6.5$ Hz, 2H, 11-H), 3.37 (t, $J = 6.6$ Hz, 14-H, (partly hidden by MeOH signal), 6.73 (d, $J = 7.9$ Hz, 1H, 6-H), 7.10 (dd, $J = 7.9$, 7.9 Hz, 1H, 5-H), 7.74 (d, $J = 7.9$ Hz, 1H, 4-H), 7.78 ppm (s, 1H, 2-H); ^{1}H NMR (600 MHz, [D$_6$]DMSO, reference: $\delta = 2.49$ ppm, 25 °C): $\delta = 1.47$ (br m, 4H, 12-H, 13-H), 3.10 (pseudo q, $J = 5.7$ Hz, 2H, 14-H), 3.16 (pseudo q, $J = 6.2$ Hz, 2H, 11-H), 6.67 (d, $J = 7.5$ Hz, 1H, 6-H), 7.01 (dd, $J = 7.8$, 7.5 Hz, 1H, 5-H), 7.53 (br t, $J = 5.7$ Hz, 1H, N15-H), 7.55 (d, $J = 7.8$ Hz, 1H, 4-H), 7.73 (s, 1H, 2-H), 8.25 (t, $J = 6.2$ Hz, 1H, N10-H), 9.83 (s, 1H, 7-OH), 11.89 (s, 1H, 17-NOH), 12.06 ppm (s, 1H, 1-OH); ^{13}C NMR (151 MHz, CD$_3$OD, reference: $\delta = 49.0$ ppm, 25 °C): $\delta = 27.0$ (C12), 27.6 (C13), 39.5 (C11), 42.0 (C14), 110.6 (C6), 111.6 (C3), 113.8 (C4), 125.2 (C7a), 125.3 (C5), 126.2 (C3a), 135.7 (C2), 145.2 (C7), 152.1 (C17), 158.5 (C16), 164.2 (C9), 185.6 ppm (C8); ^{13}C NMR (151 MHz, [D$_6$]DMSO, reference: $\delta = 39.5$ ppm, 25 °C): $\delta = 26.2$ (C12), 26.4 (C13), 38.3 (C11), 40.6 (C14), 109.3 (C6), 109.8 (C3), 111.8 (C4), 123.7 (C7a), 124.0 (C5), 124.5 (C3a), 134.1 (C2), 144.3 (C7), 151.8 (C17), 156.9 (C16), 161.9 (C9), 183.7 ppm (C8); ^{15}N NMR (60.8 MHz, [D$_6$]DMSO, reference: benzamide, $\delta_N = 73.6$): $\delta = 47.0$ (C16=NH), 55.1 (N15), 83.8 (N10), 161.0 (N1), 344.5 ppm (C17=N−OH); MS (ESI+): m/z (%): 377 (100) $[M+H]^+$; HRMS (ESI+): m/z: 377.1594 $[M+H]^+$, calcd for $C_{16}H_{21}N_6O_5$: 377.1573; HR MS/MS (ESI+, −30 eV): m/z: 359.1464 $[C_{16}H_{19}N_6O_4]^+$, 200.1140 $[C_7H_{14}N_5O_2]^+$, 184.1190 $[C_7H_{14}N_5O]^+$, 176.0339 $[C_9H_6NO_3]^+$, 157.1081 $[C_6H_{13}N_4O]^+$.

Received: January 10, 2005
Published online: April 7, 2005

Keywords: alkaloids · dyes/pigments · natural products · *N*-hydroxyoxamidines · structure elucidation

[1] R. Watling, *Fungi*, The Natural History Museum, London, **2004**.
[2] In the ESI MS/MS spectra concomitant ions were observed in very low intensity and were assigned to the corresponding N_{ind}-deoxybirnbaumins.
[3] The amidinourea end group is present in different metabolites derived from red algae: a) gigartinine: K. Ito, Y. Hashimoto, *Nature* **1966**, *211*, 417; M. V. Laycock, J. S. Craigie, *Can. J. Biochem.* **1977**, *55*, 27–30; b) gongrine: K. Ito, Y. Hashimoto, *Agric. Biol. Chem.* **1965**, *29*, 832–835; c) nicaeensin: R. Chillemi, R. Morrone, A. Patti, M. Piattelli, S. Sciuto, *J. Nat. Prod.* **1990**, *53*, 1220–1224.
[4] In Scheme 2, the compounds are shown in their nonprotonated forms. They are present, however, in the form of their trifluoroacetate salts after HPLC purification.
[5] a) For arcyroxepin A, see: W. Steglich, B. Steffan, T. Eizenhöfer, B. Fugmann, R. Herrmann, J. D. Klamann, *Ciba Found. Symp.* **1990**, *154*, 56–65; b) for nocathiacins, see: J. E. Leet, W. Li, H. A. Ax, J. A. Matson, S. Huang, R. Huang, J. L. Cantone, D. Drexler, R. A. Dalterio, K. S. Lam, *J. Antibiot.* **2003**, *56*, 232–242; T. Sasaki, T. Otani, H. Matsumoto, N. Unemi, M. Hamada, T. Takeuchi, M. Hori, *J. Antibiot.* **1998**, *51*, 715–721.
[6] M. Somei, *Adv. Heterocycl. Chem.* **2002**, *82*, 101–155.
[7] H. R. Bokesch, L. K. Pannell, T. C. McKee, M. R. Boyd, *Tetrahedron Lett.* **2000**, *41*, 6305–6308; see also: N. Lindquist, W. Fenical, *Tetrahedron Lett.* **1990**, *31*, 2521–2524.

Combinatorial Catalysis

Mixtures of Configurationally Stable and Fluxional Atropisomeric Monodentate P Ligands in Asymmetric Rh-Catalyzed Olefin Hydrogenation**

Manfred T. Reetz and Xiaoguang Li*

Several years ago it was reported that monodentate phosphites,[1] phosphonites,[2] and phosphoramidites[3] derived from 2,2′-dihydroxy-1,1′-binaphthyl (BINOL) are efficient ligands in various Rh-catalyzed asymmetric olefin-hydrogenation reactions (90–99 % *ee*). These observations were surprising, because it had been accepted that chelating bidentate P ligands are generally necessary for high levels of enantioselectivity, probably due to restricted rotation in the Rh complexes. Examples of other types of monodentate P ligands are also known.[4] Preliminary mechanistic results show that two monodentate phosphites (or phosphonites) are bonded to Rh in the transition state of hydrogenation[5] when the precatalyst is $[Rh(cod)(\mathbf{1})_2]BF_4$ (cod = cycloocta-1,5-diene). Based on these results we subsequently demonstrated that the use of a mixture of two different monodentate P ligands constitutes a new and efficient approach to combinatorial asymmetric transition-metal catalysis.[6] Once a library

[*] Prof. Dr. M. T. Reetz, Dr. X. Li
Max-Planck-Institut für Kohlenforschung
Kaiser-Wilhelm-Platz 1, 45470 Mülheim/Ruhr (Germany)
Fax: (+49) 208-306-2985
E-mail: reetz@mpi-muelheim.mpg.de

[**] Generous support by the Fonds der Chemischen Industrie is gratefully acknowledged.

 DOI: 10.1002/anie.200462612

of cheap ligands has been prepared, mixtures result in high catalyst diversity and new ligands are not needed. Although each system actually contains three (pre)catalysts in an (as yet) unpredictable ratio, namely the two homocombinations $[Rh(cod)L^aL^a]BF_4$ and $[Rh(cod)L^bL^b]BF_4$, as well as the heterocombination $[Rh(cod)L^aL^b]BF_4$, enantioselectivities of 95–99% *ee* are often possible, even though the respective homocombinations in pure form result in lower enantioselectivities. Mixtures of BINOL-derived P ligands in combination with a phosphinine (phosphabenzene) or triphenylphosphine cause reversal of enantioselectivity in a few cases.[7]

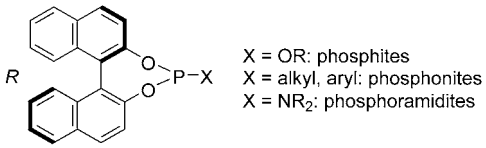

1a X = OMe
b X = *t*Bu

We now show that mixtures of appropriate chiral BINOL-derived phosphonites such as (*R*)-**1b** in combination with certain achiral P ligands or configurationally fluxional atropisomeric phosphites **2** derived from the corresponding achiral biphenols are also excellent ligand systems.

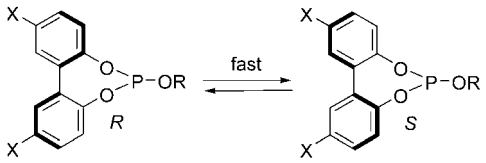

2a X = H; R = CH_3
b X = H; R = CH_2Ph
c X = H; R = *t*Bu
d X = $CH(CH_3)_2$; R = CH_2Ph

Our model reaction was the Rh-catalyzed hydrogenation of β-acylamino acrylate **3a** with formation of the β-amino acid derivative **4a** [Eq. (1)][8] In addition to **2**, the achiral

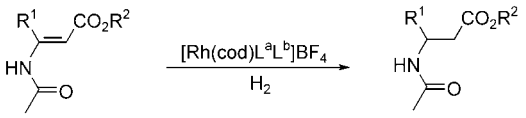

(1)

3a $R^1 = R^2 = CH_3$
b $R^1 = CH_3$; $R^2 = C_2H_5$
c $R^1 = C_2H_5$; $R^2 = CH_3$
d $R^1 = n\text{-}C_3H_7$; $R^2 = C_2H_5$
e $R^1 = Ph$; $R^2 = C_2H_5$

4

phosphines PMe_3 (**5**), P*i*Pr$_3$ (**6**), and PPh_3 (**7**) as well as the achiral phosphites $P(OMe)_3$ (**8**), $P(OiPr_3)_3$ (**9**), $P(OCH_2tBu)_3$ (**10**), and $P(OPh)_3$ (**11**) were used in combination with (*R*)-**1b** (or (*R*)-**1a**). In all cases $[Rh(cod)_2]BF_4$ was treated with a 1:1 mixture of the two monodentate P ligands (Rh/ligands = 1:2) prior to hydrogenation under standard conditions.[8]

Some remarkable results are listed in Table 1. In particular, the homocombination comprising the *tert*-butylphosphonite (*R*)-**1b** alone leads to only 45% *ee* (*S*) (entry 2), whereas the heterocombination of (*R*)-**1b** and achiral **11** results in 88% *ee* (*S*) (entry 19). Selectivities higher than those obtained with the homocombinations were also observed for several other heterocombinations (entries 7, 8, 11, 16). Dramatic effects emerged when heterocombinations of phosphonite (*R*)-**1b** and configurationally labile atropisomeric phosphites **2a**, **2b**, and **2d** were used; these systems lead to enantioselectivities of 98% *ee* (*S*), 98% *ee* (*S*), and 94% *ee* (*S*), respectively (entries 20, 21, 23).

Table 1: Rh-catalyzed hydrogenation of olefin **3a**.[a] (*R*)-BINOL derivatives led to (*S*)-**4a**.

Entry	Ligand	Conv. [%]	*ee* [%]
	Homocombinations		
1	**1a**	95	75
2	**1b**	83	45
	Heterocombinations		
3	**1a/6**	51	50
4	**1a/7**	92	14
5	**1a/8**	100	30
6	**1a/9**	96	30
7	**1a/10**	100	81
8	**1a/11**	84	79
9	**1a/2a**	83	73
10	**1a/2b**	92	67
11	**1a/2c**	57	83
12	**1a/2d**	97	65
13	**1b/5**	46	51
14	**1b/6**	67	17
15	**1b/7**	98	5
16	**1b/8**	99	84
17	**1b/9**	100	16
18	**1b/10**	89	45
19	**1b/11**	91	88
20	**1b/2a**	100	98
21	**1b/2b**	100	98
22	**1b/2c**	10	7
23	**1b/2d**	99	94

[a] Conditions: 60 bar H_2, CH_2Cl_2, RT, 20 h, Rh/**3a** = 1:50; L^a/L^b = 1:1; Rh/total ligands = 1:2).

A preliminary NMR study of the precatalyst system derived from (*R*)-**1b** and **2a** indicates the existence of a mixture of the two expected homocombinations $[Rh(cod)((R)\text{-}\mathbf{1b})_2]BF_4$ and $[Rh(cod)(\mathbf{2a})_2]BF_4$ in addition to the heterocombination $[Rh(cod)(R)\text{-}\mathbf{1b}(\mathbf{2a})]BF_4$ in a ratio of about 1:1:16 (plus a small amount of unidentified species). However, the situation is in fact more complicated, because those complexes containing the configurationally labile atropisomeric **2a** actually exist as fluxional diastereomers. Thus, the major component in the above mixture exists as a pair of diastereomers in equilibrium [Eq. (2)]. They interconvert so rapidly even at low temperatures that their relative amounts cannot be measured by NMR spectroscopy. In the extreme case only one diastereomeric form is present, but this is rather unlikely.

$$[Rh(cod)(R)\text{-}\mathbf{1b}(R)\text{-}\mathbf{2a}]BF_4 \rightleftharpoons [Rh(cod)(R)\text{-}\mathbf{1b}(S)\text{-}\mathbf{2a}]BF_4 \quad (2)$$

We postulate that diastereomer $[Rh(cod)(R)\text{-}\mathbf{1b}(R)\text{-}\mathbf{2a}]BF_4$ constitutes the matched case; cooperativity leads to

a higher hydrogenation rate and to enhanced enantioselectivity. To lend support to this hypothesis, we prepared and tested separately the structurally related heterocombinations composed of two BINOL-derived building blocks, namely [Rh(*R*)-**1b**(*R*)-**1a**]BF_4 and [Rh(*R*)-**1b**(*S*)-**1a**]BF_4, which are configurationally stable diastereomeric complexes. We have already shown that the former precatalyst leads to 99% *ee* (*S*),[8] and we now note that the latter is considerably less effective (40% *ee* (*S*); 84% yield). Of course, it must be remembered that these catalysts cannot be prepared in pure form; in other words, in each case it is the mixture of the two respective homocombinations and the heterocombination that defines the catalytic profile and thus determines the observed enantioselectivity.

The result of our combinatorial search[9] suggested that the heterocombination of **1b** and **2a** may be the optimal ligand system for Rh-catalyzed hydrogenations of β-acylamino acrylates in general. Therefore this combination was tested in the hydrogenation of the other substrates **3b–e** under standard conditions. Indeed, excellent results were obtained: **3b** (96% *ee* (*S*); 90% yield), **3c** (95% *ee* (*S*); 90% yield), **3d** (97% *ee* (*S*); 94% yield;), **3e** (84% *ee* (*R*); 69% yield).

Finally, we performed the hydrogenation of itaconic acid diester **12** (Rh/**12** = 1:1000; Rh/ligand = 1:2; 1.3 bar H_2; RT; 20 h) using the homocombination (*R*)-**1b**, which resulted in only 77% *ee* (*R*) [80% yield, Eq. (3)). For this reason we turned to the corresponding mixtures: The combinations (*R*)-**1b**/**2a** and (*R*)-**1b**/**11** gave essentially identical enantioselectivities (94% *ee* (*R*)) and quantitative yield.

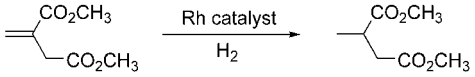

12 **13** (3)

In summary, we have shown for the first time that in Rh-catalyzed olefin-hydrogenation, mixtures comprising a BINOL-derived P ligand in combination with an achiral P compound, or a BINOL-derived P ligand in combination with a chiral but configurationally fluxional biphenol-derived phosphite can result in high enantioselectivity. The latter system is most effective and involves two rapidly interconverting diastereomers; the presumably more reactive *R*/*R* combination shows higher activity and enantioselectivity than the diastereomeric *R*/*S* form. Apart from the theoretical interest, the present results are of practical importance because half of the ligand system is derived from cheap achiral compounds such as biphenol.[10] It remains to be seen if this combinatorial approach can be extended to other reactions and ligand types.[11,12]

Received: November 15, 2004
Published online: April 12, 2005

Keywords: asymmetric catalysis · combinatorial catalysis · hydrogenation · P ligands · rhodium

[1] a) M. T. Reetz, G. Mehler, *Angew. Chem.* **2000**, *112*, 4047–4049; *Angew. Chem. Int. Ed.* **2000**, *39*, 3889–3890; b) M. T. Reetz, G. Mehler, A. Meiswinkel, Patent Application, WO 01/94278A1, **2001**.

[2] a) M. T. Reetz, T. Sell, *Tetrahedron Lett.* **2000**, *41*, 6333–6336; b) C. Claver, E. Fernandez, A. Gillon, K. Heslop, D. J. Hyett, A. Martorell, A. G. Orpen, P. G. Pringle, *Chem. Commun.* **2000**, 961–962.

[3] M. van den Berg, A. J. Minnaard, E. P. Schudde, J. van Esch, A. H. M. de Vries, J. G. de Vries, B. L. Feringa, *J. Am. Chem. Soc.* **2000**, *122*, 11539–11540.

[4] a) K. Junge, B. Hagemann, S. Enthaler, G. Oehme, M. Michalik, A. Monsees, T. Riermeier, U. Dingerdissen, M. Beller, *Angew. Chem.* **2004**, *116*, 5176–5179; *Angew. Chem. Int. Ed.* **2004**, *43*, 5066–5069; b) I. V. Komarov, A. Börner, *Angew. Chem.* **2001**, *113*, 1237–1240; *Angew. Chem. Int. Ed.* **2001**, *40*, 1197–1200; c) M. Ostermeier, J. Prieß, G. Helmchen, *Angew. Chem.* **2002**, *114*, 625–628; *Angew. Chem. Int. Ed.* **2002**, *41*, 612–617; d) Y. Chi, X. Zhang, *Tetrahedron Lett.* **2002**, *43*, 4849–4852; e) W. Chen, J. Xiao, *Tetrahedron Lett.* **2001**, *42*, 8737–8740; f) H. Huang, Z. Zheng, H. Luo, C. Bai, X. Hu, H. Chen, *J. Org. Chem.* **2004**, *69*, 2355–2361; g) A.-G. Hu, Y. Fu, J.-H. Xie, H. Zhou, L.-X. Wang, Q.-L. Zhou, *Angew. Chem.* **2002**, *114*, 2454–2456; *Angew. Chem. Int. Ed.* **2002**, *41*, 2348–2350; h) Z. Pakulski, O. M. Demchuk, J. Frelek, R. Luboradzki, K. M. Pietrusiewicz, *Eur. J. Org. Chem.* **2004**, 3913–3918; i) T. Jerphagnon, J.-L. Renaud, C. Bruneau, *Tetrahedron: Asymmetry* **2004**, *15*, 2101–2111; j) F. Lagasse, H. B. Kagan, *Chem. Pharm. Bull.* **2000**, *48*, 315–324; k) J. Ansell, M. Wills, *Chem. Soc. Rev.* **2002**, *31*, 259–268.

[5] A. Meiswinkel, Dissertation, Ruhr-Universität Bochum, Germany, **2003**.

[6] a) M. T. Reetz, T. Sell, A. Meiswinkel, G. Mehler, *Angew. Chem.* **2003**, *115*, 814–817; *Angew. Chem. Int. Ed.* **2003**, *42*, 790–793; b) M. T. Reetz, *Chim. Oggi* **2003**, *21*, 5–8; see also: c) D. Peña, A. J. Minnaard, J. A. F. Boogers, A. H. M. de Vries, J. G. de Vries, B. L. Feringa, *Org. Biomol. Chem.* **2003**, *1*, 1087–1089.

[7] M. T. Reetz, G. Mehler, *Tetrahedron Lett.* **2003**, *44*, 4593–4596.

[8] M. T. Reetz, X. Li, *Tetrahedron* **2004**, *60*, 9709–9714 and literature cited therein concerning previous work on the hydrogenation of **3**.

[9] The data shown here constitutes only about half of the total combinatorial search. Combinations of phosphonite **1** (X = CH_3) with **2** or **5**–**11** do not result in positive effects.

[10] We have previously shown that certain diphosphites composed of a chiral backbone diol and fluxional atropisomeric biphenol derivatives provide selectivities of up to 99% *ee* in olefin hydrogenation; three rapidly interconverting diastereomers are involved: a) M. T. Reetz, T. Neugebauer, *Angew. Chem.* **1999**, *111*, 134–137; *Angew. Chem. Int. Ed.* **1999**, *38*, 179–181; b) D. G. Blackmond, T. Rosner, T. Neugebauer, M. T. Reetz, *Angew. Chem.* **1999**, *111*, 2333–2335; *Angew. Chem. Int. Ed.* **1999**, *38*, 2196–2199; for related effects see: c) K. Mikami, T. Korenaga, M. Terada, T. Ohkuma, T. Pham, R. Noyori, *Angew. Chem.* **1999**, *111*, 517–519; *Angew. Chem. Int. Ed.* **1999**, *38*, 495–497; d) M. Diéguez, S. Deerenberg, O. Pàmies, C. Claver, P. W. N. M. van Leeuwen, P. Kamer, *Tetrahedron: Asymmetry* **2000**, *11*, 3161–3166; e) J. W. Faller, A. R. Lavoie, J. Parr, *Chem. Rev.* **2003**, *103*, 3345–3367; f) P. J. Walsh, A. E. Lurain, J. Balsells, *Chem. Rev.* **2003**, *103*, 3297–3344; g) K. Mikami, M. Yamanaka, *Chem. Rev.* **2003**, *103*, 3369–3400; h) M. Diéguez, O. Pàmies, A. Ruiz, S. Castillón, C. Claver, *Chem. Eur. J.* **2001**, *7*, 3086–3094; i) Z. Luo, Q. Liu, L. Gong, X. Cui, A. Mi, Y. Jiang, *Angew. Chem.* **2002**, *114*, 4714–4717; *Angew. Chem. Int. Ed.* **2002**, *41*, 4532–4535; j) A. Suárez, A. Pizzano, *Tetrahedron: Asymmetry* **2001**, *12*, 2501–2504; k) T. Ooi, Y. Uematsu, M.

Kameda, K. Maruoka, *Angew. Chem.* **2002**, *114*, 1621 – 1624; *Angew. Chem. Int. Ed.* **2002**, *41*, 1551 – 1554; l) C. Monti, C. Gennari, U. Piarulli, *Tetrahedron Lett.* **2004**, *45*, 6859 – 6862; m) H. Horibe, K. Kazuta, M. Kotoku, K. Kondo, H. Okuno, Y. Murakami, T. Aoyama, *Synlett* **2003**, 2047 – 2051; n) K. Tissot-Croset, D. Polet, A. Alexakis, *Angew. Chem.* **2004**, *116*, 2480 – 2482; *Angew. Chem. Int. Ed.* **2004**, *43*, 2426 – 2428, and references therein.

[11] Along these lines the use of mixtures of BINOL-derived phosphoramidites **1** ($X = NR_2$) and fluxional atropisomeric phosphoramidites (which we have prepared from biphenol and amines such as dimethylamine and piperidine) offers interesting perspectives.

[12] For more work on combinatorial catalysis see: M. T. Reetz, X. Li, *Angew. Chem.* **2005**, *117*, 3022–3024; *Angew. Chem. Int. Ed.* **2005**, *44*, 2962–2964.

Combinatorial Catalysis

The Influence of Mixtures of Monodentate Achiral Ligands on the Regioselectivity of Transition-Metal-Catalyzed Hydroformylation**

Manfred T. Reetz and Xiaoguang Li*

We recently reported that the use of a mixture of two different monodentate P ligands derived from 2,2′-dihydroxy-1,1′-binaphthyl (BINOL) in the asymmetric Rh-catalyzed hydrogenation of olefins can lead to drastically enhanced enantioselectivities relative to the performance of the corresponding pure ligand.[1,2] Since it is difficult to predict from structural considerations which combination is likely to be optimal, a combinatorial approach is necessary. In our original paper we also suggested that appropriate mixtures of achiral monodentate ligands may affect other catalytic parameters such as activity, *Z*/*E* selectivity, and/or regioselectivity in non enantioselective transformations.[1a] This possibility arises whenever the reactive metal species in the transition state of a catalytic reaction bears at least two ligands L. Thus, if ML_n is the reactive species, then $n \leq 2$. If ML_n is the precatalyst and ML_{n-1} the actual reactive species, then $n \leq 3$, etc. [Eq. (1)].

$$ML_n \rightleftharpoons ML_{n-1} + L \rightleftharpoons ML_{n-2} + L \qquad (1)$$

In the simplest case, a mixture leads to three catalysts that interconvert rapidly: the two homocombinations ML^aL^a and ML^bL^b and the heterocombination ML^aL^b. If ML^aL^b is more reactive than the two homocombinations, a new and different catalytic profile may emerge. Thus the application of ligand mixtures offers an alternative to the synthesis of new ligands.[3]

Here we illustrate this concept[4,5] by using mixtures of known monodentate P ligands to influence the regioselectivity of the Rh-catalyzed hydroformylation of *tert*-butyl methacrylate (**1**).[6] Although a vast number of achiral monodentate P ligands are potential candidates for such a study, we restricted the combinatorial search to a small library of 14 simple ligands (**4**–**17**) having different steric and electronic properties. Such parameters are known to affect the regioselectivity of hydroformylation in conventional catalyst systems with only one type of ligand (homocombinations).[7] Phosphines and phosphites have been used in hydroformylation for a long time,[7] whereas phosphinines of the type **16** and **17** were first introduced as ligands in such reactions in 1996 by Breit.[8]

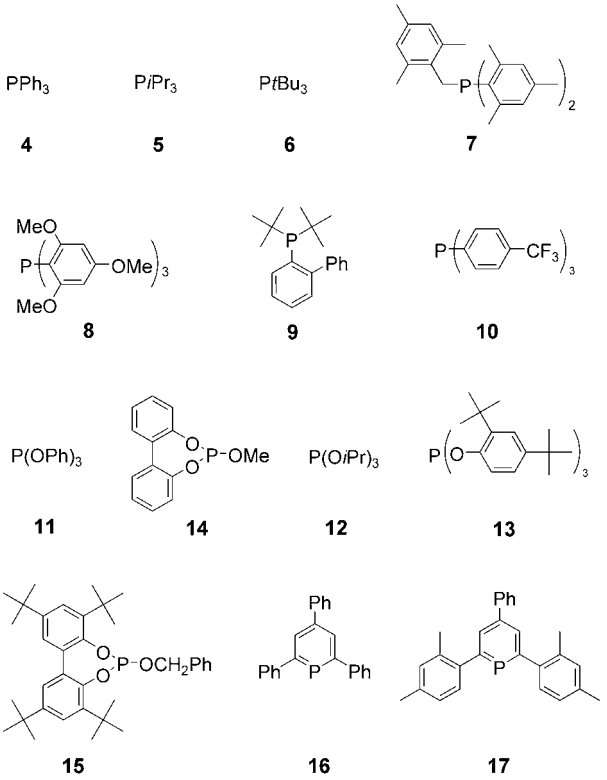

In the present study $[Rh(acac)(CO)_2]$ (acac = acetylacetonate) was used as the precatalyst under typical reaction conditions (Table 1). Although not all of the theoretically possible 91 heterocombinations were tested, the 83 mixtures examined led to the discovery of some remarkable effects. It can be seen that most homocombinations lead to the preferential formation of the linear product **3** (**2**/**3** < 1). The most notable exception is phosphite **14**,[9] which leads predominantly to the branched isomer (**2**/**3** = 2.7, Table 1, entry 11). The conventional approach to increase this regioselectivity would be to prepare and test more ligands (in addition to varying other parameters). In contrast, the present method simply involves mixing ligands already on the shelf, irrespective of the performance of the homocombinations.

[*] Prof. Dr. M. T. Reetz, Dr. X. Li
Max-Planck-Institut für Kohlenforschung
Kaiser-Wilhelm-Platz 1, 45470 Mülheim/Ruhr (Germany)
Fax: (+49) 208-306-2985
E-mail: reetz@mpi-muelheim.mpg.de

[**] Generous support by the Fonds der Chemischen Industrie is gratefully acknowledged.

  DOI: 10.1002/anie.200462613

Table 1: Hydroformylation of olefin **1**.[a]

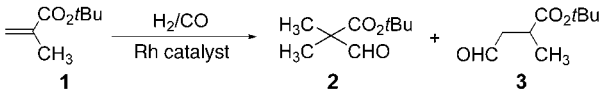

1 **2** **3**

Entry	Ligands	Conv. [%]	**2**/**3**	Hydrog. [%][b]	Entry	Ligands	Conv. [%]	**2**/**3**	Hydrog. [%][b]
				Homocombinations					
1	**4**/**4**	72	0.72	13	8	**11**/**11**	69	1.4	23
2	**5**/**5**	49	0.76	8	9	**12**/**12**	73	0.67	13
3	**6**/**6**	57	0.70	7	10	**13**/**13**	76	0.88	9
4	**7**/**7**	70	0.70	8	11	**14**/**14**	55	2.7	33
5	**8**/**8**	9	0.58	26	12	**15**/**15**	79	1.3	9
6	**9**/**9**	49	0.93	6	13	**16**/**16**	79	0.57	7
7	**10**/**10**	64	1.1	5	14	**17**/**17**	72	0.76	6
				Heterocombinations					
15	**4**/**5**	55	0.76	6	61	**8**/**9**		not studied	
16	**4**/**6**	60	0.73	7	62	**8**/**10**	53	1.6	15
17	**4**/**7**	69	1.1	27	63	**8**/**11**	61	3.1	7
18	**4**/**8**	28	3.8	10	64	**8**/**12**	15	1.3	19
19	**4**/**9**	40	2.9	9	65	**8**/**13**	22	2.6	18
20	**4**/**10**	64	0.84	6	66	**8**/**14**	32	6.4	5
21	**4**/**11**	57	1.1	17	67	**8**/**15**	28	3.3	14
22	**4**/**12**	55	1.3	7	68	**8**/**16**		not studied	
23	**4**/**13**	76	0.84	8	69	**8**/**17**		not studied	
24	**4**/**14**	38	5.3	6	70	**9**/**10**	60	1.3	9
25	**4**/**15**	69	1.2	7	71	**9**/**11**	58	2.3	13
26	**4**/**16**	37	5.4	3	72	**9**/**12**	39	1.0	9
27	**4**/**17**	39	8.4	1	73	**9**/**13**	60	1.4	11
28	**5**/**6**	63	0.68	8	74	**9**/**14**	40	3.6	4
29	**5**/**7**	66	0.73	8	75	**9**/**15**	67	1.1	5
30	**5**/**8**		not studied		76	**9**/**16**		not studied	
31	**5**/**9**	49	0.79	9	77	**9**/**17**	63	0.71	3
32	**5**/**10**	67	0.77	12	78	**10**/**11**	54	2.2	8
33	**5**/**11**	57	1.6	7	79	**10**/**12**	66	0.90	9
34	**5**/**12**	61	0.80	7	80	**10**/**13**	72	0.73	8
35	**5**/**13**	61	1.1	7	81	**10**/**14**	37	2.2	7
36	**5**/**14**	40	3.9	4	82	**10**/**15**	70	1.1	8
37	**5**/**15**	67	0.79	8	83	**10**/**16**	69	1.1	12
38	**5**/**16**	61	0.70	10	84	**10**/**17**	63	1.5	3
39	**5**/**17**	54	0.74	8	85	**11**/**12**	58	2.5	7
40	**6**/**7**	70	0.70	12	86	**11**/**13**	69	2.4	12
41	**6**/**8**		not studied		87	**11**/**14**	57	3.3	11
42	**6**/**9**	52	0.82	5	88	**11**/**15**	66	2.8	6
43	**6**/**10**	66	0.83	6	89	**11**/**16**	58	2.4	8
44	**6**/**11**	70	1.1	13	90	**11**/**17**	60	2.8	6
45	**6**/**12**	60	0.69	12	91	**12**/**13**	70	0.78	11
46	**6**/**13**	72	0.74	12	92	**12**/**14**	39	1.9	10
47	**6**/**14**	34	1.8	4	93	**12**/**15**	64	1.2	7
48	**6**/**15**	72	1.1	10	94	**12**/**16**	75	0.77	8
49	**6**/**16**	69	0.81	10	95	**12**/**17**	40	0.81	5
50	**6**/**17**	66	0.73	5	96	**13**/**14**	40	3.1	10
51	**7**/**8**		not studied		97	**13**/**15**	67	1.6	7
52	**7**/**9**		not studied		98	**13**/**16**	70	1.3	9
53	**7**/**10**	72	0.85	10	99	**13**/**17**	69	1.1	6
54	**7**/**11**	60	1.7	17	100	**14**/**15**	48	2.9	10
55	**7**/**12**	61	0.70	4	101	**14**/**16**	45	4.2	4
56	**7**/**13**	70	0.64	8	102	**14**/**17**	49	5.3	2
57	**7**/**14**	42	1.4	25	103	**15**/**16**	69	1.8	4
58	**7**/**15**	70	1.3	10	104	**15**/**17**	67	2.1	3
59	**7**/**16**	66	0.66	4	105	**16**/**17**	75	0.88	9
60	**7**/**17**	72	0.83	8					

[a] Conditions: 60 bar $CO/H_2 = 1:1$, 50 °C, 22 h, toluene as solvent, substrate/$[Rh(acac)(CO)_2] = 200:1$, $L^a/L^b = 1:1$, Rh/total ligands = 1:2.4. [b] Hydrogenated side product.

Inspection of Table 1 reveals that the mixing process results in improved regioselectivity favoring **2** in 45 cases relative to the performance of the homocombinations.

It is of particular interest that 12 heterocombinations lead to the preferential formation of the branched product **2** (Table 1, entries 17–19, 26, 27, 35, 64, 65, 73, 92, 98, and 99), despite the fact that the corresponding homocombinations all have the opposite regioselectivity favoring the linear aldehyde **3**. This observation speaks for the catalytic role of a heteroleptic rhodium complex in which two different P ligands are bonded to the metal and not for a possibly reduced concentration of one strongly binding ligand. The most prominent heterocombination in this sense is a 1:1 mixture of triphenylphosphine (**4**) and the phosphinine **17**[8] (**2**/**3** = 8.4, Table 1, entry 27). The homocombinations of **4** and **17** lead to **2**/**3** ratios of 0.72 and 0.76, respectively (Table 1, entries 1 and 14). In some cases homocombinations of two ligands favor the branched product **2** slightly (e.g., entries 8 and 12), but the heterocombination of these two ligands enhances regioselectivity (Table 1, entry 88). Of course, in some instances the mixing of two ligands decreases regioselectivity.

Table 1 reveals another interesting phenomenon, namely that the amount of undesired side product arising from olefin hydrogenation can be influenced by the choice of the heterocombination, although the effects thus far observed are small (e.g., entries 1 and 14 vs. 27).

The selectivity in favor of the branched aldehyde **2** obtained with the heterocombination **4**/**17** was then enhanced further by varying the reaction conditions (80 bar CO/H_2 = 1:1, 40 °C, 30 h, substrate/Rh = 50:1, L^a/L^b = 1:1, Rh/total ligands = 1:2.4, toluene as solvent). This led to a **2**/**3** ratio of 20, corresponding to 95 % regioselectivity (45 % conversion). Significantly, under these conditions essentially no undesired olefin hydrogenation occurs (< 0.5 %). Previously, the highest reported regioselectivity in favor of product **2** was **2**/**3** = 1.7.[6a]

In summary, we have extended the combinatorial method of using mixtures of two chiral monodentate ligands in asymmetric transition-metal catalysis. We have shown that mixtures of achiral ligands can affect regio- and chemoselectivity. Since it is at present essentially impossible to predict which heterocombinations are likely to be effective in a given case, a combinatorial approach is required. The present study was conducted with a very small library of achiral P ligands, and we do not contend that the hits found are optimal. Moreover, a given heterocombination useful for one substrate is not necessarily effective in other cases.

In the present study the heterocombinations of ligands **4**–**17** led to only small effects in hydroformylation of styrene. The use of larger libraries encompassing a greater number of structurally different monodentate P ligands is recommended here and for other transition-metal-catalyzed reactions in which at least two monodentate ligands are bonded to the metal in the transition state. Such a combinatorial procedure provides potential catalysts with a high degree of structural diversity without the preparation of new ligands. A goal for the future is to uncover the reasons for altered regioselectivity in the hydroformylations described herein and to see if activity and/or regioselectivity of other achiral transition-metal-catalyzed processes can also be influenced by the use of mixtures of monodentate ligands.[10]

Received: November 15, 2004
Published online: April 13, 2005

Keywords: combinatorial catalysis · hydroformylation · P ligands · regioselectivity · rhodium

[1] a) M. T. Reetz, T. Sell, A. Meiswinkel, G. Mehler, *Angew. Chem.* **2003**, *115*, 814–817; *Angew. Chem. Int. Ed.* **2003**, *42*, 790–793; b) M. T. Reetz, G. Mehler, A. Meiswinkel, *Tetrahedron: Asymmetry* **2004**, *15*, 2165–2167; review: c) M. T. Reetz, *Chim. Oggi* **2003**, *21*, 5–8.

[2] Following our initial report using mixtures of BINOL-derived phosphonites and phosphites,[1a] Feringa, de Vries, et al. independently described the use of the analogous phosphoramidites: a) D. Peña, A. J. Minnaard, J. A. F. Boogers, A. H. M. de Vries, J. G. de Vries, B. L. Feringa, *Org. Biomol. Chem.* **2003**, *1*, 1087–1089; b) A. Duursma, R. Hoen, J. Schuppan, R. Hulst, A. J. Minnaard, B. L. Feringa, *Org. Lett.* **2003**, *5*, 3111–3113.

[3] A mixture of two monodentate ligands in a nonenantioselective transition-metal-catalyzed chemical transformation may also lead to other effects. For example, if the catalytic cycle involves a series of distinct consecutive events, each step may require a different ligand composition for optimal efficiency which could influence rate, regio- and chemoselectivity, and/or *Z*/*E* selectivity.

[4] In the Rh-catalyzed hydroformylation of long-chain alkenes, triphenylphosphine oxide (TPPO) is used as the ligand, but before distillation of the products triphenylphosphine is added to stabilize the Rh.[7c]

[5] Of course, additives of various types have long been used in many transition-metal-catalyzed reactions; this optimization procedure differs from the approach described herein. The idea of using two identical monodentate ligands that interact with each other through hydrogen bonding or other binding phenomenon to form a formally bidentate ligand system is also different: B. Breit, W. Seiche, *J. Am. Chem. Soc.* **2003**, *125*, 6608–6609.

[6] a) M. L. Clarke, *Tetrahedron Lett.* **2004**, *45*, 4043–4045; b) It should be noted that regioselectivity is very different when methyl methacrylate is used;[4a] see also: G. Consiglio, L. Kollár, R. Kölliker, *J. Organomet. Chem.* **1990**, *396*, 375–383.

[7] a) M. Beller, J. Seayad, A. Tillack, H. Jiao, *Angew. Chem.* **2004**, *116*, 3448–3479; *Angew. Chem. Int. Ed.* **2004**, *43*, 3368–3398; b) M. Diéguez, O. Pàmies, C. Claver, *Tetrahedron: Asymmetry* **2004**, *15*, 2113–2122; c) H.-W. Bohnen, B. Cornils, *Adv. Catal.* **2002**, *47*, 1–64; d) B. Breit, W. Seiche, *Synthesis* **2001**, 1–36; e) P. W. N. M. van Leeuwen, C. Claver, *Rhodium Catalyzed Hydroformylation*, Kluwer, Dordrecht, **2000**; f) P. W. N. M. van Leeuwen, P. C. J. Kamer, J. N. H. Reek, P. Dierkes, *Chem. Rev.* **2000**, *100*, 2741–2769; For recent annual surveys, see: g) F. Ungváry, *Coord. Chem. Rev.* **2004**, *248*, 867–880; h) F. Ungváry, *Coord. Chem. Rev.* **2002**, *228*, 61–82.

[8] a) B. Breit, *Chem. Commun.* **1996**, 2071–2072; b) We thank Prof. Breit (Freiburg) for samples of **16** and **17**.

[9] It is known that sterically nonshielded phosphites can partially decompose under the reaction conditions;[7] this may influence regioselectivity, although such effects have not been studied in detail.

[10] For more work on combinatorial catalysis see: M. T. Reetz, X. Li, *Angew. Chem.* **2005**, *117*, 3019–3021; *Angew. Chem. Int. Ed.* **2005**, *44*, 2959–2962.

Cluster Compounds

From Racemic Primary Aminoalkyl(phosphanyl)ferrocene Complexes to a Lithium–Phosphorus *closo* Cluster**

*Steffen Tschirschwitz, Peter Lönnecke, Joachim Reinhold, and Evamarie Hey-Hawkins**

The first chiral phosphanylferrocene, (*R*)-*N*,*N*-dimethyl-1-[(*S*)-2-(diphenylphosphanyl)ferrocenyl]ethylamine ((*R*,*S*)-PPFA), was prepared by Hayashi et al.[1] in 1974 and was successfully applied in homogeneous catalysis two years later.[2] Since then a broad variety of phosphanylferrocene complexes has been synthesized and used for asymmetric reactions, such as hydrogenation, hydrosilylation, and aldol reactions.[3] Studies on the reaction mechanisms have shown that the asymmetric induction is mainly due to the planar chirality of the 1,2-disubstituted ferrocene complexes,[4] for which racemization is hardly possible.

To date only a few primary phosphanylferrocene complexes are known. Phosphanylferrocene, [Fe(η^5-C_5H_5)(η^5-$C_5H_4PH_2$)], was first prepared in 1989,[5] and 1,1′-bis(phosphanyl)ferrocene in 1994.[6] Both compounds are unstable when exposed to air and are oxidized within a few days in the solid state, and within a few seconds in solution. Primary phosphanylalkylferrocene complexes that have a methylene or ethylene bridge between the ferrocene moiety and the phosphanyl group are much more stable, these compounds include (phosphanylmethyl)ferrocene,[7] 1,1′-bis(phosphanylmethyl)ferrocene, 1,2-bis(phosphanylmethyl)ferrocene, and 1-phosphanyl-2-ferrocenylethane.[8]

The reactivity of the P–H bonds offers great synthetic potential. Reactions with carbonyl groups, alkyl and aryl halides, halogens, alkali metals, and Lewis acids are well known and provide many possibilities to produce functionalized, even chiral-phosphorus containing secondary or tertiary phosphines.[9] However, one of the most convenient methods is deprotonation of the primary phosphine by using organometallic compounds of the alkali metals as strong bases. Twofold deprotonations are also possible by this method. Especially primary silylphosphines with bulky organosilyl groups undergo such reactions affording phosphinediides that form alkali-metal–phosphorus clusters with spherical lithium–phosphorus frames.[10] Lithium phosphanides on the other hand are known as dimers or oligomers with ladder structures,[11] polymeric chains and helices of connected M–P units,[12] as well as more complex aggregates.[13]

Herein we present the syntheses of the first two chiral primary aminoalkyl(phosphanyl)ferrocene complexes: 2-(*N*,*N*-Dimethylaminomethyl)phosphanylferrocene (**1**) was obtained as a racemic mixture, and *N*,*N*-dimethyl-1-(2-phosphanylferrocenyl)ethylamine (**2**) with a d.r. of 96:4. Compound **1** readily undergoes twofold deprotonation with *n*BuLi to form the first known lithium–phosphorus cluster which has the structure and shows the electronic properties of a *closo* cluster according to Wade's rules.[14]

Primary phosphine **1** was obtained as a racemate according to Scheme 1 starting from *N*,*N*-dimethylaminomethylferrocene (**3**) in a two-step procedure in 66% overall yield. After *ortho*-lithiation, the phosphanyl group was introduced by using diethyl chlorophosphate. Reduction of the resulting phosphono compound with a 1:1 mixture of lithium aluminum hydride and chlorotrimethylsilane gave racemic **1** as a brown-red high-boiling-point liquid with a typical phosphine odor.

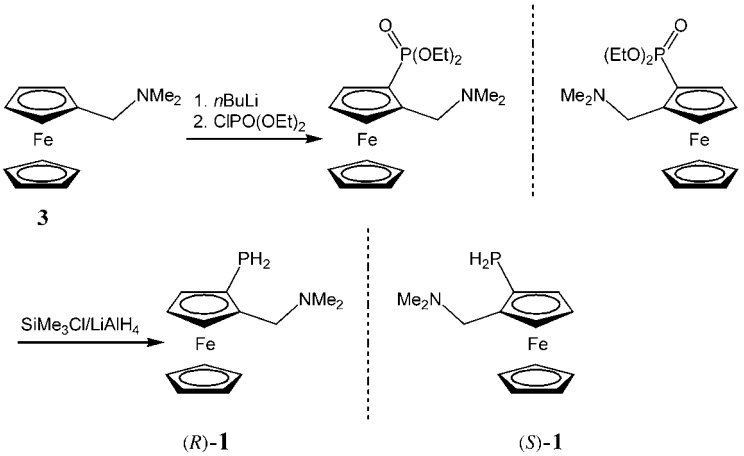

Scheme 1.

(*S*,*R*)-**2** was prepared similarly [Eq. (1)] with a d.r. of 96:4 (55% overall yield) starting from (*S*)-*N*,*N*-dimethyl-1-ferrocenylethylamine (**4**).

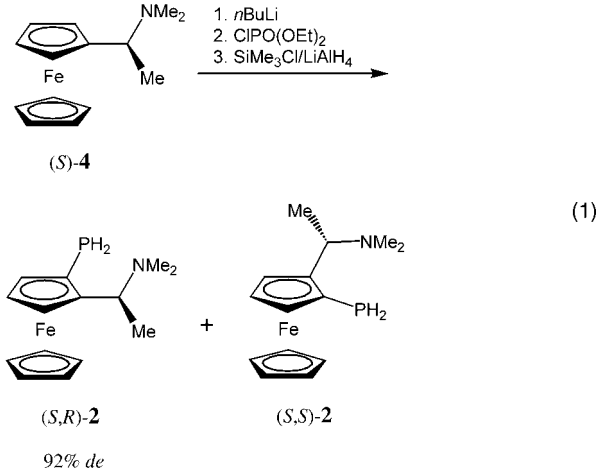

(1)

[*] Dipl.-Chem. S. Tschirschwitz, Dr. P. Lönnecke, Prof. Dr. E. Hey-Hawkins
Institut für Anorganische Chemie
Universität Leipzig
Johannisallee 29, 04103 Leipzig (Germany)
Fax: (+49) 341–973-9319
E-mail: hey@rz.uni-leipzig.de
Prof. Dr. J. Reinhold
Wilhelm-Ostwald Institut für Physikalische und Theoretische Chemie
Universität Leipzig
Johannisallee 29, 04103 Leipzig (Germany)

[**] These results were presented in part at the 21st International Conference on Organometallic Chemistry in Vancouver, Canada (25–30 July 2004).

 DOI: 10.1002/anie.200462543

cenylethylamine ((*S*)-**4**).[15] The *S*,*S* diastereomer was obtained as a side product. Analogously, (*R*,*S*)-**4** was prepared in about 56% overall yield starting from (*R*)-**4** with (*R*,*R*)-**2** as a side product.

Owing to a side-group effect of the amino group, twofold deprotonation of **1** by using two equivalents of a base was comparatively easy [Eq. (2)]. The reaction occurred at room

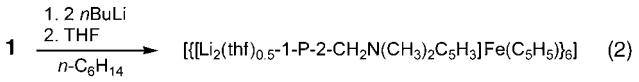

5

temperature within a few minutes. A solution of *n*-butyllithium in *n*-hexane was added slowly to a solution of **1** in *n*-hexane. The monolithium compound precipitated immediately as a red powder, but redissolved during the addition of the second equivalent of the base with formation of the dilithium phosphinediide. Partial evaporation of the solvent gave a deep red and highly pyrophoric solid (isolated in 70% yield). A solution of the dilithium phosphinediide in THF was layered with *n*-hexane to give crystals of **5**, which were investigated by X-ray diffraction.[16] Compound **5** also precipitated upon addition of a few drops of THF to a solution of the dilithium phosphinediide in *n*-hexane.

Compound **5** forms violet hexagonal prismatic crystals. The molecular structure (Figure 1) offers some novel and unexpected characteristics. One molecule consists of six dilithium phosphinediide units. All the ferrocenyl units in one molecule are planar-chiral and have the same configuration; in the case of the depicted molecule, this is the *R* configuration (Figure 1 and Figure 2). Owing to the inversion center in the monoclinic space group *P*2/*c*, all the ferrocenyl units of the second molecule in the unit cell have *S* configuration. The phosphorus atoms of three ferrocenyl

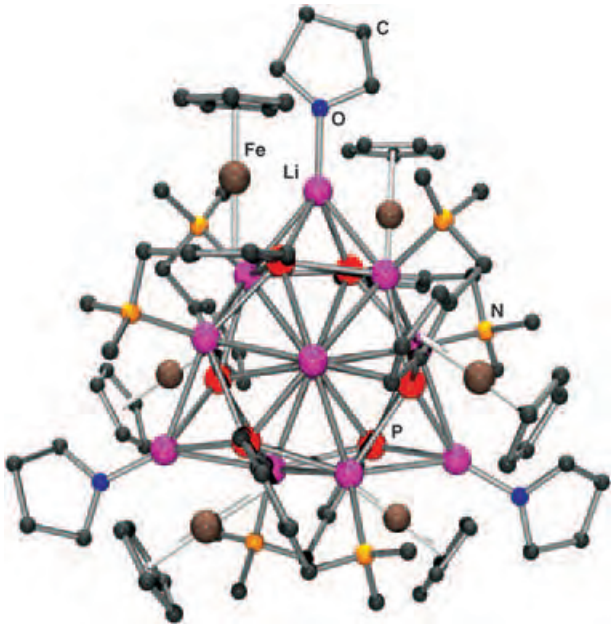

Figure 1. Molecular structure of **5**.

units and three lithium ions form a six-membered ring that has a slight chair conformation (Figure 2). Each lithium ion is additionally chelated by the dimethylamino groups of one ferrocenyl unit to form three more six-membered (Li-P-C-C-C-N) rings in a twist conformation that are anellated to the Li_3P_3 ring (Figure 2).

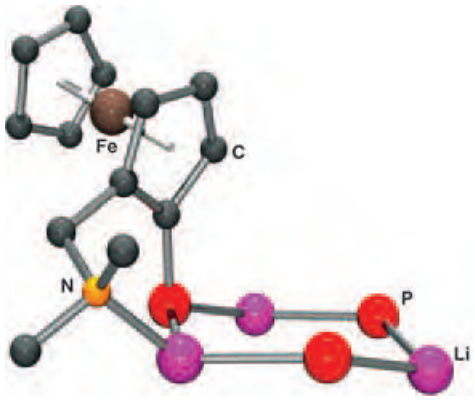

Figure 2. Fused six-membered rings in **5**.

Two of the Li_3P_3 rings are dimerized to an Li_6P_6 unit that has the structure of a distorted hexagonal antiprism in which the lithium ions have slightly distorted tetrahedral coordination geometries. Although similar structural motifs are known for lithium phosphanides and lithium amides,[17] in **5** an additional lithium ion is located in the center of the hexagonal antiprism (Figure 3) and is coordinated in a slightly distorted

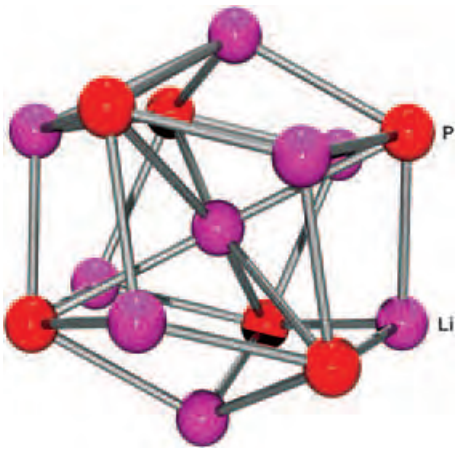

Figure 3. Li_6P_6 framework forming a distorted hexagonal antiprism with the central lithium ion and the two lithium ions capping the hexagonal faces.

octahedral fashion by the six phosphorus atoms of the Li_6P_6 unit. The central lithium ion is located on a crystallographic twofold axis. To our knowledge, **5** is the first structurally characterized lithium–phosphorus cluster with a single lithium ion in the center; alkaline-earth-metal–phosphorus clusters with alkaline-earth-metal ions in the center and

lithium–phosphorus clusters with a central Li_2O unit are known.[18]

Equally uncommon is the coordination of two additional lithium ions that cap the hexagonal faces of the Li_6P_6 antiprism (Figure 3). Owing to the shielding of these lithium ions by the ferrocenyl units they coordinate to only three phosphorus atoms and have trigonal-pyramidal coordination geometries. Three additional lithium ions are located above three of the six quadrangular Li_2P_2 faces of the distorted hexagonal Li_6P_6 antiprism. Each of these lithium ions coordinates to two phosphorus atoms and one THF molecule in a trigonal-planar fashion. Thus, the result is an $Li_{12}P_6$ cluster with 12 lithium ions and 6 ferrocenylphosphinediide units that forms an Euler deltahedron of 30 triangular planes (Figure 4).

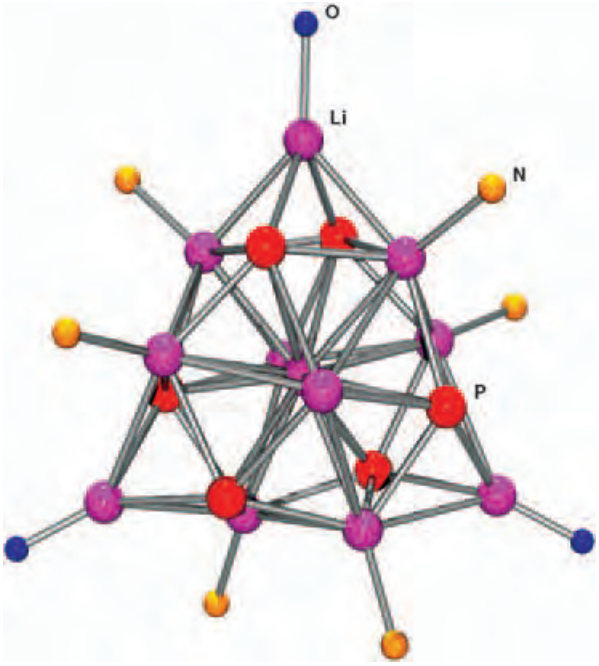

Figure 4. $Li_{12}P_6$ cluster showing all the atoms coordinating the lithium ions.

Compound **5** has the shape (30 triangular faces, $n = 17$ vertices) and electron number ($2n + 2 = 36$) of a *closo* cluster according to Wade's rules.[14] To show that **5** also has the electronic properties of a *closo* cluster, theoretical studies were carried out. To that end the $Li_{12}P_6$ cluster was considered to be composed of a 17-atom skeleton ($Li_{11}P_6$) completed by the central lithium atom. The 17 skeletal atoms occupy all of the vertices of the deltahedron. According to Wade's rule for *closo* clusters containing main-group elements, 18 (i.e., 17 + 1) skeletal bond pairs should exist. In **5**, each phosphorus atom provides four valence electrons for skeletal bonding (the fifth valence electron is involved in the terminal phosphorus–ferrocenyl bond), and each lithium atom contributes a single valence electron. This situation results in a 35-electron count, that is, one electron is missing. Usually, such an electron deficiency is compensated by a negative cluster charge. In **5**, however, the additional lithium atom in the cluster center provides the missing electron and additional stability through the electrostatic interaction between lithium and phosphorus.

To confirm this electron count, a molecular orbital (MO) calculation was performed on the model system $Li_{12}P_6H_6$, in which the terminal P–R bonds were replaced by P–H bonds (Figure 5). For this model, D_3 symmetry was adopted, which is

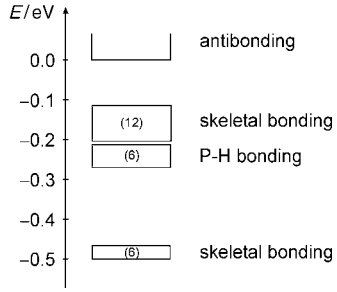

Figure 5. Number and type of molecular orbitals in various energy regions for the model compound $Li_{12}P_6H_6$ according to a DFT-B3LYP[20] calculation[21] with the minimal STO-3G basis set[22] (extended basis sets do not change the qualitative picture).

nearly that of the, albeit slightly distorted, real molecule **5**. The input structural parameters were derived as mean values from the X-ray structure. The resulting orbital energies are displayed in Figure 5. It appears that (above the core orbitals of the atoms) 24 molecular orbitals are occupied. Six of them are P–H bonding and thus not involved in skeletal bonding. The other 18 orbitals are skeletal bonding orbitals and are well separated energetically from the unoccupied antibonding orbitals; thus, the *closo* structure of the cluster is confirmed.

^{31}P and ^{7}Li NMR spectroscopy studies show that the structure of the $Li_{12}P_6$ cluster in solution is solvent-dependent. In nonpolar solvents, such as *n*-hexane, compound **5** is hardly soluble, but it dissolves when few drops of THF are added. The corresponding ^{31}P NMR spectrum shows a very broad signal at $\delta = -219$ ppm, which suggests the presence of the $Li_{12}P_6$ cluster. Upon addition of a small amount of a coordinating solvent, such as more THF, a second sharp signal at $\delta = -177.3$ ppm is observed, and, in THF alone, only this signal is observed, which we believe is due to the solvent-separated ion pairs of the dilithium phosphinediide. A similar phenomenon was revealed by ^{7}Li NMR spectroscopy investigations. A solution of **5** in *n*-hexane that contains a few drops of THF shows a broad multiplet for the $Li_{12}P_6$ cluster at $\delta =$ 0.7–5.1 ppm, this multiplet consists of several overlapping signals, and a small singlet at $\delta = 0.5$ ppm for the dilithium phosphinediide. Again the signals of the cluster decrease upon addition of THF, while the signal at $\delta = 0.5$ ppm increases. These results confirm the presence of the $Li_{12}P_6$ cluster in nonpolar solvents, while the structure is degraded in Lewis basic solvents.

Experimental Section

All procedures were performed under an inert atmosphere of pure nitrogen. The NMR spectra were recorded with an AVANCE

DRX400 spectrometer (Bruker): ^{1}H NMR (400.13 MHz): internal standard solvent, external standard TMS; ^{31}P NMR (161.9 MHz): external standard 85% H_3PO_4; ^{13}C NMR (100.16 MHz): internal standard solvent, external standard TMS; ^{7}Li NMR (155.51 MHz): internal standard solvent, external standard LiCl in D_2O. The solvents were dried and saturated with nitrogen. Compounds **3**[19] and **4**[15] were prepared by literature methods. Diethyl chlorophosphate is commercially available (ACROS Organics) and was freshly distilled before use. Elemental analyses were performed on a VARIO EL (Heraeus).

1: At room temperature *n*-butyllithium in *n*-hexane (4.8 mL, 2.05 M, 9.84 mmol, 1.2 equiv) was added to a solution of **3** (2.0 g, 8.23 mmol) in diethyl ether (20 mL). After six hours of stirring, a solution of diethyl chlorophosphate (1.7 g, 9.85 mmol, 1.2 equiv) in diethyl ether (10 mL) was added slowly at 0 °C. After a few min slow precipitation of lithium chloride was observed. After stirring overnight at room temperature, the solution was separated from the precipitate by filtration. The solvent was evaporated, and the viscous residue dried in vacuo. The reducing agent was prepared by adding a solution of chlorotrimethylsilane (2.29 g, 21.1 mmol) in THF (30 mL) to a suspension of an equimolar amount of lithium aluminum hydride (0.8 g, 21.1 mmol) in THF (10 mL) at 0 °C. The resulting suspension was stirred for 2 h at room temperature. The intermediate was dissolved in THF and slowly added to 2.5 equivalents of the reducing agent at 0 °C. After stirring overnight at room temperature, the resulting greenish suspension was hydrolyzed by slowly adding an excess of methanol (50 mL) at 0 °C. The reaction mixture was stirred for 1 h at 0 °C and then warmed to room temperature. The solvent was evaporated in vacuo, and the green-red residue extracted with *n*-pentane for 3 h. After removal of the solvent, the remaining brown-red oil was purified by fractional distillation (bath temperature: 50–60 °C, 10^{-3} mbar). The first fraction consisted mainly of residual **3**. Yield of **1**: 1.5 g (66%). ^{1}H NMR (C_6D_6): $\delta = 2.12$ (s, 6H, $N(CH_3)_2$), 3.04 (d, $^2J_{HH} = 12.0$ Hz, 1H, CH_2), 3.61 (d, $^2J_{HH} = 12.0$ Hz, 1H, CH_2), 3.72 (dd, $^1J_{PH} = 201$ Hz, $^2J_{HH} = 12.0$ Hz, 1H, PH_2), 3.86 (dd, $^1J_{PH} = 201$ Hz, $^2J_{HH} = 12.0$ Hz, 1H, PH_2), 3.90 (s, 5H, C_5H_5), 3.97 (m, 1H, C_5H_3), 4.09 (m, 1H, C_5H_3), 4.17 ppm (m, 1H, C_5H_3); ^{13}C{^{1}H} NMR (C_6D_6): $\delta = 45.0$ (s, $N(CH_3)_2$), 58.3 (d, $^3J_{CP} = 2.9$ Hz, CH_2), 66.3 (d, $^1J_{CP} = 7.6$ Hz, *i*-C1 C_5H_3), 69.2 (d, $^3J_{CP} = 3.2$ Hz, *m*-C in C_5H_3), 69.9 (s, C_5H_5), 72.9 (d, $^3J_{CP} = 2.5$ Hz, *m*-C in C_5H_3), 76.3 (d, $^2J_{CP} = 9.8$ Hz, *o*-C in C_5H_3), 89.8 ppm (d, $^2J_{CP} = 12.6$ Hz, *C*-CH_2 in C_5H_3); ^{31}P NMR (C_6D_6): $\delta = -152.2$ ppm (t, $^1J_{PH} = 200.6$ Hz); MS (FAB$^+$, 3-nitrobenzyl alcohol), *m*/*z* (%): 275 (17) $[M]^+$, 231 (100) $[M-HNMe_2]^+$, 199 (14%) $[Fe(C_5H_5)(C_5H_4CH_2)]^+$, 121 (14%) $[FeC_5H_5]^+$.

2: (*S*,*R*)-**2** was prepared analogously to **1** starting from (*S*)-**4** with a d.r. of 96:4 and an overall yield of 55%. (*R*,*S*)-**2**, was prepared similarly from (*R*)-**4** with a d.r. of 96:4 and an overall yield of 55.6%. The enantiomers (*S*,*R*)-**2** and (*R*,*S*)-**2** have identical analytical data. ^{1}H NMR (C_6D_6): $\delta = 1.18$ (d, $^3J_{HH} = 6.8$ Hz, 3H, CH_3), 2.08 (s, 6H, $N(CH_3)_2$), 3.74 (dd, $^1J_{PH} = 200$ Hz, $^2J_{HH} = 12.0$ Hz, 1H, PH_2), 3.92 (dd, $^1J_{PH} = 200$ Hz, $^2J_{HH} = 12.0$ Hz, 1H, PH_2), 3.91–4.09 ppm (m, 9H, $CH(CH_3)$, C_5H_5, C_5H_3); ^{13}C{^{1}H} NMR (C_6D_6): $\delta = 11.0$ (s, CH_3), 40.0 (s, $N(CH_3)_2$), 57.3 (d, $^3J_{CP} = 3.5$ Hz, $CH(CH_3)$), 66.3 (d, $^1J_{CP} = 6.5$ Hz, *i*-C in C_5H_3), 68.4 (d, $^3J_{CP} = 1.5$ Hz, *m*-C in C_5H_3), 69.1 (d, $^3J_{CP} = 3.1$ Hz, *m*-C in C_5H_3), 70.0 (s, C_5H_5), 75.9 (d, $^2J_{CP} = 3.2$ Hz, *o*-C in C_5H_3), 95.6 ppm (d, $^2J_{CP} = 15.2$ Hz, *C*CHMe in C_5H_3); ^{31}P NMR (C_6D_6): $\delta = -149.3$ ppm (t, $^1J_{PH} = 200.0$ Hz); MS (FAB$^+$, 3-nitrobenzylalcohol), *m*/*z* (%): 289 (17) $[M]^+$, 244 (100) $[M-HNMe_2]^+$, 186 (6) $[Fe(C_5H_5)(C_5H_5)]^+$, 121 (17) $[FeC_5H_5]^+$.

5: At 0 °C *n*-butyllithium in *n*-hexane (3.55 mL, 2.05 M, 7.28 mmol, 2 equiv) was slowly added to a solution of **1** (1.0 g, 3.64 mmol) in *n*-hexane (20 mL). Immediately after the first drop the color changed from light brown to deep red, and the monolithiated compound started to precipitate. On addition of the second equivalent of *n*-butyllithium the amount of precipitate decreased. Depending on the amount of solvent, complete dissolution could be observed. A ^{31}P NMR spectrum of the solution showed complete conversion of the starting material. After evaporation of most of the solvent, 0.73 g (70% yield) of the dilithiated compound was isolated as a red powder. The ^{31}P NMR spectrum of its THF solution showed a sharp signal at $\delta = -177.3$ ppm. Layering of the THF solution with *n*-hexane gave crystals of **5**. Crystals were also obtained by adding THF to the *n*-hexane solution of dilithiated **1**; after addition of a few drops, **5** started slowly to precipitate as an orange-red powder. More THF was added until the solid redissolved. Crystals of **5** formed slowly. In contrast to the dilithium phosphinediide, the cluster compound is hardly soluble in *n*-hexane, but soluble in a mixture of THF and *n*-hexane. ^{31}P{^{1}H} NMR: (THF): $\delta = -177.3$ ppm; (*n*-hexane/THF): $\delta = -219$ ppm (vbr); ^{7}Li NMR: (THF): $\delta = 0.5$ ppm (s); (*n*-hexane/THF): $\delta = 0.7$–5.1 ppm (m).

Received: November 8, 2004
Published online: April 8, 2005

Keywords: cluster compounds · density functional calculations · lithium · metallocenes · phosphorus

[1] T. Hayashi, K. Yamamoto, M. Kumada, *Tetrahedron Lett.* **1974**, 4405.
[2] T. Hayashi, M. Tajika, K. Tamao, M. Kumada, *J. Am. Chem. Soc.* **1976**, *98*, 3718.
[3] A. Togni, T. Hayashi, *Ferrocenes. Homogeneous Catalysis, Organic Synthesis Materials Science*, VCH, Weinheim, **1995**.
[4] T. Hayashi, M. Konishi, M. Fukushima, T. Mise, M. Kagotani, M. Tajika, M. Kumada, *J. Am. Chem. Soc.* **1982**, *104*, 180.
[5] C. Spang, F. T. Edelmann, M. Noltemeyer, H. W. Roesky, *Chem. Ber.* **1989**, *122*, 1247.
[6] M. J. Burk, M. F. Gross, *Tetrahedron Lett.* **1994**, *35*, 9363.
[7] N. J. Goodwin, W. Henderson, B. K. Nicholson, *Chem. Commun.* **1997**, 31.
[8] W. Henderson, S. R. Alley, *J. Organomet. Chem.* **2002**, *656*, 120.
[9] H. Gali, K. R. Prabhu, S. R. Karra, K. V. Katti, *J. Org. Chem.* **2000**, *65*, 676, and references therein; D. J. Brauer, M. Hingst, K. W. Kottsieper, C. Liek, T. Nickel, M. Tepper, O. Stelzer, W. S. Sheldrick, *J. Organomet. Chem.* **2002**, *645*, 14.
[10] N. Wiberg, A. Wörner, D. Fenske, H. Nöth, J. Knizek, K. Polborn, *Angew. Chem.* **2000**, *112*, 1908; *Angew. Chem. Int. Ed.* **2000**, *39*, 1838, and references therein.
[11] a) E. Hey, C. L. Raston, B. W. Skelton, A. H. White, *J. Organomet. Chem.* **1989**, *362*, 1; b) E. Hey-Hawkins, E. Sattler, *J. Chem. Soc. Chem. Commun.* **1992**, 775.
[12] a) R. A. Jones, S. U. Koschmieder, C. M. Nunn, *Inorg. Chem.* **1987**, *26*, 3610; b) E. Hey, F. Weller, *J. Chem. Soc. Chem. Commun.* **1988**, 782; c) E. Hey-Hawkins, S. Kurz, *Phosphorus Sulfur Silicon Relat. Elem.* **1994**, *90*, 281.
[13] a) S. Kurz, E. Hey-Hawkins, *Organometallics* **1992**, *11*, 2729; b) M. Driess, G. Huttner, N. Knopf, H. Pritzkow, L. Zsolnai, *Angew. Chem.* **1995**, *107*, 354; *Angew. Chem. Int. Ed. Engl.* **1995**, *34*, 316; c) T. Koch, S. Blaurock, F. Somoza, Jr., E. Hey-Hawkins, *Eur. J. Inorg. Chem.* **2000**, 2167; d) N. Wiberg, *Coord. Chem. Rev.* **1997**, *163*, 217; e) G. Fritz, P. Scheer, *Chem. Rev.* **2000**, *100*, 3341; f) K. Izod, *Adv. Inorg. Chem.* **2000**, *50*, 33.
[14] K. Wade, *Adv. Inorg. Chem. Radiochem.* **1976**, *18*, 1.
[15] Racemic **4** was synthesized and optically resolved according to the procedure developed by Ugi et al.: a) D. Marquading, H. Klusacek, G. W. Gokel, P. Hoffmann, I. K. Ugi, *J. Am. Chem. Soc.* **1970**, *92*, 5389; b) G. W. Gokel, I. Ugi, *J. Chem. Educ.* **1972**, *49*, 294.
[16] Structural data for **5**: $C_{102}H_{144}Fe_6Li_{12}N_6O_6P_6$, $M_r = 2154.43$, monoclinic, space group *P*2/*c*, $a = 1382.34(17)$, $b = 2619.4(3)$, $c = 1585.9(2)$ pm, $\beta = 107.304(2)°$, $V = 5.4825(12)$ nm^3, $Z = 2$, $\rho_{calcd} = 1.305$ Mg m^{-3}, $\mu = 0.912$ mm^{-1}, $2\theta_{max} = 46.8°$, $R = 0.0894$, $Rw = 0.1063$, three component twin (R. Sparks, GEMINI, an autoindexing program for twinned crystals, Bruker Software

Vers. 1.02), twin law by rows: 1 0 0, 0.5 0.5 −0.5, −0.5 −1 −2 and 1 0 0, −0.5 −0.5 −0.5, 0.5 1 2, twin domain ratio 0.53:0.27:0.20, 18534 measured reflections, adjacent reflections in the range from 0.007–0.030 Å were considered to be partially overlapped and ignored, 611 refined parameters, maximal residual electron density 0.53 e Å^{-3}. Data were collected with a Siemens CCD (SMART) diffractometer ($\lambda(Mo_{K\alpha}) = 71.073$ pm, $T = 203$ K). 8036 reflections from the major component were used for refinement (SAINT) of the unit cell parameters. Empirical absorption correction was carried out with SADABS (G. M. Sheldrick, SADABS, Program for Scaling and Correction of Area-detector Data). The structure was solved by direct methods (SHELXS97: G. M. Sheldrick, SHELXS-97, Program for Crystal Structure Solution, Universität Göttingen, **1997**). Fe, C, P, N, and Li atoms were refined anisotropically; the position of all H atoms were calculated and refined isotropically. CCDC-255054 (**5**) contains the supplementary crystallographic data for this paper. These data can be obtained free of charge from the Cambridge Crystallographic Data Centre via www.ccdc.cam.ac.uk/data_request/cif.

[17] a) M. A. Beswick, J. M. Goodman, C. N. Harmer, A. D. Hopkins, M. A. Paver, P. R. Raithby, A. E. H. Wheatley, D. S. Wright, *Chem. Commun.* **1997**, 1879; b) A. Bashall, A. D. Bond, A. D. Hopkins, S. J. Kidd, M. McPartlin, A. Steiner, R. Wolf, A. D. Woods, D. S. Wright, *J. Chem. Soc. Dalton Trans.* **2002**, 343.

[18] a) M. Westerhausen, S. Weinrich, G. Kramer, H. Piotrowski, *Inorg. Chem.* **2002**, *42*, 7072; b) M. Driess, U. Hoffmanns, S. Martin, K. Merz, H. Pritzkow, *Angew. Chem.* **1999**, *111*, 2906; *Angew. Chem. Int. Ed.* **1999**, *38*, 2733.

[19] J. K. Lindsay, C. R. Hauser, *J. Org. Chem.* **1957**, *22*, 355.

[20] a) A. D. Becke, *J. Chem. Phys.* **1993**, *98*, 5648; b) C. Lee, W. Yang, R. G. Parr, *Phys. Rev. B* **1988**, *37*, 785.

[21] Gaussian 03 (Revision B.03), M. J. Frisch, G. W. Trucks, H. B. Schlegel, G. E. Scuseria, M. A. Robb, J. R. Cheeseman, J. A. Montgomery, Jr., T. Vreven, K. N. Kudin, J. C. Burant, J. M. Millam, S. S. Iyengar, J. Tomasi, V. Barone, B. Mennucci, M. Cossi, G. Scalmani, N. Rega, G. A. Petersson, H. Nakatsuji, M. Hada, M. Ehara, K. Toyota, R. Fukuda, J. Hasegawa, M. Ishida. T. Nakajima, Y. Honda, O. Kitao, H. Nakai, M. Klene, X. Li, J. E. Knox, H. P. Hratchian, J. B. Cross, C. Adamo, J. Jaramillo, R. Gomperts, R. E. Stratmann, O. Yazyev, A. J. Austin, R. Cammi, C. Pomelli, J. W. Ochterski, P. Y. Ayala, K. Morokuma, G. A. Voth, P. Salvador, J. J. Dannenberg, V. G. Zakrzewski, S. Dapprich, A. D. Daniels, M. C. Strain, O. Farkas, D. K. Malick, A. D. Rabuck, K. Raghavachari, J. B. Foresman, J. V. Ortiz, Q. Cui, A. G. Baboul, S. Clifford, J. Cioslowski, B. B. Stefanov, G. Liu, A. Liashenko, P. Piskorz, I. Komaromi, R. L. Martin, D. J. Fox, T. Keith, M. A. Al-Laham, C. Y. Peng, A. Nanayakkara, M. Challacombe, P. M. W. Gill, B. Johnson, W. Chen, M. W. Wong, C. Gonzalez, J. A. Pople, Gaussian, Inc., Pittsburgh, PA, **2003**.

[22] W. J. Hehre, L. Radom, P. von R. Schleyer, J. A. Pople, *Ab-initio Molecular Orbital Theory*, Wiley, New York, **1986**.

Cage Compounds

Rational Design of a Coordination Cage with a Trigonal-Bipyramidal Shape Constructed from 33 Building Units**

Iris M. Müller and Daniela Möller*

The rapidly growing field of supramolecular coordination chemistry can be divided into two classes according to the products formed. The polymers are already well-studied because of possible applications as new materials, heterogeneous catalysts, and ion-exchange materials.[1] The other class of supramolecular entities, discrete cage molecules, are conceived by rational design and prepared from a set of molecular building blocks that fit together such that the stoichiometry and symmetry elements of the product are predestined by the starting compounds.[2] In most of the coordination cages formed by this method the corners correspond to the metal centers, which are linked by twofold bridging ligands.[2–6] The use of building blocks that cover the faces of the cage is not as common. Triangular subunits were used to form tetrahedral, octahedral, and adamantanoid coordination cages.[2–6] Cages with lower symmetry and triangular faces have been synthesized only in the past few years.[6–10] Here we report the rational design of a coordination cage with the outer shape of a trigonal bipyramid. The characterization of an intermediate gives insight into the reaction mechanism.

To our knowledge, the formation of a trigonal bipyramid consisting of five metal centers as the corners and nine ligands as twofold connecting units (M_5L_9) has not been achieved. The reason may be the different coordination requirements of the metal centers: the equatorial centers require four coordination sites while the axial ones need only three (Figure 1 a). Nevertheless, a few systems have been reported in which the equatorial edges are not covered by ligands, and coordination cages with M_5L_6 topology resulted (Figure 1 b).[7] A related system is shown in Figure 1 c, d, in which three metal centers (depicted in gray) are coordinated by two ligands with threefold symmetry. Depending on the geometry of the central atom or atom group (usually a phenyl ring) in this ligand, a trigonal bipyramid or a trigonal-prismatic system is formed. Both types of complexes have been reported a few times.[8,9] The use of triangular subunits leads to two additional means of constructing a trigonal-bipyramidal cage (Figure 1 e, f). In the M_5L_6 system of type e again the

[*] Dr. I. M. Müller, Dipl.-Chem. D. Möller
Lehrstuhl für Analytische Chemie, NC 4/27
Ruhr-Universität Bochum
44780 Bochum (Germany)
Fax: (+49) 234-321-4420
E-mail: iris.m.mueller@rub.de

[**] The authors thank Heike Schucht (Max-Planck-Institut für Bioanorganische Chemie, Mülheim) for collecting data for **1** and **2**.

Supporting information for this article is available on the WWW under http://www.angewandte.org or from the author.

 DOI: 10.1002/anie.200463034

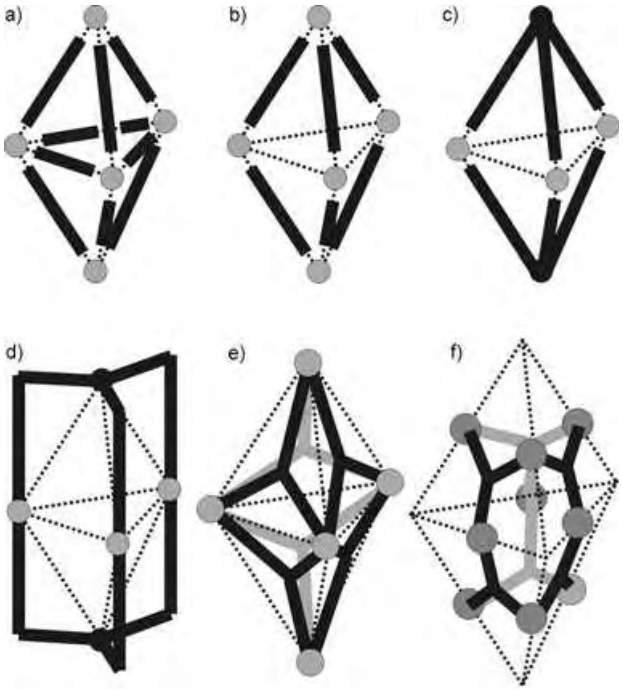

Figure 1. Schematic drawing of different trigonal-bipyramidal (tbp) cages and one related prismatic cage with different topologies; a) M_5L_9, b) M_5L_6, c) M_3L_2 (tbp), d) M_3L_2 (prismatic), e) M_5L_6, f) M_9L_6.

metal centers must adopt different coordination geometries, and again such cages have not been observed up to now. Cages in which C_3-symmetric ligands cover the six faces of the trigonal bipyramid and the metal centers represent the edges have been reported only twice. Cages with one and two metals per edge form capsules with $M_{18}L_6$ and $M_{15}L_6$ topology constructed from 24 and 21 building units, respectively.[10]

To construct larger cages with more building units, we followed this design principle, but in addition to metal centers for the linkage along the edges we used a second twofold bridging ligand. One equatorial corner in the intended trigonal bipyramid is similar to the corner in an octahedron, which we previously constructed from the ligands tris(2-hydroxybenzyl)triaminoguanidinium chloride, $[H_6L]Cl$, and sodium 5,5-diethylbarbiturate, NaHbar, which have threefold and twofold symmetry, respectively (Figure 2).[5] The obvious question is how formation of such an octahedral cage of higher symmetry can be prevented. At the corners of the octahedron close contacts between two aromatic protons were observed (2.5(2) Å).[5] The replacement of these hydrogen atoms with bulkier Br atoms should prevent the formation of the octahedral cage. Therefore, we allowed tris(5-bromo-2-hydroxybenzyl)triaminoguanidinium chloride, $[H_6Br_3L]Cl$,[11] to react with $PdCl_2$ and NaHbar under similar conditions. Dark red plates of $(Et_3NH)_6(Et_4N)_6[\{Pd_3(Br_3L)\}_6(\mu\text{-bar})_9]$ (**1**) formed; the result of the X-ray structure analysis is shown in Figure 3.[12] As expected, a trigonal bipyramid $[\{Pd_3(Br_3L)\}_6(\mu\text{-bar})_9]^{12-}$ containing a total of 33 building units was formed. Six $[Br_3L]^{5-}$ units cover the faces, and each coordinates three Pd^{2+} centers in a tridentate manner. The fourth coordination site of the square-planar metal centers is occupied by a barbiturate dianion, which bridges two adjacent faces.

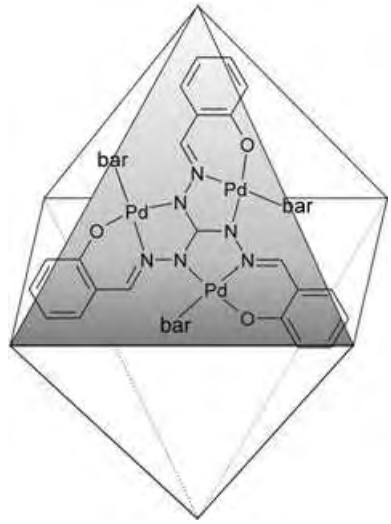

Figure 2. Schematic drawing of the octahedral cage $[(Pd_3L)_8\{\mu\text{-(bar)}\}_{12}]^{16-}$.

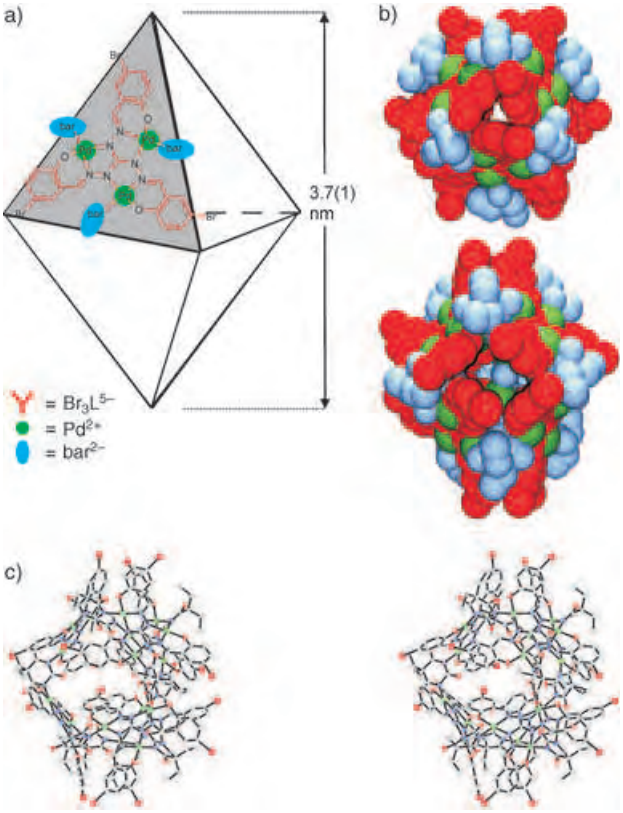

Figure 3. Crystal structure of **1**. a) Schematic drawing, b) space-filling models, and c) stereoplot (protons and counterions omitted for clarity).

The influence of the bromine atoms can be seen clearly at the corners. While at the axial corners the Br···Br distances are all equal and between 6.20(8) and 6.24(8) Å, the corners in the equatorial plane are more open with observed Br···Br distances of 5.15(8)–12.4(2) Å. The observed bond lengths

and angles in both ligands in **1** remain unchanged upon coordination, indicating that no significant distortion occurs (see Tables S1 and S2 in the Supporting Information). The cage anion in **1** is chiral; all ligands show the same screw direction of the central CN_6 core. Not surprisingly both enantiomers are present in the centrosymmetric space group *C*2/*c*. The anion in **1** has a twelvefold negative charge, and five of the counterions ($4\,Et_3NH^+$, $1\,Et_4N^+$) are present but disordered within the cage. The inside volume of the cage is estimated to be ≈ 1600 Å^3, which leaves enough space for up to 30 water molecules. Outside the cage a volume of ≈ 4500 Å^3 (or ≈ 36000 Å^3/46% of the whole unit cell) is occupied by the remaining seven cations ($2\,Et_3NH^+$, $5\,Et_4N^+$) and up to 110 disordered water molecules.

Interestingly, in addition to the dark red plates of **1** in the reaction mixture, bright red prismatic crystals of $(Et_3NH)_4(Et_4N)_4[\{Pd_3(Br_3L)\}_4(\mu\text{-bar})_4(Hbar)_4]$ (**2**) are always found. The result of their crystal structure analysis is depicted in Figure 4.[13] In one way **2** can be regarded as a tetrahedral coordination cage in which the bottom face is linked to only one and not to all three other faces. Each face is formed by a triangular $\{Pd_3(Br_3L)\}^+$ unit. The three faces that form the top of this open tetrahedron are linked by bridging bar^{2-} ligands, and the fourth face is also attached by a bridging barbiturate. In this way four Pd^{2+} centers are not involved in the linkage, and these metals each bond an $Hbar^-$ ligand at their fourth free coordination site. As a result the bottom face is not flexible but fixed in its position by strong hydrogen bonds between the protonated nitrogen atom of $Hbar^-$ and the carbonyl oxygen atom of another barbiturate ($d(N\cdots O) = 2.88(8)$ Å). The inside volume of the chiral cage is estimated to be ≈ 800 Å^3, leaving enough space for three Et_4N^+ counterions. Outside the cage a volume of ≈ 2100 Å^3 (or ≈ 4200 Å^3/31% of the whole centrosymmetric unit cell) is occupied by the remaining five cations ($1\,Et_4N^+$ and $4\,Et_3NH^+$) and roughly 40 water molecules. All bond lengths and angles in **2** fall within the expected ranges, and no significant distortions are observed (see Tables S1 and S2 in the Supporting Information).

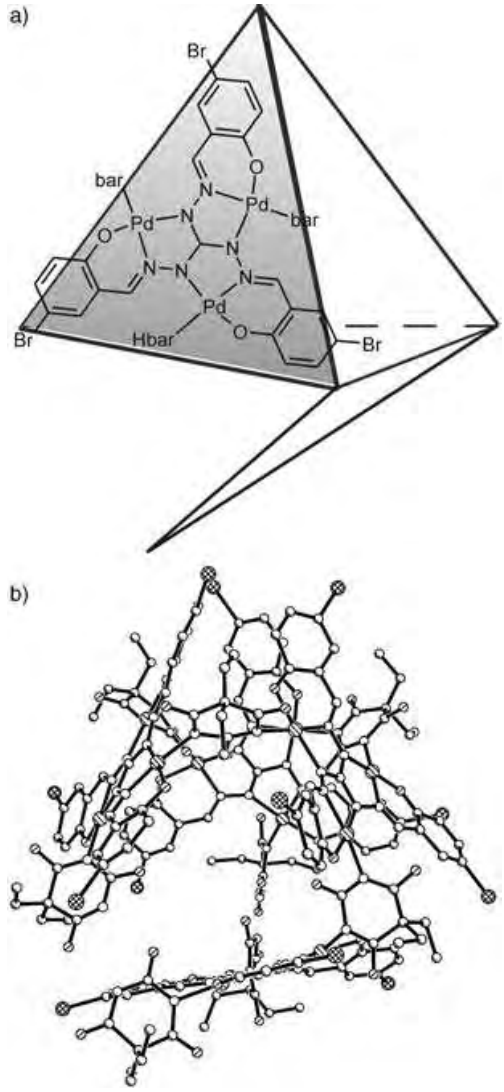

Figure 4. Crystal structure of **2**. a) Schematic drawing and b) crystal structure (protons and counterions omitted for clarity).

Cage **2** can also be seen as two-thirds of an incipient trigonal bipyramid. Only two triangular faces are missing, and all required barbiturates are already in place. Taken together with previous results, the structure of **2** provides insight into possible formation mechanism. In the first step the deprotonated ligand coordinates three square-planar metal centers. Since the free coordination sites are occupied by $Hbar^-$ ligands, the dianionic triangular building block $\{M_3(Br_3L)\}^{2-}$ results (see Figure 5a). This fragment has already been crystallized and analyzed for $M = Cu^{2+}$.[11] These units then react with each other with loss of H_2bar; this type of reaction has been confirmed under ESI conditions, again with $M = Cu^{2+}$ (see Figure 5b).[11] Linkage of three and four of these units with accompanying loss of H_2bar leads to the open trigonal pyramid and the coordination cage **2**, respectively (see Figure 5c). The subsequent introduction of two more triangular units would then lead to the formation of the trigonal bipyramid **1**.

We have succeeded in the rational, planned synthesis of the trigonal-bipyramidal coordination cage **1** with low symmetry from a set of molecular building blocks. Based on the structure of another cage compound, **2**, and previous results we suggest a possible formation mechanism.

Experimental Section

Tris(5-bromo-2-hydroxybenzyl)triaminoguanidinium chloride was prepared according to literature methods.[11] Sodium 5,5-diethylbarbiturate was purchased and used without further purification.

1 and **2**: A solution of $PdCl_2$ (48.6 mg, 0.274 mmol) and Et_4NCl (42.5 mg, 0.256 mmol) in acetonitrile (4 mL) was prepared. Solutions of tris(5-bromo-2-hydroxybenzyl)triaminoguanidinium chloride (64.7 mg, 0.0938 mmol) and sodium 5,5-diethylbarbiturate (27.6 mg, 0.134 mmol) in a mixture of acetonitrile and water (10:1, 2 mL each) were added. Then triethylamine (1 mL) was slowly diffused into the reaction mixture. After a few weeks dark red plates of **1** and red prisms of **2** formed. The two compounds were separated manually under the microscope, which resulted in lower yields of 30.8 mg (3.5×10^{-3} mmol, 23.5% relative to NaHbar) for **1** and 40.9 mg (6.5×10^{-3} mmol, 38.8% relative to NaHbar) for **2**. Elemental analyses

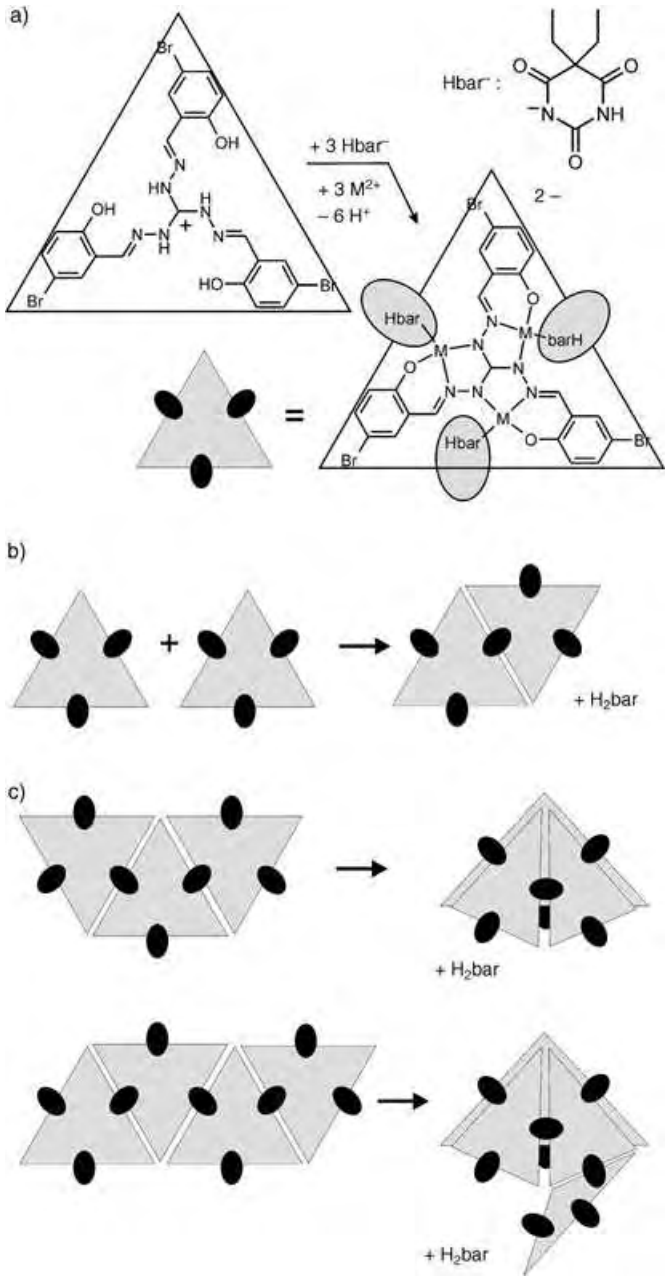

Figure 5. Possible reaction mechanism for the formation of coordination cages **1** and **2** see text for details.

[%] calcd for $C_{288}H_{378}N_{66}O_{45}Br_{18}Pd_{18}\cdot 140\,H_2O$, **1**, (11360.47): C 30.45, H 5.84, N 8.14, Pd 16.86; found: C 30.26, H 4.99, N 8.08, Pd 17.01. Elemental analyses [%] calcd for $C_{208}H_{276}N_{48}O_{36}Br_{12}Pd_{12}\cdot 30\,H_2O$, **2**, (6801.07): C 36.73, H 4.98, N 9.89, Pd 18.78; found: C 36.83, H 4.16 , N 10.02, Pd 18.45.

X-ray analysis: Intensity data were collected for **1** on a Nonius Kappa CCD ($Mo_{K\alpha}$ rotating anode) and for **2** on a Siemens SMART CCD ($Cu_{K\alpha}$ rotating anode), and in both cases the ω-scan method was employed. All data were corrected for Lorentz and polarization effects. The structures of **1** and **2** were solved by direct methods (SHELXS-97)[14] and refined by a full-matrix least-squares refinement procedure (SHELXL-97).[15] All protons were placed at geometrically estimated positions. Due to the large number of disordered counterions and solvent molecules outside the cages and the resulting low ratio of reflections to parameters, we decided to correct the X-ray data for their influence with the SQUEEZE routine in PLATON.[16] CCDC 258971–258972 contain the supplementary crystallographic data for this paper. These data can be obtained free of charge from the Cambridge Crystallographic Data Centre via www.ccdc.cam.ac.uk/data_request/cif.

Received: December 22, 2004
Published online: April 7, 2005

Keywords:
self-assembly · bridging ligands · cage compounds · palladium · solid-state structures

[1] For recent reviews, see: a) S. Kitagawa, R. Kitaura, S. Noro, *Angew. Chem.* **2004**, *116*, 2388; *Angew. Chem. Int. Ed.* **2004**, *43*, 2334; b) C. Janiak, *Dalton Trans.* **2003**, 2781; c) B. Moulton, M. J. Zaworotko, *Chem. Rev.* **2001**, *101*, 1629; d) S. R. Batten, *CrystEngComm* **2001**, *18*, 1; e) M. J. Zaworotko, *Angew. Chem.* **2000**, *112*, 3180; *Angew. Chem. Int. Ed.* **2000**, *39*, 3052; f) R. Robson, *J. Chem. Soc. Dalton Trans.* **2000**, 3735.

[2] For recent reviews, see: a) R. W. Saalfrank, B. Demleitner, H. Glaser, H. Maid, S. Reihs, W. Bauer, M. Maluenga, F. Hampel, M. Teichert, H. Krautscheid, *Eur. J. Inorg. Chem.* **2003**, 822; b) G. F. Swieger, T. J. Malefetse, *Coord. Chem. Rev.* **2002**, *225*, 91; c) S. Leininger, B. Olenyuk, P. J. Stang, *Chem. Rev.* **2000**, *100*, 853.

[3] For chiral cages, see: T. D. Hamilton, L. R. MacGillivray, *Cryst. Growth Des.* **2004**, *4*, 419.

[4] a) I. M. Müller, D. Möller, C. A. Schalley, *Angew. Chem.* **2005**, *117*, 485; *Angew. Chem. Int. Ed.* **2005**, *44*, 480; b) I. M. Müller, R. Robson, F. Separovic, *Angew. Chem.* **2001**, *113*, 4519; *Angew. Chem. Int. Ed.* **2001**, *40*, 4385.

[5] I. M. Müller, S. Spillmann, H. Franck, R. Pietschnig, *Chem. Eur. J.* **2004**, *10*, 2207.

[6] a) R. W. Saalfrank, H. Glaser, B. Demleitner, F. Hampel, M. M. Chowdhry, V. Schünemann, A. X. Trautwein, G. B. M. Vaughan, R. Yeh, A. V. Davis, K. N. Raymond, *Chem. Eur. J.* **2002**, *8*, 493; b) D. W. Johnson, J. Xu, R. W. Saalfrank, K. N. Raymond, *Angew. Chem.* **1999**, *111*, 3058; *Angew. Chem. Int. Ed.* **1999**, *38*, 2882.

[7] Recent papers: a) X. Sun, D. W. Johnson, D. L. Caulder, K. N. Raymond, E. H. Wong, *J. Am. Chem. Soc.* **2001**, *123*, 2752; b) X. Sun, D. W. Johnson, K. N. Raymond, E. H. Wong, *Inorg. Chem.* **2001**, *40*, 4504; c) C. J. Matthews, L. K. Thompson, S. R. Parsons, Z. Xu, D. O. Miller, S. L. Heath, *Inorg. Chem.* **2001**, *40*, 4448.

[8] Recent papers: a) P. S. Mukherjee, N. Das, P. J. Stang, *J. Org. Chem.* **2004**, *69*, 3526; b) Y. K. Kryschenko, S. R. Seidel, D. C. Muddiman, A. I. Nepomuceno, P. J. Stang, *J. Am. Chem. Soc.* **2003**, *125*, 9647; c) C. J. Kuehl, Y. K. Kryschenko, U. Radhakrishnan, S. R. Seidel, S. D. Huang, P. J. Stang, *Proc. Natl. Acad. Sci. USA* **2002**, *99*, 4932.

[9] Recent papers: a) C. J. Kuehl, T. Yamamoto, S. R. Seidel, P. J. Stang, *Org. Lett.* **2002**, *4*, 913; b) C.-Y. Su, Y.-P. Cai, C.-L. Chen, F. Lissner, B.-S. Kang, W. Kaim, *Angew. Chem.* **2002**, *114*, 3519; *Angew. Chem. Int. Ed.* **2002**, *41*, 3371.

[10] a) K. Umemoto, H. Tsukui, T. Kusukawa, K. Biradha, M. Fujita, *Angew. Chem.* **2001**, *113*, 2690; *Angew. Chem. Int. Ed.* **2001**, *40*, 2620; b) N. Takeda, K. Umemoto, K. Yamaguchi, M. Fujita, *Nature* **1999**, *398*, 794.

[11] I. M. Müller, D. Möller, *Eur. J. Inorg. Chem.* **2005**, 257.

[12] Crystal data for **1**: $0.09\times0.25\times0.25$ mm^3, monoclinic, $C2/c$, $a=79.90(2)$, $b=27.828(6)$, $c=36.148(7)$ Å, $\beta=102.28(3)$, $V=78534(27)$ Å^3, $\rho_{calcd}=1.495$ g cm^{-3}, $2\theta_{max}=46.04°$, $\lambda=0.71073$ Å, $T=100$ K, 212440 measured reflections, 51676 independent reflections ($R_{int}=0.1123$), 24895 observed reflec-

tions ($I > 2\sigma(I)$), $\mu = 2.70\ mm^{-1}$, empirical absorption correction, $T_{min} = 0.497$, $T_{max} = 0.785$, 2354 parameters, $R_1(I>2\sigma(I)) = 0.112$, wR_2(all data) = 0.283, max./min. residual electron density 2.33/ −1.31 e Å^{-3}.

[13] Crystal data for **2**: $0.10 \times 0.10 \times 0.15\ mm^3$, triclinic, $P\bar{1}$, $a =$ 20.224(1), $b = 21.536(1)$, $c = 35.090(2)$ Å, $\alpha = 90.074(3)$, $\beta =$ 99.291(3), $\gamma = 114.542(3)°$, $V = 13\,680(2)$ Å^3, $\rho_{calcd} =$ 1.519 g cm^{-3}, $2\theta_{max} = 135.40°$, $\lambda = 1.54178$ Å, $T = 100$ K, 72 857 measured reflections, 36 554 independent reflections ($R_{int} =$ 0.1028), 16 311 observed reflections ($I > 2\sigma(I)$), $\mu = 8.803\ mm^{-1}$, numerical absorption correction, $T_{min} = 0.236$, $T_{max} = 0.416$, 1697 parameters, $R_1(I>2\sigma(I)) = 0.1188$, wR_2(all data) = 0.3258, max./ min. residual electron density 2.84/−2.24 e Å^{-3}.

[14] G. M. Sheldrick, SHELXS-97, Program for Crystal Structure Solution, University Göttingen, **1997**.

[15] G. M. Sheldrick, SHELXL-97, Program for Crystal Structure Refinement, University Göttingen, **1997**.

[16] A. L. Spek, *Acta Crystallogr. Sect. A* **1990**, *46*, C34.

Cluster Compounds

$Ga_{10}Br_{10}$(4-*tert*-Butylpyridine)$_{10}$: A Mixed-Valent Gallium(I) Subhalide as an Intermediate during the Formation of Elemental Gallium?**

*Taike Duan, Gregor Stößer, and Hansgeorg Schnöckel**

Dedicated to Professor Gerd Becker on the occasion of his 65th birthday

Although numerous subvalent organometallic and metalloid clusters of gallium were reported in the last decade,[1] binary gallium subhalides are rare, the only exception being Ga_2X_4 species.[2] After the long known GaX_2 which is stable in aromatic solvents was shown to be a mixed-valent $Ga^+GaX_4^-$ compound,[3] many examples of donor-stabilized $Ga_2X_4(Do)_2$ (Do = donor) species could be characterized as "authentic" gallium(II) compounds.[4,5] On the way to molecular crystalline gallium(I) halides compounds only one example was known: a Ga_5Cl_7 species.[6] The first "authentic" gallium(I) compound, Ga_8I_8 (planar Ga_8 ring) was finally prepared several years ago.[7] Recently we reported the first polyhedral gallium subhalide $Ga_{24}Br_{22}$,[8] which is better described as $Ga_{12}(GaBr_2)_{10}(GaBr)_2$, in which icosahedral Ga_{12} frameworks are found both in the center and in the periphery and the mean oxidation state of gallium is only +0.92. Herein we present the compound $Ga_{10}Br_{10}$ as a further example of a gallium(I) subhalide. Similar to Ga_8I_8, the average oxidation state of the gallium atoms in this compound is +1, however, it should be interpreted as being a mixed-valent subhalide with four gallium(0), four gallium(II), and two gallium(I) atoms. The preparation, the structure, and the significance of this compound as an intermediate during the disproportionation to elemental gallium are discussed.

The co-condensation of the high-temperature molecules GaBr[9] and a solvent mixture of 4-*tert*-butylpyridine (4-*t*BuPy) and toluene (1:10) gives a dark red solution at −78 °C. The solution is concentrated at −25 °C under high vacuum and then kept at this temperature. Over several days yellowish-red platelike crystals of $Ga_{10}Br_{10}$(4-*tert*-butylpyridine)$_{10}$·4-toluene (**1**) are formed. Compound **1** is highly soluble in toluene and can also be recrystallized from this solvent. Yet the toluene solution of **1** turns pale when the temperature rises over −18 °C and above room temperature gallium metal precipitates slowly from it.[10]

The result of the X-ray structure analysis of **1**[11] is shown in Figure 1 (the data of the model compound $Ga_{10}Br_{10}(thf)_{10}$ (**1′**) determined by density functional (DFT) methods[12] are also listed). Six of the ten Ga atoms in **1** form a six-membered ring, of which two Ga atoms (Ga3 and Ga3′) are bonded to two terminal $GaBr_2$(4-*t*BuPy) entities by two-center-two electron (2c-2e) bonds; two Ga atoms are "naked", which means they are bonded only to donor molecules and other Ga atoms. The last two Ga atoms of the six-membered ring are each bonded to one Br atom and one donor molecule, therefore these atoms can be identified as gallium(I) atoms.[13]

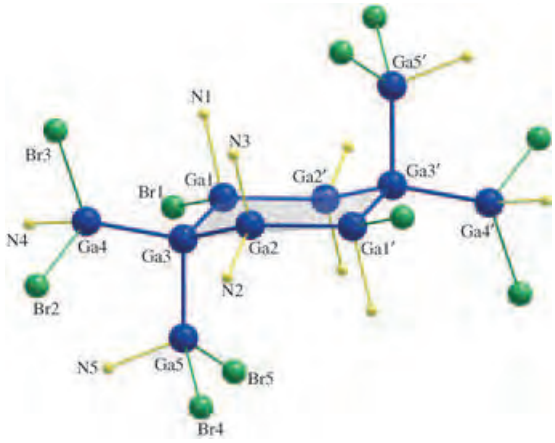

Figure 1. Results of the X-ray structure analysis of **1** (for clarity all C and H atoms are omitted) and selected bond lengths [pm] and angles [°] of **1** and the calculated model compound $Ga_{10}Br_{10}(thf)_{10}$ (**1′**; in parenthesis): Ga1-Ga2′ 249.3 (255), Ga1-Ga3 245.1 (251), Ga2-Ga3 245.6 (251), Ga3-Ga4 243.7 (250), Ga3-Ga5 244.1 (250), Ga1-Br1 249.1 (254), Ga1-N1 210.8 (216), Ga2-N2 210.4 (216), Ga2-N3 212.1 (216), Ga4-Br3 244.5 (247), Ga4-Br2 244.1 (247), Ga4-N4 208.4 (216), Ga5-Br4 241.3 (247), Ga5-Br5 243.4 (247), Ga5-N5 206.0 (216); Ga2-Ga1′-Ga3′ 119.1, Ga3-Ga2-Ga1′ 124.2, Ga2-Ga3-Ga1 106.7.

[*] T. Duan, Dr. G. Stößer, Prof. Dr. H. Schnöckel
Institut für Anorganische Chemie
Universität Karlsruhe (TH)
Engesserstrasse 15, Geb. 30.45, 76128 Karlsruhe (Germany)
Fax: (+49) 721-608-4854
E-mail: hansgeorg.schnoeckel@chemie.uni-karlsruhe.de

[**] The authors are grateful to Prof. Dr. Ingo Krossing for helpful discussions. This work was supported by the Deutsche Forschungsgemeinschaft and the Fonds der Chemischen Industrie.

 DOI: 10.1002/anie.200462075

The Ga–Ga bonds in the six-membered ring of **1** range from 249.3 to 245.1 pm and are, as expected, slightly longer than those to the terminal gallium atoms (243.8 pm). The Ga–Br bonds are consistent with expectations: the Ga^{I}–Br bond (Ga1 249.1 pm) is longer than the Ga^{II}–Br bonds (Ga4/Ga5 244 pm). Analogously, different Ga–N distances are also found for Ga1 (211 pm) and Ga4 (205 pm). Despite of the structural difference between **1** and $Ga_8I_8(Do)_6$, the average Ga–Ga bond length is similar in both compounds: **1** (245 pm) and Ga_8I_8 (246 pm).[6]

The structure of **1** and the necessary conditions for its synthesis indicate that the following mechanism for the formation and further reactions of **1** is plausible: Compound **1** is formed by the reaction of two Ga_5Br_7 entities[14] with excess GaBr(Do) under the elimination of $GaBr_3(Do)$ (Scheme 1). For the model compound **1′** such a reaction is

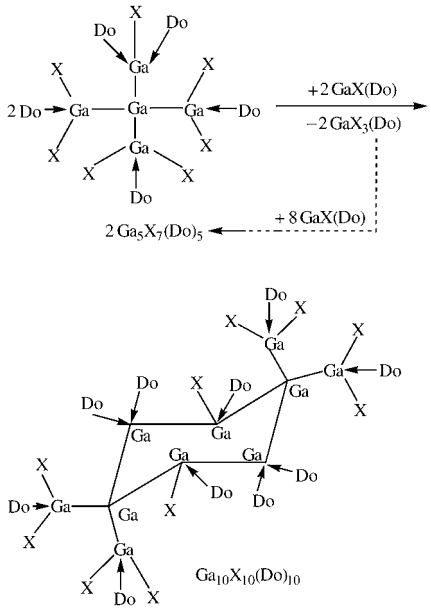

Scheme 1. The mechanism for the formation of **1** based on synthetic conditions and DFT calculations.

exothermic by $-135\ kJ\,mol^{-1}$ according to DFT calculations. The generated $GaBr_3(Do)$ molecules will be further reduced by insertion of excess GaBr(Do), and Ga_5Br_7 is formed. An analogous mechanism has been described for the formation of Al_5X_7 species.[2,15] If THF is used as donor, the reaction does not stop at **1′**; on the contrary, through the formation of additional Ga–Ga bonds and the reduction of **1** by GaBr the recently reported compound $Ga_{24}Br_{22}(thf)_{10}$ (**2**) could be formed. According to DFT calculations, the following reaction given in Equation (1) is exothermic by $-560\ kJ\,mol^{-1}$.

$$2\,Ga_{10}Br_{10}(thf)_{10}\ (\mathbf{1'}) + 5\,GaBr(thf) \rightleftharpoons Ga_{24}Br_{22}(thf)_{10}\ (\mathbf{2}) + GaBr_3(thf) + 14\,THF \quad (1)$$

Since the volatile THF released was removed by repeated evacuation during the preparation of **2**,[8] the equilibrium of Equation (1) would be clearly shifted to the right to favor the formation of the polyhedral Ga_{24} subhalide **2**. If the less volatile donor 4-*t*ert-butylpyridine[16] (b.p. 194–197 °C) instead of THF (b.p. 65–67 °C) is used and the reaction temperature is kept below −20 °C, **1** can be trapped as an intermediate during the formation of **2**. The disproportionation of **1** to **2** and finally to gallium metal and $GaBr_3$ is a chain reaction, that is, the $GaBr_3$ formed in each step reacts further with the excess GaBr species present to form Ga_5Br_7 species, which is re-introduced into the reaction cascade.

The formation of gallium metal by disproportionation is fairly restrained under −20 °C (at this temperature β-gallium and δ-gallium should be formed[1]). Probably the transformation of the puckered Ga_6 ring structure of **1** into β-gallium (planar Ga_n layers) or δ-gallium (icosahedral fragments) requires a too high activation energy. The fragmentation of **1** with the simultaneous formation of metal starts reluctantly even at −18 °C and proceeds rapidly and completely a little above room temperature. In this temperature range, however, α-gallium and liquid gallium are the stable phases. Since the topology of the Ga_6 ring in **1** is very similar to the Ga_6 framework in α-gallium (Figure 2), it seems plausible that

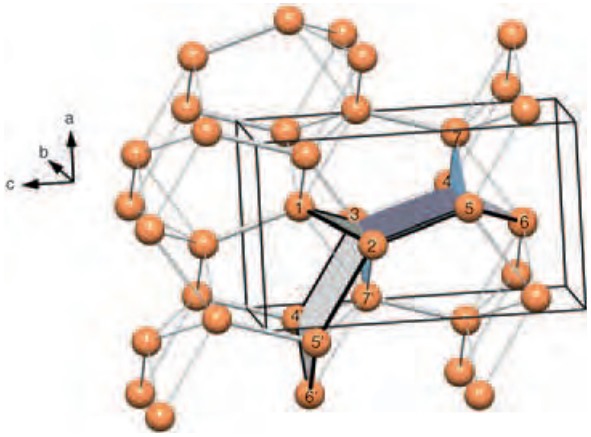

Figure 2. Ga_6 entities within α-gallium: bond lengths [pm] within the Ga_6 rings: Ga1-Ga2(Ga3)/[Ga6-Ga4(Ga5)] 279.4, Ga3-Ga4/[Ga2-Ga5] 244.8, Ga6′-Ga4′(Ga5′) 272.9, Ga4(Ga5)-Ga7/[Ga7′-Ga2(Ga3)] 272.9. The characteristic short Ga–Ga bonds (244.8 pm, for example, Ga3–Ga4) in α-gallium are highlighted; orange Ga.

the precipitation of α-gallium from **1** does not require a large activation energy. Thus, while for halides, kinetically simple insertion reactions (e.g. $4\,GaX + GaX_3 \rightarrow Ga_5X_7$) lead to their rapid disproportionation even at low temperatures and consequently to an extremely difficult isolation of the subhalides, further reactions are blocked for similar clusters protected by bulky ligands: for example, the gallium(I) compound $[Ga_6(SiPh_2Me)_8]^{2-}$ [17] with a Ga_6 framework similar to that in β-gallium does not decompose to metal even above room temperature.[18]

The isolation of **1** as an intermediate during the disproportionation of metastable GaX species in solution allows for the first time an insight into this complex process of self-organization. During this process, metalloid clusters with an increasing number of "naked" Ga^0 atoms in the core and

GaX_2 entities in the periphery grow by association, redox, and elimination reactions and could be regarded as precursors on the way to nuclei for the crystallization of the bulk metal.

Experimental Section

The high-temperature molecules GaBr (approximately, 48 mmol) were condensed together with a solvent mixture of toluene and 4-*tert*-butylpyridine (120 mL; volume ratio 10:1, ca. 1.5 equivalents of donor per Ga atom) at −196 °C.[9] The dark red solutions formed (ca. 0.41 M) are stable when kept at −78 °C. A portion (5 mL, ca. 2 mmol GaBr) of the GaBr solution was warmed from −78 °C to −20 °C overnight. The red solution was then concentrated by half at −25 °C under high vacuum and finally was kept at this temperature. During several days, yellowish-red plate crystals of $Ga_{10}Br_{10}$(4-*tert*-butylpyridine)$_{10}$·4toluene (**1**) were formed (yield: 290 mg, ca. 45 %). Compound **1** dissolves very well in toluene and can also be recrystallized from this solvent, yet it decomposes above −18 °C. Tiny single crystals of **1** were also formed directly when the GaBr solution was kept for several weeks at −78 °C and under vacuum conditions.

Received: September 22, 2004
Revised: February 14, 2005
Published online: April 8, 2005

Keywords: cluster compounds · density functional calculations · gallium · metalloid · structure determination

[1] A. Schnepf, H. Schnöckel, *Angew. Chem.* **2002**, *114*, 3683; *Angew. Chem. Int. Ed.* **2002**, *41*, 3533.
[2] H. Schnöckel, C. Klemp in *Inorganic Chemistry Highlights* (Eds.: G. Meyer, D. Naumann, L. Wesemann), Wiley-VCH, Weinheim, **2002**.
[3] G. Garton, H. M. Powell, *J. Inorg. Nucl. Chem.* **1957**, *4*, 84; H. Schmidbaur, *Angew. Chem.* **1985**, *97*, 893; *Angew. Chem. Int. Ed. Engl.* **1985**, *24*, 893.
[4] J. C. Beamish, R. W. Small, I. J. Worrall, *Inorg. Chem.* **1979**, *18*, 220; R. W. Small, I. J. Worrall, *Acta Crystallogr. Sect. B* **1982**, *38*, 250; R. W. Small, I. J. Worrall, *Acta Crystallogr. Sect. B* **1982**, *38*, 86.
[5] T. Duan, H. Schnöckel, *Z. Anorg. Allg. Chem.* **2004**, *630*, 2622.
[6] The mixed-valent Ga_5X_7 compound $Ga_5Cl_7(Et_2O)_5$ contains formally only one Ga^I atom, D. Loos, H. Schnöckel, D. Fenske, *Angew. Chem.* **1993**, *105*, 1124; *Angew. Chem. Int. Ed. Engl.* **1993**, *32*, 1059. Further $Ga_5X_7(Do)_5$ compounds: T. Duan, G. Stößer, H. Schnöckel, *Z. Anorg. Allg. Chem.* **2005**, in press.
[7] C. Doriat, M. Friesen, E. Baum, A. Ecker, H. Schnöckel, *Angew. Chem.* **1997**, *109*, 2057; *Angew. Chem. Int. Ed. Engl.* **1997**, *36*, 1969.
[8] T. Duan, E. Baum, R. Burgert, H. Schnöckel, *Angew. Chem.* **2004**, *116*, 3252; *Angew. Chem. Int. Ed.* **2004**, *43*, 3190.
[9] C. Dohmeier, D. Loos, H. Schnöckel *Angew. Chem.* **1996**, *108*, 141; *Angew. Chem. Int. Ed. Engl.* **1996**, *35*, 129.
[10] The formation of elemental gallium is evident in this and in similar studies from its melting behavior, that is, the liquid Ga is formed just above room temperature.
[11] Crystal structure analysis of **1**: $M_r = 3216.88$, triclinic, space group $P\bar{1}$, crystal dimensions: $0.20 \times 0.13 \times 0.04$ mm, $\alpha = 109.340(12)$, $\beta = 96.698(13)$, $\gamma = 96.990(13)°$; $a = 14.550(2)$, $b = 15.801(3)$, $c = 16.084(2)$ Å, $V = 3414.2(9)$ Å^3, $Z = 1$, $\rho_{calcd} = 1.565$ g cm^{-3}, $M_\mu = 4.911$ mm^{-1}, $\Theta_{max} = 20.81°$, 15436 reflections measured, of which 6848 were independent ($R_{int} = 0.1603$), 669 parameter are refined. Numerical absorption correction: (min./max. transmission 0.3534/0.7933), $R_1 = 0.0799$, $W_{R2} = 0.1568$, GOOF on $F^2 = 0.967$, completeness of $2\Theta = 95.9$ %, max./min. residual electron density peaks: 0.773/−0.731. STOE-IPDS diffractometer ($Mo_{K\alpha}$ radiation, $\lambda = 0.71071$), $T = 100$ K. The structure was solved by direct methods and refined against F^2 for all observed reflections with $\Theta_{max} = 20.81$ °C (Θ was measured untill 22.2°, all reflections over 20.81° were omitted because of their weakness by using the "Shel" instruction during the refinement). Software used: SHELXS and SHELXTL (G. M. Sheldrick, Universität Göttingen). CCDC-250131 contains the supplementary crystallographic data for this paper. These data can be obtained free of charge from the Cambridge Crystallographic Data Centre via www.ccdc.cam.ac.uk/data_request/cif.
[12] The quantum chemical calculations were carried out with the modules in the program package TURBOMOLE with DFT (BP86 functional, SVP basis set). TURBOMOLE: a) O. Treutler, R. Ahlrichs, *J. Chem. Phys.* **1995**, *102*, 346; b) Funktional BP 86: A. D. Becke, *Phys. Rev. A* **1998**, 38, 3098; J. P. Perdew, *Phys. Rev. B* **1996**, *33*, 8822; c) RIDFT: K. Eichkorn, O. Treutler, H. Öhm, M. Häser, R. Ahlrichs, *Chem. Phys. Lett.* **1995**, *242*, 652; K. Eichkorn, F. Weigend, O. Treutler, R. Ahlrichs, *Theor. Chem. Acc.* **1997**, *97*, 119.
[13] According to DFT calculations, this formal interpretation of **1′** does not describe the bonding situation sufficiently. Thus the following charges of Ga and Br atoms were determined by using Ahlrichs–Heinzmann analyses giving the following values: Ga1 −0.20; Ga2 −0.15; Ga3 −0.75; Ga4 −0.15; Ga5 0.0; Br −0.5; O −0.3. The positive charges in the overall neutral compound are found at the C and H atoms of the donor molecules.
[14] Analogous to Ga_5Cl_7 and other similar species, see ref. [6].
[15] C. Klemp, G. Stößer, I. Krossing, H. Schnöckel, *Angew. Chem.* **2000**, *112*, 3834; *Angew. Chem. Int. Ed.* **2000**, *39*, 3691.
[16] 4-*tert*-butylpyridine was chosen not just because of its high boiling point, but because of its dissolving capacity for the donor-stabilized subhalides; in contrast, polar, insoluble products are formed when pyridine was used.
[17] A. Donchev, A. Schnepf, E. Baum, G. Stößer, H. Schnöckel, *Z. Anorg. Allg. Chem.* **2001**, *628*, 157.
[18] The lower stability of the possible octahedral isomer, Ga_6R_6, has been discussed in detail in ref. [15].

Fullerene-Based Micelles

Switchable Supramolecular Organization of Structurally Defined Micelles Based on an Amphiphilic Fullerene**

Stephan Burghardt, Andreas Hirsch, Boris Schade, Kai Ludwig, and Christoph Böttcher**

Some time ago we started to investigate the synthesis and supramolecular organization of dendritic amphiphiles that contain fullerenes or calixarenes as core units.[1–3] Apart from the synthesis of structurally persistent micelles, we were particularly interested in the assembly of functionalized micelles and liposomes in order to direct the aggregation behavior of these species with an appropriate external stimulus. Results from these studies could be useful for the development of drug-delivery systems. Examples of such dendritic amphiphiles include the globular amphifullerene **1**,[1] which contains a pair of carboxy-terminated amide dendrons and five dodecyl malonate addends attached to the fullerene core in an octahedral [1:5] addition pattern, and the calixarene derivative **2**,[3] which contains analogous hydrophilic and lipophilic units. In amphiphile **1** the space required for the hydrophilic and the hydrophobic areas is balanced whereas the extended chains have free conformational mobility. This ensures a wide spectrum of energetically favorable packing motifs both for the formation of micellar structures and for extended liposomal double layers. The existence of different aggregates was confirmed by electron microscopic investigations.[2a]

By contrast, we designed amphiphile **2** as a comparatively rigid T-shaped structure[3] that does not pack to form extended ultrastructures such as liposomes. We demonstrated that the supramolecular organization of **2** yields very small and strongly bent aggregates exclusively, which are the first proven examples of structurally persistent micelles.[3] Each of these C_2-symmetrical micelles consists of exactly seven molecules of amphiphile **2**. The structure was determined by cryogenic transmission electron microscopy (cryo-TEM) and

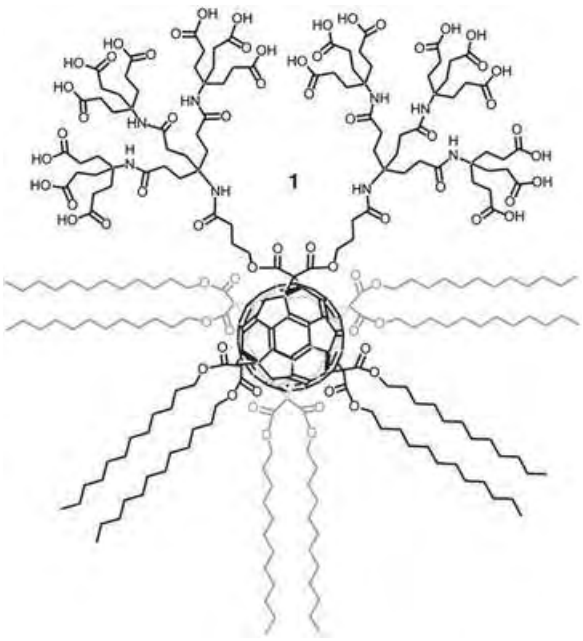

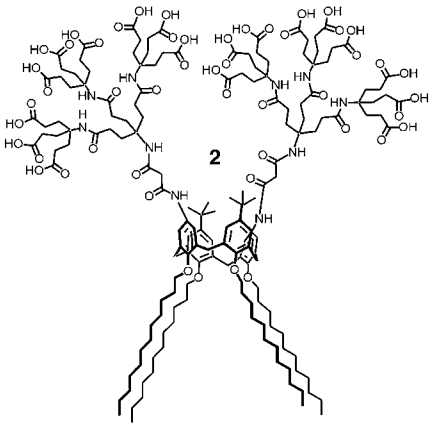

techniques for the three-dimensional reconstruction of single particles at a resolution of 12 Å.[3]

We report here for the first time on amphiphile **3** (see the Supporting Information), whose aggregation in different supramolecular organizational forms may be switched by changing the pH (Figure 1). In principle, the aggregation behavior of amphiphilic systems may be studied under quasi-native conditions by using combined methods: ultrafast cryogenic fixation of the samples ("vitrification") and direct observation by transmission electron microscopy upon simultaneous sample cooling ($\approx$120 K). The cooling rates ($>10^4$ K s^{-1}) during sample preparation are so high that molecular reorientation (e.g. formation of ice crystals) is prevented.[5,6] Ultimately, projection images of the aggregates are obtained by microscopy and thus information about their intrinsic structure is provided.

We examined amphiphile **3** at neutral pH in water (phosphate buffer pH 7.2) by these methods and found predominantly rod-shaped aggregates with a double-layer ultrastructure (Figure 2a). The diameter of these rods is 65 ±

[*] S. Burghardt, Prof. Dr. A. Hirsch
Institut für Organische Chemie
Universität Erlangen-Nürnberg
Henkestrasse 42, 91054 Erlangen (Germany)
Fax: (+49) 9131-852-6864
E-mail: andreas.hirsch@chemie.uni-erlangen.de
Dr. B. Schade, Dr. K. Ludwig, Dr. C. Böttcher
Forschungszentrum für Elektronenmikroskopie
Institut für Chemie
Freie Universität Berlin
Fabeckstrasse 36a, 14195 Berlin (Germany)
Fax: (+49) 30-838-56589
E-mail: bottcher@chemie.fu-berlin.de

[**] The authors are grateful to the Deutsche Forschungsgemeinschaft for financial support (DFG AH468/13-1 and Großgeräteinitiative to FU Berlin).

Supporting information for this article is available on the WWW under http://www.angewandte.org or from the author.

  DOI: 10.1002/anie.200462465

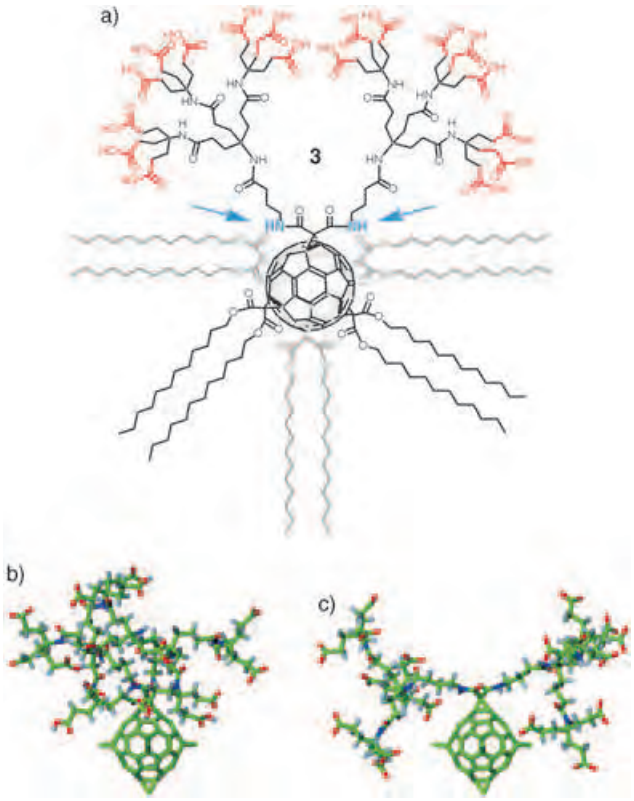

Figure 1. a) Amphiphilic fullerene dendrimer **3** with dendritic branches linked by amide bonds (blue arrow). b, c) Molecular models of differently protonated conformers of **3**, modeled with the program Tinker.[7] For clarity, the alkyl chains are not depicted. b) Dendrons partially protonated. According to earlier titration measurements on LB films, a pK_a of 7.5 is found for the chemically related dendrimer **1**.[2b] Accordingly, the simulation of **3** at pH 7.2 has been carried out by using eight negative charges (of a total of possible 18). c) Dendrons completely deprotonated (18 negative charges).

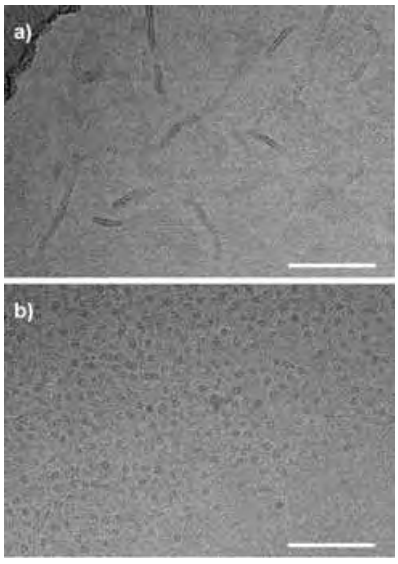

Figure 2. Representative electron micrograph showing aggregates of **3** embedded in vitrified water (scale bar: 50 Å). a) At pH 7.2 predominantly rod-shaped double-layered aggregates are found. b) At pH 9.2 exclusively globular micelles are found.

5 Å; the length is strongly variable and exceeds the diameter considerably. In addition, a few globular aggregates with a diameter of 85 ± 10 Å were found. When the pH of the neutral solution was increased to roughly 9 (borate buffer pH 9.2), those globular micelles with a diameter of 85 ± 10 Å were found exclusively (Figure 2b). Interestingly, apart from variations in diameter these globular micelles show a distinct internal structure. By analogy to our investigations on micellar structures of amphiphile **2**[3] we considered the structural motifs of the globular micelles to be an indication of structural persistence. Accordingly, each individual structure should represent a distinct spatial orientation of the aggregate. Thus, it should be possible in principle to determine the three-dimensional organization from the image data; variations in the diameters would arise from the aggregates' different orientations. By using the reconstruction techniques described earlier[3] (alignment, classification, angular reconstitution) (Figure 3a), we calculated the three-dimensional

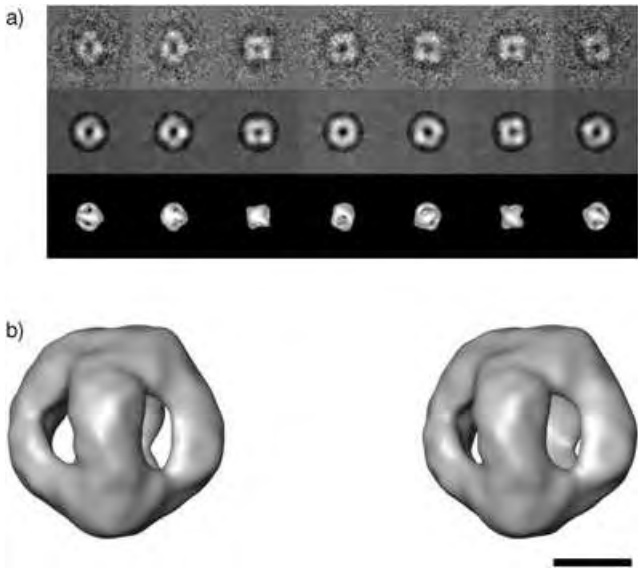

Figure 3. Three-dimensional reconstruction from electron cryogenic microscopic data of globular micelles formed by **3** at pH 9.2. a) The first row displays class sum images of micelles in various spatial orientations. Three-dimensional structural information was derived from the corresponding Euler angles at a resolution level of ≈16 Å. Back projections (second row) of the calculated volumes (third row) at identical Euler angles indicate the consistency with the experimental data. b) Stereoscopic view of the final three-dimensional reconstruction (scale bar: 25 Å).

structure for the globular micelles of **3** (Figure 3b). The successful reconstruction is evidence that the spatial molecular organization of the aggregates is identical within the achieved level of resolution (≈5000 individual aggregates were randomly extracted from the microscopic data).

To determine the possible molecular organization in the aggregates, we undertook a visual three-dimensional fitting of molecular models of **3** into the reconstructed 3D density map (Figure 4a and b). Based on a simulated conformation of **3** in its completely deprotonated form (Figure 1c) (generated with the program Tinker[7]), the globular micellar structure may be

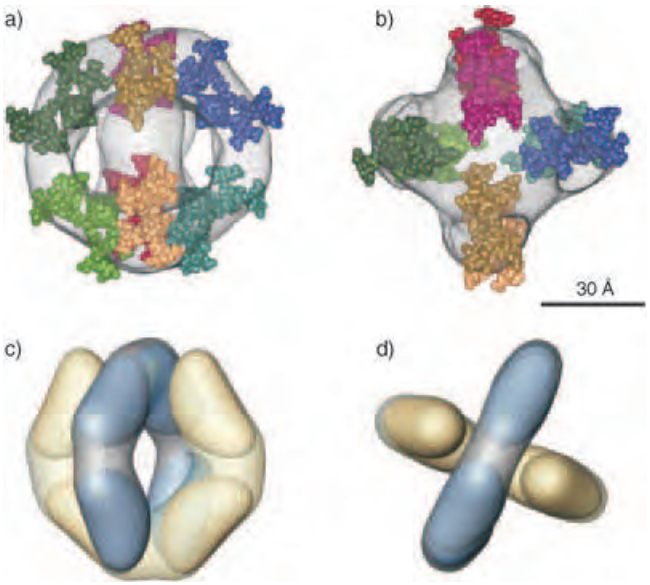

Figure 4. Interpretation of the reconstructed data. a) Eight head groups of the dendritic fullerene molecule may be fitted in a C_2-symmetrical mode into the reconstructed electron-density map. b) View of (a) tilted by 90° towards the front side. c) Schematic representation of the head-group assembly: Two planar U-shaped assemblies consisting of four molecules each (yellow and blue) are displaced by 90° along their longitudinal axes and are inserted —though not completely—into each other at their open ends. d) View of c) tilted by 90° towards the front side.

constructed from eight molecules in a C_2-symmetrical arrangement. The molecular organization of this aggregate may be described best by considering two planar U-shaped structures consisting of four molecules each. These are displaced by 90° along the longitudinal axis with respect to their open ends; however, they are not inserted completely into each other (Figure 4c and d). This molecular organization ensures a nearly spherical shape overall and thus very efficient shielding of all hydrophobic molecule parts from the aqueous environment. As was the case for the structurally persistent micelles derived from calixarene **2**, the innermost core area of the micelle formed by the hydrophobic alkyl chains is not reproduced in the reconstruction. Since individual chains do not assume a spatially defined conformation but are more or less arranged in a statistical way, this part of the aggregate is averaged out as a result of the statistical principles of the applied reconstruction method. Only the head groups, which are located easily due to the high-contrast fullerene entity, prove to be sterically persistent, thus yielding the found structural pattern.

The molecular structure of **3** encodes a supramolecular behavior representing a combination of supramolecular properties of **1** and **2**. On the one hand, and similar to **1**, the spatial demands of the hydrophilic and hydrophobic areas are well-balanced. On the other hand, and similar to **2**, the dendritic branches are linked by amide rather than ester linkages, resulting in enhanced rigidity. The significant structural change when the pH is lowered may be explained by electrostatic repulsion of the completely deprotonated carboxy groups, and enhanced solvation is a secondary effect. Accordingly, we may assume that at neutral pH the electrostatic repulsion is reduced as a consequence of partial protonation. This causes reduced solvation, which in turn leads to much closer packing as is evidenced by the smaller diameter of the rods relative to that of the globular micelles. Figure 1b shows the corresponding result of a conformational simulation of **3** in aqueous environment at neutral pH. The fact that the rod diameter is constant throughout suggests that the three-dimensional organization must be based on a circular-shaped cross-sectional area. Based on the dimensions and density profile, a double-layered molecular arrangement in a micellar cylinder can be visualized. According to this motif an appropriate radius of curvature of ca. 65 Å can be modeled by using approximately eight molecules. The corresponding model is depicted in Figure 5.

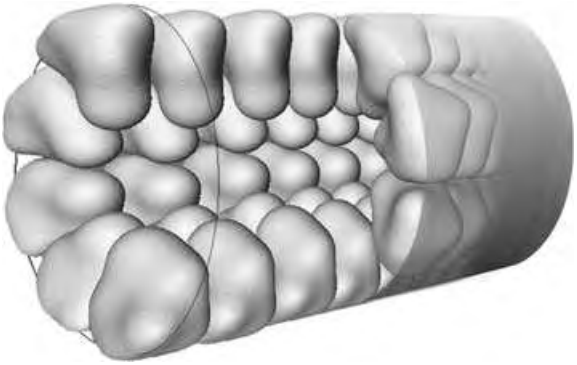

Figure 5. Proposed model of a molecular arrangement of **3** in micellar rods at neutral pH. The employed head-group volume is based on the partly protonated form shown in Figure 1b. Hydrophobic alkyl chains, which should reside at the center of the micelle, are not shown for clarity. They correspond to areas of low density in the electron microscopic images of Figure 2a.

We have demonstrated that by suitable substitution structurally persistent aggregates may be generated in a reproducible way. This opens up perspectives for the systematic investigation of the parameters responsible for aggregate formation. Fundamental investigations on the stability of the aggregates, in particular tolerance of chemical modification and functionalization of the head group, might form the basis for the synthesis of tailor-made transport systems. These may have potential for the selective deposition of drugs in living organisms.

Received: October 29, 2004
Published online: April 13, 2005

Keywords: amphiphiles · dendrimers · electron microscopy · fullerenes · micelles · self-assembly

[1] a) M. Brettreich, A. Hirsch, *Tetrahedron Lett.* **1998**, *39*, 2731–2734; b) M. Braun, S. Atalick, D. M. Guldi, H. Lanig, M. Brettreich, S. Burghardt, M. Hatzimarinaki, E. Ravanelli, M. Prato, R. Van Eldik, A. Hirsch, *Chem. Eur. J.* **2003**, *9*, 3867–3875.
[2] a) M. Brettreich, S. Burghardt, C. Böttcher, T. Bayerl, S. Bayerl, A. Hirsch, *Angew. Chem.* **2000**, *112*, 1915; *Angew. Chem. Int. Ed.*

2000, *39*, 1845 – 1848; b) A. P. Maierhofer, M. Brettreich, S. Burghardt, O. Vostrowsky, A. Hirsch, S. Langridge, T. M. Bayerl, *Langmuir* **2000**, *16*, 8884 – 8891.
[3] N. Kellermann, W. Bauer, A. Hirsch, B. Schade, K. Ludwig, C. Böttcher, *Angew. Chem.* **2004**, *116*, 3019 – 3022; *Angew. Chem. Int. Ed.* **2004**, *43*, 2959 – 2962.
[4] A. Hirsch, O. Vostrowsky, *Eur. J. Org. Chem.* **2001**, 829 – 848.
[5] M. Adrian, J. Dubochet, J. Lepault, A. W. McDowall, *Nature* **1984**, *308*, 32 – 36.
[6] J. Dubochet, M. Adrian, J.-J. Chang, J.-C. Homo, J. Lepault, A. W. McDowall, P. Schultz, *Q. Rev. Biophys.* **1988**, *21*, 129 – 228.
[7] http://dasher.wustl.edu/tinker/.

Cover Picture

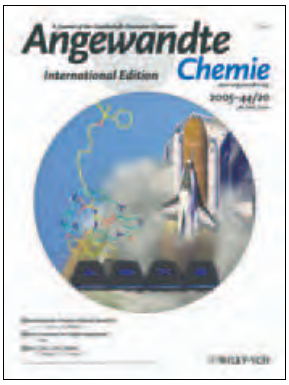

David A. Leigh,* M. Ángeles F. Morales, Emilio M. Pérez, Jenny K. Y. Wong, Carlos G. Saiz, Alexandra M. Z. Slawin,* Adrian J. Carmichael, David M. Haddleton,* A. Manfred Brouwer,* Wybren Jan Buma,* George W. H. Wurpel, Salvador León, and Francesco Zerbetto*

Molecular shuttles describe rotaxanes in which a key feature of the tertiary structure, the relative positions of the interlocked components, can be changed in response to an external input such as a solvent. The cover picture shows such an assembly as well as fluorescent patterns generated by stimuli-induced submolecular motion of the assembly in polymer films. For more details see the Communication by D. A. Leigh et al. on page 3062 ff. (The image of the space-shuttle launch was captured from the game SimCity 4: Rush Hour.)

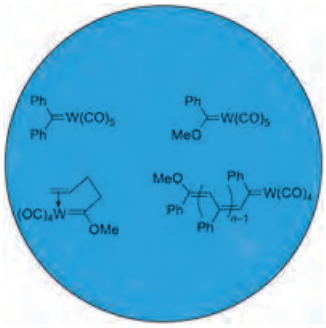

Metathesis Catalysts
The Minireview by T. J. Katz on page 3010 ff. deals with metathesis catalysts: How do carbene complexes of metals in low oxidation states compare with the commonly used high-oxidation-state analogues?

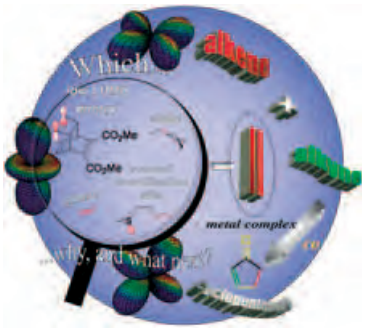

Pauson–Khand Reaction
Recent advances in the intermolecular Pauson–Khand reaction point the way to an increasingly more general and versatile reaction, as detailed by S. E. Gibson and N. Mainolfi in the Review on page 3022 ff.

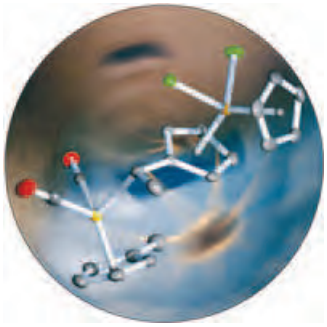

Metallocenes
A surprising kind of C–C coupling occurs when a Ti/Zr metallocene complex is treated with acid. G. A. Koutsantonis et al present the details of this process in their Communication on page 3038.

Contents

VIP ***The following Communications have been judged by at least two referees to be "very important papers" and will be published online at www.angewandte.org soon:***

Meeting Reviews

Books

Highlights

Metal-Metal Interactions

Something to zinc about: Subvalent compounds with direct metal–metal bonds have been the focus of interest for many decades. Recently the first synthesis of a molecular compound with a direct Zn–Zn bond was reported. The synthetic route, although not understood, might lead the way to other interesting compounds featuring direct metal–metal bonds, for example, of Group 2 elements.

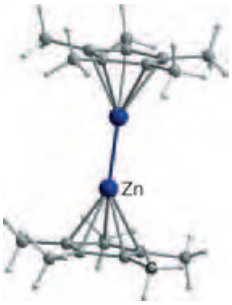

Minireviews

Olefin Metathesis

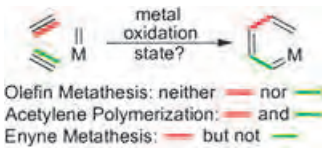

Highs and lows: Tungsten carbenes do not have to be in their highest oxidation state to initiate olefin metatheses, acetylene polymerizations, and enyne metatheses. Although low-oxidation-state metal carbenes are less active than those currently used, the former exhibit greater stereoselectivity and a broader substrate range.

Reviews

Goodbye to the weakest link: The intermolecular Pauson–Khand reaction (see scheme) has in the past been limited by the poor reactivity and selectivity of the alkene component. Concerted efforts to broaden the scope of the intermolecular Pauson–Khand reaction are critically and comprehensively covered based on the reactivity characteristics of the alkene partners, which are used to rationalize successful and failed reactions.

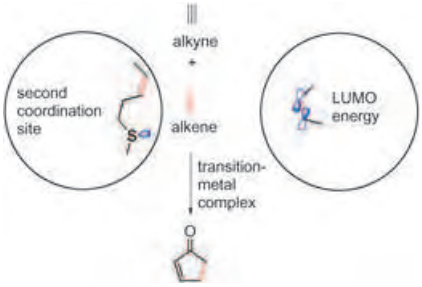

Carbocycle Synthesis

Communications

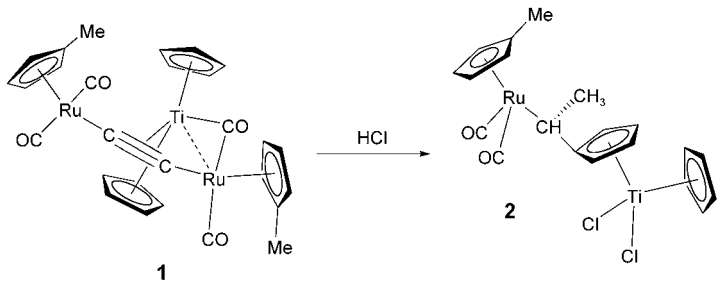

Carbon ligand transfer: Compound **1** is formed with reactive metal–ligand fragments generated from Group 4 metallocene compounds. Dropwise addition of ethanolic HCl to a solution of complex **1** in toluene affords complex **2** in a carbon–carbon bond-forming transformation that is thought to be unprecedented.

Metallocene Chemistry

Even better than the real thing? As host molecules, long synthetic nanotubes may be reasonable alternatives to single-walled nanotubes. For example, calixarene-based nanotubes effectively pack into infinite tubular bundles in the solid state (see picture), and they can be easily filled with guest molecules to form stable, but reversible, encapsulation complexes.

Host–Guest Chemistry

For the USA and Canada:
ANGEWANDTE CHEMIE International Edition (ISSN 1433-7851) is published weekly by Wiley-VCH PO Box 191161, D 69451 Weinheim, Germany. Air freight and mailing in the USA by Publications Expediting Inc. 200 Meacham Ave., Elmont, NY 11003. Periodicals postage paid at Jamaica NY 11431. US POSTMASTER: send address changes to *Angewandte Chemie*, Wiley-VCH, 111 River Street, Hoboken, NJ 07030. Annual subscription price for institutions: US$ 4948.00/4498.00 (valid for print and electronic / print or electronic delivery); for individuals who are personal members of a national chemical society, or whose institution already subscribes, or who are retired or self-employed consultants, print only: US$ 394.00. Postage and handling charges included. All Wiley-VCH prices are exclusive VAT.

The best in chemistry –

for more than a hundred years

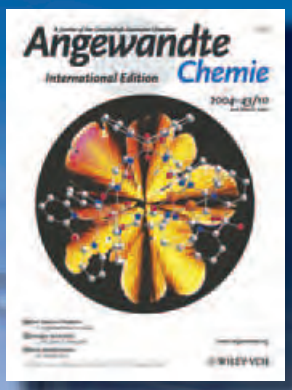

A Journal of the Gesellschaft Deutscher Chemiker

Angewandte
International Edition **Chemie**

www.angewandte.org

1888: ***The beginning of a success story***

Constant Innovations

1962: *First issue of the International Edition*
1976: *Graphical abstracts*
1979: *Cover pictures*
1988: *Centenary of Angewandte*
1989: *Routine use of color*
1991: *New section: Highlights*
1992: *Computerized editorial tracking system*
1995: *Internet service for readers*
1998: *Regular press service; full-text online*
2000: *New section: Essays; EarlyView: Communications available online ahead of the printed version*
2001: *New section: Minireviews*
2002: *Online submission of manuscripts*
2003: *Weekly publication; new section: News; new layout*
2004: *Backfiles (1962-1997); ManuscriptXpress: Online system for authors and referees*

Angewandte's advisors...

Rolf Thauer
MPI für terrestrische Mikrobiologie, Marburg

» *In 1970 Karl Decker, Kurt Jungermann, and I published a review on "Energy Production in Anaerobic Organisms" in* ***Angewandte Chemie****. We were soon surprised how many scientists from all over the world had read the article. Ever since then I have admired the broad scope, the high impact, and internationality of this Journal and I am therefore very proud, as a "chemical microbiologist", to be a member of its Editorial Board.* «

Angewandte Chemie International Edition *is a journal of the German Chemical Society (GDCh)*

GDCh

WILEY InterScience® DISCOVER SOMETHING GREAT

WILEY-VCH

11991404_gu

Formation of the vinylogous bridge between adjacent pyrrole rings (A and B) in the reaction of 5,10,15-triphenylcorrole with CI_4 affords the corresponding hemiporphycene (see structure; N blue, I pink, C white, H green). This approach allows a facile preparation of functionalized hemiporphycenes.

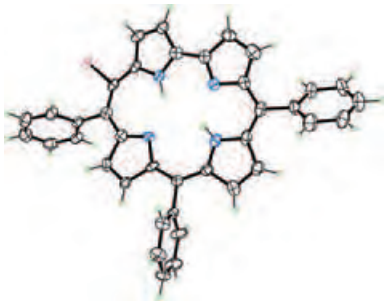

Corrole Chemistry

Raising the bar. Tethering the macrocyclic polyether to the tetracationic cyclophane in a "donor–acceptor" [2]catenane (see schematic representation) slows down the process of partial pirouetting of the crown ether around the cyclophane by a factor of 10000. This level of structural control has important consequences for the design of the next generation of molecular switches that depend on bistable "donor–acceptor" [2]catenanes.

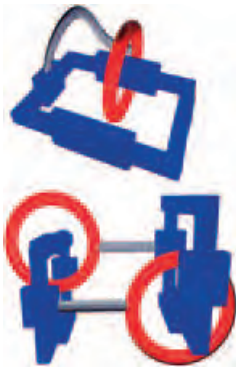

Molecular Devices

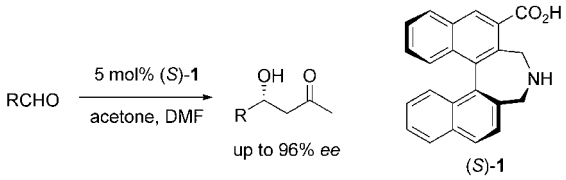

A robust binaphthyl-based amino acid ((*S*)-**1**) exhibits higher stability and selectivity than proline for the catalysis of a direct asymmetric aldol reaction between aldehydes and acetone (see scheme; DMF = *N*,*N*-dimethylformamide). Olefinic, heteroaromatic, and aromatic aldehydes were found to be suitable substrates, with the corresponding aldol adducts being obtained in good yields and excellent enantioselectivities.

Asymmetric Catalysis

Weaving with DNA: A DNA-binding protein was used to control the structure of a self-assembled 2D crystal. In the absence of protein, four oligonucleotides hybridize to form a Kagome lattice of interwoven double helices with *p*3 symmetry (see image). Addition of protein RuvA during assembly changes the symmetry and connectivity to give a DNA–protein crystal with an approximately square unit cell.

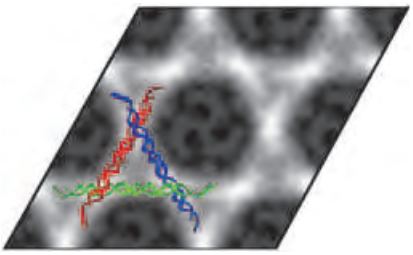

Protein–DNA Arrays

VIP

Contents

Two different types of coordination sheets made up of Co^{II} ions, 3-hydroxypicolinate, and 4,4′-bipyridine interpenetrate to form a unique molecular-based magnetic material (see picture). This material displays a low-field metamagnetic transition and spin-canted behavior.

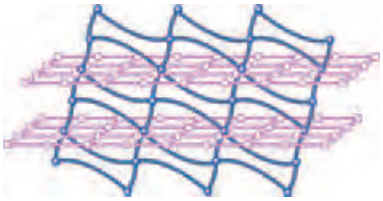

Metamagnetism

Key prenucleation species like the open-chain tetramer and the four-membered-ring structure shown are implicated in the formation of zeolites according to density functional theory calculations. The role of the solvent and the pH value is confirmed in the control of condensation reactions, particularly those favoring the formation of cyclic structures present in many zeolite structures.

Zeolite Assembly

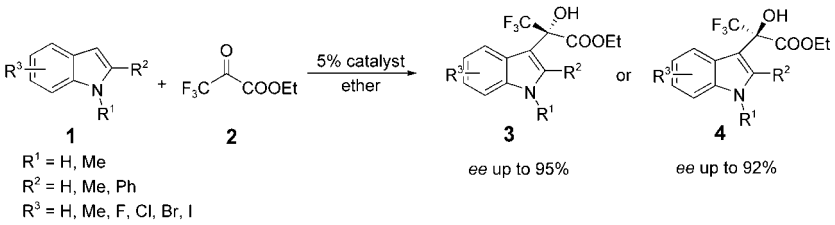

Readily available cinchona alkaloids have been used as organocatalysts in the highly efficient stereoselective hydroxyalkylation of heteroaromatics such as indoles with 3,3,3-trifluoropyruvate (**2**, see scheme).

High yields and *ee* values of both enantiomers of the products, depending on the catalyst used, indicate the usefulness of the developed methodology.

Organocatalysts

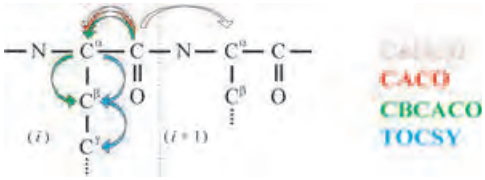

The detection of ^{13}C is now amenable to high-resolution NMR spectroscopy of proteins. A protocol for ^{13}C homonuclear decoupling in multidimensional experiments correlates carbonyl, C^{α}, and C^{β} nuclei (see picture). These techniques also allow the detection of side-chain nuclei in exclusively heteronuclear experiments, and thus the complete assignment of proteins.

Biomolecular NMR Spectroscopy

Contents

Luminous: The Au^{III} alkynyl complexes [Au(C^N^C)(C≡CR)] [HC^N^CH = 2,6-diphenylpyridine, R = C_6H_5 (**1**), C_6H_4-Cl-*p* (**2**), C_6H_4-OCH_3-*p* (**3**), C_6H_4-NH_2-*p* (**4**); HC^N^CH = 2,6-bis(4-*tert*-butylphenyl)-pyridine, R = C_6H_5 (**5**)] were prepared, and the molecular structure of **1** was characterized (see picture). Complexes **1**–**5** display luminescence in solution and in the solid state both at low and ambient temperature.

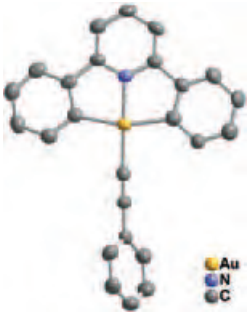

Luminescent Gold Complexes

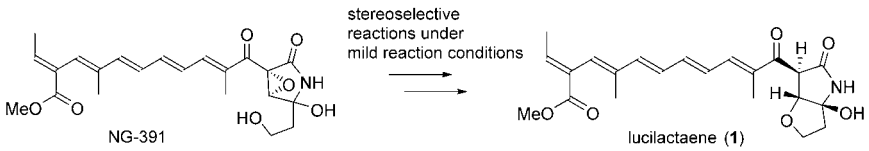

A biomimetic pathway to lucilactaene (**1**) from NG-391 has been developed which involves stereoselective reactions under very mild conditions. It was demonstrated that **1** racemizes rapidly, and the conditions under which racemization occurs were elucidated. Lucilactaene (**1**) isolated under neutral conditions is racemic, which suggests that either the natural product is racemized rapidly in the mycelia, or racemic **1** is biosynthesized.

Natural Products Synthesis

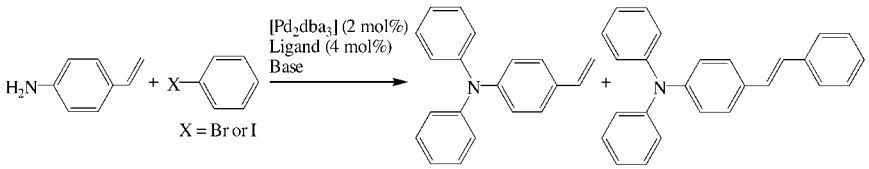

A double-amination/intermolecular-Heck-reaction sequence is used as a one-pot methodology for sequential C–N and C–C bond formations. 4-Aminostyrene was coupled with aryl bromides and aryl iodides using a [$Pd_2(dba)_3$]/proazaphosphatrane catalyst system (dba = dibenzylideneacetone; see scheme) to form *trans* 4-*N*,*N*-diaryl aminostilbene derivatives in high yields, which are comparable to those of previously reported multistep syntheses.

Arylation

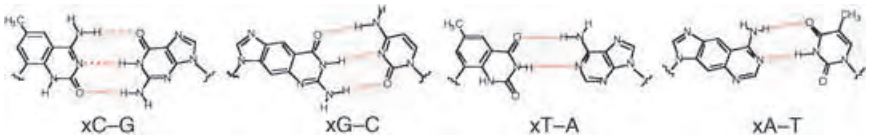

Expanding DNA: The four natural DNA nucleotides were combined with four benzo-homologous nucleotides to make self-assembling double helices (see base-paired structures). Strands of this "xDNA" form highly stable, sequence-specific duplexes with native DNA and RNA, and can expand the information capacity of DNA from a basis of four to eight characters.

Nucleic Acids

Contents

The opening or blocking of a coordination site at the lithium center (for example by attachment of THF, see picture; left) leads to diastereodivergent courses in the reactions of a highly diastereomerically enriched alkyl lithium with Me_3SnCl. At room temperature in noncoordinating solvents the reagent is configurationally stable and epimerizes in the presence of THF.

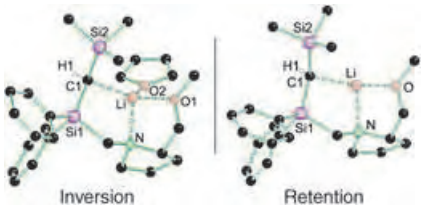

Organolithium Compounds

Favored entrance for the privileged. Two inhibitor structures to address the active site of aspartic proteases have been developed. They are equipped with a central hydroxysulfone unit and, alternatively, a pyrrolidine moiety and decorated with rationally designed side chains. The hydroxysulfones bind to HIV protease as expected, whereas the pyrrolidines display a surprising, previously unreported binding mode.

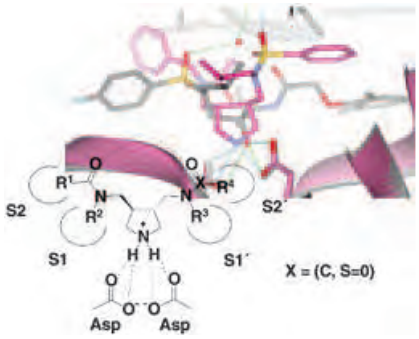

Structure Determination

NMR in gummi bears: What started as pure fun could open up interesting applications: stretched gelatin gels as chiral polymers can be used to distinguish enantiomeric solutes through their residual dipolar couplings. The method is demonstrated on a mixture of L- and D-alanine (see picture).

NMR Spectroscopy

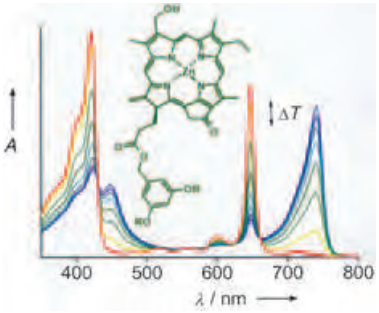

Biomimetic light-harvesting antennae are made available by noncovalent polymerization of semisynthetic zinc chlorins. The excellent solubility and the prolonged stability of the zinc chlorin aggregates enables spectroscopic investigation of their reversible formation (see picture). The rod-shaped structure of these aggregates is experimentally confirmed by atomic force microscopy.

Dyes

VIP

Service

Metal-Metal Interactions

Subvalent Compounds Featuring Direct Metal–Metal Bonds: The Zn–Zn Bond in $[Cp^*_2Zn_2]$**

Andreas Schnepf and Hans-Jörg Himmel**

Keywords:
metallocenes · metal–metal bonding · subvalent compounds · zinc

Molecular compounds featuring direct metal–metal bonds have stirred up interest for many decades now, with the nature of the bonding between the two metal centers generally being the focus of attention. In recent years interest has centered on several cluster compounds of Group 13 and 14 elements with unusual bonding properties (multiple bonds or delocalized "metal-like" bonds).[1]

In the case of Group 12 elements (Zn, Cd, Hg), compounds with direct metal–metal bonds are well known for mercury, reflecting the preference of this element for a formal oxidation state of +1.[2] As to cadmium, the compounds $Cd_2(AlCl_4)_2$[3] or $Cd_2(Tp^{Me_2})_2$[4] (Tp^{Me_2} = hydrotri(3,5-dimethylpyrazolyl)borate) have direct Cd–Cd bonds. However, owing to the increased instability of the formal oxidation state +1, the $[Cd_2]^{2+}$ ion disproportionates immediately in the presence of water to give Cd and Cd^{2+}.[2]

Thus, the ability of Group 12 elements to be engaged in direct metal–metal bonding decreases dramatically from mercury to cadmium to zinc reflecting the decreasing stability of the formal oxidation state +1. On these grounds it was for some time questionable whether it would be possible to synthesize molecular compounds featuring a direct Zn–Zn bond.

With [Cp*ZnZnCp*] (**1**; Cp* = C_5Me_5), Carmona and co-workers have now synthesized the first representative of this class of compounds. As often in the case of great advances in chemistry chance played a significant role.[5] The compound was formed unexpectedly as the product of the reaction between decamethylzincocene and diethyl zinc. At room temperature a mixture between the expected zinc(II) compound [Cp*ZnEt] (**2**) and the unexpected zinc(I) compound **1** was obtained. Depending on the reaction conditions the reaction can be manipulated to lead to either **1** or **2** as a characterizable product (Scheme 1). A new route (box in Scheme 1) now allows **1** to be prepared in a few grams, opening up the possibility to study the chemistry of this fascinating compound.[6]

Compound **1** turns out to be a colorless, pyrophoric solid. The molecular structure (Figure 1) shows a central Zn_2

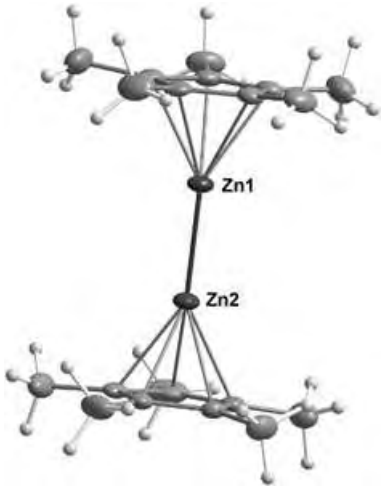

Figure 1. Molecular structure of **1**.

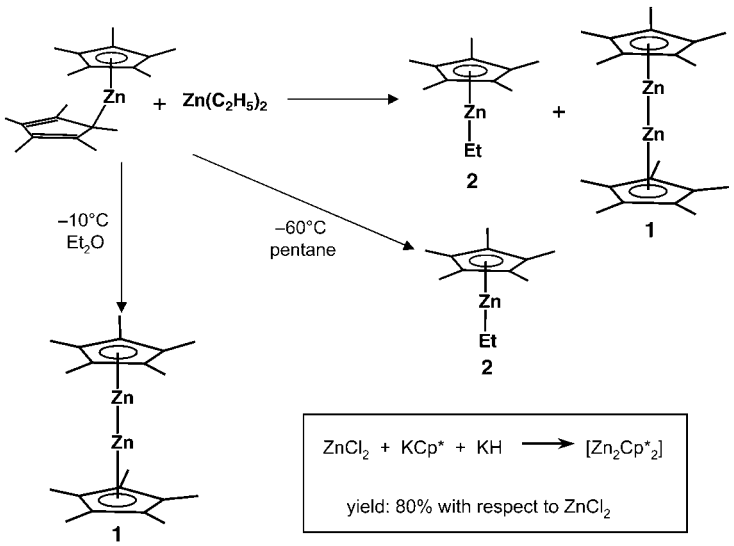

Scheme 1. Pathways leading to **1**.

[*] Dr. A. Schnepf, Priv.-Doz. Dr. H.-J. Himmel
Institut für Anorganische Chemie
Universität Karlsruhe (TH)
Engesserstrasse, Geb.30.45, 76128 Karlsruhe (Germany)
Fax: (+49) 721-608-4854
E-mail: schnepf@aoc2.uni-karlsruhe.de
himmel@chemie.uni-karlsruhe.de

[**] Cp* = C_5Me_5.

  DOI: 10.1002/anie.200500597

unit, with a very short Zn–Zn bond of 231 pm. Each of the zinc atoms is η^5 coordinated to one Cp* ligand with a distance between the zinc atom and the Cp* centroid of 204 pm. The Zn-Zn-$Cp^*_{centroid}$ angle amounts to 177.4°.

To exclude the possibility of the presence of hydrogen atoms bonded to the zinc atoms, for example, as hydrogen bridges between the two zinc atoms to give a [{Cp*Zn(μ-H)}$_2$] species, the compound was studied with several independent methods (NMR and IR spectroscopy and mass spectrometry). All these methods gave no sign of any additional hydrogen atoms. The absence of hydrogen bonded to the zinc atoms in **1** is supported by a comparison of the Zn–Zn distance (231 pm) with that found in the hydrogen-bridged compound [{RZn(μ-H)}$_2$] (R = HC(CMeNXyl)$_2$; Xyl = 2,6-$Me_2C_6H_3$; which has a Zn···Zn separation of 245 pm.[7] All methods therefore agree in that **1** indeed represents the first in substance isolated compound with a direct Zn–Zn bond.

The parent compound HZnZnH was previously generated and characterized in matrix isolation experiments as one of the products of the dimerization of two ZnH radicals in Ar, Ne, or H_2 matrices.[8] However, to date only the antisymmetric Zn–H stretching fundamental at 1740.3 cm^{-1} in Ar, 1746.8 cm^{-1} in Ne, and 1752.2 cm^{-1} in H_2 matrices could be detected. The Zn–Zn distance in the linear compound is approximately 238 pm according to quantum chemical (MP2) calculations,[9] a value which is in satisfying agreement with that measured (231 pm) and calculated (233 pm) for **1**. The quantum chemical calculations carried out for HZnZnH and **1** indicate a similar energy change of approximately +250 kJ mol^{-1} for dissociation into two ZnH and Zn(η^5-Cp*) radicals, respectively. Replacement of the H atoms in HZnZnH by more electronegative atoms or groups leads to a further increase of the bond energy. Hence, in FZnZnF the dissociation energy is higher by around 15 kJ mol^{-1}. However, disproportionation reactions are more important in judging the stability of the compounds. In the case of HZnZnH the calculated disproportionation in the gas phase leading to ZnH_2 molecules and Zn atoms is exothermic by approximately −31 kJ mol^{-1}. The corresponding disproportionation reactions for FZnZnF and ClZnZnCl are predicted to be endothermic (+37 and +30 kJ mol^{-1}, respectively). Unfortunately similar calculations on **1** are still missing. Nevertheless the results suggest that a careful choice of the ligands is essential to guide the reaction in the right direction.

In the light of the first synthesis of **1** the question arises whether or not it is also possible to synthesize derivatives of the compound HMgMgH on a preparative scale? These species should also feature metal–metal bonds with sufficiently high bond energy. Thus, according to calculations, dissociation of HMgMgH into two MgH radicals requires an energy of 197 kJ mol^{-1}.[10] HMgMgH and its isomer Mg(μ-H)$_2$Mg, which is approximately 63 kJ mol^{-1} higher in energy, were already sighted in matrix isolation experiments.[10] The antisymmetric Mg–H stretching fundamental in HMgMgH occurs at 1491.2 cm^{-1} (in Ar). A further problem is that gas-phase decomposition of HMgMgH into Mg_2 and H_2 was calculated to be exothermic by −24 kJ mol^{-1}. This result means that in addition to disproportionation there are other possible decomposition routes for these kind of compounds, which might complicate their stabilization. Fortunately owing to the relatively low reaction enthalpies for these decomposition processes in the case of the parent compound there is room for some hope that these decomposition reactions can be avoided by careful choice of the ligands.

Recently it was even possible to stabilize derivatives of the parent compound HGaGaH, which features a much weaker metal–metal bond.[11] Again, the parent compound HGaGaH was first generated and characterized in matrix isolation experiments.[12] The vibrational spectra of the matrix isolated molecule already indicated that the Ga–Ga bond in HGaGaH is most adequately described as a relatively weak donor–acceptor interaction between two GaH molecules. In agreement to this description the Ga–Ga bond in the *trans*-bent derivatives is with approximately 263 pm (as measured for ArGaGaAr, Ar = 2,6-$Dipp_2C_6H_3$; Dipp = 2,6-$iPr_2C_6H_3$)[11] relatively large, and fragmentation of the parent compound HGaGaH into two GaH fragments consumes an energy of around 57 kJ mol^{-1}.[13] In contrast to Mg_2H_2 and Zn_2H_2, the D_{2h} symmetric isomer Ga(μ-H)$_2$Ga is 50–60 kJ mol^{-1} more stable than the C_{2h} symmetric, *trans*-bent HGaGaH.[12]

In summary, the first synthesis of [Cp*ZnZnCp*] is a break through which will encourage the search for similar compounds, especially those of Group 2 elements. However, many questions still remain unsolved, especially with regard to the reaction pathway leading to this molecule. The analysis of the reaction mechanism would be very helpful for future attempts to synthesize similar species.[14] Because the compound can be synthesized in good yields one can expect to see a rich chemistry in the near future. The disproportionation reaction to Zn^{2+} and Zn metal (Scheme 2) possibly leads the way to zinc-rich cluster compounds, a strategy which has already been applied successfully in the case of Group 13 and 14 elements for the preparation of new metalloid cluster compounds.[1]

Published online: April 21, 2005

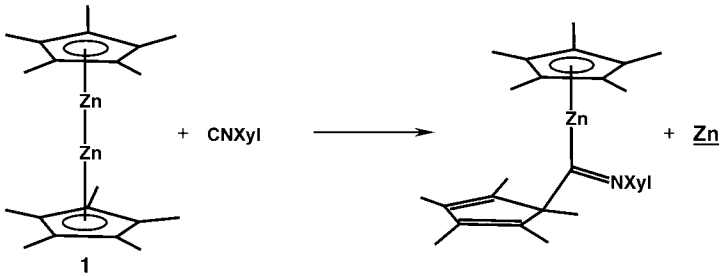

Scheme 2. Reaction of **1** with CNXyl.

[1] a) A. Schnepf, H. Schnöckel, *Angew. Chem.* **2002**, *114*, 3682; *Angew. Chem. Int. Ed.* **2002**, *41*, 3532; b) A. Schnepf, *Angew. Chem.* **2004**, *116*, 680; *Angew. Chem. Int. Ed.* **2004**, *43*, 664; c) L. Pu, A. D. Philips, A. F. Richards, M. Stender, R. S. Simons, M. M. Olmstead, P. P. Power, *J. Am. Chem. Soc.* **2003**, *125*, 11626.

[2] *Hollemann-Wiberg, Lehrbuch der Anorganischen und Allgemeinen Chemie*, 101. Aufl. (Ed.: N. Wiberg), Walter de-Gruyte, Berlin, **1995**.

[3] R. Faggiani, R. J. Gillespie, J. E. Vekris, *J. Chem. Soc. Chem. Commun.* **1986**, *7*, 517.

[4] D. L. Reger, S. S. Mason, A. L. Rheingold, *J. Am. Chem. Soc.* **1993**, *115*, 10406.

[5] I. Resa, E. Carmona, E. Gutierrez-Puebla, A. Monge, *Science* **2004**, *305*, 1136.

[6] D. del Rio, A. Galindo, I. Resa, E. Carmona, *Angew. Chem.* **2005**, *117*, 1270; *Angew. Chem. Int. Ed.* **2005**, *44*, 1244.

[7] H. Hao, C. Cui, H. W. Roesky, G. Bai, H.-G. Schmidt, M. Noltemeyer, *Chem. Commun.* **2001**, *12*, 1118.

[8] a) T. M. Greene, W. Brown, L. Andrews, A. J. Downs, G. V. Chertihin, N. Runeberg, P. Pyykkö, *J. Phys. Chem.* **1995**, *99*, 7925; b) X. Wang, L. Andrews, *J. Phys. Chem. A* **2004**, *108*, 11006.

[9] M. Kaupp, H. G. von Schnering, *Inorg. Chem.* **1994**, *33*, 4179.

[10] T. J. Tague, Jr., L. Andrews, *J. Phys. Chem.* **1994**, *98*, 8611.

[11] N. J. Hardman, R. J. Wright, A. D. Phillips, P. P. Power, *Angew. Chem.* **2002**, *114*, 2966; *Angew. Chem. Int. Ed.* **2002**, *41*, 2842.

[12] a) H.-J. Himmel, L. Manceron, A. J. Downs, P. Pullumbi, *Angew. Chem.* **2002**, *114*, 829; *Angew. Chem. Int. Ed.* **2002**, *41*, 796; b) H.-J. Himmel, L. Manceron, A. J. Downs, P. Pullumbi, *J. Am. Chem. Soc.* **2002**, *124*, 4448.

[13] H.-J. Himmel, H. Schnöckel, *Chem. Eur. J.* **2003**, *9*, 748.

[14] Which species is oxidized during the reaction has to be analyzed. One possibility is that in the first step a reductive elimination takes place ($[R_2Zn] \rightarrow Zn + R-R$) leading to Zn atoms, which react in the second step with $[Cp^*_2Zn]$ in a comproportionation reaction to give **1**. The detection of ethane as a side product in the course of the reaction might indicate the involvement of radicals. However, butane would be the expected side product under assumption of the above mentioned mechanism. The influence of the steric requirements of the Cp* ligand on the reaction also has to be evaluated. That this influence cannot be neglected is clear if the reaction of $[Cp^*_2Zn]$ is compared with that of $[Cp_2Zn]$. The reaction of $[Cp_2Zn]$ with $[Et_2Zn]$ leads almost quantitatively to the half-sandwich compound [CpZnEt].[15]

[15] J. T. B. H. Jastrzebski, J. Boersma, G. van Koten, W. J. J. Smeets, A. L. Spek, *Recl. Trav. Chim. Pays-Bas* **1988**, *107*, 263.

Olefin Metathesis

Olefin Metatheses and Related Reactions Initiated by Carbene Derivatives of Metals in Low Oxidation States

*Thomas J. Katz**

Keywords:
alkenes · alkynes · enynes · initiators · metathesis

Experiments carried out 24 years ago with tantalum carbenes have led to the much cited hypothesis that metals (other than ruthenium) must be in their highest oxidation states for their carbene derivatives to initiate olefin metatheses. The hypothesis legitimizes the uniqueness of high-oxidation-state molybdenum and tungsten carbenes as effective initiators, and it means that the Fischer tungsten carbenes that even earlier were found to initiate olefin metatheses and related transformations must be oxidized before they can be effective. The newer initiators have been termed "well-defined", the older "ill-defined". But what does the evidence show?

1. Introduction

A series of experiments published in 1976 and 1977 demonstrated for the first time that isolable metal carbenes could initiate olefin metatheses.[1] Pentacarbonyl(diphenylmethylene)tungsten (**1**; Scheme 1), a compound previously

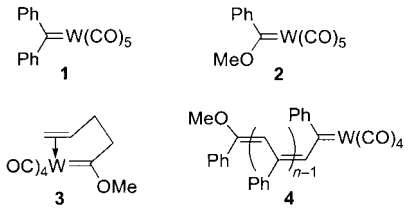

Scheme 1. Carbene initiators of olefin metathesis.

synthesized by Casey and Burkhardt[2] and at the time the most reactive metal carbene known,[3] in small amounts and at temperatures of 25 to 40 °C initiated metatheses of a variety of disubstituted cycloalkenes (cyclobutene, cyclopentene, cycloheptene, cyclooctene, and norbornene),[1c] trisubstituted cycloalkenes (1-methylcyclobutene, 1-methyl-*trans*-cyclooctene, and later 2-methylnorbornene and 1-trimethylsilylcyclobutene),[1b,e,4] 1,1-disubstituted ethylenes (2-methylpent-1-ene, 2-methylhept-1-ene),[1a] and *cis*- and *trans*-2-pentenes.[1f]

In 1980 this same metal carbene was shown to initiate polymerizations of acetylenes.[5] This was the first demonstration that isolable metal carbenes could initiate acetylene polymerizations, and in 1985 the same metal carbene was shown to initiate the enyne rearrangement [or enyne metathesis, Eq. (1)], the first demonstration of that reaction.[6]

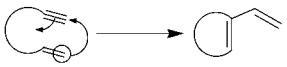

(1)

The less-reactive pentacarbonyl(methoxyphenylmethylene)tungsten (**2**), the first metal carbene to have been isolated and characterized (by Fischer and Maasböl in 1964),[7] was also shown to initiate polymerizations of acetylenes[5] and enyne rearrangements,[6a] as well as metatheses of strained olefins.[1d]

These metal carbenes offered two significant advantages over the initiating mixtures used previously:[8] 1) the ability to avert acid-catalyzed side reactions, which previously had frustrated attempts to transform trisubstituted and 1,1-disubstituted ethylenes by metathesis;[1a,b,e] and 2) uniquely high stereoselectivity both for retention of double-bond configuration in metatheses of di-[1c,d,f,g] and trisubstituted olefins[1b,e,4] and for formation of *cis* alkenes in enyne rearrangements.[6a,9]

Despite these results, a number of recent publications assert or suggest that carbene derivatives of early transition metals initiate olefin metatheses only if the metals are in their highest oxidation states.[10,11] Because these are the oxidation states of the metals in the most effective tungsten and molybdenum carbene initiators used today[12] (but not in the even more effective ruthenium carbenes[12]), it has been proposed that for Fischer tungsten carbenes to initiate olefin metatheses they must first be oxidized to ill-defined species in

[*] Prof. T. J. Katz
Department of Chemistry
Columbia University
New York, NY 10027 (USA)
Fax: (+1) 212-932-1289
E-mail: tjk1@columbia.edu

  DOI: 10.1002/anie.200462442

higher oxidation states.[10a,13] The initial compounds themselves are said[10a,b,f,14] or implied[15,16] to be ineffective. A corollary then is that high-oxidation-state tantalum [14c,17] and tungsten oxo derivatives[14c,18] were the first metal carbenes that directly initiated productive olefin metathesis. These assertions have been repeated frequently[10,13,14,16b] but never questioned. I therefore summarize herein 1) experiments demonstrating that Fischer tungsten carbenes initiate olefin metatheses, acetylene polymerizations, and enyne rearrangements; 2) evidence for the mechanisms of these transformations; 3) evidence related to the identification of well-defined initiators; and 4) possible advantages metal carbene initiators in low oxidation states might provide.

2. Fischer Tungsten Carbenes

2.1. Olefin Metatheses Initiated by Pentacarbonyl(diphenylmethylene)tungsten

As a short review was recently published of olefin metatheses, acetylene polymerizations, and enyne rearrangements initiated by Fisher metal carbenes,[1g] only orienting illustrations are provided herein. After 14–36 h in the presence of **1** (0.002–0.005 equiv) at 25–41 °C, solutions of cyclobut-, cyclopent-, cyclohept-, and cyclooctenes in toluene or benzene (≈ 3 M) were converted into the corresponding polyalkenamers in an average yield of 53 % [Eq. (2)].[1b] The number-average molecular weights ($\bar{M}_n$) of the polymers were similar, $(1.8 \pm 0.4) \times 10^5$, and their weight-average molecular weights ($\bar{M}_w$) were between 3.5×10^5 and 14×10^5. For the strained alkene norbornene, 0.0006 equivalents of the initiator sufficed, and after 18 h at room temperature (≈ 25 °C), the yield of the polymer, with $\bar{M}_n = 3.3 \times 10^5$ and $\bar{M}_w = 8.5 \times 10^5$, was 91 %.[1b,19] The number of turnovers per molecule of initiator was thus 1500 for norbornene and between 100 and 200 for the other cycloalkenes. The metatheses are not, as is sometimes asserted,[10a,c,14d] restricted to olefins that are strained.

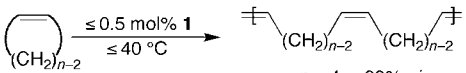

(2)

n = 4, 93% *cis*
n = 5, 86% *cis*
n = 7, >98% *cis*
n = 8, 97% *cis*

Thomas J. Katz, born in Prague, received the BA in 1956 (Wisconsin; E. E. van Tamelen) and the PhD in 1959 (Harvard; R. B. Woodward). At Columbia University, where he has been since, he has studied new structures (10π-aromatic anions, benzvalene, prismane, pentaalkylphosphoranes, helicenes), new transformations (rhodium-catalyzed cycloaddition, enyne metathesis), and new preparative and mechanistic procedures in areas such as photocyclization, isotope effects, olefin metathesis, and enantiomer discrimination.

2.1.1. Advantages of Fischer Metal Carbenes in Olefin Metathesis

The Fischer metal carbene not only initiates these metatheses, but as the polymerization of cycloheptene shows, it can be more effective than classic initiating mixtures or [W(=CH*t*Bu)(NC_6H_3-2,6-(*i*Pr)$_2$)(O*t*Bu)$_2$]. The Fischer tungsten carbene gave *cis*-polyheptenamer (> 98 % *cis*) in 66 % yield, whereas the classical WCl_6/Et_2AlCl mixture gave the *trans* product (91 % *trans*) in 18 % yield,[20] and [W(=CH*t*Bu)(NAr)(O*t*Bu)$_2$] gave no product at all.[21]

Stereospecificity is a noteworthy attribute of these Fischer tungsten carbene initiated reactions [Eq. (2)]. The double bonds in the metathesis products are 95 ± 2 % *cis* according to infrared spectroscopic analyses and 93 ± 6 % *cis* according to ^{13}C NMR spectroscopic analyses. Figure 1 illustrates one of these analyses. There is no ^{1}H NMR signal at $\delta = 32.6$ ppm, which would have identified the presence of *trans* double bonds.[1b,21] Similarly, in the 2-butene and 3-hexene initially formed from *cis*-2-pentene, the double bonds are almost exclusively *cis* (97 % and 95 %, respectively); from *trans*-2-pentene they are largely *trans* (73 % and 83 % *trans*, respectively).[1f] In the polymer formed in quantitative yield from bicyclo[4.2.0]oct-7-ene, they are 85 % *cis*.[22] Such stereoselectivity is extraordinary. It has been achieved by classic initiators only in isolated examples of metatheses of norbornene[8a,23] and other cycloalkenes,[8a,24,25] by one carbene derivative of W^{VI} for the metathesis of 2-pentene,[26,27] and by another W^{VI} carbene for the metathesis of 2,3-dicarbomethoxynorbornadiene.[28] But the Grubbs ruthenium carbenes[29] and, with one exception,[21] the Schrock tungsten[21,30] carbenes have not led to such selectivity with olefins other than norbornene.[31]

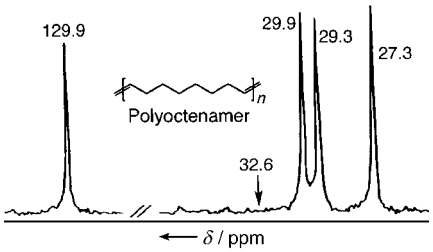

Figure 1. ^{13}C NMR spectrum (25 MHz, $CDCl_3$) of a solution of polyoctenamer prepared according to [Eq. (2)].

Pentacarbonyl(diphenylmethylene)tungsten (**1**) also initiates metatheses of trisubstituted alkenes that are cyclic and strained. In the presence of **1** (2 mol %) at 39 °C, 1-trimethylsilylcyclobutene is transformed in 80 % yield into the metathesis polymer, which within the detection limits of ^{13}C NMR spectroscopic analysis (≈ 4 %) has a perfect head-to-tail (or perfectly alternating) structure and perfect *E* ("*cis*") configuration.[4] Similarly, both 1-methyl-*trans*-cyclooctene[1e] and 2-methylnorbornene[4] give perfectly alternating polymers, the configurations of the double bonds being 76 ± 1 % *E* in the former and ≈ 60 % *Z* in the latter. 1-Methylcyclobutene,[1b] the first trisubstituted cycloalkene to be successfully polymerized by metathesis, gives, (*Z*)-"polyisoprene" (86 % *Z*;

quantitative yield) that has 90% of its units perfectly alternating.[32] Fischer metal carbene **1** also effects the exchange of methylene groups between 2-methylhept-1-ene and 2-methylpent-1-ene.[1f] Notable for all these transformations is that before they were carried out as described, no initiator was known that would bring about the metatheses of either trisubstituted or 1,1-disubstituted alkenes. The reason is that unlike **1**, all previous initiators were mixtures containing strong acids, which combine with these alkenes to form tertiary carbocations that give other products.[1a,b]

2.2. Olefin Metatheses Initiated by Other Fischer Tungsten Carbenes

Fischer metal carbenes less reactive than **1** and ineffective in initiating metatheses of many olefins are effective with olefins that are strained.[1d,4,33,34] For example, **2** (0.5 mol%) at 50°C transforms cyclobutene into *cis*-polybutenamer (90% *cis*, 60% yield) and similarly transforms other derivatives of cyclobutene as well as norbornene. The latter with 8×10^{-7} equivalents of a related initiator gave polynorbornenamer (75% *cis*, 21% yield) with $[\eta]$ (benzene, 30°C) = 3.52 dL g^{-1}.[4]

2.3. Acetylene Polymerizations

In amounts of 1–2 mol percent, both carbene complexes **1** and **2** initiate the polymerizations of acetylenes.[4,5,9,35] After 1–2 days at 50°C, the average yields of the phenyl-, methyl-, *n*-butyl-, and *tert*-butylacetylene polymers with $\bar{M}_n \approx 10^4$ were 46 ± 18%.[5] The configurations of the polymers formed when initiated by **2** were 82 ± 1% *E* (according to ^{13}C NMR spectroscopic analyses) in the case of poly(*tert*-butylacetylene) and 75 ± 10% *E* (according to infrared spectroscopic analyses) in the case of poly(phenylacetylene).[4,9] The polymerizations are slow, but the NMR spectra show that the products are notably pure.[4,5,9] Other Fischer tungsten carbenes, such as **3**, are even more reactive in polymerizing acetylenes.[36,37]

2.3.1. Advantages of Fischer Metal Carbenes in Acetylene Polymerization

Of the more recently prepared metal carbenes, [Ru(CHPh)Cl$_2$(PCy$_3$)$_2$] has not been found to polymerize any acetylenes,[38] and derivatives of [Mo(CHR)(NR″)(OR′)$_2$] polymerize only some. The latter fail, for example, with *tert*-butylacetylene.[39] In cases in which they do work,[38,40] the amounts used have been similar to or very much larger than the 1–2 mol percent of the Fischer metal carbenes used 24 years ago.

2.4. Enyne Metatheses

If, as was first suggested by Masuda,[41] the mechanism of acetylene polymerization resembles that of olefin metathesis—in simplified form if a metal carbene adds to the acetylene and is eliminated from the resulting metallacyclobutene—after metal carbene **2** has combined with *n* molecules of phenylacetylene, the product should look like structure **4**. The effect of the polymerization is to remove a stabilizing substituent,[42] the methoxy group, from the carbene center. This suggests that although **2** does not initiate metatheses of unstrained alkenes, such as 2-pentene or cyclopentene, the product **4** of its reaction with phenylacetylene, because it resembles **1**, might. In fact, when phenylacetylene in small amounts is added to a mixture of **2** and an alkene such as 2-pentene or cyclopentene, the metathesis reactions take place,[43] whereas in the absence of phenylacetylene, they do not.[44] Although the reactions are slow and low yielding, there is no question but that the addition of the acetylene actuates them. Moreover, the stereospecificities are remarkable. When the mixtures of **2** and phenylacetylene are combined with many alkenes (just as when **1** is combined with them), the double bonds in the products have the very unusual *cis* configuration: 97 ± 1% *cis* in the case of cycloheptene, 94 ± 1% *cis* in the case of cyclooctene, 95 ± 0.7% *cis* in the case of *cis*-2-pentene, and $66\%\pm8$% *cis* in the case of cyclopentene.

Related to these experiments are those in which the alkene is attached to the acetylene.[6] An example is Equation (3). Here the acetylene polymerization is terminated by an alkene after only a single cycle. Although only the phenanthrene product is observed, evidence for the presence of the other product, the methylene tungsten, is provided by similar experiments in which only small amounts of the diphenyl- or methoxyphenylmethylene tungsten reactants are used. The presumed methylene tungsten product can then compete with the diphenyl- or methoxyphenylmethylene tungsten for reaction with the enyne. The result is the enyne rearrangement [Eq. (4)].[6]

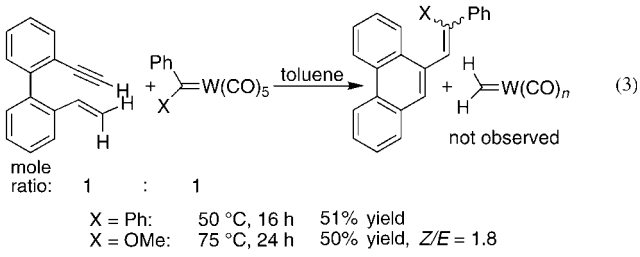

(3)

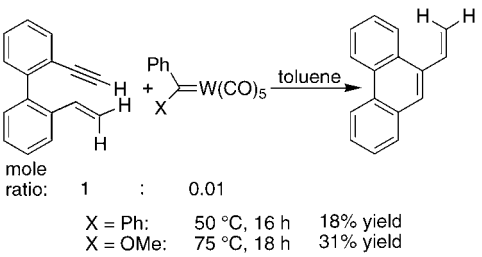

(4)

Many related experiments, one of which is summarized in Equation (5),[45] have been carried out by combining aliphatic enynes with Fischer carbene derivatives of tungsten, chromi-

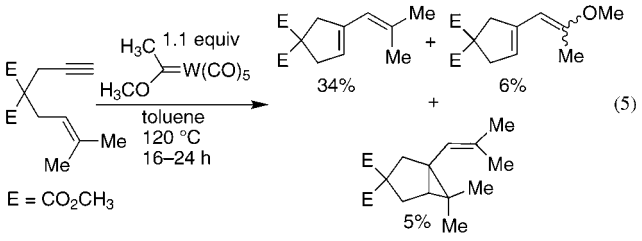

(5)

um, molybdenum, and manganese.[46a–c] These gave products analogous to those in Equations (3) and (4), as well as cyclopropanes that undoubtedly arise by a related pathway (see Section 2.5).

2.4.1. Advantages of Fischer Metal Carbenes in Enyne Metathesis

These experiments are significant not only because they demonstrated the metal-carbene-propagated enyne-metathesis reaction,[46b,c,d] but because they showed that the reaction can give the *Z* alkene with high stereoselectivity. When one of the hydrogen atoms of the methylene group of the starting material in Equation (4) is replaced by a methyl group, the propylidene group in the resulting product has the *cis* configuration (95% *cis* when the initiator is **1**, 78% *cis* when **2**).[6] The mechanistic implication is that the transformation of a metallacyclobutene into a metallabutadiene follows the path indicated in Equation (6).

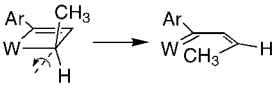

(6)

In contrast, there appears to be only one recorded example of an enyne metathesis initiated by a high-oxidation-state tungsten or molybdenum carbene.[47] There are a number of unsuccessful reactions.[47] The low-oxidation-state ruthenium carbenes have been used to great effect, but they usually give mixtures of *E* and *Z* isomers.[46d] In the presence of a ruthenium carbene plus ethylene, some alkenes give only or predominantly *E* isomers,[46d,48] but no metal carbene initiators other than the Fischer tungsten carbenes give almost pure-*Z* isomers. Remarkably, the classic olefin-metathesis initiator $MoCl_5$ combined with Ph_4Sn does also.[6b]

2.5. Evidence for the Mechanisms of These Transformations

Boiling in benzene transforms Fischer tungsten carbene [{(CH_2=$CHCH_2CH_2$)(MeO)C=}$W(CO)_5$] into **3**, by loss of CO,[49] and transforms related compounds similarly.[50] In a series of elegant mechanistic analyses, Casey et al. showed that not only do Fischer metal carbenes lose a CO ligand in this way, but to give metathesis products they *must* lose it.[51] If they do not, the metal carbenes can give cyclopropanes, but not metathesis products. Specifically, Casey et al. forced us to conclude that only when there are four carbonyl groups on the tungsten center, can **5** give the coordinatively saturated **6** (Scheme 2). When there are five carbonyl groups, it gives **7** and $[W(CO)_5]$.

The evidence was that in benzene at 22 °C, the *cis* and *trans* isomers of [{(MeOCH=$CHCH_2CH_2$O)(*p*-tolyl)C=}-$W(CO)_5$] undergo, after an induction period, autocatalytic transformations that give mainly 2-*p*-tolyl-4,5-dihydrofuran, whereas in the presence of at least equimolar amounts of coordinating ligands (Ph_3P, CH_3CN), the kinetics are first order and none of this product is formed. Only **7** is. The explanation is that **6** is produced only when a sufficient amount of a coordinatively unsaturated tungsten, formed as a product, is available to extract CO from the starting Fischer metal carbene. If it is not available, because it has been quenched by added ligand, no dihydrofuran is produced and no autocatalysis is observed. Related experiments[50b,52] and ^{1}H NMR spectroscopic evidence for the presence of the analogue of **3**[51] support these conclusions. Casey et al. pointed out the agreement between Scheme 2 and the early

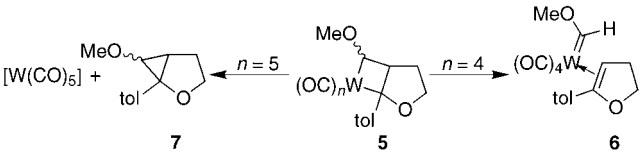

Scheme 2. The formation of products **6** and **7** from a tungsten carbene and an olefin depend on the number of ligands attached to the metal. Tol = *p*-tolyl.

observation of Fischer and Dötz[53] that CO facilitates the formation of cyclopropanes at the expense of alkenes.[51] Similarly, Casey and Cesa found, in agreement with the hypothesis, that the rates at which metal carbenes **1** and **2** exchange their carbonyl groups with isotopically labeled carbon monoxide are comparable to those of the metathesis reactions induced by the metal carbenes.[54]

Strong evidence that Fischer metal carbenes can execute the essential step of olefin metathesis was provided by the experiment of Casey and Burkhardt [Eq. (7)].[55] Among related experiments that subsequently provided similar evidence are the following: those in which **2**, now a reactant rather than a product, combines with vinyl amines to give pentacarbonyl(aminomethylene)tungsten compounds[56] and with ethyl vinyl ether under CO or with the α,β-unsaturated esters methyl cinnamate and diethyl maleate to give cyclopropanes;[53,57] those in which the chromium analogue of **2** combines with ethyl vinyl ether or *N*-vinylpyrrolidone to give **8**;[53,58] and those in which **1** with vinyl ethers other than **8** gives either **9** or analogues of **2**.[55,59,60]

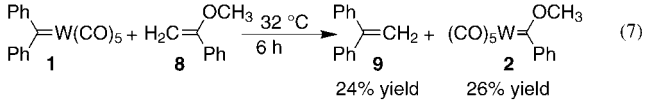

(7)

Furthermore, probably because it causes a molecule of carbon monoxide to dissociate from **1** (as it also does from **2** and from other Fischer metal carbenes),[50a,61] photoirradia-

tion brings about the exchange reaction shown in Equation (8).[62] This is a significant version of the experiment because it gives a metal carbene that has no stabilizing alkoxy group attached to the carbene center. Yet another experiment with similar significance is summarized in Equation (9): the isolation of the 1,2-diphenylcyclopropanes appears to identify a benzylidenetungsten intermediate that adds to styrene.[63]

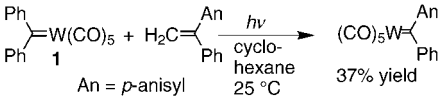

(8)

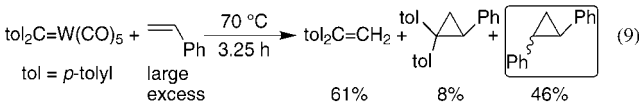

(9)

Powerful evidence for the mechanisms of initiations by Fischer metal carbenes is provided by experiments that identify a fragment of the initiator at a terminus of a ring-opening-metathesis polymerization product.[64] One is the extension of the Casey–Burkhardt experiment [Eq. (7)] shown in Equation (10).[65,66] Another, summarized in Scheme 3, yielded two materials identified as structures **10**

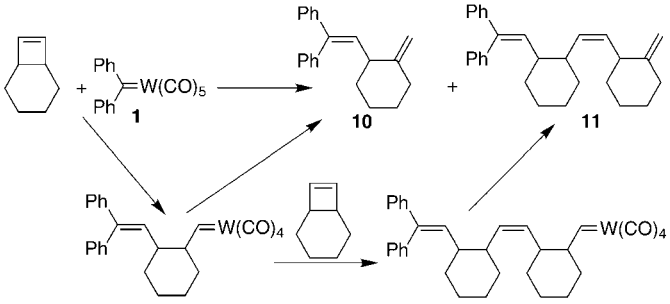

Scheme 3. Products of the reaction of the tungsten carbene **1** and an olefin that incorporate a fragment of the metal carbene.

and **11**, indications of the mechanistic steps in the scheme.[22,67] Another provided UV spectroscopic evidence for the presence of one diphenylmethylene unit (experimentally 0.8 units) per polymer chain in the product formed when the metathesis of 1-methyl-*trans*-cyclooctene is initiated by diphenylcarbene **1**.[1e]

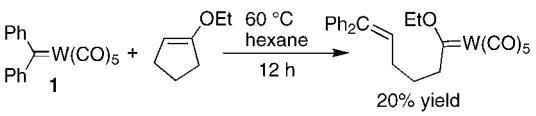

(10)

Similarly informative are the results of the experiments summarized in Equations (3) and (5) in Section 2.4. The fragments at one end of the structures formed identify how Fischer tungsten carbenes initiate enyne metatheses.

An end-group analysis also provided evidence for the related hypothesis that it is the growing acetylene polymer that initiates olefin metatheses actuated by phenylacetylene. When mixtures of this acetylene and WCl_6 initiated the polymerization of cyclopentene, a colored material was found attached to the polypentenamer formed and in an amount per chain that did not decrease when the growth of the polypentenamer chain was terminated ever earlier. The colored material (presumably polyphenylacetylene) therefore had to be attached to the initiating end of the polypentenamer chains.[68]

That Fischer metal carbenes insert into carbon–carbon multiple bonds is implied by their many stoichiometric reactions with acetylenes.[12b,69] The Dötz reaction is the best known, but Scheme 4 is cited here because it illustrates a

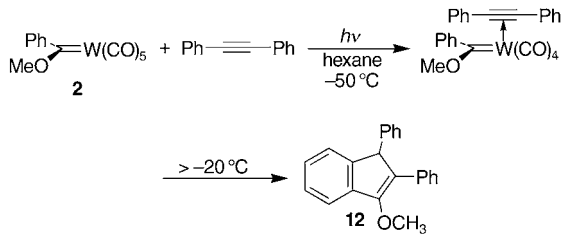

Scheme 4. Insertion of a tungsten carbene into diphenylacetylene.

reaction of a tungsten carbene and specifically one used in the work described above.[61a] Indene **12** is formed not only as indicated in the scheme, but also when mixtures of **2** with diphenylacetylene are heated.[61a] Similarly, other substituted acetylenes give analogous indenes.[70] The only explanations proposed involve acetylenes inserting into carbon–tungsten double bonds. The same is true for other transformations, such as the one in Equation (11).[71]

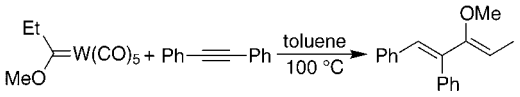

(11)

The implication of these experiments is that olefins and acetylenes insert into the carbon–metal bonds of Fischer metal carbenes, such as **1** and **2**, almost surely after a ligand is displaced from the metal. The resulting metal carbenes can combine with additional olefins and acetylenes. The consequences are olefin metatheses, acetylene polymerizations, acetylene-actuated olefin metatheses, and enyne metatheses.

3. Critique of Experiments with Fischer Metal Carbenes

3.1. Oxidation of Tungsten Carbenes

The following are reasons to question the suggestion[10a,13] that Fischer tungsten carbenes must first decompose into small amounts of high-oxidation-state alkylidene complexes before they can initiate the metathesis reactions described.

1) To carry out the experiments with **1** and **2**, solutions of the alkenes in toluene or benzene were "passed through a

column of basic alumina, degassed, and distilled from calcium hydride onto a potassium mirror and then onto pentacarbonyl(diphenylmethylene)tungsten … [then] sealed in a vacuum…"[1c] Related experiments with **3** were also carried out under vacuum.[33] The hypothesized oxidations therefore must have occurred in the absence of all but the most minuscule traces of oxidizing agents.

2) The Fischer metal carbenes are not easily decomposed or oxidized, and no significantly reactive materials have been found as products of these decompositions and oxidations.[2] The conditions described to decompose **1** were to heat it for several hours in refluxing heptane (b.p. 98 °C), whereupon it gave tetraphenylethylene, diphenylmethane, and tungsten hexacarbonyl. To oxidize it, an oxygen-saturated solution in diethyl ether was stirred under an oxygen atmosphere for 4 days to give benzophenone in 41 % yield. The methoxyphenylcarbene **2** is much more stable.[72] According to UV spectroscopic analysis, tungsten carbene **3** was unchanged after it had been heated for more than 20 times as long as it took for it to complete the metathesis of norbornene.[33]
3) The oxidation state of the tungsten does not change in the transformations summarized in Equations (7), (8), and (10) and in a related reaction.[66] These transformations mimic the essential step of olefin metatheses initiated by **1**.
4) No carbene derivative of tungsten in a higher oxidation state has yet reproduced the ability of Fischer tungsten carbenes to induce high *cis* stereospecificity in metatheses of a variety of cycloalkenes, to polymerize *tert*-butylacetylene, or to promote the metathesis of cycloheptene (see Sections 2.1.1 and 2.3.1).

Accordingly, it appears improbable that minute quantities of undetected and unspecified oxidized impurities, with properties unprecedented for oxidized species, allow Fischer metal carbenes to initiate olefin metatheses and related reactions. It also seems strange to presume that Fischer tungsten carbenes cannot propagate olefin metathesis when the most effective initiators today are carbene derivatives of Ru^{II}, which is isoelectronic with Mo^0.

3.2. Fischer Tungsten Carbenes as Chain Carriers

It is said that Fischer tungsten carbenes are unlikely to propagate metatheses because $[W(CHPh)(CO)_5]$ decomposes above −60 °C and because it does not yield metathesis products upon reaction with olefins.[10a,c] The first point is invalidated by the isolation of $[W(CHPh)(CO)_5]$ by H. Fischer et al., who handled it at room temperature,[73] and by the many transformations that seem to proceed by chain reactions even though the propagators have not been isolated. The second point contradicts Casey's conclusion,[74] summarized in Section 2.5, that the number of carbonyl ligands has to be one fewer in the propagating species than the five present in $[W(CHPh)(CO)_5]$.[75] Moreover, to exclude tungsten carbenes in low oxidation states as the propagating species in olefin metatheses seems unreasonable as they appear to be the propagating species in the enyne rearrangements discussed in Section 2.4.

3.3. Characterization of Fischer Metal Carbene Initiators

Fischer metal carbenes, it is said, do not meet criteria for an initiator to be well-defined:[10a,c,76] 1) that the propagating species either be observed in solution[16b] or be otherwise characterized;[16c] 2) that the structures of the initiators and the intermediates in the catalytic processes be essentially identical;[10c,16b] 3) that the initiators react with olefins to yield observable new carbene complexes derived from those olefins;[10c] and 4) that much of the initiator be involved in the catalytic process.[77,78]

However, as yet, no justification has been presented for these criteria, which were formulated only after the advent of recent metathesis initiators. Unexplained is why the term "initiator" should now be redefined as "well-defined initiator" and now exclude chain reactions that terminate, and why a term without previous meaning should not have been chosen for a substance that meets the new criteria.[79] Furthermore, none of the reports that provide the new definitions cite any evidence to show that the recent metathesis initiators themselves meet the new criteria. They do not seem to.

Thus in experiments with $[Mo(CH\mathit{t}Bu)(NAr)(OCMe(CF_3)_2)_2]$ (Ar = 2,6-diisopropylphenyl),[80] with $[W(CH\mathit{t}Bu)(NAr)(OCMe(CF_3)_2)_2]$,[31] and with a ruthenium carbene,[29a] only small fractions of the initiators were involved in the catalytic processes, and NMR spectra said to be those of propagating metal carbenes were detected in solution only long after the completion of the reactions in which the propagating metal carbenes were presumed to have intervened. In the experiments with $[W(CH\mathit{t}Bu)(NAr)(OCMe(CF_3)_2)_2]$, the majority of the tungsten carbene was said to have decomposed in undefined ways.[31] These results do not conform to criteria 1) and 4).

The facts are that both Fischer carbenes **1** and **2** are well-defined.[2,7,61,62,81] Their NMR, IR, UV, and mass spectra, their melting points, and their dipole moments are all defined. Their elemental compositions and molecular structures have been analyzed. They initiate olefin metatheses, acetylene polymerizations, and enyne rearrangements. The mechanisms by which they effect the initiations are compellingly made evident by experiments described in Section 2.5, which show that a ligand must be displaced from the metal, and by experiments described in Sections 2.4 and 2.5 ([Eq. (3), (5), (7), (8), (9), (10), and (11)] and Scheme 3), which identify fragments of the initiators at the termini of reaction products. The Fischer metal carbenes are not ill-defined initiators.

4. Critique of Experiments with Tantalum Carbenes

The literature on initiations by tantalum carbenes is centered on a statement repeated many times, verbatim[82] or with somewhat varied wording,[10a,c,83] that refers to the initiation of *cis*-2-pentene's metathesis by $[Ta(CH\mathit{t}Bu)Cl-$

$(OtBu)_2(PMe_3)$] and cites a preliminary communication in 1980 and a full paper in 1981:[14c,17] "This was the first time that productive metathesis of a simple olefin starting with a well-characterized carbene [or carbenoid] complex had been observed."[82] However, this initiating ability of the tantalum carbene is not described in the references cited, nor is it described anywhere else in the chemical literature.

Furthermore, experiments with this and three other tantalum carbenes are said to have demonstrated that alkoxide ligands allow, promote, encourage, or turn on the metathesis ability of tantalum carbenes.[10a,b,14a,84] *cis*-2-Pentene was the only olefin whose metathesis was mentioned, and the three other initiators were as follows: $[Ta(CHCMe_3)Cl_3(thf)_2]$, which gave a turnover of "≈ 6"; $[Ta(CHPh)Cl_3(thf)_2]$, which gave a turnover of "5–6"; and $[Ta(CHtBu)(OtBu)_3]$, which gave a turnover of "about seven".[17] Thus the basis for the statement that alkoxy substituents allow the tantalum species to function as metathesis catalysts is not strong.[85] It is weakened further by the absence of essentially any experimental details, the dissimilarity of the few mentioned,[86] and the incomplete characterization of the tantalum carbene initiators.[87,88] Six years later,[89] another tantalum carbene, which later was found to initiate the metathesis of norbornene,[89b] was said to have initiated the metathesis of 2-pentene very effectively, but there were no experimental details.

Accordingly, tantalum carbenes are known that initiate metathesis of norbornene, but there is no evidence that a well-defined and isolable tantalum carbene initiates the metathesis of any unstrained olefin.[90]

5. Summary and Outlook

There is considerable evidence that Fischer tungsten carbenes, even though their tungsten atoms are not in their highest oxidation state, initiate olefin metatheses, acetylene polymerizations, and enyne rearrangements. In contrast, members of both classes of recent initiators, $[M(CHtBu)(NAr)(OR)_2]$ (M = W or Mo) and $[Ru(CHR)Cl_2L_2]$, bring about olefin metatheses very much more quickly and with greater tolerance for accompanying functional groups. However, they do not induce the high *cis* stereoselectivity achieved by the Fischer tungsten carbenes in both olefin and enyne metatheses. Carbene derivatives of highly oxidized molybdenum or tungsten rarely initiate enyne metatheses and those of ruthenium do not initiate acetylene polymerizations. The ruthenium carbenes do initiate enyne metatheses very effectively, but their selectivities for reactions with alkenes and alkynes are usually different from those of the tungsten initiators used earlier.[91] The amounts of the initiators commonly used today are often large.[12b,d]

Thus, although the current initiators improve greatly on those discovered many years ago, further improvements should yet be possible. In searching for these, there is no reason to neglect derivatives of metals whose oxidation states are low. The differences in reactivity between the tungsten carbenes used originally and those developed more recently are similar to the differences between the currently used metal carbenes and those same metal carbenes with different ligands. If the alkoxy ligand in $[W(CHtBu)(NAr)(OR)_2]$ is $OC(CH_3)_3$ instead of $OCCH_3(CF_3)_2$,[10d,e,31] or the ligand L in $[Ru(CHR)Cl_2L_2]$ is PPh_3 instead of PCy_3,[92] the initiators are transformed from being widely effective to being effective only for the metatheses of strained olefins, such as norbornene. These differences are as great as or greater than those attributed to changes in oxidation state. Since the ligands have such large effects, the search for better initiators (e.g. those that induce high stereoselectivity) should extend beyond those classified as derivatives of Mo, W, or Re (d^0) and Ru (d^4).[93]

Received: July 26, 2004
Revised: October 27, 2004
Published online: March 31, 2005

[1] a) J. McGinnis, T. J. Katz, S. Hurwitz, *J. Am. Chem. Soc.* **1976**, *98*, 605; b) T. J. Katz, J. McGinnis, C. Altus, *J. Am. Chem. Soc.* **1976**, *98*, 606; c) T. J. Katz, S. J. Lee, N. Acton, *Tetrahedron Lett.* **1976**, *17*, 4247; d) T. J. Katz, N. Acton, *Tetrahedron Lett.* **1976**, *17*, 4251; e) S. J. Lee, J. McGinnis, T. J. Katz, *J. Am. Chem. Soc.* **1976**, *98*, 7818; f) T. J. Katz, W. H. Hersh, *Tetrahedron Lett.* **1977**, *18*, 585; g) for a review, see: T. J. Katz in *Handbook of Metathesis*, *Vol. 1* (Ed.: R. H. Grubbs), Wiley-VCH, Weinheim, **2003**, chap. 1.5, pp. 47–60.

[2] a) C. P. Casey, T. J. Burkhardt, *J. Am. Chem. Soc.* **1973**, *95*, 5833; b) C. P. Casey, T. J. Burkhardt, C. A. Bunnell, J. C. Calabrese, *J. Am. Chem. Soc.* **1977**, *99*, 2127.

[3] C. P. Casey in *Transition Metal Organometallics in Organic Synthesis*, *Vol. 1* (Ed.: H. Alper), Academic Press, New York, **1976**, chap. 3, pp. 189–233.

[4] T. J. Katz, S. J. Lee, M. A. Shippey, *J. Mol. Catal.* **1980**, *8*, 219.

[5] T. J. Katz, S. J. Lee, *J. Am. Chem. Soc.* **1980**, *102*, 422.

[6] a) T. J. Katz, T. M. Sivavec, *J. Am. Chem. Soc.* **1985**, *107*, 737; b) T. J. Katz in *Advances in Metal Carbene Chemistry* (Ed.: U. Schubert), Kluwer, Dordrecht, **1989**, p. 293.

[7] a) E. O. Fischer, A. Maasböl, *Angew. Chem.* **1964**, *76*, 645; *Angew. Chem. Int. Ed. Engl.* **1964**, *3*, 580; b) E. O. Fischer, A. Maasböl, *Chem. Ber.* **1967**, *100*, 2445.

[8] Reviews: a) K. J. Ivin, J. C. Mol, *Olefin Metathesis and Metathesis Polymerization*, Academic Press, San Diego, **1997**; b) T. J. Katz, *Adv. Organomet. Chem.* **1977**, *16*, 283.

[9] In the poly(*tert*-butylacetylene) formed under initiation by pentacarbonyl(methoxyphenylmethylene)tungsten (**2**) the configurations of the double bonds are also largely *E* (or "*cis*"): T. J. Katz, T. H. Ho, N.-Y. Shih, Y.-C. Ying, V. I. W. Stuart, *J. Am. Chem. Soc.* **1984**, *106*, 2659.

[10] a) R. R. Schrock, *J. Mol. Catal. A* **2004**, *213*, 21; b) W. C. P. Tsang, K. C. Hultzsch, J. B. Alexander, P. J. Bonitatebus, Jr., R. R. Schrock, A. H. Hoveyda, *J. Am. Chem. Soc.* **2003**, *125*, 2652; c) R. R. Schrock, A. H. Hoveyda, *Angew. Chem.* **2003**, *115*, 4740; *Angew. Chem. Int. Ed.* **2003**, *42*, 4592; d) R. R. Schrock, R. T. DePue, J. Feldman, C. J. Schaverien, J. C. Dewan, A. H. Liu, *J. Am. Chem. Soc.* **1988**, *110*, 1423; e) R. R. Schrock, *Acc. Chem. Res.* **1990**, *23*, 158; f) R. R. Schrock, *J. Organomet. Chem.* **1986**, *300*, 249.

[11] The wording in reference [10b] is ambiguous, but the statement within the reference that low-oxidation-state metal carbenes have not initiated olefin metatheses and statements in other of Schrock's writings imply the intended meaning: that the only Mo or W initiators of olefin metatheses are in a high oxidation state.

[12] a) *Handbook of Metathesis*, *Vol. 1–3* (Ed.: R. H. Grubbs), Wiley-VCH, Weinheim, **2003**; b) F. Zaragoza Dörwald, *Metal Carbenes*

in Organic Synthesis, Wiley, New York, **1999**; c) A. Fürstner, *Angew. Chem.* **2000**, *112*, 3140; *Angew. Chem. Int. Ed.* **2000**, *39*, 3012; d) K. C. Nicolaou, S. A. Snyder, *Classics in Total Synthesis II*, Wiley, New York, **2003**, chap. 7, 8, and 16.

[13] R. R. Schrock, as quoted in: A. M. Rouhi, *Chem. Eng. News* **2002**, *80*, 34.

[14] a) R. R. Schrock in *Handbook of Metathesis*, *Vol. 1* (Ed.: R. H. Grubbs), Wiley-VCH, Weinheim, **2003**, chap. 1.3, p. 8; b) R. R. Schrock, *J. Chem. Soc. Dalton Trans.* **2001**, 2541 (see p. 2546); c) R. Schrock, S. Rocklage, J. Wengrovius, G. Rupprecht, J. Fellmann, *J. Mol. Catal.* **1980**, *8*, 73; d) R. H. Grubbs, T. M. Trnka, M. S. Sanford in *Fundamentals of Molecular Catalysis* (Eds.: H. Kurosawa, A. Yamamoto), Elsevier, New York, **2003**, chap. 4, pp. 202–203.

[15] Although entitled "A Well-Characterized, Highly Active, Lewis Acid Free Olefin Metathesis Catalyst", reference [16a] does not mention previous well-characterized, less-active, Lewis acid free olefin-metathesis catalysts. Neither do references [16b,c], reviews of olefin metatheses initiated by well-defined complexes of Mo and W. Reference [16b] incorrectly asserts that the first ring-opening metathesis by a well-characterized Mo or W species was the polymerization of norbornene initiated by [W(CH*t*Bu)(NAr)(O*t*Bu)$_2$]. References [16d,e] do not consider Fischer tungsten carbenes to be single-component initiators.

[16] a) C. J. Schaverien, J. C. Dewan, R. R. Schrock, *J. Am. Chem. Soc.* **1986**, *108*, 2771; b) R. R. Schrock in *Alkene Metathesis in Organic Synthesis* (Ed.: A. Fürstner) Springer, New York, **1998**, chap. 1, pp. 1–36 (see in particular pp. 4, 5, 7, and 17); c) M. R. Buchmeiser, *Chem. Rev.* **2000**, *100*, 1565; d) T. M. Trnka, R. H. Grubbs, *Acc. Chem. Res.* **2001**, *34*, 18; e) A. Hafner, P. A. van der Schaaf, A. Mühlenbach, *Chimia* **1996**, *50*, 131; f) R. H. Grubbs, W. Tumas, *Science* **1989**, *243*, 907.

[17] S. M. Rocklage, J. D. Fellmann, G. A. Rupprecht, L. W. Messerle, R. R. Schrock, *J. Am. Chem. Soc.* **1981**, *103*, 1440.

[18] J. H. Wengrovius, R. R. Schrock, M. R. Churchill, J. R. Missert, W. J. Youngs, *J. Am. Chem. Soc.* **1980**, *102*, 4515. It is stated in this reference that in chlorobenzene [W(CH*t*Bu)(O)Cl$_2$(PEt$_3$)] alone in unspecified amounts initiates short-lived metatheses—how short is not said—of unspecified terminal and internal olefins.

[19] See Table 1.5-1 in reference [1g].

[20] a) G. Natta, G. Dall'Asta, I. W. Bassi, G. Carella, *Makromol. Chem.* **1966**, *91*, 87; b) an iridium trifluoroacetate initiator gave in 17% yield a product whose double bonds were 65% *trans*: L. Porri, P. Diversi, A. Lucherini, R. Rossi, *Makromol. Chem.* **1975**, *176*, 3121).

[21] P. Dounis, W. J. Feast, A. M. Kenwright, *Polymer* **1995**, *36*, 2787. A Schrock tungsten carbene (not fully specified) converted cyclooctene in unspecified yield into *cis*-polyoctenamer (90% *cis*). The *cis* stereoselectivities for cyclopentene, cyclodecene, and cyclododecene were 55, 20, and 20%, respectively. Cycloheptene gave no polymer. Schrock molybdenum carbenes gave polymers whose double bonds were mainly *trans*.

[22] H. Höcker, L. Reif, C. T. Thu, *Makromol. Chem. Suppl.* **1984**, *6*, 331.

[23] a) J. G. Hamilton in *Handbook of Metathesis*, *Vol. 3* (Ed.: R. H. Grubbs), Wiley-VCH, Weinheim, **2003**, chap. 3.5, pp. 143–179; b) B. Al Samak, V. Amir-Ebrahimi, D. G. Corry, J. G. Hamilton, S. Rigby, J. J. Rooney, J. M. Thompson, *J. Mol. Catal. A* **2000**, *160*, 13.

[24] See the references in references [1c] and [8b].

[25] Metatheses of acyclic alkenes by classic initiators have given only small stereoselectivities.[8a]

[26] J.-L. Couturier, C. Paillet, M. Leconte, J.-M. Basset, K. Weiss, *Angew. Chem.* **1992**, *104*, 622; *Angew. Chem. Int. Ed. Engl.* **1992**, *31*, 628. Also with one norbornene derivative, but not another, this initiator gives a polymer with double bonds largely *cis* configured.

[27] Lesser stereoselectivity was achieved by the use of two related initiators: F. Quignard, M. Leconte, J.-M. Basset, *J. Chem. Soc. Chem. Commun.* **1985**, 1816.

[28] M. B. O'Donoghue, R. R. Schrock, A. M. LaPointe, W. M. Davis, *Organometallics* **1996**, *15*, 1334.

[29] a) C. W. Bielawski, R. H. Grubbs, *Angew. Chem.* **2000**, *112*, 3025; *Angew. Chem. Int. Ed.* **2000**, *39*, 2903; b) Z. Wu, A. D. Benedicto, R. H. Grubbs, *Macromolecules* **1993**, *26*, 4975; c) V. Amir-Ebrahimi, D. A. Corry, J. G. Hamilton, J. M. Thompson, J. J. Rooney, *Macromolecules* **2000**, *33*, 717; d) K. J. Ivin, A. M. Kenwright, E. Khosravi, J. G. Hamilton, *J. Organomet. Chem.* **2000**, *606*, 37; e) K. J. Ivin, A. M. Kenwright, E. Khosravi, J. G. Hamilton, *Macromol. Chem. Phys.* **2001**, *202*, 3624; f) F. Lefebvre, X. Bories-Azeau, J. M. Basset in *Ring Opening Metathesis Polymerisation and Related Chemistry* (Eds.: E. Khosravi, T. Szymanska-Buzar), Kluwer, Dordrecht, **2002**, pp. 365–375; g) M. Buchowicz, J. C. Mol, *J. Mol. Catal. A* **1999**, *148*, 97.

[30] One of the Schrock molybdenum carbenes has transformed norbornene derivatives (but not simple cycloalkenes[21]) into *cis*-polyalkenamers: a) W. J. Feast, V. C. Gibson, E. L. Marshall, *J. Chem. Soc. Chem. Commun.* **1992**, 1157; b) E. Khosravi, A. A. Al-Hajaji, *Polymer* **1998**, *39*, 5619; c) R. R. Schrock, J.-K. Lee, R. O'Dell, J. H. Oskam, *Macromolecules* **1995**, *28*, 5933; and references [23a], [29d], and [29e].

[31] R. R. Schrock, J. Feldman, L. F. Cannizzo, R. H. Grubbs, *Macromolecules* **1987**, *20*, 1169.

[32] a) Eighteen years later the polymerization was reported again "for the first time": Z. Wu, R. H. Grubbs, *J. Mol. Catal.* **1994**, *90*, 39; their use of one of the more recently discovered initiators improved the results; b) attempts to polymerize 1-methylcyclobutene with WCl_6 combined with either Et_3Al or $EtAlCl_2$ led predominantly to saturated polymers: G. Dall'Asta, R. Manetti, *Atti Accad. Naz. Lincei Cl. Sci. Fis. Mat. Nat. Re* **1966**, *41*, 351.

[33] M. Doherty, A. Siove, A. Parlier, H. Rudler, M. Fontanille, *Makromol. Chem. Macromol. Symp.* **1986**, *6*, 33.

[34] C. T. Thu, T. Bastelberger, H. Höcker, *Makromol. Chem. Rapid Commun.* **1981**, *2*, 7.

[35] R. Nomura, K. Watanabe, T. Masuda, *Polym. Bull.* **1999**, *43*, 177.

[36] a) D. J. Liaw, A. Soum, M. Fontanille, A. Parlier, H. Rudler, *Makromol. Chem. Rapid Commun.* **1985**, *6*, 309; b) D.-J. Liaw, S.-D. Leu, C.-L. Lin, C.-F. Lin, *Polym. J. (Tokyo, Jpn.)* **1992**, *24*, 889; c) D.-J. Liaw, C.-L. Lin, *Polym. Int.* **1995**, *28*, 29; d) D.-J. Liaw, K.-R. Hu, H.-H. Chiang, E.-T. Kang, *Polym. J. (Tokyo, Jpn.)* **1995**, *27*, 262; e) D.-J. Liaw, J.-S. Tsai, *J. Polym. Sci. Part A: Polym. Chem.* **1997**, *35*, 475.

[37] a) J. Levisalles, F. Rose-Munch, H. Rudler, J.-C. Daran, Y. Dromzee, Y. Jeannin, D. Ades, M. Fontanille, *J. Chem. Soc. Chem. Commun.* **1981**, 1055; b) D. Meziane, A. Soum, M. Fontanille, H. Rudler, *Makromol. Chem.* **1985**, *186*, 367; c) D. Meziane, A. Soum, M. Fontanille, *Makromol. Chem.* **1988**, *189*, 1407.

[38] S. Koltzenburg, E. Eder, F. Stelzer, O. Nuyken, *Macromolecules* **1999**, *32*, 21.

[39] M. R. Buchmeiser, *Macromolecules* **1997**, *30*, 2274.

[40] a) R. R. Schrock, S. Luo, J. C. Lee, Jr., N. C. Zanetti, W. M. Davis, *J. Am. Chem. Soc.* **1996**, *118*, 3883; b) H. H. Fox, M. O. Wolf, R. O'Dell, B. L. Lin, R. R. Schrock, M. S. Wrighton, *J. Am. Chem. Soc.* **1994**, *116*, 2827; c) R. Schlund, R. R. Schrock, W. E. Crowe, *J. Am. Chem. Soc.* **1989**, *111*, 8004.

[41] T. Masuda, N. Sasaki, T. Higashimura, *Macromolecules* **1975**, *8*, 717.

[42] a) C. F. Bernasconi, *Adv. Phys. Org. Chem.* **2002**, *37*, 137; b) F. J. Brown, *Prog. Inorg. Chem.* **1980**, *27*, 1; c) D. J. Cardin, B. Cetinkaya, M. F. Lappert, *Chem. Rev.* **1972**, *72*, 545.

[43] T. J. Katz, S. J. Lee, M. Nair, E. B. Savage, *J. Am. Chem. Soc.* **1980**, *102*, 7940.
[44] See the footnotes to Table I in reference [43].
[45] T. R. Hoye, J. A. Suriano, *Organometallics* **1992**, *11*, 2044.
[46] For reviews, see: a) D. F. Harvey, D. M. Sigano, *Chem. Rev.* **1996**, *96*, 271; b) M. Mori in *Alkene Metathesis in Organic Synthesis* (Ed.: A. Fürstner), Springer, USA, **1998**, p. 133; c) M. Mori in *Handbook of Metathesis*, *Vol. 2* (Ed.: R. H. Grubbs), Wiley-VCH, Weinheim, **2003**, chap. 2.5, pp. 176–204; d) S. T. Diver, A. J. Giessert, *Chem. Rev.* **2004**, *104*, 1317.
[47] S.-H. Kim, W. J. Zuercher, N. B. Bowden, R. H. Grubbs, *J. Org. Chem.* **1996**, *61*, 1073.
[48] H.-Y. Lee, B. G. Kim, M. L. Snapper, *Org. Lett.* **2003**, *5*, 1855.
[49] a) C. Alvarez Toledano, J. Levisalles, M. Rudler, H. Rudler, J.-C. Daran, Y. Jeannin, *J. Organomet. Chem.* **1982**, *228*, C7; b) H. Rudler, F. Rose, M. Rudler, C. Alvarez, *J. Mol. Catal.* **1982**, *15*, 81; c) C. Alvarez Toledano, H. Rudler, J.-C. Daran, Y. Jeannin, *J. Chem. Soc. Chem. Commun.* **1984**, 574; d) A. Parlier, H. Rudler, N. Platzer, M. Fontanille, A. Soum, *J. Chem. Soc. Dalton Trans.* **1987**, 1041.
[50] a) C. P. Casey, A. J. Shusterman, N. W. Vollendorf, K. J. Haller, *J. Am. Chem. Soc.* **1982**, *104*, 2417; b) C. P. Casey, N. W. Vollendorf, K. J. Haller, *J. Am. Chem. Soc.* **1984**, *106*, 3754; c) C. Alvarez Toledano, A. Parlier, H. Rudler, J.-C. Daran, Y. Jeannin, *J. Chem. Soc. Chem. Commun.* **1984**, 576.
[51] C. P. Casey, N. L. Hornung, W. P. Kosar, *J. Am. Chem. Soc.* **1987**, *109*, 4908.
[52] C. P. Casey, A. J. Shusterman, *Organometallics* **1985**, *4*, 736.
[53] E. O. Fischer, K. H. Dötz, *Chem. Ber.* **1972**, *105*, 3966.
[54] C. P. Casey, M. C. Cesa, *Organometallics* **1982**, *1*, 87.
[55] C. P. Casey, T. J. Burkhardt, *J. Am. Chem. Soc.* **1974**, *96*, 7808.
[56] J. Barluenga, F. Aznar, A. Martin, *Organometallics* **1995**, *14*, 1429.
[57] K. H. Dötz, E. O. Fischer, *Chem. Ber.* **1972**, *105*, 1356.
[58] E. O. Fischer, B. Dorrer, *Chem. Ber.* **1974**, *107*, 1156.
[59] K. Weiss, K. Hoffmann, *J. Organomet. Chem.* **1983**, *255*, C24.
[60] W.-C. Haase, M. Nieger, K. H. Dötz, *Chem. Eur. J.* **1999**, *5*, 2014.
[61] a) H. C. Foley, L. M. Strubinger, T. S. Targos, G. L. Geoffroy, *J. Am. Chem. Soc.* **1983**, *105*, 3064; b) H.-P. Gut, N. Welte, U. Link, H. Fischer, U. E. Steiner, *Organometallics* **2000**, *19*, 2354.
[62] L. K. Fong, N. J. Cooper, *J. Am. Chem. Soc.* **1984**, *106*, 2595; the other expected product, **9**, was isolated in 22% yield from a similar reaction that was brought about by heating the reactants at 30°C for 2 weeks.
[63] C. P. Casey, H. E. Tuinstra, M. C. Saeman, *J. Am. Chem. Soc.* **1976**, *98*, 608; the formation of each mol of 1,1-ditolylethylene should be accompanied by the formation of 1 mol of benzylidene tungsten, which can lead to up to 1 mol of 1,2-diphenylcyclopropane.
[64] The statement[10a] that there are no such experiments is incorrect.
[65] J. Levisalles, H. Rudler, D. Villemin, *J. Organomet. Chem.* **1978**, *146*, 259.
[66] Similar experiments were carried out with 2-ethoxynorbornene, and the product was analyzed by X-ray diffraction as well as NMR spectroscopy: a) J. Levisalles, H. Rudler, D. Villemin, J. Daran, Y. Jeannin, L. Martin, *J. Organomet. Chem.* **1978**, *155*, C1; b) H. Rudler, *J. Mol. Catal.* **1980**, *8*, 53.
[67] Although the parent peak in the mass spectrum and the ^{1}H NMR chemical shifts and intensities are listed and the IR spectrum is displayed, the evidence for the assignment of structure **11** is incomplete, and even more so for **10**.
[68] C.-C. Han, T. J. Katz, *Organometallics* **1985**, *4*, 2186.
[69] W. D. Wulff in *Comprehensive Organometallic Chemistry II (Series* Eds.: E. W. Abel, F. G. A. Stone, G. Wilkinson), *Vol 12* (Ed.: L. S. Hegedus), Elsevier, Amsterdam, **1995**, chap. 5.3, pp. 469–547.
[70] W. D. Wulff, B. M. Bax, T. A. Brandvold, K. S. Chan, A. M. Gilbert, R. P. Hsung, J. Mitchell, J. Clardy, *Organometallics* **1994**, *13*, 102.
[71] D. W. Macomber, *Organometallics* **1984**, *3*, 1589.
[72] This is made clear for its thermal reactions: A. Wienand, H.-U. Reissig, *Organometallics* **1990**, *9*, 3133; no oxidative instability has been reported at room temperature, and no detectable change appears to occur in the air.
[73] H. Fischer, S. Zeuner, K. Ackermann, *J. Chem. Soc. Chem. Commun.* **1984**, 684.
[74] a) C. P. Casey, S. W. Polichnowski, A. J. Shusterman, C. R. Jones, *J. Am. Chem. Soc.* **1979**, *101*, 7282; b) C. P. Casey, S. W. Polichnowski, *J. Am. Chem. Soc.* **1977**, *99*, 6097.
[75] Because [(CHPh)W(CO)$_5$] reacts with olefins before it can lose a ligand, it gives cyclopropanes.
[76] a) R. H. Grubbs, *Tetrahedron* **2004**, *60*, 7117; b) R. H. Grubbs in *Handbook of Metathesis*, *Vol. 1* (Ed.: R. H. Grubbs), Wiley-VCH, Weinheim, **2003**, chap. 1.2, pp. 4–7.
[77] M. Schuster, S. Blechert, *Angew. Chem.* **1997**, *109*, 2124; *Angew. Chem. Int. Ed. Engl.* **1997**, *36*, 2036.
[78] Reference [10c] invoked the converse.
[79] Zaragoza Dörwald also noted that the term "well-defined initiator" was being associated with virtue. He objected. (F. Zaragoza Dörwald, *Angew. Chem.* **2004**, *116*, 399; *Angew. Chem. Int. Ed.* **2004**, *43*, 395).
[80] R. R. Schrock, J. S. Murdzek, G. C. Bazan, J. Robbins, M. DiMare, M. O'Regan, *J. Am. Chem. Soc.* **1990**, *112*, 3875; Whereas 15 h were required for 50% of [Mo(CH*t*Bu)(NAr)-(OCMe(CF$_3$)$_2$)$_2$] (Ar = 2,6-diisopropylphenyl) to combine with *cis*-3-hexene in benzene at an unspecified temperature and give NMR signals proposed to be from the propylidene analogue of the metal carbene, 84% of the *cis*-3-hexene isomerized to the *trans* isomer before the ^{1}H NMR spectrum of the metal carbene changed significantly and only 2 min were required for the metal carbene in toluene at 25°C to equilibrate 2-pentene, 2-butene, and 3-hexene. After 24 h, 80% of the initial metal carbene was converted into the presumed propylidene analogue, and after another 15 h all the metal carbenes had decomposed, which seems odd.
[81] a) O. S. Mills, A. D. Redhouse, *Angew. Chem.* **1965**, *77*, 1142; *Angew. Chem. Int. Ed. Engl.* **1965**, *4*, 1082; b) J. A. Connor, E. M. Jones, E. W. Randall, E. Rosenberg, *J. Chem. Soc. Dalton Trans.* **1972**, 2419; c) G. M. Bodner, S. B. Kahl, K. Bork, B. N. Storhoff, J. E. Wuller, L. J. Todd, *Inorg. Chem.* **1973**, *12*, 1071.
[82] a) See page 13 of reference [14a]; b) R. R. Schrock in *Carbene Chemistry* (Ed.: G. Bertrand), Marcel Dekker, New York, **2002**, chap. 7, p. 211; c) reference [10f], p. 251.
[83] a) G. Black, D. Maher, W. Risse in *Handbook of Metathesis*, *Vol. 3* (Ed.: R. H. Grubbs), Wiley-VCH, Weinheim, **2003**, chap. 3.2, p. 8; these authors cite reference [17] and say that [Ta(CH*t*Bu)Cl$_2$(thf)$_2$] [sic] was the first well-defined isolable tantalum alkylidene that successfully catalyzed productive metathesis of internal alkenes; b) R. R. Schrock, *Chem. Eng. News* **2003**, *81*, 140.
[84] R. R. Schrock, *Adv. Synth. Catal.* **2002**, *344*, 571.
[85] A model study[14c,17] is sometimes cited as evidence,[10a,10c,83b] although model studies, such as that of Casey and Burkardt[55] on which it is patterned, are disparaged in reference [14c].
[86] The following details were given for the experiments with [Ta(CH*t*Bu)Cl$_3$(thf)$_2$] and [Ta(CH*t*Bu)(O*t*Bu)$_3$]: the solvents were "2.5 THF, ether" for the first of these initiators and toluene for the second; ≈0.02 equivalents of the second initiator was used and an unspecified amount of the first; the temperature was 25°C for the first and unspecified for the second; the reaction time was 4 h for the first and unspecified for the second.[17]

[87] [Ta(CH*t*Bu)Cl_3(thf)$_2$] and [Ta(CH*t*Bu)(O*t*Bu)$_3$], were characterized by fragmentary spectroscopic data, but no indications of purity were published.[17,88] [Ta(CHPh)Cl_3(thf)$_2$] was presumed to form in situ when [Ta(CH_2Ph)$_2Cl_3$] was combined with *cis*-2-pentene, THF, and ether.[17] There was no spectroscopic evidence, but the formation of side products was supposed to provide evidence for its formation and provide a basis for the calculation of turnover number.[17]

[88] G. A. Rupprecht, L. W. Messerle, J. D. Fellmann, R. R. Schrock, *J. Am. Chem. Soc.* **1980**, *102*, 6236.

[89] a) K. C. Wallace, J. C. Dewan, R. R. Schrock, *Organometallics* **1986**, *5*, 2162; b) K. C. Wallace, A. H. Liu, J. C. Dewan, R. R. Schrock, *J. Am. Chem. Soc.* **1988**, *110*, 4964.

[90] The contrary, that there are highly efficient tantalum metathesis catalysts, is asserted in reference [16 f].

[91] The ruthenium carbene initiators react preferentially with alkenes,[46d] the tungsten carbene initiators with alkynes.[6a,43,68]

[92] S. T. Nguyen, R. H. Grubbs, J. W. Ziller, *J. Am. Chem. Soc.* **1993**, *115*, 9858.

[93] Reference [10a] suggests otherwise.

Carbocycle Synthesis

The Intermolecular Pauson–Khand Reaction

Susan E. Gibson and Nello Mainolfi*

Keywords:
alkenes · carbonylation · cyclopentenones · intermolecular coupling · Pauson–Khand reaction

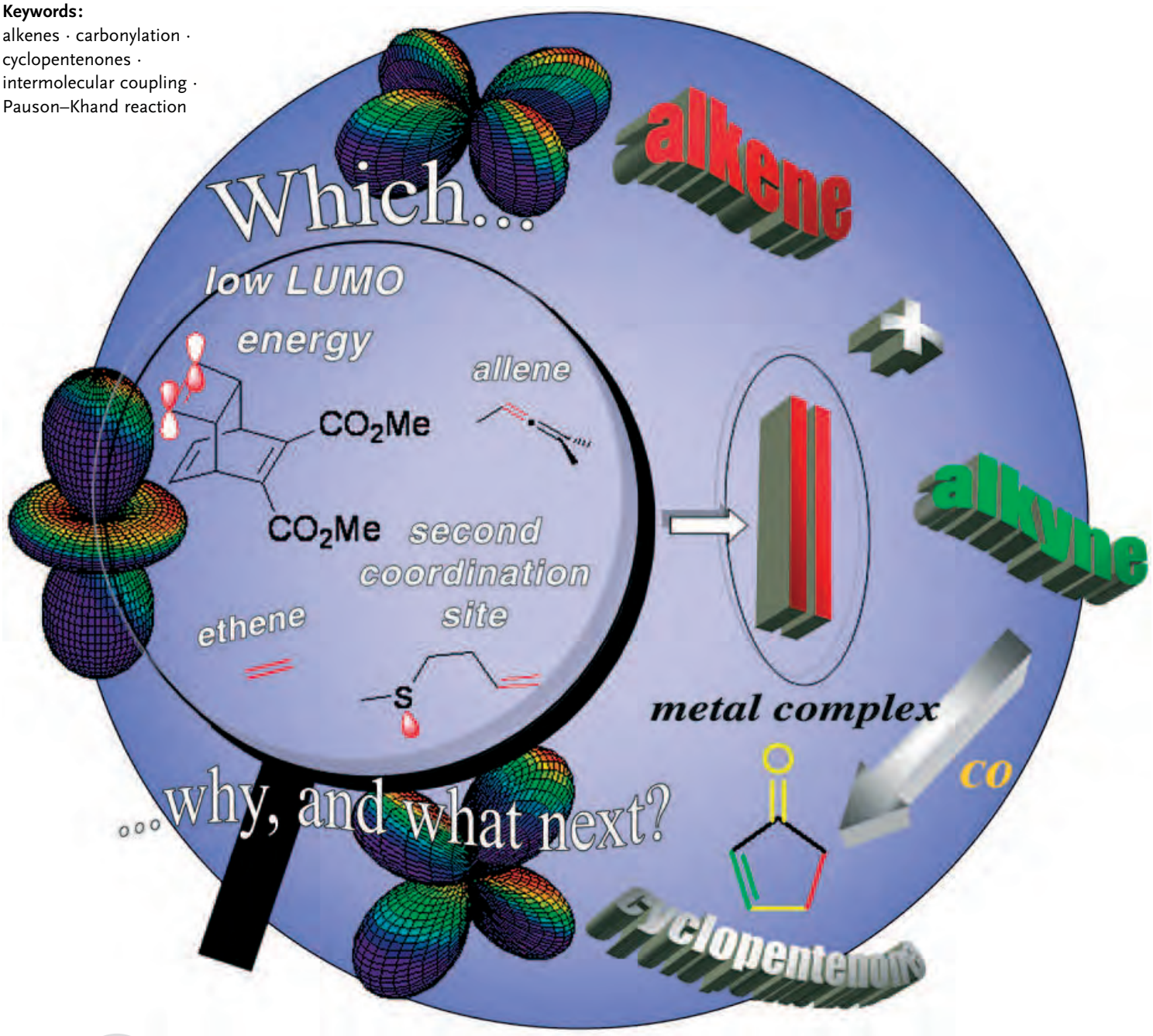

DOI: 10.1002/anie.200462235

Five membered carbocycles are important building blocks for many biologically active molecules. Moreover, substituted cyclopentenones (e.g. cyclopentenone prostaglandins) exhibit characteristic biological activity. The efficiency and atom economy of the Pauson–Khand reaction render this process potentially one of the most attractive methods for the synthesis of such compounds. Although it was discovered in its intermolecular form, the scope of the intermolecular Pauson–Khand reaction has always been limited by the poor reactivity and selectivity of the alkene component. The past decade, especially the last three years, has seen concerted efforts to broaden the scope of this reaction. In this overview, we provide a comprehensive and critical coverage of the intermolecular Pauson–Khand reaction based on the reactivity characteristics of different classes of alkenes and a rationalization of successes and misfortunes in this area.

From the Contents

1. Introduction

Metal-mediated reactions play an important role in our continuing search for improved ways of constructing complex molecules. For the synthesis of five-membered rings, there is surely no match for the Pauson–Khand reaction in terms of potential flexibility and atom economy. This reaction, discovered in 1971 by Pauson and Khand, [1] is a transition-metal-mediated coupling of an alkyne, an alkene, and a molecule of carbon monoxide that results in the formation of a cyclopentenone (Scheme 1).[2] Originally a cobalt carbonyl mediated process, the past decade has witnessed the introduction of new protocols based on titanium, rhodium, iridium, and ruthenium complexes. Furthermore, there are now many protocols based on transition-metal catalysts.[2g]

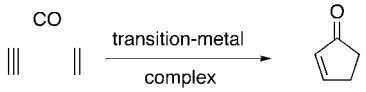

Scheme 1. The Pauson–Khand reaction.

The mechanism of the Pauson–Khand reaction has been the subject of extensive studies. It has proven difficult, however, to detect any intermediates beyond an initially formed hexacarbonylcobalt(0)–alkyne complex. A mechanism for the stoichiometric reaction, proposed by Magnus and co-workers in 1985, is still the generally accepted working mechanism (Scheme 2).[3] Starting from the initial hexacarbonyl complex **I**, the first step involves the loss of one CO ligand. This step, which is strongly endothermic, creates a vacant coordination site in intermediate **II**.[4] At this point the alkene coordinates with the cobalt and then inserts into a cobalt–carbon bond to form the cobaltacycle **III**. This is the step in which the regiochemical and stereochemical outcome is determined and is thought to be the rate-determining step.[5,9] The groups of Pericás,[5] Nakamura,[6] and Gimbert[7–9] have all performed elegant theoretical calculations on the role of the alkene in cobaltacycle formation, and these will be discussed in Section 3. The last two steps involve insertion of CO and reductive elimination to form the cyclopentenone **IV**.

Five-membered carbocycles are useful building blocks for the construction of complex biologically active molecules. Moreover, many cyclopentenones (e.g. cyclopentenone prostaglandins) exhibit a characteristic biological activity.[10] Although the Pauson–Khand reaction was discovered in its intermolecular form, the scope of the intermolecular reaction in synthetic projects has always been limited by the poor reactivity and selectivity of simple alkenes. Applications have been restricted to the use of strained alkenes such as

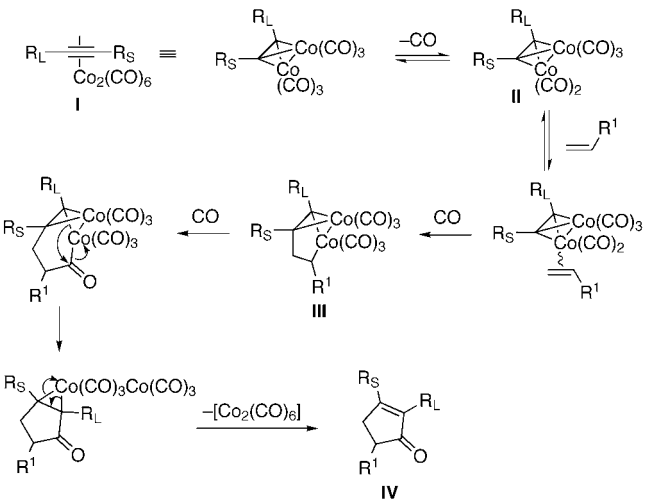

Scheme 2. The proposed mechanism for the $[Co_2(CO)_8]$-mediated Pauson–Khand reaction according to Magnus and co-workers;[3] R_L = larger group, R_S = smaller group.

[*] Prof. S. E. Gibson, N. Mainolfi
Department of Chemistry
Imperial College London
South Kensington Campus, London SW7 2AY (UK)
Fax: (+44) 207-594-5804
E-mail: s.gibson@imperial.ac.uk

 DOI: 10.1002/anie.200462235

norbornene, norbornadiene, and bicyclo[3.2.0]hept-6-ene, whilst the thermodynamically more favored intramolecular version has received most attention.[2]

The development of efficient, versatile, environmentally friendly, and possibly asymmetric catalytic *intermolecular* systems would maximize the synthetic attractiveness of the Pauson–Khand reaction and elevate this powerful reaction to a method of choice in the synthetic planning of complex biologically active molecules.[11] The past decade, and especially the past three years, has seen concerted effort from the chemistry community to broaden the scope of the intermolecular Pauson–Khand reaction.[12] In this Review we offer a comprehensive and critical coverage of the intermolecular Pauson–Khand reaction based on the reactivity characteristics of the alkene partners. By identifying reactivity patterns for different classes of alkenes, we aim to provide an overview and rationalization of successes and misfortunes in this area.

2. Reactive Alkene Partners: A Second Coordination Site

2.1. Discovery

Secondary interactions between molecules are often used to increase the rate and/or the selectivity of a reaction.[13] A preassociation of molecular partners through, for example, hydrogen bonding or Lewis acid–base interactions, is preserved during the chemical transformation and leads to a highly ordered transition state that often produces a significant enhancement in the rate and the selectivity of the reaction.

This concept was first applied to the intermolecular Pauson–Khand reaction by Krafft in 1988.[14] The use of terminal or unsymmetrically substituted alkenes usually leads to low yields and poor selectivity (Scheme 3).[2,15] Krafft and co-workers[14,16] anticipated that a heteroatom tethered to the alkene by a carbon chain would coordinate to cobalt, thus providing a bidentate complex that would lead to an increase in yield of the products and to control of the regiochemical outcome. Alkenes bearing oxygen, sulfur, and nitrogen substituents were investigated in the reaction. In contrast to alcohols and methoxymethyl ethers, which did not exhibit characteristics that would implicate heteroatom coordination,[17] sulfur and nitrogen ligands led to increased yields and excellent regiocontrol (Scheme 4).

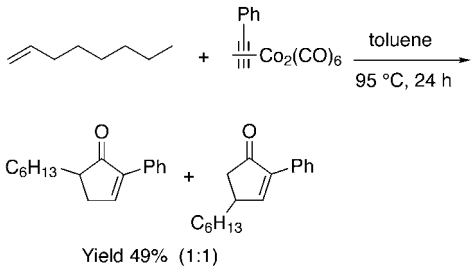

Scheme 3. An intermolecular Pauson–Khand reaction of a terminal alkene.

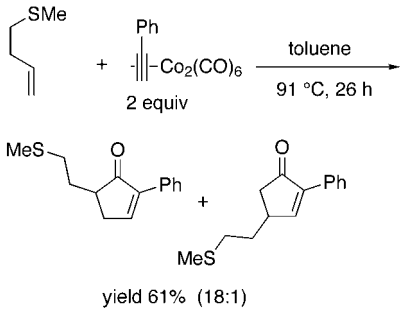

Scheme 4. An example of a substrate-directed intermolecular Pauson–Khand reaction according to Krafft and co-workers.[14]

In general allylic and bishomoallylic substrates result in poor yields and selectivities, whereas homoallylic substrates proved to be the most effective. For allylic substrates it was postulated that the tether between the heteroatom L and the alkene is too short to accommodate either a bidentate mononuclear "mode of cycloaddition" **1** (in which the heteroatom and the alkene bind to the same cobalt atom) or a bidentate binuclear "mode of cycloaddition" **3** (in which the heteroatom and the alkene each bind to different cobalt atoms) (Scheme 5). The monodentate "mode of cycloaddition" **2** (in which the heteroatom does not bind to the cobalt) is thus most likely to be the major contributor to the reaction.[18]

Sue E. Gibson obtained her first degree (1981) in Cambridge and her DPhil (1984) in Oxford (Prof. S. G. Davies). After postdoctoral studies at the ETH, Zürich (Prof. A. Eschenmoser), she lectured organic chemistry at the University of Warwick and at Imperial College, London. In 1999 she took up the Daniell Chair of Chemistry at King's College London, returning to Imperial College London and a Chair of Chemistry in 2003. Her research interests revolve around the application of transition metals in organic synthesis, especially the development and application of new asymmetric catalysts and novel chiral macrocycles.

Nello Mainolfi obtained his BSc from Queen Mary University, London, in 2001. His research project involved a new method to access substituted 2-bromophenols (Dr. Jason Eames). His PhD research (Prof. S. E. Gibson, 2001–2004) focused on the synthesis and investigations of a new class of non-racemic chiral macrocycles as ligands for asymmetric catalysis and as hosts for organic guests. He also prepared highly functionalized cyclopentenones through a new catalytic intermolecular Pauson–Khand reaction. In November 2004 he began postdoctoral studies with Prof. K. C. Nicolaou at the Scripps Research Institute.

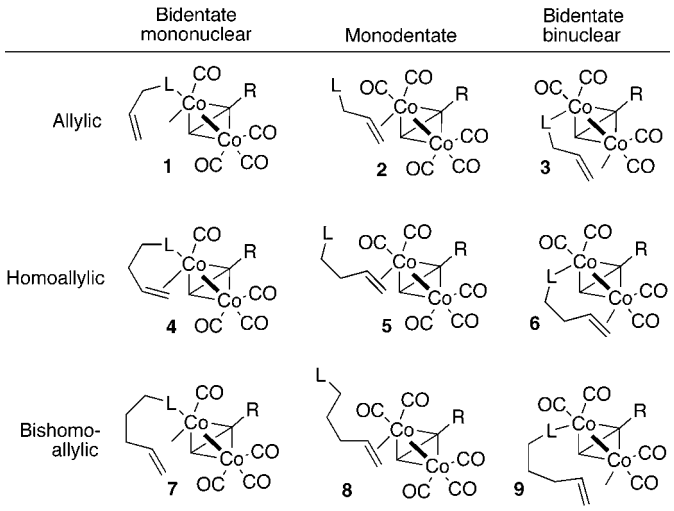

Scheme 5. Modes of cycloaddition for the substrate-directed intermolecular Pauson–Khand reaction (L = SR or NR_2) (Krafft and co-workers[16b]).

Homoallylic substrates gave very good yields of 2,5-disubstituted cyclopentenones. Therefore, it was postulated that bidentate mononuclear complex **4** (Scheme 5) is the best "mode of cycloaddition" for these substrates (the bidentate binuclear "mode of cycloaddition" **6** would give rise to the minor regioisomer). Bishomoallylic substrates exhibit a modest enhancement in yield and regioselectivity; hence "modes" **7** and **9** (Scheme 5) may well both be operating.

Krafft and Juliano explored the concept of heteroatom-directing reactions further by using tridentate alkenes (that is, alkenes bearing two heteroatoms).[19] An in-depth study of these ligands revealed that in some of the cases examined, the second tethered directing substituent enhanced the rate of the reaction (Table 1). The significantly shorter reaction times and higher yields than those for the reaction depicted in Scheme 4 and the similar to better regioselectivities observed in the reactions (Table 1, entries 1–3), could be due to the accessibility of tridentate "modes" **11** (tridentate mononuclear) and **12** (tridentate binuclear) as well as the previously discussed bidentate "mode" **10** (Scheme 6).

Table 1: Tridentate alkenes in the substrate-directed intermolecular Pauson–Khand reaction (Krafft and Juliano[19]).

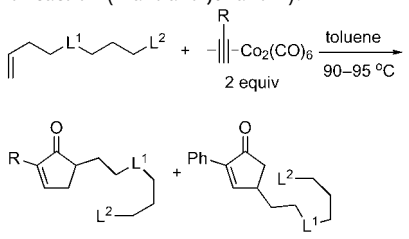

Entry	L^1	L^2	R	*t* [h]	Yield [%] (ratio)
1	S	NMe_2	Ph	6	85(15:1)
2	S	SEt	Ph	1.5	70 (8:1)
3	S	SEt	Bu	1.75	85(>40:1)

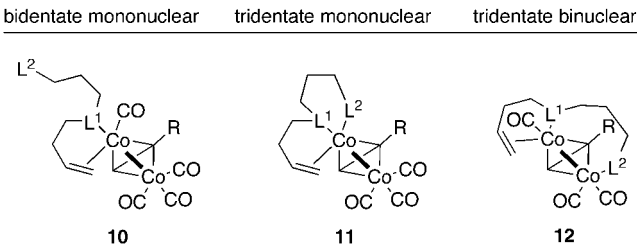

Scheme 6. Modes of cycloaddition of tridentate homoallylic substrates (Krafft and co-workers[19]).

2.2. Applications

The intermolecular Pauson–Khand reaction had to wait 10 years to benefit further from the elegant substrate-directing approach developed by Krafft and co-workers. In 2002, Itami and Yoshida reported the use of alkenyldimethyl 2-pyridylsilanes as the alkene partners for the ruthenium-catalyzed intermolecular Pauson–Khand reaction.[20] In this reaction, the pyridylsilyl group serves as a removable directing group, which facilitates the generation of desilylated cyclopentenones in moderate to excellent yields (Table 2).

Table 2: The pyridiylsilyl-directed Pauson–Khand reaction (Itami and Yoshida[20]).

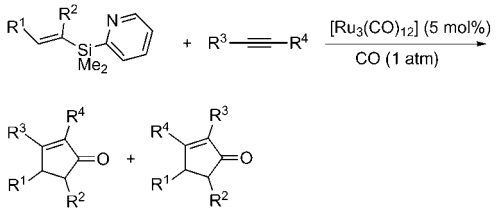

Entry	R^1	R^2	R^3	R^4	Reaction conditions	Yield [%] ratio
1	H	H	Ph	Ph	xylenes, 120 °C	88
2	H	H	H	Ph	toluene, 100 °C	55 (100:0)
3	H	H	H	C_6H_{13}	toluene, 100 °C	91 (59:41)
4	C_4H_9	H	H	Ph	xylenes, 140 °C	41 (100:0)
5	H	Me	H	C_6H_{13}	xylenes, 120 °C	40 (62:38)

Dimethyl-2-pyridylvinylsilane acted as an ethene equivalent, producing cyclopentenones in good yields and selectivity when symmetrical alkynes were used (Table 2, entry 1), but moderate yields (Table 2, entry 2) or poor regioselectivities (Table 1, entry 3) when unsymmetrical alkynes were employed.

The application of β- or α-substituted vinylsilanes resulted in the completely regioselective production of substituted cyclopentenones (for R^1 and R^2), albeit in low yields and sometimes with poor alkyne selectivity (Table 2, entries 4 and 5). This work provided an excellent example of the exploitation of a second coordination site on the alkene partner and strengthens the validity of Krafft's postulated homoallylic bidentate mononuclear "mode of cycloaddition" **4** (Scheme 5).

Another study that follows the principle of substrate-directed intermolecular Pauson–Khand reactions and further

widens the scope of this method was reported in 2003.[21] In an inspiring communication,[21a] Carretero and co-workers described the use of nonracemic chiral 2-(*N*,*N*-dimethylamino)-phenyl vinyl sulfoxide as a substrate-directing alkene partner for a stoichiometric asymmetric intermolecular Pauson–Khand reaction (Table 3). After analyzing the results of their search for an active vinyl sulfoxide they concluded that the 2-(*N*,*N*-dimethylamino)phenyl substituent on the sulfoxide yielded by far the most reactive, regio-, and diastereoselective alkene. This behavior is consistent with the operation of Krafft's bidentate mononuclear "mode of cycloaddition".[21b]

Table 3: The (*o*-dimethylamino)phenylsulfinyl-directed intermolecular Pauson–Khand reaction (Carretero and co-workers[21]).

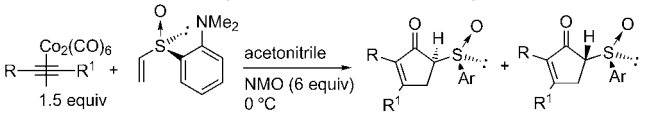

Entry	R[a]	R[1]	*t* [h]	Yield (d.r.)
1	*n*Bu	H	4	74 (93:7)
2	Bn	H	14	58 (93:7)
3	$(CH_2)_2OTIPS$	H	7	66 (>98:2)
4	CH_3	CH_3	24	no reaction
5	CH_3	CH_3	48[b]	33 (92:8)

[a] TIPS = triisopropylsilyl. [b] Pressure = 10 kbar.

In this NMO-promoted (NMO = *N*-methylmorpholine *N*-oxide)[22] intermolecular Pauson–Khand reaction the presence of the bishomoallylic dimethylamino group, aided by the sulfoxide-induced polarization of the alkene (see Section 3), promotes a highly diastereoselective, completely regioselective, and reasonable yielding reaction for terminal alkynes (Table 3, entries 1–3). No reaction occurred with an internal alkyne (Table 3, entry 4), although this limitation was partially lifted by performing the reaction at high pressure (Table 3, entry 5). The reaction has been used in the shortest reported synthesis of the antibiotic (−)-pentenomycin I.[21]

This first section of the review has highlighted the synthetic relevance of the stimulating study by Krafft and co-workers on the heteroatom-directed intermolecular Pauson–Khand reaction.[14,16,19] The two recent reports by Itami and Yoshida[20] and by Carretero and co-workers,[21] which broaden the scope of this approach to new attractive alkene partners, suggest that its synthetic potential has been underestimated for a long time.

3. Reactive Alkene Partners: The LUMO Energy

3.1. Background

Milet, Gimbert, and co-workers recently published an exciting theoretical study of the reactivity of alkenes in the intermolecular Pauson–Khand reaction.[9] After analyzing the reactivity of cyclohexene, cyclopentene, and norbornene towards the hexacarbonyldicobalt(0) complex of 1-propyne they concluded that the reactivity of the alkenes in the Pauson–Khand reaction is related to the back donation of electrons from the d orbitals of the cobalt atom to the π* orbitals of the alkene. After CDA (charge decomposition analysis) calculations they discovered that for a given alkene there was an "excellent correlation between the level of back donation and the barrier to cobaltacycle formation" (which is thought to be the rate-determining step for this reaction[9]). With norbornene they discovered a greater back donation and a lower energy barrier, whereas with cyclohexene there is little back donation and a higher barrier to cobaltacycle formation. For cyclopentene the values were similar to norbornene which is consistent with experimental observations.[23] Thus it appears that the greater the back donation, the higher the reactivity of the alkene. The common component of back donation and cobaltacycle formation is the LUMO of the alkene, and the theoretical work showed that the lower the LUMO, the higher the reactivity. The authors stated that "the LUMO of a free olefin should be generally useful as a first approximation of relative reactivity." The study also notes that a correlation exists between the C=C–C angle of the alkene (cyclohexene 128°, cyclopentene 112°, norbornene 107°) and the energy level of its LUMO: the smaller the angle, the lower the LUMO energy.

In this section we review the literature of the intermolecular Pauson–Khand reaction and we rationalize the behavior of alkene partners on the basis of this study. This not only validates this exciting work but also generates a novel set of parameters for designing new Pauson–Khand substrates.

3.2. Endocyclic Alkenes

In light of the study by Milet, Gimbert, and co-workers, reports on the use of cyclopropenes as the alkene partners in the intermolecular Pauson–Khand reaction[15f,24] come as no surprise. The C=C–C angle of cyclopropene is 64.58°,[25] and hence a low-lying LUMO and high reactivity are expected. After two reports on the use of substituted cyclopropenes[15f,24a] in the intermolecular Pauson–Khand reaction, in 2001 Pericás, Riera, and co-workers used cyclopropene itself for the first time in the cobalt-mediated version of this reaction.[24b] In this NMO-promoted coupling, cyclopropene reacted with bulky terminal alkynes to give synthetically attractive bicyclo[3.1.0]hex-3-en-2-ones **13** in good to excellent yields (Table 4, entry 1). In the case of aromatic and *n*-alkyl-substituted terminal alkynes, however, the yields were poor to moderate (Table 4, entries 2–4) and the production of tricyclic ketone **14** was observed.[26]

Based on the theoretical study of Milet, Gimbert, and co-workers, cyclobutene and its derivatives, which have a C=C–C angle of 94.2°,[27] are expected to exhibit high reactivity towards alkyne metal complexes in the intermolecular Pauson–Khand reaction. In fact, there are surprisingly few reports of cyclobutene derivatives being employed in the cobalt-mediated version of this reaction.[28] They are dominated by the bicyclo[3.2.0]hept-6-ene scaffold depicted in Scheme 7 which has been the subject of several studies that reveal very good reactivity and diastereoselectivity.[28]

Table 4: The intermolecular Pauson–Khand reaction of cyclopropene with terminal alkynes (Pericás and Riera).[24b]

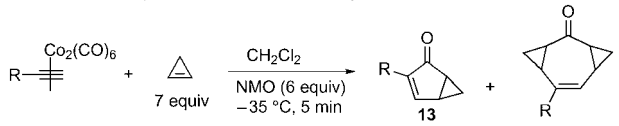

Entry	R	Yield [%]	
		13	**14**
1	*t*Bu	93	
2	Ph	50	15
3	*n*-hexyl	60	10
4	*p*-tolyl	26	23

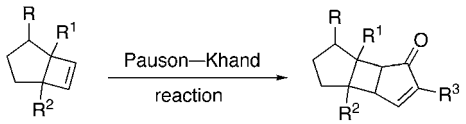

Scheme 7. The bicyclo[3.2.0]hept-6-ene scaffold in the Pauson–Khand reaction.[28]

In 2004, the use of cyclobutene derivatives was extended by our group. We reported[29] a cobalt-catalyzed intermolecular Pauson–Khand reaction of the readily available cyclobutadiene equivalent **15** (Table 5). The two-step, one-pot protocol employed a cyclobutadiene equivalent for the first time in the intermolecular Pauson–Khand reaction to provide synthetically versatile bicyclo[3.2.0]hepta-3,6-dien-2-ones **16** (Table 5, entries 1–3). A limit of this protocol is that it does not tolerate electron-withdrawing groups on the alkyne (Table 5, entry 4).

Table 5: The catalytic intermolecular Pauson–Khand reaction with a cyclobutadiene equivalent (Gibson and Mainolfi).[29]

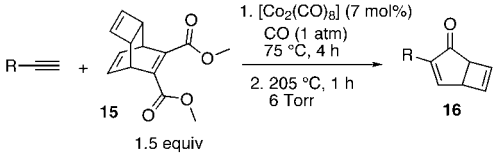

Entry	R[a]	Yield [%]
1	*n*-hexyl	98
2	Ph	75
3	$CH_2OTBDMS$	70
4	COOMe	no reaction

[a] TBDSM = *tert*-butyldimethylsilyl.

After examining cyclopropenes and cyclobutenes, our survey takes us to the cyclopentenes. The literature contains many examples of intermolecular Pauson–Khand reactions with double bonds embedded in a five-membered ring. The calculations of Milet, Gimbert, and co-workers[9] indicate that cyclopentene is activated to approximately the same extent as norbornene (the most studied alkene for this reaction). In fact, Pauson reported good reactivity for cyclopentene in his early studies of this reaction.[15a] Over the past 30 years moderate to good successes have been reported in studies on the use of 2,5-dihydrofuran **17**,[30] 2,2-dimethyl-2,5-dihydrofuran **18**,[30a] 2,3-dihydrofuran **19**,[2a,31] and cyclopentene **20**[15b,c,28f,30a,c,e–i,32,68a] (Scheme 8).

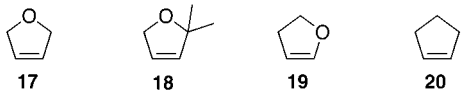

Scheme 8. Cyclopentenes used in the intermolecular Pauson–Khand reaction.

At this point it is interesting to focus on some examples in which the reactivity of the same alkene changes dramatically upon changing the reaction conditions. In the first example of the Pauson–Khand reaction of cyclopentene with phenylethyne, Pauson and Khand reported a high-temperature, moderate-yield protocol (Table 6, entry 1).[15a] A decade later Pauson and co-workers reported an improvement in the yield of this reaction when using tributylphosphine oxide as a promoter (Table 6, entry 2).[30c] A few years later, Kerr and co-workers showed that the use of an amine oxide under ultrasound conditions rendered this reaction nearly quantitative (Table 6, entry 3).[30f] In the meantime, Sugihara et al. reported the use of alkyl methyl sulfides as promoters of the Pauson–Khand reaction; under their conditions cyclopentene reacted smoothly at a relative low temperature albeit over a longer reaction time (Table 6, entry 4).[32h]

Table 6: Intermolecular Pauson–Khand reaction of cyclopentene with phenylethyne under different reaction conditions.

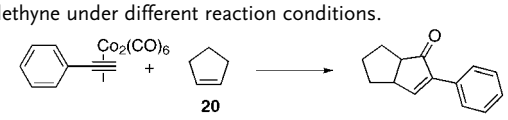

Entry	**20** [equiv]	Additive[a] ([equiv])	*t*, *T*	Yield [%]
1[15a]	5.3	none	7 h, 150–160 °C	47
2[30c]	5.9	$nBu_3P{=}O$ (1)	36 h, 69 °C	70
3[30f]	excess	TMANO (6)	10 min, RT, ultrasound	97
4[32h]	2.0	*n*BuSMe (5)	2 days, 35 °C	75

[a] TMANO = trimethylamine *N*-oxide.

An interesting subclass of cyclopentenes is the hexahydropentalenes **21** (Scheme 9). These undergo a double-bond shift prior to the Pauson–Khand reaction to access more-

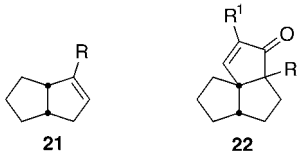

R = H (**a**), CH_3 (**b**)
$R^1 = CH_2OTBDMS$

Scheme 9. Hexahydropentalenes (**21a**)[33] and **21b**[34] and the corresponding intermolecular Pauson–Khand products **22a,b** from their reaction with a silyl-protected propargylic alcohol.

strained double bonds. Serratosa and co-workers showed[33] that the reaction of 1,2,3,3a,4,6a-hexahydropentalene (**21a**) with the hexacarbonyldicobalt(0) complex of a silyl-protected propargylic alcohol gave a single product (albeit in low yield) that corresponded to the angular fused triquinone **22a**. In an independent study Billington et al. showed that a methyl-substituted pentalene group **21b** (Scheme 9) behaved in the same way.[34] In this case the alkene shift converted a trisubstituted alkene into a tetrasubstituted alkene prior to cycloannulation.[35]

A more strained and exotic cyclopentene, benzvalene (**23**), underwent an intermolecular aminoxide-promoted Pauson–Khand reaction with moderate success (Scheme 10) in the fascinating synthesis of a $(CH)_{10}$ hydrocarbon by Christl and co-workers.[36]

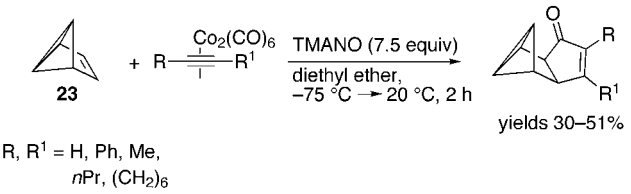

Scheme 10. Intermolecular Pauson–Khand reaction of benzvalene (**23**) with alkynes (Christl and co-workers[36]).

The theoretical studies of Milet, Gimbert, and co-workers supported by Pauson's experiments,[15a] reasoned that the poor reactivity of cyclohexene (3% yield with phenylethyne; C=C–C angle of 128° compared to 107° of norbornene) is due to a higher alkene LUMO which leads to a slightly endothermic binding energy value, in contrast to the exothermic binding energies of norbornene and cyclopentene.[9] Nevertheless, a good yield can be obtained from the reaction of cyclohexene **24** and 1-hexyne with a long reaction time and the use of *n*BuSMe as promoter (Scheme 11).[15f]

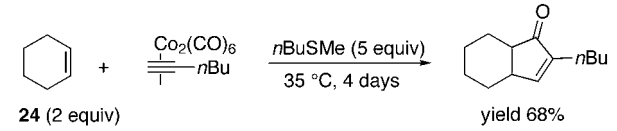

Scheme 11. Intermolecular Pauson–Khand reaction of cyclohexene (Sugihara et al.[15f]).

There are only a few examples of the use of cycloheptenes and cyclooctenes in the Pauson–Khand reaction. In their early studies,[15a] Pauson and Khand reported better reactivity for these two cyclic alkenes than for cyclohexene (41% for cycloheptene and 35% for cyclooctene in their reaction with phenylethyne) but not as good as for norbornene and cyclopentene. These experimental observations are also consistent with the results of Milet, Gimbert, and co-workers. Cycloheptene (C=C–C angle of 123°)[37,38] is predicted to have a lower-lying LUMO (and hence a higher reactivity) than cyclohexene (128°), but a higher-lying LUMO than norbornene (107°) and cyclopentene (112°). The same rationalization is valid for cyclooctene (C=C–C angle of 121.9°).[38]

As in the case of cyclohexene, a great improvement in the yield of a reaction of cycloheptene **25** was reported,[15f] again by using *n*BuSMe as a promoter (Scheme 12). It is important to note at this point that although it has proven possible to improve reactivity by changing reaction conditions, the relative rates of reactions of different alkenes are always maintained.[39]

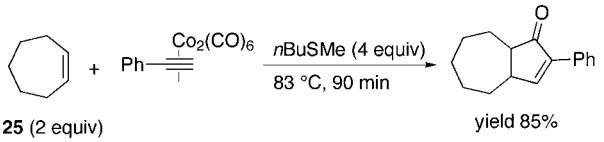

Scheme 12. A high-yielding intermolecular Pauson–Khand reaction of cycloheptene (Sugihara et al.[15f]).

Norbornene and related systems are commonly used in the intermolecular Pauson–Khand reaction. Since the early reports of Pauson and co-workers,[23a–c] in which they showed norbornenes to be the most successful alkene partners, there have been many examples of their use in the presence of different metals and under different reaction conditions,[15b–f,30c,f,32b,g,40,68a] in the asymmetric version of the reaction,[28e,h,32d,i,41] and in heterogeneous systems.[30g–i,42] Related systems such as 8-oxabicyclo[3.2.1]octenes[28b,43] and heteroatom-containing bicyclo[2.2.1]heptenes,[28f,40b,p,42a,43c,44,45] reveal similar or slightly lower levels of reactivity. As the literature contains so many examples, we have selected just two reports, one for its current importance in the field (Scheme 13) and one for its exoticism (Scheme 14).

In 2000, Shibata used norbornene in the only catalytic enantioselective intermolecular Pauson–Khand reaction reported to date based on a chiral catalyst (Scheme 13).[41p]

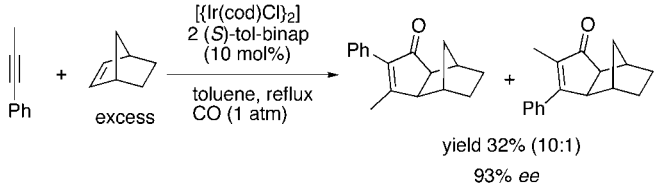

Scheme 13. The only catalytic enantioselective Pauson–Khand reaction reported to date (Shibata and Takagi[41p]).

In 1993, de Meijere and co-workers [46] reported the use of deltacyclene (**26**), a norbornadiene derivative, in a cobalt-mediated intermolecular Pauson–Khand reaction with 2-alkoxy-1-ethynylcyclopropane **27** (Scheme 14). The same group reported that the fascinating cyclic diene [2.2]paracyclophane-1,9-diene (**28**) is a good alkene partner in the intermolecular Pauson–Khand reaction.[47] With a C=C–C angle of 118.7°[48] this compound would be expected to be more reactive than cyclohexene (128°), cycloheptene (123°), and cyclooctene (121.9°), but slightly less reactive than

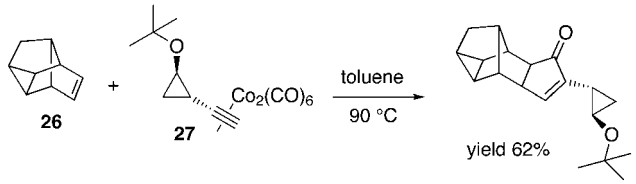

Scheme 14. Intermolecular Pauson–Khand reaction of deltacyclene (**26**) (de Meijere and co-workers[46]).

cyclopentene (112°) and norbornene (107°). This is indeed reflected in the experimental results.[47] The reaction of diene **28** with 2 equivalents of the hexacarbonyldicobalt(0) complex of phenylethyne for 1 day gave a mixture of mono- and diannulated compounds in a moderate yields (Table 7, entry 1). The reaction of the same alkene with 2.4 equivalents of the cobalt complex of trimethylsilylethyne gave the mixture in better overall yield, but only after a longer reaction time (Table 7, entry 2). In the presence of 6 equivalents of the latter alkyne complex the reaction proceeded smoothly and gave the diannulated product in high yield as a mixture of isomers (Table 7, entry 3).

Table 7: The intermolecular Pauson–Khand reaction of [2.2]paracyclophane-1,9-diene (**28**) (de Meijere and co-workers[47]).

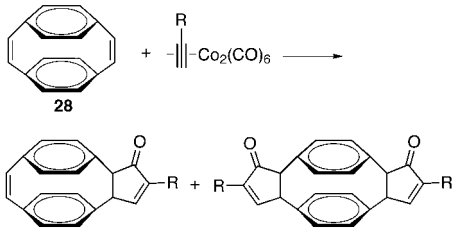

Entry	R[a] ([equiv])	*t*, *T*	Yield [%] mono[b]	di[b]
1	Ph (2)	1 day, 70 °C	27	24
2	TMS (2.4)	5 days, 90 °C	35	38
3	TMS(6)	5 days, 90 °C	0	80

[a] TMS = trimethylsilyl. [b] Yields of mono- and diannulated products.

3.3. Exocyclic Alkenes

There are only a few examples of the use of exocyclic alkenes in the intermolecular Pauson–Khand reaction. Smit et al.[49] described the use of methylenecyclopropane (**29**) in a cobalt-mediated reaction under dry, absorption conditions (SiO_2, Al_2O_3, or zeolites) (Scheme 15). The strain in **29** (C–C(=C)–C angle of 63.9°[27a]) suggests a low-lying LUMO and predicts good reactivity towards alkyne complexes in the Pauson–Khand reaction. Indeed, its reaction with 2-propyne over Al_2O_3 gave a 5:1 mixture of regioisomers in very good yield after only 2 h at 50 °C (Scheme 15, top). Predictably, the use of methylenecyclobutane (**30**) (C–C(=C)–C angle of 92°[27b]), resulted in a lower yield (Scheme 15, bottom).

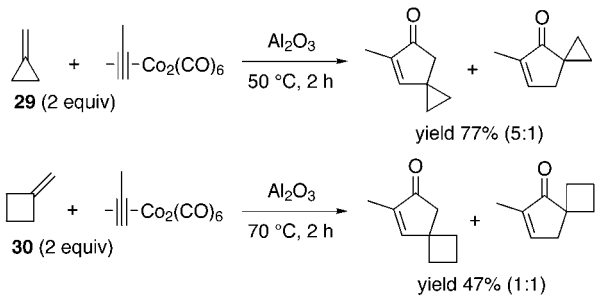

Scheme 15. Intermolecular Pauson–Khand reaction of methylenecyclopropane (**29**) and methylenecyclobutane (**30**) in the presence of solid adsorbents (Smit et al.[49]).

In 1996, Motherwell and co-workers[50] reported the use of functionalized alkylidene cyclopropanes in the NMO-assisted intermolecular Pauson–Khand reaction (Scheme 16). Interestingly, the presence of an ester group on the cyclopropane ring **31** not only reversed the regioselectivity of the reaction but also gave more-complex mixtures (Scheme 16, bottom).[51] An independent study of alkylidene cyclopropanes by Witulski and Gößmann[15g] with *N*-alkynyl amides as the alkyne partners gave similar yields and selectivities to those reported by Smit et al.[49] and Motherwell and co-workers.[50]

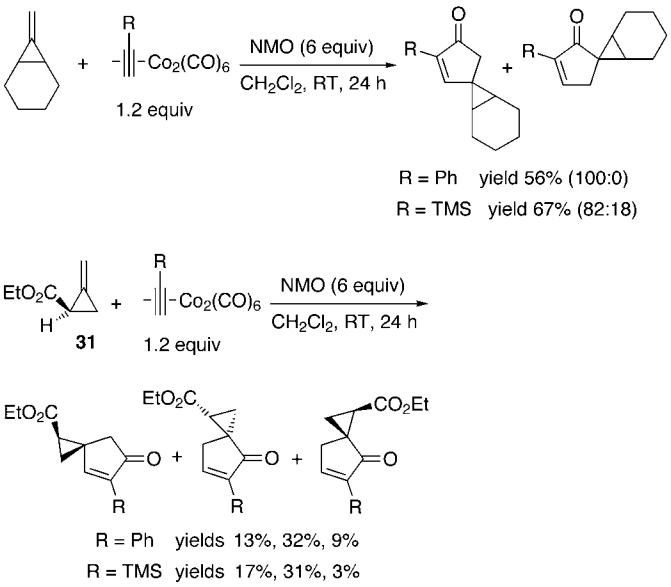

Scheme 16. Alkylidenecyclopropanes in the NMO-assisted intermolecular Pauson–Khand reaction (Motherwell and co-workers[50]).

As expected, the use of an exo methylene functionality on a six-membered ring in a thermal intermolecular Pauson–Khand reaction resulted in low yields (Table 8, entry 1).[52] However, in the presence of a large excess of the alkene (Table 8, entry 2), the desired spirocyclopentenone was produced in good yield.[53]

Table 8: Intermolecular Pauson–Khand reaction of methylene piperidines (Ishizaki, Hoshino, and co-workers[52]).

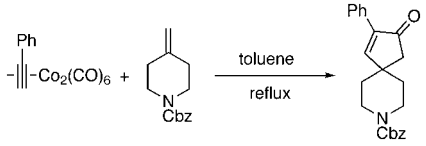

Entry	Alkene[a] [equiv]	*t* [h]	Yield [%]
1	2	5	30
2	10	3	78

CBz = benzyloxycarbonyl.

3.4. Conjugated Alkenes

Pauson and Khand examined the reactivity of conjugated alkenes in their early studies on the reaction.[54] In the case of dienes, they found that although cyclopentadiene (**32**) and fulvenes **33** reacted well,[54c] cyclohepta-1,3-diene and buta-1,3-diene (**34**) underwent a competing reaction that led to tetraenes such as **35** (hydrogen migration occurs instead of carbon monoxide insertion) (Scheme 17).[54a] They also

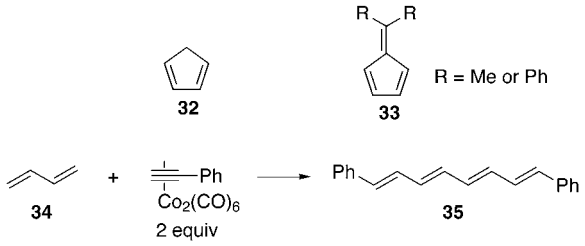

Scheme 17. Some conjugated dienes employed in the Pauson–Khand reaction (Pauson and co-workers[54a,c]).

observed[54b] that treatment of cyclohexa-1,3-diene (**36**; Scheme 18) with 2 equivalents of alkyne complex resulted first in a Diels–Alder reaction and subsequently in a Pauson–Khand reaction with the less-hindered alkene of the cycloadduct **37** (Scheme 18). When cyclohexa-1,4-diene was subjected to the same reaction conditions, a double-bond shift took place to yield **36**, which then entered the cascade sequence.[54b]

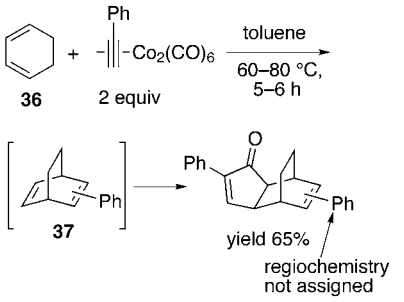

Scheme 18. A Diels–Alder/Pauson–Khand cascade reaction (Pauson and co-workers[54b]).

We believe that it is enlightening to consider these observations in the context of an extension of the hypothesis of Milet, Gimbert, and co-workers. It is known that adding conjugation to a double bond lowers the LUMO of the alkene by at least 0.5 eV.[55] Thus a conjugated diene has a lower-lying LUMO than a simple alkene, and hence should be more reactive in the Pauson–Khand reaction, if this reaction manifold can be accessed. Interestingly, a comparison of the outcome of similar reactions involving cyclopentadiene[54c] and cyclopentene[15a] suggests that the former is indeed more reactive.[56]

In 2004, Wender and co-workers have started to reveal the full potential of dienes as alkene partners in the intermolecular Pauson–Khand reaction.[57] Initially they observed that when 10 equivalents of 2,3-disubstituted-1,3-dienes such as **38** react with disubstituted alkynes in the rhodium-catalyzed intermolecular Pauson–Khand reaction at 80 °C, two other competing reactions occur: a [4+2] cycloaddition (as Pauson and co-workers observed for cyclohexadiene),[54] and a [2+2+2] coupling reaction; the desired Pauson–Khand product **39** was thus generated in low yield (Scheme 19). When the reaction was performed at 60 °C, however, a remarkable increase in selectivity was observed and led to cyclopentenones in excellent yields (Table 9, entries 1–3). Monosubstituted alkynes did not undergo cyclization.

When Pauson and co-workers investigated the reactivity of styrene **40** and its derivatives,[15a,54c,58] they discovered slightly more encouraging reactivity than with 1,3-dienes such as butadiene. Production of an unwanted coupling product still occurred through a competing pathway, but this time the Pauson–Khand product was observed. Indene (**41**), a strained version of styrene, afforded the Pauson–Khand product in improved yield (Scheme 20).[15a,54c] The two reactions showed complete regioselectivity with respect to the alkyne and the

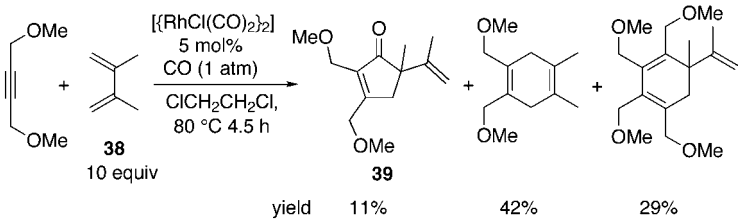

Scheme 19. Competing [2+2+1], [4+2], and [2+2+2] couplings in the reaction of a diene with a disubstituted alkyne at 80 °C (Wender and co-workers[57]).

Table 9: The intermolecular dienyl Pauson–Khand reaction (Wender and co-workers[57]).

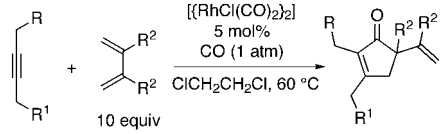

Entry	R[a]	R[1] [b]	R[2]	*t*	Yield [%]
1	OMe	OMe	Me	6	98
2	OTBS	OTBS	Me	6	87
3	OMe	OBn	Me	9	81

[a] TBS = *tert*-butyldimethylsilyl. [b] Bn = benzyl.

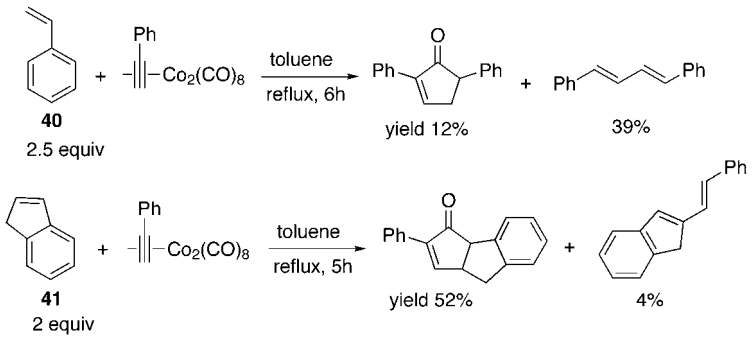

Scheme 20. Intermolecular Pauson–Khand reaction of styrene (**40**) and indene (**41**) (Pauson and Khand[15a,54c]).

alkene substituents. Although alkyne selectivity was already well-documented, the latter was noteworthy in the early years of the Pauson–Khand reaction. An explanation may be found in the polarization of the LUMO of the double bond by the arene ring which may induce the formation of the first C–C bond at the remote carbon atom of the alkene.

Control of the two observed reactivity modes of conjugated alkenes (hydrogen migration versus CO insertion) could be the key to the successful employment of a range of reactive and synthetically attractive alkene partners. The two reaction pathways can be explained in an example: The LUMO of alkenes that bear electron-withdrawing groups, for example, is very low, typically between −2 and 0 eV;[55] comparing this to the LUMO of norbornene (0.42 eV), we would expect even higher reactivity in the Pauson–Khand reaction for such alkenes. The extreme polarization of the

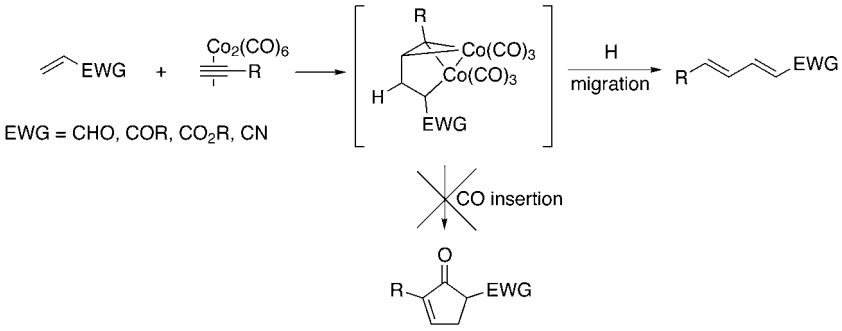

Scheme 21. Hydrogen migration (through β-hydride elimination) prevails over CO insertion in the intermolecular Pauson–Khand reaction of electron-poor alkenes. EWG = electron-withdrawing group.

double bond, however, leads to hydrogen migration and formation of dienes in preference to CO insertion and the formation of cyclopentenones (Scheme 21). In fact, reactions of members of this class of alkenes produced exclusively dienes.[59]

More recently, however, two reports on the successful employment of electron-poor alkenes have been published. In 1995, Costa and Mor[60] observed the formation of cyclopentenone products from electron-poor alkenes for the first time. Reaction of terminal alkynes and alkyl acrylates or acrylonitriles (as cosolvents) with catalytic amounts of $[Co_2(CO)_8]$ under a high pressure of CO and high temperatures forced the reactants down the CO insertion pathway and led to the isolation of cyclopentenones from a regioselective domino Pauson–Khand/Michael addition (Scheme 22).

In 1999, Cazes and co-workers reported that terminal and internal alkynes react with methyl acrylates and phenyl vinyl sulfones at lower temperatures in the stoichiometric NMO-promoted Pauson–Khand reaction.[61] They successfully exploited the anticipated high reactivity of electron-poor alkenes and suppressed the β-hydride elimination pathway by using low temperatures. In the presence of only 2 equivalents of the

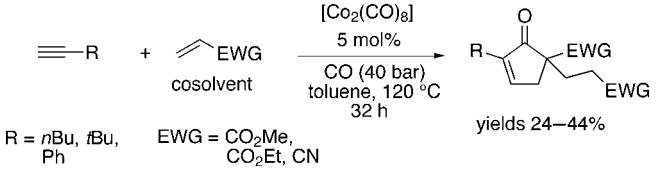

Scheme 22. The domino intermolecular Pauson–Khand/Michael addition reaction of electron-poor alkenes (Costa and Mor).[60]

alkene under mild reaction conditions (facilitated by the use of an amine oxide) only cyclopentenones were isolated (Table 10). In contrast to the results of Costa and Mor,[60] internal alkynes (Table 10, entries 1–2) result in better yields than terminal alkynes (Table 10, entries 3–4). The regioselectivity described in Scheme 22 and Table 10 is consistent with polarization of the LUMO of the alkene as mentioned above for styrene.

4. Reactive Alkene Partners: Miscellaneous

4.1. Allenes

Recent advances in the application of allenes in metal-mediated or -catalyzed reactions[62] include their use as alkene partners in the intermolecular Pauson–Khand reaction. The unusual structural and electronic characteristics of allenes[63]

Table 10: The intermolecular Pauson–Khand reaction of electron-poor alkenes (Cazes and co-workers[61]).

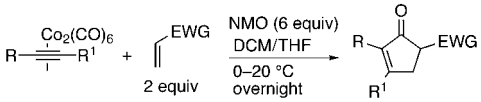

Entry	R	R^1	EWG	Yield [%]
1	CH_3	CH_3	CO_2Me	59
2	CH_3	CH_3	SO_2Ph	71
3	C_3H_7	H	CO_2Me	47
4	Ph	H	CO_2Me	41

together with the limited number of literature examples available at present have rendered it difficult to classify accurately their reactivity.

The first example of the use of an allene in the Pauson–Khand reaction was reported by Pauson in his review of 1985.[2a] He reported the smooth reactivity of cyclonona-1,2-diene with alkyne metal complexes. Apart from a report from Narasaka and co-workers,[64] in which they showed that $[Fe(CO)_4(NMe_3)]$ and irradiation promote the reaction between alkynes and allenes (Scheme 23), the major contribution to this area has originated from the Cazes group. Over the past decade they have described[65] the reactivity and regioselectivity of allenes in the NMO-promoted intermolecular Pauson–Khand reaction. They showed that the reactions depend on the substitution pattern of both acetylenic and allenic partners. The presence of an electron-donating group on the allene favors the formation of cyclopentenones **42** (Table 11, entry 1),[65b] whereas an electron-withdrawing group gives a mixture of cyclopentenones **42** and **43** (Table 11, entry 2).[65b] The reactivity of allenic hydrocarbons[65c] and their reactivity with silylated alkynes[65d] were also the subjects of extensive studies.

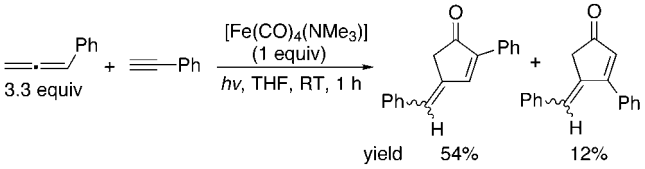

Scheme 23. Allene–alkyne intermolecular Pauson–Khand reaction in the presence of $[Fe(CO)_4(NMe_3)]$ under irradiation (Narasaka and co-workers[64]).

Table 11: The intermolecular allenyl Pauson–Khand reaction (Cazes and co-workers[65]).

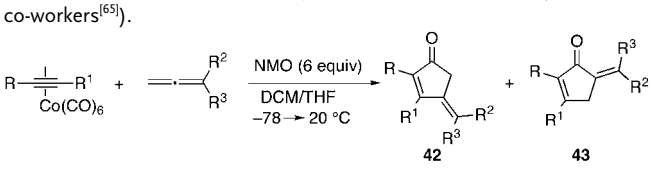

Entry	R	R^1	R^2	R^3	Yield [%] 42	43
1	CH_3	CH_3	O*t*Bu	H	30	
2	C_3H_7	C_3H_7	CO_2Me	H	33	14

Pérez-Castells and co-workers recently observed high regio- and stereoselectivity in the reactions of allene amides **44** with alkynes in the NMO-promoted version of the reaction (Scheme 24).[66] Allenes have also been used by Witulski and Gößmann,[15g] who treated 2-methylbuta-2,3-diene with an alkynyl amide in an aminoxide-promoted intermolecular Pauson–Khand reaction, and Hailes and co-workers who used undeca-5,6-diene in a key intermolecular Pauson–Khand reaction in the synthesis of novel compounds with olfactory properties.[67]

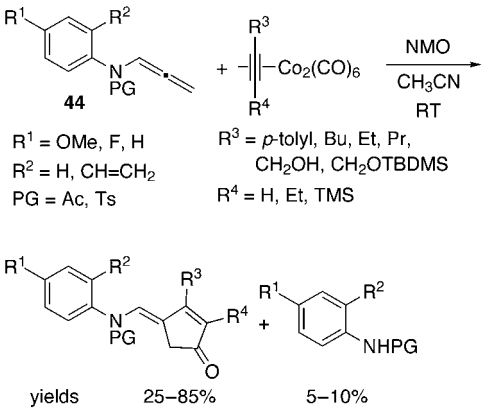

Scheme 24. Alleneamides in the intermolecular NMO-promoted Pauson–Khand reaction (Pérez-Castells and co-workers[66]). PG = protecting group; Ts = *p*-toluenesulfonyl.

4.2. Ethene

Ethene is one of the most attractive alkene partners in the Pauson–Khand reaction because of the synthetic potential of its products and it has been used since the discovery of the reaction.[2a,15a,d,30c,e,32c,40r,54a,68] However, its employment has been limited by the need for harsh reaction conditions, that is, elevated temperature and pressure. Use of the latest advances in the area such as catalysis,[68c] amine oxide promoters,[68d–f] and supercritical fluids[68g] does not remove the need to use high pressures to attain reasonable yields (Scheme 25).

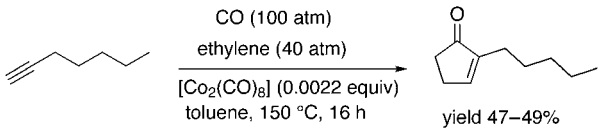

Scheme 25. A catalytic Pauson–Khand reaction under high pressures of carbon monoxide and ethene (Rautenstrauch et al.[68c]).

It was thus a significant development when Kerr and co-workers reported the first use of ethene at atmospheric pressure.[68d–f] They subsequently enhanced the practicality of the reaction even further through the discovery of an extremely convenient ethene equivalent for the intermolecular Pauson–Khand reaction.[69] During the synthesis of (+)-taylorione, Kerr and co-workers[68d–f] used $TMANO{\cdot}H_2O$ as a promoter for the annulation of alkyne metal complexes with ethene. Satisfactory yields were possible not only at a relatively low ethene pressure (25–35 atm) but also at atmospheric pressure (bubbling ethene) and room temperature (Scheme 26).

Later, Kerr discovered that vinyl esters behave as ethene equivalents when employed in the $NMO{\cdot}H_2O$-promoted stoichiometric intermolecular Pauson–Khand reaction (Table 12).[69] Interestingly, the poor reactivity of ethyl vinyl ethers had already been reported.[34,70] The change in reactivity between the ethers and the esters can be understood in terms of the molecular-orbital theory introduced in

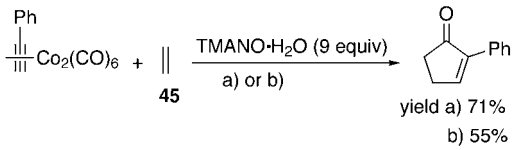

Scheme 26. TMANO-promoted Pauson–Khand reaction of ethene: a) 25–35 atm, 40 °C; b) 1 atom (bubbled), room temperature; (Kerr and co-workers[68d–f]).

Table 12: Ethene equivalents **46** in the intermolecular Pauson–Khand reaction (Kerr and co-workers[69]).

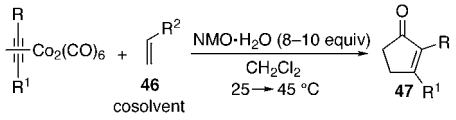

Entry	R[a]	R^1	R^2 [b]	*t* [h]	Yield [%]
1	Ph	H	OAc	1	53
2	Ph	H	OBz	16	80
3	$THPOCH_2$	H	OBz	16	87
4	CH_3	CH_3	OBz	16	5

[a] THP = tetrahydropyranyl. [b] Bz = benzoyl.

the previous section. Electron-donating groups raise the energy of the LUMO of the alkenes, thus lowering their reactivity. By converting an electron-rich vinyl ether into an electron-poor vinyl ester **46**, Kerr and co-workers not only improved the reactivity of the alkene, but also obtained the ultimate Pauson–Khand product, the deesterified cyclopentenone **47** (Table 12).[71] With this new protocol, the yields of the cyclopentenones were comparable and sometimes better than when using autoclave conditions[68d–f] (Table 12, entries 1–3). Loss of the substituent derived from the alkene may occur by the reduction of the ketone to the corresponding ketyl by low-valent cobalt species. Elimination of the ester, further reduction to the enolate, and subsequent quenching with water (contained in $NMO·H_2O$) would deliver the deesterified cyclopentenone **47**.[69b] Vinyl esters **46** showed very little reactivity towards internal alkynes, as does gaseous ethene[68] (Table 12, entry 4).

4.3. Low LUMO Energy or Coordination?

In the course of work towards the total synthesis of phorbol, Harwood and Tejera discovered that 2-furyl-substituted alkenes **48** and **50** (Scheme 27) reacted with the hexacarbonyldicobalt(0) complex of propyne **49** in good yield and regioselectivity.[72] In contrast, Pauson and co-workers showed that 2-vinylfuran reacted with phenylethyne only to produce an unwanted diene.[58a] As discussed in the previous section, this behavior is characteristic of some conjugated alkenes. In this case Harwood and Tejera showed that not only did the substituted vinyl furans **48** and **50** undergo the Pauson–Khand reaction, but also that in the case of thioether **50** the Krafft bidentate homoallylic "mode of cycloaddition" (Section 2.1, Scheme 5) was overwhelmed by the polarization of the alkene by the furyl group, thus yielding the furyl cyclopentenone as a single regioisomer.[72]

5. Summary and Outlook

We have shown how the reactivity of the alkene partners in the Pauson–Khand reaction is influenced by two major factors: the presence of other coordination sites on the alkene (Section 2) and the energy of the LUMO of the alkene (Section 3). In Section 2 it was seen that a second (and even a third) coordination site on the alkene can overcome the problems of reactivity and selectivity normally associated with the intermolecular Pauson–Khand reaction. This conclusion from a landmark study by Krafft and co-workers[14,16,19] has been underestimated for too many years, as illustrated by two recent literature reports that successfully build on this concept, and in doing so, significantly broaden the scope of the reaction.[20,21]

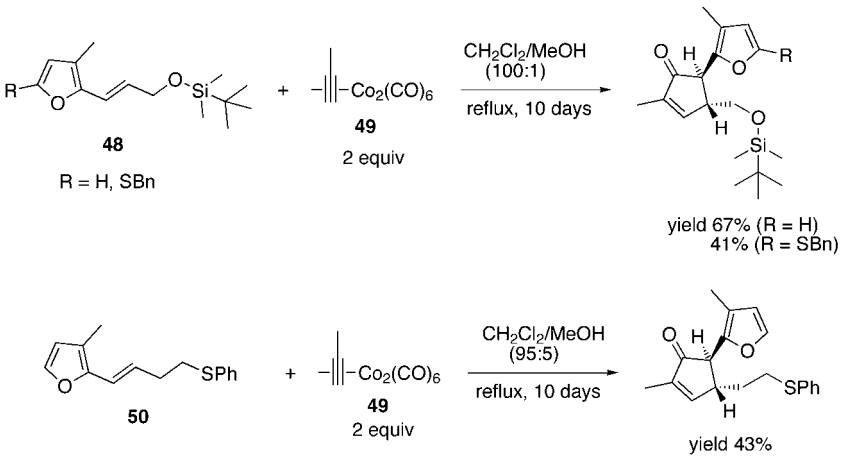

Scheme 27. The overpowering effect of the 2-furyl group in the intermolecular stoichiometric Pauson–Khand reaction (Harwood and Tejera).[72]

The second important concept is the use of the LUMO energy of the alkene to predict its relative reactivity in the Pauson–Khand reaction.[9] Our survey of intermolecular reactions in which the alkene reactivity could be rationalized with this theory has underlined the usefulness of the concept. Perhaps, more importantly, it should encourage the design and testing of many innovative Pauson–Khand substrates in the near future. As use of the intermolecular Pauson–Khand reaction in synthesis increases, it is anticipated that more examples will emerge in which electronic and coordination effects compete to determine alkene regioselectivity.

Although the journey to the perfect intermolecular Pauson–Khand reaction—efficient, versatile, environmentally friendly, asymmetric, and catalytic—is still far from over, an important step forward was very recently reported by Chung and co-workers.[73] They described a catalytic, inter-

molecular, heterogeneous (Co_2Rh_2 bimetallic nanoparticles) reaction in which an unsaturated aldehyde functions as both the alkene partner and the source of CO. It is well-documented that the reaction of aldehydes on metal surfaces releases hydrocarbons and carbon monoxide.[74,75] Chung and co-workers used this principle in the reaction of α,β-unsaturated aldehydes with terminal and internal alkynes in the presence of catalytic amounts of the nanoparticles to give cyclopentenones in moderate to good yields (Scheme 28).

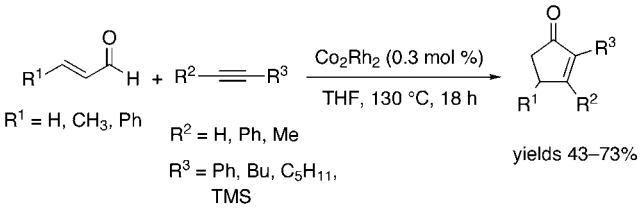

Scheme 28. The catalytic intermolecular Pauson–Khand reaction with an unsaturated aldehyde as alkene and CO source (Chung and co-workers).[73]

From a personal perspective, we hope that the report of Chung and co-workers[73] together with the insight provided herein into the reactivity problems that have, to date, been associated with the intermolecular Pauson–Khand reaction will inspire efforts to widen the scope of this potentially very powerful coupling reaction.

Received: October 7, 2004
Published online: March 31, 2005

[1] I. U. Khand, G. R. Knox, P. L. Pauson, W. E. Watts, *J. Chem. Soc. Chem. Commun.* **1971**, 36.
[2] For selected reviews, see: a) P. L. Pauson, *Tetrahedron* **1985**, *41*, 5855–5860; b) N. E. Schore, *Chem. Rev.* **1988**, *88*, 1081–1119; c) O. Geis, H.-G. Schmalz, *Angew. Chem.* **1998**, *110*, 955–958; *Angew. Chem. Int. Ed.* **1998**, *37*, 911–914; d) K. M. Brummond, J. L. Kent, *Tetrahedron* **2000**, *56*, 3263–3283; e) A. J. Fletcher, S. D. R. Christie, *J. Chem. Soc. Perkin Trans. 1* **2000**, 1657–1668; f) M. R. Rivero, J. Adrio, J. C. Carretero, *Eur. J. Org. Chem.* **2002**, 2881–2889; g) S. E. Gibson, A. Stevenazzi, *Angew. Chem.* **2003**, *115*, 1844–1854; *Angew. Chem. Int. Ed.* **2003**, *42*, 1800–1810; h) B. Alcaide, P. Almendros, *Eur. J. Org. Chem.* **2004**, 3377–3383; i) J. Blanco-Urgoiti, L. Añorbe, L. Pérez-Serrano, G. Domínguez, J. Pérez-Castells, *Chem. Soc. Rev.* **2004**, *33*, 32–42.
[3] a) P. Magnus, L.-M. Príncipe, *Tetrahedron Lett.* **1985**, *26*, 4851–4854; b) P. Magnus, C. Exon, P. Albaugh-Robertson, *Tetrahedron*, **1985**, *41*, 5861–5869.
[4] For studies on this step and detection of a pentacarbonyl dicobalt intermediate, see: C. M. Gordon, M. Kisza, I. R. Dunkin, W. J. Kerr, J. S. Scott, J. Gebicki, *J. Organomet. Chem.* **1998**, *554*, 147–154.
[5] M. A. Pericás, J. Balsells, J. Castro, I. Marchueta, A. Moyano, A. Riera, J. Vásquez, X. Verdaguer, *Pure Appl. Chem.* **2002**, *74*, 167–174.
[6] M. Yamanaka, E. Nakamura, *J. Am. Chem. Soc.* **2001**, *123*, 1703–1708.
[7] F. Robert, A. Milet, Y. Gimbert, D. Konya, A. E. Greene, *J. Am. Chem. Soc.* **2001**, *123*, 5396–5400.
[8] a) T. J. M. de Bruin, A. Milet, F. Robert, Y. Gimbert, A. E. Greene, *J. Am. Chem. Soc.* **2001**, *123*, 7184–7185; b) Y. Gimbert, D. Lesage, A. Milet, F. Fournier, A. E. Greene, J.-C. Tabet, *Org. Lett.* **2003**, *5*, 4073–4075.
[9] T. J. M. de Bruin, A. Milet, A. E. Greene, Y. Gimbert, *J. Org. Chem.* **2004**, *69*, 1075–1080.
[10] a) F. Marks, G. Fürstenberger, *Prostaglandins, Leukotrienes, and Other Eicosanoids. From Biogenesis to Clinical Application*, Wiley-VCH, Weinheim, **1999**; b) D. S. Straus, C. K. Glass, *Med. Res. Rev.* **2001**, *21*, 185–210.
[11] For the elegant use of the intermolecular Pauson–Khand reaction in the synthesis of natural products, see: a) V. Bernardes, N. Kann, A. Riera, A. Moyano, M. A. Pericás, A. E. Greene, *J. Org. Chem.* **1995**, *60*, 6670–6671; b) M. E. Krafft, Y. Y. Cheung, K. A. Abboud, *J. Org. Chem.* **2001**, *66*, 7443–7448; c) J. Chan, T. F. Jamison, *J. Am. Chem. Soc.* **2003**, *125*, 11514–11515; d) J. Chan, T. F. Jamison, *J. Am. Chem. Soc.* **2004**, *126*, 10682–10691.
[12] For recent work that significantly broadens the synthetic scope of the intermolecular Pauson–Khand reaction, see references [20, 21, 24b, 29, 57, 69].
[13] For a review on "Substrate-Directable Chemical Reactions", see: A. H. Hoveyda, D. A. Evans, G. C. Fu, *Chem. Rev.* **1993**, *93*, 1307–1370.
[14] M. E. Krafft, *J. Am. Chem. Soc.* **1988**, *110*, 968–970.
[15] For some examples, see: a) I. U. Khand, P. L. Pauson, *J. Chem. Res. Miniprint* **1977**, 168–187; b) A. Devasagayaraj, M. Periasamy, *Tetrahedron Lett.* **1989**, *30*, 595–596; c) M. Periasamy, M. R. Reddy, A. Devasagayaraj, *Tetrahedron* **1994**, *50*, 6955–6964; d) N. Jeong, Y. K. Chung, B. Y. Lee, S. H. Lee, S.-E. Yoo, *Synlett* **1991**, 204–206; e) Y. K. Chung, B. Y. Lee, N. Jeong, M. Hudecek, P. L. Pauson, *Organometallics* **1993**, *12*, 220–223; f) T. Sugihara, M. Yamada, M. Yamaguchi, M. Nishizawa, *Synlett* **1999**, 771–773; g) B. Witulski, M. Gößmann, *Synlett* **2000**, 1793–1797.
[16] a) M. E. Krafft, *Tetrahedron Lett.* **1988**, *29*, 999–1002; b) M. E. Krafft, C. A. Juliano, I. L. Scott, C. Wright, M. D. McEachin, *J. Am. Chem. Soc.* **1991**, *113*, 1693–1703.
[17] For a regioselective reaction of the tetrahydropyranyl ether of allyl alcohol and the cobalt complex of 2-butyne, see: D. C. Billington, P. L. Pauson, *Organometallics*, **1982**, *1*, 1560–1561. The origin of the selectivity was found to be the use of an internal alkyne rather than a directing effect from the heteroatoms on the alkene.[16a] The lack of rate enhancement for this particular reaction is consistent with this finding. For another example of the use of an internal alkyne to control regioselectivity, see: M. E. Krafft, R. H. Romero, I. L. Scott, *J. Org. Chem.* **1992**, *57*, 5277–5278.
[18] For poor reactivity and selectivity of allylic alcohols, see references [15b–g].
[19] M. E. Krafft, C. A. Juliano, *J. Org. Chem.* **1992**, *57*, 5106–5115.
[20] a) K. Itami, K. Mitsudo, J. Yoshida, *Angew. Chem.* **2002**, *114*, 3631–3634; *Angew. Chem. Int. Ed.* **2002**, *41*, 3481–3484; b) K. Itami, K. Mitsudo, K. Fujita, Y. Ohashi, J. Yoshida, *J. Am. Chem. Soc.* **2004**, *126*, 11058–11066.
[21] a) M. R. Rivero, J. C. de la Rosa, J. C. Carretero, *J. Am. Chem. Soc.* **2003**, *125*, 14992–14993; b) M. R. Rivero, I. Alonso, J. C. Carretero, *Chem. Eur. J.* **2004**, *10*, 5443–5459.
[22] For the first example of an aminoxide-promoted intermolecular Pauson–Khand reaction, see reference [15d].
[23] A clear order of reactivity: norbornene > cyclopentene > cyclohexene, with a major gap between the last two, was shown experimentally: a) I. U. Khand, G. R. Knox, P. L. Pauson, W. E. Watts, *J. Chem. Soc. Perkin Trans. 1* **1973**, 975–977; b) I. U. Khand, G. R. Knox, P. L. Pauson, W. E. Watts, M. I. Foreman, *J. Chem. Soc. Perkin Trans. 1* **1973**, 977–981; c) I. U. Khand, P. L. Pauson, *J. Chem. Soc. Perkin Trans. 1* **1976**, 30–32; see also reference [15a].

[24] a) S. L. Kireev, V. A. Smith, B. I. Ugrak, O. M. Nefedov, *Bull. Acad. Sci. USSR (Engl. Transl.)* **1991**, 2240 – 2246 (in this case the cyclopentenone was the minor product); b) I. Marchueta, X. Verdaguer, A. Moyano, M. A. Pericás, A. Riera, *Org. Lett.* **2001**, *3*, 3193 – 3196.

[25] W. M. Stigliani, V. W. Laurie, J. C. Li, *J. Chem. Phys.* **1975**, *63*, 1890 – 1892.

[26] It was postulated that this unprecedented adduct arises from an abnormal evolution of the key cobaltacycle intermediate of the reaction, in which a further alkene insertion competes with the normal CO insertion. The adduct was isolated as a single diastereomer whose stereochemistry could not be assigned.

[27] a) M. D. Harmony, V. W. Laurie, R. L. Kuczkowski, R. H. Schwendeman, D. A. Ramsay, F. J. Lovas, W. J. Lafferty, A. G. Maki, *J. Phys. Chem. Ref. Data* **1979**, *8*, 619 – 721; b) K. Kuchitsu, *Structure Data of Free Polyatomic Molecules: Atomic and Molecular Physics*, *Vol. 23*, Group II (Ed. Landolt-Bornstein), Springer, Berlin, **1995**.

[28] a) P. Blandon, I. U. Khand, P. L. Pauson, *J. Chem. Res. Miniprint* **1977**, 153 – 167; b) B. E. La Belle, M. J. Knudsen, M. M. Olmstead, H. Hope, M. D. Yanuck, N. E. Schore, *J. Org. Chem.* **1985**, *50*, 5215 – 5222; c) V. Sampath, E. C. Lund, M. J. Knudsen, M. M. Olmstead, N. E. Schore, *J. Org. Chem.* **1987**, *52*, 3595 – 3603; d) W. G. Dauben, B. A. Kowalczyk, *Tetrahedron Lett.* **1990**, *31*, 635 – 638; e) X. Verdaguer, A. Moyano, M. A. Pericás, A. Riera, V. Bernardes, A. E. Greene, A. Alvarez-Larena, J. F. Piniella, *J. Am. Chem. Soc.* **1994**, *116*, 2153 – 2154; f) B. A. Kowalczyk, T. C. Smith, W. G. Dauben, *J. Org. Chem.* **1998**, *63*, 1379 – 1389; g) X. Verdaguer, J. Vázquez, G. Fuster, V. Bernardes-Génisson, A. E. Greene, A. Moyano, M. A. Pericás, A. Riera, *J. Org. Chem.* **1998**, *63*, 7037 – 7052; h) E. Montenegro, A. Moyano, M. A. Pericás, A. Riera, A. Alvarez-Larena, J. F. Piniella, *Tetrahedron: Asymmetry* **1999**, *10*, 457 – 471.

[29] S. E. Gibson, N. Mainolfi, S. B. Kalindjian, P. T. Wright, *Angew. Chem.* **2004**, *116*, 5798 – 5800; *Angew. Chem. Int. Ed.* **2004**, *43*, 5680 – 5682.

[30] a) D. C. Billington, *Tetrahedron Lett.* **1983**, *24*, 2905 – 3908; b) L. Daalman, R. F. Newton, P. L. Pauson, R. G. Taylor, A. Wadsworth, *J. Chem. Res. Miniprint* **1984**, 3131 – 3149; c) D. C. Billington, I. M. Helps, P. L. Pauson, W. Thompson, D. Willison, *J. Organomet. Chem.* **1988**, *354*, 233 – 242; d) H. Brunner, A. Niedernhuber, *Tetrahedron: Asymmetry* **1990**, *1*, 711 – 714; e) C. J. Clements, D. Dumoulin, D. R. Hamilton, M. Hudecek, W. J. Kerr, M. Kiefer, P. H. Moran, P. L. Pauson, *J. Chem. Res. Miniprint* **1998**, 2658 – 2677; f) J. G. Ford, W. J. Kerr, G. G. Kirk, D. M. Lindsay, D. Middlemiss, *Synlett* **2000**, 1415 – 1418; g) D. S. Brown, E. Campbell, W. J. Kerr, D. M. Lindsay, A. J. Morrison, K. G. Pike, S. P. Watson, *Synlett* **2000**, 1573 – 1576; h) W. J. Kerr, D. M. Lindsay, S. P. Watson, *Chem. Commun.* **1999**, 2551 – 2552; i) W. J. Kerr, D. M. Lindsay, M. McLaughlin, P. L. Pauson, *Chem. Commun.* **2000**, 1467 – 1468.

[31] An intermolecular Pauson–Khand reaction with 4-methyl-2,3-dihydrofuran was employed in the elegant synthesis of (−)-terpestacin.[11c,d]

[32] a) S. Keyaniyan, M. Apel, J. P. Richmond, A. de Meijere, *Angew. Chem.* **1985**, *97*, 763 – 764; *Angew. Chem. Int. Ed. Engl.* **1985**, *24*, 770 – 771; b) A. de Meijere, *Chem. Br.* **1987**, *23*, 865 – 870; c) D. C. Billington, W. J. Kerr, P. L. Pauson, *J. Organomet. Chem.* **1988**, *341*, 181 – 185; d) V. Bernardes, X. Verdaguer, N. Kardos, A. Riera, A. Moyano, M. A. Pericás, A. E. Greene, *Tetrahedron Lett.* **1994**, *35*, 575 – 578; e) S. Fonquerna, A. Moyano, M. A. Pericás, A. Riera, *Tetrahedron* **1995**, *51*, 4239 – 4254; f) E. Montenegro, M. Poch, A. Moyano, M. A. Pericás, A. Riera, *Tetrahedron* **1997**, *53*, 8651 – 8664; g) T. Rajesh, M. Periasamy, *Tetrahedron Lett.* **1999**, *40*, 817 – 818; h) T. Sugihara, M. Yamada, M. Yamaguchi, M. Nishizawa, *Synlett* **1999**, 771 – 773; i) A. Becheanu, S. Laschat, *Synlett* **2002**, 1860 – 1864.

[33] A.-M. Montana, A. Moyano, M. A. Pericás, F. Serratosa, *Tetrahedron* **1985**, *41*, 5995 – 6003.

[34] D. C. Billington, W. J. Kerr, P. L. Pauson, C. F. Farnocchi, *J. Organomet. Chem.* **1988**, *356*, 213 – 219.

[35] In this case a mixture of cyclopentenone regioisomers of **22** was formed.

[36] M. Christl, M. Türk, E.-M. Peters, K. Peters, H. G. von Schnering, *Angew. Chem.* **1994**, *106*, 1719 – 1721; *Angew. Chem. Int. Ed. Engl.* **1994**, *33*, 1639 – 1641.

[37] The calculated angle for the chair conformation of cycloheptene is 124.40°; for the boat conformation, the angle is 120°. The value given in this case was obtained by electron diffraction.[38]

[38] M. K. Leong, V. S. Mastryukov, J. E. Boggs, *J. Mol. Struct.* **1998**, *445*, 149 – 160.

[39] In the study by Sugihara et al.,[15f] for example, the reactivity of norbornene and cyclopentene is higher than that of of cycloheptene and cyclohexene.

[40] a) L. Daalman, R. F. Newton, P. L. Pauson, A. Wadswoth, *J. Chem. Res. Miniprint* **1984**, 3150 – 3164; b) S. E. MacWhorter, V. Sampath, M. M. Olmstead, N. E. Schore, *J. Org. Chem.* **1988**, *53*, 203 – 205; c) T. Liese, A. de Meijere, *Chem. Ber.* **1986**, *119*, 2995 – 3026; d) see reference [17]; e) B. Y. Lee, Y. K. Chung, N. Jeong, Y. Lee, S. H. Hwang, *J. Am. Chem. Soc.* **1994**, *116*, 8793 – 8794; f) M. E. Krafft, R. H. Romero, I. L. Scott, *Synlett* **1995**, 577 – 578; g) N. Y. Lee, Y. K. Chung, *Tetrahedron Lett.* **1996**, *37*, 3145 – 3148; h) O. Kretschik, M. Nieger, K. H. Dötz, *Chem. Ber.* **1997**, *130*, 507 – 513; i) N. Jeong, S. H. Hwang, Y. W. Lee, J. S. Lim, *J. Am. Chem. Soc.* **1997**, *119*, 10549 – 10550; j) J. W. Kim, Y. K. Chung, *Synthesis*, **1998**, 142 – 144; k) V. Cadierno, M. P. Gamasa, J. Gimeno, J. M. Moretó, S. Ricart, A. Roig, E. Molins, *Organometallics* **1998**, *17*, 697 – 706; l) T. Sugihara, M. Yamaguchi, *Synlett* **1998**, 1384 – 1386; m) J. Balsells, A. Moyano, A. Riera, M. A. Pericàs, *Org. Lett.* **1999**, *1*, 1981 – 1984; n) M. E. Krafft, L. V. R. Boñaga, *Angew. Chem.* **2000**, *112*, 3822 – 3826; *Angew. Chem. Int. Ed.* **2000**, *39*, 3676 – 3680; o) M. E. Krafft, L. V. R. Boñaga, C. Hirosawa, *J. Org. Chem.* **2001**, *66*, 3004 – 3020; p) V. Derdau, S. Laschat, P. G. Jones, *Eur. J. Org. Chem.* **2000**, 681 – 689; q) M. Hayashi, Y. Hashimoto, Y. Yamamoto, J. Usuki, K. Saigo, *Angew. Chem.* **2000**, *112*, 645 – 647; *Angew. Chem. Int. Ed.* **2000**, *39*, 631 – 633; r) T. Kobayashi, Y. Koga, K. Narasaka, *J. Organomet. Chem.* **2001**, *624*, 73 – 87; s) A. C. Comely, S. E. Gibson, A. Stevenazzi, N. J. Hales, *Tetrahedron Lett.* **2001**, *42*, 1183 – 1185; t) S. E. Gibson, C. Johnstone, A. Stevenazzi, *Tetrahedron* **2002**, *58*, 4937 – 4942; u) R. Rios, M. A. Pericàs, A. Moyano, M. A. Maestro, J. Mahía, *Org. Lett.* **2002**, *4*, 1205 – 1208; v) R. Rios, M. A. Pericàs, A. Moyano, *Tetrahedron Lett.* **2002**, *43*, 4903 – 4906; w) J. Blanco-Urgoiti, L. Casarrubios, G. Domínguez, J. Pérez-Castells, *Tetrahedron Lett.* **2002**, *43*, 5763 – 5765; x) S. Fisher, U. Groth, M. Jung, A. Schneider, *Synlett* **2002**, 2023 – 2026; y) P. Mastrorilli, C. F. Nobile, R. Paolillo, G. P. Suranna, *J. Mol. Catal. A* **2004**, *214*, 103 – 106; z) J. Solà, A. Riera, M. A. Pericàs, X. Verdaguer, M. Maestro, *Tetrahedron Lett.* **2004**, *45*, 5387 – 5390; aa) S.-G. Lee, S.-D. Hong, Y.-W. Park, B.-G. Jeong, D.-W. Nam, H. Y. Jung, H. Lee, K. H. Song, *J. Organomet. Chem.* **2004**, *689*, 2586 – 2592.

[41] a) P. Blandon, P. L. Pauson, H. Brunner, R. Eder, *J. Organomet. Chem.* **1988**, *355*, 449 – 454; b) A. M. Hay, W. J. Kerr, G. G. Kirk, D. Middlemiss, *Organometallics* **1995**, *14*, 4986 – 4988; c) W. J. Kerr, G. G. Kirk, D. Middlemiss, *Synlett* **1995**, 1085 – 1086; d) H.-J. Park, B. Y. Lee, Y. K. Kang, Y. K. Chung, *Organometallics* **1995**, *14*, 3104 – 3107; e) S. Fonquerna, A. Moyano, M. A. Pericàs, A. Riera, *Tetrahedron* **1995**, *51*, 4239 – 4254; f) E. Montenegro, M. Poch, A. Moyano, M. A. Pericàs, A. Riera, *Tetrahedron* **1997**, *53*, 8651 – 8664; g) S. Fonquerna, A. Moyano, M. A. Pericàs, A. Riera, *J. Am. Chem. Soc.* **1997**, *119*, 10225 – 10226; h) X. Verdaguer, J. Vázquez, G. Fuster, V. Bernardes-Génisson, A. E. Greene, A. Moyano, M. A. Pericàs, A. Riera, *J.*

Org. Chem. **1998**, *63*, 7037 – 7052; i) E. Montenegro, M. Poch, A. Moyano, M. A. Pericàs, A. Riera, *Tetrahedron Lett.* **1998**, *39*, 335 – 338; j) Y. Gimbert, F. Robert, A. Durif, M.-T. Averbuch, N. Kann, A. E. Greene, *J. Org. Chem.* **1999**, *64*, 3492 – 3497; k) S. Fonquerna, R. Rios, A. Moyano, M. A. Pericàs, A. Riera, *Eur. J. Org. Chem.* **1999**, 3454 – 3478; l) A. R. Kennedy, W. J. Kerr, D. M. Lindsay, J. S. Scott, S. P. Watson, *J. Chem. Soc. Perkin Trans. 1* **2000**, 4366 – 4372; m) W. J. Kerr, D. M. Lindsay, E. M. Rankin, J. S. Scott, S. P. Watson, *Tetrahedron Lett.* **2000**, *41*, 3229 – 3233; n) D. R. Carbery, W. J. Kerr, D. M. Lindsay, J. S. Scott, S. P. Watson, *Tetrahedron Lett.* **2000**, *41*, 3235 – 3239; o) J. Balsells, J. Vázquez, A. Moyano, M. A. Pericàs, A. Riera, *J. Org. Chem.* **2000**, *65*, 7291 – 7302; p) T. Shibata, K. Takagi, *J. Am. Chem. Soc.* **2000**, *122*, 9852 – 9853; q) J. Castro, A. Moyano, M. A. Pericàs, A. Riera, A. Alvarez-Larena, J. F. Piniella, *J. Am. Chem. Soc.* **2000**, *122*, 7944 – 7952; r) K. Hiroi, T. Watanabe, *Tetrahedron Lett.* **2000**, *41*, 3935 – 3939; s) X. Verdaguer, A. Moyano, M. A. Pericàs, A. Riera, M. A. Maestro, J. Mahía, *J. Am. Chem. Soc.* **2000**, *122*, 10242 – 10243; t) I. Marchueta, E. Montenegro, D. Panov, M. Poch, X. Veraguer, A. Moyano, M. A. Pericàs, A. Riera, *J. Org. Chem.* **2001**, *66*, 6400 – 6409; u) J. Vázquez, S. Fonquerna, A. Moyano, M. A. Pericàs, A. Riera, *Tetrahedron: Asymmetry* **2001**, *12*, 1837 – 1850; v) V. Derdau, S. Laschat, *J. Organomet. Chem.* **2002**, *642*, 131 – 136; w) X. Verdaguer, M. A. Pericàs, A. Riera, M. A. Maestro, J. Mahía, *Organometallics* **2003**, *22*, 1868 – 1877; x) L. Shen, R. P. Hsung, *Tetrahedron Lett.* **2003**, *44*, 9353 – 9358; y) D. Konya, F. Robert, Y. Gimbert, A. E. Greene, *Tetrahedron Lett.* **2004**, *45*, 6975 – 6978.

[42] a) N. E. Schore, S. D. Najdi, *J. Am. Chem. Soc.* **1990**, *112*, 441 – 442; b) J. L. Spitzer, M. J. Kurth, N. E. Schore, S. D. Najdi, *Tetrahedron* **1997**, *53*, 6791 – 6808; c) A. C. Comely, S. E. Gibson, N. J. Hales, *Chem. Commun.* **1999**, 2075 – 2076; d) A. C. Comely, S. E. Gibson, N. J. Hales, *Chem. Commun.* **2000**, 305 – 306; e) A. C. Comely, S. E. Gibson, N. J. Hales, C. Johnstone and A. Stevenazzi, *Org. Biomol. Chem.* **2003**, *1*, 1959 – 1968; f) S.-W. Kim, S. U. Son, S. I. Lee, T. Hyeon, Y. K. Chung, *J. Am. Chem. Soc.* **2000**, *122*, 1550 – 1551; g) S. U. Son, S. I. Lee, Y. K. Chung, *Angew. Chem.* **2000**, *112*, 4318 – 4320; *Angew. Chem. Int. Ed.* **2000**, *39*, 4158 – 4160; h) S.-W. Kim, S. U. Son, S. I. Lee, T. Hyeon, Y. K. Chung, *Chem. Commun.* **2001**, 2212 – 2213; i) S. U. Son, K. H. Park, Y. K. Chung, *Org. Lett.* **2002**, *4*, 3983 – 3986; j) K. H. Park, S. U. Son, Y. K. Chung, *Chem. Commun.* **2003**, 1898 – 1899.

[43] a) M. E. Price, N. E. Schore, *J. Org. Chem.* **1989**, *54*, 5662 – 5667; b) M. E. Price, N. E. Schore, *Tetrahedron Lett.* **1989**, *30*, 5865 – 5868; c) A. de Meijere, L. Wessjohann, *Synlett* **1990**, 20 – 32.

[44] a) H. Primke, G. S. Sarin, S. Kohlstruck, G. Adiwidjaja, A. de Meijere, *Chem. Ber.* **1994**, *127*, 1051 – 1064; b) O. Arjona, A. G. Csákÿ, M. C. Murcia, J. Plumet, *J. Org. Chem.* **1999**, *64*, 7338 – 7341; c) M. Ahmar, B. Cazes, *Tetrahedron Lett.* **2003**, *44*, 5403 – 5406.

[45] O. Arjona, A. G. Csákÿ, R. Medel, J. Plumet, *Tetrahedron Lett.* **2001**, *42*, 3085 – 3087.

[46] H.-C. Militzer, S. Schömenauer, C. Otte, C. Puls, J. Hain, S. Bräse, A. de Meijere, *Synthesis* **1993**, 998 – 1012; de Meijere and co-workers also reported a reaction of the same alkyne with norbornene in which they obtained the cycloadduct in better yield (79%).

[47] H. Buchholz, O. Reiser, A. de Meijere, *Synlett* **1991**, 20 – 22.

[48] D. J. Cram, J. M. Cram, *Acc. Chem. Res.* **1971**, *4*, 204 – 213.

[49] W. A. Smit, S. L. Kireev, O. M. Nefedov, V. A. Tarasov, *Tetrahedron Lett.* **1989**, *30*, 4021 – 4024.

[50] H. Corlay, I. W. James, E. Fouquet, J. Schmidt, W. B. Motherwell, *Synlett* **1996**, 990 – 992.

[51] The π system of alkylidene cyclopropane is known to be delocalized over the cyclopropane ring as well as the double bond; for a discussion of the electronic changes upon metal complexation of methylenecyclopropane, see: T. A. Albright, P. R. Clemens, R. P. Hughes, D. E. Hunton, L. D. Margerum, *J. Am. Chem. Soc.* **1982**, *104*, 5369 – 5379.

[52] a) M. Ishizaki, Y. Kasama, M. Zyo, Y. Niimi, O. Hoshino, *Heterocycles* **2001**, *55*, 1439 – 1442; b) M. Ishizaki, M. Zyo, Y. Kasama, Y. Niimi, O. Hoshino, K. Nishitani, H. Hara, *Heterocycles* **2003**, *60*, 2259 – 2271.

[53] It was postulated that complete regioselectivity arises from the severe steric interactions between the alkyne–cobalt complex and the piperidine ring.

[54] a) P. L. Pauson, I. U. Khand, *Ann. N. Y. Acad. Sci.* **1977**, *295*, 2 – 14; b) I. U. Khand, P. L. Pauson, M. Habib, *J. Chem. Res. Miniprint* **1978**, 4401 – 4417; c) I. U. Khand, P. L. Pauson, M. Habib, *J. Chem. Res. Miniprint* **1978**, 4418 – 4433.

[55] a) K. N. Houk, *J. Am. Chem. Soc.* **1973**, *95*, 1973; b) I. Fleming, *Frontiers Orbitals and Organic Chemical Reactions*, Wiley, New York, **1976**, pp. 86 – 132, and references therein.

[56] Cyclopentadiene (60% yield), cyclopentene (47% yield).

[57] P. A. Wender, N. M. Deschamps, T. J. Williams, *Angew. Chem.* **2004**, *116*, 3138 – 3141; *Angew. Chem. Int. Ed.* **2004**, *43*, 3076 – 3079.

[58] a) I. U. Khand, E. Murphy, P. L. Pauson, *J. Chem. Res. Miniprint* **1978**, 4434 – 4453; b) I. U. Khand, C. A. L. Mahaffy, P. L. Pauson, *J. Chem. Res. Miniprint* **1978**, 4454 – 4470.

[59] a) I. U. Khand, P. L. Pauson, *J. Chem. Soc. Chem. Commun.* **1974**, 379; b) I. U. Khand, P. L. Pauson, *Heterocycles*, **1978**, *11*, 59 – 67.

[60] M. Costa, A. Mor, *Tetrahedron Lett.* **1995**, *36*, 2867 – 2870.

[61] M. Ahmar, F. Antras, B. Cazes, *Tetrahedron Lett.* **1999**, *40*, 5503 – 5506.

[62] a) A. S. K. Hashmi, *Angew. Chem.* **2000**, *112*, 3737 – 3740; *Angew. Chem. Int. Ed.* **2000**, *39*, 3590 – 3593; b) R. Zimmer, C. U. Dinesh, E. Nandanan, F. A. Khand, *Chem. Rev.* **2000**, *100*, 3067 – 3126; c) R. W. Bates, V. Satcharoen, *Chem. Soc. Rev.* **2002**, *31*, 12 – 21.

[63] a) S. Patai, *The Chemistry of Ketenes, Allenes, and Related Compounds*, Wiley, Chichester, **1980**; b) S. R. Landor, *The Chemistry of Allenes*, Academic Press, New York, **1982**; c) H. F. Schuster, G. M. Coppola, *Allenes in Organic Synthesis*, Wiley, New York, **1984**.

[64] T. Shibata, Y. Koga, K. Narasaka, *Bull. Chem. Soc. Jpn.* **1995**, *68*, 911 – 919.

[65] a) M. Ahmar, F. Antras, B. Cazes, *Tetrahedron Lett.* **1995**, *36*, 4417 – 4420; b) M. Ahmar, O. Chabanis, J. Gauthier, B. Cazes, *Tetrahedron Lett.* **1997**, *38*, 5277 – 5280; c) F. Antras, M. Ahmar, B. Cazes, *Tetrahedron Lett.* **2001**, *42*, 8153 – 8156; d) F. Antras, M. Ahmar, B. Cazes, *Tetrahedron Lett.* **2001**, *42*, 8157 – 8160.

[66] L. Añorbe, A. Poblador, G. Domínguez, J. Pérez-Castells, *Tetrahedron Lett.* **2004**, *45*, 4441 – 4444.

[67] H. C. Hailes, B. Isaac, M. H. Javaid, *Synth. Commun.* **2003**, *33*, 29 – 41.

[68] a) L. Daalman, R. F. Newton, P. L. Pauson, A. Wadsworth, *J. Chem. Res. Miniprint* **1984**, 3150 – 3164; b) D. C. Billington, P. Blandon, I. M. Helps, P. L. Pauson, W. Thomson, D. Willison, *J. Chem. Res. Miniprint* **1988**, 2601 – 2622; c) V. Rautenstrauch, P. Mégard, J. Conesa, W. Küster, *Angew. Chem.* **1990**, *102*, 1441 – 1444; *Angew. Chem. Int. Ed. Engl.* **1990**, *29*, 1413 – 1416; d) A. R. Gordon, C. Johnstone, W. J. Kerr, *Synlett*, **1995**, 1083 – 1084; e) C. Johnstone, W. J. Kerr, U. Lange, *J. Chem. Soc. Chem. Commun.* **1995**, 457 – 458; f) J. G. Donkervoort, A. R. Gordon, C. Johnstone, W. J. Kerr, U. Lange, *Tetrahedron* **1996**, *52*, 7391 – 7420; g) N. Jeong, S. H. Hwang, *Angew. Chem.* **2000**, *112*, 650 – 652; *Angew. Chem. Int. Ed.* **2000**, *39*, 636 – 638.

[69] a) W. J. Kerr, M. McLaughlin, P. L. Pauson, S. M. Robertson, *Chem. Commun.* **1999**, 2171 – 2172; b) W. J. Kerr, M. McLaughlin, P. L. Pauson, S. M. Robertson, *J. Organomet. Chem.* **2001**, *630*, 2171 – 2172.

[70] M. C. Croudace, N. E. Schore, *J. Org. Chem.* **1981**, *46*, 5357–5363.
[71] This behavior was observed also by Pauson and co-workers when using vinyl bromide as the alkene.[15a]
[72] L. M. Harwood, L. San Andrés Tejera, *Chem. Commun.* **1997**, 1627–1628.
[73] K. H. Park, I. G. Jung, Y. K. Chung, *Org. Lett.* **2004**, *6*, 1183–1186.
[74] a) N. F. Brown, M. A. Barteau, *J. Am. Chem. Soc.* **1992**, *114*, 4258–4265; b) R. Rupp, G. Huttner, P. Rutsch, U. Winterhalter, A. Barth, P. Kircher, L. Zsolnai, *Eur. J. Inorg. Chem.* **2000**, 523–536.
[75] For an excellent Review on carbonylation catalysis in the absence of carbon monoxide, see: T. Morimoto, K. Kakiuchi, *Angew. Chem.* **2004**, *116*, 5698–5706; *Angew. Chem. Int. Ed.* **2004**, *43*, 5580–5588.

Communications

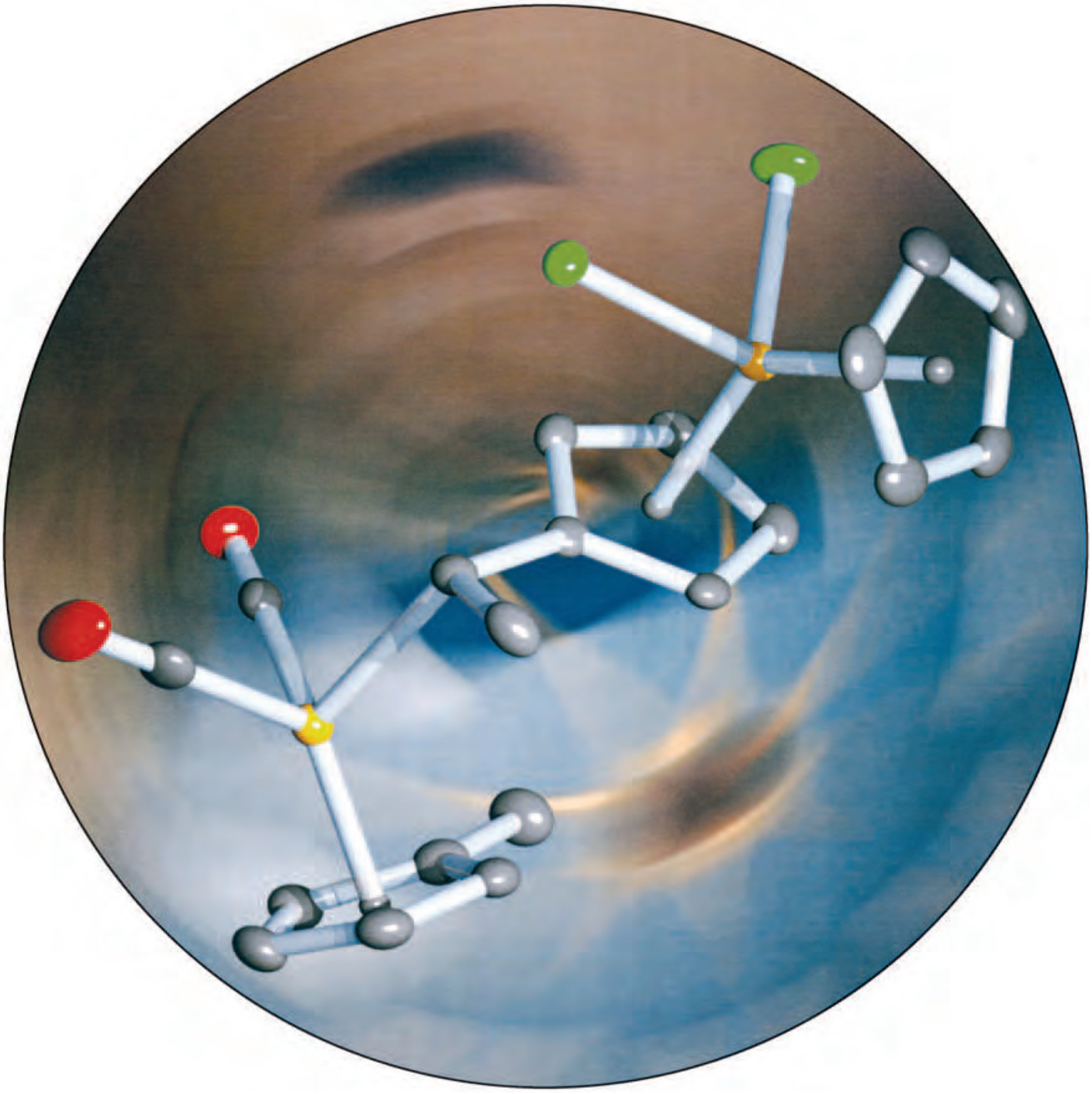

The formation of $[RuTi(\mu_2\text{-}\eta^1\text{-}\eta^5\text{-}CHMe(C_5H_4))(CO)_2(\eta\text{-}C_5H_4Me)(\eta\text{-}C_5H_5)Cl_2]$, depicted above, results from the acidic treatment of a precursor metallocene complex. This carbon–carbon bond-forming reaction is thought to be unprecedented. For more information, see the Communication by G. A. Koutsantonis and co-workers on the following pages.

  DOI: 10.1002/anie.200500224

Metallocene Chemistry

Reaction of Ruthenium Ethyne-1,2-diyl Compounds with Bis(trimethylsilyl)acetylene Complexes of Titanocene and Zirconocene: Remarkable Transfer of a C_2 Ligand**

Christopher S. Griffith, George A. Koutsantonis, Brian W. Skelton, and Allan H. White*

The chemistry of the metallocene bis(trimethylsilyl)alkyne complexes of Group 4 metals $[(\eta\text{-}C_5H_5)_2M\{\eta^2\text{-}C_2(SiMe_3)_2\}]$ (**1**, M = Ti; **2**, M = Zr·(thf)) has been initiated and pursued by Rosenthal and co-workers for a considerable amount of time.[1] These complexes provide fragments that react readily with a variety of unsaturated compounds. Such fragments have unstable 14-electron configurations in which the two unoccupied orbitals and single occupied orbital of the metallocene units provide a plausible explanation for the diverse chemistry exhibited by these complexes, which often form metallacycles.[1–7]

We, in turn, have been interested in the use of substrates reactive to sites of unsaturation as building blocks for the rational preparation of larger molecules from ruthenium ethyne-1,2-diyl compounds,[8–16] and viewed complexes **1** and **2**[6] as excellent candidates for this purpose. Both complexes contain a ligand that stabilizes the reactive metal center, but which is easily removed to allow access to the reactivity of the unsaturated metal. The displacement of $Me_3SiC{\equiv}CSiMe_3$ from the metal coordination spheres of complexes **1** and **2** has been exploited by Rosenthal and co-workers with a range of diynes and polyynes.[3]

Herein we report the reaction of the ruthenium ethyne-1,2-diyl compounds $[\{Ru(CO)_2(\eta\text{-}C_5H_4R)\}_2(\mu\text{-}C_2)]$ (**3a**, R = H; **3b**, R = CH_3) with the reactive fragments "$(\eta\text{-}C_5H_5)_2M$" derived from **1** and **2**. These reactions proceeded at ambient temperatures in tetrahydrofuran to give excellent yields of the ethynediyl-coordinated metallocenes **4** and **5**. Direct in situ reaction with Group 4 metallocene dichloride and magnesium resulted in the recovery of the known compound $[RuCl(CO)_2(\eta\text{-}C_5H_5)]$ from other indeterminate products in moderate yield. The excess of complexes **1** and **2** was removed by simple hexane extraction, but no attempt was made to isolate the liberated $Me_3SiC{\equiv}CSiMe_3$. Similar reactions performed at 40–50 °C were essentially complete after ten hours with little or no decrease in yield of the complexes. Each complex exhibits similar infrared spectra with five ν(CO) absorptions, of which the absorption at $\approx$1730 cm^{-1} was assigned to the bridging carbonyl ligand between the ruthenium and Group 4 metal centers. The ^{1}H NMR spectra of the three complexes display resonances of four magnetically inequivalent cyclopentadienyl groups. The two singlet resonances attributable to the metallocene fragment in each spectrum are significantly shifted between 1.06–1.25 ppm upfield from those of **1** or **2**. The two singlet resonances assigned to the $Ru(\eta\text{-}C_5H_5)$ moieties of **4a** and **5** are shifted with respect to that observed for **3a**, one 0.06–0.11 ppm upfield, and the other 0.35–0.30 ppm downfield. Similar changes in chemical shift values relative to those of **3b** are also observed for **4b**, with the methine ring resonances at lower field appearing as four resolved singlet resonances, and with the higher field resonances appearing as a virtual triplet. Two singlet resonances at $\delta = 1.98$ and $\delta = 1.67$ ppm are assigned to the methyl protons of the two C_5H_4Me rings. Complexes **4** and **5** are moderately air-sensitive in the solid state but more so in solution, and are best handled in an inert atmosphere.

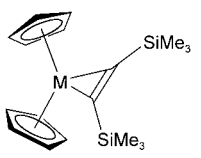

1: M = Ti
2: M = Zr • (thf)

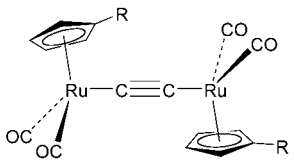

3a: R = H
3b: R= Me

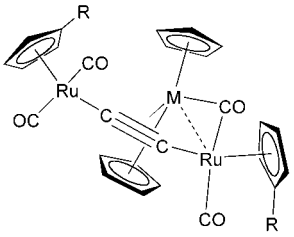

4a: M = Ti, R = H
4b: M = Ti, R= Me
5 : M = Zr, R = H

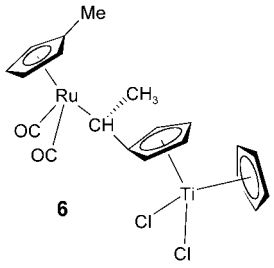

6

The ^{13}C NMR spectra measured for **4a** and **4b** contain resonances at $\delta \approx 106.0$ and $\delta \approx 105.0$ ppm, which are assigned to the titanocene moiety. The magnetic inequivalence of the $Ru(\eta\text{-}C_5H_4R)$ moieties is illustrated by the two singlet resonances at $\delta = 88.1$ and $\delta = 89.7$ ppm for **4a** and eight resolved singlet resonances at $\delta = 90.8$, 88.4, 88.0, 87.9, 86.3, 85.5, 85.3, and 85.1 ppm for **4b**. The two singlet resonances at $\delta = 114.4$ and 108.2 ppm are attributed to the *ipso* carbon atoms of the two C_5H_4Me rings. The two resonances present at $\approx$200 ppm for **4a** and **4b** are assigned to the two terminal carbonyl groups of the pendent $\{Ru(CO)_2(C_5H_4R)\}$ fragment on the basis of their chemical shifts. The resonances at $\delta =$ 203.9 and 204.4 ppm for **4a** and **4b**, respectively, are assigned to the remaining terminal carbonyl ligands coordinated to ruthenium. Downfield singlet resonances at $\delta = 305.5$ and 307.7 ppm in the spectra of **4a** and **4b**, respectively, are attributed to the bridging carbonyl group between the

[*] Dr. C. S. Griffith, Dr. G. A. Koutsantonis, Dr. B. W. Skelton, Prof. A. H. White
Chemistry, School of Chemical and Biomedical Sciences
University of Western Australia
35 Stirling Highway, Perth, WA, 6009 (Australia)
Fax: (+62) 8-6488-7247
E-mail: gak@chem.uwa.edu.au

[**] C.S.G. was the holder of an Australian Postgraduate Award.

titanium and ruthenium centers on the evidence of related semibridging carbonyl groups of the early/late transition metal heterobimetallic complexes $[Rh(\eta\text{-}C_5H_5)(\mu\text{-}CO)(\mu\text{-}\eta^1{:}\eta^2\text{-}CO)Zr(\eta\text{-}C_5Me_5)_2]$[17] and $[Ru(CO)(\mu\text{-}C(O)CH_2CH_2\text{-}(\eta\text{-}C_5H_4))(\mu\text{-}CO)Zr(\eta\text{-}C_5H_5)_2]$.[18] The carbon atoms of the coordinated ethyne-1,2-diyl unit are assigned to resonances at $\delta = 167.6$ and 93.7 ppm for **4a** and $\delta = 167.0$ and 101.6 ppm for **4b**. The connectivity of **4a** (Figure 1)[19] was established by X-ray single-crystal structure determination, and demonstrates the formation of an alkyne adduct of essentially "$Ti(C_5H_5)_2$" not unlike that of the starting material **1**. The most striking difference is that the ethyne-1,2-diyl moiety is coordinated in an unsymmetrical η^2 fashion to a titanocene fragment with a symmetrical bridging carbonyl group between the titanium atom and one of the ruthenium atoms. The ruthenium, titanium, and the alkynyl carbon atoms of the coordinated ethyne-1,2-diyl ligand are not strictly coplanar, but for the purpose of describing the overall geometry and connectivity of **4a**, they may be regarded as such. The Cp_1-Ti-Cp_2 angle of 130.8° is similar to that measured in several metallocene η^2-alkyne solid-state structures.[20] Coordination of the ethyne-1,2-diyl ligand is significantly distorted from the ideal η^2 coordination as observed from the measured Ti–C(1) and Ti–C(2) distances of 2.230(2) and 2.546(2) Å, respectively, and from a projection onto the $TiRu_2C_2$ plane as well. The measured C(1)–C(2) bond length of 1.229(3) Å is close to that of complex **3a** (1.19 Å), which indicates that substantial triple-bond character remains, and that the metallacyclopropene structure found for metallocene η^2-alkyne complexes[20–22] is not an appropriate description of the bonding situation present in **4a**. The unsymmetrical coordination of the C≡C unit to the titanium atom appears to be a direct result of the μ_2-η^1-CO ligand bridging the Ti and Ru(1) metal atoms. The separation of 2.9670(5) Å between the Ru(1) and Ti atoms is significantly larger than the sum of the metallic radii (2.81 Å), so that the presence of metal–metal bonding can be questioned. However, the range of Ti–Ru distances found in crystallographically characterized complexes ranges from ≈2.56 Å in complexes that contain unsupported metal–metal bonds stabilized by a trisilylsilane-based tripodal amido ligand,[23] ≈2.66 Å in $[(Me_2N)_3Ti\text{-}Ru(CO)_2(\eta\text{-}C_5H_5)]$,[24,25] and a significantly longer distance of ≈2.93 Å found in $Ti_2Ru_2S_4$ cubane-type clusters.[26] In these latter complexes it is believed that the electron-rich Ru atom participates in a dative-style donation to the electron-poor Ti atom. This variation in bond distance implies some ambiguity, and thus we represent the bonding between Ti and Ru centers in complexes **4** as dative, being supported by the electronic contribution from the bridging carbonyl ligand.

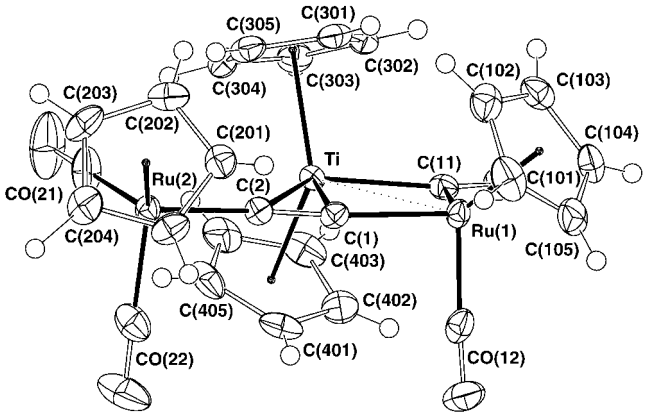

Figure 1. Molecular structure of **4a** (30% probability amplitude ellipsoids).

We were interested in the reactivity of complexes **4** and consequently conducted some reactions of those complexes with both terminal and internal alkynes, but no transformations were observed. In a manner similar to $Me_3SiC{\equiv}CSiMe_3$, the sterically encumbered ethyne-1,2-diyl ligand appears to hinder further addition of alkyne moieties to the titanium metal center, although Rosenthal and co-workers have observed varied modes of reactivity.[1,2,6]

Complex **4a** did react with carbon monoxide to afford complete transformation of the starting material with both **3a** and $[Ti(CO)_2(\eta\text{-}C_5H_5)_2]$ isolated as products. Shur and co-workers[27,28] explored the reactivity of the tolane adduct of titanocene and found that protonation of the complex by HCl/EtOH afforded *cis*-stilbene and $[TiCl_2(\eta\text{-}C_5H_5)_2]$ in essentially quantitative yield. Rosenthal and co-workers found that the Cp* ($\eta\text{-}C_5Me_5$) and ($\eta\text{-}C_5H_5$) ligands influence the reactivity of titanocene and zirconocene alkyne complexes toward water.[29] We considered protonation as a possible route to the previously unobserved ethene-1,2-diyl complexes, M-C(H)=C(H)-M and (M = $Ru(CO)_2(\eta\text{-}C_5H_4R)$). Thus, dropwise addition of ethanolic HCl to a toluene solution of complex **4b** gave the new complex **6**. The red/purple residue that remains after hexane extraction can be recrystallized to give compound **6**, $[RuTi(\mu_2\text{-}\eta^1\text{-}\eta^5\text{-}CHMe(C_5H_4))(CO)_2(\eta\text{-}C_5H_4Me)(\eta\text{-}C_5H_5)Cl_2]$, in good yield. The hexane extract of the reaction mixture afforded a pale yellow carbonyl-containing compound that has yet to be identified. Complex **6** is moderately air-sensitive in the solid state but more so in solution, and is best handled in an inert atmosphere. The spectroscopic data is consistent with the presence of at least one $\{Ru(CO)_2(\eta\text{-}C_5H_4Me)\}$ fragment. A number of likely candidate complexes, $[RuH(CO)_2(\eta\text{-}C_5H_4Me)]$, $[RuCl(CO)_2(\eta\text{-}C_5H_4Me)]$, and $[Ru(C{\equiv}CH)(CO)_2(\eta\text{-}C_5H_4Me)]$ have been discounted on the basis of their infrared and ^{1}H NMR spectra. The spectroscopic data measured for **6** is consistent with the determined single-crystal structure. The ^{1}H NMR spectrum is complicated by multiplets that are attributed to the methine protons of the substituted cyclopentadienyl ligands coordinated to ruthenium (4.99–4.91 ppm) and titanium (6.61–6.09 ppm). A singlet resonance at $\delta = 6.46$ ppm is assigned to the unsubstituted cyclopentadienyl ligand of the titanocene fragment and appears in a ratio of 5:8 to the foregoing methine resonances. The nonmethyl proton of the (CH(Me)) unit appears as a quartet ($^3J = 6.8$ Hz) at $\delta = 4.12$ ppm from coupling to the adjacent methyl protons. A doublet centered at $\delta = 1.43$ ppm displays a corresponding ^3J-coupling constant of 6.8 Hz and is assigned to the methyl protons of (CH(Me)). A singlet resonance at $\delta = 1.97$ ppm is assigned to the methyl protons of the $\eta\text{-}C_5H_4Me$ ligand. The ^{13}C NMR spectrum of **6** contains two downfield singlet resonances at $\delta = 202.6$ and

201.9 ppm, both assigned to the terminal carbonyl ligands of the {Ru(CO)$_2$(η-C$_5$H$_4$Me)} fragment. Two singlet resonances at $\delta \approx 13.0$ ppm are attributed to the methyl groups of the η-C$_5$H$_4$Me ligand and (CH(Me)) unit. A singlet resonance at $\delta = 28.5$ ppm is assigned to the tertiary carbon of the (CH(Me)) unit. Resonances assigned to the ring carbon atoms of Ru(η-C$_5$H$_4$Me) appear as four singlets between 89.9 and 88.3 ppm with a weak resonance at $\delta = 108.7$ ppm, tentatively assigned to the *ipso* carbon atom of the η-C$_5$H$_4$Me ligand. The unsubstituted η-C$_5$H$_5$ ligand of the metallocene fragment appears as a singlet resonance at $\delta =$ 119.4 ppm with four singlet resonances between 126.8 and 110.4 ppm assigned to Ti(η-C$_5$H$_4$). The corresponding *ipso* carbon gives rise to an unusual downfield singlet resonance at $\delta = 160.0$ ppm.

The structure of **6** (Figure 2)[30] is best described as a monosubstituted cyclopentadienyl titanocene dichloride fragment with a pendent {Ru(CHMe)(CO)$_2$(η-C$_5$H$_4$Me)} group.

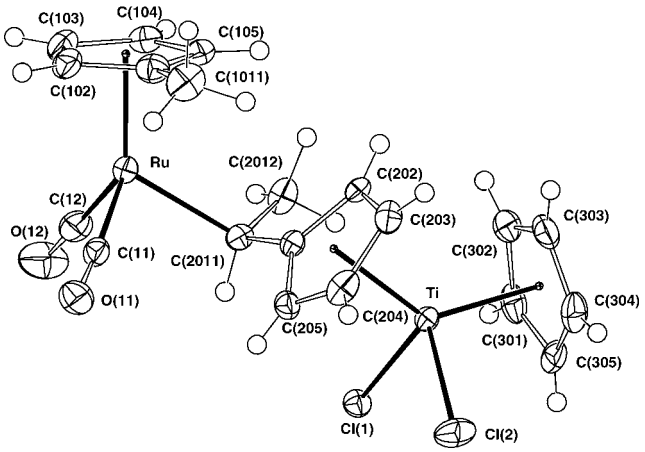

Figure 2. Molecular structure of **6** (30% probability amplitude ellipsoids).

The geometry about the titanium atom is unremarkable in comparison with [TiCl$_2$(η-C$_5$H$_5$)$_2$],[31] and the geometry about the ruthenium atom is also a typical "piano stool". The measured bond length of 2.199(5) Å for Ru–C(2011) is significantly elongated from the Ru–C(sp) bond length of 2.055(2) Å for **3b**, but compares well with the average value of 2.18 Å found for the alkyl bridged diruthenium complexes, [{Ru(CO)$_2$(η-C$_5$H$_5$)}(μ-(CH$_2$)$_x$)] ($x = 1$,[32] $x = 2$,[33] $x = 5$[34]), which implies sp^3 hybridization at C(2011). This observation is supported by the C(2011)–C(2012) distance of 1.526(5) Å which is similar to other C–C (sp^3) single bond lengths and a tetrahedral geometry about C(2011). The carbon atom (C(2011)) that bridges the ruthenium and C(201) atoms is essentially coplanar with the cyclopentadienyl ring carbon atoms (C201–205) of the titanocene dichloride fragment with a measured C(2011)–C(201) distance of 1.493(5) Å, similar to the value of 1.503(6) Å determined for C(1011)–C(101) bond distance of the methyl-substituted cyclopentadienyl ring.

We believe that the formation of **6** is unprecedented. A close examination of the connectivity reveals the apparent transfer of the now fully protonated C$_2$ unit found in **4b** (originally bound in an η^2 fashion to Ti and η^1 to the two ruthenium atoms) to a Ti(η-C$_5$H$_5$) unit. Low-valence Group 4 permethyl cyclopentadienide complexes have afforded reactivity at the (η-C$_5$Me$_5$) ring by C–H activation.[35] Formation of the {(η^1:η^5-C$_5$H$_4$)(η-C$_5$H$_5$)TiCl$_2$} fragment is also not unexpected given that the protonation of the tolane adduct of titanocene gave titanocene dichloride as a product of the reaction.[27,28] The mass balance in the reaction is essentially satisfied in the yield of **6** (Ti) and presumably with the remaining ruthenium found in the unidentified complex. Given that this other product remains unidentified, any meaningful speculation on a mechanism for the formation of **6** is difficult, but it is tempting to consider that it results from the multiple protonation of the C≡C unit of complex **4b** to give the (μ^2-η^1:η^5-C(H)(CH$_3$)(C$_5$H$_4$)) ligand bridging the two metal centers with concomitant oxidation of the titanium center. At this stage, we cannot discount the insertion of ethene derived from the dehydration of EtOH. Complex **4b** does not react with ethene and is also unreactive toward water, suggesting that reaction with EtOH is also unlikely. There are other observations made by Rosenthal and coworkers in their seminal contributions, reviewed recently,[1,6] that are relevant to the discussion of a possible mechanism. First, in the reaction of **1** with B(C$_6$F$_5$)$_3$ a zwitterionic complex, **7**, containing the B(C$_6$F$_5$)$_3$ bound to the (η-C$_5$H$_5$) ring was observed with the elimination of hydrogen, 1,2-bis(trimethylsilyl)acetylene, and importantly, 1,2-bis(trimethylsilyl)ethane. Other alkyne adducts of titanocene gave

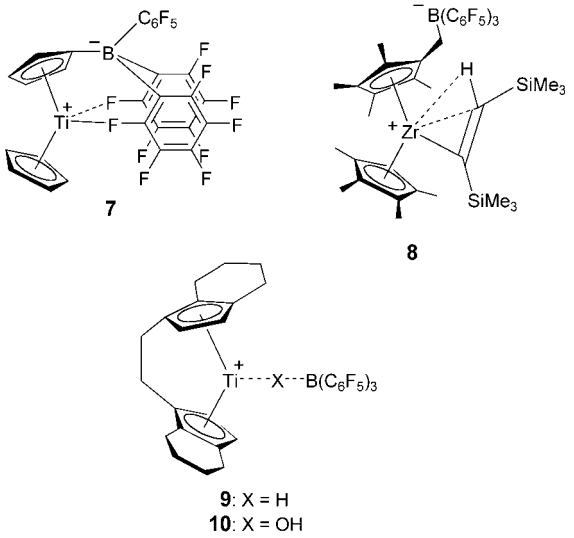

identical products. Second, in the analogous reaction of [(η-C$_5$Me$_5$)$_2$Zr(Me$_3$SiC≡CSiMe$_3$)] with B(C$_6$F$_5$)$_3$ there was no hydrogen or alkyne liberated; rather, the zwitterionic Zr^{IV} derivative, **8**, containing a σ-alkenyl ligand was isolated. Finally, the bis(trimethylsilyl)acetylene complex of *rac*-1,2-ethylene-1,1-bis(η^5-tetrahydroindenyl)titanium reacted with the Brønsted acid B(C$_6$F$_5$)$_3$·H$_2$O to give a mixture of complexes **9** and **10**. Literature precedent[36] allows the formulation of a relatively simple mechanism in which the

η^2-bound ethynediyl complex rearranges to form a bridging TiRu(μ-η^1-C≡C-Ru(CO)$_2$(η-C_5H_4R)) moiety. Subsequent hydrogen elimination from a Ti(η-C_5H_5) group leads to the formation of a bridging (μ-η^1:η^5) cyclopentadienyl ligand between the Ru and Ti atoms. Such structures are typical in organometallic chemistry and are formed by C–C homocoupling of 1,3-butadiyne and fulvene ligands. Acetylide coupling reactions[3,7,37] and cyclopentadienyl coupling reactions[6,21] are well-known in the literature. Analogous mixed heterocoupling would give either a Ru–CC–Cp unit or Ru–C(=C)–Cp intermediates, which, upon reaction with acid of the latter, lead to the observed Ru–CH(Me)–Cp moiety in **6**. Presumably, the known mobility of the C_2 group,[8,37] which we have described as bearing-like, causes discrimination between the preferred Ru–C(=C)–Cp compound over that of the Ru–CC–Cp and of Ru–CH(Me)–Cp over that of Ru–CH_2CH_2–Cp.

In spite of these observations, however, it still remains difficult to differentiate intermolecular protonation from intramolecular C–H activation. We are currently undertaking detailed isotope labeling studies that will ultimately shed light on the mechanism of formation of **6**.

In conclusion, we have compared the reactivity of our metalloalkynes, (the ruthenium ethyne-1,2-diyl complexes **3**) with that of the bulky 1,2-bis(trimethylsilyl)acetylene and found that upon coordination to titanocene, they have similar reactivity. However, upon reaction with acid, we have observed what appears to be an unprecedented transformation to give a ruthenium hydrocarbyl complex attached to titanocene dichloride. We are making a detailed examination of the reactivity of **6**, particularly with respect to its efficacy as a catalyst for the polymerization of 1-alkenes.

Experimental Section

The manipulation of oxygen- and moisture-sensitive compounds was performed under an atmosphere of high-purity argon with standard Schlenk techniques or in a dry box (Miller Howe). Infrared spectra were recorded with a Bio-Rad FTS 45 and 40 FTIR spectrometer. ^{1}H and ^{13}C NMR spectra were acquired with Varian Gemini 200 and Bruker ARX 500 spectrometers. ^{31}P NMR spectra were acquired with a Bruker ARX 500 spectrometer. ^{1}H and ^{13}C NMR spectra were referenced with respect to incompletely deuterated solvent signals. Mass spectra were obtained on a VG AutoSpec spectrometer employing a FAB ionization source in all samples unless otherwise specified. Elemental analyses were performed at The Research School of Chemistry Microanalytical Unit, Australian National University, ACT. Tetrahydrofuran was dried over sodium metal and distilled from potassium benzophenone ketyl under an atmosphere of argon. Hexanes and toluene were dried over sodium metal and distilled under an atmosphere of argon. Distilled solvents were stored over sodium or potassium mirrors until use.

4a: A solution of [Ti(η^2-$Me_3SiC{\equiv}CSiMe_3$)(η-C_5H_5)$_2$] (**1**; 42 mg, 0.121 mmol) and [{Ru(CO)$_2$(η-C_5H_5)}$_2$(μ_2-C≡C)] (**3a**; 50 mg, 0.107 mmol) in THF (20 mL) was stirred for 10 h at 50 °C. The solvent was removed in vacuo, and the dark residue was washed with *n*-hexanes (2 × 20 mL) to remove $Me_3SiC{\equiv}CSiMe_3$. Recrystallization (toluene/*n*-hexanes, −40 °C) gave dark red platelets of **4a** (58 mg, 84 %). IR (THF): $\tilde{\nu}_{CO}$ = 2032s, 1977s, 1931s, 1907w, 1733s cm^{-1}; ^{1}H NMR (C_6D_6): δ = 5.36 (s, 5H, C_5H_5Ti), 5.20 (s, 5H, C_5H_5Ti), 4.98 (s, 5H, C_5H_5Ru), 4.53 ppm (s, 5H, C_5H_5Ru); ^{13}C NMR (C_6D_6): δ = 305.5 (s, μ-CO), 203.9 (s, CO), 199.5 (s, CO), 199.2 (s, CO), 167.6 (s, (Ti)Ru*C*≡C), 106.4 (s, C_5H_5Ti), 105.1 (s, C_5H_5Ti), 93.7 (s, C≡*C*Ru(CO)$_2$(C_5H_5)), 89.7 (s, C_5H_5Ru), 88.1 ppm (s, C_5H_5Ru); elemental analysis: calcd. for $C_{26}H_{20}O_4Ru_2Ti_1$: C 48.29, H 3.12; found: C 48.19, H 2.96.

4b: A solution of [Ti(η^2-$Me_3SiC{\equiv}CSiMe_3$)(η-C_5H_5)$_2$] (**1**; 87 mg, 0.250 mmol) and [{Ru(CO)$_2$(η-C_5H_4Me)}$_2$(μ_2-C≡C)] (**3b**; 100 mg, 0.200 mmol) in THF (30 mL) was stirred for 10 h at 50 °C. The solvent was removed in vacuo, and the dark residue was washed with *n*-hexanes (2 × 20 mL) to remove $Me_3SiC{\equiv}CSiMe_3$. Recrystallization (toluene/*n*-hexanes, −40 °C sol. diff.) gave dark red crystals of **4b** (119 mg, 88 %). IR (THF): $\tilde{\nu}_{CO}$ = 2035s, 1980s, 1934s, 1907w, 1735s cm^{-1}; ^{1}H NMR (C_6D_6): δ = 5.39 (s, 5H, C_5H_5Ti), 5.24 (s, 5H, C_5H_5Ti), 4.96 (s, 1H, C_5H_4Me), 4.87 (s, 1H, C_5H_4Me), 4.84 (s, 1H, C_5H_4Me), 4.73 (s, 1H, C_5H_4Me), 4.45 (s, 1H, C_5H_4Me), 4.41 (s, 2H, C_5H_4Me), 4.37 (s, 1H, C_5H_4Me), 1.98 (s, 3H, C_5H_4*Me*), 1.67 ppm (s, 3H, C_5H_4*Me*); ^{13}C NMR (C_6D_6): δ = 307.7 (s, μ-CO), 204.4 (s, CO), 199.8 (s, CO), 199.6 (s, CO), 167.0 (s, (Ti)Ru*C*≡C), 114.4 (s, *ipso*-C), 108.2 (s, *ipso*-C), 106.5 (s, C_5H_5Ti), 105.0 (s, C_5H_5Ti), 101.6 (s, C≡*C*Ru(CO)$_2$(C_5H_5)), 90.8 (s, C_5H_4Me), 88.4 (s, *C*$_5$H$_4$Me), 88.0 (s, *C*$_5$H$_4$Me), 87.9 (s, *C*$_5$H$_4$Me), 86.8 (s, *C*$_5$H$_4$Me), 85.5 (s, *C*$_5$H$_4$Me), 85.3 (s, *C*$_5$H$_4$Me), 85.1 (s, *C*$_5$H$_4$Me), 14.0 (s, C_5H_4*Me*), 13.7 ppm (s, C_5H_4*Me*); elemental analysis: calcd. for $C_{28}H_{24}O_4Ru_2Ti_1$: C 49.86, H 3.59; found: C 49.68, H 3.56.

5: A solution of [Zr(thf)(η^2-$Me_3SiC{\equiv}CSiMe_3$)(η-C_5H_5)$_2$] (**2**; 52 mg, 0.133 mmol) and [{Ru(CO)$_2$(η-C_5H_5)}$_2$(μ_2-C≡C)] (**3a**; 50 mg, 0.107 mmol) in THF (20 mL) was stirred for 48 h at ambient temperature. The solvent was removed in vacuo and the orange residue was washed with *n*-hexanes (2 × 20 mL) to remove $Me_3SiC{\equiv}CSiMe_3$. Recrystallization (THF/*n*-hexane) gave an orange powder of **5** (38 mg, 55 %). IR (toluene): $\tilde{\nu}_{CO}$ = 2039s, 1978s, 1938s, 1909w, 1729s cm^{-1}; ^{1}H NMR (C_6D_6): δ = 5.51 (s, 5H, C_5H_5Zr), 5.36 (s, 5H, C_5H_5Zr), 4.93 (s, 5H, C_5H_5Ru(Zr)), 4.58 ppm (s, 5H, C_5H_5Ru(Zr)). The spectroscopic properties of **5** are similar to those of the Ti analogue **4a** with no indication of any other species present.

6: To a solution of [Ru_2Ti(μ_3-η^1:η^2:η^1-C≡C)(μ-CO)(CO)$_3$(η-C_5H_4Me)$_2$(η-C_5H_5)$_2$] (**4b**; 15 mg, 0.22 mmol) in toluene (10 mL) a solution of HCl/(EtOH) (0.5 mL, ≈0.006 g mL^{-1}) was added dropwise to give an immediate color change from dark to pale red. The reaction mixture was stirred for 30 min, followed by solvent removal in vacuo. The residues were washed with *n*-hexanes (50 mL) to give a yellow solution. Removal of the solvent in vacuo afforded a yellow crystalline compound, which remains unidentified (8 mg). IR (toluene): $\tilde{\nu}_{CO}$ = 2022s, 1995s cm^{-1}; ^{1}H NMR (C_6D_6): δ = 4.50 (m, 1H), 4.19 (t, 4H), 3.92 (t, 4H), 1.46 ppm (s, 6H); ^{13}C NMR (C_6D_6): δ = 197.6 (s, CO), 119.3 (s), 88.8 (s), 88.6 (s), 83.6 (s), 82.4 (s), 12.7 ppm (s); elemental analysis: found: C 38.67, H 3.48. Extraction of the remaining residues with diethyl ether (30 mL) and subsequent recrystallization (CH_2Cl_2/*n*-hexanes) gave purple rods of **6** (10 mg, 90 % with respect to Ti). IR (toluene): $\tilde{\nu}_{CO}$ = 2010s, 1957s cm^{-1}; ^{1}H NMR (CD_2Cl_2): δ = 6.61 (m, 1H, C_5H_4Ti), 6.46 (s, 5H, C_5H_5), 6.22 (m, 1H, C_5H_4Ti), 6.17 (m, 1H, C_5H_4Ti), 6.09 (m, 1H, C_5H_4Ti), 4.99–4.91 (m, 4H, C_5H_4Me), 4.12 (q, ^3J = 6.8 Hz, 1H, C*H*Me), 1.97 (s, 3H, C_5H_4*Me*), 1.43 ppm (d ^3J = 6.8 Hz, 3H, CH*Me*); ^{13}C NMR (CD_2Cl_2): δ = 202.6 (s, CO), 201.9 (s, CO), 160.0 (s, *ipso*-C(Ti)), 126.8 (s, C_5H_4Ti), 119.4 (s, unsubst. C_5H_4Ti), 110.8 (s, C_5H_4Ti), 110.4 (s, C_5H_4Ti), 108.7 (s, *ipso*-C(Ru)), 89.9 (s, C_5H_4Me), 89.4 (s, *C*$_5$H$_4$Me), 88.9 (s, *C*$_5$H$_4$Me), 88.3 (s, *C*$_5$H$_4$Me), 28.5 (s, *C*HMe), 13.4, 12.7 ppm (2 × s, C_5H_4*Me* and CH(*Me*)); MS (FAB) [*M*−(Ti(CO)(C_5H_5)Cl_2)]$^+$ *m*/*z* = 303 (100 %); experimental analysis: calcd. for $C_{20}H_{20}Cl_2O_2RuTi$: C 46.89, H 3.94; found: C 47.32, H 3.92.

Received: January 20, 2005

Keywords: cyclopentadienyl ligands · metallocenes · ruthenium · titanium · zirconium

[1] U. Rosenthal, V. V. Burlakov, P. Arndt, W. Baumann, A. Spannenberg, V. B. Shur, *Eur. J. Inorg. Chem.* **2004**, 4739 – 4749.
[2] A. Ohff, S. Pulst, C. Lefeber, N. Peulecke, P. Arndt, V. V. Burkalov, U. Rosenthal, *Synlett* **1996**, 111 – 118.
[3] U. Rosenthal, P.-M. Pellny, F. G. Kirchbauer, V. V. Burlakov, *Acc. Chem. Res.* **2000**, *33*, 119 – 129.
[4] U. Rosenthal, V. V. Burlakov, *Titanium Zirconium Org. Synth.* **2002**, 355 – 389.
[5] U. Rosenthal, P. Arndt, W. Baumann, V. V. Burlakov, A. Spannenberg, *J. Organomet. Chem.* **2003**, *670*, 84 – 96.
[6] U. Rosenthal, V. V. Burlakov, P. Arndt, W. Baumann, A. Spannenberg, *Organometallics* **2003**, *22*, 884 – 900.
[7] U. Rosenthal, *Angew. Chem.* **2004**, *116*, 3972 – 3977; *Angew. Chem. Int. Ed.* **2004**, *43*, 3882 – 3887.
[8] C. S. Griffith, G. A. Koutsantonis, B. W. Skelton, A. H. White, *Chem. Commun.* **2002**, 2174 – 2175.
[9] C. S. Griffith, G. A. Koutsantonis, B. W. Skelton, A. H. White, *J. Organomet. Chem.* **2003**, *672*, 17 – 21.
[10] C. S. Griffith, G. A. Koutsantonis, B. W. Skelton, A. H. White, *J. Organomet. Chem.* **2003**, *670*, 198 – 204.
[11] L. T. Byrne, J. P. Hos, G. A. Koutsantonis, V. Sanford, B. W. Skelton, A. H. White, *Organometallics* **2002**, *21*, 3147 – 3156.
[12] L. T. Byrne, J. P. Hos, G. A. Koutsantonis, B. W. Skelton, A. H. White, *J. Organomet. Chem.* **2000**, *598*, 28 – 35.
[13] L. T. Byrne, J. P. Hos, G. A. Koutsantonis, B. W. Skelton, A. H. White, *J. Organomet. Chem.* **1999**, *592*, 95 – 102.
[14] C. S. Griffith, G. A. Koutsantonis, B. W. Skelton, A. H. White, *Chem. Commun.* **1998**, *7*, 1805 – 1806.
[15] L. T. Byrne, C. S. Griffith, J. P. Hos, G. A. Koutsantonis, B. W. Skelton, A. H. White, *J. Organomet. Chem.* **1998**, *565*, 259 – 265.
[16] L. T. Byrne, C. S. Griffith, G. A. Koutsantonis, B. W. Skelton, A. H. White, *J. Chem. Soc. Dalton Trans.* **1998**, 1575 – 1580.
[17] P. T. Barger, J. E. Bercaw, *Organometallics* **1984**, *3*, 278.
[18] C. P. Casey, R. E. Palermo, *J. Am. Chem. Soc.* **1986**, *108*, 549.
[19] **4a:** $C_{26}H_{20}O_4Ru_2Ti$; crystal dimensions: $0.65 \times 0.35 \times 0.15$ mm^3; $M = 646.5$ monoclinic, space group $P2_1/c$, $a = 11.157(1)$, $b = 17.182(2)$, $c = 12.698(2)$ Å, $\beta = 93.880(2)°$, $V = 2429$ Å^3, $Z = 4$, $\rho_{calcd} = 1.76(8)$ g cm^{-3}, $\mu_{Mo} = 15.8$ cm^{-1}; $T_{min/max} = 0.68$ (multiscan correction); $2\theta_{max} = 58°$; $N_{total} = 27124$ reflections (full sphere CCD data, monochromatic $Mo_{K\alpha}$ radiation, $\lambda = 0.7107(3)$ Å, $T \approx 153$ K) merging to $N_{unique} = 6082$ reflections ($R_{int} = 0.027$), $N_{obs} = 5334$ ($F > 4\sigma(F)$); $R = 0.026$, $R_w = 0.034$ (weights: $(\sigma^2(F) + 0.0004F^2)^{-1}$); $(x,y,z,U_{iso})_H$ refined throughout. CCDC-261179 (**4a**) and CCDC-261180 (**6**) contain the supplementary crystallographic data for this paper. These data can be obtained free of charge from the Cambridge Crystallographic Data Centre via www.ccdc.cam.ac.uk/data_request/cif.
[20] V. V. Burlakov, A. V. Polyakov, A. I. Yanovsky, Y. T. Struchkov, V. B. Shur, M. E. Vol'pin, U. Rosenthal, H. Goerls, *J. Organomet. Chem.* **1994**, *476*, 197 – 206.
[21] U. Rosenthal, A. Ohff, M. Michalik, H. Goerls, V. V. Burlakov, V. B. Shur, *Angew. Chem.* **1993**, *105*, 1228 – 1230; *Angew. Chem.* **1993**, *31*, 1193 – 1195.
[22] C. Lefeber, A. Ohff, A. Tillack, W. Baumann, R. Kempe, V. V. Burlakov, U. Rosenthal, *J. Organomet. Chem.* **1995**, *501*, 189 – 194.
[23] L. Gade, M. Schubart, B. Findeis, S. Fabre, I. Bezougli, M. Lutz, I. J. Scowen, M. McPartlin, *Inorg. Chem.* **1999**, *38*, 5282 – 5294.
[24] W. J. Sartain, J. P. Selegue, *Organometallics* **1989**, *8*, 2153 – 2158.
[25] W. J. Sartain, J. P. Selegue, *J. Am. Chem. Soc.* **1985**, *107*, 5818 – 5820.
[26] S. Kabashima, S. Kuwata, M. Hidai, *J. Am. Chem. Soc.* **1999**, *121*, 7387 – 7845.
[27] V. B. Shur, S. Z. Bernadyuk, V. V. Burlakov, V. G. Andrianov, A. I. Yanovskii, Y. T. Struchkov, M. E. Vol'pin, *J. Organomet. Chem.* **1983**, *243*, 157 – 163.
[28] V. B. Shur, V. V. Burlakov, M. E. Vol'pin, *J. Organomet. Chem.* **1988**, *347*, 77 – 83.
[29] P.-M. Pellny, V. V. Burlakov, W. Baumann, A. Spannenberg, U. Rosenthal, *Z. Anorg. Allg. Chem.* **1999**, *625*, 910 – 918.
[30] **6** (see Ref. [19] for general details) **:** $C_{20}H_{20}Cl_2O_2RuTi$, crystal dimensions: $0.30 \times 0.08 \times 0.06$ mm^3; $M = 512.2$ monoclinic, space group $C2/c$, $a = 31.391(4)$, $b = 6.6889(9)$, $c = 20.863(3)$ Å, $\beta = 116.306(2)°$, $V = 3927$ Å^3, $Z = 8$ $\rho_{calcd} = 1.73(3)$ g cm^{-3}, $\mu_{Mo} = 14.6$ cm^{-1}; $T_{min/max} = 0.79$; $2\theta_{max} = 58°$; $N_{total} = 23281$, $N_{unique} = 4988$ ($R_{int} = 0.063$), $N_{obs} = 3634$; $R = 0.038$, $R_w = 0.039$.
[31] A. Clearfield, D. K. Warner, C. H. Saldarringa-Molina, R. Ropal, I. Bernal, *Can. J. Chem.* **1975**, *53*, 1622.
[32] Y. C. Lin, J. C. Calabrese, S. S. Wreford, *J. Am. Chem. Soc.* **1983**, *105*, 1679.
[33] M. A. Gafoor, A. T. Hutton, J. R. Moss, *J. Organomet. Chem.* **1996**, *510*, 233.
[34] K. P. Finch, J. R. Moss, M. L. Niven, *Inorg. Chim. Acta* **1989**, *166*, 181.
[35] M. Horacek, P. Stepnicka, R. Gyepes, I. Cisarova, M. Polasek, K. Mach, P.-M. Pellny, V. V. Burlakov, W. Baumann, A. Spannenberg, U. Rosenthal, *J. Am. Chem. Soc.* **1999**, *121*, 10638 – 10639.
[36] We thank Professor Uwe Rosenthal for his insightful discussion and a reviewer for helpful comments.
[37] U. Rosenthal, *Angew. Chem.* **2003**, *115*, 1838 – 1842; *Angew. Chem. Int. Ed.* **2003**, *42*, 1794 – 1798.

Host–Guest Chemistry

Supramolecular Features of Calixarene-Based Synthetic Nanotubes**

Voltaire G. Organo, Alexander V. Leontiev, Valentina Sgarlata, H. V. Rasika Dias, and Dmitry M. Rudkevich**

Filling single-walled carbon nanotubes (SWNTs) with foreign species is a quickly emerging research area.[1] The major goal is to enforce filling materials to adopt one-dimensional morphology for nanowiring, transport, and information flow. Other potential applications include the use of SWNTs

[*] V. G. Organo, Dr. A. V. Leontiev, Dr. V. Sgarlata, Prof. Dr. H. V. R. Dias, Prof. Dr. D. M. Rudkevich
Department of Chemistry & Biochemistry
The University of Texas at Arlington
Arlington, TX 76019-0065 (USA)
Fax: (+1) 817-272-3808
E-mail: dias@uta.edu
rudkevich@uta.edu

[**] V.G.O. and A.V.L. contributed equally to this work. Special thanks to Dr. Iris Thondorf for preliminary calculations. Financial support from the National Science Foundation (awards CHE-0350958 to D.M.R and CHE-0314666 to H.V.R.D.), the Alfred P. Sloan Foundation (D.M.R.), and the Robert A. Welch Foundation (grant Y-1289 to H.V.R.D.) is acknowledged.

Supporting information for this article is available on the WWW under http://www.angewandte.org or from the author.

 DOI: 10.1002/anie.200500057

as reaction vessels and gas-storage cylinders.[2] However, far-from-trivial protocols for the chemical opening of SWNTs, still not fully understood mechanisms of their filling, as well as identification of the encapsulated material are some of the problems faced in this area. Physical measurements within the interiors are also a challenge. Synthetic analogues of SWNTs have recently been introduced.[3,4] Organic synthesis offers variety of the sizes and shapes. However, most of these synthetic nanotubes are formed through self-assembly and, thus, are stable only under specific conditions. Furthermore, the stability of their encapsulation complexes is generally weak, which diminishes their capabilities as storage and transport devices and materials.

Herein, we demonstrate novel and unique features of synthetic, calixarene-based nanotubes. These nanotubes are covalently built and robust and can be prepared by conventional organic chemistry protocols. The length of the nanotubes can be controlled precisely and easily, and they effectively pack into infinite tubular bundles in the solid state. These nanotubes can also be easily filled and form kinetically and thermodynamically stable encapsulation complexes, and they can be emptied at will in a nondestructive manner. Taken together, we propose reasonable synthetic alternatives to SWNTs for filling.

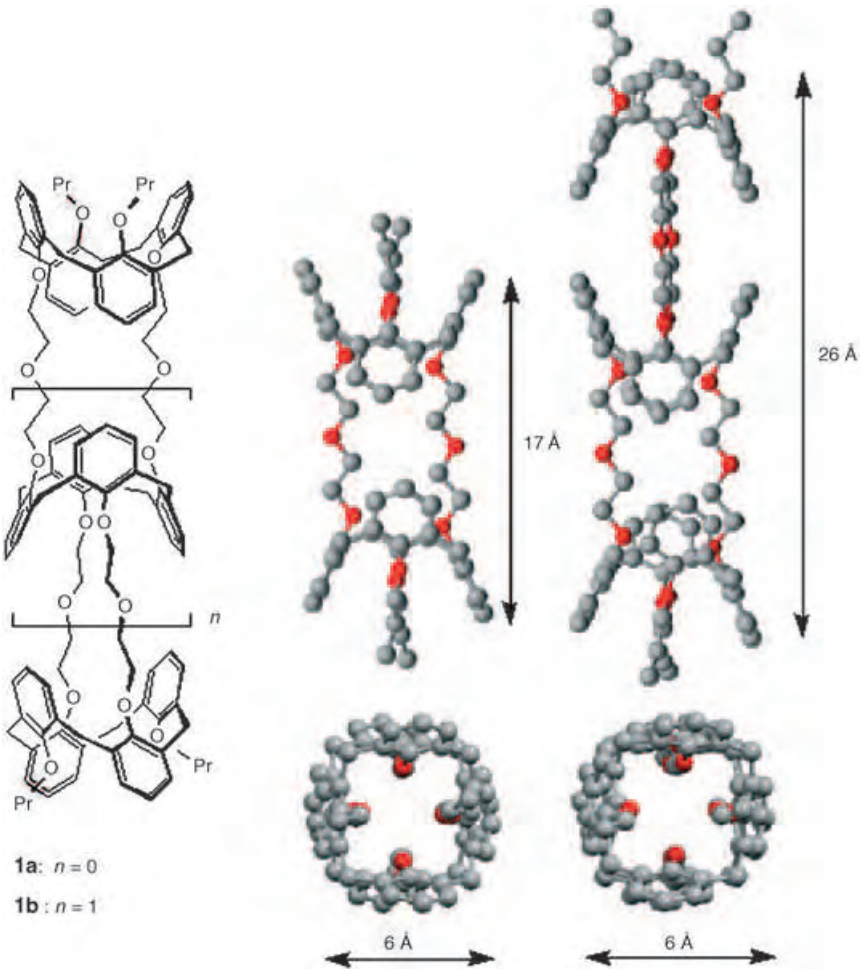

Figure 1. Left: Synthetic calixarene-based nanotubes **1a**,**b** for NO_2/N_2O_4 fixation and nitrosonium ion (NO^+) storage. Right: X-ray crystal structures of **1a**,**b** (from $CHCl_3$/MeOH; side and top views; O red, C gray). Hydrogen atoms are omitted for clarity.

Earlier we reported that simple calix[4]arenes reversibly interact with NO_2/N_2O_4 and entrap reactive nitrosonium (NO^+) cations—NO^+ is generated upon disproportionation of N_2O_4—within their π-electron-rich interiors, one per cavity.[5] Very high association constants $K_a \gg 10^6\,M^{-1}$ ($\Delta G^{295} \gg 8$ kcal mol^{-1}) for these processes were determined, and the complexes were kinetically stable. These particular properties have been used in the design of calixarene-based nanotubes **1a**,**b** (Figure 1).

The synthesis of tubes **1a**,**b** is modular (see Scheme 1 and Supporting Information). Calixarene building blocks were linked by simple, Williamson-type alkylation procedures. Alkylation of calix[4]arene diol **2a** (R = *n*Pr) with ditosylate **3** resulted in tube **1a**.[6] Reaction of diol **2b** (R = CH_2CH_2OBn) with **3** led to the formation of biscalixarene tube **4**, which has two terminal hydroxyl groups at one end. When **4** was coupled with another equivalent of ditosylate **3**, triscalixarene nanotube **1b** was isolated in 26% yield. Alternatively, nanotube **1b** could be isolated in modest yield (≈10%) from the one-step reaction of two equivalents of **3a** with tetrakisalcohol **5**. Nanotubes **1a**,**b** were characterized by high-resolution ^{1}H NMR spectroscopy and COSY and NOESY experiments, mass spectrometry, and X-ray crystallography.[7] X-ray data show that in nanotubes **1a** and **1b**, 1,3-alternate calix[4]arenes are rigidly linked with diethylene glycol bridges to form hollow cylinders with cavities of diameters of approximately 6 Å and lengths of 17 and 26 Å, respectively (Figure 1). The inner tunnels are defined by two cofacial pairs of aromatic rings oriented orthogonally along the cavity axis.

Nanotubes **1a**,**b** can be easily filled, as each calixarene unit can accommodate one NO^+ guest. Addition of excess NO_2/N_2O_4 to **1a**,**b** in tetrachloroethane in the presence of Lewis acids such as $SnCl_4$ or $BF_3{\cdot}Et_2O$ resulted in quantitative formation of nitrosonium complexes **6a**,**b** (Figure 2). Similar complexes formed when nanotubes **1a**,**b** were mixed with nitrosonium salt $NO^+SbF_6^-$ in tetrachloroethane. Adducts **6a**,**b** were identified by UV/Vis and ^{1}H NMR spectroscopy and exhibit typical features of earlier described, simpler calix[4]arene–NO^+ species.[5,8] Of particular importance is the characteristic deep purple color. The broad charge-transfer absorption bands that account for the color are observed at $\lambda_{max} \approx 550$ nm in the UV/Vis spectra. Charge transfer only occurs when NO^+ guests are tightly entrapped inside the

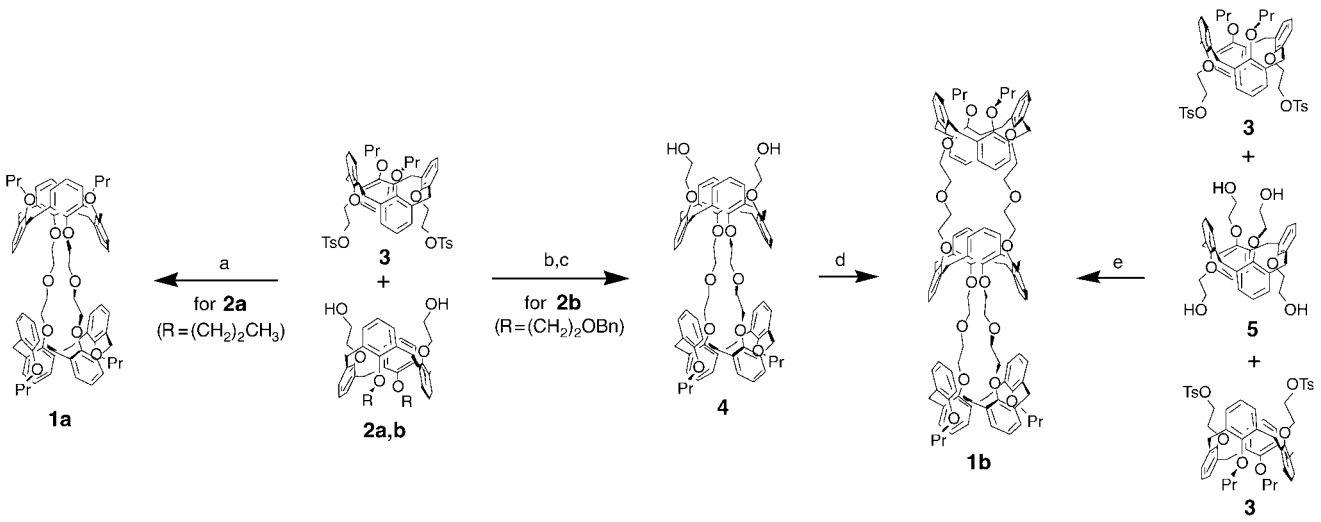

Scheme 1. a) NaH, DMF, 80 °C, 48 h, 15–20%; b) NaH, THF, reflux, 24 h, 32%; c) H_2, 10% Pd/C, THF/AcOH, 82%; d) NaH, THF, reflux, 24 h, 26%; e) NaH, THF, reflux, 3 days, 7%. Ts = *p*-toluenesulfonyl; Bn = benzyl; DMF = *N*,*N*-dimethylformamide.

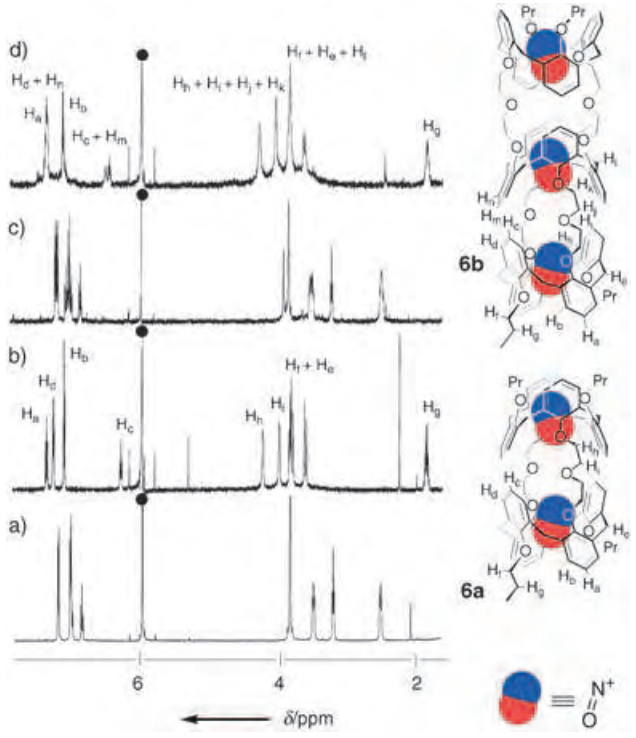

Figure 2. Partial ^{1}H NMR spectra (500 MHz, $(CDCl_2)_2$, 295 K) of a) nanotube **1a**, b) filled nanotube **6a**, c) nanotube **1b**, and d) filled nanotube **6b**. The residual solvent signals are marked with filled circles (●). The assignments were performed by COSY and NOESY experiments and supported by molecular modeling (MacroModel 7.1).

calixarene cavities.[5,8,9] Accordingly, the filling process can be monitored visually.

Upon stepwise addition of NO_2/N_2O_4 or $NO^+SbF_6^-$ in [D_2]tetrachloroethane, signals for the protons of **1a**,**b** and **6a**,**b** can be seen separately and in slow exchange by ^{1}H NMR spectroscopy. This is typical for host–guest complexes with high exchange $\Delta G^{\neq}$ barriers (>15 kcal mol^{-1}) and/or high values of association constants ($K_a > 10^6$ M^{-1}). The presence and location of the guests inside nanotubes **6a**,**b** can be deducted from conventional NMR analysis. Structural fragments that are involved in the complexation process were identified by ^{1}H NMR spectroscopy, COSY, and NOESY experiments. Although entrapped NO^+ species cannot be directly seen, chemical shifts of the methylene protons from Ar-O-CH_2 and, to a lesser extent, Ar-O-CH$_2$CH_2 and the aromatic protons are very sensitive to the encapsulation. Indeed, besides the charge transfer, strong cation–dipole interactions between the oxygen atoms of the calixarenes and the entrapped NO^+ take place.

The three signals for the protons for the propyloxy groups in **6a**,**b** appeared significantly downfield ($\Delta\delta \approx 1$ ppm) relative to empty tubes **1a**,**b** (Figure 2). This implies that two NO^+ cations are located at the ends of the nanotubes and occupy the terminal calixarene compartments. The middle calixarene in the longer tube **6b** is most probably filled as well. Downfield shifts ($\Delta\delta > 1$ ppm) of the corresponding signals for the protons of Ar-O-CH_2 and CH_2-O-CH_2 were observed for this fragment. Higher stoichiometries of NO^+ were ruled out; there is simply no room to accommodate a larger number of electrostatically repulsive cations.

According to molecular modeling studies, the nitrosonium-filled nanotubes adopt somewhat shrunken structures, with all-*gauche* conformations about the glycol C–C bonds. Such folding brings closer the aromatic rings from the neighboring calixarene units. This behavior was confirmed by NOESY for the nitrosonium-filled nonsymmetrical *O*,*O*′-dimethylated derivative of **4**. Consequently, the aromatic protons CH_c of tube **6a**, and CH_c and CH_m in tube **6b**, appear shielded and are seen somewhat upfield at $\delta \approx 6.2$–6.4 ppm (Figure 2).

Judging from the ^{1}H NMR spectra at room temperature, complexation with NO^+ does not influence the symmetry of **6a**,**b** relative to empty **1a**,**b**. Although in both cases the nonequivalence of the CH_2 protons of the calixarene methylene bridges becomes more pronounced, the number of ^{1}H NMR signals for the propyl ArOCH_2, glycol CH_2OCH_2

and $ArOCH_2$, and aromatic groups for **6a**,**b** does not change and implies that the NO^+ guests, with van der Waals dimensions of approximately 2 Å, freely rotate along the N-O axis and also tumble within the cavity.

To determine the mechanism of filling is a difficult task[1] and it remains a great challenge for SWNTs, but conventional NMR spectroscopy provides useful insights for synthetic tubes such as those prepared here. Modeling suggests that the first NO^+ ion can enter the nanotube through either its neck or one of the middle gates between the calixarenes. Upon addition of $NO^+SbF_6^-$ to tube **1a**, the intermediate half-filled 1:1 complex **1a**·NO^+ was initially observed and isolated, and the guest was found to be located between the calixarenes, within the electron-rich oxygen atoms of the crown ether.[6] The signals for the protons of the propyl Ar-O-Pr group in this complex were not shifted, which indicates that the ends of the nanotube were not occupied with NO^+. Likewise upon addition of $NO^+SbF_6^-$ to longer nanotube **1b** (at −20 °C), the intermediate partially filled species were observed. They exhibit distinct signals of all groups of protons, but the signals for the propyl Ar-O-Pr protons were not shifted downfield. These intermediate complexes were further converted into **6a**,**b** simply by addition of more NO_2/N_2O_4 or $NO^+SbF_6^-$. To avoid electrostatic repulsions, the next NO^+ ion should instead enter through the neck thus further pushing the first guest towards the end of the tube.

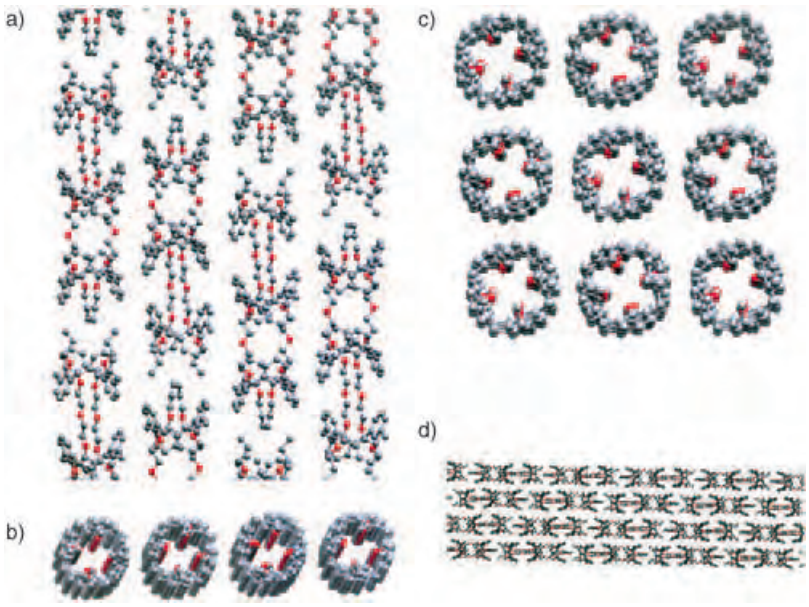

Figure 3. Side and top views of supramolecular packing of nanotube **1b** into infinite nanocylinders and the parallel stacking of neighboring nanotubes. View (d) shows the continuous tunnel of four columns of nine **1b** molecules.

Filled nanotubes **6a**,**b** are stable in anhydrous solution at room temperature for hours, but can be readily destroyed with H_2O to quantitatively regenerate free **1a**,**b** (according to ^1H NMR and UV/Vis spectral analysis). We found that the encapsulated NO^+ species can also be removed by simple addition of 18-crown-6; it is known that crown ethers form stable complexes with NO^+.[10] When 18-crown-6 ($\approx$10 equiv) was added to solutions of **6a**,**b** in [D_2]tetrachloroethane, empty nanotubes **1a**,**b** were regenerated within minutes (NMR, UV/Vis), and the deep purple color disappeared. This observation is important, as in this case foreign species are removed without decomposition and without the need to change the polarity of the solution.

Nanotube units **1a** and **1b** pack head-to-tail in straight rows to result in infinitely long cylinders. Chloroform molecules occupy the vacant spaces between the tubes. Nanotube **1b** shows a particularly appealing supramolecular structure (Figure 3) with the neighboring nanocylinders aligned parallel to each other. In each nanocylinder, molecules **1b** are twisted by 90° relative to each other, and the Ar-O-Pr propyl groups effectively occupy the voids between the adjacent molecules. In such an arrangement, the intermolecular distance between two neighboring tubes in the nanocylinder is around 6 Å, and the nanocylinders are separated from each other by about 9 Å. This supramolecular order comes with the tube length and is without precedent for conventional, shorter calixarenes. The unique linear nanostructures maximize the intermolecular van der Waals interactions in the crystal through the overall shape simplification.

In conclusion, besides SWNTs, synthetic nanotubes are now available that pack in tubular bundles and can be reversibly filled with guest molecules. At this stage only certain guests can fill the interiors, but they are charged, which is important for the design of nanowires. Given the ability of calixarenes to react with NO_x gases even in the solid state,[5,11] we will look at the flow of nitrosonium ions along the infinite nanocylinders in the solid-state bundles of **1a**,**b**. Not only would the charge be transported and detected through the changes in conductivity, but also the color of the crystals would serve as an indicator of such transport processes.[12]

Received: January 6, 2005
Published online: April 21, 2005

Keywords: calixarenes · nanotubes · nitrogen oxides · solid-state structures · supramolecular chemistry

[1] a) M. Monthioux, *Carbon* **2002**, *40*, 1809–1823; b) O. Vostrowsky, A. Hirsch, *Angew. Chem.* **2004**, *116*, 2380–2383; *Angew. Chem. Int. Ed.* **2004**, *43*, 2326–2329; c) K. Koga, G. T. Gao, H. Tanaka, X. C. Zeng, *Nature* **2001**, *412*, 802–805; d) D. A. Britz, A. N. Khlobystov, K. Porfyrakis, A. Ardavan, G. A. D. Briggs, *Chem. Commun.* **2005**, 37–39.

[2] a) A. I. Kolesnikov, J.-M. Zanotti, C.-K. Loong, P. Thiyagarajan, A. P. Moravsky, R. O. Loutfy, C. J. Burnham, *Phys. Rev. Lett.* **2004**, *93*, 035503-1–035503-4; b) C. Matranga, B. Bockrath, *J. Phys. Chem. B* **2004**, *108*, 6170–6174; c) O. Byl, P. Kondratyuk, J. T. Yates, Jr., *J. Phys. Chem. B* **2003**, *107*, 4277–4279; d) O. Byl,

P. Kondratyuk, S. T. Forth, S. A. FitzGerald, L. Chen, J. K. Johnson, J. T. Yates, Jr., *J. Am. Chem. Soc.* **2003**, *125*, 5889 – 5896; e) A. Fujiwara, K. Ishii, H. Suematsu, H. Kataura, Y. Maniwa, S. Suzuki, Y. Achiba, *Chem. Phys. Lett.* **2001**, *336*, 205 – 211.

[3] For self-assembling nanotubes, see: a) D. T. Bong, T. D. Clark, J. R. Granja, M. R. Ghadiri, *Angew. Chem.* **2001**, *113*, 1016 – 1041; *Angew. Chem. Int. Ed.* **2001**, *40*, 988 – 1011; b) S. Matile, A. Som, N. Sorde, *Tetrahedron* **2004**, *60*, 6405 – 6435; c) T. Yamaguchi, S. Tashiro, M. Tominaga, M. Kawano, T. Ozeki, M. Fujita, *J. Am. Chem. Soc.* **2004**, *126*, 10818 – 10819; d) S. Tashiro, M. Tominaga, T. Kusukawa, M. Kawano, S. Sakamoto, K. Yamaguchi, M. Fujita, *Angew. Chem.* **2003**, *115*, 3389 – 3392; *Angew. Chem. Int. Ed.* **2003**, *42*, 3267 – 3270; e) M. Tominaga, S. Tashiro, M. Aoyagi, M. Fujita, *Chem. Commun.* **2002**, 2038 – 2039; f) V. Sidorov, F. W. Kotch, G. Abdrakhmanova, R. Mizani, J. C. Fettinger, J. T. Davis, *J. Am. Chem. Soc.* **2002**, *124*, 2267 – 2278; g) L. Baldini, F. Sansone, A. Casnati, F. Ugozzoli, R. Ungaro, *J. Supramol. Chem.* **2002**, 219 – 226.

[4] For covalently linked nanotubes, see: a) A. Harada, J. Li, M. Kamachi, *Nature* **1993**, *364*, 516 – 518; b) A. Ikeda, S. Shinkai, *J. Chem. Soc. Chem. Commun.* **1994**, 2375 – 2376; c) A. Ikeda, M. Kawaguchi, S. Shinkai, *Quim. Anal. Int. Ed.* **1997**, *93*, 408 – 414; d) J.-A. Perez-Adelmar, H. Abraham, C. Sanchez, K. Rissanen, P. Prados, J. de Mendoza, *Angew. Chem.* **1996**, *108*, 1088 – 1090; *Angew. Chem. Int. Ed. Engl.* **1996**, *35*, 1009 – 1011; e) S. K. Kim, W. Sim, J. Vicens, J. S. Kim, *Tetrahedron Lett.* **2003**, *44*, 805 – 809; f) S. K. Kim, J. Vicens, K.-M. Park, S. S. Lee, J. S. Kim, *Tetrahedron Lett.* **2003**, *44*, 993 – 997; g) Y. Kim, M. F. Mayer, S. C. Zimmerman, *Angew. Chem.* **2003**, *115*, 1153 – 1158; *Angew. Chem. Int. Ed.* **2003**, *42*, 1121 – 1126.

[5] G. V. Zyryanov, Y. Kang, D. M. Rudkevich, *J. Am. Chem. Soc.* **2003**, *125*, 2997 – 3007.

[6] G. V. Zyryanov, D. M. Rudkevich, *J. Am. Chem. Soc.* **2004**, *126*, 4264 – 4270.

[7] Crystals of suitable quality of **1a** and **1b** for X-ray studies were obtained from $CHCl_3/CH_3OH$ solutions at room temperature. The X-ray intensity data were measured at 100(2) K on a Bruker SMART APEX CCD area detector system equipped with a Oxford Cryosystems 700 Series cooler, a graphite monochromator, and a $Mo_{K\alpha}$ fine-focus sealed tube ($\lambda = 0.710\,73$ Å). The data frames were integrated with the Bruker SAINT-Plus (version 6.45) software package. Structures were solved and refined using Bruker SHELXTL (version 6.14) software package. X-ray data for **1a**·2 $CHCl_3$; $C_{78}H_{86}Cl_6O_{10}$, Monoclinic, Space group $P2_1/n$; $a = 17.9825(7)$, $b = 10.6205(4)$ Å, $c = 19.8479(7)$ Å, $\beta = 111.7390(10)°$, $V = 3521.0(2)$ Å^3, $Z = 2$, $\rho_{calcd} = 1.317$ Mg m^{-3}, the hydrogen atoms were placed in idealized positions and included as riding atoms. All non-hydrogen atoms were refined anisotropically. $R1$, $wR2$ ($I > 2\sigma(I)$) = 0.0397, $wR2 = 0.1024$; $R1$, $wR2$ (all data) = 0.0465, 0.1077, GOF = 1.040. X-ray data for **1b**·4.5 $CHCl_3$; $C_{116.5}H_{124.5}Cl_{13.5}O_{16}$, Triclinic, Space group $P\bar{1}$, $a =$ 14.7634(6) Å, $b = 15.2376(6)$ Å, $c = 26.4844(11)$, Å, $\alpha =$ 75.9360(10)°, $\beta = 78.0270(10)°$, $\gamma = 80.0890(10)°$, $V =$ 5606.9(4) Å^3, $Z = 2$, $\rho_{calcd} = 1.338$ Mg m^{-3}, the hydrogen atoms were placed in idealized positions and included as riding atoms. All the chloroform molecules show severe disorder. One of the *n*-propyl groups is also disordered. These disorders were modeled reasonably well. All non-hydrogen atoms were refined anisotropically, $R1$, $wR2$ ($I > 2\sigma(I)$) = 0.0828, 0.1667; $R1$, $wR2$ (all data) = 0.1100, 0.1783, GOF = 1.105. CCDC 259477 (**1a**) and 259478 (**1b**) contain the supplementary crystallographic data for this paper. These data can be obtained free of charge from the Cambridge Crystallographic Data Centre via www.ccdc.cam.ac.uk/data_request/cif.

[8] R. Rathore, S. V. Lindeman, K. S. S. Rao, D. Sun, J. K. Kochi, *Angew. Chem.* **2000**, *112*, 2207 – 2211; *Angew. Chem. Int. Ed.* **2000**, *39*, 2123 – 2127.

[9] Experiments with wider (and more flexible) calix[5]-, calix[6]-, and calix[8]arenes did not lead to entrapment of NO^+; no characteristic color change was detected upon mixing with NO_2/N_2O_4. This observation once again rules out the possibility of coordination of NO^+ outside the calixarene cavity.

[10] a) G. S. Heo, P. E. Hillman, R. A. Bartsch, *J. Heterocycl. Chem.* **1982**, *19*, 1099 – 1103; b) S. Ricard, P. Audet, R. Savoie, *J. Mol. Struct.* **1988**, *178*, 135 – 140; c) K. Y. Lee, D. J. Kuchynka, J. K. Kochi, *Inorg. Chem.* **1990**, *29*, 4196 – 4204; d) G. I. Borodkin, V. G. Shubin, *Russ. Chem. Rev.* **2001**, *70*, 211 – 230.

[11] a) Y. Kang, D. M. Rudkevich, *Tetrahedron* **2004**, *60*, 11219 – 11225; b) Y. Kang, G. V. Zyryanov, D. M. Rudkevich, *Chem. Eur. J.* **2005**, *11*, 1924 – 1932.

[12] For guest transport in organic solids, see: a) J. L. Atwood, L. J. Barbour, A. Jerga, B. L. Schottel, *Science* **2002**, *298*, 1000 – 1002; b) O. Ohmori, M. Kawano, M. Fujita, *J. Am. Chem. Soc.* **2004**, *126*, 16292 – 16293.

Corrole Chemistry

Hemiporphycene from the Expansion of a Corrole Ring**

Roberto Paolesse, Sara Nardis, Manuela Stefanelli, Frank R. Fronczek, and Maria Graça H. Vicente*

Porphyrins are extensively studied macrocycles as their unique properties allow multiple and diverse applications in various fields ranging from medicine to the material sciences.[1] Interest in this type of compound has been further expanded by the discovery of porphyrin analogues,[2] that is, macrocycles which have a modified skeleton relative to that of porphyrin. Porphyrin analogues are interesting from both the theoretical and application points of view, as they are amenable to investigation of structure–property relationships as well as the rational modification of the macrocycle to suit a specific application. This approach mimics what happens in

[*] Prof. Dr. R. Paolesse
Dipartimento di Scienze e Tecnologie Chimiche
Università di Roma "Tor Vergata" and CNR-IMM
00133 Roma (Italy)
Fax: (+39) 067-259-4328
E-mail: roberto.paolesse@uniroma2.it

Dr. S. Nardis, M. Stefanelli
Dipartimento di Scienze e Tecnologie Chimiche
Università di Roma "Tor Vergata"
00133 Roma (Italy)

Prof. Dr. F. R. Fronczek, Prof. Dr. M. G. H. Vicente
Department of Chemistry
Lousiana State University
Baton Rouge, LA 70803 (USA)

[**] This work was supported by the MIUR-FIRB (Italy; project RBNE01KZZM).

 DOI: 10.1002/anie.200500481

natural systems, where iron porphyrins are used for oxygen transport and activation, while magnesium chlorins are exploited in photosynthetic systems.[3]

Among the large number of porphyrin analogues reported, corrole has received increased attention in recent years, although it was one of the first known members of this family of compounds with Johnson and Kay's studies on the synthesis of vitamin B_{12}.[4] Such renewed interest is in large part due to the peculiar behavior of this macrocycle, which is able to stabilize formal high oxidation states of coordinated metals,[5] thus opening interesting applications for metallocorrolates in catalysis.[6] The coordination chemistry of corrole is made even more intriguing by its non-innocent character as a ligand.[7]

The tumultuous increase of corrole-related papers in the last few years has been based on the definition of simple synthetic routes for the preparation of this macrocycle from commercially available precursors.[8] The synthesis of 5,10,15-triarylcorroles has opened the way to the study of the peripheral functionalization of the macrocycle,[9] which is a topic far less studied than its coordination chemistry.

We contributed to this field by studying the Vilsmeier formylation of free-base corroles. The reactivity of both the β-alkyl and *meso*-triaryl derivatives showed a peculiar and intriguing behavior.[10,11] In particular, 5,10,15-triphenylcorrole (**1**) afforded an unexpected and unprecedented *N*-ethane-bridged inner-core derivative as the major product in the presence of excess DMF (*N*,*N*-dimethylformamide). This compound is particularly intriguing and for this reason we decided to further study the reaction of 5,10,15-triphenylcorrole **1** with CI_4 to investigate whether a one-carbon-unit-bridged inner-core derivative could be similarly obtained. The reaction was carried out under conditions similar to those used for the Vilsmeier reaction, by heating in CH_2Cl_2/DMF at reflux.[12] Chromatography on silica gel afforded two green fractions: the first band, obtained in trace amount, was characterized as 5-iodo-10,15,20-triphenylporphyrin; the second fraction represented the major product of the reaction and was obtained in a yield of 30%.

The spectral characterization of this second compound showed the presence of a macrocycle, although its properties were different from those of corroles. For example, the UV/Vis absorption spectrum of the major product was porphyrin-like, with the presence of four Q bands, while the ^{1}H NMR spectrum showed the presence of different doublets for protons of the pyrrolic units which indicates that the product has a lower symmetry than **1**.[12] Solid-state X-ray analysis of a single crystal of the product[13] showed the presence of a two-carbon *meso* bridge, with the new carbon unit close to pyrrole B, and allowed us to identify the isomer as the 5-iodo-6,11,16-triphenylhemiporphycene (**2**; Figure 1). A similar triphenylhemiporphycene was reported by Callot et al. in 1995 as the serendipitous product obtained by a demetalation–metalation sequence carried out on a homoporphyrin.[14] Note, in that case the hemiporphycene was obtained from ring contraction of a homoporphyrin, whereas in the present case it results from the ring expansion of a corrole ring. Such a ring-expansion reaction is interesting from a synthetic point of view as it is possible to obtain the hemiporphycene from a triphenylcorrole precursor in a single step, whereas the rational synthesis developed by the groups of Vogel and Sessler requires a multistep approach.[15]

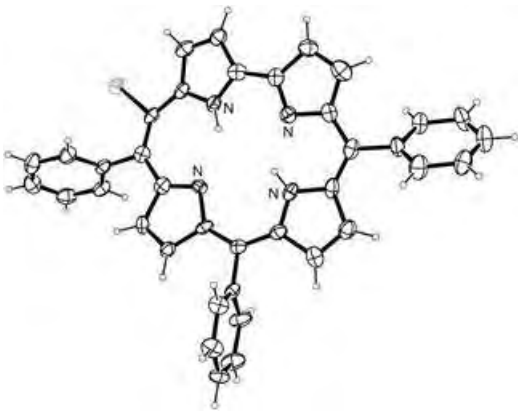

Figure 1. Crystal structure of **2** (N dark gray (labeled), I light gray, C black, H small circles).

Our unexpected result led us to further investigate the plausible reaction sequence that leads to hemiporphycene **2** from the corrole ring. To verify whether the expansion of the corrole was caused by the attack of a carbenic species, we treated the triphenylcorrole **1** with ethyldiazoacetate in bromobenzene. We obtained the corresponding *N*-21-substituted corrole **3** as the major product, as well as the hemiporphycene **4**,[14] although in very low yields, among other minor reaction products.

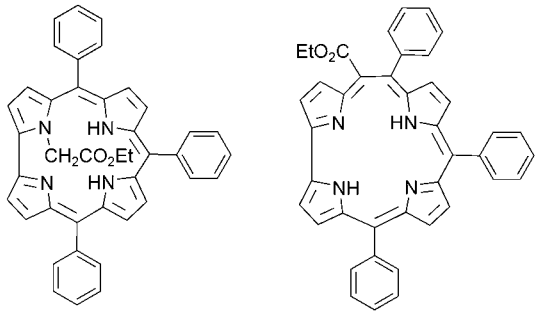

3 **4**

Similar to the stepwise conversion of the *N*-substituted porphyrin into the corresponding homoporphyrin as reported by Callot and Tschamber in 1975,[16] the *N*-21 isomer obtained from the reaction of 5,10,15-triphenylcorrole and ethyl iodoacetate was heated at reflux in bromobenzene to afford the hemiporphycene in low yields. No hemiporphycene was obtained when the *N*-22 isomer was treated under the same conditions. These results led us to hypothesize a plausible reaction mechanism for the formation of the hemiporphycene, as shown in Figure 2.

The first step involves the formation of the *N*-substituted derivative, which can then rearrange as shown to finally give the hemiporphycene ring upon loss of HI. This novel reaction represents a facile route to the hemiporphycene ring. The

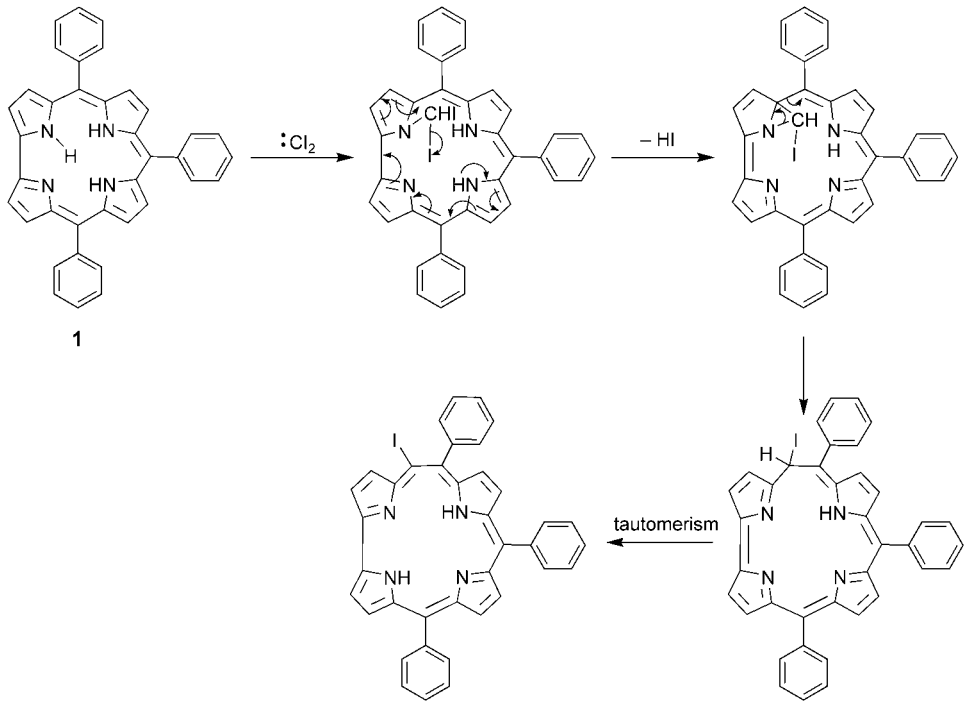

Figure 2. Proposed reaction and mechanistic pathway from **1** to **2**.

presence of an iodine atom at the vinylogous bridge offers the opportunity for further modification at this site and for exploitation of the hemiporphycene macrocycle to build more-complex molecular architectures with interesting properties for new applications.

Received: February 8, 2005
Published online: April 12, 2005

Keywords: carbenes · corroles · nitrogen heterocycles · porphyrinoids · ring expansion

[1] a) J.-H. Chou, H. S. Nalwa, M. E. Kosal, N. A. Rakow, K. Suslick in *The Porphyrin Handbook*, *Vol. 6* (Eds: K. M. Kadish, K. M. Smith, R. Guilard), Academic Press, New York, **2000**, p. 43; b) R. K. Pandey, G. Zheng in *The Porphyrin Handbook*, *Vol. 6* (Eds: K. M. Kadish, K. M. Smith, R. Guilard), Academic Press, New York, **2000**, p. 157; c) T. Malinski in *The Porphyrin Handbook*, *Vol. 6* (Eds: K. M. Kadish, K. M. Smith, R. Guilard), Academic Press, New York, **2000**, p. 231.

[2] a) J. L. Sessler, A. Gebauer, E. Vogel in *The Porphyrin Handbook*, *Vol. 2* (Eds: K. M. Kadish, K. M. Smith, R. Guilard), Academic Press, New York, **2000**, p. 1; b) J. L. Sessler, A. Gebauer, S. J. Weghorn in *The Porphyrin Handbook*, *Vol. 2* (Eds: K. M. Kadish, K. M. Smith, R. Guilard), Academic Press, New York, **2000**, p. 55.

[3] a) D. Mansuy, P. Battioni in *The Porphyrin Handbook*, *Vol. 4* (Eds: K. M. Kadish, K. M. Smith, R. Guilard), Academic Press, New York, **2000**, p. 1; b) D. Gust, T. A. Moore in *The Porphyrin Handbook*, *Vol. 8* (Eds: K. M. Kadish, K. M. Smith, R. Guilard), Academic Press, New York, **2000**, p. 153.

[4] A. W. Johnson, I. T. Kay, *J. Chem. Soc.* **1965**, 1620.

[5] C. Erben, S. Will, K. M. Kadish in *The Porphyrin Handbook*, *Vol. 2* (Eds: K. M. Kadish, K. M. Smith, R. Guilard), Academic Press, New York, **2000**, p. 233.

[6] A. Mahammed, H. B. Gray, A. E. Meier-Callahan, Z. Gross, *J. Am. Chem. Soc.* **2003**, *125*, 1162.

[7] F. A. Walker, *Inorg. Chem.* **2003**, *42*, 4526.

[8] a) R. Paolesse in *The Porphyrin Handbook*, *Vol. 2* (Eds: K. M. Kadish, K. M. Smith, R. Guilard), Academic Press, New York, **2000**, p. 201; b) D. T. Gryko, *Eur. J. Org. Chem.* **2002**, *11*, 1735.

[9] S. Nardis, D. Monti, R. Paolesse, *Mini-Reviews in Organic Chemistry*, Bentham Science Publishers Ltd., San Francisco (USA), in press.

[10] R. Paolesse, L. Jaquinod, M. O. Senge, K. M. Smith, *J. Org. Chem.* **1997**, *62*, 6193.

[11] R. Paolesse, S. Nardis, M. Venanzi, M. Mastroianni, M. Russo, F. R. Fronczek, M. G. Vicente, *Chem. Eur. J.* **2003**, *9*, 1192.

[12] A solution of 5,10,15-triphenylcorrole **1** (45 mg, 0.085 mmol), carbon tetraiodide (45 mg, 0.087 mmol), and DMF (0.9 mL, 11.6 mmol) in CH_2Cl_2 (50 mL) was heated at reflux for 1 h. The progress of the reaction was monitored by UV/Vis spectroscopy and by TLC. After disappearance of the starting material, the crude mixture was washed with water and a solution of $NaHCO_3$, and the solvent was evaporated under vacuum. Chromatography on silica gel using CH_2Cl_2 as the eluent afforded a green band as the major product, which, after crystallization from CH_2Cl_2/hexane, gave red–violet crystals of **2** (17 mg, 30%). UV/Vis (CH_2Cl_2): λ_{max} (log ε): 419 (5.28), 522 (3.8), 563 (4.15), 591 (4.02), 637 nm (4.03); ^{1}H NMR (400 MHz, $CDCl_3$, J [Hz]): $\delta = 9.37$ (d, 1H, $J = 4.4$, β-pyrrolic), 9.14 (d, 1H, $J = 4.4$, β-pyrrolic), 9.05 (d, 1H, $J = 4.5$, β-pyrrolic), 8.75 (d, 1H, $J = 4.5$, β-pyrrolic), 8.50 (d, 1H, $J = 4.4$, β-pyrrolic), 8.20 (d, 3H, $J = 6.6$, phenyl), 8.09 (d, 1H, $J = 4.4$, β-pyrrolic), 8.03 (d, 2H, $J = 7.1$, β-pyrrolic), 7.77(m, 7H, phenyl), 7.65 ppm (m, 5H, phenyl); MS (FAB): m/z (%): 664 (100), 538 (60).

[13] Single crystals of **2**, $C_{38}H_{25}N_4I$, were obtained by slow diffusion of hexane into a solution of **2** in CH_2Cl_2. The unit cell was

monoclinic, space group $P2_1/c$, $a = 24.637(5)$, $b = 10.172(3)$, $c = 24.663(6)$ Å, $\beta = 112.186(8)°$, $V = 5723(2)$ Å^3, $Z = 8$, $\rho_{calcd} = 1.542$ g cm^{-3}, $\mu_{Mo} = 1.155$ mm^{-1}, $R = 0.079$ (8718 data with $F^2 > 2\sigma F^2$), $R_w = 0.192$ (all 13574 unique data), and 775 refined parameters. A total of 39732 data were collected at $T = 100$ K to $\theta = 28.3°$ with $Mo_{K\alpha}$ radiation ($\lambda = 0.71073$ Å) on a Nonius KappaCCD diffractometer using a green blade crystal of dimensions $0.37 \times 0.12 \times 0.05$ mm^3. Absorption corrections were carried out by a multiscan method using HKL Scalepack, with transmission coefficients 0.714–0.943. Refinement was by full-matrix least squares using SHELXL, with hydrogen atoms in idealized positions. There are two independent molecules in the asymmetric unit. CCDC-258645 contains the supplementary crystallographic data for this paper. These data can be obtained free of charge from the Cambridge Crystallographic Data Centre via www.ccdc.cam.ac.uk/data_request/cif.

[14] H. J. Callot, A. Rohrer, Th. Tschamber, *New J. Chem.* **1995**, *19*, 155.

[15] E. Vogel, M. Bröring, S. J. Weghorn, P. Scholz, R. Deponte, J. Lex, H. Schrnickler, K. Schaffner, S. E. Braslavsky, M. Müller, S. Pörting, C. J. Fowler, J. L. Sessler, *Angew. Chem.* **1997**, *109*, 1725; *Angew. Chem. Int. Ed. Engl.* **1997**, *36*, 1651.

[16] H. J. Callot, Th. Tschamber, *J. Am. Chem. Soc.* **1975**, *97*, 6175.

Molecular Devices

Donor–Acceptor Pretzelanes and a Cyclic Bis[2]catenane Homologue**

*Yi Liu, Paul A. Bonvallet, Scott A. Vignon, Saeed I. Khan, and J. Fraser Stoddart**

Through its exploitation of noncovalent bonding interactions and self-assembly processes,[1] supramolecular assistance to covalent synthesis[2] has established itself as an efficient means of creating molecules with nanoscale dimensions. For two decades, researchers have harnessed the power of post-assembly covalent modification[2] to produce an array of mechanically interlocked molecular compounds,[3] some of which have been shown to behave as molecular machines[4] and switches[5] on surfaces and at interfaces, respectively. We have developed a template-directed[6] protocol for the construction of [2]catenanes[7] composed of a crown ether containing π-electron-rich aromatic ring systems and a tetracationic cyclophane comprised of two π-electron-deficient bipyridinium units. The kinetically controlled protocol relies on employing the crown ether as the template, around which the cyclophane is formed[8] from reaction of a dicationic salt with *para*-xylylene dibromide. If the crown ether is covalently tethered to this second molecule, then the resulting cyclization(s) could occur either intramolecularly and generate a pretzelane[9] or intermolecularly and generate cyclic or linear oligo/polycatenanes (Figure 1).

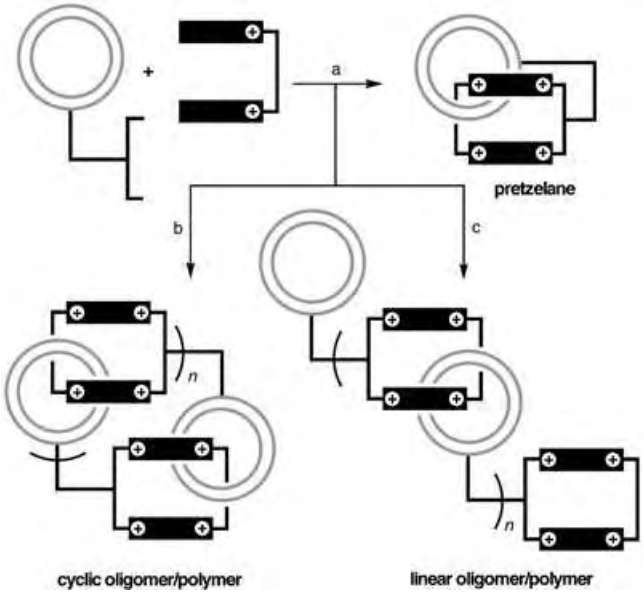

Figure 1. Graphical representations of the formation of a) a pretzelane, b) a cyclic polycatenane, and c) a linear polycatenane. The gray components are π-electron rich and the black (charged) components are π-electron deficient.

Herein, we report the synthesis of two *para*-xylylene dibromide derivatives, which have the same crown ether component[10] tethered by different linkers, and describe the outcome of their reactions with the dicationic salt. It transpires that, when the dibromide contains a longer—and more flexible—linker, a pretzelane is obtained in good yields, as suggested by (dynamic) ^{1}H NMR spectroscopic analyses in solution and confirmed by X-ray crystallographic studies in the solid state. By contrast, when the dibromide contains a shorter—and less flexible—linker, a cyclic bis[2]catenane[11] is obtained as the major product, along with lesser amounts of a pretzelane.

The synthesis of the pretzelanes **7**·4 PF_6 and **10**·4 PF_6 and the cyclic bis[2]catenane **11**·8 PF_6 are outlined in Schemes 1 and 2. Reaction of **1**,[12] which contains a symmetrically positioned carboxyl group, with an excess of **2** gave the alcohol **3**; subsequent esterification of this alcohol with another carboxylic acid derivative **4**[13] afforded the dibromide

[*] Dr. Y. Liu, Prof. P. A. Bonvallet,[+] S. A. Vignon, Dr. S. I. Khan, Prof. J. F. Stoddart
California NanoSystems Institute and
Department of Chemistry and Biochemistry
University of California, Los Angeles
405 Hilgard Avenue, Los Angeles, CA 90095-1569 (USA)
Fax: (+1) 310-206-1843
E-mail: stoddart@chem.ucla.edu

[+] Present address:
Department of Chemistry
College of Wooster, 943 College Mall
Wooster, OH 44691-2363 (USA)

[**] This work was supported by the Defense Advanced Research Projects Agency (DARPA) and the National Science Foundation (NSF) under equipment grants CHE-9974928 and CHE-0092036.

Supporting information for this article is available on the WWW under http://www.angewandte.org or from the author.

  DOI: 10.1002/anie.200500041

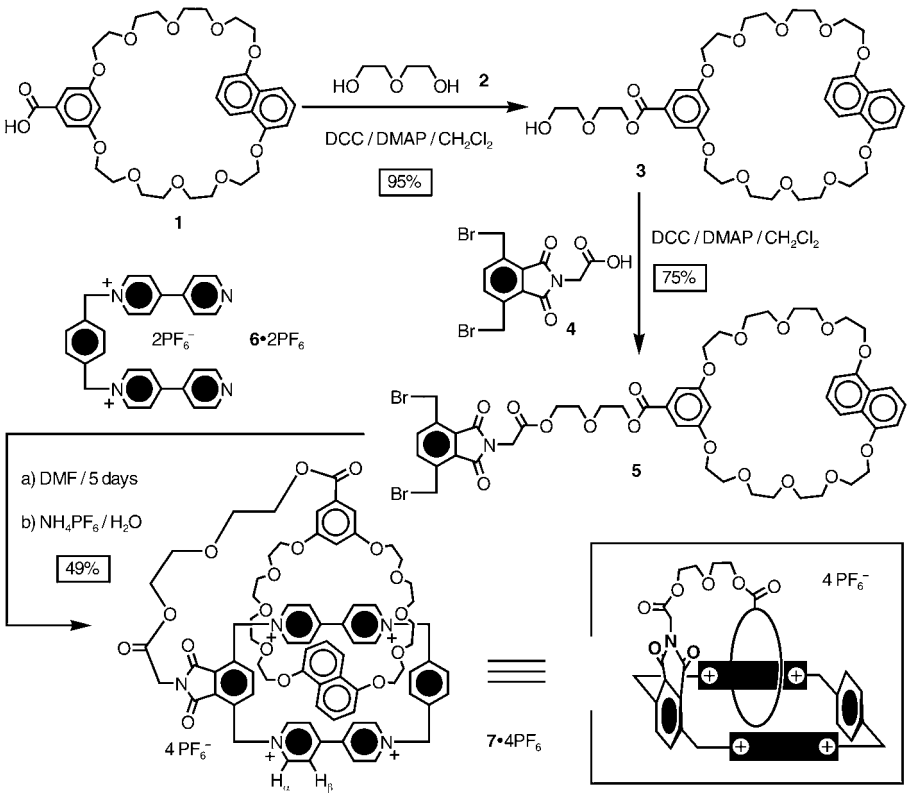

Scheme 1. The synthesis of the pretzelane **7**·4 PF_6. DCC = *N*,*N*′-dicyclohexylcarbodiimide, DMAP = 4-dimethylaminopyridine.

5 as the key intermediate. Formation of **7**·4 PF_6 was achieved in 49% yield by stirring **5** and **6**·2 PF_6[8a] in DMF (*N*,*N*′-dimethylformamide) for five days and then exchanging the counterions. In a similar fashion, the crown ether appended dibromide **9** was obtained from esterification of the crown ether **8**,[14] which carried a hydroxymethyl group, with the carboxylic acid derivative **4**. Treatment of **9** with **6**·2 PF_6 afforded a mixture of **10**·4 PF_6 and **11**·8 PF_6 in yields of 14 and 20%, respectively, after counterion exchange and column chromatography.

The pretzelane **7**·4 PF_6 contains (Figure 2) two elements of chirality, namely, planar chirality associated with the 1,5-dioxynaphthalene (DNP) ring system and helical chirality[15] arising from the relative positioning of the two interlocked rings. This helicity results from the breaking of symmetry in the tetracationic cyclophane by the phthalimido unit. It can be inverted by rotation of this phthalimido unit (process II) or by partial pirouetting of the crown ether (process III). The combination of these two chiral elements gives rise to two enantiomeric pairs of diastereoisomers. One enantiomeric pair, namely, (*pR*)-(*P*)-$\mathbf{7}^{4+}$ and (*pS*)-(*M*)-$\mathbf{7}^{4+}$, is characterized by having the oxygen atom on

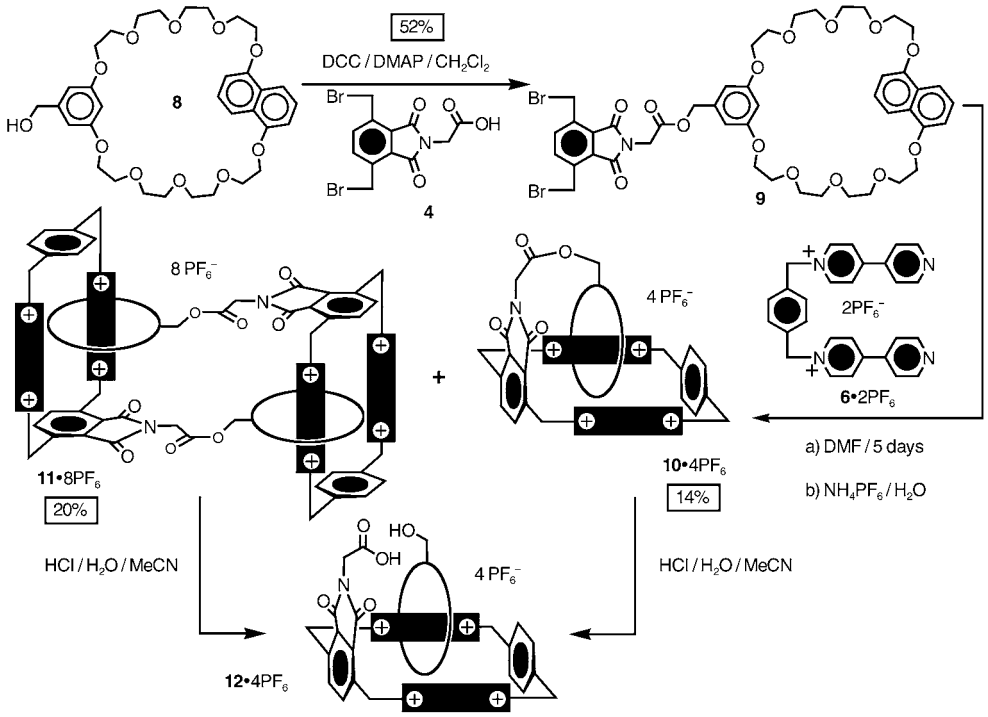

Scheme 2. The synthesis of the pretzelane **10**·4 PF_6 and the cyclic bis[2]catenane **11**·8 PF_6, followed by the hydrolysis of their esters to generate the common [2]catenane **12**·4 PF_6.

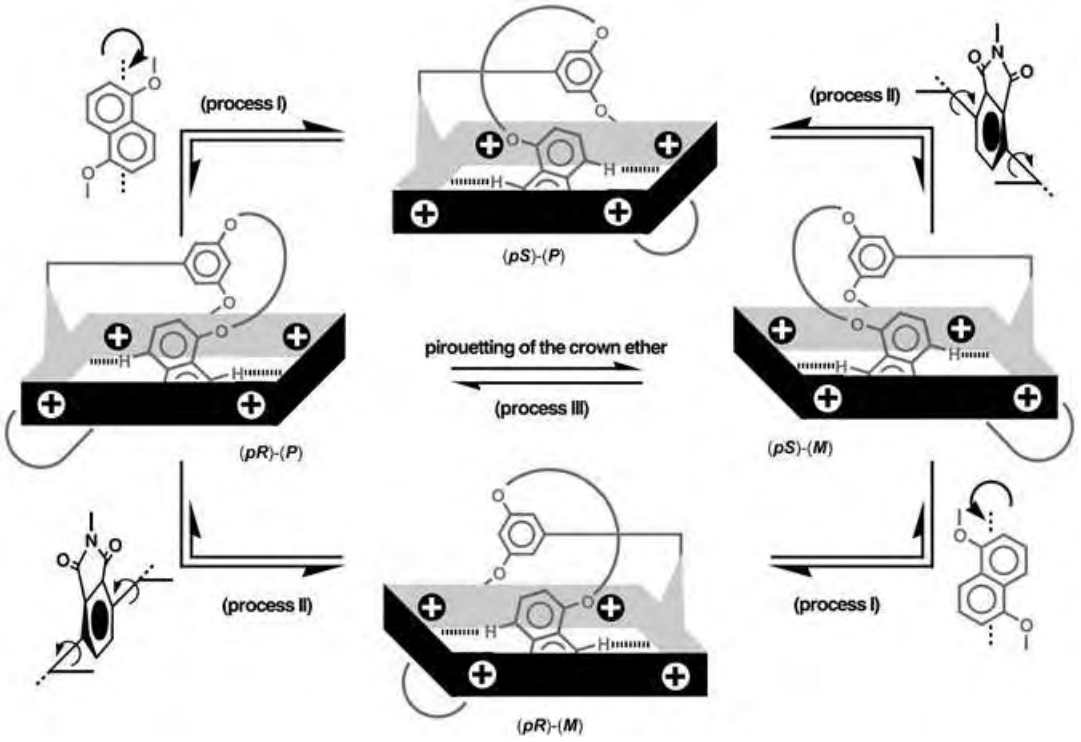

Figure 2. Graphical representations of the four possible stereoisomers of the pretzelane $\mathbf{7}^{4+}$ and the three possible dynamic processes (I, II, and III) associated with their interconversion.

the DNP ring system, which resides on the same side of the mean plane of the tetracationic cyclophane as the diimide group, pointing away from this functional group. In the case of the other enantiomeric pair, (*pS*)-(*P*)-$\mathbf{7}^{4+}$ and (*pR*)-(*M*)-$\mathbf{7}^{4+}$, this oxygen atom points toward the diimide group. Not surprisingly, the (*pR*)-(*P*) diastereoisomer is more stable than the (*pS*)-(*P*) isomer.

The X-ray structural analysis[16,17] of a single crystal obtained by vapor diffusion of $i\mathrm{Pr}_2\mathrm{O}$ into a solution of $\mathbf{7}\cdot 4\,\mathrm{PF}_6$ in MeCN identified the solid-state structure as containing an enantiomeric pair of molecules, namely, (*pR*)-(*P*)-$\mathbf{7}^{4+}$ and (*pS*)-(*M*)-$\mathbf{7}^{4+}$, and confirmed their pretzel-shaped topology (Figure 3). The tetracationic cyclophane is interlocked with the crown ether such that 1) the DNP ring system is sandwiched between the two bipyridinium units, aligned parallel to each other, with 2) one of these two units also sandwiched between the DNP ring system, also parallel, and the resorcinol ring, which is positioned alongside. The mean interplanar separations are 3.4 Å, in keeping with stabilizing π–π-stacking interactions. The conformation of the molecule is also stabilized by CH···O interactions[18] between two of the α protons on the inside bipyridinium unit and the nearby oxygen atoms in the two polyether loops of the crown ether. Furthermore, the molecular conformation is stabilized by yet another CH···O interaction between one of the oxygen atoms in the diethylene glycol linker and one of the hydrogen atoms on the appropriate methylene group at the corner of the tetracationic cyclophane. In addition, there are CH···π interactions between the naphthalene hydrogen atoms on C4 and C8 and their proximal *para*-phenylene rings. There are no discernable intermolecular stacking interactions.

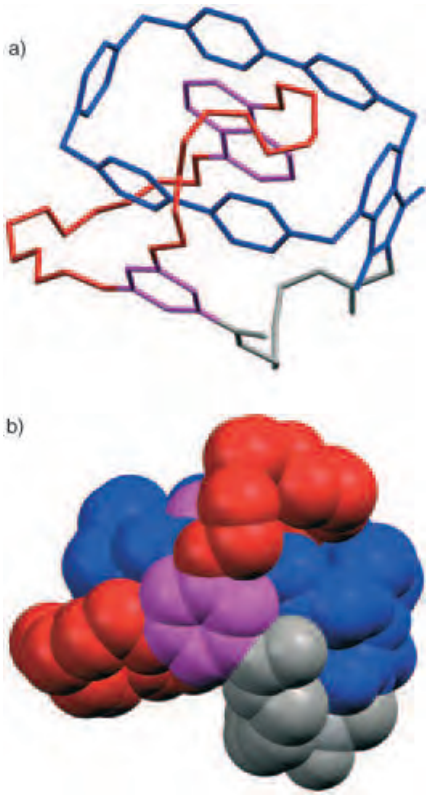

Figure 3. X-ray crystal structure of the pretzelane $\mathbf{7}^{4+}$ illustrated as a) framework and b) space-filling representations of the pretzelane. Purple: the π-donor units in the crown ether; red: the polyethylene glycol chains in the crown ether, blue: the tetracationic cyclophane; gray: the diethylene glycol chain connecting the two macrocycles.

The partial ^{1}H NMR spectrum of (Figure 4a) **7**·4 PF_6, recorded in CD_3CN, can be interpreted as a racemic modification of a single diastereoisomer. The relative stereochemistry and topology of this diastereoisomer can be

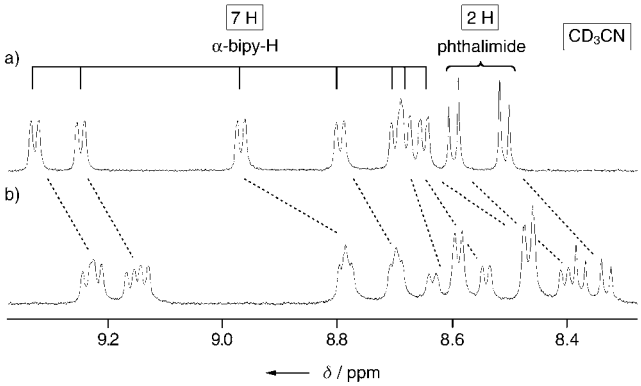

Figure 4. Partial ^{1}H NMR spectra, recorded in CD_3CN at room temperature, showing a) the signals for α-bipyridinium (bipy) and phthalimide protons in **7**·4 PF_6 and b) the change on addition of four equivalents of the chiral shift reagent Me_2NH_2·(*R*)-BINPHAT.

assigned by 2D ROESY spectroscopic analysis[19] to be the same one ((*pR*)-(*P*)-$\mathbf{7}^{4+}$/(*pS*)-(*M*)-$\mathbf{7}^{4+}$) as that observed in the solid state. The presence of these enantiomers was confirmed by recording the ^{1}H NMR spectrum (Figure 4b) in CD_3CN in the presence of a chiral shift reagent, dimethyl ammonium bis(tetrachlorobenzenediolato)mono((*R*)-[1,1′]-binaphthalenyl-2,2′-diolato)phosphate(v)[20] (Me_2NH_2·(*R*)-BINPHAT). Addition of four equivalents of Me_2NH_2·(*R*)-BINPHAT to a solution of **7**·4 PF_6 in CD_3CN results in the resonances for seven of the eight α-bipyridinium protons and the two phthalimido protons not only undergoing changes in chemical shift but also separating into two independent sets of equal intensity signals, which is commensurate with the formation of diastereoisomeric salts in approximately equal amounts.

Dynamic ^{1}H NMR spectroscopic analysis was performed on this pretzelane in CD_3SOCD_3. At room temperature, all of the protons are heterotopic and so give rise to well-resolved signals, thus indicating that any degenerate exchange processes are slow on the ^{1}H NMR timescale. Heating a CD_3SOCD_3 solution of **7**·4 PF_6 up to 120 °C (Figure 5a–d) causes the resonances[21] to begin to coalesce as a result of several site-exchange processes, including 1) reorientation (process I) of the DNP ring system outside the cyclophane's cavity, 2) a 180° rotation (process II) of the phthalimido unit about the $-CH_2ArCH_2-$ axis, and 3) pirouetting (process III) of the crown ether whereby its resorcinol unit moves from one bipyridinium unit around the tetracationic cyclophane to the other one. Since neither process I nor II are associated with degeneracy, they must occur as a pair, namely, processes I + II. The occurrence of this highly coordinated process is not unreasonable on the basis of a molecular modeling study: it suggests that the DNP ring system has to leave the cyclophane's cavity so that process II can occur.

Probe protons were chosen in $\mathbf{7}^{4+}$ to measure kinetic and thermodynamic data separately for processes I + II and

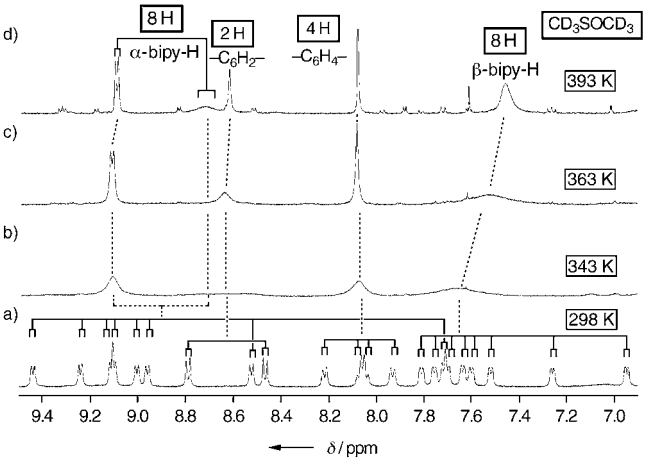

Figure 5. Partial ^{1}H NMR spectra of a solution of **7**·4 PF_6 in CD_3COCD_3 at a) 298, b) 343, c) 363, and d) 393 K, thus indicating the coalescence of the α- and β-bipyridinium protons and the phenylene protons. The unmarked, low-intensity peaks observed at 393 K are a result of decomposition of **7**·4 PF_6 at this temperature.

process III. The two diastereotopic protons on the 5-substituted resorcinol ring only undergo site exchange when processes I and II operate in tandem, while the two diastereotopic protons on the phthalimido unit experience site exchange as a result of process III. Spin-saturation transfer experiments[22] performed at 301 K on these two pairs of probe protons gave[23] ΔG values of 17.5 and 17.6 kcal mol^{-1}. The fact that these free energy barriers ($\Delta G^{\neq}$) are virtually identical (within experimental error) suggests that one process (I) is rate-limiting and that one or both of the other two processes (II and III) follow quickly.

In the case of **10**·4 PF_6 and **11**·8 PF_6, ESI mass spectrometry provided unambiguous evidence for their monomer–dimer relationship. Although they both reveal peaks at *m*/*z* 1681, 768, and 464 (Table 1), the charges carried by these ion fragments are different: the peaks for the former (**10**·4 PF_6) are singly, doubly, and triply charged, thus corresponding to the loss of one, two, and three PF_6^- ions, respectively, from a pretzelane-like constitution with a molar mass of 1826 Da, while the peaks for the latter (**11**·8 PF_6) are doubly, quadruply, and sextuply charged, thus corresponding to the loss of two, four, and six PF_6^- ions,[24] respectively, from a compound with a molar mass of 3652 Da

Table 1: Characterization[a] of **10**·4 PF_6 and **11**·8 PF_6 by ESI mass spectrometry.

Compounds	Number of PF_6^- counterions lost						
	1	2	3	4	5	6	7
10·4 PF_6	1681	768	464	312	–	–	–
(M_r = 1826)	(0.5)	(61)	(100)	(31)			
11·8 PF_6	–	1681	1072	768	586	464	377
(M_r = 3652)		(0.5)	(15)	(100)	(78)	(84)	(18)

[a] Data are presented as *m*/*z* ratio and (relative abundance (%)). Molecular weight and *m*/*z* values apply to the average mass of any isotope distribution and are based on a scale in which ^{12}C = 12.000.

and the constitution of a cyclic bis[2]catenane. To verify their mechanically interlocked topology, both compounds were subjected to acid-catalyzed hydrolysis of the ester linkage between the macrocyclic polyether and the tetracationic cyclophane. Heating **10**·4 PF_6 and **11**·8 PF_6 in CD_3CN/D_2O solutions at 70 °C for one day in the presence of one drop of HCl afforded a single product,[25] namely, the [2]catenane **12**·4 PF_6 in each case. These observations provide chemical proofs of the mechanically interlocked topologies of **10**·4 PF_6 and **11**·8 PF_6.

This exploratory study has established that the pretzelane topology can be generated[26] using appropriately CH···O-augmented donor–acceptor interactions as the recognition motif for templating the syntheses of dynamic pretzelanes. The fact that the barrier to enantiomerization between (*pR*)-(*P*)-**7**$^{4+}$ and (*pS*)-(*M*)-**7**$^{4+}$ is approximately 17.5 kcal mol^{-1} augurs well for introducing electrochemically switchable, metastable diastereoisomerism into bistable pretzelanes in which one of the bipyridinium units in the tetracationic cyclophane is replaced with a chemically modified one.

Experimental Section

7·4 PF_6: A solution of **5**[27] (0.45 g, 0.41 mmol) and the dicationic salt **6**·2 PF_6[8a] (0.39 g, 0.55 mmol) in DMF (10 mL) was stirred at room temperature for 5 days. Diethyl ether (200 mL) was added to the reaction mixture to ensure precipitation of the crude product. The precipitate was isolated by vacuum filtration and subjected to column chromatography on silica gel (MeOH/aqueous NH_4Cl (2 M)/$MeNO_2$, 7:2:1). Purple fractions containing the product were combined and concentrated. Solid NH_4PF_6 was added to the residue to precipitate **7**·4 PF_6 as a purple solid (0.39 g, 49 %). M.p. 195 °C (decomp); ^{1}H NMR (CD_3CN, 500 MHz, 298 K): δ = 9.27 (d, J = 6.6 Hz, 1 H), 9.19 (d, J = 6.6 Hz, 1 H), 8.88 (d, J = 6.6 Hz, 1 H), 8.73 (d, J = 6.6 Hz, 1 H), 8.65–8.59 (m, 3 H), 8.54 (d, J = 8.3 Hz, 1 H), 8.43 (d, J = 8.3 Hz, 1 H), 8.05 (d, J = 8.1 Hz, 1 H), 8.00–7.92 (m, 3 H), 7.43 (dd, J = 8.1, 2.4 Hz, 1 H), 7.41 (dd, J = 8.1, 2.4 Hz, 1 H), 7.38 (dd, J = 8.1, 2.4 Hz, 1 H), 7.36 (dd, J = 8.1, 2.4 Hz, 1 H), 7.28 (dd, J = 8.1, 2.4 Hz, 1 H), 7.27 (dd, J = 8.1, 2.4 Hz, 1 H), 7.00 (dd, J = 8.1, 2.4 Hz, 1 H), 6.95 (t, J = 1.5 Hz, 1 H), 6.81 (t, J = 1.5 Hz, 1 H), 6.67 (d, J = 13.7 Hz, 1 H), 6.62–6.60 (m, 2 H), 6.29 (d, J = 7.9 Hz, 1 H), 6.24 (d, J = 7.9 Hz, 1 H), 6.02 (t, J = 7.9 Hz, 1 H), 5.91–5.85 (m, 3 H), 5.78–5.73 (m, 4 H), 5.71 (t, J = 1.5 Hz, 1 H), 5.61 (t, J = 7.9 Hz, 1 H), 4.86 (d, J = 17.1 Hz, 1 H), 4.83 (dd, J = 12.5, 2.5 Hz, 1 H), 4.62 (dd, J = 12.5, 2.5 Hz, 1 H), 4.54 (d, J = 17.1 Hz, 1 H), 4.52–3.45 (m, 36 H), 3.29 (dd, J = 11.4, 2.5 Hz, 1 H), 3.07 (dd, J = 11.4, 2.5 Hz, 1 H), 2.50 (d, J = 8.1 Hz, 1 H), 2.44 ppm (d, J = 8.1 Hz, 1 H); MS(ESI): m/z 1783.4 $[M-PF_6]^+$, 818.9 $[M-2PF_6]^{2+}$, 497.6 $[M-3PF_6]^{3+}$; HRMS(ESI): m/z calcd for $C_{77}H_{81}N_5O_{17}P_3F_{18}$ $[M-PF_6]^+$: 1782.4547, found: 1782.4559.

10·4 PF_6 and **11**·8 PF_6: A solution of **9**[27] (0.31 g, 0.31 mmol) and **6**·2 PF_6[8a] (0.22 g, 0.31 mmol) in DMF (10 mL) was stirred at room temperature for 5 days. The solvent was removed under reduced pressure and the residue was subjected to column chromatography on silica gel. The fractions containing **10**·4 PF_6 were collected using MeOH/aqueous NH_4Cl (2 M)/$MeNO_2$ (7:2:1) as the eluent. The second set of fractions, containing **11**·8 PF_6, were collected using MeOH/aqueous NH_4Cl (2 M)/$MeNO_2$ (2:2:1) as the eluent. Solid NH_4PF_6 was added to the residues to precipitate **10**·4 PF_6 (76 mg, 14 %) and **11**·8 PF_6 (113 mg, 20 %) as brown solids.

10·4 PF_6: M.p. 232 °C (decomp); ^{1}H NMR ([D_6]DMSO, 500 MHz, 363 K): δ = 9.13–9.06 (m, 6 H), 8.69 (s, 2 H), 8.38 (br s, 2 H), 8.12 (s, 4 H), 7.83 (br s, 2 H), 7.81 (d, J = 7.9 Hz, 2 H), 7.66 (d, J = 6.6 Hz, 2 H), 7.59 (m, 4 H), 7.37 (t, J = 7.9 Hz, 2 H), 6.97 (d, J = 7.9 Hz, 2 H), 6.64 (br s, 2 H), 6.44 (s, 1 H), 6.22–5.80 (m, 8 H), 5.30–3.44 ppm (m, 36 H).

11·8 PF_6: M.p. 244 °C (decomp); ^{1}H NMR ([D_6]DMSO, 500 MHz, 363 K): δ = 9.22 (d, J = 6.4 Hz, 8 H), 9.01–8.78 (m, 8 H), 8.78 (s, 4 H), 8.17 (s, 8 H), 7.84–7.60 (m, 12 H), 7.10–6.93 (m, 4 H), 6.53 (s, 4 H), 6.35 (br s, 4 H), 6.30 (d, J = 8.3 Hz, 8 H), 5.90 (br. s, 8 H), 5.83 (br s, 4 H), 5.49 (s, 2 H), 5.34 (s, 4 H), 5.07 (s, 4 H), 4.45 (br s, 8 H), 4.28 (br s, 8 H), 4.11 (br s, 8 H), 4.01 (br s, 8 H), 3.93–3.46 (m, 32 H), 2.58 ppm (d, J = 8.3 Hz, 4 H).

Received: January 6, 2005
Published online: April 14, 2005

Keywords: catenanes · molecular devices · pretzelanes · self-assembly · template synthesis

[1] a) J. S. Lindsey, *New J. Chem.* **1991**, *15*, 153 – 180; b) D. Philp, J. F. Stoddart, *Angew. Chem.* **1996**, *108*, 1242 – 1286; *Angew. Chem. Int. Ed. Engl.* **1996**, *35*, 1154 – 1196; c) D. N. Reinhoudt, M. Crego-Calama, *Science* **2002**, *295*, 2403 – 2407.

[2] M. C. T. Fyfe, J. F. Stoddart, *Acc. Chem. Res.* **1997**, *30*, 393 – 401.

[3] a) G. Schill, *Catenanes, Rotaxanes, and Knots*, Academic Press, New York, **1971**; b) *Molecular Catenanes, Rotaxanes, and Knots* (Eds.: J.-P. Sauvage, C. Dietrich-Buchecker), Wiley-VCH, Weinheim, **1999**.

[4] a) V. Balzani, A. Credi, F. M. Raymo, J. F. Stoddart, *Angew. Chem.* **2000**, *112*, 3484 – 3530; *Angew. Chem. Int. Ed.* **2000**, *39*, 3348 – 3391; b) V. Balzani, A. Credi, M. Venturi, *Molecular Devices and* Machines—A *Journey into the Nano World*, Wiley-VCH, Weinheim, **2003**; c) A. H. Flood, R. J. A. Ramirez, W.-Q. Deng, R. P. Muller, W. A. Goddard III, J. F. Stoddart, *Aust. J. Chem.* **2004**, *57*, 301 – 322.

[5] a) D. W. Steuerman, H.-R. Tseng, A. J. Peters, A. H. Flood, J. O. Jeppesen, K. A. Nielsen, J. F. Stoddart, J. R. Heath, *Angew. Chem.* **2004**, *116*, 6648 – 6653; *Angew. Chem. Int. Ed.* **2004**, *43*, 6486 – 6491; b) A. H. Flood, A. J. Peters, S. A. Vignon, D. W. Steuerman, H.-R. Tseng, S. Kang, J. R. Heath, J. F. Stoddart, *Chem. Eur. J.* **2004**, *10*, 6558 – 6564; c) A. H. Flood, J. F. Stoddart, D. W. Steuerman, J. R. Heath, *Science* **2004**, *306*, 2055 – 2056.

[6] a) *Templated Organic Synthesis* (Eds.: F. Diederich, P. J. Stang), Wiley-VCH, Weinheim, **1999**; b) J. F. Stoddart, H.-R. Tseng, *Proc. Natl. Acad. Sci. USA* **2002**, *99*, 4797 – 4800.

[7] a) P.-L. Anelli, P. R. Ashton, R. Ballardini, V. Balzani, M. Delgado, M. T. Gandolfi, T. T. Goodnow, A. E. Kaifer, D. Philp, M. Pietraszkiewicz, L. Prodi, M. V. Reddington, A. M. Z. Slawin, N. Spencer, J. F. Stoddart, C. Vicent, D. J. Williams, *J. Am. Chem. Soc.* **1992**, *114*, 193 – 218; b) H.-R. Tseng, S. A. Vignon, P. C. Celestre, J. F. Stoddart, A. J. P. White, D. J. Williams, *Chem. Eur. J.* **2003**, *9*, 543 – 556.

[8] a) M. Asakawa, W. Dehaen, G. L'abbé, S. Menzer, J. Nouwen, F. M. Raymo, J. F. Stoddart, D. J. Williams, *J. Org. Chem.* **1996**, *61*, 9591 – 9595; b) G. Doddi, G. Ercolani, S. Franconeri, P. Mencarelli, *J. Org. Chem.* **2001**, *66*, 4950 – 4953; c) G. Ercolani, P. Mencarelli, *J. Org. Chem.* **2003**, *68*, 6472 – 6473; d) C. D'Acerno, G. Doddi, G. Ercolani, S. Franconeri, P. Mencarelli, A. Piermattei, *J. Org. Chem.* **2004**, *69*, 1393 – 1396.

[9] a) R. Jäger, T. Schmidt, D. Karbach, F. Vögtle, *Synlett* **1996**, *8*, 723 – 725; b) C. Yamamoto, Y. Okamoto, T. Schmidt, R. Jäger, F. Vögtle, *J. Am. Chem. Soc.* **1997**, *119*, 10547 – 10548; c) F. Vögtle, O. Safarowsky, C. Heim, A. Affeld, O. Braun, A. Mohry, *Pure Appl. Chem.* **1999**, *71*, 247 – 251; d) A. Mohry, H. Schwierz, F. Vögtle, *Synthesis* **1999**, *10*, 1753 – 1758; e) C. Heim, D. Udelhofen, F. Vögtle in *Molecular Catenanes, Rotaxanes and Knots* (Ed.: J.-P. Sauvage, C. Dietrich-Buchecker), Wiley-VCH, **1999**, pp. 177 – 222; f) C. Reuter, A. Mohry, A. Sobanski, F. Vögtle, *Chem. Eur. J.* **2000**, *6*, 1674 – 1682; g) Y. Qian, E. Vogel, A. H. Parham, M. Nieger, M. Bolte, R. Fröhlich, P. Saarenketo, K.

Rissanen, F. Vögtle, *Eur. J. Org. Chem.* **2001**, *21*, 4041 – 4049; h) M. O. Vysotsky, M. Bolte, I. Thondorf, V. Böhmer *Chem. Eur. J.* **2003**, *9*, 3375 – 3382.

[10] Q. Zhang, D. G. Hamilton, N. Feeder, S. J. Teat, J. M. Goodman, J. K. M. Sanders, *New J. Chem.* **1999**, *23*, 897 – 903.

[11] Acyclic bis[2]catenanes are known; for example: a) P. R. Ashton, A. S. Reder, N. Spencer, J. F. Stoddart, *J. Am. Chem. Soc.* **1993**, *115*, 5286 – 5287; b) P. R. Ashton, J. A. Preece, J. F. Stoddart, M. S. Tolley, *Synlett* **1994**, 789 – 792; c) P. R. Ashton, J. Huff, I. W. Parsons, J. A. Preece, J. F. Stoddart, M. S. Tolley, D. J. Williams, A. J. P. White, *Chem. Eur. J.* **1996**, *2*, 123 – 136; d) N. Armaroli, M. A. J. Rodgers, P. Ceroni, V. Balzani, C. O. Dietrich-Buchecker, J.-M. Kern, A. Bailal, J.-P. Sauvage, *Chem. Phys. Lett.* **1995**, *241*, 555 – 558.

[12] S. Menzer, A. J. P. White, D. J. Williams, M. Belohradsky, C. Hamers, F. M. Raymo, A. N. Shipway, J. F. Stoddart, *Macromolecules* **1998**, *31*, 295 – 307.

[13] Y. Liu, A. H. Flood, R. M. Moskowitz, J. F. Stoddart, *Chem. Eur. J.* **2005**, *11*, 369 – 385.

[14] P. R. Ashton, I. Baxter, S. J. Cantrill, M. C. T. Fyfe, P. T. Glink, J. F. Stoddart, A. J. P. White, D. J. Williams, *Angew. Chem.* **1998**, *110*, 1344 – 1347; *Angew. Chem. Int. Ed.* **1998**, *37*, 1294 – 1297.

[15] For a discussion of the chirality and the assignment of absolute chiralities to helices and planes, see the Supporting Information.

[16] CCDC-258912 contains the supplementary crystallographic data for this paper. These data can be obtained free of charge from the Cambridge Crystallographic Data Centre via www.ccdc.cam.ac.uk/data_request/cif.

[17] Crystal data for compound **7**·4 PF_6 ($C_{77}H_{81}N_5O_{17}P_4F_{24}$·5 MeCN): $M_r = 2133.62$, triclinic, space group $P\bar{1}$, $a = 14.443(1)$, $b = 14{,}692(1)$, $c = 24.274(2)$ Å, $\alpha = 96.324(1)$, $\beta = 95.790(1)$, $\gamma = 110.893(1)°$, $V = 4728.4(6)$ Å^3, $T = 120$ K, $Z = 2$, red platelike needles of approximate size $0.4 \times 0.2 \times 0.18$ mm, $\rho_{calcd} = 1.499$ g cm^{-3}, $\mu(Mo_{K\alpha}) = 0.198$ mm^{-1}, 42 599 reflection measured on Bruker Smart 1000 CCD diffractometer. 22 159 independent reflections, semi-empirical absorption correction from equivalents, F^2 refinement, 1355 parameters, R_1/wR_2 $[I > 2\sigma(I)] = 0.08/0.23$, $R_1/wR_2 = 0.11/0.26$ (all data).

[18] F. M. Raymo, M. D. Bartberger, K. N. Houk, J. F. Stoddart, *J. Am. Chem. Soc.* **2001**, *123*, 9264 – 9267.

[19] The assignment of relative stereochemistry to the more stable diastereoisomer of **7**·4 PF_6 using 2D ROESY is described in the Supporting Information. Also, the fact that the H-4 and H-8 protons on the dioxynaphthalene unit resonate at very high field ($\delta = 2.25$ and 2.28 ppm) indicates that this ring system is located inside the cavity of the tetracationic cyclophane.

[20] J. Lacour, A. Londez, C. Goujon-Ginglinger, V. Buss, G. Bernardinelli, *Org. Lett.* **2000**, *2*, 4185 – 4188.

[21] The pretzelane **7**·4 PF_6 begins to decompose at 120 °C in CD_3SOCD_3 solution.

[22] a) M. Feigel, H. Kessler, D. Leibfritz, *J. Am. Chem. Soc.* **1979**, *101*, 1943 – 1950; b) B. E. Mann, *J. Magn. Reson.* **1977**, *25*, 91 – 94.

[23] $\Delta G^{\neq}$ values were calculated from the rate constants k_{ex} by using the Eyring equation $\Delta G^{\neq} = R T_c \ln(k_{ex} h / k_b T_c)$, in which R is the gas constant, h is the Planck constant, and k_b is the Boltzmann constant.

[24] Furthermore, the ESI mass spectrometry of **11**·8 PF_6 also contains peaks showing the loss of three, five, and seven PF_6^- ions.

[25] The synthesis and characterization of the common [2]catenane **12**·4 PF_6 are described in the Supporting Information.

[26] A comparison of the outcomes summarized in Schemes 1 and 2 indicated that the length of the tether between the crown ether and the tetracationic cyclophane is a key parameter in determining the results of the template-directed cyclization. The longer and more flexible linker (Scheme 1) favors pretzelane formation. Higher homologues are not observed, thus reflecting the well-established fact that the entropic cost associated with generating polymeric assemblies as a result of the kinetically controlled supramolecular assistance to covalent synthesis is simply too high: small cycles are much preferred over large ones and their acyclic counterparts; see: a) R. Kramer, J.-M. Lehn, A. Marquis-Rigault, *Proc. Natl. Acad. Sci. USA* **1993**, *90*, 5394 – 5398; b) P. R. Ashton, A. N. Collins, M. C. T. Fyfe, P. T. Glink, S. Menzer, J. F. Stoddart, D. J. Williams, *Angew. Chem.* **1997**, *109*, 59 – 62; *Angew. Chem. Int. Ed. Engl.* **1997**, *36*, 59 – 62; c) D. L. Caulder, K. N. Raymond, *Angew. Chem.* **1997**, *109*, 1508 – 1510; *Angew. Chem. Int. Ed. Engl.* **1997**, *36*, 1440 – 1442; d) S. J. Cantrill, G. J. Youn, J. F. Stoddart, D. J. Williams, *J. Org. Chem.* **2001**, *66*, 6857 – 6872.

[27] The syntheses of **5** and **9** are described in the Supporting Information.

Asymmetric Catalysis

Design of an Axially Chiral Amino Acid with a Binaphthyl Backbone as an Organocatalyst for a Direct Asymmetric Aldol Reaction**

*Taichi Kano, Jun Takai, Osamu Tokuda, and Keiji Maruoka**

The direct catalytic asymmetric aldol reaction is one of the most fundamental transformations in organic synthesis, and several efficient asymmetric methodologies for this reaction using chiral metal catalysts[1] and organocatalysts[2–4] have recently been developed, of which catalysis by proline[2,3] and its derivatives[4] have been extensively explored. However, the reactivity and selectivity of some of these proline-catalyzed aldol reactions have serious limitations because of the difficulty in structurally modifying proline. Furthermore, a substoichiometric amount of proline is often necessary to achieve reasonable yields in the direct aldol reaction of aldehydes with acetone. Also, proline is known to react with electron-deficient aromatic aldehydes to form iminium salts, which undergo decarboxylation, even at room temperature.[5] Such degradation may induce the significant retardation of the proline-catalyzed aldol reactions. In this context, we were interested in designing an artificial amino acid catalyst **1** that would not undergo undesirable degradation through decar-

[*] Dr. T. Kano, J. Takai, O. Tokuda, Prof. K. Maruoka
Department of Chemistry
Graduate School of Science, Kyoto University
Sakyo, Kyoto 606-8502 (Japan)
Fax: (+81) 75-753-4041
E-mail: maruoka@kuchem.kyoto-u.ac.jp

[**] This work was partially supported by a Grant-in-Aid for Scientific Research from the Ministry of Education, Culture, Sports, Science, and Technology, Japan. We thank Tanabe Seiyaku Co., Ltd. (Japan) for providing (±)-1,1′-binaphthyl-2,2′-dicarboxylic acid.

Supporting information for this article is available on the WWW under http://www.angewandte.org or from the author.

 DOI: 10.1002/anie.200500408

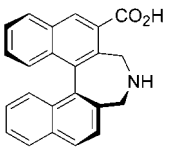

(*S*)-**1**

boxylation. Herein, we report a novel, robust amino acid catalyst **1** and its successful application to the direct asymmetric aldol reaction.

The requisite amino acid (*S*)-**1** was based on binaphthalene and prepared in a seven-step sequence from dineopentyl 1,1′-binaphthyl-2,2′-dicarboxylate ((*S*)-**2**; Scheme 1). The efficiency of this new catalyst was evaluated with the direct asymmetric aldol reaction: Reaction of 4-nitrobenzaldehyde with acetone was carried out in the

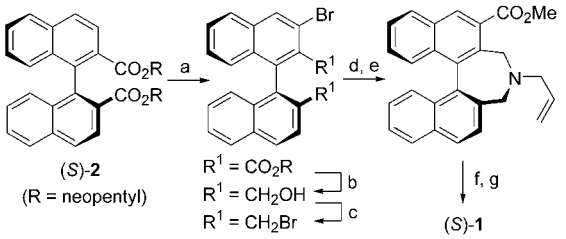

Scheme 1. Synthesis of (*S*)-**1**. Conditions: a) $Mg(TMP)_2$, THF; then Br_2; b) LAH, THF; c) BBr_3, CH_2Cl_2; d) allylamine, CH_3CN; e) 5 mol% $Pd(OAc)_2$, dppp, iPr_2NEt, CO, DMSO, MeOH; f) $Pd(OAc)_2$, PPh_3, *N*,*N*-dimethylbarbituric acid, CH_2Cl_2; g) 1 M NaOH, MeOH–THF. TMP = 2,2,6,6-tetramethylpiperidine, dppp = 1,3-bis(diphenylphosphino)propane.

presence of 5 mol% of (*S*)-**1** at room temperature in dimethyl sulfoxide (DMSO) and the aldol adduct **3** was afforded in 70% yield and 93% *ee* (Table 1, entry 1). In contrast, the reaction with L-proline under the same reaction conditions gave **3** in low yield with moderate enantioselectivity, together with 1,3-oxazolidine **4** (48% yield based on proline) derived from proline and two equivalents of 4-nitrobenzaldehyde (entry 2). It should be noted that the formation of such a by-product was not observed with **1** because of its structural stability. We also examined the solvent effect in this reaction: Changing the solvent from DMSO to acetonitrile gave **3** in low yield with slightly higher enantioselectivity (entry 3), whereas the use of amide solvents, such as *N*-methylpyrrolidone (NMP) and *N*,*N*-dimethylformamide (DMF), gave improved yields with high enantioselectivities (entries 4 and 5).

After establishing the optimal reaction conditions, the direct asymmetric aldol reaction of other electron-deficient aldehydes with acetone was carried out (Table 2). Olefinic, heteroaromatic, and aromatic aldehydes were found to be suitable substrates, with the direct aldol reactions generally giving the corresponding aldol adducts in moderate to good yields. Furthermore, excellent enantioselectivities were observed in most cases (> 95% *ee*).

The spatial distance between the amino and carboxyl groups for (*S*)-**1** was determined by MM2 calculations using CS Chem3D, and was shown to be longer than that for L-proline (Figure 1).

In summary, we have shown that the binaphthyl-based amino acid **1** is an efficient catalyst for direct asymmetric aldol reactions of aldehydes with acetone. Most successful organic catalysts for various asymmetric reactions are derived from chiral natural products, such as amino acids and

Table 1: Direct asymmetric aldol reaction of 4-nitrobenzaldehyde with acetone catalyzed by chiral amino acids.[a]

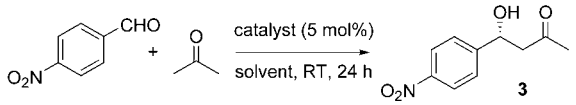

Entry	Catalyst	Solvent	Yield [%][b]	*ee* [%][c]
1	(*S*)-**1**	DMSO	70	93 (*R*)
2	L-proline	DMSO	18[d]	71 (*R*)
3	(*S*)-**1**	CH_3CN	32	95 (*R*)
4	(*S*)-**1**	NMP[e]	78	94 (*R*)
5	(*S*)-**1**	DMF	82	95 (*R*)

[a] The reaction was carried out at RT for 24 hours using 27 equivalents of acetone per equivalent of aldehyde in the presence of 5 mol% of catalyst. [b] Yield of product isolated by column chromatography. [c] The *ee* value of the product was determined by HPLC analysis using a chiral column (chiralpak AS-H, Daicel Chemical Industries). The absolute configuration was determined by comparison of the HPLC retention time of the product with reported data.[4e] [d] Bicyclic 1,3-oxazolidine **4** was isolated as a by-product in 48% yield (based on proline). [e] 1-Methyl-2-pyrrolidone.

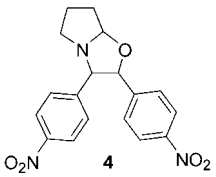

4

Table 2: Direct asymmetric aldol reaction of aldehydes with acetone catalyzed by (*S*)-**1**.[a]

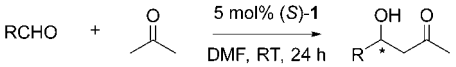

Entry	Aldehyde	R	Yield [%][b]	*ee* [%][c]
1	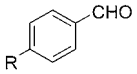	NO_2	82	95 (*R*)[d]
2		CN	80	95 (*R*)[d]
3		Ac	61	95
4	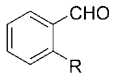	Cl	91	95 (*R*)[d]
5		OTf	81	94
6	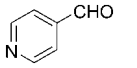	NA	76	95
7	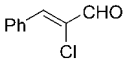	NA	73	90
8	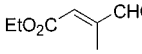	NA	81	96

[a] The reaction in DMF was carried out at RT for 24 hours using 27 equivalents of acetone per equivalent of aldehyde in the presence of 5 mol% of catalyst (*S*)-**1**. [b] Yield of product isolated by column chromatography. [c] The *ee* value of the product was determined by HPLC analysis using a chiral column (chiralpak AS-H, AD-H, or OD-H, Daicel Chemical Industries). [d] The absolute configurations were determined by comparison of the HPLC retention times of the product with reported data.[4e] OTf = triflate.

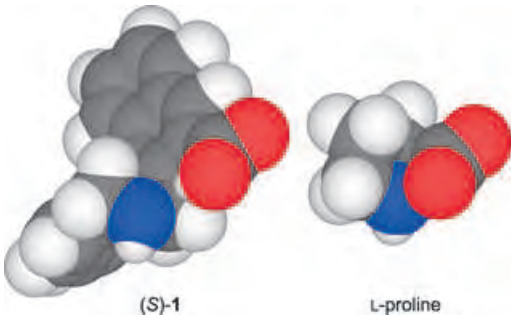

Figure 1. Space-filling models of (*S*)-**1** and L-proline by MM2 calculations.

cinchona alkaloids, and therefore there are certain limitations on possible structural modifications, especially in the design of more efficient catalysts. In this regard, the preparation and use of **1** opens up the possibility of developing structurally and electronically novel catalysts that have high reactivities and selectivities in asymmetric catalysis. Further investigations concerning the effectiveness of **1** and related catalysts for other asymmetric reactions are currently underway.

Received: February 3, 2005
Published online: April 12, 2005

Keywords: aldol reaction · amino acids · asymmetric catalysis · enantioselectivity

[1] a) M. Shibasaki, M. Kanai, K. Funabashi, *Chem. Commun.* **2002**, 1989, and references therein; b) N. Kumagai, S. Matsunaga, T. Kinoshita, S. Harada, S. Okada, S. Sakamoto, K. Yamaguchi, M. Shibasaki, *J. Am. Chem. Soc.* **2003**, *125*, 2169; c) B. M. Trost, H. Ito, E. R. Shilcoff, *J. Am. Chem. Soc.* **2001**, *123*, 3367; d) W. Yao, J. Wang, *Org. Lett.* **2003**, *5*, 1527; e) R. Mahrwald, B. Ziemer, *Tetrahedron Lett.* **2002**, *43*, 4459; f) R. Mahrwald, *Org. Lett.* **2000**, *2*, 4011; g) D. A. Evans, C. W. Downey, J. L. Hubbs, *J. Am. Chem. Soc.* **2003**, *125*, 8706.

[2] a) B. List, R. A. Lerner, C. F. Barbas III, *J. Am. Chem. Soc.* **2000**, *122*, 2395; b) W. Notz, B. List, *J. Am. Chem. Soc.* **2000**, *122*, 7386; c) B. List, P. Pojarliev, C. Castello, *Org. Lett.* **2001**, *3*, 573; d) K. Sakthivel, W. Notz, T. Bui, C. F. Barbas III, *J. Am. Chem. Soc.* **2001**, *123*, 5260; e) C. Pidathala, L. Hoang, N. Vignola, B. List, *Angew. Chem.* **2003**, *115*, 2797; *Angew. Chem. Int. Ed.* **2003**, *42*, 2785; for reviews, see: f) B. List, *Synlett* **2001**, 1675; g) B. List, *Tetrahedron* **2002**, *58*, 5573; h) B. List, *Acc. Chem. Res.* **2004**, *37*, 548; i) W. Notz, F. Tanaka, C. F. Barbas III, *Acc. Chem. Res.* **2004**, *37*, 580.

[3] a) A. Bøgevig, N. Kumaragurubaran, K. A. Jørgensen, *Chem. Commun.* **2002**, 620; b) A. B. Northrup, D. W. C. MacMillan, *J. Am. Chem. Soc.* **2002**, *124*, 6798; c) A. B. Northrup, I. K. Mangion, F. Hettche, D. W. C. MacMillan, *Angew. Chem.* **2004**, *116*, 2204; *Angew. Chem. Int. Ed.* **2004**, *43*, 2152; d) Y. Sekiguchi, A. Sasaoka, A. Shimomoto, S. Fujioka, H. Kotsuki, *Synlett* **2003**, *11*, 1655.

[4] a) H. J. Martin, B. List, *Synlett* **2003**, 1901; b) J. Kofoed, J. Nielsen, J.-L. Reymond, *Bioorg. Med. Chem. Lett.* **2003**, *13*, 2445; c) Z. Tang, F. Jiang, L.-T. Yu, L.-Z. Gong, A.-Q. Mi, Y.-Z. Jiang, Y.-D. Wu, *J. Am. Chem. Soc.* **2003**, *125*, 5262; d) Z. Tang, Z.-H. Yang, L.-F. Cun, L.-Z. Gong, A.-Q. Mi, Y.-Z. Jiang, *Org. Lett.* **2004**, *6*, 2285; e) Z. Tang, F. Jiang, X. Cui, L.-Z. Gong, A.-Q. Mi, Y.-Z. Jiang, Y.-D. Wu, *Proc. Natl. Acad. Sci. USA* **2004**, *101*, 5755; f) S. Saito, M. Nakadai, H. Yamamoto, *Synlett* **2001**, 1245; g) M. Nakadai, S. Saito, H. Yamamoto, *Tetrahedron* **2002**, *58*, 8167; h) H. Torii, M. Nakadai, K. Ishihara, S. Saito, H. Yamamoto, *Angew. Chem.* **2004**, *116*, 2017; *Angew. Chem. Int. Ed.* **2004**, *43*, 1983; for review, see: i) S. Saito, H. Yamamoto, *Acc. Chem. Res.* **2004**, *37*, 570; j) A. Berkessel, B. Koch, J. Lex, *Adv. Synth. Catal.* **2004**, *346*, 1141.

[5] F. Orsini, F. Pelizzoni, M. Forte, R. Destro, P. Gariboldi, *Tetrahedron* **1988**, *44*, 519.

Protein–DNA Arrays

Engineering a 2D Protein–DNA Crystal**

*Jonathan Malo, James C. Mitchell, Catherine Vénien-Bryan, J. Robin Harris, Holger Wille, David J. Sherratt, and Andrew J. Turberfield**

Here, we demonstrate the use of a DNA-binding protein to control the structure of a self-assembled DNA crystal. DNA self-assembly[1] has been used to create a variety of nanometer-scale objects including polyhedra,[2] simple machines,[3] two-dimensional arrays,[4] and periodic tubes.[5] Controlled construction by self-assembly is possible because the pattern of hybridization between complementary sections of oligo-

[*] J. Malo,[+] Dr. J. C. Mitchell,[+] Prof. A. J. Turberfield
Department of Physics, Clarendon Laboratory
University of Oxford, Parks Road, Oxford OX1 3PU (UK)
Fax: (+44) 1865-272-400
E-mail: a.turberfield@physics.ox.ac.uk

Dr. C. Vénien-Bryan[+]
Laboratory of Molecular Biophysics
Department of Biochemistry
University of Oxford, South Parks Road, Oxford OX1 3QU (UK)

J. Malo,[+] Prof. D. J. Sherratt
Department of Biochemistry
University of Oxford, South Parks Road, Oxford OX1 3QU (UK)

Prof. J. R. Harris
Institute of Zoology
University of Mainz, 55099 Mainz (Germany)

Prof. H. Wille
Department of Neurology and
Institute for Neurodegenerative Diseases
University of California, San Francisco, CA 94143 (USA)

[+] These authors contributed equally to this work.

[**] This work was supported by the Wellcome Trust, the MoD, and the UK research councils BBSRC, EPSRC, and MRC through the UK Bionanotechnology IRC. We thank Prof. Louise Johnson of the Laboratory of Molecular Biophysics, Oxford, for her advice, and Prof. Werner Kuhlbrandt, Dr. Janet Vonck, and Mr. Deryck Mills of the MPI for Biophysics, Frankfurt, for the use of their cryo-EM facilities and for their assistance in the cryo-EM imaging of the RuvA–HJ lattices.

Supporting information for this article is available on the WWW under http://www.angewandte.org or from the author.

 DOI: 10.1002/anie.200463027

nucleotides can be predicted. Additional control can be achieved by making use of the wide range of proteins that have evolved to manipulate DNA in order to maintain and replicate genetic information. Of these, ligases and nucleases have been used during the process of DNA nanostructure fabrication and characterization to make chemical modifications to the phosphodiester backbone.[2,4a,b,d,g] Here, we report the incorporation of a bacterial recombination protein, RuvA, as an *intrinsic* component of a DNA nanostructure. By analyzing transmission electron micrographs we have produced 2D density maps (maps of transmitted electron intensity) of both RuvA–DNA and DNA-only crystals to resolutions of less than 30 Å. Both crystals are built from the same four oligonucleotides: addition of RuvA during self-assembly completely changes the lattice symmetry and connectivity. Such specially designed 2D DNA templates, used to create ordered protein arrays, may provide a tool to determine the structure of proteins that do not readily crystallize.

Our DNA arrays are built from four oligonucleotides that assemble, by hybridization of complementary sections, to form the four arms of an immobile Holliday junction (HJ)[6] shown in Figure 1 a. Each arm has a "sticky end" that consists of six unpaired bases. Each sticky end is complementary to one other; complementary sticky ends are indicated by lock-and-key symbols in Figure 1 b and e (red pairs with green, yellow pairs with blue). Hybridization of sticky ends can bind the junctions together to form an extended array. The Kagome[7] lattice shown in Figure 1 c and d consists of DNA only and is assembled by slowly cooling a stoichiometric mixture of the four oligonucleotides from 90 °C to 20 °C over 72 h. Figure 1 d shows a transmission electron micrograph of this structure, positively stained[8] with 2 % uranyl acetate. The HJs adopt a stable antiparallel χ-stacked configuration,[9] shown schematically in Figure 1 b. Pairs of arms stack coaxially to form two quasi-continuous double helices, which meet at approximately 60° in a right-handed cross. The red and orange oligonucleotides run continuously from end to end of the two double helices with largely unperturbed helical structure; the other two oligonucleotides (green and blue) cross between helices where they meet to hold the junction together. Hybridization of complementary sticky ends joins the arms of the junctions together to form extended helices. Adjacent junctions are separated by 26 base pairs or 2.5 DNA helical turns. Three sets of parallel helices are interwoven as in Kagome basketwork (Figure 1 c), with each helix woven alternately above and below others that cross at 60° and 120°. The helices must bend as they weave, which suggests a structure with kinks at the ends of the six-base sections where sticky ends overlap to reduce the resultant strain. The plane group of the crystal is $p3$ (sixfold rotational symmetry is broken by differences between the base sequences of neighboring helices that flank the hexagons and in the positions of the nicks in the DNA backbones where sticky ends overlap). A primitive unit cell contains three junctions. Only the HJ isomer shown in Figure 1 b can be incorporated into this lattice. In the other antiparallel χ-stacked isomer, in which the blue and green oligonucleotides run continuously through the junction, complementary pairs of sticky ends are on opposite rather than adjacent arms; this isomer may assemble to create a three-dimensional periodic structure.

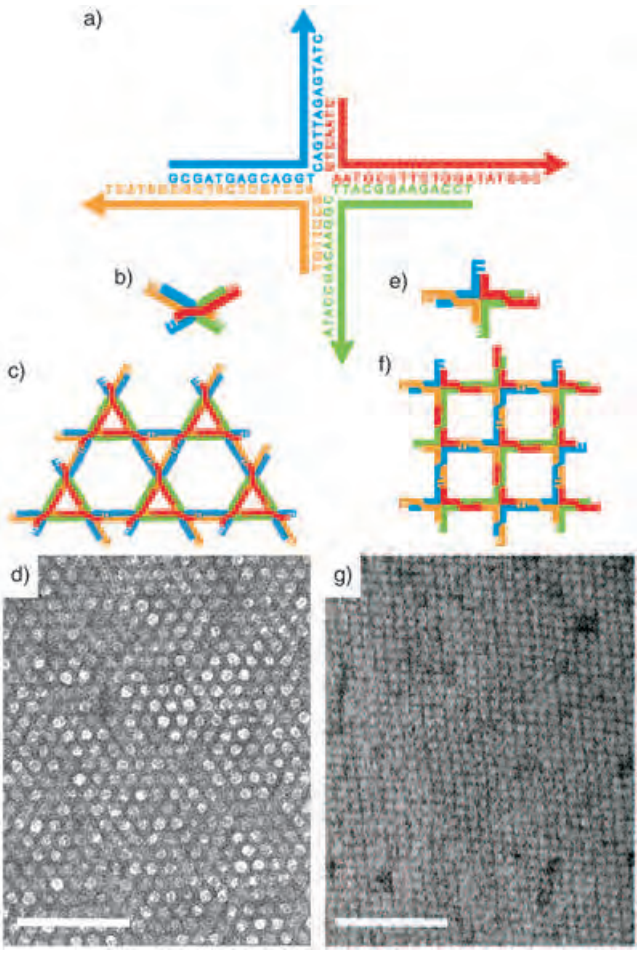

Figure 1. DNA crystals: a) The common structural unit—four oligonucleotides hybridize to form a Holliday junction (HJ) with two pairs of complementary "sticky ends". b) χ-stacked junction showing the positions of complementary sticky ends. c) Kagome lattice formed by assembly of χ-stacked junctions (for clarity, half a helical turn is shown between junctions that are, in fact, separated by 2.5 turns). d) TEM (transmission electron microscopy) image of the Kagome lattice (DNA is positively stained (dark); scale bar: 100 nm). e) Square-planar junction. f) Square lattice formed from HJs held in a square-planar configuration by protein RuvA. g) TEM image of the RuvA lattice (negatively stained: protein is lighter than background; scale bar: 100 nm).

The formation of the DNA crystal from its component oligonucleotides can be followed by measuring the decrease in A_{260}, the absorbance at 260 nm, as the mixture is slowly cooled. (A_{260} decreases as oligonucleotides hybridize.[10]) Figure 2 a shows A_{260} as a function of temperature as stoichiometric mixtures of oligonucleotides are slowly annealed and then melted. The lower pair of curves correspond to four oligonucleotides synthesized without the sticky ends that hold the junctions together. Dotted lines at 63 °C and 38 °C mark the calculated transition temperatures[11] for the assembly steps shown in Figure 2 b: first the hybridization of pairs of oligonucleotides that form the two long arms of the junction, then the coming together of these pairs to form the junction. Cooling and melting curves are overlaid, and no

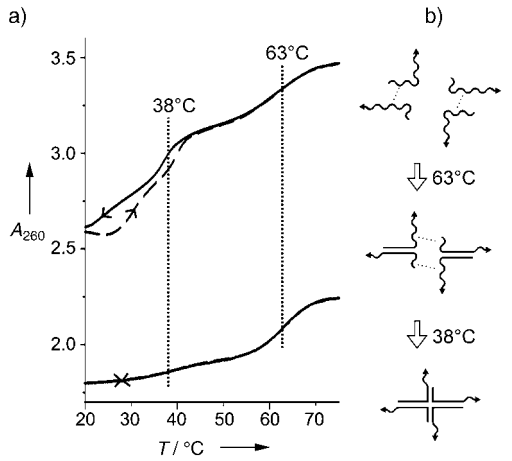

Figure 2. Monitoring self-assembly by UV/Vis absorbance spectroscopy. a) Absorbance at 260 nm (A_{260}) as a function of temperature (T) during assembly (——) and melting (-----). Hybridization is associated with a decrease in absorbance. Plots correspond to a 3 μM stoichiometric mixture of the four oligonucleotides shown in Figure 1a (upper curves) and of the same oligonucleotides with the four sticky ends removed to prevent array formation (lower curves). Rate of change of temperature: 0.1 °C min^{-1}. Dotted lines (•••••) indicate calculated transition temperatures corresponding to the assembly steps shown in part (b).

significant hysteresis is observed. The upper curves correspond to assembly and melting of the four oligonucleotides with sticky ends shown in Figure 1a. Reversible assembly of the longer arms at 63 °C is again observed, but below 42 °C there is rate-dependent hysteresis that we associate with the hybridization of sticky ends to assemble extended arrays with the structure shown in Figure 1c and d. We conclude that, as the reactants are cooled, the two more-stable pairs of oligonucleotides hybridize first then array formation begins as soon as these pairs combine to form complete junctions. This is consistent with the observation that slow cooling in the range 40–20 °C improves the size and crystalline order of the arrays, whereas slow cooling at higher temperatures does not.

The crystal shown in Figure 1f and g is made from the same four oligonucleotides to form the same HJ. In this case, however, the structure also incorporates RuvA. In vivo RuvA is part of a tripartite protein complex, the RuvABC "resolvasome",[12] which processes Holliday junctions[13] during bacterial homologous recombination. RuvA has a natural architectural role: it holds the HJ in a square-planar configuration that facilitates branch migration, driven by the ATPase RuvB,[14] and allows resolution by the endonuclease RuvC.[15] Holliday junctions are the building blocks of our DNA arrays: when RuvA binds to them during self-assembly it plays a decisive role in determining the structure and symmetry of the array. The protein is added to the cooling solution of oligonucleotides at 50 °C, at which temperature HJs have not yet formed. RuvA binds to the isolated HJs and unfolds them into a square-planar configuration[16,17] (Figure 1e). The angles between the arms are approximately 90°, the arms do not stack to form continuous helices, and the ordering of the sticky ends is different from the χ-stacked configuration (all four oligonucleotides turn at the junction to run along adjacent arms). The effect is dramatic. On further cooling the weak interactions between sticky ends assemble the units into a square lattice. In Figure 1g contrast is provided by 2% uranyl acetate which negatively stains the RuvA protein that binds each HJ.[18] The plane group of the crystal is $p1$. A primitive unit cell contains two junctions with different orientations, one of which has the major groove side upwards, and the other downwards. The connectivities of the two lattices, square and Kagome, are such that they cannot be interconverted without breaking the bonds between sticky ends that hold HJs together. Addition of RuvA at 20 °C to a ready-formed Kagome lattice does not cause detectable conversion to a square lattice.

For both crystal types, ordered domains up to 2 μm in size are observed in TEM images. Contrast between DNA or protein and background, even in the stained images shown in Figure 1d and g, is low, and the signal-to-noise ratio is limited by the need to use low electron-beam current densities to avoid damage. To obtain higher resolution structural information we have adopted two approaches to combine data from many unit cells: a process of iterative correlation mapping and averaging[19] based on the SPIDER and WEB single-particle imaging software,[20] and correction for distortion of the crystal lattice followed by reciprocal-space analysis using the MRC image-processing suite[21] designed for periodic structures. Projected density maps derived by using SPIDER are shown in Figure 3 and Figure 4 and are compared with the output of the MRC suite in the Supporting Information.

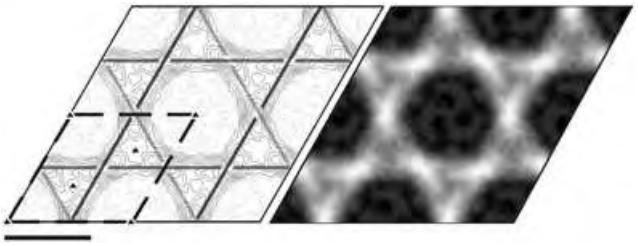

Figure 3. 2D-projected density map of a Kagome lattice composed of three interwoven DNA helices joined by χ-stacked Holliday junctions (scale bar: 10 nm). The map is derived from a negatively stained TEM image of a self-assembled DNA crystal. The contour plot and grayscale images represent the same data; woven lines indicate the positions of the helices. Dashed lines delineate a unit cell annotated with $p3$ plane group symmetry elements.

Figure 3 shows a projected density map of the DNA-only Kagome lattice. Ellipsoidal regions of high density reveal the positions of the χ-stacked HJs. The alternating orientations of the ellipses are consistent with the Kagome weaving of the helices indicated by lines in Figure 3. The distance between the junctions is 72 Å, which is 16 Å less than the contour length of the DNA duplex that joins them. We expect this distance to be shortened by strain-relieving kinks at nicks in the DNA backbone at either end of the 20 Å section that corresponds to the hybridized sticky ends. Shrinkage of the DNA caused by dehydration during grid preparation[22] may also affect this measurement.

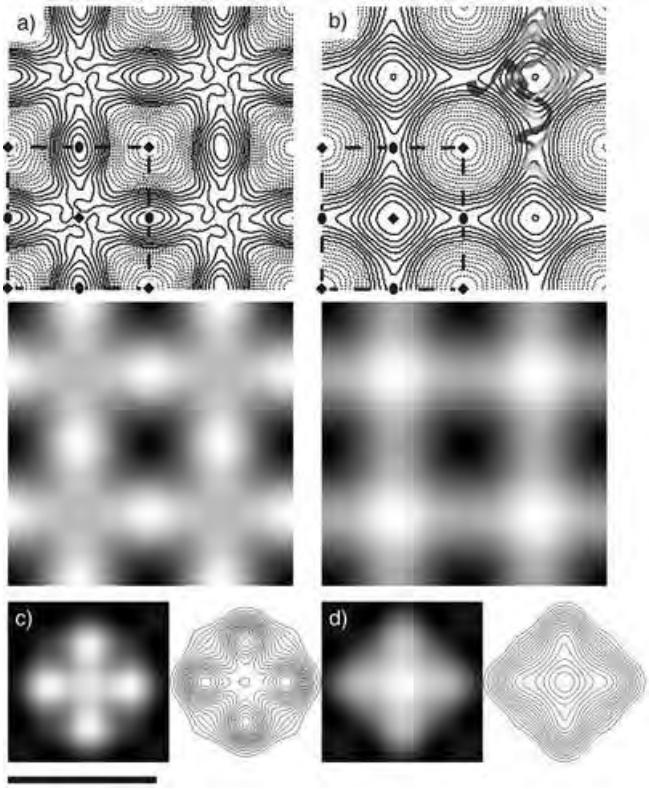

Figure 4. a, b) Projected density maps of two RuvA–DNA crystals derived from cryo-electron micrographs. Each map is represented by both a contour plot and a grayscale image. Dashed lines delineate a unit cell annotated with *p*4 plane group symmetry elements. A section of the DNA template that provides structural order is shown for illustration only. For comparison we show projection maps derived from X-ray crystal structures of Holliday junctions bound by c) a tetramer and d) an octamer of RuvA (see Supporting Information). Scale bar: 10 nm.

The protein and DNA components of the RuvA–DNA crystal shown in Figure 1g have different affinities for the uranyl acetate stain: positive staining of the DNA distorts the outline of the negatively stained RuvA complex that binds each HJ. We obtained undistorted images of this composite structure by using cryo-electron microscopy (cryo-EM) in which a thin layer of vitreous ice preserves the hydrated structure, and the image is generated by the density difference between protein and ice.[2d,23] Figure 4a and b show maps of the projected densities obtained from two RuvA–DNA crystals prepared in this way. No difference between the two differently oriented HJs in the unit cell can be resolved, so the averaged projection map has a smaller and more symmetrical unit cell than the crystal itself. The primitive unit cells of the images shown in Figure 4a and b contain one HJ and have *p*4 symmetry ($a = 95$ and 97 Å for Figure 4a and b, respectively). In Figure 4c and d, we show for comparison projected density maps derived from the X-ray crystal structures of the two known RuvA–HJ complexes, one of which incorporates a RuvA tetramer bound to one face of the junction,[16b] and the other an octamer with four molecules of RuvA bound to each face.[17] These maps have been filtered to give a resolution that is comparable to that of the cryo-EM data. The correspondence between our measured projection maps and the X-ray crystal structures is striking. We tentatively conclude that in the crystals from which the projection maps shown in Figure 4a and b were derived, which were prepared under nominally the same conditions, most HJs were bound by RuvA tetramers and octamers, respectively.

The structure of self-assembled 2D DNA crystals has previously been investigated by atomic force microscopy[4] with resolution limited to about 70 Å.[4c] To enhance the visibility of the lattice it was found necessary to add topographic features such as protruding hairpins, larger DNA domains, or streptavidin bound to biotinylated oligonucleotides,[4a,d,f,g] or to design structures with large, easily resolved gaps.[4b,c,e,h] Our micrographs demonstrate that transmission electron microscopy can provide significantly higher resolution. From computed Fourier transforms, and by comparison with the known X-ray crystal structures of the RuvA–HJ complex, we estimate the resolution of Figure 3 and Figure 4a and b to lie between 25 and 30 Å.

The use of three-dimensional DNA scaffolds[24] as templates to create artificial protein crystals for X-ray crystallography has been proposed by Seeman.[25] The structure shown in Figure 1g and Figure 4 may be regarded as a two-dimensional protein crystal whose structural order is provided by the underlying DNA scaffold rather than by interactions between protein molecules. Our density map of the RuvA–HJ complex demonstrates that a DNA-templated protein crystal can be produced with sufficient spatial order to allow measurement of protein structure. Electron microscopy of 2D crystals has achieved resolutions of 3.5 Å[26] and has the advantage that very small quantities of protein are required (typically of order 1 μg per grid). We are now working to attain higher resolution maps by improving the quality of our crystals and aim to extend the application of the DNA-scaffolding method to produce artificial crystals of other proteins, including membrane proteins that are bound to ligands attached to covalently modified oligonucleotides in a self-assembled DNA array.

Experimental Section

Purification of *E. coli* RuvA: A strain of GS566 *E. coli* that contains a RuvA-producing, ampicillin-resistant plasmid was provided by Dr. Matthew Whitby, University of Oxford. Cells were grown to OD ≈ 0.5 at 30 °C over 4 h followed by temperature-sensitive induction at 42 °C for 5 h. After lysis by sonication, purification by a series of three alternate fast-performance liquid chromatography and dialysis steps were performed to yield a solution of RuvA (80 μM, ≈ 12 mg l^{-1} of induced culture). See Supporting Information for further details.

Crystal design and assembly: Oligonucleotide sequences were designed using the program SEQUIN[27] around a symmetric sequence flanking the Holliday junction.[28] For construction of the DNA-only Kagome lattice, a stoichiometric (3 μM) mixture of the four component oligonucleotides (Sigma-Genosys; Figure 1a) was cooled from 90 °C to 20 °C over approximately 72 h in annealing buffer 1 ($MgCl_2$ (30 mM)/Tris·HCl (5 mM)/Tris acetate (20 mM)/EDTA (1 mM), pH 8.3) using a Mastercycler PCR machine (Eppendorf). The DNA–RuvA crystals were annealed using the same oligonucleotides at the same concentration in annealing buffer 2 ($MgCl_2$ (10 mM)/Tris·HCl (10 mM)/Tris acetate (40 mM)/EDTA

(1 mM), pH 8.3), also over approximately 72 h. The sample container was immersed in water in a vacuum flask, which was left to cool naturally. RuvA (24 μM) was added at 50 °C.

UV/Vis absorbance measurements: A Varian Cary 1E spectrophotometer with a 6x6 multicell-block Peltier temperature controller was used to measure the differential absorbance (A) at 260 nm between the sample, which contained a mixture of the four component oligonucleotides (3 μM) in annealing buffer 1, and a reference (only annealing buffer), both at 650 μl volume. The temperature was measured by a probe placed in a third cuvette.

Preparation of grids and electron microscopy: Specimens of the Kagome lattice were adsorbed onto 400-mesh carbon-coated copper grids and stained with 2% uranyl acetate. Electron micrographs were recorded on Kodak SO-163 film under low dose conditions using a Philips CM120 electron microscope (LMB, Oxford) at 120 kV acceleration. The defocus range was from 0.6 to 1.2 μm with a nominal magnification of ×45000. RuvA–DNA crystal specimens were applied to carbon-coated grids initially immersed in 1% tannin. These were then blotted and frozen in liquid nitrogen. Electron micrographs were recorded under low dose conditions on a JEOL 3000 electron microscope (MPI, Frankfurt) at 300 kV acceleration. The defocus range was from 0.6 to 1.2 μm with a nominal magnification of ×36000.

Image processing: Optical diffraction was used to screen and select the micrographs for crystal quality. The Kagome lattice projection map (Figure 3) was calculated from one large crystalline area ($\approx 0.6\ \mu m^2$) of an image in which the DNA was negatively stained.[18] (This image is more ordered but displays less contrast than Figure 1d in which the DNA is positively stained.[8]) The RuvA–DNA projection maps (Figure 4) were calculated using data from two separate crystals imaged under cryo-EM. Selected areas were digitized using an Optronics drum scanner (P1000) at a sampling raster of 12.5 μm that corresponds to a pixel size of 2.8 Å. A contrast transfer function (CTF) correction was applied using the CRISP software package.[29] The CTF-corrected images were processed by using correlation mapping and averaging routines[19] written for the SPIDER and WEB software packages.[20] See Supporting Information for further details.

Received: December 22, 2004
Published online: April 12, 2005

Keywords: DNA · electron microscopy · nanostructures · proteins · self-assembly

[1] N. C. Seeman, *Nature* **2003**, *421*, 427.
[2] a) J. H. Chen, N. C. Seeman, *Nature* **1991**, *350*, 631; b) Y. W. Zhang, N. C. Seeman, *J. Am. Chem. Soc.* **1994**, *116*, 1661; c) R. P. Goodman, R. M. Berry, A. J. Turberfield, *Chem. Commun.* **2004**, *12*, 1372; d) W. M. Shih, J. D. Quispe, G. F. Joyce, *Nature* **2004**, *427*, 618.
[3] a) B. Yurke, A. J. Turberfield, A. P. Mills, Jr., F. C. Simmel, J. L. Neumann, *Nature* **2000**, *406*, 605; b) H. Yan, X. Zhang, Z. Shen, N. C. Seeman, *Nature* **2002**, *415*, 62.
[4] a) E. Winfree, F. Liu, L. A. Wenzler, N. C. Seeman, *Nature* **1998**, *394*, 539; b) C. D. Mao, W. Q. Sun, N. C. Seeman, *J. Am. Chem. Soc.* **1999**, *121*, 5437; c) R. Sha, F. Liu, D. P. Millar, N. C. Seeman, *Chem. Biol.* **2000**, *7*, 743; d) T. H. LaBean, H. Yan, J. Kopatsch, F. R. Liu, E. Winfree, J. H. Reif, N. C. Seeman, *J. Am. Chem. Soc.* **2000**, *122*, 1848; e) R. Sha, F. Liu, N. C. Seeman, *Biochemistry* **2002**, *41*, 5950; f) H. Yan, S. H. Park, G. Finkelstein, J. H. Reif, T. H. LaBean, *Science* **2003**, *301*, 1882; g) H. Yan, T. H. LaBean, L. Feng, J. H. Reif, *Proc. Natl. Acad. Sci. USA* **2003**, *100*, 8103; h) L. Feng, S. H. Park, J. H. Reif, H. Yan, *Angew. Chem.* **2003**, *115*, 4478; *Angew. Chem. Int. Ed.* **2003**, *42*, 4342.
[5] a) J. C. Mitchell, J. R. Harris, J. Malo, J. Bath, A. J. Turberfield, *J. Am. Chem. Soc.* **2004**, *126*, 16342; b) P. W. K. Rothemund, E. Ekani-Nkodo, N. Papadakis, A. Kumar, D. K. Fygenson, E. Winfree, *J. Am. Chem. Soc.* **2004**, *126*, 16344.
[6] N. R. Kallenbach, R.-I. Ma, N. C. Seeman, *Nature* **1983**, *305*, 829.
[7] I. Syôzi, *Prog. Theor. Phys.* **1951**, *6*, 306.
[8] M. Beer, C. R. Zobel, *J. Mol. Biol.* **1961**, *3*, 717.
[9] a) M. Ortiz-Lombardia, A. Gonzalez, R. Eritja, J. Aymami, F. Azorin, M. Coll, *Nat. Struct. Biol.* **1999**, *6*, 913; b) B. F. Eichman, J. M. Vargason, B. H. Mooers, P. S. Ho, *Proc. Natl. Acad. Sci. USA* **2000**, *97*, 3971.
[10] R. Thomas, *Biochim. Biophys. Acta* **1954**, *14*, 231.
[11] a) N. Peyret, P. A. Seneviratne, H. T. Allawi, J. SantaLucia, Jr., *Biochemistry* **1999**, *38*, 3468; b) J. SantaLucia, Jr., *Proc. Natl. Acad. Sci. USA* **1998**, *95*, 1460.
[12] D. Zerbib, C. Mezard, H. George, S. C. West, *J. Mol. Biol.* **1998**, *281*, 621.
[13] R. Holliday, *Genet. Res.* **1964**, *5*, 282.
[14] A. Stasiak, I. R. Tsaneva, S. C. West, C. J. Benson, X. Yu, E. H. Egelman, *Proc. Natl. Acad. Sci. USA* **1994**, *91*, 7618.
[15] M. Ariyoshi, D. G. Vassylyev, H. Iwasaki, H. Nakamura, H. Shinagawa, K. Morikawa, *Cell* **1994**, *78*, 1063.
[16] a) D. Hargreaves, D. W. Rice, S. E. Sedelnikova, P. J. Artymiuk, R. G. Lloyd, J. B. Rafferty, *Nat. Struct. Biol.* **1998**, *5*, 441; b) M. Ariyoshi, T. Nishino, H. Iwasaki, H. Shinagawa, K. Morikawa, *Proc. Natl. Acad. Sci. USA* **2000**, *97*, 8257.
[17] S. M. Roe, T. Barlow, T. Brown, M. Oram, A. Keeley, I. R. Tsaneva, L. H. Pearl, *Mol. Cell* **1998**, *2*, 361.
[18] R. W. Horne in *Techniques for Electron Microscopy* (Ed.: D. H. Kay), Blackwell Scientific Publishing, Oxford, **1965**, pp. 328.
[19] H. Wille, M. D. Michelitsch, V. Guenebaut, S. Supattapone, A. Serban, F. E. Cohen, D. A. Agard, S. B. Prusiner, *Proc. Natl. Acad. Sci. USA* **2002**, *99*, 3563.
[20] J. Frank, M. Radermacher, P. Penczek, J. Zhu, Y. Li, M. Ladjadj, A. Leith, *J. Struct. Biol.* **1996**, *116*, 190.
[21] R. A. Crowther, R. Henderson, J. M. Smith, *J. Struct. Biol.* **1996**, *116*, 9.
[22] H. J. Vollenweider, A. James, W. Szybalski, *Proc. Natl. Acad. Sci. USA* **1978** *75*, 710; G. Lee, P. G. Arscott, V. A. Bloomfield, D. F. Evans, *Science* **1989**, *244*, 475.
[23] M. Adrian, J. Dubochet, J. Lepault, A. W. McDowall, *Nature* **1984**, *308*, 32.
[24] P. J. Paukstelis, J. Nowakowski, J. J. Birktoft, N. C. Seeman, *Chem. Biol.* **2004**, *11*, 1119.
[25] N. C. Seeman, *J. Theor. Biol.* **1982**, *99*, 237.
[26] R. Henderson, J. M. Baldwin, T. A. Ceska, F. Zemlin, E. Beckmann, K. H. Downing, *J. Mol. Biol.* **1990**, *213*, 899.
[27] N. C. Seeman, *J. Biomol. Struct. Dyn.* **1990**, *8*, 573.
[28] S. Zhang, N. C. Seeman, *J. Mol. Biol.* **1994**, *238*, 658.
[29] S. Hovmöller, *Ultramicroscopy* **1992**, *41*, 121.

Molecular Devices

Patterning through Controlled Submolecular Motion: Rotaxane-Based Switches and Logic Gates that Function in Solution and Polymer Films**

David A. Leigh, M. Ángeles F. Morales, Emilio M. Pérez, Jenny K. Y. Wong, Carlos G. Saiz, Alexandra M. Z. Slawin,* Adrian J. Carmichael, David M. Haddleton,* A. Manfred Brouwer,* Wybren Jan Buma,* George W. H. Wurpel, Salvador León, and Francesco Zerbetto**

The extensive use of molecular machine-like processes in biology[1] is inspiring efforts to exploit similarly well-controlled motions in functional synthetic systems.[2] Stimuli-responsive "molecular shuttles"—rotaxanes in which a key feature of the tertiary structure, the relative positions of the interlocked components, can be changed in response to an external input—constitute a basic kind of nanoscale mechanical switch,[3] capable of varying physical properties such as conductivity,[4] circular dichroism,[5] and fluorescence.[6] However, there are few examples[7] where shuttling has been demonstrated in the polymer-based media upon which many materials applications may ultimately depend, and only simple rotaxanes (not switchable molecular shuttles) have been used to create information-rich quaternary structures, such as patterned surfaces.[8] Here we report a system in which the translocation of a ring along a peptide-based thread, induced by changes in the nature of the local environment, can be used to switch the fluorescence of a rotaxane "on" or "off". Remarkably, the system not only works in solution but also in polymer films where patterns visible to the naked eye can be generated solely through controlled submolecular motion. A polymer film "INHIBIT" logic gate based on a combination of control of submolecular positioning and chemical modification (protonation) is also demonstrated.

Thread **1** consists of an anthracene fluorophore (which also acts as a "stopper") attached to a glycylglycine hydrogen-bonding binding site or "station", which, in turn, is connected to a C_{11} alkyl chain that can act as a second "solvophobic" station[9] and is terminated by a second stopper.[10] Rotaxanes **2** and **3** were prepared in 37 and 20% yields, respectively, by condensing *p*-xylylenediamine with the appropriate bis(acid chlorides) in the presence of **1** (Scheme 1).[11] Double proto-

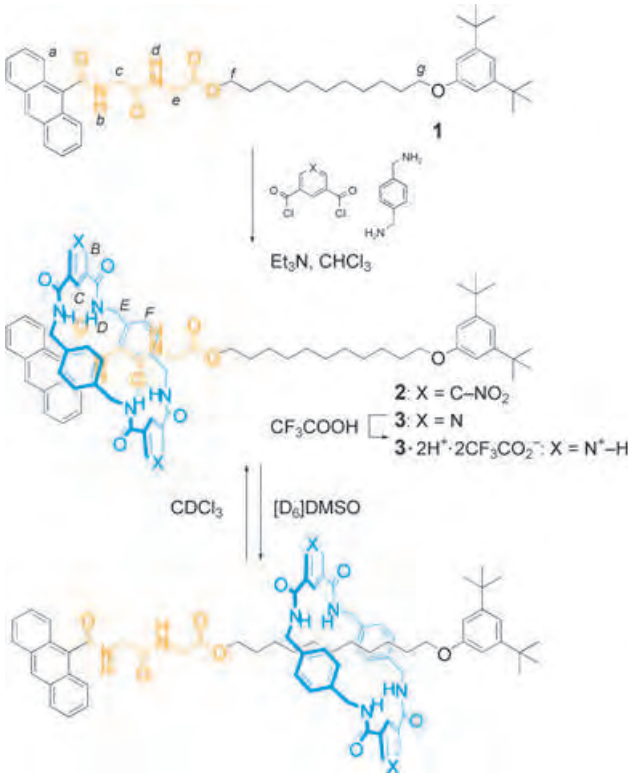

Scheme 1. Synthesis and translational isomerism exhibited by environment-switchable molecular shuttles **2**, **3**, and $\mathbf{3}\cdot 2H^+\cdot 2CF_3CO_2^-$.

nation of **3** with an excess of trifluoroacetic acid generated $\mathbf{3}\cdot 2H^+\cdot 2CF_3CO_2^-$. The macrocycles in **2** and $\mathbf{3}\cdot 2H^+$ contain nitrophenyl and pyridinium moieties, respectively, which are known to quench the fluorescence of anthracene through distance-dependent electron transfer.[6a,12]

A clear change in position of the rotaxane components of **2**, **3**, and $\mathbf{3}\cdot 2H^+\cdot 2CF_3CO_2^-$ between $CDCl_3$ and $[D_6]$DMSO (dimethylsulfoxide) is clearly apparent from ^{1}H NMR spectroscopy. Figure 1 shows the partial ^{1}H NMR spectra (400 MHz, 298 K) of thread **1** and rotaxane **2** in the different

[*] Prof. D. A. Leigh, Dr. M. Á. F. Morales, E. M. Pérez, Dr. J. K. Y. Wong
School of Chemistry, University of Edinburgh
The King's Buildings, West Mains Road, Edinburgh EH9 3JJ (UK)
Fax: (+44) 131-667-9085
E-mail: david.leigh@ed.ac.uk

Dr. C. G. Saiz, Prof. A. M. Z. Slawin
School of Chemistry, University of St. Andrews
Purdie Building, St. Andrews, Fife KY16 9ST (UK)
Fax: (+44) 1334-463-384
E-mail: amzs@st-and.ac.uk

Dr. A. J. Carmichael, Prof. D. M. Haddleton
Department of Chemistry, University of Warwick
Coventry CV4 7AL (UK)
Fax: (+44) 2476-524-112
E-mail: d.m.haddleton@warwick.ac.uk

Dr. A. M. Brouwer, Prof. W. J. Buma, Dr. G. W. H. Wurpel
Institute for Molecular Chemistry, University of Amsterdam
Nieuwe Achtergracht 129, 1018 WS Amsterdam (The Netherlands)
Fax: (+31) 20-525-5670
E-mail: fred@science.uva.nl
wybren@science.uva.nl

Dr. S. León, Prof. F. Zerbetto
Dipartimento di Chimica "G. Ciamician"
Università degli Studi di Bologna
via F. Selmi 2, 40126 Bologna (Italy)
Fax: (+39) 051-209-9456
E-mail: francesco.zerbetto@unibo.it

[**] We thank C. A. Hunter for generating the FGIP for formamide. This work was supported by the European Union.

Supporting information for this article is available on the WWW under http://www.angewandte.org or from the author.

  DOI: 10.1002/anie.200500101

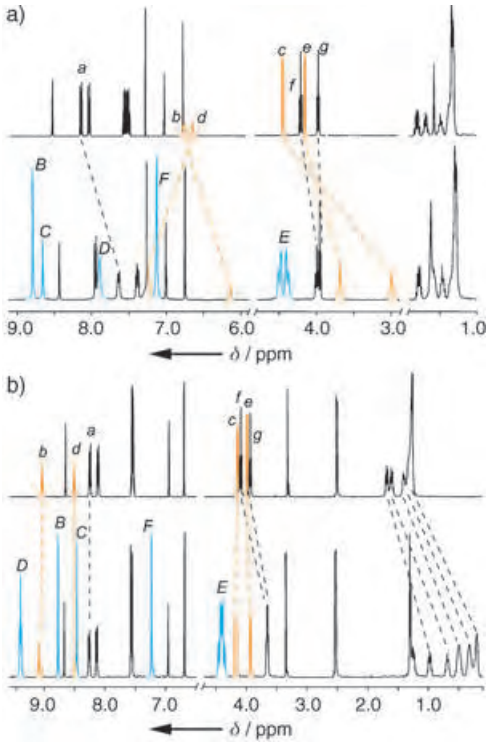

Figure 1. Partial ^{1}H NMR spectra of a) thread **1** (top) and rotaxane **2** (bottom) in $CDCl_3$, and b) thread **1** (top) and rotaxane **2** (bottom) in $[D_6]$DMSO. The assignments correspond to the lettering shown in Scheme 1 and are based on COSY and GOESY experiments (400 MHz, 298 K). In $CDCl_3$, the signals for H_c and H_e of the glycylglycine station (orange) are shielded by $\delta = 1.2$ and 0.4 ppm in the rotaxane with respect to the thread because of the aromatic rings of the macrocycle. In $[D_6]$DMSO, it is the signals that correspond to the protons of the alkyl chain that are strongly shielded, while the signals of the glycylglycine unit are essentially unchanged, which confirms the position of the macrocycle over the alkyl chain.

solvents. In $CDCl_3$ (Figure 1 a) the chemical shift differences of the glycylglycine protons between **1** and **2** indicate that the macrocycle resides principally over the peptide residue of the rotaxane.[13] The solid-state structure of a close analogue of **3** (only the non-anthracene stopper is different in **3′**) shows the macrocycle binding to the glycylglycine station through a network of intercomponent hydrogen bonds (Figure 2).[14] In contrast, in $[D_6]$DMSO (Figure 1 b) it is the signals for the protons of the alkyl chains of **2** that are shielded by up to 1.2 ppm through encapsulation by the macrocycle. The discrimination of the macrocycle for the different regions of the thread is less well expressed in solvents of polarity and hydrogen-bonding basicity that lie in-between those of $CDCl_3$ and $[D_6]$DMSO (e.g. $[D_3]$MeCN, $[D_4]$MeOH, $[D_8]$EtOAc, $[D_7]$DMF (DMF = *N*,*N*-dimethylformamide), $[D_8]$THF etc.), with smaller shifts involving more thread protons observed in the ^{1}H NMR spectra in these solvents than with $CDCl_3$ or $[D_6]$DMSO. However, the switching of the preferred translational isomer between the relatively nonpolar solvents and $[D_6]$DMSO is quite general for rotaxanes with this type of amphiphilic thread, with **3** and **3**·2 H^+·2 $CF_3CO_2^-$ exhibiting similar shift patterns to **2** (see Supporting Information).

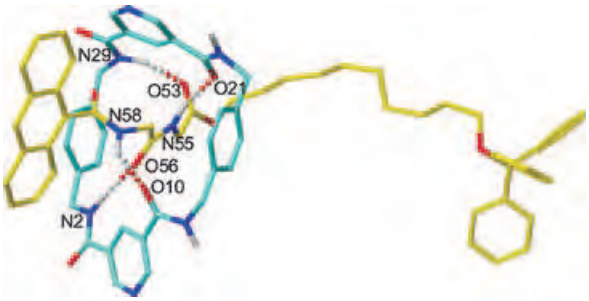

Figure 2. X-ray crystal structure[14] of **3′**, a close structural analogue of rotaxane **3** (the 3,5-di-*tert*-butylphenyl stopper in **3** is substituted for a triphenylmethyl group to give **3′**). C (macrocycle) blue, C (thread) yellow, O red, N dark blue, H white. Non-amide hydrogen atoms are omitted for clarity. Intramolecular hydrogen-bond lengths [Å] and angles [°]: N2H-O56 1.93–170.7; N58H-O10 2.16, 140.6; N55H-O21 1.96, 174.4; N29H-O53 2.03, 161.9.

The effect of the environment-induced positional change of the interlocked components on the fluorescence emission of the rotaxanes was also investigated. Fluorescence spectra ($\lambda_{ex} = 340$ nm) of 10^{-5} M solutions of rotaxanes **2** and **3**·2 H^+·2 $CF_3CO_2^-$ were recorded in benzene, CH_2Cl_2, CH_3CN, CH_3OH, DMF, DMSO, and H_2NCHO (Figure 3, Table 1). The variation in the ^{1}H NMR and fluorescence

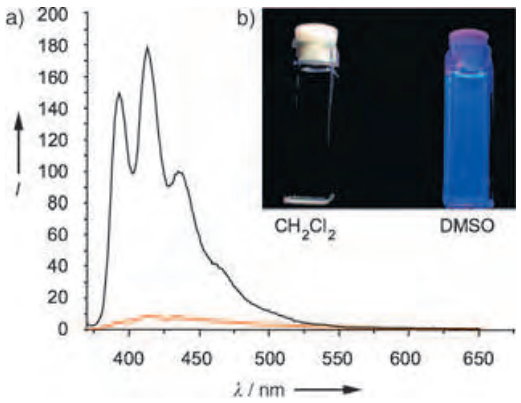

Figure 3. a) Fluorescence spectra ($\lambda_{ex} = 340$ nm, 1×10^{-5} M, 298 K) of rotaxane **2** in CH_2Cl_2 (orange) and DMSO (black). b) Photograph of the cuvettes that contain the solutions of rotaxane **2** illuminated at 254–350 nm which illustrate that the difference in fluorescence is clearly visible to the naked eye.

Table 1: Fluorescence quantum yields (φ_f) of rotaxanes **2** and **3**·2 H^+·2 $CF_3CO_2^-$ in various solvents, together with the dielectric constants (ε) and hydrogen-bond-donating (α_s)[15] and -accepting (β_s)[15] constants of the solvents.

Solvent	ε	α_s	β_s	φ_f (**2**)	φ_f (**3**·2 H^+·2 $CF_3CO_2^-$)
benzene	2.3	1.0	2.2	0.004	0.003
CH_2Cl_2	9.0	1.9	1.1	0.003	0.004
CH_3CN	37.5	1.7	4.7	0.003	0.004
DMF	37.0	1.6	8.3	0.013	0.007
CH_3OH	32.7	2.7	5.8	0.005	0.008
DMSO	49.7	0.8	8.9	0.032	0.019
H_2NCHO	109.5	2.9[a]	8.3[a]	0.029	0.042

[a] General values for the amide functional group.

spectra does not directly follow from the dielectric or hydrogen-bonding constants of the solvents, but is readily explained by considering the functional group interaction profiles (FGIP) recently introduced by Hunter (Figure 4).[15] In solvents in which the intercomponent hydrogen bonding should be strongest (benzene, CH_2Cl_2, CH_3CN) the anthracene fluorescence is virtually completely quenched, whereas in solvents with a strong solvophobic profile for alkyl chains (DMSO and NH_2CHO), UV-stimulated fluorescence is clearly visible at submicromolar concentrations. This contrasts with the trend whereby an increase in dielectric constant generally increases the efficiency of other decay pathways to result in a decrease in fluorescence intensity.[16] In fact, the very efficient quenching observed in nonpolar solvents suggests that the electron-transfer process in rotaxanes **2** and **3**·2 H^+ is close to the Marcus optimal region, where

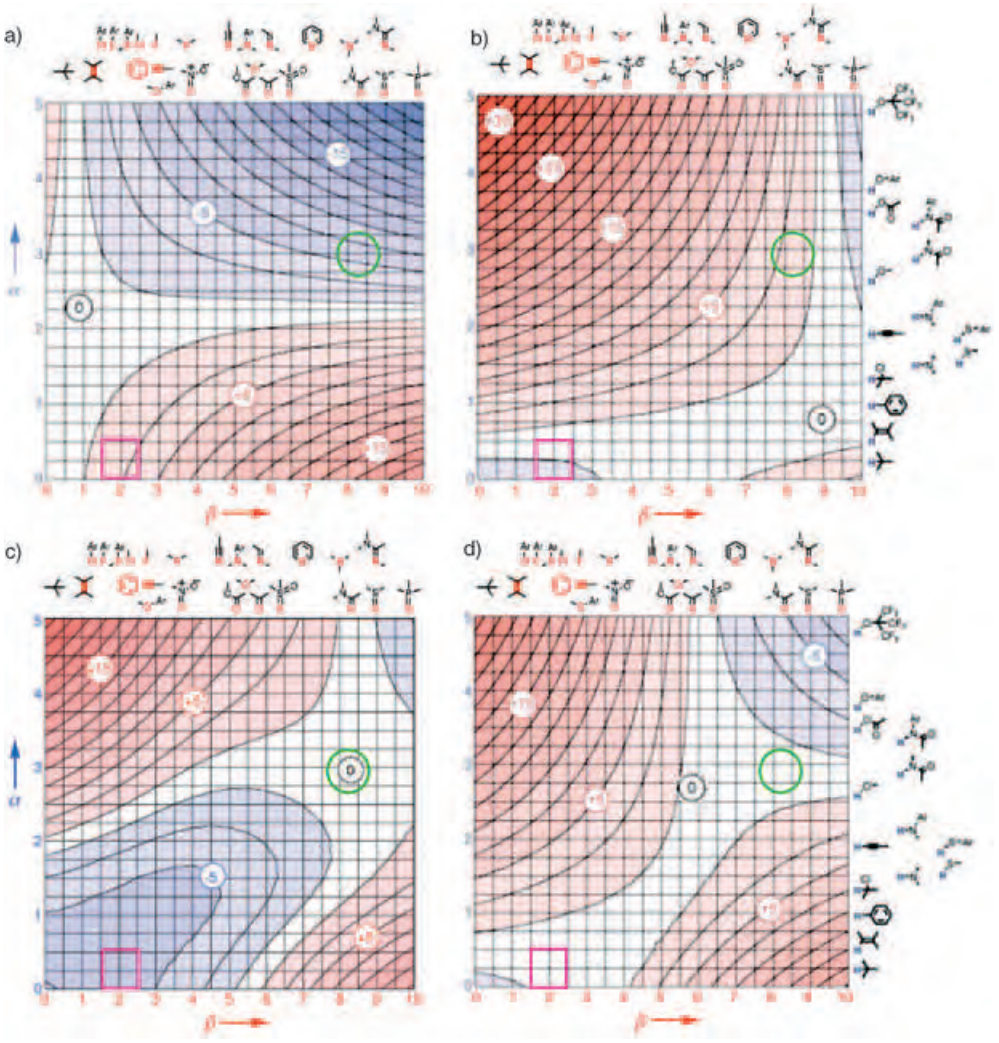

Figure 4. Functional group interaction profiles (FGIP) in a) chloroform ($\alpha_S = 2.2$, $\beta_S = 0.8$), b) DMSO ($\alpha_S = 0.8$, $\beta_S = 8.9$), c) formamide ($\alpha_S = 2.9$, $\beta_S = 8.3$),[18] and d) methanol ($\alpha_S = 0.9$ and 2.7, $\beta_S = 5.8$). Note, the FGIP of dichloromethane ($\alpha_S = 1.9$, $\beta_S = 1.1$) is very similar to that of chloroform. Blue represents a favorable interaction, and red represents an unfavorable interaction. Parts (a), (b), and (d) are reproduced with permission from Ref. [15]. The intercomponent interactions that largely determine the position and positional integrity of the macrocycle in **2**, **3**, and **3**·2 H^+·2 $CF_3CO_2^-$ are the amide–amide interaction region (highlighted with a green circle and corresponds to the peptidyl translational isomer) and the alkyl chain–phenyl ring interaction region (highlighted with a magenta square and stabilizes the alkyl translational isomer). a) Solute–solute amide–amide interactions are strongly favored and alkyl chain—phenyl ring interactions are disfavored, so we can expect the tertiary structure for the peptide-based molecular shuttles to feature the macrocycle held firmly on the peptide station by a well-defined hydrogen-bonding network, which leads to strong quenching of the anthracene fluorescence. b) Amide–amide interactions are strongly disfavored whereas alkyl chain–phenyl ring interactions in the solvent–solvent interaction dominated quadrant (bottom left) are favored, so we can expect the macrocycle to be localized on the alkyl-chain station but in a variety of positions and co-conformations owing to the general solvophobic interactions. As formamide contains both strong hydrogen-bond donors and acceptors it should display a strong solvophobic interaction in the lower left quadrant, similar to that for water. Indeed, this is the case as shown in (c), and the FGIP indicates that the solvophobic effect in NH_2CHO should be at least as strong as in DMSO, as suggested by the fluorescence measurements. d) In methanol, the amide–amide interactions are weak, but no driving force exists for alkyl-chain–phenyl-ring interactions either. So we can expect the room-temperature Boltzmann-averaged distribution to feature the macrocycle spending a significant amount of time over many positions along the entire length of the rotaxane thread; some of these conformations will lead to efficient quenching, while others do not.

the reorganization energy is equal to the $-\Delta G$ value for electron transfer (this inference is also supported by low-temperature fluorescence spectra and thermodynamic considerations, see Supporting Information). In such circumstances the electron-transfer process is barrierless and is insensitive to the polarity of the solvent.[17] We can thus conclude that the variations in intensity observed with the different solvents is caused by the change in the relative separation of the fluorophore and quencher. Although the positioning of the macrocycle on the large alkyl-chain region would be expected to be rather poorly defined through a solvophobic effect, the ratio of fluorescence quantum yields obtained solely by the average net displacement of the macrocycle along the thread is as high as 15:1 (Table 1). This is significantly less than the 200:1 on/off ratio reported recently[6a] for a light-switchable shuttle with two discrete and well-separated hydrogen-bonding stations, but is nonetheless remarkable for such a simple system and easily visible to the naked eye (Figure 3b).

To see if the same principles could be demonstrated to work in environments that are more relevant to materials applications, we synthesized well-defined polymer analogues of **2** and **3** by transition-metal-mediated living radical polymerization (often called ATRP)[19] using methyl methacrylate as a monomer and [2]rotaxanes **5** and **6** as initiators. The resulting poly(methyl methacrylate) (PMMA)-based macromolecule [2]rotaxanes **P5** and **P6** had narrow polydispersity indices (PDI) of 1.17 and 1.14, respectively, and contained approximately 10% w/w of peptide rotaxane end-groups. ^{1}H NMR studies in $CDCl_3$ and [D_6]DMSO showed that the translational isomerism of the interlocked components of polymers **P5** and **P6** in solution exactly mirrored those of the small-molecule analogues, **2** and **3**. Thin transparent films of **P5** and **P6** on quartz slides were prepared through either conventional spin-coating techniques or by the evaporation of solutions of the polymers in dichloromethane. The resulting colorless thin films were of good optical quality and behaved in a manner independent of their method of preparation.

No fluorescence was detected when slides coated with the **P5** film were illuminated with UV light (254–350 nm), which suggests that in the nonpolar environment of the PMMA-like film the macrocycle resides over the peptide portion of the thread and efficiently quenches the anthracene fluorescence. However, although exposing the **P5**-coated slides to DMSO vapor (generated by gently warming an open beaker of the solvent in the vicinity of the film for 5 min) did not result in a noticeable change to the film under natural light, upon illumination with the UV source the characteristic blue anthracene fluorescence became apparent. Masking regions of films of **P5** from DMSO vapor with aluminum grids again produced no perceptible change under natural light, but distinctly shaped and clearly visible patterns were revealed with the UV source (Scheme 2b). The system is reversible: warming the slides to 70 °C at 0.1 Torr for 15 minutes to drive off absorbed solvent resulted in the loss of the fluorescent patterning. The behavior of **P5** implies that the environment-induced change in position of the interlocked components occurs in the polymer film just as it does in solution. This view

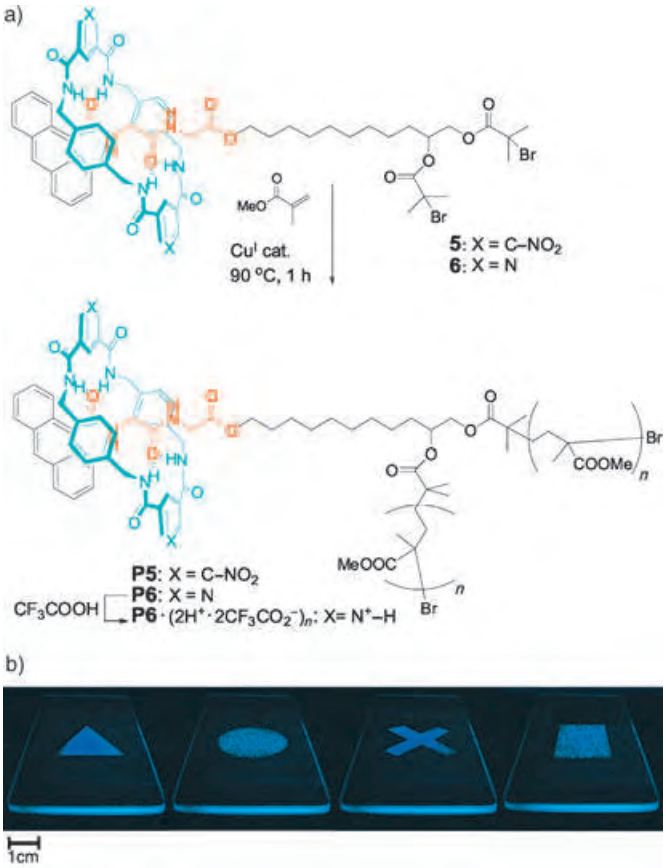

Scheme 2. a) Chemical structures of rotaxane initiators **5** and **6** and the corresponding PMMA-based polymers **P5**, **P6**, and **P6**·(2 H$^+$ 2 CF$_3$CO$_2^-$)$_n$. b) Images obtained by casting films of polymer **P5** on quartz slides, then covering the films with aluminum masks, and exposing the unmasked area to DMSO vapor for 5 minutes. The photographs were taken while illuminating the slides with an 8-watt Camag UV lamp (254–350 nm) and reveal representative triangle, circle, cross, and square symbols.

is supported by molecular dynamics simulations (see Supporting Information) in which close similarities are seen between the average intercomponent separation of **2** in CH_2Cl_2 and DMSO and **P5** in a solvent-free environment and with the addition of several molecules of DMSO.

The quartz slides coated with **P6** films were fluorescent when illuminated with UV light as the pyridine units of the macrocycle need to be protonated to quench the excited state of anthracene. Accordingly, when quartz slides coated with **P6** were exposed to CF_3CO_2H vapors (**P6**→ **P6**·(2 H$^+$·2 CF$_3$CO$_2^-$)$_n$) fluorescence was no longer observed. Figure 5b shows a distinct pattern of dark (nonfluorescent) bands resulting from thin films of **P6** upon exposure to CF_3CO_2H vapor through a striped aluminum mask (Figure 5a) and then illuminated with UV light. When the resulting dark strips of **P6**·(**2** H$^+$·2 CF$_3$CO$_2^-$)$_n$ were exposed to DMSO vapor through the same mask rotated by 90°, a criss-cross pattern was produced (Figure 5c) in which only segments that had been exposed to CF_3CO_2H vapor but not to DMSO vapor were dark when illuminated with the UV source, which suggest that displacement of the macrocycle

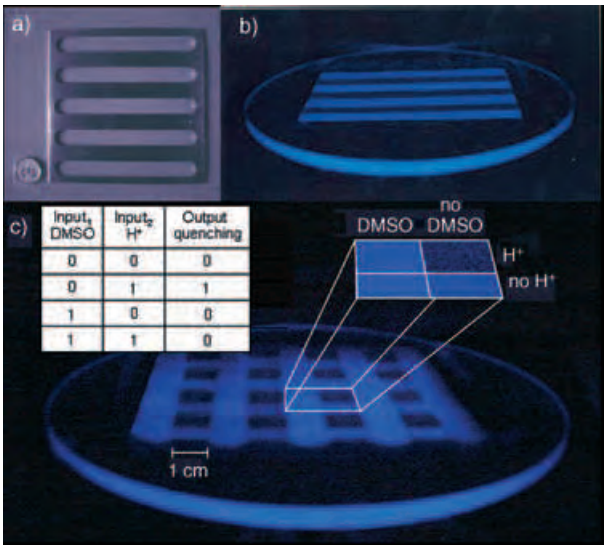

Figure 5. a) Aluminum grid used in the experiment; the coin shown for scale in the lower left corner of (a) is a UK 5 p piece. b) Pattern generated when films of **P6** were exposed to trifluoroacetic acid vapor for 5 minutes through the aluminum-grid mask. c) Criss-cross pattern obtained by rotation of the aluminum grid by 90° and exposure of the film shown in (b) to DMSO vapor for a further 5 minutes; only regions exposed to trifluoroacetic acid but not to DMSO are quenched, as shown in the magnified view. Inset: The truth table for an "INHIBIT" logic gate. The photographs of the slides were taken in the dark while illuminating with an 8-watt UV lamp (254–350 nm).

from the peptide station to the alkyl chain restores fluorescence to the exposed regions. The response of **P6** to the different combinations of two stimuli (DMSO and protons) corresponds to an "INHIBIT" Boolean logic gate.[20,21] The **P6** logic gate does not operate with full reversibility as a film, however, because although the DMSO could be removed by warming under reduced pressure (as with **P5**), the effects of the acid stimulus could not be reversed without some deterioration in the optical quality of the film. In solution, **P6** is cleanly regenerated by treatment with base, for example, triethylamine.

In conclusion, we have described a class of molecular shuttles in which translational isomerism of the components can be controlled to either permit or preclude fluorescence quenching by intercomponent electron transfer in both solution and polymer films. As the shuttling mechanism does not require a change to the covalent structure of the shuttles, the optical response can be unambiguously ascribed to changes in the relative positions of macrocycle and thread; a visible optical response from a mechanical submolecular event.[21] Although using exposure to chemical vapors as a stimulus is unlikely to be practically useful beyond sensing or, perhaps, security applications, related hydrogen-bonded shuttles can be switched in solution by using light,[23] electrochemistry,[24] changes in temperature[25] or pH,[26] and covalent-bond-forming chemical reactions.[27] The present work demonstrates that some of the switching mechanisms, properties, and logic operations established for molecular shuttles in solution can be transferred to media that are more suitable for developing materials which function through controlled submolecular motion.

Received: January 12, 2005
Published online: April 12, 2005

Keywords: fluorescence · logic gates · molecular devices · rotaxanes · solvent effects

[1] M. Schliwa, *Molecular Motors*, Wiley-VCH, Weinheim, **2003**.
[2] a) *Molecular Catenanes, Rotaxanes, and Knots*: *A Journey Through the World of Molecular Topology* (Eds.: J.-P. Sauvage, C. Dietrich-Buchecker), Wiley-VCH, Weinheim, **1999**; b) V. Balzani, A. Credi, F. M. Raymo, J. F. Stoddart, *Angew. Chem.* **2000**, *112*, 3484–3530; *Angew. Chem. Int. Ed.* **2000**, *39*, 3348–3391; c) V. Balzani, M. Venturi, A. Credi, *Molecular Devices and Machines—A Journey into the Nanoworld*, Wiley-VCH, Weinheim, **2003**; d) "Synthetic Molecular Machines": E. R. Kay, D. A. Leigh in *Functional Artificial Receptors* (Eds.: T. Schrader, A. D. Hamilton), Wiley-VCH, Weinheim, **2005**.
[3] Most shuttling mechanisms require a concomitant—and often major—change in the rotaxane primary structure (e.g. charge, oxidation state, protonation, etc). In the absence of clear controls, attributing the changes in property to the positional displacement of components rather than the change in the electronic nature or chemical composition of the molecule is not straightforward.
[4] a) A. H. Flood, R. J. A. Ramirez, W.-Q. Deng, R. P. Muller, W. A. Goddard, J. F. Stoddart, *Aust. J. Chem.* **2004**, *57*, 301–322; b) A. H. Flood, J. F. Stoddart, D. W. Steuerman, J. R. Heath, *Science* **2004**, *306*, 2055–2056.
[5] G. Bottari, D. A. Leigh, E. M. Pérez, *J. Am. Chem. Soc.* **2003**, *125*, 13360–13361.
[6] a) E. M. Pérez, D. T. F. Dryden, D. A. Leigh, G. Teobaldi, F. Zerbetto, *J. Am. Chem. Soc.* **2004**, *126*, 12210–12211; b) Q.-C. Wang, D.-H. Qu, J. Ren, K. Chen, H. Tian, *Angew. Chem.* **2004**, *116*, 2715–2719; *Angew. Chem. Int. Ed.* **2004**, *43*, 2661–2665; c) D.-H. Qu, Q.-C. Wang, J. Ren, H. Tian, *Org. Lett.* **2004**, *6*, 2085–2088.
[7] a) D. W. Steuerman, H.-R. Tseng, A. J. Peters, A. H. Flood, J. O. Jeppesen, K. A. Nielsen, J. F. Stoddart, J. R. Heath, *Angew. Chem.* **2004**, *116*, 6648–6653; *Angew. Chem. Int. Ed.* **2004**, *43*, 6486–6491; b) A. H. Flood, A. J. Peters, S. A. Vignon, D. W. Steuerman, H.-R. Tseng, S. Kang, J. R. Heath, J. F. Stoddart, *Chem. Eur. J.* **2004**, *10*, 6558–6564.
[8] M. Cavallini, F. Biscarini, S. León, F. Zerbetto, G. Bottari, D. A. Leigh, *Science* **2003**, *299*, 531.
[9] a) A. S. Lane, D. A. Leigh, A. Murphy, *J. Am. Chem. Soc.* **1997**, *119*, 11092–11093; b) T. Da Ross, D. M. Guldi, A. Farran Morales, D. A. Leigh, M. Prato, R. Turco, *Org. Lett.* **2003**, *5*, 689–691; c) J. S. Hannam, S. M. Lacy, D. A. Leigh, C. G. Saiz, A. M. Z. Slawin, S. G. Stitchell, *Angew. Chem.* **2004**, *116*, 3322–3326; *Angew. Chem. Int. Ed.* **2004**, *43*, 3260–3264; A solvent-switchable shuttle system has been developed for polyrotaxanes by Gibson and co-workers: d) C. Gong, H. W. Gibson, *Angew. Chem.* **1997**, *109*, 2426–2428; *Angew. Chem. Int. Ed. Engl.* **1997**, *36*, 2331–2333; e) C. Gong, T. E. Glass, H. W. Gibson, *Macromolecules* **1998**, *31*, 308–313; f) P. E. Mason, W. S. Bryant, H. W. Gibson, *Macromolecules* **1999**, *32*, 1559–1569.
[10] G. W. H. Wurpel, A. M. Brouwer, I. H. M. van Stokkum, A. Farran, D. A. Leigh, *J. Am. Chem. Soc.* **2001**, *123*, 11327–11328.
[11] D. A. Leigh, A. Murphy, J. P. Smart, A. M. Z. Slawin, *Angew. Chem.* **1997**, *109*, 752–756; *Angew. Chem. Int. Ed. Engl.* **1997**, *36*, 728–732.

[12] J. H. Clements, S. E. Webber, *Macromolecules* **2004**, *37*, 1531 – 1536.
[13] Several low-energy hydrogen-bonding motifs (secondary structure) of the peptide-based molecular shuttles are in equilibrium in nonpolar solvents.[10] However, the relative position of the components (tertiary structure) is similar in each.
[14] Crystal data for **3′**: $C_{78}H_{76}N_8O_9$, $M_r = 1269.47$, clear crystal of dimensions $0.005 \times 0.02 \times 0.1$ mm^3, monoclinic, $P2_1/n$ (no. 14); $a = 11.3523(3)$, $b = 35.6055(6)$, $c = 16.1772(3)$ Å; $\beta = 95.3420(10)°$, $V = 6510.5(2)$ Å^3, $\rho_{calcd} = 1.295$ Mg m^{-3}, $Z = 4$; synchrotron radiation (CLRC Daresbury Laboratory Station 9.8, silicon monochromator, $\lambda = 0.68740$ Å), $T = 160(2)$ K; 36465 reflections measured, 13843 unique. The structure was solved and refined on 881 variables, using the teXsan crystallographic package of the Molecular Structure Corporation to yield final residuals of $R = 0.215$ and $R_w = 0.332$. All hydrogen atoms on carbon atoms were placed in idealized fixed geometries. All hydrogen atoms on nitrogen atoms were located from a ΔF map and allowed to refine. CCDC-159773 contains the supplementary crystallographic data for this paper. These data can be obtained free of charge from the Cambridge Crystallographic Data Centre via www.ccdc.cam.ac.uk/data_request/cif.
[15] C. A. Hunter *Angew. Chem.* **2004**, *116*, 5424 – 5439; *Angew. Chem. Int. Ed.* **2004**, *43*, 5310 – 5324.
[16] A. P. de Silva, H. Q. N. Gunaratne, T. Gunnlaugsson, A. J. M. Huxley, C. P. McCoy, J. T. Rademacher, T. E. Rice, *Chem. Rev.* **1997**, *97*, 1515 – 1566.
[17] J. Kroon, J. W. Verhoeven, M. N. Paddon-Row, A. M. Oliver, *Angew. Chem.* **1991**, *103*, 1398 – 1404; *Angew. Chem. Int. Ed. Engl.* **1991**, *30*, 1358 – 1361.
[18] Generated by using equation 12 in Ref. [15] (C. A. Hunter, personal communication).
[19] a) D. M. Haddleton, M. C. Crossman, B. H. Dana, D. J. Duncalf, A. M. Heming, D. Kukulj, A. J. Shooter, *Macromolecules* **1999**, *32*, 2110 – 2119; b) M. Kamigaito, T. Ando, M. Sawamoto, *Chem. Rev.* **2001**, *101*, 3689 – 3745; c) F. Lecolley, C. Waterson, A. J. Carmichael, G. Mantovani, S. Harrisson, H. Chappell, A. Limer, P. Williams, K. Ohno, D. M. Haddleton, *J. Mater. Chem.* **2003**, *13*, 2689 – 2695.
[20] For a recent review on molecular-scale logic gates, see: A. P. de Silva, N. D. McClenaghan, *Chem. Eur. J.* **2004**, *10*, 574 – 586.
[21] For a polymer-based Boolean logic gate that operates in solution, see: S. Uchiyama, N. Kawai, A. P. de Silva, K. Iwai, *J. Am. Chem. Soc.* **2004**, *126*, 3032 – 3033.
[22] R. A. van Delden, N. Koumura, N. Harada, B. L. Feringa, *Proc. Natl. Acad. Sci. USA* **2002**, *99*, 4945 – 4949.
[23] a) A. M. Brouwer, C. Frochot, F. G. Gatti, D. A. Leigh, L. Mottier, F. Paolucci, S. Roffia, G. W. H. Wurpel, *Science* **2001**, *291*, 2124 – 2128; b) A. Altieri, G. Bottari, F. Dehez, D. A. Leigh, J. K. Y. Wong, F. Zerbetto, *Angew. Chem.* **2003**, *115*, 2398 – 2402; *Angew. Chem. Int. Ed.* **2003**, *42*, 2296 – 2300.
[24] A. Altieri, F. G. Gatti, E. R. Kay, D. A. Leigh, F. Paolucci, A. M. Z. Slawin, J. K. Y. Wong, *J. Am. Chem. Soc.* **2003**, *125*, 8644 – 8654.
[25] G. Bottari, F. Dehez, D. A. Leigh, P. J. Nash, E. M. Pérez, J. K. Y. Wong, F. Zerbetto, *Angew. Chem.* **2003**, *115*, 6066 – 6069; *Angew. Chem. Int. Ed.* **2003**, *42*, 5886 – 5889.
[26] C. M. Keaveney, D. A. Leigh, *Angew. Chem.* **2004**, *116*, 1242 – 1244; *Angew. Chem. Int. Ed.* **2004**, *43*, 1222 – 1224.
[27] D. A. Leigh, E. M. Pérez, *Chem. Commun.* **2004**, 2262 – 2263.

Natural Product Synthesis

Synthesis of the Tetracyclic Core of the Tetrapetalones through Transannular Oxidative [4+3] Cyclization**

*Xiang Wang and John A. Porco, Jr.**

A series of novel soybean lipoxygenase (SBL) inhibitors, tetrapetalones A–D (**1**–**4**, Scheme 1), were recently isolated

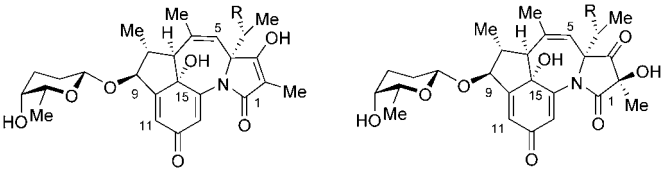

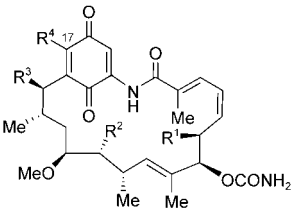

compound	R^1	R^2	R^3	R^4
macbecin (**5**)	Me	Me	OMe	H
herbimycin A (**6**)	OMe	Me	OMe	H
geldanamycin (**7**)	OMe	OH	H	OMe

Scheme 1. Chemical structures of the tetrapetalones A–D (**1**–**4**) and representative ansamycin natural products **5**–**7**.

by Komoda et al.[1] from the culture filtrate of the *Streptomyces* sp. strain USF-4727.[2] These tetrapetalones showed moderate inhibition of SBL ($IC_{50} = 190$–$360\ \mu M$ for **1**–**4**) comparable to the well-known lipoxygenase inhibitors nordihydroguaiaretic acid (NDGA, $IC_{50} = 290\ \mu M$) and kojic acid ($IC_{50} = 110\ \mu M$). The structure of tetrapetalone A (**1**) was first determined by ^1H NMR NOESY spectroscopic analysis and modified Mosher analysis,[1a] and then was subsequently revised by ^1H–^{15}N HMBC techniques, detailed NOE analysis, and chemical derivatization.[1b] The tetrapetalones B–D (**2**–**4**) were structurally characterized shortly thereafter and were shown to have similar inhibitory activities against SBL. The tetrapetalones possess an unprecedented tetracyclic skeleton bearing an appended β-rhodinosyl moiety. The unique structural feature of the tetracyclic core and its similarity to

[*] X. Wang, Prof. J. A. Porco, Jr.
Department of Chemistry and
Center for Chemical Methodology and Library Development
Boston University, 590 Commonwealth Avenue
Boston, MA 02215 (USA)
Fax: (+1) 617-353-6466
E-mail: porco@chem.bu.edu

[**] We thank Dr. J. Lee (Boston University) for assistance with NMR experiments and the National Institutes of Health (GM-62842) for research support.

Supporting information for this article is available on the WWW under http://www.angewandte.org or from the author.

 DOI: 10.1002/anie.200500247

the ansamycin antibiotics[3,4] attracted our interest and prompted consideration of synthetic approaches.

The ansamycins are important antibiotics possessing antibacterial, antifungal, and antitumor activities.[5] For example, geldanamycin (**7**) has been shown to inhibit the chaperone activity of heat shock protein 90 (Hsp 90) by noncovalent binding to its ATP/ADP binding site.[6] A synthetic analogue, 17-allylamino-17-demethoxygeldanamycin, has entered phase I clinical trials.[7] The benzylic ansamycin natural products (representative members are shown in Scheme 1) vary in oxidation level from a monophenol (for example, reblastatin),[3h] hydroquinone (for example, cytotrienin A),[3f] to a benzylquinone (for example, **5**–**7**), each bearing a highly functionalized polyketide *ansa* chain. It is likely that the biosynthesis of the benzylic ansamycins involves oxidation of the aromatic core after construction of the macrolactam unit.[8] We considered whether the tetrapetalones may be derived from a macrocyclic ansamycin precursor because of structural similarities between the tetrapetalones and the ansamycins. During oxidation of hydroquinone **8**, however, the arene-derived oxonium ion **9** may be trapped by the diene fragment, which subsequently reacts with the amide nitrogen atom to form the tetracyclic skeleton of **1**–**4** (Scheme 2).[9] It is also possible that the desired quinone **10** may undergo excited-state intramolecular proton transfer (ESIPT)[10] under UV irradiation to afford dipole **11**, which further reacts with the diene fragment to form the tetracycle. To investigate these and other possible transannular[11] [4+3] cyclization processes,[12,13] we developed a retrosynthetic analysis for tetrapetalone A to target the preparation of both hydroquinone **8** and quinone **10**. We considered ring-closing metathesis (RCM)[14] of acyclic substrate **12**, which may be derived from condensation of the acid **13** and aniline **14**, as a route to develop a convergent synthetic pathway to these precursors.

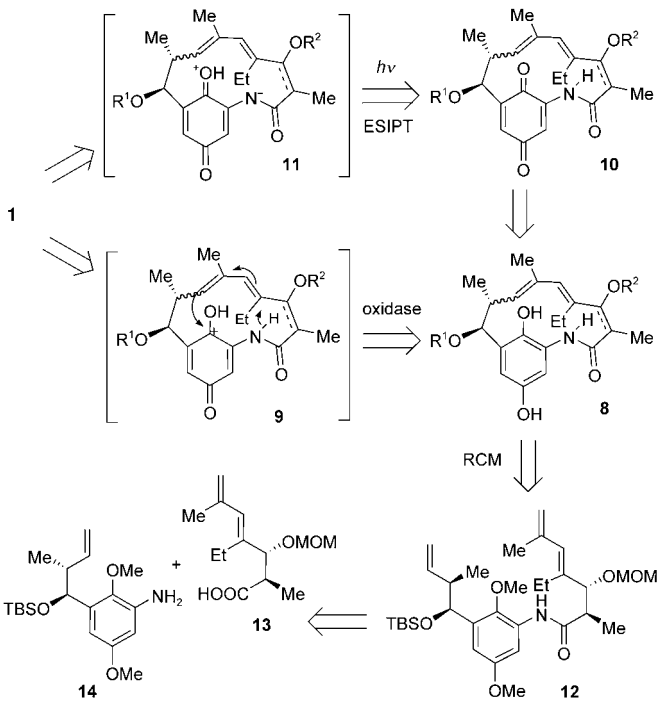

Scheme 2. Retrosynthetic analysis of tetrapetalone A (**1**). TBS = *tert*-butyldimethylsilyl. MOM = methoxymethyl.

Synthesis of the requisite diene acid **13** commenced with the Evans *syn*-aldol condensation[15] of dienal **15**[16] and chiral oxazolidinone **16** to afford chiral alcohol **17** as a single diastereomer (Scheme 3). Methoxymethyl (MOM) protection of the alcohol and hydrolysis of the chiral auxilary afforded **13** (85% yield, three steps). Asymmetric crotylation[17] of aldehyde **18**[4a] using the chiral *cis*-crotylboronate **19** derived from L-diisopropyltartrate (L-dipt) afforded chiral alcohol **20** (100% yield, single diastereomer). Silylation followed by reduction of the nitro group[18] afforded the desired aniline **14** (62% yield, two steps). Coupling of fragments **13** and **14** using *N*,*N*-bis(2-oxo-3-oxazolidinyl)phosphorodiamidic chloride (BOPCl)[19] led to epimerization of the α chiral center (C2, Scheme 3) of the amide product **12**. The use of an acid chloride proved to be feasible in the preparation of **12** (82%) without epimerization. However, treatment of acyclic triene **12** with the Grubbs second generation catalyst **21** did not produce the desired cyclic diene **22**. ^{1}H NMR spectroscopic analysis of the crude reaction mixture indicated that the ruthenium catalyst had reacted with the monosubstituted olefin, with no evidence of metathesis of the 1,1-disubstituted olefin. We believe that the 1,1-disubstituted olefin was

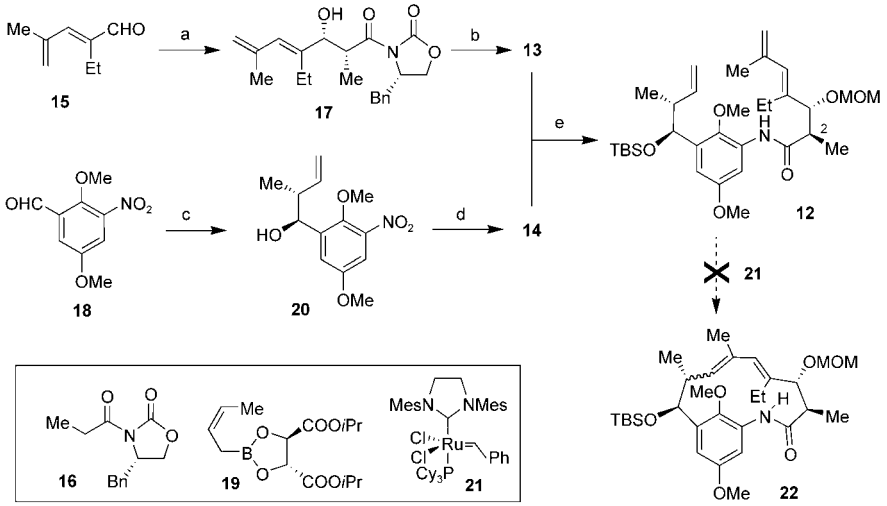

Scheme 3. RCM approach to macrolactam **22**. a) **16**, Bu_2BOTf, Et_3N, CH_2Cl_2, −78→0°C; b) 1. MOMCl, DIPEA; 2. LiOH, H_2O_2, THF, H_2O (85% yield over 3 steps); c) **19**, CH_2Cl_2, −78→25°C (100% yield); d) 1. TBSOTf, Et_3N, −78°C; 2. $NaBH_4$, S_8, THF, 65°C (62% yield over 2 steps); e) **13**, $(COCl)_2$, cat. DMF, CH_2Cl_2, 0→25°C; then **14**, Et_3N, 82% yield. MOMCl = chloromethyl methyl ether, DIPEA = diisopropylethylamine, TBSOTf = *tert*-butyldimethylsilyl triflate, DMF = *N*,*N*-dimethylformamide, Mes = mesitylene, Cy = cyclohexyl, Bn = benzyl.

unreactive in this case and that the two *meta*-substituted side chains are likely to be positioned away from each other because of "*meta* bridging" of the aromatic substituents. Therefore, the macrocyclic RCM was prohibited by both the reactivity of the olefin and the conformational strain within the substrate **12**.[4f] A conformational search on model **A** by molecular mechanics force field (MMFF) studies[20] (Scheme 4) suggested a possible rationale: the smallest

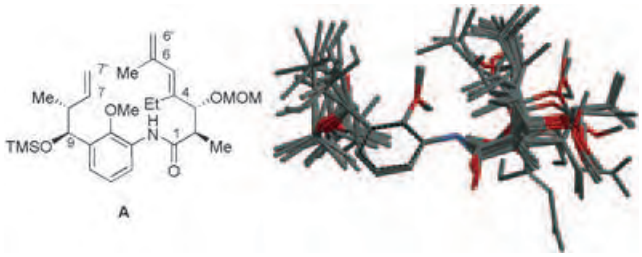

Scheme 4. Conformers of the "*meta*-bridged" acyclic model.

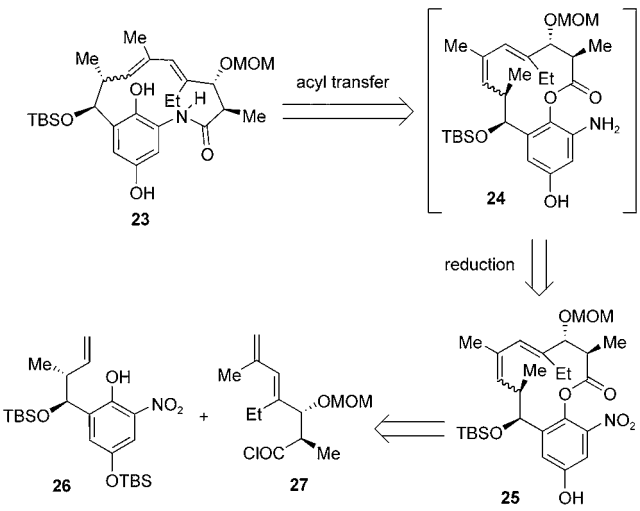

Scheme 5. Revised retrosynthetic analysis for macrolactam **23**.

distance between the C6′ and C7′ atoms is 6.2 Å among the low-energy conformers (E_{rel} = 0–5.2 kcal mol^{-1}) of model **A**. Therefore, the conformational strain of the "*meta*-bridged" framework may provide a significant barrier for macrocyclization of substrate **12**.

Since the direct macrocyclic RCM approach did not afford the desired macrocycle, we next considered that macrolactam **23** (Scheme 5) may be derived from an "*ortho*-bridged" macrolactone **24** through intramolecular acyl transfer[21] (ring expansion). Lactone **24** may be prepared from selective reduction of the nitro group of **25**, which may be obtained from nitrophenol **26** and acyl chloride **27**. A TBS group was chosen to protect the phenol of **26**, to facilitate removal at a later stage.

Synthesis of the revised C7–C15 fragment began with nitration of phenol **28**[22] followed by silylation to afford bis(silyl) ether **29** (70%, two steps; Scheme 6). Asymmetric crotylation of **29** using *cis*-crotyl boronate **19**[17] produced chiral alcohol **30** as a single diastereomer in quantitative yield. Deprotonation of the secondary alcohol of **30** using sodium hexamethyldisilazane (NaHMDS; THF, −78 °C) generated a sodium phenoxide species **31** in situ through intramolecular transfer of a silyl group.[23,24] Subsequent addition of acyl chloride **27**, Et_3N, and DMAP afforded phenol ester **32**. To our delight, triene **32** underwent smooth RCM macrocyclization to afford cyclic diene **33** after treatment with the Grubbs second generation catalyst **21** (80 °C, 30 min). NOE analysis showed that the newly formed olefin possessed a *Z* configuration. Selective desilylation of **33** (TBAF/AcOH) afforded nitrophenol **25** (85%, two steps).

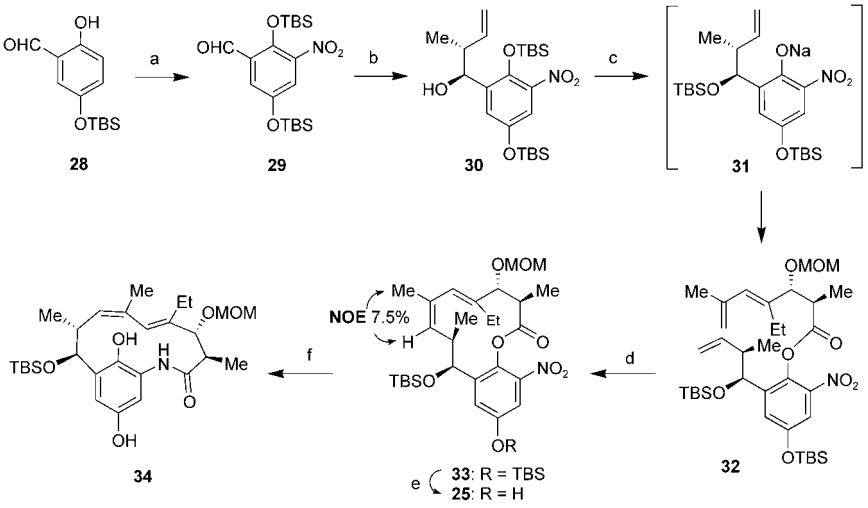

Scheme 6. Synthesis of ansamycin **34**. a) 1. $Cu(NO_3)_2 \cdot 3H_2O$, Ac_2O, 0→25 °C; 2. TBSCl, Et_3N, DMF, 70% yield over 2 steps; b) **19**, CH_2Cl_2, −78→25 °C, 99% yield; c) NaHMDS, THF, −78 °C; then **27**, Et_3N, DMAP, −78→25 °C, 85% yield; d) **21**, benzene, 80 °C; e) TBAF/HOAc, THF, 0 °C, 85% yield over 2 steps; f) $Pd/CaCO_3$, Et_3N, THF, 1 atm H_2; then silica gel, EtOAc. DMAP = 4-*N*,*N*-dimethylaminopyridine, DMF = *N*,*N*-dimethylformamide; HMDS = 1,1,1,3,3,3-hexamethyldisilazane; TBAF = tetrabutylammonium fluoride.

We next evaluated conditions for the selective reduction of the aryl nitro group in the presence of the diene functionality. We found that application of standard conditions for reduction of the nitro group, such as $SnCl_2$[25] and $NaBH_4/S_8$,[18] to substrate **25** not only reduced the nitro group but also hydrolyzed the ester, and no desired macrolactam **34** was formed. The use of Pd/C[26] or $Pd/CaCO_3$[27] in a hydrogen atmosphere was found to reduce both the diene and nitro groups. However, $Pd/CaCO_3$ chemoselectively reduced the nitro group of **25** when 10% triethylamine was employed as a cosolvent. Filtration of the reaction mixture through silica gel followed by elution with EtOAc cleanly afforded the desired acyl migration product **34**. It is interesting to note that use of the Lindlar catalyst[4b] resulted in formation of trace amounts of the desired product, presumably because of the catalyst poison PbO_2 and the sensitivity of aniline **24** to the oxidant.

With hydroquinone **34** in hand, we next evaluated the crucial biomimetic transannular oxidative [4+3] cyclization.[28] Out of the possible oxidants to effect the transformation of hydroquinones to quinones, we first chose $PhI(OAc)_2$[29] for the activation of hydroquinone. After considerable experimentation, we found that hydroquinone **34** was readily oxidized, with oxidative oligomerization as a major side reaction. Addition of a dilute solution of **34** in CH_2Cl_2 to a solution of $PhI(OAc)_2$ in CH_2Cl_2 at 0 °C over 15 minutes provided tetracycle **35** (42 %, two steps; Scheme 7). The structure of **35** was determined by NOESY spectroscopic analysis as shown in Scheme 7. Three stereocenters were formed (see inset, Scheme 7), and out of these, the configurations at the C4 and C7 atoms are the same as those of the natural products **1**–**4** but the configuration at C15 is reversed (*S*).

A conformational search of substrate **34** was performed by using MMFF studies to investigate the stereochemical outcome of this highly diastereoselective transannular [4+3] cyclization.[20] The macrocycle is positioned underneath the aromatic ring in the ground-state conformer (see inset, Scheme 7), thus establishing an *S* configuration for the C15 stereocenter. Allylic strain forces the C8–H bond to be eclipsed to the C6–C5 bond, which controls the configuration at C7. Since the ground-state conformer of **34** shows that C5–C6 is *s-trans*, we believe that the transannular cyclization may, in fact, be a stepwise process. After the diene reacts with the arene-derived oxonium ion, intermediate **36** may rotate to obtain a suitable conformation for reaction with the amide nitrogen atom. Furthermore, calculations indicated that the atropisomer of the macrolactam **34** that leads to the correct configuration at C15 is approximately 4.1 kcal mol^{-1} higher in energy than the ground-state conformer (see the Supporting Information).[30]

In summary, a novel I^{III}-promoted transannular oxidative [4+3] cyclization has been developed to construct the tetracyclic skeleton of the tetrapetalones. A convergent strategy to access the macrocyclic ansamycin precursor has been developed that involves a one-pot, base-mediated silyl transfer/acylation process for fragment coupling and a tandem reduction of the nitro group/acyl transfer process for construction of the highly strained, bicyclic system. This novel strategy provides an alternative approach to the construction of macrolactams as precursors to the ansamycin antibiotics and analogues. Synthetic studies toward the total synthesis of tetrapetalone A (**1**) and development of related oxidative [4+3] cyclization processes are currently being investigated and will be reported in due course.

Received: January 21, 2005
Published online: April 14, 2005

Keywords: acylation · antibiotics · cyclization · iodine

[1] a) T. Komoda, Y. Sugiyama, N. Abe, M. Imachi, H. Hirota, A. Hirota, *Tetrahedron Lett.* **2003**, *44*, 1659–1661; b) T. Komoda, Y. Sugiyama, N. Abe, M. Imachi, H. Hirota, H. Koshino, A. Hirota, *Tetrahedron Lett.* **2003**, *44*, 7417–7419; c) T. Komoda, K. Yoshida, N. Abe, Y. Sugiyama, M. Imachi, H. Hirota, H. Koshino, A. Hirota, *Biosci. Biotechnol. Biochem.* **2004**, *68*, 104–111; d) T. Komoda, M. Kishi, N. Abe, Y. Sugiyama, A. Hirota, *Biosci. Biotechnol. Biochem.* **2004**, *68*, 903–908.

[2] a) B. Axelrod, T. M. Cheesbrough, S. Laakso, *Methods Enzymol.* **1981**, *71*, 441–451; b) A. L. Tappel, W. O. Lumdberg, P. D. Boyer, *Arch. Biochem. Biophys.* **1953**, *42*, 293–304.

[3] Macbecin: a) H. Yamakim, S. Iguchi-Ariga, H. Ariga, *J. Antibiot.* **1989**, *42*, 604–610; b) S. Tanida, T. Hasegawa, E. Higashide, *J. Antibiot.* **1980**, *33*, 199–204; herbimycin A: c) S. Omura, Y. Iwai, Y. Takahashi, N. Sadasane, A. Nakagawa, H. Oiwa, Y. Hasegawa, T. Ikai, *J. Antibiot.* **1979**, *32*, 255–261; geldanamycin: d) K. Rinehart, K. Sasaki, G. Slomp, M. F. Grostic, E. C. Olson, *J. Am. Chem. Soc.* **1970**, *92*, 7591–7593; e) C. De Boer, P. A. Meulman, R. J. Wnuk, D. H. Peterson, *J. Antibiot.* **1970**, *23*, 442–447; cytotrienin A: f) H. Kakeya, H. Zhang, K. Kobinata, R. Onose, C. Onozawa, T. Kudo, H. Osada, *J. Antibiot.* **1997**, *50*, 370–372; mycotrienin: g) S. Hiramoto, M. Sugita, C. Ando, T. Sasaki, K. Furihata, H. Seto, N. Otake, *J. Antibiot.* **1985**, *38*, 1103–1106; reblastatin: h) P. Stead, S. Latif, A. P. Blackaby, P. J. Sidebottom,

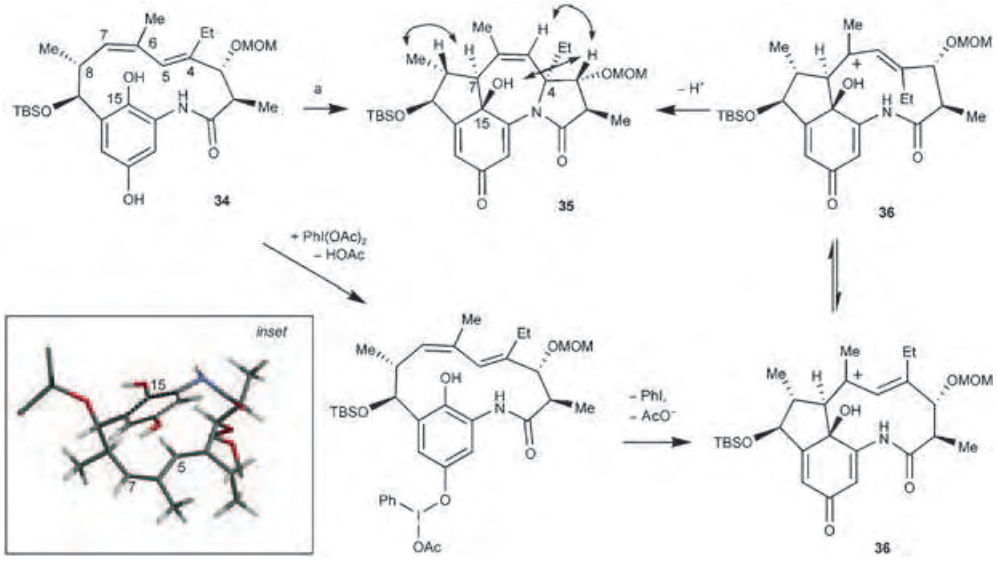

Scheme 7. I^{III}-promoted transannular oxidative [4+3] cyclization. a) $PhI(OAc)_2$, CH_2Cl_2, 0 °C (42 % yield over 2 steps).

A. Deakin, N. L. Taylor, P. Life, J. Spaull, F. Burrell, R. Jones, J. Lewis, I. Davidson, T. Mander, *J. Antibiot.* **2000**, *53*, 657 – 663.
[4] Total synthesis of macbecin: a) R. Baker, J. L. Castro, *J. Chem. Soc. Perkin Trans. 1* **1990**, 47 – 65; b) D. A. Evans, S. J. Miller, M. D. Ennis, *J. Org. Chem.* **1993**, *58*, 471 – 485; c) J. S. Panek, F. Xu, A. C. Rondon, *J. Am. Chem. Soc.* **1998**, *120*, 4113 – 4122; total synthesis of herbimycin A: d) M. Nakata, T. Osumi, A. Ueno, T. Kimura, T. Tamai, K. Tatsuta, *Tetrahedron Lett.* **1991**, *32*, 6015 – 6018; e) K. D. Carter, J. S. Panek, *Org. Lett.* **2004**, *6*, 55 – 57; total synthesis of geldanamycin: f) M. B. Andrus, E. L. Meredith, E. J. Hicken, B. L. Simmons, R. R. Glancey, W. Ma, *J. Org. Chem.* **2003**, *68*, 8162 – 8169.
[5] a) G. Lancini, M. Grandi, *Antibiotics* (New York) **1981**, *Vol.* 4, 12 – 40; b) L. Neckers, T. W. Schulte, E. Mimnaugh, *Invest. New Drugs* **1999**, *17*, 361 – 373; c) C. Najera, M. Yus, *Stud. Nat. Prod. Chem.* **2000**, *21B*, 373 – 455; d) S. Funayama, G. A. Cordell, *Stud. Nat. Prod. Chem.* **2000**, *23D*, 51 – 106.
[6] C. E. Stebbins, A. A. Russo, C. Schneider, N. Rosen, F. U. Hartl, N. P. Pavletich, *Cell* **1997**, *89*, 239 – 250.
[7] T. W. Schulte, L. M. Neckers, *Cancer Chemother. Pharmacol.* **1998**, *42*, 273 – 279.
[8] Y.-S. Hong, D. Lee, W. Kim, J.-K. Jeong, C.-G. Kim, J. K. Sohng, J.-H. Lee, S.-G. Paik, J. J. Lee, *J. Am. Chem. Soc.* **2004**, *126*, 11142 – 11143.
[9] For intramolecular trapping of an arene-derived oxonium ion with an alkene, see: A. Callinan, Y. Chen, G. Morrow, J. S. Swenton, *Tetrahedron Lett.* **1990**, *31*, 4551 – 4552.
[10] For a recent application of ESIPT in natural product synthesis, see: B. Gerald, G. Jones II, J. A. Porco, Jr., *J. Am. Chem. Soc.* **2004**, *124*, 13620 – 13621.
[11] For select examples of transannular cyclizations, see: a) A. Padwa, E. A. Curtis, V. P. Sandanayaka, *J. Org. Chem.* **1997**, *62*, 1317 – 1325; b) J. D. White, P. R. Blakemore, E. A. Korf, A. F. T. Yokochi, *Org. Lett.* **2001**, *3*, 413 – 415; for examples of transannular Diels–Alder reactions, see: c) E. M. Stocking, R. M. Williams, *Angew. Chem.* **2003**, *115*, 3186 – 3223; *Angew. Chem. Int. Ed.* **2003**, *42*, 3078 – 3115.
[12] For recent reviews, see: a) A. Padwa, A. Schoffstall, *Adv. Cycloaddit.* **1990**, *2*, 1 – 89; b) J. H. Rigby, F. C. Pigge, *Org. React.* **1997**, *51*, 351 – 478; c) F. G. West, *Adv. Cycloaddit.* **1997**, *4*, 1 – 40; d) M. Harmata, *Adv. Cycloaddit.* **1997**, *4*, 41 – 86; e) H. M. L. Davies, *Adv. Cycloaddit.* **1999**, *5*, 119 – 164; f) M. Harmata, P. Rashatasakhon, *Tetrahedron* **2003**, *59*, 2371 – 2395; g) I. V. Hartung, H. M. R. Hoffmann, *Angew. Chem.* **2004**, *116*, 1968 – 1984; *Angew. Chem. Int. Ed.* **2004**, *43*, 1934 – 1949.
[13] For intramolecular [4+3] cycloaddition reactions, see: a) H. Xiong, R. P. Hsung, C. R. Berry, C. Rameshkumar, *J. Am. Chem. Soc.* **2001**, *123*, 7174 – 7175; b) C. Rameshkumar, R. P. Hsung, *Angew. Chem.* **2004**, *116*, 625 – 628; *Angew. Chem. Int. Ed.* **2004**, *43*, 615 – 618.
[14] For recent reviews, see: a) A. Fürstner, *Angew. Chem.* **2000**, *112*, 3140 – 3172; *Angew. Chem. Int. Ed.* **2000**, *39*, 3012 – 3043; b) T. M. Trnka, R. H. Grubbs, *Acc. Chem. Res.* **2001**, *34*, 18 – 29; c) A. Deiters, S. F. Martin, *Chem. Rev.* **2004**, *104*, 2199 – 2238; for construction of a *para*-quinone macrolactam related to geldanamycin by RCM, see: d) A. Lemarchand, T. Bach, *Tetrahedron* **2004**, *60*, 9659 – 9673.
[15] D. A. Evans, J. Bartroli, T. L. Shih, *J. Am. Chem. Soc.* **1981**, *103*, 2127 – 2129.
[16] G. S. Mironov, M. I. Farberov, I. I. Bespalova, *Zh. Obshch. Khim.* **1964**, *34*, 1642 – 1645.
[17] W. R. Roush, K. Ando, D. B. Powers, A. D. Palkowitz, R. L. Halterman, *J. Am. Chem. Soc.* **1990**, *112*, 6339 – 6348.
[18] J. M. Lalancett, J. R. Freche, J. R. Brindle, M. Laliberte, *Synthesis* **1972**, 526 – 532; for application of this method, see: Ref. [4c]
[19] a) J. Diago-Meseguer, A. L. Palomo-Coll, J. R. Feemandez-Lizarbe, *Synthesis* **1980**, 547 – 551; b) C. Van Der Auwera, M. J. O. Anteunis, *Int. J. Pept. Protein Res.* **1987**, *29*, 574 – 588.
[20] All calculations were performed using Spartan '04 Windows (Wavefunction, Irvine, CA). a) "*Tutorial and User's Guide*"; b) W. J. Hehre, *A Guide to Molecular Mechanics and Quantum Chemical Calculations*, **2003**.
[21] a) O. W. Woltersdorf, Jr., H. Schwam, J. B. Bicking, S. L. Brown, S. J. DeSolms, D. R. Fishman, S. L. Graham, P. D. Gautheron, J. M. Hoffman, R. D. Larson, W. S. Lee, S. R. Michelson, C. M. Robb, N. N. Share, K. L. Shepard, A. M. Smith, R. L. Smith, J. M. Sondey, K. M. Strohmaier, M. F. Sugrue, M. P. Viaderg, *J. Med. Chem.* **1989**, *32*, 2486 – 2492; b) N. Matsumoto, H. Iinuma, T. Sawa, T. Takeuchi, *Bioorg. Med. Chem. Lett.* **1998**, *8*, 2945 – 2948.
[22] A. Liu, K. Dillon, R. M. Campbell, D. C. Cox, D. M. Huryn, *Tetrahedron Lett.* **1996**, *37*, 3785 – 3788.
[23] For a recent example of intramolecular transfer of a silyl group, see: P. Renton, L. Shen, J. Eckert, G. M. Lee, D. Gala, G. Chen, B. Pramanik, D. Schumacher, *Org. Process Res. Dev.* **2002**, *6*, 36 – 41.
[24] Nitrophenol **26** (94% *ee*) was isolated in quantitative yield after work up. HPLC analyses of **26** and *ent*-**26**: REGIS column, hexanes/2-propanol (99.5:0.5), $t_R = 7.2$ and 6.5 min, respectively.
[25] G. Subra, M. Amblard, J. Martinez, *Tetrahedron Lett.* **2002**, *43*, 9221 – 9223.
[26] P. R. Sleath, J. B. Noar, G. A. Eberlein, T. C. Bruice, *J. Am. Chem. Soc.* **1985**, *107*, 3328 – 3338.
[27] J. Smidrkal, J. Holubek, S. Jiri, J. Trojanek, *Collect. Czech. Chem. Commun.* **1985**, *50*, 861 – 868.
[28] For select examples of transannular oxidative cyclizations, see: a) M. F. Schlecht, H. J. Kim, *Tetrahedron Lett.* **1986**, *27*, 4889 – 4892; b) T. Hatta, S. Mataka, M. Tashiro, H. Suzuki, K. Numano, *J. Heterocycl. Chem.* **1991**, *28*, 289 – 293.
[29] For a review of hypervalent iodine chemistry, see: T. Wirth, *Mod. Dev. Org. Synth.* **2003**, *224*, 1 – 264.
[30] For synthesis involving atropisomers, see: a) S. Miyazaki, S. H. Kim, J. H. Wu, O. Loiseleur, S. L. Castle, *J. Am. Chem. Soc.* **1999**, *121*, 3226 – 3227; S. Miyazaki, S. H. Kim, J. H. Wu, O. Loiseleur, S. L. Castle, *J. Am. Chem. Soc.* **1999**, *121*, 10004 – 10011; b) M. E. Layton, C. M. Morales, M. D. Shair, *J. Am. Chem. Soc.* **2002**, *124*, 773 – 775; c) A. G. Myers, A. R. Hurd, P. C. Hogan, *J. Am. Chem. Soc.* **2002**, *124*, 4583 – 4585.

Iron Clusters

Coordination Chemistry of the Hexavacant Tungstophosphate $[H_2P_2W_{12}O_{48}]^{12-}$ with Fe^{III} Ions: Towards Original Structures of Increasing Size and Complexity**

*Béatrice Godin, Ya-Guang Chen, Jacqueline Vaissermann, Laurent Ruhlmann, Michel Verdaguer, and Pierre Gouzerh**

Dedicated to Professor Francis Sécheresse on the occasion of his 60th birthday

Polyoxometalates (POMs) are known to form original molecular and supramolecular structures of impressive size and complexity. This structural flexibility has been used to synthesize POMs with important chemical, biological, or physical properties.[1–3] Lacunary POMs form magnetic clusters with diverse nuclearities and original topologies.[4] The trivacant Keggin or Wells–Dawson polyoxotungstates have proven the most versatile polyoxoanion synthons for the preparation of magnetic clusters. Magnetic POMs with up to four trivacant POM subunits have been reported to date.[5,6] The largest number of first-row paramagnetic ions encapsulated in a diamagnetic POM matrix is displayed by the copper(II) polyoxotungstates $[\{(SiW_9O_{34})\{SiW_9O_{33}(OH)\}(Cu(OH))_6Cu\}_2X]^{23-}$ (X = Cl, Br) recently reported by Mialane et al.[6]

One of the goals of such studies is the search for single-molecule magnets (SMMs),[7] which are the subject of considerable interest owing to their unique physics and relevance in the development of functional nanosized materials. Their unusual properties derive from the combination of a large spin ground state with a large negative axial-type anisotropy. The current search for new SMMs is largely focused on polynuclear oxo iron[8,9] and manganese complexes.[10] Although interactions between Fe^{III} ions as well as between Mn^{III} ions, mediated by μ-oxo or μ-hydroxo bridges, are often antiferromagnetic, local ion anisotropy and particular topological arrangements can result in reasonably large spin ground states and negative *D* values. Therefore, original spin topologies and/or new SMMs can be expected from POMs with increasing size and complexity, particularly highly vacant POMs. This led us to explore the coordination chemistry of the hexavacant tungstophosphate $[H_2P_2W_{12}O_{48}]^{12-}$.

Lacunary derivatives of the Wells–Dawson anion α-$[P_2W_{18}O_{62}]^{6-}$ have been thoroughly investigated by Contant and Ciabrini,[11,12] and the related terminology (α, α_1, α_2) can be found in reference [11]. The metastable anion α-$[H_2P_2W_{12}O_{48}]^{12-}$, abbreviated as $\{P_2W_{12}\}$, could not be characterized by X-ray diffraction studies. However, its structure can be inferred from that of the condensed tetramer $[P_8W_{48}O_{184}]^{40-}$.[13] Further evidence for this structure comes from the reactions with tungstate, molybdate, and vanadate in acid media, which provide mixed tungsto-molybdo-vanadophosphates.[14] Another example of the reactivity of $\{P_2W_{12}\}$ towards d^0-transition metal ions is provided by the polyperoxo polyoxoanion $[P_2W_{12}O_{56}(NbO_2)_6]^{12-}$.[15] The reactions of $\{P_2W_{12}\}$ with lanthanides have led to the isolation of complexes that, instead of $\{P_2W_{12}\}$, contain $[P_2W_{16}O_{59}]^{16-}$ [16] or α_2-$[P_2W_{17}O_{61}]^{10-}$ [17]. In contrast, it was originally reported that $\{P_2W_{12}\}$ does not form complexes with divalent or trivalent transition-metal ions.[13] We have now succeeded in isolating several Fe^{III} and Mn^{III} complexes, and we present here our results on the $\{P_2W_{12}\}/Fe^{III}$ system.

In aqueous mixtures of lithium chloride and lithium acetate at ambient temperature, the reaction of $\{P_2W_{12}\}$ with an excess (8–14 equiv) of iron(III) chloride gives the metastable anion $[H_4P_2W_{12}Fe_9O_{56}(OAc)_7]^{6-}$ (**1**) which crystallizes as Li_2K_4-**1**·34 H_2O.[18] Upon heating in aqueous sodium acetate, **1** transforms into $[H_yP_8W_{48+x}Fe_{28-x}O_{248}]^{(84-y-3x)-}$ (**2**), which has been isolated as different salts that show slight variation in the value of *x*. A sample formulated as $Na_{16}K_{12}[H_{56}P_8W_{48}Fe_{28}O_{248}]$·ca.90 H_2O ($Na_{16}K_{12}$-**2a**·ca.90 H_2O) based on chemical analysis was obtained by heating $\{P_2W_{12}\}$ with 6 equiv of iron(III) chloride in 0.5 M sodium acetate. It was characterized by electrochemical and magnetic measurements, and by determination of the unit cell parameters. A complete X-ray diffraction study was performed on a crystal from another sample for which the formula $Na_{16}K_{10}[H_{55}P_8W_{49}Fe_{27}O_{248}]$·ca.90 H_2O ($Na_{16}K_{10}$-**2b**·ca.90 H_2O) is proposed on the basis of the structure determination. There is also some evidence of the formation of other representatives of **2** (possibly with *x* up to 4) when the Fe^{III}:$\{P_2W_{12}\}$ ratio or the pH value is lowered. However, chemical analysis and IR spectroscopy are insufficient to unequivocally determine the composition and purity of these products. When the Fe^{III}:$\{P_2W_{12}\}$ ratio is less than 4, clusters with the generalized formula $[H_yP_4W_{28+x}Fe_{8-x}O_{120}]^{(28-y-3x)-}$ (**3**) are obtained instead of **2**.[19]

The structure of **1** is shown in Figure 1. The cluster has crystallographically imposed C_2 symmetry. It derives from the hexavacant $\{P_2W_{12}\}$ anion by filling up the six vacancies with iron atoms. The substituted Wells–Dawson species $\{P_2W_{12}Fe_6\}$ thus formed supports three additional iron atoms: Two of

[*] Dr. B. Godin, Dr. Y.-G. Chen,[+] Dr. J. Vaissermann, Prof. M. Verdaguer, Prof. P. Gouzerh
Laboratoire de Chimie Inorganique et Matériaux Moléculaires, UMR CNRS 7071
Université Pierre et Marie Curie
4 Place Jussieu, 75252 Paris Cedex 05 (France)
Fax: (+33) 1-4427-3841
E-mail: pg@ccr.jussieu.fr
Dr. L. Ruhlmann
Laboratoire de Chimie Physique, UMR CNRS 8000
Université Paris-Sud
91405 Orsay Cedex (France)
[+] Present address:
Faculty of Chemistry
Northeast Normal University
Changchun (PR China)

[**] This work was supported by the CNRS and the Université Pierre et Marie Curie.

Supporting information for this article is available on the WWW under http://www.angewandte.org or from the author.

  DOI: 10.1002/anie.200463033

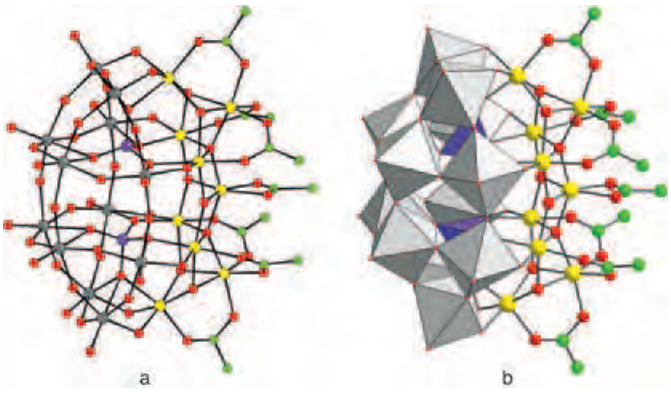

Figure 1. Ball-and-stick (a) and combined polyhedral ball-and-stick representations (b) of **1** in Li_2K_4-**1**·34 H_2O (P violet, O red, Fe yellow, W black, C green).

them are connected to three contiguous bridging oxo ligands of the $\{P_2W_{12}Fe_6\}$ subunit, while the third is connected to four bridging oxo ligands. Sixfold coordination of the Fe^{III} centers is achieved by coordination to acetate ligands. Six of the seven acetate ligands are bridging while the seventh is chelating. The Fe^{III} centers are connected through six μ_3-O and two μ_4-O units. The results of bond valence sum (BVS) calculations[20] indicate that the triply bridging oxygen atoms that do not lie in the equatorial plane are protonated. Thus the anion is formulated as $[H_4P_2W_{12}Fe_9O_{56}(OAc)_7]^{6-}$ in agreement with the results of chemical analysis. Compound **1** can be considered as bridging the gap between transition metal substituted POMs such as $[\alpha\text{-}P_2W_{15}O_{59}(FeCl)_2(FeOH_2)]^{11-}$ [21] and classic coordination clusters such as $[Fe_3O(OAc)_6(H_2O)_3]^+$.[22] Apart from the keplerates,[23a] where acetate anions act as bridging ligands for the $\{Mo_2^{V}O_4\}$ linkers, there are only a few complexes of POMs that contain acetate ligands. These include $[\gamma\text{-}SiW_{10}O_{36}(OH)Cr_2(OAc)_2(H_2O)_2]^{5-}$,[24a] $[PW_{11}O_{39}\{Rh_2(OAc)_2\}]^{5-}$,[24b] $[\{\alpha_2\text{-}P_2W_{17}O_{61}La(OAc)(H_2O)_2\}_2]^{16-}$,[17] and $[\{SiW_{11}O_{39}Ln(H_2O)(OAc)\}_2]$.[25]

The structure of **2b** is shown in Figure 2. This cluster can be viewed as a supramolecular Wells–Dawson polyoxotungstate. Each of the four $\{P_2W_{12}Fe_6\}$ subunits is connected by three Fe-O-Fe bridges to an adamantane $\{Fe_4O_6\}$ core. In addition, they are linked into pairs by three Fe-O-Fe bridges involving the three outer iron atoms. These extra bonds differentiate **2b** from the otherwise similar tetra-Keggin anion $[Nb_4O_6(\alpha\text{-}Nb_3SiW_9O_{40})_4]^{20-}$.[26] To our knowledge, there are only a few crystallographically characterized iron(III) clusters that contain an adamantane-like core: These are tetranuclear complexes with ditopic, heptadentate ligands[27] and triazacyclononane.[28]

The inner site α_2 of each Wells–Dawson subunit of **2b** is occupied either by tungsten or iron. Crystallographic refinement resulted in occupancy factors of 0.25 for W and 0.75 for Fe in this site; thus, the composition of the cluster is $\{P_8W_{49}Fe_{27}\}$. According to BVS calculations, all the Fe-O-Fe bridges are protonated, which leads to the composition $[H_{55}P_8W_{49}Fe_{27}O_{248}]^{26-}$. Only a few tetrahedral supramolecular POMs have been characterized so far. Besides the above-mentioned Nb-containing compound,[26] these include the polyoxomolybdo-europate $[Eu_4(MoO_4)(H_2O)_{16}(Mo_7O_{24})_4]^{14-}$,[29] the uranium-containing polyoxotungstate $[(UO_2)_{12}(\mu_3\text{-}O)_4(\mu_2\text{-}H_2O)_{12}(P_2W_{15}O_{56})_4]^{32-}$,[30] the tetrameric titanium(IV)-substituted Wells–Dawson polyoxotungstate $[\{Ti_3P_2W_{15}O_{57.5}(OH)_3\}_4]^{24-}$,[31] and the tetra(polyoxometalate) dendrimers $[\{P_2V_3W_{15}O_{59}(OCH_2)_3CNHCOCH_2CH_2OCH_2\}_4C]^{24-}$ [32a] and $[(SiW_{11}O_{39}GeCH_2CH_2CO_2CH_2)_4C]^{20-}$.[32b]

The cyclic voltammograms of $\{P_2W_{12}\}$, **1**, and **2a** are shown in Figure 3. The electrochemistry of $\{P_2W_{12}\}$ has been described.[33] The first reduction wave of **1** and **2a**, which is attributed to the reduction of Fe^{III} to Fe^{II}, is rather broad, particularly for **1**. However, stepwise reduction of the Fe^{III} centers is not observed, in contrast to the sandwich complexes $\alpha\beta\beta\alpha\text{-}[(Fe^{III}OH_2)_2Fe_2^{III}(X_2W_{15}O_{56})_2]^{12-}$ (X = P,[34a,b] As[34c,d]). Controlled potential coulometry under continuous argon bubbling and stirring consumes 9.3 and 27.8 electrons per molecule, respectively, for **1** at pH 3 and **2a** at pH 2. This is in satisfactory agreement with analytical and structural data. An

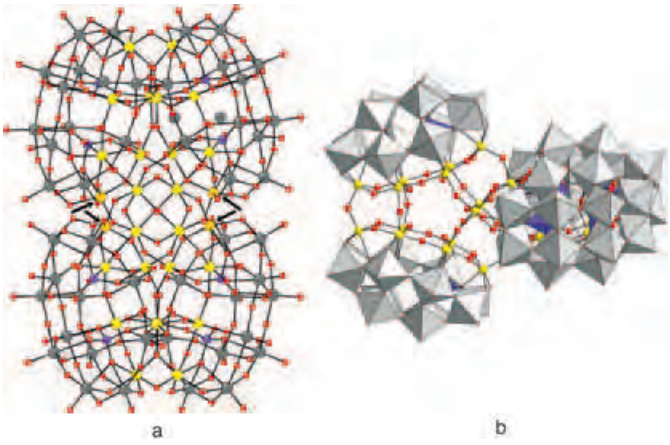

Figure 2. Ball-and-stick (a) and combined polyhedral ball-and-stick representations (b) of **2b** in $Na_{16}K_{10}$-**2b**·90 H_2O (P violet, O red, Fe yellow, W black, C green). The four inner α_2 positions (shown by the arrows) possess 75% Fe and 25% W character.

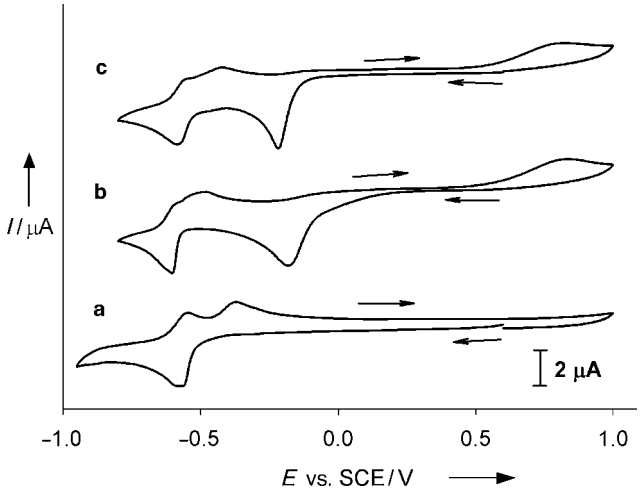

Figure 3. The cyclic voltammograms of 0.1 mM samples of $[H_2P_2W_{12}O_{48}]^{12-}$ (a), **1** (b), and **2a** (c) in 0.5 M $Li_2SO_4 + H_2SO_4$ at pH 3. The scan rate was 20 $mV\,s^{-1}$, and a glassy carbon electrode was used.

oxidation wave appears at about +0.8 V, which is attributed to the oxidation of free Fe^{II}. Demetalation of **1** and **2** upon reduction of the Fe^{III} centers parallels the behavior of multi-iron Wells–Dawson sandwich-type polyoxotungstates.[35]

The temperature dependence of the magnetization of Li_2K_4-**1**·34 H_2O was studied down to 2 K. The $\chi_M T$ product at 300 K (20 $cm^3 mol^{-1} K$) is much lower than expected for nine noninteracting Fe^{III} centers (39.4 $cm^3 mol^{-1} K$) and decreases continuously to 1.94 $cm^3 mol^{-1} K$ at 2 K. This indicates strong intramolecular antiferromagnetic coupling between the Fe^{III} centers. The magnetization was studied as a function of the applied magnetic field at 2 K: The magnetization at 50 kOe (4.2 μ_B) is consistent with a paramagnetic ground state, as expected for a cluster with an odd number of Fe^{III} centers. The magnetization data at 2 K, however, do not fit a Brillouin function for a spin $S = 5/2$, which indicates a more complex situation in the ground state. Even if the C_2 symmetry of the cluster results in a reduction in the number of nearest neighbor exchange coupling constants J in **1** to seven, the extraction of very different J values from the magnetic data is far from trivial. Accurate magnetization data, EPR characterization, and computation of the J values by density functional theory methods are in progress.[36] Magnetic studies of **2** also indicate strong antiferromagnetic coupling between the Fe^{III} centers. The residual paramagnetism in the studied sample corresponds to the presence of a species with an odd number of Fe^{III} centers, such as **2b**. Further studies are planned on this family of compounds.

In conclusion, the hexavacant tungstophosphate anion $[H_2P_2W_{12}O_{48}]^{12-}$ can accomodate six Fe^{III} centers. The $\{P_2W_{12}Fe_6\}$ species thus formed is stabilized as either **1** or **2** through further reaction with Fe^{III} centers. In addition, tungsten may substitute a part of the iron in the $\{P_2W_{12}Fe_6\}$ moiety. To our knowledge, cluster **2b**, with 27 Fe^{III} centers, is the second largest iron cluster characterized so far, being only surpassed by the $\{Mo^{VI}_{72}Fe^{III}_{30}\}$ keplerate.[23b] Manganese and nickel derivatives of $\{P_2W_{12}\}$ have been also obtained and will be reported soon.[19]

Experimental Section

1: $FeCl_3$·6 H_2O (1.21 g, 4.48 mmol) was added to a stirred solution of $K_{12}[H_2P_2W_{12}O_{48}]$·24 H_2O[12] (1.97 g, 0.50 mmol) in a mixture of 5 M LiCl (25 mL), 4 M LiOAc (9 mL), and H_2O (5 mL). The resulting mixture was stirred for 5 h and then allowed to sit. After 1 day the mixture was filtered. Dark red crystals of Li_2K_4-**1**·34 H_2O deposited from the filtrate (pH 3.7) over 1–2 d. The crystals were collected by filtration through a glass frit and washed with ice-cold water (10 mL). Yield 0.37 g (15% calculated from $\{P_2W_{12}\}$). Elemental analysis calcd (%) for $C_{14}H_{93}K_4Li_2Fe_9O_{104}P_2W_{12}$: C 3.46, K 3.21, Li 0.29, Fe 10.33, P 1.27, W 45.33; found: C 3.56, K 3.12, Li 0.33, Fe 10.13, P 1.19, W 43.37.

2: $K_{12}[H_2P_2W_{12}O_{48}]$·24 H_2O (1.0 g, 0.25 mmol) and $FeCl_3$·6 H_2O (0.405 g, 1.5 mmol) were added to a mixture of 4 M NaOAc (6 mL) and H_2O (40 mL). The resulting suspension was heated to 95 °C for 3 h and then cooled to 20 °C and filtered. Yellow-green crystals of composition $Na_{16}K_{12}$-**2a**·ca.90 H_2O deposited from the filtrate (pH 5.2) over 5 d. Yield 0.16 g (15% calculated from $\{P_2W_{12}\}$). Elemental analysis calcd (%) for $H_{238}K_{12}Fe_{28}Na_{16}O_{318}P_8W_{48}$: K 2.79, Fe 9.31, Na 2.17, P 1.47, W 52.53; found: K 2.94, Fe 9.0, Na 2.1, P 1.12, W 50.66.

The crystals thus obtained were of limited quality and only the cell parameters could be determined. Better-quality crystals, used for the crystal structure determination,[18] were obtained as follows: An aqueous solution of $Fe(ClO_4)_3$·6 H_2O (1.39 g, 3 mmol) in H_2O (10 mL) was added to a stirred suspension of $K_{12}[H_2P_2W_{12}O_{48}]$·24 H_2O (2.0 g, 0.51 mmol) in 1 M NaOAc/AcOH (20 mL, pH 6). The mixture was heated at reflux for 1 h, upon which a clear solution was obtained. The sticky solid that deposited on cooling to 20 °C was discarded and the subsequent polycrystalline fraction was recrystallized in 0.5 M NaOAc/AcOH (pH 6) to give yellow-green rods ($Na_{16}K_{10}$-**2b**·ca.90 H_2O). Both sets of crystals display similar cell parameters and IR spectra, despite small differences in the composition.

Received: December 22, 2004
Published online: April 18, 2005

Keywords: cluster compounds · electrochemistry · iron · magnetic properties · tungsten

[1] Special issue on Polyoxometalates (Guest Ed.: C. L. Hill): *Chem. Rev.* **1998**, *98*, 1–389.
[2] *Polyoxometalate Chemistry From Topology via Self-Assembly to Applications* (Eds.: M. T. Pope, A. Müller), Kluwer Academic Publishers, Dordrecht, **2001**.
[3] *Polyoxometalate Chemistry for Nano-Composite Design* (Eds.: T. Yamase, M. T. Pope), Kluwer Academic/Plenum Publishers, New York, **2002**.
[4] J. M. Clemente-Juan, E. Coronado, *Coord. Chem. Rev.* **1999**, *193–195*, 361–394.
[5] a) T. J. R. Weakley, *J. Chem. Soc. Chem. Commun.* **1984**, 1406–1407; b) J. M. Clemente-Juan, E. Coronado, J. R. Galan-Mascaros, C. J. Gomez-Garcia, *Inorg. Chem.* **1999**, *38*, 55–63.
[6] P. Mialane, A. Dolbecq, J. Marrot, E. Rivière, F. Sécheresse, *Angew. Chem.* **2003**, *115*, 3647–3650; *Angew. Chem. Int. Ed.* **2003**, *42*, 3523–3526.
[7] a) D. Gatteschi, R. Sessoli, *Angew. Chem.* **2003**, *115*, 278–309; *Angew. Chem. Int. Ed.* **2003**, *42*, 268–297.
[8] E. M. Rumberger, S. Hill, R. S. Edwards, W. Wernsdorfer, L. N. Zakharov, A. L. Rheingold, G. Christou, D. N. Hendrickson, *Polyhedron* **2003**, *22*, 1865–1870.
[9] L. F. Jones, E. K. Brechin, D. Collison, M. Helliwell, T. Mallah, S. Piligkos, G. Rajaraman, W. Wernsdorfer, *Inorg. Chem.* **2003**, *42*, 6601–6603.
[10] A. J. Tasiopoulos, A. Vinslava, W. Wernsdorfer, K. A. Abboud, G. Christou, *Angew. Chem.* **2004**, *116*, 2169–2173; *Angew. Chem. Int. Ed.* **2004**, *43*, 2117–2121.
[11] R. Contant, J.-P. Ciabrini, *J. Chem. Res. Synop.* **1977**, 222; R. Contant, J.-P. Ciabrini, *J. Chem. Res. Miniprint* **1977**, 2601–2617.
[12] R. Contant, *Inorg. Synth.* **1990**, *27*, 104–111.
[13] R. Contant, A. Tézé, *Inorg. Chem.* **1985**, *24*, 4610–4614.
[14] R. Contant, M. Abbessi, R. Thouvenot, G. Hervé, *Inorg. Chem.* **2004**, *43*, 3597–3604.
[15] D. A. Judd, Q. Chen, F. Campana, C. L. Hill, *J. Am. Chem. Soc.* **1997**, *119*, 5461–5462.
[16] A. Ostuni, M. T. Pope, *C. R. Chim.* **2000**, *3*, 199–204.
[17] U. Kortz, *J. Cluster Sci.* **2003**, *14*, 205–214.
[18] Crystal data for Li_2K_4-**1**·34 H_2O: Monoclinic, *C*2/*c* (no. 15), a = 17.566(6), b = 20.384(6), c = 26.527(16) Å, β = 103.98(4)°, V = 9217(7) Å^3, ρ_{calcd} = 3.51 g cm^{-3}, μ = 16.63 mm^{-1}, 8637 reflections (8086 unique) to 2θ = 50°, 299 refined parameters, R = 0.058, $wR(F_o^2)$ = 0.059 [2910 reflections with $I > 3\sigma(I)$], GOF = 1.13, $\Delta\rho_{max}$ = 1.93 e Å^{-3}, $\Delta\rho_{min}$ = −2.35 e Å^{-3}. Crystal data for $Na_{16}K_{10}$-**2b**·ca.90 H_2O: Triclinic, $P\bar{1}$ (no. 2), a = 21.9605(3), b = 22.4724(5), c = 28.9946(5), α = 97.590(1), β = 94.326(1), γ = 90.813(1)°, V = 14139.0(4) Å^3, ρ_{calcd} = 4.03 g cm^{-3}, μ = 21.5 mm^{-1}, 96851 reflections (68661 unique) to 2θ = 60°, 1569

refined parameters, $R = 0.068$, $wR(F_o^2) = 0.077$ [20249 reflections with $I > 3\sigma(I)$], GOF = 1.09, $\Delta\rho_{max} = 9.92\ e\,Å^{-3}$, $\Delta\rho_{min} = -2.99\ e\,Å^{-3}$. The X-ray crystallographic data were collected at room temperature either on an Enraf-Nonius MACH3 diffractometer (**1**) or on a Bruker SMART three-circle diffractometer equipped with a CCD bidimensional detector (**2b**), both with graphite-monochromated $Mo_{K\alpha}$ radiation ($\lambda = 0.71073$ Å). The structures were solved and refined by full-matrix least squares using CRYSTALS. Neutral-atom scattering factors were used with anomalous dispersion corrections applied. Hydrogen atoms were not included in the refinements. Both structures exhibit some disorder in the range of counterions and water molecules, as is often the case with polyoxometalates. Thus, only a limited number of cations and water molecules could be located. This resulted in rather high residual electron densities. CCDC-258626 contains the supplementary crystallographic data for Li_2K_4-**1**·34 H_2O. These data can be obtained free of charge from the Cambridge Crystallographic Data Centre via www.ccdc.cam.ac.uk/data_request/cif. Further details on the crystal structure investigation on $Na_{16}K_{10}$-**2b**·ca.90 H_2O may be obtained from the Fachinformationszentrum Karlsruhe, 76344 Eggenstein-Leopoldshafen, Germany (fax: (+49) 7247-808-666; e-mail: crysdata@fiz-karlsruhe.de), on quoting the depository number CSD-391310.

[19] B. Godin, J. Vaissermann, P. Herson, L. Ruhlmann, M. Verdaguer, P. Gouzerh, unpublished results..

[20] a) N. E. Beese, M. O'Keefe, *Acta Crystallogr. Sect. B* **1991**, *47*, 192; b) I. D. Brown, D. Altermatt, *Acta Crystallogr. Sect. B* **1985**, *41*, 244.

[21] T. M. Anderson, X. Zhang, K. I. Hardcastle, C. L. Hill, *Inorg. Chem.* **2002**, *41*, 2477 – 2488.

[22] a) A. Earnshaw, B. N. Figgis, *J. Chem. Soc. A* **1966**, 1656; b) K. Anzenhofer, J. J. De Boer, *Recl. Trav. Chim. Pays-Bas* **1969**, *88*, 286.

[23] a) A. Müller, E. Krickemeyer, H. Bögge, M. Schmidtmann, F. Peters, *Angew. Chem.* **1998**, *110*, 3567 – 3571; *Angew. Chem. Int. Ed.* **1998**, *37*, 3360 – 3363; b) A. Müller, S. Sarkar, S. Q. N. Shah, H. Bögge, M. Schmidtmann, S. Sarkar, P. Kögerler, B. Hauptfleisch, A. X. Trautwein, V. Shünemann, *Angew. Chem.* **1999**, *111*, 3432 – 3435; *Angew. Chem. Int. Ed.* **1999**, *38*, 3238 – 3241.

[24] a) K. Wassermann, H.-J. Lunk, R. Palm, J. Fuchs, N. Steinfeldt, R. Stösser, M. T. Pope, *Inorg. Chem.* **1996**, *35*, 3273 – 3279; b) X. Wei, M. H. Dickman, M. T. Pope, *Inorg. Chem.* **1997**, *36*, 130 – 131.

[25] P. Mialane, A. Dolbecq, E. Rivière, J. Marrot, F. Sécheresse, *Eur. J. Inorg. Chem.* **2004**, 33 – 36.

[26] G.-S. Kim, H. Zeng, D. VanDerveer, C. L. Hill, *Angew. Chem.* **1999**, *111*, 3413 – 3416; *Angew. Chem. Int. Ed.* **1999**, *38*, 3205 – 3207.

[27] a) B. P. Murch, F. C. Bradley, P. D. Boyle, V. Papaefthymiou, L. Que, Jr., *J. Am. Chem. Soc.* **1987**, *109*, 7993 – 8003; b) J. L. Sessler, J. W. Sibert, A. K. Burrell, V. Lynch, J. T. Markert, C. L. Wooten, *Inorg. Chem.* **1993**, *32*, 4277 – 4283.

[28] S. Drüeke, K. Wieghardt, B. Nuber, J. Weiss, E. L. Bominaar, A. Sawaryn, H. Winkler, A. X. Trautwein, *Inorg. Chem.* **1989**, *28*, 4477 – 4483.

[29] H. Naruke, T. Ozeki, T. Yamase, *Acta Crystallogr. Sect. C* **1991**, *47*, 489 – 492.

[30] A. J. Gaunt, I. May, D. Collison, K. T. Holman, M. T. Pope, *J. Mol. Struct.* **2003**, *656*, 101 – 106.

[31] U. Kortz, S. S. Hamzeh, S. A. Nasser, *Chem. Eur. J.* **2003**, *9*, 2945 – 2952.

[32] a) H. Zeng, G. R. Newkome, C. L. Hill, *Angew. Chem.* **2000**, *112*, 1842 – 1844; *Angew. Chem. Int. Ed.* **2000**, *39*, 1772 – 1774; b) G. Sazani, M. T. Pope, *Dalton Trans.* **2004**, 1989 – 1994.

[33] R. Contant, M. Richet, Y. W. Lu, B. Keita, L. Nadjo, *Eur. J. Inorg. Chem.* **2002**, 2587 – 2593.

[34] a) X. Zhang, Q. Chen, D. C. Duncan, R. J. Lachicotte, C. L. Hill, *Inorg. Chem.* **1997**, *36*, 4381 – 4386; b) L. Ruhlmann, L. Nadjo, J. Canny, R. Contant, R. Thouvenot, *Eur. J. Inorg. Chem.* **2002**, 975 – 986; c) U. Kortz, M. G. Savelieff, B. S. Bassim, B. Keita, L. Nadjo, *Inorg. Chem.* **2002**, *41*, 783 – 789; d) I. M. Mbomekalle, B. Keita, L. Nadjo, P. Berthet, K. I. Hardcastle, C. L. Hill, T. M. Anderson, *Inorg. Chem.* **2003**, *42*, 1163 – 1169.

[35] B. Keita, I. M. Mbomekalle, L. Nadjo, T. M. Anderson, C. L. Hill, *Inorg. Chem.* **2004**, *43*, 3257 – 3262.

[36] E. Ruiz, S. Alvarez, unpublished results.

Zeolites

Electrochemically Controlled Ion Exchange: Proton Exchange with Sodium Zeolite Y**

*Michael J. Stephenson, Stuart M. Holmes, and Robert A. W. Dryfe**

In memory of R. J. Plaisted

Zeolites are central to a number of industrially important processes, such as catalysis, gas separation, and sorption of impurities from the solution phase.[1,2] All zeolite structures, other than the purely silicaceous series end-members, contain counterions, whose nature and position can be extremely important in the aforementioned applications. Catalytic cracking of hydrocarbons, for example, is dependent upon the introduction of protons to the zeolite structure.[3] Since zeolites are frequently synthesized in their sodium form, other counterions must be introduced through ion exchange.

Zeolite Y, which has the Faujasite structure, is a principal component of cracking catalysts because of properties such as its high thermal stability and large internal surface area with easily accessible active sites. It consists of a 3D network of 12 Si or Al atoms that form circular channels 7.4 Å in diameter with cavities 11.8 Å in diameter.[4] The as-synthesized sodium form is converted into the acidic form either by direct ion exchange with dilute mineral acids or by calcination of the ammonium ion exchanged form of the zeolite to release

[*] Dr. M. J. Stephenson, Dr. R. A. W. Dryfe
School of Chemistry
University of Manchester
PO Box 88, Manchester, M601QD (UK)
Fax: (+44) 161-200-4559
E-mail: robert.dryfe@manchester.ac.uk
Dr. S. M. Holmes
School of Chemical Engineering and Analytical Science
University of Manchester
PO Box 88, Manchester, M601QD (UK)

[**] Funding from the EPSRC (GR/S11596/01) is acknowledged. Also we are grateful for the technical assistance of Mr R. J. Plaisted (1942–2005).

Supporting information for this article is available on the WWW under http://www.angewandte.org or from the author.

 DOI: 10.1002/anie.200463036

ammonia.[5] Care is needed with direct ion exchange because at low pH values acid-mediated dealumination occurs followed by structural collapse.[6] To avoid these problems, the route from the ammonium ion exchanged form to acidic zeolite Y (H−Y) is preferred. Herein, we demonstrate a novel, direct method for the preparation of H−Y by electrochemically controlled proton exchange. Importantly, we believe this method, which offers enhanced control over the degree of ion exchange, is generic, and is thus applicable to other zeolite structures and the introduction of other cations.

The novel approach described herein is derived from liquid/liquid electrochemistry, in which ions can be driven from one liquid phase into an adjacent immiscible liquid phase by application of a potential across the liquid/liquid interface.[7,8] Typically, an aqueous/organic system is employed, with solvents such as nitrobenzene or 1,2-dichloroethane (DCE) used as the organic phase. The transfer of hydrophilic ions, such as Na^+, can be facilitated by the use of a complexing agent in the organic phase (for example, crown ethers). This complexing agent stabilizes the transferred ion, and in doing so lowers the required transfer potential [see Equation (1), in which the equilibrium is potential-dependent and L denotes the complexing agent].

$$Na^+_{(aq)} + L_{(org)} \rightleftharpoons [Na^+{-}L]_{(org)} \quad (1)$$

Judicious choice of the complexing agent and organic solvent allows the selective transfer of ions from multi-ion aqueous solutions; for example, small crown ethers are more selective for small ions[9] and thioethers are more selective for transition metals.[10,11] Selective ion transfer at nonpolarized liquid/liquid interfaces is utilized for specific metal extraction (for example, electrorefining and hydrometallurgy).[12] Herein, selective ion transfer at an electrified interface is used to remove unwanted ions from the exchange medium, which in turn drives the equilibrium towards further ion exchange of the zeolite with the required counterion. With reference to Equation (2), the removal of Na^+ ions from the aqueous phase will shift the ion-exchange equilibrium to the right, which increases the amount of H^+ ions in the zeolite.

$$Na^+_{(zeolite)} + H^+_{(aq)} \rightleftharpoons H^+_{(zeolite)} + Na^+_{(aq)} \quad (2)$$

This method allows excellent control over the composition of the exchange medium, and hence exerts control over the extent of ion exchange (see Figure 1 and the Experimental Section).

The exchange process within the zeolite is predicated on its ability to sequester Na^+ ions in the organic phase with dibenzo[18]crown-6 (DB18c6). The electrochemically induced transfer of Na^+ ions occurs at a lower potential than that of H^+ ions (Figure 2). The voltammetric analysis shows that the maximum current required for the transfer of Na^+ ions is observed at an applied potential difference $\Delta\varphi$ of 0.60 V, whereas the peak current for the transfer of H^+ ions is seen at $\Delta\varphi = 0.73$ V. Therefore, if $\Delta\varphi = 0.60$ V across the exchange medium/organic interface, the transfer of Na^+ ions will be favored over the transfer of H^+ ions by a factor of $\exp(zF(0.13)/RT) \approx 150$.[7] A typical time-dependent current

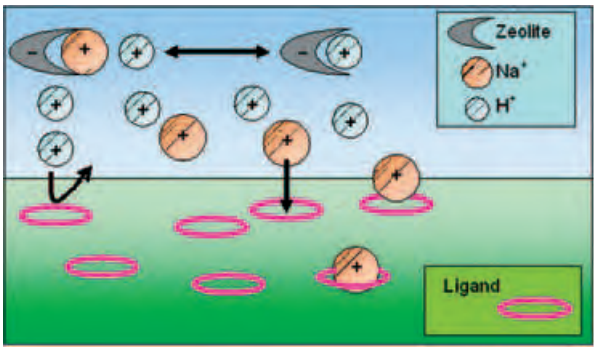

Figure 1. A schematic diagram of ion exchange in a zeolite suspended in an aqueous phase (aq) with the selective extraction of Na^+ ions into an organic phase (org), which forces the ion-exchange equilibrium [Eq. (2)] over to the right (protonated form of the zeolite).

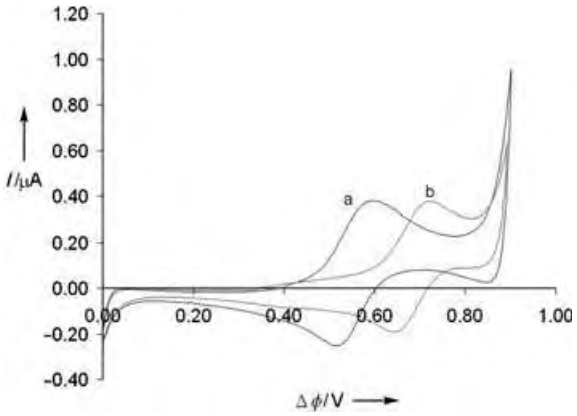

Figure 2. The cyclic-voltammetric data showing comparative transfer of Na^+ and H^+ ions facilitated by DB18c6 using a) cell 2 and b) cell 1 (see the Experimental Section) with a voltage scan rate of 0.1 Vs^{-1}.

response is shown in Figure 3 in which $\Delta\varphi = 0.60$ V across the interface. The resultant current is essentially caused by the transfer of Na^+ ions across the interface; from the magnitude of the charge passed, the amount of Na^+ ions extracted can be calculated by using Faraday's law. In this way, the removal of sodium from the exchange medium can be controlled, thus exerting control over the extent of ion exchange within the zeolite.

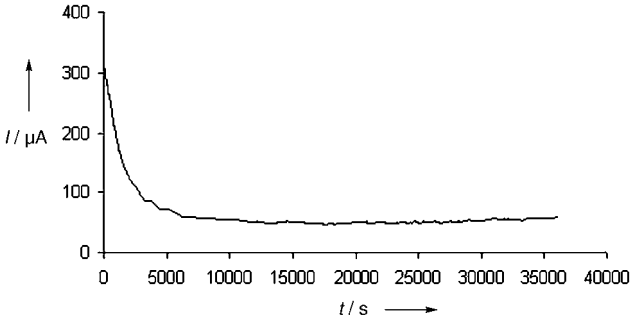

Figure 3. Chronoamperometric response of cell 3 (see the Experimental Section; X = acetic acid). The potential was stepped from 0.1 to 0.6 V and held at 0.6 V for 10 h.

The sodium and aluminum contents of the zeolite samples were then determined by inductively coupled plasma atomic emission spectroscopy (ICPAES). The proton concentration was calculated indirectly by mass balance [Eq. (3)]:

$$|H^+|_{zeo} = |AlO_2^-|_{zeo} - |Na^+|_{zeo} \quad (3)$$

The equivalent fractions of H^+ ions in the zeolite E_H, as measured experimentally, were plotted versus the charge transferred across the interface (Figure 4). The equivalent

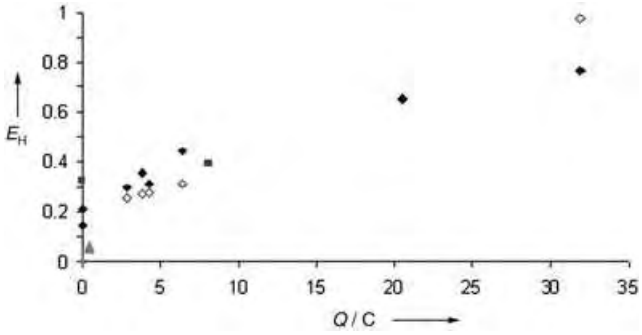

Figure 4. Graph of E_H values versus the total charged passed (Q): E_H was measured by ICPAES. Cell 3 was used (see the Experimental Section), in which X is acetic acid (filled diamonds), sulfuric acid (squares), or pure water (triangles). Data predicted by the calculations, as described in the text, are denoted with open diamonds.

fraction for ion A (E_A) was calculated with Equation (4), in which z_A is the valency of ion A, n_A is the number of moles per unit mass, and M_t is the exchange capacity of the zeolite.)

$$E_A = \frac{z_A n_A}{M_t} \quad (4)$$

The values obtained at zero Coulombs relate to the chemically exchanged samples in pure water (A), 0.02 M acetic acid (B), or 0.01 M sulfuric acid (C). These samples were left to pre-equilibrate with the zeolite for at least 14 days and were the starting points for the electrochemical experiments. Samples of type B were analyzed again after the electrochemical experiments had been completed (after approximately 2 months). For samples of type A, no proton exchange was detected after only the chemical exchange had been carried out. Subsequent electrochemical studies using pure water were hampered by resistance resulting from the aqueous phase, which made it very difficult to remove the Na^+ ions. However, partial dissociation of water allowed some H^+ ions to be incorporated, which permitted a maximum of $E_H = 0.07$ to be obtained. Note that no cations, other than H^+ ions, were present in any of the aqueous phases of the cell. For samples of type C, $E_H = 0.33$ after the chemical exchange and increased to 0.39 after 8 C of Na^+ ions had been removed from the exchange medium. For the samples of type B, $E_H = 0.15$–0.20 after the chemical exchange, which is lower than the level achieved with the sulfuric acid sample (C) and is attributed to the partial dissociation of acetic acid. However, the use of a sulfuric acid solution (C; pH = 2) might have a detrimental effect on the zeolite structure through dealumination.[13] The acetic acid solution was found to be well suited to these studies because it was sufficiently conductive to be used as an electrolyte, but was not too acidic; acted as a good source of H^+ ions; and behaved as a buffer, because it is a weak acid, giving a constant pH value of approximately 4. Figure 4 shows that there is a significant increase in the extent of the proton exchange, with increasing charge being passed. The E_H value rose to 0.77 after 32 C of Na^+ ions were extracted from the exchange medium; it is likely that this value could be improved with continual removal of Na^+ ions.

In the above experiments, it was assumed that the ion exchange was being chemically driven by transferring unwanted Na^+ ions from the exchange medium into the organic phase [Eq. (1)], which then shifts the ion-exchange equilibrium to the right [Eq. (2)]. It is conceivable that the application of an electric field at the interface may alter the ion-exchange equilibrium or remove ions directly from the zeolite; if this effect is significant, then the extent of the ion exchange will differ from that of the isotherm based just on the chemical ion-exchange process. An attempt was made to predict the extent of the ion exchange using the corrected selectivity quotient for the chemical equilibrium and the changes measured in the composition of the exchange media after electrochemical removal of the Na^+ ions (Figure 4). These predictions were then compared to the experimentally derived zeolite compositions (see the Supporting Information). The experimental values of E_H are slightly greater in most cases than the predicted values, which suggests that an electrochemical enhancement of the ion-exchange process occurs. The predicted value at 32 C is greater than the experimental value; this difference is probably because the transfer of H^+ ions begins to contribute significantly to the charge transfer at this point. At higher levels of proton exchange, the exchange medium contains a very low concentration of Na^+ ions and the selectivity of the transfer of Na^+ ions decreases, which means significant transfer of H^+ ions occurs with the transfer of Na^+ ions. However, the calculations are approximate as the corrected selectivity quotients only allow for the nonideality of the solution[13–15] and not the zeolite and only the aluminum and sodium contents are known as they are measured directly. A more accurate calculation based on the electrochemically enhanced exchange of copper ions in NaY is underway, in which both the outgoing and incoming ions can be measured directly.

The structural integrity of the samples after either chemical exchange or electrochemically enhanced ion exchange was assessed by X-ray diffraction (XRD) and N_2 sorption/desorption measurements. Exposure of samples to acid (types B and C) did not lead to the formation of amorphous regions in the XRD patterns or to any significant loss of crystallinity. The N_2 sorption isotherms showed no evidence of hysteresis, thus indicating that no secondary pore system had been formed. Secondary pores may develop with acid-induced degradation.[16] For type B samples, Barrett–Joyner–Halenda (BJH) calculations[17] of the pore-size distribution showed no significant change relative to the fresh sample. However, type C samples developed some pores

approximately 100 Å in diameter following two weeks of exposure to acid. Brunauer–Emmett–Teller (BET) surface-area measurements revealed an approximate decrease in the internal surface area for the chemically exchanged samples of type C, compared to the fresh sample after two weeks of exposure to sulfuric acid; $E_H = 0.3$ after two weeks. For type B samples, both the extent of the ion exchange and the change in the surface area were small following two weeks of exposure to acetic acid. However, extraction of 2.8 C of charge from this sample caused the E_H value to rise to 0.3. Significantly, the amount of H^+ ions needed to achieve this rise could be introduced into the sample with a decreased level of concomitant change (ca. 10%) in the surface area, as measured by BET studies, compared to the type C samples.

In summary, ion exchange can be readily controlled in microporous materials through the use of electrified interfaces: protons can be incorporated into these materials using weak acids, without the need for repeated washing. Therefore, this method is very useful for zeolites that are pH sensitive. We are currently applying this technique to zeolites with high aluminum contents, that is, NaA and NaX. This new method is very effective at removing small concentrations of unwanted ions from exchange media, and so is able to complete the exchange more efficiently than repeated washing. The exchange of ions with poor selectivity also benefits from this method, as small traces of unwanted counterions can be removed and there is no need to continually refresh the exchange medium; furthermore, the direct ion exchange of preformed membranes that are sensitive to thermal treatment is allowed. This phenomenon has been found to be useful in the final stages of copper(II) ion exchange with NaY. In addition, judiciously chosen complexing agents allow the electrochemically enhanced ion exchange of nearly every possible combination of ions. The tertiary Li^+/Ca^{2+}/NaX system is also currently being studied. The preliminary data reported herein suggest that the electrochemically enhanced ion-exchange process yields greater ion exchange than would be expected from just a chemical exchange.

Experimental Section

Method: The zeolite powder (2.5 wt% NaY; Crossfield Chemicals, Warrington, UK) was suspended in the aqueous phase of the cell (cells 1–3). The Na^+ ion content of the as-purchased zeolite sample was greater than 98%; the remaining ions were protons. ICPAES analysis was performed on the fresh sample, the level of the initial proton impurities was below the experimental error of ICPAES. The water/DCE interface was supported within a polyethylene terephthalate "track-etched" membrane (0.1 μm pore diameter; Osmonics Inc., Livermore, CA, USA). The organic phase electrolyte in all cases was bis(triphenylphosphoranylidene) ammonium tetrakis(pentafluoro)phenylborate (BTPPA $TPBF_{20}$). The water/DCE interface was polarized using a four-electrode potentiostat (Autolab PGSTAT 100; Eco-chemie, Utrecht, Netherlands). The organic phase was stirred at 4 Hz with a magnetic stirring device; other cell details have been reported previously.[18] For these experiments, the organic solution was renewed every 10 h. Typical currents were approximately 50 μA, which could be increased by using a higher interfacial area and/or by stirring both phases. The experiments were performed at ambient laboratory temperature (293(±)2 K).

The electrochemical cells used can be written as:

Cell 1

$Ag_{(S)} \,|\, AgTPB_{(S)} \,|\, 0.02\,\text{M}$ $BTPPATPBF_{20}$, $1 \times 10^{-3}\,\text{M}$ $DB18c6_{(DCE)} \,||\, 0.01\,\text{M}$ $H_2SO_{4(aq)} \,|\, Ag_2SO_{4(S)} \,|\, Ag_{(S)}$

Cell 2

$Ag_{(S)} \,|\, AgTPB_{(S)} \,|\, 0.02\,\text{M}$ $BTPPATPBF_{20}$, $1 \times 10^{-3}\,\text{M}$ $DB18c6_{(DCE)} \,||\, 0.01\,\text{M}$ H_2SO_4, $0.01\,\text{M}$ $Na_2SO_{4(aq)} \,|\, Ag_2SO_{4(S)} \,|\, Ag_{(S)}$

Cell 3

$Ag_{(S)} \,|\, AgTPB_{(S)} \,|\, 0.02\,\text{M}$ $BTPPATPBF_{20}$, $0.01\,\text{M}$ $DB18c6_{(DCE)} \,||$ 2.5 wt% NaY, $0.01\,\text{M}$ $X_{(aq)} \,|\, Ag_2SO_{4(S)} \,|\, Ag_{(S)}$

Received: December 22, 2004
Published online: April 12, 2005

Keywords: electrochemistry · interfaces · ion exchange · liquids · zeolites

[1] P. M. M Blauwhoff, J. W. Gosselink, E. P. Kieffer, S. T. Sie, W. H. J. Stork in *Catalysis and Zeolites: Fundamentals and Applications* (Eds. J. Weitkamp, L. Puppe), Springer, Berlin, **1999**, pp. 437–538.
[2] C. Colella in *Handbook of Porous Solids*, *Vol. 2* (Eds.: F. Schüth, K. S. W. Sing, J. Weitkamp), Wiley-VCH, Weinheim, **2002**, pp. 1156–1189.
[3] I. E. Maxwell, W. H. J. Stork in *Studies in Surface Science and Catalysis*, *Vol. 137*, 2nd ed. (Eds.: H. van Bekkum, E. M. Flanigen, P. A. Jacobs, J. C. Jansen), Elsevier, Amsterdam, **2001**, pp. 747–820.
[4] C. Baerlocher, W. M. Meier, D. H. Olson, *Atlas of Zeolite Framework Types*, 5th ed., Elsevier, Amsterdam, **2001**, p. 132.
[5] A. P. Bolton, M. A. Lanewala, *J. Catal.* **1970**, *18*, 154–163.
[6] R. Szostak, *Stud. Surf. Sci. Catal.* **2001**, *137*, 261–297.
[7] H. H. J. Girault, D. J. Schiffrin in *Electroanalytical Chemistry*, *Vol. 15* (Ed.: A. J. Bard), Marcel Dekker, New York, **1989**, pp. 1–141.
[8] P. Vanýsek, *Electrochim. Acta* **1995**, *40*, 2841–2847.
[9] A. Dassie, A. M. Baruzzi, *J. Electroanal. Chem.* **2000**, *492*, 94–102.
[10] G. Lagger, L. Tomaszewski, M. D. Osborne, B. J. Seddon, H. H. Girault, *J. Electroanal. Chem.* **1998**, *451*, 29–37.
[11] M. J. Stephenson, S. M. Holmes, R. A. W. Dryfe, *Electrochem. Commun.* **2004**, *6*, 294–298.
[12] W. J. Albery, R. A. Choudhery, *J. Phys. Chem.* **1988**, *92*, 1142–1151.
[13] B. E. Conway, *Electrochemical Data*, Elsevier, Amsterdam, **1952**, p. 63.
[14] R. A. Robinson, R. H. Stokes, *Electrolyte Solutions*, 2nd ed., Butterworths, London, **1959**, p. 230.
[15] E. Glueckauf, *Nature* **1949**, *163*, 414–415.
[16] J. Lynch, F. Raatz, P. Dufresne, *Zeolites* **1987**, *7*, 333–340.
[17] E. P. Barrett, L. G. Joyner, P. P. Halenda, *J. Am. Chem. Soc.* **1951**, *73*, 373–380.
[18] B. Kralj, R. A. W. Dryfe, *Phys. Chem. Chem. Phys.* **2001**, *3*, 5274–5282.

Metamagnetism

Spin Canting and Metamagnetism in a 3D Homometallic Molecular Material Constructed by Interpenetration of Two Kinds of Cobalt(II)-Coordination-Polymer Sheets**

*Ming-Hua Zeng, Wei-Xiong Zhang, Xian-Zhong Sun, and Xiao-Ming Chen**

Molecular magnetism—such as ferromagnetic, ferrimagnetic, and antiferromagnetic long-range ordering properties at low temperatures—has been observed for many transition-metal complexes.[1] In contrast, only a few magnetically ordered complexes exhibit metamagnetic phase transitions,[1b,c] and most of them are heterometallic[2] or homometallic compounds[3] or metal-radical materials[4] that display low dimensionality (one- or two-dimensional structures). In particular, homometallic three-dimensional metamagnets have only been documented in several azide-bridged complexes[5] and metal phosphonates[6] or metal carboxylates.[7]

Complicated magnetic anisotropy has significant influence on the bulk magnetic properties.[8,9] Furthermore, there is a close relationship to metamagnets, which are antiferromagnets with a strong anisotropy (without a spin-flop phase) and a net magnetic moment.[9] It is well known that a pure 1D system cannot present long-range magnetic ordering at $T \neq 0$ K.[8] Only interchain interactions can lead to ordering with spontaneous magnetization, and in a 2D system long-range ordering occurs only in the Ising limit.[9] Coupling of the magnetic ordering is a consequence of the 3D structure. So far the design of polynuclear metal complexes and extended networks with predictable magnetic properties is still a challenge in the field of molecular magnetism.[1] A great deal of work is required to understand the structural factors that govern the exchange coupling between paramagnetic centers, since such a relationship is complex and so far remains elusive.[1,8]

Recently we reported synthetic approaches to homometallic coordination polymers of different dimensionalities that show weak ferromagnetic or ferrimagnetic behavior.[10] Now we have used 3-hydroxypicolinate (pico)[11] as a bischelating ligand to construct alternating chains of metal ions. Similar to phenyleneoxamate,[2a] pico should be able to mediate electronic effects between paramagnetic metal ions,[12] and may favor antiferromagnetic coupling through the *anti–anti* carboxylate bridges.[7d] Owing to the predictable lack of compensation of the individual spin moments through the bridging and asymmetrical exchanging mode of pico ligands, weakly ferromagnetic 1D chains may be created.[9,12] Employment of additional bridging 4,4′-bipyridine (4,4′-bpy) ligands can further interconnect these chains into a 2D structure, which may lead to stabilization of the magnetic ordering.[9] Clearly, the key structural or electronic characteristics control the resulting magnetic ground states and result in modulated bulk magnetic properties.[9,12] Hydrothermal treatment of Co^{II} ions and the organic ligands provided $[Co_4(pico)_4(4,4'\text{-bpy})_3(H_2O)_2]_n \cdot 2nH_2O$ (**1**), a 3D network consisting of two different, interpenetrating 2D neutral polymers. With strong anisotropy from single ions arranged in the chains, sheets, and finally the 3D structure, **1** exhibits spin canting and typical metamagnetism.

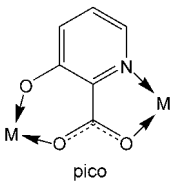

Crystal-structure determination by X-ray crystallography showed that each of the four Co^{II} ions in the asymmetric unit of **1** is located in a distorted octahedron. Atom Co1 is coordinated by two O,N-chelating sites of two pico ligands and two 4,4′-bpy ligands, whereas Co2 is coordinated by two O,O′-chelating sites of two pico ligands and two 4,4′-bpy ligands (Figure 1, left). The two kinds of Co^{II} ions are alternatively bridged by pico ligands to form A-type zigzag chains $[Co_2(pico)_2(H_2O)_2]_n$ (Co1···Co2 5.638(1) Å). These chains are further interlinked through 4,4′-bpy ligands into A-type sheets $[Co_2(pico)_2(4,4'\text{-bpy})(H_2O)_2]_n$ (Co···Co 11.220(2) Å), in which the pair of pyridyl groups in each 4,4′-bpy ligand is significantly twisted with a dihedral angle of about 16° (Figure 2a). The curved conformation of the 4,4′-bpy ligands in the corrugated sheets leads to the existence of two kinds of meshes (atom–atom distance ca. 11.2 × 7.3, 11.2 × 3.5 Å).

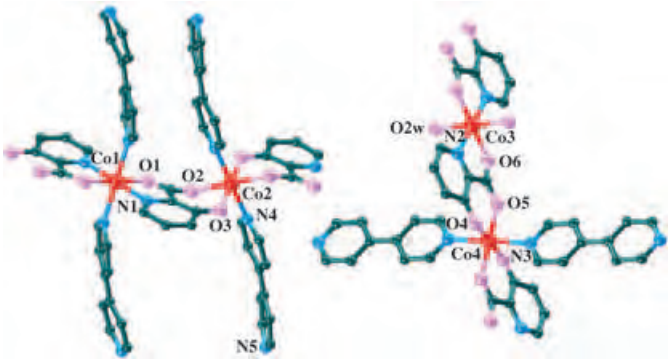

Figure 1. Perspective views of the coordination environments of Co1 and Co2 (left) and Co3 and Co4 (right) in **1**.

Atom Co3 is coordinated by two pico N,O-chelating sites and two *trans* aqua ligands, whereas Co4 is coordinated by

[*] Dr. M.-H. Zeng, W.-X. Zhang, X.-Z. Sun, Prof. Dr. X.-M. Chen
School of Chemistry and Chemical Engineering
Sun Yat-Sen University
Guangzhou 510275 (P.R. China)
Fax: (+86) 20-8411-2245
E-mail: cescxm@zsu.edu.cn
Dr. M.-H. Zeng
Research Institute of Bioinorganic Chemistry
Department of Chemistry and Chemical Engineering
GuangXi Normal University
Guilin 541004 (P.R. China)

[**] This work was supported by the NSFC (no. 20131020) and the Scientific and Technological Bureau of Guangdong Province (no. 04205405).

Supporting information for this article is available on the WWW under http://www.angewandte.org or from the author.

 DOI: 10.1002/anie.200462463

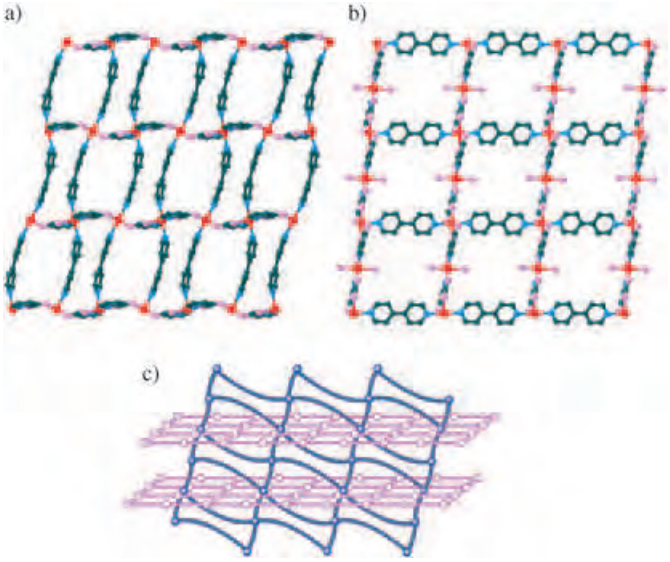

Figure 2. Views of the a) A-type and b) B-type sheets found in **1** (C green, N blue, O pink, Co red). c) A schematic representation of the interpenetrated sheets (A-type sheet blue, B-type sheet pink).

two O,O′-chelating sites of two pico ligands and two 4,4′-bpy ligands (Figure 1, right). The pico ligands alternatively bridge Co^{II} ions to form B-type zigzag chains $[Co_2(pico)_2]_n$ (Co3···Co4 5.804(1) Å), which are further bridged by the 4,4′-bpy ligands into B-type sheets $[Co_2(pico)_2(4,4'\text{-bpy})_2]_n$ (Figure 2b; Co···Co 11.538(2) Å). This results in a square net with a uniform mesh size (atom–atom distance ca. 11.5 × 11.6 Å) different than that in the A-type sheets.

Interestingly, the two types of sheets are interpenetrated in a parallel/diagonal inclined fashion with the bigger windows of the A-type nets enclosing the 4,4′-bpy rods of the B-type nets. In addition the windows of the B-type nets contain the nodes (B chain) of the A-type nets in a 1:1 ratio.[13] This leads to a unique, compact, 3D extended network (Figure 2c and Supporting Information), featuring a strong structural anisotropy (from single-ion anisotropy to anisotropic chains, sheets, and the final 3D structure).[8,9]

Hydrogen-bonding interactions are present between the sheets. The lattice water molecules participate in moderately strong hydrogen bonds with the pico oxygen atoms in the A-type chains (O–H···O 2.828, 3.005 Å; see Supporting Information). The aqua oxygen atoms O2w in the B-type chains form strong hydrogen bonds with the pico O2 and O3 atoms in the A-type chains of the adjacent sheets (2.711, 2.728 Å; see Supporting Information). Strong edge-to-face aromatic interactions (3.56 Å) also exist between adjacent 4,4′-bpy groups of different sheets. Although the 2D→3D parallel or inclined interpenetration of layers is not very unusual, the intertwining of different sheets is extremely rare in both inorganic and coordination polymer chemistry.[13] Complex **1** is the first example of the inclined interpenetration of two types of sheets with different composites that have the same topology (4,4-net).

The magnetic susceptibility of **1** was measured in the 2–320-K range at 100 Oe by using a polycrystalline powder sample (Figure 3a). The temperature dependence of the

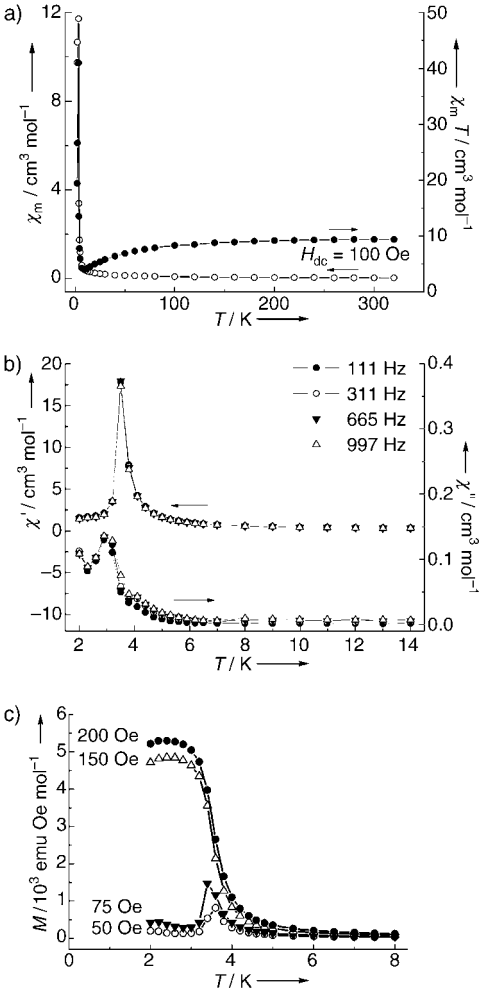

Figure 3. a) Plot of $\chi_M T$ versus T for **1**. The field strength used was $H = 100$ Oe per $\{Co^{II}\}_4$. b) The temperature dependence of the in-phase (χ') and the out-of-phase (χ'') ac magnetic susceptibilities for **1**. c) Plot of magnetization M versus T at 50, 75, 150, and 200 Oe for **1**.

reciprocal susceptibility (χ_M^{-1}) above 20 K follows the Curie–Weiss law with a Weiss constant θ of −20.4 K, thus indicating an overall strong antiferromagnetic interaction and/or spin–orbital coupling between the Co^{II} ions. The value of $\chi_M T$ at 300 K is 9.37 emu K mol^{-1} and thus higher than the spin-only value of 7.49 emu K mol^{-1} expected for four magnetically isolated high-spin Co^{II} ions. The product $\chi_M T$ first decreases smoothly to a rounded minimum of 4.03 emu K mol^{-1} at 9.0 K, then increases rapidly to a very high and sharp maximum of 41.0 emu K mol^{-1} at 3.5 K (characteristic of a magnetic long-range ordering), and finally decreases more rapidly on further cooling. The behavior above 3.5 K is characteristic of a canted antiferromagnetic chain, and that below 3.5 K may be attributed to interchain antiferromagnetic interactions and/or the saturation effect.[3]

The temperature dependence of the ac susceptibility measured in a field of 6 Oe shows the same features (Figure 3b). The maximum of χ' observed at $T_c = 3.5$ K, in agreement with the above results, confirms the occurrence of a phase transition. The absence of an out-of-phase signal (χ'') at this temperature points to a long-range antiferromagnetic

order. However, the imaginary component χ'' presents a peak at 3.0 K, which is the signature of a magnetized state, thus indicating that a partly canted antiferromagnetic structure exists below this temperature.[7a] No frequency dependence of these transitions is observed.

The temperature dependence of the magnetization of **1** at various fields is shown in Figure 3c. For applied fields below 100 Oe, the field-cooled (FC) curves present a maximum at 3.5 K, thus indicating that some interlayer antiferromagnetic interactions are operative. However, a magnetic field above 150 Oe is sufficient to overcome these weak interactions, and **1** presents a field-induced transition from an antiferromagnetic to a ferromagnetic-like state.[2–4,9] The magnetization was also measured in the range of 2–30 K (see Supporting Information). The field-cooled magnetization (FCM), measured under an applied field of 10 G, increases rapidly on cooling to 3.5 K and then diminishes. The zero-field-cooled magnetization (ZFCM) shows a maximum at 3.5 K and decreases rapidly as the temperature is further increased. This behavior implies metamagnetic ordering.[2–4,9]

Interestingly, in the *M*–*H* curve of **1** around the transition temperatures and magnetic hysteresis (Figure 4a), the magnetization curves for different temperatures below the transition temperature exhibit a sigmoidal shape with a common crossing point for $H = 160$ Oe; the 2.5-K isotherm indicates clearly that the saturation is not reached even with 70 kOe ($M = 4.35\,N\mu_B$; N = Avogadro number, μ_B = Bohr magneton). The low-field magnetization presents a small butterfly-shaped hysteresis with a metamagnetic-like transition around 160 Oe (Figure 4b), in agreement with the *FC* results. All these facts clearly confirm a metamagnetic behavior of **1** with a critical temperature T_c of 3.5 K and a critical field H_c of about 160 Oe. This reversal involves an increase of around 0.8 μ_B per Co_4 unit.

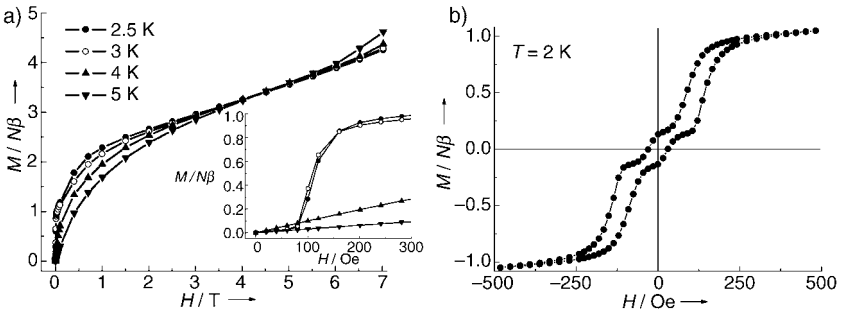

Figure 4. Plots of a) the first magnetization at 2–5 K (the inset shows the detail in a low field (0–300 Oe) at 2–5 K) and b) the hysteresis loop at 2 K.

All the structural factors in **1** diminish the antiferromagnetic interaction to a greater extent to favor the ferromagnetic interaction observed.[9] The magneto–structural correlation indicates that there exists a strong structural anisotropy in **1** and, consequently, anisotropy in competitions between the exchange interactions of the 3D motif, which result in a typical metamagnetism. The antiferromagnetic interactions operate between Co^{II} ions of adjacent sheets, possibly through electrostatic (dipolar) interactions and hydrogen bonding between the interpenetrated adjacent sheets.[3,13] The reason why the transition fields are so low in **1** is not yet clear, but the contribution of the substantial hydrogen bonding and dipolar interaction between the interpenetrated sheets and of the conjugated bridging ligands, as well as spin canting in the crystal lattice, may play a role in this phenomenon.[3,4,8]

In conclusion, the bridging pico ligand can be used to prepare a molecular-based magnetic material constructed by unusual interpenetration of two types of coordination sheets, which leads to a beautiful low-field metamagnetic transition and spin-canted behavior. This work demonstrates the importance of the crystal engineering of coordination polymers in the field of molecular-based magnetic materials.

Experimental Section

Synthesis: In a typical experiment, H_2pico (0.139 g, 1 mmol) in an aqueous solution (6 mL) of NaOH (0.080 g, 2 mmol) was mixed with 4,4′-bpy (0.117 g, 0.75 mmol) in EtOH (2 mL); the mixture was then added to an aqueous solution (2 mL) of $Co(NO_3)_2{\cdot}6H_2O$ (0.291 g, 1 mmol). The new mixture was placed in a 23-mL Teflon-lined autoclave and heated at 160 °C for 160 h. The autoclave was then cooled over a period of 12 h at a rate of 5 K h^{-1}. Orange crystals of **1** were collected by filtration, washed with water, and dried in air. Phase-pure **1** was obtained by manual separation (final yield: 185 mg, 56% based on Co). C,H,N analyses of **1**: calcd (%): C 48.96, H 3.35, N 10.57; found: C 48.94, H 3.38, N 10.52. IR (KBr disk): $\tilde{\nu} = 3391$ m, 1585 vs, 1533 vs, 1465 m, 1248 m, 810 m, 713 m, 624 cm^{-1} m.

Crystal data for **1**: $M_r = 662.36$, triclinic, space group $P\bar{1}$, $a = 11.275(2)$, $b = 11.538(2)$, $c = 11.609(2)$ Å, $\alpha = 80.181(3)°$, $\beta = 71.909(3)°$, $\gamma = 73.148(2)°$, $V = 1368.5(3)$ $Å^3$, $T = 293$ K, $Z = 2$, $\rho_{calcd} = 1.930$ g cm^{-3}; of 5267 unique reflections, 4005 were observed with $I \geq 2\sigma(I)$. Crystal size: $0.27 \times 0.19 \times 0.14$ mm^3. The structure was solved by direct methods and refined by the full-matrix least-squares method on F^2 using SHELXTL.[14] Structural plots were generated with OLEX.[15] Refinement of 385 variables with anisotropic thermal parameters for all non-hydrogen atoms gave $R1 = 0.0619$, $Rw2 = 0.1152$, and $S = 1.075$. CCDC-253952 contains the supplementary crystallographic data for this paper. These data can be obtained free of charge from The Cambridge Crystallographic Data Centre via www.ccdc.cam.ac.uk/data_request/cif.

Magnetic measurements: The magnetic measurements were carried out with Quantum Design SQUID MPMS XL-7 instruments. The diamagnetism of the sample and sample holder were taken into account.

Received: October 29, 2004
Revised: January 13, 2005
Published online: March 16, 2005

Keywords: cobalt · magnetic properties · metamagnets · N ligands · O ligands

[1] a) E. Coronado, F. Palacio, J. Veciana, *Angew. Chem.* **2003**, *115*, 2674–2676; *Angew. Chem. Int. Ed.* **2003**, *42*, 2570–2572; b) C. Janiak, *Dalton Trans.* **2003**, 2781–2804; c) "Metal-Organic and

Organic Molecular Magnets": P. Day, A. E. Underhill, *Philos. Trans. R. Soc. London Ser. A* **1999**, *357*, 2849 – 3184.
[2] a) C. L. M. Pereira, E. F. Pedroso, H. O. Stumpf, M. A. Novak, L. Ricard, R. Ruiz-García, E. Rivière, Y. Journaux, *Angew. Chem.* **2004**, *116*, 974 – 976; *Angew. Chem. Int. Ed.* **2004**, *43*, 956 – 958; b) Y.-Z. Zhang, S. Gao, H.-L. Sun, G. Su, Z.-M. Wang, S.-W. Zhang, *Chem. Commun.* **2004**, 1906 – 1907; c) S. Ohkoshi, Y. Arimoto, T. Hozumi, H. Seino, Y. Mizobe, K. Hashimoto, *Chem. Commun.* **2003**, 2772 – 2773.
[3] a) E.-Q. Gao, Y.-F. Yue, S.-Q. Bai, Z. He, C.-H. Yan, *J. Am. Chem. Soc.* **2004**, *126*, 1419 – 1429; b) L.-M. Zheng, S. Gao, H.-H. Song, S. Decurtins, A. J. Jacobson, X.-Q. Xin, *Chem. Mater.* **2002**, *14*, 3143 – 3147; c) P. S. Mukherjee, S. Dalai, E. Zangrando, F. Lloret, N. R. Chaudhuri, *Chem. Commun.* **2001**, 1444 – 1445; d) X. Hao, Y.-G. Wei, S.-W. Zhang, *Chem. Commun.* **2000**, 2271 – 2272; e) M. Monfort, I. Resino, J. Ribas, H. Stoeckli-Evans, *Angew. Chem.* **2000**, *112*, 197 – 199; *Angew. Chem. Int. Ed.* **2000**, *39*, 191 – 193.
[4] a) H. Kumagai, K. Inoue, *Angew. Chem.* **1999**, *111*, 1694 – 1696; *Angew. Chem. Int. Ed.* **1999**, *38*, 1601 – 1603; b) C. Aoki, T. Ishida, T. Nogami, *Inorg. Chem.* **2003**, *42*, 7616 – 7625.
[5] E.-Q. Gao, Z.-M. Wang, C.-H. Yan, *Chem. Commun.* **2003**, 1748 – 1749.
[6] a) P. Yin, L.-M. Zheng, S. Gao, X.-Q. Xin, *Chem. Commun.* **2001**, 2346 – 2347; b) W.-K. Chang, R.-K. Chiang, Y.-C. Jiang, S.-L. Wang, S.-F. Lee, K.-H. Lii, *Inorg. Chem.* **2004**, *43*, 2564 – 2568.
[7] a) Z.-L. Huang, M. Drillon, N. Masciocchi, A. Sironi, J.-T. Zhao, P. Rabu, P. Panissod, *Chem. Mater.* **2000**, *12*, 2805 – 2812; b) H. Kumagai, C. J. Kepert, M. Kurmoo, *Inorg. Chem.* **2002**, *41*, 3410 – 3422; c) R.-H. Wang, E.-Q. Gao, M.-C. Hong, S. Gao, J.-H. Luo, Z.-Z. Lin, L. Han, R. Cao, *Inorg. Chem.* **2003**, *42*, 5486 – 5488; d) T.-F. Liu, H.-L. Sun, S. Gao, S.-W. Zhang, T.-C. Lau, *Inorg. Chem.* **2003**, *42*, 4792 – 4794.
[8] O. Kahn, *Molecular Magnetism*, VCH, New York, **1993**.
[9] a) J.-P. Renard in *Organic and Inorganic Low Dimensional Crystalline Materials* (Eds.: M. Drillon, P. Delhaes), Plenum, New York, **1987**, p. 125; b) R. L. Carlin, *Magnetochemistry*, Springer, Berlin, **1986**.
[10] a) H.-J. Chen, Z.-W. Mao, S. Gao, X.-M. Chen, *Chem. Commun.* **2001**, 2320 – 2321; b) M.-H. Zeng, S. Gao, X.-L. Yu, X.-M. Chen, *New J. Chem.* **2003**, *27*, 1599 – 1602; c) M.-H. Zeng, S. Gao, X.-M. Chen, *Inorg. Chem. Commun.* **2004**, *7*, 864 – 867.
[11] S. M. O. Quintal, H. I. S. Nogueira, V. Félix, M. G. B. Drew, *New J. Chem.* **2000**, *24*, 511 – 517.
[12] a) K. Itoh, M. Minoshita, *Molecular Magnetism, New Magnetic Materials*, Gordon Breach-Kodansha, Tokyo, **2000**; b) J. B. Goodenough, *Magnetism and the Chemical Bond*, Wiley, New York, **1963**.
[13] B. Moulton, M. J. Zaworotko, *Chem. Rev.* **2001**, *101*, 1629 – 1658, and references therein; b) S. R. Batten, R. Robson, *Angew. Chem.* **1998**, *110*, 1558 – 1595; *Angew. Chem. Int. Ed.* **1998**, *37*, 1460 – 1494; c) M. J. Zaworotko, *Chem. Commun.* **2001**, 1 – 9; d) S. R. Batten, *CrystEngComm* **2001**, *18*, 1 – 7; e) L. Carlucci, G. Ciani, D. M. Proserpio, *New J. Chem.* **1998**, *22*, 1319 – 1321.
[14] SHELXTL 6.10, Bruker Analytical Instrumentation, Madison, Wisconsin, USA, **2000**.
[15] O. V. Dolomanov, A. J. Blake, N. R. Champness, M. Schroder, *J. Appl. Crystallogr.* **2003**, *36*, 1283 – 1284.

Zeolite Assembly

Oligomerization and Cyclization Processes in the Nucleation of Microporous Silicas**

Miguel J. Mora-Fonz, C. Richard A. Catlow, and Dewi W. Lewis**

The nucleation and growth of zeolites and other microporous solids continues to pose many questions.[1,2] Whilst the general features of self-assembly through condensation polymerization are understood for siliceous systems, the conditions under which both natural and synthetic zeolites form render such a complex process extremely difficult to characterize experimentally. Thus, whilst the species initially present in silicate gels can be characterized by NMR spectroscopy with some certainty,[3,4] their charge state is more difficult to probe.[5] Similarly, although scattering methods can be used to tentatively identify larger (possibly nucleation) species,[6,7] the relative stability and lifetime of the smallest clusters, significant in zeolitic structures, such as four-membered rings, remain unclear. Furthermore, in the postnucleation regime, there is much debate as to which species are responsible for crystal growth: small oligomers or larger subunits. Indeed, it has been suggested that the growth of silicalite-1 (MFI zeolite) is controlled by a unique nanocluster,[8] although there is some debate about this proposal.[9] Moreover, characterization of zeolite surfaces suggests that much smaller units are responsible for surface growth.[10]

Here, we describe quantum chemical calculations that model some of the species present prior to nucleation and attempt to examine the pathways by which such key species may form and hence rationalize the assembly of zeolitic structures. In particular, we discuss the factors that drive the condensation polymerization of silicate oligomers and that favor the cyclization of such species: pH and solvent.

In the past decade there have been a number of computational studies of model structures involved in the nucleation process of silicates. Structures and energies for small clusters containing up to five silicon atoms were obtained by Pereira et al.[11,12] One conclusion that can be drawn from these results is that linear silicate species are favored over cyclic structures—a situation not conducive to the formation of zeolitic structures but instead one that favors the formation of amorphous silicates.[11] These early calculations were performed using a local DFT method and considered only neutral species, although solvation effects were included using the COSMO method.[13] The roles of water and organic templates in prenucleation gels were studied by Lewis et al.[14] and Catlow et al.[15] by more approximate molecular mechan-

[*] M. J. Mora-Fonz, C. R. A. Catlow, D. W. Lewis
Centre for Theoretical and Computational Chemistry
Department of Chemistry, University College London
20 Gordon Street, London WC1H 0AJ (UK)
Fax: (+44) 20-7679-7463
E-mail: d.w.lewis@ucl.ac.uk

[**] CONACyT and UCL are acknowledged for funding of this work.

  DOI: 10.1002/anie.200462524

ics methods. They identified key roles for template molecules—preventing the collapse of large hydrophobic silicate clusters to more dense structures—and for charge interactions between anionic silicates and templating cations—maintaining intimate cluster–template interactions.

The formation of small cyclic species can be considered as central to the nucleation and growth of siliceous zeolites, since four-, five, and six-membered rings dominate such structures. However, as we have seen, ab initio calculations suggested that linear silicate oligomers are favored.[11] Herein we attempt to answer the following key questions: how does the cyclization process occur and what is the role of pH and solvation in forming such prenucleation species?

Details of the methods used are described in the Experimental Section and result from a systematic survey of available methods and tools. Further details of our evaluations will be published elsewhere, where the methods chosen will be shown to provide a good and self-consistent description of the geometry and energetics of these silicate systems. For example, trends in the successive deprotonation energies of monomeric and dimeric species are quantitatively reproduced.[16]

Experimentally, high pH is required for condensation reactions to occur: under such conditions the dominant silicate species will be anionic.[5] The basic reaction is given in Equation (1); further deprotonation gives $H_2SiO_4^{2-}$ and so

$$Si(OH)_4 + OH^- \rightarrow (OH)_3SiO^- + H_2O \quad (1)$$

on, and is also possible with larger oligomers. For some of the small clusters present in the first stages of nucleation, we have calculated the relative stability of the various possible anionic species in both the gas phase and in solution (modeled by the COSMO solvation model; Table 1). The results show that it is thermodynamically favorable for an OH^- ion to deprotonate the monomeric species to form the monocharged anion $(OH)_3SiO^-$, both in the gas phase and in solution. Further deprotonation is, however, significantly less favorable, suggesting that such species will be present in lower concentrations and will likely be highly reactive.

The change in free energy for the removal of a single proton by OH^- in the gas phase is quite large for all the linear oligomers considered; however, this value is reduced by a factor of three or four when a description of the solvent is included in the reaction. The role of the solvent is even more important for the second deprotonation. This emphasizes the important role of the water in stabilizing multiply charged anions, which is key in the condensation reactions and considered next. Whilst some of the free energies of deprotonation in our solvation model remain positive, they are clearly significantly lower than the corresponding gas-phase results. We estimate that our model may overestimate these energies by at most $\approx 25\ kJ\,mol^{-1}$ based on a comparison with experimental equilibrium constants for the deprotonation of $Si(OH)_4$.[17] Such an offset can be attributed to many factors such as solvation and dilution, which we are currently investigating further.[16].

We therefore limit ourselves to a semiquantitative discussion of the reaction energetics and compare only relative energies, which we expect to be reasonably accurate for all the species considered. We also note that, as yet, these calculations do not consider interactions with charge-balancing cations, for example, H_3O^+ and Na^+, nor with organic templating agents. However, the presence of such species is likely to increase the stability of the more deprotonated species.

We now consider the condensation reactions of some of these clusters, both neutral and charged, again in the gas phase and in the presence of the solvation model (Figure 1, Table 2). The simplest condensation reaction, that of the dimerization of silicic acid [Eq. (2)] is found to be favorable in

$$2\,Si(OH)_4 \rightarrow (OH)_3SiOSi(OH)_3 + H_2O \quad (2)$$

the gas phase for both neutral and charged species. However, when solvation is included, the free energy of the reaction is significantly less favorable for the neutral species than when charged species are considered. Similar trends are also observed for the condensation of larger oligomers. Our results, therefore, highlight the role of pH, which is also observed experimentally, in driving the initial polymerization processes to give these small oligomers. However, the reaction of two $Si(OH)_3O^-$ species ($M^- + M^-$) is very unfavorable, suggesting that stabilization of such species by cationic species or mechanisms for rearrangement by means of proton transfer will be significant. But it should also be noted that very high pH is not conducive to zeolite nucleation.[18]

Thus, our calculated condensation energies show how dimers, trimers, and larger oligomers can be readily formed, as in experiment, but only when the model includes a description of an aqueous medium at high pH. In particular, we note that condensation of neutral species is strongly disfavored beyond the formation of the dimer. Thus, at low

Table 1: Calculated Gibbs free energies [$kJ\,mol^{-1}$] for the deprotonation of silica species in the gas phase and in solution. The ΔG value is given for the formation of the deprotonated species from the reaction of its parent species with OH^-; water is the other product.[a]

Species	$\Delta G_{deprot.}$		Species	$\Delta G_{deprot.}$	
	Gas	Soln		Gas	Soln
M^-	−229	−64	$3r^{3-}$	391	−46
M^{2-}	284	2	T^-	−375	−127
M^{3-}	814	66	T^{2-}	−8	−76
D^-	−294	−92	T^{3-}	315	−33
D^{2-}	116	−23	$4r^-$	−341	−123
D^{3-}	527	−21	$4r^{2-}$	7	−69
Tr^-	−342	−100	$4r^{3-}$	344	−33
Tr^{2-}	53	−63	P^-	−408	−141
Tr^{3-}	404	−4	$5r^-$	−384	−130
$3r^-$	−299	−60	H^-	−412	−135
$3r^{2-}$	57	−64	$6r^-$	−382	−115

[a] Codes used: M = monomer, D = dimer, Tr = timer, 3r = 3-ring, T = tetramer, 4r = 4-ring, P = pentamer, 5r = 5-ring, 6r = 6-ring, H = hexamer. The charge of the deprotonated species is given by the usual superscript. Thus, for example, the first entry is the deprotonation of a neutral monomer, $Si(OH)_4$ (M in our notation) by reaction with OH^- to give $(OH_3)SiO^-$ (M^- in our notation) and H_2O.

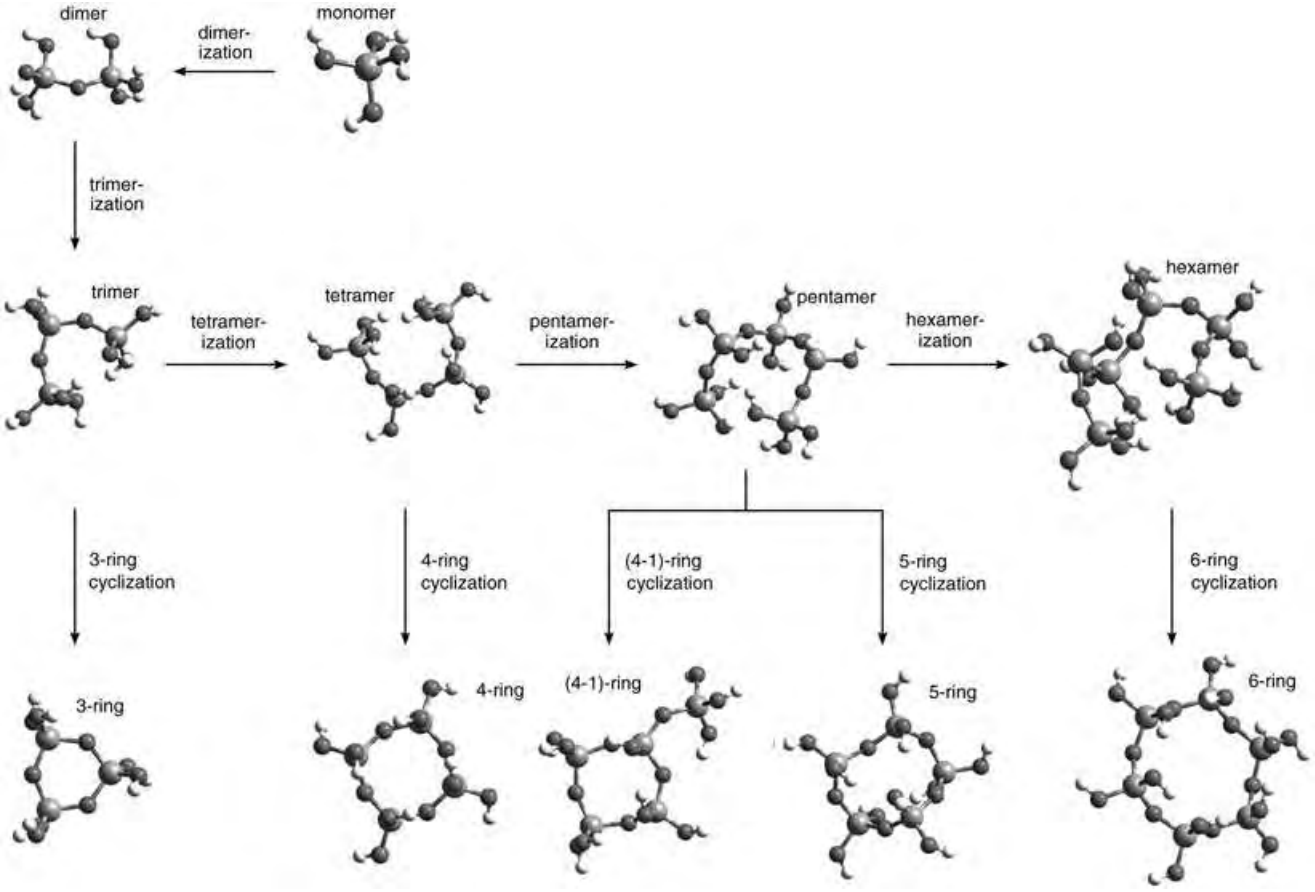

Figure 1. Condensation reactions for silicate clusters from monomer to hexameric species. For linear growth (e.g. tetramerization) the values are for the reaction of a silicate species with a monomeric species to give water as a product. For internal condensations leading to rings the other product is also water. The species codes are given in Table 1.

Table 2: Calculated energies [kJ mol^{-1}] for the condensation reactions depicted in Figure 1 forming silicate clusters from monomeric to hexameric species. For linear growth (e.g. tetramerization) the values are for the reaction of a silicate species with a monomeric species to give water as a product. For internal condensations leading to rings the other product is also water. The species codes are given in Table 1.

	Dimerization		
	Reactants	$T\Delta S$	ΔG
Gas	M,M	3	-14
	M$^-$,M	-14	-78
	M$^-$,M$^-$	-22	267
Soln	M,M	-8	0
	M$^-$,M	-14	-28
	M^{2-},M	-21	-53
	M$^-$,M$^-$	-28	13

	Trimerization		
	Reactants	$T\Delta S$	ΔG
Gas	D,M	-22	5
	D,M$^-$	-41	-107
	D$^-$,M	-25	-43
Soln	D,M	-20	6
	D,M$^-$	-39	-30
	D^{2-},M	-19	-42

	Tetramerization		
	Reactants	$T\Delta S$	ΔG
Gas	Tr,M	-20	-3
	Tr,M$^-$	-34	-149
	Tr$^-$,M	-15	-36
Soln	Tr,M	-21	12
	Tr,M$^-$	-24	-50
	Tr^{2-},M	-17	-27

	Pentamerization		
	Reactants	$T\Delta S$	ΔG
Gas	T,M	-17	-4
	T,M$^-$	-43	-183
	T$^-$,M	-29	-37
Soln	T,M	-20	3
	T,M$^-$	-19	-74
	T^{2-},M	-15	-13

	Hexamerization		
	Reactants	$T\Delta S$	ΔG
Gas	P,M	-14	-19
	P,M$^-$	-25	-201
	P$^-$,M	1	-22
Soln	P,M	-2	-5
	P,M$^-$	-26	-76
	P^{2-},M	-15	-40

	3-Ring Cyclization		
	Reactants	$T\Delta S$	ΔG
Gas	Tr	68	-37
	Tr$^-$	63	6
Soln	Tr	77	-61
	Tr$^-$	70	-21
	Tr^{2-}	67	-22

	4-Ring Cyclization		
	Reactants	$T\Delta S$	ΔG
Gas	T	83	-59
	T$^-$	62	-25
Soln	T	55	-48
	T$^-$	62	-44
	T^{2-}	69	-37

	(4-1)-Ring Cyclization		
	Reactants	$T\Delta S$	ΔG
Gas	P	80	-45
	P$^-$	76	-7
Soln	P	82	-55
	P$^-$	61	-21
	P^{2-}	69	-22

	5-Ring Cyclization		
	Reactants	$T\Delta S$	ΔG
Gas	P	80	-51
	P$^-$	74	-27
Soln	P	77	-65
	P$^-$	62	-53
	P^{2-}	30	-55

	6-Ring Cyclization		
	Reactants	$T\Delta S$	ΔG
Gas	H	72	-38
	H$^-$	64	-8
Soln	H	47	-40
	H$^-$	66	-20
	H^{2-}	50	-4

pH, where anionic species are less prevalent, polymerization is inhibited. We also note that for the trimerization reaction (and for the formation of higher oligomers) the dominant contribution to the free energy is a favorable change in enthalpy, which overcomes the adverse negative change in entropy.

Once trimers are formed, however, there is also the possibility of internal condensation to form rings, key zeolitic structural units. The lowest energy conformation for the trimer is almost cyclic, suggestive of an easy route for internal condensation to form a three-membered ring. Indeed, all our results suggest that the formation of a three-membered ring is

likely, in accordance with NMR experiments where this cluster is observed.[8] However, the seeming ease of 3-ring formation raises the question of the role of this species in nucleation and subsequent growth processes, since these rings are extremely rare in siliceous zeolites. However, we should note that the formation of a linear tetramer from the trimer is more favorable than the closure of the 3-ring when doubly charged trimers are considered, in other words, those likely to be present at higher pH. Furthermore, the overall formation energy of a four-membered ring by means of the reaction of the more likely 3-ring species (i.e. charged) with a monomer is favorable. For example, the free energies of formation of a 4-ring (in solvation) from an anionic 3-ring with monomer and anionic monomer are -37 and $-42\ kJ\,mol^{-1}$ respectively, whilst the reaction of a dianionic 3-ring and an anionic monomer (giving a trianionic 4-ring) is also exergonic by $11\ kJ\,mol^{-1}$. In contrast, the reopening of 4-rings by reaction with further monomers is strongly unfavorable. We are currently investigating the activation barrier to trimer cyclization and also routes for subsequent ring opening. It is also of note that cyclization processes are favored by the entropic contribution.

As with the trimer, the tetramer can either polymerize further or form a ring. The free energy released, in each of the charge states considered, clearly indicates that cyclization is strongly preferred over further linear growth. Given the prevalence of the 4-ring in so many zeolite structures, we might expect its formation and stability to be very significant in zeolite nucleation and growth. We might also expect the process of (any) cyclization reaction to be kinetically favored, as it is unimolecular. Clearly we also need to consider reaction barriers, calculation of which are now underway.[16] Again, we note that ring formation is favorable, with little variation in Gibbs energy, in a number of charge states. However, the formation of neutral 4-rings is unlikely, not due to the energetics of the cyclization itself, but rather since neutral tetramers are unlikely to be present. In contrast, there is significant variation in the reaction free energies for further addition of silicate species (giving a pentamer), depending on the exact charge state.

Thus, from a consideration of the energetics of the reactions determined here, for formation of species up to tetramers, we would expect a large population of dimers, 3-rings, and 4-rings, primarily singly and doubly charged. However, further linear polymerization will be competing with condensation onto these smaller species, particularly the 4-ring. Thus, whilst formation of larger linear oligomers remains energetically favored, we do not expect such species to be present in large amounts, owing to the other, even more favored, competing processes. Indeed, internal cyclization of a pentamer is more likely to lead to the formation of a 4-1 unit rather than the 5-ring, in excellent agreement with experiment, where the former species is considered to be present, with little evidence of the formation of the 5-ring.[3] Similarly, the 6-ring is unlikely to form as a solution species (from a linear hexamer), since internal cyclization to form smaller rings is more favorable.

From these initial calculations we can draw a number of conclusions and inferences. Firstly, we find excellent agreement between the overall energetics of the processes considered and the experimental observations of small oligomers in solution. We find a pH dependence for polymerization and the formation of small rings. Thus, we may conclude, tentatively, that the methods selected, in which solvation is included (albeit as a continuum) and pH is treated by considering anionic silicate species, give a reasonable description of the system. Future work will establish whether more sophisticated (and necessarily more expensive) models are required: for example, the inclusion of explicit water to describe the mechanism of condensation and the solvation of counter ions such as Na^+. Secondly, the formation of cyclic fragments is clearly favored—in agreement with experiment and with the expectation of the formation of zeolite-like nucleation species. Furthermore, the cyclization is driven by high pH—again well-known experimentally in silicate chemistry.[19,20] It is therefore unlikely that larger noncyclic oligomers play a significant role in either nucleation or crystal growth. Hence, growth is much more likely to occur by condensation of relatively small units, particularly those that lead to rings, in either nucleation species or in subsequent surface growth. We note that there is clear evidence that surfaces with complete (small) rings are prevalent from both high-resolution transmission electron microscopy and computational studies of siliceous zeolite surfaces.[21] Thirdly, it is clear that large single (>5- and even 5-) rings are not formed as free species in solution, although bridged species need to be considered, and result from the condensation of smaller units.

We are now considering larger species that are expected to form in solution (such as double-4-rings) and the mechanisms by which they may form (for example, double-6-rings can be constructed from 4-rings). Similarly, we are considering the reaction barriers for growth condensations and internal condensations. We believe that such studies will provide insight into the mechanisms of nucleation, assist the interpretation of experimental studies of nucleation phenomena, and also contribute to our understanding of subsequent crystal growth of siliceous zeolites.

Experimental Section

Theoretical method: All the calculations were performed using DMOL^3, version 2.2,[22,23] using a numeric DNP basis set. All final structures were optimized using the BLYP functional. Water was considered by means of the COSMO solvation approach[13,24] and gas-phase structures were subsequently reoptimized in the presence of the solvation model. To avoid bias (as many of the fragments were taken initially from zeolite crystal structures) and to avoid local minima, a simulated annealing strategy was adopted to search for the lowest energy structures. Structures were subjected to a quantum molecular dynamics simulation run at 700 K for 3000 steps of 0.46 fs, using a low-cost basis set and the PWC functional. The final structure from such runs was then optimized at the BLYP/DNP level, first in the gas phase and then in COSMO. The Gibbs free energy was calculated by standard statistical mechanical methods; a temperature of 450 K was assumed, which is typical of zeolite synthesis.

Received: November 5, 2004
Published online: April 13, 2005

Keywords: density functional calculations · silicates · sol–gel processes · zeolites

[1] C. S. Cundy, P. A. Cox, *Chem. Rev.* **2003**, *103*, 663.
[2] D. P. Serrano, R. v. Grieken, *J. Mater. Chem.* **2001**, *11*, 2391–2407.
[3] C. T. G. Knight, S. D. Kinrade, *J. Phys. Chem. B* **2002**, *106*, 3329.
[4] C. E. A. Kirschhock, R. Ravishankar, F. Verspeurt, P. J. Grobet, P. A. Jacobs, J. A. Martens, *J. Phys. Chem. B* **2002**, *106*, 3333.
[5] A. R. Felmy, H. Cho, J. R. Rustad, M. J. Mason, *J. Solution Chem.* **2001**, *30*, 509.
[6] P.-P. E. A. de Moor, T. P. M. Beelen, R. A. van Santen, L. W. Beck, M. E. Davis, *J. Phys. Chem. B* **2000**, *104*, 7600.
[7] P.-P. E. A. de Moor, T. P. M. Beelen, R. A. van Santen, K. Tsuji, M. E. Davis, *Chem. Mater.* **1999**, *11*, 36.
[8] C. E. A. Kirschhock, R. Ravishankar, F. Verspeurt, P. J. Grobet, P. A. Jacobs, J. A. Martens, *J. Phys. Chem. B* **1999**, *103*, 4965.
[9] D. D. Kragten, J. M. Fedeyko, K. R. Sawant, J. D. Rimer, D. G. Vlachos, R. F. Lobo, M. Tsapatsis, *J. Phys. Chem. B* **2003**, *107*, 10006.
[10] J. R. Agger, N. Hanif, C. S. Cundy, A. P. Wade, S. Dennison, P. A. Rawlinson, M. W. Anderson, *J. Am. Chem. Soc.* **2003**, *125*, 830.
[11] J. C. G. Pereira, C. R. A. Catlow, G. D. Price, *J. Phys. Chem. A* **1999**, *103*, 3268.
[12] J. C. G. Pereira, C. R. A. Catlow, G. D. Price, *J. Phys. Chem. A* **1999**, *103*, 3252.
[13] A. Klamt, *J. Phys. Chem.* **1995**, *99*, 2224.
[14] D. W. Lewis, C. R. A. Catlow, J. M. Thomas, *Faraday Discuss.* **1997**, *106*, 451.
[15] C. R. A. Catlow, D. S. Coombes, D. W. Lewis, J. C. G. Pereira, *Chem. Mater.* **1998**, *10*, 3249.
[16] M. J. Mora-Fonz, C. R. A. Catlow, D. W. Lewis, unpublished results.
[17] J. Efík, A. V. McCormick, *Chem. Eng. Sci.* **1999**, *54*, 3513.
[18] P.-P. E. A. d. Moor, T. P. M. Beelen, B. U. Komanschek, P. W. Larry, W. Beck, M. E. Davis, R. A. v. Santen, *Chem. Eur. J.* **1999**, *5*, 2083.
[19] R. K. Iler, *The Chemistry of Silica : Solubility, Polymerization, Colloid and Surface Properties, and Biochemistry*, Wiley, New York, **1979**.
[20] C. J. Brinker, *J. Non-Cryst. Solids* **1988**, *100*, 31.
[21] B. Slater, C. R. A. Catlow, Z. Liu, T. Ohsuna, O. Terasaki, M. A. Camblor, *Angew. Chem.* **2002**, *114*, 1283; *Angew. Chem. Int. Ed.* **2002**, *41*, 1235.
[22] B. Delley, *J. Chem. Phys.* **1990**, *92*, 508.
[23] B. Delley, *J. Chem. Phys.* **2000**, *113*, 7756.
[24] K. Baldridge, A. Klamt, *J. Chem. Phys.* **1997**, *106*, 6622.

Organocatalysts

Highly Enantioselective Organocatalytic Hydroxyalkylation of Indoles with Ethyl Trifluoropyruvate**

Béla Török, Mohammed Abid, Gábor London, Joseph Esquibel, Marianna Török, Shilpa C. Mhadgut, Ping Yan, and G. K. Surya Prakash**

Dedicated to Professor George A. Olah

Over the years, the application of organofluorine compounds has received extensive attention in the pharmaceutical industry and in materials science owing to the unique properties of fluorinated compounds.[1] Trifluoromethylated compounds are particularly interesting as the strong electron-withdrawing effect of the CF_3 group leads to exceptional properties. These molecules are frequently applied as drugs or chiral resolution agents as examples.[1,2] Despite the numerous methodologies, the synthesis of trifluoromethylated compounds are still in great demand.[3] The Friedel–Crafts alkylation of aromatic compounds with activated carbonyl compounds is one of the most important C–C bond-forming reactions.[4] Despite its importance, the number of asymmetric Friedel–Crafts reactions is limited and mostly based on the use of chiral Lewis acids.[5] A recently developed organocatalytic Friedel–Crafts alkylation reaction represents an important addition to this field.[6]

Herein, we describe the first highly enantioselective organocatalytic Friedel–Crafts hydroxyalkylation reaction. We demonstrate that with the application of pseudoenantiomeric cinchona alkaloids as catalysts in the reaction of substituted indoles and ethyl 3,3,3-trifluoropyruvate, the synthesis of both enantiomeric products is possible (Scheme 1).

[*] Prof. Dr. B. Török, M. Abid, G. London, J. Esquibel, Dr. M. Török, S. C. Mhadgut
Department of Chemistry
Michigan Technological University
1400 Townsend Drive, Houghton, MI 49931 (USA)
Fax: (+1) 906-487-2061
E-mail: btorok@mtu.edu
Dr. P. Yan, Prof. Dr. G. K. S. Prakash
Loker Hydrocarbon Research Institute and
Department of Chemistry
University of Southern California
University Park, Los Angeles, CA 90089-1661 (USA)
Fax: (+1) 213-740-6270
E-mail: gprakash@usc.edu

[**] Dedicated to Professor George A. Olah on the occasion of the 10th anniversary of his Nobel Prize. Financial support by the NSF (CHE-9512445) at Michigan Technological University and by the Loker Hydrocarbon Research Institute at USC is gratefully acknowledged. Professor Tse Lok Ho of National Chiao Tung University, Taiwan, is thanked for useful discussions.

Supporting information for this article is available on the WWW under http://www.angewandte.org or from the author.

  DOI: 10.1002/anie.200462877

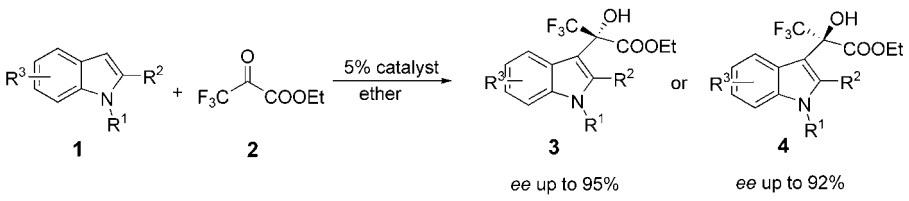

1 2 3 4

Scheme 1. Synthesis of chiral 3,3,3-trifluoro-2-(indol-3-yl)-2-hydroxylpropionic acid esters through catalysis by cinchona alkaloids. R^1 = H, Me; R^2 = H, Me, Ph; R^3 = H, Me, F, Cl, Br, I.

The target compounds are related to the well-known Mosher's acid,[2] and many of them have recently been synthesized as racemic mixtures by a superacid-catalyzed process.[7] In another recent attempt, a chiral copper(II)–bisoxazoline complex was used as a catalyst in the reaction of activated aromatics and ethyl 3,3,3-trifluoropyruvate and yielded the *S* enantiomer of the products.[8] Our present approach is based on the interaction between **2** and chiral alcohols including cinchona alkaloids.[9] By using these auxiliaries, a chiral intermediate can be obtained which can induce effective enantiodifferentiation in an organocatalytic process that is free of Lewis acids.[10] Cinchona alkaloids are very effective catalysts in many areas of asymmetric synthesis, such as chiral-base or phase-transfer catalysis, and organometallic reactions.[11] However, there are no data available concerning their use as chiral auxiliaries in Friedel–Crafts-type reactions. Our above hypothesis was tested in the reaction of indole (**1a**) and **2** with several optically active alcohols (e.g. menthol, α-methyl and α-trifluoromethyl benzyl alcohols) and aminoalcohols (e.g. prolinols, hydroxyprolines), including cinchona alkaloids and some of their derivatives (see Table 1), as chiral auxiliaries.

Cinchona alkaloids were found to be excellent catalysts for the test reaction, while the other chiral auxiliaries resulted in both poor yields and enantioselectivities of the products. As such, cinchona alkaloids were selected for further studies. After optimizing the reaction conditions (solvent, temperature, cinchona/trifluoropyruvate/indole ratios), the activity and selectivity of cinchona derivatives were compared. The optimized conditions and summarized results are shown in Table 2.

Table 2 shows that cinchonidine (CD) was the best catalyst towards the formation of **3a**, while cinchonine (CN) gave the highest yield and *ee* value for **4a**. Both catalysts provided excellent yields and enantioselectivities (up to 99% yield, 95% *ee*) in providing the opposite enantiomers. The initial reaction rates indicate that the application of cinchona alkaloids as catalysts significantly increases the reaction rates; in the case of CD the hydroxyalkylation takes place with rates that are more than two orders of magnitude higher than in the absence of catalyst. This observation unambiguously indicates that the enantiodifferentiation is a kinetic phenomenon in this reaction. Furthermore, the data obtained with *O*- and *N*-substituted cinchona derivatives clearly demonstrate that both the nitrogen atom of the quinuclidine ring and the 9-hydroxyl group play a vital role in the enantiodifferentiation. Blocking any of these two moieties results in very low enantioselectivities. On

Table 2: Enantioselective hydroxyalkylation of indole with ethyl 3,3,3-trifluoropyruvate in ether at −8 °C catalyzed by different cinchona alkaloids.

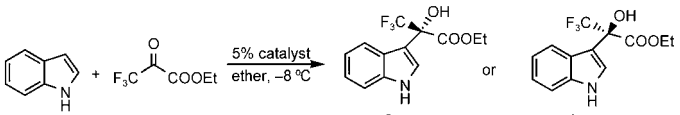

1a 2 3a 4a

Catalyst	*t* [h][a]	Major product	Reaction rate [mmol h^{-1}][b]	Yield [%][c]	*ee* [%][d]
–	90	**3a**+**4a** (racemic)	5.2×10^{-3}	95	0
CD	2	**3a**	8.2×10^{-1}	99	95
CN	2	**4a**	6.5×10^{-1}	98	90
QN	2.5	**3a**	3.4×10^{-1}	98	92
QD	3	**4a**	1.4×10^{-1}	98	87
DHQD	3	**3b**	1.2×10^{-1}	98	83
NBnCD	8	**3a**	8.3×10^{-2}	98	4
NBnCN	24	**4a**	2.1×10^{-2}	98	6
AcOCD	16	**3a**	4.2×10^{-2}	97	7
AcOCN	17	**4a**	3.9×10^{-2}	97	3

[a] Time needed to complete the reaction; [b] Initial rates; [c] Isolated yields; [d] Average of five parallel reactions.

Table 1: Structures of cinchona alkaloids and their derivatives, used as catalysts for enanatioselective hydroxylations of indole with ethyl-3,3,3-trifluoropyruvate.

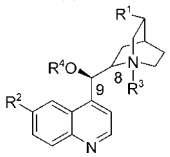

R^1	R^2	R^3	R^4	C8	C9	Catalyst	
vinyl	H	–	H	*R*	*S*	cinchonidine	CD
vinyl	H	–	H	*S*	*R*	cinchonine	CN
vinyl	OCH_3	–	H	*R*	*S*	quinine	QN
vinyl	OCH_3	–	H	*S*	*R*	quinidine	QD
Et	OCH_3	–	H	*S*	*R*	dihydroquinidine	DHQD
vinyl	H	Bn	H	*R*	*S*	*N*-benzylcinchonidine	NBnCD
vinyl	H	Bn	H	*S*	*R*	*N*-benzylcinchonine	NBnCN
vinyl	H	–	Ac	*R*	*S*	9-*O*-acetylcinchonidine	AcOCD
vinyl	H	–	Ac	*S*	*R*	9-*O*-acetylcinchonine	AcOCN

Bn = benzyl.

the basis of these results CD and CN were selected for the synthesis of *S* and *R* isomeric products, respectively. A wide range of substituted indoles were studied, and representative results are tabulated in Table 3.

Table 3: Enantioselective hydroxyalkylation of substituted indoles with ethyl 3,3,3-trifluoropyruvate in ether at −8 °C catalyzed by cinchona alkaloids.

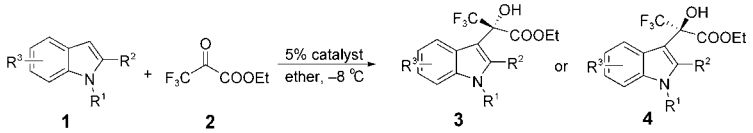

1 **2** **3** **4**

Reactant	R^1	R^2	R^3	Catalyst	Product	Yield [%][a]	*ee* [%][b]
1a	H	H	H	CD	**3a**	99	95
	H	H	H	CN	**4a**	99	90
1b	H	H	5-Me	CD	**3b**	98	93
	H	H	5-Me	CN	**4b**	99	92
1c	H	H	6-Me	CD	**3c**	97	95
	H	H	6-Me	CN	**4c**	98	90
1d	H	H	5-F	CD	**3d**	97	92
	H	H	5-F	CN	**4d**	98	86
1e	H	H	5Cl	CD	**3e**	96	90
	H	H	5-Cl	CN	**4e**	98	86
1f	H	H	5-Br	CD	**3f**	97	87
	H	H	5-Br	CN	**4f**	96	85
1g	H	H	5-I	CD	**3g**	97	87
	H	H	5-I	CN	**4g**	97	85
1h	H	H	5-COOMe	CD	**3h**	96	88
	H	H	5-COOMe	CN	**4h**	97	85
1j	H	H	5-OMe	CD	**3j**	98	83
	H	H	5-OMe	CN	**4j**	96	83

[a] Isolated yields. [b] Average of five parallel reactions.

Results of Table 3 indicate that both enantiomers of the products can be synthesized with high yields and enantioselectivities by appropriate selection of the catalyst. As a limitation of the approach it is worth mentioning that 1-methyl-indole derivatives ($R^1 = Me$) always gave good yields, but only racemic mixtures of products. It was also observed that the substituent in the 2-position of indole also played a crucial role. When R^2 is a relatively small group (2-Me-indole), the *ee* value of the product decreases to 75% (from 95%) with CD and 64% (from 90%) with CN. When R^2 is bulkier (2-Ph-indole), enantiodifferentiation is not observed and a racemic mixture of products is obtained.

Although it is premature to provide a detailed mechanistic explanation at this level, the major observations regarding the mechanism are as follows: 1) The indole NH, cinchona 9-OH, and quinuclidine N groups cannot be blocked; 2) Substituents in the 2-position of aromatics hinder or block enantiodifferentiation; 3) ^{19}F NMR investigations, in agreement with the literature,[9] clearly showed that **2** forms hemiketals with cinchona alkaloids through the 9-hydroxyl group. Such intermediates, however, are not effective electrophiles. The reaction of the hemiketal (prepared from a 1:1 mixture of **2** and CD) and indole gave low *ee* values in an extremely slow reaction (64% yield after 20 h, 47% *ee*); 4) The enantiodifferentiation is a kinetic phenomenon in this system (see reaction rate data in Table 2). We propose that the alkaloid forms a weak hydrogen-bonded complex with indole and then anchors **2** to form an active hydrogen-bonded intermediate. Thus the alkaloid provides a chiral environment and also activates the electrophilic carbonyl group of **2**.

In conclusion, an unprecedented cinchona alkaloid catalyzed, highly enantioselective organocatalytic Friedel–Crafts hydroxyalkylation of indole derivatives has been developed. Besides the isolation of products in high yields and enantioselectivities, the major advantages of the process are that the reactions are clean and fast and that commercially available economic catalysts can provide both enantiomers of the products, as desired. The application of this new method carries the potential of also being extended to several other reactions.

Received: December 10, 2004
Revised: January 21, 2005
Published online: April 21, 2005

Keywords: alkylation · C–C coupling · cinchona alkaloids · enantioselectivity · nitrogen heterocycles

[1] *Biomedical Frontiers of Fluorine Chemistry* (Eds.: I. Ojima, J. R. McCarthy, J. T. Welch), American Chemical Society, Washington, DC, **1996**; *Enantiocontrolled Synthesis of Fluoroorganic Compunds: Stereochemical Challenges and Biomedicinal Targets* (Ed.: V. A. Soloshonok), Wiley, New York, **1999**; *Asymmetric Fluoroorganic Chemistry* (Ed.: P. V. Ramachandran), American Chemical Society, Washington, DC, **2000**, ACS Symp. Ser.; *Organofluorine Compounds* (Ed.: T. Hiyama), Springer, Heidelberg, **2001**; P. Kirsch, *Modern Fluoroorganic Chemistry: Synthesis, Reactivity, and Applications*, Wiley-VCH, New York, **2004**.

[2] J. A. Dale, H. S. Mosher, *J. Am. Chem. Soc.* **1968**, *90*, 3732; J. A. Dale, H. S. Mosher, *J. Am. Chem. Soc.* **1973**, *95*, 512; W. H. Pirkle, D. J. Hoover, *Top. Stereochem.* **1982**, *13*, 264.

[3] G. K. S. Prakash, A. Yudin, *Chem. Rev.* **1997**, *97*, 757; P. Lin, J. Jiang, *Tetrahedron* **2000**, *56*, 3635; G. K. S. Prakash, M. Mandal, *J. Fluorine Chem.* **2001**, *112*, 123; G. K. S. Prakash, M. Mandal, G. A. Olah, *Org. Lett.* **2001**, *3*, 2847; G. K. S. Prakash, M. Mandal, G. A. Olah, *Angew. Chem.* **2001**, *113*, 609; *Angew. Chem. Int. Ed.* **2001**, *40*, 589.

[4] *Friedel–Crafts and Related Reactions* (Ed.: G. A. Olah), Wiley, New York, **1965**; G. A. Olah, R. Krisnamurthy, G. K. S. Prakash, *Friedel–Crafts Alkylation* in *Comprehensive Organic Synthesis, Vol. III, 1st ed.* (Eds.: B. M. Trost, I. Fleming), Pergamon, Oxford, **1991**, p. 293.

[5] W. Zhuang, T. Hansen, K. A. Jørgensen, *Chem. Commun*, **2001**, 347; K. B. Jensen, J. Thorhauge, R. G. Hazell, K. A. Jørgensen, *Angew. Chem.* **2001**, *113*, 164; *Angew. Chem. Int. Ed.* **2001**, *40*, 160; K. A. Jørgensen, *Synlett* **2003**, 1117; M. Bandini, A. Melloni, R. Umani-Ronchi, *Angew. Chem.* **2004**, *116*, 560; *Angew. Chem. Int. Ed.* **2004**, *43*, 550, and references therein.

[6] N. A. Paras, D. W. C. MacMillan, *J. Am. Chem. Soc.* **2001**, *123*, 4370, P. I. Dalko, L. Moissan, *Angew. Chem.* **2001**, *113*, 3840; *Angew. Chem. Int. Ed.* **2001**, *40*, 3726.

[7] G. K. S. Prakash, P. Yan, B. Török, G. A. Olah, *Synlett* **2003**, 527.

[8] W. Zhuang, N. Gathergood, R. G. Hazell, K. A. Jørgensen, *J. Org. Chem.* **2001**, *66*, 1009.
[9] M. von Arx, T. Mallat, A. Baiker in *Supported Catalysts and Their Applications* (Eds.: D. C. Sherrington, A. P. Kybett), Royal Society of Chemistry, Cambridge, **2001**, p. 247.
[10] B. List, *Synlett* **2001**, 1675; B. List, *Tetrahedron* **2002**, *58*, 5573; H. Groger, *Chem. Rev.* **2003**, *103*, 2795; N. Halland, P. S. Aburel, K. A. Jørgensen, *Angew. Chem.* **2003**, *115*, 685; *Angew. Chem. Int. Ed.* **2003**, *42*, 661; B. List, *Acc. Chem. Res.* **2004**, *37*, 548.
[11] H. Wynberg, *Top. Stereochem.* **1986**, *16*, 87; K. Kacprzak, J. Gawronski, *Synthesis* **2001**, 961; S. K. Tian, Y. Chen, J. Hang, L. Tang, P. McDaid, L. Deng, *Acc. Chem. Res.* **2004**, *37*, 621.

Biomolecular NMR Spectroscopy

Complete Assignment of Heteronuclear Protein Resonances by Protonless NMR Spectroscopy**

Wolfgang Bermel, Ivano Bertini, Luminita Duma, Isabella C. Felli, Lyndon Emsley, Roberta Pierattelli, and Paul R. Vasos*

The complete assignment of the resonances of a protein is key to the determination of its solution structure by NMR spectroscopy and for the study of protein–protein and protein–ligand interactions. The proton-based assignment strategy usually starts with the correlation of individual resonances of each amino acid residue through scalar connectivities followed by linking them one after the other.[1,2] Although many different triple-resonance NMR spectroscopy experiments have been designed for full assignments,[2] spectral overlap can still lead to ambiguities. This poses a significant limiting factor in the cases of large and/or paramagnetic biomolecules.[3]

After the pioneering report of ^{13}C NMR spin-system assignments of ^{13}C-enriched *Anabaena* 7120 ferredoxin by Markley and co-workers,[4] heteronuclear NMR spectroscopy experiments were progressively abandoned in favor of ^{1}H-detection experiments. However, as was recently pointed out, heteronuclear NMR spectroscopy decreases the effect of detrimental transverse relaxation, which is typical of large or paramagnetic proteins.[5–17] For this reason, several heteronuclear NMR spectroscopy experiments for backbone assignment have been proposed for fully ^{13}C- and ^{15}N-enriched proteins.[13,14,17] Furthermore, backbone sequence-specific assignment by the recently-designed CANCO experiment has also been reported.[18] We present herein an extension of the set of *exclusively heteronuclear* experiments to protein side chain resonances for the complete heteronuclear assignment of a protein. With a novel CBCACO experiment the carbonyl carbon (CO) is linked to the C^{β} and to the C^{α} nuclei; the connection to the rest of the amino acid side chain is achieved through a ^{13}C–^{13}C TOCSY experiment with C^{α} detection. In these experiments, we have successfully implemented spin-state selection methods for the removal of signal splitting in the acquisition dimension which is caused by multiple ^{13}C–^{13}C scalar couplings. This makes ^{13}C detection an amenable tool for high-resolution NMR spectroscopy. The proposed assignment strategy is summarized in Figure 1. A

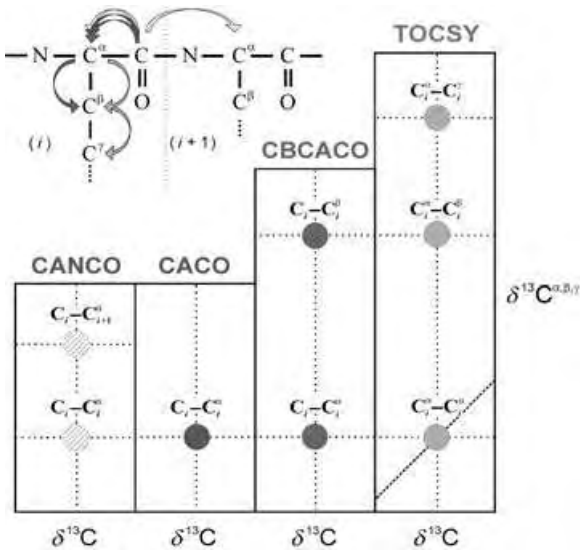

Figure 1. Illustration of the assignment procedure for ^{13}C NMR spectroscopy experiments. The assignment starts with analysis of the CACO experiment, which provides the correlation between the carbonyl carbon (CO) and the C^{α} nuclei of each amino acid. The spin-system assignment is extended to the C^{β} nuclei with the CBCACO experiment, and the process is completed with the TOCSY experiment, which provides correlation between the C^{α} and the other carbon nuclei of the amino acid side chain. The amino acid spin systems are finally assigned in a sequence-specific manner with the aid of a CANCO experiment,[18] which provides the correlation of each CO to the two neighboring C^{α} nuclei.

[*] Prof. I. Bertini
CERM and Department of Chemistry
University of Florence
Via Luigi Sacconi 6, 50019 Sesto Fiorentino (Italy)
Fax: (+39) 055-457-4271
E-mail: bertini@cerm.unifi.it
Dr. W. Bermel
Bruker BioSpin GmbH, Rheinstetten (Germany)
Dr. L. Duma, Prof. L. Emsley
Laboratoire de Chimie, UMR 5182 CNRS
Ecole Normale Superieure de Lyon (France)
Dr. I. C. Felli, Prof. R. Pierattelli, Dr. P. R. Vasos
CERM and Department of Chemistry
University of Florence (Italy)

[**] The authors are grateful to Dr. Alan Stern and Dr. Frank Delaglio for useful comments. L.D. was supported by the EC Marie Curie Fellowship (Contract HPMT-2000-000137). This work was supported in part by the EC Contracts HPRI-CT-2001-50026, HPRN-CT-2000-00092, and QLG2-CT-2002-00988. All NMR pulse sequences written for the Bruker Avance series spectrometers are available upon request.

Supporting information for this article is available on the WWW under http://www.angewandte.org or from the author.

 DOI: 10.1002/anie.200461794

detailed description of CBCACO and other novel experiments presented herein are provided in the Supporting Information.

Figure 2c shows the 2D version of the CBCACO spectrum recorded with isotopically enriched (70% ^{2}H, 98% ^{13}C and ^{15}N), reduced human Cu,Zn superoxide dismutase (SOD),[19] a dimeric protein of $M_W = 32000$. The 55-Hz CO line splitting due to the C^{α}–CO scalar coupling is removed by separation of the two multiplet components with the in-phase/anti-phase (IPAP) scheme,[20,21] followed by their recombination to increase the sensitivity of the spectrum[22] (Supporting Information). Upon comparison with the IPAP–CACO spectrum (Figure 2a), the additional cross-peaks in the IPAP–CBCACO spectrum allow identification of the types of amino acid groups present in the protein on the basis of the chemical shift of C^{β}.[23] Moreover, the resolution is enhanced through the chemical-shift dispersion of C^{β} resonances ($\approx$70 ppm), which are larger than those of C^{α} ($\approx$35 ppm). Notably, this single spectrum reveals all C^{α} and C^{β} signals that have been previously assigned.[24] Furthermore, the correlations of carbonyl and carboxylate nuclei of Asp, Asn, Glu, and Gln residues, which may be important in the study of surface properties in protein–protein interactions, are easily assigned, as they are observed in a specific region of the spectrum (centered at $\omega_2 = 180$ ppm and $\omega_1 = 35$ ppm). The IPAP–CBCACO experiment is designed for easy expansion

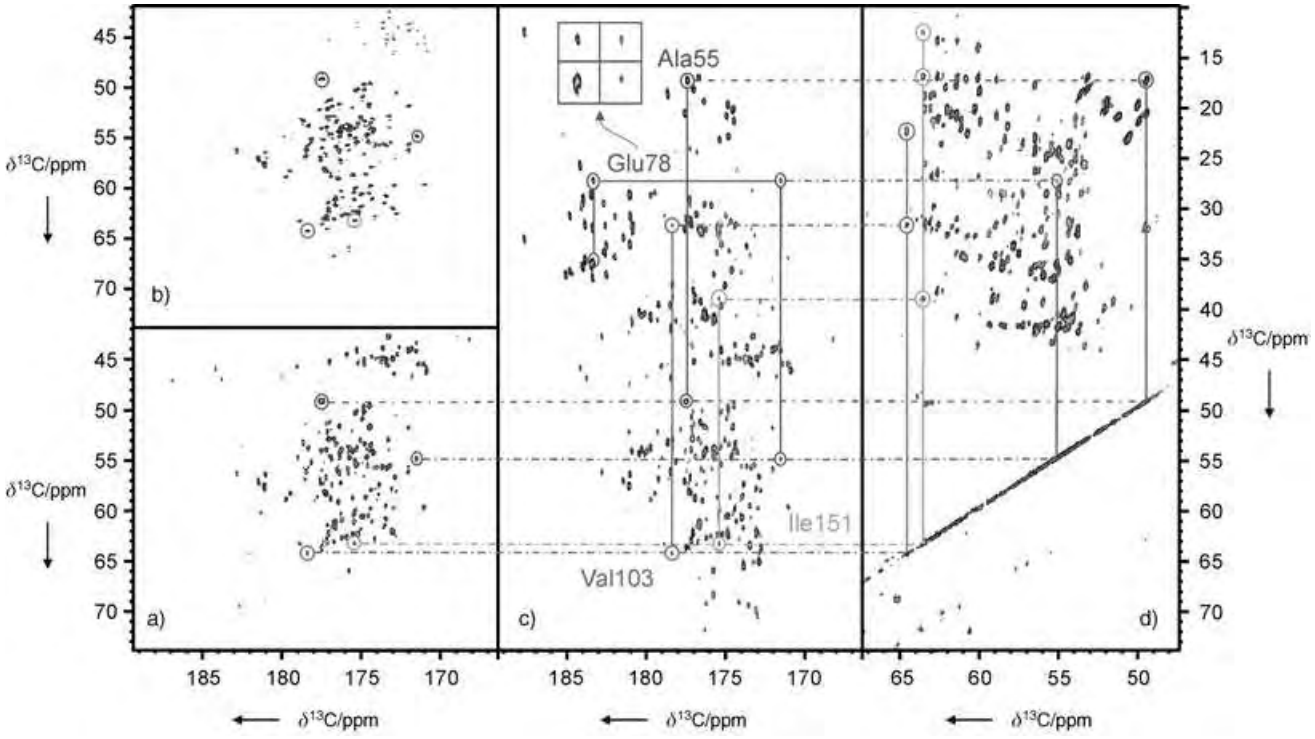

Figure 2. a) IPAP–CACO spectrum, b) DIPAP–COCA spectrum, c) 2D version (^{13}CO–$^{13}C^{\alpha/\beta}$) of the IPAP–CBCACO spectrum, and d) ^{13}C–^{13}C DIPAP–TOCSY spectrum recorded at 298 K with reduced Cu,Zn SOD (70% ^{2}H, 98% ^{13}C and ^{15}N) on a Bruker Avance NMR spectrometer (16.4 T, 700.06 MHz for ^{1}H, 176.03 MHz for ^{13}C) equipped with a ^{13}C-{^{1}H,^{15}N}TXO probe head. Chemical shifts were referenced to external 2,2-dimethyl-2-silapentane-5-sulfonic acid. The protein sample (2 mM) was prepared as previously reported[38] in phosphate buffer (20 mM, pH 5.0). The direct links between the different correlations in the spectra of panels a), c), and d) are reported for four different amino acid types. For comparison, panel b) shows the DIPAP–COCA spectrum rotated by 90°; the connectivities shown in panel a) are circled as well. The inset in panel c) shows an expansion of the four cross-peaks present in the IPAP–CBCACO spectrum for Glu78. For the spectra in panel a) and c), matrices of 1024×128 and 1024×192 complex points, respectively, in the ^{13}CO and $^{13}C^{\alpha/\beta}$ dimensions were acquired with 256 transients per increment and a recycle delay of 1.25 s; ^{1}H, ^{2}H, and ^{15}N were decoupled during the whole sequence. For each time increment in the indirect dimension, two FIDs were stored separately, one each for the anti-phase and in-phase components. The FIDs were then added and subtracted to separate the two multiplet components. These were then shifted to the center of the original multiplet by ($J_{CO-C^{\alpha}}$/2) Hz and again added to obtain a singlet.[22] Prior to Fourier transformation, an expansion to 2048×512 by linear prediction in the indirect dimension, together with zero filling and squared-sine-multiplication functions shifted by $\pi/4$ were applied in the t_2 and t_1 dimensions. For the spectrum in panel b) a matrix of 1024×96 complex points in the $^{13}C^{\alpha}$ and ^{13}CO dimensions was acquired, with 256 transients per increment and a recycle delay of 1.25 s; ^{1}H, ^{2}H, and ^{15}N were decoupled during the whole sequence. For each time increment in the indirect dimension, four FIDs were stored separately, and the resulting submatrices were added and subtracted in pairs to separate the four multiplet components, and then shifted by ($\pm J_{CO-C^{\alpha}}$/2) Hz and ($\pm J_{C^{\alpha}-C^{\beta}}$/2) Hz and added again to obtain a singlet.[22] Prior to Fourier transformation, an expansion to 2048×512 by linear prediction in the indirect dimension, together with zero filling and squared-sine-multiplication functions shifted by $\pi/4$ were applied in the t_2 and t_1 dimensions. For spectrum in panel d) a matrix of 1024×256 complex points was acquired, with 256 transients per increment and a recycle delay of 1.25 s; ^{1}H, ^{2}H, and ^{15}N were decoupled during the whole sequence, except during the DIPSI-3[39] spin lock of 23 ms. The processing of data for the four DIPAP submatrices was performed as described for panel b). Prior to Fourier transformation, an expansion of 2048×512 with zero filling and squared-sine-multiplication functions shifted by $\pi/4$ and $\pi/2$ were applied in the t_2 and t_1 dimensions, respectively.

into a 3D version by evolving the C^{α} chemical shift in the third dimension.

The IPAP filter can be implemented in a CBCACO experiment without introducing additional delays and it offers a gain in sensitivity with respect to other methods of *J*-coupling suppression.[*] The IPAP filter can, of course, be easily included in the CACO experiment.[**]

The extension of heteronuclear assignments through a ^{13}C–^{13}C TOCSY experiment[11,15] is conveniently performed by detection of the C^{α} resonances, which experience splitting from the coupling of the C^{α} nuclei to both the CO and the C^{β} nuclei. Therefore, a double IPAP (DIPAP) scheme[28] was implemented to remove the double splitting present on the C^{α} signal. As nuclear relaxation is a dominant limitation in complex pulse sequences, we succeeded in merging the two IPAP blocks into a single short building block. An example of C^{α} detection is provided by the DIPAP–COCA spectrum recorded on the same SOD sample (Figure 2b) at 16.4 T. It is nearly identical to the IPAP–CACO spectrum (Figure 2a) in terms of resolution and number of signals, except for signals that do not show the secondary coupling such as those of Gly residues. Furthermore, C^{α} detection is expected to be better than the detection of CO at high fields, as CO relaxation is dominated by the chemical-shift anisotropy (CSA) interaction that increases with the square of the magnetic field.[29,30] The detailed pulse sequence is reported in the Supporting Information.

Figure 2b shows that the DIPAP building block is quite effective. It allows one to successfully record highly resolved ^{13}C–^{13}C TOCSY spectra, as shown in Figure 2d. In the present case, the DIPAP–TOCSY experiment allowed a significant extension of the assignments for SOD[24] (expected C' and C^{α}, 100%; C^{β}, 98%; C^{γ}, 93%; C^{δ}, 89%; C^{ε}, 82%; side-chain CO, 100%).[***]

The same set of experiments was performed on a sample of ^{13}C,^{15}N-enriched oncomodulin (2.5 mM), a small Ca-binding protein of $M_W = 11\,500$. This enabled the assignment of all the resonances already obtained by standard ^{1}H-based NMR spectroscopy.[31] With this method of spin-state-selective detection, the assignments were expanded to almost all complete spin systems that were expected on the basis of the protein primary sequence (expected C', C^{α} and C^{β}, 100%; C^{γ} and C^{δ}, 98%; C^{ε}, 73%; side-chain CO, 100%;).[***]

In conclusion, the data presented herein show that removal of ^{13}C–^{13}C splitting in the acquisition dimension creates a significant step forward in direct-detection-^{13}C NMR spectroscopy and opens new prospects in the resolution of biomolecular NMR spectroscopic data. Indeed, there are a large number of experiments that could benefit from the present approach, including 3D experiments that are important to reduce spectral overlap typical of large molecules. Notably, a 3D-IPAP–CBCACO experiment on a sample of oncomodulin (2.5 mM) requires 16 scans, which is not an unreasonably long duration in comparison with standard proton-based 3D experiments at the same field. Similarly, the DIPAP–TOCSY experiment is highly sensitive and an optimal data set can be obtained in less than 24 h. The ^{13}C–^{13}C experiments presented herein can thus be included in any standard biomolecular NMR spectroscopy protocol for structure determination.

The measurement of ^{13}C–^{13}C couplings to determine residual dipolar couplings for the purposes of structure determination[32] can be performed by analysis of the individual submatrices obtained in the IPAP and DIPAP experiments, even if the resolution is still not ideal. Simultaneous decoupling of the different nuclei limits the effective RF field strength available for each nucleus as well as the duration of the acquisition time. Care should be taken to minimize overheating the sample during experiments. ^{13}C homodecoupling[10] is no longer necessary, making these experiments possible with any standard NMR spectrometer equipped for triple resonance experiments. The increase in sensitivity expected with the use of cryogenic technology in probe design, which is not yet fully exploited in ^{13}C NMR spectroscopy, will further assist in the establishment of direct-detection ^{13}C NMR as a routine technique for protein investigations and also for samples that are more dilute than those used in the experiments reported herein.

These experiments are also advantageous to the study of unfolded, highly mobile, and exchangeable systems in which the broadening of the NH signals cannot be recovered through the TROSY approach. In general, direct-detection ^{13}C NMR experiments are the only source of information for cases in which the ^{1}H resonances are broadened beyond detection through relaxation or exchange effects. Finally, ^{13}C NMR spectroscopy is the appropriate solution to paramagnetic relaxation as has been previously shown;[10,16] indeed this has been proven in studies of lanthanide-substituted oncomodulin, as a continuation of this research. In this case, a number of structural restraints based on paramagnetism are also available for solution-structure determination.[12,33–37]

[*] Several methods have been proposed to remove *J* splitting from the acquisition dimension, such as band-selective homodecoupling,[10] maximum entropy reconstruction,[25] and other post-acquisition methods.[26] We propose the method based on spin-state-selective schemes with the IPAP sequence[20,21] as an example, because it provides the best signal-to-noise ratio (S/N) in comparison with other methods (not shown). The gain in S/N compared with the most intense component of the coupled spectrum is close to that theoretically expected of SQRT(2), owing to the uniform *J*-coupling values found in ^{13}C signals. For band-selective homodecoupling, the lower S/N obtained results mainly from the higher intrinsic level of noise introduced by the acquisition method, rather than from unsatisfactory decoupling efficiency. Maximum entropy reconstruction apparently gives higher signal than the homodecoupled and nondecoupled spectra which comes at the expense of a nonuniform noise that surrounds the reconstructed peaks if the *J* coupling is not exactly matched.[25]

[**] Similarly, a S^3E filter[27] can be used, which is an even more compact way to obtain spin-state selection. The corresponding sequence and spectrum are reported in the Supporting Information.

[***] In the case of aromatic amino acids, an additional experiment is necessary to conveniently assign the aromatic ring carbon nuclei that resonate around 130 ppm.[23]

Received: August 26, 2004
Revised: December 16, 2005
Published online: April 14, 2005

Keywords: carbon NMR spectroscopy · NMR spectroscopy · protein structures · proteins · spin-state selection

[1] G. Wagner, *Prog. Nucl. Magn. Reson. Spectrosc.* **1990**, *22*, 101 – 139.
[2] M. Sattler, J. Schleucher, C. Griesinger, *Prog. Nucl. Magn. Reson. Spectrosc.* **1999**, *34*, 93 – 158.
[3] M. Salzmann, K. Pervushin, G. Wider, H. Senn, K. Wüthrich, *J. Am. Chem. Soc.* **2000**, *122*, 7543 – 7548.
[4] B.-H. Oh, W. M. Westler, P. Darba, J. L. Markley, *Science* **1988**, *240*, 908 – 911.
[5] U. Kolczak, J. Salgado, G. Siegal, M. Saraste, G. W. Canters, *Biospectroscopy* **1999**, *5*, S19-S32.
[6] I. Bertini, Y.-M. Lee, C. Luchinat, M. Piccioli, L. Poggi, *ChemBioChem* **2001**, *2*, 550 – 558.
[7] Z. Serber, C. Richter, V. Dötsch, *ChemBioChem* **2001**, *2*, 247 – 251.
[8] M. Kostic, S. S. Pochapsky, T. C. Pochapsky, *J. Am. Chem. Soc.* **2002**, *124*, 9054 – 9055.
[9] T. E. Machonkin, W. M. Westler, J. L. Markley, *J. Am. Chem. Soc.* **2002**, *124*, 3204 – 3205.
[10] W. Bermel, I. Bertini, I. C. Felli, R. Kümmerle, R. Pierattelli, *J. Am. Chem. Soc.* **2003**, *125*, 16423 – 16429.
[11] A. Eletsky, O. Moreira, H. Kovacs, K. Pervushin, *J. Biomol. NMR* **2003**, *26*, 167 – 179.
[12] F. Arnesano, L. Banci, I. Bertini, I. C. Felli, C. Luchinat, A. R. Thompsett, *J. Am. Chem. Soc.* **2003**, *125*, 7200 – 7208.
[13] I. Bertini, I. C. Felli, R. Kümmerle, D. Moskau, R. Pierattelli, *J. Am. Chem. Soc.* **2004**, *126*, 464 – 465.
[14] I. Bertini, I. C. Felli, R. Kümmerle, C. Luchinat, R. J. Pierattelli, *J. Biomol. NMR* **2004**, *30*, 245 – 251.
[15] B. Vögeli, H. Kovacs, K. Pervushin, *J. Am. Chem. Soc.* **2004**, *126*, 2414 – 2420.
[16] T. E. Machonkin, W. M. Westler, J. L. Markley, *J. Am. Chem. Soc.* **2004**, *126*, 5413 – 5426.
[17] E. Babini, I. Bertini, F. Capozzi, I. C. Felli, M. Lelli, C. Luchinat, *J. Am. Chem. Soc.* **2004**, *126*, 10496 – 10497.
[18] I. Bertini, L. Duma, I. C. Felli, M. Fey, C. Luchinat, R. Pierattelli, P. R. Vasos, *Angew. Chem.* **2004**, *116*, 2307 – 2309; *Angew. Chem. Int. Ed.* **2004**, *43*, 2257 – 2259.
[19] L. Banci, I. Bertini, F. Cramaro, R. Del Conte, A. Rosato, M. S. Viezzoli, *Biochemistry* **2000**, *39*, 9108 – 9118.
[20] M. Ottiger, F. Delaglio, A. Bax, *J. Magn. Reson.* **1998**, *131*, 373 – 378.
[21] P. Andersson, J. Weigelt, G. Otting, *J. Biomol. NMR* **1998**, *12*, 435 – 441.
[22] N. C. Nielsen, H. Thøgersen, O. W. Sørensen, *J. Am. Chem. Soc.* **1995**, *117*, 11365 – 11366.
[23] H. Zhang, S. Neal, D. S. Wishart, *J. Biomol. NMR* **2003**, *25*, 173 – 195.
[24] L. Banci, I. Bertini, F. Cramaro, R. Del Conte, M. S. Viezzoli, *Eur. J. Biochem.* **2002**, *269*, 1905 – 1915.
[25] N. Shimba, A. S. Stern, C. S. Craik, J. C. Hoch, V. Dötsch, *J. Am. Chem. Soc.* **2003**, *125*, 2382 – 2383.
[26] K. Pervushin, A. Eletsky, *J. Biomol. NMR* **2003**, *25*, 147 – 152.
[27] A. Meissner, J. O. Duus, O. W. Sørensen, *J. Magn. Reson.* **1997**, *128*, 92 – 97.
[28] L. Duma, S. Hediger, B. Brutscher, A. Bockmann, L. Emsley, *J. Am. Chem. Soc.* **2003**, *125*, 11816 – 11817.
[29] L. Zeng, M. W. F. Fischer, E. R. P. Zuiderweg, *J. Biomol. NMR* **1996**, *7*, 157 – 162.
[30] K. T. Dayie, G. Wagner, *J. Am. Chem. Soc.* **1997**, *119*, 7797 – 7806.
[31] E. Babini, I. Bertini, F. Capozzi, C. Del Bianco, D. Holleder, T. Kiss, C. Luchinat, A. Quattrone, *Biochemistry* **2004**, *43*, 16076 – 16085.
[32] A. Bax, G. Kontaxis, N. Tjandra, *Methods Enzymol.* **2001**, *339*, 127 – 174.
[33] I. Bertini, C. Luchinat, G. Parigi, *Concepts Magn. Reson.* **2002**, *14*, 259 – 286.
[34] I. Bertini, A. Donaire, B. Jimenez, C. Luchinat, G. Parigi, M. Piccioli, L. Poggi, *J. Biomol. NMR* **2001**, *21*, 85 – 98.
[35] G. Pintacuda, A. Moshref, A. Leonchiks, A. Sharipo, G. Otting, *J. Biomol. NMR* **2004**, *29*, 351 – 361.
[36] R. Barbieri, C. Luchinat, G. Parigi, *ChemPhysChem* **2004**, *5*, 797 – 806.
[37] T. Ikegami, L. Verdier, P. Sakhaii, S. Grimme, P. Pescatore, K. Saxena, K. M. Fiebig, C. Griesinger, *J. Biomol. NMR* **2004**, *29*, 339 – 349.
[38] E. D. Getzoff, D. E. Cabelli, C. L. Fisher, H. E. Parge, M. S. Viezzoli, L. Banci, R. A. Hallewell, *Nature* **1992**, *358*, 347 – 351.
[39] A. J. Shaka, C. J. Lee, A. Pines, *J. Magn. Reson.* **1988**, *77*, 274 – 293.

Biradical Intermediates

Generation of the Elusive *meta*-Benzoquinone in the Gas Phase**

Jana Roithová, Detlef Schröder, and Helmut Schwarz*

Dedicated to Professor Josef Michl on the occasion of his 65th birthday

meta-Benzoquinone (**1**) is a challenging molecule that belongs to the family of biradicaloid *meta*-disubstituted benzenes.[1] While numerous experimental and theoretical studies have been devoted to the closely related *meta*-xylylene (**2**),[2–4] *meta*-benzoquinone has been studied only theoretically.[4–6] Extensive (σ-S, π-SD)QCI calculations con-

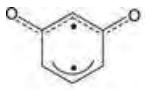

1

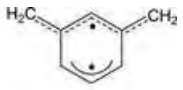

2

[*] Dr. J. Roithová,[+] Dr. D. Schröder, Prof. Dr. H. Schwarz
Institut für Chemie der Technischen Universität Berlin
10623 Berlin (Germany)
Fax: (+49) 30-314-21102
E-mail: Detlef.Schroeder@TU-Berlin.de

[+] Permanent address:
J. Heyrovský Institute of Physical Chemistry
Academy of Sciences
18223 Prague 8 (Czech Republic)

[**] This work was supported by the Deutsche Forschungsgemeinschaft, the European Commission (MCInet), the Fonds der Chemischen Industrie, and the Gesellschaft von Freunden der Technischen Universität Berlin. We thank Waltraud Zummack for experiments on the oxidation of resorcinol with KIO_3 as reported in ref. [10].

Supporting information for this article is available on the WWW under http://www.angewandte.org or from the author.

  DOI: 10.1002/anie.200461783

ducted by Fort et al.[4] predict a $^3B_2$ ground state of neutral **1**. The first excited singlet state ($^1B_2$) also has a biradicaloid structure and has been calculated to be 0.4 eV higher in energy.[7] There have been attempts to prepare derivatives of *meta*-benzoquinone, but probably due to the suggested rapid decarbonylation, none of the substituted *meta*-benzoquinones has been isolated so far.[8–10] This work reports the generation of *meta*-benzoquinone by means of neutralization–reionization (NR) mass spectrometry, a technique proved efficient for the generation and characterization of elusive molecules.[11,12]

Neutralization–reionization mass spectrometry consists of three steps. First, an ion of the desired structure is generated in the gas phase. Next, the mass-selected ion is neutralized in high-energy collision with an appropriate gas and all remaining charged species are deflected. In the third step, the beam of neutral species—the parent molecule and its fragments—is reionized in a second time-delayed collision to facilitate mass analysis, detection, and structural characterization based on the fragmentation pattern. As amply demonstrated,[11,12] in an ideal case an NR experiment is a convenient means for the generation and detection of otherwise hardly accessible neutral molecules. However, a conventional NR spectrum contains not only signals indicative for the neutral target molecule, rather it constitutes a superposition of fragmentations of neutral and ionic species involved in the sequential collision events. The problem of extracting the desired information specific to the neutral molecule in question has been addressed by several approaches,[11,13] of which the neutral and ion decomposition difference (NIDD) method[14] is applied here.

The first step towards *meta*-benzoquinone concerns the generation of a suitable ionic precursor.[15] The present study is confined to the corresponding anion, because experiments with the molecular cation $\mathbf{1}^{\bullet+}$ are considered ambiguous as far as the ion structure is concerned due to facile Wagner–Meerwein and other rearrangements in cationic species.[18] The anion $\mathbf{1}^{\bullet-}$ (Scheme 1) is generated by chemical ionization of resorcinol (1,3-dihydroxybenzene) using N_2O as reagent gas, where ionization of the latter provides $O^{\bullet-}$, which serves as the ionizing agent. Formation of $\mathbf{1}^{\bullet-}$ requires the elimination of both hydrogen atoms from the hydroxy groups of the precursor; of course, the singly deprotonated ion $C_6H_5O_2^-$ is observed as well. However, hydrogen may also be abstracted from the ring carbons, which would then lead to the putative anions $\mathbf{3}^{\bullet-}$–$\mathbf{6}^{\bullet-}$ (Scheme 1). According to B3LYP calculations,[19] these tautomers are about 1.5 eV higher in energy than $\mathbf{1}^{\bullet-}$. Therefore, the contribution of ring-deprotonated isomers is very likely to be small—if there is any—compared to $\mathbf{1}^{\bullet-}$. Abstraction of both hydrogen atoms from C–H bonds only as well as ring-opening would lead to anions with even considerably higher relative energies; these structures are therefore not considered any further in the discussion.

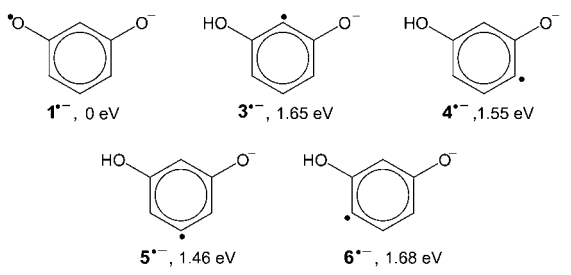

Scheme 1. Various isomers of $C_6H_4O_2^{\bullet-}$ and their energies $E_{0K} = E_{tot} + E_{ZPV}$ relative to $\mathbf{1}^{\bullet-}$; $E_{tot}(\mathbf{1}^{\bullet-}) = -381.628204$ Hartree, E_{ZPV} (zero-point vibration energy) $(\mathbf{1}^{\bullet-}) = 0.081688$ Hartree.

The connectivity of the $C_6H_4O_2^{\bullet-}$ anion generated from resorcinol was examined by recording its metastable ion (MI) and collisional activation (CA) mass spectra (Figure 1). The

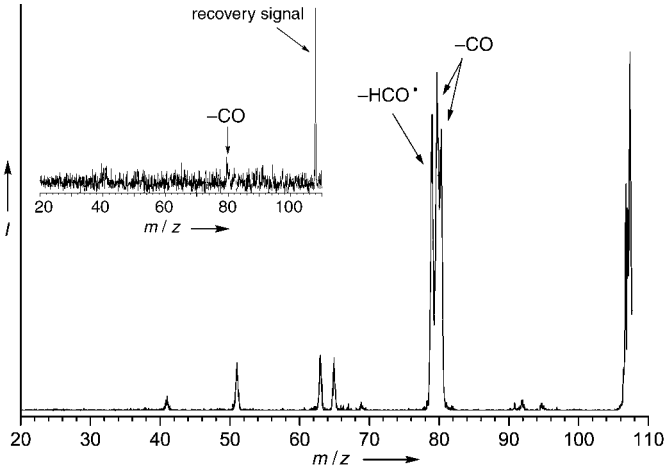

Figure 1. CA mass spectrum of $C_6H_4O_2^{\bullet-}$ generated by chemical ionization of resorcinol using N_2O as a reagent gas. The inset shows the $^-NR^-$ mass spectrum of $C_6H_4O_2^{\bullet-}$.

most dominant feature in both spectra corresponds to the loss of carbon monoxide with a characteristic peak shape that indicates a significant reverse activation barrier. The kinetic energy release associated with this process is estimated as 0.53 eV from the horn-to-horn distance of the composite peak in an energy-resolved experiment.[23] However, as the fragmentation pattern in the CA spectrum cannot be associated unambiguously with a particular connectivity of the parent ion, the CA and charge reversal ($^-CR^+$) spectra of $C_6H_4O_2^{\bullet-}$ generated by chemical ionization of $(O\text{-D})_2$- resorcinol[24,25] and 1,3-bis(trimethylsilyloxy)benzene, respectively, were acquired as well; N_2O was used as reagent gas. If mixtures of isomers were formed, the relative populations of isomers should be precursor-dependent and hence lead to differences in the spectra. Experimentally, the CA and $^-CR^+$ spectra of $C_6H_4O_2^{\bullet-}$ generated from resorcinol, its $(O\text{-D})_2$ analogue, and 1,3-bis(trimethylsilyloxy)benzene are identical within experimental uncertainty. Thus, we conclude that only the most stable isomer $\mathbf{1}^{\bullet-}$ is formed, irrespective of the precursor employed. Even if other isomers were generated initially,[26] the experimental findings imply that isomerization to $\mathbf{1}^{\bullet-}$ must have occurred either inside the ion source or within the time elapsed during mass selection (ca. 25 μs). The eventual isomerization to other benzoquinone isomers, that is, *ortho* and *para* isomers, is excluded on the basis of different CA as well as $^-CR^+$ spectra of the respective anions (see the

Supporting Information). Specifically, the base peak in the $^{-}CR^{+}$ spectrum of *para*-benzoquinone, the thermodynamically most stable isomer, corresponds to C_2H_2 elimination (*m*/*z* 82). This fragmentation is completely missing in the $^{-}CR^{+}$ spectra of either *ortho* or *meta* isomer. On the other hand, the $^{-}CR^{+}$ spectrum of *meta*-benzoquinone anion shows intense loss of $C_3H_3^{\bullet}$ (*m*/*z* 69), which is missing in the spectra of the two other isomers. Therefore, the occurrence of skeletal rearrangements leading to the formation of a mixture of benzoquinone isomers can certainly be ruled out.[27] Accordingly, the experimental results imply that $\mathbf{1}^{\bullet-}$ serves as the major, if not exclusive, contributor to the beam of mass-selected $C_6H_4O_2^{\bullet-}$ ions.

Collisional neutralization by electron transfer at keV energies is considered to occur on the femtosecond timescale as a vertical process and is thus governed by Franck–Condon factors.[11–13] The efficiency of the transition between an ion and the corresponding neutral counterpart together with the associated amount of internal excitation can be estimated from the difference of the vertical and adiabatic energies ($\Delta E_{v/a}$) of the corresponding transitions (Scheme 2). Generation of triplet ground state of *meta*-benzoquinone ($^3B_2$) from the anion $\mathbf{1}^{\bullet-}$ is associated with a calculated $\Delta E_{v/a}(\mathbf{1}^{\bullet-}/^3\mathbf{1})$ of 0.12 eV; likewise, $\Delta E_{v/a}(\mathbf{1}^{\bullet-}/^1\mathbf{1}) = 0.20$ eV results for the formation of singlet $^1B_2$ (Scheme 2).[28] These rather small values suggest favorable Franck–Condon factors for electron detachment from $\mathbf{1}^{\bullet-}$. The probability of $\mathbf{1}^{\bullet-}$ to survive an NR sequence has been probed by a $^{-}NR^{-}$ experiment.[17] Despite a rather poor signal-to-noise ratio, the $^{-}NR^{-}$ spectrum of $\mathbf{1}^{\bullet-}$ clearly shows the recovery ion as the major signal (inset in Figure 1). In agreement with the theoretical predictions, neutral *meta*-benzoquinone (**1**) can thus be generated from its anion without undergoing complete dissociation during the time interval of about 1 μs required for the passage from the neutralization to the reionization cell, which defines a minimum lifetime of **1**.

The $^{-}NR^{+}$ spectrum (Figure 2a) differs largely from the $^{-}NR^{-}$ spectrum (Figure 1, inset) in that extensive fragmentation processes are observed, for which two explanations can be put forward. First, the ionization cross sections for fragments formed at the neutral stage differ substantially for reionization to anions and reionization to cations.[29] Secondly, excessive fragmentation often takes place at the cationic stage which is also reflected in the charge-reversal spectrum ($^{-}CR^{+}$, Figure 2b).[30] Information about fragmentations of the neutral molecules can be extracted from a comparison of the $^{-}NR^{+}$ signals, resulting as a superposition of fragmentations of both, ions and neutrals, with the $^{-}CR^{+}$ spectrum, in which mostly fragmentations of ionic species are sampled.[13,14] In the resulting $^{-}NIDD^{+}$ spectrum, positive signals are due to fragmentations occurring at the neutral stage, while negative signals originate from preferential decompositions of ionic species. According to Figure 2c, the most intense fragmentation of neutral **1** is associated with loss of carbon monoxide concomitant with generation of cyclopentadienone, which is then reionized (*m*/*z* 80). Formation of cyclopentadienone is further supported by the positive $^{-}NIDD^{+}$ signal of a subsequent CO loss, which implies the generation of C_4H_4 (*m*/*z* 52);[31] the latter can further lose molecular hydrogen under NR conditions (*m*/*z* 50).[32]

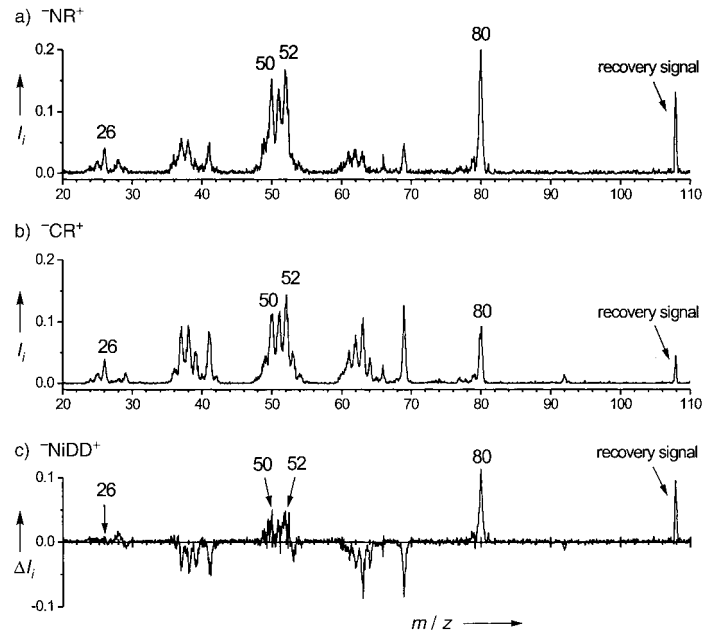

Figure 2. a) $^{-}NR^{+}$ ($\Sigma I_i = 1$), b) $^{-}CR^{+}$ ($\Sigma I_i = 1$), and c) $^{-}NIDD^{+}$ ($\Sigma I_i = 0$) mass spectra of $C_6H_4O_2^{\bullet-}$ ($\mathbf{1}^{\bullet-}$) generated by chemical ionization of resorcinol using N_2O as reagent gas.

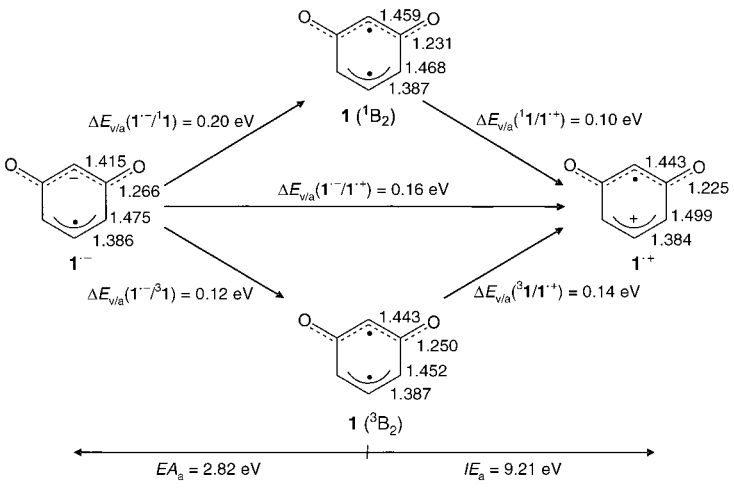

Scheme 2. Redox energies relevant in the neutralization–reionization and charge-reversal experiments. Relative energies and bond lengths [Å] were obtained from calculations.[19]

To corroborate the experimental findings, we also considered the reaction pathway for CO loss from *meta*-benzoquinone (**1**) computationally (Scheme 3). For the triplet ground state **1** ($^3B_2$), the rate-determining barrier is quite significant (2.56 eV), and decarbonylation to afford triplet cyclopentadienone is endothermic. On the singlet surface, however, the initial barrier is much lower ($E_{rel} = 1.02$ eV) and the asymptote **8** + CO is lower in energy than **1** ($^3B_2$).

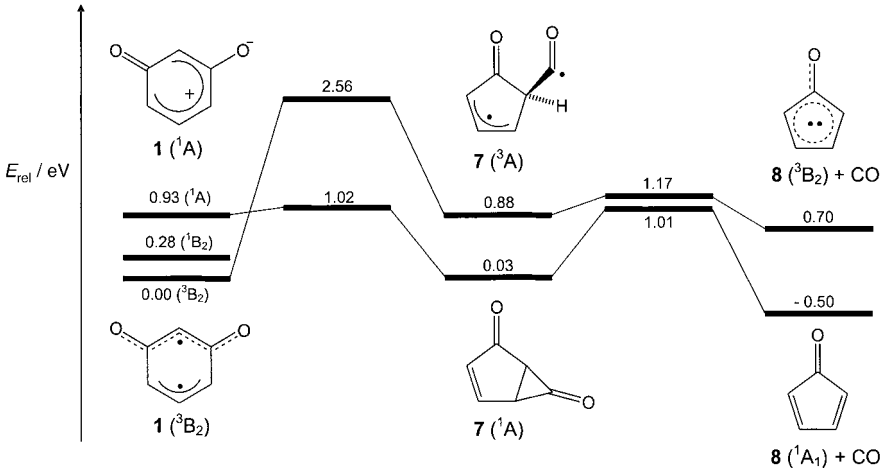

Scheme 3. Calculated reaction pathways for the decarbonylation of the singlet and triplet states of *meta*-benzoquinone (**1**). Energies are given at 0 K and related to $\mathbf{1}(^3B_2)$; $E_{tot}(^3\mathbf{1}) = -381.524990$ Hartree, $E_{ZPV}(^3\mathbf{1}) = 0.0822234$ Hartree).

Accordingly, decarbonylation of **1** ($^3B_2$) can be assisted by a spin change along the reaction coordinate.[33]

In conclusion, the elusive *meta*-benzoquinone (**1**) has been generated in the gas phase by means of neutralization–reionization mass spectrometry. The main fragmentation channel of the neutral molecule leads to loss of carbon monoxide concomitant with cyclopentadienone as the most probable product. The present experimental and theoretical results pose no fundamental objections against the generation of *meta*-benzoquinone under different conditions. Matrix isolation of this molecule, which appears feasible, could then provide the ultimate spectroscopic characteristics of **1**.

Received: August 25, 2004
Revised: November 10, 2004
Published online: April 13, 2005

Keywords: decarbonylation · density functional calculations · mass spectrometry · quinones · radical ions

[1] M. S. Platz, *Quinodimethanes and Related Diradicals*, *Vol. 1* (Ed.: W. T. Borden), Wiley, New York, **1982**, p. 195.
[2] L. A. Hammad, P. G. Wenthold, *J. Am. Chem. Soc.* **2000**, *122*, 11203.
[3] B. B. Wright, M. S. Platz, *J. Am. Chem. Soc.* **1983**, *105*, 628.
[4] R. C. Fort, Jr., S. J. Getty, D. A. Hrovat, P. M. Lahti, W. T. Borden, *J. Am. Chem. Soc.* **1992**, *114*, 7549.
[5] P. M. Lahti, A. R. Rossi, J. A. Berson, *J. Am. Chem. Soc.* **1985**, *107*, 2273.
[6] See also: a) D. E. Seeger, P. M. Lathi, A. R. Rossi, J. A. Berson, *J. Am. Chem. Soc.* **1986**, *108*, 1251; b) M. Fischer, P. Wan, *J. Am. Chem. Soc.* **1999**, *121*, 4555; c) H. T. Le, P. C. Nam, V. L. Dao, T. Veszpremi, M. T. Nguyen, *Mol. Phys.* **2003**, *101*, 2347.
[7] See also: J. Gräfenstein, D. Cremer, *Phys. Chem. Chem. Phys.* **2000**, *2*, 2091.
[8] W. H. Starnes, D. A. Plank, J. C. Floyd, *J. Org. Chem.* **1975**, *40*, 1124.
[9] Oxidation of resorcinol with KIO_3 was reported to produce a "dirty yellow solid" which was assigned as a quinone based on its chemical behavior.[10] However, neither precise details of the reaction conditions and yields nor spectroscopic data were provided; the major interest in ref. [10] was the reaction kinetics. Further, we note that the reported melting points of the isolated solid (120–121 °C) and its mono-2,4-dinitrophenylhydrazone (185–187 °C) are close to the corresponding values of *para*-benzoquinone and its hydrazone derivative, respectively (115 °C and 186 °C, respectively). Several attempts in our laboratory to reproduce the reported procedure failed and instead led to iodoresorcinols as well as phenol-coupling products; *para*-benzoquinone was not even detected as a by-product.
[10] J. F. Iyun, P. O. Ukoha, *Int. J. Chem.* **1999**, *38*, 180.
[11] F. Tureček, *Top. Curr. Chem.* **2003**, *225*, 77.
[12] N. Goldberg, H. Schwarz, *Acc. Chem. Res.* **1994**, *27*, 347.
[13] C. A. Schalley, G. Hornung, D. Schröder, H. Schwarz, *Chem. Soc. Rev.* **1998**, *27*, 91.
[14] C. A. Schalley, G. Hornung, D. Schröder, H. Schwarz, *Int. J. Mass Spectrom. Ion Processes* **1998**, *172*, 181.
[15] The experiments were performed with a modified VG ZAB/HF/AMD four-sector mass spectrometer of BEBE configuration (B stands for magnetic and E for electric sector).[16] $\mathbf{1}^{\bullet-}$ was generated by negative-ion chemical ionization of resorcinol, 1,3-bis(trimethylsiloxy)benzene, and 1,3-dimethoxybenzene, using N_2O as reagent gas, accelerated to a kinetic energy of 8 keV and mass-selected by means of B(1)/E(1). The structure of the anion was probed by its metastable ion and collisional activation (CA) mass spectra. To this end, the unimolecular fragmentations of anions and their fragmentations upon collision with helium (80 % transmission, *T*), respectively, in the field-free region preceding the second magnet (3rd FFR) were recorded by scanning B(2). NR and charge reversal (CR) spectra were obtained by using a tandem of differentially pumped collision cells located in the 3rd FFR equipped with a deflector placed in between the cells. For NR experiments, both cells were filled (80 % *T*) by appropriate gases (O_2/Xe in $^-NR^-$ and O_2/O_2 in $^-NR^+$, respectively)[17] and the deflector was switched on. For $^-CR^+$ experiments, only the first cell was filled with O_2 (80 % *T*) and the deflector was grounded. Usually 10–50 scans were averaged to improve the signal-to-noise ratio, and the final data were derived from two to six independent measurements.
[16] R. Srinivas, D. Sülzle, T. Weiske, H. Schwarz, *Int. J. Mass Spectrom. Ion Processes* **1991**, *107*, 368.
[17] According to the charge states of the projectile and recovery ions, the NR spectra are denoted as $^+NR^+$, $^+NR^-$, $^-NR^+$, and $^-NR^-$, as suggested by: A. W. McMahon, S. K. Chowdhury, A. G. Harrison, *Org. Mass Spectrom.* **1989**, *24*, 620.
[18] D. Kuck, *Int. J. Mass Spectrom.* **2002**, *213*, 101.
[19] The calculations were performed using the density functional method B3LYP[20] in conjunction with 6-311 + G(2d,p) basis sets as implemented in Gaussian 98.[21] For all optimized structures, a frequency analysis was performed in order to assign them as genuine minima or transition structures and to determine the zero-point vibrational energies (E_{ZPV}). All transition structures were characterized by intrinsic reaction coordinate calculations.[22] The calculations of the anions $\mathbf{1}^{\bullet-}$ and $\mathbf{3}^{\bullet-}$–$\mathbf{6}^{\bullet-}$ were restricted to doublet states. The energies given in Schemes 1–3 are obtained as $E_{0K} = E_{tot} + E_{ZPV}$.

[20] a) A. D. Becke, *J. Chem. Phys.* **1993**, *98*, 5648; b) C. Lee, W. Yang, R. G. Parr, *Phys. Rev. B* **1988**, *37*, 785; c) B. Miehlich, A. Savin, H. Stoll, H. Preuss, *Chem. Phys. Lett.* **1989**, *157*, 200; d) S. H. Vosko, L. Wilk, M. Nusair, *Can. J. Phys.* **1980**, *58*, 1200.
[21] Gaussian 03 (Revision B.04), M. J. Frisch,. G. W. Trucks, H. B. Schlegel, G. E. Scuseria, M. A. Robb, J. R. Cheeseman, J. A. Montgomery, Jr., T. Vreven, K. N. Kudin, J. C. Burant, J. M. Millam, S. S. Iyengar, J. Tomasi, V. Barone, B. Mennucci, M. Cossi, G. Scalmani, N. Rega, G. A. Petersson, H. Nakatsuji, M. Hada, M. Ehara, K. Toyota, R. Fukuda, J. Hasegawa, M. Ishida, T. Nakajima, Y. Honda, O. Kitao, H. Nakai, M. Klene, X. Li, J. E. Knox, H. P. Hratchian, J. B. Cross, C. Adamo, J. Jaramillo, R. Gomperts, R. E. Stratmann, O. Yazyev, A. J. Austin, R. Cammi, C. Pomelli, J. W. Ochterski, P. Y. Ayala, K. Morokuma, G. A. Voth, P. Salvador, J. J. Dannenberg, V. G. Zakrzewski, S. Dapprich, A. D. Daniels, M. C. Strain, O. Farkas, D. K. Malick, A. D. Rabuck, K. Raghavachari, J. B. Foresman, J. V. Ortiz, Q. Cui, A. G. Baboul, S. Clifford, J. Cioslowski, B. B. Stefanov, G. Liu, A. Liashenko, P. Piskorz, I. Komaromi, R. L. Martin, D. J. Fox, T. Keith, M. A. Al-Laham, C. Y. Peng, A. Nanayakkara, M. Challacombe, P. M. W. Gill, B. Johnson, W. Chen, M. W. Wong, C. Gonzalez, J. A. Pople, Gaussian, Inc., Pittsburgh, PA, **2003**.
[22] a) C. Gonzalez, H. B. Schlegel, *J. Chem. Phys.* **1989**, *90*, 2154; b) C. Gonzalez, H. B. Schlegel, *J. Phys. Chem.* **1990**, *94*, 5523.
[23] R. G. Cooks, J. H. Beynon, R. M. Caprioli, G. R. Lester, *Metastable Ions*, Elsevier, Amsterdam, **1973**.
[24] The hydrogen atoms of the hydroxy groups of resorcinol were exchanged by its reaction with CH_3OD at room temperature. Due to facile keto–enol tautomerization, the sample contains also a small amount of D_3-resorcinol (< 4 %).
[25] The $^{-}CR^{+}$ spectra of O-deprotonated nonlabeled and O-bisdeuterated resorcinol (*m*/*z* 109 and 110, respectively) show characteristic losses of O$^{\bullet}$ atoms and OH$^{\bullet}$ and OD$^{\bullet}$ groups, respectively. Instead, the $^{-}CR^{+}$ spectrum of $C_6H_4O_2^{\bullet -}$ (Figure 2b) shows only the loss of O$^{\bullet}$ atom, which is yet further evidence for the suggested connectivity of $C_6H_4O_2^{\bullet -}$, rather than ring-deprotonated forms.
[26] In the studies of *meta*-xylylene, the radical anion $\mathbf{2}^{\bullet -}$ was generated by hydrogen abstraction from *meta*-xylene with $O^{\bullet -}$.[2] The authors claim generation of 75 % of desired *meta*-xylylene and 25 % of anions with one of the hydrogen atoms eliminated from the ring.
[27] In the context of a possible contribution of the ring-deprotonated isomers $\mathbf{3}^{\bullet -}$–$\mathbf{6}^{\bullet -}$, it is also worth mentioning that generation of *para*-benzoquinone anion by CI from either *para*-benzoquinone or hydroquinone leads to identical $C_6H_4O_2^{\bullet -}$ ions.
[28] The results for the $^1B_2$ state should be taken with some caution because the description of an open-shell singlet state with single reference methods, like B3LYP, inevitably encounters spin-contamination by the triplet state.
[29] D. Schröder, K. Schroeter, W. Zummack, H. Schwarz, *J. Am. Soc. Mass Spectrom.* **1999**, *10*, 878.
[30] M. M. Bursey, *Mass Spectrom. Rev.* **1990**, *9*, 555.
[31] H. Wang, K. Brezinsky, *J. Phys. Chem. A* **1998**, *102*, 1530.
[32] M.-Y. Zhang, B. K. Carpenter, F. W. McLafferty, *J. Am. Chem. Soc.* **1991**, *113*, 9499.
[33] a) R. Poli, J. N. Harvey, *Chem. Soc. Rev.* **2003**, *32*, 1; b) H. Schwarz, *Int. J. Mass Spectrom.* **2004**, *237*, 75.

Synthetic Methods

1,3-Dipolar Cycloadditions of Carbonyl Ylides to Aldimines: A Three-Component Approach to *syn*-α-Hydroxy-β-amino Esters**

*Staffan Torssell, Marcel Kienle, and Peter Somfai**

The β-amino alcohol and α-hydroxy-β-amino acid moieties are found in a large variety of biologically important compounds and natural products[1] as well as in a growing number of ligands and chiral auxiliaries for asymmetric synthesis.[2] Existing synthetic routes towards enantiopure *vic*-amino alcohols have traditionally relied on derivatization of the chiral pool of amino acids for the most part; however, there is an inherent limitation of accessible targets.[3] Considerable efforts have been made in developing asymmetric routes to β-amino alcohols to circumvent these drawbacks; these can be divided into two strategically different approaches.[4] Most commonly, the amino alcohol functionality is introduced into a pre-existing carbon skeleton, and this can be accomplished by Sharpless aminohydroxylation[5] or by ring opening of epoxides[4,6,7] or aziridines[4,7,8] with appropriate nucleophiles. More effectively, the amino alcohol moiety can be constructed by concomitant formation of a new carbon–carbon bond and two vicinal stereogenic centers in a single step. This approach has been realized by addition of glycine-derived enolates to aldehydes to yield *anti*-β-amino alcohols[1b,9] or by addition of α-alkoxy enolates to aldimines in a Mannich-type reaction.[1a,10] Although several methods are currently available for the stereo- and enantioselective formation of *vic*-amino alcohols, there is clearly a demand for simple and efficient entries to this interesting class of substance.

It was envisioned that *vic*-amino alcohols **A** could be obtained by hydrolysis of the corresponding oxazolidines **B**, and that these heterocycles could be prepared from the 1,3-dipolar cycloaddition of a carbonyl ylide **C** to an imine **D** (Scheme 1).[11] The carbonyl ylide **C**, in turn, could be prepared from insertion of the carbene derived from **E** into aldehyde **F**. Herein, we report the realization of this strategy by detailing the first example of such a three-component protocol for the synthesis of *syn*-α-hydroxy-β-amino esters and its application to the asymmetric synthesis of the C13 taxol side chain.

[*] S. Torssell, M. Kienle, Prof. P. Somfai
Organic Chemistry
KTH Chemistry, Royal Institute of Technology
10044 Stockholm (Sweden)
Fax: (+46) 8791-2333
E-mail: somfai@kth.se

[**] This work was supported financially by AstraZeneca Södertälje, the Swedish Research Council, and the Knut and Alice Wallenberg Foundation.

Supporting information for this article is available on the WWW under http://www.angewandte.org or from the author.

  DOI: 10.1002/anie.200500296

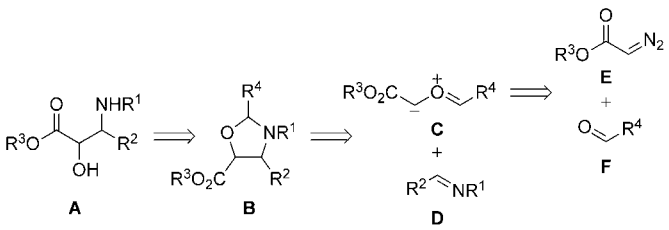

Scheme 1. Retrosynthetic analysis of the α-hydroxy-β-amino ester synthesis.

Initially, a mixture of benzylidenebenzylamine (**1a**), benzaldehyde (**2**), and $Rh_2(OAc)_4$ in CH_2Cl_2 was stirred at room temperature (Scheme 2). Addition of ethyl diazoacetate (EDA; **3**) over 1 h at room temperature afforded the desired cycloadduct **4**, which yielded *vic*-amino alcohol **5a** (*syn*/*anti* 93:7) in 82% yield (*syn*; Table 1, entry 1) on hydrolysis.[12] The relative stereochemistry of **5a** was verified by its conversion into the corresponding oxazolidinone by ^{1}H NMR spectroscopic analysis of the relevant coupling constants.[13]

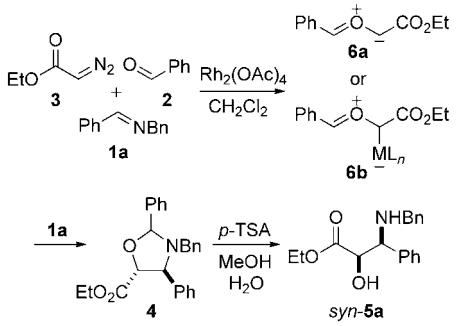

Scheme 2. 1,3-Dipolar cycloaddition to benzylidenebenzylamine. *p*-TSA = *para*-toluenesulfonic acid, Bn = benzyl.

With the reaction conditions established, it was of interest to optimize the key components of the reaction. First, the choice of metal catalyst was examined. $Cu(OTf)_2$ is known to be a suitable catalyst for the decomposition of **3**, but unfortunately this only led to recovery of **1a** (entry 2), probably because of coordination of the metal to the basic imine nitrogen atom with concomitant inhibition of the carbenoid formation.[11c,d,14] Next, the substituent on the imine was varied to investigate if this would influence the reaction outcome. When using imine **1b**, which was derived from aniline and **2**, a complex reaction mixture was obtained with no trace of the desired product (entry 3), whereas attempts with **1c** gave only recovered starting material (entry 4). Aldehyde **2** could be exchanged for other aromatic aldehydes, but this did not improve the reaction outcome so the remaining experiments were performed with **2**. The performances of other aldimines under the optimized reaction conditions are summarized in Table 1. In all cases, the reaction proceeded cleanly to provide the desired *syn*-α-hydroxy-β-amino ester in high yield and excellent diastereoselectivity.[15] Several benzylidenebenzylamine derivatives containing electron-withdrawing (entries 5–8) or electron-donating substituents (entries 9–11) in the *meta* or *para*-positions gave comparable yields and diastereoselectivities irrespective of the steric or electronic properties of the aryl substituent. The furfural-derived imine **1k** afforded the corresponding product **5k** in high yield and diastereoselectivity (entry 12), which is of interest as the furan moiety can be readily derivatized into several useful functional groups. The reaction of ethyl glyoxalate imine (**1l**) gave *syn*-β-hydroxyaspartate (**5l**), a potent blocker of glutamate transporters,[16] in high yield and good diastereoselectivity (entry 13), thus indicating that the reaction is not only restricted to aromatic imines and the scope of the transformation can be widened.

Table 1: 1,3-Dipolar cycloaddition of carbonyl ylides to aldimines.[a]

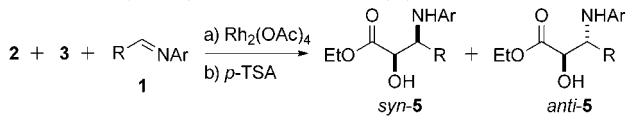

Entry	**1** (R/Ar)	d.r. (*syn*/*anti*)[b]	Yield of *syn*-**5** [%][c]
1	**a** (Ph/Bn)	93:7	**a** (82)
2[d]	**a** (Ph/Bn)	N.A.	**a** (0)[e]
3	**b** (Ph/Ph)	N.A.	**b** (0)[f]
4	**c** (Ph/4-$MeOC_6H_4$)	N.A.	**c** (0)[e]
5[g]	**d** (4-$NO_2C_6H_4$/Bn)	91:9	**d** (61)
6	**e** (4-ClC_6H_4/Bn)	98:2	**e** (75)
7	**f** (4-FC_6H_4/Bn)	97:3	**f** (78)
8	**g** (4-$MeOC_6H_4$/Bn)	98:2	**g** (77)
9	**h** (4-MeC_6H_4/Bn)	97:3	**h** (87)
10[g]	**i** (4-$MeOC_6H_4$/Bn)	94:6	**i** (78)
11	**j** (2-naphthyl/Bn)	98:2	**j** (83)
12[g,h]	**k** (2-furyl/Bn)	92:8	**k** (75)
13[g,h]	**l** (CO_2Et/Bn)	83:17	**l** (64)

[a] The reaction was carried out with imine **1** (1.0 equiv), benzaldehyde (1.5 equiv), $Rh_2(OAc)_4$ (2.0 mol%), and powdered 4-Å molecular sieves in CH_2Cl_2 at RT with addition of ethyl diazoacetate (1.5 equiv) over 1 h. Hydrolysis was performed with *p*-TSA (2 equiv) in MeOH/H_2O (95:5). [b] Determined by NMR spectroscopic analysis of the crude product; *syn* and *anti* diastereoisomers were separated with flash chromatography. [c] Yield of isolated product. [d] $Cu(OTf)_2$ (5 mol%) in THF. [e] Only imine and hydrolyzed imine. [f] Complex mixture of by-products. [g] Addition time = 10 h. [h] 0 °C. N.A. = not available.

The mechanism of the reaction proceeds through a chemoselective insertion of the metallocarbene into benzaldehyde to form either a metal-free[11a,17a] **6a** or a metal-associated ylide[17] **6b**, both of which can then undergo a 1,3-dipolar cycloaddition with the aldimine yielding the *trans*-substituted oxazolidine **4**, which can then be hydrolyzed to the corresponding *syn*-α-hydroxy-β-amino ester **5** (Scheme 2). To ascertain if ylide **6** is metal-associated, the generation of the ylide and its subsequent reaction with imine **1a** was performed with $[Rh_2(hfb)_4]$ (hfb = heptafluorobutyrate) and $[Rh_2\{(S)\text{-dosp}\}_4]$ ((*S*)-dosp = (*S*)-*N*-dodecylbenzenesulfonyl prolinate), respectively. When $[Rh_2(hfb)_4]$ was used, **5a** was obtained in only 13% yield with lower diastereoselectivity (*syn*/*anti* = 88:12 compared to entry 1, Table 1), whereas with $[Rh_2\{(S)\text{-dosp}\}_4]$ **5a** was obtained in 62% yield with excellent diastereoselectivity (*syn*/*anti* = 94:6) and modest enantiose-

lectivity (24% *ee*). These preliminary results support the formation of a metal-associated ylide in this case. It is interesting to note that no products derived from the formation of azomethine ylides, by combination of **1** with **3**, was observed in these reactions.[11c,d]

It was also of interest to develop an asymmetric protocol for the synthesis of enantiomerically enriched *syn*-α-hydroxy-β-amino esters and to apply it to the synthesis of the taxol C13 side chain **9** (Scheme 3),[5,18] which is known to be important

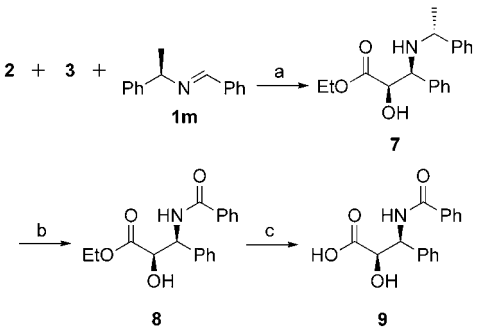

Scheme 3. Asymmetric synthesis of the C13 side chain of taxol. Reagents and conditions: a) 1) $Rh_2(OAc)_4$ (2 mol%), 4-Å molecular sieves, CH_2Cl_2, 0°C; 2) *p*-TSA, MeOH/H_2O (95:5), RT (77%, 2 steps, d.r. 8:1:1); b) 1) H_2, [$Pd(OH)_2$], EtOH, 3 M HCl, RT; 2) PhCOCl, $NaHCO_3$, EtOAc, 0°C (77% over 2 steps); c) LiOH·H_2O, THF/MeOH/H_2O (10:5:4), RT (89%).

for the antitumor activity of taxol.[18] Initial attempts with (−)-8-phenylmenthyl diazoacetate[19] as the carbene source with **1a** and **2** gave none of the desired product. Gratifyingly, however, reaction of the enantiomerically pure imine **1m**, derived from (+)-α-methylbenzylamine, with **2** and **3** gave the desired *syn*-amino alcohol **7** in good yield (77%) and selectivity (*syn*/*syn*/*anti* = 8:1:1) after hydrolysis (Scheme 3). Compound **7** was readily isolated from the two minor isomers by flash chromatography, and subsequent catalytic hydrogenolysis of this compound followed by benzoylation under Schotten–Baumann conditions afforded amide **8** (77% yield, two steps). Finally, hydrolysis of **8** using LiOH yielded the taxol side chain **9** as a white solid in five steps and an overall yield of 42%. Analytical data of **9** were in good agreement with previously reported data.[5,18]

In conclusion, we have developed an efficient protocol for the synthesis of *syn*-β-amino alcohols and *syn*-α-hydroxy-β-amino acid derivatives based on a highly diastereoselective three-component coupling of imines, benzaldehyde, and EDA. The methodology was applied to a short enantioselective synthesis of the C13 side chain of taxol.

Received: January 26, 2005
Published online: April 12, 2005

Keywords: amino alcohols · carbenoids · cycloaddition · multicomponent reactions · ylides

[1] a) S. Kobayashi, H. Ishitani, M. Ueno, *J. Am. Chem. Soc.* **1998**, *120*, 431–432; b) J. Kobayashi, M. Nakamura, Y. Mori, Y. Yamashita, S. Kobayashi, *J. Am. Chem. Soc.* **2004**, *126*, 9192–9193; c) H.-S. Lee, S. H. Kang, *Synlett* **2004**, 1673–1685, and references therein.

[2] D. J. Ager, I. Prakash, D. R. Schaad, *Chem. Rev.* **1996**, *96*, 835–875.

[3] M. T. Reetz, *Angew. Chem.* **1991**, *103*, 1559–1573; *Angew. Chem. Int. Ed. Engl.* **1991**, *30*, 1531–1546.

[4] S. C. Bergmeier, *Tetrahedron* **2000**, *56*, 2561–2576.

[5] G. Li, H.-T. Chang, K. B. Sharpless, *Angew. Chem.* **1996**, *108*, 449–452; *Angew. Chem. Int. Ed. Engl.* **1996**, *35*, 451–454.

[6] J. F. Larrow, S. E. Schaus, E. N. Jacobsen, *J. Am. Chem. Soc.* **1996**, *118*, 7420–7421.

[7] B. Olofsson, U. Khamrai, P. Somfai, *J. Org. Chem.* **2002**, *67*, 8574–8583.

[8] a) G.-I. Hwang, J.-H. Chung, W. K. Lee, *J. Org. Chem.* **1996**, *61*, 6183–6188; b) X. E. Hu, *Tetrahedron* **2004**, *60*, 2701–2743.

[9] With glycine derived enolates: a) M. Horikawa, J. Busch-Petersen, E. J. Corey, *Tetrahedron Lett.* **1999**, *40*, 3843–3846; b) N. Yoshikawa, M. Shibasaki, *Tetrahedron* **2002**, *58*, 8289–8298; c) T. Ooi, M. Taniguchi, M. Kameda, K. Maruoka, *Angew. Chem.* **2002**, *114*, 4724–4726; *Angew. Chem. Int. Ed.* **2002**, *41*, 4542–4544.

[10] Mannich-type reaction: a) B. List, P. Pojarliev, W. T. Biller, H. J. Martin, *J. Am. Chem. Soc.* **2002**, *124*, 827–833; b) A. Córdova, W. Notz, G. Zhong, J. M. Betancort, C. F. Barbas III, *J. Am. Chem. Soc.* **2002**, *124*, 1842–1843; c) B. M. Trost, L. R. Terrell, *J. Am. Chem. Soc.* **2003**, *125*, 338–339; d) S. Matsunaga, N. Kumagai, S. Harada, M. Shibasaki, *J. Am. Chem. Soc.* **2003**, *125*, 4712–4713.

[11] For three-component reactions using diazo compounds for carbonyl ylides, see: a) C.-D. Lu, Z.-Y. Chen, H. Liu, W.-H. Hu, A.-Q. Mi, *Org. Lett.* **2004**, *6*, 3071–3074; b) A. E. Russell, J. Brekan, L. Gronenberg, M. P. Doyle, *J. Org. Chem.* **2004**, *69*, 5269–5274; for azomethine ylides, see: c) K. B. Hansen, N. S. Finney, E. N. Jacobsen, *Angew. Chem.* **1995**, *107*, 750–752; *Angew. Chem. Int. Ed. Engl.* **1995**, *34*, 676–678; d) C. V. Galliford, M. A. Beenen, S. T. Nguyen, K. A. Scheidt, *Org. Lett.* **2003**, *5*, 3487–3490; e) M. Yan, N. Jacobsen, W. Hu, L. S. Gronenberg, M. P. Doyle, J. T. Colyer, D. Bykowski, *Angew. Chem.* **2004**, *116*, 6881–6884; *Angew. Chem. Int. Ed.* **2004**, *43*, 6713–6716; for oxonium ylides, see: f) C.-D. Lu, H. Liu, Z.-Y. Chen, W.-H. Hu, A.-Q. Mi, *Org. Lett.* **2005**, *7*, 83–86; for ammonium ylides, see: g) Y. Wang, Y. Zhu, Z. Chen, A. Mi, W. Hu, M. P. Doyle, *Org. Lett.* **2003**, *5*, 3923–3926.

[12] Addition of powdered activated 4-Å molecular sieves gave higher yields and more reproducible results, see: C.-D. Lu, Z.-Y. Chen, H. Liu, W.-H. Hu, A.-Q. Mi, M. P. Doyle, *J. Org. Chem.* **2004**, *69*, 4856–4859.

[13] The $J(4,5) = 5.1$ Hz coupling constant is consistent with 4,5-*trans* relative stereochemistry, see: C. H. Heathcock, T. A. Blumenkopf, K. M. Smith, *J. Org. Chem.* **1989**, *54*, 1548–1562.

[14] M. P. Doyle, M. Yan, W. Hu, L. S. Gronenberg, *J. Am. Chem. Soc.* **2003**, *125*, 4692–4693.

[15] The *syn* and *anti* diastereoisomers where readily separated by flash chromatography for all substrates.

[16] K. Shimamoto, Y. Shigeri, Y. Yasuda-Kamatani, B. Lebrun, N. Yumoto, T. Nakajima, *Bioorg. Med. Chem. Lett.* **2000**, *10*, 2407–2410.

[17] For discussions about metal-associated ylides, see: a) M. P. Doyle, D. C. Forbes, M. N. Protopopova, S. A. Stanley, M. M. Vasbinder, K. R. Xavier, *J. Org. Chem.* **1997**, *62*, 7210–7215; b) S. Kitagaki, M. Anada, O. Kataoka, K. Matsuno, C. Umeda, N. Watanabe, S.-I. Hashimoto, *J. Am. Chem. Soc.* **1999**, *121*, 1417–1418; c) D. M. Hodgson, A. H. Labande, F. Y. T. M.

Pierard, M. Á. Expósito Castro, *J. Org. Chem.* **2003**, *68*, 6153–6159.
[18] For the shortest synthesis of the C13 side chain of taxol, see Ref. [5] a) L. Deng, E. N. Jacobsen, *J. Org. Chem.* **1992**, *57*, 4320–4323; b) D.-M. Gou, Y.-C. Liu, C.-S. Chen, *J. Org. Chem.* **1993**, *58*, 1287–1289; c) V. K. Aggarwal, J.-L. Vasse, *Org. Lett.* **2003**, *5*, 3987–3990.
[19] For the synthesis of (−)-8-phenylmenthyl diazoacetate, see: A. V. Bedekar, E. B. Koroleva, P. G. Andersson, *J. Org. Chem.* **1997**, *62*, 2518–2526.

Semiconductors

Photonic Crystals with Thermally Switchable Stop Bands Fabricated from Se@Ag_2Se Spherical Colloids**

*Unyong Jeong and Younan Xia**

Self-assembly of monodispersed spherical colloids into highly ordered lattices has attracted considerable attention due to the potential use of these periodic structures as photonic crystals.[1] Despite intensive study on this subject, the building blocks available to form long-range ordered lattices have been mainly limited to polymer latexes and silica beads.[2] To obtain wider photonic band gaps by increasing the contrast in refractive index, processing materials with refractive indices greater than 2 into monodispersed spherical colloids is of the utmost necessity.[3] Although a number of semiconductors (e.g., ZnS, CdS, and TiO_2) with relatively high refractive indices have been recently synthesized as monodispersed spheres and then crystallized into 3D opaline lattices with strong stop bands in the visible region,[4] the diversity of materials still needs to be greatly expanded to fully capitalize on the advantages and exploit the potential brought by the large contrast in refractive index. Very recently, we developed a solution-phase method for the large-scale production of monodispersed amorphous selenium (*a*-Se) spherical colloids with readily controllable sizes.[5] Herein we demonstrate that the high reactivity of Se towards Ag atoms could be used to generate monodispersed spherical colloids consisting of *a*-Se cores and Ag_2Se shells. More interestingly, the reversible phase transition associated with Ag_2Se provides a new platform for fabricating photonic crystals with thermally switchable stop bands.

As a semiconductor with a narrow band gap, Ag_2Se has a range of interesting and useful properties. It undergoes a phase transition at 133 °C with a remarkable change in the electronic property.[6] The low-temperature β-phase crystallizes in an orthorhombic lattice and acts as a semiconductor. It is a good candidate for thermoelectric applications due to its low lattice thermal conductivity ($\approx 5\ mW\,cm^{-1}\,K$), high electrical conductivity ($\approx 2000\ S\,cm^{-1}$), and hence a relatively large Seebeck coefficient (about $-150\ \mu V\,K^{-1}$).[7] It was also demonstrated that slight changes in stoichiometry to $Ag_{2+\delta}Se$ (in the same orthorhombic lattice) can induce appreciable magnetoresistance.[8] An explanation to account for this property considers the existence of small silver clusters in the crystal lattice.[9] Nonstoichiometric solids have also been reported to exist in tetragonal, face-centered cubic (fcc), monoclinic, or triclinic structures at room temperature.[10] Recently, Alivisatos and co-workers reported the use of a cation-exchange reaction to transform Ag_2Se nanocrystals into CdSe without causing any change to the morphology.[11] The high-temperature phase, α-Ag_2Se, has a body-centered cubic (bcc) structure and is a good superionic conductor as a result of the high mobility of silver cations and the low activation energy for diffusion and conduction.[12] The polymorphic transition between the β- and α-phases has been shown to be reversible.

We note that photonic crystals with tunable stop bands have been exploited as sensors to detect and monitor the variation in temperature, strain, and concentration of a chemical or biochemical species.[13–16] Recently, our group also demonstrated color writing and printing by embedding photonic crystals in elastomeric matrices.[17] The essence of this research is to take advantage of the reversible, polymorphic transition of a solid material to fabricate photonic crystals with stop bands that can be reversibly switched between two spectral positions. Such a system can potentially serve as an optical switch or a thermally printable medium.

It has been demonstrated that β-Ag_2Se nanowires could be produced by reacting nanowires of trigonal selenium (*t*-Se, serving as a chemical template) with $AgNO_3$ in an aqueous solution at room temperature [Eq. (1)].[18] In this particular

$$3\,Se_{(s)} + 6\,Ag^{+}_{(aq)} + 3\,H_2O \rightarrow 2\,Ag_2Se_{(s)} + Ag_2SeO_{3(s)} + 6\,H^{+}_{(aq)} \quad (1)$$

route, the formation of monoclinic Ag_2SeO_3 as a by-product was inevitable.

Herein we wish to report a new process, in which $AgNO_3$ is reduced by ethylene glycol to generate Ag atoms that further react with spherical colloids of *a*-Se to form monodispersed colloids consisting of *a*-Se cores and β-Ag_2Se shells. The *a*-Se colloids with smooth surfaces and controllable sizes are, in turn, synthesized by using a chemical solution-phase method based on the reduction of selenious acid with excessive hydrazine in ethylene glycol.[5] After residual hydrazine has been removed, $AgNO_3$ dissolved in ethylene glycol is added to generate *a*-Se@Ag_2Se core–shell colloids.

[*] Dr. U. Jeong, Prof. Y. Xia
Department of Chemistry, University of Washington
Seattle, WA 98195-1700 (USA)
Fax: (+1) 206-685-8665
E-mail: xia@chem.washington.edu

[**] This work was supported in part by the STC Program of the National Science Foundation (NSF) under Agreement Number DMR-0120967 and a Fellowship from the David and Lucile Packard Foundation. Y.X. is an Alfred P. Sloan Fellow (2000) and a Camille Dreyfus Teacher Scholar (2002). U.J. has also received partial support from the Post-Doctoral Fellowship Program of the Korean Science and Engineering Foundation (KOSEF).

Supporting information for this article is available on the WWW under http://www.angewandte.org or from the author.

 DOI: 10.1002/anie.200462906

The extent of conversion from *a*-Se to Ag_2Se can be controlled by adjusting the molar ratio of $AgNO_3$ to *a*-Se.

The formation of Ag_2Se was first confirmed by powder X-ray diffraction (XRD, Philips PW-1710 diffractometer). As shown in Figure 1 A, the as-synthesized colloids of *a*-Se

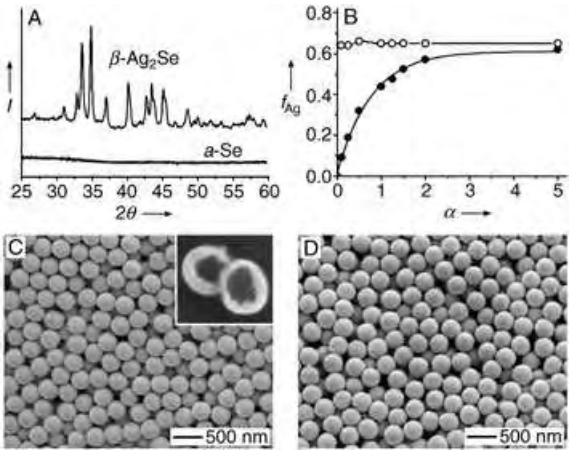

Figure 1. A) XRD patterns taken from the as-synthesized *a*-Se and *a*-Se@Ag_2Se colloids (with $f_{Ag} = 0.32$). All peaks were indexed to orthorhombic β-Ag_2Se. B) Plots showing how f_{Ag} of the core–shell colloids changed as the molar ratio (α) of $AgNO_3$ to Se varied. Solid circles and open circles represent f_{Ag} values measured by using EDX before and after removal of the Se cores with hydrazine, respectively. C) SEM image of core–shell colloids synthesized with $\alpha = 0.5$. The inset shows a SEM image of two broken colloids after the *a*-Se cores had been dissolved with hydrazine. D) SEM image of another batch of core–shell colloids synthesized with $\alpha = 2.0$.

displayed no diffraction peak in the entire 2θ range from 25 to 60°, which indicates an amorphous structure. The XRD pattern taken from the product (synthesized with a molar ratio of 0.5 $AgNO_3$ to 1.0 Se) matched the orthorhombic lattice of β-Ag_2Se (lattice constants: $a = 4.33$, $b = 7.06$, $c = 7.76$ Å). The XRD patterns were essentially the same regardless of the ratio of $AgNO_3$ to Se involved in the synthesis. It is worth mentioning that no impurity such as Ag_2SeO_3 was detected in the as-synthesized product; this lack of impurity is because ethylene glycol was able to reduce Ag^+ cations to Ag atoms, which then diffused quickly into the lattice of *a*-Se to generate β-Ag_2Se as the sole product [Eq. (2)].

$$2\,Ag + Se \rightarrow Ag_2Se \qquad (2)$$

For the as-obtained core–shell colloids, we used energy-dispersive X-ray spectra (EDX, Genesis 2000, EDAX Inc., Mahwah, NJ) to determine the elemental composition, or the atomic fraction of silver (f_{Ag}). To improve the signal-to-noise ratio and thus obtain reliable data, we used a thick slab (≈ 6 μm) of the colloid sample deposited on a silicon wafer in combination with a beam spot of > 100 μm^2. EDX peaks that corresponded to the L shell of Ag and Se were employed for all quantitative analyses. Figure 1 B shows the change in f_{Ag} (solid circles) with increasing molar ratio of $AgNO_3$ to Se ($\alpha = [AgNO_3]/[Se]$) and demonstrates a monotonic increase as α changed from 0 to 5. To determine the atomic fraction of Ag in the shells only, the Se cores were selectively removed by immersing the sample in hydrazine for 18 h. As the Ag_2Se shells were polycrystalline, the Se cores were slowly etched away by hydrazine through the grain boundaries. The atomic fractions of Ag for the etched samples are presented as open circles in Figure 1 B; essentially the same value ($\approx 65\%$) was obtained regardless of the α value. This percentage matches the stoichiometry of Ag_2Se, which indicates that the Ag_2Se shells were very pure. The plots also show that the *a*-Se colloids can only be completely converted into Ag_2Se when the molar ratio of $AgNO_3$ to Se is higher than 5.

Figure 1 C and D show scanning electron microscopy (SEM, Siron XL, FEI, Hillsboro, OR) images of two typical samples obtained at different molar ratios of $AgNO_3$ to Se: 0.5:1 and 2:1. As with the *a*-Se colloids, the core–shell particles were spherical, monodispersed, and had featureless surfaces. The inset in Figure 1 C gives a SEM image of the same sample after the unconverted *a*-Se cores had been selectively removed by extraction with hydrazine. On the basis of both SEM and XRD results, we concluded that the as-obtained products were composed of Se cores (amorphous) and β-Ag_2Se shells (polycrystalline). Once the f_{Ag} value of a sample had been determined by EDX, both the shell thickness and the dimensional change involved in this template-engaged reaction was estimated. For instance, the calculated diameter and shell thickness of the colloids displayed in Figure 1 C are 310 and 22 nm, respectively, which are in good agreement with the results from TEM studies. The derivation of these values is provided as Supporting Information, together with experimental results.

Both Se and Ag_2Se transform into different phases as the temperature is raised from room temperature to about 150 °C: Se undergoes a transition from amorphous to trigonal phase at 31 °C whereas Ag_2Se has a phase transition (from β to α) around 133 °C. We have followed the phase transitions of both cores and shells with XRD. In a typical experiment, a thick film (≈ 1 mm) was cast on a glass slide from an aqueous suspension of core–shell colloids and dried in air. The sample was annealed at various temperatures ranging from room temperature to 150 °C with increasing steps of ≈ 10 °C. The sample was annealed at each set temperature for 10 min and then quenched by placing it on a cold metal plate. XRD measurements were taken immediately after quenching and were completed within 10 min. Figure 2 shows XRD patterns taken from the same sample as that given in Figure 1 D ($f_{Ag} = 0.56$). The diffraction pattern at room temperature was similar to that shown in Figure 1 A, although different values of f_{Ag} were involved. After the sample had been annealed at 110 °C, a small new peak (indicated by the asterisk in Figure 2) appeared at $2\theta = 28.5°$, which corresponds to the (101) diffraction of *t*-Se. After the sample had been annealed at 150 °C, the peaks associated with β-Ag_2Se mostly disappeared and a characteristic peak of α-Ag_2Se (with a bcc structure) appeared at $2\theta = 35.2°$ (indicated by the triangular in Figure 2); this peak was indexed to the (200) diffraction. The sample reverted to the β-Ag_2Se structure when it was cooled slowly to 110 °C. It is worth pointing out that the peak from *t*-Se remained the same in the β↔α transition for the

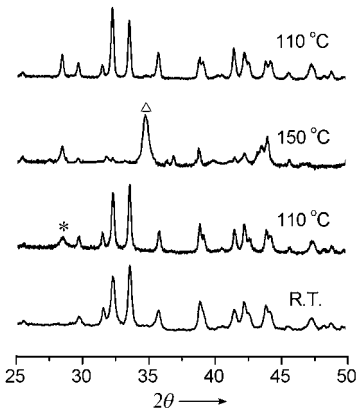

Figure 2. XRD patterns taken from a sample of Se@Ag_2Se core–shell colloids at room temperature, which were then heated to 110 and 150 °C, followed by cooling to 110 °C. The sample was annealed at each temperature for 10 min and quenched on a cold metal plate and XRD measurement was taken within 10 min. ⋆ and △ represent the peaks for *t*-Se and α-Ag_2Se, respectively.

Ag_2Se shells. These results indicate that the Se core was well preserved inside the Ag_2Se shell as the sample underwent thermal annealing. The XRD results confirm that the phase transition between orthorhombic and bcc structure for the Ag_2Se shells is reversible. SEM studies also showed that the spherical shape of these core–shell colloids was maintained through multiple cycles of such phase transitions when $f_{Ag} = 0.56$. In comparison, the shells with $f_{Ag} = 0.32$ were broken in the annealing process and the Se leaked from the shells and aggregated into large, irregular structures.

The thermally reversible transition between two different states for the Ag_2Se shells implies that these core–shell colloids could be used as building blocks to fabricate photonic crystals with reversibly switchable stop bands. To this end, we have crystallized core–shell colloids ($f_{Ag} = 0.56$) into 3D opaline lattices on glass substrates by using a previously reported method.[19] Figure 3 shows the cross-sectional SEM images of a typical sample, which displays an fcc structure with its {111} planes oriented parallel to the surface of the supporting substrate. Figure 3 A shows an image of the as-obtained sample, and Figure 3 B shows the same sample after it had been annealed at 150 °C for 10 min, then quenched to room temperature by placing it on a cold metal plate. Even though the core–shell colloids went through two phase transitions from *a*-Se to *t*-Se and from β-Ag_2Se to α-Ag_2Se, the spherical shape of the colloids and the long-range order of the lattice were both essentially retained. As long as the Se cores did not leak out (or if they were removed in advance), the phase transition between β- and α-Ag_2Se could go through many cycles of heating and cooling without causing significant changes to the opaline lattices.

Figure 4 shows the near-IR reflection spectra taken from an opaline lattice assembled from core–shell colloids with $f_{Ag} = 0.56$. The spectra were recorded by using a fiber-optic spectrometer (NIR-128, Control Development, South Bend, IN) with an incident and detection angle of 10° from the normal to the surface. The opaline lattice was annealed at various temperatures up to 150 °C with a step increase of

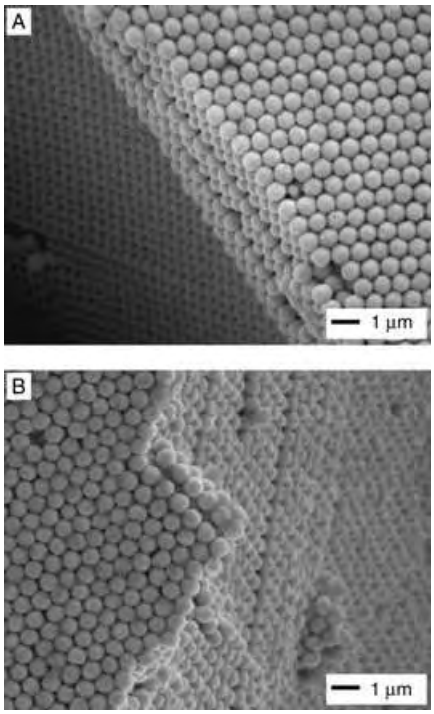

Figure 3. A) Cross-sectional SEM image of an opaline lattice assembled from *a*-Se@Ag_2Se colloids with $f_{Ag} = 0.56$. B) The same sample, after it had been annealed at 150 °C for 10 min.

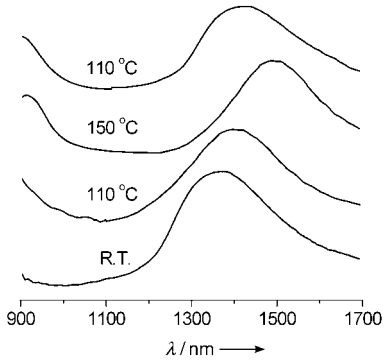

Figure 4. Reflection spectra in the near-IR region taken from an opaline lattice consisting of Se@Ag_2Se core–shell colloids with $f_{Ag} = 0.56$. The temperature was increased from room temperature to 110 and 150 °C, and then reduced to 110 °C. After the sample had been annealed at each temperature for 10 min, it was quenched to preserve the high-temperature phases.

10 °C. After annealing for 10 min at each temperature, the sample was quenched (by placing it on a cold metal plate) to preserve the high-temperature phases. We did not observe any significant change in the peak position until 70 °C. When the annealing temperature was increased to 80 °C, the peak suddenly red-shifted to 1392 nm and then showed little change as the temperature was further raised to 130 °C. This change was attributed to the increase in the refractive index when the cores were converted from *a*-Se into *t*-Se. In the range of 130–140 °C, the peak was red-shifted again to 1497 nm as the Ag_2Se shells underwent a transition from

the β- to the α-phase. The peak shifted back to 1415 nm when the sample was annealed at 110 °C, and then quenched to room temperature.

The observed reflectance peaks and shifts can be explained on the basis of the Bragg diffraction equation. The refractive index of β-Ag_2Se was obtained by plotting the data reported for the UV/Vis region[20] and fitting them with the first-order Sellmeier equation (Eq. (3)),[21] in which $A =$

$$n^2(\lambda) = A + B[\lambda^2/(\lambda^2 - C)] \quad (3)$$

5.20, $B = 3.62$, and $C = 0.13$; and the unit for λ is μm. From this equation, the refractive index of β-Ag_2Se was calculated as 2.98 at $\lambda = 2$ μm. The Moss relationship, $n^4 E_g = 95$,[22] could not be applied to this system as the value of the band gap (E_g) of β-Ag_2Se is still being disputed. The reported values, −0.17,[23] 1.33,[24] 1.58,[25] and 2.17 eV,[26] would suggest very different refractive indices: 4.86, 2.90, 2.88, and 2.44, respectively. The volume fraction of the shell and the core were calculated (see the Supporting Information). For core–shell colloids with $f_{Ag} = 0.56$, the volume fraction of the core (X_{core}) was 23 %. The dielectric constant of the core–shell colloids was calculated by assuming a linear relationship between the dielectric constant and the volume fraction [Eq. (4)].[27] With

$$n = n_{core} X_{core} + n_{shell}(1 - X_{core}) \quad (4)$$

the reported refractive index of 2.45 for *a*-Se,[28] a value of 2.86 was obtained for the refractive index of core–shell colloids with $f_{Ag} = 0.56$.

Based on the assumption of a closely packed structure (26 % air), the reflectance peak centered at ≈1365 nm for the sample annealed at room temperature was assigned to the diffraction from (111) lattice planes. From the Bragg diffraction equation,[29] the peak position was calculated as 1358 nm with a refractive index of 2.86 for the core–shell colloids. The higher refractive index of *t*-Se (2.8 at 2 μm versus 2.45 for *a*-Se)[30] increased the refractive index of the core–shell particles to 2.94. This increase in refractive index led to a red shift for the (111) peak to ≈1395 nm, which matched the experimental result. After the sample had been annealed at 150 °C, the (111) diffraction peak was further shifted to ≈1497 nm and a new peak appeared at ≈919 nm. The red shift was induced by the phase transition from β- to α-Ag_2Se, that is, from a semiconductor to a superionic state. From the peak position of the (111) plane, the refractive index of α-Ag_2Se was estimated to be 3.26. This refractive index could be used to assign the peak at ≈919 nm as the diffraction from (220) lattice planes (calculation: 916 nm). The Moss relationship[22] predicted a band-gap energy of 0.84 eV for α-Ag_2Se, which is much lower than that of β-Ag_2Se obtained from our refractive index value (1.20 eV). Note that the band gap of α-Ag_2Se is still in the range of semiconductors. The increase in conductivity accompanying the transition from the β- to the α-phase mainly results from the enhanced mobility of the Ag cations. When the sample was cooled down to 110 °C, the diffraction peaks were recovered with some slight thermal hysteresis: 1415 nm for the (111) diffraction and below 900 nm for the (220) diffraction. The peaks did not shift anymore when the sample was annealed again at temperatures below 110 °C, which suggests that the phase transition between *a*-Se and *t*-Se was irreversible.

This study focuses on how thermally induced polymorphic transitions can lead to changes in the photonic band gap. Photonic crystals with a band gap in the visible region can serve as photonic papers, which is one of the primary uses for core–shell colloids. For example, a phase transition of the photonic crystals can be induced in a confined region with the aid of a laser and subsequent quenching to room temperature can preserve the kinetically trapped patterns. These altered regions will diffract light of longer wavelengths than will do other regions, thus enabling colored patterns to be recorded. If the photonic crystals are annealed at an elevated temperature, the patterns can be readily erased. In addition, the electrical conductivity of β-Ag_2Se ($\approx 2000\ S\,cm^{-1}$) is exceptionally high relative to those of other semiconductors.[7] This value can be further increased to $\approx 6000\ S\,cm^{-1}$ in the α-Ag_2Se phase.[7c] These unique properties will make the *a*-Se@Ag_2Se core–shell colloids potentially useful in thermoelectric applications.

In summary, we have exploited the high reactivity of *a*-Se towards Ag atoms to produce core–shell spherical colloids in the form of *a*-Se@Ag_2Se. Upon heating, the cores and shells change phase from *a*-Se to *t*-Se and from β-Ag_2Se to α-Ag_2Se, respectively. When the shells were sufficiently thick (55 nm, or with $f_{Ag} = 0.56$), the core–shell colloids maintained their spherical shape while undergoing multiple cycles of phase transitions between β-Ag_2Se and α-Ag_2Se. This feature has been used to fabricate photonic crystals with thermally switchable stop bands.

Experimental Section

In a typical synthesis, hydrazine hydrate (55 % N_2H_4; Aldrich) in ethylene glycol (0.35 M, 80 mL) was added to pure ethylene glycol (400 mL; J. T. Baker) in a 1000-mL Erlenmeyer flask. After the mixture had been stirred for 10 min, H_2SeO_3 (Aldrich, 99.99 %) in ethylene glycol (0.07 M, 80 mL) was introduced and the reaction was allowed to proceed for 2 h. As hydrazine can also reduce $AgNO_3$ to Ag nanoparticles and agglomerates, all remaining hydrazine in the suspension of *a*-Se colloids was removed by vacuum distillation before $AgNO_3$ was added to the reaction system. To form Ag_2Se, a solution of poly(vinylpyrrolidone) (PVP; 15 mL, $\bar{M}_w = 55\,000$, 3 g per 200 mL; Aldrich) in ethylene glycol was added at room temperature to the *a*-Se that had been suspended in ethylene glycol (30 mL). Adding a solution of $AgNO_3$ (Aldrich, 99.9 %) in ethylene glycol to this suspension resulted in a change from red to dark brown then dark blue as the ratio between $AgNO_3$ and *a*-Se increased. The reaction mixture was diluted with water (100 mL) and the core–shell colloids were collected by centrifugation. To remove ethylene glycol and excess PVP, the product was again diluted with water (100 mL) and separated by centrifugation. This washing cycle was repeated several times before the product was dried in air. The colloids were stable in air and did not aggregate.

Received: December 11, 2004
Published online: April 12, 2005

Keywords: colloids · selenium · semiconductors · silver

[1] See, for example: a) C. López, *Adv. Mater.* **2003**, *15*, 1679; b) special issue "Materials Science Aspects of Photonic Crystals": A. Polman, P. Wiltzius, *MRS Bull.* **2001**, *26*, 608; c) special issue "Photonic Crystals": Y. Xia, *Adv. Mater.* **2001**, *13*, 369; d) O. D. Velev, A. M. Lenhoff, *Curr. Opin. Colloid Interface Sci.* **2000**, *5*, 56; e) A. Stein, R. C. Schroden, *Curr. Opin. Solid State Mater. Sci.* **2001**, *5*, 553; f) Y. A. Vlasov, X. Z. Bo, J. C. Sturm, D. J. Norris, *Nature* **2001**, *414*, 289; g) J. F. Bertone, P. Jiang, K. S. Hwang, D. M. Mittleman, V. L. Colvin, *Phys. Rev. Lett.* **1999**, *83*, 300; h) D. Wang, R. A. Caruso, F. Caruso, *Chem. Mater.* **2001**, *13*, 364; i) W. M. Lee, S. A. Prunziski, P. V. Braun, *Adv. Mater.* **2002**, *14*, 271.

[2] a) R. Arshady, *Colloid Polym. Sci.* **1992**, *270*, 717; b) W. Stöber, A. Fink, E. Bohn, *J. Colloid Interface Sci.* **1968**, *26*, 62.

[3] J. D. Joannopoulos, R. D. Meade, J. N. Winn, *Photonic Crystals*, Princeton University, Princeton, **1995**.

[4] a) E. Matijević, D. Murphy-Wilhelmy, *J. Colloid Interface Sci.* **1982**, *86*, 476; b) D. Murphy-Wilhelmy, E. Matijević, *J. Chem. Soc. Faraday Trans.* **1984**, *80*, 563; c) K. P. Velikov, A. van Blaaderen, *Langmuir* **2001**, *17*, 4779; d) M. L. Breen, A. D. Dinsmore, R. H. Pink, S. B. Qadri, B. R. Ratna, *Langmuir* **2001**, *17*, 903; e) X. Jiang, T. Herricks, Y. Xia, *Adv. Mater.* **2003**, *15*, 1205.

[5] U. Jeong, Y. Xia, *Adv. Mater.* **2005**, *17*, 102.

[6] a) Y. Kumashiro, T. Ohachi, I. Taniguchi, *Solid State Ionics* **1996**, *86*, 761; b) M. C. Santhosh Kumar, B. Pradeep, *Bull. Mater. Sci.* **2002**, *25*, 407.

[7] a) M. Ferhat, J. Nagao, *J. Appl. Phys.* **2000**, *88*, 813; b) V. Damodars Das, D. Karunakaran, *J. Appl. Phys.* **1990**, *67*, 15; c) M. C. S. Kumar, B. Pradeep, *Bull. Mater. Sci.* **2002**, *25*, 407.

[8] a) R. Xu, A. Husmann, T. F. Rosenbaum, M.-L. Saboungi, J. E. Enderby, P. B. Littlewood, *Nature* **1997**, *390*, 57; b) G. Beck, J. Janek, *Phys. B* **2001**, *308*, 1086.

[9] a) A. A. Abrikosov, *Phys. Rev. B* **1998**, *58*, 2788; b) A. A. Abrikosov, *Europhys. Lett.* **2000**, *49*, 789.

[10] a) T. Okabe, K. Ura, *J. Appl. Crystallogr.* **1994**, *27*, 140; b) L. V. Constantinescu, *Thin Solid Films* **1976**, *32*, 333; c) Y. Saito, M. Sato, M. Shiojiri, *Thin Solid Films* **1981**, *79*, 257; d) A. G. Abdullayev, R. B. Shafizade, E. S. Krupnikov, K. V. Kiriluk, *Thin Solid Films* **1983**, *106*, 175.

[11] D. H. Son, S. M. Hughes, Y. Yin, A. P. Alivisatos, *Science* **2004**, *306*, 1009.

[12] a) M. A. Hamilton, A. C. Barnes, W. S. Howells, H. E. Fischer, *J. Phys. Condens. Matter* **2001**, *13*, 2425; b) J. P. Rino, Y. M. Hornos, G. A. Antonio, I. Ebbsjö, R. K. Kalia, P. Vashishta, *J. Chem. Phys.* **1988**, *89*, 7542.

[13] a) J. M. Weissman, H. B. Sunkara, A. S. Tse, S. A. Asher, *Science* **1996**, *274*, 959; b) S. Valkama, H. Kosonen, J. Ruokolainen, T. Haatainen, M. Torkkeli, R. Serimaa, G. T. Brinke, O. Ikkala, *Nat. Mater.* **2004**, *3*, 872; c) Z. B. Hu, X. H. Lu, J. Gao, *Adv. Mater.* **2001**, *13*, 1708; d) J. D. Bebord, S. Eustis, S. B. Debord, M. T. Lofye, L. A. Lyon, *Adv. Mater.* **2002**, *14*, 658.

[14] a) J. H. Holtz, S. A. Asher, *Nature* **1997**, *389*, 829; b) C. E. Reese, M. E. Baltusavich, J. P. Keim, S. A. Asher, *Anal. Chem.* **2001**, *73*, 5038; c) C. F. Blanford, R. C. Schroden, M. Al-Daous, A. Stein, *Adv. Mater.* **2001**, *13*, 26.

[15] a) T. Cassagneau, F. Caruso, *Adv. Mater.* **2002**, *14*, 1629; b) Z.-Z. Gu, R. Horie, S. Kubo, Y. Yamada, A. Fijishima, O. Sato, *Angew. Chem.* **2002**, *114*, 1201; *Angew. Chem. Int. Ed.* **2002**, *41*, 1153.

[16] a) S. H. Foulger, P. Jiang, A. C. Lattam, D. W. Smith, J. Ballato, *Langmuir* **2001**, *17*, 6023; b) K. Sumioka, H. Kayashima, T. Tsutsui, *Adv. Mater.* **2002**, *14*, 1284.

[17] a) H. Fudouzi, Y. Xia, *Adv. Mater.* **2003**, *15*, 892; b) H. Fudouzi, Y. Xia, *Langmuir* **2003**, *19*, 9653.

[18] a) B. Gates, Y. Wu, Y. Yin, P. Yang, Y. Xia, *J. Am. Chem. Soc.* **2001**, *123*, 11500; b) B. Gates, B. Mayers, B. Cattle, Y. Xia, *Adv. Funct. Mater.* **2002**, *12*, 219.

[19] S. H. Park, D. Qin, Y. Xia, *Adv. Mater.* **1998**, *10*, 1028.

[20] V. Hönig, A. Thomas, *Phys. Status Solidi A* **1987**, *100*, K81.

[21] D. T. F. Marple, *J. Appl. Phys.* **1964**, *35*, 539.

[22] T. S. Moss, *Phys. Status Solidi B* **1985**, *131*, 415.

[23] A. G. Abdullayev, R. B. Shafizade, E. S. Kruprikov, K. V. Kiriluk, *Thin Solid Films* **1983**, *106*, 175.

[24] A. B. Kulkarni, M. D. Uplane, C. D. Lokhande, *Thin Solid Films* **1995**, *120*, 14.

[25] M. C. Santhosh Kumar, B. Pradeep, *Semicond. Sci. Technol.* **2002**, *17*, 261.

[26] R. Harpeness, O. Palchik, A. Gedanken, V. Palchik, S. Amiel, M. A. Slifkin, A. M. Weiss, *Chem. Mater.* **2002**, *14*, 2094.

[27] H. Takeda, K. Yoshino, *Appl. Phys. Lett.* **2002**, *80*, 24.

[28] a) P. Nagels, E. Sleeckx, R. Callaerts, E. Márquez, J. M. González, A. M. Bernal-Oliva, *Solid State Commun.* **1997**, *102*, 539; b) T. Innami, T. Miyazaki, A. Adachi, *J. Appl. Phys.* **1999**, *86*, 1382.

[29] a) P. L. Flaugh, S. E. O'Donnell, S. A. Asher, *Appl. Spectrosc.* **1984**, *38*, 847; b) J. Jethmalani, W. Ford, *Chem. Mater.* **1996**, *8*, 2146.

[30] E. D. Palik in *Handbook of Optical Constants of Solid*, *Vol. 2* (Ed.: E. D. Palik), Academic Press, Orlando, **1985**, p. 691.

Gas Sensors

Organic–Inorganic Hybrid Sol–Gel Materials Incorporating Functionalized Cobalt(III) Corroles for the Selective Detection of CO**

Jean-Michel Barbe, Gabriel Canard, Stéphane Brandès, and Roger Guilard**

Corroles and their metal derivatives continue to attract increasing interest because of their potential applications in many fields[1–3] and because of the development of new straightforward and powerful syntheses.[4–9] For example, it is now possible to functionalize the corrole macrocycle at the *meso* positions with several groups,[9,10] thus allowing it be anchored on various solid supports. Nanostructured organic–inorganic hybrid materials have also been developed, and these offer the possibility to incorporate many different organic chelates and complexes into their framework.[11–14] Moreover, immobilized complexes within the material are expected to be more stable than analogous isolated com-

[*] Dr. J.-M. Barbe, Dr. G. Canard, Dr. S. Brandès, Prof. Dr. R. Guilard
LIMSAG, UMR 5633
Faculté des Sciences "Gabriel"
Université de Bourgogne
6 Boulevard Gabriel, 21100 Dijon (France)
Fax: (+33) 380-396-117
E-mail: jmbarbe@u-bourgogne.fr
roger.guilard@u-bourgogne.fr

[**] This work was supported by the CNRS and Air Liquide. G.C. gratefully acknowledges the "Région Bourgogne" and Air Liquide for financial support.

Supporting information for this article is available on the WWW under http://www.angewandte.org or from the author.

 DOI: 10.1002/anie.200463009

plexes. Therefore, applications in different fields such as catalysis,[15] optical sensors,[16,17] and metal-ion separation processes, especially for transition metals,[18] heavy metals,[19,20] and actinides,[21] have been developed. Many examples of gas separation devices with hybrid organic–inorganic membranes based on a gas-diffusion process have been described,[22–24] but only a few examples of gas separation through the formation of chemical bonds between gas molecules and solid supports are known;[14,25] gas-detection studies with hybrid organic–inorganic materials are also rare.[17,26]

We recently reported the high affinity and infinite selectivity of cobalt(III) corroles for CO over O_2 and N_2.[27] Hybrid xerogels are able to combine the textural and the structural properties of the inorganic matrix such that the gas-binding properties of immobilized Co^{III} corroles can be tuned. Furthermore, the incorporation of these Co complexes in a solid inorganic network stabilizes the active species and the resulting materials are well adapted to the preparation of powders, fibers, or thin films. Unusual adsorption properties may arise by combining the intrinsic reactivity of the metallo–organic complex with the properties of the inorganic framework[28] as the arrangement of the organic moieties gives rise to short-range organization.[29,30] In this regard, corrole macrocycles were immobilized, for the first time, in a silica matrix through one Si–C covalent bond. The anchoring of one hydrolysable $-Si(OEt)_3$ terminal group to the corrole allowed the preparation of hybrid materials through a sol–gel process. Herein, we describe the synthesis, physicochemical characterization, and adsorption properties of these materials.

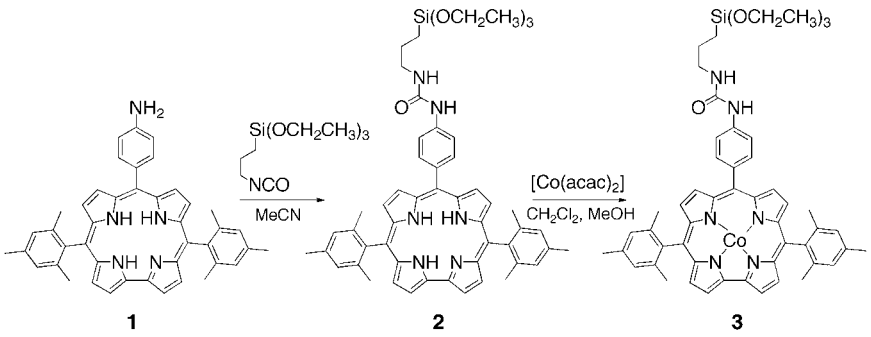

Scheme 1. Synthesis of the alkoxysilylated corrole precursors.

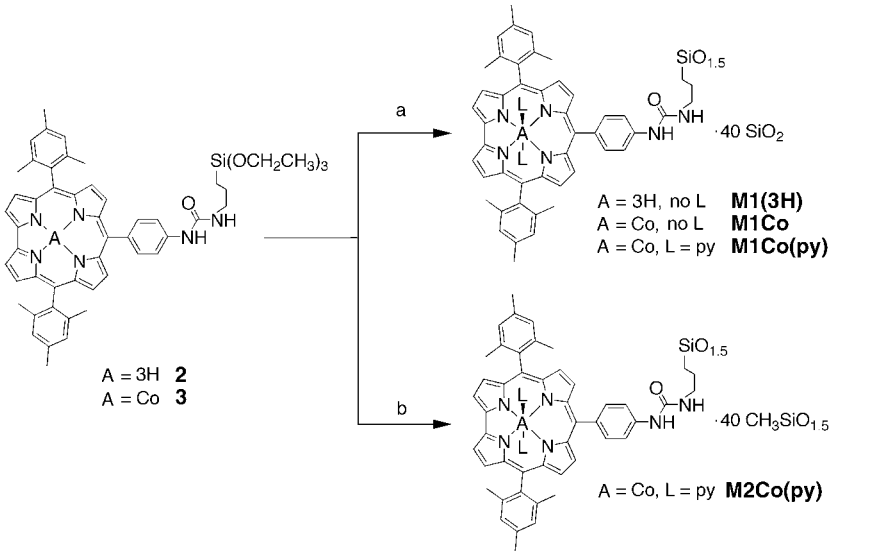

Scheme 2. Preparation of the materials: a) 40 equiv TEOS, distilled H_2O, TBAF, THF (with or without pyridine); b) 40 equiv MTEOS, distilled H_2O, TBAF, py, THF. L = axial pyridine ligand.

Complex **3** was prepared in two steps starting from corrole **1** (Scheme 1).[31] The reaction of 3-(triethoxysilyl)propyl isocyanate on **1** led to the formation of **2** in 4 days with a yield of 68%. Metalation of the free base **2** with cobalt(II) acetylacetonate afforded the precursor **3** in 96% yield (Scheme 1). These derivatives were characterized by ^{1}H NMR and UV/Vis spectroscopies, MALDI-TOF MS, and elemental analysis (see the Supporting Information).

Two types of materials were made: **M1** was prepared by co-polycondensation of **2** or **3** with 40 equivalents of tetraethoxysilane (TEOS); **M2** was prepared by co-polycondensation of **3** with 40 equivalents of methyltriethoxysilane (MTEOS; Scheme 2).[31] In the case of **M1**, the gelation process was performed at room temperature in THF by adding a stoichiometric amount of distilled water to the reaction mixture in the presence of tetrabutylammonium fluoride (TBAF, 1 mol% with respect to silicon) as catalyst. Under these conditions, **M1(3H)** and **M1Co**, which were obtained from **2** and **3**, respectively, gelled rapidly and the resulting monolithic gels were aged for 7 days. Upon addition of an excess of pyridine (py) during the gelation reaction of **3** with TEOS, **M1Co(py)** was synthesized (see Scheme 2 and the Supporting Information). The sol–gel process was further explored by treating the alkoxysilylated metallocorrole precursor **3** with 40 equivalents of MTEOS to prepare homogeneous molecular materials with enhanced stability of the cobalt(III) corrole in a moist atmosphere. A 14-day procedure led to the formation of **M2Co(py)** from a mixture of **3**, MTEOS, distilled water, a large excess of pyridine, and a catalytic amount of TBAF (5 mol% with respect to Si) at room temperature (Scheme 2). A larger TBAF/Si ratio was needed to initiate the sol–gel reaction for the formation of **M2Co(py)** than was needed for **M1Co(py)**.

The axial positions of the Co ion were protected during the sol–gel process by pyridine. The challenge was to make the Co^{III} coordination sites available for CO binding after removal of the pyridine ligands and to create a cavity for optimal accessibility of the gas. Thus, this protective method prevents inactivation of cobalt(III) corrole sites that occurs

through coordination of free silanol and siloxane groups on the material surface. The interaction of the cobalt ions with these groups cannot occur in **M2Co(py)** as there are mainly methyl groups present at the surface of the material.

The analytical and spectroscopic data for the silylated precursors and the hybrid xerogels are consistent with the structures presented in Scheme 2 and demonstrate that the corrole is incorporated into the solids. The metallocorrole concentration in the materials was deduced from elemental analyses (see the Supporting Information). For **M1Co**, the presence of the organic functional moieties in the mesopores and the condensation rate of the solids were evidenced by their ^{29}Si CP/MAS NMR spectra exhibiting one set of resonances at $\delta = -58$ and -63 ppm for the hybrid parts T^2 ($CSi[(OSi)_2OH]$) and T^3 ($CSi[(OSi)_3]$) substructures, respectively, and by the presence of a second set of resonances at $\delta = -101$ and -110 ppm corresponding to Q^3 ($Si[(OSi)_3OH]$) and Q^4 ($Si[(OSi)_4]$) inorganic substructures. Although the ^{29}Si CPMAS/NMR spectra could not be analyzed quantitatively, evidence of the major T^3 and Q^3 substructures was in accordance with a high condensation level for the solids.[32] Conversely, for **M2Co(py)**, only one sharp signal for the T^3 substructure was observed at $\delta = -66$ ppm, which is indicative of a polycondensed solid. The absence of signals between $\delta = -90$ ppm and -110 ppm suggests that no Si–C bond cleavage occured during the hydrolysis–polycondensation process.

The electronic spectra in the diffuse reflectance mode for **M1Co(py)** and **M1Co** materials resemble those of Co^{III} corroles in solution, with a single Soret band near 400 nm and very broad Q bands (500–650 nm; see the Supporting Information). These results indicate that the coordinating pyridine molecules are removed when the materials are put under vacuum. Conversely, the spectrum of **M2Co(py)** exhibits a new band close to 620 nm, which is characteristic of a hexacoordinated cobalt(III) corrole with two pyridine ligands.[33] Therefore, severe conditions are needed to remove pyridine molecules from **M2Co(py)**.

The surface area and pore diameters of the xerogels were determined by using nitrogen adsorption experiments according to BET and BJH calculations.[34,35] In general, the specific area is an important physical criteria for controlling accessibility of the gas molecules to the active sites. The texture of the free-base and cobalt(III) corrole materials obtained by co-gelation with TEOS was neither highly dependent on the presence of the metal in the macrocycle nor on the use of the protecting base. Thus, the surface areas of **M1(3H)**, **M1Co**, and **M1Co(py)** range between 450 and 520 $m^2 g^{-1}$. The N_2 adsorption/desorption isotherms of these samples were of type II with no hysteresis loop, which is characteristic of macroporous materials.[36] In contrast, the **M2Co(py)** xerogel prepared with MTEOS was almost nonporous (12 $m^2 g^{-1}$), even when more drastic aging conditions were used.

The CO adsorption was investigated concomitantly with O_2 and N_2 adsorption measurements to determine the selectivity of the materials towards CO versus O_2 and N_2. The equilibrium constant related to the CO binding affinity K_i and the adsorption capacity V_i ($i = N_2$ or O_2) was calculated by considering two different adsorption processes: selective chemisorption on the Co^{III} ion and nonselective physisorption resulting from dissolution and diffusion of the gas into the solid material.[27] The experimental isotherms corresponding to the CO adsorption were thus analyzed by using a model based on three Langmuir-type isotherms [Eq. (1)] and the N_2 and O_2 isotherms with a single Langmuir-type isotherm model [Eq. (2)].

$$V_{CO} = \frac{V_1 K_1 P}{1 + K_1 P} + \frac{V_2 K_2 P}{1 + K_2 P} + K_3 P \quad (1)$$

$$V_{i_{tot}} = \frac{V_i K_i P}{1 + K_i P} \quad (2)$$

An example of the CO adsorption adjustment by the isotherm model for **M1Co(py)** is given in Figure 1 along with experimental isotherms related to O_2 and N_2 adsorption. The main data relating to the CO adsorption for the four materials are reported in Table 1.

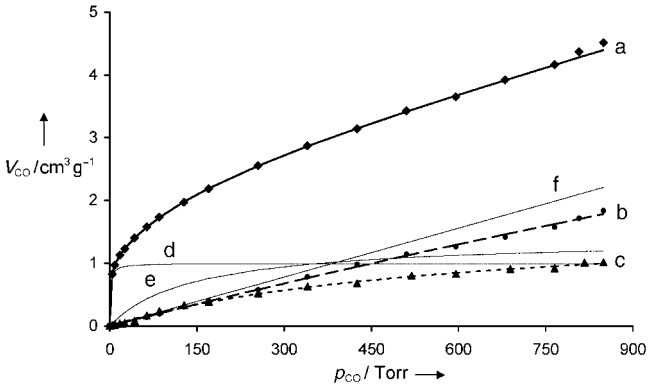

Figure 1. a) CO, b) N_2, and c) O_2 adsorption isotherms for **M1Co(py)** recorded at 293 K; d), e), and f) represent the first, second, and third components, respectively, of the calculated isotherms for CO adsorption (see [Eq. (1)].

Table 1: Experimental and calculated CO adsorption data for the xerogels

Material	V_{CO}[a] [$cm^3 g^{-1}$]	V_1 [$cm^3 g^{-1}$]	$(P_{1/2})_1$[b] [Torr]	V_2 [$cm^3 g^{-1}$]	$(P_{1/2})_2$[b] [Torr]	$K_3 \times 10^3$ [$Torr^{-1}$]	[Co][c] [$mmol g^{-1}$]	% CO[d]
M1(3H)	0.84	2.42	895	–	–	–	–	–
M1Co	5.92	0.54	1.12	0.75	138	6.19	0.186	31
M1Co(py)	4.16	1.00	1.22	1.39	141	2.60	0.202	53
M2Co(py)	3.06	1.30	0.40	0.58	73	1.61	0.219	38

[a] Experimental volume adsorbed at 760 Torr. [b] $(P_{1/2})_i = 1/K_i$. [c] Concentration of cobalt in the materials. [d] Percentage of active sites calculated from $V_1 + V_2$ and [Co].

For CO adsorption, the first two Langmuir components are related to the chemisorption of CO on accessible cobalt(III) corroles located at the surface of the material (K_1) and on less accessible complexes inside the solid (K_2), K_1 being by far larger than K_2. Physisorption of CO on the solid is given by a third component (K_3). Figure 1 clearly shows that the N_2 (b) and O_2 (c) adsorptions correspond to physisorption of the

gases on the porous material ($P_{1/2}^{N_2 \text{ or } O_2} > 500$ Torr) as well as the third component of the CO experimental adsorption isotherm curve. Another key feature is the selectivity of the CO adsorption compared to those of O_2 and N_2. Indeed, these values, which are calculated from $(P_{1/2})_1^{O_2 \text{ or } N_2}/(P_{1/2})_1^{CO}$, are about 470 and 5600 for CO/O_2 and CO/N_2 respectively. These significant values represent the adsorption phenomenon at a very low partial pressure of CO and therefore at a very low CO content. However, from a chemical point of view, the CO/O_2 and CO/N_2 selectivities are infinite as O_2 and N_2 cannot bind to the Co^{III} ion.[27] Such an attribute is significant for a CO gas detector to be used under ambient conditions.

The adsorption of CO by **M1(3H)** (Table 1 and the Supporting Information) is very low and results only from physisorption on the solid. This is not surprising as **M1(3H)** incorporates a free-base corrole, therefore no chemisorption of CO can occur. Furthermore, it is clear that the introduction of pyridine during the gelation process significantly increases the accessibility of the Co^{III} sites as demonstrated by the higher V_1 and lower $(P_{1/2})_1$ values for **M1Co(py)** and **M2Co(py)** compared with **M1Co** (see Table 1). Moreover, the use of MTEOS instead of TEOS induces an important decrease in the physisorption of CO, which is reflected by a lower K_3 value (Table 1) while maintaining a high accessibility of the metallocorroles, as shown by the low V_2 value with respect to V_1. Thus, a large surface area is not a prerequisite for a material that is very reactive towards CO.

In conclusion, very high affinities for CO compared with O_2 and N_2 were obtained for Co^{III} corroles incorporated into silica matrices. The sol–gel process led to new organic–inorganic hybrid composite materials. By this flexible process, devices with different shapes might be prepared, such as thin films coated on a solid support through a gelation reaction. This development facilitates the elaboration of a gas sensor and enhances the long-term stability of the device.

Received: December 21, 2004
Published online: April 14, 2005

Keywords: carbon monoxide sensors · cobalt · organic–inorganic hybrid composites · porphyrinoids · sol–gel processes

[1] R. Paolesse in *The Porphyrin Handbook*, *Vol. 2* (Eds.: K. M. Kadish, K. M. Smith, R. Guilard), Academic Press, New York, **2000**, p. 201.
[2] C. Erben, S. Will, K. M. Kadish in *The Porphyrin Handbook*, *Vol. 2* (Eds.: K. M. Kadish, K. M. Smith, R. Guilard), Academic Press, New York, **2000**, p. 233.
[3] R. Guilard, J. M. Barbe, C. Stern, K. M. Kadish in *The Porphyrin Handbook*, *Vol. 18* (Eds.: K. M. Kadish, K. M. Smith, R. Guilard), Elsevier, New York, USA, **2003**, p. 303.
[4] Z. Gross, N. Galili, I. Saltsman, *Angew. Chem.* **1999**, *111*, 1530; *Angew. Chem. Int. Ed.* **1999**, *38*, 1427.
[5] D. T. Gryko, *Chem. Commun.* **2000**, 2243.
[6] R. Paolesse, S. Nardis, F. Sagone, R. G. Khoury, *J. Org. Chem.* **2001**, *66*, 550.
[7] D. T. Gryko, K. Jadach, *J. Org. Chem.* **2001**, *66*, 4267.
[8] D. T. Gryko, K. E. Piechota, *J. Porphyrins Phthalocyanines* **2002**, *6*, 81.
[9] D. T. Gryko, B. Koszarna, *Org. Biomol. Chem.* **2003**, *1*, 350.
[10] R. Guilard, D. T. Gryko, G. Canard, J. M. Barbe, B. Koszarna, S. Brandès, M. Tasior, *Org. Lett.* **2002**, *4*, 4491.
[11] G. Dubois, C. Reyé, R. J. P. Corriu, S. Brandès, F. Denat, R. Guilard, *Angew. Chem.* 2001, 113, 1121; *Angew. Chem. Int. Ed.* **2001**, *40*, 1087.
[12] R. J. P. Corriu, F. Embert, Y. Guari, C. Reyé, R. Guilard, *Chem. Eur. J.* **2002**, *8*, 5732.
[13] M. G. Basallote, E. Blanco, M. Blazquez, M. J. Fernandez Trujillo, R. Litran, M. A. Manez, M. R. del Solar, *Chem. Mater.* **2003**, *15*, 2025.
[14] R. J. P. Corriu, E. Lancelle-Beltran, A. Mehdi, C. Reyé, S. Brandès, R. Guilard, *Chem. Mater.* **2003**, *15*, 3152.
[15] A. Adima, J. J. E. Moreau, M. Wong Chi Man, *Chirality* **2000**, *12*, 411.
[16] S. Blair, R. Kataky, D. Parker, *New J. Chem.* **2002**, *26*, 530.
[17] C. Sanchez, B. Lebeau, F. Chaput, J.-P. Boilot, *Adv. Mater.* **2003**, *15*, 1969.
[18] H. J. Im, Y. Yang, L. R. Alain, C. E. Barnes, S. Dai, Z. Xue, *Environ. Sci. Technol.* **2000**, *34*, 2209.
[19] A. G. S. Prado, L. N. H. Arakaki, C. Airoldi, *J. Chem. Soc. Dalton Trans.* **2001**, 2206.
[20] A. Walcarius, C. Delacote, S. Sayen, *Electrochim. Acta* **2004**, *49*, 3775.
[21] S. Bourg, J.-C. Broudic, O. Conocar, J. J. E. Moreau, D. Meyer, M. W. C. Man, *Chem. Mater.* **2001**, *13*, 491.
[22] C. Guizard, A. Bac, M. Barboiu, N. Hovnanian, *Sep. Purif. Technol.* **2001**, *25*, 167.
[23] D.-W. Lee, B. Sea, K.-Y. Lee, K.-H. Lee, *Ind. Eng. Chem. Res.* **2002**, *41*, 3594.
[24] K. Kuraoka, Y. Tanaka, M. Yamashita, T. Yazawa, *Chem. Commun.* **2004**, 1198.
[25] G. Dubois, R. Tripier, S. Brandès, F. Denat, R. Guilard, *J. Mater. Chem.* **2002**, *12*, 2255.
[26] E. S. Ribeiro, Y. Gushikem, J. C. Biazzotto, O. S. Serra, *J. Porphyrins Phthalocyanines* **2002**, *6*, 527.
[27] J.-M. Barbe, G. Canard, S. Brandès, F. Jérôme, G. Dubois, R. Guilard, *Dalton Trans.* **2004**, 1208.
[28] R. Corriu, C. Reye, A. Mehdi, G. Dubois, C. Chuit, F. Denat, B. Roux-Fouillet, R. Guilard, G. Lagrange, S. Brandès, WO Pat. 9937656, **1999**; J. Goulon, C. Goulon-Ginet, A. Rogalev, F. Wilhelm, N. Jaouen, D. Cabaret, Y. Joly, G. Dubois, R. J. P. Corriu, G. David, S. Brandès, R. Guilard, *Eur. J. Inorg. Chem.*, in press.
[29] B. Boury, R. J. P. Corriu, *Chem. Commun.* **2002**, 795.
[30] B. Boury, R. J. P. Corriu, *Chem. Rec.* **2003**, *3*, 120.
[31] Abbreviations: compound **1**: 5,15-dimesityl-10-(4-aminophenyl)corrole; compound **2**: 5,15-dimesityl-10-{4-phenyl-[3-(3-triethoxysilyl)propyl]urea}corrole; compound **3**: [5,15-dimesityl-10-{4-phenyl-[3-(3-triethoxysilyl)propyl]urea}corrolato] cobalt(III); acac: acetylacetonate; TEOS: tetraethoxysilane; MTEOS: methyltriethoxysilane; TBAF: tetrabutylammonium fluoride.
[32] D. A. Loy, K. J. Shea, *Chem. Rev.* **1995**, *95*, 1431.
[33] R. Guilard, C. P. Gros, F. Bolze, F. Jérôme, Z. Ou, J. Shao, J. Fischer, R. Weiss, K. M. Kadish, *Inorg. Chem.* **2001**, *40*, 4845.
[34] S. Brunauer, P. H. Emmet, E. Teller, *J. Am. Chem. Soc.* **1938**, *60*, 309.
[35] E. Barrett, L. G. Joyner, P. P. Halenda, *J. Am. Chem. Soc.* **1951**, *73*, 373.
[36] K. S. W. Sing, D. H. Everett, R. A. W. Haul, L. Moscou, R. A. Pierotti, J. Rouquérol, T. Siemieniewska, *Pure Appl. Chem.* **1985**, *57*, 603.

Luminescent Gold Complexes

Luminescent Gold(III) Alkynyl Complexes: Synthesis, Structural Characterization, and Luminescence Properties**

Vivian Wing-Wah Yam, Keith Man-Chung Wong, Ling-Ling Hung, and Nianyong Zhu*

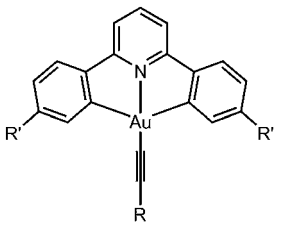

R' = H; R = C_6H_5 (**1**)
C_6H_4-Cl-*p* (**2**)
C_6H_4-OCH_3-*p* (**3**)
C_6H_4-NH_2-*p* (**4**)
R' = *t*Bu; R = C_6H_5 (**5**)

Scheme 1.

In contrast to the related gold(I)[1–3] and the isoelectronic platinum(II) compounds,[4,5] which are known to show rich luminescence properties, luminescent gold(III) compounds are rare, with very few exceptions that emit at room temperature in solution.[6] The reasons for the lack of luminescence in gold(III) species are probably the presence of low-energy d–d ligand field (LF) states and the electrophilicity of the gold(III) center. The presence of a nonemissive low-lying d–d state would quench the luminescence excited state by thermal equilibration or energy transfer.[7] Coupling of strong σ-donating alkynyl ligands to gold(III) should render the metal center more electron rich, with the additional advantage of raising the energy of the d–d states, which would result in enhanced luminescence by increasing the chances of populating the emissive state for the construction of luminescent organometallic materials. Despite the fact that alkynyl complexes of gold(I)[3] and the isoelectronic platinum(II)[5] are known and have been shown to display rich photoluminescence properties, to our surprise, alkynyl complexes of gold(III) are extremely rare.[8] Although there is increasing interest in the use of gold(III) compounds for catalysis of organic synthetic reactions of alkynes,[9] the chemistry of gold(III) alkynyls is essentially unexplored and underdeveloped, and their luminescence properties are virtually unknown.

Herein we describe the synthesis of a novel series of biscyclometalated gold(III) alkynyl complexes [Au(C^N^C)(C≡CR)] [HC^N^CH = 2,6-diphenylpyridine, R = C_6H_5 (**1**), C_6H_4-Cl-*p* (**2**), C_6H_4-OCH_3-*p* (**3**), C_6H_4-NH_2-*p* (**4**); HC^N^CH = 2,6-bis(4-*tert*-butylphenyl)pyridine, R = C_6H_5 (**5**)], which are the first of their kind (Scheme 1). The molecular structure of **1** was determined by X-ray crystallography. The photophysical properties of **1**–**5** were also studied.

Unlike most other gold(III) compounds, which exhibit luminescence only at low temperature or are nonemissive, complexes **1**–**5** display luminescence in various media at both low and ambient temperature.

Figure 1 shows the crystal structure of **1**, in which the gold(III) center adopts a distorted square-planar coordination geometry with C(9)-Au(1)-C(25) and N(1)-Au(1)-C(1) angles of 162.0(3) and 178.5(3)°, respectively, as is characteristic of d^8 metal complexes. The C^N^C ligand and the gold(III) center are essentially coplanar, with the plane lying at a dihedral angle of 64.97° with respect to the ethynylbenzene moiety. The bond lengths about the gold(III) center and the C^N^C

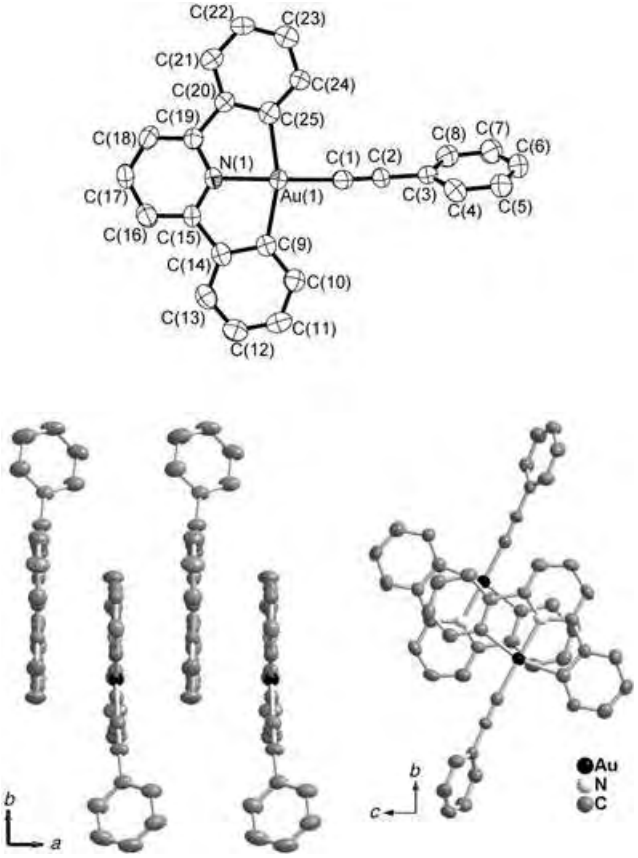

Figure 1. Top: Crystal structure of **1** with atomic numbering scheme. Hydrogen atoms are omitted for clarity. Thermal ellipsoids are drawn at the 40% probability level. Selected bond lengths [Å] and angles [°]: Au(1)–C(1) 1.979(7), Au(1)–C(9) 2.073(7), Au(1)–C(25) 2.071(7), Au(1)–N(1) 1.999(5), C(1)–C(2) 1.185(9); C(9)-Au(1)-C(25) 162.0(3), N(1)-Au(1)-C(1) 178.5(3), Au(1)-C(1)-C(2) 176.6(7), C(1)-C(2)-C(3) 177.6(9). Bottom: Crystal packing showing the π···π stacking arrangement in different views.

[*] Prof. Dr. V. W.-W. Yam, Dr. K. M.-C. Wong, L.-L. Hung, Dr. N. Zhu
Centre for Carbon-Rich Molecular and
Nano-Scale Metal-Based Materials Research
Department of Chemistry
The University of Hong Kong
Pokfulam Road, Hong Kong (P. R. China)
Fax: (+852) 2857-1586
E-mail: wwyam@hku.hk

[**] V.W.-W.Y. acknowledges support from the University Development Fund of The University of Hong Kong and The University of Hong Kong Foundation for Educational Development and Research Limited. The work described in this paper has been supported by a CERG Grant from the Research Grants Council of Hong Kong Special Administrative Region, China (Project No. HKU 7022/03P). L.-L.H. acknowledges the receipt of a postgraduate studentship from The University of Hong Kong.

 DOI: 10.1002/anie.200500253

ligand [Au(1)–C(9) 2.073(7), Au(1)–C(25) 2.071(7), Au(1)–N(1) 1.999(5) Å] are similar to the Au–C and Au–N distances in related gold(III) bis-cyclometalated complexes[10] and are also comparable to the Pt–C and Pt–N distances in analogous platinum(II) complexes.[5c–f] The Au–C(1) and C(1)–C(2) bond lengths of 1.979(7) and 1.185(9) Å, respectively, as well as the Au(1)-C(1)-C(2) bond angle of 176.6(7)° are comparable to those found in gold(I) alkynyl[3] and analogous platinum(II) alkynyl complexes.[5c–f] The shortest Au···Au distance of 5.003(1) Å indicates the absence of significant Au···Au interaction. However, the crystal packing of **1** (Figure 1) reveals the presence of partially staggered [Au^{III}-C^N^C] units with interplanar distances of 3.384 Å between the adjacent C^N^C ligands, suggestive of the presence of aromatic π···π stacking interactions.

All complexes exhibit an intense absorption band at 312–323 nm and a moderately intense vibronic-structured absorption band at 362–412 nm in dichloromethane. The photophysical data of **1**–**5** are collected in Table 1, and the electronic absorption spectra of **1**, **4**, and **5** are shown in Figure 2. The vibrational progressional spacings of 1310–1380 cm^{-1} in the lower energy absorption band correspond to the skeletal vibrational frequency of the C^N^C ligand. The absorption energy was found to be rather insensitive to the nature of the alkynyl ligand. In addition, the observation of similar absorption bands for the chloro counterpart [Au(C^N^C)Cl] is suggestive of the lack of involvement of the alkynyl ligands in this transition. In view of this, and the nonreducing nature of gold(III), such low-energy absorptions are assigned as metal-perturbed intraligand (IL) π–π* transition of the C^N^C ligand, involving some charge transfer from the phenyl moiety to the pyridyl unit. This is further supported by the lower absorption energy of **5** compared to **1** with the same alkynyl ligand. The observation of a lower energy metal-perturbed IL π–π* transition in **5** is ascribed to the better electron-donating properties of the *tert*-butyl group on the phenyl rings, which raises the energy of the HOMO localized on the phenyl ring and thus narrows the gap between the HOMO and the pyridine-localized LUMO. Similar assignments were also suggested for other related gold(III) complexes.[10] Interestingly, an additional shoulder was observed in the electronic absorption spectrum of **4** at about 415 nm (Figure 2). Since the alkynyl ligand with an electron-rich amino substituent has better electron-donating ability, the presence of a low-lying alkynyl-to-diarylpyridine

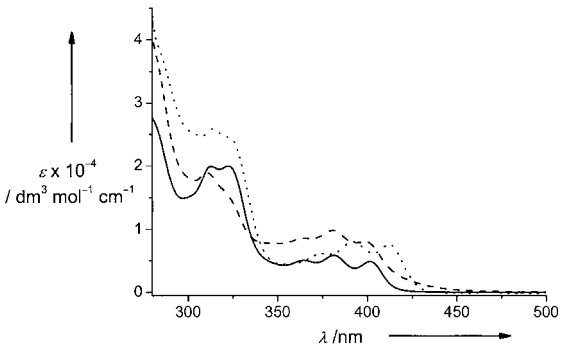

Figure 2. Electronic absorption spectra of **1** (——), **4** (----), and **5** (•••••) in dichloromethane solution at room temperature.

Table 1: Photophysical data for **1**–**5**.

Complex	Absorption λ_{max} [nm] (ε_{max} [dm^3 mol^{-1} cm^{-1}])[a]	Medium (T [K])	Emission λ_{max} [nm] (τ_0 [μs])	Φ_{em}[b]
1	312 (19890), 322 (19980), 364 (5050), 381 (5870), 402 (4870)	CH_2Cl_2 (298)[c]	476, 506, 541, 582 (< 0.05)	1.0×10^{-3}
		solid (298)	588	
		thin film (298)[d]	568	
		solid (77)	496 (28.3, 310.4)[f]	
		glass (77)[c,e]	470, 503, 537, 585 (194)	
2	312 (19400), 322 (19640), 365(4640), 382 (5170), 402 (4305)	CH_2Cl_2 (298)[c]	476, 506, 539, 584 (< 0.05)	0.2×10^{-3}
		solid (298)	550 (< 0.05)	
		solid (77)	500 (25.3, 256.6)[f]	
		glass (77)[c,e]	470, 504, 534, 590 (151)	
3	312 (13820), 322 (13455), 362 (6400), 380 (6245), 400 (4190)	CH_2Cl_2 (298)[c]	474, 505, 539, 584 (< 0.05)	0.5×10^{-3}
		solid (298)	555 (< 0.05)	
		solid (77)	485 (28.4, 268.2)[f]	
		glass (77)[c,e]	470, 503, 536, 585 (137)	
4	310 (19195), 322 sh (15680), 365 (8855), 381 (10100), 399 (8300), 415 sh (3410)	CH_2Cl_2 (298)	611 (0.3)	2.0×10^{-3}
		solid (298)	585 (0.2)	
		solid (77)	548 (0.3, 1.7)[f]	
		glass (77)[c,e]	470, 503, 535, 587 (107)	
5	313 (26190), 323 (24460), 374 (6130), 392 (8035), 412 (7465)	CH_2Cl_2 (298)[c]	484, 514, 548, 593 (0.1)	6.0×10^{-3}
		solid (298)	550 (< 0.05)	
		solid (77)	503 (18.2, 171.9)[f]	
		glass (77)[c,e]	478, 512, 548, 600 (200)	

[a] In dichloromethane at 298 K. [b] Luminescence quantum yield, measured at room temperature with $[Ru(bpy)_3]^{2+}$ as standard. [c] Vibronic-structured emission band. [d] Prepared by vacuum deposition. [e] In CH_2Cl_2/EtOH/MeOH (1:40:10). [f] Double-exponential decay.

ligand-to-ligand charge-transfer (LLCT) transition is possible. Thus, the low-energy absorptions in **4** are assigned as an admixture of intraligand (IL) π–π*(C^N^C)/LLCT π(C≡C-C_6H_4-NH_2-*p*)→π*(C^N^C) transitions.

Unlike most other gold(III) compounds, which are non-emissive or only show luminescence at low temperature, **1**–**5** display intense luminescence at 468–611 nm in solution on excitation at $\lambda \geq 360$ nm at room temperature (Table 1). This supports the idea that introduction of strong σ-donating alkynyl ligands into gold(III) compounds would enhance the luminescence properties by increasing the d–d splitting, as opposed to the observation of emission only in low-temperature glasses of the chloro analogue [Au(C^N^C)Cl].[10] The long-lived emission with lifetimes in the microsecond range is suggestive of a triplet parentage. In general, the emission energies of the compounds were found to be rather insensitive to the nature of the alkynyl ligands. A vibronic-structured emission band with band maximum at around 480 nm was observed for **1**–**3** and **5** in dichloromethane at room temperature (Figure 3). The vibrational progressional spacings of

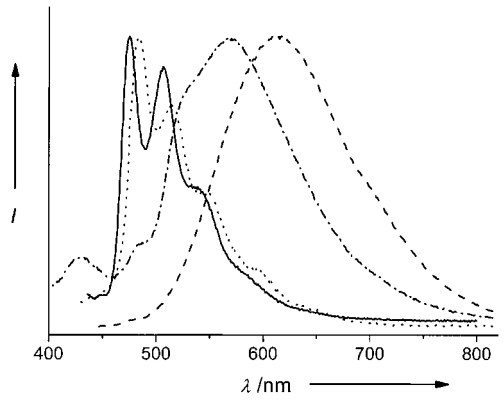

Figure 3. Normalized emission spectra of **1** (——), **4** (----), **5** (••••) in degassed CH_2Cl_2 and **1** in the solid state (thin film, –•–•) at 298 K.

about 1300 cm^{-1} are in line with the C=C and C=N stretching frequencies of the tridentate ligand, indicative of the involvement of the tridentate ligand in the excited state origin. The luminescence is assigned as originating from a metal-perturbed IL ^{3}[π-π*] state of the tridentate C^N^C ligand. Similar to the low-energy absorption band in the electronic absorption studies, **5** emits at lower energy than **1**, since the electron-rich *tert*-butyl groups on the phenyl rings of the C^N^C ligand in **5** lead to a higher energy phenyl-localized HOMO and hence a lower energy ^{3}[π-π*] excited state. In contrast to **1**–**3** and **5**, which show a vibronic-structured emission band in dichloromethane, **4** exhibits a structureless emission band at 611 nm even in dilute solution (5×10^{-6} mol dm^{-3}; Figure 3). On the basis of the energetically higher lying π(C≡C-C_6H_4-NH_2-*p*) orbital, the lower energy emission band in **4** is tentatively assigned as derived from an LLCT ^{3}[π(C≡C-C_6H_4-NH_2-*p*)→π*(C^N^C)] excited state. It is noteworthy that the emission spectra of **1**–**5** in the solid state show a low-energy structureless band at 550–585 nm (Figure 3). The red shift of the solid-state emission relative to that in solution is attributed to dimeric or excimeric emission arising from the π···π stacking of the C^N^C ligand, probably due to the ordered packing of the molecules in the solid state, as supported by the observation of such π···π stacking in the crystal packing of **1** (Figure 1).

Experimental Section

Complexes **1**–**5** were synthesized by reaction of [Au(C^N^C)Cl] with various terminal alkynes in the presence of a catalytic amount of copper(I) iodide in triethylamine and dichloromethane. Pale yellow crystals were obtained by slow diffusion of diethyl ether vapor into a dichloromethane solution of the complexes after column chromatography on silica gel with dichloromethane as eluent. **1**: Yield: 88%. ^{1}H NMR (300 MHz, CH_2Cl_2, 298 K, relative to Me_4Si): $\delta = 8.04$ (dd, $J = 7.4$, 1.0 Hz, 2H, C^N^C), 7.92 (t, $J = 8.0$ Hz, 1H, C^N^C), 7.62 (m, 4H, C^N^C and C_6H_5), 7.54 (d, $J = 8.0$ Hz, 2H, C^N^C), 7.26–7.44 ppm (m, 7H, C^N^C and C_6H_5); positive EI-MS: *m/z*: 527 $[M]^+$; IR (KBr): $\tilde{\nu} = 2147$ cm^{-1} ν(C≡C); elemental analysis (%) calcd for $C_{25}H_{16}NAu$ (found): C 56.93 (56.57), H 3.04 (3.05), N 2.66 (2.66). **2**: Yield: 85%. ^{1}H NMR (300 MHz, CH_2Cl_2, 298 K, Me_4Si): $\delta = 8.00$ (dd, $J = 7.2$, 1.0 Hz, 2H, C^N^C), 7.90 (t, $J = 8.0$ Hz, 1H, C^N^C), 7.50–7.60 (m, 6H, C^N^C and C_6H_4), 7.25–7.42 ppm (m, 6H, C^N^C and C_6H_4); positive EI-MS: *m/z*: 562 $[M]^+$; IR (KBr): $\tilde{\nu} = 2157$ cm^{-1} ν(C≡C); elemental analysis (%) calcd for $C_{25}H_{15}NClAu \cdot 0.5\,H_2O$ (found): C 52.59 (52.85), H 2.80 (2.66), N 2.45 (2.40). **3**: Yield: 86%. ^{1}H NMR (400 MHz, CH_2Cl_2, 298 K, Me_4Si): $\delta = 8.02$ (dd, $J = 7.6$, 1.0 Hz, 2H, C^N^C), 7.90 (t, $J = 8.0$ Hz, 1H, C^N^C), 7.60 (dd, $J = 7.6$, 1.0 Hz, 2H, C^N^C), 7.50–7.56 (m, 4H, C^N^C and C_6H_4), 7.40 (dt, $J = 7.3$, 1.3 Hz, 2H, C^N^C), 7.27 (dt, $J = 7.3$, 1.3 Hz, 2H, C^N^C), 6.91 (d, $J = 8.9$ Hz, 2H, C_6H_4), 3.88 ppm (s, 3H, OCH_3); positive EI-MS: *m/z*: 557 $[M]^+$; IR (KBr): $\tilde{\nu} = 2157$ cm^{-1} ν(C≡C); elemental analysis (%) calcd for $C_{26}H_{18}NOAu \cdot 0.5\,H_2O$ (found): C 55.12 (55.15), H 3.36 (3.28), N 2.47 (2.48). **4**: Yield: 80%. ^{1}H NMR (300 MHz, CH_2Cl_2, 298 K, Me_4Si): $\delta = 8.07$ (dd, $J = 7.4$, 1.0 Hz, 2H, C^N^C), 7.92 (t, $J = 8.0$ Hz, 1H, C^N^C), 7.65 (dd, $J = 7.4$, 1.0 Hz, 2H, C^N^C), 7.56 (d, $J = 8.0$ Hz, 2H, C^N^C), 7.39–7.45 (m, 4H, C^N^C and C_6H_4), 7.30 (dt, $J = 7.5$, 1.3 Hz, 2H, C^N^C), 6.67 (d, $J = 8.6$ Hz, 2H, C_6H_4), 3.84 ppm (s, 2H, NH_2); positive EI-MS: *m/z*: 542 $[M]^+$; IR (KBr): $\tilde{\nu} = 2143$ cm^{-1} ν(C≡C); elemental analysis (%) calcd for $C_{25}H_{17}N_2Au \cdot 0.5\,H_2O$ (found): C 54.45 (54.59), H 3.27 (3.13), N 5.08 (5.04). **5**: Yield: 85%. ^{1}H NMR (400 MHz, CH_2Cl_2, 298 K, Me_4Si): $\delta = 8.18$ (d, $J = 2.0$ Hz, 2H, C^N^C), 7.86 (t, $J = 8.0$ Hz, 1H, C^N^C), 7.60 (d, $J = 7.6$ Hz, 2H, C_6H_5), 7.56 (d, $J = 8.0$ Hz, 2H, C^N^C), 7.46 (d, $J = 8$ Hz, 2H, C^N^C), 7.35 (m, 5H, C^N^C and C_6H_5), 1.39 (s, 9H, *t*Bu), 1.53 ppm (s, 18H, *t*Bu); positive EI-MS: *m/z*: 640 $[M]^+$; IR (KBr): $\tilde{\nu} = 2149$ cm^{-1} ν(C≡C); elemental analysis calcd for $C_{33}H_{32}NAu \cdot 0.5\,H_2O$ (found): C 61.11 (61.02), H 5.09 (5.08), N 2.16 (2.17).

Crystal data for **1**: $C_{25}H_{16}AuN$, $M_r = 527.35$, crystal dimensions $0.4 \times 0.2 \times 0.2$ mm, orthorhombic, space group $P2_12_12_1$, $a = 6.735(1)$, $b = 14.265(3)$, $c = 19.583(4)$ Å, $V = 1881.4(6)$ $Å^3$, $Z = 4$, $\rho_{calcd} = 1.862$ g cm^{-3}, $\mu(Mo_{K\alpha}) = 7.827$ mm^{-1}, $F(000) = 1008$, $T = 253$ K. Final $R = 0.0262$, $wR = 0.0555$ with $I > 2\sigma(I)$; $R = 0.0339$, $wR = 0.0569$ for all data; GOF = 0.925 for 244 parameters and a total of 10500 reflections, of which 3283 were independent ($R_{int} = 0.0377$). MAR diffractometer, $Mo_{K\alpha}$ radiation ($\lambda = 0.71073$ Å); collection range $2\theta_{max} = 50.62°$ with 3° oscillation step of ϕ, 300 s exposure time, and scanner distance of 120 mm. 54 images were collected. CCDC-260767 (**1**) contains the supplementary crystallographic data for this paper. These data can be obtained free of charge from the Cambridge Crystallographic Data Centre via www.ccdc.cam.ac.uk/data_request/cif.

Received: January 22, 2005
Published online: April 14, 2005

Keywords: alkynyl ligands · gold · luminescence

[1] a) P. C. Ford, A. Vogler, *Acc. Chem. Res.* **1993**, *26*, 220; b) *Gold: Progress in Chemistry, Biochemistry, and Technology* (Ed.: H. Schmidbaur), Wiley, Chichester, **1999**; c) V. W. W. Yam, K. K. W. Lo, *Chem. Soc. Rev.* **1999**, *28*, 323; d) V. W. W. Yam, K. K. W. Lo in *Multimetallic and Macromolecular Inorganic Photochemistry*, *Vol. 4* (Eds.: V. Ramamurthy, K. S. Schanze), Marcel Dekker, New York, **1999**, pp. 31 – 112; e) J. M. Forward, J. P. Fackler, Jr., Z. Assefa in *Optoelectronic Properties of Inorganic Compounds* (Eds.: D. M. Roundhill, J. P. Fackler, Jr.), Plenum, New York, **1999**, pp. 195 – 229.

[2] a) J. C. Vickery, M. M. Olmstead, E. Y. Fung, A. L. Balch, *Angew. Chem.* **1997**, *109*, 1227; *Angew. Chem. Int. Ed. Engl.* **1997**, *36*, 1179; b) K. H. Leung, D. L. Phillips, M. C. Tse, C. M. Che, V. M. Miskowski, *J. Am. Chem. Soc.* **1999**, *121*, 4799; c) M. A. Rawashdeh-Omary, M. A. Omary, J. P. Fackler, Jr., R. Galassi, B. R. Pietroni, A. Burini, *J. Am. Chem. Soc.* **2001**, *123*, 9689; d) V. W. W. Yam, E. C. C. Cheng, N. Zhu, *Angew. Chem.* **1999**, *111*, 193; *Angew. Chem. Int. Ed.* **1999**, *38*, 197; e) V. W. W. Yam, E. C. C. Cheng, Z. Y. Zhou, *Angew. Chem.* **2000**, *112*, 1749; *Angew. Chem. Int. Ed.* **2000**, *39*, 1683; f) V. W. W. Yam, E. C. C. Cheng, N. Zhu, *Angew. Chem.* **2001**, *113*, 1813; *Angew. Chem. Int. Ed.* **2001**, *40*, 1763; g) W. F. Fu, K. C. Chan, K. K. Cheung, C. M. Che, *Chem. Eur. J.* **2001**, *7*, 4656; h) R. L. White-Morris, M. M. Olmstead, F. Jiang, D. S. Tinti, A. L. Balch, *J. Am. Chem. Soc.* **2002**, *124*, 2327; i) Y. Lee, R. Eisenberg, *J. Am. Chem. Soc.* **2003**, *125*, 7778; j) A. Kishimura, T. Yamashita, T. Aida, *J. Am. Chem. Soc.* **2005**, *127*, 179.

[3] a) D. Li, X. Hong, C. M. Che, W. C. Lo, S. M. Peng, *J. Chem. Soc. Dalton Trans.* **1993**, 2929; b) T. E. Müller, S. W. K. Choi, D. M. P. Mingos, D. Murphy, D. J. Williams, V. W. W. Yam, *J. Organomet. Chem.* **1994**, *484*, 209; c) V. W. W. Yam, S. W. K. Choi, K. K. Cheung, *Organometallics* **1996**, *15*, 1734; d) W. J. Hunks, M. A. MacDonald, M. C. Jennings, R. J. Puddephatt, *Organometallics* **2000**, *19*, 5063; e) H. Y. Chao, W. Lu, M. C. W. Chan, C. M. Che, K. K. Cheung, N. Zhu, *J. Am. Chem. Soc.* **2002**, *124*, 14696; f) W. Lu, N. Zhu, C. M. Che, *J. Am. Chem. Soc.* **2003**, *125*, 16081; g) S. K. Yip, E. C. C. Cheng, L. H. Yuan, N. Zhu, V. W. W. Yam, *Angew. Chem.* **2004**, *116*, 5062; *Angew. Chem. Int. Ed.* **2004**, *43*, 4954.

[4] a) D. M. Roundhill, H. B. Gray, C. M. Che, *Acc. Chem. Res.* **1989**, *22*, 55; b) V. H. Houlding, V. M. Miskowski, *Coord. Chem. Rev.* **1991**, *111*, 145; c) J. A. Zuleta, M. S. Burbery, R. Eisenberg, *Coord. Chem. Rev.* **1990**, *97*, 47; d) D. R. McMillin, J. J. Moore, *Coord. Chem. Rev.* **2002**, *229*, 113.

[5] a) V. W. W. Yam, *Acc. Chem. Res.* **2002**, *35*, 555; b) M. Hissler, J. E. McGarrah, W. B. Connick, D. K. Geiger, S. D. Cummings, R. Eisenberg, *Coord. Chem. Rev.* **2000**, *208*, 115; c) V. W. W. Yam, R. P. L. Tang, K. M. C. Wong, K. K. Cheung, *Organometallics* **2001**, *20*, 4476; d) V. W. W. Yam, K. M. C. Wong, N. Zhu, *J. Am. Chem. Soc.* **2002**, *124*, 16081; e) V. W. W. Yam, K. M. C. Wong, N. Zhu, *Angew. Chem.* **2003**, *115*, 1438; *Angew. Chem. Int. Ed.* **2003**, *42*, 1400; f) W. Lu, B. X. Mi, M. C. W. Chan, Z. Hui, C. M. Che, N. Zhu, S. T. Lee, *J. Am. Chem. Soc.* **2004**, *126*, 4958.

[6] a) V. W. W. Yam, S. W. K. Choi, T. F. Lai, W. K. Lee, *J. Chem. Soc. Dalton Trans.* **1993**, 1001; b) C. W. Chan, W. T. Wong, C. M. Che, *Inorg. Chem.* **1994**, *33*, 1266.

[7] A. Vogler, H. Kunkely, *Coord. Chem. Rev.* **2001**, *219–221*, 489.

[8] a) A. Johnson, R. J. Puddephatt, *J. Chem. Soc. Dalton Trans.* **1977**, 1384; b) M. A. Cinellu, G. Minghetti, M. V. Pinna, S. Stoccoro, A. Zucca, M. Manassero, *J. Chem. Soc. Dalton Trans.* **1999**, 2823; c) L. A. Méndez, J. Jiménez, E. Cerrada, F. Mohr, M. Laguna, *J. Am. Chem. Soc.* **2005**, *127*, 852.

[9] a) N. Asao, T. Nogami, S. Lee, Y. Yamamoto, *J. Am. Chem. Soc.* **2003**, *125*, 10921; b) A. S. K. Hashmi, *Gold Bull.* **2003**, *36*, 3.

[10] K. H. Wong, K. K. Cheung, M. C. W. Chan, C. M. Che, *Organometallics* **1998**, *17*, 5305.

Natural Products Synthesis

Determination by Asymmetric Total Synthesis of the Absolute Configuration of Lucilactaene, a Cell-Cycle Inhibitor in p53-Transfected Cancer Cells**

*Junichiro Yamaguchi, Hideaki Kakeya, Takao Uno, Mitsuru Shoji, Hiroyuki Osada, and Yujiro Hayashi**

The tumor-suppressor gene p53 is involved in important cellular events, such as cell-cycle control and apoptosis.[1] The p53 gene is lost or mutated in many types of human tumors. Small molecules that induce cell-cycle arrest or apoptosis in a p53-independent manner or allow mutant p53 to alter a conformationally active form of p53 may be good candidates for treating various types of cancers.[2] Recently we isolated lucilactaene (**1**), which arrests cell-cycle progression in the G1 phase at the nonpermissive temperature of 37 °C in Hl299/tsp53 cells, from *Fusarium* sp. RK97-94.[3] Lucilactaene (**1**) is a synthetically challenging molecule because of its rare hexahydro-3a-hydroxy-5-oxo-2*H*-furo[3,2-b]pyrrol-6-yl ring system and its substituted and conjugated *E*,*E*,*E*,*E*,*E* pentaene moiety, which is unstable to acid, base, and light.

Along with lucilactaene (**1**), we isolated a known neuronal-cell-protecting compound, NG-391 (**2**),[4] which possesses the same pentaene portion but a different γ-lactam moiety, and which is probably biosynthesized from the same intermediate as **1**.[3] These natural products **1** and **2** are close structural relatives of fusarins A and C,[5] nonmutagenic metabolites of *Fusarium moniliforme*. Though the biosynthetic pathways that lead to **1** and **2** remain unclear, the following is a plausible pathway based on the proposed biosynthetic route to fusarin C:[5] The fully elaborated polyketide reacts with homoserine aldehyde by an intramolecular Knoevenagel reaction to form the unmodified 1,5-dihydropyrrol-2-one **3**, a possible common key intermediate of **1** and **2**, after cleavage of the thioester (NADPH reduction) and condensation (Scheme 1). In the case of NG-391 (**2**), the remaining steps are epoxidation and oxidation to form the hemiaminal, either by ether hydroxylation α to the nitrogen atom or oxidation to an imine and addition of water (the

[*] J. Yamaguchi, T. Uno, Dr. M. Shoji, Prof. Dr. Y. Hayashi
Department of Industrial Chemistry
Faculty of Engineering, Tokyo University of Science
Kagurazaka, Shinjuku-ku, Tokyo 162-8601 (Japan)
Fax: (+81) 3-5261-4631
E-mail: hayashi@ci.kagu.tus.ac.jp
Dr. H. Kakeya, Prof. Dr. H. Osada
Antibiotics Laboratory, Discovery Research Institute
RIKEN, 2-1 Hirosawa, Wako, Saitama 351-0198 (Japan)

[**] This work was partially supported by a Grand-in-Aid for Scientific Research on Priority Areas (A): "Creation of Biologically Functional Molecules", from the Ministry of Education, Culture, Sports, Science, and Technology of Japan. We are indebted to a referee for a useful suggestion concerning the mechanism of racemization of **1**.

Supporting information for this article is available on the WWW under http://www.angewandte.org or from the author.

  DOI: 10.1002/anie.200500060

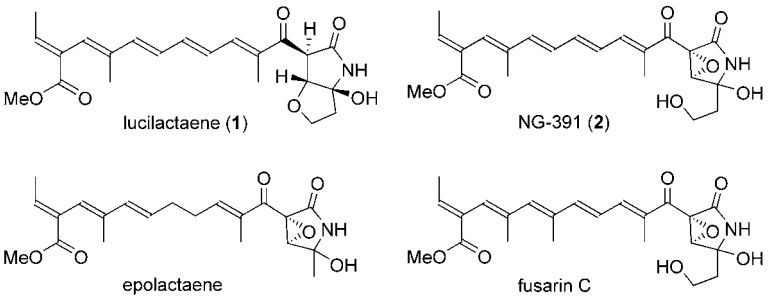

reactions might occur in the reverse order). In the case of lucilactaene (**1**), an intramolecular Michael reaction and oxidation to form the hemiaminal are the remaining reactions (again the order of reactions might be reversed). Another possibility for the biosynthesis of **1** is via **2** through intramolecular epoxide-ring opening by the primary hydroxy group, followed by reduction.

A similar side chain is also found in epolactaene, a neuritogenic compound isolated from the fungal strain *Penicillium* sp. BM-1689-P.[6] Clarification of the structure–activity relationships of lucilactaene (**1**), NG-391 (**2**), epolactaene, and their derivatives is highly desirable for elucidating their mechanism of action. We completed the first total syntheses of **2**[7] and epolactaene,[8] and developed a biologically more potent molecule, epolactaene tertiary butyl ester (ETB).[9] Recently, we revealed that both epolactaene and ETB bind to human Hsp60 and inhibit Hsp60 chaperon activity in vitro and in cultured cells,[9] whereas Kobayashi and co-workers reported that epolactaene is an inhibitor of mammalian topoisomerases α and β in vitro.[10]

The absolute configuration of NG-391 (**2**) was determined by us by asymmetric total synthesis.[7] The optical rotation of lucilactaene (**1**) is zero in two different solvents (methanol and chloroform), which indicates the possibility that **1** is racemic. That **1** should be racemic appears strange when one considers its structural resemblance with **2**. Because of the interesting biological properties of **1**, its lability, and its rare structure, and because of the puzzle concerning its absolute configuration, we have investigated its asymmetric total synthesis by a biomimetic route.

On the basis of the proposed biosynthetic pathway, we planned to synthesize **1** from the key intermediate **4**, which corresponds to the key biosynthetic intermediate **3**. We had already synthesized **2** from **4**.[7] The remaining steps from **4** to lucilactaene (**1**) would be hydrolysis of the nitrile group, an intramolecular Michael reaction with the hydroxy group (R′ = H) as the nucleophile, and functional-group transformations (Scheme 2). However, all attempts, including changing of the order in which the reactions were carried out, were unsuccessful.

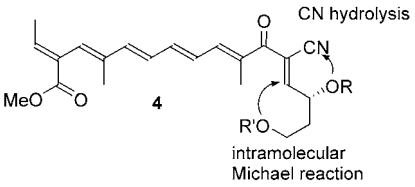

Scheme 2. Proposed synthetic approach to lucilactaene from **4**.

We therefore considered an approach to **1** from NG-391 (**2**)[7] (Scheme 3). The formation of methyl ether **6**, followed by reductive removal of the epoxide to give an alkene **5**, an intramolecular Michael reaction, and deprotection would afford lucilactaene (**1**). For this approach to be successful the reactions would have to proceed under mild conditions to avoid decomposition of the labile pentaene moiety. Methyl ether formation and the Michael reaction must proceed with

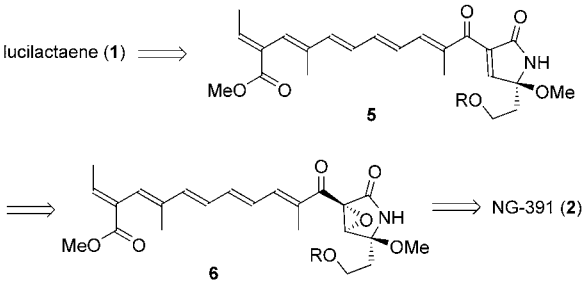

Scheme 3. Retrosynthetic analysis of lucilactaene.

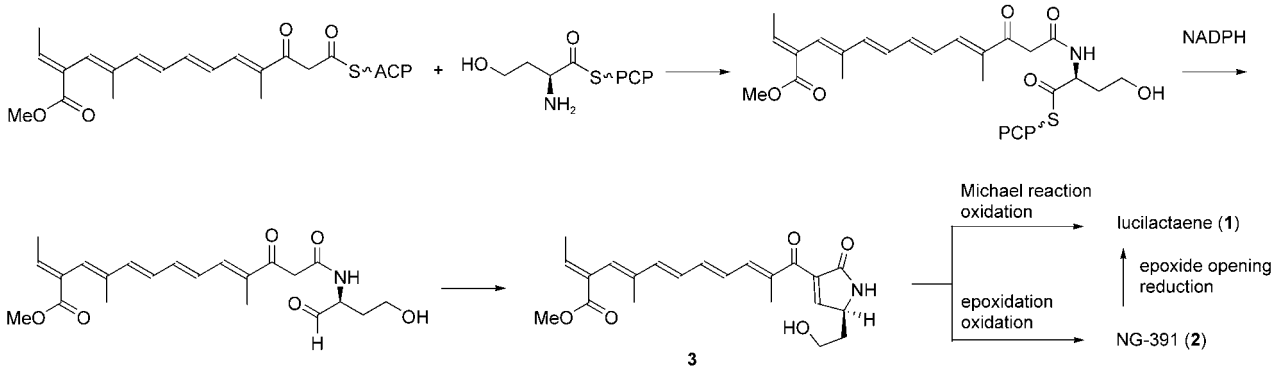

Scheme 1. Proposed biosynthesis of lucilactaene (**1**) and NG-391 (**2**). ACP = acyl carrier protein, NADPH = nicotinamide adenine dinucleotide phosphate, PCP = peptidyl carrier protein.

high diastereoselectivity for **1** to be generated with high enantiomeric excess.

The methyl ether was formed stereoselectively by the treatment of **2** with a catalytic amount of $TsOH{\cdot}H_2O$ in MeOH to afford β-methoxide **7** as a single isomer in which methanol had captured the acyliminium ion intermediate from the opposite face to that occupied by the epoxide (Scheme 4).[11] The next planned transformation was the reductive removal of the epoxide. Although SmI_2 is known to convert α,β-epoxyketones into α,β-unsaturated ketones,[12] in this case reductive demethoxylation is faster than epoxide removal. When epoxylactam **7** was treated with SmI_2, a 5-(2-hydroxyethyl)-2-pyrrolidone derivative was formed. After some experimentation, it was found that the protecting group on the nitrogen atom of the amide affects the reactivity of the compound towards reductive demethoxylation. Thus, **7** was treated with Boc_2O in the presence of triethylamine and a catalytic amount of DMAP to give the bis-Boc-protected derivative **8** in 69% yield over two steps. The reductive removal of the epoxide with SmI_2 (2 equiv) now proceeded efficiently at low temperature without affecting the methoxy group to afford **9** in 75% yield. The two Boc protecting groups were then removed by treatment with CF_3CO_2H (TFA) in CH_2Cl_2 at room temperature, whereupon a spontaneous Michael reaction and the conversion of the methyl ether into a hydroxy group gave lucilactaene (**1**) in 28% yield, along with lucilactaene methyl ether (**10**) in 55% yield. Synthetic **1** exhibited identical spectroscopic properties to those of the natural product (^1H NMR, ^{13}C NMR, IR).

The optical rotation of this synthetic lucilactaene (**1**) was zero, identical to that of the isolated natural product and markedly different to that of **10** ($[\alpha]_D$ +36.6 ($c = 0.17$, MeOH)). Lucilactaene methyl ether (**10**) can also be converted into **1** in 60% yield by treatment with TFA in CH_2Cl_2; again the optical rotation of the product is zero. The large difference in optical rotation between **1** and its methyl ether **10** strongly suggests that the lucilactaene (**1**) formed is racemic. If racemization occurs during the synthesis, it must be during the final treatment with acid. To better understand the facile racemization of **1**, the synthesis of optically pure **1** was investigated.

To avoid possible racemization, the final cleavage of the hemiaminal protecting group should be conducted under neutral conditions. To this end we developed a novel deprotection method. When NG-391 (**2**) was treated with $PhSeCH_2CH_2OH$[13] in the presence of a catalytic amount of $TsOH{\cdot}H_2O$ in CH_2Cl_2 for 3 h at room temperature, phenylselenylethyl ether **11** was formed in 31% yield as a single isomer; **2** was recovered in 67% yield (Scheme 5). Although decomposition occurred upon longer treatment of **2** with acid, the repeated exposure of recovered **2** to acid led to its conversion into **11** in a high overall yield of 94%. Both the amide and the hydroxy groups were protected with Boc_2O to afford **12** in 73% yield. The sequence of steps involving reductive removal of the epoxide with SmI_2, removal of the Boc groups, and the Michael reaction proceeded as efficiently as for the methyl ether derivative **8** to afford the bicyclic compound **14** as a single isomer in 36% yield over two steps. The transformation of the 2-phenylselenylethoxy group into a hydroxy group could be carried out under mild reaction conditions in three novel steps: 1) The oxidation of the selenide to the selenoxide, which was isolated in good yield, proceeded smoothly at low temperature on treatment with dimethyldioxirane (DMD),[14] without affecting the pentaene moiety. 2) The elimination of benzeneselenenic acid occurred at 60 °C in the presence of dabco to provide vinyl ether **16**.[15] 3) Final oxidative removal of the vinyl substituent was performed under neutral conditions by the use of DMD at low temperature (−78 °C) to afford lucilactaene (**1**) in 56% yield from **15** *in optically pure form* ($[\alpha]_D$ +39.5 ($c = 0.10$, MeOH)).[16]

It is clear from the asymmetric total synthesis that isolated natural lucilactaene (**1**) is racemic. The facile racemization raises another question: There is the possibility that natural **1** is optically active but that racemization proceeds during the purification process. To investigate this possibility, it was necessary to isolate **1** under nonracemizing conditions. We

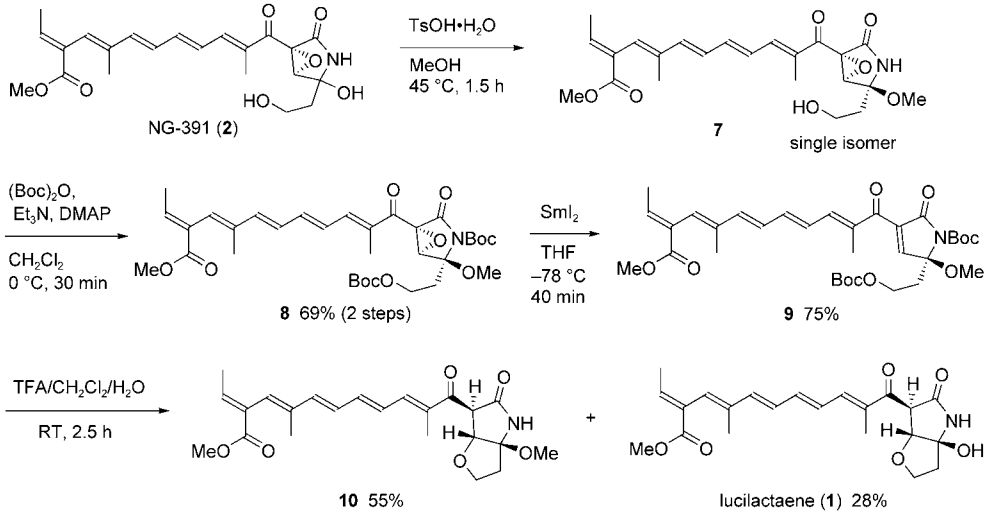

Scheme 4. Synthesis of lucilactaene. Boc = *tert*-butoxycarbonyl, DMAP = 4-dimethylaminopyridine, Ts = *p*-toluenesulfonyl.

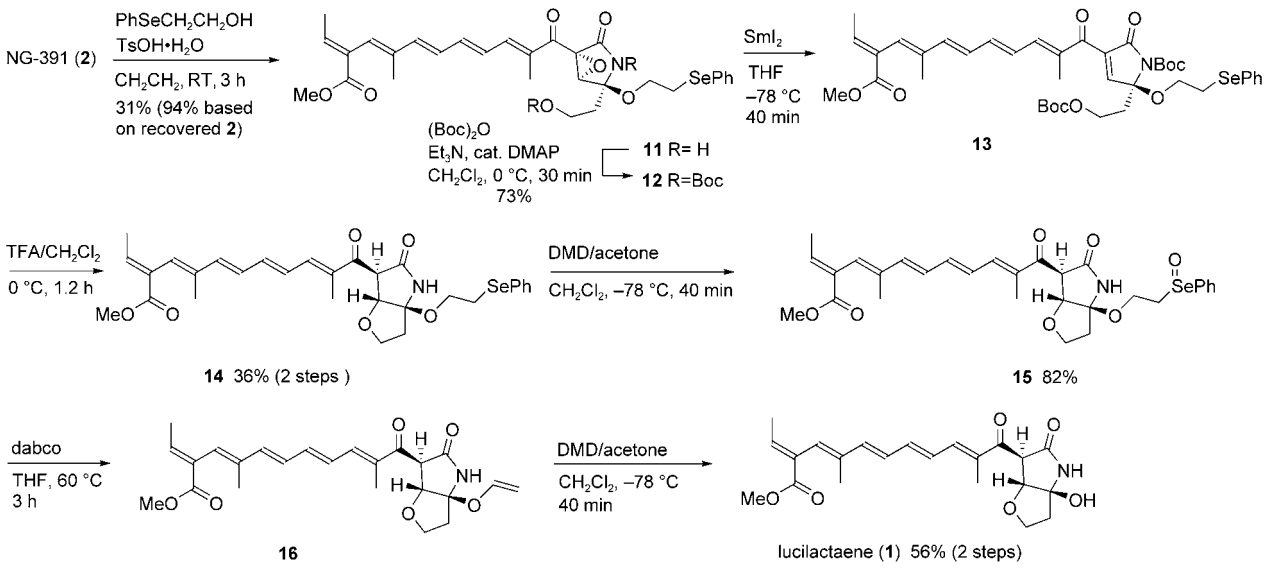

Scheme 5. Synthesis of optically pure lucilactaene; dabco = 1,4-diazabicyclo[2.2.2]octane.

chose to use bicycle **17** as a model compound to establish such conditions.

Optically pure **17**, prepared by the same method as that used for **1**, was treated with various reagents, and after a certain period of time the optical purity of the recovered **17** was measured by HPLC analysis on a chiral phase; the results are summarized in Table 1. Under weakly acidic or basic conditions, for example, in the presence of PPTS in MeOH or NEt_3 in CH_2Cl_2, no racemization was observed. However, racemization occurred when **17** was treated with TFA/CH_2Cl_2 or K_2CO_3 in MeOH. It was also confirmed that no racemization occurred in the medium in which the fermentation was carried out. These results indicate that the purification of lucilactaene (**1**) should be performed under nearly neutral, mild reaction conditions. The racemization might occur via intermediates such as **18** or **19**, which arise from a reversible retro-Michael reaction, followed by acyliminium ion formation or keto–amide formation, though the order of the reactions might be different (Scheme 6).

As information about the racemization under a variety of conditions had been obtained, the production profile of lucilactaene (**1**) by *Fusarium* sp. RK97-94 was investigated further. All experiments were performed as rapidly as possible, with the temperature and pH value controlled carefully. The ethyl acetate extracts of the broth (supernatant) and the mycelia, which were obtained by centrifugation, were prepared under mild conditions at pH 7.0. The production profile of **1** in the broth is summarized in Table 2. The optical purity of **1** in the broth was very low (ca. 10% *ee*) throughout the fermentation. Moreover, the lucilactaene (**1**) in the mycelia was also nearly racemic (data not shown).

As shown in Scheme 1, lucilactaene (**1**) and NG-391 (**2**) may be biosynthesized from the same intermediate **3**. Epoxidation and oxidation to form the hemiaminal produce **2**; these two reactions proceed in this order, as **2** would otherwise be racemic. The absolute configura-

Table 1: Racemization of the lucilactaene model **17**.

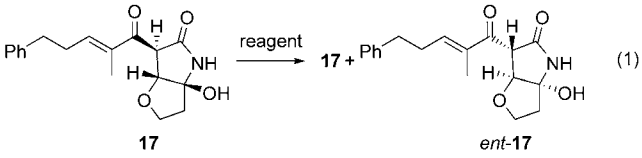

Entry	Reagent	*T* [°C]	*t* [h]	*ee* [%][a]
1	none	23	24	100
2	AcOH/CH_2Cl_2 (1:20)	23	3	100
3	PPTS in MeOH (0.005 M)	23	3	100
4	DMD in acetone (0.07 M)	−78	0.5	100
5	Et_3N/CH_2Cl_2 (1:4)	23	3	100
6	TFA/CH_2Cl_2 (1:100)	0	0.1	98
7	TFA/CH_2Cl_2 (1:20)	0	0.25	57
8	TsOH·H_2O in CH_2Cl_2 (0.013 M)	23	3	48
9	K_2CO_3 in MeOH (0.15 M)	23	3	2
10	TFA/CH_2Cl_2 (1:4)	0	2.5	0
11	culture medium[b]	28	48	100

[a] Optical purity was determined by HPLC analysis on a chiral phase (chirapak AD-H). [b] Culture medium: 2% glucose, 1% soluble starch, 0.3% meat extract, 2.5% yeast extract, 0.05% NaCl, 0.005% K_2HPO_4, 0.05% $CaCO_3$, and 0.05% $MgSO_4$·H_2O adjusted to pH 7.2. PPTS = pyridinium *p*-toluenesulfonate.

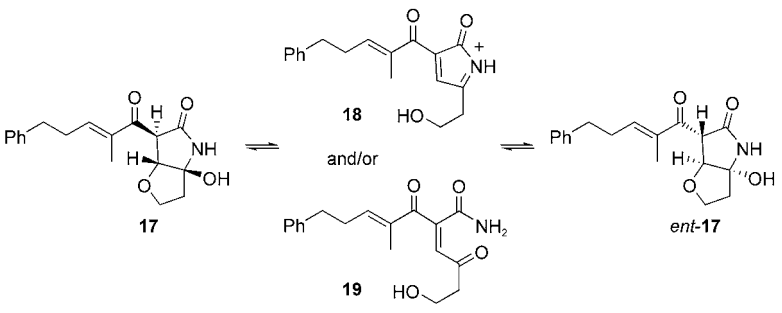

Scheme 6. Racemization of **17** via **18** and/or **19**.

Table 2: Production profile of **1** by *Fusarium sp.* RK97-94 in the broth.

Entry	*t* [h]	pH[a]	PCV[b] [%]	Production of **1** [μg mL^{-1}]	*ee* [%][c]
1	24	7.4	10	0	n.d.[d]
2	48	7.2	30	0.014	10.0
3	72	8.3	45	0.084	10.3
4	96	8.5	50	0.71	6.9

[a] pH value of the fermentation broth. [b] Packed-cell volume (*v*/*v*). [c] Optical purity was determined by HPLC analysis on a chiral phase (chiralcel OD-RH). [d] Not determined.

tion of the epoxide can also be explained reasonably as arising from the selective epoxidation from the opposite face to that with the hydroxyethyl substituent. In the synthesis of **1**, a Michael reaction and oxidation to form the hemiaminal are the remaining steps. Should the Michael reaction be the first step, then we suspect that racemization must occur during the subsequent oxidation step, because the internal Michael addition is a spontaneous reaction, as demonstrated for the synthetic conversion of **13** into **14** without racemization. That is, there is an acidic moiety in the enzyme responsible for this oxidation which causes racemization. If oxidation is the first step, a subsequent racemization process is conceivable (Scheme 7): Intermediate **3** may undergo tautomerism to a

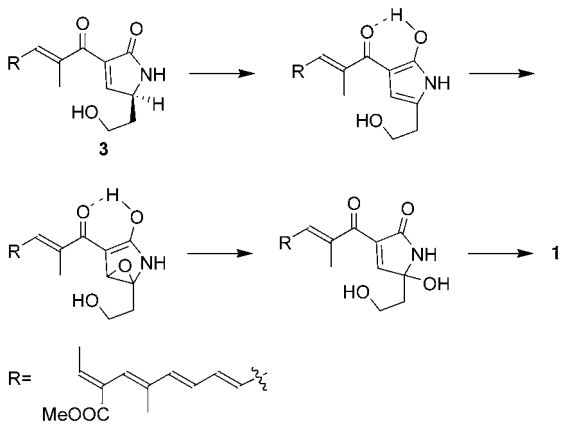

Scheme 7. Possible racemization mechanism in the biosynthesis of lucilactaene.

2-hydroxypyrrole derivative, which could undergo epoxidation and isomerization. Racemization could occur via the achiral pyrrole tautomer. A subsequent Michael reaction would then afford racemic lucilactaene (**1**).

In summary, the labile natural product lucilactaene (**1**), which readily undergoes racemization, has been synthesized for the first time in optically pure form via a biomimetic pathway. The conditions under which racemization occurs were elucidated during this total synthesis. The careful isolation of lucilactaene (**1**) from both the broth and the mycelia under neutral, nonracemizing conditions demonstrated that the isolable natural product is in fact itself racemic. This total synthesis, which enabled verification of the absolute configuration of **1**, has several noteworthy features: All the reactions from NG-391 (**2**) are mild enough not to affect the labile *E*,*E*,*E*,*E*,*E* pentaene moiety; ether formation from **2** to **7** and **11** and the intramolecular Michael reaction from **9** to **10** or from **13** to **14** are both highly stereoselective; the reductive removal of the epoxide with SmI_2 without effecting demethoxylation, and the deprotection of a hemiaminal under neutral, oxidative conditions via vinyl ether **16** by using a newly developed phenylselenylethyl protecting group, are also useful transformations. Detailed biological studies on both enantiomers of lucilactaene are underway, the results of which will be reported in due course.

Received: January 7, 2005
Published online: April 14, 2005

Keywords: asymmetric synthesis · biosynthesis · lucilactaene · racemization · total synthesis

[1] a) B. A. Forster, H. A. Coffey, M. J. Morin, F. Rastinejad, *Science* **1999**, *286*, 2507; b) B. Vogelstein, D. Lane, A. J. Levine, *Nature* **2000**, *408*, 307.
[2] a) A. J. Levine, *Cell* **1997**, *88*, 323; b) D. Hanahan, R. A. Weinberg, *Cell* **2000**, *100*, 57.
[3] H. Kakeya, S.-I. Kageyama, L. Nie, R. Onose, G. Okada, T. Beppu, C. J. Norbury, H. Osada, *J. Antibiot.* **2001**, *54*, 850.
[4] T. Sugawara, H. Shinonaga, H. Simura, R. Yoshikawa, K. Yamamoto, Jpn. Kokai Tokkyo Koho 319289, (December 3, **1996**).
[5] a) W. C. A. Gelderblom, W. F. O. Marasas, P. S. Steyn, P. G. Thiel, K. J. Merwe, P. H. Rooyen, R. Vleggaar, P. L. Wessels, *J. Chem. Soc. Chem. Commun.* **1984**, 122; b) P. S. Steyn, R. J. Vleggaar, *J. Chem. Soc. Chem. Commun.* **1985**, 1189; c) Z. Song, R. J. Cox, C. M. Lazarus, T. J. Simpson, *ChemBioChem* **2004**, *5*, 1196.
[6] H. Kakeya, I. Takahashi, G. Okada, K. Isono, H. Osada, *J. Antibiot.* **1995**, *48*, 733.
[7] Y. Hayashi, J. Yamaguchi, M. Shoji, *Tetrahedron* **2002**, *58*, 9839.
[8] a) Y. Hayashi, K. Narasaka, *Chem. Lett.* **1998**, 313; b) Y. Hayashi, J. Kanayama, J. Yamaguchi, M. Shoji, *J. Org. Chem.* **2002**, *67*, 9443; for total syntheses by other research groups, see: c) S. Marumoto, H. Kogen, S. Naruto, *J. Org. Chem.* **1998**, *63*, 2068; d) S. Marumoto, H. Kogen, S. Naruto, *Tetrahedron* **1999**, *55*, 7129; e) S. Marumoto, H. Kogen, S. Naruto, *Tetrahedron* **1999**, *55*, 7145; f) K. Kuramochi, H. Itaya, S. Nagata, K.-i. Takano, S. Kobayashi, *Tetrahedron Lett.* **1999**, *40*, 7367; g) K. Kuramochi, S. Nagata, H. Itaya, K.-i. Takano, S. Kobayashi, *Tetrahedron Lett.* **1999**, *40*, 7371; h) K. Kuramochi, S. Nagata, H. Itaya, Y. Matsubara, T. Sunoki, H. Uchiro, K.-i. Takao, S. Kobayashi, *Tetrahedron* **2003**, *59*, 9743.
[9] Y. Nagumo, H. Kakeya, J. Yamaguchi, T. Uno, M. Shoji, Y. Hayashi, H. Osada, *Bioorg. Med. Chem. Lett.* **2004**, *14*, 4425.
[10] Y. Mizushima, S. Kobayashi, K. Kuramochi, S. Nagata, F. Sugawara, K. Sakaguchi, *Biochem. Biophys. Res. Commun.* **2000**, *273*, 784; b) J. Nakai, K. Kawada, S. Nagata, K. Kuramochi, H. Uchiro, S. Kobayashi, M. Ikekita, *Biochim. Biophys. Acta* **2002**, *1581*, 1; c) K. Kuramochi, Y. Mizushima, S. Nagata, F. Sugawara, K. Sakaguchi, S. Kobayashi, *Bioorg. Med. Chem.* **2004**, *12*, 1983.
[11] The determination of the stereostructure of **7** is described in the Supporting Information.
[12] J. M. Concellon, E. Bardales, *Org. Lett.* **2002**, *4*, 189.
[13] J. E. Baldwin, R. M. Adlington, M. B. Mitchell, J. Robertson, *Tetrahedron* **1991**, *47*, 5901.
[14] A. Ishii, S. Matsubayashi, T. Takahashi, J. Nakayama, *J. Org. Chem.* **1999**, *64*, 1084.

[15] a) L. Engman, *J. Org. Chem.* **1989**, *54*, 884; b) K. Haraguchi, H. Tanaka, H. Maeda, Y. Itoh, S. Saito, T. Miyasaka, *J. Org. Chem.* **1991**, *56*, 5401; c) M. Tiecco, L. Testaferri, M. Tingoli, F. Marini, *J. Org. Chem.* **1993**, *58*, 1349, and references therein.

[16] The optical purity was determined by HPLC analysis on a chiral phase (chiralcel OD-RH column, H_2O/CH_3CN (100:45), 1.0 mL min^{-1}; t_R ((−)-**1**): 27.7 min, t_R ((+)-**1**): 40.2 min).

Arylation

One-Pot Sequential N and C Arylations: An Efficient Methodology for the Synthesis of *trans* 4-*N*,*N*-Diaryl Aminostilbenes**

*Mecheril V. Nandakumar and John G. Verkade**

N,*N*-Diaryl aminostilbenes and *N*,*N*-diaryl aminostyrenes are versatile compounds that have found exciting applications in the field of photochemistry; most of these compounds are patented and they are widely used as electro-photographic photoconductors and photoreceptors.[1] Recent reports have demonstrated, for example, that these compounds can exhibit an amino-conjugation effect in their fluorescence enhancement spectra[2] and can act as ionophores for transition metals,[3] and have several other applications.[4] The synthetic routes to these compounds begin from aniline and the corresponding aryl halides through a three-step process involving an Ullmann/Vilsmeier/Wittig[5] reaction sequence or from triphenylamine through a Vilsmeir/Wittig/palladium-catalyzed arylation sequence.[6] Recently, the synthesis of *trans* 4-*N*,*N*-diaryl aminostilbenes from the corresponding halostilbenes or aminostilbenes by palladium-catalyzed amination reactions has also been reported.[2,3]

Palladium-catalyzed cross-coupling reactions, facilitated by a variety of ligands, are exceedingly powerful and reliable methods for C–C[7] and C–heteroatom[8] bond formations and have a vast number of applications in the pharmaceutical,[9] dye,[10] agriculture,[11] and polymer[12] industries. In recent years, our studies of commercially available proazaphosphatranes,[13] such as **1**, which were first synthesized by us, have shown them to be efficient ligands in palladium-catalyzed N arylations[14] and the Suzuki[15] and Stille[16] couplings. The substrates for these coupling reactions included aryl chlorides, which encompassed electron-poor, neutral, and electron-rich examples. Moreover, proazaphosphatranes can also function as strong non-ionic stoichiometric bases that facilitate a variety of useful organic transformations.[17]

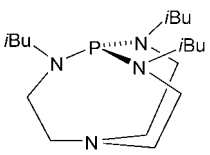

1

Herein, we report a one-pot synthesis of *trans* 4-*N*,*N*-diaryl aminostilbenes from commercially available starting materials using a double Buchwald–Hartwig amination/intermolecular Heck reaction sequence in the presence of $[Pd_2(dba)_3]$/**1** (dba = dibenzylideneacetone) as the catalytic system. Recently, transition-metal-catalyzed sequential C–C and C–heteroatom bond-forming reactions have attracted synthetic chemists because of their ability to facilitate the formation of more than one bond in a one-pot reaction. Reports of palladium-catalyzed amination/intramolecular cyclization reaction sequences for the synthesis of indole derivatives[18] illustrate the importance of such coupling reactions. A one-pot two-catalyst synthesis of 1,3-diphenylindazoles using a combination of copper-catalyzed N-arylation and palladium-catalyzed C-arylation reactions has also been reported.[19] To the best of our knowledge, a one-pot double amination/intermolecular Heck reaction sequence has not been described to date. Herein, we present the preliminary results of such a one-pot protocol.

Our studies commenced with the coupling of 4-aminostyrene with bromobenzene under the conditions given in Scheme 1. Optimization studies were carried out (Table 1),

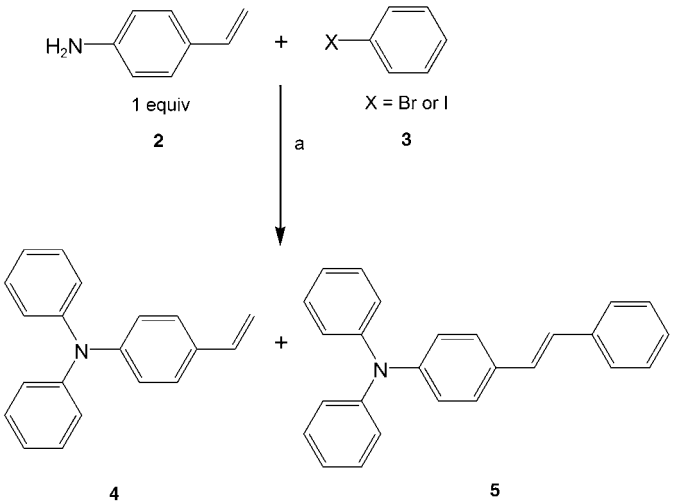

Scheme 1. a) $[Pd_2(dba)_3]$ (2 mol%), **1** (4 mol%), NaO*t*Bu (3.5 equiv), aryl halide (3.2 equiv), dry toluene (10 mL), under argon atmosphere.

and it was initially found that when the reaction was carried out at 60 °C with ligand **1** over 3 h (entry 1), the only coupling observed was a double amination (product **4**); the Heck reaction required a minimum of 110 °C for the protocol to be efficient (entry 3). When iodobenzene was used instead, the Heck reaction occurred at 100 °C (entries 7 and 8) but faster conversion was realized at 110 °C (entry 9). In addition, other phosphines, such as davephos (2-dicyclohexylphosphino-2′-(*N*,*N*-dimethylamino)biphenyl), tBu_3P, and *rac*-binap (2,2′-

[*] Dr. M. V. Nandakumar, Prof. Dr. J. G. Verkade
Department of Chemistry
Iowa State University
Ames, IA 50011-3111 (USA)
Fax: (+1) 515-294-0105
E-mail: jverkade@iastate.edu

[**] We thank the National Science Foundation for support of this work and Aldrich for research samples.

Supporting information for this article is available on the WWW under http://www.angewandte.org or from the author.

 DOI: 10.1002/anie.200462938

Table 1: Optimization of the one-pot double amination/intermolecular Heck reaction.

Entry	Aryl halide	Ligand	*t* [h]	*T* [°C]	Yield [%][a] 4	5	Total yield [%] 4+5
1		**1**	3	60	90	0	90
2			12	100	92	2	94
3			16	110	9	83	92
4		davephos	3	60	53	0	53
5			16	110	69	14	83
6		*rac*-binap	16	110	56	34	90
7		**1**	12	100	32	66	98
8			24	100	0	94 (78)[b]	94
9			16	110	0	93	93
10		tBu_3P	16	110	74	11	85
11		*rac*-binap	16	110	0	56	56
12		davephos	16	110	27	61	88

[a] Yield of isolated product. [b] Reported yield for a two-step, two-pot synthesis.[2]

bis(diphenylphosphino)-1,1′-binapthyl), were found to be inefficient ligands (entries 4–6 and 10–12).

Next, we examined the coupling of a variety of aryl bromides and iodides with 4-aminostyrene to test the generality of this methodology (Table 2). The major products formed were *trans N*,*N*-diaryl aminostilbenes **5**, except when 4-bromoanisole and 3-bromoanisole were the substrates (entries 5 and 6, respectively). The yields of **5** from 4-bromotoluene and 4-iodotoluene as the substrates (entries 1 and 9, respectively) were similar to those reported previously,[20] whereas the yields of **5** from 4-bromoanisole and 4-iodoanisole were poor (entries 5 and 8). On the other hand, the yields of **5** from 4-bromotoluene and 4-iodotoluene (entries 1 and 9) were superior to the overall yield (55%) from a three-step procedure involving an Ullmann/Vilsmeier/Wittig reaction series.[20,21] All other products derived from this reaction series have not been previously reported (entries 2–4, 6 and 7).

It is evident from the results of optimization experiments given in Table 1 that the reaction pathway to **5** is a double amination followed by an intermolecular Heck reaction. As the amination reactions were completed within 3 h at 60°C and the Heck reactions required an elevated temperature and a longer reaction time, we were able to utilize this difference in coupling activity for the one-pot synthesis of **5** with two identical aryl groups at the nitrogen atom and a different one at the opposite terminus of **5** (Scheme 2). The first step of this one-pot procedure afforded the bisamination product in three hours, as monitored by TLC. The addition of 4-bromotoluene (1.2 equiv) in the second step afforded **6a** in very good yield. Reaction of 4-aminostyrene with 4-bromoanisole and bromobenzene under the same conditions gave the analogous product **6b** in moderate yield (Scheme 2). Our yield of **6a** (86%) is comparable to that reported in a patented procedure (89%) involving the single-step reaction of 4-methyldiethylbenzylphosphonate with 4-*N*,*N*-diphenylaminobenzaldehyde.[22a] However, our yield of **6a** is substantially better than the yield achieved through a Wittig reaction of 4-methylbenzyltriphenylphosphonium chloride with the aforementioned aldehyde (72%)[22a] and the overall yield (46%) of a previously reported three-step synthesis.[22bc] Although **6b** has been reported previously, no yield was given.[1]

In a similar manner, unsymmetrically *N*-substituted diaryl aminostilbenes **7a,b** were synthesized in very good yields by using aryl iodides instead of aryl bromides

Table 2: One-pot double amination/intermolecular Heck reactions of 4-aminostyrene with aryl bromides and aryl iodides.

Entry	Aryl halide	Yield [%][a] 4	5	Total yield [%] 4+5
1	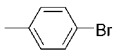	11	84	95
2	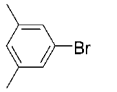	37	61	98
3	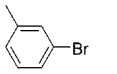	28	60	88
4	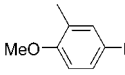	27	59	86
5	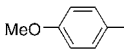	47	34	81
6	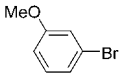	60	34	94
7	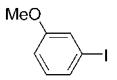	32	63	95
8	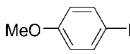	0	41	41
9	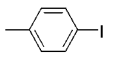	0	87 (83%)[b]	87

[a] Yield of isolated product. Reaction conditions: $[Pd_2(dba)_3]$ (2 mol%), **1** (4 mol%), NaO*t*Bu (3.5 equiv), aryl halides (3.2 equiv), dry toluene (10 mL), 110°C, 16 h, under argon atmosphere. [b] Reported yield.[20]

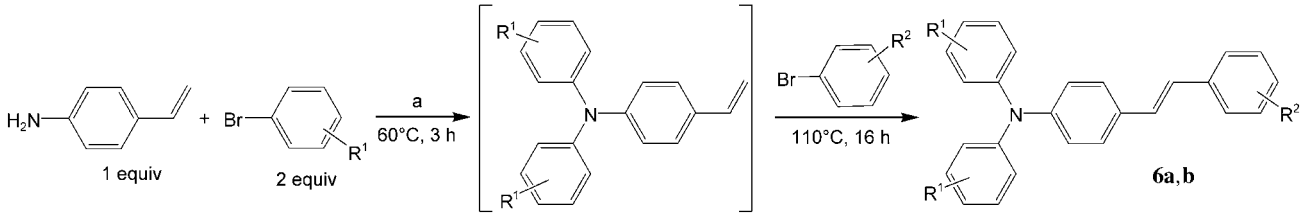

Scheme 2. a) $[Pd_2(dba)_3]$ (2 mol%), **1** (4 mol%), NaO*t*Bu (3.5 equiv), dry toluene (10 mL), in an argon atmosphere. **6a**, $R^1 = H$, $R^2 = CH_3$ (86%); **6b**, $R^1 = 4\text{-OMe}$, $R^2 = H$ (60%).

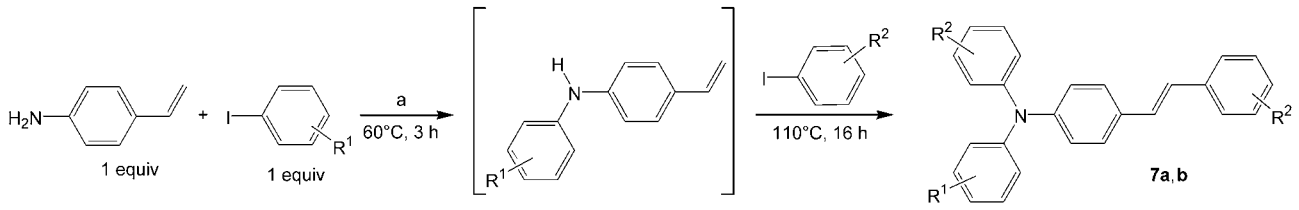

Scheme 3. a) $[Pd_2(dba)_3]$ (2 mol%), **1** (4 mol%), NaO*t*Bu (3.5 equiv), dry toluene (10 mL), in an argon atmosphere. **7a**, $R^1 = CH_3$, $R^2 = H$ (78%); **7b**, $R^1 = 4$-OMe, $R^2 = H$ (79%).

(Scheme 3). Our yield of 78% for **7a** is lower than that of a previously reported synthesis involving the reaction of 4-(*N*-(4-methylphenyl)-*N*-phenylamino)benzaldehyde and diethylbenzylphosphonate (91%).[1] It should be noted that this higher yield was achieved in a single reaction involving two reactants, one of which required prior synthesis. When this requirement is taken into consideration, the overall yield is 50%[21] compared with our yield of 78% from a one-pot procedure. Although **7b** has been reported previously, no yield was given.[1]

In summary, we have developed a novel one-pot methodology for the synthesis of *trans* 4-*N*,*N*-diaryl aminostilbenes **5**, which hitherto have always been synthesized in multipot processes. It is also of note that: 1) the same catalyst system is used for both the amination and the intermolecular Heck coupling in a loading that is quite low (2 mol% of $[Pd_2(dba)_3]$ and 4 mol% of the ligand); 2) ligand **1** is superior to others in our protocol and is commercially available; 3) selective coupling of aryl halides with the nitrogen atom and the double bond of the styrenyl substrate can be achieved in a one-pot reaction by merely adding aryl halides sequentially at different temperatures. This strategy has significant potential for the design and synthesis of many complex molecules and for combinatorial libraries in which moieties with both C–N and C–C bonds are present; 4) higher overall yields than those reported previously have been achieved; 5) the reduction in the number of steps in such syntheses permit these types of transformations to be potentially more economical and environmentally friendly. Studies are under way with heteroaryl halides and additional aryl halides (including chlorides) as reagents in the methodology reported herein and will be reported in due course.

Received: December 15, 2004
Published online: April 14, 2005

Keywords: amination · C–C coupling · cross-coupling · Heck reaction · palladium

[1] a) M. Sasaki (Ricoh Co., Japan), Ger. Offen., **1983**, *97*, Patent Application DE 83-3315437 19830428*Chem. Abstr.* **1985**, *100*, 112236; b) Y. Oda, T. Homma, F. Yoshihide, *Denshi Shashin Gakkaishi* **1990**, *29*, 250–258; c) Y. Fujimaki, H. Tadokoro, Y. Oda, H. Yoshioka, T. Homma, H. Moriguchi, K. Watanabe, A. Konishita, N. Hirose, *J. Imaging Technol.* **1991**, *17*, 202–206.

[2] J. S. Yang, S. Y. Chiou, K. L. Lia, *J. Am. Chem. Soc.* **2003**, *125*, 2518–2527.

[3] J. S. Yang, Y. H. Lin, C. S. Yang, *Org. Lett.* **2002**, *4*, 777–780.

[4] a) J. S. Yang, C. Y. Hwang, C. C. Hsich, S. Y. Chiou, *J. Org. Chem.* **2004**, *69*, 719–726; b) J. S. Yang, Y. D. Lin, F. L. Liao, *J. Org. Chem.* **2004**, *69*, 3517–3525; c) J. S. Yang, K. L. Liau, C. M. Wang, C. Y. Hwang, *J. Am. Chem. Soc.* **2003**, *125*, 12325–12335.

[5] X. D. Cao, X. Q. Zhou, Q. M. Dong, Q. He, D. Z. Liu, *Jingxi Huagong* **2003**, *20*, 452–454.

[6] a) S. Sengupta, S. K. Sadhukaran, S. Muhuri, *Tetrahedron Lett.* **2002**, *43*, 3521–3524; b) T. C. Lin, G. S. He, P. N. Prasad, L. S. Tan, *J. Mater. Chem.* **2004**, *14*, 982–991.

[7] For general references, see; a) J. Tsuji, *Palladium Reagents and Catalysis: Innovations in Organic Synthesis*, Wiley, Chichester, **1995**; b) *Handbook of Organopalladium Chemistry for Organic Synthesis* (Eds.: E.-I. Negishi, A. de Meijere), *Vols. 1 and 2*, Wiley, New York, **2002**.

[8] a) J. F. Hartwig, *Acc. Chem. Res.* **1998**, *31*, 852–860; b) J. F. Hartwig, *Angew. Chem.* **1998**, *110*, 2154–2177; *Angew. Chem. Int. Ed.* **1998**, *37*, 2046–2067; c) J. P. Wolfe, S. Wagaw, J. F. Marcoux, S. L. Buchwald, *Acc. Chem. Res.* **1998**, *31*, 805–818; d) A. R. Muci, S. L. Buchwald, *Top. Curr. Chem.* **2002**, *219*, 131–209.

[9] F. A. Beland, F. F. Kadlubar, *Handbook of Experimental Pharmacology, Carcinogenesis and Mutagenesis*, Grove, Springer, Heidelberg, **1990**.

[10] D. R. Waring, G. Hallas, *The Chemistry and Application of Dyes*, Plenum, New York, **1990**.

[11] *CRC Handbook of Pesticides* (Ed.: G. W. Milne), CRC, Boca Raton, FL, **1994**.

[12] a) T. Mukundan, *Macromol. Mater. Eng.* **2002**, *287*, 442; b) T. A. Skotheim, R. L. Elsenbaumer, J. R. Reynolds, *Handbook of Conducting Polymers*, 2nd ed., Marcel Dekker, New York, **1997**.

[13] Proazaphosphatranes, such as **1**, are commercially available from Aldrich, Strem, and Digital Specialty Chemicals.

[14] a) S. Urgaonkar, M. Nagarajan, J. G. Verkade, *J. Org. Chem.* **2003**, *68*, 452–459; b) S. Urgaonkar, M. Nagarajan, J. G. Verkade, *Org. Lett.* **2003**, *5*, 815–818.

[15] S. Urgaonkar, M. Nagarajan, J. G. Verkade, *Tetrahedron Lett.* **2002**, *43*, 8921–8924.

[16] a) W. Su, S. Urgaonkar, J. G. Verkade, *Org. Lett.* **2004**, *6*, 1421–1424; b) W. Su, S. Urgaonkar, J. G. Verkade, *J. Am. Chem. Soc.* **2004**, *126*, 16433–16439.

[17] For recent reviews, see: a) J. G. Verkade, *Top. Curr. Chem.* **2003**, *223*, 1–44; b) J. G. Verkade, P. B. Kisanga, *Aldrichimica Acta* **2004**, *37*, 3–14; c) J. G. Verkade, P. B. Kisanga, *Tetrahedron* **2003**, *59*, 7819–7853.

[18] a) S. D. Edmondson, A. Mastraechio, E. R. Parmee, *Org. Lett.* **2000**, *2*, 1109–1112; b) P. Matyus, B. U. W. Maes, Z. Riedl, G. Hajos, G. L. F. Lemiere, P. Tapolcsanyi, K. Monsieurs, O. Elias, R. A. Dommisse, G. Krajsovszky, *Synlett* **2004**, *7*, 1123–1139; c) G. Cuny, M. B. Choussy, J. Zgu, *Angew. Chem.* **2003**, *115*, 4922–4925; *Angew. Chem. Int. Ed.* **2003**, *42*, 4774–4777; d) V. Khedkar, A. Tillack, M. Michalik, M. Beller, *Tetrahedron Lett.* **2004**, *45*, 3123–3126; e) H. Siebeneicher, I. Bytschkov, S. Doye, *Angew. Chem.* **2003**, *115*, 3151–3153; *Angew. Chem. Int. Ed.* **2003**, *42*, 3042–3044; f) K. Yamazaki, Y. Nakamura, Y. Kondo, *J. Chem. Soc. Perkin Trans. 1* **2002**, 2137–2138.

[19] V. Collot, P. R. Bovy, S. Rault, *Tetrahedron Lett.* **2000**, *41*, 9053 – 9057.
[20] Y. Fujimaki, Y. Takei, Y. Suzuki, H. Nomori, Eur. Pat. Appl., **1985**, Patent No. EP0144791*Chem. Abstr.* **1985**, *103*, 132358.
[21] M. Behl, E. Hattemer, M. Brehmer, *Macromol. Chem. Phys.* **2002**, *203*, 503 – 510.
[22] a) M. Sasaki, Ger. Offen., **1984**, Patent Application. DE 3342724A1–19840530*Chem. Abstr.* **1984**, *101*, 219792; b) A. S. Gajare, K. Toyota, M. Yoshifuji, F. Ozawa, *Chem. Commun.* **2004**, *17*, 1994 – 1995; c) H. J. Lee, J. Sohn, J. Hwang, S. Y. Park, H. Choi. M. Cha, *Chem. Mater.* **2004**, *16*, 456 – 465.

Nucleic Acids

Assembly of the Complete Eight-Base Artificial Genetic Helix, xDNA, and Its Interaction with the Natural Genetic System**

*Jianmin Gao, Haibo Liu, and Eric T. Kool**

Much recent research has focused on the design of new base pairs that function in natural DNA.[1–11] Beyond this, a few recent studies have begun to explore the possibility of replacing *all* the base pairs of DNA, an approach which may eventually lead to entirely new genetic systems.[12–22] In addition to testing the limits of human-designed biological systems, such work might shed new light on the influence of base pairs on the storage and transfer of genetic information in DNA. Moreover, the resulting DNA-like molecules may be useful as experimental probes of physical interactions in enzyme active sites and at protein–DNA interfaces.

Toward these ends, a recent report described the pairing of benzo-homologated forms of adenine (xA) and thymine (xT) with natural thymine and adenine, respectively, to form a right-handed helical complex with a diameter approximately 2.4 Å larger than that of natural DNA.[12] The study revealed that in some cases these expanded DNA (xDNA) duplexes are more stable than the analogous sequence of natural DNA. Another report described the preparation and properties of the analogously expanded forms of cytosine and guanosine (xC and xG) as well.[16] All four expanded nucleobases were found to be inherently fluorescent, which makes them potentially applicable as biophysical tools.

[*] J. Gao,[+] H. Liu,[+] Prof. Dr. E. T. Kool
Department of Chemistry, Stanford University
Stanford, CA 94305-5080 (USA)
Fax: (+1) 650-725-0259
E-mail: kool@leland.stanford.edu

[+] These persons contributed equally to this work.

[**] This work was supported by the US National Institutes of Health (GM63587). J.G. and H.L. acknowledge Stanford Graduate Fellowships.

Supporting information for this article is available on the WWW under http://www.angewandte.org or from the author.

The combination of the four natural bases with their four expanded analogues—potentially yielding an eight-base artificial pairing system—has not been tested; this is of interest in part because of the large information storage and processing potential of such a molecular system.[23–28] Furthermore, the concept of interfacing the artificial xDNA genetic system with the natural one is intriguing, as the larger helices may have enhanced stability and inherent fluorescence. Targeting natural DNA or RNA sequences would require combination of the full set of four xDNA bases on one strand, which has not yet been explored. With these possibilities in mind, we describe herein the first studies of the full set of xDNA genetic building blocks.

We employed previously described methods to prepare the four xDNA deoxyribosides (Figure 1) as suitably protected phosphoramidite derivatives.[12,16,29] These were incorporated into a number of oligomeric sequences for testing helical assembly properties. Sequences contained the eight bases xC, xG, xA, xT, C, G, A, and T in various combinations (Table 1 and Supporting Information). The stability of the resulting helices was evaluated by optically monitored thermal denaturation; curve fitting and concentration studies were used to derive estimates of free energy (Supporting Information). Buffers contained Na·PIPES (10 mM, pH 7.0), Na^+ (100 mM) and Mg^{2+} (10 mM). CD spectra of putative helices (and DNA controls) were also recorded (Supporting Information).

The initial results with four different eight-base contexts revealed stable self-assembly into bimolecular complexes. Table 1 shows data for these first sequences. The thermal melting experiments revealed apparent all-or-none melting behavior and sigmoidal transitions that are similar in shape to those of the corresponding DNA control helices, but with generally higher transition temperatures (T_m) (Figure 2). The three strongest xDNA complexes gave increases in T_m (12–21 °C) as well as in estimated free energy (2.3–3.0 kcal mol^{-1} at 37 °C) relative to the native DNA helices. These three sequences include two cases in which xDNA bases were scattered on both strands, and one in which they were present on one strand only. The remaining sequence context (Figure 2d) also restricted the xDNA bases to one strand, but was further specialized, as purine and pyrimidine bases were segregated to opposite ends of each strand. Thermal stability in this case was slightly (2.9 °C) lower than that of the corresponding native DNA sequence, and the estimated free energy fell within experimental error of the control. The stoichiometry of the complexes was tested with mixing experiments in which the molar ratios of strand pairs were varied in regular increments. Plots for three of the sequence contexts are available in the Supporting Information; changes in absorbance for the fourth sequence were too small to yield reliable data. The results for the three plots gave strand stoichiometry values of 0.50:0.50, 0.45:0.55, and 0.49:0.51. Thus the data were most consistent with a double-stranded stoichiometry in all three complexes. However, as the hyper- and hypochromicity values were small, the stoichiometric assignments should be considered preliminary.

The success of the natural DNA genetic system rests not only in its ability to form double helices, but importantly, in its

  DOI: 10.1002/anie.200500069

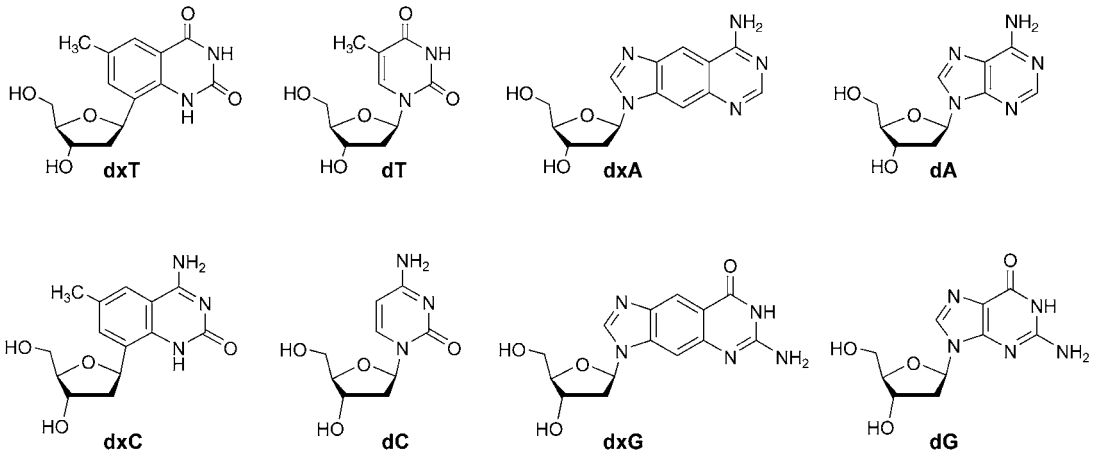

Figure 1. Structures of the eight nucleoside components of expanded DNA (xDNA).

Table 1: Thermal melting data and estimated free energies for decamer xDNA duplexes containing eight different bases.[a]

Entry	Sequence	T_m[b] [°C]	ΔG°_{37}[c] [kcal mol^{-1}]
1	5′-**A T** C A **C** T **G T** G C 3′-T A **G T** G **A** C A **C G**	59.9 ± 0.5	−12.8 ± 0.3
	5′-A T C A C T G T G C 3′-T A G T G A C A C G	44.6 ± 0.5	−10.0 ± 0.1
2	5′-**A C G T T A G T C G** 3′-T G C A A T C A G C	53.1 ± 0.5	−11.5 ± 0.2
	5′-A C G T T A G T C G 3′-T G C A A T C A G C	41.5 ± 0.5	−9.2 ± 0.1
3	5′-**T** G **T** A **C G** C **A G** T 3′-A **C** A **T** G C **G** T C **A**	63.4 ± 0.5	−11.9 ± 0.2
	5′-T G T A C G C A G T 3′-A C A T G C G T C A	40.3 ± 0.5	−8.9 ± 0.1
4	5′-**T C T T C G G A A G** 3′-A G A A G C C T T C	36.1 ± 0.5	−8.3 ± 0.1
	5′-T C T T C G G A A G 3′-A G A A G C C T T C	39.0 ± 0.5	−8.7 ± 0.1
5	5′-**A C G T T A G T C G** 3′-*U G C A A U C A G C*	47.8 ± 0.5	−9.4 ± 0.2
	5′-A C G T T A G T C G 3′-*U G C A A U C A G C*	42.6 ± 0.5	−9.5 ± 0.1
6	5′-**T C T T C G G A A G** 3′-*A G A A G C C U U C*	43.0 ± 0.5	−9.8 ± 0.2
	5′-T C T T C G G A A G 3′-*A G A A G C C U U C*	43.2 ± 0.5	−9.6 ± 0.1

[a] Benzo-homologated bases are represented in boldface; native DNA controls are shown for each sequence; entries 5 and 6: xDNA–RNA duplexes in which the RNA strand bases are italicized. Conditions: NaCl (100 mM), $MgCl_2$ (10 mM), and Na·PIPES (10 mM, pH 7.0). All DNA and xDNA sequences are 3′-phosphorylated (omitted for clarity). [b] Oligonucleotide concentration = 5.0 μM. [c] Averages of values from van't Hoff and curve-fitting methods.

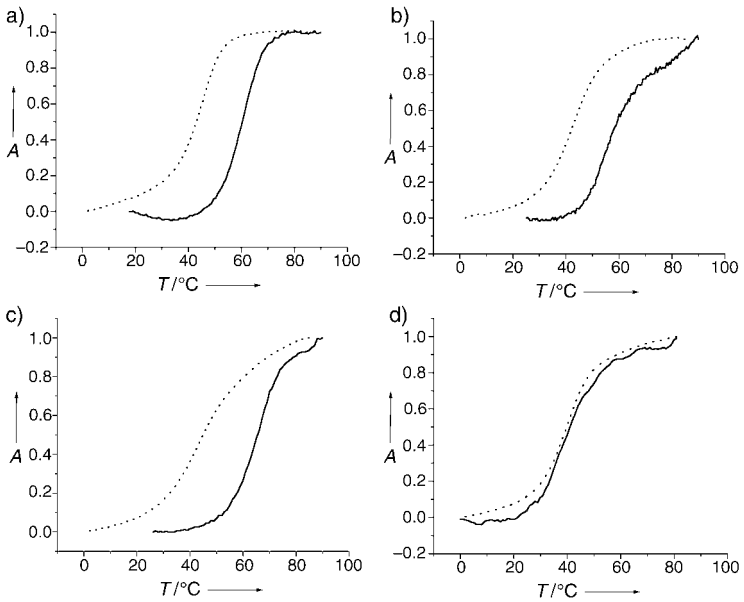

Figure 2. Normalized thermal denaturation plots for four different expanded DNA duplexes: a) d(xAxTCAxCTxGxTGCp)·d(xGxCACxAGxTxGATp) versus d(ATCACTGTGCp)·d(GCACAGTGATp); b) d(xAxCxGxTxTxAxGxTxCxGp)·d(CGACTAACGTp) versus d(ACGTTAGTCGp)·d(CGACTAACGTp); c) d(xTGxTAxCxGCxAxGTp)·d(xACTxGCGxTAxCAp) versus d(TGTACGCAGTp)·d(ACTGCGTACAp); d) d(xTxCxTxTxCxGxGxAxAxGp)·d(CTTCCGAAGAp) versus d(TCTTCGGAAGp)·d(CTTCCGAAGAp) for which the xDNA data were smoothed from five adjacent points to minimize noise from the small change in absorbance. Experimental conditions for data from both xDNA (——) and natural DNA (----): oligonucleotide (5 μM), NaCl (100 mM), $MgCl_2$ (10 mM), Na·PIPES buffer (10 mM, pH 7.0).

ability to do so with high specificity in sequence recognition. Thus it was of interest to test whether expanded-diameter xDNA helices could also exhibit sequence discrimination. This was done by evaluating the thermal stability of all possible natural-base mismatches of the four expanded bases. Figure 3 shows data from the analysis of all four matched pairs and the twelve possible mismatches. The same set of measurements were taken with native DNA as a control, so that a direct comparison of base-mismatch selectivities could

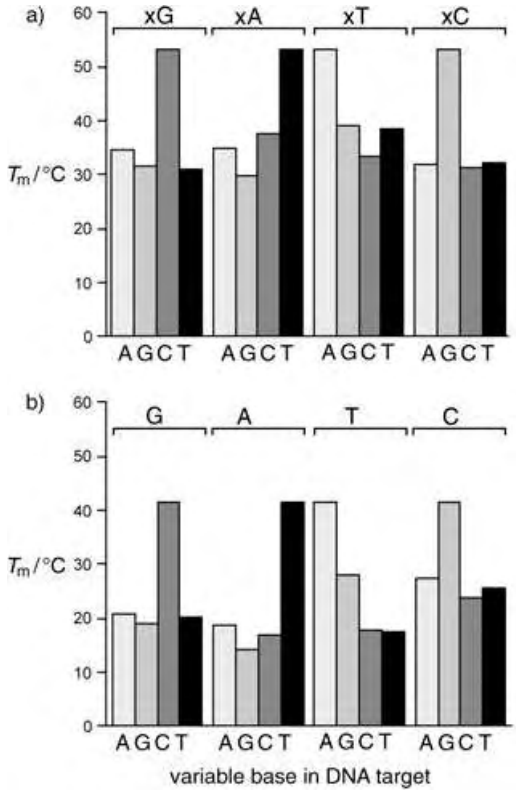

Figure 3. Histograms showing similar sequence selectivity for a) xDNA and b) native DNA of analogous sequence. Thermal melting temperatures are shown for singly mismatched and matched sequences in the context of a decamer duplex. (Details and conditions provided in Supporting Information).

be made (numerical data available in Supporting Information).

The results show that the four xDNA bases have surprisingly similar mismatch selectivity as natural DNA. Remarkably, the overall profiles of relative selectivities of xDNA had almost the same shape as those of native DNA double helices (Figure 3), which indicates that the two have similar mismatch preferences. The data show T_m values that are decreased by 13.9–23.4 °C for single xDNA mismatches, which are nearly the same as the respective decreased T_m range of 13.6–24.5 °C for mismatched bases in natural DNA. Therefore, oligonucleotide strands composed entirely of the four xDNA bases can recognize naturally structured DNA with high sequence selectivity and with high affinity.

In a search for evidence of helicity, CD was performed on all four double-stranded xDNA complexes (sequences shown in Table 1) in addition to the analogous DNA sequences as a comparison (Supporting Information). The xDNA spectra were clearly different from those of the control DNA, and also varied from sequence to sequence. Because the benzo-expanded DNA bases are electronically different from natural nucleobases, the excitonic interactions with stacked neighbors are different. However, CD spectra did reveal induced chirality in the xDNA that is consistent with helical complexes. An early structural study of a two-base xDNA system showed right-handed helicity,[17] which suggests that the present complexes also likely adopt a right-handed form. The variability in the xDNA spectra may arise from the fact that the sequences are complex: there are 64 possible nearest neighbors in this eight-base system (compared with only 16 in DNA). Thus these short xDNA sequences vary much more than native DNA in nearest-neighbor composition, which results in different electronic interactions.

Finally, full xDNA strands were tested for their ability to bind complementary RNA sequences. This was tested preliminarily in two all-xDNA strand contexts (Table 1, entries 5 and 6). Note that incorporation of the expanded bases into both strands of the duplexes was not possible, as "xRNA" nucleosides are not yet available. Representative denaturation curves for the xDNA–RNA complexes are given in the Supporting Information. The data showed clearly that both xDNA strands formed the predicted complexes with the decamer RNA target strands. In one case the xDNA–RNA complex was slightly more stable than the analogous DNA–RNA control, with an increase in T_m of 5.2 °C. In the other context, the thermal stabilities of the xDNA–RNA and DNA–RNA complexes were equal. Overall, the xDNA–RNA complexes were less stable than xDNA–DNA complexes (Table 1), which suggests that the expanded helices may prefer a B-like over an A-like helical conformation.

To our knowledge, this is the first report of a new genetic form that encodes as many as eight fundamental units of information. Previous studies from other research groups have focused on new hydrogen-bonded base pairs that are designed to function within the context of the natural genetic system.[1,5] Such artificial pairs, of which isoC–isoG and kappa–pi are examples, have been shown to pair selectively in naturally structured oligonucleotides.[30] Recent experiments with DNA polymerases have shown that such pairs may be replicated with sufficient selectivity to function properly in PCR amplifications.[31] The work reported herein is distinct from that precedent in two primary ways: first, all the current size-expanded base pairs adopt a structure that differs from the natural purine–pyrimidine base-pair structure, and second, the system presented herein is designed in its entirety, whereas the previous systems were meant to function in the natural context.

The current experiments illustrate a way for the xDNA artificial genetic system to interface with the natural biological genetic system. In the design of xDNA, the large base homologs can either be distributed among both strands (to yield the eight-base system described above), or they can be segregated into one of the two strands. In the latter scenario, the non-expanded strand is composed of natural DNA or RNA. The present results have confirmed for the first time that xDNA can recognize natural DNA and RNA in a sequence-dependent manner.

Finally, the eight-base xDNA design may lend itself to the storage and transfer of high-density information. Recent experiments have shown that natural DNA can be useful in encoding structural and computational information in designed nanostructures, computing systems, and machines.[23–28,32–39] The sequence complexity of natural DNA scales with 4^n, in which n = sequence length, whereas that of xDNA scales with 8^n. Thus the information density of xDNA is 2^n greater; for example, there are 262144 possible

hexamer sequences of xDNA, and only 4096 hexamer sequences of DNA. This high information density may be useful for data encryption and processing,[23–28] and in assembled structural designs of greater complexity than can be generated with DNA.

Experimental Section

The deoxynucleoside phosphoramidite derivatives of the four benzo-homologated nucleosides were prepared as described previously.[16,29] For synthesis of oligomers, the eight nucleosides described herein (Figure 1) were incorporated into oligonucleotides with automated solid-phase methods. All xDNA and DNA control sequences contained a 3′ phosphate group to avoid the need for eight different support resins, and were prepared with a "3′-phosphate-ON" controlled-pore glass support (Glen Research). Oligonucleotides were synthesized on an Applied Biosystems 392 DNA/RNA synthesizer in the trityl-off mode with standard β-cyanoethylphosphoramidite chemistry. Prolonged coupling times were used, which gave average stepwise yields of $>93\%$ by trityl monitoring. After synthesis, oligonucleotides were deprotected and removed from solid supports in the conventional manner. Oligomer products were purified by HPLC and quantified by UV/Vis absorption. Molar extinction coefficients were calculated by the nearest-neighbor method,[40] and those for oligonucleotides containing artificial residues were calculated by adding the extinction coefficient of the artificial nucleoside to the that of the core duplex. Previous reports have confirmed that the four modified xDNA nucleotides can be incorporated intact into oligonucleotides.[12,14,16] To confirm this for our work, we characterized two sequences by MALDI-TOF mass spectrometry: one with all four modified bases and the other with all eight bases, and the expected masses were observed. RNA oligonucleotides were purchased from Dharmacon. They were deprotected according to the manufacturer's protocol, then purified with denaturing preparative gel electrophoresis.

Thermal denaturation studies were conducted with sample concentrations that ranged between 1 and 40 μM in volumes of 1 mL in NaCl (100 mM), $MgCl_2$ (10 mM), and Na·PIPES (10 mM, pH 7.0). Solutions were then heated at 90 °C for 5 min and annealed by slow cooling to room temperature and then to 0 °C. Melting studies were carried out in teflon-capped quartz cells (path length = 1 cm) under N_2 atmosphere on a UV/Vis spectrophotometer (Varian Cary 1) equipped with a Peltier temperature controller. Absorbance was monitored at $\lambda = 320$ nm (xDNA) or $\lambda = 260$ nm (control DNA) during a temperature increase from 5 to 90 °C at a rate of 0.5 °C min^{-1}.

Melting temperatures (T_m) were determined by computer fit (Meltwin 3.5) of the first derivative of absorbance with respect to $1/T$. Uncertainty of T_m is estimated at ± 0.5 °C based on repetitions of experiments. Free energy values were estimated with two methods: 1) computer-fitting denaturation data with an algorithm that employs linear sloping baselines by using the two-state approximation for melting, and 2) van't Hoff thermodynamic parameters derived from linear plots of $1/T_m$ as a function of $\ln(C_T)$ by measuring T_m at varied concentrations (C_T = total DNA concentration). Values shown are averages from these two methods. They should be considered preliminary estimates only, as they rely on the assumption of a constant heat capacity (Cp) value,[41] which is not known to be the case for xDNA.

Received: January 7, 2005
Published online: April 18, 2005

Keywords: benzopurines · benzopyrimidines · DNA structures · nucleic acids · structure–activity relationships

[1] S. A. Benner, T. R. Battersby, B. Eschgfaller, D. Hutter, J. T. Kodra, S. Lutz, T. D. K. Baschlin, M. Blattler, M. Egli, C. Hammer, H. A. Held, J. Horlacher, Z. Huang, B. Hyrup, T. F. Jenny, S. C. Jurczyk, M. Konig, U. von Krosigk, M. J. Lutz, L. J. MacPherson, S. E. Moroney, E. Muller, K. P. Nambiar, J. A. Piccirilli, C. Y. Switzer, J. J. Vogel, C. Richert, A. L. Roughton, J. Schmidt, K. C. Schneider, J. Stackhouse, *Pure Appl. Chem.* **1998**, *70*, 263–266.
[2] E. T. Kool, *Acc. Chem. Res.* **2002**, *35*, 936–943.
[3] A. A. Henry, F. E. Romesberg, *Curr. Opin. Chem. Biol.* **2003**, *7*, 727–733.
[4] T. Mitsui, A. Kitamura, M. Kimoto, T. To, A. Sato, I. Hirao, S. Yokoyama, *J. Am. Chem. Soc.* **2003**, *125*, 5298–5307.
[5] H. P. Rappaport, *Nucleic Acids Res.* **1988**, *16*, 7253–7267.
[6] S. Atwell, E. Meggers, G. Spraggon, P. G. Schultz, *J. Am. Chem. Soc.* **2001**, *123*, 12364–12367.
[7] K. Tanaka, Y. Yamada, M. Shionoya, *J. Am. Chem. Soc.* **2002**, *124*, 8802–8803.
[8] H. Weizman, Y. Tor, *J. Am. Chem. Soc.* **2001**, *123*, 3375–3376.
[9] C. Brotschi, C. J. Leumann, *Angew. Chem.* **2003**, *115*, 1694–1697; *Angew. Chem. Int. Ed.* **2003**, *42*, 1655–1658.
[10] J. Parsch, J. W. Engels, *Nucleosides Nucleotides Nucleic Acids* **2001**, *20*, 815–818.
[11] G. Mathis, J. Hunziker, *Angew. Chem.* **2002**, *114*, 3335–3338; *Angew. Chem. Int. Ed.* **2002**, *41*, 3203–3205.
[12] H. Liu, J. Gao, S. R. Lynch, Y. D. Saito, L. Maynard, E. T. Kool, *Science* **2003**, *302*, 868–871.
[13] N. Minakawa, N. Kojima, S. Hikishima, T. Sasaki, A. Kiyosue, N. Atsumi, Y. Ueno, A. Matsuda, *J. Am. Chem. Soc.* **2003**, *125*, 9970–9982.
[14] N. J. Leonard, *Acc. Chem. Res.* **1982**, *15*, 128–135.
[15] H. Liu, J. Gao, E. T. Kool, *J. Am. Chem. Soc.* **2005**, *127*, 1396–1402.
[16] H. Liu, J. Gao, E. T. Kool, *J. Org. Chem.* **2005**, *70*, 639–647.
[17] H. Lu, K. He, E. T. Kool, *Angew. Chem.* **2004**, *116*, 5958–5960; *Angew. Chem. Int. Ed.* **2004**, *43*, 5834–5836.
[18] A. H. F. Lee, E. T. Kool, *J. Org. Chem.* **2005**, *70*, 132–140.
[19] H. Liu, S. R. Lynch, E. T. Kool, *J. Am. Chem. Soc.* **2004**, *126*, 6900–6905.
[20] K. Tanaka, A. Tengeiji, T. Kato, N. Toyama, M. Shionoya, *Science* **2003**, *299*, 1212–1213.
[21] F. Seela, A. Melenewski, C. Wei, *Bioorg. Med. Chem. Lett.* **1997**, *7*, 2173–2176.
[22] K. Groebke, J. Hunziker, W. Fraser, L. Peng, U. Diederichsen, K. Zimmermann, A. Holzner, C. Leumann, A. Eschenmoser, *Helv. Chim. Acta* **1998**, *81*, 375–474.
[23] L. M. Adleman, *Science* **1994**, *266*, 1021–1024.
[24] B. Shimanovsky, J. Feng, M. Potkonjak, *Inform. Hiding Lect. Notes Comput. Sci.* **2003**, *2578*, 373–386.
[25] X. P. Su, L. M. Smith, *Nucleic Acids Res.* **2004**, *32*, 3115–3123.
[26] A. Okamoto, K. Tanaka, I. Saito, *J. Am. Chem. Soc.* **2004**, *126*, 9458–9463.
[27] L. Gao, X. Yang, W. B. Liu, J. Xu, *Prog. Nat. Sci.* **2004**, *14*, 705–709.
[28] K. A. Schmidt, C. V. Henkel, G. Rozenberg, H. P. Spaink, *Nucleic Acids Res.* **2004**, *32*, 4962–4968.
[29] H. Liu, J. Gao, L. Maynard, Y. D. Saito, E. T. Kool, *J. Am. Chem. Soc.* **2004**, *126*, 1102–1109.
[30] C. R. Geyer, T. R. Battersby, S. A. Benner, *Structure* **2003**, *11*, 1485–1498.
[31] A. M. Sismour, S. Lutz, J. H. Park, M. J. Lutz, P. L. Boyer, S. H. Hughes, S. A. Benner, *Nucleic Acids Res.* **2004**, *32*, 728–735.
[32] D. S. Liu, S. Balasubramanian, *Angew. Chem.* **2003**, *115*, 5912–5914; *Angew. Chem. Int. Ed.* **2003**, *42*, 5734–5736.

[33] P. Yin, H. Yan, X. G. Daniell, A. J. Turberfield, J. H. Reif, *Angew. Chem.* **2004**, *116*, 5014 – 5019; *Angew. Chem. Int. Ed.* **2004**, *43*, 4906 – 4911.
[34] T. Ye, C. D. Mao, *J. Am. Chem. Soc.* **2004**, *126*, 11410 – 11411.
[35] W. B. Sherman, N. C. Seeman, *Nano Lett.* **2004**, *4*, 1203 – 1207.
[36] W. U. Dittmer, A. Reuter, F. C. Simmel, *Angew. Chem.* **2004**, *116*, 3634 – 3637; *Angew. Chem. Int. Ed.* **2004**, *43*, 3550 – 3553.
[37] Y. Chen, C. D. Mao, *J. Am. Chem. Soc.* **2004**, *126*, 8626 – 8627.
[38] Y. Chen, M. S. Wang, C. D. Mao, *Angew. Chem.* **2004**, *116*, 3638 – 3641; *Angew. Chem. Int. Ed.* **2004**, *43*, 3554 – 3557.
[39] Y. Chen, S. H. Lee, C. Mao, *Angew. Chem.* **2004**, *116*, 5449 – 5452; *Angew. Chem. Int. Ed.* **2004**, *43*, 5335 – 5338.
[40] M. J. Cavaluzzi, P. N. Borer, *Nucleic Acids Res.* **2004**, *32*, e13.
[41] A. Tikhomirova, N. Taulier, T. V. Chalikian, *J. Am. Chem. Soc.* **2004**, *126*, 16387 – 16394.

Cluster Compounds

Polyhedral Vanadium Oxide Cages: Infrared Spectra of Cluster Anions and Size-Induced d Electron Localization**

Knut R. Asmis, Gabriele Santambrogio, Mathias Brümmer, and Joachim Sauer**

The size-dependent properties of transition metal oxide clusters have been intensely studied not only because of interest in this peculiar state of matter, but also because of their relevance as building blocks for nanostructured materials. Vanadium oxides, in particular, are important in supported catalysts,[1] as cathode materials in lithium batteries,[2] in bolometric detectors,[3] and as ferromagnetic nanotubes.[4] While the structural characterization of vanadium oxide clusters deposited on surfaces[5] has reached atomic resolution, it remains a major experimental challenge in the gas phase.[6] Infrared photodissociation[7] paired with quantum chemistry is currently the most generally applicable approach for cluster ions even though it requires intense and tunable infrared radiation sources. Below 2000 cm^{-1}, in the fingerprint region of metal oxide clusters, only free-electron lasers meet these demands.[8]

Herein we report the first experimental infrared spectra of transition metal oxide cluster anions in the gas phase. We combine infrared multiple photon dissociation (IRMPD) spectroscopy with density functional theory (DFT) to characterize the geometric and electronic structures of a representative series of vanadium oxide cluster anions, $(V_2O_5)_n^-$ ($n = 2$, 3, or 4).[9] Compelling evidence is produced that these anions have the polyhedral cage structures that have been predicted before, but have eluded spectroscopic detection until now.[10,11] Evidence is also found for a size-induced localization of the extra electron in this series of anions.

The IRMPD spectra of mass-selected $V_4O_{10}^-$, $V_6O_{15}^-$, and $V_8O_{20}^-$ are shown on the left in Figure 1. They were measured by irradiating vibrationally cold, mass-selected parent ions with intense, tunable IR radiation from the free-electron laser FELIX[12] and monitoring the mass-selected fragment ion yield as a function of laser wavelength. Only when the radiation is resonant with a fundamental vibrational transition can the cluster ions absorb photons, thereby initiating a sequential multiphoton absorption process[13] which leads to heating of the cluster ion and eventually to photodissociation. The simplicity of the $V_4O_{10}^-$ spectrum is striking and immediately suggests a structure of higher symmetry with degenerate transitions. The dominant feature is a single, rather narrow intense band at 990 cm^{-1}. Based on our previous measurements on vanadium oxide cluster cations it is assigned to a vanadyl stretching mode.[14] The weaker signal below 750 cm^{-1} is attributed to a V–O–V stretch. The IRMPD spectrum of $V_8O_{20}^-$ is markedly different. While the vanadyl band stays nearly unchanged, a new band, much broader and roughly four times stronger than the vanadyl band, is observed centered at 870 cm^{-1}. The appearance of the $V_6O_{15}^-$ spectrum is intermediate between the spectra described above. An intense vanadyl band, somewhat broader and red-shifted, is followed by a four times less intense band at 830 cm^{-1}. No signal is observed below 700 cm^{-1} for the two larger clusters.

To understand these vibrational spectra we performed DFT calculations (B3LYP functional[15,16]) of cluster geometries and vibrational spectra (see Figure 1). All three anions are open-shell systems with a single unpaired electron. For $V_4O_{10}^-$ we find a tetragonal D_{2d} structure (**1**) which is minimally Jahn–Teller distorted from the T_d structure. Each vanadium atom is fourfold coordinated, forming one short V=O bond (159 pm) and three V–O bonds (181 pm). The four symmetry-equivalent vanadyl bond stretches combine to give three IR-active b_2 and e modes, which are quasi-degenerate and explain the single intense vanadyl band in the IRMPD spectrum. The six symmetric V–O–V bond stretches also give rise to three IR-active e and b_2 modes (629 and 609 cm^{-1}, respectively), and they have a cumulative oscillator strength that is about 1/3 that of the vanadyl bands, in good agreement with experiment. The modes resulting from the six antisym-

[*] Dr. K. R. Asmis
Fritz-Haber-Institut der Max-Planck-Gesellschaft
Faradayweg 4–6, 14195 Berlin (Germany)
Fax: (+49) 308-413-5603
E-mail: asmis@fhi-berlin.mpg.de
Prof. Dr. J. Sauer
Institut für Chemie, Humboldt-Universität Berlin
Unter den Linden 6, 10099 Berlin (Germany)
Fax: (+49) 302-093-7136
E-mail: js@chemie.hu-berlin.de
Dipl.-Phys. G. Santambrogio, Dipl.-Ing. M. Brümmer
Institut für Experimentalphysik, Freie Universität Berlin
Arnimallee 14, 14195 Berlin (Germany)

[**] This work was supported by the German Research Foundation (DFG) as part of the Collaborative Research Center 546. We gratefully acknowledge the support of the "Stichting voor Fundamenteel Onderzoek der Materie (FOM)" in providing the required beam time on FELIX and highly appreciate the skilful assistance of the FELIX staff. We thank L. Wöste and G. Meijer for their continuous support and A. Fielicke for helpful discussions.

Supporting information for this article is available on the WWW under http://www.angewandte.org or from the author.

  DOI: 10.1002/anie.200462894

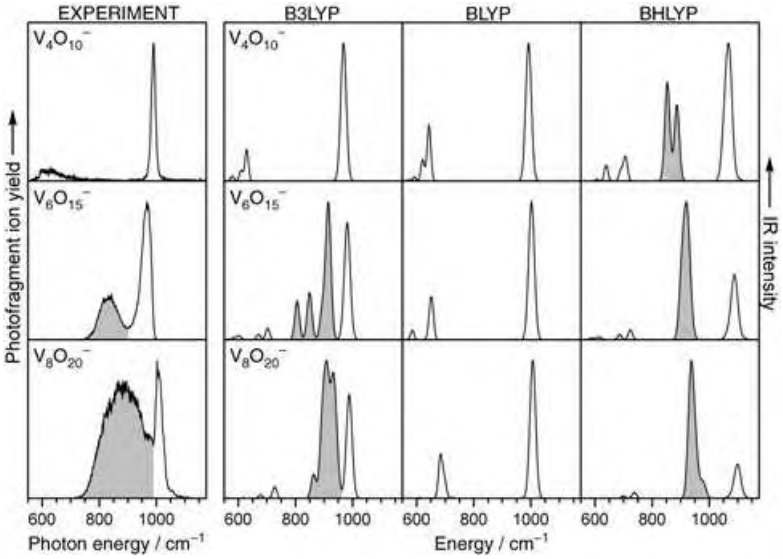

Figure 1. Experimental and simulated vibrational spectra of vanadium oxide cluster anions in the region of the V–O and V=O bond stretch modes. IRMPD spectra (left) of $V_4O_{10}^-$, $V_6O_{15}^-$, and $V_8O_{20}^-$ were measured from 550 to 1175 cm^{-1} by monitoring the dominant fragmentation channel, which leads to the formation of $V_3O_8^-$, $V_4O_{10}^-$, and $V_4O_{10}^-$, respectively. Simulated spectra (right) were obtained from scaled harmonic frequencies and oscillator strengths employing the B3LYP, BLYP, and BHLYP functionals. The calculated stick spectra were convoluted for better comparison with the experiment. Gray shaded peaks indicate localization of the unpaired d electron (see text).

metric V–O–V bond stretches are below 600 cm^{-1} and have vanishingly low intensities.

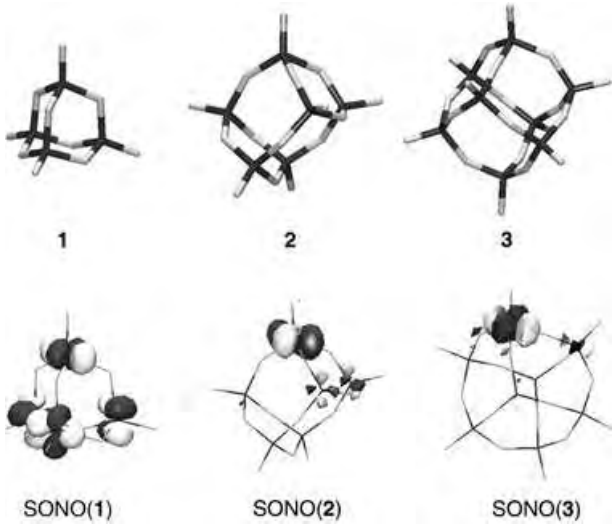

In $V_4O_{10}^-$ the unpaired electron is completely delocalized over d-states of all four vanadium sites, as illustrated by its singly-occupied natural orbital SONO(**1**). In contrast, in the larger anions the unpaired electron is localized at a single vanadium site, which lowers the symmetry of their structures to C_s. For $V_6O_{15}^-$ and $V_8O_{20}^-$ we find the distorted trigonal prism and cube structures **2** and **3**. Their singly occupied natural orbitals, SONO(**2**) and SONO(**3**), reflect the localization of the unpaired electron. Compared to $V_4O_{10}^-$, the average V–O(–V) bond distances in $V_8O_{20}^-$ are longer at the electron localization site (189 pm), but shorter at the other sites (177–178 pm), while the V=O bond distances are similar and not affected by the localization. Unlike the closed-shell neutral parent compounds, the D_{3h} structure (trigonal prism) of $V_6O_{15}^-$ and the D_{2d} structure (cube) of $V_8O_{20}^-$ are higher-order saddle points that are 45 and 21 kJ mol^{-1}, respectively, above the ground state. For both $V_6O_{15}^-$ and $V_8O_{20}^-$ first-order saddle points with C_{2v} symmetry are found 9.8 and 8.7 kJ mol^{-1}, respectively, above the ground state. They represent transition structures for the interconversion of two equivalent C_s-minimum structures and have the additional electron delocalized over two sites.

The effects of symmetry breaking are directly observed in the vibrational spectra of these species (indicated by the gray-shaded area in Figure 1). Upon localization of the unpaired electron intense V–O–V stretch transitions appear at around 100–200 cm^{-1} below the strong vanadyl band, which replace the weak V–O–V feature more than 350 cm^{-1} below the vanadyl band in the spectrum of the delocalized case ($V_4O_{10}^-$). The calculated ratio of the cumulative oscillator strengths of the V–O–V modes and the V=O modes is 3.3 for $V_8O_{20}^-$ and 0.3 for $V_4O_{10}^-$; these values compare well to the experimental values of 4.4 and 0.4 respectively. The vanadyl modes are not affected by the electron localization and therefore their position and width remain nearly unchanged. Comparison with the experimental infrared spectra confirms the general predictions of the B3LYP model, in particular the pronounced, qualitative changes upon electron localization when the size of the cluster is increased.[17]

Figure 1 shows not only the B3LYP results discussed so far, but also the results of DFT calculations with the BLYP[16,18] and BHLYP[16,19] functionals. The increasing admixture of Fock exchange (0, 20, and 50% in BLYP, B3LYP, and BHLYP, respectively) leads to an increasing tendency for symmetry breaking.[20–22] BHLYP (right column in Figure 1) yields localization of the unpaired electron for all three cage-type anions, and also for $V_4O_{10}^-$. Consequently, the calculated BHLYP spectrum of $V_4O_{10}^-$ shows additional bands between 800 and 900 cm^{-1} that are absent from the experimental spectrum. In contrast, BLYP predicts delocalization of the unpaired electron for all three cage-type anions studied and C_{2v} and D_{2d} structures become the ground states of $V_6O_{15}^-$ and $V_8O_{20}^-$, respectively. All three BLYP spectra show no bands between 750 and 950 cm^{-1}, which is in clear contrast with the experimental spectra of $V_6O_{15}^-$ and $V_8O_{20}^-$. In summary, Figure 1 shows that only B3LYP reproduces correctly the transition from symmetric (delocalized) to broken-symmetry (localized) structures when passing from $V_4O_{10}^-$ to $V_6O_{15}^-$ in this series of $(V_2O_5)_n^-$ cluster anions.

Figure 2 compares the gas-phase IRMPD spectrum of $V_8O_{20}^-$ with the electron energy loss spectrum of a V_2O_5

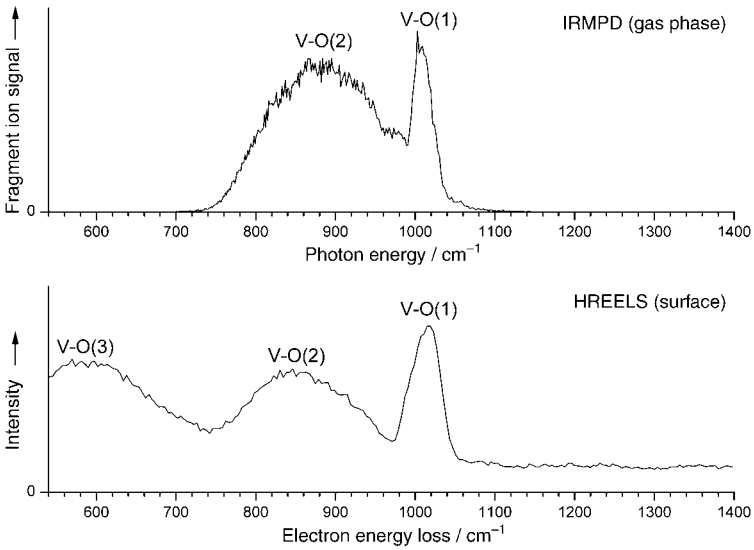

Figure 2. Vibrational spectra of different forms of vanadium oxide: The IRMPD spectrum of the gas-phase cluster anion $V_8O_{20}^-$ (top) and the spectrum of a freshly cleaved 001 surface of V_2O_5 (bottom), measured by high resolution electron energy loss spectroscopy (see text).

surface,[23] which also probes vibrational states. The spectra are surprisingly similar in the region above 740 cm^{-1}, with both displaying two bands of similar width and relative intensity. Their assignment is identical, that is, to vibrational modes of singly and doubly coordinated oxygen atoms. The third broad band of the surface spectrum is not observed in the gas phase. This can easily be rationalized because this band is assigned[11,24] to triply coordinated oxygen sites, which do not exist in the $V_8O_{20}^-$ cluster anion. Hence, the vibrational spectra reflect clearly the common (V=O and V–O–V bonds) and the discriminating (triply coordinated O) structural features of gas-phase clusters and solid surfaces.[25,26]

In this communication the polyhedral cage structures of $(V_2O_5)_n^-$ clusters ($n = 2$, 3, 4) have been identified spectroscopically for the first time by IRMPD spectroscopy. We have also found evidence for size-dependent charge localization in these clusters. Symmetry-breaking localization is observed in many other chemical systems for the reverse process—creation of an electron hole.[21] For example, the electron hole created in quartz when doped with Al is not delocalized over all four oxygen sites of the AlO_4 defect site, but localized at one oxygen only.[22] The proper description of electron (hole) localization phenomena by DFT depends on the functional used. In the present case we use the measured IRMPD spectra as the criteria for selecting the proper functional and find that only B3LYP has the right admixture of Fock exchange to reproduce the size-dependent change from delocalized to localized d electron states in vanadium oxide cages correctly. Even though the largest cluster anion studied here, $V_8O_{20}^-$, is still rather small, it reveals some striking similarities with the properties of a vanadium oxide single-crystal surface, making it an interesting gas-phase model for surface adsorption and reactivity studies.

Experimental Section

The present experiments were carried out on a previously described tandem mass spectrometer–ion trap system.[27] Vanadium oxide clusters were prepared by pulsed laser vaporization of a vanadium rod in the presence of O_2 seeded in He. The beam of negative ions was collimated and mass-selected by a quadrupole mass filter. Mass-selected cluster ions were accumulated and cooled to 15 K in a linear radio-frequency ion trap. IR photodissociation spectra were obtained by photoexcitation of the trapped cold ions with pulsed radiation from the FELIX,[12] and subsequent monitoring of the mass-selective ion yield. A FELIX bandwidth (RMS) of less than 0.3% of the central wavelength and pulse energies up to 60 mJ per macropulse were used.

Unrestricted Kohn–Sham calculations were performed with TURBOMOLE.[28] Triple-zeta valence plus polarization basis sets (TZVP) were applied.[29] Harmonic vibrational frequencies were obtained from second analytic derivatives[30] and were scaled using standard procedures (see Supporting Information).

Received: December 10, 2004
Published online: April 13, 2005

Keywords: cluster compounds · density functional calculations · electronic structure · IR spectroscopy · vanadium

[1] B. M. Weckhuysen, D. E. Keller, *Catal. Today* **2003**, *78*, 25–46.
[2] M. S. Whittingham, *Chem. Rev.* **2004**, *104*, 4271–4301.
[3] L. A. L. de Almeida, G. S. Deep, A. M. N. Lima, I. A. Khrebtov, V. G. Malyarov, H. Neff, *Appl. Phys. Lett.* **2004**, *85*, 3605–3607.
[4] L. Krusin-Elbaum, D. M. Newns, H. Zeng, V. Derycke, J. Z. Sun, R. Sandstrom, *Nature* **2004**, *431*, 672–676.
[5] a) J. Schoiswohl, G. Kresse, S. Surnev, M. Sock, M. G. Ramsey, F. P. Netzer, *Phys. Rev. Lett.* **2004**, *92*, 206103; b) N. Magg, B. Immaraporn, J. B. Giorgi, T. Schroeder, M. Bäumer, J. Döbler, Z. L. Wu, E. Kondratenko, M. Cherian, M. Baerns, P. C. Stair, J. Sauer, H.-J. Freund, *J. Catal.* **2004**, *126*, 88–100.
[6] a) A. Dinca, T. P. Davis, K. J. Fisher, D. R. Smith, G. D. Willett, *Int. J. Mass Spectrom.* **1999**, *182*/183, 73–84; b) R. C. Bell, K. A. Zemski, D. R. Justes, A. W. Castleman, Jr., *J. Chem. Phys.* **2001**, *114*, 798–811; c) H. J. Zhai, L.-S. Wang, *J. Chem. Phys.* **2002**, *117*, 7882–7888; d) A. Pramann, K. Koyasu, A. Nakajima, K. Kaya, *J. Chem. Phys.* **2002**, *116*, 6521–6528.
[7] M. A. Duncan, *Int. J. Mass Spectrom.* **2000**, *200*, 545–569.
[8] G. von Helden, D. van Heijnsbergen, G. Meijer, *J. Phys. Chem. A* **2003**, *107*, 1671–1688.
[9] A systematic study of vanadium oxide cluster anions containing two to eight vanadium atoms will be reported shortly.
[10] S. F. Vyboishchikov, J. Sauer, *J. Phys. Chem. A* **2000**, *104*, 10913–10922.
[11] S. F. Vyboishchikov, J. Sauer, *J. Phys. Chem. A* **2001**, *105*, 8588–8598.
[12] D. Oepts, A. F. G. van der Meer, P. W. van Amersfoort, *Infrared Phys. Technol.* **1995**, *36*, 297–308.
[13] J. Oomens, G. Meijer, G. von Helden, *J. Phys. Chem. A* **2001**, *105*, 8302–8309.
[14] K. R. Asmis, G. Meijer, M. Brümmer, C. Kaposta, G. Santambrogio, L. Wöste, J. Sauer, *J. Chem. Phys.* **2004**, *120*, 6461–6470.
[15] A. D. Becke, *J. Chem. Phys.* **1993**, *98*, 5648–5652.
[16] C. Lee, W. Yang, R. G. Parr, *Phys. Rev. B* **1988**, *37*, 785–789.
[17] Some discrepancies between experimental and simulated spectra remain and are attributed to the approximate nature of the calculations, which neglect the multiphotonic nature of the absorption process and assume that the potentials are single-well and harmonic.

[18] A. D. Becke, *Phys. Rev. A* **1988**, *38*, 3098 – 3100.
[19] A. D. Becke, *J. Chem. Phys.* **1993**, *98*, 1372 – 1377.
[20] C. D. Sherrill, M. S. Lee, M. Head-Gordon, *Chem. Phys. Lett.* **1999**, *302*, 425 – 430.
[21] M. Sodupe, J. Bertran, L. Rodriguez-Santiago, E. J. Baerends, *J. Phys. Chem. A* **1999**, *103*, 166 – 170.
[22] G. Pacchioni, F. Frigoli, D. Ricci, J. A. Weil, *Phys. Rev. B* **2001**, *63*, 054102; X. Solans-Monfort, V. Branchadell, M. Sodupe, M. Sierka, J. Sauer, *J. Chem. Phys.* **2004**, *121*, 6034 – 6041.
[23] B. Tepper, B. Richter, A. C. Dupuis, H. Kuhlenbeck, C. Hucho, P. Schilbe, M. A. bin Yarmo, H.-J. Freund, *Surf. Sci.* **2002**, *496*, 64 – 72.
[24] V. Brázdová, M. V. Ganduglia-Pirovano, J. Sauer, *Phys. Rev. B* **2004**, *69*, 165420.
[25] In solid compounds, mixed-valence polyvanadate species, such as $V_{15}O_{36}^{5-}$, are found which also have a cage structure with terminal V=O groups, but contain triply coordinated O in addition to V–O–V bonds. See ref. [26].
[26] A. Müller, E. Krickemeyer, M. Penk, H.-J. Walberg, H. Bögge, *Angew. Chem.* **1987**, *99*, 1060 – 1061; *Angew. Chem. Int. Ed. Engl.* **1987**, *26*, 1045 – 1046.
[27] K. R. Asmis, M. Brümmer, C. Kaposta, G. Santambrogio, G. von Helden, G. Meijer, K. Rademann, L. Wöste, *Phys. Chem. Chem. Phys.* **2002**, *4*, 1101 – 1104.
[28] a) R. Ahlrichs, M. Bär, M. Häser, H. Horn, C. Kölmel, *Chem. Phys. Lett.* **1989**, *162*, 165 – 169; b) O. Treutler, R. Ahlrichs, *J. Chem. Phys.* **1995**, *102*, 346 – 354; c) K. Eichkorn, O. Treutler, H. Öhm, M. Häser, R. Ahlrichs, *Chem. Phys. Lett.* **1995**, *242*, 652 – 660.
[29] A. Schäfer, C. Huber, R. Ahlrichs, *J. Chem. Phys.* **1994**, *100*, 5829 – 5835.
[30] P. Deglmann, F. Furche, R. Ahlrichs, *Chem. Phys. Lett.* **2002**, *362*, 511 – 518.

Oxidative Heck Reaction

Palladium-Catalyzed Intermolecular Alkenylation of Indoles by Solvent-Controlled Regioselective C–H Functionalization**

*Neil P. Grimster, Carolyn Gauntlett, Christopher R. A. Godfrey, and Matthew J. Gaunt**

Over the past three decades the Heck reaction has become one of the most fundamental metal-catalyzed C–C bond-forming processes for the synthesis of complex molecules.[1] It has had a huge impact on organic synthesis despite the disadvantage that the overall coupling of the two fragments requires two discrete activation steps: 1) the formation of an aryl or vinyl halide and 2) the palladium(0)-catalyzed union of the reaction partners [Eq. (1)]. A direct oxidative Heck

Conventional Heck reaction

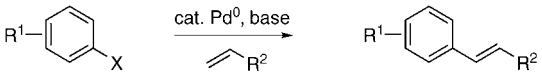

(1)

reaction would bypass the need for preactivated reaction partners and lead to a more efficient process. To this end, Fujiwara, Moritani et al. developed an efficient coupling of arenes and activated alkenes through an oxidative palladium(II)-catalyzed process, and this transformation has found widespread use in synthesis [Eq. (2)].[2]

Fujiwara–Moritani oxidative Heck reaction

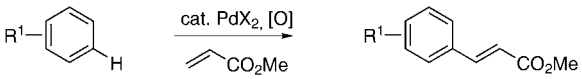

(2)

We are interested in the development of catalytic processes that exploit selective and controllable C–H functionalization[3] to elaborate simple aromatic compounds to useful products. The catalytic functionalization of aromatic heterocycles is an important transformation, and methods for the synthesis and elaboration of indoles in particular have received significant attention.[4] The indole motif is a ubiquitous feature of alkaloid and peptide natural products and represents an important structural element for the pharmaceutical industry. As a result, many useful and practical processes exist for the modification of the indole structure, and, as previously mentioned, metal-catalyzed coupling reactions are of particular utility, although these methods often require a prefunctionalized indole unit for each elaboration.[4,5] Surprisingly, the development of an oxidative C3 alkenylation of free (NH) indoles has received little attention,[6] and to the best of our knowledge there is no example of an intermolecular oxidative C2 alkenylation of a free (NH) indole.[7] Nor is there a method to select between the two positions of the important fundamental motif. Herein we describe a general direct oxidative Heck reaction that exploits a novel, selective, solvent-controlled, palladium-catalyzed C–H functionalization of free (NH) indoles and leads to the elaboration of the heteroaromatic core at either the 2- or the 3-position [Eq. (3)].

The natural reactivity of indole suggested that palladation and Heck coupling would take place preferentially at the 3-

New switchable solvent-controlled regioselective palladium-catalyzed indole alkenylation by C–H functionalization

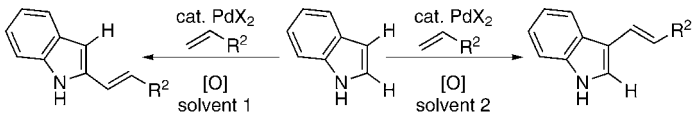

(3)

[*] N. P. Grimster, C. Gauntlett, Dr. M. J. Gaunt
Department of Chemistry, University of Cambridge
Lensfield Road, Cambridge CB21EW (UK)
Fax: (+44) 1223-336-362
E-mail: mjg32@cam.ac.uk
Dr. C. R. A. Godfrey
Syngenta Crop Protection Research AG, WRO 1060.2.06
Schwazaldallee 215, 4002 Basel (Switzerland)

[**] We gratefully acknowledge Syngenta and the EPSRC for an Industrial Case Award (to N.P.G.), the Royal Society for a University Research Fellowship (to M.J.G.), and Professor Steven Ley for support and useful discussions.

Supporting information for this article is available on the WWW under http://www.angewandte.org or from the author.

 DOI: 10.1002/anie.200500468

position.[6] However, we speculated that it might be possible to control the selectivity of the reaction by the use of different solvents and additives. Fundamental to this hypothesis was the knowledge that the migration of groups from the 3- to the 2-position of indole has been observed in the alkylation of 3-substituted indoles (Scheme 1).[8] By analogy, we anticipated that a migration of the C3–PdX bond to the 2-position would enable a complementary C–H functionalization process.

We began by screening the reaction between indole (**1a**, R^1 = H) and *n*-butyl acrylate (**4a**) in the presence of $Pd(OAc)_2$ as a catalyst with a variety of solvents and $Cu(OAc)_2$ as the oxidant.[9] Reactions in polar solvents gave exclusively the C3-functionalized indoles **3a** (Table 1, entries 1–2), except when 1,4-dioxane was used (Table 1, entry 3), in which case no reaction was observed, perhaps because of the insolubility of $Cu(OAc)_2$ in this solvent. The use of *tert*-butyl benzoyl peroxide (*t*BuOOBz) as the soluble reoxidizing agent, however, led to a reaction in 1,4-dioxane, but with a surprising reversal of selectivity to produce a 2:1 mixture of the C2- and C3-substituted indoles **2a** and **3a**, respectively (Table 1, entry 4). Careful monitoring of the reaction showed that **3a** predominated at the beginning of the reaction with **2a** only starting to form as the reaction proceeded. Benzoic acid is produced as a result of the reoxidation of Pd^0 by *t*BuOOBz, and it was believed that the increasing concentration of acid may be responsible for the switch in selectivity as the reaction progresses. This hypothesis was supported by the result of the reaction in DMF/AcOH, which led to a 1:1 mixture of isomers (Table 1, entry 5), whereas only **3a** was formed in DMF alone. To our delight, the use of AcOH as a cosolvent with 1,4-dioxane led to a 7:1 ratio of **2a**:**3a** (Table 1, entry 6) and demonstrated that the regioselectivity of palladium-catalyzed indole alkenylation could be controlled.

Further optimization showed that the use of DMSO as a cosolvent with DMF improved the yield of **3a** (Table 1, entry 7), thus suggesting that DMSO may prevent the precipitation of Pd^0 in the reaction mixture prior to reoxidation.[10a] Although no further improvements to the C2 functionalization reaction were made,[11] we found that the use of MeCN/AcOH switched the selectivity back in favor of the 3-position (Table 1, entry 8), as did the addition of DMSO to the reaction in 1,4-dioxane/AcOH (Table 1, entry 9).[10b] It is remarkable that the addition of a polar coordinating cosolvent seems to promote a total switch in the selectivity of the reaction, and investigations into the nature of this selectivity are ongoing.

Table 1: Optimization studies for indole functionalization.[a]

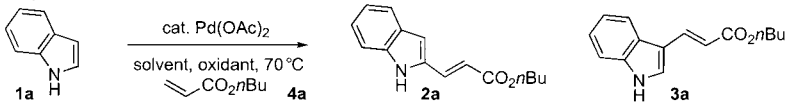

Entry	Catalyst loading [%]	Oxidant (equiv)	Solvent (*v*/*v*)	Yield of **2**+**3** [%][b]	**3a**/**2a**
1	10	$Cu(OAc)_2$ (1.8)	DMF	54	>95:5
2	10	$Cu(OAc)_2$ (1.8)	DMSO	66	>95:5
3	10	$Cu(OAc)_2$ (1.8)	1,4-dioxane	n.r.	–
4	10	*t*BuOOBz (0.9)	1,4-dioxane	48	1:2
5	10	$Cu(OAc)_2$ (1.8)	DMF/AcOH (3:1)	54	1:1
6	20	*t*BuOOBz (0.9)	1,4-dioxane/AcOH (3:1)	58	1:7
7	10	$Cu(OAc)_2$ (1.8)	DMF/DMSO (10:1)	79	>95:5
8	10	*t*BuOOBz (0.9)	MeCN/AcOH (3:1)	65	>95:5
9	10	*t*BuOOBz (0.9)	1,4-dioxane/AcOH/DMSO (3:1:0.4)	66	>95:5

[a] For all reactions the mixture (0.4 M) was stirred for 18 h. [b] Yields after isolation and purification by flash silica-gel chromatography. n.r. = no reaction. Bz = benzoyl, DMF = *N*,*N*-dimethylformamide, DMSO = dimethyl sulfoxide.

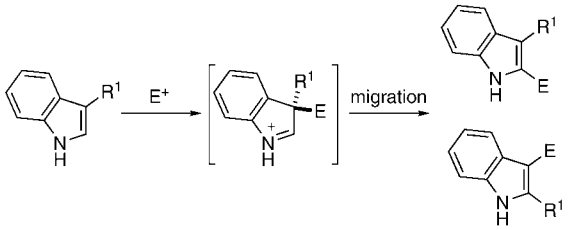

Scheme 1. Electrophilic attack on indoles.

Although at this stage we can not be certain of the mechanism of this process, we propose plausible pathways for the two reactions in Scheme 2. Palladation at C3 is thought to occur via intermediate **I**, and following rearomatization to **II** a Heck-type reaction forms the C3-functionalized indole **3**. Under neutral conditions, the acetate ion formed from the attack of indole on $Pd(OAc)_2$ will readily remove a proton from **I** to form the C3-palladated species **II**. In contrast, under acidic reaction conditions we propose that this deprotonation would be slowed, which could allow a migration of the C3–PdX bond in **I** to the highly activated 2-position of the iminium intermediate to give intermediate **III** and ultimately **IV**.[12] The effect of the cosolvent, as well as the presence of

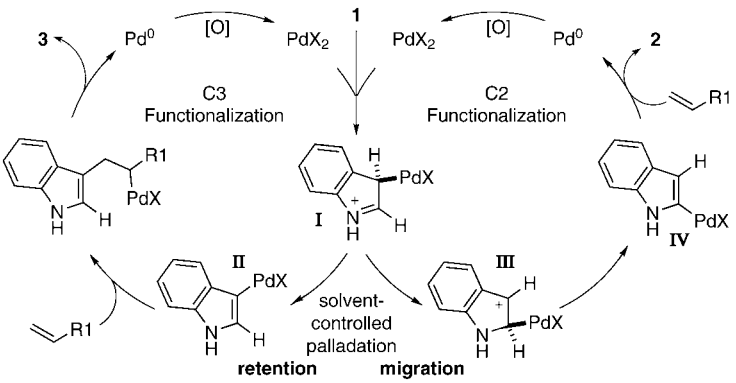

Scheme 2. Proposed mechanism of C–H functionalization.

AcOH, is also important since the results in Table 1 suggest that strongly coordinating solvents (DMSO, MeCN) override any effect that the presence of acid may have, thus leading to C3 selectivity. However, with weakly coordinating 1,4-dioxane as a solvent the proposed migration still appears to be facile, even without the addition of acid, thus leading to the C2-functionalized indole **2** as the major isomer. It is also possible that the C3 palladation is reversible, and that the intermediate derived from C2 palladation is ultimately formed prior to coupling. In this case the C2-palladated species must be thermodynamically more stable and the rate of insertion into the alkene slow. Mechanistic investigations are currently underway, and these results will be reported in due course.

Table 2 shows that a range of indoles and alkenes participate in the regioselective oxidative coupling reaction. Importantly, free (NH) indoles are suitable substrates for this process. The C3-functionalization process worked well for electron-deficient alkenes, such as **4a–d**, which reacted with **1a** to form indoles **3a–d** in good yield. Indole phosphonate **3e** could also be generated from vinyl phosphonate **4e** in good yield. The reaction of **1a** with lactone **4f** produced a mixture of alkenyl indole regioisomers **3f** (1:1) in 66% combined yield. The non-activated alkenes styrene (**4g**) and cyclohexene (**4h**) reacted with **1a** to form the corresponding indoles **3g** and **3h** (after hydrogenation) in good yield. The *N*-methyl indole derivative **1b** reacted with **4a** to form **3i** in 75% yield, and 5-nitroindole **1c** was smoothly converted into **3j** in 76% yield. Of particular note was the use of 5-bromoindole (**1d**); the highly versatile product **3k** was isolated in 75% yield with the aryl bromide moiety intact. Thus, this first general method for the direct oxidative Heck coupling at C3 of free (NH) indoles can be applied to a range of indoles and alkenes.

Table 2: Regioselective C3 functionalization of indoles.

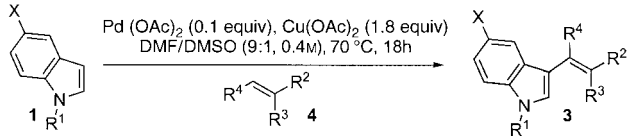

Entry	Alkene		Indole	Product[a]		Yield [%][b]
1	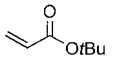	**4b**	X, R^1 = H **1a**	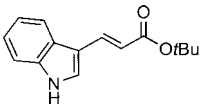	**3b**	91
2	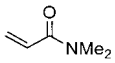	**4c**	X, R^1 = H **1a**	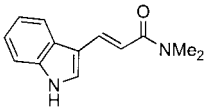	**3c**	70
3	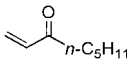	**4d**	X, R^1 = H **1a**	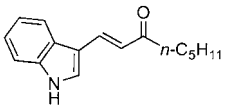	**3d**	68
4	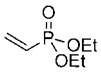	**4e**[d]	X, R^1 = H **1a**	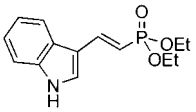	**3e**	70
5		**4f**	X, R^1 = H **1a**	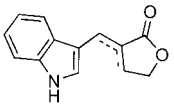	**3f**	66[c]
6		**4g**[e]	X, R^1 = H **1a**	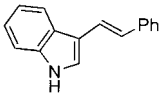	**3g**	62
7		**4h**[f]	X, R^1 = H **1a**	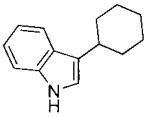	**3h**	62
8	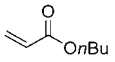	**4a**	X = H, R^1 = Me **1b**	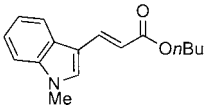	**3i**	75
9	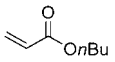	**4a**	X = NO_2, R^1 = H **1c**	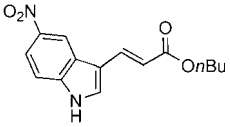	**3j**	76
10	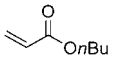	**4a**	X = Br, R^1 = H **1d**	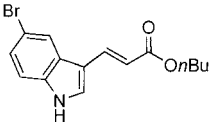	**3k**	75

[a] Only the C3-functionalized isomer was produced. [b] Yields of products after purification. [c] A 1:1 mixture of isomers was produced. [d] **4e**: 5 equivalents. [e] **1a**: 2 equivalents, **4g**: 1 equivalent. [f] **4h**: 10 equivalents used because of its volatility; yield after hydrogenation.

We next turned our attention to the development of the corresponding catalytic C2 alkenylation. When the reactions were performed with dioxane/AcOH as the solvent (Table 1, entry 6) the regioselectivity of the oxidative process was switched in favor of reaction at the 2-position (Table 3). However, the yields were generally lower in these cases, presumably as a result of competitive oxidative decomposition of indole **1a** and the product **2** under these reaction conditions. Nevertheless, indole alkenylation occurred selectively at the C2 position with all substrates tested, in generally good yields for this type of transformation. Interestingly, the use of *N*-methylindole (**1b**) resulted in no alkenylation at either C2 or C3 under these conditions, thus highlighting a potentially crucial role of the free NH moiety in these reactions.

It was also possible to further derivatize the indole products through C–H functionalization (Scheme 3). Indole **3b** reacted with **4a** to form **5** in a moderate 41% yield as the

Table 3: Regioselective C2 functionalization of indoles.

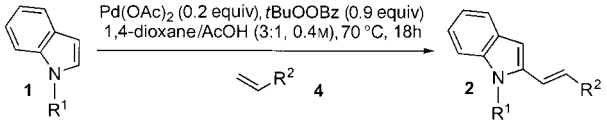

Entry	Alkene		Indole	Product[a]		Yield [%][b]
1	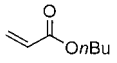	**4a**	$R^1 = H$ **1a**	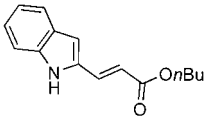	**2a**	51[c]
2	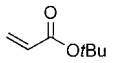	**4b**	$R^1 = H$ **1a**	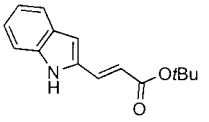	**2b**	57
3	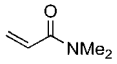	**4c**	$R^1 = H$ **1a**	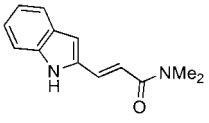	**2c**	34
4	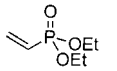	**4e**	$R^1 = H$ **1a**	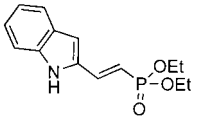	**2e**	51
5	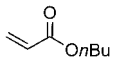	**4a**	$R^1 = Me$ **1b**	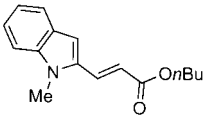	**2i**	n.r.

[a] Only the C2-functionalized isomer was produced. [b] Yields of products after purification. [c] A 7:1 mixture of **2**/**3** was produced; 51% is the yield of isolated **2a**.

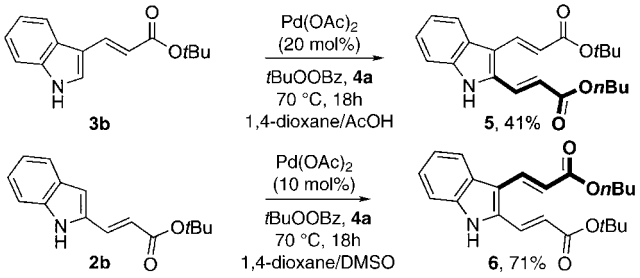

Scheme 3. Formation of bis(alkenyl)indoles.

sole product, whereas indole **2b** was converted into diene **6** in 71% yield through reaction with **4a** in 1,4-dioxane/DMSO. This strategy thus allows the selective installation of substituents at either position in any order and provides access to highly functionalized indoles by catalytic methods.

In summary, we have developed a general method for the selective intermolecular alkenylation of indoles through a palladium-catalyzed C–H functionalization reaction. The nature of the solvent determines the regioselectivity of the reaction, so that the alkenylation can be directed to either the 2- or the 3-position of free (NH) indoles. This discovery could have important consequences for the selective elaboration of other heteroaromatic core structures. Current efforts are directed towards the improvement of the efficiency and scope of the reaction, a more detailed mechanistic investigation, and application to other types of heteroaromatic compounds.

Experimental Section

General procedure for C3 alkenylation: Palladium acetate (0.1 equiv) was added to a mixture of the alkene (2 equiv), copper(II) acetate (1.8 equiv), and the indole (1 equiv) in DMF/DMSO (9:1, 0.4 M), and the reaction mixture was stirred at 70 °C. After 18 h the reaction mixture was cooled to room temperature and partitioned between water and ethyl acetate, then filtered through a plug of celite. The layers were separated, and the organic layer was washed with aqueous saturated brine solution, dried over $MgSO_4$, filtered, and concentrated under reduced pressure. Purification by flash chromatography afforded the C3-alkenylated indole.

General procedure for C2-alkenylation: Palladium acetate (0.2 equiv) was added to a mixture of the alkene (2 equiv), *t*BuOOBz (0.9 equiv), and the indole (1 equiv) in 1,4-dioxane/AcOH (3:1, 0.4 M), and the reaction mixture was stirred at 70 °C. After 18 h the reaction mixture was cooled to room temperature and neutralized with aqueous sodium hydrogen carbonate solution, diluted with ethyl acetate, and filtered through a plug of celite. The layers were separated, and the organic layer was washed with aqueous sodium hydrogen carbonate solution and aqueous saturated brine solution, dried over $MgSO_4$, filtered, and concentrated under reduced pressure. Purification by flash chromatography afforded the C2-alkenylated indole.

Received: February 7, 2005
Published online: April 12, 2005

Keywords: C–C coupling · Heck reaction · indoles · palladium · regioselectivity

[1] For recent reviews, see: a) A. B. Dounay, L. E. Overman, *Chem. Rev.* **2003**, *103*, 2945; b) I. P. Beletskaya, A. V. Cheprakov, *Chem. Rev.* **2000**, *100*, 3009; c) A. de Meijere, F. E. Meyer, *Angew. Chem.* **1994**, *106*, 2473; *Angew. Chem. Int. Ed. Engl.* **1994**, *34*, 2379.

[2] a) I. Moritani, Y. Fujiwara, *Tetrahedron Lett.* **1967**, 1119; b) Y. Fujiwara, I. Moritani, S. Danno, R. Asano, S. Teranishi, *J. Am. Chem. Soc.* **1969**, *91*, 7166; for a recent intramolecular application of this reaction, see: c) H. Zhang, E. M. Ferreira, B. M. Stoltz, *Angew. Chem.* **2004**, *116*, 6270; *Angew. Chem. Int. Ed.* **2004**, *43*, 6144, and references therein.

[3] The term C–H functionalization is used in a general sense to describe the activation and transformation of a C–H bond. This term was described by Sames and co-workers; see: a) B. Sezen, D. Sames, *J. Am. Chem. Soc.* **2003**, *125*, 10580; see also: b) A. E. Shilov, G. B. Shul'pin, *Chem. Rev.* **1997**, *97*, 2879; c) V. Ritleng, C. Sirlin, M. Preffer, *Chem. Rev.* **2002**, *102*, 1731; d) G. Dyker, *Angew. Chem.* **1999**, *111*, 1808; *Angew. Chem. Int. Ed.* **1999**, *38*, 1698.

[4] a) R. J. Sundberg, *Indoles*, Academic Press, New York, **1996**; b) L. S. Hegedus, *Angew. Chem.* **1988**, *100*, 1147; *Angew. Chem. Int. Ed.* **1988**, *27*, 1113; c) G. W. Gribble, *J. Chem. Soc. Perkin Trans. 1* **2000**, 1045; for a recent metal-catalyzed synthesis of indoles, see: d) M. C. Willis, G. N. Brace, I. P. Holmes, *Angew. Chem.* **2005**, *117*, 407; *Angew. Chem. Int. Ed.* **2005**, *44*, 403.

[5] For examples of the palladium-catalyzed intramolecular C–H functionalization of indoles, see: a) E. M. Ferreira, B. M. Stoltz, *J. Am. Chem. Soc.* **2003**, *125*, 9578; b) C. Liu, X. Han, X. Wang, R. A. Widenhoefer, *J. Am. Chem. Soc.* **2004**, *126*, 3700; c) G. Abbiati, E. M. Becalli, G. Broggini, C. Zoni, *J. Org. Chem.* **2003**, *68*, 7625; for direct palladium-catalyzed arylation reactions, see: d) B. Sezen, D. Sames, *J. Am. Chem. Soc.* **2003**, *125*, 5274; e) B. S. Lane, D. Sames, *Org. Lett.* **2004**, *6*, 2897; for a gold-catalyzed coupling reaction, see: f) A. Arcadi, G. Bianchi, M. Chiarini, G. D'Anniballe, F. Marinelli, *Synlett* **2004**, 944; for a stoichiometric palladium-catalyzed alkenylation, see: g) T. Itahara, M. Ikeda, T. Sakakibara, *J. Chem. Soc. Perkin Trans. 1* **1983**, 1361.

[6] J. Chengguo, W. Lu, T. Kitamura, Y. Fujiwara, *Org. Lett.* **1999**, *1*, 2097.

[7] During the preparation of this manuscript we became aware of a report relating to a C2 alkenylation of an indole that contains a metal-directing group on the indole nitrogen atom: E. Capito, J. M. Brown, A. Ricci, *Chem. Commun.* **2005**, in press.

[8] a) R. J. Sundberg, *The Chemistry of Indoles*, Academic Press, New York, **1970**, pp. 78–83; b) A. H. Jackson, B. Naidoo, P. Smith, *Tetrahedron* **1968**, *24*, 6119.

[9] For an overview of oxidative palladium-catalyzed transformations, see: M. S. Sigman, M. Schultz, *J. Org. Biomol. Chem.* **2004**, *2*, 2551.

[10] a) B. A. Steinhoff, S. R. Fix, S. S. Stahl, *J. Am. Chem. Soc.* **2002**, *124*, 766; b) for an effect of DMSO, see: M. S. Chen, C. M. White, *J. Am. Chem. Soc.* **2004**, *126*, 1346.

[11] Conditions reported by Ferreira and Stoltz (reference [5a]) for an intramolecular process gave **2a** in 34% yield.

[12] For a recent example of Pd migrations, see: M. A. Campo, Q. Huang, T. Yoa, Q. Tian, R. C. Larock, *J. Am. Chem. Soc.* **2003**, *125*, 11507.

Transition-Metal Complexes

The Myth of Cyanide Always Being a Strong-Field Ligand: Synthesis and Structural Characterization of Homoleptic $S = 2$ Pentacyanochromate(II), $[Cr^{II}(CN)_5]^{3-}$, and Nonacyanodichromate(II), $[Cr^{II}_2(CN)_9]^{5-}$**

*Kendric J. Nelson, Ian D. Giles, William W. Shum, Atta M. Arif, and Joel S. Miller**

Dedicated to Harry B. Gray

Crystal field theory has provided detailed insight into the structure, spectroscopic, and magnetic properties of transition-metal coordination complexes since its inception. The empirical genesis of the spectrochemical series, which identifies strong π-acceptor ligands as strong-field ligands, is understood on the basis of molecular orbital theory. Cyanide is deeply entrenched as being a strong-field ligand, as revealed by low-spin ground states for its homoleptic complexes: for example, $[M(CN)_6]^{n-}$ ($n = 2$, 3, 4)[1] and $[M^{II}(CN)_5]^{3-}$ (M = Co, Ni).[2] Furthermore, they do not violate the $18e^-$ rule by exceeding 18 electrons about the metal center M. The only high-spin example is the unusual $13e^-$ $S = 5/2$ complex $[Mn^{II}(CN)_4]^{2-}$,[3] which being tetrahedral has a substantially reduced crystal-field stabilization energy, Δ, of $^4/_9$ the value expected for the $17e^-$ $S = 1/2$ complex $[Mn^{II}(CN)_6]^{4-}$. As part of our ongoing studies toward molecule-based magnets,[4] we sought to prepare Prussian blue structured magnets based upon $[Cr^{II}(CN)_6]^{4-}$ for comparison with those derived from $[Cr^{III}(CN)_6]^{3-}$, which magnetically order at temperatures as high as 100 °C (approximately).[5]

$K_4[Cr^{II}(CN)_6]$ has been prepared from aqueous media, but owing to the lability of the d^4 Cr^{II} state, excess cyanide is required in solution. Despite undergoing a Jahn–Teller distortion, $16e^-$ $K_4[Cr^{II}(CN)_6]$ is low-spin $S = 1$. Owing to the need for excess cyanide, aqueous routes to Prussian blue structured materials would be unproductive, so we sought a nonaqueous source of $[Cr^{II}(CN)_6]^{4-}$ and targeted $(NEt_4)_4[Cr^{II}(CN)_6]$. The reaction of either $Cr^{II}_2(OAc)_4$[6] or $[Cr^{II}(MeCN)_4(BF_4)_2]$[7] with as much as a twofold excess of NEt_4CN in MeCN led to dark purple block crystals of composition $(NEt_4)_3[Cr^{II}(CN)_5]\cdot MeCN\cdot{}^1/_8\,THF$ (**1**). In the solid state **1** exhibits a broad $\nu_{C\equiv N}$ absorption at 2086 cm^{-1} (half-width at half height: 9.2 cm^{-1}, see Figure 1). This is comparable to 2080 cm^{-1} reported for $[Co^{II}(CN)_5]^{3-}$,[8] but differs from the absorptions at 2095 (m), 2111 (vs), and 2123 cm^{-1} (vs) reported for $[Ni^{II}(CN)_5]^{3-}$,[9] and is higher in energy than the broad $\nu_{C\equiv N}$ absorption at 2020 cm^{-1} observed for $K_4[Cr^{II}(CN)_6]$.[10] The electronic spectrum (5000–30000 cm^{-1}) of a solution of $(NEt_4)_3[Cr^{II}(CN)_5]$ (1.30 mM) in MeCN comprises an absorption at 22120 cm^{-1} ($\lambda = 452$ nm, $\varepsilon = 122\,M^{-1}cm^{-1}$; Figure 1). However, **1** does not obey Beer's

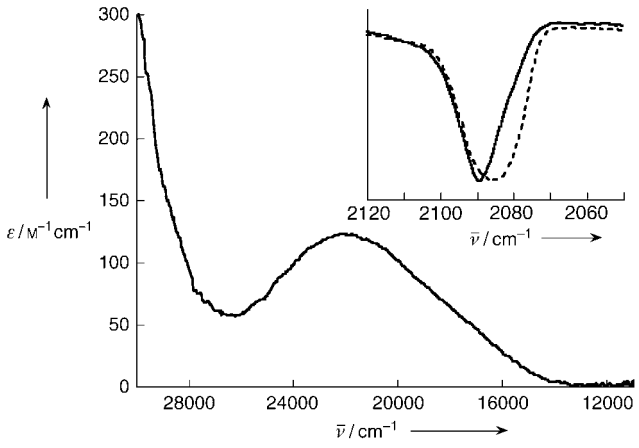

Figure 1. Electronic absorption spectrum of $(NEt_4)_3[Cr^{II}(CN)_5]$ (1.30 mM in MeCN). Inset: $\nu_{C\equiv N}$ vibrational spectra of $(NEt_4)_3[Cr^{II}(CN)_5]$ (-----) and $(NEt_4)_8[Cr^{II}(CN)_5][Cr^{II}_2(CN)_9]$ (——) in KBr.

[*] K. J. Nelson, I. D. Giles, W. W. Shum, Dr. A. M. Arif, Prof. J. S. Miller
Department of Chemistry
University of Utah
Salt Lake City, UT 84112-0850 (USA)
Fax: (+1) 801-581-8433
E-mail: jsmiller@chem.utah.edu

[**] The authors gratefully acknowledge fruitful discussions with R. D. Ernst and partial support from the U.S. DOE (grant no. DE FG 03-93ER45504) and the ACS PRF (grant no. 36165-AC5). Dedicated to Harry B. Gray for his pioneering studies in the area of homoleptic metallocyanides.

 DOI: 10.1002/anie.200462763

law, as the electronic absorption spectrum of the solution changes as a function of cyanide concentration (the details of this equilibrium are under investigation).

The asymmetric unit cell[11] contains four $[Cr^{II}(CN)_5]^{3-}$ units (Figure 2), twelve Et_4N^+ cations, as well as four molecules of MeCN and half a molecule of THF of solvation, which arises from the diffusion of THF into a solution of **1** in MeCN to obtain the crystals. Each Cr^{II} center is pentacoordinate, with both square-pyramidal and distorted trigonal bipyramid structures present. The low barrier for interconversion between the limiting square-pyramidal and trigonal bipyramid five-coordinate structures leads to the formation of several local structures,[12] as has been reported for $[Ni^{II}(CN)_5]^{3-}$ even within the same unit cell.[13] For the square-pyramidal structures the apical Cr–C bond lengths range from 2.229(5) to 2.238(6) Å (av 2.23 Å) and the basal Cr–C bond lengths range from 2.110(7) to 2.135(5) Å (av 2.12 Å). The C_{apical}-Cr-C_{basal} angle ranges from 93.6(2) to 108.2(3)° (av 99.0°), and the *trans* C_{basal}-Cr-C_{basal} angle ranges from 155.9(2) to 166.9(2)° (av 161.9°). The Cr atom lies 0.33 Å above the plane formed by the four basal carbon atoms. These values are similar to those found for $[M^{II}(CN)_5]^{3-}$ (M = Co, Ni; see Table 1),[14] except that the Cr–C bonds are the longest, as expected for an early first-row transition metal. In the distorted trigonal bipyramidal structure the axial Cr–C bond lengths range from 2.094(6) to 2.118(6) Å (av 2.11 Å) while the equatorial Cr–C bond lengths range from 2.113(6) to 2.188(5) Å (av 2.15 Å). The axial Cr–C bonds are shorter than the equatorial Cr–C bonds, as reported for the distorted trigonal bipyramidal $[Ni^{II}(CN)_5]^{3-}$ structure.[13]

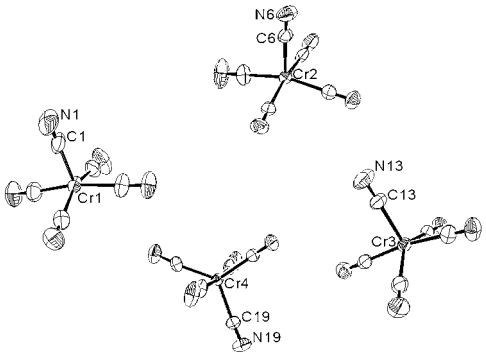

Figure 2. ORTEP labeling diagram of $(NEt_4)_3[Cr^{II}(CN)_5]\cdot MeCN\cdot{}^1/_8\,THF$ (**1**; 50% probability level; cations and solvent molecules are omitted for clarity).

Owing to formation of solely the pentacyanide complex even in the presence of excess cyanide ion, the reaction was carried out with 5 equivalents of CN^- per Cr^{II} ion, and dark brown needlelike crystals of $(NEt_4)_8[Cr^{II}(CN)_5][Cr^{II}_2(CN)_9]\cdot 2\,MeCN$ (**2**) were isolated. In the solid state **2** exhibits a broad $\nu_{C\equiv N}$ absorption at 2090 cm^{-1} (half-width at half height: 6.9 cm^{-1}), which is comparable to that observed for $(NEt_4)_3[Cr^{II}(CN)_5]$ (Figure 1). Furthermore, similar to $(NEt_4)_3[Cr^{II}(CN)_5]$, **2** also does not obey Beer's law (the details of this equilibrium are also under investigation).

The asymmetric unit cell[15] of **2** contains one $[Cr^{II}(CN)_5]^{3-}$ unit, one $[Cr_2^{II}(CN)_9]^{5-}$ unit (see Figure 3), eight Et_4N^+ cations, and two molecules of MeCN of solvation. Each Cr^{II} center is pentacoordinate, with a distorted square-pyramidal local C_{4v} symmetry. The Cr center in the distorted square-pyramidal $[Cr^{II}(CN)_5]^{3-}$ unit lies 0.40 Å above the plane formed by the four basal carbon atoms, and the apical Cr–C bond length is 2.23 Å, while the average basal Cr–C bond length is 2.12 Å. $[Cr^{II}_2(CN)_9]^{5-}$ is composed of two square-pyramidal $[Cr^{II}(CN)_4]^{2-}$ moieties bridged by a cyanide ion. The bridging cyanide is disordered, with average Cr–C and Cr–N bond lengths of 2.20 Å observed. The Cr center lies 0.37 Å above the plane formed by the four basal carbon atoms, and the basal Cr–C bond length is 2.13 Å on average. To the best of our knowledge, this structural motif has not been previously reported.

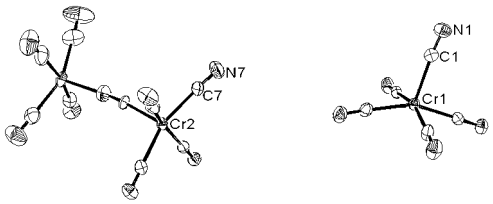

Figure 3. ORTEP labeling diagram of $(NEt_4)_8[Cr^{II}(CN)_5]$-$[Cr^{II}_2(CN)_9]\cdot 2\,MeCN$ (**2**; 50% probability level; cations and solvent molecules are omitted for clarity).

The magnetic susceptibility, χ, was measured for both $(NEt_4)_3[Cr^{II}(CN)_5]$ and $(NEt_4)_8[Cr^{II}(CN)_5][Cr^{II}_2(CN)_9]$ from 5 to 300 K. $(NEt_4)_3[Cr^{II}(CN)_5]$ has an effective room temper-

Table 1: Comparison of geometries of d^4, d^7, and d^8 square-pyramidal, distorted square-pyramidal, and distorted trigonal bipyramid $[M^{II}(CN)_5]^{3-}$ (M = Cr, Co, Ni) structures.

	$[Cr^{II}(CN)_5]^{3-}$ (**1**)	$[Cr^{II}(CN)_5]^{3-}$ (**2**)	$[Cr^{II}_2(CN)_9]^{5-}$ (**2**)	$[Co^{II}(CN)_5]^{3-}$ [14]	$[Ni^{II}(CN)_5]^{3-}$ [14]
d^n	4	4	4	7	8
S	2	2	[a]	1/2	0
M–C_{apical} [Å]	2.23	2.23	2.20	2.010	2.140
M–C_{basal} [Å] (av)	2.12	2.12	2.13	1.894	1.890
trans C_{basal}-M-C_{basal} [°] (av)	161.9	157.8	158.9	164.7	161.5
C_{apical}-M-C_{basal} [°] (av)	98.96	100.7	100.5	97.60	99.00
deviation (M–basal plane) [Å]	0.33	0.40	0.37	0.25	0.30
M–C_{axial} [Å]	2.11	–	–	–	1.84[13a]
M–$C_{equatorial}$ [Å]	2.15	–	–	–	1.94[13a]

[a] Singlet ground state, nonet excited state.

ature magnetic moment, $\mu_{eff} = (8\chi T)^{1/2}$, of 4.90 μ_B (corrected for temperature-independent paramagnetism (TIP); see Figure 4). This value significantly exceeds the expected spin-only moment of 2.83 μ_B for $S = 1$ low-speed Cr^{II}, but it is in

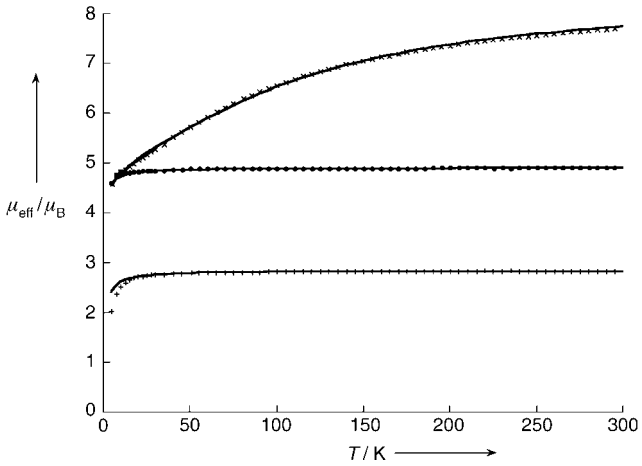

Figure 4. Temperature dependence of the effective magnetic moment, $\mu_{eff} = (8\chi T)^{1/2}$, of $K_4[Cr^{II}(CN)_6]$ (+), $(NEt_4)_3[Cr^{II}(CN)_5]$ (●), and $(NEt_4)_8[Cr^{II}(CN)_5][Cr^{II}_2(CN)_9]$ (×). The solid lines are fits, as discussed in the text.

excellent agreement with the expected spin-only value of 4.90 μ_B for $S = 2$ high-spin Cr^{II}. Above 5 K, $\chi(T)$ could be fitted to the Curie–Weiss expression, $\chi \propto (T-\theta)^{-1}$, with $g = 2.00$, $\theta = -0.79$ K, and a TIP value of 50×10^{-6} emu mol^{-1}. In contrast, the room temperature μ_{eff} value for $K_4[Cr^{II}(CN)_6]$ is 2.82 μ_B (corrected for TIP). Above 5 K, $\chi(T)$ could also be fitted to the Curie–Weiss expression with $g = 2.00$, $\theta = -1.9$ K, and a TIP value of 150×10^{-6} emu mol^{-1} (Figure 4). The room temperature μ_{eff} value is consistent with the low-spin $S = 1$ ground state previously reported.[16] Hence, $[Cr^{II}(CN)_5]^{3-}$ is a rare example of a high-spin homoleptic cyanide complex.

The magnetic behavior of $(NEt_4)_8[Cr^{II}(CN)_5][Cr^{II}_2(CN)_9]$ is more complex (Figure 4) as a result of contributions from $[Cr^{II}(CN)_5]^{3-}$ and dinuclear $[Cr^{II}_2(CN)_9]^{5-}$. The observed data can be modeled with an $S = 2$ Curie–Weiss expression and a Bleaney–Bower-like $S = 2$ term,[17] with $g = 2.00$, $J/k = -19.1$ K, $\theta = -0.79$ K, and a TIP value of 150×10^{-6} emu mol^{-1}. Hence, **2** exhibits moderate intradimer antiferromagnetic coupling of -19.1 K (-13.3 cm^{-1}), and the nonet excited state lies 266 cm^{-1} (0.76 kcal mol^{-1}) above the singlet ground state.

Formation of $[Cr^{II}(CN)_5]^{3-}$ and $[Cr^{II}_2(CN)_9]^{5-}$, but not the sought $(NEt_4)_4[Cr^{II}(CN)_6]$, is quite surprising as $K_4[Cr^{II}(CN)_6]$ as well as $Na_4[Cr^{II}(CN)_6]$ are known low-spin octahedral compounds.[10,18] Furthermore, why does $(NEt_4)_3[Cr^{II}(CN)_5]$, but not $(NEt_4)_4[Cr^{II}(CN)_6]$, form in the presence of excess cyanide? We attribute the formation of $[Cr^{II}(CN)_5]^{3-}$ to the initial formation of $[Cr^{II}(CN)_6]^{4-}$, which is expected to have a reduced $\Delta(Cr^{II})$ value with respect to $\Delta(Cr^{III})$ and which makes a high-spin state more accessible. High-spin $t_{2g}^3e_g^1$ $[Cr^{II}(CN)_6]^{4-}$ would have an electron in an antibonding orbital that weakens the Cr^{II}–C bonds and destabilizes the system, and when the large tetranegative charge is considered—although, $(NEt_4)_4[Fe^{II}(CN)_6]$ is known to have a shorter M–C bond[19]—loss of a cyanide ion is favored to form the observed $[Cr^{II}(CN)_5]^{3-}$ species. Presumably $A_4[Cr^{II}(CN)_6]$ (A = Na, K) is stabilized through electrostatic interactions between the alkali-metal cation (and water molecules) and the nitrogen centers of the cyanide units.

Experimental Section

1: In a DryBox (< 0.5 ppm O_2) $Cr^{II}_2(OAc)_4$ (274.8 mg, 0.8078 mmol) was dissolved in deoxygenated MeCN (50 mL) to give an orange–red solution, which was then added dropwise to a stirring colorless solution of NEt_4CN (1.510 g, 9.563 mmol) in MeCN (50 mL). After stirring for 30 min, the dark purple solution was filtered and concentrated to 20 mL under reduced pressure. Dark purple crystalline blocks were obtained by diffusion of THF (yield: 62%) and characterized by single-crystal X-ray diffraction. The crystallographic sample was maintained in contact with the mother liquor to prevent solvent loss. Thermogravimetric analysis showed the sample was stable up to 160 °C and could be desolvated at lower temperatures (i.e. heating at 110 °C under reduced pressure) to form the desolvated $(NEt_4)_3[Cr^{II}(CN)_5]$. Selected IR data (KBr): $\tilde{\nu} = 2986$ (s), 2950 (m), 2892 (w), 2086 (s), 1488 (s), 1461 (s), 1396 (s), 1375 (w), 1311 (w), 1186 (m), 1175 (s), 1080 (w), 1055 (w), 1035 (m), 1005 (s), 787 cm^{-1} (s).

2: $Cr^{II}_2(OAc)_4$ (55.94 mg, 0.1644 mmol) dissolved in MeCN (20 mL) was added dropwise to a solution of NEt_4CN (256.3 mg, 1.640 mmol) in MeCN (20 mL). After stirring for 30 min, the reddish purple solution was filtered and concentrated to 15 mL under reduced pressure. Brown needlelike crystals were obtained by diffusion of THF (yield: 24%) and characterized by single-crystal X-ray diffraction. The crystallographic sample was maintained in contact with the mother liquor to prevent solvent loss. Selected IR data (KBr): $\tilde{\nu} =$ 2986 (s), 2949 (m), 2894 (w), 2248 (w), 2090 (s), 1484 (s), 1461 (s), 1396 (s), 1377 (w), 1310 (w), 1185 (m), 1175 (s), 1080 (w), 1057 (w), 1036 (m), 1005 (s), 789 cm^{-1} (s).

Received: December 1, 2004
Revised: February 1, 2005
Published online: April 14, 2005

Keywords: crystal field theory · cyanides · magnetic properties · transition metals

[1] J. J. Alexander, H. B. Gray, *J. Am. Chem. Soc.* **1968**, *90*, 4260.
[2] J. J. Alexander, H. B. Gray, *J. Am. Chem. Soc.* **1967**, *89*, 3356.
[3] W. E. Buschmann, A. M. Arif, J. S. Miller, *Angew. Chem.* **1998**, *110*, 813; *Angew. Chem. Int. Ed.* **1998**, *37*, 781.
[4] J. S. Miller, J. L. Manson, *Acc. Chem. Res.* **2001**, *34*, 563.
[5] S. Ferlay, T. Mallah, R. Ouahes, P. Veillet, M. Verdaguer, *Nature* **1995**, *378*, 701; S. M. Holmes, G. S. Girolami, *J. Am. Chem. Soc.* **1999**, *121*, 5593; Ø. Hatlevik, W. E. Buschmann, J. Zhang, J. L. Manson, J. S. Miller, *Adv. Mater.* **1999**, *11*, 914.
[6] J. H. Balthis, Jr., J. C. Bailar, Jr., *Inorg. Synth.* **1939**, *1*, 122; M. Kranz, A. Witkowska, *Inorg. Synth.* **1960**, *6*, 144.
[7] R. T. Henriques, E. Herdtweck, F. E. Kühn, A. D. Lopes, J. Mink, C. C. Ramão, *J. Chem. Soc. Dalton Trans.* **1998**, 1293; W. E. Buschmann, A. M. Arif, J. S. Miller, *Chem. Eur. J.* **1998**, *4*, 1731.
[8] D. A. White, A. J. Solodar, M. M. Baizer, *Inorg. Chem.* **1972**, *11*, 2160.
[9] W. P. Griffith, J. R. Lane, *J. Chem. Soc.* **1972**, 158.
[10] J. P. Eaton, D. Nicholls, *Transition Met. Chem.* **1981**, *6*, 203.
[11] Crystal data for $(NEt_4)_3[Cr^{II}(CN)_5]\cdot MeCN\cdot{}^1/_8 THF$ (**1**): $C_{126}H_{256}Cr_4N_{36}O_{0.5}$ triclinic, space group: $P\bar{1}$, $a = 17.8172(3)$ Å,

$b = 20.8318(6)$ Å, $c = 21.5756(5)$ Å, $\alpha = 87.6399(9)°$, $\beta = 84.4486(13)°$, $\gamma = 71.9031(14)°$, $V = 7575.7(3)$ Å^3, $Z = 2$, $T = 150$ K, $\rho_{calcd} = 1.092$ Mg m^{-3}. The structure was solved by a combination of direct methods and heavy atoms using SIR 97. All non-hydrogen atoms were refined with anisotropic displacement coefficients. Hydrogen atoms were assigned isotropic displacement coefficients $U(H) = 1.2\,U(C)$ or $1.5\,U(C_{Me})$, and their coordinates were allowed to ride on their respective carbons using SHELXL97. The asymmetric unit contains four $[Cr(CN)_5]^{3-}$ and twelve $[NEt_4]^+$ units, as well as four molecules of acetonitrile and half a molecule of tetrahydrofuran. Most of the cations and half of the acetonitrile units exhibit orientation disorder (50:50). Only one anion, $[Cr^{II}(CN)_5]^{3-}$, of the asymmetric unit exhibits orientation disorder in one of the cyanide ligands (C18–N18 and C18′–N18′) on atom Cr4 (50:50). This is not surprising as both square-pyramidal and distorted trigonal bipyramid structures are present in the unit cell. The weighting scheme employed was $w = 1/[\sigma^2(F_o^2) + (0.1366P)^2 + 10.5826P]$, where $P = (F_o^2 + 2F_c^2)/3$. The refinement converged to $R1 = 0.0842$, $wR2 = 0.218$, and $S = 1.036$ for 16467 reflections with $1 > 2\sigma(I)$, and $R1 = 0.1396$, $wR2 = 0.2649$, and $S = 1.036$ for 26638 unique reflections and 1831 parameters. The maximum Δ/σ value in the final cycle of the least-squares treatment was zero, and the residual peaks on the final difference-Fourier map ranged from -0.504 to 1.677 e$^-$ Å^{-3}.

[12] A. R. Rossi, R. Hoffmann, *Inorg. Chem.* **1975**, *14*, 365.

[13] K. N. Raymond, P. W. R. Corfield, J. A. Ibers, *Inorg. Chem.* **1968**, *7*, 1362; J. J. Sokol, M. P. Shores, J. R. Long, *Angew. Chem.* **2001**, *113*, 242; *Angew. Chem. Int. Ed.* **2001**, *40*, 236.

[14] L. D. Brown, K. N. Raymond, *Inorg. Chem.* **1975**, *14*, 2590.

[15] Crystal data for $(NEt_4)_8[Cr^{II}(CN)_5][Cr_2^{II}(CN)_9]\cdot 2MeCN$ (**2**): $C_{82}H_{166}Cr_3N_{24}$ triclinic, space group: $P\bar{1}$, $a = 10.2618(2)$ Å, $b = 22.4902(5)$ Å, $c = 23.4526(4)$ Å, $\alpha = 114.5636(8)°$, $\beta = 90.3961(11)°$, $\gamma = 101.8783(10)°$, $V = 4791.3(2)$ Å^3, $Z = 2$, $T = 150$ K, $\rho_{calcd} = 1.140$ Mg m^{-3}. The structure was solved by a combination of direct methods and heavy atoms using SIR 97. All non-hydrogen atoms were refined with anisotropic displacement coefficients. Hydrogen atoms were assigned isotropic displacement coefficients $U(H) = 1.2\,U(C)$ or $1.5\,U(C_{Me})$, and their coordinates were allowed to ride on their respective carbons using SHELXL97. There are two distinctly different anions, $[Cr^{II}(CN)_5]^{3-}$ and $[Cr_2^{II}(CN)_9]^{5-}$. Three out of the eight $(NEt_4)^+$ cations exhibit unequal (67:33) orientation disorder. The asymmetric unit contains two noncoordinating molecules of acetonitrile. The weighting scheme employed was $w = 1/[\sigma^2(F_o^2) + (0.0944P)^2 + 4.5597P]$ where $P = (F_o^2 + 2F_c^2)/3$. The refinement converged to $R1 = 0.0671$, $wR2 = 0.1662$, and $S = 1.019$ for 14333 reflections with $1 > 2\sigma(I)$, and $R1 = 0.1131$, $wR2 = 0.1971$, and $S = 1.019$ for 21857 unique reflections and 1138 parameters. The maximum Δ/σ value in the final cycle of the least-squares treatment was zero, and the residual peaks on the final difference-Fourier map ranged from -0.595 to 1.286 e$^-$ Å^{-3}. CCDC-253631 (**1**) and 257172 (**2**) contain the supplementary crystallographic data for this paper. These data can be obtained free of charge from the Cambridge Crystallographic Data Centre via www.ccdc.cam.ac.uk/data_request/cif.

[16] E. A. Boudreaux, L. N. Mulay, *Theory and Applications of Molecular Paramagnetism*, Wiley-Interscience, New York, **1976**, p. 177.

[17] C. J. O'Connor, *Prog. Inorg. Chem.* **1982**, *29*, 203. The equation used for this binuclear spin 2–2 system is ($\boldsymbol{H} = -2JS_1S_2$):

$$\chi = \frac{Ng^2\mu_B^2}{k(T-\theta)}\left[\frac{2e^{\frac{2J}{kT}} + 10e^{\frac{6J}{kT}} + 28e^{\frac{12J}{kT}} + 60e^{\frac{20J}{kT}}}{(1 + 3e^{\frac{2J}{kT}} + 5e^{\frac{6J}{kT}} + 7e^{\frac{12J}{kT}} + 9e^{\frac{20J}{kT}})} + 2\right],$$

with T = temperature, N = Avogadro's number, k = Boltzmann's constant, μ_B = Bohr Magneton, θ = Weiss constant, J = coupling constant, and S = spin state.

[18] When the reaction was carried out in deoxygenated water in the presence of excess cyanide ion, the complex $[Cr^{II}(CN)_5]^{3-}$ formed ($\nu_{C\equiv N} = 2089$ cm^{-1}; half-width at half height: 9.4 cm^{-1}).

[19] J. C. Eppich, K. J. Nelson, A. M. Arif, unpublished results.

Boron–Magnesium Reagents

Preparation and Selective Reactions of Mixed Bimetallic Aromatic and Heteroaromatic Boron–Magnesium Reagents**

*Oliver Baron and Paul Knochel**

Dedicated to Professor Peter Stanetty on the occasion of his 60th birthday

The selective functionalization of aryl and heteroaryl compounds is an important synthetic task. The resulting polyfunctional (hetero)aryl derivatives are often essential building blocks in the synthesis of pharmaceuticals, agrochemicals, and new organic materials.[1] We envisaged that bimetallic[2] aromatic derivatives of type **1**, which bear two metal-centered substituents of distinctly different reactivity, would be useful reagents. Their stepwise reaction with two electrophiles E^1 and E^2 would provide products of type **2** and **3** (Scheme 1).

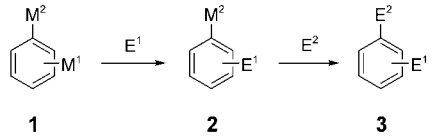

Scheme 1. Reactivity of bimetallic aryl derivates.

Unfortunately, the reaction of *para*-iodoboronic ester **4a**[3] with *i*PrMgCl afforded only the corresponding isopropylboronate, which results from the attack of the Grignard reagent at the boronic ester functionality. However, the reaction with the new reagent *i*PrMgCl·LiCl[4] (−78 °C, 2 h) furnished the desired magnesiated boronic ester **5a**, which reacted with a variety of electrophiles to provide boronic esters of type **6** in good yields (Scheme 2, Table 1). Thus, the reaction of **5a** with allylic bromides in the presence of a catalytic amount of CuCN·2 LiCl[5] furnished the expected allylated boronic esters **6a** and **6b** in 77 and 67 % yield, respectively (Table 1, entries 1 and 2). Acylation reactions proceeded best when the Grignard reagents **5a** and **5b** were transmetalated stoichiometrically with CuCN·2 LiCl. Both aliphatic and aromatic acid chlorides reacted smoothly to give the keto-substituted boronic esters **6c**, **6d**, and **6i** in 72, 73, and 71 % yield, respectively (Table 1, entries 3, 4, and 9). The magnesiated

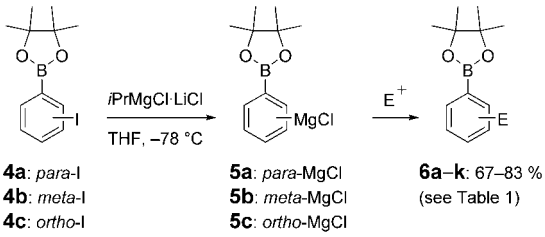

Scheme 2. Synthesis of boronic esters of type **6** by the treatment of magnesiated boronic esters **5** with electrophiles.

boronic esters **5a–b** also added directly to benzaldehyde to provide the hydroxy-substituted boronic esters **6e** and **6h** in 83 and 71 % yield, respectively (Table 1, entries 5 and 8). The boronic ester cuprates underwent a smooth addition–elimination reaction with 3-iodocyclohexenones to furnish the expected β-substituted unsaturated ketones **6f** (78 %), **6g** (79 %), and **6j** (76 %; Table 1, entries 6, 7, and 10). Preliminary experiments showed that the *ortho*-magnesiated phenylboronic ester **5c** displayed a lower reactivity towards electrophiles. However, its allylation gave the boronic ester **6k** in 71 % yield (Table 1, entry 11).

By using the readily available heterocyclic diiodides **7**,[6] **8**,[7] and **9**,[8] it was possible to prepare the iodoheteroaryl boronic esters **11** (76 %), **12** (76 %), and **13** (81 %) by an I/Mg exchange followed by treatment with the dioxaborolane **10** (Scheme 3). These boronic esters were readily converted by treatment with *i*PrMgCl·LiCl at −78 °C into the related magnesiated species **14–16**, which reacted with various electrophiles as found for the magnesiated carbocyclic boronic esters. Thus, the copper(I)-catalyzed allylation of **14** and **16** provided the allylated heterocyclic boronic esters **17a** and **17c** in 83 and 91 % yield, respectively (Table 2, entries 1 and 3). Transmetalation of the magnesiated 2-indolyl boronic ester **15** with CuCN·2 LiCl, followed by treatment with

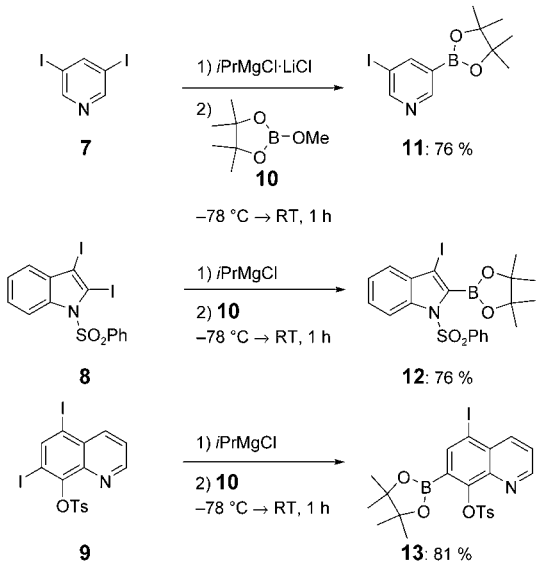

Scheme 3. Synthesis of iodo-substituted heterocyclic boronic esters **11–13** by I/Mg exchange. Ts = *p*-toluenesulfonyl.

[*] Dipl.-Chem. O. Baron, Prof. Dr. P. Knochel
Department Chemie und Biochemie
Ludwig-Maximilians-Universität München
Butenandtstrasse 5–13, Haus F, 81377 München (Germany)
Fax: (+49) 89-2180-77680
E-mail: paul.knochel@cup.uni-muenchen.de

[**] We thank the Fonds der Chemischen Industrie and Merck Research Laboratories (MSD) for financial support. We also thank Chemetall and BASF for generous gifts of chemicals.

Supporting information for this article is available on the WWW under http://www.angewandte.org or from the author.

 DOI: 10.1002/anie.200462928

Table 1: Preparation of boronic esters of type **6** by the reaction of the magnesiated aryl boronic esters **5a–c** with electrophiles.

Entry	5	Electrophile	6	Yield [%][a]
	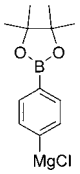		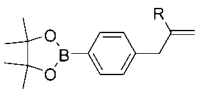	
1	**5a**	R = H	**6a**: R = H	77
2	**5a**	R = CO_2Et	**6b**: R = CO_2Et	67
			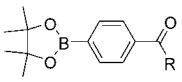	
3	**5a**	PhCOCl	**6c**: R = Ph	72
4	**5a**	BuCOCl	**6d**: R = Bu	73
			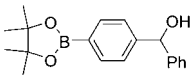	
5	**5a**	PhCHO[b]	**6e**	83
			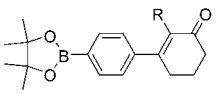	
6	**5a**	R = H	**6f**: R = H	78
7	**5a**	R = Me	**6g**: R = Me	79
	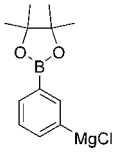		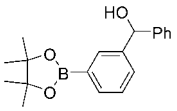	
8	**5b**	PhCHO[b]	**6h**	71
			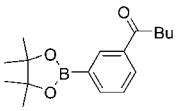	
9	**5b**	BuCOCl	**6i**	71
			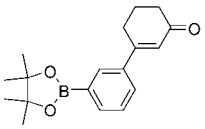	
10	**5b**		**6j**	76
	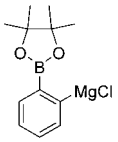		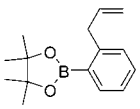	
11	**5c**		**6k**	71

[a] Yield of analytically pure isolated product. [b] This reaction does not require a transmetalation step with CuCN·2 LiCl.

propionyl chloride, furnished the keto-substituted indolyl boronic ester **17b** in 81% yield (Table 2, entry 2). The reaction of magnesiated species **16** with benzaldehyde gave the corresponding alcohol directly in 78% yield (Table 2, entry 4).

All new polyfunctional boronic esters underwent smooth Suzuki cross-coupling reactions. Thus, boronic ester **6h** (Table 1, entry 8) reacted readily with 4-bromobenzonitrile in the presence of [$PdCl_2$(dppf)] (5 mol%; dppf = 1,1′-bis(diphenylphosphanyl)ferrocene)[9] and K_2CO_3 (3 equiv) in THF at 60 °C (9 h) to give the cross-coupling product **18** in 92% yield (Scheme 4). In a convenient one-pot procedure, the iodoboronic ester **4a** was treated first with *i*PrMgCl·LiCl (−78 °C, 2 h) and then with benzaldehyde to provide the magnesium alcoholate **19**, which was submitted directly to Suzuki cross-coupling conditions.[8] This sequence afforded the terphenyl derivative **20**, which was isolated in 73% yield (Scheme 4). Similarly, magnesiation of the *meta*-substituted iodoboronic ester **4b**, transmetalation with CuCN·2 LiCl, and treatment with 3-iodo-2-methylcyclohexenone led to the polyfunctional boronic ester **21**, which reacted with 4-bromoisoquinoline under palladium catalysis to provide the heterocyclic product **22** in 52% overall yield (Scheme 4).

In summary, we have prepared magnesiated aryl and heteroaryl boronic esters by an I/Mg exchange. These reagents provided access to a broad array of polyfunctional boronic esters, which underwent smooth Suzuki cross-coupling reactions. Further extensions of this methodology are currently being studied in our laboratories.

Experimental Section

Typical procedure: Synthesis of **12**: *i*PrMgCl (1.48 mL, 1.3 mmol, 0.88 M in THF) was added dropwise over 5 min to a solution at −78 °C of **8** (0.611 g, 1.2 mmol) in THF (8 mL) in a dry, argon-flushed 25-mL Schlenk tube equipped with a magnetic stirring bar and a septum. The reaction mixture was stirred at this temperature for 2 h, until completion of the I/Mg exchange was detected by GC analysis of reaction aliquots, then **10** (0.158 g, 1.0 mmol) was added. The resulting mixture was allowed to warm to room temperature and stirred until full conversion into the boronic ester **12** was indicated by GC analysis. The reaction mixture was then quenched with a small amount of a saturated, aqueous solution of NH_4Cl and extracted with Et_2O (4 × 10 mL), and the extracts were dried over Na_2SO_4. After filtration, the solvent was evaporated in vacuo. Recrystallization from CH_2Cl_2 yielded **12** (387 mg, 76%) as a colorless solid.

Synthesis of **17b**: *i*PrMgCl·LiCl (1.46 mL, 1.4 mmol, 0.96 M in THF) was added dropwise over 15 min to a solution at −78 °C of **12** (0.611 g, 1.2 mmol) in THF (25 mL) in a dry, argon-flushed 100-mL

Table 2: Synthesis of polyfunctional heterocyclic boronic esters of type **17** by the reaction of magnesiated heterocyclic boronic esters with electrophiles.

Entry	Magnesiated boronic ester	Electrophile	**17**	Yield[a] [%]
1	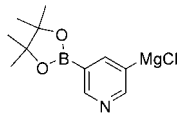 **14**	allyl bromide	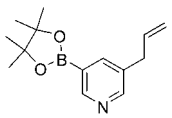 **17a**	83
2	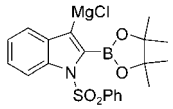 **15**	EtCOCl	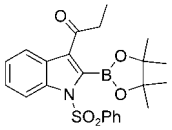 **17b**	81
3	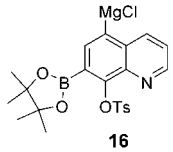 **16**	allyl bromide	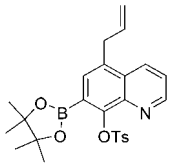 **17c**	91
4	**16**	PhCHO[b]	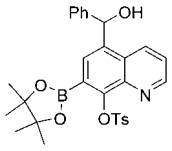 **17d**	78

[a] Yield of analytically pure isolated product. [b] This reaction does not require a transmetalation step with CuCN·2 LiCl.

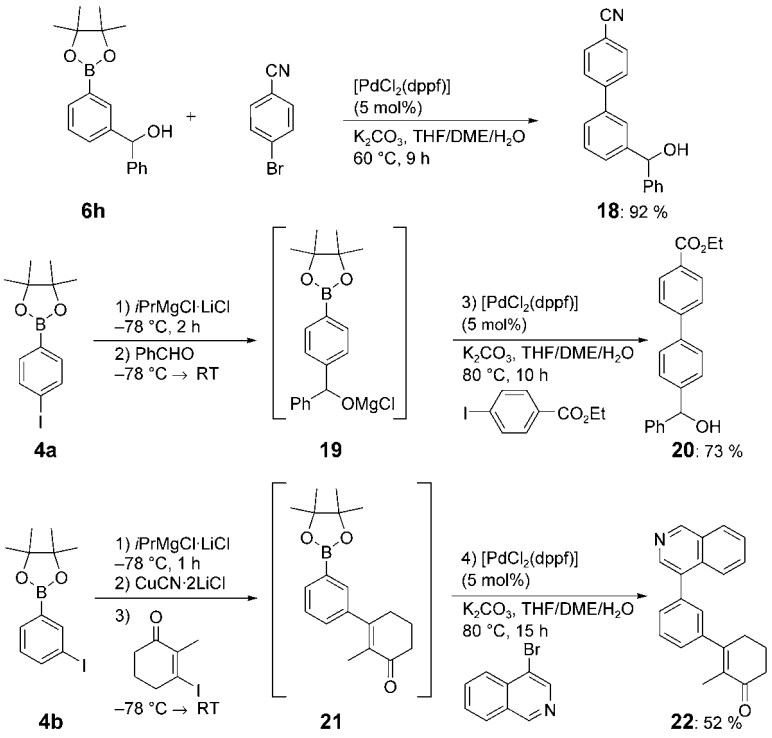

Scheme 4. One-pot magnesiation, reaction with an electrophile, and Suzuki cross-coupling. DME = 1,2-dimethoxyethane.

Schlenk tube equipped with a magnetic stirring bar and a septum. The reaction mixture was stirred at this temperature for 1 h, until completion of the I/Mg exchange was detected by GC analysis of reaction aliquots, then CuCN·2 LiCl (1.2 mL, 1.2 mmol, 1.0 M in THF) was added, and the resulting mixture was stirred at −78 °C for an additional 20 min. Propionyl chloride (0.093 g, 1.0 mmol) was then added, and the reaction mixture was allowed to warm to room temperature and stirred until full conversion into the boronic ester **17b** was indicated by GC analysis. The reaction mixture was then quenched with a small amount of a saturated, aqueous solution of NH_4Cl and extracted with Et_2O (4 × 10 mL) and CH_2Cl_2 (3 × 10 mL), and the extracts were dried over Na_2SO_4. After filtration, the solvent was evaporated in vacuo. Recrystallization from CH_2Cl_2 yielded the indolyl boronic ester **17b** (356 mg, 81 %) as a colorless solid.

Received: December 14, 2004
Published online: April 12, 2005

Keywords: boronic esters · cross-coupling · heterocycles · magnesium · palladium

[1] For recent advances in the selective functionalization of aromatic systems, see: a) J. Clayden, *Organolithiums: Selectivity for Synthesis*, Pergamon, New York, **2002**; b) M. C. Whisler, S. MacNeil, V. Snieckus, P. Beak, *Angew. Chem.* **2004**, *116*, 2256; *Angew. Chem. Int. Ed.* **2004**, *43*, 2206; c) R. R. Milburn, V. Snieckus, *Angew. Chem.* **2004**, *116*, 906; *Angew. Chem. Int. Ed.* **2004**, *43*, 888; d) M. G. Debije, J. Piris, M. P. De Haas, J. M. Warman, Z. Tomovic, C. D. Simpson, M. D. Watson, K. Müllen, *J. Am. Chem. Soc.* **2004**, *126*, 4641; e) J. Qu, C. Kohl, M. Pottek, K. Müllen, *Angew. Chem.* **2004**, *116*, 1554; *Angew. Chem. Int. Ed.* **2004**, *43*, 1528; f) J. T. Suri, D. B. Cordes, F. E. Cappuccio, R. A. Wessling, B. Singaram, *Angew. Chem.* **2003**, *115*, 6037; *Angew. Chem. Int. Ed.* **2003**, *42*, 5857.

[2] a) I. Marek, *Chem. Rev.* **2000**, *100*, 2887; b) I. Marek, *Tetrahedron* **2002**, *58*, 9463.

[3] The iodoaryl boronic esters **4a–c** were prepared by the treatment of the corresponding iodoaryl magnesium chlorides, obtained in turn by I/Mg exchange, with **10** (THF, −78→25 °C, 1–3 h, 86–91 %); see Supporting Information. a) A. Finch, P. J. Gardner, E. J. Pearn, *Recl. Trav. Chim. Pays-Bas* **1964**, *83*, 1314; b) R. W. Hoffmann, A. Endesfelder, H.-J. Zeiss, *Carbohydr. Res.* **1983**, *123*, 320.

[4] a) A. Krasovskiy, P. Knochel, *Angew. Chem.* **2004**, *116*, 3396; *Angew. Chem. Int. Ed.* **2004**, *43*, 3333; b) F. Kopp, A. Krasovskiy, P. Knochel, *Chem. Commun.* **2004**, 2288; c) H. Ren, A. Krasovskiy, P. Knochel, *Org. Lett.* **2004**, *6*, 4215.

[5] P. Knochel, M. C. P. Yeh, S. C. Berk, J. Talbert, *J. Org. Chem.* **1988**, *53*, 2390.

[6] M. Winkler, B. Cakir, W. Sander, *J. Am. Chem. Soc.* **2004**, *126*, 6135.

[7] a) B. Witulski, N. Buschmann, U. Bergsträßer, *Tetrahedron* **2000**, *56*, 8473; b) M. G. Saulnier, G. W. Gribble, *J. Org. Chem.* **1982**, *47*, 757.

[8] A. Staubitz, W. Dohle, P. Knochel, *Synthesis* **2003**, 233.

[9] a) N. Miyaura, A. Suzuki, *Chem. Rev.* **1995**, *95*, 2457; b) G. A. Molander, B. Biolatto, *J. Org. Chem.* **2003**, *68*, 4302.

Organolithium Compounds

A Highly Diastereomerically Enriched, Silyl-Substituted Alkyl Lithium, Configurationally Stable at Room Temperature**

Carsten Strohmann, Bors C. Abele, Klaus Lehmen, and Daniel Schildbach*

Dedicated to Professor Johann Weis on the occasion of his 60th Birthday

Over the last 20 years, a number of enantiomerically and diastereomerically enriched[1] alkyl lithium compounds have been reported.[2,3] For most of the compounds the configuration of the metalated stereogenic carbon center is only stable at low temperatures (−78 °C). However, more recently, corresponding compounds have been synthesized which have proved to be configurationally stable for a few minutes at higher temperatures, including examples from Hoppe et al. and from our own group.[2,4,5] In a few cases the absolute configuration of the alkyl lithium and the reaction products have been determined unambiguously by single-crystal X-ray structural analysis,[6] which allows conclusions that are free from speculation to be drawn on the stereochemical course of the reaction of the alkyl lithium with electrophilic reaction partners. We recently described the highly stereoselective lithiation of an (aminomethyl)benzylsilane, the molecular structure of the corresponding alkyl lithium compound, and the stereochemical course of its reactions.[5,6g,7]

We now report the synthesis of the highly diastereomerically enriched silyl-substituted alkyl lithium compound (*R*,*S*)-**6**, its different structures in the solid state, determined on crystals from coordinating and non-coordinating solvent mixtures, and the diastereodivergent stereochemical course of the reactions of (*R*,*S*)-**6** with chlorotrimethylstannane in relation to the solvent used. Diastereodivergent reactions of alkyl lithium compounds by variation of the electrophile have already been described, however a control of the stereochemical course of the reaction by choice of solvent is to our knowledge unknown.

The synthesis of the starting compound, the optically active (aminomethyl)[(trimethylsilyl)methyl]silane (*S*)-**5**, occurs in good yields in four steps starting from dichloro(chloromethyl)silane **1**. A chlorine–iodine exchange by a Finkelstein reaction is necessary in the second step for the introduction of the optically active amine (*S*)-2-(methoxymethyl)pyrrolidine (SMP; Scheme 1).

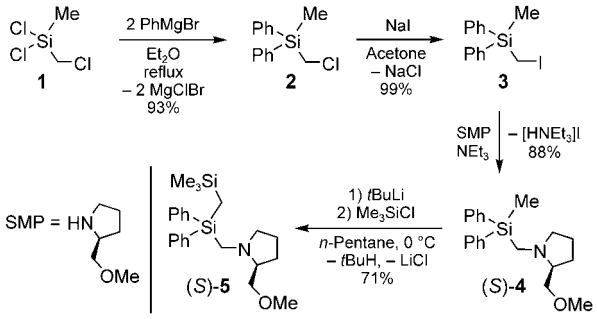

Scheme 1. Synthesis of the starting compound (*S*)-**5**. For full experimental details see the Supporting Information.

The lithiation of (*S*)-**5** occurred in the first case by reaction with *sec*-butyllithium in toluene/cyclohexane over 30 days at −80 °C (Schema 2, path 1). After warming to room temperature and being left to stand for 60 min the mixture was cooled to −90 °C and treated with chlorotrimethylstannane (Me_3SnCl reacts rapidly as a selective trapping reagent even at low temperatures). The ^1H NMR spectra of the crude product **7** showed a diastereomeric ratio d.r. = 91:9 for the tin compound (Scheme 2). The absolute configuration of the main stereoisomer (*R*,*S*)-**7** was determined by derivatization to the ammonium stannate $[Ph_2\{(Me_3Si)(Me_3Sn)CH\}SiCH_2N(H)C_6H_{12}O][Me_3SnCl_2]$ ((*R*,*S*)-**8**) and subsequent single-crystal X-ray analysis.[8]

If the described procedure of lithiation and substitution was carried out in toluene/cyclohexane but after the addition of *sec*-butyllithium warming to room temperature was carried out within only 5 min, the tin compounds were formed with a diastereomeric ratio of only d.r. = 63:37 (Scheme 2, path 2). This diastereomeric relationship was not influenced by the standing time of the lithium compound (*R*,*S*)-**6** at room temperature, since the reactions of the lithium compound with the electrophile both immediately after warming to room temperature and after 60 min standing time at room temperature gave the same result. It follows from this result that the diastereomeric ratio of the lithium compound **6** is dependent almost exclusively upon the conditions of the deprotonation (kinetically controlled diastereotopos-differentiating deprotonation). In addition, it can be deduced that the configuration at the stereogenic, metalated carbon center of (*R*,*S*)-**6** is stable for at least 60 min at room temperature (Scheme 2).

We made a striking observation on the stereochemical course of the lithiation–substitution sequence when it was carried out in a toluene/cyclohexane/THF mixture under otherwise identical conditions (Scheme 2, path 3). The single-crystal X-ray structural analysis of the two alkyl lithium compounds (*R*,*S*)-**6** and (*R*,*S*)-**6**·THF do indeed show in each case an *R* configured metalated carbon center (Figures 1 and 2). The ^1H NMR spectroscopic investigation of the crude product of the reaction of (*R*,*S*)-**6**·THF with chlorotrimethyl-

[*] Priv.-Doz. Dr. C. Strohmann, Dr. B. C. Abele, Dr. K. Lehmen, Dr. D. Schildbach
Institut für Anorganische Chemie
Universität Würzburg
Am Hubland, 97074 Würzburg (Germany)
Fax: (+49) 931-888-4605
E-mail: mail@carsten-strohmann.de

[**] We thank the Deutsche Forschungsgemeinschaft, the Graduiertenkolleg 690, and the Fonds der Chemischen Industrie for the financial support of this work and Wacker-Chemie GmbH for generous gifts of chemicals.

Supporting information for this article (full experimental details) is available on the WWW under http://www.angewandte.com or from the author.

  DOI: 10.1002/anie.200462141

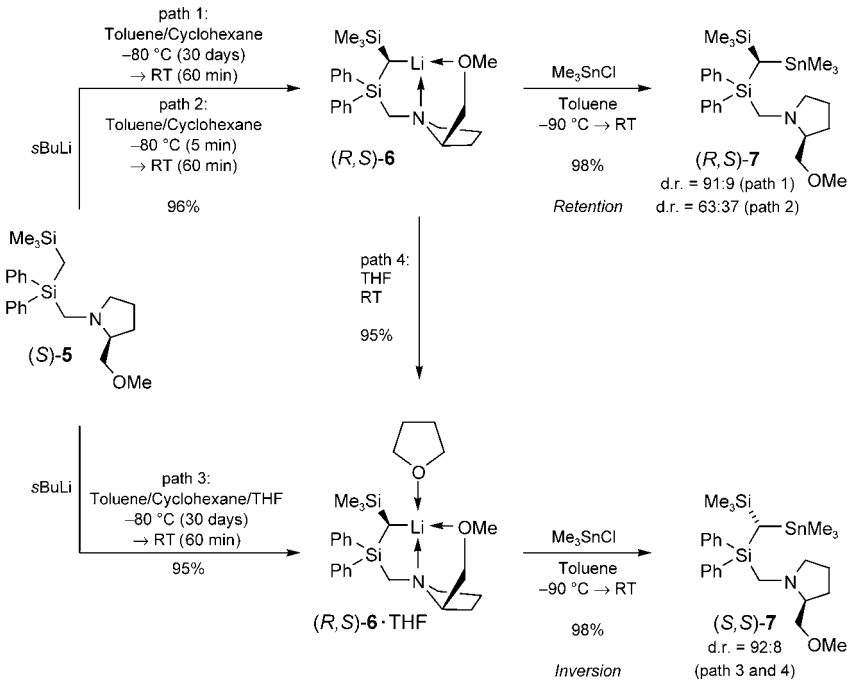

Scheme 2. Lithiation of (*S*)-**5** and diastereodivergent reaction pathway. For full experimental details see the Supporting Information.

stannane shows, however, a diastereomeric ratio of d.r. = 92:8 for the tin compound formed in favor of the (*S*,*S*)-**7** diastereomer. Thus the substitution with (*R*,*S*)-**6** in the presence of THF occurs with inversion of the configuration, whereas in the noncoordinating toluene/cyclohexane mixture retention of configuration is observed. Moreover, the addition of a few drops of THF to the only slightly diastereomerically enriched sample of (*R*,*S*)-**6** (d.r. = 63:37) at room temperature in an analogous trapping reaction at −90 °C also produces the tin compound (*S*,*S*)-**7** with d.r. = 92:8 (Scheme 2, path 4). Thus, this fourth form of the reaction is a thermodynamically controlled epimerization at room temperature. Reactions of isolated (*R*,*S*)-**6** in toluene and (*R*,*S*)-**6**·THF in THF gave the same results.

The molecular structures of (*R*,*S*)-**6** (Figure 1) and (*R*,*S*)-**6**·THF (Figure 2) were determined by single-crystal X-ray structural analysis. The stereochemical homogeneity of the samples was confirmed in that identical lattice constants were obtained for each of ten randomly chosen crystals.[8] Both (*R*,*S*)-**6** and (*R*,*S*)-**6**·THF crystallize as monomers with only one C–Li contact of 2.176(6) ((*R*,*S*)-**6**) and 2.195(8) Å ((*R*,*S*)-**6**·THF). Both molecules have an *R* configuration at the metalated carbon center C1. The lithium centers show in each case a contact to the metalated carbon center C1 and are also coordinated by both a nitrogen and oxygen center of the SMP ligand. A fourth coordination site on the lithium in (*R*,*S*)-**6**·THF is occupied by a THF molecule from the solvent, whereas in the case of (*R*,*S*)-**6** short contacts to the hydrogen atoms H3b (2.281 Å) and H3c (2.014 Å) of a methyl group of the neighboring molecule are observed with formal formation of a coordination polymer. Common to both structures are short Si1–C1 and Si2–C1 bonds of between 1.789 and 1.808 Å, which result from the polarization-induced charge stabilization by the silicon centers (α effect). The sum of the angles of 348.2 and 345.6° for the "carbanionic units" of (*R*,*S*)-**6** and (*R*,*S*)-**6**·THF show a pyramidalization of the metalated center, which is illustrated by the Si1-C1-Si2 bond angles of 127.2(2) and 125.6(2)°. In (*R*,*S*)-**6** the shortest contact involving the lithium center (1.970(7) Å) is to the oxygen atom of the SMP handle. In (*R*,*S*)-**6**·THF the shortest Li–O contact of 1.955(8) Å is to the coordinated THF molecule, the distance to the oxygen atom of the SMP handle is increased to 2.079(8) Å.

Whereas (*R*,*S*)-**6** is the result of a kinetically controlled diastereotopos-differentiating deprotonation, (*R*,*S*)-**6**·THF can be formed in a thermodynamically controlled epimerization at room temperature. Examination of the C1–Li bond axis shows that in the stereoisomer (*R*,*S*)-**6**·THF, the trimethylsilyl group and the THF molecule distance themselves spatially from each other and the crystallized

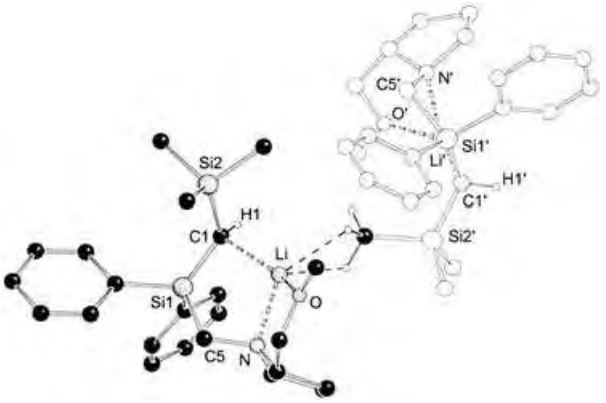

Figure 1. Molecular structure of compound (*R*,*S*)-**6** (Schakal representation).[9a] Selected bond lengths [Å] and angles [°]: Si1-C1 1.800(4), Si2-C1 1.808(4), Li-C1 2.176(6), N-Li 2.098(7), O-Li 1.970(7); C1-Si1-C5 109.7(2).

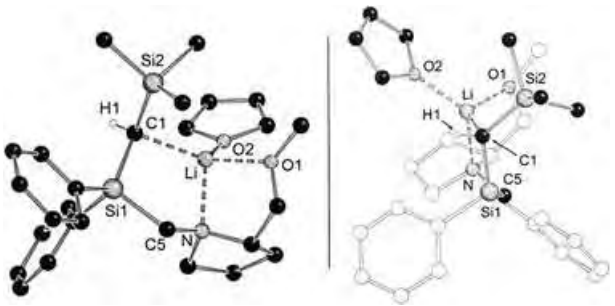

Figure 2. Molecular structure of compound (*R*,*S*)-**6**·THF (left), detail representation (right; Schakal representation).[9a] Selected bond lengths [Å] and angles [°]: Si1-C1 1.789(4), Si2-C1 1.797(4), Li-C1 2.195(8), N-Li 2.106(7), O1-Li 2.079(8), O2-Li 1.955(8); C1-Si1-C5 109.6(2).

diastereomer thus represents the thermodynamically most stable isomer (Figure 2 right). A quantum chemical estimation of the relative energies of (*R*,*S*)-**6**·THF and (*S*,*S*)-**6**·THF at the B3LYP/6-31+G(d) level shows an energetic preference for (*R*,*S*)-**6**·THF over (*S*,*S*)-**6**·THF of 8 kJ mol^{-1}, which corresponds to the trend found experimentally.[10]

The ^{13}C NMR spectrum of (*R*,*S*)-**6**·THF in [D$_6$]benzene at room temperature shows only one set of signals in which a quartet with $^{1}J_{^{13}C,^{7}Li} = 16.0$ Hz is observed for the metalated carbon center (Figure 3). The line shape of the quartet is

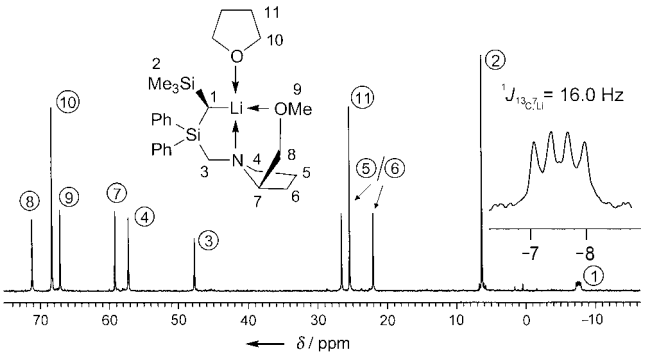

Figure 3. Section from the ^{13}C NMR spectrum of (*R*,*S*)-**6**·THF in [D$_6$]benzene at room temperature.

produced by superimposition of the ^{13}C–^{7}Li coupling pattern with the ^{13}C–^{6}Li coupling pattern. This result suggests the presence of **6** as a monomer in solution with the lithium center static on the NMR time scale at room temperature. NMR spectroscopy studies by Fraenkel and Reich in polar solvents, usually THF, show that inversion barriers which play a role in the racemization of chelated alkyl lithium compounds lie in an energy range of 18–80 kJ mol^{-1},[11], however an SMP handle allows particularly strong chelation. Thus, fixation of the lithium center in THF and the high stability of the configuration in nonpolar solvents for (*S*)-**5** are not surprising.

In contrast a ^{13}C–^{7}Li coupling could not be resolved for (*R*,*S*)-**6** in [D$_8$]toluene, neither at room temperature nor between 20 and −50 °C. Owing to the high quadrupole moment of ^{7}Li (nuclear spin $I = {}^{3}/_{2}$) corresponding couplings are not always observed, even in "frozen" exchange processes. Through the shortening of the carbon–lithium contact during a reduction in temperature, the resolution of the C–Li coupling, which is caused by the increasing quadrupole interaction, becomes worse and the coupling pattern often disappears again.[12] The same effect is observed in low-temperature ^{13}C NMR spectroscopy investigations with (*R*,*S*)-**6**·THF in [D$_8$]toluene, in which a strong broadening of the signal for the metalated carbon center is observed with falling temperature.

How can the experimentally observed stereochemical course be explained? In the case of a coordinated donor molecule, as in (*R*,*S*)-**6**·THF, it emerges that a rear attack of the electrophile with inversion of configuration is possible. This possibility is also shown by visualization of (*R*,*S*)-**6**·THF (optimized at the B3LYP/6-31+G(d) level) with the corresponding HOMO (the orbital coefficients at C1 are almost equally large; Figure 4). In contrast, with a free coordination site, substitution with retention of configuration is conceivable after precoordination at the formally triply coordinated

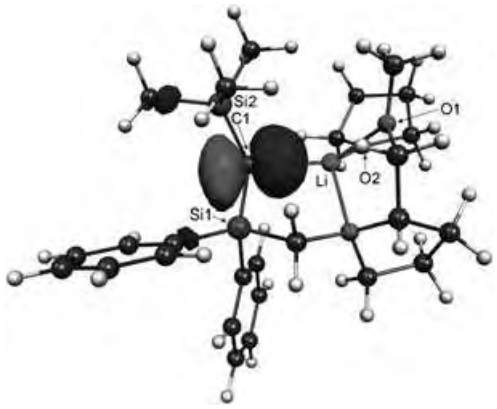

Figure 4. B3LYP/6-31+G(d)-optimized structure of (*R*,*S*)-**6**·THF and visualization of the highest occupied molecular orbital (Molekel representation; [9b] the numbering corresponds to that in Figure 1).

lithium center in solution (just as high selectivities in deprotonations can be explained by complex-induced proximity effects (CIPE)).[13] Thus the choice of solvent, and with it the coordination sphere of the lithium center, decides the stereochemical course of the reaction of (*R*,*S*)-**6** with the electrophile Me$_3$SnCl.

Our studies show that the choice of the solvent can have a considerable effect on the (stereochemical) reaction behavior of an alkyl lithium. Therefore only an unambiguous experimental determination of the absolute configuration can form the basis for an explanation of the stereochemical course of the reaction of diastereomerically enriched alkyl lithium compounds. Quantum mechanical methods can be of assistance in comparing the mechanisms involved. The next question is whether this observation in our system (*R*,*S*)-**6** can be confirmed by reactions with other electrophiles.

Received: September 28, 2004
Revised: January 2, 2005
Published online: April 18, 2005

Keywords: carbanions · chirality · lithium · silanes

[1] In general we refer to the stereogenic metalated carbon center when we speak of "enantiomerically enriched" alkyl lithium compounds, however, compounds of this type are in fact diastereomerically enriched alkyl lithium compounds.

[2] a) A. Basu, S. Thayumanavan, *Angew. Chem.* **2002**, *114*, 740–763; *Angew. Chem. Int. Ed.* **2002**, *41*, 716–738; b) D. Hoppe, T. Hense, *Angew. Chem.* **1997**, *109*, 2376–2410; *Angew. Chem. Int. Ed. Engl.* **1997**, *36*, 2282–2316; c) D. Hoppe, G. Christoph in *The Chemistry of Organolithium Compounds* (Eds.: Z. Rappoport, I. Marek), Wiley, Chichester, **2004**, p. 1055–1164; d) D. Hoppe, F. Marr, M. Brüggemann, *Top. Organomet. Chem.* **2003**, *6*, 61–137; e) R. E. Gawley, I. Coldham in *The Chemistry of Organolithium*

Compounds (Eds.: Z. Rappoport, I. Marek), Wiley, Chichester, **2004**, p. 997–1053; f) P. Beak, D. R. Anderson, M. D. Curtis, J. M. Laumer, D. J. Pippel, G. A. Weisenburger, *Acc. Chem. Res.* **2000**, *33*, 715–727; g) P. Beak, T. A. Johnson, D. D. Kim, S. H. Lim, *Top. Organomet. Chem.* **2003**, *6*, 139–176.

[3] a) T. H. Chan, P. Pellon, *J. Am. Chem. Soc.* **1989**, *111*, 8737–8738; b) T. H. Chan, S. Lamothe, *Tetrahedron Lett.* **1991**, *32*, 1847–1850; c) T. H. Chan, K. T. Nwe, *J. Org. Chem.* **1992**, *57*, 6107–6111.

[4] a) B. Kaiser, D. Hoppe, *Angew. Chem.* **1995**, *107*, 344–346; *Angew. Chem. Int. Ed. Engl.* **1995**, *34*, 323–325; b) D. Hoppe, B. Kaiser, O. Stratmann, R. Fröhlich, *Angew. Chem.* **1997**, *109*, 2872–2874; *Angew. Chem. Int. Ed. Engl.* **1997**, *36*, 2784–2786; c) F. Marr, R. Fröhlich, D. Hoppe, *Org. Lett.* **1999**, *1*, 2081–2083.

[5] C. Strohmann, K. Lehmen, K. Wild, D. Schildbach, *Organometallics* **2002**, *21*, 3079–3081.

[6] a) G. Boche, M. Marsch, J. Harbach, K. Harms, B. Ledig, F. Schubert, J. C. W. Lohrenz, H. Ahlbrecht, *Chem. Ber.* **1993**, *126*, 1887–1894; b) M. Marsch, K. Harms, O. Zschage, D. Hoppe, G. Boche, *Angew. Chem.* **1991**, *103*, 338–339; *Angew. Chem. Int. Ed.* Engl. **1991**, *30*, 321–323; c) I. Hoppe, M. Marsch, K. Harms, G. Boche, D. Hoppe, *Angew. Chem.* **1995**, *107*, 2328–2330; *Angew. Chem. Int. Ed. Engl.* **1995**, *34*, 2158–2160; d) H. Ahlbrecht, G. Boche, K. Harms, M. Marsch, H. Sommer, *Chem. Ber.* **1990**, *123*, 1853–1858; e) R. I. Papasergio, B. W. Skelton, P. Twiss, A. H. White, C. L. Raston, *J. Chem. Soc. Dalton Trans.* **1990**, 1161–1172; f) see ref. [5]; g) C. Strohmann, D. H. M. Buchold, T. Seibel, K. Wild, D. Schildbach, *Eur. J. Inorg. Chem.* **2003**, 3453–3463.

[7] C. Strohmann, D. H. M. Buchold, K. Wild, D. Schildbach in *Organosilicon Chemistry V* (Eds.: N. Auner, J. Weis), Wiley-VCH, Weinheim, **2003**, p. 155–166.

[8] Diffractometer: StoeIPDS; $Mo_{K\alpha}$ radiation, $\lambda = 0.71073$ Å, $T = 173$ K; all structures were refined anisotropically against F^2 (G. M. Sheldrick, SHELXS-90 and SHELXL-97, Universität Göttingen, **1990** and **1997**); the refinement of the absolute structure was additionally ensured by refinement of the Flack parameter for the determination of the relative configuration. a) (*R*,*S*)-**6**·THF (colorless plates from *n*-pentane/THF, $0.3 \times 0.3 \times 0.2$ mm^3): $C_{27}H_{42}LiNO_2Si_2$, $M_r = 475.74$, orthorhombic, space group $P2_12_12_1$, $a = 10.7958(16)$, $b = 14.037(3)$, $c = 18.920(3)$ Å, $V = 2867.2(8)$ Å^3, $Z = 4$, $\rho = 1.102$ Mg m^{-3}, 2θ range: 4.3–48.0°. 24064 reflections, of which 4501 were independent ($R_{int} = 0.2199$). $R_1 = 0.0661$, $wR_2 = 0.1188$ (all data). Flack parameter: −0.01(18); b) (*R*,*S*)-**6** (orange-yellow needles from *n*-pentane, $0.4 \times 0.4 \times 0.3$ mm^3): $C_{23}H_{34}LiNOSi_2$, $M_r = 403.63$, monoclinic, space group $P2_1$, $a = 10.971(7)$, $b = 10.677(6)$, $c = 11.162(8)$ Å, $\beta = 112.07(7)$, $V = 1211.7(13)$ Å^3, $Z = 2$, $\rho = 1.106$ Mg m^{-3}, 2θ range: 4.4–54.0°. 8374 reflections, of which 4441 were independent ($R_{int} = 0.0544$). $R_1 = 0.0458$, $wR_2 = 0.0899$ (all data). Flack parameter: 0.02(14); c) (*R*,*S*)-**8** (colorless needles, $0.4 \times 0.3 \times 0.2$ mm^3): $C_{29}H_{53}Cl_2NOSi_2Sn_2$, $M_r = 796.18$, triclinic, space group $P1$, $a = 9.504(2)$, $b = 10.292(3)$, $c = 10.865(4)$ Å, $\alpha = 68.70(4)$, $\beta = 70.81(4)$, $\gamma = 81.71(3)$°, $V = 934.7(5)$ Å^3, $Z = 1$, $\rho = 1.414$ Mg m^{-3}, 2θ range: 4.2–52.0°. 13687 reflections, of which 6918 independent ($R_{int} = 0.0507$). $R_1 = 0.0434$, $wR_2 = 0.1169$ (all data). Flack parameter: −0.02(3). CCDC-250458 ((*R*,*S*)-**6**), CCDC-250459 ((*R*,*S*)-**6**·THF), and CCDC-250460 ((*R*,*S*)-**8**) contain the detailed crystallographic data for this publication. The data can be obtained free of charge from the Cambridge Crystallographic Data Centre under www.ccdc.cam.ac.uk/data_request/cif.

[9] a) E. Keller, Schakal99, Universität Freiburg, **1999**; b) S. Portmann, Molekel, ETH Zürich, Schweiz, **2001**.

[10] Gaussian 98 (Revision A.7), M. J. Frisch, G. W. Trucks, H. B. Schlegel, G. E. Scuseria, M. A. Robb, J. R. Cheeseman, V. G. Zakrzewski, J. A. Montgomery, R. E. Stratmann, J. C. Burant, S. Dapprich, J. M. Millam, A. D. Daniels, K. N. Kudin, M. C. Strain, O. Farkas, J. Tomasi, V. Barone, M. Cossi, R. Cammi, B. Mennucci, C. Pomelli, C. Adamo, S. Clifford, J. Ochterski, G. A. Petersson, P. Y. Ayala, Q. Cui, K. Morokuma, D. K. Malick, A. D. Rabuck, K. Raghavachari, J. B. Foresman, J. Cioslowski, J. V. Ortiz, B. B. Stefanov, G. Liu, A. Liashenko, P. Piskorz, I. Komaromi, R. Gomperts, R. L. Martin, D. J. Fox, T. Keith, M. A. Al-Laham, C. Y. Peng, A. Nanayakkara, C. Gonzalez, M. Challacombe, P. M. W. Gill, B. G. Johnson, W. Chen, M. W. Wong, J. L. Andres, M. Head-Gordon, E. S. Replogle, J. A. Pople, Gaussian, Inc., Pittsburgh, PA, **1998**; energy minimization and calculation at the HF/3-21G(d) level gave the same conformers as calculations at the B3LYP/6-31 + G(d) level. All the frequency calculations were carried out at the HF/3-21G(d) level because of size they were not used for the zero-point correction of the calculated energies and showed no negative frequencies. A zero correction resulting from these frequency calculations increased the energy difference between (*R*,*S*)-**6**·THF and (*S*,*S*)-**6**·THF by 0.9 kJ mol^{-1}. Absolute electronic energies without zero correction (B3LYP/6-31 + G(d)) from the quantum chemical calculations in atomic units: (*R*,*S*)-**6**·THF: −1846.00502703, (*S*,*S*)-**6**·THF: −1846.00192466; energy difference: 8.1 kJ mol^{-1}.

[11] a) H. J. Reich, K. J. Kulicke, *J. Am. Chem. Soc.* **1995**, *117*, 6621–6622; b) H. J. Reich, W. S. Goldenberg, A. W. Sanders, C. C. Tzschucke, *Org. Lett.* **2001**, *3*, 33–36; c) G. Fraenkel, J. H. Duncan, K. Martin, J. Wang, *J. Am. Chem. Soc.* **1999**, *121*, 10538–10544.

[12] a) G. Fraenkel, A. Chow, R. Fleischer, H. Liu, *J. Am. Chem. Soc.* **2004**, *126*, 3983–3995; b) J. Zabicky in *The Chemistry of Organolithium Compounds* (Eds.: Z. Rappoport, I. Marek), Wiley, Chichester, **2004**, p. 311–433; c) D. Johnels, H. Günther in *The Chemistry of Organolithium Compounds* (Eds.: Z. Rappoport, I. Marek), Wiley, Chichester, **2004**, p. 137–203; d) W. Bauer, W. R. Winchester, P. von R. Schleyer, *Organometallics* **1987**, *6*, 2371–2379.

[13] M. C. Whisler, S. MacNeil, V. Snieckus, P. Beak, *Angew. Chem.* **2004**, *116*, 2256–2276; *Angew. Chem. Int. Ed.* **2004**, *43*, 2206–2225.

Structure Determination

An Old Target Revisited: Two New Privileged Skeletons and an Unexpected Binding Mode For HIV-Protease Inhibitors**

*Edgar Specker, Jark Böttcher, Hauke Lilie, Andreas Heine, Andreas Schoop, Gerhard Müller, Nils Griebenow, and Gerhard Klebe**

HIV protease is probably the most vigorously studied enzymatic target for therapeutic intervention in the short history of structure-based drug design.[1] For over a decade, attempts to find new efficient inhibitors have attracted and absorbed the curiosity, talents, and energy of many scientists.[2] No other protein has been scrutinized as often in crystal structures of protein–ligand complexes; in the publicly available Protein Data Bank more than 200 individual structures have been deposited.[3] As a result of these impressive efforts, nine approved drugs have been launched that improve both the quality of life and life expectancy for an increasing number of HIV-infected patients.[4] However, the initial euphoria surrounding these major achievements has decreased due to the occurrence of viral resistance to the prescribed therapy based on these drugs.[5] As a consequence, novel inhibitors with alternative frameworks are being sought to circumvent resistance development.

Can we expect any new inhibitory principles to be discovered in the case of such an exhaustively studied member of the aspartyl protease family? In an attempt to develop novel privileged building blocks to address the conserved binding epitope of aspartyl protease, we have designed and synthesized two novel parent structures, the aminohydroxysulfones and pyrrolidinemethaneamines. Both skeletons were designed to address, across the entire family of aspartyl proteases, the conserved catalytic diad and the peptide recognition motif, which features the proteases for proper recognition and arrest of their substrates. Furthermore, both skeletons were designed with the impetus to give easy access to multiple decorations using side chains tailored to systematically explore and specifically address the various substrate recognition pockets exhibited by this class of proteases.

Up to now a plethora of privileged building blocks have been incorporated successfully into HIV-protease inhibitors (Figure 1). The first generation of inhibitors comprises motifs

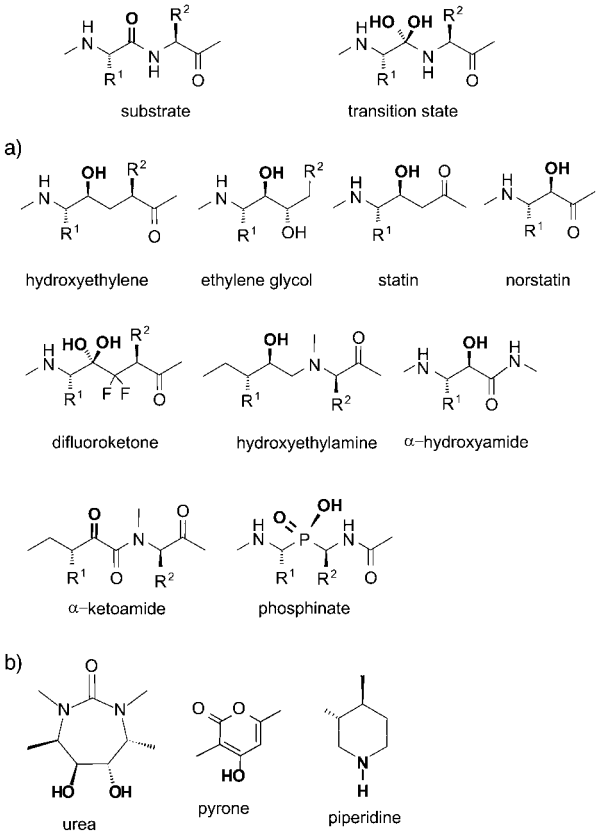

Figure 1. Privileged skeletons frequently used to address the conserved catalytic center in aspartyl protease. a) Classical transition-state analogues usually incorporated into peptidomimetics; b) newly discovered scaffolds that address aspartyl proteases, in particular HIV protease.

classified as transition-state analogues, which closely resemble the tetrahedral intermediate formed along the reaction pathway. The second generation of lead compounds departed from closely imitating the transition state, and they frequently tried to incorporate the position of the structural water.[6,7] This water mediates in case of the substrate analogue inhibitors the protein–ligand interaction. In the late 1990s researchers at Roche discovered by screening studies the piperidine moiety as a novel privileged skeleton for addressing the catalytic center of aspartyl proteases.[8]

Our rational design of the aminohydroxysulfones was inspired by four skeletons of already known inhibitors targeting distinct aspartyl proteases (Scheme 1). Our aminohydroxysulfones are derived from the hydroxyethyleneamine core of the HIV-protease inhibitor amprenavir (**1**),[9] by replacing the *sec*-butyl-substituted nitrogen atom in the α-

[*] Dr. E. Specker,[+] J. Böttcher,[+] Dr. A. Heine, Prof. G. Klebe
Institut für Pharmazeutische Chemie
Philipps-Universität Marburg
Marbacher Weg 6, 35032 Marburg (Germany)
Fax: (+49) 6421-282-994
E-mail: klebe@mailer.uni-marburg.de
Dr. H. Lilie
Institut für Biotechnologie
Martin-Luther-Universität Halle-Wittenberg
Kurt-Mothes-Strasse 3, 06120 Halle/Saale (Germany)
Dr. A. Schoop
Boehringer Ingelheim, Vienna (Austria)
Dr. G. Müller
Axxima Pharmaceuticals AG, München (Germany)
Dr. N. Griebenow
Bayer AG, Elberfeld (Germany)
[+] Equally contributing authors

[**] The authors are grateful to Bayer AG, Wuppertal (Germany), for financial support. The clone of the protease was kindly provided by Prof. Helena Danielson, University of Uppsala, Department of Biochemistry.

  DOI: 10.1002/anie.200462643

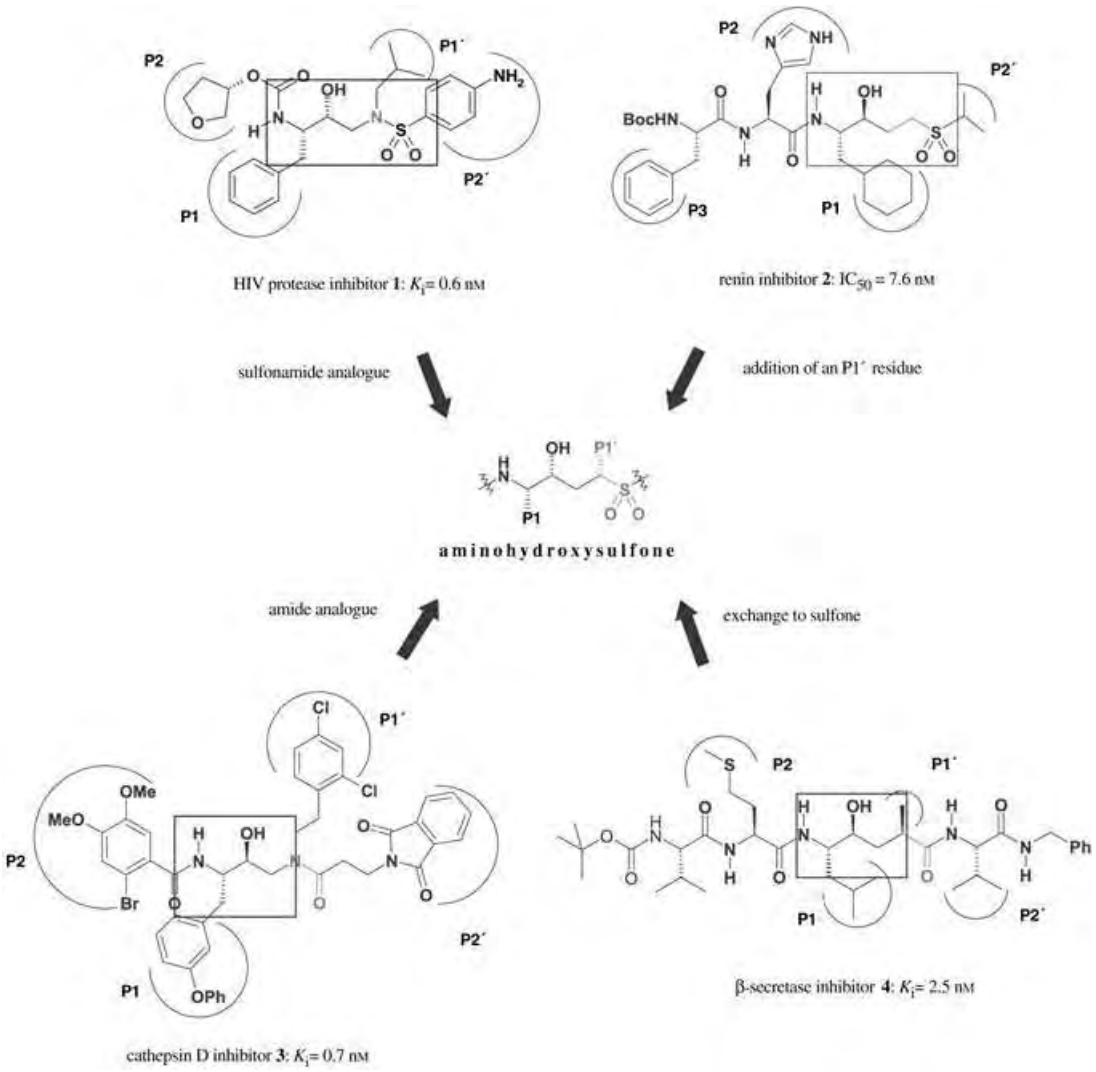

Scheme 1. Design of the aminohydroxysulfones based on the structural elements of known aspartyl protease inhibitors.

position with a carbon atom. The related sulfone core of the renin inhibitor **2**[10] lacks a substitution in α-position to address the P1′ pocket. In the aminohydroxysulfones the central scaffolds of the cathepsin D inhibitor **3**[11] and the β-secretase inhibitor **4**[12] are changed from an amide bond and a keto group, respectively, to a methylenesulfone moiety. To assess the potential of the aminohydroxysulfones as novel lead structures for the inhibition of aspartyl proteases, we decorated the central core with the previously optimized substituents found in the inhibitors **1**–**4**, which address the S2–S2′ subsites.

In our design of the novel pyrrolidinemethaneamines we intended to combine two key structural elements present in the classical peptidomimetic substrate-analogue inhibitors such as pepstatin (**5**, Scheme 2)[13,14] and the newly discovered type of cyclic amines (see Figure 1) to directly address the pivotal position between both catalytic aspartates.

The hydroxy group of statin directly coordinates to the two opposing aspartic acids. We decided to replace this privileged core fragment by a pyrrolidine moiety capable of being symmetrically extended towards the C- and N-terminal subsites by using molecular scaffolds frequently incorporated into substrate-analogue inhibitors. As apparent from the multiple crystal structures with such peptidomimetics (e.g. pepstatin **5**, Scheme 2), important hydrogen bonds are formed by the peptide-like backbone of the inhibitor to the flap regions of these proteases. In the case of HIV protease, this contact is mediated by a water molecule in hydrogen bonds with the amide functions of Ile A50 and Ile B50; for cathepsin D the inhibitor is directly hydrogen-bonded to the amide functions of Gly 79 and Asp 87. To evaluate the inhibitory potential of the new pyrrolidinemethaneamines we decorated the central pyrrolidine moiety with side chains already optimized for the HIV-protease inhibitor amprenavir (**1**). Diastereoselective syntheses yielded racemic mixtures of the designed target compounds. The synthesis and characterization of the new inhibitors will be described elsewhere.

In the series of aminohydroxysulfones the racemate of **6** (Figure 2) exhibited a K_i value of 80 nM for HIV-protease inhibition. Resolution of the racemic mixture revealed the more potent enantiomer to have a K_i value of 45 nM. To validate whether the binding of **6** follows the initial design

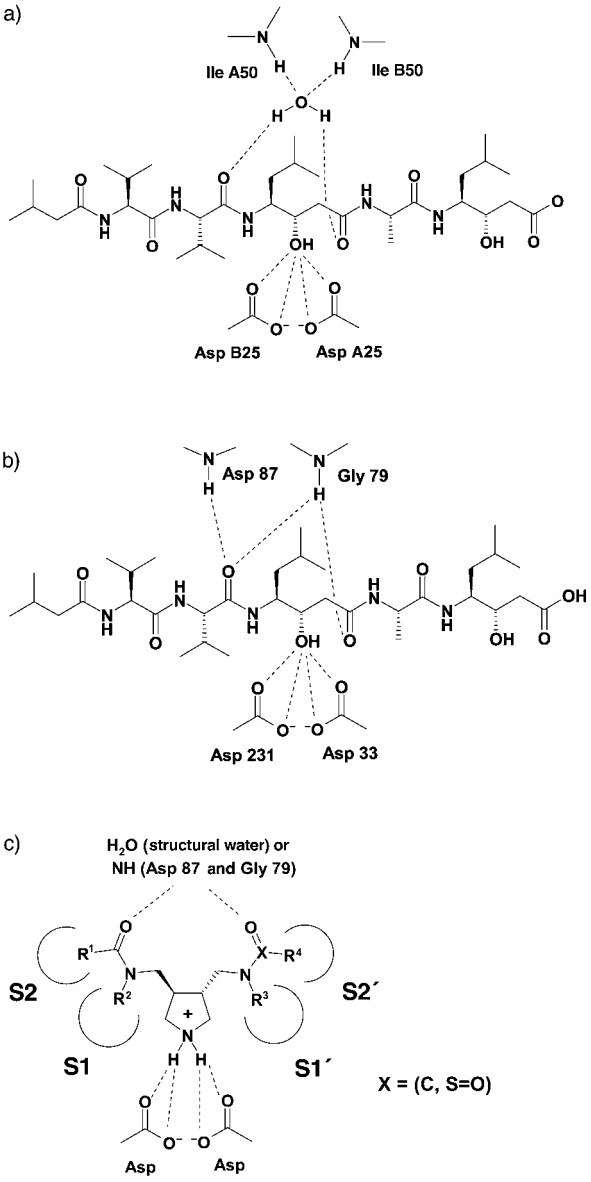

Scheme 2. a) Hydrogen bonds of pepstatin (**3**) in the active site of HIV protease; b) hydrogen bonds of peptstatin (**3**) in the active site of cathepsin D; c) a pyrrolidinemethaneamine unit and its hydrogen bonds in the active site of an aspartyl protease.

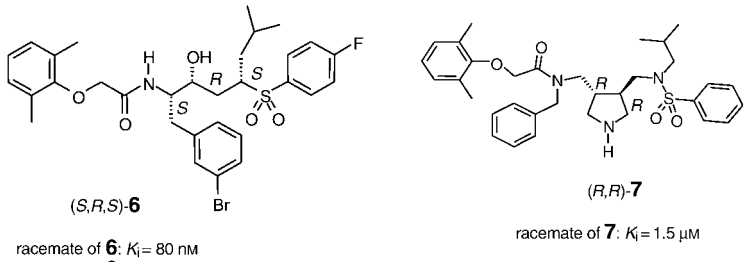

Figure 2. Structural formulae of (*S*,*R*,*S*)-**6** and (*R*,*R*)-**7** and the K_i values for inhibition of HIV1 protease.

concept and its stereochemistry, we determined the crystal structure of the complex with HIV1 protease (Table 1).

Table 1: Data collection and refinement statistics for the complexes with **6** and **7**.

	HIV1 complex with **6**	HIV1 complex with **7**
Resolution [Å]	25–1.73	20–1.5
Space group	$P2_12_12$	$P2_12_12_1$
Cell dimensions [Å]	$a=57.9$	$a=51.9$
	$b=85.8$	$b=57.7$
	$c=46.8$	$c=62.2$
Highest resolution shell [Å]	1.76–1.73	1.53–1.5
Measured reflections	101 892	109 029
Independent reflections	24 462	29 849
Completeness of data [%]	97.6 (79.2)[a]	97.5 (77.3)[a]
I/σ	12.8 (1.7)[a]	18.6 (1.6)[a]
R_{sym} [%]	7.8 (45.2)[a]	6.3 (54.0)[a]
Refined residues	198	198
Refined ligand atoms	40	41
Refined water molecules	207	190
Refined glycerol molecules	–	2
Refined Cl^- ions	3	2
Resolution in refinement [Å]	8–1.73	8–1.5
R_{cryst} ($F>4\sigma F_o$; F_o)	16.7; 20.1	16.7; 18.1
R_{free} ($F>4\sigma F_o$; F_o)	21.0; 24.7	22.0; 23.6
Mean B-factor [Å^2]	17.2; 14.6	16.7; 19.0
(peptide chain A; B)		
Main chain [Å^2]	12.8; 11.4	13.1;15.8
Side chains [Å^2]	22.1; 18.0	20.6; 22.5
Ligand [Å^2]	23.0	33.0
Water [Å^2]	28.1	29.0
Glycerol molecules [Å^2]	–	52.8
Cl^- ions [Å^2]	18.3	20.2
Ramachandran plot		
Most favored geometry [%]	95.6	94.9
Additionally allowed [%]	4.4	5.1
Generously allowed [%]	0	0
Disallowed [%]	0	0

[a] Values in parentheses refer to the shell of highest resolution.

Figure 3a shows the binding mode of the more potent enantiomer, (*S*,*R*,*S*)-**6**, superimposed with the complex of amprenavir (**1**). The latter inhibitor served as one of the references in our design concept. Both inhibitors bind with their central OH group between the two aspartates, and either their carbonyl or sulfonyl groups form hydrogen bonds to the structural water of the protease. The S1 pocket (Leu A23, Pro A81, Val A82, Ile A84) is occupied nearly identically by the benzyl and bromobenzyl moieties in **1** and **6**, respectively. The bulky *meta*-bromine substituent in **6** extends into the adjacent solvent environment, thus not provoking any induced-fit adaptations. Similarly the S2′ subsite accommodates the *para*-aminophenyl (**1**) and the *para*-fluorophenyl (**6**) groups in nearly indistinguishable fashion. However, the fluorine substituent in **6** cannot form a hydrogen bond with the adjacent Asp 30 as is observed in the complex with **1**. The *sec*-butyl substituents at the amino group of **1** and on the α-C atom of the sulfone group of **6** orient their terminal methyl groups in very similar fashion into the S1′ site (Leu A23, Gly A27, Ile B81, Val B82, Ile B84) and achieve comparable occupancy. The two inhibitors differ in the size of their substitutents hosted in the S2 subsite (Ala B28, Val B32, Ile B47, Ile A50). Amprenavir (**1**) exhibits a terminal tetrahy-

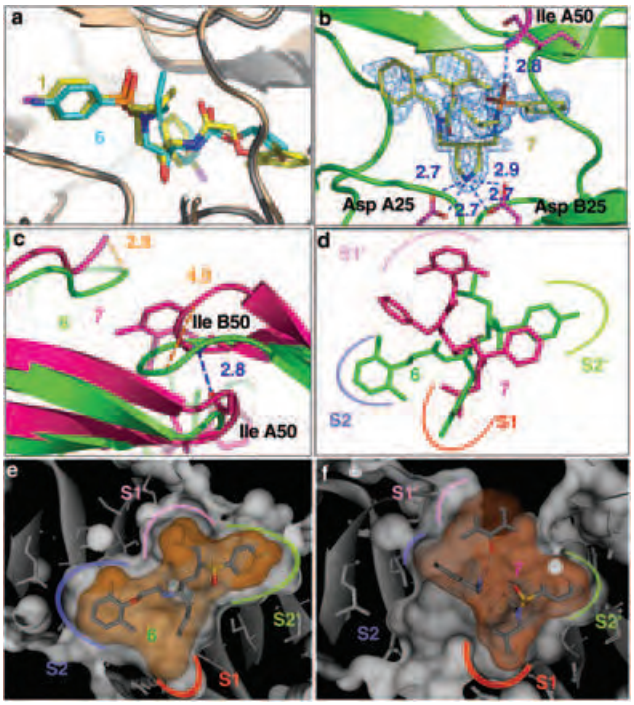

Figure 3. a) Superposition of the binding mode of (*S*,*R*,*S*)-**6** with the structure of **1** in complex with HIV1 protease. b) Binding mode of **7** with the protease showing the pyrrolidino nitrogen in the pivotal position between the two aspartates; the difference electron density (contour level 1σ) is indicated as blue chicken wire. c) Superposition of the complex of **6** and **7** depicting the strong distortion of the flap region for the latter complex. d) Ligands **6** and **7** are mutually aligned to show the addressing of subsites S2–S2′ of the protease. Sections of the complex with **6** (e) and **7** (f) showing the occupation of S2 to S2′ by the side chains of the inhibitor; protein surface in white, ligand surface in orange.

drofuran moiety, whereas **6** is decorated with a 2,6-dimethylphenoxy portion. The latter sterically more demanding substituent requires more space in the S2 pocket[15] and extends beyond the region filled by **1** into the bordering solvent. Nevertheless, it achieves a better occupation of this subpocket. Despite these differences, both complexes show hardly any conformational differences and no induced-fit adaptations of the enzyme.

The aminohydroxysulfone moiety of **6**, developed from a rather conservative design concept from already known inhibitors, exhibits the expected binding mode. The 75-fold decrease in affinity relative to that of amprenavir is supposedly due to the bromine atom of the *meta*-bromobenzyl portion, which remains partly exposed to solvent in the bound state. This incomplete desolvation is possibly detrimental to binding. Furthermore, most likely the close contact of the *para*-aminophenyl moiety in **1** is more favorable than the short distance of the negatively polarized *para*-fluorophenyl group in **6** to the carboxy group of Asp30.

While our rather conservative design of the aminohydroxysulfone template closely resembles the underlying parent substrate structure of an extended peptide chain with protruding side chains, the pyrrolidinemethaneamine core exhibits little if any structural resemblance to a peptide. Docking suggested the binding to be similar to that of the classical substrate-like inhibitors; however, significant crowding in the central region was indicated. Among the derivatives synthesized, **7** (Figure 2), specifically decorated to address HIV protease, shows a K_i value of 1.5 μM as a racemate. Cocrystallization of HIV protease with racemic **7** revealed that the *R*,*R* enantiomer binds to the enzyme (Table 1). As expected, the nitrogen atom of the pyrrolidine ring, likely protonated in the bound state, occupies the pivotal position between the two aspartates. As expected, it is a perfect substitute for the hydroxy group of, for example, **6** (Figure 3b). Even though the side chains of (*R*,*R*)-**7** are similar to those of (*S*,*R*,*S*)-**6**, the pyrrolidine-based inhibitor adopts a new and surprising binding mode. First of all, it repells the structural water from the binding site and forms one direct hydrogen bond to the backbone NH of Ile A50 with one of its sulfoxy oxygens. The carbonyl group of the amide functionality remains unsatisfied without forming any further polar contacts to the enzyme. As a consequence, the NH backbone functionality of Ile B50 finds a hydrogen-bonding partner in the carbonyl group of the amide bond of Ile A50 of the neighboring polymer chain. This additional contact to the neighboring flap loop stabilizes the dimer in the flap region. Possibly this surprising further hydrogen bond is a surrogate for the missing contact originally formed by the bridging structural water which has been repelled from the complex. This unusual geometry of the flap parallels a significant distortion (up to 4.9 Å) of the polymer chain in this region compared to, for example, the complex formed with **6** (Figure 3c).

The decorating side chains of **7** were designed to address, like **6**, the four subsites S2–S2′. However, the overall orientation of the inhibitor in the complex is rotated relative that of **6**. To some extent similarity in the occupation of the S1 and S2′ subsites (Figure 3d–f) can be recognized. The S1 pocket (Leu A23, Val A82, Val A84, Gly B48, Gly B49) accommodates the *sec*-butyl group of **7** and the *meta*-bromobenzyl moiety of **6** in a similar fashion. Likewise, the phenylsulfonamide substitutent is hosted by the S2′ pocket (Ala A28, Val A32, Ile A84, Ile B50). In case of **6**, this site is filled by the *para*-fluorophenyl group. The remaining two decorations, the *N*-benzyl- and dimethylphenoxy group, are placed next to each other; they extensively occupy the S1′ pocket and penetrate into the bordering solvent environment. The *N*-benzyl substituent barely permeates into the S2 pocket, which remains virtually unoccupied. The site accommodating the latter two side chains of **7** is bound by the residues Ile A50, Val B32, Ile B47, Ile B54, Thr B80, Pro B81, Val B82, and Ile B84.

Interestingly enough **6** and **7** crystallize in two distinct space groups, $P2_12_12$ and $P2_12_12_1$, respectively. Accordingly, it is questionable whether the observed differences are provoked by crystal packing. However, in structures of other complexes found in either space groups, distortions of the flap region similar to that observed for **7** were not observed. Next, we compared the size of the ligand-surface portion that is buried upon complex formation.[16] For **1** and **6** 95% of the ligand surface is in close contact with the protein, whereas for **7** only 85% of the surface is buried upon complexation. This

significantly smaller value for **7** is in agreement with the solvent exposure of the bulky dimethylphenoxy moiety in S1′. The latter extends with one of its faces significantly into the neighboring solvent area; inhibitor **6** places a short *sec*-butyl group into this pocket largely avoiding solvent exposure.

Two new skeletons have been discovered to successfully address the conserved binding motif of aspartyl proteases: the aminohydroxysulfones and the pyrrolidinemethanamines. Crystal structure analyses of the new privileged scaffolds decorated with side chains intended for HIV-protease inhibition reveal their binding modes. The binding mode of the aminohydroxysulfone was not surprising. However, the pyrrolidine derivative adopts a surprising and rather unexpected binding mode. Detailed analysis of its bound conformation and the contacts formed with the protein will provide further insights to explain the adopted binding mode. Furthermore, it will guide the structure-based optimization of this new inhibitor skeleton to improve its binding affinity. Supposedly, the new inhibitor skeleton also provides challenging opportunities to combat resistance. The new type of inhibitor achieves good inhibition although one subsite is left virtually unoccupied. Thus, the virus has at least one less option for mutational adaptation. Furthermore, the induced perturbation in the flap region also occurs in an area most likely out of range for the virus to mutate without significant loss in functionality of its protease.

The present study is a lesson in drug design. The binding mode of **6**,[17] derived by a rather conservative design concept, was correctly predicted including the assignment of stereocenters. Side chains transferred from other potent inhibitors were actually found in the expected subsites. The opposite has to be conceived for **7**. In rational design of **7** the hydroxy function in the transition-state analogue was correctly replaced by a pyrrolidino nitrogen. Furthermore, the inhibitor was equipped symmetrically with two polar acceptor groups to address the flap water. However, this water is repelled from the complex. The side chains were selected analogously to those of **6**, but they actually accommodate different subsites. It has to be admitted that design and docking were unable to predict the correct binding mode. Nevertheless, a potent class of ligands has been created. While the binding geometry of the heterocyclic scaffolds matches the prediction, the mounted side chains deviate substantially from the expected orientation. Without crystallography we would never have detected this discrepancy. With some good luck, an elaborate and tediously collected, however nonconclusive structure–activity relationship could have been indicative. This clearly points to the limits of computer design and stresses the importance of experiments. Only if both go hand in hand, can successful structure-based design be accomplished. The two novel scaffolds can be added to the toolbox of medicinal chemistry. They meet the stringent definition of privileged structures: they address the target family-wide molecular recognition commonalities and simultaneously offer a modular chemistry for peripheral decoration with required special orientation.

Received: November 17, 2004
Published online: April 8, 2005

Keywords: drug design · HIV protease · inhibitors · proteins · structure determination

[1] R. E. Babine, S. L. Bender, *Chem. Rev.* **1997**, *97*, 1359 – 1472.
[2] S. Thaisvivongs, J. W. Strohbach, *Biopolym. Pep. Sci.* **1999**, 51, 51 – 58.
[3] J. Vondrasek, A. Wlodawer, *Proteins Struct. Funct. Genet.* **2002**, *49*, 29 – 31.
[4] D. D. Richman, *Nature* **2001**, *410*, 995 – 1001.
[5] L. Romano, G. Venturi, S. Giomi, L. Pippi, P. E. Valensin, M. Zazzi, *J. Med. Virol.* **2002**, *66*, 143 – 150.
[6] E. De Clercq, *Int. J. Biochem. Cell Biol.* **2004**, *36*, 1800 – 1822.
[7] A. Brik, C.-H. Wong, *Org. Biomol. Chem.* **2003**, *1*, 5 – 14.
[8] E. Vieira, A. Binggeli, V. Breu, D. Bur, W. Fischli, R. Güller, G. Hirth, H. P. Märki, M. Müller, C. Oefner, M. Scalone, H. Stadler, M. Wilhelm, W. Wostl, *Bioorg. Med. Chem. Lett.* **1999**, *9*, 1397 – 1402.
[9] E. E. Kim, C. T. Baker, M. D. Dwyer, M. A. Murcko; B. G. Rao, R. D. Tung, M. A. Navia, *J. Am. Chem. Soc.* **1995**, *117*, 1181 – 1182.
[10] G. Bolis, A. K. L. Fung, J. Greer, H. D. Kleinert, P. A. Marcotte, T. J. Perun, J. J. Plattner, H. H. Stein, *J. Med. Chem.* **1987**, *30*, 1729 – 1737.
[11] E. C. Lee, E. K. Kick, J. A. Ellman, *J. Am. Chem. Soc.* **1998**, *120*, 9735 – 9747.
[12] A. K. Ghosh, G. Bilcer, C. Harwood, R. Kawahama, D. Shin, K. A. Hussain, L. Hong, J. A. Loy, C. Nguyen, G. Koelsch, J. Ermolieff, J. Tang, *J. Med. Chem.* **2001**, *44*, 2865 – 2868.
[13] P. M. D. Fitzgerald, B. M. McKeever, J. F. van Middlesworth, J. P. Springer, J. C. Heimbach, C-T. Leu, W. K. Herber, R. A. F. Dixon, P. L. Darke, *J. Biol. Chem.* **1990**, *265*, 14209 – 14219.
[14] E. T. Baldwin, T. N. Bhat, S. Gulnik, M. V. Hosur, D. Sowder, R. E. Cachau, J. Collins, A. M. Silva, J. W. Erickson, *Proc. Natl. Acad. Sci. USA* **1993**, *90*, 6796 – 6799.
[15] P. L. Beaulieu, P. C. Anderson, D. R. Cameron, G. Croteau, V. Gorys, C. Grand-Maître, D. Lamarre, F. Liard, W. Paris, L. Plamondon, F. Soucy, D. Thibeault, D. Wernic, C. Yoakim, *J. Med. Chem.* **2000**, *43*, 1094 – 1108.
[16] M. L. Connolly, *J. Appl. Crystallogr.* **1983**, *16*, 548 – 558.
[17] The structure data of **6** and **7** are available from the Protein Data Bank (PDB) under the codes 1XL2 and 1XL5, respectively.

NMR Spectroscopy

Stretched Gelatin Gels as Chiral Alignment Media for the Discrimination of Enantiomers by NMR Spectroscopy**

*Kyryl Kobzar, Horst Kessler, and Burkhard Luy**

Verification of the enantiomeric purity of a product and measurement of enantiomeric excess is an everyday problem in modern organic chemistry. Therefore, the development of a convenient method of measurement for this purpose is desirable. Classical NMR spectroscopic techniques that discriminate enantiomers depend on chiral auxiliaries such as chiral derivatizing agents, lanthanide chiral-shift reagents, and chiral solvating agents.[1,2] These methods work only for functionalized chiral molecules of interest that can interact with the auxiliaries to build detectable diastereomeric compounds or adducts. In contrast, chiral orienting media permit enantiomer discrimination through the differential ordering effect of enantiomers within the chiral phase.[3,4] Therefore, even compounds that lack polar groups, such as saturated chiral hydrocarbons[5] and even prochiral elements in symmetrical molecules,[6,7] can be distinguished by NMR spectroscopy in such media.

So far, only surfactant bilayers,[8–10] various chiral liquid-crystalline media,[11–15] and achiral liquid crystals with chiral cages[16] have been reported to be suitable for enantiomeric discrimination. Such media are usually difficult to prepare and operate only within certain temperature ranges. Furthermore, their induced orientation depends on the strength of the magnetic field. In contrast, covalently cross-linked, stretched-polymer gels[17–19] are relatively easy to handle and provide field-independent orientation.

The aim of the studies presented herein was to obtain partial alignments in stretched chiral gels. Gelatin in the form of *gummibärchen* (the famous German sweets) was used for the initial proof of principle that alignment is possible with this kind of polymer. In further experiments we were able to show that stretched gelatin gels as chiral alignment media not only make it possible to obtain structural information through residual dipolar couplings,[20,21] but also provide a way to discriminate between enantiomers and to measure enantiomeric excess. Gelatin therefore represents a new subtype of alignment media: polymer gels in which the spatial structure is almost solely stabilized by hydrogen bonds.

Gummibärchen were swollen in deionized water to about twice their original dimensions (Figure 1) and subsequently cut into roughly cylindrical shapes. They were then dried on a glass capillary and inserted into NMR tubes with D_2O. After equilibration for two days, deuterium NMR spectra were acquired with a clearly visible quadrupolar splitting in the range of $\approx$20 Hz (Figure 2A).

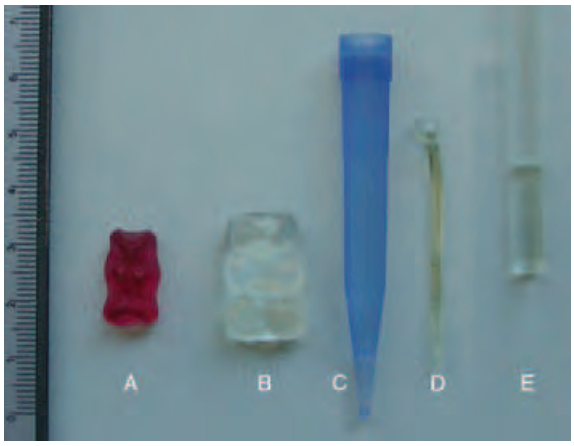

Figure 1. Various stages of the preparation of stretched gelatin samples: A) gummibärchen; B) gummibärchen swollen in water; C) gelatin gel (10%) prepared in a pipette tip; D) gel after drying in the pipette tip; E) equilibrated gelatin sample with a D_2O deuterium splitting of 117 Hz (Figure 2B); left: centimeter scale.

After this successful proof that partial alignment is possible with gelatin-based gels, further experiments with household gelatin were conducted. Heated gelatin solution ($\approx$10% w/v) was poured into a standard pipette tip with a sealed end and dried for eight weeks under refrigeration (Figure 1). From this, solid sticks with diameters of $\approx$1.9 mm and uniform appearance were collected, put into NMR tubes, and subjected to constrained swelling by direct addition of D_2O in a procedure similar to that described earlier for polystyrene sticks.[19] After swelling for a couple of days and a single solvent exchange to wash out unwanted substances, the gel showed a quadrupolar splitting for D_2O of 117 Hz at 25°C (Figure 2B). A mixture of L-alanine (30 mg) and D-alanine (25 mg; 9% *ee*) was added to the sample and allowed to diffuse into the gel. Although its spatial structure is largely stabilized by hydrogen bonds, the gel, in the presence of polar solutes over a two-month period, exhibited no change in the deuterium quadrupolar splitting of the solvent. A specially designed *J*-coupling experiment (Figure 3) was acquired that allowed separation of the two enantiomers.

In principle, any order-dependent NMR interaction can be used for the distinction of enantiomers. So far, mostly 1D[3,4,10,11,13,14,16,24–30] and 2D[4,5,31–33] ^{2}H NMR spectra of non-isotopically enriched samples have been reported in which use was made of the difference in residual quadrupolar couplings in chiral orienting media. However, the low natural abundance of deuterium nuclei requires either long acquisition times or the use of deuterated compounds.

Recently, *J*-coupling spectroscopy on ^{1}H[31] and ^{13}C[34] nuclei was proposed as an alternative technique in which the different residual dipolar couplings (RDCs) of enantiomers lead to distinguishable NMR spectroscopic signals. However, the lower limit of alignment in known liquid-

[*] Dipl.-Chem. K. Kobzar, Prof. Dr. H. Kessler, Dr. B. Luy
Department Chemie
Lehrstuhl für Organische Chemie II
Technische Universität München
Lichtenbergstrasse 4, 85747 Garching (Germany)
Fax: (+49) 89-289-13210
E-mail: burkhard.luy@ch.tum.de

[**] B.L. and H.K. thank the Fonds der Chemischen Industrie and the DFG (Emmy Noether fellowship LU 835/1-1; Ke 147/37-1) for financial support. We also thank W. Rist and F. Rist for support.

 DOI: 10.1002/anie.200462736

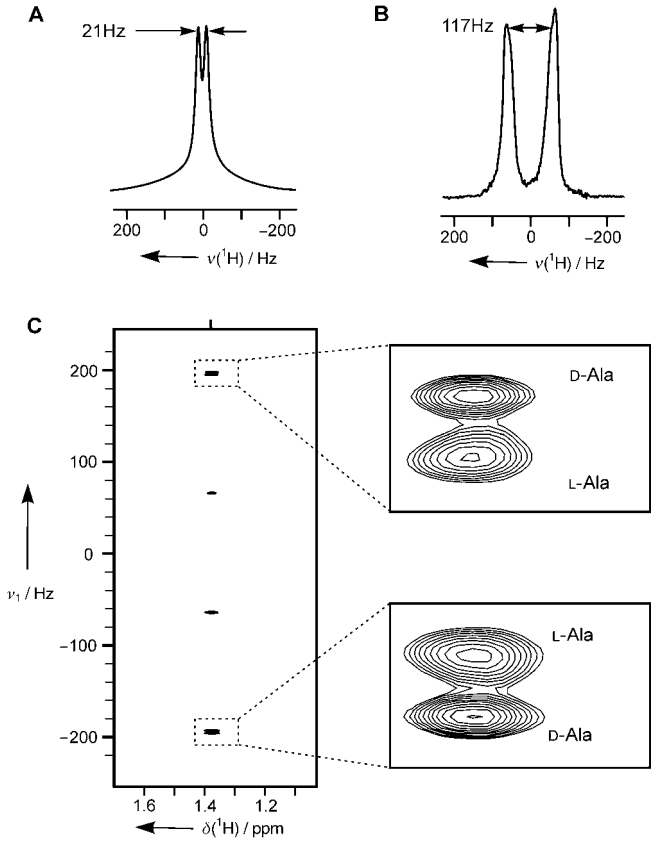

Figure 2. NMR spectra acquired on stretched gelatin samples: A) ^{2}H NMR spectrum of a stretched gummibärchen sample swollen in D_2O; B) ^{2}H NMR spectrum of a sample of household gelatin (see text for details); C) ^{1}H,^{13}C-BIRD^{d,X}-*J*-coupling spectrum of L-Ala/D-Ala (1.2:1): the two enantiomers can be clearly distinguished. The spectrum was acquired with the sequence described in Figure 3 with 2048 t_1 increments and processed in both dimensions in phase-sensitive mode.

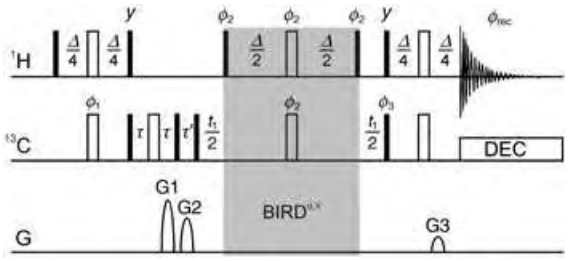

Figure 3. ^{1}H,^{13}C-BIRD^{d,X}-*J*-coupling experiment for the phase-sensitive, high-resolution detection of single-bond ($D_{CH}+{}^1J_{CH}$) couplings. 90° and 180° pulses are indicated by black and white bars, respectively. Unless otherwise indicated, the pulses are *x*-phase. Phase cycles are $\phi_1 = y, y, y, y, -y, -y, -y, -y$; $\phi_2 = x, x, -x, -x$; $\phi_3 = x, -x$; $\phi_{rec} = x, -x, x, -x, -x, x, -x, x$. Delays: $\Delta = 1/({}^1J_{CH}+D_{CH})$, τ and τ' are delays for gradient application (1.2 ms). The ratio of gradient strengths are G1:G2:G3 = 80:30:20.1. The BIRD^{d,X} element for suppression of long-range ^{1}H,^{13}C-couplings is shaded gray. Phase-sensitive absorption (States-TPPI) is possible by cycling ϕ_1. Alternatively, simple t_1-incrementation can be applied with the processing procedure described previously in references [22, 23].

crystalline media results in considerable RDCs that can easily reach the size of $^1J_{CH}$-coupling constants,[35] which therefore limits one to very basic NMR spectroscopic experiments with known disadvantages: ^{1}H *J*-coupling spectra are not phase-sensitive and broadened line widths from ^{1}H,^{1}H-RDCs lead to spectra that in many cases are hardly interpretable. Directly detected ^{13}C *J*-coupling spectra, on the other hand, have the disadvantage of a low signal-to-noise ratio.

In contrast, stretched gels with relatively weak induced alignments permit the use of conventional heteronuclear pulse-sequence building blocks, as the condition $D_{CH} \ll {}^1J_{CH}$ can be easily fulfilled. We were therefore able to design a ^{1}H-excited and detected ^{13}C,^{1}H-correlated pulse sequence with an additional BIRD^{d,X} element[36] for the suppression of long-range ^{13}C,^{1}H scalar and dipolar couplings (Figure 3). This experiment has acceptable sensitivity. Phase-sensitive detection and decreased cross-peak multiplicity decrease the signal width in the indirect dimension sufficiently to separate very small differences in single-bond D_{CH} coupling constants.

The pulse sequence applied to the mixture of L-alanine/D-alanine (1.2:1) diffused in a stretched gelatin gel gave two multiplets for the β-CH_3 groups with a well-resolved difference in outer *J*-multiplet components of 2.5 Hz (Figure 2C). A control experiment with a sample prepared with L-alanine revealed only one signal at the same position as the stronger component of the mixed sample. This is clear evidence that the difference of the D_{CH} RDCs of the enantiomers in chiral stretched gelatin is the origin of the split signal (data not shown). The spectrum of the enantiomeric mixture is so well-resolved that by cross-peak integration, an enantiomeric excess of $7 \pm 5\,\%$ was obtained which is very close to the expected value. Notably, the observed signal intensity is dependent not only on the concentration of a single enantiomer, but also on the efficiency of coherence transfer via scalar and dipolar couplings with the function: $\sin^2(\pi[{}^1J_{CH}+D_{CH}]\Delta/2)\cos(\pi[{}^1J_{CH}+D_{CH}]\Delta)$. For the case shown in Figure 2C this leads to a very low systematic error of less than 0.3 % *ee*.

We have shown the usefulness of gelatin gels for the partial alignment of molecules in aqueous environments. They form three-dimensional networks of polypeptide chains from the partial renaturation of native collagen,[37] which eliminates the need for any added cross-linking agent to connect the polymer chains, as is the case for other gels used for the same purpose.[17–19,38–40] Interestingly, this polymer structure, which is held together almost solely through a network of hydrogen bonds, is able to withstand the forces present in the constrained swollen gels. However, household gelatin gels are generally not stable at temperatures above $\approx 35\,°C$,[37] and the chemical stability of stretched gels with respect to solutes must be studied in greater detail. At neutral pH values and at room temperature, our samples did not change alignment properties after more than two months.

Chiral alignment media lead to the differential orientation of enantiomers and therefore allow discrimination of enantiomeric mixtures by NMR spectroscopy.[4] To our knowledge, gelatin is the first chiral alignment medium that combines the possibility of enantiomeric resolution with the advantages of partial alignment through mechanical stretching. The easily scalable alignment reported herein holds potential for the

application of more sophisticated pulse sequences with greater sensitivity and decreased signal width due to reduced multiplet patterns. The combination of chiral gel-based alignment media, field-independent alignment, and field-independent *J*-coupling-based measurement techniques may eventually allow these measurements to be taken on low-field, low-cost NMR spectrometers, as long as chemical-shift resolution is not necessary.

This approach toward enantiomeric resolution is not limited to gelatin polymers and is probably transferable to other chiral gels or achiral gels with chiral cages, which would permit enantiomer discrimination in nonaqueous solutions as well.

Received: November 26, 2004
Revised: January 21, 2005
Published online: April 18, 2005

Keywords: chirality · enantiomeric discrimination · gels · NMR spectroscopy · polymers

[1] T. J. Wenzel, J. D. Wilcox, *Chirality* **2003**, *15*, 256 – 270.
[2] D. Parker, *Chem. Rev.* **1991**, *91*, 1441 – 1457.
[3] E. Sackmann, S. Meiboom, L. C. Snyder, *J. Am. Chem. Soc.* **1968**, *90*, 2183.
[4] M. Sarfati, P. Lesot, D. Merlet, J. Courtieu, *Chem. Commun.* **2000**, 2069 – 2081.
[5] M. Sarfati, J. Courtieu, P. Lesot, *Chem. Commun.* **2000**, 1113 – 1114.
[6] D. Merlet, J. W. Emsley, P. Lesot, J. Courtieu, *J. Chem. Phys.* **1999**, *111*, 6890 – 6896.
[7] C. Aroulanda, D. Merlet, J. Courtieu, P. Lesot, *J. Am. Chem. Soc.* **2001**, *123*, 12059 – 12066.
[8] A. S. Tracey, P. Diehl, *FEBS Lett.* **1975**, *59*, 131 – 132.
[9] A. S. Tracey, *Mol. Phys.* **1977**, *33*, 339 – 350.
[10] K. Baczko, C. Larpent, P. Lesot, *Tetrahedron: Asymmetry* **2004**, *15*, 971 – 982.
[11] E. Lafontaine, J. P. Bayle, J. Courtieu, *J. Am. Chem. Soc.* **1989**, *111*, 8294 – 8296.
[12] E. Lafontaine, J. M. Pechine, J. Courtieu, C. L. Mayne, *Liq. Cryst.* **1990**, *7*, 293 – 298.
[13] I. Canet, J. Courtieu, A. Loewenstein, A. Meddour, J. M. Pechine, *J. Am. Chem. Soc.* **1995**, *117*, 6520 – 6526.
[14] B. E. Weiss-Lopez, M. Azocar, R. Montecinos, B. K. Cassels, R. Araya-Maturana, *Langmuir* **2001**, *17*, 6910 – 6914.
[15] C. Aroulanda, M. Sarfati, J. Courtieu, P. Lesot, *Enantiomer* **2001**, *6*, 281 – 287.
[16] J. M. Pechine, A. Meddour, J. Courtieu, *Chem. Commun.* **2002**, 1734 – 1735.
[17] R. Tycko, F. J. Blanco, Y. Ishii, *J. Am. Chem. Soc.* **2000**, *122*, 9340 – 9341.
[18] H. J. Sass, G. Musco, S. J. Stahl, P. T. Wingfield, S. Grzesiek, *J. Biomol. NMR* **2000**, *18*, 303 – 309.
[19] B. Luy, K. Kobzar, H. Kessler, *Angew. Chem.* **2004**, *116*, 1112 – 1115; *Angew. Chem. Int. Ed.* **2004**, *43*, 1092 – 1094.
[20] N. Tjandra, A. Bax, *Science* **1997**, *278*, 1111 – 1114.
[21] J. R. Tolman, J. M. Flanagan, M. A. Kennedy, J. H. Prestegard, *Proc. Natl. Acad. Sci. USA* **1995**, *92*, 9279 – 9283.
[22] B. Luy, G. Hauser, A. Kirschning, S. J. Glaser, *Angew. Chem.* **2003**, *115*, 1338 – 1341; *Angew. Chem. Int. Ed.* **2003**, *42*, 1300 – 1302.
[23] B. Luy, J. P. Marino, *J. Magn. Reson.* **2003**, *163*, 92 – 98.
[24] A. Solgadi, A. Meddour, J. Courtieu, *Tetrahedron: Asymmetry* **2004**, *15*, 1315 – 1318.
[25] P. Lesot, D. Merlet, A. Loewenstein, J. Courtieu, *Tetrahedron: Asymmetry* **1998**, *9*, 1871 – 1881.
[26] A. Meddour, P. Berdague, A. Hedli, J. Courtieu, P. Lesot, *J. Am. Chem. Soc.* **1997**, *119*, 4502 – 4508.
[27] I. Canet, A. Meddour, J. Courtieu, J. L. Canet, J. Salaun, *J. Am. Chem. Soc.* **1994**, *116*, 2155 – 2156.
[28] W. Smadja, S. Auffret, P. Berdague, D. Merlet, C. Canlet, J. Courtieu, J. Y. Legros, A. Boutros, J. C. Fiaud, *Chem. Commun.* **1997**, 2031 – 2032.
[29] M. Tavasli, J. Courtieu, R. J. M. Goss, A. Meddour, D. O'Hagan, *Chem. Commun.* **2002**, 844 – 845.
[30] P. Lesot, D. Merlet, M. Sarfati, J. Courtieu, H. Zimmermann, Z. Luz, *J. Am. Chem. Soc.* **2002**, *124*, 10071 – 10082.
[31] J. Farjon, D. Merlet, P. Lesot, J. Courtieu, *J. Magn. Reson.* **2002**, *158*, 169 – 172.
[32] D. Merlet, B. Ancian, J. Courtieu, P. Lesot, *J. Am. Chem. Soc.* **1999**, *121*, 5249 – 5258.
[33] P. Lesot, M. Sarfati, J. Courtieu, *Chem. Eur. J.* **2003**, *9*, 1724 – 1745.
[34] J. Farjon, J.-P. Baltaze, P. Lesot, D. Merlet, J. Courtieu, *Magn. Reson. Chem.* **2004**, *42*, 594 – 599.
[35] C. M. Thiele, S. Berger, *Org. Lett.* **2003**, *5*, 705 – 708.
[36] D. Uhrin, T. Liptaj, K. E. Kover, *J. Magn. Reson. Ser. A* **1993**, *101*, 41 – 46.
[37] *The Science and Technology of Gelatin* (Eds.: A. G., Ward, A. Courts), Academic Press, New York, **1977**.
[38] J. C. Freudenberger, S. Knör, K. Kobzar, D. Heckmann, T. Paululat, H. Kessler, B. Luy, *Angew. Chem.* **2005**, *117*, 427 – 430; *Angew. Chem. Int. Ed.* **2005**, *44*, 423 – 426.
[39] P. Haberz, J. Farjon, C. Griesinger, *Angew. Chem.* **2005**, *117*, 431 – 433; *Angew. Chem. Int. Ed.* **2005**, *44*, 427 – 429.
[40] J. C. Freudenberger, P. Spiteller, R. Bauer, H. Kessler, B. Luy, *J. Am. Chem. Soc.* **2004**, *126*, 14690 – 14691.

Dyes

Reversible Self-Organization of Semisynthetic Zinc Chlorins into Well-Defined Rod Antennae**

*Valerie Huber, Martin Katterle, Marina Lysetska, and Frank Würthner**

Dedicated to Professor Franz Effenberger on the occasion of his 75th birthday

The light-harvesting rod-shaped antennae in the chlorosomes of green phototrophic bacteria (e.g. *Chloroflexus aurantiacus*) are one of the most fascinating examples of self-organized functional assemblies. In contrast to other plant or bacterial light-harvesting systems, chlorosome antennae solely consist

[*] V. Huber, Dr. M. Katterle, Dr. M. Lysetska, Prof. Dr. F. Würthner
Institut für Organische Chemie
Universität Würzburg
Am Hubland, 97074 Würzburg (Germany)
Fax: (+49) 931-888-4756
E-mail: wuerthner@chemie.uni-wuerzburg.de

[**] This work was supported by the Fonds der Chemischen Industrie.

 DOI: 10.1002/anie.200462762

of bacteriochlorophylls (BChl) and do not require any protein to control their self-organization. Holzwarth, Schaffner, Tamiaki, and co-workers have investigated these natural systems and developed a simple model compound **1** for the main constituents, namely BChl *c*, of these light-harvesting antennae.[1]

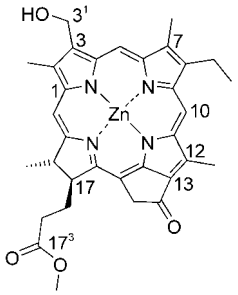

1

Both BChl *c* and the model compound **1** self-organize in nonpolar solvents, such as *n*-hexane, into extended dye aggregates which exhibit the highest exciton diffusion length of all dye assemblies reported to date.[2] This property is of fundamental importance for the high efficiency of the light-harvesting antennae in chlorosomes of green bacteria and instructive for the design of organic solar cells.

The micelle-type aggregates of BChl *c* and its model compound **1** are prone to further macroscopic aggregation in solution leading to precipitation of less-defined agglomerates.[3] Thus, it is difficult to handle these compounds and to deduce their structure–function relationships. Herein we introduce compounds developed on the basis of **1** which self-organize into well-defined rod aggregates of excellent solubility. The formation of these aggregates is completely reversible and can be triggered simply by variation of solvent polarity. Hence, for the first time an easy to use biomimetic antennae model for the more complex natural systems is made available.

Scheme 1 illustrates our strategy for the design of highly soluble artificial rod-shaped antennae which do not agglomerate. In natural chlorosome systems, each chlorin unit contains only one nonpolar chain (e.g. farnesyl).[1b] The rod aggregates formed by self-organization of these chlorins are surrounded by neighboring rod aggregates as well as by a lipid monolayer membrane covering the chlorosome. In both cases the neighboring alkyl chains interpenetrate and thereby accomplish a "fusion" which holds the aggregate together.[4] Consequently, isolated BChl *c* dissolved in water or organic solvents tend to agglomerate. In contrast, increasing the number of alkyl chains in 17^3 position of the chlorin unit should lead to highly soluble rod aggregates in the form of cylindrical micelles with a significantly reduced propensity for agglomeration. For the evaluation of this concept, the zinc chlorins **6a–c** containing one (**6a**), two (**6b**), or three (**6c**) alkyl chains were prepared. These new biomimetic compounds may be helpful for the structural elucidation of the natural antennae aggregates, and also provide spectroscopically uniform functional structures.

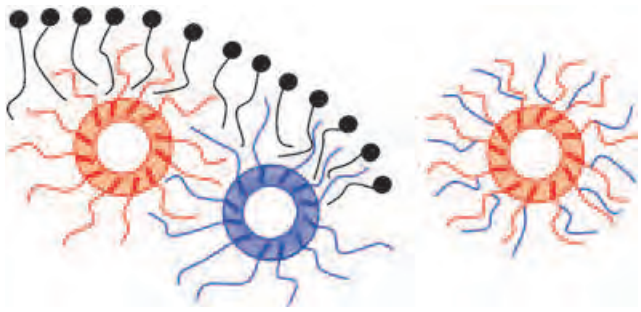

Scheme 1. Left: Model of a chlorosome: Lipid monolayer (black), rod aggregates of BChl *c* containing one nonpolar side chain per chlorin unit (red and blue). Right: Isolated rod aggregate in solution containing two nonpolar side chains per chlorin unit (compare **6b**).

The zinc chlorins were synthesized by derivatization of Chl *a* which was extracted from the algae *Spirulina maxima*.[5] Scheme 2 shows the synthesis of the desired zinc chlorins **6a–c** starting with the pheophorbide **2**, which was obtained from Chl *a*.[6]

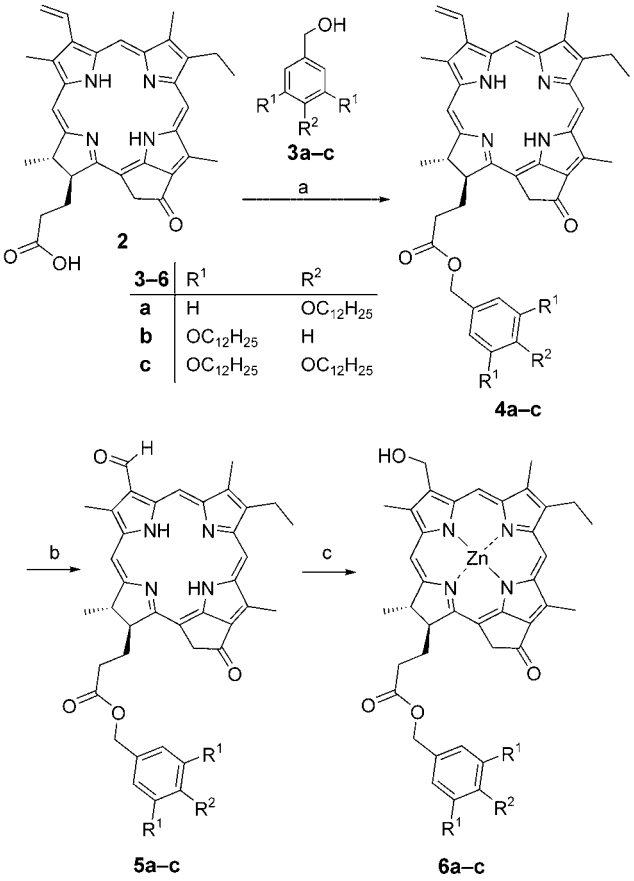

Scheme 2. a) DCC, DMAP, DPTS, *N*-ethyldiisopropylamine, CH_2Cl_2, RT, 3 h, 40–61 %; b) OsO_4, $NaIO_4$, AcOH, THF/H_2O, RT, 5 h, 80–98 %; c) $BH_3(t\text{Bu})NH_2$, THF, RT, 4 h; $Zn(OAc)_2$, MeOH, RT, 3 h, 60–85 %. DCC = dicyclohexylcarbodiimide, DMAP = 4-dimethylaminopyridine, DPTS = 4-dimethylaminopyridinium-*p*-toluenesulfonate.

The carboxylic acid in 17^3 position of 13^2-demethoxycarbonylmethylpheophorbide *a* (**2**) was esterified with the alcohols **3a–c** by activation with DCC, DMAP, DPTS, and *N*-ethyldiisopropylamine in dichloromethane. Oxidative cleavage of the 3^1 vinyl group of **4a–c** by osmium tetroxide and sodium periodate afforded the respective formyl derivates **5a–c**. The formyl group in **5a–c** was selectively reduced with borane *tert*-butylamine to the alcohol, and the desired zinc

chlorins **6a–c** were obtained by subsequent addition of a methanolic solution of zinc acetate.[7,8]

Characteristic for the dye aggregates in chlorosomes of *Chloroflexus aurantiacus* and for the in vitro aggregates of BChl *c* is a bathochromic shift of the Q_y band with respect to the corresponding absorption in the monomer.[1b] This red shift can be ascribed to the interaction between metallochlorins which is comparable to that in Scheibe aggregates (J-aggregates).[9] Three structural characteristics of metallochlorins are important for the formation of tubular J-aggregates:[3] A central metal ion for the coordination with the oxygen atom of the 3^1 hydroxy group, an extended π system for effective π–π interactions, and hydrogen-bond donor (3^1 OH) and hydrogen-bond acceptor (13^1 keto) groups. The first two interactions mentioned above lead to a slipped type of π–π stacking as in the case of J-aggregates (see Scheme 3), whereas hydrogen bonding induces the tubular

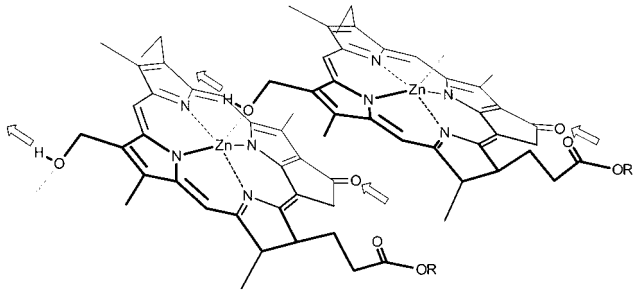

Scheme 3. Interactions between zinc chlorins **6a–c**. Zn—O coordination bonds that direct J-type stacks are marked in gray. Hydrogen bonds that connect these stacks to give tubes are shown by arrows.

structure in which all the alkyl chains are oriented towards the outside (inverse cylinder micelle).[10] Like BChl *c*, the zinc chlorins **6a–c** also have these structural characteristics and, thus, their Q_y-band should also be bathochromically shifted because of J-aggregate formation. Indeed, for the zinc chlorins **6a–c** the characteristic red shift of the Q_y-band from 648 nm to 742 nm was observed as the UV/Vis spectra show (Figure 1). Also characteristic is the very small Stokes

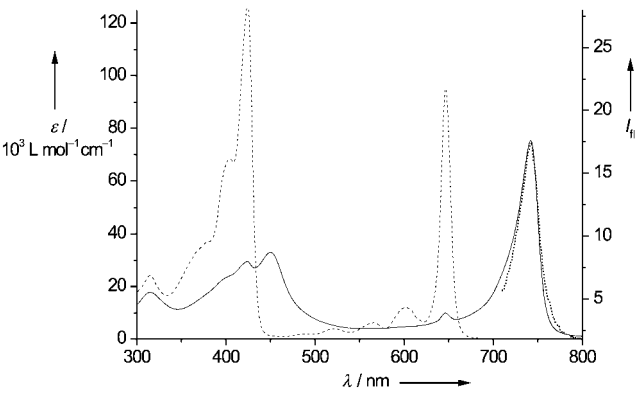

Figure 1. UV/Vis spectra of **6b**. Monomer dissolved in THF, $c = 2.3 \times 10^{-5}$ mol L^{-1} (-----); aggregate dissolved in hexane with <1% THF, $c = 4.6 \times 10^{-5}$ mol L^{-1} (——). Fluorescence spectrum ($\lambda_{ex} = 690$ nm) of **6b** dissolved in hexane with <1% THF (••••).

shift (<1 nm) which indicates resonance fluorescence behavior of J-aggregates of the zinc chlorins **6a–c** (see fluorescence spectrum in Figure 1).

In contrast to model compound **1**, both zinc chlorins **6b** and **c** with two and three alkyl chains, respectively, form in nonpolar solvents, soluble aggregates that are stable for a prolonged time. As expected from our concept, at least two alkyl chains are necessary to enable good solubility, since zinc chlorin **6a** as well as model compound **1** agglomerate within hours to days and finally precipitate (Figure 2).

Figure 2. Color and solubility of zinc chlorin **6b** in THF (left) and in heptane with 1% THF after 8 days (right) compared to that of model compound **1** (middle, also in heptane with 1% THF after 8 days).

To gain more insight into the aggregation process, zinc chlorin **6b** was dissolved in di-*n*-butyl ether and heptane (20:80) and temperature-dependent (15–95 °C) UV/Vis spectroscopic measurements were performed. Preliminary experiments showed that a steady state is achieved after about 1 h at lower temperatures; therefore, the samples were equilibrated for 1.5 h prior to each measurement. The variable temperature UV/Vis absorption studies have revealed that with increasing temperature, the Q_y-band of aggregates at 742 nm decreases and accordingly the monomer band of chlorins at 648 nm increases (Figure 3). On subsequent cooling of the sample, the Q_y-band of the aggregate is completely recovered, demonstrating the reversibility of aggregate formation. The fact that no precipitation was observed on warming or on cooling indicates that the aggregate structures of zinc chlorins are thermodynamically stable and, thus, they differ from numerous other self-organized dye aggregates.[11] As can been seen in the inset of Figure 3, the absorption versus temperature (*A* vs. *T*) plot provides sigmoidal curves with a melting temperature of about 60 °C for the aggregates of zinc chlorin **6b**. The dissociation of the aggregates can also be induced by addition of small amounts of protic solvents, such as methanol, which weaken hydrogen bonding as well as coordinative interactions (Scheme 3).

A distinct feature for natural BChl *c* rod aggregates is, besides bathochromic shift of the long-wavelength UV/Vis absorption bands, an induced circular dichroism (CD) effect. This effect occurs on chiral excitonic coupling of transition

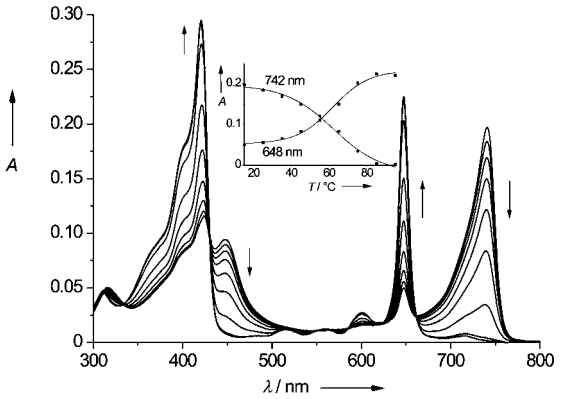

Figure 3. Temperature-dependent UV/Vis spectra of **6b** in di-*n*-butyl ether/heptane (20:80; $c = 3 \times 10^{-6}$ mol L^{-1}). Initial temperature 15 °C, increased successively by 10 °C in 1.5 h intervals up to 95 °C; arrows indicate changes upon increasing temperature. Inset: the decrease of the Q_y-band of aggregates at 742 nm and the increase of the monomer band at 648 nm upon increasing temperature.

dipole moments and consists of two bands with opposite signs (exciton couplet).[12] Surprisingly, different CD spectra of isolated chlorosomes and in vitro generated aggregates of BChl *c* have been reported.[2,13] Griebenow et al. have categorized the observed CD spectra into three types (type I: the sign of the CD curve changes from positive at shorter wavelengths to negative at longer wavelengths [+/−], type II: opposite behavior to type I [−/+], and the mixed-type: [−/+/−]).[14] In a theoretical approach, Holzwarth and co-workers proposed that the different types of CD spectra result from a size effect.[15] According to this approach, at an aggregate length of more than 30 molecules of BChl *c*, the type II converts into the mixed-type. On the other hand, previously mentioned uncontrolled agglomeration of in vitro aggregates of BChl *c* and **1** could lead to artifacts in CD spectra. Therefore, it is interesting to note that zinc chlorin **6b** exhibits an exciton couplet, which is very similar to that of the model compound **1**. This exciton couplet reversibly arises and disappears on temperature change (see Figure 4) and does not undergo any time-dependent changes at a particular temperature.

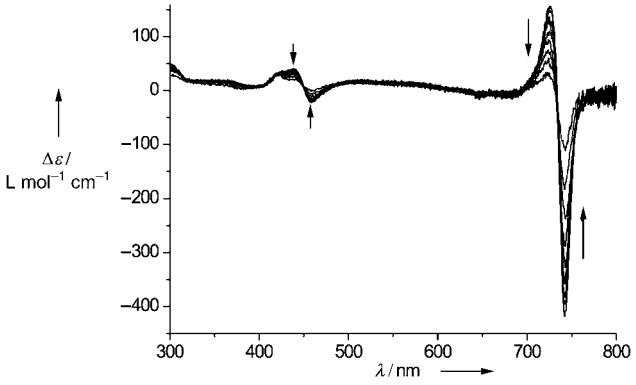

Figure 4. Temperature-dependent (15–95 °C) CD spectra of **6b** ($c = 1 \times 10^{-5}$ mol L^{-1}) in di-*n*-butyl ether/heptane (20:80). The temperature was increased in 10 °C intervals after 1.5 h equilibration time; arrows indicate changes upon increasing temperature.

The data presented reveal that the aggregates of zinc chlorins **6b** and **c** have spectral properties comparable to those of the natural light-harvesting systems in chlorosomes. Encouraged by these results, atomic force microscopy (AFM) studies were carried out to elucidate the structural properties of **6b** and **c**. Figure 5a shows an AFM image of a sample,

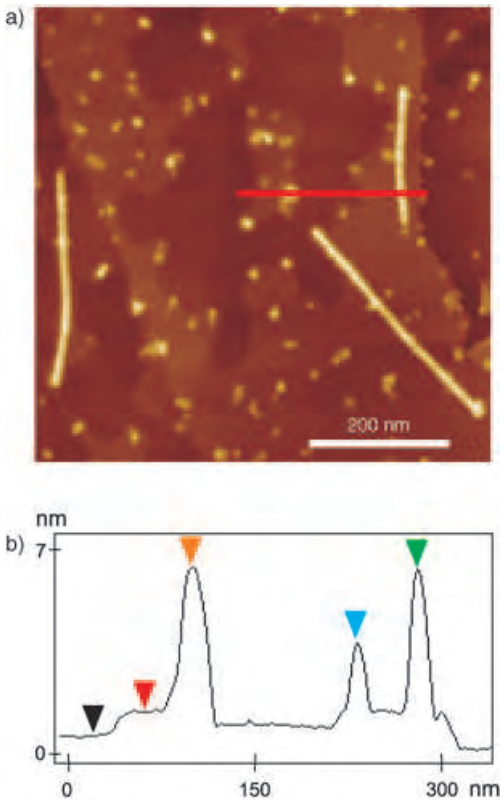

Figure 5. a) AFM image in tapping mode of **6b**. The sample was prepared by spin-coating of a solution of **6b** ($c = 4.6 \times 10^{-5}$ mol L^{-1}) in hexane/THF (100:1) onto HOPG and measured in air. b) Profile of the red line in (a), details are given in the text.

which was prepared by spin-coating of a solution of **6b** in hexane/THF onto HOPG (highly ordered pyrolytic graphite). As can be seen in this image, zinc chlorin **6b** self-organizes into rigid rods. The length of the rods is 300 ± 97 nm and the height is 5.8 ± 0.4 nm (vertical distance between the black and green triangle, Figure 5b). It is remarkable that all the observed rod-like antennae are isolated. This structural behavior corroborates our concept illustrated in Scheme 1. The measured height of about 6 nm of these biomimetic zinc chlorin aggregates is in agreement with electron microscopy data of the BChl *c* rod aggregates in chlorosomes (*Chloroflexus aurantiacus*)[16] and also comply with the tubular model postulated by Holzwarth and Schaffner.[10] Spectroscopic data and theoretical calculations[10,15] already suggested the presence of rod-shaped structures, but now, by AFM measurements, microscopic evidence is obtained for the first time for the supramolecular organization of this class of chromophores.

Besides rod-shaped structures, smaller (3.1 ± 0.6 nm in height, vertical distance between the black and blue triangle,

Figure 5b) and bigger (5.6 ± 0.7 nm in height, vertical distance between the black and orange triangle) globular objects are visible in the AFM image shown in Figure 5. Future studies should clarify, whether these globular micelle structures are caused by preparation process of the sample or if they already co-exist with the rod aggregate in solution. Furthermore, a molecular monolayer of 0.5 ± 0.1 nm thickness (vertical distance between the black and red triangle, Figure 5b) is visible on HOPG surface, which may indicate the self-organization of zinc chlorin **6b** monomers induced by the graphite surface.

Preliminary experiments indicate that our strategy demonstrated in Scheme 2 can also be applied to prepare rod aggregates of zinc chlorins in water, since the Q_y-band of zinc chlorin **7** (in water/THF 100:1) is also red-shifted from 648 nm to 744 nm. Further investigations with this compound are in progress.

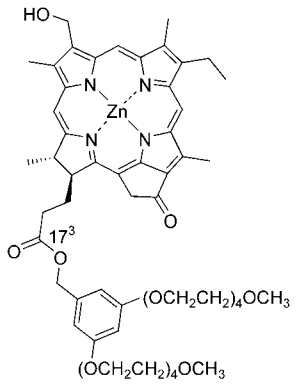

7

In summary, with the newly developed compounds **6b** and **6c**, zinc chlorins are made available whose self-organized rod-shaped antennae exhibit excellent solubility in nonpolar solvents. This favorable property enabled spectroscopic investigations that confirm the reversible formation of these biological important dye assemblies. For the first time AFM enabled isolated rod aggregates to be observed whose diameter is in good agreement with electron microscopic data of BChl *c* aggregates in chlorosomes.

Received: November 30, 2004
Published online: April 21, 2005

Keywords: aggregation · chlorins · dyes/pigments · scanning probe microscopy · self-organization

[1] a) H. Tamiaki, A. R. Holzwarth, K. Schaffner, *J. Photochem. Photobiol. B* **1992**, *15*, 355–360; b) A. R. Holzwarth, K. Griebenow, K. Schaffner, *J. Photochem. Photobiol. A* **1992**, *65*, 61–71.

[2] a) D. C. Brune, G. H. King, A. Infosino, T. Steiner, M. L. W. Thewalt, R. E. Blankenship, *Biochemistry* **1987**, *26*, 8652–8658; b) S. Savikhin, Y. Zhu, R. E. Blankenship, W. S. Struve, *J. Phys. Chem.* **1996**, *100*, 3320–3322; c) V. I. Prokhorenko, D. B. Steensgaard, A. R. Holzwarth, *Biophys. J.* **2000**, *79*, 2105–2120.

[3] a) T. S. Balaban, J. Leitich, A. R. Holzwarth, K. Schaffner, *J. Phys. Chem. B* **2000**, *104*, 1362–1372; b) T. S. Balaban, A. D. Bhise, M. Fischer, M. Linke-Schaetzel, C. Roussel, N. Vanthuyne, *Angew. Chem.* **2003**, *115*, 2190–2194; *Angew. Chem. Int. Ed.* **2003**, *42*, 2140–2144.

[4] J. M. Olson, *Photochem. Photobiol.* **1998**, *67*, 61–75.

[5] K. M. Smith, D. A. Goff, D. J. Simpson, *J. Am. Chem. Soc.* **1985**, *107*, 4946–4954.

[6] H. Tamiaki, M. Amakawa, Y. Shimono, R. Tanikaga, A. R. Holzwarth, K. Schaffner, *Photochem. Photobiol.* **1996**, *63*, 92–99.

[7] Data for **6b**: dark green solid; m.p. 241 °C; ^{1}H NMR (400 MHz, $CDCl_3$, [D_5]pyridine, 25 °C): $\delta = 9.58$ (s, 1H, CH), 9.41 (s, 1H, CH), 8.33 (s, 1H, CH), 6.38–6.36 (m, 3H, CH), 5.87 (s, 2H, CH_2), 5.22 (d, ^2J(H,H) = 19.7 Hz, 1H, CH_2), 5.05 (d, ^2J(H,H) = 19.6 Hz, 1H, CH_2), 4.97 (d, ^2J(H,H) = 12.4 Hz, 1H, CH_2), 4.92 (d, ^2J(H,H) = 12.4 Hz, 1H, CH_2), 4.38 (dq, ^3J(H,H) = 7.3 Hz, ^3J(H,H) = 2.1 Hz, 1H, CH), 4.22 (td, ^3J(H,H) = 7.2 Hz, ^3J(H,H) = 2.5 Hz, 1H, CH), 3.84 (t, ^3J(H,H) = 6.6 Hz, 4H, CH_2), 3.75 (q, ^3J(H,H) = 7.6 Hz, 2H, CH_2), 3.70 (s, 3H, CH_3), 3.30 (s, 3H, CH_3), 3.19 (s, 3H, CH_3), 2.63–2.55 und 2.45–2.29 und 1.99–1.91 (m, 4H, CH_2), 1.72–1.65 (m, 9H, CH_3, CH_2), 1.38–1.25 (m, 36H, CH_2), 0.88 ppm (t, $^3J = 7.0$ Hz, 6H, CH_3); UV/Vis (THF): $\lambda_{max}(\varepsilon)$ = 648 nm (95000 L mol^{-1} cm^{-1}); MS (FAB, NBA): 1058.7 $[M-2H]^+$.

[8] To avoid demetallation, we have used zinc ions instead of the magnesium ions present in natural (bacterio)chlorophylls, and thereby increased the chemical stability of chlorins.

[9] a) D. Möbius, *Adv. Mater.* **1995**, *7*, 437–444; b) A. Pawlik, S. Kirstein, U. De Rossi, S. Dähne, *J. Phys. Chem. B* **1997**, *101*, 5646–5651; c) H. von Berlepsch, C. Böttcher, A. Ouart, C. Burger, S. Dähne, S. Kirstein, *J. Phys. Chem. B* **2000**, *104*, 5255–5262; d) S. Dähne, *Bunsen Magazin* **2002**, *4*, 81–92.

[10] a) A. R. Holzwarth, K. Schaffner, *Photosynth. Res.* **1994**, *41*, 225–233; b) K. Schaffner, A. R. Holzwarth, *Leopoldina* **1997**, *42*, 205–220.

[11] a) F. Würthner, C. Thalacker, A. Sautter, W. Schärtl, W. Ibach, O. Hollricher, *Chem. Eur. J.* **2000**, *6*, 3871–3886; b) F. Würthner, S. Yao, *J. Org. Chem.* **2003**, *68*, 8943–8949; c) C. Thalacker, A. Miura, S. De Feyter, F. C. De Schryver, F. Würthner, *Org. Biomol. Chem.* **2005**, *3*, 414–422.

[12] N. Berova, K. Nakanishi in *Circular Dichroism: Principles and Applications* (Eds.: N. Berova, K. Nakanishi, R. Woody), VCH, New York, **2000**, pp. 337–368.

[13] a) M. Miller, T. Gillbro, J. M. Olson, *Photochem. Photobiol.* **1993**, *57*, 98–102; b) R. Frese, U. Oberheide, I. van Stokkum, R. van Grondelle, M. Foidl, J. Oelze, H. van Amerongen, *Photosynth. Res.* **1997**, *54*, 115–126.

[14] K. Griebenow, A. R. Holzwarth, F. van Mourik, R. van Grondelle, *Biochim. Biophys. Acta* **1991**, *1058*, 194–202.

[15] V. I. Prokhorenko, D. B. Steensgaard, A. R. Holzwarth, *Biophys. J.* **2003**, *85*, 3173–3186.

[16] L. A. Staehelin, J. R. Golecki, R. C. Fuller, G. Drews, *Arch. Mikrobiol.* **1978**, *119*, 269–277.

Cover Picture

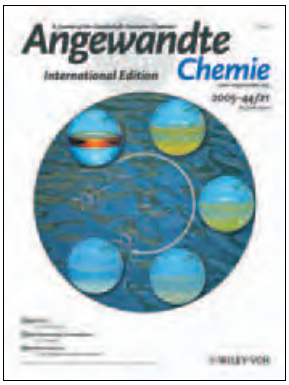

Sridhar Narayan, John Muldoon, M. G. Finn, Valery V. Fokin, Hartmuth C. Kolb, and K. Barry Sharpless*

Reactions "on water" offer ease of product isolation and may be substantially faster than the same reactions performed in organic solvents. The cover picture shows the time course of an ene reaction between (*S*)-β-pinene and diethyl azodicarboxylate performed on water. The insoluble reactants float on water, whereas the product descends under the water layer and is isolated as a colorless oil. For more details on these reactions, see the Communication by K. B. Sharpless and co-workers on page 3275 ff.

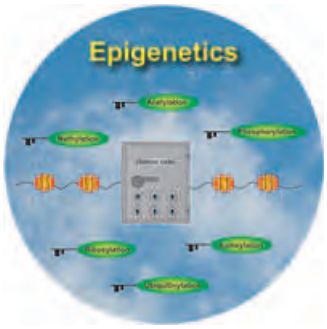

Epigenetics
A. Giannis and co-workers delve into the secrets of the histone code in their Review on page 3186. What influence do histones have on the activation and inactivation of gene sequences?

Crystal Growth
Two growth processes, habit formation and branching growth, determine the crystal shape of electrochemically generated Cu_2O crystals. In their Communication on page 3218 ff., K.-S. Choi and M. J. Siegfried explain how these processes can be controlled.

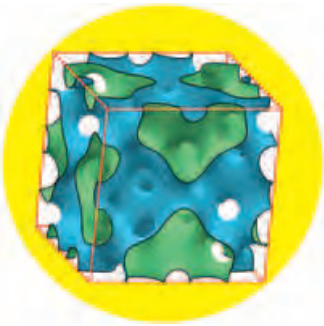

Mesoporous Materials
The mesoporous silica superstructure SBA-1 was studied to obtain a formulation in terms of curvature, which is important for surfactant structures and the mechanism of formation of inorganic replicas. The results are presented by M. W. Anderson and co-workers on page 3243 ff.

Contents

VIP *The following Communications have been judged by at least two referees to be "very important papers" and will be published online at www.angewandte.org soon:*

News

Books

Highlights

Fullerenes

Breaking with convention: In the textbook aromatic annulenes the p orbitals are oriented perpendicular to the ring plane. In trannulenes the p orbitals form a cyclic, conjugated π system within the ring plane (see scheme). This concept of "in-plane" aromaticity was first recognized in 1979, and now representative compounds have been synthesized. The all-*trans* configuration of the annulene ring is stabilized by a fullerene framework, and the novel physicochemical properties of trannulenes open new opportunities for the design of light-harvesting compounds.

Combinatorial Chemistry

Decoding technology: Besides mainstream applications in transcription profiling, DNA microarrays are currently being explored as tools for the deconvolution of synthetic libraries. Current examples include the discovery of a new type of organic reaction and the screening of peptide nucleic acid encoded inhibitor libraries to investigate new proteolytic activities from dust mite extracts (see picture).

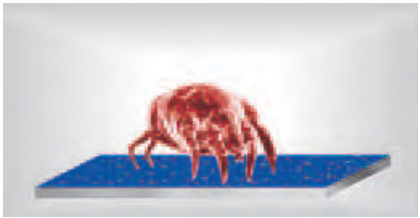

Reviews

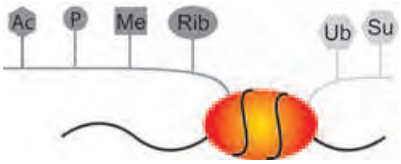

Wrapped around the finger! It has been known for a long time that histones organize the structure of cellular DNA. The news, however, is that histones are also able to influence elementary DNA-dependent processes. The type and number of specific histone modifications (examples rendered in gray) determine in advance if and when a gene is transcribed. The first modulators of histone-modifying enzymes have already become promising drugs.

Communications

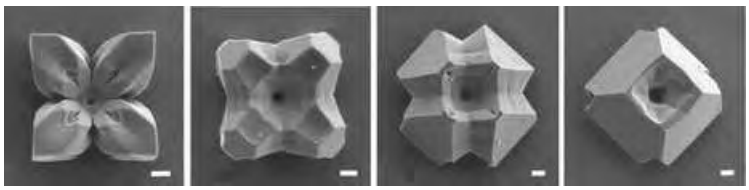

A new level of programmability and freedom in directing the crystal growth of cuprous oxide was demonstrated by controlling the degree of branching and crystal habit in a systematic manner during electrodeposition. Examples of Cu_2O crystals in which these features were directed by rationally designing a growth condition and growth history are shown (scale bar = 1 μm).

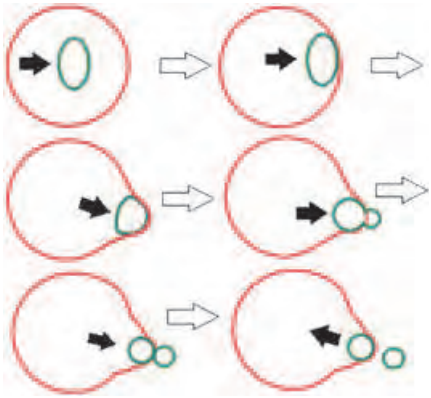

Cooperation of mother and daughter vesicles, which are self-assembled from an ill-defined hyperbranched copolymer, leads to fission of the daughter membrane in a cytomimetic process (see picture; red: mother vesicle, green: daughter vesicle). This is the first example of giant polymer vesicles (5–200 μm) being used as model membranes.

For the USA and Canada:
ANGEWANDTE CHEMIE International Edition (ISSN 1433-7851) is published weekly by Wiley-VCH PO Box 191161, D 69451 Weinheim, Germany. Air freight and mailing in the USA by Publications Expediting Inc. 200 Meacham Ave., Elmont, NY 11003. Periodicals postage paid at Jamaica NY 11431. US POSTMASTER: send address changes to *Angewandte Chemie*, Wiley-VCH, 111 River Street, Hoboken, NJ 07030. Annual subscription price for institutions: US$ 4948.00/4498.00 (valid for print and electronic / print or electronic delivery); for individuals who are personal members of a national chemical society, or whose institution already subscribes, or who are retired or self-employed consultants, print only: US$ 394.00. Postage and handling charges included. All Wiley-VCH prices are exclusive VAT.

www.angewandte.org

1888: ***The beginning of a success story***

Constant Innovations

1962: *First issue of the International Edition*
1976: *Graphical abstracts*
1979: *Cover pictures*
1988: *Centenary of Angewandte*
1989: *Routine use of color*
1991: *New section: Highlights*
1992: *Computerized editorial tracking system*
199

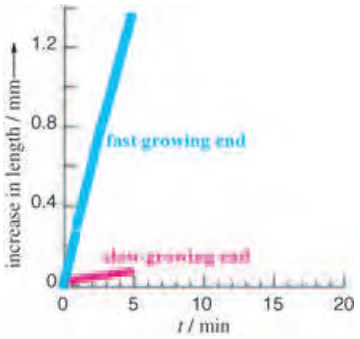

Crystallization of the thermodynamically metastable β glycine is explained on the basis of its growth at the opposite poles of the crystal (see graph) and by considering the structure of the relevant surfaces of the three polymorphs and their interactions with solvent molecules.

Crystal Growth

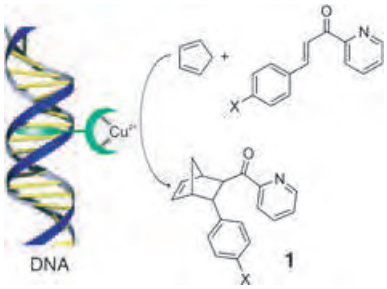

A twist in catalysis! The chirality of DNA is transferred directly to a Diels–Alder reaction by using a DNA-tethered catalyst. A catalytically active copper complex with achiral ligands self-assembles with DNA to give products with up to 90% *ee*, as is the case for the *exo* isomer of product **1**.

Asymmetric Catalysis

Cross-correlated relaxation (CCR) can be used to describe the structure and dynamics of biomolecules (see picture). By combining theoretical and experimental techniques in the study of proteins, for example, it is possible to acquire detailed information concerning the local anisotropic motion of the peptide plane

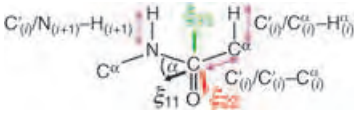

from a single cross-correlation: the C′/N–H CCR rate.

NMR Spectroscopy

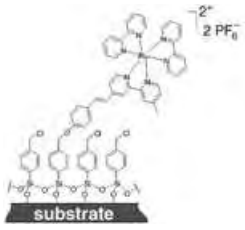

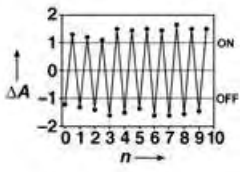

Don't forget to write! Electrochemical charge storage in a ruthenium-based monolayer on a hydrophilic substrate (for example, indium tin oxide coated glass) produces redox switching of the optical properties of the system (see picture).

This read/write process can be carried out at low voltage in air and monitored by UV/Vis spectrophotometry. This makes the monolayer system a suitable candidate for nonvolatile memory devices.

Molecular Devices

Contents

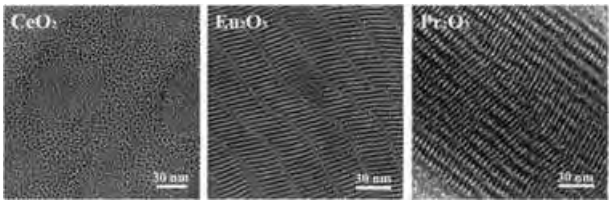

Thermolysis of benzoylacetonate complexes proved successful in the synthesis of rare-earth oxide nanocrystals. CeO_2 nanopolyhedra, Eu_2O_3 nanodisks, and Pr_2O_3 nanoplates display 2D ordering on copper grids (see figure), and the former two show interesting optical properties arising from surface-modification effects.

Nanocrystals

Hydrogen bonding and π–π interactions are the driving forces for the self-assembly of a diamide organogelator into nanotubes in organic solution. Freeze-fracture electron microscopy (see image) and small angle neutron scattering studies show the tubes have a diameter of (24.2 ± 0.3) nm with a wall thickness of (3.3 ± 0.4) nm and an aspect ratio of 1:50 or higher.

Self-Assembly

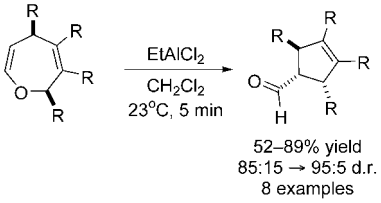

A room-temperature diastereoselective [1,3] rearrangement results from treatment of 2,5-dihydrooxepins with $EtAlCl_2$ (see scheme). A modular synthesis of dihydrooxepins allows substituents to be incorporated at any position on the ring, which means that various polysubstituted cyclopentenes can be prepared through this Lewis acid mediated [1,3] ring contraction.

Synthetic Methods

Ready cleavage of dioxygen and its selective insertion into Rh–alkene bonds occurs in the presence of $[\{Rh(PhN_3Ph)(C_8H_{12})\}_n]$ ($n = 1$ and 2). The structure of the resulting dirhodadioxetane complex (see picture) and kinetic measurements support a dimetallic mechanism for this process that occurs with 100% atom economy.

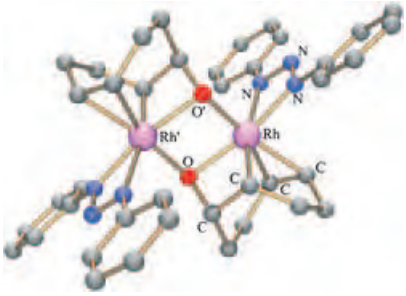

O–O Activation

Contents

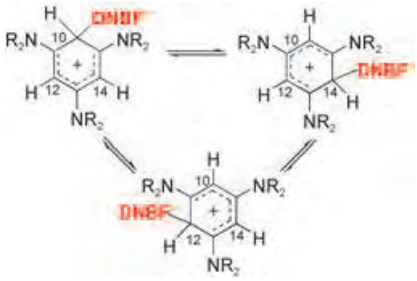

Proposal accepted: NMR experiments have shown unequivocally that the previously only proposed zwitterionic carbon–carbon Meisenheimer–Wheland complexes are formed in the reaction of 4,6-dinitrobenzofuroxan (DNBF) with 1,3,5-tris(*N*,*N*-dialkylamino)benzenes. Increasing the temperature results in a rapid exchange between three homomeric forms of the complex (see scheme; NR_2 = piperidyl, morpholinyl, pyrrolidinyl).

Reactive Intermediates

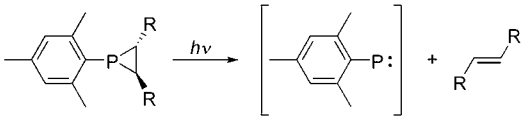

1 R = Me
2 R = H

3

Monitoring the cleavage of phosphiranes **1** and **2** by using a variety of low-temperature and time-resolved spectroscopic techniques has shown that triplet mesitylphosphinidene (**3**) is the principal product of this photolytic reaction (see scheme). Results obtained by using laser flash photolysis show that **3** is readily quenched by reactive π systems.

Radicals

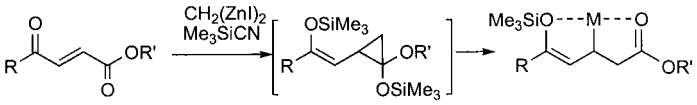

1 **2**

Enolate–homoenolate equivalents 1 can be prepared in one step by the title reaction. They act as functionalized *Z*-γ-siloxyallyl zinc reagents **2** by undergoing ring opening in the presence of a Lewis acid. Addition of **2** to tosylimines gives *vic*-amino alcohols with high diastereoselectivity, presumably due to a fixed conformation resulting from coordination of the metal atom.

Organozinc Reagents

Disguise tactics: Peptide–polymer hybrid nanotubes are constructed in which self-assembled cyclic peptides govern the structure, and a synthetic polymer coating determines the surface chemistry. Formation of the latter is initiated in situ from preorganized peptide building blocks. The picture shows an AFM image of nanotubes on a silicon wafer.

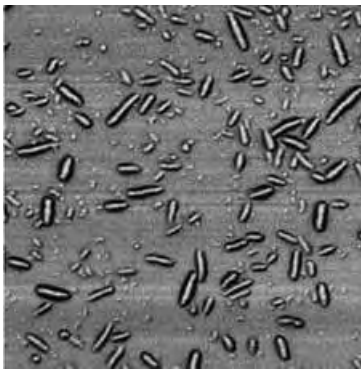

Nanotubes

Contents

The issues for May 2005 appeared online on the following dates
Issue 17: April 21 · Issue 18: April 25 · Issue 19: May 3 · Issue 20: May 9

Service

Fullerenes

Trannulenes with "In-Plane" Aromaticity: Candidates for Harvesting Light Energy**

*Glenn A. Burley**

Keywords:
annulenes · aromaticity · fullerenes · trannulenes

Dedicated to Paul von Ragué Schleyer on the occasion of his 75th birthday

Annulenes are defined as cyclic conjugated polyenes with their ring size indicated by a numerical prefix (e.g. [6]annulene for benzene).[1] Annulenes adhering to Hückel's $4n+2$ π-electron rule are termed aromatic.[2] Up until 2001 all experimentally observed annulenes comprised C–C double bonds with either an all-*cis* (such as benzene) or a *cis,trans* configuration (for example [10]annulene). In these annulenes the p orbitals are oriented perpendicular to the annulene ring plane (Figure 1 a).

Conversely, trannulenes (annulenes in which the C–C double bonds in the ring are exclusively of *trans* configuration) (e.g. **1**, Figure 2), have a completely different the p-orbitals orientation: they lie parallel to the ring plane (Figure 1 b).[3,4] This p-orbital overlap pattern, termed "in-plane" aromaticity, was predicted as early as 1979 by Schleyer et al. in a publication describing the 3,5-didehydrophenyl cation, the first double-aromatic system.[5] To support the existence of trannulenes, which are higher energy annulene isomers, Schleyer et al. elegantly predicted that a supporting molecular framework such as a dodecahedrapentaene (**2**, Figure 2) would provide a suitable three-dimensional setting for such "in-plane" aromaticity.[4]

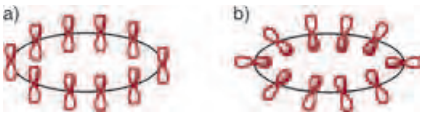

Figure 1. Visualization of the orbital overlap in a) conventional annulenes where the overlap is perpendicular to the ring plane, and in b) trannulenes where the overlap is parallel to the ring plane ("in-plane" aromaticity). This situation should not to be confused with that in [4*n*] Möbius systems, which are aromatic structures with enforced phase discontinuity. Möbius aromatic systems have been regarded as a combination of normal annulenic conjugation (a) and belt-shaped conjugation (b).[19]

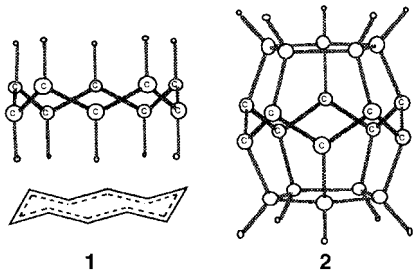

Figure 2. The [10]trannulenes: all-*trans*-cyclodecapentaene (**1**) and the central unit of dodecahedrapentaene (**2**) as computed by Schleyer et al. to be energy minima at the B3LYP/6-31G* level.[3]

The serendipitous realization of the first trannulene structure **3** by Taylor et al. (Figure 3) proved to fulfil Schleyer's theoretical predictions.[6] Indeed, **3** comprised an [18]trannulene within a three-dimensional [60]fullerene framework. The most notable structural feature of trannulene **3** is the presence of an 18π trannulene belt formed as a result of a threefold S_N2'' nucleophilic displacement of the three outermost fluorine atoms of $C_{60}F_{18}$ by the tertiary carbanion derived from diethyl bromomalonate.[6,7] Additionally, a central aromatic benzenoid ring (present in the $C_{60}F_{18}$ starting structure) is retained within the fluorinated region, and a nonplanar triphenylene substructure is formed within the nonfluorinated region, yielding a new type of double-aromatic system.[8]

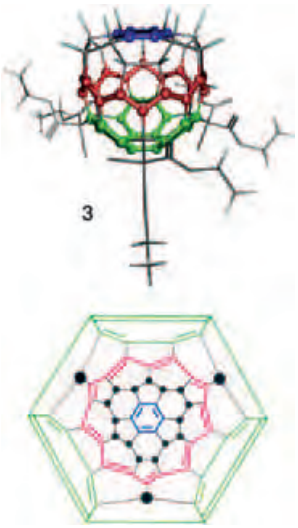

Figure 3. Top: X-ray crystal of trannulene **3**, which is prepared from the reaction of $C_{60}F_{18}$ and the carbanion of diethyl bromomalonate.[6] The [18]trannulene ring is depicted in red, the central benzene ring in blue, and the triphenylene substructure in green. Bottom: Schlegel diagram of **3**. Large black circles mark the site of functionalization (diethyl bromomalonate), whereas the smaller black circles represent fluorine atoms.

Computational investigations concerning the p-orbital arrangement and aromaticity of **3** further complemented Schleyer's theoretical predictions. Both the experimental (**3**) and theoretical (**2**) trannulenes adhere to Hückel's rule. On the basis of magnetic properties (magnetic diatropicity),[9,10] structure (small

[*] Dr. G. A. Burley
Fakultät Chemie und Pharmazie
Ludwig-Maximilians Universität
Butenandtstrasse 5–13 (Haus F)
81377 München (Germany)
Fax: (+49) 89-2180-77756
E-mail:
glenn.burley@cup.uni-muenchen.de

[**] G.A.B. thanks Armin Berndt, Roger Taylor, Johannes Gierlich, and Thomas Carell. This work was supported by the Alexander von Humboldt Foundation.

  DOI: 10.1002/anie.200500362

C–C bond alternation of the trannulene substructure),[6] and stability (more stable than other known fluorofullerenes) considerations,[11] these trannulene structures are indeed aromatic.

Recently the trannulene family has welcomed two new members. The drum-shaped $C_{60}Cl_{30}$ **4** reported by Troshin et al.[12] displays an equatorial trannulene belt flanked by two benzenoid substructures situated at the poles of the fullerene (Figure 4). Equally impressive is the unexpected discovery of a mild preparative route to a nonhalogenated trannulene by sixfold alkylation of the C_{60}^{6-} anion.[*] The resulting trannulene **5** discovered by Chiang et al. comprises a central trannulene belt flanked by two highly distorted triphenylene units (Figure 5).[14]

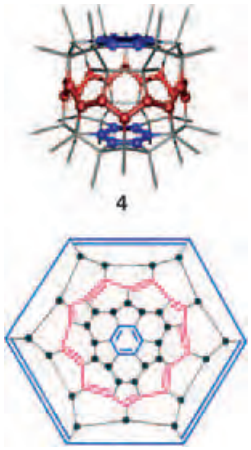

Figure 4. Top: X-ray crystal structure of trannulene **4**, which is prepared by the reaction of C_{60} with $SbCl_5$ at 220–250 °C.[12] The [18]trannulene ring is depicted in red, and the benzenoid structures are depicted in blue. Bottom: Schlegel diagram of **4**. The small black circles represent chlorine atoms.

Currently a total of three trannulenes have been discovered. Trannulenes **3**–**5** arise from three distinct preparative routes and exhibit three distinct topologies and π-conjugated substructures, which will most likely transcribe into quite distinct and tunable physicochemical properties. For example, the presence of an [18]trannulene moiety in the nonhalogenated trannulene **5** leads to significant absorptions in the near-IR region ($\lambda_{max} = 760$ and 850 nm), although the first reduction potential ($E_1^{Red} = -0.49$ V vs. Ag/AgCl) remains similar to that of [60]fullerene.[14] The presence of fifteen fluorine atoms in trannulene **3** results in a blue shift of the absorption spectrum ($\lambda_{max} = 612$ and 658 nm) and a dramatic increase in electron affinity, resulting in an anodic shift of the first reduction potential ($E_1^{Red} = -0.05$ V vs. SCE).[9,11,15,16] Although limited physicochemical data has been reported for chlorotrannulene **4**, the presence of thirty chlorine atoms in close proximity to the trannulene ring would most probably cause an even greater increase in electron affinity relative to that of **3** and **5**. The dark-orange color of **4** is an initial indicator of a more dramatic blue-shift compared with that of fluorofullerene **3**.

Hence the potential tunability of the physicochemical properties along with the low reorganization energy of the [60]fullerene cage makes these structures potential electron-acceptors for harvesting light energy.[17] Indeed the first donor–acceptor dyad comprising a fluorofullerene trannulene confirmed the ability of these remarkable molecules to accept a charged entity and store the resultant excitation energy in a long-lived charge-separated state.[15] Recent investigations have also demonstrated that the photophysics of a trannulene dyad series can be tuned from electron transfer to energy transfer as a function of the photoactive substituent, thus providing an additional level of molecular tailoring for specific applications.[18] Additionally, the mild conditions required for the preparation of trannulenes **3** and **5** will allow the incorporation of further functionalities through derivatization of the addends, thereby enabling these systems to be used as modular building blocks.

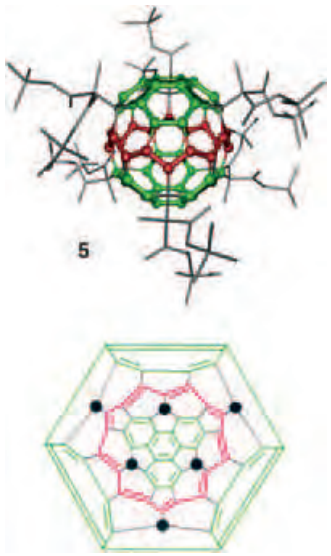

Figure 5. Top: X-ray crystal structure of trannulene **5**, which is prepared by the reaction of C_{60}^{6-} with diethyl 2-bromo-2-methylmalonate.[14] The [18]trannulene ring is depicted in red and the triphenylene substructure in green. Bottom: Schlegel diagram of **4**. The large black circles mark the sites of functionalization.

Synthetic organic chemists have now synthesized the first trannulenes, which were predicted by Schleyer et al.[4] The discoveries that followed have led to new branches of both fullerenes and of organic chemistry, and it is likely that the coming years will bring forth numerous derivatives and trannulene types exhibiting fascinating topologies and novel physicochemical properties.

[*] The C_{60}^{6-} anion is a three-dimensional aromatic species as judged by its large NICS value of −48.7.[13]

[1] a) F. Sondheimer, *Acc. Chem. Res.* **1972**, *5*, 81–91; b) H. Hopf, *Classics in Hydrocarbon Chemistry*, Wiley-VCH, Weinheim, **2000**.

[2] a) E. Hückel, *Z. Phys.* **1931**, *70*, 204; E. Hückel, *Z. Phys.* **1931**, *72*, 310; b) E. Hückel, *Z. Phys.* **1932**, 628; c) E. Hückel, *Grundzüge der Theorie ungesättigter und aromatischer Verbindungen*, Verlag Chemie, Berlin, **1938**.

[3] A. B. McEwen, P. von R. Schleyer, *J. Org. Chem.* **1986**, *51*, 4357–4368.

[4] A. A. Fokin, H. Jiao, P. von R. Schleyer, *J. Am. Chem. Soc.* **1998**, *120*, 9364–9365.

[5] a) J. Chandrasekhar, E. D. Jemmis, P. von R. Schleyer, *Tetrahedron Lett.* **1979**, *39*, 3707–3710; b) P. von R. Schleyer, H. Jiao, M. N. Glukhovtsev, J. Chandrasekhar, E. Kraka, *J. Am. Chem. Soc.* **1994**, *116*, 10129–10134.

[6] X.-W. Wei, A. D. Darwish, O. V. Boltalina, P. B. Hitchcock, R. Taylor, *Angew. Chem.* **2001**, *113*, 3077–3080; *Angew. Chem. Int. Ed.* **2001**, *40*, 2989–2992.

[7] X.-W. Wei, A. G. Avent, O. V. Boltalina, A. D. Darwish, P. W. Fowler, J. P. B. Sandall, J. M. Street, R. Taylor, *J. Chem. Soc. Perkin Trans. 2* **2002**, 41–46.

[8] For experimental verification of double-aromatic systems see: a) M. Unverzagt, G. Subramanian, M. Hofmann, P. von R. Schleyer, S. Berger, K. Harms, W. Massa, A. Berndt, *Angew. Chem.* **1997**, *109*, 1567–1569; *Angew. Chem. Int. Ed.*

Engl. **1997**, *36*, 1469 – 1472; b) H.-J. Zhai, A. E. Kuznetsov, A. I. Boldyrev, L.-S. Wang, *ChemPhysChem* **2004**, *5*, 1885 – 1891, and references therein.
[9] G. A. Burley, P. W. Fowler, A. Soncini, J. P. B. Sandall, R. Taylor, *Chem. Commun.* **2003**, 3042 – 3043.
[10] R. W. A. Havenith, A. Rassat, P. W. Fowler, *J. Chem. Soc. Perkin Trans. 2* **2002**, 723 – 727.
[11] G. A. Burley, A. G. Avent, I. V. Gol'dt, P. B. Hitchcock, H. l-Matar, D. Paolucci, F. Paolucci, P. W. Fowler, A. Soncini, J. M. Street, R. Taylor, *Org. Biomol. Chem.* **2004**, *2*, 319 – 329.
[12] P. Troshin, R. N. Lyubovskaya, I. N. Ioffe, N. B. Shustova, E. Kemnitz, S. I. Troyanov, *Angew. Chem.* **2005**, *117*, 238 – 241; *Angew. Chem. Int. Ed.* **2005**, *44*, 234 – 237.
[13] a) A. Hirsch, H. Jiao, Z. Chen, *Angew. Chem.* **2000**, *112*, 4079 – 4081; *Angew. Chem. Int. Ed.* **2000**, *39*, 3915 – 3917.
[14] T. Canteenwala, P. A. Padmawar, L. Y. Chiang, *J. Am. Chem. Soc.* **2005**, *127*, 26 – 27.
[15] G. A. Burley, A. G. Avent, O. V. Boltalina, I. V. Gol'dt, D. M. Guldi, M. Marcaccio, F. Paolucci, D. Paolucci, R. Taylor, *Chem. Commun.* **2003**, 148 – 149.
[16] G. A. Burley, O. V. Boltalina, T. Drewello, I. V. Gol'dt, M. Marcaccio, F. Paolucci, D. Paolucci, J. M. Street, R. Taylor, *Org. Biomol. Chem.* **2003**, *1*, 2015 – 2023.
[17] D. M. Guldi, *Chem. Soc. Rev.* **2002**, *31*, 22 – 36.
[18] D. M. Guldi, G. A. Burley, M. Marcaccio, F. Paolucci, D. Paolucci, J. Ramey, R. Taylor, *Chem. Eur. J.*, submitted.
[19] a) D. Ajami, O. Oeckler, A. Simon, R. Herges, *Nature* **2003**, *426*, 819 – 821; b) T. Kawase, M. Oda, *Angew. Chem.* **2004**, *116*, 4496 – 4498; *Angew. Chem. Int. Ed.* **2004**, *43*, 4396 – 4398; c) C. Castro, Z. Chen, C. S. Wannere, H. Jiao, W. L. Karney, M. Mauksch, R. Puchta, N. J. R. van Eikema Hommes, P. von R. Schleyer, *J. Am. Chem. Soc.* **2005**, *127*, 2425 – 2432.

Combinatorial Chemistry

DNA Microarrays as Decoding Tools in Combinatorial Chemistry and Chemical Biology**

*Marina Lovrinovic and Christof M. Niemeyer**

Keywords:
combinatorial chemistry · DNA · immobilization · microarrays · proteins

Over the last few years, laterally microstructured arrays of DNA[1] and protein probes[2–4] have been developed as tools for high-throughput experimentation in biomedical research. These devices have the advantage of spatial addressability of the probes and require only small amounts of analyte. The development of protein microarrays is still obstructed by the intrinsic instability of many proteins, which leads to the loss of functionality during their automated deposition onto chemically activated surfaces. However, the application of DNA arrays is almost routine nowadays, as they are chemically stable and are often available off-the-shelf through academic and commercial suppliers. Hence, the application of DNA microarrays toward investigations of gene expression by quantitation of mRNA levels under variable environmental conditions offers a well-established approach in the fundamental and industrial research of biological systems.[5] In addition to these mainstream applications of DNA chips in genomics, alternative uses of these devices as tools for decoding combinatorial libraries in chemistry and chemical biology are currently emerging.

Figure 1. DNA-directed immobilization of DNA–protein conjugates with surface-bound capture oligomers of a DNA microarray.

As an example, DNA arrays can be used as programmed matrices for the site-selective immobilization of DNA oligomer-tagged proteins and small molecules (Figure 1). This approach, termed DNA-directed immobilization (DDI), offers a chemically mild procedure for the site-selective, highly parallel, and reversible attachment of protein libraries to solid supports.[6] As a particular advantage, the proteins retain their biological activity because they are attached to the surface through a short double-stranded DNA linker rather than being directly fixed at the surface by multiple covalent or noncovalent contacts, which may restrict their conformational freedom and could lead to (partial) denaturation of tertiary structure.[6b] The advantage of the DDI method for the fabrication of protein microarrays has been demonstrated for antibodies,[6c,f,g] receptors[6d] and enzymes.[6b,i]

Winssinger and co-workers have applied the principle of nucleic acid-directed immobilization to the screening of small-molecule libraries for compounds that bind to protein targets.[7–10] The technology is based on peptide nucleic acid (PNA)-encoded small-molecule probes, which are accessible through solid-phase combinatorial syntheses (Figure 2). The small-molecule portion of the probe is designed to bind to proteins in a mechanism-dependent manner, therefore discriminating between active proteins and proteins that are present in a latent or inactive form. The PNA portion of the probes functions as a code for the synthetic history of the small-molecule portion, and therefore permits deconvolution of the probe through hybridization at an oligonucleotide microarray. Array-based deconvolution allows the simultaneous analysis of multiple probes in a miniaturized format and has the potential of screening up to 400000 probes in a solution volume of less than 300 μL. The initial validation of this approach was carried out with specific inhibitor probes whose design was based on the peptide substrate specificity of known proteases, such as cathepsins[7] and caspase.[8]

Recently, this methodology was applied to the discovery of new proteolytic activities in dust mite extracts.[10] House dust mites are a major source of allergens and contribute to the increased incidence of allergenic diseases such as bronchial asthma. Some of these allergens have protease activity, which has long been known to produce an allergic response. To elucidate the cellular mechanisms behind the development

[*] Dipl.-Chem. M. Lovrinovic, Prof. Dr. C. M. Niemeyer
Universität Dortmund
Fachbereich Chemie
Biologisch-Chemische Mikrostrukturtechnik
Otto-Hahn Strasse 6, 44227 Dortmund (Germany)
Fax: (+49) 231-755-7082
E-mail: christof.niemeyer@uni-dortmund.de

[**] We acknowledge financial support of our work by Deutsche Forschungsgemeinschaft (DFG) and by the research program "Molecular Basics of Biosciences" of the University of Dortmund.

DOI: 10.1002/anie.200500645

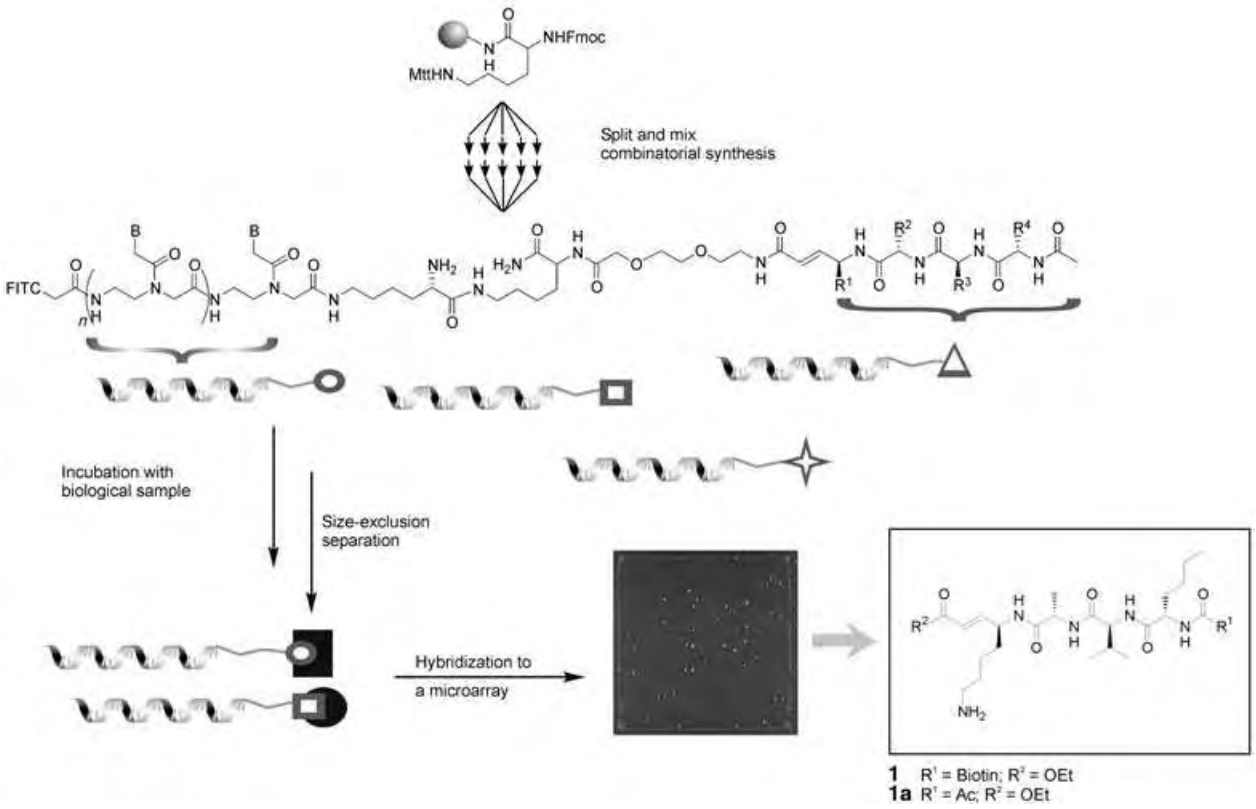

Figure 2. Synthesis and deconvolution of a PNA-encoded library (adapted from Ref. [10]). The fluorescein isothiocyanate (FITC) group enables fluorescence detection of the binding of all members of the library to the spatially encoded DNA array. Mtt = 4-methyltrityl; Fmoc = 9-fluorenylmethoxycarbonyl.

of allergies, it is essential to profile the activity of the proteases involved.

To this end, a 4000-member PNA-encoded tetrapeptide inhibitor library designed to target cysteine proteases was synthesized by combinatorial split-and-mix synthesis (Figure 2). The library was incubated with dust mite lysate, and the unbound probes were subsequently separated by spin filtration through a 30-kDa molecular weight cut-off filter. The retained samples that contained the protein-bound probes were hybridized to an oligonucleotide array containing capture oligomers for all members of the PNA-encoded inhibitor library. Fluorescence imaging allowed the identification of tetrapeptides that had bound to protease targets. Active inhibitors contained lysine and norleucine at position P1 and alanine at position P2 (Figure 2). Positions P3 and P4 of the inhibitor appeared to be less important for target binding; the most striking feature was that compounds with histidine, phenylalanine, or proline at position P3 were completely inactive as inhibitors. The probe with the highest intensity on the microarray had the inhibitor sequence Nle-Val-Ala-Lys (P1–P4). This probe (compound **1** in Figure 2) was re-synthesized with a biotinylated linker to isolate and identify the interacting proteins. Following incubation of **1** with the dust mite lysate, the probe and proteins attached to it were captured with streptavidin and the proteins were sequenced my mass spectrometry.

Two major proteins, Derp1 and Derp10 were identified. Derp1 is a 25-kDa protein homologous to the papain family of cysteine proteases, and Derp10 is a 33-kDa protein that is homologous to tropomyosin. Isolated Derp1 was then prepared from house mite fecal pellets by immunoaffinity chromatography by using an immobilized monoclonal antibody, and its substrate specificity was profiled with the tetrapeptide substrate library in a positional scanning format. The results confirmed that the major substrate specificity determinant for Derp1 is in the P2 position for the alanine residue. Moreover, a slight preference of Derp1 for basic amino acids in positions P1 and P3 was observed, as well as a preference for aliphatic amino acids such as isoleucine, proline, valine, leucine, and norleucine in position P4. Finally, the authors demonstrated the phenotypic relevance of Derp1 function in allergy progression by the inhibition of cleavage of CD25 (the α chain of the interleukin 2 cell-surface receptor) from T-cells with the tetrapeptide inhibitor **1a**.[9]

In a related approach, Melkko et al. used DNA-encoded self-assembling chemical (ESAC) libraries for the facile identification of small molecules that bind macromolecular targets.[11] In this case, libraries of organic molecules linked to individual DNA oligomers were assembled with DNA strands that contain complementary sequence stretches, thereby providing a code associated with each organic moiety. After incubation of the ESAC libraries with a protein of interest attached to a solid support and removal of unbound mate-

rials, the coding sequences of the selected compounds were decoded with a DNA microarray. Repetition of the selection cycle led to the affinity maturation of compounds that bind human serum albumin and bovine carbonic anhydrase with dissociation constants in the nanomolar range.[11]

The above examples impressively demonstrate how DNA microarrays can be used for the decoding of nucleic acid encoded small-molecule libraries. Hu et al. have recently applied DNA microarrays to the high-throughput screening of expressed enzyme libraries (Figure 3).[12] Their strategy, termed "Expression Display", is based on the ribosome-display technique, which allows the in-vitro expression of proteins in a cell-free translation reaction. The resulting polypeptides are thereby tagged with their own coding mRNAs.[13] The proteins were expressed from a cDNA library containing 384 different open-reading frames (ORFs) from yeast, four of which encoded known protein tyrosine phosphatases (PTPs), through in-vitro transcription and translation (steps 1 and 2 in Figure 3). The resulting library of ribosomal complexes was incubated with the activity-based probe **2** that had been immobilized on streptavidin magnetic beads, and which specifically and irreversibly binds PTPs (step 3). The mRNA was eluted and reverse-transcribed to generate the corresponding fluorescently labeled cDNA. The resulting cDNA library was then hybridized to the decoding DNA microarray (containing 384 cDNAs) for the parallel identification of functional PTPs. Positives were identified by the location of fluorescent spots on the array (Figure 3). Indeed, microarray analysis revealed the selective detection of the four PTPs from the library, which also contained ORFs for other enzyme classes (proteases, kinases, oxidoreductases) and nonenzyme proteins. Hence, this example of combining activity-based probes and array-based high-throughput identification suggests that it should be possible to screen thousands of proteins, all in a single reaction without the need for parallel cloning, expression, purification, and characterization of individual proteins.[12]

DNA microarrays have also been used recently in synthetic organic chemistry as a selection tool for the discovery of a new type of chemical reaction: the Pd-catalyzed carbon-carbon bond-forming reaction that generates an enone from an alkyne and alkene (Figure 4).[14] To this end, Liu and co-workers, whose work is focused on the development of DNA-templated organic syntheses,[15] prepared two pools of DNA-linked small-molecule substrates, each of which contains 12 different potentially reactive functional groups covalently linked to either the 5′- (pool A) or 3′-end (pool B) of an oligonucleotide. Pool A oligomers contain a "coding region" that uniquely identifies the substrate as well as one of 12 different "annealing regions". Pool B oligomers also contain a "coding region" which encodes the substrate and complements one of the 12 annealing regions in pool A (Figure 4a).

When pools A and B are combined in a single aqueous solution at nanomolar concentrations, specific Watson–Crick base-pairing assembles the compounds into 12×12 discrete pairs of substrates, which experience effective concentrations in the millimolar range. Substrates linked to noncomplementary oligomers experience nanomolar solution concentrations and hence do not react with each other at a significant rate. To allow the separation of reactive pairs, each substrate of pool B was covalently linked to its corresponding oligomer by a linker containing a biotin group and a cleavable disulfide bond (Figure 4b). After incubation under a set of chosen reaction conditions, the disulfide bonds were cleaved and the biotin group remained covalently linked only to pool A compounds after a bond-forming reaction between pool A and pool B substrates had occurred. Avidin affinity selection of the resulting solution separated biotinylated from non-biotinylated compounds. Reactive substrate pairs were then amplified by PCR. Because PCR amplification is extremely sensitive, femtomole quantities of substrate were sufficient for the entire reaction discovery process.

As both pools each contained 12 substrates, 144 different DNA-linked substrates of pool A were prepared to encode all heterocoupling combinations. Furthermore, DNA-linked substrates

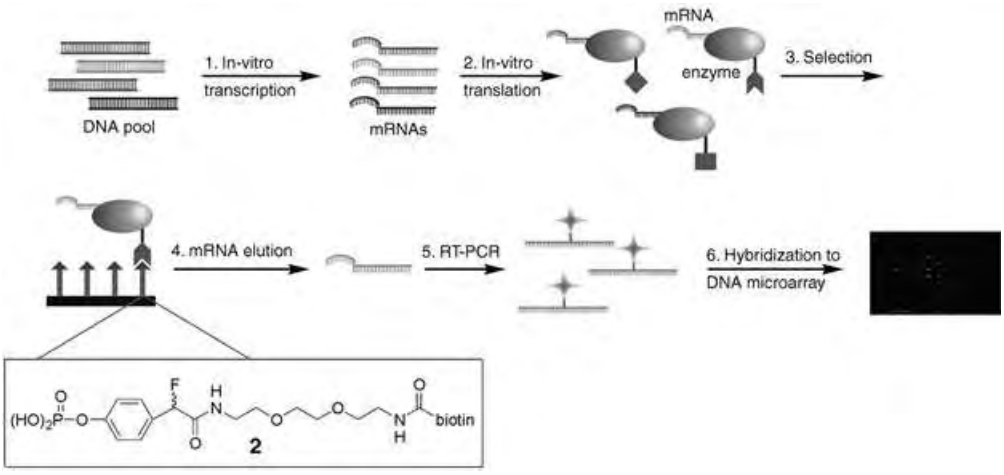

Figure 3. Expression display of an enzyme library (RT = reverse transcription). Also shown is the structure of the protein tyrosine phosphatase (PTP)-specific activity-dependent probe **2** (adapted from Ref. [12]).

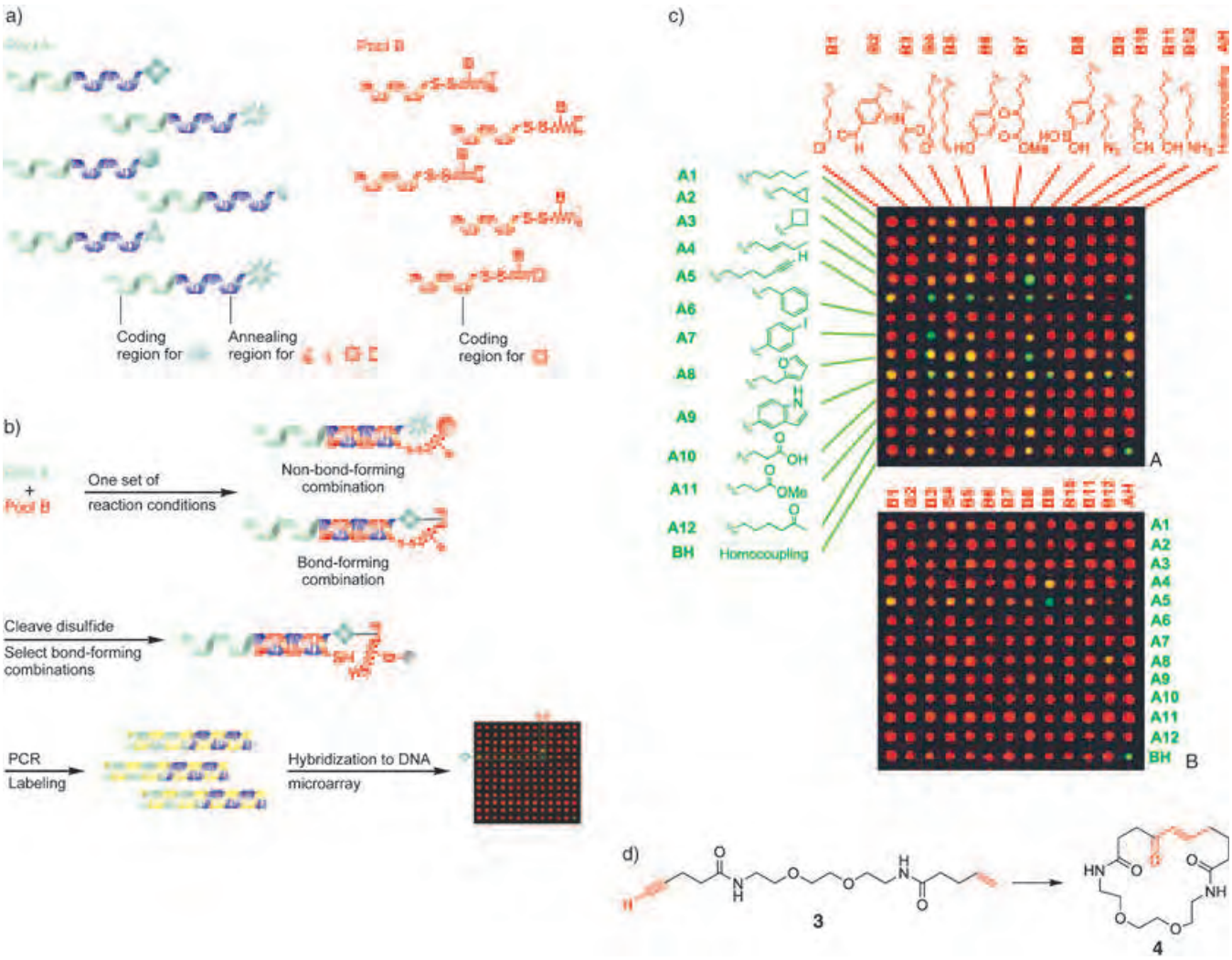

Figure 4. Discovery of a new type of chemical reaction that takes advantage of DNA-templated reactions (adapted from Ref. [14], array data reproduced with kind permission).

that encoded for the homocoupling of any of the 24 different substrates were prepared, bringing the total number of unique substrate combinations to 168. Although this approach required the preparation of a large number of DNA-linked substrates, these are typically synthesized at the nanomole-scale, and therefore, provide sufficient material for more than 1000 reaction discovery processes.

To enable a semiquantitative analysis of bond-forming efficiency, the mixture of the two pools A and B was amplified twice by PCR. Prior to bond formation and selection, PCR was carried out with Cy5-labeled primers while the post-selection mixture was amplified with Cy3-labelled primers. Equal amounts of the two PCR products were combined and hybridized to the DNA array containing all possible sequence combinations. The ratios of Cy3 (green) to Cy5 (red) fluorescence was determined for all array locations, and spots with green/red fluorescence ratios above 1.5 were considered positive. A pre-quantified internal standard (bottom right corner of the array in Figure 4c) was used as a positive control and as a reference to compare different arrays.

Initial validation tests were carried out with the known reaction between an alkyne (A5) and an azide (B9) in the presence of Cu^{I}. The observation of a single green spot (green/red ratio = 8.5) indicated the feasibility of the reaction discovery method (bottom array in Figure 4c). Similarly, the selection for bond formation after treatment of the pools with EDC/NHS (EDC = 1-ethyl-3-(3-dimethylaminopropyl)carbodiimide, NHS = *N*-hydroxysuccinimide) led to the formation of a single positive spot, indicating a reaction between the amine (B12) and the carboxylic acid (A10) compound (green/red ratio = 15.6). After the successful "rediscovery" of known bond-forming reactions, the authors then examined the reactivity of the library in the presence of Pd^{II}. The first reaction, carried out for one hour at 37 °C, led to five strong positives (A7 + B3, A5 + B3, A4 + B8, A5 + B5, and A5 homocoupling), in addition to five weaker positives (A9 + B3, A8 + B3, A8 + B8, A5 + B8, and A5 + B9; top array in Figure 4c). The 10 putative bond-forming reactions were then examined in separate DNA-templated reactions, and gel electrophoretic analysis indicated that all five strong positives and three of the weak positives indeed

corresponded to authentic DNA-templated reactions, whereas two weak positives (A9 + B3 and A5 + B9) showed little or no product formation.

Repetition of the selection experiment under more stringent conditions (20 min at 25 °C) decreased the number of positive signals and suggested that Pd^{II}-mediated carbon-carbon bond formation between the terminal alkyne (A5) and terminal alkene (B5) proceeds efficiently to generate an enone product. For the detailed investigation of this reaction in a non-DNA-templated version, small-molecule substrate **3** was synthesized and subjected to intramolecular cyclization to yield enone **4** in the presence of Pd^{II}. It was observed that this macrocyclization occurs at the milligram scale with Na_2PdCl_4 (5 mol %) in the presence of 1 equivalent $CuCl_2$ in various solvents with yields larger than 90 %. Hence, the discovery of this alkyne–alkene coupling reaction indicates the value of searching a large number of substrate combinations for unexpected reactions. The authors anticipate that similar schemes will lead to the discovery of additional bond-forming reactions between simple and relatively unreactive functional groups.[14]

In conclusion, these examples demonstrate the versatility of DNA microarrays as tools for the decoding of complex libraries of DNA-tagged small-molecules[16] as well as biomolecular compounds. These developments have been made feasible through the extraordinary physicochemical stability of nucleic acids, their availability by solid-phase synthesis, and the resulting steady progress in DNA array technologies over the past 15 years. Although DNA chips have since become routine tools, many problems have yet to be solved, for instance, the accurate prediction and quantitation of hybridization efficiencies of individual probes. Far more challenging, however, is the extension of applications similar to those described herein to protein microarrays. This may allow even deeper insight into biological systems on a proteome-wide scale. Owing to the exquisite and delicate architecture of nature's universal tools, however, steps toward this goal will surely constitute a fascinating research area for creative chemical biologists in the near future.

Published online: April 28, 2005

[1] For reviews on DNA microarray technology, see: a) U. R. Mueller, D. V. Nicolau, *Microarray Technology and Its Applications*, Springer, Berlin, **2005**; b) R. L. Stears, T. Martinsky, M. Schena, *Nat. Med.* **2003**, *9*, 140 – 145; c) M. C. Pirrung, *Angew. Chem.* **2002**, *114*, 1326 – 1341; *Angew. Chem. Int. Ed.* **2002**, *41*, 1276; d) C. M. Niemeyer, D. Blohm, *Angew. Chem.* **1999**, *111*, 3039 – 3043; *Angew. Chem. Int. Ed.* **1999**, *38*, 2865 – 2869; e) E. M. Southern, K. Mir, M. Shchepinov, *Nat. Genet.* **1999**, *21*, 5 – 9.

[2] M. F. Templin, D. Stoll, M. Schrenk, P. C. Traub, C. F. Vohringer, T. O. Joos, *Trends Biotechnol.* **2002**, *20*, 160 – 166.

[3] D. S. Wilson, S. Nock, *Angew. Chem.* **2003**, *115*, 510 – 517; *Angew. Chem. Int. Ed.* **2003**, *42*, 494 – 500.

[4] D. S. Yeo, R. C. Panicker, L. P. Tan, S. Q. Yao, *Comb. Chem. High Throughput Screening* **2004**, *7*, 213 – 221.

[5] DNA microarray technology is a well-established tool in chemical genomics for the profiling of whole-genome transcripts for the identification and validation of targets of small molecules such as kinase inhibitors. For examples, see: a) C. Kung, K. M. Shokat, *ChemBioChem* **2005**, *6*, 523 – 526; b) D. W. Provance, Jr., C. R. Gourley, C. M. Silan, L. C. Cameron, K. M. Shokat, J. R. Goldenring, K. Shah, P. G. Gillespie, J. A. Mercer, *Proc. Natl. Acad. Sci. USA* **2004**, *101*, 1868 – 1873; c) K. M. Specht, K. M. Shokat, *Curr. Opin. Cell Biol.* **2002**, *14*, 155 – 159; d) A. S. Carroll, A. C. Bishop, J. L. DeRisi, K. M. Shokat, E. K. O'Shea, *Proc. Natl. Acad. Sci. USA* **2001**, *98*, 12578 – 12583.

[6] a) C. M. Niemeyer, T. Sano, C. L. Smith, C. R. Cantor, *Nucleic Acids Res.* **1994**, *22*, 5530 – 5539; b) C. M. Niemeyer, L. Boldt, B. Ceyhan, D. Blohm, *Anal. Biochem.* **1999**, *268*, 54 – 63; c) C. M. Niemeyer, B. Ceyhan, *Angew. Chem.* **2001**, *113*, 3798 – 3801; *Angew. Chem. Int. Ed.* **2001**, *40*, 3685 – 3688, ; d) M. Lovrinovic, R. Seidel, R. Wacker, H. Schroeder, O. Seitz, M. Engelhard, R. Goody, C. M. Niemeyer, *Chem. Commun.* **2003**, 822 – 823; e) U. Feldkamp, R. Wacker, W. Banzhaf, C. M. Niemeyer, *ChemPhysChem* **2004**, *5*, 367 – 372; f) R. Wacker, C. M. Niemeyer, *ChemBioChem* **2004**, *5*, 453 – 459; g) R. Wacker, H. Schroeder, C. M. Niemeyer, *Anal. Biochem.* **2004**, *330*, 281 – 287; h) F. Kukolka, C. M. Niemeyer, *Org. Biomol. Chem.* **2004**, *2*, 2203 – 2206; i) L. Fruk, C. M. Niemeyer, *Angew. Chem.* **2005**, *117*, DOI: 10.1002/anie.200462567; *Angew. Chem. Int. Ed.* **2005**, *44*, DOI: 10.1002/ange.200462567.

[7] N. Winssinger, J. L. Harris, B. J. Backes, P. G. Schultz, *Angew. Chem.* **2001**, *113*, 3254 – 3258; *Angew. Chem. Int. Ed.* **2001**, *40*, 3152 – 3155.

[8] N. Winssinger, S. Ficarro, P. G. Schultz, J. L. Harris, *Proc. Natl. Acad. Sci. USA* **2002**, *99*, 11139 – 11144.

[9] N. Winssinger, R. Damoiseaux, D. C. Tully, B. H. Geierstanger, K. Burdick, J. L. Harris, *Chem. Biol.* **2004**, *11*, 1351 – 1360.

[10] J. Harris, D. E. Mason, J. Li, K. W. Burdick, B. J. Backes, T. Chen, A. Shipway, G. Van Heeke, L. Gough, A. Ghaemmaghami, F. Shakib, F. Debaene, N. Winssinger, *Chem. Biol.* **2004**, *11*, 1361 – 1372.

[11] S. Melkko, J. Scheuermann, C. E. Dumelin, D. Neri, *Nat. Biotechnol.* **2004**, *22*, 568 – 574.

[12] Y. Hu, G. Y. Chen, S. Q. Yao, *Angew. Chem.* **2005**, *117*, 1072 – 1077; *Angew. Chem. Int. Ed.* **2005**, *44*, 1048 – 1053.

[13] A related technology is based on the in-vitro translation of mRNA derivatized with a puromycin group at its 3′-end. The peptidyl-acceptor antibiotic puromycin covalently couples the mRNA with the encoded polypeptide chain formed at the ribosome, which results in the specific conjugation of the informative (mRNA) with the functional (polypeptide) moiety. Such covalent nucleic acid–protein conjugates have potential for the fabrication of protein microarrays: P. A. Lohse, M. C. Wright, *Curr. Opin. Drug Discovery Dev.* **2001**, *4*, 198 – 204; M. Kurz, K. Gu, A. Al-Gawari, P. A. Lohse, *ChemBioChem* **2001**, *2*, 666 – 672.

[14] M. W. Kanan, M. M. Rozenman, K. Sakurai, T. M. Snyder, D. R. Liu, *Nature* **2004**, *431*, 545 – 549.

[15] X. Li, D. R. Liu, *Angew. Chem.* **2004**, *116*, 4956 – 4979; *Angew. Chem. Int. Ed.* **2004**, *43*, 4848 – 4870.

[16] J. J. Diaz-Mochon, L. Bialy, L. Keinicke, M. Bradley, *Chem. Commun.* **2005**, 1384 – 1386.

Gene Regulation

Epigenetics—An Epicenter of Gene Regulation: Histones and Histone-Modifying Enzymes

*Markus Biel, Veit Wascholowski, and Athanassios Giannis**

Keywords:
DNA · enzymes · epigenetics · gene regulation · histone code

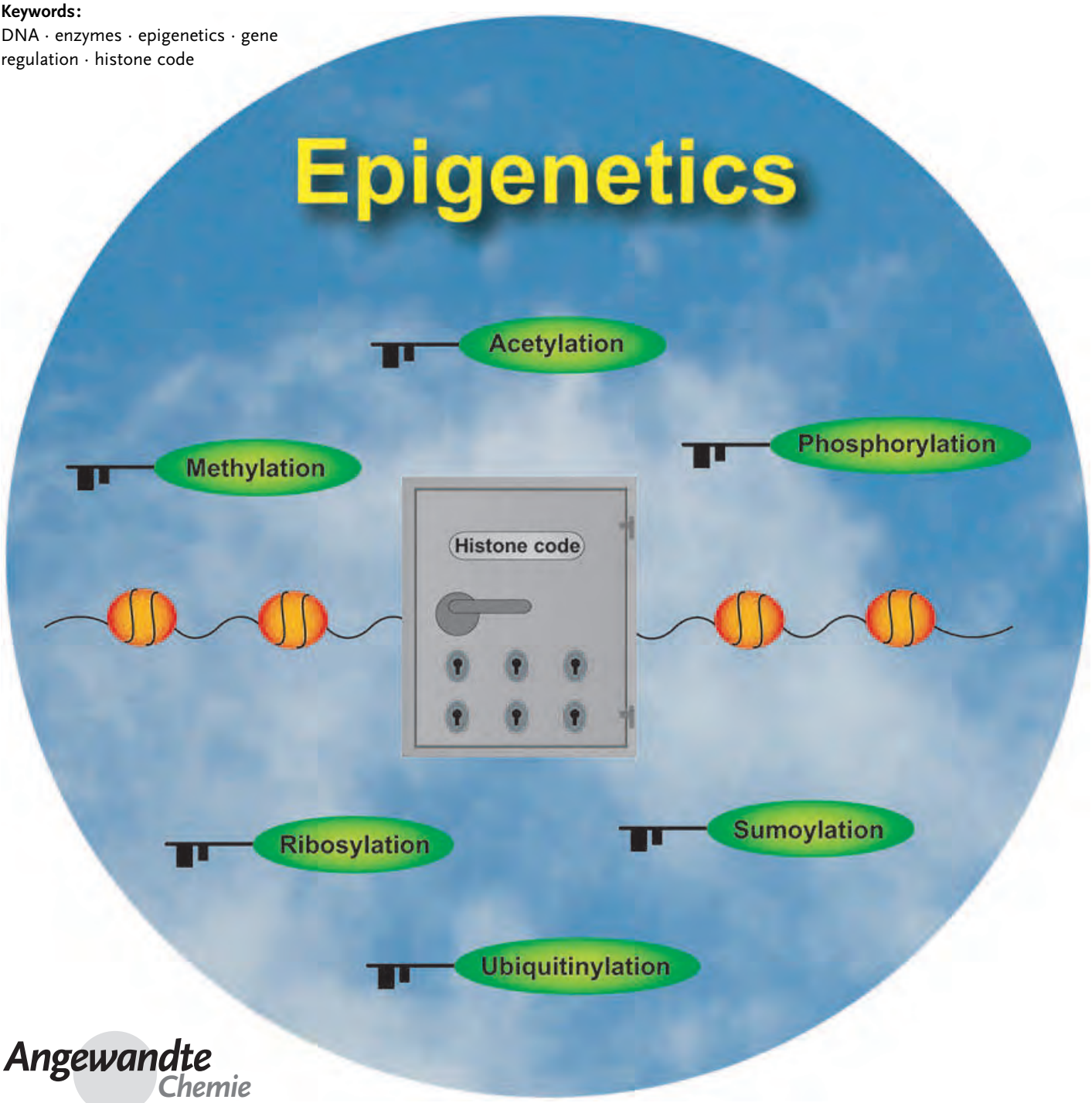

DOI: 10.1002/anie.200461346

The treatment of cancer through the development of new therapies is one of the most important challenges of our time. The decoding of the human genome has yielded important insights into the molecular basis of physical disorders, and in most cases a connection between failures in specific genes and the resulting clinical symptoms can be made. The modulation of epigenetic mechanisms enables, by definition, the alteration of cellular phenotype without altering the genotype. The information content of a single gene can be crucial or harmful, but the prerequisite for a cellular effect is active gene transcription. To this end, epigenetic mechanisms play a very important role, and the transcription of a given gene is directly influenced by the modification pattern of the surrounding histone proteins as well as the methylation pattern of the DNA. These processes are effected by different enzymes which can be directly influenced through the development of specific modulators. Of course, all genetic information is written as a four-character code in DNA. However, epigenetics describes the art of reading between the lines.

From the Contents

1. Introduction

The entire genetic information of an organism is extremely heterogeneous when it comes to the expression of single genes. Whereas some genes are transcribed frequently, other areas of the genome are silenced. As genetic information is highly regulated and organized, it is possible to change the phenotype of a cell without altering its genotype. This is done by epigenetic mechanisms, which operate in advance of actual gene transcription events and are encoded in various patterns of DNA methylation and histone modification.

1.1. The Histone Code Hypothesis

In the nucleus of a cell, the eukaryotic genome is condensed into structures of higher order called chromatin. The fundamental repeating unit of chromatin is the nucleosome,[1] in which 145–147 DNA base pairs are wrapped left-handed around a core histone protein, which consists of two of each of the four histone protein subunits: H2A, H2B, H3 and H4.[2] The linker histone H1 completes the nucleosome and allows the condensation of this fundamental unit to structures of higher order, which are visible under the microscope as chromosomes during metaphase of the cell cycle. The structure of each core histone is essentially a globular domain;[3] only the highly conserved amino termini of the histone proteins are presented as flexible chains at the surface of the nucleosome, where they are frequent targets for various posttranslational modifications.[4,5] Such modifications include the acetylation of specific lysine residues by histone acetyltransferases (HATs), the methylation of lysine and arginine residues by histone methyltransferases (HMTs), and the phosphorylation of specific serine groups by histone kinases (HKs). Further histone modifications include the attachment of ubiquitin (Ub), small ubiquitin-like modifiers (SUMOs), and poly(ADP-ribose) (PAR) units (Figure 1).

Furthermore, enzymes responsible for the cleavage of some histone modifications, such as histone deacetylases (HDACs), histone phosphatases (PPs), ubiquitin hydrolases (Ubps) and poly(ADP-ribose)glycohydrolases (PARGs), have already been identified.[6–8] Particularly in the case of histone H3, it was shown that its posttranslational modifications are closely related to fundamental cellular events like the activation and repression of transcription.[9] In general, acetylation of H3 at lysine 14 (H3-K14), phosphorylation of serine 10 (H3-S10), and methylation of H3-K4 lead to transcriptional activation. In contrast, the repression of certain genes is linked to deacetylation of H3-K14 and methylation of H3-K9.[10,11]

These modifications mutually affect each other in many cases to generate specific, well-regulated patterns (Figure 2). In yeast, for example, phosphorylation of H3-S10 by the histone kinase Snf1 facilitates the yGcn5-mediated acetylation of H3-K14.[12] On the other hand, methylation of H3-K9 is directly dependent on a second modification: if H3-S10 is phosphorylated, methylation of H3-K9 by the histone methyltransferase SUV39 is blocked; these effects are conversely related as well.[13] From these observations came the histone code hypothesis: the various modifications made to one or more histone termini act in a combinatorial and sequence-dependent manner to yield specific downstream events; these modifications are therefore used as a cellular vocabulary for the regulation of different transcription-based processes.[14]

[*] Dipl.-Chem. M. Biel, Dipl.-Chem. V. Wascholowski, Prof. Dr. A. Giannis
University of Leipzig, Institute of Organic Chemistry
Johannisallee 29, 04103 Leipzig (Germany)
Fax: (+49) 0341-973-6599
E-mail: giannis@chemie.uni-leipzig.de

 DOI: 10.1002/anie.200461346

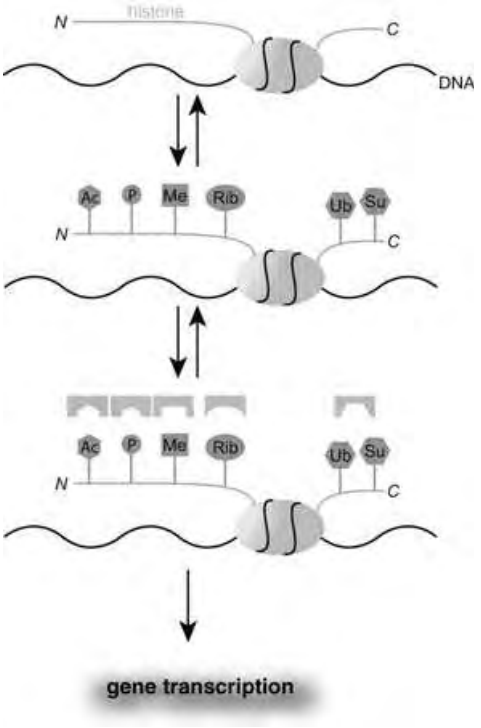

Figure 1. The formation of specific modification patterns at the histone termini results in the recruitment of regulatory units that translate the histone code into specific downstream events.

One way to read this language is through the recruitment of regulatory proteins with certain protein modules, which can recognize one or more histone modifications within a specific context. The acetylation of H3-K14 is a signal for the binding of proteins that possess a bromo domain, which is able to recognize acetylated lysine residues, and which is present in proteins such as Swi2/Snf, TAFII250, and Gcn5.[15] Swi2/Snf is responsible for the partial ATP-dependent opening of the chromatin structure, which makes the DNA more accessible to transcription machinery. Methylated lysine residues are bound by proteins equipped with a chromo domain. The heterochromatin-associated protein 1 (HP1) for example, belongs to the group of chromo domain-containing proteins that specifically interact with methylated H3-K9. This process is linked to the silencing of genes.[10]

Histone proteins not only fulfill the structural requirements of DNA, but also serve as a matrix for the establishment of a code that regulates its accessibility. This observation has moved the postulated histone code into the center of attention within the scientific community. It is an important starting point for the development of new therapies for diseases that are caused by abnormalities in the complexly regulated epigenetic network.[16]

Changing the epigenetic code through the development of small molecules that can modulate the properties of histone-modifying enzymes is an important challenge that could lead to the prevention of oncogene transcription and the activation of tumor repressors, which can induce apoptosis in tumor cells, force them to undergo cell-cycle arrest, or force their transition into differentiation. This article describes the known histone modifications and discusses the possible applications of modulators of histone-modifying enzymes in the fields of biology and medicine.

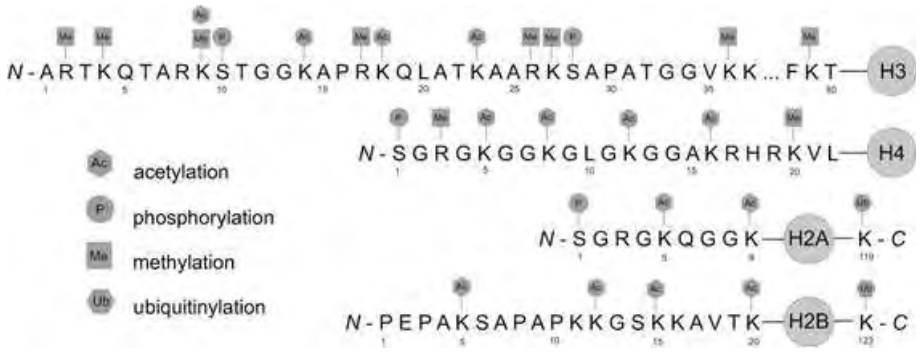

Figure 2. Posttranslational modifications of the histone proteins H3, H4, H2A, and H2B.

2. Histone Acetylation

Histone acetylation is one of the best understood histone modifications and takes place at the ε-

Markus Biel was born in Karlsruhe in 1973. He studied chemistry at the University of Karlsruhe and received his diploma in 2000. As a PhD student in the research group of Prof. A. Giannis, he moved from Karlsruhe to the Institute of Organic Chemistry of the University of Leipzig in 2002. He is engaged in the synthesis and biological evaluation of inhibitors of histone acetyltransferase and modulators of protein palmitoylation.

Veit Wascholowski was born in Braunschweig in 1975. He studied chemistry at the University of Karlsruhe and completed his diploma in 2000. Since that time he has been carrying out PhD studies in the research group of Prof. A. Giannis, first at Karlsruhe and since 2002 at the University of Leipzig. His field of interest is problems in chemical biology. He is therefore engaged in the synthesis and biological evaluation of new ceramide analogues and modulators of apoptosis.

amino groups of conserved lysine residues.[17] The highly regulated activities of HATs and HDACs are responsible for the control of specific acetylation levels.[18] One of the earliest discoveries in this context is that histones within the expanded, actively transcribed regions of chromatin (euchromatin) are acetylated to a higher degree than those in condensed regions (heterochromatin), which are not accessible to the transcription machinery.[19,20] This effect, that the temporary extent of gene transcription depends on its position with respect to accessible or inaccessible chromatin surroundings is called position effect variegation (PEV).[10,21–23] Genes that encode products which suppress PEV (and hence transcription) belong to the *su(var)* (suppressors of variegation) group, of which the products HDAC and HP1 are members.[24,25] In contrast, products of members of the *e(var)* (enhancers of variegation) gene group, such as the HATs, are PEV modulators that enhance variegation.[26,27]

2.1. Histone Acetyltransferases (HATs)

Many known transcription factors possess an intrinsic HAT activity.[28] These proteins are grouped into different enzyme family classes through sequence homologies and similarities in their biological functions (Table 1).[29]

Table 1: HAT families and functions of selected members.

HAT	organism	function
GNAT family		
Gcn5	yeast, human	coactivator
PCAF	human	coactivator
Elp3	yeast	elongation
ATF-2	yeast, human	activator
MYST family		
MOZ	human	coactivator
Ybf2/Sas3	yeast	elongation
Sas2	yeast	silencing
Tip60	human	DNA-repair, apoptosis
Esa1	yeast	cell cycle progression
MOF	fruit fly	dosage compensation[a]
CBP/p300 family	worm, human	global coactivator

[a] dosage compensation: a regulatory process to ensure that female and male organisms have the same amount of X-chromosome products.

Athanassios Giannis was born in Drama, Greece in 1954. From 1972 to 1980 he studied chemistry, and from 1978 to 1988, medicine at the University of Bonn. After his diploma work with Prof. M. T. Reetz, he completed his PhD on the synthesis of C-glycosides with Prof. K. Sandhoff in 1986. In 1992 he received his university lectureship in Organic Chemistry and Biochemistry; in 1997 he was appointed Professor at the University of Karlsruhe. He has been a full Professor of Organic Chemistry and Natural Products Chemistry at the University of Leipzig since May of 2002. His focus is in angiogenesis, apoptosis, epigenetic mechanisms, and signal transduction; he is researching new antitumor agents.

The GNAT family includes a relatively small number of HATs. In addition to a C-terminal catalytic HAT domain of ≈160 residues, each member possesses a bromo domain for specific interaction with acetylated lysine groups.[30–32] Members of the CBP/p300 family are less substrate-specific and serve more as global modulators of transcription.[33] They each have a 500-residue catalytic HAT domain, a bromo domain, and a cysteine-rich motif, which likely facilitates protein–protein interactions.[34] Members of the MYST family are involved in a much broader range of biological processes.[35–38] They have a 250-amino acid catalytic domain that includes a zinc-binding region, a cysteine-rich motif, and an N-terminal chromo domain for the specific recognition of methylated lysine groups.[39,40] In addition to these three main HAT groups, there are over a dozen proteins also known to have acetyltransferase activity.[41]

Histone acetyltransferases are always present in the form of large multiprotein complexes in vivo, which serves to control substrate selectivity.[42] In yeast, for example, the HAT yGcn5 is part of the multiprotein complexes Ada and SAGA.[43] Together with the proteins Ada2 and Ada3, the catalytic subunit is formed.[44] Recombinant Gcn5 is able to acetylate free histones, but the modification of native, nucleosomal histones usually succeeds only under the control of the large multiprotein complex. It directs the substrate selectivity and specificity of HAT activity. Free Gcn5 acetylates histone proteins chiefly at H3-K14, whereas within the Ada complex Gcn5 accepts H3 lysine residues 9, 14, and 18 as substrates.[45] Furthermore, complex formation regulates HAT function in transcription processes. Depending on the specific complex formed, HATs are recruited to certain promoter regions through interactions with different activators, which leads to the acetylation of surrounding histones and subsequent induction of transcription. Establishment of such activator contact in yeast is mediated by the protein Tra1, which is part of the SAGA and NuA4 complexes.[46,47] The human homologue TRAP is present in the complexes STAGA[48] and Tip60,[49] where it mediates contact with the cell-cycle-regulating protein c-Myc and with the E2F family of transcriptional activators.[50,51]

Ultimately, such an assembly of functional units leads to the transcription of the gene of interest. The regulation of the human interferon (IFN)-β gene is a good example (Figure 3). Following viral infection, the progressive acetylation of histones near the IFN-β gene promoter can be observed.[52] The enhancer region, upstream of the gene, binds a multiprotein complex that includes three transcription factors (NF-κB, IRFs, ATF-2/c-Jun) and a scaffold protein (HMG I(Y)).[53] This so-called enhanceosome recruits the HAT Gcn5, which acetylates H4-K8 and H3-K9. Furthermore, a prerequisite for the acetylation at H3-K14 is the phosphorylation of H3-S10 by an unknown kinase. This developed histone code ultimately activates transcription by the subsequent binding of the transcription complexes SWI/SNF and TFIID through their bromo domains.[54] The acetylation at H4-K8 is necessary for binding SWI/SNF, whereas acetylation at H3-K9 and H3-K14 is essential for recruiting the transcription factor TFIID. Both results support the existence of the postulated histone code.[55]

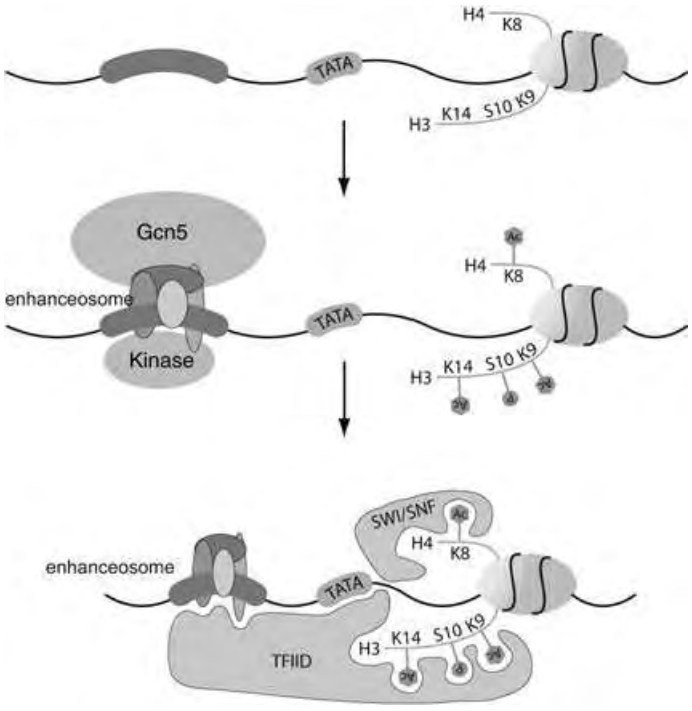

Figure 3. The transcription of the human interferon-β genes as an example of the control of transcription through specific histone acetylation. Following viral infection, a multiprotein complex (enhanceosome) is formed at the enhancer region and recruits the HAT Gcn5, which acetylates H4-K8 and H3-K9. After phosphorylation of H3-S10 by an unknown kinase, Gcn5 also acetylates H3-K14. The written histone code leads to the accumulation of the transcription complexes SWI/SNF and TFIID. Both proteins possess the requisite bromo domains for this interaction. Moreover, TFIID contacts both the TATA-box element of the DNA and the enhanceosome.

The influence of HATs on chromatin-dependent events such as transcription suggests that other DNA-based mechanisms could be influenced by HAT activity as well.[56] Examples include cell-cycle progression,[57–61] DNA recombination,[62,63] and DNA repair and apoptosis.[49] Furthermore, HATs influence DNA replication[59], elongation,[64,65] and the transcriptional silencing of genes.[66,67] Some HATs also recognize protein substrates other than histones. For example, p300 acetylates the tumor suppressor protein p53,[68–70] and therefore affects its ability to interact with DNA. Acetylation also modulates the activity of general transcription factors like TFIIβ and TFIIF,[71] the DNA-binding transcription factors GATA-1,[72] GATA-3,[73] ELKF,[74] MyoD,[75] E2F,[76] cMyb,[77] and dTCF,[78] as well as the chromatin-associated proteins HMG(Y),[79] HMG-14,[80] HMG-17,[81] CDP/cut,[82] and HIV Tat.[83] Therefore, acetylation is analogous to phosphorylation, which is an important tool in controlling the activity of kinase-mediated signal-transduction cascades.

Owing to the broad presence of HATs in different biological processes, there are some diseases which are caused by dysfunctional, mutated HATs. The Rubinstein–Taybi syndrome was first mentioned in 1957, and six years later Rubinstein and Taybi described a study of seven children with wide thumbs, broad, large toes, typical face courses, and retarded mental development. This disorder is the result of a mutation in the *crebbp* gene, which encodes the histone acetyltransferase CBP.[84,85]

A characteristic of human leukemia is chromosomal translocation, which leads to the expression of fusion proteins. Such proteins exhibit altered properties from their wild-type counterparts, and the transcription of genes, controlled by an abnormal HAT fusion protein, functions incorrectly. For example, in acute myelogenous leukemia (AML),[36,86] the amino terminus of CBP is fused with the MOZ protein—a HAT of the MYST family—and the resulting fusion protein is rendered useless.

2.1.1. *Structure and Catalytic Mechanism of the HAT Gcn5*

The results of kinetic studies[87–90] show that the acetylation mechanism of Gcn5 proceeds via a ternary complex of histone H3, enzyme, and acetyl-CoA.[91] As a result, the acetyl group is transferred directly to the amino group of the lysine residue without the formation of an acetylated enzyme intermediate. The central enzyme core domain is responsible for catalysis and acetyl-CoA binding, whereas the N- and C-terminal segments appear to be necessary for the interaction with the histone substrate.

X-ray crystallographic structure analysis[92–96] shows that the pantothen chain and the pyrophosphate groups are responsible for the binding of acetyl-CoA, whereas the adenine base does not make a considerable contribution. The H3 substrate of Gcn5 from *tetrahymena* (*t*Gcn5) binds in a groove above the core domain, and is flanked on both sides by the C- and N-terminal protein chains. Most of the contacts are present along the H3 backbone, whereby three quarters are on K14 and the five residues in the C-terminal direction, which narrows the H3 recognition motif down to GKXP. Furthermore, Glu 122 is a highly conserved basic group in *t*Gcn5 which has hydrophobic surroundings and is close to a region of negative electrostatic potential. This results in an increased pK_a value for Glu 122, and facilitates the binding of the positively charged lysine residue. The water molecule between Glu 122 and the protonated amino group of K14 is held in place by a hydrogen bond to the backbone amide of Val 123 and the hydroxy function of Tyr 160. During catalysis Glu 122 deprotonates the ammonium function of H3-K14 and enables a direct attack of the ideally positioned acetyl-CoA (Figure 4). The tetrahedral intermediate is stabilized by a hydrogen bond to the backbone amide of Leu 126 and decomposes under release of the desired products.

2.1.2. *Modulators of HAT Activity*

The first reports of selective peptide inhibitors of the HATs p300 and PCAF were published in 2000.[97–99] They were designed as disubstrate analogues of H3 and acetyl-CoA. The observed mode of inhibition reflects the substrate specificity of the particular HAT studied. Whereas p300 was inhibited by the structurally simple Lys-CoA (**1**), sufficient inhibition of the more specific PCAF was possible only with the 20-amino acid peptide H3-CoA-20 (**2**; Figure 5). The most crucial disadvantages of these inhibitors are their low cell permeability and metabolic instability, which decreases their suitability for investigations in vivo.[100] In 2003, anacardic acid (**3**) was identified as a HAT inhibitor through a broad

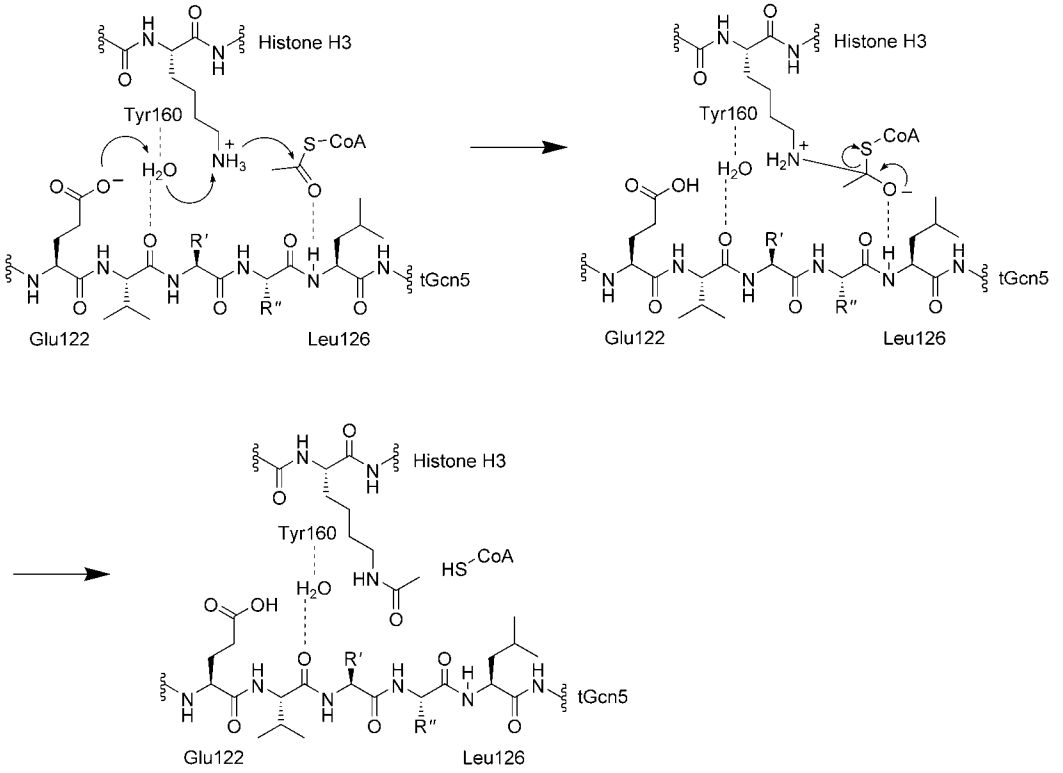

Figure 4. Catalytic mechanism of the HAT *t*Gcn5: Glu122 serves as a general base and supports nucleophilic attack of the ε-amino function of the lysine residue on the precoordinated acetyl-CoA. The transition state is stabilized through the amide function of Leu126 and decomposes with the release of CoASH and the acetylated lysine product (derived from [94]).

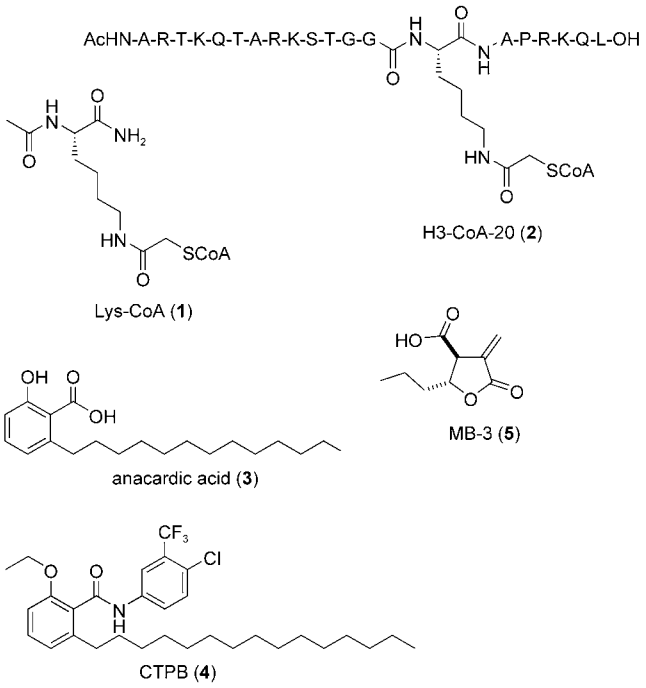

Figure 5. Modulators of the HATs: Lys-CoA (**1**) is a bisubstrate analogue and inhibits the HAT p300, whereas the peptide H3-CoA-20 (**2**) is described as an inhibitor of PCAF. Anacardic acid (**3**) inhibits both p300 and PCAF, whereas the amide derivative CTBP (**4**) represents an activator of the enzyme. MB-3 (**5**) is a small, cell-permeable inhibitor of the human Gcn5.

screen of plant extracts with antitumor activity.[101] This was the first report of a small-molecule inhibitor of the HATs p300 and PCAF. Interestingly, amidation of the carboxylic acid group leads to compound **4**, which is an activator of p300. Anacardic acid had been previously identified as an inhibitor of DNA polymerase β,[102] and therefore the biological selectivity could be limited.

In the meantime, our group developed MB-3 (**5**),[103] a small, cell-permeable inhibitor of the human Gcn5 which is based structurally on the α-methylene-γ-butyrolactone motif—a common substructure element in many natural products.[104] This privileged structure had been previously used for the design of an inhibitor for fatty acid synthase,[105] another enzyme involved in the transfer of acetyl-CoA. The development of MB-3 was brought about by the appropriate derivatization of the basic butyrolactone motif without the arbitrary screening of large compound libraries. Interestingly, the length of the aliphatic side chain is crucial for biological activity.

Alongside these efforts, nature has already developed ways to modulate HAT activity. For example, the activity of CBP/p300 is regulated through different posttranslational modifications.[106] The stimulation of CBP through phosphorylation by cycline E/CDK2 facilitates the progression of the cell through S-phase.[107] Phosphorylation within another region of the enzyme (the GF-box) allows binding of the transcription factor AP1,[108] whereas methylation within the CREB-binding domain decreases CPB affinity for the

phosphorylated CREB protein.[109] Moreover, after sumoylation (Section 6), p300 is able to interact with HDAC6.[110]

2.2. Histone Deacetylases (HDACs)

As a part of multiprotein complexes, HDACs catalyze the cleavage of acetyl functions from proteins, particularly from histones.[111] The importance of these enzymes is underscored by their evolutionary conservation from insects to humans.[112] So far, 18 different HDACs have been identified and divided into three distinct enzyme classes.[113] Enzymes of class I are originally derived from the yeast HDAC yRPD3. In humans, the HDACs 1, 2, 3, 8 and 11 are members of class I,[114] as they share the same compact structure and are expressed in the nuclei of most cell lines and tissue types.[115] Class II enzymes are expressed in a small number of cell types and are homologous to yHFA1. In contrast to class I HDACs, the subcellular location of class II HDACs is not limited to the nucleus; they are also present in cytoplasm.[113,116] Both classes have a highly conserved catalytic domain of 390 amino acids, but differ in overall composition and size. Mechanistically, the hydrolytic cleavage of the acetyl function proceeds through the activation of a water molecule by a zinc ion in the active site.[117] Class III enzymes (sirtuins) share a common ancestry with the yeast transcription repressor Sir2 (silent information regulator 2), and are subdivided into five classes.[118] Members share a common active site of 275 amino acids, and employ nicotinamide adenine dinucleotide (NAD^+) as a cofactor necessary for catalysis.[119] Moreover, class III HDACs possess two CXXC motifs (zinc-finger domains) and at least one hydrophobic region (leucine zipper) which facilitate protein–protein and protein–DNA interactions.[118,120]

2.2.1. Class I and Class II HDACs

The deacetylation of histones leads to closed chromatin structures, which are no longer accessible to the transcription machinery. To mediate this type of gene silencing, HDACs must be recruited to different promoter regions, as they cannot interact directly with DNA or associated histone proteins.[121,122] For this reason, HDACs are always part of protein complexes, which bind to specified regions of DNA (Figure 6).

In some cases, HDACs are recruited to the DNA through complex formation with different transcription factors. For example, HDAC1 associates with YY1,[123] whereas HDACs 4, 5, 7, and 9 bind to the MEF family of transcription factors, which interact with specific promoter regions and therefore transport the enzymes to their proper areas of action.[124] The HAT p300 and HDAC4 compete for the same binding site of MEF2. The transcription factor can therefore function either as a repressor or as an activator of gene expression, depending on the enzyme bound. The switch in activity is calcium dependent; the MEF2 binding site on HDAC4 overlaps with that of calmodulin. If the intracellular

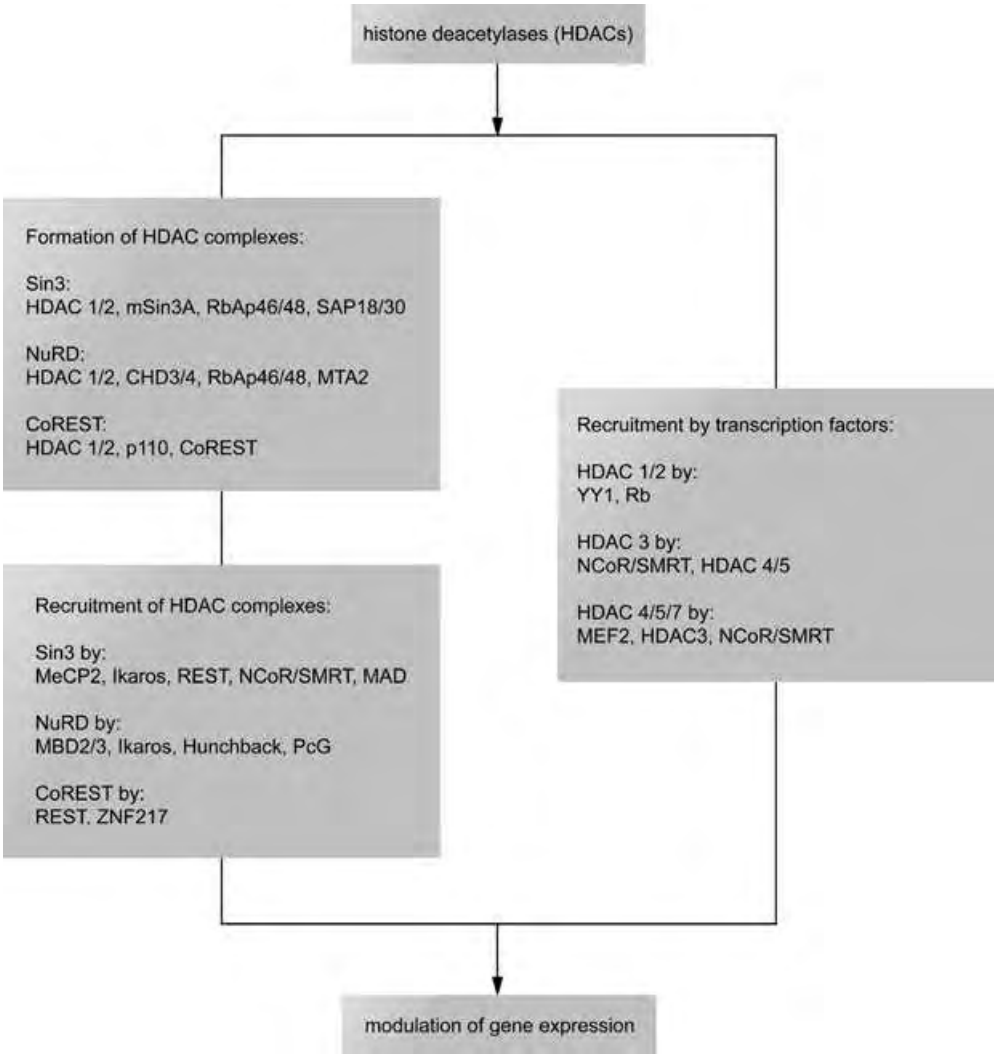

Figure 6. HDACs form complexes with other proteins to fulfill their biological functions. For example, HDAC1 and HDAC2 form the Sin3 complex with mSin3A, RpAp46/48, and SAP18/30. This is recruited to the DNA by MeCP2 and leads to silencing of the target gene. The same is true for the NuRD and CoREST complexes. In addition, HDACs are able to interact directly with transcription factors like YY1, MEF2, and the nuclear corepressor NCoR, as well as with other HDACs.

calcium level favors calmodulin binding to HDAC4, the enzyme loses its ability to interact with MEF2. In that case the transcription factor recruits p300 and gene expression is activated through acetylation of chromatin.[124] Moreover, HDAC4 as well as HDAC5 and HDAC7 possess three 14-3-3 binding sites, which can be phosphorylated at specific serine residues. Phosphorylation interrupts the HDAC–MEF contact and enables the binding of 14-3-3 proteins. As a result, the HDAC is transported from the nucleus to the cytoplasm, where the enzyme is inactive. Also in this case, p300 binds to the MEF2 transcription factor and activates gene expression.[124] Furthermore, the association of HDAC4 with Erk1 and Erk2, and the observation that activation of the Ras–MAPK pathway increases the localization of deacetylases in the nucleus are important hints that there could be cross-talk between the two pathways.[125]

There are other examples in which HDACs are able to bind transcription factors only as members of protein complexes. For HDAC1 and HDAC2, the complexes Sin3,[126,127] NuRD[128] and CoREST[129–131] have been characterized. Sin3, for example, consists of HDACs1/2 and the histone-binding proteins RpAp46/48, which together form the core complex, which is also a substructure element of the NuRD complex. The Sin3 complex also includes the stabilizers SAP18, SAP30, and mSin3A, which mediate the interactions with many DNA-binding proteins and direct the complex to specific DNA regions.

The fundamental structure[117] of the HDAC classes I and II consists of a single domain that is structurally related to the class of the open α/β hydrolases. A deep, tubular pocket widens into an internal cavity that houses the enzyme active site. Whereas the channel-like structure is lined with numerous hydrophobic amino acids, the active site is able to coordinate the central zinc ion through several polar histidine and aspartate residues. The catalytic mechanism[112] shows similarities to other metallo- and serine proteases: the carbonyl oxygen of the acetyl function coordinates to the zinc ion and is positioned in close proximity to a water molecule, which is activated for nucleophilic attack at the carbonyl group by interaction with the zinc ion (Figure 7). The tetrahedral oxyanion intermediate is probably stabilized through an interaction with the zinc ion and a hydrogen bond to a neighboring tyrosine group. After the spontaneous decomposition of this intermediate, the desired products are released, and a new catalytic cycle can start.

In 1976 the natural product trichostatin A (TSA, **6**) (Figure 8) was isolated from *Streptomyces hygroscopicus* and identified as a fungistatic antibiotic.[132] After approximately 20 years, it was also identified as a potent inhibitor of class I and class II HDACs ($K_i = 3.4$ nM).[133] Before that time, short-chain fatty acids such as the antiepilepsy drug valproic acid (**14**) and phenyl butyrate (**15**) were characterized as weak inhibitors of HDACs, with IC_{50} values in the millimolar range.[134,135] In contrast, hydroxamic acid derivatives like TSA (**6**), SAHA (**7**), and CBHA (**8**) inhibit HDACs at nanomolar concentrations, and are distinguished by longer half-lives and better bioavailability.

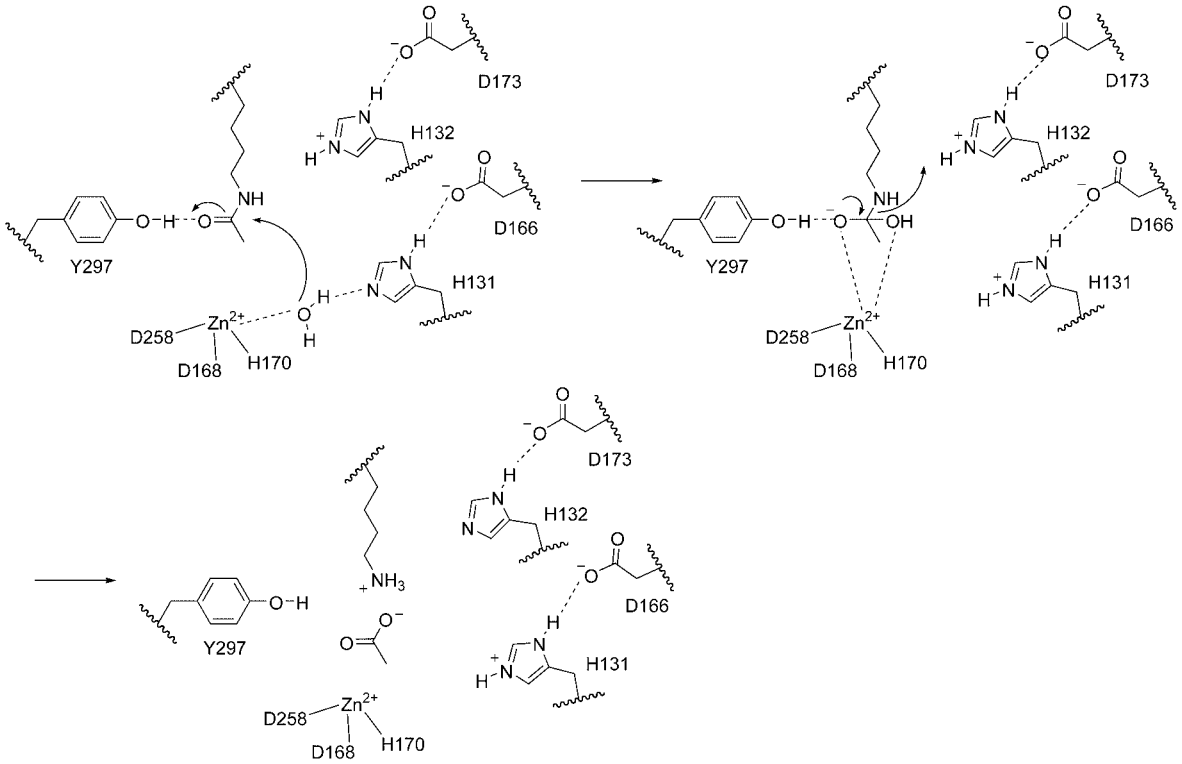

Figure 7. Catalytic mechanism of class I and II HDACs: the acetylated substrate is activated by the interaction with the hydroxy function of Y297. Meanwhile, the nucleophilic strength of the water molecule, which is necessary for amide hydrolysis, is increased through both the central zinc ion and the basic system, H131–D166. The oxyanion forms a hydrogen bond to Y297 and is coordinated by the central zinc ion to stabilize the tetrahedral intermediate. The proton required for the decomposition of the intermediate is provided by the system, H132–D173.

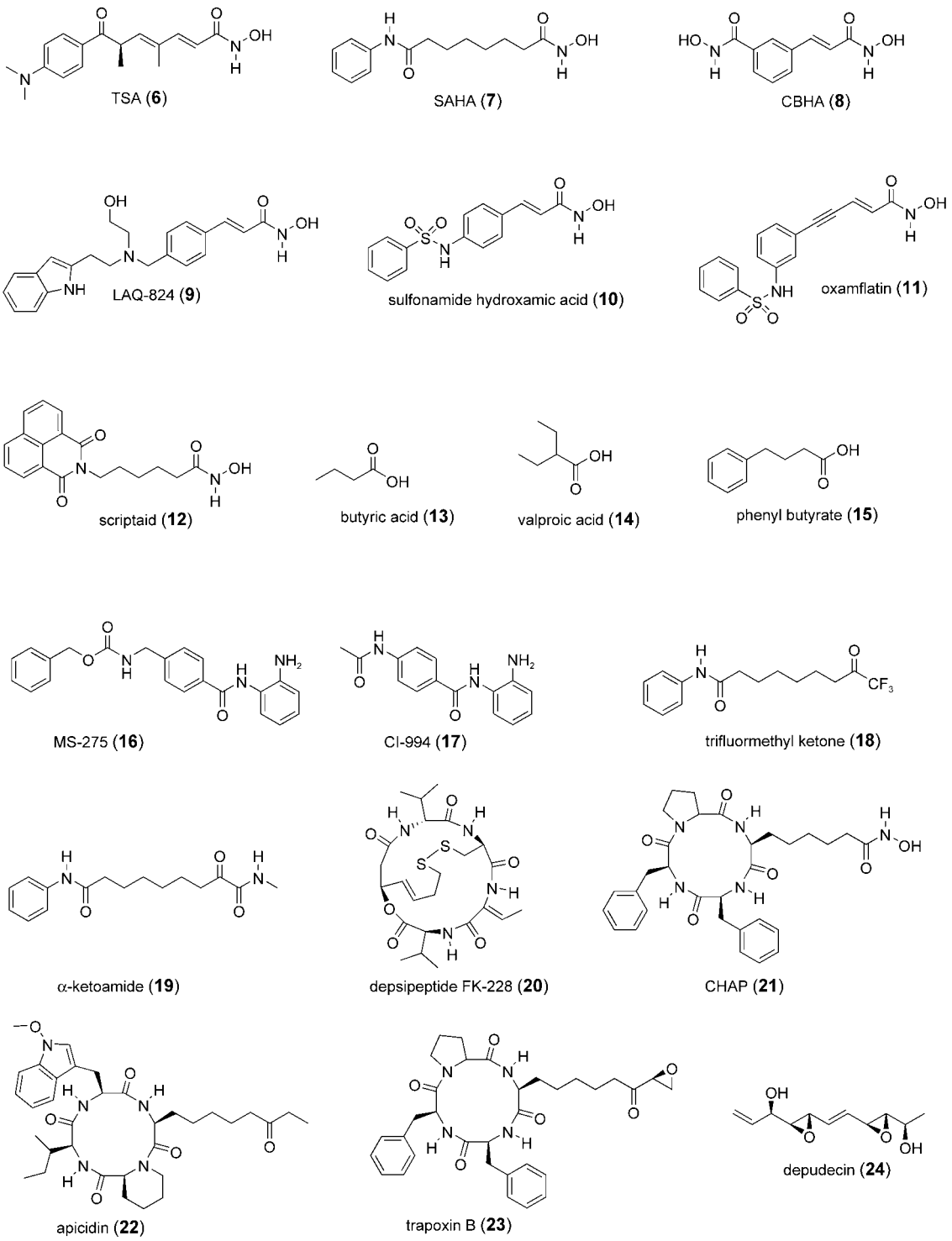

Figure 8. Examples of identified HDAC inhibitors, which can be grouped into five different structural classes: hydroxamates, **6**–**12**; aliphatic acids, **13**–**15**; benzamides, **16**–**17**; electrophilic ketones, **18**–**19**; cyclic tetrapeptides, **20**–**23**; and other molecules like **24**.

The potency of this class of inhibitors is explained by the X-ray crystallographic structure of HDAC cocrystallized with TSA,[117] as an almost perfect active-site fit is observed: the terminal hydroxamic acid function efficiently coordinates the catalytically essential zinc ion of the active site (Figure 9). As expected, trichostatic acid, the carboxylic acid analogue of TSA is biologically inactive.[136]

The aliphatic chain of TSA enables numerous van der Waals contacts with the hydrophobic residues of the tubular channel of the HDAC enzymes. The aromatic component of TSA mimics the amino acids that surround the lysine group in the natural substrate, and also acts as a surface element that caps and effectively closes the channel to the active site. This information served as a basis for the development of new

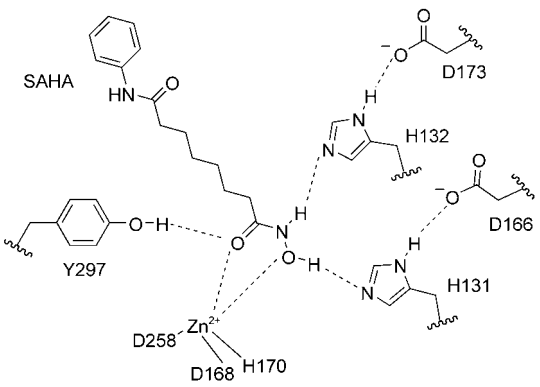

Figure 9. SAHA (**7**), a simple derivative of TSA, shows a perfect interaction with the central amino acid residues of the HDAC active site.

inhibitors that share the fundamental structure of TSA (surface element–aliphatic chain–complexing group), and provided detailed insight into the mode of inhibition through the study of structure–activity relationships (SAR).[137,138]

In addition to the hydroxamic acids, other HDAC-inhibiting compounds such as phenylenediamines (MS-275, **16**) and epoxides (trapoxin A, **23**) are well-known. Whereas the length of the aliphatic chain is limited to five or six carbon atoms (in **6** and **7**), isosteric substitution with an appropriate aromatic system (as in **8**) is allowed.[139–143] The cap should be a small, planar group (in **6**) or a tetrapeptidic structure as in apicidin (**22**); structure type affects inhibitory activity. For example, a compound with a small, planar cap and a carboxylic acid group as the functional unit leads to an ineffective inhibitor, whereas the same molecule with a cyclic tetrapeptide as a surface element is potent.[139,140] If the stereochemistry of TSA is changed, it is rendered completely inactive.[136,144] The synthetic hybrid CHAP (**21**), which has hydroxamic acid as a functional unit and a tetrapeptide as a cap structure, is a potent inhibitor at nanomolar concentrations.[145,140] Furthermore, some natural products, like depudecin (**24**), do not fit the structural motif of TSA, yet are moderately active HDAC inhibitors.[146–148]

To evaluate the biological functions of each and every HDAC enzyme, it is important to identify new and selective inhibitors. Most HDACs possess a highly conserved catalytic domain, but have a certain variation among the amino acids that do not directly interact with TSA. For this reason, a specific modulation of the capping structure enables access to selective inhibitors.[112] The sense of this strategy is the fact that HDAC6 is not inhibited by compounds with cyclic peptides as surface elements. The most pronounced differences between HDAC6 and the other HDACs lie in the vicinity of Tyr91, which is located at the entrance of the tubular channel and interacts directly with the cap portion of TSA.

The reason for the continued search for improved HDAC inhibitors is their potential use as tumor therapeutics. Although histone acetylation plays a global role in the regulation of gene expression, HDAC inhibitors only affect the transcription of a small subset of genes that are associated with the control of cell growth.[149] The explanation for such a small range of action could be attributed to the fact that according to the model of the histone code, other types of covalent histone modifications could also affect transcription.[8] In addition to histone deacetylation, histone methylation also directs gene silencing, which is not blocked by the application of HDAC inhibitors. The same principle applies to DNA methylation (Section 3.1.2).[150]

Nevertheless, HDAC inhibitors are able to stop the proliferation of leukemias and solid tumors, and can induce cell differentiation. The molecular basis for this has, until now, been only partially understood.[138,151–154] In most tumor cells, HDAC inhibitors activate transcription of the CDK inhibitor WAF1 (p21, coded by CDKN1A).[155] Moreover, the inhibition of different cyclins as well as the hypophosphorylation of the retinoblastoma tumor-suppressor protein Rb results in the inhibition of S-phase progression and subsequently in a cell-cycle arrest at G1.[156] This blocks apoptosis and directs the cell to differentiation. Tumor cells that show no G1 arrest after the application of HDAC inhibitors (for example, cells that lack CDKN1A)[157,158] replicate their DNA to the double set of chromosomes and pass into apoptosis.[159–162] One explanation for this phenomenon could be that the hyperacetylation of histones disturbs the centromere and kinetochore functions during cell-cycle progression, which would result in different lethal dysfunctions. In contrast, normal cells induce a G2 checkpoint after treatment with HDAC inhibitors, which leads to a cell-cycle arrest with less toxicity (Figure 10).[159]

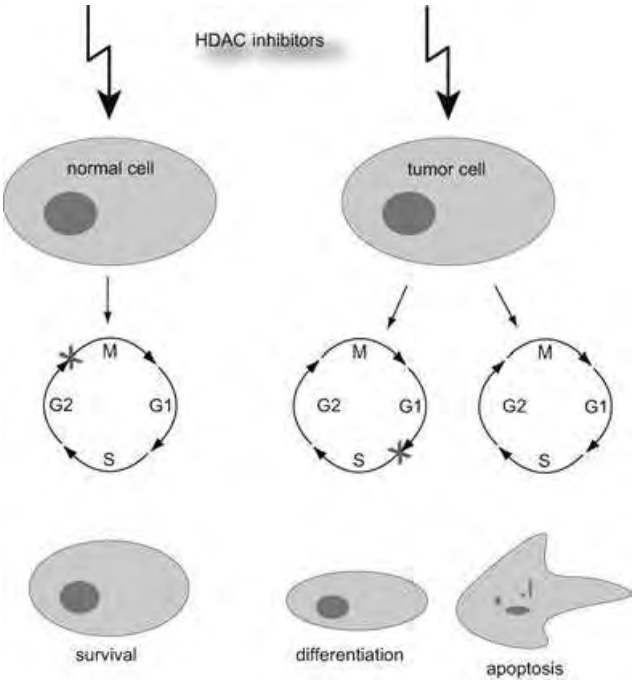

Figure 10. Biological effects of HDAC inhibitors: in normal cells, the application of HDAC inhibitors leads to the induction of a G2 checkpoint, which results in cell-cycle arrest with less toxicity. Under the influence of HDAC inhibitors, many tumor cells increase transcription of the CDK inhibitor WAF1, which leads to a cell-cycle arrest at G1 and directs the cell into differentiation. Cells that do not respond with an arrest at G1 replicate their DNA and induce apoptosis.

The treatment of various tumor cells with HDAC inhibitors induces apoptosis.[152,156,160,161,163] The inhibitors activate both the extrinsic and intrinsic apoptotic signaling pathways. For example, apicidin (**22**) and CBHA (**8**) stimulate expression of the death receptor CD95 and its ligand CD95L.[161,162] Furthermore, after the application of HDAC inhibitors, an increase in the expression of pro-apoptotic Bcl2 proteins (BAX/BAK) and a decrease of anti-apoptotic factors can be observed.[154,164,165] Both pathways result in the activation of caspases.

Beyond this, HDAC inhibitors show further antitumor activities, such as the enhanced transcription of genes that encode MHC I and MHC II to stimulate immune cell recognition and activation.[166–169] Furthermore, TSA (**6**) inhibits the expression of VEGF, which is normally induced by hypoxia, thereby preventing angiogenesis.[170]

These investigations show that HDAC inhibitors are potent antitumor agents, which exhibit only minimal side effects. For this reason they represent a dramatic change in the treatment of cancer diseases. Already, the potent HDAC inhibitors SAHA (**7**), the depsipeptide FK-228 (**20**), MS-275 (**16**), and LAQ-824 (**9**) have shown promising results in phases I and II of clinical trials.

2.2.2. *Class III HDACs: Sirtuins*

The namesake of all sirtuins is the silent information repressor 2 (Sir2) of yeast, a NAD^+-dependent histone deacetylase that is not subject to inhibition by TSA.[118,171] Initial analyses indicated that the enzyme uses a stoichiometric quantity of NAD^+ for the removal of acetyl groups from acetylated lysine residues. The NAD^+ group typically serves as a redox cofactor in biological systems, but in the case of Sir2 it is used as an acetyl group acceptor after hydrolysis of the nicotinamide moiety.[172] Detailed structural studies have shown that Sir2 possess a central core domain with a Rossman fold at both ends and a flexible zinc-binding motif. These structural elements are linked through a series of loops that form a cleft in the central region of the core domain. The acetylated lysine substrate and the NAD^+ cosubstrate bind at opposite sides of this cleft.[173–176]

The X-ray crystallographic structure of the Sir2 homologue of *Saccharomyces cerevisiae* (yHst2), cocrystallized with acetylated H4 and a stable NAD^+ analogue in which the ribose ring is replaced with a 2,3-dihydroxycyclopentane group (carba-NAD^+), has shed new light on the catalytic mechanism of the class III enzymes (Figure 11).[177] Based on this structural information, it is likely that nicotinamide is hydrolyzed in an initial step, and that the resulting oxycation intermediate is stabilized by a water molecule coordinated to Asn116. In a second step, the activated ribose is subject to nucleophilic attack by the carbonyl oxygen of the acetyl lysine function, and the resulting imine-like intermediate is captured by a second nucleophilic attack by the ribose 2′-OH group, facilitated by His135. Subsequent hydrolysis of the acetal-analogue structure gives free lysine and 2′-*O*-acetyl-ADP-ribose. This reaction is made possible by a water molecule coordinatively fixed at Asn116, with the participation of protonated His135. During catalysis, the ribose ring of the cosubstrate and the highly conserved β1-α2 loop of the enzyme clearly change their positions.

Sir2 is associated with the silencing of certain genes.[178] In the case of ySir2p, there are three different regions in the yeast genome that are mainly subject to silencing: those adjacent to the telomeres, regions of ribosomal DNA (rDNA), and regions of the silent mating-type loci.[179] To fulfill these functions, Sir2 is present in two different complexes.[179] The complex Sir2/Sir3/Sir4 (SIR-complex) is responsible for silencing at the telomeres, and could play an important role in the formation of heterochromatin.[180] A

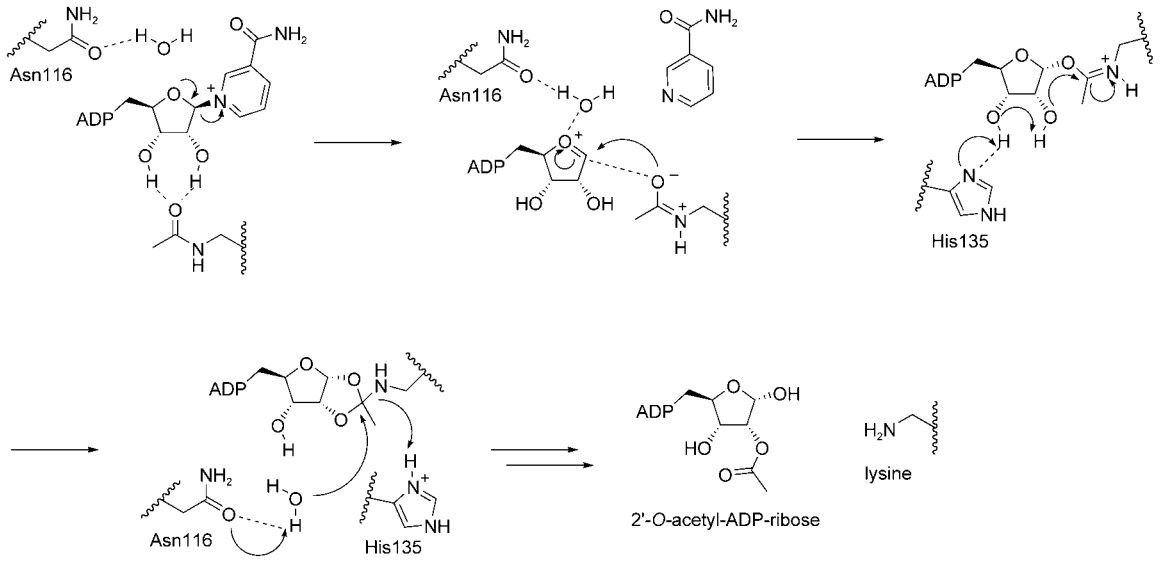

Figure 11. Catalytic mechanism of sirtuins: as the acetyl lysine substrate is precoordinated at both hydroxy functions of the ribose group, the nicotinamide unit is cleaved through the influence of a water molecule, which is coordinatively fixed at Asn116, and stabilizes the ribose oxycation intermediate. The nucleophilic attack of acetyl lysine forms a imine-analogue structure, which is trapped by a second nucleophilic attack of the 2′-OH-ribose function, mediated by His135. After hydrolysis, lysine and 2′-*O*-acetyl-ADP-ribose are released.

deletion of Sir3 or Sir4 results in truncated telomeres and misdirected mitosis, whereas the overexpression of Sir4 leads to the extension of telomeres (Figure 12).[180]

The other complex, Sir2/Net1/Cdc14, is responsible for the formation of closed chromatin structures at regions of ribosomal DNA (rDNA).[179] There are approximately 100–200 copies of genes that encode rRNA. The multiple repeats in DNA sequence enables a splicing process which forms extrachromosomal circles (ERCs), which are toxic and shorten the lifespan of a cell.[191] This effect can be demonstrated by the artificial introduction of ERCs. In contrast, lifespan can be increased by the introduction of an additional copy of Sir2, as silencing of the rDNA region represses the formation of toxic ERCs.[192] Surprisingly, in many organisms the restriction of glucose also increases lifespan.[193] An explanation for this is the direct link between Sir2 activity and the concentration of NAD^+, which reflects the metabolic state of a cell.[194] A low glucose intake leads to a decrease in metabolic activity and therefore to the oxidation of NADH to NAD^+. An increased NAD^+ concentration gives rise to enhanced Sir2 activity, and as a result, the increased silencing of rDNA represses the formation of toxic ERCs. As a control experiment in yeast has shown, a mutation in the NAD^+ biosynthetic pathway decreases lifespan, which can be reversed neither by a mutation in the glucose metabolic pathway, nor by Sir2.[194]

Small-molecule modulators of the sirtuins are absolutely required for investigations of the biological functions of these enzymes with a chemical–genetic approach. The first reported sirtuin inhibitor was a nonhydrolyzable NAD^+ analogue that is cell impermeable and of limited utility.[172] Schreiber and coworkers identified sirtinol (**25**) as an inhibitor with a central 2-hydroxy-1-naphthol unit that is necessary and sufficient for inhibition (Figure 13).[193] A recent screen of a 6000-com-

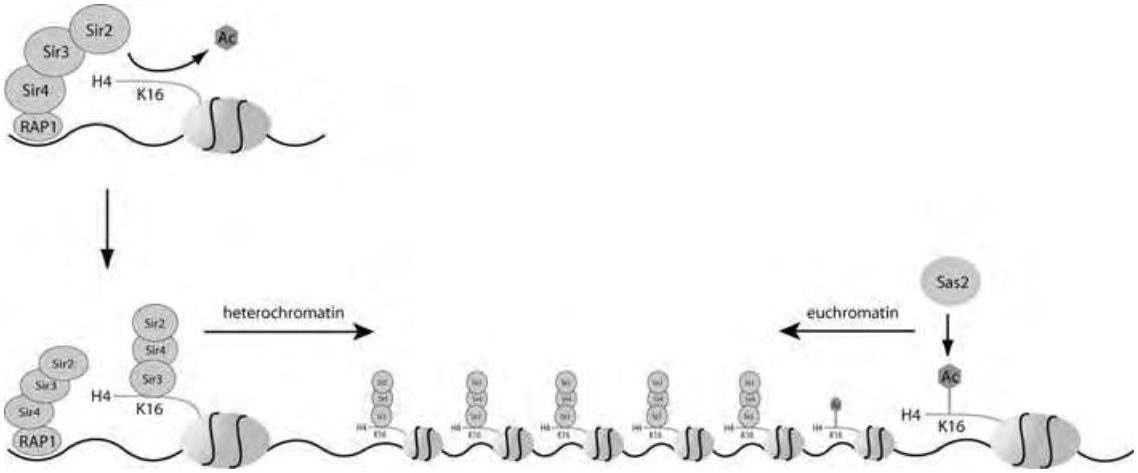

Figure 12. Sir2-mediated gene silencing at the telomeres: the DNA binding protein Rap1 recruits the HDACs Sir4, Sir3, and Sir2.[181–184] Sir2 subsequently deacetylates the closest histone H4 at K16, which creates an available site for the formation of another sirtuin complex, and the cycle can repeat again.[185–187] The spread of heterochromatin in this manner is countered by a second process mediated by the HAT Sas2, which is responsible for the active acetylation of H4-K16.[188–190] The degree of heterochromatin extension at the telomere regions is determined by the equilibrium of these opposing processes.

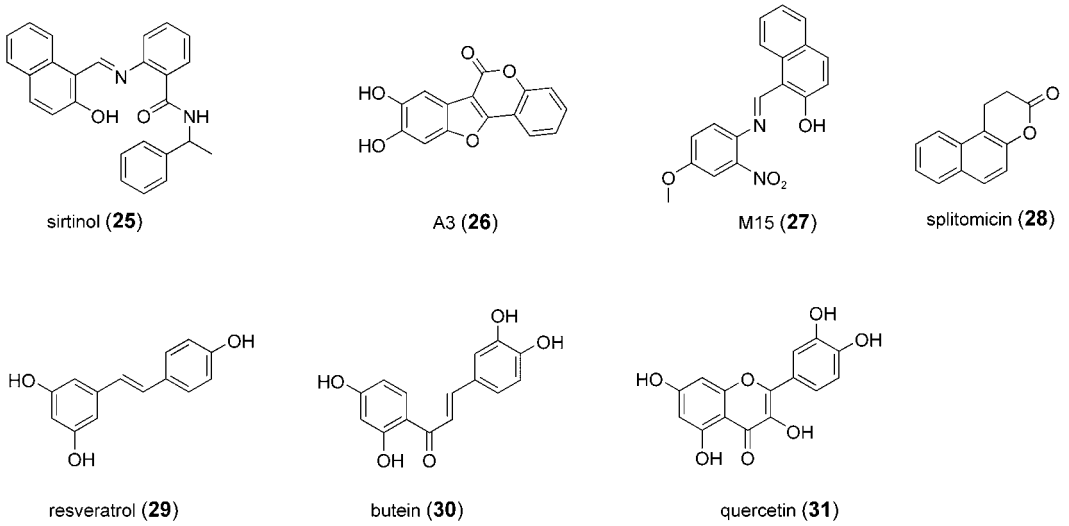

Figure 13. Modulators of sirtuins: sirtinol (**25**), A3 (**26**), M15 (**27**), and splitomicin (**28**) are sirtuin inhibitors, whereas resveratrol (**29**), butein (**30**), and the flavone derivative quercetin (**31**) are activators of these enzymes.

pound library identified splitomicin (**28**) as an inhibitor of Sir2, effective at micromolar concentrations. Splitomicin has a hydrolysis-sensitive lactone, which is crucial for biological activity.[195] Moreover, with resveratrol (3,5,4′-trihydroxy-(*E*)-stilbene, **29**) a potent stimulator of sirtuins was discovered.[196] Resveratrol is an ingredient of red wine that belongs to the group of secondary plant metabolites.[197] With the chalcone derivative butein (**30**) and the flavone derivative quercetin (**31**), other members of the family of sirtuin activating compounds (STACS) were identified, but shown to be less effective than resveratrol.

3. Histone Methylation

Although histone methylation was discovered over 30 years ago, only quite recently was it pushed into the center of scientific attention as an important part of gene regulation.[198] Since 2000, many histone methyltransferases (HMTs) have been identified, and the interactions among histone modifications have been characterized.[199,200]

Specific methylation of lysine residues is known to occur on histone H3 at K4, K9, K27, K36, K79 and on histone H4 at K20. Arginine methylation takes place within the tails of histone H3 at R2, R17, R26 and histone H4 at R3. Furthermore, the N-terminus of H1 is methylated at lysine residues[201] and the methylation of nonhistone proteins has been documented as well.[202,203]

Histone methylation is a stable epigenetic mark that does not alter the overall charge of the histone tails. However, with increasing methylation (Figure 14)[8] comes an increase in basicity, hydrophobicity, and an influence on the affinity for anionic molecules like DNA.[204,205] HMTs display remarkable specificity in the level of methylation they catalyze, and the latest findings suggest that this could have functional significance in transcription.[206]

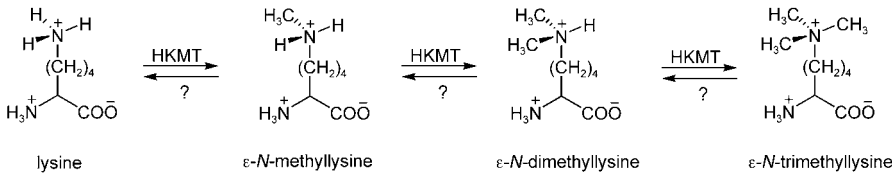

Figure 14. Structure of lysine and its methylated derivatives: HKMT = histone lysine methyltransferase; ? = unknown demethylating mechanism.

Similar to histone acetylation, histone methylation can modulate histone interaction with DNA and chromatin-associated proteins, which results in an alteration of nucleosomal structures and functions, and ultimately contributes to different biological processes.[207]

3.1. Histone Lysine Methyltransferases (HKMTs)

In 2000, SUV39 from *Drosophila* was identified as the first histone lysine methyltransferase, which is specific for H3-K9.[13] HKMTs use *S*-adenosylmethionine (SAM) as a cofactor.[207] Interestingly, the cofactor-binding region is unrelated to the classical SAM-binding folds of DNA- and arginine methyltransferases.[208]

The HKMT catalytic motif was mapped to an evolutionarily conserved, globular domain of approximately 130 amino acid residues, termed the SET domain after the three *Drosophila* genes involved in epigenetic processes (*s*u(var)3-9, *e*nhancer-of-zeste, and *t*rithorax). Cysteine-rich regions of higher sequence variation (PRE-SET- or POST-SET-domains) flank the SET domain, and are required for enzyme activity.[200,208,209] Close inspection of the SET domains has identified three specific, highly conserved amino acids (Asn241, His242, and Tyr283) that influence enzyme activity.[208,210–212] Also, mutation of Asn241 affects the binding of the SAM cofactor.[208]

To date, over 300 proteins have been identified that contain SET domains,[199] and which can be grouped into four major classes: SUV39, SET1, SET2, und RIZ-SET. Their classification is based foremost on sequence similarity between the SET domains and secondarily on their relationship to SET domains in the yeast *S. cerevisiae*.[200,213] Furthermore, each enzyme family shows other common structural features, such as bromo-, chromo-, PRE-SET- and POST-SET domains; it appears that all of them have the same substrate specificity.[200,208,209]

Only the SUV39 family possesses a PRE-SET and a chromo domain, which does not bind methylated H3-K9. However, it is possible that it recognizes other methylated lysine residues or proteins.[200] Such differences in the binding specificity of chromo domains have been observed in other proteins and it is possible that the methylation level regulates binding preferences.[214,215] The methyltransferase MLL, a SET1 family member, has a bromo domain and a methyl-binding domain (MBD).[216] Also, the SET2 family member ASH1 possesses a bromo domain and can associate with the CBP acetyltransferase, as MLL (Section 2.1).[217,218]

The members of the retinoblastoma-interacting zinc finger family (RIZ-family) are transcriptional regulators. They control differentiation, and are involved in various cancers.[200,219–222] To date, no known RIZ proteins possess methyltransferase activity.

In the meantime, X-ray crystallographic structure data are available for HKMTs such as Dim-5,[210] Clr4,[223] LSMT,[212] as well as four separate SET7/9 structures in different configurations.[211,224–226] Not all SET proteins are HKMTs, but they may represent evolutionary deactivated HKMTs.[10,209]

In 2002, the first non-SET HKMT was identified, termed Dot1. It exhibits specificity for H3-K79.[227] For this reason, HKMTs should not be classified by sequence homology, but instead on the basis of epigenetic criteria regarding their histone specificity (Table 2). At this point it is not known how different HKMTs control their catalysis of mono-, di-, and trimethylation, and in which way this varied substitution pattern correlates with transcription.[228]

Table 2: Specificity of histone lysine methyltransferases.

specificity	histone lysine methyltransferase[a]
H3-K4	ySet1,[229] Trx,[230] Ash1,[230,231] Set7/9,[224,232] ALL-1,[233] MLL,[234] ALR,[235] ALR-1,[235] SMYD3[236]
H3-K9	SUV39,[237] Suv39h1,[13,238] Suv39h2,[239] Clr4,[13,215,240] Dim-5,[210,241] G9a,[242] Eu-HMTase I,[243] ESET,[244] SETDB1,[245] Ash1[230,231]
H3-K27	E(Z),[b][246] Ezh2,[247] G9a[242]
H3-K36	ySet2,[248] NSD1[249]
H3-K79	Dot1,[227,250] Dot1L,[227,251] Dot1p[252]
H4-K20	PR-Set7,[c][253] Ash1,[230,231] NSD1,[249] Suv4–20h1/2[254]

[a] ALL-1: acute lymphoblastic leukemia 1; ALR: ALL-related gene; Ash1: absent, small, or homeotic discs 1; Clr4: cryptic loci regulator; Dot1: disrupter of telomeric silencing; Dot1L: disrupter of telomeric silencing-like; E(Z): enhancer of zeste; ESET: ERG-associated protein with SET domain (ERG = ets-related gene); Eu-HMTase I: euchromatic histone methyltransferase 1; Ezh2: enhancer of zeste homologue 2, ySet1: yeast SET-domain-containing 1; ySet2: yeast SET-domain-containing 2; MLL: mixed-lineage leukemia; NSD1: nuclear receptor-binding SET-domain protein 1; PR-Set7: PR-SET-containing protein 07; Set7/9: SET domain-containing 7/9; SET 8: SET-domain-containing 8; SETDB1: SET-domain-bifurcated 1; SMYD3: SET- and MYND-domain-containing protein 3; SUV39: suppressor of variegation 3-9; Suv39h: SUV39 homologue; Trx: Trithorax. [b] E(Z) methylates H3-K9 in the native complex as well.[255] [c] also known as SET 8.[253c]

3.1.1. *Histone Methylation and Gene Repression (H3-K9, H3-K27, H4-K20)*

The histone position H3-K9 seems to be of particular significance for epigenetic modification, as it is a site for both acetylation and methylation. Euchromatin or heterochromatin is formed depending on the type of modification. Also, methylation at H3-K27 and H4-K20 mediates gene repression, such as X-chromosome inactivation.

The histone binding protein HP1 (heterochromatin-associated protein 1) plays an essential role in epigenetic silencing through the formation of heterochromatin. This conserved process is based on the functional cooperation between HDACs, HKMTs and HP1 (Figure 15). After methylation of H3-K9 by SUV39, the transcriptional repressor HP1 (a product of the second *su(var)* gene, Su(var)2-5) binds through selective recognition by its chromo domain.[214,215,256] The HP1 protein possesses two highly conserved regions: the chromo- and the chromo-shadow domains.[257] With its chromo domain, HP1 recognizes and binds methylated H3-K9, whereas the chromo-shadow domain may be responsible for other protein interactions, such as that with SUV39.[256–259] More H3-K9 methylation events are caused by this interaction, and HP1 mediates the propagation of heterochromatin by spreading over wide chromosomal ranges.[260]

It has been shown in yeast as well, that the recruitment of HP1 to centromeric heterochromatin by the SUV39 homologue Clr4 is necessary for transcriptional silencing.[215,240c] Until now, it has not been known how HP1 generates highly compact chromatin structures and functions as a transcriptional repressor.[10,261] One possible mechanism for the propagation of heterochromatin is the dimerization of HP1 through chromo-shadow domain interactions.[207]

Several reports have shown that the methylation of H3-K9 and H3-K27 correlates with X-chromosome inactivation (Xi).[262–266] In this process, the recruitment of HP1 does not occur. It seems that Xi is established by an RNA-dependent process in which an Ezh2 complex is recruited for subsequent methylation of H3-K9 and H3-K27.[247a,255,266–272] However, the significance of histone methylation and Xi awaits clarification. Likewise, RNA is also involved in the propagation of heterochromatin. It could create binding sites for HMTs, or mediate the formation of higher order chromatin structures.[273,274] The acetylation of H3-K9 and H3-K14, as well as the phosphorylation of H3-S10 generally prevent the formation of heterochromatin (Section 1.1).[13,240c,275]

As mentioned above, the specific methylation of H3 creates docking sites for repressor proteins, which ultimately recruit a core repressor complex. However, the process that dictates specific gene repression by HKMTs, including the methylation of H3-K9, H3-K27, and H4-K20, is not as well-characterized. For example, the polycomb (PC) protein binds specifically to methylated H3-K27 with its chromo domain. This results in the specific formation of an active polycomb repressor complex.[247a,255,269,276–278]

Another example of transcriptional repression at euchromatic regions is the retinoblastoma (Rb) protein, which recruits the repressive SUV39/HP1 complex to the genes that control the cell cycle like cyclin E (Figure 16).[259,279,280] Cyclin E is necessary for regulation of the G1/S-phase transition in the cell cycle. Downregulation of Rb leads to cell proliferation and may be involved in tumor growth.[281]

In this case, Rb is recruited to promoters through its interaction with the cell-cycle regulatory, DNA-specific-binding protein E2F.[282,283] SUV39 subsequently binds, the appropriate H3 tails are methylated, and HP1 is localized to these specific promoters. In this manner, HP1 mediates the repression of transcription without the formation of heterochromatin.

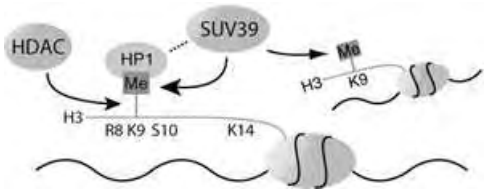

Figure 15. Gene silencing through histone methylation: deacetylation at H3-K9 by specific HDACs is necessary for subsequent methylation by HKMT activity, such as that of SUV39. HP1 selectively recognizes methylated H3-K9. The propagation of heterochromatin and gene repression is mediated by HP1 recruitment of SUV39 and additional H3-K9 methylation.

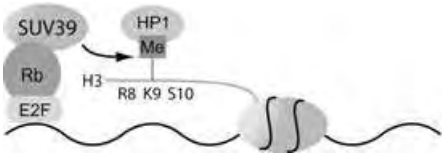

Figure 16. Histone methylation and transcriptional repression: E2F/Rb localize the histone lysine methyltransferase SUV39 at specific promoter sequences, and HP1 initiates transcriptional repression at euchromatin.

Mutation of the Rb protein disrupts the association of Rb and SUV39, the cyclin E promoter is undermethylated at H3-K9, and as a result, HP1 is not associated with the cyclin E promoter.[259] These results highlight the fact that specific methylation at H3-K9 around certain promoter regions occurs through the mediation of repressor proteins like Rb. This process is probably HDAC-dependent for deacetylation of H3-K9 prior to its methylation.[13,237b,284]

Also unclear is the role of HP1. If SUV39 is necessary for the repression of cyclin E and other Rb-regulated genes like dihydrofolate reductase (DHFR) promoters, HP1 binding is assumed to be the repressive event.[242,279] One possible mechanism could be that HP1 recruits other regulators to the promoter to mediate silencing; indeed, HP1 has been shown to associate with deacetylases and ATPases.[257] Alternatively, HP1 may protect methylated H3-K9 sites from catabolism by a demethylase activity that has yet to be characterized. If HP1 is involved in silencing of cyclin E, then its association with the promoter would have to be transient, as cyclin E is activated during S-phase. This association may be controlled by phosphorylation events, as HP1 is known to be highly phosphorylated.[258] However, the phosphorylation of Rb may disrupt the association with SUV39, so that other kinases may be involved.[279] As a result of phosphorylation, E2F is released and transcription is activated.[285] HP1 is not only involved in the regulation of Rb-dependent genes, but also associates with several transcriptional regulators,[257] such as the Ikaros protein[286,287] and the KRAB-associated protein 1 (KAP1).[288–290]

Another histone methylation that correlates with transcriptional repression is the methylation of H4-K20. In *Drosophila* this specific methylation is carried out by the HKMT PRSet7, and corresponds to condensed chromosomal regions.[253a,b,291] Furthermore, studies in vitro and in vivo have shown that methylation at H4-K20 inhibits the acetylation of H4-K16, which is a mark for the hyperactive male X chromosome in *Drosophila*,[292] and transcriptionally active chromatin in human cells.[293] Further investigations are necessary, as H4-K20 can be present in mono-, di-, and trimethylated states.[294]

3.1.2. Histone and DNA Methylation

The aberrant DNA methylation of promoter regions seems to be contribute substantially to tumorigenesis.[295–299] This could result from methylation errors that occur during DNA replication, de novo DNA methylation events, and faulty DNA-repair processes.[300] Enzymatic DNA methylation at the C5 position of cytosine residues leads directly to gene silencing, yet the fundamentals of this process remain unknown.

A recent observation in the fungus *Neurospora crassa* led to the discovery that DNA methylation is dependent on specific histone methylation events,[301,302] and a similar finding was also reported in *Arabidopsis thaliana*.[303] In *N. crassa* a methyltransferase specific for H3-K9 (Dim-5) was identified, and determined to be necessary for DNA methylation and gene silencing.[241a]

SUV39 and G9a were also reported in to be in connection with DNA methylation.[304–307] Furthermore, it is known that DNA methyltransferases (DNMTs) can associate with HP1 homologues.[303,308–310] In an initial stage, Dim-5 trimethylates[311] H3-K9, and HP1 binds through its chromo domain. Next, HP1 recruits additional DNMTs[312,313] to chromatin which methylate DNA. It was shown recently that trimethylated H3-K9[311] and HP1[314] are essential for DNA methylation in *N. crassa*. HP1 may act as an adapter between histone and DNA methylation.

A further phase in these gene-silencing processes involves the recruitment of methyl-binding proteins (MBPs), which contain an MBD domain that recognizes methylated DNA. Like MeCP2, MBPs subsequently recruit HDACs, which deacetylate lysine tails and make the substrate accessible for further methylation events (Section 2.2.1).[315–318] Recently it has been shown both in vitro and in vivo that MeCP2 is able to not only recruit HDACs, but also a histone methyltransferase, which is specific for methylation of H3-K9.[319] The identity of this recruited HKMT is not yet known, but MBP also interacts with the Suv39h1-HP1 complex.[320] Mutations in the gene sequences that code for MeCP2 lead to Rett syndrome, which is characterized by mental disabilities in young girls.[321–323] It is remarkable that such mutations do not cause a global gene derepression; the effect is limited to neuronal genes which explains the corresponding pathology.[324,325]

Furthermore, there are reports of methyltransferases that possess MBD domains for the recognition of methylated DNA, such as the human SETDB1 and its murine homologue ESET.[315] Likewise, SETDB1 is involved in H3-K9 methylation during DNA replication.[326] A new HKMT, SMYD3 has been identified, which recognizes and binds specific DNA sequences.[327] Surprisingly, DNMTs are able to associate in vitro and in vivo with H3-K9-specific HKMTs, such as Suv39h1. As a result, further histone methylations are possible.[308] These continual cycles of histone and DNA methylation lead to gene silencing (Figure 17).[200]

Interestingly, this connection between the methylation of DNA and that of H3-K9 has not been observed in other species, such as *S. cerevisiae*.[10,328] This implies that the connection between histone methylation and that of DNA may not apply to all organisms. In the fruit fly *Drosophila*

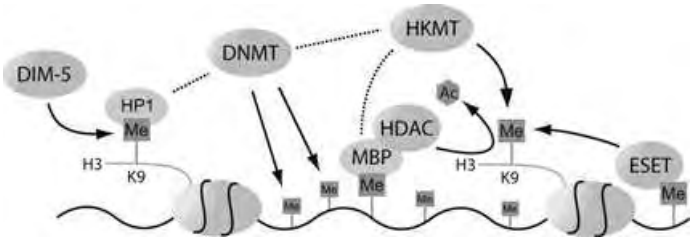

Figure 17. The complex interplay of histone and DNA methylation: after binding of HP1 at methylated H3-K9, DNA methyltransferases (DNMTs) are recruited, which subsequently methylate DNA. MBP proteins recognize this DNA methylation und recruit HDACs, which deacetylate additional histones for subsequent methylation by HKMTs equipped with methyl-binding domains, like ESET. Recent results show that MBP proteins and DNMTs are able to recruit histone-lysine methyltransferases.

melanogaster and in the yeast *Schizosaccharomyces pombe*, regions of DNA methylation have not been observed, yet these organisms do have signaling pathways that operate through histone methylation.[240] In such cases, gene silencing is associated with histone deacetylation, histone methylation, and the binding of repressor proteins, such as HP1.[214,215,240,258]

The combination of enhanced histone and DNA methylation may also occur to silence one of the two copies of the X chromosome in female mammals.[301]

Inhibitors of DNA methylation rapidly reactivate the expression of genes that have undergone epigenetic silencing, particularly if this silencing has occurred in a pathological situation. The DNA methylation inhibitors 5-azacytidine[329] (5-aza-CR, **32**), and 5-aza-2′-deoxycytidine[330] (5-aza-CdR, **33**) induce gene expression and differentiation in cultured cells.[331,332] However, a disadvantage of these azanucleosides is their instability in aqueous solution. In addition, they are toxic and not orally active. For this reason, more potent analogues 5-fluoro-2′-deoxycytidine[333] (FCDR, **34**) and zebularine[334] (**35**) were developed (Figure 18).[335]

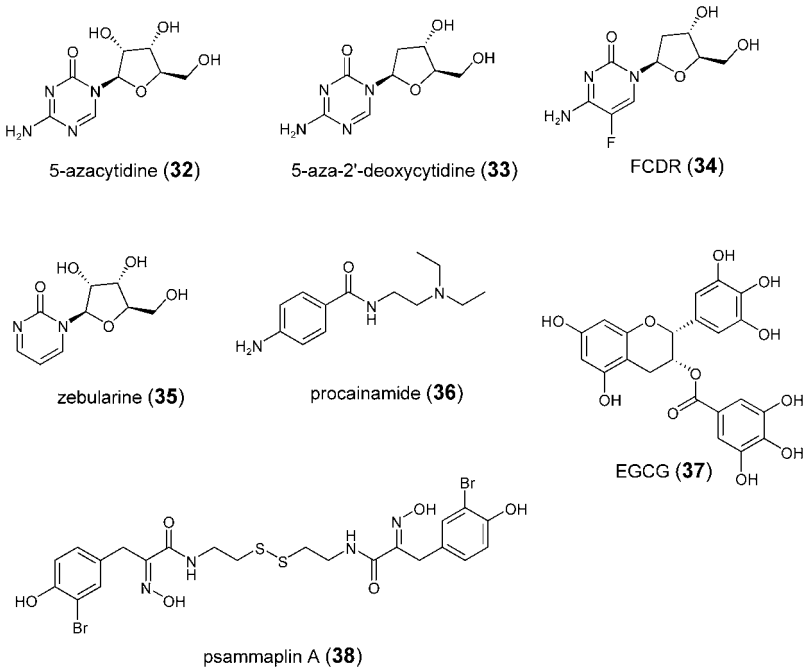

Figure 18. Structures of DNA methylation inhibitors: 5-azacytidine (5-aza-CR, **32**); 5-aza-2′-deoxycytidine (5-aza-CdR, **33**); 5-fluoro-2′-deoxycytidine (FCDR, **34**); zebularine (**35**); procainamide[336] (**36**); epigallocatechin[337] (EGCG, **37**); und psammaplin A[338] (**38**).

The fact that epigenetic silencing is almost universally associated with histone deacetylation resulted in the development of combination therapies, in which inhibitors of both HDAC and DNA methylation are present; this shows remarkable success against tumor cells.[339–343] A recent study with mice demonstrated a strong synergy between 5-aza-CdR (**33**) and the HDAC inhibitor, phenyl butyrate (**15**; Figure 8).[344] Combination preparations of **33** and HDAC inhibitors are now in clinical trials (Section 2.2.1).[16]

3.1.3. Histone Methylation and Activated Transcription (H3-K4, H3-K36, H3-K79)

Transcriptionally active euchromatin is methylated at three positions: H3-K4, H3-K36, and H3-K79. Furthermore, the methylation level at H3-K4 appears to play an important role.[199] Methylation of H3-K4 by Set7/9 impairs the Suv39h1-mediated methylation of H3-K9, and thereby the formation of heterochromatin is hindered (Figure 19).[232b] Moreover, the binding of the histone deacetylase repression complex NuRD (Section 2.2.1) to H3 is precluded by methylation at H3-K4.[345] Dimethylation at H3-K4 may serve as a global epigenetic mark in euchromatin and mediates these general mechanisms, whereas trimethylation at H3-K4 correlates with activated transcription.[228,346] Interestingly, SET7/9 catalyzes only the monomethylation of H3-K4[224,225] and ySet1 mediates only the di- and trimethylations.[228] Methylations at H3-K4 are correlated with euchromatin and activated transcription.[347,348] This is additionally supported by acetylation at H3-K9. Furthermore, the methylation of H3-K4 is highly conserved evolutionarily; methylation of H3-K4 in heterochromatin has not yet been observed.[349,350]

Similarly, Dot1-mediated methylation of H3-K79 can block the development of heterochromatin,[250] a process in which sirtuins are involved (Section 2.2.2).[227,252] On the other hand, sirtuin binding impairs Dot1-mediated methylation of H3-K79.[250,252]

The synthesis of mRNA in eukaryotic organisms is a highly regulated key biological process. Various studies have shown that histone methylation at H3-K4, H3-K36, and H3-K79 by specific HKMTs is functionally linked to RNA polymerase II (RNAP II) and transcriptional elongation.[351–355]

It seems clear that methylation of H3-K4 and H3-K9 corresponds to different biological events. However, there are forms of HKMT, such as a truncated version of the *Drosophila* Ash1 HKMT, which methylate both H3-K4 and H3-K9.[231a,232a] This particular type of dual modification may result in the induction of genes which are normally repressed.[199] More investigations are nec-

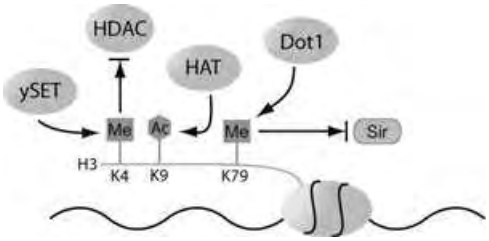

Figure 19. Histone methylation and activated transcription: both H3-K4 methylation and H3-K9 acetylation result in activated transcription. Methylation at H3-K79 by Dot1 also blocks Sir-mediated silencing.

essary for a clearer explanation of this unusual methylation pattern.

3.2. Histone Arginine Methyltransferases (HRMTs)

Methylation of arginine groups occurs on histone H3 at R2, R17, R26 and on H4 at R3. The arginine guanidino function can be either mono- or dimethylated (Figure 20). For this, HRMTs are grouped into two major enzyme classes.

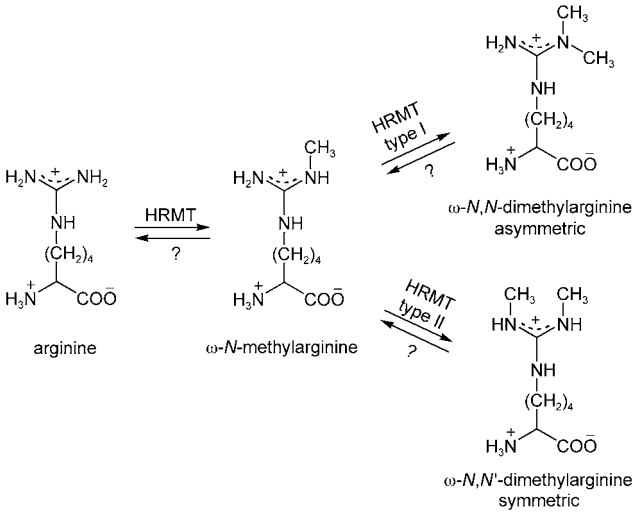

Figure 20. The structure of arginine and its methylated derivatives: HRMT = histone arginine methyltransferase; ? = unknown demethylating mechanism.

Type I enzymes catalyze the formation of symmetric ω-N^G,$N^{G'}$-dimethylarginine tails, whereas the type II enzymes catalyze the formation of asymmetric ω-N^G,N^G-dimethylarginine tails.

At this point, seven mammalian protein arginine methyltransferases (PRMTs) have been identified, and all of them share a highly conserved catalytic domain (Table 3). Nine *Drosophila* arginine methyltransferases (DARTs) have been identified in that organism.

Table 3: Known histone arginine methyltransferases (HRMTs).[200] [a]

HRMT[b]	specificity	type of methylation
PRMT1[363–365]	H4-R3	asymmetric
PRMT4/CARM1[366,367]	H3-R2, H3-R17, H3-R26	asymmetric
PRMT5/JBP1[368,369]	H2A, H4	symmetric

[a] PRMT2 is not identified as an enzyme;[8,356] PRMT3,[357–359] 6,[360] and 7[361,362] are not known as HRMTs. [b] PRMT = protein arginine N-methyltransferase; CARM = coactivator-associated arginine methyltransferase; JBP = Janus kinase-binding protein.

In contrast to histone lysine methyltransferases, PRMTs bear few domains beside the catalytic domain. PRMT3 possesses a zinc-finger structure and PRMT2 has a SH3 domain, which may be responsible for substrate specificity.[200] Nonhistone proteins are also methylated at arginine residues,[356] and are involved in signal transduction,[370–373] mRNA splicing,[374,375] RNA transport[376–378] and mediate protein–protein interactions.[379]

Furthermore, methylation of an arginine residue of the HAT CBP/p300 by PRMT4/CARM1 has been identified in vivo. This event blocks the association of CBP/p300 with the CREB transcription factor and therefore influences transcriptional regulation (Section 2.1.1).[109]

The arginine methyltransferase CARM1/PRMT4 specifically methylates H3-R2, H3-R17 and H3-R26 in vitro, and is a coactivator of nuclear receptors.[366,367,380] PRMT1 methylates H4-R3 in vivo,[364,381] yet the corresponding target promoters have not yet been identified. PRMT5 has a preference for H2A and H4 in vitro, but the region of methylation remains unknown.[200] Furthermore, methylation at H4-R3 enhances the subsequent acetylation of H4.[381] Both arginine methylation and histone acetylation are histone modifications that give rise to transcriptional activation.

In 2004, the first arginine methyltransferase inhibitor, AMI-1 (**39**), was identified that does not influence histone lysine methylation (Figure 21).[382] Moreover, AMI-1 is cell-

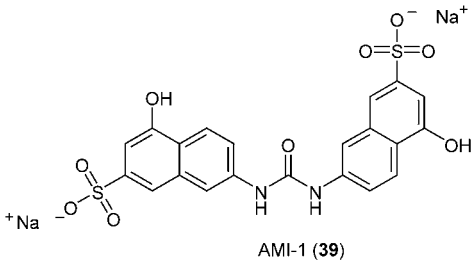

Figure 21. Structure of the specific PRMT inhibitor AMI-1 (**39**).

permeable and appears to interact with the HRMT substrate binding site. Recently, AMI-1 was described as a selective HIV-1 reverse transcriptase inhibitor; this study also demonstrated that this compound is not cytotoxic.[383] In this context, eight more inhibitors and two activators of PRMTs were identified. However, their selectivities against PRMT isoforms are varied.[382]

3.3. Histone Demethylation

As repressive histone methylation occurs at both heterochromatin and euchromatin, the stability of this modification comes into question. Under thermodynamic conditions, methylation is much more stable than acetylation or phosphorylation. The latter two are cleavable by HDACs and phosphatases (PPs) and are thus reversible. Active histone demethylases (HDMases) are as yet unknown. In 2002, a HAT was identified whose N-terminal domain has sequence similarity to an enzyme superfamily in which SAM is used as a cofactor in radical reactions. Based on this similarity, a radical-dependent demethylating activity was postulated.[384] Indeed, demethylases with nonhistone substrates have been

identified.[385–387] Such enzyme activity results in the production of formaldehyde. Thus, the demethylation process probably occurs through an oxidative mechanism.[388]

Repeated cycles of DNA replication may effectively dilute histone methylation.[10,207] An alternative mechanism for decreasing methylation density is through the replacement of methylated histones with unmodified forms, such as histone variants.[389] Another potential demethylating event is the proteolytic cleavage of histone N-termini, which has been observed in *Tetrahymena*.[10,201] Ubiquitinylation could also take part in histone demethylation.[10,390]

Recently, a demethylating mechanism for arginine groups in histones was described. The peptidylarginine deiminase 4 (PAD4/PADI4)[391] can catalyze the conversion of both mono- and unmethylated arginine groups to citrulline in vitro and in vivo. Dimethylated histone arginine residues are not substrates of PAD4/PADI4 and are therefore not demethylated. Whether citrulline-modified histones elicit any effect on chromatin structure, or if they are recognized and bound by other proteins are questions that should be explored.[392–394] However, a specific demethylating mechanism has yet to be identified, and thus continued research in this area is necessary.

4. Histone Phosphorylation

Histone phosphorylation was initially reported in the 1960s.[395] Since that time, phosphorylation has been shown to occur on all histones. Important phosphorylation sites such as H3-S10 and H3-S28 were identified to be involved in cell-cycle processes during mitosis[396,397] and meiosis, as well as in transcriptional gene activation during interphase, although these fundamental cell-cycle processes elicit opposite effects toward the structure of chromatin. Furthermore, all phosphorylated serine residues are located within the highly conserved amino acid sequence, Ala-Arg-Lys-Ser (ARKS).[398]

4.1. H3 Phosphorylation in Mitosis and Meiosis

Phosphorylation at H3-S10 is involved in chromosomal condensation and cell division during mitosis and meiosis.[6,397] H3-S28[399] and H3-T11[400] have also been identified as mitosis-specific phosphorylation sites. It remains unknown whether these modifications are causally linked. Histone phosphorylation is also necessary for chromosome condensation in mammals[401] and in *T. thermophila*.[396]

Phosphorylation of H3-S10 begins during the late G2/M-phase transition at pericentric heterochromatin and spreads throughout the genome until late prophase.[402,403] Ultimately this is followed by general dephosphorylation during the progression through cell division to telophase.[397]

Mitotic phosphorylation at H3-S10 is mediated by members of the aurora kinase family, such as Ipl1 kinase in yeast and nematodes,[404] aurora B in *Drosophila*,[405] and aurora B (and A) in mammals.[406] The aurora B kinases are also involved in mitotic phosphorylation at H3-S28[407] and are regarded as the true H3-S10 kinases, as their subcellular localization[408] seems better suited than that of aurora A, which is a centromeric protein.[409] These kinases are also thought to be required for the proper recruitment of the condensin complex and assembly of the mitotic spindle.[405]

The balance of the phosphorylation level, as well as the exact chromosomal condensation during cell division is mediated by type 1 phosphatases (PP1).[404,410–412] A set of data indicate that phosphorylation of H3 is not essential during mitosis/meiosis,[413–416] and the role of this is increasingly under controversy.[417] It is possible that H3 phosphorylation is not directly involved in chromosome condensation, but instead plays an indirect role in the complex mechanisms of chromosomal rearrangement.[417]

4.2. H3 Phosphorylation during Transcription

In mammals, histone phosphorylation is involved in the transcriptional activation of immediate early-response genes, such as *c-fos*, *c-myc*, and *c-jun* during interphase.[417–420] These genes are directly linked to signaling cascades, without a requirement for the biosynthesis of new proteins.[398] This stimulus-dependent H3 phosphorylation is fast, transient, and concerns only a particular group of genes. In addition, these phosphorylated H3 histones are susceptible to hyperacetylation,[421] which links both modifications during the activation of transcription through a MAP kinase signaling cascade.[422–424] Therefore, this cascade not only phosphorylates transcription factors and coactivators, but histones as well.[425] However, other signaling cascades are present which may be involved in the activation of immediate early-response genes, like the Janus kinase/signal transducer and activator of transcription (JAK/STAT)[426] or the nuclear factor κB (NF-κB).[427] Studies with relatively specific MAP kinase inhibitors and other inhibitors have shown that in mammals, H3 phosphorylation is mediated by the ERK or p38 MAP kinase pathways, depending on the nature of the stimulus, but is not mediated through the JNK/SAPK pathway.[423,424,428,429]

Although these two signaling pathways are involved in phosphorylation, histone phosphorylation is effected by downstream kinases and not by MAP kinases themselves. In this case, kinases of the RSK[430–432] and MSK families[428,433,434] may be activated,[398] yet it appears that the latter family represents those designated for H3 phosphorylation.[398,434,435] MSK1/2 are localized in the nucleus and are activated by both the ERK and the p38 MAP kinase pathways (Figure 22).[436] Furthermore, studies in vitro have shown that MSK1 phosphorylates H3 with a much higher efficiency than RSK1/2.[398] Mutations in RSK2 are found in the human genetic disease known as the Coffin–Lowry syndrome, which has the same clinical symptoms as Rubinstein–Taybi syndrome (Section 2.1).[437,438] Other histone kinases linked to transcription have been identified, such as Snf1,[12] PKB/Akt,[439,440] and IKB kinase-α (IKK-α).[441,442]

The stimulation-dependent phosphorylation of H3-S28 by a MAP kinase has been described.[434,443,444] However, a direct link between phosphorylation at H3-S28 and activated tran-

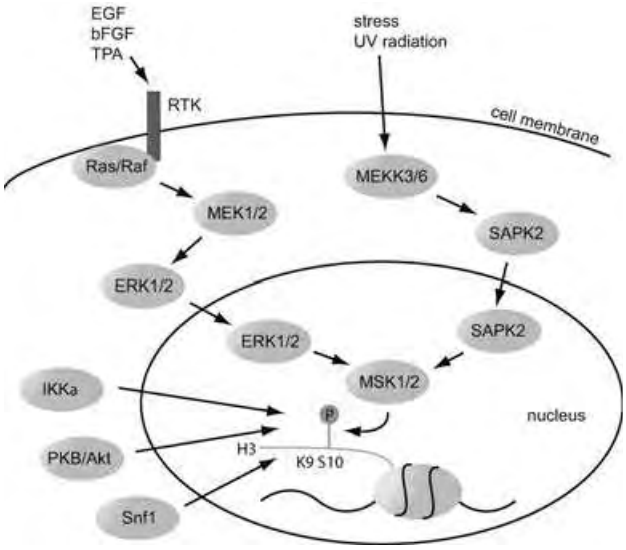

Figure 22. Signaling pathways that lead to H3-S10 phosphorylation and gene expression: activation of the MAP-kinase cascade or the p38 cascade by mitogens, growth factors, stress, or UV irradiation leads to the activation of MSK1/2 kinases, which phosphorylate H3-S10 and result in the activation of genes, such as *c-fos* and *c-jun*. The activation of IKK-α, PKB/Akt and Snf1 is also possible with subsequent H3-S10 phosphorylation. EGF = epidermal growth factor; ERK = extracellular signal-regulated kinase; FGF = fibroblast growth factor; IKKα = IKB Kinase-α; MEK = mitogen-activated protein kinase; MEKK = mitogen-activated protein kinase/ERK kinase kinase; MSK = mitogen- and stress-response kinase; PKB = protein kinase B; Raf = ras-activated factor; RAS = rat sarcoma; RKT = receptor tyrosine kinase; SAPK = stress-activated protein kinase; Snf1 = sucrose non-fermented 1; TPA = 12-*O*-tetradecanoylphorbol-13-acetate.

scription has not yet been established. [398] The H3-S10 residue is located in a region of the protein that is also subject to other modifications. For example, H3-K9 and H3-K14 can be acetylated, which normally correlates with active transcription. On the other hand, methylation at H3-K9 leads to the formation of heterochromatin and gene silencing. Experiments performed in vitro and in vivo support this conclusion of such a mutual interaction (Section 1.1).[445]

4.3. Phosphorylation and Acetylation

Phosphorylation and acetylation of histones are both linked to the activation of transcription. Antibody-based experiments have shown that the dually modified H3 isoform is present in vivo.[275,446] Precisely what role this functional interrelationship of these two modifications plays remains unclear; two models have been proposed: the synergistic model and the parallel-independent model.

4.3.1. Synergistic Model

Experiments conducted in vitro reveal that the HAT yGcn5 shows a preference for binding to phosphorylated H3-S10.[275,446,447] The crystal structure data of Gcn5 from yeast[447] and *Tetrahymena*[96] has allowed the identification of essential amino acid interactions. The yeast version (yGcn5) has a six- to tenfold higher substrate specificity for H3-S10.[275,447] This enhanced substrate specificity is the result of a higher K_M value and a k_{cat} value that is relatively unchanged, which shows that phosphorylation at H3-S10 enhances the binding affinity of yGcn5 rather than its catalytic turnover.

Promoters of MAP-kinase-activated genes, such as *c-fos*, are populated by acetylated and phosphorylated H3 histones.[275] Together, both modifications elicit a synergistic effect in which the MAP signaling pathway leads to phosphorylation at H3-S10. This phosphorylated serine group is then preferentially bound by Gcn5, which acetylates H3-K14 and induces transcriptional activation (Figure 23).[447]

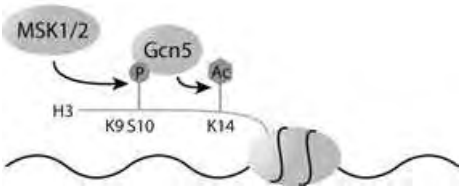

Figure 23. Synergistic model: MSK1/2 phosphorylates H3-S10, which increases the binding affinity for Gcn5. Once bound, the HAT activity of Gcn5 results in the acetylation of H3-K14, which activates transcription.

In contrast, chromatin immunoprecipitation (ChIP) assays for several yeast promoters have shown that Gcn5 acetylates all available sites of H3, except K14.[448] Furthermore, Gcn5 in the native SAGA complex (Section 2.1) exhibits preference for H3 neither in its phosphorylated nor nonphosphorylated states.[449] A possible explanation for this difference could be that the subunits of SAGA mediate binding.

4.3.2 Parallel-Independent Model

The stimulation of mouse fibroblasts with EGF leads to phosphorylation and acetylation of H3. However, both modifications occur independently of each other.[446] This shows that phosphorylation at H3-S10 is not an inevitable signal for a subsequent acetylation at K14. Analysis of the induction of *c-jun* genes supports this finding.[450] MAP-kinase-dependent phosphorylation at H3 was also identified in active, previously acetylated regions of gene expression. Acetylation is a dynamic process that is kept in balance by the action of HATs and HDACs (Figure 24).[450]

Phosphorylation of H3 is dramatically decreased by mutations in MSK kinases or by the inhibition of MSK1/2, whereas histone acetylation in these gene regions remains relatively unaffected.[434,451,452] This supports the model that in some cases the presence of a modification is not required for additional histone modifications.

The genome-wide distribution of histone H3-K14 acetylation and H3-S10 phosphorylation during the heat shock response were examined in *Drosophila*.[453] Thermal stress leads to the global inactivation of transcription and to the induction of genes that are involved in heat shock.[454,455] These results suggest that the genomic distribution of acetylation on histones H3 and H4 remains more or less

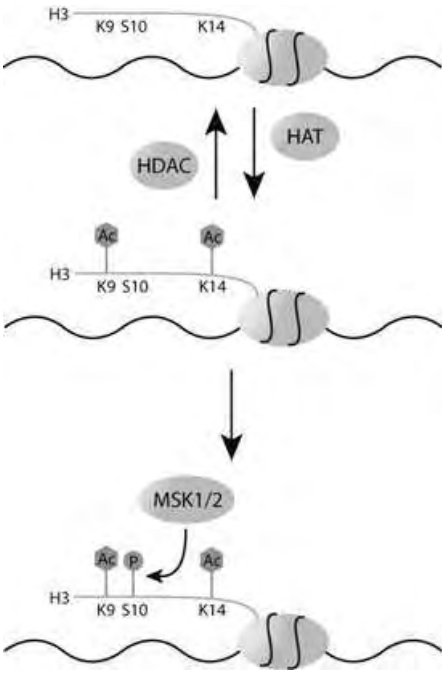

Figure 24. Parallel-independent model: acetylation at H3-K9 and H3-K14 is maintained by an equilibrium established by the activities of HATs and HDACs. MSK1/2 phosphorylates a previously acetylated histone H3 tail at K9 and K14. This results in activated transcription.

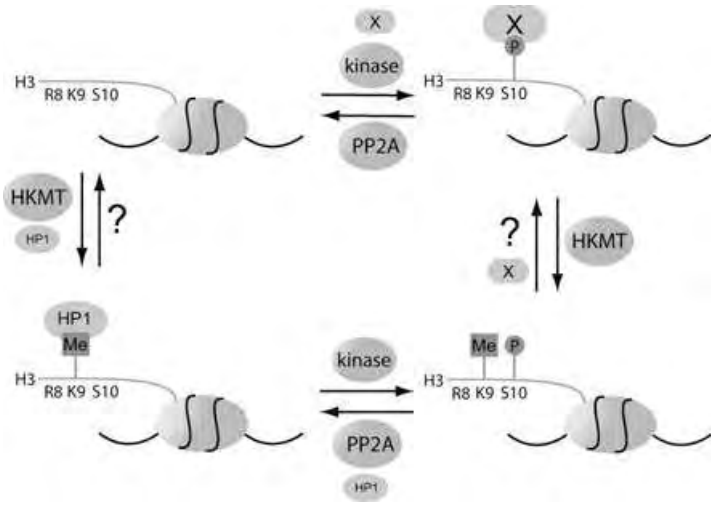

Figure 25. Binary switch hypothesis: posttranslational modification of histones results in the recruitment of effector proteins, like HP1 and X. Additional modifications in close proximity to an existing modification, such as HKMT-directed methylation at H3-K9, leads to loss of the effector protein and the associated biological effect. ? = unknown demethylating mechanism, PP2A = protein phosphatase type 2, X = postulated phosphorylation binding protein.

static. However, the distribution of histone phosphorylation changes dramatically and is only detected at those regions that contain actively transcribed heat shock genes. The kinase responsible has not yet been identified, but a possible candidate is Jil-1, a new tandem kinase with some similarity to members of the human MSK kinase family.[456–458]

The results show that in *Drosophila*, histone phosphorylation is intimately linked to transcriptional activation and the presence of acetylated histones may not necessarily denote regions of actively transcribed genes.[459]

4.4. Phosphorylation and Methylation

How are cells able to change a repressive modification, such as the methylation of H3-K9, to reach an activated state of transcription? The binary switch hypothesis is based on the observation that most repressive methylation events at H3 are adjacent to serine or threonine residues.[445] This concept postulates that phosphorylation blocks the binding of repressive proteins that normally recognize histone methylation. This is supported through the coexistence of methylation and phosphorylation in HeLa cells.[445] The phosphorylation at H3-S10 blocks the kinetically controlled binding of HP1 at H3-K9[260,460] and allows other enzymes, like HATs, to acetylate other sites to override the repressed state. In addition, the repressed state is quickly recovered by dynamic dephosphorylation (Figure 25). Another possibility is that phosphorylation creates binding sites for several enzymes, such as demethylases that have not yet been identified, which demethylate H3-K9. Subsequent acetylation at this position would then be possible. However, all these proposals remain hypothetical and must be demonstrated experimentally.

If this concept is correct, other combinations of modifications, such as acetylation/phosphorylation and ubiquitinylation/phosphorylation, could extend the potential pattern of the histone code.

4.5. Histone Dephosphorylation

The presence of kinase–phosphatase pairs that maintain proper phosphorylation levels during mitosis leads to the proposal that similar mechanisms are also present in the processes of transcriptional activation and inactivation. After heat shock in *Drosophila*, the transcriptional activation of heat shock genes is accompanied by the de-novo phosphorylation of H3-S10, whereas this modification disappears from the rest of the genome. Treatment of cells with phosphatase type 2 (PP2A) inhibitors, or mutations in genes that code for PP2A decrease the dephoshorylation of H3. This demonstrates that gene expression during heat shock depends on the phosphorylation level of H3, which may be regulated through changes in PP2A activity.[461]

5. Histone Ubiquitinylation

Ubiquitin (Ub) is a highly conserved protein of 76 amino acids. Its name reflects the broad presence of Ub in all eukaryotic cells.[462] The covalent attachment of Ub to other proteins was observed 30 years ago with histones.[463] The exact purpose of this modification is still under investigation. In most cases, ubiquitinylation serves as a mark for the proteolytic, ATP-dependent degradation of proteins by the

proteasome.[464] In this process, several Ub units are transferred to the target protein by a succession of three enzymatic steps.[465] Through ATP hydrolysis, the ubiquitin-activating enzyme E1 binds the C-terminus of Ub as a reactive thioester and subsequently catalyzes the transfer of the activated Ub protein to the ubiquitin-conjugating enzyme E2 in a transesterification reaction. The ubiquitin ligase E3 next transfers the Ub group from E2 to the ε-amino function of a lysine residue in the target protein to generate a new isopeptide bond. At position 48, Ub itself possess an internal lysine residue with which the catalytic bond-forming cascade is repeated, and several Ub units can be bound as a chain at the target protein.[466]

There are many hints that ubiquitinylation is more than a simple mark for the degradation of useless or defective proteins. Like phosphorylation, it serves as a signal for various cellular processes[467,468] and plays an important role in cell-cycle regulation, transcription, signal transduction, DNA repair, endocytosis, apoptosis, and the immune response.[468] In 2004, Chiechanover, Hershko, and Rose received the Nobel prize in chemistry for their fundamental contributions to ubiquitinylation research.

The histone protein H2B is monoubiquitinylated at the highly conserved Lys123 residue in the C-terminal region.[469,470] This particular modification is not linked to proteasome-directed degradation; instead, it is most likely an additional letter in the alphabet of the histone code.[471] The attachment of the Ub moiety follows the aforementioned enzymatic cascade: the ubiquitin-conjugating enzyme E2 was identified as Rad6 and Ubc2,[472] whereas Bre1 was found to serve as the Ub ligase E3.[473–476] Additionally, the so-called PAF complex is also associated with H2B ubiquitinylation.[477] Rad6 (E2) is recruited to a specific promoter region by Bre1 (E3), whereas the PAF complex regulates the activity of Rad6 during the monoubiquitinylation of H2B.[478]

Although the information coded through histone ubiquitinylation is not yet fully understood, it is clear that this modification is equally as important as the other letters of the histone code. Like acetylation, ubiquitinylation is a dynamic process,[479–482] and 17 different Ub hydrolases (UBPs) have been identified in yeast.[483] Furthermore, Ubp8 represents a stoichiometric subunit of the SAGA complex[484] and this is one of the reasons for describing this enzyme in the context of other histone-modifying enzymes.

Recently, it was demonstrated that ubiquitinylation of H2B influences the methylation of H3: deletion of the *rad6* gene or an appropriate mutation in the H2B ubiquitinylation sequence prevents methylation of H3-K4 and H3-K79, which is normally catalyzed by Set1 and Dot1.[227,229a,b,252,388,485–488] The ubiquitinylated histone could be bound by HMTs with a special ubiquitin-interacting domain,[489–491] which has been identified in numerous other factors. Furthermore, PAF is not only necessary for H2B ubiquitinylation, but is also decisive for the methylation at H3-K4 and H3-K79.[352] Methylation at lysine side chains will take place only if the PAF complex activates Rad6/Bre1 for monoubiquitinylation at H2B.[352] In this manner, ubiquitinylation of H2B is a regulating element for the methylation of H3-K4 and H3-K79, and preserves transcriptionally active euchromatin (Figure 26).

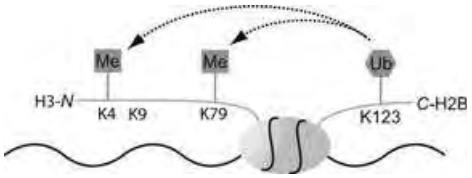

Figure 26. Ubiquitinylation of H2B-K123 influences histone methylation at H3-K4 and H3-K79.

6. Histone Sumoylation

The abbreviation SUMO (small ubiquitin-like modifier) designates a group of small proteins that are related to Ub through secondary and tertiary structure elements.[492] Their mechanism of attachment to target proteins is also similar to that of Ub. A SUMO-activating enzyme E1 (SAE1/SAE2) binds SUMO with concomitant ATP hydrolysis as a reactive thioester, which is transesterified to the SUMO-conjugating enzyme E2 (Ubc9). The last step is likely to be the transfer of the SUMO group from E2 to the ε-amino function of a lysine residue by the action of a ligase E3.[493]

Ub and SUMO proteins differ substantially in their primary structures, with a sequence homology of only 18%. This results in a completely different surface charge distribution. Furthermore, sumoylation does not represent a mark for the degradation of proteins.[494] Examples of the large group of sumoylated proteins[495] are p53 and H4. The histone is not modified at the usual consensus sequence, γ-Lys-X-Glu (γ = bulky hydrophobic amino acid; X = any amino acid).

Whereas histone ubiquitinylation is generally linked with active chromatin, there is increasing evidence that sumoylation elicits a contrary effect.[496] For example, the expression of a reporter is decreased by the SUMO-conjugating enzyme Ubc9. A simultaneous decrease in H3 acetylation and a significant increase of the heterochromatin-associated protein HP1, which is directly linked to gene silencing, can be observed.[496] From these results, a model has been developed to describe the mode of action of sumoylation.[497] As the acetylation of histone proteins increases, so does the sumoylation of H4. This serves as a signal for the termination of gene expression that had been originally induced through acetylation. The recruitment of HDAC activity clears the acetylated position for subsequent methylation, and allows the binding of the repressor protein HP1. The extent to which histone sumoylation actually plays a fundamental role must be clarified through future investigations. Some results show that sumoylation has a more indirect influence on these processes. In the case of p300/CREB, the acetyltransferase itself is sumoylated, and shows a stronger binding to HDAC6.[110] Another example is the transcription factor Elk-1; its sumoylation leads to the recruitment of HDAC activity to the Elk-1 promoter. The subsequent decrease in histone acetylation results in the repression of transcription.[498]

7. Histone Poly-ADP-Ribosylation

Like numerous other proteins, histones are modified by the successive attachment of anionic ADP-ribose monomers to generate poly(ADP-ribose) (PAR) chains (Figure 27).[499] Seven different PARPs (PAR polymerases) have been identified in mammals, from which PARP-1 is preferably expressed.[500]

From a mechanistic point of view, PARP-1 catalyzes the transfer of ADP-ribose units from the donor NAD^+ to an acceptor protein.[501] The first unit is attached to the carboxyl group of a glutamic or aspartic acid residue by an ester bond, whereas additional ADP-ribose units extend the chain through glycosidic bonds with the hydroxy function of the preceding ribose molecule. This is the same manner with which linear or branched polymers of up to 200 units are generated. The *parp-1* gene is highly conserved and codes for an N-terminal double zinc finger DNA binding domain, a central automodification domain, and a C-terminal NAD^+-binding domain.[502]

Like the sirtuins, which are NAD^+-dependent, PARP-1 is sensitive to the physiological state of a cell. Moreover, the activity of the enzyme is regulated by an allosteric mechanism.[503] The binding of DNA, especially damaged DNA, increases the activity. PARP-1 is also able to interact with two DNA helices simultaneously; it is therefore likely that the enzyme binds at locations where DNA exits the nucleosome. Moreover, PARP-1 activity is increased through the interaction of the automodification domain with transcription factors like YY1, which are able to bind DNA.[504] In contrast, an automodification in this region of PARP-1 inhibits DNA binding and ADP-ribosyltransferase activity.[503]

The influence of PARP-1 on the regulation of transcription processes is based on two important mechanisms: first, PAR modification of histones leads to an altered chromatin structure;[505] second, PARP-1 facilitates the binding of other factors to DNA in many cases, which activates transcription through the formation of a enhanceosome. Highly inducible genes are good examples of this.[506] The expression of heat shock proteins and the induction of immune system genes depends heavily on PARP-1 activity. In general, areas of high transcriptional activity or regions of decondensed chromatin are those with a high probability for the presence of PARP-1. However, there are some examples to the contrary:[507] PARP-1 is necessary for chromatin condensation and transcription repression. It appears that the effect of PARP-1 on chromatin structure depends on the neighboring chromatin. Whereas genes with euchromosomal surroundings, like *hsp70*, are activated by PARP-1, the same enzyme represses genes with a heterochromatin environment, such as *copia*.[507]

Under physiological conditions PAR modification is reversible[508] and its cleavage occurs rapidly after termination of the stimulus. PAR polymers, induced by heat shock, show a complete turnover within 25 minutes after termination of induction.[506] The reason for this is the presence of a specific poly(ADP-ribose) glycohydrolase (PARG). The activity of this enzyme seems to be proportional to the length of the polymer substrate.

The inclusion of PARP-1 into the group of chromatin-modifying enzymes is justified by some similarities to HATs, for example.[509] PARP-1 affects various DNA-based processes like transcription, replication, and DNA repair; it also participates directly in the assembly of transcription complexes at enhancers and promoters.[510] In addition, the PAR modification is part of a synergism that is typical for the histone code: nucleosomes can be modified simultaneously by acetyl groups and PAR residues.[511]

8. Conclusion

The length of the DNA of the human genome in its free, double helical form is approximately one meter. To be stably compressed for storage in cell nuclei, it must be organized into a structure of higher order. At the same time, this condensation naturally restricts accessibility to the DNA. However, nature uses this restriction very effectively as a way to regulate transcription. Histone proteins and nucleosomes are necessary for the generation of DNA structures of higher order and furthermore, they serve as templates to establish the histone code, an epigenetic mechanism for the regulation of transcription. The various histone modifications are analogous to a repertoire of letters, whose mutual dependence and influence on each other creates a sort of grammar. The fundamental establishment of the histone code is brought

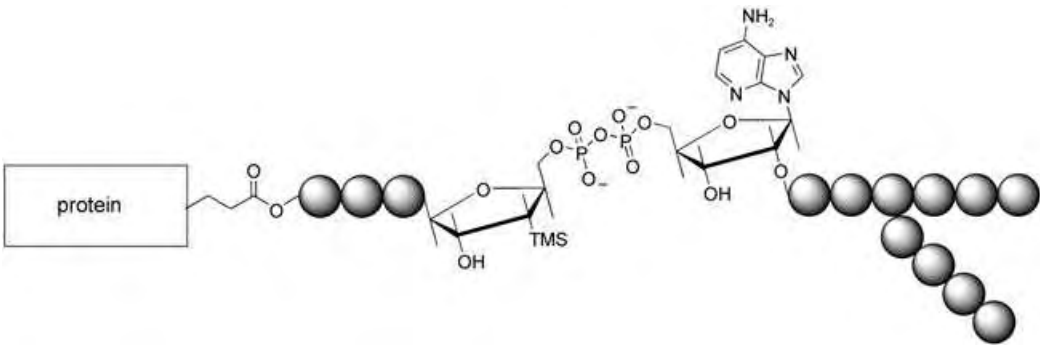

Figure 27. Poly(ADP-ribosyl)ation of proteins: the initial ADP-ribosyl unit is attached at a glutamic or aspartic acid residue of the target protein through an ester bond. Extension ensues through formation of glycosidic bonds, which enable the formation of branched structures. The spheres represent ADP-ribose units.

about by the different enzyme families involved: HATs, HDACs, HMTs, HKs, and PPs, as well as the enzymes that control ubiquitinylation, sumoylation, and PAR modification. Despite the growing knowledge concerning the histone code, a abundance of questions still remain. Particularly, histone methylation, which is an important component of transcriptional regulation and the direction of other cellular processes, is not yet well-understood. The contradictory biological outputs of methylation at different lysine and arginine residues of the histones are also of emerging importance. The publication of some HMT crystallographic structure information should be a sufficient impetus for the development of chemical tools to assist in the study of these processes. Imitations of natural structures, for example, through bisubstrate analogues or simple peptide mimetics[512] could be the first steps in this approach.

The same type of exploration is necessary for the HATs. To date, the entire scope of their biological properties and interactions is only partially understood after the development of the first enzyme modulators; additional modulators will be helpful for further investigations. The different families of histone acetyltransferases and histone deacetylases mediate different biological processes. Therefore, the use of special modulators to selectively address these enzymes would be very helpful. Histone demethylation remains a topic that awaits clarification altogether.

In principle, the development of modulators of histone-modifying enzymes would enable the urgently-needed decoding of the histone code and, above all, the control of this code from the outside. This would enable the development of new therapies and new drugs for the treatment of tumors. This is supported by the fact that some HDAC inhibitors, in combination with inhibitors of DNA methylation, are already in clinical trials.

The investigation of epigenetic mechanisms is an important and new area of biomedical research. The development of the necessary modulators for epigenetic systems requires the active participation of chemistry. A clarification of the molecular details of epigenetic mechanisms will lead to a better understanding of pathological processes and will enable the development of completely new therapeutic drugs and concepts. Those in the fields of bioorganic and medicinal chemistry should recognize this as one of their most important research tasks.

Addendum (April 22, 2005)

During the printing of this Review, some important papers have been published in the area of epigenetics.

The dogma that histone methylation is irreversible has now been disproved with the identification of lysine-specific histone demethylase (LSD1), also known as KIAA0601.[513] LSD1 is a FAD-dependent amine oxidase that is able to specifically demethylate mono- and dimethylated H3-K4 in an oxidative manner.[514] LSD1 is associated with the CoREST repressor complex and represses transcription.[513] In this way, histone methylation is a dynamic process like histone acetylation or phosphorylation.

The type-II methyltransferase PRMT7 is specific for histones H2A and H4.[515] Analyses for the control of HKMT product specificity has been investigated.[516]

H3-T3 is an additional mitosis-specific phosphorylation mark, and the specific kinase for this is haspin.[517]

Ultraviolet B radiation (UVB) induces the phosphorylation of H3-S10 which is mediated by a Fyn kinase.[518] However, the phosphorylation of H3-S28 is mediated by MLTK-α (mixed-lineage kinase-like mitogen-activated protein triple kinase-α).[519]

With curcumin, another specific inhibitor of the histone acetyltransferase CBP has been identified.[520]

The ubiquitin hydrolase Ubp8 represents a new functional module within the SAGA multiprotein complex that is involved in gene regulation through the deubiquitinylation of H2B.[521]

Another report describes that the ubiquitin hydrolase Ubp10 targets H2B as substrate for deubiquitinylation, which helps to localize Sir2 to the telomeres.[522]

There is evidence that PARP-1 functions as both a structural component of chromatin and as a modulator of chromatin structure through its intrinsic enzymatic activity.[523]

Received: July 17, 2004

[1] a) S. Khorasanizadeh, *Cell* **2004**, *116*, 259–272; b) G. Arents, R. W. Burlingame, B. C. Wang, W. E. Love, E. N. Moudrianakis, *Proc. Natl. Acad. Sci. USA* **1991**, *88*, 10148–10152; c) G. Arents, E. N. Moudrianakis, *Proc. Natl. Acad. Sci. USA* **1993**, *90*, 10489–10493.
[2] R. D. Kornberg, Y. Lorch, *Cell* **1999**, *98*, 285–294.
[3] K. Luger, A. W. Mader, R. K. Richmond, D. F. Sargent, T. J. Richmond, *Nature* **1997**, *389*, 251–260.
[4] V. G. Allfrey, R. Faulkner, A. E. Mirsky, *Proc. Natl. Acad. Sci. USA* **1964**, *61*, 786–794.
[5] H. T. Spotswood, B. M. Turner, *J. Clin. Invest.* **2002**, *110*, 577–582.
[6] P. Cheung, C. D. Allis, P. Sassone-Corsi, *Cell* **2000**, *103*, 263–271.
[7] B. M. Turner, *Cell* **2002**, *111*, 285–291.
[8] Y. Zhang, D. Reinberg, *Genes Dev.* **2001**, *15*, 2343–2360.
[9] M. Grunstein, *Nature* **1997**, *389*, 342–352.
[10] T. Jenuwein, C. D. Allis, *Science* **2001**, *293*, 1074–1080.
[11] S. L. Schreiber, B. E. Bernstein, *Cell* **2002**, *111*, 771–778.
[12] W. S. Lo, L. Duggan, N. C. Tolga, W. S. Lane, R. Shiekhattar, S. L. Berger, *Science* **2001**, *293*, 1142–1146.
[13] S. Rea, F. Eisenhaber, D. O'Carroll, B. D. Strahl, Z. W. Sun, M. Schmid, S. Opravil, K. Mechtler, C. P. Ponting, C. D. Allis, T. Jenuwein, *Nature* **2000**, *406*, 593–599.
[14] B. D. Strahl, C. D. Allis, *Nature* **2000**, *403*, 41–45.
[15] A. H. Hassan, P. Prochasson, K. E. Neely, S. C. Galasinski, M. Chandy, M. J. Carrozza, J. L. Workman, *Cell* **2002**, *111*, 369–379.
[16] G. Egger, G. Liang, A. Aparicio, P. A. Jones, *Nature* **2004**, *429*, 457–463.
[17] J. A. Johnson, B. M. Turner, *Semin. Cell Dev. Biol.* **1999**, *10*, 179–188.
[18] S. K. Kurdistani, M. Grunstein, *Nat. Rev. Mol. Cell Biol.* **2003**, *4*, 276–284.
[19] T. R. Hebbes, A. W. Thorne, C. Crane-Robinson, *EMBO J.* **1988**, *7*, 1395–1403.
[20] S. W. Brown, *Science* **1966**, *151*, 417–425.

[21] G. Reuter, P. Spierer, *Bioessays* **1992**, *14*, 605 – 612.
[22] G. Thon, A. J. S. Klar, *Genetics* **1992**, *131*, 287 – 296.
[23] R. C. Allshire, J.-P. Javerzat, N. J. Readhead, G. Cranston, *Cell* **1994**, *76*, 157 – 169.
[24] L. L. Wallrath, *Curr. Opin. Genet. Dev.* **1998**, *8*, 147 – 153.
[25] J. C. Eissenberg, *Proc. Natl. Acad. Sci. USA* **1990**, *87*, 9923 – 9927.
[26] T. Tsukiyama, C. Wu, *Curr. Opin. Genet. Dev.* **1997**, *7*, 182 – 191.
[27] A. J. Kal, T. Mahmoudi, N. B. Zak, C. P. Verrijzer, *Genes Dev.* **2000**, *14*, 1058 – 1071.
[28] J. E. Brownell, J. Zhou, T. Ranalli, R. Kobayashi, D. G. Edmondson, S. Y. Roth, C. D. Allis, *Cell* **1996**, *84*, 843 – 851.
[29] S. Y. Roth, J. M. Denu, C. D. Allis, *Annu. Rev. Biochem.* **2001**, *70*, 81 – 120.
[30] C. Dhalluin, J. E. Carlson, L. Zheng, C. He, A. K. Aggarwal, M. M. Zhou, *Nature* **1999**, *399*, 491 – 496.
[31] R. H. Jacobson, A. G. Ladurner, D. S. King, R. Tjian, *Science* **2000**, *288*, 1422 – 1425.
[32] P. Ornaghi, P. Ballario, A. M. Lena, A. Gonzalez, P. Filetici, *J. Mol. Biol.* **1999**, *287*, 1 – 7.
[33] N. Shikama, J. Lyon, N. B. LaThangue, *Trends Cell Biol.* **1997**, *7*, 230 – 236.
[34] R. Marmorstein, *J. Mol. Biol.* **2001**, *311*, 433 – 444.
[35] C. Reifsnyder, J. Lowell, A. Clarke, L. Pillus, *Nat. Genet.* **1996**, *14*, 44 – 49.
[36] J. Borrow, V. P. Stanton, J. M. Andresen, R. Becher, F. G. Behm, R. S. K. Chaganti, C. I. Civin, *Nat. Genet.* **1996**, *14*, 33 – 41.
[37] M. Carapeti, R. C. T. Aguiar, A. E. Watmore, J. M. Goldman, N. C. P. Cross, *Cancer Genet. Cytogenet.* **1999**, *113*, 70 – 72.
[38] A. Hilfiker, D. Hilfiker-Kleiner, A. Pannuti, J. C. Lucchesi, *EMBO J.* **1997**, *16*, 2054 – 2060.
[39] R. T. Utley, J. Côte, *Curr. Top. Microbiol. Immunol.* **2003**, *274*, 203 – 236.
[40] S. Takechi, T. Nakayama, *Biochem. Biophys. Res. Commun.* **1999**, *266*, 405 – 410.
[41] X.-J. Yang, *Nucleic Acids Res.* **2004**, *32*, 959 – 976.
[42] M. J. Carrozza, R. T. Utley, J. L. Workman, J. Côte, *Trends Genet.* **2003**, *19*, 321 – 329.
[43] P. A. Grant, L. Duggan, J. Cote, S. M. Roberts, J. E. Brownell, R. Candau, R. Ohba, T. Owen-Hughes, C. D. Allis, F. Winston, S. L. Berger, J. L. Workman, *Genes Dev.* **1997**, *11*, 1640 – 1650.
[44] R. Balasubramanian, M. G. Pray-Grant, W. Selleck, P. A. Grant, S. Tan, *J. Biol. Chem.* **2002**, *277*, 7989 – 7995.
[45] P. A. Grant, A. Eberharter, S. John, R. G. Cook, B. M. Turner, J. L. Workman, *J. Biol. Chem.* **1999**, *274*, 5895 – 5900.
[46] P. A. Grant, D. Schieltz, M. G. Pray-Grant, J. R. Yates, J. L. Workmann, *Mol. Cell* **1998**, *2*, 863 – 867.
[47] S. Allard, R. T. Utley, J. Savard, A. Clarke, P. Grant, C. J. Brandl, L. Pillus, J. L. Workman, J. Cote, *EMBO J.* **1999**, *18*, 5108 – 5119.
[48] E. Martinez, V. B. Palhan, A. Tjernberg, E. S. Lymar, A. M. Gamper, T. K. Kundu, B. T. Chait, R. G. Roeder, *Mol. Cell. Biol.* **2001**, *21*, 6782 – 6795.
[49] T. Ikura, V. V. Ogryzko, M. Grigoriev, R. Groisman, J. Wang, M. Horikoshi, R. Scully, J. Qin, Y. Nakatani, *Cell* **2000**, *102*, 463 – 473.
[50] S. B. McMahon, M. A. Wood, M. D. Cole, *Mol. Cell. Biol.* **2000**, *20*, 556 – 562.
[51] S. E. Lang, S. B. McMahon, M. D. Cole, P. Hearing, *J. Biol. Chem.* **2001**, *276*, 32627 – 32634.
[52] T. Agalioti, S. Lomvardas, B. Parekh, T. Maniatis, D. Thanos, *Cell* **2000**, *103*, 667 – 678.
[53] M. Merika, D. Thanos, *Curr. Opin. Gent. Dev.* **2001**, *11*, 205 – 208.
[54] S. Lomvardas, D. Thanos, *Cell* **2001**, *106*, 685 – 696.
[55] T. Agalioti, G. Chen, D. Thanos, *Cell* **2002**, *111*, 381 – 392.
[56] H. Chen, M. Tini, R. M. Evans, *Curr. Opin. Cell Biol.* **2001**, *13*, 218 – 224.
[57] E. R. Smith, A. Eisen, W. Gu, M. Sattah, A. Pannuti, J. Zhou, R. G. Cook, J. C. Lucchesi, C. D. Allis, *Proc. Natl. Acad. Sci. USA* **1998**, *95*, 3561 – 3565.
[58] A. S. Clarke, J. E. Lowell, S. J. Jacobsen, L. Pillus, *Mol. Cell. Biol.* **1999**, *19*, 2515 – 2526.
[59] M. Iizuka, B. Stillman, *J. Biol. Chem.* **1999**, *274*, 23027 – 23034.
[60] S. Ait-Si-Ali, A. Polesskaya, S. Filleur, R. Ferreira, A. Duquet, P. Robin, A. Vervish, D. Trouche, F. Cabon, A. Harel-Bellan, *Oncogene* **2000**, *19*, 2430 – 2437.
[61] J. E. Krebs, C. J. Fry, M. Samuels, C. L. Peterson, *Cell* **2000**, *102*, 587 – 598.
[62] M. S. Schlissel, *Science* **2000**, *287*, 438 – 440.
[63] M. T. McMurry, M. S. Krangel, *Science* **2000**, *287*, 495 – 498.
[64] G. Otero, J. Fellows, Y. Li, T. de Bizemont, A. M. Dirac, C. M. Gustafsson, H. Erdjument-Bromage, P. Tempst, J. Q. Svejstrup, *Mol. Cell* **1999**, *3*, 109 – 118.
[65] B. O. Wattschieben, G. Otero, T. de Bizemont, J. Fellows, H. Erdjument-Bromage, R. Ohba, Y. Li, C. D. Allis, P. Tempst, J. Q. Svejstrup, *Mol. Cell* **1999**, *4*, 123 – 128.
[66] A. E. Ehrenhofer-Murray, D. H. Rivier, J. Rine, *Genetics* **1997**, *145*, 923 – 934.
[67] C. Reifsnyder, J. Lowell, A. Clarke, L. Pillus, *Nat. Genet.* **1996**, *14*, 42 – 49.
[68] W. Gu, R. G. Roeder, *Cell* **1997**, *90*, 595 – 606.
[69] L. Liu, D. M. Scolnick, R. C. Trievel, H. B. Zhang, R. Marmorstein, T. D. Halazonetis, S. L. Berger, *Mol. Cell. Biol.* **1999**, *19*, 1202 – 1209.
[70] K. Sakaguchi, J. E. Herrera, S. Saito, T. Miki, M. Bustin, A. Vassilev, C. W. Anderson, E. Appella, *Genes Dev.* **1998**, *12*, 2831 – 2841.
[71] A. Imhof, X. J. Yang, V. V. Ogryzko, Y. Nakatani, A. P. Wolffe, H. Ge, *Curr. Biol.* **1997**, *7*, 689 – 692.
[72] J. Boyes, P. Byfield, Y. Nakatani, V. Ogryzko, *Nature* **1998**, *396*, 594 – 598.
[73] T. Yamagata, K. Mitani, H. Oda, T. Suzuki, H. Honda, T. Asai, K. Maki, T. Nakamoto, H. Hirai, *EMBO J.* **2000**, *19*, 4676 – 4687.
[74] W. Zhang, J. J. Bieker, *Proc. Natl. Acad. Sci. USA* **1998**, *95*, 9855 – 9860.
[75] V. Sartorelli, P. L. Puri, Y. Hamamori, V. Ogryzko, G. Chung, Y. Nakatani, J. Y. Wang, L. Kedes, *Mol. Cell* **1999**, *4*, 725 – 734.
[76] M. A. Martinez-Balbas, U. M. Bauer, S. J. Nielsen, A. Brehm, T. Kouzarides, *EMBO J.* **2000**, *19*, 662 – 671.
[77] A. Tomita, M. Towatari, S. Tsuzuki, F. Hayakawa, H. Kosugi, K. Tamai, T. Miyazaki, T. Kinoshita, H. Saito, *Oncogene* **2000**, *19*, 444 – 451.
[78] L. Waltzer, M. Bienz, *Nature* **1998**, *395*, 521 – 525.
[79] N. Munshi, M. Merika, J. Yie, K. Senger, G. Chen, D. Thanos, *Mol. Cell* **1998**, *2*, 457 – 467.
[80] M. Bergel, J. E. Herrera, B. J. Thatcher, M. Prymakowska-Bosak, A. Vassilev, Y. Nakatani, B. Martin, M. Bustin, *J. Biol. Chem.* **2000**, *275*, 11514 – 11520.
[81] J. E. Herrera, K. Sakaguchi, M. Bergel, L. Trieschmann, Y. Nakatani, M. Bustin, *Mol. Cell. Biol.* **1999**, *19*, 3466 – 3473.
[82] S. Li, B. Aufiero, R. L. Schiltz, M. J. Walsh, *Proc. Natl. Acad. Sci. USA* **2000**, *97*, 7166 – 7171.
[83] R. E. Kiernan, C. Vanhulle, L. Schiltz, E. Adam, H. Xiao, F. Maudoux, C. Calomme, A. Burny, Y. Nakatani, K. T. Jeang, M. Benkirane, C. Van Lint, *EMBO J.* **1999**, *18*, 6106 – 6118.
[84] T. Murata, R. Kurokawa, A. Krones, K. Tatsumi, M. Ishii, T. Taki, M. Masuno, H. Ohashi, M. Yanagisawa, M. G. Rosenfeld, C. K. Glass, Y. Hayashi, *Hum. Mol. Genet.* **2001**, *10*, 1071 – 1076.

[85] I. Coupry, C. Roudaut, M. Stef, M. A. Delrue, M. Marche, I. Burgelin, L. Taine, C. Cruaud, D. Lacombe, B. Arveiler, *J. Med. Genet.* **2002**, *39*, 415 – 421.
[86] R. H. Goodman, S. Smolik, *Genes Dev.* **2000**, *14*, 1553 – 1577.
[87] K. G. Tanner, R. C. Trievel, M.-H. Kuo, R. M. Howards, S. L. Berger, C. D. Allis, R. Marmorstein, J. M. Denu, *J. Biol. Chem.* **1999**, *274*, 18157 – 18160.
[88] O. D. Lau, A. D. Courtney, A. Vassilev, L. A. Marzilli, R. J. Cotter, Y. Nakatani, P. A. Cole, *J. Biol. Chem.* **2000**, *275*, 21953 – 21959.
[89] K. G. Tanner, M. R. Langer, J. M. Denu, *Biochemistry* **2000**, *39*, 11961 – 11969.
[90] K. G. Tanner, M. R. Langer, Y. Kim, J. M. Denu, *J. Biol. Chem.* **2000**, *275*, 22048 – 22055.
[91] F. Dyda, D. C. Klein, A. B. Hickman, *Annu. Rev. Biophys. Biomol. Struct.* **2000**, *29*, 81 – 103.
[92] R. C. Trievel, J. R. Rojas, D. E. Sterner, R. N. Venkataramani, L. Wang, J. Zhou, C. D. Allis, S. L. Berger, R. Marmorstein, *Proc. Natl. Acad. Sci. USA* **1999**, *96*, 8931 – 8936.
[93] Y. Lin, C. M. Fletcher, J. Zhou, C. D. Allis, G. Wagner, *Nature* **1999**, *400*, 86 – 89.
[94] J. R. Rojas, R. C. Trievel, J. Zhou, Y. Mo, X. Li, S. L. Berger, C. D. Allis, R. Marmorstein, *Nature* **1999**, *401*, 93 – 98.
[95] A. Clements, J. R. Rojas, R. C. Trievel, L. Wang, S. L. Berger, R. Marmorstein, *EMBO J.* **1999**, *18*, 3521 – 3532.
[96] A. Clements, A. N. Poux, W.-S. Lo, L. Pillus, S. L. Berger, R. Marmorstein, *Mol. Cell* **2003**, *12*, 461 – 473.
[97] O. D. Lau, T. K. Kundu, R. E. Soccio, S. Alt-Si-Ali, E. M. Khalil, A. Vassilev, A. P. Wolffe, Y. Nakatani, R. G. Reoder, P. A. Cole, *Mol. Cell* **2000**, *5*, 589 – 595.
[98] P. R. Thompson, H. Kurooka, Y. Nakatani, P. A. Cole, *J. Biol. Chem.* **2001**, *276*, 33721 – 33729.
[99] A. N. Poux, M. Cebrat, C. M. Kim, P. A. Cole, R. Marmorstein, *Proc. Natl. Acad. Sci. USA* **2002**, *99*, 14065 – 14070.
[100] A. Costanzo, P. Merlo, N. Pediconi, M. Fulco, V. Sartorelli, P. A. Cole, G. Fontemaggi, M. Fanciulli, L. Schiltz, G. Blandino, C. Balsano, M. Levrero, *Mol. Cell* **2002**, *9*, 175 – 186.
[101] K. Balsubramanyam, V. Swaminathan, A. Ranganathan, T. K. Kundu, *J. Biol. Chem.* **2003**, *278*, 19134 – 19140.
[102] J. Chen, Y.-H. Zhang, L.-K. Wang, S. J. Sucheck, A. M. Snow, S. M. Hecht, *Chem. Commun.* **1998**, 2769 – 2770.
[103] M. Biel, N. Kretsovali, E. Karatzali, J. Papamatheakis, A. Giannis, *Angew. Chem.* **2004**, *116*, 4065 – 4067; *Angew. Chem. Int. Ed.* **2004**, *43*, 3974 – 3976.
[104] H. M. R. Hoffmann, J. Rabe, *Angew. Chem.* **1985**, *97*, 96 – 112; *Angew. Chem. Int. Ed. Engl.* **1985**, *24*, 94 – 110.
[105] F. P. Kuhajda, E. S. Pizer, J. N. Li, N. S. Mani, G. L. Frehywot, C. A. Townsend, *Proc. Natl. Acad. Sci. USA* **2000**, *97*, 3450 – 3454.
[106] G. Legube, D. Trouche, *EMBO Rep.* **2003**, *4*, 944 – 947.
[107] S. Ait-Si-Ali, *Nature* **1998**, *396*, 184 – 186.
[108] K. Zanger, S. Radovick, F. E. Wondisford, *Mol. Cell* **2001**, *7*, 551 – 558.
[109] W. Xu, H. Chen, K. Du, H. Asahara, M. Tini, B. M. Emerson, M. Montminy, R. M. Evans, *Science* **2001**, *294*, 2507 – 2511.
[110] D. Girdwood, D. Bumpass, O. A. Vaughan, A. Thain, L. A. Anderson, A. W. Snowden, E. Garcia-Wilson, N. D. Perkins, R. T. Hay, *Mol. Cell* **2003**, *11*, 1043 – 1054.
[111] G. G. Gray, T. J. Ekstrom, *Exp. Cell Res.* **2001**, *262*, 75 – 83.
[112] C. M. Grozinger, S. L. Schreiber, *Chem. Biol.* **2002**, *9*, 3 – 16.
[113] E. Verdin, F. Dequiedt, H. G. Kasler, *Trends Genet.* **2003**, *19*, 286 – 293.
[114] C. M. Grozinger, C. A. Hassig, S. L. Schreiber, *Proc. Natl. Acad. Sci. USA* **1999**, *96*, 4868 – 4873.
[115] W. Fischle, V. Kiermer, F. Dequiedt, E. Verdin, *Biochem. Cell Biol.* **2001**, *79*, 337 – 348.
[116] W. Fischle, S. Emiliani, M. J. Hendzel, T. Nagase, N. Nomura, W. Voelter, E. Verdin, *J. Biol. Chem.* **1999**, *274*, 11713 – 11720.
[117] M. S. Finnin, J. R. Donigian, A. Cohen, V. M. Richon, R. A. Rifkind, P. A. Marks, N. P. Pavletich, *Nature* **1999**, *401*, 188 – 193.
[118] R. A. Frye, *Biochem. Biophys. Res. Commun.* **2000**, *273*, 793 – 798.
[119] S. Imai, C. Armstrong, L. Guarente, *Nature* **2000**, *403*, 795 – 800.
[120] C. B. Brachmann, J. M. Sherman, S. E. Devine, E. E. Cameron, L. Pillus, J. D. Boeke, *Genes Dev.* **1995**, *9*, 2888 – 2902.
[121] L. J. Burke, A. Baniahmad, *FASEB J.* **2000**, *14*, 1876 – 1888.
[122] P. A. Wade, *Hum. Mol. Genet.* **2001**, *10*, 693 – 698.
[123] W. M. Yang, C. Inouye, Y. Zeng, D. Bearss, E. Seto, *Proc. Natl. Acad. Sci. USA* **1996**, *93*, 12845 – 12850.
[124] H. D. Youn, C. M. Grozinger, J. O. Liu, *J. Biol. Chem.* **2000**, *275*, 22563 – 22567.
[125] C. M. Grozinger, S. L. Schreiber, *Proc. Natl. Acad. Sci. USA* **2000**, *97*, 7835 – 7840.
[126] Y. Zhang, H. H. Ng, H. Erdjument-Bromage, P. Tempst, A. Bird, D. Reinberg, *Genes Dev.* **1999**, *13*, 1924 – 1935.
[127] D. E. Ayer, *Trends Cell Biol.* **1999**, *9*, 193 – 198.
[128] P. S. Knoepfler, R. N. Eisenman, *Cell* **1999**, *99*, 447 – 450.
[129] R. Aasland, A. F. Stewart, T. Gibson, *Trends Biochem. Sci.* **1996**, *21*, 87 – 88.
[130] A. You, J. K. Tong, C. M. Grozinger, S. L. Schreiber, *Proc. Natl. Acad. Sci. USA* **2001**, *98*, 1454 – 1458.
[131] G. W. Humphrey, Y. Wang, V. R. Russanova, T. Hirai, J. Qin, Y. Nakatani, B. H. Howard, *J. Biol. Chem.* **2001**, *276*, 6817 – 6824.
[132] N. Tsuji, M. Kobayashi, K. Nagashima, Y. Wakisaka, K. Koizumi, *J. Antibiot.* **1976**, *29*, 1 – 6.
[133] M. Yoshida, M. Kijima, M. Akita, T. Beppu, *J. Biol. Chem.* **1990**, *265*, 17174 – 17179.
[134] M. Gottlicher, S. Minucci, P. Zhu, O. H. Kramer, A. Schimpf, *EMBO J.* **2001**, *20*, 6969 – 6978.
[135] J. S. Chen, D. V. Faller, *Curr. Cancer Drug Targets* **2003**, *3*, 219 – 236.
[136] M Yoshida, Y. Hoshikawa, K. Koseki, K. Mori, T. Beppu, *J. Antibiot.* **1990**, *43*, 1101 – 1106.
[137] W. K. Kelly, O. A. O'Connor, P. A. Marks, *Expert Opin. Invest. Drugs* **2002**, *11*, 1695 – 1713.
[138] P. A. Marks, R. A. Rifkind, V. M. Richon, R. Breslow, T. Miller, W. K. Kelly, *Nat. Rev. Cancer* **2001**, *1*, 194 – 202.
[139] M. Jung, G. Brosch, D. Kolle, H. Scherf, C. Gerhauser, P. Loidl, *J. Med. Chem.* **1999**, *42*, 4669 – 4679.
[140] R. Furumai, Y. Komatsu, N. Nishino, S. Khochbin, M. Yoshida, S. Horinouchi, *Proc. Natl. Acad. Sci. USA* **2001**, *98*, 87 – 92.
[141] V. M. Richon, Y. Webb, R. Merger, T. Sheppard, B. Jursic, L. Ngo, F. Civoli, R. Breslow, R. A. Rifkind, P. A. Marks, *Proc. Natl. Acad. Sci. USA* **1996**, *93*, 5705 – 5708.
[142] V. M. Richon, S. Emiliani, E. Verdin, Y. Webb, R. Breslow, R. A. Rifkind, P. A. Marks, *Proc. Natl. Acad. Sci. USA* **1998**, *95*, 3003 – 3007.
[143] T. Suzuki, T. Ando, K. Tsuchiya, N. Fukazawa, A. Saito, Y. Mariko, T. Yamashita, O. Nakanishi, *J. Med. Chem.* **1999**, *42*, 3001 – 3003.
[144] K. Mori, K. Koseki, *Tetrahedron* **1998**, *54*, 1101 – 1106.
[145] Y. Komatsu, K. Y. Tomizaki, M. Tsukamoto, T. Kato, N. Nishino, S. Sato, T. Yamori, T. Tsuruo, R. Furumai, M. Yoshida, S. Horinouchi, H. Hayashi, *Cancer Res.* **2001**, *61*, 4459 – 4466.
[146] H. J. Kwon, T. Owa, C. A. Hassig, J. Shimada, S. L. Schreiber, *Proc. Natl. Acad. Sci. USA* **1998**, *95*, 3356 – 3361.
[147] M. Jung, *Curr. Med. Chem.* **2001**, *8*, 1505 – 1511.
[148] M. L. Curtin, *Expert Opin. Ther. Pat.* **2002**, *12*, 1375 – 1384.
[149] J. M. Mariadason, G. A. Corner, L. H. Augenlicht, *Cancer Res.* **2000**, *60*, 4561 – 4572.
[150] E. E. Cameron, K. E. Bachman, S. Myohanen, J. G. Herman, S. B. Baylin, *Nat. Genet.* **1999**, *21*, 103 – 107.

[151] P. A. Marks, V. M. Richon, R. Breslow, R. A. Rifkind, *Curr. Opin. Oncol.* **2001**, *13*, 477 – 483.
[152] U. H. Weidle, A. Grossmann, *Anticancer Res.* **2000**, *20*, 1471 – 1485.
[153] P. A. Marks, V. M. Richon, R. A. Rifkind, *J. Natl. Cancer Inst.* **2000**, *92*, 1210 – 1216.
[154] O. H. Kramer, M. Gottlicher, T. Heinzel, *Trends Endocrinol. Metab.* **2001**, *12*, 294 – 300.
[155] S. Y. Archer, S. Meng, A. Shei, R. A. Hodin, *Proc. Natl. Acad. Sci. USA* **1998**, *95*, 6791 – 6796.
[156] M. M. Lipinski, T. Jacks, *Oncogene* **1999**, *18*, 7873 – 7882.
[157] V. Sandor, A. Senderowicz, S. Mertins, D. Sackett, E. Sausville, M. V. Blagosklonny, S. E. Bates, *Br. J. Cancer* **2000**, *83*, 817 – 825.
[158] R. R. Rosato, Z. Wang, R. V. Gopalkrishnan, P. B. Fisher, S. Grant, *Int. J. Oncol.* **2001**, *19*, 181 – 191.
[159] L. Qiu, A. Burgess, D. P. Fairlie, H. Leonard, P. G. Parsons, B. G. Gabrielli, L. Qiu, *Mol. Cell. Biol.* **2000**, *20*, 2069 – 2083.
[160] A. A. Ruefli, M. J. Ausserlechner, D. Bernhard, V. R. Sutton, K. M. Tainton, R. Kofler, M. J. Smyth, R. W. Johnstone, *Proc. Natl. Acad. Sci. USA* **2001**, *98*, 10833 – 10838.
[161] S. H. Kwon, S. H. Ahn, Y. K. Kim, G.-U. Bae, J. W. Yoon, S. Hong, H. Y. Lee, Y.-W. Lee, H.-W. Lee, J.-W. Han, *J. Biol. Chem.* **2001**, *276*, 2073 – 2080.
[162] R. D. Glick, S. L. Swendeman, D. C. Coffey, R. A. Rifkind, P. A. Marks, V. M. Richon, M. P. La Quaglia, *Cancer Res.* **1999**, *59*, 4392 – 4399.
[163] J. A. Vrana, R. H. Decker, C. R. Johnson, Z. Wang, W. D. Jarvis, V. M. Richon, M. Ehinger, P. B. Fisher, S. Grant, *Oncogene* **1999**, *18*, 7016 – 7025.
[164] T. Suzuki, H. Yokozaki, H. Kuniyasu, K. Hayashi, K. Naka, S. Ono, T. Ishikawa, E. Tahara, W. Yasui, *Int. J. Cancer* **2000**, *88*, 992 – 997.
[165] X. X. Cao, I. Mohuiddin, F. Ece, D. J. McConkey, W. R. Smythe, *Am. J. Respir. Cell Mol. Biol.* **2001**, *25*, 562 – 568.
[166] T. Maeda, M. Towatari, H. Kosugi, H. Saito, *Blood* **2000**, *96*, 3847 – 3856.
[167] W. J. Magner, A. L. Kazim, C. Stewart, M. A. Romano, G. Catalano, C. Grande, N. Keiser, F. Santaniello, T. B. Tomasi, *J. Immunol.* **2000**, *165*, 7017 – 7024.
[168] N. Mishra, D. R. Brown, I. M. Olorenshaw, G. M. Kammer, *Proc. Natl. Acad. Sci. USA* **2001**, *98*, 2628 – 2633.
[169] E. Shestakova, M. T. Bandu, J. Doly, E. Bonnefoy, *J. Virol.* **2001**, *75*, 3444 – 3452.
[170] M. S. Kim, H. J. Kwon, Y. M. Lee, J. H. Baek, J.-E. Jang, S.-W. Lee, E.-J. Moon, H.-S. Kim, S.-K. Lee, H. Y. Chung, C. W. Kim, K.-W. Kim, *Nature Med.* **2001**, *7*, 437 – 443.
[171] R. A. Frye, *Biochem. Biophys. Res. Commun.* **1999**, *260*, 273 – 279.
[172] J. Landry, J. T. Slama, R. Sternglanz, *Biochem. Biophys. Res. Commun.* **2000**, *278*, 685 – 690.
[173] J. L. Avalos, I. Celic, S. Muhammad, M. S. Cosgrove, J. D. Boeke, C. Wolberger, *Mol. Cell* **2002**, *10*, 523 – 535.
[174] M. S. Finnin, J. R. Donigian, N. P. Pavletich, *Nat. Struct. Biol.* **2001**, *8*, 621 – 625.
[175] K. Zhao, X. Chai, A. Clements, R. Marmorstein, *Nat. Struct. Biol.* **2003**, *10*, 864 – 871.
[176] J. Min, J. Landry, R. Sternglanz, R. M. Xu, *Cell* **2001**, *105*, 269 – 279.
[177] K. Zhao, R. Harshaw, X. Chai, R. Marmorstein, *Proc. Natl. Acad. Sci. USA* **2004**, *101*, 8563 – 8568.
[178] D. Moazed, *Curr. Opin. Cell Biol.* **2001**, *13*, 232 – 238.
[179] M. R. Gartenberg, *Curr. Opin. Microbiol.* **2000**, *3*, 132 – 137.
[180] F. Palladino, T. Laroche, E. Gilson, A. Axelrod, L. Pillus, S. M. Gasser, *Cell* **1993**, *75*, 543 – 555.
[181] P. Moretti, K. Freeman, L. Coodly, D. Shore, *Genes Dev.* **1994**, *8*, 2257 – 2269.
[182] K. Luo, M. A. Vega-Palas, M. Grunstein, *Genes Dev.* **2002**, *16*, 1528 – 1539.
[183] G. J. Hoppe, J. C. Tanny, A. D. Rudner, S. A. Gerber, S. Danaie, S. P. Gygi, D. Moazed, *Mol. Cell. Biol.* **2002**, *22*, 4167 – 4180.
[184] L. N. Rusche, A. L. Kirchmaier, J. Rine, *Mol. Biol. Cell* **2002**, 2207 – 2222.
[185] A. Hecht, T. Laroche, S. Strahl-Bolsinger, S. M. Gasser, M. Grunstein, *Cell* **1995**, *80*, 583 – 592.
[186] P. S. Kayne, U. J. Kim, M. Han, J. R. Mullen, F. Yoshizaki, M. Grunstein, *Cell* **1988**, *55*, 27 – 39.
[187] J. S. Thompson, X. Ling, M. Grunstein, *Nature* **1994**, *369*, 245 – 247.
[188] H. Renauld, O. M. Aparicio, P. D. Zierath, B. L. Billington, S. K. Chhablani, D. E. Gottschling, *Genes Dev.* **1993**, *7*, 1133 – 1145.
[189] N. Suka, K. Luo, M. Grunstein, *Nat. Genet.* **2002**, *32*, 378 – 383.
[190] A. Kimura, T. Umehara, M. Horikoshi, *Nat. Genet.* **2002**, *32*, 370 – 377.
[191] L. Guarente, *Genes Dev.* **2000**, *14*, 1021 – 1026.
[192] M. Kaeberlein, M. McVey, L. Guarente, *Genes Dev.* **1999**, *13*, 2570 – 2580.
[193] C. M. Grozinger, E. D. Chao, H. E. Blackwell, D. Moazed, S. L. Schreiber, *J. Biol. Chem.* **2001**, *276*, 38837 – 38843.
[194] S. J. Lin, P. A. Defossez, L. Guarente, *Science* **2000**, *289*, 2126 – 2128.
[195] J. Posakony, M. Hirao, S. Stevens, J. A. Simon, A. Bedalov, *J. Med. Chem.* **2004**, *47*, 2635 – 2644.
[196] K. T. Howitz, K. J. Bitterman, H. Y. Cohen, D. W. Lamming, S. Lavu, J. G. Wood, R. E. Zipkin, P. Chung, A. Kisielewski, L.-L. Zhang, B. Scherer, D. A. Sinclair, *Nature* **2003**, *425*, 191 – 196.
[197] a) M. Jang, L. Cai, G. O. Udeani, K. V. Slowing, C. F. Thomas, C. W. W. Beecher, H. H. S. Fong, N. R. Farnsworth, A. D. Kinghorn, R. G. Mehta, R. C. Moon, J. M. Pezzuto, *Science* **1997**, *275*, 218 – 220; b) S. Quideau, *ChemBioChem* **2004**, *5*, 427 – 430.
[198] K. Murray, *Biochemistry* **1964**, *3*, 10 – 15.
[199] R. J. Sims, K. Nishioka, D. Reinberg, *Trends Genet.* **2003**, *19*, 629 – 639.
[200] T. Kouzarides, *Curr. Opin. Genet. Dev.* **2002**, *12*, 198 – 209.
[201] K. E. van Holde, *Chromatin*, 1st ed., Springer, New York, **1989**.
[202] Q. Zheng, E. J. Simel, P. E. Klein, M. T. Royer, R. L. Houtz, *Protein Expression Purif.* **1998**, *14*, 104 – 112.
[203] B. Polevoda, M. R. Martzen, B. Das, E. M. Phizicky F. Sherman, *J. Biol. Chem.* **2000**, *275*, 20508 – 20513.
[204] C. S. Baxter, P. Byvoet, *Biochem. Biophys. Res. Commun.* **1975**, *63*, 286 – 291.
[205] P. Byvoet, G. R. Shepherd, J. M. Hardin, B. J. Noland, *Arch. Biochem. Biophys.* **1972**, *148*, 558 – 567.
[206] B. M. Turner, *Nat. Cell Biol.* **2003**, *5*, 390 – 393.
[207] J. C. Rice, C. D. Allis, *Curr. Opin. Cell Biol.* **2001**, *13*, 263 – 273.
[208] R. Marmorstein, *Trends Biochem. Sci.* **2003**, *28*, 59 – 62.
[209] R. Schneider, A. J. Bannister, T. Kouzarides, *Trends Biochem. Sci.* **2002**, *27*, 396 – 402.
[210] X. Zhang, H. Tamaru, S. I. Khan, J. R. Horton, L. J. Keefe, E. U. Selker, X. Cheng, *Cell* **2002**, *111*, 117 – 127.
[211] J. R. Wilson, C. Jing, P. A. Walker, S. R. Martin, S. A. Howell, G. M. Blackburn, S. J. Gamblin, B. X. Wilson, *Cell* **2002**, *111*, 105 – 115.
[212] R. C. Trievel, B. M. Beach, L. Dirk, R. L. Houtz, J. H. Hurley, *Cell* **2002**, *111*, 91 – 103.
[213] M. Lachner, T. Jenuwein, *Curr. Opin. Cell Biol.* **2002**, *14*, 286 – 298.
[214] M. Lachner, D. O'Carroll, S. Rea, K. Mechtler, T. Jenuwein, *Nature* **2001**, *410*, 116 – 120.
[215] A. J. Bannister, P. Zegerman, J. F. Partridge, E. A. Miska, J. O. Thomas, R. C. Allshire, T. Kouzarides, *Nature* **2001**, *410*, 120 – 124.

[216] C. Caldas, M.-H. Kim, A. MacGregor, D. Cain, S. Aparicio, L. M. Wiedemann, *Oncogene* **1998**, *16*, 3233 – 3241.
[217] P. Ernst, J. Wang, S. J. Korsmeyer, *Curr. Opin. Hematol.* **2002**, *9*, 282 – 287.
[218] F. Bantignies, R. H. Goodman, S. M. Smolik, *Mol. Cell. Biol.* **2000**, *20*, 9317 – 9330.
[219] C. Abbondanza, N. Medici, V. Nigro, V. Rossi, L. Gallo, G. Piluso, A. Belsito, A. Roscigno, P. Bontempo, A. A. Puca, A. M. Molinari, B. Moncharmont, G. A. Puca, *Proc. Natl. Acad. Sci. USA* **2000**, *97*, 3130 – 3135.
[220] G. Steele-Perkins, W. Fang, X.-H. Yang, M. Van Gele, T. Carling, J. Gu, I. M. Buyse, J. A. Fletcher, J. Liu, R. Bronson, R. B. Chadwick, A. de la Chapelle, X.-K. Zhang, F. Speleman, S. Huang, *Genes Dev.* **2001**, *15*, 2250 – 2262.
[221] S. Fears, C. Mathieu, N. Zeleznik-Le, S. Huang, J. D. Rowley, G. Nucifora, *Proc. Natl. Acad. Sci. USA* **1996**,*93*, 1642 – 1647.
[222] G.-L. Jiang, S. Huang, *Cancer Res.* **2001**, *61*, 1796 – 1798.
[223] J. Min, X. Zhang, X. Cheng, S. Grewal, R.-M. Xu, *Nat. Struct. Biol.* **2002**, *9*, 828 – 832.
[224] B. Xiao, C. Jing, J. R. Wilson, P. A. Walker, N. Vasisht, G. Kelly, S. Howell, I. A. Taylor, G. M. Blackburn, S. J. Gamblin, *Nature* **2003**, *421*, 652 – 656.
[225] T. Kwon, J. H. Chang, E. Kwak, C. W. Lee, A. Joachimiak, Y. C. Kim, J. W. Lee, Y. Cho, *EMBO J.* **2003**, *22*, 292 – 303.
[226] S. A. Jacobs, J. M. Harp, S. Devarakonda, Y. Kim, F. Rastinejad, S. Khorasanizadeh, *Nat. Struct. Biol.* **2002**, *9*, 833 – 838.
[227] Q. Feng, H. Wang, H. H. Ng, H. Erdjument-Bromage, P. Tempst, K. Struhl, Y. Zhang, *Curr. Biol.* **2002**, *12*, 1052 – 1058.
[228] H. Santos-Rosa, R. Schneider, A. J. Bannister, J. Sherriff, B. E. Bernstein, N. C. T. Emre, S. L. Schreiber, J. Mellor, T. Kouzarides, *Nature* **2002**, *419*, 407 – 411.
[229] a) S. D. Briggs, M. Bryk, B. D. Strahl, W. L. Cheung, J. K. Davie, S. Y. Dent, F. Winston, C. D. Allis, *Genes Dev.* **2001**, *15*, 3286 – 3295; b) M. Bryk, S. D. Briggs, B. D. Strahl, M. J. Curcio, C. D. Allis, F. Winston, *Curr. Biol.* **2002**, *12*, 165 – 170; c) J. Sollier, W. Lin, C. Soustelle, K. Suhre, A. Nicolas, V. Geli, C. de La Roche Saint-André, *EMBO J.* **2004**, *23*, 1957 – 1967.
[230] T. Klymenko, J. Muller, *EMBO Rep.* **2004**, *5*, 373 – 377.
[231] a) C. Beisel, A. Imhof, J. Greene, E. Kremmer, F. Sauer, *Nature* **2002**, *419*, 857 – 862; b) K. N. Byrd, A. Shearn, *Proc. Natl. Acad. Sci. USA* **2003**, *100*, 11535 – 11540.
[232] a) H. Wang, R. Cao, L. Xia, H. Erdjument-Bromage, C. Borchers, P. Tempst, Y. Zhang, *Mol. Cell* **2001**, *8*, 1207 – 1217; b) K. Nishioka, S. Chuikov, K. Sarma, H. Erdjument-Bromage, C. D. Allis, P. Tempst, D. Reinberg, *Genes Dev.* **2002**, *16*, 479 – 489; c) A. Kouskouti, E. Scheer, A. Staub, L. Tora, I. Talianidis, *Mol. Cell* **2004**, *14*, 175 – 182.
[233] T. Nakamura, T. Mori, S. Tada, W. Krajewski, T. Rozovskaia, R. Wassell, G. Dubois, A. Mazo, C. M. Croce, E. Canaani, *Mol. Cell* **2002**, *10*, 1119 – 1128.
[234] T. A. Milne, S. D. Briggs, H. W. Brock, M. E. Martin, D. Gibbs, C. D. Allis, J. L. Hess, *Mol. Cell* **2002**, *10*, 1107 – 1117.
[235] Y. H. Goo, Y. C. Sohn, D. H. Kim, S. W. Kim, M. J. Kang, D. J. Jung, E. Kwak, N. A. Barlev, S. L. Berger, V. T. Chow, R. G. Roeder, D. O. Azorsa, P. S. Meltzer, P. G. Suh, E. J. Song, K. J. Lee, Y. C. Lee, J. W. Lee, *Mol. Cell. Biol.* **2003**, *23*, 140 – 149.
[236] R. J. Sims III, D. Reinberg, *Nat. Cell Biol.* **2004**, *6*, 685 – 687.
[237] a) G. Schotta, A. Ebert, V. Krauss, A. Fischer, J. Hoffmann, S. Rea, T. Jenuwein, R. Dorn, G. Reuter, *EMBO J.* **2002**, *21*, 1121 – 1131; b) B. Czermin, G. Schotta, B. B. Hulsmann, A. Brehm, P. B. Becker, G. Reuter, A. Imhof, *EMBO Rep.* **2001**, *2*, 915 – 919.
[238] A. H. Peters, D. O'Carroll, H. Scherthan, K. Mechtler, S. Sauer, C. Schofer, K. Weipoltshammer, M. Pagani, M. Lachner, A. Kohlmaier, S. Opravil, M. Doyle, M. Sibilia, T. Jenuwein, *Cell* **2001**, *107*, 323 – 337.
[239] D. O'Carroll, H. Scherthan, A. H. Peters, S. Opravil, A. R. Haynes, G. Laible, S. Rea, M. Schmid, A. Lebersorger, M. Jerratsch, L. Sattler, M. G. Mattei, P. Denny, S. D. Brown, D. Schweizer, T. Jenuwein, *Mol. Cell. Biol.* **2000**, *20*, 9423 – 9433.
[240] J. Nakayama, J. C. Rice, B. D. Strahl, C. D. Allis, S. I. Grewal, *Science* **2001**, *292*, 110 – 113.
[241] a) H. Tamaru, E. U. Selker, *Nature* **2001**, *414*, 277 – 283; b) E. U. Selker, M. Freitag, G. O. Kothe, B. S. Margolin, M. R. Rountree, C. D. Allis, H. Tamaru, *Proc. Natl. Acad. Sci. USA* **2002**, *99*, 16485 – 16490.
[242] a) M. Tachibana, K. Sugimoto, T. Fukushima, Y. Shinkai, *Biol. Chem.* **2001** *276*, 25309 – 25317; b) J. C. Rice, S. D. Briggs, B. Ueberheide, C. M. Barber, J. Shabanowitz, D. F. Hunt, Y. Shinkai, C. D. Allis, *Mol. Cell* **2003**, *12*, 1591 – 1598.
[243] H. Ogawa, K.-I. Ishiguro, S. Gaubatz, D. M. Livingston, Y. Nakatani, *Science* **2002**, *296*, 1132 – 1136.
[244] a) L. Yang, L. Xia, D. Y. Wu, H. Wang, H. A. Chansky, W. H. Schubach, D. D. Hickstein, Y. Zhang, *Oncogene* **2002**, *21*, 148 – 152; b) J. E. Dodge, Y. K. Kang, H. Beppu, H. Lei, E. Li, *Mol. Cell. Biol.* **2004**, *24*, 2478 – 2486.
[245] D. C. Schultz, K. Ayyanathan, D. Negorev, G. G. Maul, F. J. Rauscher, *Genes Dev.* **2002**, *16*, 919 – 932.
[246] a) J. Muller, C. M. Hart, N. J. Francis, M. L. Vargas, A. Sengupta, B. Wild, E. L. Miller, M. B. O'Connor, R. E. Kingston, J. A. Simon, *Cell* **2002**, *111*, 197 – 208; b) R. Cao, Y. Zhang, *Curr. Opin. Genet. Dev.* **2004**, *14*, 155 – 164.
[247] a) R. Cao, L. Wang, H. Wang, L. Xia, H. Erdjument-Bromage, P. Tempst, R. S. Jones, Y. Zhang, *Science* **2002**, *298*, 1039 – 1043; b) S. Erhardt, I. H. Su, R. Schneider, S. Barton, A. J. Bannister, L. Perez-Burgos, T. Jenuwein, T. Kouzarides, A. Tarakhovsky, M. A. Surani, *Development* **2003**, *130*, 4235 – 4248.
[248] a) B. D. Strahl, P. A. Grant, S. D. Briggs, Z. W. Sun, J. R. Bone, J. A. Caldwell, S. Mollah, R. G. Cook, J. Shabanowitz, D. F. Hunt, C. D. Allis, *Mol. Cell. Biol.* **2002**, *22*, 1298 – 1306; b) N. J. Krogan, M. Kim, A. Tong, A. Golshani, G. Cagney, V. Canadien, D. P. Richards, B. K. Beattie, A. Emili, C. Boone, A. Shilatifard, S. Buratowski, J. Greenblatt, *Mol. Cell. Biol.* **2003**, *23*, 4207 – 4218.
[249] a) G. V. Rayasam, O. Wendling, P. O. Angrand, M. Mark, K. Niederreither, L. Song, T. Lerouge, G. L. Hager, P. Chambon, R. Losson, *EMBO J.* **2003**, *22*, 3153 – 3163; b) A. L. Nielsen, P. Jorgensen, T. Lerouge, M. Cervino, P. Chambon, R. Losson, *Mol. Cell. Biol.* **2004**, *24*, 5184 – 5196.
[250] H. H. Ng, D. N. Ciccone, K. B. Morshead, M. A. Oettinger, K. Struhl, *Proc. Natl. Acad. Sci. USA* **2003**, *100*, 1820 – 1825.
[251] J. Min, Q. Feng, Z. Li, Y. Zhang, R. M. Xu, *Cell* **2003**, *112*, 711 – 723.
[252] F. van Leeuwen, P. R. Gafken, D. E. Gottschling, *Cell* **2002**, *109*, 745 – 756.
[253] a) K. Nishioka, J. C. Rice, K. Sarma, H. Erdjument-Bromage, J. Werner, Y. Wang, S. Chuikov, P. Valenzuela, P. Tempst, R. Steward, J. T. Lis, C. D. Allis, D. Reinberg, *Mol. Cell* **2002**, *9*, 1201 – 1213; b) J. C. Rice, K. Nishioka, K. Sarma, R. Steward, D. Reinberg, C. D. Allis, *Genes Dev.* **2002**, *16*, 2225 – 2230; c) E. Julien, W. Herr, *Mol. Cell* **2004**, *14*, 713 – 725.
[254] G. Schotta, M. Lachner, K. Sarma, A. Ebert, R. Sengupta, G. Reuter, D. Reinberg, T. Jenuwein, *Genes Dev.* **2004**, *18*, 1251 – 1262.
[255] B. Czermin, R. Melfi, D. McCabe, V. Seitz, A. Imhof, V. Pirrotta, *Cell* **2002**, *111*, 185 – 196.
[256] L. Aagaard, G. Laible, P. Selenko, M. Schmid, R. Dorn, G. Schotta, S. Kuhfittig, A. Wolf, A. Lebersorger, P. B. Singh, G. Reuter, T. Jenuwein, *EMBO J.* **1999**, *18*, 1923 – 1938.
[257] D. O. Jones, I. G. Cowell, P. B. Singh, *Bioessays* **2000**, *22*, 124 – 137.
[258] J. C. Eissenberg, S. C. R. Elgin, *Curr. Opin. Genet. Dev.* **2000**, *10*, 204 – 210.

[259] S. J. Nielsen, R. Schneider, U.-M. Bauer, A. J. Bannister, A. Morrison, D. O'Carroll, R. Firestein, M. Cleary, T. Jenuwein, R. E. Herrera, T. Kouzarides, *Nature* **2001**, *412*, 561 – 565.
[260] T. Cheutin, A. J. McNairn, T. Jenuwein, D. M. Gilbert, P. B. Singh, T. Misteli, *Science* **2003**, *299*, 721 – 725.
[261] G. Wang, A. Ma, C. Chow, D. Horsley, N. R. Brown, I. G. Cowell, P. B. Singh, *Mol. Cell. Biol.* **2000**, *20*, 6970 – 6983.
[262] E. Heard, C. Rougeulle, D. Arnaud, P. Avner, C. D. Allis, D. L. Spector, *Cell* **2001**, *107*, 727 – 738.
[263] B. A. Boggs, P. Cheung, E. Heard, D. L. Spector, A. C. Chinault, C. D. Allis, *Nat. Genet.* **2002**, *31*, 73 – 76.
[264] J. E. Mermoud, B. Popova, A. Peters, T. Jenuwein, N. Brockdorff, *Curr. Biol.* **2002**, *12*, 247 – 251.
[265] A. Peters, J. E. Mermoud, D. O'Carroll, M. Pagani, D. Schweizer, N. Brockdorff, T. Jenuwein, *Nat. Genet.* **2002**, *31*, 77 – 80.
[266] K. Plath, J. Fang, S. K. Mlynarczyk-Evans, R. Cao, K. A. Worringer, H. Wang, C. C. de la Cruz, A. P. Otte, B. Panning, Y. Zhang, *Science* **2003**, *300*, 131 – 135.
[267] J. Wang, J. Mager, Y. Chen, E. Schneider, J. C. Cross, A. Nagy, T. Magnuson, *Nat. Genet.* **2001**, *28*, 371 – 375.
[268] W. Mak, J. Baxter, J. Silva, A. E. Newall, A. P. Otte, N. Brockdorff, *Curr. Biol.* **2002**, *12*, 1016 – 1020.
[269] A. Kuzmichev, K. Nishioka, H. Erdjument-Bromage, P. Tempst, D. Reinberg, *Genes Dev.* **2002**, *16*, 2893 – 2905.
[270] J. Silva, W. Mak, I. Zvetkova, R. Appanah, T. B. Nesterova, Z. Webster, A. Peters, T. Jenuwein, A. P. Otte, N. Brockdorff, *Dev. Cell* **2003**, *4*, 481 – 495.
[271] J. Müller, C. M. Hart, N. J. Francis, M. L. Vargas, A. Sengupta, B. Wild, E. L. Miller, M. B. O'Connor, R. E. Kingston, J. A. Simon, *Cell* **2002**, *111*, 197 – 208.
[272] P. Avner, E. Heard, *Nat. Rev. Genet.* **2001**, *2*, 59 – 67.
[273] C. Maison, D. Bailly, A. Peters, J.-P. Quivy, D. Roche, A. Taddei, M. Lachner, T. Jenuwein, G. Almouzni, *Nat. Genet.* **2002**, *31*, 329 – 334.
[274] S. I. S. Grewal, D. Moazed, *Science* **2003**, *301*, 798 – 802.
[275] P. Cheung, K. G. Tanner, W. L. Cheung, P. Sassone-Corsi, J. M. Denu, C. D. Allis, *Mol. Cell* **2000**, *5*, 905 – 915.
[276] Z. Shao, F. Raible, R. Mollaaghababa, J. R. Guyon, C. Wu, W. Bender, R. E. Kingston, *Cell* **1999**, *98*, 37 – 46.
[277] F. Lyko, R. Paro, *Bioessays* **1999**, *21*, 824 – 832.
[278] V. Pirrotta, *Cell* **1998**, *93*, 333 – 336.
[279] L. Vandel, E. Nicolas, O. Vaute, R. Ferreira, S. Ait-Si-Ali, D. Trouche, *Mol. Cell. Biol.* **2000**, *20*, 6484 – 6494.
[280] A. Huwe, R. Mazitschek, A. Giannis, *Angew. Chem.* **2003**, *115*, 2170 – 2187; *Angew. Chem. Int. Ed.* **2003**, *42*, 2122 – 2138.
[281] T. Owa, H. Yoshino, K. Yoshimatsu, T. Nagasu, *Curr. Med. Chem.* **2001**, *8*, 1487 – 1503.
[282] E. Nicolas, C. Roumillac, D. Trouche, *Mol. Cell. Biol.* **2003**, *23*, 1614 – 1622.
[283] C. Seum, A. Spierer, D. Pauli, J. Szidonya, G. Reuter, P. Spierer, *Development* **1996**, *122*, 1949 – 1956.
[284] A. Brehm, T. Kouzarides, *Trends Genet.* **1999**, *15*, 142 – 145.
[285] D. Hanahan, R. A. Weinberg, *Cell* **2000**, *100*, 57 – 70.
[286] K. E. Brown, S. S. Guest, S. T. Smale, K. Hahm, M. Merkenschlager, A. G. Fisher, *Cell* **1997**, *91*, 845 – 854.
[287] J. Koipally, A. Renold, J. Kim, K. Georgopoulos, *EMBO J.* **1999**, *18*, 3090 – 3100.
[288] K. Ayyanathan, M. S. Lechner, P. Bell, G. G. Maul, D. C. Schultz, Y. Yamada, K. Tanaka, K. Torigoe, F. J. Rauscher, *Genes Dev.* **2003**, *17*, 1855 – 1869.
[289] M. Abrink, J. A. Ortiz, C. Mark, C. Sanchez, C. Looman, L. Hellman, P. Chambon, R. Losson, *Proc. Natl. Acad. Sci. USA* **2001**, *98*, 1422 – 1426.
[290] R. F. Ryan, D. C. Schultz, K. Ayyanathan, P. B. Singh, J. R. Friedman, W. J. Fredericks, F. J. Rauscher, *Mol. Cell. Biol.* **1999**, *19*, 4366 – 4378.
[291] J. Fang, Q. Feng, C. S. Ketel, H. Wang, R. Cao, L. Xia, H. Erdjument-Bromage, P. Tempst, J. A. Simon, Y. Zhang, *Curr. Biol.* **2002**, *12*, 1086 – 1099.
[292] B. M. Turner, A. J. Birley, J. Lavender, *Cell* **1992**, *69*, 375 – 384.
[293] C. A. Johnson, L. P. O'Neill, A. Mitchell, B. M. Turner, *Nucleic Acids Res.* **1998**, *26*, 994 – 1001.
[294] B. Sarg, E. Koutzamani, W. Helliger, I. Rundquist, H. H. Lindner, *J. Biol. Chem.* **2002**, *277*, 39195 – 39201.
[295] P. A. Jones, S. B. Baylin, *Nat. Rev. Genet.* **2002**, *3*, 415 – 428.
[296] J. A. Tsou, J. A. Hagen, C. L. Carpenter, I. A. Laird-Offringa, *Oncogene* **2002**, *21*, 5450 – 5461.
[297] K. P. Nephew, T. H. Huang, *Cancer Lett.* **2003**, *183*, 125 – 328.
[298] M. Szyf, *Ageing Res. Rev.* **2003**, *2*, 299 – 328.
[299] P. W. Laird, *Nat. Rev. Cancer* **2003**, *3*, 253 – 266.
[300] R. L. Momparler, *Oncogene* **2003**, *22*, 6479 – 6483.
[301] J. C. Rice, C. D. Allis, *Nature* **2001**, *414*, 258 – 261.
[302] K. E. Bachman, B. H. Park, I. Rhee, H. Rajagopalan, J. G. Herman, S. B. Baylin, K. W. Kinzler, B. Vogelstein, *Cancer Cell* **2003**, *3*, 89 – 95.
[303] J. P. Jackson, A. M. Lindroth, X. Cao, S. E. Jacobsen, *Nature* **2002**, *416*, 556 – 560.
[304] B. Lehnertz, Y. Ueda, A. Derijck, U. Braunschweig, L. Perez-Burgos, S. Kubicek, T. Chen, E. Li, T. Jenuwein, A. Peters, *Curr. Biol.* **2003**, *13*, 1192 – 1200.
[305] Z. Xin, M. Tachibana, M. Guggiari, E. Heard, Y. Shinkai, J. Wagstaff, *J. Biol. Chem.* **2003**, *278*, 14996 – 15000.
[306] T. Hashimshony, J. Zhang, I. Keshet, M. Bustin, H. Cedar, *Nat. Genet.* **2003**, *34*, 187 – 192.
[307] K. W. Makar, C. B. Wilson, *Nat. Immunol.* **2004**, *5*, 241 – 242.
[308] F. Fuks, P. J. Hurd, R. Deplus, T. Kouzarides, *Nucleic Acids Res.* **2003**, *31*, 2305 – 2312.
[309] A. M. Lindroth, X. Cao, J. P. Jackson, D. Zilberman, C. M. McCallum, S. Henikoff, S. E. Jacobsen, *Science* **2001**, *292*, 2077 – 2080.
[310] E. Li, *Nat. Rev. Genet.* **2002**, *3*, 662 – 673.
[311] H. Tamaru, X. Zhang, D. McMillen, P. B. Singh, J. Nakayama, S. I. Grewal, C. D. Allis, X. Cheng, E. U. Selker, *Nat. Genet.* **2003**, *34*, 75 – 79.
[312] T. H. Bestor, *Hum. Mol. Genet.* **2000**, *9*, 2395 – 2402.
[313] K. E. Bachman, M. R. Rountree, S. B. Baylin, *J. Biol. Chem.* **2001**, *276*, 32282 – 32287.
[314] M. Freitag, P. C. Hickey, T. K. Khlafallah, N. D. Read, E. U. Selker, *Mol. Cell* **2004**, *13*, 427 – 434.
[315] H. H. Ng, A. Bird, *Curr. Opin. Genet. Dev.* **1999**, *9*, 158 – 163.
[316] P. L. Jones, G. J. Veenstra, P. A. Wade, D. Vermaak, S. U. Kass, N. Landsberger, J. Strouboulis, A. P. Wolffe, *Nat. Genet.* **1998**, *18*, 187 – 191.
[317] A. El-Osta, A. P. Wolffe, *Gene Expression* **2000**, *9*, 63 – 75.
[318] X. Nan, H. H. Ng, C. A. Johnson, C. D. Laherty, B. M. Turner, R. N. Eisenman, A. Bird, *Nature* **1998**, *393*, 386 – 389.
[319] F. Fuks, P. J. Hurd, D. Wolf, X. Nan, A. P. Bird, T. Kouzarides, *J. Biol. Chem.* **2003**, *278*, 4035 – 4040.
[320] N. Fujita, S. Watanabe, T. Ichimura, S. Tsuruzoe, Y. Shinkai, M. Tachibana, T. Chiba, M. Nakao, *J. Biol. Chem.* **2003**, *278*, 24132 – 24138.
[321] H. F. Jorgensen, A. Bird, *Ment. Retard. Dev. Disabil. Res. Rev.* **2002**, *8*, 87 – 93.
[322] R. E. Amir, I. B. Van den Veyver, M. Wan, C. Q. Tran, U. Francke, H. Y. Zoghbi, *Nat. Genet.* **1999**, *22*, 185 – 188.
[323] R. Klose, A. Bird, *Science* **2003**, *302*, 793 – 795.
[324] W. G. Chen, Q. Chang, Y. Lin, A. Meissner, A. E. West, E. C. Griffith, R. Jaenisch, M. E. Greenberg, *Science* **2003**, *302*, 885 – 889.
[325] K. Martinowich, D. Hattori, H. Wu, S. Fouse, F. He, Y. Hu, G. Fan, Y. E. Sun, *Science* **2003**, *302*, 890 – 893.
[326] S. A. Sarraf, I. Stancheva, *Mol. Cell* **2004**, *15*, 595 – 605.

[327] R. Hamamoto, Y. Furukawa, M. Morita, Y. Iimura, F. P. Silva, M. Li, R. Yagyu, Y. Nakamura, *Nat. Cell Biol.* **2004**, *6*, 731 – 740.
[328] R. K. Mann, M. Grunstein, *EMBO J.* **1992**, *11*, 3297 – 3306.
[329] F. Sorm, A. Piskala, A. Cihak, J. Vesely, *Experientia* **1964**, *20*, 202 – 203.
[330] J. K. Christman, *Oncogene* **2002**, *21*, 5483 – 5495.
[331] P. G. Constantinides, P. A. Jones, W. Gevers, *Nature* **1977**, *267*, 364 – 366.
[332] P. A. Jones, S. M. Taylor, *Cell* **1980**, *20*, 85 – 93.
[333] S. Schmidt, C. D. Pein, H. J. Fritz, D. Cech, *Nucleic Acids Res.* **1992**, *20*, 2421 – 2426.
[334] L. Zhou, X. Cheng, B. A. Connolly, M. J. Dickman, P. J. Hurd, D. P. Hornby, *J. Mol. Biol.* **2002**, *321*, 591 – 599.
[335] J. C. Cheng, C. B. Matsen, F. A. Gonzales, W. Ye, S. Greer, V. E. Marquez, P. A. Jones, E. U. Selker, *J. Natl. Cancer Inst.* **2003**, *95*, 399 – 409.
[336] A. Villar-Garea, M. F. Fraga, J. Espada, M. Esteller, *Cancer Res.* **2003**, *63*, 4984 – 4989.
[337] M. Z. Fang, Y. Wang, N. Ai, Z. Hou, Y. Sun, H. Lu, W. Welsh, C. Yang, *Cancer Res.* **2003**, *63*, 7563 – 7570.
[338] I. C. Pina, J. T. Gautschi, G.-Y.-S. Wang, M. L. Sanders, F. J. Schmitz, D. France, S. Cornell-Kennon, L. C. Sambucetti, S. W. Remiszewski, L. B. Perez, K. W. Bair, P. Crews, *J. Org. Chem.* **2003**, *68*, 3866 – 3873.
[339] A. J. Boivin, L. F. Momparler, A. Hurtubise, R. L. Momparler, *Anti-Cancer Drugs* **2002**, *13*, 869 – 874.
[340] J. Gagnon, S. Shaker, M. Primeau, A. Hurtubise, R. L. Momparler, *Anti-Cancer Drugs* **2003**, *14*, 193 – 202.
[341] R. L. Momparler, J. Ayoub, *Lung Cancer* **2001**, *34*, S111-S115.
[342] M. Primeau, J. Gagnon, R. L. Momparler, *Int. J. Cancer* **2003**, *103*, 177 – 184.
[343] S. Shaker, M. Bernstein, L. F. Momparler, R. L. Momparler, *Leuk. Res.* **2003**, *27*, 437 – 444.
[344] S. A. Belinsky, D. M. Klinge, C. A. Stidley, J. P. Issa, J. G. Herman, T. H. March, S. B. Baylin, *Cancer Res.* **2003**, *63*, 7089 – 7093.
[345] P. Zegerman, B. Canas, D. Pappin, T. Kouzarides, *J. Biol. Chem.* **2002**, *277*, 11621 – 11624.
[346] H. H. Ng, F. Robert, R. A. Young, K. Struhl, *Mol. Cell* **2003**, *11*, 709 – 719.
[347] B. D. Strahl, R. Ohba, R. G. Cook, C. D. Allis, *Proc. Natl. Acad. Sci. USA* **1999**, *96*, 14967 – 14972.
[348] R. Schneider, A. J. Bannister, F. A. Myers, A. W. Thorne, C. Crane-Robinson, T. Kouzarides, *Nat. Cell Biol.* **2004**, *6*, 73 – 77.
[349] M. D. Litt, M. Simpson, M. Gaszner, C. D. Allis, G. Felsenfeld, *Science* **2001**, *293*, 2453 – 2455.
[350] K. Noma, C. D. Allis S. I. S. Grewal, *Science* **2001**, *293*, 1150 – 1155.
[351] M. Hampsey, D. Reinberg, *Cell* **2003**, *113*, 429 – 432.
[352] N. J. Krogan, J. Dover, A. Wood, J. Schneider, J. Heidt, M. A. Boateng, K. Dean, O. W. Ryan, A. Golshani, M. Johnston, J. F. Greenblatt, A. Shilatifard, *Mol. Cell* **2003**, *11*, 721 – 729.
[353] B. Li, L. Howe, S. Anderson, J. R. Yates III, J. L. Workman, *J. Biol. Chem.* **2003**, *278*, 8897 – 8903.
[354] T. Xiao, H. Hall, K. O. Kizer, Y. Shibata, M. C. Hall, C. H. Borchers, B. D. Strahl, *Genes Dev.* **2003**, *17*, 654 – 663.
[355] M. Gerber, A. Shilatifard, *J. Biol. Chem.* **2003**, *278*, 26303 – 26306.
[356] a) A. E. McBride, P. A. Silver, *Cell* **2001**, *106*, 5 – 8; b) C. Qui, J. Chang, Y. Zhu, A. V. Yeldandi, S. M. Rao, Y. J. Zhu, *J. Biol. Chem.* **2002**, *277*, 28624 – 28630.
[357] J. Tang, J. D. Gary, S. Clarke, H. R. Herschman, *J. Biol. Chem.* **1998**, *273*, 16935 – 16945.
[358] A. Frankel, S. Clarke, *J. Biol. Chem.* **2000**, *275*, 32974 – 32982.
[359] F. Bachand, P. A. Silver, *EMBO J.* **2004**, *23*, 2641 – 2650.
[360] A. Frankel, N. Yadav, J. Lee, T. L. Branscombe, S. Clarke, M. T. Bedford, *J. Biol. Chem.* **2002**, *277*, 3537 – 3543.
[361] T. B. Miranda, M. Miranda, A. Frankel, S. Clarke, *J. Biol. Chem.* **2004**, *279*, 22902 – 22907.
[362] L. Gros, C. Delaporte, S. Frey, J. Decesse, B. R. de Saint-Vincent, L. Cavarec, A. Dubart, A. V. Gudkov, A. Jacquemin-Sablon, *Cancer Res.* **2003**, *63*, 164 – 171.
[363] J. Tang, A. Frankel, R. J. Cook, S. Kim, W. K. Paik, K. R. Williams, S. Clarke, H. R. Herschman, *J. Biol. Chem.* **2000**, *275*, 7723 – 7730.
[364] B. D. Strahl, S. D. Briggs, C. J. Brame, J. A. Caldwell, S. S. Koh, H. Ma, R. G. Cook, J. Shabanowitz, D. F. Hunt, M. R. Stallcup, C. D. Allis, *Curr. Biol.* **2001**, *11*, 996 – 1000.
[365] W. An, J. Kim, R. G. Roeder, *Cell* **2004**, *117*, 735 – 748.
[366] D. Chen, H. Ma, H. Hong, S. S. Koh, S.-M. Huang, B. T. Schurter, D. W. Aswad, M. R. Stallcup, *Science* **1999**, *284*, 2174 – 2177.
[367] H. Ma, C. T. Baumann, H. Li, B. D. Strahl, R. Rice, M. A. Jelinek, D. W. Aswad, C. D. Allis, G. L. Hager, M. R. Stallcup, *Curr. Biol.* **2001**, *11*, 1981 – 1985.
[368] T. L. Branscombe, A. Frankel, J.-H. Lee, J. R. Cook, Z. Yang, S. Pestka, S. Clarke, *J. Biol. Chem.* **2001**, *276*, 32971 – 32976.
[369] J. Rho, S. Choi, Y. R. Seong, W.-K. Cho, S. H. Kim, D.-S. Im, *J. Biol. Chem.* **2001**, *276*, 11393 – 11401.
[370] L. Altschuler, J. O. Wook, D. Gurari, J. Chebath, M. Revel, *J. Interferon Cytokine Res.* **1999**, *19*, 189 – 195.
[371] J. Tang, P. N. Kao, H. R. Herschman, *J. Biol. Chem.* **2000**, *275*, 19866 – 19876.
[372] M. T. Bedford, A. Frankel, M. B. Yaffe, S. Clarke, P. Leder, S. Richard, *J. Biol. Chem.* **2000**, *275*, 16030 – 16036.
[373] K. A. Mowen, J. Tang, W. Zhu, B. T. Schurter, K. Shuai, H. R. Herschman, M. David, *Cell* **2001**, *104*, 731 – 741.
[374] W. J. Friesen, S. Massenet, S. Paushkin, A. Wyce, G. Dreyfuss, *Mol. Cell* **2001**, *7*, 1111 – 1117.
[375] F. M. Boisvert, J. Cote, M. C. Boulanger, P. Cleroux, F. Bachand, C. Autexier, S. Richard, *J. Cell Biol.* **2002**, *159*, 957 – 969.
[376] E. C. Shen, M. F. Henry, V. H. Weiss, S. R. Valentini, P. A. Silver, M. S. Lee, *Genes Dev.* **1998**, *12*, 679 – 691.
[377] C. Y. Yun, X. D. Fu, *J. Cell Biol.* **2000**, *150*, 707 – 718.
[378] J. Cote, F. M. Boisvert, M. C. Boulanger, M. T. Bedford, S. Richard, *Mol. Biol. Cell* **2003**, *14*, 274 – 287.
[379] W. J. Friesen, S. Paushkin, A. Wyce, S. Massenet, G. S. Pesiridis, G. Van Duyne, J. Rappsilber, M. Mann, G. Dreyfuss, *Mol. Cell. Biol.* **2001**, *21*, 8289 – 8300.
[380] U. M. Bauer, S. Daujat, S. J. Nielsen, K. Nightingale, T. Kouzarides, *EMBO Rep.* **2002**, *3*, 39 – 44.
[381] H. Wang, Z. Q. Huang, L. Xia, Q. Feng, H. Erdjument-Bromage, B. D. Strahl, S. D. Briggs, C. D. Allis, J. Wong, P. Tempst, Y. Zhang, *Science* **2001**, *293*, 853 – 857.
[382] D. Cheng, N. Yadav, R. W. King, M. S. Swanson, E. J. Weinstein, M. T. Bedford, *J. Biol. Chem.* **2004**, *279*, 23892 – 23899.
[383] A. G. Skillman, K. W. Maurer, D. C. Roe, M. J. Stauber, D. Eargle, T. J. Ewing, A. Muscate, E. Davioud-Charvet, M. V. Medaglia, R. J. Fisher, E. Arnold, H. Q. Gao, R. Buckheit, P. L. Boyer, S. H. Hughes, I. D. Kuntz, G. L. Kenyon, *Bioorg. Chem.* **2002**, *31*, 443 – 458.
[384] Y. Chinenov, *Trends Biochem. Sci.* **2002**, *27*, 115 – 117.
[385] W. K. Paik, S. Kim, *Arch. Biochem. Biophys.* **1974**, *165*, 369 – 378.
[386] P. Khanna, M. S. Jorns, *Biochemistry* **2001**, *40*, 1441 – 1450.
[387] M. A. Wagner, M. S. Jorns, *Biochemistry* **2000**, *39*, 8825 – 8829.
[388] A. J. Bannister, R. Schneider, T. Kouzarides, *Cell* **2002**, *109*, 801 – 806.
[389] T. H. Thatcher, J. MacGaffey, J. Bowen, S. Horowitz, D. L. Shapiro, M. A. Gorovsky, *Nucleic Acids Res.* **1994**, *22*, 180 – 186.
[390] V. J. Palombella, O. J. Rando, A. L. Goldberg, T. Maniatis, *Cell* **1994**, *78*, 773.

[391] E. R. Vossenaar, A. J. Zendman, W. J. van Venrooij, G. J. Pruijn, *Bioessays* **2003**, *25*, 1106 – 1118.
[392] Y. Zhang, *Nature* **2004**, *431*, 637 – 639.
[393] Y. Wang, J. Wysocka, J. Sayegh, Y.-H. Lee, J. R. Perlin, L. Leonelli, L. S. Sonbuchner, C. H. McDonnald, R. G. Cook, Y. Dou, R. G. Roeder, S. Clarke, M. R. Stallcup, C. D. Allis, S. A. Coonrod, *Science* **2004**, *306*, 279 – 283.
[394] G. L. Cuthbert, S. Daujat, A. W. Snowden, H. Erdjument-Bromage, T. Hagiwara, M. Yamada, R. Schneider, P. D. Gregory, P. Tempst, A. J. Bannister, T. Kouzarides, *Cell* **2004**, *118*, 545 – 553.
[395] R. M. Gutierrez, L. S. Hnilica, *Science* **1967**, *157*, 1324 – 1325.
[396] Y. Wei, C. A. Mizzen, R. G. Cook, M. A. Gorovsky, C. D. Allis, *Proc. Natl. Acad. Sci. USA* **1998**, *95*, 7480 – 7484.
[397] L. R. Gurley, J. A. D'Anna, S. S. Barham, L. L. Deaven, R. A. Tobey, *Eur. J. Biochem.* **1978**, *84*, 1 – 15.
[398] A. L. Clayton, L. C. Mahadevan, *FEBS Lett.* **2003**, *546*, 51 – 58.
[399] H. Goto, Y. Tomono, K. Ajiro, H. Kosako, M. Fujita, M. Sakurai, K. Okawa, A. Iwamatsu, T. Okigaki, T. Takahashi, M. Inagaki, *J. Biol. Chem.* **1999**, *274*, 25543 – 25549.
[400] U. Preuss, G. Landsberg, K. H. Scheidtmann, *Nucleic Acids Res.* **2003**, *31*, 878 – 885.
[401] A. Van Hooser, D. W. Goodrich, C. D. Allis, B. R. Brinkley, M. A. Mancini, *J. Cell Sci.* **1998**, *111*, 3497 – 3506.
[402] M. J. Hendzel, Y. Wei, M. A. Mancini, A. Van Hooser, T. Ranalli, B. R. Brinkley, D. P. Bazett-Jones, C. D. Allis, *Chromosoma* **1997**, *106*, 348 – 360.
[403] D. M. Sauve, H. J. Anderson, J. M. Ray, W. M. James, M. Roberge, *Cell Biol.* **1999**, *145*, 225 – 235.
[404] J. Y. Hsu, Z. W. Sun, X. Li, M. Reuben, K. Tatchell, D. K. Bishop, J. M. Grushcow, C. J. Brame, J. A. Caldwell, D. F. Hunt, R. Lin, M. M. Smith, C. D. Allis, *Cell* **2000**, *102*, 279 – 291.
[405] R. Giet, D. M. Glover, *J. Cell Biol.* **2001**, *152*, 669 – 682.
[406] C. Crosio, G. M. Fimia, R. Loury, M. Kimura, Y. Okano, H. Zhou, S. Sen, C. D. Allis, P. Sassone-Corsi, *Mol. Cell. Biol.* **2002**, *22*, 874 – 885.
[407] H. Goto, Y. Yasui, E. A. Nigg, M. Inagaki, *Genes Cells* **2002**, *7*, 11 – 17.
[408] Y. Terada, M. Tatsuka, F. Suzuki, Y. Yasuda, S. Fujita, M. Otsu, *EMBO J.* **1998**, *17*, 667 – 676.
[409] G. Gopalan, C. S. Chan, P. J. Donovan, *J. Cell Biol.* **1997**, *138*, 643 – 656.
[410] M. E. Murnion, R. R. Adams, D. M. Callister, C. D. Allis, W. C. Earnshaw, J. R. Swedlow, *J. Biol. Chem.* **2001**, *276*, 26656 – 26665.
[411] F. Hans, S. Dimitrov, *Oncogene* **2001**, *20*, 3021 – 3027.
[412] L. Francisco, W. Wang, C. S. Chan, *Mol. Cell. Biol.* **1994**, *14*, 4731 – 4740.
[413] A. E. de la Barre, V. Gerson, S. Gout, M. Creaven, C. D. Allis, S. Dimitrov, *EMBO J.* **2000**, *19*, 379 – 391.
[414] R. R. Adams, H. Maiato, W. C. Earnshaw, M. Carmena, *J. Cell Biol.* **2001**, *153*, 865 – 880.
[415] D. E. MacCallum, A. Losada, R. Kobayashi, T. Hirano, *Mol. Biol. Cell* **2002**, *13*, 25 – 39.
[416] E. K. Speliotes, A. Uren, D. Vaux, H. R. Horvitz, *Mol. Cell* **2000**, *6*, 211 – 223.
[417] C. Prigent, S. Dimitrov, *J. Cell Sci.* **2003**, *116*, 3677 – 3685.
[418] L. C. Mahadevan, A. C. Willis, M. J. Barratt, *Cell* **1991**, *65*, 775 – 783.
[419] P. Allegra, R. Sterner, D. F. Clayton, V. G. Allfrey, *J. Mol. Biol.* **1987**, *196*, 379 – 388.
[420] T. A. Chen, V. G. Allfrey, *Proc. Natl. Acad. Sci. USA* **1987**, *84*, 5252 – 5256.
[421] M. J. Barratt, C. A. Hazzalin, E. Cano, L. C. Mahadevan, *Proc. Natl. Acad. Sci. USA* **1994**, *91*, 4781 – 4785.
[422] S. Thomson, L. C. Mahadevan, A. L. Clayton, *Semin. Cell Dev. Biol.* **1999**, *10*, 205 – 214.
[423] C. A. Hazzalin, E. Cano, A. Cuenda, M. J. Barratt, P. Cohen, L. C. Mahadevan, *Curr. Biol.* **1996**, *6*, 1028 – 1031.
[424] C. A. Hazzalin, A. Cuenda, E. Cano, P. Cohen, L. C. Mahadevan, *Oncogene* **1997**, *15*, 2321 – 2331.
[425] J. M. Kyriakis, J. Avruch, *Physiol. Rev.* **2001**, *81*, 807 – 869.
[426] J. E. Darnell, *Science* **1997**, *277*, 1630 – 1635.
[427] P. A. Baeuerle, D. Baltimore, *Cell* **1996**, *87*, 13 – 20.
[428] S. Thomson, A. L. Clayton, C. A. Hazzalin, S. Rose, M. J. Barratt, L. C. Mahadevan, *EMBO J.* **1999**, *18*, 4779 – 4793.
[429] J. M. English, M. H. Cobb, *Trends Pharmacol. Sci.* **2002**, *23* ,40 – 45.
[430] P. Sassone-Corsi, C. A. Mizzen, P. Cheung, C. Crosio, L. Monaco, S. Jacquot, A. Hanauer, C. D. Allis, *Science* **1999**, *285*, 886 – 891.
[431] M. Frodin, S. Gammeltoft, *Mol. Cell. Endocrinol.* **1999**, *151*, 65 – 77.
[432] H. G. Yntema, B. van den Helm, J. Kissing, G. van Duijnhoven, F. Poppelaars, J. Chelly, C. Moraine, J. P. Fryns, B. C. Hamel, H. Heilbronner, H. J. Pander, H. G. Brunner, H. H. Ropers, F. P. Cremers, H. van Bokhoven, *Genomics* **1999**, *62*, 332 – 343.
[433] I. S. Strelkov, J. R. Davie, *Cancer Res.* **2002**, *62*, 75 – 78.
[434] A. Soloaga, S. Thomson, G. R. Wiggin, N. Rampersaud, M. H. Dyson, C. A. Hazzalin, L. C. Mahadevan, J. S. Arthur, *EMBO J.* **2003**, *22*, 2788 – 2797.
[435] G. R. Wiggin, A. Soloaga, J. M. Foster, V. Murray-Tait, P. Cohen, J. S. Arthur, *Mol. Cell. Biol.* **2002**, *22*, 2871 – 2881.
[436] M. Deak, A. D. Clifton, L. M. Lucocq, D. R. Alessi, *EMBO J.* **1998**, *17*, 4426 – 4441.
[437] J. Ausio, D. B. Levin, G. V. De Amorim, S. Bakker, P. M. Macleod, *Clin. Genet.* **2003**, *64*, 83 – 95.
[438] A. Hanauer, I. D. Young, *J. Med. Genet.* **2002**, *39*, 705 – 713.
[439] C. Crosio, N. Cermakian, C. D. Allis, P. Sassone-Corsi, *Nat. Neurosci.* **2000**, *3*, 1241 – 1247.
[440] L. M. Salvador, Y. Park, J. Cottom, E. T. Maizels, J. C. R. Jones, R. V. Schillace, D. W. Carr, P. Cheung, C. D. Allis, J. L. Jameson, M. Hunzicker-Dunn, *J. Biol. Chem.* **2001**, *276*, 40146 – 40155.
[441] Y. Yamamoto, U. N. Verma, S. Prajapati, Y. T. Kwak, R. B. Gaynor, *Nature* **2003**, *423*, 655 – 659.
[442] V. Anest, J. L. Hanson, P. C. Cogswell, K. A. Steinbrecher, B. D. Strahl, A. S. Baldwin, *Nature* **2003**, *423*, 659 – 663.
[443] S. Zhong, C. Jansen, Q. B. She, H. Goto, M. Inagaki, A. M. Bode, W. Y. Ma, Z. Dong, *J. Biol. Chem.* **2001**, *276*, 33213 – 33219.
[444] S. Zhong, Y. Zhang, C. Jansen, H. Goto, M. Inagaki, Z. Dong, *J. Biol. Chem.* **2001**, *276*, 12932 – 12937.
[445] W. Fischle, Y. Wang, C. D. Allis, *Nature* **2003**, *425*, 475 – 479.
[446] A. L. Clayton, S. Rose, M. J. Barratt, L. C. Mahadevan, *EMBO J.* **2000**, *19*, 3714 – 3726.
[447] W. S. Lo, R. C. Trievel, J. R. Rojas, L. Duggan, J. Y. Hsu, C. D. Allis, R. Marmorstein, S. L. Berger, *Mol. Cell* **2000**, *5*, 917 – 926.
[448] N. Suka, Y. Suka, A. A. Carmen, J. Wu, M. Grunstein, *Mol. Cell* **2001**, *8*, 473 – 479.
[449] M. A. Shogren-Knaak, C. J. Fry, C. L. Peterson, *J. Biol. Chem.* **2003**, *278*, 15744 – 15748.
[450] S. J. Nowak, V. G. Corces, *Trends Genet.* **2004**, *20*, 214 – 220.
[451] S. Thomson, A. L. Clayton, L. C. Mahadevan, *Mol. Cell* **2001**, *8*, 1231 – 1241.
[452] B. Lefebvre, K. Ozato, P. Lefebvre, *EMBO Rep.* **2002**, *3*, 335 – 340.
[453] S. J. Nowak, V. G. Corces, *Genes Dev.* **2000**, *14*, 3003 – 3013.
[454] M. E. Mirault, M. Goldschmidt-Clermont, L. Moran, A. P. Arrigo, A. Tissieres, *Cold Spring Harb. Symp. Quant. Biol.* **1978**, *42*, 819 – 827.
[455] A. Spradling, S. Penman, M. L. Pardue, *Cell* **1975**, *4*, 395 – 404.
[456] Y. Jin, Y. Wang, D. L. Walker, H. Dong, C. Conley, J. Johansen, K. M. Johansen, *Mol. Cell* **1999**, *4*, 129 – 135.

[457] Y. Jin, Y. Wang, J. Johansen, K. M. Johansen, *J. Cell Biol.* **2000**, *149*, 1005 – 1010.
[458] Y. Wang, W. Zhang, Y. Jin, J. Johansen, K. M. Johansen, *Cell* **2001**, *105*, 433 – 443.
[459] M. Labrador, V. G. Corces, *Genes Dev.* **2003**, *17*, 43 – 48.
[460] R. Festenstein, S. N. Pagakis, K. Hiragami, D. Lyon, A. Verreault, B. Sekkali, D. Kioussis, *Science* **2003**, *299*,719 – 721.
[461] S. J. Nowak, C. Y. Pai, V. G. Corces, *Mol. Cell. Biol.* **2003**, *23*, 6129 – 6138.
[462] C. M. Pickart, *Cell* **2004**, *116*, 181 – 190.
[463] I. L. Goldknopf, H. Busch, *Proc. Natl. Acad. Sci. USA* **1977**, *74*, 864 – 868.
[464] J. Adams, *Nat. Rev. Cancer* **2004**, *4*, 349 – 360.
[465] A. Hershko, *J. Biol. Chem.* **1988**, *263*, 15237 – 15240.
[466] A. F. Kisselev, A. L. Goldberg, *Chem. Biol.* **2001**, *8*, 739 – 758.
[467] L. Sun, Z. J. Chen, *Curr. Opin. Cell Biol.* **2004**, *16*, 119 – 126.
[468] L. A. Passmore, D. Barford, *Biochem. J.* **2004**, *379*, 513 – 525.
[469] K. Robzyk, J. Recht, M. A. Osley, *Science* **2000**, *287*, 501 – 504.
[470] A. W. Thorne, P. Sautiere, G. Briand, C. Crane-Robinson, *EMBO J.* **1987**, *6*, 1005 – 1010.
[471] M. A. Osley, *Biochim. Biophys. Acta* **2004**, *1677*, 74 – 78.
[472] C. Hoege, B. Pfander, G. L. Moldovan, G. Pyrowolakis, S. Jentsch, *Nature* **2002**, *419*, 135 – 141.
[473] B. Bartel, I. Wunning, A. Varshavsky, *EMBO J.* **1990**, *9*, 3179 – 3189.
[474] R. E. Johnson, S. T. Henderson, T. D. Petes, S. Prakash, M. Bankmann, L. Prakash, *Mol. Cell. Biol.* **1992**, *12*, 3807 – 3818.
[475] V. Bailly, S. Lauder, S. Prakash, L. Prakash, *J. Biol. Chem.* **1997**, *272*, 23360 – 23365.
[476] C. A. Joazeiro, A. M. Weissman, *Cell* **2000**, *102*, 549 – 552.
[477] H. H. Ng, S. Dole, K. Struhl, *J. Biol. Chem.* **2003**, *278*, 33625 – 33628.
[478] A. Wood, J. Schneider, J. Dover, M. Johnston, A. Shilatifard, *J. Biol. Chem.* **2003**, *278*, 34739 – 34742.
[479] E. M. Bradbury, *BioEssays* **1992**, *14*, 9 – 16.
[480] R. L. Seale, *Nucleic Acids Res.* **1981**, *9*, 3151 – 3158.
[481] R. S. Wu, K. W. Kohn, W. M. Bonner, *J. Biol. Chem.* **1981**, *256*, 5916 – 5920.
[482] I. L. Goldknopf, S. Sudhakar, F. Rosenbaum, H. Busch, *Biochem. Biophys. Res. Commun.* **1980**, *95*, 1253 – 1260.
[483] A. Y. Amerik, S. J. Li, M. Hochstrasser, *Biol. Chem.* **2000**, *381*, 981 – 992.
[484] K. W. Henry, A. Wyce, W. S. Lo, L. J. Duggan, N. C. Emre, C. F. Kao, L. Pillus, A. Shilatifard, M. A. Osley, S. L. Berger, *Genes Dev.* **2003**, *17*, 2648 – 2663.
[485] S. D. Briggs, T. Xiao, Z. W. Sun, J. A. Caldwell, J. Shabanowitz, D. F. Hunt, C. D. Allis, B. D. Strahl, *Nature* **2002**, *418*, 498.
[486] J. Dover, J. Schneider, M. A. Tawiah-Boateng, A. Wood, K. Dean, M. Johnston, A. Shilatifard, *J. Biol. Chem.* **2002**, *277*, 28368 – 28371.
[487] Z. W. Sun, C. D. Allis, *Nature* **2002**, *418*, 104 – 108.
[488] H. H. Ng, R.-M. Xu, Y. Zhang, K. Struhl, *J. Biol. Chem.* **2002**, *277*, 34655 – 34657.
[489] A. Buchberger, *Trends Cell Biol.* **2002**, *12*, 216 – 221.
[490] G. Prag, S. Misra, E. A. Jones, R. Ghirlando, B. A. Davies, B. F. Horazdovsky, J. H. Hurley, *Cell* **2003**, *113*, 609 – 620.
[491] R. S. Kang, C. M. Daniels, S. A. Francis, S. C. Shih, W. J. Salerno, L. Hicke, I. Radhakrishnan, *Cell* **2003**, *113*, 621 – 630.
[492] F. Melchior, *Annu. Rev. Cell Dev. Biol.* **2000**, *16*, 591 – 626.
[493] J.-S. Seeler, A. Dejean, *Nat. Rev. Mol. Cell Biol.* **2003**, *4*, 690 – 699.
[494] R. T. Hay, *Trends Biochem. Sci.* **2001**, *26*, 332 – 333.
[495] S. Müller, A. Ledl, D. Schmidt, *Oncogene* **2004**, *23*, 1998 – 2008.
[496] Y. Shiio, R. N. Eisenman, *Proc. Natl. Acad. Sci. USA* **2003**, *100*, 13225 – 13230.
[497] D. Nathan, D. E. Sterner, S. L. Berger, *Proc. Natl. Acad. Sci. USA* **2003**, *100*, 13118 – 13120.
[498] S.-H. Yang, A. D. Sharrocks, *Mol. Cell* **2004**, *13*, 611 – 617.
[499] J.-C. Amé, E. L. Jacobson, M. K. Jacobson in *From DNA Damage and Stress Signalling to Cell Death—Poly ADP-Ribosylation Reactions*, (Eds.: G. de Murcia, S. Shall), Oxford University Press, New York, **2000**, pp. 1 – 34.
[500] P. O. Hassa, M. O. Hottinger, *Cell. Mol. Life Sci.* **2002**, *59*, 1534 – 1553.
[501] D. D'Amours, S. Desnoyers, I. D'Silva, G. G. Poirier, *Biochem. J.* **1999**, *342*, 249 – 268.
[502] V. Rolli, A. Ruf, A. Augustin, G. E. Schulz, J. Ménissier-de Murcia, G. Murcia in *From DNA Damage and Stress Signalling to Cell Death—Poly ADP-Ribosylation Reactions* (Eds.: G. de Murcia, S. Shall), Oxford University Press, New York, **2000**, pp. 35 – 79.
[503] W. L. Kraus, J. T. Lis, *Cell* **2003**, *113*, 677 – 683.
[504] J. Griesenbeck, M. Ziegler, N. Tomilin, M. Schweiger, S. L. Oei, *FEBS Lett.* **1999**, *443*, 20 – 24.
[505] A. Huletsky, G. de Murcia, S. Muller, M. Hengartner, L. Menrad, D. Lamarre, G. G. Poirier, *J. Biol. Chem.* **1989**, *264*, 8878 – 8886.
[506] A. Tulin, A. Spradling, *Science* **2003**, *299*, 560 – 562.
[507] A. Tulin, D. Stewart, A. C. Spradling, *Genes Dev.* **2002**, *16*, 2108 – 2119.
[508] L. Davidovich, M. Vodenicharov, E. B. Affar, G. G. Poirier, *Exp. Cell Res.* **2001**, *268*, 7 – 13.
[509] A. Vaquero, A. Loyola, D. Reinberg, *Sci. Aging Knowledge Environ.* **2003**, *14*, RE4.
[510] W. L. Kraus, J. Wong, *Eur. J. Biochem.* **2002**, *269*, 2275 – 2283.
[511] N. Malik, M. Smulson, *Biochemistry* **1984**, *23*, 3721 – 3725.
[512] A. Giannis, T. Kolter, *Angew. Chem.* **1993**, *105*, 1303 – 1326; *Angew. Chem. Int. Ed. Engl.* **1993**, *32*, 1244 – 1267.
[513] a) S. Kubicek, T. Jenuwein, *Cell* **2004**, *119*, 903 – 906; b) Y. Shi, F. Lan, C. Matson, P. Mulligan, J. R. Whetstine, P. A. Cole, R. A. Casero, Y. Shi, *Cell* **2004**, *119*, 941 – 953.
[514] F. Forneris, C. Binda, M. A. Vanori, A. Mattevi, E. Battaglioli, *FEBS Lett.* **2005**, *579*, 2203 – 2207.
[515] J.-H. Lee, J. R. Cook, Z. H. Yang, O. Mirochnitchenko, S. L. Gunderson, A. M. Felix, N. Herth, R. Hoffmann, S. Pestka, *J. Biol. Chem.* **2005**, *280*, 3656 – 3664.
[516] R. E. Collins, M. Tachibana, H. Tamaru, K. M. Smith, D. Jia, X. Zhang, E. U. Selker, Y. Shinkai, X. Cheng, *J. Biol. Chem.* **2005**, *280*, 5563 – 5570.
[517] J. Dai, S. Sultan, S. S. Taylor, J. M. Higgins, *Genes Dev.* **2005**, *19*, 472 – 488.
[518] Z. He, Y. Y. Cho, W. Y. Ma, H. S. Choi, A. M. Bode, Z. Dong, *J. Biol. Chem.* **2005**, *280*, 2446 – 2456.
[519] H. S. Choi, B. Y. Choi, Y. Y. Cho, F. Zhu, A. M. Bode, Z. Dong, *J. Biol. Chem.* **2005**, *280*, 13545 – 13553.
[520] K. Balasubramanyam, R. A. Varier, M. Altaf, V. Swaminathan, N. B. Siddappa, U. Ranga, T. K. Kundu, *J. Biol. Chem.* **2004**, *279*, 51163 – 51173.
[521] K. Ingvarsdottir, N. J. Krogan, N. C. Emre, A. Wyce, N. J. Thompson, A. Emili, T. R. Hughes, J. F. Greenblatt, S. L. Berger, *Mol. Cell Biol.* **2005**, *25*, 1162 – 1172.
[522] N. C. Emre, K. Ingvarsdottir, A. Wyce, A. Wood, N. J. Krogan, K. W. Henry, K. Li, R. Marmorstein, J. F. Greenblatt, A. Shilatifard, S. L. Berger, *Mol. Cell.* **2005**, *17*, 585 – 594.
[523] M. Y. Kim, S. Mauro, N. Gevry, J. T. Lis, W. L. Kraus, *Cell* **2004**, *119*, 735 – 736.

Communications

A basic crystal shape is determined by habit formation and branching growth. Control of these processes leads to an enormous degree of synthetic freedom in generating crystal shapes. The vast array of architectures obtained for cuprous oxide during electrochemical growth is shown. For more details see the Communication by K.-S. Choi and M. J. Siegfried on the following pages.

  DOI: 10.1002/anie.200463018

Crystal Engineering

Directing the Architecture of Cuprous Oxide Crystals during Electrochemical Growth**

*Matthew J. Siegfried and Kyoung-Shin Choi**

A basic crystal shape is determined by two growth processes: habit formation and branching growth.[1–7] Crystal habit is determined by the relative order of surface energies of different crystallographic planes of a crystal.[1,2] The fastest crystal growth will occur in the direction perpendicular to the face with the highest surface energy. This results in elimination or reduction of higher energy surfaces, while lower energy surfaces increase in area. Therefore, a habit can be modified when the relative order of surface energies can be altered or when crystal growth along certain directions is selectively hindered.[3] Alternatively, branching growth is created by a diffusion effect.[4,5] When a crystal grows, ions or molecules near the surface are consumed by the growing crystal and a concentric diffusion field forms around the crystal.[6,7] This makes the apexes of a polyhedral crystal, which protrude further into the region of higher concentration, grow faster than the central parts of facets, thus forming branches. The branching growth, however, generates rough and unstable surfaces between branches that have many surface dangling bonds. This can rapidly increase the growth kinetic coefficient in these regions and compensate for the diffusion effect to result in faceting growth that develops flat and smooth faces.[4,5] Therefore, preference for branching and faceting can be altered by growth conditions that amplify or minimize the diffusion effect.

The ability to tune the shapes of materials directly relates to the ability to tune their properties and stabilities because the crystal shape dictates the interfacial atomic arrangement of the material. To date, many efforts have been made to stabilize various habits or branching growth of inorganic materials.[3,8–17] However, most earlier efforts focused on stabilizing specific forms rather than providing a strategy to systematically and freely direct the crystal morphology. Recently, we reported a methodical habit modification of electrochemically deposited Cu_2O crystals by using the pH-dependence of preferential adsorption of sodium dodecyl sulfate (SDS) on the {111} faces of Cu_2O crystals.[18] We have been specifically interested in understanding and controlling the shape-guiding processes in electrodeposition because electrodeposition allows the growth of various semiconducting and metallic crystals directly from a conducting substrate with good electrical contact, which can be easily integrated into devices. Here, we elucidate synthetic parameters that can systematically control branching or faceting growth in electrodeposition. By coupling this understanding with an ability to independently control habit, we demonstrate a new level of programmability and freedom in directing the morphology of Cu_2O crystals.

For supersaturation-based crystallization, temperature and concentration are the main factors that affect the basic shape-guiding processes. For example, in nature snow crystals can grow into thousands of different forms with varying crystal habits and degrees of branching by subtle changes in temperature and humidity.[19–25] Therefore, we first investigated the effects of the temperature of deposition and the concentration of Cu^{2+} ions on the branching or faceting growth of Cu_2O crystals on an ITO (indium tin oxide) working electrode. Figure 1 shows scanning electron microscopy (SEM) images of crystals of Cu_2O grown from the medium that stabilizes an octahedral habit (see Experimental Section for detailed conditions)[18] at varying deposition temperatures (40, 50, 60, and 70 °C) by using both potentiostatic deposition (constant potential) and galvanostatic deposition (constant current density). When potentiostatic deposition is used ($E = 0.09$ V), branching is more pronounced as the temperature increases. However, under galvanostatic deposition ($I = 0.1$ mA cm^{-2}) the degree of branching diminishes as the temperature increases. Similar conflicting trends were observed for crystals of Cu_2O deposited from a range of concentrations of Cu^{2+} ions (0.005, 0.01, 0.02, and 0.04 M; images not shown). When potentiostatic deposition was used ($E = 0.09$ V), branching was favored in a more dilute solution (≤ 0.02 M), while under galvanostatic deposition ($I = 0.1$ mA cm^{-2}), more-pronounced branching was observed as the concentration increased (≥ 0.01 M). These opposite tendencies for potentio- and galvanostatic depositions indicate

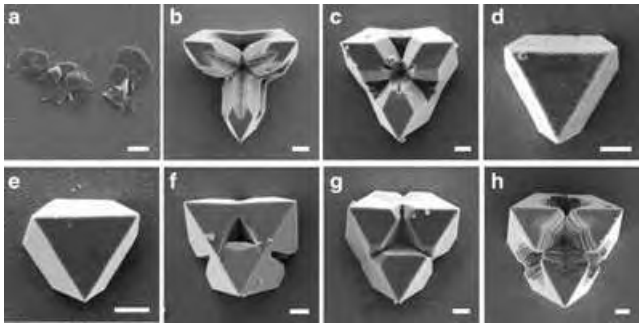

Figure 1. SEM images of octahedral Cu_2O crystals grown at varying deposition temperatures showing opposing trends of branching or faceting for potentio- and galvanostatic depositions. Potentiostatic depositions ($E = 0.09$ V) at a) 40 °C (no crystalline Cu_2O can be deposited under this condition), b) 50 °C, c) 60 °C, and d) 70 °C. Galvanostatic depositions ($I = 0.1$ mA cm^{-2}) at e) 40 °C, f) 50 °C, g) 60 °C, and h) 70 °C (scale bar = 1 μm). See Supporting Information for low-magnification SEM images that show the uniformity of crystal morphology over the electrodes.

[*] M. J. Siegfried, Prof. Dr. K.-S. Choi
Department of Chemistry
Purdue University
West Lafayette, IN 47907 (USA)
Fax: (+1) 765-494-0239
E-mail: kchoi1@purdue.edu

[**] This work was supported by the Purdue Research Foundation and made use of the Life Science Microscopy Facility at Purdue University.

Supporting information for this article is available on the WWW under http://www.angewandte.org or from the author.

that temperature and concentration are not the primary factors that exert homogeneous effects on branching in electrocrystallization. As the deposition temperature and the concentration of Cu^{2+} ions affect the deposition potential and current in a systematic manner, the changes in deposition potential and current caused by the variation of the temperature and concentration of Cu^{2+} ions needed to be examined in conjunction with the degree of branching.

Figure 2 shows the deposition potential and current used to deposit each crystal shown in Figure 1. In this plot, the

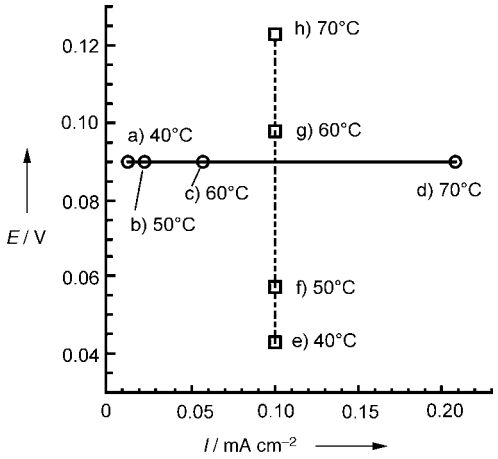

Figure 2. Plot of the deposition potential versus the current used to deposit each crystal shown in Figure 1. The effects of temperature on the deposition potential for galvanostatic deposition (-----) and the current for potentiostatic deposition (——) are clearly shown.

effect of temperature on the potentials for galvanostatic deposition and the currents for potentiostatic deposition is clearly illustrated. Generally speaking, an increase in the temperature improves the reaction kinetics and results in an increase in reaction rates, which in electrodeposition translates into an increase in deposition current. Therefore, when potentiostatic deposition is used, an increase in temperature causes an increase in deposition current (solid line in Figure 2). Accordingly, when galvanostatic deposition is used, an increase in temperature causes a decrease in the deposition potential; with a faster deposition rate, less potential (equivalent to a more positive potential for cathodic depositions) is required to keep the same level of deposition current (dashed line in Figure 2).

This understanding revealed that it was not the temperature but the deposition potential and current varied by the temperature that were directly responsible for the systematic change in the degree of branching. The most-significant branching is produced in regions of low potentials or currents (Figure 2b,h), below which no crystalline cuprous oxide can be deposited. As the overpotential or current increases (to increase the overpotential for cathodic depositions is equivalent to shifting the deposition potential toward more-negative values), the degree of branching decreases by a more-pronounced filling-in process to seal the gaps between the branches (Figure 2c,f,g). When the potential and current values reach $I = 0.2\ mA\,cm^{-2}$ and $V = 0.05\ V$ (Figure 2d,e), crystals grow as perfectly faceted polyhedra with no sign of branching. An identical trend was observed for the experiments with varying concentrations of Cu^{2+}; an increase in Cu^{2+} concentration causes an increase in deposition current for the potentiostatic deposition while causing a decrease in the deposition potential for the galvanostatic deposition. This observation again confirms that it is the changes in potential and current caused by the variation of concentration of Cu^{2+} that affect the degree of branching in a consistent manner.

On the basis of this realization, we attempted to control the preferences for branching or faceting solely by manipulating the deposition potential and current. Figure 3 shows

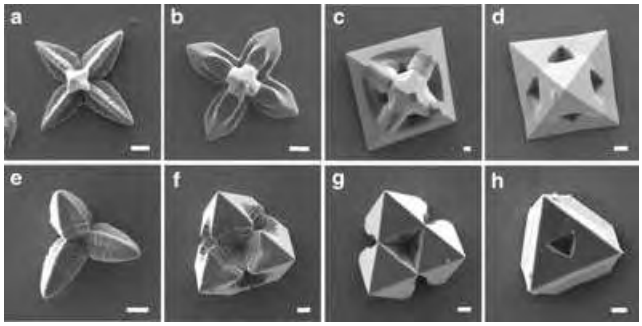

Figure 3. SEM images of deposited octahedral Cu_2O crystals that display systematically varying degrees of branching with (100) planes parallel to the substrate (a–d) and with (111) planes parallel to the substrate (e–h; scale bar = 1 μm). These crystals were obtained at a constant temperature (60 °C) and concentration of Cu^{2+} (0.02 M) and by applying deposition conditions of $0.10\ mA\,cm^{-2} \le I \le 0.12\ mA\,cm^{-2}$ and $0.08\ V \le E \le 0.12\ V$.

branched crystals obtained under constant temperature (60 °C) and concentration of Cu^{2+} (0.02 M) by applying deposition conditions that were identified from Figure 2 to induce branching growth ($0.10\ mA\,cm^{-2} \le I \le 0.12\ mA\,cm^{-2}$ and $0.08\ V \le E \le 0.12\ V$). Various stages of branching and filling-in processes were captured by finely tuning the conditions, modes (i.e. galvano- or potentiostatic), and times of deposition. All the deposition conditions we have investigated and their effect on branching and faceting are summarized in Figure 4, which composes a well-defined potential–current (I vs. V) diagram for faceting and branching growth. The degree of branching in the branching region diminishes gradually as the potential and current move toward the border of the faceting region.

This tendency for branching and faceting is quite the opposite of what one would normally expect for electrodeposition in which only the concentration of the species to be reduced creates a diffusion-limited condition. For example, dendrite or branching growth of metals will most likely occur at a high potential or deposition rate owing to a rapid depletion of M^{n+} ions near the growing crystals ($M^{n+} + n\,e^- \leftrightarrow M^0$). However, deposition of Cu_2O is quite unique in that it involves two distinctive processes for crystallization: reduction of Cu^{2+} ions ($Cu^{2+} + e^- \leftrightarrow Cu^+$, $E^0 = 0.153\ V$) and precipitation of Cu^+ ions ($2\,Cu^+ + H_2O \leftrightarrow Cu_2O + 2\,H^+$, $\log(Cu^+) = -0.84 - pH$; (Cu^+) = activity of Cu^+ ion).[26] Therefore, changes in concentrations of Cu^+

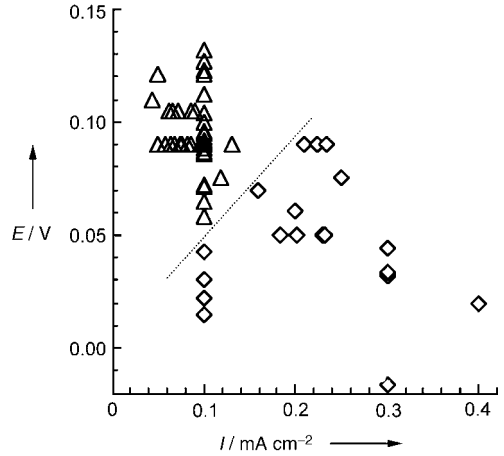

Figure 4. A deposition potential–current diagram summarizing the effect of electrochemical conditions on branching (△) and faceting (◇) growth. The electrochemical conditions plotted here were obtained either by directly adjusting the potential or current or by changing them indirectly through variation of temperature and concentrations of Cu^{2+} ion. The medium that stabilizes an octahedral habit was exclusively used to collect the data shown here.

and H^+ as well as Cu^{2+} and the site of reduction or deposition need to be studied in conjunction with changes in deposition potential and current to understand branching or faceting growth of Cu_2O crystals. More experiments are currently being carried out to derive a precise mechanism for branching in regions of low potential or current.

All the crystals discussed up to this point display the same octahedral habit as the degree of branching was independently controlled from habit. By combining the deposition conditions identified in Figure 4 with chemical conditions to regulate crystal habit (see Experimental Section for detailed compositions of media),[18] simultaneous manipulation of habit and branching become possible. Figure 5a–c show the results of branching control performed in a medium that stabilizes the {100} faces of Cu_2O crystals and, therefore, a cubic habit. Conversely, Figure 5d shows branched crystals obtained by using a medium that precisely tunes the growth ratio, R (the growth rate along the ⟨100⟩ direction/growth rate along the ⟨111⟩ direction), to obtain a truncated octahedral habit as the final morphology.[18,27] To the best of our knowledge, this level of synthetic freedom and programmability in controlling both the degree of branching and habit has not previously been demonstrated for any semiconducting system.

More complexity can be introduced to the architecture of Cu_2O crystals when different media are used for the branching and filling-in processes. This strategy mimics the growth of snow crystals in nature that leads to thousands of unique crystal morphologies. When developing snow crystals fall from the sky, they pass through many atmospheric regions of varying humidity and temperature. As each region has different preferences for habit and branching, the journey of snow crystals creates complexity in their growth history and, therefore, complexity in their final morphologies.[19,25] Electrodeposition is ideal for creating an equivalent complex growth history because the crystal growth can be paused at

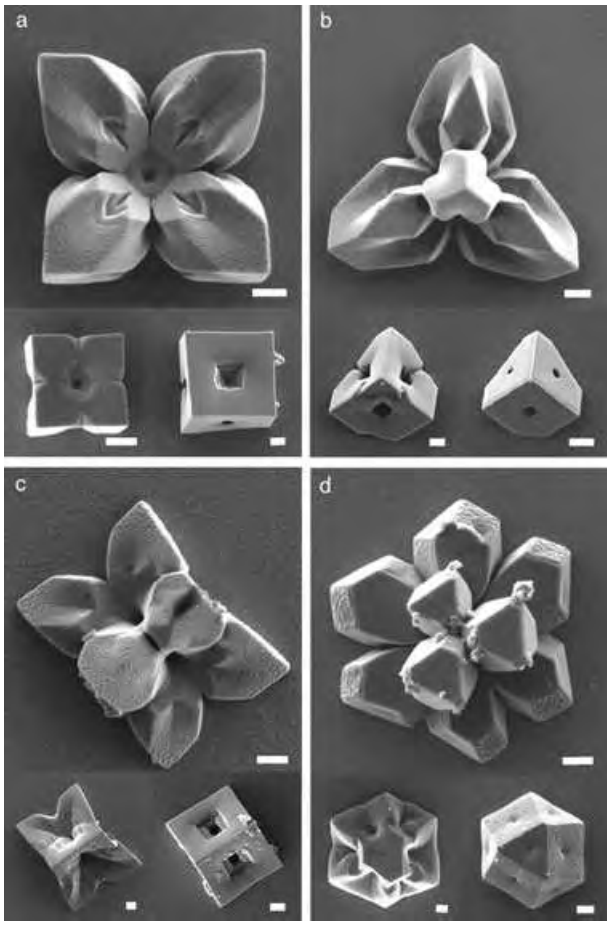

Figure 5. SEM images of branched Cu_2O crystals with varying crystal habit. Cubic crystals grown with a) (100) planes, b) (111) planes, and c) (110) planes parallel to the substrate. d) Cuboctahedral crystals with (111) planes parallel to the substrate. Insets for each image show crystals of the same habit and orientation with gradually increasing filling-in processes that are controlled by the deposition conditions identified in Figure 4 (scale bar = 1 μm). See Experimental Section for detailed compositions of the media.

any moment and resumed in a new medium. Figure 6a–c show how branched octahedral crystals transform when the filling-in process is continued in a new medium that stabilizes {100} faces. Since the initial branches are positioned to form an octahedral skeleton, a quick transition to a single cube is extremely difficult. Therefore, the tips of the branches that would otherwise become the apexes of an octahedron rapidly develop {100} faces and each branch forms its own cube and expose only {100} faces at the interfaces. Then these individual cubes eventually fuse together to form one seamless cube to attain a minimum surface energy. Figure 6d–f show the opposite case; branches were built in a medium that stabilizes cubic shapes, and the filling-in process was continued in a medium to grow octahedral crystals. Again various novel and exquisite surface patterns are generated when the crystals are forced to develop {111} faces by using branches that point to the apexes of a cube to eventually transform into a simple octahedral crystal. This observation implies endless possibilities of designing new crystal mor-

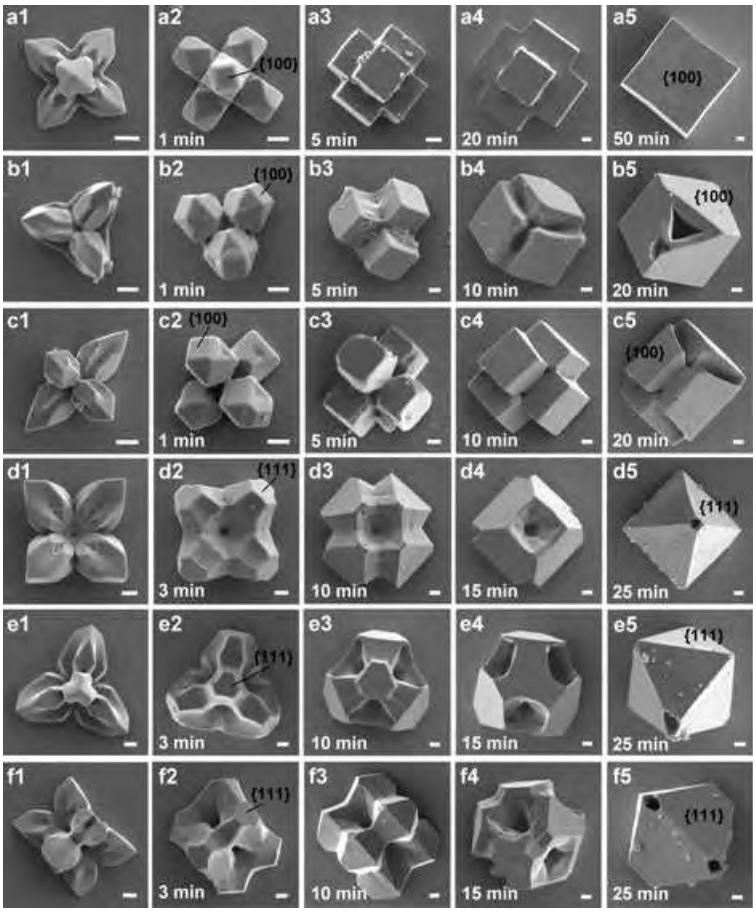

Figure 6. SEM images of novel Cu_2O crystal morphologies constructed through the addition of complex growth histories. a–c) Branched crystals were first deposited in a medium that stabilizes an octahedral habit for 3 minutes (column 1), and the filling-in process was resumed in a new medium that stabilizes a cubic habit for the time depicted in each figure (columns 2–5). d–f) Branched crystals were first deposited in a medium that stabilizes a cubic habit for 12 minutes (column 1), and the filling-in process was resumed in a new medium that stabilizes an octahedral habit for the time depicted in each figure (columns 2–5). Crystals are shown with (100) planes (a, d), (111) planes (b, e), and (110) planes (c, f) parallel to the substrate (scale bar = 1 μm). All the crystals shown here were grown under constant temperature (60 °C) and concentration of Cu^{2+} ion (0.02 M). Galvanostatic depositions of $I = 0.1$ mA cm^{-2} and 0.3 mA cm^{-2} were used for the initial branching and resumed filling processes, respectively.

phologies by combining multiple growth media and growth conditions.

In summary, we have demonstrated a methodical and simultaneous tuning of the habit and the degree of branching of Cu_2O crystals by elucidating and manipulating key conditions that control shape-guiding processes in electrocrystallization. By combining this understanding with the unique capability of electrodeposition to pause and resume crystallization at any stage, it was possible to assemble numerous unprecedented crystal architectures by rationally designing the growth conditions and growth history. The programmability and synthetic freedom demonstrated in this work will not only provide valuable information for the study of electrochemical crystal growth mechanisms[23,28,29] but also build a foundation for the study of directed crystal growth of various semiconducting crystals on a conducting substrate. These systems will be useful for a broad range of applications such as sensors, optoelectronics, and catalysis.

Experimental Section

Cu_2O crystals were prepared by cathodic deposition from aqueous solutions of 0.005–0.04 M $Cu(NO_3)_2$ ($2Cu^{2+} + H_2O + 2e^- \rightarrow Cu_2O + 2H^+$) by using a conventional three-electrode setup. For the counter electrode, 100 Å of titanium followed by 500 Å of platinum were deposited on clean glass slides by sputter-coating. ITO (sheet resistance = $15 \pm 5\ \Omega\,cm^{-2}$), purchased from Delta Techologies, Limited, was used as a working electrode. The reference electrode was Ag/AgCl in a solution of KCl (4 M), against which all potentials reported here were measured. The electrolyte used to stabilize the octahedral shape (shown in Figures 1 and 3) contains 5 wt% sodium dodecyl sulfate (SDS) as a habit modifier (pH 4.9 before the addition of SDS) to stabilize {111} faces of Cu_2O crystals. The medium used to stabilize a cubic habit (Figure 5a–c) was composed of a solution of $Cu(NO_3)_2$ (0.02 M) without SDS (pH 4.9), and the medium used to grow truncated octahedral habit (Figure 5d) was composed of a solution of $Cu(NO_3)_2$ (0.02 M) and 5 wt% SDS (the pH was adjusted to 4.3 before the addition of SDS).[18] The range of deposition conditions to promote faceting growth in a solution of Cu^{2+} (0.02 M) is $E \leq 0.07$ V and $I \geq 0.15$ mA cm^{-2} at 60 °C. Branching growth can be stabilized at $0.07\ V < E \leq 0.14$ V and $0.04\ mA\,cm^{-2} \leq I < 0.15\ mA\,cm^{-2}$ with more-significant branching induced at a more-positive potential and lower current. Both potential and current are required to be in these specific ranges to stabilize branching growth. When $E > 0.14$ V and $I < 0.04$ mA cm^{-2}, no crystalline Cu_2O can be deposited. The compositional purity of the Cu_2O crystals shown in this study was confirmed by powder X-ray diffraction, details of which are provided in the Supporting Information.

Received: December 22, 2004

Keywords: crystal growth · electrochemistry · semiconductors · solid-state structures

[1] J. W. Mullin, *Crystallization*, Butterworths, London, **1971**.
[2] H. E. Buckley, *Crystal Growth*, Wiley, New York, **1951**.
[3] S. Mann, *Angew. Chem.* **2000**, *112*, 3532–3548; *Angew. Chem. Int. Ed.* **2000**, *39*, 3393–3406.
[4] A. A. Chernov, *J. Cryst. Growth* **1974**, *24/25*, 11–31.
[5] T. Kudora, T. Irisawa, A. Ookawa, *J. Cryst. Growth* **1977**, *42*, 41–46.
[6] W. F. Berg, *Proc. R. Soc. London Ser. A* **1938**, *164*, 79–96.
[7] C. W. Bunn, *Discuss. Faraday Soc.* **1949**, *5*, 132–144.
[8] J. H. Adair, E. Suvaci, *Curr. Opin. Colloid Interface Sci.* **2000**, *5*, 160–167.
[9] Y. Sun, Y. Xia, *Science* **2002**, *298*, 2176–2179.
[10] C. A. Orme, A. Noy, A. Wierzbicki, M. T. McBride, M. Grantham, H. H. Teng, P. M. Dove, J. J. De Yoreo, *Nature* **2001**, *411*, 775–779.
[11] T. K. Sau, C. J. Murphy, *J. Am. Chem. Soc.* **2004**, *126*, 8648–8649.
[12] V. F. Puntes, K. M. Krishnan, A. P. Alivisatos, *Science* **2001**, *291*, 2115–2117.
[13] R. Liu, F. Oba, E. W. Bohannan, F. Ernst, J. A. Switzer, *Chem. Mater.* **2003**, *15*, 4882–4885.
[14] Z.-L. Xiao, C. Y. Han, W.-K. Kwok, H.-W. Wang, U. Welp, J. Wang, G. W. Crabtree, *J. Am. Chem. Soc.* **2004**, *126*, 2316–2317.
[15] H. Yan, R. He, J. Pham, P. Yang, *Adv. Mater.* **2003**, *15*, 402–405.
[16] S.-M. Lee, Y.-W. Jun, S.-N. Cho, J. Cheon, *J. Am. Chem. Soc.* **2002**, *124*, 11244–11245.

[17] S. Chen, Z. L. Wang, J. Ballato, S. H. Foulger, D. L. Carroll, *J. Am. Chem. Soc.* **2003**, *125*, 16186 – 16187.
[18] M. J. Siegfried, K.-S. Choi, *Adv. Mater.* **2004**, *16*, 1743 – 1746.
[19] U. Nakaya, *Snow Crystals: Natural and Artificial*, Harvard University Press, Cambridge, **1954**.
[20] T. Kobayashi in *Physics of Snow and Ice*, *Part 1* (Ed.: H. Oura), Institute of Low Temperature Science, Hokkaido University, Sapporo, **1967**.
[21] J. Hallett, B. J. Mason, *Proc. R. Soc. London Ser. A* **1958**, *247*, 440 – 453.
[22] T. Kuroda, R. Lacmann, *J. Cryst. Growth* **1982**, *56*, 189 – 205.
[23] E. Yokoyama, T. Kudora, *Phys. Rev. A* **1990**, *41*, 2038 – 2049.
[24] R. Lacmann, I. N. Stranski, *J. Cryst. Growth* **1971**, *13*, 236 – 240.
[25] K. G. Libbrecht, *Eng. Sci.* **2001**, *LXIV(1)*, 10 – 19.
[26] M. Pourbaix, Atlas of Electrochemical Equilibria in Aqueous Solutions, Pergamon, New York, **1966**.
[27] A. L. Wang, *J. Phys. Chem. B* **2000**, *104*, 1153 – 1175.
[28] H. Jónsson, A *nnu. Rev. Phys. Chem.* **2000**, *51*, 623 – 653.
[29] A. C. Levi, M. Kotrla, *J. Phys. Condens. Matter* **1997**, *9*, 299 – 344.

Cytomimetic Chemistry

Real-Time Membrane Fission of Giant Polymer Vesicles**

*Yongfeng Zhou and Deyue Yan**

Vesicle transformations that mimic cellular processes have become a specific topic of interest in recent years.[1] Lipid vesicles (liposomes), surfactant vesicles, and block-copolymer vesicles are conventional and useful model membranes for living cells.[2–5] Most model membranes reported are submicroscopic (20–500 nm) in nature and conclusions concerning these membranes are often based on inference rather than on direct observation. Menger and co-workers have successfully used giant vesicles (5–200 μm), which have the advantage of being microscopic and therefore visible, to directly observe real-time shape transformations of vesicles that mimic cellular morphology. They coined the term "cytomimetic chemistry" to describe the visible cell-like morphologies of giant vesicles.[6] Up to now, many interesting cell-like activities such as birth, budding, endocytosis, exocytosis, fusion, and fission have been reported in studies of cytomimetic behavior.[6–8] However, all of the vesicles that have been used so far in cytomimetic chemistry are giant liposomes, and no real-time transformations of polymer vesicles have been observed. Herein, we present work to develop the cytomimetic chemistry into the field of polymers by using giant polymer vesicles as model membranes ("cytomimetic macromolecular chemistry"). We also describe a new and sequential membrane fission process by displaying a series of high-resolution and real-time transformation images of individual vesicles.

Membrane fission is very important and common in various biological processes such as endocytosis. However, there has been little experimental work on vesicle fission that mimics cell fission at the phenomenological level. Luisi and co-workers found evidence of fission of larger vesicles by adding fresh surfactant into preformed vesicles; they called this phenomenon "the matrix effect" to stress that the pre-existing vesicles or liposomes act as a matrix for the formation of new vesicles.[2] Nolte and co-workers also detected vesicle fission by adding calcium ions into synthetic phospholipid vesicles and presented a possible mechanism.[3b] Eisenberg and co-workers also proposed a fission sequence by carefully arranging several images selected from a large number of TEM micrographs of submicroscopic block copolymer vesicles.[5c,d] The mechanisms for vesicle fission mentioned above are speculative and based on characterization data obtained from TEM and light scattering. In contrast, Döbereiner, Sackmann, and co-workers—the pioneers of cytomimetic chemistry—used optical microscopy to monitor the real-time fission of giant lipid vesicles induced by heating and osmotic deflation.[8] Kitamura also presented images of real-time fission of giant lipid vesicles induced by a laser.[9] Unfortunately, these images in are low-resolution or segmental. To understand similar behavior in living cells, it is necessary to obtain high-resolution, real-time, sequential images of individual vesicles undergoing fission. In addition, the use of giant polymer vesicles as model membranes in cytomimetic chemistry is a new and exciting area of research.

Compared with liposomes, polymer vesicles are very stabile. Eisenberg and co-workers reported a type of polymer vesicle called "crew-cut micelles", which are obtained by the self-assembly of block copolymers that have small hydrophilic fractions ($<20\,\%$) in a mixture of solvents.[5] Discher and co-workers reported another type of polymer vesicle termed "polymersomes" from block copolymers that have a hydrophilic fraction ($35\pm10\,\%$) similar to those of liposomes.[10] Very recently, we reported a new sort of polymer vesicle called "branched polymersomes". These branched polymersomes were synthesized through molecular self-assembly of an ill-defined hyperbranched copolymer, HBPO–star–PEO (HPBO is hyperbranched poly(3-ethyl-3-oxetanemethanol); PEO is polyethylene oxide), which has a higher hydrophilic fraction ($>60\,\%$) in water.[11] HBPO–star–PEO is an amphiphilic multiarm copolymer with a hydrophobic hyperbranched HBPO core and a large population of hydrophilic PEO arms.[11] Three giant polymer vesicles, HB3, HB2, and HB1, with average diameters of 4.0 μm, 22.6 μm, and 112.8 μm, respectively, were obtained[11b] The molecular self-assembly process of vesicles HB1–3 involved directly putting the polymer into stirred deionized water (polymer concen-

[*] Dr. Y. Zhou, Prof. Dr. D. Yan
College of Chemistry and Chemical Engineering
State Key Laboratory of Metal Matrix Composites
Shanghai Jiao Tong University
800 Dongchuan Road, Shanghai 200240 (P.R. China)
Fax: (+86) 21-5474-1297
E-mail: dyyan@sjtu.edu.cn

[**] Financial support from the National Natural Science Foundation of China (no. 20274024, 50233030) and from the basic research foundation of Shanghai Science and Technique Committee (no. 03JC14046, 04JC14057) is acknowledged.

Supporting information for this article is available on the WWW under http://www.angewandte.org or from the author.

 DOI: 10.1002/anie.200462622

tration 10 mg mL^{-1}) at room temperature. HB1–3 vesicles not only have the advantages of polymer vesicles but are also visible under the microscope as are giant lipid vesicles. Thus, HB1–3 vesicles are ideal model membranes for cytomimetic chemistry.

HB2 vesicles were chosen to investigate the real-time cytomimtetic behavior under an optical microscope. Detailed structures of the HB2 molecules and vesicles are described in the Supporting Information. Membrane fission of a daughter vesicle inside a mother vesicle was observed by adding glucose to the HB2 vesicle solution (Figure 1). The daughter

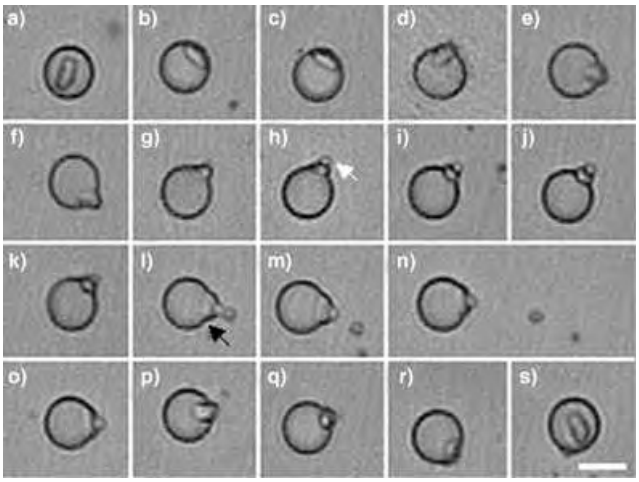

Figure 1. A series of images showing the interaction of a daughter vesicle inside its mother vesicle during fission. The scale bar represents 25 μm. The time of image (a) is set as 0, and the elapsed times for the images are 33 (b), 64 (c), 105 (d), 130 (e), 134 (f), 165 (g), 170 (h), 179 (i), 182 (j), 190 (k), 243 (l), 246 (m), 263 (n), 273 (o), 421 (p), 620 (q), 719 (r), and 920 s (s), respectively. Images (a–g), (h–o), and (p–s) are defined as the prophase, metaphase, and anaphase of fission, respectively. For the fission experiment, glucose (15 mM) was added to an aqueous solution of HB2 vesicles. After the glucose had dissolved, the sample was subjected to ultrasound for 10 min before being transferred to a culture dish for optical microscopy measurements (Leica Dmlp, TMS94) at 20°C.

vesicle underwent five fission steps: suspension inside the mother vesicle (Figure 1 a); coalescence with the mother vesicle (Figure 1 b,c); protrusion from the membrane of the mother vesicle to form a pear shape (Figure 1 d–i); fission (Figure 1 m,n); retraction into the mother vesicle (Figure 1 o–s); suspension of the daughter vesicle for several minutes until the fission cycle ends or repeats itself (Figure 1 s). We have observed one daughter vesicle inside a mother vesicle undergoing three fission cycles, with each cycle taking longer to complete than the previous. We observed at least eight vesicles displaying similar fission behavior to that shown in Figure 1.

Clearly, it is the daughter vesicle that undergoes membrane fission. Experimental evidence to support this claim comes from three sources. First, we have not observed spontaneous budding from a single vesicle without the presence of an inner daughter vesicle. Second, the sequential images (Figure 1 a–l) suggest that the daughter vesicle passes through the mother vesicle to form the pear-shaped structure (Figure 1 h–l), and it is the deformation of this structure that results in membrane fission (Figure 1 l–o). We also find that formation of a pear-shaped structure is not certain to lead to vesicle fission; sometimes the vesicles maintain the pear shape for a relatively long time without further fission. Instead, there is a gradual retraction of pear shape into the mother vesicle and the intact daughter vesicle is formed again (see the Supporting Information). The images in Figure 1 (Figure 1 a–l) combined with those in the Supporting Information confirm that the pear-shaped structure, from which the fission takes place, is formed from the daughter vesicle. The third piece of evidence comes from the change in size of the daughter vesicle before and after membrane fission. The daughter vesicle is irregular but can be regarded as quasi-ellipse. Thus, we can define the daughter vesicle in terms of the length of the major and minor axes. The major axis of the daughter vesicle before fission (≈ 7 μm) is longer than that of the daughter vesicle after fission (< 6 μm), as is the minor axis. Nevertheless, the daughter vesicle is not a regular ellipse, so it would be better to find a more precise way of comparing the volume of the vesicles. We overlapped the daughter vesicle before and after fission by using a computer program (see the Supporting Information) and the result clearly show that the size of the daughter vesicle decreased after fission.

How does the vesicle fission shown in Figure 1 take place? We believe that the osmotic pressure and the mother vesicle induce the fission. Similar to biological membranes, liposomes are semipermeable and are much more permeable to water than to glucose. It is well known that polymer vesicles are less permeable than liposomes.[5] Therefore, it is conceivable that water can easily permeate the HB2 vesicle membrane, however, permeation of glucose, a larger molecule, through the vesicle membrane is more difficult. In fact, the semipermeable membrane property of the HB1–3 vesicle has been verified by a vesicle-shrinkage experiment in another hyperosmotic solution (results not shown). So the addition of glucose greatly increases the difference in osmotic pressure between the aqueous interior of the HB2 vesicle and the bulk solution, which drives water and the daughter vesicle out of the mother vesicle.

During the fission, the daughter vesicle moves towards the mother vesicle and often part of the daughter breaks through (Figure 1 a–d). However, it does not directly penetrate the mother vesicle because of the intrinsically high stability of the polymer vesicle.[5,10] The membrane of the mother vesicle works as a tough elastic barrier, thus preventing the daughter vesicle from completely breaking out. The daughter and mother vesicles make contact and at that point the mother vesicle, driven by the movement of the daughter vesicle, deforms into a bud structure (Figure 1 e–g). A comparison of the mother vesicle before and after deformation (Figure 1 a and f; see also the Supporting Information) shows that the surface of the mother vesicle increases after forming the bud. This expansion of the membrane should lead to an increase in surface tension.[12] Figure 2 a–f shows the models to illustrate the deformation of the daughter vesicle and mother vesicle to form the bud. Details of the interaction between the mother and daughter vesicles are still under investigation in our lab and will be reported in due course.

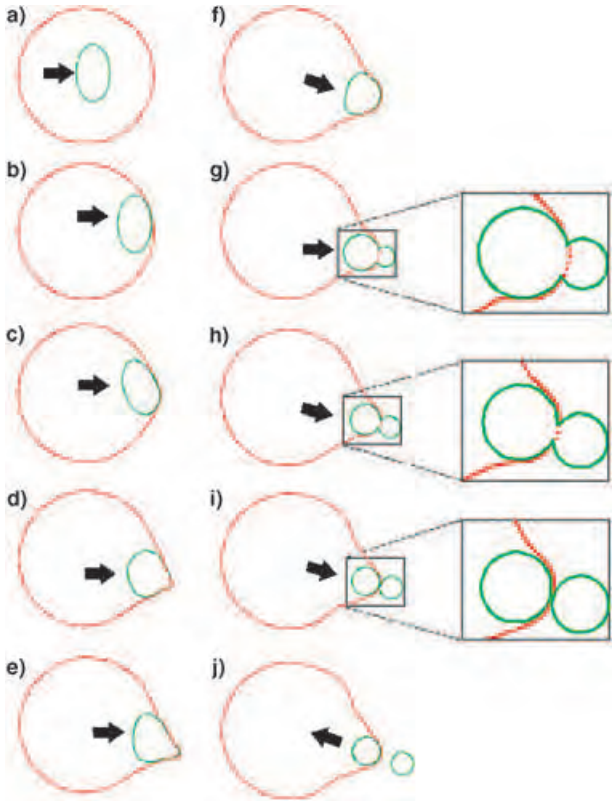

Figure 2. Models of vesicle transformations during membrane fission shown in Figure 1. The mother vesicle is in red and the daughter vesicle is in green. Black arrows show the movement of the daughter vesicle. The red dashed curves in (g) and (h) show the intersecting line resulting from the penetration of the mother vesicle by the daughter vesicle.

Figure 1 h shows an important intermediate: the partial penetration of the daughter vesicle through the mother vesicle. Figure 1 shows the mother vesicle in black and the daughter vesicle in gray. The black profiles of the vesicle image in Figure 1 a–g indicate that the daughter vesicle is enveloped by the mother vesicle during these changes in morphology. However, in Figure 1 h the gray vesicle has partly passed through the black vesicle (white arrow). From a comparison of the volume of the daughter vesicle in Figure 1 h with that in Figure 1 a, it is clear that the gray membrane located outside the black vesicle in Figure 1 h comes from the daughter vesicle. Evidently, the daughter vesicle has partly penetrated the mother vesicle by the force of osmotic pressure. It is conceivable for the daughter vesicle to break through the mother vesicle if the tension induced by the movement of the daughter has exceeded the tolerance of the mother. Further evidence of the penetrating ability of the daughter vesicle came from experiments with a higher glucose concentration (25 mM): the daughter vesicle was observed to completely pass through the mother vesicle forced by the higher osmotic pressure (see the Supporting Information). This process is similar to the birthing process reported by Menger and Gabrielson.[6b,c]

Figure 1 i–l shows the sequential deformation of the daughter vesicle inside and outside the mother vesicle. The penetration by the daughter leads to a "wound" in the mother vesicle and the mother heals the wound spontaneously.[6b,c] In addition, the daughter vesicle continues to penetrate the mother vesicle driven by osmotic pressure. Figure 2 g–i shows the possible changes of the daughter vesicle during the penetration. Figure 2 g shows that the daughter vesicle is divided into two by the mother vesicle and a neck is formed in the interface, which shapes the daughter vesicle into a pearlike structure. As the wound in the mother vesicle heals and the penetration by the daughter vesicle continues, the neck becomes narrower and narrower (Figure 2 h). Then the daughter becomes two vesicles that are in contact with each other as shown in Figure 1 l and Figure 2 i.

The strong deformation of the mother vesicle in Figure 1 l is of particular interest. Figure 1 l shows the mother vesicle at the point of greatest deformation (indicated by the black arrow; see also Figure 2 i), which leads to the large tension that retracts the part of the daughter vesicle retained inside the mother. Thus, complete fission takes place (Figures 1 m, 1 n, and 2 j). We have found that vesicle fission will only occur after the deformation of the mother and daughter vesicles has reached the state shown in Figure 1 l, which is the critical morphology for vesicle fission. The deformation of the mother vesicle decreases after releasing a small vesicle (Figure 1 m–o), the mother vesicle gradually recovers its spherical morphology (Figure 1 p–s), and the daughter vesicle is fully retracted.

Fission processes reported previously involve only one vesicle, whereas the fission described herein is new as it involves two vesicles. There is a strong interaction between mother and daughter vesicles during fission and deformation of the mother occurs with concomitant fission of the daughter. We have called this process "cooperative fission".

The "spontaneous curvature" and "area difference elasticity" models developed by Döbereiner, Sackmann, Seifert, and others have been successfully used to forecast, explain, and analyze the budding and fission of lipid vesicles.[8] The theoretical models mostly deal with a fission process that involves only one vesicle. The participation of a mother vesicle greatly increases the complexity of the studied "cooperative fission". A modified physical model that takes into account the geometrical and mechanical constraints of the mother vesicle is needed. Nevertheless, since both the theoretical and experimental results with lipid vesicles have stressed the pear structure and its importance in subsequent membrane fission, the behavior of lipid vesicles and polymer vesicles overlap here in membrane fission.

In conclusion, we have presented a novel real-time membrane fission process, called cooperative fission, by using giant polymer vesicles as model membranes. A mother vesicle with a daughter vesicle within shows a cooperative effect during membrane fission, which is caused by osmotic pressure combined with the stability of the mother polymer vesicle. Our finding extends the field of cytomimetic chemistry into polymers. These results along with previous reports on liposomes and surfactant vesicles,[2–6,8,9] lead us to the conclusion that membranes—regardless of the composition, whether they involve small molecules or macromole-

cules, whether synthetic or natural—can undergo this cytomimetic process in the absence of a protein.

Received: November 16, 2004
Revised: February 5, 2005
Published online: April 21, 2005

Keywords: copolymers · membranes · self-assembly · vesicle fission

[1] a) *Giant Vesicles, Perspectives in Supramolecular Chemistry* (Eds.: P. L. Luisi, P. Walde), Wiley, Chichester, **2000**; b) J.-M. Lehn, *Science* **2002**, *295*, 2400; c) H. Ringsdorf, B. Schlarb, J. Venzmer, *Angew. Chem.* **1988**, *100*, 117; *Angew. Chem. Int. Ed. Engl.* **1988**, *27*, 113.

[2] a) N. Berclaz, M. Müller, P. Walde, P. L. Luisi, *J. Phys. Chem. B* **2001**, *105*, 1056; b) N. Berclaz, E. Blöchliger, M. Müller, P. L. Luisi, *J. Phys. Chem. B* **2001**, *105*, 1065; c) J. W. Szostak, D. P. Bartel, P. L. Luisi, *Nature* **2001**, *409*, 387; d) S. Rasi, F. Mavelli, P. L. Luisi, *J. Phys. Chem. B* **2003**, *107*, 14068.

[3] a) D. M. Vriezema, J. Hoogboom, K. Velonia, K. Takazawa, P. C. M. Christianen, J. C. Maan, A. E. Rowan, R. J. M. Nolte, *Angew. Chem.* **2003**, *115*, 796; *Angew. Chem. Int. Ed.* **2003**, *42*, 772; b) N. A. J. M. Sommerdijk, T. H. L. Hoeks, M. Synak, M. C. Feiters, R. J. M. Nolte, B. Zwanenburg, *J. Am. Chem. Soc.* **1997**, *119*, 4338.

[4] G. Cevc, H. Richardsen, *Adv. Drug Delivery Rev.* **1999**, *38*, 207–232.

[5] a) L. Zhang, A. Eisenberg, *Science* **1995**, *268*, 1728; b) L. Zhang, A. Eisenberg, *Science* **1996**, *272*, 1777; c) L. Luo, A. Eisenberg, *Langmuir* **2001**, *17*, 6804; d) D. E. Discher, A. Eisenberg, *Science* **2002**, *297*, 967.

[6] a) F. M. Menger, N. Balachander, *J. Am. Chem. Soc.* **1992**, *114*, 5862; b) F. M. Menger, K. Gabrielson, *J. Am. Chem. Soc.* **1994**, *116*, 1567; c) F. M. Menger, K. D. Gabrielson, *Angew. Chem.* **1995**, *107*, 2260; *Angew. Chem. Int. Ed. Engl.* **1995**, *34*, 2091; d) F. M. Menger, M. I. Angelova, *Acc. Chem. Res.* **1998**, *31*, 789; e) F. M. Menger, J. S. Keiper, *Adv. Mater.* **1998**, *10*, 888; f) F. M. Menger, V. A. Seredyuk, A. A. Yaroslavov, *Angew. Chem.* **2002**, *114*, 1406; *Angew. Chem. Int. Ed.* **2002**, *41*,1350; g) F. M. Menger, V. A. Seredyuk, *J. Am. Chem. Soc.* **2003**, *125*, 11800.

[7] a) A.-S. Cans, N. Wittenberg, R. Karlsson, L. Sombers, M. Karlsson, O. Orwar, *Proc. Natl. Acad. Sci. USA* **2003**, *100*, 400; b) F. Nomura, M. Nagata, T. Inaba, H. Hiramatsu, H. Hotani, K. Takiguchi, *Proc. Natl. Acad. Sci. USA* **2001**, *98*, 2340; c) F. Nomura, T. Inaba, S. Ishikawa, M. Nagata, S. Takahashi, H. Hotani, K. Takiguchi, *Proc. Natl. Acad. Sci. USA* **2004**, *101*, 3420.

[8] a) J. Käs, E. Sackmann, *Biophys. J.* **1991**, *60*, 825; b) H.-G. Döbereiner, J. Käs, D. Noppl, I. Sprenger, E. Sackmann, *Biophys. J.* **1993**, *65*, 1396; c) E. Sackmann in *Handbook of Biological Physics*, *Vol. 1A* (Eds.: R. Lipowsky, E. Sackmann), Elsevier, New York, **1995**, pp. 213–305; d) H.-G. Döbereiner, E. Evans, M. Kraus, U. Seifert, M. Wortis, *Phys. Rev. E* **1997**, *55*, 4458; e) U. Seifert, *Adv. Phys.* **1997**, *46*, 13; f) H.-G. Döbereiner, *Curr. Opin. Colloid Interface Sci.* **2000**, *5*, 256.

[9] N. Kitamura, N. Sekiguchi, H.-B. Kim, *J. Am. Chem. Soc.* **1998**, *120*, 1942.

[10] a) B. M. Discher, Y.-Y. Won, D. Ege, J. C.-M. Lee, F. S. Bates, D. E. Discher, D. A. Hammer, *Science* **1999**, *284*, 1143; b) B. M. Discher, D. A. Hammer, F. S. Bates, D. E. Discher, *Curr. Opin. Colloid Interface Sci.* **2000**, *5*, 125.

[11] a) D. Yan, Y. Zhou, J. Hou, *Science* **2004**, *303*, 65; b) Y. Zhou, D. Yan, *Angew. Chem.* **2004**, *116*, 5004; *Angew. Chem. Int. Ed.* **2004**, *43*, 4896.

[12] E. Evans, W. Rawicz, *Phys. Rev. Lett.* **1990**, *64*, 2094.

Crystal Growth

Solvent Effect on Crystal Polymorphism: Why Addition of Methanol or Ethanol to Aqueous Solutions Induces the Precipitation of the Least Stable β Form of Glycine

Isabelle Weissbuch, Vladimir Yu. Torbeev, Leslie Leiserowitz,* and Meir Lahav**

Dedicated to Professor J. Michael McBride on the occasion of his 65th birthday

Crystal polymorphism, which embodies the ability of molecules to form diverse packing arrangements displaying different physical and chemical characteristics, is of paramount importance in fields such as pharmacology, solid-state chemistry, and material science.[1] However, the conditions to induce the precipitation of various (metastable) polymorphs is invariably achieved by "mix and try" methods, which are kinetically driven. Various factors should be considered in trying to understand these complex processes, for example, the formation of structured clusters in solution prior to crystallization, the structure of growing surfaces that delineate emerging nuclei, the interaction between these surfaces and the solvent, as well as solvent–solute and solute–solute interactions. Herein, we attempt to unravel some of these factors to rationalize the preferred crystallization of the β form of glycine (gly) in water–alcohol solutions as opposed to the more stable α or γ polymorphs.

The thermodynamic stability of the three polymorphs of glycine at room temperature is in the order $\gamma > \alpha > \beta$.[2–5] The α form[6] (space group $P2_1/n$), grown from supersaturated aqueous solutions (33.3 g/100 mL water) at 25 °C, has a bipyramidal habit and is composed of centrosymmetric bilayers formed by strong NH···O hydrogen-bonding interactions between cyclic hydrogen-bonded zwitterionic molecular pairs. These bilayers are related along the *b* axis by glide symmetry through weak CH···O interactions (Figure 1 a). Previous studies indicated that α-gly crystallizes primarily in aqueous solutions through hydrogen-bonded cyclic dimer growth units: Diffusion-coefficient[7] measurements of supersaturated aqueous solutions of glycine point to the formation of clusters with an average of 1.8 molecular growth units. Furthermore, atomic force microscopy (AFM) and phase interferometry microscopy measurements established that steps approximately 1 nm in size were formed, which correspond to the thickness of a glycine bilayer.[8,9] Grazing-incidence X-ray diffraction studies on growing α-gly {010}

[*] Dr. I. Weissbuch, V. Yu. Torbeev, Prof. Dr. L. Leiserowitz, Prof. Dr. M. Lahav
Department of Materials and Interfaces
The Weizmann Institute of Science
76100-Rehovot (Israel)
Fax: (+972) 8-934-4138
E-mail: isabelle.weissbuch@weizmann.ac.il
leslie.leiserowitz@weizmann.ac.il
meir.lahav@weizmann.ac.il

  DOI: 10.1002/anie.200500164

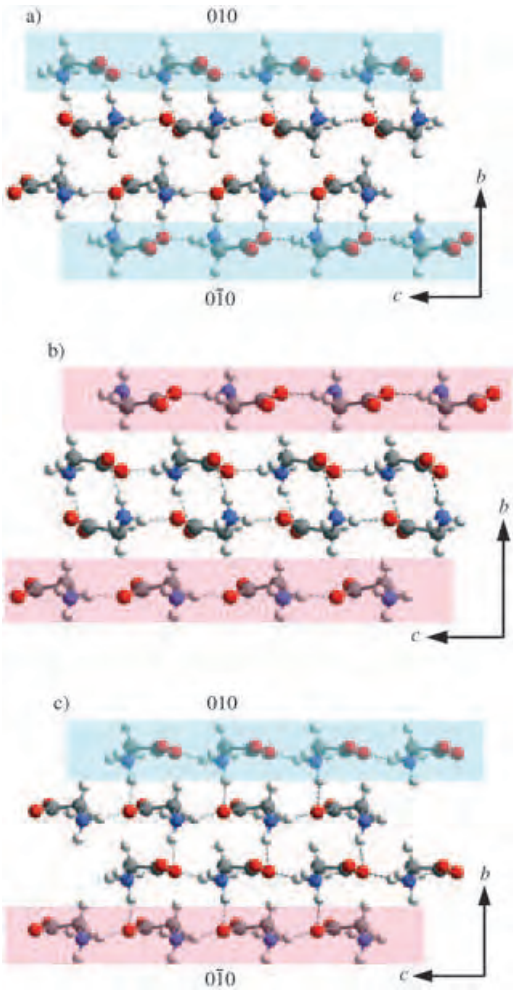

Figure 1. Packing arrangements of the a), b) α and c) β polymorphs of glycine. a), b) α-Gly exposing either weak solvent-binding C–H bonds to the solution at the (010) surface (azure) or strong solvent-binding N–H bonds to the solution at the (010) surface (pink). c) β-Gly exposing (010) "azure" and (0–10) "pink" surfaces, similar to that in α-gly, but at the two opposite poles of the crystal.

crystal faces[10] showed that the crystals primarily had exposed C–H bonds, thus indicating that glycine cyclic dimers are the growth units for α-gly formation.[9]

The first crystallization of β-gly from water–alcohol solutions was reported by Fischer.[11] The crystal structure[12,13] is polar (space group $P2_1$) and comprises hydrogen-bonded layers, which are akin to those observed in the α form, but which are interlinked by NH···O and CH···O interactions through a twofold screw-symmetry axis perpendicular to the layer plane (Figure 1c). The addition of alcohol reduces the solubility of glycine from 25.0 g/100 mL water (25 °C) to 2.65 g/100 mL solvent in 50.1 % (v/v) ethanol–water mixtures. This reduced solubility should result in an increased concentration of solvated glycine monomers relative to that of hydrogen-bonded cyclic dimers. Such behavior is apparently consistent with the preferred precipitation of β-gly from alcohol–water solutions because the crystal structure consists of hydrogen-bonded monomer units, as opposed to α-gly which comprises cyclic hydrogen-bonded pairs.

Long needles of β-gly were grown in water–ethanol mixtures containing 50, 26.1, and 10 % (v/v) ethanol and also from 1:1 water–methanol mixtures containing 4.0, 19.0, 35.9, and 5.0 g gly/100 mL solvent, respectively (Figure 2a).

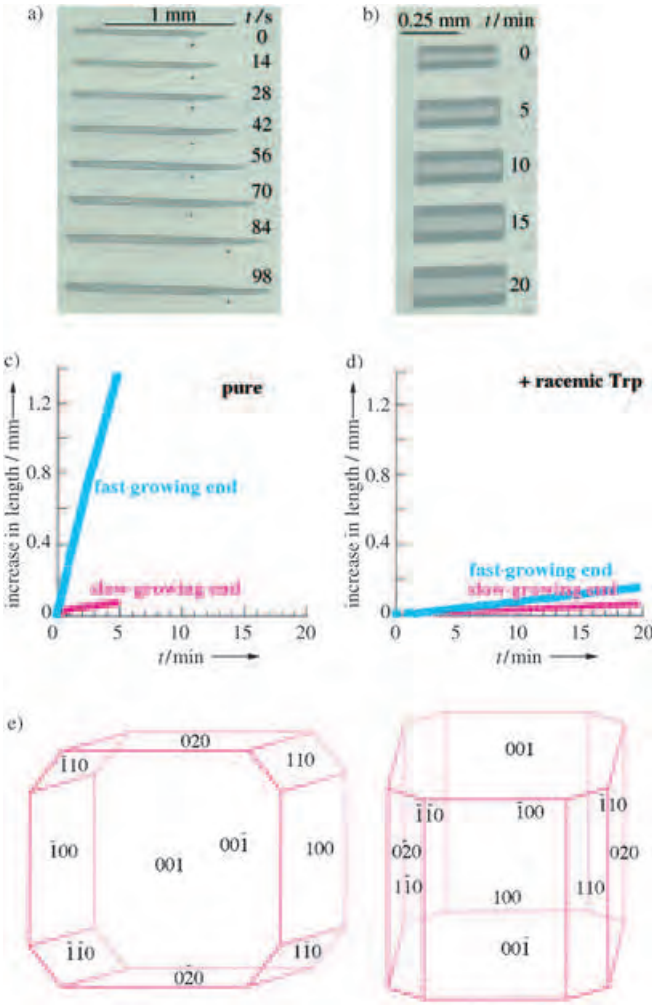

Figure 2. Photographs showing the growth of β-gly crystals in a 1:1 water–ethanol solution in a) the absence and b) the presence of 5 % (w/w) racemic Trp. c, d) Corresponding increase in length at opposite ends of the β-gly crystals. e) The theoretical growth form of β-gly viewed along the *c* and *a* axes.

Therefore, we were faced with the conundrum that the more thermodynamically stable α- and γ-gly polymorphs do not generally precipitate in aqueous solutions containing methanol or ethanol under the specified experimental conditions. We thought that an answer to this problem might be gleaned from the growth kinetics of the three polymorphs of glycine coupled with an analysis of the action of the solvent at the various crystal faces.

Growth kinetic measurements of single β-gly crystals in 1:1 water–ethanol solutions at 25 °C reveal a fast growth at one pole of the needle and a very slow growth at the opposite end (Figure 2a, c). We determined the absolute polarity[14] of

β-gly by employing "tailor-made" additives, in this case racemic tryptophane (Trp). The packing arrangement of β-gly (Figure 1c) dictates that an (*R*)-tryptophane additive may occupy the site of a glycine molecule at the end of the (010) crystal with exposed C–H bonds and subsequently retard its growth. If this end is the faster growing of the two crystal poles, tryptophane would induce the formation of short prismatic crystals, as observed experimentally (Figure 2b, d). Therefore, we conclude that β-gly grows faster at the side with exposed C–H bonds (colored azure) than at the opposite side with exposed N–H bonds (colored pink; Figure 1c). Previous studies have shown that the relative rates of growth at the opposite ends of polar crystals in polar solvents can be correlated directly with the relative rates by which solvent molecules are stripped from the opposite ends.[15–18] The faster growth rate at the β-gly pole with exposed C–H bonds is in agreement with this model; the water or alcohol solvent molecules can be attached more effectively to the slow-growing glycine surface with exposed N–H bonds through strong $OH_{sol}\cdots O_{gly}^-$ and $NH_{gly}\cdots O_{sol}$ interactions than to the fast-growing β-gly pole with exposed C–H bonds with strong $OH_{sol}\cdots O_{gly}^-$ interactions but only weak $CH_{gly}\cdots O_{sol}$ interactions. The surface of the fast- and slow-growing ends of β-gly (Figure 1c) are very similar in structure to the {010} surfaces of α-gly with either exposed C–H or N–H bonds, as shown in Figure 1a, b, respectively.[19] On the basis of the realistic assumption, which is supported by experimental evidence,[8,9] that glycine molecules in aqueous solution dock onto the crystal surface primarily as hydrogen-bonded cyclic glycine pairs, it is thought that an {010} face will expose the faster-growing surface with exposed C–H bonds to a much larger extent than the slower-growing surface with exposed N–H bonds. We anticipated that the reduced solubility of glycine in solution caused by the presence of ethanol would lead to a higher proportion of solvated glycine monomer units docking onto the α-gly {010}-surface sites with exposed N–H bonds. Thus, the time required to strip the overlying solvent molecules, prior to formation of the glycine cyclic dimer growth units and propagation of the glycine bilayer with exposed C–H bonds on its {010} surface, would lead to an overall reduction in growth rate along the $\pm b$ directions of the α-gly crystal. Indeed, the α-gly crystals obtained from a 9:1 water–ethanol solution tended to display more well developed {010} faces (Figure 3a) than crystals obtained from purely aqueous solutions. Therefore, embryonic α-crystallites would expose slow-growing {010} surfaces at higher concentrations of the alcohol in contrast to β nuclei, which has only one slow-growing polar end and so results in a preferred kinetic precipitation of the latter.

A further consequence of the pronounced effect of solvent on the crystal morphology of β-gly can be observed by comparing its needlelike habit (Figure 2a) with the regular shape resulting from the theoretical growth form (Figure 2e), which was computed by using Cerius[2] according to the attachment energy hypothesis by Hartman and Perdock.[20,21] Thus, water or alcohol as solvent impedes growth normal on the {*h*0*l*} faces of the needle crystals as a result of strong solvent attachment to these faces through $OH_{sol}\cdots O_{gly}$ and $NH_{gly}\cdots O_{sol}$ hydrogen-bonding interactions.

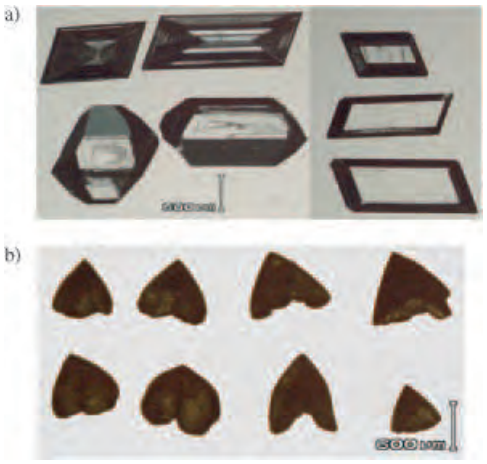

Figure 3. a) α-Gly crystals grown from 9:1 water–ethanol. b) γ-Gly crystals observed in several crystallizations from a 1:1 water–ethanol solution.

The absence of the stable γ-gly form[22] in crystals formed in alcohol–water solutions may be explained by examination of its growth properties. The polar crystal structure of γ-gly (space group $P3_1$; Figure 4), which is not composed of cyclic glycine pairs, is delineated by a (00–1) face at which CO_2^- groups emerge and capped crystal faces at the opposite end that expose NH_3^+ groups. Previous studies[23] have shown

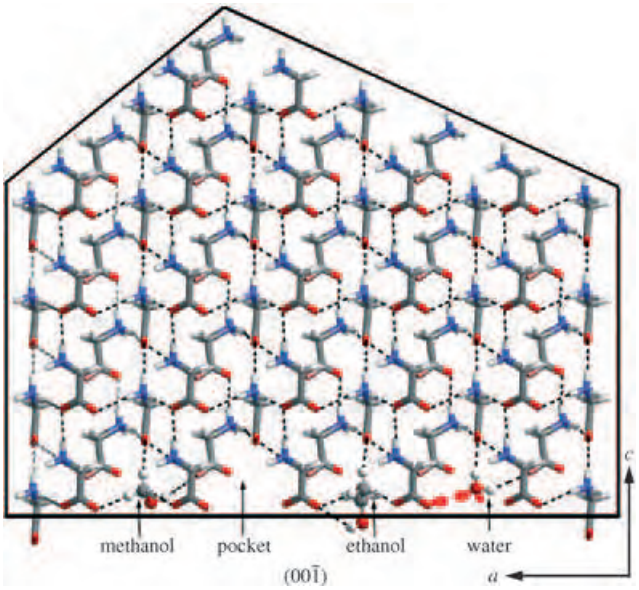

Figure 4. Packing arrangement of γ-gly showing the pockets on the fast-growing (00–1) face that are poisoned by the adsorption of ethanol and methanol molecules (shown as "balls and sticks"). In addition to the $OH_{sol}\cdots O_{gly}^-$ interaction, three $CH_{sol}\cdots O_{gly}^-$ interactions are formed that are similar in geometry to, but weaker than, the three $N{-}H_{gly}\cdots O_{gly}^-$ interactions that glycine would make. Note that a water molecule within the pocket is only weakly bound as the two possible $OH_{sol}\cdots O_{gly}^-$ hydrogen-bonding interactions would be counterbalanced by a lone-pair $O_{sol}\cdots O_{gly}^-$ repulsion (shown in red); therefore, the pocket is relatively accessible to approaching glycine molecules.

that γ-gly, grown in aqueous solutions and in the presence of auxiliaries that inhibit the crystallization of α-gly, appear as [001] needles that grow along the polar *c* axis much faster at the end of the crystal with the CO_2^- groups than at the opposite capped end. This unidirectional growth was interpreted in terms of a "relay" mechanism, according to which the corrugated face at the CO_2^- end will have ridges covered by bound water and pockets that are weakly hydrated, if at all. These pockets are then amenable to being quickly filled with NH_3^+ groups from glycine molecules that, in turn, will induce stripping of the water molecules from the ridged surfaces.[16] However, ethanol and methanol solvent molecules can reside within the pockets through $OH_{sol}\cdots O_{gly}^-$ and $CH\cdots O_{gly}^-$ hydrogen-bonding interactions, thus inhibiting growth at the CO_2^- end of the crystal (Figure 4). In several of the crystallization experiments carried out in water–ethanol mixtures, the few γ-gly crystals that were observed exhibited a morphology in keeping with the proposed inhibition by ethanol or methanol of growth along the otherwise fast-growing CO_2^- end of the crystal (Figure 2b).

In conclusion, the analysis of the growth kinetics of different polymorphs in terms of their crystal structures and solvent–surface, solute–solvent, and solute–solute interactions allows a rationale to be proposed for understanding the crystallization of kinetically controlled polymorphs.[24] Herein, focus was placed on the interplay between the various solute species[25] and solvent–surface interactions to account for the polymorph precipitated. These results also support the established model that removal of the solvent molecules is an important rate-determining step in the growth of a given face. The ideas presented herein should be relevant for understanding and controlling crystal morphology and the polymorphism of systems that form hydrogen-bonding patterns, such as amino acids, carboxylic acids, and primary and secondary amides.

Experimental Section

Crystallization experiments were performed in covered crystallizing dishes at room temperature without stirring. α-Gly crystals were grown from aqueous solutions containing 33.3 g gly/100 mL water. β-Gly crystals were grown from ethanol/water solutions (50, 26.1, and 10% ethanol (v/v)) and 50% (v/v) methanol/water solutions containing 4.0, 19.04, 35.9, and 5.0 g gly/100 mL solvent, respectively. X-ray single-crystal and powder-diffraction measurements were used to characterize the crystals. Crystals of β-gly were also grown in the absence and in the presence of racemic tryptophane in crystallizing dishes on the stage of an optical microscope with an attached digital video camera. Snapshots taken every 7 s were used to determine the growth of β-gly at both ends of the needlelike crystals by measuring on each image the increase in length at each end of the specimen crystals relative to a reference point.

Received: January 16, 2005
Published online: April 21, 2005

[1] J. Bernstein, *Polymorphism in Organic Crystals*, Clarendon, Oxford, **2002**.
[2] H. Onuma, H. Hosogai, T. Kawakita, *J. Cryst. Growth* **1992**, *116*, 421.
[3] K. Allen, R. J. Davey, E. Ferrari, C. Towler, G. J. Tiddy, M. O. Jones, R. G. Pritchard, *Cryst. Growth Des.* **2002**, *2*, 523.
[4] S. Chongprasert, S. A. Knopp, S. Nail, *J. Pharm. Sci.* **2001**, *90*, 421.
[5] G. L. Perlovich, L. K. Hansen, A. Bauer-Brandl, *J. Therm. Anal. Calorim.* **2001**, *66*, 699.
[6] J.-P. Legros, Å. Kvick, *Acta Crystallogr. Sect. B* **1980**, *36*, 3052.
[7] A. S. Myerson, P. Y. Lo, *J. Cryst. Growth* **1990**, *99*, 1048.
[8] P. W. Carter, A. C. Hillier, M. D. Ward, *J. Am. Chem. Soc.* **1994**, *116*, 944.
[9] D. Gidalevitz, R. Feidenhans'l, S. Matlis, D. M. Smilgies, M. J. Christensen, L. Leiserowitz, *Angew. Chem.* **1997**, *109*, 991; *Angew. Chem. Int. Ed. Engl.* **1997**, *36*, 955.
[10] {010} denotes (010) and (0−10) symmetry-related faces.
[11] E. Fisher, *Ber. Dtsch. Chem. Ges.* **1905**, *38*, 2917.
[12] Y. Iitaka, *Acta Crystallogr.* **1960**, *13*, 35.
[13] E. S. Ferrari, R. G. Davey, W. I. Cross, A. L. Gillon, C. S. Towler, *Cryst. Growth Des.* **2003**, *3*, 53.
[14] Z. Berkovitch-Yellin, L. Addadi, M. Idelson, L. Leiserowitz, M. Lahav, *Nature* **1982**, *296*, 27.
[15] F. C. Wireko, L. J. W. Shimon, F. Frolow, Z. Berkovitch-Yellin, M. Lahav, L. Leiserowitz, *J. Phys. Chem.* **1987**, *91*, 472.
[16] L. J. W. Shimon, M. Vaida, L. Addadi, M. Lahav, L. Leiserowitz, *J. Am. Chem. Soc.* **1990**, *112*, 6215.
[17] J.-L. Wang, L. Leiserowitz, M. Lahav, *J. Phys. Chem.* **1992**, *96*, 15.
[18] M. Hussain, J. Anwar, *J. Am. Chem. Soc.* **1999**, *121*, 8583.
[19] The poorly developed end faces of β-gly were observed to be of the type {110} or {011}.
[20] P. Hartman, W. G. Perdock, *Acta Crystallogr.* **1955**, *8*, 49.
[21] P. Hartman, *J. Cryst. Growth* **1980**, *49*, 157.
[22] Y. Iitaka, *Acta Crystallogr.* **1961**, *14*, 1.
[23] I. Weissbuch, L. Leiserowitz, M. Lahav, *Adv. Mater.* **1994**, *6*, 952.
[24] I. Weissbuch, L. Leiserowitz, M. Lahav, *Cryst. Growth Des.* **2003**, *3*, 125.
[25] C. S. Towler, R. J. Davey, R. W. Lancaster, C. J. Price, *J. Am. Chem. Soc.* **2004**, *126*, 13347.

Keywords: crystal growth · glycine · polymorphism · solvent effects

Asymmetric Catalysis

DNA-Based Asymmetric Catalysis**

Gerard Roelfes and Ben L. Feringa**

The ubiquitous right-handed double helix of DNA is arguably the most elegant example of chirality in nature, yet chirality in biocatalysis is almost exclusively the domain of the enzymes encoded by DNA.[1] The direct transfer of chiral information from DNA to chemical reactions will require the use of DNA-based catalysts. In marked contrast to catalytic RNAs, which have been employed successfully in a wide range of reactions including enantioselective catalysis,[2,3] the synthetic repertoire of "DNAzymes" is still very modest.[4] The limited applicability of catalytic DNA has occasionally been attributed to the absence of the 2′-OH functional group in the sugar-phosphate backbone and the propensity for natural DNA to adopt a double-helical duplex structure, which precludes the formation of catalytically competent tertiary structures.[4] Although the catalytic power of DNA has been enhanced by the incorporation of nucleotide bases with extended functionality,[5] enantioselective catalysis based on DNA has yet to be reported. However, the reported chirality transfer from DNA in stoichiometric DNA-templated synthesis, which leads to diastereoselectivity in chemical reactions and enantioselection of chiral substrates,[6] suggests the potential of DNAzymes in asymmetric catalysis.

Herein, we demonstrate that the chirality of the DNA double helix can be transferred directly to a metal-catalyzed reaction, in the present case the copper(II)-catalyzed Diels–Alder reaction (Figure 1). This can be done by positioning a nonchiral or racemic catalyst in intimate contact with DNA and using the chiral information of the DNA double helix to generate reaction products with an excess in one of their enantiomers. These artificial DNAzymes can be generated through the propensity of small aromatic molecules to intercalate in a noncovalent, yet kinetically stable and stereoselective fashion, which enables the anchoring of metal complexes to DNA.[7] This noncovalent and modular approach allows rapid structural variation and optimization of the catalytic system.

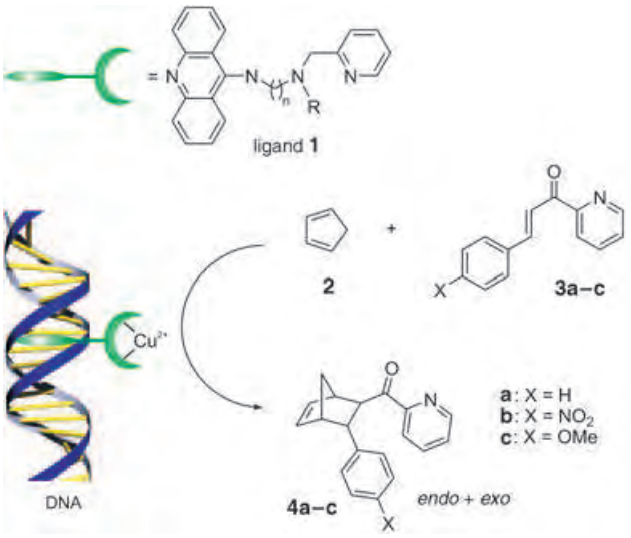

Figure 1. Schematic representation of the asymmetric Diels–Alder reaction of cyclopentadiene (**2**) with aza-chalcone **3**, catalyzed by copper complexes of ligand **1** in the presence of DNA.

The catalyst is a complex formed in situ from copper(II) with ligand **1**, which contains three key structural features: a DNA-intercalating moiety such as 9-aminoacridine, a spacer component, and a metal-binding group. The ligands were prepared in an efficient and straightforward fashion starting from monoprotected diamines (Supporting Information).[8] The copper(II) complex has a characteristic green color, with a weak UV/Vis spectroscopic absorbance at $\lambda_{max} = 620$ nm ($\varepsilon = 50\,M^{-1}cm^{-1}$) in the case of ligand **1a** (Supporting Information). This absorption, which is typical for copper di- and polyamine complexes,[9] is slightly red-shifted in the presence of DNA ($\lambda_{max} = 660$ nm). The addition of extra copper salt did not give a significant increase in this absorption. The combination of DNA with either $Cu(NO_3)_2$ or the free ligand does not have discernable features in this wavelength region, which demonstrates that DNA does not sequester the copper(II) ion from the ligand. Although complexation of these achiral ligands to copper generates chiral complexes, they are formed as a racemic mixture; thus any enantiomeric excess found in the product of the catalyzed reaction originates from DNA.[10]

The Diels–Alder reaction between cyclopentadiene (**2**) and the aza chalcone **3** in water[11] was catalyzed by copper(II) complexes of ligand **1** in the presence of salmon testes or calf thymus DNA, both of which are readily available and inexpensive. The reaction was allowed to proceed until $>80\,\%$ conversion. Product **4** was obtained as a mixture of the *endo* (major) and *exo* (minor) isomers, both with a significant enantiomeric excess, depending on the ligand used (Table 1). A series of control experiments established that the combination of ligand, copper salt, and DNA is required to obtain both efficient catalysis and enantioselectivity (Supporting Information).

[*] Dr. G. Roelfes
Department of Organic Chemistry, Stratingh Institute and Department of Biochemistry
Groningen Biomolecular Sciences and Biotechnology Institute
University of Groningen
Nijenborgh 4, 9747 AG Groningen (The Netherlands)
Fax: (+31) 50-363-4296
E-mail: j.g.roelfes@rug.nl
Prof. Dr. B. L. Feringa
Department of Organic Chemistry, Stratingh Institute
University of Groningen
Nijenborgh 4, 9747 AG Groningen (The Netherlands)
Fax: (+31) 50-363-4296
E-mail: b.l.feringa@rug.nl

[**] The authors thank W. R. Browne and Professor D. B. Janssen for valuable discussions. This research was supported by a Veni grant from the Netherlands Organization for Scientific Research (NWO) to G.R.

Supporting information for this article is available on the WWW under http://www.angewandte.org or from the author.

  DOI: 10.1002/anie.200500298

Table 1: Results of the catalytic Diels–Alder reaction with 1-naphthylmethyl- and 3,5-dimethoxybenzyl-substituted ligand **1**.[a]

Entry	Ligand	Ligand **1** R	*n*	Dienophile	Diels–Alder Product **4** *endo*/*exo*	*endo* [% *ee*]	*exo* [% *ee*]
1	**1a**		3	**3a**	98:2	49	18
2[b]	**1a**		3	**3a**	97:3	49	23
3[c]	**1a**		3	**3a**	98:2	47	23
4	**1a**		3	**3b**	96:4	37	16
5	**1a**		3	**3c**	98:2	48	24
6	**1b**		4	**3a**	98:2	33	19
7	**1c**		5	**3a**	97:3	<5	<5
8	**1d**		2	**3a**	96:4	−48	−37
9	**1e**		3	**3a**	98:2	−37	−7
10	**1f**	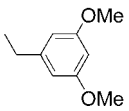	2	**3a**	92:8	−37	−78
11[b]	**1f**		2	**3a**	92:8	−34	−74
12[c]	**1f**		2	**3a**	92:8	−35	−82
13[d]	**1f**		2	**3a**	82:18	−34	−80
14	**1f**		2	**3b**	88:12	−47	−78
15	**1f**		2	**3c**	91:9	−53	−90

[a] All experiments were carried out with salmon testes DNA under the standard conditions (see Experimental Section) unless noted otherwise. [b] Conditions: catalyst (0.18 mM), dienophile (4 mM), cyclopentadiene (34 mM). [c] Calf thymus DNA. [d] DNA = synthetic duplex $d(GACT)_2$-$(AGTC)_2$ (0.39 mM), cyclopentadiene (21 mM), buffer contained NaCl (75 mM).

The substituent R and the spacer length *n* of the ligand are crucial for both the observed enantioselectivity and the enantiopreference (that is, which enantiomer is formed in excess). A screen of ligands with a fixed spacer length ($n = 3$) revealed the importance of the R group and specifically, the requirement for it to contain an aromatic (arylmethyl) group (Supporting Information). This suggests the involvement of π–π interactions between the substituent and the dienophile, as was previously described in the case of catalysts based on amino acids.[11] The best results in the series examined were obtained for ligands with R = 1-naphthylmethyl (**1a**), for which an *endo*/*exo* ratio of 98:2 and 49% *ee* for the *endo* isomer were found (Table 1, entry 1). Comparison of these results with those from ligand with R = 2-naphthylmethyl, which did not produce any significant enantiomeric excess, demonstrates the subtlety of the interaction of the substituent of the ligand with the dienophile.

Elongation of the spacer in **1a** resulted in a rapid decrease of the enantioselectivity; for $n = 5$ (**1c**) no significant enantiomeric excess was observed (Table 1, entry 7). In contrast, a decrease in spacer length to $n = 2$ (**1d**) gave a value similar to **1a** (48% *ee*), but surprisingly of the opposite enantiomer (entry 8). These findings demonstrate that intimate contact between the DNA double helix and the catalyst is required for efficient chirality transfer. They therefore offer compelling evidence for DNA as the source of chirality in these reactions.

The special case of R = 3,5-dimethoxybenzyl gave the same enantiomer of the product in excess regardless of spacer length ($n = 2$ or 3). In the case of ligand **1f** ($n = 2$) relatively more of the *exo* isomer was formed (*endo*/*exo* = 92:8), with 37% *ee* for the *endo* and 78% *ee* for the *exo* isomer (Table 1, entry 10).

The difference in behavior of the catalyst based on ligands **1a** and **1f** is also evident from the reactions with substrates **3b** and **3c**, which contain a nitro and a methoxy group, respectively, on position 4 of the phenyl ring. Although the conversions observed with these substrates were generally lower ($\approx 50\%$) than those obtained with **3a** (a possible result of their lower solubility), similar results with **3c** and slightly lower *ee* values with **3b** were obtained with ligand **1a** (Table 1, entries 4 and 5). In contrast, the complex with ligand **1f** gave a much improved enantiomeric excess for both substrates; in the case of the methoxy-substituted substrate **3c**, up to 53 and 90% *ee* were observed for the *endo* and *exo* isomers, respectively (entry 15). These values represent the highest *ee* values obtained thus far with this system. These results provide strong evidence that the interaction of the substituent R with the dienophile is important for the stereochemical outcome of the reaction. However, the exact nature of this interaction and in particular, the differences between R = 1-naphthylmethyl and R = 3,5-dimethoxybenzyl are the subject of further study.

Neither the substrate/catalyst ratio, which could be increased to 4 mM:0.18 mM dienophile/catalyst (that is, catalyst at 4.5 mol% with respect to substrate, giving up to 22 turnover events; Table 1, entries 2 and 11) nor the source of the DNA used (salmon testes versus calf thymus DNA; entries 3 and 12) had a significant effect on the results. A small synthetic dsDNA (the self-complementary 16-mer $d(GACT)_2(AGTC)_2$) also gave a similar enantioselectivity for **1f** (entry 13), which rules out any possible residual impurity in the DNA from natural sources as influencing the catalytic reaction. Interestingly, in this case the *exo* product was favored even more.

The results presented herein demonstrate that the chirality of DNA can be transferred directly to a catalytic reaction. Despite the invariance of the chirality of the DNA employed, both enantiomers of the Diels–Alder product are accessible by a judicious choice of ligand. The key strengths of the present system are its modular nature, which together with the noncovalent binding of the catalytic moiety to DNA and the use of achiral ligands, allows rapid structural variation and optimization of catalysts for new reactions. An additional advantage of the present approach is the isolation of the product from the reaction mixture. The use of a DNA intercalator in the catalytic system creates a very tightly bound Cu–ligand–DNA complex, which remains in the aqueous phase during extraction of the products. The possibility to address specific DNA sequences in both natural and synthetic DNA, for example, by using a selective DNA binding moiety tethered to the catalyst, is particularly appealing for the future design of DNA-based catalysts.

Experimental Section

Catalytic Diels–Alder reactions: DNA-bound catalyst in buffered solution (salmon testes DNA (1.3 mg mL^{-1}), catalyst (0.3 mM, ligand/Cu^{2+} = 1.3), and MOPS (20 mM, pH 6.5))[12] was prepared by mixing salmon testes DNA (2 mg mL^{-1}) in solution with MOPS (30 mM) in a

volume of 10 mL (prepared 24 h in advance) with a solution of the preformed catalyst: $Cu(NO_3)_2$ (0.9 mM) and ligand **1a** (1.17 mM) in a volume of 5 mL. An aliquot of a stock solution of dienophile **3a** in CH_3CN (0.5 M, 30 μL) was added to a final concentration of 1 mM and the mixture was cooled to 5 °C. The reaction was started with the addition of cyclopentadiene (5 mM, 7 μL) and mixed by continuous inversion for 3 days, followed by extraction of the product with diethyl ether. After ^{1}H NMR spectroscopic analysis the percent *ee* value was determined by chiral HPLC (Daicel chiralcel-ODH column, elution with heptane/*i*PrOH 98:2). Selected products were purified by column chromatography and analyzed on an Daicel chiralpak-AD column to confirm the results obtained from analysis of the crude product.

Received: January 26, 2005
Published online: April 21, 2005

Keywords: asymmetric catalysis · copper · cycloaddition · deoxyribozymes · DNA

[1] a) K. Faber, *Biotransformations in Organic Synthesis, 4th ed.*, Springer, Berlin, **2000**; b) M. T. Reetz, *Proc. Natl. Acad. Sci. USA* **2004**, *101*, 5716 – 5722.
[2] a) J. A. Doudna, T. R. Cech, *Nature* **2002**, *418*, 222 – 228; b) T. M. Tarasow, E. Kellogg, B. L. Holley, D. Niewlandt, S. L. Tarasow, B. E. Eaton, *J. Am. Chem. Soc.* **2004**, *126*, 11 843 – 11 851.
[3] a) B. Seelig, S. Keiper, F. Stuhlmann, A. Jäschke, *Angew. Chem.* **2000**, *112*, 4764 – 4768; *Angew. Chem. Int. Ed.* **2000**, *39*, 4576 – 4579; ; b) F. Stuhlmann, A. Jäschke, *J. Am. Chem. Soc.* **2002**, *124*, 3238 – 3244.
[4] S. K. Silverman, *Org. Biomol. Chem.* **2004**, *2*, 2701 – 2706.
[5] a) G. F. Joyce, *Annu. Rev. Biochem.* **2004**, *73*, 791 – 836; b) J. A. Bittker, K. J. Phillips, D. R. Liu, *Curr. Opin. Chem. Biol.* **2002**, *6*, 367 – 374; c) J. P. May, R. Ting, R. Lerner, J. M. Tomas, Y. Roupioz, D. M. Perrin, *J. Am. Chem. Soc.* **2004**, *126*, 4145 – 4156.
[6] a) X. Li, D. R. Liu, *J. Am. Chem. Soc.* **2003**, *125*, 10 188 – 10 189; b) I. A. Kozlov, L. E. Orgel, P. E. Nielson, *Angew. Chem.* **2000**, *112*, 4462 – 4465; *Angew. Chem. Int. Ed.* **2000**, *39*, 4292 – 4295; ; c) M. Bolli, R. Micura, A. Eschenmoser, *Chem. Biol.* **1997**, *4*, 309 – 320.
[7] a) G. Roelfes, M. E. Branum, Li Wang, L. Que, Jr., B. L. Feringa, *J. Am. Chem. Soc.* **2000**, *122*, 11 517 – 11 518; b) K. E. Erkkila, D. T. Odom, J. K. Barton, *Chem. Rev.* **1999**, *99*, 2777 – 2796.
[8] See Supporting Information.
[9] a) M. E. Quiroz-Castro, G. A. Van Albada, I. Mutikainen, U. Turpeinen, J. Reedijk, *Inorg. Chim. Acta* **2000**, *297*, 129 – 133; b) D.-H. Lee, N. N. Murthy, K. D. Karlin, *Inorg. Chem.* **1997**, *36*, 5785 – 5792; c) A. W. Addison, H. M. J. Hendriks, J. Reedijk, L. K. Thompson, *Inorg. Chem.* **1981**, *20*, 103 – 110.
[10] Enantiomeric enrichment through selective binding of the product to DNA was excluded. See Supporting Information.
[11] a) S. Otto, J. B. F. N. Engberts, *J. Am. Chem. Soc.* **1999**, *121*, 6798 – 6806; b) S. Otto, G. Boccaletti, J. B. F. N. Engberts, *J. Am. Chem. Soc.* **1998**, *120*, 4238 – 4239.
[12] MOPS buffers are known to have negligible interaction with copper ions; see: H. E. Mash, Y.-P. Chin, L. Sigg, R. Hari, H. Xue, *Anal. Chem.* **2003**, *75*, 671 – 677.

NMR Spectroscopy

Local Structure and Anisotropic Backbone Dynamics from Cross-Correlated NMR Relaxation in Proteins**

Phineus R. L. Markwick, Remco Sprangers, and Michael Sattler**

The molecular function of biomacromolecules is determined by both their 3D structure and conformational dynamics. NMR cross-correlated relaxation (CCR) contains information about local structure and local anisotropic dynamics. CCR arises from the interference of two relaxation mechanisms such as chemical shift anisotropy (CSA) and dipole–dipole (DD) interactions, which are described by tensors in 3D space, and contains information about the relative orientation of these tensors and their correlated motion.[1–4] In this respect, CCR rates involving CSA tensors are most useful, as they sample local structure and dynamics along three orthogonal axes. Over the past few years, numerous NMR experiments have been designed to measure cross-correlated relaxation rates to determine local molecular geometry,[3,5] to study local dynamics,[6–9] and to characterize chemical-shift tensors in solution.[10–12] Different models of anisotropic local motion of the peptide plane have been discussed.[7,9,13–15]

Whereas CCR processes in principle contain an enormous amount of information, the interpretation of these relaxation rates must be treated with great care. For example, a CSA/DD relaxation process depends on many factors, including the local molecular structure, the magnitude of the CSA and orientation of the shift tensor in the fixed molecular frame, and local anisotropic dynamics.[2] To simplify this problem, the magnitude of the CSA and orientation of the shift tensor, both of which are difficult to access experimentally and theoretically, are often treated as fixed invariable parameters. Alternatively, the effect of dynamics is included through a generalized (isotropic) order parameter, which represents a considerable simplification to the complex hierarchy of internal anisotropic dynamic modes that characterize the local motion of the peptide plane. Recently, the vector fluctuations of N–H and $C'–C^{\alpha}$ bonds were monitored by studying the temperature dependence of cross-correlated relaxation rates rather than their absolute values, thereby diminishing the influence of uncertainties in CSA parameters.[9]

[*] Dr. P. R. L. Markwick, Dr. R. Sprangers, Dr. M. Sattler
European Molecular Biology Laboratory (EMBL)
Meyerhofstrasse 1, 69117 Heidelberg (Germany)
Fax: (+49) 6221-387-306
E-mail: markwick@embl.de
sattler@embl.de

[**] We thank Dr. M. Nilges, Professor R. Brüschweiler, Dr. B. Simon and C. Roome for discussions, P.R.L.M. acknowledges an EMBO fellowship. This work was supported by the DFG and the EU (D-LAB).

Supporting information for this article is available on the WWW under http://www.angewandte.org or from the author.

  DOI: 10.1002/anie.200462495

With extended DFT calculations, we previously found significant site-specific variations in both the magnitude of the C′ CSA (the relative magnitudes of the three principal components of the shift tensor δ_{11}, δ_{22}, and δ_{33}) and the orientation of the C′ chemical-shift tensor (with principal axes ξ_{11}, ξ_{22}, and ξ_{33}; Figure 1). We formulated a simple model for the C′ CSA, which depends only on the isotropic chemical shift, δ_{iso}.[16] The δ_{11} and δ_{33} components are ostensibly

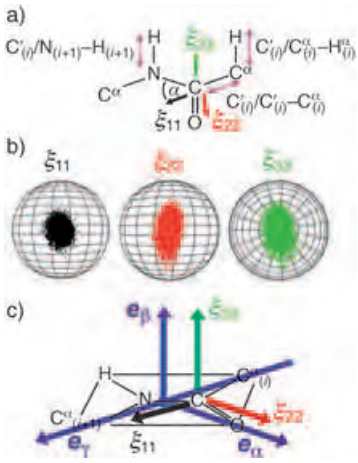

Figure 1. a) Schematic representation of the three C′ CSA/DD CCR rates studied. The average orientation of the C′ chemical-shift tensor (angle α) is also indicated (principal axes ξ_{11}, ξ_{22}, and ξ_{33}). The ξ_{33} axis lies perpendicular to the peptide plane, whereas the ξ_{11} and ξ_{22} axes lie in the peptide plane. b) Temporal fluctuations of the peptide plane of Val126 over the MD simulation. c) Representation of the average orientation of the C′ chemical-shift tensor (principal axes ξ_{11}, ξ_{22}, and ξ_{33}) and average GAF principal axes ($\boldsymbol{e}_\alpha$, $\boldsymbol{e}_\beta$, and $\boldsymbol{e}_\gamma$) in the local molecular frame.

invariable with average values of 247 ± 2 ppm and 85 ± 1 ppm, whereas the δ_{22} component varies linearly with the isotropic chemical shift ($\delta_{22} = 3\delta_{iso} - 332$ ppm). The parameterization of our CSA model[16] is notably improved in comparison with previous proposals,[17,18] and is supported by a recent analysis of experimental CCR rates, although local anisotropic motion was not explicitly considered in this study.[12] We also found that the orientation of the shift tensor is site-specific with the average α angle (the angle between ξ_{11} and the C′–N bond; Figure 1) varying from 22°–46°.[16]

Herein we combine classical molecular dynamics (MD) and extended DFT simulation methods with multidimensional NMR spectroscopy to study transverse C′ CSA/DD CCR processes. The extended DFT calculations provide an accurate representation of the C′ CSA magnitude and the orientation of the chemical-shift tensor in the fixed molecular frame. The MD simulation contains information about local anisotropic dynamics. Thus, by combining DFT and MD we can consider the relevant factors that affect the CCR rates and dissect their relative contributions.[2] Employing the Gaussian Axial Fluctuation (GAF) model,[19,20] we study local anisotropic fluctuations of the peptide plane orientation and provide an efficient method to determine these from cross-correlated relaxation.

We have measured three CSA/DD cross-correlated relaxation rates involving the carbonyl CSA: $C'_{(i)}$/ $C^{\alpha}_{(i)}$–$H^{\alpha}_{(i)}$, $C'_{(i)}$/$N_{(i+1)}$–$H_{(i+1)}$, and $C'_{(i)}$/$C'_{(i)}$–$C^{\alpha}_{(i)}$ (Figure 1) for the 55-residue Tudor domain. A CSA/DD CCR rate, $\Gamma^{(CSA/DD)}$, associated with the interference of a chemical-shift tensor centered at nucleus J and a magnetic dipole–dipole interaction between nuclei K and L is given by:[1,3,4]

$$\Gamma^{(CSA/DD)}{}_{J/K-L} = 2\,d\,c \sum_i \{\delta_{ii}\, 4J^{cc}_{ii,K-L}(0)\} \tag{1}$$

in which $d = \sqrt{(1/8)}\,(\mu_0/4\pi)\,(h/2\pi)\,\gamma_K\,\gamma_L\,\langle r^{-3}_{K\text{-}L}\rangle$ and $c = \sqrt{(1/8)}\,\gamma_J B_0$ are constant factors for the dipolar and CSA interactions, respectively (Supporting Information).[*]

The cross-correlated spectral density functions, $J^{cc}_{ii,K-L}(\omega)$, are associated with the average relative orientation and temporal correlated motion between the i^{th} principal axis of the chemical-shift tensor and the K–L dipolar interaction. Assuming time-scale separation for slow isotropic rotation diffusion with an associated correlation time, τ_c, and fast local anisotropic motion, the spectral density function can be obtained by Fourier transformation of the associated cross-correlation function as:[1,3,4]

$$J^{cc}_{ii,K-L}(\omega) = 2\int_0^{\infty} C_{ii,K-L}(t)\,cos\,\omega t\,dt \tag{2a}$$

$$C_{ii,K-L}(t) = 1/5^{(t/\tau_c)}\,C^{int}_{ii,K-L}(t) \tag{2b}$$

$$C^{int}_{ii,K-L}(t) = \langle \boldsymbol{d}_{K-L}(0)\,\xi_{ii}(t)\rangle \equiv \langle P_2\,(cos\,\theta_{ii,K-L}(t))\rangle \tag{2c}$$

The first and second terms on the right side of Equation (2b) describe the correlation functions for internal motion assuming overall isotropic tumbling, which is a reasonable assumption for the Tudor domain (the ratio of $D_{\parallel}/D_{\perp} = 1.02$). The description of anisotropic rotational diffusion involves rather complex spectral densities,[3,21] and under certain limits the influence of anisotropic rotational diffusion can be approximated.[21] The values $\boldsymbol{d}_{K-L}$ and ξ_{ii} represent the orientation of the dipole–dipole interaction (K–L) and the principal chemical-shift tensor axes, respectively. $\theta_{ii,K-L}$ is the projection angle between the dipole–dipole vector and the i^{th} principal axis of the chemical-shift tensor. Herein, the spectral density functions in Equation (1) are derived numerically from the MD simulation according to Equation (2).

The cross-correlation functions can be expressed analytically with the model-free approach,[22,23] in which the average relative orientation and amplitude of the correlated motion of the two interaction vectors is defined by a single parameter, $S^2_{ii,K-L}$, known as the order parameter (Supporting Information). In the 3D GAF model, the anisotropic order parameter $S^2_{ii,K-L}$ is described by assuming Gaussian fluctuations around three principal axes, which are rigidly attached to the peptide plane. The 3D GAF parameters for the Tudor domain (principal axes $\boldsymbol{e}_\alpha$, $\boldsymbol{e}_\beta$, and $\boldsymbol{e}_\gamma$) and the standard deviation of

[*] Note that if K = J, that is, for a CCR that involves the CSA of spin J and a dipole–dipole interaction between spins J and L, $\Gamma^{(CSA/DD)}_{J,J-L} = 2\,d\,c \sum_i \{\delta_{ii}\,(4J^{cc}_{ii,J-L}(0) + 3J^{cc}_{ii,J-L}(\omega_J)\}$.

the angular fluctuations (σ_α, σ_β, σ_γ) have been extracted from a MD trajectory.[19,20]

Figure 2a shows the correlation between the simulated [Eq. (1) and Eq. (2)] and experimental C′/C$^\alpha$–H$^\alpha$ cross-correlated relaxation rates. In general, an excellent agreement between the experimental and simulated data is observed. Deviations are found for residues in loop regions, which, apart from Asp96, exhibit a low heteronuclear {^{1}H}–^{15}N NOE (<0.65). Presumably, these differences between simulation and experiment arise from incomplete sampling of ψ angles averaged over the MD simulation. Particularly in secondary structure elements, the motion of the C′ chemical-shift tensor principal axes and the C$^\alpha$–H$^\alpha$ bond vector is highly correlated, and the associated cross-correlation functions extracted from the MD trajectory exhibit almost no decay.

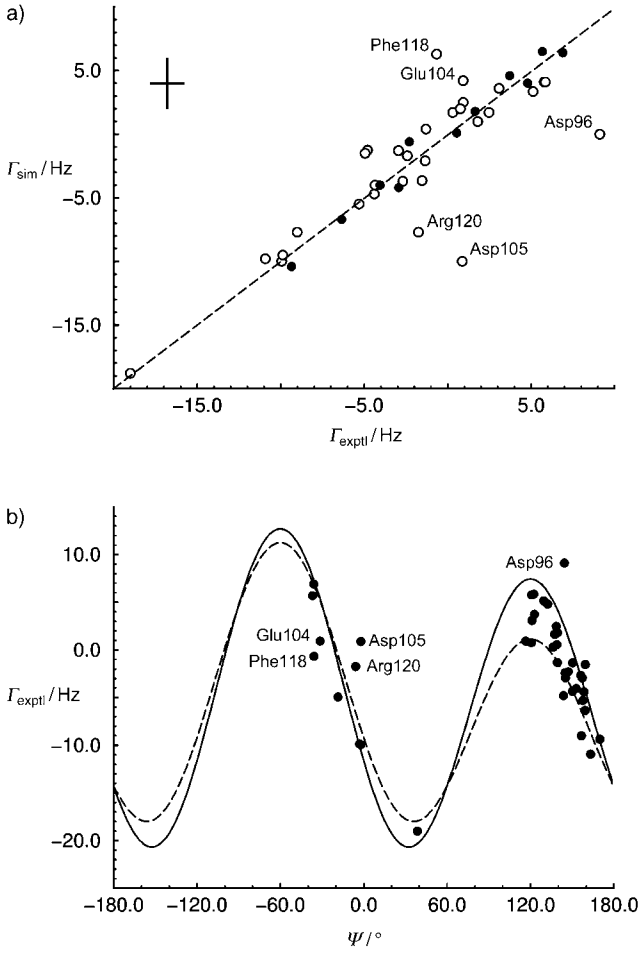

Figure 2. a) Experimental and simulated C′/C$^\alpha$–H$^\alpha$ CCR rates (Γ) for all residues in the Tudor domain excluding terminal residues and glycine residues. Filled and empty circles represent residues whose chemical-shift tensors were calculated with the extended DFT method or with the C′ CSA model, respectively. Under the model, the orientation of the shift tensor was fixed with $\alpha = 34°$. For five residues (labeled) the correlation between experiment and theory is poor. Each of these residues is in a loop region and, except for Asp96, exhibits a low heteronuclear {^{1}H}–^{15}N NOE (<0.65). b) Experimental C′/C$^\alpha$–H$^\alpha$ CCR rates plotted with respect to the ψ angle taken from the X-ray crystallographic structure.[34] Lines indicate the expected CCR rates assuming an C′ isotropic chemical shift of 168 ppm (-----) and 180 ppm (——). In both cases the orientation of the C′-shift tensor is fixed with $\alpha = 34°$.

This CCR process is predominantly dependent on the ψ angle, which determines the average orientation between the principal axes of the C′ shift tensor and the C$^\alpha$–H$^\alpha$ bond vector.[24–27] However, as can be observed in Figure 2b, site-specific variations of the C′ chemical-shift tensor also have an effect on the resulting relaxation rates, particularly when $60° < \psi < 180°$ for residues in β sheet secondary structure elements. Considering all residues studied in the Tudor domain, observed CCR rates vary between $-19.0\ s^{-1}$ and $+9.0\ s^{-1}$. The effect of C′ CSA variations causes a change in the relaxation rate of up to $7\ s^{-1}$ (25% of the total observed range), whereas the effect of dynamics (in secondary structure elements) only produces a change in the CCR rate of up to $2\ s^{-1}$ (7% variation). The orientation of the C′ chemical-shift tensor relative to the peptide plane has a small effect on the relaxation rate ($<3\ s^{-1}$) and is observed only in α-helical regions (Supporting Information).

This analysis indicates that when C′/C$^\alpha$–H$^\alpha$ CSA/DD CCR rates are used for refining the backbone angle ψ in secondary structure elements,[27,28] local dynamics has only a small effect on the measured rates. However, site-specific variations of the C′ CSA should clearly be taken into account. This can be addressed easily with the CSA model based on the isotropic C′ chemical shift.[16]

The C′/N–H CCR process depends predominantly on the C′ CSA (the magnitude of the δ_{22} component) and local anisotropic dynamics. This is highlighted in Figure 3, in which experimental and simulated CCR rates are compared with a fixed shift tensor[29] (Figure 3a) and our site-specific shift tensor[16] (Figure 3b); each case presents the simulated results with and without the inclusion of dynamics. On average, the ω angle is $180° \pm 5°$ in all residues studied, and such small variations in this angle have a negligible effect on the relaxation rates. Similarly, variations in the orientation of the C′-shift tensor in the fixed molecular frame (the α angle) have a very small effect on this CCR process (Supporting

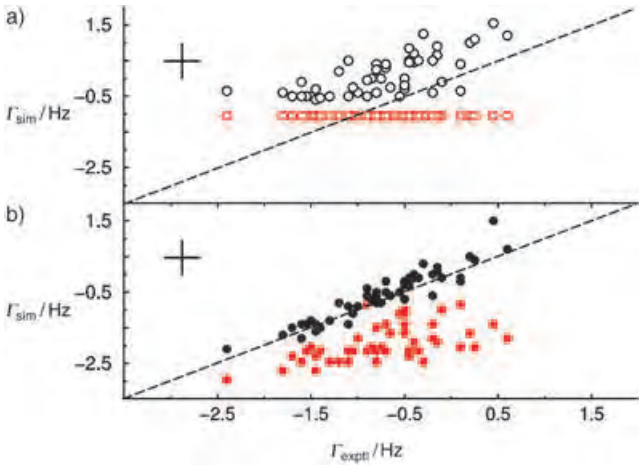

Figure 3. a) Experimental and simulated C′/N–H CCR rates assuming a fixed invariant C′ CSA[29] excluding (red ○) and including (black ○) the effect of local anisotropic dynamics. b) Experimental and simulated C′/N–H CCR rates with the site-specific C′-shift tensor excluding (red ●) and including (black ●) the effect of local anisotropic dynamics. In all cases a N–H bond length of 1.02 Å is employed, and the orientation of the C′ chemical-shift tensor is fixed with $\alpha = 34°$.

Information). This relaxation rate has been used previously to characterize local anisotropic dynamics—that of the peptide plane.[8,30] The analysis presented herein strongly argues that site-specific CSA variations have to be considered before extracting dynamic parameters from this CCR rate, as discussed below.

Experimental and simulated C′/C′–C$^{\alpha}$ cross-correlated relaxation rates for the 12 carbonyl groups studied with our extended DFT procedure are shown in Figure 4. This CCR

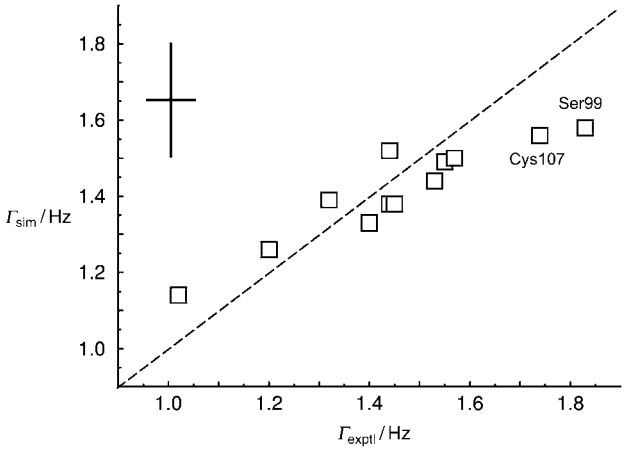

Figure 4. Correlation between experimental and simulated C′/C′–C$^{\alpha}$ CCR rates for the 12 residues studied with the extended DFT chemical-shift calculation.[16] The C′/C′–C$^{\alpha}$ CCR rate depends strongly on the orientation of the chemical-shift tensor (the α angle). Large CCR rates such as those of Ser99 and Cys107 are observed when the α angle is very large (>42°). Unfortunately, it is difficult to accurately estimate the magnitude of the site-specific α angle. The α angle of each residue is therefore obtained directly from the DFT calculations.

process depends primarily on the orientation of the shift tensor in the molecular frame. A change in the α angle alone (Figure 1) from 20° to 50° causes a change in the C′/C′–C$^{\alpha}$ CCR rate of 0.6 s^{-1}, which covers the range of relaxation rates measured. Local anisotropic dynamics leads to variations that change the relaxation rate by up to 0.30 s^{-1} (50% of the total observed range). The variation in the carbonyl CSA can cause a change in the relaxation rate of up to 0.15 s^{-1} (25% of the total range). Therefore, local anisotropic dynamics contributes only partially to the observed variations in this CCR rate, and variations in the α angle have to be considered.

For C′/N–H and C′/C′–C$^{\alpha}$ CCR processes, local anisotropic motion of the peptide plane has a considerable effect on the observed relaxation rates. To further investigate the effect of local anisotropic motion on these CCR processes, we employed the 3D GAF model of Brüschweiler and coworkers.[20] This model is particularly useful, as it describes the motion of the peptide plane in terms of physically meaningful geometrical parameters. For all residues in the Tudor domain we found that the principal axis $\boldsymbol{e}_{\beta}$ sits perpendicular to the peptide plane and the $\boldsymbol{e}_{\gamma}$ axis lies at an angle of 36°–40° relative to the C′–N bond. The 3D GAF principal axes of rotation are therefore almost exactly co-oriented with the average DFT calculated principal axes of the C′-shift tensor in the fixed peptide frame (Figure 1). The standard deviations of amplitude fluctuations (σ_{α}, σ_{β}) over the MD trajectory of 10 ns change very little from residue to residue, with average values in the β-sheet regions (6±2°, 4.5±2°), in the 3_{10} helix (5±2°, 4±2°) and in the loop regions (11°±3°, 8°±3°). A significantly larger variation was observed in the fluctuation of σ_{γ} from 9° to 17° in the secondary structure elements and up to 25° in the more flexible loop regions. These results are similar to a previous analysis of ubiquitin based on a set of autocorrelated relaxation rates.[15]

Through simplification of the 3D GAF model to an effective 1D GAF model, in which $\sigma_{\alpha}=\sigma_{\beta}=5°\equiv\sigma_{\alpha\beta}$ (the global average value for all residues in secondary structure elements) and by using the average orientation of the 3D GAF principal rotation axes, we have calculated the effect of the variation of σ_{γ} on the C′/N–H CCR rate. The resulting 2D CCR map (Figure 5), which includes the effect of site-specific

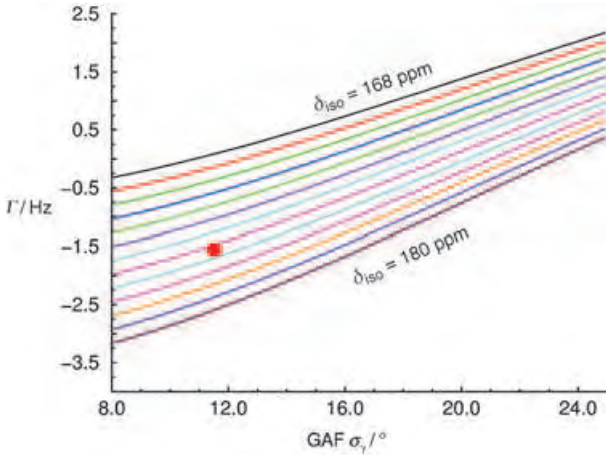

Figure 5. A 2D CCR map for C′/N–H CCR. From top to bottom, the isotropic C′ chemical shift varies from 168 to 180 ppm with lines drawn every 1 ppm; $\sigma_{\alpha\beta}$ is fixed at 5°. For a given C′/N–H CCR rate, the corresponding σ_{γ} can be extracted from the 2D map, as shown for Val126 (δ_{iso} = 175.3 ppm; C′/N–H CCR rate = −1.6 Hz).

C′ CSA variations, allows the accurate estimation of σ_{γ} from a given experimental C′/N–H CCR rate. As shown in detail in the Supporting Information, variations in the orientation of the C′-shift tensor and $\sigma_{\alpha\beta}$ generally have a negligible effect on this CCR process. The resulting σ_{γ} amplitude fluctuations correlate very well with the autocorrelated ^{15}N order parameter calculated from ^{15}N relaxation data with TENSOR2[31] (Figure 6). This important result demonstrates that the different relaxation rates provide a consistent description of the local anisotropic dynamics. This observation also argues that out-of-plane motion of the N–H bond vector[9,32] does not have a strong effect on these relaxation rates.[*] Given the larger amplitude of σ_{γ} compared with $\sigma_{\alpha\beta}$, our GAF analysis is

[*] In fact, this is indicated by comparing C′/N–H cross-correlated order parameters calculated numerically from the MD simulation [Eq. (1) and Eq. (2)] with the order parameters extracted from the 3D GAF analysis of the same simulation. The difference in the numerically calculated order parameters (which include N–H out-of-plane motion) and the 3D GAF order parameters (which do not sense N–H out-of-plane motion) is less than 0.03, resulting in a negligible change in the associated CCR rates.

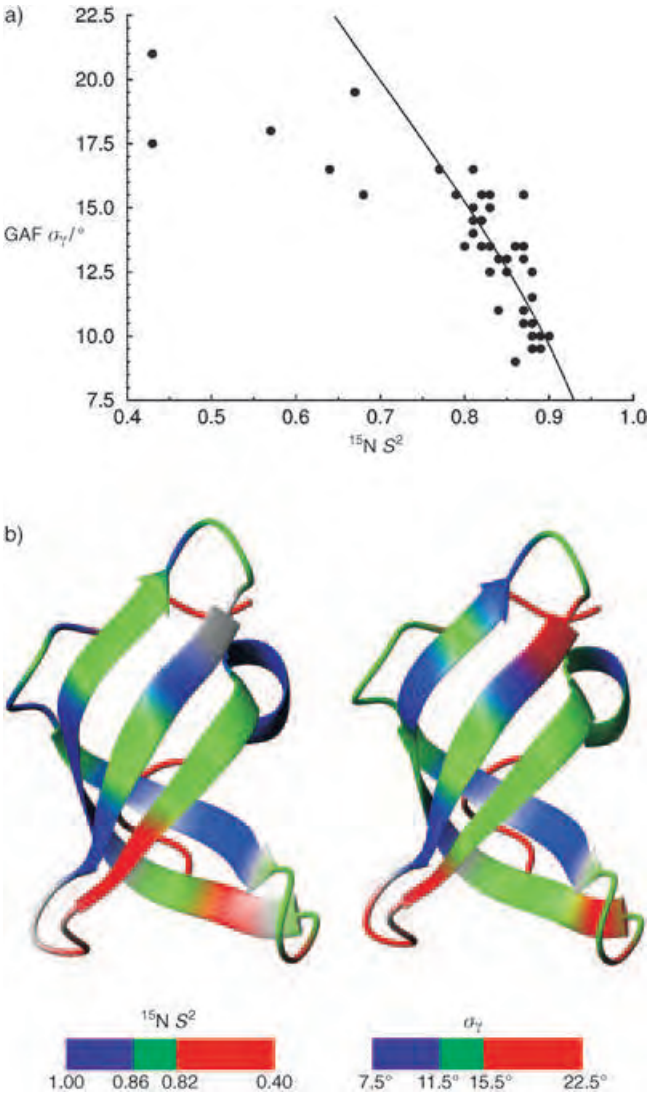

Figure 6. a) Correlation between the order parameter S^2 extracted from ^{15}N autorelaxation rates and σ_γ, which is extracted from the analysis of C′/N–H cross-correlated relaxation data. Assuming that $\sigma_\alpha = \sigma_\beta = 5°$, the theoretically expected correlation[19,20] is indicated by the solid line. For residues in secondary structure elements with the ^{15}N order parameter $S^2 = 0.75$, the result is in good agreement with the expected correlation. For the more flexible residues in terminal loop regions, a distinct deviation is observed. This results partly from the fact that for these residues, $\sigma_{\alpha\beta}$ is much larger than 5°, and also from the fact that for these very flexible regions, the 3D GAF model breaks down. b) Representation of the variations of the ^{15}N order parameter S^2 and σ_γ visualized on the Tudor domain. Residues for which no experimental data are available are rendered in gray.

consistent with so-called crankshaft motions around the $C^\alpha_{(i)} \cdots C^\alpha_{(i+1)}$ axis (Figure 1c).[7,13–15] We have also calculated 2D CCR maps for the C′/C′–C$^\alpha$ CCR rate, which demonstrate the strong dependence of this rate on the orientation of the C′-shift tensor and variations in $\sigma_{\alpha\beta}$ (Supporting Information).

In summary, we have performed a detailed analysis of C′ CSA/DD CCR rates by combining classical MD and extended DFT simulation methods. We have found that the C′/C$^\alpha$–H$^\alpha$ CCR rate depends primarily on the local protein structure (the ψ angle), but is also affected by variations in the C′ CSA. In contrast, the C′/C′–C$^\alpha$ CCR rate strongly depends on the orientation of the carbonyl chemical-shift tensor in the fixed molecular frame and local anisotropic dynamics, but C′ CSA variations also play a role. The C′/N–H CCR rate depends principally on the carbonyl CSA (the magnitude of δ_{22}) and local anisotropic dynamics and is thus most useful for the characterization of such motions. Employing the 3D GAF model, it is possible to acquire detailed information concerning the local anisotropic motion of the peptide plane from a single cross-correlation: the C′/N–H CCR rate.

Cross-correlated relaxation processes contain a wealth of information concerning both the structure and dynamics of biomolecular systems and are exploited in the design of relaxation-optimized NMR experiments.[33] The improved description of the parameters presented herein will be useful for future studies of the characterization of local anisotropic dynamics. A dissection of the relaxation data into different contributing factors demonstrates the power of combining theoretical and experimental techniques to probe the structure and dynamics of biomacromolecules.

Received: November 2, 2004
Revised: January 10, 2005
Published online: April 21, 2005

Keywords: chemical shift anisotropy · density functional calculations · molecular dynamics · NMR spectroscopy · structure elucidation

[1] M. W. F. Fischer, A. Majumdar, E. R. P. Zuiderweg, *Prog. Nucl. Magn. Reson. Spectrosc.* **1998**, *33*, 207.
[2] C. Scheurer, N. R. Skrynnikov, S. F. Lienin, S. K. Straus, R. Brüschweiler, R. R. Ernst, *J. Am. Chem. Soc.* **1999**, *121*, 4242.
[3] H. Schwalbe, T. Carlomagno, M. Hennig, J. Junker, B. Reif, C. Richter, C. Griesinger, *Methods Enzymol.* **2001**, *338*, 35.
[4] D. Frueh, *Prog. Nucl. Magn. Reson. Spectrosc.* **2002**, *41*, 305.
[5] B. Reif, M. Hennig, C. Griesinger, *Science* **1997**, *276*, 1230.
[6] M. W. F. Fischer, L. Zeng, Y. X. Pang, W. D. Hu, A. Majumdar, E. R. P. Zuiderweg, *J. Am. Chem. Soc.* **1997**, *119*, 12629.
[7] M. W. F. Fischer, L. Zeng, A. Majumdar, E. R. P. Zuiderweg, *Proc. Natl. Acad. Sci. USA* **1998**, *95*, 8016.
[8] T. Carlomagno, M. Maurer, M. Hennig, C. Griesinger, *J. Am. Chem. Soc.* **2000**, *122*, 5105.
[9] T. Wang, S. Cai, E. R. P. Zuiderweg, *J. Am. Chem. Soc.* **2003**, *125*, 8639.
[10] Y. Pang, E. R. P. Zuiderweg, *J. Am. Chem. Soc.* **2000**, *122*, 4841
[11] D. Fushman, D. Cowburn, *Methods Enzymol.* **2001**, *339*, 109.
[12] F. Cisnetti, K. Loth, P. Pelupessy, G. Bodenhausen, *ChemPhysChem* **2004**, *5*, 807.
[13] A. R. Fadel, D. Q. Jin, G. T. Montelione, R. M. Levy, *J. Biomol. NMR* **1995**, *6*, 221.
[14] R. M. Levy, M. Karplus, *Biopolymers* **1979**, *18*, 2465.
[15] S. F. Lienin, T. Bremi, B. Brutscher, R. Brüschweiler, R. R. Ernst, *J. Am. Chem. Soc.* **1998**, *120*, 9870.
[16] P. R. L. Markwick, M. Sattler, *J. Am. Chem. Soc.* **2004**, *126*, 11424.
[17] T. G. Oas, C. Y. Hartzell, T. J. McMahon, G. P. Drobny, F. W. Dahlquist, *J. Am. Chem. Soc.* **1987**, *109*, 5956.
[18] N. Asakawa, S. Kuroki, H. Kurosu, I. Ando, A. Shoji, T. Ozaki, *J. Am. Chem. Soc.* **1992**, *114*, 3261.
[19] R. Brüschweiler, P. E. Wright, *J. Am. Chem. Soc.* **1994**, *116*, 8426.
[20] T. Bremi, R. Brüschweiler, *J. Am. Chem. Soc.* **1997**, *119*, 6672.

[21] M. Deschamps, *J. Phys. Chem. A* **2002**, *106*, 2438.
[22] G. Lipari, A. Szabo, *J. Am. Chem. Soc.* **1982**, *104*, 4546.
[23] G. Lipari, A. Szabo, *J. Am. Chem. Soc.* **1982**, *104*, 4559.
[24] D. Yang, R. Konrat, L. E. Kay, *J. Am. Chem. Soc.* **1997**, *119*, 11938.
[25] D. Yang, L. E. Kay, *J. Am. Chem. Soc.* **1998**, *120*, 9880.
[26] E. Chiarparin, P. Pelupessy, R. Ghose, G. Bodenhausen, *J. Am. Chem. Soc.* **1999**, *121*, 6876.
[27] R. Sprangers, M. J. Bottomley, J. P. Linge, J. Schultz, M. Nilges, M. Sattler, *J. Biomol. NMR* **2000**, *16*, 47.
[28] B. Reif, A. Diener, M. Hennig, M. Maurer, C. Griesinger, *J. Magn. Reson.* **2000**, *143*, 45.
[29] Q. Teng, M. Iqbal, T. A. Cross, *J. Am. Chem. Soc.* **1992**, *114*, 5312.
[30] B. Brutscher, N. R. Skrynnikov, T. Bremi, R. Brüschweiler, R. R. Ernst, *J. Magn. Reson.* **1998**, *130*, 346.
[31] P. Dosset, J. C. Hus, M. Blackledge, D. Marion, *J. Biomol. NMR* **2000**, *16*, 23.
[32] T. S. Ulmer, B. E. Ramirez, F. Delaglio, A. Bax, *J. Am. Chem. Soc.* **2003**, *125*, 9179.
[33] K. Pervushin, R. Riek, G. Wider, K. Wüthrich, *Proc. Natl. Acad. Sci. USA* **1997**, *94*, 12366.
[34] R. Sprangers, M. R. Groves, I. Sinning, M. Sattler, *J. Mol. Biol.* **2003**, *327*, 507.

Molecular Devices

Electrochemical Addressing of the Optical Properties of a Monolayer on a Transparent Conducting Substrate**

*Atindra D. Shukla, Amitava Das, and Milko E. van der Boom**

Thin-film chemistry and surface engineering, in particular the generation of new molecular electronic and photonic materials, are attracting considerable interest.[1] The development of a fundamental understanding of molecular interactions, orientation, and function is essential for the formation of device-quality organic mono- and multilayers.[2] Direct control of thin-film properties might lead to a wide range of applications in molecular-based optics and electronics. For instance, low-voltage redox-active molecules may be potentially useful for the design of new monolayers for charge-storage memory devices.[3,4] These molecular-based memories, bound to Si(100), withstand operation and device-processing temperatures.[4] However, many challenges need to be addressed before such systems will become readily available. It has been very difficult to predict and to switch reversibly the monolayer properties for a given molecular building block. Much effort has been devoted to the development of molecular switches in solution,[5–7] whereas such systems immobilized on substrate surfaces is a rapidly developing field.[3,4,8–11] Recently Di Bella and co-workers reported the first example of a redox switch self-assembled on an optically transparent Pt electrode.[9] The optical properties of the thiol-based monolayers can be controlled by chemical oxidation and reduction. Herein, we demonstrate electrochemical switching of the optical properties of a ruthenium-based monolayer, which is covalently attached to a transparent conducting substrate surface.

The molecular building block consists of a tris(bipyridyl)-ruthenium module for charge storage and a phenol unit for covalent surface attachment (Figure 1). Functional thin films are formed by covalent assembly of the previously reported ruthenium-based molecular building block at an organic interface (Figure 1).[12] The siloxane-based coupling layers (CL) were prepared on freshly cleaned float glass, Si(100), and glass-coated with indium tin oxide (ITO). Substrates were treated with a dry pentane solution of *p*-chloromethylphenyltrichlorosilane (1:100, v/v) at room temperature for 30 min

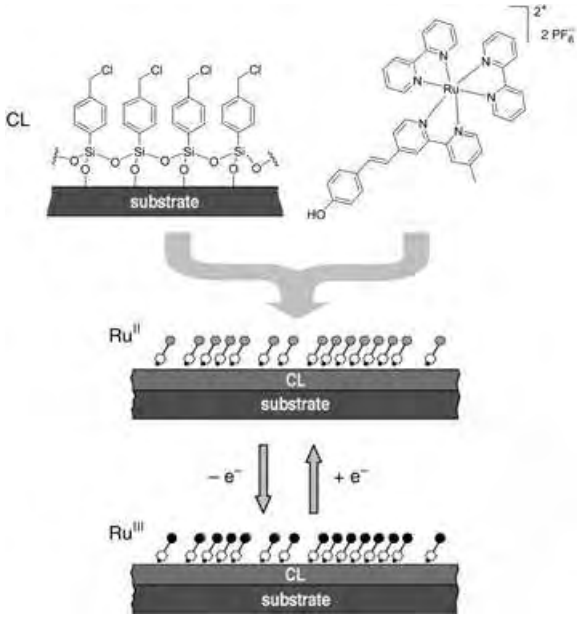

Figure 1. Formation of ruthenium-based monolayers on ITO-coated glass, glass, and silicon substrate surfaces functionalized with a chlorobenzyl-based coupling layer (CL). Electrochemical and spectroelectrochemical measurements were performed on glass coated with ITO on a single side. Monolayers were assembled only on the ITO side of the glass substrate by mechanical protection of the glass surface.

[*] Dr. A. D. Shukla, Dr. M. E. van der Boom
Department of Organic Chemistry
The Weizmann Institute of Science
76100 Rehovot (Israel)
Fax: (+972) 8-934-4142
E-mail: milko.vanderboom@weizmann.ac.il
Dr. A. Das
Central Salt and Marine Chemicals Research Institute
Gujarat (India)

[**] This research was supported by the Helen and Martin Kimmel Center for Molecular Design, the Yigal-Alon Fellowship program, MINERVA, the German BMBF, and the MJRG for Molecular Materials and Interface Design (M.E.v.d.B). A.D. thanks DST (India) for financial assistance. A.D.S. is the recipient of the Reva G. Stone Postdoctoral Fellowship. We thank M. Altman and H. Cohen (WIS) for the AFM and XPS measurements, respectively. M.E.v.d.B. is the incumbent of the Dewey David Stone and Harry Levine career development chair.

Supporting information for this article is available on the WWW under http://www.angewandte.org or from the author.

 DOI: 10.1002/anie.200461958

under N_2. The substrates were then thoroughly washed with copious amounts of dry pentane and dried at 115 °C for about 15 min. Subsequently, the colorless chlorobenzyl-functionalized substrates were immersed in a 2.0 mM toluene/CH_2Cl_2 (6:4, v/v) solution of the ruthenium complex, and heated for 48 h at 80 °C under N_2 by using glass pressure tubes. The resulting chromophore films were washed and sonicated (1 min) with copious amounts of CH_2Cl_2, acetone, and isopropyl alcohol, and dried under a gentle stream of N_2. Similar surface coupling reactions of benzyl halide interfaces with phenols or pyridine moieties to form ether linkages or pyridinium salts, respectively, have been reported.[13,14] The new monolayers strongly adhere to the glass and silicon substrates, are insoluble in common organic solvents, and cannot be removed by either the "Scotch-tape decohesion" test or by CO_2 snowjet cleaning.

Freshly prepared samples were characterized by a combination of semicontact atomic force microscopy (AFM), optical transmission (UV/Vis) spectrometry, X-ray photoelectron spectroscopy (XPS), electrochemistry, and spectroelectrochemistry.[14] The latter technique was used to vary and to read the optical properties of the system. XPS measurements of the Ru^{II}-based monolayer on ITO-coated glass revealed a Si/N ratio of about 1:2.1, which indicates that about 35 % of the CL molecules reacted. This is not uncommon.[15] The relatively small footprint of the CL molecules prohibits a quantitative reaction with the larger ruthenium complex. The film thickness derived from angle-resolved XPS is estimated to be 13 ± 2 Å. Semicontact AFM measurements on films grown on Si(100) substrates show an essentially smooth film surface with no evident grain boundaries. The root-mean-square surface roughness is about 0.1 nm for $1 \times 1\ \mu m^2$ scan areas (see the Supporting Information). Electrochemical measurements were performed to evaluate the redox activity of the monolayers. Figure 2 a shows the cyclic voltammograms of the monolayer on ITO-coated glass at different voltage scan rates (ν). The half-wave redox potential $E_{1/2}$ remains constant within $\nu = 100$–$1000\ mV s^{-1}$. The peak-to-peak separation (ΔE) is about 64 mV for $\nu = 500\ mV s^{-1}$. Figure 2 b shows the linear correlation of the peak current I_p versus ν. Apparently, a reversible redox process occurs involving a one-electron transfer. The ΔE value is expected to be about 60 mV for a Ru^{II}/Ru^{III} couple in solution.[16] The potential of the Ru^{II}/Ru^{III} couple $E_{1/2}$ is 0.95 V with respect to the ferrocene/ferrocenium standard.

After the initial conditioning scans, continuous cyclic voltammetry (CV) measurements show a repetitive redox behavior for at least 45 cycles. The magnitude of the ruthenium-centered oxidation current decreases slightly with the first six successive sweeps, possibly as a result of deactivation or reordering of the molecular components (Figure 3).

The UV/Vis optical absorbance measurements of the Ru^{II}-based films on glass and on ITO-coated glass substrates show a ligand-based π–π* transition band at $\lambda_{max} = 314$ nm. The low-energy metal-to-ligand charge-transfer (MLCT) band appears at $\lambda = 462$ nm. Increasing the reaction time to 72 h does not affect the intensity of these absorbance bands. In situ spectroelectrochemistry performed in air showed a

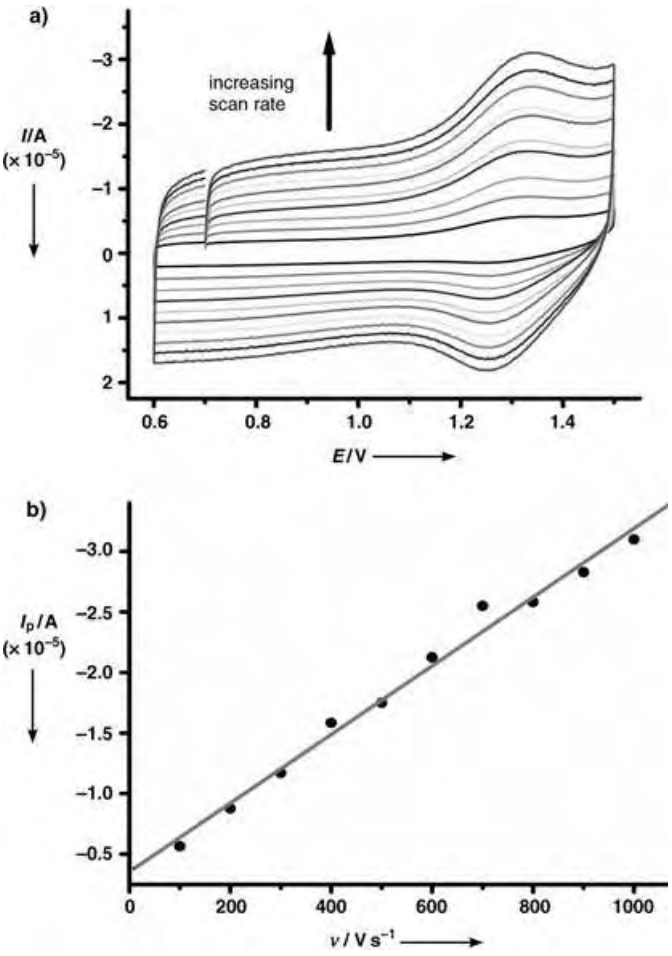

Figure 2. a) Representative cyclic voltammetric responses at different scan rates of the ruthenium-based monolayer on ITO-coated glass, which operates as the working electrode. Pt wires were used as reference and counter electrodes. The electrochemical (EC) experiments were carried out at room temperature in dry acetonitrile containing 20 mM nBu_4NPF_6 with a CHI660A potentiostat. The voltage scan rate was varied from 100 to 1000 $mV s^{-1}$ with steps of 100 $mV s^{-1}$. b) Linear correlation ($R^2 = 0.988$) of the peak current I_p versus the scan rate ν.

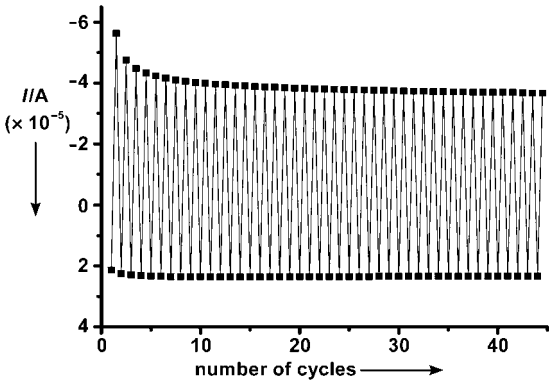

Figure 3. Representative EC redox switching as a function of redox cycles. The CV experiments were conducted at a sweep rate of 1000 $mV s^{-1}$. The lines are drawn as a guide to the eye.

significant reversible change in the intensity of the absorbance band at $\lambda_{max} = 314$ nm upon alternation of the metal

oxidation state, Ru^{II}/Ru^{III} (Figure 4). Nine repetitions of the phenomenon are shown in the inset of Figure 4; they demonstrate the possibility of optical readout of the charge storage. The MLCT band is too weak for accurate monitoring by transmission UV/Vis spectrometry.

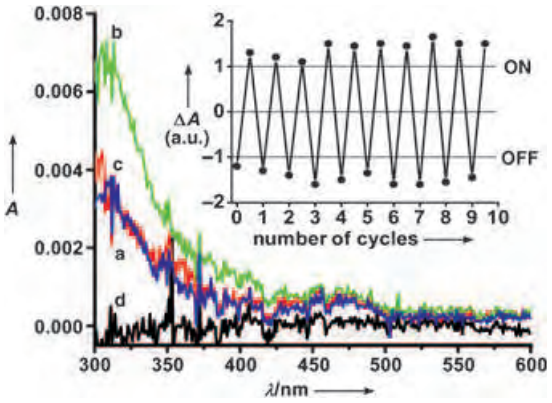

Figure 4. Absorption spectra for the optical switching of the ruthenium-based monolayer on ITO at $\lambda = 314$ nm for 10 min: a) Ru^{II}, b) Ru^{III}, c) Ru^{II}, d) baseline. The inset shows the EC on/off switching of the intensity change of the absorbance band at $\lambda = 314$ nm (ΔA, a.u.) versus the number of Ru^{II}/Ru^{III} cycles. The lines are drawn as a guide to the eye. EC oxidation was carried out by bulk electrolysis at 1.4 V, while reduction was performed at −0.1 V (20 min each). UV/Vis spectra were recorded in situ on a Cary 100 spectrophotometer after each oxidation state change.

In summary, the formation and characterization of a ruthenium-based monolayer on hydrophilic substrates, including ITO-coated glass, is described. Electrochemical variation of the metal oxidation state of the covalently surface-bound molecular building blocks triggers a reversible change in the optical properties of the ligand module. This read/write process can be carried out conveniently in air and monitored with a standard UV/Vis spectrophotometer. The low-voltage operation and the stability of the monolayer may make it a suitable candidate for nonvolatile memory devices. Extension of the scope of the work presented herein to mono- and multilayers of other metal-based chromophores, as well as to modulation of luminescence intensity and nonlinear optical responses, is in progress.

Received: September 12, 2004
Revised: January 27, 2005
Published online: April 8, 2005

Keywords: molecular devices · monolayers · ruthenium · switches · thin films

[1] a) A. Nitzan, M. A. Ratner, *Science* **2003**, *300*, 1384; b) A. Salomon, D. Cahen, S. Lindsay, J. Tomfohr, V. B. Engelkes, C. D. Frisbie, *Adv. Mater.* **2003**, *15*, 1883; c) M. E. van der Boom, *Angew. Chem.* **2002**, *114*, 3511; *Angew. Chem. Int. Ed.* **2002**, *41*, 3363.

[2] For examples of functional mono- and multilayers, see: a) P. Zhu, H. Kang, A. Facchetti, G. Evmenenko, P. Dutta, T. J. Marks, *J. Am. Chem. Soc.* **2003**, *125*, 11496; b) T. van der Boom, G. Evmenenko, P. Dutta, M. R. Wasielewski, *Chem. Mater.* **2003**, *15*, 4068; c) A. Facchetti, A. Abbotto, L. Beverina, M. E. van der Boom, P. Dutta, G. Evmenenko, T. J. Marks, G. A. Pagani, *Chem. Mater.* **2002**, *14*, 4996; d) G. A. Neff, M. R. Helfrich, M. C. Clifton, C. J. Page, *Chem. Mater.* **2000**, *12*, 2363; e) M. S. Johal, Y. W. Cao, X. D. Chai, L. B. Smilowitz, J. M. Robinson, T. J. Li, D. McBranch, D.-Q. Li, *Chem. Mater.* **1999**, *11*, 1962; f) V. Burtman, A. Zelichenok, S. Yitzchaik, *Angew. Chem.* **1999**, *111*, 2078; *Angew. Chem. Int. Ed.* **1999**, *38*, 2041; g) A. Ulman, *Chem. Rev.* **1996**, *96*, 1533; h) H. E. Katz, W. L. Wilson, G. Scheller, *J. Am. Chem. Soc.* **1994**, *116*, 6636.

[3] Q. Li, G. Mathur, M. Homsi, S. Surthi, V. Misra, V. Malinovskii, K.-H. Schweikart, L. Yu, J. S. Lindsey, Z. Liu, R. B. Dabke, A. Yasseri, D. F. Bocian, W. G. Kuhr, *Appl. Phys. Lett.* **2002**, *81*, 1495.

[4] a) Z. Liu, A. A. Yasseri, J. S. Lindsey, D. F. Bocian, *Science* **2003**, *302*, 1543; b) R. L. Carroll, C. B. Gorman, *Angew. Chem.* **2002**, *114*, 4556; *Angew. Chem. Int. Ed.* **2002**, *41*, 4378.

[5] a) A. P. de Silva, D. B. Fox, T. S. Moody, S. M. Weir, *Trends Biotechnol.* **2001**, *19*, 27; b) *Molecular Switches* (Ed.: B. L. Feringa), Wiley-VCH, Weinheim, **2001**; c) I. Willner, E. Katz, *Angew. Chem.* **2000**, *112*, 1230; *Angew. Chem. Int. Ed.* **2000**, *39*, 1180; d) special issue on "Photochromism: Memories and Switches": *Chem. Rev.* **2000**, *100*, 1683; e) B. J. Coe, *Chem. Eur. J.* **1999**, *5*, 2464.

[6] For an electrochemically driven metal-based switch in solution, see: D. Kalny, M. Elhabiri, T. Moav, A. Vaskevich, I. Rubinstein, A. Shanzer, A.-M. Albrecht-Gary, *Chem. Commun.* **2002**, 1426.

[7] a) G. Fabbrini, E. Menna, M. Maggini, A. Canazza, G. Marcolongo, M. Meneghetti, *J. Am. Chem. Soc.* **2004**, *126*, 6239; b) J. T. M. Kennis, I. H. M. van Stokkum, S. Crosson, M. Gauden, K. Moffat, R. van Grondelle, *J. Am. Chem. Soc.* **2004**, *126*, 4512; c) M. P. Debreczeny, W. A. Svec, M. R. Wasielewski, *Science* **1996**, *274*, 584; d) L. Zelikovich, J. Libman, A. Shanzer, *Nature* **1995**, *374*, 790.

[8] a) S. Yasutomi, T. Morita, Y. Imanishi, S. Kimura, *Science* **2004**, *304*, 1944; b) M. J. Cook, A.-M. Nygård, Z. Wang, D. A. Russell, *Chem. Commun.* **2002**, *10*, 1056; c) C. P. Collier, G. Mattersteig, E. W. Wong, Y. Luo, K. Beverly, J. Sampaio, F. M. Raymo, J. F. Stoddart, J. R. Heath, *Science* **2000**, *289*, 1172.

[9] For chemical switching of the optical properties of a thiol-based monolayer on ultrathin Pt electrodes, see: S. Sortino, S. Petralia, S. Conoci, S. Di Bella, *J. Am. Chem. Soc.* **2004**, *126*, 1122.

[10] The use of optical spectroscopy to measure the redox state of noncovalently bound organic films on transparent electrodes is known; however, to the best of our knowledge only very few studies have been reported on thiol-based monolayers.[9] For examples of spectroelectrochemistry on noncovalently bound (adsorbed) organic films, see: a) D. R. Dunphy, S. B. Mendes, S. S. Saavedra, N. R. Armstrong, *Anal. Chem.* **1997**, *69*, 3086; b) S. C. Paulson, C. M. Elliot, *Anal. Chem.* **1996**, *68*, 1711; c) J. W. Perry, A. J. McQuillan, F. C. Anson, A. H. Zewail, *J. Phys. Chem.* **1983**, *87*, 1480; d) for an example of spectroelectrochemistry on a multilayer based on electrostatic interactions, see: Z. Guo, Y. Shen, M. Wang, F. Zhao, S. Dong, *Anal. Chem.* **2004**, *76*, 184.

[11] J. Lahann, S. Mitragotri, T.-N. Tran, H. Kaido, J. Sundaram, I. S. Choi, S. Hoffer, G. A. Somorjai, R. Langer, *Science* **2003**, *299*, 371.

[12] A. J. Amoroso, A. Das, J. A. McCleverty, M. D. Ward, F. Barigelletti, L. Flamigni, *Inorg. Chim. Acta* **1994**, *226*, 171.

[13] a) R. Yerushalmi, A. Scherz, M. E. van der Boom, *J. Am. Chem. Soc.* **2004**, *126*, 2700; b) A. Gulino, P. Mineo, E. Scamporrino, D. Vitalini, I. Fragala, *Chem. Mater.* **2004**, *16*, 1838; c) W. J. Dressick, M. S. Chen, S. L. Brandow, *J. Am. Chem. Soc.* **2000**,

122, 982; d) D.-Q. Li, B. I. Swanson, J. M. Robinson, M. A. Hoffbauer, *J. Am. Chem. Soc.* **1993**, *115*, 6975.
[14] Monolayer characterization will be reported in a full paper; for details of the XPS and AFM instrumentation and analysis procedures, see: A. D. Shukla, D. Strawser, A. C. B. Lucassen, D. Freeman, H. Cohen, D. A. Jose, A. Das, G. Evmenenko, P. Dutta, M. E. van der Boom, *J. Phys. Chem. B* **2004**, *8*, 17505.
[15] W. Lin, W. Lin, G. K. Wong, T. J. Marks, *J. Am. Chem. Soc.* **1996**, *118*, 8034.
[16] *Electrochemical Methods: Fundamentals and Applications, 2nd ed.* (Eds.: A. J. Bard, L. R. Faulkner), Wiley, New York, **2001**.

Vapochromism

Vapochromic Behavior Accompanied by Phase Transition between Charge-Polarization and Charge-Density-Wave States in a Quasi-One-Dimensional Iodine-Bridged Dinuclear Platinum Compound**

Hiroyuki Mastuzaki, Hideo Kishida, Hiroshi Okamoto,* Kouichi Takizawa, Satoshi Matsunaga, Shinya Takaishi, Hitoshi Miyasaka, Ken-ichi Sugiura, and Masahiro Yamashita*

One-dimensional (1D) materials have attracted great attention for several decades in the fields of chemistry and physics, because they exhibit characteristic optical properties that originate from 1D electronic structures as well as magnetic and transport properties.[1] Some 1D materials have been reported to show striking and reversible changes in color and/or luminescence upon exposure to volatile organic compounds and water vapor. This spectroscopic change in the presence of vapor is called vapochromism, which is a promising phenomenon for chemical-vapor-sensing devices.[2] Typical vapochromic materials are the series of compounds $[Pt(CNR)_4][Pt(CN)_4]$ ($R = p$-CN-C_6H_4-C_nH_{2n+1}; $n = 1, 2, 6, 10, 12, 14$), which are square-planar Pt^{II} compounds that form linear chains of alternating $[Pt(CNR)_4]^{2+}$ dications and $[Pt(CN)_4]^{2-}$ dianions.[2b,d] The vapochromism of these complexes is suggested to be a result of the change in the Pt···Pt distance,[2d] which is not related to instabilities of 1D electronic structures such as Peierls and spin-Peierls instabilities. Herein, we report a new type of vapochromism driven by the phase-transition characteristic of 1D electronic systems. A 1D halogen-bridged dinuclear platinum compound was studied, which displays a reversible phase transition on exposure to water vapor with a remarkable change in structural and optical properties. This compound has a 1D chain structure composed of repeating metal–metal–halogen (MMX) units, in which M = Pt and X = I, called an MMX chain.

A 1D electronic structure is formed in the MMX chain compound by the d_{z^2} orbitals of the M atoms and the p_z orbitals of the X atoms. The formal valence of M is 2.5+, and three electrons exist per two d_{z^2} orbitals. The following four charge-ordering (CO) states are theoretically expected in this system:[3]

a) -$M^{2.5+}$-$M^{2.5+}$-X-$M^{2.5+}$-$M^{2.5+}$-X-
average-valence (AV) state

b) ···M^{2+}-M^{2+}···X-M^{3+}-M^{3+}-X···
charge-density-wave (CDW) state

c) ···M^{2+}-M^{3+}-X···M^{2+}-M^{3+}-X···
charge-polarization (CP) state

d) ···M^{2+}-M^{3+}-X-M^{3+}-M^{2+}···X···
alternating charge-polarization (ACP) state

Two families of the MMX chain compounds, namely, $A'_4[Pt_2(pop)_4X]\cdot n H_2O$ ($A' = K$, NH_4; $pop = P_2O_5H_2^{2-}$; $X =$ Cl, Br)[4] and $[M_2(dta)_4I]$ ($M = Pt$, Ni; $dta = CH_3CS_2^-$),[5] were reported in the early stage of the studies. The ground state of the former was revealed to be the CDW state. For $[Pt_2(dta)_4I]$, a transition from the CP to the ACP state was suggested to occur at 80 K,[5d] while $[Ni_2(dta)_4I]$ was considered to have the AV state.[5c] The I-bridged compounds have a larger hybridization between the p orbital of the X atom and the d orbital of the M atom than the Cl- or Br-bridged compounds, so various CO states are expected to be stabilized. In preceding papers,[6,7] we reported on the synthesis of about 20 compounds of the type $A'_4[Pt_2(pop)_4I]\cdot n H_2O$ and $A''_2[Pt_2(pop)_4I]\cdot n H_2O$, with different countercations ($A' = Na$, NH_4, Rb, Cs, $C_nH_{2n+1}NH_3$, and $(C_nH_{2n+1})_2NH_2$; $A'' = NH_3(C_nH_{2n})NH_3$). We demonstrated that substitution of these compounds widely changes the Pt···I···Pt distance (d(Pt-I-Pt)) and that the electronic structures of PtPtI chains are controlled between the diamagnetic CDW and paramagnetic CP states. Moreover, we reported the pressure- and photoinduced phase transition between the CP and CDW states in $[(C_2H_5)_2NH_2]_4[Pt_2(pop)_4I]$.[7] The target material in the present study is $[NH_3(C_4H_8)NH_3]_2[Pt_2(pop)_4I]\cdot 4H_2O$ (**1**), which shows vapochromic behavior accompanied by a transition between the paramagnetic CP state and the diamagnetic CDW state.

[*] Dr. H. Mastuzaki, Dr. H. Kishida, Prof. Dr. H. Okamoto
Department of Advanced Materials Science
Graduate School of Frontier Sciences, University of Tokyo
5-1-5 Kashiwanoha, Kashiwa, Chiba 277-8561 (Japan)
and
CREST (JST), Kawaguchi, Saitama 332-0012 (Japan)
Fax: (+81) 4-7136-3773
E-mail: matsu@okalab.k.u-tokyo.ac.jp
okamotoh@k.u-tokyo.ac.jp
K. Takizawa, S. Matsunaga, Dr. S. Takaishi, Dr. H. Miyasaka, Prof. Dr. K.-i. Sugiura, Prof. Dr. M. Yamashita
Department of Chemistry, Graduate School of Science
Tokyo Metropolitan University
1-1 Minamiohsawa, Hachioji, Tokyo 192-0397 (Japan)
and
CREST (JST),Kawaguchi, Saitama 332-0012 (Japan)

[**] This work was partly supported by a Grant-in-Aid for Creative Scientific Research from the Ministry of Education, Culture, Sports, Science, and Technology.

  DOI: 10.1002/anie.200500091

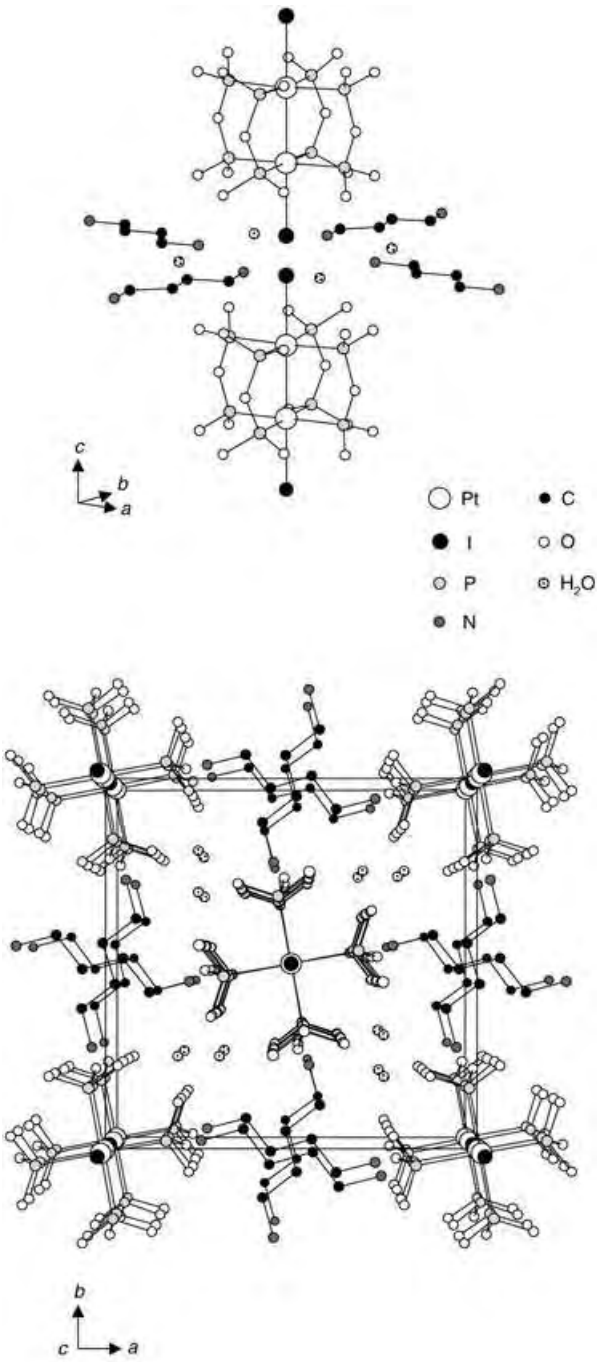

Figure 1. Crystal structure of **1**. H atoms have been omitted for clarity.

Figure 1 shows a perspective view of the crystal structure of **1** at 296 K. Two Pt atoms are linked by four pop ligands to form a $\{Pt_2(pop)_4\}$ unit. The two neighboring $\{Pt_2(pop)_4\}$ units are bridged by I ions, thus forming a PtPtI linear chain along the *c* axis. The bridging I ions are disordered with half occupancies from the midpoints between the neighboring Pt–Pt units, because the displacement of I ions is not three-dimensionally ordered. Therefore, it is difficult to determine from the X-ray structural analysis whether the ground state of **1** is the CDW or CP state. The Pt···Pt distance is 2.837 Å, which is between between that in $K_4[Pt_2^{II}(pop)_4]\cdot 2H_2O$ (2.925 Å)[8a] and that in $K_4[Pt_2^{III}(pop)_4I_2]$ (2.754 Å),[8b] and the Pt···I distance is 2.722 Å. The countercations $[NH_3(C_4H_8)NH_3]^{2+}$ are located in the spaces among the four chains and form hydrogen bonds to the pop ligands. Four H_2O molecules are also located in the spaces.

Raman spectra were measured to obtain information about the CO structure of **1**. Figure 2a shows the polarized

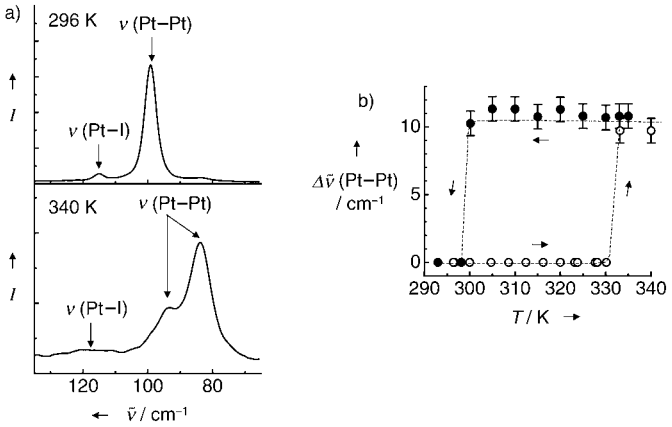

Figure 2. a) Polarized Raman spectra for the polarization of $z(x,x)z$ ($x \| c$ axis) at 296 and 340 K. b) Temperature dependence of the magnitude of splitting in the Pt–Pt stretching Raman band $\Delta\tilde{\nu}$(Pt–Pt).

Raman spectra of **1** in the usual laboratory humidity at 296 and 340 K. The strong signals at 80–100 cm^{-1} are attributed to the Pt–Pt stretching mode ν(Pt–Pt) of the Pt–Pt unit. An overtone progression of ν(Pt–Pt) up to fourth order is observed in both spectra. At 296 K, a single ν(Pt–Pt) band is observed at 98 cm^{-1}, which indicates the formation of only one kind of Pt–Pt unit. A relatively weak band is also observed at around 115 cm^{-1}. This band can be assigned to the Pt–I stretching mode, which is activated by the displacement of I ions from the midpoint between the neighboring Pt–Pt units. This fact is consistent with the crystal structure of **1** discussed above. Therefore, the ground state of **1** at 296 K can be considered as the CP state. The ν(Pt–Pt) band clearly splits into two components when the temperature is increased from 296 to 340 K, which indicates that there are two kinds of Pt–Pt units, in the present case Pt^{II}–Pt^{II} (86 cm^{-1}) and Pt^{III}–Pt^{III} (94 cm^{-1}), while the Pt–I stretching mode seems to be still activated. Therefore, the electronic phase at 340 K is reasonably classified as the CDW phase.

The temperature dependence of the magnitude of splitting in the Pt–Pt stretching Raman band $\Delta\tilde{\nu}$(Pt–Pt) is shown in Figure 2b. When heated from room temperature, $\Delta\tilde{\nu}$(Pt–Pt) remains at zero within the temperature range from 296 to 330 K but abruptly increases to about 10 cm^{-1} at 333 K. In the cooling run, $\Delta\tilde{\nu}$(Pt–Pt) does not change even at 333 K, but returns to zero at 300 K. This result indicates that the CDW phase can return to the original CP phase by cooling the crystal to room temperature. We confirmed this reversibility by repeating the heating and cooling processes several times. It should be noted that the reversibility largely depends on the humidity. In fact, the CDW phase does not recover to the CP phase on lowering the temperature in a fully dry atmosphere.

We can, however, revive the reversibility by exposing the crystal to water vapor. Thus, the reversibility is not a simple function of temperature. Further studies will be necessary to clarify how the transition between the CP and CDW phases depends on the values of temperature and humidity.

The most striking feature of **1** is that the CP-to-CDW transition is accompanied by a marked color change of the crystal. The polarized reflectivity spectra and corresponding microscope images of the sample are presented in Figure 3a.

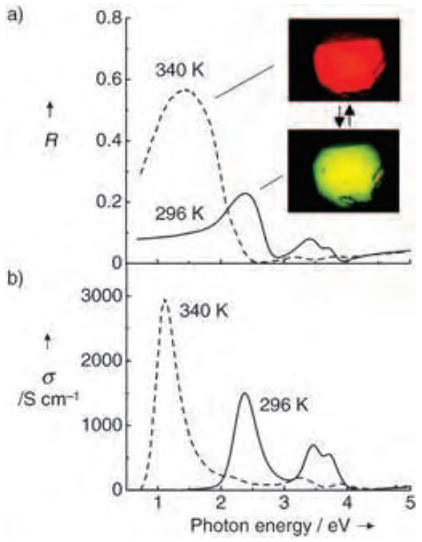

Figure 3. a) Polarized reflectivity and b) optical conductivity spectra with polarization of light parallel to the *c* axis in **1** at 296 and 340 K. The insets in (a) show the corresponding microscope images for the single crystal taken in reflection mode.

Compound **1** is yellow–green at 296 K as a result of the peak at 2.37 eV; on increasing the temperature up to about 340 K, the color changes to red–brown. This color is primarily a result of the strong reflection band from the near-infrared to the visible region. Such clear chromism is also confirmed by the optical conductivity (σ) spectra (Figure 3b). The peak energy of the lowest charge-transfer (CT) band (E_{CT}) drastically shifts from 2.37 (520 nm) to 1.12 eV (1110 nm). This spectral change is anomalously larger than that of the previously reported vapochromic materials. From a previous theoretical study on the optical excitation in the MMX chain compounds,[3c] the lowest CT band observed at 2.37 eV in the CP phase can be assigned to intradimer CT excitation from [-I···Pt^{2+}-Pt^{3+}-I···Pt^{2+}-Pt^{3+}-I-] to [-I-Pt^{3+}-Pt^{2+}···I···Pt^{2+}-Pt^{3+}-I-], while the CT band at 1.12 eV in the CDW phase is attributable to the interdimer CT band from [-I···Pt^{2+}-Pt^{2+}···I-Pt^{3+}-Pt^{3+}-I-] to [-I···Pt^{2+}-Pt^{3+}-I···Pt^{2+}-Pt^{3+}-I-]. The CP-to-CDW transition and the resultant change of the origin for the optical gap are responsible for the observed chromism. The gap energy $E_{CT} = 1.12$ eV at 340 K is nearly equal to that of other compounds in the CDW phase.[7] The *d*(Pt-I-Pt) value is relatively small in the CDW compounds compared to that in the CP compounds. Therefore, it is reasonable to consider that the observed CP-to-CDW transition is driven by the decrease in the value of *d*(Pt-I-Pt).

Thermogravimetric analysis (TGA) was performed in a dry nitrogen atmosphere to gain an insight into the mechanism of the phase transition (Figure 4). Compound **1** shows a gradual weight loss when the temperature is increased from

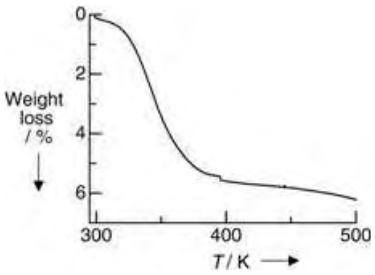

Figure 4. TGA trace of **1** under a dry nitrogen purge at 5 K min^{-1}.

room temperature, and has lost 5.450 % of its weight at 395 K. This value is in good agreement with that calculated (5.365 %) for the loss of four H_2O molecules per formula unit. The compound then shows a minor weight loss (< 0.5 %) up to approximately 500 K. There is a discrepancy in the temperature dependence of the water losses observed in TGA (Figure 4) and the valence changes observed in the Raman spectra (Figure 2b). This discrepancy is considered to be for the following reason: It is natural to consider that the water molecules near the surface of the crystal are lost more readily than those inside the crystal. The total water loss of the sample is probed in the TGA measurement, whereas the Raman spectra sensitively reflect changes in the penetration depth of the pump light (1.96 eV), which is much smaller than the thickness of the crystal (≫ 10 μm). These optical and TGA results demonstrate that the transition between the CP and CDW states is triggered by desorption and absorption of water molecules. Powder X-ray diffraction measurements were also performed to investigate the vapochromic structural changes. The diffraction pattern of **1** heated at 353 K in vacuum shows that the crystal has converted into some new, and as yet unidentified, crystal structure. Further studies will be necessary to determine the details of this structural transition.

In conclusion, we have found a novel reversible vapochromic behavior accompanied by a phase transition between the paramagnetic CP state and the diamagnetic CDW state in the MMX compound $[NH_3(C_4H_8)NH_3]_4[Pt_2(pop)_4I]\cdot 4H_2O$. The results presented here lead us to expect that the MMX chain compound is a versatile candidate for future chemical-vapor-sensing devices.

Experimental Section

The starting compounds $K_4[Pt_2(pop)_4]\cdot 2H_2O$ and $K_4[Pt_2(pop)_4I_2]$ were prepared according to the methods previously described.[4b] Single crystals of **1** were grown by the standard diffusion method using an H-shaped glass cell. Aqueous solutions (2 mL each) of $[NH_3(C_4H_8)NH_3]SO_4$ (2 mg) and of $K_4[Pt_2(pop)_4]\cdot 2H_2O$ (20 mg) and $K_4[Pt_2(pop)_4I_2]$ (20 mg) were loaded at the ends of the cell and allowed to slowly diffuse in water at room temperature. After about a week, yellow–green needle crystals were obtained. Elemental anal-

ysis (%) calcd for $C_{10}H_{48}IN_4O_{24}P_8Pt_2$: C 7.14, H 3.30, N 4.16; found: C 7.15, H 3.20, N 4.13.

X-ray structural analysis of **1** was performed by using a Rigaku RAXIS-RAPID imaging-plate diffractometer with graphite monochromated $Mo_{K\alpha}$ radiation ($\lambda = 0.7107$ Å). Crystal data for **1** at 296 K: $M_r = 1343.31$, tetragonal, space group $I4/m$, $a = 13.3474(8)$, $c = 9.8091(7)$ Å, $V = 1747.5(2)$ Å^3, $Z = 2$, $\rho_{calcd} = 2.553$ g cm^{-3}, final $R = 0.0351$, $wR = 0.138$, GOF = 1.587 with $I > 3.00\sigma(I)$. CCDC-245189 contains the supplementary crystallographic data for this paper. These data can be obtained free of charge from the Cambridge Crystallographic Data Centre via www.ccdc.cam.ac.uk/data_request/cif.

Polarized Raman spectra of **1** were measured by using a Renishaw Ramascope 1000B Raman spectrometer with a continuous-wave He–Ne laser (1.96 eV) and an optical microscope. Polarized reflectivity spectra were obtained by using a specially designed spectrometer with a 25-cm-grating monochromator and an optical microscope. TGA was carried out under a dry nitrogen atmosphere using the Rigaku Thermo plus2 TG 8120 analyzer.

Received: January 11, 2005
Published online: April 11, 2005

Keywords: chain structures · phase transitions · platinum · Raman spectroscopy · vapochromism

[1] *Extended Linear Chain Compounds*, *Vols. 1–3* (Ed.: J. S. Miller), Plenum, New York, **1982**.

[2] a) C. L. Exstrom, J. R. Sowa, Jr., C. A. Daws, D. Janzen, K. R. Mann, *Chem. Mater.* **1995**, *7*, 15–17; b) C. A. Daws, C. L. Exstrom, J. R. Sowa, Jr., K. R. Mann, *Chem. Mater.* **1997**, *9*, 363–368; c) M. A. Mansour, W. B. Connick, R. J. Lachicotte, H. J. Gysling, R. Eisenberg, *J. Am. Chem. Soc.* **1998**, *120*, 1329–1330; d) C. E. Buss, K. R. Mann, *J. Am. Chem. Soc.* **2002**, *124*, 1031–1039.

[3] a) S. A. Borsch, K. Prassides, V. Robert, A. O. Solonenko, *J. Chem. Phys.* **1998**, *109*, 4562–4568; b) S. Yamamoto, *Phys. Rev. B* **2001**, *64*, R140102-1–R125124-4; c) M. Kuwabara, K. Yonemitsu, *J. Mater. Chem.* **2001**, *11*, 2163–2175.

[4] a) M. Kurmoo, R. J. H. Clark, *Inorg. Chem.* **1985**, *24*, 4420–4425; b) N. Kimura, H. Ohki, R. Ikeda, M. Yamashita, *Chem. Phys. Lett.* **1994**, *220*, 40–45; c) C.-M. Che, F. H. Herbstein, W. P. Schaefer, R. E. Marsch, H. B. Gray, *J. Am. Chem. Soc.* **1983**, *105*, 4604–4607.

[5] a) C. Bellitto, A. Flamini, L. Gastaldi, L. Scaramuzza, *Inorg. Chem.* **1983**, *22*, 444–449; b) C. Bellitto, G. Dessy, V. Fares, *Inorg. Chem.* **1985**, *24*, 2815–2820; c) M. Yamashita, Y. Wada, K. Toriumi, T. Mitani, *Mol. Cryst. Liq. Cryst.* **1992**, *216*, 207–212; d) H. Kitagawa, N. Onodera, T. Sonoyama, M. Yamamoto, T. Fukawa, T. Mitani, M. Seto, Y. Maeda, *J. Am. Chem. Soc.* **1999**, *121*, 10068–10080.

[6] M. Yamashita, S. Miya, T. Kawashima, T. Manabe, T. Sonoyama, H. Kitagawa, T. Mitani, H. Okamoto, R. Ikeda, *J. Am. Chem. Soc.* **1999**, *121*, 2321–2322.

[7] H. Matsuzaki, T. Matsuoka, H. Kishida, K. Takizawa, H. Miyasaka, K. Sugiura, M. Yamashita, H. Okamoto, *Phys. Rev. Lett.* **2003**, *90*, 046401-1–046401-4.

[8] a) M. A. Filomena Dos Remedios Pinto, P. J. Sadler, S. Neidle, M. R. Sanderson, A. Subbiah, R. Kuroda, *J. Chem. Soc. Chem. Commun.* **1980**, 13–15; b) K. A. Alexander, S. A. Bryan, F. R. Fronczek, W. C. Fultz, A. L. Rheingold, D. M. Roundhill, P. Stein, S. F. Watkins, *Inorg. Chem.* **1985**, *24*, 2803–2808.

Mesoporous Materials

A New Minimal Surface and the Structure of Mesoporous Silicas**

Michael W. Anderson, Chrystelle C. Egger, Gordon J. T. Tiddy, John L. Casci, and Kenneth A. Brakke*

The formation of complex inorganic superstructures in nature relies on the interaction between organic and inorganic species to direct the inorganic form away from its "usual" morphology. During synthesis the superstructures are soft and dynamic which makes a study of the nature of the ephemeral interface difficult.[1] However, the inorganic skeletons formed are stable and consequently amenable to detailed examination. In 1992 researchers at Mobil[2] and in Japan[3] made the remarkable discovery that the subtle forms of mesoscopic organization of surfactant molecules could be imprinted on oxide structures. Herein we report our studies of the structure of the surfactant-templated, cubic, mesoporous silica superstructure, SBA-1[3] and provide a formulation in terms of curvature that has important repercussions for both surfactant structures and the mechanism of formation of inorganic replicas. We establish that the crucial interface that determines the inorganic structure is between the silica and water adsorbed at the micelle surface, not between silica and surfactant, thus challenging the present synthesis mechanisms.[4] We adopt a general protocol for understanding the surface curvature and energy which could be applied widely

[*] Prof. M. W. Anderson,[$] Dr. C. C. Egger[+ #]
Department of Chemistry, UMIST
Manchester, M601QD (UK)
Fax: (+44) 161-200-4511
E-mail: m.anderson@manchester.ac.uk
Prof. G. J. T. Tiddy[$]
Department of Chemical Engineering, UMIST
Manchester, M601QD (UK)
Prof. J. L. Casci
Synetix
Johnson Matthey
Billingham, TS231LB (UK)
Prof. K. A. Brakke
Mathematics Department, Susquehanna University
Selinsgrove, PA 17870 (USA)
[+] current address:
Institut de Science et d'Ingénierie Supramoléculaires
ISIS-Groupe BASF
8, allée Gaspard Monge, 67083 Strasbourg (France)
[$] M.W.A. and G.J.T.T. are now at the University of Manchester, after unification of the Victoria University of Manchester with UMIST on October 1, 2004.
[#] These authors contributed equally to this work.
[**] We are grateful to Vladimir Zholobenko for assistance with the synchrotron X-ray diffraction measurements.

Supporting information for this article is available on the WWW under http://www.angewandte.org or from the author.

 DOI: 10.1002/anie.200462295

to the growth of inorganic structures in biology, including nonperiodic and disordered structures.

Currently there are a number of ways to address the mesophase structure of these mesoporous silicas. Terasaki and co-workers[5] adopted the direct structure elucidation approach by using electron crystallography. With this method they were able to reconstruct an electron density map directly with electron micrographs recorded along several zone axes. This has the distinct advantage that no predefined knowledge is required and that the diffraction intensities are optimized through the observation of individual particles. However, its disadvantage is that the electron density map does not easily yield clues about the synthesis mechanism. The technique is also technically very demanding and is only suitable for highly organized 3D structures that are stable in the electron microscope. It is not a routine technique and cannot be used to monitor many sample preparations, or to look at preparations in situ.

Another route, first adopted by Anderson and Alfredsson,[6] and more recently by Solovyov and co-workers,[7] and Schüth and co-workers,[8,9] involves the determination of a structural model from some known data followed by its refinement according to certain parameters, for instance, against X-ray diffraction patterns or electron micrographs. This method has the advantage that it is flexible and can be applied to a variety of preparations; the results also give information about synthesis mechanisms. The disadvantage is that the process does require input from other techniques and some prior knowledge. Also, the powder X-ray diffractogram is an average technique and as a consequence, it is important that the sample is relatively homogeneous. Herein we introduce a general mathematical approach to the modeling of mesoporous silicas, which allows easy generation of electron density maps and diffraction patterns for comparison with experimental data.

SBA-1 was synthesized in HCl (4 M) with hexadecyltriethylammonium bromide (HTEABr) as surfactant and tetraethylorthosilicate (TEOS) as a source of silica. The structure is known from electron crystallography[10] to belong to the space group $P_{m\bar{3}n}$ and consists of cages connected through windows. The corresponding surfactant phase is known as the I_1^3 (or Q^{223} referring to the space group number, or *Pm3n* as an identifier for $P_{m\bar{3}n}$[11]) phase which is a cubic, isotropic, micellar phase. Curiously, the I_1^3 phase was not observed in the phase behavior of HTEABr,[12] in which a hexagonal phase occurs at the micellar solution boundary. Consequently, we studied the phase behavior of this surfactant with a temperature-programmed penetration scan (Supporting Information). This shows that in the presence of impurities that are likely to remain from the surfactant synthesis, such as bromohexadecane, a cubic phase is induced below $\approx 32\,^{\circ}C$. Significantly, this phase occurs between the hexagonal phase and isotropic solution, which suggests a higher curvature of the micellar phase. More importantly, when HTEABr is exchanged with chloride ions to make HTEACl the penetration scan reveals the presence of three cubic mesophases. HTEACl is probably the templating agent in SBA-1 preparations owing to the large excess of chloride anions in the preparation.

The essence of our approach herein was first to build the structure essentially by hand. This requires some knowledge of the possible structures of the I_1^3 surfactant phase; some that have been discussed in the literature are illustrated in Figure 1. However, close inspection of electron micrographs

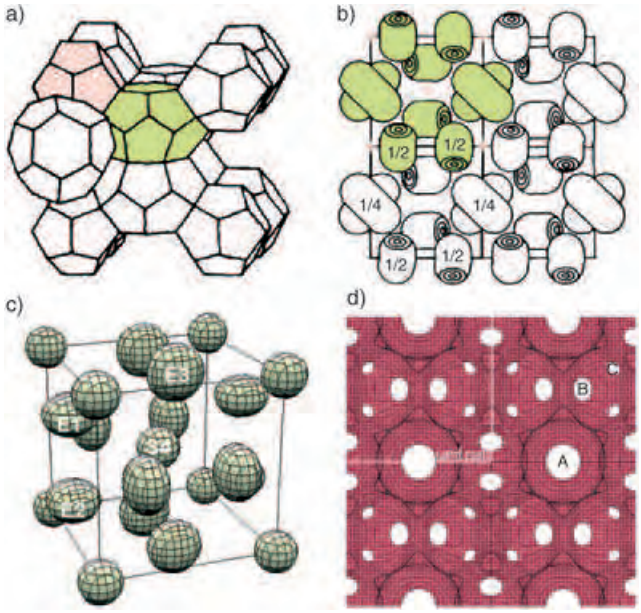

Figure 1. Various representations of the I_1^3 structure with $P_{m\bar{3}n}$ symmetry: a) model of Charvolin and Sadoc[13], which displays two polyhedra (12-hedron and 14-hedron) defining volumes that contain micelle plus associated water; b) rod-type micelles of Fontell and co-workers[14]; c) single exponential function displaying 21 micelles: 9 spherical and 12 oblate ellipsoidal, according to exponential mathematics, equivalent to model adopted by Vargas and co-workers;[15] d) continuous surface created by an exponential function as the radii of the micelles are increased, displaying the three different window types (A, B, and C) in SBA-1—2×2 unit cells viewed along [100]. To create a continuous surface, 12 extra virtual ellipsoids are placed in adjacent cells to ensure that there are no edge effects.

reported previously[10] quickly discounts the possibility of rodlike micelles as the structure-directing agent, and consequently we choose the approach of Vargas and co-workers,[15] which uses spherical and oblate ellipsoidal micelles arranged on a cubic lattice. To describe such structures, a useful and simple exponential mathematics is available to "hand build" structures, as described in detail by Jacob and Andersson,[16] and as outlined in the Experimental Section below. A remarkably good fit is produced between experimental and theoretical diffraction patterns as shown in Figure 2. However, there is some discrepancy between the calculated void volume and that determined experimentally, suggesting that the model needs further refinement. The model works well for both as-prepared and calcined samples (Supporting Information). Upon calcination the unit cell shrinks by $\approx 9\,\%$ but the relative diffraction intensity changes very little. This indicates that 1) the structure remains essentially intact, and 2) there is no need to consider an electron-density profile other than silica walls and voids. The content of the void, which will be mobile, is not a significant

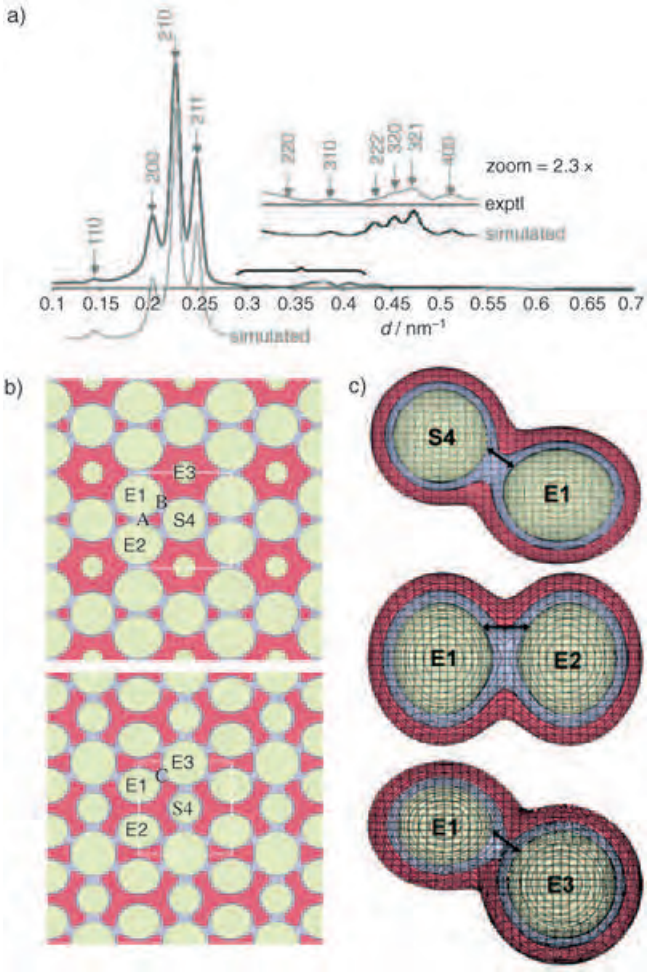

Figure 2. Calculated X-ray diffraction pattern and model from the analytical function: a) Experimental and simulated X-ray diffraction pattern for as-prepared SBA-1 with an analytical expression of $r_1 = r_2 = 0.229$ for a unit cell, for example, 19.5 Å (based on a unit cell of 85 Å) and an oblateness of 1.2; $C = 0.01$. b) Slices through the unit cell of SBA-1: red = hydroxylated silica wall structure, yellow = micellar structure, and blue = adsorbed water. The slice through the middle of the unit cell ($z = 0.5$, top) illustrates the A windows between the flat sides of two oblate ellipsoids and the B windows between a spherical and an elliptical micelle. The slice at $z = 0.375$ (bottom) shows the C windows between the tips of two ellipsoidal micelles. c) Illustration of how the window size in SBA-1 is related to the curvature in which the micelles meet, in terms of the thickness of the adsorbed water layer between the micelles; the contact angle between micelles will be different.

factor to determine the relative diffraction intensity. Nevertheless, a number of important features are immediately apparent from this approach. First, the radius of the spherical micelle must be similar to that of the short radius of the oblate ellipsoidal micelles, otherwise the [110] reflection becomes unacceptably large. This is reasonable, as these radii will both be governed by the length of the surfactant paraffin chain. Second, there is an interesting correlation between the window size and the geometry of adjacent micelles that cause the window formation. SBA-1 has three different windows and, as can be observed in Figure 1 d, the window size is greatest when the contact angle between touching micelles is smallest; alternatively, the thickness of the adsorbed water layer on the micelles which excludes the silica wall is a constant (Figure 2). This suggests mechanisms to control window size through control over the curvature of micelles.

A number of the important micellar and bicontinuous surfactant phases have been described previously in terms of infinite periodic minimal surfaces (IPMS).[17] Such surfaces are continuous in 3D space and have the property that the mean curvature at all points on the surface is zero. A number of the micellar phases have been described in this regard, but the I_1^3 structure has not yet been correlated with any known IPMS. A convenient method to explore possible IPMS structures is to use the *Surface Evolver* software from Brakke[18] which refines a surface either to minimal area or to minimal squared-mean curvature. A number of cubic IPMS have recently been explored with this approach.[19] We used this package with the "hand-built" structure as the starting point for refinement, and refined the squared-mean curvature under the constraints of defined void volume (determined from nitrogen adsorption and helium pycnometry experiments). The results are remarkable. First, without volume constraint, a new minimal surface is generated at a void volume of 55%. The surface is shown in Figure 3 and has almost exactly zero-mean curvature at every point on the surface. The surface may be characterized as a smoothed version of the analytic surface by using decreasing squared-mean curvature as a smoother. An X-ray diffraction pattern produced from such a surface is in excellent agreement with that observed experimentally. The fit is further improved by constraining the void volume to that observed experimentally (58%), and the surface produced still has close to constant and zero-mean curvature (Figure 4). In this case the surface can either be refined to constant-mean curvature or to minimal integrated-square-mean curvature. The latter approach was found to give the best agreement between experiment and simulation. The mesopore sizes are consistent with previously reported work from Terasaki and co-workers,[10] and consequently the model is consistent with X-ray diffraction, electron microscopy, and gas adsorption experiments. We have not tried to further improve the diffraction fits with the methods of Solovyov et al.,[7] as we believe that the number of variables relative to the number of fitting parameters precludes an improvement in accuracy.

This result has important repercussions for both the structure and mechanism of formation of SBA-1 and mesoporous silicas in general and also, by analogy, for the structure of surfactant mesophases. SBA-1 is formed from a low-concentration surfactant solution, which is above the critical micelle concentration (CMC) but an order of magnitude below that normally required for mesophase formation. The solution has high ionic strength which alone is not sufficient to salt out the mesophase. The precipitation only occurs in the presence of silica species. The precise nature of these silica species is unknown, although they will be positively charged at this low pH. However, the mechanism must be cooperative between the micelle species and the silica species. Before mesophase formation, the micelles must have a substantial shell formed from silica species to supply all the silica in the final product. After mesophase formation and reorganization,

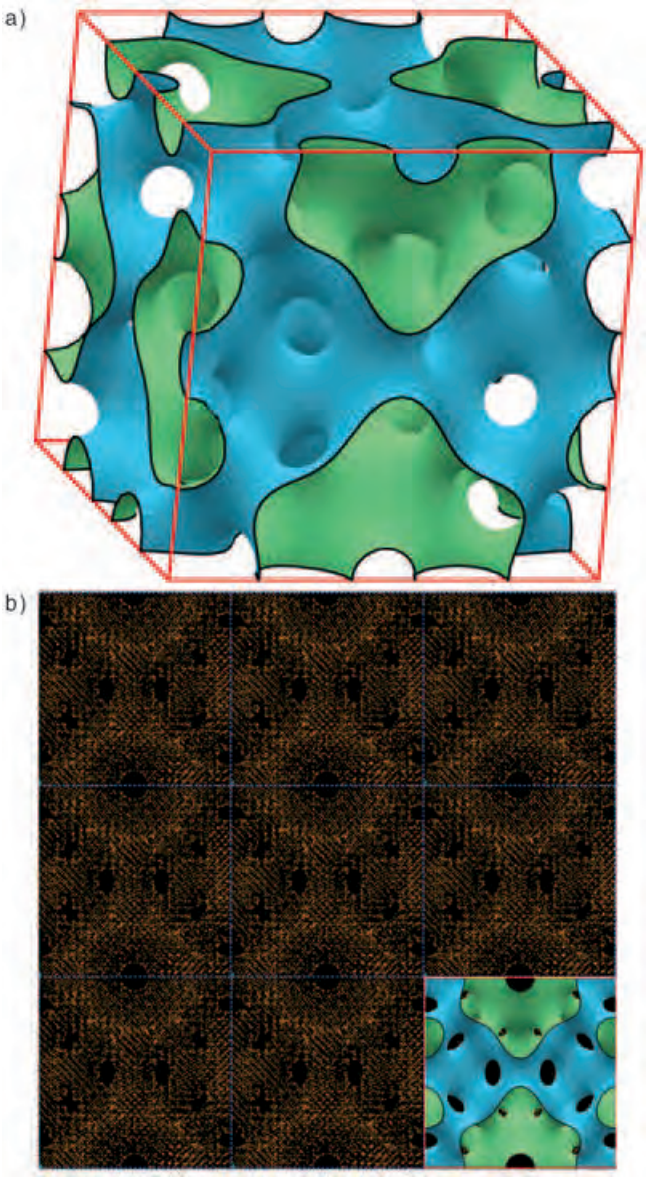

Figure 3. $P_{m\bar{3}n}$ symmetry surface with zero-mean curvature at all points: a) oblique view and b) view along [100] superimposed on 3×3 unit cells of the atomistic model used to calculate the diffraction patterns. In SBA-1 the green volume represents the inorganic hydroxylated silica wall of the material, and the blue volume contains micellar surfactant surrounded by a layer of adsorbed water. In the I_1^3 surfactant mesophase, the free water would occupy the green volume.

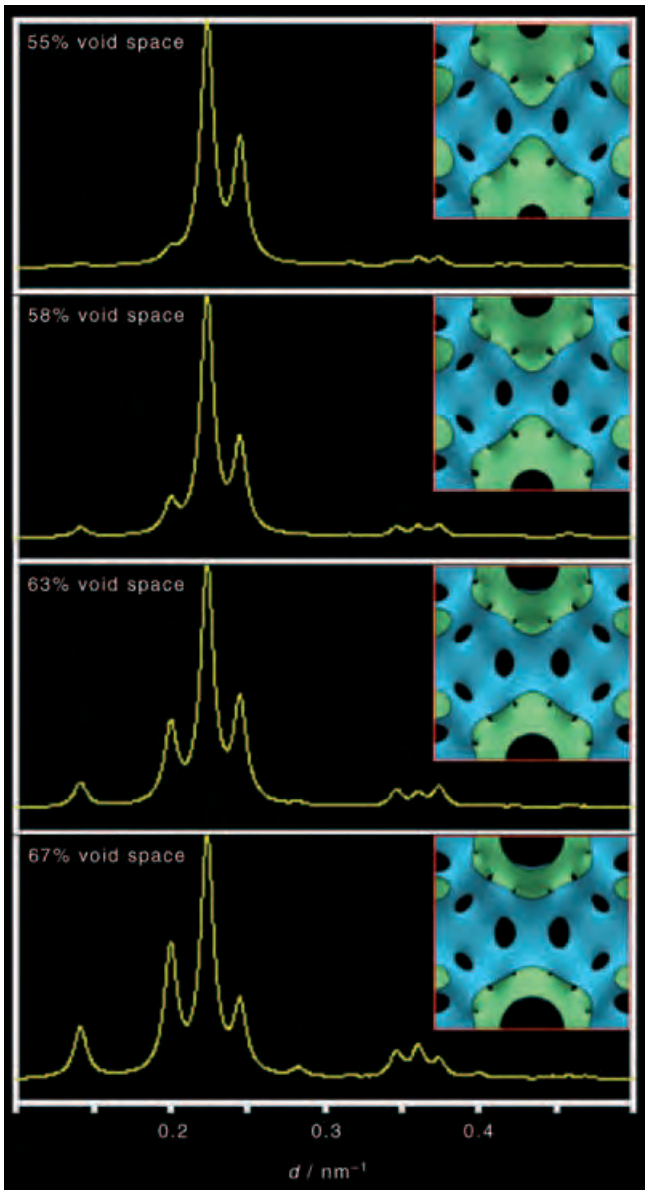

Figure 4. Calculated X-ray diffraction patterns for structures refined with *Surface Evolver*.[18] The wall volume in green is filled with uniform electron density and the void space is empty. A void volume of 55% is the surface closest to a minimal surface with near zero-mean curvature; 58% void volume represents a slightly thinner wall still, with very low curvature which most closely resembles as-prepared SBA-1.

the SBA-1 structure reveals that the silica has retracted from the micellar surface (creating windows) and that the mean curvature of the silica surface is close to zero. Yet in a micellar mesophase the mean curvature of the micelles is very large. Moreover, the Gaussian curvature (the product of the maximum and minimum curvature) of the micelles is positive, whereas the Gaussian curvature of the final structure is negative at every point. We make the assumption on geometric grounds that the micelles do not merge to form a continuous phase, as they are simply too long to be accommodated in the window region of the structure. The window sizes are less than ≈13 Å and the surfactant molecules are >20 Å, requiring a window of at least 40 Å for a bilayer (n.b.: 1) surfactant length is about 75% of all trans length; 2) the surface wrapping is complex, and therefore the notion of a bilayer is not correct, but illustrates the size that the window would need to be if the micelles were to "fuse"). Consequently, the interface of the silica is clearly not at the interface with the surfactant micelle, but at the interface with the adsorbed hydration layer surrounding the micelle (Figure 2). Although it is possible that there are other related zero-mean-curvature surfaces for such a tortuous surface, the one found fits the experimental data and is therefore a valid description for this structure in terms of curvature. As has been suggested before for other cubic

micellar mesophases (specifically Q^{225} and Q^{229}) this interface between the adsorbed water and the free water, in pure surfactant/water systems, is usually a zero-mean-curvature surface (surfaces F-RD and I-WP respectively).[17] Herein we have established, through the structure of the inorganic precipitate, that a similar picture of a high-curvature micellar structure with an adsorbed water layer extending to a zero-curvature surface and then a free water region on the other side of the surface is valid for the I_1^3 or Q^{223} structure. The silica in the structure of SBA-1, and probably many other mesoporous silica structures, develops its final form in the free water. Such a mechanism would not be inconsistent with the hexagonal MCM-41 type structure in which the surfactant is present as long rods but with substantial free water between the rods (the hexagonal phase can accommodate a larger variation in water concentration than the cubic phases). The packing constraints in the hexagonal phase would also favor thicker walls simply on geometric grounds—there is less surface area to pack the silica without thickening. As a result, there are no exclusion zones in which windows will occur, and the surfactant rods are essentially covered with silica species. Such a mechanism is, however, at substantial variance with the previously proposed mechanisms of mesoporous silica formation,[4] which rely heavily upon the direct close interaction between silica species and surfactant. We suggest this interaction is crucial only in the initial precipitation process, but the combination of other interactions is far more important to the structure of the final mesophase observed. With this general method of building structures by hand followed by curvature refinement according to experimental constraints, it should be possible to derive accurate models for all inorganic mesoporous structure types. Even disordered structures could be built, as the method of constructing surfaces by hand allows any starting arrangement and micelle shape (although this would be clearly more demanding and would require information about the nature of the disorder). The same methods can also be applied toward the growth of inorganic structures in biology.

Experimental Section

Hexadecyltriethylammonium bromide (HTEABr) was prepared by mixing 1-bromohexadecane (98%, Lancaster) and triethylamine (99%, Jansen Chimica) in absolute ethanol under reflux conditions for 24 h. Ethanol was then removed with a rotary evaporator until a white, viscous paste was obtained. The resulting gel was recrystallized by minimal addition of chloroform, then ethyl acetate until the whole solid precipitated. SBA-1 was prepared with tetraethylorthosilicate (TEOS; 98%, Aldrich) as a source of silica, HTEABr (made in-house), distilled water, and aqueous HCl (33 wt%, BDH). Molar ratios for a typical SBA-1 synthesis were HTEABr/H_20/HCl/TEOS = 1:3500:280:5. After an aging time of 1 week at 4 °C, the mixture was heated to 100 °C within 10 min for 1 h. These conditions were optimal for the generation of homogeneous stable materials that have probably reached an equilibrium as a soft solid before solidification in the final heating at 100 °C. We have established by ^{29}Si-MAS NMR spectroscopy that at these low pH conditions, cross-linking is retarded, which is consistent with the work of Brinker and Scherer.[20] Ethanol is liberated during the hydrolysis of TEOS ($\approx$1.5 wt%) but this has little influence on the processes occurring, as the ethanol resides mainly in the water. (Low ethanol levels (<1 mol dm^{-3}) are known to have only a minimal influence on CMC values, hence only a small amount of ethanol is found in the micelles.) The surfactant moiety was finally burned out by calcination at 550 °C for several hours, with a slow temperature-ramp rate (0.5 °C min^{-1}). Hand-built structures were formulated with *Mathematica* software; the atomistic structures were generated with a *Fortran* program; X-ray diffraction patterns were calculated with *Cerius II* software from Accelerys; *Mathematica* contour surfaces were translated for input into *Surface Evolver* with a *Fortran* program.

The basis for the initial hand-built structures is that a sphere can be expressed not only as $x^2+y^2+z^2=C$ but also in the exponential scale by

$$e^{-(x^2+y^2+z^2)} = C \quad (1)$$

The radius of the sphere is determined by the constant C, and the center of the sphere can be moved to any coordinate h, k, or l by the following transformation:

$$e^{-[(x-h)^2+(y-k)^2+(z-l)^2]} = C \quad (2)$$

The sphere can be elongated or squashed in any dimension to produce, for instance, an oblate ellipsoid by the following transformation:

$$e^{-[b_1(x-h)^2+b_2(y-k)^2+b_3(z-l)^2]} = C \quad (3)$$

Finally, an object with a different radius can be formed by adding a constant, a, within the exponential, thus:

$$e^{a-[b_1(x-h)^2+b_2(y-k)^2+b_3(z-l)^2)} = C \quad (4)$$

The utility of working in the exponential scale is that multiple objects can be incorporated in a single expression by adding exponential functions together (Supporting Information). Furthermore, as isolated objects approach, a continuously wrapped surface is produced with the smoothness of the wrapping governed by the value of C. Jacob and Andersson[16] have demonstrated that this approach can be extended to describe many objects with complex shape. The arrangement of micelles in the $P_{m\bar{3}n}$, I_1^3 structure is given by adding 21 objects together according to the following equation:

$$\sum_{h,k,l} e^{-\{(x-h)^2+(y-k)^2+(z-l)^2\}} + \sum_{h',k',l'} e^{|a-\{b_1(x-h')^2+b_2(y-k')^2+b_3(z-l')^2\}|} = C \quad (5)$$

and this is shown in Figure 1c. Then, by increasing the radius of the micelles relative to the unit cell size, a continuously wrapped surface is produced (Figure 1d), which represents the structure of SBA-1. To test the validity of the model, an atomistic structure of SBA-1 was produced by placing silicon atoms randomly on one side of this continuous surface; X-ray diffraction patterns were generated for varying values of the micelle radius and the degree of oblateness of the micelles.

Received: October 13, 2004
Revised: December 14, 2005
Published online: April 21, 2005

Keywords: mesoporous materials · minimal surface · molecular modeling · SBA-1 · structure elucidation

[1] S. Hyde, S. Andersson, K. Larsson, Z. Blum, T. Landh, S. Lidin, B. W. Ninham, *The Language of Shape*, Elsevier Science B. V., Amsterdam, **1997**.
[2] C. T. Kresge, M. E. Leonowicz, W. J. Roth, J. C. Vartuli, J. S. Beck, *Nature* **1992**, *359*, 710–712.

[3] S. Inagaki, Y. Fukushima, K. Kuroda, *J. Chem. Soc. Chem. Commun.* **1993**, 680–682.
[4] Q. Huo, D. I. Margolese, U. Ciesla, D. G. Demuth, P. Feng, T. E. Gier, P. Sieger, A. Firouzi, B. F. Chmelka, F. Schüth, G. D. Stucky, *Chem. Mater.* **1994**, *6*, 1176–1191.
[5] A. Carlsson, M. Kaneda, Y. Sakamoto, O. Terasaki, R. Ryoo, S. H. Joo, *J. Electron Microsc.* **1999**, *48*, 795–798.
[6] V. Alfredsson, M. W. Anderson, *Chem. Mater.* **1996**, *8*, 1141–1146.
[7] L. A. Solovyov, S. D. Kirik, A. N. Shmakov, V. N. Romannikov, *Microporous Mesoporous Mater.* **2001**, *44*, 17–23.
[8] J. Sauer, F. Marlow, F. Schüth, *Phys. Chem. Chem. Phys.* **2001**, *3*, 5579–5584.
[9] S. Schacht, M. Janicke, F. Schüth, *Microporous Mesoporous Mater.* **1998**, *22*, 485–493.
[10] Y. Sakamoto, M. Kaneda, O. Terasaki, D. Y. Zhao, J. M. Kim, G. Stucky, H. J. Shin, R. Ryoo, *Nature* **2000**, *408*, 449–453.
[11] P. Sakya, J. M. Seddon, R. H. Templer, R. J. Mirkin, G. J. T. Tiddy, *Langmuir* **1997**, *13*, 3706–3714.
[12] E. S. Blackmore, G. J. T. Tiddy, *J. Chem. Soc. Faraday Trans. 2* **1988**, *84*, 1115–1127.
[13] J. Charvolin, J. F. Sadoc, *J. Phys.* **1988**, *49*, 521–526.
[14] K. Fontell, K. K. Fox, E. Hansson, *Mol. Cryst. Liq. Cryst.* **1985**, *1*, 9–17.
[15] R. Vargas, P. Mariani, A. Gulik, V. Luzzati, *J. Mol. Biol.* **1992**, *225*, 137–145.
[16] M. Jacob, S. Andersson, *The Nature of Mathematics and the Mathematics of Nature*, Elsevier Science B.V., Amsterdam, **1998**.
[17] V. Luzzati, H. Delacroix, A. Gulik, *J. Phys. 2* **1996**, *6*, 405–418.
[18] K. A. Brakke, *Philos. Trans. R. Soc. London Ser. A* **1996**, *354*, 2143–2157.
[19] E. A. Lord, A. L. Mackay, *Curr. Sci.* **2003**, *85*, 346–362.
[20] C. J. Brinker, G. W. Scherer, *Sol-Gel Science*, *Academic Press*, **1990**.

Host–Guest Systems

Ditopic Complexation and Release of Neutral Guest Molecules by a Hydrogen-Bonded "*Endo–Exo*" Receptor

Miguel A. Mateos-Timoneda, Jessica M. C. A. Kerckhoffs, Mercedes Crego-Calama, and David N. Reinhoudt**

The highest level of sophistication in noncovalent chemistry is found in living systems, where elegant supramolecular assemblies make up the machinery that enables and supports functions important for life. The understanding of the mechanism for (bio)molecular recognition is also crucial in the development of new drugs and for the mimicry of the activity of biosystems.[1–3] The principles of biomolecular recognition[4] have successfully been extended to synthetic receptors[5] that are able to bind guest species such as cations,[6] anions,[7] or small neutral molecules.[8] The study of different degrees of complexity in the molecular recognition process is also important for the understanding of different biomolecular processes. For example, at the active site of enzymes, strict recognition of the transition state by the enzyme is required (selective *endo* recognition), whereas the initial protein–protein recognition can be more loose and flexible (nonselective *exo* recognition). Nevertheless, and to the best of our knowledge, there are no synthetic examples in the literature that exploit the diverse levels (that is, *endo/exo*, selective/nonselective) of molecular recognition encountered in nature.

Further control over the complexity of the molecular recognition process can also be achieved through the formation of multiple interactions at different areas of the host molecule, as observed at antibody–antigen interfaces,[9] as well as by the interaction of one host with two or more different guest molecules.[10] There are only a few examples of synthetic receptors capable of complexing two different types of guest molecules, usually cations and anions.[11] However, the covalent synthesis of these receptors remains elusive and time consuming because of the complexity of the functionalities needed to complex the two different types of guest. Self-assembly provides a simpler and faster way to bring together the desired functionalities for the recognition of the guest,[12] but it is necessary to avoid interfering with the required functionalities during the self-assembly of the receptor. Thus, the complexation of two (or more) different neutral guest molecules with one synthetic receptor is rare and has only been achieved in the interior of capsulelike assemblies (*endo* receptors)[13] and other cavities by using the principles of crystal engineering.[14]

Herein, we report the first (noncovalent) receptor able to act simultaneously as an *endo* and *exo* receptor for neutral molecules (Figure 1). This hydrogen-bonded receptor is able to *selectively* encapsulate a neutral noncovalent trimer in the pocket situated in between two subdomains (floors) of the receptor (*endo* complexation) while simultaneously complexing different neutral guest molecules at the periphery of the assembly (*exo* complexation), thus resembling the different degrees of complexity encountered in biorecognition.[15] The receptor is formed by the self-assembly of nine components (three calix[4]arenes dimelamines and six barbiturate/cyanurate derivatives) through 36 cooperative hydrogen bonds. The periphery of the self-assembled receptor is decorated with six pyridyl groups that are able to complex a variety of dicarboxylic acids (nonselective process) in a 1:3 fashion through two-point hydrogen-bonding interactions. The receptor can simultaneously encapsulate a noncovalent trimer of alizarin through π–π stacking interactions. This self-assembly of the receptor and the recognition processes of the guests bring together 15 molecules with total specificity. Surprisingly, the order in which these guest molecules are added is very

[*] M. A. Mateos-Timoneda, Dr. J. M. C. A. Kerckhoffs, Dr. M. Crego-Calama, Prof. D. N. Reinhoudt
Laboratory of Supramolecular Chemistry and Technology
MESA+ Institute for Nanotechnology and
Faculty of Science and Technology
University of Twente
P.O. Box 217, 7500 AE Enschede (The Netherlands)
Fax: (+31) 53-489-4645
E-mail: m.cregocalama@utwente.nl
d.n.reinhoudt@utwente.nl

  DOI: 10.1002/anie.200500134

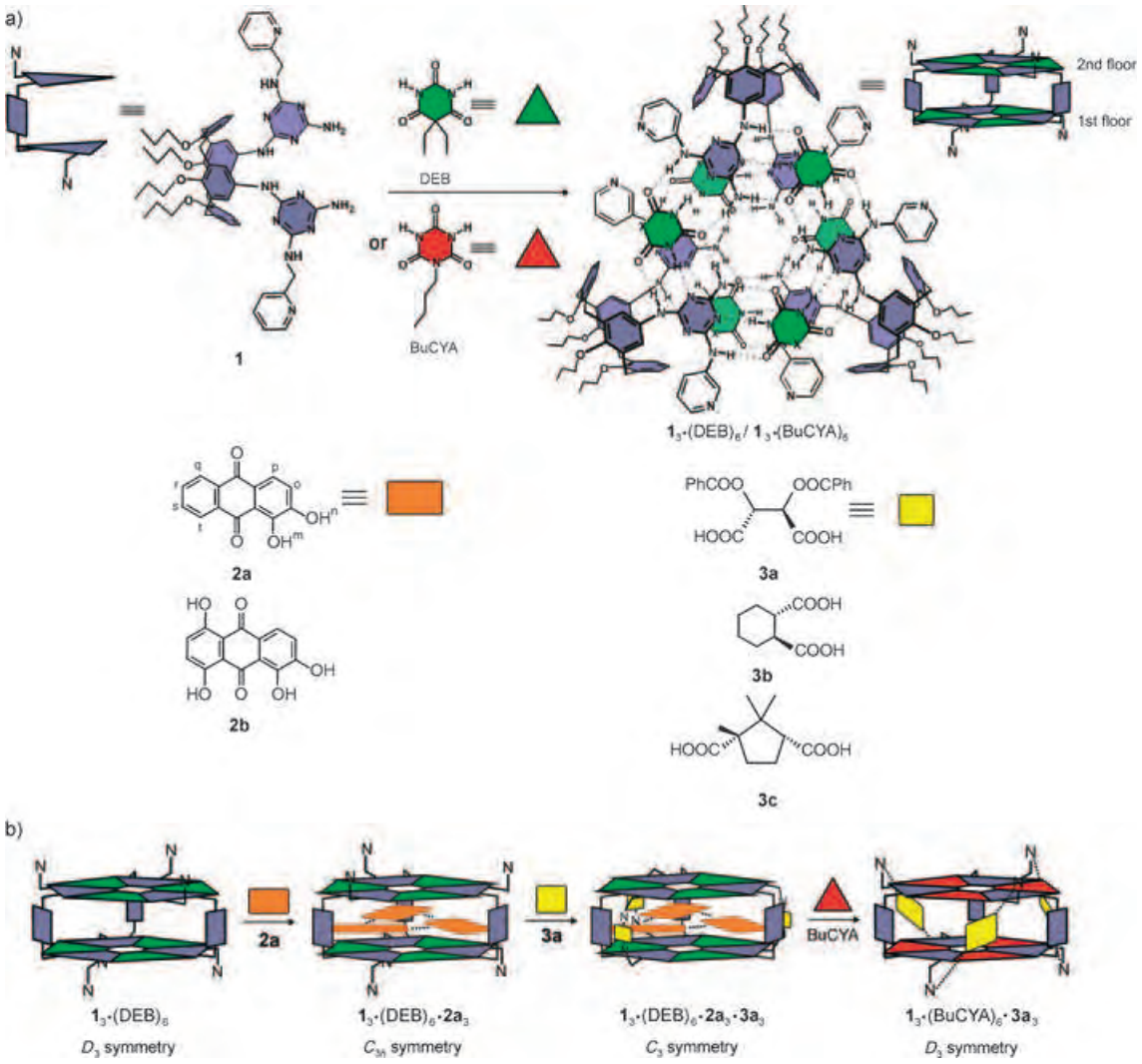

Figure 1. a) Molecular and schematic (side view) representations of the building blocks and the corresponding hydrogen-bonded assemblies $\mathbf{1}_3\cdot(DEB)_6/\mathbf{1}_3\cdot(BuCYA)_6$ and guest molecules **2a–b** and **3a–c**. b) Schematic representation of the recognition of guest **2a** and **3a** by $\mathbf{1}_3\cdot(DEB)_6/\mathbf{1}_3\cdot(BuCYA)_6$ receptors, and the release of **2a**. The corresponding symmetry of the assemblies is also given: assemblies with D_3 symmetry ($\mathbf{1}_3\cdot(DEB)_6$ and $\mathbf{1}_3\cdot(BuCYA)_6\cdot\mathbf{3a}_3$) have the two melamine rings in each calix[4]arene in a staggered orientation while these rings in assemblies with C_{3h} and C_3 symmetry ($\mathbf{1}_3\cdot(DEB)_6\cdot\mathbf{2a}_3$ and $\mathbf{1}_3\cdot(DEB)_6\cdot\mathbf{2a}_3\cdot\mathbf{3a}_3$, respectively) have a parallel orientation.

important for the outcome of the recognition and encapsulation processes. Furthermore, the receptor has the ability to selectively release the guest molecules complexed in the internal cavity (when it receives the appropriate stimuli) while the guest molecules at the periphery remain complexed to the receptor.

Hydrogen-bonded receptors $\mathbf{1}_3\cdot(DEB)_6$ and $\mathbf{1}_3\cdot(BuCYA)_6$ are formed spontaneously upon mixing calix[4]arene dimelamine **1** and barbiturate (DEB) or cyanurate (BuCYA) derivatives, respectively, in a 1:2 ratio in apolar solvents (Figure 1).[16] The self-assembly process is driven by the cooperative formation of 36 hydrogen bonds, which leads to assemblies with a high thermodynamic stability, even at concentrations of 10^{-4} M. Despite the negative entropy arising from the assembly of nine components, the formation of the assembly is enthalpically driven ($\Delta H^{o} < 0$) as a result of the formation of the 36 hydrogen bonds between the complementary hydrogen-bonding arrays of **1** and DEB or BuCYA.

The first step in achieving the *endo–exo* complexation is the encapsulation of alizarin (**2a**) within the two rosette layers of the receptor. The ^{1}H NMR spectrum of a 1.0 mM solution of the hydrogen-bonded receptor $\mathbf{1}_3\cdot(DEB)_6$ in [D_8]toluene shows that nearly all the signals are shifted, both for the host assembly and for the guest molecules (Figure 2b), upon addition of three equivalents of alizarin (**2a**). For example, the signals of the NH_{DEB} protons (H^a and H^b) involved in the hydrogen-bonding array shift upfield from $\delta = 14.85$ and 14.08 to 14.43 and 13.81 ppm, respectively. Similarly, proton H^i of the 2-methylpyridine substituents of the melamine rings undergoes an upfield shift of approximately 0.5 ppm upon addition of alizarin. Molecular simulation studies (Quanta 97, CHARMm 24.0) suggest that H^i is pointing towards the center of the receptor, thus resulting in the observed upfield shift in the ^{1}H NMR spectrum. Large upfield shifts were also observed for the aromatic protons of the guest molecules **2a** (> 3.0 ppm), which indicates their encapsulation in the

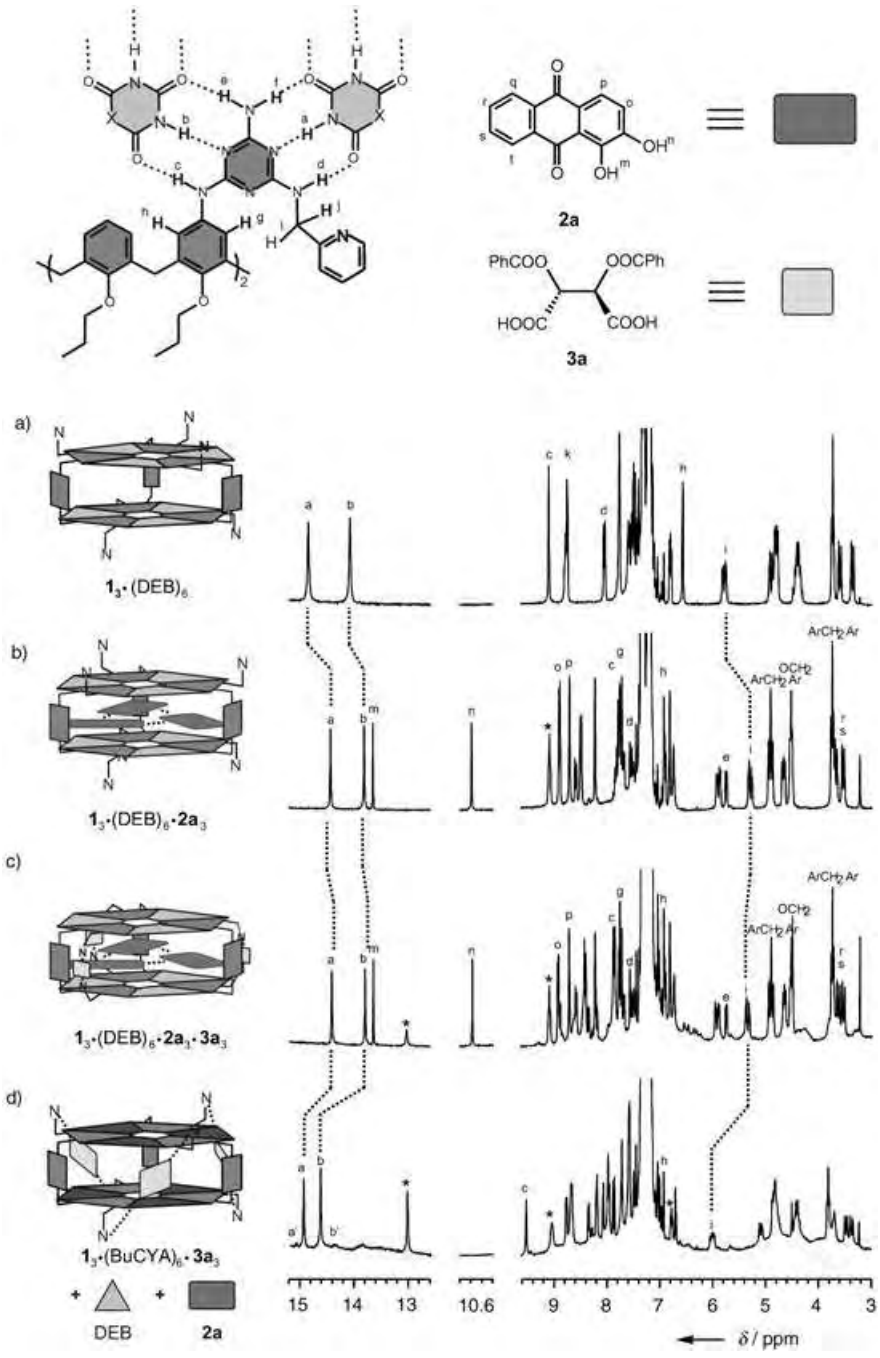

Figure 2. Parts of the ^{1}H NMR spectra (300 MHz) of a) assembly $\mathbf{1}_3\cdot(DEB)_6$ (1 mM), b) $\mathbf{1}_3\cdot(DEB)_6$ + 3 equiv **2a**, c) $\mathbf{1}_3\cdot(DEB)_6\cdot\mathbf{2a}_3$ + 3 equiv **3a**, and d) $\mathbf{1}_3\cdot(DEB)_6\cdot\mathbf{2a}_3\cdot\mathbf{3a}_3$ + 6 equiv BuCYA. Signals marked with * belong to the free **2a**. All spectra were recorded at 298 K in [D_8]toluene.

interior of the assembly. Moreover, the downfield shift observed for alizarin hydroxyl OH^n proton ($\Delta\delta \approx 3.6$ ppm) indicates the formation of intermolecular hydrogen bonds between the carbonyl and hydroxy groups of adjacent guest molecules. These ^{1}H NMR studies shows clearly the encapsulation (*endo* complexation) of a noncovalent trimer of **2a** by receptor $\mathbf{1}_3\cdot(DEB)_6$ to give the complex $\mathbf{1}_3\cdot(DEB)_6\cdot\mathbf{2a}_3$. The encapsulation of alizarin is very selective and sensitive to small structural changes. For example, no complexation was observed when protons H^q and H^t of alizarin **2a** were replaced by hydroxy groups (1,2,5,8-anthraquinone, **2b**, Figure 1).[17] The encapsulation is accompanied by a change in the symmetry of the host assembly, from D_3 to C_{3h} symmetry.[18,19]

After the encapsulation of $\mathbf{2a}_3$ in $\mathbf{1}_3\cdot(DEB)_6$ had been achieved (*endo* complexation), the role of $\mathbf{1}_3\cdot(DEB)_6\cdot\mathbf{2a}_3$ as an *exo* receptor was studied. Addition of three equivalents of dibenzoyl-D-tartaric acid (**3a**) to the complex $\mathbf{1}_3\cdot(DEB)_6\cdot\mathbf{2a}_3$ resulted in upfield shifts of the signals H^a and H^b from $\delta = 14.43$ and 13.81 to 14.38 and 13.76 ppm, respectively (Figure 2c). The signal for proton H^i undergoes a downfield shift of approximately 0.1 ppm. The signal of H^i at $\delta = 5.40$ ppm is indicative of the formation of hydrogen bonds between the 2-methylpyridyl substituents of the calix[4]arene dimelamine and the diacid **3a**.[20] The stoichiometry of the complexation of **3a** by $\mathbf{1}_3\cdot(DEB)_6\cdot\mathbf{2a}_3$ is not clear from these ^{1}H NMR studies. However, circular dichroism (CD) studies (data not shown) on the complexation of **3a** by receptor $\mathbf{1}_3\cdot(BuCYA)_6$ clearly showed the formation of a complex with 1:2 stoichiometry as the major species, although complexes with 1:1 and 1:3 stoichiometries were also present as minor species, probably because of steric effects or allosteric conformational changes.[21] The acids interact with the receptor through two-point interactions. These interactions are only possible "sideways", that is, each diacid interacts with both floors of the double rosette (Figure 1b), with one carboxylic acid of the guest hydrogen bonded to the pyridyl ring of the calix[4]arene dimelamine in the first floor while the other acid group of the same guest interacts with the other pyridyl group of the same calix[4]arene dimelamine (second floor).

The *exo* complexation is not very substrate selective: other diacids with different chemical structure, such as (1*R*,2*R*)-cyclohexane-1,2-dicarboxylic acid (**3b**) and (1*S*,3*R*)-camphoric acid (**3c**, Figure 1a), are also complexed in a similar fashion (data not shown).

Hence, the data show the complexation of six molecules of two different neutral guest molecules (alizarin **2a** and diacid **3a**). The hydrogen-bonded trimer $\mathbf{2a}_3$ is encapsulated in the internal cavity of the receptor $\mathbf{1}_3\cdot DEB_6$ while three molecules of guest **3a** are complexed at the periphery of the host assembly. The receptor has two different degrees of selectivity in the molecular recognition process; that is, the *endo* recognition is very selective and sensitive to the structure of the guest while the *exo* recognition is not structurally very demanding. The relative

orientation of the melamine groups (eclipsed) is preserved during the complexation of **3a** and results in the complex $\mathbf{1}_3\cdot(DEB)_6\cdot\mathbf{2a}_3\cdot\mathbf{3a}_3$ with C_3 symmetry.

The controlled release of the guest molecules from the hydrogen-bonded complex $\mathbf{1}_3\cdot(DEB)_6\cdot\mathbf{2a}_3\cdot\mathbf{3a}_3$ was subsequently studied.[22] Cyanurates form stronger hydrogen bonds with melamines than do barbiturates, thus allowing the exchange of DEB for BuCYA.[23] The addition of the BuCYA to the complex $\mathbf{1}_3\cdot(DEB)_6\cdot\mathbf{2a}_3\cdot\mathbf{3a}_3$ results in the selective release of the hydrogen-bonded trimer $\mathbf{2a}_3$ to give the complex $\mathbf{1}_3\cdot(BuCYA)_6\cdot\mathbf{3a}_3$ in which the guest molecules at the periphery remain complexed. The release of the three guest molecules **2a** is achieved because cyanurate-based assemblies are not able to encapsulate **2a** as a result of geometrical differences between barbiturate- and cyanurate-based assemblies.[17] The release was proven by ^{1}H NMR and CD spectroscopy (Figure 2d and 3, respectively). Addition of six equivalents of BuCYA (with respect to complex $\mathbf{1}_3\cdot(DEB)_6\cdot\mathbf{2a}_3\cdot\mathbf{3a}_3$) to a solution of the complex $\mathbf{1}_3\cdot(DEB)_6\cdot\mathbf{2a}_3\cdot\mathbf{3a}_3$ in [D$_8$]toluene generated a ^{1}H NMR spectrum in which all the signals of $\mathbf{1}_3\cdot(DEB)_6\cdot\mathbf{2a}_3\cdot\mathbf{3a}_3$ had disappeared and only signals corresponding to complex $\mathbf{1}_3\cdot(BuCYA)_6\cdot\mathbf{3a}_3$ and free **2a** and DEB could be seen. For example, the signal at $\delta = 10.58$ ppm (which corresponds to OH^n when it forms intermolecular hydrogen bonds in the trimer $\mathbf{2a}_3$) is not present in the spectrum.[24] Moreover, the signals for protons H^a and H^b are split and shifted downfield from $\delta = 14.38$ and 13.76 ppm to $\delta = 14.95$ and 14.64 ppm, respectively (Figure 2d). The splitting of the signals arises from the transfer of chirality from the chiral guest (**3a**) to the assembly.[19] This induction of chirality is not complete, and therefore the two possible diastereomers (*P* and *M*) are formed.[25]

Additional proof for the complexation and selective release of guest molecules from $\mathbf{1}_3\cdot(DEB)_6\cdot\mathbf{2a}_3\cdot\mathbf{3a}_3$ was obtained from CD spectroscopy (Figure 3). Receptor $\mathbf{1}_3\cdot(DEB)_6$ with D_3 symmetry exists as a racemic mixture of *P* and *M* enantiomers[19] and is therefore CD inactive. As mentioned earlier, the formation of the complex $\mathbf{1}_3\cdot(DEB)_6\cdot\mathbf{2a}_3$ is accompanied by a change in the symmetry

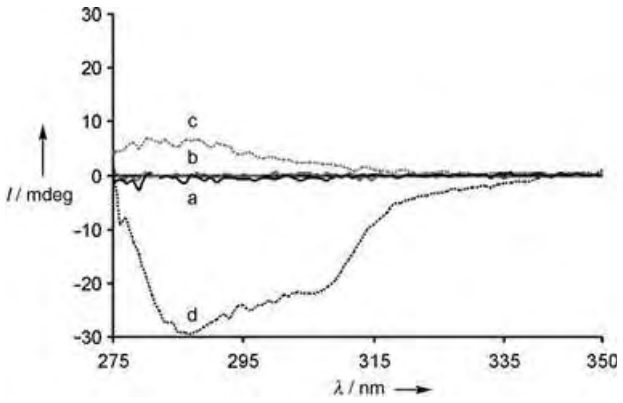

Figure 3. CD spectrum of a) $\mathbf{1}_3\cdot(DEB)_6$ (1.0 mM solution), b) $\mathbf{1}_3\cdot(DEB)_6$ + 3 equiv of **2a**, c) $\mathbf{1}_3\cdot(DEB)_6\cdot\mathbf{2a}_3$ + 3 equiv of **3a**, and d) $\mathbf{1}_3\cdot(DEB)_6\cdot\mathbf{2a}_3\cdot\mathbf{3a}_3$ + 6 equiv of BuCYA. The spectra were recorded at 298 K in [D$_8$]toluene.

of the hydrogen-bonded receptor from D_3 to C_{3h}. In the C_{3h} symmetry, the two melamine moieties adopt an eclipsed conformation, thus resulting in an achiral complex. Addition of **3a** to $\mathbf{1}_3\cdot(DEB)_6\cdot\mathbf{2a}_3$ results in the appearance of a small CD signal (Figure 3) arising from the complexation and transfer of the chirality from **3a** to $\mathbf{1}_3\cdot(DEB)_6\cdot\mathbf{2a}_3$ which causes a change in the symmetry from C_{3h} for the complex $\mathbf{1}_3\cdot(DEB)_6\cdot\mathbf{2a}_3$ to C_3 for $\mathbf{1}_3\cdot(DEB)_6\cdot\mathbf{2a}_3\cdot\mathbf{3a}_3$.[26] Moreover, addition of BuCYA to $\mathbf{1}_3\cdot(DEB)_6\cdot\mathbf{2a}_3\cdot\mathbf{3a}_3$ leads to a new signal in the CD spectrum. This signal is very similar to that observed in the CD spectrum of $\mathbf{1}_3\cdot(BuCYA)_6\cdot\mathbf{3a}_3$ formed by direct mixing of assembly $\mathbf{1}_3\cdot(BuCYA)_6$ and three equivalents of **3a**,[19] thus proving the release of the trimeric $\mathbf{2a}_3$ and the change of symmetry from C_3 back to D_3. In this case, the chirality of **3a** has been transferred to the complex $\mathbf{1}_3\cdot(BuCYA)_6\cdot\mathbf{3a}_3$ which results in the formation of one of the two possible diastereomeric assemblies ((P)-$\mathbf{1}_3\cdot(BuCYA)_6\cdot\mathbf{3a}_3$), and thus a signal is observed in the CD spectrum.[19]

Interestingly, changing the order in which the guest molecules **2a** and **3a** are added has a large influence on the self-assembling behavior of the system. Addition of three equivalents of **3a** directly to a solution of assembly $\mathbf{1}_3\cdot(DEB)_6$ in [D$_8$]toluene (1.0 mM) results in almost complete disassembly (only 8% remains intact) of the host assembly as can be seen by the disappearance of the signals for protons H^a and H^b in the ^{1}H NMR spectrum (Figure 4a,b). The higher acidity of the guest **3a** relative to DEB[27] possibly enables **3a** to form stronger hydrogen bonds with the calix[4]arene dimelamine building blocks **1**, thus leading to the destruction of the assembly. Nevertheless, the subsequent addition of three equivalents of **2a** to this solution results in a ^{1}H NMR spectrum that is identical to the one obtained previously when the guest molecules were added in reversed order (see Figures 2c and 4c). Thus, the host assembly is surprisingly reassembled by templation of the guest **2a** even in the presence of diacid **3a**. Moreover, the encapsulation of guest **2a** also allows the subsequent complexation of the guest **3a** in a similar fashion as described above, thus resulting in the quantitative formation $\mathbf{1}_3\cdot(DEB)_6\cdot\mathbf{2a}_3\cdot\mathbf{3a}_3$ (Figure 4c). The reassembling of the host receptor is probably a result of the stabilizing effect of the π–π interactions between the guest **2a** and the calix[4]arene and dimelamine rings of **1**.[28] Further addition of six equivalents of BuCYA to $\mathbf{1}_3\cdot(DEB)_6\cdot\mathbf{2a}_3\cdot\mathbf{3a}_3$ also leads to the exchange of DEB for BuCYA and release of the trimer $\mathbf{2a}_3$ (Figure 4d). The complexation of **3a** by $\mathbf{1}_3\cdot(BuCYA)_6$ after the exchange of DEB for BuCYA has also been proven by CD spectroscopy.[29]

Herein, we have demonstrated the complexation/encapsulation of two different kinds of neutral guest molecules in which perfect control is shown over the molecular recognition process at two different levels. The noncovalent host molecules $\mathbf{1}_3\cdot(DEB)_6$ display two different modes of complexation, that is, as an nonselective-*exo* receptor for three molecules of carboxylic acid **3a** at the periphery of the assembly and as an selective-*endo* receptor that templates the formation of a noncovalent hydrogen-bonded trimer of alizarin **2a** in the interior cavity of the assembly. The self-assembly of the receptor and the recognition processes bring together, using

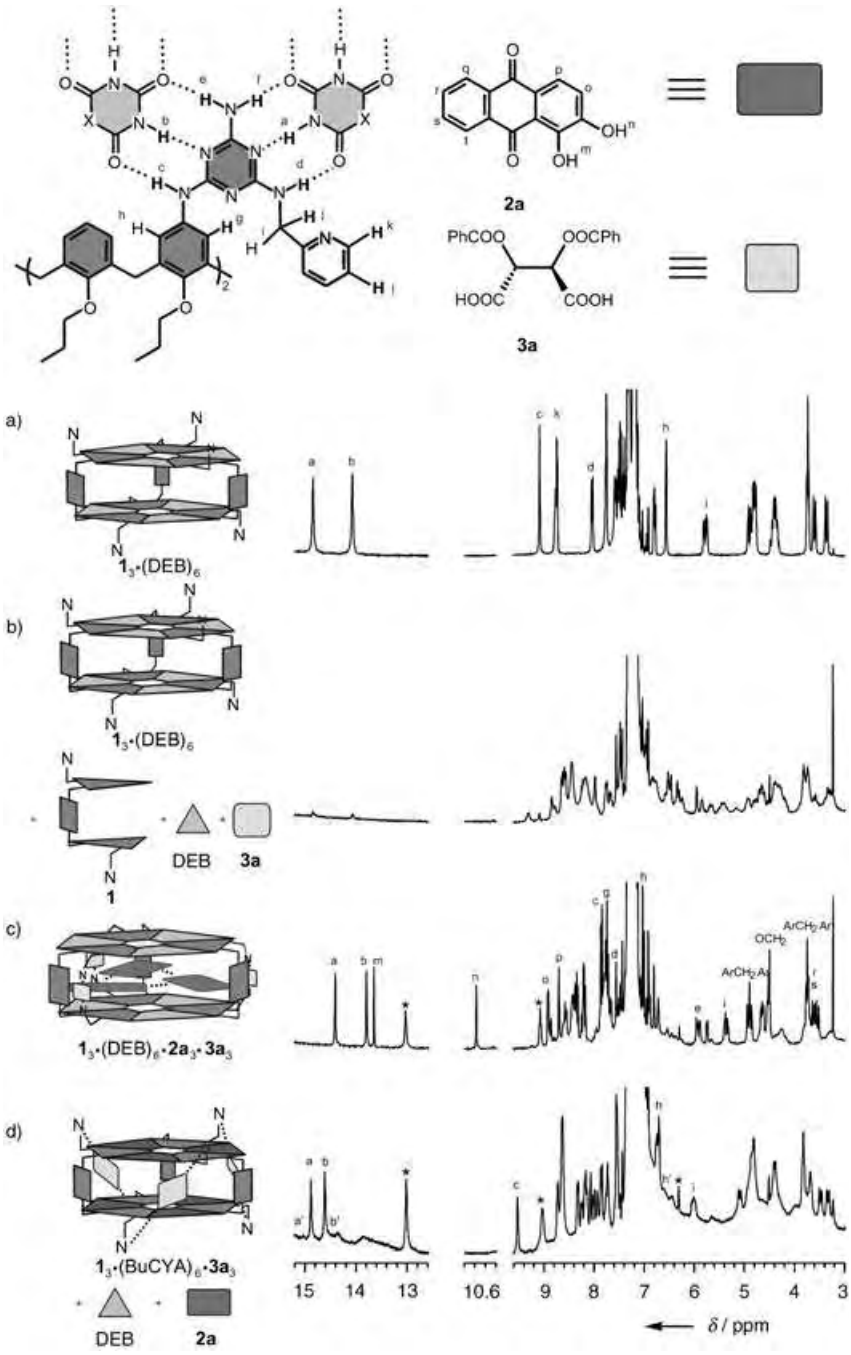

Figure 4. Parts of the ^{1}H NMR spectra (300 MHz) of a) assembly $\mathbf{1}_3\cdot(DEB)_6$ (1 mM), b) $\mathbf{1}_3\cdot(DEB)_6$ + 3 equiv **3a**, c) $\mathbf{1}_3\cdot(DEB)_6$ + 3 equiv **3a** + 3 equiv **2a**, and d) $\mathbf{1}_3\cdot(DEB)_6\cdot\mathbf{2a}_3\cdot\mathbf{3a}_3$ + 6 equiv BuCYA. Signals marked with * belong to the free guest **2a**. All spectra were recorded at 298 K in [D_8]toluene.

the same noncovalent interactions, nine building blocks of the receptor and six guest molecules with absolute control over their spatial disposition to form the complex $\mathbf{1a}_3\cdot(DEB)_6\cdot\mathbf{2a}_3\cdot\mathbf{3a}_3$. Moreover, the addition of BuCYA leads to the release of the noncovalent trimer, while the other guest molecules remain complexed. It has also been demonstrated that the order in which the different building blocks are added is very important for the outcome of the self-assembly process. This observation might have important consequences for noncovalent synthesis in general.

Received: January 13, 2005
Published online: April 21, 2005

Keywords: *endo–exo* complexation · host–guest systems · hydrogen bonds · selective release · self-assembly

[1] E. A. Meyer, R. K. Castellano, F. Diederich, *Angew. Chem.* **2003**, *115*, 1244 – 1287; *Angew. Chem. Int. Ed.* **2003**, *42*, 1210 – 1250.
[2] R. Fiammengo, M. Crego-Calama, D. N. Reinhoudt, *Curr. Opin. Chem. Biol.* **2001**, *5*, 660 – 673.
[3] J. Ohkanda, J. W. Lockman, M. A. Kothare, Y. Qian, M. Blaskovich, S. Sebti, A. D. Hamilton, *J. Med. Chem.* **2002**, *45*, 177 – 188.
[4] *Principles of Molecular Recognition* (Eds.: A. D. Buckingham, A. C. Legon, S. M. Roberts), Blackie, London, **1993**.
[5] J. H. Harley, T. D. James, C. J. Ward, *J. Chem. Soc. Perkin Trans. 1* **2000**, 3155 – 3184.
[6] a) D. J. Cram, T. Kaneda, R. C. Helgeson, B. Brown, C. B. Knobler, E. Meverick, K. N. Trueblood, *J. Am. Chem. Soc.* **1985**, *107*, 3645 – 3657; b) L. Fabbrizzi, A. Poggi, *Chem. Soc. Rev.* **1995**, *24*, 197 – 202; c) T. W. Bell, A. B. Khasanov, M. G. B. Drew, A. Filikov, T. L. James, *Angew. Chem.* **1999**, *111*, 2705 – 2709; *Angew. Chem. Int. Ed.* **1999**, *38*, 2543 – 2547.
[7] a) S. L. Tobey, E. V. Anslyn, *J. Am. Chem. Soc.* **2003**, *125*, 10963 – 10970; b) P. A. Gale, *Coord. Chem. Rev.* **2001**, *213*, 79 – 128; c) C. Suksai, T. Tuntulani, *Chem. Soc. Rev.* **2003**, *32*, 192 – 202; d) J. L. Sessler, S. Camiolo, P. A. Gale, *Coord. Chem. Rev.* **2003**, *240*, 17 – 55; e) J. M. Linares, D. Powell, K. Bowman-James, *Coord. Chem. Rev.* **2003**, *240*, 57 – 75; f) K. H. Choi, A. D. Hamilton, *Coord. Chem. Rev.* **2003**, *240*, 101 – 110; g) L. Fabbrizzi, M. Licchelli, G. Rabaioli, A. Taglietti, *Coord. Chem. Rev.* **2000**, *205*, 85 – 108.
[8] a) O. Middel, W. Verboom, D. N. Reinhoudt, *Eur. J. Org. Chem.* **2002**, *16*, 2587 – 2597; b) A. S. Droz, F. Diederich, *J. Chem. Soc. Perkin Trans. 1* **2000**, 4224 – 4226; c) S. Tamaru, S. Shinkai, A. B. Khasanov, T. W. Bell, *Proc. Natl. Acad. Sci. USA* **2002**, *99*, 4972 – 4976; d) B. P. Orner, X. Salvatella, J. S. Quesada, J. de Mendoza, E. Giralt, A. D. Hamilton, *Angew. Chem.* **2002**, *114*, 125 – 127; *Angew. Chem. Int. Ed.* **2002**, *41*, 117 – 119; e) M. Almaraz, C. Raposo, M. Martín, M. C. Caballero, J. R. Moran, *J. Am. Chem. Soc.* **1998**, *120*, 3516 – 3517.
[9] a) A. G. Amit, R. A. Marinzza, S. E. V. Phillips, R. J. Poljak, *Science* **1986**, *233*, 747 – 753; b) R. A. Lerner, S. J. Benkovic, P. G. Schultz, *Science* **1991**, *252*, 659 – 667, and references therein.
[10] a) M. Mammen, S.-K. Choi, G. M. Whitesides, *Angew. Chem.* **1998**, *110*, 2908 – 2953; *Angew. Chem. Int. Ed.* **1998**, *37*, 2754 – 2794; b) J. Huskens, A. Mulder, T. Auletta, C. A. Nijhuis, M. J. W. Ludden, D. N. Reinhoudt, *J. Am. Chem. Soc.* **2004**, *126*, 6784 – 6797.
[11] a) X. D. Shi, K. M. Mullaugh, J. C. Fettinger, Y. Jiang, S. A. Hofstadler, J. T. Davis, *J. Am. Chem. Soc.* **2003**, *125*, 10830 –

10841; b) A. Casnati, C. Massera, N. Pelizzi, I. Stibor, E. Pinkassik, F. Ugozzoli, R. Ungaro, *Tetrahedron Lett.* **2002**, *43*, 7311 – 7314; c) L. A. J. Chrisstoffels, F. de Jong, D. N. Reinhoudt, S. Sivelli, L. Gazzola, A. Casnati, R. Ungaro, *J. Am. Chem. Soc.* **1999**, *121*, 10142 – 10151; d) N. Pelizzi, A. Casnati, A. Friggeri, R. Ungaro, *J. Chem. Soc. Perkin Trans. 2* **1998**, 1307 – 1311; e) D. G. Hilmey, L. A. Paquete, *J. Org. Chem.* **2004**, *69*, 3262 – 3270.

[12] F. W. B. Van Leeuwen, W. Verboom, X. Shi, J. T. Davis, D. N. Reinhoudt, *J. Am. Chem. Soc.* **2004**, *126*, 16575 – 16581.

[13] a) M. H. K. Ebbing, M.-J. Villa, J.-M. Valpuesta, P. Prados, J. de Mendoza, *Proc. Natl. Acad. Sci. USA* **2002**, *99*, 4962 – 4966; b) L. J. Barbour, M. R. Caira, T. le Roex, L. R. Nassimbeni, *J. Chem. Soc. Perkin Trans. 2* **2002**, 1973 – 1979; c) T. Heinz, D. M. Rudkevich, J. Rebek, Jr., *Nature* **1998**, *394*, 764 – 766; d) S. K. Körner, F. C. Tucci, D. M. Rudkevich, T. Heinz, J. Rebek, Jr., *Chem. Eur. J.* **2000**, *6*, 187 – 195; e) A. Shivanyuk, J. Rebek, Jr., *J. Am. Chem. Soc.* **2002**, *124*, 12074 – 12075; f) J. Chen, J. Rebek, Jr., *Org. Lett.* **2002**, *4*, 327 – 329; g) S. D. Starnes, D. M. Rudkevich, J. Rebek, Jr., *J. Am. Chem. Soc.* **2001**, *123*, 4659 – 4669.

[14] a) J. L. Atwood, L. J. Barbour, A. Jerga, *Proc. Natl. Acad. Sci. USA* **2002**, *99*, 4837 – 4841; b) K. Biradha, C. Seward, M. J. Zaworotko, *Angew. Chem.* **1999**, *111*, 584 – 587; *Angew. Chem. Int. Ed.* **1999**, *38*, 492 – 495.

[15] J. A. McCammon, *Curr. Opin. Struct. Biol.* **1998**, *8*, 245 – 249.

[16] a) R. H. Vreekamp, J. P. M. van Duynhoven, M. Hubert, W. Verboom, D. N. Reinhoudt, *Angew. Chem.* **1996**, *108*, 1306 – 1309; *Angew. Chem. Int. Ed. Engl.* **1996**, *35*, 1215 – 1218; b) P. Timmerman, R. H. Vreekamp, R. Hulst, W. Verboom, D. N. Reinhoudt, K. Rissanen, K. A. Udachin, J. Ripmeester, *Chem. Eur. J.* **1997**, *3*, 1823 – 1832.

[17] J. M. C. A. Kerckhoffs, PhD Thesis, University of Twente (NL), **2003**.

[18] J. M. C. A. Kerckhoffs, F. W. B. van Leeuwen, A. L. Spek, H. Kooijman, M. Crego-Calama, D. N. Reinhoudt, *Angew. Chem.* **2003**, *115*, 5895 – 5900; *Angew. Chem. Int. Ed.* **2003**, *42*, 5717 – 5722.

[19] L. J. Prins, K. A. Jolliffe, R. Hulst, P. Timmerman, D. N. Reinhoudt, *J. Am. Chem. Soc.* **2000**, *122*, 3617 – 3627.

[20] T. Ishi-i, M. Crego-Calama, P. Timmerman, D. N. Reinhoudt, S. Shinkai, *J. Am. Chem. Soc.* **2002**, *124*, 14631 – 14641.

[21] S. Shinkai, M. Ikeda, A. Sugasaki, M. Takeuchi, *Acc. Chem. Res.* **2001**, *34*, 494 – 503.

[22] a) K. Park, *Controlled Drug Delivery: Challenges and Strategies*, American Chemical Society, Washington, DC, **1997**; b) T. Douglas, M. Young, *Nature* **1998**, *393*, 152 – 155; c) N. K. Mal, M. Fujiwara, Y. Tanaka, *Nature* **2003**, *421*, 350 – 353.

[23] A. G. Bielejewska, C. E. Marjo, L. J. Prins, P. Timmerman, F. de Jong, D. N. Reinhoudt, *J. Am. Chem. Soc.* **2001**, *123*, 7518 – 7533.

[24] The ^{1}H NMR spectrum of the receptor complexing both $\mathbf{2a}_3$ and $\mathbf{3a}_3$ after the addition of BuCYA is similar to the ^{1}H NMR spectrum of $\mathbf{1}_3\cdot(\text{BuCYA})_6\cdot\mathbf{3a}_3$ formed by direct mixing of assembly $\mathbf{1}_3\cdot(\text{BuCYA})_6$ and three equivalents of **3a** (data not shown).

[25] In the absence of chiral auxiliary, the receptor is presented as a racemic mixture of *P* and *M* enantiomers and therefore only two signals (ca. 13–15 ppm) are expected for the NH protons of the barbiturate/cyanurate componets in the ^{1}H NMR spectrum. However, the addition of chiral diacids (D or L) leads to the formation of diastereomeric ((*P*)-D or (*M*)-L) assemblies (induction of chirality), and therefore four signals are expected, two signals for each diastereomeric receptor.

[26] The encapsulation of alizarin **2a** by assemblies bearing chiral building blocks leads to a change of symmetry from D_3 to C_3.[17] The CD spectrum of these assemblies resembles the CD spectrum obtained for complex $\mathbf{1}_3\cdot(\text{DEB})_6\cdot\mathbf{2a}_3\cdot\mathbf{3a}_3$.

[27] The pK_a value of DEB is 7.4 and of guest **3a** is 2.99 (see: a) R. M. C. Dawson, *Data for biochemichal research*, Clarendon Press, Oxford, **1959**; b) N. Chidambaram, D. J. Burgess, *AAPS PharmSciTech* **2000**, *2*, 1 – 11).

[28] a) C. A. Hunter, J. K. M. Sanders, *J. Am. Chem. Soc.* **1990**, *112*, 5525 – 5534; b) M. G. J. ten Cate, J. Huskens, M. Crego-Calama, D. N. Reinhoudt, *Chem. Eur. J.* **2004**, *10*, 3632 – 3639.

[29] Addition of BuCYA to $\mathbf{1}_3\cdot(\text{DEB})_6\cdot\mathbf{2a}_3\cdot\mathbf{3a}_3$ results in the appearance of a negative CD signal similar to the signal obtained by direct mixing of assembly $\mathbf{1}_3\cdot(\text{BuCYA})_6$ and three equivalents of **3a**. Thus, addition of BuCYA results in the release of the trimeric species of **2a**.

Organic Synthesis

Intermolecular Tandem Pd-Catalyzed Cross-Coupling/[4+4] and [4+2] Cycloadditions: A One-Pot, Five-Component Assembly of Bicyclo[6.4.0]dodecanes**

Phil Ho Lee and Kooyeon Lee*

Tandem reactions have long been established as efficient methods for the rapid synthesis of complex compounds starting from simple, readily available substrates in relatively few steps.[1–3] Although many intramolecular tandem reactions have been reported for constructing complex organic molecules, the corresponding highly efficient intermolecular reactions remain an important challenge for synthetic organic chemists. A range of strategies involving the sequential generation of radical and anionic species has been used for such intermolecular transformations.[4,5] However, relatively few transition-metal-catalyzed intermolecular tandem processes[6] have been developed for the synthesis of complex cyclic compounds.[7] Recently, we reported a method for the synthesis of substituted allenes, polyallenes, and unsymmetrical bis(allenes) from allenylindium reagents generated in situ.[8] With this result in hand, we envisioned that a Pd-catalyzed cascade process involving sequential cross-coupling between vinyl bromides or triflates and propargyl halides followed by [4+4] and [4+2] cycloadditions should provide structurally diverse carbocycles. Herein, we describe the development of tandem Pd-catalyzed cross-coupling/[4+4]

[*] Prof. Dr. P. H. Lee, Dr. K. Lee
Department of Chemistry, Kangwon National University
Chunchon 200-701 (Republic of Korea)
Fax: (+82) 33-253-7582
E-mail: phlee@kangwon.ac.kr

[**] This work was supported by the CMDS at KAIST and grant no. R02-2003-000-10023-0 of the Basic Research Program of the KOSEF. We thank Prof. Tom Livinghouse of Montana State University for proofreading this manuscript.

 DOI: 10.1002/anie.200461957

and [4+2] cycloadditions as an efficient approach to bicyclo-[6.4.0]dodecane derivatives (Scheme 1).[9]

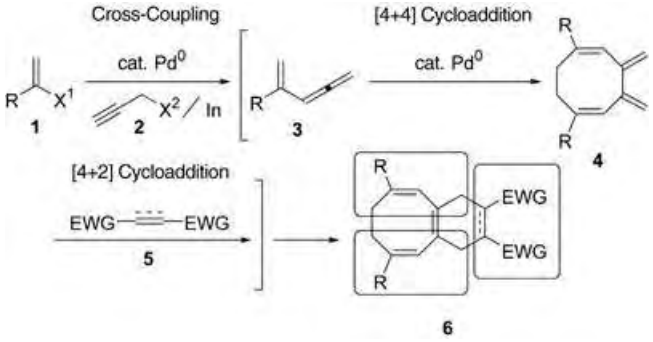

Scheme 1. EWG = electron-withdrawing group.

The tandem process was first examined with α-bromostyrene, propargyl bromide, and tetracyanoethylene (TCE). The organoindium reagent obtained from one equivalent of indium and 1.5 equivalents of propargyl bromide was added to a solution of one equivalent of α-bromostyrene in the presence of 4 mol % of $[Pd(PPh_3)_4]$ and three equivalents of LiCl,[8,10] and the solution was stirred at 50 °C for 2 h. In the ^{1}H NMR spectrum of the crude product mixture, 3,4-dimethylene-1,6-diphenyl-1,5-cyclooctadiene (**4ba**) was observed as the major compound, thus indicating that a sequential cross-coupling/[4+4] cycloaddition had taken place to produce **4ba** in 94 % yield. Because **4ba** is a 1,3-diene, we further attempted a [4+2] cycloaddition reaction with crude **4ba**. Thus, **4ba** was treated with 1.5 equivalents of TCE (70 °C, benzene, 18 h) to afford **6baa** in 84 % yield. This transformation shows that five components can be assembled in an intermolecular cascade cross-coupling/[4+4] and [4+2] cycloaddition sequence (Scheme 2).

A Pd-catalyzed [4+4] cycloaddition reaction with a vinyl allene as the starting material was reported recently.[11] In this reaction, the vinyl allene was obtained from the reaction of 1-phenylvinylmagnesium bromide with propargyl bromide in the presence of a Pd^0 catalyst.[12] However, preparation of the vinyl allene in situ by inversion of the charge polarization of the reaction components (α-bromostyrene and propargyl bromide) was applied in the present method.

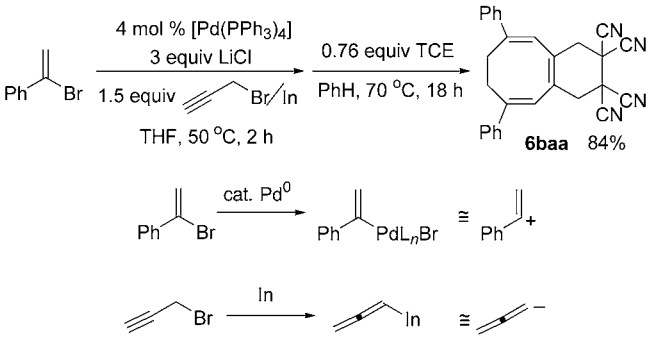

Scheme 2.

The results of several one-pot, five-component assembly reactions are summarized in Table 1. With **5b**, **5c**, **5e**, and **5g** as dienophiles, **4ba** gave bicyclo[6.4.0]dodecane derivatives in good yields (entries 2–5). Similarly, **4ba** reacted with maleimide (**5f**) to produce **6baf** in 79 % yield (entry 6). For a vast number of α-bromovinylarenes as organic electrophiles, the presence of various substituents, for example, 4-trifluoromethyl, 4-methoxy, and 2-chloro on the aromatic ring, did not affect the efficiency of the tandem reactions. The reaction also worked equally well with α-bromovinylarenes containing free hydroxy and amino groups (entries 9 and 11). Treatment of **4ga** with two equivalents of naphthoquinone afforded **6gad** in 64 % yield (entry 7). Reaction of **4da** with glyoxylic acid ethyl ester produced **6dah** in 69 % yield, and the enol triflate of 3-bromoacetophenone underwent the cascade reaction to afford **6hae** in 66 % yield (entry 12).

(α-Bromovinyl)trimethylsilane reacted with propargyl bromide to produce **4aa** in 71 % yield under the optimized conditions. Unfortunately, the desired bicyclo[6.4.0]dodecane derivative was not obtained, because of the instability of **4aa** under the conditions of the [4+2] cycloaddition reaction. With propargyl halides as nucleophilic cross-coupling partners, the presence of a methyl substituent at the α position has little effect on either the reaction rate or the product yield.[13] In the case of 3-chloro-3-methyl-1-butyne (**2b**), **4bb**, **4cb**, **4eb**, and **4gb**, with four methyl substituents on the exocyclic C=C bonds, were obtained in 63–91 % yield. However, these compounds did not undergo the [4+2] cycloaddition because of steric hindrance.

Although the mechanism of the present reaction has not been established, a possible reaction pathway is shown in

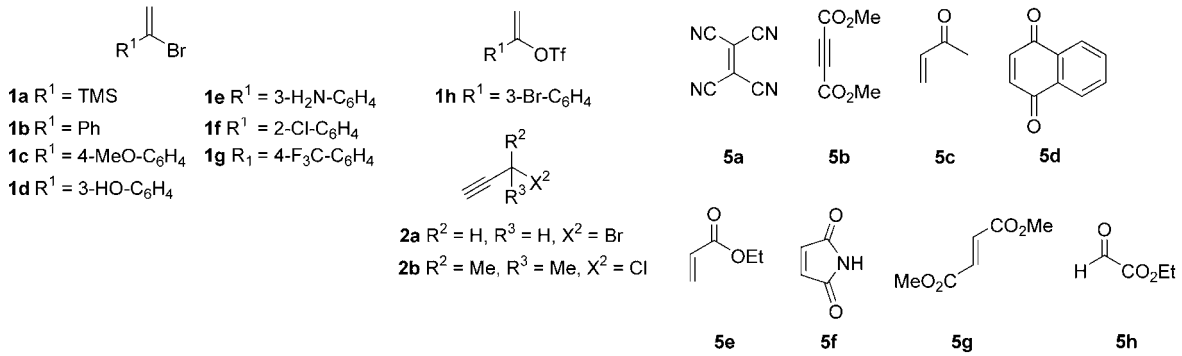

Table 1: Cascade cross-coupling/[4+4] and [4+2] cycloaddition.[a]

Entry	Reagents	Product	Yield [%][b]	Entry	Reagents	Product	Yield [%][b]	Entry	Reagents	Product	Yield [%][b]
1	**1b**, **2a**, **5a**	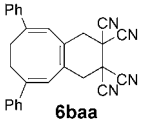 **6baa**	84	5	**1b**, **2a**, **5g**	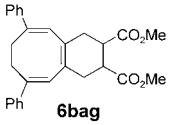 **6bag**	74	9	**1e**, **2a**, **5a**	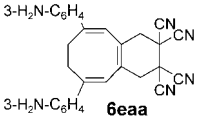 **6eaa**	65
2	**1b**, **2a**, **5b**	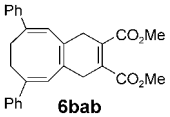 **6bab**	76	6	**1b**, **2a**, **5f**	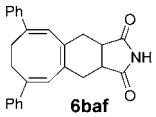 **6baf**	79	10	**1f**, **2a**, **5c**	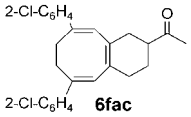 **6fac**	72[c]
3	**1b**, **2a**, **5c**	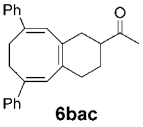 **6bac**	72[c]	7	**1g**, **2a**, **5d**	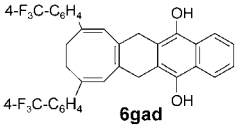 **6gad**	64	11	**1d**, **2a**, **5h**	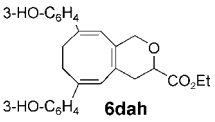 **6dah**	69
4	**1b**, **2a**, **5e**	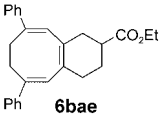 **6bae**	71	8	**1c**, **2a**, **5c**	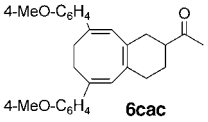 **6cac**	79[c]	12	**1h**, **2a**, **5e**	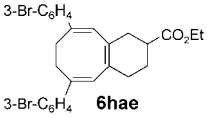 **6hae**	66

[a] Cross-coupling/[4+4] cycloaddition: Compound **1** (0.5 mmol) was treated with **2** (0.75 mmol) and indium (0.5 mmol) in THF (2 mL), in the presence of 4 mol% of $[Pd(PPh_3)_4]$ and LiCl (1.5 mmol) under N_2 at 50°C for 2 h. [4+2] Cycloaddition: Crude **4** was treated with **5** (0.38 mmol) in benzene (2 mL) at 70°C for 18 h. [b] Yield of isolated product. [c] 2.5 equiv of methyl vinyl ketone was used.

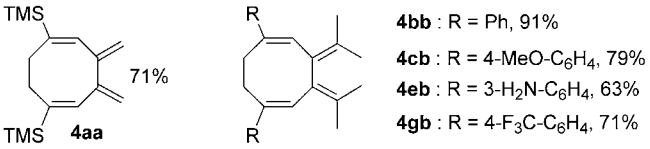

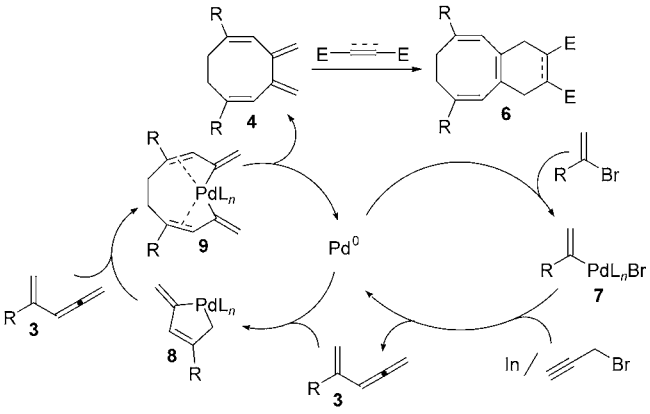

Scheme 3.

Scheme 3. Oxidative addition of the vinyl bromide to a Pd^0 complex and subsequent transmetalation with the organoindium reagent, followed by reductive elimination, affords the vinylallene **3**. Subsequent insertion of Pd^0 into the vinyl allene produces a five-membered palladacycle **8**, which reacts with another molecule of the vinyl allene to generate the di(σ-alkenyl) palladium complex **9**. Final reductive elimination would then give the 3,4-dimethylene-1,5-cyclooctadiene **4**.[8,11] [4+2] Cycloaddition of the 1,3-diene **4** with representative dienophiles produces the observed bicyclo[6.4.0]dodecane derivatives **6**.

In conclusion, this study has led to the development of a novel tandem Pd-catalyzed cross-coupling/[4+4] and [4+2] cycloaddition sequence that allows the rapid synthesis of bicyclo[6.4.0]dodecane derivatives starting from α-bromovinylarenes, propargyl bromides, and dienophiles in one reaction vessel. It is noteworthy that five components are assembled into one molecule in this procedure. In addition, the present process is one of the comparatively few examples in which a Pd^0 catalyst is simultaneously involved in two catalytic cycles.[2,3]

Experimental Section

Typical experimental procedure: **6baa**: α-Bromostyrene (**1b**, 102.0 mg, 0.5 mmol) was added at room temperature, under nitrogen, to a suspension of $[Pd(PPh_3)_4]$ (4 mol%, 23.1 mg) and lithium chloride (63.5 mg, 1.5 mmol) in dry THF (1 mL). After 15 min the allenylindium reagent, which was generated from propargyl bromide (**2a,** 80% (w/w) in toluene, 89.2 mg, 0.75 mmol) and indium (57.0 mg, 0.5 mmol) in dry THF (1 mL), was added. The solution was stirred at 50°C under nitrogen for 2 h, and then the solvent was removed under reduced pressure. A solution of tetracyanoethylene (**5a,** 48 mg, 0.38 mmol) in dry benzene (2 mL) was added to the residue. After heating at 70°C under nitrogen for 18 h, the resulting solution was quenched with saturated aqueous $NaHCO_3$. The aqueous layer was extracted with diethyl ether (3 × 20 mL), and the combined organic phases were washed with water and brine, dried with $MgSO_4$, filtered, and concentrated under reduced pressure. The residue was purified by silica-gel column chromatography with EtOAc/hexane (1:10) as eluent to produce 6,9-diphenyl-7,8-dihydro-1*H*,4*H*-benzocyclooctene-2,2,3,3-tetracarbonitrile (**6baa**; 87.0 mg, 84%). ^1H NMR (400 MHz, $CDCl_3$, 25°C, TMS): $\delta = 7.34$–7.30 (m, 10H), 5.94 (s, 2H), 3.28 (s, 4H), 2.88 ppm (s, 4H); ^{13}C NMR (100 MHz, $CDCl_3$): $\delta =$ 147.3, 141.9, 128.6, 128.3, 126.2, 124.2, 124.0, 110.6, 37.9, 36.6,

30.4 ppm; IR (film): $\tilde{\nu}$ = 3055, 1941 cm^{-1}; HRMS (EI) calcd for $C_{28}H_{20}N_4M^+$ 412.1688; found 412.1689.

Received: September 12, 2004
Revised: February 11, 2005
Published online: April 21, 2005

Keywords: cross-coupling · cycloaddition · indium · palladium · tandem reactions

[1] N. Hall, *Science* **1994**, *266*, 32.
[2] a) T.-L. Ho, *Tandem Organic Reactions*, Wiley-Interscience, New York, **1992**; b) T.-L. Ho, *Tactics of Organic Synthesis*, Wiley-Interscience, New York, **1994**, p. 79; c) L. F. Tietze, F. Haunert in *Stimulating Concepts in Chemistry* (Eds.: F. Vögtle, J. F. Stoddart, M. Shibasaki), Wiley-VCH, Weinheim, **2000**, p. 39.
[3] a) L. F. Tietze, U. Beifuss, *Angew. Chem.* **1993**, *105*, 137; *Angew. Chem. Int. Ed. Engl.* **1993**, *32*, 131; b) R. A. Bunce, *Tetrahedron* **1995**, *51*, 13103; c) E. Negishi, C. Coperet, S. Ma, S.-H. Liou, F. Liu, *Chem. Rev.* **1996**, *96*, 365; d) L. F. Tietze, *Chem. Rev.* **1996**, *96*, 115.
[4] a) I. Ryu, H. Yamazaki, A. Ogawa, N. Kambe, N. Sonoda, *J. Am. Chem. Soc.* **1993**, *115*, 1187; b) K. Tsuchii, M. Doi, T. Hirao, A. Ogawa, *Angew. Chem.* **2003**, *115*, 3614; *Angew. Chem. Int. Ed.* **2003**, *42*, 3490.
[5] a) T. Shono, I. Nishiguchi, M. Sasaki, *J. Am. Chem. Soc.* **1978**, *100*, 4314; b) K. Takai, T. Ueda, N. Ikeda, T. Moriwake, *J. Org. Chem.* **1996**, *61*, 7990; c) K. Takai, N. Matsukawa, A. Takahashi, T. Fujii, *Angew. Chem.* **1998**, *110*, 160; *Angew. Chem. Int. Ed.* **1998**, *37*, 152; d) J. Terao, K. Saito, S. Nii, N. Kambe, N. Sonoda, *J. Am. Chem. Soc.* **1998**, *120*, 11822.
[6] a) M. Lautens, W. T. Klute, *Chem. Rev.* **1996**, *96*, 49; b) L. Yet, *Chem. Rev.* **2000**, *100*, 2963; c) S.-I. Ikeda, *Acc. Chem. Res.* **2000**, *33*, 511; d) J. Montgomery, *Acc. Chem. Res.* **2000**, *33*, 467; e) Y. M. Dong, W. C. MacMillan, *J. Am. Chem. Soc.* **2001**, *123*, 2448; f) P. A. Wender, G. G. Gamber, M. J. C. Scanio, *Angew. Chem.* **2001**, *113*, 4013; *Angew. Chem. Int. Ed.* **2001**, *40*, 3895; g) S. Ikeda, *J. Synth. Org. Chem. Jpn.* **2001**, *59*, 960; h) L. W. A. van Berkom, G. J. T. Kuster, F. Kalmoua, R. de Gelder, H. W. Scheeren, *Tetrahedron Lett.* **2003**, *44*, 5091; i) K. Inanaga, K. Takasu, M. Ihara, *J. Am. Chem. Soc.* **2004**, *126*, 1352; j) A. Ajamian, J. L. Gleason, *Angew. Chem.* **2004**, *116*, 3842; *Angew. Chem. Int. Ed.* **2004**, *43*, 3754.
[7] a) T. K. Devon, A. I. Scott, *Handbook of Naturally Occurring Compounds*, *Vol. II*, Academic Press, New York, **1972**; b) D. J. Faulkner, *Nat. Prod. Rep.* **1984**, *1*, 251, 551; D. J. Faulkner, *Nat. Prod. Rep.* **1986**, *3*, 1; D. J. Faulkner, *Nat. Prod. Rep.* **1987**, *4*, 539; D. J. Faulkner, *Nat. Prod. Rep.* **1988**, *5*, 613; c) T. Oishi, Y. Ohtsuka, *Studies in Natural Products Chemistry* (Ed.: Atta-ur-Rahman), Elsevier, Amsterdam, **1989**, p. 73; d) C. J. Moody, *Studies in Natural Products Chemistry* (Ed.: Atta-ur-Rahman), Elsevier, Amsterdam, **1992**, pp. 201–239.
[8] K. Lee, D. Seomoon, P. H. Lee, *Angew. Chem.* **2002**, *114*, 4057; *Angew. Chem. Int. Ed.* **2002**, *41*, 3901.
[9] For a review on eight-membered ring carbocycle construction, see: a) N. A. Petasis, M. A. Patane, *Tetrahedron* **1992**, *48*, 5757; b) S. M. Sieburth, N. T. Cunard, *Tetrahedron* **1996**, *52*, 6251; c) G. Mehta, V. Singh, *Chem. Rev.* **1999**, *99*, 881.
[10] a) P. H. Lee, S.-Y. Sung, K. Lee, *Org. Lett.* **2001**, *3*, 3201; b) K. Lee, J. Lee, P. H. Lee, *J. Org. Chem.* **2002**, *67*, 8265; c) P. H. Lee, D. Seomoon, K. Lee, S. Kim, H. Kim, H. Kim, E. Shim, M. Lee, S. Lee, M. Kim, M. Sridhar, *Adv. Synth. Catal.* **2004**, *346*, 1641.
[11] a) M. Murakami, K. Itami, Y. Ito, *Angew. Chem.* **1998**, *110*, 3616; *Angew. Chem. Int. Ed.* **1998**, *37*, 3418; b) M. Murakami, K. Itami, Y. Ito, *Synlett* **1999**, 951; c) Thermal dimerization of vinylallene: R. Schneider, H. Siegel, H. Hopf, *Liebigs Ann. Chem.* **1981**, 1812.
[12] When α-bromostyrene is treated with propargyl bromide in the presence of Mg and Pd^0, α-bromostyrene and propargyl bromide act as synthons of a vinyl anion and allenyl cation, respectively, to produce a vinyl allene: M. Murakami, K. Thami, Y. Ito, *Organometallics* **1999**, *18*, 1326.

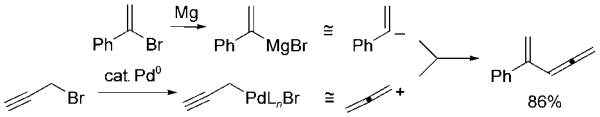

[13] The use of 3-bromo-1-butyne produced the corresponding [4+4] adduct in 90% yield. The product consisted of three stereoisomers (1.3:1.0:1.3) with respect to the orientation of the two methyl groups on the exocyclic double bonds.

Nanocrystals

Rare-Earth Oxide Nanopolyhedra, Nanoplates, and Nanodisks**

Rui Si, Ya-Wen Zhang, Li-Ping You, and Chun-Hua Yan**

The synthesis of colloidal nanocrystals has attracted rapidly growing interest not only due to their remarkable size- and shape-dependent chemical and physical properties but also because of their self-assembly potential for device applications.[1–7] For the preparation of nanomaterials with desirable properties, it remains a challenge to explore robust pathways and unify principles towards the systematic manipulation of their crystal size and shape in different systems. The thermolysis of various organometallic precursors and treatment in surfactant solutions have been regarded as powerful

[*] R. Si, Prof. Dr. Y.-W. Zhang, Prof. Dr. C.-H. Yan
State Key Laboratory of Rare-Earth Materials
Chemistry and Applications
PKU-HKU Joint Lab for Rare-Earth Materials
and Bioinorganic Chemistry
Peking University
Beijing 100871 (P.R. China)
Fax: (+86) 10-6275-4179
E-mail: ywzhang@pku.edu.cn
yan@pku.edu.cn
Prof. L.-P. You
Electron Microscopy Laboratory
Peking University, Beijing 100871 (P.R. China)

[**] Grants-in-aid from NSFC (nos. 20171003, 20221101, 20490210, and 20423005) and the Founder foundation of PKU are gratefully acknowledged.

Supporting information for this article is available on the WWW under http://www.angewandte.org or from the author.

  DOI: 10.1002/anie.200462573

pathways to synthesize size- and shape-controlled nanoparticles,[1,2,5,7–19,22] nanorods,[2,6,13,14,16,20,21] and nanodisks and nanoplates[14,21–23] of metals,[2,6,8,9,11,13,22] semiconductors,[1,5,14,21] and metal oxides.[7,10,12,15–20,23]

More recently, surface-modified rare-earth compound nanocrystals have drawn more attention due to their unique properties and promising applications in, for example, UV shielding, luminescent displays, optical communication, biochemical probes, and medical diagnostics. For instance, Sato et al. obtained ZnO- and CaO-doped CeO_2 nanoparticles in water at 40 °C that show a significantly reduced catalytic activity in oxidation and excellent UV-absorption capability.[24] Haase et al. have prepared colloidal $CePO_4$:Tb/$LaPO_4$ core-shell nanoparticles in diphenyl ether at 200 °C that display green emission with a high quantum yield of 70 %,[4] and van Veggel et al. have reported the synthesis of redispersible Er^{3+}-, Nd^{3+}-, and Ho^{3+}-doped LaF_3 nanoparticles with modified near-infrared emission.[3]

However, an important family of rare-earth compounds, namely colloidal rare-earth oxide nanocrystals (other than ceria), have rarely been synthesized, possibly due to the difficulty in choosing appropriate precursor complexes.[23,25–27] Therefore, to develop a versatile route towards colloidal rare-earth oxide nanocrystals is of some urgency. We report here a novel and general synthesis of rare-earth oxide nanocrystals by thermolysis of their benzoylacetonate complexes in oleic acid/oleylamine solvents to give, depending upon the nature of the metal cations and the selective adsorption effects of the solvents employed, highly dispersible and crystalline rare-earth oxide nanopolyhedra, nanoplates, and nanodisks. Optical characterization showed that the CeO_2 nanopolyhedra and Eu_2O_3 nanodisks have interesting optical properties.

The crystal structure and morphology of the products synthesized under optimal conditions were determined by powder X-ray diffraction (XRD) and transmission electron microscopy (TEM), respectively (Table 1). All the dry, trivalent rare-earth oxides (Ln_2O_3, Ln = La–Y) have a body-centered cubic (*bcc*) structure (space group: *Ia*3), whereas dry CeO_2 has a face-centered cubic (*fcc*) structure (space group: *Fm*3*m*). Figure 1 shows the XRD patterns of four samples.

Table 1: Crystal structures and morphologies of the as-obtained rare-earth oxides synthesized by thermolysis of $Ln(BA)_3(H_2O)_2$ (Ln = La–Y) or $Ce(BA)_4$ in oleic acid (OA)/oleylamine (OM) at 250–330 °C for 20–60 min.[a]

	OA/OM	*T* [°C]	*t* [min]	Structure	Morphology
La_2O_3	1:7	330	60	*Ia*3	7 nm nanoplate
CeO_2	0	250	20	*Fm*3*m*	2.6 nm nanopolyhedron
Pr_2O_3	3:5	310	60	*Ia*3	20 nm nanoplate
Nd_2O_3	3:5	310	60	*Ia*3	11 nm nanoplate
Sm_2O_3	3:5	310	60	*Ia*3	11 nm nanoplate 26 nm nanodisk
Eu_2O_3	3:5	310	60	*Ia*3	12 nm nanoplate 32 nm nanodisk
Gd_2O_3	3:5	310	60	*Ia*3	30 nm nanodisk
Tb_2O_3	3:5	310	60	*Ia*3	34 nm nanodisk
Er_2O_3	3:5	310	60	*Ia*3	43 nm nanodisk
Y_2O_3	3:5	310	60	*Ia*3	65 nm nanodisk

[a] Determined by powder X-ray diffraction (Rigaku D/MAX-2000, $Cu_{K\alpha}$ radiation) and transmission electron microscopy (Philips Tecnai F30, 300 kV).

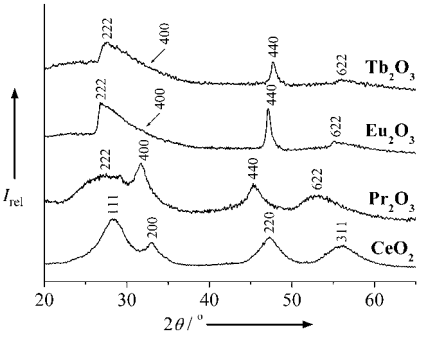

Figure 1. XRD patterns of dry CeO_2, Pr_2O_3, Eu_2O_3, and Tb_2O_3. The calculated lattice constant *a* is 5.4516(3), 11.36(1), 10.97(1), and 10.90(1) Å for CeO_2 (JCPDS: 34-0394), Pr_2O_3,[28] Eu_2O_3 (JCPDS: 34-0392), and Tb_2O_3 (JCPDS: 23-1418), respectively.

The TEM image shown in Figure 2a reveals that the as-obtained CeO_2 nanopolyhedra have a uniform size of 2.6 nm and form a two-dimensional (2D) superlattice structure on the copper grids. The HRTEM image (inset in Figure 2a) shows that each CeO_2 nanopolyhedron is a truncated octahedron enclosed by the (111) and (200) planes.[29]

Figure 2b is the TEM image of the as-obtained Eu_2O_3 redissolved in cyclohexane. Nanodisks with a diameter of about 32 nm have formed, and some of them assemble through their round surface to produce rail-like nanoarrays (see also the Supporting Information). Each slightly flexural Eu_2O_3 nanodisk comprises six (222) layers and has a thickness of 1.6 nm according to the HRTEM image of the side-surface (inset in Figure 2b). The ($\bar{4}40$) planes are perpendicular to (222), and thus the preferential growth direction of the nanodisks is [110]. Each as-obtained Eu_2O_3 nanodisk has a 2D growth structure that is confined along the [111] direction. Figure 2c displays the 2D Eu_2O_3 nanoarrays in a large area. The array axis is [111] and the distance between two adjacent nanodisks is 2.3 nm. Figure 2d shows the TEM image of the Eu_2O_3 nanocrystals redissolved in toluene/hexane (1:1); square nanoplates with a side-size of about 12 nm have formed (see also the Supporting Information). Figure 2e shows that the surface of a nanoplate is composed of the (400) and (040) planes. Each Eu_2O_3 nanoplate is constructed from four (004) layers and has a thickness of 1.0 nm, as determined from the HRTEM image of its side-surface (bottom inset in Figure 2e). The angle between the (222) and (004) planes is close to 60°, which is consistent with the calculated value. The as-obtained Eu_2O_3 nanoplate has a 2D growth structure that is confined along the [001] direction due to symmetry breaking, similar to the case of Gd_2O_3 square nanoplates.[23]

Figures 2f and g show the TEM images of the as-obtained Er_2O_3 and Pr_2O_3, respectively. Pure nanodisks with a diameter of 43 nm are present for Er_2O_3, while pure square nanoplates with a side-size of 20 nm have formed for Pr_2O_3. Figure 2h shows the 2D Pr_2O_3 nanoarrays produced on the copper grids. The array axis is [001] and the distance between two adjacent nanodisks is 2.9 nm.

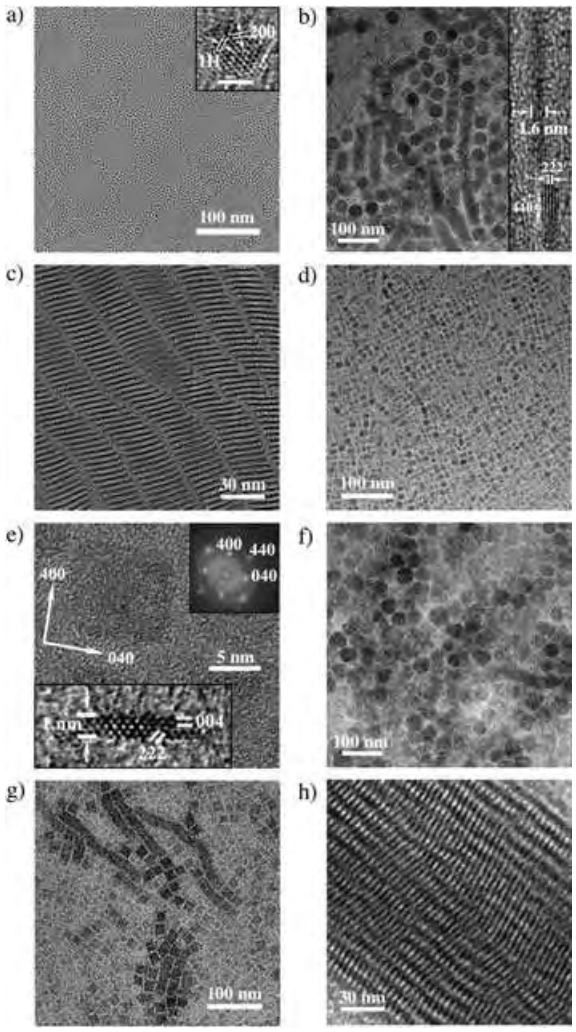

Figure 2. a) TEM image of the as-obtained CeO_2; the inset shows the HRTEM image of a CeO_2 nanopolyhedron (scale bar: 2 nm); b) TEM image of the as-obtained Eu_2O_3 redissolved in cyclohexane; the inset shows the side-surface HRTEM image of a nanodisk; c) TEM image of the 2D Eu_2O_3 nanoarrays; d) TEM image of the as-obtained Eu_2O_3 redissolved in toluene/hexane (1:1); e) The surface and side-surface HRTEM images of an Eu_2O_3 nanoplate; the inset shows the fast Fourier transformation of the surface HRTEM image; f) TEM image of the as-obtained Er_2O_3; g) TEM image of the as-obtained Pr_2O_3; h) TEM image of the 2D Pr_2O_3 nanoarrays.

The mechanism of shape-controlled synthesis of nanocrystals is currently being investigated intensively.[6,12–14,16,17,20–22] During the thermolysis of the precursor complexes the capping ligand (variety, concentration, and selective adsorption onto particular crystallographic facets) plays a critical role in the shape-control process. In our case, experiments show that oleic acid binds more strongly than oleylamine to the surface atoms of the nanocrystals, due to its higher oxophilicity. Increasing the amount of oleic acid gradually dissolved the CeO_2 and greatly improved the solubility of the Ln_2O_3 products in nonpolar solvents. Capping ligands also have distinct effects on the shape of the products formed during the crystal-growth process (Figure 3a).

The thermolysis of rare-earth benzoylacetonate complexes releases a large number of rare-earth oxide nuclei in which the oxygen comes from the chelating ligand.[5] In the *fcc* CeO_2 crystals, the density of surface atoms follows the order $\{111\} > \{100\} > \{110\}$. Generally, the face with a higher density of surface atoms is blocked by the adsorption of surfactants during the crystal growth of colloidal nanocrystals, and the growth along this facet is therefore considerably restricted. However, since oleylamine is characterized by its nonselective adsorption on these faces, the CeO_2 nuclei grow in a 3D mode to generate nanopolyhedra enclosed by both the (111) and (200) planes. The *bcc* structure of Ln_2O_3 can be derived from the *fcc* structure of CeO_2 by removing one-fourth of the oxygen atoms from specific lattice sites. The surface density of atoms in the facets of this structure follows the order $\{100\} > \{111\} > \{110\}$. The former two denser facets are selectively capped by oleic acid, which means that the nuclei grow in a 2D mode to produce nanoplates with confined (001) planes or nanodisks with confined (111) planes. The confinement effect of oleic acid on the specific facets in this case can be demonstrated in the synthesis of Eu_2O_3 nanodisks: decreasing the amount of oleic acid (OA/OM = 1:7) led to some of the Eu_2O_3 nanoparticles showing 3D growth (see Figure 3b). The shape evolution from square nanoplate (La_2O_3–Eu_2O_3) to nanodisk (Sm_2O_3–Y_2O_3) is possibly caused by the change of relative growth rate along {100} to {111} across the Ln_2O_3 series.

Further experiments showed that the size of our rare-earth oxide nanocrystals can be tuned by changing the synthetic parameters, such as the reaction time and temperature. For Eu_2O_3, for example, shortening the reaction time

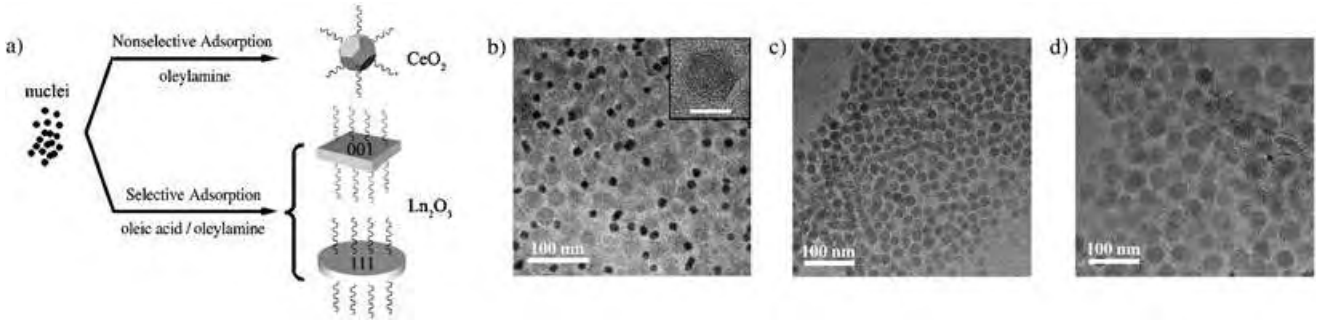

Figure 3. a) Formation of rare-earth oxide nanopolyhedra, nanoplates, and nanodisks. b)–d) TEM images of the as-obtained Eu_2O_3: b) OA/OM = 1:7, 310 °C, 1 h (inset: HRTEM image of an Eu_2O_3 nanoparticle; scale bar: 10 nm); c) OA/OM = 3:5, 310 °C, 20 min; d) OA/OM = 3:5, 330 °C, 1 h.

from 1 h to 20 min caused a decrease in the diameter of the nanodisks from 32 to 20 nm at a reaction temperature of 310 °C (Figure 3c). Upon increasing the reaction temperature from 310 to 330 °C, the size of the nanodisks increased from 32 to 41 nm with a reaction time of 1 h (Figure 3d).

Figure 4a shows the UV/Vis absorption spectrum of the colloidal CeO_2 nanopolyhedra. The spectrum exhibits a strong absorption band at about 300 nm due to the charge-transfer transition from the O 2p to the Ce 4f orbital in CeO_2. Its absorption edge is blue-shifted compared to that of the aggregated CeO_2 nanocrystals in our previous work.[30] Furthermore, the direct bandgap energy, E_d,[31] of the dispersible CeO_2 is 3.60 eV, much larger than that of the aggregated one (3.42 eV). As both CeO_2 samples have the same cubic structure and particle size (2.6 nm), the blue shift of the UV absorption observed for the present monodisperse CeO_2 nanopolyhedra must be related to a modification of the surface state by surface passivation arising from the capping oleylamine ligands.[30]

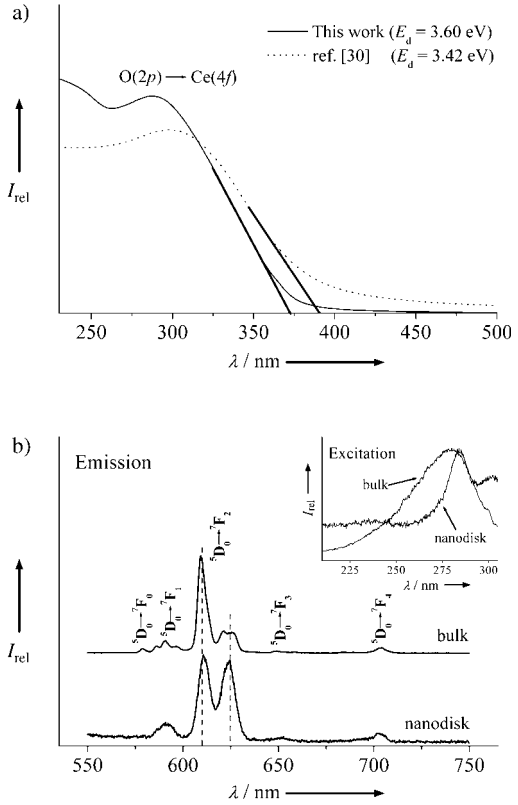

Figure 4. a) UV/Vis absorption spectra (Hitachi U-3010) of the monodisperse CeO_2 nanopolyhedra (solid line) obtained in this work and the aggregated CeO_2 ones of ref. [30] (dotted line). b) Room-temperature fluorescence emission spectra (Hitachi F-4500) of the Eu_2O_3 nanodisks and commercial Eu_2O_3 powders (λ_{ex} = 285 nm); the inset shows their excitation spectra (λ_{em} = 610 nm).

Figure 4b shows the room-temperature emission spectra of Eu_2O_3 nanodisks redissolved in cyclohexane and commercial Eu_2O_3 (99.99%) powder after excitation at a wavelength of 285 nm. The spectra are described by the $^5D_0 \rightarrow {}^7F_j$ line emissions (J = 0, 1, 2, 3, and 4) of the Eu^{3+} ion.[32] An interesting feature is that the intensity ratio of the peak at 625 nm to the peak at 610 nm is greatly enhanced in the emission spectrum of the Eu_2O_3 nanodisks compared with that of the cubic Eu_2O_3 powders. The emission spectrum of the cubic Eu_2O_3 nanodisks is very similar to that of the monoclinic Eu_2O_3 polycrystalline powders, in which the Eu^{3+} ion occupies a site of lower symmetry.[33] It is known that surface atoms, which have a lower coordination number, usually have lower symmetry than bulk ones. In the present Eu_2O_3 nanodisks, two out of six (222) planes are surface ones and thus the surface fraction of Eu^{3+} ions is very high ($> 1/3$). Therefore, this unusual spectrum is considered to result from the higher fraction of surface Eu^{3+} ions, which occupy a different symmetric site due to their lower coordination number than that of the bulk atoms in the Eu_2O_3 nanodisks.

In summary, we have demonstrated a general synthesis of dispersible rare-earth oxide nanocrystals by thermolysis of their benzoylacetonate complexes in oleic acid/oleylamine, which may represent a general route to nanocrystals of other metal oxides. Due to the selective adsorption of the capping ligands on certain cubic faces during crystal growth, nanocrystals with different morphologies, such as nanopolyhedra, nanoplates, and nanodisks, are created, which exhibit a striking ability to self-assemble into large-area nanoarrays. These novel nanometric architectures with unusual optical properties that result from surface-modification effects are expected to enrich the field of lanthanide chemistry, benefit the development of a shape-control theory for nanocrystals, and promise the fabrication of advanced rare-earth functional materials with new applications.

Experimental Section

Oleylamine (OM, Acros), oleic acid (OA, Alfa), and 1-benzoylacetone (HBA, Acros) were used as received.

Rare-earth complexes: La_2O_3, $Ce_2(CO_3)_3$, Pr_6O_{11}, Nd_2O_3, Sm_2O_3, Eu_2O_3, Gd_2O_3, Tb_4O_7, Er_2O_3, or Y_2O_3 (metal content 6 mmol) was dissolved in 40 mL of deionized water by adding HNO_3. HBA (24 mmol) was dissolved in 80 mL of ethanol by adding $NH_3{\cdot}H_2O$. The above two solutions were mixed together whilst stirring and dilute aqueous NH_3 was then added dropwise (final pH: 6–7). The solution was aged at room temperature for 12 h and then filtered. The precipitate was collected, washed with deionized water, and then dried in vacuo at 40 °C overnight. The yields of the complexes were 40–60%.

Dispersible rare-earth oxides: To obtain Ln_2O_3 (Ln = La, Pr, Nd, Sm, Eu, Gd, Tb, Er, or Y), $Ln(BA)_3(H_2O)_2$ (0.2 mmol) was added to 15 mL of OA/OM (Table 1) in a three-necked flask at room temperature. Ar was bubbled through the solution for 20 min and then the solvents were removed under vacuum at about 100 °C for 30 min. The flask was then heated to 310–330 °C at a heating rate of 20 K min^{-1} with vigorous magnetic stirring in a temperature-controlled electromantle, and was maintained at this temperature for 1 h under Ar. To obtain CeO_2, $Ce(BA)_4$ (0.5 mmol in 1 mL of OM) was injected into 15 mL of OM at 250 °C and heated for 20 min under Ar. When the reaction was complete, an excess amount of ethanol was poured into the solution at about 70 °C. The resultant mixture was centrifugally separated and the products were collected. The as-precipitated nanocrystals were washed several times with ethanol and then dried in vacuo at 70 °C overnight. The yield of nanocrystals obtained was

about 75%. The as-precipitated nanocrystals could be redissolved in nonpolar solvents such as hexane, toluene, and cyclohexane.

Received: November 10, 2004
Revised: March 3, 2005
Published online: April 21, 2005

Keywords: crystal growth · fluorescence · nanostructures · rare-earth oxides · UV/Vis spectroscopy

[1] C. B. Murray, D. J. Norris, M. G. Bawendi, *J. Am. Chem. Soc.* **1993**, *115*, 8706.
[2] S.-J. Park, S. Kim, S. Lee, Z. G. Khim, K. Char, T. Hyeon, *J. Am. Chem. Soc.* **2000**, *122*, 8581.
[3] J. W. Stouwdam, F. C. J. M. van Veggel, *Nano Lett.* **2002**, *2*, 733.
[4] K. Kömpe, H. Borchert, J. Storz, A. Lobo, S. Adam, T. Möller, M. Haase, *Angew. Chem.* **2003**, *115*, 5672; *Angew. Chem. Int. Ed.* **2003**, *42*, 5513.
[5] W. S. Seo, H. H. Jo, K. Lee, J. T. Park, *Adv. Mater.* **2003**, *15*, 795.
[6] F. Dumestre, B. Chaudret, C. Amiens, M.-C. Fromen, M.-J. Casanove, P. Renaud, P. Zurcher, *Angew. Chem.* **2002**, *114*, 4462; *Angew. Chem. Int. Ed.* **2002**, *41*, 4286.
[7] T. Hyeon, S. S. Lee, J. Park, Y. Chung, H. B. Na, *J. Am. Chem. Soc.* **2001**, *123*, 12798.
[8] D. P. Dinega, M. G. Bawendi, *Angew. Chem.* **1999**, *111*, 1906; *Angew. Chem. Int. Ed.* **1999**, *38*, 1788.
[9] E. V. Shevchenko, D. V. Talapin, H. Schnablegger, A. Kornowski, O. Festin, P. Svedlindh, M. Haase, H. Weller, *J. Am. Chem. Soc.* **2003**, *125*, 9090.
[10] M. Yin, S. O'Brien, *J. Am. Chem. Soc.* **2003**, *125*, 10180.
[11] N. R. Jana, X. Peng, *J. Am. Chem. Soc.* **2003**, *125*, 14280.
[12] J. Cheon, N.-J. Kang, S.-M. Lee, J.-H. Lee, J.-H. Yoon, S. J. Oh, *J. Am. Chem. Soc.* **2004**, *126*, 1950.
[13] V. F. Puntes, K. M. Krishnan, A. P. Alivisatos, *Science* **2001**, *291*, 2115.
[14] M. Monge, M. L. Kahn, A. Maisonnat, B. Chaudret, *Angew. Chem.* **2003**, *115*, 5479; *Angew. Chem. Int. Ed.* **2003**, *42*, 5321.
[15] W. S. Seo, H. H. Jo, K. Lee, B. Kim, S. J. Oh, J. T. Park, *Angew. Chem.* **2004**, *116*, 1135; *Angew. Chem. Int. Ed.* **2004**, *43*, 1115.
[16] N. R. Jana, Y. Chen, X. Peng, *Chem. Mater.* **2004**, *16*, 3931.
[17] H. Zeng, P. M. Rice, S. X. Wang, S. Sun, *J. Am. Chem. Soc.* **2004**, *126*, 11458.
[18] F. X. Redl, C. T. Black, G. C. Papaefthymiou, R. L. Sandstrom, M. Yin, H. Zeng, C. B. Murray, S. P. O'Brien, *J. Am. Chem. Soc.* **2004**, *126*, 14583.
[19] J. Park, K. An, Y. Hwang, J.-G. Park, H.-J. Noh, J.-Y. Kim, J.-H. Park, N.-M. Hwang, T. Hyeon, *Nat. Mater.* **2004**, *3*, 891.
[20] P. D. Cozzoli, A. Kornowski, H. Weller, *J. Am. Chem. Soc.* **2003**, *125*, 14539.
[21] A. Ghezelbash, M. B. Sigman, Jr., B. A. Korgel, *Nano Lett.* **2004**, *4*, 537.
[22] V. F. Puntes, D. Zanchet, C. K. Erdonmez, A. P. Alivisatos, *J. Am. Chem. Soc.* **2002**, *124*, 12874.
[23] Y. C. Cao, *J. Am. Chem. Soc.* **2004**, *126*, 7456.
[24] R. Li, S. Yabe, M. Yamashita, S. Momose, S. Yoshida, S. Yin, T. Sato, *Solid State Ionics* **2002**, *151*, 235.
[25] W. P. Hsu, L. Rönnquist, E. Matijević, *Langmuir* **1988**, *4*, 31.
[26] M. Yada, M. Mihara, S. Mouri, M. Kuroki, T. Kijima, *Adv. Mater.* **2002**, *14*, 309.
[27] X. Wang, X. M. Sun, D. P. Yu, B. S. Zou, Y. D. Li, *Adv. Mater.* **2003**, *15*, 1442.
[28] G. V. Samsonov, *The Oxide Handbook*, 2nd ed., IFI/Plenum, New York, **1982**, p. 13.
[29] Z. L. Wang, X. Feng, *J. Phys. Chem. B* **2003**, *107*, 13563.
[30] Y. W. Zhang, R. Si, C. S. Liao, C. H. Yan, C. X. Xiao, Y. Kou, *J. Phys. Chem. B* **2003**, *107*, 10159.
[31] R. A. Van Leeuwen, C.-J. Hung, D. R. Kammler, J. A. Switzer, *J. Phys. Chem.* **1995**, *99*, 15247.
[32] G. Blasse, B. C. Grabmaier, *Luminescent Materials*, Springer, Berlin, **1994**.
[33] K. C. Sheng, G. M. Korenowski, *J. Phys. Chem.* **1988**, *92*, 50.

Self-Assembly

Self-Assembled Diamide Nanotubes in Organic Solvents**

*Nancy Díaz, François-Xavier Simon, Marc Schmutz, Michel Rawiso, Gero Decher, Jacques Jestin, and Philippe J. Mésini**

In the field of nanomaterials, high aspect ratio objects such as fibers and nanotubes are interesting since they can form 3D networklike gels, they can be effectively oriented, and can be used to transport electrons or particles in a 1D fashion. Supramolecular chemistry has proved to be very useful for building such objects. Besides carbon nanotubes and biological macromolecules, many fibrillar structures have been assembled from supramolecular self-association of small molecules.[1] The self-assembly process offers crucial advantages in the formation of gels by low-mass organic gelators,[2] such as thermoreversibility, easy processing, and high purity. However, chemical design and synthesis also permits the addition of further functionality to threadlike assemblies for applications such as biomineralization[3] and the selective binding of protein on lipidic tubes.[4] Tubular structures offer additional properties because of the presence of an inner cavity, which can be used as nanocargo devices or nanoreactors.[5] They have also been used to template inorganic tubular structures by sol–gel processes[6] and multilayered polyelectrolyte tubes upon layer-by-layer adsorption.[7]

Numerous molecules can self-assemble to form 1D objects such as ribbons or fibrils;[8] however, only a few of

[*] N. Díaz, F.-X. Simon, Dr. M. Schmutz, Dr. M. Rawiso, Prof. G. Decher, Dr. P. J. Mésini
Institut Charles Sadron
6 rue Boussingault, 67083 Strasbourg Cedex (France)
Fax: (+33) 388-414-099
E-mail: mesini@ics.u-strasbg.fr
Dr. J. Jestin
Laboratoire Léon Brillouin
CEA-Saclay
91191 Gif-sur-Yvette Cedex (France)

[**] This work was supported by a CONACyT fellowship (N.D.) and by a MESR fellowship (F.-X.S.). We thank Dr. P. Schultz for the use of the cryofracturing apparatus developed by Dr. J.-C. Homo at the IGBMC UMR 7104, Illkirch, France; Benoît Heinrich for WAXS spectra; and Dr. P. Baxter for critical reading of the manuscript.

Supporting information for this article is available on the WWW under http://www.angewandte.org or from the author.

  DOI: 10.1002/anie.200500536

them form hollow tubes.[9] Some such tubes formed from lipids[10] and bile acids[11] have diameters on the order of micrometers and are polydisperse. Recent work has enabled the discovery of new self-assembled tubes, such as from sugar derivatives,[12] bolaamphiphiles,[13] lipids,[4] steroids,[14] peptides,[15] and hexabenzocoronene derivatives,[16] with diameters that fill the gap between the micrometer scale and the diameter of the carbon nanotubes (1 to 3 nm). Such tubes are always found along with helical ribbons, which are precursors to the closed tubes and were previously identified by Kunitake and co-workers.[17] These impressive objects have stimulated much theoretical work in which their assembly into ribbons that can further wind up into helical ribbons, and ultimately form tubes, was modeled.[18] In relation to the above-mentioned studies, we report a new compound, with a simple chemical structure, which is able to self-assemble into nanotubes in organic solvents. We also report the characterization of these tubes.

Many diamides self-assemble in organic solvents to form fibrillar aggregates through formation of hydrogen-bonding interactions.[19] The morphology of these aggregates is strongly influenced by the directionality of the hydrogen bonds as well as steric factors. We prepared a diamide bearing a bulky aromatic-decyl ester to study its influence on the shape of the aggregates. Compound **1** was synthesized in two

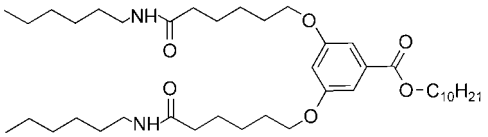

1

steps on a gram scale (see Supporting Information) and isolated as a powder that is insoluble at room temperature in most organic solvents (toluene, benzene, alkanes, methanol, ethanol) but soluble in chloroform and dichloromethane. The formation of gels at low concentration was observed when **1** was suspended in aliphatic solvents or toluene, heated until completely dissolved, and the resulting solution cooled back at 25 °C. The formation of the gel could be observed above concentrations of 0.05 wt % in cyclohexane. Gel formation is thermally reversible: heating the gel results in an isotropic sol phase. This behavior arises from the formation of aggregates through reversible bonds.

The nature of these bonds was explored by spectroscopic techniques. Examination of the **1**/cyclohexane gels by FTIR spectroscopy showed an NH stretching band at 3302 cm^{-1} (Figure 1 a) and an amide I band at 1642 cm^{-1} (Figure 1 b) characteristic of H-bonded amides. In chloroform, in which **1** is soluble at all concentrations, the IR spectra showed only an H-free NH band at 3450 cm^{-1} and a CO band at 1663 cm^{-1}. When the gels are heated from 26 to 64 °C, which is above the melting temperature of the gel (59 °C), the amide A band (Figure 1 a) at 3302 cm^{-1} and the amide I and II bands at 1642 and 1551 cm^{-1} (Figure 1 b) disappear gradually while shifted bands appear at 3457, 1660, and 1520 cm^{-1}, respectively. These bands are characteristic of H-free amides and their intensities increase with temperature. These measurements

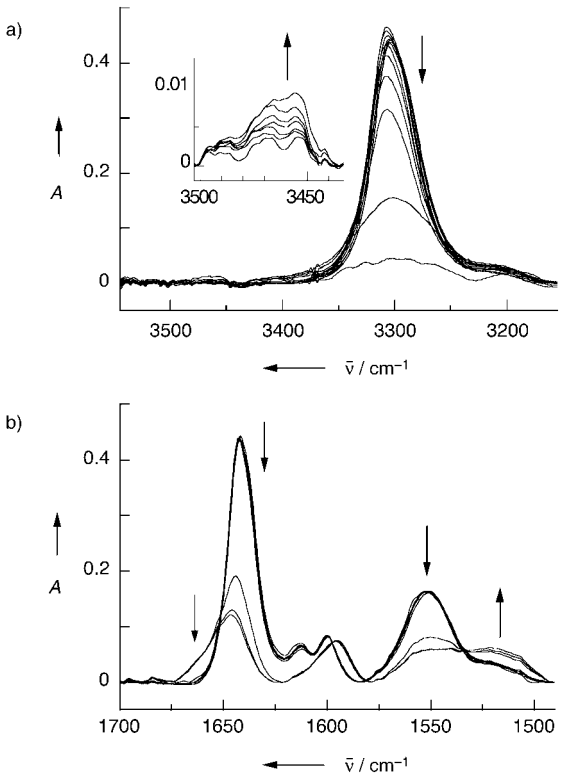

Figure 1. IR spectra of **1** gels in cyclohexane (2 wt %) at temperatures from 26 to 64 °C: a) ν_{NH} region, b) ester and amide I and II region.

confirm that hydrogen bonds between the amide groups contribute to the association process. We previously showed[20] that compounds lacking the amide groups cannot aggregate in alkane solvents. Raising the temperature of the gel also strongly affects the molecular spectra (Figure 2). For example, the absorption band at 223 nm shifts to 207 nm and the bands at 264 and 258 nm transform into a single band at 251 nm. The UV spectrum of **1** in cyclohexane at higher temperatures is similar to the spectrum in chloroform (absorption bands at 254 and 308 nm, not shown). These modifications arise from π interactions between the aromatic rings. Such interactions also contribute to the self-assembly process. The presence of marked isosbestic points in the

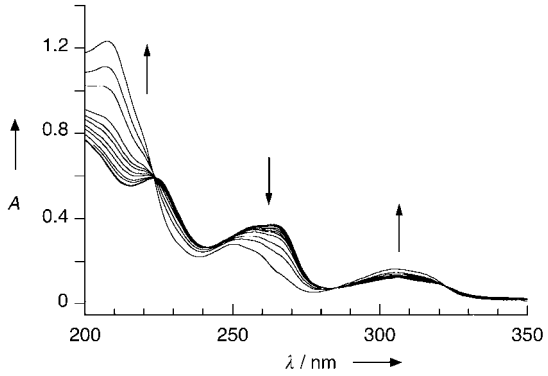

Figure 2. UV spectra of **1** gels in cyclohexane (0.3 wt %) at temperatures from 27 to 62 °C.

spectra shows that there is an equilibrium between aggregated and isolated species and that the position of this equilibrium depends on the temperature. Also, the intermediate species which lie between infinite aggregates and single molecules must have the same molar extinction coefficient. This would not be the case for the smallest aggregates, which would be expected to exhibit spectra which are different from both single molecules and larger aggregates. The stable isosbestic points, therefore, strongly suggest that the major intermediates comprise an equilibrium mixture of large aggregates.

The structure of the gels in cyclohexane has been investigated by electron microscopy (Figure 3). The gel was rapidly frozen to keep the solvent matrix in an amorphous state. Samples were fractured and Pt-shadowed (Figure 3a). Direct TEM could not be used because of the sample thickness and presence of organic solvent. This study revealed that the gels comprise cylindrical aggregates with a very large aspect ratio: their lengths are of the order of a micrometer, and their widths are about 20–30 nm with little dispersity. In a few samples the fracture occurred in a plane perpendicular to the cylinders axis, thus showing their cross-sections (Figure 3b). The white spot in the middle of the cylinder corresponds to an area that cannot be reached by the metal particles, and shows that it is lower than the surrounding rim. The cylinders are therefore hollow. The wall thickness was estimated from longitudinal fractures to be (4 ± 3) nm, the high uncertainty resulting mainly from the thickness of the evaporated metal. No branching structures were observed. Diluted solutions of **1** (below the concentration resulting in the gel) were rotary shadowed after deposition on carbon grids (Figure 3c) and found to contain mainly helical tapes. The mean diameter of those helices is (30 ± 4) nm, which lies in the same range as that of the cylinders. Tubules with helical defects can also be observed in the same solutions. They represent the last step of the self-assembly process, before the formation of the perfectly closed tubes, and emphasize again the link between the closed tubes and helical tapes. As the concentration increases, the lateral width of the helical tapes increases until the tubes are closed. In these samples, right-handed and left-handed helices are present in equal quantities, thus resulting in an overall racemic mixture. A few features structurally different to those discussed above were identified as ribbons. Their thickness was equal to that of the cylinders and they represent the first stage of tube formation.

Small-angle scattering experiments provided definitive evidence of the existence of the proposed tubular structure. The technique has been used successfully to elucidate the structure of nanotubes.[14,21] We recorded the intensities of neutron scattering by low concentration **1**/[D_{12}]cyclohexane gels in the range of $q = 0.008$–0.6 Å^{-1} (Figure 4). When interparticle correlations are negligible, the intensity scattered by a sample is given by Equation (1), in which Φ_v is the

$$I(q) = \Phi_v \, \Delta\rho^2 \, V_p \, P(q) \tag{1}$$

volume fraction of the particles, V_p is the volume of one particle (Å^3), $\Delta\rho^2$ is the contrast of the particle (cm^{-4}), and $P(q)$ is the form factor of the particle. Figure 4 represents the intensity normalized to the contrast and the volume fraction as a function of the scattering vector q.

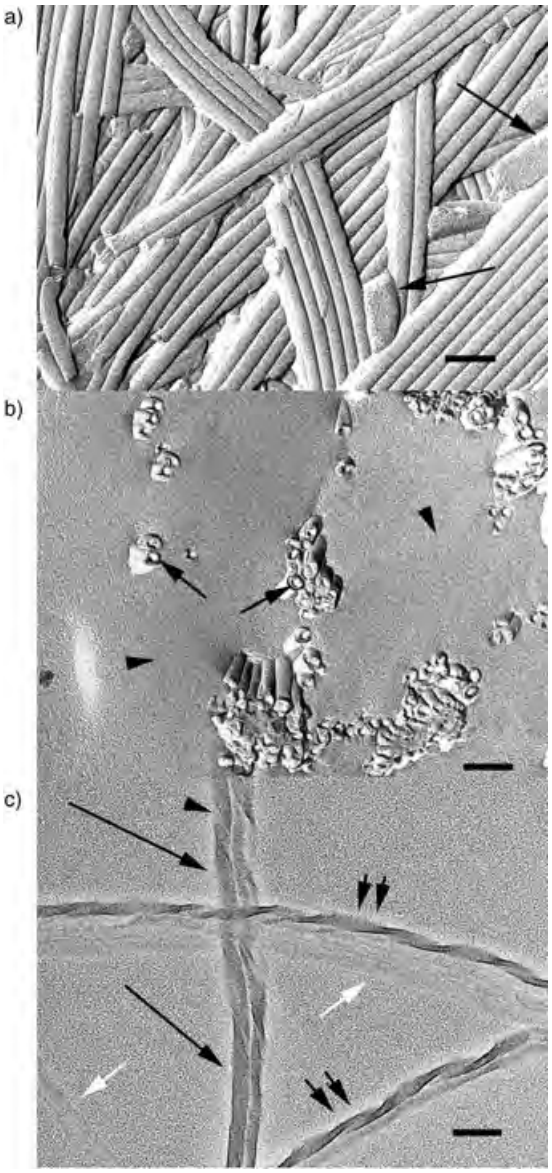

Figure 3. Electron micrographs of self-assembled **1** in cyclohexane. Scale bar is 100 nm. a) Replica of a freeze fracture of **1**-cyclohexane gels (2 wt% concentration). Diameters of the tubes approximately 25–30 nm. Arrow: solvent area. b) Same as (a) with a fracture plane nearly perpendicular to the main axis of the tubes. Arrows: sections of the tubes, which are clearly hollow. Arrowheads: amorphous solvent. c) TEM image of adsorbed diluted solution of **1** in cyclohexane (0.01 wt%) and rotary shadowed. White arrow: single tape. Double arrow: helical tape with a helical pitch of 120 nm. Long arrow: tubule showing only helical groove (arrow head).

The form factor for a long cylinder[22] can be approximated by Equation (2), where L is the length, R_o and R_i are

$$P(q) = \frac{\pi}{qL} \frac{4(R_o J_1(qR_o) - R_i J_1(qR_i))^2}{q^2(R_o^2 - R_i^2)^2} \tag{2}$$

the outer and inner radii of the cylinder, respectively, and J_1 is the Bessel function of the first order. The first factor

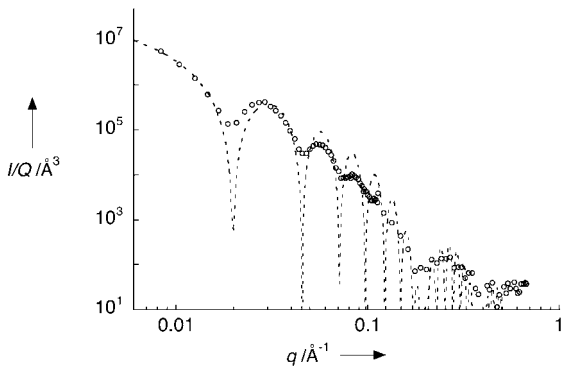

Figure 4. SANS data for **1** gels in [D_{12}]cyclohexane. ○: experimental data. -----: fit according to Equation (2): mean diameter $R_o + R_i = 242$ Å; thickness $R_o - R_i = 33$ Å.

corresponds to the form factor of the rigid rod and can be observed only at low q values, namely for $q < 1/R$. When R_o tends to R_i, which corresponds to infinitely thin hollow cylinders, the second factor in Equation (2) tends to $(J_0(qR))^2$ where J_0 represents the Bessel function of zero order. The curve exhibits a series of oscillations where the minima follow the progression of the zeros of the Bessel function of the zeroth order (ca. $3\pi/4R$, $7\pi/4R$, $11\pi/4R$ ...), which is strong evidence for hollow cylinders having a thin wall thickness. Fitting the positions of the minima and maxima enabled measurement of the mean diameter of the cylinders $2R = (R_o + R_i)$, which is equal to (24.2 ± 0.3) nm. The oscillations fit into an envelop curve that decreases and is minimal around 0.19 Å^{-1}. This envelop curve can be fitted by adjusting the thickness of the wall $R_o - R_i$, while the mean radius is kept constant. The thickness was found to be (3.3 ± 0.4) nm. The maximal length of the fully stretched molecule of **1** is estimated to be 3.6 nm by force-field calculations. The differences between the theoretical and experimental form factor may indicate a certain dispersity of tube diameters or a slight anistropy of the section.

The X-ray scattering at wide angles by the gels showed Bragg peaks (Figure 5). The spectrum confirmed that the tubes have a crystalline array, which differentiates them from micelles. Fuhrhop and co-workers also found crystalline order in self-assembled tubes of octylgluconamide.[23] Although it is not possible to establish a model for the wall structure at a molecular level, any proposed model should be coherent with the following experimental facts: the molecules are linked together by hydrogen bonds between amides and by π interactions between aromatic rings. More studies are in progress to elucidate further the inner structure of the tube wall.

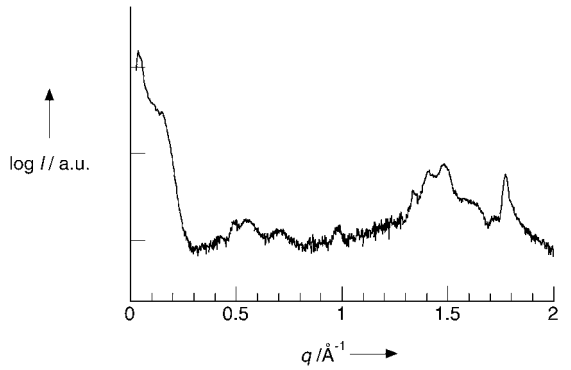

Figure 5. WAXS data of **1** gel in cyclohexane (6.4 wt%).

In summary, we have demonstrated that very simple molecules can be used to prepare well-defined nanotubes in organic solvents. The mean diameter of the tubes is (24.2 ± 0.3) nm as measured by small-angle neutron scattering studies (SANS). The interactions between molecules were assigned to hydrogen bonds between amides as well as aromatic π interactions on the basis of IR and UV spectroscopic studies. Analogues of **1** are under study to elucidate the molecular parameters that influence the shape and the size of the nanotubes.

Experimental Section

Synthesis of **1**: see the Supporting Information.

IR spectra were performed in NaCl cells on a IFS 88 apparatus equipped with a thermostated cell holder. The UV spectra were recorded on a 500 spectrometer. The neutron scattering experiments were performed at the LLB in Saclay on the PAXE spectrometer. Correction, reduction, and normalization of the data were carried out as described previously.[24] The wide-angle X-ray scattering (WAXS) experiments were carried out at the IPCMS, in Strasbourg on an Inel diffractometer, using $Cu_{K\alpha 1}$ radiation.

Freeze-fracture and electron microscopy experiments were performed as described previously for other self-associating systems.[25]

Received: February 12, 2005
Published online: April 21, 2005

Keywords: colloids · materials science · nanotubes · self-assembly · supramolecular chemistry

[1] a) J.-M. Lehn, *Science* **2002**, *295*, 2400; b) J. H. Fuhrhop, J. Koning, *Membranes and Molecular Assemblies: The Synkinetic Approach*, The Royal Society of Chemistry, Cambridge, **1998**; c) G. M. Whitesides, J. P. Mathias, C. T. Seto, *Science* **1991**, *254*, 1312.
[2] P. Terech, R. G. Weiss, *Chem. Rev.* **1997**, *97*, 3133.
[3] J. D. Hartgerink, E. Beniash, S. I. Stupp, *Science* **2001**, *294*, 1684.
[4] a) P. Ringler, W. Muller, H. Ringsdorf, A. Brisson, *Chem. Eur. J.* **1997**, *3*, 620; b) E. M. Wilson-Kubalek, R. E. Brown, H. Celia, R. A. Milligan, *Proc. Natl. Acad. Sci. USA* **1998**, *95*, 8040.
[5] a) W. Han, P. Kohler-Redlich, C. Scheu, F. Ernst, M. Ruhle, N. Grobert, M. Terrones, H. W. Kroto, D. R. M. Walton, *Adv. Mater.* **2000**, *12*, 1356; b) H. C. Pham, N. Keller, C. Estournes, G. Ehret, J. M. Greneche, M. J. Ledoux, *Phys. Chem. Chem. Phys.* **2003**, *5*, 3716.
[6] a) K. J. C. van Bommel, A. Friggeri, S. Shinkai, *Angew. Chem.* **2003**, *115*, 1010; *Angew. Chem. Int. Ed.* **2003**, *42*, 980; b) J. H. Jung, Y. Ono, K. Hanabusa, S. Shinkai, *J. Am. Chem. Soc.* **2000**, *122*, 5008.
[7] A. A. Mamedov, N. A. Kotov, M. Prato, D. M. Guldi, J. P. Wicksted, A. Hirsch, *Nat. Mater.* **2002**, *1*, 190.
[8] J. H. Fuhrhop, W. Helfrich, *Chem. Rev.* **1993**, *93*, 1565.
[9] J. M. Schnur, *Science* **1993**, *262*, 1669.
[10] J. M. Schnur, B. R. Ratna, J. V. Selinger, A. Singh, G. Jyothi, K. R. K. Easwaran, *Science* **1994**, *264*, 945.

[11] D. S. Chung, G. B. Benedek, F. M. Konikoff, J. M. Donovan, *Proc. Natl. Acad. Sci. USA* **1993**, *90*, 11341.
[12] a) D. A. Frankel, D. F. O'Brien, *J. Am. Chem. Soc.* **1994**, *116*, 10057; b) G. John, M. Masuda, Y. Okada, K. Yase, T. Shimizu, *Adv. Mater.* **2001**, *13*, 715.
[13] J. H. Fuhrhop, D. Spiroski, C. Boettcher, *J. Am. Chem. Soc.* **1993**, *115*, 1600.
[14] P. Terech, Y. Talmon, *Langmuir* **2002**, *18*, 7240.
[15] a) S. Vauthey, S. Santoso, H. Gong, N. Watson, S. Zhang, *Proc. Natl. Acad. Sci. USA* **2002**, *99*, 5355; b) C. Valery, M. Paternostre, B. Robert, T. Gulik-Krzywicki, T. Narayanan, J. C. Dedieu, G. Keller, M. L. Torres, R. Cherif-Cheikh, P. Calvo, F. Artzner, *Proc. Natl. Acad. Sci. USA* **2003**, *100*, 10258.
[16] J. P. Hill, W. Jin, A. Kosaka, T. Fukushima, H. Ichihara, T. Shimomura, K. Ito, T. Hashizume, N. Ishii, T. Aida, *Science* **2004**, *304*, 1481.
[17] N. Nakashima, S. Asakuma, T. Kunitake, *J. Am. Chem. Soc.* **1985**, *107*, 509.
[18] a) J. V. Selinger, F. C. MacKintosh, J. M. Schnur, *Phys. Rev. E* **1996**, *53*, 3804; b) C. M. Chen, *Phys. Rev. E* **1999**, *59*, 6192; c) A. Aggeli, I. A. Nyrkova, M. Bell, R. Harding, L. Carrick, T. C. B. McLeish, A. N. Semenov, N. Boden, *Proc. Natl. Acad. Sci. USA* **2001**, *98*, 11857; d) I. A. Nyrkova, A. N. Semenov, A. Aggeli, M. Bell, N. Boden, T. C. B. McLeish, *Eur. Phys. J. B* **2000**, *17*, 499.
[19] a) K. Tomioka, T. Sumiyoshi, S. Narui, Y. Nagaoka, A. Iida, Y. Miwa, T. Taga, M. Nakano, T. Handa, *J. Am. Chem. Soc.* **2001**, *123*, 11817; b) J. Schneider, C. Messerschmidt, A. Schulz, M. Gnade, B. Schade, P. Luger, P. Bombicz, V. Hubert, J. H. Fuhrhop, *Langmuir* **2000**, *16*, 8575.
[20] R. Schmidt, F. B. Adam, M. Michel, M. Schmutz, G. Decher, P. J. Mesini, *Tetrahedron Lett.* **2003**, *44*, 3171.
[21] a) K. Sakurai, Y. Ono, J. H. Jung, S. Okamoto, S. Sakurai, S. Shinkai, *J. Chem. Soc. Perkin Trans. 2* **2001**, 108; b) T. Imae, K. Funayama, M. P. Krafft, F. Giulieri, T. Tada, T. Matsumoto, *J. Colloid Interface Sci.* **1999**, *212*, 330.
[22] J. M. Deutch, *Macromolecules* **1981**, *14*, 1826.
[23] S. Svenson, J. Koening, J. H. Fuhrhop, *J. Phys. Chem.* **1994**, *98*, 1022.
[24] R. Schmidt, M. Schmutz, A. Mathis, G. Decher, M. Rawiso, P. Mésini, *Langmuir* **2002**, *18*, 7167.
[25] R. Schmidt, M. Schmutz, M. Michel, G. Decher, P. Mésini, *Langmuir* **2002**, *18*, 5668.

Synthetic Methods

Stereoselective Lewis Acid Mediated [1,3] Ring Contraction of 2,5-Dihydrooxepins as a Route to Polysubstituted Cyclopentenes**

*Christopher G. Nasveschuk and Tomislav Rovis**

The Diels–Alder reaction is a cornerstone of organic synthesis, and its ability to enable the production of cyclohexenes in a stereocontrolled manner is unparalleled. In contrast, no method exists for the synthesis of cyclopentanes that matches the scope and power of the Diels–Alder reaction in spite of the prevalence of these ring systems in natural products. Among numerous methods that have been used to target these cores, vinylcyclopropane ring-expansion strategies have been intensively investigated and have provided some spectacular successes.[1,2] Nevertheless, most reports result in mono- or disubstituted cyclopentanes and cyclopentenes, while approaches to polysubstituted systems are rare.[3] We were interested in addressing this deficiency and developing a diastereoselective approach to tri-, tetra-, and pentasubstituted cyclopentanes from readily available precursors, and herein we report our results.

We have previously reported the [1,3] rearrangement of vinyl acetals which proceeds through a metalloenolate and oxocarbenium ion pair.[4] To extend this concept to other stabilized cations, we initiated a program to study the [1,3] rearrangement of allylvinyl ethers that would form a metalloenolate and an allylic cation ion pair under Lewis acidic conditions. However, we were mindful that these substrates could also undergo a Lewis acid (LA) accelerated Claisen rearrangement, which if concerted, would form the [3,3] rearrangement product exclusively.[5] A number of workers have documented that the Lewis acid mediated Claisen rearrangement proceeds stepwise[6] and occasionally provides the [1,3] adduct with some selectivity.[7] To favor the [1,3] over the [3,3] product, we envisioned that a cyclic allylvinyl ether or 2,5-dihydrooxepin could provide access to densely functionalized cyclopentenes under ionizing conditions as the [3,3] rearrangement should be disfavored because of ring strain in the cyclopropane product [Eq. (1)]. We report the successful implementation of this strategy, in which a unique Lewis acid promoted ring contraction of 2,5-dihydrooxepins to cyclopentenes was used.

[*] C. G. Nasveschuk, Prof. T. Rovis
Department of Chemistry
Colorado State University
Fort Collins, CO 80523 (USA)
Fax: (+1) 970-491-1801
E-mail: rovis@lamar.colostate.edu

[**] Financial support was provided by the National Institute of General Medical Sciences (GM65407). We also thank Merck Research Laboratories, GlaxoSmithKline, Amgen, and Eli Lilly for unrestricted support. We thank Professor Andre Charette (Montreal) for helpful discussions.

Supporting information for this article is available on the WWW under http://www.angewandte.org or from the author.

  DOI: 10.1002/anie.200500088

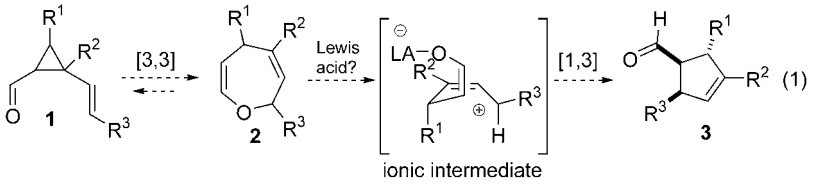

Despite their apparent complexity, 2,5-dihydrooxepins are readily prepared by a retro-Claisen reaction of the corresponding cyclopropyl aldehyde **1**, itself available by a modular approach using established methods (see below).[8,9] An equilibrium between **1** and **2** has been predicted computationally,[10] and may be shifted towards the 2,5-dihydrooxepin with π-stabilizing substituents [Eq. (2); EDG = electron-donating group, EWG = electron-withdrawing group].[9]

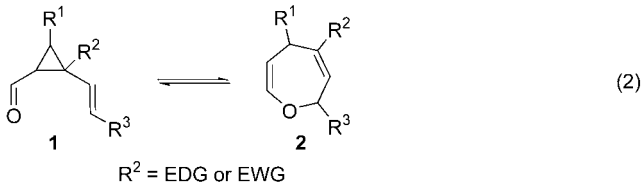

(2)

We began our investigations by developing a highly modular approach to the 2,5-dihydrooxepin skeleton. A representative synthesis is illustrated in Scheme 1. A Sonogashira cross-coupling between propargyl alcohol and aryl halides provided **4**.[11] Selective formation of the (*Z*)-vinyl iodide **5** was effected with red-Al/I_2,[12] and a Negishi coupling was then employed to insert an additional alkene.[13] A directed Simmons–Smith cyclopropanation afforded **7** in near quantitative yield as a single regioisomer.[14] We felt that **7** could be converted into **9** in a one-pot oxidation/retro-Claisen sequence and, after some optimization, it was found that 1.5 equivalents of the Dess–Martin periodinane in CH_2Cl_2 at 40 °C provided the desired 2,5-dihydrooxepin. The nature of the equilibrium meant that the unrearranged aldehyde **8** could be isolated and subsequently converted into **9** by heating overnight in toluene at 110 °C.

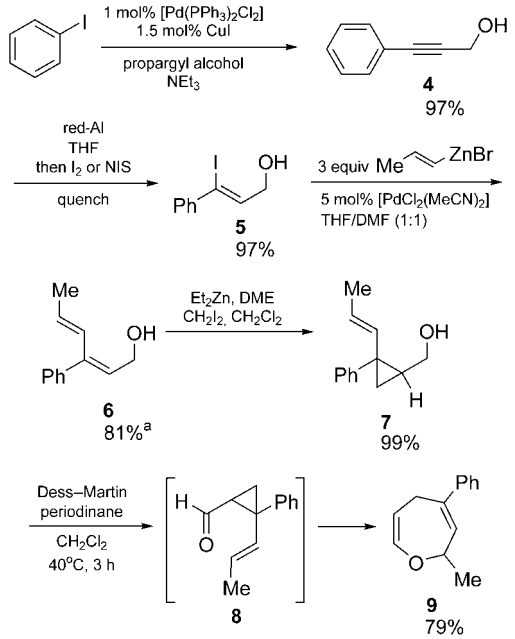

Scheme 1. Synthetic approach to the 2,5-dihydrooxepins.

With a convergent approach to the requisite 2,5-dihydrooxepins in hand, we began our studies on the stereoselective [1,3] ring contraction by conducting a brief screen of Lewis acids. $Cu(OTf)_2$, $TiCl_4$, and $SnCl_4$ yielded no product under a variety of conditions (Table 1, entries 1–3). In the presence of $EtAlCl_2$ (entries 4–6), the starting material was consumed with the formation of uncharacterized oligomeric products. We hypothesized that this could happen in one of two ways: 1) vinyl ether **9** could polymerize before ionization of the C–O bond or 2) the zwitterionic intermediate generated from the ionization of C–O is stable enough so that intramolecular ring closure is slower than the bimolecular reaction. Thus, cyclopentene **10** was isolated in 89% yield with 90:10 (*cis*/*trans*) selectivity (entry 7) when **9** was subjected to dilute Lewis acid at ambient temperature. We further note that slow addition of dilute 2,5-dihydrooxepin to the Lewis acid generally provides an incremental increase in selectivity (entry 8).

Table 1: Optimization of [1,3] ring contraction.

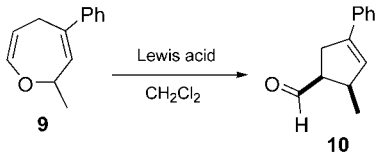

Entry	Lewis acid	Conditions	Yield [%] (*cis*/*trans*)
1	$Cu(OTf)_2$	various	NP[a]
2	$TiCl_4$	various	NP[a]
3	$SnCl_4$	various	NP[a]
4	$EtAlCl_2$	0.1 M, −78 °C, 30 min	NP[a]
5	$EtAlCl_2$	0.1 M, 23 °C, 30 min	NP[a]
6	$EtAlCl_2$	0.001 M, −78 °C, 60 min	NP[a]
7	$EtAlCl_2$	0.001 M, 23 °C, 5 min	89 (90:10)
8	$EtAlCl_2$	0.02 M, 23 °C, 5 min[b]	53 (93:7)

[a] Starting material consumed. [b] Slow addition of substrate to dilute Lewis acid. NP = no product.

We then evaluated the scope of the [1,3] ring contraction of the 2,5-dihydrooxepins. Electron-donating and electron-withdrawing groups in the *para* position of the aromatic ring are tolerated and give products in comparable yield and selectivity (Table 2, entries 1–3). Additional substitution on the dihydrooxepin unit is well-tolerated, with substrate **15** furnishing tetrasubstituted cyclopentene **16** in good selectivity. An increase in the steric bulk of the substituent from a methyl group (**9**) to a phenethyl group (**17**) or protected alcohol (**19**) results in a slight decrease in the yield and selectivity, but still provides synthetically useful amounts of product. Lastly, the use of aldehyde **21** as a substrate indicates

Table 2: Reaction scope.

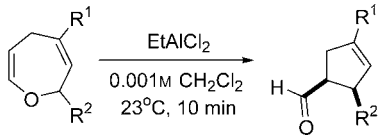

Entry	substrate	Product	Yield [%]	*cis*/*trans*
1	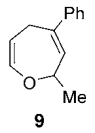 **9**	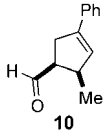 **10**	89	90:10
2	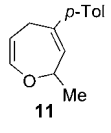 **11**	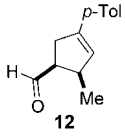 **12**	85	93:7
3	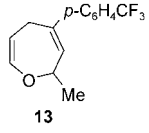 **13**	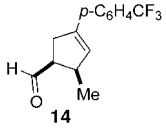 **14**	75	87:13
4	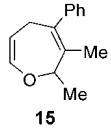 **15**	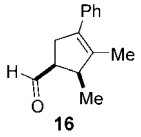 **16**	58	88:12
5	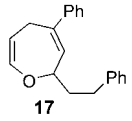 **17**	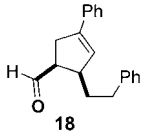 **18**	73	85:15
6	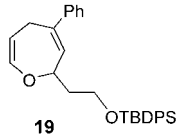 **19**	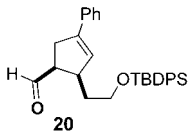 **20**	52	85:15
7	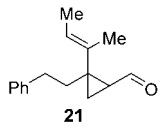 **21**	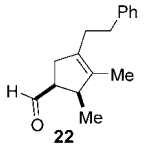 **22**	59	89:11

p-Tol = *para*-toluene, TBDPS = *tert*-butyldiphenylsilyl.

Table 3: Aldehyde epimerization.

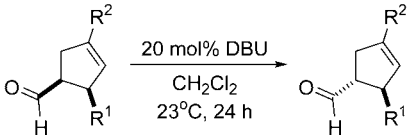

Entry	Substrate (R^1, R^2)	Product	Yield [%]	*cis*/*trans*
1	**12** (Me, *p*-Tol)	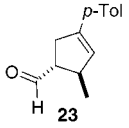 **23**	68	12:88
2	**18** ($-CH_2CH_2Ph$, Ph)	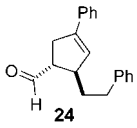 **24**	81	3:97

jected to the optimized reaction conditions, **26** was isolated in 70% yield and 95% *ee* [Eq. (3)]. The pre-existing stereo-

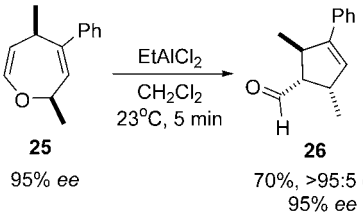

(3)

center controls the diastereoselective course of the reaction, and the observed selectivity can be rationalized by our proposed model (Figure 1). There is an interplay of minimi-

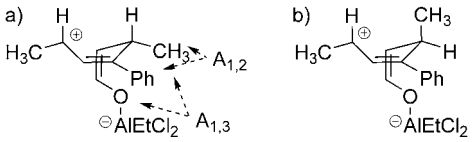

Figure 1. Proposed stereochemical model for the diastereoselective rearrangement of **25**. a) Minimization of the $A_{1,2}$ and $A_{1,3}$ strains and b) the favored model brought about by this process.

that formation of the dihydrooxepin is not necessary to achieve reaction. Furthermore, this substrate lacks the aryl stabilization evident in the other substrates, thus suggesting that aliphatic stabilization is sufficient in some cases. These disubstituted cyclopentene carboxaldehydes are readily epimerized[14] to form the *trans* diastereomer upon treatment with 1,8-diazabicyclo[5.4.0]undec-7-ene (DBU; Table 3, entries 1 and 2).

A considerable advantage of this method is the ability to introduce substitution at every position of the dihydrooxepin ring. With this approach in mind, we sought to apply the protocol of Charette et al.[15] as a means of introducing further substitutents onto the cyclopropane and affording a tetrasubstituted cyclopentene on [1,3] rearrangement. 2,5-Dihydrooxepin **25** was synthesized in an enantioenriched form using the Charette–Simmons–Smith protocol.[15] When **25** was subzation between the $A_{1,2}$ strain, between the phenyl group on the allyl cation and the adjacent methyl, and the $A_{1,3}$ strain, between the alkoxide on the enolate and the methyl group, that presumably leads to the observed levels of diastereoselectivity.

As noted above, we may also use the aldehydes as precursors for the rearrangement [Table 2, entry 7; Eq. (4)].

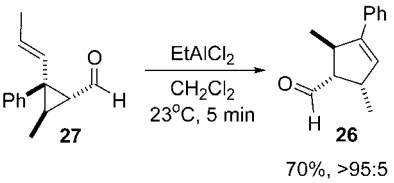

(4)

We suggest that this arises from the initial Lewis acid catalyzed retro-Claisen rearrangement that gives the 2,5-dihydrooxepin prior to [1,3] bond migration. Another possibility is that the Lewis acid accelerates the Claisen/retro-Claisen equilibrium so that a Curtin–Hammett situation is formed where the cyclopentene product is siphoned off from either the 2,5-dihydrooxepin or the cyclopropyl aldehyde. Although the exact mechanism at this stage remains unclear, this observation makes the overall procedure operationally simpler.

The presence of the olefin in the cyclopentene allows for further diastereoselective functionalization. We investigated one such approach and found that diastereoselective dihydroxylation produces a pentasubstituted cyclopentane in modest yield but excellent selectivity [Eq. (5), NMO = 4-methylmorphoöine *N*-oxide].[16]

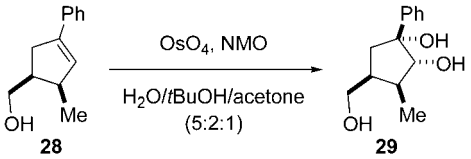

(5)

In summary, we have developed a novel room-temperature Lewis acid mediated diastereoselective [1,3] ring contraction of 2,5-dihydrooxepins. Our modular approach to these seven-membered heterocycles allows for the installation of a variety of groups at every position. The reaction provides access to *cis* and *trans* cyclopentene carboxaldehydes with good selectivities, and can lead to tetrasubstituted cyclopentenes in high enantiomeric excess and diastereoselectivity.

Received: January 11, 2005
Published online: April 21, 2005

Keywords: cyclopentenes · diastereoselectivity · Lewis acids · rearrangement · ring contraction

[1] a) T. Hudlicky, T. M. Kutchan, S. M. Naqvi, *Org. React.* **1985**, *33*, 247–335; b) T. Hudlicky, J. D. Price, *Chem. Rev.* **1989**, *89*, 1467–1486; c) H. N. C. Wong, M.-Y. Hon, C.-W. Tse, Y.-C. Yip, *Chem. Rev.* **1989**, *89*, 165–198; d) T. Hudlicky, J. W. Reed, *Comprehensive Organic Synthesis*, *Vol. 5* (Eds. B. Trost, I. Fleming, L. A. Paquette), Pergamon, Oxford, **1991**, pp. 899–970; e) H.-U. Reißig, R. Zimmer, *Chem. Rev.* **2003**, *103*, 1151–1196.

[2] a) S. D. Larsen, P. V. Fisher, B. E. Libby, R. M. Jensen, S. A. Mizsak, W. Watt, W. R. Ronk, S. T. Hill, *J. Org. Chem.* **1996**, *61*, 4725–4738; b) G. Zuo, J. Louie, *Angew. Chem.* **2004**, *116*, 2327–2329; *Angew. Chem. Int. Ed.* **2004**, *43*, 2277–2279.

[3] H. M. Davies, B. Xiang, N. Kong, D. G. Stafford, *J. Am. Chem. Soc.* **2001**, *123*, 7461–7462.

[4] Y. Zhang, N. T. Reynolds, K. Manju, T. Rovis, *J. Am. Chem. Soc.* **2002**, *124*, 9720–9721.

[5] Examples of [1,3] rearrangements of allyl vinyl ethers: a) K. Nonoshita, H. Banno, K. Maruoka, H. Yamamoto, *J. Am. Chem. Soc.* **1990**, *112*, 316–322; b) P. A. Grieco, J. D. Clark, C. T. Jagoe, *J. Am. Chem. Soc.* **1991**, *113*, 5488–5489; c) A. Gänsauer, D. Fielenbach, C. Stock, *Adv. Synth. Catal.* **2002**, *344*, 845–848; d) A. Gänsauer, D. Fielenbach, C. Stock, D. Geich-Gimbel, *Adv. Synth. Catal.* **2003**, *345*, 1017–1030.

[6] K. Nonoshita, H. Banno, K. Maruoka, H. Yamamoto, *J. Am. Chem. Soc.* **1990**, *112*, 316–322.

[7] P. A. Grieco, J. D. Clark, C. T. Jagoe, *J. Am. Chem. Soc.* **1991**, *113*, 5488–5489.

[8] a) B. Hofmann, H.-U. Reißig, *Synlett* **1993**, 27–29; b) B. Hofmann, H.-U. Reißig, *Chem. Ber.* **1994**, *127*, 2327–2335.

[9] R. K. Boeckman, Jr., M. D. Shair, J. R. Vargas, L. A. Stolz, *J. Org. Chem.* **1993**, *58*, 1295–1297.

[10] D. Sperling, H.-U. Reißig, J. Fabian, *Liebigs Ann.* **1997**, 2443–2449.

[11] E. E. Scott, E. T. Donnelly, M. E. Welker, *J. Organomet. Chem.* **2003**, *673*, 67–76.

[12] J. A. Marshall, B. S. DeHoff, *J. Org. Chem.* **1986**, *51*, 863–872.

[13] M. Abarbri, J. Thibonnet, J.-L. Parrain, A. Duchêne, *Synthesis* **2002**, 543–551.

[14] H. Frauenrath, J. Runsink, *J. Org. Chem.* **1988**, *53*, 1860–1862.

[15] A. B. Charette, H. Juteau, H. Lebel, C. Molinaro, *J. Am. Chem. Soc.* **1998**, *120*, 11943–11952.

[16] I. Coldham, K. N. Price, R. E. Rathmell, *Org. Biomol. Chem.* **2003**, *1*, 2111.

O—O Activation

Dimetallic Dioxygen Activation Leading to a Doubly Oxygen-Bridged Dirhodium Complex**

Cristina Tejel, Miguel A. Ciriano, Eduardo Sola, M. Pilar del Río, Gustavo Ríos-Moreno, Fernando J. Lahoz, and Luis A. Oro*

Catalytic oxygenation constitutes an important method of converting readily available alkenes into chemicals with high added value. These oxygenations should preferably use the cheap and environmentally benign dioxygen as oxidant, and incorporate both oxygen atoms into the substrate molecules, thus optimizing atom economy.[1] However, with the exception of the Wacker process, such practical use of oxygen seems nowadays restricted to a few heterogeneous catalysts,[2]

[*] Dr. C. Tejel, Prof. M. A. Ciriano, Dr. E. Sola, M. P. del Río, Dr. G. Ríos-Moreno, Prof. F. J. Lahoz, Prof. L. A. Oro
Departamento de Química Inorgánica
Instituto de Ciencia de Materiales de Aragón
C.S.I.C.-Universidad de Zaragoza
50009 Zaragoza (Spain)
Fax: (+34) 976-761-187
E-mail: ctejel@unizar.es

Prof. L. A. Oro
Instituto Universitario de Catálisis Homogénea
Universidad de Zaragoza
50009 Zaragoza (Spain)

[**] The generous financial support from MCyT(DGI)/FEDER (Projects BQU2002-00074 and BQU2003-05412) is gratefully acknowledged.

 DOI: 10.1002/anie.200463073

although important progress towards this goal has been reported in the chemistry of soluble metal complexes.[3]

A recent review by Gal and co-workers[4] analyzes in detail the reactivity of rhodium and iridium complexes relevant to alkene oxygenation. Often, the use of peroxides as oxidants leads to facile monooxygenation reactions, through C–O bond-forming steps, to afford reactive 2-metallaoxetane intermediates.[5–7] In contrast, the more scarce C–O bond-forming reactions using dioxygen are assumed to involve the initial formation of 3-metalla-1,2-dioxolanes,[8] from which the evolution to oxygenated products seems to follow unselective routes and most often requires the presence of sacrificial reductants.[4] An exception to this inconvenient behavior has been reported for the 1,5-cyclooctadiene dianionic complex $[Ir(P_3O_9)(C_8H_{12})]^{2-}$, in which the formation of a 2-metallaoxetane intermediate from 0.5 molar equivalents of dioxygen has been suggested to be the consequence of a dimetallic O–O bond cleavage.[9] Herein we provide further evidence for the feasibility of this atom-economic dimetallic oxygenation route, by describing the facile formation of a dinuclear 2-metallaoxetane compound from dioxygen and an equilibrium mixture of the mono- and dinuclear rhodium complexes $[Rh(PhN_3Ph)(C_8H_{12})]$ ($\mathbf{1_M}$) and $[\{Rh(\mu\text{-}PhN_3Ph)(C_8H_{12})\}_2]$ ($\mathbf{1_D}$).

The bis(phenyl)triazenide rhodium(I) compound $[\{Rh(PhN_3Ph)(C_8H_{12})\}_n]$ (**1**), first reported by Knoth,[10] was easily prepared by treating $[\{Rh(\mu\text{-}OMe)(C_8H_{12})\}_2]$ with bis(phenyl)triazene in toluene. By comparison with rhodium triazenide compounds previously characterized by X-ray diffraction studies,[11] it was likely that the red solid obtained from the reaction was a dinuclear compound with bridging triazenide ligands. However, the NMR spectra of the compound dissolved in $[D_6]$benzene is indicative of an equilibrium mixture of the mono- and dinuclear complexes shown in Scheme 1. The dissociation equilibrium constant K_{eq} was estimated by NMR spectroscopic analysis to be 0.092 mol L^{-1} at 293 K.

Exposure of **1** to dioxygen in toluene at 293 K and atmospheric pressure gave the dinuclear dirhodadioxetane complex $[\{Rh(PhN_3Ph)(OC_8H_{12})\}_2]$ (**2**, Scheme 1) in 90% yield. Volumetric gas-burette measurements with O_2 indicated a consumption of 0.5 molecules of gas per atom of rhodium (0.51 ± 0.03 equiv), thus showing that all the reacting dioxygen was incorporated into **2**. The molecular structure of complex **2** (Figure 1)[12] confirms that, despite the presence of

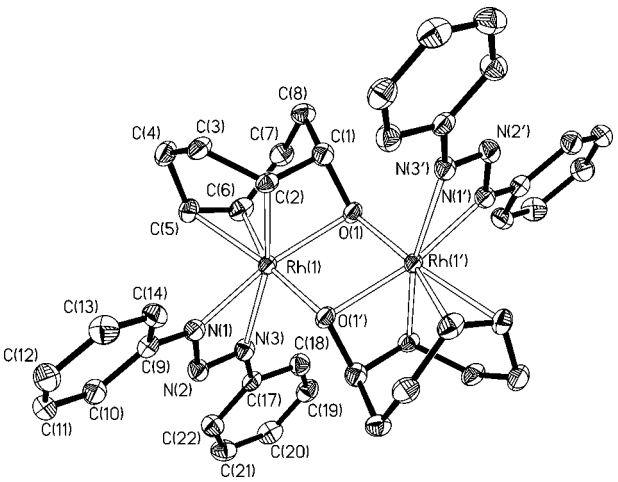

Figure 1. Solid-state structure of the dinuclear complex **2**. Selected bond distances [Å] and angles [°]: Rh(1)-N(1) 2.040(3), Rh(1)-N(3) 2.347(3), Rh(1)-O(1) 2.076(3), Rh(1)-O(1′) 2.064(3), Rh(1)-C(2) 2.037(4), Rh(1)-C(5) 2.223(4), Rh(1)-C(6) 2.206(4); N(1)-Rh(1)-O(1) 167.42(11), N(3)-Rh(1)-C(2) 167.62(13), O(1′)-Rh(1)-C(5) 162.51(12).

potentially bridging triazenide ligands, the dinuclear structure is held by bridging oxygen atoms—a feature by itself suggestive of a dimetallic activation of dioxygen. Moreover, among the few 2-metallaoxetane moieties resulting from insertion of oxygen atoms into metal–alkene bonds,[5,6,9] compound **2** constitutes the first example of a bridging one.

Complex **2** was found to be kinetically unstable in solution, slowly evolving to $[\{Rh(PhN_3Ph)(HO\text{-}C_8H_{11})\}_n]$ ($\mathbf{3_n}$, Scheme 1). The transformation was found to be complete in about three days at room temperature in dichloromethane. As confirmed by the solid-state structure shown in Figures 2 and 3,[13] the transformation involves the isomerization of the (η^2-

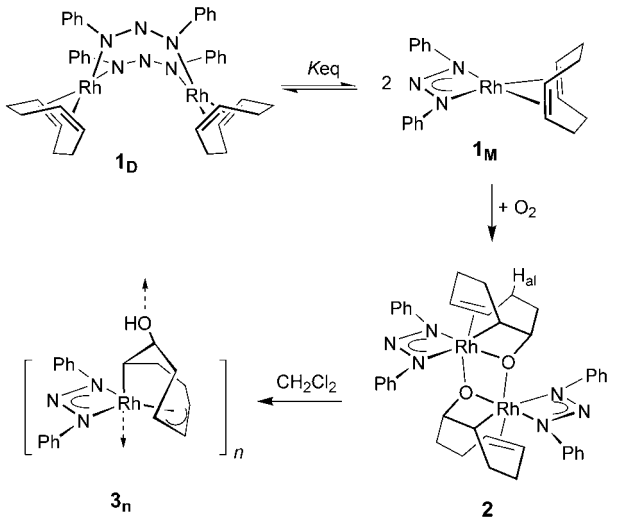

Scheme 1. Equilibration between the mono- and dinuclear complexes, and the products of the reaction of **1** with dioxygen.

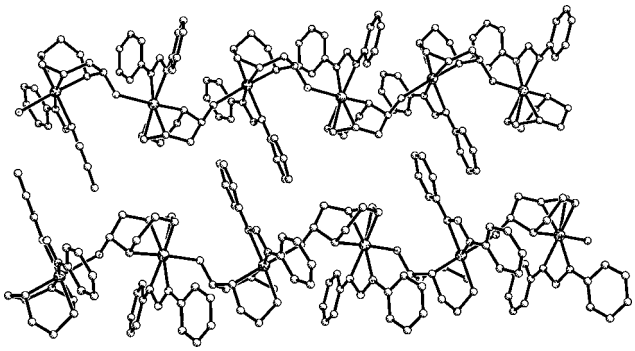

Figure 2. Polymeric chains formed in the crystal structure of complex $\mathbf{3_n}$ by the two independent dimeric units.

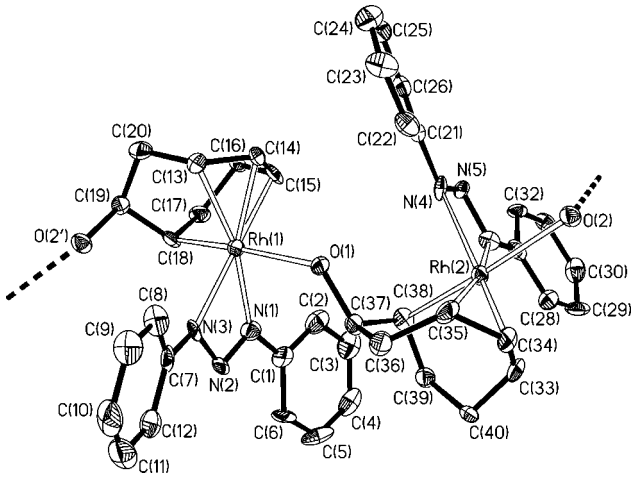

Figure 3. Solid-state structure of one of the two independent dimeric moieties of $\mathbf{3_n}$. Selected bond distances [Å] and angles [°] (mean values for the four equivalent parameters)[11]: Rh-N(1) 2.121(4), Rh-N(3) 2.139(4), Rh-O(1) 2.359(3), Rh-C(18) 2.051(5), Rh-C(13) 2.163(5), Rh-C(14) 2.080(5), Rh-C(15) 2.163(5); N(1)-Rh-C(13) 168.8(2), N(3)-Rh-C(15) 170.4(2), O(1)-Rh-C(18) 175.8(2).

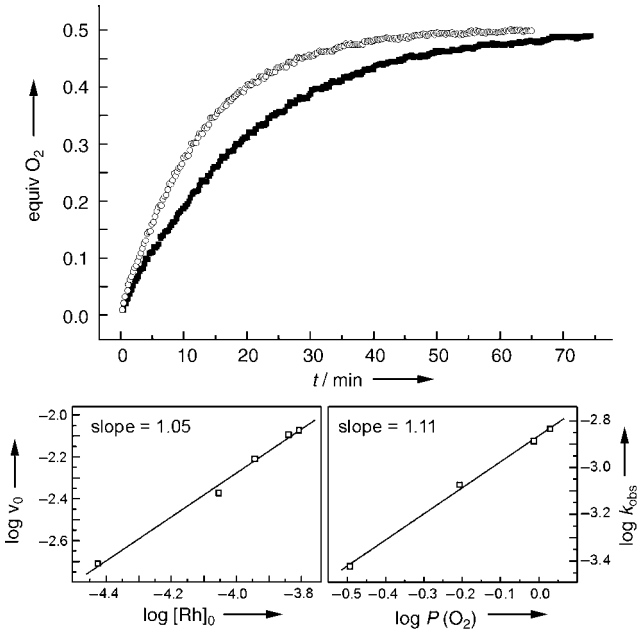

Figure 4. Top: Examples of O_2 uptake experiments in solutions of **1** in toluene ($[Rh]_0 = 6.18\times10^{-3}$ mol L^{-1}) at 293 K; ○: $P = 1.00$ bar; ■: $P = 0.65$ bar. Bottom: Dependence of the initial reaction rates upon the initial concentration of **1** (left) and dependence of the pseudo-first-order rate constants k_{obs} upon the O_2 partial pressure (right).

κ-*O*,*C*-OC_8H_{12}) ligand of **2** into a hydroxyallyl (η^3-κ-*C*-$(HO)C_8H_{11}$) isomeric ligand (Scheme 1). Such an isomerization has been proposed to involve a metal-mediated activation of an allylic C–H bond followed by the transfer of the activated hydrogen atom to the alkoxy oxygen atom.[5,6,9]

The solid-state structure of $\mathbf{3_n}$ consists of a polymeric chain of mononuclear complexes (Figure 2) connected by Rh–O bonds (mean Rh–O(1) bond lengths 2.359(3) Å). Such bonds are long and presumably fragile, since they take place at a rhodium coordination position strongly labilized by the large *trans* effect of a σ-sp^3 carbon atom. Therefore, it seems unlikely that such a polymeric structure could remain in solution.

Accordingly, the NMR spectra of solutions of $\mathbf{3_n}$ are indicative of two equivalent phenyl groups, a feature hardly compatible with the polymeric structure, but likely for a potentially fluxional 16-electron Rh^{III} fragment.

The dioxygen activation reaction leading to complex **2** has been investigated kinetically by O_2-uptake experiments on solutions of **1** in toluene at 293 K. The initial concentrations of **1** in these solutions, expressed as concentrations of rhodium atoms $[Rh]_0$, were about 5×10^{-3} mol L^{-1}. At these concentrations and below, the equilibrium between $\mathbf{1_D}$ and $\mathbf{1_M}$ is greatly shifted toward the mononuclear compound, so that the concentration of $\mathbf{1_M}$ approaches a linear dependence upon that of rhodium, namely $[\mathbf{1_M}] \approx [Rh]$. In turn, that of $\mathbf{1_D}$ is better described by the expression of the equilibrium constant, namely $[\mathbf{1_D}] \approx [Rh]^2/K_{eq}$, thus depending upon the square of the rhodium concentration. Figure 4 and Table 1 shows examples for the reaction profiles obtained under constant pressure of dioxygen, which correspond well to those expected for a first-order dependence upon complex concentration. The logarithmic representation of the initial reaction rates (v_0) versus $[Rh]_0$ indicates a linear dependence, therefore confirming the mononuclear complex $\mathbf{1_M}$, rather than $\mathbf{1_D}$, to be the kinetically relevant species in this oxygenation. The dependence of the pseudo-first-order rate constants k_{obs} upon dioxygen pressure confirms that the oxygenation rate is also first order in dioxygen.

Table 1: Kinetic data for the reaction of **1** with dioxygen.

$[Rh]_0$ [$\times10^{-3}$ M]	$P(O_2)$ [bar]	v_0 [mmol O_2 s^{-1}]	k_{obs} [$\times10^{-3}$ s^{-1}]
8.48	0.97	1.56×10^{-4}	1.34
8.08	0.97	1.45×10^{-4}	1.27
6.18	0.97	1.14×10^{-4}	1.29
4.24	0.97	8.84×10^{-5}	1.28
1.94	0.97	3.76×10^{-5}	1.27
8.08	1.07	3.76×10^{-5}	1.43
8.08	0.62	3.76×10^{-5}	0.83
8.08	0.32	3.76×10^{-5}	0.37

These kinetic data discount any mechanism initiated by reaction of dioxygen with the dinuclear complex $\mathbf{1_D}$, and evidence a reaction of dioxygen with the mononuclear complex $\mathbf{1_M}$ as the most likely rate-determining step in the process (Scheme 2). This conclusion is compatible with the mechanism previously proposed by Klemperer and co-workers for the aforementioned singular example of dioxygen activation.[9] Adaptation of this proposal to our reaction in Scheme 2 would result in a mononuclear complex coordinating dioxygen, which undergoes the attack by an intact mononuclear complex ($\mathbf{1_M}$) to complete a dimetallic dioxygen cleavage. In our system, such a dimetallic activation step seems to be fast; likely as a consequence of the unsaturated character of the triazenide–rhodium complex $\mathbf{1_M}$. The coordination requirements of the Klemperer's tridentate $P_3O_9^{3-}$ ancillary ligand were proposed to favor the splitting of the

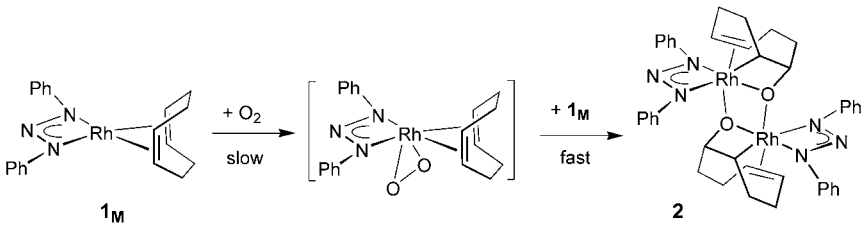

Scheme 2. Proposed mechanism for the reaction of dioxygen with **1**.

dinuclear species resulting after dioxygen activation, a feature not required in our triazenide oxygenation product, which remains dinuclear (Scheme 2).

Although the above mechanism could be within the reach of other unsaturated mononuclear complexes or fragments, our preliminary investigation of rhodium compounds isoelectronic and very closely related to **1** indicates that this dioxygen activation is far from general. Actually, the complex [{Rh(μ-PhNCHNPh)(C_8H_{12})}$_2$],[13] which remains dinuclear at all concentration ranges, did not undergo reaction with dioxygen under the conditions described for **1**, while the mononuclear species [Rh(PhNC(Ph)NPh)(C_8H_{12})],[14] which does not form detectable dimers in solution, did not activate dioxygen either. These observations might suggest a correlation between the ability of unsaturated mononuclear fragments to reversibly form dinuclear species in solution and its activity in these dioxygen cleavage reactions. Whether or not this correlation exists is currently being investigated within our search for oxygenation catalysts, which can benefit from such facile, selective, and atom-economic dioxygen dimetallic activation.

Experimental Section

1: The addition of PhNNNHPh (165.7 mg, 0.84 mmol) to a yellow solution of [{Rh(μ-OMe)(cod)}$_2$] (203.4 mg, 0.42 mmol; cod = cycloocta-1,5-diene) in toluene (10 mL) produced a red solution from which a red solid precipitated in a few minutes. Hexane (5 mL) was added after 30 min to complete the precipitation of the solid. The solid was filtered under argon, washed with hexane (2 × 4 mL), and vacuum-dried. Yield: 290.8 mg (85 %). Elemental analysis (%) calcd for $C_{20}H_{22}N_3Rh$: C 58.97, H 5.44, N 10.32; found: C 59.19, H 5.34, N 10.31; ^{1}H NMR ([D$_6$]benzene, 25 °C) for $\mathbf{1_M}$: δ = 7.33 (br d, J(H,H) = 7.7 Hz, 4H), 7.14 (t, J(H,H) = 6.9 Hz, 4H) and 6.93 (tt, J(H,H) = 7.4, 1.1 Hz, 2H; C_6H_5), 4.32 (br s, 4H, =CH), 2.05 (m, 4H, CH_2^{exo}), 1.36 (q, J(H,H) = 7.9 Hz, 4H, CH_2^{endo}); for $\mathbf{1_D}$: δ = 7.77 (br s, 8H), 7.23 (t, J(H,H) = 8.3 Hz, 8H) and 7.03 (tt, J(H,H) = 7.4, 1.1 Hz, 4H; C_6H_5), 4.64 (br s, 4H) and 4.11 (br s, 4H; =CH), 2.76 (m, 4H) and 2.18 (m, 4H; CH_2^{exo}), 1.70 (q, J(H,H) = 7.7 Hz, 4H) and 1.47 (q, J(H,H) = 7.9 Hz, 4H; CH_2^{endo}); ^{13}C{^{1}H} NMR ([D$_6$]benzene, 25 °C) for $\mathbf{1_M}$: δ = 149.5 (C^{ipso}-C_6H_5), 129.2 (C^{meta}-C_6H_5), 124.1 (C^{para}-C_6H_5), 117.2 (C^{ortho}-C_6H_5), 80.3 (d, J(C,Rh) = 12 Hz, =CH), 30.6 (CH); for $\mathbf{1_D}$: δ = 152.9 (C^{ipso}-C_6H_5), 128.4 (C^{meta}-C_6H_5), 124.9 (C^{para}-C_6H_5), 124.1 (C^{ortho}-C_6H_5), 87.6 (br) and 76.8 (br; =CH), 31.1 and 30.8 (CH); MS: m/z (%): 814 (20) [M^+] ($\mathbf{1_D}$), 407 (100) [M^+] ($\mathbf{1_M}$).

2: A suspension of [{Rh(PhNNNPh)(C_8H_{12})}$_n$] (150.0 mg) in toluene (8 mL) was stirred in an oxygen atmosphere for 2 h. The initial dark red suspension evolved to an orange solution, which was concentrated to about 3 mL. Hexane (15 mL) was added to complete the precipitation of the solid, which was filtered off, washed with hexane (2 × 5 mL), and vacuum-dried. Yield: 156 mg (90 %). Elemental analysis (%) calcd for $C_{40}H_{44}N_6O_2Rh_2$: C 56.75, H 5.24, N 9.93; found: C 57.01, H 5.03, N 9.79; ^{1}H NMR ($CDCl_3$, 25 °C) (assigned from ^{1}H,^{1}H-COSY spectrum) δ = 7.47 (m, 8H, H^{ortho}-C_6H_5), 7.36 (t, J(H,H) = 7.5 Hz, 4H) and 7.32 (t, J(H,H) = 8.2 Hz, 4H; H^{meta}-C_6H_5), 7.11 (t, J(H,H) = 7.3 Hz, 2H) and 7.04 (t, J(H,H) = 7.2 Hz, 2H; H^{para}-C_6H_5), 6.25 (t, J(H,H) = 7.4 Hz, 2H) and 5.00 (m, 2H; =CH), 5.25 (t, J(H,H) = 6.9 Hz, 2H; HC-O-Rh), 4.78 (m, 2H; HC-Rh), 2.62 (m, 2H), 2.38 (m, 2H), 1.91 (m, 8H), 1.50 (m, 2H) and 0.80 (m, 2H; CH_2); ^{13}C{^{1}H} NMR ($CDCl_3$, 25 °C) δ = 149.6 and 148.4 (C^{ipso}-C_6H_5), 129.1 and 128.6 (C^{meta}-C_6H_5), 123.7 and 123.3 (C^{para}-C_6H_5), 119.2 and 117.7 (C^{ortho}-C_6H_5), 100.5 (d, J(C,Rh) = 8 Hz) and 95.7 (d, J(C,Rh) = 7 Hz; =CH), 94.6 (d, J-(C,Rh) = 2 Hz; HC-O-Rh), 33.6 (d, J(C,Rh) = 17 Hz; HC-Rh), 33.9, 27.8, 24.8 and 20.6 (CH_2); MS: m/z (%): 847 (12) [M^+], 423 (100) [(M/2)$^+$].

3: An orange solution of **2** (100 mg, 0.12 mmol) in CH_2Cl_2 (10 mL) became green over 72 h in an argon atmosphere. Concentration of the solution to about 2 mL and addition of hexane (10 mL) afforded the product as a green solid, which was separated by filtration and dried under vacuum. Yield: 70 mg (70 %). Elemental analysis (%) calcd for $C_{20}H_{22}N_3O_1Rh_1$: C 56.75, H 5.24, N 9.93; found: C 56.85, H 5.23, N 9.75; ^{1}H NMR ($CDCl_3$, 25 °C): (assigned from ^{1}H,^{1}H-COSY spectrum) δ = 7.56 (d, J(H,H) = 7.8 Hz, 4H; H^{ortho}-C_6H_5), 7.34 (t, J(H,H) = 7.8 Hz, 4H; H^{meta}-C_6H_5), 7.06 (t, J(H,H) = 7.2 Hz, 2H; H^{para}-C_6H_5), 5.15 (m, 2H; H^4 and H^6), 4.01 (t, J(H,H) = 8.7 Hz, 1H; H^5), 3.52 (m, 1H; H^1), 2.68 (m, 1H; H^8), 2.36 (d, J(H,H) = 9.0 Hz, 1H; OH), 2.03 (m, 3H; H^{2a}, H^{3a}, H^{7a}), 1.32 (m, 1H; H^{7b}), 1.27 (m, 1H; H^{3b}), 0.67 (m, 1H; H^{2b}); MS: m/z (%): 423 (100) [M^+].

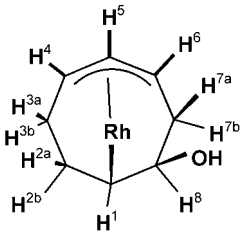

Kinetic measurements: Dioxygen uptake experiments were performed in an apparatus consisting of a (7.99 mL) stainless-steel gas reservoir triply connected to a high-pressure dioxygen source, a pressure transmitter, and an electronic pressure meter/controller (EL-Press, Bronkhorst HI-TEC). The outlet of the pressure controller was connected to a 100-mL reaction flask, also connected to a Schlenk manifold to allow for manipulation of the reaction and degassing. In a typical reaction, a solution of **1** at the desired concentration in toluene was transferred to the reaction flask, degassed in vacuo over 30 s, and then exposed to dioxygen at the desired total pressure. The pressure was programmed at the computer connected to the pressure controller. The reaction flask was shaken vigorously during reaction. Consumption of dioxygen was registered as a pressure decrease in the closed reservoir, by means of the pressure transmitter, at intervals of 15 s. The pressure decrease was converted into the moles of dioxygen consumed by using the precalibrated volume of the reservoir and considering an ideal gas behavior. Initial rates were obtained through a least-square fitting of the initial 10 % of the reactions. Pseudo-first-order rate constants k_{obs} were calculated by fitting the experimental reaction profiles to exponentials. The toluene vapor pressure at the temperature of the system was considered in calculating dioxygen partial pressures.[16].

Received: December 27, 2004
Revised: March 2, 2005
Published online: April 21, 2005

Keywords: metallacycles · N ligands · O—O activation · oxidation · rhodium

[1] D. H. R. Barton, *The Activation of Dioxygen and Homogeneous Catalytic Oxidation*, Plenum, New York, **1993**.

[2] W. N. M. Van Leeuwen, *Homogeneous Catalysis*, Kluwer Academic Publisher, Dordrecht, **2004**.

[3] a) S. S. Stahl, *Angew. Chem.* **2004**, *116*, 3480; *Angew. Chem. Int. Ed.* **2004**, *43*, 3400; b) "Catalysis by Metal Complexes": *Advances in Catalytic Activation of Dioxygen by Metal Complexes*, *Vol. 26* (Ed.: L. I. Simándi), Kluwer Academic Publisher, Dordrecht **2003**; c) A. L. Gavrilova, C. J. Qin, R. D. Sommer, A. L. Rheingold, B. Bosnich, *J. Am. Chem. Soc.* **2002**, *124*, 1714.

[4] B. De Bruin, P. H. M. Budzelaar, A. W. Gal, *Angew. Chem.* **2004**, *116*, 4236; *Angew. Chem. Int. Ed.* **2004**, *43*, 4142.

[5] a) B. De Bruin, J. A. E. Verhagen, C. H. J. Shouten, A. W. Gal, D. Feichtinger, D. A. Plattner, *Chem. Eur. J.* **2001**, *7*, 416; b) B. De Bruin, M. J. Boerakker, J. A. W. Verhagen, R. De Gelder, J. M. M. Smits, A. W. Gal, *Chem. Eur. J.* **2000**, *6*, 298.

[6] T. C. Flood, M. Iimura, J. M. Perotti, A. L. Rheingold, T. E. Concolino, *Chem. Commun.* **2000**, 1681.

[7] a) T. Sciarone, J. Hoogboom, P. P. J. Schlebos, P. H. M. Budzelaar, R. de Gelder, J. M. M. Smits, A. W. Gal, *Eur. J. Inorg. Chem.* **2002**, 457; b) B. De Bruin, J. A. Brands, J. J. J. M. Donners, M. P. J. Donners, R. De Gelder, J. M. M. Smits, A. W. Gal, A. L. Spek, *Chem. Eur. J.* **1999**, *5*, 2921.

[8] a) M. Krom, T. P. J. Peters, R. G. E. Coumans, T. J. J. Sciarone, J. Hoogboom, S. I. ter Beek, P. P. J. Schlebos, J. M. M. Smits, R. de Gelder, A. W. Gal, *Eur. J. Inorg. Chem.* **2003**, 1072.

[9] V. W. Day, W. G. Klemperer, S. P. Lockledge, D. J. Main, *J. Am. Chem. Soc.* **1990**, *112*, 2031.

[10] W. H. Knoth, *Inorg. Chem.* **1973**, *12*, 38.

[11] 3D Search and Research using the Cambridge Structural Database, F. H. Allen, O. Kennard, *Chem. Des. Auto. News* **1993**, *8*, 31.

[12] Crystal data for **2**·3 C_7H_8: $C_{40}H_{44}N_6O_2Rh_2$·3 C_7H_8, $M_r = 1123.04$, prismatic crystal ($0.16 \times 0.05 \times 0.05$ mm), triclinic, space group $P\bar{1}$, $a = 9.7616(11)$, $b = 11.5598(13)$, $c = 12.4273(14)$ Å, $\alpha = 86.458(2)$, $\beta = 68.865(2)$, $\gamma = 87.552(2)°$, $V = 1305.2(3)$ Å^{-3}, $Z = 1$, $\rho_{calcd} = 1.429$ g cm^{-3}, $F(000) = 582.0$, $T = 100(2)$ K, $Mo_{K\alpha}$ radiation ($\lambda = 0.71073$ Å, $\mu = 0.682$ mm^{-1}). Data collected with a Bruker SMART APEX CCD diffractometer. Of 15557 measured reflections (2θ: 3.5–55°, ω scans 0.3°), 5903 were unique ($R_{int} = 0.0406$); a multiscan absorption correction was applied (SADABS program) with min./max. transmission factors of 0.932/0.955. Structure solved by Patterson and difference-Fourier maps; refined using SHELXTL. A disordered toluene molecule was found in the asymmetric unit. Final agreement factors were $R1 = 0.0506$ (5226 obs. reflections, $F^2 > 4\sigma(F^2)$) and $wR2 = 0.1086$; data/restrains/parameters 5903/0/454; GOF = 1.112. CCDC-258836 (**2**) and CCDC-258837 (**3**) contain the supplementary crystallographic data for this paper. These data can be obtained free of charge from the Cambridge Crystallographic Data Centre via www.ccdc.cam.ac.uk/data_request/cif.

[13] Crystal data for **3**: $C_{20}H_{22}N_3ORh$, $M_r = 423.31$, monoclinic, space group $P2_1/n$, $a = 10.7068(11)$, $b = 16.5017(18)$, $c = 40.470(4)$ Å, $\beta = 95.299(2)°$, $V = 7119.7(13)$ Å^{-3}, $Z = 16$, $\rho_{calcd} = 1.580$ g cm^{-3}, $F(000) = 3456$, $T = 100(2)$ K, $Mo_{K\alpha}$ radiation ($\lambda = 0.71073$ Å, $\mu = 0.972$ mm^{-1}). Data collected as described for **2** with an irregular prism ($0.084 \times 0.054 \times 0.054$ mm). Of 38220 measured reflections (2θ: 2–50°), 12544 were unique ($R_{int} = 0.1048$); a multiscan absorption correction was performed (SADABS program) with min./max. transmission factors of 0.923/0.942. Structure solution and refinement as described for **2**. Two independent, but chemically equivalent, dimeric complexes were found in the asymmetric unit. Final agreement factors were $R1 = 0.068$ (6315 observed reflections) and $wR2 = 0.1737$. Data/restrains/parameters 12544/42/901; GOF = 0.998. All residual peaks above 1 e Å^{-3} were found in close proximity to the rhodium metal and have no chemical sense.

[14] P. Piraino, G. Tresoldi, F. Faraone, *J. Organomet. Chem.* **1982**, *224*, 305.

[15] F. J. Lahoz, A. Tiripicchio, M. Tiripicchio-Camellini, L. A. Oro, M. T. Pinillos, *J. Chem. Soc. Dalton Trans.* **1985**, 1487.

[16] *TRC Thermodynamic Tables*, Vol. VIII, p. Kb-3290.

Phosphazanes

Synthesis and Solid-State Structure of a Metal Complex of a Diphosphineimine**

Leonard E. Anagho, Jamie F. Bickley, Alexander Steiner, and Lothar Stahl**

Dedicated to Professor Michael Veith on the occasion of his 60th birthday

Diphosphineimine compounds of the general structure R_2P-PR_2=NR [**A**; Eq. (1)] have been known for some time,[1] but

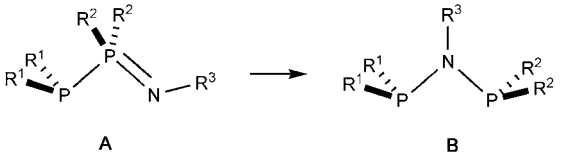

(1)

the pronounced tendency of these molecules to rearrange to the isomeric diphosphinoamines **B** has hampered the development of their chemistry and relegated them to structural curiosities. For example, the diphosphineimine iPr$_2$P(=N-Ph)PEt$_2$ was reported to completely rearrange to diphosphinoamine iPr$_2$P-NPh-PEt$_2$ in the presence of electrophiles or nucleophiles.[1d] Similarly, the attempted synthesis of a palladium dichloride complex of Ph_2P-PPh_2=N{C_6H_4(o-CN)} only furnished the diphosphinoamine complex *cis*-[$PdCl_2${(o-CN)C_6H_4N(PPh_2)$_2$}].[2b] Diphosphinoamines, of course, have a

[*] J. F. Bickley, Dr. A. Steiner
Department of Chemistry
University of Liverpool
Crown Street, Liverpool, L69 7ZD (UK)
Fax: (+44) 151-794-3588
E-mail: a.steiner@liverpool.ac.uk
L. E. Anagho, Professor Dr. L. Stahl
Department of Chemistry
University of North Dakota
Grand Forks, ND 58202 (USA)
Fax: (+1) 701-777-2331
E-mail: lstahl@chem.und.edu

[**] The Chevron Phillips Chemical Company (L.S.) and the EPSRC (A.S.) are acknowledged for financial support.

 DOI: 10.1002/anie.200462588

long history as ligands for transition metals and as stable molecules in their own right.[3] They have been used in late-transition-metal homogeneous polyolefin catalysis because they impart a greater stability to the complexes than the more conventional diimines.[4,5] The asymmetric diphosphineimines have both electron-donating imine and electron-accepting phosphine functionalities, as exemplified in the ylidic form **C**, which may combine the best features of diimines and diphosphines and, thus, be superior ligands. Furthermore, these hemilabile phosphorus(III)/phosphorus(V) molecules should have applications in other important catalytic transformations, such as hydroformylation and hydrogenation reactions,[6] thus making the search for stable diphosphineimines an area of interest.

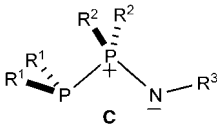

C

Herein, we report the synthesis and solid-state structure of the first diphosphineimine that is kinetically stable enough to allow the isolation of a transition-metal complex. Our investigations also furnished the first solid-state structure of a diphosphineimine sulfide and of a metal complex in which the diphosphineimine has isomerized to the corresponding diphosphinoamine, thereby providing the rare opportunity to compare coordination compounds of both structural isomers.

Diphosphineimines are occasionally formed when amidophosphines are treated with halophosphines in the attempted synthesis of diphosphinoamines.[1,2] Symmetrical diphosphinediimines can also be synthesized by the oxidative coupling of amidophosphines.[7] The addition of $\{Me_2Si(\mu\text{-}NtBu)_2PNPh\}Li$ to Ph_2PCl in THF resulted in the nucleophilic attack of $\{Me_2Si(\mu\text{-}NtBu)_2PNPh\}^-$ on the phosphorus atom of Ph_2PCl to afford $Me_2Si(\mu\text{-}NtBu)_2P(=NPh)PPh_2$ (**1**) as the only phosphorus-containing product [Eq. (2)]. Treatment of

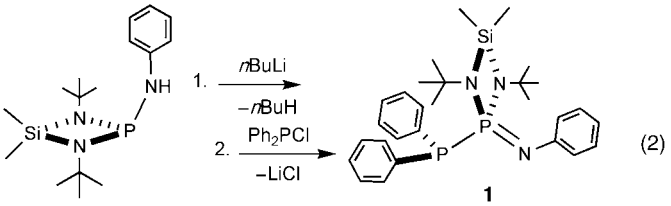

(2)

1

$(Ph_2PNPh)Li$ with $Me_2Si(\mu\text{-}NtBu)_2PCl$,[8] in contrast, gave only an intractable mixture.

A direct P–P bond in **1** was suggested by an AB pattern of doublets in the ^{31}P NMR spectrum at $\delta = 49.9$ and 44.9 ppm, respectively ($J(P,P) = 182$ Hz), but later findings showed that coupling constants of this magnitude are not diagnostic for direct P–P bonds in these systems (see below). A single-crystal X-ray analysis of the colorless product confirmed the assumed structure of **1**.

Figure 1 shows one of the two independent molecules, whose metric parameters are identical within experimental uncertainties. The P–P and P=N bonds (2.2092(7) and 1.5568(15) Å, respectively) are somewhat shorter than those of the previously characterized diphosphineimine of the type $(o\text{-}X)C_6H_4N{=}PPh_2\text{-}PPh_2$ (X = CF_3, Ph, CN) in which they

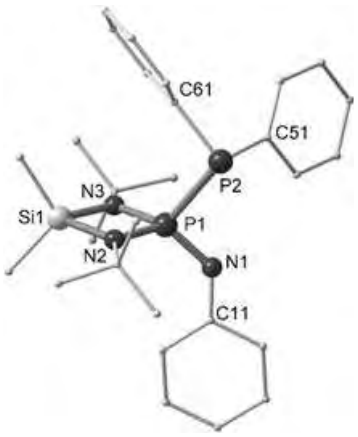

Figure 1. Solid-state structure of **1** (hydrogen atoms have been omitted). Selected bond lengths [Å] and angles [°]: P(1)-P(2) 2.2092(7), P(1)-N(1) 1.5568(15), P(1)-N(2) 1.6761(15), P(1)-N(3) 1.6804(16); N(1)-P(1)-P(2) 97.12(6), N(2)-P(1)-N(3) 86.67(8), C(61)-P(2)-P(1) 104.01(6), C(51)-P(2)-P(1) 106.44(7), C(51)-P(2)-C(61) 102.84(8).

ranged from 2.2379(16) to 2.2498(18) Å and from 1.571(3) to 1.578(3) Å, respectively.[2] These bond-length contractions may be a reflection of the greater stability of **1**, which proved to be unusually thermally robust: it exhibited no tendency to decompose or rearrange to the corresponding diphosphinoamine on heating to reflux in toluene (24 hours).

Diphosphineimines are normally kinetic products that isomerize to the corresponding diphosphinoamines during attempted chemical transformations and metal coordination.[1d,2] In notable contrast, the reaction of **1** with elemental sulfur produced the colorless compound **2** as the only product [Eq. (3)]. To the best of our knowledge, this diphosphine-

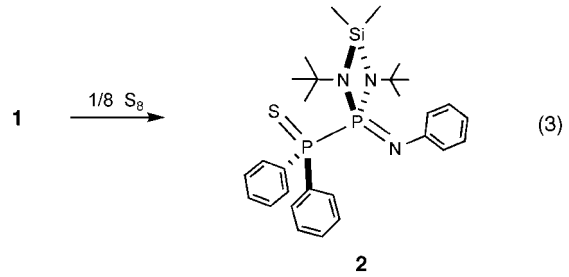

(3)

2

imine sulfide is only the second of its kind to have been reported and the first to have been characterized by X-ray structural analysis.[1c]

The solid-state structure of **2** confirmed that the P–P bond had remained intact during the reaction (Figure 2). The molecule adopted a staggered conformation to minimize nonbonding interactions: the bulkiest substituent on one phosphorus atom is in a *gauche* conformation with the smallest substituents on the opposite phosphorus atom. This conformation renders **2** almost perfectly mirror-symmetric, with the phosphorus, sulfur, silicon, and nitrogen (imino) atoms all lying in a noncrystallographic mirror plane. The comparatively short P=S and P=N(imino) bonds (1.9563(8) and 1.5507(19) Å, respectively) form a torsion angle of

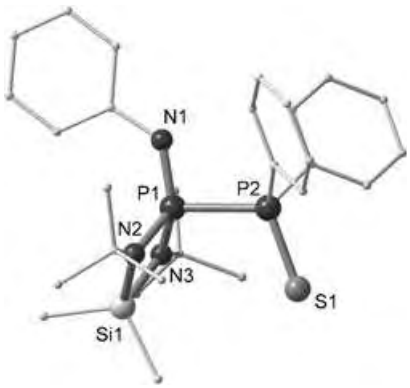

Figure 2. Solid-state structure of **2** (hydrogen atoms have been omitted). Selected bond lengths [Å] and angles [°]: P(1)-P(2) 2.2332 (7), P(1)-N(1) 1.5507(19), P(2)-S(1) 1.9563(8), P(1)-N(2) 1.6684(18), P(1)-N(3) 1.6677(17); N(1)-P(1)-P(2) 99.72(7), P(1)-P(2)-S(1) 110.71(3), N(2)-P(1)-N(3) 87.54(9), C(41)-P(2)-C(51) 103.19(10).

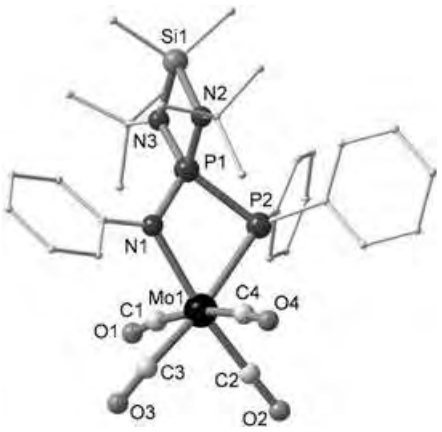

Figure 3. Solid-state structure of **3**. (Only one of the two independent molecules is shown; the toluene molecule and the hydrogen atoms have been omitted.) Selected bond lengths [Å] and angles [°]: Mo(1)-P(2) 2.4915(9), Mo(1)-N(1) 2.321(2), Mo(1)-C(1) 2.032(3), Mo(1)-C(2) 1.946(3), Mo(1)-C(3) 1.976(3), Mo(1)-C(4) 2.042(3), P(1)-P(2) 2.2362(11), P(1)-N(1) 1.599(2), P(1)-N(2) 1.661(2), P(1)-N(3) 1.669(2); N(1)-P(1)-P(2) 91.29(9), Mo(1)-N(1)-P(1) 111.16(11), Mo(1)-P(2)-P(1) 86.99(3).

approximately 179° about the slightly elongated P–P bond (2.2332(7) Å).

Compound **1** did not isomerize on heating and oxidation, which encouraged us to explore its coordination chemistry. Treatment of **1** with *cis*-[$Mo(CO)_4$(piperidine)$_2$] in THF and heating to reflux afforded the light-yellow molybdenumtetracarbonyldiphosphineimine [**3**; Eq. (4)]. The infrared spectrum exhibited three ν(CO) bands at 2010, 1890, and 1850 cm^{-1}, respectively, as is common for many molybdenumtetracarbonyl complexes with local C_{2v} symmetry. These carbonyl stretching vibrations are lower than for most complexes of the *cis*-[$Mo(CO)_4$(PP)] type (PP refers to alkanediyl- or amine-bridged bisphosphines),[9] thus suggesting that **1** is the expected electron-rich chelating ligand.

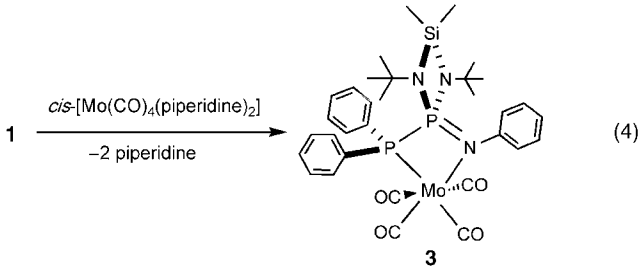

(4)

Complex **3**, which crystallizes as a monotoluene solvate with two independent molecules in the asymmetric unit, was analyzed by single-crystal X-ray analysis. The spirocyclic molecule is composed of two almost-planar four-membered rings (Figure 3), but the trapezoidal Mo-P-P-N ring is much more irregular than the rhombus of the diazasilaphosphetidine. Thus, the *cis*-configured Mo–P and Mo–N bonds are 2.4915(9) and 2.321(2) Å, respectively, while the P–P and P=N bond lengths are 2.2362(11) and 1.599(2) Å, respectively. The Mo–P bond length is similar to those in the related *cis*-[$Mo(CO)_4$(PP)] and *cis*-[$Mo(CO)_4$(PN)] complexes,[9,10] but the Mo–N and P=N bonds are rather long for an sp^2-hybridized nitrogen atom,[10] possibly because of ring strain. There is a distinct asymmetry in the Mo–CO bond lengths as the axial bonds are significantly longer than the equatorial ones. Notably, the Mo–CO bond *trans* to the best electron donor, namely the imino nitrogen atom, is the shortest one of the four Mo–CO bonds. The bond parameters within the diazasilaphosphetidine are unremarkable and similar to those in related compounds.[11]

Despite the direct P–P bond, the P–P coupling constant of **3** is only a third of the magnitude (ca. 69 Hz) as that of **1**, for reasons that are not yet clear.

Although the surprising thermal and chemical stabilities of **1** suggested that this diphosphineimine might be thermodynamically stable with respect to its isomer, its interaction with nickel salts proved otherwise. Compound **1** was treated with *cis*-[$NiBr_2$(diglyme)] (diglyme = diethyleneglycol dimethyl ether) to furnish the diphosphinoaminenickel dibromide complex **4** as the only product, even at room temperature [Eq. (5)].

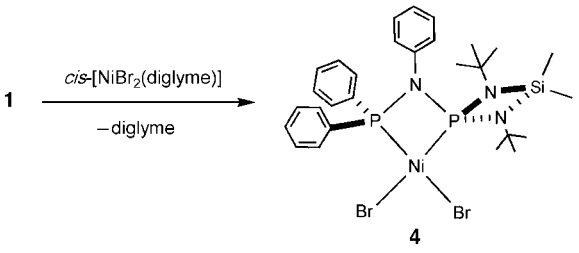

(5)

The diamagnetism of the compound had indicated a square-planar coordination geometry about the nickel ion, and this arrangement was confirmed by the solid-state structure of **4** (Figure 4). The two planes defined by the nickel and phosphorus and the nickel and bromide atoms, respectively, are nearly coplanar (dihedral angle = 6°) and perpendicular to the diazasilaphosphetidine ring. Despite the dissimilar substituents on both phosphorus atoms, the Ni–P

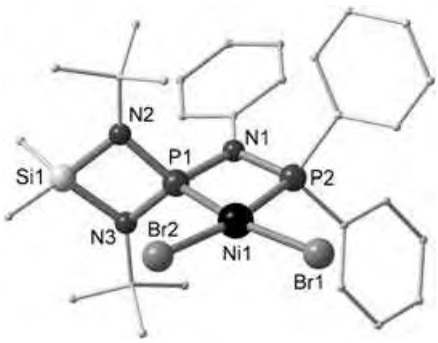

Figure 4. Solid-state structure of **4** (the THF molecule and the hydrogen atoms have been omitted). Selected bond lengths [Å] and angles [°]: Ni(1)-P(1) 2.1270(10), Ni(1)-P(2) 2.1151(10), Ni(1)-Br(1) 2.3481(6), Ni(1)-Br(2) 2.3302(6), P(1)-N(1) 1.714(3), P(2)-N(1) 1.714(3), P(1)-N(2) 1.658(3), P(1)-N(3) 1.670(3); P(1)-N(1)-P(2) 97.17(14), P(1)-Ni(1)-P(2) 74.62(4), Br(1)-Ni(1)-Br(2) 98.07(2), N(2)-P(1)-N(3) 87.67(15).

bonds are almost equidistant (the Ni–P1 and Ni–P2 bond lengths are 2.1270(10) and 2.1151(10) Å) and are slightly shorter than those in the related *cis*-[$NiBr_2${$Ar_2PN(Me)PAr_2$}] ($Ar = o$-$tBuC_6H_4$), which features symmetrical Ni–P bonds (2.1611(6) Å).[4a] This latter nickel complex, with its bulky bis(diphenylphosphine)amine ligand, was shown to be a very good polyolefin catalyst, and the more electron-rich **4** may exhibit a similar reactivity.

The ^{31}P NMR spectrum gave no indication that the isomerization of **1** had occurred as it showed two doublets at $\delta = 55.8$ and 43.9 ppm for the P1 and P2 atoms, respectively, with larger coupling constants ($J(P,P) = 137$ Hz) than those seen in **3**. Thus, ^{31}P NMR spectroscopy, which is usually considered a diagnostic tool, was neither reliable for predicting the connectivity in these phosphorus–nitrogen compounds nor did it show a correlation between the coupling constants and the P–P bond lengths. These results are in keeping with earlier studies that showed large and variable two-bond P–P coupling constants in diphosphinoamines that ranged from 15 to 665 Hz.[12]

Given the catalytic activity of nickel and the inertness of the [$Mo(CO)_4$] moiety, it is not surprising that **1** isomerized in the presence of $NiBr_2$ even at room temperature, although it was unaffected by [$Mo(CO)_4$] when they were heated together to reflux in THF. However, it is surprising that the soft {$Mo(CO)_4$} fragment is coordinated by the hard nitrogen atom, although the harder $NiBr_2$ moiety is coordinated by the soft phosphorus atoms. This disparity further underlines the kinetic control demonstrated in Equations (4) and (5). Our results also suggest that attempts to stabilize diphosphineimines with certain Group 10 metal compounds, as had been done previously, may cause isomerization instead.[2a] The ease with which **1** isomerizes in the presence of $NiBr_2$ clearly rules out its use as a diphosphineimine ligand in Group 10 metal catalysis.

In summary, the syntheses and solid-state structures of a kinetically stable diphosphineimine, its molybdenum complex, and its sulfide analogue have been reported. Whether the electronic properties or the cyclic structure of the diazasilaphosphetidine give this particular diphosphineimine its unique stability remains to be seen. The potential rewards for finding stable diphosphineimines are clear, and we are currently exploring the reaction chemistry of **1** to understand the properties of these intriguing molecules.

Experimental Section

1: A solution of $Me_2Si(\mu$-$NtBu)_2PN(H)Ph$[11a] (11.2 mmol) in hexanes (20 mL) was treated dropwise at 0 °C with *n*BuLi (11.3 mmol) in hexanes (15 mL). The reaction mixture was heated at reflux for 1 h, cooled to RT, and then treated dropwise with a solution of Ph_2PCl (11.2 mmol) in hexanes. This caused a white precipitate to form. The mixture was stirred overnight and then filtered to afford a colorless, clear solution from which colorless, rectangular crystals separated upon cooling; yield: 3.69 g (64.9 %). M.p. 170–172 °C; elemental analysis (%) calcd for $C_{28}H_{39}N_3P_2Si$: C 66.24, H 7.74, N 8.28; found: C 66.01, H 7.84, N 8.11; ^1H NMR (500.1 MHz, CD_2Cl_2, 21 °C): $\delta = 7.94$ (m, 4H, Ph), 7.37 (m, 6H, Ph), 7.15 (t, $J = 7.1$ Hz, 2H, Ph), 7.06 (d, $J = 8.1$ Hz, 2H, Ph), 6.72 (t, $J = 7.1$ Hz, 1H, Ph), 1.13 (s, 18H, *t*Bu), 0.56 (s, 3H, Me), 0.20 ppm (s, 3H, Me); $^{31}P[^1H]$ NMR (202.5 MHz, CD_2Cl_2, 21 °C): $\delta = 2.66$ (d, $J(P,P) = 182.4$ Hz), −30.82 ppm (d, $J(P,P) = 182.8$ Hz).

2: Compound **1** (0.235 g, 0.486 mmol) and elemental sulfur (0.016 g, 0.50 mmol) were dissolved in THF (20 mL), and the mixture was heated at reflux for 3 h. Following removal of THF, the ensuing white powder was dissolved in toluene to afford colorless crystals upon cooling; yield: 0.213 g (81.2 %). M.p. 202–206 °C; elemental analysis (%) calcd for $C_{28}H_{39}N_3P_2SSi$: C 62.31, H 7.28, N 7.79; found: C 61.94, H 7.35, N 7.72; ^1H NMR (500.1 MHz, C_6D_6, 21 °C): $\delta = 9.178$ (dd, $J = 12.4$, 8.0 Hz, 4H, Ph), 7.43 (d, $J = 8.3$ Hz, 2H, Ph), 7.34 (t, $J = 7.5$ Hz, 2H, Ph), 7.11 (td, $J = 8.0$, 3.2 Hz, 2H, Ph), 6.99 (t, $J = 7.4$ Hz, 2H, Ph), 6.95 (t, $J = 7.3$ Hz, 1H, Ph), 0.94 (s, 18H, *t*Bu), 0.83 (s, 3H, Me), 0.38 ppm (s, 3H, Me); $^{31}P[^1H]$ NMR (202.5 MHz, CD_2Cl_2, 21 °C): $\delta = 10.94$ (d, $J(P,P) = 238.8$ Hz), −8.40 ppm (d, $J(P,P) = 238.8$ Hz).

3: Compound **1** (0.250 g, 0.500 mmol) and *cis*-[$Mo(CO)_4$(piperidine)$_2$] (0.195 g, 0.500 mmol) were dissolved in THF (50 mL) and the mixture was heated at reflux for 3 h. A yellow powder precipitated upon cooling, which was recrystallized from toluene to afford light-yellow crystals; yield: 0.263 g (65.1 %). M.p. 176 °C (decomp); elemental analysis (%) calcd for $C_{39}H_{47}MoN_3O_4P_2Si$: C 57.99, H 5.86, N 5.20; found: C 58.04, H 5.98, N 5.34; ^1H NMR (500.1 MHz, CD_2Cl_2, 21 °C): $\delta = 8.09$ (m, 4H, Ph), 7.52 (s, 6H, Ph), 7.39 (t, $J = 7.6$ Hz, 2H, Ph), 7.22 (m, 4H, Ph), 6.91 (t, $J = 7.3$ Hz, 1H, Ph), 2.34 (s, 3H, Me), 0.84 (s, 21H, *t*Bu, Me), 0.66 ppm (s, 3H, Me); $^{31}P[^1H]$ NMR (202.5 MHz, CD_2Cl_2, 21 °C): $\delta = 49.93$ (d, $J(P,P) = 69.5$ Hz), 44.97 ppm (d, $J(P,P) = 69.0$ Hz); $^{13}C[^1H]$ NMR (CD_2Cl_2), 121.5 MHz, 21 °C): $\delta = 221.4$ (s, CO_{eq}), 218.3 (d, $J = 32.9$ Hz, CO_{eq}), 210.2 (d, $J = 8.5$ Hz, CO_{ax}), 132.8 (d, $J = 26.4$ Hz, Ph), 131.9 (s, Ph), 129.6 (s, Ph), 128.9 (s, Ph), 126.1 (s, Ph), 122.4 (s, Ph), 32.4 (s, *t*Bu), 5.0 (s, Me), 4.4 ppm (s, Me); IR (nujol): $\tilde{\nu} = 2010.4$ (s), 1889.9 (vs), 1850.4 cm^{-1} (vs).

4: A suspension of *cis*-[$NiBr_2$(diglyme)] (0.321 g, 0.912 mmol) in THF (10 mL) was treated dropwise with a solution of **1** (0.398 g, 0.816 mmol) in THF (25 mL) at RT. The ensuing orange mixture slowly turned red and was stirred overnight. The dark red–brown solution was filtered through a medium-porosity frit and stored in a freezer. Several crops of red–brown, needle-shaped crystals formed upon cooling; yield: 0.369 g (59.0 %). M.p. 273–282 °C; elemental analysis (%) calcd for $C_{32}H_{47}Br_2N_3NiOP_2Si$: C 48.15, H 5.93, N 5.26; found: C 47.91, H 5.98, N 5.23; ^1H NMR (500.1 MHz, CD_2Cl_2, 21 °C): $\delta = 8.11$ (dd, $J = 12.4$, 7.9 Hz, 4H, Ph), 7.77 (s, 2H, Ph), 7.49 (s, 4H, Ph), 7.23 (s, 4H, Ph), 7.01 (s, 3H, Ph), 3.58 (s, 4H, THF), 1.85 (s, 4H, THF) 1.50 (s, 18H, *t*Bu) 0.78 (s, 3H, Me), 0.401 ppm (s, 3H, Me);

$^{31}P\{^1H\}$ NMR (202.5 MHz, CD_2Cl_2, 21 °C): $\delta = 55.81$ (d, $J(P,P) = 137.0$ Hz), 43.88 ppm (d, $J(P,P) = 137.0$ Hz).

Crystal data for **1**, **3**, and **4** were collected on a Bruker Smart Apex CCD and those for **2** on a Stoe IPDS diffractometer using graphite monochromated $Mo_{K\alpha}$ radiation ($\lambda = 0.71069$ Å). The structures were solved with direct methods and refined by full-matrix least-squares against F^2 using the SHELXTL program.

Crystal data for **1**: $C_{28}H_{39}N_3P_2Si$, triclinic, space group $P\bar{1}$ (no. 2), $a = 12.1274(7)$, $b = 15.3090(9)$, $c = 16.1150(9)$ Å, $\alpha = 81.0053(11)$, $\beta = 72.7523(10)$, $\gamma = 82.8704(10)$°, $V = 2812.6(3)$ Å^3, $Z = 4$, $\rho_{calcd} = 1.199$ g cm^{-3}, $T = 100$ K, $2\theta_{max} = 50$°, $\mu = 0.218$ mm^{-1}, 13774 reflections measured, of which 9783 were unique ($R_{int} = 0.0632$), final R indices: $R1 = 0.0365$, ($I > 2\sigma(I)$), $wR2 = 0.0904$ (all data).

Crystal data for **2**: $C_{28}H_{39}N_3SiP_2S$, monoclinic, space group $P2_1/n$ (no. 14), $a = 9.0459(10)$, $b = 9.7581(9)$, $c = 33.246(4)$ Å, $\beta = 93.604(13)$°, $V = 2928.8(5)$ Å^3, $Z = 4$, $\rho_{calcd} = 1.224$ g cm^{-3}, $T = 200$ K, $2\theta_{max=}48$°, $\mu = 0.282$ mm^{-1}, 18452 reflections measured, of which 4522 were unique ($R_{int} = 0.0502$), final R indices: $R1 = 0.0370$ ($I > 2\sigma(I)$), $wR2 = 0.0997$ (all data).

Crystal data for **3**: $C_{39}H_{47}MoN_3O_4P_2Si$, monoclinic, space group $P2_1/n$ (no. 14), $a = 19.2663(16)$, $b = 11.4770(10)$, $c = 36.889(3)$ Å, $\beta = 103.3213(14)$°, $V = 7937.3(12)$ Å^3, $Z = 8$, $\rho_{calcd} = 1.352$ g cm^{-3}, $T = 100$ K, $2\theta_{max} = 50$°, $\mu = 0.483$ mm^{-1}, 40213 reflections measured, of which 13998 were unique ($R_{int} = 0.0500$), final R indices: $R1 = 0.0401$ ($I > 2\sigma(I)$), $wR2 = 0.1006$ (all data).

Crystal data for **4**: $C_{32}H_{47}Br_2N_3NiOP_2Si$, monoclinic, space group $P2_1/c$ (no. 14), $a = 18.3666(13)$, $b = 12.1328(8)$, $c = 16.1095(11)$ Å, $\beta = 90.4750(14)$°, $V = 3589.7(4)$ Å^3, $Z = 4$, $\rho_{calcd} = 1.477$ g cm^{-3}, $T = 100$ K, $2\theta_{max=}50$°, $\mu = 2.918$ mm^{-1}, 18367 reflections measured, of which 6325 were unique ($R_{int} = 0.0375$), final R indices: $R1 = 0.0351$ ($I > 2\sigma(I)$), $wR2 = 0.0859$ (all data).

CCDC-254120–254123 (**1**–**4**, respectively) contain the supplementary crystallographic data for this paper. These data can be obtained free of charge from The Cambridge Crystallographic Data Centre via www.ccdc.cam.ac.uk/data_request/cif.

Received: November 12, 2004
Published online: April 21, 2005

Keywords: heterocycles · molybdenum · N,P ligands · nickel · phosphazanes

[1] a) O. J. Scherer, W. M. Janssen, *J. Organomet. Chem.* **1969**, *20*, 111; b) A. Schmidpeter, H. Rossknecht, *Z. Naturforsch. B* **1971**, *26*, 81; c) H. Rossknecht, W. P. Lehmann, A. Schmidpeter, *Phosphorus* **1975**, *5*, 195; d) V. L. Foss, Y. A. Veits, T. E. Chernykh, I. F. Lutsenko, *Zh. Obshch. Khim.* **1984**, *12*, 2670.

[2] a) Z. Fei, R. Scopelliti, P. J. Dyson, *Dalton Trans.* **2003**, 2772; b) Z. Fei, R. Scopelliti, P. J. Dyson, *Eur. J. Inorg. Chem.* **2004**, 530.

[3] a) M. S. Balakrishna, V. Sreenivasa Reddy, S. S. Krishnamurthy, J. F. Nixon, J. C. T. R. Burckett St. Laurent, *Coord. Chem. Rev.* **1994**, *129*, 1; b) T. R. Prout, T. W. Imiolczyk, F. Barthelmey, S. M. Young, R. C. Haltiwanger, A. D. Norman, *Inorg. Chem.* **1994**, *33*, 1783; c) H. Schmidbaur, S. Lauteschläger, F. H. Köhler, *J. Organomet. Chem.* **1984**, *271*, 173; d) D. S. Payne, J. A. A. Mokuolu, J. C. Speakman, *Chem. Commun.* **1965**, 599.

[4] a) N. A. Cooley, S. M. Green, D. F. Wass, K. Heslop, A. G. Orpen, P. G. Pringle, *Organometallics* **2001**, *20*, 4769; b) S. J. Dossett, A. Gillon, A. G. Orpen, J. S. Fleming, P. G. Pringle, D. F. Wass, M. D. Jones, *Chem. Commun.* **2001**, 699.

[5] L. K. Johnson, C. M. Killian, M. Brookhart, *J. Am. Chem. Soc.* **1995**, *117*, 6414.

[6] a) C. D. Frohning, C. W. Kohlpaintner in *Applied Homogeneous Catalysis with Organometallic Compounds* (Eds.: B. Cornils, W. A. Herrmann), VCH, Weinheim, **1996**, pp. 29–104; b) H. Brunner in *Applied Homogeneous Catalysis with Organometallic Compounds* (Eds.: B. Cornils, W. A. Herrmann), VCH, Weinheim, **1996**, pp. 201–216.

[7] a) J. Ellermann, P. Gabold, F. A. Knoch, M. Moll, A. Schmidt, M. Schütz, *Z. Naturforsch. B* **1996**, *51*, 201; b) P. Braunstein, R. Hasselbring, A. Tiripicchio, F. Ugozzoli, *J. Chem. Soc. Chem. Commun.* **1995**, 37.

[8] a) M. Veith, M. Grosser, V. Huch, *Z. Anorg. Allg. Chem.* **1984**, *513*, 89; b) M. Veith, B. Bertsch, V. Huch, *Z. Anorg. Allg. Chem.* **1988**, *599*, 73.

[9] a) S. L. Mukerjee, S. P. Nolan, C. D. Hoff, R. Lopez de la Vega, *Inorg. Chem.* **1988**, *27*, 81; b) M. S. Balakrishna, T. K. Prakasha, S. S. Krishnamurthy, U. Siriwardane, N. S. Hosmane, *J. Organomet. Chem.* **1990**, *390*, 203; c) I. Bernal, G. M. Reisner, G. D. Dobson, C. B. Dobson, *Inorg. Chim. Acta* **1986**, *121*, 199.

[10] D. Walther, S. Liesicke, L. Böttcher, R. Fischer, H. Görls, G. Vaughan, *Inorg. Chem.* **2003**, *42*, 625.

[11] a) D. C. Haagenson, D. F. Moser, L. Stahl, R. J. Staples, *Inorg. Chem.* **2002**, *41*, 1245; b) O. J. Scherer, M. Püttmann, C. Krüger, G. Wolmershäuser, *Chem. Ber.* **1982**, *115*, 2076.

[12] I. J. Colquhoun, W. McFarlane, *J. Chem. Soc. Dalton Trans.* **1977**, 1674.

Organic Chemistry

"On Water": Unique Reactivity of Organic Compounds in Aqueous Suspension**

*Sridhar Narayan, John Muldoon, M. G. Finn, Valery V. Fokin, Hartmuth C. Kolb, and K. Barry Sharpless**

Water is a desirable solvent for chemical reactions for reasons of cost, safety, and environmental concerns, and the study of organic reactions in aqueous solvents has an intriguing history.[1] Most notably, certain pericyclic reactions such as

[*] Dr. S. Narayan, Dr. J. Muldoon, Prof. M. G. Finn, Prof. V. V. Fokin, Prof. H. C. Kolb, Prof. K. B. Sharpless
Department of Chemistry and
the Skaggs Institute of Chemical Biology
The Scripps Research Institute
10550 North Torrey Pines Road
La Jolla, CA 92037 (USA)
Fax: (+1) 619-554-6738
E-mail: sharples@scripps.edu

[**] We thank Dr. Vladislav Litosh for carrying out preliminary work. Support from the National Institutes of Health, National Institute of General Medical Sciences (GM 28384), the National Science Foundation (CHE9985553), the Skaggs Institute for Chemical Biology, and the W. M. Keck Foundation is gratefully acknowledged. S.N. thanks the Skaggs Institute for a postdoctoral fellowship. We also thank Dr. Suresh Suri, Edwards Air Force Base, California, for a generous gift of quadricyclane. We urge our fellow chemists to float their problematic reactions on water and to send observations of success or failure to us at onwater@scripps.edu for public dissemination with attribution.

Supporting information for this article is available on the WWW under http://www.angewandte.org or from the author.

 DOI: 10.1002/anie.200462883

Diels–Alder cycloadditions[2] and Claisen rearrangements[3] of hydrophobic compounds have been found to be accelerated in dilute aqueous solution. Yet, either organic cosolvents and/or substrate modifications are almost always employed in preparative-scale reactions performed in water,[1] as it is assumed that solubility is required for efficient reaction. Not only do these strategies detract from the simplicity and advantages sought from the use of water in the first place, but, as we report here, the venerable assumption "corpora non agunt nisi soluta" (substances do not interact unless dissolved) can be distinctly counterproductive.

In recent years, we have focused on modular synthetic techniques that rely on a few nearly perfect reaction types.[4] In the course of this work, we have noticed that many such reactions often proceed optimally in pure water,[5] and particularly when the organic reactants are insoluble in the aqueous phase.[6] We present here several examples that illustrate a remarkable phenomenon: substantial rate acceleration when insoluble reactants are stirred in aqueous suspension, denoted here as "on water" conditions. Even when the rate acceleration is negligible, the use of water as the only supporting medium has other advantages including ease of product isolation and above all, safety, thanks to its high heat capacity[7] and unique redox stability.

In connection with our studies on the reactivity of strained olefins, we explored the preparation of 1,2-diazetidines from quadricyclane (**1**) by the $2\sigma+2\sigma+2\pi$ cycloaddition with azodicarboxylates, discovered by Lemal and co-workers.[8] The typical reaction conditions involve heating **1** with dimethyl azodicarboxylate (DMAD, **2**) in toluene or benzene at 80 °C for 24 h or longer.[8,9] In contrast, when a mixture of DMAD and quadricyclane is vigorously stirred "on water", the reaction is complete within a few minutes at ambient temperature. The corresponding neat (solvent-free) reaction of these two liquids takes nearly two days to reach completion, which shows that the rate acceleration is not the sole consequence of an increase in the effective concentration of reagents (Table 1).

As the cycloaddition of DMAD with quadricyclane demonstrates, the "on water" method consists simply of stirring the reactant(s) with water to generate an aqueous suspension. Nonpolar liquids that separate from water into a clear organic phase are ideal candidates for these reactions. Solid reactants can also be utilized, provided one reaction partner is a liquid and adequate mixing is ensured. Vigorous stirring promotes the reaction, most likely by increasing the area of surface contact between the organic and aqueous phases. The observed rate acceleration does not depend on the amount of water used, as long as sufficient water is present for clear phase separation to occur.[10] The product is isolated simply by phase separation or filtration. In cases where clear phase separation does not occur, such as in small-scale reactions, liquid–liquid extraction may be necessary.

Seeking insight into the origin of rate acceleration in the DMAD–quadricyclane cycloaddition, the reaction between **1** and **2** was carried out under a variety of conditions and the time to completion was monitored (Table 2). Under homogenous conditions, polar protic solvents accelerate the reaction, with observed reaction rates in the following order: $MeOH/H_2O$ (3:1) > MeOH > DMSO > $CH_3CN \approx CH_2Cl_2$ > EtOAc ≈ toluene.[11] This trend suggests that hydrogen bonding, charge stabilization, and dipolar effects may each be important for rate acceleration.[12] While water contributes to such properties in homogeneous mixtures, heterogeneity was crucial for observing large rate accelerations. Thus, the presence or absence of methanol in a heterogeneous reaction made little difference, but the rate slowed considerably when enough methanol was used to make the reaction homogeneous. However, heterogeneity in itself is not responsible for rate acceleration as the reaction "on" perfluorohexane was only slightly faster than the neat reaction. Interestingly, a significant solvent isotope effect was also observed: the reaction slowed noticeably when D_2O was used in place of water.

Table 1: Reaction of quadricyclane (**1**) with dimethyl azodicarboxylate (**2**).

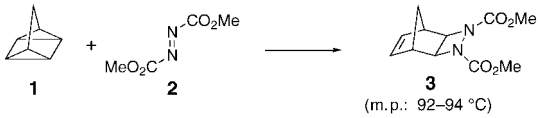

1 **2** **3** (m.p.: 92–94 °C)

Solvent	Conc. [M]	*T* [°C]	*t*	Yield [%][a]
neat	4.53[b]	0	2 h	0[c]
neat	4.53[b]	23	48 h	85
toluene	1	80	24 h	74
on H_2O	**4.53[d]**	**0**	**1.5 h**	**93**
on H_2O	**4.53[d]**	**23**	**10 min**	**82**

[a] Yields are of isolated pure products. [b] Calculated from the measured density of a 1:1 mixture of **1** and **2**. [c] No product discernible after 2 h. [d] The maximum effective concentration "on water" is assumed to be the same as that of the neat reaction.

Table 2: Reaction of quadricyclane (**1**) with dimethyl azodicarboxylate in various solvents.[a]

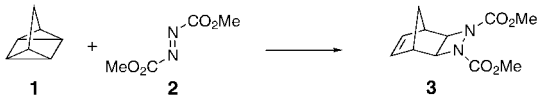

1 **2** **3**

Solvent	Conc. [M][b]	Time to completion
toluene	2	> 120 h
EtOAc	2	> 120 h
CH_3CN	2	84 h
CH_2Cl_2	2	72 h
DMSO	2	36 h
MeOH	2	18 h
neat	4.53	48 h
on D_2O	4.53	45 min
on C_6F_{14}	4.53	36 h
on H_2O	**4.53**	**10 min**
$MeOH/H_2O$ (3:1, homogeneous)	2	4 h
$MeOH/H_2O$ (1:1, heterogeneous)	4.53	10 min
$MeOH/H_2O$ (1:3, heterogeneous)	4.53	10 min

[a] Compound **3** was the only product observed in each case. [b] Concentrations of the neat and heterogeneous reactions are calculated from the measured density of a 1:1 mixture of **1** and **2**. DMSO = dimethylsulfoxide.

Acceleration of reactions "on water" is evident even when a nonpolar solvent comprises a part or most of the organic phase as shown in Table 3. Thus, the reaction of quadricyclane (**1**) with diethyl azodicarboxylate (DEAD, **4**), carried out simply by stirring a toluene solution of DEAD with **1** "on water", proceeds at a considerably higher rate than when the reaction is carried out in toluene alone.

Table 3: Cycloaddition of quadricyclane (**1**) performed with DEAD (commercial reagent in toluene) "on water".[a]

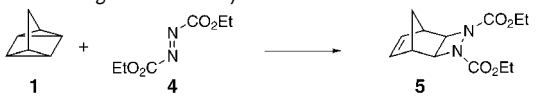

1 **4** **5**

t [h]	Conversion [%][b]	
	toluene[c]	**toluene on H_2O**[d]
3	4	**42**
6	8	**56**
17	18	**69**

[a] Isolated yield after 24 h at 23 °C: toluene, 24%; toluene "on water", 72%. [b] Determined by ^{1}H NMR spectroscopy using acetophenone as internal standard. [c] Commercial DEAD in toluene used (49%, 2.86 M). [d] As [c], except for the presence of an equal volume of water to toluene.

We have found that the high reactivity of azodicarboxylates "on water" is not limited to their cycloaddition reactions: the ene reactions of these compounds respond similarly to conditions of aqueous suspension relative to organic solution. Leblanc et al. have used the ene reaction of bis(trichloroethyl) azodicarboxylate (**7**) to achieve the allylic amination of olefins under thermal conditions.[13] In nonpolar solvents such as benzene, prolonged heating at 80 °C was reportedly required to attain useful levels of reactivity with simple olefins such as cyclohexene (**6**). In the absence of solvent, the reaction of liquid **6** and solid **7** was found to proceed at 50 °C, but still required 36 h for completion as well as the presence of excess cyclohexene. In contrast, the reaction performed "on water" was complete within eight hours at 50 °C and afforded the product in 91% yield (see Table 4). The neat reaction between **6** and **7** not only appeared to be slower, but the reaction mixture was also considerably harder to mix uniformly. In contrast, when heated to 50 °C "on water" the reaction mixture initially formed a molten organic phase, which gave way to the product as a white precipitate. In practical terms, reactions of solid components in aqueous suspension are more reproducible and convenient than in the absence of solvent, as water provides for efficient "mixing" of the reactants without the dilution cost of a true solvent. Furthermore, the effective melting point of solid reaction mixtures is noticeably lowered in the presence of water, such that a fused organic phase is often formed.

Table 4: Ene reaction of cyclohexene (**6**) with bis(trichloroethyl) azodicarboxylate (**7**) "on water".

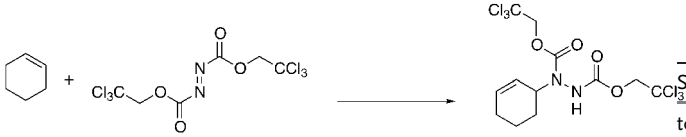

6 **7** **8**

Solvent	*T* [°C]	*t* [h]	Yield [%]
benzene	80	24	70[a]
neat	50	36[b]	62
on H_2O	**50**	**8**	**91**

[a] Data from Ref. [13]. [b] Additional **6** added after 24 h.

The notion of the special nature of water as a solvent for organic reactions began with examples of Diels–Alder reactions more than fifty years ago.[14] The first quantitative data were reported by Rideout and Breslow, who showed that Diels–Alder reactions between nonpolar compounds proceeded at much higher rates in water (dilute homogeneous solution) than in organic solvents.[15] Rate accelerations as high as 200-fold were noted in certain cases. Breslow et al. also noted the high *endo* selectivity of certain Diels–Alder reactions carried out in water, under both homogeneous and heterogeneous conditions.[16] Although rate acceleration and selectivity were ascribed primarily to hydrophobic effects, it has since been appreciated that hydrogen bonding plays an important role.[17] Ironically, much of the careful quantitative work on the process does not directly apply to synthetic chemistry, as the experiments reported by Breslow, Engberts, and others were conducted at low concentrations (mM or less) to maintain homogeneity in water, while preparative reactions usually require much higher concentrations. In a rare example of a heterogeneous process, Grieco et al. reported the Diels–Alder reaction of an acyclic diene bearing a carboxylic acid group to occur in aqueous suspension faster than in organic solution.[18] The best results were obtained in the reactions of diene carboxylate salts with various dienophiles in water, and the rate accelerations due to water were ascribed to micellar catalysis.[19] As some of these reactions were carried out under conditions similar to ours, we evaluated the effectiveness of the "on water" protocol for Diels–Alder reactions.

We performed the cycloaddition of the water-insoluble *trans*,*trans*-2,4-hexadienyl acetate (**9**) and *N*-propylmaleimide (**10**) under various conditions (Table 5). As before, a protic solvent (methanol) was better than nonprotic solvents, and

Table 5: Comparison of water versus organic solvents for a typical Diels–Alder reaction.

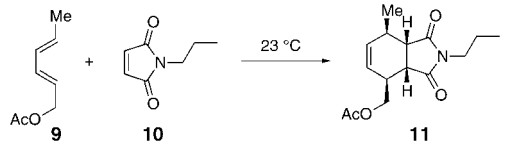

9 **10** **11**

Solvent	Conc. [M]	Time to completion [h]	Yield [%]
toluene	1	144	79
CH_3CN	1	>144	43[a]
MeOH	1	48	82
neat	3.69[b]	10	82
H_2O	**3.69**[b]	**8**	**81**

[a] Yield after chromatographic purification. Other yields are of crude products, which were >95% pure by ^{1}H NMR spectroscopy. [b] Calculated from the measured density of a 1:1 mixture of **9** and **10**.

the reaction in aqueous suspension showed substantial rate acceleration over homogeneous solution. Consistent with the results of Grieco et al.[18] and in contrast to the reaction of **1** + **2** described above, the neat Diels–Alder addition of **9** to **10** (both liquids) was approximately as fast as in water suspension.[20]

Claisen rearrangements are another significant class of reactions for which the accelerating effect of water is well-recognized.[21] The initial discovery appears to have been made during mechanistic studies of the chorismate–prephenate rearrangement, a key step in the biosynthesis of shikimic acid.[22] Brandes, Grieco, and Gajewski then performed a kinetic study on the rearrangement of an allyl vinyl ether substrate with an attached carboxylate functionality.[23] The rate of rearrangement of the carboxylate salt in water was found to be about two orders of magnitude higher than that of the methyl ester in nonpolar solvents.[24] These findings were exploited further by Grieco et al., who used the accelerating influence of water to promote difficult rearrangements.[25]

In contrast to the aliphatic Claisen rearrangements, the effect of water on the analogous aromatic Claisen rearrangement is little known.[26] We have made preliminary measurements on naphthyl ether **12**, which undergoes rearrangement at an appreciable rate even at room temperature. Table 6

Table 6: Comparison of solvents for an aromatic Claisen rearrangement (0.28–0.46 M), performed at room temperature.[a]

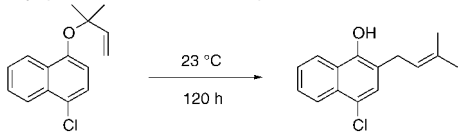

12 **13** (m.p.: 54–56 °C)

Solvent	Yield [%][b]
toluene	16
DMF	21
CH_3CN	27
MeOH	56[c]
neat	73
on H_2O	**100**

[a] Conversion was monitored by ^{1}H NMR analysis of aliquots. [b] Except in the case of MeOH, no other products were detected by ^{1}H NMR spectroscopy. [c] 14% of 4-chloro-1-naphthol was also observed.

shows the effect of various solvents on this process. After five days at 23 °C, the sample of **12** in aqueous suspension had completely rearranged to **13**, while the rearrangement was considerably slower in organic solvents. The neat reaction was again closest in rate to water and required one further day to reach completion. As with Diels–Alder reactions, the "on water" protocol provides the best set of conditions in terms of efficiency, convenience, and safety, even when rate accelerations are not large.

Non-pericyclic reactions such as the opening of epoxides and aziridines with heteroatom nucleophiles also derive unique benefits from the "on water" environment. Hydrogen bonding is crucial for the activation of such electrophiles, making these ring-opening processes autocatalytic and difficult to control under neat conditions. Instead, protic solvents such as alcohols and especially alcohol/water mixtures provide good homogeneous media for these transformations.[4] Here too, we find that water alone is the medium of choice. The reactions are completed in shorter times than in other protic solvents, and the pure product often precipitates, to be isolated by simple filtration.

The reaction of cyclohexadiene monoepoxide (**14**) with *N*-(3-chlorophenyl)piperazine (**15**) is illustrative (Table 7).

Table 7: Application of the "on water" method to the nucleophilic opening of an epoxide.

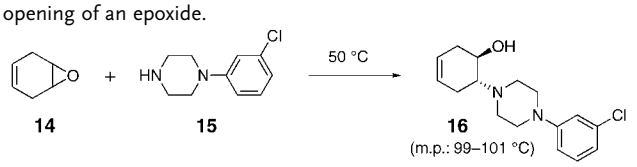

14 **15** **16** (m.p.: 99–101 °C)

Solvent	Conc. [M]	*t* [h]	Yield [%]
toluene	1	120	< 10[a]
neat	3.88[b]	72	76
EtOH	1	60	89
on H_2O	**3.88[b]**	**12**	**88**

[a] Determined by ^{1}H NMR spectroscopic analysis of the crude reaction mixture. [b] Calculated from the measured density of a 1:1 mixture of **14** and **15**.

When heated at 50 °C, the reaction "on water" was completed overnight, while the reactions in solution in ethanol or without solvent required approximately three days to reach completion. In toluene, less than 10% conversion occurred after five days at the same temperature. Thus, taking into account the concentrations of the reagents, the rates of reactions "on water" and in ethanol appeared to be approximately the same, and greater than that for the reaction performed in the absence of solvent.

Thus, a variety of reactions can be efficiently carried out in aqueous suspension, with the most dramatic effects observed for the addition of azodicarboxylates to unsaturated hydrocarbons. To the best of our knowledge, these examples represent some of the largest rate accelerations due to water observed under preparative conditions, that is, at molar concentrations. A central theme in the field of aqueous organic chemistry has been the need to promote solubility in these reactions. Clearly, solubility is not essential.

Although the reactivity phenomenon described here has immediate practical implications, its origins are presently unclear; nevertheless, a few preliminary remarks are in order. For example, it is possible that reactions "on water" actually proceed through small amounts of dissolved solutes. Rate acceleration in homogeneous aqueous solution has been attributed to a variety of effects such as hydrophobic aggregation,[2,15] cohesive energy density,[27] or ground-state destabilization.[28,29] Breslow et al. have invoked solution-phase hydrophobic effects to explain the high *endo* selectivity of certain Diels–Alder reactions in aqueous suspension and solution.[2a,16] Engberts and co-workers made a fundamental point by providing evidence that, in cycloaddition reactions, hydrophobic destabilization will have a considerably greater

impact on the ground state than on the transition state.[29,30] The importance of hydrogen bonding in the acceleration of Diels–Alder reactions in aqueous solution is supported by both experimental[31] and theoretical[32] studies.

However, it seems that many of the reactions described above are simply too fast for the acceleration to be solely due to solution-phase phenomena. In this regard, the observed requirement for heterogeneity and the finding that the rates of reactions "on water" often exceed those of the same reactions performed in the absence of solvent demand attention. Perhaps the unique properties of molecules at the macroscopic phase boundary between water and insoluble hydrophobic oils play a role.[33] The same principles that contribute to solution-phase effects may be amplified at such phase boundaries, but other factors, such as the redistribution of surface species driven by surface-tension energetics,[34] may also be relevant. We plan to keep exploring the "on water" phenomenon both for practical applications and mechanistic understanding.

Received: December 10, 2004
Published online: April 21, 2005

Keywords: click chemistry · cycloaddition · interfaces · rearrangement · water chemistry

[1] a) *Organic Synthesis in Water* (Ed.: P. A. Grieco), Blackie, London, **1998**; b) C.-J. Li, *Chem. Rev.* **1993**, *93*, 2023; c) U. M. Lindstrom, *Chem. Rev.* **2002**, *102*, 2751.
[2] a) R. Breslow, *Acc. Chem. Res.* **1991**, *24*, 159; b) *"Structure and Reactivity in Aqueous Solution"*, R. Breslow, *ACS Symp. Ser.* **1994**, *568*, 291.
[3] J. J. Gajewski, *Acc. Chem. Res.* **1997**, *30*, 219.
[4] H. C. Kolb, M. G. Finn, K. B. Sharpless, *Angew. Chem.* **2001**, *113*, 2056; *Angew. Chem. Int. Ed.* **2001**, *40*, 2004.
[5] V. V. Fokin, K. B. Sharpless, *Angew. Chem.* **2001**, *113*, 3563; *Angew. Chem. Int. Ed.* **2001**, *40*, 3455.
[6] Z. M. Wang, K. B. Sharpless, *J. Org. Chem.* **1994**, *59*, 8302; Z. P. Demko, K. B. Sharpless, *J. Org. Chem.* **2001**, *66*, 7945.
[7] At 4.18 $J\,cm^{-3}\,K$, water has an unusually high heat capacity for a liquid; see: *NIST Chemistry WebBook* (Eds.: P. J. Linstrom, W. G. Mallard), NIST Standard Reference Database Number 69, March 2003, National Institute of Standards and Technology, Gaithersburg MD, 20899 (http://webbook.nist.gov).
[8] N. Rieber, J. Alberts, J. A. Lipsky, D. M. Lemal, *J. Am. Chem. Soc.* **1969**, *91*, 5668.
[9] R. Platz, W. Fuchs, N. Rieber, U.-R. Samuel, J. Jung (BASF AG), DE 2615878, **1977** [*Chem. Abstr.* **1978**, *88*, 37803].
[10] The amount of water used can be chosen to best balance/control the exothermicity of the reaction, as the resulting increase in total reaction volume does not constitute dilution of the reaction zone.
[11] For an example of solvent effect on the cycloaddition of quadricyclane with azodicarbonyl compounds, see: M. E. Landis, J. C. Mitchell, *J. Org. Chem.* **1979**, *44*, 2288.
[12] A. Rodgman, G. F. Wright, *J. Org. Chem.* **1953**, *18*, 465. For the only reported example, to our knowledge, of the accelerating influence of water on the reactions of azodicarboxylates, see: L. E. Gast, E. W. Bell, H. M. Teeter, *J. Am. Oil Chem. Soc.* **1956**, *33*, 278.
[13] Y. Leblanc, R. Zamboni, M. A. Bernstein, *J. Org. Chem.* **1991**, *56*, 1971; For Lewis acid mediated ene reactions of azodicarboxylates at −60 °C, see: M. A. Brimble, C. H. Heathcock, *J. Org. Chem.* **1993**, *58*, 5261.
[14] R. B. Woodward, H. Baer, *J. Am. Chem. Soc.* **1948**, *70*, 1161; H. Hopff, C. W. Rautenstrauch, US 2262002, **1939** [*Chem. Abstr.* **1942**, *36*, 10469].
[15] D. C. Rideout, R. Breslow, *J. Am. Chem. Soc.* **1980**, *102*, 7816.
[16] R. Breslow, U. Maitra, D. Rideout, *Tetrahedron Lett.* **1983**, *24*, 1901.
[17] For an excellent recent review of the role of hydrophobic effects on reactivity, see: S. Otto, J. B. F. N. Engberts, *Org. Biomol. Chem.* **2003**, *1*, 2809.
[18] P. A. Grieco, P. Garner, Z. He, *Tetrahedron Lett.* **1983**, *24*, 1897.
[19] P. A. Grieco, K. Yoshida, P. Garner, *J. Org. Chem.* **1983**, *48*, 3137; However, see: R. Breslow, U. Maitra, *Tetrahedron Lett.* **1984**, *25*, 1239, and Ref. [28b].
[20] As both starting materials and the product are oils, the neat reaction is not prone to physical "mixing" issues, which can arise when one of the reactants is a solid. Even when mixing is not an issue, we have encountered a few cases where the reactions "on water" are two- to threefold faster than the corresponding neat reaction, although the example shown here is typical.
[21] J. J. Gajewski in *Organic Synthesis in Water* (Ed.: P. A. Grieco), Blackie, London, **1998**, p. 82.
[22] a) S. D. Copley, J. R. Knowles, *J. Am. Chem. Soc.* **1987**, *109*, 5008; b) R. M. Coates, B. D. Rogers, S. J. Hobbs, D. R. Peck, D. P. Curran, *J. Am. Chem. Soc.* **1987**, *109*, 1160; c) J. J. Gajewski, J. Jurayj, D. R. Kimbrough, M. E. Gande, B. Ganem, B. K. Carpenter, *J. Am. Chem. Soc.* **1987**, *109*, 1170; d) B. Ganem, *Angew. Chem.* **1996**, *108*, 1015; *Angew. Chem. Int. Ed. Engl.* **1996**, *35*, 937.
[23] E. Brandes, P. A. Grieco, J. J. Gajewski, *J. Org. Chem.* **1989**, *54*, 515.
[24] Grieco subsequently reported that the rearrangement of the same methyl ester in aqueous suspension was qualitatively comparable in rate and efficiency to that of the carboxylate salt in homogeneous solution. See Ref. [25].
[25] P. A. Grieco, E. B. Brandes, S. McCann, J. D. Clark, *J. Org. Chem.* **1989**, *54*, 5849.
[26] a) W. N. White, E. F. Wolfarth, *J. Org. Chem.* **1970**, *35*, 2196; b) J. An, L. Bagnell, T. Cablewski, C. R. Strauss, R. W. Trainor, *J. Org. Chem.* **1997**, *62*, 2505.
[27] a) G. Desimoni, G. Faita, P. P. Righetti, L. Toma, *Tetrahedron* **1990**, *46*, 7951; b) J. J. Gajewski, *J. Org. Chem.* **1992**, *57*, 5500; "*Structure and Reactivity in Aqueous Solution: Characterization of Chemical and Biological Systems*", J. J. Gajewski, N. L. Brichford, *ACS Symp. Ser.* **1994**, *568*, 229.
[28] a) W. Blokzijl, J. B. F. N. Engberts, *Angew. Chem.* **1993**, *105*, 1610; *Angew. Chem. Int. Ed. Engl.* **1993**, *32*, 1545; b) "*Structure and Reactivity in Aqueous Solution*", W. Blokzijl, J. B. F. N. Engberts, *ACS Symp. Ser.* **1994**, *568*, 303.
[29] A. Meijer, S. Otto, J. B. F. N. Engberts, *J. Org. Chem.* **1998**, *63*, 8989.
[30] W. Blokzijl, J. B. F. N. Engberts, *J. Am. Chem. Soc.* **1992**, *114*, 5440.
[31] a) S. Otto, W. Blokzijl, J. B. F. N. Engberts, *J. Org. Chem.* **1994**, *59*, 5372; b) G. K. van der Wel, J. W. Wijnen, J. B. F. N. Engberts, *J. Org. Chem.* **1996**, *61*, 9001.
[32] J. Chandrasekhar, S. Shariffskul, W. L. Jorgensen, *J. Phys. Chem. B* **2002**, *106*, 8078.
[33] a) R. U. Lemieux, *Acc. Chem. Res.* **1996**, *29*, 373; b) D. N. Shin, J. W. Wijnen, J. Engberts, A. Wakisaka, *J. Phys. Chem. B* **2001**, *105*, 6759; c) D. N. Shin, J. W. Wijnen, J. Engberts, A. Wakisaka, *J. Phys. Chem. B* **2002**, *106*, 6014; d) S. K. Pal, J. Peon, A. H. Zewail, *Proc. Natl. Acad. Sci. USA* **2002**, *99*, 1763; e) L. R. Pratt, A. Pohorille, *Chem. Rev.* **2002**, *102*, 2671.
[34] J. T. Koberstein, *J. Polym. Sci. Part B* **2004**, *42*, 2942.

Biomimetic Synthesis

Biomimetic Synthesis of Grossularines-1**

*Fumiko Y. Miyake, Kenichi Yakushijin, and David A. Horne**

Dedicated to Professor Peter B. Dervan on the occasion of his 60th birthday

Isolated in only small amounts from the Britannia marine tunicate *Dendrodoa grossularia* (Styelidae), grossularine-1 (**1**) represents one of the more structurally intriguing members of a relatively small but potent class of α-carboline metabolites that exhibit pronounced effects against solid human tumor cell lines.[1] The limited material available from nature as well as synthetic sources, however, have hampered further investigations in vivo. Closely related to **1** is *N,N*-didesmethylgrossularine-1 (**2**) (from the Chuuk Atoll tunicate *Polycarpa aurata*) whose structure was established by X-ray crystallographic analysis.[2]

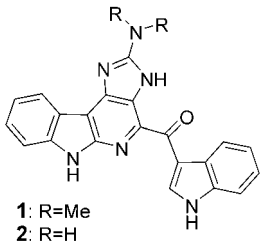

1: R=Me
2: R=H

In contrast to the well-known class of β-carboline-derived natural products, grossularines represent the first examples of naturally occurring α-carbolines. Despite the promising biological activity of **1**, only one total synthesis has been completed.[3] In the approach of Hibino and co-workers, the construction of the tetracyclic pyrido[2,3-*b*]indole ring system proceeded in a linear manner through the use of Pd-catalyzed cross-coupling reactions of halogenated indoles and metallated imidazoles. A formal synthesis of **1** has been reported by Molina et al.[4] that intersects the key intermediate reported by Hibino and co-workers. Herein we describe a remarkably concise biomimetic synthesis of **1** and **2** that is based on a novel oxidative dimerization–electrocyclization sequence of 2-amino-4-(3-indolyl)imidazoles **5** and **6** derived from oxotryptamine (**3**).

Oxotryptamine (**3**) continues to serve as an important cornerstone in indole heterocyclic construction. In previous work reported by our research group, a practical procedure for the preparation of **3** was developed that avoids the use of protecting groups and DDQ oxidation, and was applied to the synthesis of various bis-indole marine natural products.[5] In a formal sense, grossularine **1** and its didesmethyl congener **2** consist of two oxotryptamine units that are linked by an oxidative coupling between the two carbon centers of the amino-bearing termini. Although such a mode of dimerization is difficult to envisage with oxotryptamine per se, the use of an electron-rich aromatic surrogate based on 2-aminoimidazoles **5** and **6** seemed plausible, particularly in view of the oxidized analogue, 2-dimethylamino-5-(3-indolyl)imidazol-4-one (**4**).[6] This derivative was co-isolated with **1** from the same tunicate. The presence of this oxidized metabolite

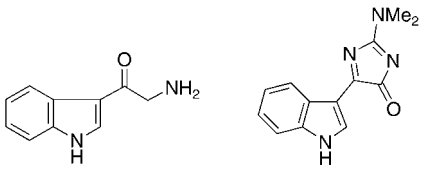

3 **4**

along with the fact that 2-aminoimidazoles are readily converted into imidazolones through oxidation [Eq. (1)],[7] suggests that 2-aminoimidazoles **5** and **6** could serve as potential biosynthetic forerunners.

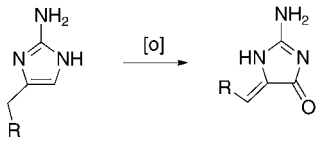

(1)

The synthesis begins with the preparation of 2-aminoimidazoles **5** and **6** by using the classical cyclocondensation of α-amino carbonyl compounds and cyanamide (Scheme 1).[8] Condensation of oxotryptamine (**3**) and dimethylcyanamide in the absence of air produced 2-dimethylamino-4-(3-indolyl)imidazole (**5**).[9,10] Attempts to purify **5** as the free base by flash chromatography were unsuccessful owing to its instability; however, **5** can be obtained in relatively pure form

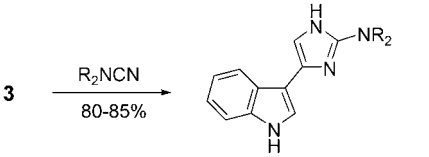

5: R=Me (as HCl salt)
6: R=H

Scheme 1. Preparation of 2-amino-4-(3-indolyl)imidazoles (**5**) and (**6**).

[*] F. Y. Miyake, Dr. K. Yakushijin, Dr. D. A. Horne
Department of Chemistry, Oregon State University
Corvallis, OR 97331 (USA)
Fax: (+1) 541-737-2062
E-mail: horned@onid.orst.edu

[**] Financial support from the National Institutes of Health (GM71985) and Chugai Pharmaceutical Co. is gratefully acknowledged. We thank Rodger Kohnert for assistance with NMR spectroscopic data acquisition and Jeff Morre of the Mass Spectrometry Facility of the Environmental Health Science Center (NIEHS P30 ES00210) at Oregon State University for recording mass data.

Supporting information for this article is available on the WWW under http://www.angewandte.org or from the author.

  DOI: 10.1002/anie.200500055

as the hydrochloride salt. On the other hand, 2-amino-4-(3-indolyl)imidazole (**6**), which lacks the dimethyl substituent, can be secured as the free base by the condensation of **3** with cyanamide followed by chromatographic purification over silica. These findings are consistent with observations made by Snyder and co-workers during their investigations of Diels–Alder reactions of 2-aminoimidazoles, in which greater thermal and air sensitivity of 2-dimethylaminoimidazole was observed.[11]

The instability of **5** normally would not be judged very significant on its own; however, further investigation was inspired by the fact that this 2-aminoimidazole derivative is quite sensitive to air and that an oxidative coupling event could, in principle, deliver conjoined indole units as a means to potentially access the α-carboline core. We were quite surprised to find that upon exposure of **5**·HCl to a methanol solution saturated with ammonia, α-carboline **8** was produced (Scheme 2).[12] During the course of the reaction, dimer **7** partially precipitated from solution after 1 day as a dark violet solid. Collection and resubjection of **7** to the reaction conditions afforded **8**. To explain these results, one mechanistic pathway might involve initial oxidative dimerization of **5** to yield dimer **7**. Upon standing in a methanol-saturated ammonia solution, **7** undergoes an electrocyclization–aromatization event via tautomer **7a**. Oxidation of the resulting intermediate **7b** to **7c** followed by facile aminolysis results in the loss of dimethylguanidine and the formation of α-carboline **8**. The sequence is remarkably efficient, delivering **8** directly in one pot and good overall yield from **5**. Aromatic imine **8** was found to be quite stable and required fairly rigorous hydrolysis conditions to yield grossularine-1 (**1**) as a yellow solid. All spectral data of synthetic **1** were in excellent agreement with data reported for the natural product.[1]

Similarly, treatment of **6** under analogous MeOH–NH_3 conditions produced fused pentacyclic dimer **9** as a dark violet to black solid (Scheme 3). Upon further standing in MeOH–NH_3, **9** underwent aminolysis to afford imine **10**. Hydrolysis of the imine functionality of **10** gave *N*,*N*-didesmethylgrossularine-1 (**2**). Alternatively, **2** can be obtained directly from the hydrolysis of **9**. All spectral data of synthetic **2** were in excellent agreement with those reported for the natural product.[2] In noting differences between dimethylaminoimidazole **5** and its didesmethylamino analogue **6**, the precyclized desmethylamino dimer corresponding to **7** was not obtained in the case of **6**. This outcome is attributed to the greater solubility of the putative desmethyl intermediate in methanolic ammonia. In the case of **5**, the *N*,*N*-dimethylamino analogue **7c** corresponding to **9** also was not obtained. The greater propensity toward aminolysis of this putative guanidinium ion intermediate explains this result.

Although electron-rich aromatic heterocycles such as indoles are known to undergo autoxidative coupling,[13] the oxidative dimerization of 2-aminoimidazoles under simple aerobic conditions is unprecedented. The structurally and biologically significant α-carboline natural products **1** and **2** were produced in excellent overall yields with an operationally simple, three-pot sequence starting from oxotryptamine. The chemistry and brevity of this novel sequence support a plausible biogenetic con-

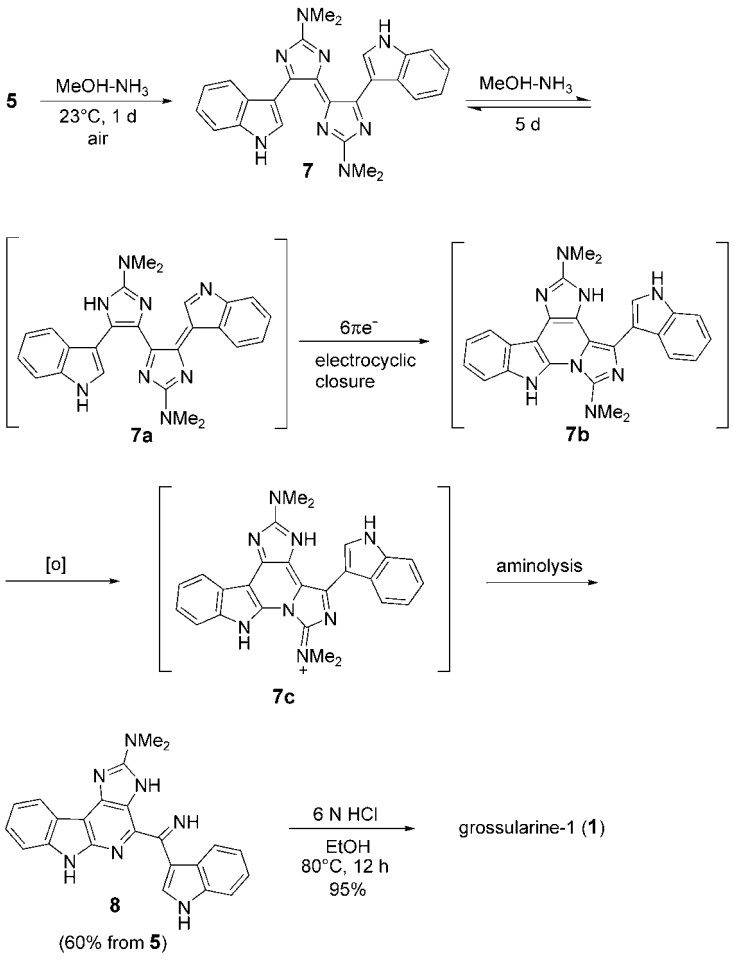

Scheme 2. Synthesis of grossularine-1 (**1**).

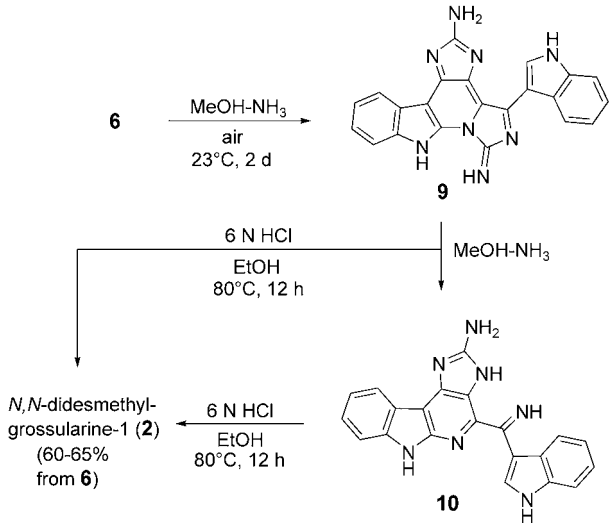

Scheme 3. Synthesis of *N*,*N*-didesmethylgrossularine-1 (**2**).

nection that explains these and several other structurally related members this α-carboline family.

Received: January 6, 2005
Published online: April 28, 2005

Keywords: alkaloids · biomimetic synthesis · dimerization · natural products · oxidation

[1] a) C. Moquin-Pattey, M. Guyot, *Tetrahedron* **1989**, *45*, 3445 – 3450; b) A. Loukaci, M. Guyot, *Magn. Reson. Chem.* **1996**, *34*, 143 – 145; c) N. Helbecque, C. Moquin, J.-L. Bernier, E. Morel, M Guyot, J.-P. Henichart, *Cancer Biochem. Biophys.* **1987**, *9*, 271 – 279.
[2] S. A. Abas, M. B. Hossain, D. van der Helm, F. J. Schmitz, M. Laney, R. Cabuslay, R. C. Schatzman, *J. Org. Chem.* **1996**, *61*, 2709 – 2712.
[3] T. Choshi, S. Yamada, E. Sugino, T. Kuwada, S. Hibino, *J. Org. Chem.* **1995**, *60*, 5899 – 5904.
[4] P. Molina, P. M. Fresneda, M. A. Sanz, C. Foces-Foces, M. C. R. de Arellano, *Tetrahedron* **1998**, *54*, 9623 – 9638.
[5] a) F. Y. Miyake, K. Yakushijin, D. A. Horne, *Org. Lett.* **2000**, *2*, 2121 – 2123; b) F. Y. Miyake, K. Yakushijin, D. A. Horne, *Org. Lett.* **2000**, *2*, 3185 – 3187; c) F. Y. Miyake, K. Yakushijin, D. A. Horne, *Org. Lett.* **2002**, *4*, 941 – 943.
[6] M. Guyot, M. Meyer, *Tetrahedron Lett.* **1986**, *27*, 2621 – 2622.
[7] a) A. Olofson, K. Yakushijin, D. A. Horne, *J. Org. Chem.* **1998**, *63*, 1248 – 1253; b) A. C. Barrios-Sosa, K. Yakushijin, D. A. Horne, *J. Org. Chem.* **2000**, *65*, 610 – 611; c) A. C. Barrios-Sosa, K. Yakushijin, D. A. Horne, *J. Org. Chem.* **2002**, *67*, 4498 – 4500.
[8] a) A. Lawson, *J. Chem. Soc.* **1956**, 307 – 310; b) G. C. Lancini, E. Lazzari, *J. Heterocycl. Chem.* **1966**, *3*, 152 – 166.
[9] In contrast to the more commonly observed 2-aminoimidazole unit found in nature, the *N,N*-dimethylaminoimidazole derivative has been less frequently encountered. For a five-step synthesis of *N,N*-dimethylaminoimidazole from benzyl isocyanate, see: A. Dalkafouki, J. Ardisson, N. Kunesch, L. Lacombe, J. E. Poisson, *Tetrahedron Lett.* **1991**, *32*, 5325 – 5328.
[10] Structural identity for all new compounds was established on the basis of ^{1}H and ^{13}C NMR spectra and HRMS analysis.
[11] B. R. Lahue, Z.-K. Wan, J. K. Snyder, *J. Org. Chem.* **2003**, *68*, 4345 – 4354.
[12] Autoxidation of **5**·HCl took place upon standing in a MeOH solution to yield 2-dimethylamino-5-(3-indolyl)imidazol-4-one (**4**) as a yellow solid which was identical, by comparison of ^{1}H and ^{13}C NMR spectral data, to natural and synthetic material reported in references [6] and [9], respectively.
[13] For an example of unsymmetrical dimer formation resulting from autoxidation of the indolic neurotoxin 5,6-dihydroxytryptamine, see S. Singh, J.-F. Jen, G. Dryhurst, *J. Org. Chem.* **1990**, *55*, 1484 – 1489.

Metallofullerenes

2D NMR Characterization of the La@C_{82} Anion**

Takahiro Tsuchiya, Takatsugu Wakahara, Yutaka Maeda, Takeshi Akasaka, Markus Waelchli, Tatsuhisa Kato, Hiroshi Okubo, Naomi Mizorogi, Kaoru Kobayashi, and Shigeru Nagase**

Endohedral metallofullerenes have attracted special interest as new spherical molecules, and intensive effort has been made to disclose their structures and electronic properties.[1] Although NMR spectroscopy is a powerful tool for elucidating the structure of a given compound,[2] its application to endohedral metallofullerenes such as La@C_{82} is very difficult because of their paramagnetic nature.[3,4] Recently, we reported the determination of the cage symmetry in paramagnetic metallofullerenes such as La@C_{82}-A(C_{2v}),[5] La@C_{82}-B(C_s),[6] Pr@C_{82}-A(C_{2v}),[7] and Ce@C_{82}-A(C_{2v})[8] by ^{13}C NMR measurements on their anionic forms [M@C_{82}]$^-$. However, it remains an important goal to verify the bond connectivity and assign the NMR lines, as this is essential for full characterization of the structures of endohedral metallofullerenes. We now report the first mapping of the bond connectivity in the carbon cage of [La@C_{82}-A]$^-$ and definitive assignment of the NMR lines by 2D INADEQUATE (incredible natural abundance double quantum transfer experiment) NMR measurements.[9–11] The bonding nature

[*] T. Tsuchiya, T. Wakahara, T. Akasaka
Center for Tsukuba Advanced Research Alliance
University of Tsukuba
Tsukuba, Ibaraki 305-8577 (Japan)
Fax: (+81) 29-853-6409
E-mail: akasaka@tara.tsukuba.ac.jp

N. Mizorogi, K. Kobayashi, S. Nagase
Institute for Molecular Science
Myodaiji, Okazaki 444-8585 (Japan)
E-mail: nagase@ims.ac.jp

Y. Maeda
Department of Chemistry, Tokyo Gakugei University
Koganei, Tokyo 184-8501 (Japan)

M. Waelchli
Bruker Biospin, Co. Ltd.
Tsukuba, Ibaraki 305-0051 (Japan)

T. Kato
Department of Chemistry, Josai University
Sakado, Saitama 350-0295 (Japan)

H. Okubo
Technical Development Department, Toyo Tanso Co. Ltd.
Kagawa, 769-1612 (Japan)

[**] This work was supported in part by a Grant-in-Aid, the 21st Century COE Program, Nanotechnology Support Project, and NAREGI Nanoscience Project from the Ministry of Education, Culture, Sports, Science, and Technology of Japan. This work was partly supported by a grant from the Kurata Memorial Hitachi Science and Technology Foundation.

Supporting information for this article is available on the WWW under http://www.angewandte.org or from the author.

  DOI: 10.1002/anie.200500039

of the carbon cage in $[La@C_{82}\text{-}A]^-$ was revealed from the carbon–carbon coupling constants $^1J_{CC}$. The position of La was also confirmed by measurements of relaxation time T_1.

Figure 1 shows the 2D INADEQUATE NMR spectrum of $[La@C_{82}\text{-}A]^-$. Two-bonded carbon atoms share a double

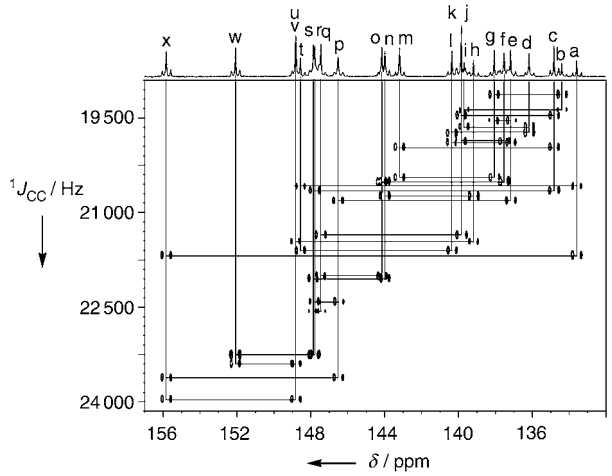

Figure 1. 2D INADEQUATE NMR spectrum of $[La@C_{82}\text{-}A]^-$.

quantum frequency in the vertical dimension, and each peak appears at the two respective chemical shifts in the horizontal dimension. To assign the 2D INADEQUATE NMR spectrum at an early stage, the ^{13}C NMR chemical shifts of $[La@C_{82}\text{-}A]^-$ were calculated at the B3LYP-GIAO/6-31G(d)//B3LYP/6-311+G(d) level. It was shown that the C atom designated no. 8 in Table 1 has the most upfield ^{13}C NMR signal. Therefore, we started the ^{13}C NMR assignment and bond

Table 1: Peak assignment and chemical shifts (δ) for the ^{13}C NMR spectrum of $[La@C_{82}]^-$.

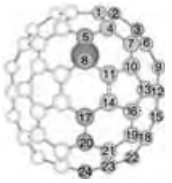

Carbon no.[a]	Signal no.[b]	δ [ppm]	Carbon no.[a]	Signal no.[b]	δ [ppm]
1	d	136.5	13	r	148.1
2	i[c]	140.0	14	u	149.1
3	b[c]	134.7	15	k	140.1
4	l	140.6	16	w	152.4
5	t[c]	148.9	17	v[c]	149.1
6	g	138.4	18	q	147.8
7	e	137.5	19	s	148.2
8	a[c]	133.9	20	h[c]	139.5
9	m	143.5	21	n	144.3
10	p	146.8	22	o	144.4
11	x	156.1	23	f	137.8
12	c	135.1	24	j[c]	140.1

[a] Carbon atoms are numbered in order of distance from La atom. The optimized structure of $[La@C_{82}\text{-}A]^-$ was obtained at the B3LYP/6-311+G(d) level. [b] Assigned in Figure 1. [c] Half-intensity peak.

connectivity from the most upfield signal a in Figure 1, that is, from carbon no. 8. As shown in Table 1, all C atoms in $[La@C_{82}\text{-}A]^-$ are completely assigned, as the first example for fullerenes apart from C_{60}, C_{70}, and their derivatives.

In the 2D INADEQUATE NMR spectrum, each peak is split into a doublet by the relevant carbon–carbon coupling constant $^1J_{CC}$. It is well known that $^1J_{CC}$ increases with shortening bond length and increasing π-bond order.[12] The 5,6 and 6,6 ring-fusion bonds of empty fullerenes such as C_{60} and C_{70} are considered to have single- and double-bond character, respectively.[13] Figure 2a plots the C–C bond

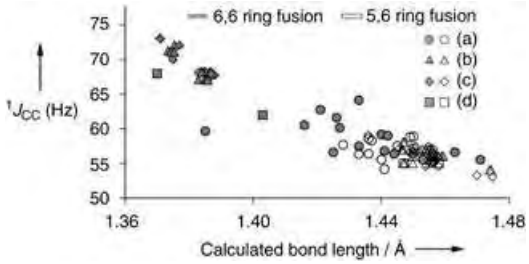

Figure 2. Plots of calculated carbon–carbon bond lengths [Å] vs $^1J_{CC}$ [Hz] for a) $[La@C_{82}\text{-}A]^-$, b) C_{60} *trans*-3 bis-adduct,[10b,c] c) C_{60} *trans*-4 bis-adduct,[10b,c] and d) C_{70}.[11b]

lengths calculated for $[La@C_{82}\text{-}A]^-$ at the B3LYP/6-311+G(d) level against the observed $^1J_{CC}$ values. To compare $[La@C_{82}\text{-}A]^-$ with empty fullerenes, the plots for *trans*-3 and *trans*-4 Bingel bis-adducts of C_{60}[10b,c] and pristine C_{70}[11b] are also shown in Figure 2b–d. For the empty fullerenes, the C–C bonds with larger $^1J_{CC}$ values and shorter calculated bonds correspond to the 6,6 ring-fusion bonds, and these plots do not overlap with those for the 5,6 ring-fusion bonds. However, the plots of 6,6 and 5,6 ring-fusion bonds for $[La@C_{82}\text{-}A]^-$ overlap with each other. In this context, it may be concluded that the 5,6 and 6,6 ring-fusion bonds in $[La@C_{82}\text{-}A]^-$ are shortened and elongated, respectively, and the classification of single- and double-bond character of $[La@C_{82}\text{-}A]^-$ is less clear than that of empty fullerenes. Shortening of the 5,6 ring-fusion bonds and the elongation of the 6,6 ring-fusion bonds were also calculated for $C_{82}(C_{2v})$ (Figure 3). However, the extent of shortening and elongation in $[La@C_{82}\text{-}A]^-$ is much larger than

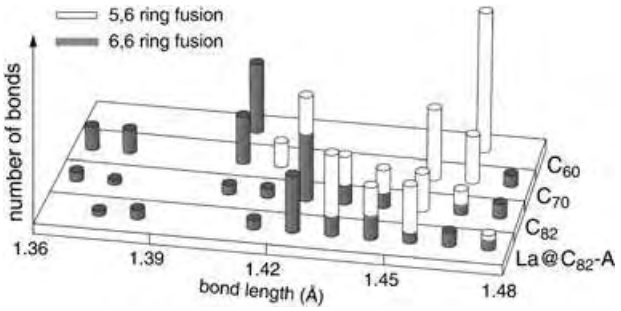

Figure 3. Histogram of 5,6 and 6,6 ring-fusion bond lengths calculated for C_{60}, C_{70}, $C_{82}(C_{2v})$, and La@C_{82}-A at the B3LYP/6-311+G(d) level.

that in pristine C_{82}, as a result of three-electron transfer from La to the LUMO and LUMO+1 of C_{82}, which have antibonding character.[4]

Important information about the position of La in $[La@C_{82}\text{-}A]^-$ is also obtainable from ^{13}C NMR measurements. Calculations on $[La@C_{82}\text{-}A]^-$ show that the C–C bonds in the vicinity of La are elongated (Figure 4) because of electron

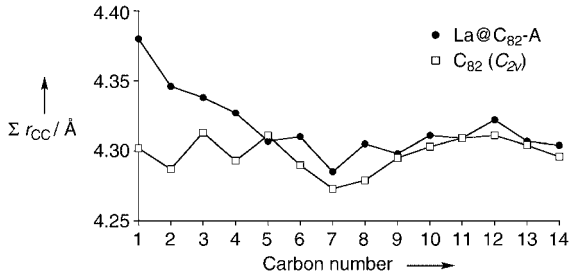

Figure 4. Plots of the sum of the calculated carbon–carbon distances to neighboring carbon atoms for $[La@C_{82}\text{-}A]^-$ and C_{82} (C_{2v}) at the B3LYP/6-311+G(d) level. Carbon atoms are numbered in order of distance from La atom, as shown in Table 1.

transfer from La to C_{82}.[4] It is known that the relaxation time T_1 governed by dipole–dipole relaxation is proportional to the sixth power of the internuclear distance.[14,15] It is noticeable that carbon no. 1 in Table 1, which is calculated to be the nearest to La in $[La@C_{82}\text{-}A]^-$, has the largest T_1 value and gives the largest value for the sum of the sixth power of the C–C bond lengths (see Supporting Information).[16] Thus, T_1 measurements support that La is located at the position predicted by calculations.[4,5]

In conclusion, the 2D INADEQUATE NMR spectrum of $[La@C_{82}\text{-}A]^-$ yields the bonding topology, coupling constants, and full assignment of the ^{13}C NMR spectrum. In other words, the 2D INADEQUATE NMR measurement can be used as an alternative method to X-ray crystallographic analysis for the structural characterization of endohedral metallofullerenes.

Experimental Section

A 13% ^{13}C-enriched $La@C_{82}$-A sample was prepared according to the reported procedure by using an arc vaporization method with a composite anode containing ^{13}C-enriched graphite and lanthanum oxide.[17] $[La@C_{82}\text{-}A]^-$ was prepared electrochemically as described before.[5] The 2D INADEQUATE NMR spectrum was measured in $[D_6]$acetone/CS_2 (1/1) at 125 MHz on a Bruker DRX 500 spectrometer with a CryoProbe system. All calculations were performed with Gaussian 03.[18]

Received: January 5, 2005
Published online: April 18, 2005

Keywords: fullerenes · lanthanum · metallofullerenes · NMR spectroscopy · structure elucidation

[1] For recent reviews, see *Endofullerenes: A New Family of Carbon Clusters* (Eds.: T. Akasaka, S. Nagase), Kluwer, Dordrecht, **2002**.
[2] a) J. E. Peralta, V. Barone, G. E. Scuseria, R. H. Contreras, *J. Am. Chem. Soc.* **2004**, *126*, 7428; b) T. Kodama, R. Fujii, Y. Miyake, K. Sakaguchi, H. Nishikawa, I. Ikemoto, K. Kikuchi, Y. Achiba, *Chem. Phys. Lett.* **2003**, *377*, 197.
[3] Y. Chai, T. Guo, C. Jin, R. E. Haufler, L. P. F. Chibante, J. Fure, L. Wang, J. M. Alford, R. E. Smalley, *J. Phys. Chem.* **1991**, *95*, 7564.
[4] K. Kobayashi, S. Nagase, *Chem. Phys. Lett.* **1998**, *282*, 325.
[5] T. Akasaka, T. Wakahara, S. Nagase, K. Kobayashi, M. Waelchli, K. Yamamoto, M. Kondo, S. Shirakura, S. Okubo, Y. Maeda, T. Kato, M. Kako, Y. Nakadaira, R. Nagahata, X. Gao, E. Van Caemelbecke, K. M. Kadish, *J. Am. Chem. Soc.* **2000**, *122*, 9316.
[6] T. Akasaka, T. Wakahara, S. Nagase, K. Kobayashi, M. Waelchli, K. Yamamoto, M. Kondo, S. Shirakura, Y. Maeda, T. Kato, M. Kako, Y. Nakadaira, X. Gao, E. Van Caemelbecke, K. M. Kadish *J. Phys. Chem. B* **2001**, *105*, 2971.
[7] T. Wakahara, S. Okubo, M. Kondo, Y. Maeda, T. Akasaka, M. Waelchli, M. Kako, K. Kobayashi, S. Nagase, T. Kato, K. Yamamoto, X. Gao, E. V. Caemelbecke, K. M. Kadish, *Chem. Phys. Lett.* **2002**, *360*, 235.
[8] T. Wakahara, J. Kobayashi, M. Yamada, Y. Maeda, T. Tsuchiya, M. Okamura, T. Akasaka, M. Waelchli, K. Kobayashi, S. Nagase, T. Kato, M. Kako, K. Yamamoto, K. M. Kadish, *J. Am. Chem. Soc.* **2004**, *126*, 4483.
[9] A. Bax, R. Freeman, S. P. Kempsell, *J. Am. Chem. Soc.* **1980**, *102*, 4851.
[10] a) M. S. Meier, H. P. Spielmann, R. G. Bergosh, R. C. Haddon, *J. Am. Chem. Soc.* **2002**, *124*, 8090; b) G. A. Burley, P. A. Keller, S. G. Pyne, G. E. Ball, *J. Org. Chem.* **2002**, *67*, 8316; c) G. A. Burley, P. A. Keller, S. G. Pyne, G. E. Ball, *Chem. Commun.* **2000**, 1717; d) W. T. Ford, T. Nishioka, F. Qiu, F. D'Souza, J.-P. Choi, *J. Org. Chem.* **2000**, *65*, 5780; e) T. Akasaka, Y. Maeda, T. Wakahara, T. Mizushima, W. Ando, M. Waelchli, T. Suzuki, K. Kobayashi, S. Nagase, M. Kako, Y. Nakadaira, M. Fujitsuka, O. Ito, Y. Sasaki, K. Yamamoto, T. Erata, *Org. Lett.* **2000**, *2*, 2671; f) J. M. Hawkins, S. Loren, A. Meyer, R. Nunlist, *J. Am. Chem. Soc.* **1991**, *113*, 7770.
[11] a) T. Sternfeld, R. E. Hoffman, I. Aprahamian, M. Rabinovitz, *Angew. Chem.* **2001**, *113*, 469; *Angew. Chem. Int. Ed.* **2001**, *40*, 455; b) R. D. Johnson, G. Meijer, J. R. Salem, D. S. Bethune, *J. Am. Chem. Soc.* **1991**, *113*, 3619.
[12] a) S. Berger, *Org. Magn. Reson.* **1984**, *22*, 47; b) C. J. Unker, R. E. London, T. W. Waley, G. H. Daub, *J. Am. Chem. Soc.* **1983**, *105*, 733; c) P. E. Hansen, *Org. Magn. Reson.* **1979**, *12*, 109.
[13] A. Hirsch, *Top. Curr. Chem.* **1999**, *199*, 1.
[14] To disclose the position of La in $[La@C_{82}\text{-}A]^-$, ^{139}La–^{13}C NOE measurements were performed. However, no NOE was observed between them. This may be due to the very fast relaxation of La.
[15] G. C. Levy, D. J. Kerwood in *Encyclopedia of Nuclear Magnetic Resonance*, *Vol. 2* (Eds.: D. M. Grant, R. K. Harris), Wiley, New York, **1996**, pp. 1147–1157.
[16] Spin-rotation relaxation is known to be in inverse proportion to temperature.[15] The T_1 values of each C atom for $[La@C_{82}\text{-}A]^-$ increase with increasing temperature (see Supporting Information). This result rules out spin-rotation relaxation.
[17] K. Yamamoto, H. Funasaka, T. Takahashi, T. Akasaka, T. Suzuki, Y. Maruyama, *J. Phys. Chem.* **1994**, *98*, 12831.
[18] Gaussian 03 (Revision C.01), M. J. Frisch, G. W. Trucks, H. B. Schlegel, G. E. Scuseria, M. A. Robb, J. R. Cheeseman, J. A. Montgomery, Jr., T. Vreven, K. N. Kudin, J. C. Burant, J. M. Millam, S. S. Iyengar, J. Tomasi, V. Barone, B. Mennucci, M. Cossi, G. Scalmani, N. Rega, G. A. Petersson, H. Nakatsuji, M.

Hada, M. Ehara, K. Toyota, R. Fukuda, J. Hasegawa, M. Ishida, T. Nakajima, Y. Honda, O. Kitao, H. Nakai, M. Klene, X. Li, J. E. Knox, H. P. Hratchian, J. B. Cross, C. Adamo, J. Jaramillo, R. Gomperts, R. E. Stratmann, O. Yazyev, A. J. Austin, R. Cammi, C. Pomelli, J. W. Ochterski, P. Y. Ayala, K. Morokuma, G. A. Voth, P. Salvador, J. J. Dannenberg, V. G. Zakrzewski, S. Dapprich, A. D. Daniels, M. C. Strain, O. Farkas, D. K. Malick, A. D. Rabuck, K. Raghavachari, J. B. Foresman, J. V. Ortiz, Q. Cui, A. G. Baboul, S. Clifford, J. Cioslowski, B. B. Stefanov, G. Liu, A. Liashenko, P. Piskorz, I. Komaromi, R. L. Martin, D. J. Fox, T. Keith, M. A. Al-Laham, C. Y. Peng, A. Nanayakkara, M. Challacombe, P. M. W. Gill, B. Johnson, W. Chen, M. W. Wong, C. Gonzalez, J. A. Pople, Gaussian, Inc., Pittsburgh, PA, **2004**.

Reactive Intermediates

Evidence for Carbon–Carbon Meisenheimer–Wheland Complexes between Superelectrophilic and Supernucleophilic Carbon Reagents**

Carla Boga, Erminia Del Vecchio, Luciano Forlani, Andrea Mazzanti, and Paolo E. Todesco*

The observation, or the isolation (when it is possible), of intermediates in nucleophilic aromatic substitution[1a] (S_NAr; the so-called Meisenheimer complexes M) and in electrophilic aromatic substitution[1b,c] (the so-called Wheland complexes W) reactions is an important confirmation of the proposed mechanisms. Our interest has, in the past, focused on intermediates in the S_NAr reaction[2] and, more recently, also on electrophilic aromatic substitution reactions[3] (Wheland intermediates). Both kinds of σ complexes (M and W) have appreciable stability when a number of strong electron-withdrawing groups or electron-donating groups, respectively, are present on the aromatic ring. 4,6-Dinitrobenzofuroxan (DNBF) is a powerful carbon electrophilic reagent[4] and 1,3,5-tris(*N*,*N*-dialkylamino)benzenes are powerful carbon nucleophilic reagents.[5] Herein, we report that these couples act as superelectrophilic[6,7] and supernucleophilic reagents, thus providing evidence of a carbon–carbon coupling reaction with formation of Meisenheimer–Wheland zwitterionic complexes. This kind of adduct was, up until now, only proposed,[7] but not observed experimentally.

Addition of solutions of 1,3,5-tris(*N*-piperidyl)benzene (**1**), 1,3,5-tris(*N*-morpholinyl)benzene (**2**), or 1,3,5-tris(*N*-pyrrolidinyl)benzene (**3**) in CD_2Cl_2 to a solution of DNBF in CD_2Cl_2 at −70 °C in an NMR tube resulted in the signals of the starting materials in the ^1H NMR spectra disappearing and the appearance of new signals, which are ascribed to compounds **4**, **5**, and **6** (Scheme 1). Acidification of solutions of **4** in $[D_6]$DMSO by addition of DCl afforded a spectrum containing exclusively the signals of the starting materials, namely **1** (in a protonated form) and DNBF.

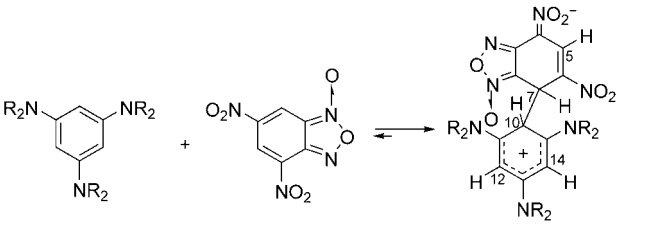

NR2 = *N*-piperidyl **1**
NR2 = *N*-morpholinyl **2**
NR2 = *N*-pyrrolidinyl **3**

DNBF

NR2 = *N*-piperidyl **4**
NR2 = *N*-morpholinyl **5**
NR2 = *N*-pyrrolidinyl **6**

Scheme 1. Reaction of 1,3,5-tris(*N*,*N*-dialkylamino)benzenes with 4,6-dinitrobenzofuroxan to produce carbon–carbon zwitterionic complexes.

Scheme 1 illustrates the observed reactions with formation of Wheland–Meisenheimer complexes **4**–**6**, whose structures are in agreement with the spectral data obtained at low temperature. Detailed analyses of the reaction products **4**–**6** by variable-temperature NMR spectroscopy revealed an unexpected behavior of these W–M compounds which deserves some special consideration. We describe herein the study carried out on compound **6** in detail; similar behavior was obtained with **4** and **5** (full spectral data for compounds **4**–**6** are shown in Tables 1 and 2).

The mixing of cooled (−70 °C) solutions of DNBF and 1,3,5-tris(*N*-pyrrolidinyl)benzene (**3**) in CD_2Cl_2 afforded a new product (**6**) immediately. The ^1H NMR spectrum of this solution (maintained at −70 °C) shows four separate signals in the range $\delta = 4.3$–5.1 ppm, three of which correspond to the three hydrogen atoms belonging to the tris(*N*-pyrrolidinyl)-benzene moiety and one ascribed to the furoxanic ring. The other hydrogen atom, which is hydrogen bonded to the furoxanic ring, was found at $\delta = 8.60$ ppm (Table 1).

Direct proton to carbon correlation (gHSQC sequence, Figure 1, left) obtained at −70 °C shows that two of the four hydrogen atoms which resonate at $\delta = 4.61$ and 4.43 ppm are connected to two carbon atoms at $\delta = 87.22$ and 88.28 ppm; these chemical shifts are in the range typical for sp^2-hybridized carbon atoms of 1,3,5-tris(*N*-pyrrolidinyl)benzene. In contrast, the two remaining proton signals ($\delta = 4.32$ and 5.00 ppm) are connected directly to carbon atoms resonating at $\delta = 45.09$ and 40.87 ppm, respectively, which is clear evidence for the sp^3 hybridization of these carbon atoms.

[*] Dr. C. Boga, Dr. E. Del Vecchio, Prof. Dr. L. Forlani, Dr. A. Mazzanti, Prof. Dr. P. E. Todesco
Dipartimento di Chimica Organica "A. Mangini"
Facolta' di Chimica Industriale
Universita' di Bologna
Viale Risorgimento, 4-40136 Bologna (Italy)
Fax: (+39) 051-209-3654
E-mail: forlani@ms.fci.unibo.it

[**] This work was supported by the University of Bologna (ex 60% MIUR and funds for selected research topics A.A. 2003–2004) and the Ministero dell'Università e della Ricerca Scientifica e Tecnologica.

Supporting information for this article is available on the WWW under http://www.angewandte.org or from the author.

 DOI: 10.1002/anie.200500238

Table 1: ^{1}H NMR spectral data in CD_2Cl_2.

Compound	T [°C]	δ_{H5}	δ_{H7}	δ_{H10}	δ_{H12}[a]	δ_{H14}[a]	δ_{NCH_2}	$\delta_{others\ CH_2}$
1	+25			6.00			3.00–3.10 (m, 12H)	1.60–1.70 (m, 12H), 1.46–1.56 (m, 6H)
2	+25			6.00			3.05–3.10 (m, 12H)	3.75–3.82 (m, 12H)
3	+25			5.18			3.19–3.27 (m, 12H)	1.88–1.98 (m, 12H)
DNBF	+25	9.11 (d, J = 1.9 Hz)	8.84 (d, J = 1.9 Hz)					
4	−70	8.77	4.97 (d, J = 4.7 Hz)	4.68 (d, J = 4.7 Hz)	5.26	5.11	2.70–4.25 (m, 12H)	1.30–1.95 (m, 18H)
4	+ 25	8.78	5.15	5.22[b]	5.22[b]	5.22[b]	3.28–3.52 (m, 12H)	1.60–1.80 (m, 18H)
5	−70	8.81	5.05 (d, J = 3.8 Hz)	4.66	5.16	5.30		2.85–4.25 (m, 24H)
5	−25	8.83	5.30	5.23[b]	5.23[b]	5.23[b]		3.10–4.00 (m, 24H)
6	−70	8.60	5.00 (d, J = 3.6 Hz)	4.32 (d, J = 3.6 Hz)	4.61	4.43	2.70–4.25 (m, 12H)	1.60–2.20 (m, 12H)
6	+25	8.67 (d, J = 0.9 Hz)	5.14	4.58[b]	4.58[b]	4.58[b]	3.15–3.60 (m, 12H)	1.80–2.15 (m, 12H)

[a] Interchangeable assignments. [b] Broad singlet.

Proton to proton correlation obtained at −70 °C (gCOSY sequence, Figure 1, right) shows that the signal at δ = 5.00 ppm is correlated with the furoxanic hydrogen atom at δ = 8.60 ppm and to one of the three tris(*N*-pyrrolidinyl)benzene hydrogen atoms at δ = 4.32 ppm (J = 3.6 Hz).

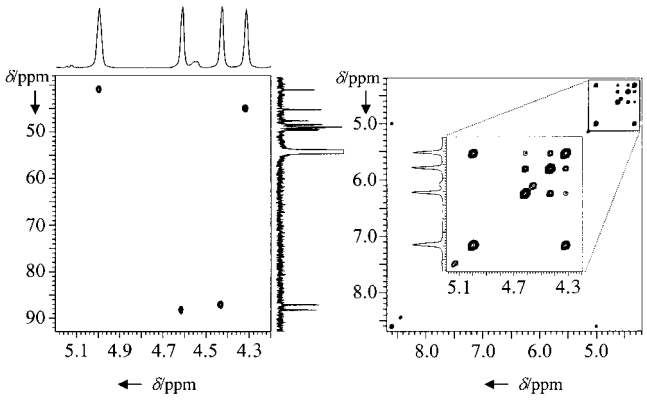

Figure 1. Left: gHSQC spectrum of compound **6** in CD_2Cl_2 at −70 °C. Right: gCOSY spectrum of compound **6** in CD_2Cl_2 at −70 °C.

All the mentioned NMR data, recorded at −70 °C, agree with a Wheland–Meisenheimer (W–M) structure that is produced in the reaction between DNBF and tris(*N*-pyrrolidinyl)benzene.[8]

In the Wheland–Meisenheimer structure (Scheme 1) C12 and C14 are sp^2 hybridized, while C10 and C7 are sp^3 hybridized, thus accounting for the two high-field ^{13}C NMR signals at δ = 45.09 and 40.87 ppm, respectively. The presence of two distinct hydrogen (and carbon) signals for the two other CH groups (C12 and C14) of the tris(*N*-pyrrolidinyl)-benzene can be easily explained because of the presence of an asymmetric carbon center (C7) and a "C_2 center" (C10);[9] under these conditions the two CH atoms are diastereotopic and thus appear as anisochronous signals in both the ^{1}H and ^{13}C NMR spectra. The same effect can be observed for the aromatic quaternary carbon atoms, which show three separated signals, and for the pyrrolidinic rings (six signals for the six α-nitrogen carbon atoms).

On raising the temperature, neither the ^{13}C nor ^{1}H NMR spectra change until −30 °C (−30 °C and −40 °C for **4** and **5**, respectively). Above −30 °C the three signals ascribed to the hydrogen atoms of the tris(*N*-pyrrolidinyl)benzene moiety show line broadening as a result of an exchange process. The signals coalesce at −1 °C and appear as a single signal at +20 °C (Figure 2). In contrast, the other signal (H7) always remains sharp.

It is worth noting that the dynamic process observed is reversible: warming the solution from −30 °C to room temperature and cooling again to −30 °C gives a spectrum that is identical to the starting one. Satisfactory line-shape simulation (Figure 2) was obtained using only one rate constant, which shows that $\Delta G^{\neq}$ is not constant with temperature and indicates that the $\Delta S^{\neq}$ value is not negligible. An accurate analysis by means of the Eyring equation[10] yields $\Delta H^{\neq} = 22.7 \pm 0.2$ kcal mol^{-1} and $\Delta S^{\neq} = 32 \pm 5$ e.u. for **6** ($\Delta H^{\neq} = 17.6 \pm 0.2$ kcal mol^{-1}, $\Delta S^{\neq} = 18 \pm 6$ e.u. for **4** and $\Delta H^{\neq} = 10.4 \pm 0.3$ kcal mol^{-1}, $\Delta S^{\neq} = 10 \pm 6$ e.u. for **5**).

The same dynamic process can also be observed in the ^{13}C NMR spectra: the coalescence of the three quaternary carbon atoms C11, C13, and C15 can be clearly seen above −30 °C, and they appear as a single line above −1 °C. However, the coalescence and the single averaged line cannot be observed for the three carbon atoms at δ = 87.22, 88.28, and 45.09 ppm because of the very large chemical shift difference between the signals (a line width of about 3 KHz is expected assuming $\Delta G^{\neq} \approx 13$ kcal mol^{-1} at room temperature). As in the proton spectra, the fourth signal, belonging to the C7 atom of the furoxanic ring, is always sharp irrespective of the temper-

Table 2: ^{13}C NMR spectral data in CD_2Cl_2.

Comp.	T [°C]	$\delta_{C4,C6,C8,C9}$[a]	δ_{C5}	δ_{C7}	δ_{C10}	$\delta_{C12,C14}$[a]	$\delta_{C11,C13,C15}$[a]	δ_{NCH_2}	$\delta_{NCH_2CH_2}$ and $NCH_2CH_2CH_2$
1	+25				99.32	99.32, 99.32	154.80	52.15	25.29, 26.94
2	+25				97.64	97.64, 97.64	154.06	50.72	67.69
3	+25				86.67	86.67, 86.67	150.67	48.46	26.12
DNBF	+25	116.65, 138.46, 145.19, 151.19	126.42	120.14					
4	−70	109.61, 113.43, 119.28, 150.43	135.47	41.99	39.47	88.24, 90.09	158.51, 159.85, 159.89	48.33, 48.76 49.08, 49.80(2 sig. ov.), 49.85	23.78, 24.22, 24.26, 24.56, 24.88, 26.15, 26.26, 26.51, 27.33
4	+25	110.92, 114.21, 120.00, 151.21	135.70	43.75			160.34	50.44	26.53, 24.72
5	−70	109.44, 113.44, 118.34, 150.33	135.51	42.94	39.17	89.52, 91.23	159.87, 160.27, 160.94	46.75, 47.36, 47.60, 47.90, 48.37, 48.71	65.00, 65.56, 66.12, 66.20, 66.56, 66.97
6	−70	109.36, 113.62, 119.16, 150.95	133.78	40.87	45.09	87.22, 88.28	154.91, 155.29, 157.94	47.54, 48.37, 48.86, 49.03, 49.37, 49.55	24.83, 24.97, 25.01, 25.43, 25.88, 26.17
6	+25	110.25, 114.54, 119.46, 151.79	134.60	42.28			157.86[b]	49.79	25.96

[a] Interchangeable assignments. [b] Broad signals.

ature, thus showing that the furoxanic anion is still present at room temperature.[11]

Hence, the dynamic NMR data suggest the existence, above the coalescence temperature, of a Wheland–Meisenheimer complex in three homomeric structures (Scheme 2) with bonds C7/C10, C7/C12, and C7/C14 rapidly exchanging. The positive value of $\Delta S^{\neq}$ also agrees with a mechanism in which a bond involved in the W–M complex is broken. It should be noted that the activation parameters obtained for **6** are quite different from those obtained for **4** and **5**. A possible explanation can be hypothesized by considering the different steric environments involved in the W–M complexes: although the steric effects of the six-membered rings are almost the same in **4** and **5**, the smaller and more flexible five-membered rings in **6** lead to a stabilization of the W–M structure and hence affords greater $\Delta H^{\neq}$ and $\Delta S^{\neq}$ values.

The existence of a π–π charge-transfer (CT) complex between DNBF and tris(amino)benzene derivatives could also occur, but experimental spectral data obtained for

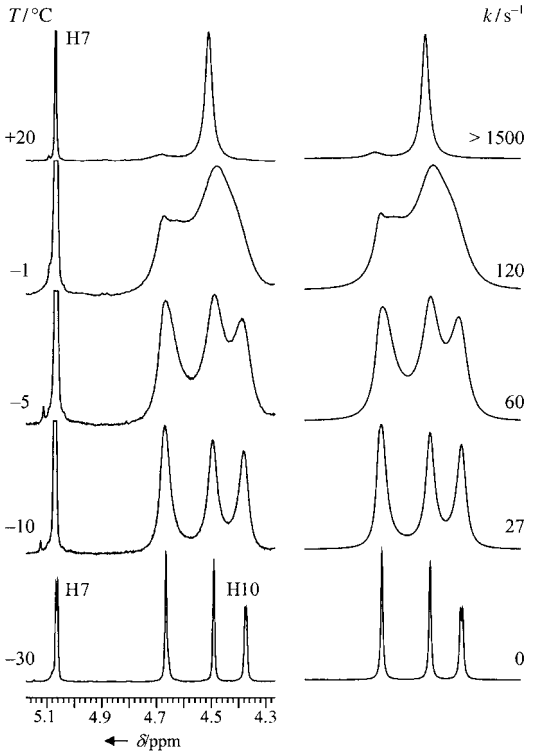

Figure 2. Left: experimental variable-temperature NMR spectra of **6**. Right: line-shape simulation obtained with the rate constant indicated. NR_2 = piperidyl, morpholinyl, pyrrolidinyl.

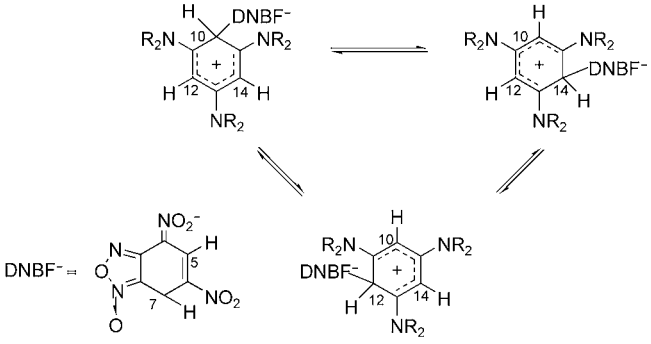

Scheme 2. Proposed interconversion pathway for the observed reversible and temperature-dependent transformation of W–M structures **4**–**6**.

compounds **4** and **6** clearly show (also at room temperature) the presence of sp^3 hybridization at the C7-position of the DNBF moiety (^{13}C NMR signal at $\delta = 40.87$ ppm). If such a CT complex existed, this carbon atom should revert back to sp^2 hybridization and hence a ^{13}C NMR signal at around $\delta =$ 90 ppm would be observed in the ^{13}C NMR spectrum at +25 °C.

In conclusion, the reaction between a superelectrophilic reagent such as DNBF and powerful carbon nucleophilic reagents such as 1,3,5-tris(*N*,*N*-dialkylamino)benzenes have given the possibility to characterize, for the first time, zwitterionic carbon–carbon Meisenheimer–Wheland complexes, whose structures were ascertained by one- and two-dimensional NMR experiments. A dynamic NMR study of these species also showed, through observation of coalescence, that increasing the temperature results in the formation of a Wheland–Meisenheimer complex in three homomeric structures with bonds C7/C10, C7/C12, and C7/C14 rapidly exchanging. Very strongly activated systems often give unexpected results, and this is the case here.

Experimental Section

Compounds **1** and **2** were prepared as reported in ref. [3]. Compound **3** was prepared in a similar manner from 1,3,5-trichlorobenzene and pyrrolidine. DNBF was prepared as reported in ref. [8]. NMR spectra were recorded on Varian Gemini 300, Mercury 400, or Inova 600 spectrometers operating at 300, 400, or 600 MHz (for ^1H NMR) or 75.46, 100.56, or 150.80 MHz (for ^{13}C NMR), respectively. Signal multiplicities were established by DEPT experiments. Chemical shifts were referenced to the solvent [($\delta = 5.30$ and 54.2 ppm for CD_2Cl_2), ($\delta = 7.27$ and 77.0 ppm for $CDCl_3$), ($\delta = 2.0$ and 0.3 ppm for CD_3CN), ($\delta = 2.6$ and 39.5 ppm for [D_6]DMSO) for ^1H and ^{13}C NMR, respectively]. The variable-temperature NMR spectra and 2D low-temperature spectra were recorded on the Inova 600 with a direct PFG Probe. The temperatures were calibrated by substituting the sample with a precision Cu/Ni thermocouple before the measurements. Complete fitting of dynamic NMR line shapes was carried out using a PC version of the DNMR-6 program.[12]

The low-temperature samples for NMR experiments were prepared directly in the NMR tube by mixing two cooled (−70 °C) solutions of DNBF (0.006 M) and **1**, **2**, or **3** (0.006 M) in CD_2Cl_2.

The behavior observed for compounds **4**–**6** on changing the temperature and the reversibility of the process was also observed in $CDCl_3$ solutions.

Mixing **1**, **2**, or **3** with DNBF in acetonitrile at low temperature (−30 °C) resulted in the precipitation of a coral-red solid. Heating the resulting solids, which were isolated by filtration, in a melting point apparatus resulted in them gradually darkening (133–140 °C, 118–125 °C, and 129–135 °C for compounds **4**–**6**, respectively) then decomposing. However, their ^1H and ^{13}C NMR spectra were identical to those obtained for compounds **4**–**6**, formed directly in an NMR tube and recorded at 25 °C.

Received: January 21, 2005
Published online: April 18, 2005

Keywords: carbanions · carbocations · electrophilic addition · nucleophilic addition · zwitterions

[1] a) M. B. Smith, J. March, *March's Advanced Organic Chemistry, Reactions, Mechanisms, and Structure*, 5th ed., Wiley, New York, **2001**, chap. 13, pp. 850–893, and references therein; b) M. B. Smith, J. March, *March's Advanced Organic Chemistry, Reactions, Mechanisms, and Structure*, 5th ed., Wiley, New York, **2001**, chap. 11, pp. 675–758, and references therein; c) D. Lenoir, *Angew. Chem.* **2003**, *115*, 880–883; *Angew. Chem. Int. Ed.* **2003**, *42*, 854–857.

[2] a) G. Collina, L. Forlani, *J. Phys. Org. Chem.* **1988**, *1*, 351–357; b) L. Forlani, A. Ferrara, A. Lugli, P. E. Todesco, *J. Chem. Soc. Perkin Trans. 2* **1994**, 1703–1707; c) C. Boga, L. Forlani, *J. Chem. Soc. Perkin Trans. 2* **1998**, 2155–2157.

[3] C. Boga, E. Del Vecchio, L. Forlani, *Eur. J. Org. Chem.* **2004**, 1567–1571.

[4] F. Terrier, *Nucleophilic Aromatic Displacement*, VCH, New York, **1991**.
[5] F. Effenberger, *Acc. Chem. Res.* **1989**, *22*, 27 – 35.
[6] a) F. Terrier, R. Goumont, M.-J. Pouet, J.-C. Hallé, *J. Chem. Soc. Perkin Trans. 2* **1995**, 1629 – 1637; b) E. Buncel, R. A. Renfrow, M. J. Strauss, *J. Org. Chem.* **1987**, *52*, 488 – 495.
[7] a) S. Kurbatov, P. Rodrigues-Dafonte, R. Gaumont, F. Terrier, *Chem. Commun.* **2003**, 2150 – 2151; b) G. A. Olah, *Angew. Chem.* **1993**, *105*, 805 – 827; *Angew. Chem. Int. Ed. Engl.* **1993**, *32*, 767 – 788.
[8] Recently, we studied the formation of σ complexes between nitrobenzofuroxans and amines and found that reaction of DNBF with 1,4-diazabicyclo[2.2.2]octane (DABCO) or piperidine affords Meisenheimer complexes which show ^{1}H NMR signals (in [D$_6$]DMSO) corresponding to protons bonded to the sp^3-hybridized C7 atom at $\delta = 6.8$ ppm and 6.2–6.4 ppm, respectively. When DNBF reacts with 1,8-diazabicyclo[5,4,0]undec-7-ene (DBU) the positive charge is delocalized over the two nitrogen atoms, and the ^{1}H NMR signal of the proton on the sp^3-hybridized C7 atom appears at $\delta = 5.3$ ppm, which is very similar to values reported here for **4**–**6**; see C. Boga, L. Forlani, *J. Chem. Soc. Perkin Trans. 2* **2001**, 1408 – 1413.
[9] a) W. B. Jennings, *Chem. Rev.* **1975**, *75*, 307 – 322; b) K. Mislow, M. Raban, *Top. Stereochem.* **1967**, *1*, 1 – 38.
[10] J. Sandström, *Dynamic NMR Spectroscopy*, Academic Press, London, **1982**, p. 99.
[11] This observation also excludes the hypothesis that the starting reagents could be involved in the transition state because, if this is true, an exchange between the H7 signal of the W–M complex and the H7 signal of DNBF should be observed.
[12] QCPE program no. 633, Indiana University, Bloomington, IN, USA.

Radicals

Infrared, UV/Vis, and W-band EPR Spectroscopic Characterization and Photochemistry of Triplet Mesitylphosphinidene**

Götz Bucher, Mark L. G. Borst, Andreas W. Ehlers, Koop Lammertsma, Stefano Ceola, Martina Huber, Dirk Grote, and Wolfram Sander*

Although many simple carbenes (R_2C)[1] and nitrenes (RN)[2–4] have been detected by various spectroscopic techniques, analogous phosphinidenes (RP) have not.[5–7] In sharp contrast to the abundant examples of transition-metal complexed phosphinidenes,[8–10] evidence of noncomplexed phosphinidines has remained elusive except for a recent matrix-IR study by Glatthaar and Maier[11] on H_3SiP, which was generated by the reaction of atomic silicon with phosphine, and an earlier electron paramagnetic resonance (EPR) study by Gaspar and co-workers[12] on mesitylphosphinidene (2,4,6-$Me_3C_6H_2P$; MesP; **3**), which was obtained by photolysis of *trans*-1-mesityl-2,3-dimethylphosphirane (**1**) in methylcyclohexane at $T = 77$ K (Scheme 1). No other direct experimental confirmation has been obtained for the existence of **3**.

Theoretical studies concur with the spectroscopic observation that a strongly preferred triplet ground state is predicted for aryl phosphinidene.[13,14] From the X-band

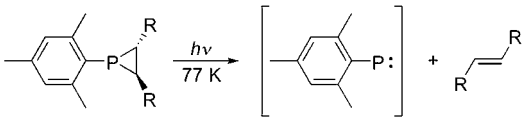

1 R = Me
2 R = H

3

Scheme 1. Photochemical formation of triplet MesP (**3**).

[*] M. L. G. Borst, Dr. A. W. Ehlers, Prof. Dr. K. Lammertsma
Department of Organic and Inorganic Chemistry
Faculty of Sciences
Vrije Universiteit
De Boelelaan 1083, 1081 HV Amsterdam (The Netherlands)
Fax: (+31) 20-598-7488
E-mail: k.lammertsma@few.vu.nl

Priv.-Doz. Dr. G. Bucher, D. Grote, Prof. Dr. W. Sander
Lehrstuhl für Organische Chemie II
Ruhr-Universität Bochum
Universitätsstr. 150, 44801 Bochum (Germany)

Dr. S. Ceola, Dr. M. Huber
Department of Molecular Physics
University of Leiden
Huygens Lab
2300 RA Leiden (The Netherlands)

[**] G.B. thanks K. Gomann for his help with the X-band EPR measurements, and the Dr. O. Röhm-Gedächtnisstiftung for financial support. This work was supported in part by the Council for Chemical Sciences of the Netherlands Organization for Scientific Research (M.B. and K.L.).

Supporting information for this article is available on the WWW under http://www.angewandte.org or from the author.

 DOI: 10.1002/anie.200462862

EPR spectrum, a zero-field-splitting (ZFS) parameter, D, of $|D/hc| = 3.521\ cm^{-1}$ was determined,[12] which is much larger than that for triplet phenylnitrenes ($\approx 1\ cm^{-1}$) and triplet phenylcarbenes ($\approx 0.5\ cm^{-1}$). The unusually large value of D was attributed to second-order spin–orbit contributions. Recent calculations on spin–orbit coupling in alkyl nitrenes, phosphinidenes, and arsinidenes yielded a D value of $|D/hc| = 3.46\ cm^{-1}$ for triplet methyl phosphinidene,[15] in line with the results of Gaspar and co-workers.[12] However, it should also be noted that on photolysis of more congested phosphiranes, Yoshifuji and co-workers[16] were unable to obtain an EPR signal in the reported region other than a weak signal at 5 K that was believed to be due to triplet oxygen.

We have investigated the photochemistry of **1** and **2** by using matrix-isolation spectroscopy and laser flash photolysis; herein we report EPR, infrared, and UV/Vis data that unequivocally support the formation of mesitylphosphinidene **3**.

Initially, using an X-band EPR spectrometer, we tried in vain to reproduce the EPR spectrum reported by Gaspar and co-workers.[12] Photolysis (248 nm, KrF-excimer, or 254 nm) of **2**, which was matrix-isolated in glassy methylcyclohexane ($T = 5$ K), resulted in the formation of yellow matrices but the corresponding spectra only showed strong doublet signals around $g = 2$ (g is the g factor) without EPR transitions attributable to triplet **3**. However, employing a W-band (95 GHz) EPR spectrometer, we detected a very weak signal exactly at the place predicted (4926 mT, Figure 1) for a triplet species with the ZFS parameters reported by Gaspar and co-workers; a background scan without sample showed no transitions in this spectral region.

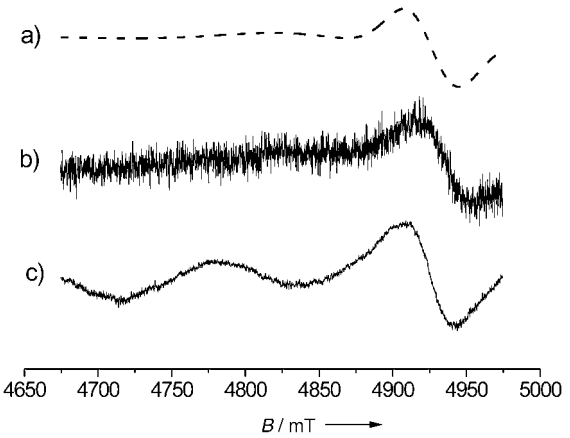

Figure 1. W-band EPR spectra of a sample of **2** in polycrystalline cyclohexane ($T = 5$ K), irradiated for 60 min with $\lambda = 254$ nm. a) Simulated spectrum. Simulation parameters: line width = 10 mT, $D = -3770.6$ mT ($|D/hc| = 3.521\ cm^{-1}$). b) Experimental spectrum obtained by sweeping the magnetic field from lower to higher values and c) from higher to lower values.

Monitoring by IR spectroscopy of the photolysis ($\lambda_{exc} =$ 254 nm, 48 h) of **1** or **2**, which were matrix-isolated in Ar at 10 K, showed slow disappearance of the phosphirane IR bands and formation of very weak new bands. Some of these bands are attributable to *trans*-2-butene (from **1**) or ethylene (from **2**), whose IR spectra were also recorded independently by matrix isolation of these alkenes. The remaining bands are assigned to triplet **3** based on a comparison with the IR spectrum calculated at the B3LYP/6-31G(d) level (Table 1).

Table 1: Calculated and experimental IR data of **3** (range 1700 to 500 cm^{-1}).

No.	$\tilde{\nu}_{calcd}$ [cm^{-1}]	$\tilde{\nu}_{calcd}$ (×0.97) [cm^{-1}]	Calcd intensity [km mol^{-1}]	$\tilde{\nu}_{exp.}$ [cm^{-1}]	Exp. intensity	Description[a]
46	1644.7	1595.0	50.2			8A
45	1575.9	1528.6	4.7	1532.4	vw	8B + τ *p*-CH_3
44	1527.6	1481.8	8.3	–	–	δ_{as} *o*-CH_3
43	1523.0	1477.3	33.0			δ_{as} *o*-CH_3
42	1516.5	1471.0	5.6	–	–	δ_{as} *p*-CH_3
41	1515.9	1470.4	9.3	–	–	δ_{as} *p*-CH_3
40	1512.6	1467.2	0.2	–	–	τ *o*-CH_3
39	1511.5	1466.2	15.9	1431.1	w	τ *o*-CH_3
38	1457.6	1413.9	1.6	1407.3	vw	19B + τ *p*-CH_3
37	1445.8	1402.4	3.1	1398.9	w	δ_s CH_3
36	1443.3	1400.0	1.4			δ_s CH_3
35	1443.3	1400.0	1.0	–	–	19A + δ_s CH_3
34	1439.2	1396.0	1.2	–	–	δ_s CH_3
33	1319.2	1279.6	1.6	1296.0	vw	14
32	1309.9	1270.6	9.4	1286.2	w	13
31	1271.5	1233.4	0.8	1237.8	vw	3
30	1206.5	1170.3	0.3	1170.5	vw	9A
29	1074.9	1042.7	2.2	–	-	17B + ρ CH_3
28	1070.8	1038.7	0.0	–	–	17A + ρ CH_3
27	1068.3	1036.3	5.0	1033.3	w	ρ CH_3
26	1065.3	1033.3	19.2			ρ CH_3
25	1059.7	1027.9	0.7	–	–	ρ CH_3
24	1041.9	1010.6	0.0	–	–	ρ CH_3
23	1026.8	996.0	1.9	993.0	vw	ρ CH_3
22	973.9	944.7	1.1	–	–	ρ CH_3
21	941.1	912.9	0.3	–	–	ρ CH_3
20	898.0	871.1	0.0	–	–	10A
19	874.0	847.8	12.5	849.8	m	5
18	725.5	703.7	0.9	709.7	w	4
17	630.5	611.6	4.8	625.8	w	6A
16	572.8	555.6	0.03	542.9	vw	12

[a] Descriptions are analogous to those of the vibrations of benzene as proposed by Pitzer and Scott.[17]

When the sample was subjected to further irradiation ($\lambda_{exc} = 385$–420 nm or $\lambda_{exc} > 455$ nm, 90 min), the IR bands associated with both triplet **3** and *trans*-2-butene or ethylene disappeared, while those of the starting materials **1** or **2** partially re-emerged, together with a new set of IR bands.[18a] The new photoproduct showed a broad IR band at $\tilde{\nu} = 2261.2\ cm^{-1}$, thus indicating the presence of a P–H bond. By comparison with a calculated IR spectrum (B3LYP/6-31G(d)), the product could be identified as 1*H*,2*H*-dihydrobenzophosphete **4** (Figure 2; see also the Supporting Information).[18b] Intramolecular C–H insertion of the phosphorus center of supermesitylphosphinidene (2,4,6-*t*$Bu_3(C_6H_2)$P; Mes*P) into the *ortho*-*t*Bu group to give a phosphaindane is common[6–7] and λ^5-benzophosphetes have been reported previously.[19] The new dihydro-λ^3-benzophosphete **4**, which is energetically favored over triplet **3**, may be formed similarly or via phosphaquinone methide **5** (Scheme 2).

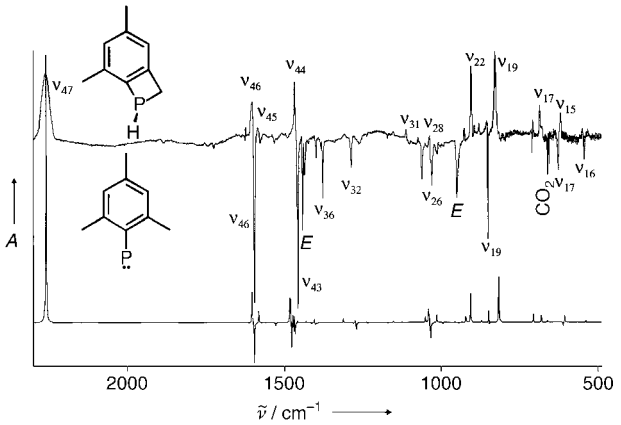

Figure 2. Top: Difference IR spectrum (Ar, 10 K) of the spectra obtained after photolysis of **2** at $\lambda_{exc} = 254$ nm (48 h) and subsequently at $\lambda_{exc} > 385$ nm (90 min). Bands pointing down disappear on photolysis at $\lambda_{exc} > 385$ nm and are attributed to a mixture of ethylene (E) and triplet **3**. The splitting of phosphinidene bands at $\tilde{\nu} = 1028.6$ and 1061.3 cm^{-1} (ν_{26}) is likely due to Fermi resonance.[18b] Several very weak bands remain unassigned. Bands pointing up are attributed to the secondary photoproduct **4** and traces of **2**. The highest intensity of the difference spectrum amounts to ca. 0.1. The assignment of a number of selected bands has been indicated by giving the transition numbers (see Tables 1 and S1). Bottom: calculated IR difference spectrum (0.97 × scaling, (U)B3LYP/6-31G(d)) of **4** minus triplet **3**.

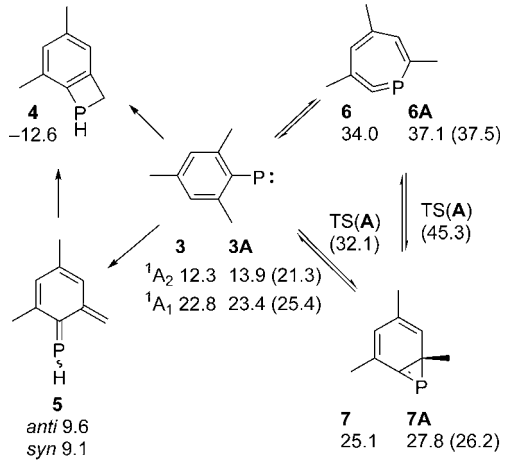

Scheme 2. B3LYP/6-31G(d) energies [kcal mol^{-1}] for the $C_9H_{11}P$ and unsubstituted C_6H_5P (**A**) isomers relative to triplet **3** and **3A**. CASPT2-(8/8)/6-31G(d) energies for **A** are given in parentheses.

The UV/Vis spectrum further supports the photochemical formation of **3** from matrix-isolated phosphiranes **1** (and **2**). Photolysis ($\lambda_{exc} = 254$ nm, 80 min, Ar, 10 K) gave rise to two new strong absorptions at $\lambda = 278$ and 292 nm, three weaker absorptions around 350, 370, and 390 nm, and a weak, broad absorption with fine structure between 420 and 470 nm. Subsequent long-wavelength photolysis ($\lambda_{exc} > 455$ nm) resulted in depletion of the absorptions at $\lambda = 278$, 292, 350, and > 420 nm, while those at $\lambda = 370$ and 390 nm initially increased in intensity (Figure 3). Extended near-UV photolysis ($\lambda_{exc} = 360$–400 nm, 2 h) resulted in bleaching of all absorptions with $\lambda > 300$ nm.

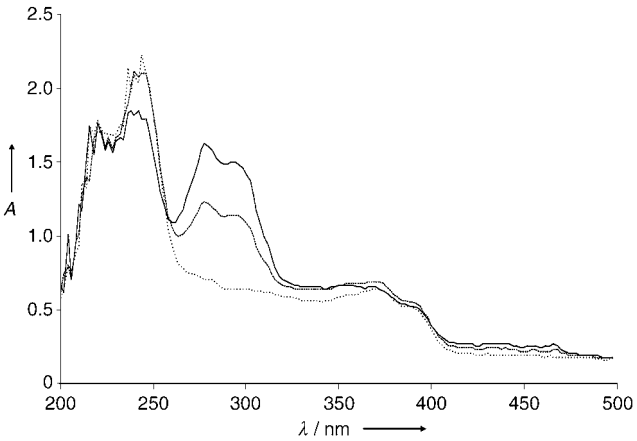

Figure 3. UV/Vis spectra (Ar, 10 K) obtained after photolysis of **1** after photolysis at $\lambda_{exc} = 254$ nm for 80 min (——), after subsequent photolysis at $\lambda_{exc} > 455$ nm for 10 min (-----), and after extended photolysis at $\lambda_{exc} > 455$ nm for 100 min (••••).

These observations are rationalized by assigning the absorptions $\lambda = 278$, 292, 350, and 420–470 nm to triplet mesitylphosphinidene **3**, and those at $\lambda = 370$ and 390 nm to a secondary photoproduct other than **4**. The UV/Vis spectrum of **3**, with a weak, structured broad band extending to $\lambda =$ 470 nm, strongly resembles the UV/Vis spectra of known triplet aryl nitrenes.[4a] The intense excitations at $\lambda = 285$, 310, 340, 415, and 440 nm calculated with time-dependent B3LYP/6-311 + G(d,p)[20] for triplet mesitylphosphinidene provide convincing evidence that triplet **3** is indeed formed upon photolysis of matrix-isolated mesitylphosphiranes **1** and **2**,[21] albeit in small yield.[22] The origin of the absorptions at 370 and 390 nm cannot be attributed to secondary photoproduct **4** because its calculated UV/Vis spectrum (TD-B3LYP/6-311 + G(d,p)) gives a longest-wavelength absorption at $\lambda_{max} =$ 255 nm. Among the compounds considered, the calculated spectrum of didehydrophosphepine **6** ($\lambda_{max} = 360$ and 385 nm) matches best the experimental data.[23,24] Formation of **6** from **3** may occur by ring enlargement, either directly,[25] or via bicyclic phosphirene **7**.[26] Borden and co-workers showed by using multiconfigurational second-order perturbation theory (CASPT2) that the ring expansion of singlet phenylphosphinidene **3A** to **6A** (via **7A**) is endothermic with sizeable barriers (Scheme 2);[27] our calculations at the B3LYP/6-31G(d) level give similar results, except for the state $^1A_2$ of the parent molecule.[28] The tentative assignment of didehydrophosphepine **6** as a minor photoproduct may appear surprising as it is the least-stable isomer of those considered, though bulky linear phospha-allenes are known.[29] However, steady-state irradiation under conditions of matrix-isolation spectroscopy frequently allows for the observation of processes that are thermodynamically unfavorable and whose outcome mostly depends on the concentration of photostationary equilibriums.

Finally, we explored the laser flash photolysis (LFP) of an argon-purged cyclohexane solution of **1** at ambient temperature with an excitation of 266 nm and nanosecond time resolution. The resulting transient spectrum (Figure 4) contained a single species with absorptions at $\lambda_{max} = 285$ nm (vs)

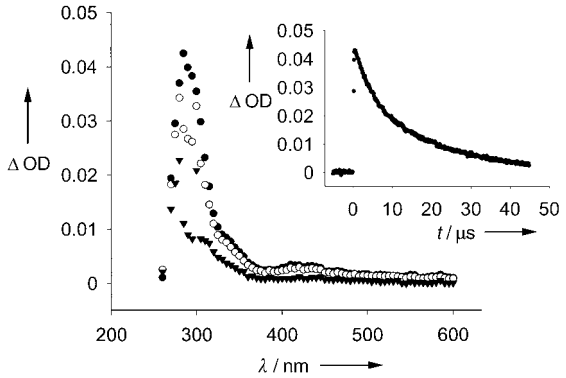

Figure 4. Transient spectra, recorded after LFP ($\lambda_{exc} = 266$ nm) of phosphirane **1** in cyclohexane under Ar atmosphere. Black circles: 470 ns after LFP, white circles: 1.7 μs after LFP, black triangles: 75 μs after LFP. Inset: transient trace, monitored at $\lambda = 285$ nm.

and 400–475 nm (broad, weak) and a lifetime $\tau = 13$ μs, which we assign to phosphinidene **3** based on the similarity with the UV/Vis spectrum of the matrix-isolated species at 10 K (Figure 3). The transient species could be quenched with oxygen,[30] and it reacted with the π-systems ethyl propiolate HC≡CCOOEt ($k_{ETP} = (7.7 \pm 1.1) \times 10^6$ L mol^{-1} s^{-1}) and tetramethylallene ($k_{TMA} = (5.0 \pm 0.8) \times 10^6$ L mol^{-1} s^{-1}, see the Supporting Information) but not with 1-hexene. This reactivity supports the formation of triplet **3**, which is expected to give an allylic triplet diradical with tetramethylallene, whereas such stabilization cannot occur with hexene as a reaction partner.

In conclusion, we have unequivocally identified triplet mesitylphosphinidene **3** as the primary reaction product in the photolytic cleavage of phosphiranes **1** and **2** by using a variety of low-temperature and time-resolved spectroscopic techniques. Under conditions of matrix isolation, **3** is formed in very low yield only, which is likely to be due to the efficient photoinduced addition of **3** to the alkene still present in the matrix cage. Upon further irradiation, **3** rearranges into 1*H*,2*H*-dihydrobenzophosphete **4**. Results obtained by using laser flash photolysis provide further support for the formation of **3**, and show that **3** will readily be quenched by reactive π-systems. Further studies on the photochemistry of **1**, **2**, and related compounds are in progress.

Experimental Section

The matrix isolation setup used in this work has been described before.[31] As light sources, a Hg low-pressure lamp ($\lambda = 254$ nm; Gräntzel, Germany) and Hg high-pressure lamps (Osram, 500 W, Oriel housing) in combination with cut-off filters were used. Argon (Messer-Griesheim, 99.999%) was used as the matrix material. Compounds **1** and **2** were synthesized according to reported procedures.[32] Deposition was performed by using the slow-spray-on technique at a sample temperature of 20 °C. *Trans*-2-butene (99%) was supplied by Matheson and deposited as 0.1%/99.9% mixture with Ar. X-band EPR-spectroscopic measurements were performed by using a Bruker Elexsys E500 EPR spectrometer with an ER077R magnet (75 mm pole cap distance) and an ER047 XG-T microwave bridge. Frozen solutions of **2** in methylcyclohexane were irradiated both within the resonator cavity ($T = 5$ K) by using a Lambda-Physik Compex 110 excimer laser operated with Kr/F_2 (248 nm, 200 mJ per pulse) or externally ($T = 77$ K) by using $\lambda = 254$ nm (Hg low-pressure lamp). W-band EPR-spectroscopic measurements employed a Bruker Elexsys E680 spectrometer. Prior to measurement, a degassed solution of **2** in cyclohexane was irradiated ($\lambda = 254$ nm, 60 min, $T = 77$ K) in a quartz capillary cooled to 77 K in a quartz dewar and transferred frozen into the precooled cryostat. Experimental parameters: frequency = 94.185061 GHz, microwave power = 15 dB, modulation amplitude = 0.1 mT, modulation frequency = 100 kHz. Simulations were performed by using the Easyspin routine[33] and all the parameters entering the simulation are given in the figure caption.

The setup used for laser flash photolysis has been described before.[34] Solutions (ca. 0.1 mM) of **1** in cyclohexane (Baker, spectroscopic grade) were purged with Ar for 20 min prior to the experiment. Tetramethylallene (Aldrich) and ethyl propiolate (Fluka) were of the highest purity commercially available and were used as received. 1-Hexene (Aldrich) was freshly distilled immediately prior to use.

All calculations were performed with Gaussian 98.[35] All geometry optimizations and frequency calculations (scaled by 0.97)[36] were performed at the (U)B3LYP/6-31G(d) level of theory. UV spectra were calculated using time-dependent density functional theory (TDDFT; B3LYP/6-311 + G(d,p)).

Received: December 9, 2004
Published online: April 21, 2005

Keywords: EPR spectroscopy · laser spectroscopy · matrix isolation · photolysis · radicals

[1] W. Sander, G. Bucher, S. Wierlacher, *Chem. Rev.* **1993**, *93*, 1583–1621.
[2] "Photochemical Reactivity of Azides": G. Bucher, *CRC Handbook of Photochemistry*, 2nd ed., CRC Press, Boca Raton, FL, **2003**, chap. 44.
[3] G. B. Schuster, M. S. Platz, in *Advances in Photochemistry, Vol. 17* (Eds.: D. H. Volman, G. Hammond, D. C. Neckers), Wiley, New York, **1992**, pp. 69–143.
[4] a) M. S. Platz, *Acc. Chem. Res.* **1995**, *28*, 487–492; b) M. S. Platz in *Reactive Intermediate Chemistry* (Eds.: R. A. Moss, M. S. Platz, M. Jones, Jr.), Wiley, Hoboken, NJ, **2003**, chap. 11.
[5] U. Schmidt, *Angew. Chem.* **1975**, *87*, 535–540; *Angew. Chem. Int. Ed. Engl.* **1975**, *14*, 523–528.
[6] M. Yoshifuji, T. Sato, N. Inamoto, *Chem. Lett.* **1988**, 1735–1738.
[7] K. D. Dillon, F. Mathey, J. F. Nixon, *Phosphorus: The Carbon Copy*, Wiley, Chichester, **1998**, chap. 2.
[8] K. Lammertsma, *Top. Curr. Chem.* **2003**, *229*, 95–119.
[9] K. Lammertsma, M. J. M. Vlaar, *Eur. J. Org. Chem.* **2002**, 1127–1138.
[10] F. Mathey, N. H. Tran Huy, A. Marinetti, *Helv. Chim. Acta* **2001**, *84*, 2938–2957.
[11] J. Glatthaar, G. Maier, *Angew. Chem.* **2004**, *116*, 1314–1317; *Angew. Chem. Int. Ed.* **2004**, *43*, 1294–1296.
[12] X. Li, S. I. Weissman, T.-S. Lin, P. P. Gaspar, A. H. Cowley, A. I. Smirnov, *J. Am. Chem. Soc.* **1994**, *116*, 7899–7900.
[13] M. T. Nguyen, A. Van Keer, L. G. Vanquickenborne, *J. Org. Chem.* **1996**, *61*, 7077–7084.
[14] A. W. Ehlers, K. Lammertsma, E. J. Baerends, *Organometallics* **1998**, *17*, 2738–2742.
[15] Z. Havlas, M. Kývala, J. Michl, *Collect. Czech. Chem. Commun.* **2003**, *68*, 2335–2343.
[16] K. Tsuji, S. Sasaki, M. Yoshifuji, *Heteroat. Chem.* **1998**, *9*, 607–613.
[17] K. S. Pitzer, D. W. Scott, *J. Am. Chem. Soc.* **1943**, *65*, 803–829.
[18] a) The ratio between **1** (or **2**) and **4** after photolysis of **3** in the presence of the alkene in the matrix cage decreases with longer

irradiation times. b) The observed spectrum of **3** has two medium intensity bands at $\tilde{\nu} = 1040$–$1070\ cm^{-1}$ but only one is calculated. This may be due to Fermi resonance between the bands at $\tilde{\nu}_{calcd} = 1065.3\ cm^{-1}$ (A′) and $\tilde{\nu}_{calcd} = 572.8\ cm^{-1}$ (A′, $\tilde{\nu}_{exp.} = 542.9\ cm^{-1}$), which would split the band at $\tilde{\nu}_{calcd} = 1065.3\ cm^{-1}$ into the two components observed at 1028.6 and $1061.3\ cm^{-1}$.

[19] U. Heim, H. Pritzkow, U. Fleischer, H. Grützmacher, M. Sanchez, R. Réau, G. Bertrand, *Chem. Eur. J.* **1996**, *2*, 68–74.

[20] Recent studies reported favorably on the use of TDDFT for open-shell species, particularly for the lower excitations: a) B. Dai, K. Deng, J. Yang, Q. Zhu, *J. Chem. Phys.* **2003**, *118*, 9608–9613; b) P. W. Thulstrup, L. Broge, E. Larsen, J. Springborg, *J. Chem. Soc. Dalton Trans.* **2003**, 3199–3204; c) R. Andreu, J. Garín, J. Orduna, *Tetrahedron* **2001**, *57*, 7883–7892.

[21] The formation of a triplet diradical by cleavage of only one P–C bond is considered unlikely. Not only is the triplet diradical 5.2 kcal mol^{-1} less stable than triplet **3**, its calculated IR spectrum and UV spectrum do not correlate well with the experimental spectra. See the Supporting Information for details.

[22] The reversibility of the phosphirane cleavage indicates that the low yield of **3** is due to an unfavorable photostationary equilibrium rather than a very low quantum yield or pronounced filter effects.

[23] The observation of an extremely weak IR band at $\tilde{\nu} = 1723.7\ cm^{-1}$ supports the formation of **6** (C=C=P stretching mode: $\tilde{\nu}_{calcd} = 1712.9\ cm^{-1}$ (scaled by 0.97, weak).

[24] Phosphaquinone methide **5** (*anti*-**5**: $\lambda_{max,\,calcd} = 482$ nm; *syn*-**5**: $\lambda_{max,\,calcd} = 495$ nm) and bicyclic phosphirene **7** ($\lambda_{max,\,calcd} = 334$ and 494 nm) are less likely candidates.

[25] J. C. Hayes, R. S. Sheridan, *J. Am. Chem. Soc.* **1990**, *112*, 5879–5881.

[26] An example of a stable 2*H*-phosphirene: O. Wagner, G. Maas, M. Regitz, *Angew. Chem.* **1987**, *99*, 1328–1330; *Angew. Chem. Int. Ed. Engl.* **1987**, *26*, 1257–1259.

[27] J. M. Galbraith, P. P. Gaspar, W. T. Borden, *J. Am. Chem. Soc.* **2002**, *124*, 11669–11674.

[28] A spin-projection correction was applied, see E. Goldstein, B. Beno, K. N. Houk, *J. Am. Chem. Soc.* **1996**, *118*, 6036–6043.

[29] a) M. Yoshifuji, K. Toyota, K. Shibayama, N. Inamoto, *Tetrahedron Lett.* **1984**, *25*, 1809–1812; b) R. Appel, P. Fölling, B. Josten, M. Siray, V. Winkhaus, F. Knoch, *Angew. Chem.* **1984**, *96*, 620–621; *Angew. Chem. Int. Ed. Engl.* **1984**, *23*, 619–620.

[30] When the sample was briefly brought into contact with air, the transient lifetime was significantly reduced. Due to the instability of **1** towards oxygen, no systematic quenching study was attempted.

[31] W. W. Sander, *J. Org. Chem.* **1989**, *54*, 333–339.

[32] X. Li, D. Lei, M. Y. Chiang, P. P. Gaspar, *J. Am. Chem. Soc.* **1992**, *114*, 8526–8531.

[33] S. Stoll, *Spectral Simulations in Solid-State ESR*, PhD thesis, ETH Zürich, **2003**.

[34] G. Bucher, *Eur. J. Org. Chem.* **2001**, 2463–2475.

[35] Gaussian 98 (Revision A.3): M. J. Frisch et al., see Supporting Information.

[36] In the spectral region of interest, a scaling factor of 0.97 for the fundamental frequencies was used because of its better correlation with observed values than the 0.9614 recommended in A. P. Scott, L. Radom, *J. Phys. Chem.* **1996**, *100*, 16502–16513.

Organozinc Reagents

Preparation of Enolate–Homoenolate Species as (*Z*)-γ-Siloxyallylmetal Equivalents: Sequential 1,4-Addition of Bis(iodozincio)methane to 1,4-Dicarbonylbutenes and Cyclopropanation**

*Takaharu Hirayama, Koichiro Oshima, and Seijiro Matsubara**

gem-Dizinc reagents, which have two nucleophilic sites on a carbon atom, have been used for a variety of molecular transformations based on repetition of C–C bond formation on the same carbon atom.[1] In our series of investigations on their reactivity, we have also found that 1,4-addition of bis(iodozincio)methane (**1**) to *s-cis*-α,β-unsaturated ketones such as chalcone or phenyl 1-propenyl ketone in the presence of chlorotrimethylsilane gives (*Z*)-trimethylsilyl enol ethers of γ-iodozincioketone stereoselectively.[2] If we can force migration of the iodozincio group from the γ position to the β position stereospecifically, (*Z*)-3-siloxyallylmetal species, which are considered to be a useful synthetic tool, will become available (Scheme 1). Various 3-alkoxyallylmetal

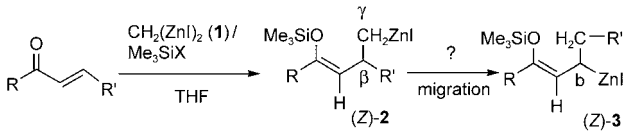

Scheme 1. Preparation of (*Z*)-3-siloxyallylzinc species (*Z*)-**3** by 1,4-addition of bis(iodozincio)methane (**1**) via (*Z*)-**2**.

species have been reported.[3,4] As achiral 3-alkoxyallylmetal reagents which give *vic*-diols diastereoselectively by reaction with aldehyde, derivatives of B,[5] In,[6] Sn,[7] Al,[8] Fe,[9] and Cr[10] have been shown to be valuable. The corresponding optically active reagents based on Al,[11] Sn,[12] Ti,[13] and B[14] have also been applied for the enantioselective synthesis of *vic*-diols. In all cases, some limitation arises from preparation of the stereochemically defined 3-alkoxyallylmetal reagent. Using our method (Scheme 1), we can prepare diastereoselectively (*Z*)-3-alkoxyallylmetal reagents containing an additional functional group R′. Here we describe a novel method

[*] T. Hirayama, Prof. Dr. K. Oshima, Prof. Dr. S. Matsubara
Department of Material Chemistry
Graduate School of Engineering
Kyoto University
Kyoutodaigaku-Katsura, Nishikyo, Kyoto 615-8501 (Japan)
Fax: (+81) 75-383-2438
E-mail: matsubar@orgrxn.mbox.media.kyoto-u.ac.jp

[**] This work was supported financially by the Japanese Ministry of Education, Science, Sports, and Culture. The financial support provided by Chugai Pharmaceutical Co., Ltd. and by the Takahashi Industrial and Economical Research Foundation is acknowledged.

Supporting information for this article is available on the WWW under http://www.angewandte.org or from the author.

 DOI: 10.1002/anie.200500133

to prepare the *Z* isomers of 3-siloxyallylzinc reagents as well as their highly diastereoselective reaction with tosylimines.

To promote migration of the iodozincio group from the γ- to the β-position (i.e., (*Z*)-**2**→(*Z*)-**3** in Scheme 1), we planned to use ring opening of a cyclopropanol. As shown in Scheme 2, our approach was to prepare enolate–homoenolate

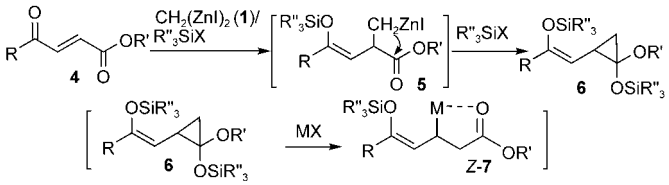

Scheme 2. Reaction concept for preparation of enolate–homoenolate equivalent **6**.

derivative **6**[15] by 1,4-addition of **1** to β-carboalkoxy α,β-unsaturated ketone **4**. The 1,4-addition of **1** to **4** in the presence of trimethylsilyl cyanide would afford the (*Z*)-trimethylsilyl enol ether of γ-iodozincio ketone **5** in situ, as shown in Scheme 2. Intramolecular nucleophilic attack on the ester group would give cyclopropane derivative **6**. This is an equivalent of enolate–homoenolate derivative (*Z*)-**7**, since 1-alkoxy-1-trialkylsiloxycyclopropane undergoes a ring-opening reaction in the presence of Lewis acid as a mediator to give a homoenolate, as reported by Nakamura.[16]

A mixture of ketoester **4a** (R = Ph, R′ = Et; 1.0 mmol), triethylamine (2.5 mmol), and trimethylsilyl cyanide (1.1 mmol) in THF was treated with **1** (1.2 mmol) at 25 °C for 5 min. Some additional trimethylsilyl cyanide (1.1 mmol) was added and the mixture was stirred for 10 min at room temperature. Triethylamine was added to prevent hydrolysis of silyl enol ether during aqueous workup. After aqueous workup, enolate–homoenolate equivalent **6a** (R = Ph, R′ = Et) was obtained in 99% yield. In the same way, enolate–homoenolate equivalents **6b–e** in Scheme 3 were obtained in good yields. When chlorodimethylphenylsilane was used as silylating reagent instead of trimethylsilyl cyanide, the corresponding phenyldimethylsilyl ether derivatives **6f–i** were obtained (Scheme 3). Products **6a–i** in Scheme 3 were obtained as equimolar mixtures of two diastereomers. Although the C=C bonds of these enol ethers were exclusively in the *Z* configuration,[17] formation of the cyclopropane ring (**5**→**6** in Scheme 2) did not proceed diastereoselectively.

Following the procedure for preparation of **6a** in Scheme 3 without addition of triethylamine, we added the tosylimine of benzaldehyde before aqueous workup and then raised the reaction temperature to 80 °C. As shown in Scheme 4, β-siloxylamine derivative **8a** was obtained as a single diastereomer after 4 h. The structure was also determined by X-ray analysis (Figure 1). The enolate–homoenolate equivalent **6a** reacted as (*Z*)-3-trimethylsiloxyallylmetal (*Z*)-**7**, since the 1-trimethylsiloxy-1-ethoxycyclopropane group in **6a** was converted to the homoenolate by the mediation of divalent zinc salts such as zinc(II) iodide and cyanide that were present in the reaction mixture. Examples

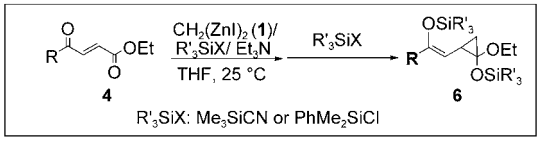

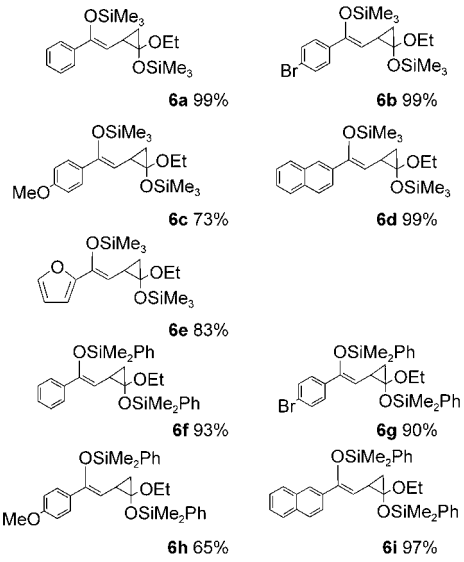

Scheme 3. Synthesis of trialkylsilyl enolate–homoenolates **6**.

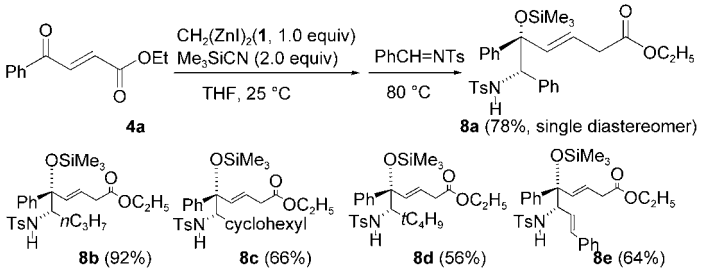

Scheme 4. Reaction of enolate–homoenolate prepared from **4a** with various imines.

Figure 1. X-ray structure of **8a**.

of the reaction of **6a** with other tosylimines are also shown in Scheme 4. In all cases, the *threo*-β-siloxylamines were obtained with high diasteroselectivity.[18]

The reason for these extraordinarily high diasteroselectivities in the reaction of **6a** with imines in Scheme 4 is not clear. One possible explanation is that **6a** transforms into the β-zincioester (*Z*)-**7a**, which may have a fixed conformation due to coordination (Figure 2). If β-zincioester (*Z*)-**7a** reacts with (*E*)-tosylimine with activation by Lewis acid, as in **9**, the *threo* isomer **8a** will be a major product.

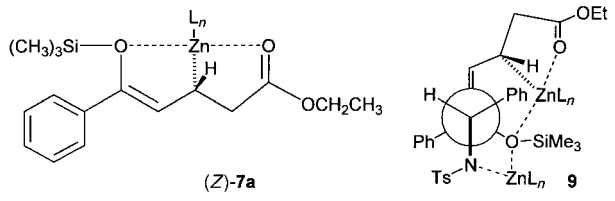

Figure 2. Proposed conformation of (*Z*)-**7a** and the transition state **9**.

Mediation with copper salt was required for reaction of *gem*-dizinc reagent **1** with aliphatic derivatives of **4** (Scheme 5; **10**, R = alkyl). Treatment of **1** with copper salt

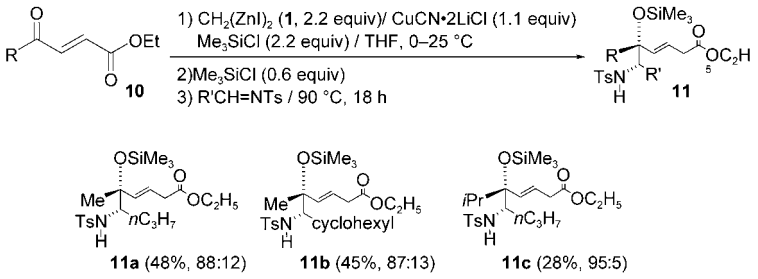

Scheme 5. Reaction of enolate–homoenolate prepared from aliphatic enone **10** with various imines.

in THF at −50 °C gave a copper reagent, which adds to aliphatic enone as we reported previously.[2] Treatment of **10** with the copper reagent from **1** in the presence of silylating agent gave enolate–homoenolate in situ, which added to tosylimines at 80 °C. The diastereoselectivities were inferior to those obtained with the aromatic substrates shown in Scheme 4 but were sill good.

Thus, the results allow us to propose a novel method to prepare stereochemically defined γ-siloxyallyl zinc species using 1,4-addition reactions of a *gem*-dizinc reagent. In addition, these zinc reagents add to tosylimines with high diastereoselectivity.

Experimental Section

1: A mixture of Zn (25 mmol), diiodomethane (1.0 mmol), and $PbCl_2$ (0.005 mmol) in THF (2.0 mL) was sonicated for 1 h in an ultrasonic cleaner bath under Ar. Diiodomethane (10 mmol) in THF (20 mL) was added dropwise to the mixture over 15 min at 10 °C with vigorous stirring. The mixture was stirred for 2 h at 25 °C. After the stirring was stopped, the reaction vessel was allowed to stand undisturbed for several hours. Excess zinc was separated by sedimentation. The ^{1}H NMR spectra of the obtained supernatant showed a broad singlet at −1.2 ppm at 0 °C corresponding to the methylene proton of **1**. The concentration was determined by ^{1}H NMR spectroscopy with 2,2,3,3-tetramethylbutane as an internal standard. The supernatant was used for further reaction as a solution of **1** in THF (0.4–0.5 M). In a sealed vessel, a solution of **1** can be stored at room temperature at least for two months.

6a (general procedure for **6**): A solution of **1** (0.4 M, 3.0 mL, 1.2 mmol) in THF was added dropwise to a solution of **4a** (0.2 g, 1.0 mmol), triethylamine (0.35 mL, 2.5 mmol), and trimethylsilyl cyanide (0.14 mL, 1.1 mmol) in THF (2.0 mL) at 25 °C. After the mixture had been stirred for 5 min, some additional trimethylsilyl cyanide (0.14 mL, 1.1 mmol) was added and stirring was continued for 10 min at 25 °C. Water (0.5 mL) was added to the reaction mixture at 0 °C. The mixture was extracted with diethyl ether. The combined organic layers were washed with brine and dried over anhydrous sodium sulfate. After chromatography on a short silica-gel column with hexane/ether/triethylamine as eluent, **6a** was obtained in 97% yield as a mixture of two diastereomers (55:45). These diastereomers arised from the configuration of the cyclopropane ring. ^{1}H NMR (500 MHz, $CDCl_3$): δ = 7.42–7.48 (m, 2H), 7.26–7.31 (m, 2H), 7.19–7.24 (m, 1H), 5.08 (d, J = 9.6 Hz, 0.55H), 5.07 (d, J = 9.6 Hz, 0.45H), 3.60–3.76 (m, 2H), 2.18 (ddd, J = 6.5, 10.0, 10.0 Hz, 0.55H), 2.16 (ddd, J = 6.0, 9.6, 10.5 Hz, 0.45H), 1.39 (dd, J = 5.5, 10.5 Hz, 0.55H), 1.28 (dd, J = 5.5, 10.5 Hz, 0.45H), 1.21 (t, J = 9.0 Hz, 1.35H), 1.20 (t, J = 9.0 Hz, 1.65H), 0.88 (dd, J = 5.5, 6.0 Hz, 0.45H), 0.76 (dd, J = 5.5, 6.0 Hz, 0.55H), 0.22 (s, 5H), 0.20 ppm (s, 4H), 0.16 (s, 9H); ^{13}C NMR (125 MHz, $CDCl_3$): minor product δ = 149.6, 139.0. 128.2, 127.4, 125.2, 109.7, 89.5, 62.1, 25.4, 23.7, 22.2, 15.5, 0.94, 0.83 ppm; major product δ = 149.5, 139.0. 128.2, 127.4, 125.2, 110.0, 89.9, 61.9, 25.4, 23.7, 22.6, 15.5, 0.94, 0.83 ppm; MS (ESI): m/z: 387 [M^+($C_{19}H_{32}O_3Si_2$)+Na^+].

8b (general procedure for **8**): A solution of **1** in THF (0.4 M, 3.0 mL, 1.2 mmol) was added dropwise to a solution of **4a** (0.2 g, 1.0 mmol) and trimethylsilyl cyanide (0.14 mL, 1.1 mmol) in THF (2.0 mL) at 25 °C. After the mixture had been stirred for 5 min, trimethylsilyl cyanide (0.14 mL, 1.1 mmol) was added, and stirring was continued for 10 min at 25 °C. A solution of the *N*-tosylimine of butanal (0.27 g, 1.2 mmol) in THF (1.5 mL) was added to the mixture at 25 °C, and the mixture was warmed to 80 °C and stirred at this temperature for 5 h. The resulting mixture was cooled to 0 °C. After addition of water, the resulting mixture was extracted with ethyl acetate. The combined organic layers were washed with brine, dried over anhydrous sodium sulfate, and concentrated in vacuo. The residue was purified by column chromatography on silica gel to provide **8b** as a single diastereomer in 92% yield. Single-crystal X-ray analysis determined the stereochemistry of the product. ^{1}H NMR ($CDCl_3$): δ = 7.69 (d, J = 6.5 Hz, 2H), 7.33 (d, J = 6.5 Hz, 2H), 7.2–7.3 (m, 5H), 5.99 (d, J = 15.5 Hz, 1H), 5.76 (dt, J = 7.0, 15.5 Hz, 1H), 4.55 (d, J = 9.0 Hz, 1H), 4.14 (q, J = 7.5 Hz, 2H), 3.76 (ddd, J = 2.5, 9.0, 9.0 Hz, 1H), 3.08 (d, J = 7.0 Hz, 2H), 2.39 (s, 3H), 1.20–1.42 (m, 2H), 1.27 (t, J = 7.5 Hz, 3H), 1.06–1.19 (m, 1H), 0.85–0.95 (m, 1H), 0.71(t, J=7.0 Hz, 3H), 0.16 ppm (s, 9H); ^{13}C NMR (125 Hz, $CDCl_3$): δ = 171.5, 142.7, 142.3, 139.8, 135.8, 129.6, 128.2. 127.9, 127.8, 127.1, 126.8, 81.5, 63.7, 61.1, 38.1, 34.6, 21.7, 19.9, 14.4, 14.1, 2.2 ppm; m.p. 80.0 °C (recrystallized from CH_3CN); HRMS (FAB): m/z: calcd for $C_{27}H_{40}NO_5SiS$: 518.2396 [(M+1)$^+$]; found: 518.2405. Crystal structure data: Triclinic, a = 10.842(10), b = 12.134(11), c = 13.608(13) Å, β = 110.316(15)°, V = 1489(2) Å^3, Z = 2, ρ_{calcd} = 1.154 Mg m^{-3}, λ($Mo_{K\alpha}$) = 0.71073 Å, T = 296 K, θ_{max} = 54.0°, R = 0.051 for 6267 reflections ($I > 2\sigma(I)$).

Received: January 13, 2005
Published online: April 21, 2005

Keywords: allylic compounds · amino alcohols · cyclization · diastereoselectivity · zinc

[1] a) P. Knochel, J.-F. Normant, *Tetrahedron Lett.* **1986**, *27*, 4427; P. Knochel, J.-F. Normant, *Tetrahedron Lett.* **1986**, *27*, 4431; b) I. Marek, J.-F. Normant, *Chem. Rev.* **1996**, *96*, 3241; c) S. Matsubara, K. Oshima, *Proc. Jpn. Acad. Ser. B* **2003**, *79*, 71; S. Matsubara, K. Oshima, K. Utimoto, *J. Organomet. Chem.* **2001**, *617–618*, 39; S. Matsubara, *J. Synth. Org. Soc. Jpn.* **2000**, *58*, 118; d) P. Knochel in *Handbook of Grignard Reagents* (Eds.: G. S. Silverman, P. E. Rakita), Marcel Dekker, New York, **1996**, chap. 30; e) F. Berttini, P. Gasselli, G. Zubiani, G. Cainelli, *Tetrahedron* **1970**, *26*, 1281; f) B. J. J. van de Heisteeg, M. A. Schat, G. Tinga, O. S. Akkerman, F. Bickelhaupt, *Tetrahedron Lett.* **1986**, *27*, 6123; g) E. Nakamura, K. Kubota, G. Sakata, *J. Am. Chem. Soc.* **1997**, *119*, 5457; h) A. Hirai, M. Nakamura, E. Nakamura, *J. Am. Chem. Soc.* **2000**, *122*, 11791.

[2] a) S. Matsubara, D. Arioka, K. Utimoto, *Synlett* **1999**, 1253; b) S. Matsubara, H. Yamamoto, D. Arioka, K. Utimoto, K. Oshima, *Synlett* **2000**, 1202.

[3] A. R. Katritzky, M. Piffl, H. Lang, E. Anders, *Chem. Rev.* **1999**, *99*, 665.

[4] M. Lombardo, S. Licciulli, C. Trombini, *Pure Appl. Chem.* **2004**, *76*, 657.

[5] a) R. W. Hoffmann, J. Krüger, D. Brückner, *New J. Chem.* **2001**, *25*, 102; b) R. W. Hoffmann, B. Kemper, *Tetrahedron Lett.* **1981**, *22*, 5263; c) R. W. Hoffmann, R. Metternich, *Liebigs Ann. Chem.* **1985**, 2390; d) T. Moriya, A. Suzuki, N. Miyaura, *Tetrahedron Lett.* **1995**, *36*, 1887; e) W. R. Roush, M. R. Michaelides, D. F. Tai, B. M. Laser, W. K. M. Chong, D. J. Harris, *J. Am. Chem. Soc.* **1989**, *111*, 2984.

[6] T. Hirashita, T. Kamei, T. Horie, H. Yamamura, M. Kaway, S. Araki, *J. Org. Chem.* **1999**, *64*, 172.

[7] a) S. Waterlot-Bourdea, J.-L. Parrain, J.-P. Quintard, *J. Org. Chem.* **1999**, *64*, 172; b) G. C. Micalizio, A. N. Pinchuck, W. R. Roush, *J. Org. Chem.* **2000**, *65*, 8730; c) G. E. Keck, D. E. Abbott, M. R. Wiley, *Tetrahedron Lett.* **1987**, *28*, 139.

[8] Y. Yamamoto, K. Komatsu, K. Maruyama, *J. Organomet. Chem.* **1985**, *285*, 31.

[9] S. Jiang, G. E. Agoston, T. Chen, M. P. Cabal, E. Turos, *Organometallics* **1995**, *14*, 4697.

[10] a) K. Takai, K. Nitta, K. Utimoto, *Tetrahedron Lett.* **1988**, *29*, 5263; b) W. R. Roush, T. D. Bannister, M. D. Wendt, J. A. Jablonowski, K. A. Scheidt, *J. Org. Chem.* **2002**, *67*, 4275.

[11] J.-I. Chika, H. Takei, *Tetrahedron Lett.* **1998**, *39*, 605.

[12] a) J. A. Marshall, *Chem. Rev.* **1996**, *96*, 31; b) J. A. Marshall, K. W. Hinkle, *J. Org. Chem.* **1996**, *61*, 105; c) W. R. Roush, M. S. Van Nieuwenhze, *J. Am. Chem. Soc.* **1994**, *116*, 8536; d) G. E. Keck, K. A. Savi, E. N. Cressman, D. E. Abbott, *J. Org. Chem.* **1994**, *59*, 7889; e) I. Kadota, K. Kobayashi, H. Okano, N. Asao, Y. Yamamoto, *Bull. Soc. Chim. Fr.* **1995**, *132*, 615.

[13] J. Cossy, C. Willis, V. Bellosta, L. Saint-Jalmes, *Synthesis* **2002**, 951.

[14] a) H. C. Brown, P. K. Jadhav, K. S. Bhat, *J. Am. Chem. Soc.* **1988**, *110*, 1535; b) J. A. Hunt, W. R. Roush, *J. Org. Chem.* **1997**, *62*, 1112.

[15] α,β-Dilithium salts of ketones: I. Ryu, H. Nakahira, M. Ikebe, N. Sonoda, S. Yamamoto, M. Komatsu, *J. Am. Chem. Soc.* **2000**, *122*, 1219.

[16] E. Nakamura, S. Aoki, K. Sekiya, H. Oshino, I. Kuwajima, *J. Am. Chem. Soc.* **1987**, *109*, 8056.

[17] A conjugated addition of bis(iodozincio)methane to 4-phenyl-4-oxo-2-butene in the presence of chlorotrimethylsilane gave (*Z*)-trimethylsilylenol ether diastereoselectively.[2a] An NOE experiment also supported *Z* configuration of **6a**.

[18] For X-ray diffraction, a crystal was mounted on a glass fiber coated with epoxy resin. Measurements were made on a Rigaku Mercury charge-coupled device (CCD) system with graphite monochromated $Mo_{K\alpha}$ radiation.

Nanotubes

Peptide–Polymer Hybrid Nanotubes**

*Julien Couet, J. D. Jeyaprakash S. Samuel, Alexey Kopyshev, Svetlana Santer, and Markus Biesalski**

Since the discovery of carbon nanotubes,[1] there has been a growing interest in organic tubular structures with very small dimensions. The number of possible applications of these microstructures has also grown, particularly in the fields of microelectronics,[2,3] separation technology,[4] and biomedical technology.[5] There is an increased use of so-called bottom-up strategies for the design of organic nanotubes and nanofibers.[6] Some promising examples of this include the self-assembly of amphiphilic molecules (small lipids,[7] di-[8] and triblock,[9] and coil-ring-coil[10] block copolymers), polymeric foldamers,[11] as well as the self-assembly of cyclic peptides to form peptide nanotubes.[12–14]

Cyclic peptides that consist of an even number of D- and L-amino acids exhibit a pronounced tendency to self-assemble into tubular structures in which a large number of peptide subunits are held in place by intermolecular hydrogen bonds.[12–14] Through their design principle, these cyclic molecules maintain a flat conformation in which the amide functional groups lie perpendicular to the plane of the molecular ring. This allows the formation of an extended network of hydrogen bonds, preferably in an antiparallel β-sheet structure.[15] As a result of the peptide configuration, all the side-chain functional groups are located on the ring periphery. This imparts the nanotubes with a defined hollow core and enables simple access to the functional groups for modification of the surface chemistry. The side-chain functional groups of the peptide can have an influence on the formation of either single-peptide nanotubes, or higher-order 3D aggregates.[16]

Since the pioneering work by Ghadiri and co-workers,[12] such self-assembled peptide nanotubes have been applied as novel antibiotics[17] and as artificial ion channels.[18] The range of application of peptide nanotubes is determined mainly by their surface chemistry. As shown by Ghadiri and co-workers,[12–14] the surface chemistry can be tuned by individually synthesizing cyclic peptides with different primary sequences. An alternative way to adjust the surface chemistry is through the attachment of synthetic macromolecules to the surface of the structure after self-assembly, thus embedding the peptide nanotube in a polymeric shell. In this case, the structure of the resulting hybrid material is governed by both the peptide nanotube core as well as the polymeric shell, and the surface chemistry is determined by the choice of grafted synthetic macromolecules.

The assembly of cyclic peptide precursors into nanotubes with subsequent surface-induced polymerization around the nanotubes offers a novel approach toward the preparation of a large number of shape-persistent hybrid materials that are not easily accessed by any other technique. An interesting aspect of this strategy is that defined structural information can be transferred from a biologically derived module to a synthetic polymer (and vice versa).

Recently, it was shown that synthetic peptides can be modified with polymerization initiators, which can subsequently initiate reactions that link peptides into covalent polymers.[19–21] For example, such modified peptides have been used as initiators for nitroxide-mediated controlled radical polymerizations[19] and atom-transfer radical polymerizations (ATRP).[20,21]

In our work, we have taken advantage of the ability of distinct cyclic peptides to self-organize into defined tubular structures, as discussed above. In particular, we have used peptide nanotubes as structurally defined templates to prepare nanometer-sized peptide–polymer hybrid nanotubes. Figure 1 schematically outlines this approach. Cyclic peptides composed of eight amino acids that are arranged with alternating D- and L-configurations are modified with certain chemical groups at distinct side-chain positions. These groups can serve as initiation sites for controlled free-radical polymerization by the ATRP technique. The cyclic-peptide initiators self-assemble into peptide nanotubes in a fashion analogous to that described above. A subsequent polymerization reaction of *N*-isopropylacrylamide (NIPAM) in aqueous dispersion is triggered by the surface-attached initiator groups to yield a novel class of polymeric hybrid nanostructures in which the peptide core is covalently attached to a functional polymeric shell.

The process begins with a solution of the cyclic-peptide initiator in pure trifluoroacetic acid (TFA). The precursors slowly self-assemble and precipitate from solution in the form of nanotubes upon a gradual increase in the amount of water added to the TFA phase. The nanotubes can be isolated through a simple centrifugation procedure, followed by rinsing with water. The products are then characterized with respect to chemical identity, surface chemistry, internal structure, and morphology. Analysis by FTIR spectroscopy

[*] J. Couet, A. Kopyshev, Dr. S. Santer,[+] Dr. M. Biesalski
Institute for Microsystem Technology (IMTEK)
University of Freiburg
Georges-Köhler-Allee 103, 79110 Freiburg (Germany)
Fax: (+49) 761-203-7163
E-mail: biesalsk@imtek.de
Dr. J. D. J. S. Samuel
IBM Almaden Research Center
San Jose, CA95120 (USA)
[+] Previous surname: Prokhorova

[**] We thank the following people for their assistance with the analysis of cyclic peptides and polymer hybrid materials: Dr. J. Wörth and C. Warth (ESI MS and LC–MS), Dr. M. Ade (X-ray diffraction), Dr. R. Thomann and A. Neub (TEM), and K. Shroff (automated peptide synthesis). Financial support came from the Deutsche Forschungsgemeinschaft (Emmy Noether Programm), the Landesstiftung Baden-Württemberg (Eliteförderprogramm Nachwuchswissenschaftler), and the Fonds der Chemischen Industrie. J.C. thanks the DAAD for a fellowship with the postgraduate student exchange program. We thank Prof. J. Rühe and Dr. O. Prucker for valuable support and stimulating discussions.

Supporting information for this article is available on the WWW under http://www.angewandte.org or from the author.

 DOI: 10.1002/anie.200462993

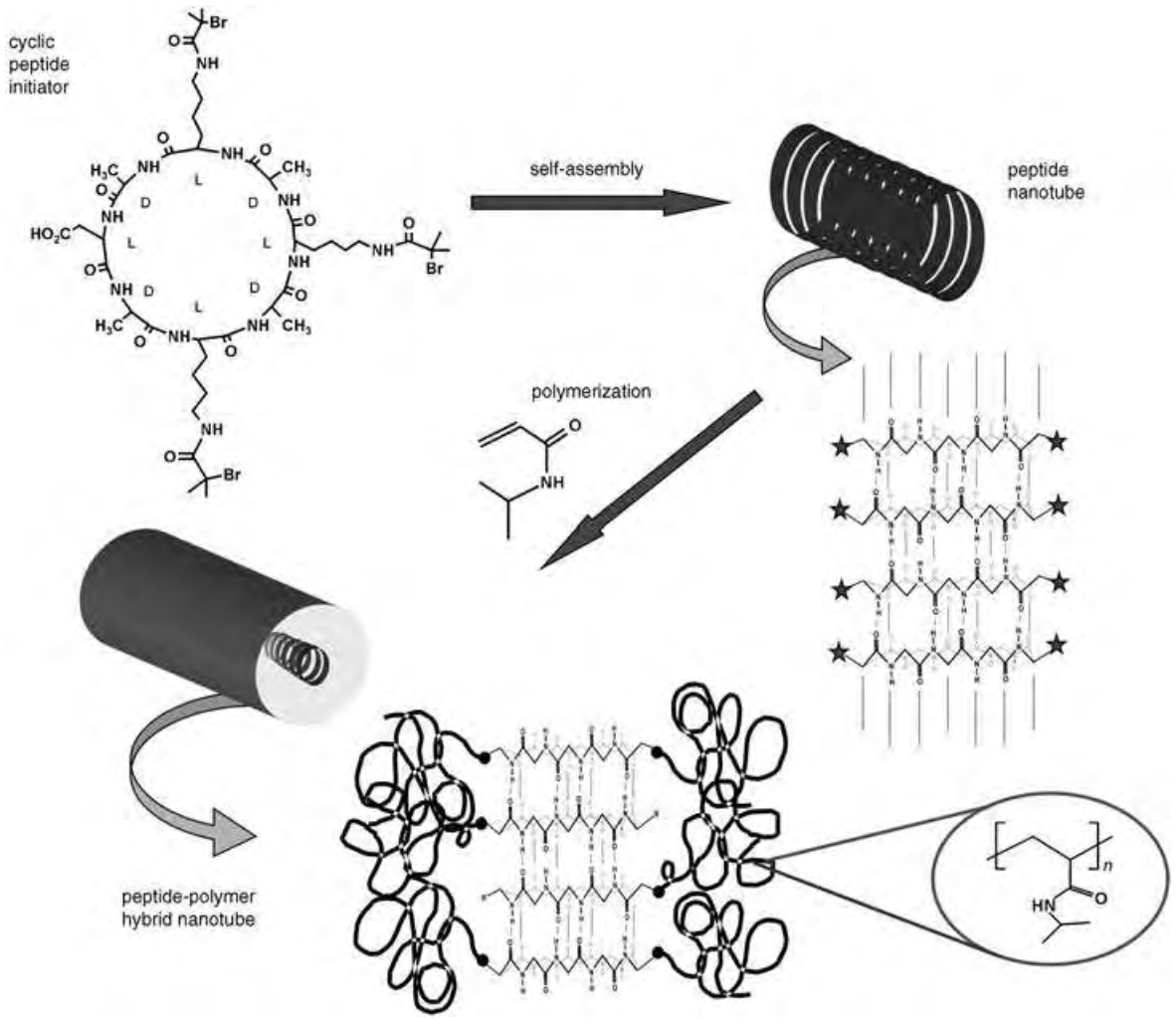

Figure 1. Schematic outline of the synthesis of peptide–polymer hybrid nanotubes. A cyclic peptide with polymerization initiator groups at distinct side chains self-assembles to form a peptide nanotube that has the initiator groups exclusively at the outer surface. A subsequent surface-initiated polymerization in the presence of NIPAM monomer coats the peptide core with a covalently bound PNIPAM polymer shell.

shows the presence of closely packed peptides that are stacked in a β-sheet structure held together through intermolecular hydrogen bonds.[22] Furthermore, X-ray photoelectron spectroscopy proves the presence of the bromine groups that are required for the nanotube surface-initiated polymerization.[22] The morphology of the cyclic-peptide nanotubes was studied by AFM and TEM. A representative AFM image of nanotubes that were drop cast from an aqueous dispersion onto a silicon wafer is shown in Figure 2. Both single nanotubes and 2D aggregates were observed on the surface. The average height of a cyclic-peptide nanotube, determined by statistical analysis of AFM cross-section data, is 1.7 ± 0.2 nm (Figure 2c). The length of the peptide nanotubes ranges between 100 and 500 nm. Both values are consistent with experimental and theoretical studies of single-peptide nanotubes consisting of eight-membered rings of D- and L-amino acids.[16] The height of the 2D fibrous aggregates, shown in Figure 2, is equal to those of single-peptide nanotubes which implies that the aggregates are most likely formed during the surface drying procedure. Clear experimental support for this is still pending, however.

The cyclic-peptide initiator nanotubes were dispersed into a mixture of water, monomer, and polymerization additives by which a surface-induced ATRP reaction was initiated at room temperature. NIPAM was chosen as the monomer, as it yields peptide–polymer nanotubes with a nontoxic polymer (PNIPAM) coating and displays interesting physical properties, such as a lower critical solution temperature. After a defined polymerization time, the cyclic-peptide–PNIPAM nanotubes were washed extensively with water to remove any physisorbed polymer generated from the transmission of surface-bound radicals to NIPAM monomers in solution.

Figure 3b shows AFM images of the cyclic-peptide–PNIPAM nanotubes adsorbed to a silicon wafer (the sample has been drop cast from aqueous solution). Notably, 2D aggregates are no longer observed; the nanotubes are present as distinct rod-shaped structures that are 80 ± 20 nm in length and 12 ± 3 nm in height as determined by the statistical analysis of more than 400 nanotubes (Figures 3c and d). A cross-section of a single polymer–peptide nanotube (Figures 3e and f) shows that the polymer shell surrounds the peptide core in a very homogeneous manner. The presence of

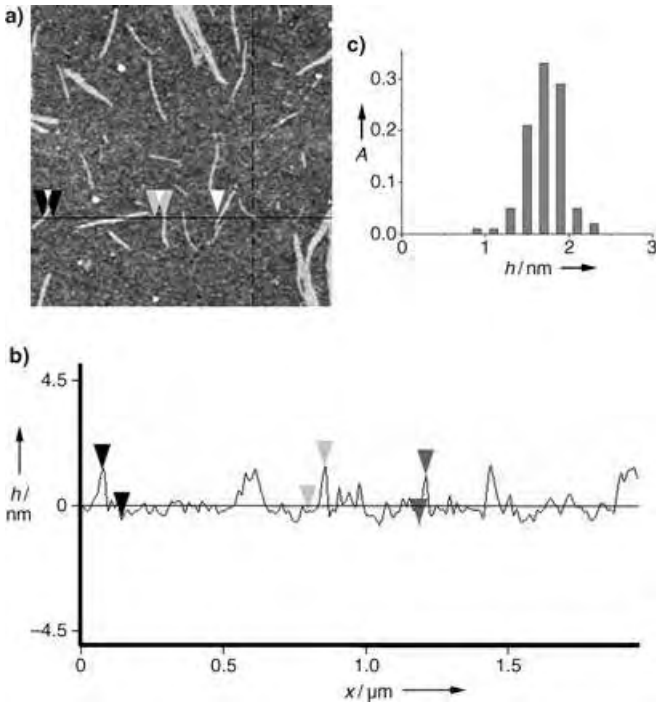

Figure 2. Analysis of the self-assembled cyclic-peptide initiator nanotubes: a) AFM image of peptide nanotubes adsorbed on a silicon wafer (scale: 2 μm; height: 5 nm); b) cross-section of the marked positions in part a); c) height distribution from the statistical analysis of adsorbed nanotubes (relative abundance *A* as a function of measured height *h*).

the PNIPAM polymer is proven by FTIR[22] spectroscopy and NMR spectroscopy. Furthermore, FTIR analysis of the cyclic-peptide–PNIPAM nanotubes suggests that the internal peptide assembly is an intact β-sheet structure.[22] Finally, as can be observed in the AFM phase image, a black halo surrounds each rodlike structure, indicative of a softer polymeric shell covering the peptide nanotube core (Figure 3a).

To demonstrate that the polymer is covalently bound to the peptides, control experiments were performed by mixing free PNIPAM polymer in solution with similar peptide nanotubes that lack initiator groups at the surface (Figure 4a). In this case the purely physisorbed macromolecules can be completely removed through simple solvent extraction. AFM analysis demonstrates that the unmodified peptide nanotubes can be recovered after solvent extraction. This indicates that the nanotubes described above consist of an assembly of covalently linked peptide–polymer hybrid molecules.

In summary, the strategy introduced herein for the design and preparation of functional peptide–polymer hybrid nanostructures allows the preparation of a novel class of nanotubes whose structure is governed primarily through the biomolecular component (peptide), and whose surface chemistry can be adjusted by the grafted synthetic polymer. AFM analysis demonstrates that the PNIPAM polymeric shell coats the peptide nanotube core in a highly homogeneous manner, and, as it is covalently attached to the cyclic peptide subunits, it cannot be removed by simple solvent extraction. Beside the peptide core, the internal structure of the polymeric shell is an

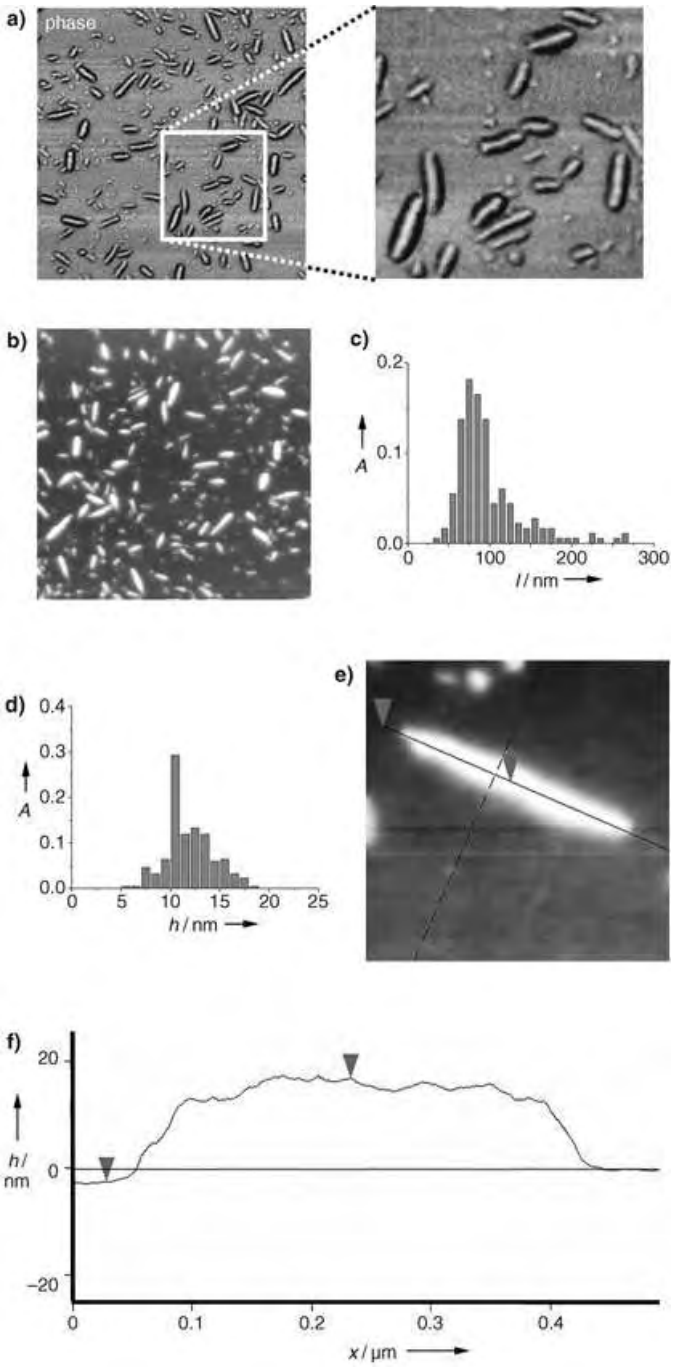

Figure 3. Analysis of the peptide–PNIPAM nanotubes: a) AFM phase image of cyclic-peptide nanotubes adsorbed on a silicon wafer (scale: 2 μm); an enlarged area of the phase image is shown (scale: 0.8 μm); b) AFM image (scale: 2 μm; height 50 nm); c) relative abundance *A* as a function of the length *l* and d) height *h* as determined by statistical analysis of the of the nanotubes; e) AFM image (scale: 0.5 μm, height: 25 nm) and f) cross-section analysis along the marked positions in part e) of a cyclic-peptide–PNIPAM nanotube.

important factor that governs the structure of this novel class of polymeric hybrid materials. Presumably, the molar mass and the conformation of the peptide-bound polymer chains can be controlled by adjusting the appropriate polymerization conditions. Additionally, the graft density may be controlled

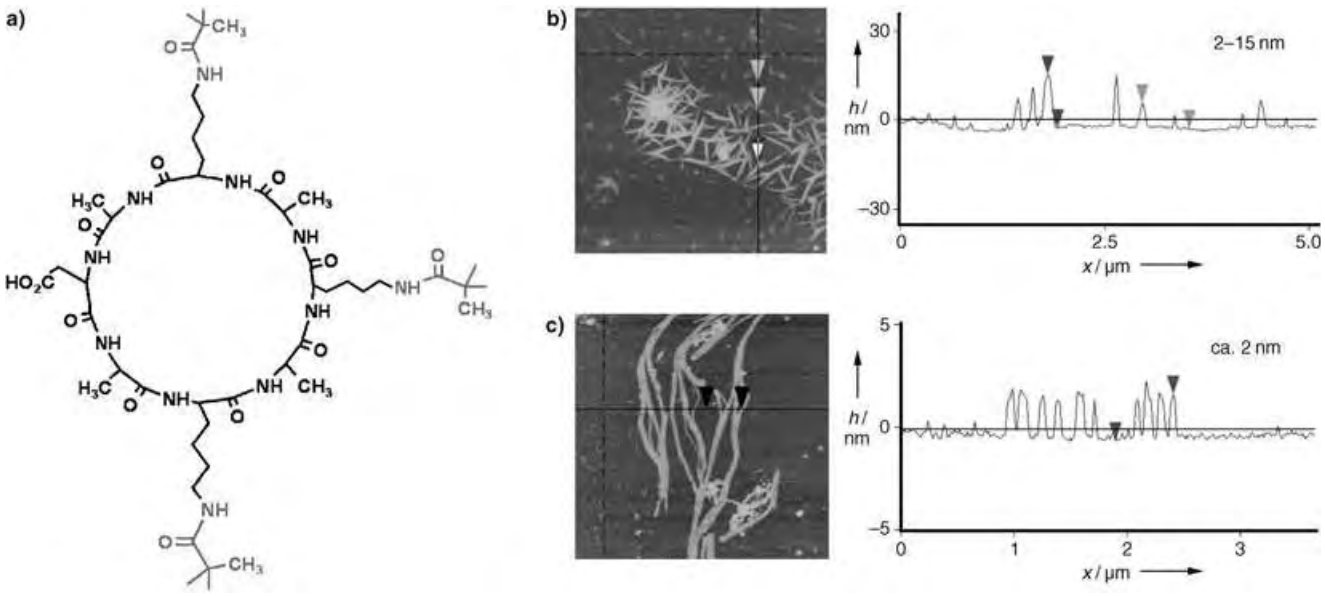

Figure 4. a) Schematic image of a cyclic peptide (CPB) that was synthesized for control experiments. It was allowed to self-assemble to form similar peptide nanotubes, which were then mixed with free PNIPAM polymer, and adsorbed to the surface of a silicon wafer, and analyzed by AFM both before and after extraction with water. b) AFM image (size: 5 μm, height: 35 nm) and cross-section analysis of polymer–CPB nanotubes before and c) after extraction with water.

by the dilution of initiator sites; systematic studies of these issues will be reported in forthcoming communications. Notably, one would expect neighboring chains to repel each other more strongly with an increase in the molecular mass and graft density of the polymers. If such forces were to overcome those that hold the cyclic-peptide subunits together, the point at which self-assembled peptide–polymer nanotubes break up into shorter aggregates may be determined. This may become a way to gain control of the length of such hybrid nanotubes.

Experimental Section

All cyclic peptides were prepared with standard Fmoc (Fmoc = 9-fluorenylmethoxycarbonyl) chemistry protocols for solid-phase peptide synthesis. Cyclization of the linear peptide (HOOC-L-Asp-(OAll)-[D-Ala-L-Lys(Mtt)]-D-Ala-NH_2) and the attachment of functional groups (the ATRP initiators) were carried out directly on the solid phase (All = allyl, Mtt = 4-methyltrityl). The cyclic peptides were cleaved from the resin and purified by recrystallization from TFA/water and preparative reversed-phase HPLC (C_{18}, CH_3CN/H_2O elution gradient). Characterization of the cyclic-peptide precursor product was carried out with ESI MS, NMR spectroscopy, and FTIR spectroscopy.[22]

Peptide nanotube surface-initiated ATRP reactions were carried out in dispersed aqueous phase similar to a recently published protocol by Kizhakkedathu and co-workers.[23] In brief, the monomer, solvent, and HMTETA (HMTETA = 1,1,4,7,10,10-hexamethyltriethylenetetramine) were mixed and degassed by repeated freeze/thaw cycles under vacuum. Subsequently, Cu^{I}, Cu^{II}, and Cu^{0} were added under frozen conditions and the reaction mixture was allowed to slowly warm to room temperature. The peptide initiator nanotubes were dispersed in an aqueous solution and added to a polymerization chamber. Polymerization was carried out at 20 ± 1.0 °C under an atmosphere of inert gas. After 90 min, the reaction was quenched by addition of excess Cu^{II} and dilution with excess water. The molar ratio of monomer/initiator was 200:1, and the monomer conversion, as determined by HPLC, was ≈ 0.7. At this point, the polymer-modified peptide nanotubes were still in a dispersed phase (the solution maintained a hazy appearance); workup could therefore be done by repeated centrifugations and extensive washings with cold water, which ensures the removal of all physisorbed macromolecules from the polymer–peptide hybrids.

The control experiment was carried out with peptide nanotubes generated from a cyclic peptide that lacks polymerization initiation groups at the surface. These reference nanotubes were mixed with free PNIPAM polymer in aqueous dispersion and analyzed by AFM without further solvent extraction. The aggregates were then repeatedly washed with water, and analyzed again by AFM for any remaining polymer physisorbed to the peptide nanotubes.

Received: December 20, 2004
Published online: April 14, 2005

Keywords: nanotechnology · nanotubes · peptides · polymers · supramolecular chemistry

[1] S. Iijima, *Nature* **1991**, *354*, 56–58.
[2] J. Li, C. Papadopoulos, J. M. Xu, M. Moskovits, *Appl. Phys. Lett.* **1999**, *75*, 367–369.
[3] H. S. P. Wong, *IBM J. Res. Dev.* **2002**, *46*, 133–168.
[4] G. L. Che, B. B. Lakshmi, E. R. Fisher, C. R. Martin, *Nature* **1998**, *393*, 346–349.
[5] C. R. Martin, P. Kohli, *Nat. Rev.* **2002**, *2*, 29–37.
[6] D. T. Bong, T. D. Clark, J. R. Granja, M. R. Ghadiri, *Angew. Chem.* **2001**, *113*, 1016–1041; *Angew. Chem. Int. Ed.* **2001**, *40*, 988–1011.
[7] J. M. Schnur, *Science* **1993**, *262*, 1669–1676.
[8] K. Yu, A. Eisenberg, *Macromolecules* **1998**, *31*, 3509–3518.
[9] J. Grumelard, A. Taubert, W. Meier, *Chem. Commun.* **2004**, *13*, 1462–1463.
[10] S. Höger, *Chem. Eur. J.* **2004**, *10*, 1320–1329.
[11] S. Hecht, A. Khan, *Angew. Chem.* **2003**, *115*, 24–26; *Angew. Chem. Int. Ed.* **2003**, *42*, 6021–6024.

[12] M. R. Ghadiri, J. R. Granja, R. A. Milligan, D. E. McRee, N. Khazanovich, *Nature* **1993**, *366*, 324 – 327.
[13] J. D. Hartgerink, J. R. Granja, R. A. Milligan, M. R. Ghadiri, *J. Am. Chem. Soc.* **1996**, *118*, 43 – 50.
[14] M. R. Ghadiri, *Adv. Mater.* **1995**, *7*, 675 – 677.
[15] M. R. Ghadiri, K. Kobayashi, J. R. Granja, R. K. Chadha, D. E. McRee, *Angew. Chem.* **1995**, *107*, 76 – 78; *Angew. Chem. Int. Ed. Engl.* **1995**, *34*, 93 – 95.
[16] T. Nakanishi, H. Okamoto, Y. Nagai, K. Takeda, I. Obataya, H. Mihara, H. Azehara, Y. Suzuki, W. Mizutani, K. Furukawa, K. Torimitsu, *Phys. Rev. B* **2002**, *66*, 165417.
[17] S. Fernandez-Lopez, H. S. Kim, E. C. Choi, M. Delgado, J. R. Granja, A. Khasanov, K. Kraehenbuehl, G. Long, D. A. Weinberger, K. M. Wilcoxen, M. R. Ghadiri, *Nature* **2001**, *412*, 452 – 455.
[18] M. R. Ghadiri, J. R. Granja, L. K. Buehler, *Nature* **1994**, *369*, 301 – 304.
[19] M. L. Becker, J. Liu, K. L. Wooley, *Chem. Commun.* **2003**, *2*, 180 – 181.
[20] H. Rettig, E. Krause, H. G. Börner, *Macromol. Rapid Commun.* **2004**, *25*, 1251 – 1256.
[21] Y. Mei, K. L. Beers, H. C. Michelle Byrd, D. L. van der Hart, N. R. Washburn, *J. Am. Chem. Soc.* **2004**, *126*, 3472 – 3476.
[22] See Supporting Information.
[23] J. N. Kizhakkedathu, R. Norris-Jones, D. E. Brooks, *Macromolecules* **2004**, *37*, 734 – 743.

Porphyrin Complexes

Asymmetric Spin Density Distribution in the Copper(II) Complex of N-Confused Tetraphenylporphyrin: A Multifrequency Continuous-Wave and Pulse EPR Study**

*George Mitrikas, Carlos Calle, and Arthur Schweiger**

The relevance of metalloporphyrins in catalysis, biology, medicine, and materials science has been well documented during the past decades.[1] Recently, N-confused porphyrins (NCP), a new family of porphyrin isomers that contain an inverted pyrrole ring in the macrocycle connected at its α- and β′-positions, have received increased attention.[2,3] These novel artificial porphyrins exhibit unique physical and chemical properties, for instance, the ability to stabilize unusual oxidation states of metals as a result of the reactivity of the inverted pyrrole.[4]

N-confused porphyrins form stable organometallic macrocycles with transition-metal centers.[5] One of the first described is the copper(II) complex with N-confused tetraphenylporphyrin [Cu^{II}-(nctpp)] (Scheme 1).[6] This organocopper(II) species is of particular interest as a model compound in studies of the reaction mechanisms of metalloenzymes. Its properties are directly related to the electronic structure, and consequently the delocalization of the unpaired electron over the complex can be used as a probe to study the reaction mechanisms.

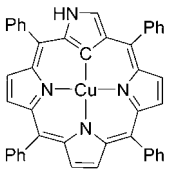

Scheme 1. Structure of [Cu^{II}(nctpp)].

In this communication we describe a combined multifrequency continuous-wave (CW) and pulse EPR study of [Cu^{II}(nctpp)] focusing on the elucidation of the magnetic interactions between the unpaired electron of the complex and the nitrogen donors of the porphyrin ring. Pulse EPR methods can give more detailed information than CW EPR spectroscopy about the electronic structure through an elaborate mapping of the hyperfine and nuclear quadrupole interactions.[7]

The nctpp macrocycle was prepared by the one-flask synthesis of Lindsey and co-workers.[8] The X-band EPR spectrum of [Cu^{II}(nctpp)] in frozen THF displays features that are typical for Cu^{II} complexes (Figure 1a). No ligand hyperfine structure was observed along $g_{\|}$ because of inhomogeneous broadening and strain effects related to the solvent. When the complex is magnetically diluted in zinc(II) tetra-

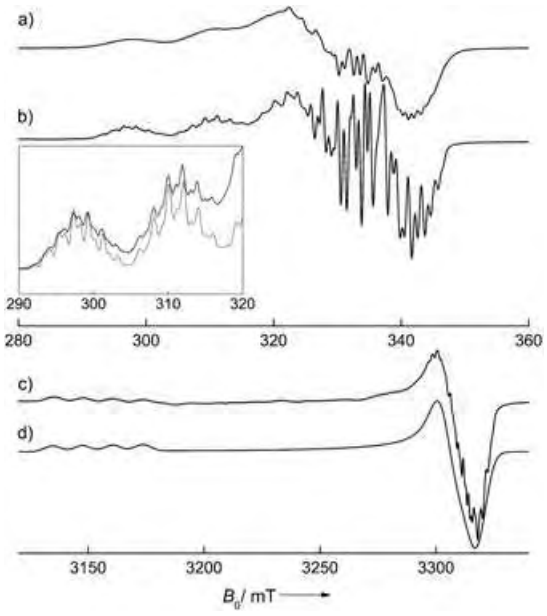

Figure 1. EPR spectra of [Cu^{II}(nctpp)]. a) X-band, in frozen THF solution (T = 50 K). b) X-band, diluted in [Zn(tpp)] powder (T = 150 K). Inset: Low-field region of (b) showing the copper and nitrogen hyperfine couplings. Upper trace (black): experiment; lower trace (gray): simulation. c) W-band, diluted in [Zn(tpp)] powder (T = 100 K). d) Simulation of spectrum (c) (for simulation parameters see text).

[*] Dr. G. Mitrikas, C. Calle, Prof. Dr. A. Schweiger
Laboratorium für Physikalische Chemie
ETH-Hönggerberg, 8093 Zürich (Switzerland)
Fax: (+41) 1-632-1021
E-mail: schweiger@esr.phys.chem.ethz.ch

[**] This work was supported by the Swiss National Science Foundation. We thank Bruno Mancosu for preparing the nctpp ligand and Dr. Piotr J. Chmielewski for providing us with the nctpp ligand as a reference for testing our sample.

Supporting information for this article is available on the WWW under http://www.angewandte.org or from the author.

 DOI: 10.1002/anie.200500155

phenylporphyrin [Zn(tpp)] powder, a remarkably well-resolved ligand hyperfine structure is observed (Figure 1b). The low-field region of the spectrum can be accurately simulated assuming two nitrogen nuclei with hyperfine values $A_{\parallel} \approx (59 \pm 3)$ MHz and one nitrogen nucleus with $A_{\parallel} \approx (29.5 \pm 3)$ MHz (Figure 1, inset).[9] This observation is clear-cut proof that the three nitrogen donors of the porphyrin core are no longer equivalent, in contrast to the case in [Cu^{II}-(tpp)].[10]

The W-band EPR spectrum shown in Figure 1c indicates that the $\boldsymbol{g}$ matrix is axial even with the high resolution obtained at 94.3 GHz. From a simulation of this spectrum (Figure 1d) we determined the g principal values $g_{\parallel} = 2.137 \pm 0.001$ and $g_{\perp} = 2.036 \pm 0.001$, and the ^{63}Cu hyperfine couplings $|A_{\parallel}| = (379 \pm 5)$ MHz and $|A_{\perp}| = (110 \pm 20)$ MHz. The g principal values are in line with the unpaired electron being in the $d_{x^2-y^2}$ orbital but are smaller than those reported for [Cu^{II}(tpp)] ($g_{\parallel} = 2.190$, $g_{\perp} = 2.045$).[10] This observation together with the smaller copper hyperfine coupling ($|A_{\parallel}| = 615$ MHz for [Cu^{II}(tpp)]) indicates that in [Cu^{II}(nctpp)] the metal–ligand bond has a stronger covalent character than in [Cu^{II}(tpp)].

A more detailed study of the hyperfine and nuclear quadrupole couplings of the two equivalent nitrogens is provided by pulse ENDOR spectroscopy.[7] Figure 2 shows

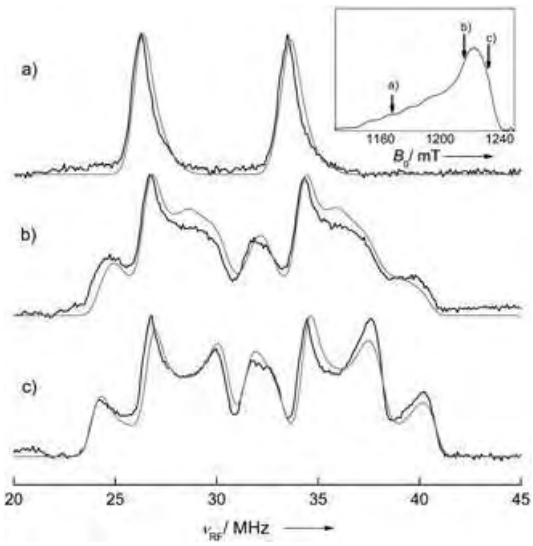

Figure 2. Q-band Davies-ENDOR spectra of [Cu^{II}(nctpp)] diluted in [Zn(tpp)] powder measured at different observer positions. Black traces: experiments; gray traces: simulations (for simulation parameters see text). Inset: FID-detected Q-band EPR spectrum ($T = 20$ K).

Davies-ENDOR spectra measured at Q-band frequencies.[11] The spectrum measured close to $g_{\parallel}$ (trace a) consists of a doublet centered at 30 MHz with the two peaks split by twice the ^{14}N Larmor frequency, $2\nu_N = 7.2$ MHz. Consequently, these two peaks are assigned to strongly coupled nitrogens with a hyperfine coupling of 60 MHz and an unresolved nuclear quadrupole interaction along this orientation. ENDOR measurements at different observer positions (Figure 2, black traces) and their spectral simulations (Figure 2, gray traces) provide the complete determination of the principal values of the hyperfine, $\boldsymbol{A}$, and nuclear quadrupole, $\boldsymbol{P}$, coupling tensors: $(A_1, A_2, A_3) = (71.5, 58.3, 59.5)$ MHz ± 0.2 MHz and $(P_1, P_2, P_3) = (-0.87, 1.00, -0.13)$ MHz ± 0.1 MHz.

The hyperfine interactions of the third ^{14}N nucleus of the porphyrin core and of the outer or "inverted" ^{14}N nucleus were studied with HYSCORE spectroscopy at Q-band. Figure 3 shows the single-crystal-like matched HYSCORE[7]

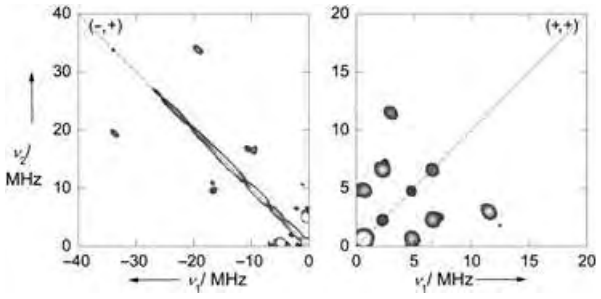

Figure 3. Matched Q-band HYSCORE spectrum of [Cu^{II}(nctpp)] diluted in [Zn(tpp)] powder; observer position at $g_{\parallel}$, $T = 20$ K. For clarity the $(-,+)$ and $(+,+)$ quadrants have different scales.

spectrum at $g_{\parallel}$. The peaks observed in the $(-,+)$ quadrant originate from strong ^{14}N interactions. The crosspeaks around $(-17, 10)$ MHz and $(-10, 17)$ MHz are assigned to single-quantum transitions, whereas the two crosspeaks at $(-33.7, 19.3)$ MHz and $(-19.3, 33.7)$ MHz are assigned to double-quantum transitions with $\Delta m_I = 2$. The latter transitions are to first order independent of the nuclear quadrupole interaction, differ by $4\nu_N = 14.4$ MHz, and are centered on the hyperfine coupling of 26.5 MHz along this orientation. HYSCORE measurements at additional observer positions (not shown here) give the following values for the hyperfine coupling tensor of the third ^{14}N nucleus of the porphyrin core: $(A_1, A_2, A_3) = (26.5, 35, 26.5)$ MHz ± 0.5 MHz.

The correlation peaks in the $(+,+)$ quadrant of the HYSCORE spectrum correspond to weak ^{14}N interactions and therefore can be assigned to the remote ^{14}N nucleus of the inverted pyrrole. The crosspeaks at (3.0, 11.5) MHz and (11.5, 3.0) MHz represent double-quantum transitions from which a hyperfine coupling of $|A_{\parallel}| = (4.3 \pm 0.2)$ MHz is estimated. In addition, the crosspeaks at (6.6, 2.3) MHz and (2.3, 6.6) MHz, as well as those at (0.7, 4.8) MHz and (4.8, 0.7) MHz are assigned to single-quantum transitions and give a nuclear quadrupole coupling of $P_3 = (0.6 \pm 0.1)$ MHz. A complete study of the magnetic parameters for this remote nitrogen nucleus will be published elsewhere.

In summary, we have shown for the first time that in [Cu^{II}(nctpp)] the three nitrogens of the porphyrin core are not equivalent, in contrast to [Cu^{II}(tpp)] where all four nitrogens are described by the same principal values of the hyperfine tensor, $(A_1, A_2, A_3) = (54.2, 42.8, 44.1)$ MHz.[10] More specifically, in [Cu^{II}(nctpp)] two of the core nitrogen nuclei are magnetically equivalent and have a considerably larger hyperfine coupling, $(A_1, A_2, A_3) = (71.5, 58.3, 59.5)$ MHz, whereas a much smaller hyperfine coupling of $(A_1, A_2, A_3) =$

(26.5, 35, 26.5) MHz is found for the third nitrogen nucleus. Thus, we conclude that the inversion of the pyrrole ring in [Cu^{II}(nctpp)] is followed by a strong asymmetric distribution of the electron spin density on the three nitrogen nuclei, demonstrating the breaking of the D_{4h} symmetry. This is in good agreement with preliminary results obtained by DFT computations.[12] On the basis of these findings it is tempting to study which other changes and special features of the electronic structure of this rare organometallic compound can be observed.

Received: January 14, 2005
Published online: April 28, 2005

Keywords: copper · ENDOR spectroscopy · EPR spectroscopy · porphyrins

[1] L. R. Milgrom, *The Colours of Life: An Introduction to the Chemistry of Porphyrins and Related Compounds,* Oxford University Press, Oxford, **1997**.
[2] L. Latos-Grażyński in *The Porphyrin Handbook*, *Vol. 2* (Eds.: K. M. Kadish, K. M. Smith, R. Guilard), Academic Press, San Diego, **2000**, chap. 14.
[3] H. Furuta, H. Maeda, A. Osuka, *Chem. Commun.* **2002**, 1795 – 1804.
[4] H. Maeda, Y. Ishikawa, T. Matsuda, A. Osuka, H. Furuta, *J. Am. Chem. Soc.* **2003**, *125*, 11822 – 11823.
[5] J. D. Harvey, C. J. Ziegler, *Coord. Chem. Rev.* **2003**, *247*, 1 – 19.
[6] P. J. Chmielewski, L. Latos-Grażyński, I. Schmidt, *Inorg. Chem.* **2000**, *39*, 5475 – 5482.
[7] A. Schweiger, G. Jeschke, *Principles of Pulse Electron Paramagnetic Resonance*, Oxford University Press, Oxford, **2001**.
[8] G. R. Geier III, D. M. Haynes, J. S. Lindsey, *Org. Lett.* **1999**, *1*, 1455 – 1458.
[9] All simulations were performed using the EasySpin package (http://www.esr.ethz.ch).
[10] T. G. Brown, B. M. Hoffman, *Mol. Phys.* **1980**, *39*, 1073 – 1109.
[11] I. Gromov, J. Shane, J. Forrer, R. Rakhmatoullin, Yu. Rozentzwaig, A. Schweiger, *J. Magn. Reson.* **2001**, *149*, 196 – 203.
[12] DFT computation gives hyperfine couplings of two ^{14}N nuclei with $(A_1, A_2, A_3) = (80, 65, 66)$ MHz and one with $(A_1, A_2, A_3) = (28, 35, 28)$ MHz.

Stereoselective Reactions

Efficient 1,5-Chirality Transfer in Palladium-Catalyzed Allylic Alkylations of Chelated Amino Acid Ester Enolates**

Uli Kazmaier and Thomas Lindner*

Dedicated to Professor Franz Effenberger on the occasion of his 75th birthday

Of the palladium-catalyzed reactions, allylic alkylations are especially popular, not least because of a number of stereoselective variants.[1] In general, heteronucleophiles are used as well as symmetric stabilized carbanions such as malonates as C nucleophiles. The advantage of the latter is that in the C–C coupling step only one stereogenic center is created, that is, that in the allyl fragment. In contrast, the use of unsymmetrical nucleophiles (Nu) such as β-ketoesters[2] and imines of amino acid esters[3] in general results in mixtures of diastereomers. Therefore, most examples in the literature dealing with the stereochemical outcome of the allylic alkylation focus on 1,3-disubstituted allylic systems (Scheme 1). In reactions of substrates **A**, which form a symmetric achiral π-allyl palladium complex **B**, the stereochemical outcome can be controlled by chiral ligands (L*). In contrast, unsymmetric substrates **C** give rise to the chiral allyl complex **D**, and stereogenic information is transferred from the starting material **C** to the product **E**.[1] The only snag is the

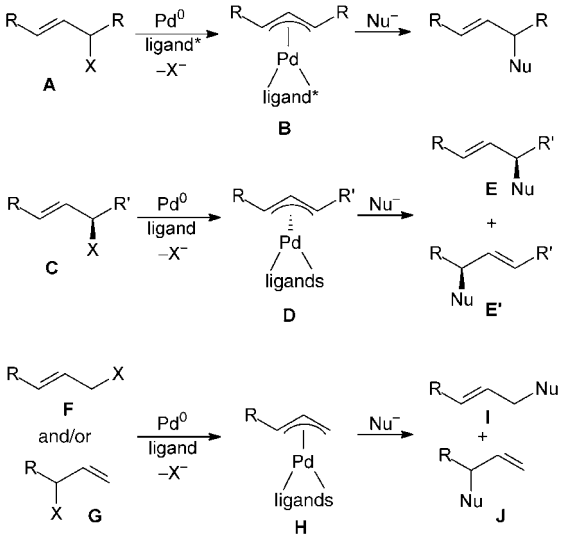

Scheme 1. Asymmetric palladium-catalyzed allylic alkylations.

[*] Prof. Dr. U. Kazmaier, Dipl.-Chem. T. Lindner
Institut für organische Chemie
Universität des Saarlandes
Im Stadtwald, Geb. 23.2, 66123 Saarbrücken (Germany)
Fax: (+49) 681-302-2409
E-mail: u.kazmaier@mx.uni-saarland.de

[**] This work was supported by the Deutsche Forschungsgemeinschaft (SFB 247 and Ka 880/5) and the Fonds der Chemischen Industrie.

 DOI: 10.1002/anie.200500095

problem of regioselectivity. Especially the reaction of substrates bearing very similar substituents R and R′ results in the formation of product mixtures (**E** + **E**′).[4]

This problem is less significant with substrates **F** and **G**, which form the terminal π-allylpalladium complexes **H**, since these allyl complexes are usually attacked at the sterically least hindered position (→**I**). Therefore, for stereoselective synthesis these substrates are uninteresting, because in reactions of symmetrical nucleophiles only achiral products are obtained, while the application of unsymmetrical nucleophiles gives rise to racemic mixtures. Even the use of enantiomerically pure substrates **G** is not a solution to this problem, because the chiral information is lost nearly immediately through π-σ-π isomerization.[5] To the best of our knowledge a suitable protocol for transferring chiral information from the allyl substrate to the stereogenic center in the attacking nucleophile has not yet been reported.

Terminal complexes such as **H** can be converted into optically active products **J** only if the nucleophilic attack can be directed towards the sterically more hindered position. According to Pfaltz et al. this goal can be reached by switching the reaction mechanism from an S_N2-type towards a more S_N1-type mechanism.[6] For example, with phosphite ligands[7] instead of phosphanes, the branched products **J** are formed preferentially. These can be obtained in an enantiomerically enriched form when chiral ligands such as phosphite oxazolines[6] and sterically demanding monophosphanes are used.[8] Other metals such as molybdenum,[9] tungsten,[10] and iridium[11] also have a higher tendency for the formation of branched product **J**. It is known that rhodium complexes in general do not undergo π-σ-π isomerization, and therefore they facilitate chirality transfer from an optically active substrate to the product **J**.[12]

Our group is investigating reactions of chelated amino acid ester enolates **K** and also their application as nucleophiles in palladium-catalyzed allylic alkylations.[13] These nucleophiles react under much milder conditions than the "standard nucleophiles". In addition, they also allow the generation of a second stereogenic center, and this generally in a highly stereoselective fashion. Because these chelated enolates already react at −78 °C, π-σ-π isomerization can be suppressed nearly completely.[14] Therefore, *Z*-configurated allyl substrates **L** can be converted into the corresponding *syn*/*anti* allyl complex **M** (without isomerization), which then is attacked by **K** regioselectively at the "*anti* position" (Scheme 2). This allows a chirality transfer from **L** to **N**. The diastereoselectivity of the formation of the allylation product **N** depends on the substituent R and increases with the decreasing bulk of R.

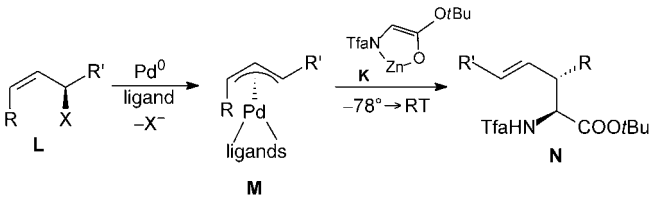

Scheme 2. Palladium-catalyzed allylic alkylations of chelated enolates. Tfa = trifluoroacetyl.

One might therefore expect the best selectivity for R = H. In this case only one stereogenic center is formed, and we hoped that the high selectivity of the nucleophilic attack on the allyl complex could be used for chirality transfer directly to the α-position of the amino acid formed. But with R = H the problems discussed above take effect, and the very fast π-σ-π isomerization of terminal π-allyl palladium complexes prevents chirality transfer from **L** to **N**. Therefore we focused our attention on reactions of substrates such as **1** which are easily obtained from lactic acid. We investigated the influence of the O-protecting group (PG) on the stereochemical outcome of the reaction (Scheme 3, Table 1). We chose

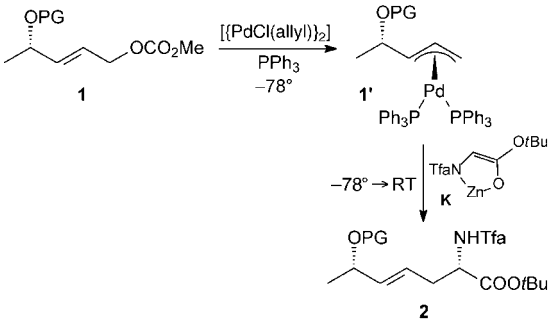

Scheme 3. Diastereoselective allylation of chelated enolates; see also Table 1.

Table 1: Diastereoselective allylation of chelated enolates; see also Scheme 3.

Entry	Substrate	PG[a]	Yield [%]	ds [%][a]
1	**1a**	MOM	89	71[b]
2	**1b**	THP	96	80[b]
3	**1c**	Bn	99	87[b]
4	**1d**	TBDMS	99	84[c]
5	**1e**	TBDPS	93	96[c]
6	**1f**	Trt	–	
7	**1g**	Piv	85	93[b]

[a] MOM = methoxymethyl, THP = tetrahydropyranyl, Bn = benzyl, TBDMS = *tert*-butyldimethylsilyl, TBDPS = *tert*-butyldiphenylsilyl, Trt = trityl, Piv = pivaloyl, ds = diastereoselectivity. [b] Determined by ^{13}C NMR spectroscopy. [c] Determined by HPLC.

methyl carbonate as the leaving group and trifluoroacetyl-protected *tert*-butyl glycinate as the nucleophile. The yields were excellent and nearly independent of the O-protecting group used; only with the tritylated substrate (Table 1, entry 6) was no reaction observed. It seems in this case that the coordination of the palladium to the alkene is hindered for steric reasons. Apparently the coordination occurs from the face opposite to the oxygen atom, giving rise to allyl complex **1**′, which then is attacked by the chelated enolate **K** from the backside. The diastereoselectivities obtained nicely correlate with the size of the O-protecting group, which is especially significant in the switch from the TBDMS to the sterically more demanding TBDPS protecting group. The latter protecting group gave 96 % ds, an excellent result especially when one considers that this is an example of 1,5-induction.

An equally good result was obtained with the pivaloyl derivative **1g**. This substrate is quite interesting because it has two leaving groups, which should both be replaceable. The primary carbonate leaving group is the significantly more reactive one. With one equivalent of nucleophile the monosubstitution product **2f** was formed exclusively, while with 2.6 equivalents of **K** a mixture of **2f** (55%) and the disubstituted product **3f** (44%, 75% ds) in almost quantitative overall yield was obtained. In principle it should be possible to use the pivaloate group in the first step to control the configuration at the α-position of the amino acid before it is replaced in the second step by various other nucleophiles.

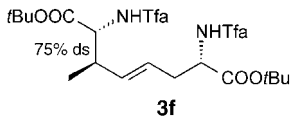

3f

To get an impression of how fast the π-σ-π isomerization of these terminal allyl substrates occurs, we also subjected the *Z* substrate *rac*-**4e** to the same reaction conditions (Scheme 4). As mentioned earlier, with 1,3-disubstituted substrates of type **L** (Scheme 2) the isomerization was suppressed completely.[14] If this is also true with terminal allyl complexes one might expect (Z)-**2e** as the substitution product. In contrast, *rac*-**2e** was formed with exactly the same selectivity as obtained from **1e**. This clearly indicates that in terminal π-allyl complexes the π-σ-π isomerization is even faster than the substitution with these highly reactive nucleophiles.

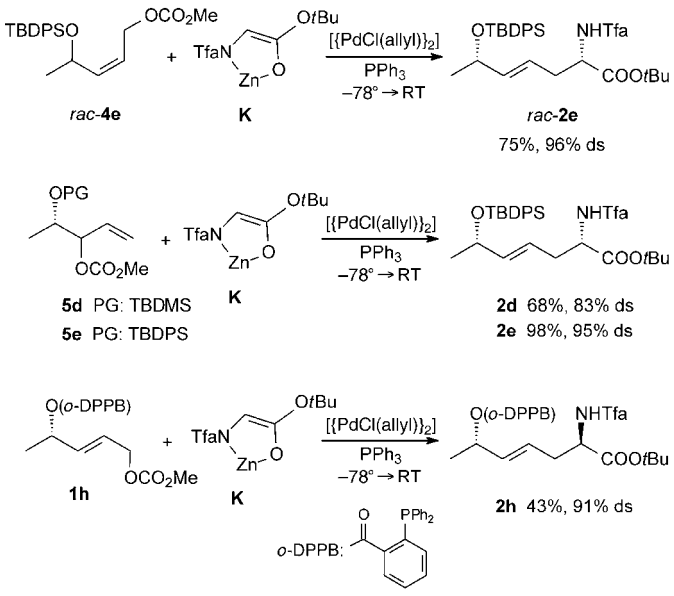

Scheme 4. Diastereoselective allylation of chelated enolates.

With this in mind one should expect that analogous substrates **5** with a secondary leaving group should provide the same substitution products, independent of the configuration of the leaving group. This is a very interesting option, because these substrates are easily accessible. Therefore we investigated the reaction of the two silyl-protected derivatives **5d** and **5e**, and indeed, the selectivities obtained were exactly the same as with the linear substrates **1d** and **1e**.

In all examples investigated so far, the *syn*-configurated product was obtained preferentially. To provide the corresponding *anti* isomer, the palladium must be coordinated to the opposite face of the alkene, in other words, the face of the O-substituent. Breit et al. reported for hydroformylation reactions that coordinating protecting groups such as the diphenylphosphanylbenzoate (*o*-dppb) are especially suitable for this purpose.[15] As illustrated with the *o*-dppb-protected substrate **1h**, such a directing effect can also be used for stereoselective allylations. By this synthetic protocol both stereoisomeric products can be obtained from one substrate (allylic alcohol) in a highly stereoselective fashion.

To test the generality of this concept we also subjected substrate **6a** (with the sterically demanding isopropyl group) and the **6b** (with a ketal protecting group) to our reaction conditions (Scheme 5). Indeed, the results were comparable to those obtained with the corresponding methyl-substituted derivatives **1**.

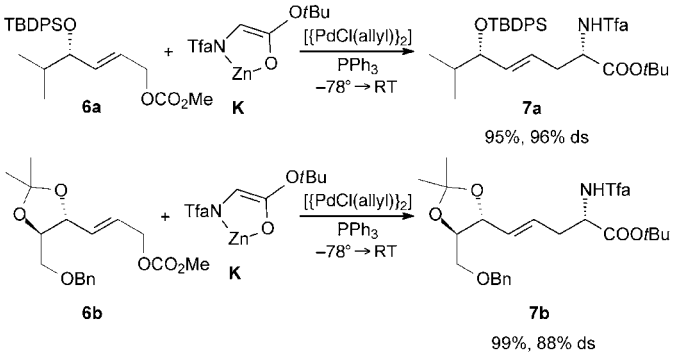

Scheme 5. Reactions of substituted allylic substrates.

In conclusion we could show that chelated enolates are good nucleophiles for stereoselective allylations of both 1,3-disubstituted and also terminal allylic substrates. Neither the position and configuration of the leaving group nor the olefin geometry influences on the stereochemical outcome of the reaction. This is exclusively controlled by the O-protecting group used. Further investigations are in progress.

Experimental Section

General procedure for palladium-catalyzed allylic alkylations: Hexamethyldisilazane (226 mg, 1.40 mmol) was dissolved in THF (1.5 mL) in a Schlenk flask under argon. After the solution had been cooled to −78 °C, *n*BuLi (1.6 M, 0.80 mL, 1.25 mmol) was added slowly. The reaction mixture was stirred for 20 min at this temperature, and then the cooling bath was removed and stirring was continued for further 15 min. In a second Schlenk flask *N*-trifluoroacetyl *tert*-butyl glycinate (114 mg, 0.50 mmol) was dissolved in THF (3 mL). The solution was cooled to −78 °C, before the fresh prepared lithium hexamethyldisilazanide solution was added. After 15 min a solution of dried $ZnCl_2$ (75 mg, 0.55 mmol) in THF (0.5 mL) was added, and stirring was continued for 30 min.

A solution was prepared from [{PdCl(allyl)}$_2$] (10 mg, 0.025 mmol) and PPh_3 (30 mg, 0.113 mmol) in THF (5 mL). After this solutionwas stirred for 15 min at room temperature, it was added to the chelated enolate at −78 °C. At the same temperature the allyl substrate (0.3 mmol) was added in THF (0.5 mL) before the mixture was allowed to warm to room temperature overnight. The solution was diluted with ether before 1 M $KHSO_4$ was added (NH_4Cl for ketal-protected substrates). After separation of the layers, the aqueous layer was extracted three times with ether, and the combined organic layers were dried over Na_2SO_4. The solvent was evaporated in vacuo, and the crude product was purified by flash chromatography.

Received: January 11, 2005
Published online: April 25, 2005

Keywords: allylation · amino acids · chelates · enolates · palladium

[1] Reviews: a) S. A. Godleski in *Comprehensive Organic Synthesis*, *Vol. 4* (Eds.: B. M. Trost, I. Fleming), Pergamon, Oxford, **1991**, pp. 585 – 661; b) T. Lübbers, P. Metz in *Houben-Weyl—Stereoselective Synthesis*, (Eds.: G. Helmchen, R. W. Hoffmann, J. Mulzer, E. Schaumann), Thieme, Stuttgart, **1996**, pp. 2371 – 2473; c) B. M. Trost, D. L. VanVranken, *Chem. Rev.* **1996**, *96*, 395 – 422; d) J. M. J. Williams, *Synlett* **1996**, 705 – 710; e) U. Kazmaier, M. Pohlman in *Metal Catalyzed C-C and C-N Coupling Reactions* (Eds.: A. de Meijere, F. Diederich), Wiley-VCH, Weinheim, **2004**, pp. 531 – 584, and references therein.

[2] a) I. Shimizu, M. Toyoda, T. Terashima, M. Oshima, H. Hasegawa, *Synlett* **1992**, 301 – 302; b) N. Greeves, J. S. Torode, *Synthesis* **1993**, 1109 – 1112; c) T. Hayashi, A. Ohno, S. Lu, Y. Matsumoto, E. Fukuyo, K. Yanagi, *J. Am. Chem. Soc.* **1994**, *116*, 4221 – 4226; d) K. Hiroi, A. Hidaka, R. Sezaki, Y. Imamura, *Chem. Pharm. Bull.* **1997**, *45*, 769 – 777.

[3] a) D. Ferroud, J. P. Genet, R. Kiolle, *Tetrahedron Lett.* **1986**, *27*, 23 – 26; b) J. C. Baldwin, J. M. J. Williams, R. P. Beckett, *Tetrahedron: Asymmetry* **1995**, *6*, 1515 – 1518.

[4] a) B. M. Trost, T. R. Verhoeven in: *Comprehensive Organometallic Chemistry*, *Vol. 8* (Eds.: G. Wilkinson, F. G. A. Stone, E. W. Abel), Pergamon, Oxford, **1982**, pp. 799 – 938; b) L. S. Hegedus in *Organometallics in Synthesis* (Ed.: M. Schlosser), Wiley, Chichester, **1994**, pp. 427 – 444; c) J. Tsuji, *Palladium Reagents and Catalysts—Innovations in Organic Synthesis*, Wiley, Chichester, **1995**.

[5] P. Corradini, G. Maglio, A. Musco, G. Paiaro, *Chem. Commun.* **1966**, 618 – 619.

[6] R. Prétôt, A. Pfaltz, *Angew. Chem.* **1998**, *110*, 337 – 339; *Angew. Chem. Int. Ed.* **1998**, *37*, 323 – 325.

[7] J. Ansell, M. Wills, *Chem. Soc. Rev.* **2002**, *31*, 259 – 268.

[8] a) T. Hayashi, M. Kawatsura, Y. Uozumi, *Chem. Commun.* **1997**, 561 – 562; b) T. Hayashi, *J. Organomet. Chem.* **1999**, *576*, 195 – 202.

[9] a) B. M. Trost, M. Lautens, *Tetrahedron* **1987**, *43*, 4817 – 4840; b) B. M. Trost, I. Hachiya, *J. Am. Chem. Soc.* **1998**, *120*, 1104 – 1105; c) B. M. Trost, S. Hildbrand, K. Dogra, *J. Am. Chem. Soc.* **1999**, *121*, 10416 – 10417; d) F. Glorius, A. Pfaltz, *Org. Lett.* **1999**, *1*, 141 – 144; e) A. v. Malkov, I. R. Baxendale, D. J. Mansfield, P. Kocovsky, *J. Chem. Soc. Perkin Trans. 1* **2001**, 1234 – 1240; f) F. Glorius, M. Neuburger, A. Pfaltz, *Helv. Chim. Acta* **2001**, *84*, 3178 – 3196.

[10] a) B. M. Trost, M. H. Hung, *J. Am. Chem. Soc.* **1983**, *105*, 7757 – 7759; b) J. Lehmann, G. C. Lloyd-Jones, *Tetrahedron* **1995**, *51*, 8863 – 8874; c) G. C. Lloyd-Jones, A. Pfaltz, *Angew. Chem.* **1995**, *107*, 534 – 536; *Angew. Chem. Int. Ed. Engl.* **1995**, *34*, 462 – 464.

[11] a) R. Takeuchi, M. Kashio, *Angew. Chem.* **1997**, *109*, 268 – 270; *Angew. Chem. Int. Ed. Engl.* **1997**, *36*, 263 – 265; b) R. Takeuchi, M. Kashio, *J. Am. Chem. Soc.* **1998**, *120*, 8647 – 8655; c) B. Bartels, G. Helmchen, *Chem. Commun.* **1999**, 741 – 742; d) K. Fuji, N. Kinoshita, K. Tanaka, T. Kawabata, *Chem. Commun.* **1999**, 2289 – 2290.

[12] a) P. A. Evans, J. D. Nelson, *J. Am. Chem. Soc.* **1998**, *120*, 5581 – 5582; b) P. A. Evans, L. J. Kennedy, *Org. Lett.* **2000**, *2*, 2213 – 2215; c) P. A. Evans, L. J. Kennedy, *J. Am. Chem. Soc.* **2001**, *123*, 1234 – 1235.

[13] a) U. Kazmaier, F. L. Zumpe, *Angew. Chem.* **1999**, *111*, 1572 – 1574; *Angew. Chem. Int. Ed.* **1999**, *38*, 1468 – 1470; b) U. Kazmaier, D. Schauß, M. Pohlman, *Org. Lett.* **1999**, *1*, 1017 – 1019; c) U. Kazmaier, M. Pohlman, D. Schauß, *Eur. J. Org. Chem.* **2000**, 2761 – 2766; d) T. D. Weiss, G. Helmchen, U. Kazmaier, *Chem. Commun.* **2002**, 1270 – 1271; e) U. Kazmaier, *Curr. Org. Chem.* **2003**, 317 – 328.

[14] a) U. Kazmaier, F. L. Zumpe, *Angew. Chem.* **2000**, *112*, 805 – 807; *Angew. Chem. Int. Ed.* **2000**, *39*, 802 – 804; b) U. Kazmaier, F. L. Zumpe, *Eur. J. Org. Chem.* **2001**, 4067 – 4076; c) U. Kazmaier, M. Pohlman, *Synlett* **2004**, 623 – 626.

[15] B. Breit, P. Demel, C. Studte, *Angew. Chem.* **2004**, *116*, 3874 – 3877; *Angew. Chem. Int. Ed.* **2004**, *43*, 3786 – 3789.

Molecular Magnets

Magnetic Moments of the Endohedral Cluster Fullerenes $Ho_3N@C_{80}$ and $Tb_3N@C_{80}$: The Role of Ligand Fields

*Manfred Wolf, Karl-Hartmut Müller, Yurii Skourski, Dieter Eckert, Petra Georgi, Matthias Krause, and Lothar Dunsch**

The electronic and magnetic properties of endohedral fullerenes $M_k@C_{2n}$ for different metals M (such as lanthanides R, Group 3 and Group 2 metals) is a current area of endohedral fullerene research.[1] The influence of the electron transfer from M to the carbon cage, the geometric structure of the $M_k@C_{2n}$, as well as the location of the metal ion(s) in the cage on the magnetic properties are commonly studied. As shown by ESR spectroscopy, photoemission or Mössbauer spectroscopy, R ions are trivalent in most cases as in $Er_k@C_{82}$ for $k = 1$ and 2[2,3] and $Dy@C_{2n}$ ($2n = 80$, 82, 84).[4] Detailed studies of the fullerene magnetization versus applied field and temperature have confirmed these results.[5–11] On the other hand europium was found to be divalent in fullerenes for $2n = 74$ or

[*] Dr. M. Wolf, Dr. K.-H. Müller, Dr. D. Eckert, Dr. P. Georgi, Dr. M. Krause, Prof. Dr. L. Dunsch
IFW Dresden
POB 270116, 01171 Dresden (Germany)
Fax: (+49) 351-465-9811
E-mail: l.dunsch@ifw-dresden.de
Dr. Y. Skourski
Max-Planck-Institut für Physik komplexer Systeme Dresden
Nöthnitzer Strasse 38, 01187 Dresden (Germany)

  DOI: 10.1002/anie.200461500

82.[9,10] The formal valency of an ion M depends also on the number of the ions encaged: For $Sc_k@C_{82}$ ($k=1, 2, 3$) Takata et al.[12] reported scandium to be divalent for $k=1$ or 2, whereas for $k=3$ the whole trimer has a charge of $+3$, $(Sc_3)^{3+}$, that is, the formal valency of scandium is $+1$. Endohedral thulium is divalent in $Tm@C_{82}$,[13,14] whereas a $+3$ state is discussed for $Tm_2@C_{82}$.[15,16] Structural studies on $Sc_2@C_{84}$,[17] $Sc_3@C_{82}$,[12] $La@C_{82}$[18] and $Er_2@C_{82}$[3] show the metal ions in an off-center position in the cage causing a low symmetry of the fullerene. In $Sc_3@C_{82}$ the scandium ions form a (nearly) equilateral triangle.[12]

A new type of endohedral fullerene was introduced with the nitride cluster fullerenes such as $Sc_3N@C_{80}$ which are stable endohedral structures of carbon cages, and are almost as stable as empty cages. In $Sc_3N@C_{80}$, the nitrogen atom is bonded to the three scandium atoms in a triangular planar configuration.[19,20] The entire Sc_3N cluster is bonded to the C_{80} cage, the shortest Sc–C_{80} distances being of the order of 2.3 to 2.5 Å.[19,20] This bond configuration which is measured in a short-time-scale experiment may be hidden in experiments with a longer time scale. For example, ^{13}C NMR spectroscopy indicated a time-averaged structural picture of a non-interacting I_h-C_{80} cage and an isotropic Sc_3N cluster.[19] More detailed investigations revealed a complex diffusion dynamics of the encaged cluster at room temperature.[21]

The interest in endohedral fullerenes encapsulating lanthanide ions is related to the unfilled 4f shell of the lanthanide ions, which gives rise to large magnetic moments and a variety of interesting magnetic properties. Also, these materials have a great potential for applications as contrast agents for magnetic resonance or X-ray investigations, biological tracing agents, and radiopharmaceuticals.[22,23] Some of these applications are closely related to the unique magnetic properties of these materials. For the first time, we present herein a new magnetic structure for the R_3N clusters (R = Ho, Tb) in the systems $Ho_3N@C_{80}$ and $Tb_3N@C_{80}$, and explain the unexpected values observed for the magnetic moments of the encapsulated nitride clusters. These results provide information on the interaction between the magnetic moments of rare-earth metals encapsulated in the fullerene cage. The magnetic properties are used to determine the oxidation state of R in $R_3N@C_{80}$.

By using a new preparative route[24] for nitride cluster fullerenes, $Ho_3N@C_{80}$ and $Tb_3N@C_{80}$ were synthesized in high yields and with an outstanding selectivity. As demonstrated by HPLC analysis of the holmiumnitride fullerene soot (Figure 1), $Ho_3N@C_{80}$ is the main component in the fullerene soot and can be easily isolated by one HPLC run. Besides $Ho_3N@C_{80}$ small amounts of the endohedral structure $Ho_3N@C_{82}$ and higher cage sizes were produced. The high purity of the isolated samples is confirmed by mass spectrometric data (Figure 1, inset). The fullerenes C_{60} and C_{70} appeared as byproducts of the reaction. $Ho_3N@C_{80}$ and $Tb_3N@C_{80}$ are large-energy-gap fullerenes having optical gaps of approximately 1.75 eV.[24] By Vis-NIR and FTIR analysis both cluster fullerenes were assigned to the carbon cage C_{80}:7 with icosahedral symmetry I_h.[24] Electron spin resonance experiments revealed that both structures are diamagnetic at room temperature.

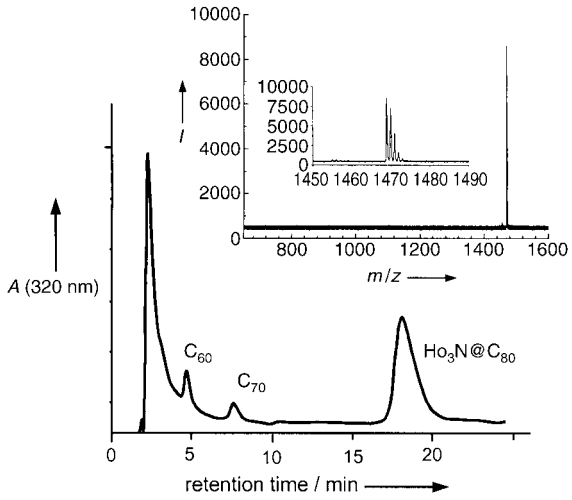

Figure 1. HPLC trace of the $Ho_3N@C_{2n}$ soot on a Buckyprep column with toluene as an eluent. The chromatogram shows the dependence of the optical absorption at $\lambda = 320$ nm on the retention time, which reveals that $Ho_3N@C_{80}$ is the main component of the soot. Inset: LD-TOF mass spectrum confirming the high purity of the $Ho_3N@C_{80}$ sample.

The results of our magnetic studies are presented in Figures 2 and 3. The field dependence of magnetization

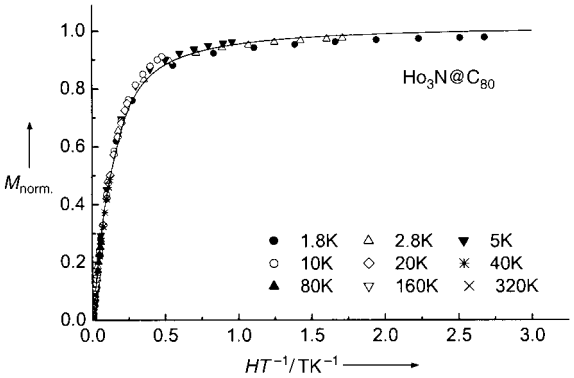

Figure 2. The experimental data $M(H,T)$ for $Ho_3N@C_{80}$ (symbols) corrected for the diamagnetic contribution and normalized to the saturation. The solid line represents the fitted Langevin function with a magnetic moment $\mu = 21\ \mu_B$.

$M(H,T)$ of $Ho_3N@C_{80}$ and $Tb_3N@C_{80}$ was measured at various temperatures. For both structures the $M(H,T)$ data fit well with a simple dependence on only one variable, HT^{-1}, pointing to an ideal Curie paramagnetism. The observed magnetization curves can be described by the Langevin function $M(H/T) = m_s L(\mu H/k_B T)$, with μ as the moment of the fullerene molecule and k_B as the Boltzmann constant. The as determined values of μ are 21 μ_B for $Ho_3N@C_{80}$ and 17 μ_B for $Tb_3N@C_{80}$ (μ_B = Bohr's magneton). The large values of μ justify the neglect of quantum effects, that is, the description of the magnetic behavior by a Langevin function. These moments for the fullerene molecules are quite different from those of non-interacting Ho^{3+} ions (10 μ_B) or Tb^{3+} ions (9 μ_B). Also, they cannot be explained by a linear antiferromagnetic

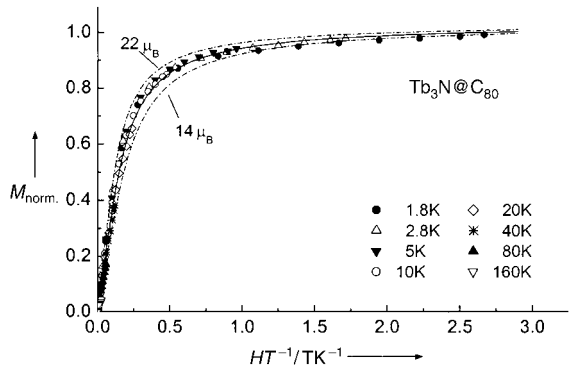

Figure 3. The experimental data $M(H,T)$ for $Tb_3N@C_{80}$ (symbols) corrected for the diamagnetic contribution and normalized to the saturation. The solid line represents the fitted Langevin function with a magnetic moment $\mu = 17\,\mu_B$. The broken lines correspond to the normalized magnetization for $\mu = 14\,\mu_B$ and $\mu = 22\,\mu_B$.

or ferromagnetic alignment of the three moments in the cages. A ferromagnetic linear alignment would result in $30\,\mu_B$ for $Ho_3N@C_{80}$ and $27\,\mu_B$ for $Tb_3N@C_{80}$.

The field and temperature dependence of the magnetization of $Ho_3N@C_{80}$ and $Tb_3N@C_{80}$ can be understood by assuming a stable configuration of the magnetic moments the three atoms R, which is unchanged in the temperature and field range under investigation. These net magnetic moments μ do not experience any significant magnetic anisotropy. Otherwise the field and temperature dependence of magnetization would deviate from that shown in Figure 2 and Figure 3.[25,26]

A comparison with the literature data on $Sc_3@C_{82}$,[12] $Er_xSc_{3-x}@C_{80}$,[29] $Lu_3N@C_{80}$,[23] and $Sc_3N@C_{80}$[20] allows the following conclusions to be drawn: 1) the three Ho or Tb ions form a nearly equilateral triangle with one N^{3-} species in its center as shown in Figure 4a, and 2) both in $Ho_3N@C_{80}$ and $Tb_3N@C_{80}$ each of the rare-earth ions is in the +III state. Such a charge distribution is supported by HPLC, Vis-NIR, and FTIR data.[23] On taking up six electrons the C_{80} cage attains a closed-shell like that found for $Sc_3N@C_{80}$.[19,20,27,28] No contributions of N^{3-} and $[C_{80}]^{6-}$ to the magnetic moment are expected and the magnetic behavior is governed only by the cluster $(Ho^{3+})_3N^{3-}$ or $(Tb^{3+})_3N^{3-}$. As the cage has no spin, contrary to the case of endohedral monometallofullerenes,[30] no coupling between the R magnetic moments and the cage has to be taken into account.

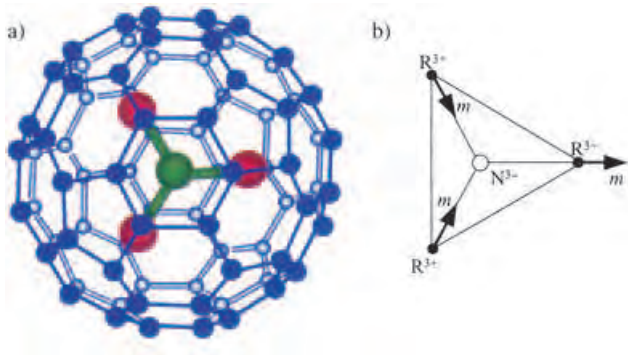

Figure 4. a) Structure of a $R_3N@C_{80}$ molecule according to ref. [18], blue: carbon, green: nitrogen, and red: rare earth atoms; b) orientation of the individual R magnetic moments m (arrows) in the R_3N cluster in $R_3N@C_{80}$ (R = Ho, Tb).

The total magnetic moments μ of $Ho_3N@C_{80}$ and $Tb_3N@C_{80}$ do not experience any detectable magnetic anisotropy. Taking into account the diffusion dynamics of R_3N and that "static" magnetic measurements have a longer time scale than NMR spectroscopy experiments, this situation is in agreement with the current model for $Sc_3N@C_{80}$.[19–21] However, the single R ions are subjected to ligand fields resulting in a magnetic anisotropy of the individual R magnetic moments with respect to local directions within the R_3N cluster. The ligand field of the nitrogen ion in the R_3N cluster causes the preferred direction of the R magnetic moments with respect to the R–N bonds. If these R–N bonds are "magnetically easy directions" and the magnetic anisotropy caused by the ligand fields is relatively strong compared to the exchange interaction between the R magnetic moments, the direction of these moments will be "pinned" along the bond directions. For ferromagnetic exchange the configuration of the three magnetic moments is shown in Figure 4b. A vector addition of the three (classical) R magnetic moments m results in the magnitude $2\,|m|$, that is, $20\,\mu_B$ for the Ho_3N cluster and $18\,\mu_B$ for Tb_3N, which is in good agreement with the results given above. Antiferromagnetic exchange can be excluded as it would result in a vanishing total moment of the $R_3N@C_{80}$ molecule. The charge distribution of these cluster fullerenes can be formally described as $(R^{3+})_3N^{3-}@C_{80}^{6-}$. Because the N^{3-} as well as C_{80}^{6-} ions do not contribute to the magnetic moment and the R magnetic moments are shielded by a carbon cage which has a filled electron shell, $Ho_3N@C_{80}$ and $Tb_3N@C_{80}$ do not show a finite paramagnetic Curie temperature, and magnetic hysteresis as well as differences between zero field and field cooling conditions do not occur. The vanishing (or very small) magnetic anisotropy is suggested to be related to the closed shell of the C_{80}^{6-} ion. This situation is in contrast to results on endohedral monometallofullerenes, for which the contribution of the π electron has to be taken into account.[31]

In summary, the net magnetic moments of the encaged (R_3N) trimer (R = Ho, Tb) can not be explained either by non-interacting magnetic moments from R, nor by a dominant ferromagnetic or antiferromagnetic exchange interaction between the R moments. The net moments of $21\,\mu_B$ ($Ho_3N@C_{80}$) and $17\,\mu_B$ ($Tb_3N@C_{80}$) are explained by a new model for the magnetic structure of $Ho_3N@C_{80}$ and $Tb_3N@C_{80}$, in which strong ligand fields within the (R_3N) cluster act on the ferromagnetically exchange-coupled moments of R. As a result of this combination of different types of interaction the individual R moments are not collinearly aligned but are parallel to the R–N bonds (R = Ho or Tb).

Experimental Section

The cluster fullerenes were prepared using a modified Krätschmer–Huffman arc burning method. Two modifications of this process were

applied: In a first version a solid nitrogen source was used by adding varying amounts of calcium cyanamide to the metal/graphite powder mixture. As the main and second synthetic route the concept of the reactive arc atmosphere[32] was applied to improve the ratio of trimetal nitride fullerenes to empty fullerenes. In general, graphite rods filled with a metal/graphite or metaloxide/graphite powder mixture were used. The soot of the arc burning process was soxhlet extracted with CS_2 for 20 h. After extraction non-fullerene products such as polycyclic aromatic hydrocarbons and other low molecular structures were removed from the extract by washing with acetone.

High performance liquid chromatography (HPLC) was used for fullerene purification and analysis (BuckyPrep column, Nacalai Tesque). Owing to the high content of the $R_3N@C_{80}$ structure (R = Ho or Tb) in the fullerene extract these fullerenes were isolated by a single separation step using a 4.6×250 mm BuckyPrep column. The resulting purity was over 95%.

The mass spectrometric characterization was by MALDI-TOF mass spectrometry using the Biflex II spectrometer (Bruker, Germany) and 9-nitroanthracene as the matrix. Positive and negative ions of the fullerenes were detected.

The magnetic measurements were performed on a SQUID magnetometer at temperatures T from 1.8 K to room temperature in magnetic fields H up to 5 Tesla. As the mass of the investigated samples was very small (about 60 μg in the case of $Ho_3N@C_{80}$, 40 μg for $Tb_3N@C_{80}$) the as measured magnetization values $M_{exp}(H,T)$ data revealed a remarkable diamagnetic contribution to the susceptibility, χ_{dia}, from the encapsulating glass ampoule and a two-step analysis had to be done. In a first step χ_{dia} was determined from a fit of $m_s L(\mu H/k_B T) + \chi_{dia} H$ to M_{exp}. The magnetization values $M(H,T)$ of the fullerene powder is then given by $M(H,T) = M_{exp} - \chi_{dia} H$. The final values of m_s and μ were determined by fitting $m_s L(\mu H/k_B T)$ to these $M(H,T)$ values. The very small changes in m_s and μ demonstrated the consistency of the procedure. Furthermore it is noted, that such small fullerene amounts were "smeared" over the walls of the encapsulating glass ampoule in the SQUID magnetometer. Therefore the absolute value of the magnetization of the sample could not be determined sufficiently precisely. However the dependence of the magnetization $M(H,T)$ normalized to m_s on field and temperature could be determined with an accuracy of typically 1% as confirmed by repeated measurements. Regarding μ, the fitting results have been verified by a comparison of the fitted magnetization curve with theoretical curves for assumed μ values of 22 μ_B and 14 μ_B in the case of $Tb_3N@C_{80}$ (see Figure 3).

Received: July 31, 2004
Revised: January 10, 2005
Published online: April 28, 2005

Keywords: endohedral fullerenes · lanthanides · magnetic moment · molecular magnets · paramagnetism

[1] H. Shinohara, *Rep. Prog. Phys.* **2000**, *63*, 843.
[2] M. E. J. Boonman, P. H. M. van Loosdrecht, D. S. Bethune, I. Holleman, G. J. M. Meijer, P. J. M. van Bentum, *Phys. B* **1995**, *211*, 323.
[3] R. M. Macfarlane, G. Wittmann, P. H. M. van Loosdrecht, M. de Vries, D. S. Bethune, St. Stevenson, H. C. Dorn, *Phys. Rev. Lett.* **1997**, *79*, 1397.
[4] Yu. S. Grushko, E. G. Alekseev, V. S. Kozlov, L. I. Molkanov, G. Wortmann, H. Giefers, K. Rupprecht, M. A. Khodorkovskii, *Hyperfine Interact.* **2000**, *126*, 121.
[5] H. J. Huang, S. H. Yang, X. X. Zhang, *J. Phys. Chem. B* **2000**, *104*, 1473.
[6] H. J. Huang, S. H. Yang, X. X. Zhang, *J. Phys. Chem. B* **1999**, *103*, 5928.
[7] B. Diggs, A. Zhou, C. Silva, S. Kirkpatrick, N. T. Nuhfer, M. E. McHenry, D. Petasis, S. A. Majetich, B. Brunett, J. O. Artman, S. W. Staley, *J. Appl. Phys.* **1994**, *75*, 5879.
[8] A. Bartl, L. Dunsch, J. Fröhner, G. Seifert, D. Eckert, M. Wolf, K.-H. Müller, *SPIE J.* **1997**, *3142*, 36.
[9] L. Dunsch, D. Eckert, J. Fröhner, A. Bartl, P. Kuran, M. Wolf, K.-H. Müller, *Electrochem. Soc. Proc.* **1998**, *6*, 955.
[10] K.-H. Müller, L. Dunsch, D. Eckert, M. Wolf, A. Bartl, *Synth. Met.* **1999**, *103*, 2417.
[11] H. Funasaka, K. Sakurai, Y. Oda, K. Yamamoto, T. Takahashi, *Chem. Phys. Lett.* **1995**, *232*, 273.
[12] M. Takata, E. Nishibori, M. Sakata, M. Inakuma, E. Yamamoto, H. Shinohara, *Phys. Rev. Lett.* **1999**, *83*, 2214.
[13] T. Pichler, M. S. Golden, M. Knupfer, J. Fink, U. Kirbach, P. Kuran, L. Dunsch, *Phys. Rev. Lett.* **1997**, *79*, 3026.
[14] T. Pichler, M. Knupfer, M. S. Golden, T. Böske, J. Fink, U. Kirbach, P. Kuran, L. Dunsch, C. Jung, *Appl. Phys. A* **1998**, *66*, 281.
[15] "Nanonetwork Materials" K. Kikuchi, K. Sakaguchi, O. Norio, T. Kodama, H. Nishikawa, I. Ikemoto, K. Kohdate, D. Matsumura, T. Yokoyama, T. Ohta, *AIP Conf. Proc.* **2001**, *590*, 473.
[16] K. Kikuchi, K. Akiyama, K. Sakaguchi, T. Kodama, H. Nishakawa, I. Ikemoto, T. Ishigaki, Y. Achiba, K. Sueki, H. Nakahara, *Chem. Phys. Lett.* **2000**, *319*, 472.
[17] M. Takata, E. Nishibori, B. Umeda, M. Sakata, M. Inakuma, E. Yamamoto, H. Shinohara, *Phys. Rev. Lett.* **1997**, *78*, 3330.
[18] W. Andreoni, A. Curioni, *Phys. Rev. Lett.* **1996**, *77*, 834.
[19] S. Stevenson, G. Rice, T. Glass, K. Harich, F. Cromer, M. R. Jordan, J. Craft, E. Hadju, R. Bible, M. M. Olmstead, K. Maitra, A. J. Fisher, A. L. Balch, H. C. Dorn, *Nature* **1999**, *401*, 55.
[20] M. Krause, H. Kuzmany, P. Georgi, L. Dunsch, K. Vietze, G. Seifert, *J. Chem. Phys.* **2001**, *115*, 6596.
[21] "Structural and Electronic Properties of Molecular Nanostructures" K. Vietze, G. Seifert, *AIP Conf. Proc.* **2002**, *633*, 39.
[22] M. Mikawa, H. Kato, M. Okumura, M. Narataki, Y. Kanazawa, N. Miwa, H. Shinohara, *Bioconjugate Chem.* **2001**, *12*, 510.
[23] E. B. Iezzi, J. C. Duchamp, K. R. Fletcher, T. E. Glass, H. C. Dorn, *Nano Lett.* **2002**, *2*, 1187.
[24] L. Dunsch, M. Krause, J. Noack, P. Georgi, *J. Phys. Chem. Solids* **2004**, *65*, 309.
[25] H. D. Williams, K. O'Grady, M. El Hilo, R. W. Chantrell, *J. Magn. Magn. Mater.* **1993**, *122*, 129.
[26] M. Respaud, *J. Appl. Phys.* **1999**, *86*, 556.
[27] J. M. Campanera, C. Bo, M. M. Olmstead, A. L. Balch, J. M. Poblet, *J. Phys. Chem. A* **2002**, *106*, 12356.
[28] T. Akasaka, S. Nagase, K. Kobayashi, M. Wälchli, K. Yamamoto, H. Funasaka, M. Kako, T. Hoshino, T. Erata, *Angew. Chem.* **1997**, *109*, 1716; *Angew. Chem. Int. Ed. Engl.* **1997**, *36*, 1643.
[29] R. M. Macfarlane, D. S. Bethune, S. Stevenson, H. C. Dorn, *Chem. Phys. Lett.* **2001**, *343*, 229.
[30] K. Furukawa, S. Okubo, H. Kato, H. Shinohara, T. Kato, *J. Phys. Chem. A* **2003**, *107*, 10933.
[31] M. Inakuma, H. Kato, A. Taninaka, H. Shinohara, T. Enoki, *J. Phys. Chem. B* **2003**, *107*, 6965.
[32] L. Dunsch, P. Georgi, F. Ziegs, H. Zöller, German patent, DE 10301722A1, **2003**.

Microbubbles

Gas-Filled Polyelectrolyte Capsules**

Dmitry G. Shchukin, Karen Köhler, Helmuth Möhwald, and Gleb B. Sukhorukov*

In the last decade material chemists have been very interested in spatially confined, engineered micro- and nanosystems containing various species (e.g., catalysts, DNA, drugs, enzymes) that are applicable in diagnostics, catalysis, therapy, and bioengineering in both aqueous and nonaqueous media. Most successful examples of such micro- and nanocontainers are liposomes,[1] micelles and microemulsions,[2–5] lipid bilayers,[6] polymer microcapsules,[7] and inorganic hosts.[8–11] The advantages of these structures are their small (and usually variable) size and low toxicity, and the controlled permeability of the microcontainer wall. In general, the inner lumen of emulsions, liposomes, capsules, etc. is composed of either solution or solid material. The only exception among the materials containing gaseous lumen are the so-called ultrasonic contrast agents[12–14] (for a survey of commercial ultrasonic contrast agents see ref. [15]). The fabrication of ultrasonic contrast agents is based on the spontaneous formation of a microbubble polydispersion in a solution containing a mixture of block copolymers or other amphiphilic materials by either shaking in a laboratory blender or, more effectively, by ultrasonic agitation.[12–15] However, the main drawbacks of such self-assembled microbubbles are their low stability in water and in salt solution (up to 10–12 h), and the difficulty in modifying their shell by introducing a desired material in order to attain additional functionality.

On the other hand, polyelectrolyte multilayers are an effective barrier to prevent or drastically decrease gas diffusion. As shown by B. Tieke, M. L. Bruening, T. J. McCarthy et al.,[16–19] poly(allylamine hydrochloride), poly(styrene sulfonate), polyacrylic acid, polyethylenimine, and poly(diallyldimethylammonium chloride) multilayers reduce the diffusion of oxygen, nitrogen, CO_2, and other gases by up to 150-fold relative to their diffusion in water, and they can be used as gas-separation membranes with good selectivity for O_2 and N_2.[17] The reduced gas permeability through polyelectrolyte multilayers is explained by the dense and rigid packing of the polyelectrolytes.[16] Thus, microcontainers built from polyelectrolyte multilayers or, at least, containing polyelectrolytes in the shell can be a good tool for gas entrapment.

Polyelectrolyte microcapsules, which are fabricated by layer-by-layer (LbL) deposition[20–22] of oppositely charged polyelectrolytes,[23] can be considered as confined microvolumes with a gaseous lumen. The main features of the polyelectrolyte capsules distinguishing them from other microcontainers are their multifunctionality and the straightforward modification of the shell on the nanometer scale. Macromolecules, drugs, fluorescent labels, and nanoparticles can be enriched in the inner volume of the capsules because of the switchable permeability of the capsule shell.[24,25] Polyelectrolyte capsules with a gaseous lumen (core) could be of interest as contrast agents for ultrasonic diagnostics, as gas-dispersing containers, as components of fuel cells, and in chemical catalysis.

Herein we describe the application of polyelectrolyte multilayers for air encapsulation and the formation of polyelectrolyte microcapsules with a gaseous interior. Our work also provides an example of LbL technology used for polyelectrolyte assembly on spherical water/air interfaces (in which the "air" core serves as the template). The resulting air-containing polyelectrolyte capsules possess all characteristics of air-in-water microemulsions; however, they are more stable and can be easily treated and transferred from one solution to another by filtration or centrifugation. Besides reduction of gas diffusion and, as a consequence, higher capsule stability, the assembled polyelectrolyte multilayers can bear additional functionality (molecular recognition, magnetic and/or fluorescent properties) providing special characteristics to the "air" capsules.

We combined the self-assembly of the gas microbubbles in aqueous media with stepwise LbL deposition of oppositely charged polyelectrolytes onto the resulting "air" core. In the first step, self-organized formation of an air microdispersion in water was performed according to a known procedure[12,13] (Figure 1a). This initial air suspension is stable for 4–5 h. Then, poly(allylamine hydrochloride) (PAH) and poly(styrene sulfonate) (PSS) layers were adsorbed in alternation starting from a positively charged PAH layer (Figure 1b,c). The resulting capsules with entrapped air are less dense than water and can be collected easily at the top of the vial (see photograph in Figure 1) upon centrifugation at low rpm (<500) or by "reverse" sedimentation. Higher rotation speeds lead to capsule coalescence and shell rupture. A more detailed description of the capsule preparation can be found in the Supporting Information.

The ζ-potential (Malvern Zetasizer 4) of the initial Tween:Span air microbubbles is slightly negative (see Figure 2a). Further electrophoretic measurements indicate the charging of the air microbubbles coated with the adsorbed polyelectrolyte multilayer upon each added layer. Figure 2a shows a drastic increase of the surface charge after deposition of the first PAH layer (≈ 50 mV) followed by alternating changes of ≈ 15 mV after each subsequent layer. In fact, there

[*] Dr. D. G. Shchukin, K. Köhler, Prof. Dr. H. Möhwald, Dr. G. B. Sukhorukov
Max Planck Institute of Colloids and Interfaces
14424 Potsdam (Germany)
Fax: (+49) 331-567-9202
E-mail: dmitry.shchukin@mpikg.mpg.de
Dr. G. B. Sukhorukov
The IRC in Biomedical Materials
Queen Mary University of London
Mile End Road, London, E1 4NS (UK)

[**] D.G.S. acknowledges the Alexander von Humboldt Foundation for an individual research fellowship. The authors thank Dr. Jürgen Hartman and Rona Pitschke for transmission electron microscopy analysis, Anne Heilig for atomic force microscopy analysis, and Roy Knocke for Raman spectra.

Supporting information for this article is available on the WWW under http://www.angewandte.org or from the author.

  DOI: 10.1002/anie.200462889

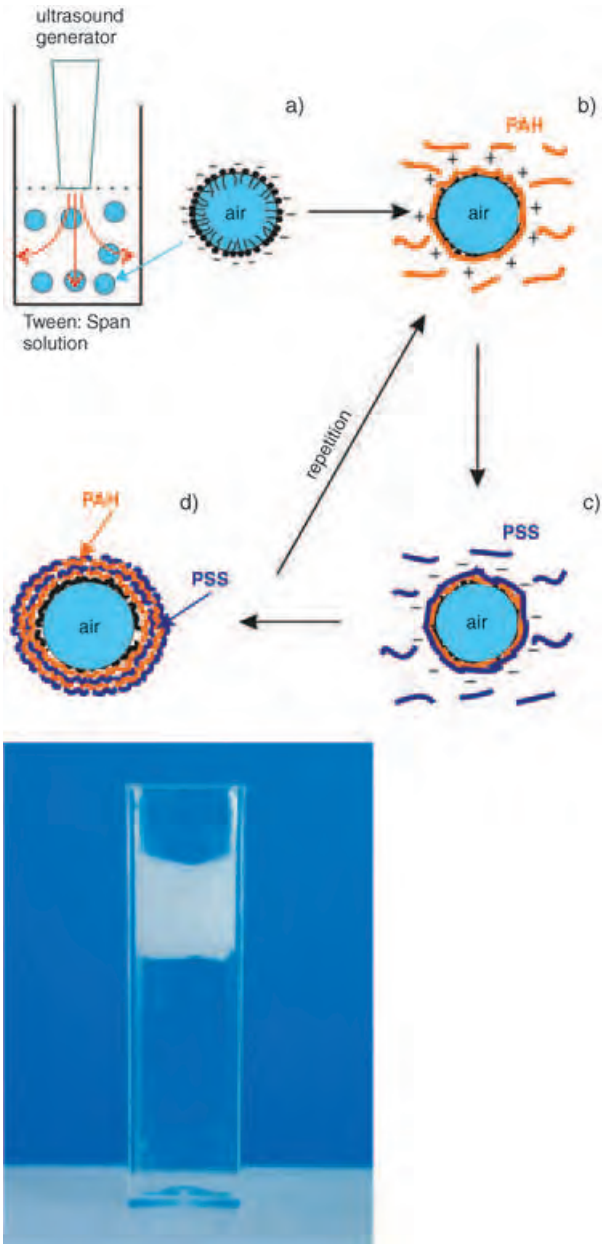

Figure 1. Schematic illustration of the formation of polyelectrolyte capsules on an "air" core. The Tween:Span mixture, which is used to form air microbubbles (a), is further stabilized by the electrostatic assembly of PAH/PSS multilayers (b–d). Bottom: a photograph of air-containing polyelectrolyte capsules in aqueous solution after centrifugation.

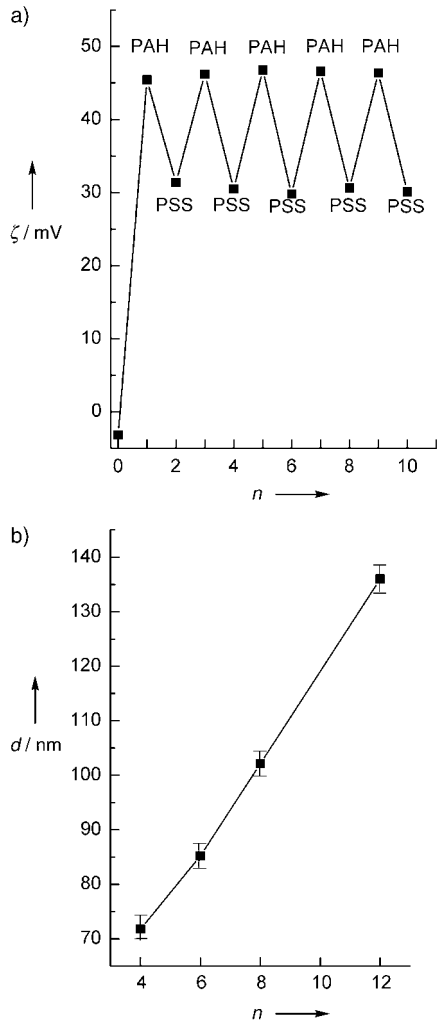

Figure 2. a) ζ-potential as a function of the number of layers, *n*, in the air-containing polyelectrolyte capsules. b) Thickness, *d*, of the capsule shell as a function of layer number (derived from AFM measurements).

is no complete recharging of the microbubble surface during the deposition of the positively and negatively charged polyelectrolytes. A possible explanation of this phenomenon is that during deposition of the first PAH layer PAH molecules deeply penetrate the initial Tween:Span shell forming a branched thick layer with an excess of positive charge inside, which cannot be completely compensated by the next PSS layer deposited onto the surface. The following PAH/PSS layers change the ζ-potential in the usual way with the same values for the assembled layers of the same evenness.

To obtain additional evidence of the growth of PAH/PSS multilayers on air microbubbles, we examined air-containing capsules with different numbers of layers by atomic force microscopy (AFM). As seen in Figure 2b, the average thickness of the capsule shell obtained from the height measurements gradually increases with the layer number in increments of about 8 nm per layer. This unambiguously confirms LbL assembly of the oppositely charged polyelectrolytes on the surface of air microbubble. However, it is not possible to study air-containing capsules with less than four layers by AFM because of their instability during drying—only polyelectrolyte debris was observed. Extrapolation of the AFM data estimates the average thickness of the first Tween:Span/PAH layer at ≈48 nm, which is six times greater than the thickness of the subsequently deposited polyelectrolyte layers and in good agreement with the drastic increase of the ζ-potential after PAH deposition onto the Tween:Span shell (Figure 2a).

The AFM image shows the continuous morphology of the shell film (Figure 3). Creases and folds resulting from capsule

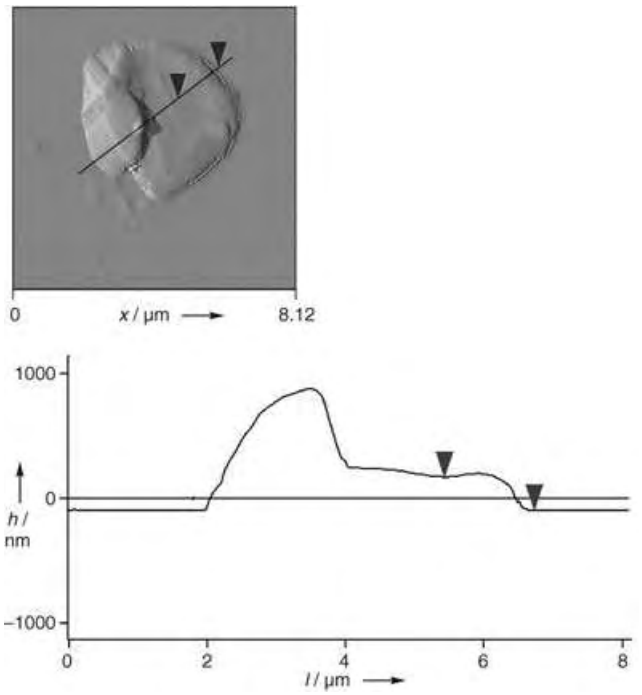

Figure 3. AFM image and height profile of an air-$(PAH/PSS)_6$ microcapsule. Vertical distance between the tip and the surface: 271.84 nm.

collapse after drying are observed, which coincide well with scanning electron microscopy observations (SEM, Figure 4a). Dried air-PAH/PSS capsules collapse to form flat structures (Figure 4a), which are rougher and bulkier than the flat structures obtained after the water-filled polyelectrolyte capsules are dried.[26] This discrepancy can be explained by different mechanisms of the capsule collapse: Shell deformation of the water-filled polyelectrolyte capsules occurs gradually as water evaporates from the capsule interior, resulting in smooth and flat films. In contrast, the air-filled capsules collapse immediately after the surrounding solution has been evaporated, forming less ordered, bulky structures.

Confocal microscopic images (Leica TCS SP, 100× oil-immersion objective) of air-containing polyelectrolyte capsules were recorded in fluorescence and transmission modes (Figure 4b,c). The capsules are polydisperse and their size varies from 1 to 20 µm; they are spherical and no aggregation is observed. Fluorescence is detected only from the capsule wall, indicating the presence of PAH labeled with fluorescein isothiocyanate (FITC) only in the shell and not in the volume. Air-containing PAH/PSS capsules can be expanded after 5 min of heating by a microscope lamp because of the high thermal expansion coefficient of the gaseous lumen (core). At elevated temperatures the shell explodes and the capsule is destroyed (Figure 5).

Raman spectra (CRM200, Witec) recorded for both the air-containing polyelectrolyte capsules and the surrounding water are shown in Figure 6a. A number of peaks observed for the polyelectrolyte capsules within the range 700–3000 cm^{-1} can be assigned to the vibration and stretching modes of PSS, Span, and Tween molecules.[27] The intensity of the broad band at 3200–3600 cm^{-1}, which corresponds to the

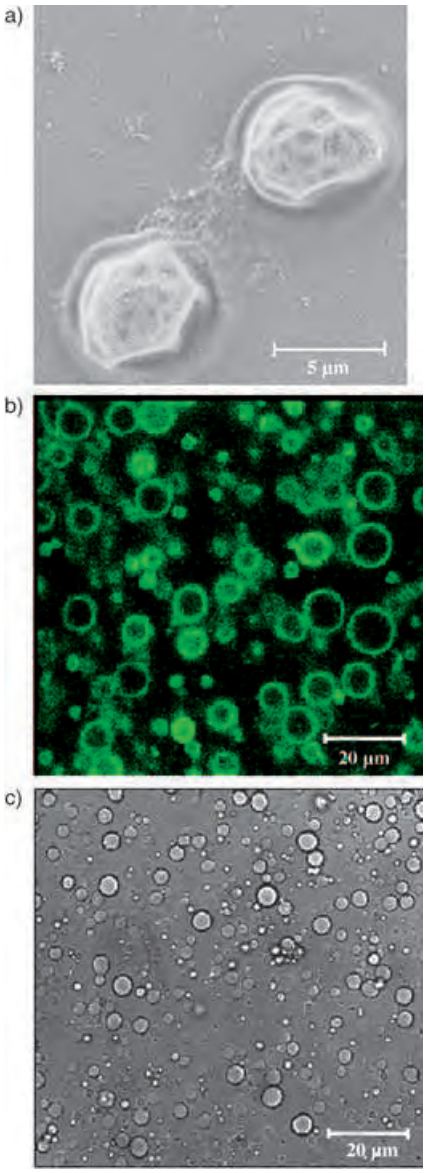

Figure 4. a) SEM image of air-$(PAH/PSS)_6$ microcapsules; b,c) confocal microscopy images of air-$(PAH/PSS)_6$ microcapsules made in FITC mode (signal from fluorescein isothiocyanate-labeled PAH) and bright-field mode, respectively.

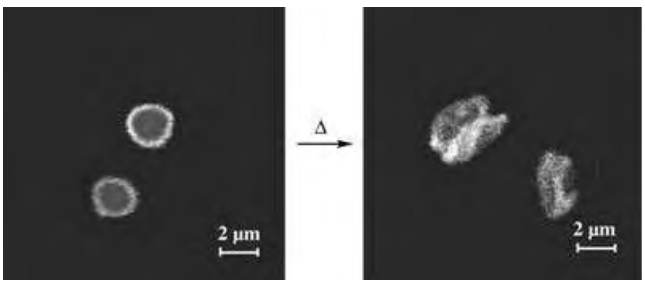

Figure 5. Confocal microscopy images of air-$(PAH/PSS)_6$ microcapsules made in FITC mode (signal from FITC-labeled PAH) before and after heating by a microscope lamp.

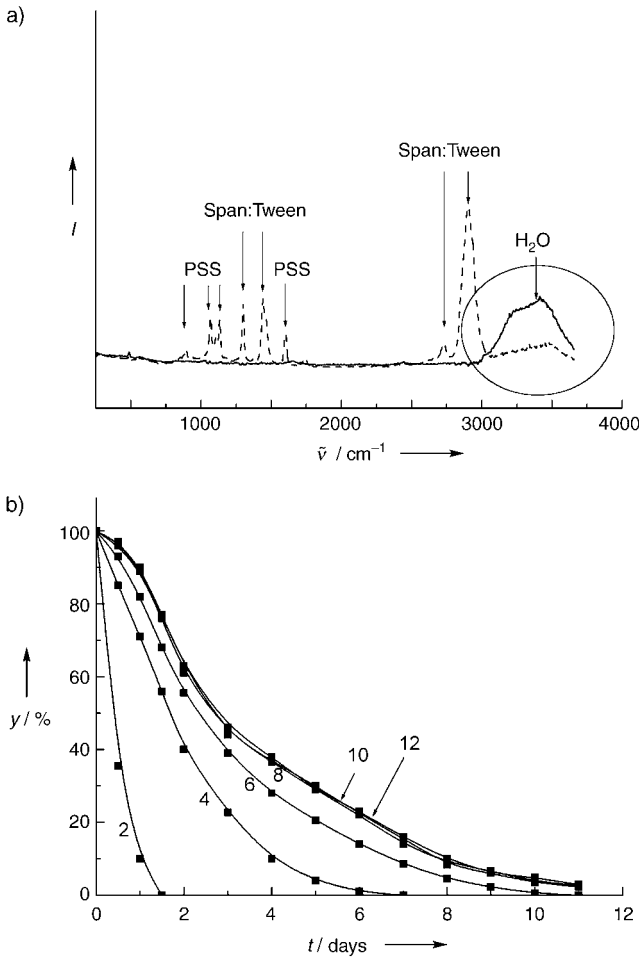

Figure 6. a) Raman confocal microscopy spectra from an air-containing polyelectrolyte capsule (dashed line) and surrounding water solution (solid line). b) Fraction *y* of intact air-containing polyelectrolyte capsule measured by counting confocal microscopy images. Numbers on the curves are the numbers of PAH and PSS layers deposited onto air microbubble.

vibration of OH groups of water, is considerably lower for polyelectrolyte capsules than for the surrounding solution. The gaseous core of the capsules does not contribute to the Raman signal at these wavenumbers, and the small intensity of the peaks observed at 3200–3600 cm^{-1} is caused by the water molecules entrapped inside the polyelectrolyte shell, which can contain up to 40 % v/v water according to Estrela-Lopis et al.[28] Hence, both confocal and Raman measurements prove the air/PAH/PSS structure of the resulting polyelectrolyte capsules.

Air-containing polyelectrolyte capsules have a higher stability against collapse in aqueous suspension than either the gas suspensions developed for ultrasonic contrasting[12–15] or the initial Span:Tween suspension. The stability of the capsules, which was estimated by confocal microscopy as the number of intact capsules after a certain time period divided by total number of capsules prepared, gradually increases with the number of polyelectrolyte layers; however, at eight or more polyelectrolyte layers the effect of the next layers becomes lower and approaches zero at 12 layers (Figure 6b). This could be associated with the looser packing of polyelectrolyte molecules at higher layer numbers accompanied by the strengthening of the first three to four layers by the following polyelectrolyte layers. The first polyelectrolyte layers are densely packed. Thus mass transfer through the shell is decreased, and consequently, the dissolution of the gaseous core in water is prevented to some extent.[29] In contrast, the last layers have a more porous structure, which has negligible influence on the gas diffusion. A similar effect of the shell thickness on the permeability properties was observed by Antipov et al.[30] for conventional "aqueous" polyelectrolyte capsules.

Electrostatic layer-by-layer assembly of polyelectrolyte multilayers was successfully accomplished on the surface of an air microbubble (core). The resulting polyelectrolyte shell stabilizes the overall air microsuspension against collapse and prevents air dissolution in water media. Air-containing poly(allylamine)/poly(styrene sulfonate) microcapsules have a wide size distribution (1–20 μm) and gaseous interior, and are stable for at least one week. These capsules have potential as contrast agents in ultrasonic diagnostics. Moreover, because of the high density gradient across the water/polyelectrolyte/air interface, air-containing polyelectrolyte capsules could be sensitive to low-power ultrasonic irradiation. This would make it feasible to use them as delivery agents capable of ultrasonically triggered remote release of the compounds entrapped within the shell of microbubbles. Additional properties could be imparted to the air-containing polyelectrolyte capsules by introducing inorganic nanoparticles (fluorescent, magnetic, bioactive) as one of the shell components (layer) or by performing a chemical reaction directly in the shell. We are currently studying ultrasonically sensitive capsules containing an air core and a polyelectrolyte shell modified by drug or metal nanoparticles.

Received: December 10, 2004
Revised: February 23, 2005
Published online: April 21, 2005

Keywords: emulsions · interfaces · microbubbles · polyelectrolytes · self-assembly

[1] A. Graff, M. Winterhalter, W. Meier, *Langmuir* **2001**, *17*, 919.
[2] B. J. Forrest, L. W. Reeves, *Chem. Rev.* **1981**, *81*, 1.
[3] R. Ball, A. D. J. Haymet, *Phys. Chem. Chem. Phys.* **2001**, *3*, 4753.
[4] S. Klingelhofer, W. Heitz, M. Antonietti, *J. Am. Chem. Soc.* **1997**, *119*, 10116.
[5] M. V. Seregina, L. M. Bronstein, M. Antonietti, *Chem. Mater.* **1997**, *9*, 923.
[6] W. Shenton, S. Mann, H. Cölfen, A. Bacher, M. Fisher, *Angew. Chem.* **2001**, *113*, 456; *Angew. Chem. Int. Ed.* **2001**, *40*, 442.
[7] E. D. Sudol, M. S. El-Aasser in *Emulsion Polymerization and Emulsion Polymers* (Eds.: P. A. Lovell, M. S. El-Aasser), Chichester, England, **1997**, p. 699.
[8] G. A. Ozin, S. Oliver, *Adv. Mater.* **1995**, *7*, 943.
[9] G. J. de A. A. Soler-Illia, C. Sanchez, B. Lebeau, J. Patarin, *Chem. Rev.* **2002**, *102*, 4093.
[10] M. Vettraino, B. Ye, X. He, D. M. Antonelli, *Aust. J. Chem.* **2001**, *54*, 85.

[11] M. Wark, M. Ganschow, Y. Rohlfing, G. Schulz-Ekloff, D. Wohrle, *Stud. Surf. Sci. Catal.* **2001**, *135*, 160.
[12] D. M. El-Sherif, M. A. Wheatley, *J. Biomed. Mater. Res. Part A* **2003**, *66*, 347.
[13] D. H. Kim, M. J. Costello, P. B. Duncan, D. Needham, *Langmuir* **2003**, *19*, 8455.
[14] A. L. Klibanov, *Adv. Drug Delivery Rev.* **1999**, *37*, 139.
[15] a) F. Calliada, R. Campani, O. Bottinelli, A. Bozzini, M. G. Sommaruga, *Eur. J. Radiol.* **1998**, *27*, 157; b) E. G. Schutt, D. H. Klein, R. M. Mattrey, J. G. Riess, *Angew. Chem.* **2003**, *115*, 3336; *Angew. Chem. Int. Ed.* **2003**, *42*, 3218.
[16] K. P. Xiao, J. J. Harris, A. Park, C. M. Martin, V. Pradeep, M. L. Bruening, *Langmuir* **2001**, *17*, 8236.
[17] J.-M. Levasalmi, T. J. McCarthy, *Macromolecules* **1997**, *30*, 1752.
[18] L. Krasemann, B. Tieke, *Mater. Sci. Eng. C* **1999**, *8–9*, 513.
[19] F. Van Ackern, L. Krasemann, B. Tieke, *Thin Solid Films* **1998**, *327–329*, 762.
[20] G. Decher, J. D. Hong, J. Schmitt, *Thin Solid Films* **1992**, *210*/211, 831.
[21] J. S. Shi, F. Hua, T. H. Cui, Y. M. Lvov, *Chem. Lett.* **2003**, *32*, 316.
[22] M. Olek, J. Ostrander, S. Jurga, N. Kotov, K. Kempak, M. Giersig, *Nano Lett.* **2004**, *4*, 1889.
[23] G. B. Sukhorukov, E. Donath, S. Davis, H. Lichtenfeld, F. Caruso, V. I. Popov, H. Möhwald, *Polym. Adv. Technol.* **1998**, *9*, 759.
[24] G. Ibarz, L. Dahne, E. Donath, H. Möhwald, *Adv. Mater.* **2001**, *13*, 1324.
[25] A. A. Antipov, G. B. Sukhorukov, H. Möhwald, *Langmuir* **2003**, *19*, 2444.
[26] G. B. Sukhorukov, D. G. Shchukin, W. F. Dong, H. Möhwald, V. V. Lulevich, O. I. Vinogradova, *Macromol. Chem. Phys.* **2004**, *205*, 530.
[27] B. Schrader, *Raman Infrared Atlas of Organic Compounds*, 2nd ed., VCH, Weinheim, **1989**.
[28] I. Estrela-Lopis, S. Leporatti, S. Moya, A. Brandt, E. Donath, H. Möhwald, *Langmuir* **2002**, *18*, 7861.
[29] M. A. Borden, M. L. Longo, *Langmuir* **2002**, *18*, 9225.
[30] A. A. Antipov, G. B. Sukhorukov, E. Donath, H. Möhwald, *J. Phys. Chem. B* **2001**, *105*, 2281.

Cover Picture

De-Liang Long, Hamera Abbas, Paul Kögerler, and Leroy Cronin*

Upon thermal stimulation the two templating sulfite anions embedded in the "Trojan Horse" polyoxometalate cluster shown in the cover picture release electron "soldiers" to the cluster's surface, turning the cluster from colorless to blue (background). The formation of the mixed-valence cluster shell is commensurate with the oxidation of the sulfite to sulfate anions. More details about this coupled structural and electronic rearrangement are given in the Communication by L. Cronin et al. on page 3415 ff.

Cellulose Chemistry
In view of the strong growth in cellulose research worldwide, D. Klemm, H.-P. Fink, and co-workers take stock of the latest developments in cellulose chemistry and current perspectives on its applications in their Review on page 3358.

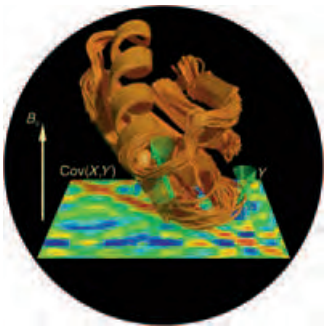

Molecular Dynamics Simulations
The correlated motions determined in NMR relaxation studies of protein solution structures can be consistently simulated with molecular dynamics. This technique is described in the Communication by B. de Groot and co-workers on page 3394 ff.

History of Chemistry
The Essay by E. Vaupel on page 3344 ff. covers the life and work of the Jewish chemist and industrialist Arthur Eichengrün, the father of the German cellulose acetate industry.

Contents

VIP ***The following Communications have been judged by at least two referees to be "very important papers" and will be published online at www.angewandte.org soon:***

Books

Highlights

Organocatalysis

Nature knows best: Recently developed enantioselective organocatalytic methods for the reduction of olefins under transfer-hydrogenation conditions are discussed (see scheme). The metal-free, amine-catalyzed reductions described have been inspired by the way natural systems perform reduction reactions.

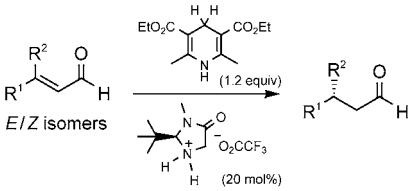

Essays

History of Chemistry

The life and achievements of the Jewish chemist and entrepreneur Arthur Eichengrün, a trailblazer in the German cellulose acetate industry, have been unjustly forgotten as a long-term consequence of National Socialism. Newly examined sources give detailed insight into his tragic biography, which was illustrative of the times.

Reviews

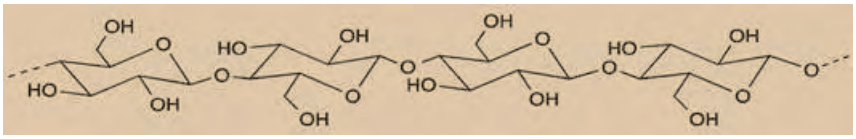

The trend toward renewable resources has led to a global renaissance of cellulose research over the past ten years. This review describes the highlights of the progress made in this area, which has provided a better understanding of the structure of cellulose derivatives, the tailoring of cellulose products, alternative production processes for cellulose regenerates, and new pathways for the formation of supramolecular architectures.

Communications

Correlated motions probed? A recently reported NMR relaxation experiment promised to probe correlated motions in proteins. However, molecular dynamics simulations imply that this is not the case. The simulations agree well with data obtained through two independent and established NMR spectroscopic methods and thus provide an alternative and consistent access to correlated protein motions (see picture) from NMR techniques.

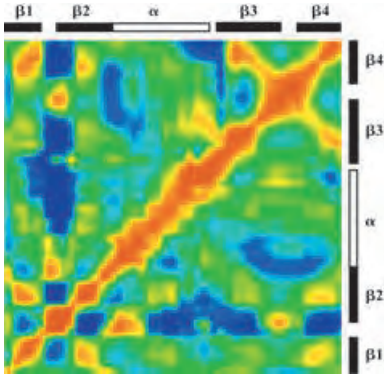

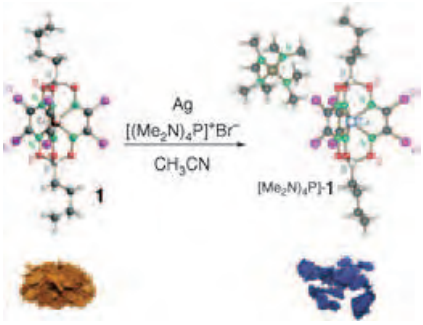

A grip on what's inside: A clathrochelate ligand controls the oxidation state of the encapsulated cobalt ion in complex **1**. This complex can be reduced chemically in acetonitrile solution by treatment with silver in the presence of tetraalkylammonium or tetra(dimethylamido)phosphonium halides to the dark-blue reduced complex [$(NMe_2)_4$P]-**1** in high yield (see scheme).

For the USA and Canada:
ANGEWANDTE CHEMIE International Edition (ISSN 1433-7851) is published weekly by Wiley-VCH PO Box 191161, D 69451 Weinheim, Germany. Air freight and mailing in the USA by Publications Expediting Inc. 200 Meacham Ave., Elmont, NY 11003. Periodicals postage paid at Jamaica NY 11431. US POSTMASTER: send address changes to *Angewandte Chemie*, Wiley-VCH, 111 River Street, Hoboken, NJ 07030. Annual subscription price for institutions: US$ 4948.00/4498.00 (valid for print and electronic / print or electronic delivery); for individuals who are personal members of a national chemical society, or whose institution already subscribes, or who are retired or self-employed consultants, print only: US$ 394.00. Postage and handling charges included. All Wiley-VCH prices are exclusive VAT.

The best in chemistry –

for more than a hundred years

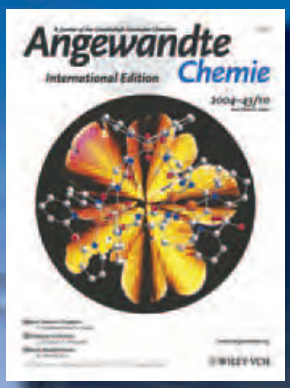

A Journal of the Gesellschaft Deutscher Chemiker

Angewandte
International Edition **Chemie**

www.angewandte.org

1888: ***The beginning of a success story***

Constant Innovations

1962: *First issue of the International Edition*
1976: *Graphical abstracts*
1979: *Cover pictures*
1988: *Centenary of Angewandte*
1989: *Routine use of color*
1991: *New section: Highlights*
1992: *Computerized editorial tracking system*
1995: *Internet service for readers*
1998: *Regular press service; full-text online*
2000: *New section: Essays; EarlyView: Communications available online ahead of the printed version*
2001: *New section: Minireviews*
2002: *Online submission of manuscripts*
2003: *Weekly publication; new section: News; new layout*
2004: *Backfiles (1962-1997); ManuscriptXpress: Online system for authors and referees*

Angewandte's advisors...

Manfred Reetz
Max-Planck-Institut für Kohlenforschung, Mülheim

*»**Angewandte Chemie** is extremely well-balanced in providing various types of information to the academic and industrial chemical community. If you inadvertently miss an issue, the mishap will catch up with you sooner or later.«*

Angewandte Chemie International Edition *is a journal of the German Chemical Society (GDCh)*

GDCh

WILEY InterScience® DISCOVER SOMETHING GREAT

WILEY-VCH

1881404_gu

An anion-exchange strategy was used to prepare two helical structures made up of cucurbituril and asymmetric copper(II) complexes containing 8-hydroxyquinoline-5-sulfonate and 3,5-diiodosalicylate (right half of picture) or 3-iodobenzoate (left half). The shape-matching interactions between cucurbituril and the copper complexes were assisted by the iodo substituents.

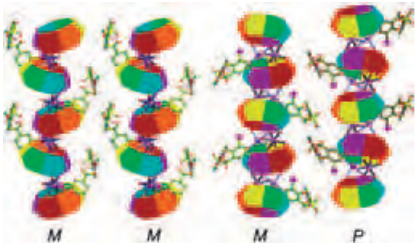

Cucurbituril Polymers

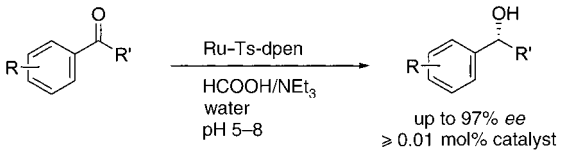

Much faster, more enantioselective, and more-productive catalysis was attained in the asymmetric transfer hydrogenation of aromatic ketones with the Noyori–Ikariya Ru–Ts-dpen catalyst in water under slightly basic conditions (see scheme). At low pH values, the reaction was much less efficient and appears to operate through a different mechanism.

Transfer Hydrogenation

The global dynamics of the TAR RNA from HIV-1 bound to two distinctly charged molecules have been characterized by NMR studies of residual dipolar couplings (see picture). While neomycin B (NeoB: +5) arrests global motions in TAR, the small organic molecule acetylpromazine (AcP: +1) does not. Results indicate that electrostatic interactions are critical for arresting global motions in RNA.

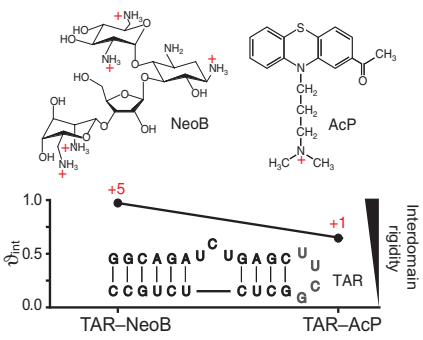

RNA Recognition

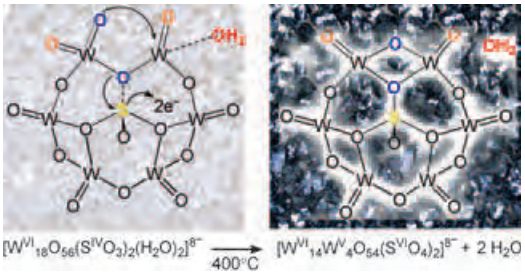

Cores and effect: Heating the cluster $[W_{18}O_{56}(SO_3)_2(H_2O)_2]^{8-}$ causes an electron transfer from the core sulfite anions to the cluster shell resulting in a color change from colorless to dark blue (see backgrounds). The electron transfer is coupled with a structural reorganization of the cluster shell and oxidation of the sulfite to sulfate anions (see scheme).

Cluster Compounds

Contents

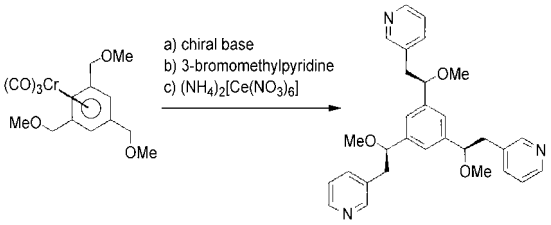

Chiral-base chemistry has been used to introduce multiple elements of chirality around an (arene)tricarbonylchromium(0) complex. Three stereogenic centers could be installed in one operation to synthesize a nonracemic chiral C_3-symmetric triphosphine and a nonracemic chiral C_3-symmetric tripyridine (see scheme).

Asymmetric Synthesis

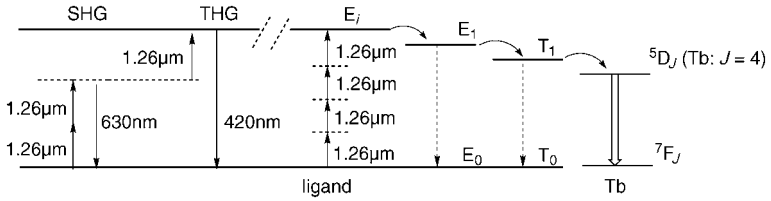

Red, green, and blue emissions are observed simultaneously for an organoterbium complex that displays remarkable multiphoton upconversion when excited by a near-infrared light source. The system undergoes two nonlinear optics processes simultaneously: second and third harmonic generation (SHG: red emission; THG: blue), and four-photon upconversion (green) for excitation at $\lambda \approx 1.26$ (see diagram).

Luminescence

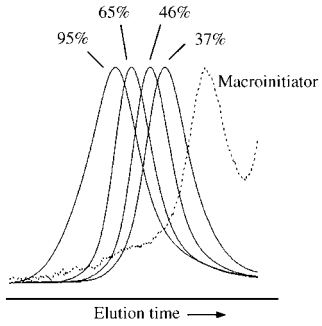

A poly(vinyl acetate) macroinitiator, preformed by a cobalt-mediated technique, facilitates controlled radical polymerization of vinyl acetate (VAc) in suspension in water. The molar mass increases with monomer conversion, as demonstrated by size exclusion chromatograms (see picture), and the polydispersity remains low at 1.2–1.4. Moreover, the VAc polymerization rate is much higher in suspension than in the bulk.

Controlled Radical Polymerization

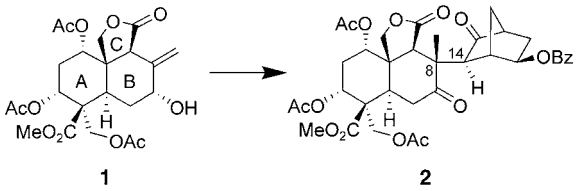

The advanced decalin intermediate 1 was synthesized and elaborated into the potential azadirachtin precursor **2**. The challenging synthesis involved several protecting-group manipulations and coupling of **1** with an appropriate norbornene unit.

Natural Products Synthesis (1)

Contents

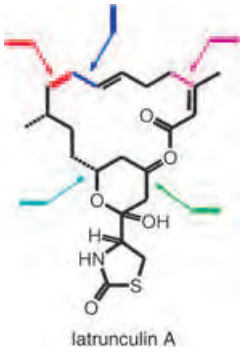

latrunculin A

Selective actin-binding is the most prominent biochemical property of the scarce marine natural product latrunculin A (see formula). Modern metal-catalyzed C–C bond-formation reactions, including a ring-closing enyne–yne metathesis (shown in red), now open a convenient, flexible, and productive entry to this important probe molecule for chemical biology.

Natural Product Synthesis

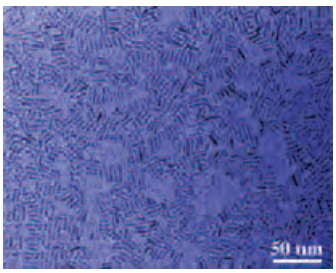

High-temperature nonhydrolytic aminolysis has been developed as an approach to monodisperse titania nanocrystals by exploiting the chemical modification of reactive titanium isopropoxide with oleic acid as the chelating ligand. Its capabilities for the anisotropic growth of highly crystalline anatase titania nanocrystals (see picture) with controlled size and shape have been demonstrated.

Nanostructures

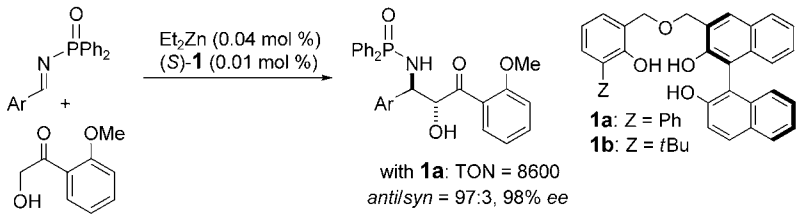

An achiral unit is shown to be better than a chiral unit in promoting an asymmetric reaction. Non-C_2-symmetric linked-binols **1** with one chiral 1,1′-bi-2-naphthol unit and one flexible achiral unit are employed as ligands in direct catalytic asymmetric Mannich-type reactions (see scheme; TON = turnover number). With as little as 0.01 mol % of ligand **1a** and 0.04 mol % of Et_2Zn, the reaction proceeded smoothly to give the product in 98 % *ee*.

Asymmetric Catalysis

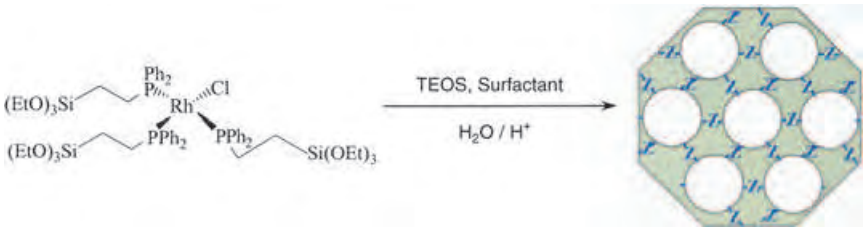

Covalently imprisoned within pore walls of mesostructured porous silica, organophosphanyl transition-metal complexes (Z, see picture) are still able to effect heterogeneous hydrogenation catalysis. The key to the synthetic protocol that leads to the well-defined metal sites lies in silylation of the material prior to extraction of the surfactant template. TEOS = tetraethylorthosilicate.

Mesoporous Materials

Contents

Service

Organocatalysis

Organocatalytic Hydride Transfers: A New Concept in Asymmetric Hydrogenations

*Hans Adolfsson**

Keywords:
asymmetric catalysis · enantioselectivity · hydrogen transfer · organocatalysis · reduction

Asymmetric hydrogenation of unsaturated organic compounds, such as olefins, carbonyls, and imines, is currently becoming a standard procedure in both academic laboratories and industrial applications.[1,2] On the basis of the vast number of biologically active compounds in which a hydrogen substituent is part of the stereogenic center, it is not surprising that the development of efficient enantioselective reduction reactions has been the main focus within the area of asymmetric catalysis. The early discoveries in the 1960s by Knowles and co-workers, who revealed that chiral rhodium complexes based on the Wilkinson catalyst were able to catalyze the hydrogenation of unsaturated carboxylic acids with a slight enantiomeric excess under homogenous conditions, opened the door to an intensive hunt for more efficient and more selective catalysts.[3] A number of milestones have been reached since the initial experiments were performed, and today we are equipped with a plethora of different methods for the enantioselective reduction of unsaturated organic compounds.

Until now, all the methods developed for the reduction of organic compounds have been dominated by the use of metal catalysts surrounded by proper stereodiscriminating chiral ligands. Highly efficient catalysts based on rhodium(I) or ruthenium(II) complexes with chiral diphosphine ligands have been introduced for the enantioselective olefin reduction of enamines and unsaturated carboxylic acids with molecular hydrogen.[1,4] More recently, iridium complexes with chiral P,N ligands have been used for the enantioselective reduction of nonfunctionalized olefins.[5,6] The asymmetric reduction of ketones and imines are commonly performed by using molecular hydrogen and chiral ruthenium(II) catalysts.[4] A mild alternative for the latter reductions is to perform the reactions under hydrogen-transfer conditions.[7] Metal-catalyzed hydrogen-transfer reactions using isopropyl alcohol or formic acid as sources of hydrogen have been extensively studied during the last decade.[8] Highly enantioselective processes, in particular for the reduction of ketones, have been established using catalysts based on vicinal amino alcohols, diamines, or pseudodipeptides in combination with Ru^{II}–arene precursors.[8–10]

The common denominator in the systems described above is that the principal center of reactivity is positioned on a (transition) metal hydride or dihydride. However, a shift of this paradigm was recently made by the discovery that simple ammonium salts of secondary amines were able to catalyze the chemoselective reduction of α,β-unsaturated aldehydes in the presence of a dihydropyridine as the hydride donor.[11] In biological systems reductions are made in cascade reactions that involve metalloenzymes and organic hydride reduction cofactors such as nicotinamide adenine dinucleotide (NADH) or flavin adenine dinucleotide ($FADH_2$). Inspired by the way natural systems perform reduction reactions, List and co-workers recently reported that Hantzsch ester **1** worked as a good NADH mimic in the hydride-transfer reaction to the iminium ion formed from 2-nitrocinnamyl aldehyde **2** and a catalytic amount of dibenzylammonium trifluoroacetate (**4**; Scheme 1).[11] The reaction proved to be highly chemoselective and high yielding (94%) to afford the saturated aldehyde **3**. In a series of experiments it was shown that different ammonium salts of secondary amines, including pyrrolidine and piperidine, efficiently catalyzed the transformation. The screening of different enal substrates using catalyst **4** and the NADH mimic **1** demonstrated that mono- or disubstitution of a wide range of groups (aryl or alkyl) at the β position was tolerated and gave the corresponding saturated aldehydes in good yields. However, enals that contain an additional substituent in the α position were not reduced under these conditions. The successful results obtained when ammonium salts of cyclic secondary amines were used as catalysts indicated that chiral cyclic amines such as the com-

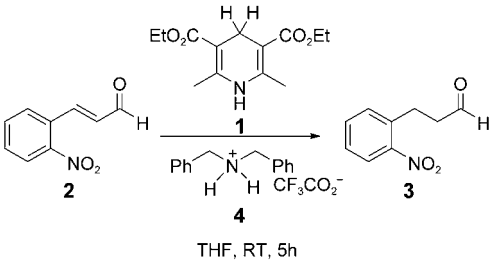

Scheme 1. Organocatalytic chemoselective reduction of enal **2**.

[*] Dr. H. Adolfsson
Department of Organic Chemistry
Stockholm University
The Arrhenius Laboratory
10691 Stockholm (Sweden)
Fax: (+46) 8-154-908
E-mail: hansa@organ.su.se

  DOI: 10.1002/anie.200500827

monly used organocatalyst **5**[12] would catalyze the reaction and perhaps be able to induce asymmetry in the hydride-transfer step. List and co-workers were indeed rewarded in the reduction of enal **6** by using a substoichiometric amount of the HCl salt **5** as catalyst, as product **7** was obtained in 81% yield with 81% enantiomeric excess (Scheme 2).[11] This is the first example of an enantioselective metal-free transfer hydrogenation of an olefin, and with this result yet another color was added to the constantly growing palette of organocatalyzed asymmetric reactions.[13,14]

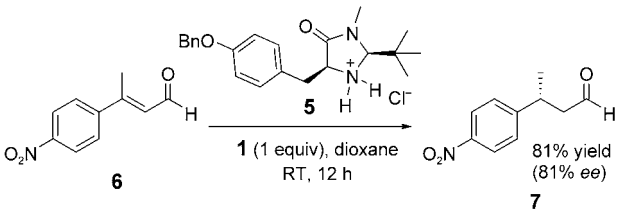

Scheme 2. Enantioselective reduction of enal **6** catalyzed by ammonium salt **5**. Bn = benzyl.

In further studies on iminium-catalyzed asymmetric hydride transfers to olefins, the groups of MacMillan and List almost concurrently reported that β,β-disubstituted aldehydes could be reduced in good yields and with excellent enantioselectivity.[15,16] The catalysts used by both groups were based on the same imidazolidinone skeleton and differed only in the ring substituents. MacMillan and co-workers reported that superior levels of enantiomeric excess were obtained by employing the amine triflate salt **8** in chloroform at −30 °C.[15] Under these conditions a number of different trisubstituted α,β-unsaturated aldehydes were reduced in high yields (74–95%) with enantioselectivities of up to 97% *ee* (Scheme 3). Most interestingly, irregardless of whether an *E* or a *Z* olefin was used as substrate, they both converged into the same *S* enantiomer of the product. This result is in direct contrast to many metal-catalyzed hydrogenations in which the geometry of the olefin generally dictates the outcome of the reaction. The reason for the observed stereoconvergence is believed to result from a fast *E*–*Z* isomerization reaction mediated by the catalyst prior to the selective reduction of the *E* olefin.

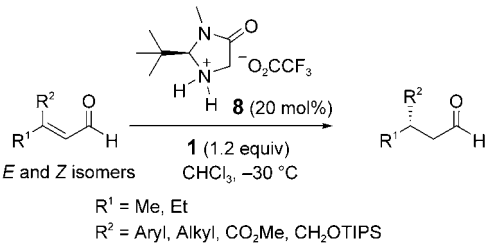

Scheme 3. Organocatalytic enantioselective transfer hydrogenation of α,β-unsaturated aldehydes. TIPS- = triisopropylsilyl.

In the report by List and co-workers, the trichloroacetate salt of a derivative of **5** (10 mol%) was used as catalyst in the reduction of different β,β-arylmethyl enals.[16] When the reaction was performed in dioxane at 13 °C using a slight excess of a modified version of **1** (1.02 equiv), the saturated aldehydes were obtained in high yields (77–90%) with enantioselectivities of up to 96%. In accordance with the results reported by MacMillan and co-workers, List's group observed similar enantioconvergence when the reduction was performed on mixtures of *E*/*Z* substrates. From a practical point of view, mixtures of *E*/*Z* isomers obtained from either Wittig-type or olefin metathesis reactions can be used directly in the reductions without initial separations. The reaction is believed to proceed by the mechanism depicted in Scheme 4.

The iminium ion is initially formed in a reaction between the imidazolidinone catalyst and the enal. Depending on the geometry of the starting olefin, *E*- and *Z*-configured ions are formed. The reason for the excellent stereoconvergence observed in the reaction is explained by a rapid interconversion of the two iminium ions prior to the rate-determining hydride attack from the dihydropyridine. The hydride ion is then selectively transferred to the *E*-configured olefin from the least sterically hindered face to produce the *S* isomer of the product.

In conclusion, List and MacMillan and their respective co-workers have opened a novel field in the area of reduction chemistry by demonstrating that asymmetric transfer-hydrogenation reactions of unsaturated aldehydes can be performed solely by organic catalysts. At its current stage, the reaction is limited to only aldehyde substrates, but it is reasonable to expect that the scope will be extended to also cover unsaturated ketones. In addition, lower catalyst loadings would make this reduction protocol even more attractive. However, the simplicity of the method in combination with the obtained high levels of enantioselectivity suggest that this method will become a standard

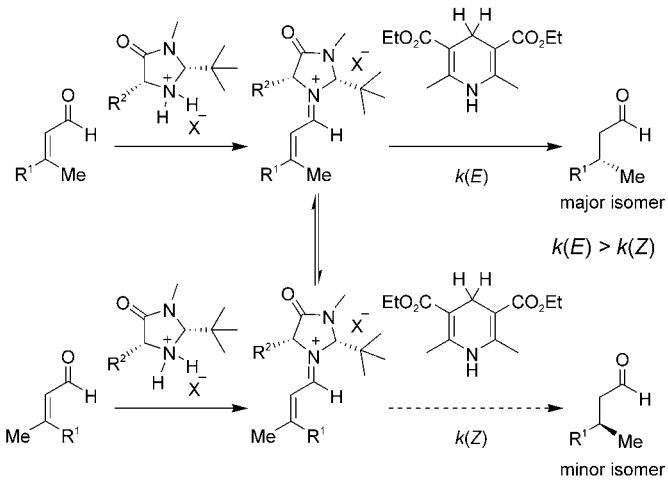

Scheme 4. Proposed mechanism for the organocatalytic enantioselective transfer hydrogenation of *E*/*Z* olefins.

technique for chemoselective asymmetric reductions of α,β-unsaturated aldehydes.

Published online: May 2, 2005

[1] H. U. Blaser, C. Malan, B. Pugin, F. Spindler, H. Steiner, M. Studer, *Adv. Synth. Catal.* **2003**, *345*, 103 – 151.

[2] R. Noyori, M. Kitamura, T. Ohkuma, *Proc. Natl. Acad. Sci. USA* **2004**, *101*, 5356 – 5362.

[3] W. S. Knowles, *Angew. Chem.* **2002**, *114*, 2096 – 2107; *Angew. Chem. Int. Ed.* **2002**, *41*, 1998 – 2007.

[4] R. Noyori, *Angew. Chem.* **2002**, *114*, 2108 – 2123; *Angew. Chem. Int. Ed.* **2002**, *41*, 2008 – 2022.

[5] A. Lightfoot, P. Schnider, A. Pfaltz, *Angew. Chem.* **1998**, *110*, 3047 – 3050; *Angew. Chem. Int. Ed.* **1998**, *37*, 2897 – 2899.

[6] K. Källström, C. Hedberg, P. Brandt, A. Bayer, P. G. Andersson, *J. Am. Chem. Soc.* **2004**, *126*, 14308 – 14309.

[7] G. Zassinovich, G. Mestroni, S. Gladiali, *Chem. Rev.* **1992**, *92*, 1051 – 1069.

[8] M. J. Palmer, M. Wills, *Tetrahedron: Asymmetry* **1999**, *10*, 2045 – 2061.

[9] R. Noyori, S. Hashiguchi, *Acc. Chem. Res.* **1997**, *30*, 97 – 102.

[10] A. Bøgevig, I. M. Pastor, H. Adolfsson, *Chem. Eur. J.* **2004**, *10*, 294 – 302.

[11] J. W. Yang, M. T. Hechavarria Fonseca, B. List, *Angew. Chem.* **2004**, *116*, 6829 – 6832; *Angew. Chem. Int. Ed.* **2004**, *43*, 6660 – 6662.

[12] K. A. Ahrendt, C. J. Borths, D. W. C. MacMillan, *J. Am. Chem. Soc.* **2000**, *122*, 4243 – 4244.

[13] P. I. Dalko, L. Moisan, *Angew. Chem.* **2001**, *113*, 3840 – 3864; *Angew. Chem. Int. Ed.* **2001**, *40*, 3726 – 3748.

[14] P. I. Dalko, L. Moisan, *Angew. Chem.* **2004**, *116*, 5248 – 5286; *Angew. Chem. Int. Ed.* **2004**, *43*, 5138 – 5175.

[15] S. G. Ouellet, J. B. Tuttle, D. W. C. MacMillan, *J. Am. Chem. Soc.* **2005**, *127*, 32 – 33.

[16] J. W. Yang, M. T. Hechavarria Fonseca, B. List, *Angew. Chem.* **2005**, *117*, 110 – 112; *Angew. Chem. Int. Ed.* **2005**, *44*, 108 – 110.

History of Chemistry

Arthur Eichengrün—Tribute to a Forgotten Chemist, Entrepreneur, and German Jew

*Elisabeth Vaupel**

Keywords:
aspirin · cellulose acetate · history of chemistry · pharmaceutical chemistry · plastics industry

The Jewish chemist and entrepreneur Arthur Eichengrün (1867–1949), a trailblazer in the German cellulose acetate industry, was widely known in professional circles and highly respected in both Imperial Germany and its successor, the Weimar Republic. The German Empire was indebted to him for numerous inventions and patents, some of which had considerable military value, especially during the First World War. One of the long-term consequences of the subsequent Nazi dictatorship in Germany is that Eichengrün's life and work have unjustly been forgotten. Newly examined sources from the archives of the Bayer corporation in Leverkusen and the district court in Charlottenburg, together with documents preserved by the Eichengrün family, have made it possible for the first time to reconstruct in detail key circumstances in the life of this versatile chemist—revealing a tragic story, but one illustrative of the times and important for historical research at several levels.[1]

Chemist—The Perfect Profession for a Social Climber

Arthur Eichengrün was born in 1867 into a Germany undergoing industrialization at a feverish pace. When in 1885 he elected to study chemistry it was clear that the chemical industry was on the verge of joining mechanical engineering and the electrical sector as one of the leading elements in the Imperial German economy. Especially the manufacturers of coal-tar and aniline dyes had enhanced the German chemical industry's international reputation. It was not at all unusual in this era that Eichengrün, scion of a Jewish cloth-manufacturing family from Aachen, would opt for training as a chemist.[2] A significant number of chemistry students in Imperial Germany toward the end of the 19th century were Jewish, many from families that owned textile mills, including Carl Liebermann (1842–1914) and Victor Meyer (1868–1897). Apparently it was widely appreciated that the study of chemistry, especially if directed toward chemical technology and dye chemistry, offered a singularly versatile educational platform for young people expecting someday to assume a role in the family firm. A chemical education opened for a Jew, in particular, an important door to full participation in the steady advance of the chemical industry in Germany. Despite the fact that Jews had relatively recently (1871) been granted full legal rights in all parts of the German Reich, establishing a career was still very difficult in many respects. Especially in chemistry it was possible through commercially attractive inventions and lucrative patents for one rapidly to amass a fortune, and through financial success to achieve an enviable social status.

Eichengrün decided upon training of a very practical sort and embarked on a professional career as a pharmaceutical chemist, later turning to photochemistry before finally establishing himself as a pioneer in plastics. He enrolled first at the technical institute in his hometown of Aachen, then transferred for a year to Berlin where he studied not only at the university—specifically under Prof. August Wilhelm Hofmann (1818–1892)—but also at the Charlottenburg Technical Institute. There he was taken under the wing of Carl Liebermann (1842–1914), a cousin of the painter Max Liebermann and himself a chemist with a Jewish family background. In the winter semester 1888/89 Eichengrün returned to Aachen to pursue a doctorate under Alfred Einhorn (1857–1917), who, like many of his favorite professors, was also a Jew. The young instructor Einhorn would later supervise the doctoral studies of Richard Willstätter (1872–1942), but already he was one of the rising stars in the scientific firmament. His research on the structure of cocaine, the first local anesthetic adopted by the medical profession, had, for example, attracted a considerable amount of attention.[3] Cocaine was introduced in this context in 1884 by Karl Koller (1857–1944) at the suggestion of Sigmund Freud (1856–1939), and it had opened up exciting new prospects in surgery. In particular, cocaine made it possible to perform painless operations on the eye.[4] Until 1899, technical institutes were not authorized to confer doctoral degrees, so Eichengrün could not submit his dissertation in Aachen directly but was forced instead to locate a university willing to accept the work. Einhorn helped him establish contact with Otto Fischer (1852–1932) at Erlangen, under whom Eichengrün was awarded a doctoral degree in 1890 as an "external candidate".[5] With this achievement behind him—a highly significant one in the title-hungry social world of Wilhelminic Germany—he had reached the first rung

[*] Priv.-Doz. Dr. E. Vaupel
Deutsches Museum
Museumsinsel 1
80306 München (Germany)
E-mail: e.vaupel@deutsches-museum.de

  DOI: 10.1002/anie.200462959

on the social ladder, a challenging obstacle for a Jew.

In his doctoral work with Einhorn, which is noteworthy in the history of pharmacy especially for including a synthesis of the local anesthetic Novocaine, Eichengrün was pointing the way toward a new subdiscipline that was only beginning to take shape: pharmaceutical chemistry. He therefore launched his career not with one of the dye works, as might have been anticipated, but rather in the pharmaceutical industry. The first position he accepted was with the firm of C. H. Boehringer & Son in Ingelheim am Rhein, where in 1892 he was assigned the task of establishing a facility for the isolation and purification of cocaine. Cocaine preparations had become extremely interesting from an economic standpoint with the alkaloid's debut as a local anesthetic. Only a year later Eichengrün moved on, however, joining up successively with two small pharmaceutical concerns that no longer exist. The first was the recently (1888) established Balzer & Co. in Grünau near Berlin, which was in the hands of Liebermann's family, shortly thereafter, the firm of Dr. L. C. Marquardt in Beuel, a highly regarded manufacturer since 1846 of both pharmaceutical products and chemicals. The amateurish approach both companies took to research and marketing so disconcerted him, however, that Eichengrün made up his mind to seek a place instead with a large company. On January 10, 1896, he took a position with the Farbenfabrik Bayer, formerly Friedrich Bayer & Co., in Elberfeld, the forerunner of today's massive Bayer complex in Leverkusen (Figure 1). Bayer had already begun to evolve from a classical dye works into a successful producer of pharmaceuticals on the strength of a novel pain reliever, Phenacetin, introduced in 1887.[6] Eichengrün was the first chemist Bayer engaged to work exclusively in the pharmaceuticals area. He was entrusted with the further development of the new pharmaceutical research division, which in terms of personnel was already undergoing rapid expansion (Figure 2). Eichengrün's strategy for devising new drugs was as ingenious as it was simple: he kept close watch on the pharmaceutical market, noting what preparations competitors like Hoechst, Knoll, Merck, Schering, and others were introducing, at the same time monitoring the various ailments and classes of compounds in which they displayed interest.[7] He quickly latched onto promising advances, including the quest for better disinfectants during a period that witnessed the flourishing of bacteriology as well as development of new medications for treatment of the then rampant sexually transmitted diseases. Diligence, systematic research within a restricted field, sometimes the barely legitimate imitation from a patent standpoint of a competitor's product, and a healthy measure of that indispensable commodity, luck—all these played significant roles in Eichengrün's striking success as a pharmaceutical chemist.

Figure 1. Arthur Eichengrün, ca. 1896, when he was applying for a position at Bayer. Photo: Bayer-Archiv, Leverkusen.

A Pharmaceutical Patent Makes Eichengrün Rich

Among the many drugs developed and subsequently marketed by Bayer during Eichengrün's tenure there, two major successes warrant special mention. The first is the silver protein formulation Protargol (Figure 3), a disinfectant introduced for therapeutic use in 1897. This became the standard agent for treating gonorrhea (known colloquially as "tripper" ; English slang: "the clap"), at the time the most prevalent of the sexually transmitted diseases.[8] Protargol quickly replaced for this purpose the corrosive silver nitrate, and remained the classic treatment for gonorrhea for more than fifty years until the advent of sulfonamides and penicillin. With huge demand both at home and abroad, including an enormous market within the military, royalties from Protargol alone made Eichengrün a wealthy man, his social ascent of course benefiting from this financial prominence. According to the terms of his contract he

Figure 2. View into the first pharmaceutical research laboratory at Bayer. Eichengrün is the slender, tall man in front on the right. Photo: Bayer-Archiv, Leverkusen.

Figure 3. Bottle of Protargol, the Bayer drug for treating gonorrhea. Photo: Bayer-Archiv, Leverkusen.

was entitled to 5% of the net profits from any patented product of which he was the sole developer, including Protargol. No other pharmaceutical discovery rewarded him as richly as Protargol. His royalties exclusively from this medication—far from the only one he devised—amounted in the year 1907 to the fantastic sum of 13309 marks, followed by 11811 marks in 1908 and 13687 marks in 1909. That was equivalent to more than twice his 1896 annual starting salary of 5000 marks, which increased by 500 marks a year such that it reached 10000 marks per annum by the time he left Bayer in 1908.[9] By way of comparison, a teacher in those days earned between 1200 and 1500 marks a year, a factory worker roughly 50 marks a month.

Eichengrün, the Intellectual Father of Aspirin

Eichengrün's name is also associated with Bayer's world-famous signature drug, the pain reliever Aspirin, even though synthesis of the active ingredient, acetylsalicylic acid, (on August 10, 1897) was not conducted by Eichengrün himself, but by his laboratory associate Felix Hoffmann (1868–1946).[10] Nevertheless, Eichengrün was probably involved in the project, since the synthesis and marketing of Aspirin certainly was the work of a team, not a single person. The inspiration behind attempting to modify the characteristics of the well-known salicylic acid through acetylation, in the hope of creating a substance more readily tolerated, probably stemmed from Eichengrün. It was actually not an especially original idea, because at that time acetylation was a favorite derivatization technique and virtually a matter of routine, a step that had already led to a host of valuable medicinal agents. For example, the important antipyretic agent Antifebrin, from Hoechst, was obtained by the acetylation of aniline. Also, in 1887 Bayer had introduced the successful antipyretic Phenacetin, prepared by acetylation of *p*-aminophenetidine, and in 1897, shortly before the key Aspirin synthesis, Bayer began supplying heroin, similarly acquired through an acetylation.[11]

Eichengrün maintained in later years—first rather casually in 1930 in the "Reichshandbuch der deutschen Gesellschaft" ("Imperial Handbook of German Society") and then quite emphatically in 1949 in the journal "Die Pharmazie"—that he had been the co-discoverer of Aspirin along with Hoffmann.[12] These claims, promulgated decades after the drug's introduction,[13] repeatedly stirred up controversy, most recently in 1999 when the British historian of pharmacy Walter Sneader confirmed Eichengrün's role in the development of the Aspirin.[14] Research in the Bayer archives has shown that Bayer's assignment of sole rights of discovery to Hoffmann was based strictly on the available documentary evidence. That the synthesis of Aspirin was in all likelihood a team effort, so in fairness the party responsible for suggesting the decisive synthetic strategy should also be identified—this argument never came into play simply because there were no relevant records to support it. Moreover, a similar lack of documentary evidence meant that nothing came of Eichengrün's further allegation that, had he not intervened, the Bayer pharmacologist Heinrich Dreser (1860–1924) would have prevented clinical testing of acetylsalicylic acid on the grounds of its supposed coronary toxicity, and only through his personal efforts to counter Dreser's rejective stance was the drug ever marketed. In summary, Eichengrün's contention that he was a co-discoverer of Aspirin, while plausible, is nowhere supported in writing.

Bayer had Eichengrün to thank not only for his role in the expansion of the pharmaceutical research division, but also for the company's diversification in the photochemical direction, a rather belated move (not further considered here), at least when compared with analogous efforts on the part of other chemical manufacturers.[15] Highlights from this phase of Eichengrün's career include the synthesis of the photographic developer Edinol and the first preparation starting from cellulose acetate of a nonflammable safety film for movies, which we revisit in some detail below. During his years with Bayer, Eichengrün submitted a total of 35 patent applications.[16] There can be no argument about his having been a versatile, inventive, bustling chemist with a sure instinct for promising research topics as well as marketable products. In reviewing his personnel files in the Bayer archives one is also struck by his business acumen as reflected in the close watch Eichengrün kept over his personal interests in negotiating with his employer.

Eichengrün's Battle for the Future of Cellulose Acetate

A crucial factor in Eichengrün's ensuing career was his work starting in 1900 with cellulose acetate, originally with the goal of providing Bayer with a foothold in artificial silk production. From that point on he increasingly fell under the spell of this substance, which although first prepared in 1865 by Paul Schützenberger (1829–1897) was largely ignored until the turn of the century.[17] In the years that followed, Eichengrün established a profile as a practitioner and empiricist dedicated wholly to the exploitation of cellulose acetate chemistry. He made no contribution whatsoever to the scientific study of cellulose itself, which went on during the 1920s especially in the laboratories of Hermann Staudinger (1881–1965) and at the Kaiser Wilhelm Institute for Fibrous Materials, founded in 1920 in Berlin-Dahlem.

Industrial interest in cellulose acetate was first kindled in 1904/05 when the American George Miles (1868–1939) and, independently, Arthur Eichengrün succeeded in preparing an acetone-soluble, plasticizable form of the material, the so-called secondary acetate, through partial saponification of the chloroform-soluble triacetate ("primary acetate"). Bayer began marketing this acetone-soluble cellulose acetate in 1905 under the tradename Cellit.[18]

Although Eichengrün actively searched for potential applications for Cellit, in every conceivable direction and always making sure that he secured appropriate patent protection, industrial-scale development posed serious problems for many years. Eichengrün's initial idea was to promote cellulose acetate as a replacement for the highly flammable cellulose nitrate in its principal applications. By contrast, the acetate could be induced to burn only with difficulty, suggesting that there should be a huge market for Cellit in the manufacture of plastics, transparent sheeting, photographic film, fibers, and lacquers. The basic idea clearly demonstrated foresight, but Eichengrün failed to reckon with what proved to be a very lengthy period of development attributable to the fact that, despite apparent similarities between cellulose nitrate and cellulose acetate, their chemical behaviors differed greatly. It was thus not possible to adapt for cellulose acetate the methods most commonly employed in cellulose nitrate processing (such as the choice of solvent, plasticizer, etc.).

A Laborious Initiation through Acetate Rayon

Eichengrün and his co-workers applied in 1904 for a patent for the dry spinning of acetate rayon. In 1907, working on the basis of this patent, the Kunstseidenfabrik Jülich attempted to initiate industrial-scale production of such a material. The project was quickly abandoned, however, despite encouraging results: the expenses were simply too great, especially given the high cost of acetic acid and problems associated with its recovery. Another drawback was the fact that no way could be found to dye the resulting acetate rayon using the coloring agents available at that time.

A commercially viable acetate rayon made its appearance only much later, in 1920, in conjunction with development by René Clavel (1886–1969), a chemist and industrialist from Basel, of the first acetate dyes. The late onset of acetate rayon production has an interesting historical origin: During the First World War, cellulose acetate was utilized extensively in the preparation of airplane lacquer (as elaborated below). When the war ended and the market for this critical defense commodity suddenly collapsed, it was essential that new products be sought to take advantage of existing manufacturing capacity. A determined quest for promising applications was thus initiated. It was this call for innovation that provided the necessary incentive for renewed attempts to commercialize acetate rayon.[19]

Visions of a Nonflammable Movie Film

Eichengrün was confident early on that his hard-to-ignite cellulose acetate could eventually evolve into a replacement for conventional nitrocellulose-based movie films, which were so highly flammable that they had been responsible for numerous theater fires. He expended considerable effort on this seminal idea during a period when he was in charge of the Bayer photo works in Düsseldorf, but his attempts were thwarted by the limited mechanical stability of cellulose acetate film relative to the nitrocellulose analogue, coupled with its greater sensitivity to water, higher cost, and poor retention of applied photochemical layers (Figure 4).[20] As in the case of acetate rayon, and for similar reasons, success in preparing a safety film based on cellulose acetate came only after the First World War, by which time Eichengrün was no longer engaged with the problem. Indeed, universal adoption of film of this type occurred only after the Second World War.[21]

In recognizing the great potential inherent in cellulose acetate, Eichengrün was years ahead of his time. Despite the problems encountered with both acetate rayon fabric and the elusive movie films he remained certain that the future for cellulose acetate was bright,

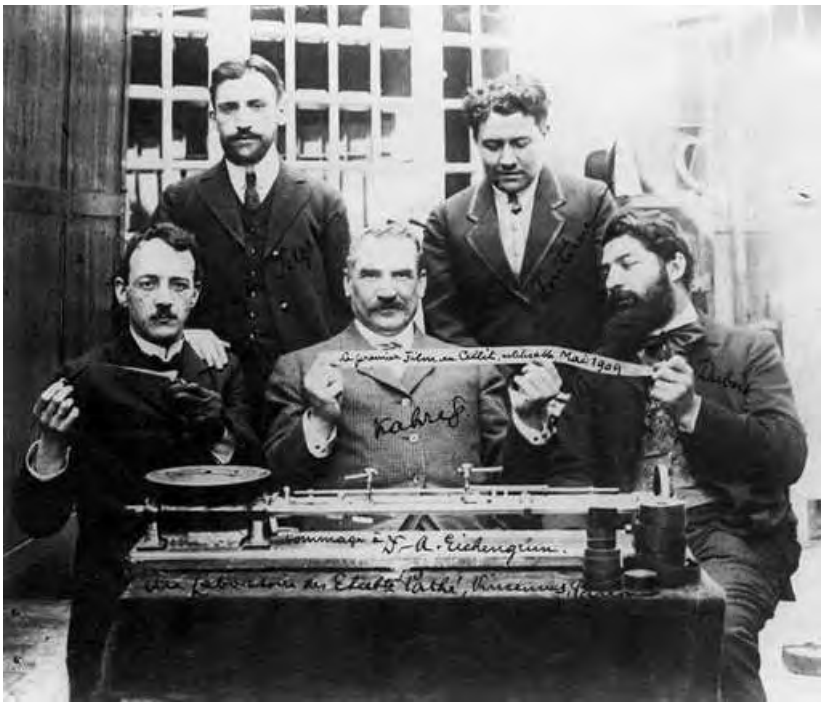

Figure 4. Tribute to Eichengrün, inventor of the first nonflammable movie film made from cellulose acetate (Cellit), which was first successfully employed in 1909 by the film company Pathé Fréres in Vincennes near Paris. Photo: Bayer-Archiv, Leverkusen.

and in fact he was critical of Bayer for not being willing to stay the course through the necessarily long phase of development, when costs would of course greatly exceed benefits. His professional frustrations were further complicated by private issues: the physically attractive Eichengrün had since 1894 been married to an American, Elizabeth Fechheimer, and was the father of four children, but he had in the meantime become involved with a Dutch woman, Madeleine Bickenbach née Mijnssen, who also was married. Even though in June of 1905 he wedded his new love, and proceeded to have two additional children with her, his turbulent private life had created a number of enemies for him in puritanical Elberfeld. The accumulating professional and personal problems culminated in his leaving Bayer at the end of 1908. Thanks to the formidable wealth he had amassed he was able to establish himself independently in Berlin with a private laboratory of his own. There he concentrated exclusively on cellulose acetate and its potential applications, still on the best of terms with his former employer. By 1915 Eichengrün's private laboratory had already evolved into what amounted to a small chemical plant with a staff of 14, and in 1919 the company, now boasting nearly 70 employees, was renamed "Cellon-Werke Dr. Arthur Eichengrün" (Figure 5).[22]

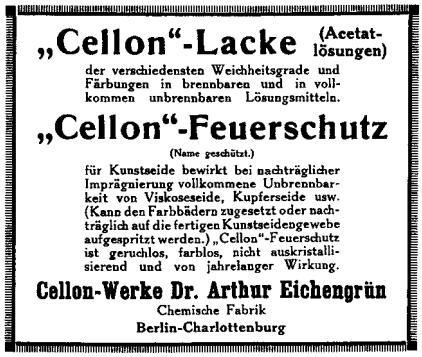

Figure 5. Advertisement for the "Cellon-Werke Dr. Arthur Eichengrün", which existed from 1919 to 1933. From: H. Stadlinger, *Das Kunstseiden-Taschenbuch*, 2nd ed., Finanz-Verlag GmbH, Berlin, **1930**, preceding p. 415.

Figure 6. Multiple "Cellonization" of the external surface of a zeppelin made it impervious to gases and weather resistant, as well as conferring upon it streamlining characteristics. Photo: Archiv für Luftschiffbau Zeppelin GmbH, Friedrichshafen.

Lacquers and Plastics as Critical War Materials

The astonishing metamorphosis of a one-man laboratory into a flourishing midsized enterprise, especially during the First World War, can be attributed above all to two of Eichengrün's inventions: cellulose-acetate lacquer and a combustion-resistant plastic, also from cellulose acetate, known as Cellon.[23] In contrast to acetate rayon and the safety film for movies, where developmental work was interrupted by the war and thus delayed for several years, the war actually served as a remarkable stimulus to the introduction of cellulose acetate in lacquers and plastics.

In the early days of aviation, airplane wings, as well as zeppelins, were covered with a linen or cotton fabric that was made water-repellant, gas-tight, and resistant to both mechanical and chemical degradation by impregnation with rubber. In 1909 Eichengrün recognized the advantages cellulose acetate lacquer might offer in this application. The lacquers he subsequently prepared not only saved weight, but they also circumvented the demand for rubber, an especially scarce commodity during wartime because it had to be imported from abroad. In the course of drying, fabric coverings that had been "cellonized" became tight as a drum, which also made the aircraft more streamlined.[24] After 1910 the rapidly expanding aviation industry became the principal consumer of cellulose acetate lacquers. Eichengrün arranged for their manufacture by the Berlin firm of Dr. Quittner & Co. using his patented process, an arrangement that proved especially lucrative during the war years. Apart from the air force, another major customer for tensioning lacquers was the navy with its fleet of zeppelins (Figure 6). Had the war not ended in 1918, Eichengrün would have been the beneficiary of yet another military contract: for the manufacture of cellulose acetate impregnated clothing as protection against the skin corrosion inflicted by the mustard gas "Lost".

Eichengrün profited from military contracts during the First World War in other contexts as well. As previously noted, cellulose acetate was useful not only in tensioning lacquers but also for plastics manufacture. The most important product of this type was known by the trade name Cellon. It had been produced since 1911 according to Eichengrün's patented method through a license agreement with the Rheinisch-Westfälische Sprengstoff AG, later known as the Dynamit-Nobel-Actien-Gesellschaft but originally Alfred Nobel & Co., located in Troisdorf near Cologne. A substantial market for this transparent, nonflammable, shatterproof plastic developed in conjunction with goggles for aviators and gas masks. The latter were in especially great demand in consequence of gas warfare. Before the advent of acrylic glass Cellon was also used in the fabrication of windows for automobiles, zeppelins, aircraft cockpits, and naval vessels.[25] For a time during the First World War there was even sporadic interest in the idea of exploiting Cellon's transparency to create a transparent airplane, which in the sky would be nearly invisible. Initially a top-secret project, the notion was eventually conceded to be technologically utopian (Figure 7).

Eichengrün's Cellon factories survived Germany's defeat in the war relatively unscathed and were not constrained by the restrictions of the Versailles Treaty, which had a devastating effect on the aircraft industry in general. This favorable outcome could be attrib-

Figure 7. A nearly invisible military aircraft with a Cellon covering, together with a plane covered as usual with cloth. The "*transparent airplane characterized by a weather-resistant covering consisting of roughly 1/10 cellulose derivative and 9/10 camphor substitute and gelatinizing agent*" was patented during World War I, but remained an object of technical utopia. Photo: Bayer-Archiv, Leverkusen.

uted in large measure to the creative entrepreneur's talent for never losing sight of civil applications for his inventions. Most of his patents were employed under licensing agreements. In his own facilities he produced only cellulose acetate lacquer, for which he had captured a significant commercial market through collaboration with subcontractors working for Berlin's electrical engineering firms, especially AEG. There was a strong demand for insulating lacquer, developed in response to wartime shortages of rubber and guttapercha.[26] Cellulose acetate also found a niche in several other relatively crisis-proof applications, such as fireproofing impregnation and substitution for plaster of Paris in the preparation of casts and related bandaging materials employed for immobilizing broken bones.[27]

Injection Molding of Thermoplastic Materials

As noted previously, Eichengrün worked closely during the period of the Weimar Republic with the Rheinisch-Westfälische-Sprengstoff AG, which had introduced to the market his plastic known as Cellon. The company actually began as a producer of nitrocellulose, primarily for gun cotton, but because of fluctuating demand for the latter (high only in wartime) they had since 1903 also been processing the material into celluloid. Gun-cotton production was abandoned entirely in 1919 in compliance with the terms of the Versailles Treaty, at which point the entire powder factory was refitted for the manufacture of plastics.[28] The company's product spectrum was limited essentially to celluloid and Cellon. This change in orientation, dictated by political circumstances, created in Germany a boom in the infant synthetic materials sector. It is thus no coincidence that the year 1919 saw Eichengrün develop a new type of synthetic, one based on cellulose acetate modified by plasticizers. This became the first thermoplastic material in synthetics history amenable to injection molding. A corresponding patent application was submitted in the same year. The preparation was marketed initially under the trade name Lonarit, but this was changed to Trolit after Eichengrün's patent was acquired by the Rheinisch-Westfälische-Sprengstoff AG.[29]

Eichengrün was responsible not only for the ground-breaking development of the first injection-molding substrate with plastic characteristics, but also for the associated processing technology. In 1919 he patented a "*device for the fabrication of moldings from cellulose esters in which the heated mass is forced under pressure through channels, with the distinctive feature that the compression mold adheres to the channel wall, within which the hot-fluid mass then solidifies to become the molded object*".[30] In other words, Eichengrün developed the first plunger-type injection-molding machine for thermoplastic materials. Based on the two Eichengrün patents referred to above, the firm of Eckert & Ziegler in Cologne became the first manufacturer of injection-molding equipment. In 1926 Eckert & Ziegler became a subsidiary of the Rheinisch-Westfälische-Sprengstoff AG, which is therefore regarded as the industrial trailblazer in the injection molding of plastics.[31] Eichengrün's achievement in perfecting both a new processing material and the associated manufacturing technology made possible the mass-production of various plastic articles on the basis of cellulose acetate, despite the fact that injection molding was initially constrained to small items in the range of 10 to 25 grams. Cellulose acetate quickly displaced celluloid in many applications, and improvements in injection-molding technology soon made it possible to produce objects in the 250–300-gram range. Injection-molded articles established an especially firm foothold in the rapidly developing electrical engineering industry, which encompassed not only civilian applications but later under the Third Reich also played a major role in arms manufacture.

"Aryanization" of the Cellon-Werke Dr. Arthur Eichengrün

The National Socialist party assumed power in Germany in January 1933. By March of that year Eichengrün had already been forced by the "Kampfbund des gewerblichen Mittelstandes" ("Fighting Union of the Industrial Middle Class") to hand over management of his company to an Aryan trustee. The Kampfbund was infamous for its especially virulent antisemitism. In 1933 (i.e.,

remarkably early) he also modified the corporate structure of the firm, transforming it into a "GmbH": the Cellon-Werke GmbH (Figure 8).[32] In the process, the Jewish-sounding name "Eichengrün" thus disappeared entirely so the enterprise would appear from the outside to be safely Aryan—a deftly arranged bit of subterfuge with the objective of keeping the firm out of Nazi hands. Eichengrün sold 51% of the company to business associates classed unambiguously as Aryans, retaining for himself the residual 49%. A board of directors made up of influential persons, some of them members of the NSDAP, was expected to shield the operation from further trespass on the part of the state.

Figure 8. Advertisement for the Cellon company after its conversion into a GmbH. Eichengrün's name no longer appears (cf. Figure 5). From: K. Mienes, *Celluloseester und Celluloseäther unter besonderer Berücksichtigung der Benzylcellulose*, Chem.-techn. Verlag Dr. Bodenbender, Berlin, **1934**, p. A VI.

Later, Eichengrün began to receive threats that after December 31, 1937 the Cellon-Werke GmbH would no longer be eligible for government contracts unless it were completely transferred into Aryan hands. Such a ban would have been catastrophic, since in the meantime the Reichsbahn (German Railroad) had become its principal client, accounting for up to 90% of total sales. In desperation he finally disposed of his remaining share in the business. The signed sales agreement, executed on January 12, 1938, predated by nine months the horrible November pogrom.[33] Thanks to this timely and rigorous Aryanization of what had been a Jewish firm, Eichengrün was able to negotiate for himself comparatively favorable terms, and also hand-select a sympathetic set of business partners. Only after November 9, 1938 did a Jew's ability to maneuver in situations like this essentially disappear altogether. Looking back, Eichengrün nevertheless recognized that he could have arranged a significantly better set of conditions had he acted even sooner: *"I would have been much better off if, when first ordered in the spring of 1933 to liquidate the Cellon works and leave them in Aryan hands, I had at once complied and stepped aside."*[34]

The Cellon-Werke GmbH was purchased by the Chemische Fabrik Dr. Joachim Wiernik & Co. AG, situated in Berlin-Waidmannslust, which on January 1, 1940 acquired the new name Diwag Chemische Fabriken AG.[35] Eichengrün maintained that Diwag always fulfilled its stated commitments "*in the most loyal way*", even though "*it was not possible to follow through*" on his aspirations to "*continue the pursuit of inventive activities in the framework of the company and with its support*".[36] Eichengrün managed to ensure, however, that he would be forced to transfer to Diwag only a portion of his patents, procedures, production techniques, and formulations. In addition, Diwag agreed to retain all personnel employed longer than ten years, including Eichengrün's son Edgar from his first marriage, who according to the terms of the Nuremberg Laws was considered only half-Jewish and, in contrast to his siblings, had foregone emigration. Eichengrün utilized his remaining freedom of action to safeguard from the National Socialists to the best of his ability the 254922 reichsmarks he received for selling the business. For example, he arranged to have Diwag set aside 92% of the money to be dispensed in the form of annual payments extending through 1955.[37] But despite these precaution his windfall quickly shrank. Commissions and legal and notary fees alone swallowed up 16000 reichsmarks. Additional outlays were required to cover compulsory tariffs imposed on all Jewish citizens in the wake of the pogrom of November 9, 1938. The sum of 125000 reichsmarks in the form of a "Jewish property tax" fell due in 1939. This particular levy, initially set at 20% of assets, was later increased to 25%. In January 1940 he was forced to pay an additional 27000 reichsmarks as an "emigrant tax for the Jewish congregation of Berlin", even though Eichengrün had officially declared his withdrawal from the Jewish community as early as September 20, 1894 and no longer regarded himself a member of the Jewish faith. Finally, in October 1940, he was obligated to surrender 83000 reichsmarks in "flight from the Reich tax". The latter was to be deposited into a blocked account, from which it could be confiscated by the tax authorities if Eichengrün were ever to leave the country. This actually transpired when he was deported to the Theresienstadt concentration camp, which technically classified as "flight" to Czechoslovakia. In other words, he was compelled to finance out of his own pocket what amounted to his kidnapping![38]

In 1933 when the Cellon-Werke was transformed into a GmbH, Eichengrün skillfully exploited a legal loophole and arranged to isolate and retain for himself a small private office and research laboratory under the name "Cellon-Werke Dr. Arthur Eichengrün". From here he supervised his remaining patents and licenses, dedicating all his consulting activities to Diwag. Put candidly, this entailed "armaments-related experiments in the interest of both the high command and the navy".[39] Eichengrün and his wife lived off royalties from the obviously numerous patents that remained his. Nevertheless, even the private office and laboratory eventually fell under National Socialist scrutiny. Using the argument that his firm was ineligible for registration under the applicable commercial statutes since it was engaged only in the exploitation of patent rights and asset administration, and neither manufactured nor marketed any products, the "Cellon-Werke Dr. Arthur Eichengrün" was expunged from the commercial register on February 3, 1942.[40]

Eichengrün failed to recognize until roughly 1938/39 how precarious his situation had become. One is left to speculate about why this might have been the case: perhaps this passionate tinkerer and inventor simply succeeded

in deluding himself, still possible because after he reorganized his firm into a GmbH in 1933 and disposed of it entirely in 1938 he was allowed to proceed largely undisturbed in his research and patent-application activities. It could also be that he believed himself immune because of the military significance of his discoveries, in conjunction with personal contacts he enjoyed with various ministries and high-ranking personalities—including his immediate neighbor, Hermann Göring (1893–1946)—and his fruitful collaboration with Diwag, a company perceived as important from a military standpoint.[41] Eichengrün was clever enough to create the impression that he and his private research laboratory were themselves indispensable on the grounds of defense contracts and various patents crucial to the military, such as that for the Cellon sheathing the navy relied on for ship propellers.[42] Despite having to pay the exorbitant Jewish property tax mentioned above, Eichengrün continued to do relatively well from a financial standpoint. Soon after November 9, 1938 he transferred all his rights from the corporate sales agreement with Diwag to his third wife, the ("Aryan") Lucie Bartsch: "*Therefore, acting on advice from lawyers, notaries, and industrialists, shortly after November 9, 1938 I conveyed my rights from the Wiernik contracts … to my wife, and a year later in Munich took the same steps in notarized form with respect to license income from various other contracts, along with all my household effects, including personal collections. … In any event, through these donations to my wife, my entire income, apart from a single contract with the Dynamit Nobel A.G., devolved upon my wife and thus came into Aryan possession and—insofar as one could foresee at the time—safe hands.*"[43]

The ever-increasing pressure of chicanery and harassment was not enough to induce Eichengrün to emigrate, even though he could have afforded to do so and most of the children from his first and second marriages had already made this choice. The staunchly apolitical Eichengrün evidently refused quite consciously to be intimidated by the Nazis. His compulsive self-assertiveness was presumably undergirded by the fact that monetary policies of the National Socialist state made emigration extremely unattractive, as he could have transferred only a fraction of his wealth abroad. But prosperity was for Eichengrün a source of great pride, a symbol of the social status he had achieved and one that could be put on display. He took pleasure in the fact that his wealth made possible a luxurious lifestyle and the acquisition of a valuable art collection (albeit one reflecting a rather conventional taste).[44] His preoccupation with social prestige was evident from the outset in a weakness for aristocratic addresses. He had long been drawn toward places where celebrities congregated. Even in the days when he worked for Bayer he resided in the same neighborhood as his superior Carl Duisberg (1861–1935), and as a young, successful Berlin industrialist he became the owner of a gorgeous villa in Berlin-Grunewald, although he was forced to sell it later when inflation ran rampant. In 1915 he acquired a vacation home on the Obersalzberg, but this too had to be sold in 1932 on account of increasingly intolerable anti-Semitic badgering.[45] After 1928 Eichengrün lived in an elegant house at Kaiserdamm 34 in Charlottenburg. In 1932 a new neighbor moved into the apartment below his: Hermann Göring, Speaker of the Reichstag (the German Parliament). In April 1933 the latter was appointed Prime Minister of Prussia, and in the following month he took over the new Imperial Aviation Ministry, from which position, in March 1935, he assumed supreme command of the Air Force, quickly ensuring its expansion. One can only speculate that, given their involvement in aviation, Eichengrün and Göring would have discussed their common interests. Both also had a fondness for luxurious surroundings, and their art collections might well have constituted another point of contact. In 1939 Göring was subjected to public pressure from comrades in the party because of what they perceived to be his unbearable domestic living situation. The result was that Eichengrün had to give up the Charlottenburg residence. After this expulsion Eichengrün was nevertheless able to afford moving for a year and a half (in 1940/41) to Munich, known as the "Capital of the [Nazi] Movement"—albeit after the "surrender of 5% of his annual income to an agency in Munich"—where he and his wife resided in the elegant Regina Palasthotel.[46] In 1941 he returned to Berlin, ultimately occupying a moderate apartment on the Pommersche Strasse in Wilmersdorf, a neighborhood that at the time was characterized by a conspicuously high proportion of Jewish residents, and where the family of his son Edgar also lived.

The ever-increasing discrimination, which in turn led to social isolation and exclusion from scientific, commercial, and civil organizations, was especially hard on someone as concerned with social acceptance as Eichengrün. "*The oppression and gradual segregation from the world of the living, and above all the transformation of good friends and scientific acquaintances into utterly indifferent and in some cases hostile figures, as well as the things one was forced to suffer in everyday life, cannot be depicted in words*", he wrote in retrospect.[47] He regarded the state's intrusion into his opulent lifestyle as especially discriminating, namely the confiscation of what had become for him cherished status symbols. For example, since September 20, 1939 it had been illegal for Jews to possess radio; they would simply be appropriated by the state with no compensation whatsoever, so Eichengrün was forced to relinquish his costly and beloved Telefunken receiver. He was equally bitter about the obligatory sale of his eight-cylinder Ford—he who had once been a proud member of the Automobile Club of Germany. There was really no choice, because since the end of 1938 Jews were not allowed to own or operate motor vehicles.[48] In the past he had also been a member of the prestigious Motor Yacht Club of Germany, but again he was compelled to sell his stately motor vessel with its American motor.

Eichengrün was deeply alarmed when he learned of the first deportations of Jewish citizens from Baden and the Palatinate under a decree issued on October 15, 1940. Report of this catastrophe triggered desperate efforts on his part to counter his escalating loss of rights on account of his "Jewishness". In a traumatic letter he appealed to Dr. Paul Müller (1876–1945), managing director of Dynamit Nobel in Troisdorf,

the company that produced his Cellon plastic (a substance of critical importance to the military) and was exploiting as well 15 additional Eichengrün patents relevant to armaments manufacture under the Third Reich, above all ones concerning the injection-molding process and related substrates. Referring explicitly to both earlier and current personal inventions with wartime relevance, he pleaded for support of his application for recognition under the terms of the Nuremberg Laws as a "citizen" despite his Jewish heritage. Quite remarkably, exceptions were sometimes granted to provisions of the German Nationality Act of September 15, 1935 so long as these were seen to be "in the interest of the public at large".[49] Full-blooded Jews or others practicing Judaism ("Geltungsjuden") could therefore under certain circumstances be declared "first-degree half-castes" or even "German-blooded". In seeking exemption from the Nationality Act, an applicant would normally attempt to demonstrate either a special set of skills and significance or else meritorious service on behalf of the fatherland, appending references solicited from persons or institutions of lofty stature and reputation within the Nazi state. What follow are several quotes (in translation) selected from Eichengrün's February 1941 letter to Paul Müller. For purposes of clarity it is worth noting that at this point Eichengrün had already been expelled from his residence on the Kaiserdamm in Charlottenburg and was living in the Regina Palasthotel in Munich:

"*As you know, I have been living here in Munich for the past year and a half. … I was supposed to be expelled from the hotel some time ago; the corresponding order from the local 'District Office for Aryanization' [Gaustelle für Arisierung] was subsequently withdrawn, however, and I have stayed here unmolested. … We recently learned in confidence from an absolutely reliable source that in the very near future the same sort of action will be initiated in Munich as … in Baden. My wife has succeeded in presenting the situation to a highly placed party official and supplying him above all with information regarding my contributions to commerce, aviation, and the four-year plan, and to the acquisition of foreign currency, as well as my current activities. The gentleman displayed increasing interest, and offered the following advice: 'Travel to Berlin and arrange to contact responsible parties in both the Ministry of Aviation and the Ministry of Economics. But first secure letters or testimonials from leading figures in industry, in particular from I.G. [Farben] if possible. These letters must state that Dr. E. in nearly 50 years of service has achieved a record of exceptional merit in the most diverse aspects of industrial chemistry, that the author of the letter is familiar with the benefits Dr. E.'s inventions have brought the German economy, and that one also anticipates additional benefits from his recent work. German industry would be incapable of understanding it if such a man were to be pulled from his path, and sees it of the greatest importance that he be permitted to pursue without hindrance or limitations his current projects, which have already led to several patent applications and are in some cases already undergoing tests in industrial settings.' … This is almost word-for-word the view expressed by the high party official in question. It follows that the sword of Damocles hovering over my head can only be restrained by the intervention of industry, in part through reference to the value and somewhat unusual current state of development of my inventions (e.g., acetate rayon, the injection-molding process, Cellit) and in part—and apparently this is regarded as extremely important—to the work I am pursuing at the moment and successes it may produce. … I therefore believe it would not be a wasted effort if you were to direct such a letter—which must of course contain references to applications of Cellon for the army and to the significance of the injection-molding technique (for the four-year plan)—to the Ministry of Economics. … I hope you will not be offended by my calling upon you in an unusual matter like this. I know that it is not appreciated when one deals in a friendly way with someone like me, and I realize that a great many in industry and science who once knew and valued me would take offense at such an unreasonable request. But you have always displayed such a friendly disposition toward me that I am confident you will help me. This has to do not simply with a courtesy or an ordinary favor for a friend, but rather with actual life or death. Because I will never allow myself to be carried away alive, so if this solitary open passageway involving a letter of exemption is closed off, I am left only with the bitter end.*"[50]

Eichengrün's petition to be exempted from the provisions of the German Nationality Act, had it been approved, would at least have conferred upon him the status of "provisional citizen" (i.e., that of a "Jewish half-caste"), and in an ideal case even that of full citizenship (i.e., one of "German blood"), thereby screening him from further persecution. But it was denied, even though leading representatives of IG Farben interceded on his behalf. Eichengrün remained a Jew in the sense of the Nuremberg Laws, and thus retained the inferior status of a "German national", who was denied essential rights of citizenship.

Denunciation and Deportation to Theresienstadt

In August 1941 Eichengrün submitted another application for the granting of an exception. It had to do with the status of his marriage to his third wife, Lucie Bartsch, an "Aryan". This time Eichengrün was more fortunate in his quest. The Minister of the Interior recognized his June 4, 1942 marriage as "privileged", even though being childless it would actually have qualified only as a simple "mixed marriage" under the laws of the National Socialists.[51] This "privileged mixed marriage" provided Eichengrün with a certain, although shaky, measure of protection; in most cases the Jewish partner escaped deportation.

After the autumn of 1942 the situation for mixed German–Jewish families and half-castes deteriorated dramatically. Early in 1943 threats were issued that Jewish partners in German–Jewish mixed marriages were also to be deported and included in the "final solution".[52] This applied especially to Berlin, the city with the most people in that category. Instead of evacuating all Jews with German partners as a single group, the tactic adopted was to charge each individual Jew in a mixed marriage insofar as possible with an alleged

breach of the law; given the hundreds of interdictions to which Jews were subject it was not difficult to identify some piece of trivia that could be exaggerated into a crime. The person in question was then taken into "protective custody" and deported to a concentration camp. In this final stage of persecution of the Jews, Eichengrün, supposedly protected by his "privileged mixed marriage", also became one of the victims of the Nazi regime. In October 1942 Eichengrün was denounced before the prosecutor's office by Dr. Georg Klauer, at that time Director of the German Patent Office and known for his rigorous application of anti-Semitic law. On the basis of Klauer's denunciation he was accused of submitting two letters to the Patent Office, dated December 1941 and January 1942, that lacked the obligatory name "Israel" in the signature, a label which had been mandatory for Jews since January 1, 1939. Through an "embezzled signature" he had thus "fraudulently attempted to accrue the honors conferred upon an inventor".[53] Eichengrün protested that neither case had involved a personal signature, but rather the official designation for his private office and laboratory, "Cellon-Werke Dr. Arthur Eichengrün", which continued to be listed in the official commercial registry until February 2, 1942. Company names were explicitly excluded from the requirement of the obligatory name "Israel", but he was nevertheless arrested, ordered to serve a prison sentence, and deported in May 1944 to Theresienstadt. His wife actually made matters worse, in that her plea for release of her husband was unfortunately submitted on company stationery from the "Cellon-Werke Dr. Arthur Eichengrün", a nonexistent entity since February 1942. The rule of law no longer being in force in Germany, her plea for mercy was ignored.

Eichengrün remained in Theresienstadt until the liberation of the concentration camp by the Red Army. Despite his advanced age and his being a diabetic he survived the confinement, though visibly weakened, with little bodily harm (Figure 9). When the war ended he returned to Berlin, where he found his home ravaged and plundered. Yet his drive was unbroken. In his new home he set up a makeshift laboratory

Figure 9. Eichengrün after his release from the concentration camp. Photo: E. Eichengrün, Königswinter.

in which he improved some of his old formulations and developed new ones. For example, based on his experiences in Theresienstadt he devised an agent against bed bugs.

Friends and colleagues went out of their way after 1945 to see that belated honors were bestowed on Eichengrün as "compensation" for the injustices he had suffered. Thus, at the initiative of Rudolf Pummerer (1882–1973), once a student of Willstätter, the University of Erlangen in August 1946 commemorated the award of his doctoral degree, six years later than would have been customary. The archives of the University of Erlangen include the revealing annotation that this commemoration of the 50th anniversary of a degree conferral was observed in 1946 rather than 1940 because Eichengrün's Jewish faith would have made a timely ceremony impossible.[54]

Eichengrün was a victim of National Socialism at several levels, even though the stepwise "Aryanization" of his firm was somewhat atypical, and quite remarkably he successively defended his art collection from the Nazis' grasp. Although especially in the early 1930s he managed to soften somewhat the blows from constant escalation of the anti-Semitic decrees through adroit and clever tactics, probably with the help of numerous opportune warnings and scraps of information, in the long run it made little difference. Today he is largely unknown by those in the plastics industry, and his name is an unfamiliar one even among acknowledged historians of chemistry and pharmacy. This is due not only to his having as a practitioner, inventor, and industrialist left less of an imprint on scientific history than colleagues whose contributions were in the more theoretical aspects of science. His consignment to oblivion is instead largely an outcome of the most dismal chapter in German history.

I wish to express my deep appreciation to Prof. Dr. Dr. h.c. Fritz Eiden, Munich, and Prof. Dr. Otto Krätz, Starnberg, for supplementary information, suggestions, and many informative discussions. With respect to acquiring archival material I am much indebted to Ernst Eichengrün, Königswinter, Ulrich Chaussy, Munich, Dr. Jost Lemmerich, Berlin, and the staff of the Bayer Archives in Leverkusen.

Published online: March 30, 2004

Translated by Dr. William Russey Huntingdon, PA (USA)

[1] Cf. the following brief biographies: A. Eichengrün, *Reichshandbuch der Deutschen Gesellschaft*, Vol. *1*, Berlin, **1930**, pp. 378–379; E. Eichengrün, *Kunststoffe* **1947**, *37*, 24; H. Stadlinger, *Die Pharmazie* **1947**, *2*, 383–384; H. G. Bodenbender, *Angew. Chem. Ausg. A* **1948**, *60*, 111–112; E. Eichengrün, *Neue Deutsche Biographie*, Vol. *4*, Berlin, **1959**, pp. 373–374.

[2] Regarding Eichengrün's career as a chemist cf. his interview with Philipp Manes conducted at the KZ Theresienstadt in: *Philipp Manes Document Collection, Theresienstadt/Tatsachenberichte/Heft 8*, The Institute of Contemporary History and Wiener Library, London, Document No. 1346.

[3] With respect to Einhorn cf.: E. Uhlfelder, *Chem.-Ztg.* **1917**, *41*, 373–374; E. Uhlfelder, *Ber. Dtsch. Chem. Ges.* **1917**, *50*, 668–670; W. Schneider, *Pharm. Ind.* **1956**, *18*, 85–88.

[4] On the discovery of cocaine's effectiveness as a local anesthetic and its impact on morphinism see H. Honegger, H. Hessler, *Pharm. Ztg.* **1972**, *117*, 1153–1195; J. G. Reicheneder, *Sudhoffs Arch.* **1988**, *72*, 170–184.

[5] A. Eichengrün, *Ueber das Methoxy-oxydihydrocarbostyril*, Diss. phil. Friedrich

Alexander-Universität zu Erlangen, Aachen **1890**, Archives of the University of Erlangen-Nürnberg C4/3b Nr. 1318. The doctoral degree certificate is dated March 7, 1890.

[6] W. Wimmer, "*Wir haben fast immer was Neues": Gesundheitswesen und Innovationen der Pharma-Industrie in Deutschland, 1880–1935*, Duncker & Humblot, Berlin, **1994**, pp. 123–133; W. Bartmann, *Zwischen Tradition und Fortschritt. Aus der Geschichte der Pharmabereiche von Bayer, Hoechst und Schering von 1935–1975*, Franz Steiner, Stuttgart, **2003**, pp. 87 – 93.

[7] A. Eichengrün, *Z. Angew. Chem.* **1898**, *11*, 900 – 904; A. Eichengrün, *Z. Angew. Chem.* **1899**, *12*, 219 – 226; A. Eichengrün, *Z. Angew. Chem.* **1899**, *12*, 1147 – 1153; A. Eichengrün, *Z. Angew. Chem.* **1901**, *14*, 261 – 270; A. Eichengrün, *Z. Angew. Chem.* **1902**, *15*, 217 – 225; A. Eichengrün, *Z. Angew. Chem.* **1913**, *26*, 49 – 56.

[8] A. Eichengrün, *Chem.-Ztg.* **1897**, *21*, 940; A. Eichengrün, *Pharm. Centralbl.* **1897**, *38*, 639 – 640; O. Anselmino, E. Gilg, *Kommentar zum Deutschen Arzneibuch 6. Ausgabe 1926*, Vol. *1*, Springer, Berlin, **1928**, pp. 278 – 280; H. P. Kaufmann, *Arzneimittel-Synthese*, Springer, Berlin, **1953**, p. 588.

[9] Personnel files of A. Eichengrün, Bayer-Archiv Leverkusen.

[10] R. Schmitz, *Med. Welt* **1983**, *34*, 799 – 803; J. R. McTavish, *Pharm. Hist.* **1987**, *29*, 103 – 115; T. J. Rinsema, *Gesch. Pharm.* **1999**, *51*, 33 – 39 (supplement to the *Deutsche Apotheker-Zeitung*).

[11] M. de Ridder, *Heroin. Vom Arzneimittel zur Droge*, Campus Verlag, Frankfurt, **2000**, pp. 20 – 21.

[12] A. Eichengrün, *Die Pharmazie* **1949**, *4*, 582 – 584.

[13] A. Eichengrün, Pharmazeutisch-wissenschaftliche Abteilung, *Farbenfabriken Bayer & Co. ("Böttinger-Schrift")*, Vol. 2, Elberfeld, **1918**, pp. 409–416, Bayer-Archiv, Leverkusen 1/6.1 and Library of the Deutsches Museum, Munich 1971 C 23. In this essay on the history of his department it is noteworthy that Eichengrün makes no claim to a role in the synthesis of Aspirin, whereas he discusses his other pharmaceutical discoveries in detail. That he began to publicize his contribution to the Aspirin synthesis specifically in 1930 could be accounted for by his increasing persecution as a Jew, which forced him in self-defense to cite all his accomplishments in as much detail as possible.

[14] Cf. The report "Aspirin-Entdecker von Nazis nicht anerkannt", *Süddeutsche Zeitung* no. 206 from September 7, **1999**, p. 14; "L'inventeur de l'aspirine: un ursurpateur?", *Le Soir* from September 8, **1999**. Moreover: W. Sneader, *Br. Med. J.* **2000**, *321*, 1591 – 1594.

[15] A. Eichengrün, *Z. Angew. Chem.* **1901**, *14*, 1017 – 1071; A. Eichengrün, *Verh. Ges. Dtsch. Naturforsch. Aerzte* **1901**, *73*, 140 – 145; A. Eichengrün, *Z. Angew. Chem.* **1902**, *15*, 1114 – 1116; A. Eichengrün, Photographische und technische Abteilung, *Farbenfabriken Bayer & Co. ("Böttinger-Schrift")*, Vol. 2, Elberfeld, **1918**, pp. 457–462 (see note [13]).

[16] Personnel files of A. Eichengrün, Bayer-Archiv Leverkusen.

[17] A. Eichengrün in *Enzyklopädie der technischen Chemie,* keyword "Acetylcellulosen", 1st ed., Vol. *1* (Ed.: F. Ullmann), Urban & Schwarzenberg, Berlin, **1915**, pp. 114 – 130; A. Eichengrün in *Enzyklopädie der technischen Chemie,* keyword "Acetylcellulosen", 2nd ed., Vol. *1* (Ed.: F. Ullmann), Urban & Schwarzenberg, Berlin, **1928**, pp. 116 – 141.

[18] A. Eichengrün in *Enzyklopädie der technischen Chemie,* keyword "Cellit", 1st ed., Vol. *3* (Ed.: F. Ullmann), Urban & Schwarzenberg, Berlin, **1916**, p. 301; A. Eichengrün in *Enzyklopädie der technischen Chemie,* keyword "Cellit", 2nd ed., Vol. *3* (Ed.: F. Ullmann), Urban & Schwarzenberg, Berlin, **1929**, pp. 119 – 120; A. Eichengrün, *Chem.-Ztg.* **1927**, *51*, 25 – 26.

[19] A. Eichengrün in *Technologie der Textilfasern*, Vol. *7* (Ed.: R. O. Herzog), Julius Springer, Berlin, **1927**, pp. 189 – 211.

[20] A. Eichengrün, K. Mienes in *Celluloseverbindungen und ihre besonders wichtigen Verwendungsgebiete dargestellt an Hand der Patent-Weltliteratur*, Vol. *1* (Ed.: O. Faust), Julius Springer, Berlin, **1935**, pp. 1205 – 1206.

[21] A. Ossenbrunner, *Kunststoffe* **1952**, *42*, 232 – 235.

[22] See records of the *Cellon-Werke Dr. Arthur Eichengrün*, Amtsgericht Charlottenburg, 90 HRA 94620 alt; O. Wenzel, *Adressbuch und Warenverzeichnis der chemischen Industrie des Deutschen Reiches* **1923**, *15*, 44; **1928**, *16*, 42; **1930/31**, *17*, 45.

[23] A. Eichengrün, *Verhandlungen des Vereins zur Beförderung des Gewerbfleißes* **1920**, *99*, 78 – 104.

[24] M. Bottler, *Kunststoffe* **1916**, *6*, 56 – 58; Dr. Quittner & Co. , *Kunststoffe* **1916**, *6*, 99; A. Eichengrün, *Kunststoffe* **1916**, *6*, 151 – 152.

[25] A. Rost, *Kunststoffe* **1913**, *3*, 150 – 152; H. Stadlinger, *Chem.-Ztg.* **1929**, *53*, 77 – 78; R. Röhm, *Kunststoffe* **1937**, *27*, 60 – 62; R. Röhm, *"Cellon". Fabrikation, Eigenschaften und Verarbeitung*, [no publ., no loc.] **1939**, pp. 1 – 12, Library of the Deutsches Museum, Munich 1945 B 24.

[26] A. Eichengrün in *Die Isolierstoffe der Elektrotechnik* (Ed.: H. Schering), Julius Springer, Berlin, **1924**, pp. 311 – 336.

[27] A. Eichengrün, *Z. Angew. Chem.* **1929**, *42*, 214 – 217.

[28] F. Trimborn, *Explosivstoffabriken in Deutschland. Ein Nachschlagewerk zur Geschichte der Explosivstoffindustrie*, 2nd ed., Verlag Locher, Cologne, **2002**, pp. 233 – 236, 259–261.

[29] H. B. Willers, *Kunststoffe* **1924**, *14*, 36 – 37; H. B. Willers, *Mix & Genest Nachrichten* **1924**, *1*, 30 – 35; H. B. Willers, *Mix & Genest Nachrichten* **1929**, *6*, 1 – 9.

[30] Lonarit-Gesellschaft m.b.H. , DRP 441 023 from January 26, 1919; Cellon-Werke Dr. Arthur Eichengrün, DRP 393 873 from January 26, 1919.

[31] H. Stadlinger, *Chem.-Ztg.* **1932**, *56*, 409 – 411, 431 – 432; E. M. Lais, *Kunststoffe* **1937**, *27*, 70 – 75; E. M. Lais, *Kunststoffe* **1938**, *28*, 62; K. Mienes, A. Krause, *Kunststoffe* **1940**, *30*, 1 – 3; H. Gastrow, *Kunststoffe* **1940**, *30*, 203 – 206; M. E. Laeis, *Der Spritzguss thermoplastischer Massen*, 2nd ed., Carl Hanser, Munich, **1959**, p. 18; R. Sonntag, *Kunststoffe* **1985**, *75*, V–XIV.

[32] O. Wenzel, *Adressbuch und Warenverzeichnis der Chemischen Industrie des Dritten Reiches* **1935**, *8*, 46.

[33] E. Eichengrün, *Verkauf der Cellon-Werke*, Berlin April **1951**, archives of the Eichengrün family, Königswinter. It is quite apparent that in the January 1938 sale of his share in the firm Eichengrün was acting in anticipation of the edict from the Ministry of Economics issued on March 1, 1938 prohibiting Jews from being awarded government contracts, cf. J. Walk, *Das Sonderrecht für die Juden im NS-Staat. Eine Sammlung der gesetzlichen Maßnahmen und Richtlinien – Inhalt und Bedeutung*, C. F. Müller Juristischer Verlag, Heidelberg, **1981**, p. 217.

[34] A. Eichengrün, Erläuterungen zu meinem Testament, Wilmersdorf December 12, 1942, Eichengrün family archives, Königswinter. On the subject of Aryanization see the essay by F. Bajohr in *"Arisierung" im Nationalsozialismus. Volksgemeinschaft, Raub und Gedächtnis* (Ed.: Fritz Bauer Institut), Campus Verlag, Frankfurt, **2000**, pp. 15 – 30.

[35] *Handbuch der deutschen Aktiengesellschaften* **1936**, *41/6*, 8317; **1937**, *42/5*, 6865–6866; **1938**, *43/2*, 1947–1948; **1939**, *44/5*, 6264–6265; **1940**, *45/6*, 6738–6739; **1941**, *46/6*, 6580–6581. Diwag was among the companies classified as militarily important suppliers to the army high command; cf.: *Liste der Fertigungskennzeichen für Waffen, Munition und Gerät,* Oberkommando des Heeres, Berlin, **1944**, p. 771.

[36] A. Eichengrün, Erläuterungen zu meinem Testament, Wilmersdorf December 30, 1942, Eichengrün family archives, Königswinter.
[37] Declaration of Dipl.-Kaufmann Runk from August 11, 1938 regarding sale of interests in the Cellon-Werke G.m.b.H.; Transcripts nos. 4,5,6 of the notary index for 1938, transacted in Berlin on January 12, 1938; Copy of a letter from A. Eichengrün to Diwag, Bad Wiessee June 27, 1949, Eichengrün family archives, Königswinter. Noteworthy is the great discrepancy between the negotiated selling price and the estimated gross value of the Cellon-Werke GmbH according to the balance sheet of December 31, 1938, listed as 449 792,20 reichsmarks, cf. Zentralfinanzamt Berlin to the Amtsgericht Berlin, Amtsgericht Charlottenburg, Cellon-Werke Dr. Arthur Eichengrün, 90 HRA 94620 alt.
[38] A. Eichengrün, Further details listed on p. 2 of the questionnaire related to the report of asset losses attributable to Nazi law or other actions of the Nazi regime, Berlin May 3, 1946; E. Eichengrün, Sale of the Cellon-Werke, Berlin April 1951; Wilhelm Schulz to the United States Department of Justice, Overseas Branch, Berlin-Dahlem, Berlin May 22, 1953, Eichengrün family archives, Königswinter.
[39] A. Eichengrün to the Amtsgericht Berlin, Berlin-Charlottenburg August 11, 1941, Amtsgericht Charlottenburg 90 HRA 94620 alt.
[40] Amtsgericht Charlottenburg, Cellon-Werke Dr. Arthur Eichengrün, 90 HRA 94620 alt. A copy of the deletion notice is also in the Eichengrün family archives, Königswinter.
[41] Hermann Göring and Arthur Eichengrün occupied the house at Kaiserdamm 34 in Berlin-Charlottenburg, cf. Berliner Adressbuch, Vol. 1, August Scherl Deutsche Adressbuch-Gesellschaft m.h.H., Berlin, **1933**, p. 517 (Eichengrün) und p. 771 (Göring), Library of the Deutsches Museum, Munich ZB 1860.
[42] DRP 701 170 from March 24, 1937, issued on August 2, 1941. See also Cellon-Werke Dr. Arthur Eichengrün to the Amtsgericht Berlin-Charlottenburg, Berlin-Charlottenburg September 18, 1941, Amtsgericht Charlottenburg, Cellon-Werke Dr. Arthur Eichengrün, 90 HRA 94620 alt. Corvette captain Walther of the navy high command is explicitly cited here as the partner working with Eichengrün.
[43] A. Eichengrün, Erläuterungen zu meinem Testament, Wilmersdorf December 30, 1942, Eichengrün family archives, Königswinter.
[44] Dr. Eichengrün's collection survived the Second World War nearly intact—only a few pictures and sculptures needed to be sold in the early post-war period—and was disposed of at auction after Eichengrün's death by his heirs through Leo Spik, Berlin, in Lot 374 on April 20/21, 1950. Regarding the collection see also the letter from A. Eichengrün to Herrn Thiemann, Berlin, April 12, 1948, Eichengrün family archives, Königswinter.
[45] See U. Chaussy, *Nachbar Hitler. Führerkult und Heimatzerstörung am Obersalzberg*, 4th ed., C. Links, Berlin, **2004**, pp. 40–44, 58–60, 123–128.
[46] A. Eichengrün to P. Müller, Charlottenburg February 12, 1941, Bayer-Archiv Leverkusen, Eichengrün personnel files
[47] A. Eichengrün to Herrn Thiemann, Berlin April 12, 1948, Eichengrün family archives, Königswinter.
[48] See ref. [38].
[49] J. M. Steiner, J. Frh. v. Cornberg, *Vierteljahreshefte fuer Zeitgeschichte* **1998**, *46*, 143–187; B. Meyer, "*Jüdische Mischlinge". Rassenpolitik und Verfolgungserfahrung 1933–1945*, Dölling und Galitz, Hamburg, **1999**, pp. 105–108.
[50] See ref. [46]. Müller supported Eichengrün's cause, cf.: P. Müller, W. Pungs to the Wirtschaftsgruppe Chemische Industrie, Troisdorf August 22, 1941, as well as the equally supportive letter from Dr. Hörlein and Dr. Brüggemann, IG Leverkusen, Leverkusen October 14, 1941, to the Wirtschaftsgruppe Chemische Industrie, Bayer-Archiv Leverkusen, Eichengrün personnel files. Müller emphasized the "far-reaching importance" flowing out of "the work of Dr. Eichengrün with respect to the German economy during the World War as well as especially in this war".
[51] The police commissioner in Berlin, Sec. II, to A. Eichengrün, Berlin June 11, 1942, Eichengrün family archives, Königswinter.
[52] Cf.N. Stoltzfus, *Widerstand des Herzens. Der Aufstand der Berliner Frauen in der Rosenstraße – 1943*, Deutscher Taschenbuch Verlag, Munich, **2002**, pp. 276–283.
[53] L. Eichengrün to the Gestapo headquarters in Berlin, Berlin February 1, 1944; A. Eichengrün: Was ich den Nazis zu verdanken habe ("What I have to thank the Nazis for"), Berlin June 1947, Eichengrün family archives, Königswinter. When Klauer was summoned in 1948 to appear before the Denazification Authorities he committed suicide. With respect to Klauer's role in National Socialism see: R. Spencer, *J. Pat. Off. Soc.* **1949**, 31, 79–87.
[54] University of Erlangen Archives C5/1 no. 45.

Polymer Science

Cellulose: Fascinating Biopolymer and Sustainable Raw Material

Dieter Klemm, Brigitte Heublein, Hans-Peter Fink,* and Andreas Bohn*

Keywords:
cellulose chemistry · polymer materials · polysaccharides · supramolecular chemistry · sustainable raw materials

Dedicated to Professor Burkart Philipp

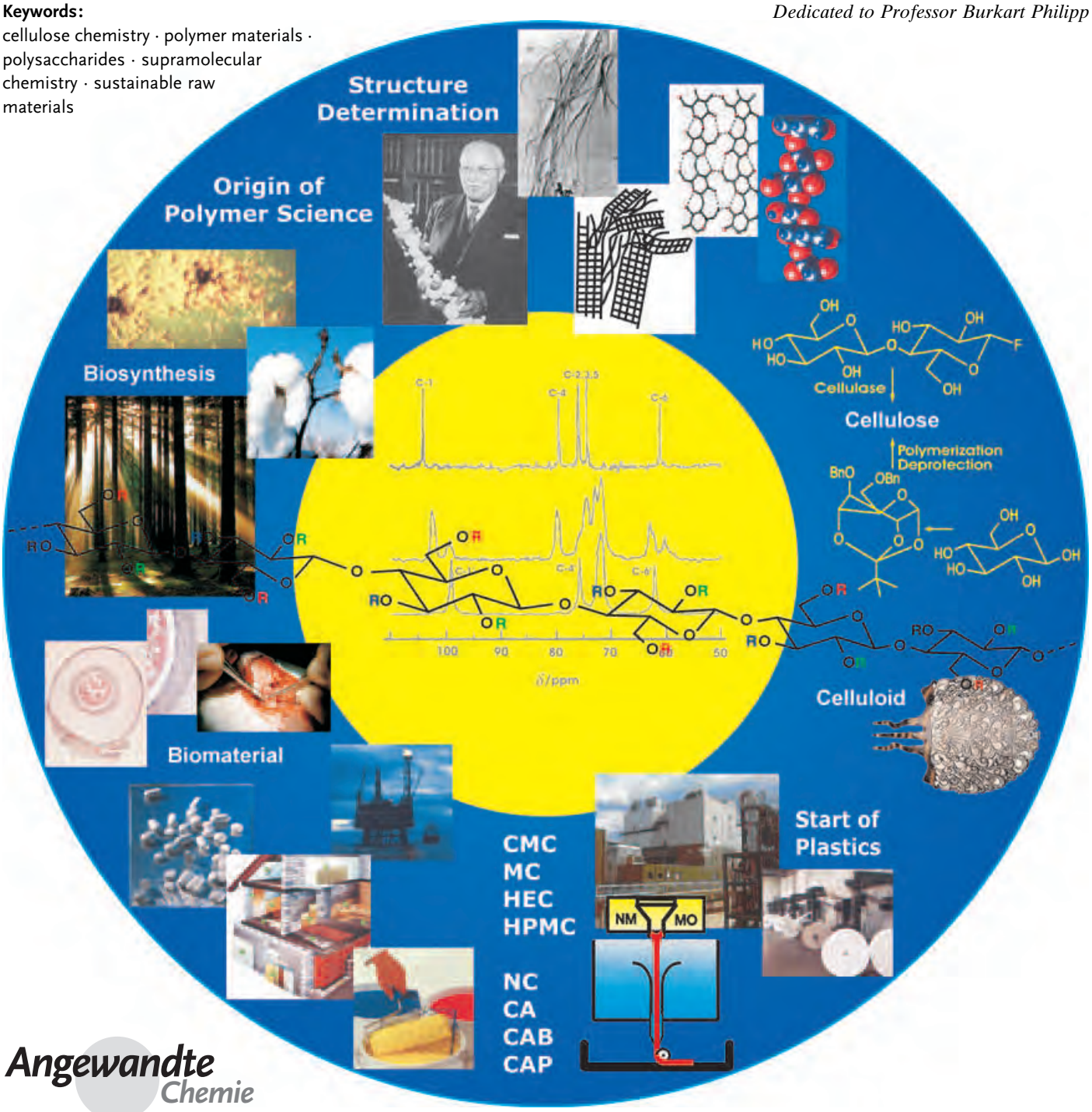

DOI: 10.1002/anie.200460587

As the most important skeletal component in plants, the polysaccharide cellulose is an almost inexhaustible polymeric raw material with fascinating structure and properties. Formed by the repeated connection of D-glucose building blocks, the highly functionalized, linear stiff-chain homopolymer is characterized by its hydrophilicity, chirality, biodegradability, broad chemical modifying capacity, and its formation of versatile semicrystalline fiber morphologies. In view of the considerable increase in interdisciplinary cellulose research and product development over the past decade worldwide, this paper assembles the current knowledge in the structure and chemistry of cellulose, and in the development of innovative cellulose esters and ethers for coatings, films, membranes, building materials, drilling techniques, pharmaceuticals, and foodstuffs. New frontiers, including environmentally friendly cellulose fiber technologies, bacterial cellulose biomaterials, and in-vitro syntheses of cellulose are highlighted together with future aims, strategies, and perspectives of cellulose research and its applications.

From the Contents

1. Introduction

In 1838 the French chemist Anselme Payen described a resistant fibrous solid that remains behind after treatment of various plant tissues with acids and ammonia, and after subsequent extraction with water, alcohol, and ether.[1] He determined the molecular formula to be $C_6H_{10}O_5$ by elemental analysis, and observed the isomerism with starch. The term "cellulose" for this plant constituent was first used in 1839 in a report of the French academy on the work of Payen.[2]

Thousands of years prior to the discovery of the "sugar of the plant cell wall", cellulose was used in the form of wood, cotton, and other plant fibers as an energy source, for building materials, and for clothing. Since the Egyptian papyri, a considerable part of human culture has been shaped by cellulose materials.

As a chemical raw material, cellulose has been used for about 150 years. The formation of cellulose nitrate by reaction with nitric acid[3] and the corresponding technical synthesis of the first thermoplastic polymer material called celluloid (camphor used as plasticizer) by the Hyatt Manufacturing Company in 1870 demonstrated that new materials could be produced on an industrial scale by the chemical modification of cellulose.[4] With this knowledge came an increased use of synthetic fibers based on wood cellulose, instead of native cellulose fibers, for textiles and technical products. The first example herein is the production of regenerate cellulose filaments by spinning a solution of cellulose in a mixture of copper(II) hydroxide and aqueous ammonia, in which tetraamminecopper(II) hydroxide (cuprammonium hydroxide) $[Cu(NH_3)_4](OH)_2$ is formed,[5] followed by the currently most important large-scale technical process in fiber production, the viscose process.[6] In this process, cellulose is transformed into cellulose xanthogenate (see Scheme 16 and Figure 18) followed by spinning its solution in aqueous sodium hydroxide (viscose).

From the current point of view, cellulose is the most common organic polymer, representing about 1.5×10^{12} tons of the total annual biomass production, and is considered an almost inexhaustible source of raw material for the increasing demand for environmentally friendly and biocompatible products.[7] Wood pulp remains the most important raw material source for the processing of cellulose, most of which is used for the production of paper and cardboard. Approximately 2% ($\approx$3.2 million tons in 2003) were used for the production of cellulose regenerate fibers and films, as well as for the synthesis of a large number of cellulose esters and ethers. Such cellulose derivatives produced on an industrial scale (see Schemes 16 and 17 in Section 4) are used for coatings, laminates, optical films and sorption media, as well as for property-determining additives in building materials, pharmaceuticals, foodstuffs, and cosmetics. In the field of synthetic fibers, the Lyocell process made an industrial breakthrough as an environmentally friendly alternative to the viscose process, whereby cellulose is regenerated from

[*] Prof. Dr. D. Klemm, Dr. B. Heublein
Institut für Organische Chemie und Makromolekulare Chemie
Friedrich-Schiller-Universität Jena
07743 Jena (Germany)
Fax: (+49) 3641-948202
E-mail: Dieter.Klemm@uni-jena.de
Dr. habil. H.-P. Fink, Dr. A. Bohn
Fraunhofer-Institut für Angewandte Polymerforschung
14476 Potsdam-Golm (Germany)
Fax: (+49) 331-568-3815
E-mail: fink@iap.fhg.de

 DOI: 10.1002/anie.200460587

solution in *N*-methylmorpholine-*N*-oxide (NMMO) monohydrate by spinning (Section 5). Numerous new applications of cellulose take advantage of its biocompatibility and chirality for the immobilization of proteins,[8] antibodies,[9] and heparin,[10] and for the separation of enantiomeric molecules[11] as well as the formation of cellulose composites with synthetic polymers and biopolymers.[12]

The fascination of the cellulose biopolymer is a result of its specific structure, which is described in more detail in the following section. The fusion of both carbohydrate and polymer chemistry in a macromolecule composed of repeating glucose units generates surprising specificity and impressively diverse architectures, reactivities and functions. In contrast to carbohydrates of low molar mass, the reactions and properties of cellulose are determined by intermolecular interactions, cross-linking reactions, chain lengths, chain-length distribution, and by the distribution of functional groups on the repeating units and along the polymer chains. Cellulose differs from synthetic polymers by virtue of its distinct polyfunctionality, its high chain stiffness, and its sensitivity toward the hydrolysis and oxidation of the chain-forming acetal groups, which determine its chemistry and handling.

The elucidation of the polymeric structure of cellulose can be traced back to 1920 with the pioneering work of Hermann Staudinger.[13] Through acetylation and deacetylation of cellulose, he recognized that its structure does not merely consist of an aggregation of D-glucose units. Rather, the glucose units were found to be linked to each other covalently to form long molecular chains. This, along with Staudinger's research with other chain molecules, marked the discovery of the polymeric state of molecules and of the corresponding reactions that are unique to polymers and represents the origin of polymer science.

Figure 1 shows the molecular structure of cellulose as a carbohydrate polymer generated from repeating β-D-glucopyranose molecules that are covalently linked through acetal functions between the equatorial OH group of C4 and the C1 carbon atom (β-1,4-glucan), which is, in principle, the manner in which cellulose is biogenetically formed. As a result, cellulose is an extensive, linear-chain polymer with a large number of hydroxy groups (three per anhydroglucose (AGU) unit) present in the thermodynamically preferred $^4C_1$ conformation. To accommodate the preferred bond angles of the acetal oxygen bridges, every second AGU ring is rotated 180° in the plane. In this manner, two adjacent structural units define the disaccharide cellobiose.

The chain length of cellulose expressed in the number of constituent AGUs (degree of polymerization, DP) varies with the origin and treatment of the raw material. In case of wood

Dieter Klemm received his master's degree (diploma) in 1964 from the University of Jena, and received his PhD in 1968 from work in the stereospecific synthesis of nitrogen-containing steroids conducted with Prof. G. Drefahl at the Institute of Organic Chemistry. He obtained his habilitation in 1977 after conducting research in synthetic polymer chemistry with H.-H. Hörhold. After work in the pharmaceutical industry and initial activities in polysaccharides as a university lecturer, he has been a professor of organic chemistry at the University of Jena since 1987. He is associate editor of the journal Cellulose and columnist of Polymer News. In 2004 he became the first German scientist to receive the Anselme Payen Award of the American Chemical Society for contributions to the development of new cellulose-based materials.

Brigitte Heublein studied chemistry at the Friedrich Schiller University of Jena and received her master's degree (diploma) in 1969 with her investigations of cationic polymerization of vinyl monomers. She received her PhD in 1974 from research into the control of cationic polymerizations of vinyl monomers with Prof. G. Heublein at the Institute of Organic and Macromolecular Chemistry, and was associated with that research group until 1989. Since 1990 she has been working in organic natural products and polysaccharide chemistry under the direction of Prof. D. Klemm.

Hans-Peter Fink studied physics at Rostock University, where he received his diploma in 1973 and his PhD in 1977 under Prof. G. Becherer on X-ray diffraction analysis of glass ceramics. Between 1975 and 1992 he worked at the Institute for Polymer Chemistry in Teltow–Seehof, conducting structural investigations of cellulose which was also the topic of his habilitation (1991, Rostock University). He has been employed at the Fraunhofer Institute for Applied Polymer Research since its foundation in 1992, and he currently heads the Division of Natural Polymers of the Institute. He has been awarded repeatedly for his contributions to the field of cellulose research, most recently in 2002, with the Jisuke Hayashi Award of the Cellulose Society of Japan.

Andreas Bohn studied mineralogy at the universities of Münster and Berlin, where he graduated in 1994 from the Hahn–Meitner Institute with a diploma thesis on X-ray and neutron scattering investigations of the structure of proton conductors. Since 1995 he has been working in the department of structure characterization at the Fraunhofer Institute for Applied Polymer Research in Teltow and Potsdam (Golm). In 2000 he received his PhD degree with a thesis on X-ray diffraction investigations of the structure and orientation of bacterial cellulose and regenerated cellulose films. He has since headed the group of X-ray structure characterization at the Institute.

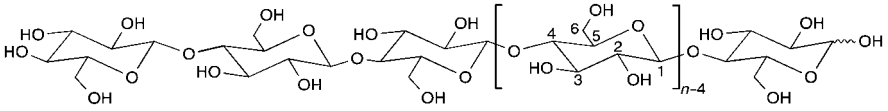

Figure 1. Molecular structure of cellulose (n = DP, degree of polymerization).

pulp, the values are typically 300 and 1700. Cotton and other plant fibers have DP values in the 800–10000 range, depending on treatment; similar DP values are observed in bacterial cellulose. Regenerate fibers from cellulose contain 250–500 repeating units per chain. By acid treatment and cellulase-catalyzed hydrolysis, cellulose can be quantitatively decomposed to D-glucose. Partial chain degradation yields powdery cellulose substrates of the microcrystalline cellulose type[14] (such as Avicel) with DP values between 150 and 300. A β(1→4) linked glucan with 20–30 repeating units offers all properties of cellulose.[15]

The cellulose chain consists at one end of a D-glucose unit with an original C4-OH group (the nonreducing end); the other end is terminated with an original C1-OH group, which is in equilibrium with the aldehyde structure (the reducing end). Technical celluloses, such as bleached wood pulp, contain additional carbonyl and carboxy groups as a result of the isolation and purification processes that play a significant role in the processing of cellulose.[16]

The molecular structure imparts cellulose with its characteristic properties: hydrophilicity, chirality, degradability, and broad chemical variability initiated by the high donor reactivity of the OH groups (Section 3). It is also the basis for extensive hydrogen bond networks, which give cellulose a multitude of partially crystalline fiber structures and morphologies (Section 2). The properties of cellulose are therefore determined by a defined hierarchical order in supramolecular structure and organization.

Scheme 1 presents the four different pathways by which cellulose is accessed today. As described above, the dominant pathway is the production of cellulose from plants. In the seed hairs of cotton, cellulose is available in almost pure form. In contrast, wood cellulose forms a native composite material with lignin and other polysaccharides (hemicelluloses) from which it is isolated by large-scale chemical pulping, separation, and purification processes.

Apart from plants, certain bacteria, algae, and fungi produce cellulose as well. Because of their specific supramolecular structures, these cellulose forms are frequently used as model substances for further research on cellulose structure, crystallinity, and reactivity, as well as for the development of new materials and biomaterials (Section 6). On this basis, the biosynthesis of cellulose has been investigated in detail over the past decades.[17] Therefore, it is known that the biosynthesis of cellulose has been part of the life cycle of cyanobacteria for over 3.5 billion years.[18]

The synthesis of cellulose in vitro should be highlighted as an additional important development in recent years.[15] The first reported cellulase-catalyzed formation of cellulose was based on cellobiosyl fluoride,[19] and the first chemosynthesis was carried out through a ring-opening polymerization of substituted D-glucose pivalate moieties, followed by deprotection (Section 7).[20]

A considerable stimulation of scientific and technological research in the field of cellulose has been triggered over the past 10 years in response to the growing global importance in renewable resources and environmentally compatible materials. With its foundations in the knowledge contained in monographs, books and review articles,[21] this review presents important current developments and discusses the aims, strategies, and perspectives in the field of cellulose. The topics highlighted herein were chosen for their current importance to the field of cellulose research and the nature of the innovative impetus associated with a given development; their selection reflects the experience of the authors. Thus, a collection of current cellulose research and development has been created that combines discussions of structure, synthesis, innovative products, and new frontiers in an updated contribution to the scientific literature.

2. Structure and Properties of Cellulose in the Solid State and in Solution

The hierarchical structure of cellulose, formed by the hydrogen bond network between hydroxy groups, has been the subject of intense research for more than 100 years, marked with frequent controversy over results and a consistent supply of new insight.[22] Directly from the beginning, progress was closely connected with the introduction and continued development of structure-analysis methods, such as X-ray diffraction, electron microscopy, high-resolution ^{13}C solid state NMR spectroscopy, and neutron diffraction

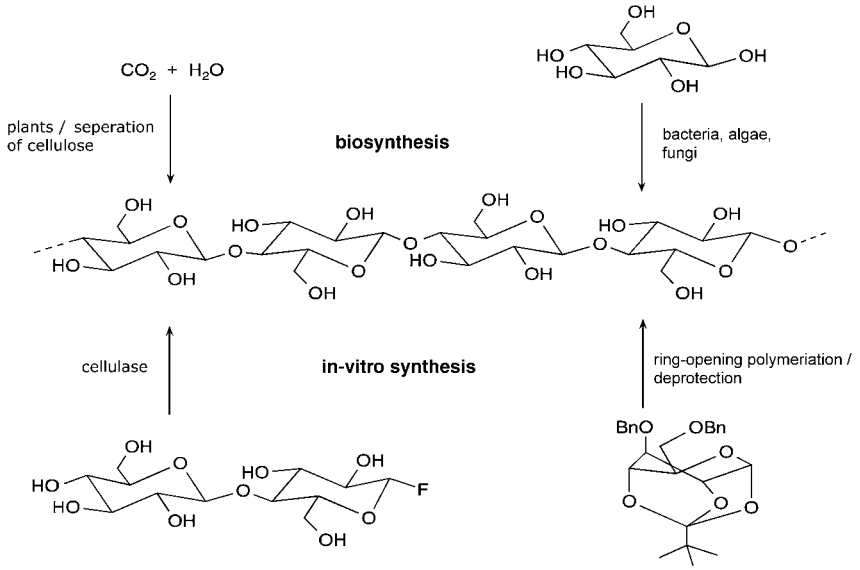

Scheme 1. Principle pathways to cellulose formation.

analysis. A detailed analysis and modeling of the various structural levels of cellulose is essential for synthetic reaction procedures, and for the controlled structure formation and properties of cellulose-based chemical products (man-made cellulosics).

2.1. Solid-State Structures of Native Cellulose

As shown in the molecular structure represented in Figure 1, the hydroxy groups of β-1,4-glucan cellulose are placed at positions C2 and C3 (secondary, equatorial) as well as C6 (primary). The CH_2OH side group is arranged in a *trans-gauche* (*tg*) position relative to the O5–C5 and C4–C5 bonds. As a result of the supramolecular structure of cellulose, the solid state is represented by areas of both high order (crystalline) and low order (amorphous).

2.1.1. Crystal Structure

As a first approximation, the crystal structure of native cellulose (cellulose I) determined by X-ray diffraction can be described by a monoclinic unit cell (space group $P2_1$) which contains two cellulose chains in a parallel orientation with a twofold screw axis.[23] In the 1980s, ^{13}C-CP/MAS NMR spectroscopy was used in the initial discovery that native cellulose is present in two different crystalline cellulose I modifications (I_α and I_β), which can be found alongside each other; the I_α/I_β ratio depends on the origin of the cellulose.[24] Investigations with electron microbeam diffraction[25] and combined X-ray and neutron diffraction[26] recently revealed the corresponding crystalline structures to have triclinic (I_α) and monoclinic (I_β) unit cells. Figure 2 shows a schematic representation of the I_β crystal structure. In the side view (Figure 2b) of the central chains of a unit cell, two intramolecular, chain-stiffening hydrogen bonds are revealed. Notably, one of the most recent reports on the I_β structure[27] describes different conformations for neighboring chains as well as different H-bonding systems inside neighboring molecular layers.

Apart from the thermodynamically less stable cellulose I, cellulose may occur in other crystal structures (cellulose II, III, and IV),[21] of which cellulose II (Figure 2) is the most stable structure of technical relevance. It can be formed from cellulose I by treatment with aqueous sodium hydroxide (mercerization) or by dissolution of the cellulose and

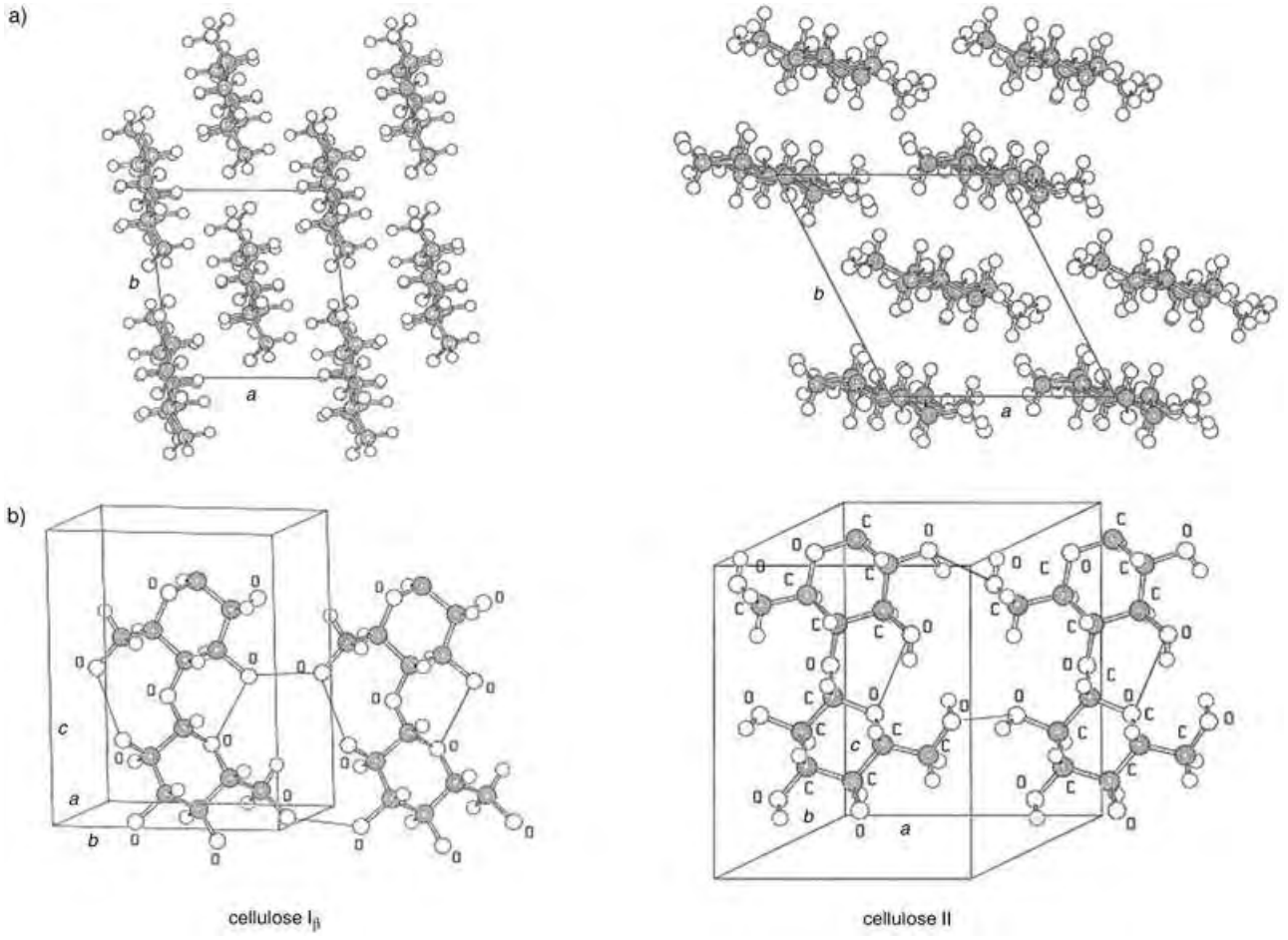

Figure 2. Crystal structures of cellulose I_β and cellulose II: a) projection of the unit cell (UC) along the *a*–*b* plane; b) projection of the UC parallel to the (100) lattice plane (cellulose I) and the (010) lattice plane (cellulose II).[22c]

subsequent precipitation/regeneration, as is done in the formation of fiber and film. This monoclinic crystal structure[28] with two antiparallel chains in the unit cell is characterized by the specific unit cell geometry with a modified H-bonding system. The alkalization of cellulose is of considerable importance to commercial-scale cellulose production as a method for increasing the reactivity (activation) of subsequent reactions as well as for the mercerization of cotton. Depending on the concentration of lye, the temperature, and mechanical load, it is possible to convert cellulose I into various crystalline alkali forms, each with a different crystal structure and variable NaOH and water content.[29] All forms will then convert into crystalline "hydrato cellulose" (water cellulose) during washout, and to cellulose II through drying (Figure 3). It is not yet understood how the parallel chain arrangement of cellulose I undergoes transition into the antiparallel orientation of cellulose II without an intermediate dispersion of cellulose molecules.

There are currently only a few reports on the structure of noncrystalline random cellulose chain segments.[30] More knowledge in this area is required, as these structure elements have a significant influence on the accessibility and reactivity of cellulose, as well as on the properties of man-made cellulose fibers.

2.1.2. *Morphology*

The biological function and numerous applications of cellulose are based on its distinct fiber morphology. The morphological hierarchy is defined by elementary fibrils, microfibrils, and microfibrillar bands.[31] The lateral dimensions of these structural units are between 1.5 and 3.5 nm (elementary fibrils), between 10 and 30 nm (microfibrils), and on the order of 100 nm (microfibrillar bands). The length of the microfibrils is on the order of several hundred nm. Figure 4 shows electron micrographs of the fibrillar structure of samples of varying origin; a structural model of an initially hydrated bacterial cellulose sample is shown in Figure 28 (Section 6.1).

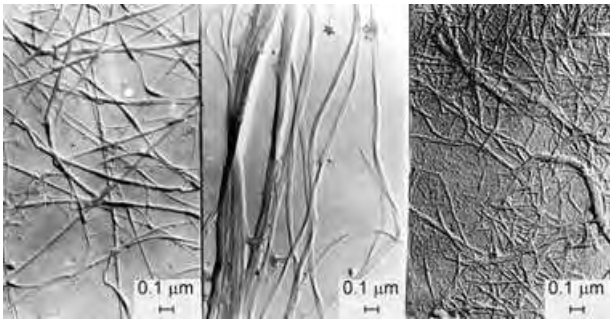

Figure 4. Electron micrographs of cellulosic microfibrils of varying origins:[32] left, *Valonia* spp. (algae) cellulose; center, cotton linters; right, spruce sulfite pulps.

The fringed fibrillar model with crystalline regions of varying dimensions (crystallites) and noncrystalline regions has proven successful for the description of the structure of microfibrils and the partial crystalline structure of cellulose in connection with the reactivity of this polymer[29c] (Figure 5).

The degree of crystallinity of cellulose and the dimensions of the crystallites have been the subject of extensive investigations for many years;[33] some results of X-ray diffraction measurements of native celluloses have been compiled in

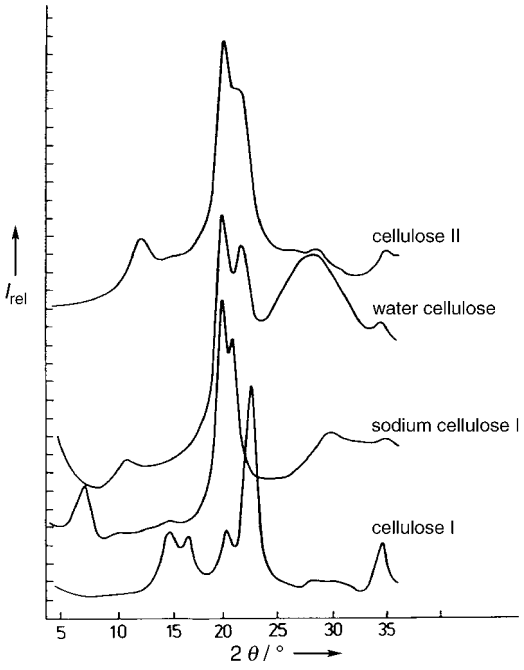

Figure 3. X-ray wide-angle scattering curves of cellulose modifications formed during alkalization and regeneration[29c] (I_{rel} = relative intensity, 2θ = diffraction angle).

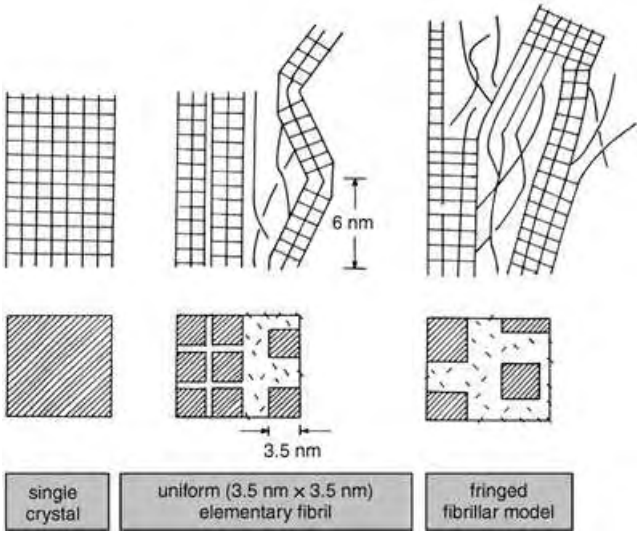

Figure 5. Various models of the supramolecular structure of cellulose microfibrils.[29c]

Table 1: Degrees of crystallinity (x_c), crystallite sizes ($D_{(hkl)}$), and lateral dimensions (d) of microfibrils of native celluloses

Cellulose Source	x_c [%]	crystallite sizes [nm]			d [nm]
		$D_{(1\bar{1}0)}$	$D_{(110)}$	$D_{(020)}$	
algal cellulose	>80%	10.1	9.7	8.9	10–35
bacterial cellulose	65–79	5.3	6.5	5.7	4–7
cotton linters	56–65	4.7	5.4	6.0	7–9
ramie	44–47	4.6		5.0	3–12
flax	44 (56)[a]	4–5	4–5	4–5	3–18
hemp	44 (59)[a]	3–5	3–5	3–5	3–18
dissolving pulp	43–56			4.1–4.7	10–30

[a] Degree of crystallinity relative to cellulose.

Table 1. The corresponding values of regenerated cellulose in the form of filaments and films are given in Table 4 (Section 5.5.1).

Notably, the lateral crystallite dimensions of regenerated cellulose (cellulose II) are in the range of ≈4–5 nm regardless of the production process (Table 4), whereas in native celluloses, values of up to 20 nm have been observed. The reasons for the formation of nearly uniform cross-sectional dimensions of these cellulose II crystallites from different structure-forming processes still have to be clarified.

The pore structure can be considered the counterpart to the fibril morphology of cellulose. It is considerably important for the accessibility in chemical reactions and enzymatic degradation.[34] The controlled variation of pore structures enables cellulose products to meet the needs of a wide range of applications, from highly specialized membrane and carrier materials to consumer goods, such as nonwovens[35] with excellent absorption properties.

2.1.3. *Growth Architectures and Material Design*

As the skeletal component in all plants, cellulose is organized in a cellular hierarchical structure. In combination with the accompanying substances hemicelluloses, lignin, and pectin, this structure leads to the extraordinary properties of native composite materials, such as wood, cotton, flax, and hemp. Figure 6 schematically illustrates the cell walls of cotton and wood with differently structured layers, in which the secondary cell-wall layer S2 contains the main quantity of cellulose.

The cellulose molecules organized in the cell walls in the form of microfibrils have characteristic orientations (helix angles), which differ as a function of the cell wall layer, and according to the plant type as well. Figure 7 shows X-ray fiber diffraction patterns of cotton and bast fibers (flax, hemp, and jute), which reflect the different average orientations of the crystalline spectra of these natural fibers.

The lower orientation of the cellulose microfibrils in cotton fibers (helix angle ≈18°) gives rise to a smaller module of elasticity and a higher elongation at breakage compared with bast fibers, which have a much higher microfibril orientation (helix angle ≈4°–5°) and fiber strength. The adaptation of the mechanical properties of wood to environmental conditions through corresponding helix angles is fascinating, and has yet to be rivaled in technical composite materials.[37] However, it is already possible to adapt the parameters of cellulosic man-made fibers to user requirements through a targeted influence on the orientation (with particular respect to the noncrystalline chain segments). It is therefore possible to develop man-made cellulose fibers similar to cotton with low orientation (high elongation), and technical fibers with high orientation and a high modulus of elasticity, similar to bast fibers.

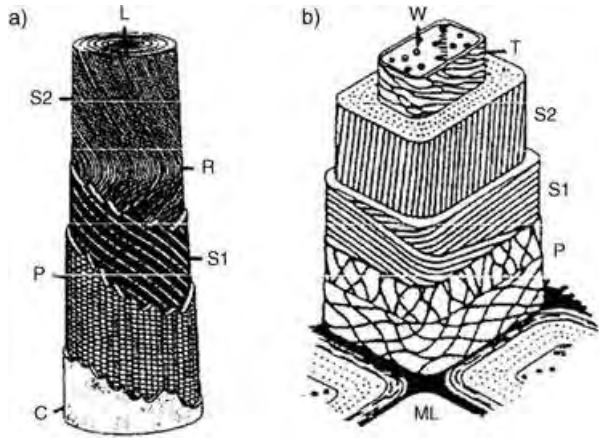

Figure 6. Structural design of plant cell walls exemplified by a) cotton and b) wood fibers:[21b] C = cuticula layer, L = lumen, ML = middle lamella, P = primary cell wall layer, R = reversing point, S1 = secondary cell wall layer 1, S2 = secondary cell wall layer 2, *T* = tertiary cell wall, W = wart layer.

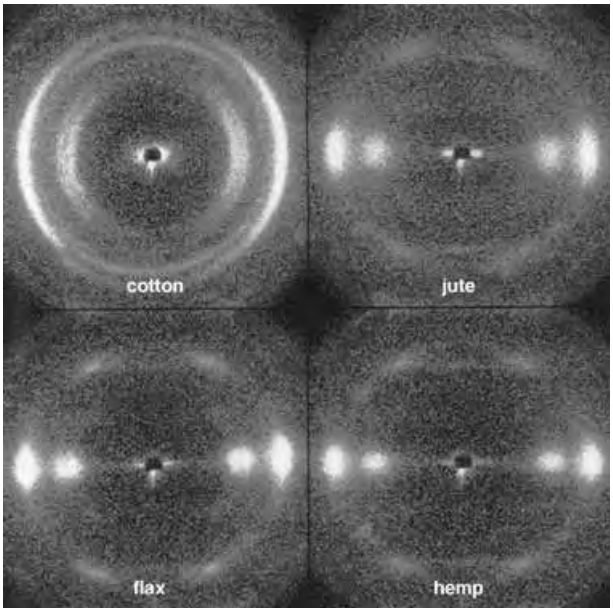

Figure 7. X-ray fiber diagrams of various natural cellulosic fibers.[36]

2.2. *Solution Structures of Cellulose and Cellulose Derivatives*

An understanding of the structure of cellulose and cellulose derivatives in solution is not only a matter of scientific interest, but has great practical importance as well.

Examples include the shaping of cellulose from spinning solutions,[38] modification of the synthesis of cellulose derivatives (Section 3) and the properties of water-soluble cellulose ethers (Section 4), which all are dependent on the solution structure. For this reason, questions regarding the structure of cellulose in solution have been the subject of intense research and discussion over the past decades. According to Schurz,[38a] a differentiation is made initially between molecularly dispersed and network solutions, to which a portion of gel particles may be added. Figure 8 illustrates suggested models of the different solution states of cellulose derivatives, which may depend on the type of solvent, polymer concentration, chain length distribution, and the type, pattern, and degree of cellulose substitution.

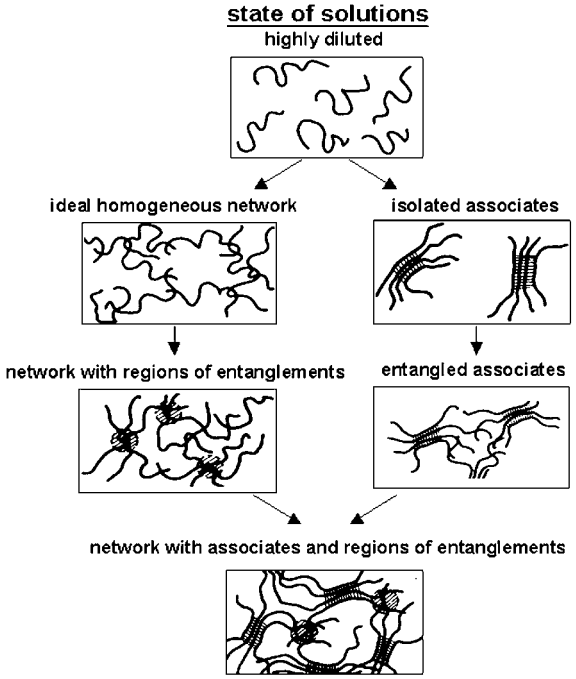

Figure 8. Scheme of the potential dissolution states of cellulose.[38a]

As a rule, cellulose derivatives with free OH groups are not molecularly dispersible. Investigations with partially substituted cellulose carbanilates and benzoates revealed, however, that aggregate-free solutions can occur through specific polymer–solvent (e.g. DMF) interactions.[39] On the other hand, completely substituted products (such as cellulose tricarbanilates) can be molecularly soluble or, owing to strong intermolecular interactions, insoluble as is the case with trimethylsilyl cellulose with DS 3.0.

Whereas highly diluted solutions have been used for fundamental research of solution structures, applied practices, such as the viscous process, employ concentrated systems with polymer concentrations of 8–12%, which are described as network solutions with gel-particle portion in accordance with model assumptions.[38b,c] Apart from rheological examinations, gel-particle characterizations are also normally carried out to determine the quality of a given spinning solution.[38]

Over the past few years the research group of Burchard, in particular, has carried out extensive fundamental research into the structure of cellulose and cellulose derivatives in solution by means of static and dynamic light scattering.[40] With regioselective modified cellulose ethers, new insight was gained into the entropy effect during the dissolution of cellulose derivatives (Section 3.2.3).[39,40]

The initial research results on the solution state of cellulose in *N*-methylmorpholine-*N*-oxide (NMMO) monohydrate as a technically relevant system (Section 5) substantiate the presence of bimodal molecule aggregations with up to 1000 chains, which can be attributed to incomplete dissolution of crystal structures of the starting cellulose material.[41] In the first approximation, the average number of molecules in the smaller aggregates corresponds to that of crystallites (50–100), whereas the average number of molecules in larger aggregates correlates with the number of molecules found in a microfibril (250–1000).[42] In a ternary solvent system composed of NMMO, water, and diethylenetriamine [bis-(2-aminoethyl)-amine], cellulose is molecularly soluble within a temperature range of 25–60 °C. Therefore, the average molar mass and other properties of the dissolved molecules could be determined by means of light scattering.[43]

2.3. Liquid-Crystalline Cellulose Structures

Owing to chain stiffness, cellulose and certain cellulose derivatives in solutions of higher concentration may form cholesteric (chiral-nematic) structures. Since the discovery of the lyotropic liquid-crystalline state of hydroxypropyl cellulose in water,[44] a multitude of cellulose derivatives were found, which produce lyotropic or thermotropic liquid-crystalline phases.[45] Chiral-nematic films and gels are formed from the solutions. The influence of the solvent and of the chain stiffness on the pitch and handedness of the chiral-nematic structures was examined.[46]

Regioselectively substituted (position 2, 3 or 6 of the AGU) cellulose phenylurethanes with F, Cl, or CH_3 groups in the phenyl ring form lyotropic liquid-crystalline mesophases in highly concentrated solutions, the structure and optical properties of which depend strongly on the site of substitution, as well as on the concentration and temperature of the solution.[46] The photo-cross-linking of cellulose-(3-chlorophenyl)-urethanes in mixtures with acrylate monomers produces semi-interpenetrating polymer networks, which can change their selective reflection under compression.[47] Cellulose urethanes with azo-dye substituents and acrylates of hydroxypropyl cellulose are other well-analyzed lyotropic liquid-crystalline cellulose products. The latter form gels in water through photo-cross-linking, and their resulting color is determined by the water content.[47] The optical properties that can be controlled by the pitch of cholesteric phases open up important fields of application, such as color pigments in car paints and as copy protection color for document papers.

Liquid-crystalline states of unsubstituted cellulose are significant with particular respect to new spinning methods and the production of high-performance fibers. Suitable

solvents for this include NMMO, a mixture of trifluoroacetic acid and chlorinated alkanes, DMA/LiCl, ammonium rhodanide in liquid ammonia,[48] and concentrated phosphoric acid. However, any spinning process based in these liquid-crystalline systems has yet to gain industrial acceptance. The cellulose concentrations in NMMO used in the Lyocell process are below the liquid-crystalline phase range (Section 5).

Recently, developments appear to have emerged in conjunction with the possible production of chiral-nematic suspensions from cellulose crystallites or microfibrils.[46a]

3. Cellulose Chemistry: New Syntheses, Products and Supramolecular Architectures

3.1. Specific Features of the Reactions of Cellulose

The insolubility of cellulose in water and in most organic solvents caused by its supramolecular structure is the reason behind the fact that all commercially available products are currently produced through reactions of cellulose in the solid, or more or less swollen state (heterogeneous reactions).[49] Because each repeating unit of cellulose has three hydroxy groups available for reaction, and the stability of the chain-forming acetal groups toward various reagents, oxygen, and mechanical and thermal load is limited, additional questions emerge over substituent distribution in the product and over chain degradation during synthesis.

In case of heterogeneous reactions, the accessibility and reactivity of the OH groups are clearly determined by hydrogen bond-breaking activation steps (through alkaline compounds such as NaOH, Section 2.1.1)[50] and by interaction with the reaction media (e.g. swelling).[51] Thus, the "linear" transfer of the typical reactions of organic chemistry to cellulose is not easily done. However, the control of cellulose activation and of the type of heterogeneous reaction permits effective synthesis of cellulose products with desired degrees of reaction, reproducible substitution patterns, and targeted properties at both the laboratory and production scales. There remain important aspects of the synthesis procedure that are understood only partially. Therefore, a lot of experience and the right "feeling" are still required in cellulose syntheses.

Through the use of specific cellulose solvents,[21a] which disrupt hydrogen bonds and thus dissolve the adducts formed, the influence of the supramolecular structure of cellulose on the reaction procedure is eliminated almost completely. In this context, a solution of LiCl in DMA (DMA/LiCl) is one of the most important solvent systems for cellulose in organic syntheses[52] as well as for analytical purposes.[53] The structure of this binary medium, the mechanism of dissolution, the influence of water on the dissolving activity, and the state of dissolution of cellulose have been investigated in detail.[40,54]

Over the past few years, it was demonstrated that tetrabutylammonium fluoride trihydrate in DMSO (DMSO/TBAF) effectively dissolves cellulose and is very useful for homogeneous syntheses.[55] Fundamental progress has also been made in the classical field of metal-containing cellulose solvents like cuprammonium hydroxide.[56] In doing so, the solution structure of cellulose in this copper-containing medium was elucidated (Scheme 2).[53]

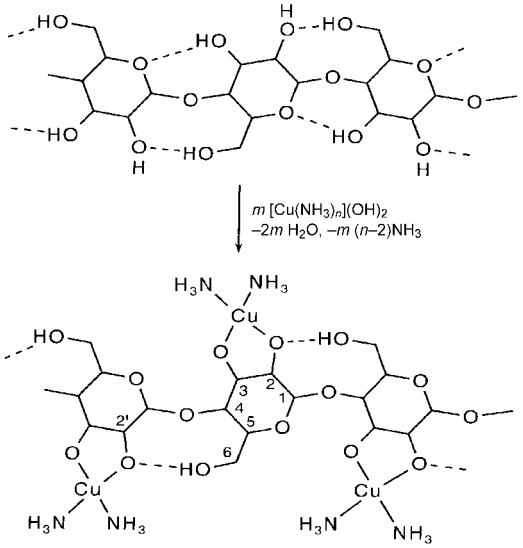

Scheme 2. Complex formation of cellulose in cuprammonium hydroxide.[53]

Extensive preparative work on the laboratory scale has been carried out over the past 20 years with cellulose solvent systems. As a result, new types of cellulose derivatives have been synthesized and the knowledge of reaction mechanisms, reaction control, structure–property relationships (solubility, film formation, stability), and structure analysis has been increased.[57] Until now, it has not been possible to transfer the homogeneous reactions to technical scale, as the handling of aprotic dipolar media and salt components poses an obstacle.

Of course, partially substituted soluble cellulose derivatives are also good substrates for reactions under homogeneous conditions (see Sections 3.2.1 and 3.2.4 as well).[58] Cellulose ethers have proven particularly useful as intermediates and regioselective protecting groups. Typical examples include trityl,[59] methoxy-substituted trityl,[60,61] bulky silyl (Section 3.2.3), as well as allyl and benzyl ethers.[62] Table 2 contains example data for trityl protecting groups.[60]

Table 2: Trityl and methoxytrityl ethers as O6-selective protecting groups.

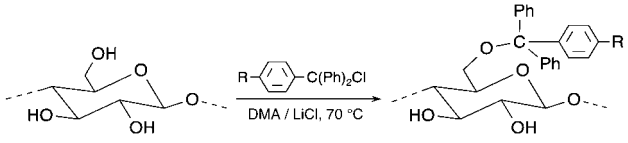

Polymer R	t [h]	DS 6	3	2	Σ
H	48	0.96	0.01	0.13	1.10
OCH_3	4	0.97	0.00	0.06	1.03
OCH_3	48	0.96	0.00	0.10	1.06

Limited chain degradation can be accepted in most reactions of cellulose without loss of the product properties, if chain lengths beyond the convergence range of the material parameters are not obtained. Transformation of cellulose with phenyl isocyanate (carbanilation) and silylation (Section 3.2.3) take place without chain degradation, for example.[58]

3.2. New Cellulose Products and Selective Syntheses

The wide range of preparative and structure-analytical studies over the past 10 years includes characterization of the donor–acceptor properties of cellulose substrates and derivatives by means of solvatochromic EDA complexes[63] and investigations of cellulose thiosulfates and self-assembling derivatives.[64] Part of this work also includes studies of celluloses with reduced functionality (at O2 and O3 as ether-protected substrates for subsequent reactions at C6-OH groups)[61] as well as cellulose products with covalently fixed dyes (e.g. azulene carboxylic acid ester) and their optoelectronic properties[65] (Scheme 3).

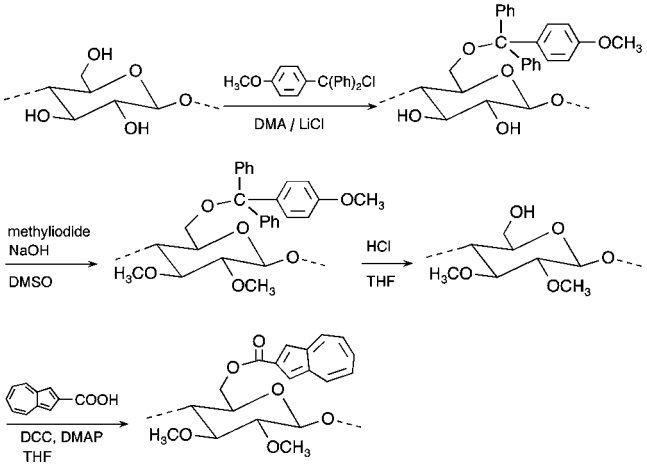

Scheme 3. 2,3-Methyl ether as a regioselective control element in the formation of celluloses with optoelectronic properties.

Products of current research include specifically modified cellulose derivatives for applications in enantioselective chromatography[66] and as biomaterials,[67] as are new types of cellulose products produced by acylysis and "retrosynthesis".[68] There are also reports of structure change and modification of cellulose in low-temperature salt melts/ionic solvents,[69] structure analysis of cellulose and substituted cellulose derivatives,[70] and determination of the polymer dynamics of cellulose derivatives in solution by dielectric relaxation spectroscopy.[71] The viscoelastic and rheo-optical properties of water-soluble cellulose derivatives and their ultrasonic degradation to smaller units with well-defined molar masses has also been investigated.[72]

A special challenge for synthetic work are the selective reactions of the OH groups of the repeating cellulose units and along the polymer chains. This problem is, of course, typical in polysaccharide chemistry. Horton and Yalpani have presented pioneering work in this area.[73] Results with the regiochemistry of cellulose are also the subject of review articles.[74]

The difference in reactivity between the primary hydroxy group at C6 (highly accessible) and the secondary hydroxy group at C2 (highly acidic and in close proximity to the acetal function) is exploited for selective reactions of cellulose, but is overshadowed by the hydrogen bridge networks described in Section 2. Furthermore, AGUs can be activated along the cellulose chains in a manner to favor reaction preferentially at certain chain segments ("reactive microstructures"). At the laboratory scale, regioselective syntheses of cellulose products are particularly successful with protecting group techniques and the selective involvement of OH groups in discrete solvation and activation states, by specific downstream reactions, by enzymatic transformations of reactive cellulose derivatives, and by chemosynthesis with functionalized glucose as starting material.

Cellulose derivatives with functionalization patterns of high uniformity are important not only for comparison with statistically modified celluloses, but are particularly important as products with new properties and applications. Their importance also lies with respect to questions that remain open about the solution structure of cellulose derivatives and for the design of supramolecular architectures (Section 3.3). Typical examples include 6-*O*- and 2,3-di-*O*-acetyl-6-*O*-triphenylmethylcellulose,[75] 2,6-di-*O*-thexyldimethylsilylcellulose, and 3-*O*-alkylcelluloses,[76] as well as methyl ethers regioselectively modified with fluorescent benzyl ether groups.[77]

3.2.1. Progress in the Synthesis of Cellulose Esters

During the past decade, cellulose sulfates have undergone intense investigation,[21a] as their water-soluble sodium salts offer excellent rheological and gel-forming properties, which has increased their importance as film-forming materials, anionic polyelectrolytes, and biologically active polymers. In view of this application potential, cellulose sulfates are also mentioned in Scheme 16, Section 4, although they have not been used technically to a large extent. One priority with these products has also been the synthesis of cellulose sulfates with a regioselective distribution of substituents, which is possible by sulfation of cellulose ester and cellulose ether intermediates, including the use of protecting groups.[21a,78]

Scheme 4 highlights typical examples of this. For cellulose nitrites and trimethylsilyl ethers, sulfation takes place through the substitution of these functional groups. In the cases of acetate, trifluoroacetate, and trityl ether, sulfation occurs by transformation of the free OH groups. The acetate route proceeds through the selective diamine-catalyzed hydrolysis of cellulose triacetate to the preferentially formed 6-acetate intermediate. The regioselectivities illustrated in Scheme 4 are supported by published DS (degree of substitution) data.[21a] Whereas the reversibility of the direct sulfation of cellulose leads to a statistic distribution along the polymer chain, regioselective sulfations are successful with partially protected precursors, which render inputs irreversible, and

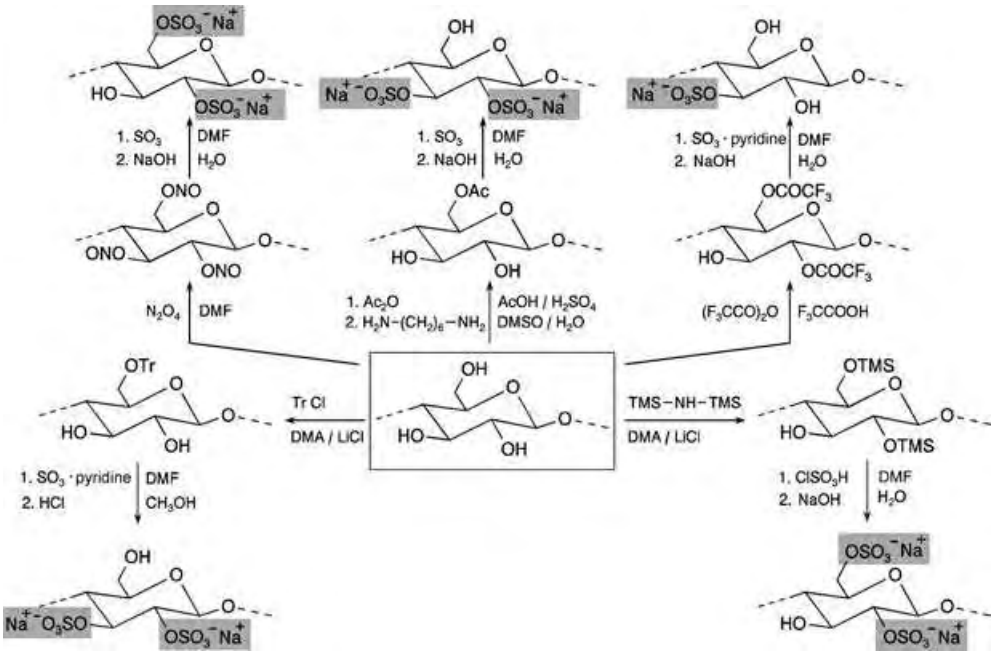

Scheme 4. Synthesis pathways to cellulose sulfates with regioselective distribution of ionic groups.

result from kinetically controlled reactions. A further option toward regioselectivity involves the conversion of reactive intermediates.

In view of their thermoplastic behavior and self-organization, cellulose esters of long-chain carboxylic acids were systematically studied.[79] In this context, composites and nanocomposites of cellulose and its derivatives with lignin as well as supramolecular architectures play an important role as natural composite wood substitute materials.[79] Cellulose esters of aliphatic, aromatic, bulky, and functionalized carboxylic acids are available through the activation of free acids in situ with tosyl chloride, *N*,*N*′-carbonyldiimidazole, and iminium chloride under homogeneous acylation with DMA/LiCl or DMSO/TBAF. From this, a wide range in the degree of substitution, various substituent distributions, and interesting properties (bioactivity, thermal and dissolution behavior) are possible (Scheme 5).[80]

The successful deacetylation of cellulose acetates (CAs) by means of acetyl esterases was recently reported.[81] Regioselectively C6-substituted CAs with a low degree of substitution (DS) can be produced by enzymes of the carbohydrate esterase (CE) family 1. Esterases of the CE 5 family lead to regioselectively 3,6-di-*O*-acetylated CAs, whereas the regioselective modification at position 3 is possible with CE 4 enzymes. Systematic investigations dem-

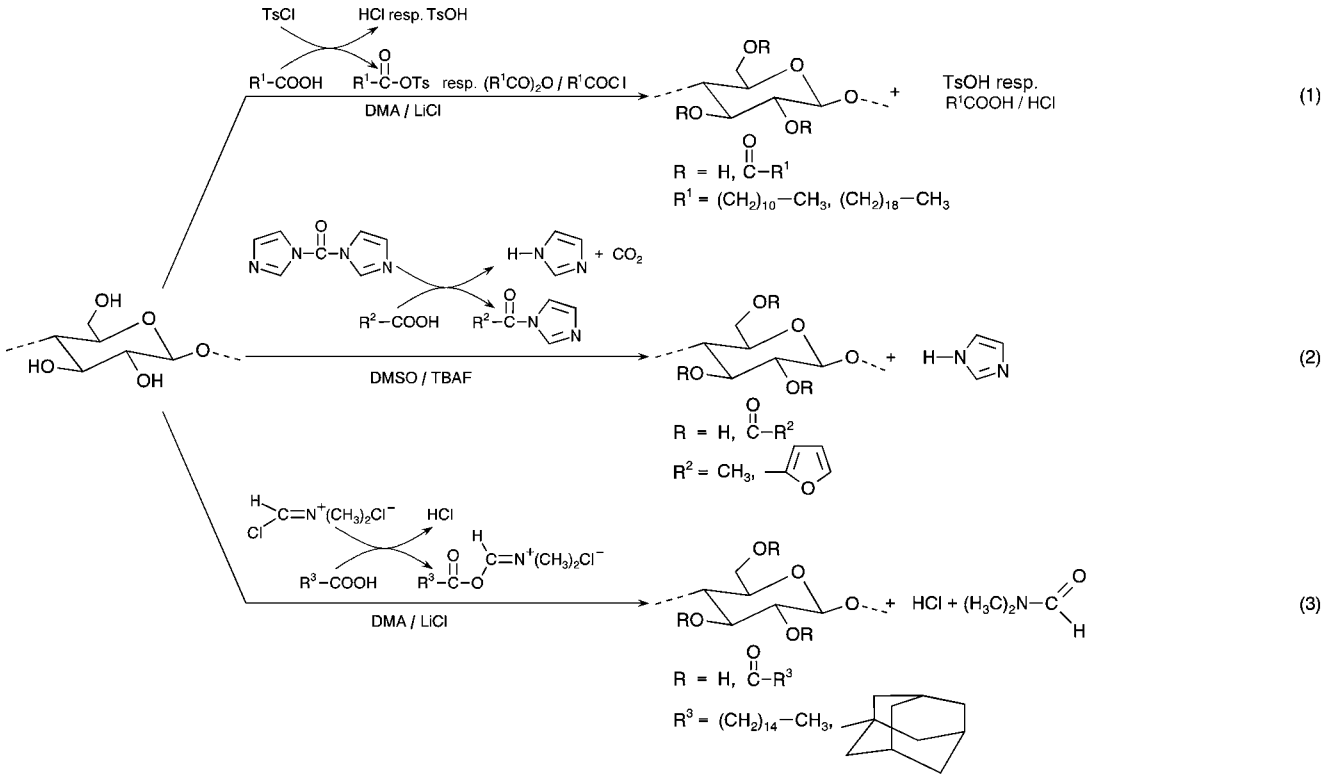

Scheme 5. Esterification of cellulose by the in-situ activation of the carboxylic acid by (1) tosyl chloride, (2) *N*,*N*′-carbonyldiimidazole, and (3) iminium chloride.

onstrate that the distribution of acetate groups within the AGU and along the cellulose chains of the starting acetates influences the effect of the enzymes. Acetate groups at position 2 are particularly active. The acetylase of *Aspergillus niger* catalyzes preferential deacetylation of cellulose acetate (CA) to form a product that is C6-acetylated along the polymer chain.[81a,82]

3.2.2. Cellulose Ethers with Nonstatistical Substituent Distribution along the Chains

Blocklike carboxymethyl celluloses (CMCs)[83] can be created by using the concept of reactive structure fractions.[84] This term was applied to activated noncrystalline areas of cellulose, which by treatment with low concentrations of aqueous sodium hydroxide, permit a selective attack on the alkylation reagent. This connection exploits the fact that the activation of the cellulose by aqueous sodium hydroxide is dependent on the concentration of base and on the lateral dimensions of the ordered areas. Therefore, with appropriate concentrations of base, noncrystalline chain segments can react in a blocklike manner. Another possible route to CMCs with unconventional substituent distributions is through the derivatization of cellulose in reactive microstructures, which are formed by induced-phase separation.[80a] In this case, NaOH used for activation is added in the form of anhydrous particles to a solution of cellulose in DMA/LiCl, which initiates a phase separation under gel formation. At the solution–particle interface, active cellulose is regenerated (reactive microstructures) in the chain segments with sodium monochloroacetate to give CMCs with DS values up to 2.2 in one reaction step. Structure analysis of these CMC products revealed a distribution of substituents that deviates significantly from statistical prediction.[80a]

The phase-separation principle can also be extended to other solvent systems (DMSO, TBAF, and NMMO), various cellulose intermediates (CA and TMSC; Figure 9), as well as other cellulose ether syntheses (Figure 10). In all cases, blocklike functionalization patterns occur and thus the formation of products with new properties. The curves

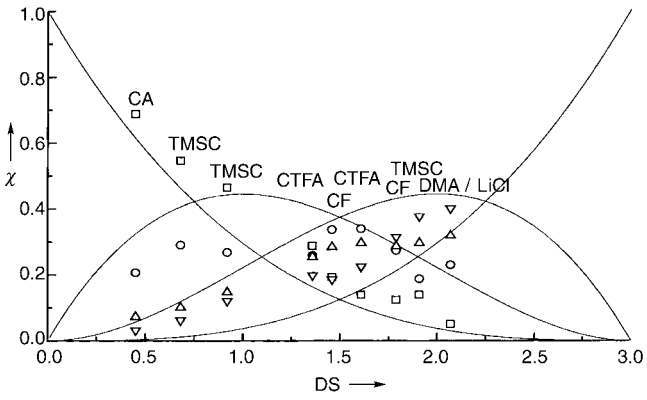

Figure 9. Mole fractions χ of glucose (○), mono-*O*-carboxymethyl glucoses (□), di-*O*-carboxymethyl glucoses (△), and 2,3,6-tri-*O*-carboxymethylglucose (▽) in hydrolyzed carboxymethyl cellulose samples as a function of the degree of substitution (DS) determined by HPLC. Starting from cellulose acetate (CA), trimethylsilyl cellulose (TMSC), cellulose trifluoroacetate (CTFA), cellulose formate (CF), and cellulose dissolved in DMA/LiCl, the polymers were synthesized by induced-phase separation.[80a]

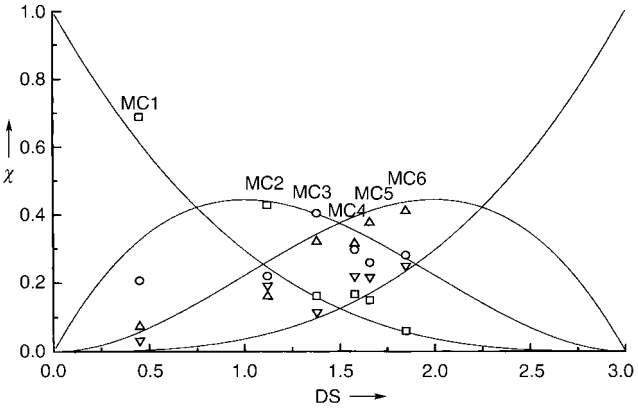

Figure 10. Mole fractions χ of glucose (○), mono-*O*-methyl glucoses (□), di-*O*-methyl glucoses (△), and 2,3,6-tri-*O*-methylglucose (▽) in hydrolyzed methyl cellulose (MC) samples as a function of the degree of substitution (DS) determined by HPLC.[80a]

presented in the Figures correspond to the molar fractions, which were calculated by a simplified statistical model by Spurlin.[80e] This model is based on the assumption of uniform reactivity between the OH groups of C2, C3 and C6, independent of the DS value already present. Whereas the mole fractions of heterogeneously synthesized cellulose ethers agree with model calculations,[80f] the mole fractions of samples produced by induced-phase separation deviate from this model. In all cases, the portion of unsubstituted and trisubstituted AGUs is extremely high. The resulting blocklike functionalization pattern is also reflected in the new properties of these products. The partial DS values of positions 2, 3 and 6 of the carboxymethyl celluloses can be calculated from the ^{1}H NMR spectra of the carboxymethyl glucoses obtained by chain degradation.[80f]

3.2.3. Silyl Celluloses

The silylation of polar protic groups (such as OH) with chlorosilanes and silazanes leads to silyl ethers which are characterized by a remarkable increase in thermal stability, lipophilic behavior and a lack of hydrogen bonds. Owing to the simple cleavage of the silyl ethers under acidic conditions, or through nucleophilic attack, they can be used as selective protecting groups in organic synthesis.[85] Therefore, the introduction of silyl groups and the properties of silyl ethers are very attractive in carbohydrate and polysaccharide chemistry.

The silylation of cellulose has been known for about 50 years.[86] During the last decade, it proved to be a suitable way to prepare silyl celluloses for the formation of supramolecular structures (Section 3.3.1) and to differentiate between the three OH groups of the AGU in regioselective syntheses with silicon-containing protecting groups.[87,88]

As shown in Scheme 6, trimethylsilylation with hexamethyldisilazane (HMDS) in liquid ammonia results in a complete conversion of all hydroxy groups to form 2,3,6-tri-*O*-trimethylsilyl cellulose with a DS value of 3.0.[89] The

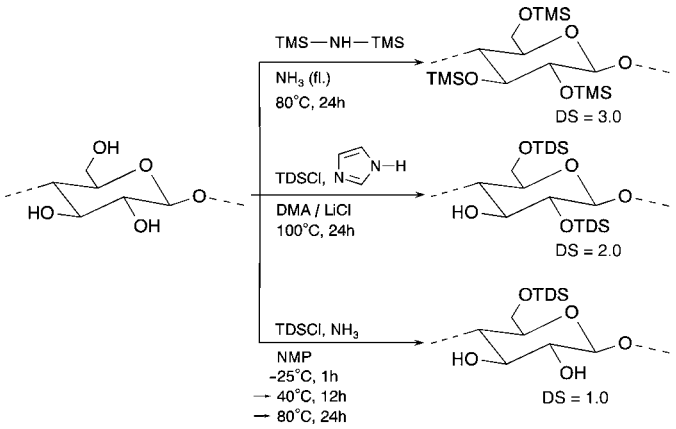

Scheme 6. Various reactivities of the hydroxy groups of cellulose during silylation.

activation of the cellulose with liquid ammonia takes about 30 min. In this process, the accessibility of the OH groups reaches such degree that the rate of silylation (with saccharin as catalyst)[88b,c] follows first-order kinetics up to 50%, although the reaction takes place heterogeneously at the suspended cellulose. During the silylation and desilylation reactions described below, no degradation of the cellulose chain occurs.[88]

If the OH groups are made accessible by dissolving the polymer in DMA/LiCl (homogeneous reaction) and if the synthesis takes place in the presence of imidazole, the bulky silylation reagent thexyldimethylchlorosilane (TDSCl) will lead to complete silylation at O6 and O2 (DS value = 2.0), which means that the primary and the most reactive secondary OH groups are converted.[90] If silyl ether formation starts with the same reagent in cellulose suspension in aprotic dipolar media such as *N*-methylpyrrolidone (NMP), which contain gaseous ammonia, a specific solution state of the silyl cellulose is observed after silylation of all primary C6-OH groups, and after evaporation of the ammonia at about 40 °C. This state does not permit any further reaction of the secondary hydroxy groups, even in cases of large reagent excess, increased temperature, and very long reaction times.[88a]

Structure analysis of the regioselectively substituted silyl celluloses has been particularly successful with 2D NMR spectroscopy after methylation of all free OH groups, complete desilylation, and acetylation of all OH functions created (Scheme 7).[88a] Such analysis is also possible after a simplified analogous process in which acetylation is carried out on the hydroxy groups not converted during the silylation.

Through this complex sample preparation, a remarkable improvement in spectral resolution is observed. In this manner, the structure of 2,6-di-*O*-TDS cellulose could be determined by NMR spectroscopy of 2,6-di-*O*-acetyl-3-*O*-

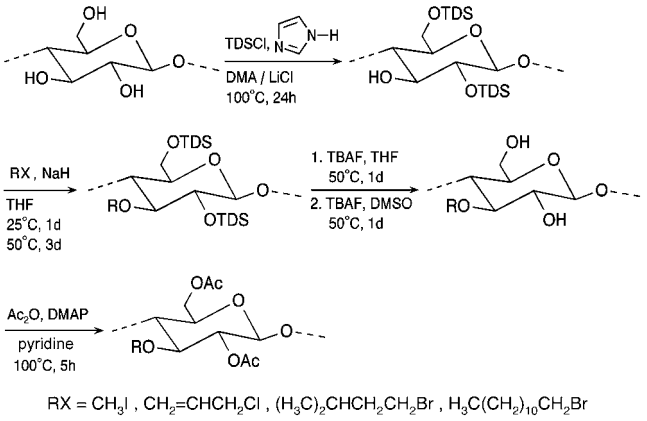

Scheme 7. Synthesis of 3-*O*-ethers of cellulose from 2,6-di-*O*-thexyldimethylsilylcellulose.

methyl cellulose. Likewise, the structure of 6-*O*-TDS cellulose was determined with 2,3-di-*O*-acetyl-6-*O*-TDS cellulose under spectroscopic analysis. An exact correlation between the signals and the protons of the AGU can made with the resultant cross-peaks. The downfield signal shifts of H-2 (4.94 ppm) and H-3 (4.58 ppm) verify the subsequent acetylation of the secondary OH groups. The methylene protons of the AGU reveal a typical high-field shift of H-6a (3.64 ppm) and H-6b (3.14 ppm) as a result of O6 silylation.[88a]

A permethylation analysis was carried out in parallel, with chain degradation of the methylated samples by aqueous trifluoroacetic acid and HPLC analysis of the methyl glucoses.[91] Furthermore, analysis of the silicon content in a classical manner by the elementary analysis of SiO_2 has proven to be very useful and reliable.

The desilylation of cellulose silyl ethers can lead to completely desilylated cellulose regenerates (films, particles, and filaments), to partially silylated celluloses with an alternative distribution of silyl groups,[89b,c] or to regioselectively substituted cellulose derivatives by using the protecting group technique.[90] Typical examples are the syntheses of 3- and 2,3-alkyl ethers of cellulose (Scheme 7 and 8).

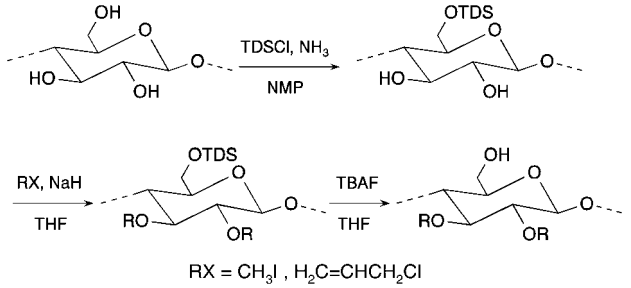

Scheme 8. Synthesis of 2,3-di-*O*-alkylcelluloses by the protecting group techniques.

The structure of these regioselectively functionalized celluloses can be determined by ^{13}C NMR spectroscopy (Figure 11), 2D ^{1}H–^{1}H and ^{1}H–^{13}C techniques (Figure 12) and COSY-DQF spectra (Figure 13). ^{1}H NMR spectroscopy requires the acetylation of the free OH groups.

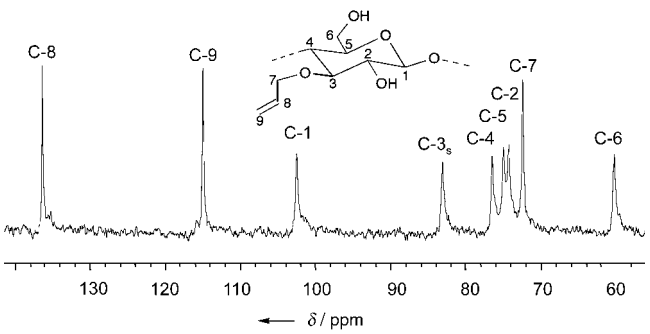

Figure 11. ^{13}C NMR spectrum of 3-*O*-allyl cellulose in [D_6]DMSO at 60 °C.[88a]

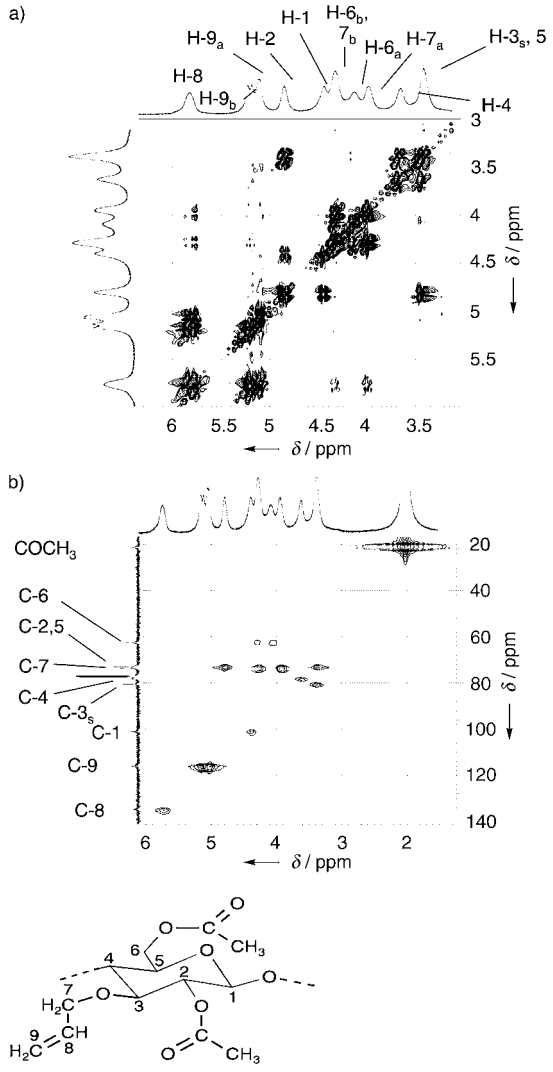

Figure 12. a) ^{1}H–^{1}H NMR spectrum and b) ^{1}H–^{13}C-HMQC measurement of 3-*O*-allyl-2,6-di-*O*-acetylcellulose in $CDCl_3$ at 40 °C.[88a]

Regular selectively functionalized celluloses are important for gaining new insight into the solubility and solution structure of cellulose derivatives. The use of aliphatic O3 cellulose ethers with various alkyl group lengths, it was demonstrated that short alkyl residues (e.g. pentyl) at the stiff cellulose backbone leads to insolubility, whereas long alkyl chains (e.g. dodecyl) result in molecularly soluble products. Together with other facts, these results indicate that entropic effects affect solubility to a much greater extent than enthalpic factors that have been considered in the interpretation of the solvation effects up to this point in time.[39,40,76]

3.2.4. *Cellulose Sulfonates*

The synthesis of organosulfonic acid esters (sulfonates) by simple esterification of the OH groups of cellulose with the corresponding sulfonic acid chlorides or anhydrides is an effective way to attach (in contrast to all cellulose derivatives important up to now) nucleofuge groups to cellulose. The cellulose sulfonates therefore open a wide range of substituted products, which are not available through the conventional methods of "O chemistry" of cellulose (that is, attack of the O atom donor of the OH groups to electrophiles). Moreover, they also have interesting polymeric and material properties, creating new fields of application.[92]

The most frequently synthesized and used cellulose sulfonates are the *p*-toluenesulfonates (tosylates) followed by the methanesulfonates (mesylates), *p*-bromobenzenesulfonates (brosylates), and trifluoromethanesulfonates (triflates). The current knowledge of the synthesis, properties, and subsequent reactions of the cellulose sulfonates is subject of a review.[93]

The synthesis of cellulose sulfonates (Scheme 9) has been previously carried out in suspension (heterogeneous). The homogeneous esterification is successful in solutions of cellulose in DMA/LiCl. In this case, the preparation of cellulose tosylate can be optimized to an extent that permits control of the DS value and the formation of polymers that are free of by-products. At temperatures of +7 °C, for example, cellulose tosylate with a maximum DS value of 2.3 can be synthesized with tosyl chloride in the presence of triethylamine, which can also be controlled by the molar ratio of tosyl chloride/AGU of the cellulose. Scheme 10 demonstrates examples of important downstream reactions of cellulose tosylate.

3.2.5. *Aminocelluloses*

The term aminocellulose refers to aminodeoxy derivatives that bear the nitrogen function directly on the cellulose skeleton, in contrast to the well-known amino acid esters and amino ethers of cellulose.[21a] Corresponding halogen derivatives and sulfonates are typical starting materials for the synthesis of aminodeoxycelluloses.

Cellulose derivatives with amino anchor groups for the immobilization of enzymes and other proteins were obtained through a specific structural design based on cellulose tosylates. In a typical example, cellulose tosylate (DS = 2.3) reacts with 1,4-phenylenediamine (PDA) in DMSO at 100 °C in the presence of TEA[94] (Scheme 11).

To ensure the S_N2 alkylation of only one of the PDA amino groups in homogeneous solution, and to obtain colorless products, a molar ratio of 9:1 PDA/AGU was used. Under these conditions, PDA cellulose is formed with

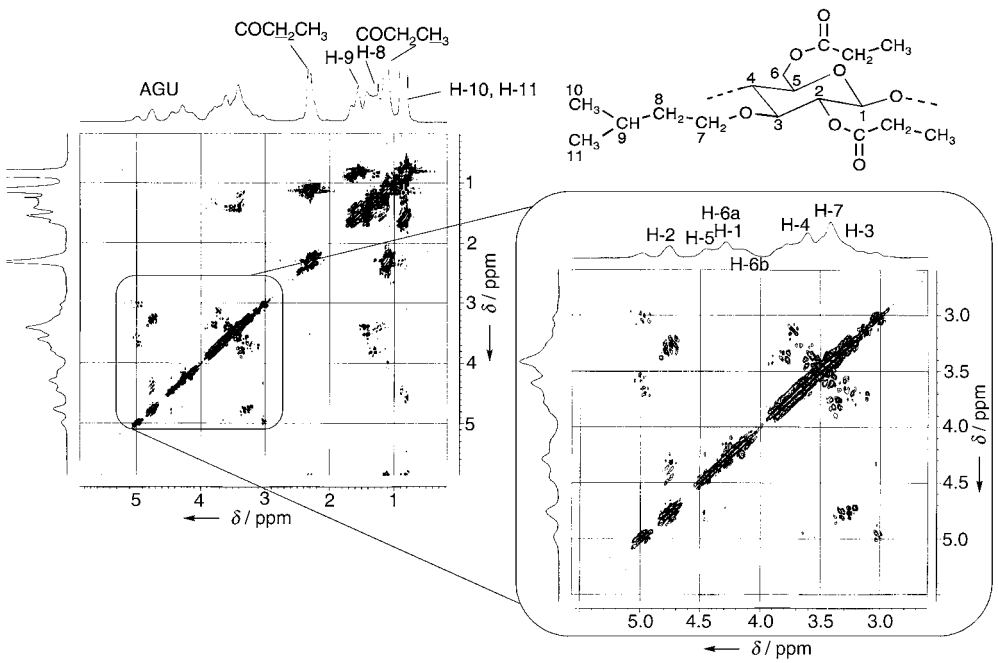

Figure 13. COSY-DQF spectrum of 3-*O*-isopentyl-2,6-di-*O*-propionyl cellulose in $CDCl_3$ at 40 °C.[88a]

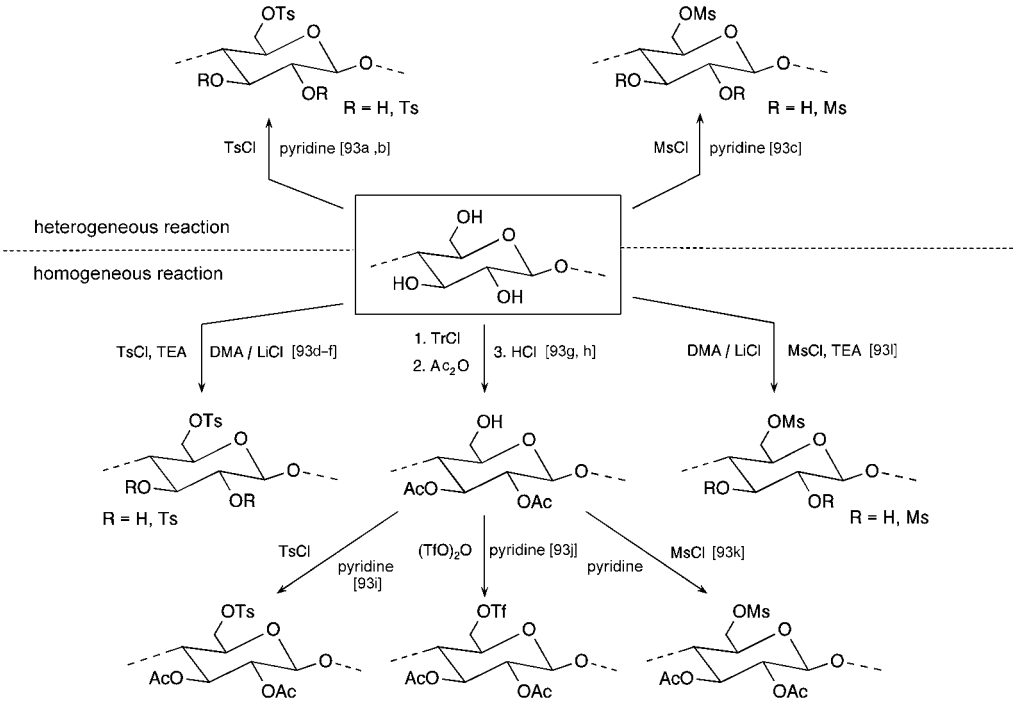

Scheme 9. Synthesis routes for cellulose sulfonates.[93]

$DS_{PDA} = 0.75$ and $DS_{tosylate} = 1.30$. The ^{13}C NMR spectroscopic data reveal that the transformation occurs at the 6-tosylate group of the starting polymer. The remaining secondary tosylate groups assist in the solubility and film formation of the product.

The PDA celluloses are suitable polymer carriers for the immobilization of enzymes with, for example, glutaraldehyde, diazo coupling, or ascorbic acid, and for the combined fixation of redox-active dyes by oxidative coupling (Figure 14). The potential of PDA cellulose films was investigated by the immobilization of oxidoreductases, such as glucose oxidase, peroxidase, and lactate oxidase. High enzyme activities of 206 mU cm^{-2} were obtained during the immobilization of peroxidase with glutaraldehyde, for example.[95] These properties of PDA celluloses have triggered broad investigations on the application of such aminocelluloses as polymer supports in fiber-optical biosensors.[96]

In comparison, aliphatic diamino groups can be introduced into cellulose with diaminoalkanes (H_2N–$(CH_2)_n$–NH_2; $n = 2, 4, 8, 12$) (Scheme 12),[97] by using the S_N2 reaction of cellulose tosylate derivatives (2,3-benzoate, 2,3-carbanilate, and 2,3-methyl ether). Aminocellulose carbanilates produced from 1,2-diaminoethane and 1,4-diaminobutane with $DS_{amin} < 0.4$ are soluble in DMA and DMSO, for example, and the corresponding 2,3-methoxy derivatives are soluble in water, ethanol, and DMSO. Figure 15 shows a typical ^{13}C NMR spectrum of 6-(4-aminobutyl)-6-deoxy-2,3-di-*O*-methyl aminocellulose in D_2O in part b) compared with the spectrum of the starting tosylate in part a).

The films formed from these solutions are suitable for the immobilization of enzymes. In this manner, glucose oxidase was immobilized onto an aminocellulose carbanilate ($DS_{aminobutyl} = 0.49$, $DS_{carbanilate} = 0.58$, $DS_{tosylate} = 0.08$) with an activity of 205 mU cm^{-2} by using benzoquinone as the immobilizing reagent.[97] Aminocelluloses of araliphatic diamines have also been used as enzyme supports.[98]

The synthesis of aminocelluloses based on aliphatic monoamines has been known for a long time, as the following examples illustrate. After the initial investigations between 1978 and 1980,[99a,b] the reaction of cellulose tosylates with monoamines was investigated systematically.[99c–e] Open questions were primarily with regard to the inhibition of crosslinking by multiple reactions of the amine, the extent of aminolysis reactions of the toluene sulfonic acid ester under

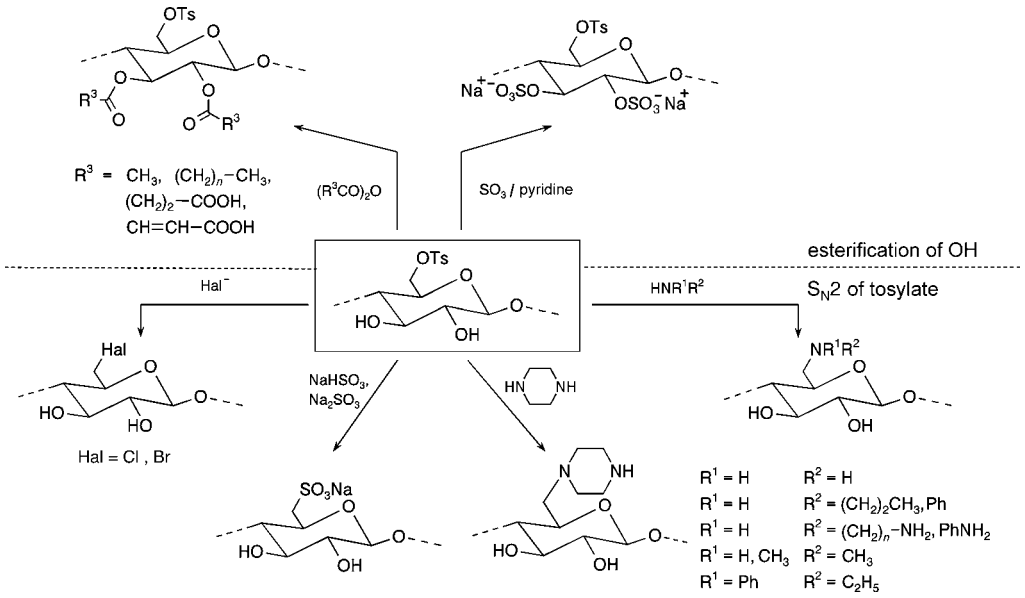

Scheme 10. Subsequent reactions of cellulose tosylate.[93]

the regeneration of OH groups, as well as the selective conversion of primary and secondary tosylate groups. Tosyl cellulose with DS values of 0.1 to 1.1 synthesized under homogeneous reaction conditions reacts with methylamine to form the corresponding methylaminocellulose with comparable degrees of substitution. These cellulose derivatives are to be used as adsorbents for the extracorporeal purification of blood.[99f] Long-chain aliphatic amines can be introduced by the same methods (Scheme 13).[100]

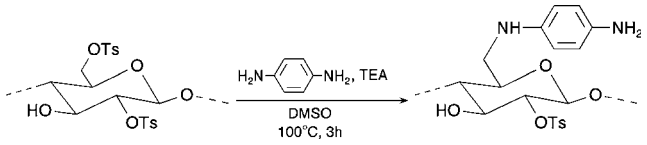

Scheme 11. Synthesis of PDA-cellulose by reaction of cellulose tosylate with 1,4-phenylenediamine (PDA).

3.3. Supramolecular Architectures

The past 10 years of cellulose research have also been characterized by expanding activity in the design of the supramolecular structure of cellulose derivatives. As a molecular basis in this respect, regioselectively functionalized celluloses have become very important. Preparative and application-oriented work has led to the formation of colloidal superstructures through selective topochemical reactions on crystallites formed by acid-catalyzed hydrolytically degraded cellulose,[101] for example, and to the formation of ultrathin layers of phosphorylated cellulose derivatives on metal surfaces.[102] The following examples are given to illustrate other routes to the formation of supramolecular cellulose architectures and their properties.

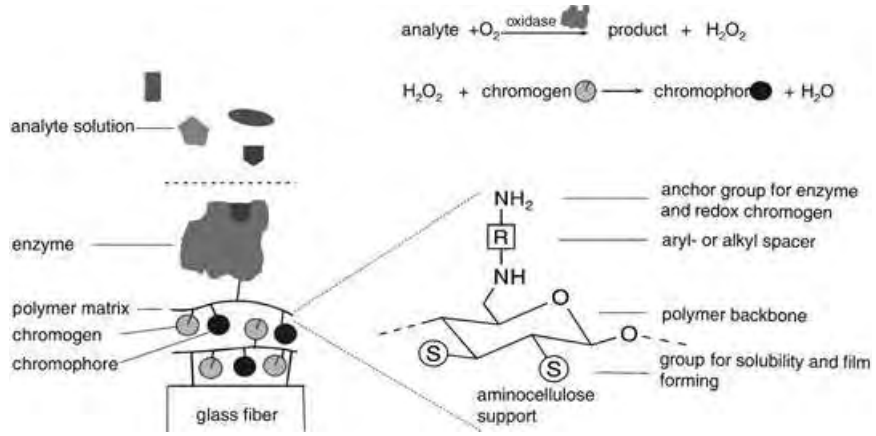

Figure 14. Scheme of an enzyme sensor and structural elements of the aminocellulose support.

3.3.1. Hair–Rod Nanocomposites

Ultrathin mono- and multilayer systems of high order can be constructed with the Langmuir–Blodgett technique from isopentyl cellulose (DS = 2.9), [5-(9-anthrylmethoxy)pentyl]-isopentyl cellulose ($DS_{isopentyl} = 2.8$, $DS_{anthryl} = 0.1$), fumarate-modified isopentyl cellulose, and trimethylsilyl celluloses (DS > 2.5) (Figure 16).[103]

The architecture of these layers is best described by the embedding of molecular rods—in this case, the cellulose polymer backbone—into the matrix of the side-group segments (ether substituents; hair–rod polymers). By subsequent reactions (photo-cross-linking and cycloaddition) or the

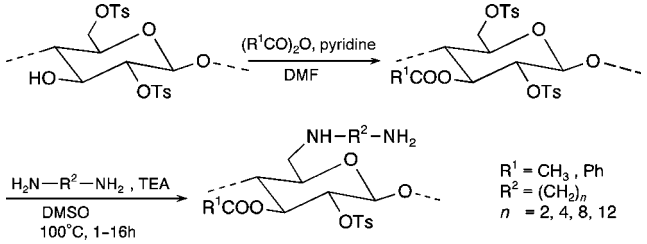

Scheme 12. Aminocelluloses synthesized from aliphatic diamines and cellulose tosylate.

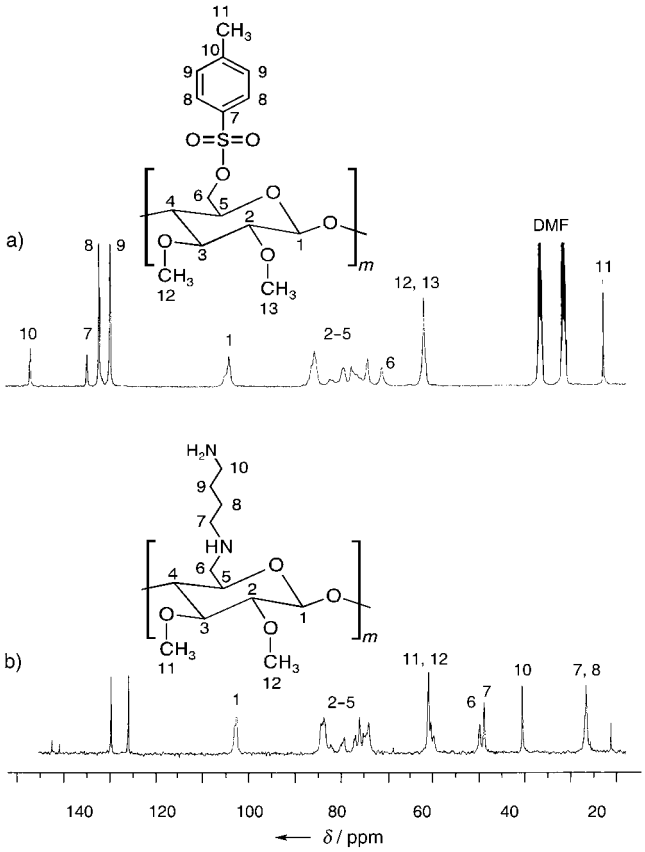

Figure 15. ^{13}C NMR spectra of a) 2,3-di-*O*-methyl-6-*O*-tosyl cellulose in [D_7]DMF and b) 6-(4-aminobutyl)-6-deoxy-2,3-di-*O*-methyl aminocellulose in D_2O.[97]

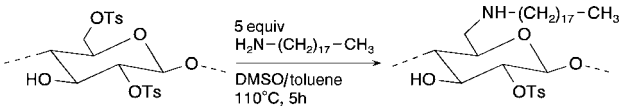

Scheme 13. Synthesis of 6-(*N*-octadecylamino)-6-deoxycellulose tosylate.

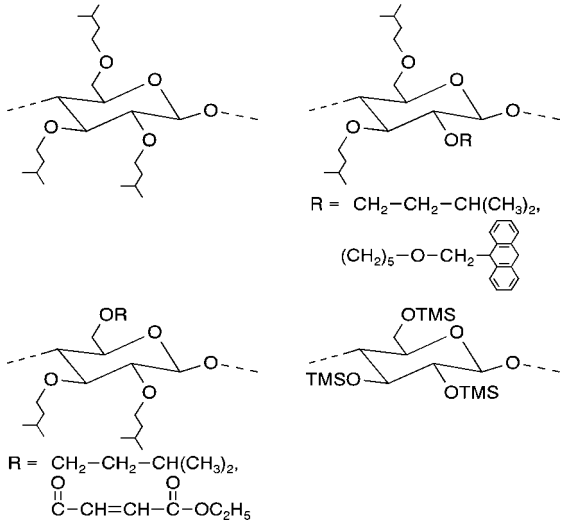

Figure 16. Typical hair–rod cellulose ethers for the construction of nanostructured layers.

regeneration of cellulose through acidic hydrolysis of the TMS-cellulose layers, 3D networks and ultrathin cellulose layers are formed.[104] The latter are important as insoluble and stable hydrophilic films for the adsorption of dyes as well as of synthetic and biogenic polymers. By subsequent introduction of succinate groups into the cellulose films, this behavior can be further amplified.[105] Therefore, ultrathin cellulose layers are very good substrates for diagnostic and analytical purposes. Corresponding 2D cellulose architectures are used for the design of structured ultrathin peptide layers and their use in neurophysiologic growth studies.[106]

3.3.2. NTA Cellulose Films for Protein Fixation

During the course of investigations on the interaction of cellulose and cellulose derivatives with proteins, it was possible to covalently bind nitrilotriacetic acid (NTA) groups onto cellulose.[107a] NTA-cellulose forms thin films on glass substrates from solution in DMSO, which enables a stoichiometric binding of nickel to the NTA substituents upon incubation with an aqueous solution of $NiSO_4$. Treatment of these films with solutions of histidine and fluorescently labeled model proteins, followed by a thorough rinsing to wash away unbound protein yields model protein that is specifically bound to the Ni-NTA groups of cellulose, as substantiated by inverse microscopy. Proteins can then be eluted from the surface by treatment with an imidazole solution (1M).

Figure 17 illustrates the principle assembly of the cellulose–protein complex, containing two histidine units bound at the NTA-modified cellulose film through a Ni^{2+} ion. The

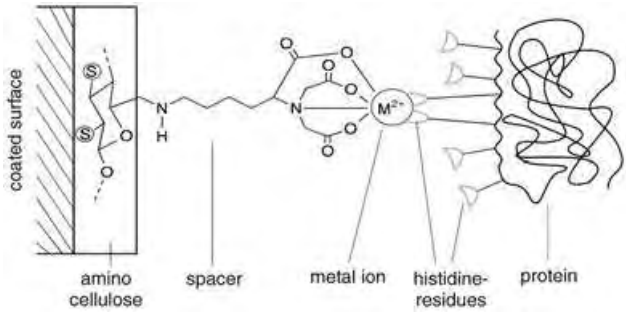

Figure 17. Schematic representation of the immobilization of histidine and fluorescently labeled proteins onto nitrilotriacetic acid (NTA)-modified aminocellulose films by metal complexes (M = Ni, S = control element for solubility and film formation).

synthesis of the cellulose support involved dissolution of cellulose (DP = 800) in DMA/LiCl and tosylation with tosyl chloride in the presence of triethylamine (DS: 1.2–2.0). To introduce the NTA groups, a corresponding H_2N-terminal derivative was prepared. Starting with N_ε-benzyloxycarbonyl-L-lysine, the N_α position was dicarboxymethylated, the protecting group was removed from the N_ε position and persilylated with trimethylchlorosilane in toluol in the presence of triethylamine (for the separation of by-products and improvement of the following S_N2 reaction). In reaction

with the cellulose tosylate in a DMSO/toluene mixture, the nitrilotriacetic acid derivative was synthesized in 24 h at 90 °C (Scheme 14). The His_6 (6 histidine units) and fluorescently labeled model protein were synthesized according to published methods.[107b]

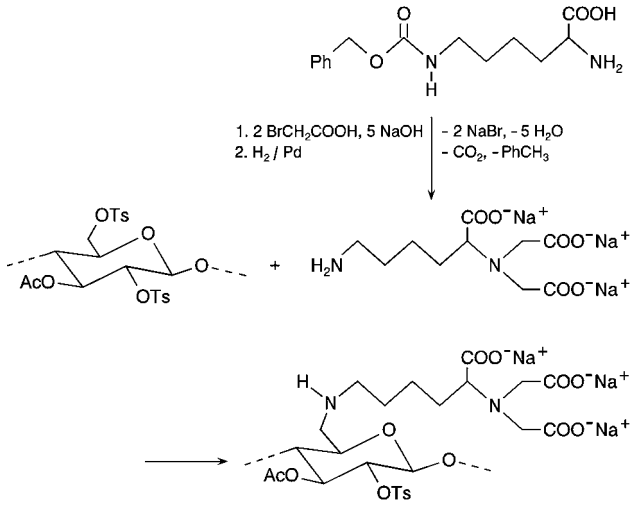

Scheme 14. Synthesis of nitrilotriacetic acid (NTA)-modified aminocellulose.

3.3.3. *Monolayers of Reactive Cellulose Derivatives*

By addition of tetrathionate to 6-*O*-(3-allyloxy-2-hydroxy)-propylcellulose, water-soluble thiosulfates of cellulose can be synthesized to form dense monolayers with a thickness of 4 ± 1 nm on gold surfaces by chemisorption.[108] These layers have been characterized by ellipsometry, AFM, FTIR- and X-ray photoelectron spectroscopy, as well as contact-angle measurements. These investigations have revealed that the thiosulfate groups are homolytically cleaved, and stable gold thiolate anchor groups are formed via thioradical intermediates. The interaction of these cellulose derivatives immobilized on gold surfaces with proteins was investigated. Cellulose thiosulfates of water-soluble carboxymethyl celluloses were included in this work (Scheme 15).

In summary, it was shown that self-assembled monolayers (SAMs) of cellulose derivatives with reactive groups can be synthesized rapidly and with uniform quality. Biomolecules can be linked to these SAMs directly, with controlled density, and with only a small amount of nonspecific interactions. Such SAMs are therefore a suitable platform for the study of molecular recognition on surfaces and for the development of biosensors.

4. Innovative Commercial Esters and Ethers of Cellulose

Cellulose esters of inorganic and organic acids (Scheme 16) as well as cellulose ethers (Scheme 17) were pioneer compounds of cellulose chemistry, and remain the most important technical derivatives of cellulose.[4,21a,d,109] Present developments are therefore aimed at a more detailed understanding of the structure–property relationships, an improved adaptation of these cellulose products to specific and new applications, and to the decreased use of chemicals from an economical and ecological perspective. Continuous investments into the improvement of technical syntheses (pilot and production plants), into sophisticated analysis, and into improved testing methods determine the course of these developments.

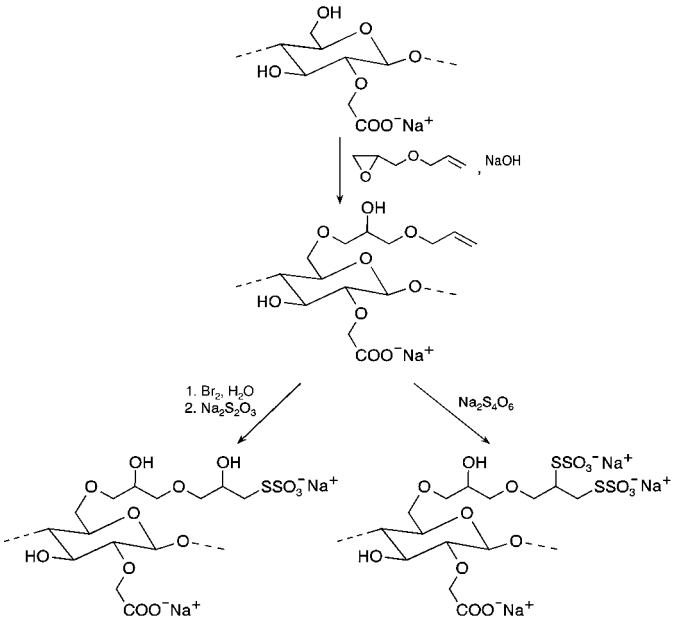

Scheme 15. Synthesis of thiosulfates of carboxymethyl cellulose (CMC).

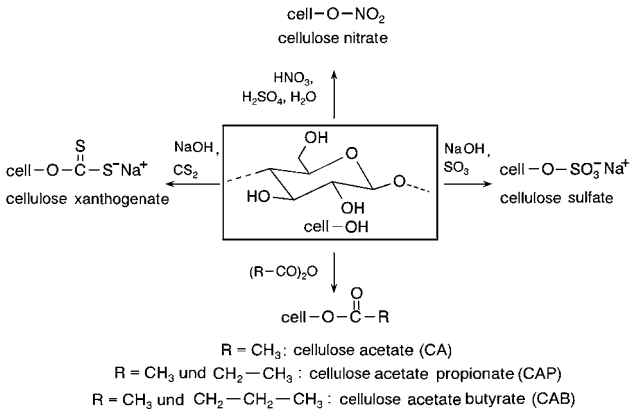

Scheme 16. Typical technical cellulose esters.

4.1. *Progress in the Development and Application of Cellulose Esters*[110a]

4.1.1. *Coatings and Controlled-Release Systems*

Materials such as metal, plastic, wood, paper, and leather are coated with polymers primarily for protection and for the improvement of their properties. For this purpose, cellulose

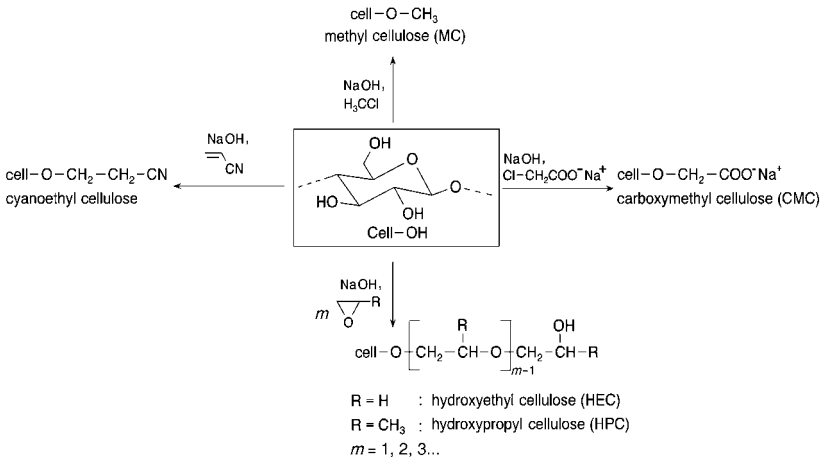

Scheme 17. Examples of commercial cellulose ethers.

acetate (CA), cellulose acetate propionate (CAP) and cellulose acetate butyrate (CAB) are the most important classical and solvent-based cellulose esters of the coating industry.

To decrease the amount of organic solvents used in coating systems, there has been an increased development over the past few years of high solid-content coatings, water-based coatings, powder coatings, and radiation-curable polymers as key elements in new technologies. These technologies now meet the requirements of commercial products as well. In view of the EU directive on volatile organic compounds (VOC), solvent-based lacquers are under special scrutiny. In the case of nitrocellulose (NC) lacquers, the aim is to retain these solvent-containing lacquers as powerful alternatives within the provisions of the EU directive through the establishment of a solvent management system.[111a]

Various concepts were pursued in the development of water-based cellulose ester coatings. Notable examples include the use of conventional as well as high hydroxy group-containing esters in water, the introduction of carboxy groups by radical-initiated graft copolymerization,[112] acylation with dicarboxylic acid anhydrides, and the esterification of carboxymethyl cellulose (Table 3). As the complex structures of these commercial products cannot be characterized completely in many cases, the functional groups are listed without information about their distributions along the polymer. The DS values of the various residues are used for product descriptions. A cellulose acetate butyrate succinate is thus characterized with $DS_{acetate} = 0.09$, $DS_{butyrate} = 1.94$, $DS_{OH} = 0.58$ and $DS_{succinate} = 0.38$. Radiation-curable coatings are synthesized from common cellulose esters by introduction of polymerizable and cross-linkable functionalities (Table 3).

In the field of controlled-release systems, cellulose ester is in an excellent position as a result of its established process and application safety, its readiness toward chemical modifications, and its good handling properties.[110a] New systems were therefore developed on this basis as enteric coatings, hydrophobic matrices, and semipermeable membranes for applications in pharmacy, agriculture, and cosmetics.

4.1.2. Composites, Films, and Membranes

Since the commercial production of celluloid, the classical application of cellulose esters has been as thermoplastic materials, and is currently under intense advancement for the creation of high-performance materials that are based on renewable resources.[110a] Topics include the production of

Table 3: Examples of water-based and radiation-curable cellulose ester coatings.

Substrate	Reagent	Product, R in cell-OR			
cellulose acetate propionate (CAP)	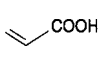	H	H_3CCO	H_3CCH_2CO	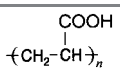
cellulose acetate butyrate (CAB)	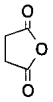	H	H_3CCO	$H_3CCH_2CH_2CO$	$OCCH_2CH_2COOH$
cellulose acetate (CA)		H	H_3CCO	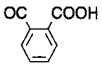	
carboxymethyl cellulose (CMC)	$(H_3CCO)_2O$, $(CH_3CH_2CH_2CO)_2O$	H	H_3CCO	$H_3CCH_2CH_2CO$	$H_2CCOO^-Na^+$
cellulose butyrate succinate (CB-SU)	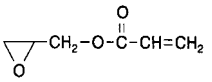	H	$H_3CCH_2CH_2CO$	$OCCH_2CH_2C(O)OCH_2CH(OH)CH_2OC(O)CH{=}CH_2$	
cellulose acetate propionate (CAP)	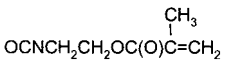	H	H_3CCO	H_3CCH_2CO	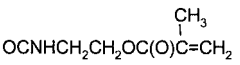
cellulose acetate propionate (CAP)	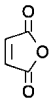	H	H_3CCO	H_3CCH_2CO	$OCCH{=}CHCOOH$

long-chain cellulose esters and the development of blends with other polymers. Cellulose esters are widely used in composites and laminates as binder, filler, and laminate layers. In combination with natural fibers, they can be used to some extent as composites from sustainable raw materials with good biodegradability.

Cellulose ester films have been used in large quantities as optical media by virtue of their very good mechanical and optical properties and ease of accessibility.[110a] Although other products with a favorable balance of performance and cost have partially replaced cellulose esters in this field, cellulose acetates in particular continue to be an excellent material for photographic films owing to their excellent properties. The development of LCDs were a result of innovations in this field.

An additional domain of cellulose esters is their use as membranes and other separation media.[110a] Cellulose nitrate and cellulose acetate were the first materials to be fabricated into useful membranes. Today, cellulose esters are used in all techniques of separation. Their applications concern water supply, food and beverage processing, as well as applications in medicine and in bioscience research. They cover the entire filtration spectrum from particle-, micro- and ultrafiltration up to nano- and hyperfiltration (reverse osmosis). Superabsorbers are also a form of sorption media in the broadest sense, characterized by their high swelling and water retention capacities and insolubility (through cross-linking).[110b]

4.2. Developments in the Field of Cellulose Ethers[111]

The synthesis of cellulose ethers is an important aspect of commercial cellulose derivatization. The production of methylcellulose (MC) was described for the first time in 1905, followed by other nonionic alkyl ethers of cellulose in 1912, and of carboxymethyl cellulose (CMC) and hydroxyethyl cellulose (HEC) after 1920. Shortly thereafter, the industrial production of these most important cellulose ethers was started.

They have the outstanding properties good solubility and high chemical stability, and are toxicologically innocuous. The especially important matter of water solubility can be controlled to a certain extent by the constitution and combination of the ether groups, the degree of substitution, and the distribution of substituents. Cellulose ethers are processed in a dissolved or highly swollen state. They are the dominant polymers in numerous industrial applications and in convenience goods for matters in which consistency in the quality of aqueous media and water-containing systems is required.

Etherification of cellulose on the industrial scale is performed in aqueous alkaline media in which cellulose is present in a highly swollen state. The dominant approach for this process is O-alkylation with alkyl halides according to Williamson; other approaches include epoxide addition and Michael addition of reagents with activated double bonds. Scheme 17 highlights some typical examples. In contrast to methyl cellulose, carboxymethyl cellulose, and hydroxyalkyl cellulose, the commercial importance of cyanoethyl cellulose remains limited to a few special applications: as an additive in the paper and textile industry, and in the formation of membranes.

4.2.1. Cellulose Ethers for Drilling Technologies and Building Materials[111a]

The use of cellulose ethers as additives to drilling fluids for consistency control is of considerable importance to the drilling of wells for mineral oil, natural gas, and water. Drilling fluids supplemented with cellulose ethers keep rock dust in suspension, cool the drilling head, and stabilize the bore.

Another significant core business in which cellulose ethers are used is the building materials market, which involves a multitude of tailor-made versions of methylhydroxyethyl (MHEC) and methylhydroxypropyl celluloses (MHPC) that control the rheology and processing of plaster systems. As additives that are admixed to the mortar in the range of 0.02–0.70% by mass, they make up a market share of about 90%. Cellulose ether permits the silo transport and machine processing of dry mortar as well as the effective handling of gypsum plasters, knifing fillers, tile adhesives, and joint fillers. They determine the water requirement, the water-retaining power, and the development of consistency in plaster systems.

4.2.2. Pharmaceuticals, Cosmetics, and the Food Market[111a]

In addition to carboxymethyl cellulose, high-purity hydroxypropylmethyl cellulose (HPMC) was synthesized and introduced onto the market for this demanding area of application. HPMC binds water, has good stability in freeze/thaw cycles, mediates the viscosity of liquids, and is odorless and tasteless. In products of this kind, purity and permanent quality play a critical role, as their production must adhere to GMP standards.

Carboxymethyl cellulose is used as a stabilizer in beverages. It has improved the consistency, texture and storage quality of milk products, and ensures that the solids added are kept in suspension. It is also used to stabilize whey-based beverages.

5. Regenerated Cellulose: Environmentally Friendly Technologies on the Advance

5.1. Present Situation

The most important segment by volume in the chemical–technical processing of cellulose is represented by products made of regenerated cellulose (man-made cellulosics), which primarily include regenerated fibers, but also films, membranes, and sponges. At an annual world production of about 2.2 million tons (2002), the viscose method,[113] well over 100 years old, still dominates production methods in which pulp with CS_2 is converted into cellulose xanthogenate as a metastable intermediate. The xanthogenate is soluble in aqueous sodium hydroxide, and can be formed as a viscose solution in a wet process. After precipitation of the shaped

product, the substituent is cleaved off, and high-purity cellulose is regenerated. Viscose fibers (Rayon) have excellent properties for a broad product range, from wet-strength cottonlike textile fibers (Modal fibers) to technical fibers in the form of cord (Rayon) for use in high-performance tires. Viscose technology is still in use today for film (cellophane) production, which is particularly important for food casing products.

The viscose route, however, is technologically complex (see processing scheme in Figure 18), requires highest-quality dissolving pulp, and leads to problematic environmental loads from the use of CS_2, heavy metal compounds (in the precipitation process), and resultant by-products. To decrease emissions and to meet the environmental standards, different methods can be applied.

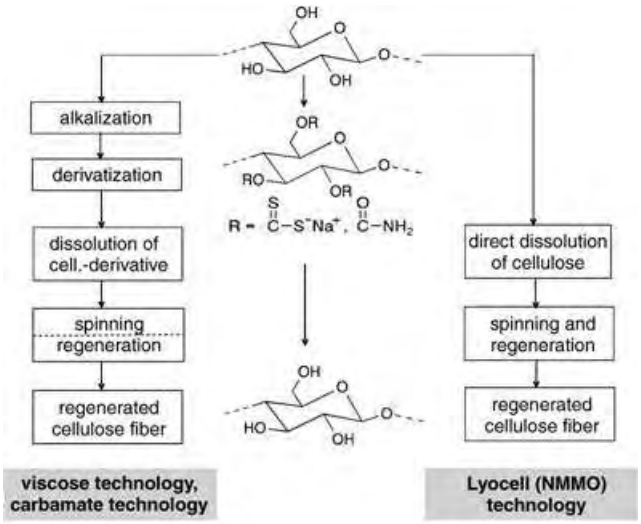

Figure 18. Process principles in regenerated cellulose technologies: left, derivate methods; right, direct methods.

The first (and rather unspectacular) variant to this end is to improve the existing viscose production by optimizing the consumption of chemicals, with particular regard to minimizing the use of CS_2.[114] This variant also includes the refitting of exhaust gas and waste water cleaning equipment, which has been implemented continuously in the viscose industries in western Europe, where today the emissions either meet or lie below the threshold values in place.[115] It is advantageous that existing facilities can still be used for the production of highly sophisticated types of fiber that have been introduced to the market. The increased cost of viscose technology incurred by the purification of exhaust gas and waste water is a disadvantage that must be weighed against the product advantages, in particular, in case of the installation of new production capacities.

Alternate processing technologies should be simpler than the viscose process, and environmentally hazardous materials and side products in general must be avoided (Figure 18). An alternate derivatization method that has been developed to commercial maturity without the use of sulfur-containing compounds, but that retains the viscose spinning technology, is the CarbaCell process,[116] in which a new reaction variant employs urea to convert cellulose into cellulose carbamate, which can be subsequently processed on existing viscose spinning systems.

The direct dissolution and shaping of cellulose without derivatization is possible with copper ammonia technology,[117] which originated as a very early spinning route of cellulose (Cupro silk, Cuprophane). It is rarely used anymore, as it poses environmental hazards. Among others, it has been suggested that the dissolution and shaping of cellulose could be carried out by DMA/LiCl or zinc chloride and in aqueous solution with NaOH (CELSOL process),[118] or phosphoric acid as a direct solvent to spin high-strength cellulose filaments.[119] However, the most advanced development took place beginning in the 1980s with a process based on the NMMO monohydrate solvent system, which was taken to commercial maturity and which made the current industrial breakthrough known as the Lyocell process.[120] This process offers the potential for a revolutionary development in cellulose processing, as it is comparatively simple (Figure 18) and is practically free from emissions as almost all the solvent involved is recovered.

5.2. The CarbaCell Process

The starting point of this development is founded in previous studies[121] of the transformation of cellulose with urea (after urea breakdown) to form cellulose carbamate (Scheme 18), which is soluble and shapeable in sodium

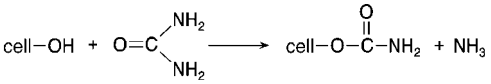

Scheme 18. Formation of cellulose carbamate by transformation of cellulose with urea.

hydroxide solution. The patented CarbaCell technology is based on a synthesis of the cellulose carbamate in xylene as a transfer medium.[116] The technical sequence is similar to the viscose method (Figure 18). The starting cellulose material is initially alkalized and pre-ripened (partial chain degradation); in the synthesis stage it is subsequently derivatized and dissolved in sodium hydroxide solution. The spinning solution is filtered and deaerated prior to wet spinning in an acidic precipitation bath, followed by a salt-containing alkaline decomposition bath for the hydrolysis of the carbamate groups at elevated temperature. The structural changes of the cellulose during processing are clearly illustrated in Figure 19 with ^{13}C-CP/MAS solid-state NMR spectra.

Depending on the derivatization procedure, the transformation of the alkalized cellulose with urea leads to structures that are similar to the cellulose modifications II and IV, and that have either blocklike or statistic distributions of the substituents along the cellulose chain.[38e] Apart from

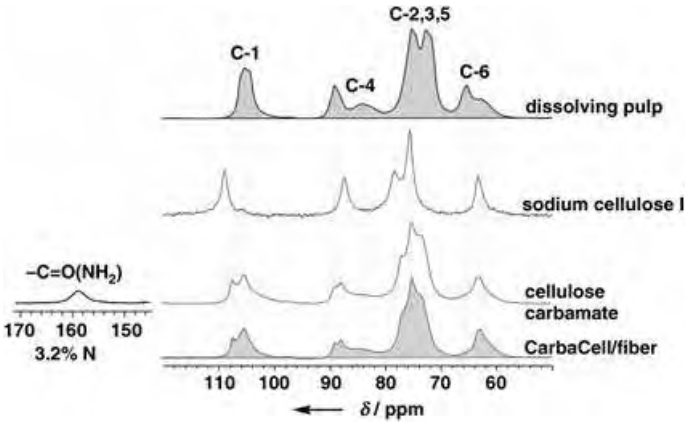

Figure 19. Structural changes of cellulose in the carbamate process as observed with ^{13}C-CP/MAS NMR spectroscopy.[122]

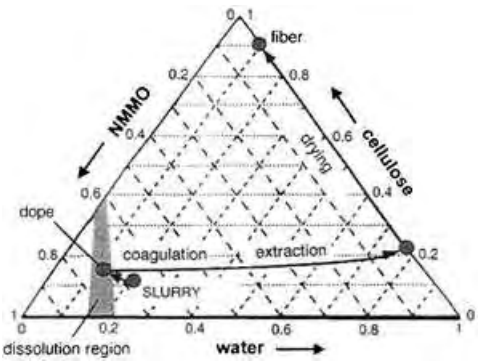

Figure 20. Phase diagram: cellulose/NMMO/water.[124a]

the use of the innocuous urea as a substitute for the toxic CS_2, the advantage of the carbamate process is that the cellulose carbamate is relatively stable at room temperature, which permits storage times of more than a year without loss of quality. Thus, the synthesis of cellulose carbamate can be carried out on a large scale in a central location, from which products can then be shipped to decentralized facilities for processing (such as spinning factories). Industrial tests have shown that cellulose carbamate can be processed without any problems on viscose spinning machines. Despite the advantages of the carbamate process, which could possibly be used for other products such as high-absorbent nonwovens, hollow fibers, sponges, and carpet cleaners, industrial cellulose carbamate production sites have not yet been established.

5.3. The NMMO (Lyocell) Process

Owing to its strong N–O dipole, *N*-methylmorpholine-*N*-oxide (NMMO) in combination with water can dissolve cellulose without prior activation or derivatization. With a water content of 13.3 % by mass and a decreased melting point of about 74 °C, NMMO monohydrate is significant as a solvent, from a technical standpoint, compared with pure NMMO. The breakthrough of this system for technical applications came with the introduction of stabilizers such as propylgallate, which suppresses the radical separation of the NMMO and scission of the cellulose chain at the required processing temperatures.[123] Solutions with cellulose content of up to 23 % can be produced starting with the dispersion of conventional cellulose in NMMO with a high water content (such as 50 %). Subsequent concentration of the suspension at higher temperature until the NMMO monohydrate composition is made permits dissolution of the cellulose. In the ternary phase diagram of Figure 20, the path of the cellulose during the solutions production and the technological stages of the NMMO processes (cf. Figure 18) can be followed.

The shaping of the cellulose/NMMO/water solution into fibers takes place at temperatures between 80 and 120 °C, at which the semiliquid system (dope), with a cellulose content of 8–23 %, is extruded from a nozzle over an air gap with a length of 10–250 mm into an aqueous precipitation bath. There, the cellulose precipitates almost instantaneously. In a closed circle, the industrial recovery of NMMO is 99.6–99.7 % from the precipitation bath, with its upgrade and cleaning by an ion-exchange process. In the dry jet/wet-spinning process, any deformation in the region of the nozzle and the following air gap section elicits a significant influence on structure formation (particularly the orientation state) of the thread and its resulting properties. The fundamentals of crystallization and structure formation of the cellulose after precipitation from NMMO solutions were initially analyzed by Chanzy and co-workers,[125] and Dubé and co-workers.[126] A list of the extensive literature concerning the structure formation of cellulose regenerated materials made from NMMO solutions available since the seminal work is given in Ref. [42]

Compared with conventional viscose fibers, today's generation of commercial Lyocell fibers spun from NMMO solution have outstanding properties in certain respects, such as strength in both wet and dry states, modulus of elasticity, sorption behavior, wearing properties, gloss, and touch. However, the distinct wet fibrillation behavior is predominantly disadvantageous, and its suppression still requires additional processing, such as subsequent cross-linking steps (Section 5.5).

The fact that the cellulose/NMMO/water solution can be deformed in the nozzle and the air gap, similar to a melt, opened up the initial possibility to produce cellulose films in a blow-extrusion process[127] (basic sketch in Figure 21). Spun fleeces (melt-blown nonwovens) [128] can also be manufactured analogously to synthetic polymers (polyethylene, polypropylene, and polyethyleneterephthalate) shaped from melt. The blown-film process permits the setting of longitudinal and transverse properties by means of the corresponding orientation states, a feature still not feasible in this manner for cellulose films, on the one hand. On the other hand, the morphology and pore structure of the film can be influenced by the subsequent precipitation process, which is not possible in melt-extruded films from synthetic polymers. This results in versatile application possibilities for the blown films from cellulose, which range from packaging materials and food casings, to dialysis membranes.

Another advantage of the NMMO process is that less expensive cellulose of lower purity (higher hemicellulose

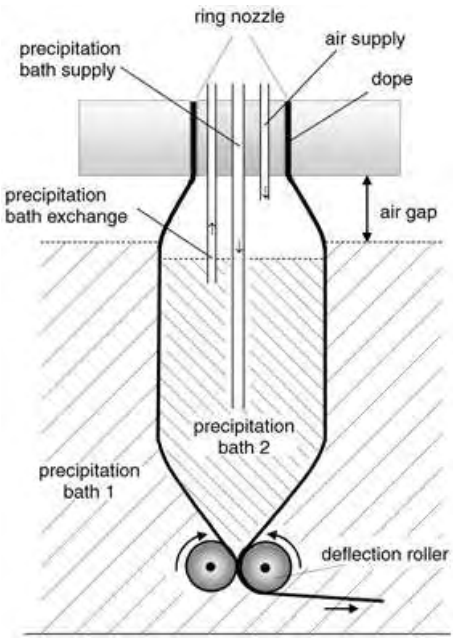

Figure 21. Basic sketch on blow-extrusion of cellulose films made from NMMO solution.

content) can be used; this is a significant benefit for the development and production of melt-blown nonwovens.[128] The pioneering significance of the cellulose/NMMO/water system is also made clear by the fact that apart from classical fibers and films, numerous new products can be produced, thus opening a gigantic field of application for the sustainable polymer raw material cellulose. Developments are currently in progress, including lyophane membranes for water purification,[124b] precursor filaments for carbon fibers,[129] and cellulose-based functional materials[130] such as conductive and piezoelectric fibers, ceramic hollow fibers, pearl cellulose for encapsulation, and highly porous materials for various applications.

Special emphasis must also be placed on the fact that through the industrially applied Lyocell fiber process and the emission-free technical NMMO recovery system developed in this field, a significant drawback to the previous cellulose technologies has been removed. This achievement was acknowledged by awarding the Austrian company Lenzing AG the EU Environmental Award 2000 for the Lyocell process.

5.4. The Chemistry of the NMMO/Cellulose System

Like all amine-*N*-oxides, NMMO is well-known as an oxidizing agent in organic chemistry. Therefore, its application in an industrial process is not unproblematic. Against this background, systematic and detailed investigations on the chemistry of NMMO were carried out in a series of studies.[131a]

All homolytic reactions of NMMO start with cleavage of the N–O bond with formation of aminium (aminyl) radicals (Scheme 19). In the absence of oxygen, these radicals undergo

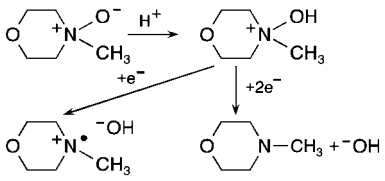

Scheme 19. Homolytic and heterolytic bond cleavage of *N*-methylmorpholine-*N*-oxide (NMMO).[131a]

disproportionation or react in redox processes that finally produce *N*-methylmorpholine, morpholine, and formaldehyde (Scheme 20, top). These processes are induced by transition metal ions. In the presence of oxygen, the radicals react with the latter (Scheme 20, top).

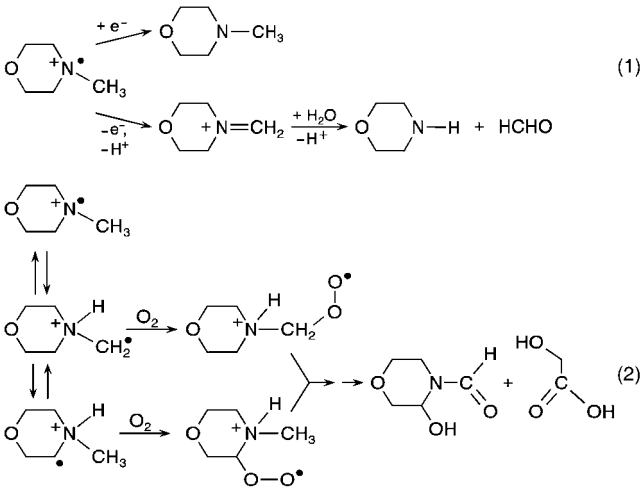

Scheme 20. Reactions in the NMMO/cellulose system starting from the aminyl radicals; products of redox processes in the (1) absence and (2) presence of oxygen.[131a]

The heterolytic reactions in NMMO solution proceed either by reductive deoxygenation of NMMO, which produces *N*-methylmorpholine with concomitant oxidation of reductants such as cellulose, or by the formation of morpholine and formaldehyde by Polonowski-type reactions in intramolecular redox processes (Scheme 21). A third pathway induced by carbenium-iminium ions as an autocatalytic process can cause the quantitative decomposition of NMMO.

The current knowledge of the potential reactions in the cellulose/NMMO/water solvent system is of considerable significance for the safe and economically effective production of cellulose fibers according to the aminoxide process. The strict exclusion of heavy metals such as copper, even at the smallest concentrations, as well as a tightly controlled temperature system are basic safety requirements.

5.5. Structures and Properties of Cellulose Regenerate Fibers and Films

The high stage of development and the vast range of today's viscose products are founded on decades of research

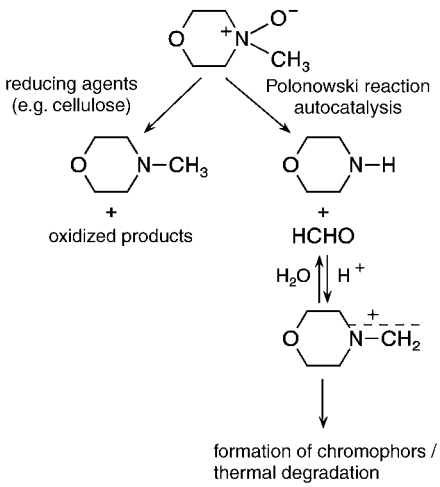

Scheme 21. Reductive deoxygenation and carbenium-iminium ion formation in the NMMO/cellulose system.[131a]

efforts. It results from a largely empirical understanding of the complicated processes of cellulose derivative structure formation from solution which have not always been published, and which are mastered today only by a few specialists in industry and research institutes. The development of new, possibly superior products manufactured through application of the latest environmentally compatible technologies can be realized only through a comparatively thorough understanding of the structure formation process and the connections between manufacturing conditions, structures, and properties. The differences between viscose, carbamate, and Lyocell fibers based on different structure formation conditions are described below. From this, the targets of the structure–property relationships of new products can be derived.

5.5.1. *Cellulose Regenerate Fibers*

Electron micrographs of ultrathin sections of the various regenerate fibers reveal that textile viscose fibers have a lobed cross-section and a skin–core morphology, whereas the round to oval cross-sectional shapes and the homogeneous morphologies of carbamate and Lyocell fibers are distinctly different, and are similar to each other (Figure 22). In the latter case, it is apparent that a fast "hard" precipitation takes place without hydrolysis of the carbamate groups, whereas the precipitation conditions of the viscose process are "softer"; the precipitation, the substituent removal, as well as the transport of the reaction products during regeneration take

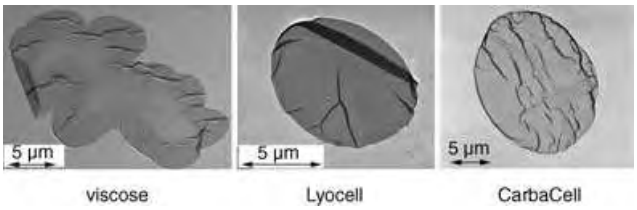

Figure 22. TEM images of cross-sections of various kinds of cellulosic fibers.

Table 4: Degrees of crystallinity (x_c) and crystallite sizes ($D_{(hkl)}$) of regenerated cellulose fibers.

Fiber Type		x_c [%]	$D_{1\bar{1}0}$ [nm]	D_{110} [nm]	D_{004} [nm]
viscose		27–31			
	technical yarn		6.6	3.9	9.7
	textile yarn		5.1	4.5	9.8
Lyocell	filament	35	4.4	3.3	17.5
carbamate	filament	34–43	3.6–4.1	4.1–5.3	10.0–12.4

place as competing processes. Table 4 shows that the degrees of crystallinity (WAXS, Ruland–Vonk method)[132] for carbamate and Lyocell fibers range between 35 and 40 %, above the respective value for viscose fibers of lower crystallinity (≈30 %). A comparison of the crystallite dimensions, also determined by X-ray diffraction and given in Table 4, demonstrates that the Lyocell fiber has narrower and particularly longer crystallites (in the fiber direction).

Distinct differences between the types of fibers are also revealed in their state of orientation, which has significant influence on the mechanical properties. Figure 23 compares the overall orientation (f_t; obtained by birefringence measurements), the orientation of the crystalline ranges (f_c; X-ray

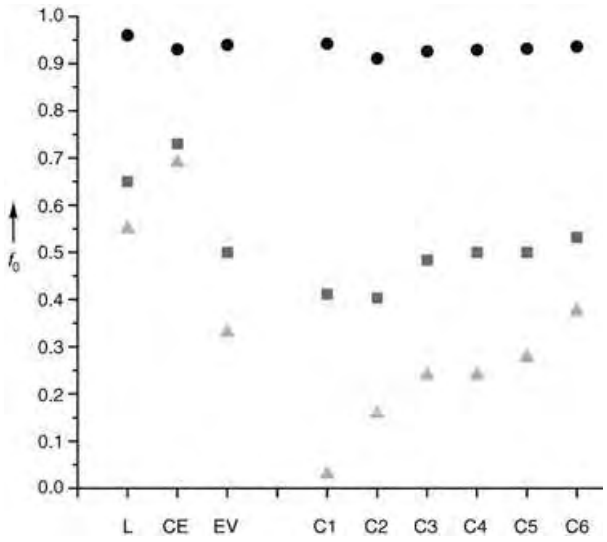

Figure 23. Orientation parameters of different cellulose regenerate fibers:[122] orientation factor, f_o; overall orientation, f_t (■); orientation of crystalline ranges, f_c (●); orientation of noncrystalline chain segments, f_a (▲); fiber types: Lyocell, L; CordEnka, CE; EnkaViskose, EV; Carbamate, C1–C6.

diffraction), as well as the orientation factors calculated for the noncrystalline chain segments (f_a) of commercial fibers and a number of development patterns from the carbamate program.

It is clear that the stiff and fibrillating behavior of the Lyocell fibers is caused by their high orientation in the noncrystalline regions—similar to technical fibers—the lowering of which in combination with a decrease in the degree of crystallinity was, and still is, a central task in the continued development of Lyocell fibers. In the development of

carbamate fibers, however, the problem was to increase the low orientation of the noncrystalline chain segments at the beginning. This problem has been solved in the meantime; today carbamate fibers can be produced with an orientation state and property profile almost identical to those of viscose.

The decrease of crystallinity and orientation of Lyocell fibers is possible by a "softer" precipitation in alcoholic baths. Fibers with a firm, highly oriented core and a soft, non-fibrillating shell can be produced through a two-stage precipitation in alcohol and water (Figure 24).[133]

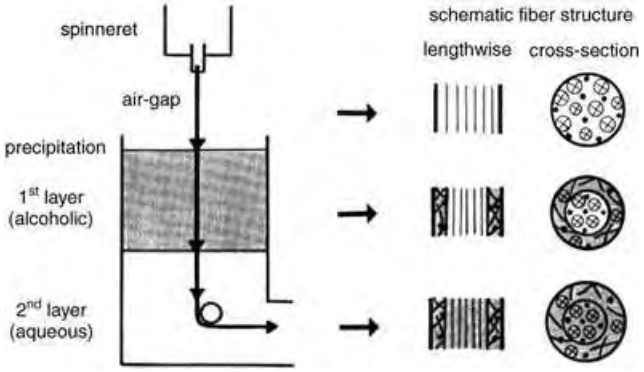

Figure 24. Basic sketch of the double-bath precipitation for Lyocell fibers with a core–shell structure.

This example demonstrates, that knowledge of fiber structures and an understanding of the structure-forming process are important prerequisites for the development of products with the desired properties. A wide range of alternate possibilities for influencing fiber structure and properties, including the downstream cross-linking of molecules in the fiber, can be found in the patent literature. The full potential capacity for such process control, however, has certainly not yet been tapped by the methods currently in use. Therefore, a more thorough understanding of these structure-forming processes is urgently required.

5.5.2. Blown Films Made of Cellulose

As with Lyocell fibers, the precipitation process, which in this case includes inner and outer precipitation baths (see basic sketch, Figure 21), offers considerable possibilities to influence the morphology and pore structure of the product films. Symmetrical (identical precipitation baths inside and outside) and asymmetrical (different precipitation baths inside and outside) film structures can be produced without difficulty (Figure 25). Compared with cellophane and cuprophane films on the market, blown films produced according to the Lyocell process have somewhat lower degrees of crystallinity ($\approx 40\,\%$) and only slightly smaller lateral crystallite dimensions.

An advantage of the blow-extrusion process, which can be transferred to cellulose films as well, is the ability to control the orientation in the machine direction and transverse

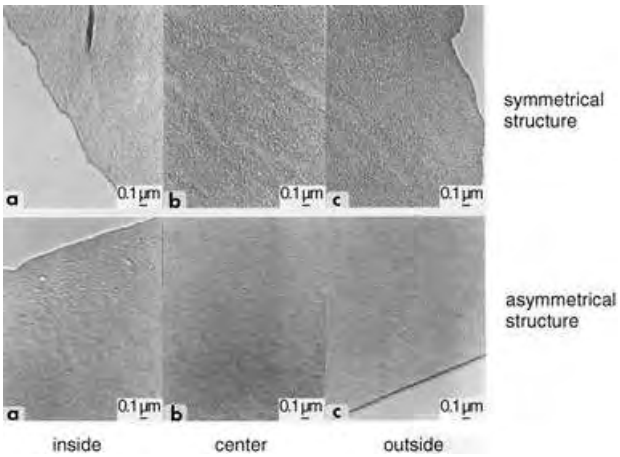

Figure 25. TEM micrographs of symmetrical and asymmetrical structures of blown films.

direction without any problems by means of the draw-down and blow-up ratio. Figure 26 shows the X-ray pole figures in a uniplanar orientation of the $(1\bar{1}0)$ lattice plane, whereby suitably adjusted draw-down and blow-up ratios[127] can be used to produce different orientation states up to almost balanced films (compare longitudinal and transverse strength values of Figure 26).

The orientation distribution of the crystallite longitudinal axis (chain direction) in the film plane can be approximated with the (110) pole figures. Figure 27 shows the corresponding distribution functions of the longitudinal chain axis of differently produced blown films (BF7, 10, and 13) in comparison with commercial cellophane and cuprophane, which substantiates the control possibilities described. It should be emphasized as well that the mechanical properties of the blown films are superior to those of conventional products, and that the separating properties of Lyocell-based films, such as the dialysis and flow rates, are outstanding as a result of their pore structures.[124a]

6. Bacterial Cellulose as a Model Compound and High-Performance Material

6.1. Formation and Structure

The biosynthesis of cellulose takes place not only in plants, but, as already mentioned in Section 1, also in bacteria (such as *Acetobacter*, *Acanthamoeba*, and *Achromobacter* spp.), algae (*Valonia, Chaetamorpha* spp.), and fungi.[134] The formation of cellulose by laboratory bacterial cultures is an interesting and attractive access to pure cellulose for both organic and polymer chemists. By selecting the substrates, cultivation conditions, various additives, and finally the bacterial strain, it is possible to control the molar mass, the molar mass distribution, and the supramolecular structure. Thus it is possible to control important cellulose properties, and also the course of biosynthesis (e.g. kinetics, yield, and other metabolic products).

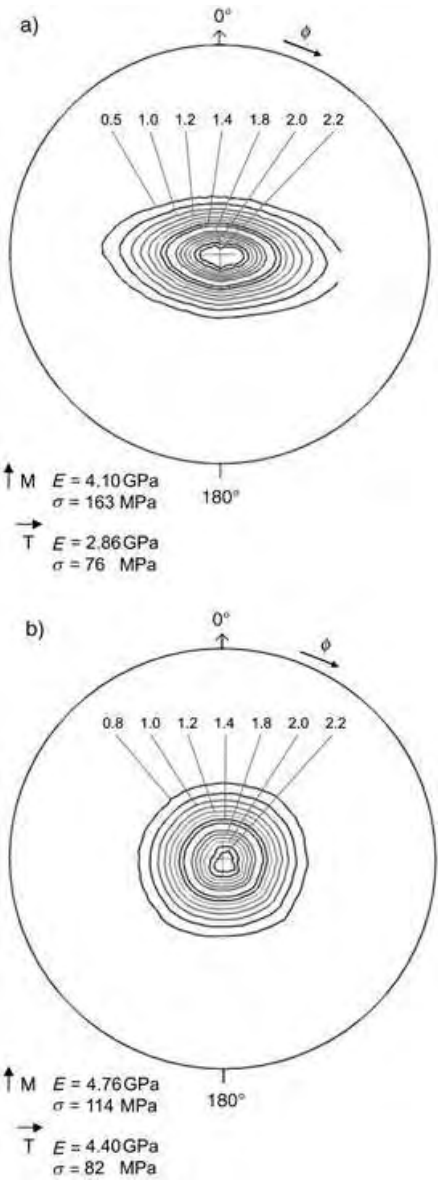

Figure 26. (1$\bar{1}$0) Pole figures and mechanical properties of differently produced cellulose blown films: a) draw-down in machine direction larger than transverse (BF7); b) drawing balanced in longitudinal and transverse direction (BF13).

Amongst the cellulose-forming bacteria, *Acetobacter* strains (reclassified as the genus *Gluconacetobacter*) are especially suitable for the production and investigation of cellulose. These gram-negative and strictly aerobic bacteria form ellipsoidal, straight, or slightly bent rods in the size range of 0.6–0.8 × 1.0–4.0 μm. They are not pathogenic and are commonly found on naturally grown fruits and in fruit products. Strains of the *Acetobacter xylinus* species produce extracellular cellulose that is easily isolated as fiber material. Under static immersed cultivation conditions, a biofilm of varying thickness (fleece) is produced which helps the colonized bacteria to maintain a high oxygen content near the surface, and which serves as a protective barrier against drying, natural enemies, and radiation.

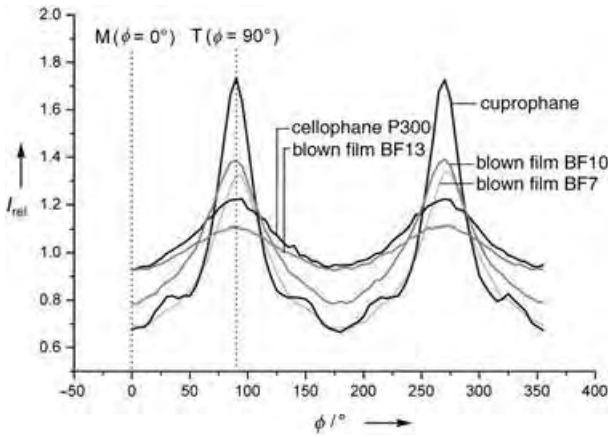

Figure 27. Orientation of the cellulose chains in the film plane (ϕ scan of the (110) pole figure at $\chi = 85°$).

The metabolic products of *A. xylinus* were initially described by A. J. Brown in 1886.[135] He identified a gelatinous mass, formed on the culture solution during the course of vinegar fermentation as cellulose. Thanks to systematic and comprehensive research over the past decades,[17] recent knowledge about the formation and structure of bacterial cellulose is extensive. Moreover, this work is an important part of research investigations of the integration of biotechnological synthesis methods in polysaccharide chemistry and the development of cellulose products with new properties and application potentials.

The synthesis of the bacterial cellulose occurs between the outer and plasma membranes of the cell by a cellulose-synthesizing complex (terminal complex) starting with uridine diphosphate glucose (UDP glucose).[136] This complex is associated with bacterial cell surface pores, which have a diameter of about 3.5 nm. Cellulose synthase catalyzes the addition of UDP glucose to the end of the growing cellulose chain, which exits the cell as an elementary fibril, and then forms a 3D network with other elementary fibrils through formation of microfibrils and ribbons.[136] Crystallization and polymerization of the elementary fibrils are closely linked. One single cell can convert over 100 glucose molecules into cellulose per hour. As the culture medium contains millions of bacteria, the polymer is synthesized practically "before your eyes". The details of the polymerization catalyzed by cellulose synthase have been the subject of controversy.[137] The latest studies seem to indicate that the β-(1→4) linkage starts with the formation of cellobiose as an intermediate at a dual UDP glucose binding site.

A detailed model of the structure (Figure 28) of the bacterial cellulose of *A. xylinus* (strain NCIB 8034) in a never-dried state was determined by synchrotron X-ray diffraction experiments and studies carried out by electron microscopy.[138] Anhydrous units (nanofibrils) with cross-sectional dimensions in the nm range appear hydrated as a whole, and are aggregated to flat microfibrils with a width of 70–150 nm. This model was basically substantiated by means of small-angle X-ray diffraction, and was expanded by the fact

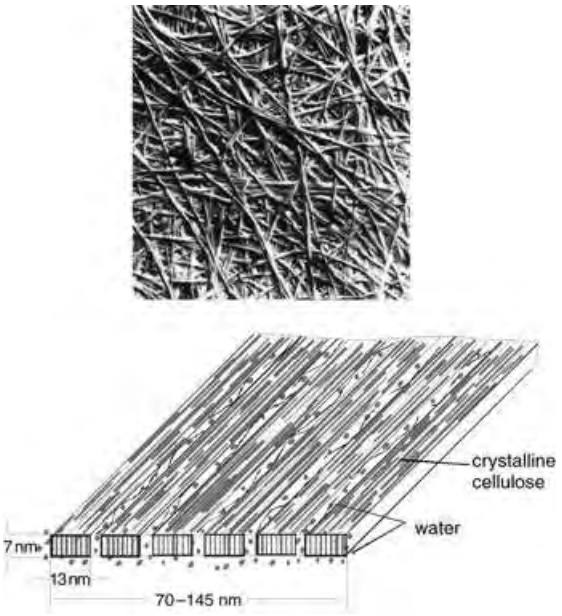

Figure 28. SEM image of dried bacterial cellulose (top) and model of an initially hydrated bacterial cellulose microfibril (bottom).

that a shell of noncrystalline cellulose chains passes around neighboring microfibrils to produce a microfibril band with a width of about 500 nm.[139] After drying, the initially wet and highly swollen cellulose fleece becomes a uniplanar oriented foil with microfibrils partially twisted around the longitudinal axis (Figure 28) which consist of $\approx 80\%$ I_α cellulose.

6.2. Properties and Applications

Although identical to cellulose of plant origin in terms of molecular formula, bacterial cellulose is quite different. The degree of polymerization is very high, with DP values of 2000–8000. Crystallinity is also high, with values of 60–90%. Bacterial cellulose is characterized by its high purity (no association with accompanying substances like hemicelluloses, lignin, or pectin) and by an extremely high water content of 90% or more. Upon complete removal of water by air drying, the bacterial cellulose will only rehydrate to the same low extent as that of plant celluloses after re-exposure to water: about 6%. After gentle freeze-drying, however, it can absorb up to 70% of the original water content by re-swelling.[140a] Through a stepwise exchange of water for other solvents, it is possible to introduce methanol, acetone, or *n*-hexane, for example, at the same volume as water in bacterial cellulose, while maintaining the hollow space and network structure.[140a]

Bacterial cellulose highly swollen with water gives well-resolved ^{13}C NMR spectra without additional pretreatment with conventional techniques (CP/MAS) of solid-state NMR spectroscopy.[138,140a,d,e] Figure 29 shows a typical example. Detailed NMR spectroscopic examinations of bacterial cellulose and of its biosynthetic route were carried out by using ^{13}C-labeled D-glucose.[141a]

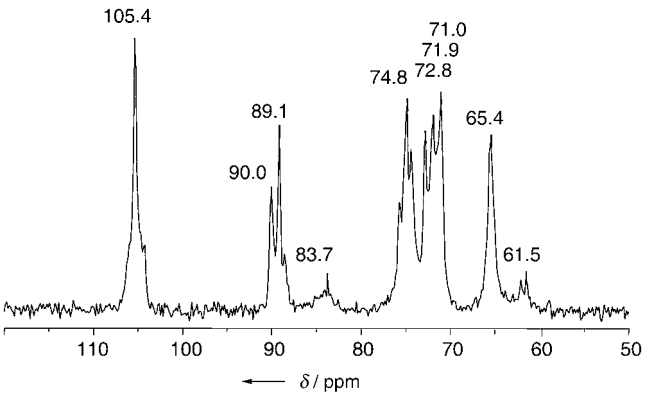

Figure 29. ^{13}C-CP/MAS NMR spectrum of a purified never-dried bacterial cellulose fleece (swelling agent: water).[140a,e]

Because of its crystalline nano- and microfibril structure, bacterial cellulose has excellent mechanical properties[142] (Table 5). It is therefore well-suited as a reinforcing agent for paper and fibers made from glass, carbon, phenol resin, and silicon at small quantities (5%). Owing to the high modulus of elasticity in combination with a large internal loss factor, it is also a superior material for headphone and loudspeaker membranes (Sony Corp.).

Table 5: Mechanical properties of bacterial cellulose and other organic layer materials (from Gilbert[142]).

Material	Young's Modulus [GPa]	Tensile Strength [MPa]	Elongation [%]
bacterial cellulose (BC)	15–35	200–300	1.5–2.0
polypropylene (PP)	1–1.5	30–40	100–600
polyethylene terephthalate (PET)	3–4	50–70	50–300
cellophane	2–3	20–100	15–40

Over the past few years, there has been an increased interest in commercial applications of bacterial cellulose. Important examples include supports for proteins, cell cultures and microorganisms, products for temporary skin and tissue replacement (Biofill, Bioprocess, and Gengiflex), calorie-free food such as Coco de Nata, and additives in the production of lattices and paper. These activities are accompanied by the isolation of new bacterial strains, genetic modifications, and a wide variation of all laboratory culture parameters.[143]

6.3. Biotechnological Synthesis of Blood Vessels from Dextrose

The investigations described below required for the formation, characterization and application of innovative biomaterials for surgery[140] have taken advantage of the powerful *A. xylinus* AX5 strain as a particularly suitable "cellulose factory in the laboratory".[140a] As shown in Figure 30, this strain produces water-soluble D-glucose (dex-

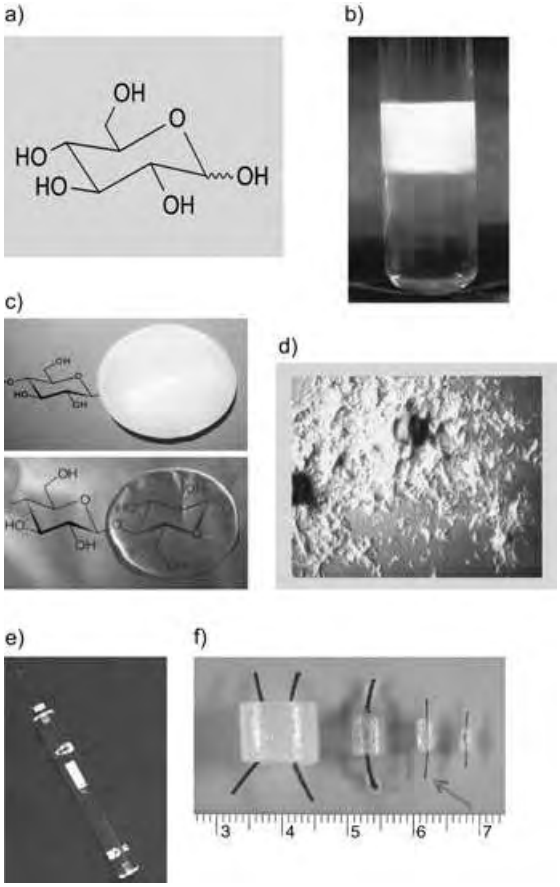

Figure 30. Biotechnological synthesis of bacterial cellulose of varying design: a) substrate D-glucose; b) static culture with cellulose fleece at the interface between Schramm–Hestrin culture medium and air after eight days of cultivation at 28 °C; c) never-dried (top) and completely air dried (bottom) cellulose fleece viewed from the top; d) colony of an *Acetobacter xylinus* strain; e) glass matrix for shaping the bacterial cellulose directly in the culture medium with cellulose tubes formed (see Figure 31); f) cellulose tubes of different dimensions after removal from the matrix and purification (arrow: implants for experimental microsurgery; scale values in cm).[140a]

trose) in static culture with the conventional Schramm–Hestrin culture medium[140a] within eight days, with a yield of 40 % cellulose in the form of a high swollen fleece at the interface between the culture medium and air.

Thus it was demonstrated that bacterial cellulose can be suitably shaped for application during biosynthesis. With the patented matrix reservoir technology developed for this purpose, it is possible to synthesize the cellulose in the shape of formed hollow bodies directly in the culture medium without subsequent treatment.[144] Figure 31 shows a schematic diagram of the cultivation vessel, in which the glass matrix is immersed in a larger volume of nutrient solution. The tube-shaped bacterial cellulose is produced in the nutrient medium which has entered between the outer and inner matrices, and is supplied with oxygen by a second opening to the air space.

The cellulose tubes (brand name BASYC, Bacterial Synthesized Cellulose) formed biotechnologically in this way were investigated for their application as a new type of

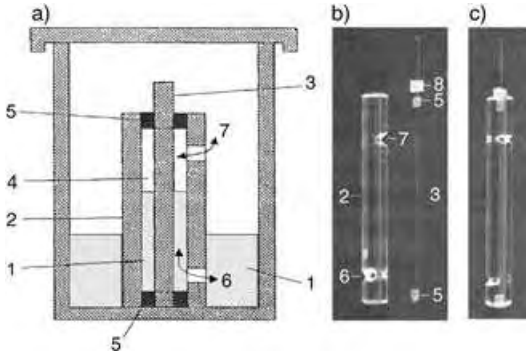

Figure 31. Matrix reservoir cultivation technique for the production of shaped bacterial cellulose (BASYC): a) basic sketch; b) example of the building units of a glass matrix: (1) Schramm–Hestrin culture medium in the reservoir and within the matrix, (2) outer matrix, (3) inner matrix, (4) cultivation space between outer and inner matrix, (5) spacer, (6) opening to the reservoir, (7) opening to the air, (8) stopper; c) ready-to-use matrix.[140a]

biomaterial for microsurgery in a cooperative effort between physicians, biologists and chemists.[140c] Tubular implants with an internal diameter of less than 3 mm were used (Figure 30 f, arrow). This application is derived from new microsurgical techniques that can repair nerves and blood vessels by sutures in a very small diameter range with optical equipment. The well-known synthetic implant materials from the surgery of larger vessels made of polytetrafluoroethylene, polyethylene terephthalate, polyethylene, and polyurethane have been insufficient for the requirements of microsurgery, often resulting in thromboses.

The wall of the BASYC tubes consist of the bacterial cellulose loaded with water at 90 % or greater in the nanofiber network, as described above. The hollow spaces of the BASYC material transport water, monovalent ions, and small molecules, but not biopolymers or corpuscular blood constituents. The stored water not only stabilizes the cellulose network, it also contributes to the tissue and hemocompatibility of BASYC.

For the BASYC vessel implants, the low roughness of the inner surface (feature variations of ≈ 15 nm) is especially significant, and can be obtained with the matrix-reservoir technique. This degree of roughness is within the order of magnitude of that for typical blood vessels in rats. BASYC tubes also meet other significant demands for microvessel replacement: they have a constant shape, are sufficiently stable against internal and external pressure, are flexible and elastic, and are capable of handling a tight microsurgical suture. Figure 32 a shows an example of the microsurgical work with shaped cellulose material. Results of investigations of the microsurgery of nerves and vessels of the rat as an experimental model are shown in Figure 32 b–f.

Upon dissection of the *nervus ischiadicus* and subsequent reconnection by a microsurgical suture, a protective cover (cuff) of BASYC prevents connective tissue from growing into the nerve gap, and favors the adhesion of the fascicles, which facilitates early regeneration of the nerve and a rapid return of muscle function. The good incorporation of bacterial cellulose-forming connective tissue and new blood

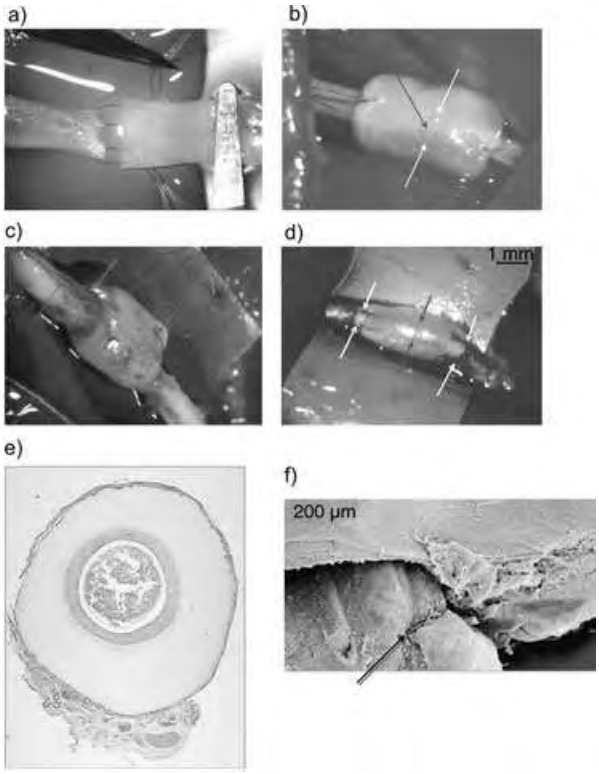

Figure 32. Application of bacterial cellulose tubes (BASYC) for training in microsurgical techniques and for animal experimental microsurgery on nerves and vessels: a) end-in-end connection (anastomosis) of BASYC tubes; b) *nervus ischiadicus* of the rat directly after operation of the dissected nerve (white arrows: anastomosis, black arrow: suture) with BASYC protective cover; c) operating field 10 weeks after the nerve dissection (arrows: new connective tissue and new blood vessels); d) BASYC implant in the carotid artery of the rat directly after operation (white arrows: anastomosis, black arrows: free blood flow, visible through the cellulose tube); e) cross-section of the middle part of a BASYC implant from the carotid artery of the rat after four weeks of residence time in the body as a histological preparation (cf. text); f) SEM image of a longitudinally cut BASYC implant with a homogeneous surface in the cellulose (left) and natural vessel region (arrow: remaining suture material). Magnification: 10×: (a, b, c); 6×: (d); and 32×: (e).[140c]

vessels on the surface of the protective cover is worthy of particular emphasis.

Upon reconnection of a dissected carotid artery (in a rat model) with a BASYC tube, the internal surface of the BASYC material becomes completely covered by an endothelial cell layer after a residence time of four weeks, as determined by histological examination of the preparation along with a specific test for endothelial cells (Figure 32e). Blood remnants can be found in the lumen. As observed by electron microscopy, the complete colonization of the BASYC region with endothelial cells covering both parts of the suture (Figure 32f) can be substantiated. Apparently, the BASYC material is a good substrate for the anchoring of autologous cells.

Upon coverage of longitudinally cleaved tubes with bovine endothelial cells in cell culture tests, a distinct sprouting of the initially spherical cells takes place within 24 h. Electron microscopy shows that the resulting filaments barely differ from the fibers of bacterial cellulose (Figure 33). This structure apparently also benefits the rapid endothelial colonization of BASYC.

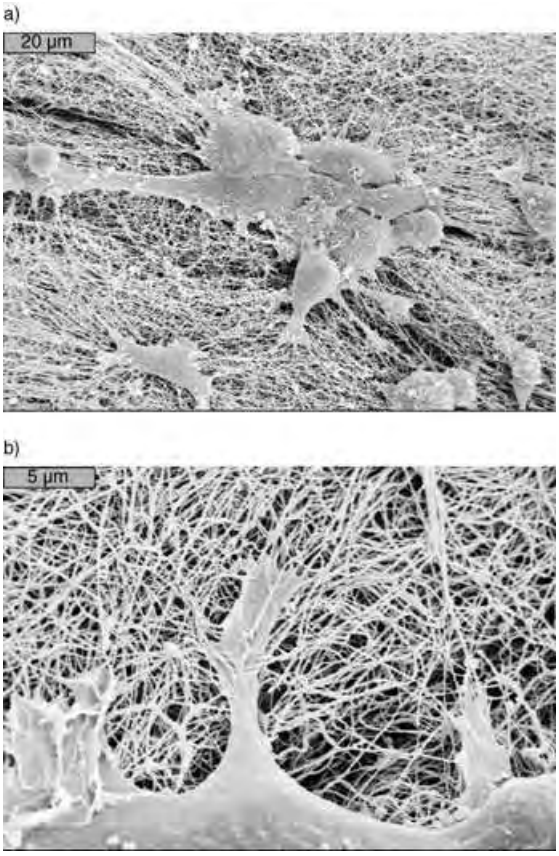

Figure 33. Scanning electron microscopy of the growth of bovine endothelial cells on a BASYC surface 24 h after spreading: a) overview; b) section at 4× enlargement.[140c]

Notably, further investigations have shown that BASYC microvessel implants can be applied toward vessels under low or high pressure, and that in all cases, thromboses were never observed.

6.4. Bacterial Cellulose for Veterinary Medicine and Cosmetics

The supramolecular structure of bacterial cellulose depends on the method of formation applied. Apart from the methods employed in static cultures and by the matrix-reservoir technique described above, an optimized surface cultivation of *A. xylinus* has been developed.[145] This cultivation system overcomes the transport barrier at the interface between nutrient solution and air for the introduction of the necessary nutrients (carbon and nitrogen sources, inorganic salts, and oxygen) as well as for the removal of the products formed by spraying a substrate aerosol directly on the surface of the immersed culture without causing a mechanical impairment. The cellulose layers of about 10 cm thickness

thus obtained are tested and respectively used for veterinary and cosmetic applications.[146]

7. In-Vitro Syntheses: Ways to New Horizons

The synthesis of a polysaccharide requires frequently repeated glycosylations, including the total control of the configuration at the anomer C atom and of the regioselectivity of the reacting hydroxy group. For this reason, it has only been within the past few years that cellulose could be produced synthetically.

7.1. Enzyme-Catalyzed Cellulose Structure

After many attempts to synthesize cellulose outside organisms, Kobayashi and co-workers[19b] succeeded in 1992 with the enzymatic polymerization of β-cellobiosyl fluoride in the presence of purified cellulase as catalyst in an acetonitrile/buffer solution at 30 °C. Cellulose with a yield of 54 % and a DP value of 22 was formed. The polymer structure as determined by ^{13}C and ^{1}H NMR spectroscopy corresponds well with that of natural cellulose.

Scheme 22 demonstrates that this in-vitro synthesis principle can also be extended to the preparation of amylose and chitin.[19] In continuation of this synthesis work, the in-vitro formation of crystalline cellulose I in an optimized solution system with purified cellulase has been described for the first time.[19d] The generation of this thermodynamically less stable allomorph had been known up to this point in living cells only.

7.2. Ring-Opening Polymerization of Glucose Derivatives

By stepwise synthesis[147] and particularly by cationic ring-opening polymerization of glucose orthoesters, cellulose was synthesized in a purely chemical manner by Nakatsubo and Kamitakahara in 1996 for the first time.[20] Starting with 3-*O*-benzyl-α-D-glucopyranose-1,2,4-orthopivalates with different groups at position 6, cellulose (after deprotection) is accessible according Scheme 23, as well as regioselectively substituted cellulose derivatives.

Scheme 24 shows the corresponding synthesis of uniform methyl celluloses. The DP values of these celluloses are in the range of 20–50. The influence of the glucose substituents on the regio- and stereochemistry of the polymerization could be identified and optimized through systematic work, as well as the availability of the glucose derivatives required and the deprotection chemistry of the product.[148]

8. Summary and Outlook

Science and technology continue to move toward renewable raw materials and more environmentally friendly and sustainable resources and processes. Cellulose, cellulose derivatives, and polysaccharides as a whole are of growing importance in the development and application of polymer materials. This progression has triggered a distinct renaissance of cellulose research and application all over the world over the past 10 years. In this context, it has been essential to increase the current knowledge of organic and polymer chemistries as well as in the chemistry of low-molecular-weight carbohydrates and other polysaccharides in the basic and application-oriented work in the field of cellulose. Moreover, it has been important to intensify the interdisciplinary interactions between biology, physics, pharmacy, medicine, and the wood industry and chemical engineering.

In consequence of this expanding development, groundbreaking insight has been gained on the complex structure of cellulose and cellulose derivatives in the solid state and in solution, on cellulose reactivity, reaction control, and selective syntheses, and regarding supramolecular structure formation as well as the biosynthesis and in-vitro synthesis of cellulose. This includes the rapid development of polysaccharide instrumental analysis and a deeper understanding of the relation between reaction conditions, product structure, and application-oriented properties. Thus, it has been possible to develop new types of cellulose esters and ethers as "polymers

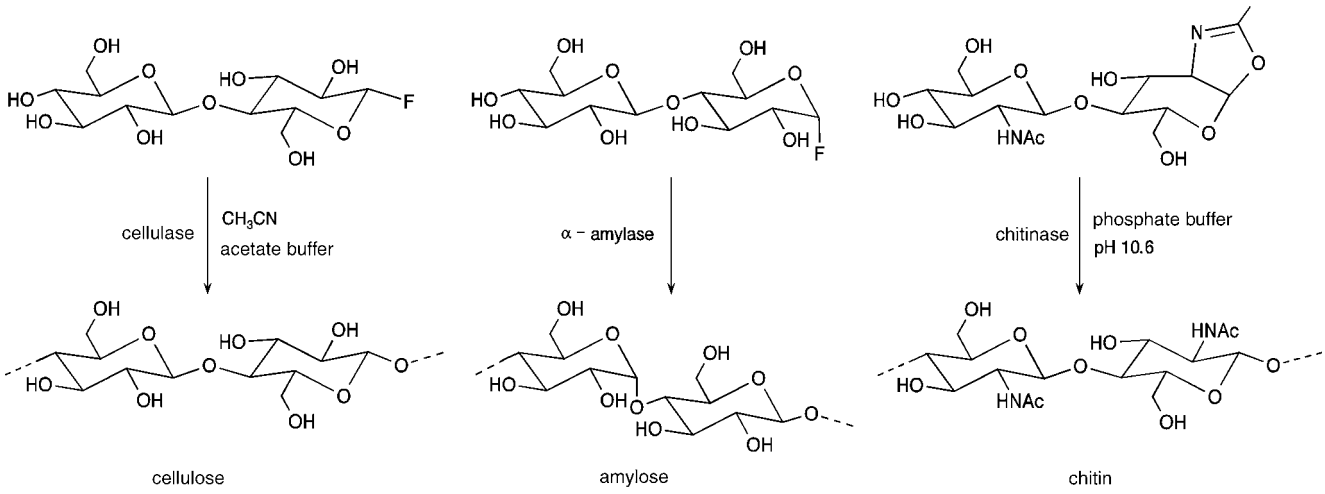

Scheme 22. Enzyme-catalyzed in-vitro synthesis of cellulose and related polysaccharides.

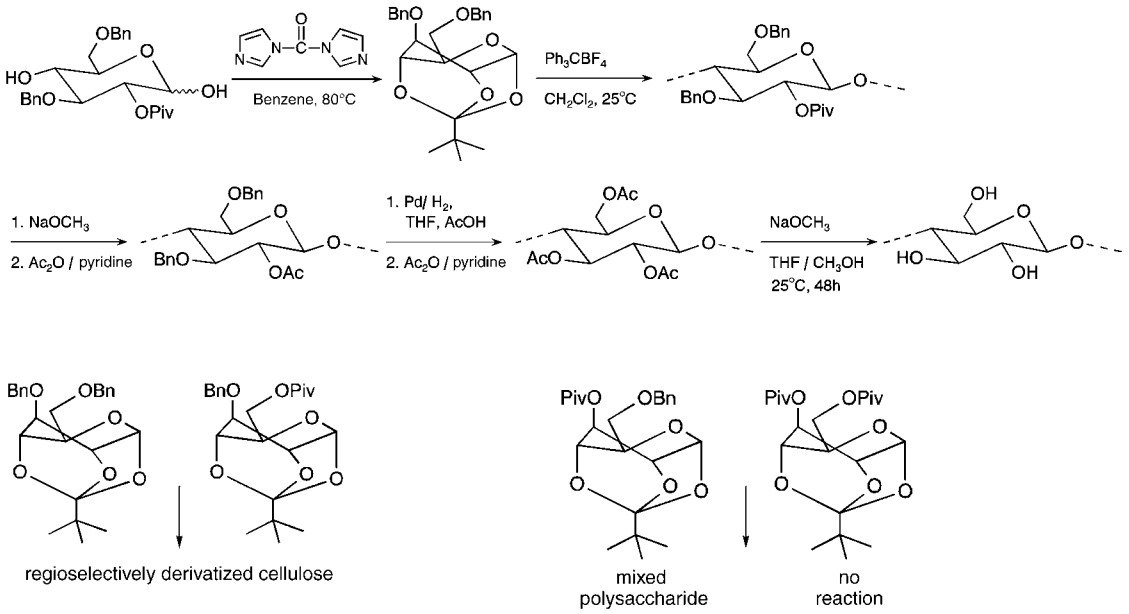

Scheme 23. Chemosynthesis of cellulose by ring-opening polymerization of 3,6-di-*O*-benzyl-α-D-glucopyranose-1,2,4-orthopivalate and the influence of substituents at positions 2 and 3 on the course of the reaction.

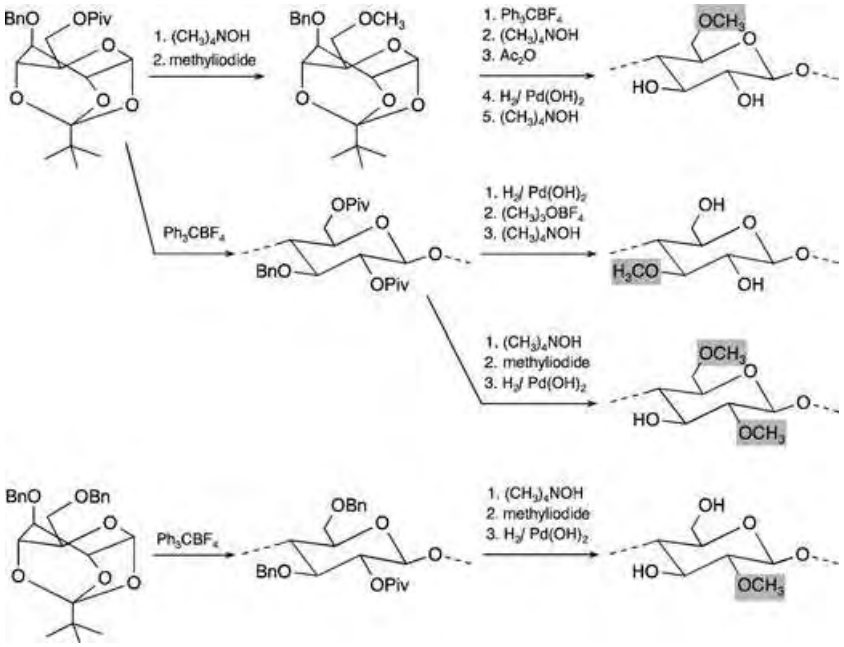

Scheme 24. Synthesis of regioselectively substituted methyl celluloses starting from 3-*O*-benzyl-α-D-glucopyranose-1,2,4-orthopivalates.

of the future", for example, toward a wide range of high-quality applications on the industrial scale, which have been established in the market. Fundamental research on the cellulose/NMMO/water system has led to a novel, environmentally friendly technology (Lyocell process) for the production of cellulose regenerate products, which has revolutionized the processing of cellulose, and has at least partially removed the previous disadvantages in comparison with the process steps in the production of synthetic polymers.

All signs and symptoms seem to indicate that the impressive rate of development in the field of cellulose will continue or will even accelerate. The establishment of centers of excellence, new pilot, process, and production plants, the expansion of large-scale technical products, a close cooperation of fundamental and applied research, as well as an effective international cooperation of scientists and facilities are distinct evidence of this fact. New insight into the processes of wood pulping and overall wood processing, into the production of cellulose from other plants as well as into the analysis of cellulose products will help to ensures that the quality, variety of products, and ecological acceptance of the starting materials will grow, along with the consistent ecological orientation of industrial cellulose chemistry.

Fundamental changes regarding the access to cellulose as a raw material are predictable because of the fast growth in understanding cellulose biosynthesis. Indeed, efforts are being made to purify and sequence cellulose synthase and associated proteins to generate a reproducible cell-free system capable of generating crystalline cellulose. By introducing genes to modify cellulose biosynthesis in important cellulose-forming organisms (trees, cotton crops, and bacteria), it should be possible to tailor various types of cellulose for pulp, paper, building materials, textiles, and other fields of application.

If cellulose-forming bacteria could be cultivated on a large technical scale, the requirement of cellulose could be satisfied entirely by this source in the future.

The aim of this paper is to demonstrate the current state of development in the field of cellulose research and application through examples. It should be also pointed out that cellulose as a natural product belongs to the polymers, which hold an impressive future potential for fundamental knowledge as

well as for large-scale production in a wide range of applications.

Glossary

AGU	anhydroglucose unit
BF	blow film
CMC	carboxymethyl cellulose
CA	cellulose acetate
CAB	cellulose acetate butyrate
CAP	cellulose acetate propionate
CE	carbohydrate esterase
CF	cellulose formate
CTFA	cellulose trifluoracetate
DCC	dicyclohexylcarbodiimide
DP	degree of polymerization
DS	degree of substitution
HEC	hydroxyethyl cellulose
HMDS	hexamethyldisilazane
HPC	hydroxypropyl cellulose
HPMC	hydroxypropylmethyl cellulose
MC	methyl cellulose
Ms	mesyl
NC	nitrocellulose
NMMO	*N*-methylmorpholine-*N*-oxide
NMP	*N*-methylpyrrolidone
NTA	nitrilotrieacetic acid
PDA	1,4-phenylenediamine
Piv	pivalate
TDS	thexyldimethylsilyl
TEA	Triethylamine
Thexyl	1,2-dimethyl-butyl-1
TMS	trimethylsilyl
TMSC	trimethylsilyl cellulose
Tr	triphenylmethyl, Trityl
Ts	tosyl
Tf	triflyl
UDP	uridine diphosphate

We gratefully acknowledge the Deutsche Forschungsgemeinschaft for the financial support of the Priority Program "Cellulose and Cellulose Derivatives—Molecular and Supramolecular Structure Design" from 1996 to 2002 as well as for the support by the Fachagentur Nachwachsende Rohstoffe and the German Federal Ministries BUEL and BMBF. A lot of the work described herein was carried out on this basis. Moreover, we express our gratitude for the effective and helpful cooperation with the colleagues in these programs as well as for the stimulating interaction with Professor Dieter Schumann (Clinic of Maxillofacial and Plastic Surgery, University of Jena), Professor Wolfgang Glasser (Virginia Polytechnic Institute, Blacksburg, USA), Professor R. Malcolm Brown (University of Texas, Austin, USA), and Professor Fumiaki Nakatsubo (Kyoto University, Kyoto, Japan). We thank Wolff Cellulosics GmbH (Germany), the German subsidiaries of the Acordis-Group, Lenzing AG (Austria), and Eastman Chemicals Company (Kingsport, TN, USA) for the trusting cooperation and for the versatile information on commercial products and processes.

Received: May 7, 2004
Published online: April 28, 2005

[1] a) A. Payen, *C. R. Hebd. Seances Acad. Sci.* **1838**, *7*, 1052; A. Payen, *C. R. Hebd. Seances Acad. Sci.* **1838**, *7*, 1125; b) K. Hess, *Zellst. Pap.* **1938**, *18*, 302–305.
[2] A. Brogniart, A. B. Pelonze, R. Dumas, *Comptes Rendus* **1839**, *8*, 51–53.
[3] C. F. Schönbein, *Ber. Naturforsch. Ges. Basel* **1847**, *7*, 27.
[4] K. Balser, L. Hoppe, T. Eichler, M. Wendel, A.-J. Astheimer, *Ullmann's Encyclopedia of Industrial Chemistry*, *Vol. A5* (Eds.: W. Gerhartz, Y. S. Yamamoto, F. T. Campbell, R. Pfefferkorn, J. F. Rounsaville), VCH, Weinheim, **1986**, pp. 419–459.
[5] H. Krässig, R. G. Steadman, K. Schliefer, W. Albrecht, *Ullmann's Encyclopedia of Industrial Chemistry*, *Vol. A5* (Eds.: W. Gerhartz, Y. S. Yamamoto, F. T. Campbell, R. Pfefferkorn, J. F. Rounsaville), VCH, Weinheim, **1986**, pp. 413–415.
[6] C. F. Cross, B. T. Bevan, C. Beadle, *Ber. Dtsch. Chem. Ges.* **1893**, *26*, 1090–1097; C. F. Cross, B. T. Bevan, C. Beadle, *Ber. Dtsch. Chem. Ges.* **1893**, *26*, 2520–2533.
[7] a) D. Klemm, H.-P. Schmauder, T. Heinze in *Biopolymers*, *Vol. 6* (Eds.: E. Vandamme, S. De Beats, A. Steinbüchel), Wiley-VCH, Weinheim, **2002**, pp. 290–292; b) D. L. Kaplan in *Biopolymers from Renewable Resources*, (Ed.: D. L. Kaplan), Springer, Berlin, **1998**, pp. 1–29.
[8] a) A. J. Martinez, S. Manolache, V. Gonzalez, R. A. Young, F. J. Denes, *J. Biomater. Sci. Polym. Ed.* **2000**, *11*, 415–438; b) C. Kauffmann, O. Shoseyov, E. Shpigel, E. A. Bayer, R. Lamed, Y. Shoham, R. T. Mandelbaum, *Environ. Sci. Technol.* **2000**, *34*, 1292–1296.
[9] F. Loescher, T. Ruckstuhl, S. Seeger, *Adv. Mater.* **1998**, *10*, 1005–1009.
[10] M. Erdtmann, R. Keller, H. Baumann, *Biomaterials* **1994**, *15*, 1043–1048.
[11] a) F. Ling, E. Bramachary, M. Xu, F. Svec, J. M. J. Fréchet, *J. Sep. Sci.* **2003**, *26*, 1337–1346; b) P. Franco, A. Senso, L. Oliveros, C. Minguillon, *J. Chromatogr. A* **2001**, *906*, 155–170; c) G. Felix, *J. Chromatogr.* **2001**, *906*, 171–184; d) G. Goetmar, D. Zhou, B. J. Stanley, G. Guiochon, *Anal. Chem.* **2004**, *76*, 197–202; e) Y. Toga, K. Tachibana, A. Ichida, *J. Liq. Chromatogr. Relat. Techn.* **2003**, *26*, 3235–3248.
[12] a) A. Amash, P. Zugenmaier, *Polymer* **1999**, *41*, 1589–1596; b) A. Amash, F.-I. Hildebrandt, P. Zugenmaier, *Desig. Monom. Polym.* **2002**, *5*, 385–399; c) A. P. Linder, R. Bergman, A. Bodin, P. Gatenholm, *Langmuir* **2003**, *19*, 5072–5077; d) A. Henriksson, P. Gatenholm, *Holzforschung* **2001**, *55*, 495–502; e) J. O. Karlsson, A. Henriksson, J. Michalek, P. Gatenholm, *Polymer* **2000**, *41*, 1551–1559.
[13] H. Staudinger, *Ber. Dtsch. Chem. Ges.* **1920**, *53*, 1073–1085.
[14] a) W. M. Humphreys in *Handbook of Fat Replacers*, (Eds.: S. Roller, S. A. Jones), CRC, Boca Raton, **1996**, pp. 131–144; b) H. Jiijma, K. Takeo in *Handbook of Hydrocolloids* (Eds.: G. O. Phillips, P. A. Williams), Woodhead, Cambridge, **2000**, pp. 331–346.
[15] S. Kobayashi, J. Sakamoto, S. Kimura, *Prog. Polym. Sci.* **2001**, *26*, 1525–1560.
[16] J. Röhrling, A. Potthast, T. Rosenau, H. Sixta, P. Kosma, *Lenzinger Ber.* **2002**, *81*, 89–97.
[17] a) R. M. Brown, Jr., T. K. Scott, *Science* **1999**, *71*, 204–212; b) R. M. Brown, Jr., *J. Macromol. Sci. Pure Appl. Chem.* **1996**, *33*, 1345–1373; c) R. M. Brown, Jr., *Pure Appl. Chem.* **1999**, *71*, 204–212; d) T. Kondo, E. Togawa, R. M. Brown, Jr., *Biomac-*

romolecules **2001**, *2*, 1324 – 1330; e) D. Klemm, H.-P. Schmauder, T. Heinze in *Biopolymers*, *Vol. 6* (Eds.: E. Vandamme, S. De Beats, A. Steinbüchel), Wiley-VCH, Weinheim, **2002**, pp. 285 – 290; f) S. Kimura, T. Kondo, *J. Plant Res.* **2002**, *115*, 297 – 302; g) I. M. Saxena, R. M. Brown, Jr., *Prog. Biotechnol.* **2001**, *18*, 69 – 76; h) U. Roemling, *Res. Microbiol.* **2002**, *153*, 205 – 212; i) R. M. Brown, Jr., I. M. Saxena, *Plant Physiol. Biochem.* **2000**, *38*, 57 – 67.

[18] D. Nobles, D. Romanovicz, R. M. Brown, Jr., *Plant Physiol.* **2001**, *127*, 529 – 542.

[19] a) S. Kobayashi, K. Kashiwa, T. Kawasaki, S. Shoda, *J. Am. Chem. Soc.* **1991**, *113*, 3079 – 3084; b) S. Kobayashi, K. Kashiwa, J. Shimada, T. Kawasaki, S. Shoda, *Macromol. Symp.* **1992**, *54/55*, 509 – 518; c) S. Kobayashi, S. Shoda, H. Uyama, *Adv. Polym. Sci.* **1995**, *121*, 1 – 30; d) S. Kobayashi, H. Uyama, M. Ohmae, *Bull. Chem. Soc. Jpn.* **2001**, *74*, 613 – 635.

[20] F. Nakatsubo, H. Kamitakahara, M. Hori, *J. Am. Chem. Soc.* **1996**, *118*, 1677 – 1681.

[21] a) D. Klemm, B. Philipp, T. Heinze, U. Heinze, W. Wagenknecht, *Comprehensive Cellulose Chemistry*, *1st ed.*, *Vol. 1* und 2, Wiley-VCH, Weinheim, **1998**; b) H. A. Krässig, *Cellulose-Structure, Accessibility, and Reactivity*, Gordon and Breach, Amsterdam, **1993**; c) D. N.-S. Hon, *Chemical Modification of Lignocellulosic Materials*, *1st ed.*, Marcel Dekker, New York, **1996**; d) D. Klemm, H.-P. Schmauder, T. Heinze in *Biopolymers*, *Vol. 6* (Eds.: E. Vandamme, S. De Beats, A. Steinbüchel), Wiley-VCH, Weinheim, **2002**, pp. 275 – 319; e) F. Horii in *Wood and Cellulosic Chemistry*, *2. ed.* (Eds.: D. N-S. Hon, N. Shiraishi), Marcel Dekker, New York, **2001**, pp. 83 – 107; f) A. Isogai in *Wood and Cellulosic Chemistry*, *2. ed.* (Eds.: D. N-S. Hon, N. Shiraishi), Marcel Dekker, New York, **2001**, pp. 599 – 625; g) *Prog. Polym. Sci.* **2001**, *26*, 1337 – 1971, (Special Issue: Cellulose and Related Polysaccharides); h) A. Richter, D. Klemm, *Cellulose* **2003**, *10*, 133 – 138;

[22] a) "The Structures of Cellulose": R. H. Atalla, *ACS Symp. Ser.* **1987**, *340*; b) A. C. O'Sullivan, *Cellulose* **1997**, *4*, 173 – 207; c) P. Zugenmaier, *Prog. Polym. Sci.* **2001**, *26*, 1341 – 1417.

[23] K. H. Gardner, J. Blackwell, *Biopolymers* **1974**, *13*, 1975 – 2001.

[24] R. H. Atalla, D. L. Van der Hart, *Science* **1984**, *223*, 283 – 285.

[25] J. Sugiyama, R. Vuong, H. Chanzy, *Macromolecules* **1991**, *24*, 4168 – 4175.

[26] V. L. Finkenstadt, R. P. Millane, *Macromolecules* **1998**, *31*, 7776 – 7783.

[27] Y. Nishiyama, P. Langan, H. Chanzy, *J. Am. Chem. Soc.* **2002**, *124*, 9074 – 9082.

[28] P. Langan, Y. Nishiyama, H. Chanzy, *Biomacromolecules* **2001**, *2*, 410 – 416.

[29] a) T. Okano, A. Sarko, *J. Appl. Polym. Sci.* **1985**, *30*, 325 – 332; b) H.-P. Fink, E. Walenta, J. Kunze, G. Mann in *Cellulose and Cellulose Derivates: Physico-Chemical Aspects and Industrial Applications* (Eds.: J. F. Kennedy, G. O. Phillips, P. A. Williams, L. Piculell), Woodhead, **1995**, pp. 523 – 528; c) H.-P. Fink, D. Hoffmann, B. Philipp, *Cellulose* **1995**, *2*, 51 – 70.

[30] a) O. Ellefsen, J. Gjonnes, N. Norman, *Nor. Skogind.* **1959**, *13*, 411; b) H.-P. Fink, B. Philipp, D. Paul, R. Serimaa, T. Paakkari, *Polymer* **1987**, *28*, 1265; c) T. Paakkari, R. Serimaa, H.-P. Fink, *Acta Polym.* **1989**, *40*, 731.

[31] D. Fengel, G. Wegener, *Wood*, Walter de Gruyter, Berlin, **1989**.

[32] H.-P. Fink, D. Hoffmann, H. J. Purz in *Cellulosics: Pulp, Fibre and Environmental Aspects* (Eds.: J. F. Kennedy, G. O. Phillips, P. A. Williams), Ellis Horwood, New York, **1993**, pp. 165 – 170.

[33] J. Ganster, H.-P. Fink, *Polymer Handbook*, *4th ed.* (Eds.: J. Brandrup, E. H. Immergut, E. A. Grulke, A. Abe, D. Bloch), Wiley, New York, **1999**, pp. 135 – 157.

[34] a) S. Westermarck, *Eur. J. Pharm. Biopharm.* **2000**, *50*, 319 – 325; b) J. Crawshaw, R. E. Cameron, *Polymer* **2000**, *41*, 4691 – 4698; c) R. R. Nigmatullin, M. T. Bruk, Y. P. Gomza, V. V. Shilov, *Dokl. Akad. Nauk Ukr. SSR Ser. B* **1989**, *10*, 46 – 50.

[35] M. Janura, Vorträge der 98. Hauptversammlung des Vereins Zellcheming und Cellulose-Chemiker-Rundgespräch, Baden-Baden, Germany, June 17 – 19, 2003, CD (*Papier* **2004**, *4*).

[36] H.-P. Fink, E. Walenta, J. Kunze, *Papier* **1999**, *9*, 534 – 542.

[37] P. Fratzl, *Phys. J.* **2002**, *1*, 49 – 55.

[38] a) J. Schurz, *Papier* **1979**, *33*, 558 – 561; b) E. Gruber, *Cellul. Chem. Technol.* **1979**, *13*, 259 – 278; c) E. Treiber, I. Uneback, *Papier* **1988**, *42*, 679 – 682; d) T. Karstens, *Papier* **1988**, *42*, 665 – 672; e) J. Gensrich, H.-P. Fink, J. Kunze, E. Schaaf, Proceeding der Zellcheming-Konferenz, Baden-Baden, June 24 – 27, 2002, CD (*Papier* **2003**, *5*) [*Chem. Abstr.* **2003**, *139*, 215686].

[39] P. Zugenmaier, K. Schmidt, *Abstr. Pap. Am. Chem. Soc.* **2000**, 219: 159 Cell Part 1 [*Chem. Abstr. Plus* **2000**, *328*, 018].

[40] a) W. Burchard, *Papier* **1994**, *48*, 755 – 764; b) W. Burchard, *Cellulose* **2003**, *10*, 213 – 225.

[41] a) B. Morgenstern, T. Röder, *Papier* **1998**, *52*, 713 – 717; b) T. Röder, B. Morgenstern, *Polymer* **1999**, *40*, 4143 – 4147.

[42] H.-P. Fink, P. Weigel, H. J. Purz, J. Ganster, *Prog. Polym. Sci.* **2001**, *26*, 1473 – 1524.

[43] U. Drechsler, S. Radosta, W. Vorweg, *Macromol. Chem. Phys.* **2000**, *201*, 2023 – 2030.

[44] R. S. Werbowyj, D. G. Gray, *Mol. Cryst. Liq. Cryst.* **1976**, *34*, 97 – 103.

[45] a) D. G. Gray, *Faraday Discuss. Chem. Soc.* **1985**, *79*, 257 – 264; b) R. D. Gilbert, *ACS Symp. Ser.* **1990**, *433*, 259 – 272; c) P. Zugenmaier in *Handbook of Liquid Crystals*, *Vol. 3* (Ed.: D. Demus), Wiley-VCH, Weinheim, **1998**, pp. 453 – 482; d) M. Siekmeyer, H. Steinmeier, P. Zugenmaier, *Macromol. Chem.* **1989**, *190*, 1037 – 1045.

[46] a) D. G. Gray, *Carbohydr. Polym.* **1994**, *14*, 277 – 284; b) Ch. Derleth, P. Zugenmaier, *Macromol. Chem. Phys.* **1997**, *198*, 3799 – 3814.

[47] M. Müller, R. Zentel, *Macromol. Chem. Phys.* **2000**, *201*, 2055 – 2063.

[48] J.-X. Guo, D. G. Gray in *Cellulosic Polymers—Blends and Composites* (Ed.: R. Gilbert), Hanser/Gardnerr, Munich, **1994**, pp. 25 – 45.

[49] D. Klemm, B. Philipp, T. Heinze, U. Heinze, W. Wagenknecht, *Comprehensive Cellulose Chemistry*, *1st ed.*, *Vol. 1*, Wiley-VCH, Weinheim, **1998**, pp. 130 – 155.

[50] D. Klemm, B. Philipp, T. Heinze, U. Heinze, W. Wagenknecht, *Comprehensive Cellulose Chemistry*, *1st ed.*, *Vol. 2*, Wiley-VCH, Weinheim, **1998**, pp. 31 – 71.

[51] D. Klemm, B. Philipp, T. Heinze, U. Heinze, W. Wagenknecht, *Comprehensive Cellulose Chemistry*, *1st ed.*, *Vol. 1*, Wiley-VCH, Weinheim, **1998**, pp. 43 – 82.

[52] T. R. Dawsey, C. L. Mc Cormick, *J. Macromol. Sci. Rev. Macromol. Chem. Phys.* **1990**, *30*, 405 – 440.

[53] W. Burchard, N. Habermann, P. Klüfers, B. Seger, U. Wilhelm, *Angew. Chem.* **1994**, *106*, 936 – 939; *Angew. Chem. Int. Ed. Engl.* **1994**, *33*, 884 – 887.

[54] A. Potthast, T. Rosenau, R. Buchner, T. Röder, G. Ebner, H. Bruglachner, H. Sixta, P. Kosma, *Cellulose* **2002**, *9*, 41 – 53.

[55] G. T. Ciacco, T. F. Liebert, E. Trollini, T. J. Heinze, *Cellulose* **2003**, *10*, 125 – 132.

[56] K. Saalwächter, W. Burchard, P. Klüfers, G. Kettenbach, P. Mayer, D. Klemm, S. Dugarmaa, *Macromolecules* **2000**, *33*, 4094 – 4107.

[57] D. Klemm, B. Philipp, T. Heinze, U. Heinze, W. Wagenknecht, *Comprehensive Cellulose Chemistry*, *1st ed.*, *Vol. 1*, Wiley-VCH, Weinheim, **1998**, pp. 155 – 165.

[58] M. Vieira, T. Liebert, T. Heinze in *Recent Advances in Environmentally Compatible Polymers* (Ed.: J. F. Kennedy), Woodhead, Cambridge, **2001**, pp. 53 – 60.

[59] a) J. W. Green in *Methods in Carbohydrate Chemistry*, (Eds.: R. L. Whistler, J. W. Green, J. N. Be Miller, M. L. Wolfram), Academic Press, New York, **1963**, pp. 327 – 345; b) B. R. Hakness, D. G. Gray, *Macromolecules* **1990**, *23*, 1452 – 1457; c) T. Kondo, D. G. Gray, *Carbohydr. Res.* **1991**, *220*, 173 – 183; d) T. Kondo, *J. Polym. Sci. Part B: Polym. Phys.* **1997**, *35*, 717 – 723.

[60] J. A. Camacho-Gomez, U. W. Erler, D. Klemm, *Macromol. Chem. Phys.* **1996**, *197*, 953 – 964.

[61] a) H. Kern, S. W. Choi, G. Wenz, *Polym. Prepr. Am. Chem. Soc. Div. Polym. Chem.* **1998**, *39*, 80 – 81; b) H. Kern, S. W. Choi, G. Wenz, J. Heinrich, L. Ehrhardt, P. Mischnik, P. Garidel, A. Blume, *Carbohydr. Res.* **2000**, *326*, 67 – 79.

[62] T. Kondo, A. Isogai, A. Ishizu, J. Nakano, *J. Appl. Polym. Sci.* **1987**, *34*, 55 – 63.

[63] a) K. Fischer, S. Spange, S. Fischer, C. Bellmann, J. Adams, *Cellulose* **2002**, *9*, 31 – 40; b) S. Spange, K. Fischer, S. Pranse, T. Heinze, *Cellulose* **2003**, *10*, 201 – 212.

[64] a) D. F. S. Petri, S. W. Choi, H. Beyer, T. Schimmel, M. Bruns, G. Wenz, *Polymer* **1999**, *40*, 1593 – 1601; b) G. Wenz, P. Liepold, N. Bordeanu, *Macromol. Symp.*, **2004**, *210*, 203 – 208.

[65] F. X. Redl, O. Köthe, K. Röckl, W. Bauer, J. Daub, *Macromol. Chem. Phys.* **2000**, *201*, 2091 – 2100.

[66] M. Acemoglu, E. Kusters, J. Baumann, I. Hernandez, C. P. Mak, *Chirality* **1998**, *10*, 294 – 306.

[67] Ch. Liu, H. Baumann, *Carbohydr. Res.* **2002**, *337*, 1297 – 1307.

[68] P. Arndt, K. Bockholt, R. Gerdes, S. Huschens, J. Pyplo, H. Redlich, K. Samm, *Cellulose* **2003**, *10*, 75 – 83.

[69] a) S. Fischer, H. Leipner, K. Thümmler, E. Brendler, J. Peters, *Cellulose* **2003**, *10*, 227 – 236; b) S. Fischer, W. Voigt, K. Fischer, *Cellulose* **1999**, *6*, 213 – 219.

[70] a) P. Mischnick, J. Heinrich, M. Gohdes, O. Wilke, N. P. Rogmann, *Macromol. Chem. Phys.* **2000**, *201*, 1985 – 1995; b) P. Mischnick, *Angew. Chem.* **2000**, *112*, 1274 – 1276; *Angew. Chem. Int. Ed.* **2000**, *39*, 1222 – 1224; c) P. Mischnick, *Cellulose* **2001**, *8*, 245 – 257; d) P. Mischnick, Ch. Henning, *Biomacromolecules* **2001**, *2*, 180 – 184; e) P. Mischnick, J. Heinrich, M. Gohdes, *Papier* **1999**, *53*, 729 – 743; f) J. Heinrich, P. Mischnick, *J. Polym. Sci. Part A: Polym. Chem.* **1999**, *37*, 3011 – 3016; g) K. Fischer, R. Koch, M. Fischer, I. Schmidt, *Papier* **1999**, *53*, 722 – 727; h) U. Drechsler, S. Radosta, W. Vorweg, *Macromol. Chem. Phys.* **2000**, *201*, 2023 – 2030; i) A. Cohen, H. Schagerlof, C. Nilsson, C. Melander, F. Tjerneld, L. Gorton, *J. Chromatogr. A* **2004**, *1029*, 87 – 95; j) P. W. Arisz, H. J. Kauw, J. J. Boon, *Carbohydr. Res.* **1995**, *271*, 1 – 14; k) S. Horner, J. Puls, B. Saake, E.-A. Klohr, *Carbohydr. Polym.* **1999**, *19*, 1 – 7; l) J. Puls, S. Horner, T. Kruse, B. Saake, T. Heinze, *Papier* **1998**, *52*, 743 – 747.

[71] J. Einfeldt, D. Meißner, A. Kwasniewski, *Prog. Polym. Sci.* **2001**, *26*, 1419 – 1472.

[72] a) C. Clasen, W.-M. Kulicke, *Prog. Polym. Sci.* **2001**, *26*, 1839 – 1919; b) N. Schittenhelm, W.-M. Kulicke, *Macromol. Chem. Phys.* **2000**, *201*, 1976 – 1984.

[73] a) D. Horton in *New Developments in Industrial Polysaccharides* (Eds.: V. Crescenzi, I. C. M. Dea, S. Stivala), Gordon and Breach, New York, **1985**, pp. 173 – 205; b) M. Yalpani, *Tetrahedron* **1985**, *41*, 2957 – 3020.

[74] a) B. Philipp, D. Klemm, U. Heinze, *Polym. News* **1999**, *24*, 305 – 308; b) D. Klemm, L. Einfeldt, *Macromol. Symp.* **2001**, *163*, 35 – 47.

[75] Y. Tsunashima, K. Hattori, H. Kawanihi, F. Horii, *Biomacromolecules* **2001**, *2*, 911 – 1000.

[76] K. Petzold, D. Klemm, B. Heublein, W. Burchard, G. Savin, *Cellulose* **2004**, *11*, 177 – 193.

[77] H. Itagaki, M. Tokai, T. Kondo, *Polymer* **1997**, *38*, 4201 – 4205.

[78] a) A. Richter, D. Klemm, *Cellulose* **2003**, *10*, 133 – 138; b) H. Baumann, Ch. Liu, V. Faust, *Cellulose* **2003**, *10*, 65 – 74.

[79] a) C. Vaca-Garcia, G. Gozzelinoi, W. G. Glasser, M. E. Borredon, *J. Polym. Sci. Part B* **2003**, *401*, 281 – 288; b) A. Franko, K. C. Seaveg, J. Gumaer, W. G. Glasser, *Cellulose* **2001**, *8*, 171 – 179; c) H. Matsumura, W. G. Glasser, *J. Appl. Polym. Sci.* **2000**, *78*, 2254 – 2261; d) I. Ghosh, K. R. Jain, W. G. Glasser, *J. Appl. Polym. Sci.* **1999**, *74*, 448 – 457; e) W. G. Glasser, R. Taib, R. K. Jain, R. Kander, *J. Appl. Polym. Sci.* **1999**, *73*, 1329 – 1340; f) C. M. Buchanan, N. L. Buchanan, J. S. Debenham, P. Gatenholm, M. Jacobsson, M. C. Shelton, T. L. Watterson, M. D. Wood, *Carbohydr. Polym.* **2003**, *23*, 345 – 357; g) G. Toriz, R. Arvidsson, M. Westin, P. Gatenholm, *J. Appl. Polym. Sci.* **2003**, *88*, 337 – 345.

[80] a) T. Heinze, T. Liebert, *Prog. Polym. Sci.* **2001**, *26*, 1689 – 1762; b) T. Heinze, T. Liebert, K. Pfeiffer, M. A. Hussain, *Cellulose* **2003**, *10*, 283 – 296; c) M. A. Hussain, T. Liebert, T. Heinze, *Polym. News* **2004**, *29*, 14 – 17; d) M. A. Hussain, Dissertation, Universität Jena, **2004**; e) H. M. Spurlin, *J. Am. Chem. Soc.* **1939**, *61*, 2222 – 2227; f) T. Heinze, Habilitationsschrift, Universität Jena, **1997**.

[81] a) C. Altaner, B. Saake, J. Puls, *Cellulose* **2001**, *8*, 259 – 265; b) C. Altaner, B. Saake, J. Puls, *Cellulose* **2003**, *10*, 85 – 95; c) C. Altaner, B. Saake, M. Tenkanen, J. Eyzaguirre, C. B. Faulds, P. Biely, V. L. Viikari, M. Siika-aho, J. Puls, *J. Biotechnol.* **2003**, *105*, 95 – 104.

[82] a) C. Altaner, B. Saake, J. Puls, *Cellulose* **2003**, *10*, 391 – 395; b) R. Bayer, H. Lutz, *Ullmann's Encyclopaedia of Industrial Chemistry*, *Vol. 9* (Eds.: W. Gerhartz, Y. S. Yamamoto, F. T. Campbell, F. Pfefferkorn, J. F. Rounsaville), VCH, Weinheim, **1986**, pp. 1 – 26.

[83] G. Mann, J. Kunze, F. Loth, H.-P. Fink, *Polymer* **1998**, *39*, 3155 – 3165.

[84] H.-P. Fink, H. Dautzenberg, J. Kunze, B. Philipp, *Polymer* **1986**, *27*, 944 – 948.

[85] T. W. Greene, P. G. M. Wuts, *Protective Groups in Organic Synthesis*, *2nd ed.*, Wiley-Interscience, New York, **1991**, pp. 69 – 83.

[86] H. A. Schuyten, J. W. Weaver, J. D. Reid, F. J. Jürgens, *J. Am. Chem. Soc.* **1948**, *70*, 1919 – 1920.

[87] a) H. Bartl, J. Falbe, *Methoden Org. Chem. (Houben Weyl) 4th ed.*, *Vol. E20*, **1987**; b) W. P. Pawlowski, R. D. Gilbert, R. E. Forness, S. T. Purington, *J. Polym. Sci. Part B: Polym. Phys.* **1988**, *26*, 1101 – 1110; c) D. Klemm, B. Philipp, T. Heinze, U. Heinze, W. Wagenknecht, *Comprehensive Cellulose Chemistry*, *Vol. 2*, *1st ed.*, Wiley-VCH, Weinheim, **1998**, pp. 274 – 294.

[88] a) K. Petzold, A. Koschella, D. Klemm, B. Heublein, *Cellulose* **2003**, *10*, 251 – 269; b) W. Mormann, *Cellulose* **2003**, *10*, 271 – 281; c) C. A. Brugnes, T. K. Jurrienes, *J. Org. Chem.* **1982**, *47*, 3966 – 3969.

[89] a) W. Mormann, J. Demeter, *Macromolecules* **1999**, *32*, 1706 – 1710; b) W. Mormann, J. Demeter, T. Wagner, *Macromol. Symp.* **2001**, *163*, 48 – 57; c) W. Mormann, J. Demeter, *Macromol. Chem. Phys.* **2000**, *201*, 1963 – 1968.

[90] A. Koschella, T. Heinze, D. Klemm, *Macromol. Biosci.* **2001**, *1*, 49 – 54.

[91] P. Mischnick, M. Lange, M. Gohdes, A. Stein, K. Petzold, *Carbohydr. Res.* **1995**, *277*, 179 – 187.

[92] a) K. Rahn, M. Diamantoglou, D. Klemm, H. Berghmans, T. Heinze, *Angew. Makromol. Chem.* **1996**, *238*, 143 – 163; b) T. Heinze, K. Rahn, *Papier* **1996**, *12*, 721 – 729.

[93] a) E. Heuser, M. Heath, W. H. Shockley, *J. Am. Chem. Soc.* **1950**, *72*, 670; b) S. I. Takahashi, T. Fujimoto, B. M. Barna, T. Miyamoto, H. Inagaki, *J. Polym. Sci. Part A: Polym. Chem.* **1986**, *24*, 2981 – 2993; c) R. W. Roberts, *J. Am. Chem. Soc.* **1957**, *79*, 1175 – 1178; d) C. L. Mc Cormick, T. R. Dawsey, J. K. Newman, *Carbohydr. Res.* **1990**, *208*, 183 – 191; e) T. R. Dawsey in *Polymer and Fiber Science: Recent Advances* (Eds.: R. E. Fornes, R. D. Gilbert), VCH, New York, **1992**,

pp. 157–176; f) K. Rahn, M. Diamantoglou, D. Klemm, M. Berghmans, Th. Heinze, *Angew. Makromol. Chem.* **1996**, *238*, 143–163; g) R. Hofmann (IG Farben), DE 526479, **1929** [*Chem. Abstr.* **1931**, *25*, 39014]; R. Hofmann (IG Farben), DE 528821, **1929** [*Chem. Abstr.* **1931**, *25*, 44504]; h) T. Eicher, W. Fischer, *Ullmanns Enzyklopädie der technischen Chemie*, *Vol. 9* (Eds.: E. Bartholomé, E. Biekert, H. Hellmann, H. Ley, W. M. Weigert), VCH, Weinheim, **1975**, pp. 227–246; i) F. B. Cramer, C. B. Purves, *J. Am. Chem. Soc.* **1939**, *61*, 3458–3462; j) C. J. Biermann, R. Narayan, *Carbohydr. Res.* **1986**, *153*, C1–C3; k) M. L. Wolfrom, J. C. Sowden, E. A. Metcalf, *J. Am. Chem. Soc.* **1941**, *63*, 1688–1691; l) C. E. Frazier, W. G. Glasser, *Polym. Prepr. Am. Chem. Soc. Div. Polym. Chem.* **1990**, *31*, 634–635; m) G. Siegmund, D. Klemm, *Polym. News* **2002**, *27*, 84–89.

[94] a) J. Tiller, P. Berlin, D. Klemm, *Macromol. Chem. Phys.* **1999**, *200*, 1–9; b) J. Tiller, P. Berlin, D. Klemm, *J. Appl. Polym. Sci.* **2000**, *75*, 904–915.

[95] P. Berlin, D. Klemm, J. Tiller, R. Rieseler, *Macromol. Chem. Phys.* **2000**, *201*, 2070–2082.

[96] a) J. Tiller, P. Berlin, D. Klemm, *Biotechnol. Appl. Biochem.* **1999**, *30*, 155–162; b) J. Tiller, R. Rieseler, P. Berlin, D. Klemm, *Biomacromolecules* **2002**, *3*, 1021–1029; c) P. Berlin, D. Klemm, A. Jung, H. Liebegott, R. Rieseler, J. Tiller, *Cellulose* **2003**, *10*, 343–367.

[97] J. Tiller, D. Klemm, P. Berlin, *Design. Monom. Polym.* **2001**, *4*, 315–328.

[98] J. Becher, H. Liebegott, P. Berlin, D. Klemm, *Cellulose* **2004**, *11*, 119–126.

[99] a) T. Teshirogi, H. Yamamoto, M. Sakamoto, *Sen'i Gakkaishi* **1978**, *34*, 510–515; b) S. Imai, M. Murai, A. Hamaguchi, R. Matushita, M. Koyama, *Anal. Chim. Acta* **1980**, *113*, 139–147; c) K. Arai, Y. Kanou, *Sen'i Gakkaishi* **1999**, *55*, 356–360; d) T. Heinze, A. Koschella, L. Magdaleno-Maiza, A. S. Ulrich, *Polym. Bull.* **2001**, *46*, 7–13; e) U. Mais, S. Knaus, W. H. Binder, H. Gruber, *Lenzinger Ber.* **2000**, *79*, 71–76; f) S. Knaus, U. Mais, W. H. Binder, *Cellulose* **2003**, *10*, 139–150.

[100] G. Siegmund, Dissertation, Universität Jena, **2002**.

[101] E. Sipahi-Saglam, M. Gelbrich, E. Gruber, *Cellulose* **2003**, *10*, 237–250.

[102] a) T. Kowalik, H.-J. Adler, A. Plagge, M. Stratmann, *Macromol. Chem. Phys.* **2000**, *201*, 2064–2069; b) E. Jaehne, T. Kowalik, H.-J. Adler, A. Plagge, M. Stratmann, *Macromol. Symp.* **2002**, *177*, 97–109.

[103] G. Wegner, *Macromol Chem. Phys.* **2003**, *204*, 347–357.

[104] a) M. Schaub, G. Wenz, G. Wegner, A. Stein, D. Klemm, *Adv. Mater.* **1993**, *5*, 919–922; b) V. Buchholz, G. Wegner, S. Strainme, L. Ödberg, *Adv. Mater.* **1996**, *8*, 399–402.

[105] V. Buchholz, P. Adler, M. Bäcker, W. Hölle, A. Simon, G. Wegner, *Langmuir* **1997**, *13*, 3206–3209.

[106] a) F. Loescher, S. Seeger, DE 19736736, **1999**, [*Chem. Abstr.* **1999**, *130*, 198049]; b) F. Loescher, T. Ruckstuhl, T. Jaworek, G. Wegner, S. Seeger, *Langmuir* **1998**, *14*, 2786–2789.

[107] a) S. Diekmann, G. Siegmund, A. Roecker, D. Klemm, *Cellulose* **2003**, *10*, 53–63; b) P. Steinrücke, U. Aldinger, O. Hill, A, Hillisch, R. Basch, S. Diekmann, *Anal. Biochem.* **2000**, *286*, 26–34.

[108] D. F. S. Petri, S. W. Choi, H. Beyer, T. Schimmel, M. Bruns, G. Wenz, *Polymer* **1999**, *40*, 1593–1601.

[109] T. Brock, M. Groteklaes, P. Mischke, *Europ. Coat. J.* **2002**, *5*, 70–72.

[110] a) K. J. Edgar, C. M. Buchanan, J. S. Debenham, P. A. Rundquist, B. D. Seiler, M. C. Shelton, D. Tindall, *Prog. Polym. Sci.* **2001**, *26*, 1605–1688; b) R. Toung, *Text. Sci. Technol.* **2003**, *13*, 233–281.

[111] a) H.-G. Poersch-Parcke, R. Kirchner, *Solutions*, *2nd ed* (Ed.: Wolff Cellulosics GmbH), **2003** (www.wolff-cellulosics.de); b) R. Doenges, *Papier* **1997**, *51*, 653–660; c) L. Brandt in *Industrial Polymers Handbook*, *Vol. 3* (Ed.: E. S. Wilks), Wiley-VCH, Weinheim, **2001**, pp. 1569–1613.

[112] D. Klemm, B. Philipp, T. Heinze, U. Heinze, W. Wagenknecht, *Comprehensive Cellulose Chemistry*, *1st ed.*, *Vol. 1*, Wiley-VCH, Weinheim, **1998**, pp. 17–27.

[113] K. Götze, *Chemiefasern nach dem Viskoseverfahren*, *3rd ed.*, *Vol. 1*, Springer, Heidelberg, **1967**, pp. 1–778.

[114] J. Gensrich, H. Schleicher in *Cellulosic Man-made Fibres*, *Proceedings of the Singapore Viscose Chemistry's Seminar*, Akzo-Nobel, April 22–24, **1997**.

[115] C. Reisinger in *Cellulosic Man-made Fibres*, *Proceedings of the Singapore Viscose Chemistry's Seminar*, Akzo-Nobel, April 22–24, **1997**.

[116] M. Voges, M. Brück, H.-P. Fink, J. Gensrich in *Proceedings of the Akzo-Nobel Cellulosic Man-made Fibre Seminar*, Stenungsund, **2000**.

[117] K. Nishiyama in *Cellulosic Man-made Fibres*, *Proceedings of the Singapore Viscose Chemistry's Seminar*, Akzo-Nobel, April 22–24, **1997**.

[118] a) M. Vehviläinen, P. Nousiainen in *Cellulosic Man-made Fibres*, *Proceedings of the Singapore Viscose Chemistry's Seminar*, Akzo-Nobel, April 22–24, **1997**; b) C. Yamane, M. Mori, M. Saito, K. Okajima, *Polym. J.* **1996**, *28*, 1039–1047.

[119] H. Boerstoel, H. Maatman, J. B. Westerink, B. M. Koenders, *Polymer* **2001**, 7371–7379.

[120] H. Firgo, M. Eibl, D. Eichinger, *Lenzinger Ber.* **1995**, *75*, 47–50.

[121] K. Ekman, V. Eklund, J. Fors, J. I. Huttunen, J.-F. Selin, O. T. Turunen in *Cellulose Structure, Modification and Hydrolysis* (Eds.: R. A. Young, R. M. Rowell), Wiley, New York, **1986**, pp. 131–148.

[122] H.-P. Fink, J. Gensrich, R. Rihm, M. Voges, M. Brück in *Proceedings of the 6th Asian Textile Conference*, Hong Kong, August 22–24, **2001**, 1–7.

[123] F. A. Buijtenhuijs, M. Abbas, A. J. Witteveen, *Papier* **1986**, *40*, 615–619.

[124] a) U. Wachsmann, M. Diamantoglou, *Papier* **1997**, *51*, 660–665; b) H. Harms, *Materialwiss. Werkstofftech.* **2003**, *34*, 267–271.

[125] H. Chanzy, M. Dubé, R. H. Marchessault, *J. Polym. Sci. Lett. Ed.* **1979**, *17*, 219–226.

[126] M. Dubé, R. H. Blackwell in *Proceedings of the International Dissolving and Speciality Pulps Conference*, Boston, Tappi Press, **1983**, S. 111–119.

[127] a) P. Weigel, H.-P. Fink, *Lenzinger Ber.* **1997**, *76*, 115–118; b) H.-P. Fink, P. Weigel, A. Bohn, *Lenzinger Ber.* **1997**, *76*, 119–125.

[128] W. Y. Luo, *Proceedings of the 11th Annual International TANDEC Nonwovens Conference*, P4.2, Knoxville, **2001**.

[129] S. Peng, H. Shao, X. Hu, *J. Appl. Polym. Sci.* **2003**, *90*, 1941–1947.

[130] F. Meister, D. Vorbach, F. Niemz, T. Schulze, E. Taeger, *Materialwiss. Werkstofftech.* **2003**, *34*, 262–266.

[131] a) T. Rosenau, A. Potthast, H. Sixta, P. Kosma, *Prog. Polym. Sci.* **2001**, *26*, 1763–1837; b) T. Rosenau, A. Potthast, I. Adorjan, A. Hofinger, H. Sixta, H. Firgo, P. Kosma, *Cellulose* **2002**, *9*, 283–291; c) T. Rosenau, A. Potthast, A. Hofinger, H. Sixta, P. Kosma, *Holzforschung* **2002**, *56*, 199–208; d) A. Potthast, T. Rosenau, P. Kosma, *Lenzinger Ber.* **2000**, *79*, 92–96; e) I. Adorjan, J. Sjoberg, T. Rosenau, A. Hofinger, P. Kosma, *Carbohydr. Res.* **2004**, *339*, 1899–1906; f) T. Rosenau, A. Hofinger, A. Potthast, P. Kosma, *Polymer* **2003**, *44*, 6153–6158.

[132] a) W. Ruland, *Acta Crystallogr.* **1961**, *14*, 1180–1185; b) C. G. Vonk, *J. Appl. Crystallogr.* **1973**, *6*, 148–152; c) H.-P. Fink, E. Walenta, *Papier* **1994**, *48*, 739–748.

[133] H.-P. Fink, P. Weigel, H.-J. Purz, *Lenzinger Ber.* **1998**, *78*, 41 – 44.

[134] a) E. J. Vandamme, S. De Baets, A. Vanbaelen, K. Joris, P. De Wulf, *Polym. Degrad. Stab.* **1998**, *59*, 93 – 99; b) R. Jonas, L. F. Farah, *Polym. Degrad. Stab.* **1998**, *59*, 101 – 106; c) R. E. Cannon, S. M. Anderson, *Crit. Rev. Microbiol.* **1991**, *17*, 435 – 447.

[135] A. J. Brown, *J. Chem. Soc.* **1886**, *49*, 432 – 439.

[136] a) P. De Wulf, K. Jores, E. Vandamme, *J. Chem. Technol. Biotechnol.* **1996**, *67*, 376 – 380; b) R. M. Brown, Jr., K. Kudlicka, S. Cousins, R. Nagy, *Am. J. Bot.* **1992**, *79*, 1247 – 1258; c) S. Yamanaka, K. Watanabe in *Cellulosic Polymers — Blends and Composites* (Ed.: R. D. Gilbert), Hanser, München **1994**, pp. 207 – 215; d) R. Jonas, L. F. Farah, *Polym. Degrad. Stab.* **1998**, *59*, 101 – 106; e) C. Tokoh, K. Takabe, M. Fujita, H. Saiki, *Cellulose* **1998**, *5*, 249 – 261.

[137] a) N. S. P. Hau, J. F. Robyt, *Carbohydr. Res.* **1998**, *313*, 125 – 133; b) N. Carpita, C. Vergara, *Science* **1998**, *279*, 672 – 673; c) S. Salmon, S. M. Hudson, *J. Macromol. Sci. Rev. Macromol. Chem. Phys.* **1997**, *37*, 99 – 276.

[138] H.-P. Fink, H. J. Purz, A. Bohn, J. Kunze, *Macromol. Symp.* **1997**, *120*, 207 – 217.

[139] O. M. Astley, A. Chanliaud, A. M. Donald, M. J. Gidley, *Int. J. Biol. Macromol.* **2001**, *29*, 193 – 202.

[140] a) U. Udhardt, Dissertation, Universität Jena, **2004**; b) D. Klemm, D. Schumann, U. Udhardt, S. Marsch, *Prog. Polym. Sci.* **2001**, *26*, 1561 – 1603; c) S. Marsch, Dissertation, Universität Jena, **2004**; d) M. Seifert, S. Hesse, V. Kabrelian, D. Klemm, *J. Polym. Sci. Part A: Polym. Chem.* **2004**, *42*, 463 – 470; e) S. Hesse, Dissertation, Universität Jena, **2005**.

[141] a) T. Erata, T. Shikano, M. Fujiwara, M. Takai in *Proceedings of the 11th International Cellucon Conf*erence, Tsukuba, **1999**, 261 – 268 [*Chem. Abstr.* **2003**, *139*, 86827]; b) M. Fujiwara, Y. Osada, S. Yunoki, H. Hono, T. Erata, M. Takai in *Recent Advances in Environmentally Compatible Polyenes* (Ed.: J. F. Kennedy), Woodhead, Cambridge, **2001**, pp. 359 – 364.

[142] "Applications of Bacterial Cellulose": S. Yamanaka, K. Watanabe in *Cellulosic Polymers — Blends and Composites* (Ed.: R. Gilbert), Hanser Gardner, München, **1994**, pp. 207 – 215.

[143] a) J. K. Park, Y. H. Park, J. Y. Jung, *Biotechnol. Bioprocess Eng.* **2003**, *8*, 83 – 88; b) S. Moonmangmee, H. Toyama, O. Adachi, G. Theeragool, N. Lotonge, K. Matsushita, *Biosci. Biotechnol. Biochem.* **2002**, *66*, 777 – 783; c) T. Nakai, N. Tonouchi, T. Konishi, Y. Kojima, T. Tsuchida, F. Yoshinaga, F. Sakai, T. Hayashi, *Proc. Natl. Acad. Sci. USA* **1999**, *96*, 14 – 18; d) Y. K. Yang, S. H. Park, J. W. Hwang, Y. R. Pyun, Y. S. Kim, *J. Ferment. Bioeng.* **1998**, *85*, 312 – 317.

[144] D. Klemm, S. Marsch, D. Schumann, U. Udhardt (SurA Chemicals GmbH), Pat.-Nr. W 2001/61026 A 1/2001 [*Chem. Abstr.* **2001**, 618187].

[145] K. Frankenfeld, M. Hornung, B. Lindner, M. Ludwig, A. Muelversted, H.-P. Schmauder (Forschungszentrum für Medizintechn. und Biotechnologie e.V.), DE 10022751, **2000** [*Chem. Abstr.* **2001**, *134*, 152442].

[146] a) M. Hornung, M. Ludwig, H.-P. Schmauder, *Chem. Ing. Tech.* **2002**, *74*, 667; b) S. Mutafov, B. Angelova, H.-P. Schmauder, T. Avramowa, L. Boyadijeva, *Biotechnol. Bioeng.* **2003**, *84*, 160 – 169.

[147] T. Nishimura, T. Takano, F. Nakatsubo, K. Murahami, *Mokuzai Gakkaishi* **1993**, *39*, 40 – 47.

[148] a) F. Nakatsubo in *Wood Cellulose Chemistry, 2nd ed.* (Eds.: D. N.-S. Hon, N. Shiraishi), Marcel Dekker, New York, **2001**, pp. 627 – 654; b) M. Hori, F. Nakatsubo, *Macromolecules* **2001**, *34*, 2476 – 2481.

Communications

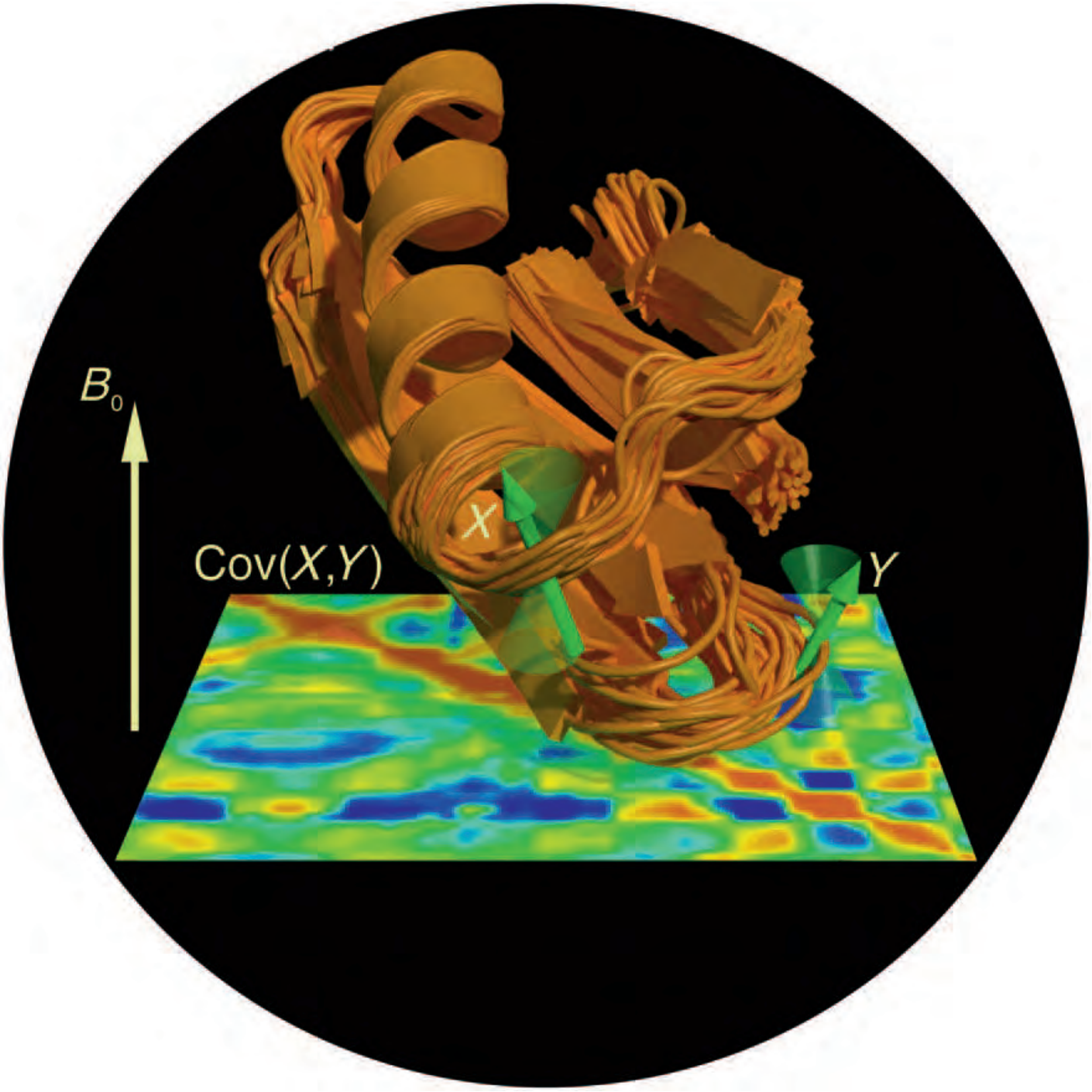

Correlated motions can be accurately extracted from molecular dynamics (MD) simulations that are compatible with the measured NMR spectroscopic data (NOE and order parameters) for two different proteins (Cov: covariance matrix). B. de Groot and co-workers discuss the results of MD simulations on a fragment of protein G in their Communication on the following pages.

  DOI: 10.1002/anie.200462957

Molecular Dynamics Simulations

Molecular Dynamics Simulations of Protein G Challenge NMR-Derived Correlated Backbone Motions**

*Oliver F. Lange, Helmut Grubmüller, and Bert L. de Groot**

Protein function is fundamentally linked to underlying structural and molecular dynamics.[1] Many biological functions such as enzymatic activity and ligand binding are controlled or even realized through conformational motions,[2] which are typically collective in nature, as is the case with allosteric effects and domain motions.[3] Conformational motions determine energetics, kinetics, and the strength of thermodynamic driving forces through conformational entropy.[4–6]

NMR relaxation studies provide a powerful and established method to gain experimental access to fast protein dynamics in atomic detail.[7–9] Model-free analysis of NMR relaxation times, in particular, yields generalized order parameters for individual bond vectors[10] which allows the extraction of information about flexibility and timescales of the motions of individual backbone sites[11] and side chains.[12] Until recently, however, NMR relaxation experiments could only probe the flexibility of individual bond vectors, whereas correlated motions could not be probed. A recently proposed method by Mayer et al.[13] promises to overcome this limitation by measuring the covariation of backbone motion by NMR relaxation studies. Specifically, the authors "propose a general approach to the detection of correlated changes in internal protein motions, which are expected to reflect the underlying influence of correlated dynamics".[13] In this approach, NMR relaxation data for a small domain of protein G were obtained for 10 mutants at the same sequence position. The resulting perturbations were reported to cause changes in the measured order parameters, which were recorded for each individual residue. For many residue pairs, these changes are significantly correlated (Figure 1a), which led the authors to suggest that the observed covariances reflect underlying correlated atomic motions.[13] Whether and how the measured covariations actually reflect correlated atomic motion cannot be resolved by experiment alone, which prevents the direct atomistic interpretation of these types of measurements. To address this issue, we present sub-microsecond molecular dynamics (MD) simulations which, together with the NMR experimental data, provide a comprehensive picture of the correlated atomic dynamics of the protein G domain.

We carried out two MD simulations of the B1 domain of protein G, with lengths of 100 and 200 ns, referred to as MD1 and MD2, respectively. Correlations of atomic motions were quantified by correlation matrices calculated from the MD simulations. Figure 1c shows correlation matrices obtained from MD1 (above the diagonal) and MD2 (below the diagonal). The similarity of the two matrices shows that the computed correlations are largely well-converged. Full convergence is not reached for residues 37–42, which constitute the loop that connects the α helix with the β3 strand. Closer inspection revealed long timescale contributions to the loop dynamics. However, the relevant sub-microsecond timescale probed by NMR relaxation experiments[14] is well-sampled in our simulations.

The matrix is dominated by strong correlations between neighboring residues, and appears as a band along the diagonal. The broad region of high correlation between residues 22 and 38 is caused by the 1–4 contacts of the central α helix. The two bands of high correlation perpendicular to the diagonal result from the contacts between different strands of the four-stranded β sheet. Strong correlations and anticorrelations are also found between residues 10–15 of the first hairpin loop and the rest of the molecule. They are caused by a kinking-out motion of the turn between strands β1 and β2 together with part of the β sheet. This motion, hinged around residues 8 and 15, is the main contribution to the principal collective motion (Figure 2), as revealed by principal component analysis.[15,16]

To test for a direct connection between the covariation of NMR order parameters and the computed correlated atomic motion observed in the simulation, we compared the computed correlation matrices (Figure 1c) with the S^2- and the τ_e-based covariation matrices derived by Mayer et al.[13] (Figure 1a). Overall, the level of correspondence is low. The only feature shared with the MD simulations is the band of anticorrelated motion between residues 10–14, which is present in the experimental results derived from covariations in τ_e order parameters, but which is not observed in the S^2-derived correlations. Apart from this detail, the overall lack of similarity is striking. The nature of this discrepancy deserves closer inspection.

An important question is whether the MD simulations describe atomic motions with sufficient accuracy. Potential artifacts include force-field inaccuracies and convergence problems. Therefore, we compared the root mean squared fluctuations (RMSF) of the two MD trajectories (MD1 and MD2) with the RMSF of a structural ensemble of the B1 domain of protein G obtained from NMR spectroscopic NOE data[17] (PDB entry 3gb1, Experimental Section). The RMSF profiles obtained form the MD simulation agree well with the NOE ensemble (Figure 3). Moreover, the correlation matrices obtained from the simulations (Figure 1c) are in good agreement with that obtained from the NOE ensemble (Figure 1b). These agreements between the simulation- and NOE-derived results are quantified by correlation coefficients of 0.77 and 0.81 for MD1 and MD2, respectively. In

[*] O. F. Lange, Priv.-Doz. Dr. H. Grubmüller, Dr. B. L. de Groot
Theoretical and Computational Biophysics Department
Max Planck Institute for Biophysical Chemistry
Am Fassberg 11, 37077 Göttingen (Germany)
Fax: (+49) 551-2012302
E-mail: degroot@gwdg.de

[**] We thank Christian Griesinger, Sander Nabuurs, and Martin Stone for carefully reading the manuscript.

Supporting information for this article is available on the WWW under http://www.angewandte.org or from the author.

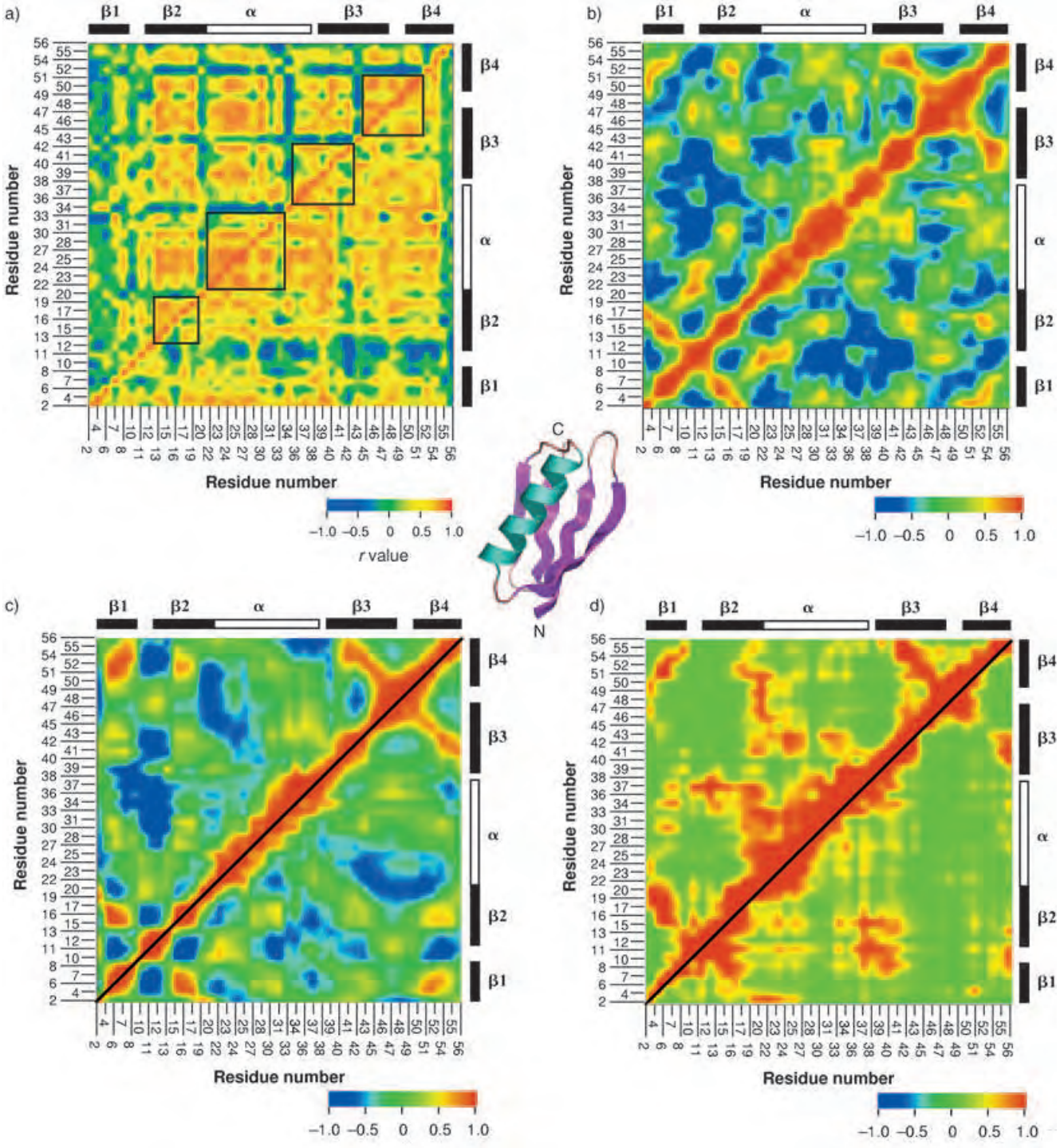

Figure 1. Correlation matrices from NMR experiments and MD calculations. a) Correlation matrices taken with permission from Mayer et al.;[13] data for S^2 covariations are shown above the diagonal, whereas those for τ_e covariations are shown below the diagonal (the black boxes are irrelevant for the present discussion). b) Correlation matrix computed from an NMR–NOE structural ensemble. c) Correlation matrices computed from MD simulations. The correlations computed from MD1 are shown above the diagonal; correlations derived from MD2 are below the diagonal. d) Generalized correlations computed from MD2 (above the diagonal); correlations computed for N–H vector motions (below the diagonal). The simulated B1 domain of protein G is depicted in the center.

contrast, the correlation coefficients between all of these matrices and the covariance matrix computed from order parameters (Figure 1a) are much smaller: 0.06 and 0.04 for the two MD matrices, and 0.05 for the NOE matrices. The good agreement between MD and the NOE ensemble in terms of the atomic fluctuations and particularly their correlations makes it unlikely that the discrepancy with the covariance matrix obtained from order parameters is caused

Figure 2. Main collective motion of the B1 domain of protein G as revealed by the principal component analysis described in the text.

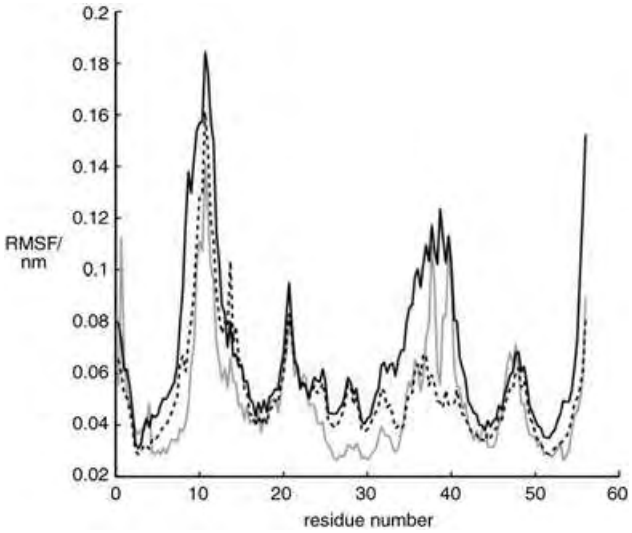

Figure 3. RMSF of backbone atoms observed in the NMR ensemble (gray line), and RMSF computed from the two different MD trajectories (MD1, ——; MD2, -----): the positions of the major RMSF peaks agree well with the experimental data. The fluctuations of the largest motion (residues 8–15) and of the α helix are slightly overestimated by the MD simulations but overall, the flexibility of the remaining regions of the molecule is well-reproduced.

by simulation artifacts. That this agreement is not just anecdotal is indicated by a correlation coefficient of 0.82 for the NOE and MD covariance matrix obtained for a different protein, ubiquitin (Supporting Information), and by a correlation coefficient of 0.8 obtained with a different NMR data set for protein G (PDB entry 1gb1).

Because order parameters form the basis for the covariances determined by Mayer et al., it is necessary to check if the motions probed by order parameters are accurately described by the MD simulations as well. To this end, we compared the experimentally obtained order parameters[18] for protein G with those computed from the MD trajectories (Figure 4a). Within the error bars, the simulations agree with each other as well as with the measured order parameters. The inset of Figure 4 shows that most differences between the observed and computed order parameters are below 0.1 with

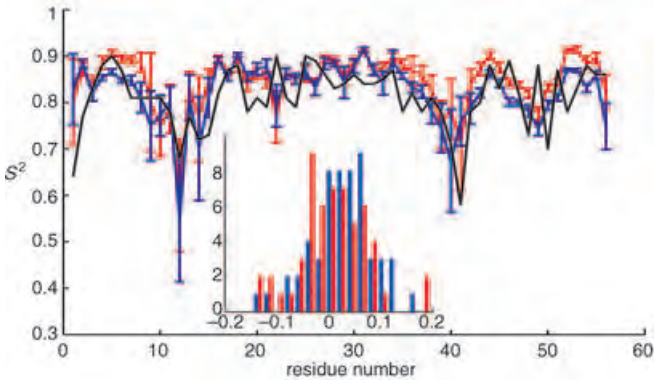

Figure 4. Comparison of the generalized order parameters (S^2) between the MD simulations and the NMR data set.[18] Computed order parameters (in color) with error bars are compared with experimentally observed order parameters (black). Inset: histogram of the order parameter differences between the MD data sets and the experimental results.

few outliers below 0.2. Overall, the agreement is good and is in line with earlier observations.[19–22]

We therefore conclude that the simulations provide a comprehensive and accurate picture of the correlated atomic motion within the protein G domain that is consistent with the available experimental data. The remaining unexplained discrepancy with the covariances derived from NMR experimental order parameters suggests that these two quantities are, in fact, not directly related. Comparison of all elements of the MD correlation matrix with the respective covariations of NMR order parameters as a scatter plot (Figure 5a) confirms this finding. Furthermore, the absence of any detectable structure in this plot suggests the absence of any relation to this measure of linearly correlated atomic motion.

At this point, it is important to note that the correlation coefficients as used in the matrices shown in Figures 1b and 1c, although widely used, detect only part of all possible correlated atomic motions. For instance, two atoms oscillating with a $\pi/2$ phase shift will give rise to a vanishing correlation matrix element $\langle \sin(\omega t)\sin(\omega t+\pi/2)\rangle = 0$, and thus, this highly correlated motion would not be detected. This simple example shows that the results discussed so far do not rule out the possibility that the measured covariations of NMR order parameters relate to such "hidden" correlated motions. To detect those as well, we employed a second, more general correlation measure derived from information theory.

To this end, we consider the information S_i contained within the motion of each individual atom i as well as the joint information $S_{i,j}$ contained within the (possibly correlated) motion of each pair of atoms i and j. As any type of correlation, hidden or not, will decrease $S_{i,j}$ with respect to $S_i + S_j$, the excess $C_{i,j} = S_i + S_j - S_{i,j}$ serves as a generalized and very sensitive measure to detect all correlations within atomic motions. We note that an equivalent formulation of the same method would rest on the fact that only for statistically independent data sets X and Y, their joint probability is given by $P(X,Y) = P(X)\,P(Y)$. For the calculation of the information contents from MD trajectories, see the Supporting Information and Ref. [34].

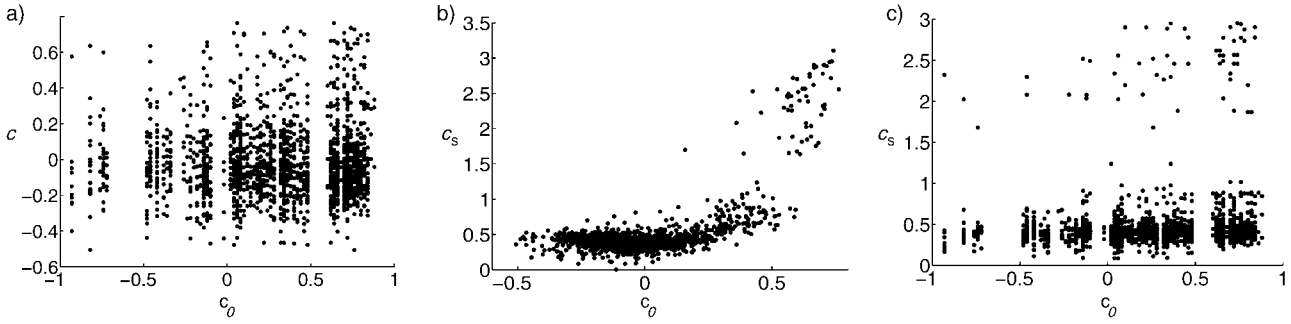

Figure 5. Scatter plots of covariation and correlation matrix elements in which two of the correlation matrices shown in Figure 1 are compared; each point represents the two different correlations obtained with the respective methods for the same residue pair. a) Correlations obtained from MD simulation *c*, as depicted in Figure 1 c, are plotted against the covariations of order parameters c_0, shown in Figure 1 a. b) Generalized correlations c_S (Figure 1 d) obtained from the MD simulation are plotted against c_0 (Figure 1 c), the correlations obtained from MD simulation in the established way. c) Generalized correlations c_S (Figure 1 d) computed from simulation MD2 plotted against measured covariations of order parameters c_0 (Figure 1 a).

Figure 1 d (above the diagonal) shows the obtained generalized correlation matrix. Although the overall structure appears similar, minor but significant differences to the linear Pearson correlation matrix (Figure 1 c) are observed, which result from the "hidden" correlations now detected by the information theoretical approach. Quantitative comparison of the Pearson matrix elements with the generalized elements (Figure 5 b) confirms that the two measures are related (with a correlation coefficient of 0.65). In contrast, no such relation is observed to the covariances derived from the NMR order parameters (Figure 5 c; correlation coefficient 0.07), which suggests that no significant information on correlated atomic motion in Cartesian space is contained within these NMR spectroscopic data.

It might be argued that a more direct comparison between MD and NMR data would rest on an analysis of the correlation in the orientational fluctuations of N–H bond vectors, which are probed by the NMR order parameters, rather than on the Cartesian coordinates. However, these fluctuations are already included within the generalized correlation measure described above and hence, similar results are expected. Figure 1 d (below the diagonal) shows that this is indeed the case as quantified by the low correlation coefficient of 0.05 between N–H vector fluctuations in MD and the covariances derived from the NMR order parameters.

In summary, we have demonstrated that for two different proteins, correlated motions can be accurately extracted from MD simulations that are compatible with the measured NMR data (NOE and order parameters). However, the correlated atomic motions described by our sub-microsecond MD simulations of the B1 domain of protein G are unrelated to covariations derived from order parameters, even though different measures of correlated motion have been applied. The obtained agreement with independent NMR spectroscopic NOE data and with N–H order parameters provides strong evidence that the simulations accurately describe the atomic motions and their correlations at the experimentally relevant timescale. This is further supported by the good qualitative agreement with the results of recently published residual dipolar coupling experiments.[23] Taken together, the results render it unlikely that the observed covariances in measured order parameters reflect the underlying influence of the correlated atomic dynamics for the wild-type protein. Instead, we speculate that the measured covariances are caused by correlated structural changes that result from the introduced point mutations, which in turn, affect the atomic mobilities. In this framework, the experiments would probe remarkably correlated structural plasticities rather than correlated atomic motions. Further simulations of all 10 mutants studied will therefore be required to test this hypothesis and to structurally characterize the properties of this proposed nonlocal plasticity.

Experimental Section

MD simulations were started from the crystal structure of the B1 domain of streptococcal protein G[24] (PDB entry 1PGB). Simulations were carried out with the OPLS all-atom force field.[25] The protein was solvated in 4651 TIP4P water molecules. Four sodium ions were added to the simulation system to compensate for the net negative charge of the protein. The total system size comprised 19463 atoms. The simulation was carried out in a cubic box with a minimal distance between solute and box edge of 0.8 nm. Periodic boundary conditions were used. All MD simulations were carried out with the Gromacs simulation suite.[26] LINCS and Settle[27,28] were applied to constrain covalent bond lengths, allowing an integration step of 2 fs. Electrostatic interactions were calculated with the particle-mesh Ewald method.[29] The temperature was kept constant by separately coupling ($\tau = 0.1$ ps) the peptide and solvent to an external temperature bath.[30] The pressure was kept constant by weak isotropic coupling ($\tau = 1.0$ ps) to a pressure bath.[30] Simulations were run for 100 ns (MD1) and 200 ns (MD2).

An NMR–NOE structure ensemble of 30 structures was generated with the standard simulated annealing protocol in CNS,[31] applying the NOE distance bounds as available from the PDB entry 3GB1.[32] In short, individual structures were generated by slow cooling from high-temperature simulations starting from an extended structure and different sets of starting velocities. Each annealing cycle consisted of 15 ps of torsion-angle MD at high temperature (50000 K) followed by an annealing phase (15 ps) to zero temperature with torsion-angle MD and an annealing phase (15 ps) with Cartesian dynamics from 2000 to 0 K. Finally, each structure was energy-minimized by 10 cycles of 200 steepest-decent steps. Default parameters for the scaling of the individual energy terms were used, including the NOE energy term.

To analyze the data in the molecular coordinate frame, all structures were fitted to the backbone of the crystal structure. RMSF for each ensemble were calculated as $RMSF_i = \sqrt{\langle r_i^2 \rangle}$, in which r_i is the distance of the i^{th} C^α atom from its average position, and the $\langle\,\rangle$ denote the average over the whole trajectory with snapshots recorded every picosecond. The correlation matrices were computed as $C_{i,j} = \langle \mathbf{x}_i \cdot \mathbf{x}_j \rangle / (\langle \mathbf{x}_i^2 \rangle \langle \mathbf{x}_j^2 \rangle)^{1/2}$, in which $\mathbf{x}_i$ and $\mathbf{x}_j$ are difference vectors between the i^{th} and j^{th} C^α atom, respectively, and their average positions in the molecule-fixed frame. To enhance visibility of small differences, the correlations were weighted by the sigmoidal function $W(x) = 2/[1 + \exp(-\lambda x)] - 1$, with $\lambda = 5.5$ before plotting. The enhancement coefficient λ was set as strong as possible under the constraint that only statistically significant fluctuations become apparent.

Order parameters S^2 were defined as the asymptotic value of internal correlation functions.[10] The internal correlation function $C_{int}(t)$ of the N–H bond vector motion is given by $C_{int}(t) = \langle P_2(\cos\chi(t)) \rangle$, where $\chi(t)$ is the angle between the internuclear vectors $r(t)$ and $r(0)$, and r is measured in the molecule-fixed frame. $P_2(x) = (3x^2 - 1)/2$ denotes the second Legendre polynomial. Fluctuations in the internuclear separation were not included, because the length of all covalent bonds were fixed by LINCS[27] throughout the simulation. It has been shown previously that the effect of such constraints on order parameters calculated from simulations is negligible.[33]

To estimate statistical errors in the obtained order parameters, the MD trajectories were divided into N fragments of length 1 ns each. For each fragment s, internal correlation functions $C_{int}^{s,i}(t)$ were computed for each bond vector i with snapshots taken every picosecond. Parameters $\chi_{s,i}$ were computed as the average from 480 to 500 ps of the internal correlation function $C_{int}^{s,i}(t)$. The order parameter of bond vector k was computed as the mean of $\chi_{s,i}$ over all the fragments, that is $S_i^2 = (\sum_s^N \chi_s^i)/N$, with the error bars given by:

$$\Delta S_i^2 = \frac{1}{\sqrt{N(N-1)}} \left[\sum_s^N \chi_{s,i}^2 - \left(\sum_t^N \chi_{t,i} \right)^2 \right]^{1/2} \quad (1)$$

The results do not change significantly if the fragmentation length is changed from 1 ns to longer time intervals (data not shown).

To obtain the generalized correlation measure $C_{i,j} = S_i + S_j - S_{i,j}$ between the C^α atoms i and j, we computed for all atom pairs (i,j) the information S_i of the motion of atom i in its $d = 3$ dimensional configurational space as well as the information $S_{i,j}$ of the combined motion of atoms i and j in their $d = 6$ dimensional configurational space. Herein, only a sketch of the approach is given; for details, see the Supporting Information and Ref. [34].

Our approach is based on a combination of kernel density estimation and nearest-neighbor estimation. For every snapshot k of the trajectory, an effective neighbor distance σ_s is determined by requiring $T = \sum_t^N e^{(\mathbf{x}_t - \mathbf{x}_s)^2/(2\sigma_s^2)}$ for a given and fixed $T = 20$. In this case, N denotes the number of snapshots, and values of $\mathbf{x}$ represent vectors in the d dimensional configurational space considered. This isotropic averaging over local snapshots typically suffers from highly anisotropic configurational space densities, that is, drastically differing widths of the configurational snapshot ensemble in different directions. Particularly problematic and inaccurate were those directions for which the widths are smaller than σ_s. We therefore treated those l_s narrow directions separately by a Gaussian-derived estimate $S_G = 1/2 \sum_{h=1}^{l_s} \log \lambda_h^s$, which is particularly suitable for those small-amplitude degrees of freedom of width $\lambda_{h=1\ldots l_s}^s$, respectively. Taken together, the information was computed by:

$$S = \frac{\log N}{N} - \frac{1}{N} \sum_{s=1}^{N} (\log \alpha(d - l_s) - (d - l_s) \log \sigma_s - S_G) \quad (2)$$

in which $\alpha(d_s)$ denotes a proportionality factor dependent on the local dimension $d_s = d - l_s$, which relates the nearest-neighbor statistics σ_s to the information measure S. We used 10000 snapshots taken every 20 ps from trajectory MD2 for this analysis.

The correlations in the motion of N–H bond vectors were computed by applying the generalized correlation measure to pairs of the normalized internuclear vectors rather than to pairs of atomic positions.

Received: December 16, 2004
Revised: January 28, 2005

Keywords: conformation analysis · correlated motions · molecular dynamics · NMR spectroscopy · proteins

[1] A. J. Wand, *Nat. Struct. Biol.* **2001**, *8*, 926.
[2] S. J. Benkovic, S. Hammes-Schiffer, *Science* **2003**, *301*, 1196.
[3] P. K. Agarwal, S. R. Billeter, P. T. R. Rajagopalan, S. J. Benkovic, S. Hammes-Schiffer, *Proc. Natl. Acad. Sci. USA* **2002**, *99*, 2794.
[4] J. N. Onuchic, Z. Luthey-Schulten, P. G. Wolynes, *Annu. Rev. Phys. Chem.* **1997**, *48*, 545.
[5] J. D. Forman-Kay, *Nat. Struct. Biol.* **1999**, *6*, 1086.
[6] A. L. Lee, A. J. Wand, *Nature* **2001**, *411*, 501.
[7] R. Ishima, D. A. Torchia, *Nat. Struct. Biol.* **2000**, *7*, 740.
[8] A. G. Palmer, *Annu. Rev. Biophys. Biomol. Struct.* **2001**, *30*, 129.
[9] V. A. Daragan, K. H. Mayo, *Prog. Nucl. Magn. Reson. Spectrosc.* **1997**, *31*, 63.
[10] G. Lipari, A. Szabo, *J. Am. Chem. Soc.* **1982**, *104*, 4546.
[11] L. E. Kay, D. A. Torchia, A. Bax, *Biochemistry* **1989**, *28*, 8972.
[12] A. G. Palmer, M. Rance, P. E. Wright, *J. Am. Chem. Soc.* **1991**, *113*, 4371.
[13] K. L. Mayer, M. R. Earley, S. Gupta, K. Pichumani, L. Regan, M. J. Stone, *Nat. Struct. Biol.* **2003**, *10*, 962.
[14] A. G. Palmer, Chem. Rev. **2004**, *104*, 3623.
[15] A. E. Garcia, *Phys. Rev. Lett.* **1992**, *68*, 2696.
[16] A. Amadei, A. B. M. Linssen, H. J. C. Berendsen, *Proteins Struct. Funct. Genet.* **1993**, *17*, 412.
[17] A. M. Gronenborn, D. R. Filipula, N. Z. Essig, A. Achari, M. Whitlow, P. T. Wingfield, G. M. Clore, *Science* **1991**, *253*, 657.
[18] D. Idiyatullin, V. A. Daragan, K. H. Mayo, *J. Phys. Chem. B* **2003**, *107*, 2602.
[19] M. Philippopoulos, C. Lim, *J. Mol. Biol.* **1995**, 254, 771.
[20] D. C. Chatfield, A. Szabo, B. R. Brooks, *J. Am. Chem. Soc.* **1998**, *120*, 5301.
[21] M. Philippopoulos, A. M. Mandel, A. G. Palmer, C. Lim, *Proteins Struct. Funct. Genet.* **1997**, *28*, 481.
[22] D. A. Case, *Acc. Chem. Res.* **2002**, *35*, 325.
[23] G. M. Clore, C. D. Schwieters, *Biochemistry* **2004**, 43, 10678.
[24] T. Gallagher, P. Alexander, P. Bryan, G. L. Gilliland, *Biochemistry* **1994**, *33*, 4721.
[25] W. L. Jorgensen, D. S. Maxwell, J. Tirado-Rives, *J. Am. Chem. Soc.* **1996**, *118*, 11225.
[26] E. Lindahl, B. Hess, D. Van der Spoel, *J. Mol. Model.* **2001**, *7*, 306; internet: http://www.gromacs.org.
[27] B. Hess, H. Bekker, H. J. C. Berendsen, J. G. E. M. Fraaije, *J. Comput. Chem.* **1997**, *18*, 1463.
[28] S. Miyamoto, P. A. Kollman, *J. Comput. Chem.* **1992**, 13, 952.
[29] T. Darden, D. York, L. Pedersen, *J. Chem. Phys.* **1993**, *98*, 10089.
[30] H. J. C. Berendsen, J. P. M. Postma, A. DiNola, J. R. Haak, *J. Chem. Phys.* **1984**, *81*, 3684.
[31] A. T. Brünger, P. D. Adams, G. M. Clore, W. L. DeLano, P. Gros, R. W. Grosse-Kunstleve, J. S. Jiang, J. Kuszewski, N. Nilges, N. S. Pannu, R. J. Read, L. M. Rice, T. Simonson, G. L. Warren, *Acta Crystallogr. Sect. D* **1998**, *54*, 905.
[32] J. Kuszewski, A. M. Gronenborn, G. M. Clore, *J. Am. Chem. Soc.* **1999**, *121*, 2337.
[33] S. Pfeiffer, D. Fushman, D. Cowburn, *J. Am. Chem. Soc.* **2001**, *123*, 3021.
[34] O. Lange, H. Grubmüller, *unpublished results.*

Coordination Compounds

Tuning a Metal's Oxidation State: The Potential of Clathrochelate Systems**

Yan Z. Voloshin, Oleg A. Varzatskii, Ivan I. Vorontsov, and Mikhail Yu. Antipin*

"Oxidation state" is one of most fundamental concepts in chemistry. The stabilization of previously unknown or unusual oxidation states of metal ions allows us to obtain results that are important both for theoretical inorganic chemistry and for the design of new molecular electronic devices, electrochromic materials, and electron-storage systems.

Complexes with a metal ion encapsulated in a three-dimensional macropolycyclic ligand cavity have undoubted promise in stabilizing unusual oxidation states of such caged ions. This is due to the fact that an encapsulated and coordinatively saturated metal ion is completely isolated from environmental factors (in particular, effects of solvation and additional coordination that exclude occurrence of redox processes by bridge mechanisms). The size of a three-dimensional ligand cavity may be controlled by changing the nature of the capping and chelating fragments of the macropolycyclic framework, and donor atoms (groups) that are optimal for stabilization of a desired electronic configuration of this ion may be chosen.[1]

Varying the substituents on a clathrochelate framework is thought to be a new and unique opportunity to stabilize unusual oxidation states of an encapsulated metal ion: although the apical substituents in the capping fragments of the same type affect the electronic characteristics of ligand donor atoms (and, therefore, the encapsulated metal ion) to a very minor extent,[2] the influence of electron-donating (electron-withdrawing) substituents in chelate (ribbed) fragments with a system of conjugated π-bonds may prove to be crucial.[3] We suppose that the electron-withdrawing substituents in such fragments of a clathrochelate ligand stabilize the lowest oxidation states of an encapsulated metal ion. A new approach to the synthesis of cobalt(I) complexes uses a macrobicyclic hexachloride ligand with six strongly electron-withdrawing substituents in chelating π-conjugated α-dioximate fragments. The template condensation of dichloroglyoxime with the corresponding boron-containing Lewis acid on a Co^{2+} ion matrix leads to formation of the brown *n*-butylborane-capped hexachloride cobalt(II) clathrochelate [Co{$(Cl_2Gm)_3(Bn\text{-}C_4H_9)_2$}] (**1**) in high yield (Gm = glyoxime).

We were unable to oxidize, either chemically or electrochemically, the clathrochelate **1** to the corresponding cobalt(III) complex (the process is irreversible and is accompanied by destruction of the clathrochelate structure), but **1** easily undergoes a chemical reduction in acetonitrile solution with silver in the presence of tetraalkylammonium or tetra(dimethylamido)phosphonium halides to produce the dark-blue complex $\mathbf{1}^-$ in high yield (Scheme 1). Analogous reductions

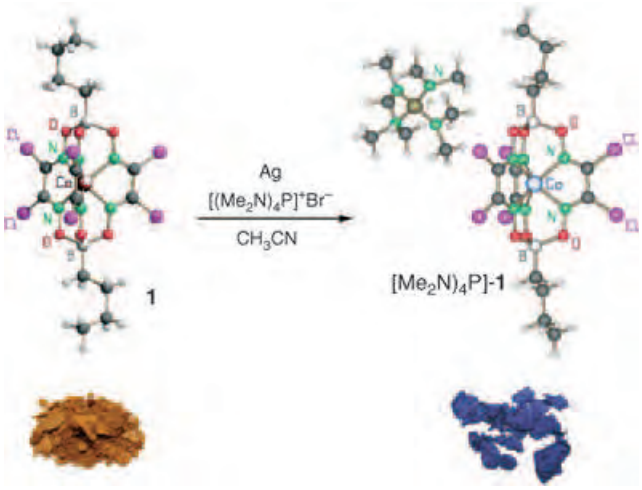

Scheme 1. Reduction of cobalt(II) clathrochelate **1** affords cobalt(I) clathrochelate $[(NMe_2)_4P]$-**1**.

were also carried out for phenylboronic and fluoroboronic hexachloride cobalt(II) clathrochelates. The resulting tetraalkylammonium and tetra(dimethylamido)phosphonium salts of clathrochelate anions with an encapsulated Co^+ ion proved to be air-stable as solid for several months.

The X-ray crystallography data for **1** and $[(NMe_2)_4P]$-**1** indicate that the Co–N distance changes very little on passing from a cobalt(II) clathrochelate **1** to a cobalt(I) clathrochelate anion $\mathbf{1}^-$ (1.984(1) vs. 2.003(3) Å, respectively), as is the case for the previously studied pair $[Co^{II}(bipy)_3]^{2+}/[Co^{I}(bipy)_3]^+$ (2.128 vs. 2.11(2) Å[4]; bipy = 2,2′-bipyridyl) due to an appreciable contribution of Co^I-to-cage charge transfer (πd→π*cage back donation). However, the Co–N distance in the synthesized clathrochelate complexes with a rigid cage framework, as in the case of macrobicyclic iron(II) compounds,[1] is substantially shorter than that in their nonmacrocyclic analogs.[4]

The coordination polyhedra of nonmacrocyclic tris-diiminate complexes and their clathrochelate analogs are also appreciably different: cobalt(II) and cobalt(I) tris-bipyridinates display a trigonal-antiprismatic (TAP) configuration

[*] Prof. Y. Z. Voloshin
Nesmeyanov Institute of Organoelement Compounds
119991 Moscow (Russia)
Fax: (+7) 095-135-5085
E-mail: voloshin@ineos.ac.ru
voloshin@cc.nifhi.ac.ru
and
Karpov Institute of Physical Chemistry
10 Vorontsovo Pole, 105064 Moscow (Russia)
Fax: (+7) 095-975-2450
Dr. O. A. Varzatskii
Vernadskii Institute of General and Inorganic Chemistry
Kiev-142 03680 (Ukraine)
Dr. I. I. Vorontsov, Prof. M. Yu. Antipin
Nesmeyanov Institute of Organoelement Compounds
119991 Moscow (Russia)

[**] The authors gratefully acknowledge support of the Russian Foundation for Basic Research (grant nos. 03-03-32214, 03-03-32531, and 04-03-32206) and the Russian Science Support Foundation.

  DOI: 10.1002/anie.200463070

with distortion angles φ (in passing from TAP ($\varphi = 60°$) to a trigonal prism (TP; $\varphi = 0°$)) of 44.9° and 45.2°, respectively, whereas the geometry of the cage complexes obtained is close to the value for a TP (φ value of 7.8° and 1.3° for cobalt(II) and cobalt(I) cages, respectively). Such a geometry in the case of macrobicyclic systems is due to the large ionic (Shannon) radius of the Co^{2+} ion, which fits the cavity size of the TAP clathrochelate ligand poorly. A change in the ligand geometry from TAP, characteristic of cobalt(III) clathrochelates,[1] to TP leads to an increase in the cavity size, and this facilitates encapsulation of the Co^{2+} ion. A further rotary–translationary extension of the clathrochelate framework permits the encapsulation of a Co^{+} ion with a higher Shannon radius.

It should also be emphasized that the Co^{2+} ion is shifted (by 0.3 Å) from the cavity center towards one of the three chelating fragments (probably due to the structural Jahn–Teller effect for a low-spin d^7 configuration: according to the magnetic susceptibility data for **1**, $\mu_{eff} = 1.55\ \mu_B$ and $S = 1/2$). On the other hand, the clathrochelate of the Co^{+} ion (d^8 configuration) is a high-spin complex ($\mu_{eff} = 2.85\ \mu_B$ and $S = 1$). The X-band EPR spectrum of **1** recorded at 10 K for a powdered sample of an isostructural diamagnetic iron(II) clathrochelate containing the same ligand that was doped with 1% of **1** shows the strong anisotropy of the *g*-factor as well as the hyperfine coupling constant. This spectrum can be described in terms of an $S = 1/2$ spin doublet interacting with a single ^{59}Co nucleus ($I = 7/2$, natural abundance 100%) and is typical of low-spin d^7 systems.[5] The EPR spectral parameters are $g_x = 2.252$, $g_y = 2.070$, and $g_z = 1.984$ and $A_{xx} = 125 \times 10^{-4}$, $A_{yy} = 9 \times 10^{-4}$, and $A_{zz} = 50 \times 10^{-4}\ cm^{-1}$. We failed to observe the EPR spectra of paramagnetic complexes $\mathbf{1}^-$ down to 4 K because of both the long spin–lattice relaxation time and the magnitude and sign of the spin–orbital interaction and their ligand-field symmetry.[6] On the other hand, the absence of EPR signals undoubtedly excludes the formation of organic radicals (i.e., the reduced cage).

XPS was used to directly probe the cobalt ion oxidation states in **1** and $\mathbf{1}^-$. For this ion there is a noticeable (0.9 eV) decrease in the $Co\,2p_{3/2}$ binding energy in $\mathbf{1}^-$ (main peak at 780.8 eV) compared to **1** (main peak at 781.7 eV).

The UV/vis spectra of these clathrochelates in solution are different (Figure 1): the spectrum of the dark-blue solution of $\mathbf{1}^-$ contains two intense bands at $\lambda = 544$ ($\varepsilon = 6.6 \times 10^3\ mol^{-1}\,L\,cm^{-1}$) and 680 nm ($\varepsilon = 8.0 \times 10^3$), whereas the brown color of **1** is determined by two less-intense bands at $\lambda = 421$ ($\varepsilon = 640$) and 468 nm ($\varepsilon = 1550$). The intense bands in the visible spectra of cobalt(I) complexes with azomethine ligands were assigned in earlier studies[7] to charge-transfer bands (first of all to MLCT bands).

The electrochemical behavior of $\mathbf{1}^-$ in dichloromethane solution is characterized by two consecutive oxidations. The first wave, at $E_{1/2} = -440$ mV, is reversible on both glassy carbon and Pt electrodes: the Tomeš criterion value, which was determined from the cyclic voltammogram on a Pt ultramicroelectrode, is equal to 60 mV, and the ratio of peak currents for direct (anodic) and reverse (cathodic) waves on a glassy carbon electrode is close to 1. This process is assigned to a metal-based $Co^{+/2+}$ redox couple. The second wave, which is observed at higher potential ($E_{1/2} = 630$ mV), is most probably irreversible since the Tomeš criterion value is 130 mV and the above-mentioned ratio is less than 1. This process is assigned to the $Co^{2+/3+}$ redox couple.

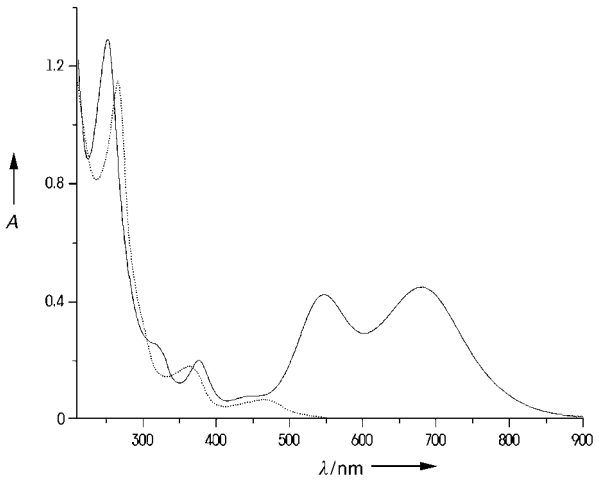

Figure 1. UV/vis spectra of acetonitrile solutions of **1** (••••) and $[(NMe_2)_4P]$-**1** (——) at the same concentrations.

The cobalt(II) clathrochelate can be both irreversibly oxidized and reversibly reduced electrochemically. The location and shape of the reduction wave for this complex coincide with the first oxidation wave for the cobalt(I) compound. The oxidation wave for **1** coincides with the second oxidation wave for $\mathbf{1}^-$.

Our results suggest wider possibilities for the stabilization of the lowest and highest (including unusual and previously unknown) oxidation states by introducing electron-withdrawing (in particular, halide, alkoxy and aryloxy) and electron-donating (especially amine) substituents in the chelating fragments of a macrobicyclic ligand.

Experimental Section

Single crystals of complexes **1** and $[(NMe_2)_4P]$-**1** were grown at room temperature from benzene/isooctane and dichloromethane/benzene mixtures, respectively.

Crystallographic measurements were performed at 110 K (**1**) and 120 K ($[(NMe_2)_4P]$-**1**) with a Bruker SMART 1 K CCD area detector using $Mo_{K\alpha}$ radiation ($\lambda = 0.71073$ Å).[8] Reflection intensities were integrated with SAINT software[8] and corrected by a semi-empirical method (SADABS program).[9] The structures were solved by direct methods and refined by full-matrix least-squares in the anisotropic approximation for non-hydrogen atoms using SHELXTL.[10] The position of the hydrogen atoms was calculated geometrically and refined using the riding model with isotropic temperature factors $U_{iso} = n\,U_{eq}(C)$, where $n = 1.5$ for methyl groups and 1.2 for the other ones and U_{eq} is the equivalent isotropic displacement parameter of the corresponding pivot carbon atoms.

Crystal data for **1**: $C_{14}H_{18}B_2Cl_6CoN_6O_6$, $M_r = 659.59$, monoclinic, space group $C2/c$, $a = 17.347(4)$, $b = 8.102(2)$, $c = 17.172(3)$ Å, $\beta = 91.936(4)°$, $V = 2411.9(8)$ Å^3, $Z = 4$, $\rho_{calcd} = 1.816\ g\,cm^{-3}$, $2\theta_{max} = 50.0°$, 11685 unique data, $R_1 = 0.0466$, $R_w = 0.1311$.Crystal data for $[(NMe_2)_4P]$-**1**: $C_{28}H_{48}B_2Cl_6CoN_{10}O_6P$, $M_r = 944.98$, monoclinic, space group $P2_1/c$, $a = 15.405(2)$, $b = 12.381(2)$, $c = 22.627(3)$ Å, $\beta = 102.162(3)°$, $V = 4218.6(9)$ Å^3, $\rho_{calcd} = 1.488\ g\,cm^{-3}$, $2\theta_{max} = 54.1°$, 9152 unique data, $R_1 = 0.0539$, $R_w = 0.1364$. CCDC-213266 (**1**) and -213265 ($[(NMe_2)_4P]$-**1**) contain the supplementary crystallographic

data for this paper. These data can be obtained free of charge from the Cambridge Crystallographic Data Centre via www.ccdc.cam.ac.uk/data_request/cif.

Received: December 27, 2004
Published online: April 21, 2005

Keywords: cobalt · EPR spectroscopy · macrocyclic ligands · oxidation state · reduction

[1] Y. Z. Voloshin, N. A. Kostromina, R. Krämer, *Clathrochelates: Synthesis, Structure and Properties*, Elsevier, Amsterdam, **2002**.
[2] A. M. Sargeson, *Coord. Chem. Rev.* **1996**, *151*, 89–114; Y. Z. Voloshin, O. A. Varzatskii, A. I. Stash, V. K. Belsky, Y. N. Bubnov, I. I. Vorontsov, K. A. Potekhin, M. Y. Antipin, E. V. Polshin, *Polyhedron* **2001**, *20*, 2721–2733; Y. Z. Voloshin, O. A. Varzatskii, I. I. Vorontsov, M. Y. Antipin, A. Y. Lebedev, A. S. Belov, A. V. Palchik, *Russ. Chem. Bull.* **2003**, *52*, 1552–1561.
[3] Y. Z. Voloshin, O. A. Varzatskii, A. V. Palchik, A. I. Stash, V. K. Belsky, *New J. Chem.* **1999**, *23*, 355–357; Y. Z. Voloshin, O. A. Varzatskii, T. E. Kron, V. K. Belsky, V. E. Zavodnik, A. V. Palchik, *Inorg. Chem.* **2000**, *39*, 1907–1918; Y. Z. Voloshin, V. E. Zavodnik, O. A. Varzatskii, V. K. Belsky, A. V. Palchik, N. G. Strizhakova, I. I. Vorontsov, M. Y. Antipin, *J. Chem. Soc. Dalton Trans.* **2002**, 1193–1202; Y. Z. Voloshin, O. A. Varzatskii, T. E. Kron, V. K. Belsky, V. E. Zavodnik, N. G. Strizhakova, V. A. Nadtochenko, V. A. Smirnov, *J. Chem. Soc. Dalton Trans.* **2002**, 1203–1211; Y. Z. Voloshin, O. A. Varzatskii, A. V. Palchik, N. G. Strizhakova, I. I. Vorontsov, M. Y. Antipin, D. I. Kochubey, B. N. Novgorodov, *New J. Chem.* **2003**, *27*, 1148–1155.
[4] D. J. Szalda, C. Creutz, D. Mahajan, N. Sutin, *Inorg. Chem.* **1983**, *22*, 2372–2379; M.-C. Liaw, M.-C. Cheng, S.-M. Peng, *Bull. Inst. Chem. Acad. Sin.* **1991**, *38*, 55–61.
[5] A. Rockenbauer, E. B. Zahonyi, L. I. Simandi, *J. Chem. Soc. Dalton Trans.* **1975**, 1729; A. Rockenbauer, E. B. Zahonyi, L. I. Simandi, *J. Coord. Chem.* **1972**, *2*, 53; K. A. Lance, K. A. Goldsby, D. H. Busch, *Inorg. Chem.* **1990**, *29*, 4537–4544; K. Wang, R. B. Jordan, *Inorg. Chem.* **2000**, *39*, 1823–1827.
[6] W. Low, *Paramagnetic Resonance in Solids*, Academic Press, New York, **1960**; J. W. Orton, *Electron Paramagnetic Resonance*, Iliffe Books, London, **1968**; *Electron Paramagnetic Resonance* (Ed.: S. Geschwind), Plenum, New York, **1972**; R. L. Carlin, *Magnetochemistry*, Springer, Berlin, **1986**.
[7] Y. Kaizu, T. Yazaki, Y. Torii, H. Kobayashi, *Bull. Chem. Soc. Jpn.* **1970**, *43*, 2068–2071; Y. Kaizu, Y. Torii, H. Kobayashi, *Bull. Chem. Soc. Jpn.* **1970**, *43*, 3296–3297; A. B. P. Lever, *Inorganic Electronic Spectroscopy*, Elsevier, Amsterdam, **1984**.
[8] *SMART and SAINT, Release 5.0, Area detector control and integration software*, Bruker AXS, Analytical X-ray Instruments, Madison, Wisconsin, USA, **1998**.
[9] G. M. Sheldrick, *SADABS: A program for exploiting the redundancy of area-detector X-ray data*, University of Göttingen, Germany, **1999**.
[10] G. M. Sheldrick, *SHELXTL-97. Program for the Solution and Refinement of Crystal Structures*, Bruker AXS Inc., Madison, Wisconsin, USA, **1997**.

Cucurbituril Polymers

Iodine-Assisted Assembly of Helical Coordination Polymers of Cucurbituril and Asymmetric Copper(II) Complexes**

Feng Zhang, Tatsuo Yajima, Yi-Zhi Li, Guo-Zheng Xu, Hui-Lan Chen, Qi-Tao Liu,* and Osamu Yamauchi**

Iodine has long been paid considerable attention for its fascinating chemical behavior[1,2] and biological essentiality.[3] The use of iodine as electrical conductor in the synthesis of donor–acceptor charge-transfer materials is well known.[4] In recent years, iodine in various forms has found applications in catalysis[5] as well as the creation of novel structures[6] and materials.[7] When covalently bound to an aromatic ring, iodine and other halogen atoms are versatile, assembly-organizing factors that direct extended networks[8,9] and induce helical aggregation of copper(II) complexes.[9,10] Furthermore, iodine is an essential element and plays an important role in the life processes of mammals and most vertebrates by forming the iodophenol moieties of thyroid hormones, growth hormones that function by binding to nuclear receptors.[11–13] The effect of the iodo substituent on these biological events has yet to be understood.

Cucurbituril (CB6) is a pumpkin-shaped macrocyclic compound synthesized by acid-catalyzed condensation of glycoluril and formaldehyde.[14] It is composed of six symmetrically arranged glycoluril units covalently linked by twelve methylene bridges to form a rigid, annular, hollow cavitand with two highly polar carbonyl openings.[15] CB6 has

[*] Dr. F. Zhang, Dr. Y.-Z. Li, Prof. H.-L. Chen
State Key Laboratory of Coordination Chemistry
Nanjing University
22 Hankou Road, Nanjing 210093 (P.R. China)
Fax: (+86) 25-8331-4502
E-mail: hlchen@netra.nju.edu.cn

Dr. F. Zhang, G.-Z. Xu, Prof. Q.-T. Liu
Institute of Chemistry and Engineering
Liaoning University
Huanggu, Shenyang 110036 (P.R. China)
Fax: (+86) 24-8685-4241
E-mail: qtliu@lnu.edu.cn

Dr. T. Yajima, Prof. O. Yamauchi
Faculty of Engineering
Kansai University
Suita, Osaka 564-8680 (Japan)
Fax: (+81) 6-6330-3770
E-mail: osamuy@ipcku.kansai-u.ac.jp

[**] F.Z. gratefully thanks Prof. Kimoon Kim of Pohang University of Science and Technology for his kind direction on postdoctoral research during 2001–2002 in CSS. This work was supported by grants from the Natural Science Foundation of China (no. 29971014 to F.Z. and nos. 20071017 and 50272027 to H.-L.C.), the State Postdoctoral Foundation of China (F.Z.), and a Grant-in-Aid for Scientific Research from the Ministry of Education, Culture, Sports, Science, and Technology of Japan (no. 16350036 to O.Y.).

Supporting information for this article is available on the WWW under http://www.angewandte.org or from the author.

  DOI: 10.1002/anie.200463071

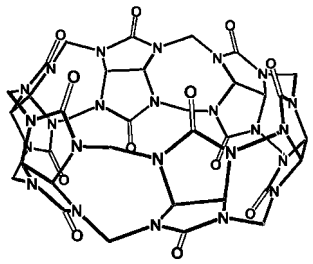

Cucurbituril (CB6)

received much interest in the last two decades as synthetic receptor[16–22] and has found discrete uses in inclusion catalysis,[20] interlocked architectures,[21] and functional molecular devices.[22] The guest-binding properties and inclusion mechanisms of CB6 have been investigated in detail.[16,18] Recently, various CB6 homologues, CB7 and CB8 in particular,[23] have been used for the development of functional molecular devices.[17c,24]

To date, investigations of the weak interactions leading to CB6-mediated molecular assembly are still lacking. The chemical behavior of the convex-shaped outer walls of CB6 and its homologues remains unknown and needs to be explored for the development of novel structures and functional materials incorporating cucurbiturils with transition metal complexes. CB6 can form more stable complexes with alkali metal ions[18] than with transition metal ions,[19g] and thus drives the assembly of alkali metal one-dimensional coordination polymers through wall-to-wall, shape-matching interactions of CB6.[19c,d] A negatively charged transition metal complex with aromatic moieties can bind to a positively charged CB6–alkali metal complex in aqueous solution and compete with CB6 self-recognition. This leads to a hybrid assembly of the CB6–alkali metal coordination polymer incorporating the transition metal complex.

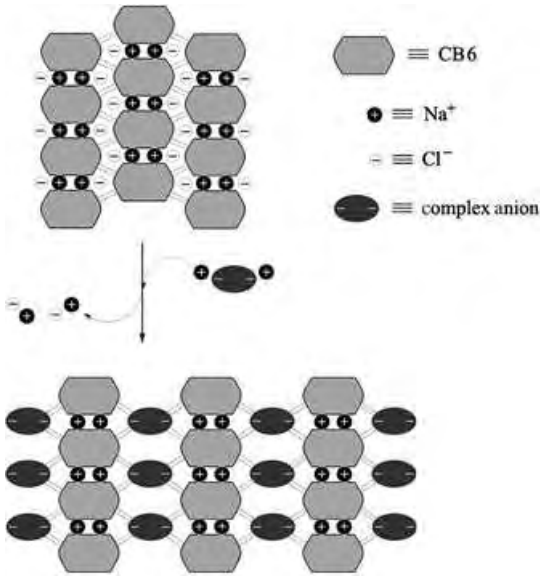

Scheme 1. Schematic representation of the anion-exchange strategy involving CB6 self-recognition (top) and CB6–ligand recognition (bottom).

Herein we report two novel helical structures that are synthesized by an anion-exchange strategy based on asymmetric, shape-matching recognition (Scheme 1). The anionic copper(II) complexes $[Cu(I_2sal)(Hqs)]^{2-}$ and $[Cu(Ibz)(Hqs)Cl]^{2-}$ (I_2sal = 3,5-diiodosalicylate, Ibz = 3-iodobenzoate, Hqs = 8-hydroxyquinoline-5-sulfonate) display a four-coordinate N_1O_3 and a five-coordinate N_1O_3Cl asymmetric structure, respectively, and are recognized by the cationic CB6–sodium(I) 1D coordination polymer. According to the structures of the two molecular assemblies, the convex-shaped glycoluril backbones of CB6 exhibit a much higher affinity to the iodoaromatic moieties of the copper(II) complexes than to the other CB6 units. This results in formation of the helical 1D polymer arrays with the assistance of the iodo substituents.

Compound **1** was isolated as rod-shaped colorless crystals from an aqueous NaCl solution of CB6. A dilute 1:1:1:1 mixture of **1** with Cu^{II}, Hqs, and I_2sal or Ibz in aqueous NaCl solution afforded complexes **2** or **3** as prismatic or needle-shaped green crystals (see the Experimental Section). The structures of **1**–**3** were determined by X-ray crystallography.[25]

$[Na_4(CB6)_2(H_2O)_{16}]Cl_4 \cdot 6H_2O$ **1**

$[Na_2(CB6)(H_2O)_2][Cu(I_2sal)(Hqs)] \cdot 6.5H_2O$ **2**

$[Na_2(CB6)(H_2O)_2][Cu(Ibz)(Hqs)Cl] \cdot 5.5H_2O$ **3**

In the crystal structure of **1**, the CB6 molecules display C_{2h} symmetry and are connected by twofold O(1)-Na^I-O(1) coordination linkages to form a linear 1D polymer (Figure 1a). The CB6 molecules in **2** and **3** are asymmetric in the presence of the complex anions. They are connected by asymmetric $O_{\mu2}$(water)–Na^I dinuclear clusters with formation of O–Na chelates for one of the carbonyl openings and one Na(1)-$O(12)_{\mu2}$-Na(2) bridging and two O–Na coordination bonds for the other. The resulting 1D polymers in **2** and **3** exhibit a zig-zag, folded helical conformation; neighboring CB6 molecules in the same polymer are in close contact with each other (Figure 1b,c). The closest distances between the carbonyl O(3) atom of the glycoluril unit G3 and the carbonyl C(12) atom of unit G6 are 3.07 and 3.13 Å, with corresponding CB6–CB6 tilting angles of 31.1° and 32.6° for **2** and **3**, respectively.

The 1D polymer in **2** exists as a pair of helical enantiomers, and the enantiomeric CB6 molecules of the *P* and *M* helices bind with the corresponding enantiomeric $[Cu(I_2sal)(Hqs)]^{2-}$ anions along the same $P2_1$ axis through asymmetric shape-matching interactions between the aromatic moieties of $Cu(I_2sal)(Hqs)$ and the outer walls of the CB6 molecules. The 1D polymer in **3**, on the other hand, exists only as an *M*-type helix, whose CB6 molecules are closely contacted by the $[Cu(Ibz)(Hqs)Cl]^{2-}$ anions through *P*-type helical shape-matching accommodation. The complex anions of **2** and **3** assume a rigid skew-bent conformation connected by asymmetric Cu^{II} ion centers with a distorted square-planar coordination geometry for $[Cu(I_2sal)(Hqs)]^{2-}$ and a distorted square-pyramidal coordination geometry for $[Cu(Ibz)(Hqs)Cl]^{2-}$ (Figure 2); the dihedral angles between the

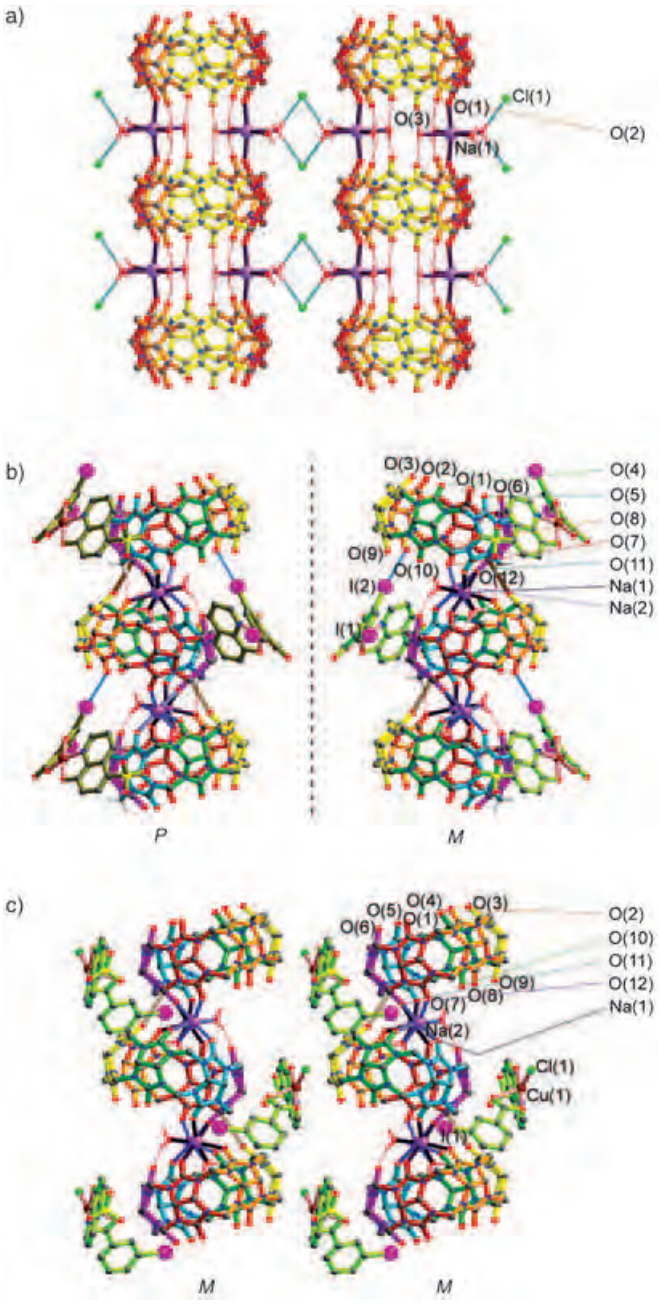

Figure 1. Ball-and-stick representations for the linear 1D-polymer in **1** (a) and the helical 1D polymers in **2** (b) and **3** (c) with the asymmetric glycoluril units G1–G6 (G1 red, G2 orange, G3 yellow, G4 green, G5 cyan, G6 purple).[26]

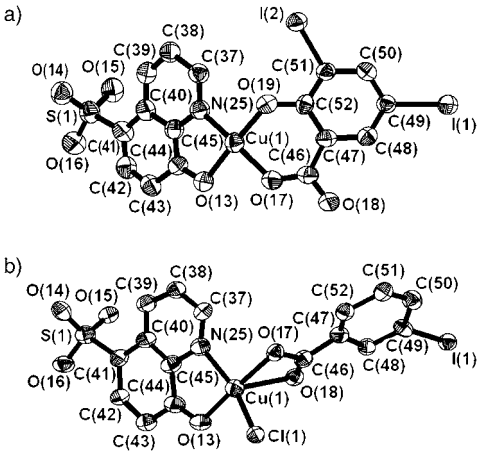

Figure 2. ORTEP views of a) $[Cu(I_2sal)(Hqs)]^{2-}$ in **2** and b) $[Cu(Ibz)(Hqs)Cl]^{2-}$ in **3** with the thermal ellipsoids at the 50% probability level.[26]

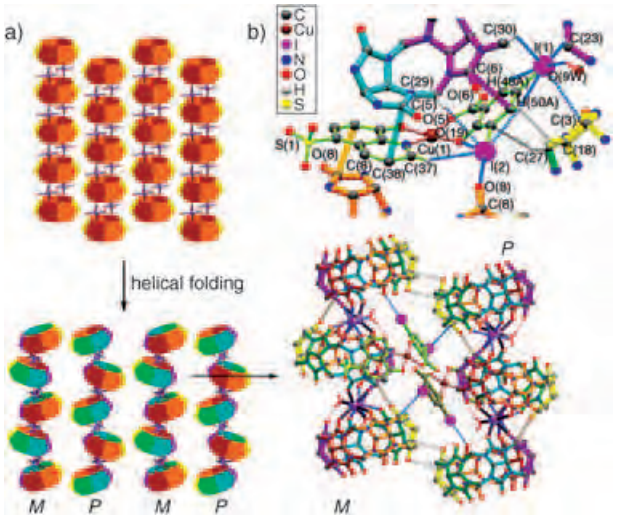

Figure 3. a) Schematic representation of the polymer 2D layer in **1**, the 2D open-cavity framework in **2** (left), and the structure for the accommodation of $Cu(I_2sal)(Hqs)$ into the homocenter-symmetric open cavity (lower right). b) The host–guest shape-matching mode in **2** involving I–O, I–C, and I–H weak interactions.[26]

coordinated aromatic rings are 130.3 and 106.1°, respectively. It is these discrete and properly skew-bent conformations that allow the asymmetric shape-matching and thus result in the discrete helical structures (Figures 3 and 4). The skew-bent conformations are reminiscent of that of thyroid hormones, whose inner and outer phenol rings are asymmetrically bridged by an ether oxygen atom instead of the Cu^{II} ion of the complexes presented here.[3b]

In complex **2**, the positively charged *P* and *M* polymer helices are alternately packed with opposite orientations (Figure 3a) and assembled as a two-dimensional layer structure with open cavities. Each cavity is composed of the half walls of three CB6 enantiomer pairs through shape-matching interactions between the G3 semi-glycoluril rings of two CB6 enantiomer pairs with a ring–ring distance of 3.29 Å. Most importantly, each open cavity holds homocenter symmetry, tightly accommodating a pair of $[Cu(I_2sal)(Hqs)]^{2-}$ enantiomers in the same symmetry. To our knowledge, this is the first example of a helical enantiomeric host–guest assembly constructed from an asymmetric transition metal complex anion (guest) and the outer walls of CB6 molecules within the cavity-forming cation aggregates (host) through asymmetric shape-matching interactions.

The skew-bent form of $[Cu(I_2sal)(Hqs)]^{2-}$ in **2** is arranged in such a way that the inward I_2sal and Hqs ring faces fit to the semi-glycoluril rings of units G6 and G5, respectively, of the same CB6 molecule. The outward I_2sal and Hqs ring faces

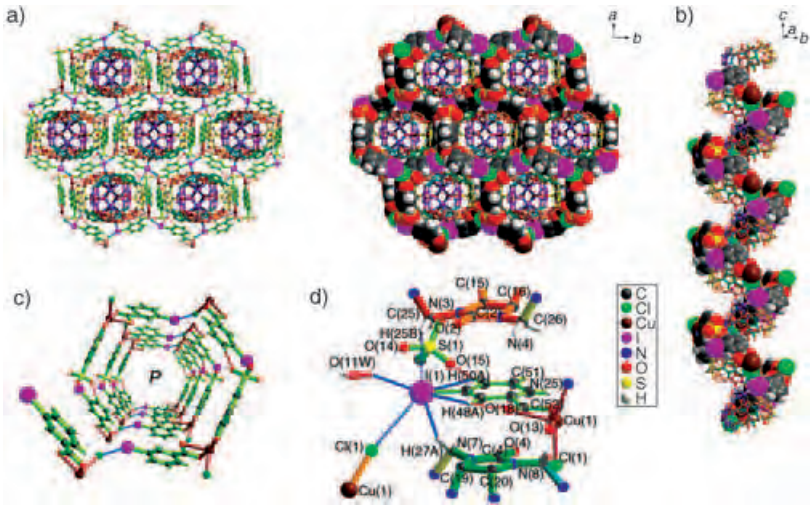

Figure 4. a) Top views for the helical inclusion structure of **3**. b) Side view for the complex anion-wrapped polymer helix in **3**. c) Top view for the *P*-type anionic helical net channel. d) Representation of the asymmetric shape-matching mode of Ibz to G2 (orange) and G4 (green) involving I–H and I–Cl weak interactions.[26]

contact with the semi-glycoluril rings of units G3 and G2, respectively, of the CB6 molecules in the neighboring polymers (Figure 3b). The inward G6–I_2sal and G5–Hqs and outward Hqs–G2 matching pairs form face-to-face π–π stacking interactions, with closest ring–ring distances of 3.38, 3.47, and 3.43 Å and ring–ring tilting angles of 19.6, 5.9, and 5.8°, respectively. In contrast, the outward I_2sal–G3 matching pair is achieved by complementary iodine–G3 ring charge transfer and C–H···π interactions between a G3 hydrogen atom and the I_2sal ring. This places the I_2sal and G3 rings in edge-to-edge contact with a closest ring–ring distance and angle of 3.50 Å and 15.7°.

In **3**, unique helical polymer-inclusion assembly by the $[Cu(Ibz)(Hqs)Cl]^{2-}$ anion is achieved with formation of helical networks (Figure 4). The complex anion is arranged leaning toward the corresponding hinge site of the polymer helix, with the inward Ibz and Hqs ring faces contacting the semi-glycoluril rings of units G2 and G6, respectively, of the neighboring CB6 molecules. The outward Ibz and Hqs ring faces close to G4 and G3, respectively, of the CB6 molecules in the neighboring polymer (Figure 1c and 4d). The closest ring–ring distances are 3.67, 3.46, 3.60, and 3.44 Å, respectively, for the G2–Ibz, G6–Hqs, Ibz–G4, and Hqs–G3 matching pairs with corresponding ring–ring angles of 3.3, 4.6, 1.5, and 4.2°, indicating face-to-face π–π stacking interactions.

The same striking point for compounds **2** and **3** is the assembly-assisting role of the iodo substituents, whose multiple weak interactions with CB6 amplify the asymmetry and enhance the stability of the asymmetric shape-matching interactions. In **2**, the iodo substituents are involved in multiple hydrogen-bonding interactions with the G6 methine and the hydrogen atoms of the C(29) and C(30) methylene groups as well as charge-transfer interactions with the ureido G2 oxygen and G3 carbon atoms (Figure 3b). The interatomic distances for I(1)–C(3), I(2)–O(8), and I–H(23A, 30A, 9WA, 29B, 37A) are 3.78, 3.34, and 3.25–3.30 Å, respectively, and thus all lie within the corresponding van der Waals distances[27] of 3.85, 3.55, and 3.35 Å, respectively. The interatomic distances involving the iodo substituent in **3** (Figure 4d), that is, I(1)–H(25B) (2.98 Å) and I(1)–H(27A) (3.07 Å), are distinctly shorter than the van der Waals distance for I–H. All these distances are comparable with those previously observed for other systems (I–C 3.63–3.82, I–O 3.08–3.37, I–H 2.85–3.20 Å)[9] and some thyroactive species (I–O 2.99–3.45 Å).[3c] In addition, the iodo substituent in **3** also contacts the coordinated Cl^- anion within the van der Waals distance and favors the hydrogen-bonding interaction of its *ortho*-hydrogen atom with the sulfonate oxygen atom of Hqs (O···C 3.37, O···H 2.39 Å; ∢O···H–C 176.2°). These results suggest that the iodine atoms of coordinated I_2sal and Ibz may play an important role in the formation of **2** and **3** by serving as an efficient asymmetric weak-binding knot and template.

In conclusion we present two novel helical structures established by iodine-assisted asymmetric shape-matching interactions between the convex outer walls of CB6 and the aromatic moieties of asymmetric copper(II) complexes. The synthetic strategy may also be suitable for other hybrid structures and the construction of cucurbiturils incorporating various transition metal complexes. Our results suggest that the iodo substituent may exert a profound effect on its covalently bound aromatic moiety in specific asymmetric recognition to a given structural environment through selective shape-matching interactions. The observed structural change due to the interactions between CB6 and the iodophenol moiety may suggest the possible function of thyroid hormones as an iodine-assisted asymmetric template in the hormone–receptor binding switches inducing the biologically active conformation of the receptor.

Experimental Section

CB6 was synthesized following a literature procedure[15] and obtained as a white powder in 40–45% yield after drying at 110°C. Elemental analysis calcd for $(C_{36}H_{36}N_{24}O_{12})\cdot 9H_2O$ [%]: C 37.31, H 4.70, N 29.01; found: C 37.68, H 4.84, N 28.70; ^{1}H NMR (Bruker, 500 MHz, in D_2O): $\delta = 5.65$ (s, CH), 5.74 (d, CHH), 4.38 ppm (d, CHH).

1: A solution of CB6 (0.5 mmol) in 0.2 M aqueous NaCl was concentrated to near saturation followed by slow vapor diffusion of ethanol into the solution at room temperature for one week. The colorless rod-shaped crystals were dried in air at room temperature (60–70% yield). Elemental analysis calcd for $(C_{72}H_{104}N_{48}Na_4O_{40})Cl_4\cdot 6H_2O$ [%]: C 32.96, H 4.46, N 25.62; found: C 33.12, H 4.32, N 25.76.

2: Compound **1** (0.05 mmol) was dissolved in 0.2 M aqueous NaCl and the solution was added dropwise to an aqueous 1:1:1 mixture of $CuCl_2$, I_2sal, and Hqs (0.05 mmol) at pH 6 under stirring. Slow evaporation of the filtrate over two weeks provided prismatic green crystals of **2** (40–50% yield based on CB6). Elemental analysis calcd for $(C_{52}H_{47}N_{25}I_2SNa_2O_{21}Cu)\cdot 6.5H_2O$ [%]: C 33.39, H 3.23, N 18.72; found: C 33.67, H 3.02, N 18.90.

3: Compound **3** was prepared in a similar manner to **2** with Ibz in place of I_2sal. Slow evaporation of the filtrate for two weeks provided needle-shaped green crystals of **3** (40–50% yield based on CB6). Elemental analysis calcd for $(C_{52}H_{49}N_{25}O_{20}SICuClNa_2)\cdot 5.5H_2O$ [%]: C 35.75, H 3.46, N 20.04; found: C 36.07, H 3.09, N 20.25.

Received: December 27, 2004
Revised: February 5, 2005
Published online: April 21, 2005

Keywords: copper · helical structures · iodine · polymers · supramolecular chemistry

[1] P. Y. Cheng, D. Zhong, A. H. Zewail, *Chem. Phys. Lett.* **1995**, *242*, 369–379, and references therein.
[2] a) M. C. Aragoni, M. Arca, F. A. Devillanova, A. Garau, F. Isaia, V. Lippolis, G. Verani, *Coord. Chem. Rev.* **1999**, *184*, 271–290; b) P. Deplano, J. R. Ferraro, M. L. Mercuri, E. F. Trogu, *Coord. Chem. Rev.* **1999**, *188*, 71–95.
[3] a) N. L. Eberhardt, J. W. Apriletti, J. D. Baxter in *Biochemical Actions of Hormones*, *Vol. 7* (Ed.: G. Litwack), Academic Press, New York, **1980**, pp. 311–394; b) V. Cody, *Endocr. Rev.* **1980**, *1*, 140–166; c) V. Cody, P. Murray-Rust, *J. Mol. Struct.* **1984**, *112*, 189–199; d) R. M. Evans, *Science* **1988**, *240*, 889–895; e) C. K. Glass, J. M. Holloway, *Biochim. Biophys. Acta* **1990**, *1032*, 157–176.
[4] J. R. Ferraro, J. M. Williams in *Introduction to Synthetic Electrical Conductors*, Academic Press, New York, **1987**.
[5] See for example: a) S. Nakanishi, Y. Mukouyama, Y. Nakato, *J. Phys. Chem. B* **2001**, *105*, 5751–5756; b) L. Liao, Y. Pang, L. Ding, F. E. Karasz, *Macromolecules* **2002**, *35*, 6055–6059; c) R. A. Periana, O. Mirinov, D. J. Taube, S. Gamble, *Chem. Commun.* **2002**, 2376–2377; d) J. S. Yadav, P. K. Chand, S. Anjaneyulu, *Tetrahedron Lett.* **2002**, *43*, 3783–3784; e) J. Sun, Y. Dong, L. Cao, X. Wang, S. Wang, Y. Hu, *J. Org. Chem.* **2004**, *69*, 8932–8934.
[6] See for example: a) A. J. Blake, F. A. Devillanova, R. O. Gould, W. S. Li, V. Lippolis, S. Parsons, C. Radek, M. Schröder, *Chem. Soc. Rev.* **1998**, *27*, 195–205; b) W. W. Mont, F. Ruthe, *Coord. Chem. Rev.* **1999**, *189*, 101–133; c) R. Makiura, I. Nagasawa, N. Kimura, S. Ishimaru, H. Kitagawa, R. Ikeda, *Chem. Commun.* **2001**, 1642–1643; d) C. J. Horn, A. J. Blake, N. R. Champness, A. Garau, V. Lippolis, C. Wilson, M. Schröder, *Chem. Commun.* **2003**, 312–313; e) L. Jongen, A. V. Mudring, A. Möller, G. Meyer, *Angew. Chem.* **2004**, *116*, 3245–3248; *Angew. Chem. Int. Ed.* **2004**, *43*, 3183–3185.
[7] See for example: a) R. R. Tykwinski, K. Kamada, D. Bykowski, K. Ohta, R. McDonald, *Adv. Mater.* **2000**, *12*, 133–137; b) Q. Chu, Z. Wang, Q. Huang, C. Yan, S. Zhu, *J. Am. Chem. Soc.* **2001**, *123*, 11069–11070; c) Y. Shimazaki, T. Nogami, F. Tani, A. Odani, O. Yamauchi, *Angew. Chem.* **2001**, *113*, 3977–3980; *Angew. Chem. Int. Ed.* **2001**, *40*, 3859–3862; d) A. T. Yordanov, A. L. Lodder, E. K. Woller, M. J. Cloninger, N. Patronas, D. Milenic, M. W. Brechbiel, *Nano Lett.* **2002**, *2*, 595–599; e) Y. Cai, S. L. Bernasek, *J. Am. Chem. Soc.* **2003**, *125*, 1655–1659.
[8] See for example: a) E. Corradi, S. V. Meille, M. T. Messina, P. Metrangolo, G. Resnati, *Angew. Chem.* **2000**, *112*, 1852–1856; *Angew. Chem. Int. Ed.* **2000**, *39*, 1782–1785; b) P. Metrangolo, G. Resnati, *Chem. Eur. J.* **2001**, *7*, 2511–2519; c) A. De Santis, A. Forni, R. Liantonio, P. Metrangolo, T. Pilati, G. Resnati, *Chem. Eur. J.* **2003**, *9*, 3974–3983; d) T. Caronna, R. Liantonio, T. A. Logothetis, P. Metrangolo, T. Pilati, G. Resnati, *J. Am. Chem. Soc.* **2004**, *126*, 4500–4501; e) H. L. Nguyen, P. N. Horton, M. B. Hursthouse, A. C. Legon, D. W. Bruce, *J. Am. Chem. Soc.* **2004**, *126*, 16–17.
[9] a) T. Sugimori, H. Masuda, O. Yamauchi, *Bull. Chem. Soc. Jpn.* **1994**, *67*, 131–137; b) F. Zhang, A. Odani, H. Masuda, O. Yamauchi, *Inorg. Chem.* **1996**, *35*, 7148–7155; c) F. Zhang, T. Yajima, H. Masuda, A. Odani, O. Yamauchi, *Inorg. Chem.* **1997**, *36*, 5777–5784; d) F. Zhang, Y. Z. Li, X. Gao, H. L. Chen, Q. T. Liu, A. Odani, O. Yamauchi, *Chem. Lett.* **2004**, *33*, 556–557; e) F. Zhang, Y. Y. Zhang, X. Gao, X. D. Zhang, Y. Z. Li, H. L. Chen, Q. T. Liu, *Chem. J. Chin. Univ.* **2004**, *25*, 1422–1424; f) F. Zhang, S. Y. Sang, Y. Y. Zhang, X. D. Zhang, Y. Z. Li, H. L. Chen, Q. T. Liu, *Acta Chim. Sin.* **2004**, *62*, 2055–2061.
[10] See Figure S1 in the Supporting Information.
[11] D. Voet, J. G. Voet, *Biochemistry*, 2nd ed., Wiley, New York, **1995**, pp. 1261–1265.
[12] a) W. W. Chin in *Nuclear Hormone Receptors* (Ed: M. G. Parker), Academic Press, New York, **1991**, pp. 79–102; b) C. K. Glass, *Endocr. Rev.* **1994**, *15*, 391–407.
[13] a) R. L. Wagner, J. W. Apriletti, M. E. McGrath, B. L. West, J. D. Baxter, R. J. Fletterick, *Nature* **1995**, *378*, 690–697; b) A. J. Hörlein, A. M. Näär, T. Heinzel, J. Torchia, B. Gloss, R. Kurokawa, A. Ryan, Y. Kamei, M. Söderström, C. K. Glass, M. G. Rosenfeld, *Nature* **1995**, *377*, 397–404; c) R. C. J. Rebeiro, J. W. Apriletti, B. L. West, R. L. Wagner, R. J. Fletterick, F. Schaufele, J. D. Baxter, *Ann. N. Y. Acad. Sci.* **1995**, *758*, 366–389.
[14] R. Behrend, E. Meyer, F. Rusche, *Justus Liebigs Ann. Chem.* **1905**, *339*, 1–37.
[15] W. A. Freeman, W. L. Mock, N. Y. Shih, *J. Am. Chem. Soc.* **1981**, *103*, 7367–7368.
[16] W. L. Mock in *Comprehensive Supramolecular Chemistry*, *Vol. 2* (Ed.: F. Vögtle), Pergamon, Oxford, **1996**, pp. 477–493.
[17] a) K. Kim, *Chem. Soc. Rev.* **2002**, *31*, 96–107; b) J. W. Lee, K. Kim, *Top. Curr. Chem.* **2003**, *228*, 111–140; c) J. W. Lee, S. Samal, N. Selvapalam, H. J. Kim, K. Kim, *Acc. Chem. Res.* **2003**, *36*, 621–630.
[18] a) C. Márquez, R. R. Hudgins, W. M. Nau, *J. Am. Chem. Soc.* **2004**, *126*, 5806–5816; b) C. Márquez, W. M. Nau, *Angew. Chem.* **2001**, *113*, 3248–3254; *Angew. Chem. Int. Ed.* **2001**, *40*, 3155–3160.
[19] a) D. Whang, J. Heo, J. H. Park, K. Kim, *Angew. Chem.* **1998**, *110*, 83–85; *Angew. Chem. Int. Ed.* **1998**, *37*, 78–80; b) B. D. Wagner, A. I. MacRae, *J. Phys. Chem. B* **1999**, *103*, 10114–10119; c) J. Heo, S. Y. Kim, D. Whang, K. Kim, *Angew. Chem.* **1999**, *111*, 675–678; *Angew. Chem. Int. Ed.* **1999**, *38*, 641–643; d) J. Heo, J. Kim, D. Whang, K. Kim, *Inorg. Chim. Acta* **2000**, *279*, 307–312; e) M. N. Sokolov, A. V. Virovets, D. N. Dybtsev, O. A. Gerasko, V. P. Fedin, R. Hernandez-Molona, W. Clegg, A. G. Sykes, *Angew. Chem.* **2000**, *112*, 1725–1727; *Angew. Chem. Int. Ed.* **2000**, *39*, 1659–1661; f) V. P. Fedin, V. Gramlich, M. Worle, T. Weber, *Inorg. Chem.* **2001**, *40*, 1074–1077; g) H. J. Buschmann, E. Cleve, K. Jansen, E. Schollmeyer, *Anal. Chim. Acta* **2001**, *437*, 157–163; h) X. Y. He, G. Li, H. L. Chen, *Inorg. Chem. Commun.* **2002**, *5*, 633–636; i) F. Pichierri, *Chem. Phys. Lett.* **2004**, *390*, 214–219.
[20] W. L. Mock, T. A. Irra, J. P. Wepsiec, M. Adhya, *J. Org. Chem.* **1989**, *54*, 5302–5308.
[21] a) K. M. Park, D. Whang, E. Lee, J. Heo, K. Kim, *Chem. Eur. J.* **2002**, *8*, 498–508; b) K. M. Park, S. Y. Kim, J. Heo, D. Whang, S. Sakamoto, K. Yamaguchi, K. Kim, *J. Am. Chem. Soc.* **2002**, *124*, 2140–2147; c) S. G. Roh, K. M. Park, S. Sakamoto, K. Yamaguchi, K. Kim, *Angew. Chem.* **1999**, *111*, 671–675; *Angew. Chem. Int. Ed.* **1999**, *38*, 638–641.
[22] a) H. Isobe, N. Tomita, J. W. Lee, H. J. Kim, K. Kim, E. Nakamura, *Angew. Chem.* **2000**, *112*, 4427–4430; *Angew. Chem. Int. Ed.* **2000**, *39*, 4257–4260; b) S. I. Jun, J. W. Lee, S. Sakamoto, K. Yamaguchi, K. Kim, *Tetrahedron Lett.* **2000**, *41*, 471–475; c) J. W. Lee, K. P. Kim, K. Kim, *Chem. Commun.* **2001**, 1042–1043; d) Y. J. Jeon, H. J. Kim, S. Y. Jon, N. Selvapalam,

D. H. Oh, I. Seo, C. S. Park, S. R. Jung, D. S. Koh, K. Kim, *J. Am. Chem. Soc.* **2004**, *126*, 15944 – 15945.

[23] a) H. J. Kim, I. S. Jung, S. Y. Kim, E. Lee, J. K. Kang, S. Sakamoto, K. Yamaguchi, K. Kim, *J. Am. Chem. Soc.* **2000**, *122*, 540 – 541; b) A. Day, A. P. Arnold, R. J. Blanch, B. Snushall, *J. Org. Chem.* **2001**, *66*, 8094 – 8100.

[24] See for example: a) C. Márquez, W. M. Nau, *Angew. Chem.* **2001**, *113*, 4515 – 4518; *Angew. Chem. Int. Ed.* **2001**, *40*, 4387 – 4390; b) W. S. Jeon, H. J. Kim, C. Lee, K. Kim, *Chem. Commun.* **2002**, 1828 – 1829; c) H. J. Kim, W. S. Jeon, Y. H. Ko, K. Kim, *Proc. Natl. Acad. Sci. USA* **2002**, *99*, 5007 – 5011; d) Y. J. Jeon, P. K. Bharadwaj, S. W. Choi, J. W. Lee, K. Kim, *Angew. Chem.* **2002**, *114*, 4654 – 4656; *Angew. Chem. Int. Ed.* **2002**, *41*, 4474 – 4476; e) Y. Miyahara, K. Abe, T. Inazu, *Angew. Chem.* **2002**, *114*, 3146 – 3149; *Angew. Chem. Int. Ed.* **2002**, *41*, 3020 – 3023; f) W. Ong, A. E. Kaifer, *Angew. Chem.* **2003**, *115*, 2214 – 2217; *Angew. Chem. Int. Ed.* **2003**, *42*, 2164 – 2167; g) C. Márquez, U. Pischel, W. M. Nau, *Org. Lett.* **2003**, *5*, 3911 – 3914; h) K. Moon, A. E. Kaifer, *Org. Lett.* **2004**, *6*, 185 – 188; i) F. Constabel, K. E. Geckeler, *Tetrahedron Lett.* **2004**, *45*, 2071 – 2073.

[25] The crystal structures of **1**–**3** were determined with a Bruker P4 four-circle diffractometer with graphite-monochromatic $Mo_{K\alpha}$ radiation ($\lambda = 0.71073$ Å). Data were collected at room temperature (293 K) in the range $1.53 \le \theta \le 25.00°$ for **1**, $1.33 \le \theta \le 24.99°$ for **2**, and $1.36 \le \theta \le 26.00°$ for **3**. The structures were solved by direct methods and refined using full-matrix least squares on F^2 (SHELXTL, Bruker, 2000). All non-hydrogen atoms were refined anisotropically, and hydrogen atoms were generated geometrically or determined from the difference Fourier map and refined isotropically. Crystal data for **1**: monoclinic, space group $C2/m$, $a = 23.363(8)$, $b = 10.680(2)$, $c = 14.530(3)$ Å, $\beta = 113.36(4)°$, $V = 3328(2)$ Å^3, $Z = 1$, $\rho_{calcd} = 1.309$ g cm^{-3}, $\mu = 0.196$ mm^{-1}, $R_1 = 0.0465$ for 2611 reflections with $I > 2\sigma(I)$, and $wR_2 = 0.1445$ for 3114 unique reflections. Crystal data for **2**: monoclinic, space group $P2_1/n$, $a = 17.180(3)$, $b = 18.550(4)$, $c = 25.950(3)$ Å, $\beta = 99.34(3)°$, $V = 8160(3)$ Å^3, $Z = 4$, $\rho_{calcd} = 1.523$ g cm^{-3}, $\mu = 1.148$ mm^{-1}, $R_1 = 0.0481$ for 8816 reflections with $I > 2\sigma(I)$, and $wR_2 = 0.1243$ for 14307 unique reflections. Crystal data for **3**: orthorhombic, space group $P2_12_12_1$, $a = 25.270(5)$, $b = 16.410(3)$, $c = 18.570(4)$ Å, $V = 7701(3)$ Å^3, $Z = 1$, $\rho_{calcd} = 1.507$ g cm^{-3}, $\mu = 0.847$ mm^{-1}, $R_1 = 0.0424$ for 15130 reflections with $I > 2\sigma(I)$, and $wR_2 = 0.1210$ for 15130 unique reflections. CCDC 257203, 257204, and 227936 (for **1**, **2**, and **3**, respectively) contain the supplementary crystallographic data for this paper. These data can be obtained free of charge from The Cambridge Crystallographic Data Centre via www.ccdc.cam.ac.uk/data_request/cif.

[26] For ORTEP views of the structure and details concerning the weak interactions, see the Supporting Information.

[27] Based on Pauling radii; see L. Pauling, *The Nature of the Chemical Bond*, Cornell University Press, Ithaca, **1960**, p. 260.

Transfer Hydrogenation

Insight into and Practical Application of pH-Controlled Asymmetric Transfer Hydrogenation of Aromatic Ketones in Water**

*Xiaofeng Wu, Xiaoguang Li, Frank King, and Jianliang Xiao**

Dedicated to Professor Ryoji Noyori

Catalysis in water represents a major area of intense research in modern chemistry.[1] Water is inexpensive, readily available, and environmentally benign, and is thus an ideal solvent for chemical reactions. We recently reported that asymmetric transfer hydrogenation of aromatic ketones with the Ru–(*R*,*R*)-Ts-dpen catalyst (Ts-dpen = *N*-(*p*-toluenesulfonyl)-1,2-diphenylethylenediamine) or its polymer-supported analogue

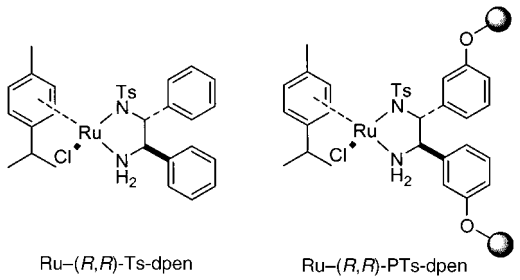

Ru–(*R*,*R*)-Ts-dpen Ru–(*R*,*R*)-PTs-dpen

Ru–(*R*,*R*)-PTs-dpen (PTs-dpen = poly(ethylene glycol)-supported Ts-dpen) can be considerably accelerated by using water as solvent and in the case of Ru–(*R*,*R*)-PTs-dpen, the catalyst was recycled more than 10 times without loss of enantioselectivity.[2,3] The reducing agent used in those studies was HCOONa. To our surprise, when the often-used HCOOH–NEt_3 azeotrope was adopted as reductant for the same reaction in water, a much slower reaction was observed. This prompted us to investigate whether the reaction was affected by the pH value of the solution. Although Benyei and Joó reported that the rate of transfer hydrogenation of benzaldehyde by aqueous HCOONa with a water-soluble

[*] X. Wu, Dr. X. Li, Prof. Dr. J. Xiao
Liverpool Centre for Materials and Catalysis
Department of Chemistry, University of Liverpool
Liverpool L69 7ZD (UK)
Fax: (+44) 151-794-3589
E-mail: j.xiao@liv.ac.uk
Prof. Dr. F. King
Johnson Matthey
Billingham, Cleveland TS23 1LB (UK)

[**] We thank the DTI MMI project and its industrial/academic partners (Prof. R. Catlow, Royal Institution; Dr. A. Danopoulos, University of Southampton; Dr. F. Hancock and Dr. A. Zanotti-Gerosa, Johnson Matthey; Dr. P. Levett and Dr. A. Pettman, Pfizer; Dr. P. Hogan and Dr. M. Purdie, AstraZeneca; Dr. P. Ravenscroft, GlaxoSmithKline) for financial support and valuable suggestions. We also thank Dr. N. Winterton for helpful suggestions.

 DOI: 10.1002/anie.200500023

Ru^{II}–phosphine catalyst is independent of the pH value of the solution under basic conditions,[4] recent work from Ogo et al. revealed a strong pH dependence in the rate of the reduction of ketones by HCOONa with $[(\eta^6\text{-}C_6M_6)Ru(bpy)(H_2O)]^{2+}$ (bpy = bipyridyl) in water.[5] However, there appear to be no reported studies on how the pH values may affect asymmetric transfer hydrogenation in aqueous media.

Asymmetric transfer hydrogenation of ketones is a powerful alternative to asymmetric hydrogenation for the production of chiral alcohols.[6] Among the various chiral catalysts reported, the most notable is the Ru–Ts-dpen catalyst developed by Noyori, Ikariya, Hashiguchi, and co-workers.[7] This catalyst and the related variants have been successfully applied by Noyori, Ikariya, and others to a wide range of prochiral ketones and imines.[3,7–9] The reaction is most often performed in 2-propanol or the HCOOH–NEt_3 azeotropic mixture; they act as both solvents and hydrogen sources. However, the transfer hydrogenation under such conditions tends to be sluggish, accompanied with low productivity. We herein report that asymmetric transfer hydrogenation with the Noyori–Ikariya catalyst is pH dependent and can be effected in faster rates, with little compromise on enantioselectivities, by a smaller amount of HCOOH–NEt_3 in water. Our preliminary observations concerning why the reduction is pH dependent are also presented.

Following on from our finding that aromatic ketones can be reduced more rapidly by HCOONa in water than in HCOOH–NEt_3 with the Ru–Ts-dpen catalyst,[2] we wondered whether similar acceleration in rates could be achieved with the azeotrope in water as solvent. We set out by examining the asymmetric transfer hydrogenation of acetophenone to 1-phenylethanol. As before,[2a] the precatalyst was generated by treating (*R*,*R*)-Ts-dpen (0.012 mmol) with $[\{RuCl_2(p\text{-cymene})\}_2]$ (0.005 mmol) in water (1 mL) at 40 °C for 1 h, and the reduction started by introducing the HCOOH–NEt_3 azeotrope (1.0 mL; molar ratio HCOOH/NEt_3 = 2.5:1) and acetophenone with a substrate/catalyst (S/C) ratio of 100:1. Surprisingly, less than 2% conversion was observed after reduction at 40 °C for 1 h; the conversion rose to 98% after a prolonged time of 12 h. This is in stark contrast to the observation made with HCOONa in water, under which the ketone was fully converted into (*R*)-1-phenylethanol in 1 h albeit with a lower enantioselectivity (94 vs. 97% *ee*). The most discernable difference between the two systems was the pH value of the solution. The pH value of the azeotrope–water system was 3 at the beginning of the reaction; the aqueous HCOONa solution was far more basic (pH 7). Thus the question arose: Was the reaction rate affected by pH values, and if so, could the reduction be accelerated by adjusting the pH value?

To address this issue, we measured the initial rates of the reduction of acetophenone (1.0 mmol) in water (0.5 mL) at various initial solution pH values by adjusting the HCOOH/NEt_3 molar ratios; the total solution volume remained constant at 1.0 mL, however. Figure 1 shows the initial turnover frequency (TOF) as a function of the starting pH values. Our speculations were confirmed as the reaction barely took place at low pH values; it accelerated at pH 3.9, with the acceleration slowing down at approximately pH 4.8.

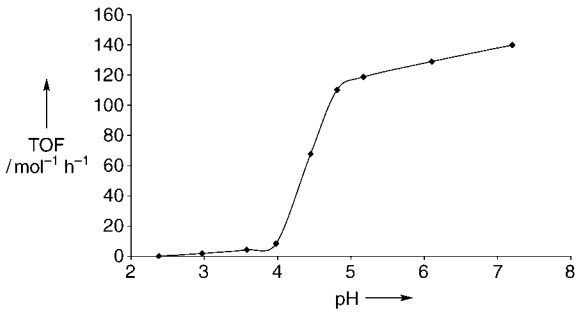

Figure 1. Initial TOF against initial solution pH values for the reduction of acetophenone (1 M, assuming the solution is homogeneous) by HCOOH–NEt_3 in water (1 mL total volume) with Ru–(*R*,*R*)-Ts-dpen at 40 °C. The initial pH values were determined by varying the HCOOH/NEt_3 molar ratios from 4.6:1.0 to 0.37:1.0.

The rate appeared to level off at pH > 7. However, examination of the effect of a further pH increase on the rate was difficult under the chosen conditions. The aforementioned $[(\eta^6\text{-}C_6M_6)Ru(bpy)(H_2O)]^{2+}$ resulted in a decreased rate at pH > 6 in the reduction of ketones.[5] This was attributed to the formation of a Ru^{II}–OH complex by deprotonation of a coordinated H_2O. The less significant effect of higher pH on the reduction in this case may stem from the higher basicity of Ts-dpen than that of bipyridine.[10]

The higher rates at pH values greater than 4 could be due to the increased concentration of $HCOO^-$. At pH > 4, HCOOH ($pK_a = 3.6$) exists predominately as $HCOO^-$, which is needed to form the ruthenium formato complex (Scheme 1, see below). This would be in line with our previous report that the rate of the reduction of acetophenone by HCOONa increases with the formate concentration in water when [formate] < 5 M.[2a] However, there appears to be no correlation of TOF with $[HCOO^-]$ in this study. Thus, for example, the initial TOF increased 8 times when the initial pH value changed from 4.0 to 4.5; the corresponding change in the calculated initial $[HCOO^-]$ was only from 3.1 to 2.9 M, suggesting that the observed TOF–pH correlation cannot simply be ascribed to the variation in formate concentration.

To address the issue raised above further, we followed the reduction of acetophenone starting at pH 2.3. As can be seen from Figure 2, the reduction barely occurred before the pH value increased to approximately 3.5, which seems to support the notion that the reduction is governed by the concentration of formate. The observed increase in solution pH with time is a consequence of the decomposition of HCOOH by Ru–Ts-dpen and its consumption in the reduction of the ketone. The decomposition gave rise to CO_2 and H_2, as shown by MS in the absence of ketone. However, the most surprising observation is that the enantioselectivity varied with the pH value as well (Figure 2). This observation suggests that there might be a competing pathway in operation under acidic conditions, which is less selective than that at higher pH values and becomes insignificant under basic conditions. A similar change in *ee* values with time was noticed by Carmona, Oro, Joó, and co-workers, but the cause was less clear.[11]

The observed change in reaction rates with solution pH values suggests that the rates can be modulated by the pH.

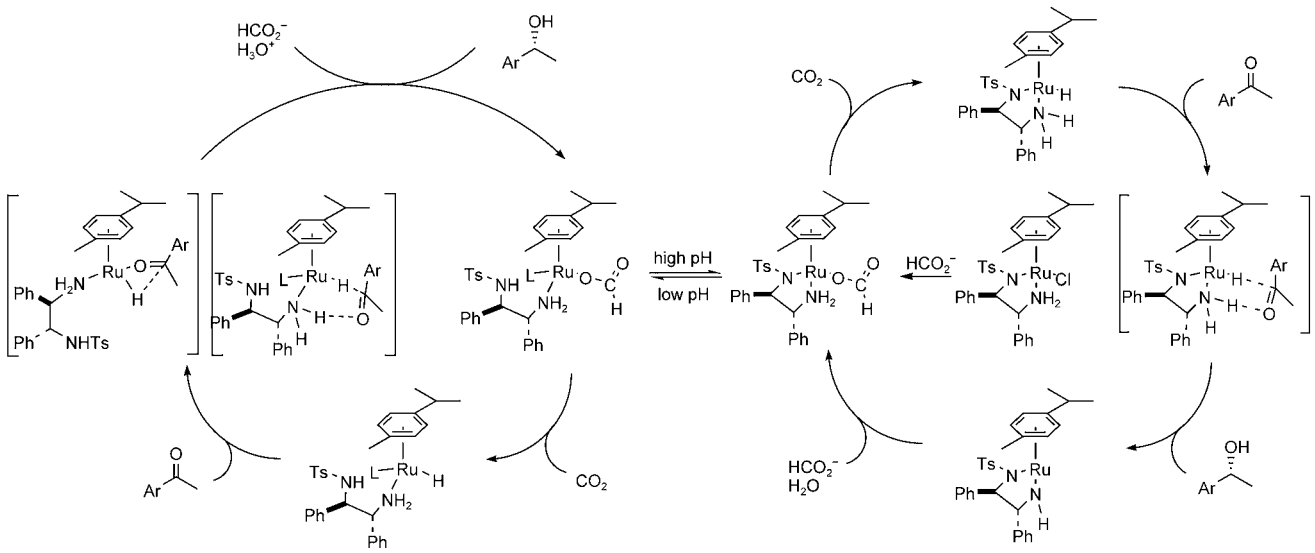

Scheme 1. Proposed catalytic cycles for the reduction of ketones under acidic and basic conditions. L may be a water molecule.

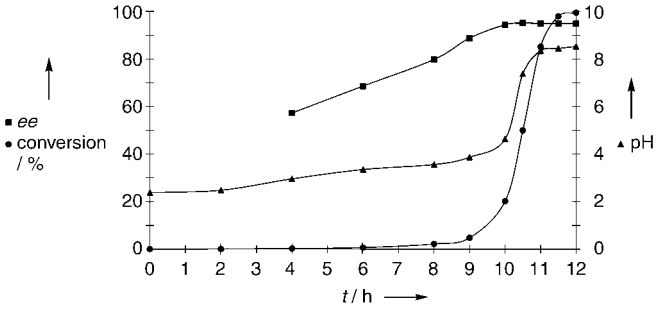

Figure 2. Graph of conversion (●), enantioselectivity (■), and pH (▲) versus time for the reduction of acetophenone (1 M) by HCOOH–NEt_3 (initial molar ratio: 4.6:1.0; 0.5 mL) in water (0.5 mL) with Ru–(*R*,*R*)-Ts-dpen at 40 °C.

This is indeed the case. Thus, as illustrated in Figure 3, the reduction of acetophenone could be rapidly initiated by raising the pH value by simple adding NEt_3 and suppressed by adding HCOOH. The reversible rise and fall in rates against

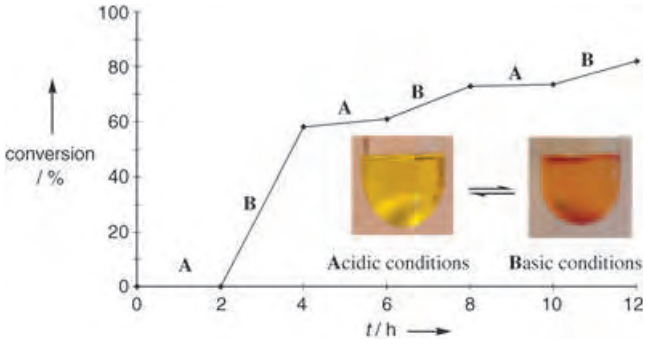

Figure 3. Graph of conversion versus time for the reduction of acetophenone (1 M) by HCOOH–NEt_3 in water (1:1 initial volume ratio, 0.5 mL water) with Ru–(*R*,*R*)-Ts-dpen at 40 °C. In regions A the initial HCOOH/NEt_3 molar ratio was maintained at 4.6:1.0 (pH 2.8), whereas in regions B HCOOH/NEt_3 = 2.3:1.0 (pH 3.7).

pH may partly result from the fluctuation of formate concentration; but there could be another explanation, that is, there may exist two interchangeable catalytic pathways, with their proportion determined by solution pH. Consistent with this, the aqueous solution changed color reversibly; the solution was yellow under acidic conditions and orange under basic conditions (Figure 3).

Taken the above observations together, we propose that the Ru–Ts-dpen catalyst operates through two catalytic cycles (Scheme 1). The cycle under basic conditions follows the concerted mechanism proposed by Noyori et al.,[12,13] whereas that at low pH values starts with the protonation of the coordinated Ts-dpen. The low rates and low *ee* values in the latter case can be interpreted as resulting from the conventional, stepwise reduction of ketones[12b,14] and/or from a similar concerted mechanism with a less-well-organized transition state. The Ru^{II}–Cl precatalyst is probably hydrolyzed with displacement of the chloride by water,[15] thus explaining its solubility in water. The question concerning which nitrogen atom is protonated is not yet clear but may be addressed from the following observations. The pK_a value of the amido nitrogen group in Ts-dpen has been measured to be 7.4,[10] and a lanthanide complex that contains a related NTs unit (pK_a = 6.4) has been shown to undergo a pH-dependent on-and-off process.[16] It is also known that the amino chelate rings in Ru^{II}–en (en = ethylenediamine) complexes are stable under conditions that are far more acidic than those used in this study.[17] Furthermore, the Ru^{II}–NTs bond is longer than the Ru^{II}–NH_2 bond in the precatalyst.[18] These observations suggest that the amido rather than the amino nitrogen atom is protonated.

If the (*R*,*R*)-Ts-dpen ligand is protonated under acidic conditions, introduction of the opposite enantiomer, (*S*,*S*)-Ts-dpen, to the solution could be expected to generate a mixture of Ru–(*R*,*R*)-Ts-dpen and Ru–(*S*,*S*)-Ts-dpen and lead to a racemic product. Furthermore, the ligand substitution process should be pH dependent, as the chelating effect of (*R*,*R*)-Ts-dpen would come into play at higher pH values (Scheme 2).

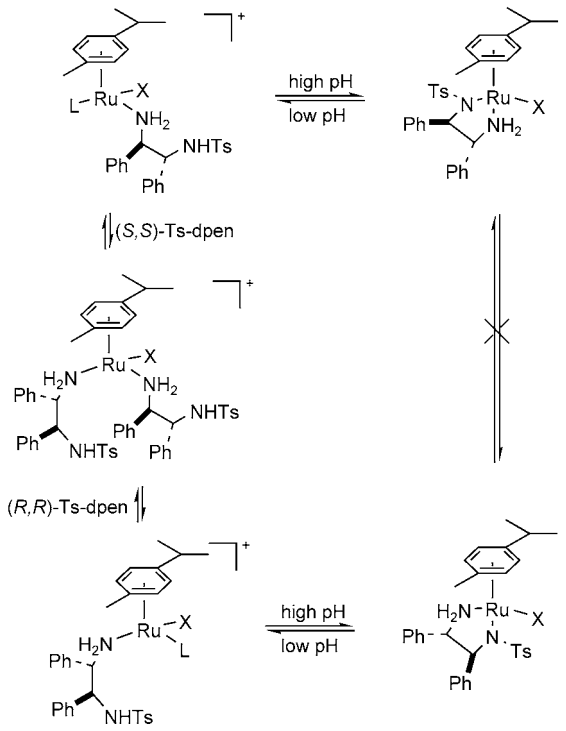

Scheme 2. Proposed ligand substitution as a function of pH. X may be a hydride or formate.

This is indeed the case, as shown in Figure 4 for the reduction of acetophenone. Thus, the addition of (*S*,*S*)-Ts-dpen (1 equiv) into an aqueous solution containing Ru–(*R*,*R*)-Ts-dpen (pH 4.6) lowered the enantioselectivity dramatically from the initial value of 98% *ee* at 5% conversion to 5% *ee* when the reaction was complete (Figure 4a). This corresponds to an *ee* value of 5% for the reduction upon the introduction of (*S*,*S*)-Ts-dpen and indicates that the subsequent reduction was virtually non-enantioselective. In sharp contrast, no significant effects on either the rate or *ee* values were noticed when the same ligand was introduced at a higher pH value of 7.7 (Figure 4b). These kinetic profiles are similar to those observed without the additional ligand, suggesting that the active catalytic species in the presence of additional (*S*,*S*)-Ts-dpen are the same Ru–(*R*,*R*)- or (*S*,*S*)-Ts-dpen complex. Further evidence in support of the mechanism is seen in the reaction by adding bipyridine, which inhibited the reduction of acetophenone only under acidic conditions.

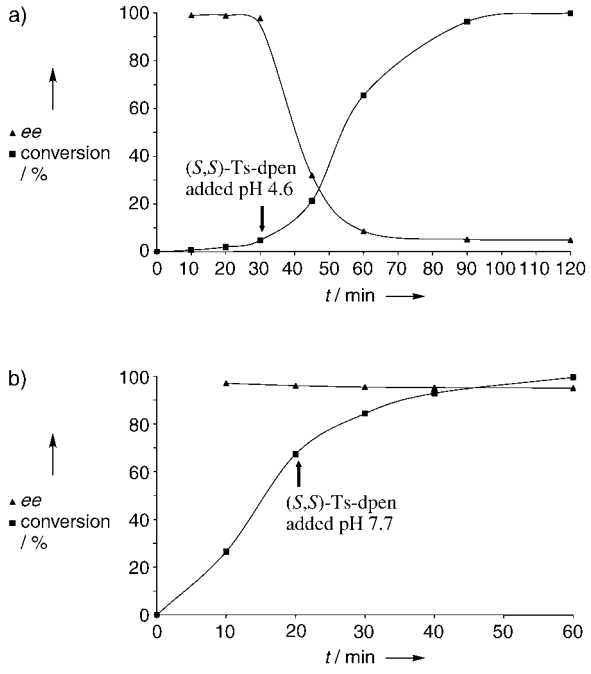

Figure 4. Effect of (*S*,*S*)-Ts-dpen (1 equiv added at the pH indicated) on the conversion (■) and enantioselectivity (▲) of the reduction of acetophenone (1 M) by HCOOH–NEt_3 in water (1:1 volume ratio) with Ru–(*R*,*R*)-Ts-dpen at 40°C. The initial HCOOH/NEt_3 molar ratio was 2.3:1.0 (a) and 0.7:1.0 (b).

With these findings in hand, it was then easy to address the issue of slow reaction rates faced when combining the HCOOH–NEt_3 azeotrope with water.[19] Thus, instead of simply adding the azeotrope mixture to water, we used an aqueous solution of HCOOH and NEt_3, in which the amine acted as a pH modulator, thus ensuring that the pH value of the solution was maintained between 5 and 8 during any reduction. Under such conditions, aromatic ketones could be reduced with Ru–(*R*,*R*)-Ts-dpen to secondary alcohols in water at much faster rates and with little loss in enantioselectivities; some examples are given in Table 1. In comparison with the original conditions described by Noyori and coworkers,[7a] the current method affords similar conversions and *ee* values in much shorter times by using much smaller amounts of HCOOH and NEt_3.

Table 1: Asymmetric transfer hydrogenation of ketones by HCOOH–Et_3N with Ru–(*R*,*R*)-Ts-dpen in water.[a]

Ketones	*t* [h]	Conversion [%][b]	*ee* [%][b]
acetophenone	1.5	100	97
4′-fluoroacetophenone	1.5	100	92
4′-trifluoromethylacetophenone	1.3	100	95
4-acetylbenzonitrile	1.5	99	89
4′-nitroacetophenone	2	>99	85
4′-methoxyacetophenone	5	>99	97
3′-methoxyacetophenone	2.5	99	95
4-acetylpyridine	2	>99	96
2-acetylthiophene	2	>99	96
4′-methylpropiophenone	3	99	92

[a] The reactions were carried out in a mixture of H_2O (0.5 mL) and HCOOH–Et_3N (0.5 mL; molar ratio 1.2:1.0; initial pH 5) at 40°C, with ketone (1 mmol) at a S/C ratio of 100:1. [b] Determined by GC. The configuration of the alcohol was *R*.

One of the limitations of the Ru–Ts-dpen catalyst and related variants was their low productivity, with most applications having S/C ratios of ≈200:1.[7–9] This limitation can now be effectively circumvented by employing the current method. As is seen from Table 2, by controlling the pH to a range of 5–8 by simply adjusting the HCOOH/NEt_3 ratios, aromatic ketones can be readily reduced at S/C ratios of 1000:1–10000:1 in water to afford the chiral alcohols with little compromise in enantioselectivities.

Table 2: Asymmetric transfer hydrogenation of ketones in water at higher S/C ratios.[a]

Ketones	S/C	*t* [h]	Conversion [%][b]	*ee* [%][b]
Acetophenone	1000	9	>99	96
4′-chloroacetophenone	1000	11	>99	93
4′-methoxyacetophenone	1000	32	99	95
2-acetylfuran	1000	8	>99	96
2′-acetonaphthone	1000	11	>99	95
acetophenone	5000[c]	57	98	96
acetophenone	10000[d]	110	98	94

[a] The reactions were carried out in a mixture of H_2O (2.5 mL) and HCOOH–Et_3N (2.5 mL; 1.2:1.0) at 40 °C with 10 mmol of ketone at pH 5–8. [b] Determined by GC analysis. The configuration of the alcohol was *R*. [c] The volume of the mixture of water and HCOOH–Et_3N was 10 mL (1:1 volume ratio); ketone: 50 mmol. [d] Water (10 mL), HCOOH (initially 5 mL), Et_3N (20 mL), and ketone (0.1 mol) were used.

In summary, the results presented herein demonstrate that aqueous-phase asymmetric transfer hydrogenation of aromatic ketones by formic acid with the Noyori–Ikariya Ru–Ts-dpen catalyst is modulated by the solution pH. By controlling the pH value, much faster rates and higher turnover numbers in conjunction with excellent *ee* values can be delivered. Evidence is presented that suggests that there may be two competing catalytic cycles, and hence the reaction rates and enantioselectivities are a function of solution pH values.

Experimental Section

$[\{RuCl_2(p\text{-cymene})\}_2]$ (3.1 mg, 0.005 mmol) and (*R,R*)-Ts-dpen (4.4 mg, 0.012 mmol) were dissolved in degassed water (0.5 mL). After stirring at 40 °C for 1 h, HCOOH (0.13 mL, 3.3 mmol), Et_3N (0.37 mL, 2.7 mmol), and acetophenone (120 mg, 1.0 mmol) were added to the solution. Following degassing three times, the mixture was allowed to react at 40 °C for a certain period of time. The workup was the same as before[2] and the product was analyzed by GC (Chrompack Chirasil-Dex CB column).

The reduction at S/C = 10000:1 was carried out as follows: After preparation of the precatalyst in water (10 mL), HCOOH (5 mL, 0.13 mol), Et_3N (20 mL, 0.14 mol), and acetophenone (12 g, 0.10 mol) were introduced. The reaction was conducted in a way similar to that above, except that during the reduction HCOOH was periodically added to keep the pH value between 5 and 8.

The reduction could also be performed in the absence of water. An example under comparable conditions is given here. The catalyst was prepared in a similar way in degassed HCOOH–NEt_3 (1 mL; molar ratio = 0.9:1). The reduction started with the introduction of acetophenone (120 mg, 1 mmol; S/C = 100:1) and resulted in a complete reaction at 40 °C in 7 h with 97 % *ee*.

Received: January 4, 2005
Published online: April 25, 2005

Keywords: acidity · asymmetric catalysis · ketones · ruthenium · transfer hydrogenation

[1] For recent reviews, see: a) T. Dwars, G. Oehme, *Adv. Synth. Catal.* **2002**, *344*, 239–260; b) D. Sinou, *Adv. Synth. Catal.* **2002**, *344*, 221–237; c) F. Joó, *Acc. Chem. Res.* **2002**, *35*, 738–745; d) U. M. Lindström, *Chem. Rev.* **2002**, *102*, 2751–2772.

[2] a) X. F. Wu, X. G. Li, W. Hems, F. King, J. Xiao, *Org. Biomol. Chem.* **2004**, *2*, 1818–1821; b) X. G. Li, X. F. Wu, W. P. Chen, F. E. Hancock, F. King, J. Xiao, *Org. Lett.* **2004**, *6*, 3321–3324.

[3] For recent examples of asymmetric transfer hydrogenation in water, see: a) P. N. Liu, J. G. Deng, Y. Q. Tu, S. H. Wang, *Chem. Commun.* **2004**, 2070–2071; b) Y. Himeda, N. Onozawa-Komatsuzaki, H. Sugihara, H. Arakawa, K. Kasuga, *J. Mol. Catal. A* **2003**, *195*, 95–100; c) Y. P. Ma, H. Liu, L. Chen, X. Cui, J. Zhu, J. G. Deng, *Org. Lett.* **2003**, *5*, 2103–2106.

[4] A. Benyei, F. Joó, *J. Mol. Catal.* **1990**, *58*, 151–163.

[5] S. Ogo, T. Abura, Y. Watanabe, *Organometallics* **2002**, *21*, 2964–2969.

[6] For recent reviews, see: a) H.-U. Blaser, B. Pugin, F. Spindler, H. Steiner, M. Studer, *Adv. Synth. Catal.* **2003**, *345*, 103–151; b) K. Everaere, A. Mortrex, J.-F. Carpentier, *Adv. Synth. Catal.* **2003**, *345*, 67–77.

[7] a) A. Fujii, S. Hashiguchi, N. Uematsu, T. Ikariya, R. Noyori, *J. Am. Chem. Soc.* **1996**, *118*, 2521–2522; b) S. Hashiguchi, A. Fujii, J. Takehara, T. Ikariya, R. Noyori, *J. Am. Chem. Soc.* **1995**, *117*, 7562–7563.

[8] a) T. Hamada, T. Torri, K. Izawa, T. Ikariya, *Tetrahedron* **2004**, *60*, 7411–7417; b) M. Watanabe, K. Murata, T. Ikariya, *J. Org. Chem.* **2002**, *67*, 1712–1715, and references therein.

[9] For some recent examples, see: a) J. Hannedouche, G. J. Clarkson, M. Wills, *J. Am. Chem. Soc.* **2004**, *126*, 986–987; b) T. J. Geldbach, P. J. Dyson, *J. Am. Chem. Soc.* **2004**, *126*, 8114–8115; c) D. Sterk, M. S. Stephan, B. Mohar, *Tetrahedron Lett.* **2004**, *45*, 535–537; d) P. N. Liu, P. M. Gu, F. Wang, Y. Q. Tu, *Org. Lett.* **2004**, *6*, 169–172; e) X. G. Li, W. P. Chen, W. Hems, F. King, J. Xiao, *Tetrahedron Lett.* **2004**, *45*, 951–953; f) X. Sun, G. Manos, J. Blacker, J. Martin, A. Gavriilidis, *Org. Process Res. Dev.* **2004**, 8, 909–914.

[10] B. Mohar, A. Valleix, J.-R. Desmurs, M. Felemez, A. Wagner, C. Mioskowski, *Chem. Commun.* **2001**, 2572–2573.

[11] D. Carmona, F. J. Lahoz, R. Atencio, L. A. Oro, M. P. Lamata, F. Viguri, E. S. Jose, C. Vega, J. Reyes, F. Joó, A. Katho, *Chem. Eur. J.* **1999**, *5*, 1544–1564.

[12] a) T. Koike, T. Ikariya, *Adv. Synth. Catal.* **2004**, *346*, 37–41; b) R. Noyori, M. Yamakawa, S. Hashiguchi, *J. Org. Chem.* **2001**, *66*, 7931–7944.

[13] a) D. A. Alonso, P. Brandt, S. J. M. Nordin, P. G. Andersson, *J. Am. Chem. Soc.* **1999**, *121*, 9580–9588; b) D. G. I. Petra, J. N. H. Reek, J. W. Handgraaf, E. J. Meijer, P. Dierkers, P. C. J. Kamer, J. Brussee, H. E. Schoemaker, P. W. N. M. van Leeuwen, *Chem. Eur. J.* **2000**, *6*, 2818–2829.

[14] G. Zassinovich, G. Mestroni, S. Gladiali, *Chem. Rev.* **1992**, *92*, 1051–1069.

[15] F. Wang, H. Chen, Dr. S. Parsons, I. D. H. Oswald, J. E. Davidson, P. J. Sadler, *Chem. Eur. J.* **2003**, *9*, 5810–5820.

[16] M. P. Lowe, D. Parker, O. Reany, S. Aime, M. Botta, G. Castellano, E. Gianolio, R. Pagliarin, *J. Am. Chem. Soc.* **2001**, *123*, 7601–7609.

[17] For examples, see: a) J. K. Beattie, H. Elsbernd, *J. Am. Chem. Soc.* **1969**, *91*, 4573–4574; b) J. A. Broomhead, L. Kane-Maguire, D. Wilson, *Inorg. Chem.* **1975**, *14*, 2575–2577.

[18] K. J. Haack, S. Hashiguchi, A. Fujii, T. Ikariya, R. Noyori, *Angew. Chem.* **1997**, *109*, 297–300; *Angew. Chem. Int. Ed. Engl.* **1997**, *36*, 285–288.

[19] In neat HCOOH–NEt_3, the reduction was faster when the HCOOH/NEt_3 ratio decreased, but slower than that in the aqueous solution (see Experimental Section).

RNA Recognition

Evidence that Electrostatic Interactions Dictate the Ligand-Induced Arrest of RNA Global Flexibility**

*Stephen W. Pitt, Qi Zhang, Dinshaw J. Patel, and Hashim M. Al-Hashimi**

Arresting flexibility to prevent RNA from undergoing functionally important conformational transitions is an established strategy for developing RNA-targeting therapeutics.[1] To understand the role of RNA flexibility in adaptive recognition[2] is also important for the rational design of small molecules that bind their RNA target with high affinity and specificity.[3] Yet few studies have quantitatively examined how RNA-binding therapeutics affect the flexibility of their RNA targets. As a result, little is known about the RNA–ligand interactions that are important for arresting different types of RNA functional flexibility. Here, we provide direct evidence by using NMR residual dipolar couplings (RDCs)[4] that electrostatic interactions play a primary role in dictating the degree to which small molecules arrest global motions in RNA.

The transactivation response element (TAR) RNA from HIV-1 (Figure 1a) is a primary RNA target for developing anti-HIV therapeutics[5] and its molecular flexibility is implicated in its function. Upon binding to its cognate target, the transactivator protein (Tat), TAR undergoes large conformational changes that involve reorientation of two helical domains from a bent to a coaxially aligned state.[6] By using RDCs, we previously reported evidence for significant interdomain flexibility in free TAR which may play a direct role in mediating the conformational changes in TAR that accompany Tat recognition.[7a,b] We also demonstrated that Mg^{2+} or the ligand mimic of Tat, argininamide, can bind TAR and completely arrest these interdomain motions.[7c,d]

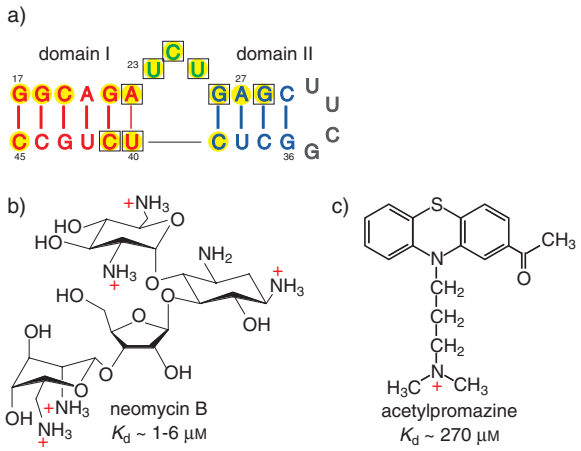

Figure 1. a) Secondary structure of TAR (transactivation response element) RNA in which the wild-type loop is replaced by a UUCG counterpart. The highlighted residues undergo $\Delta\delta > 0.1$ ppm changes in ^{1}H NMR chemical shifts upon binding to neomycin B (yellow) and acetylpromazine (□). b, c) Structures and TAR-dissociation constants (K_d) for neomycin B (b; NeoB)[9,11] and acetylpromazine (c; AcP).[14]

The RDC methodology and TAR provide a unique opportunity to examine RNA–ligand interactions that are particularly important for arresting a general class of RNA motions, which involve global reorientation of helical domains. Numerous studies on RNA–aminoglycoside recognition have demonstrated that electrostatic interactions between cationic groups on the ligand and regions of high negative-charge density in the RNA can contribute significantly to aminoglycoside-binding affinities and specificities.[8] As global motions in RNA originate from local mobility in the negatively charged backbone and as functional groups from many residues can be involved in forming pockets of high negative-charge density in RNA, we reasoned that similar electrostatic interactions are also likely to be important for arresting RNA global motions.

To examine this hypothesis, we employed RDC NMR methodology to characterize the conformational dynamics of TAR when it is bound to two molecules that have different electrostatic charges: the aminoglycoside neomycin B (NeoB),[9] which bears five positively charged ammonium groups, and the small organic molecule acetylpromazine (AcP),[10] which carries a single positive charge (Figure 1b,c). Both NeoB and AcP bind TAR and inhibit its interaction with Tat.[9,10] A previously reported NOE-based NMR spectroscopic study of the structure of the TAR–NeoB complex[11] showed that NeoB binds TAR in the minor groove and stabilizes a coaxially stacked conformation similar to that observed for TAR bound to Tat peptides and Arg (arginine).[6a,b,d] In contrast, the NMR-determined structure of the TAR–AcP complex indicates that AcP induces minor changes in the conformation of TAR and that it binds a cavity at the interdomain interface.[12] Both NMR studies did not report on the global dynamics of TAR in the ligand-bound state.

[*] Q. Zhang, Prof. H. M. Al-Hashimi
Department of Chemistry and Biophysics Research Division
University of Michigan
Ann Arbor, MI 48109 (USA)
Fax: (+1) 734-647-4865
E-mail: hashimi@umich.edu

Dr. S. W. Pitt
Department of Pharmacology
Weil Medical College of Cornell University
New York, NY 10021 (USA)

Prof. D. J. Patel
Cellular Biochemistry and Biophysics Program
Memorial Sloan-Kettering Cancer Center
1275 York Avenue, New York, NY 10021 (USA)

[**] We thank Prof. H. Schwalbe, Dr. J. Wöhnert (University of Frankfurt), Dr. A. Phân (MSKCC), and Prof. O. Yaghi (University of Michigan) for stimulating discussions. H.M.A. was a visiting professor supported by SFB 579 at the University of Frankfurt in the group of H. Schwalbe during part of this work. D.J.P. acknowledges funding from the NIH (CA46778).

Supporting information for this article (correlation plots for RDCs measured in two different experiments; measured and back-calculated RDCs; impact of choice of RDCs on order tensor analysis; table of measured RDCs) is available on the WWW under http://www.angewandte.org or from the author.

  DOI: 10.1002/anie.200500075

Shown in Figure 2 are the RDC-derived best-fit generalized degrees of order (ϑ)[13] determined for each domain in the two TAR complexes. The generalized degree of order describes the degree of alignment experienced by each domain which should be identical if the domains are held rigid relative to one another.[13] Results are shown when different input domain structures were used in the order tensor calculations, including idealized A-form helices generated by using Insight II (Molecular Simulations Inc.) and the previous NOE-based NMR spectroscopically determined structures of TAR–NeoB (pdb 1QD3)[11] and TAR–AcP (pdb 1LVJ).[12] Also shown are the values of the root-mean-square deviation (rmsd) between measured and back-calculated RDC values which provide a measure of agreement between a domain structure and measured RDC values.

In the structure determined from NMR spectroscopic studies, NeoB induces local distortions in domain I.[11] Accordingly, most NMR models for domain I in TAR–NeoB yield rmsd values that are lower than the idealized A-form helix (Figure 2a). More importantly, the ϑ value determined for the two domains in TAR–NeoB are similar, particularly for domains that yield the lowest rmsd values (Figure 2a). The best-fit ϑ_{int} value ($\vartheta_{domain\,I}/\vartheta_{domain\,II}$),[13] which provides a measure of interdomain motional amplitudes, is close to unity ($\vartheta_{int} = 0.94$) and thus indicates that NeoB arrests interdomain motions in TAR (Figure 2c). Remarkably, this is not the case for TAR bound to AcP. As previously observed for free TAR,[7a] the ϑ value for domain I is significantly smaller than that for domain II (Figure 2b), and the best-fit ϑ_{int} value (0.69) for TAR–AcP is only slightly higher than that previously reported for free TAR (0.59; Figure 2c). The low ϑ_{int} value for TAR–AcP cannot be attributed to errors in the input domain structures because the best-fit domains yield rmsd values that are equal to or smaller than the experimental uncertainty in the RDC values (see Figure 2b and Supporting Information) and because low ϑ_{int} values are observed independent of both input domain structure (Figure 2b) and RDCs (see Supporting Information). The low ϑ_{int} value for TAR–AcP could arise from fast exchange between free and AcP-bound TAR states. On the basis of the concentrations of TAR ($\approx$1 mM) and AcP ($\approx$2 mM) used in the RDC measurements and the binding constant (K_a) of $K_a \approx 270$ μm,[14] approximately 81% of TAR is computed to be in the bound state. If a population-weighted average of free and bound ϑ_{int} values is assumed (although, strictly, averages over RDCs should be considered), then a similar population-corrected ϑ_{int} value for TAR–AcP of 0.71 is obtained. In agreement with this analysis, an ϑ_{int} value of 0.71 was determined for molar ratios of about 1:5 for TAR/AcP in which the bound state is approximately 94% populated (data not shown). Rather, the low ϑ_{int} value determined for TAR–AcP argues that unlike NeoB, AcP only marginally arrests global motions in TAR.

In Figure 2d, we compare the average domain–domain orientations determined for TAR–NeoB and TAR–AcP by using RDCs with counterparts determined previously for free TAR[7a] and TAR bound to Mg^{2+}[7c] and Arg.[7d] The more coaxially stacked TAR–NeoB conformation is similar to those of TAR–Arg and TAR–Mg, whereas TAR–AcP is very similar to free TAR. The RDC-derived global conformations for TAR–NeoB and TAR–AcP are also in excellent agreement with the corresponding results of NOE-based structural NMR studies (Figure 2e).[11,12]

Our results allude to a correlation between the average domain–domain orientation of TAR and dynamics with bent interdomain alignments being more globally flexible than their coaxially stacked counterparts (Figure 2c,d). Furthermore, all of the ligands that arrest global motions in TAR

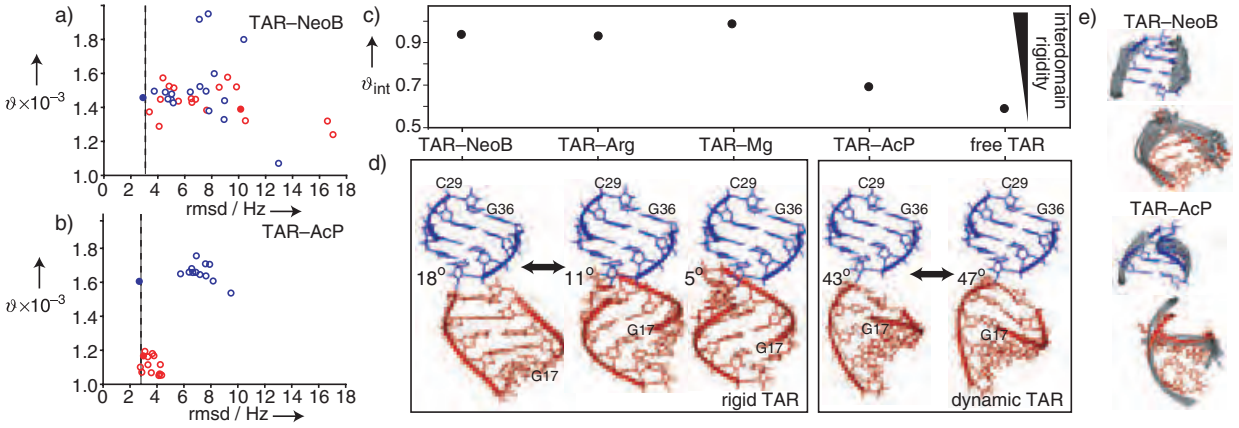

Figure 2. The global structural dynamics of TAR–NeoB and TAR–AcP. The best-fit generalized degree of order (ϑ) for domains I and II in a) TAR–NeoB and b) TAR–AcP as a function of the root-mean-square deviation (rmsd) between measured residual dipolar couplings (RDCs) and values back-calculated by using the best-fit order tensor (red unfilled circle: domain I NMR models; red filled circle: domain I idealized; blue unfilled circle: domain II NMR models; blue filled circle: domain II idealized). The experimental uncertainty (rmsd) in RDCs (see Supporting Information) is indicated by a dashed vertical line. c) The internal generalized degree of order, $\vartheta_{int} = \vartheta_{domain\,I}/\vartheta_{domain\,II}$, determined for TAR–NeoB and TAR–AcP and a comparison with previous values determined for free TAR,[7a] TAR–Mg,[7c] and TAR–Arg.[7d] d) The best-fit relative domain orientation in TAR–NeoB and TAR–AcP determined by superimposing order tensor frames and a comparison with free TAR,[7a] TAR—Mg,[7c] and TAR–Arg.[7d] Domain II (blue) is superimposed and the best-fit interhelical angle is shown next to each structure. The residues for the bulge are not shown. The estimated uncertainty in the interhelical angle is less than $\pm 6°$. e) Comparison of the RDC-derived interdomain alignment (red and blue) with structures as determined by NOE-based NMR spectroscopy (in gray) of TAR–NeoB (pdb 1QD3) and TAR–AcP (pdb 1LVJ).

(NeoB, Arg, and Mg^{2+}) are known to be involved in intermolecular electrostatic interactions. In the structure determined from NMR studies,[11] the five positively charged amino groups in NeoB are in close proximity to many backbone phosphate groups of TAR and other electronegative groups that belong to domains I and II and the bulge (U-C-U). The positively charged guanidinium group of Arg interacts with phosphate groups in domain I (A22) and the bulge (U23) as well as basic electronegative groups in domain II (G26).[6a,b,d] Recent studies indicate that two Arg ligands may be involved in electrostatic interactions with two regions of negative-charge density in TAR.[15] The crystal structure of TAR in the presence of Mg^{2+} and Ca^{2+} shows a network of inner- and outer-sphere interactions between three divalent ions and functional groups that span domains I (A22) and II (G26, A27, and G28) as well as the bulge (U23, C24, U25).[6e] In sharp contrast, the structure determined from NMR studies of TAR–AcP indicates that the RNA–ligand intermolecular contacts primarily involve stacking and hydrophobic interactions between the three-membered ring and base moieties in the bulge and neighboring residues.[12] There is also evidence that the aliphatic side chain that harbors the single positive charge is flexible and protrudes in and out of the TAR binding pocket.[14]

Our results can therefore be rationalized in part on the basis of electrostatic interactions between negatively charged pockets in TAR that can be formed by backbone phosphate groups as well as other sugar/base electronegative groups and cationic groups in the ligand. Such interactions can uniquely stabilize the negatively charged backbone that is responsible for activating global motions in TAR and/or allow simultaneous clamping interactions with electronegative groups that belong to residues that span the interdomain interface. In TAR, formation of such negatively charged pockets appears to require a degree of coaxial stacking which likely serves to bring backbone phosphates and other electronegative groups in the bulge and neighboring residues into spatial proximity.[15] In this manner, electrostatic interactions may simultaneously arrest global motions and stabilize coaxially aligned conformations of TAR.

To our knowledge, the results reported here for TAR–AcP represent the first example in which global motions are observed in an RNA complex. This illustrates how ligand binding in itself is not sufficient for arresting RNA global motions, even if the RNA-binding site is at a critical junction that intersperses helical domains. Our results also indicate that electrostatic interactions offer one approach for stabilizing the global alignment of RNA domains that are separated by flexible linkers. The RDC approach presented in this work provides insight into such dynamical features underlying RNA–small-molecule recognition that are critical to rational drug design and that are not available from static three-dimensional structures.

Experimental Section

Uniformly $^{15}N/^{13}C$-labeled TAR was prepared by in vitro transcription. Samples for NMR studies contained TAR ($\approx$1.0 mM), sodium phosphate (15 mM), sodium sulfate (25 mM), and EDTA (ethylenediaminetetraacetic acid, 0.1 mM) at pH 6.0–6.2. The samples of TAR–NeoB and TAR–AcP also contained NeoB (2 mM, MP Biomedical Inc.) or AcP (2 mM, Research Diagnostics), respectively. Identical samples that contained Pf1 phage ($\approx$25 mg mL^{-1}, ASLA Ltd) were also prepared for NMR studies.[16] NMR spectroscopy experiments were recorded at 600 MHz at 25 °C. One-bond RDCs for C1′–H1′, C2–H2, C5–H5, C6–H6, C8–H8, N1–H1, and N3–H3 were measured twice by using experiments that yield splittings along either the direct (^{1}H) and indirect ($^{13}C/^{15}N$) dimension, as previously described.[7d] Average RDC values were used whenever possible. Order tensors were computed using ORDERTEN SVD[17a] and REDCAT.[17b] A total of 20/18 and 21/19 RDCs were measured in domains I/II in TAR–NeoB and TAR–AcP, respectively. In all cases, RDCs from terminal residues G17 and C45 in domain I were omitted from analysis to avoid complications resulting from end-fraying effects. For NMR models of TAR–AcP, five RDC interactions from G18 and C44 had to be omitted owing to differences between the secondary structure of domain I in the two TAR constructs.

Received: January 9, 2005
Published online: April 28, 2005

Keywords: conformation analysis · drug design · NMR spectroscopy · RNA

[1] a) B. T. Porse, I. Leviev, A. S. Mankin, R. A. Garrett, *J. Mol. Biol.* **1998**, *276*, 391–404; b) T. Pape, W. Wintermeyer, M. V. Rodnina, *Nat. Struct. Biol.* **2000**, *7*, 104–107.
[2] a) J. R. Williamson, *Nat. Struct. Biol.* **2000**, *7*, 834–837; b) N. Leulliot, G. Varani, *Biochemistry* **2001**, *40*, 7947–7956.
[3] a) T. Hermann, *Biochimie* **2002**, *84*, 869–875; b) Q. Vicens, E. Westhof, *ChemBioChem* **2003**, *4*, 1018–1023.
[4] a) J. R. Tolman, J. M. Flanagan, M. A. Kennedy, J. H. Prestegard, *Proc. Natl. Acad. Sci. USA* **1995**, *92*, 9279–9283; b) N. Tjandra, A. Bax, *Science* **1997**, *278*, 1111–1114.
[5] a) A. Krebs, V. Ludwig, O. Boden, M. W. Gobel, *ChemBioChem* **2003**, *4*, 972–978; b) M. Froeyen, P. Herdewijn, *Curr. Top. Med. Chem.* **2002**, *2*, 1123–1145.
[6] a) J. D. Puglisi, R. Tan, B. J. Calnan, A. D. Frankel, J. R. Williamson, *Science* **1992**, *257*, 76–80; b) F. Aboul-ela, J. Karn, G. Varani, *J. Mol. Biol.* **1995**, *253*, 313–332; c) F. Aboul-ela, J. Karn, G. Varani, *Nucleic Acids Res.* **1996**, *24*, 3974–3981; d) A. S. Brodsky, J. R. Williamson, *J. Mol. Biol.* **1997**, *267*, 624–639; e) J. A. Ippolito, T. A. Steitz, *Proc. Natl. Acad. Sci. USA* **1998**, *95*, 9819–9824.
[7] a) H. M. Al-Hashimi, Y. Gosser, A. Gorin, W. Hu, A. Majumdar, D. J. Patel, *J. Mol. Biol.* **2002**, *315*, 95–102; b) Q. Zhang, R. Throolin, S. W. Pitt, A. Serganov, H. M. Al-Hashimi, *J. Am. Chem. Soc.* **2003**, *125*, 10530–10531; c) H. M. Al-Hashimi, S. W. Pitt, A. Majumdar, W. Xu, D. J. Patel, *J. Mol. Biol.* **2003**, *329*, 867–873; d) S. W. Pitt, A. Majumdar, A. Serganov, D. J. Patel, H. M. Al-Hashimi, *J. Mol. Biol.* **2004**, *338*, 7–16.
[8] a) Y. Tor, T. Hermann, E. Westhof, *Chem. Biol.* **1998**, *5*, 277–283; b) T. Hermann, E. Westhof, *J. Mol. Biol.* **1998**, *276*, 903–912; c) T. Hermann, E. Westhof, *J. Med. Chem.* **1999**, *42*, 1250–1261; d) Y. Tor, *ChemBioChem* **2003**, *4*, 998–1007.
[9] a) S. Wang, P. W. Huber, M. Cui, A. W. Czarnik, H. Y. Mei, *Biochemistry* **1998**, *37*, 5549–5557; H.-Y. Mei, A. A. Galan, N. S. Halim, D. P. Mack, D. W. Moreland, K. B. Sanders, H. N. Truong, A. W. Czarnik, *Bioorg. Med. Chem. Lett.* **1995**, *5*, 2755–2760.
[10] a) A. V. Filikov, V. Mohan, T. A. Vickers, R. H. Griffey, P. D. Cook, R. A. Abagyan, T. L. James, *J. Comput.-Aided Mol. Des.* **2000**, *14*, 593–610; b) K. E. Lind, Z. Du, K. Fujinaga, B. M. Peterlin, T. L. James, *Chem. Biol.* **2002**, *9*, 185–193.
[11] C. Faber, H. Sticht, K. Schweimer, P. Rösch, *J. Biol. Chem.* **2000**, *275*, 20660–20666.

[12] Z. Du, K. E. Lind, T. L. James, *Chem. Biol.* **2002**, *9*, 707 – 712.
[13] J. R. Tolman, H. M. Al-Hashimi, L. E. Kay, J. H. Prestegard, *J. Am. Chem. Soc.* **2001**, *123*, 1416 – 1424.
[14] M. Mayer, T. L. James, *J. Am. Chem. Soc.* **2004**, *126*, 4453 – 4460.
[15] B. Davis, M. Afshar, G. Varani, A. I. Murchie, J. Karn, G. Lentzen, M. Drysdale, J. Bower, A. J. Potter, I. D. Starkey, T. Swarbrick, F. Aboul-ela, *J. Mol. Biol.* **2004**, *336*, 343 – 356.
[16] a) M. R. Hansen, L. Mueller, A. Pardi, *Nat. Struct. Biol.* **1998**, *5*, 1065 – 1074; b) G. M. Clore, M. R. Starich, A. M. Gronenborn, *J. Am. Chem. Soc.* **1998**, *120*, 10571 – 10572.
[17] a) J. A. Losonczi, M. Andrec, M. W. F. Fischer, J. H. Prestegard, *J. Magn. Reson.* **1999**, *138*, 334 – 342; b) H. Valafar, J. H. Prestegard, *J. Magn. Reson.* **2004**, *167*, 228 – 241.

Cluster Compounds

Confined Electron-Transfer Reactions within a Molecular Metal Oxide "Trojan Horse"**

*De-Liang Long, Hamera Abbas, Paul Kögerler, and Leroy Cronin**

Dedicated to Professor Xin-Quan Xin on the occasion of his 70th birthday.

Heteropolyoxometalates (HPOMs) are molecular metal oxide clusters characterized by a vast structural diversity,[1] rich electrochemistry,[2] and versatile catalytic activities.[3] HPOMs frequently are derived from archetypal metal oxide cages of the general composition $(MO_3)_x$ (M = Mo, W) that incorporate structurally vital tetrahedral anions (e.g., $[SO_4]^{2-}$, $[PO_4]^{3-}$, $[SiO_4]^{4-}$). Yet since the first structural elucidation of the archetypal Keggin HPOM $[(MO_3)_{12}PO_4]^{3-}$ in 1933, and after many thousands of publications on developments in the HPOM area,[4–6] the role of the central template in these exceptionally stable molecules has primarily remained a structural one.[6]

[*] Dr. D.-L. Long, H. Abbas, Dr. L. Cronin
Department of Chemistry
The University of Glasgow
Glasgow, G12 8QQ (UK)
Fax: (+44) 141-330-4888
E-mail: L.Cronin@chem.gla.ac.uk
Dr. P. Kögerler
Ames Laboratory and Department of Physics & Astronomy
Iowa State University
Ames, IA 50011 (USA)

[**] This work was supported by the Leverhulme Trust (London), The Royal Society and The University of Glasgow. The EPSRC provided funds for the X-ray diffractometer. Ames Laboratory is operated for the U.S. Department of Energy by Iowa State University Contract No. W-7405-Eng-82.

Supporting information for this article is available on the WWW under http://www.angewandte.org or from the author.

One particularly interesting family of HPOMs is based on the very stable Dawson structural type ($[M_{18}O_{54}(XO_4)_2]^{m-}$; M = Mo or W, X = main-group element) which contains two tetrahedral anions and a metal oxide framework structure $(MO_3)_{18}$. This class of HPOM cluster was first structurally characterized fifty years ago and since then the subject of many hundreds of papers.[2,7] We are interested in the design of new fundamental types of isopolyoxometalates[8,9] as well as non-conventional HPOM clusters[10] that incorporate two pyramidal anions,[11] similar to the Dawson archetype, as such clusters may exhibit unprecedented properties arising from the intramolecular electronic interactions between the encapsulated anions, thus providing a novel route to manipulate the physical properties of the $\{M_{18}\}$ Dawson-type clusters.

In an attempt to develop internally switchable molecular clusters based on polyoxometalates, we have recently discovered the sulfite-based Dawson-type polyoxomolybdates α- and β-$[Mo^{VI}{}_{18}O_{54}(SO_3)_2]^{4-}$ (**1a** and **1b**, respectively). They incorporate two adjacent sulfite anions in a configuration causing a short, yet non-bonding intramolecular S···S interaction between the sulfite anions and exhibit unusual reversible thermochromic properties over the temperature range 77 to 500 K.[10] In an extension of this work we succeeded in synthesizing the first two examples of polyoxotungstate clusters incorporating the sulfite anion,[12] $[W^{VI}{}_{18}O_{54}(SO_3)_2]^{4-}$ (**2a**), the isostructural tungstate analogue to **1a**, and $[W^{VI}{}_{18}O_{56}(SO_3)_2(H_2O)_2]^{8-}$ (**3a**; see Figure 1). They were isolated as $(Bu_4N)_4[W^{VI}{}_{18}O_{54}(SO_3)_2]$ (**2**) and $K_7Na[W^{VI}{}_{18}O_{56}(SO_3)_2(H_2O)_2]\cdot 20H_2O$ (**3**) and characterized by single crystal X-ray structure analysis,[13] elemental analysis, IR and UV-Vis spectroscopy, bond valence sum (BVS) and DFT calculations.[14]

Interestingly, **3a** has a curious structure including two terminal water ligands which is unknown for closed-shell HPOM clusters of any type.[15] Moreover, **3** also demonstrates unprecedented electronic properties: the cluster anion **3a**, $[W_{18}O_{56}(SO_3)_2(H_2O)_2]^{8-}$, undergoes a unique electron-transfer reaction when heated, in which a structural re-arrangement allows the two embedded pyramidal sulfite ($S^{IV}O_3^{2-}$) anions to release up to four electrons (analogous to the "soldiers" hidden inside the "Trojan Horse") to the surface of the cluster generating the sulfate-based, deep blue, mixed-valence cluster $[W_{18}O_{54}(SO_4)_2]^{8-}$. Although electron-transfer reactions and structural rearrangements are very well known for HPOMs,[6] this is the first example of a coupled structural-rearrangement and electron-transfer process, whereby the electrons are "released" from the core of the cluster. It is also the first example of a fully characterized unimolecular reaction involving an HPOM.

To fully explore and understand these properties we must consider the structural differences between the cluster anions **2a** and **3a**. The structures of both clusters consist of two $\{W_9(SO_3)\}$ halves which contain six equatorial and three capping metal positions. The two halves are joined by linking each of the six equatorial metal atoms of each half together through six bridging oxo ligands (Figure 1 and Figure 2). The key structural differences between these two cluster families are primarily based on the relative orientation of their two sulfite groups (Figure 2) whereby the base of the pyramid

 DOI: 10.1002/anie.200500541

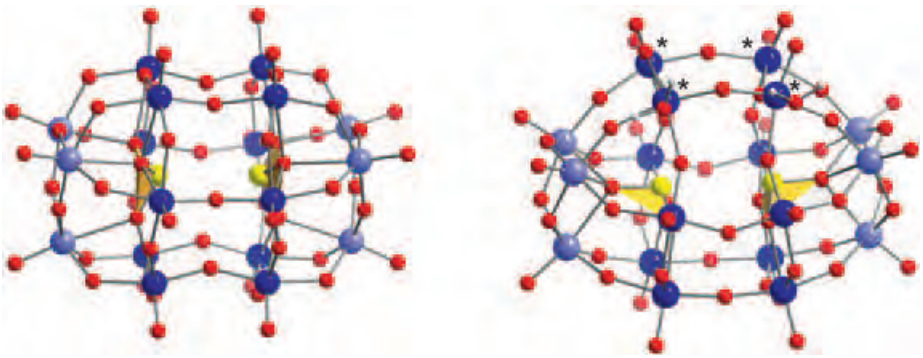

Figure 1. Ball-and-stick representations of the structures of the D_{3h}-symmetric α-$[W_{18}O_{54}(SO_3)_2]^{4-}$ (**2a**, left) and the C_{2v}-symmetric $[W_{18}O_{56}(SO_3)_2(H_2O)_2]^{8-}$ (**3a**, right) cluster anions; light blue spheres represent capping $\{W_3\}$, dark blue spheres represent equatorial $\{W_6\}$, red O, gray H, yellow S. Yellow polyhedra represent the pyramidal SO_3 units and emphasize their different relative orientations within each framework; * marks tungsten units that are not coordinated to the sulfite groups and thus have two terminal oxo ligands.

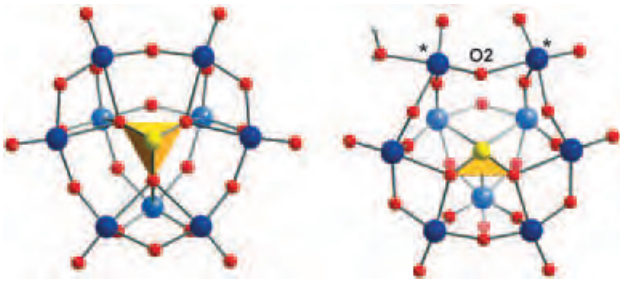

Figure 2. Schematic comparison of the SO_3 coordination mode in **2a** (left) and **3a** (right). Only one $\{W_9(SO_3)\}$ half is shown, viewed along the long axis of the cluster. Colors are as in Figure 1.

formed by the trigonal-pyramidal SO_3 group in **2a** is centrally aligned and binds to all nine metal centers of each $\{W_9(SO_3)\}$ fragment, whereas in compound **3a** the SO_3 pyramids are tilted so that only seven of the nine metal centers of each $\{W_9(SO_3)\}$ fragment are connected.

This arrangement leaves four neighboring equatorial tungsten positions in **3a** uncoordinated to the templating sulfite groups and thereby reduces the overall molecular symmetry from D_{3h} (**1a** and **2a**) to C_{2v} with the loss of a number of mirror planes and the C_3 axis for **3a**. The significantly different orientations of the sulfite ions in **3a** compared to **1a** and **2a** is also reflected by the S···S distance of 3.61(2) Å in **3a** which is significantly longer than the distance of 3.19(1) Å in **2a** and 3.27(1) Å in **1a**.

The second major structural difference between **2a** and **3a** lies in the number of terminal oxo ligands present in each cluster type. All of the metal atoms present in **2a** (as well as in **1a**) only support one terminal oxo ligand that is not shared by other metal atoms, however cluster **3a** contains four tungsten units (labeled as W* in Figures 1 and 2), each with two terminal ligands. This situation arises because these four tungsten units are not bonded to the embedded sulfite groups. The two terminal ligands and four bridging μ_2-oxo (O^{2-}) ligands per W* center complete a slightly distorted octahedral coordination geometry. Structural analysis (including bond valence sum analysis) reveals that while two of the four unique W* centers each have two terminal oxo ligands (W=O ca. 1.7 Å), the other two W* centers each have one terminal oxo ligand and one terminal water ligand (W=O ca. 1.7 Å and W–OH_2 ca. 2.2 Å). There is a slight disorder but the presence of two water ligands and two oxo ligands is confirmed by the average bond valence sums as well as chemical and thermal analysis. Furthermore the bridging oxo group (O2 in Figure 2) between the two W* positions of a $\{W_9(SO_3)\}$ half is now folded into the cluster and points towards the vacant site of the SO_3 pyramid with a O2···S distance of 2.96(2) Å, whereas the equivalent position in **1a** and **2a** points outwards.

The structure of **3a** is already prearranged for an internal reorganization and a concurrent internal redox reaction, in which the encapsulated sulfite anions act as embedded reducing agents, and are oxidized to sulfate when heated to over 400 °C. In the course of this reaction a maximum of four electrons could be transferred to the metal oxide framework, causing the color change from colorless ($\{W^{VI}_{18}\}$) to blue ($\{W^{VI}_{14}W^{V}_{4}\}$). The overall reaction is accompanied by the release of the two coordinated water ligands from the W* centers. Because the reduction of the metal oxide shell by four electrons is balanced by the internal oxidation of the two sulfite anions (to sulfate groups), the overall charge of the cluster remains identical to give $[W^{VI}_{14}W^{V}_{4}O_{54}(SO_4)_2]^{8-}$ (**4a**). The reaction can be summarized as shown in Equation (1).

$$[W^{VI}_{18}O_{56}(S^{IV}O_3)_2(H_2O)_2]^{8-} \rightarrow \alpha\text{-}[W^{VI}_{14}W^{V}_{4}O_{54}(S^{VI}O_4)_2]^{8-} + 2\,H_2O \quad (1)$$

This reaction mechanism is confirmed by a variety of experiments which includes the observation of the loss of two water molecules at 400 °C, indicated in the IR spectrum and quantified by thermogravimetric analysis (TGA). The formation of the two sulfate moieties is shown by the IR and Raman spectra (emergence of an additional band at 650 cm^{-1}, attributed to sulfate) and in differential scanning calorimetry (DSC) traces, a sharp exothermic process associated with the onset of the internal redox reaction and the formation of sulfate at ca. 400 °C (Figure 3).

Analysis of compound **4** ($K_7Na[W_{18}O_{54}(SO_4)_2]$) also confirms its formula, and the four-electron reduced polyoxotungstate shell which is also indicated by the transformation of colorless **3** into deep blue **4**. This data also confirms that **4a** is not protonated, which is confirmed by the loss of the H(-O) signal in solid-state ^1H magic angle spinning (MAS) NMR spectrum. Given the unambiguous analytical data for the formation of **4** it is unfortunate that crystals suitable for single-crystal X-ray diffraction could not be obtained and that it is exceptionally reactive, but **4** is stable for many weeks if sealed in an evacuated glass tube. However, we are able to confidently suggest that the mixed-valence framework of the

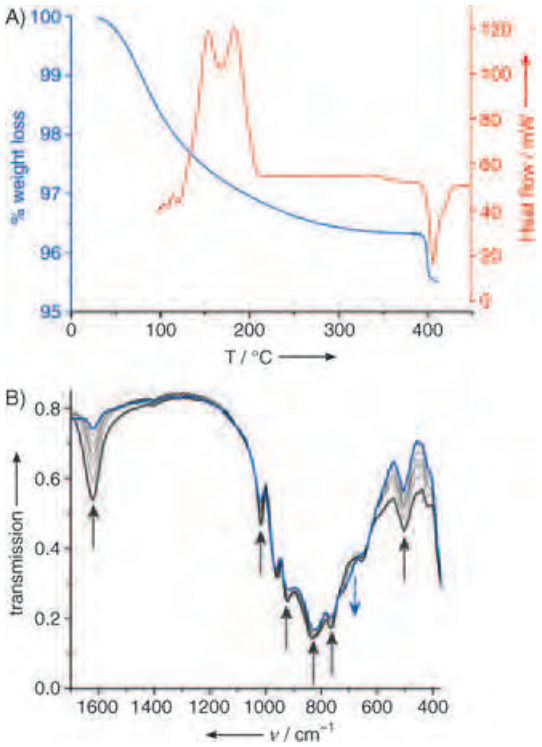

Figure 3. A) TGA (blue line) and DSC (red line) results. B) the IR spectrum of **3** (dark gray line) and the product **4** (blue line). Arrows indicate the changes going from **3** to **4**. The weight loss of just under 0.9% at 400°C correlates with the loss of two water molecules. The exothermic peak in the DSC curve at 400°C is consistent with the formation of the sulfate groups.

product α-$[W_{18}O_{54}(SO_4)_2]^{8-}$ (**4a**) is equivalent to the fully oxidized framework of the conventional sulfate-based Dawson cluster α-$[W_{18}O_{54}(SO_4)_2]^{4-}$ (**5a**), which can be synthesized by the reaction of tungstate in the presence of sulfate anions.[16] This structural hypothesis follows from a comparison of the structure of the cluster anion **5a** with that of the starting species **3a**. Overlaying the two structures reveals that the positions of all the tungsten and sulfur centers are identical to within 0.30(2) Å. We therefore hypothesize that the frameworks of the reduced product **4a** and oxidized **5a** are virtually isostructural; this idea is also supported by the fact that almost all other $\{M_{18}\}$ clusters with tetrahedral templates (over 80 are reported) display the same metal oxide framework geometry and may only differ in the relative orientation of the capping $\{M_3\}$ units giving several isomeric possibilities.

To examine this hypothesis, the preliminary energetic features of a pathway for the reaction in Equation (1) can be established from ab initio density functional theory (DFT) calculations.[14] Owing to the complexity of the system, the complete energy hyper-surface cannot be obtained and we thus used an approximate transition state. This transition-state geometry was obtained from geometrical arguments by interpolation between the atomic coordinates in **3a** and **5a**. Although the results can only be interpreted semi-quantitatively, they agree with the existence of a substantial activation barrier requiring heating and a subsequent exothermic step. The energy difference between **3a** and the transition state (plus two water molecules), that is, the reaction state representing the thermodynamic barrier, is approximately 200 kJ mol^{-1}, while the step from the transition state to the final state is characterized by an energy gain of approximately 450 kJ mol^{-1}, rendering the final state (**4a** + 2 H_2O) around 250 kJ mol^{-1} more stable than **3a**. The energy release during the exothermic process at 400°C (when **3** transforms to **4**) measured using DSC (288 kJ mol^{-1}) coincides within 15% with the theoretical result. This comparison therefore provides a striking link between theory and experiment.[17] The initial step of the reaction in Equation (1) requires movement of some of the terminal and bridging oxygen ligands of the W1 and W2 centers (Figure 4). First, the O1, O2 (both blue) and the O3, O4 (orange) positions shown in Figure 4A and 4B rotate clockwise about the central tungsten atoms through the transition state (Figure 4A, center) until the terminal O1 (bound to W1) position is within bonding distance of W2 and

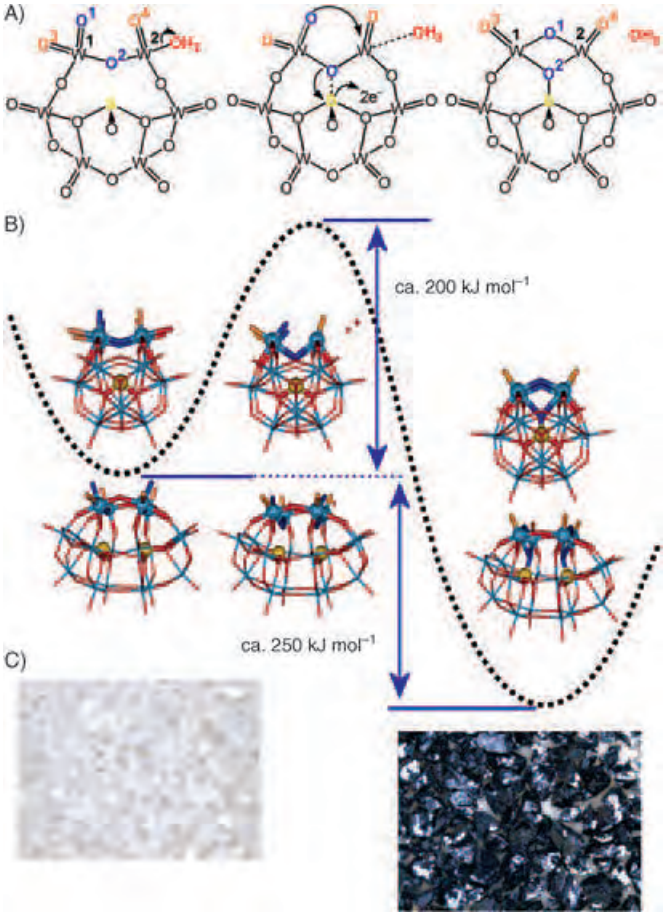

Figure 4. A) Scheme illustrating the proposed reaction mechanism. For clarity only the equatorial cluster "belts" and the central sulfur position of a $\{W_9(SO_3)\}$ fragment are shown. B) The structures of the cluster reactant **3a**, the transition state, and the product **4a** are shown and are superimposed on the suggested energy pathway (both a top view and side view of the clusters are shown for clarity with the red O, light blue W, yellow S). A common color scheme is used in (A) and (B) for the oxygen atoms that move during the transformation. C) Photographs of the crystals of the reactant **3** (colorless; left) and the product **4** (blue; right).

the bridging O2 center moving towards the sulfur atom reaches bonding distance with this center.

As can be seen in Figure 4A and 4B, the oxygen trajectories during the transformation are extremely (O1 $\Delta = 1.8$ Å; 66°), (O2 $\Delta = 1.5$ Å; 37°), (O3 $\Delta = 1.2$ Å; 30°), (O4 $\Delta = 1.2$ Å; 37°). Finally, as the bond is being made between O1 and W2 the *trans*-positioned water ligand on W2 is cleaved off (an animation of this transformation, generated by the interpolation of the coordinates between **3a** and **5a**, is present in the Supporting Information).

In conclusion, the enclosure of sulfite anions with a "correct" orientation in an HPOM cluster shell transforms these anions from "innocent" structural templates to electronically reactive, functional units. The sulfite ions can now release electrons to the cluster shell upon activation by heat (the sulfite groups in cluster **3a** are "activated" whereas those in **2a** are not). Therefore this new class of "activated" metal oxide cluster shows promise for the development of novel functional metal oxides, and **3a** is the first characterized inorganic cluster to undergo a concerted reaction in which a unimolecular process is characterized by a coupled structural and electronic rearrangement. Although the transformation of **3** to **4** does not appear reversible we will seek to extend this system, for example, by the replacement of the water groups for other ligands.

Experimental Section

2: $Na_2WO_4{\cdot}2H_2O$ (6.6 g, 20 mmol) and Na_2SO_3 (2.4 g, 19 mmol) were dissolved in water (25 mL). Hydrochloric acid (37%, 5 mL) was added to the stirred solution and the pH value of the solution was adjusted to 1.9 using diluted hydrochloric acid. The solution was then heated under reflux for 72 h. After cooling, the solution was added to a solution of Bu_4NBr (6.0 g, 18.6 mmol) in water (200 mL). A white precipitate was collected by centrifuging, washed with water and ethanol, and dried in vacuum. Recrystallization of the solid in acetonitrile afforded cream yellow crystals of **2** (yield 2.3 g, 39%). IR (KBr disk): $\tilde{\nu} = 3434$, 2961, 2873, 1625, 1482, 1379, 1151, 1105, 993, 915, 877, 779 cm^{-1}; elemental analysis (%) calcd for $C_{64}H_{144}W_{18}N_4O_{60}S_2$: C 14.5, H 2.7, N 1.1, W 62.4; found: C 14.2, H 2.6, N 1.2, W 63.0.

3: Compound **3** was produced in the same procedure as **2** except that in the final step solid KCl (5.0 g, 67 mmol) was added to the reaction mixture instead of a Bu_4NBr solution and the mixture was stirred for 2 h to yield a white precipitate, which was collected and then recrystallized in minimum water (ca. 140 mL) with the addition of KCl (2 g) and drops of diluted hydrochloric acid to keep the pH value at 2.0. After the solution was concentrated to about 100 mL (by evaporation in air), the colorless crystals of **3** were collected (yield 2.3 g, 41%). IR (KBr disk): $\tilde{\nu} = 3434$, 1623, 1017, 917, 800 cm^{-1}; elemental analysis (%) calcd for $H_{44}K_7NaO_{84}S_2W_{18}$: K 5.4, Na 0.45, W 65.4%; found: K 4.8, Na 0.40, W 66.1. The purity of the bulk phases was confirmed by powder diffraction.

Received: February 14, 2005
Published online: May 4, 2005

Keywords: electron transfer · polyoxometalates · rearrangement · sulfur · tungsten

[1] A. Müller, S. Roy, *Coord. Chem. Rev.* **2003**, *245*, 153; A. Müller, P. Kögerler, C. Kuhlmann, *Chem. Commun.* **1999**, 1347.
[2] P. J. S. Richardt, R. W. Gable, A. M. Bond, A. G. Wedd, *Inorg. Chem.* **2001**, *40*, 703; T. Ruther, V. M. Hultgren, B. P. Timko, A. M. Bond, W. R. Jackson, A. G. Wedd, *J. Am. Chem. Soc.* **2003**, *125*, 10133.
[3] W. B. Kim, T. Voitl, G. J. Rodriguez-Rivera, S. T. Evans, J. A. Dumesic, *Angew. Chem.* **2005**, *117*, 788; *Angew. Chem. Int. Ed.* **2005**, *44*, 778.
[4] T. M. Anderson, W. A. Neiwert, M. L. Kirk, P. M. B. Piccoli, A. J. Schultz, T. F. Koetzle, D. G. Musaev, K. Morokuma, R. Cao, C. L. Hill, *Science* **2004**, *306*, 2074.
[5] *Polyoxometalate Chemistry: from Topology via Self-assembly to Applications* (Eds.: M. T. Pope, A. Müller), Kluwer: Dordrecht, **2001**, pp. 1–467; K. Wassermann, M. H. Dickman, M. T. Pope, *Angew. Chem.* **1997**, *109*, 2552; *Angew. Chem. Int. Ed. Engl.* **1997**, *36*, 1445.
[6] T. Yamase, *Chem. Rev.* **1998**, *98*, 307; F. Hussain, B. S. Bassil, L.-H. Bi, M. Reicke, U. Kortz, *Angew. Chem.* **2004**, *116*, 3567; *Angew. Chem. Int. Ed.* **2004**, *43*, 3485.
[7] B. Dawson, *Acta Crystallogr.* **1953**, *6*, 113; M. Holscher, U. Englert, B. Zibrowius, W. F. Holderich, *Angew. Chem.* **1994**, *106*, 2552; *Angew. Chem. Int. Ed. Engl.* **1994**, *33*, 2491.
[8] D.-L. Long, P. Kögerler, L. J. Farrugia, L. Cronin, *Angew. Chem.* **2003**, *115*, 4312; *Angew. Chem. Int. Ed.* **2003**, *42*, 4180.
[9] D.-L. Long, H. Abbas, P. Kögerler, L. Cronin, *J. Am. Chem. Soc.* **2004**, *126*, 13880.
[10] D.-L. Long, P. Kögerler, L. Cronin, *Angew. Chem.* **2004**, *116*, 1853; *Angew. Chem. Int. Ed.* **2004**, *43*, 1817.
[11] Surprisingly, there are few examples of $\{M_{18}\}$ Dawson-like clusters that host non-tetrahedral anions, presumably due to size restrictions, examples include a single pyramidal anion ($[BiO_3]^{3-}$ or $[AsO_3]^{3-}$) in each cluster (see Y. Ozawa, Y. Sasaki, *Chem. Lett.* **1987**, 923 and Y. Jeannin, J. Martin-Frere, *Inorg. Chem.* **1979**, *18*, 3010) or a di-tetrahedral anion ($[P_2O_7]^{4-}$, two PO_4 tetrahedra sharing one corner, see S. Himeno, A. Saito, T. Hori, *Bull. Chem. Soc. Jpn.* **1990**, *63*, 1602 and U. Kortz, M. T. Pope, *Inorg. Chem.* **1994**, *33*, 5643).
[12] The compounds reported herein are the first examples of tungstosulfites and it should be noted that structurally characterized molybdosulfites are also rare, in addition to reference [10] see: M. J. Manos, J. D. Woollins, A. M. Z. Slawin, T. A. Kabanos, *Angew. Chem.* **2002**, *114*, 2925; *Angew. Chem. Int. Ed.* **2002**, *41*, 2801, and references therein.
[13] Crystal data and structure refinements for **2**: $C_{64}H_{144}N_4O_{60}S_2W_{18}$ $M_r = 5303.25$ g mol^{-1}; a block crystal ($0.24 \times 0.14 \times 0.08$ mm^3) was analyzed with a Kappa CCD diffractometer using $Mo_{K\alpha}$ radiation ($\lambda = 0.71073$ Å) at 150(2) K. Orthorhombic, space group $Pnn2$, $a = 26.7514(5)$, $b = 28.5677(5)$, $c = 15.7284(2)$ Å, $V = 12020.1(3)$ Å^3, $Z = 4$, $\rho = 2.931$ g cm^{-3}, $\mu(Mo_{K\alpha}) = 17.26$ mm^{-1}, $F(000) = 9600$, 44592 reflections measured, of which 21004 are independent, 1228 refined parameters, $R1 = 0.0371$, $wR2 = 0.0766$. **3**: $H_{44}K_7Na_1O_{84}S_2W_{18}$, $M_r = 5058.46$ g mol^{-1}; block crystal: $0.16 \times 0.10 \times 0.05$ mm^3; $T = 120(2)$ K. Monoclinic, space group $P2_1/c$, $a = 22.2248(4)$, $b = 12.6847(2)$, $c = 28.2393(5)$ Å, $\beta = 96.0234(7)°$, $V = 7817.1(2)$ Å^3, $Z = 4$, $\rho = 4.244$ g cm^{-3}, $\mu(Mo_{K\alpha}) = 26.58$ mm^{-1}, $F(000) = 8896$, 65801 reflections measured, of which 15487 are independent, 1078 refined parameters, $R1 = 0.0562$, $wR2 = 0.1202$. CCDC 249657 and CSD 414366 contain the supplementary crystallographic data for this paper. These data can be obtained free of charge from the Cambridge Crystallographic Data Centre via www.ccdc.cam.ac.uk/data_request/cif.
[14] Computation details: Density functional theory calculations (including Löwdin and Mulliken population analysis) using the TURBOMOLE5.6 package required TZVPP basis sets and

hybrid B3-LYP exchange-correlation functionals to converge. All structures (C_1 symmetry) were allowed to briefly equilibrate until a small, consistent mean energy gradient $|dE/dxyz|$ was reached. The mean shift for each atomic position generated by the free geometric equilibration amounted to 0.007 Å. Initial structures for the starting and the final reagent were obtained from crystallographic data for **3** and **5**, respectively, with two water molecules added to the final geometry.

[15] This is, to our knowledge, the first example of a non-lacunary HPOM which includes tungsten centers with more than one terminal ligand.

[16] S. Himeno, H. Tatewaki, M. Hashimoto, *Bull. Chem. Soc. Jpn.* **2001**, *74*, 1623.

[17] Other characteristic electronic properties support the suggested reaction pathway as well: A gradual transfer of charge density from the sulfite groups in the initial state **3a** to the tungsten positions in the final state is reflected by a continuous decrease in the HOMO–LUMO energy gap and a gradual decrease of the tungsten partial atomic net charges. In the final product, the four electrons are delocalized over all 18 tungsten positions, resulting in nearly uniform Löwdin partial charges (with standard deviations of 2%). Throughout the series, the Löwdin charges of the sulfur positions successively increase from 0.173 (**3a**) to 0.186 (transition state) to 0.198 (final product), a pattern corresponding to the oxidation of the sulfite groups.

Biosensors

AFM-Tip-Integrated Amperometric Microbiosensors: High-Resolution Imaging of Membrane Transport**

Angelika Kueng, Christine Kranz, Alois Lugstein, Emmerich Bertagnolli, and Boris Mizaikoff*

The mapping of molecular transport across membranes at the single-cell level is one of the major challenges in cell physiology. Miniaturized biosensors offer many advantages by combining the selectivity of biological recognition with well-established principles of transduction. To date, the combination of biosensing with atomic force microscopy (AFM) is mainly based on the mass-sensitive detection of binding events that change the deflection of a cantilever which is surface-modified with immobilized bioreceptors. Many biochemically relevant processes are based on the electrochemical conversion of molecules; therefore, techniques for obtaining laterally resolved information on coupled oxidation–reduction processes with correlation in space and time are of particular interest.[1] Scanning electrochemical microscopy (SECM) has proven to be a versatile tool for spatially resolved measurements of molecular transport across porous membranes.[2–4] Spatially resolved electrochemical information on interface processes is provided by combining electroanalytical techniques with the principle of scanning a microelectrode in close vicinity across the sample surface.[5] Few applications of miniaturized scanning biosensors combined with SECM are described in the literature.[6,7] A main limitation is the achievable lateral resolution, which is not comparable to that of AFM or consistent with the targeted imaging of membrane-transport processes at a molecular level.

A major step toward overcoming these limitations was recently made with the integration of micro- and nanoelectrodes into AFM tips.[8,9] An electroactive area with defined geometry, which is recessed from the apex of an AFM tip (Figure 1a and b), allows integration of SECM[10–12] functionality into AFM by correlating the current measured at the integrated electrode with the topographical information obtained by the AFM tip. These combined AFM–SECM probes retain the integrity of both techniques, and can be applied in dynamic-mode operation at soft biological samples.[13]

Herein, well-established protocols for the immobilization of biological recognition elements, such as enzymes, are applied to integrate micro- and nanobiosensors into AFM tips. The defined electrode geometry and the employed immobilization techniques result in a confined immobilization of the biological recognition element at the electrode surface. Enzymatic conversion of electroactive and -inactive species generated at the sample surface is possible by the immobilization of enzymes through self-assembled thiol monolayers with reactive headgroups[14] (Figure 1b(B)) or polymer-film entrapment[15,16] (Figure 1b(A)). Hence, simultaneous imaging of surface morphology and biologically relevant analytes involved in surface processes significantly extends the applicability of this technology. This integrated approach, along with the high sensitivity and fast response time of amperometric micro- and nanobiosensors, provides the spatial and temporal resolution for the investigation of cellular processes at the nanometer scale.

A synthetic model was selected to mimic glucose transport through cellular membranes. The high-resolution mapping of glucose membrane transport was carried out by immobilizing glucose oxidase at the surface of the AFM-tip-integrated electrode by electrochemically induced, localized precipitation of enzyme-containing polymer suspensions.[15] Glucose biosensors fabricated with this technology exhibit excellent sensitivity, response time, reproducibility, and long-term stability.

Figure 1c shows a schematic representation of the imaging mode for laterally resolved mapping of glucose membrane

[*] Dr. A. Kueng, Dr. C. Kranz, Prof. Dr. B. Mizaikoff
School of Chemistry and Biochemistry
Georgia Institute of Technology
Atlanta, GA 30332-0400 (USA)
Fax: (+1) 404-385-6447
E-mail: christine.kranz@chemistry.gatech.edu
Dr. A. Lugstein, Prof. Dr. E. Bertagnolli
Solid State Electronics Institute
Vienna University of Technology
Floragasse 7, 1040 Vienna (Austria)

[**] This work is supported by NSF (grant 0216368) within the program "Biocomplexity in the Environment", the National Institute of Health (grant EB000508), and the "Fonds zur Förderung der wissenschaftlichen Forschung" Austria (grants P14122-CHE and J2230). PCT patent on this technology: WO0194877A1.

 DOI: 10.1002/anie.200461556

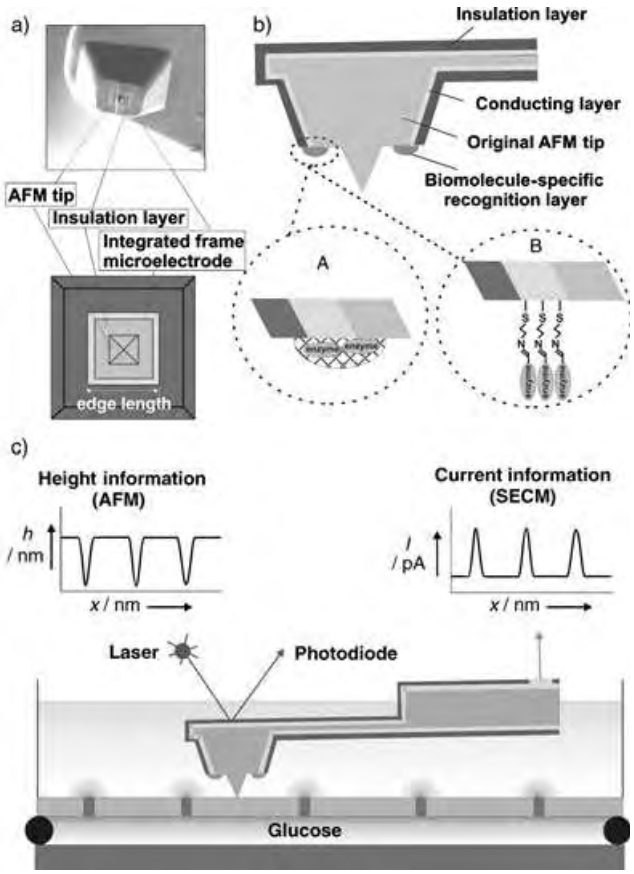

Figure 1. a) SEM image and schematic top view of an AFM-tip-integrated frame electrode; b) schematic cross section of an AFM-tip-integrated biosensor. Enzymes can be immobilized at the surface of the scanning-probe tip-integrated electrode through self-assembled thiol monolayers with functionalized headgroups (A) or through electrochemical deposition of enzyme-containing polymer films (B). c) Schematic cross section of the experimental setup for imaging glucose transport through a porous membrane during simultaneous AFM mapping.

transport with AFM-tip-integrated glucose biosensors. Images were recorded in AFM dynamic mode,[17] a prerequisite for the investigation of soft biological samples, and in SECM generation/collection (G/C) mode.[12] In G/C operation, the current response arises from an electroactive species generated at the sample surface. The integrated electrode or microbiosensor acts as a sensor that establishes concentration profiles of individual species near the sample surface. The signal traces in Figure 1c schematically illustrate schematically the expected qualitative height and current signals recorded with the bifunctional probe scanned in the x direction above a synthetic membrane with 200-nm pores. As the reshaped AFM tip is imaging the pores, which corresponds to a decrease in the height signal, glucose is diffusing through the pores toward the immobilized glucose oxidase layer, which catalyzes the conversion of glucose into gluconolactone. The corresponding reactions are summarized in Figure 2a. The resulting current measured at the integrated electrode arises from the oxidation of the enzymatically generated by-product H_2O_2, which is oxidized at the electrode surface at a bias voltage of 650 mV versus Ag/AgCl. Therefore, the current signal increases during imaging of the pores as a result of glucose diffusion from the donor into the receptor compartment.

Prior to application, the AFM-tip-integrated enzyme electrodes were characterized in an electrochemical cell by constant-potential amperometry. The calibration function obtained for the AFM-tip-integrated glucose biosensor is shown in Figure 2b and exhibits adequate linearity with an R^2 value of 0.9889 in the concentration range of 0.5–2.5 mM glucose in aqueous solution.

Simultaneously recorded AFM topography (Figure 2c) and SECM current images in the presence (Figure 2d) and absence (Figure 2f) of glucose in the donor compartment, and exemplary line scans of the height and current response (Figure 2e) are also presented. The current recorded at the AFM-tip-integrated glucose biosensor during the imaging of the pores increases as a result of the localized production of H_2O_2. The glucose signal response in the electrochemical image corresponds to the topography measured simultaneously with the AFM tip. The SECM current image of the porous membrane represents a contour map of the glucose concentration after emergence of the aqueous solution of

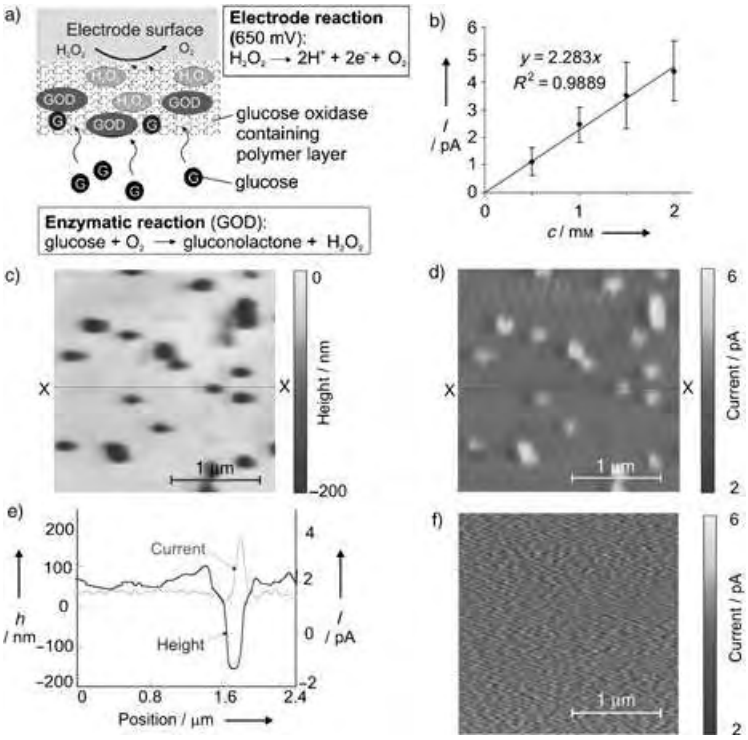

Figure 2. a) Reactions for glucose detection with a biosensor based on glucose oxidase (GOD). b) Glucose calibration of an AFM-tip-integrated biosensor (edge length: 800 nm) fabricated by entrapment of glucose oxidase within a polymer film. Simultaneously recorded c) height and d) current images of glucose diffusion through a porous polycarbonate membrane (pore size: 200 nm); images recorded in AFM dynamic mode. e) Exemplary corresponding line scans of height and current. f) Current image recorded without glucose in the donor compartment.

glucose from the membrane pore and free diffusion into the receptor-compartment solution. As is evident in the control experiment, the measured current is negligible without glucose in the donor compartment (Figure 2 f).

Quantification of the current signal obtained requires precise knowledge of the electrode geometry and the absolute distance between the electrochemical probe and the sample surface, which is provided by the bifunctional AFM–SECM probes. Furthermore, by applying a simple single-pore model previously described for the analysis of SECM images at membranes,[2,18] the flux of glucose away from the pore opening is assumed to be dominated by radial diffusion in the absence of an appreciable convective flow. The glucose transport rate can be obtained by assuming that the pore opening is hemispherical and solving the continuity equation by using Fick's law at appropriate boundary conditions.[19–22]

The concentration profile $C(r)$ at a radius r above the hemispherical pore opening can be described by Equation (1), where C_S represents the concentration of the molecule at the surface of the pore opening. Earlier results demonstrated that the radial divergence of the diffusive flux from a microscopic pore, regardless of its real shape, results in the pore appearing as if it were hemispherical in shape.[19] For a disk-shaped pore with radius a, the radius of the corresponding hemispherical pore r_0 can be described by Equation (2).

$$C(r) = (r_0/r)C_S \quad (1)$$

$$r_0 = 2a/\pi \quad (2)$$

On the basis of this approach, the theoretical glucose concentration at a distance (r) of 310 nm, which corresponds to the reshaped AFM tip height, above a pore opening with a radius of 100 nm (a) is estimated to be 0.62 mM for a 3 mM glucose solution. The evaluation of the current response in the SECM image (Figure 2 d) results in an average peak current of 1.5 ± 0.3 pA. According to the linear regression of the glucose calibration obtained at the AFM-tip-integrated electrode (Figure 2 b), the measured glucose concentration is estimated to be 0.66 ± 0.13 mM. This semiquantitative value corresponds well to the theoretically estimated concentration of 0.62 mM.

To demonstrate the versatility of the proposed technique for a wider range of applications, horseradish peroxidase (HRP) was immobilized at the surface of an AFM-tip-integrated electrode through self-assembled thiol monolayers with reactive headgroups (Figure 1 b (B)).[14] Simultaneously recorded topographical (AFM-tip) and electrochemical (substrate-generated) images were obtained by immobilizing a peroxidase layer at the surface of an AFM-tip-integrated electrode. The reactions involved are shown schematically in Figure 3. The peroxidase activity was imaged in the tip-generation/substrate-collection mode of SECM (see Figure 3 a) during AFM contact-mode operation. At the AFM-tip-integrated electrode, the enzyme-catalyzed reduction of H_2O_2 involves ferrocene methanol (Fc) as an electron donor. Ferrocenium methanol (Fc^+, which contains Fe^{2+}), the electroactive by-product of the HRP-catalyzed reaction,

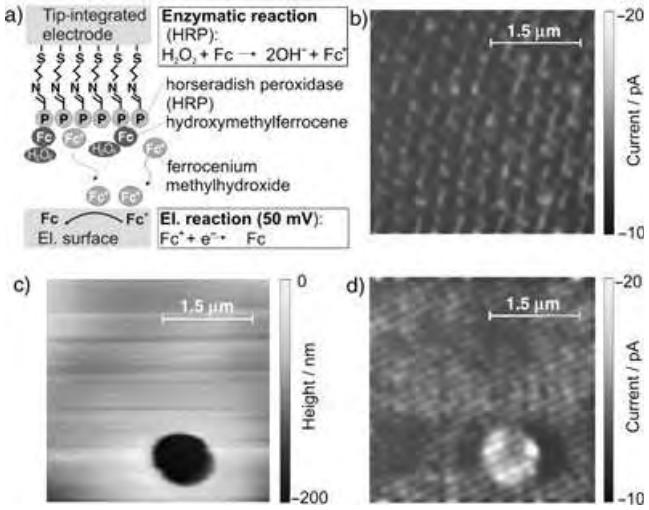

Figure 3. a) Reactions and detection scheme of the experiment in the tip-generation/substrate-collection mode for imaging with an AFM-tip-integrated biosensor based on horseradish peroxidase (HRP). Topographical information and tip-integrated peroxidase activity is recorded simultaneously by contact-mode AFM operation. The current measured at the microelectrode array reflects the enzyme activity of the HRP biosensor integrated into the AFM tip. Top view of the height (c) and simultaneously recorded current in the presence (d) and absence (b) of H_2O_2 in solution. El. = electrode.

diffuses to the biased sample surface, which comprises a microstructured electrode array where Fc^+ is reduced at a selected potential not amenable to any other species in solution. The simultaneously obtained topography of an individual microstructured disk electrode and the local (electro)chemical activity are shown in Figure 3 c and 3 d, respectively. Comparison with the control experiment in the absence of H_2O_2 (Figure 3 b) demonstrates the successful application of tip-integrated enzyme layers in bifunctional SECM–AFM probes for SECM tip generation/substrate collection.

AFM-tip-integrated imaging biosensors are a promising concept that combine the advantages of high selectivity provided by amperometric microbiosensors with high-resolution scanning probe microscopy based on microfabricated multifuntional scanning probes. High reproducibility of the fabrication process and the size of the integrated sensors in the micro- to nanodomain make them a versatile tool for future applications in probing a wide range of biologically relevant processes at a cellular level. The presented technology provides a concept for the simultaneous detection of surface morphology and (electro)chemical activity with high selectivity and high lateral resolution, on the basis of this concept of "imaging nanobiosensors". Accurate positioning and scanning of nanobiosensors at a defined distance above the sample surface provides quantitative kinetic parameters with high lateral and temporal resolution. Given the flexibility of the technology, there is considerable scope for the extended use of multifunctional scanning probes for a wide range of biological specimens and processes.

Experimental Section

AFM-tip-integrated gold electrodes (thickness of the gold layer: 100 nm, parylene C insulation layer: 800 nm) were fabricated and characterized as previously described.[8,9] All measurements were carried out with a Pico Plus AFM (Molecular Imaging, Tempe, AZ). The output signal of the bipotentiostat (A-832, CH Instruments, Austin, TX) was read at an additional AD/DA channel offered by the AFM instrument. The faradaic current recorded at the integrated electrode was obtained simultaneously with the topographical information provided by the reshaped AFM tip.

Imaging of glucose membrane transport with an AFM-tip-integrated biosensor based on glucose oxidase: The AFM–SECM tip used for imaging glucose diffusion through the synthetic porous membrane had an edge length of 800 nm and a reshaped tip height of 310 nm. Selective electrode-surface modification was performed by the pH-shift-induced polymerization of enzyme-containing films.[15] For polymer-film formation, a potential-pulse profile (2200 mV for 0.2 s, 800 mV for 1 s, and 0 mV for 5 s versus Ag/AgCl) was applied for one cycle, which led to the formation of an enzyme-containing polymer layer selectively deposited on the electrode surface.

Calibration of the tip-integrated biosensor was carried out by constant-potential amperometry by using a bipotentiostat (A832, CH Instruments, Austin, TX) and an electrochemical cell equipped with a Pt counter electrode and an Ag/AgCl reference electrode containing 10 mL of phosphate-buffered saline (PBS) solution at pH 7.4. The enzyme-modified electrode was operated at a potential of 650 mV versus Ag/AgCl to oxidize the H_2O_2 formed during the reaction catalyzed by glucose oxidase. After the current signal reached a steady-state value, aliquots of a glucose standard solution (0.2 M) were injected and the increase in current was monitored.

To study glucose membrane transport, a porous polycarbonate membrane (200-nm pore size, Osmonics Inc., Minnetonka, MN) was mounted in a custom-built vertical diffusion cell that separated aqueous solutions in the donor and receptor compartments (see Figure 1c). Measurements were performed in PBS solution (pH 7.4). The donor solution (bottom) contained glucose (3 mM). All measurements were carried out in a three-electrode setup with an Ag/AgCl reference electrode and a platinum-wire counter electrode at room temperature. The integrated biosensor was biased at a potential of 650 mV to oxidize evolving H_2O_2. Scan area: 2450 × 2450 nm, scan rate: 1 line s^{-1}, drive frequency: 32 kHz, tip potential: 650 mV versus Ag/AgCl.

Imaging with an AFM-tip integrated biosensor based on horseradish peroxidase: The AFM–SECM tip (edge length: 860 nm, tip height: 410 nm) was cleaned in H_2SO_4/H_2O_2 (70:30 v/v) for 30 s, rinsed three times with water, and then immediately immersed in cystaminium dichloride (0.1M in acetate buffer; pH 5.5) for 30 min. After rinsing the probe five times with deionized water, HRP (1 mg) in phosphate buffer (100 μL, pH 7.0) containing 2.5% (v/v) glutaraldehyde was immobilized on the integrated gold electrode for 2 h. The probe was thoroughly rinsed with buffer solution several times, and the sample was stored at 4 °C prior to use.

The AFM–SECM experiment was carried out in AFM contact and SECM tip-generation/substrate-collection modes in ferrocene methanol (Fc, 2 mmol) in phosphate buffer (0.1M, pH 7.0) with KCl (0.1M) as the electrolyte in the presence and absence of the enzymatic substrate H_2O_2 (0.5 mmol). The microstructured gold sample (Quantifoil Micro Tools, Jena, Germany) was biased at a potential of 50 mV versus Ag/AgCl to reduce ferrocenium methanol (Fc^+). Scan area: 4 × 4 μm, scan rate: 1 line s^{-1}.

Received: August 5, 2004
Revised: February 28, 2005
Published online: April 28, 2005

Keywords: biosensors · glucose · membranes · scanning probe microscopy

[1] J. K. H. Horber, M. J. Miles, *Science* **2003**, *302*, 1002.
[2] B. D. Bath, H. S. White, E. R. Scott, *Scanning Electron Microsc.* **2001**, 343.
[3] O. D. Uitto, H. S. White, K. Aoki, *Anal. Chem.* **2002**, *74*, 6131.
[4] B. D. Bath, R. D. Lee, H. S. White, E. R. Scott, *Anal. Chem.* **1998**, *70*, 1047.
[5] A. J. Bard, F. R. F. Fan, D. T. Pierce, P. R. Unwin, D. O. Wipf, F. Zhou, *Science* **1991**, *254*, 68.
[6] A. Hengstenberg, C. Kranz, W. Schuhmann, *Chem. Eur. J.* **2000**, *6*, 1547.
[7] B. R. Horrocks, D. Schmidtke, A. Heller, A. J. Bard, *Anal. Chem.* **1993**, *65*, 3605.
[8] C. Kranz, G. Friedbacher, B. Mizaikoff, A. Lugstein, J. Smoliner, E. Bertagnolli, *Anal. Chem.* **2001**, *73*, 2491.
[9] A. Lugstein, E. Bertagnolli, C. Kranz, A. Kueng, B. Mizaikoff, *Appl. Phys. Lett.* **2002**, *81*, 349.
[10] R. C. Engstrom, M. Weber, D. J. Wunder, R. Burgess, S. Winquist, *Anal. Chem.* **1986**, *58*, 844.
[11] R. C. Engstrom, T. Meaney, R. Tople, R. M. Wightman, *Anal. Chem.* **1987**, *59*, 2005.
[12] C. Lee, J. Kwak, F. C. Anson, *Anal. Chem.* **1991**, *63*, 1501.
[13] A. Kueng, C. Kranz, A. Lugstein, E. Bertagnolli, B. Mizaikoff, *Angew. Chem.* **2003**, *115*, 3358; *Angew. Chem. Int. Ed.* **2003**, *42*, 3238.
[14] T. Wilhelm, G. Wittstock, R. Szargan, *Fresenius J. Anal. Chem.* **1999**, *365*, 163.
[15] C. Kurzawa, A. Hengstenberg, W. Schuhmann, *Anal. Chem.* **2002**, *74*, 355.
[16] A. Kueng, C. Kranz, B. Mizaikoff, *Biosens. Bioelectron.* **2004**, *19*, 1301.
[17] P. K. Hansma, J. P. Cleveland, M. Radmacher, D. A. Walters, P. E. Hillner, M. Bezanilla, M. Fritz, D. Vie, H. G. Hansma, C. B. Prater, J. Massie, L. Fukunaga, J. Gurley, V. Eilings, *Appl. Phys. Lett.* **1994**, *64*, 1738.
[18] A. Kueng, C. Kranz, B. Mizaikoff, *Biosens. Bioelectron.* **2004**, in press; published in ASAP section.
[19] E. R. Scott, H. S. White, J. B. Phipps, *Anal. Chem.* **1993**, *65*, 1537.
[20] J. Crank, *The Mathematics of Diffusion*, Oxford University Press, New York, **1956**.
[21] E. L. Cussler, *Diffusion: Mass Transfer in Fluid Systems*, Cambridge University Press, New York, **1997**.
[22] A. J. Bard, L. R. Faulkner, *Electrochemical Methods*, Wiley, New York, **1980**.

Supported Catalysts

Heterotrimetallic RuMnMn Species on a Hydrotalcite Surface as Highly Efficient Heterogeneous Catalysts for Liquid-Phase Oxidation of Alcohols with Molecular Oxygen**

*Kohki Ebitani, Ken Motokura, Tomoo Mizugaki, and Kiyotomi Kaneda**

The creation of a well-defined, active metal site on a solid surface not only opens up an avenue to materials that boost catalytic performance but also aids an understanding of the molecular basis of heterogeneous catalysis.[1] Modifying the coordination sphere of a metal species with other metals as ligands, which is a basic approach in organometallic and bioinorganic chemistry,[2] is also being applied to heterogeneous catalysis[3] because of the potential of performing unique catalytic reactions based on cooperation between diverse metals within a regular arrangement. In addition, this allows local compositional modeling for the strong metal–support interactions (SMSI) seen in supported metal catalysts.[4]

Hydrotalcite (HT), which is a layered, mixed hydroxide of Mg and Al,[5] has received attention as a material for advanced heterogeneous catalysts[6,7] because of the cation-exchange ability of the Brucite layer, the anion-exchange ability of the interlayer, its adjustable surface basicity, and adsorption capacity. Recently, we created a monomeric Ru^{IV}-OH species on the HT (Ru/HT) surface by adsorption which turned out to be an excellent heterogeneous catalyst for the one-pot synthesis of α-alkylated nitriles by a Ru-catalyzed alcohol oxidation coupled with a base-promoted aldol reaction.[7d] As part of our ongoing project on the functionalization of supported Ru catalysts to achieve environmentally friendly ("green") organic syntheses, we present a novel HT-bound heterotrimetallic $Ru^{IV}Mn^{IV}Mn^{IV}$ species that has been structurally characterized on the atomic scale by X-ray absorption spectroscopy.[8] This material is an excellent solid catalyst for liquid-phase alcohol oxidation under mild conditions. This protocol to create a supported mixed-metal species can provide catalytically active compounds that are uniform in composition and distribution on a solid surface by applying concepts from coordination chemistry, and bridges the gap between homogeneous and heterogeneous catalysis.[9]

We obtained well-defined, heterotrimetallic RuMnMn species on the HT surface ($RuMn_2$/HT) by immobilizing Mn cations onto Ru/HT. The Ru/HT was prepared by treating HT with an aqueous solution of $RuCl_3 \cdot n\,H_2O$.[7d] The retention of the HT interlayer distance (3.0 Å), as shown by XRD (X-ray diffraction),[10] indicated that both metal species are accommodated on the HT surface. The K-edge XANES (X-ray absorption near-edge structure) spectrum of the Ru and Mn of $RuMn_2$/HT reveals that the surface Ru and Mn cations are in the oxidation state +IV. In the Fourier transformation of the Ru K-edge k^3-weighted EXAFS (extended X-ray absorption fine structure) spectrum of $RuMn_2$/HT (Figure 1b) a peak near 3.5 Å, corresponding to the contiguous Ru sites (Ru–O–Ru),[11] was barely detected.

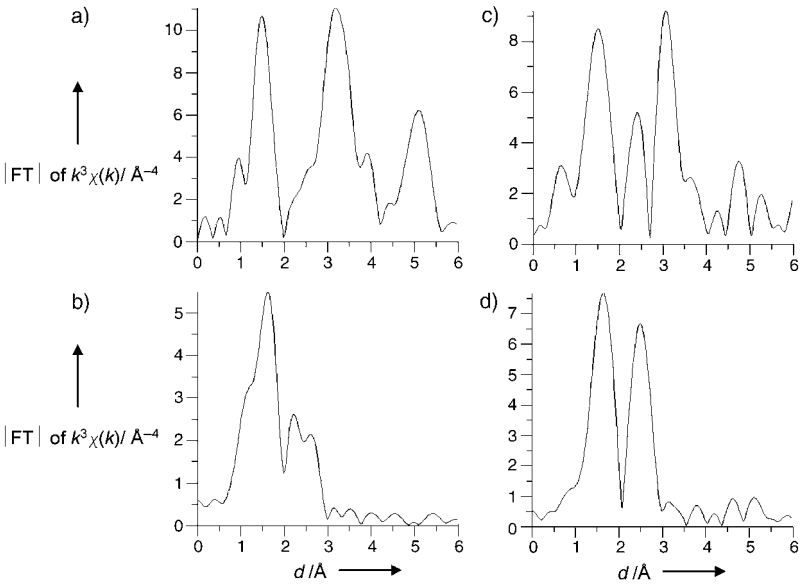

Figure 1. Fourier transformation (FT) of the k^3-weighted K-edge EXAFS spectrum of a) RuO_2, b) $RuMn_2$/HT (Ru K-edge), c) β-MnO_2, and d) $RuMn_2$/HT (Mn K-edge). The phase shift was not corrected.

The coordination number (CN), distance (R), and Debye–Waller factor ($\Delta\sigma$) of the Ru–O, Ru–Mg, and Ru–Mn bonds, as estimated by a curve-fitting analysis,[8] are listed in Table 1. The Ru^{IV} species of $RuMn_2$/HT are surrounded by six oxygen atoms with different bond distances. The shortest Ru–O bond was assigned to a Ru^{IV}–OH moiety.[12] Two bonds of Ru–Mg and Ru–Mn shells, with CNs of 0.9 and 1.9, respectively, prove that the Ru^{IV} species is in the vicinity of the Mg cation within the Brucite-like sheets and two Mn cations on the HT surface. Furthermore, a Mn–Mn shell with a distance of 2.32 Å and CN of 1.1 shows the formation of dimeric Mn^{IV} cation species.[13]

The above results show a $Ru^{IV}Mn^{IV}Mn^{IV}$ trimetallic species on the HT surface, as shown in Figure 2, in which dimeric Mn–Mn species are connected to a single Ru^{IV} cation through OH groups and water. To our knowledge, this is the first report of the preparation of heterotrimetallic species

[*] Dr. K. Ebitani, K. Motokura, Dr. T. Mizugaki, Prof. Dr. K. Kaneda
Graduate School of Engineering Science, Osaka University
1–3 Machikaneyama, Toyonaka Osaka 560-8531 (Japan)
Fax: (+81) 6-6850-6260
E-mail: kaneda@cheng.es.osaka-u.ac.jp

[**] This work was supported by a Grant-in-Aid for Scientific Research from the Ministry of Education, Culture, Sports, Science and Technology of Japan. We thank Prof. M. Nomura (KEK, PF) and Dr. T. Uruga (SPring-8) for XAFS measurements.

Supporting information for this article is available on the WWW under http://www.angewandte.org or from the author.

 DOI: 10.1002/anie.200462600

Table 1: Curve-fitting results for K-edge EXAFS of Ru and Mn.

Sample	Shell	CN[a]	*R* [Å][b]	Δσ [Å^2][c]
$RuMn_2$/HT	Ru-K			
	Ru–O(1)	2.1	1.97	−0.0079
	Ru–O(2)	2.1	2.07	−0.0045
	Ru–O(3)	1.1	1.83	−0.0088
	Ru–O(4)	0.6	2.61	−0.0087
	Ru–Mg	0.9	3.19	−0.1023
	Ru–Mn	1.9	3.28	0.0499
	Mn-K			
	Mn–O(1)	2.6	1.85	−0.0030
	Mn–O(2)	3.1	1.98	−0.0060
	Mn–Mn	1.1	2.32	−0.0017
RuO_2[d]	Ru–O(1)	2	1.94	–
	Ru–O(2)	4	1.98	–
β-MnO_2[e]	Mn–O	6	1.89	–
	Mn–Mn(1)	2	2.87	–
	Mn–Mn(2)	8	3.42	–

[a] Coordination number. [b] Interatomic distance. [c] Δσ is the difference between the Debye–Waller factor of the sample and that of the reference sample. [d] Taken from the crystallographic data.[11] [e] Taken from the crystallographic data.[26]

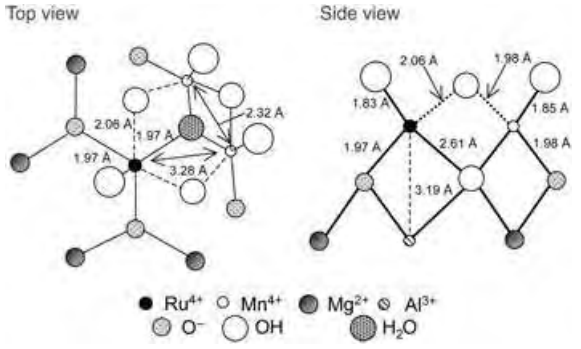

Figure 2. Proposed structure of the heterotrimetallic RuMnMn species on HT.

Table 2: Oxidation of benzyl alcohol (**1**) in the presence of various Ru catalysts under 1 atm O_2.[a]

Entry	Catalyst	Conv. [%][b]	Yield [%][b]
1	$RuMn_2$/HT	100	99
2	reuse 1[c]	100	99
3	reuse 2[c]	100	98
4	reuse 3[c]	100	99
5	Ru/HT	66	66
6	Ru/Al_2O_3[d]	56	55
7	$RuO_2 \cdot n H_2O$	5	4
8	Mn_2/HT[e]	0	0
9	HT	0	0

[a] Reaction conditions: catalyst (3 mol% Ru), benzyl alcohol (1 mmol), toluene (5 mL), 60°C, 1 atm O_2, 1 h. [b] Conversions and yields were determined by GC analysis using an internal standard method based on benzyl alcohol. [c] Catalyst recovered and reused. [d] Prepared by the reported procedure.[15c] [e] 6 mol% Mn.

consisting of metal cations on a support involving metal oxide and metal hydroxides,[14] whereas the preparation of supported heterobimetallic or metal alloy species have been reported.[3] Adjusting the basicity of the hydroxy groups around the Ru^{IV} cation, produced by reaction of the surface OH groups of HT with $RuCl_3$ species,[7d] brought about selective immobilization of Mn cations in the vicinity of the Ru species to give the unique $Ru^{IV}Mn^{IV}Mn^{IV}$ sites.

The catalytic ability of the RuMnMn species was explored in the oxidation of alcohol with O_2 at atmospheric pressure (Table 2).[15,16] The trimetallic $RuMn_2$/HT shows a higher catalytic activity than Ru/HT,[7d] Ru/Al_2O_3,[15c,e] and RuO_2,[15a] which are typical heterogeneous Ru catalysts for the oxidation of benzyl alcohol (**1**).[17] Benzyl alcohol was oxidized to benzaldehyde (**2**) quantitatively within 1 h in the presence of the $RuMn_2$/HT catalyst.[18]

The initial turnover frequency based on Ru for $RuMn_2$/HT (140 h^{-1}) is almost five times larger than that for Ru/HT. On a 10-mmol scale oxidation of **1** in the presence of 0.1 mol% Ru, the turnover number based on Ru reached 840 at 90°C. Moreover, the high catalytic ability of $RuMn_2$/HT was demonstrated by the quantitative oxidation of **1** within 10 h, even at 40°C.

As displayed in Table 3, the $RuMn_2$/HT catalyst selectively oxidizes a wide variety of alcohols. Primary and secondary benzylic alcohols are converted into the corresponding carbonyl compounds in high yield (entries 1–3). The catalysis is also chemoselective; $RuMn_2$/HT preferentially oxidizes primary over secondary hydroxy groups, as shown by the selective oxidation of 1-[(4′-hydroxymethyl)phenyl]ethanol to 1-[(4′-formyl)phenyl]ethanol in 98% yield (Scheme 1).

In the case of cyclopropyl(phenyl)methanol, the hydroxy group was oxidized without cleavage of the cyclopropyl ring

Table 3: Oxidation of various alcohols catalyzed by $RuMn_2$/HT in the presence of O_2.[a]

Entry	Alcohol	Product	*t* [h]	Conv. [%]	Yield [%][b]
1	Benzyl alcohol (**1**)	Benzaldehyde (**2**)	1	100	99
2	1-Phenylethanol	Acetophenone	3.5	100	92
3	Benzhydrol	Benzophenone	2	94	93
4	Cyclopropyl(phenyl)methanol	Cyclopropyl phenyl ketone	6	100	99
5	Cinnamyl alcohol	Cinnamaldehyde	1.5	100	97
6	(2-Hydroxymethyl)thiophene	2-Thiophenecarboxaldehyde	2	100	89
7	2-Aminobenzyl alcohol	2-Aminobenzaldehyde	21	100	100

[a] Reaction conditions: catalyst (2 mol% Ru), alcohol (1 mmol), toluene (5 mL), 60°C, O_2 flow. [b] Yields were calculated based on alcohols.

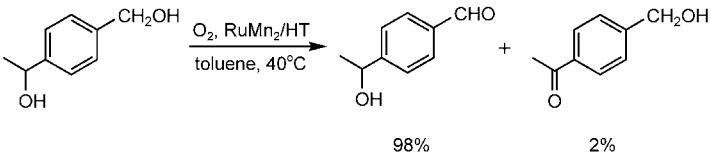

Scheme 1. Selective oxidation of primary hydroxy groups by $RuMn_2$/HT catalyst.

(entry 4). Oxidation of cinnamyl alcohol proceeded smoothly without affecting the carbon–carbon double bond (entry 5). Furthermore, $RuMn_2$/HT effectively catalyzes the oxidation of (2-hydroxymethyl)thiophene, a heteroaromatic alcohol, to 2-thiophenecarboxaldehyde, in high yield (entry 6), and the oxidation of 2-aminobenzyl alcohol to 2-aminobenzaldehyde, quantitatively (entry 7), in contrast to the homogeneous Pd and Ru complexes.[16]

The spent $RuMn_2$/HT catalyst could be readily separated from the reaction mixture by filtration. The EXAFS spectrum of the recovered $RuMn_2$/HT catalyst confirmed retention of the original RuMnMn structure, and ICP (inductively coupled plasma) analysis of the filtrate indicated no leaching of Ru and Mn species during the oxidation. The $RuMn_2$/HT catalyst could be reused while maintaining the same high catalytic activity and selectivity (Table 2, entries 2–4). When the catalyst was removed at about 50% conversion of the alcohol, no further oxidation was detected in the filtrate after 3 h under 1 atm O_2 which shows that the present alcohol oxidations proceed at the interface between the catalyst surface and the liquid phase.

To the best of our knowledge, $RuMn_2$/HT is the most effective, environmentally benign Ru catalyst for the oxidation of benzylic and aromatic allylic alcohols in the liquid phase[15,16c,d,19] with the advantages of 1) high catalytic activity, even with O_2 at 1 atm as the sole oxidant, 2) wide applicability to alcohols, including those containing heteroatoms, 3) simple preparation and work-up procedures, and 4) reusability as a solid catalyst.

The Mn cations in the RuMnMn species evidently play a pivotal role in improving the Ru-catalyzed alcohol oxidation since Mn_2/HT does not catalyze the reaction (Table 2, entry 8). We have proposed a catalytic cycle for the alcohol oxidation (Scheme 2)[20] that proceeds via a ruthenium alkoxide intermediate, which undergoes β-hydrogen elimination to produce the carbonyl compound and a ruthenium hydride species, as observed by IR spectroscopy.[10] Reaction of this hydride with O_2 and subsequent ligand-exchange with the alcohol completes the catalytic cycle.[15b,c]

A rate equation based on a Michaelis–Menten-type model[21] for this proposed mechanism [Eq. (1)] agrees well with the kinetic data.

$$\mathrm{Ru{-}OH + RCH_2OH} \underset{k_{-1}}{\overset{k_1}{\rightleftharpoons}} \mathrm{[Ru{-}OCH_2R]} \xrightarrow{k_2} \mathrm{Ru{-}H + RCHO} \qquad (1)$$

For the $RuMn_2$/HT-catalyzed oxidation of **1**, K_M and k_2 were calculated to be 2.96 mM and 0.047 s^{-1}, respectively, at 60 °C. The rate constant (k_2) of β-hydrogen elimination from the ruthenium alkoxide intermediate is therefore almost twice that for the Mn-free Ru/HT. The β-hydrogen elimination is considered as the rate-determining step in the overall alcohol oxidation from the primary kinetic isotope effect in the competitive oxidation of **1** and $C_6D_5CD_2OH$ (4.2).[15b,e] Thus, the Mn cations in the heterotrimetallic sites facilitate β-hydrogen elimination from the ruthenium alkoxide intermediate. Removing the water molecule that binds the Ru and Mn cations improves the situation of the Ru species during β-hydrogen elimination by, for example, producing a coordinately unsaturated Ru site.[16c]

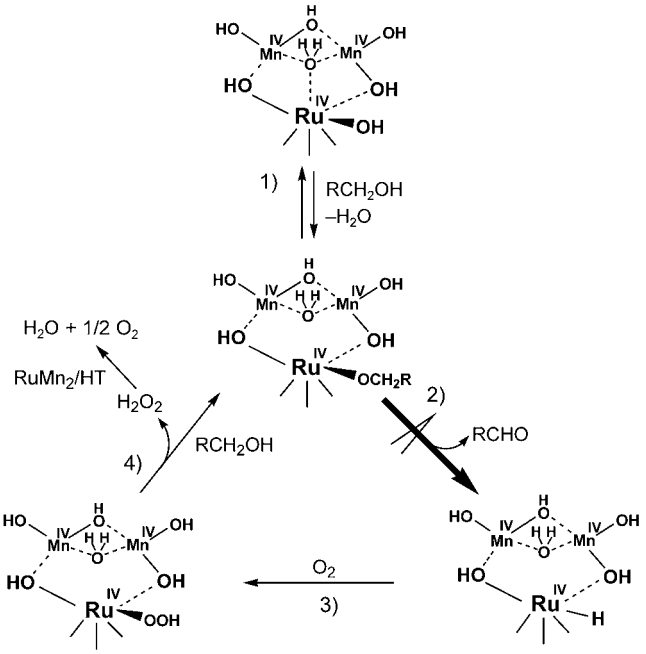

Scheme 2. A proposed mechanism for the oxidation of a primary alcohol by trimetallic RuMnMn sites.

For the secondary alcohol 1-phenylethanol, K_M and k_2 were found to be 133 mM and 0.026 s^{-1}, respectively, at 60 °C. Importantly, the K_M value is significantly greater than that for the oxidation of **1**, which is reflected in the preferential oxidation of primary hydroxy groups by this species.[22] The formation of metal alkoxide intermediates of primary alcohols is favored over secondary alcohols in the ligand-exchange step.[23]

In summary, a robust heterotrimetallic $Ru^{IV}Mn^{IV}Mn^{IV}$ species coordinated to a hydrotalcite surface as a macroligand facilitates the highly efficient aerobic oxidation of alcohols. Such cooperative action among high-valence metal cations in a heterometallic species on a solid surface provides a unique protocol for the preparation of functionalized heterogeneous catalysts for environmentally benign organic syntheses.[24] Ongoing efforts are focused on creating high-valence Ru cation species, that is, Ru^{VI} and Ru^{VII}, based on the redox interaction within a heterometallic site for highly efficient epoxidation and dihydroxylation reactions of alkenes with molecular oxygen.

Experimental Section

Ru/HT[7d] was treated with an aqueous solution of $MnCl_2{\cdot}4H_2O$ to afford $RuMn_2$/HT.[10] Elemental analysis (%) calcd for $Ru_{0.071}Mn_{0.142}/Mg_6Al_2(OH)_{16}CO_3$: Ru 1.03, Mn 1.12, Mg 21.0, Al, 8.14; found: Ru 1.05, Mn 1.20, Mg 21.4, Al 7.9.

The X-ray absorption spectra were recorded at the BL01B1 beamline in SPring-8 of JASRI, Japan (2003B0944-UXa-np and 2004A489-NXa-np) and at the BL-10B beamline of PF at KEK, Japan (2001G143 and 2002G102). The data were reduced using computer

systems at the Data Processing Center of Kyoto University according to a previously reported procedure.[25]

Received: November 13, 2004
Revised: December 29, 2004
Published online: April 28, 2005

Keywords: alcohols · heterogeneous catalysis · oxidation · ruthenium · supported catalysts

[1] a) A. M. Argo, J. F. Odzak, F. S. Lai, B. C. Gates, *Nature* **2002**, *415*, 623; b) A. Suzuki, A. Yamaguchi, T. Chihara, Y. Inada, M. Yuasa, M. Abe, M. Nomura, Y. Iwasawa, *J. Phys. Chem. B* **2004**, *108*, 5609.

[2] a) N. Wheatley, P. Kalck, *Chem. Rev.* **1999**, *99*, 3379; b) B. H. Holm, E. I. Solomon, *Chem. Rev.* **2004**, *104*, 347.

[3] *Handbook of Heterogeneous Catalysis* (Eds.: G. Ertl, H. Knözinger, J. Weitkamp), VCH, Weinheim, **1997**.

[4] S. J. Tauster, S. C. Fung, L. R. Garten, *J. Am. Chem. Soc.* **1978**, *100*, 170.

[5] F. Cavani, F. Trifirò, A. Vaccari, *Catal. Today* **1991**, *11*, 173.

[6] For typical catalysis of hydrotalcites as solid bases, see: B. M. Choudary, M. L. Kantam, B. Kavita, C. V. Reddy, K. K. Rao, F. Figueras, *Tetrahedron Lett.* **1998**, *39*, 3555; T. Honma, M. Nakajo, T. Mizugaki, K. Ebitani, K. Kaneda, *Tetrahedron Lett.* **2002**, *43*, 6229.

[7] For typical heterogeneous metal catalysts based on HT, see: a) B. Sels, D. De Vos, M. Buntinx, F. Pierard, A. Kirsch-De Mesmaeker, P. A. Jacobs, *Nature* **1999**, *400*, 8565; b) T. Nishimura, N. Kakiuchi, M. Inoue, S. Uemura, *Chem. Commun.* **2000**, 1245; c) B. M. Choudary, N. S. Choudary, S. Madhi, M. L. Kantam, *Angew. Chem.* **2001**, *113*, 4755; *Angew. Chem. Int. Ed.* **2001**, *40*, 4619; d) K. Motokura, D. Nishimura, K. Mori, T. Mizugaki, K. Ebitani, K. Kaneda, *J. Am. Chem. Soc.* **2004**, *126*, 5662.

[8] *X-ray Absorption: Principles, Applications, and Techniques of EXAFS, SEXAFS, and XANES* (Eds.: D. C. Köningsberger, R. Prins), Wiley, New York, **1988**.

[9] For a recent review on immobilization of metal species, see: C. Copéret, M. Chabanas, R. P. Saint-Arroman, J.-M. Basset, *Angew. Chem.* **2003**, *115*, 164; *Angew. Chem. Int. Ed.* **2003**, *42*, 156.

[10] See Supporting Information.

[11] P. Triggs, *Helv. Phys. Acta* **1985**, *58*, 657.

[12] Two Ru–O bonds of 1.83 and 2.07 Å are assigned to Ru–OH and Ru–OH_2, respectively. See: P. Dubourdeaux, M. Tavarès, A. Grand, R. Ramasseul, J.-C. Marchon, *Inorg. Chim. Acta* **1995**, *240*, 657; A. Liobet, D. J. Hodgson, T. Meyer, *Inorg. Chem.* **1990**, *29*, 3760.

[13] The Mn–Mn distance is slightly shorter than that in bis-(hydroxo)-bridged Mn^{IV} dimers (2.73–2.93 Å). See: M. J. Baldwin, T. L. Stemmler, P. J. Riggs-Gelasco, M. L. Kirk, J. E. Penner-Hahn, V. L. Pecoraro, *J. Am. Chem. Soc.* **1994**, *116*, 11349.

[14] Generation of heterometallic species has not been reported on HT containing Pd, Os, or W.[7c]

[15] For selected heterogeneous Ru catalysts for alcohol oxidation, see: a) M. Matsumoto, M. Watanabe, *J. Org. Chem.* **1984**, *49*, 3435; b) K. Yamaguchi, K. Mori, T. Mizugaki, K. Ebitani, K. Kaneda, *J. Am. Chem. Soc.* **2000**, *122*, 7144; c) K. Yamaguchi, N. Mizuno, *Angew. Chem.* **2002**, *114*, 4720; *Angew. Chem. Int. Ed.* **2002**, *41*, 4538; d) M. Musawir, P. N. Davey, G. Kelly, I. V. Kozhevnikov, *Chem. Commun.* **2003**, 1414; e) K. Yamaguchi, N. Mizuno, *Chem. Eur. J.* **2003**, *9*, 4353. See also T. Mallat, A. Baiker, *Chem. Rev.* **2004**, *104*, 3037 as a recent review.

[16] For representative aerobic alcohol oxidations by homogeneous metal complexes, see: a) A. Hanyu, E. Takezawa, S. Sakaguchi, Y. Ishii, *Tetrahedron Lett.* **1998**, *39*, 5557; b) G.-J. ten Blink, I. W. C. E. Arends, R. A. Sheldon, *Science* **2000**, *287*, 1636; c) P. A. Shapley, N. Zhang, J. L. Allen, D. H. Pool, H.-C. Liang, *J. Am. Chem. Soc.* **2000**, *122*, 1079; d) A. Dijksman, A. Marino-González, A. Mairata i Payeras, I. W. C. E. Arends, R. A. Sheldon, *J. Am. Chem. Soc.* **2001**, *123*, 6826.

[17] See the Supporting Information for typical time courses for the oxidation of **1**.

[18] A control experiment was performed using benzaldehyde in the presence of $RuMn_2$/HT and water at 60 °C in toluene under oxygen. Benzaldehyde was quantitatively recovered showing that it is not oxidized further under these conditions. See Supporting Information.

[19] $RuMn_2$/HT is highly effective for the oxidation of benzylic and aromatic allylic alcohols, but not for primary aliphatic alcohols; the oxidation of 1-octanol with $RuMn_2$/HT (2 mol-% Ru) afforded octanal in 62% yield at 60 °C after 5 h. A CoCeRu trimetallic catalyst shows a high activity for the aerobic oxidation of primary aliphatic alcohols: H.-B. Ji, T. Mizugaki, K. Ebitani, K. Kaneda, *Tetrahedron Lett.* **2002**, *43*, 7179; K. Ebitani, H.-B. Ji, T. Mizugaki, K. Kaneda, *J. Mol. Catal. A* **2004**, *212*, 161.

[20] 1) The addition of a radical scavenger (2,6-di-*tert*-butyl-*p*-cresol) did not affect the rate of the oxidation. 2) Treatment of $RuMn_2$/HT with **1** under argon afforded an IR signal of a Ru–H species at 2120 cm^{-1}.[10,16d] This species disappeared upon exposure to O_2. 3) During the oxidation of **1**, the ratio of O_2 consumed to **2** was 1:2.

[21] R. W. Missen, C. A. Mims, B. A. Saville, *Introduction to Chemical Reaction Engineering and Kinetics*, Wiley, New York, **1999**. The initial rate of oxidation of **1** is proportional to the amount of $RuMn_2$/HT and independent of the oxygen pressure.

[22] If the second step in Equation (1) is the rate-determining step, the K_M value can be regarded as a dissociation equilibrium constant (k_{-1}/k_1) of the first step. See ref. [21].

[23] A similarly high chemoselectivity for primary alcohols has been observed in the $Zr(OAc)_2$-catalyzed oxidation of alcohols: K. Kaneda, Y. Kawanishi, S. Teranishi, *Chem. Lett.* **1984**, 1481.

[24] P. T. Anastas, J. C. Warner, *Green Chemistry; Theory and Practice*, Oxford University Press, Oxford, **1998**.

[25] T. Yamamoto, T. Tanaka, S. Takenaka, S. Yoshida, T. Onari, Y. Takahashi, T. Kosaka, S. Hasegawa, M. Kudo, *J. Phys. Chem. B* **1999**, *103*, 2385.

[26] H. W. Baur, *Acta Crystallogr., Sect. B* **1976**, *32*, 220.

Enzymes

Synthesis of Luciferyl Coenzyme A: A Bioluminescent Substrate for Firefly Luciferase in the Presence of AMP**

*Hugo Fraga, Rui Fontes, and Joaquim C. G. Esteves da Silva**

Firefly luciferase (EC 1.13.12.7) is an oxidoreductase that catalyzes the bioluminescent reaction of luciferin (LH_2), ATP, and oxygen [Eq. (1) and (2)].[1,2] Research has been focused

$$LH_2 + ATP\text{-}Mg \rightleftharpoons LH_2\text{-}AMP + PPi \quad (1)$$

$$LH_2\text{-}AMP + O_2 \rightarrow Oxyluciferin + AMP + CO_2 + h\nu \quad (2)$$

on the clarification of the mechanism behind light emission, and as a consequence of its high quantum yield,[3] this reaction was defined as a model for the optimization of chemiluminescence systems.[4] The applications of firefly luciferase reactions range from ATP determination to the standard use of the *luc* gene in molecular biology.[5–7]

McElroy et al.[8] described the similarities between the mechanism of firefly luciferase reactions [Eq. (1)–(4)] and

$$LH_2\text{-}AMP + CoA \rightleftharpoons LH_2\text{-}CoA + AMP \quad (3)$$

$$L\text{-}AMP + CoA \rightleftharpoons L\text{-}CoA + AMP \quad (4)$$

those of the acyl-CoA synthetases [Eq. (5) and (6)]. This

$$fatty\ acid + ATP\text{-}Mg \rightleftharpoons acyl\text{-}AMP + PPi \quad (5)$$

$$acyl\text{-}AMP + CoA \rightleftharpoons acyl\text{-}CoA + AMP \quad (6)$$

relationship was supported by the luciferase formation of the intermediate luciferyl adenylate (LH_2-AMP) and the production of dehydroluciferyl coenzyme A (L-CoA) from dehydroluciferyl adenylate (L-AMP); the latter compound is an oxidation product of LH_2-AMP (Supporting Information). Since then, several experimental observations have provided support for the McElroy hypothesis: the synthesis of dinucleoside polyphosphates (observed in acyl-CoA synthetases),[9] the high primary degree of sequence identity with rat long chain acyl-CoA synthetase (35.8%),[10] and recently the ability of luciferase to catalyze directly acyl-CoA formation [Eq. (5) and (6)].[11]

Herein we report the chemical synthesis and characterization of a new product in the firefly luciferase mechanism, namely, luciferyl coenzyme A (LH_2-CoA). The luciferase-catalyzed formation of LH_2-CoA from LH_2-AMP and coenzyme A [Eq. (3)] in anoxic media was recently advanced.[12] In that work, however, the unequivocal characterization of the enzymatically produced compound was not performed owing to the low catalytic activity that made the isolation of the formed compound impractical.

The chemical synthesis methodology employed in this work to obtain LH_2-CoA was based on the procedures of Simon and Shemin and of Wieland and Rueff (Scheme 1),[13,14] in which an acid anhydride is allowed to

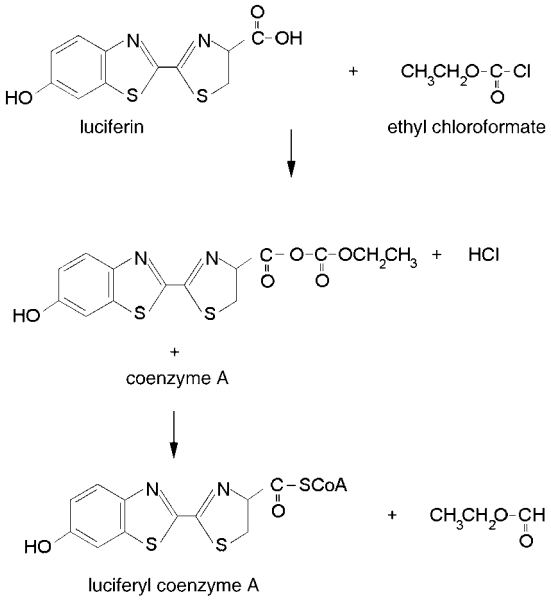

Scheme 1. Chemical synthesis of LH_2-CoA.

react with a thiol in cold aqueous solution. As luciferin anhydride is not readily available, a mixed anhydride obtained from luciferin and ethyl chloroformate was used (Scheme 1).[15] By using this synthetic scheme we synthesized LH_2-CoA and confirmed its identity as the firefly luciferase product, which has already been detected.[12]

The formation of acyl-CoA catalyzed by acyl-CoA synthetases is readily reversible,[16] and the same was observed in the case of the luciferase-catalyzed formation of L-CoA.[2,17] Both the reverse and direct reactions occur through the same adenylated intermediates: L-AMP and acyl-AMP for luciferase and acyl-CoA synthetases, respectively [Eq. (4) and (6)]. In the case of LH_2-CoA, the corresponding adenylate is LH_2-AMP, which is also the direct intermediate in the bioluminescent reaction [Eq. (2) and (3)].

If Equation (3) could be reversed, luciferase would catalyze the conversion of AMP and LH_2-CoA into LH_2-AMP. This adenylate in the presence of oxygen would be oxidized to oxyluciferin, the light emitter. This hypothesis was

[*] Dr. H. Fraga,[+] Dr. R. Fontes,[+] Prof. Dr. J. C. G. Esteves da Silva
LAQUIPAI, Chemistry Department
Faculdade de Ciências da Universidade do Porto
R. Campo Alegre 687, 4169-007 Porto (Portugal)
Fax: (+351) 226-082-959
E-mail: jcsilva@fc.up.pt

[+] Additional address:
Biochemistry Department (U38-FCT)
Faculdade de Medicina da Universidade do Porto
4200-319 Porto (Portugal)

[**] This study was supported by the Fundação para a Ciência e Tecnologia (Lisbon) (FSE-FEDER): project POCTI/QUI/37768/2001 and PhD grant SFRH/BD/1395.

Supporting information for this article is available on the WWW under http://www.angewandte.org or from the author.

 DOI: 10.1002/anie.200462934

confirmed by the observed light production when LH_2-CoA and AMP were mixed in the presence of firefly luciferase (Figure 1). No light was emitted in the controls performed with LH_2-CoA and without AMP injection, thus confirming that the conversion of this compound into LH_2-AMP is essential for light emission.

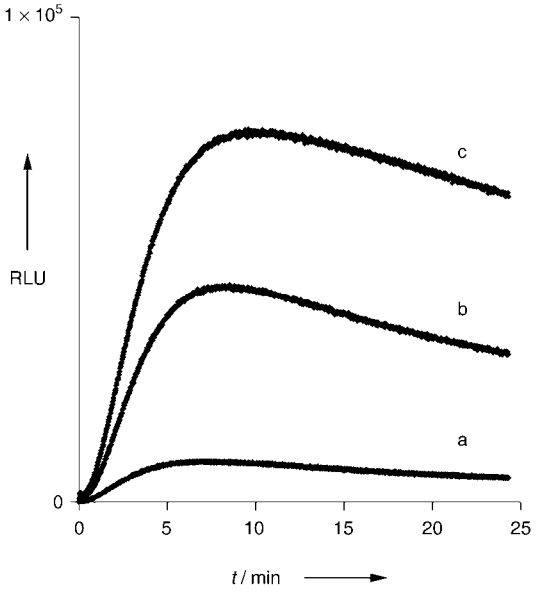

Figure 1. Bioluminescence from LH_2-CoA and AMP. The reaction mixtures contained purified and desalted LH_2-CoA (4 mM), EDTA (10 mM), hepes pH 7.5 (50 mM), and luciferase (0.04 mg protein mL^{-1}) in a final volume of 100 μL. The reactions were initiated with the injection of AMP. Curves a, b and c correspond to 62.5, 250, and 500 μM AMP, respectively (final concentrations).

The synthesized LH_2-CoA was purified but still contained traces of LH_2 as contaminant. In the presence of LH_2 any residual ATP would generate light through the direct adenylation of LH_2 [Eq. (1) and (2)]. To confirm that bioluminescence resulted from LH_2-CoA and AMP, the assays were supplemented with EDTA (10 mM). The presence of EDTA in this relatively high concentration prevented any possibility of direct adenylation because this process is Mg^{2+} dependent [Eq. (1)].[1,2]

The light emitted during the assay time was directly proportional to the concentration of AMP (up to 500 μM, Figure 2). Under our experimental conditions, that is, in the presence of 10 mM EDTA, the response obtained with ATP (5 mM, the highest AMP concentration used) was negligible (less than 5%).

The kinetic profile of LH_2-CoA + AMP bioluminescence (Figure 1) was markedly different from the flash profile of the LH_2 + ATP-Mg^{2+} (classic) bioluminescent reaction. In LH_2-CoA + AMP bioluminescence the rate of light production increased with incubation time, reaching a maximum at 10–20 min. Slow rise time patterns have already been described for LH_2-AMP analogues and luciferase mutants.[18]

As we have worked with native enzyme, and LH_2-AMP is a common intermediate in LH_2-CoA + AMP and classic bioluminescence, we deduce that the light profile obtained should be a consequence of the slow kinetics of the reaction of formation of LH_2-AMP from LH_2-CoA and AMP [Eq. (3)].

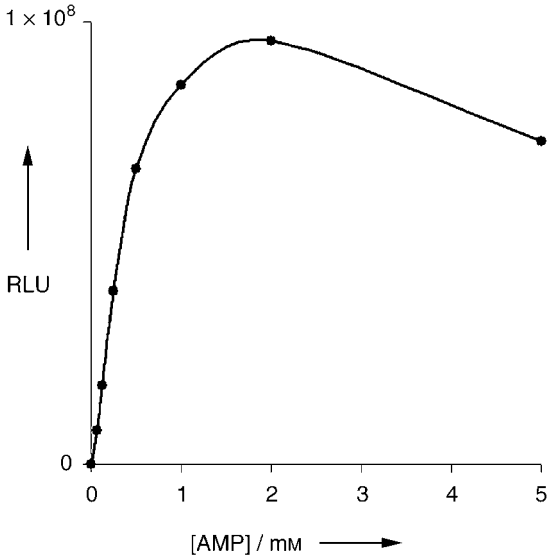

Figure 2. Total light output during the assay time (25 min) as a function of added AMP.

We had previously observed that the conversion of LH_2-AMP into LH_2-CoA is a relatively slow process.[12]

The identification of a new bioluminescent substrate for luciferase opens perspectives for the development of new bioanalytical methodologies for AMP detection. Moreover, the results presented herein are strong evidence for an evolutionary relationship between luciferase and acyl-CoA synthetases. From Equations (1)–(6) it is clear that if we exclude the light-production reaction [Eq. (2)], the mechanisms presented by firefly luciferase are in all ways similar to those of this class of enzymes.

Experimental Section

A stock solution of commercial luciferase (L8506) was prepared by dissolving the lyophilized powder (15 mg lyophilisate mL^{-1}) in hepes pH 7.5 (500 mM; 15 mg lyophilisate mL^{-1}) and stored at −20 °C. A stock solution of EDTA was prepared in hepes pH 7.5 (500 mM). Firefly luciferin, firefly luciferase, AMP, ATP, coenzyme A, EDTA, and hepes were purchased from Sigma, ethyl chloroformate from Aldrich, and triethylamine from Fluka.

Identification of enzyme-produced LH_2-CoA: The reaction mixture (15 μL) for the luciferase (Lase) synthesis of LH_2-CoA used ATP (1 mM), LH_2 (30 μM), coenzyme A (1 mM), $MgCl_2$ (2 mM), hepes pH 7.5 (100 mM), and Lase (1 mg protein mL^{-1}). All the solutions were prepared and kept under N_2. The reaction was initiated by the addition of Lase and was performed at ambient temperature. After 30 min of incubation, the enzyme reaction was stopped by the addition of aqueous methanol (15 μL; 66% v/v), centrifuged (13400 rpm, 2 min), and the supernatant was analyzed by reversed-phase HPLC. The chromatographic system consisted of a HP-1100 isocratic pump, a Rheodyne manual injection valve, a Chromolith C18 (Merck) column, and a Unicam Crystal 250 UV/Vis diode array detector. The eluent was an aqueous solution of 20% methanol, 4 mM phosphate buffer (pH 7.0), and the flux rate was set to 1 mL min^{-1}. Although a different order of elution could be obtained by using other phosphate buffer concentrations, under the above conditions LH_2-CoA (12 min) eluted after LH_2 (7 min). The spectra obtained for LH_2-CoA was similar to that reported previously,[12] with maxima at 262 and 340 nm ($A_{260}/A_{340} = 1.15:1$); see Supporting Information.

Chemical synthesis of luciferyl coenzyme A: The synthesis of luciferyl coenzyme A was based on previously reported methods for acyl-CoA thioester preparation.[13–15] LH_2 (50 mg, 0.178 mmol) in THF (15 mL) was mixed with triethylamine (25 μL, 0.178 mmol) at 0 °C. Ethyl chloroformate (17 μL, 0.178 mmol) was then added, and the mixture was left at 0 °C for 30 min. The volume of the reaction mixture was reduced to a half under a stream of N_2, and a mixture of coenzyme A (68.7 mg; 0.09 mmol) and $NaHCO_3$ (20 mg) in THF/H_2O (2:1; 10 mL) was added. The pH value was maintained at 7.5–8. After stirring for 30 minutes the reaction mixture was analyzed by reversed-phase HPLC as described for the identification of enzyme-produced LH_2-CoA. This system allowed the resolution of reactants and products, and the reaction was monitored at regular time intervals until no more LH_2-CoA formation was observed (120 min).

The retention time observed for the chemically synthesized compound was the same as that observed with enzyme-produced LH_2-CoA (Supporting Information). The THF was evaporated, and the aqueous solution was acidified to pH 3–4 by the addition of small amounts of a cation-exchange resin (Amberlite IR-120-H^+). The resin was removed by filtration, and the filtrate was extracted with diethyl ether (2×20 mL) to remove unconverted LH_2. The aqueous phase and organic phase were analyzed by reversed-phase HPLC, and as expected, no LH_2-CoA was detected in the diethyl ether.

The aqueous phase was lyophilized and a green fluorescent powder was obtained. LH_2-CoA was purified by reversed-phase HPLC by using a Supelco semipreparative column (LC-18, 25 cm × 10 mm, 5 μm) with a solution of methanol (40%) and phosphate buffer (11–15 mM; pH 7.0) as eluent; the flux rate was set to 3 mL min^{-1}. MALDI TOF analysis of purified LH_2-CoA was performed at RIAIDT, Unidad de Espectroscopia de Masas, Santiago de Compostela, Spain, and confirmed the calculated mass for $C_{32}H_{42}N_9O_{18}P_3S_3$, $M_w = 1029.842$ g mol^{-1} (Supporting Information). Prior to MS analysis and bioluminescence assays, LH_2-CoA solutions were desalted by using a ZipTip from Millipore; the phosphate content on the treated sample was verified by a variation of the molybdate method.[19] Purified LH_2-CoA stored at −20 °C was stable during the period of the bioluminescent assays (2 weeks), as confirmed by reversed-phase HPLC.

Bioluminescence from LH_2-CoA and AMP: The bioluminescence tests were performed in a homemade luminometer by using a Hammamatsu HCL35 photomultiplier tube. The reaction mixtures contained purified and desalted LH_2-CoA (4 μM), EDTA (10 mM), hepes pH 7.5 (50 mM), and luciferase (0.04 mg protein mL^{-1}); final volume: 100 μL. The reactions were initiated with the injection of AMP. The assays were carried out in duplicate, and control assays with water and ATP (5 mM, with and without EDTA (10 mM)) were also performed. Light was measured for 25 minutes with integrations at 1-s intervals.

Received: December 14, 2004
Published online: April 28, 2005

Keywords: adenosine monophosphate · bioluminescence · enzymes · firefly luciferase · total synthesis

[1] K. V. Wood, *Photochem. Photobiol.* **1995**, *62*, 662–673.
[2] W. C. Rhodes, W. D. McElroy, *J. Biol. Chem.* **1958**, *233*, 1528–1537.
[3] H. H. Seliger, W. D. McElroy, *Arch. Biochem. Biophys.* **1960**, *88*, 136–141.
[4] W. Adam, D. Reinhardt, C. R. Saha-Moller, *Analyst* **1996**, *121*, 1527–1531.
[5] B. L. Strehler, J. R. Totter, *Arch. Biochem. Biophys.* **1952**, *40*, 28–41.
[6] A. Lundin, *Methods Enzymol.* **2000**, *305*, 346–370.
[7] I. Bronstein, J. Fortin, P. E. Stanley, G. S. A. B. Stewart, L. J. Krika, *Anal. Biochem.* **1994**, *219*, 169–181.
[8] W. D. McElroy, M. DeLuca, J. Travis, *Science* **1967**, *156*, 150–160.
[9] A. Sillero, M. A. Sillero, *Pharmacol. Ther.* **2000**, *87*, 91–102.
[10] H. Suzuki, Y. Kawarabayasi, J. Kondo, A. Takaaki, K. Nishikawa, S. Kimura, T. Hashimoto, T. Yamamoto, *J. Biol. Chem.* **1990**, *265*, 15, 8681–8685.
[11] Y. Oba, M. Ojika, S. Inouye, *FEBS Lett.* **2003**, *540*, 251–254.
[12] H. Fraga, J. C. G. Esteves da Silva, R. Fontes, *ChemBioChem* **2004**, *5*, 110–115.
[13] E. J. Simon, D. Shemin, *J. Am. Chem. Soc.* **1953**, *75*, 2520.
[14] T. Wieland, L. Rueff, *Angew. Chem.* **1953**, *65*, 186.
[15] E. Stadtman, *Methods Enzymol.* **1957**, *3*, 931–941.
[16] T. L. Webster, *J. Biol. Chem.* **1967**, *242*, 6, 1232–1240.
[17] H. Fraga, J. C. G. Esteves da Silva, R. Fontes, *Tetrahedron Lett.* **2004**, *45*, 2117–2120.
[18] B. R. Branchini, M. H. Murtiashaw, R. A. Magyar, N. C. Portier, M. C. Ruggiero, J. G. Stroh, *J. Am. Chem. Soc.* **2002**, *124*, 2112–2113.
[19] B. N. Ames, *Methods Enzymol.* **1966**, *8*, 115–118.

Coordination Polymers

Supramolecular Interactions as Determining Factors of the Geometry of Metallic Building Blocks: Tetracarboxylate Dimanganese Species**

Abdessamad Grirrane, Antonio Pastor, Agustín Galindo, Diego del Río, Annabella Orlandini, Carlo Mealli,* Andrea Ienco, Andrea Caneschi, and Javier Fernández Sanz*

Notwithstanding the richness of manganese carboxylate chemistry,[1] dimanganese tetracarboxylate species with a copper acetate-like core have been characterized only

[*] A. Grirrane, Dr. A. Pastor, Prof. A. Galindo, Dr. D. del Río
Departamento de Química Inorgánica
Universidad de Sevilla
Aptdo 553, 41071 Seville (Spain)
Fax: (+34) 95-455-7153
E-mail: galindo@us.es

Dr. A. Orlandini, Dr. C. Mealli, Dr. A. Ienco
ICCOM, CNR
Via Madonna del piano, 50019 Sesto Fiorentino, Firenze (Italy)
Fax: (+39) 055-5225203
E-mail: carlo.mealli@iccom.cnr.it

Dr. A. Caneschi
Dipartimento di Chimica and INSTM RU of Firenze
Università di Firenze
Via della Lastruccia 3, 50019 Sesto Fiorentino (Italy)

Dr. J. Fernández Sanz
Departamento de Química Física
Universidad de Sevilla
41071 Seville (Spain)

[**] This work was supported by DGESIC (BQU2001-3715) and the Junta de Andalucía, and by EC RTN QUEMOLNA (FP6-504880) and the Italian MIUR with an FIRB grant. We thank Dante Masi for technical assistance with the X-ray analyses.

Supporting information for this article is available on the WWW under http://www.angewandte.org or from the author.

 DOI: 10.1002/anie.200462965

recently.[2] At the time of our report on $[Mn(tda)(bipy)]_n$ (**1**) (tda = thiodiacetate = $S(CH_2COO)_2^{2-}$; bipy = 2,2′-bipyridine),[2] the only other known examples either lacked detailed structural information ($[Mn_2(C_3F_7CO_2)_4(bipy)_2]$[3]) or had not been deposited in the Cambridge Structural Database[4] ($[Mn_2(Ph_2XCCO_2)_4(quinoline)_2]$;[5] X = H, Me). Another example, $[Mn_2(\mu\text{-}OOCtBu)_4\{OC(tBu)OHNEt_3\}_2]$, has appeared recently.[6] In **1**, the bimetallic $\{Mn_2(\mu\text{-carboxylate})_4\}$ units, completed by two terminal bipy ligands and interconnected by pairs of CH_2SCH_2 spacers, form linear chains which further organize into a supramolecular structure through noncovalent interactions.[7,8] Copper acetate itself and other metal carboxylate synthons often generate metal-organic frameworks (MOF) through coordinative bonds,[7] whereas the overall architecture of **1** stems from the interactions between the 1D polymeric chains. In fact, the bipy ligands of adjacent chains, which are all parallel to each other, are π-stacked in a gearlike arrangement with the formation of compacted 2D sheets. In order to understand better the correlations between the geometry of the building blocks and the given supramolecular structure, we have tried to combine the Mn–tda unit with other N-donor chelating ligands.

X-ray studies of complexes obtained with 1,10-phenanthroline[9] and 4,4′-dimethoxy-2,2′-bipyridine showed that they are not isostructural with **1**, possibly because of the steric requirements of the different ligands (see the Supporting Information). To minimize these, we selected the ligands 4,4′-dimethyl-2,2′-bipyridine (4,4′-Me_2bipy) and 5,5′-dimethyl-2,2′-bipyridine (5,5′-Me_2bipy), which contain a pair of the smallest alkyl substituents, CH_3 groups, that are not adjacent to the N donors. The synthetic procedure was maintained as close as possible to that of **1**: we treated each of the above ligands with $[Mn(tda)(H_2O)]_n$ (**2**), which is obtainable in good yields by the reaction of aerobic aqueous solutions of $MnCl_2$ with a 1:1 mixture of Na_2CO_3 and thiodiacetic acid.[2] Two new compounds were crystallized that, like **1**, exhibit a 1:1:1 ratio of Mn, tda, and the N-chelate. From X-ray analyses, both products were shown to be one-dimensional polymers of formula $[\{Mn(N\text{-}N)\}_2(\mu\text{-}tda)_2(\mu\text{-}H_2O)]_n$ (N-N = 4,4′-Me_2bipy, **3**; 5,5′-Me_2bipy, **4**), formed by binuclear units with a core different from that of copper acetate. Both compounds exhibit antiferromagnetic behavior (see the Supporting Information for details). The estimated value of J ($5.5 \pm 0.1\ cm^{-1}$) matches those of other binuclear Mn^{II} species with structures similar to **3** and **4** (i.e., similar local coordination, Mn–Mn separation, and a unique Mn–O–Mn bridge).[10–12] The larger J value found for **1** ($8.2\ cm^{-1}$)[2] indicates that the exchange interaction is more efficient with four rather than two *syn-syn* carboxylato and one μ-H_2O bridges.[13]

As shown in Figure 1,[14] the structure of **3** (that of **4** is similar, see the Supporting Information) consists of extended ribbons formed by binuclear Mn_2 units linked through pairs of CH_2SCH_2 spacers. In contrast to **1**, two of the four carboxylate groups coordinated to the Mn_2 unit adopt monodentate coordination to each metal atom, thereby affording an unprecedented bridging mode (μ_3-κ^1(O),κ^1(O′)-κ^1(O″)) for the tda ligand. In the binuclear core, a bridging water molecule (O9) forms two strong hydrogen bonds with the uncoordinated oxygen atoms of the two monodentate carboxylate groups (the contacts O2···O9 and O6′···O9 are 2.547 and 2.561 Å, respectively). Finally, two terminal Me_2bipy ligands, which are now almost orthogonal to each other (dihedral angle 72°) rather than parallel, complete a pseudo-octahedral geometry at each metal. With respect to **1**, the loss of the trigonal-prismatic coordination (TP) does not affect the Mn···Mn separation, which remains nonbonding (3.581(1) Å and 3.502(1) Å, in **3** and **1**, respectively). The arrangement $[\{M(\kappa^1\text{-}OOCR)L_2\}_2(\mu\text{-}OOCR)_2(\mu\text{-}H_2O)]$ (L_2 = two monodentate N-donor ligands or a bidentate one) is common for divalent metal ions,[15] and includes four manganese examples.[10,11,16] One of these, which contains the ligand 4,4′-Me_2bipy,[11] has been proposed as a model for the active site of dimanganese enzymes.[17]

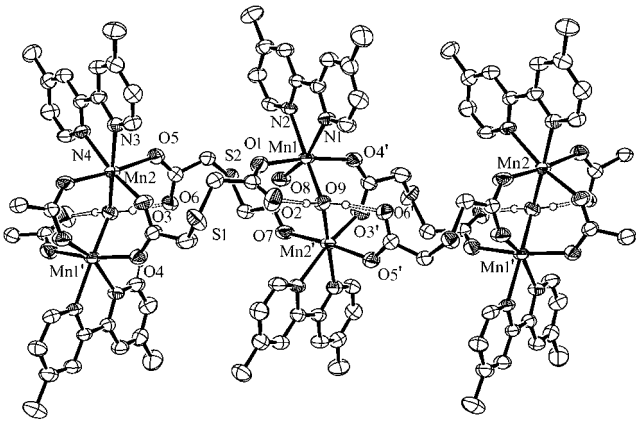

Figure 1. ORTEP drawing of polymer **3** propagated along the *y* axis. The H atoms have been omitted for clarity. Selected bond lengths [Å] and angles [°]: Mn1–O1 2.203(4), Mn1–O8 2.113(4), Mn1–O4′ 2.166(3), Mn1–O9 2.218(3), Mn2–O3 2.140(3), Mn2–O5 2.182(4), Mn2′–O7 2.136(4), Mn2′–O9 2.234(4), Mn1···Mn2′ 3.581(1); Mn1-O9-Mn2′ 107.1(2). The symbol ′ corresponds to the transformation $-x+{}^1/_2, y+{}^1/_2, -z+{}^1/_2$.

The fact that the structure of **1** differs from those of **3** and **4** seems attributable to the methyl substituents on the bipyridine ligand in **3** and **4**. As highlighted before,[2] the threading of the ribbons in **1** stems from a head-to-tail interpenetration of the parallel bipy ligands and the formation of extended 2D sheets. The degree of π-stacking is definitely more compact here than that described for similar systems.[18] In this respect, the interaction mode between the bipy ligands in **3** and **4** is evidently different from that in **1** (see the Supporting Information). First, the nonparallel disposition of the two bipy ligands in each binuclear unit determines the presence of an extended 3D packing rather than 2D sheets. Moreover, the presence of methyl substituents does not allow the same degree of interpenetration between the parallel bipy ligands of adjacent chains. The loss of compactness with respect to **1** is confirmed by the lower crystal densities of **3** and **4**, in spite of their 10% larger molecular weights (1.520, 1.540, and $1.705\ g\,cm^{-3}$ for **3**, **4**, and **1**, respectively). The different situation can be qualitatively appreciated by looking at the projections of two facing bipy ligands down their normal vectors (Figure 2).

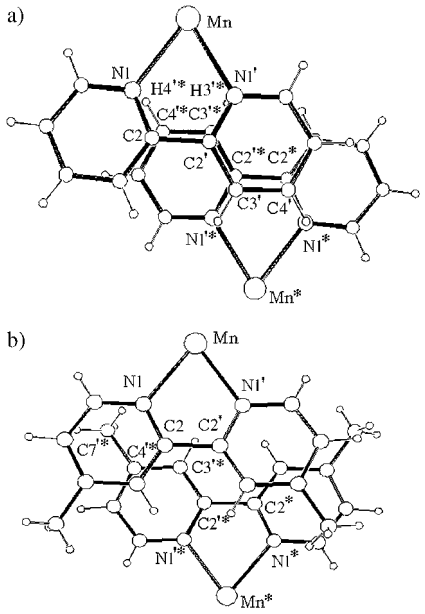

Figure 2. Comparative projections of the facing {Mn(bipy)} and {Mn(4,4′-Me_2bipy)} fragments in **1** (a) and **3** (b) down axes perpendicular to the bipy ligands. The atom of the bipy skeleton are indicated by standard labeling (the applied symmetry operations (*) are: $-x$, $1-y$, $1-z$ and $-x+{}^1/_2$, $-y+{}^1/_2$, $-z$ for compounds **1** and **3**, respectively).

In **1**, five C–C bonds of two stacked bipy ligands are mutually eclipsed, as are seven C–H bonds. Conversely, a slippage of the two projected ligands in **3** elongates the separation between the symmetry-related Mn atoms by about 0.4 Å with respect to **1**. This avoids a shortened contact between one CH_3 group and the coordination sphere of the facing metal atom (e.g., the atom Mn and the group at C7′* in **3**). If, in the lattice of **1**, the H4′* atom was replaced by a CH_3 group, the latter would clash with the coordination sphere of the facing Mn atom (contacts <2 Å). Another aspect of the bipy geometry in **1** is the 10° twisting of the two six-membered rings around the connecting C2–C2′ bond. As a consequence, the contacts between the eclipsing atoms N1/H4′* and N1′/H3′* (and their symmetry equivalents) are significantly shorter (3.15 and 3.45 Å) than the separation of the bipy mean squares planes (4.01 Å). Although not exceptionally short, the latter N···H distances suggest that an important contribution to the overall stacking originates from the four π–σ interactions between the H atoms and the p_π-orbitals of the N atoms for any pair of bipy ligands.[18] Finally, another possible contribution to the compactness of the interpenetrating ribbons in **1** may be due to a residual interaction between the thioether sulfur atom and a bipy C–H bond (3.32 Å). Conversely, the slippage in **3** minimizes such a hydrogen bonding (if any), since the S···H–C separation increases to 3.71 Å.

Comparative DFT calculations were performed for the discrete binuclear units of **1** and **3**, with no methyl substituents in either case. The optimized geometry of $[Mn_2(OOCH)_2(bipy)_2(\mu\text{-}OOCH)_2(\mu\text{-}H_2O)]$ (**3a**) satisfactorily reproduces that of the building block in **3**, including the two quasi-orthogonal bipy ligands (84°). The $[Mn_2(\mu\text{-}OOCH)_4(bipy)_2]$ unit was first optimized by imposing D_{2h} symmetry (model **1a**). The computed parameters are sufficiently similar to those of the actual compound **1** (see the Supporting Information), but the number of imaginary frequencies suggested that **1a** is not a minimum. A new optimization without symmetry constraints provided an actual minimum, **1b**, with a different coordination geometry. In particular, the local coordination at the Mn atoms is no longer TP but almost octahedral (one of the O–Mn–O angles opens to 166°), and the terminal bipy ligands are far from being coplanar (dihedral angle of about 66°). Energetically, **1b** is more stable than **1a** by only 1.2 kcal mol^{-1}, a result which is consistent with the zero crystal-field stabilization energy for d^5 high-spin metal systems and their facile and subtle adaptation to alternative coordination environments.[19] In contrast, the comparison of the energies associated with **3a** and **1a** is very significant as the former species is more stable with respect to the system **1a** + H_2O by as much as 20.4 kcal mol^{-1}. While the entropic factor should favor separated components, complex **3a** must receive a considerable amount of stabilization from the intramolecular hydrogen bonding between water and free carboxylate oxygen atoms. Since the structure of **3** is not experimentally observed in the presence of the bipy ligand, the formation of complex **1** can only be caused by more-energetic noncovalent interactions between the coordination polymers.

In conclusion, this study provides evidence that the noncovalent interactions between coordination polymers in a supramolecular system can ultimately affect the primary structure of the metallic building blocks. In general, metallic building blocks are used in supramolecular chemistry to generate specific directional patterns, while the present case reverses such a paradigm. In fact, the geometry of the building block adapts to support the most-stabilized supramolecular architecture.

Experimental Section

3: A solution of **2**[2] (0.113 g, 0.5 mmol) in 20 mL of water was treated with a solution of 4,4′-Me_2bipy (0.092 g, 0.5 mmol) in 20 mL of ethanol. The mixture was heated at 90 °C for 2 h and then it was concentrated to a volume of 15 mL. The resultant solution was filtered and yellow crystals of **3** suitable for single-crystal X-ray structure analysis were obtained after slow evaporation of the solvent at ambient temperature for several days. Yield: 0.12 g (60 %). IR (Nujol mull on NaCl plates): $\tilde{\nu}=3588$–3249 (br), 1970 (br, m), 1619 (s), 1553 (s), 1528 (s), 1486 (m), 1454 (s), 1397 (s), 1306 (m), 1289 (w), 1236 (m), 1209 (s), 1166 (w), 1130 (w), 1096 (w), 1037 (w), 1012 (s), 936 (m), 919 (m), 887 (m), 843 (w), 830 (s), 792 (m), 767 (w), 718 (w), 686 (s), 675 (s), 665 (m) cm^{-1}. Elemental analysis (%) calcd for $C_{16}H_{17}MnN_2O_{4.5}S$: C 48.49, H 4.32, N 7.07; found C 47.90, H 4.26, N 6.80.

Complex **4** was obtained by a similar synthetic procedure as yellow crystals (0.17 g, 82 % yield). IR (Nujol mull on NaCl plates): $\tilde{\nu}=3029$ (br, s), 1970 (br, m), 1615 (s), 1569 (s), 1526 (s), 1499 (s), 1484 (s), 1446 (s), 1387 (s), 1319 (m), 1245 (m), 1234 (m), 1212 (s), 1181 (m), 1164 (m), 1153 (m), 1089 (m), 1043 (s), 990 (w), 953 (w), 938 (m), 892 (m), 843 (m), 832 (m), 810 (w), 793 (m), 771 (m), 734 (m), 670 (s), 648 (m) cm^{-1}. Elemental analysis (%) calcd for $C_{16}H_{17}MnN_2O_{4.5}S$: C 48.49, H 4.32, N 7.07, S 8.09; found C 48.38, H 4.18, N 7.15, S 8.13.

The geometries of the complexes $[Mn_2(\mu\text{-}OOCH)_4(bipy)_2]$ (**1a** and **1b**) and $[Mn_2(OOCH)_2(bipy)_2(\mu\text{-}OOCH)_2(\mu\text{-}H_2O)]$ (**3a**) were

computed by density functional calculations at the unrestricted BP86[20] level of theory using the 6-31G* basis set. The multiplicity was imposed to $S=5$, in agreement with the experimental data recorded at room temperature. Vibrational frequency calculations by diagonalization of the analytically computed Hessian were carried out for all models. Structures **1b** and **3a** (both optimized without symmetry constraints) correspond to real minima in the potential-energy surface. Conversely, **1a** (imposed D_{2h} symmetry) is characterized by six imaginary frequencies that involve displacement of some atoms in order to break the imposed symmetry (all of them smaller than 60 cm^{-1}). For the energy differences, single-point calculation on the previously optimized structures were carried out with the 6-311+G** basis set. All calculations were performed with the Gaussian 98 package of programs.[21]

Received: December 16, 2004
Revised: March 10, 2005
Published online: April 25, 2005

Keywords: carboxylate ligands · density functional calculations · manganese · stacking interactions · supramolecular chemistry

[1] See, for example: *Comprehensive Coordination Chemistry*, *Vol. 4* (Eds.: G. Wilkinson, R. D. Gillard, J. A. McCleverty), Pergamon, **1987**, chap. 1.
[2] A. Grirrane, A. Pastor, A. Galindo, A. Ienco, C. Mealli, P. Rosa, *Chem. Commun.* **2003**, 512.
[3] a) S. Menage, PhD Thesis, University of Paris Sud, Orsay, France, **1988**, and private communication; b) an ORTEP diagram is shown in: H. Mimoun, L. Sausine, S. Menage, J.-J. Girerd in *New Developments in Selective Oxidation* (Eds.: G. Centi, F. Trifiro), Elsevier, Amsterdam, **1990**.
[4] Cambridge Structural Database: F. H. Allen, O. Kennard, *Chem. Des. Autom. News* **1993**, *8*, 31.
[5] M. Nakashima, H. Maruo, T. Hata, T. Tokii, *Chem. Lett.* **1999**, 1277.
[6] E. V. Amel'chenkova, T. O. Desinova, S. E. Nefedov, *Mendeleev Commun.* **2004**, *3*, 1.
[7] a) L. Brammer, *Chem. Soc. Rev.* **2004**, *33*, 476; b) C. Janiak, *Dalton Trans.* **2003**, 2781; c) M. Eddaoudi, D. B. Moler, H. Li, B. Chen, T. M. Reineke, M. O'Keeffe, O. M. Yaghi, *Acc. Chem. Res.* **2001**, *34*, 319; d) L. Brammer, M. D. Burgard, C. S. Rodger, J. K. Swearingen, N. P. Rath, *Chem. Commun.* **2001**, 2468.
[8] Selected examples of the influence of noncovalent interactions on structure include: a) H. Adams, J.-L. Jiménez Blanco, G. Chessari, C. A. Hunter, C. M. R. Low, J. M. Sanderson, J. G. Vinter, *Chem. Eur. J.* **2001**, *7*, 3494; b) J. W. Steed, K. Johnson, C. Legido, P. C. Junk, *Polyhedron* **2003**, *22*, 769.
[9] A Mn–tda complex containing a phen ligand has been characterized recently by X-ray crystallography: J. Marek, Z. Travnicek, P. Kopel, *Acta Crystallogr. Sect. C* **2003**, *59*, m429.
[10] B.-H. Ye, T. Mak, I. D. Williams, X.-Y. Li, *Chem. Commun.* **1997**, 1813.
[11] S.-B. Yu, S. J. Lippard, I. Shweky, A. Bino, *Inorg. Chem.* **1992**, *31*, 3502.
[12] A. Caneschi, F. Ferraro, D. Gatteschi, M. C. Melandri, P. Rey, R. Sessoli, *Angew. Chem.* **1989**, *101*, 1408; *Angew. Chem. Int. Ed. Engl.* **1989**, *28*, 1365.
[13] A dependence of *J* on the nature of the carboxylate bridge in manganese(II) complexes has been reported recently: S. Durot, C. Policar, G. Pelosi, F. Bisceglie, T. Mallah, J.-P. Mahy, *Inorg. Chem.* **2003**, *42*, 8072.
[14] Diffraction data for **3** and **4** were collected at room temperature on a Philips PW 1100 ($\lambda=1.54180$ Å) and an Enraf Nonius CAD4 ($\lambda=0.71073$ Å) automatic diffractometer, respectively. Crystallographic data for **3**: $C_{32}H_{34}Mn_2N_4O_9S_2$, $M_r=792.63$, monoclinic, $C2/c$, $a=21.120(4)$, $b=17.270(5)$, $c=22.467(4)$ Å, $\beta=122.29(2)°$, $V=6927(3)$ Å^3, $Z=8$, $\rho_{calcd}=1.520$ Mg m^{-3}, $\mu=7.560$ mm^{-1}, reflections collected/unique 4679/4365, $R=0.0516$ ($I>2\sigma(I)$), $Rw=0.1271$. Crystallographic data for **4**: $C_{32}H_{34}Mn_2N_4O_9S_2$, $M_r=792.63$, monoclinic, $P2_1/n$, $a=12.4650(14)$, $b=17.101(6)$, $c=16.1130(19)$ Å, $\beta=95.42(1)°$, $V=3419.4(13)$ Å^3, $Z=4$, $\rho_{calcd}=1.540$ Mg m^{-3}, $\mu=0.920$ mm^{-1}, reflections collected/unique 4936/4746, $R=0.0369$ ($I>2\sigma(I)$), $Rw=0.0848$. CCDC-257325 (**3**) and -257326 (**4**) contain the supplementary crystallographic data for this paper. These data can be obtained free of charge from the Cambridge Crystallographic Data Centre via www.ccdc.cam.ac.uk/data_request/cif.
[15] CCDC search: 38 hits.
[16] B.-H. Ye, I. D. Williams, X.-Y. Li, *J. Inorg. Biochem.* **2002**, *92*, 128.
[17] For a recent review on this subject see, for example: A. J. Wu, J. E. Penner-Hahn, V. L. Pecoraro, *Chem. Rev.* **2004**, *104*, 903.
[18] For a critical account on π–π stacking see, for example: C. Janiak, *J. Chem. Soc. Dalton Trans.* **2000**, 3885.
[19] See, for example: N. N. Greenwood, A. Earnshaw, *Chemistry of the Elements*, 2nd ed., Pergamon, Oxford, **1997**.
[20] a) A. D. Becke, *Phys. Rev. A* **1988**, *38*, 3098; b) J. O. Perdew, *Phys. Rev. B* **1986**, *33*, 8822.
[21] Gaussian 98 (Revision A.7): M. J. Frisch et al., see Supporting Information

Asymmetric Synthesis

Introduction of Multiple Elements of Chirality around an Aromatic Core and an Approach to Enantiomerically Pure C_3-Symmetric Ligands

M. Paola Castaldi, Susan E. Gibson, Matthew Rudd, and Andrew J. P. White*

Nonracemic chiral ligands that possess planar chirality and C_2 and C_3 symmetry have delivered excellent results in the field of asymmetric catalysis.[1–4] In particular, the application of ligands that possess C_3 symmetry in asymmetric catalysis is currently attracting interest, despite the challenges associated with the synthesis of such ligands.[5–8] Having discovered a chiral-base-mediated reaction that efficiently generates a single stereogenic center,[9] we wondered whether this reaction could be used to generate multiple stereocenters in a one-pot reaction, and thus create ligands with some of the more synthetically challenging configurations that perform so well in asymmetric catalysis. The results of our study are presented herein, and their potential application in the field of ligand synthesis is illustrated by the synthesis of a C_3-symmetric

[*] M. P. Castaldi, Prof. S. E. Gibson, M. Rudd, A. J. P. White
Department of Chemistry
Imperial College London
South Kensington Campus, London SW7 2AY (UK)
Fax: (+44) 207-594-5804
E-mail: s.gibson@imperial.ac.uk

  DOI: 10.1002/anie.200500020

enantiomerically pure triphosphine and a C_3-symmetric enantiomerically pure tripyridine.

Tricarbonylchromium(0) complexes of alkyl benzyl ethers, such as **1**, give chiral ether complexes **3** in high yield and enantiomeric excess upon treatment with *n*-butyllithium and a chiral diamine **2** followed by an electrophile (Scheme 1).[9] The enantiomer (+)-(*R*,*S*,*S*,*R*)-**2**,[10] which is derived from (*R*)-α-methylbenzylamine, leads to an *R* configuration at the new stereocenter, presumably because the base will preferentially abstract the pro-*R* benzylic proton.

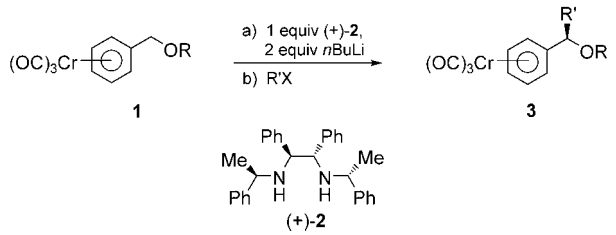

Scheme 1. Use of a chiral diamide to create a single stereocenter.

Our first experiment to determine whether this reaction could be used more than once on a single aromatic core was performed with a tricarbonylchromium(0) complex of a 1,2-disubstituted arene. As shown in Scheme 2, complex **4** was

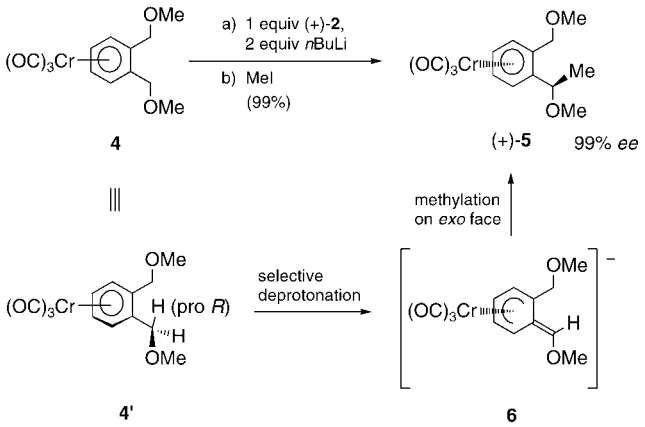

Scheme 2. Creation of central and planar chirality by selective alkylation.

used with iodomethane as a model for the electrophile.[11] Reaction of **4** with one equivalent of diamine (+)-**2** (the *R*,*S*,*S*,*R* enantiomer) and two equivalents of *n*-butyllithium followed by quenching with iodomethane gave one monomethylated species in 99% yield and with 99% *ee*, as determined by HPLC analysis.[12,13]

The selective monomethylation of **4** can be explained as follows: first, it was assumed that the two methoxymethyl substituents adopt conformations that minimize their steric interactions. It was apparent that the pro-*R* proton in **4** (indicated in structure **4′**) is the most accessible of the four benzylic protons to the base because removal of benzylic protons is favored by an antiperiplanar relationship between the proton and the tricarbonylchromium(0) unit,[14] and the chiral base (*R*,*S*,*S*,*R* configuration) is known to selectively remove pro-*R* protons. Thus, deprotonation leads to anion **6**, which is subsequently methylated on its *exo* face (that is, antiperiplanar to the tricarbonylchromium(0) unit) to give the monomethylated product (+)-**5**. Further methylation is disfavored as the conformation that would place the remaining pro-*R* proton antiperiplanar to the tricarbonylchromium(0) unit gives rise to severe steric interactions between the two groups attached to the arene ring, as illustrated by structure **5′**. Thus, although the desired multiple selective alkylation did

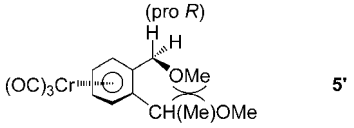

not occur with this substrate, the chiral base did differentiate between the four hydrogen atoms and the monomethylation of the resulting anion generated an enantiomerically pure product with not only central chirality at one of the benzylic sites but also planar chirality that arises from the two different substituents on the chromium-complexed arene ring.

In contrast to the monomethylation described above, the treatment of complex **7**,[15] which is derived from 1,3-benzenedimethanol, with one equivalent of diamine (+)-**2** and two equivalents of *n*-butyllithium followed by quenching of the reaction with iodomethane gave a dimethylated product in 71% yield and with 99% *ee* (Scheme 3), as

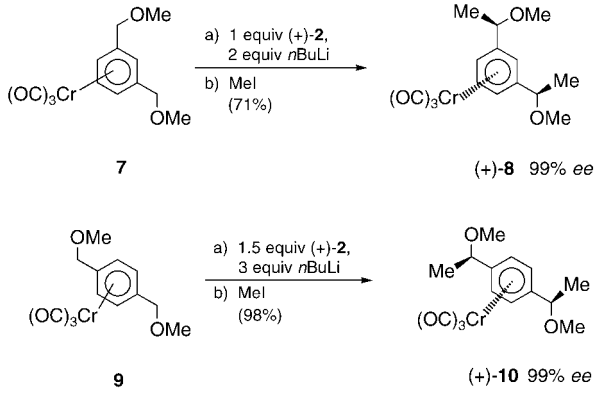

Scheme 3. Creation of two stereocenters by using a chiral diamide.

determined by HPLC analysis. In this case, the two pro-*R* hydrogen atoms can readily adopt an antiperiplanar relationship to the tricarbonylchromium(0) unit, so that both are cleanly removed by the chiral base. Quenching of the resulting dianion leads to the dimethylated product (+)-**8**. It was anticipated that the use of electrophiles that contain groups such as phosphines and subsequent removal of the tricarbonylchromium(0) unit (see below) would provide rapid access to enantiomerically pure C_2-symmetric pincer ligands.[16] The 1,4-disubstituted complex **9** behaved in a similar manner to the 1,3-disubstituted complex **7** (Scheme 3). In this case, the yield and the enantiomeric excess of the C_2-

symmetric product (+)-**10** were optimized by using 1.5 equivalents of diamine **2** and 3 equivalents of *n*-butyllithium.[17]

To determine whether three stereoselective alkylations could be carried out in a one-pot reaction, we turned our attention to the 1,3,5-trisubstituted complex **11**.[18] After optimization of the reaction conditions with the iodomethane quench, it was found that three chiral centers could be installed to give the complex (+)-**12** in good yield and with high enantioselectivity (Scheme 4).

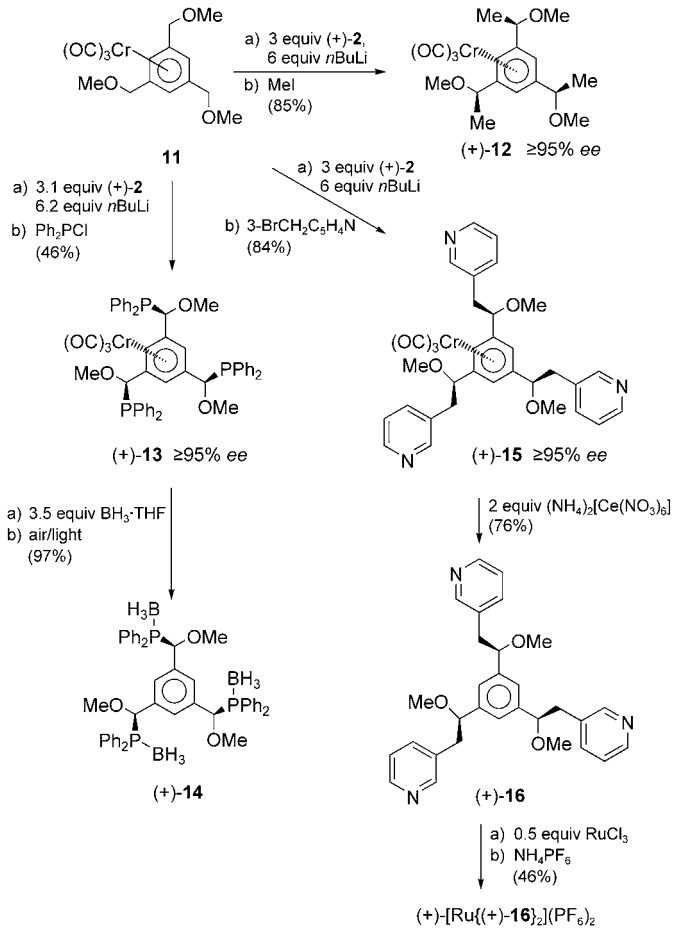

Scheme 4. Creation of three stereocenters by using a chiral diamide.

To demonstrate the potential of the reactions described above for the preparation of structurally distinct ligands for application in asymmetric catalysis, we introduced phosphine and pyridine moieties into the electrophile and applied the resulting compounds to the most challenging reaction in which the model electrophile had been used: the trifunctionalization of **11**. Pleasingly, when chlorodiphenylphosphane was used as the electrophile in the reaction of **11**, the C_3-symmetrical triphosphine (+)-**13** was formed in reasonable yield and with high enantiomeric excess (Scheme 4 and Figure 1). Similarly, when the reaction was quenched with 3-bromomethylpyridine, the C_3-symmetric tripyridine (+)-**15** was prepared in very good yield and with high enantiomeric excess.[19] The subsequent oxidative removal of the tricarbonylchromium(0) unit proceeded smoothly to give enantiomerically pure products (+)-**14** and (+)-**16**. Heating (+)-**16** with $RuCl_3$ followed by anion exchange gave (+)-[Ru{(+)-**16**}$_2$](PF$_6$)$_2$, which is the first example of a structurally characterized chiral bis(tripyridyl)ruthenium complex (Figure 2).

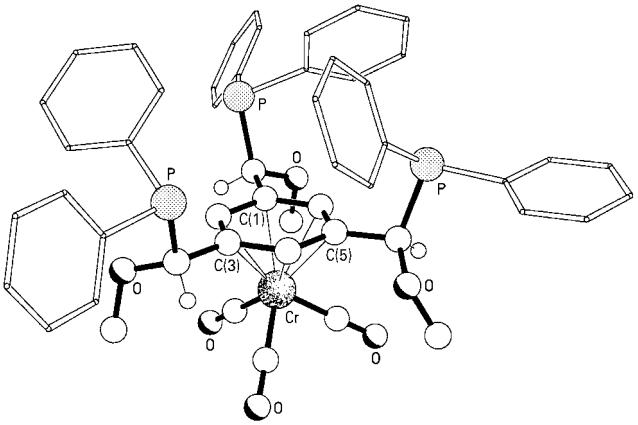

Figure 1. The molecular structure of (+)-**13**.[20]

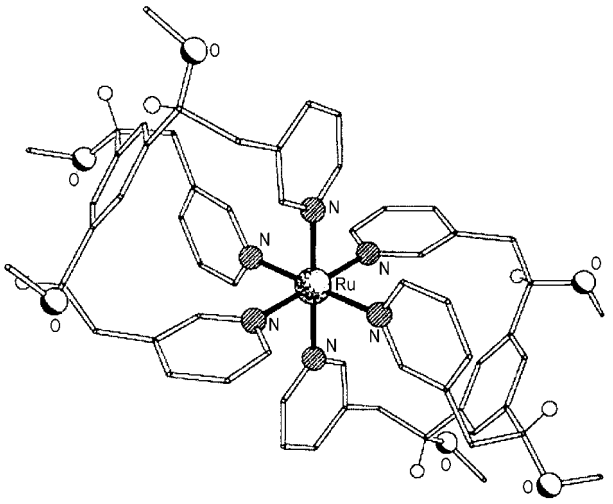

Figure 2. The molecular structure of (+)-[Ru{(+)-**16**}$_2$](PF$_6$)$_2$.[21]

In summary, we have demonstrated that chiral bases can be used to readily generate a range of stereochemical arrays around an aromatic core. Initial experiments reveal that replacement of the model electrophile that was used as a quench with other electrophiles that can introduce important donor groups, such as phosphanes and pyridines, leads to structurally distinct enantiomerically pure chiral ligands. Finally, the reactions described may also be applied to the synthesis of chiral cores of organometallic and organic dendrimers.

Experimental Section

(+)-**13**: *n*-Butyllithium (1.49 mL, 2.50 M in hexanes, 3.72 mmol, 6.2 equiv) was added dropwise to a stirred solution of diamine **2** (208 mg, 1.86 mmol, 3.1 equiv) in dry THF (100 mL) at −78 °C. The

solution was then allowed to warm to room temperature over a period of 30 min to allow the formation of a diamide. The resulting deep-red solution was cooled to −78 °C, and a solution of lithium chloride (80 mg, 1.86 mmol, 3.1 equiv; dried with a heat gun) in THF (10 mL) was added through a cannula. The reaction mixture was stirred for a further 5 min before a precooled solution (−78 °C) of **11** (208 mg, 0.6 mmol, 1.0 equiv) in THF (10 mL) was introduced dropwise through a short cannula. Stirring was continued for a period of 60 min before chlorodiphenylphosphane (0.99 mL, 5.4 mmol, 9.0 equiv) was added in one portion through a syringe. The reaction was then stirred for 1 h at −78 °C followed by a further 2 h at −40 °C before methanol (2 mL) was added and the solvent removed in vacuo. Purification of the residue by flash column chromatography on silica gel (hexane/diethyl ether, 99:1–90:10) afforded (+)-**13** (253 mg, 0.28 mmol, 47 % yield) as a yellow solid. The enantiomeric excess was determined by HPLC analysis (chiralcel OD-H; *n*-hexane/2-propanol, 99.6:0.4, 1.0 $cm^3 min^{-1}$, 330 nm); *S* enantiomer: t_R = 12.5 min (minor); *R* enantiomer: t_R = 20.6 min (major): ≥ 95 % *ee*; $[\alpha]_D^{20} = +226.9$ ($c = 0.67$, CH_2Cl_2); m.p. 155–157 °C; ^{1}H NMR (500 MHz, $CDCl_3$): $\delta = 3.43$ (s, 9H; OCH_3), 4.75 (d, $J = 4.7$ Hz, 3H; $CHPPh_2$), 5.54 (s, 3H; $C_{Cr}H$), 7.28–7.40 (m, 24H; PPh_2), 7.46–7.51 ppm (m, 6H; PPh_2); ^{31}P NMR (202 MHz, $CDCl_3$): $\delta = 13.38$ ppm (PPh_2); ^{13}C NMR (125 MHz, $CDCl_3$): $\delta = 61.0$ (OCH_3), 83.6 (d, J = 24 Hz; $CHPPh_2$), 89.8 (d, $J = 10$ Hz; $C_{Cr}H$), 107.2 (d, $J = 19$ Hz; $C_{Cr}CHPPh_2$), 128.3–128.5 (m; C_{Ar}), 128.9, 129.5 (C_{Ar}), 132.2 (d, J = 15 Hz; C_{Ar}), 133.2 (d, $J = 19$ Hz; C_{Ar}), 135.2 (d, $J = 20$ Hz; C_{Ar}), 135.9 (d, $J = 15$ Hz; C_{Ar}), 233.6 ppm (CO); IR ($\tilde{\nu}_{max}$, CH_2Cl_2): 1967 (CO), 1882 (CO) cm^{-1}; MS(FAB): *m/z* (%): 898 (72) [M^+], 814 (100) [M^+−3 CO], 629 (38) [M^+−3 CO−PPh_2]; elemental analysis (%) calcd for $C_{51}H_{45}O_6P_3Cr$ (898.833): C 68.15, H 5.05; found: C 68.15, H 4.96.

Received: January 4, 2005
Published online: April 28, 2005

Keywords: asymmetric synthesis · chiral bases · phosphines · symmetry · tripyridines

[1] I. Ojima, *Catalytic Asymmetric Synthesis*, Wiley-VCH, New York, **2000**.
[2] W. Tang, X. Zhang, *Chem. Rev.* **2003**, *103*, 3029–3070.
[3] T. J. Colacot, *Chem. Rev.* **2003**, *103*, 3101–3118.
[4] S. E. Gibson, H. Ibrahim, *Chem. Commun.* **2002**, 2465–2473.
[5] C. Moberg, *Angew. Chem.* **1998**, *110*, 260–281; *Angew. Chem. Int. Ed.* **1998**, *37*, 248–268.
[6] C. Dro, S. Bellemin-Laponnaz, R. Welter, L. H. Gade, *Angew. Chem.* **2004**, *116*, 4579–4582; *Angew. Chem. Int. Ed.* **2004**, *43*, 4479–4482.
[7] G. Bringmann, R.-M. Pfeifer, C. Rummey, K. Hartner, M. Breuning, *J. Org. Chem.* **2003**, *68*, 6859–6863.
[8] For the use of C_3-symmetric tripodal oxazolines as receptors, see: S.-G. Kim, K.-H. Kim, Y. K. Kim, S. K. Shin, K. H. Ahn, *J. Am. Chem. Soc.* **2003**, *125*, 13819–13824.
[9] E. L. M. Cowton, S. E. Gibson, M. J. Schneider, M. H. Smith, *Chem. Commun.* **1996**, 839–840.
[10] K. Bambridge, M. J. Begley, N. S. Simpkins, *Tetrahedron Lett.* **1994**, *35*, 3391–3394.
[11] Complex **4** was synthesized in two steps by heating 1,2-benzenedimethanol with hexacarbonylchromium(0) (81 % yield) and then stirring the resultant complex with acidic methanol (90 % yield).
[12] A sample of (±)-**5** was prepared for HPLC analysis by the treatment of **4** with *tert*-butyllithium followed by iodomethane.[13] Treatment of **7**, **9**, and **11** with *tert*-butyllithium and an electrophile led to complex mixtures, so products (+)-**8**, (+)-**10**, (+)-**12**, (+)-**13**, and (+)-**15** were analyzed by using samples of their respective enantiomers prepared by using the chiral base derived from (−)-(*S*,*R*,*R*,*S*)-**2**.
[13] J. Blagg, S. G. Davies, N. J. Holman, C. A. Laughton, B. E. Mobbs, *J. Chem. Soc. Perkin Trans. 1* **1986**, 1581–1589.
[14] S. G. Davies, T. D. McCarthy in *Comprehensive Organometallic Chemistry II*, *Vol. 12*, Pergamon, Oxford, **1995**, pp. 1057–1060.
[15] Satisfactory spectroscopic (IR, ^{1}H NMR, ^{13}C NMR), low-resolution mass-spectrometric, and microanalytical data were obtained for the novel compounds **7**–**16**.
[16] Pincer complexes exhibit a rich and varied chemistry, but surprisingly little attention has been paid to the development of nonracemic chiral versions of these compounds; for reviews, see: a) M. E. van der Boom, D. Milstein, *Chem. Rev.* **2003**, *103*, 1759–1792; b) M. Albrecht, G. van Koten, *Angew. Chem.* **2001**, *113*, 3866–3898; *Angew. Chem. Int. Ed.* **2001**, *40*, 3750–3781.
[17] HPLC analysis of products (+)-**8** and (+)-**10** from some experiments revealed small amounts (< 5 %) of the corresponding *meso* complexes.
[18] Complex **11** was synthesized in four efficient steps by esterification of the commercially available benzene-1,3,5-tricarboxylic acid with acidic methanol (99 %), reduction with $LiAlH_4$ (98 %), methylation with sodium hydride/iodomethane (99 %), and heating with hexacarbonylchromium(0) (98 %).
[19] Products (+)-**12**, (+)-**13**, (+)-**14**, (+)-**15**, and (+)-**16** were diastereoisomerically pure (determined by high-field NMR spectroscopic analysis) after isolation by column chromatography.
[20] Crystal data for (+)-**13**: $C_{51}H_{45}CrO_6P_3$, $M_r = 898.78$, orthorhombic, space group $P2_12_12_1$ (no. 19), $a = 11.497(5)$, $b = 17.024(8)$, $c = 23.651(10)$ Å, $V = 4629(3)$ Å^3, $Z = 4$, $\rho_{calcd} = 1.290$ g cm^{-3}, $\mu(Cu_{K\alpha}) = 3.403$ mm^{-1}, $T = 293$ K, yellow plates; 4388 independent measured reflections, F^2 refinement, $R_1 = 0.060$, wR_2 = 0.149, 3294 independent observed absorption-corrected reflections ($|F_o| > 4\sigma(|F_o|)$, $2\theta_{max} = 130°$), 479 parameters. The absolute structure of (+)-**13** was determined by a combination of *R*-factor tests ($R_1^+ = 0.0601$, $R_1^- = 0.0928$) and by use of the Flack parameter ($x^+ = 0.000(14)$). CCDC-246809 contains the supplementary crystallographic data for this paper. These data can be obtained free of charge from the Cambridge Crystallographic Data Center via www.ccdc.cam.ac.uk/data_request/cif.
[21] Crystal data for (+)-[Ru{(+)-**16**}$_2$](PF_6)$_2$: $[C_{60}H_{66}N_6O_6Ru](PF_6)_2 \cdot 2CH_2Cl_2$, $M_r = 1528.05$, monoclinic, space group $P2_1$ (no. 4), $a = 10.5334(5)$, $b = 18.2106(8)$, $c = 17.6404(9)$ Å, β = 90.877(4)°, $V = 3383.4(3)$ Å^3, $Z = 2$, $\rho_{calcd} = 1.500$ g cm^{-3}, $\mu_{MoK\alpha}$ = 0.524 mm^{-1}, $T = 173$ K, yellow shards; 21626 independent measured reflections, F^2 refinement, $R_1 = 0.108$, $wR_2 = 0.182$, 20273 independent observed absorption-corrected reflections ($|F_o| > 4\sigma(|F_o|)$, $2\theta_{max} = 66°$), 838 parameters. The absolute structure of (+)-[Ru{(+)-**16**}$_2$](PF_6)$_2$ was determined by a combination of *R*-factor tests ($R_1^+ = 0.1075$, $R_1^- = 0.1091$) and by use of the Flack parameter ($x^+ = 0.11(4)$, $x^- = 0.89(4)$). CCDC-264307 contains the supplementary crystallographic data for this paper. These data can be obtained free of charge from the Cambridge Crystallographic Data Center via www.ccdc.cam.ac.uk/data_request/cif.

Luminescence

Simultaneous Observation of Green Multiphoton Upconversion and Red and Blue NLO Processes from Polymeric Terbium(III) Complexes**

Ka-Leung Wong, Ga-Lai Law, Wai-Ming Kwok, Wing-Tak Wong, and David Lee Phillips**

Photoexcitation at a certain wavelength in the near-infrared (NIR) region followed by luminescence at a shorter wavelength in the visible domain is called near-infrared-to-visible photon upconversion. This is a rather unusual process as low-energy photons are "converted" into higher energy photons: two or three photons of NIR light are required to generate one photon of visible light.[1] Nonlinear optics (NLO) is another mechanism that can lead to the generation of light at a frequency that is either twice or integral-multiples of the incident light.[2] The phenomena of two- or three-photon upconversion, and second or third harmonic generation (SHG or THG) on organic materials have received considerable attention since fluorescence detection became popular in applications such as photodynamic therapy, optical data storage, and microfabrication.[3]

Multiphoton excitation allows molecules that typically absorb in the UV region to be excited with red or NIR light. The photoluminescence processes from organolanthanide complexes are usually induced by an organic chromophoric ligand that absorbs incident light and transfers its resultant excitation energy to the lanthanide ion.[4] Until now, only a few multiphoton processes in organolanthanide complexes have been observed owing to the limitations of experimental measurements.[5] Although there have been reports on lanthanide complexes that display second harmonic generation, these have been limited and focused only on glassy doped lanthanide materials.[6] In recent years, our group[7] and others[8] have investigated several high-order multiphoton processes from organic ligands and metal complexes. Herein we report, to the best of our knowledge, the first observation of rare multiphoton upconversion emission from a lanthanide complex as well as SHG and THG transmission phenomena, which occur simultaneously from the same excitation source in the IR region at $\lambda \approx 1.26$ and 1.34 μm.

The N-tripodal ligand **L** was treated with terbium nitrate to give the complex $[Tb(\mathbf{L})(NO_3)_3]$ (**1**, see Figure 1), which is

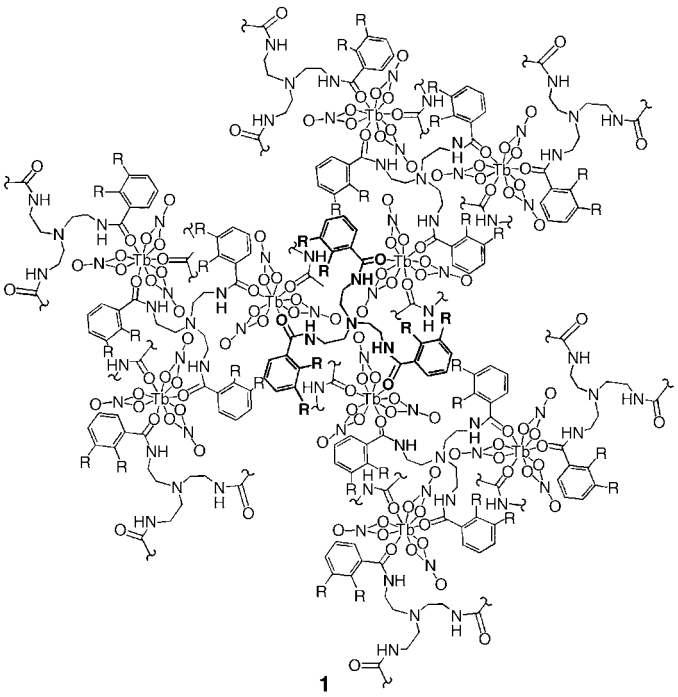

1

Figure 1. Polymeric structure of complex **1**. Ligand **L** is highlighted in bold at the center of the structure. R = OCH_3.

thermally stable up to 300 °C, as shown by thermogravimetric analysis (see Supporting Information). Single crystals of **1** were isolated through the slow evaporation of a solution of **1** in THF/MeCN at room temperature over a few days. The crystal structure of **1** was determined by X-ray crystallography and is shown in Figure 2. The coordination geometry of the metal center in **1** can be described as a tricapped trigonal prism, in which each Tb^{3+} ion is coordinated by three carbonyl (amide) groups from three separate but identical tripodal ligands, and doubly coordinated by three nitrate ions. Upon complexation, the tripodal ligand adopts a polymetallic dendritic form, as the branches contain oxygen groups for binding with lanthanide ions. The ensemble of the tripodal ligand and its connectivity with the lanthanide ion, which itself is preorganized as a result of its coordination to three chromophores, forms a metallodendrimer. The metal takes on a "metal as ligand, metal as complex" approach in this dendritic architecture.[8]

Complex **1** exhibits both strong linear and nonlinear luminescence at room temperature and acts as the gain medium. The chromophores and complexes are known to absorb two or more photons ($\lambda_{ex} = 650$ and 800 nm) and be excited to higher energy states with further energy transfer to the terbium center to produce green f–f emission (Figure 3a).[7] Ligand **L** shows upconversion emission in the blue region ($S_1 \rightarrow S_0$) upon three-photon absorption at $\lambda \approx 800$ nm and four-photon absorption at $\lambda \approx 1.26$ μm (see Supporting

[*] K.-L. Wong, G.-L. Law, Dr. W.-M. Kwok, Prof. Dr. W.-T. Wong, Prof. Dr. D. L. Phillips
Department of Chemistry
The University of Hong Kong
Pokfulam Road, Hong Kong, (P.R. China)
Fax: (+86) 852-2547-2933
E-mail: wtwong@hkucc.hku.hk
phillips@hkucc.hku.hk

[**] The authors acknowledge the financial support of the Hong Kong Research Grants Council (HKU 1/01C) and The University of Hong Kong. K.-L.W. and G.-L.L. acknowledge postgraduate studentships administered by The University of Hong Kong. W.-M.K. acknowledges a research assistant professorship administered by The University of Hong Kong. NLO = nonlinear optics.

Supporting information for this article is available on the WWW under http://www.angewandte.org or from the author.

  DOI: 10.1002/anie.200500031

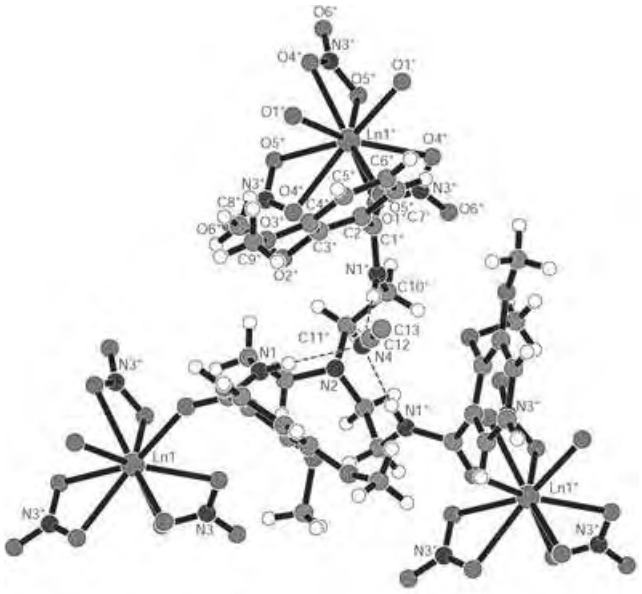

Figure 2. ORTEP drawing of **1** (Ln = Tb) and **2** (Ln = Gd).

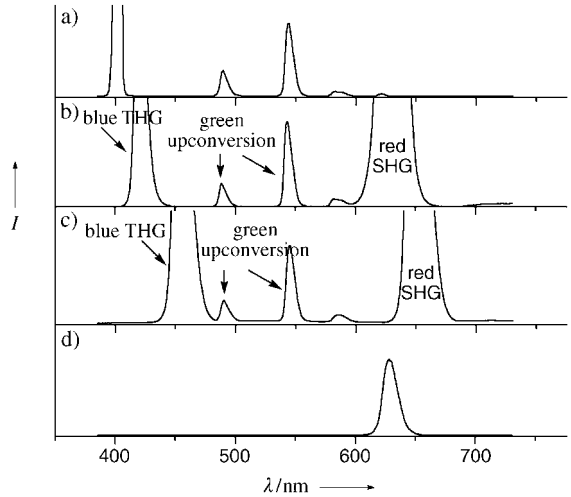

Figure 3. Spectra of the upconversion ($\lambda_{em} = 545$ nm, $^5D_4 \rightarrow {}^7F_5$) and NLO emissions produced upon multiphoton absorption in complex **1**: a) Three-photon upconversion ($\lambda_{ex} = 800$ nm); b, c) simultaneous green four-photon upconversion and red SHG and blue THG processes upon excitation at $\lambda \approx 1.26$ μm (b) and $\lambda \approx 1.34$ μm (c) with a NIR irradiation source; d) SHG spectrum of urea, which was used as the standard, upon excitation at $\lambda \approx 1.26$ μm with the NIR irradiation source.

Information). Complex **1** exhibits a strong multiphoton absorption when excited by ultrashort laser pulses at $\lambda \approx 1.26$ μm to produce the green structured upconversion emission bands of **1** that arise from the f–f transitions of the $^5D_4 \rightarrow {}^7F_J$ ($J = 6$–3) states of terbium. This upconversion process occurs simultaneously with two other nonlinear processes, namely SHG and THG, to generate two additional colors, blue and red, under the same excitation process in the NIR region (Figure 3b). Furthermore, by adjusting the wavelength and intensity of the source, the second and third color elements can be continuously tuned around $\lambda \approx 1.34$ μm, while the green upconversion is still detected (Figure 3c). From the observed behavior, the complexes seem to be extremely wavelength-sensitive and provide an effective tunable system. The red SHG effect can be visually observed as it is the more dominant process, however, a suitable filter can be used to cut-off the red SHG emission while the green upconversion and blue THG are still observed.

The ligand and complex appeared to have no linear absorption in the spectral range from 400 nm to 1.34 μm. However, the blue and green upconversion luminescence from both the ligand and the lanthanide complex can be seen under excitation at $\lambda = 1.26$ and ≈ 1.34 μm when generated by a Ti:sapphire laser. The chromophore absorbs at $\lambda \approx 330$ nm (30303 cm^{-1}), [7] which indicates that the absorption of at least four photons is required for upconversion upon excitation at $\lambda \approx 1.26$ μm (7937 cm^{-1}) and ≈ 1.34 μm (7462 cm^{-1}), whereas for the ligand the accumulation of more than three photons is needed upon excitation at $\lambda \approx 1.34$ μm to reach its lowest emitting state for upconversion emission. The Soga equation[9] is used in auxiliary to verify these SHG, THG, and upconversion processes (Figure 4a–d). The gradients

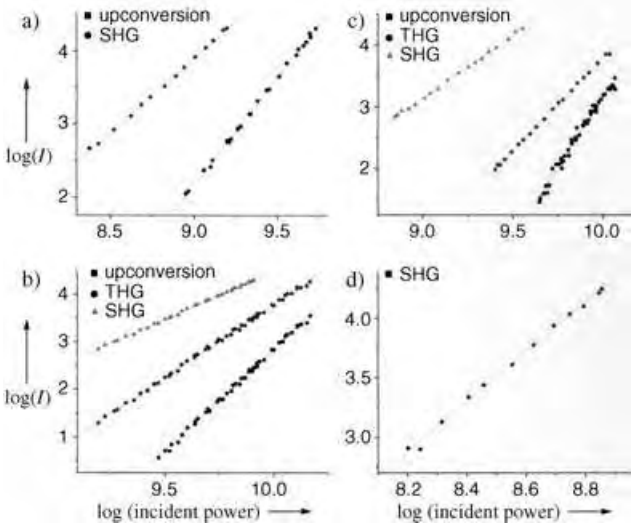

Figure 4. Power dependence of the emission intensities of a) three-photon upconversion ($\lambda_{ex} = 800$ nm) and b), c) four-photon upconversion ($^5D_4 \rightarrow {}^7F_5$), SHG, and THG processes in **1** upon excitation at $\lambda \approx 1.26$ μm (b) and $\lambda \approx 1.34$ μm (c); d) spectrum of SHG of urea as standard ($\lambda_{ex} \approx 1.26$ μm).

obtained for logarithmic plots of incident power versus intensity are 4.28 (Figure 4b, $\lambda_{ex} = 1.26$ μm) and 4.51 (Figure 4c, $\lambda_{ex} = 1.34$ μm). These double-logarithmic representations are therefore in good agreement with the multiphoton-upconversion processes, while the slopes in Figure 4b and c for the THG and SHG processes are 3 and 2, respectively, in the region of $\lambda \approx 1.26$ and ≈ 1.34 μm and agree with the theoretical values of photons needed.

The suggested energy-transfer diagram for the various multi-NLO processes of the Tb complex **1** is shown in Figure 5. For upconversion: First, the energy provided from either a visible or NIR pulse promotes the ligand from the ground state S_0 to a higher energy excited singlet state S_i after absorption of four photons. Then, the electrons in S_i return to

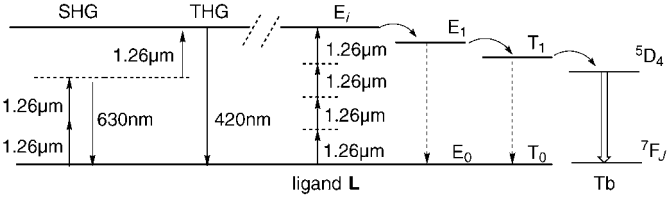

Figure 5. The proposed energy-transfer diagram for the various processes (four-photon upconversion, SHG, THG) in **1**. E_i is a higher energy singlet excited state; E_1 is the radiative lower energy singlet excited state; T_1 is the lowest energy triplet excited state; E_0 and T_0 both refer to the ground state. Linear arrows indicate radiative energy-transfer processes; curly arrows represent nonradiative energy-transfer processes.

the lowest energy excited singlet state S_1 and further, through intersystem crossing, to the lowest energy triplet excited state T_1. This mechanism was further supported by the energies of the S_1 and T_1 states determined for the Gd complex [Gd(**L**)-$(NO_3)_3$] (**2**).[4a,10] As a result of the ligand being attached to a heavy-metal ion such as terbium, the rate of intersystem crossing ($S_1 \rightarrow T_1$) is enhanced.[11] Finally, the electrons from the ligand T_1 state transfer their excess energy to Tb^{III} through either nonresonant phonon-assisted energy transfer or resonant energy transfer, which leads to promotion of Tb^{III} to the $^5D_4$ state. Finally, Tb^{III} relaxes to the ground-state ^7F_J configuration and emits its characteristic green luminescence. Meanwhile, the mechanism for the two other NLO processes involves direct accumulation of two or three photons for SHG and THG, respectively, to result in the two other emissions (red and blue) in the visible region (Figure 5).

We previously reported crystallographic details for a ligand that is similar to **L** but differs in its mode of coordination to Tb to consequently give rise to a different center of symmetry. Only green multiphoton upconversion was observed in that particular system (see Supporting Information). Therefore, the geometry and symmetry of the complex, as controlled by the configuration of coordination of the chromophore to Tb, together with the exceptional properties of the chromophore bring about this unique multiphoton process.

In summary, we have reported tunable second and third harmonic generation with simultaneous indirect multiphoton-upconversion-sensitized luminescence processes in a terbium complex. This phenomenon occurs when the Tb^{III} center has an appropriate symmetry center and is sensitized with a suitable organic ligand. Complex **1** appears to be a very good system for multiple-photon nonlinear photoluminescence and may be useful in future designs of new multiphoton materials. The novel simultaneous multiphoton processes described here may allow the further development of organolanthanide complexes as probe molecules.

Experimental Section

N-[2-(bis{2-[(2,3-dimethoxybenzoyl)amino]ethyl}-amino)ethyl]-2,3-dimethoxybenzamide (**L**) was prepared according to a reported method.[12]

1: $Tb(NO_3)_3 \cdot 6H_2O$ (47 mmol) and **L** (141 mmol) were dissolved in methanol (15 mL), and the mixture was allowed to heat at reflux for 24 h to give complex **1** (62%). Single crystals of **1** were obtained by slow evaporation of a solution of **1** in THF/MeCN. Elemental analysis: calcd for $C_{33}H_{42}N_7O_{18}Tb$: C 40.28, H 4.27, N 9.97; found: C 40.29, H 4.26, N 9.96; FAB-MS: *m/z*: 797 $[M-3NO_3]^+$, 645 $[M-3NO_3-Tb]^+$. Crystal data for **1**·MeCN: $C_{35}H_{45}N_8O_{18}Tb$, $M=1024.71$, trigonal, $P3c1$, $a=10.877(1)$, $c=21.360(2)$ Å, $V=2188.5(3)$ Å^3, $T=298$ K, $Z=2$, $\mu(Mo_{K\alpha})=16.94$ cm^{-1}, 13728 reflections measured, 1960 unique, 1468 observed reflections [$I>1.5\sigma(I)$] were used in all of the calculations, $R=0.0977$, $R_w=0.0822$. Although the crystal data were not of high quality, the crystal structure is essentially isomorphous with the Gd complex **2** and other complexes of **L** with the middle members of the lanthanide series.

2: $Gd(NO_3)_3 \cdot 6H_2O$ (47 mmol) and **L** (141 mmol) were dissolved in methanol (15 mL), and the mixture was heated at reflux for 24 h to give **2** (66%). Single crystals of **2** were obtained by slow evaporation of a solution of **2** in THF/MeCN. Elemental analysis: calcd for $C_{35}H_{45}N_7O_{18}Gd$: C 41.06, H 4.40, N 9.57; found: C 41.08, H 4.41, N 9.58; FAB-MS: *m/z*: 792 $[M-3NO_3]^+$, 643 $[M-3NO_3-Gd]^+$. Crystal data for **2**·MeCN: $C_{35}H_{45}N_7O_{18}Gd$, $M=1023.03$, trigonal, $P3c1$, $a=10.885(1)$, $c=21.403(2)$ Å, $V=2196.1(3)$ Å^3, $T=298$ K, $Z=2$, $\mu(Mo_{K\alpha})=15.95$ cm^{-1}, 13901 reflections measured, 1497 unique, 1468 observed reflections with [$I>2\sigma(I)$] were used in all of the calculations, $R=0.0963$, $R_w=0.0871$. CCDC 258846 (**1**) and 258847 (**2**) contain the supplementary crystallographic data for this paper. These data can be obtained free of charge from the Cambridge Crystallographic Data Centre via www.ccdc.cam.ac.uk/data_request/cif.

The 800-nm pump source was generated from the fundamental of a femtosecond mode-locked Ti:Sapphire laser system (output beam: ≈150-fs duration and 1-kHz repetition rate). The 1.26–1.34 μm pump wavelengths were generated from a homebuilt optical parametric amplifier, which was pumped by the SHG of the 800-nm femtosecond pulses.[13] The lasers were focused to a spot size of ca. 50 μm by means of a lens ($f=10$ cm) onto the sample. The emitting light was collected with a backscattering configuration into a 0.5-m spectrograph and detected by a liquid-nitrogen-cooled CCD detector.

Received: January 5, 2005
Revised: February 2, 2005
Published online: April 28, 2005

Keywords: energy transfer · lanthanides · luminescence · nonlinear optics · tripodal ligands

[1] a) F. Auzel, *Chem. Rev.* **2004**, *104*, 139–174; b) P. Gerner, C. Reinhard, H. U. Güdel, *Chem. Eur. J.* **2004**, *10*, 4735–4741.
[2] a) G. de la Torre, P. Vázquez, F. Agulló-López, T. Torres, *Chem. Rev.* **2004**, *104*, 3723–3750; b) G. Rojo, F. Agulló-López, G. A. Carriedo, F. J. García Alonso, J. I. Fidalgo Martinez, *Synth. Met.* **2001**, *124*, 201–203.
[3] a) K. D. Belfield, K. J. Schafer, W. Mourad, B. A. Reinhardt, *J. Org. Chem.* **2000**, *65*, 4475–4481; b) B. Paci, C. Schmidit, C. Fiorini, J.-M. Nunzi, C. Arbez-Gindre, C. G. Screttas, *J. Chem. Phys.* **1999**, *111*, 7486–7492; c) T. J. Marks, M. A. Ratner, *Angew. Chem.* **1995**, *107*, 167–186; *Angew. Chem. Int. Ed.* **2004**, *43*, 155–173.
[4] a) H. C. Aspinal, *Chem. Rev.* **2002**, *102*, 1807–1850; b) G. F. Sá, O. L. Malta, C. Mello Dongeá, A. M. Simas, R. L. Longo, P. A. SantaCruz, E. F. Silva, Jr., *Coord. Chem. Rev.* **2000**, *196*, 165–195.
[5] a) J. S. Shirk, J. R. Lindle, F. J. Bartoll, M. E. Boyle, *J. Phys. Chem.* **1992**, *96*, 5847–5882; b) L.-M. Fu, X.-F. Wen, X.-C. Ai, Y. Sun, Y.-S. Wu, J.-P. Zhang, Y. Wang, *Angew. Chem.* **2005**, *117*, 757–760; *Angew. Chem. Int. Ed.* **2005**, *44*, 747–750.

[6] a) G. Dominiak-Dzik, W. Ryba-Romanowski, S. Golab, L. Macalik, J. Hanuza, A. Pajaczkowska, *J. Mol. Struct.* **2000**, *555*, 213 – 225; b) W.-T. Dong, H.-G. Zhang, Q. Su, Y.-H. Lin, S.-M. Wang, C.-S. Zhu, *J. Solid State Chem.* **1999**, *148*, 302 – 307; c) M. T. Anderson, M. L. F. Phillips, G. D. Stucky, *J. Non-Cryst. Solids* **1994**, *178*, 120 – 128.

[7] a) K.-L. Wong, W.-M. Kwok, W.-T. Wong, D. L. Phillips, K.-W. Cheah, *Angew. Chem.* **2004**, *116*, 4759 – 4762; *Angew. Chem. Int. Ed.* **2004**, *43*, 4659 – 4662; b) L. Luo, W. P.-W. Lai, K.-L. Wong, W.-T. Wong, K.-F. Li, K.-W. Cheah, *Chem. Phys. Lett.* **2004**, *398*, 372 – 376; c) W. P.-W. Lai, W.-T. Wong, K.-F. Li, K.-W. Cheah, *New J. Chem.* **2002**, *26*, 576 – 581.

[8] a) D. W. Brousmiche, J. M. Serin, J. M. J. Fréchet, G.-S. He, T.-C. Lin, S.-J. Chung, P. N. Prasad, *J. Am. Chem. Soc.* **2003**, *125*, 1448 – 1449; b) G.-S. He, P. P. Markowlez, T.-C. Lin, P. N. Prasad, *Nature* **2002**, *415*, 767 – 770.

[9] S. Tanabe, K. Tamai, K. Hirao, N. Soga, *Phys. Rev. B* **1993**, *47*, 2507 – 2514.

[10] C. Yang, L.-M. Wang, J.-P. Zhang, W.-T Wong, X.-C. Ai, Y.-F. Qiao, B.-S. Zou, L.-L. Gui, *Angew. Chem.* **2004**, *116*, 5120 – 5123; *Angew. Chem. Int. Ed.* **2004**, *43*, 5010 – 5013.

[11] G. S. Maciel, K.-S. Kim, S.-J. Chung, J. Swiatkiewicz, G.-S. He, P. N. Prasad, *J. Phys. Chem. B* **2001**, *105*, 3155 – 3157.

[12] S. M. Cohen, M. Meyer, K. N. Raymond, *J. Am. Chem. Soc.* **1998**, *120*, 6277 – 6286.

[13] a) M. Towrie, A. W. Parker, W. Shaikh, P. Matousek, *Meas. Sci. Technol.* **1998**, *9*, 816 – 823; b) C. Ma, W. M. Kwok, W. S. Chan, P. Zuo, J. T. W. Kary, P. H. Toy, D. L. Phillips, *J. Am. Chem. Soc.* **2005**, *127*, 4163 – 4172.

Controlled Radical Polymerization

Effective Cobalt Mediation of the Radical Polymerization of Vinyl Acetate in Suspension**

*Antoine Debuigne, Jean-Raphaël Caille, Christophe Detrembleur, and Robert Jérôme**

Controlled radical polymerization (CRP)[1] is a common technique for the synthesis of (co)polymers with well-defined molecular parameters (M_n, M_w/M_n), reactive end groups, composition, and architecture. Radical polymerization of a variety of monomers can be controlled by three mechanisms: nitroxide-mediated polymerization (NMP),[2] atom-transfer radical polymerization (ATRP),[3] and radical addition/fragmentation chain-transfer (RAFT).[4] However, control of the radical polymerization of vinyl acetate remains a concern, even though substantial progress by degenerative chain transfer,[5] ATRP,[6,7] and RAFT based on xanthates[8,9] and dithiocarbamates[10] has been reported. Additional effort needs to be devoted to this issue, because vinyl acetate can be polymerized only by a radical process and poly(vinyl acetate) (PVAc) is widely used, for example, as precursor of the water-soluble and otherwise inaccessible poly(vinyl alcohol).[11] Therefore, molecular engineering of PVAc and development of suitable techniques are of utmost importance for the production of novel polymeric materials.

Controlled radical polymerization is most often carried out in bulk or in solution in organic solvents. However, the use of water as dispersion medium may have a number of advantages, including better control of heat transfer, absence of volatile organic solvents, fast polymerization, and possibly high monomer conversion and production of high molar mass polymers. For all these reasons, ever-increasing attention is being paid to the extension of CRP to heterogeneous polymerization techniques, that is, suspension, emulsion, and miniemulsion polymerization.[12–14]

Recently, we reported a system based on cobalt acetylacetonate [$Co(acac)_2$] that imparts control to the radical polymerization of vinyl acetate initiated by 2,2′-azobis(4-methoxy-2,4-dimethyl valeronitrile), V-70, in the bulk at 30 °C.[15] The molar mass of poly(vinyl acetate) indeed changes linearly with monomer conversion, in good agreement with the predicted values (Table 1, entry 1). Moreover, the polydispersity is as low as 1.2. These observations are consistent with a mechanism based on reversible addition of the growing radicals to the cobalt complex and establishment of an equilibrium between alkylcobalt(III) and cobalt(II) complexes, that is, the dormant and the active species, respectively (Scheme 1). A similar mechanism was previously proposed for acrylate polymerization mediated by cobalt porphyrin[16–18] and cobaloxime complexes.[19]

Because of the advantages of using water as a continuous phase, cobalt-mediated radical polymerization of vinyl acetate was tentatively conducted in suspension in water. Therefore, in addition to [$Co(acac)_2$] and V-70, water and a poly(vinyl alcohol-*co*-vinyl acetate) dispersant (0.16 wt% in water) were added to vinyl acetate to give a dispersion in water of the azo initiator (V-70) and the monomer (Scheme 2). Under these conditions, the cobalt-mediated radical polymerization of vinyl acetate remains controlled, as assessed by the clear increase of the molar mass with monomer conversion (Table 1, entry 2). In parallel, the polydispersity increases rapidly with monomer conversion (from 1.3 to 2.35), and the experimental molar masses exceed the theoretical values calculated from the [VAc]/[$Co(acac)_2$] molar ratio, which indicates a loss of control as the polymerization progresses. The poor solubility of the [$Co(acac)_2$] complex in the organic phase (vinyl acetate) is thought to be the reason for the low polymerization efficiency ($M_{n,theor}$/

[*] A. Debuigne, C. Detrembleur, Prof. R. Jérôme
Center for Education and Research on Macromolecules (CERM)
University of Liège
Sart-Tilman, B6, 4000 Liège (Belgium)
Fax: (+32) 4-366-3497
E-mail: rjerome@ulg.ac.be
Dr. J.-R. Caille
Solvay Research and Technology
rue de Ransbeek 310, 1120 Brussels (Belgium)

[**] The authors gratefully acknowledge Solvay for financial support. We thank V. Bodart, F. Declercq, and A. Momtaz (Solvay) for fruitful discussions and Wakko for providing us with V-70. A.D., C.D., and R.J. are indebted to the "Belgian Science Policy" for financial support and to CERM in the framework of the "Interuniversity Attraction Poles Programme (PAI V/03)—Supramolecular Chemistry and Supramolecular Catalysis". C.D. is "Chercheur Qualifié" by the FNRS, Belgium.

 DOI: 10.1002/anie.200500112

Table 1: Radical polymerization of vinyl acetate initiated by V-70 in the presence of $[Co(acac)_2]$ at 30 °C in bulk and in suspension in water.

Entry	Conditions[a]	t [h]	Conv. [%][b]	$M_{n,SEC}$[c] [g mol^{-1}]	$M_{n,theor}$[d] [g mol^{-1}]	$M_{n,theor}/M_{n,SEC}$	M_w/M_n
1	bulk	20	11	7500	5100	0.68	1.25
		22	21	12000	9800	0.82	1.20
		25	36	19500	16800	0.86	1.20
		28	51	24000	23800	0.99	1.20
		44	70	30000	32700	1.09	1.40
2	suspension	4	5	21500	2300	0.11	1.30
		5.5	16	40000	7500	0.19	1.45
		7.5	32	54500	14900	0.27	1.55
		24	>99	95500	46200	0.48	2.35

[a] Bulk: $[Co(acac)_2]/[V\text{-}70]/[VAc]$ 1:3.25:542; Suspension: VAc/H_2O 2.5:3 (v/v), PVOH-*co*-PVAc in water (0.16 wt%). [b] Monomer conversion was determined gravimetrically after removal of the unconverted monomer in vacuo. [c] Determined by size exclusion chromatography (SEC) with polystyrene calibration. [d] $M_{n,theor} = ([M]_0/[Co]_0) \times M_{mono} \times$ conv.

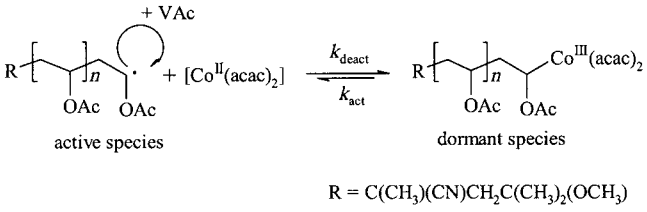

Scheme 1. Equilibrium between dormant and active species in the cobalt-mediated radical polymerization of vinyl acetate.

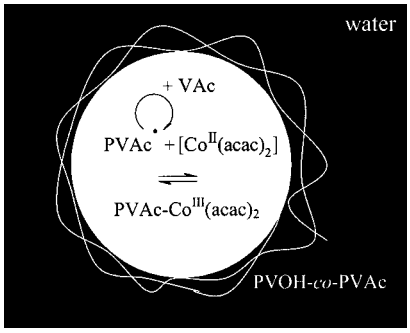

Scheme 2. Equilibrium between dormant and active species within vinyl acetate droplets in suspension polymerization.

$M_{n,SEC}$). The partition coefficient of the cobalt complex between vinyl acetate and water was determined by weighing the solid residue left by each liquid phase after decantation. The concentration of $[Co(acac)_2]$ in water was ten times higher than in the monomer, consistent with the color of the aqueous phase, which had the typical purple color of $[Co(acac)_2]$. That only a small part of the cobalt complex is available in the monomer droplets is confirmed by the polymerization kinetics. Plots of $\ln([M]_0/[M])$ versus time are shown in Figure 1 for bulk and suspension CRP of vinyl acetate. The induction period is much shorter for suspension polymerization (3 h) than for bulk polymerization (19 h). Because this period is the time required for the growing radicals to add to the cobalt complex with formation of dormant species (Scheme 1), the shorter induction time qualitatively agrees with the smaller amount of cobalt in the monomer phase in suspension polymerization.

To increase the polymerization efficiency and to restrict the extent of irreversible termination, the concentration of the cobalt complex in the organic phase must be increased to increase the amount of dormant species (Scheme 2). For this purpose, suspension polymerization of vinyl acetate was initiated by a poly(vinyl acetate) macroinitiator, end-capped by $[Co^{III}(acac)_2]$ and preformed in the bulk, in the presence of the cobalt complex and V-70, at low monomer conversion. This prereacted mixture, which consists of poly(vinyl acetate) chains in unconverted monomer, was merely poured

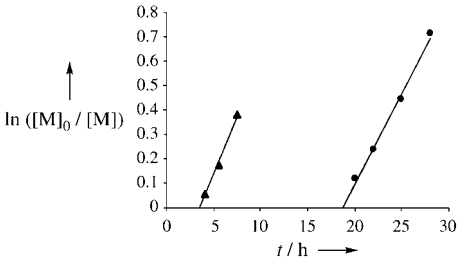

Figure 1. Plot of $\ln([M]_0/[M])$ versus time for the vinyl acetate polymerization initiated by V-70 in the presence of $[Co(acac)_2]$ at 30 °C in bulk (●) and in suspension in water (▲) (Table 1).

into an aqueous solution of poly(vinyl alcohol-*co*-vinyl acetate) under vigorous stirring at 30 °C. According to this strategy, the $[Co(acac)_2]$ complex, covalently bonded as an end group to the dormant chains, is located in the vinyl acetate droplets, that is, where it must be present to efficiently mediate the polymerization. This technique was tested at two $[VAc]/[Co(acac)_2]$ molar ratios (Table 2). Under these conditions, the molar mass increases with reaction time, and the molar mass distribution is rather narrow ($M_w/M_n = 1.2$–1.4), even at high monomer conversion (90%; Table 2, Figure 2). As expected, compared to suspension polymerization in the presence of $[Co(acac)_2]$, the use of a PVAc-$Co(acac)_2$ macroinitiator results in a much higher efficiency ($M_{n,theor}/M_{n,SEC} \approx 0.7$; see entry 2 in Table 1 and data in Table 2). Dependence of the molar mass on monomer conversion is linear, and the molecular weight of PVAc is dictated by the $[VAc]/[PVAc\text{-}Co(acac)_2]$ molar ratio, as is the case for a controlled process. Figure 3 illustrates the shift of the size exclusion chromatogram with polymerization time. Importantly, very high molecular weight PVAc with a rather low polydispersity ($M_{n,SEC} = 100000$ g mol^{-1}, $M_w/M_n = 1.40$, Table 2, entry 2) can be prepared. Moreover, the cobalt-mediated polymerization of vinyl acetate in suspension is very fast at low temperature (30 °C) and is quasicomplete 2 h after addition of the prereaction mixture to the aqueous solution of dispersant. Indeed, the slope of monomer conversion versus time

Table 2: Radical polymerization of vinyl acetate initiated at 30 °C by a low molar mass poly(vinyl acetate) macroinitiator in suspension in water.[a]

Entry	[VAc]/[Co]	t [min][b]	Conv. [%][c]	$M_{n,SEC}$[d] [g mol^{-1}]	$M_{n,theor}$[e] [g mol^{-1}]	$M_{n,theor}/M_{n,SEC}$	M_w/M_n
1	542	0	1	–	–	–	–
		30	37	26000	17300	0.67	1.20
		60	46	33500	21500	0.64	1.20
		120	65	44000	30300	0.69	1.20
		240	95	60500	44300	0.73	1.35
2	1084	0	9	14000	8400	0.60	1.20
		25	36	49000	33600	0.69	1.35
		40	48	66000	44800	0.68	1.30
		70	75	100000	70000	0.70	1.40
		240	99	99000	92400	0.93	1.80

[a] Prereaction in bulk: [Co(acac)$_2$]/[V-70] 1:3.25. PVOH-*co*-PVAc in water (0.16 wt%). 1) 22 h of prepolymerization in bulk, [VAc]/[Co] 542:1. 2) 14 h of prepolymerization in bulk, [VAc]/[Co] 1084:1. [b] t_0: time of addition of the prepolymerized VAc to a PVOH-*co*-PVAc aqueous solution, VAc/H_2O 2.5:3 (v/v). [c] Monomer conversion was determined gravimetrically after removal of the unconverted monomer in vacuo. [d] Determined by SEC with PS calibration. [e] $M_{n,theor} = ([M]_0/[Co]_0) \times M_{mono} \times$ conv.

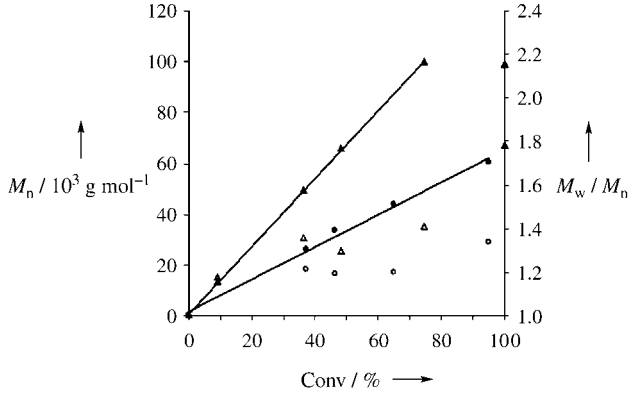

Figure 2. Dependence of M_n (filled symbols) and M_w/M_n (open symbols) on monomer conversion for VAc polymerization initiated at 30 °C by a low molar mass poly(vinyl acetate) macroinitiator in suspension in water (Table 2). VAc/H_2O = 5:6 (v/v), PVOH-*co*-PVAc in water (0.16 wt%). ●: $M_{n,SEC}$ for [Co(acac)$_2$]/[V-70]/[VAc] 1:3.25:542; ▲: $M_{n,SEC}$ for [Co(acac)$_2$]/[V-70]/[VAc] 1:3.25:1084; ○: M_w/M_n for [Co(acac)$_2$]/[V-70]/[VAc] 1:3.25:542; △: M_w/M_n for [Co(acac)$_2$]/[V-70]/[VAc] 1:3.25:1084.

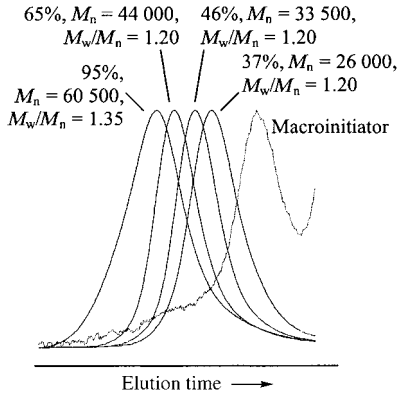

Figure 3. Size exclusion chromatograms for poly(vinyl acetate) initiated by PVAc oligomers end-capped by [Co(acac)$_2$] at 30 °C in the presence of water and PVOH-*co*-PVAc (0.16 wt%) as stabilizer. [Co(acac)$_2$]/[V-70]/[VAc] 1:3.25:542 (Table 2, entry 1).

increases drastically when the prepolymerized medium is poured into water (Figure 4). This spectacular increase in polymerization rate may be attributed to the diffusion of [Co(acac)$_2$] from the monomer droplets to the aqueous phase, which induces a shift of the equilibrium towards the active species (Scheme 2). Finally, poly(vinyl acetate) beads, with a diameter in the millimeter range, are obtained at high monomer conversion, as observed by optical microscopy (Figure 5).

For the first time, the radical polymerization of vinyl acetate can be easily controlled in suspension in water to give poly(vinyl acetate) with predictable molecular weight and low polydispersity up to very high molecular weight and high monomer conversion. Because the reactivity of vinyl acetate is comparable to that

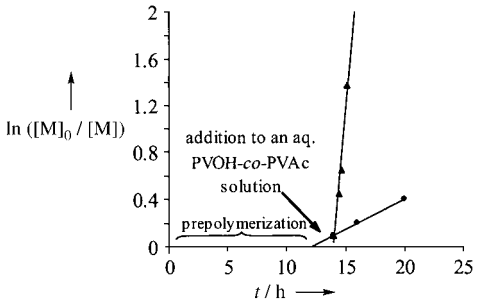

Figure 4. Conversion versus time for VAc bulk polymerization initiated by V-70 in the presence of [Co(acac)$_2$] at 30 °C (●) on addition of the polymerization medium at 10% conversion to an aqueous solution of PVOH-*co*-PVAc (▲; Table 2, entry 2). [Co(acac)$_2$]/[V-70]/[VAc] 1:3.25:1084.

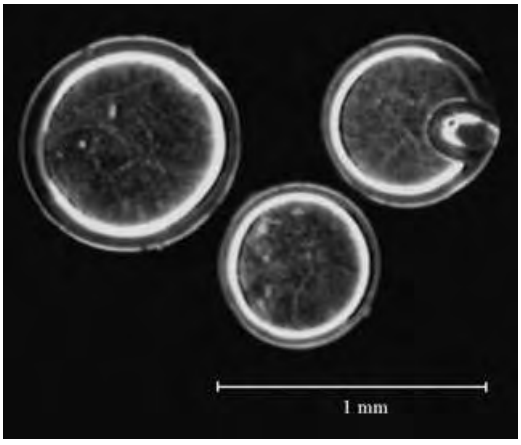

Figure 5. Poly(vinyl acetate) beads prepared by cobalt-mediated polymerization of VAc initiated by a low molar mass PVAc macroinitiator in the presence of water and a PVOH-*co*-PVAc dispersant at 30 °C (Table 2, entry 1, 95%).

of vinyl chloride, this new process will be extended to the radical polymerization of vinyl chloride in the near future.

Experimental Section

Materials: Vinyl acetate (>99%, Acros) was dried over calcium hydride, degassed by several freeze/thaw cycles, distilled under reduced pressure, and stored under argon. Doubly distilled water was degassed by several freeze/thaw cycles. Cobalt(II) acetylacetonate ($[Co(acac)_2]$, >98%, Merck), poly(vinyl alcohol-*co*-vinyl acetate) (72.5% hydrolyzed, Alcotex), and 2,2′-azobis(4-methoxy-2,4-dimethyl valeronitrile) (V-70, Wakko) were used as received. Size exclusion chromatography (SEC) was carried out in THF (flow rate: 1 mL min^{-1}) at 40°C with a Waters 600 liquid chromatograph equipped with a 410 refractive-index detector and styragel columns (four columns HP PL gel 5 μL 10^5 Å, 10^4 Å, 10^3 Å, 10^2 Å). Polystyrene (PS) standards were used for calibration. The molar mass of PVAc determined by SEC with PS calibration was in good agreement with that determined by ^{1}H NMR whenever the α end group of the initiator ($-OCH_3$ at $\delta = 3.13$ ppm) could be observed and compared to the $-CHOCOCH_3$ proton at $\delta = 4.8$ ppm of the monomer unit. An optical microscope (Zeiss) was used to observe the PVAc beads.

Cobalt-mediated radical polymerization of vinyl acetate in the bulk: $[Co(acac)_2]$ (25.7 mg, 10^{-4} mol) and V-70 (100 mg, 3.25×10^{-4} mol) were added to a glass tube capped by a three-way stopcock. The reactor was purged by three vacuum/argon cycles before addition of vinyl acetate (5 mL, 542×10^{-4} mol). The reaction mixture was heated in an oil bath thermostatically controlled at 30°C. No polymerization occurred for a few hours, after which the viscosity increased. Samples were withdrawn at different reaction times, and the vinyl acetate conversion was determined by weighing the polymer collected on removal of the unconverted monomer in vacuo at 50°C.

Cobalt-mediated radical polymerization of vinyl acetate in suspension in water: $[Co(acac)_2]$ (78 mg, 3×10^{-4} mol) and V-70 (300 mg, 9.75×10^{-4} mol) were added to a glass tube capped by a three-way stopcock. The reactor was purged by three vacuum/argon cycles before vinyl acetate (15 mL, 1626×10^{-4} mol) was added. Then known volumes (2.5 mL) of the purple reaction mixture were added to a degassed aqueous solution of PVOH-*co*-PVAc (3 mL, 0.16 wt%) in several round-bottom flasks, previously purged by argon and containing a magnetic stirrer. All these flasks were heated in an oil bath thermostatically controlled at 30°C with vigorous stirring (1000 rpm). Samples were taken from the flasks at different reaction times, the monomer conversion was determined gravimetrically as descibed above, taking into account the amount of water and stabilizer.

Cobalt-mediated radical polymerization of vinyl acetate initiated by a PVAc macroinitiator in suspension in water: $[Co(acac)_2]$ (78 mg, 3×10^{-4} mol) and V-70 (300 mg, 9.75×10^{-4} mol) were added to a glass tube capped by a three-way stopcock. The reactor was purged by three vacuum/argon cycles before vinyl acetate (15 mL, 1626×10^{-4} mol) was added. The flask was heated to 30°C for a few hours, during which the color turned green-brown. Samples (2.5 mL) of this reaction mixture were added to a degassed aqueous solution of PVOH-*co*-PVAc (3 mL, 0.16 wt%) in several round-bottom flasks, previously purged with argon. All these flasks were heated in an oil bath thermostatically controlled at 30°C with vigorous stirring (1000 rpm). At high monomer conversion, PVAc beads were collected by filtration, washed with water, and dried in vacuo.

Received: January 12, 2005
Published online: April 28, 2005

Keywords: cobalt · poly(vinyl acetate) · radical reactions · suspension polymerization

[1] G. Moad, E. Rizzardo, D. H. Solomon, *Macromolecules* **1982**, *15*, 909.
[2] C. J. Hawker, A. W. Bosman, E. Harth, *Chem. Rev.* **2001**, *101*, 3661.
[3] K. Matyjaszewski, J. Xia, *Chem. Rev.* **2001**, *101*, 2921.
[4] G. Moad, J. Chiefari, Y. K. Chong, J. Krstina, R. T. A. Mayadunne, A. Postma, E. Rizzardo, S. H. Thang, *Polym. Int.* **2000**, *49*, 993.
[5] M. C. Iovu, K. Matyjaszewski, *Macromolecules* **2003**, *36*, 9346.
[6] J. Xia, H.-J. Paik, K. Matyjaszewski, *Macromolecules* **1999**, *32*, 8310.
[7] M. Wakioka, K.-Y. Baek, T. Ando, M. Kamigaito, M. Sawamoto, *Macromolecules* **2002**, *35*, 330.
[8] E. Rizzardo, J. Chiefari, R. T. A. Mayadunne, G. Moad, S. H. Thang, *Polym. Prepr. Am. Chem. Soc. Div. Polym. Chem.* **1999**, *40*, 342.
[9] E. Rizzardo, J. Chiefari, R. Mayadunne, G. Moad, S. Thang, *Macromol. Symp.* **2001**, *174*, 209.
[10] M. Destarac, D. Charmot, X. Franck, S. Z. Zard, *Macromol. Rapid Commun.* **2000**, *21*, 1035.
[11] W. H. McDowell, W. O. Kenyon, *J. Am. Chem. Soc.* **1940**, *62*, 415.
[12] J. Qiu, B. Charleux, K. Matyjaszewski, *Prog. Polym. Sci.* **2001**, *26*, 2083.
[13] M. F. Cunningham, *Prog. Polym. Sci.* **2002**, *27*, 1039–1067.
[14] S. W. Prescott, M. J. Ballard, E. Rizzardo, G. Gilbert, *Aust. J. Chem.* **2002**, *55*, 415.
[15] A. Debuigne, J.-R. Caille, R. Jérôme, *Angew. Chem.* **2005**, *117*, 1125; *Angew. Chem. Int. Ed.* **2005**, *44*, 1101.
[16] B. B. Wayland, G. Poszmik, S. L. Mukerjee, M. Fryd, *J. Am. Chem. Soc.* **1994**, *116*, 7943.
[17] B. B. Wayland, L. Basickes, S. L. Mukerjee, M. Wei, M. Fryd, *Macromolecules* **1997**, *30*, 8109.
[18] Z. Lu, M. Fryd, B. B. Wayland, *Macromolecules* **2004**, *37*, 2686.
[19] L. D. Arvanitopoulos, M. P. Greuel, H. J. Harwood, *Polym. Prepr. Am. Chem. Soc. Div. Polym. Chem.* **1994**, *35*, 549.

Natural Products Synthesis (1)

Studies toward the Synthesis of Azadirachtin, Part 1: Total Synthesis of a Fully Functionalized ABC Ring Framework and Coupling with a Norbornene Domain**

K. C. Nicolaou, Pradip K. Sasmal, A. J. Roecker, Xiao-Wen Sun, Sunil Mandal, and Antonella Converso*

We recently embarked on a program directed towards the total synthesis of azadirachtin (**1**, Scheme 1), the remarkable

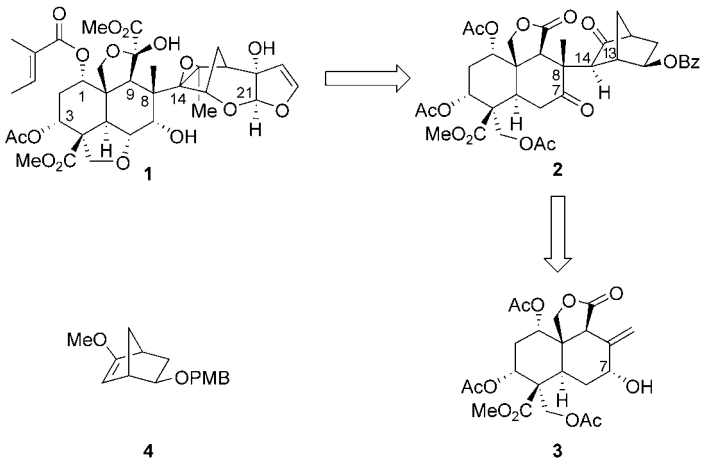

Scheme 1. Retrosynthetic analysis of azadirachtin (**1**).

antifeedant agent isolated from the Neem tree[1] and currently in use as an insecticide.[2] Our radical-based approach towards this unusually challenging target molecule (see Scheme 1) was validated by a number of model studies,[3–5] which, however, left much to be desired in terms of functionalities on the crowded decalin system of the natural product. Herein we report the total synthesis of a fully functionalized ABC decalin intermediate **3** and its coupling with a suitable norbornene system **4** to afford a C7–C13 linked product, which was elaborated into the advanced intermediate **2** and whose structural disposition might allow its eventual conversion into azadirachtin (**1**). In the following Communication in this issue,[6] we describe both the total synthesis and semisynthesis of a different decalin intermediate and its elaboration into a close precursor of the target molecule, as well as some interesting reactions made possible by the special proximity effects that uniquely characterize the azadirachtin structural motif.[7]

According to our previously disclosed strategy,[3–5] azadirachtin (**1**) was to be approached through a path marked by key intermediates such as **2**, **3**, and **4** as retrosynthetically outlined in Scheme 1. Crucial to the success of such a plan is the availability of fully functionalized advanced decalin systems such as **3**, which have the potential to yield azadirachtin upon coupling with norbornene derivatives such as **4** followed by appropriate elaboration.

The fundamental strategy for the synthesis of the norbornene precursor **4** has already been reported in a previous Communication.[5] The construction of the fully functionalized decalin system **3** in its enantiomerically pure form is depicted in Scheme 2. Thus, starting from enantiopure compound **5**,[5] ketone **6** was produced by dibenzylation (for abbreviations and conditions, see legends in schemes) followed by desilylation and Swern oxidation of the resulting secondary alcohol. Ketone **6** was then converted into enone **7** in 81% overall yield for the three-step sequence with a regioselectivity of approximately 10:1. Subsequent functionalization of **7** by Mander carboxylation[8] followed by aldol reaction of the resulting β-ketoester with paraformaldehyde in the presence of $Yb(OTf)_3$ led to the corresponding hydroxyester, whose hydroxy group was protected as a TBS ether (69% yield for three steps). Subsequent epoxidation of the enone moiety of the so-obtained intermediate by TBHP in the presence of triton B furnished, stereoselectively, epoxide **8** in 87% yield. The required 1,3-diaxial diol system within the growing substrate was established first by regioselective opening of the epoxide moiety of **8** (91% yield) with PhSeNa (generated in situ from PhSeSePh and $NaBH_4$)[9] and then stereoselective reduction ($NaBH_4$) of the intermediate hydroxyketone to afford the desired compound **9** in 63% yield. Selective removal of the TBS group, peracetylation, debenzylation, and finally, regioselective monoprotection of the primary alcohol of the resulting diol as a TES ether yielded alcohol **10** in 74% yield over four steps. The hydroxy compound **10** was then oxidized with DMP, and the resulting ketone was olefinated with $Ph_3P=CH_2$ prior to removal of the TES group in the presence of catalytic DDQ.[10] The primary alcohol was then oxidized to the corresponding aldehyde **11** (once again with DMP) in 65% overall yield over the four steps. The targeted coupling partner **3** was finally obtained from the latter intermediate **11** in 48% overall yield,[11] by the following sequence: 1) oxidation with $NaClO_2$, 2) exposure to ethanolic HCl (0.5 M), and 3) allylic oxidation with SeO_2 and TBHP.

[*] Prof. Dr. K. C. Nicolaou, Dr. P. K. Sasmal, A. J. Roecker, Dr. X.-W. Sun, Dr. S. Mandal, Dr. A. Converso
Department of Chemistry and
The Skaggs Institute for Chemical Biology
The Scripps Research Institute
10550 North Torrey Pines Road, La Jolla, CA 92037 (USA)
Fax: (+1) 858-784-2469
E-mail: kcn@scripps.edu
and
Department of Chemistry and Biochemistry
University of California, San Diego
9500 Gilman Drive, La Jolla, CA 92093 (USA)

[**] We thank Dr. D. H. Huang and Dr. G. Siuzdak for NMR spectroscopic and mass spectrometric assistance, respectively. Financial support for this work was provided by grants from the National Institutes of Health (USA) and the Skaggs Institute for Chemical Biology, and a predoctoral fellowship from the Division of Organic Chemistry of the American Chemical Society sponsored by Novartis (to A.J.R.).

 DOI: 10.1002/anie.200500216

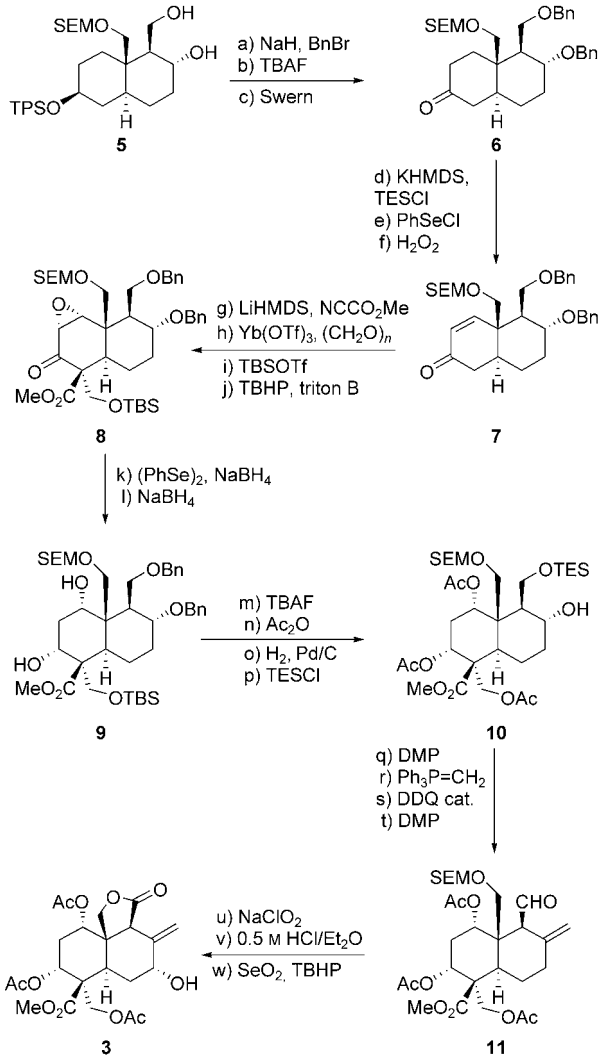

Scheme 2. Construction of decalin fragment **3**. Reagents and conditions: a) NaH (6.0 equiv), BnBr (4.0 equiv), nBu$_4$NI (0.2 equiv), THF/DMF (3:1), 25 °C, 24 h; b) TBAF (2.0 equiv), THF, 25 °C, 15 h, 91 % over two steps; c) $(COCl)_2$ (1.5 equiv), DMSO (3.0 equiv), Et_3N (6.0 equiv), −78→25 °C, CH_2Cl_2, 1 h, 89%; d) KHMDS (1.5 equiv), TESCl (1.5 equiv), THF, −78 °C, 30 min; e) PhSeCl (1.1 equiv), CH_2Cl_2, −78 °C, 30 min; f) H_2O_2 (30% v/v, 3.0 equiv), THF, 0→25 °C, 1 h, 80% over three steps; g) LiHMDS (2.0 equiv), $NCCO_2Me$ (1.5 equiv), THF, −78 °C, 6 h, 93 %; h) $(CH_2O)_n$ (20 equiv), $Yb(OTf)_3$ (2.0 equiv), THF, 25 °C, 2 h; i) TBSOTf (1.5 equiv), 2,6-lutidine (2.5 equiv), CH_2Cl_2, −78 °C, 30 min, 74% over two steps; j) triton B (2.0 equiv), aqueous TBHP (70%; 10 equiv), THF, 25 °C, 16 h, 87%; k) $(PhSe)_2$ (3.0 equiv), $NaBH_4$ (6.0 equiv), EtOH, 25 °C, 0.5 h, 91%; l) $NaBH_4$ (8.0 equiv), MeOH/CH_2Cl_2 (1:15), 25 °C, 24 h, 63 %; m) TBAF (1.5 equiv), THF, 0→25 °C, 1 h; n) Ac_2O (6.0 equiv), Et_3N (10 equiv), DMAP (0.4 equiv), CH_2Cl_2, 25 °C, 6 h, 92% over two steps; o) Pd/C (10%; 20 wt%), H_2 (1 atm), EtOH, 25 °C, 16 h, 98%; p) TESCl (1.0 equiv), Et_3N (2.0 equiv), CH_2Cl_2, 0→25 °C, 2 h, 82%; q) DMP (1.5 equiv), $NaHCO_3$ (1.5 equiv), CH_2Cl_2, 0→25 °C, 2 h, 91 %; r) $Ph_3P=CH_2$ (5.0 equiv), diethyl ether, 25 °C, 2 h, 80%; s) DDQ (0.1 equiv), THF/H_2O (9:1), 25 °C, 2 h, 97%; t) DMP (1.5 equiv), CH_2Cl_2, 0→25 °C, 2 h, 92%; u) $NaClO_2$ (4.0 equiv), NaH_2PO_4 (4.0 equiv), 2-methyl-2-butene (75 equiv), THF/tBuOH/H_2O (2:4:1), 25 °C, 1 h; v) 0.5 M HCl, EtOH/Et_2O (1:1), 0→25 °C, 6 h, solvent evaporated; then, Ac_2O (6.0 equiv), Et_3N (10 equiv), DMAP (0.4 equiv), CH_2Cl_2, 25 °C, 6 h, 94% over two steps; w) SeO_2 (5.0 equiv), TBHP (10 equiv), CH_2Cl_2, 25 °C, 6 h, 51 %. Bn = benzyl, DMF = *N*,*N*-dimethylformamide, TBAF = tetra-*n*-butylammonium fluoride, DMSO = dimethyl sulfoxide, HMDS = hexamethyldisilazane, TES = triethylsilyl, OTf = trifluoromethanesulfonate, TBS = *tert*-butyldimethylsilyl, triton B = benzyltrimethylammonium hydroxide, TBHP = *tert*-butyl hydroperoxide, DMAP = 4-(dimethylamino)pyridine, DMP = Dess–Martin periodinane, DDQ = 2,3-dichloro-5,6-dicyano-*p*-benzoquinone.

With **3** in hand, we were now poised to test the key bromoketalization[12] reaction between this substrate and norbornene enol ether **4**, a reaction that had shown rather capricious behavior during our previous model studies. Upon considerable experimentation, it was found that the optimum conditions for this coupling required addition of Br_2 to norbornene derivative **4** in CH_2Cl_2 at −78 °C followed by the sequential addition of *N*,*N*-dimethylaniline and allylic alcohol **3**, and warming slowly to 0 °C. Chromatographic resolution of the rather complex mixture of products led to the isolation and characterization of two diastereomeric bromoketals (ca. 1:1 ratio, 80 % combined yield), whose NMR spectroscopic analysis revealed structures **12** and **13** (Scheme 3). The ratio of the two isomers was found to be dependent on reaction time, temperature, and, apparently, on the steric environment around the attacking allylic alcohol moiety, since previous[4,5] and subsequent[6] experiments with other decalin allylic alcohol substrates led to different results. Scheme 4 provides a possible explanation for these results by invoking an oxonium ion intermediate **4b** derived from the rupture of the initially formed bromonium ion **4a** as the temperature is raised to 0 °C. Attack on oxonium ion **4b** from the *exo* face is now possible, and leads to the formation of the *epi*-C13 bromoketal (azadirachtin numbering) **4d** (Scheme 4) or **13** (Scheme 3).

Both bromoketals **12** and **13** were subjected to radical cyclization conditions[13] to afford the desired hexacyclic products **17** and **18** (Table 1) in 70 and 76 % yield, respectively (Scheme 3). The structures and stereochemistries of **17** and **18** were unambiguously assigned by NMR spectroscopy (^{1}H,^{13}C-COSY, ROESY, and HMQC). Interestingly, only compound **13** generated the desired polycycle **18** upon treatment with nBu$_3$SnH–Et$_3$B[14] at room temperature, whereas compound **12** gave, exclusively, reduction to **16**. This observation suggests that, while the radical formed from **12** (i.e. **14**) requires higher temperature to access the appropriate transition state for ring closure, the radical obtained from **13** resides in a more privileged position to attain the required transition state for cyclization, which apparently takes place even at ambient temperature.

Interestingly, the primary radicals initially formed from **14** and **15** only undergo the 5-*exo*-trig mode of ring closure. The alternative 6-*endo*-trig mode of reaction is also available in principle and, indeed, is observed with other substrates, as we shall describe in more detail in the following Communication in this issue.[6] In the present instance the secondary radical thus formed through the action of $(Me_3Si)_3SiH$–AIBN undergoes ring closure, leading to a primary radical, which in turn undergoes an intramolecular 1,5-H shift (see 30-H (azadirachtin numbering) in structures **14** and **15**) to afford ketone **17**, in the case of **14**, or undergoes an intermolecular quench to yield PMB ether **18** in the case of **15**.

The stereochemistry of the newly generated stereogenic centers within **18** was confirmed by ^{1}H NMR NOE studies (see Scheme 3). As further proof of its structure, compound **17** was also constructed from the previously synthesized[5] intermediate **19** as shown in Scheme 5. Thus, **19** was converted into compound **20** by protection as a BOM ether, desilylation, and oxidation under Swern conditions. Regioselective unsa-

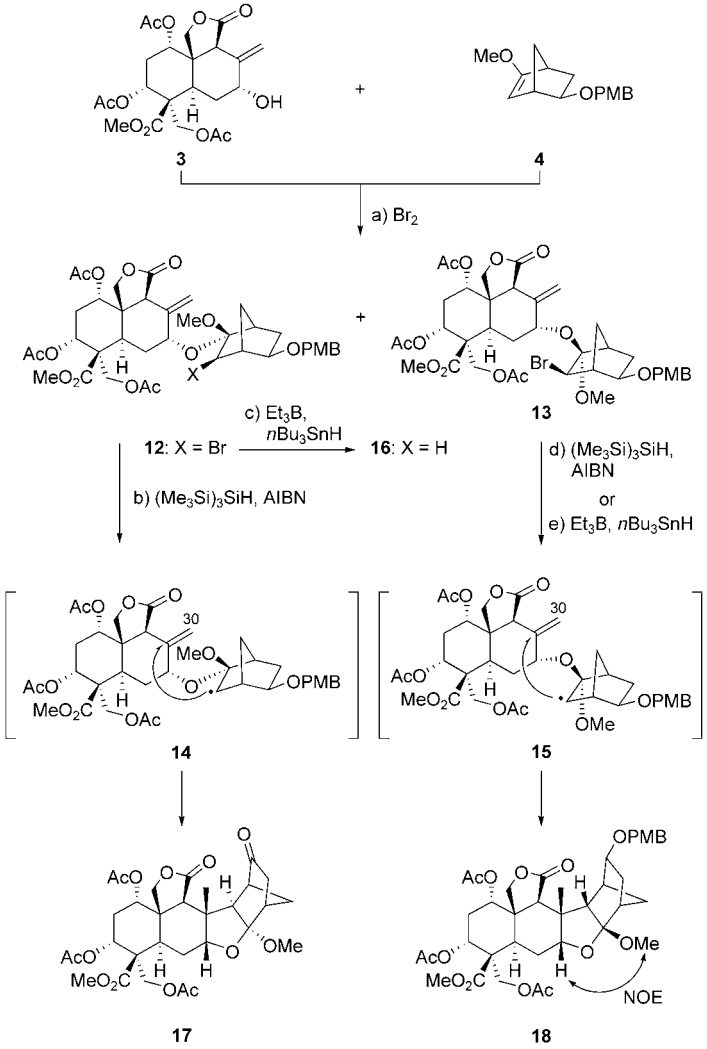

Scheme 3. Coupling of decalin system **3** with norbornene derivative **4** and synthesis of hexacyclic compounds **17** and **18**. Reagents and conditions: a) Br_2 (1.5 equiv), *N*,*N*-dimethylaniline (2.0 equiv), **4** (2.0 equiv), CH_2Cl_2, −78 °C, 10 min; then **3**, −78→0 °C over 2 h, 0 °C, 1 h, **12** (38%) and **13** (42%); b) $(Me_3Si)_3SiH$ (2.0 equiv), AIBN (1.0 equiv), toluene (0.007 M), 110 °C, 30 min, 70%; c) Et_3B (5.0 equiv), nBu_3SnH (5.0 equiv), CH_2Cl_2, 25 °C, 1 h, 80%; d) $(Me_3Si)_3SiH$ (2.0 equiv), AIBN (1.0 equiv), toluene (0.007 M), 110 °C, 30 min, 76%; e) Et_3B (5.0 equiv), nBu_3SnH (5.0 equiv), CH_2Cl_2, 25 °C, 1 h, 80%. AIBN = 2,2′-azobisisobutyronitrile.

turation of ketone **20** with IBX,[15] followed by sequential treatment with LiHDMS/$NCCO_2Me$ and $Yb(OTf)_3/(CH_2O)_n$, furnished hydroxyenone **21**, whose protection with TBS, stereoselective epoxidation, and reductive epoxide opening (PhSeNa, 81% over two steps) led to β-hydroxyketone **22**. Following stereoselective reduction (30%) of **22** with $NaBH_4$, desilylation and then peracetylation of the resulting triol afforded triacetate **23**. Finally, hydrogenolysis of the BOM protecting group from intermediate **23** followed by oxidation with DMP furnished the desired hexacyclic ketone **17**, whose spectroscopic and chromatographic properties matched those of a sample obtained from the more convergent and expedient route depicted in Scheme 3.

In the final phase of this study, it was important to demonstrate the cleavage of the temporary bridge that was so

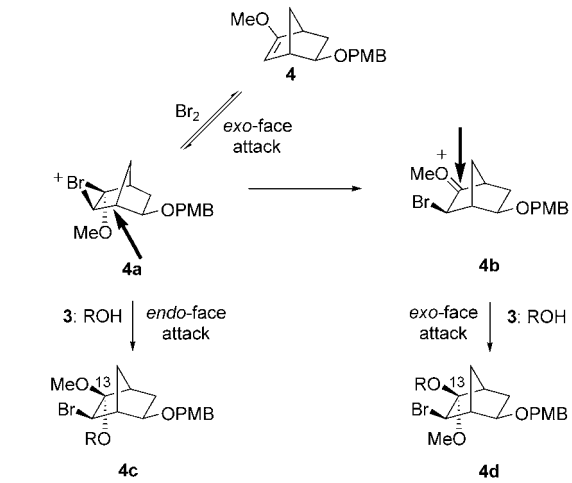

Scheme 4. Proposed mechanism for bromoketalization of **3** and **4**.

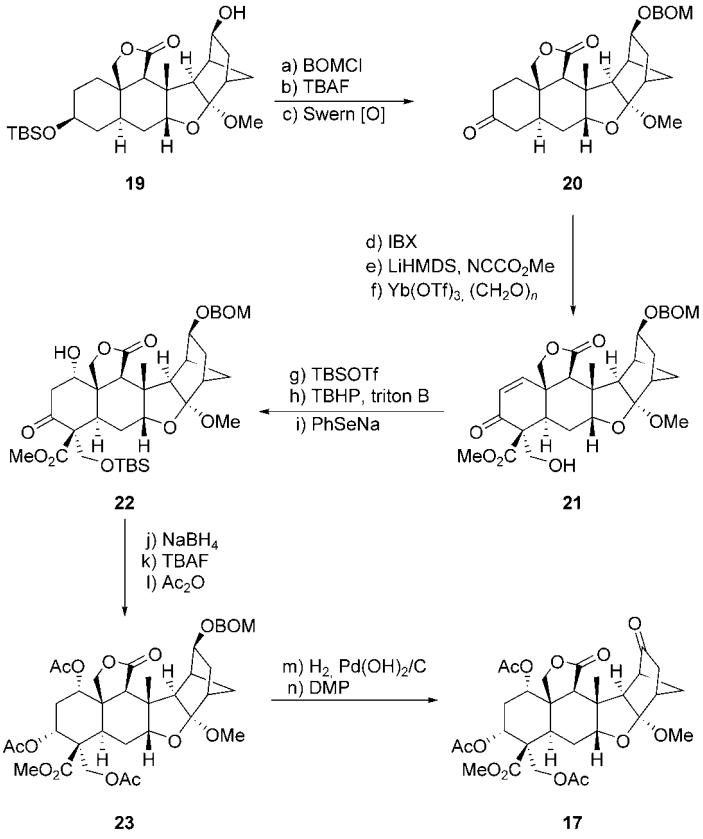

Scheme 5. Construction of hexacyclic compound **17** from **19**. Reagents and conditions: a) BOMCl (5.0 equiv), iPr_2NEt (10 equiv), DMF, 40 °C, 24 h, 96%; b) TBAF (2.0 equiv), THF, 25 °C, 12 h, 94%; c) $(COCl)_2$ (2.0 equiv), DMSO (3.0 equiv), Et_3N (4.0 equiv), −78→25 °C, CH_2Cl_2, 1 h, 74%; d) IBX (1.5 equiv), DMSO, 65 °C, 36 h, 75%; e) LiHMDS (1.5 equiv), $NCCO_2Me$ (1.2 equiv), HMPA (1.5 equiv), THF, −78 °C, 3 h, 65%; f) $(CH_2O)_n$ (5.0 equiv), $Yb(OTf)_3$ (2.0 equiv), THF, 25 °C, 1 h, 72%; g) TBSOTf (1.1 equiv), 2,6-lutidine (2.0 equiv), CH_2Cl_2, −78 °C, 1 h, 90%; h) triton B (2.0 equiv), aqueous TBHP (70%; 10 equiv), THF, 25 °C, 16 h; i) PhSeNa (3.0 equiv), EtOH, 25 °C, 4 h, 81% over two steps; j) $NaBH_4$ (8.0 equiv), THF, 25 °C, 30 min, 30%; k) TBAF (1.5 equiv), THF, 0→25 °C, 1 h; l) Ac_2O (6.0 equiv), Et_3N (10 equiv), DMAP (0.4 equiv), CH_2Cl_2, 25 °C, 6 h, 80% over two steps; m) $Pd(OH)_2/C$ (20%; 10 wt%), H_2 (1 atm), EtOH, 25 °C, 1 h; n) DMP (2.0 equiv), CH_2Cl_2, 0→25 °C, 2 h, 90% over two steps. BOM = benzyloxymethyl, IBX = *o*-iodoxybenzoic acid, HMPA = hexamethylphosphoramide.

instrumental in forming the challenging C8–C14 bond as a prelude to further advances toward azadirachtin. Towards this end, the hexacyclic compound **18** was first converted into the benzoate **24** (by protecting-group exchange through hydrogenolysis and benzoylation) and followed by hydrolysis to hemiketal **25** in 75% overall yield (Scheme 6). Finally, hemiketal **25** was oxidized with PCC to afford diketone **2** (Table 1) in 80% yield. Diastereomer **17** has not, as yet, been advanced further.

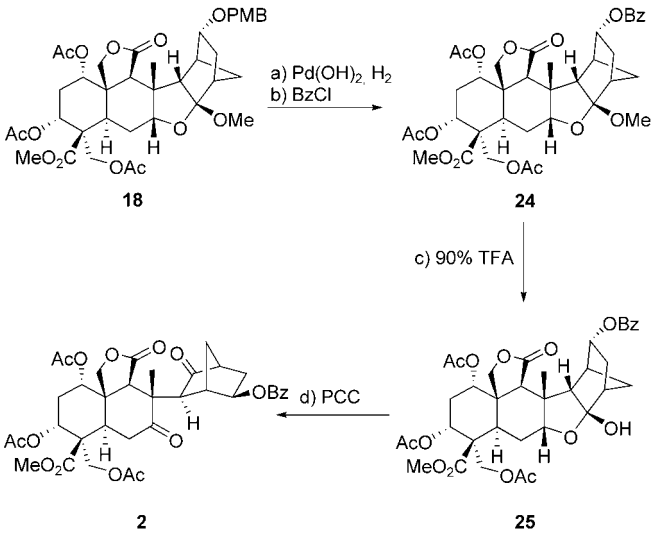

Scheme 6. Conversion of hexacyclic compound **18** into advanced pentacyclic intermediate **2**. Reagents and conditions: a) $Pd(OH)_2/C$ (20%; 10 wt%), H_2 (1 atm), EtOH, 25 °C, 1 h; b) BzCl (3.0 equiv), Et_3N (6.0 equiv), DMAP (0.1 equiv), CH_2Cl_2, 0→25 °C, 4 h; c) aqueous TFA (90%), 65 °C, 3 h, 75% over three steps; d) PCC (15 equiv), DCE, 65 °C, 16 h, 80%. Bz = benzoyl, TFA = trifluoroacetic acid, PCC = pyridinium chlorochromate, DCE = 1,2-dichloroethane.

The described chemistry provides solutions to a number of challenges posed by the decalin domain of azadirachtin (**1**) and brings the realization of the synthesis of this molecule within close range. In the following Communication in this issue,[6] we describe further studies that place this goal even closer, but from a different angle.

Received: January 19, 2005
Published online: April 21, 2005

Keywords: asymmetric synthesis · natural products · protecting groups · radical reactions · total synthesis

Table 1: Selected physical properties for compounds **2**, **17**, and **18**.

2: $R_f = 0.29$ (silica gel, EtOAc/hexanes 1:1); $[\alpha]_D^{32} = -28.0$ ($c = 0.6$, CH_2Cl_2); IR (film): $\tilde{\nu}_{max} = 2923, 2851, 1780, 1745, 1717, 1451, 1376, 1231, 1112, 1048, 963\ cm^{-1}$; ^1H NMR (500 MHz, C_6D_6): $\delta = 8.02$ (d, $J = 7.7$ Hz, 2H), 7.58 (t, $J = 7.7$ Hz, 1H), 7.46 (t, $J = 7.7$ Hz, 2H), 5.52 (t, $J = 2.9$ Hz, 1H), 5.16 (d, $J = 7.0$ Hz, 1H), 4.83 (t, $J = 2.9$ Hz, 1H), 4.41 (A of ABq, $J = 10.6$ Hz, 1H), 4.35 (B of ABq, $J = 10.6$ Hz, 1H), 4.29 (A of ABq, $J = 10.5$ Hz, 1H), 4.00 (B of ABq, $J = 10.5$ Hz, 1H), 3.82 (s, 3H), 3.22–3.09 (m, 2H), 2.97 (br s, 1H), 2.93 (d, $J = 2.2$ Hz, 1H), 2.67 (dd, $J = 15.7$, 2.9 Hz, 1H), 2.65 (s, 1H), 2.58 (d, $J = 4.0$ Hz, 1H), 2.44 (dt, $J = 17.0$, 3.5 Hz, 1H), 2.38–2.30 (m, 2H), 2.13–1.95 (m, 3H), 2.07 (s, 3H), 2.06 (s, 3H), 1.99 (s, 3H), 1.29 ppm (s, 3H); ^{13}C NMR (125 MHz, C_6D_6): $\delta = 214.3, 207.3, 174.0, 172.4, 170.2, 169.9, 169.5, 166.1, 133.4, 130.0, 129.7, 128.6, 77.0, 69.5, 67.3, 66.3, 65.8, 53.9, 53.3, 51.0, 49.2, 48.0, 47.6, 41.6, 34.8, 33.0, 32.9, 32.8, 29.9, 27.6, 23.2, 21.2, 21.0, 20.6$ ppm; HRMS (MALDI): calcd for $C_{36}H_{40}O_{14}Na$: 719.2310 [M+Na^+], found 719.2311

17: $R_f = 0.11$ (silica gel, EtOAc/hexane 1:1); $[\alpha]_D^{32} = -44.5$ (CH_2Cl_2, $c = 0.14$); IR (film): $\tilde{\nu}_{max} = 2954, 2922, 2851, 1778, 1743, 1730, 1439, 1375, 1320, 1234, 1050, 938, 736, 604\ cm^{-1}$; ^1H NMR (600 MHz, C_6D_6): $\delta = 5.63$ (br s, 1H), 4.89 (br s, 1H), 4.39 (d, $J = 10.5$ Hz, 1H), 4.23 (d, $J = 10.5$ Hz, 1H), 3.76 (d, $J = 9.6$ Hz, 1H), 3.63 (s, 1H), 3.42 (d, $J = 9.6$ Hz, 1H), 3.14 (s, 3H), 3.10 (s, 3H), 3.05 (s, 1H), 2.98 (dd, $J = 13.8$, 3.6 Hz, 1H), 2.85 (d, $J = 4.8$ Hz, 1H), 2.46 (br s, 1H), 2.28 (br s, 1H), 2.21–2.17 (m, 2H), 2.05 (dt, $J = 13.8$, 3.6, 1H), 1.69 (s, 3H), 1.68 (s, 3H), 1.67–1.66 (m, 1H), 1.62 (s, 3H), 1.59–1.51 (m, 3H), 1.14 (s, 3H), 1.09 ppm (d, $J = 10.2$ Hz, 1H); ^{13}C NMR (150 MHz, C_6D_6): $\delta = 214.9, 175.3, 172.5, 169.7, 169.1, 168.6, 115.3, 84.4, 69.6, 67.4, 67.4, 66.8, 66.1, 53.9, 51.9, 51.4, 50.3, 50.0, 46.4, 41.4, 40.4, 39.7, 38.7, 27.8, 27.7, 22.3, 20.5, 20.5, 20.1, 16.3$ ppm; HRMS (ESI-TOF): calcd for $C_{30}H_{38}O_{13}Na^+$ [M+Na^+]: 629.2204; found: 629.2205

18: $R_f = 0.26$ (silica gel, EtOAc/hexane 1:1); $[\alpha]_D^{32} = +1.4$ (CH_2Cl_2, $c = 0.14$); IR (film): $\tilde{\nu}_{max} = 2934, 2851, 1777, 1745, 1612, 1513, 1440, 1372, 1318, 1231, 1182, 1047, 823, 736\ cm^{-1}$; ^1H NMR (600 MHz, C_6D_6): $\delta = 7.27$ (d, $J = 8.4$ Hz, 2H), 6.80 (d, $J = 8.4$ Hz, 2H), 5.69 (br s, 1H), 4.82 (br s, 1H), 4.44 (d, $J = 11.4$ Hz, 1H), 4.43 (d, $J = 10.2$ Hz, 1H), 4.41 (d, $J = 10.2$ Hz, 1H), 4.36 (d, $J = 11.4$ Hz, 1H), 3.95 (br s, 1H), 3.87 (d, $J = 10.0$ Hz, 1H), 3.63 (d, $J = 6.0$ Hz, 1H), 3.56 (d, $J = 10.0$ Hz, 1H), 3.33 (s, 3H), 3.24 (s, 1H), 3.13 (br s, 1H), 3.11 (s, 3H), 3.04 (s, 3H), 3.02 (dd, $J = 13.8$, 3.0 Hz, 1H), 2.40 (d, $J = 3.6$ Hz, 1H), 2.36 (br d, $J = 16.8$ Hz, 1H), 2.08 (br d, $J = 16.8$ Hz, 1H), 2.03–1.96 (m, 4H), 1.91 (d, $J = 9.6$ Hz, 1H), 1.68 (s, 3H), 1.60 (s, 3H), 1.53 (br s, 1H), 1.48 (dd, $J = 9.6$, 3.0 Hz, 1H), 1.44 (s, 3H), 1.11 ppm (s, 3H); ^{13}C NMR (150 MHz, C_6D_6): $\delta = 176.1, 172.6, 169.6, 169.0, 168.9, 159.6, 131.3, 129.7, 117.1, 114.0, 81.3, 81.2, 71.0, 70.8, 67.1, 66.6, 66.5, 63.6, 54.7, 52.0, 50.6, 50.2, 46.4, 43.6, 43.0, 42.0, 37.9, 33.2, 33.0, 28.5, 27.5, 25.8, 22.2, 20.7, 20.3, 20.0$ ppm; HRMS (ESI-TOF): calcd for $C_{38}H_{48}O_{14}Na^+$ [M+Na^+]: 751.2936; found: 751.2932

[1] For isolation, see: a) J. H. Butterworth, E. D. Morgan, *J. Chem. Soc. Chem. Commun.* **1968**, 23–24; for structure determination, see: b) J. N. Bilton, H. B. Broughton, P. S. Jones, S. V. Ley, Z. Lidert, E. D. Morgan, H. S. Rszepa, R. N. Sheppard, A. M. Z. Slawin, D. J. Williams, *Tetrahedron* **1987**, *43*, 2805–2815; c) W. Kraus, M. Bokel, A. Bruhn, R. Cramer, I. Klaiber, A. Klenk, G. Nagl, H. Pohnl, H. Sadlo, B. Vogler, *Tetrahedron* **1987**, *43*, 2817–2830; d) C. J. Turner, M. S. Tempesta, R. B. Taylor, M. G. Zagorski, J. S. Termini, D. R. Schroeder, K. Nakanishi, *Tetrahedron* **1987**, *43*, 2789–2804.

[2] a) V. H. Guerrini (Australia), PCT Int. Appl., WO 19901211, **1991** [*Chem. Abstr.* **1991**, *116*, 2316]; b) P. H. Hull (Australia), PCT Int. Appl., WO 9105561, **1991** [*Chem. Abstr.* **1991**, *115*, 108578]; c) J. A. Klocke, M. S. Lee, R. B. Yamasaki (Native Plants, Inc., USA)., Eur. Pat. Appl., EP 308044, **1989** [*Chem. Abstr.* **1989**, *112*, 153732]; d) Z. Lidert (Rohm and Haas Co., USA), Eur. Pat. Appl. EP 311284, **1989** [*Chem. Abstr.* **1989**, *111*, 92333]; e) G. Stix, *Sci. Am.* **1992**, *266*, 132; f) B. Corradi (Italy), Eur. Pat. Appl., Ep 1293122, **2003** [*Chem. Abstr.* **2003**, *138*, 200347]; g) T. R. Govindachari, G. Gopalakrishnan, *J. Indian Chem. Soc.* **1998**, *75*, 655–661; h) H. Gong, H. Xu, (People Rep. China), application CN 1468625, **2004**; i) A. J. Mordue, *Neem: Today and in the New Millennium* **2004**, 229–242; j) E. D.

Morgan, *Neem: Today and in the New Millennium* **2004**, 21 – 32; k) P. D. K. Jayanthi, A. Verghese, *Entomon* **2004**, *29*, 45 – 50; l) S. R. Moorty, A. D. Kumar (Fortune Bio-Tech Limited, India), application US 6733802, **2004** [*Chem. Abstr.* **2004**, *140*, 352064].

[3] K. C. Nicolaou, M. Follmann, A. J. Roecker, K. W. Hunt, *Angew. Chem.* **2002**, *114*, 2207 – 2210; *Angew. Chem. Int. Ed.* **2002**, *41*, 2103 – 2106.

[4] K. C. Nicolaou, A. J. Roecker, M. Follmann, R. Baati, *Angew. Chem.* **2002**, *114*, 2211 – 2214; *Angew. Chem. Int. Ed.* **2002**, *41*, 2107 – 2110.

[5] K. C. Nicolaou, A. J. Roecker, H. Monenschein, P. Guntupalli, M. Follmann, *Angew. Chem.* **2003**, *115*, 3765 – 3770; *Angew. Chem. Int. Ed.* **2003**, *42*, 3637 – 3642.

[6] K. C. Nicolaou, P. K. Sasmal, T. V. Koftis, A. Converso, E. Loizidou, F. Kaiser, A. J. Roecker, C. C. Dellios, X.-W. Sun, G. Petrovic, *Angew. Chem.* **2005**, *117*, 3513 – 3518; *Angew. Chem. Int. Ed.* **2005**, *44*, 3447 – 3452, following Communication in this issue.

[7] For earlier synthetic studies from other groups, see: a) A. Murai, *J. Toxicol. Toxin Rev.* **2003**, *22*, 617 – 632; b) T. Fukuzaki, S. Kobayashi, T. Hibi, T. Ikuma, J. Ishihara, N. Kanoh, A. Murai, *Org. Lett.* **2002**, *4*, 2877 – 2880; c) T. Durand-Reville, L. B. Gobbi, B. L. Gray, S. V. Ley, J. S. Scott, *Org. Lett.* **2002**, *4*, 3847 – 3850; d) Y. Yamamoto, J. Ishihara, N. Kanoh, A. Murai, *Synthesis* **2000**, 1894 – 1906; e) S. V. Ley, C. E. Gutteridge, A. R. Pape, C. D. Spilling, C. Zumbrunn, *Synlett* **1999**, 1295 – 1297; f) H. Schlesiger, E. Winterfeld, *Chirality* **1997**, *9*, 454 – 458; g) H. Watanabe, T. Watanabe, K. Mori, T. Kitahara, *Tetrahedron Lett.* **1997**, *38*, 4429 – 4432; h) A. A. Denholm, L. Jennens, S. V. Ley, A. Wood, *Tetrahedron* **1995**, *51*, 6591 – 6604; i) K. J. Henry Jr., B. Fraser-Reid, *J. Org. Chem.* **1994**, *59*, 5128 – 5129; j) S. V. Ley, A. A. Denholm, A. Wood, *Nat. Prod. Rep.* **1993**, *10*, 109 – 157; k) H. Kolb, S. V. Ley, *Tetrahedron Lett.* **1991**, *32*, 6187 – 6190; l) Y. Nishikimi, T. Iimori, M. Sodeoka, M. Shibasaki, *J. Org. Chem.* **1989**, *54*, 3354 – 3359; m) M. G. Brasca, H. B. Broughton, D. Craig, S. V. Ley, A. A. Somovilla, P. L. Toogood, *Tetrahedron Lett.* **1988**, *29*, 1853 – 1856.

[8] S. R. Crabtree, W. L. A. Chu, L. N. Mander, *Synlett* **1990**, 169 – 170.

[9] M. Miyashita, T. Suzuki, A. Yoshikoshi, *Tetrahedron Lett.* **1987**, *28*, 4293 – 4296.

[10] K. Tanemura, T. Suzuki, T. Horaguchi, *J. Chem. Soc. Perkin Trans. 1* **1992**, 2997 – 2998.

[11] A. F. Barrero, S. Arseniyadis, J. F. Quilez Dell Moral, M. Mar Herrador, M. Valdivia, D. Jimenez, *J. Org. Chem.* **2002**, *67*, 2501 – 2508.

[12] For selected previous bromoketalization reactions, see: a) A. Srikrishna, G. Sundarababu, *Tetrahedron* **1990**, *46*, 7901 – 7910; b) J. D. White, P. Theramongkol, C. Kuroda, J. R. Engebrecht, *J. Org. Chem.* **1988**, *53*, 5909 – 5921; c) G. Stork, R. Mook, Jr., S. A. Biller, S. D. Rychnovsky, *J. Am. Chem. Soc.* **1983**, *105*, 3741 – 3742; d) G. Stork, R. Mook, Jr., *J. Am. Chem. Soc.* **1983**, *105*, 3720 – 3722.

[13] J. M. Kanabus-Kaminska, J. A. Hawari, D. Griller, C. Chatgilialoglu, *J. Am. Chem. Soc.* **1987**, *109*, 5267 – 5268.

[14] K. Miura, Y. Ichinose, K. Nozaki, K. Fugami, K. Oshima, K. Utimoto, *Bull. Chem. Soc. Jpn.* **1989**, *62*, 143 – 147.

[15] K. C. Nicolaou, T. Montagnon, P. S. Baran, Y. L. Zhong, *J. Am. Chem. Soc.* **2002**, *124*, 2245 – 2258.

Studies toward the Synthesis of Azadirachtin, Part 2: Construction of Fully Functionalized ABCD Ring Frameworks and Unusual Intramolecular Reactions Induced by Close-Proximity Effects**

K. C. Nicolaou, Pradip K. Sasmal, Theocharis V. Koftis, Antonella Converso, Eriketi Loizidou, Florian Kaiser, A. J. Roecker, Constantinos C. Dellios, Xiao-Wen Sun, and Goran Petrovic*

In the preceding Communication in this issue[1] we described the total synthesis of a potential decalin precursor to azadirachtin (**1**),[2] its coupling to a suitable norbornene fragment **4** (Scheme 1), and the elaboration of the product to an advanced intermediate along the path to this synthetic target. Herein we report the total synthesis and semisynthesis from azadirachtin of a more advanced decalin system **3**, its coupling to the same norbornene fragment **4**, and the elaboration of the resulting product to an advanced intermediate for the total synthesis of azadirachtin (Scheme 1). This report also includes a number of unusual reactions induced by proximity effects and special steric factors highlighting the unique characteristics of the azadirachtin scaffold.

Having successfully synthesized tricyclic decalin system **5**, (Scheme 1) and explored its chemistry toward azadirachtin (**1**) as described in the preceding Communication,[1] we turned our attention to the more advanced tetracyclic decalin precursor **3**, which bears the tetrahydrofuran ring system of **1** within its structure. Our plan to synthesize the targeted intermediate **3** required key building block **6** (Scheme 2) as

[*] Prof. Dr. K. C. Nicolaou, Dr. P. K. Sasmal, Dr. T. V. Koftis, Dr. A. Converso, Dr. F. Kaiser, A. J. Roecker, Dr. C. C. Dellios, Dr. X.-W. Sun, Dr. G. Petrovic
Department of Chemistry and
The Skaggs Institute for Chemical Biology
The Scripps Research Institute
10550 North Torrey Pines Road, La Jolla, CA 92037 (USA)
Fax: (+1) 858-784-2469
E-mail: kcn@scripps.edu
and
Department of Chemistry and Biochemistry
University of California, San Diego
9500 Gilman Drive, La Jolla, CA 92093 (USA)
E. Loizidou
Department of Chemistry
San Diego State University
5500 Campanile Drive, San Diego, CA 92182 (USA)

[**] We thank Dr. D. H. Huang, Dr. G. Siuzdak, and Dr. R. Chadha for NMR spectroscopic, mass spectrometric, and X-ray crystallographic assistance, respectively. Financial support for this work was provided by grants from the National Institutes of Health (USA) and the Skaggs Institute for Chemical Biology, a postdoctoral fellowship from the Alexander von Humboldt Foundation (to F.K.), and a predoctoral fellowship from the Division of Organic Chemistry of the American Chemical Society sponsored by Novartis (to A.J.R.).

 DOI: 10.1002/anie.200500217

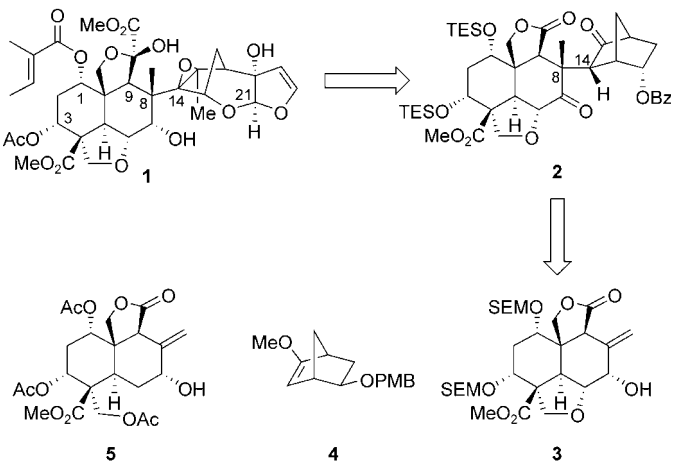

Scheme 1. Structure of azadirachtin (**1**) and possible precursors **3** and **5**.

the starting point, a compound that had been encountered as an enantiopure substance in our previous expeditions.[1] This diol **6** was first protected as a cyclohexanone ketal, the two benzyl protecting groups were cleaved, the resulting primary hydroxy group was selectively silylated, and finally the remaining secondary alcohol was oxidized with DMP to afford ketone **7** in 58% overall yield. Compound **7** was then converted into enone **8** by the standard, three-step protocol in 95% overall yield and thence into mesylate **10** via hydroxy compound **9** by desilylation followed by mesylation of the primary alcohol. The OsO_4–NMO-induced dihydroxylation of enone **10** proceeded stereoselectively from the less-hindered α face and was accompanied by internal S_N2-type mesylate displacement, affording the expected tetrahydrofuran derivative in 95% yield over two steps. Desilylation of the latter intermediate with TBAF furnished dihydroxyketone **11** in 96% yield. This substance was then converted into the exocyclic olefin **13** via its diacetate **12** (95%) by a Wittig reaction with $Ph_3P{=}CH_2$ (93%) followed by deacetylation with K_2CO_3 in MeOH (92%). This three-step process was adopted after encountering difficulties with the attempted, but failed, direct olefination of **11**. The primary alcohol of diol **13** was selectively oxidized to the corresponding hydroxyaldehyde through a TEMPO-catalyzed oxidation procedure (75%).[3] The remaining secondary hydroxy function was protected as an acetoxy group, and the aldehyde moiety was further oxidized to the acetate carboxylic acid. Exposure of the latter to 0.5 M ethanolic HCl gave the dihydroxylactone **14** through cleavage of both the ketal and the silyl protecting groups and ring closure (69% overall yield). Lactone **14** crystallized from CH_2Cl_2/hexanes as colorless crystals (m.p. 240–241 °C) and X-ray crystallographic analysis[4] confirmed the ring framework and stereochemical features of this compound (Figure 1). Finally, protection of both free hydroxy groups within **14** with SEMCl (89% yield) followed by treatment with K_2CO_3 in MeOH led to the coveted hydroxylactone **3** in 99% yield.

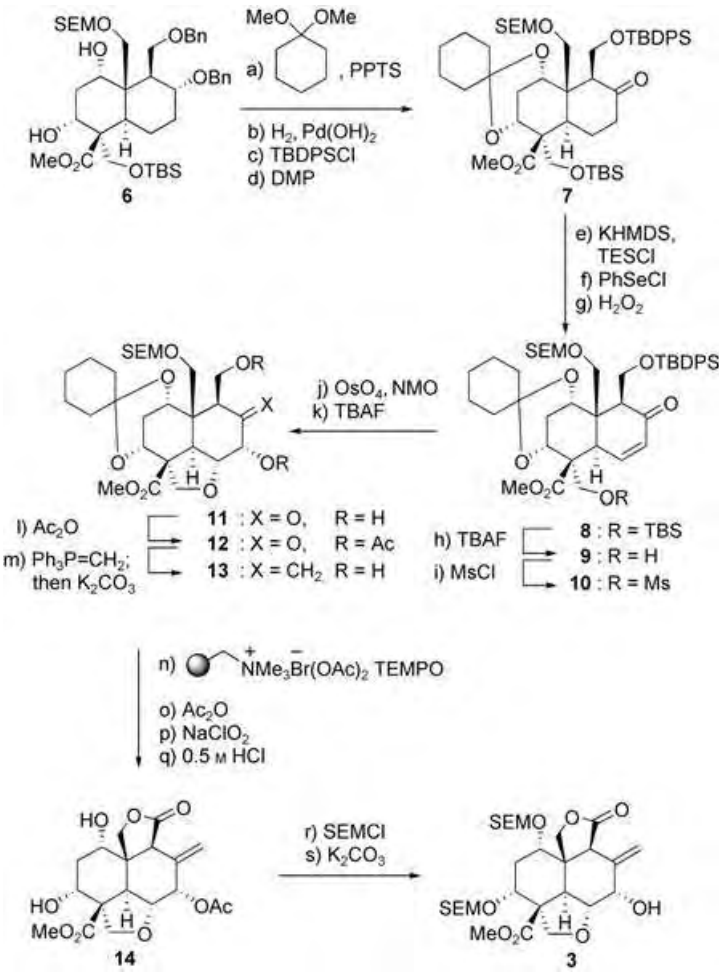

Scheme 2. Total synthesis of hydroxylactone **3**. Reagents and conditions: a) 1,1-dimethoxycyclohexane (4.0 equiv), PPTS (8.0 equiv), benzene, 80 °C, 4 h, 74%; b) Pd/C (10%; 40 wt%), $NaHCO_3$ (10 equiv), H_2 (1 atm), EtOAc, 25 °C, 24 h, 91%; c) TBDPSCl (1.5 equiv), Et_3N (3.0 equiv), DMAP (0.1 equiv), CH_2Cl_2, 0 °C, 2 h, 94%; d) DMP (1.5 equiv), $NaHCO_3$ (2.0 equiv), CH_2Cl_2, 0→25 °C, 2 h, 91%; e) KHMDS (1.5 equiv), TESCl (1.5 equiv), THF, −78 °C, 30 min; f) PhSeCl (1.1 equiv), CH_2Cl_2, −78 °C, 30 min; g) H_2O_2 (3.0 equiv), THF, 0→25 °C, 1 h, 95% over three steps; h) TBAF (1.5 equiv), THF, 0→25 °C, 2 h, 94%; i) MsCl (2.0 equiv), Et_3N (4.0 equiv), DMAP (0.1 equiv), CH_2Cl_2, 0 °C, 2 h; j) OsO_4 (0.2 equiv), NMO (2.0 equiv), *t*BuOH/THF/H_2O (5:5:1), 25 °C, 24 h, 95% over two steps; k) TBAF (1.5 equiv), THF, 25 °C, 3 h, 96%; l) Ac_2O (8.0 equiv), Et_3N (12 equiv), DMAP (0.2 equiv), CH_2Cl_2, 0→25 °C, 2 h, 95%; m) 1. $Ph_3P{=}CH_2$ (8.0 equiv), Et_2O, 0→25 °C, 6 h, 93%; 2. K_2CO_3 (6.0 equiv), MeOH, 25 °C, 5 h, 92%; n) TEMPO (0.8 equiv), polystyrene-supported bromite resin (6.0 equiv), CH_2Cl_2, 0 °C, 2 h, 75%; o) Ac_2O (5.0 equiv), Et_3N (10 equiv), DMAP (0.2 equiv), CH_2Cl_2, 0→25 °C, 1 h, 92%; p) $NaClO_2$ (4.0 equiv), NaH_2PO_4 (5.0 equiv), 2-methyl-2-butene (75 equiv), THF/*t*BuOH/H_2O (2:4:1), 25 °C, 1 h; q) HCl (0.5 M), EtOH/Et_2O (1:1), 0→25 °C, 3 h, 75% over two steps; r) SEMCl (6.0 equiv), *i*Pr_2NEt (12 equiv), *n*Bu_4NI (4.0 equiv), $CHCl_3$, 61 °C, 8 h, 89%; s) K_2CO_3 (10 equiv), MeOH, 25 °C, 2 h, 99%. PPTS = pyridinium *p*-toluene sulfonate, TBDPS = *tert*-butyldiphenylsilyl, DMAP = 4-(dimethylamino)pyridine, DMP = Dess–Martin periodinane, HMDS = hexamethyldisilazide, TES = triethylsilyl, TBAF = tetra-*n*-butylammonium fluoride, Ms = mesyl, NMO = *N*-methylmorpholine *N*-oxide, TEMPO = 2,2,6,6-tetramethyl-1-piperidinyloxyl radical, SEM = 2-(trimethylsilyl)ethoxymethyl.

Having completed the construction of hydroxylactone **3**, we then contemplated obtaining this same key intermediate

from the natural product **1** through semisynthesis. The aim of the degradation exercise of azadirachtin (**1**) to this key decalin fragment was not only to enrich our supplies of the target compound **2** for the purposes of our total synthesis efforts, but also to discover certain, unexpected or suspected, intricacies of the azadirachtin molecule that may be either of general interest or prove to be of some use in aiding our sail towards the natural product. In our search for an expedient route to **3** from **1** we made use of the work of Ley and coworkers,[5–7] who developed a four-step degradation sequence from **1** to **15**,[6] the tetracyclic compound that served as a beachhead for our expeditions (Scheme 3). Thus, the two hydroxy groups within **15** were protected as SEM ethers by reaction with SEMCl in the presence of iPr$_2$NEt, and the resulting bis-SEM-protected ketone was converted into olefin **17** by a regioselective transformation into the corresponding triflate **16** and then reduction of the latter compound with Et$_3$SiH in the presence of [Pd(PPh$_3$)$_4$] (47% overall yield for three steps). Manual molecular modeling suggested the α face of the double bond of **17** as the more accessible site, and this bias was greatly enhanced by the asymmetric dihydroxylation of this compound with K_2OsO_4 and (DHQD)$_2$PHAL in the presence of $MeSO_2NH_2$ in 96% yield, leading to 1,2-diol **18** as the exclusive product. Landing an acetate group on the secondary alcohol of **18** proved trivial, as treatment of this compound with Ac$_2$O, DMAP and Et$_3$N furnished monoacetate **19** (98% yield) as expected. Debenzylation of compound **19** required carefully controlled conditions (10% Pd(OH)$_2$/C, MeOH-H$_2$O, pH 7, H$_2$), otherwise an unusual reaction took place, namely the reduction of the benzene ring to afford the corresponding cyclohexylmethyl ether derivative **19**-H$_6$ (10% Pd(OH)$_2$/C, EtOH, H$_2$, 98% yield, **23**/**19**-H$_6$ ≈ 2.6:1). The origin of this remarkable mode of reactivity of benzyl ether derivative **19** remains unknown. Facilitated by the neighboring hydroxy group, the reduction with NaBH$_4$ of the carbomethoxy group of the debenzylation product derived from **19** proceeded smoothly to afford triol **20** in good yield. The Pb(OAc)$_4$-induced cleavage of the 1,2-diol system within **20** gave γ-lactone **21** in 70% overall yield from **19** for the three steps. Finally, exposure of **21** to SOCl$_2$ in the presence of pyridine led to the corresponding exocyclic olefin, which was treated with K$_2$CO$_3$ to give the targeted allylic alcohol **3** in 85% overall yield.

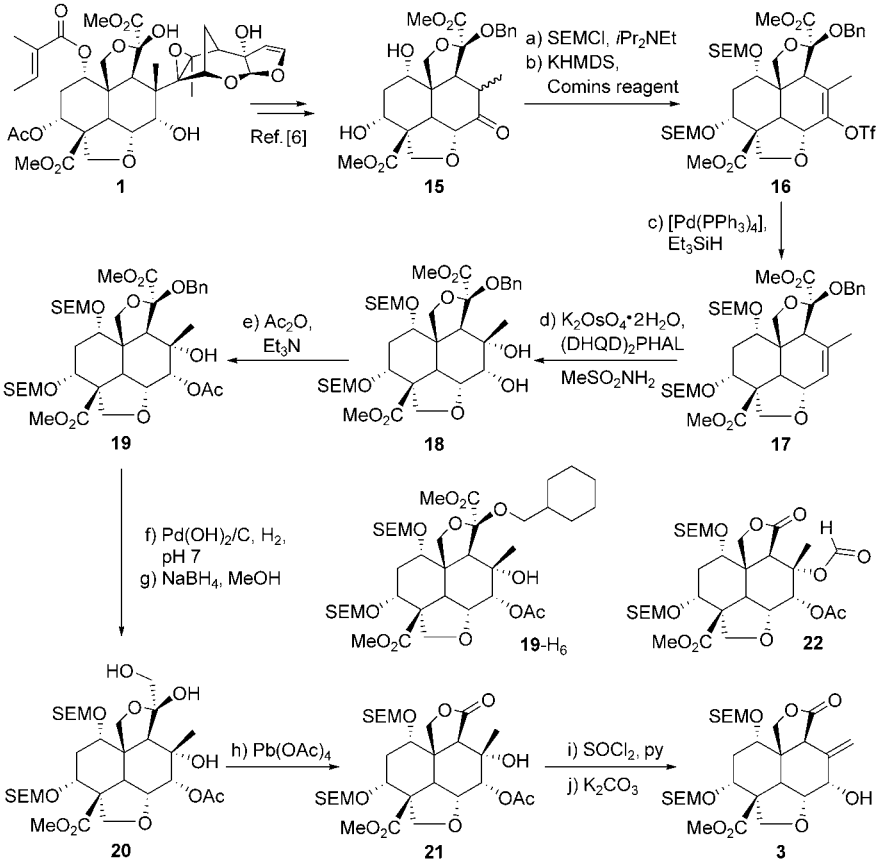

Scheme 3. Semisynthesis of hydroxylactone fragment **3** from **1**. Reagents and conditions: a) SEMCl (6.0 equiv), iPr$_2$NEt (12 equiv), nBu$_4$NI (4.0 equiv), CHCl$_3$, 60 °C, 8 h, 89%; b) Comins reagent (2.0 equiv), KHMDS (0.5 M in toluene, 2.0 equiv), THF, −78 °C, 30 min, 56%; c) [Pd(PPh$_3$)$_4$] (0.2 equiv), Et$_3$SiH (3.0 equiv), LiCl (3.0 equiv), DMF, 55 °C, 24 h, 95%; d) K_2OsO_4·H$_2$O (0.2 equiv), (DHQD)$_2$PHAL (0.5 equiv), K$_3$Fe(CN)$_6$ (3.0 equiv), $MeSO_2NH_2$ (1.0 equiv), K$_2$CO$_3$ (3.0 equiv), tBuOH/H$_2$O (3:2), 2 h, 96%; e) Ac$_2$O (5.0 equiv), Et$_3$N (10 equiv), DMAP (1.0 equiv), CH$_2$Cl$_2$, 0→25 °C, 8 h, 98%; f) Pd(OH)$_2$/C (1:1 w/w), H$_2$O/MeOH (1:2), pH 7, H$_2$, 25 °C, 2 h; g) NaBH$_4$ (10 equiv), MeOH, 0→25 °C, 4 h; h) Pb(OAc)$_4$ (2.0 equiv), CH$_2$Cl$_2$, 0 °C, 2 h, 70% over three steps; i) SOCl$_2$ (20 equiv), py, 0→25 °C, 8 h, 86%; j) K$_2$CO$_3$ (10 equiv), MeOH, 25 °C, 2 h, 99%. Comins reagent = 2-[*N*,*N*-bis(trifluoromethylsulfonyl)amino]-5-chloropyridine, DMF = *N*,*N*-dimethylformamide, (DHQD)$_2$PHAL = 1,4-bis(9-*O*-dihydroquinidinyl)phthalazine, py = pyridine.

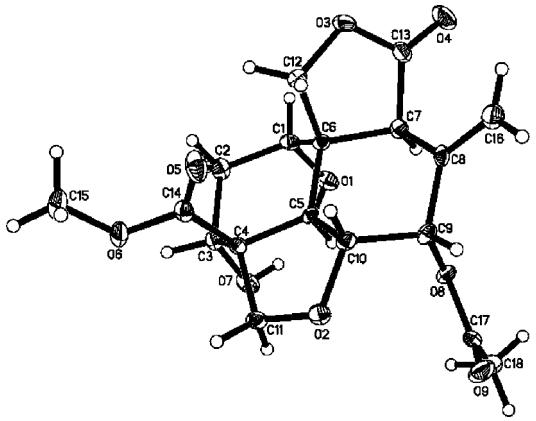

Figure 1. ORTEP drawing of **14** at the 30% probability level.

En route to allylic alcohol **3** from compound **19**, a noteworthy reaction was observed which led to a number of subsequent developments of equal interest. When the crude reaction mixture from hydrogenation of **19** was subjected to the intended reduction of the methyl ester with NaBH$_4$ followed by 1,2-diol cleavage with Pb(OAc)$_4$ on a large scale, the γ-lactone formate **22** was obtained, together with the desired γ-lactone alcohol **21** in approximately equimolar amounts and good overall yield. As shown in Scheme 4, we

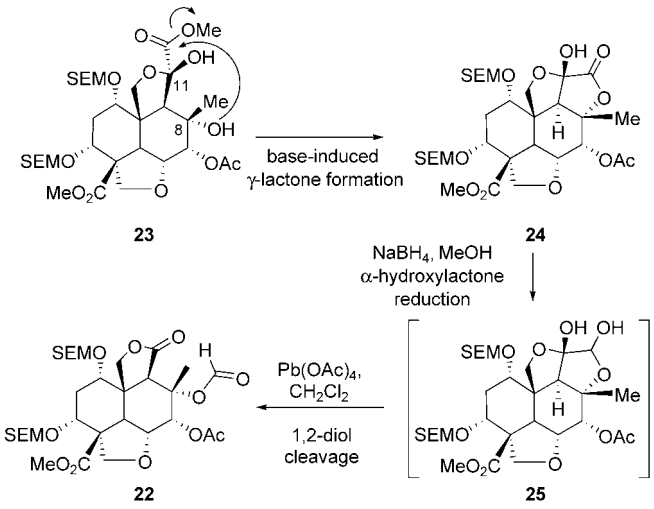

Scheme 4. An unexpected $Pb(OAc)_4$-induced carbonyl migration and preparation of formate **22**. Reagents and conditions: $NaBH_4$ (10 equiv), MeOH, 0 °C→25 °C, 30 min; then $Pb(OAc)_4$ (10 equiv), CH_2Cl_2, 0→25 °C, 2 h, 95% over three steps.

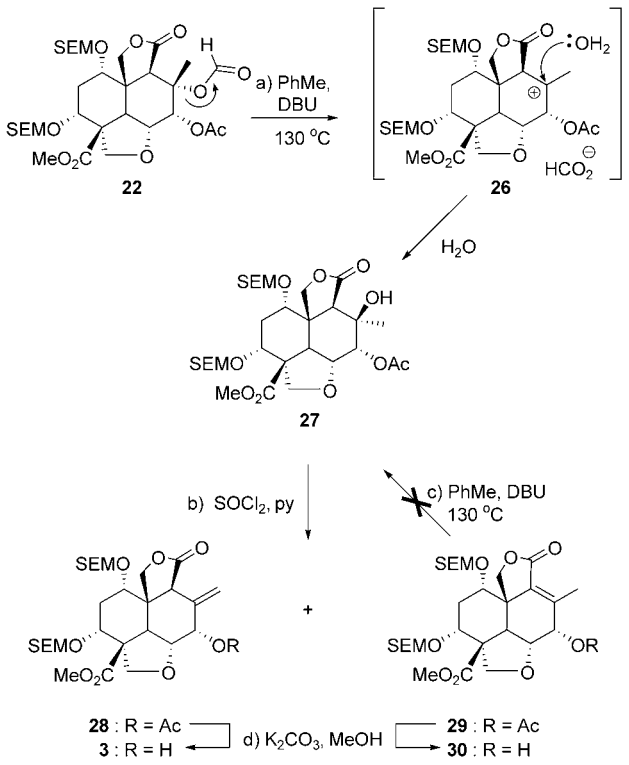

Scheme 5. An unexpected, DBU-induced inversion of configuration and preparation of 8-*epi* hydroxy compound **27** and allylic acetates **28** and **29**. Reagents and conditions: a) DBU (20 equiv), toluene, reflux, 4 h, 70%; b) $SOCl_2$ (20 equiv), py, 0→25 °C, 8 h, 71%; c) DBU (20 equiv), toluene, reflux, 10 h; d) K_2CO_3 (10 equiv), MeOH, 25 °C, 2 h, 99%. DBU = 1,8-diazabicyclo[5.4.0]undec-7-ene.

hypothesized that this rather unusual outcome might be due to the propensity of the incipient diol **23** to form pentacyclic lactone **24** by attack of the C8 tertiary hydroxy group at the neighboring C11-carbomethoxy moiety with subsequent expulsion of a molecule of MeOH. Exposure of **24** to $NaBH_4$ would then result in the C11-OH-assisted reduction of the newly formed γ-lactone ring, yielding bis-hemiketal **25**, which could be oxidatively cleaved in the next step by $Pb(OAc)_4$ to give the observed formate lactone **22**. In support of this hypothesis we synthesized the postulated intermediate **24** from **23** and converted it exclusively into formate **22** by the proposed two-step sequence in 95% overall yield.

The fortuitous availability of formate **22** inspired a potential entry into the α,β-unsaturated γ-lactone series of decalin fragments (e.g. compound **30**, Scheme 5) as possible partners in coupling reactions with the norbornene-type precursors of azadirachtin (e.g. **4**). Thus, **22** was heated in refluxing toluene in the presence of DBU in the hope that the α,β-unsaturated lactone **29** would be obtained by elimination of the formate ester group (see Scheme 5). Instead, however, compound **27** was observed as the only product (70%). This C8-inverted tertiary alcohol **27** is presumably the product of ionization of the formate group to carbocation **26** followed by its immediate quenching by traces of moisture present in the reaction medium (**22**→**26**→**27**, Scheme 5). The nonpolar nature of the solvent employed (toluene) accounts for the observed inversion of configuration at C8, the tight ion pair formed between the decalin cationic domain and the leaving formate anion ensuring total blockade of the already hindered decalin α face. An alternative plausible mechanism, namely that involving stereoselective conjugate addition of water to an initially formed α,β-unsaturated γ-lactone (i.e. **29**, the compound targeted in the first place), has been ruled out by the failure of **29** to undergo addition of water upon exposure to the same reaction conditions. Unexpected as it was, the C8-*epi* alcohol **27** offers the only point of entry found so far, even after considerable experimentation, into the α,β-unsaturated γ-lactone series of decalin fragments. This was converted into **29** by exposure to $SOCl_2$ in the presence of pyridine in a reaction that also produced the exocyclic olefinic acetate **28** in a combined yield of 71% (**28**/**29** ≈ 2:1). Allylic alcohols **3** and **30**, obtained by treatment of this mixture with K_2CO_3 in MeOH, were conveniently separated by silica gel chromatography.

Allylic alcohol **3**, which was now available through two different routes, was then subjected to bromoketalization with norbornene derivative **4** under the conditions described in the preceding Communication[1] and remarkably afforded a single bromoketal **31** in 76% yield (Scheme 6).[10] It is interesting to recall that the bromoketalization of the previously employed decalin substrate **5**, which lacks the tetrahydrofuran system, led to a mixture of two diastereomeric bromoketals in approximately 1:1 ratio.[1] From this contrast, it is apparent that the distribution of the two isomers in these reactions is dictated not only by the reaction time and temperature, but also, and most profoundly, by the nature of the decalin partner.[8]

It was again found that $(Me_3Si)_3SiH$ served as an excellent H-atom donor in the radical-based cyclization of bromoketal **31**, yielding heptacyclic compounds **35** and **36** (Table 1) in 32 and 42% yield, respectively.[9] In this case, the secondary radical **32**, initially generated from **31**, underwent both the 6-*endo*-trig and the 5-*exo*-trig modes of ring closure,[8] thus leading to the tertiary and primary radicals **33** and **34**. These,

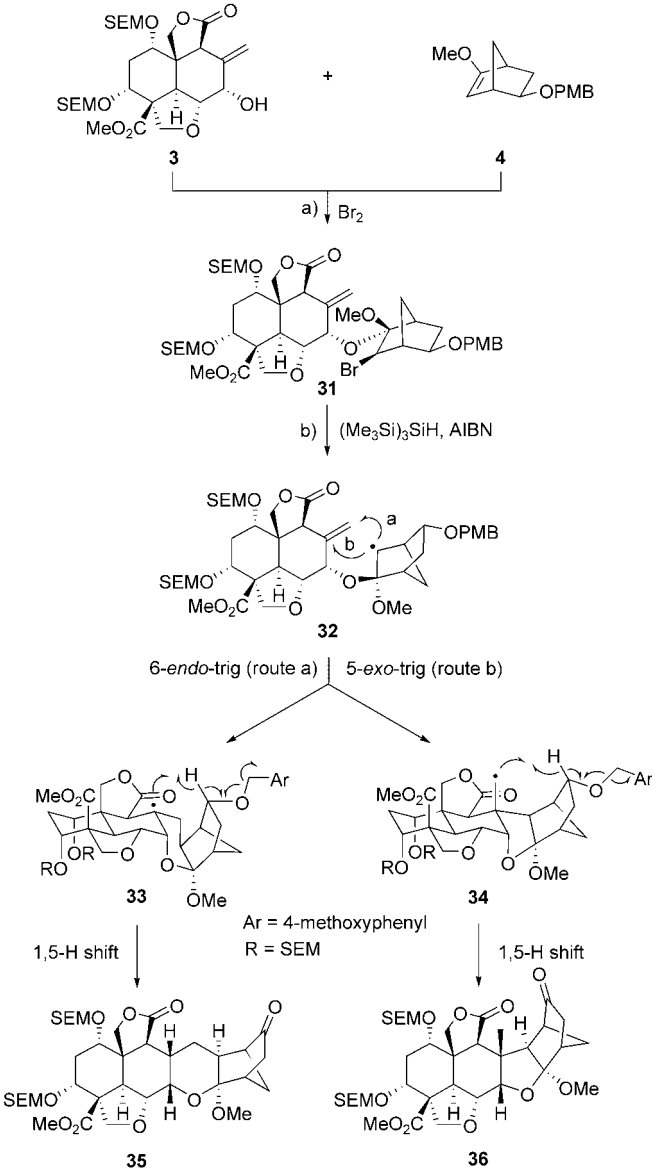

Scheme 6. Bromoketalization of hydroxylactone **3** with norbornene derivative **4** and elaboration of the product into **35** and **36**. Reagents and conditions: a) Br_2 (1.5 equiv), *N*,*N*-dimethylaniline (2.0 equiv), K_2CO_3 (10 equiv), **4** (2.0 equiv), CH_2Cl_2, −78 °C, 10 min; then **3**, −78→0 °C over 2 h, 0 °C, 1 h, 76%; b) $(Me_3Si)_3SiH$ (2.0 equiv), AIBN (1.0 equiv), toluene (0.007 M), 110 °C, 30 min, **35** (32%) **36** (42%); AIBN = 2,2′-azobisisobutyronitrile.

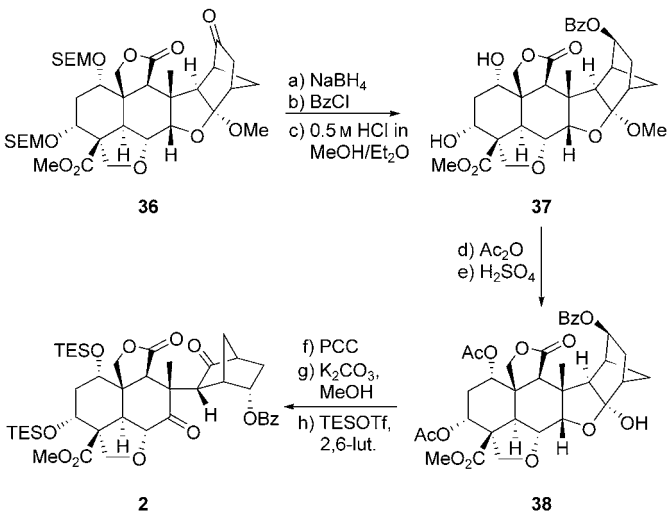

Scheme 7. Conversion of heptacyclic compound **36** into advanced system **2**. Reagents and conditions: a) $NaBH_4$ (5.0 equiv), MeOH, 0 °C, 15 min, 88%; b) BzCl (7.0 equiv), DMAP (5.0 equiv), pyridine, 60 °C, 5 h; c) 0.5 M HCl, MeOH/Et_2O (1:1), 0→25 °C, 6 h, 72% over two steps; d) Ac_2O (8.0 equiv), Et_3N (12 equiv), DMAP (0.4 equiv), CH_2Cl_2, 0→25 °C, 6 h, 79%; e) H_2SO_4 (5.0 equiv), CH_2Cl_2, 0 °C, 30 min; f) PCC (15 equiv), DCE, 65 °C, 16 h, 60% over two steps; g) K_2CO_3 (10 equiv), MeOH, 25 °C, 30 min; h) TESOTf (10 equiv), 2,6-lutidine (20 equiv), CH_2Cl_2, −78→25 °C, 24 h, 62% over two steps. Bz = benzoyl, PCC = pyridinium chlorochromate, DCE = 1,2-dichloroethane, OTf = trifluoromethanesulfonate.

in turn, undergo a 1,5-H shift (as shown in Scheme 6), to afford ketones **35** and **36**, respectively, upon oxidative cleavage of the PMB ether group. This behavior again reveals the controlling power of the decalin system in deciding the fate of these chemical species.

From the two intermediates **35** and **36**, only the latter is potentially productive in the campaign towards azadirachtin. To this end, we needed to demonstrate the facile cleavage of the temporary bridge that enabled the formation of the crucial C8–C14 bond in the first place. The heptacyclic ketone **36** (Scheme 7) was reduced with $NaBH_4$ in MeOH, exclusively from the *exo* side, to afford the corresponding alcohol, which was benzoylated and then desilylated under acidic conditions to furnish dihydroxy benzoate **37** in 63% overall yield. Exposure of diol **37** to Ac_2O, Et_3N, and DMAP gave the corresponding bisacetate (79% yield), which was subsequently converted into hemiketal **38**. Finally, oxidation of **38** with PCC, cleavage of the acetate group, and TES protection furnished diketone **2** (Table 1) in 37% yield for the four steps.

In the course of our drive towards azadirachtin (**1**), we became keenly, and sometimes painfully, aware of the unique behavior of this natural product due to the oxygen-rich nature of its skeleton and the close proximity of its numerous functional groups. In addition to the above-mentioned incidents, we consider it of interest to reveal one more example that speaks to this point. Scheme 8 shows the outcome of the reaction of diketone **2** with MeLi. It became apparent that initial loss of the benzoyl protecting group at C21 unmasked the secondary alcohol function, which was then in a position to attack the C7 carbonyl group, presumably forming a hemiketal. The existence of the latter compound was evidently transient under the reaction conditions, as a further ring closure ensued, this time on the C13 carbonyl carbon atom, to give the highly congested cagelike ketal/hemiketal **40** in 72% overall yield. Lactone **40** did not constitute the end of the journey in this cascade in the presence of $CeCl_3$. In this case, further attack by MeLi at the C11 lactone carbonyl function produced a free primary alcohol group, which was then able to reach across the decalin system to attack the C4 carbomethoxy residue to generate a second lactone ring with the expulsion of a methoxy group, furnishing, upon further addition of MeLi, the impressively

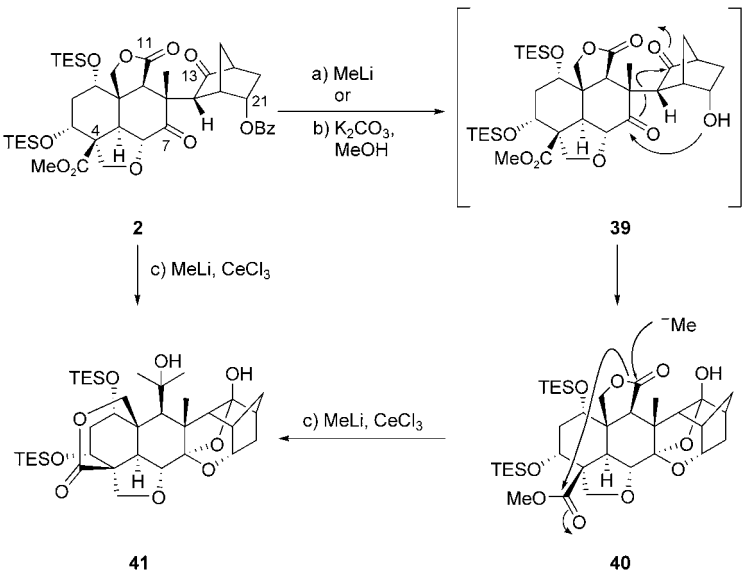

Scheme 8. Intriguing cascade sequences with azadirachtin-type scaffolds. Reagents and conditions: a) MeLi (5.0 equiv), Et_2O, −78 °C, 2 h, 72%; b) K_2CO_3 (10 equiv), MeOH, 25 °C, 36 h, 91%; c) MeLi (5.0 equiv), $CeCl_3$ (5.0 equiv), Et_2O, 0 °C, 8 h, 80%.

compact polycycle **41** in 80% overall yield from **2**. The stable ketal/hemiketal **40** was also the exclusive product (91% yield) of the reaction of benzoate **2** with K_2CO_3 in MeOH.

The described chemistry represents our most recent and important advancements toward the total synthesis of azadirachtin (**1**) and at the same time reveals some of the inner intricacies of this uniquely crowded and highly functionalized molecular architecture. Further progress towards congeners of azadirachtin is sure to be frustrated or facilitated by these intricacies.

Received: January 19, 2005
Published online: April 22, 2005

Keywords: asymmetric synthesis · degradation · natural products · radical reactions · total synthesis

Table 1: Selected physical properties for compounds **2**, **35**, and **36**.

2: $R_f = 0.50$ (silica gel, EtOAc/hexane 1:2); $[\alpha]_D^{32} = -23.0$ ($c = 0.3$, $CHCl_3$); IR (film) $\tilde{\nu}_{max} = 2955, 2876, 1782, 1763, 1752, 1742, 1717, 1458, 1273, 1162, 1113, 1019, 874, 813, 716\ cm^{-1}$; ^1H NMR (600 MHz, C_6D_6): $\delta = 7.87$ (d, $J = 7.5$ Hz, 2H), 7.51 (t, $J = 7.5$ Hz, 1H), 7.42 (t, $J = 7.5$ Hz, 2H), 5.57 (ddd, $J = 10.2$, 9.0, 4.2 Hz, 1H), 5.01 (d, $J = 14.4$ Hz, 1H), 4.62 (d, $J = 10.5$ Hz, 1H), 4.44 (br s, 1H), 4.13 (d, $J = 8.4$ Hz, 1H), 4.06 (d, $J = 8.4$ Hz, 1H), 3.91 (s, 1H), 3.83 (d, $J = 10.5$ Hz, 1H), 3.76 (s, 3H), 3.73 (br s, 1H), 3.11 (br d, $J = 3.0$ Hz, 1H), 3.02 (br s, 1H), 2.99 (d, $J = 14.4$ Hz, 1H), 2.85 (br d, $J = 4.8$ Hz, 1H), 2.66 (dt, $J = 13.2$, 4.2 Hz, 1H), 2.41 (ddd, $J = 13.2$, 10.2, 4.8 Hz, 1H), 2.02 (br d, $J = 15.6$ Hz, 1H), 1.90 (br d, $J = 15.6$ Hz, 1H), 1.87 (br d, $J = 10.8$ Hz, 1H), 1.78 (br d, $J = 10.8$ Hz, 1H), 1.37 (s, 3H), 0.97 (t, $J = 7.8$ Hz, 9H), 0.96 (t, $J = 8.4$ Hz, 9H), 0.66 (q, $J = 7.8$ Hz, 6H), 0.61 ppm (q, $J = 8.4$ Hz, 6H); ^{13}C NMR (150 MHz, C_6D_6): $\delta = 212.7, 202.0, 175.4, 174.0, 166.7, 132.9, 130.0, 129.5, 128.5, 76.1, 74.4, 74.3, 70.8, 69.9, 66.5, 56.5, 55.3, 54.5, 53.3, 52.6, 52.0, 48.0, 45.0, 42.6, 36.6, 36.2, 30.8, 20.8, 7.0, 7.0, 4.7$ ppm; HRMS (ESI TOF): calcd for $C_{42}H_{61}O_{11}Si_2^+$ [M+H^+]: 797.3747; found: 797.3748

35: $R_f = 0.25$ (silica gel, EtOAc/hexanes 1:1); $[\alpha]_D^{31} = -30.0$ ($c = 0.3$, CH_2Cl_2); IR (film): $\tilde{\nu}_{max} = 2952, 2926, 1780, 1743, 1724, 1437, 1249, 1163, 1054, 836\ cm^{-1}$; ^1H NMR (500 MHz, C_6D_6): $\delta = 4.75$ (d, $J = 7.0$ Hz, 1H), 4.70 (dd, $J = 9.2$, 1.0 Hz, 1H), 4.63 (d, $J = 6.6$ Hz, 1H), 4.56 (d, $J = 6.6$ Hz, 1H), 4.45 (t, $J = 2.6$ Hz, 1H), 4.32 (d, $J = 11.0$ Hz, 1H), 4.31 (d, $J = 6.6$ Hz, 1H), 4.23 (dd, $J = 11.0$, 1.5 Hz, 1H), 4.17 (d, $J = 7.7$ Hz, 1H), 3.93 (ddd, $J = 10.6$, 9.5, 5.8 Hz, 1H), 3.79 (d, $J = 8.1$ Hz, 1H), 3.69–3.62 (m, 3H), 3.53–3.44 (m, 3H), 3.41 (s, 3H), 3.39 (dd, $J = 11.5$, 1.5 Hz, 1H), 3.15 (s, 3H), 2.50 (d, $J = 2.5$ Hz, 1H), 2.34 (dd, $J = 5.1$, 2.2 Hz, 1H), 2.23–2.13 (m, 4H), 1.72 (br d, $J = 11.3$ Hz, 1H), 1.53 (dd, $J = 17.8$, 4.5 Hz, 1H), 1.51 (br d, $J = 12.0$ Hz, 1H), 1.42 (dd, $J = 12.8$, 3.8 Hz, 1H), 1.35 (dt, $J = 16.2$, 2.9 Hz, 1H), 1.23 (br d, $J = 10.6$ Hz, 1H), 1.19–1.05 (m, 2H), 0.87 (d, $J = 7.7$ Hz, 1H), 0.85 (d, $J = 8.1$ Hz, 1H), 0.08 (s, 9H), −0.04 ppm (s, 9H); ^{13}C NMR (125 MHz, C_6D_6): $\delta = 214.1, 177.6, 173.9, 116.8, 93.5, 93.2, 88.0, 77.4, 73.0, 71.3, 70.0, 69.2, 66.1, 65.6, 59.9, 57.7, 54.9, 51.6, 51.4, 48.5, 43.9, 40.8, 40.1, 38.6, 37.2, 36.6, 29.4, 26.9, 18.1, 18.0, −1.3, −1.4$ ppm; HRMS (MALDI): calcd for $C_{36}H_{58}O_{12}Si_2Na$: 761.3359 [M+Na^+]; found: 761.3350

36: $R_f = 0.36$ (silica gel, EtOAc/hexanes 1:1); $[\alpha]_D^{31} = -24.0$ ($c = 0.3$, CH_2Cl_2); IR (film): $\tilde{\nu}_{max} = 2953, 2924, 1766, 1741, 1725, 1438, 1317, 1248, 1169, 1098, 1032, 836\ cm^{-1}$; ^1H NMR (500 MHz, C_6D_6): $\delta = 4.76$ (d, $J = 7.0$ Hz, 1H), 4.61 (d, $J = 7.0$ Hz, 1H), 4.59 (d, $J = 6.6$ Hz, 1H), 4.39–4.37 (m, 1H), 4.37 (d, $J = 6.6$ Hz, 1H), 4.33–4.27 (m, 3H), 4.17 (d, $J = 10.3$ Hz, 1H), 4.07 (d, $J = 7.7$ Hz, 1H), 3.96 (ddd, $J = 11.0$, 9.5, 5.9 Hz, 1H), 3.71 (s, 1H), 3.64 (ddd, $J = 11.0$, 9.9, 5.9 Hz, 1H), 3.56 (br t, $J = 2.4$ Hz, 1H), 3.54–3.46 (m, 4H), 3.37 (s, 3H), 3.10 (s, 3H), 3.05 (d, $J = 4.4$ Hz, 1H), 2.42 (d, $J = 3.7$ Hz, 1H), 2.38 (d, $J = 4.0$ Hz, 1H), 2.31 (dd, $J = 18.0$, 4.8 Hz, 1H), 2.13 (dt, $J = 16.1$, 2.6 Hz, 1H), 1.68–1.61 (m, 1H), 1.48 (dd, $J = 18.0$, 4.8 Hz, 1H), 1.39 (dt, $J = 16.1$, 2.9 Hz, 1H), 1.21 (s, 3H), 1.18–1.05 (m, 3H), 0.88 (d, $J = 8.4$ Hz, 1H), 0.87 (d, $J = 7.7$ Hz, 1H), 0.10 (s, 9H), 0.03 ppm (s, 9H); ^{13}C NMR (125 MHz, C_6D_6): $\delta = 215.0, 176.3, 174.1, 116.0, 93.6, 92.5, 85.0, 73.9, 72.8, 72.3, 70.5, 69.8, 67.3, 66.2, 65.6, 53.9, 53.8, 51.6, 51.1, 49.1, 47.5, 46.6, 42.0, 39.9, 38.9, 35.2, 27.1, 18.2, 18.1, 16.5, −1.3, −1.4$ ppm; HRMS (MALDI): calcd for $C_{36}H_{58}O_{12}Si_2Na$: 761.3359 [M+Na^+]; found: 761.3366

[1] K. C. Nicolaou, P. K. Sasmal, A. J. Roecker, X.-W. Sun, S. Mandal, A. Converso, *Angew. Chem.* **2005**, *117*, 3509–3513; *Angew. Chem. Int. Ed.* **2005**, *44*, 3443–3447, preceding Communication in this issue.
[2] For the isolation, structural elucidation, and previous synthetic studies in the area of azadirachtin (**1**), see literature cited in reference [1].
[3] G. Sourkouni-Argirusi, A. Kirschning, *Org. Lett.* **2000**, *2*, 3781–3784.
[4] CCDC-261 286 contains the supplementary crystallographic data for this paper. These data can be obtained free of charge from the Cambridge Crystallographic Data Centre via www.ccdc.cam.ac.uk/data_request/cif.
[5] S. V. Ley, P. J. Lovell, S. C. Smith, A. Wood, *Tetrahedron Lett.* **1991**, *32*, 6183–6186.
[6] S. V. Ley, P. J. Lovell, A. M. Z. Slawin, S. C. Smith, D. J. Williams, A. Wood, *Tetrahedron* **1993**, *49*, 1675–1700.
[7] A. A. Denholm, L. Jennens, S. V. Ley, A. Wood, *Tetrahedron* **1995**, *51*, 6591–6604.
[8] C. Anies, L. Billot, J.-Y. Lallemand, A. Pancrazi, *Tetrahedron Lett.* **1995**, *36*, 7247–7250.
[9] The structures and stereochemistries of compounds **31**, **35**, and **36** were unambiguously assigned by spectroscopic analysis (^1H, ^{13}C, COSY, ROESY, HMQC, and HMBC).
[10] **Note added in proof**: After submission of this manuscript, we isolated the other bromoketal diastereomer in approximately 10% yield from experiments carried out on a larger scale.

Polymer Films

Environmentally Stable Super Water-Repellent Poly(alkylpyrrole) Films**

Hu Yan, Kazutomo Kurogi, Hiroyuki Mayama, and Kaoru Tsujii**

It is well-known that the wettability of a solid surface by a liquid is governed by two factors: a chemical component and a geometric component of the solid surface.[1] Super liquid repellency is crucially important in daily life and in industry. Several kinds of super water- or oil-repellent surfaces with contact angles larger than 150° have been realized by a combination of chemical and geometric approaches.[2–12] The main approach for the chemical factor is a coating of fluorinated compounds with low surface energy, whereas the geometric factor is governed by the formation of fractal or rough surface structures.

In nature the leaves of some plants, such as the lotus, show super water repellency only by the geometric factor.[13] The surface of the leaf is geometrically a fractal, but chemically is a wax composed mainly of fatty acid esters and alcohols. The legs of water striders also show super water repellency by the geometric factor only.[14]

The alkylketene dimer (AKD) surface, which geometrically is a fractal with a dimension of 2.29 but chemically is just a wax, is only one artificial super water-repellent surface with a large contact angle, in this case 174°.[2,3] A series of studies on the AKD fractal structures provide much insight into the theoretical origins of the super water repellency that occurs in nature in plant leaves or insects. The AKD surface, however, has the drawback of poor durability from the standpoint of practical applications. The AKD surface is environmentally weak, mainly because it is soluble in organic solvents and its melting point is as low as 67 °C.[3] Therefore, creation of environmentally stable super water-repellent surfaces which do not contain any fluorinated compounds but are geometrically rough or fractal structures is crucially significant, from both the academic and practical aspects.

Conductive polymers have attracted great attention because of their unique electrical properties and the easy synthesis of film-shaped products coupled with good thermal stability.[15–17] Therefore, the synthetic methods are well-established.[18,19] Conventionally, conductive polymers are electrochemically synthesized as films with various surface features according to the reaction conditions.[19] Therefore, in principle, conductive polymer films with a fractal structure or rough morphology are easily synthesized by simple optimization of the reaction conditions. Kossmehl et al. reported poly(2,2′-bithienyl-5,5′-diyl) (PBT) layers, which were synthesized by an electrochemical method and showed super water repellency and good thermal stability.[20,21] Herein, we report on super water-repellent poly(alkylpyrrole) films (contact angle larger than 150°), which showed excellent environmental stability to both temperature and organic solvents or oils.

The electrochemical polymerization of alkylpyrrole was performed in a beaker by using two electrodes (Figure 1; see

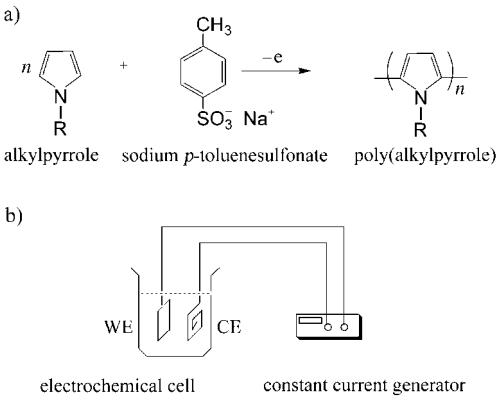

Figure 1. a) Chemical structures of monomeric alkylpyrrole, sodium *p*-toluenesulfonate electrolyte, and the polymer produced; b) setup of the electrochemical synthesis (WE = working electrode, CE = counter electrode).

Experimental Section). Figure 2 shows the poly(alkylpyrrole) film that was electrochemically synthesized with 1-*n*-octadecylpyrrole and sodium *p*-toluenesulfonate as monomer and electrolyte, respectively. "Needle"-like poly(alkylpyrrole) structures grew perpendicularly to the surface of the indium tin oxide (ITO) electrode. Thousands of the poly(alkylpyrrole) needles, which were approximately 5 μm in diameter and 40 μm in length, were arrayed in an orderly manner on the surface of the ITO electrode. The needle-shaped array is similar to an array of polyacrylonitrile nanofibrils previously reported by Feng et al.[8] However, these nanofibril arrays were fabricated by using a template. The surface of the array of polyacrylonitrile nanofibrils showed super water repellency, with a contact angle larger than 150°. Martin et al. first reported the template-guided electrochemical synthesis of an array of polypyrrole microtubes by using a porous poly-

[*] Dr. H. Yan, Dr. H. Mayama, Prof. Dr. K. Tsujii
Research Institute for Electronic Science (RIES)
Hokkaido University
Sapporo 001-0021 (Japan)
Fax: (+81) 11-706-9357
E-mail: yanhu@es.hokudai.ac.jp
tsujik@es.hokudai.ac.jp
Prof. Dr. K. Tsujii
CREST, JST (Japan)
K. Kurogi
Faculty of Science
Hokkaido University (Japan)

[**] H.Y. acknowledges fellowship support from the 21st century COE program "Center of Excellence for Advanced Life Science on the Base of Bioscience and Nanotechnology" of Hokkaido University, Japan. This work was supported by a Grant-in-Aid for Scientific Research (B) (No. 16310077) from the Ministry of Education, Culture, Sports, Science, and Technology, Japan, and was partly supported by NOASTEC, Japan. We thank Dr. S. Shibuichi of Kao Corporation for his preliminary but pioneering investigation and helpful advice on this work.

Supporting information for this article is available on the WWW under http://www.angewandte.org or from the author.

 DOI: 10.1002/anie.200500266

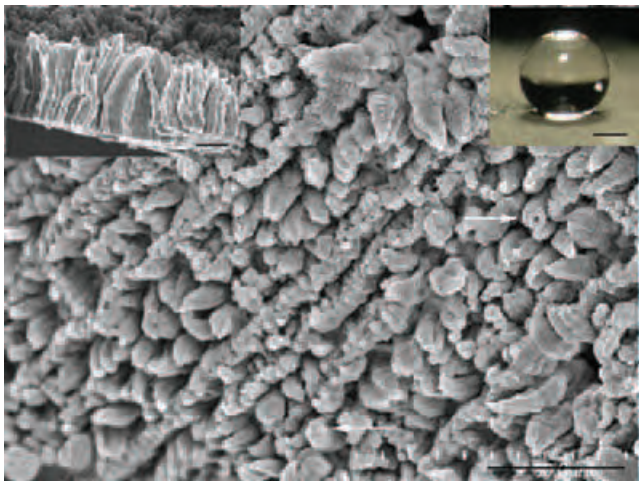

Figure 2. Scanning electron microscopic (SEM) image of the super water-repellent poly(alkylpyrrole) film (scale bar: 15 μm). Left inset: SEM image of the cross section of the film (bar: 15 μm). Right inset: digital camera image of a water droplet on the film (bar: 500 μm). The synthetic conditions were as follows: 1-*n*-octadecylpyrrole/*p*-toluenesulfonate (10:1 molar ratio); 1-*n*-octadecylpyrrole (0.005 mol dm^{-3}); reaction time, 60 min; applied voltage, 22.5 V; working electrode, ITO glass.

carbonate membrane as a template.[22] In the work described herein, the poly(alkylpyrrole) array grew without any template and, on close inspection, the single needle-like poly(alkylpyrrole) structures may be microtubes (arrows in Figure 2). Qiu et al. previously reported that microtube-like polypyrrole is formed in the electrochemical polymerization of pyrrole without template materials.[23] Recently Yan et al. also independently reported the formation of polypyrrole microtubes during the electrochemical polymerization of pyrrole without a template.[24–26] However, in these two cases, the microtubes do not array in an orderly and dense fashion, and the diameters and lengths are much larger than those reported herein.[22–25] Therefore, we believe that our work is the first to show an array of needle-like or capped microtubes of conductive polymer that was electrochemically synthesized without a template. The features of the array indicate that it should show super water repellency in principle, as in the case of polyacrylonitrile nanofibrils.[9] Furthermore, the array should show high stability to heating and organic solvents, because conductive polymers normally consist of long-range-conjugated aromatic rings which are thermally stable and poorly soluble in the usual organic solvents.[19]

Actually, the surface of the poly(alkylpyrrole) film showed super water repellency with a contact angle larger than 150° (right inset of Figure 2). The surface of a cross section of the poly(alkylpyrrole) film was subjected to a preliminary analysis by a box counting method,[2,3] and was found to be a fractal with a dimension of 2.23 (left inset of Figure 2).

The reaction conditions such as concentration and molar ratio of the reactants, applied voltage, reaction time, and working electrode significantly influence the surface structure, that is, the water repellency of the poly(alkylpyrrole) film. Detailed results will be reported elsewhere.

The influence of treatment temperature on the wettability was systematically investigated to evaluate the thermal stability of the films in terms of contact angle to water (Figure 3). The contact angle of the film was nearly constant

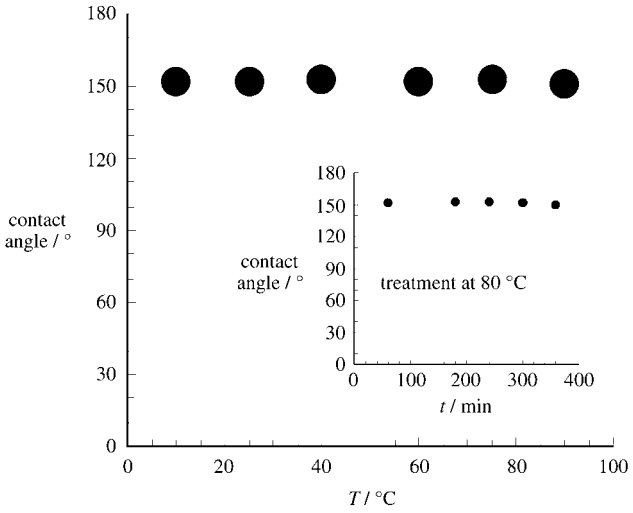

Figure 3. Thermal stability of the super water-repellent poly(alkylpyrrole) film treated at various temperatures for 2 h. The inset shows the thermal stability of a film treated at 80 °C for various treatment times.

even when the temperature was increased. The inset of Figure 3 shows the effects of the treatment time at 80 °C on the film. Similarly, the contact angle of the film was also nearly constant when the treatment time was increased. Poly(alkylpyrrole) is one of the conductive polymers that usually consist of aromatic rings and conjugated π bonds on the main polymer chain. Therefore, the polymer has enough thermal stability of chemical composition in the experimental range of temperature and treatment time. The needle-like shape of the poly(alkylpyrrole) structures may also have high thermal stability, similar to the case of polypyrrole microtubes.[26] We consider that the high thermal stability of the film in terms of contact angle can be explained by the thermally stable chemical and geometric factors (see Supporting Information).

Similarly, the influence of treatment with organic solvents and oils on the wettability was systematically investigated to evaluate the durability of the films to these substances in terms of contact angle to water. Figure 4 shows the effects of various organic solvents and oils on the water repellency of the film. The contact angle of the film did not change even after treatment. On the basis of the dark color of the film, the poly(alkylpyrrole) could be a doped conductive polymer, which usually consists of conjugated π bonds with π electrons that are delocalized on the main polymer chains.[19] Doped conductive polymers are normally insoluble in any organic solvents.[19] Therefore, the film has sufficient durability of chemical composition and morphology when treated with organic solvents and oils. We consider that the durability of the film in terms of contact angle can also be explained by the highly stable chemical and geometric factors.

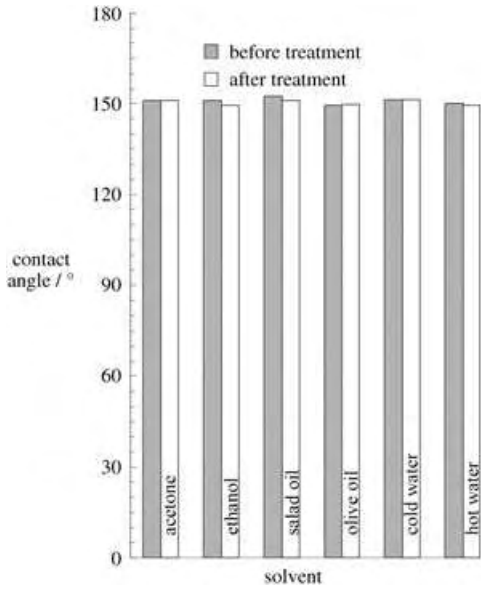

Figure 4. Durability of the super water-repellent poly(alkylpyrrole) film on treatment with organic solvent and oil. See text for the treatment conditions.

In conclusion, we have succeeded in the electrochemical synthesis of super water-repellent poly(alkylpyrrole) films with a contact angle larger than 150°. The SEM images show that the surface of the film consists of a perpendicular alignment of thousands of "needle"-like poly(alkylpyrrole) structures. On the basis of a preliminary analysis by a box counting method, the surface was considered to be a fractal with a dimension of 2.23. In contrast to AKD, the super water-repellent poly(alkylpyrrole) films had excellent environmental stability to both heating and organic solvent treatments in terms of the contact angle to water. These results may be of considerable significance as both fundamental and industrial guiding principles. Moreover, the feature of the film which consists of a vertical alignment of needle-like conductive polymer can be extended to nanotechnological or biotechnological applications, such as electronic devices[22] and substrates for cell culture.[27]

Experimental Section

Synthesis of poly(alkylpyrrole) films: The electrochemical synthesis was performed in a two-electrode cell containing an acetonitrile solution of alkylpyrrole and sodium *p*-toluenesulfonate, by using a constant-current generator (Yokogawa programmable DC source) at room temperature (Figure 1). The alkylpyrrole chosen was 1-*n*-octadecylpyrrole. Synthesis was carried out under the following conditions: working electrode, ITO glass; 1-*n*-octadecylpyrrole (5 mmol); sodium *p*-toluenesulfonate (0.5 mmol); applied voltage, 22.5 V; reaction time, 60 min. The films obtained were extensively washed with acetonitrile to eliminate reactants, and finally dried overnight at room temperature under reduced pressure. The reaction conditions were optimized in terms of contact angle of the film to water by changing the concentrations and molar ratios of alkylpyrrole and sodium *p*-toluenesulfonate, and the applied voltage, time, and working electrode.

Environmental stability of the films in terms of contact angle: Thermal stability was evaluated by treating the films at various temperatures for 2 hours. After the thermal treatments the contact angles were measured at room temperature. The treatment at 80 °C, however, was carried out for various treatment times. The durability to organic solvents or oils was evaluated by immersing the films in an organic solvent and then drying at 80 °C under a reduced pressure. The oils were placed on the films, which were then washed with acetone and finally dried as above. The contact angle was measured on the dried films.

SEM and contact angle measurements: Scanning electron microscopy (SEM) of the films was carried out with a field-emission SEM (Hitachi S-5200) after covering them with a thin layer of sputtered alloy of gold and palladium. The contact angles of the films to water droplets ($\approx$1 mm in diameter) were measured with an optical contact angle meter (Kyowa DropMaster) at room temperature and humidity.

Received: January 24, 2005
Published online: April 28, 2005

Keywords: fractals · hydrophobic effect · polymers · surface chemistry · thin films

[1] K. Tsujii in *Surface Activity: Principles, Phenomena, and Applications* (Ed.: T. Tanaka), Academic Press, New York, **1998**, pp. 52–54.
[2] T. Onda, S. Shibuichi, N. Satoh, K. Tsujii, *Langmuir* **1996**, *12*, 2125–2127.
[3] S. Shibuichi, T. Onda, N. Satoh, K. Tsujii, *J. Phys. Chem.* **1996**, *100*, 19512–19517.
[4] K. Tsujii, T. Yamamoto, T. Onda, S. Shibuichi, *Angew. Chem.* **1997**, *109*, 1042–1044; *Angew. Chem. Int. Ed. Engl.* **1997**, *36*, 1011–1012.
[5] S. Shibuichi, T. Yamamoto, T. Onda, K. Tsujii, *J. Colloid Interface Sci.* **1998**, *208*, 287–294.
[6] K. Tadanaga, N. Katata, T. Minami, *J. Am. Ceram. Soc.* **1997**, *80*, 1040–1042.
[7] K. Tadanaga, N. Katata, T. Minami, *J. Am. Ceram. Soc.* **1997**, *80*, 3213–3216.
[8] L. Feng, S. Li, Y. Li, H. Li, J. Zhai, L. Zhang, Y. Song, L. Jiang, D. Zhu, *Angew. Chem.* **2002**, *114*, 1269–1271; *Angew. Chem. Int. Ed.* **2002**, *41*, 1221–1223.
[9] L. Feng, S. Li, Y. Li, H. Li, L. Zhang, J. Zhai, Y. Song, B. Liu, L. Jiang, D. Zhu, *Adv. Mater.* **2002**, *14*, 1857–1860.
[10] L. Feng, Z. Zhang, Z. Mai, Y. Ma, B. Liu, L. Jiang, D. Zhu, *Angew. Chem.* **2004**, *116*, 2046–2048; *Angew. Chem. Int. Ed.* **2004**, *43*, 2012–2014.
[11] T. Sun, G. Wang, L. Feng, B. Liu, Y. Ma, L. Jiang, D. Zhu, *Angew. Chem.* **2004**, *116*, 361–364; *Angew. Chem. Int. Ed.* **2004**, *43*, 357–360.
[12] H. Yan, K. Tsujii, JP patent, Application No. P2004-378147.
[13] C. Neinhuis, W. Barthlott, *Ann. Bot.* **1997**, *79*, 667–677.
[14] X. Gao, L. Jiang, *Nature* **2004**, *432*, 36.
[15] S. Asavapiriyanont, G. K. Chandler, G. A. Gunawardena, D. Pletcher, *J. Electroanal. Chem.* **1984**, *177*, 229–244.
[16] P. G. Pickup, R. A. Osteryoung, *J. Am. Chem. Soc.* **1984**, *106*, 2294–2299.
[17] R. E. Noftleand, D. Pletcher, *J. Electroanal. Chem.* **1987**, *227*, 229–235.
[18] M. Satoh, K. Kaneto, K. Yoshino, *Synth. Met.* **1986**, *14*, 289–296.
[19] *Handbook of Conjugated Polymers* (Eds.: T. A. Skotheim, R. L. Elsenbaumer, J. R. Reynolds), Marcel Dekker, New York, **1996**.
[20] G. Kossmehl, M. Niemitz, *Synth. Met.* **1991**, *41–43*, 1065–1071.
[21] M. Niemitz, G. Kossmehl, *Angew. Makromol. Chem.* **1991**, *185*, 147–154.
[22] C. R. Martin, L. S. Van Dyke, Z. H. Cai, W. B. Liang, *J. Am. Chem. Soc.* **1990**, *112*, 8976–8977.

[23] L.-T. Qiu, G.-Q. Shi, J.-Y. Yuan, G.-Y. Han, F.-E. Chen, *J. Electroanal. Chem.* **2004**, *561*, 149 – 156.
[24] H. Yan, T. Ishida, N. Toshima, *Chem. Lett.* **2001**, 816 – 817.
[25] H. Yan, M. Inokuchi, S. Ariyoshi, M. Kinoshita, N. Toshima, *Synth. Met.* **2003**, *135–136*, 269 – 270.
[26] H. Yan, M. Inokuchi, M. Kinoshita, N. Toshima, *Synth. Met.* **2005**, *148*, 93 – 98.
[27] H. Yan, H. Shiga, E. Ito, K. Tsujii, *Int. J. Nanosci.* **2005**, in press.

P,N Ligands

Quadruple Deprotonation of 2-Aminophenylphosphane with a p-Block-Metal/Alkali-Metal Base**

Felipe García, Simon M. Humphrey, Richard A. Kowenicki, Eric J. L. McInnes, Christopher M. Pask, Mary McPartlin, Jeremy M. Rawson, Matthew L. Stead, Anthony D. Woods, and Dominic S. Wright**

The application of superbases, such as the well-known Schlosser base consisting of *t*BuOK and RLi, in the deprotonation of organic substrates is well established.[1] Recently, Mulvey investigated the structural chemistry and applications of related mixed-metal amide reagents.[2] These species show remarkable activity and specificity in their reactions with aromatic hydrocarbons and ferrocene (Cp_2Fe; Cp = cyclopentadienyl).[3,4] For example, the treatment of Cp_2Fe with a mixture of iPr_2NH/Bu_2Mg and *n*BuNa results in a double 1,3-deprotonation of the two Cp rings.[3] We recently observed that the stepwise reaction of $MesPH_2$ (Mes = 2,4,6-$Me_3C_6H_2$) with BnNa (Bn = benzyl) and $[Sn(NMe_2)_2]$ results in the unusual stannate ion $[Sn(2\text{-}CH_2\text{-}4,6\text{-}Me_2C_6H_2)(PMes)]^{3-}$, which arises from the intermolecular deprotonation of a methyl group (Scheme 1).[5] We wanted to examine the activity of this type of p-block-metal/alkali metal reaction

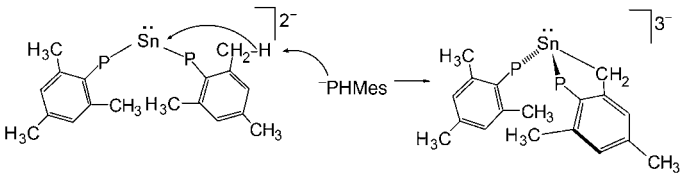

Scheme 1. Formation of $[Sn(2\text{-}CH_2\text{-}4,6\text{-}Me_2C_6H_2)(PMes)]^{3-}$ through intermolecular *ortho* deprotonation of a C–H bond.

system further because this Sn^{II}/BnNa system effectively acts as a superbase and there is a close relationship between this C–H activation reaction and activation reactions mediated by transition metals.[6] Herein, we present the observation that the reaction of 2-aminophenylphosphane (1-PH_2-2-$NH_2C_6H_4$) with *n*BuLi (1 equiv) followed by the addition of $[Sn(NMe_2)_2]$ (1 equiv) results in remarkable quadruple deprotonation of the ligand (Scheme 2) and generates the unusual paramagnetic Sn^{II}-centered cage $[\{[Sn(L)(NMe_2)Li(thf)][Sn(L)Li(thf)_3]Sn\}_2]$ (**1**) containing L^{4-} and $L^{3-\cdot}$ ions (L = ligand; see the Experimental Section).

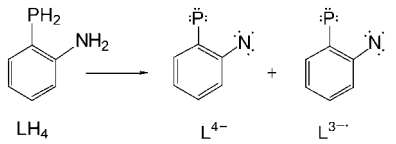

Scheme 2. The deprotonation of LH_4 by $[Sn(NMe_2)_2]$/*n*BuLi. LH_4 = 1-PH_2-2-$NH_2C_6H_4$, L = ligand.

No N–H or P–H stretching bands are found in the IR spectrum of solid **1**, thus showing that the NH_2 and PH_2 groups of the ligand have been completely deprotonated. As far as we can gauge, neither $[Sn(NMe_2)_2]$ nor *n*BuLi alone will cause deprotonation to this extent. The surprising paramagnetic character of **1** was indicated initially by ^1H and ^{31}P NMR spectroscopic studies: only a broad resonance in the aromatic region appears in the ^1H NMR spectrum at room temperature, and a very broad singlet appears at approximately $\delta = 10$–15 ppm in the $^{31}P\{^1H\}$ NMR spectrum. Compound **1** in the solid state exhibits a strong signal in the EPR spectrum at both the X and K bands (Figure 1). The spectral width is identical at both frequencies, which means that this signal can not be interpreted as a rhombic set of *g* values. Therefore, we attempted to simulate the spectra on the basis of 1) hyperfine coupling in which the two unpaired electrons are independent of each other and 2) hyperfine coupling with an exchange interaction (a biradical system). It was not possible to reproduce the relative intensities of the transitions by assuming coupling to ^{31}P or $^{117,119}Sn$ nuclei[7] for any set of parameters that were tried (including the number of nuclei), nor was it possible to simulate the spectra on the basis of a biradical system with coupling to these isotopes or the

[*] F. García, S. M. Humphrey, R. A. Kowenicki, Dr. C. M. Pask, Dr. J. M. Rawson, M. L. Stead, Dr. A. D. Woods, Dr. D. S. Wright
Chemistry Department
University of Cambridge
Lensfield Road, Cambridge CB21EW (UK)
Fax: (+44) 1223-336-362
E-mail: dsw1000@cus.cam.ac.uk
Dr. E. J. L. McInnes
The EPSRC cw EPR Service Centre
University of Manchester
Oxford Road, Manchester M13 9PL (UK)
Prof. M. McPartlin
Department of Health and Human Sciences
London Metropolitan University
Holloway Road, London N78DB (UK)

[**] We thank the EPSRC (S.M.H., C.M.P., M.M., J.M.R., and D.S.W); St. Catharine's College, Cambridge (fellowship for A.D.W.); The Cambridge European Trust and Newton Trust (F.G.); the States of Guernsey; and The Domestic and Millennium Fund (R.A.K.) for financial support. Acknowledgment is made to the donors of the American Chemical Society Petroleum Research Fund for partial support of this research (M.L.S.). We also thank Dr. J. E. Davies (Cambridge) for collecting X-ray data for compound **1**.

  DOI: 10.1002/anie.200500340

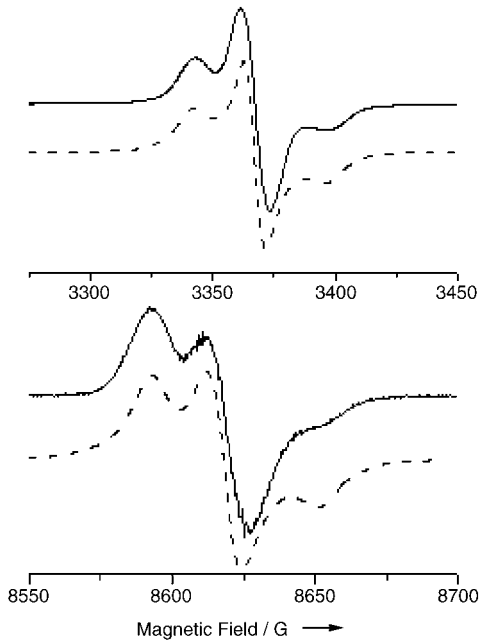

Figure 1. Experimental (solid lines) and simulated (from parameters in the text; dashed lines) EPR spectra of a powdered sample of **1** at 295 K; top: at the X band (9.448 GHz) and bottom: at the K band (24.167 GHz).

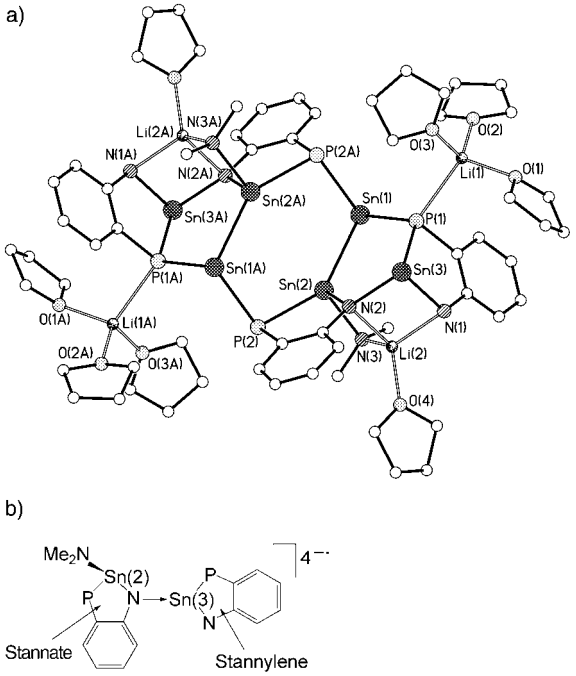

Figure 2. a) Molecular structure of **1**. Hydrogen atoms and lattice-bound THF molecules have been omitted for clarity; disorder of the THF molecules is not shown. Selected bond lengths [Å] and angles [°]: Sn(1)–P(1) 2.603(4), Sn(1)–P(2A) 2.607(4), Sn(1)–Sn(2) 2.885(1), Sn(2)–N(2) 2.10(1), Sn(2)–N(3) 2.18(1), Sn(3)–N(1) 2.18(1), Sn(3)–N(2) 2.17(1), Sn(3)–P(1) 2.566(4), Li(1)–P(1) 2.56(3), Li(2)–N 2.00(3)–2.14(3); angles about Sn(1): 86.21(9)–103.58(9), Sn(2): 88.4(3)–145.9(1), Sn(3): 81.0(3)–99.7(3). b) Schematic representation of the stannate/stannylene $[Sn_2(L)_2(NMe_2)]^{4-}$ ion of **1**.

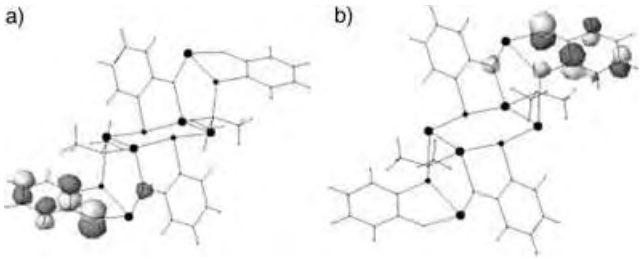

Figure 3. Representation of the semiempirical component PM5-derived frontier MOs of **1**, which illustrates their ligand-based π character: a) the HOMO and b) the LUMO. Large spheres = Sn atoms, small spheres = P atoms.

^{14}N isotope. The only good simulations were obtained by assuming coupling of each unpaired electron to a single ^{14}N nucleus (with no interaction between the two unpaired electrons) with the parameters $g_{x,y} = 2.004$, $g_z = 2.002$, $A_z = 27 \times 10^{-4}\ cm^{-1}$, and $A_{x,y}$ held at an arbitrarily small value of $1x10^{-4}\ cm^{-1}$. The $A_z(^{14}N)$ value places an upper limit of approximately 45% on the unpaired electron density in the 2p orbital of the N atom. The lack of resolution of the ^{31}P nuclei coupling in the EPR spectrum suggests that this coupling constant is smaller than the experimentally obtained linewidths (ca. 10 G).

The low-temperature X-ray crystal structural analysis of **1**[8] (combined with the previous spectroscopic data) shows that the complex consists of centrosymmetric molecules with the formula $[\{[Sn(L)(NMe_2)Li(thf)][Sn(L)Li(thf)_3]Sn\}_2]$ (Figure 2a). Consistent with the main conclusion drawn from the EPR studies, semiempirical calculations on the $[Sn_6(L)_4(NMe_2)_2]^{4-}$ ion of **1** (see Figure 3, in which the tris-THF-solvated Li^+ ions and the THF solvation have been omitted) show that the frontier orbitals are ligand based (85%) rather than Sn based.[9] Furthermore, the majority of the spin density is found on the nitrogen centers of the ligands located at the periphery of the cage (as indicated in Figure 3). The calculated spin density of 30% on the nitrogen centers of these ligands is in good agreement with the upper estimate of 45% based on EPR studies. Interestingly, the spin densities on the nitrogen and phosphorus centers of the ligands within the central portion of the molecule are an order of magnitude less (no greater than 5%). This distribution explains why the complex behaves as a biradical, in which there is no interaction between the unpaired electrons. The major deduction drawn from the spectroscopic and molecular orbital (MO) studies is that to attain electronic neutrality the hexanuclear Sn_6 arrangement of **1** must consist of six Sn^{II} centers together with two tetraanions L^{4-} and two radical trianions $L^{3-\cdot}$, as well as two NMe_2 groups, rather than the potential metal-centered alternative consisting of two Sn^{III} and four Sn^{II} ions and four L^{4-} ions.

The biradical arrangement of **1** consists of two symmetry-related stannylene/stannate fragments (Figure 2b) that are connected by two Sn^{II} centers within the central $(Sn_2P)_2$ ring of **1** through Sn–Sn and Sn–P bonds. The Sn–Sn bonds within the $(Sn_2P)_2$ ring (Sn(2)–Sn(1) = 2.885(1) Å) are best described as dative bonds between eight-electron stannate

(donor) and Sn^{II} centers (acceptor). These bonds are considerably shorter than the dative Sn–Sn bonds in $[ArSn^{II}\rightarrow Sn^{II}\{1,8\text{-}(NR)_2C_{10}H_6\}]$ ($Ar = 2,6\text{-}(Me_2N)_2C_6H_3$; Sn–Sn = 3.087(2) Å),[10] but similar in length to the bonds in the most closely related species $[(Me_3Si)_3Sn^{II}\rightarrow Sn^{II}\{2\text{-}[(Me_3Si)_2C]C_5H_4N\}]$ (Sn–Sn = 2.8689(5) Å).[11] The Sn–P and Sn–N bond lengths (2.497(4)–2.607(4) and 2.10(1)–2.18(1) Å, respectively) are within the range observed for structurally characterized Sn^{II}–P and Sn^{II}–N compounds.[12] The shortest of the Sn–P and Sn–N bond lengths in **1** are in the {Sn(N–C⋯C–P)} chelate rings, with Sn(1)–P bonds (mean = 2.605(4) Å) being the longest bonds of this type in the structure. This Sn(1) centre has a highly distorted pyramidal geometry (range of angles about Sn(1) = 86.21(9)–103.58(9)°), which is similar to that found at the stannylene center Sn(3) (range = 81.0(3)–99.7(3)°). The neutrality of the molecular arrangement of **1** is completed by four Li^+ ions that are located at the periphery of the cage. The $Li(1)(thf)_3$ center is bonded to a P atom (Li(1)–P(1) = 2.56(3) Å), and the Li(2)(thf) center is coordinated by three N centers of the core (Li(2)–N = 2.00(3)–2.14(3) Å).

Although symmetrical N-heterocyclic germylenes,[13] silylenes,[14] and stannylenes[15] have been studied extensively in the past decade, and noncyclic N–Sn–O and N–Sn–C stannylenes are known,[16,17] the N,P-stannylene arrangement found in **1** is unique for a heterocyclic species. To the best of our knowledge, the extent of the deprotonation observed in this study is without precedent for a simple organic acid when treated with a base in solution. The deprotonation of both the NH_2 and PH_2 groups of 2-aminophenylphosphane is particularly dramatic bearing in mind the large negative charge that develops in the resulting L^{4-} and $L^{3-\cdot}$ ions. The results reported herein show that multiple deprotonation of organic acids by mixed alkali-metal organometallic/p-block-metal dimethylamide reagents is a promising area for future study.

Experimental Section

*n*BuLi (3.1 mL, 1.6 mol L^{-1} in hexanes, 5.0 mmol) was added to 2-aminophenylphosphane (0.47 mL, 5.0 mmol) in THF (20 mL) was carried out at −78 °C. The reaction mixture was warmed to room temperature and stirred for 4 h to yield a red solution. The reaction mixture was then cooled to −78 °C, and $[Sn(NMe_2)_2]$ (1.10 g, 5.0 mmol) was added as a solution in THF (10 mL). The reaction mixture was warmed to room temperature and stirred for 16 h to yield a dark-red solution. The solvent was reduced in volume to 5–10 mL and filtered. Complex **1** (0.20 g, 10% yield based on Sn) was crystallized from the filtrate at −30 °C (ca. 1 week). IR (nujol): $\tilde{\nu}$ = 1583 (m), 1020 (s), 816 (m), 765 (w), 735 cm^{-1} (m); ^1H NMR (25 °C, 500.16 MHz, $[D_8]$THF): $\delta = 7.5$–5.7 (collection of overlapping multiplets), 3.50 (m, -CH_2-, THF), 1.70 ppm (m, -CH_2-O, THF) the aromatic resonances were not resolved when the temperature was lowered to −80 °C; ^{31}P NMR (25 °C, 161.975 MHz, $[D_8]$THF, reference: 85% H_3PO_4/D_2O): δ = 10–15 ppm (v br s); elemental analysis (%) calcd for $C_{64}H_{100}Li_4N_6O_9P_4Sn_6$: C 37.7, H 4.8, N 4.4, P 5.9; found C 39.2, H 5.1, N 4.3, P 6.3. The X-ray crystallographic analysis of **1** was carried out on batches of crystals from two separate reactions to confirm the reproducibility and consistency of the product obtained. Although the yield of **1** is low, the paramagnetic nature of the other products of this reaction that are present in solution made it impossible to obtain further NMR spectroscopic data on them (through, the absence of crystalline material). However, other products may well be expected if one bears in mind that the 1:1:1 reaction stoichiometry of nBuLi/$[Sn(NMe_2)_2]$/LH_4 is different from the observed stoichiometry of the components in **1**.

Received: January 28, 2005
Published online: April 28, 2005

Keywords: deprotonation · lithium · metal–metal bonding · tin · X-ray diffraction

[1] L. Lochmann, *Eur. J. Inorg. Chem.* **2000**, *39*, 115.
[2] R. E. Mulvey, *Chem. Commun.* **2001**, 1049.
[3] D. R. Armstrong, A. R. Kennedy, R. E. Mulvey, R. B. Rowlings, *Angew. Chem.* **1999**, *111*, 231; *Angew. Chem. Int. Ed.* **1999**, *38*, 131.
[4] W. Clegg, K. W. Henderson, A. R. Kennedy, R. E. Mulvey, C. T. O'Hara, R. B. Rowlings, D. M. Tooke, *Angew. Chem.* **2001**, *113*, 4020; *Angew. Chem. Int. Ed.* **2001**, *40*, 3902.
[5] M. McPartlin, A. D. Woods, C. M. Pask, T. Vogler, D. S. Wright, *Chem. Commun.* **2003**, 1524.
[6] Z. Hou, D. W. Stephan, *J. Am. Chem. Soc.* **1992**, *114*, 10088; Z. Hou, T. L. Breen, D. W. Stephan, *Organometallics* **1993**, *12*, 3158.
[7] Although the observed g value is within the range previously observed for Sn-centred radicals (g = 1.988–2.077) there is no evidence for hyperfine coupling to the Sn nuclei; previously reported coupling constants ($a(^{117,119}Sn)$ = 329–3426 G) are much greater than the linewidth of 10–15 G observed in the spectrum of **1**; J. Iley, *The Chemistry of Organic Germanium, Tin and Lead* (Ed.: S. Patai), Wiley, New York, **1993**, chap. 5; A. Sekiguchi, T. Fukawa, V. Y. Lee, M. Nakamoto, *J. Am. Chem. Soc.* **2003**, *125*, 9250.
[8] Crystal data for **1**: $C_{64}H_{100}Li_4N_6O_9P_4Sn_6$, M_r = 1961.28, monoclinic, space group $C2/c$, $Z = 4$, a = 33.0513(16), b = 17.4337(7), c = 16.6854(9) Å, β = 98.209(2)°, V = 9515.7(8) $Å^3$, $\mu(Mo_{K\alpha})$ = 1.661 mm^{-1}, ρ_{calcd} = 1.370 $Mg\,m^{-3}$, T = 180(2) K. Data were collected on a Nonius KappaCCD diffractometer. Of a total of 14976 reflections collected, 4813 were unique (R_{int} = 0.151). The structure was solved by direct methods and refined by full-matrix least-squares on F^2 (G. M. Sheldrick, *SHELX-97*, Göttingen, Germany, **1997**). Final $R1 = 0.079$ ($I > 2\sigma(I)$) and $wR2 = 0.213$ (all data). CCDC-261960 contains the supplementary crystallographic data for this paper. These data can be obtained free of charge from the Cambridge Crystallographic Data Centre via www.ccdc.cam.ac.uk/data_request/cif.
[9] Single-point semiempirical calculations were performed by using MOPAC implemented through the quantum cache version 5.0 (Fujitsu). PM5 parameters were employed on the assumption of an RHF state (neglecting electron–electron correlation). This process yielded a near-degenerate pair of singly occupied MOs with an energy separation of 0.056 eV (5.4 kJ mol^{-1}). These MOs comprise the in-phase and out-of-phase combinations ($\sqrt{2}$-($\Phi_a \pm \Phi_b$)) of the frontier MOs depicted in Figure 3, which were calculated from a closed-shell configuration. Further SCF calculations confirmed that the structure is a minimum on the potential-energy surface.
[10] C. Drost, P. B. Hitchcock, M. F. Lappert, *Angew. Chem.* **1999**, *111*, 1185; *Angew. Chem. Int. Ed.* **1999**, *38*, 1113.
[11] C. J. Cardin, D. J. Cardin, S. P. Constantine, A. K. Todd, S. J. Teat, S. Coles, *Organometallics* **1998**, *17*, 2144.
[12] Conquest Software for searching the Cambridge Structural Database and visualizing crystal structures: I. J. Bruno, J. C. Cole, P. R. Edgington, M. Kessler, C. F. Macrae, P. McCabe, J. Pearson, R. Taylor, *Acta Crystallogr. Sect. B* **2002**, *58*, 389.
[13] M. Denk, R. Lennon, R. Hayashi, R. West, A. V. Belyakov, H. P. Verne, A. Haaland, M. Wagner, N. Metzier, *J. Am. Chem. Soc.*

1994, *116*, 2691; B. Gerrhus, M. F. Lappert, J. Heinicke, R. Boese, D. Blaser, *J. Chem. Soc. Chem. Commun.* **1995**, 1931; B. Gerrhus, M. F. Lappert, J. Heinicke, R. Boese, D. Blaser, *J. Organomet. Chem.* **1996**, *521*, 211; D. F. Moser, I. A. Guzei, R. West, *Main Group Met. Chem.* **2001**, *24*, 811.

[14] J. Pfeiffer, W. Maringgele, M. Noltemeyer, A. Meler, *Chem. Ber.* **1989**, *122*, 245; W. Hermann, M. Denk, J. Behm, W. Scherer, F.-R. Klingan, H. Bock, B. Solouki, M. Wagner, *Angew. Chem.* **1992**, *104*, 1489; *Angew. Chem. Int. Ed. Engl.* **1992**, *31*, 1485; O. Kuhl, P. Lonnecke, J. Heinicke, *Polyhedron* **2001**, *20*, 221.

[15] a) H. Braunschweig, B. Gerrhus, P. B. Hitchcock, M. F. Lappert, *Z. Anorg. Allg. Chem.* **1995**, *621*, 1922; b) F. E. Hahn, L. Wittenbecher, M. Kuhl, T. Lugger, R. Frohlich, *J. Organomet. Chem.* **2001**, *617*, 629; c) T. Gans-Eichler, D. Gudat, M. Nieger, *Angew. Chem.* **2002**, *114*, 1966; *Angew. Chem. Int. Ed.* **2002**, *41*, 1888.

[16] L. Pu, M. M. Olmstead, P. P. Power, *Organometallics* **1998**, *17*, 5602; H. Braunschweig, R. W. Chorley, P. B. Hitchcock, M. F. Lappert, *J. Chem. Soc. Chem. Commun.* **1992**, 1311.

[17] See also: M. Driess, R. Janoschek, H. Pritzkow, U. Winkler, *Angew. Chem.* **1995**, *107*, 1746; *Angew. Chem. Int. Ed. Engl.* **1995**, *34*, 1614.

Inverse Crown Compounds

Selective *Meta*-Deprotonation of Toluene by Using Alkali-Metal-Mediated Magnesiation**

Prokopis C. Andrikopoulos, David R. Armstrong, David V. Graham, Eva Hevia, Alan R. Kennedy, Robert E. Mulvey, Charles T. O'Hara, and Christine Talmard*

Deprotonative metalation, whereby a proton is substituted by a metal cation to transform a parent organic compound to a more reactive metallic intermediate, which, in turn, can be used to transfer the organic fragment to another molecule, is one of the fundamental synthetic tools that chemists employ to construct compounds.[1] Thus this indispensable tool is put to labor on a daily basis in laboratories across the world, both in academia, for general synthesis, and in industry, for the manufacture of fine chemicals and pharmaceuticals. With polyatomic organic compounds containing two or more hydrogen atoms, there is often a requirement to be selective in choosing the specific hydrogen atom to be removed to generate the desired organic fragment. Owing largely to their polar nature, alkali-metal alkyl ("RM") and amide ("R_2NM") compounds, especially those of lithium, are often the best reagents for effecting deprotonative metalation, but there are limits to their selectivity.[2,3]

A primary source of aromatic compounds, alkylbenzenes, typified by toluene, offer several sites for metalation: the alkyl side chain or the *ortho*, *meta*, or *para* ring sites.[4] However, in practice, toluene is almost exclusively metalated on the CH_3 substituent by common reagents such as BuLi-(tmeda) (tmeda is *N*,*N*,*N*′,*N*′-tetramethylethylenediamine), BuNa, or BuK.[5–7] This situation follows conventional wisdom as the newly formed benzyl "carbanion" ($PhCH_2^-$) is resonance stabilized, and thus in these mainstream monometallic systems it is the most thermodynamically stable of the four isomers possible when a proton is abstracted from toluene. All of the relevant studies hitherto have achieved metalation at kinetic ring sites to only a very minor, synthetically useless, extent, and anyway this is usually followed by isomerization to the thermodynamic benzyl structure. For this reason, metalation reactions of toluene have had a limited scope of usefulness within organic synthesis. Given this background, chemists will be surprised to learn that it is now possible to reverse this order of thermodynamic stability in favor of ring as opposed to methyl deprotonation of toluene by using a special synergic (bimetallic)[8] approach. Moreover, this approach enables regioselective metalation at the *meta* position, to contrast with the normal *ortho*-, *para*-directing effect that the methyl group of toluene exerts in reactions such as electrophilic aromatic substitution. Thus we report the selective *meta* deprotonation of toluene in the mixed sodium–magnesium amido complex [(tmeda)Na(μ-$C_6H_4CH_3$)(μ-tmp)Mg(tmp)] (**1**; where tmp is 2,2,6,6-tetramethylpiperidide). We describe the synthesis and characterization of **1**, as well as reporting the results of theoretical calculations on model compounds, which can offer an explanation for this unexpected *meta* selectivity.

As part of a study working towards the development of new mixed-metal amide-based reagents which can display remarkable synergic reactivities, we recently introduced the bimetallic sodium-magnesium monoalkyl bisamido complex [(tmeda)Na(μ-Bu)(μ-tmp)Mg(tmp)] (**2**).[9] This new reagent is best prepared by combining the individual monometallic alkyl compounds and treating the mixture with equimolar amounts of the parent cyclic amine tmp(H) and the chelating auxiliary tmeda (Scheme 1). In this way **2** is produced in near-quantitative yields in a pure, crystalline form ideal for synthetic utilization. We anticipated that **2** could have special Brønsted basic properties as it has a number of characteristics of different existing bases, but all combined within a single molecule: these include bulky amide ligands (as in Li(tmp)), a strongly nucleophilic alkyl ligand (as in BuLi or BuNa) but one within a unique sterically hindered environment, a mixed-metal mixed-anion set (as in the Lochmann–Schlosser, lithium carbon potassium alkoxide (LICKOR) superbases), and a diamine molecule known to activate alkali metal reagents in many reactions.[1] Furthermore, **2** is soluble in many common organic solvents (such as hydrocarbons). Its

[*] P. C. Andrikopoulos, Dr. D. R. Armstrong, D. V. Graham, Dr. E. Hevia, Dr. A. R. Kennedy, Prof. R. E. Mulvey, Dr. C. T. O'Hara, C. Talmard
Department of Pure and Applied Chemistry
University of Strathclyde
Glasgow, G1 1XL (UK)
Fax: (+44) 141-552-0876
E-mail: r.e.mulvey@strath.ac.uk

[**] This work was supported by the U.K. EPSRC through grant award no. GR/R81183/01, the E.U. through a Marie Curie Fellowship to E.H., and the Royal Society/Leverhulme Trust through a Fellowship to R.E.M.

Supporting information for this article is available on the WWW under http://www.angewandte.org or from the author.

 DOI: 10.1002/anie.200500379

$$2\,BuNa + 2Bu_2Mg + 2tmp(H) + 2tmeda \xrightarrow{-BuH} [(tmeda)Na(Bu)(tmp)Mg(tmp)] + NaMgBu_3(tmeda)$$

2

$$[(tmeda)Na(Bu)(tmp)Mg(tmp)] + C_6H_5CH_3 \xrightarrow{-BuH} [(tmeda)Na(C_6H_4CH_3)(tmp)Mg(tmp)]$$

1

Scheme 1. Synthesis of the bimetallic base **2** and its reaction with toluene to form **1**.

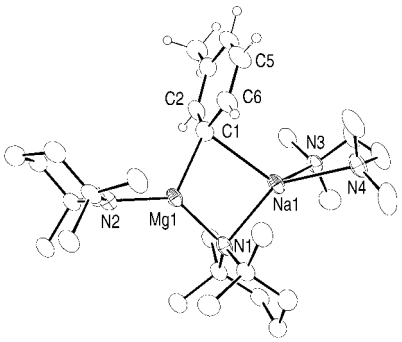

Figure 1. Molecular structure of **1**. Hydrogen atoms, apart from those of the tolyl group, are omitted for clarity.

deprotonative ability was first demonstrated with benzene, which was readily converted into $C_6H_5^-$ within the product [(tmeda)Na(μ-C_6H_5)(μ-tmp)Mg(tmp)] (**3**).[9] Regioselectivity was not an issue in this case. Deprotonation of toluene (Scheme 1) also proved straightforward, by simply adding it to a hexane solution of **2** and heating the mixture to reflux. The solid product of the reaction was colorless, crystalline **1** (58% yield), the formation of which was accompanied by butane gas evolution. When the reaction was repeated using a stoichiometric amount of toluene instead of a tenfold excess, **1** was still obtained in a 30% yield. Characterized by both ^1H and ^{13}C NMR spectroscopic studies (recorded in [D_6]benzene solution), **1** displays a pattern in the aromatic region of the ^1H NMR spectrum (a singlet, two doublets, and a triplet) consistent with *meta*-deprotonated toluene (i.e., corresponding to the *ortho**-, *ortho*/*para*-, and *meta*-hydrogen atoms respectively). This assignment is confirmed by the presence of the CH_3 resonance of toluene and the absence of a benzylic CH_2 resonance. Furthermore, there is no sign of other possible regioisomers of metalated toluene, each of which, if present, would give rise to distinctive resonance patterns in the aromatic region. The spectra also reveal that at ambient temperature both types of tmp ligand are equivalent and that the tmeda coligand remains coordinated to the sodium center. It should be noted that in the absence of tmeda, a 1:1:3 mixture of BuNa, Bu_2Mg, and tmp(H), thought to generate "[{tmp(H)}Na(Bu)$(tmp)_2$Mg]" in situ,[9] reacts with toluene to give [$(tmp)_6Na_4Mg_2${C_6H_3(Me)}][10] in which toluene is dideprotonated in the 2,5-positions. The low yield of this product and the new discovery of **1**, suggests that this twofold deprotonation is a subsequent reaction effected by strong heating, which probably involves intramolecular deprotonation of a monodeprotonated toluene species and elimination of $Mg(tmp)_2$ as the Na:Mg ratio changes from 1:1 in **1** to 2:1 in the other product.

X-ray crystallographic studies established the molecular structure of **1** (Figure 1).[11] A four-element NaNMgC ring, with a mixed tmp/$C_6H_4CH_3$ bridging ligand set, forms the central feature of the structure, which is completed by a terminal tmp on magnesium and a bidentate attached tmeda on sodium. Thus its basic connectivity is the same as that in **2** and **3**, with only the identity of the carbon bridge changing ($C_6H_4CH_3$ in **1**, Bu in **2**, C_6H_5 in **3**). In **1** (as in **3**), the central NaNMgC ring is essentially planar (sum of endocyclic bond angles, 359.94°), whereas in **2** there is a deviation from planarity (corresponding sum, 356.33°). This distinction reflects the aromatic/aliphatic nature of the carbon bridge and its hybridization (sp^2/sp^3, on discounting the long contacts to Na). In forming a short, strong bond to the *meta*-C1 atom (2.197(5) Å), close to coplanarity with the tolyl ring plane (as shown by the Mg1C1C6C5 torsion angle, −168.9(4)°), the Mg1 atom in **1** in effect refills the position vacated by the abstracted proton. This result implies intriguingly that the metalation reaction is formally a magnesiation as opposed to a sodiation, which runs counter to the normal reactivity order of organomagnesium versus organosodium compounds (i.e., that organosodium compounds are orders of magnitude more reactive).[12] Contrary to the parallel orientation of Mg1, Na1 lies almost perpendicular to the tolyl ring plane (Na1-C1-Mg1 bond angle, 80.78(16)°). The shortest Na1-tolyl contact is to the *meta* C1 (2.681(5) Å), where most of the negative charge resides, but the proximate C atoms also lie close by (Na1-C6, 3.147(5)Å; Na1-C2, 3.333(5) Å). This bonding distinction between magnesium and sodium with respect to the deprotonated substrate, signifying more σ character for magnesium and more π character for sodium, is also found in inverse crown complexes.[13,14]

The origin of this unexpected *meta* selectivity was probed by theoretical calculations. Preliminary geometry optimizations on all molecules were performed at the Hartree–Fock level, using the 6-13G* basis set, then the optimized structure so obtained was re-refined at the density functional theory (DFT) level, employing the B3LYP method and the 6-311G** basis set.[13] The reaction between **2** and toluene to give **1** (Scheme 1) was calculated to be exothermic by 8.21 kcal mol^{-1}. Four regioisomers of the model compound [Na(μ-tolyl)(μ-tmp)Mg(tmp)] (**1A**–**1D**; Figure 2), where tolyl represents a toluene molecule singly deprotonated in the *ortho* (**1A**), *meta* (**1B**), *para* (**1C**), or *methyl* (**1D**) positions, were examined. Consistent with the experimental structure of **1**, the most stable theoretical structure is calculated to be the *meta* isomer **1B** (relative energy, 0.00 kcal mol^{-1}). The next lowest energy structure is the *para* isomer **1C** (at +2.35 kcal mol^{-1}) followed by the *ortho* isomer **1A** (at 5.12 kcal mol^{-1}). Somewhat surprisingly, the least stable structure of all is the benzyl isomer **1D**, which is 7.77 kcal mol^{-1} less stable than **1B**. Comparing the dimensions of **1B** and **1D**, it is clear that the major contribution to the energetic preference for **1B** lies not in Mg–C σ bonding but in

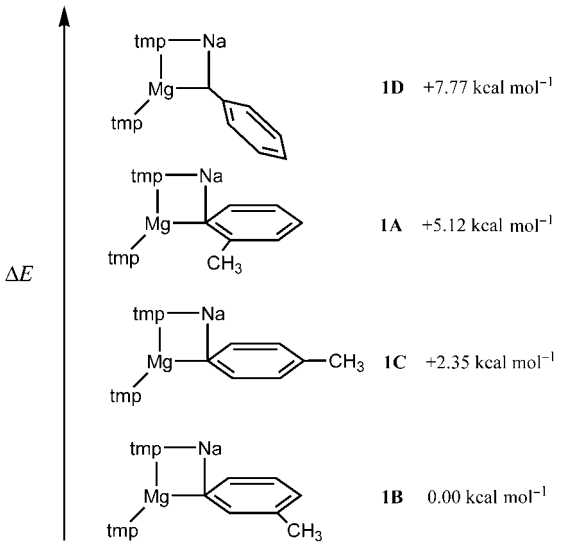

Figure 2. The theoretical structures **1A**–**1D**, in order of decreasing stability.

Na–C π interactions: thus the Mg–C bond in **1B** (2.232 Å) is only modestly shorter than that in **1D** (2.279 Å); but whereas **1B** displays several short-to-medium length Na–C π interactions (2.453 Å, 2.915 Å, and 2.960 Å to *meta*, *para*, and *ortho* C atoms, respectively), the orientation of the benzyl ring in **1D** is such that there are no Na–C π contacts below 4.8 Å (the Na–C benzylic bond length is 2.475 Å). While each individual Na–C π interaction in **1B** may be weak, collectively they must contribute significantly to its overall stability. Hence the normal order of thermodynamic stability of toluene metalation products (side-chain isomer > ring-site isomer) has been reversed by using this special bimetallic approach. When tmeda is included in the calculations, the benzyl isomer is still less stable than the *meta* isomer, but by a reduced margin ($+1.99$ kcal mol^{-1}); also the *para* isomer is fractionally more stable than the *meta* isomer (relative energies, 0.00 and $+0.05$ kcal mol^{-1}, respectively). However, *meta*-deprotonation has also been observed in tmeda-free solutions in the synthesis of the dideprotonated complex $[Na_4Mg_2(C_6H_3CH_3)(tmp)_6]$, so the tmeda-free models **1A**–**1D** probably provide a reasonable guide to the experimental reaction. Noting that conventional magnesium bases are generally too weak to metalate toluene, this new synergic mixed-metal methodology that opens a direct route to *meta*-substituted toluenes,[15,16] is perhaps best regarded as alkali-metal-mediated magnesiation, a new form of magnesiation with greatly enhanced basic powers.[17]

To test its ability to be intercepted by electrophiles, **1** was treated with three molar equivalents of trimethylsilyl triflate in [D$_6$]benzene solution. A white precipitate formed instantaneously, and was removed by filtration. A ^{1}H NMR spectrum of the filtrate showed that **1** had converted essentially quantitatively into trimethyl *meta*-tolylsilane, as established by comparison with an authentic sample of trimethyl *meta*-tolylsilane.[16] This promising result confirms that **1** should be an excellent precursor to *meta*-substituted tolyl compounds.

Experimental Section

All reactions were carried out under a protective argon atmosphere.

1: Freshly prepared [(tmeda)Na(μ-Bu)(μ-tmp)Mg(tmp)] (**2**) (1.0 g, 2 mmol) was dissolved in hexane (10 mL). Next toluene (2 mL; 20 mmol) was added and the pale yellow solution obtained was heated to reflux for 90 min. The flask containing the resulting light orange solution was placed in a Dewar flask of hot water and allowed to cool slowly to room temperature affording colorless crystals of **1** (yield, 0.62 g, 58 %). ^{1}H NMR (400 MHz, 25 °C, [D$_6$]benzene): $\delta = 7.75$ (H_{ortho*}, C_6H_4-CH_3), 7.62 (H_{para}, C_6H_4-CH_3), 7.10 (H_{meta}, C_6H_4-CH_3), 6.92 (H_{ortho}, C_6H_4-CH_3), 2.19 (CH_3, C_6H_4-CH_3), 1.90 (m, 4H, tmp), 1.64 (s, 24H, CH_3, tmp), 1.56 (s, 12H, CH_3, tmeda), 1.48 (m, 4H, CH_2, tmeda), 1.35 ppm (m, 8H, tmp); ^{13}C{^{1}H} NMR (100.63 MHz, 25 °C, [D$_6$]benzene): $\delta = 172.83$ (Mg-C_{meta*}), 142.29 (C_{ortho*}), 137.48 (C_{para}), 135.76 (C_{ipso}), 127.04 (C_{meta}), 126.13 (C_{ortho}), 57.23 (CH_2, tmeda), 52.60 (N-*C*, tmp), 46.26 (CH_3, tmeda), 42.71 (tmp), 36.24 (CH_3, tmp), 22.45 (CH_3, C_6H_4-CH_3), 20.70 ppm (tmp).

Received: February 1, 2005
Published online: April 21, 2005

Keywords: deprotonation · inverse crown compounds · magnesium · metalation · sodium

[1] M. Schlosser, *Organometallics in Synthesis* (Wiley, Chichester, 2nd ed., **2002**, chap. 1. For an authoritative review on hydrogen–metal interconversion reactions in aromatic systems see: M. Schlosser, *Angew. Chem.* **2005**, *117*, 380; *Angew. Chem. Int. Ed.* **2005**, *44*, 376.
[2] B. J. Wakefield, *The Chemistry of Organolithium Compounds*, Pergamon, Oxford, 1st ed., **1974**.
[3] P. G. Williard, *Comprehensive Organic Synthesis*, *Vol. 1*, Pergamon, New York, **1991**, p. 1.
[4] R. T. Morrison, R. N. Boyd, *Organic Chemistry*, Prentice Hall, New Jersey, 6th ed., **1992**, chap. 16.
[5] A. J. Chalk, T. J. Hoogeboom, *J. Organomet. Chem.* **1968**, *11*, 615.
[6] C. D. Broaddus, *J. Am. Chem. Soc.* **1966**, *88*, 4174.
[7] C. D. Broaddus, *J. Org. Chem.* **1970**, *35*, 10. Note that this paper reports that using BuLi(tmeda), the *meta* position of toluene is the most reactive "kinetic" site of the ring, but the best yield of deprotonation obtained is only 9 %.
[8] For recent examples of other studies dealing with deprotonation of aromatics using related bimetallic systems see: a) Y. Kondo, M. Shilai, M. Uchiyama, T. Sakamoto, *J. Am. Chem. Soc.* **1999**, *121*, 359; b) H. Awad, F. Mongin, F. Trécourt, G. Quéguiner, F. Marsais, F. Blanco, B. Abarca, R. Ballesteros, *Tetrahedron Lett.* **2004**, *45*, 6697.
[9] E. Hevia, D. J. Gallagher, A. R. Kennedy, R. E. Mulvey, C. T. O'Hara, C. Talmard, *Chem. Commun.* **2004**, 2422.
[10] D. R. Armstrong, A. R. Kennedy, R. E. Mulvey, R. B. Rowlings, *Angew. Chem.* **1999**, *111*, 231; *Angew. Chem. Int. Ed.* **1999**, *38*, 131.
[11] Crystal data for **1**: $C_{31}H_{59}MgN_4Na$, $M_r = 535.12$. All measurements were made at 123 K on a Nonius Kappa CCD diffractometer. These gave, triclinic, space group $P\bar{1}$, $a = 9.8562(4)$, $b = 11.3668(4)$, $c = 16.0733(7)$ Å, $\alpha = 69.568(2)$, $\beta = 83.965(2)$, $\gamma = 83.558(2)$°, $V = 1672.59(12)$ Å^3, $Z = 2$, $\lambda = 0.71073$ Å, $\mu = 0.090$ mm^{-1}; 16555 reflections, 4467 unique, R_{int} 0.087; final refinement to convergence on F^2 gave $R = 0.0870$ (F, 3274 obs. data only) and $R_w = 0.2343$ (F^2, all data), GOF = 1.099. Diffraction intensity fell sharply beyond $2\theta = 45.5$° and this had an adverse impact on the quality of the data collection and refinement. Atomic coordinates, bond lengths, and angles.

CCDC-257597 (**1**) contains the supplementary crystallographic data for this paper. These data can be obtained free of charge from the Cambridge Crystallographic Data Centre via www.ccdc.cam.ac.uk/data_request/cif.

[12] C. Elschenbroich, A. Salzer, *Organometallics A Concise Introductio*, VCH, New York, 2nd ed., **1992**, chap. 5, p. 6.

[13] R. E. Mulvey, *Chem. Commun.* **2001**, 1049.

[14] P. C. Andrikopoulos, D. R. Armstrong, W. Clegg, C. J. Gilfillan, E. Hevia, A. R. Kennedy, R. E. Mulvey, C. T. O'Hara, J. A. Parkinson, D. M. Tooke, *J. Am. Chem. Soc.* **2004**, *126*, 11612.

[15] For full details of the theoretical calculations see Supporting Information.

[16] H. J. Reich, J. E. Holladay, J. D. Mason, W. H. Sikorski, *J. Am. Chem. Soc.* **1995**, *117*, 12137.

[17] H. Richey, Jr., *Grignard Reagents: New Developments*, Wiley, Chichester, **2000**.

Natural Product Synthesis

Concise and Practical Synthesis of Latrunculin A by Ring-Closing Enyne–Yne Metathesis**

Alois Fürstner and Laurent Turet*

Incubation of eukaryotic cells with micromolar concentrations of the marine natural product latrunculin A (**1**) or its ring-contracted congener

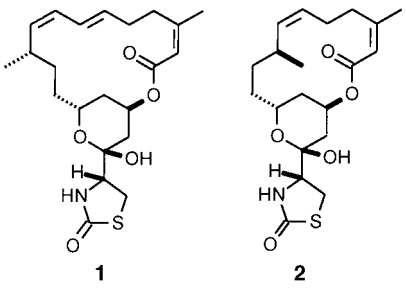

latrunculin B (**2**) results in a selective perturbation or even complete disruption of the actin cytoskeleton.[1,2] Thereby, the potency and rapid onset of action are highly reminiscent of genetic knockout experiments, and thus allow study of the many biological properties of actin by what might be considered a prototype "chemical genetics" approach.[3] This crucial and highly complex subcellular protein network determines the shape and mechanical properties of the cells and is responsible for motility processes as fundamental as exo- and endocytosis. The recent discovery of an actin-dependent checkpoint in mitosis also relied on the use of **1**, thus increasing the interest in this and related probe molecules even further.[4]

It is hardly surprising, therefore, that this family of scarce macrolides has also attracted the interest of the synthetic community to culminate in three successful total synthesis campaigns.[5–7] In this context, we reported an efficient route to latrunculin B (**2**) based upon the use of ring-closing alkyne metathesis (RCAM)[8,9] for the formation of the macrocycle.[7] Although this approach is inherently flexible and should therefore be amenable to the synthesis of all other members of this series, two important aspects deserved further consideration before it was adapted to the total synthesis of the parent compound **1**.

While access to **2** relies on a regular RCAM reaction[8,9] of a properly protected diyne of type **B** to cycloalkyne **A** followed by Lindlar reduction, the envisaged extension of this strategy to the synthesis of **1** implies a metathetic event between an alkyne and a conjugated enyne (**D**→**C**, Scheme 1). Only if this transformation occurs strictly chemoselectively at the triple bonds without affecting the adjacent olefin[10] might latrunculin A come into reach. Such alkyne-selective enyne–yne metathesis reactions were disclosed only recently and have never been used in a similarly complex setting.[11] Moreover, as the resulting products are necessarily strained, the efficiency of this reaction strongly depends on the ring size formed, with the smallest successful example reported to date comprising 18 ring atoms.[11] It was therefore by no means clear if this methodology was applicable to the

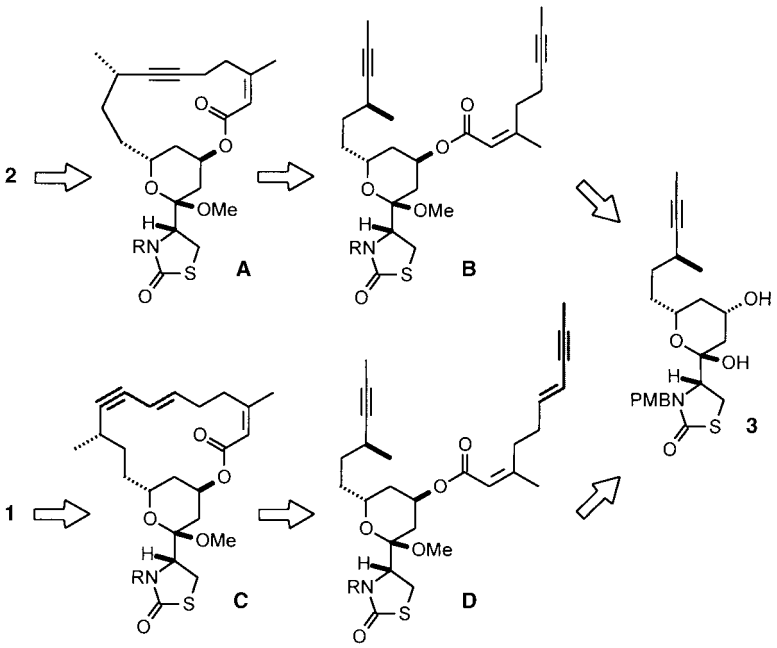

Scheme 1. Retrosynthetic analyses of latrunculin A and B which both converge to the common building block **3**. PMB = *para*-methoxybenzyl.

[*] Prof. A. Fürstner, Dr. L. Turet
Max-Planck-Institut für Kohlenforschung
45470 Mülheim/Ruhr (Germany)
Fax: (+49) 208-306-2994
E-mail: fuerstner@mpi-muelheim.mpg.de

[**] Generous financial support by the MPG, the Fonds der Chemischen Industrie, and the Merck Research Council is gratefully acknowledged. We thank Dr. D. De Souza for helpful comments and discussions and Dipl.-Chem. J. T. Jensen for preliminary experiments on the synthesis of the acid segment.

  DOI: 10.1002/anie.200500390

stereoselective formation of the diene moiety of **1** which is embedded into the 16-membered ring of a rigid bicyclic skeleton.

The second aspect that deserves further consideration is of practical relevance. While compound **3** as the key building block en route to **2** can also be used for the total synthesis of **1** (see Scheme 1), its preparation relies on an aldol reaction which is not fully satisfactory. Specifically, exposure of aldehyde **4** to the titanium enolate derived from ketone **5** at −78 °C provides product **6** as an inseparable 2:1 mixture of the corresponding diastereomers (Scheme 2).[7] This mixture equilibrates to a more favorable ≈7:1 ratio of isomeric hemiketals on acid-catalyzed cleavage of the O-TBS group at C-11 (latrunculin B numbering), most likely by a retro-Michael/Michael manifold that involves a transient oxocarbenium ion.[7,12] If this mechanistic hypothesis is correct, however, it might be possible to obtain **3** also from the α,β-unsaturated ketone **7** by protonation and addition of water through a sterically and stereoelectronically preferred equatorial trajectory. It seemed lucrative to pursue this idea as it

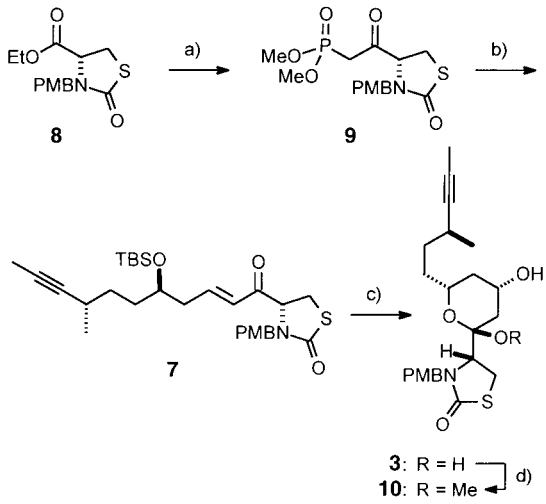

Scheme 3. Improved synthesis of the key building block **3**: a) $(MeO)_2P(O)CH_3$, *n*BuLi, THF, −78 °C, 60%; b) $Ba(OH)_2 \cdot 8H_2O$ (activated at 140 °C), THF, aldehyde **4**, 75%; c) aq. HCl, THF, 63%; d) MeOH, camphorsulfonic acid (cat.), quantitative.

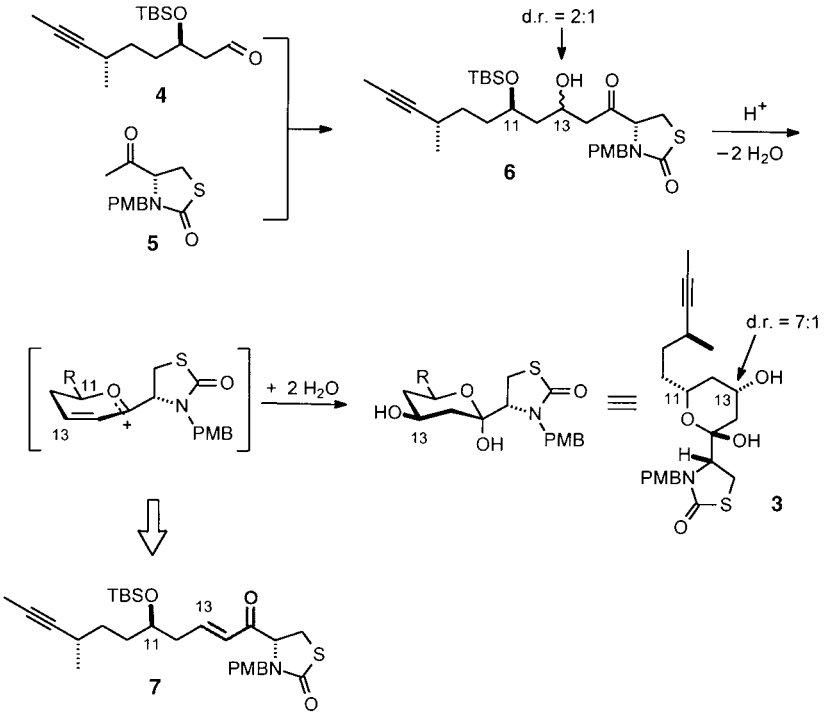

Scheme 2. Established aldol route to the key building block **3** and rationale for the stereochemical equilibration observed upon hemiketal formation. TBS = *tert*-butyldimethylsilyl.

may allow us to replace the somewhat capricious aldol reaction by a simple olefination, which requires neither the handling of sensitive compounds nor the use of low temperatures and should therefore be much more robust, practical, and scaleable.

As shown in Scheme 3, this strategy turned out highly rewarding. Thus, reaction of ester **8** (derived from cysteine in two high-yielding steps)[7] with deprotonated $(MeO)_2P(O)CH_3$ afforded ketophosphonate **9**, ready for condensation with aldehyde **4** (obtained in multigram quantities from (+)-citronellene in seven steps, as previously described).[7] After some experimentation it was found that this Horner–Wadsworth–Emmons reaction proceeded best when activated $Ba(OH)_2$ was used as the base.[13] Exposure of the resulting alkene **7** to aqueous HCl gave the desired hydrated hemiketal **3** in approximately 9:1 ratio; the individual isomers were separable after transformation into the corresponding methyl glycosides **10**. Importantly, this outcome does not only corroborate the proposed equilibration mechanism (see Scheme 2) but also opens a convenient route to this essential building block.

The required acid part was obtained from enol triflate **12**[14] by using iron-catalyzed cross-coupling chemistry previously developed in our laboratory (Scheme 4).[15,16] To this end, substrate **12** was treated with the commercially available organomagnesium reagent **13** in the presence of $[Fe(acac)_3]$ as a cheap and benign precatalyst to give product **14** on a multigram scale.[17] Cleavage of the acetal, conversion of the resulting aldehyde **15** into the corresponding alkyne **17** with the aid of the Ohira–Bestmann reagent **16**,[18] followed by hydrozirconation/iodination[19] provided the desired alkenyl iodide **18** as a single isomer.[20] Conversion of this compound into enyne **19** turned out to be surprisingly difficult, and only the "9-methoxy-9-BBN" variant of the Suzuki reaction (9-MeO-9-BBN, MeC≡CNa, $[Pd(PPh_3)_4]$ catalyst), as previously described by our group, gave satisfactory and reproducible results.[21] Enyne **19** was saponified with KOH in aqueous THF, whereas other bases commonly used for ester hydrolyses led to the decomposition of the material and/or partial epimerization of its *Z*-configured enoate moiety.

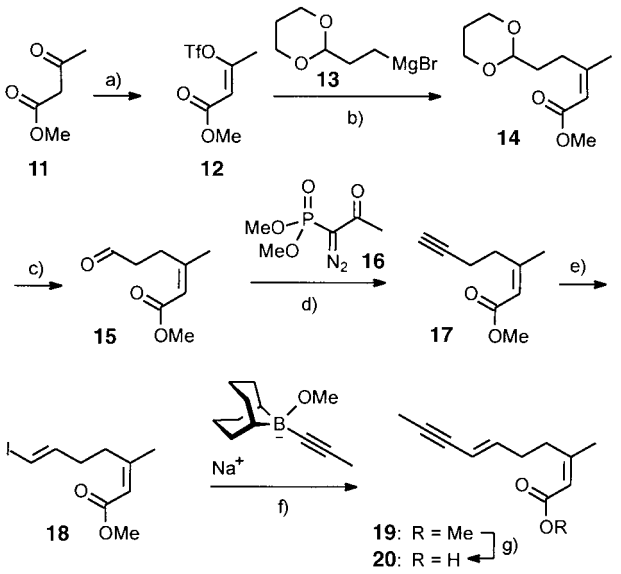

Scheme 4. Preparation of the acid part: a) (1) NaH, CH_2Cl_2; (2) Tf_2O, 82%; b) Grignard reagent **13**, [Fe(acac)$_3$] (15 mol%), −30°C, THF, 67–83%; c) aq. HCOOH, reflux; d) reagent **16**, K_2CO_3, MeOH, 80% (over both steps); e) [$Cp_2Zr(H)Cl$], CH_2Cl_2, then I_2, 56%; f) 9-MeO-9-BBN, NaC≡CMe, [$Pd(PPh_3)_4$] (5 mol%), THF, reflux, 77%; g) KOH, aq. THF, 82%. Tf = trifluoromethanesulfonyl, acac = acetylacetonate, Cp = cyclopentadienyl, BBN = borabicyclo[3.3.1]nonane.

Coupling of the fragments now in hand required the consecutive formation of triflate **21** and substitution with the sodium salt of acid **20** (see Scheme 5). All attempts to perform this esterification under Mitsunobu conditions were unrewarding. We were pleased to note that the resulting product **22** underwent productive enyne–yne metathesis to give the desired product **23** in the presence of catalytic amounts of [Mo{N(*t*Bu)(Ar)}$_3$] (**26**), activated in situ with CH_2Cl_2 as previously described.[22,23] This success, however, was thwarted by our inability to cleave the remaining N-PMB group from the thiazolidinone ring with either 2,3-dichloro-5,6-dicyano-1,4-benzoquinone (DDQ) or cerium ammonium nitrate (CAN). Although we were apprehensive that this step might be problematic,[24] it seemed likely that the high ring strain of the cyclic enyne **23** promotes its degradation by rendering the single-electron oxidation of this reactive entity more facile than the cleavage of the PMB group.

To test this hypothesis, cleavage of the N-PMB group prior to ring closure was attempted. It was gratifying to note that this change in the order of events paved the way to the target. Thus, treatment of the acyclic enyne **22** with CAN afforded product **24** in acceptable yield. Although this compound could not be cyclized owing to the known incompatibility of complex **26** with N-unprotected amides,[22] conversion into the Teoc derivative **25** allowed the crucial enyne–yne metathesis to proceed with rigorous chemoselectivity at the triple bonds to form the highly strained 16-membered cyclic product **27** in 70% yield. Not only is this the smallest ring size ever to be formed by ring-closing enyne–yne metathesis[11] but the compatibility with the dense and diverse array of functional groups also attests to the excellent application profile of this emerging methodology. *Z*-Selective semihydrogenation of the triple bond in **27** with Lindlar's catalyst in the presence of a large excess of quinoline to suppress overreduction followed by consecutive cleavage of the Teoc group and the methyl glycoside in **28** under standard conditions furnished latrunculin A (**1**). The spectroscopic and analytical data for the product were in excellent agreement with those already reported.[1,5,6]

In summary, a concise and efficient synthesis of the strongly actin-binding marine natural product latrunculin A has been achieved. The chosen route features the first successful implementation of a ring-closing enyne–yne metathesis reaction into a total synthesis and is largely catalysis-based overall. Furthermore, a practical solution for the preparation of the key intermediate **3** has been developed that clearly surpasses prior art. As this building block can also serve as a convenient platform for the preparation of non-natural analogues of both **1** and **2**, we are now in a favorable position for a synthesis-driven evaluation of the still largely unknown structure–activity profile of this important class of bioactive macrolides. Our investigations along these lines will be reported shortly.

Received: February 1, 2005
Published online: April 21, 2005

Keywords: alkynes · cross-coupling · macrocycles · metathesis · natural products

[1] Isolation: a) I. Neeman, L. Fishelson, Y. Kashman, *Mar. Biol.* **1975**, *30*, 293–296; b) A. Groweiss, U. Shmueli, Y. Kashman, *J. Org. Chem.* **1983**, *48*, 3512–3516; c) Y. Kashman, A. Groweiss, R. Lidor, D. Blasberger, S. Carmely, *Tetrahedron* **1985**, *41*, 1905–1914; d) R. K. Okuda, P. J. Scheuer, *Experientia* **1985**, *41*, 1355–1356; e) Y. Kakou, P. Crews, G. J. Bakus, *J. Nat. Prod.* **1987**, *50*, 482–484; f) N. K. Gulavita, S. P. Gunasekera, S. A. Pomponi, *J. Nat. Prod.* **1992**, *55*, 506–508; g) J. Tanaka, T. Higa, G. Bernardinelli, C. W. Jefford, *Chem. Lett.* **1996**, 255–256; h) D. Mebs, *J. Chem. Ecol.* **1985**, *11*, 713–716; i) T. R. Hoye, S.-E. N. Ayyad, B. M. Eklov, N. E. Hashish, W. T. Shier, K. A. El Sayed, M. T. Hamann, *J. Am. Chem. Soc.* **2002**, *124*, 7405–7410.

[2] I. Spector, N. R. Shochet, Y. Kashman, A. Groweiss, *Science* **1983**, *219*, 493–495.

[3] Selected reviews: a) K.-S. Yeung, I. Paterson, *Angew. Chem.* **2002**, *114*, 4826–4847; *Angew. Chem. Int. Ed.* **2002**, *41*, 4632–4653; b) J. R. Peterson, T. J. Mitchison, *Chem. Biol.* **2002**, *9*, 1275–1285; c) I. Spector, N. R. Shochet, D. Blasberger, Y. Kashman, *Cell Motil. Cytoskeleton* **1989**, *13*, 127–144; d) W. M. Morton, K. R. Ayscough, P. J. McLaughlin, *Nat. Cell Biol.* **2000**, *2*, 376–378, and references therein.

[4] a) Y. Gachet, S. Tournier, J. B. A. Millar, J. S. Hyams, *Nature* **2001**, *412*, 352–355; b) see also: Y. Nakaseko, M. Yanagida, *Nature* **2001**, *412*, 291–292.

[5] a) A. B. Smith, J. W. Leahy, I. Noda, S. W. Remiszewski, N. J. Liverton, R. Zibuck, *J. Am. Chem. Soc.* **1992**, *114*, 2995–3007; b) A. B. Smith, I. Noda, S. W. Remiszewski, N. J. Liverton, R. Zibuck, *J. Org. Chem.* **1990**, *55*, 3977–3979; c) R. Zibuck, N. J. Liverton, A. B. Smith, *J. Am. Chem. Soc.* **1986**, *108*, 2451–2453.

[6] a) J. D. White, M. Kawasaki, *J. Org. Chem.* **1992**, *57*, 5292–5300; b) J. D. White, M. Kawasaki, *J. Am. Chem. Soc.* **1990**, *112*, 4991–4993.

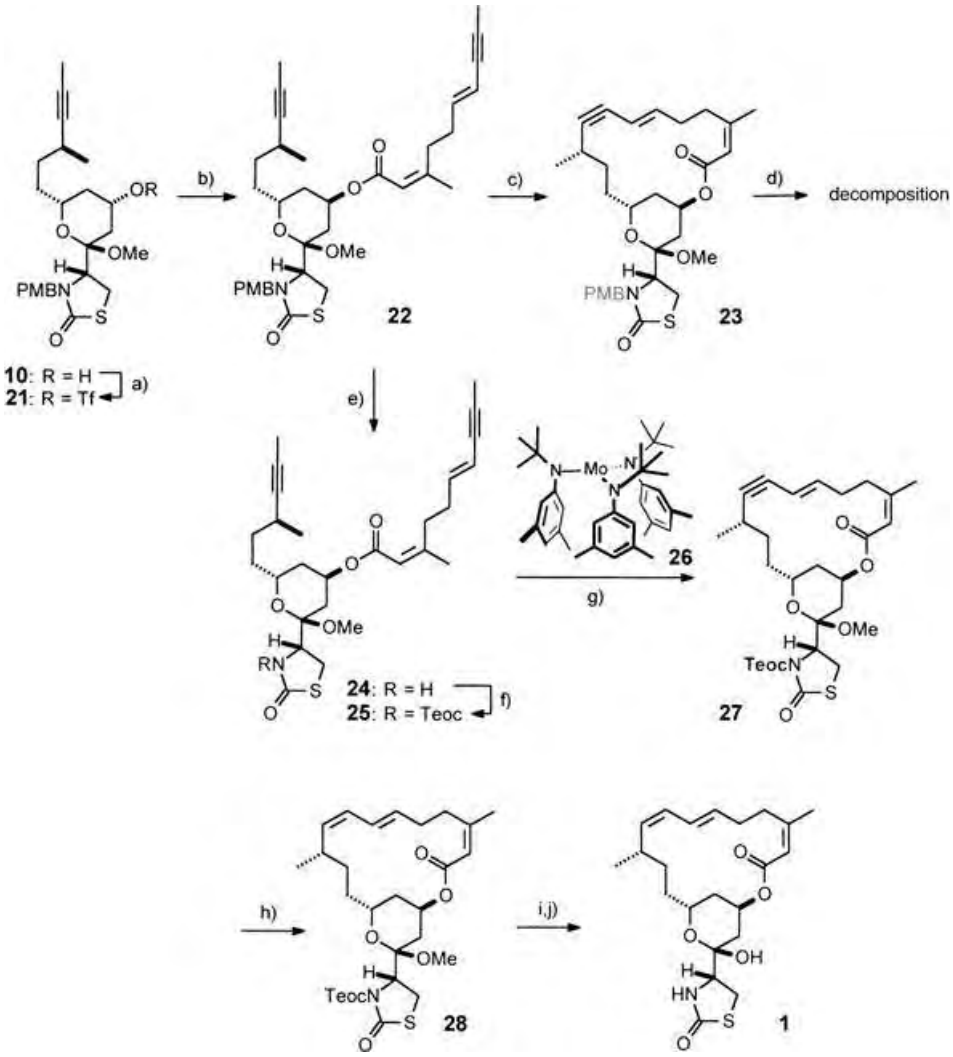

Scheme 5. Ring-closing enyne–yne metathesis and completion of the total synthesis of **1**: a) Tf_2O, pyridine, CH_2Cl_2, −78 °C; b) sodium salt of **20**, 15-crown-5, THF, 74% (over both steps); c) complex **26** (10 mol%), CH_2Cl_2/toluene, 80 °C, 36% (unoptimized); d) CAN, MeCN/H_2O, 0 °C→RT; e) CAN, MeCN/H_2O, 54%; f) $Me_3SiCH_2CH_2OH$, triphosgene, pyridine, CH_2Cl_2, then compound **24**, DMAP/$(iPr)_2NEt$, 81%; g) complex **26** (10 mol%), CH_2Cl_2/toluene, 80 °C, 70%; h) H_2 (1 atm), Lindlar catalyst, quinoline, CH_2Cl_2, 82%; i) TBAF, THF, 62%; j) aq. HOAc, 60 °C, 80%. Teoc = trichloroethoxycarbonyl, CAN = cerium ammonium nitrate, DMAP = 4-dimethylaminopyridine, TBAF = tetra-*n*-butylammonium fluoride.

[7] A. Fürstner, D. De Souza, L. Parra-Rapado, J. T. Jensen, *Angew. Chem.* **2003**, *115*, 5516–5518; *Angew. Chem. Int. Ed.* **2003**, *42*, 5358–5360.

[8] a) A. Fürstner, G. Seidel, *Angew. Chem.* **1998**, *110*, 1758–1760; *Angew. Chem. Int. Ed.* **1998**, *37*, 1734–1736; b) A. Fürstner, O. Guth, A. Rumbo, G. Seidel, *J. Am. Chem. Soc.* **1999**, *121*, 11108–11113.

[9] A. Fürstner, P. W. Davies, *Chem. Commun.*, in press.

[10] In this context, it is worth mentioning that standard alkene metathesis catalysts do not distinguish between alkenes and alkynes, but attack both types of π systems with similar ease. For example, see: a) S. T. Diver, A. J. Giessert, *Chem. Rev.* **2004**, *104*, 1317–1382; b) A. Fürstner, *Angew. Chem.* **2000**, *112*, 3140–3172; *Angew. Chem. Int. Ed.* **2000**, *39*, 3012–3043.

[11] F. Lacombe, K. Radkowski, G. Seidel, A. Fürstner, *Tetrahedron* **2004**, *60*, 7315–7324.

[12] Similar observations were previously reported by Smith et al. in ref. [5], and Kashman and co-workers in: D. Blasberger, S. Carmely, M. Cojocaru, I. Spector, N. R. Shochet, Y. Kashman, *Liebigs Ann. Chem.* **1989**, 1171–1188.

[13] I. Paterson, K.-S. Yeung, J. B. Smaill, *Synlett* **1993**, 774–776.

[14] Enol triflate **12** was previously formed in 61% yield from methyl acetoacetate and $PhN(Tf)_2$ with KHMDS as the base (see ref. [7]). Note that the new protocol that employs NaH and Tf_2O is significantly more productive (82%) and readily scaleable (8 g).

[15] B. Scheiper, M. Bonnekessel, H. Krause, A. Fürstner, *J. Org. Chem.* **2004**, *69*, 3943–3949.

[16] a) A. Fürstner, A. Leitner, M. Méndez, H. Krause, *J. Am. Chem. Soc.* **2002**, *124*, 13856–13863; b) A. Fürstner, A. Leitner, *Angew. Chem.* **2002**, *114*, 632–635; *Angew. Chem. Int. Ed.* **2002**, *41*, 609–612; c) A. Fürstner, A. Leitner, *Angew. Chem.* **2003**, *115*, 320–323; *Angew. Chem. Int. Ed.* **2003**, *42*, 308–311; d) B. Scheiper, F. Glorius, A. Leitner, A. Fürstner, *Proc. Natl. Acad. Sci. USA* **2004**, *101*, 11960–11965; e) R. Martin, A. Fürstner, *Angew. Chem.* **2004**, *116*, 4045–4047; *Angew. Chem. Int. Ed.* **2004**, *43*, 3955–3957; f) A. Fürstner, R. Martin, *Chem. Lett.* **2005**, *34*, 624–628.

[17] A more direct approach to **19** by cross-coupling of enol triflate **12** with bromide **29** was unsuccessful as the latter could not be converted into the corresponding Grignard reagent.

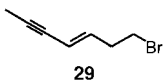

29

[18] a) S. Ohira, *Synth. Commun.* **1989**, *19*, 561 – 564; b) S. Müller, B. Liepold, G. J. Roth, H. J. Bestmann, *Synlett* **1996**, 521 – 522.
[19] J. Schwartz, J. A. Labinger, *Angew. Chem.* **1976**, *88*, 402 – 409; *Angew. Chem. Int. Ed. Engl.* **1976**, *15*, 333 – 340.
[20] More-direct alternatives for the formation of **18**, such as the Takai–Utimoto olefination of aldehyde **15** with $CHI_3/CrCl_2$, furnished an inseparable mixture of the *E* and *Z* isomers, details of which will be reported in a forthcoming full paper.
[21] a) A. Fürstner, G. Seidel, *Tetrahedron* **1995**, *51*, 11165 – 11176; b) for a recent application, see: O. Lepage, E. Kattnig, A. Fürstner, *J. Am. Chem. Soc.* **2004**, *126*, 15970 – 15971.
[22] a) A. Fürstner, C. Mathes, C. W. Lehmann, *J. Am. Chem. Soc.* **1999**, *121*, 9453 – 9454; b) A. Fürstner, C. Mathes, C. W. Lehmann, *Chem. Eur. J.* **2001**, *7*, 5299 – 5317.
[23] Previous applications: a) A. Fürstner, K. Grela, C. Mathes, C. W. Lehmann, *J. Am. Chem. Soc.* **2000**, *122*, 11799 – 11805; b) A. Fürstner, K. Radkowski, J. Grabowski, C. Wirtz, R. Mynott, *J. Org. Chem.* **2000**, *65*, 8758 – 8762; c) A. Fürstner, C. Mathes, K. Grela, *Chem. Commun.* **2001**, 1057 – 1059; d) A. Fürstner, F. Stelzer, A. Rumbo, H. Krause, *Chem. Eur. J.* **2002**, *8*, 1856 – 1871.
[24] Smith et al. reported that they failed to deprotect the *N*-PMB group from the corresponding macrocyclic diene prepared by an entirely different route (see ref. [5]).

Nanostructures

Aminolysis Route to Monodisperse Titania Nanorods with Tunable Aspect Ratio**

*Zhihua Zhang, Xinhua Zhong, Shuhua Liu, Dongfei Li, and Mingyong Han**

Nanocrystalline titanium dioxide (titania) has been investigated extensively, as it plays a prominent role in fundamental studies and has both potential and demonstrated applications in solar energy conversion,[1] photocatalysis,[2] photochromic devices,[3] and gas sensing.[4,5] Among the three natural crystalline forms of titanium dioxide (anatase, brookite, and rutile), rutile is the most stable phase, whereas anatase has superior optoelectronic and photochemical properties.[6] There have been a number of recent reports on the preparation of nanoscaled anatase titania in the form of nanoparticles, nanorods, nanowires, and nanotubes for significantly increasing its specific surface area and delocalization of carriers, which may enhance the performance of this material in highly efficient sensors, photocatalysts, and photovoltaic cells as compared with planar solids or powders.[5,7] To realize these promising high-performance applications, the various nanosized titanias and their derivatives must also fulfill a wide variety of requirements in terms of particle size, size distribution, shape and morphology, crystallinity, and phase purity. The current challenge is to control and tailor all these parameters and properties simultaneously in one synthetic approach or process.

Among the various synthetic routes developed in the last decades, the most general and versatile solution-phase synthetic strategy is based on the hydrolysis and condensation of titanium alkoxides to create nanosized titania with diameters that range from a few tens to several hundreds of nanometers.[8] Owing to extreme moisture or water sensitivity, in most cases, the very fast hydrolytic process at low temperature yields amorphous products with polydisperse size and mixed phases, and subsequent hydrothermal processing or calcination is necessary to induce crystallization. The high reactivity of tetrafunctional titanium alkoxides $Ti(OR)_4$ can be chemically modified by using carboxylic acids such as oleic acid as chelating ligands to decrease the number of TiOR groups available for violent hydrolysis by ligand substitution/exchange.[9] Chemical modification can decrease precursor reactivity and yield more controllable hydrolysis and condensation processes under mild reflux. Volatile water is maintained in a closed system at an elevated temperature of 80–100 °C, and long aging times of 6–12 h or more are required to promote further hydrolysis and improve crystallization of the final nanoproducts. Until now, an alternative high-temperature nonhydrolytic strategy was still preferred to make highly crystalline nanoparticles[10] because the amorphous form is usually inactive in various light-responsive properties such as photocatalysis.[11] The main conventional nonhydrolytic routes reported involve the elimination reaction between titanium tetrachloride and oxygen-donor molecules such as titanium alkoxides and organic ethers which yield environmentally unfavorable, volatile alkyl chlorides or hydrogen chloride. The fast formation of nanosized titania may also limit systematic morphological control in the presence of organic surfactants. Therefore, it is useful to explore and design new preparative reactions to avoid the existing specific problems encountered in conventional hydrolytic or nonhydrolytic routes.

Herein we present a novel high-temperature, nonhydrolytic synthetic approach to anatase titania nanocrystals. It was developed on the basis of a well-known ester aminolysis reaction that involves the nucleophilic attack of an amine group on the carbonyl carbon atom of titanium carboxylate derivatives[12] and the chemical modification of reactive molecular precursors with OLA as the chelating ligand. The high-temperature aminolysis of titanium carboxylate (titanium oleate) complexes can be well-controlled by using high-boiling long-chain oleylamine rather than volatile water. In addition to the preparation of size-tunable anatase TiO_2 nanodots, the "greener" aminolysis route can also provide much better control of the anisotropic growth and can be used

[*] Dr. X. H. Zhong, Dr. D. F. Li, Prof. Dr. M. Y. Han
Institute of Materials Research and Engineering
3 Research Link, Singapore 117602 (Singapore)
Fax: (+65) 6872-0785
E-mail: my-han@imre.a-star.edu.sg
biehanmy@nus.edu.sg
Dr. Z. H. Zhang, Dr. S. H. Liu, Prof. Dr. M. Y. Han
Department of Materials Science
National University of Singapore
Lower Kent Ridge Road, Singapore 119260 (Singapore)

[**] This work was supported by National University of Singapore and Institute of Materials Research & Engineering.

Supporting information for this article is available on the WWW under http://www.angewandte.org or from the author.

  DOI: 10.1002/anie.200500410

to readily prepare monodisperse anatase TiO_2 nanorods with tunable length and diameter. An added benefit is that anatase TiO_2 nanorods can also be used as ideal host matrices for the preparation of transparent dilute magnetic oxides that have promising applications such as magneto-optical devices.[13]

A mixture of titanium isopropoxide (TIP; 1 mmol) and oleic acid (OLA; 5 mmol) was used to generate OLA complexes of titanium at 80 °C in 1-octadecene (ODE; 6 mL), followed by the injection of a predetermined amount of oleylamine (OA; 1–10 mmol) at 260 °C to give various nanosized TiO_2 preparations. TiO_2 nanorods were characterized by TEM (Figure 1 a–c); their length depends on the amount of OA used. When the OA content was increased from 1 to 2 to 3 mmol, monodisperse TiO_2 nanorods with lengths of 12, 30, and 16 nm were obtained, respectively, all with a diameter of about 2 nm. The use of OA at 4 mmol in the presence of the unchanged molar ratio of TIP (1 mmol) and OLA (5 mmol), spherical TiO_2 nanoparticles of $\approx$2.3 nm in diameter were obtained (Figure 1 d). Large excesses of OA only generate white titania precipitate. The high-resolution TEM image of a single nanorod (16 nm) shows the single-crystalline structure (Figure 1 c, inset). The lattice spacing of 0.35 nm corresponds to the *d* spacing between adjacent (101) crystallographic planes of anatase TiO_2 nanorods. The as-synthesized anatase nanorods were elongated along the [001] direction; the long axis of the nanorods is parallel to the [001] direction. These surface-capped nanorods can be well-spaced on the copper grid, and some of them are self-assembled with identical distance between them, as shown in Figure 1 a–c. The XRD patterns show a pure anatase phase without other titanium oxide polymorphs (Figure 2). The (004) diffraction peak becomes much stronger and sharper with an increase in length of the nanorods, whereas other peaks remain similar in shape and intensity. The strong peak intensity and narrow width of the ⟨004⟩ reflection and relatively lower intensity and broader width for the other reflections indicate preferred anisotropic growth along the *c* axis of the anatase lattice.

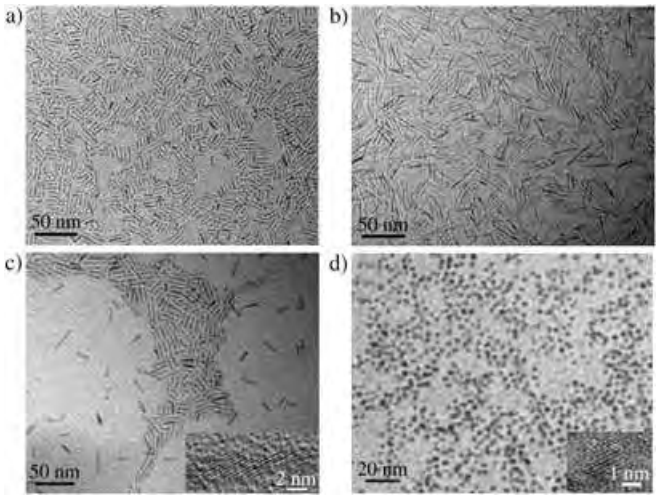

Figure 1. TEM images of length-tunable TiO_2 nanorods with lengths of a) 12, b) 30, and c) 16 nm, prepared at 260 °C with 1, 2, and 3 mmol of OA, respectively; the molar ratio of TIP (1 mmol) and OLA (5 mmol) was kept unchanged. d) TEM image of TiO_2 nanodots of 2.3 nm obtained at 260 °C with 4 mmol OA; the molar ratio of TIP and OLA was kept as described for parts a)–c). Inset in part c): HR-TEM image of a single titania nanorod (16 nm).

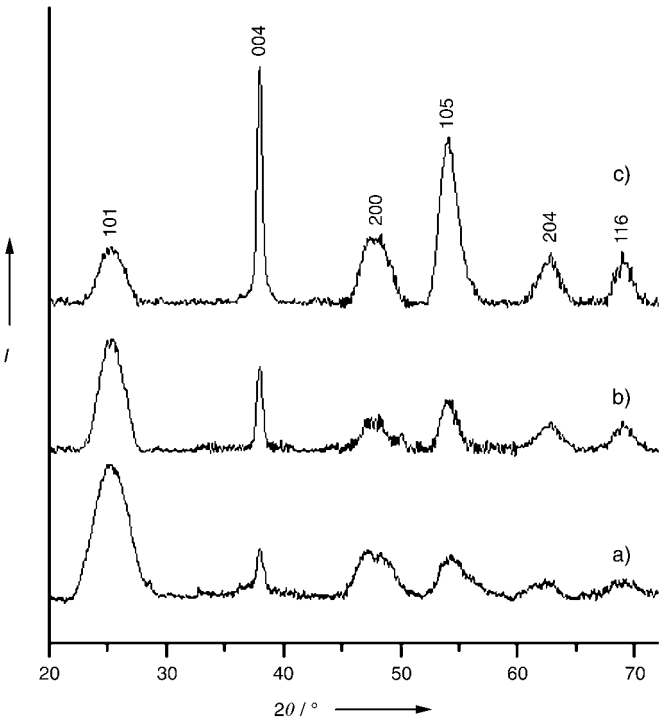

Figure 2. Powder XRD patterns of TiO_2 samples: a) spherical particles of diameter 2.3 nm (molar ratio TIP/OLA/OA = 1:5:4); b) 16-nm nanorods (molar ratio TIP/OLA/OA = 1:5:3); c) 30-nm nanorods (molar ratio TIP/OLA/OA = 1:5:2).

To elucidate the mechanism of titania nanorod formation, we investigated the respective roles of OA and OLA in the noncoordinating ODE system under the optimized conditions for preparing 30-nm titania nanorods with a TIP/OLA/OA molar ratio of 1:5:2. Interestingly, when either OLA or OA is used alone, TiO_2 cannot be obtained even at 260 °C. This observation indicates a synergistic effect of OA and OLA in generating titania nanorods. As reported in the literature, TIP ($Ti(OiPr)_4$) can readily react with OLA ($C_{17}H_{33}COOH$) to generate yellow OLA–titanium complexes $(C_{17}H_{33}COO)_xTi(OiPr)_{4-x}$ at 80 °C in which one or more isopropoxide groups is replaced with an oleate ligand with concomitant release of isopropyl alcohol.[9,14] Although heating the resulting titanium carboxylates at 260 °C does not produce TiO_2, the subsequent injection of a predetermined amount of OA ($C_{18}H_{35}NH_2$) can "decompose" it to form monodisperse anatase titania nanorods. We note that similar reaction systems were also used for the preparation of metal oxide or chalcogenide nanoparticles such as Fe_2O_3, Fe_3O_4, $MnFe_2O_4$, $CoFe_2O_4$, and ZnSe with fatty acid as a stabilization/coordination reagent, and primary amine as an efficient activation reagent to accelerate the formation of nanoparticles.[15]

The mechanism of formation of nanosized TiO_2 was further studied systematically by FTIR spectroscopy. Figures 3 a and b show the FTIR spectra of pure OLA and the mixture of TIP (1 mmol) and OLA (2 mmol) after 20 min at

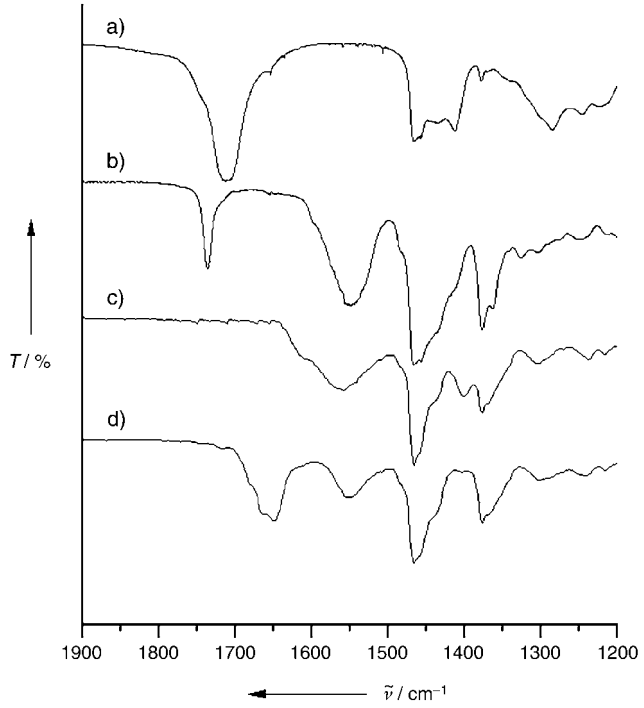

Figure 3. FTIR spectra of a) OLA; b) a mixture of OLA and TIP after treatment at 80 °C; c) the same mixture after washing with acetone and hexane; d) the mixture after further aminolysis to generate nanosized TiO_2.

80 °C. A characteristic C=O stretching band of OLA appears at 1710 cm^{-1} in Figure 3a. The disappearance of the free C=O stretching band at 1710 cm^{-1} in Figure 3b shows that OLA reacts completely with TIP (or excludes the presence of unionized OLA). The resulting oleate anion ($C_{17}H_{33}COO^-$) is expected to show asymmetric and symmetric COO^- stretching bands at $\approx$1565 and $\approx$1434 cm^{-1}, respectively, as were observed in titanium acetate.[16–18] The latter is normally more difficult to locate as a result of its overlap with C–H bending vibrations at 1467, 1450, and 1375 cm^{-1} (attributed to symmetric CH_2, asymmetric CH_3, and symmetric CH_3 in oleate (or OLA), respectively).[16] In our case, the new strong band at $\approx$1555 cm^{-1}, attributed to the asymmetric stretching vibration of carboxylate anions, indicates the coordination of OLA to titanium centers to form titanium oleate complexes by ligand exchange/substitution.[16]

The characteristic C=O stretching vibration of isopropyl oleate at 1736 cm^{-1} in Figure 3b is clearly distinguished from that of titanium oleate complexes. The by-product, isopropyl oleate, was generated either by nonhydrolytic elimination/condensation of unstable carboxylatotitanium alkoxide $(C_{17}H_{33}COO)_xTi(OiPr)_{4-x}$, which can remove some of the oleate and isopropoxide ligands together, or a slow esterification reaction between the reactant OLA and the released isopropyl alcohol. Figure 3c shows the FTIR spectrum of the reaction mixture of OLA with TIP after washing with hexane/acetone (1:1) to remove isopropyl oleate for further reaction. As a result, only the asymmetric COO^- stretching frequency at $\approx$1560 cm^{-1} appeared after the complete removal of isopropyl oleate from the reaction system. Further reaction was carried out at 260 °C for 20 min after the injection of 2 mmol of OA into the reaction mixture. In comparison with Figure 3c, the new stretching vibrations at 1651 and 1550 cm^{-1} in Figure 3d are attributed to different carbonyl stretches in single-substituted amide, which is discussed further below. Almost the same evidence was also obtained when acetic acid was used to replace OLA to prepare titania particles (Supporting Information). The above results indicate that the carbonyl groups of titanium carboxylate precursors can undergo nucleophilic attack by OA to form amides, as opposed to water, which attacks the highly electron-deficient/electrophilic Ti^{IV} center and thus hydrolyzes titanium alkoxides. This process is similar to the conventional aminolysis reaction of organic esters.[12] The conventional aminolysis mechanism of esters may resemble an S_N2 reaction with a tetrahedral transition state or intermediate, which requires a nucleophile ($R'NH_2$) to collide with the electropositive carbonyl carbon in the ester to form an organic amide ($RC(O)NHR'$). In our case, the resulting tetrafunctional titanium carboxylate (titanium oleate) complexes $(C_{17}H_{33}COO)_xTi(OiPr)_{4-x}$ were aminolyzed by OA to form unstable hydroxyalkoxides $(C_{17}H_{33}COO)_{x-1}Ti(OH)(OiPr)_{4-x}$ via a tetrahedral transition state through nucleophilic attack by OA on the carbonyl carbon atom of titanium oleate complexes (Scheme 1). Consequently, the subsequent polycondensation reaction of the resulting hydroxylated titanium precursors produces extensive Ti–O–Ti networks covalently capped with carboxylates.[19]

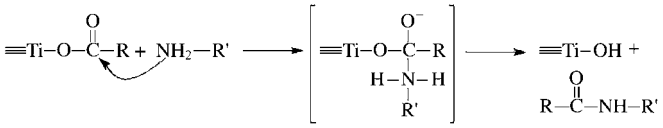

Scheme 1. Aminolysis reaction between titanium carboxylate complexes and primary amine.

During the growth of TiO_2 nanocrystals, as (001) planes have higher surface energy or are more chemically reactive than others,[20] carboxylate groups coordinated to (001) faces could be more easily aminolyzed under the attack of OA and form or extend the Ti–O–Ti network along the [001] direction. Less reactive titanium carboxylate precursors are also helpful in maintaining high monomer concentrations in the reaction solution for elongated growth of titania nanocrystals, as has been suggested.[21] Various amounts of OLA were used to optimize the preparation conditions of titania nanorods, and more than 4 mmol of OLA was necessary to prepare soluble TiO_2 nanocrystals in the noncoordinating ODE system. It was also observed that upon increasing the amount of OA from 1 to 2 mmol, the length of the resulting monodisperse titania nanorods increased from 12 to 30 nm. However, with the further increase of OA content to 3 mmol, nanorod length was decreased to 16 nm, which indicates suppression of anisotropic growth at higher OA contents. Finally, only spherical nanoparticles were formed when 4 mmol of OA was used, and aggregated particles were produced when $\gg$5 mmol of OA was used; this indicates the

decreased stabilization that results from the consumption of surface-coordinated oleate ligands on particle surfaces. Moreover, the increased OA content can accelerate the aminolysis reaction to form nanoparticles.

Although monodisperse TiO_2 nanocrystals with a tunable aspect ratio ranging from 1 to 13 (nanodots to nanorods) have been prepared, the resulting length-tunable TiO_2 nanocrystals have only a very small diameter of $\approx$2.0 nm, a result of the tight binding of OLA on the titania surface, which restrains its growth.[9,10c] To prepare diameter-tunable TiO_2 nanorods, a weaker capping agent, cetyltrimethylammonium bromide (CTAB), was used to decrease/balance the strong binding affinity of OLA on the anatase surface. With 1 mmol of TIP, 1 mmol of OA, and 5 mmol of OLA, only very narrow TiO_2 nanorods of diameter $\approx$2.0 nm were obtained (Figure 1a). By introducing larger amounts of CTAB and maintaining a similar TIP/OA/OLA molar ratio, larger, diameter-tunable TiO_2 nanorods of 2.9, 3.8, and 4.6 nm (Figure 4a–c) were produced under optimized conditions. From the above results, it is now known that higher OA content is required to prepare TiO_2 nanodots (Figure 1d). Hence, to prepare larger TiO_2 nanodots, an larger amount of CTAB and a smaller amount of OLA were used to balance the stabilization of nanoparticles while retaining the TIP/OA molar ratio of 1:3. Thus, size-tunable TiO_2 nanodots of 2.3, 3.0, 4.2, and 6.0 nm were prepared under various reaction conditions (Figure 1d and Figure 4c–d). In comparison with bulk anatase titania (3.2 eV), a blue-shift of the absorption onset of anatase titania nanodots was observed. The blue-shift increased with decreasing size of the particles, which exhibit size-dependent optical properties (Supporting Information).

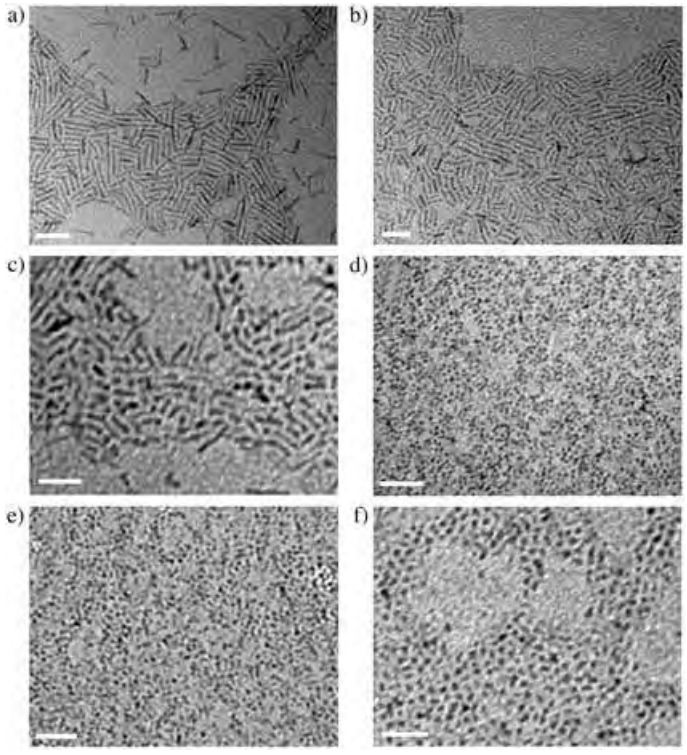

Figure 4. TEM images of diameter-tunable TiO_2 nanorods of length a) 2.9, b) 3.8, and c) 4.6 nm and size-tunable TiO_2 nanodots of size d) 3.0, e) 4.2, and f) 6.0 nm, prepared at different TIP/OA/OLA/CTAB molar ratios and temperatures (1 mmol of TIP was used for all the preparations): a) 1:1:5:3, 260°C; b) 1:1:5:6, 260°C; c) 1:1:4:6, 280°C; d) 1:3:5:3, 260°C; e) 1:3:4:5, 260°C; f) 1:3:3:5, 300°C. Scale bar: 50 nm.

In conclusion, a high-temperature nonhydrolytic aminolysis approach has been developed, and its capability to produce highly crystalline, monodisperse anatase nanocrystals with controlled size and shape in a reasonable size range was demonstrated. By combining the advantage of chemical modification of reactive titanium isopropoxide by oleic acid, the high-temperature aminolysis reaction of titanium oleate complexes with decreased reactivity can be controlled very well for the anisotropic growth of titania nanorods with high-boiling-point oleylamine rather than volatile water. Weaker CTAB ligands were further used to balance the strong binding affinity of OLA ligands for producing larger titania nanodots and thicker titania nanorods. The aminolysis route is much greener because, unlike conventional nonhydrolytic routes, it does not form environmentally unfavorable, volatile alkyl chlorides or hydrogen chloride. In addition to the preparation of size-tunable anatase titania nanodots ranging from 2.3 to 6.0 nm, the "greener" aminolysis route can also provide much better control of anisotropic growth and allows ready preparation of monodisperse titania nanorods with tunable lengths and diameters that range between 2.3–30 nm and 2.0–4.6 nm, respectively. Meanwhile, our synthetic method has been extended further for the preparation of various oxide nanocrystals (e.g., ZrO_2) from different carboxylate precursors.

Experimental Section

Titanium isopropoxide (98%, Acros), oleic acid (90%, Aldrich), oleylamine (70%, Aldrich), octylamine (99%, Aldrich), 1-octadecene (90%, Aldrich), cetyltrimethylammonium bromide (99%, Acros), hexane (99%, Tedia), and acetone (HPLC grade, Tedia) were used as received. All experiments were carried out by standard oxygen-free techniques under nitrogen flow.

In a typical preparation of length-tunable TiO_2 nanorods with a diameter of $\approx$2.0 nm, OLA (1.6 mL, 5 mmol) in 1-ODE (6 mL) was dried and degassed at 80°C in a 50-mL three-neck flask for 1 h. Then TIP (0.3 mL, 1 mmol) was injected into the mixed solution and heated for 20 min. The solution gradually turned from colorless to a pale yellow, indicating the formation of titanium carboxylate complexes. Gaseous isopropyl alcohol was rapidly released while the mixture was heated at 260°C for 10 min. The aminolysis reaction was then initiated by rapid injection of a predetermined amount of OA ranging from 1 to 4 mmol (0.32–1.28 mL) with vigorous stirring. After 1 h, the resulting solution was allowed to cool to room temperature. The resulting crude solution of TiO_2 nanorods was diluted with hexane (10 mL) followed by precipitation with acetone (20 mL). The crude product was recovered by centrifugation, dispersed in hexane (20 mL), and subjected to a second round of purification. The white powders obtained can be redispersed easily in nonpolar solvents such as hexane, toluene, and chloroform for further characterization. For the preparation of diameter-tunable TiO_2 nanorods and size-tunable TiO_2 nanodots, a certain amount of CTAB was mixed with OLA in 1-ODE, and the mixture was dried and degassed for 1 h. Then TIP (0.3 mL, 1 mmol) was injected into the mixed solution, which was heated for 20 min. The remaining procedure is identical to that described above, but with different experimental parameters as

appropriate. TIP (0.3 mL, 1 mmol) was used for all the above preparations.

Powder XRD was performed with a Siemens D5005 X-ray powder diffractometer. XRD samples were prepared by dropping the a TiO_2 nanocrystal solution onto a silicon (100) wafer and drying at room temperature. TEM and HR TEM images were obtained with a JEOL 1010 and a Philips 3010 operating at accelerating voltages of 100 and 300 kV, respectively. TEM samples were prepared by placing a drop of a nanorod solution in hexane onto Formvar carbon-coated copper grids and drying in a desiccator. FTIR spectra were recorded with a FTS 165 Bio-Rad FTIR spectrophotometer in the range of 4000–400 cm^{-1} with KBr plates.

Received: February 3, 2005
Published online: April 25, 2005

Keywords: high-temperature chemistry · nanostructures · nonhydrolytic synthesis · titania · titanium

[1] a) B. O'Regan, M. Gratzel, *Nature* **1991**, *353*, 737; b) P. Wang, S. M. Zakeeruddin, R. Humphry-Baker, J. E. Moser, M. Gratzel, *Adv. Mater.* **2003**, *15*, 2010; c) S. Nakade, M. Matsuda, S. Kambe, Y. Saito, T. Kitamura, T. Sakata, Y. Wada, H. Mori, S. Yanagida, *J. Phys. Chem. B* **2002**, *106*, 10004.

[2] a) M. R. Hoffmann, S. T. Martin, W. Choi, D. W. Bahnemann, *Chem. Rev.* **1995**, *95*, 69; b) L. Gao, Q. H. Zhang, *Scr. Mater.* **2001**, *44*, 1195; c) S. Y. Chae, M. K. Park, S. K. Lee, T. Y. Kim, S. K. Kim, W. I. Lee, *Chem. Mater.* **2003**, *15*, 3326.

[3] a) K. Naoi, Y. Ohko, T. Tatsuma, *J. Am. Chem. Soc.* **2003**, *125*, 3664; b) Y. Ohko, T. Tatsuma, T. Fujii, K. Naoi, C. Niwa, Y. Kubota, A. Fujishima, *Nat. Mater.* **2003**, *2*, 29.

[4] Y. Zhu, J. Shi, Z. Zhang, C. Zhang, X. Zhang, *Anal. Chem.* **2002**, *74*, 120.

[5] N. Wu, S. Wang, I. A. Rusakova, *Science* **1999**, *285*, 1375.

[6] U. Diebold, *Surf. Sci. Rep.* **2003**, *48*, 53.

[7] a) M. Adachi, Y. Murate, S. Yoshikawa, *Chem. Lett.* **2000**, *8*, 942; b) S. Uchida, R. Chiba, M. Tomiha, N. Masaki, M. Shirai, *Electrochemistry* **2002**, *70*, 418; c) J. A. Byrne, B. R. Eggins, *J. Electroanal. Chem.* **1998**, *457*, 61; d) J. E. G. Wijinhoven, W. L. Vos, *Science* **1998**, *281*, 802.

[8] a) Y. J. Liu, R. O. Claus, *J. Am. Chem. Soc.* **1997**, *119*, 5273; b) M. M. Wu, J. B. Long, A. H. Huang, Y. J. Luo, S. H. Feng, R. R. Xu, *Langmuir* **1999**, *15*, 8822.

[9] P. D. Cozzoli, A. Kornowski, H. Weller, *J. Am. Chem. Soc.* **2003**, *125*, 14539.

[10] a) T. J. Trentler, T. E. Denler, J. F. Bertone, A. Agrawal, V. L. Colvin, *J. Am. Chem. Soc.* **1999**, *121*, 1613; b) J. N. Hay, H. M. Raval, *Chem. Mater.* **2001**, *13*, 3396; c) Y. W. Jun, M. F. Casula, J. H. Sim, S. Y. Kim, J. Cheon, A. P. Alivisatos, *J. Am. Chem. Soc.* **2003**, *125*, 15981.

[11] B. Ohtani, Y. Ogawa, S. Nishimoto, *J. Phys. Chem. B* **1997**, *101*, 3746.

[12] a) H. Adalsteinsson, T. C. Bruice, *J. Am. Chem. Soc.* **1998**, *120*, 3440; b) T. C. Bruice, S. J. Benkovic, *Bioorganic Mechanisms*, W. A. Benjamin, New York, **1966**; c) A. Williams, *Acc. Chem. Res.* **1989**, *22*, 387.

[13] Y. Matsumoto, M. Murakami, T. Shono, T. Hasegawa, T. Fukumura, M. Kawasaki, P. Ahmet, T. Chikyow, S. Koshihara, H. Koinuma, *Science* **2001**, *291*, 854.

[14] T. J. Boyle, R. P. Tyner, T. M. Alam, B. L. Scott, J. W. Ziller, B. G. Potter, *J. Am. Chem. Soc.* **1999**, *121*, 12104.

[15] a) T. Hyeon, S. S. Lee, J. Park, Y. Chung, H. B. Na, *J. Am. Chem. Soc.* **2001**, *123*, 12798; b) S. H. Sun, H. Zeng, *J. Am. Chem. Soc.* **2002**, *124*, 8204; c) S. H. Sun, H. Zeng, D. B. Robinson, S. Raoux, P. M. Rice, S. X. Wang, G. X. Li, *J. Am. Chem. Soc.* **2004**, *126*, 273; d) H. Zeng, P. M. Rice, S. X. Wang, S. H. Sun, *J. Am. Chem. Soc.* **2004**, *126*, 11458; e) N. R. Jana, Y. F. Chen, X. G. Peng, *Chem. Mater.* **2004**, *16*, 3931; f) J. Park, K. An, Y. Hwang, J. G. Park, H. J. Noh, J. Y. Kim, J. H. Park, N. M. Hwang, T. Hyeon, *Nat. Mater.* **2004**, *3*, 891; g) L. S. Li, N. Pradhan, Y. J. Wang, X. G. Peng, *Nano Lett.* **2004**, *4*, 2261.

[16] L. J. Bellamy, *The Infrared Spectra of Complex Molecules*, Chapman and Hall, London, **1975**.

[17] S. Doeuff, M. Henry, C. Sanchez, J. Livage, *J. Non-Cryst. Solids* **1987**, *89*, 206.

[18] P. J. Thistlethwaite, M. S. Hook, *Langmuir* **2000**, *16*, 4993.

[19] Y. Murakami, T. Matsumoto, Y. Takasu, *J. Phys. Chem. B* **1999**, 103, 1836.

[20] R. L. Penn, J. F. Banfield, *Geochim. Cosmochim. Acta* **1999**, *63*, 1549.

[21] X. G. Peng, *Adv. Mater.* **2003**, *15*, 459.

Asymmetric Catalysis

Non-C_2-Symmetric, Chirally Economical, and Readily Tunable Linked-binols: Design and Application in a Direct Catalytic Asymmetric Mannich-Type Reaction**

Takamasa Yoshida, Hiroyuki Morimoto, Naoya Kumagai, Shigeki Matsunaga, and Masakatsu Shibasaki**

Asymmetric catalysis employing chiral metal complexes is one of the most general and flexible methods in asymmetric synthesis.[1] In the development of asymmetric metal catalysts for highly enantioselective and reactive reactions, the design of chiral ligands for the metal center is of key importance: the activity and selectivity of the metal centers can be tuned by chiral ligands. A delicate balance between the steric and electronic properties of the catalyst determines the reaction efficiency. Thus, a chiral ligand with a readily tuneable framework is desirable.[2]

We recently reported the preparation of a series of chiral ligands termed "linked-binols" (**1a**–**c**; Scheme 1).[3,4] These linked-binols consist of two chiral 1,1′-bi-2-naphthol units connected at the 3 and 3″-positions by a flexible linker containing one heteroatom. Linked-binols often provide a better chiral environment than 1,1′-bi-2-naphthol (**2**;

[*] T. Yoshida, H. Morimoto, N. Kumagai, Dr. S. Matsunaga, Prof. Dr. M. Shibasaki
Graduate School of Pharmaceutical Sciences
The University of Tokyo
Hongo, Bunkyo-ku, Tokyo 113-0033 (Japan)
Fax: (+81) 3-5684-5206
E-mail: smatsuna@mol.f.u-tokyo.ac.jp
mshibasa@mol.f.u-tokyo.ac.jp

[**] This work was supported by a Grant-in-Aid for Specially Promoted Research and a Grant-in-Aid for Encouragements for Young Scientists (B) (for S.M.) from JSPS and MEXT.

Supporting information for this article is available on the WWW under http://www.angewandte.org or from the author.

  DOI: 10.1002/anie.200500425

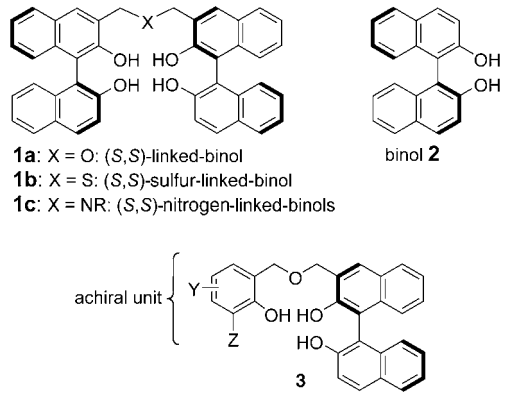

Scheme 1. Structures of (*S*,*S*)-linked-binols **1a–c**, 1,1′-bi-2-naphthol **2**, and new ligands **3**.

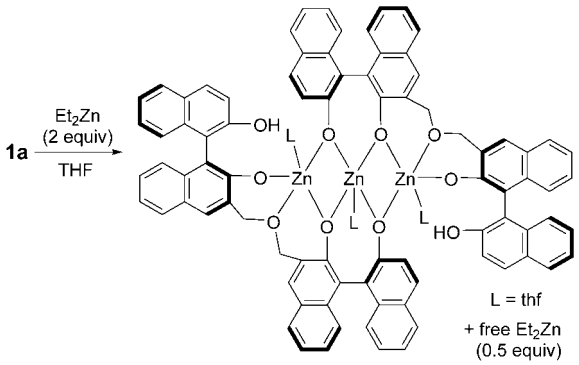

Scheme 2. Structure of a Zn/**1a** (3:2) complex.

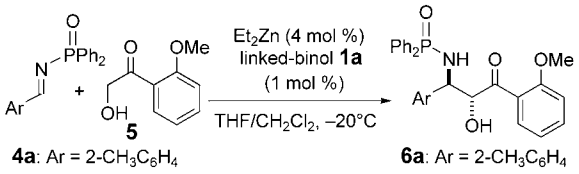

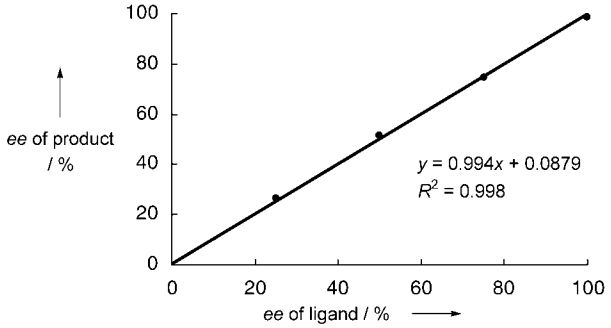

Figure 1. Linear relationship between Mannich-adduct **6a** and (*S*,*S*)-linked-binol **1a** observed in a direct Mannich-type reaction of **4a** with **5**.

Scheme 1), as was demonstrated in various catalytic asymmetric reactions, such as epoxide openings,[3a] a direct aldol reaction,[5] Michael reactions,[6,7] and direct Mannich-type reactions.[8] Although they are conformationally rigid, two chiral binaphthyl units seem essential to provide an efficient chiral environment for high enantioselectivity; however, they also impose severe limitations on ligand design. So far, the properties of linked-binol complexes could only be tuned by changing the heteroatom of the linker (**1a–c**).[3] Electronic and steric modifications of the binaphthyl moiety is tedious and lengthy because of the presence of two chiral units. Thus, improving the performance of ligands with the original linked-binol framework in catalytic reactions is a formidable challenge. For example, many steps are required when modifying the electronic properties by preparing 6,6′,6″,6‴-tetrasubstituted C_2-symmetric linked-binols. A simple, more flexible strategy is required to overcome this intrinsic dilemma and tune the properties of linked-binols. Herein, we report a readily tuneable, non-C_2-symmetric linked-binol **3** with only one chiral 1,1′-bi-2-naphthol unit and one flexible achiral unit (Scheme 1).[9] On the basis of our mechanistic studies on the Et_2Zn/linked-binol **1a** catalytic system, new ligands were designed and evaluated in direct catalytic asymmetric Mannich-type reactions. The introduction of an achiral unit was not only economical in terms of chirality[10] but also afforded comparable enantioselectivity and a much higher reaction rate than the original linked-binol **1a** with two chiral 1,1′-bi-2-naphthol units.

For the design and evaluation of the new linked-binols, a Et_2Zn/**1a** complex was used for reference because its structure and reactivity had been previously studied. The structure of the Zn/**1a** (3:2) precatalyst, prepared from Et_2Zn/**1a** (2:1; Scheme 2), was determined by X-ray crystallographic, NMR spectroscopic, and ESI mass-spectrometric analysis.[11] In the Zn/**1a** (3:2) complex, neither of the linked-binol units had a C_2-symmetric environment and one of the phenolic OH groups remained unchanged, even in the presence of a slight excess of Et_2Zn. On the other hand, there was a linear relationship between the enantiomeric excess of product **6a** and that of the chiral ligand **1a** used in the Mannich-type reaction of diphenylphosphanoylimine (**4a**) and hydroxyketone **5** (Figure 1).[12] The structure of the Zn/**1a** (3:2) complex (Scheme 2) and the results shown in Figure 1 suggested that 1) C_2 symmetry in linked-binol **1a** is not important, 2) one phenolic OH group is not required, and 3) a homochiral complex is more favorable than a heterochiral complex. We hypothesized that one of the chiral binaphthol units could be replaced with an achiral unit, such as an atropisomeric biphenol or an achiral phenol derivative. Chirality should be then transferred to the flexible achiral unit on complexation with a zinc center, and a similar chiral environment should be obtained with a ligand that was economical in terms of chirality.

The structures of ligands **3a–k** are shown in Scheme 3.[13] The catalytic potential of these ligands was evaluated in a direct asymmetric Mannich-type reaction of imine **4a** and hydroxyketone **5** using 5 mol% of ligand **3** and 20 mol% of Et_2Zn at −20°C in THF/CH_2Cl_2 ([imine] = 150 mM, [**3**] = 7.5 mM). When the original ligand **1a** was used, the reaction was completed within 1 h and the Mannich adduct **6a** was obtained in 99% yield with *anti*/*syn* selectivity of 98:2 in >99% *ee* (Table 1, entry 1). A control experiment with 10 mol% of binol **2** had a much lower reaction rate and

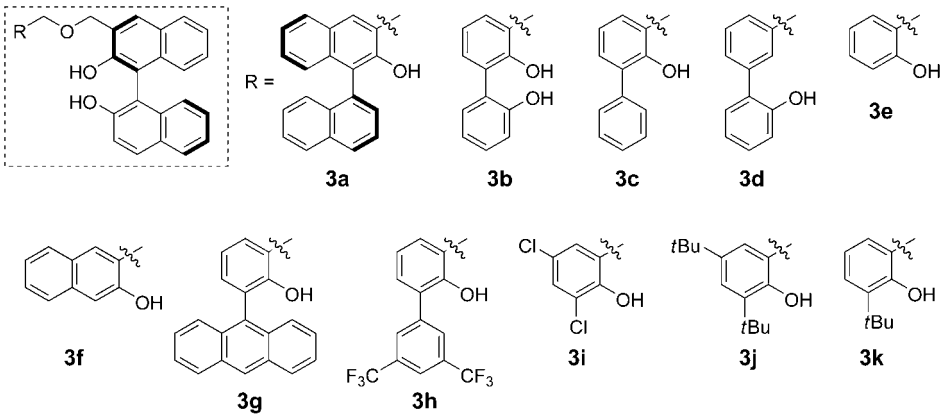

Scheme 3. Structures of non-C_2-symmetric (*S*)-linked-binol derivatives **3a–k** containing one achiral unit and one chiral binaphthol unit.

Table 1: Catalytic asymmetric Mannich-type reaction using various chiral ligands (**1a**, **2**, and **3a–k**).

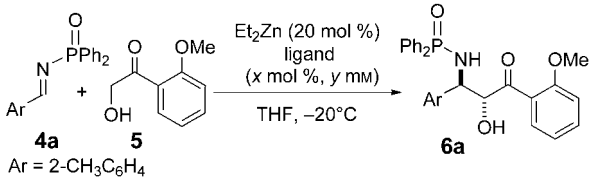

Entry	Ligand (mol%)	[Ligand] [mM]	*t* [h]	Yield [%]	*anti*/*syn*	*ee* [%]
1	**1a** (5)	7.5	1	99	97:3	>99
2	**2** (10)	15	68	85	87:13	24
3	**3a** (5)	7.5	1	99	94:6	99
4	**3b** (5)	7.5	1	98	98:2	98
5	**3c** (5)	7.5	1	99	97:3	99
6	**3d** (5)	7.5	23	74	91:9	9
7	**3e** (5)	7.5	11	92	95:5	90
8	**3f** (5)	7.5	5	93	95:5	87
9	**3g** (5)	7.5	1	98	96:4	99
10	**3h** (5)	7.5	1	95	98:2	98
11	**3i** (5)	7.5	1	94	98:2	98
12	**3j** (5)	7.5	1	96	98:2	98
13	**3k** (5)	7.5	1	95	98:2	98

ee value (68 h, 24% *ee*; entry 2). Ligand **3a**, which lacks one phenolic OH group, gave results similar to those obtained with **1a** (entry 3). Ligand **3b** with an atropisomeric biphenol unit was also efficient (entry 4), thus suggesting that the chirality of the biphenol unit was controlled by complexation with the zinc center.[14] Even an achiral unit, such as **3c**, gave excellent results (1 h, 99% yield, 99% *ee*; entry 5), whereas ligand **3d**, which has a phenolic OH group in the 2′-position, had a low reaction rate and poor enantioselectivity (23 h, 74% yield, 9% *ee*; entry 6). Ligands **3e** and **3f** also produced unsatisfactory yields and modest enantioselectivities (entries 7 and 8). The results shown in entries 5–8 imply that both the phenolic OH group at the proper position and a substituent on the aromatic ring are required. To evaluate the effects of substituents on the phenol ring, ligands **3g–k** were used, and all of them showed a high reactivity and enantioselectivity (entries 9–15). The achiral units in ligands **3i–k** were readily accessible from commercially available salicylic aldehyde derivatives.[15]

Although many ligands in Scheme 3 gave high enantioselectivities (Table 1), it was difficult to compare their performance precisely in terms of reaction rate. Generally, catalyst concentration becomes rather low when catalyst loading is reduced to <0.1 mol% because of substrate-solubility limitations. Thus, high turnover frequencies (TOF) and turnover numbers (TON) under dilute conditions are required to lower the catalyst loading. To evaluate the ligands quantitatively, the reaction for each ligand was monitored under dilute conditions ([imine] = 31 mM, [**3**] = 0.31 mM, 1 mol%; Table 2 and Figure 2). The initial rate of the reaction with each ligand (**1a**, **2**, and **3a–k**) is summarized in Table 2, and the profiles of the reactions with ligands **1a**, **2**, **3c**, **3j**, and **3k** are shown in Figure 2.[16] It is of note that many ligands with achiral units (shown in Scheme 3) gave a better reaction rate than the original linked-binol **1a** that contained two chiral units (initial

Table 2: Initial reaction rate with various chiral ligands (**1a**, **2**, and **3a–k**) under dilute conditions.

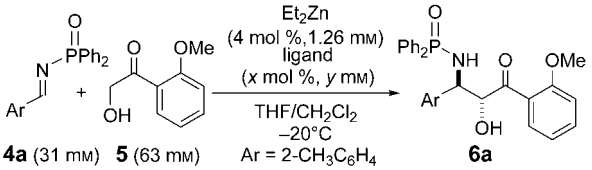

Entry	Ligand (mol%)	[Ligand] [mM]	Initial rate [mM min^{-1}]
1	**1a** (1)	0.31	0.199
2	**2** (2)	0.62	0.015
3	**3a** (1)	0.31	0.333
4	**3b** (1)	0.31	0.354
5	**3c** (1)	0.31	0.696
6	**3d** (1)	0.31	0.019
7	**3e** (1)	0.31	0.096
8	**3f** (1)	0.31	0.135
9	**3g** (1)	0.31	0.375
10	**3h** (1)	0.31	0.455
11	**3i** (1)	0.31	0.435
12	**3j** (1)	0.31	0.742
13	**3k** (1)	0.31	0.848

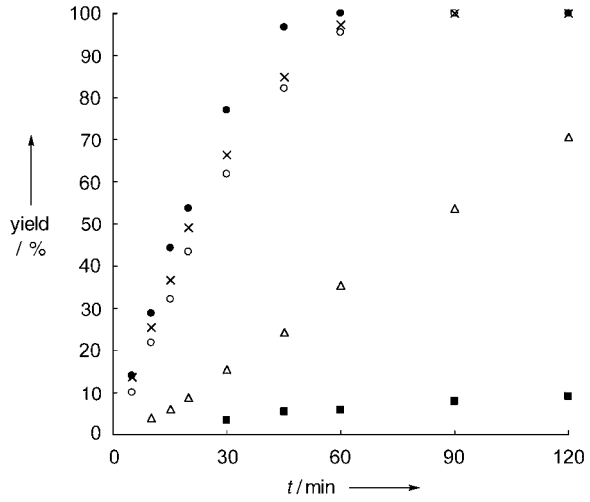

Figure 2. Reaction profiles with chiral ligands: **1a** (△ = 0.31 mM), **2** (■ = 0.62 mM), **3c** (○ = 0.31 mM), **3j** (× = 0.31 mM), and **3k** (● = 0.31 mM).

rate = 0.199 mM min^{-1}). Ligands **3j** and **3k** with electron-donating *t*Bu groups gave the highest reaction rates (**3j** = 0.742 mM min^{-1}, **3k** = 0.848 mM min^{-1}), and ligand **3c** also produced a comparable reaction rate (**3c** = 0.696 mM min^{-1}). Ligand **3g**, with a bulky aromatic substituent, had lower reactivity than **3c** but higher reactivity than **1a**. An electron-withdrawing group also had a lower reaction rate (**3h** and **3i**). These results suggested that an appropriate group at the *ortho* position of the phenolic OH group and a relatively less acidic phenolic OH group were suitable substituents on the ligands for the present Mannich-type reaction. These results demonstrated the usefulness of the present strategy to sterically and electronically fine-tune complexes of metal and linked-binols.

The utility of ligand **3c** was further demonstrated, as shown in Schemes 4 and 5. The catalyst loading for **3c** was successfully lowered: the Mannich-type reaction proceeded smoothly with as little as 0.01 mol% of **3c**, with the product being afforded in good yield and selectivity at 0 °C after 36 h (86%, 98% *ee*, TON = 8600; this is the highest TON value achieved in the catalytic asymmetric Mannich-type reaction so far.[17,18]) The reaction proceeded smoothly even with low concentrations of the ligand ([**3c**] = 0.095 mM). The broad substrate range of ligand **3c** is also summarized in Scheme 5.

Although a Et_2Zn/ligand stoichiometry of 4:1 was used for the Mannich-type reaction, characterization of the reaction

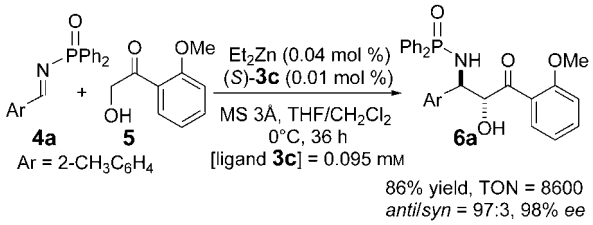

Scheme 4. Catalytic asymmetric Mannich-type reaction using 0.01 mol% of **3c**. MS 3 Å = molecular sieves (3 Å).

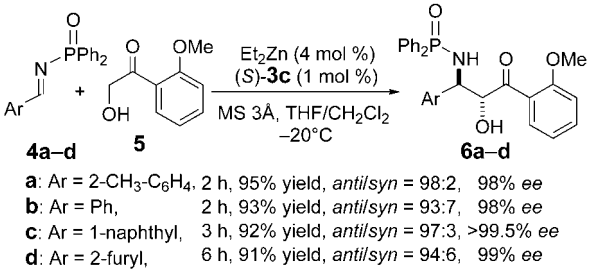

Scheme 5. Catalytic asymmetric Mannich-type reaction of imines **4a–d** using **3c**.

mixture was difficult for both **1a** and **3c**. Thus, we investigated the structures of precatalysts of a Et_2Zn/ligand mixture in a 2:1 ratio for a preliminary evaluation of the properties of **3c** relative to **1a**.[19] The complex formed in the Et_2Zn/**3c** (2:1) mixture was confirmed to be similar to that in the Et_2Zn/**1a** (2:1) mixture (Zn/**1a** = 3:2; Scheme 2) by ESI mass-spectrometric analysis. The ESIMS spectrum of the Et_2Zn/**3c** (2:1) mixture showed major peaks at *m*/*z* 1183–1194,[20] which correspond to a Zn/**3c** (3:2) complex. The ^{1}H and ^{13}C NMR spectroscopic analysis of the Et_2Zn/**3c** (2:1) mixture indicated eight different benzylic protons and four benzylic carbon atoms,[20] thus suggesting that the Zn/**3c** (3:2) complex does not have C_2 symmetry, and that two molecules of **3c** were differentially involved, possibly in a head-to-tail fashion. Further investigations to determine the structure of the Zn/**3c** complex unequivocally are ongoing. Although the structure of the actual active species formed under the reaction conditions is not clear at the moment, we speculate that the coordination site at the zinc center would be sterically less crowded in the Zn/**3c** complex than in the Zn/**1a** complex, thus accelerating the rate-limiting exchange step[21] between the product and ketone **5** to regenerate the Zn/ligand/ketone complex. Further mechanistic studies are in progress.

In summary, we have developed readily tuneable, economical in terms of chirality, non-C_2-symmetric linked-binol derivatives. The new design overcomes the drawbacks inherent in the original C_2-symmetric ligand **1a** with two chiral binaphthol units. The present strategy has been useful to fine-tune metal/linked-binol complexes in a direct catalytic asymmetric Mannich-type reaction. Further application of these new sterically and electronically tuneable ligands to other asymmetric reactions, in which the original linked-binol **1a** produced unsatisfactory results, is currently ongoing.

Received: February 4, 2005
Published online: April 28, 2005

Keywords: amino alcohols · asymmetric catalysis · chiral ligands · Mannich reaction · zinc

[1] For general reviews, see: a) *Comprehensive Asymmetric Catalysis* (Eds.: E. N. Jacobsen, A. Pfaltz, H. Yamamoto), Springer, Berlin, **1999**, and **2003**; b) *Catalytic Asymmetric Synthesis*, *2nd ed.* (Ed.: I. Ojima), Wiley-VCH, New York, **2000**.

[2] For recent reviews on asymmetric catalysis using sterically and electronically modified binol derivatives, see: a) Y. Chen, S.

Yekta, A. K. Yudin, *Chem. Rev.* **2003**, *103*, 3155; b) P. Kocovsky, S. Vyskocil, M. Smrcina, *Chem. Rev.* **2003**, *103*, 3213.

[3] For the oxygen-linked-binol **1a**, see: a) S. Matsunaga, J. Das, J. Roels, E. M. Vogl, N. Yamamoto, T. Iida, K. Yamaguchi, M. Shibasaki, *J. Am. Chem. Soc.* **2000**, *122*, 2252; b) S. Matsunaga, T. Ohshima, M. Shibasaki, *Adv. Synth. Catal.* **2002**, *344*, 4; for the sulfur-linked-binol **1b**, see: c) N. Kumagai, S. Matsunaga, T. Kinoshita, S. Harada, S. Okada, S. Sakamoto, K. Yamaguchi, M. Shibasaki, *J. Am. Chem. Soc.* **2003**, *125*, 2169; for the nitrogen-linked-binol **1c**, see: d) K. Majima, R. Takita, A. Okada, T. Ohshima, M. Shibasaki, *J. Am. Chem. Soc.* **2003**, *125*, 15837.

[4] For the design and application of related chiral ligands, see: a) E. M. Vogl, S. Matsunaga, M. Kanai, T. Iida, M. Shibasaki, *Tetrahedron Lett.* **1998**, *39*, 7917; b) H. Ishitani, T. Kitazawa, S. Kobayashi, *Tetrahedron Lett.* **1999**, *40*, 2161; c) T. Harada, Y. Hiraoka, T. Kusukawa, Y. Marutani, S. Matsui, M. Nakatsugawa, K. Kanda, *Org. Lett.* **2003**, *5*, 5059; d) S. Kobayashi, K. Arai, H. Shimizu, Y. Ihori, H. Ishitani, Y. Yamashita, *Angew. Chem.* **2005**, *117*, 771; *Angew. Chem. Int. Ed.* **2005**, *44*, 761.

[5] a) N. Kumagai, S. Matsunaga, N. Yoshikawa, T. Ohshima, M. Shibasaki, *Org. Lett.* **2001**, *3*, 1539; b) N. Yoshikawa, N. Kumagai, S. Matsunaga, G. Moll, T. Ohshima, T. Suzuki, M. Shibasaki, *J. Am. Chem. Soc.* **2001**, *123*, 2466; see also Ref. [3c]

[6] a) S. Harada, N. Kumagai, T. Kinoshita, S. Matsunaga, M. Shibasaki, *J. Am. Chem. Soc.* **2003**, *125*, 2582; b) S. Matsunaga, T. Kinoshita, S. Okada, S. Harada, M. Shibasaki, *J. Am. Chem. Soc.* **2004**, *126*, 7559.

[7] Y. S. Kim, S. Matsunaga, J. Das, A. Sekine, T. Ohshima, M. Shibasaki, *J. Am. Chem. Soc.* **2000**, *122*, 6506; see also Ref. [3d]

[8] a) S. Matsunaga, N. Kumagai, S. Harada, M. Shibasaki, *J. Am. Chem. Soc.* **2003**, *125*, 4712; b) S. Matsunaga, T. Yoshida, H. Morimoto, N. Kumagai, M. Shibasaki, *J. Am. Chem. Soc.* **2004**, *126*, 8777.

[9] For selected, recent, related examples using a conformationally flexible biphenyl unit in asymmetric catalysis, see: a) K. Mikami, T. Korenaga, M. Terada, T. Ohkuma, T. Pham, R. Noyori, *Angew. Chem.* **1999**, *111*, 517; *Angew. Chem. Int. Ed.* **1999**, *38*, 495; b) J. Balsells, P. J. Walsh, *J. Am. Chem. Soc.* **2000**, *122*, 1802; c) T. Ooi, Y. Uematsu, M. Kameda, K. Maruoka, *Angew. Chem.* **2002**, *114*, 1621; *Angew. Chem. Int. Ed.* **2002**, *41*, 1551; d) Z. Luo, Q. Liu, L. Gong, X. Cui, A. Mi, Y. Jiang, *Angew. Chem.* **2002**, *114*, 4714; *Angew. Chem. Int. Ed.* **2002**, *41*, 4532; for other examples, see: e) K. Mikami, M. , Yamanaka, *Chem. Rev.* **2003**, *103*, 3369; f) P. J. Walsh, A. E. Lurain, J. Balsells, *Chem. Rev.* **2003**, *103*, 3297; g) J. W. Faller, A. R. Lavoie, J. Parr, *Chem. Rev.* **2003**, *103*, 3345; h) A. Alexakis, C. Benhaim, *Eur. J. Org. Chem.* **2002**, 3221.

[10] For "chiral economy" in total synthesis, see: A. Fischli, *Chimia* **1976**, *30*, 4; for "chirality economy" in asymmetric catalysis, see Ref. [9c]

[11] For characterization of the Zn/linked-binol **1a** (3:2) complex, see Ref. [3c]: mechanistic studies conducted therein reported that the actual active species was supposed to have a more complicated structure that incorporated hydroxy ketone **5**; ESI-mass-spectrometric analysis revealed that a Zn/linked-binol/ketone **5** (7:3:4) complex could be an active species under the reaction conditions.

[12] For reviews on nonlinear effects, see: a) C. Girard, H. B. Kagan, *Angew. Chem.* **1998**, *110*, 3088; *Angew. Chem. Int. Ed.* **1998**, *37*, 2922; b) H. B. Kagan, *Adv. Synth. Catal.* **2001**, *343*, 227; c) D. G. Blackmond, *Acc. Chem. Res.* **2000**, *33*, 402.

[13] For the synthesis and spectra of ligands **3a–k**, see the Supporting Information.

[14] The initial reaction rate of the Mannich-type reaction with a *meso*-linked-binol derivative prepared from (*S*)-binol and (*R*)-binol units was estimated relative to that of (*S*,*S*)-linked-binol **1a**. A similar initial reaction rate was observed for **1a** and the *meso*-linked-binol. The chirality of ligand **3b** should be controlled by (*S*)-biphenol-(*S*)-binol on complexation with the zinc center because the pseudo-*meso*-(*R*)-biphenol-(*S*)-binol-type complex would afford products in low enantiomeric excess.

[15] In terms of cost efficiency, **3b** and **3c** are also superior to **1a**: 2,2′-biphenol (500 g; Aldrich) and 2-phenylphenol (500 g; Aldrich).

[16] The reaction profiles with other ligands are summarized in the Supporting Information.

[17] For reviews of catalytic asymmetric Mannich-type reactions, see: a) S. Kobayashi, M. Ueno in *Comprehensive Asymmetric Catalysis Supplement I* (Eds.: E. N. Jacobsen, A. Pfaltz, H. Yamamoto), Springer, Berlin, **2003**, chap. 29.5, p. 143; b) A. Córdova, *Acc. Chem. Res.* **2004**, *37*, 102; for selected recent examples of direct catalytic asymmetric Mannich(-type) reactions, see also; c) B. List, P. Pojarliev, W. T. Biller, H. J. Martin, *J. Am. Chem. Soc.* **2002**, *124*, 827; d) A. Córdova, W. Notz, G. Zhong, J. M. Betancort, C. F. Barbas III, *J. Am. Chem. Soc.* **2002**, *124*, 1842; e) A. Córdova, S.-I. Watanabe, F. Tanaka, W. Notz, C. F. Barbas III, *J. Am. Chem. Soc.* **2002**, *124*, 1866; f) K. Juhl, N. Gathergood, K. A. Jørgensen, *Angew. Chem.* **2001**, *113*, 3083; *Angew. Chem. Int. Ed.* **2001**, *40*, 2995; g) B. M. Trost, L. R. Terrell, *J. Am. Chem. Soc.* **2003**, *125*, 338; h) Y. Hayashi, W. Tsuboi, I. Ashimine, T. Urushima, M. Shoji, K. Sakai, *Angew. Chem.* **2003**, *115*, 3805; *Angew. Chem. Int. Ed.* **2003**, *42*, 3677; i) W. Zhuang, S. Saaby, K. A. Jørgensen, *Angew. Chem.* **2004**, *116*, 4576; *Angew. Chem. Int. Ed.* **2004**, *43*, 4476; j) D. Uraguchi, M. Terada, *J. Am. Chem. Soc.* **2004**, *126*, 5356, and references therein.

[18] The best TON was achieved using 0.02 mol% of **1a** ([ligand **1a**] = 0.21 mM, TON = 4900)[8b]; however, the concentration of **1a** had to be >0.2 mM to promote the reaction efficiently. Under similar conditions given in Scheme 2 ([ligand **1a**] = 0.1 mM, 0.01 mol%), TON < 4000.

[19] In the present Mannich-type reaction, the ratio of Et_2Zn/ligand (**1a** or **3c**) did not affect enantioselectivity. Et_2Zn/**1a** (2 mol% of **1a**): 2:1 (>99% *ee*, d.r. 98:2, 2 h, >95% yield), 3:1 (>99% *ee*, d.r. 98:2, 1 h, >95% yield), 4:1 (>99% *ee*, d.r. 98:2, 1 h, >95% yield); Et_2Zn/**3c** (2 mol% of **3c**): 2:1 (99% *ee*, d.r. 99:1, 1 h, >95% yield), 3:1 (98% *ee*, d.r. 98:2, 1 h, >95% yield), 4:1 (98% *ee*, d.r. 98:2, 1 h, >95% yield); thus, we assumed that a similar active species formed under these reaction conditions, and that the structural information obtained with Et_2Zn/ligand (2:1) would give some insight into the properties of **3c**.

[20] ESI mass spectra as well as the ^1H NMR and ^{13}C NMR spectra of Et_2Zn/**3c** (2:1) are given in the Supporting Information. The ESI mass-spectrometric analysis showed several signals that correspond to the Zn/**3c** (3:2) trinuclear complex, depending on the natural-isotope distribution pattern of zinc.

[21] The rate-limiting step of the Mannich-type reaction of **4a** with **5** was determined to be a catalyst-turnover step by kinetic studies on the initial rate; see Ref. [8b]

Mesoporous Materials

Organometallic Chemistry Inside the Pore Walls of Mesostructured Silica Materials**

Véronique Dufaud, France Beauchesne, and Laurent Bonneviot**

Recently a new class of porous organic–inorganic hybrid materials was prepared through the surfactant-templated polycondensation of bridged silsesquioxane organic molecules. These new materials, which are also referred to as periodic mesoporous organosilicas (PMOs), are unique as their channel walls contain both inorganic and organic fragments.[1] These fragments are uniformly distributed within the framework by covalent bonding of two or more terminal silyl groups, which leaves the void space unoccupied after template removal. This new approach extends the field of mesoporous materials into the chemistry of channel walls. Through choice or design of the organic functionality, one may create new materials that have truly unique properties and behaviors. These embedded fragments are readily accessible for chemical reaction, thus opening the possibility of using such materials as catalysts.[2]

Herein, we report the development of new methodologies for the preparation of inorganic–organometallic hybrid materials in which the organometallic complexes, which are structurally well defined at the molecular level, are integrated within the pore walls of highly ordered mesostructured silicas. This integration of the complex into the solid, rather than the grafting of a complex to the surface, should reduce some of the problems commonly associated with supported homogeneous systems, notably, catalyst leaching, pore blockage, and distribution inhomogeneity.

The first step in the accomplishment of this goal was the synthesis of an organometallic precursor that had multiple polycondensable organosiloxane functionalized donor ligands.[3] The rhodium organophosphine complex **1** was chosen to provide a wide range of potential catalytic applications (e.g., hydrogenation, hydroformylation).

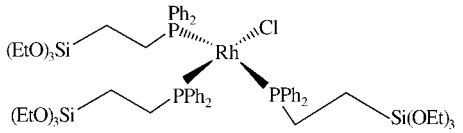

1

We wished to use this precursor directly in the synthesis of a hybrid MCM-type silica by cohydrolysis and polycondensation of **1** with tetraethylorthosilicate (TEOS) in the presence of cetyltrimethylammonium bromide (CTAB) as a structure-directing agent (SDA), but this precursor (and indeed, many catalytically interesting transition-metal complexes) was insoluble in water and unlikely to be stable under the classical aqueous basic conditions of this process.[4] Thus, we adapted the condensation reaction under the mild, acidic conditions reported by Stucky and co-workers (which led to the formation of SBA-3 mesostructured silicas)[5] to add an organic cosolvent, acetonitrile,[6] to better dissolve the transition-metal complex. Various combinations of **1**, TEOS, water, acetonitrile, CTAB, and HCl were attempted. The best results were obtained with 7.5 % wt acetonitrile, which led to materials that had a rhodium content of up to a 2 % wt in a highly ordered solid and contained the structure-directing agent CTAB in the channels.[7]

To render the organometallic sites of the as-made solid accessible, the surfactant template was removed by extraction.[8] It was found that if the extraction was performed directly on the as-made materials, all the structural order was lost. This instability, which is likely to be a consequence of the low temperature at which the condensation reaction was performed, disappeared when the as-made material was first silylated with $(CH_3)_3SiCl$ or $(CH_3)_2SiCl_2$ before the CTAB was extracted.[9]

The solids thus obtained were characterized by methods appropriate to molecular species (e.g., solid-state ^{13}C, ^{31}P, and ^{29}Si NMR spectroscopy, IR spectroscopy, and elemental analysis) as well as techniques more commonly associated with the characterization of mesoporous solids (nitrogen sorption isotherms, powder X-ray diffraction (XRD), thermogravimetric analysis (TGA), transmission electron microscopy (TEM), and energy dispersive X-ray (EDX) analysis). The characterization of one material (**2**, lot 1), which had been silylated with $(CH_3)_3SiCl$ and was shown by microanalysis to have 1.7 % wt Rh is presented below.

Mesoscopic order within **2** was shown to have been maintained after extraction of the SDA. The powder XRD pattern of **2** showed three clear peaks in the 2θ range of 1–10°, which is characteristic of 2D hexagonal ordered mesophases, with the d(10) spacing changing from 30 to 37 Å because of extraction of the template (Figure 1).[10] At this stage, the IR spectrum of **2** showed very little absorption in the 3000–2800 cm^{-1} range, thus indicating that the SDA had been removed.

Ordering was also clearly evident in the TEM image of **2** (Figure 2). Long-range ordering of the channels was observed with a spacing periodicity of approximately 3 nm. The TEM/EDX data were also important as they showed that metal complexes were localized in well-ordered phases of the solid

[*] Dr. V. Dufaud, Prof. L. Bonneviot
Laboratoire de Chimie
UMR CNRS–ENS 5182
Ecole Normale Supérieure de Lyon
46 allée d'Italie, 69364 Lyon cedex 07 (France)
Fax: (+33) 4-7272-8860
E-mail: vdufaud@ens-lyon.fr
laurent.bonneviot@ens-lyon.fr
Dr. F. Beauchesne
Institut de Recherches sur la Catalyse
2 avenue A. Einstein, 69626 Villeurbanne cedex (France)

[**] The authors thank François Theillet for his participation in the catalytic experiments and Frédéric Lefebvre, Gérard Bergeret, and William Desquesnes for help in the physical and textural characterization measurements.

Supporting information for this article is available on the WWW under http://www.angewandte.org or from the author.

 DOI: 10.1002/anie.200500454

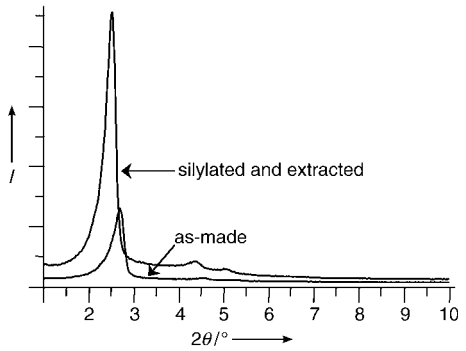

Figure 1. XRD pattern of rhodium-containing SBA-3 silica before and after extraction of the SDA.

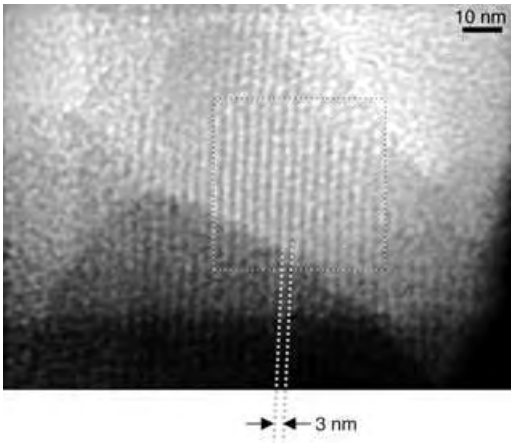

Figure 2. TEM micrographs of the extracted rhodium-modified hybrid material **2** (lot 1).

and the ligand-to-metal ratio (i.e., the P/Rh ratio) of the molecular precursor was maintained at 3 ± 0.3 (see the Supporting Information). This observation was confirmed over a large number of sample areas of the surface that was tested. Note that the elemental analysis of a sample of material on the milligram scale showed a P/Rh ratio of 2.96.[11]

The ^{31}P cross-polarization magic-angle spinning (CP-MAS) NMR spectroscopy showed a single signal at $\delta = 40.4$ ppm, which corresponds to a coordinated phosphine ligand. The ^{13}C CP-MAS NMR spectrum exhibited all of the aryl and alkyl resonances for the phosphine ligand as well as a strong signal at $\delta = -1.0$ ppm associated with the methyl of $(CH_3)_3Si-$ fragment, but no significant signal that could be associated with the CTAB template molecule was present. The ^{13}C CP-MAS NMR spectrum also showed evidence of a trace of the ethoxy fragment of the molecular precursor, which would indicate that some of the ethoxysilane was incompletely condensed. In the ^{29}Si CP-MAS NMR spectrum, the presence of T^2 and T^3 sites, as indicated by signals at $\delta = -60$ and 67.4 ppm, suggests that the precursor is not simply encapsulated but rather integrated into the silica network. Other signals were also observed in the $\delta = -90$ to -115 ppm spectral region (silica Q sites) and at $\delta = 15$ ppm ($(CH_3)_3Si-$ fragment).[12]

The TGA profile showed four regions of weight loss.[13] At temperatures up to about 100 °C, weight loss was accompanied by an endothermic differential thermal analysis (DTA) peak, which was presumably because of desorption of water. A second region of weight loss followed at temperatures between 200 and 550 °C, which, may be considered n inspection of the first derivative of the profile as a peak centered at 360 °C and a shoulder at around 460 °C, both arising from the decomposition and desorption of volatile organic species. The embedded complex is thermally stable up to 200 °C. The weight loss taken between 200 and 460 °C, and attributed to the ligand, is in good agreement with the metal loading and the stoichiometry of the molecular precursor. Above 460 °C, the weight loss is mainly because of the decomposition of the trimethylsilyl groups and accounts for approximately two $(CH_3)_3Si-$ fragments per rhodium atom. Further weight loss occurred at temperatures above 650 °C, which is probably because of the condensation of silanols of the silica framework.

The results of the analysis of the adsorption–desorption isotherms and the pore-size-distribution curves of the extracted unmodified and rhodium-modified materials are shown in Figure 3. Both samples show a type IV isotherm, which is characteristic of mesoporous solids. Relatively

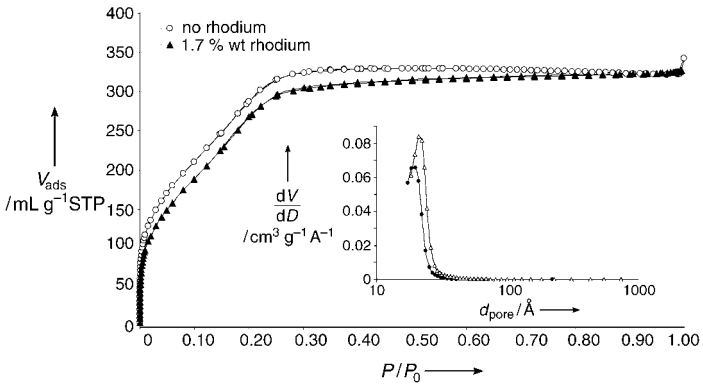

Figure 3. Nitrogen adsorption–desorption isotherms and pore-size distributions (from the Barret–Joiner–Halenda (BJH) calculations) of unmodified and rhodium-modified SBA-3 silicas.

narrow pore–diameter distributions were observed for both materials and the average pore diameter did not vary significantly between the two samples (2.0–2.2 nm), which would seem to indicate that the rhodium had indeed been incorporated into the walls of the silica rather than remaining in the pores or the channels. The Brunauer–Emmett–Teller (BET) specific surface area measured for the rhodium-modified material ($930\ m^2 g^{-1}$) was also quite similar to that of the unmodified analogue ($1090\ m^2 g^{-1}$).[14]

Thus, we have a material in which intact triphosphanylrhodium chloride fragments have been covalently bound to the silica framework without the overall porosity or the degree of order of the material being affected. The complexes seem to be homogeneously distributed and embedded in the channel walls. The question remained whether the metal-containing sites of **2** were accessible for catalytic chemical reactions and

whether the rhodium complex would exhibit typical behavior associated with its homogeneous analogue.

The catalytic activity of several hybrid materials for hydrogenation was evaluated by using substrates of varying steric encumbrance and compared to the activity of a homogeneous catalyst, [$RhCl(PPh_3)_3$]. Among the materials tested were two different lots of a model system prepared by postsynthetic grafting of precursor **1** onto calcined SBA-15 silica **3**. Results obtained for the catalytic tests are given in Table 1.

Table 1: Hydrogenation of alkenes by different rhodium-based catalysts.[a]

Substrate	Catalyst	% wt Rh[b]	Substrate/Rh	Conv [%]	TOF [h^{-1}]
styrene	**3**	0.8	7600	85	2150
	2	0.7	8500	93	2650
cyclohexene	**3**	0.8	7550	100	2590
	2	0.7	8560	100	2850
acrolein	**3**	0.8	7500	4	97
	2	0.7	8890	4	104
crotonaldehyde	**3**	1.1	5500	≈7[c]	20[c]
	2	1.7	3400	≈5[c]	9[c]
styrene	[$RhCl(PPh_3)_3$]	3.5×10^{-4} M solution	6600	75[d]	3300[d]

[a] Conditions: $P(H_2)=20$ bar, 70 °C, 3 h in benzene. TOF = turnover frequency, conv = conversion. [b] From elemental analysis. [c] 19 h. [d] Homogeneous catalysis, 1.5 h.

In all cases, the modified SBA-3 materials, including **2**, exhibited similar activity to that of model system **3**; thus, it is clear that the rhodium centers are available for catalysis. Indeed, for styrene hydrogenation, the activity is in the same range as that observed for the homogeneous complex. Furthermore, catalytic activity was observed even for the more hindered double bonds of cyclohexene and crotonaldehyde (see Table 1. The chemoselectivity (100%) of the catalyst for the carbon–carbon double bond in α,β-unsaturated aldehydes is the same as that reported for the homogeneous catalyst.[15] Limited attempts at recycling the catalyst have shown that catalytic activity is undiminished over several cycles, but more rigorous testing is needed.

In summary, we have developed a new synthetic protocol that allows the incorporation of phosphine-ligated transition-metal complexes into SBA-3 type silicas without significant loss of the mesoscopic order of the silica framework or the coordination environment and catalytic activity of the transition-metal complex. Key novel aspects of the protocol are the use of acetonitrile as a cosolvent, the acidic conditions, the relatively low temperatures, and silylation of the material prior to extraction of the SDA. The method has been successfully extended to incorporate other siloxy organophosphanyl transition-metal complexes into hybrid materials, notably those of platinum and palladium. The evaluation of these materials, in terms of activity and stability, for a variety of catalytic applications is ongoing.

Received: February 6, 2005
Published online: April 28, 2005

Keywords: heterogeneous catalysis · hydrogenation · mesoporous materials · rhodium · silicates

[1] a) S. Inagaki, S. Guan, Y. Fukushima, T. Ohsuna, O. Terasaki, *J. Am. Chem. Soc.* **1999**, *121*, 9611; b) T. Asefa, M. J. MacLachlan, N. Coombs, G. A. Ozin, *Nature* **1999**, *402*, 867; c) C. Yoshima-Ishii, T. Asefa, N. Coombs, M. J. MacLachlan, G. A. Ozin, *Chem. Commun.* **1999**, 2539.

[2] S. Inagaki, S. Guan, T. Ohsuna, O. Terasaki, *Nature* **2002**, *416*, 304.

[3] The transition-metal precursor, [$RhCl\{PPh_2(CH_2)_2Si(OCH_2CH_3)_3\}_3$] (**1**), was prepared by treating [{RhCl(cod)}$_2$] (cod = 1,5-cyclooctadiene) with $PPh_2(CH_2)_2Si(OCH_2CH_3)_3$ according to the procedure reported: O. Kröcher, R. A. Köppel, M. Fröba, A. Baiker, *J. Catal.* **1998**, *178*, 284.

[4] a) J. S. Beck, J. C. Vartuli, W. J. Roth, M. E. Leonowicz, C. T. Kresge, K. D. Schmitt, C. T.-W. Chu, D. H. Olson, E. W. Sheppard, S. B. McCullen, J. B. Higgins, J. L. Schlenker, *J. Am. Chem. Soc.* **1992**, *114*, 10834; b) C. T. Kresge, M. E. Leonowicz, W. J. Roth, J. C. Vartuli, J. S. Beck, *Nature* **1992**, *359*, 710.

[5] Q. Huo, D. I. Margolese, U. Ciesla, D. G. Demuth, P. Feng, T. E. Gier, P. Sieger, A. Firouzi, B. F. Chmelka, F. Schüth, G. D. Stucky, *Chem. Mater.* **1994**, *6*, 1176.

[6] In a typical procedure, CTAB was first dissolved in water, HCl, and half of the amount of acetonitrile used in the gel composition. TEOS was then prehydrolyzed over 15 min at room temperature prior to the addition of the organometallic precursor that had been dissolved in the remaining portion of acetonitrile. The resulting solution was stirred for 3 h at room temperature. The solid product was collected by filtration, washed with water, and dried under vacuum overnight at 25 °C.

[7] Optimized molar composition: TEOS 1; H_2O 120; CH_3CN 4.3; HCl 9.2; CTAB 0.12. When a siloxane-containing transition-metal complex is used, the calculation of the molar composition is based on the total number of condensable silicon centers, from TEOS and the complex.

[8] The template was removed from the as-made material by batch extraction with dry ethanol at 50 °C for 2 h. Three extraction cycles were necessary to complete the process.

[9] The postsilylation reaction was performed in dry toluene at 50 °C for 1 h using either $(CH_3)_3SiCl$ or $(CH_3)_2SiCl_2$ as the silylating agents.

[10] The expansion of the structure upon silylation and extraction, indicated by the increase of the d(10) spacing is likely to be related to the decreased degree of hydrogen-bonding interactions between the surface hydroxy groups, which leads to a partial release of the internal surface tension.

[11] Elemental analysis: 1.5% wt P and 1.7% wt Rh.

[12] D. W. Sindorf, G. E. Maciel, *J. Am. Chem. Soc.* **1983**, *105*, 3767.

[13] Thermogravimetric analyses were conducted from 25 to 1000 °C in air at a heating rate of 5 °C min^{-1}.

[14] We have demonstrated for an SBA-15 material that the postsynthetic grafting of the rhodium complex onto the surface of unmodified calcined silica dramatically reduces the specific area and the median pore-size diameter and that the effect varies inversely with rhodium loading (see the Supporting Information).

[15] a) P. N. Rylander, *Hydrogenation Methods*, Academic Press, London, **1985**; b) J. M. Grosselin, C. Mercier, G. Allmang, F. Grass, *Organometallics* **1991**, *10*, 2126; c) P. Clause, *Top. Catal.* **1998**, *5*, 51.

Natural Product Synthesis

Catalytic Enantioselective Total Syntheses of Bisorbicillinolide, Bisorbicillinol, and Bisorbibutenolide**

*Ran Hong, Yonggang Chen, and Li Deng**

Dedicated to Professor Eric N. Jacobsen

The remarkable structural complexity and broad range of interesting biological activitiesis of bisorbicillinoids have made them attractive synthetic targets. Although structurally diverse, it was postulated that bisorbicillinoids were biosynthetically generated from a common intermediate, sorbicillinol (**1a**), through several fascinating and chemically distinct dimerizations of **1a** (Scheme 1).[1,2] This notion was confirmed in pioneering synthetic studies of bisorbicillinoids by the research groups of Corey and Nicolaou that culminated in the successful biomimetic total syntheses of bisorbicillinol (**2**) and trichodimerol (**3**) through a [4+2] dimerization and a Michael reaction/ketalization dimerization, respectively.[1,2] Furthermore, the Corey and Nicolaou groups showed that dimerization of optically active sorbicillinol (**1a**), prepared by hydrolysis of the optically active 6-acetylsorbicillinol (**1b**; obtained through preparative HPLC resolution of its racemic counterpart), led to the formation of **2** and **3** in the optically active form.[2a,d] Nicolaou et al. also demonstrated that bisorbicillinol (**2**) could be converted into bisorbibutenolide (**4**),[2c,d] thus supporting the proposal of Abe et al. that bisorbicillinol (**2**) is a biosynthetic precursor to other more structurally complex bisorbicillinoids.[3] Although Abe et al. postulated that intermediate **5**, which is formed during the conversion of **2** into **4**, could also give rise to bisorbicillinolide (**6**),[3b] the total synthesis of **6**, in either its racemic or optically active form, has not yet been reported.

These inspiring synthetic studies underscored the importance of developing a highly enantioselective synthesis of sorbicillinol derivatives (**1**). The presence of a single heteroatom-substituted quaternary stereocenter and densely packed sensitive functionalities apparently render this task highly challenging, as no enantioselective total synthesis of any member of the bisorbicillinoids has been reported.[4] Herein, we describe a catalytic, enantioselective, and flexible synthesis of sorbicillinol derivatives **1** and the enantioselective total syntheses of bisorbicillinolide (**6**), bisorbicillinol (**2**), and bisorbibutenolide (**4**).

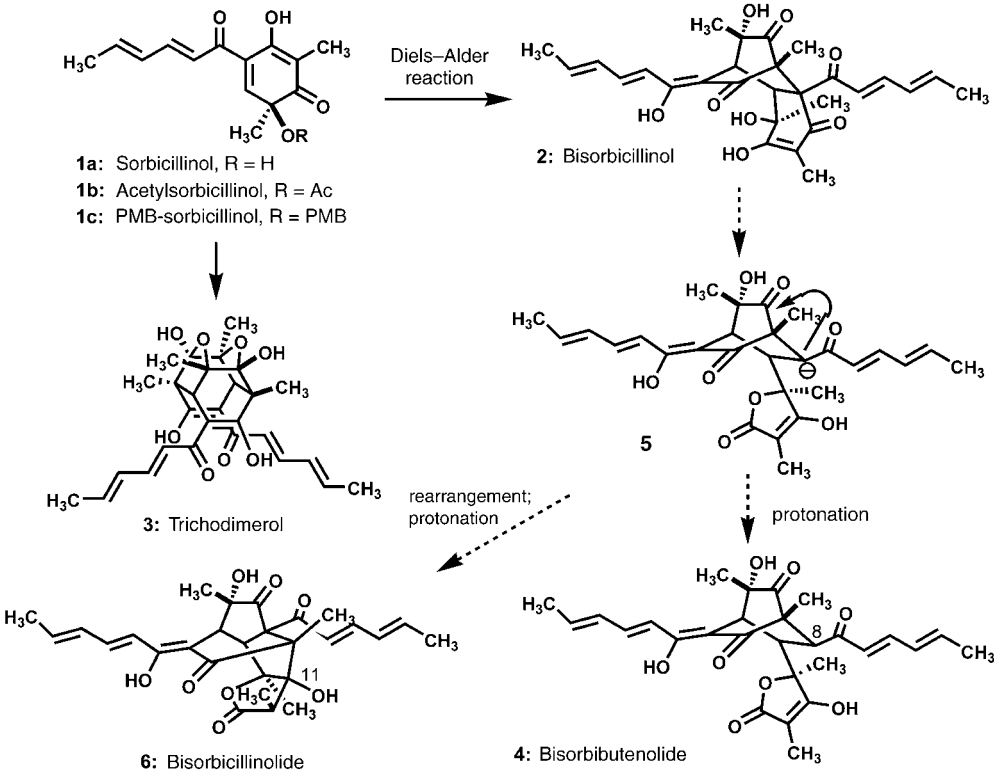

Scheme 1. Selected bisorbicillinoids and the biosynthesis hypothesis.

Our synthetic plan, outlined in Scheme 2 featured a catalyst-controlled enantioselective construction of the het-

[*] Dr. R. Hong, Y. Chen, Prof. L. Deng
Department of Chemistry
Brandeis University
Waltham, MA 02454-9110 (USA)
Fax: (+1) 781-736-2516
E-mail: deng@brandeis.edu

[**] This work was financially supported by the National Institutes of Health (GM-61591).

Supporting information for this article is available on the WWW under http://www.angewandte.org or from the author.

  DOI: 10.1002/anie.200500480

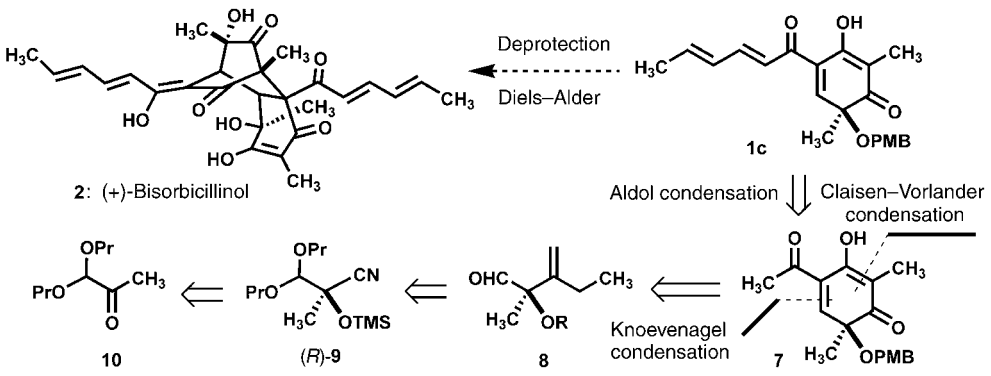

Scheme 2. Retrosynthetic analysis of bisorbicillinol (**2**). TMS = trimethylsilyl.

eroatom-substituted quaternary stereocenter in sorbicillinol derivative **1c**. Considering the sensitive nature of the dienone side chain,[5] we planned to introduce it at a later stage in our synthesis of **1c**. We envisaged that quinol **7** could be derived from aldehyde **8** through a Knoevenagel condensation and a subsequent Claisen–Vorländer condensation.[6] Aldehyde **8** could be prepared from cyanohydrin (*R*)-**9**, which was prepared in 92% *ee* and quantitative yield on a multigram scale by a modified cinchona alkaloid catalyzed enantioselective cyanosilylation of acetal ketone **10** (Scheme 3).[7]

The addition of Grignard reagent EtMgBr to the optically active cyanohydrin **9** in THF/Et_2O proceeded smoothly to form α-hydroxy ketone **11** in nearly quantitative yield (Scheme 3).[8] After masking the ketone as a methylene group through a Wittig olefination,[9] the tertiary alcohol was protected as a *para*-methoxybenzyl (PMB) ether to furnish **12**.[10] The acetal group of **12** was readily hydrolyzed in excellent yield with aqueous HCl to provide aldehyde **8**, which was required for the critical Knoevenagel condensation. A modification of the procedure developed by Lehnert[11] was used for the $TiCl_4$-promoted Knoevenagel condensation of aldehyde **8** with ethyl acetoacetate, which proceeded to generate **13** as a 7:1 mixture of isomers (*Z*/*E*). The desired *Z* isomer was isolated in 85% yield. Ozonolysis in the presence of pyridine at −72 °C provided diketone ester **14** in 80% yield.[12] Gratifyingly, the Claisen–Vorländer condensation with NaOH in dry dimethyl sulfoxide (DMSO) furnished the PMB-protected chiral quinol **7** in 67% yield.

Having secured an eight-step enantioselective route for the construction of the chiral quinol ring, we turned our attention to the installation of the dienone side chain to form the PMB-protected sorbicillinol **1c**. Unfortunately, all attempts to accomplish this task through either an aldol condensation or a two-step sequence[5b] of allylation followed by dehydrogenation were unsuccessful because of the propensity of **7** to undergo decomposition under basic conditions. We then began to explore an alternative strategy involving the introduction of all the carbon atoms required for the construction of sorbicillinol derivatives **1** before the formation of the quinol ring. We envisaged using the readily accessible ynone ester **15**[13] instead of ethyl acetoacetate for the Knoevenagel condensation (Scheme 4) with subsequent isomerization of the alkynone to a dienone.

The Knoevenagel condensation of **15** with aldehyde **8** proceeded in the presence of *N*-methylmorpholine (NMM)[11b] with exceedingly high Z selectivity ($Z/E > 50{:}1$) to afford **16** in 93% yield. Following the ozonolysis of **16**, the isomerization of ynone **17** to dienone **18** was accomplished in 92% yield with a modified Trost–Lu protocol[14] utilizing palladium acetate and tri-*p*-tolylphosphine. The outcome of the Claisen–Vorländer cyclization of **18** depended critically on the base used for the generation of the enolate, as **18** readily underwent decomposition with either lithium diisopropylamide (LDA) or NaH, whereas no reaction occurred with lithium bis(trimethylsilyl)amide (LiHMDS) or sodium bis(trimethylsilyl)amide (NaHMDS). After numerous experi-

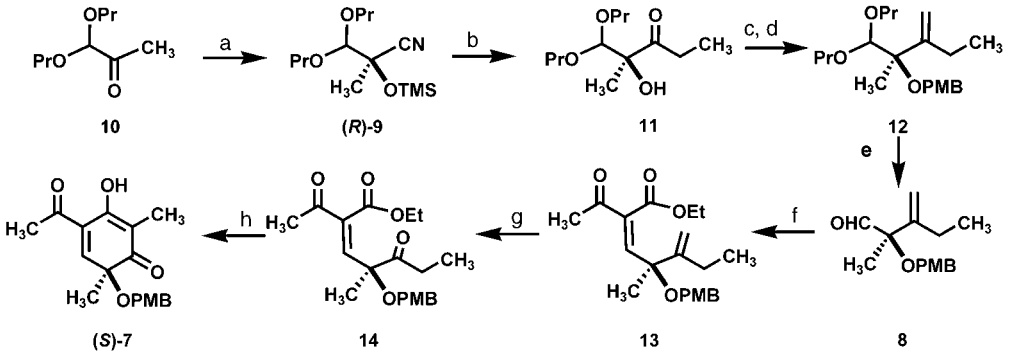

Scheme 3. Conditions: a) TMSCN, $(DHQ)_2AQN$ (2 mol%), $CHCl_3$, 100%, 92% *ee*; b) EtMgBr, Et_2O/THF (4:1), 98%; c) Ph_3PCH_3Br, $Et(Me)_2COK$, benzene, 82%; d) PMBOC(=NH)CCl_3, TfOH (cat.), Et_2O, 92% (based on the recovered starting material); e) 3 N HCl (aq), acetone, 90%; f) ethyl acetoacetate, $TiCl_4$, pyridine, THF, 85%; g) ozone, pyridine, CH_2Cl_2, 80%; h) NaOH, DMSO, 67%. $(DHQ)_2AQN$ = 1,4-bis(dihydroquinyl)anthraquinone, TfO = trifluoromethanesulfonate; PMB = *para*-methoxybenzyl.

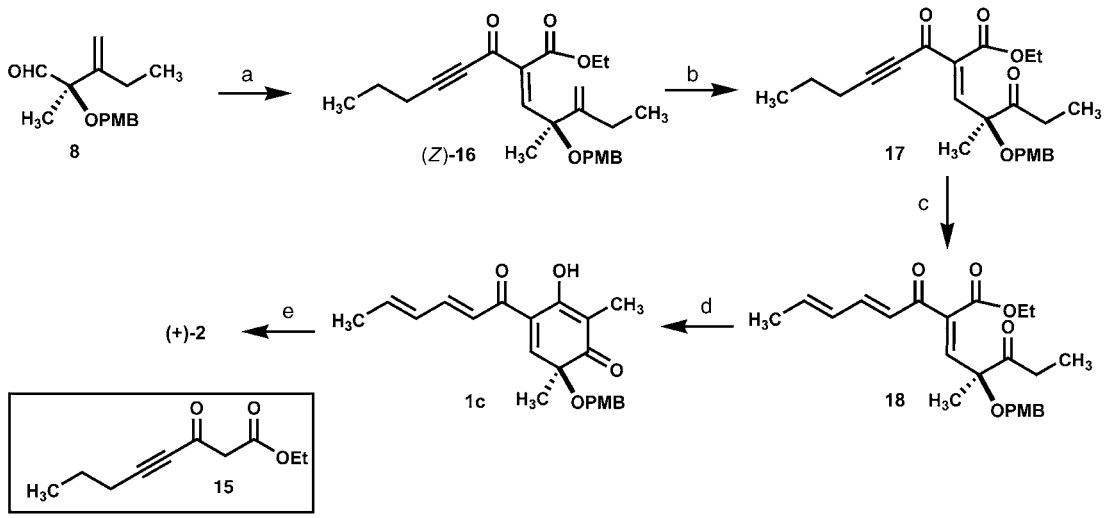

Scheme 4. Conditions: a) **15**, $TiCl_4$, NMM, THF, 93%; b) ozone, pyridine, CH_2Cl_2, 99%; c) $Pd(OAc)_2$ (cat.), *p*-tol_3P, benzene, 92%; d) Ph_3COH, KH, THF, 90%; e) TFA, CH_2Cl_2, 54%. tol = tolyl.

ments, we found that the cyclization proceeded cleanly with Ph_3COK to afford PMB-protected sorbicillinol **1c** in 90% yield. Treatment of **1c** with trifluoroacetic acid (TFA) at room temperature[15] accomplished the removal of the PMB group and the [4+2] dimerization of the resulting sorbicillinol **1a** in one pot to afford (+)-bisorbicillinol (**2**) in 54% yield after isolation. The conversion of (+)-**2** into (+)-**4** following the procedure reported by Nicolaou et al.[2c,d] allowed us to complete an 11-step enantioselective synthesis of **4** in 15% overall yield.[16,17]

In light of the proposal by Abe et al. that bisorbicillinol (**2**) is the possible biosynthetic precursor for bisorbicillinolide (**6**),[3b] we attempted the conversion of synthetic (+)-**2** into (+)-**6**. We were pleased to observe that (+)-**2**, on standing in methanol for 48 hours, rearranged to give (+)-**6** and (+)-**4** as a 4:1 mixture, which after isolation gave these compounds in 64% and 10% yield, respectively (Scheme 5). Thus, the first total synthesis of bisorbicillinolide (**6**) was completed.[16,17]

In conclusion, the first enantioselective total syntheses of bisorbicillinolide (**6**), bisorbicillinol (**2**), and bisorbibutenolide (**4**) have been accomplished in 10/11 steps and 12–19% overall yields by using a modified cinchona alkaloid catalyzed cyanosilylation as the stereochemistry-defining step.[18] Moreover, the rearrangement of **2** into **6** sheds light on the biosynthesis of **6**. Further exploration of the potential for modified cinchona alkaloid catalyzed enantioselective ketone cyanosilylations in target-oriented synthesis are now underway. These investigations are being carried out in the context of asymmetric total syntheses of other complex natural products and biosynthetically related analogues of chiral quinols **7** or sorbicillinol derivatives **1**.

Received: February 8, 2005
Published online: April 28, 2005

Keywords: bisorbicillinoids · natural products · rearrangement · sorbicillinol · total synthesis

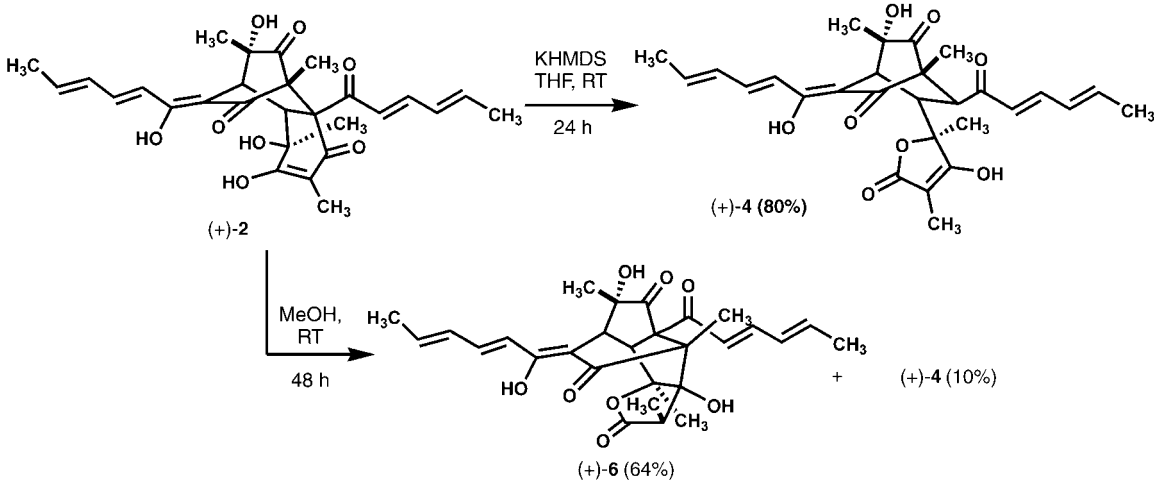

Scheme 5. Total synthesis of bisorbicillinolide (**6**).

[1] K. C. Nicolaou, S. A. Snyder, *Classics in Total Synthesis II*, Wiley-VCH, Weinheim, **2003**, chap. 11, p. 351.

[2] a) D. Barnes-Seeman, E. J. Corey, *Org. Lett.* **1999**, *1*, 1503; b) K. C. Nicolaou, R. Jautelat, G. Vassilikogiannakis, P. S. Baran, K. B. Simonsen, *Chem. Eur. J.* **1999**, *5*, 3651; c) K. C. Nicolaou, K. B. Simonsen, G. Vassilikogiannakis, P. S. Baran, V. P. Vidali, E. N. Pitsinos, E. A. Couladouros, *Angew. Chem.* **1999**, *111*, 3762; *Angew. Chem. Int. Ed.* **1999**, *38*, 3555; d) K. C. Nicolaou, G. Vassilikogiannakis, K. B. Simonsen, P. S. Baran, Y. L. Zhong, V. P. Vidali, E. N. Pitsinos, E. A. Couladouros, *J. Am. Chem. Soc.* **2000**, *122*, 3071.

[3] a) N. Abe, O. Sugimoto, K.-I. Tanji, A. Hirota, *J. Am. Chem. Soc.* **2000**, *122*, 12606; b) N. Abe, O. Sugimoto, T. Arakawa, K.-I. Tanji, A. Hirota, *Biosci. Biotechnol. Biochem.* **2001**, *65*, 2271.

[4] a) A total synthesis of (+)-bisorbicillinol (**2**) in 51 % *ee* has been reported, see: L. H. Pettus, R. W. Van de Water, T. R. R. Pettus, *Org. Lett.* **2001**, *3*, 905; b) for a chiral-auxiliary-directed synthesis of chiral quinols bearing a heteroatom-substituted quaternary center, see: L. H. Mejorado, C. Hoarau, T. R. R. Pettus, *Org. Lett.* **2004**, *6*, 1535; c) for a comprehensive review, see: D. Magdziak, S. Meek, T. R. R. Pettus, *Chem. Rev.* **2004**, *104*, 1383.

[5] a) R. Andrade, W. A. Ayer, P. P. Mebe, *Can. J. Chem.* **1992**, *70*, 2526; b) J. L. Wood, B. D. Thompson, N. Yusuff, D. A. Pflum, M. S. P. Matthäus, *J. Am. Chem. Soc.* **2001**, *123*, 2097.

[6] a) L. Claisen, O. Lowman, *Ber. Dtsch. Chem. Ges.* **1887**, *20*, 651; b) D. Vorländer, *Ber. Dtsch. Chem. Ges.* **1894**, *27*, 2053; c) D. Vorländer, *Justus Liebigs Ann. Chem.* **1897**, *294*, 253.

[7] S.-K. Tian, R. Hong, L. Deng, *J. Am. Chem. Soc.* **2003**, *125*, 9900.

[8] a) T. Holm, *Tetrahedron Lett.* **1966**, *7*, 3329; b) E. C. Ashby, *Q. Rev. Chem. Soc.* **1967**, *21*, 259.

[9] A. B. Simth III, P. J. Jerris, *J. Org. Chem.* **1982**, *47*, 1845.

[10] N. Nakajima, K. Horita, R. Abe, O. Yonemitsu, *Tetrahedron Lett.* **1988**, *29*, 4139.

[11] a) W. Lehnert, *Tetrahedron Lett.* **1970**, *11*, 4723; b) W. Lehnert, *Tetrahedron* **1972**, *28*, 663.

[12] G. Slomp, Jr, J. L. Johnson, *J. Am. Chem. Soc.* **1958**, *80*, 915.

[13] Alkynonyl ester **15** is prepared in quantitative yield from the reaction of commercially available ethyl malonyl chloride with 1-pentynylmagnesium chloride (see the Supporting Information).

[14] a) D. Ma, Y. Lin, X. Lu, Y. Yu, *Tetrahedron Lett.* **1988**, *29*, 1045; b) B. M. Trost, T. Schmidt, *J. Am. Chem. Soc.* **1988**, *110*, 2301; c) Y. Inoue, S. Imaizumi, *J. Mol. Catal.* **1988**, *49*, L19; for applications in syntheses, see: d) D. Desmaële, *Tetrahedron* **1992**, *48*, 2925; e) K. Matsuo, Y. Sakaguchi, *Chem. Pharm. Bull.* **1997**, *45*, 1620.

[15] L. Yan, D. Kahne, *Synlett* **1995**, 523.

[16] Synthetic (+)-**2**, (+)-**4**, and (+)-**6** were spectroscopically identical to reported natural products (see the Supporting Information for details). (+)-**2**: $[\alpha]_D = +181°$ ($c = 0.23$, MeOH) (Ref. [17a]: $+195.2°$ ($c = 0.5$, MeOH)); (+)-**6**: $[\alpha]_D = +310°$ ($c = 0.05$, MeOH) (Ref. [17b]: $+318°$ ($c = 0.1$, MeOH)); (+)-**4**: $[\alpha]_D = +128.6°$ ($c = 0.14$, MeOH) (Ref. [17b]: $+124.4°$ ($c = 0.5$, MeOH)).

[17] a) N. Abe, T. Murata, A. Hirota, *Biosci. Biotechnol. Biochem.* **1998**, *62*, 661; b) N. Abe, T. Murata, A. Hirota, *Biosci. Biotechnol. Biochem.* **1998**, *62*, 2120.

[18] The absolute configuration of cyanohydrin **9** has been determined to be *R*;[7] consequently, the current asymmetric syntheses with (*R*)-**9** as an intermediate provide direct experimental evidence confirming the previous assignment of the absolute configurations for (+)-**2**, (+)-**4**, and (+)-**6** based on their biosynthesis hypothesis (see the Supporting Information).

Natural Product Synthesis

Total Synthesis of 2-(5,6-Epoxyisoprostane A_2)phosphorylcholine and Elucidation of the Relative Configuration of the Isoprostane Moiety**

*Hukum P. Acharya and Yuichi Kobayashi**

1-Palmitoyl-2-(5,6-epoxyisoprostane E_2)-*sn*-glycero-3-phosphorylcholine (**1**) and the related molecule **2** with 5,6-epoxyisoprostane A_2 at the *sn*-2 position (Scheme 1) are

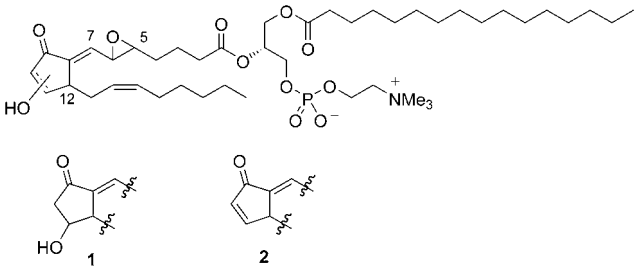

Scheme 1. Aortic oxidation products of 2-arachidonoylphosphorylcholine.

oxidation products of 1-palmitoyl-2-arachidonoyl-*sn*-glycero-3-phosphorylcholine (PAPC)[1] that are found in interleukin-1β-stimulated human aortic endothelial cells (HAEC) and in mildly oxidized low-density lipoproteins (ox-LDL).[2] These molecules stimulate HAEC to release interleukin-8 and monocyte chemotactic protein-1. The monocytes activated by these chemokines[2,3] enter the vessel wall, where they initiate and cause the progression of atherosclerotic lesion.[3,4] The whole structures of **1** and **2**, and in particular the vinyl epoxide moiety of the isoprostane unit, are important for this activity.[5]

In contrast to the considerable progress made in the biological study of these compounds, the structures of the epoxyisoprostane parts of **1** and **2** had not been elucidated fully. Thus, although the connectivities and geometries of the epoxy and Δ^{14} olefinic moieties had been determined unambiguously by ^{1}H NMR spectroscopy and mass spectrometry,[1] the *E* geometry of the Δ^7 alkene and the relative configura-

[*] H. P. Acharya, Prof. Y. Kobayashi
Department of Biomolecular Engineering
Tokyo Institute of Technology
Box B-52, 4259 Nagatsuta-cho
Midori-ku, Yokohama 226-8501 (Japan)
Fax: (+81) 45-924-5789
E-mail: ykobayas@bio.titech.ac.jp

[**] We thank NOF Corporation, Japan, for a generous supply of 1-palmitoyl lysophosphorylcholine. This work was supported by a Grant-in-Aid for Scientific Research from the Ministry of Education, Science, Sports, and Culture of Japan and the Sasakawa Scientific Research Grant from The Japan Science Society.

Supporting information for this article is available on the WWW under http://www.angewandte.org or from the author.

 DOI: 10.1002/anie.200500534

tion of the epoxy moiety and C12 were assigned for **2** by analogy with a structurally related compound.[6] Whereas it is believed that the configuration of the glycerol moiety of compounds **1** and **2** is the same as in *sn*-glycerol-3-phosphate, there was no information about the configuration of the 4 (for **1**) or 3 (for **2**) stereocenters in the respective isoprostane moieties. As **2** is the dehydration product of **1** and was isolated with **1** from the same origin, it seems reasonable to assume that the epoxyisoprostane portions of **1** and **2** share the same configuration at C5, C6, C12, and the Δ^7 olefin. Consequently, we chose to synthesize the epoxyisoprostane A_2 **3**—that is, the cyclopentenone-containing carboxylic acid constituent of compound **2**—to elucidate the relative configuration (Scheme 2).[7]

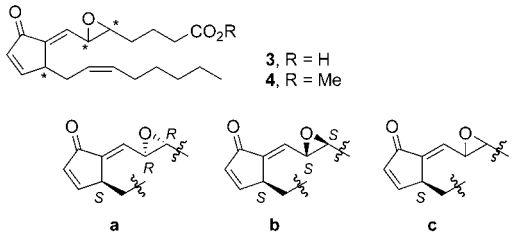

Scheme 2. 5,6-Epoxyisoprostanes A_2 that we have synthesized.

Methyl ester **6**, with a similar structure to acid **3**, was synthesized by Jung et al. by a three-component coupling strategy[8] starting from enone **5** (TBS = *tert*-butyldimethylsilyl). The same relative configuration as in **6** was assigned to **2**

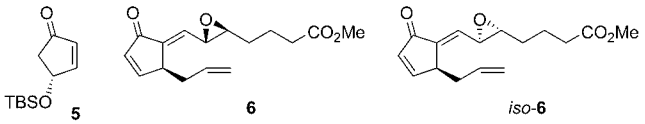

(i.e., **2b**) by comparison of their ^{1}H NMR spectra.[6] The results reported in the following prove that this assignment was wrong—the error having occurred mostly because Jung et al. did not include the isomer *iso*-**6** in their study—and that the natural product **2** either has the stereostructure **2a** or is the enantiomer of **14**.

Our approach to the epoxyisoprostane A_2 stereoisomers **3a–c**, which involves the combination of enone **7** and epoxyaldehydes **8a–c** in an aldol reaction, is summarized in Scheme 3. First, ester **9** was synthesized on a multigram scale from the TBS ether of **10**[9] (> 95% *ee*) through a palladium-catalyzed reaction with dimethyl malonate/*t*BuOK followed by decarboxylation,[10] and was converted into olefin **11** stereoselectively by reduction with DIBAL and subsequent Wittig reaction of the resulting aldehyde in 86% yield (Scheme 4). The silyl group was removed with TBAF, and oxidation of the resulting alcohol with PCC afforded **7** in 83% yield.

The aldol reaction of **7** with the epoxyaldehyde **8a**[11] afforded **12** as a mixture of the *anti* and *syn* aldol products. Without separation, the mixture was converted into the corresponding mesylate, which was exposed to Al_2O_3[12] to

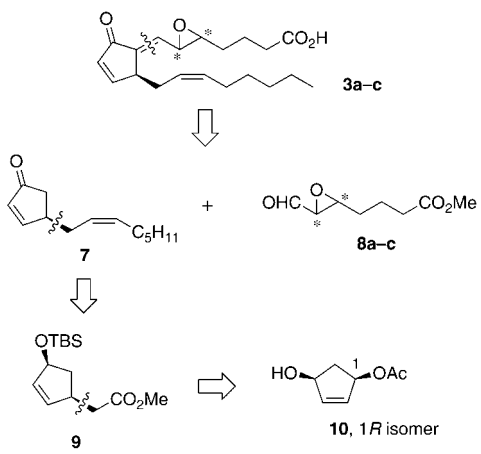

Scheme 3. Retrosynthetic analysis of **3**.

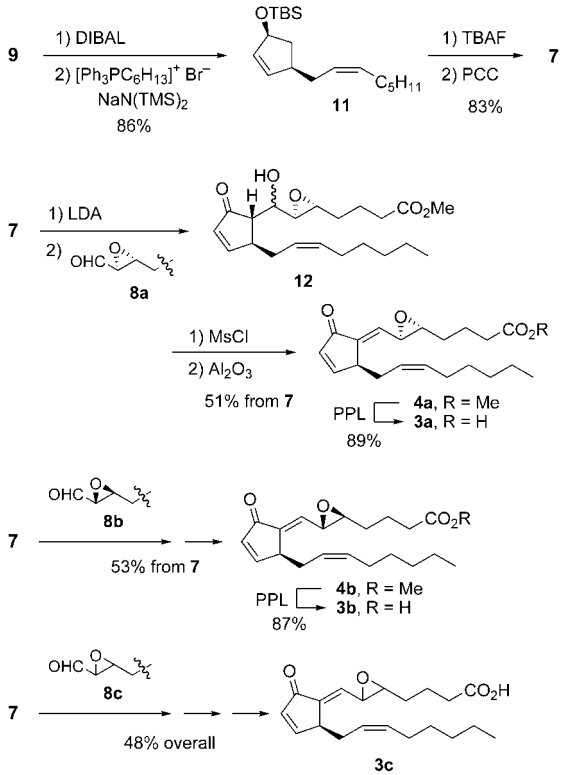

Scheme 4. Stereoselective synthesis of **3a**, **3b**, and **3c** via enone **7**. DIBAL = diisobutylaluminum hydride, LDA = lithium diisopropylamide, Ms = methanesulfonyl, TBAF = tetrabutylammonium fluoride, TMS = trimethylsilyl, PCC = pyridinium chlorochromate.

produce the 7*E* alkene–methyl ester **4a** in 51% yield from **7**.[13] No signal was observed for the hydrogen atom at C7 of the *Z* isomer in the expected 0.5–1-ppm upfield region.[14] Finally, the hydrolysis of **4a** with porcine pancreatic lipase (PPL) furnished epoxyisoprostane **3a** in 89% yield. Similarly, the aldol reaction of **7** with epoxyaldehyde **8b**[11] followed by hydrolysis with PPL afforded **3b** in 46% yield from **7**. The diastereomeric mixture **3c** (a 1:1 mixture of **3a** and **3b**) was synthesized from **7** and the racemic epoxide **8c**.

Expanded ^{1}H NMR spectra of **3a**, **3b**, **3c** (a 2:3 mixture of **3a** and **3b**), [15] and natural **3** that include the signals for the diagnostic 7-H atom ($\delta = 6.1$–6.2 ppm) and the less variable 10-H atom ($\delta = 6.3$–6.4 ppm) are presented in Figure 1.[16,17] For comparison, the spectrum of the analogue **6** is also sketched, but in two possible ways, since the chemical shift of residual $CHCl_3$ ($\delta = 7.24$ or 7.26 ppm) in $CDCl_3$, which was used as the reference, is not reported. The observed baseline separation of the signals for the 7-H atom in **3a** and **3b**, and the negligible drift in the chemical shifts for 7-H and 10-H of **3a** and **3b** in the mixture **3c**, show the high reliability of this method for the elucidation. Clearly, the spectrum of **3a** is coincident with that of natural **3**, thus allowing the determination of the 5*R**,6*R**,12*S** relative configuration and the 7*E* olefin geometry for natural **3**. This configuration is different from that assigned by analogy with the analogue **6**.[6]

Finally, the synthesis of the isoprostane phosphorylcholine **2a** was investigated. From the methods available for the synthesis of phospholipids,[18,19] we chose the direct esterification of **3a** with 1-palmitoyl-2-lyso-PC (**13**; PC = phosphorylcholine) since the reagents or conditions established for the other methods seemed incompatible with **3a**. Unfortunately, an attempted esterification of **3a** and the lyso-PC **13** with the standard reagent (DCC/DMAP)[19] did not take place even upon treatment at elevated temperatures for several days.[20] However, the treatment of **3a** and **13** with the Yamaguchi reagent[21,22] in CH_2Cl_2[23] at room temperature for 36 h afforded **2a** in 53% yield after chromatography on silica gel to obtain a mixture of **2a** and DMAP, and then reversed-phase chromatography to separate the mixture (Scheme 5).

According to the literature, the formation of **2** in vivo from 1-palmitoyl-2-arachidonoyl-PC may be a non-enzymatic process;[2,5] therefore, **2** is probably a diastereomeric mixture

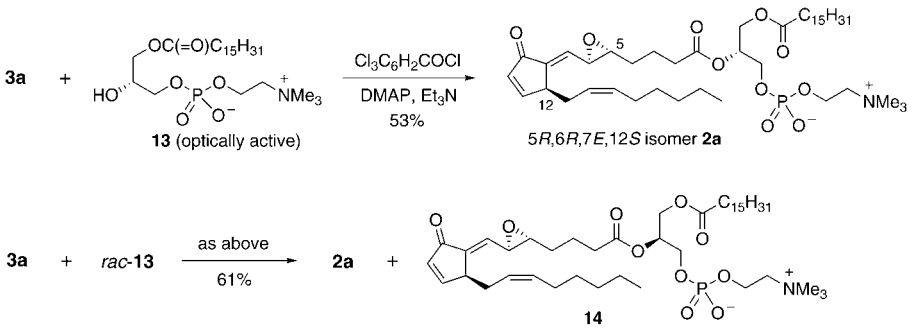

Scheme 5. Synthesis of two diastereomers of **2**. DMAP = 4-dimethylaminopyridine.

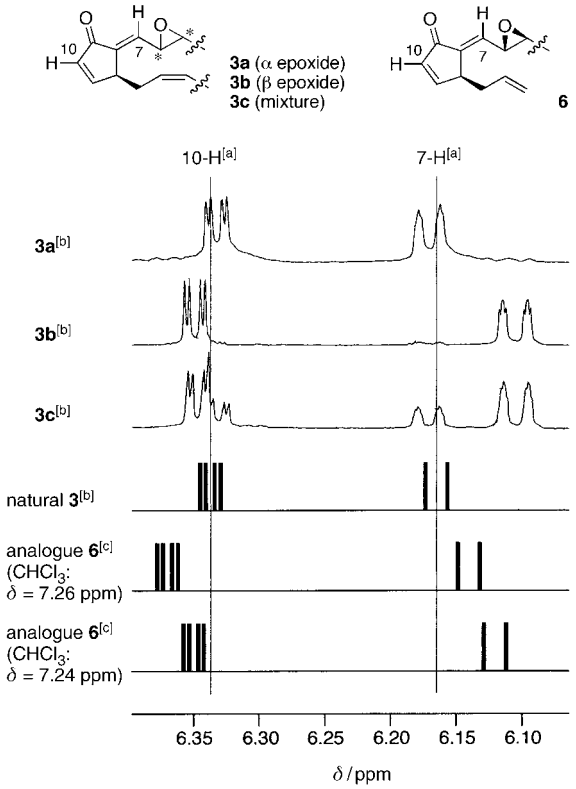

Figure 1. Expanded ^{1}H NMR spectra (500 MHz, $CDCl_3$) of **3a–c**, natural **3**, and the analogue **6**. [a] Reference lines that cross the center of the signals for natural **3**. [b] As residual $CHCl_3$, used as a reference in the ^{1}H NMR spectrum (500 MHz) of natural **3**, is set at $\delta = 7.24$ ppm, the spectra of **3a**, **3b**, and **3c** were referenced in the same way. [c] As the chemical shift of $CHCl_3$ is not reported, two spectra of **6** are represented in which it is assumed that the signal for $CHCl_3$ is observed at $\delta = 7.26$ or 7.24 ppm in the original spectrum.

in which both possible substituents derived from the carboxylic acids **3a** and *ent*-**3a** are present at the *sn*-2 position. To obtain spectroscopic and chromatographic information about the diastereomer derived from *ent*-**3a**, the condensation of **3a** and *rac*-**13**[24] was carried out under the above conditions to synthesize **2a** and **14**, the latter of which is the enantiomer of the compound in question. The mixture (**2a** and **14**), produced in 61% yield, was inseparable by TLC and column chromatography. Furthermore, the ^{1}H NMR (500 MHz) spectrum of the mixture was superimposable on that of pure **2a**.

In conclusion, we have established the relative configuration of the epoxyisoprostane component of **2** as **3a**. Moreover, **2a** was successfully constructed from **3a** and 1-palmitoyl lyso-PC (**13**) by using the Yamaguchi reagent. The present method would also be applicable to the synthesis of the regioisomers of **2** that were described recently.[5] We believe that the biological study of atherosclerosis will be spurred by the stereodefinition of 2-(5,6-epoxyisoprostane A_2)phosphorylcholine.

Received: February 12, 2005
Published online: April 28, 2005

Keywords: aldol reaction · isoprostanes · phospholipids · phosphorylcholine · total synthesis

[1] A. D. Watson, G. Subbanagounder, D. S. Welsbie, K. F. Faull, M. Navab, M. E. Jung, A. M. Fogelman, J. A. Berliner, *J. Biol. Chem.* **1999**, *274*, 24787–24798.

[2] a) A. D. Watson, N. Leitinger, M. Navab, K. F. Faull, S. Hörkkö, J. L. Witztum, W. Palinski, D. Schwenke, R. G. Salomon, W. Sha, G. Subbanagounder, A. M. Fogelman, J. A. Berliner, *J. Biol.*

Chem. **1997**, *272*, 13597 – 13607; b) J. A. Berliner, *Vasc. Pharmacol.* **2002**, *38*, 187 – 191; c) A. Jerlich, R. J. Schaur, A. R. Pitt, C. M. Spickett, *Free Radical Res.* **2003**, *37*, 645 – 653.

[3] a) N. Leitinger, T. R. Tyner, L. Oslund, C. Rizza, G. Subbanagounder, H. Lee, P. T. Shih, N. Mackman, G. Tigyi, M. C. Territo, J. A. Berliner, D. K. Vora, *Proc. Natl. Acad. Sci. USA* **1999**, *96*, 12010 – 12015; b) J. A. Berliner, G. Subbanagounder, N. Leitinger, A. D. Watson, D. Vora, *Trends Cardiovasc. Med.* **2001**, *11*, 142 – 147.

[4] L. Boring, J. Gosling, M. Cleary, I. F. Charo, *Nature* **1998**, *394*, 894 – 897.

[5] G. Subbanagounder, J. W. Wong, H. Lee, K. F. Faull, E. Miller, J. L. Witztum, J. A. Berliner, *J. Biol. Chem.* **2002**, *277*, 7271 – 7281.

[6] M. E. Jung, A. Kers, G. Subbanagounder, J. A. Berliner, *Chem. Commun.* **2003**, 196 – 197. It is uncertain that the 1,4-addition of the *cis*-2-heptenyl anion to enone **5** would proceed at the terminal carbon atom of the anion regioselectively with retention of the *cis* olefin geometry.

[7] For recent reviews of other isoprostane syntheses, see: a) G. Helmchen, M. Ernst, G. Paradies, *Pure Appl. Chem.* **2004**, *76*, 495 – 506; b) L. G. Quana, J. K. Cha, *Chem. Phys. Lipids* **2004**, *128*, 3 – 14; c) T. Durand, A. Guy, O. Henry, A. Roland, S. Bernad, S. E. Fangour, J.-P. Vidal, J.-C. Rossi, *Chem. Phys. Lipids* **2004**, *128*, 15 – 33; d) J. Rokach, S. Kima, S. Bellone, J. A. Lawson, D. Praticò, W. S. Powell, G. A. FitzGerald, *Chem. Phys. Lipids* **2004**, *128*, 35 – 56; e) D. F. Taber, R. S. Hoerrner, R. J. Herr, D. M. Gleave, K. Kanai, R. Pina, Q. Jiang, M. Xu, *Chem. Phys. Lipids* **2004**, *128*, 57 – 67.

[8] a) R. Noyori, M. Suzuki, *Angew. Chem.* **1984**, *96*, 854 – 882; *Angew. Chem. Int. Ed. Engl.* **1984**, *23*, 847 – 876; b) R. Noyori, M. Suzuki, *Chemtracts: Org. Chem.* **1990**, *3*, 173 – 197; c) M. Suzuki, Y. Morita, H. Koyano, M. Koga, R. Noyori, *Tetrahedron* **1990**, *46*, 4809 – 4822; d) M. Suzuki, T. Kawagishi, A. Yanagisawa, T. Suzuki, N. Okamura, R. Noyori, *Bull. Chem. Soc. Jpn.* **1988**, *61*, 1299 – 1312.

[9] a) T. Sugai, K. Mori, *Synthesis* **1988**, 19 – 22; b) K. Laumen, M. P. Schneider, *J. Chem. Soc. Chem. Commun.* **1986**, 1298 – 1299.

[10] H. P. Acharya, Y. Kobayashi, *Tetrahedron Lett.* **2004**, *45*, 1199 – 1202.

[11] The epoxyaldehydes **8a** and **8b** were prepared from the corresponding allylic alcohol in two steps according to a literature procedure with modification of the second step (1) *t*BuOOH, D-(−)-DIPT or L-(+)-DIPT (diisopropyl tartrate), $Ti(OPr)_4$; 2) SO_3-pyridine): A. M. Kornilov, A. E. Sorochinskii, I. A. Butovich, V. P. Kukhar, *Zh. Org. Khim.* **1987**, *23*, 2470 – 2471; A. M. Kornilov, A. E. Sorochinskii, I. A. Butovich, V. P. Kukhar, *J. Org. Chem. USSR* **1987**, *23*, 2183 – 2184.

[12] a) G. H. Posner, G. M. Gurria, K. A. Babiak, *J. Org. Chem.* **1977**, *42*, 3173 – 3180; b) K. Yamada, T. Arai, H. Sasai, M. Shibasaki, *J. Org. Chem.* **1998**, *63*, 3666 – 3672.

[13] The Al_2O_3-assisted elimination generally produces the thermodynamically stable alkene (see reference [10] and the references cited therein).

[14] a) G. L. Bundy, D. R. Morton, D. C. Peterson, E. E. Nishizawa, W. L. Miller, *J. Med. Chem.* **1983**, *26*, 790 – 799; b) S. Sugiura, T. Toru, T. Tanaka, A. Hazato, N. Okamura, K. Bannai, K. Manabe, S. Kurozumi, R. Noyori, *Chem. Pharm. Bull.* **1984**, *32*, 4658 – 4661; c) J. Zhu, J.-Y. Yang, A. J. H. Klunder, Z.-Y. Liu, B. Zwanenburg, *Tetrahedron* **1995**, *51*, 5847 – 5870.

[15] This 2:3 mixture of diastereomers was synthesized by another sequence of reactions: 1) aldol reaction of **7** with $MeO_2C(CH_2)_3CH{=}CHCHO$; 2) epoxidation of the resulting *anti* aldol product with *t*BuOOH/$Ti(OiPr)_4$; 3) mesylation; 4) elimination of the mesylate group with Al_2O_3.

[16] The ^{1}H NMR spectra of **3a**, **3b**, and **3c** were recorded under identical conditions to those reported[1] for natural **3** (500 MHz, $CDCl_3$, residual $CHCl_3$ set at $\delta = 7.24$ instead of 7.26 ppm).

[17] The exposure of **3a** to silica gel afforded lactone **I**, whose signals in the ^{1}H NMR spectrum overlap with another diagnostic multiplet at $\delta = 2.5$–2.7 ppm; therefore we used the clearly resolved region $\delta = 6.0$–6.2 ppm for the assignment. Furthermore, the signals for the lactone can be seen in the reported spectrum of **3**[1] at $\delta \approx 4.40$ and 4.80 ppm as the isolated signals and at $\delta = 6.35$ and 7.55 ppm as shoulders. Compound **I** is probably formed by epoxide-ring opening by H_2O under weakly acidic conditions (silica gel and/or DCl in $CDCl_3$) and subsequent lactonization of the resulting diol.

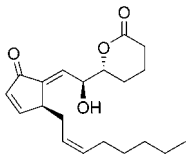

I

[18] a) F. Ramirez, J. E. Marecek, *Synthesis* **1985**, 449 – 488; b) J. M. Delfino, S. L. Schreiber, F. M. Richards, *Tetrahedron Lett.* **1987**, *28*, 2327 – 2330; c) J. Xia, Y.-Z. Hui, *Chem. Pharm. Bull.* **1999**, *47*, 1659 – 1663; d) F. S. Roodsari, D. Wu, S. G. Pum, J. Hajdu, *J. Org. Chem.* **1999**, *64*, 7727 – 7737; e) P. R. J. Gaffney, C. B. Reese, *J. Chem. Soc. Perkin Trans. 1* **2001**, 192 – 205.

[19] For recent examples, see: a) F. M. Menger, Y.-L. Wong, *J. Org. Chem.* **1996**, *61*, 7382 – 7390; b) J. Lindberg, J. Ekeroth, P. Konradsson, *J. Org. Chem.* **2002**, *67*, 194 – 199; c) M. Sun, Y. Deng, E. Batyreva, W. Sha, R. G. Salomon, *J. Org. Chem.* **2002**, *67*, 3575 – 3584; d) X. Gu, M. Sun, B. Gugiu, S. Hazen, J. W. Crabb, R. G. Salomon, *J. Org. Chem.* **2003**, *68*, 3349 – 3761; DCC = *N*,*N*′-cyclohexylcarbodiimide.

[20] Prior to the attempted esterification mentioned in the text, we succeeded in the condensation of linoleic acid with 1-palmitoyl lyso-PC in the presence of DCC and DMAP in CH_2Cl_2 to afford the product in 77% yield.

[21] a) J. Inanaga, K. Hirata, H. Saeki, T. Katsuki, M. Yamaguchi, *Bull. Chem. Soc. Jpn.* **1979**, *52*, 1989 – 1993; b) K. Makino, N. Nakajima, S. Hashimoto, O. Yonemitsu, *Tetrahedron Lett.* **1996**, *37*, 9077 – 9080.

[22] We have used the Yamaguchi reagent for the macrocyclization of macrosphelides C, F, G, and H: a) Y. Kobayashi, H. P. Acharya, *Tetrahedron Lett.* **2001**, *42*, 2817 – 2820; b) Y. Kobayashi, Y.-G. Wang, *Tetrahedron Lett.* **2002**, *43*, 4381 – 4384.

[23] Because of the low solubility of the lyso-PC, toluene, the standard solvent for the Yamaguchi reaction, was not used.

[24] Prepared from racemic glycidol according to a literature method; see reference [19b].

Natural Product Synthesis

Total Synthesis of (+)-Dactylolide through an Efficient Sequential Peterson Olefination and Prins Cyclization Reaction**

*Danielle L. Aubele, Shuangyi Wan, and Paul E. Floreancig**

Dedicated to Professor Peter Dervan on the occasion of his 60th birthday

Dactylolide (**1**, Figure 1) is a bicyclic macrolactone that was isolated from the Vanuatu sponge *Dactylospongia* in 2001 by Riccio and co-workers.[1] While dactylolide is moderately cytotoxic toward L1210 (lymphatic leukemia) and SK-OV-3 (ovarian cancer) cells, causing 63% and 40% growth inhibition, respectively, at 3.2 $\mu g\,mL^{-1}$ (8.3 μM), the structurally related natural product zampanolide (**2**)[2] shows significantly greater cytotoxic activity, with IC_{50} values of 1–5 nM against several cell lines. Upon completing the syntheses of **1** and **2**,[3] Smith et al. concluded, on the basis of optical rotation data, that the common macrolide cores of these compounds have opposite absolute configurations. The incongruence in optical rotations between natural ($[\alpha]_D = +30°$, $c = 1$, MeOH) and synthetic ($[\alpha]_D = +235°$, $c = 0.52$, MeOH[3] or $-128°$, $c = 0.39$, MeOH, antipode[4]) dactylolide, however, preclude a firm conclusion regarding its absolute stereochemistry. Hoye and Hu's demonstration[4] that dactylolide can be converted into zampanolide through an aza-aldol addition shows that both compounds can be accessed through a common strategy, provided the route can be used to access either enantiomer. Herein, we report a convergent and efficient route to dactylolide that employs an acetal linkage to fuse two complex fragments and a Prins reaction that proceeds under remarkably mild conditions to form the methylene tetrahydropyran group. In this sequence stereogenicity is derived from asymmetric catalysts that are readily available as either enantiomer, which makes the route also applicable to the synthesis of zampanolide.

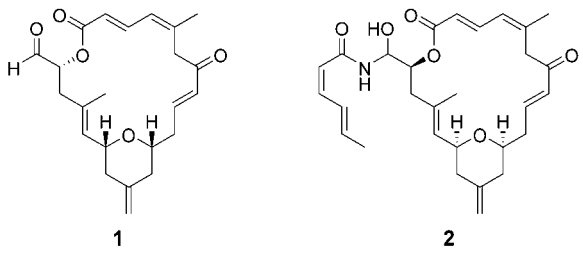

Figure 1. (+)-Dactylolide and (−)-zampanolide.

We established two key objectives for the synthesis of dactylolide (Figure 2): to maximize convergency by coupling two functionalized subunits at a reasonably late stage in the sequence, and to minimize the number of carbon–carbon bond-forming reactions. We postulated that the former objective could result from the union of two advanced fragments through an acetal linkage.[5] This somewhat underutilized approach to increasing molecular complexity is quite attractive in both the efficiency of the coupling and the capacity for acetals to serve as precursors for structurally diverse ethers. We envisioned asymmetric vinylogous Mukaiyama aldol reactions[6] to be effective vehicles for achieving the latter objective. Thus **1** can be accessed from diol **3**, which, in turn, results from transposed allylic alcohol **4** (Figure 2). Acetal **5**, prepared through the union of **6** and **7**, serves as the precursor for the methylene tetrahydropyran. We recently reported[7] that acetals of this general structure undergo Prins reactions under very mild conditions, with promotion of the process in water by Lewis acid surfactant catalysts.[8] Sequences that employ catalytic, asymmetric vinylogous Mukaiyama aldol reactions can be designed to access **6** and **7** from *p*-methoxybenzyloxyacetaldehyde and 2-butynol, respectively.

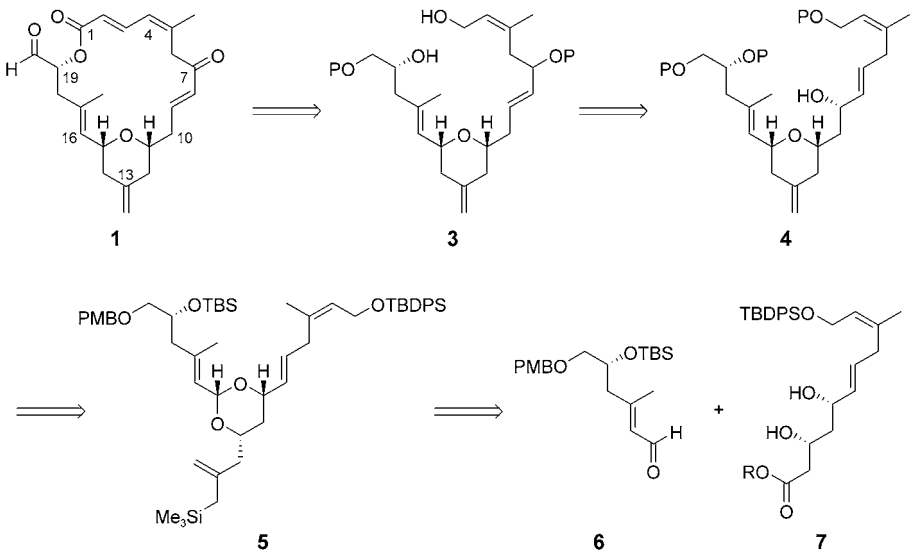

Figure 2. Retrosynthetic analysis of dactylolide. P = protecting group, PMB = *p*-methoxybenzyl, TBS = *tert*-butyldimethylsilyl, TBDPS = *tert*-butyldiphenylsilyl.

[*] D. L. Aubele,[+] S. Wan, Prof. Dr. P. E. Floreancig
Department of Chemistry
University of Pittsburgh
Pittsburgh, PA 15260 (USA)
Fax: (+1) 412-624-8611
E-mail: florean@pitt.edu

[+] Current address:
Elan Pharmaceuticals, Inc.
800 Gateway Blvd.
South San Francisco, CA 94080 (USA)

[**] We thank the National Institutes of Health (GM-62924) for generous financial support of this work.

Supporting information for this article is available on the WWW under http://www.angewandte.org or from the author.

 DOI: 10.1002/anie.200500564

The synthesis of **6** (Scheme 1) requires a high level of control over both the stereocenter at C19 and the geometry of the trisubstituted alkene. Our route to **6** follows the sequence devised by Evans et al. in their synthesis of callipeltoside.[9]

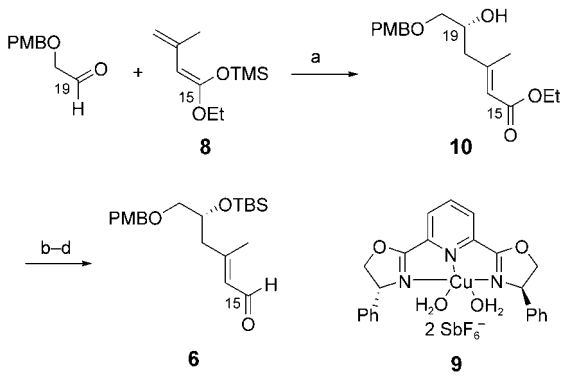

Scheme 1. a) **9**, CH_2Cl_2, −78 °C, 82 %, 95 % *ee*; b) TBSCl, imidazole, DMF, 89 %; c) $LiAlH_4$, Et_2O; d) MnO_2, CH_2Cl_2, 80 %, 2 steps. DMF = *N*,*N*-dimethylformamide.

Condensation of silyl ketene acetal **8** with *p*-methoxybenzyloxyacetaldehyde in the presence of Cu·pybox catalyst **9**[10] provided **10** in 82 % yield and 95 % *ee*, with the alkene formed as a single isomer. Conversion of **10** into **6** proceeded through a straightforward three-step sequence of protection, reduction, and oxidation.

As an entry into **7** (Scheme 2), the geometry of the $\Delta^{4,5}$-trisubstituted olefin was set through a hydroalumination reaction of 2-butynol with Red-Al[11] followed by quenching with Bu_3SnCl to form vinyl stannane **11** in 93 % yield. Following protection of the primary hydroxyl group, palladium-mediated coupling[12] with bromide **12**[13] and acetal hydrolysis in situ provided enal **13** in 80 % yield. To the best of our knowledge, this is the first report of **12** serving as an electrophilic surrogate for crotonaldehyde in a cross-coupling reaction. The absence of a chelating group in **13** precluded the use of the Cu·pybox complex as a promoter of aldol chemistry. Therefore we utilized Denmark's bisphosphoramide catalytic system **15**[14] and $SiCl_4$ to effect coupling between **13** and ketene acetal **14** to yield alcohol **16** in 93 % *ee* and 67 % yield at 83 % conversion (83 % yield based on recovered starting material). Notably, this reaction proceeded with even higher selectivity than the corresponding reaction with cinnamaldehyde that was reported in the original manuscript,[15] which suggests that this catalyst is well suited for applications in the synthesis of complex molecules. Thermolysis of **16** in BuOH followed by *syn*-reduction of the resulting keto ester with Et_2BOMe and $NaBH_4$[16] completed the synthesis of diol **7**.

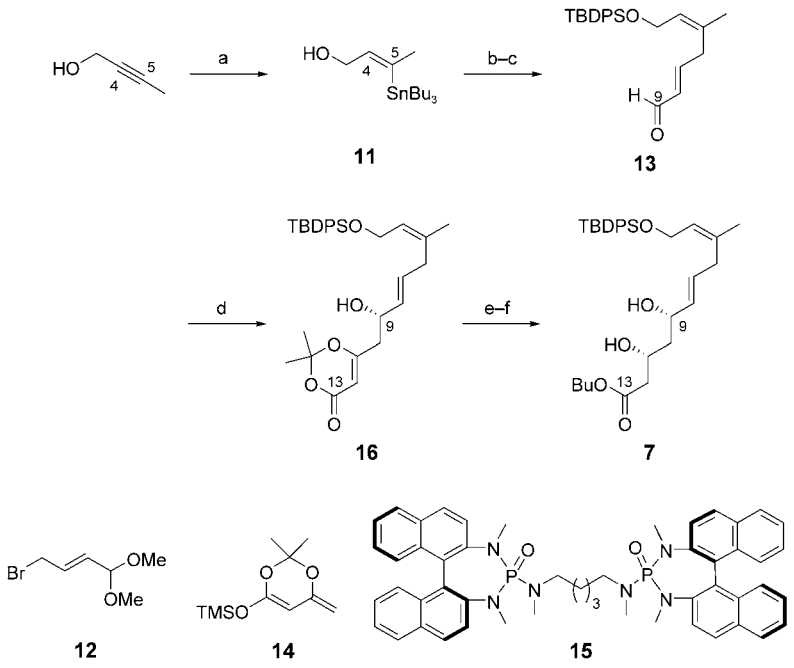

Scheme 2. a) Red-Al, THF, then Bu_3SnCl, 93 %; b) TBDPSCl, imidazole, DMF, 87 %; c) **12**, $[(CH_3CN)_2PdCl_2]$, PPh_3, $CHCl_3$, 65 °C, then HCO_2H, CH_2Cl_2, 80 %; d) **15**, $SiCl_4$, **14**, CH_2Cl_2, −78 °C, 67 % at 83 % conversion, 93 % *ee*; e) *n*BuOH, reflux, 74 %; f) Et_2BOMe, $NaBH_4$, THF, −78 °C, 83 %. Red-Al = sodium bis(2-methoxyethoxy)aluminumhydride.

Formation of the acetal linkage between **6** and **7** (Scheme 3) through standard acid catalysis was complicated by competitive isomerization of the trisubstituted alkene in the enal. Conversion of **7** into its bis-trimethylsilyl ether and coupling with **6** using Noyori's TMSOTf-mediated protocol,[17] however, provided acetal **17** in high yield and without isomerization. In preparation for the Prins reaction, we subjected **17** to excess $TMSCH_2MgCl$ and $CeCl_3$ followed by an acidic workup.[18] To our surprise the major product isolated from this reaction was methylene tetrahydropyran **19**, the desired subunit of dactylolide, which resulted from allylsilane formation, followed by acetal ionization to provide oxocarbenium ion **18**, and cyclization. After conducting a series of experiments designed to elucidate the initiator for the Prins reaction, we concluded that weakly Lewis acidic cerium salts are not completely removed in the aqueous workup and initiate ionization and cyclization upon evaporation of the organic solvent. While this process was quite direct, the yields proved to be irreproducible. A more reliable protocol for this transformation was devised in which the addition of alkylcerium was quenched with aqueous $NaHCO_3$ and a solution of the resulting crude tertiary alcohol in CH_2Cl_2 was subjected to pyridinium triflate and $MgSO_4$ to effect a sequential Peterson olefination and Prins cyclization. This remarkably mild process routinely provided **19** in 75 % yield from **17**. The desiccant and the non-nucleophilic triflate ion were both necessary to promote cyclization without causing protodesilylation of the allylsilane. Although acetal ionization can occur to form two oxocarbenium ions, **18** can proceed through a kinetically facile 6-*endo* pathway while cyclization through the alternative ion would proceed through a less favorable 8-*endo* pathway. Therefore the observed selectivity strongly suggests that cyclization is the product-determining step rather than ionization.[19]

Transposition of the C9 allylic alcohol that was formed in the Prins reaction was required to complete the synthesis of dactylolide (Scheme 4) and was achieved through conversion of the hydroxyl group of **19**

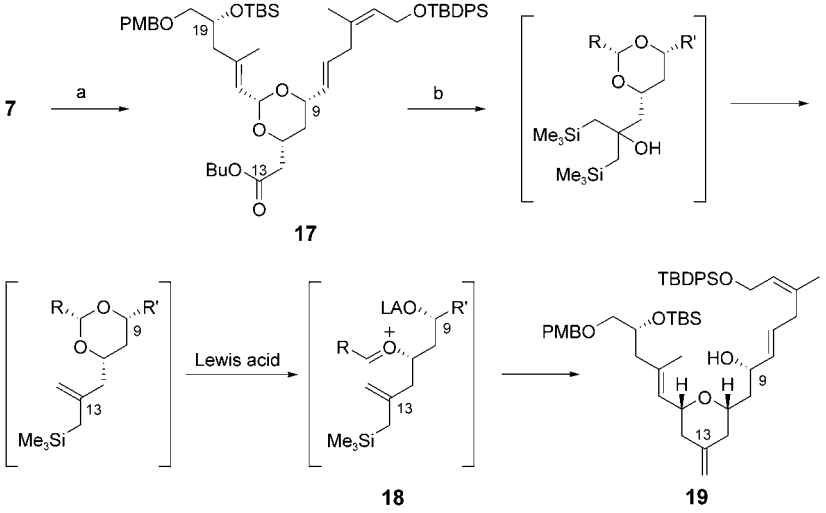

Scheme 3. a) (1) TMSCl, imidazole, DMAP, DMF; (2) **6**, TMSOTf, CH_2Cl_2, −78 °C, 83 %; b) 1) Me_3SiCH_2MgCl, $CeCl_3$, THF, −78 °C→RT; 2) Py·HOTf, $MgSO_4$, CH_2Cl_2, 75 %. TMS = trimethylsilyl, DMAP = 4-dimethylaminopyridine, Tf = trifluoromethanesulfonyl, Py (py) = pyridine, LA = Lewis acid.

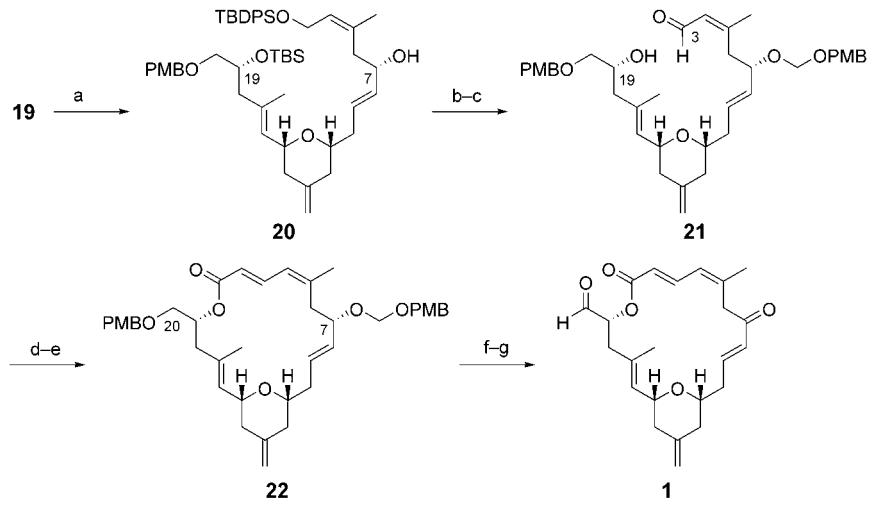

Scheme 4. a) (1) PhSeCN, Bu_3P, THF; (2) H_2O_2, py, THF, −30 °C, 62 %; b) (1) $PMBOCH_2Cl$, iPr_2NEt, CH_2Cl_2; (2) HF·Py, py, THF, 80 %; c) $PhI(OAc)_2$, TEMPO, CH_2Cl_2, 87 %; d) Diethylphosphonoacetic acid, DCC, DMAP, CH_2Cl_2, 95 %; e) NaHMDS, THF, −78 →0 °C, 73 %; f) DDQ, CH_2Cl_2, buffer (pH 7), 63 % (14 % C7 ketone); g) Dess–Martin periodinane, CH_2Cl_2, 77 %. TEMPO = 2,2,6,6-tetramethylpiperidinyl-1-oxyl, DCC = dicyclohexyl carbodiimide, HMDS = hexamethyldisilazide, DDQ = 2,3-dichloro-5,6-dicyano-1,4-benzoquinone.

into a selenide with PhSeCN and Bu_3P[20], with no complication from the S_N2' pathway. Oxidation of the crude selenide with H_2O_2 in the presence of pyridine induced a selenium variant[21] of the Mislow–Evans rearrangement[22] to provide allylic alcohol **20** in 62 % yield over the two-step sequence.[23] While the stereochemical outcome of this reaction was not rigorously established, mechanistic analogy[24] strongly suggests that the nascent alcohol is oriented as shown in Scheme 4. Attempts to form the PMB ether of the hydroxyl group at C7 under basic (NaH, PMBCl, NaI) or acidic ($PMBOC(NH)CCl_3$, $BF_3{\cdot}OEt_2$, or TfOH) conditions resulted in low conversions and significant decomposition. Formation of the *p*-methoxybenzyloxymethyl ether[25] ($PMBOCH_2Cl$, iPr_2NEt), however, proceeded much more efficiently. Desilylation of the resulting ether with Py·HF yielded the C3,C19 diol in 80 % yield from **20**. Selective oxidation of the primary allylic C3 alcohol with TEMPO and $PhI(OAc)_2$[26] formed aldehyde **21** in 87 % yield. Macrolactone formation was most conveniently accomplished through an intramolecular Horner–Emmons reaction, a parallel of Smith's approach[3] to this system. Acylation of the hydroxyl group at C19 with diethylphosphonoacetic acid and DCC provided the corresponding phosphonoacetate, which, upon deprotonation with NaHMDS, engaged in an intramolecular condensation reaction to provide macrolactone **22** in 73 % yield from **21**. The synthesis was completed by an oxidative cleavage of both protecting groups with DDQ. This process provided the C7,C20 diol along with variable amounts of the C7 ketone. The allylic oxidation proved to be inconsequential as the following step was a double oxidation of the diol with the Dess–Martin periodinane[27] to provide dactylolide in 77 % yield ($[\alpha]_D = +163°$, $c = 0.29$, MeOH).

In summary, we have reported an efficient total synthesis of dactylolide. Key steps in the sequence include two enantioselective vinylogous Mukaiyama reactions, fragment coupling through acetal formation, a sequential Peterson olefination/Prins cyclization reaction that proceeds under very mild conditions, and a Mislow–Evans rearrangement to effect the transposition of an allylic alcohol. The linear sequence was kept as brief as possible by minimizing carbon–carbon bond-forming reactions and employing a convergent approach. As both antipodes of the catalysts that were used to establish stereogenicity are available, this sequence is also applicable to the synthesis of zampanolide through the use of Hoye's aza-aldol reaction.

Received: February 15, 2005
Published online: April 21, 2005

Keywords: allylic compounds · asymmetric synthesis · carbocations · natural products · rearrangement

[1] A. Cutignano, I. Bruno, G. Bifulco, A. Casapullo, C. Debitus, L. Gomez-Paloma, R. Riccio, *Eur. J. Org. Chem.* **2001**, 775–778.

[2] J.-i. Tanaka, T. Higa, *Tetrahedron Lett.* **1996**, *37*, 5535 – 5538.
[3] a) A. B. Smith, III, I. G. Safanov, *Org. Lett.* **2002**, *4*, 635 – 637; b) A. B. Smith, III, I. G. Saonov, R. M. Corbett, *J. Am. Chem. Soc.* **2002**, *124*, 11102 – 11113.
[4] T. R. Hoye, M. Hu, *J. Am. Chem. Soc.* **2003**, *125*, 9576 – 9577.
[5] For several elegant examples of the utility of acetals in synthesis, see: L. E. Overman, L. D. Pennington, *J. Org. Chem.* **2003**, *68*, 7143 – 7157.
[6] For a review, see: G. Casiraghi, F. Zanardi, G. Appendino, G. Rassu, *Chem. Rev.* **2000**, *100*, 1929 – 1972.
[7] D. L. Aubele, C. A. Lee, P. E. Floreancig, *Org. Lett.* **2003**, *5*, 4521 – 4523.
[8] S. Kobayashi, K. Manabe, *Acc. Chem. Res.* **2002**, *35*, 209 – 217.
[9] D. A. Evans, E. Hu, J. D. Burch, G. Jaeschke, *J. Am. Chem. Soc.* **2002**, *124*, 5654 – 5655.
[10] D. A. Evans, M. C. Kozlowski, J. A. Murray, C. S. Burgey, K. R. Campos, B. T. Connell, R. J. Staples, *J. Am. Chem. Soc.* **1999**, *121*, 669 – 685.
[11] S. E. Denmark, T. K. Jones, *J. Org. Chem.* **1982**, *47*, 4595 – 4597.
[12] F. K. Sheffy, J. P. Godschalx, J. K. Stille, *J. Am. Chem. Soc.* **1984**, *106*, 4833 – 4840.
[13] O. Gaonac'h, J. Maddaluno, J. Chauvin, L. Duhamel, *J. Org. Chem.* **1991**, *56*, 4045 – 4048.
[14] S. E. Denmark, T. Wynn, G. L. Beutner, *J. Am. Chem. Soc.* **2002**, *124*, 13405 – 13407.
[15] S. E. Denmark, G. L. Beutner, *J. Am. Chem. Soc.* **2003**, *125*, 7800 – 7801.
[16] K.-M. Chen, G. E. Hardtmann, K. Prasad, O. Repic, M. J. Shapiro, *Tetrahedron Lett.* **1987**, *28*, 155 – 158.
[17] R. Noyori, S. Murata, M. Suzuki, *Tetrahedron* **1981**, *37*, 3899 – 3910.
[18] a) T. V. Lee, J. A. Channon, C. Cregg, J. R. Porter, F. S. Roden, H. T.-L. Yeoh, *Tetrahedron* **1989**, *45*, 5877 – 5886; b) B. A. Narayanan, W. H. Bunnelle, *Tetrahedron Lett.* **1987**, *28*, 6261 – 6264.
[19] For a related example, see: Y. Hu, D. J. Skalitzky, S. D. Rychnovsky, *Tetrahedron Lett.* **1996**, *37*, 8679 – 8682.
[20] P. A. Grieco, S. Gilman, M. Nishizawa, *J. Org. Chem.* **1976**, *41*, 1485 – 1486.
[21] H. J. Reich, *J. Org. Chem.* **1975**, *40*, 2570 – 2572.
[22] D. A. Evans, G. C. Andrews, *Acc. Chem. Res.* **1974**, *7*, 147 – 155.
[23] For the an excellent application of this strategy in complex-molecule synthesis, see: A. K. Mapp, C. H. Heathcock, *J. Org. Chem.* **1999**, *64*, 23 – 27.
[24] H. J. Reich, K. E. Yelm, *J. Org. Chem.* **1991**, *56*, 5672 – 5679.
[25] A. P. Kozikowski, J.-P. Wu, *Tetrahedron Lett.* **1987**, *28*, 5125 – 5128.
[26] A. De Mico, R. Margarita, L. Parlanti, A. Vescovi, G. Piancatelli, *J. Org. Chem.* **1997**, *62*, 6974 – 6977.
[27] a) D. B. Dess, J. C. Martin, *J. Am. Chem. Soc.* **1991**, *113*, 7277 – 7287; b) D. B. Dess, J. C. Martin, *J. Org. Chem.* **1983**, *48*, 4155 – 4156.

Silyl Ethenes

Regio- and Stereoselective Approach to 1,2-Di- and 1,1,2-Trisilylethenes by Cobalt-Mediated Reaction of Silyl-Substituted Dibromomethanes with Silylmethylmagnesium Reagents**

*Hirohisa Ohmiya, Hideki Yorimitsu, and Koichiro Oshima**

Vinylsilanes are useful organometallic reagents in organic synthesis because the C(sp^2)–Si bonds undergo numerous transformations.[1] Multiply silylated ethenes are thus likely to represent platforms for a variety of highly substituted ethenes. Moreover, multiply silylated ethenes themselves attract considerable attention from the viewpoint of structural organic chemistry.[2] Despite their importance, there is a limited number of access routes to multiply silylated ethenes. Hydrosilylation of silylacetylenes[3] and bissilylation of acetylenes[4] are most convenient procedures.[5] Scheme 1 (top)

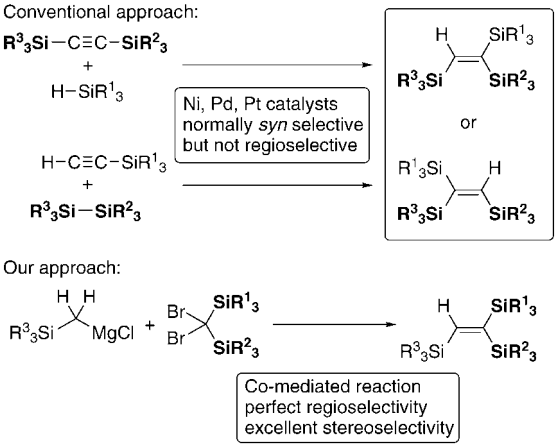

Scheme 1. Conventional and novel approaches toward 1,2-di- and 1,1,2-trisilylethenes.

shows representative approaches, for instance, to trisilylethenes with three different silyl groups. However, difficulties are often encountered in such synthetic strategies in terms of regioselectivity and the occurrence of several side reactions.

During the course of our studies into cobalt-mediated reactions of organic halides with Grignard reagents,[6] we

[*] H. Ohmiya, Dr. H. Yorimitsu, Prof. Dr. K. Oshima
Department of Material Chemistry
Graduate School of Engineering
Kyoto University
Kyoto-daigaku Katsura, Nishikyo-ku, Kyoto 615-8510 (Japan)
Fax: (+81) 75-383-2438
E-mail: oshima@orgrxn.mbox.media.kyoto-u.ac.jp

[**] This work was supported by Grants-in-Aid for Scientific Research for Young Scientists and COE Research from the Ministry of Education, Culture, Sports, Science, and Technology, Japan.

Supporting information for this article is available on the WWW under http://www.angewandte.org or from the author.

  DOI: 10.1002/anie.200500576

serendipitously found that the reaction of dibromomethane with dimethyl(phenyl)silylmethylmagnesium chloride in the presence of a cobalt salt provided dimethyl(phenyl)vinylsilane in excellent yield [Eq. (1)]. This observation encouraged us to explore the potential of silylated dibromomethanes[7] as precursors for multiply silylated ethenes (Scheme 1, bottom). Herein we report an inherently regioselective and, fortunately, stereoselective preparation of 1,2-di- and 1,1,2-trisilylethenes by means of a cobalt salt, thus creating a novel approach toward multiply silylated ethenes.[8,9]

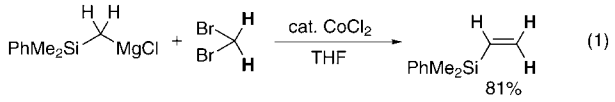

(1)

After optimization of reaction conditions, the synthesis of 1,2-disilylethene proved to require cobalt(II) chloride (10 mol%) and a Grignard reagent (3 equiv). THF was the solvent of choice, while ether, dioxane, and HMPA were far inferior. The best results were found at a reaction temperature of 20 °C. Table 1 summarizes the syntheses of various 1,2-disilylethenes. All the reactions resulted in the exclusive formation of (*E*)-1,2-disilylethenes **1** in high yields. The steric hindrance of the silyl groups such as $MePh_2Si$ and $tBuMe_2Si$ had virtually no adverse influence on the synthesis. Interestingly, isopropoxy- and allyl-substituted silylmethyl Grignard reagents participated in this reaction.

Table 1: Synthesis of (*E*)-1,2-disilylethenes **1**.

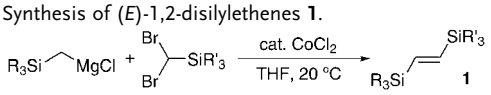

Entry	R_3Si	R′Si	**1**	Yield [%]
1	Me_3Si	Me_2PhSi	**a**	87
2	Me_3Si	$MePh_2Si$	**b**	86
3	Me_3Si	$tBuMe_2Si$	**c**	70
4	Me_2PhSi	Me_3Si	**a**	90
5	Me_2PhSi	Me_2PhSi	**d**	78
6	$(iPrO)Me_2Si$	Me_2PhSi	**e**	88
7	$(CH_2{=}CHCH_2)Me_2Si$	Me_2PhSi	**f**	79

The high efficiency of this method prompted us to examine dibromodisilylmethanes as starting materials. Contrary to our expectation, the catalytic conditions did not give satisfactory results. Instead, stoichiometric use of a cobaltate reagent $[(R^3{}_3SiCH_2)_4Co(MgCl)_2]$,[10,11] prepared from Co^{II} chloride and a Grignard reagent (4 equiv), allowed the efficient synthesis of 1,1,2-trisilylethenes (Table 2). The reactions of $(Me_3Si)_2CBr_2$ proceeded smoothly to afford **2a** and **2b** in good yields (Table 2, entries 1 and 2). The bulkier $MePh_2Si$- and $tBuMe_2Si$-substituted precursors were also converted into **2** in reasonable yields (Table 2, entries 3–7). The reactions were clean, and the main by-products were $(R^1{}_3Si)(R^2{}_3Si)C(H)Br$, $(R^1{}_3Si)(R^2{}_3Si)CH_2$, and $(R^1{}_3Si)(R^2{}_3Si)C{=}CH_2$, which were readily separated from the desired products by size-exclusion chromatography (see below). Gratifyingly, treatment of unsymmetrically substituted dibromodisilylmethanes under similar conditions yielded (*E*)-**2e**–**2g** with three different silyl groups stereoselectively (Table 2, entries 5–7). The reaction of a dibromosilylstannylmethane furnished the corresponding (*Z*)-1,2-disilyl-1-stannylethene **2h** with good stereoselectivity (Table 2, entry 8). There are few facile methods for the stereo- and regioselective synthesis of ethenes with different Group 14 metal substituents. Unfortunately, the attempted synthesis of tetrasilylethene from $(R_3Si)_2CBr_2$ and $(R_3Si)_2CHMgCl$ did not succeed.

Table 2: Synthesis of 1,1,2-trisilylethenes **2**.

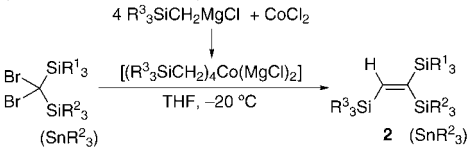

Entry	$R^1{}_3Si$	$R^2{}_3Si$	$R^3{}_3Si$	**2**	Yield [%]	*E*/*Z*
1	Me_3Si	Me_3Si	Me_3Si	**a**	75	–
2	Me_3Si	Me_3Si	Me_2PhSi	**b**	73	–
3	$MePh_2Si$	$MePh_2Si$	Me_3Si	**c**	55	–
4	$tBuMe_2Si$	Me_3Si	Me_3Si	**d**	58	100:0[a]
5	$MePh_2Si$	Me_3Si	$(iPrO)Me_2Si$	**e**	48	90:10[a]
6	$MePh_2Si$	Me_3Si	Me_2PhSi	**f**	54	94:6[a]
7	$MePh_2Si$	Me_3Si	$(CH_2{=}CHCH_2)Me_2Si$	**g**	53	94:6[a]
8	$MePh_2Si$	(Bu_3Sn)	Me_3Si	**h**	51	8:92[b]

[a] Determined by NOE experiments. [b] Judged by $J_{Sn\text{-}H}$.

We propose a mechanism for the stoichiometric reaction as shown in Scheme 2. Halogen–cobalt exchange initially takes place to produce intermediate **3**. One of the silylmethyl groups on the cobalt center migrates to generate **4** with concomitant liberation of bromide.[12] β-Hydride elimination finalizes the formation of 1,1,2-trisilylethene **2**. The major *E* stereoisomers in Table 2 would originate from the more stable eclipsed conformer upon β-hydride elimination. The formation of the by-product $(R^1{}_3Si)(R^2{}_3Si)C{=}CH_2$ can stem from β-silyl elimination.[13]

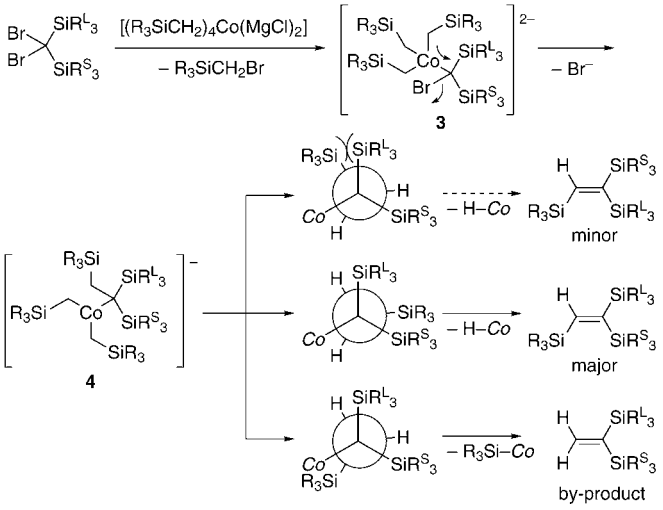

Scheme 2. Proposed mechanism for the formation of 1,1,2-trisilylethenes in the presence of stoichiometric amounts of the cobaltate complex.

In summary, we have developed a novel method for the synthesis of 1,2-di- and 1,1,2-trisilylethenes in a regio- and stereoselective manner. The products are not only useful as precursors for various alkenes but are also structurally interesting. Further improvement of this strategy will allow access to a wide range of ethenes that are multifariously substituted with Group 14 metals.

Experimental Section

General procedure (**1a**): Anhydrous cobalt(II) chloride (6.5 mg, 0.05 mmol) was placed in a 20-mL reaction flask and heated with a hair dryer in vacuo for 2 min. After the cobalt salt turned blue, anhydrous THF (3.0 mL) was added under argon. The mixture was stirred for 3 min at room temperature. Dibromo(dimethyl(phenyl)-silyl)methane (154 mg, 0.50 mmol) and a solution of trimethylsilyl-methylmagnesium chloride in diethyl ether (1.0 M; 1.5 mL, 1.5 mmol) were successively added dropwise to the reaction mixture at 0 °C. While the Grignard reagent was being added, the mixture turned brown. After being stirred for 1 h at 20 °C, the reaction mixture was poured into water. The product was extracted with hexane (2 × 20 mL). The combined organic layer was dried over sodium sulfate and concentrated. Purification of the crude oil by silica-gel column chromatography (hexane) provided the corresponding (*E*)-1,2-di-silylethene **1a** (102 mg, 0.43 mmol) in 87 % yield.

2b: Anhydrous cobalt(II) chloride (97.5 mg, 0.75 mmol) was placed in a 30-mL reaction flask and dried in vacuo for 2 min. Anhydrous THF (5.0 mL) was added under argon, and the mixture was stirred for 3 min at room temperature. A solution of dimethyl-(phenyl)silylmethylmagnesium chloride in diethyl ether (0.95 M; 3.16 mL, 3.0 mmol) was added dropwise to the reaction mixture at −20 °C. After the mixture was stirred for 15 min at −20 °C, dibromobis(trimethylsilyl)methane (159 mg, 0.50 mmol) was added dropwise to the reaction mixture at −20 °C. After being stirred for an additional 1 h at −20 °C, the reaction mixture was poured into water. The product was extracted with hexane (2 × 20 mL). The combined organic layer was dried over sodium sulfate and concentrated. Silica-gel column chromatography (hexane) followed by gel-permeation chromatography (toluene, to remove by-products described above) provided the corresponding 1,1,2-trisilylethene **2b** (111 mg, 0.36 mmol) in 73 % yield.

Received: February 16, 2005
Published online: April 28, 2005

Keywords: alkenes · cobalt · Grignard reagents · silicon · synthetic methods

[1] a) K. Oshima in *Science of Synthesis (Houben-Weyl)*, *Vol. 4* (Ed.: I. Fleming), Georg Thieme, Stuttgart, **2002**, chap. 4.4.34; b) K. Miura, A. Hosomi in *Main Group Metals in Organic Synthesis*, *Vol. 2* (Eds.: H. Yamamoto, K. Oshima), Wiley-VCH, Weinheim, **2004**, chap. 10.4; c) J. S. Panek in *Comprehensive Organic Chemistry*, *Vol. 1* (Eds.: B. M. Trost, I. Fleming), Pergamon, Oxford, **1991**, chap. 2.5; d) M. A. Brook, *Silicon in Organic, Organometallic, and Polymer Chemistry*, Wiley-VCH, New York, **2000**.

[2] a) H. Sakurai, K. Ebata, K. Sakamoto, Y. Nakadaira, C. Kabuto, *Chem. Lett.* **1988**, 965 – 968; b) H. Schmidbaur, J. Ebenhoech, *Z. Naturforsch. B* **1987**, *42*, 1543 – 1548; c) M. Kira, H. Nakazawa, H. Sakurai, *J. Am. Chem. Soc.* **1983**, *105*, 6983 – 6987; d) H. Sakurai, Y. Nakadaira, H. Tobita, T. Ito, K. Toriumi, H. Ito, *J. Am. Chem. Soc.* **1982**, *104*, 300 – 302.

[3] a) T. Suzuki, P. Y. Lo, *J. Organomet. Chem.* **1990**, *391*, 19 – 25; b) E. Lukevics, Z. V. Belyakova, M. G. Pomerantseva, M. G. Voronkov, *J. Organomet. Chem. Libr.* **1977**, *5*, 1 – 179; c) I. Ojima in *The Chemistry of Organic Silicon Compounds* (Eds.: S. Patai, Z. Rappoport), Wiley, Chichester, **1989**, pp. 1479 – 1526; d) *Comprehensive Handbook on Hydrosilylation* (Ed.: B. Marciniec), Pergamon, Oxford, **1992**; e) T. Hiyama, T. Kusumoto in *Comprehensive Organic Chemistry*, *Vol. 8* (Eds.: B. M. Trost, I. Fleming), Pergamon, Oxford, **1991**, chap. 3.12; f) K. A. Horn, *Chem. Rev.* **1995**, *95*, 1317 – 1350.

[4] a) M. Suginome, Y. Ito, *Chem. Rev.* **2000**, *100*, 3221 – 3256; b) J. Hibino, S. Nakatsukasa, K. Fugami, S. Matsubara, K. Oshima, H. Nozaki, *J. Am. Chem. Soc.* **1985**, *107*, 6416 – 6417; c) H. Watanabe, M. Kobayashi, M. Saito, Y. Nagai, *J. Organomet. Chem.* **1981**, *216*, 149 – 157.

[5] For the disproportionation of vinylsilane, see: a) B. Marciniec, E. Walczuk-Gusciora, P. Blazejewska-Chadyniak, *J. Mol. Catal. A* **2000**, *160*, 165 – 171; b) B. Marciniec, J. Guliñski, *J. Organomet. Chem.* **1984**, *266*, C19-C21; for Ru-catalyzed dehydrogenative silylation of vinylsilanes, see: c) Y. Seki, K. Takeshita, K. Kawamoto, *J. Organomet. Chem.* **1989**, *369*, 117 – 123.

[6] a) K. Wakabayashi, H. Yorimitsu, K. Oshima, *J. Am. Chem. Soc.* **2001**, *123*, 5374 – 5375; b) Y. Ikeda, T. Nakamura, H. Yorimitsu, K. Oshima, *J. Am. Chem. Soc.* **2002**, *124*, 6514 – 6515; c) T. Tsuji, H. Yorimitsu, K. Oshima, *Angew. Chem.* **2002**, *114*, 4311 – 4313; *Angew. Chem. Int. Ed.* **2002**, *41*, 4137 – 4139; ; d) T. Fujioka, T. Nakamura, H. Yorimitsu, K. Oshima, *Org. Lett.* **2002**, *4*, 2257 – 2259; e) K. Mizutani, H. Shinokubo, K. Oshima, *Org. Lett.* **2003**, *5*, 3959 – 3961; f) K. Mizutani, H. Yorimitsu, K. Oshima, *Chem. Lett.* **2004**, *33*, 832 – 833; g) T. Nishikawa, H. Yorimitsu, K. Oshima, *Synlett* **2004**, 1573 – 1574; h) H. Ohmiya, H. Yorimitsu, K. Oshima, *Chem. Lett.* **2004**, *33*, 1240 – 1241; i) H. Ohmiya, T. Tsuji, H. Yorimitsu, K. Oshima, *Chem. Eur. J.* **2004**, *10*, 5640 – 5648; j) Y. Ikeda, H. Yorimitsu, H. Shinokubo, K. Oshima, *Adv. Synth. Catal.* **2004**, *346*, 1631 – 1634; k) H. Shinokubo, K. Oshima, *Eur. J. Org. Chem.* **2004**, 2081 – 2091.

[7] A. Inoue, J. Kondo, H. Shinokubo, K. Oshima, *Chem. Lett.* **2001**, 956 – 957, and references therein.

[8] For the cobalt-mediated reaction of dibromocyclopropane with methyl and butyl Grignard reagents, see: Y. Nishii, K. Wakasugi, Y. Tanabe, *Synlett* **1998**, 67 – 69.

[9] We previously reported the manganese-catalyzed reaction of dibromo(silyl)methane with alkyl Grignard reagents to form 1-silyl-1-alkene, and only one example of the synthesis of 1,2-disilylethene was described. However, the reaction is not very efficient (*t*BuMe$_2$SiCH=CHSiMe$_3$, 57 % yield by using a stoichiometric amount of a manganate complex [(Me$_3$SiCH$_2$)$_3$MnMgCl]): a) H. Kakiya, R. Inoue, H. Shinokubo, K. Oshima, *Tetrahedron Lett.* **1997**, *38*, 3275 – 3278; b) H. Kakiya, H. Shinokubo, K. Oshima, *Bull. Chem. Soc. Jpn.* **2000**, *73*, 2139 – 2147.

[10] The exact structure of the species [(R$^3_3$SiCH$_2$)$_4$Co(MgCl)$_2$] in solution is not clear. For convenience, we use this expression. Several organocobaltate(II) compounds were characterized by X-ray crystallographic analysis: R. S. Hay-Motherwell, G. Wilkinson, B. Hussain, M. B. Hursthouse, *Polyhedron* **1990**, *9*, 931 – 937.

[11] For a review on cobaltate complexes, see: T. Kauffmann, *Angew. Chem.* **1996**, *108*, 401 – 418; *Angew. Chem. Int. Ed. Engl.* **1996**, *35*, 386 – 403.

[12] For examples of halogen–metal exchange between *gem*-dihaloalkane and ate complexes followed by alkyl migration, see: A. Inoue, J. Kondo, H. Shinokubo, K. Oshima, *Chem. Eur. J.* **2002**, *8*, 1730 – 1740, and references therein.

[13] a) F. Kakiuchi, A. Yamada, N. Chatani, S. Murai, N. Furukawa, Y. Seki, *Organometallics* **1999**, *18*, 2033 – 2036; b) Y. Wakatsuki, H. Yamazaki, M. Nakano, Y. Yamamoto, *J. Chem. Soc. Chem. Commun.* **1991**, 703 – 704; see also reference [5].

Cover Picture

Rolf Schiffmann, Andreas Heine, Gerhard Klebe, and Christian D. P. Klein*

Metalloenzymes are often studied in the presence of unphysiologically high concentrations of metal ions. This situation may lead to artifacts in assays if the binding of an inhibitor is made possible through additional metal ions; such compounds would appear highly potent in vitro, but may not possess activity in vivo. In their Communication on page 3620 ff., C. D. P. Klein and co-workers describe this effect with the enzyme methionine aminopeptidase as an example. (Mouse image provided by the U.S. National Park Service.)

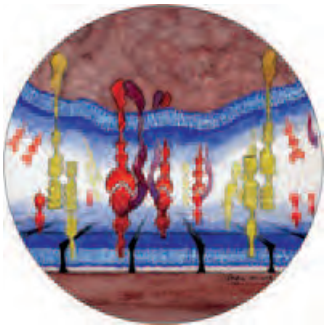

Surface Chemistry of Membranes
The interactions between neighboring membranes that lead to the formation of protein patterns perform important biological functions. In his Review on page 3524 ff. J. T. Groves discusses these processes through the use of model systems and measurement techniques.

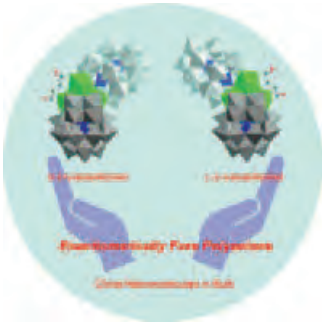

Chirality Transfer
A small organic molecule can transfer chirality to a large polyoxometalate cluster. How this transfer occurs is reported by C. L. Hill and co-workers in their Communication on page 3540 ff.

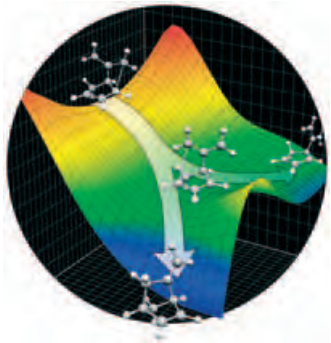

Reaction Mechanisms
K. N. Houk and co-workers describe computational studies of the thermal rearrangement of 6-methylenebicyclo[3.2.0]hept-2-ene in their Communication on page 3548 ff. The results suggest a bifurcation of reaction trajectories which explains the product ratios observed.

Contents

VIP ***The following Communications have been judged by at least two referees to be "very important papers" and will be published online at www.angewandte.org soon:***

Meeting Reviews

Books

Highlights

C–H Aminations

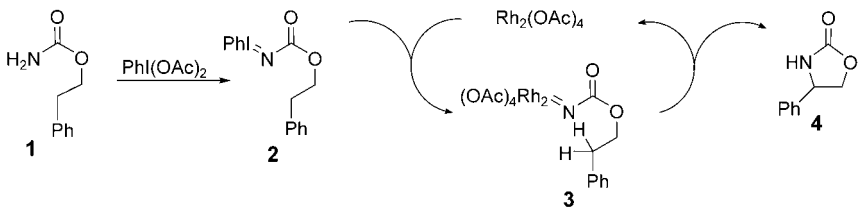

C–N bond formation by nitrene-induced C–H amination is an elegant class of reaction (see scheme). The Highlight describes how such intramolecular processes are catalytic with transition metals and display enantioselectivity to provide a powerful synthetic tool ideally suited to the synthesis of natural products.

Lab on a Chip

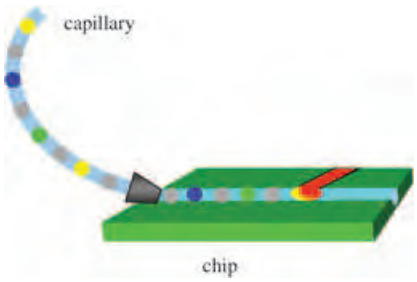

Chipping in for microlabs: A capillary with segmented sample droplets was coupled to a microfluidic chip for the high-throughput screening of samples on the nanoliter scale. A three-phase system was developed for the segmentation; the sample droplets are surrounded by a fluorinated carrier fluid and additionally separated by gas bubbles. The ultimate goal in this area of research is a pocket-sized laboratory.

Reviews

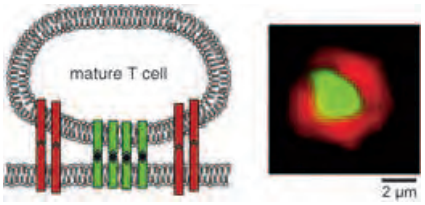

Informative patterns: Cell membranes can respond to chemical interactions with the surface in ways not seen with inorganic materials. One example is the formation of a spatial pattern at membrane junctions during intercellular signaling. The formation of such a pattern in immunological synapses (see picture; right: fluorescence image) is examined in this Review through the use of model systems and imaging technologies.

Communications

Small but influential: Chirality transfer from a small chiral organic unit (D- or L-tartrate) to a very large metal–oxide framework is demonstrated by the enantiomerically pure, nonracemizing polytungstates D- or L-**1** (see picture, the central part is shown in polyhedral form; purple Zr, gray W, blue P, black C, red O). The tartrate unit determines the absolute configuration of the inorganic moiety, offering a new method to control the chirality of polyoxoanions.

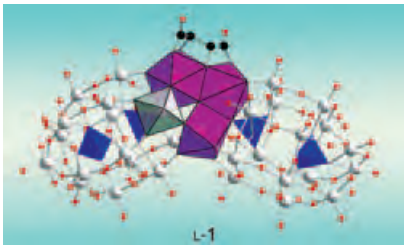

Split into seven sizes: Highly ordered cleavage of supercoiled plasmid DNA by S1 nuclease was accomplished through DNA complexation with water-soluble cationic block copolymers (see schematic representation). The results provide insights into the mechanisms of endogenous protein-induced modification of DNA and into the design of artificial restriction enzymes through the supramolecular assembly of synthetic macromolecules.

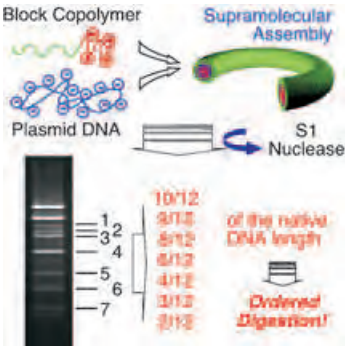

For the USA and Canada:
ANGEWANDTE CHEMIE International Edition (ISSN 1433-7851) is published weekly by Wiley-VCH PO Box 191161, D 69451 Weinheim, Germany. Air freight and mailing in the USA by Publications Expediting Inc. 200 Meacham Ave., Elmont, NY 11003. Periodicals postage paid at Jamaica NY 11431. US POSTMASTER: send address changes to *Angewandte Chemie*, Wiley-VCH, 111 River Street, Hoboken, NJ 07030. Annual subscription price for institutions: US$ 4948.00/4498.00 (valid for print and electronic / print or electronic delivery); for individuals who are personal members of a national chemical society, or whose institution already subscribes, or who are retired or self-employed consultants, print only: US$ 394.00. Postage and handling charges included. All Wiley-VCH prices are exclusive VAT.

The best in chemistry –

for more than a hundred years

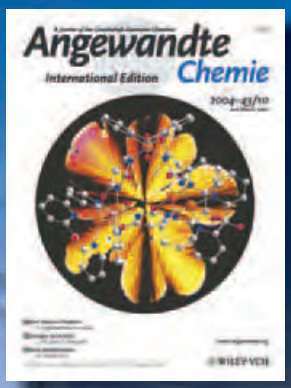

A Journal of the Gesellschaft Deutscher Chemiker

Angewandte International Edition **Chemie**

www.angewandte.org

1888: ***The beginning of a success story***

Constant Innovations

1962: *First issue of the International Edition*
1976: *Graphical abstracts*
1979: *Cover pictures*
1988: *Centenary of Angewandte*
1989: *Routine use of color*
1991: *New section: Highlights*
1992: *Computerized editorial tracking system*
1995: *Internet service for readers*
1998: *Regular press service; full-text online*
2000: *New section: Essays; EarlyView: Communications available online ahead of the printed version*
2001: *New section: Minireviews*
2002: *Online submission of manuscripts*
2003: *Weekly publication; new section: News; new layout*
2004: *Backfiles (1962-1997); ManuscriptXpress: Online system for authors and referees*

Angewandte's advisors...

Roald Hoffmann
Cornell University
(Photo: Lois Anshus)

» As an applied theoretical chemist, I love it that the best chemical journal in the world has „applied" in its title. It's history, I know. But there is also the implication in this adjective that these sterling accounts of the new, these just-in-time reviews, these incisive essays that ***Angewandte Chemie*** *contains – that they all are of true utility, and are really used, by the finest chemists of our time. «*

Angewandte Chemie International Edition *is a journal of the German Chemical Society (GDCh)*

GDCh

WILEY InterScience® DISCOVER SOMETHING GREAT

WILEY-VCH

11951404_gu

Deuterium labeling experiments on the rearrangement of methylenebicycloalkene **1** to **3** show stereoselectivity despite the intermediacy of a stabilized diradical structure **2**. A theoretical model built from computational studies explains the observed product ratios. Stereoselectivity among [3,3] (minor) products implicates an unusual bifurcation of reaction trajectories after the initial bond-breaking transition state.

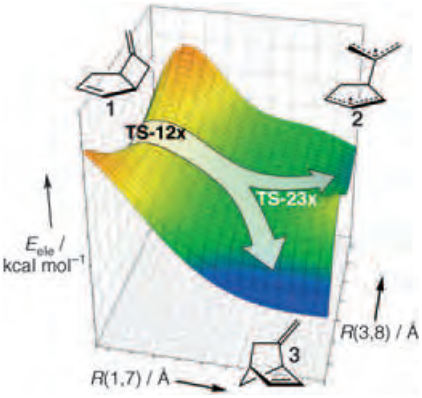

Reaction Dynamics

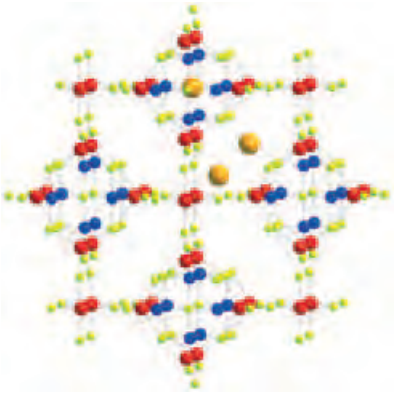

Like zeolites, $K_6Sn[Zn_4Sn_4S_{17}]$ (see structure) has remarkable ion-exchange properties and forms $CsK_5Sn[Zn_4Sn_4S_{17}]$ and $RbK_5Sn[Zn_4Sn_4S_{17}]$ in the presence of the Cs^+ and Rb^+ ions, respectively. These compounds have an open framework comprising $[Zn_4Sn_4S_{17}]^{10-}$ clusters linked by Sn^{4+} centers and are remarkably stable. One-fifth of the K^+ ions play an important templating role in stabilizing the framework. Zn blue, Sn red, S yellow, K orange.

Ion Exchange

Group 5 telluride nanostructures have been grown through chemical vapor transport from the elements. The novel nanostructured chalcogenide Nb_3Te_4 (a cluster of Nb_3Te_4 nanowires is pictured) is the first example of this type of nanowire grown with a pseudo-1D structural basis. The wires are single crystalline with longitudinal axes aligned along the crystallographic *c* axis. The nanowires are metallic but do not exhibit superconductivity above 1.8 K.

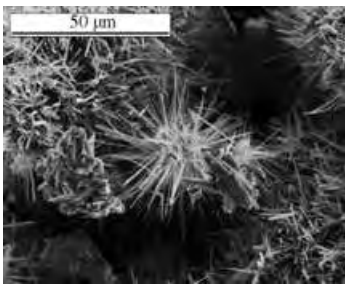

Nanostructures

Contents

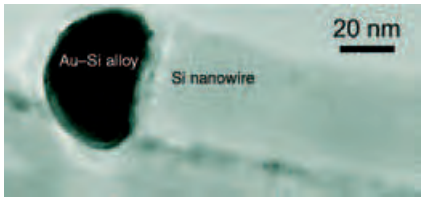

Under pressure! The synthesis of crystalline silicon nanowires can be carried out in organic solvents at reaction temperatures of up to 450–500°C under high-pressure conditions. Gold particles are used as seeds, and organosilanes are employed as the silicon source. The decomposition chemistry of the organosilanes determines the quality of the nanowires formed (see picture of an Si nanowire with an Si/Au tip).

Nanostructures

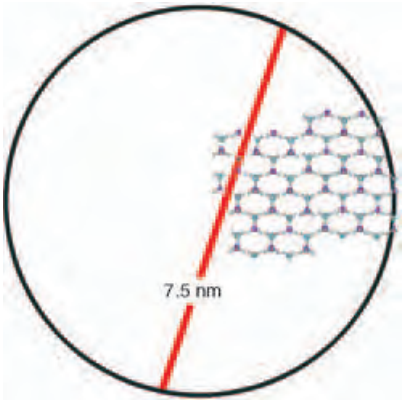

Hydrogen-rich materials infused in nanoscaffolds offer a promising approach to on-board hydrogen storage. A mesoporous scaffold decreases the temperature for hydrogen release from ammonia borane (AB), a conventional hydrogen-storage material, to below 80 °C and leads to an increase in the purity of the hydrogen released. (See schematic representation of a hydrogen-bonded AB network in the cross-section of a single pore.)

Hydrogen Storage

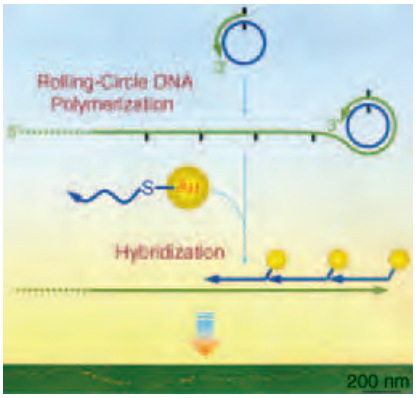

Strands of gold: Extended one-dimensional arrays of gold nanoparticles up to 4 μm long can be assembled by hybridization between thiolated DNA/nanoparticle 1:1 conjugates and long DNA templates, which were prepared by rolling-circle polymerization (see picture). The linear self-assembled structures could link the nanometric properties of materials with the convenience of micrometric manipulation.

Nanoparticle Arrays

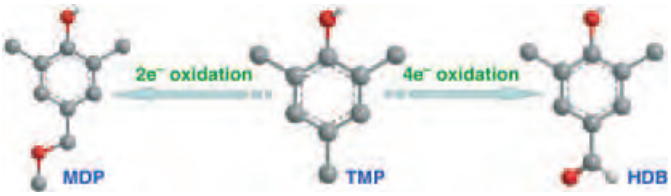

An environmentally friendly procedure has been developed for the oxidation of 2,4,6-trimethylphenol (TMP) at the *para* C_{sp^3}–H bond. Upon reaction with H_2O_2 in the presence of catalytic amounts of Cu^{II} and neocuproine in methanol at 65 °C, 4-(methoxymethyl)-2,6-dimethylphenol (MDP) or 4-hydroxy-3,5-dimethylbenzaldehyde (HDB) is formed (see reaction).

C–H Activation

Contents

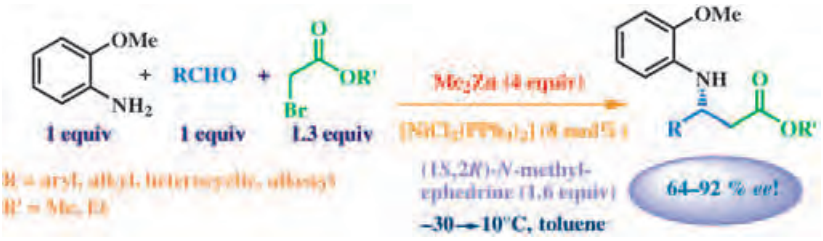

A key to molecular diversity is the preparation of new frameworks in multicomponent condensations of three or more reactants. A new highly enantioselective one-pot, three-component, nickel-catalyzed, imino-Reformatsky reaction affords β-amino esters with 64–92% *ee* (see scheme). The simplicity and broad scope of our method provide a practical access to useful building blocks.

Multicomponent Reactions

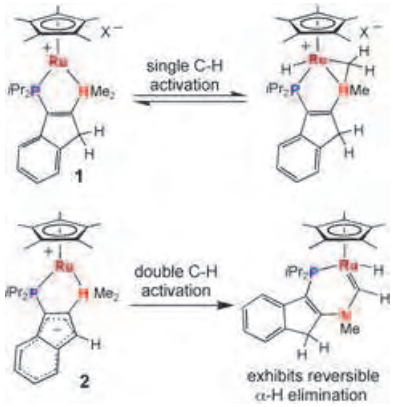

A masked variant of the first coordinatively unsaturated [Cp*Ru(κ²-*P*,*N*)]⁺ cation (**1**) is reported, which has proven capable of single intramolecular C–H activation. In contrast, the isostructural zwitterionic complex **2** apparently rearranges to a hydridocarbene by way of a remarkably facile, ligand-assisted double C–H bond activation process (see scheme).

C–H Activation

Appropriate linking of Lewis acidic and Lewis basic components—in this case boronic acid and tertiary amine functionalities—allows the construction of a robust organometallic receptor capable of selectively binding hydrogen fluoride. This system can differentiate between exposure to HF and to related acids, such as HCl, by providing opposing electrochemical responses (see picture).

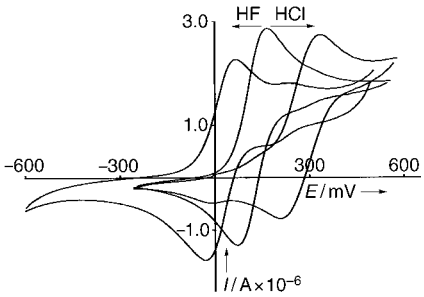

Sensors

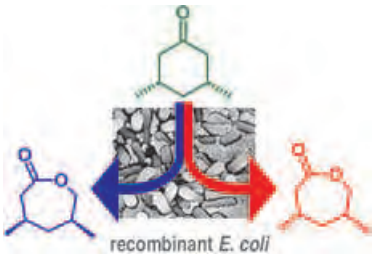

The identification of enzyme pairs with overlapping substrate specificity and enantiocomplementary transformations is a key challenge in biocatalysis. Enantio- and regiodivergent Baeyer–Villiger oxidations were successfully carried out by using a small library of recombinant *Escherichia coli* strains expressing monooxygenases of various microbial origin (see picture). The clustering of enzymes based on stereopreference is in good agreement with phylogenetic similarity.

Biotransformations

Contents

Service

Corrigendum

Amino Acids—Valuable Organocatalysts in Carbohydrate Synthesis

Angew. Chem. Int. Ed. **2005**, *44*

DOI 10.1002/anie.200462873

In this Highlight, the reaction scheme for a proline-catalyzed carbohydrate synthesis was rendered incorrectly at the bottom of Scheme 4. The correct Scheme is shown, and the sentence that begins at the bottom of the first column on page 2188 should read: "For example, the 2-methyl-2-deoxymannose derivative **21** was obtained as a single stereoisomer from α-benzyloxyacetaldehyde (**20**) and propionaldehyde (**6**)."

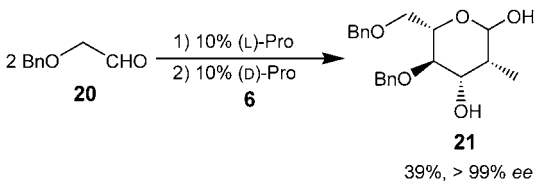

Stretched Gelatin Gels as Chiral Alignment Media for the Discrimination of Enantiomers by NMR Spectroscopy

Angew. Chem. Int. Ed. **2005**, *44*

DOI 10.1002/anie.200462736

In Figure 3 of this Communication, the label for ϕ_1 was positioned incorrectly. The correct figure is shown here.

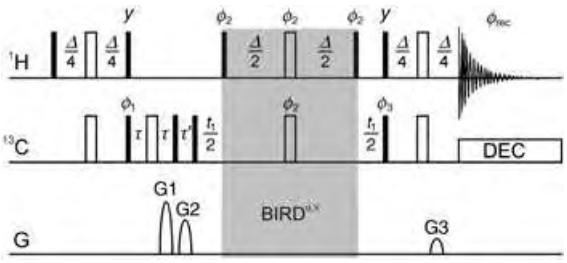

Swiss Delight: Bürgenstock 2005**

Martin Oestreich*

Spectacular Bürgenstock, a haven of tranquility almost 1000 meters above Lake Lucerne, is the traditional venue for the EUCHEM Conference on Stereochemistry. Under the presidency of Alain Krief (Université de Namur) some 140 junior and senior chemists from academia and industry met for the 40th anniversary of the "Bürgenstock Conference" in April.

The president and the organizing committee [Hans-Beat Bürgi (Universität Bern), François Diederich (ETH Zürich), E. Peter Kündig (Université de Genève), and Klaus Müller (F. Hoffmann-LaRoche)] provided a well-balanced interdisciplinary program of 14 invited lectures and three poster sessions including five selected short oral communications each as appetizers. As a special teaser, the program was only revealed to the participants upon arrival!

The scientific portion commenced with a guided tour by Jonathan Clayden (University of Manchester) through synthetic and stereochemical aspects of amide chemistry. The asymmetric metallation of amides coupled with spontaneous dearomatizing cyclization is the key step in his enantioselective total synthesis of kanoid amino acids. Another focus of his research group is the use of sterically hindered and thus atropisomeric aromatic amides as stereochemical controllers. With this system, it is possible to impart remote stereocontrol over the impressive distance of more than 20(!) bond lengths (**1**→**2**; Scheme 1).

Charles Mioskowski (Université Louis Pasteur) reported on the high-throughput screening of catalysts for enantioselective carbonyl reduction (benzoyl formic acid → mandelic acid) with competitive enzyme immunoassays. The enantiomeric excess was determined by measuring the concentration of one enantiomer with an enantiospecific antibody. In the second part of his talk, he discussed the synthesis of the bis(pulvinic acid) norbadione A and its complexation of radioactive cesium-137 in comparison with related pulvinic acids. In the evening lecture, David E. Cane (Brown University) presented the detailed synthetic and enzymological elucidation of polyketide biosynthesis, namely that of the broad-spectrum antibiotic erythromycin A. A direct study of enzyme-mediated polyketide chain elongation clarified the conversion of acetate and propionate building blocks into macrolides.

Guy C. Lloyd-Jones (University of Bristol) gave an excellent talk on isotopic "hidden" desymmetrization as a stereochemical probe in transition-metal-catalyzed processes. Realized through the site-specific introduction of stable isotopes (^{2}H or ^{13}C), this technology was successfully applied to the mechanistic elucidation of palladium- and molybdenum-catalyzed asymmetric alkylation reactions. By using isotopic labeling, his research group has also shed light on the ruthenium-catalyzed enyne metathesis, which likely follows an "yne-then-ene" rather than an "ene-then-yne" pathway. Continuing the theme of catalysis, yet from an entirely different angle, Keiji Maruoka (Kyoto University) described the evolution of structurally simple but powerful quaternary ammonium salts as chiral phase-transfer catalysts. The application of such organocatalysts (**5**, Scheme 2)—some of which are now commercially available—to the asymmetric alkylation of α-amino acid derivatives permits the preparation of important unnatural secondary and tertiary α-amino acids (**3** → **4**; Scheme 2). Among other transformations, these catalysts also promote highly enantio- and diastereoselective direct aldol reactions.

Baptized a "Zn-ing Mg-ician", Paul Knochel (Universität München) presented a selection of novel Grignard reagents with distinctly graduated reactivity for the halogen–magnesium exchange at unsaturated carbon centers. With this methodology at hand, a plethora of functionalized magnesium organometallic compounds are now accessible and have been subsequently

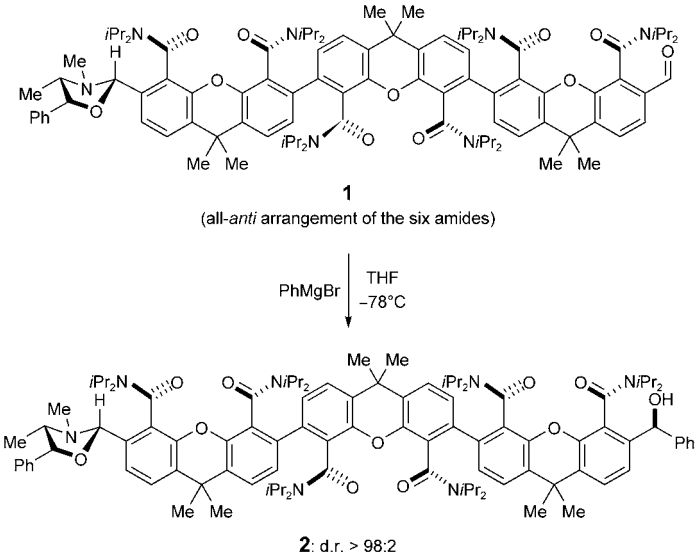

Scheme 1. Remote stereocontrol along a carbon chain with atropisomeric amides.

[*] Dr. M. Oestreich
Institut für Organische Chemie
und Biochemie
Albert-Ludwigs-Universität Freiburg
Albertstrasse 21
79104 Freiburg (Germany)
Fax (+49) 761-203-6100
E-mail: martin.oestreich@orgmail.chemie.uni-freiburg.de

[**] 40th EUCHEM Conference on Stereochemistry, sponsored by the European Association for Chemical and Molecular Sciences (EuCheMS), Bürgenstock (Switzerland), April 16–22, 2005.

  DOI: 10.1002/anie.200501433

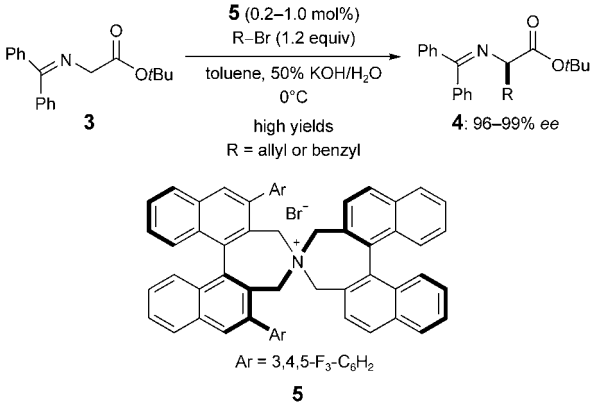

Scheme 2. Asymmetric phase-transfer catalysis.

implemented in cross-coupling reactions.

The third day kicked off with a talk by Ian A. Wilson (The Scripps Research Institute) about studies of antibody–antigen complexes with X-ray crystallography. As an example, insight has been gained into the recognition of HIV-1 proteins which could advance efforts toward an effective HIV-1 vaccine. An informative historical background on the Spanish flu epidemic of 1918 served as an introduction for his approach toward answering the question of why this particular avian influenza was so disastrous. In an instructive talk, Thomas Carell (Universität München) focused on genome maintenance systems and the molecular machinery involved in recognizing and repairing oxidative and photoinduced lesions. Synthetic and crystallographic efforts have shed light on the mechanisms that counteract such DNA damage.

The morning session of the following day was devoted to organic molecules as functional materials. Klaus Müllen (MPI Mainz) enticed his audience into the aesthetic electronic world of two- and three-dimensional benzenes: rods, discs, spheres, and dendrimers. Later, Masahiro Irie (Kyushu University) gave a fascinating talk on photochromism "spiced up" with several experiments demonstrating the reversible photochemical transformation of two defined, thermally stable compounds (**6** ⇄ **7**; Scheme 3). The application of photochromic reactions in solution and in solid state, even at a molecular level, provides opportunities for the design of optoelectronic devices.

Catherine L. Drennan (MIT) reported on the (structural) elucidation of vitamin biosynthesis by AdoMet (*S*-adenosyl-L-methionine) radical metalloproteins such as biotin synthase (BioB) (**8** → **9**; Scheme 4). She also emphasized the substantial role of bifunctional carbon monoxide dehydrogenase/acetyl-CoA synthase (CODH/ACS) in the global carbon cycle and presented insight into the mechanisms of carbon dioxide fixation.

The final morning session was opened by Mikiko Sodeoka (Tohoku University) in a presentation of her efforts toward the development of selective inhibitors of protein phosphatases and necrotic cell death. The understanding of the mode of action of these inhibitors was supported through structure–activity relationships. With the unique polycyclic structures of the phomoidrides (**10**; Figure 1) as a starting point, John L. Wood (Yale University) told an intriguing story about the interplay of target-oriented synthesis and the occasionally serendipitous discovery of novel reactions.

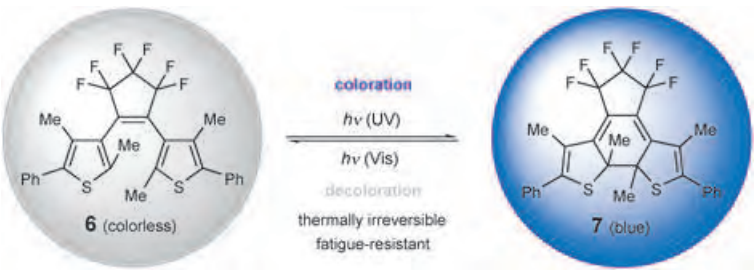

Scheme 3. A photochromic reaction.

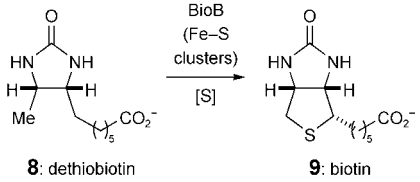

Scheme 4. Biotin synthase-catalyzed insertion of sulfur.

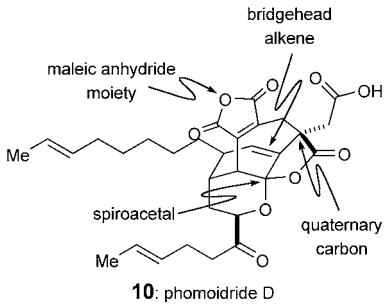

Figure 1. Synthetic challenges in **10**.

The privilege of the final scientific talk was granted to David A. Evans (Harvard University). In a highly scholarly talk on asymmetric Lewis acid catalysis employing chiral bis(oxazoline) (box) and bis(oxazolinyl)pyridine (pybox) metal complexes, he delineated the importance of the metal center (the inorganic chemist's perspective) besides ligand design (the organic chemist's perspective). As tidbits, several elegant applications of novel methodologies in natural product synthesis were also included.

On the entertaining side, an "enchanting" Koji Nakanishi (Columbia University) performed as a magician with some of the invited speakers as victims of his magic. The final words belonged to Klaus Müller who improvised an amusing, not-so-serious summary of the week.

The perfect blend of scientific exchange and recreation had again set the stage for an extraordinarily pleasant experience. The president and the "four gnomes of Bürgenstock" (C&EN, April 11, 2005) organized a flawless conference. If there had been a downside, it was the weather; when Alain Krief handed the baton to president-elect Bernhard Kräutler (Universität Innsbruck), he roguishly selected an umbrella!

C–H Aminations

Recent Advances in Catalytic Intramolecular C–H Aminations

Huw M. L. Davies and Matthew S. Long*

Keywords:
amination · C–H activation · insertion · synthetic methods · transition metals

Installation of an amine functionality is a fundamental operation in organic synthesis and can, of course, be performed in many ways, but ultimately the majority of methods involve reaction of a nitrogen-based nucleophile with an electrophilic carbon center. From a strategic standpoint, the preparation of amines by amination of C–H bonds would be an extremely attractive alternative [Eq. (1)].[1] Pioneering work by Breslow

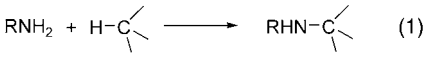

(1)

and Gellman in the 1980s demonstrated that the metal-catalyzed reaction of tosylimidophenyliodinane (TsN=IPh, tosyl (Ts) = *p*-toluenesulfonyl) generated metal nitrenes that were capable of aminating cyclohexane.[2] In recent years considerable advances have been made in the development of this chemistry into a generally useful C–H amination process by using improved catalysts and protocols in which readily available amines or amides are used as the starting substrates. This report highlights these advances and illustrates the elegant applications of the amination of C–H bonds in total synthesis.

One of the drawbacks with the early methods of amination of C–H bonds was the requirement of preforming the rather labile aryliodinane intermediates.[1] Recently, the groups of Che[3] and Du Bois[4] independently reported that the formation of aryliodinanes and the insertion of metallonitrenoids into C–H bonds can be conducted in a one-pot procedure. While Che and co-workers initially focused on intermolecular reactions,[3] Espino and Du Bois demonstrated that carbamates are efficiently converted into the corresponding oxazolidinones through an intramolecular nitrenoid C–H insertion pathway.[4] Initially the primary carbamate **1** is oxidized to the corresponding iodoimine **2**, which is in turn decomposed by a dirhodium complex to generate the metallonitrene **3**; this reactive intermediate then undergoes a C–H insertion event to furnish the cyclic product **4** and releases the rhodium complex to continue the catalytic cycle (Scheme 1).

The intramolecular reactions may exhibit impressive levels of stereo- and regiocontrol. The formation of five-membered rings is strongly favored, and the nitrenoid will preferentially insert into an activated benzylic site over an alkyl site. More-hindered methine C–H bonds are also amenable to insertion by the nitrenoid. In all the examples reported, the cyclic carbamates are generated with *syn* diastereoselectivity and with retention of stereochemistry at the insertion site (Scheme 2).

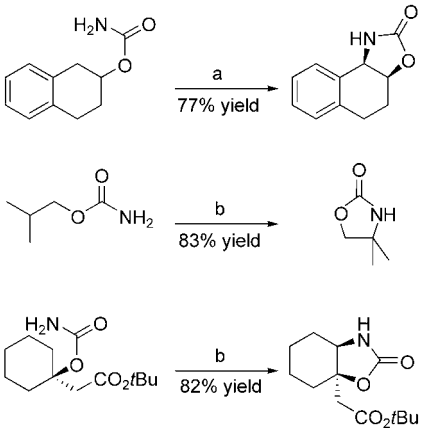

Scheme 2. a) $PhI(OAc)_2$, $Rh_2(tpa)_4$ (5 mol%), MgO, CH_2Cl_2, 40 °C; b) $PhI(OAc)_2$, $Rh_2(OAc)_4$ (5 mol%), MgO, CH_2Cl_2, 40 °C. tpa = triphenylacetate.

When sulfamate esters such as **5** are used as substrates, six-membered-ring formation is favored and results in the selective formation of 1,2,3-oxathiazinane-2,2-dioxide heterocycles **6**.[5] In general the reactions are high yielding and proceed with elevated levels of diastereoselectivity (Scheme 3).[6]

A very elegant expansion of the synthetic utility of the intramolecular amination reaction has been insertion reactions into ethereal C–H bonds.[7] Du Bois and co-workers have exploited this reactivity to prepare cyclic sulfamates **7**–**10** that are then used as iminium ion equivalents. Upon treatment

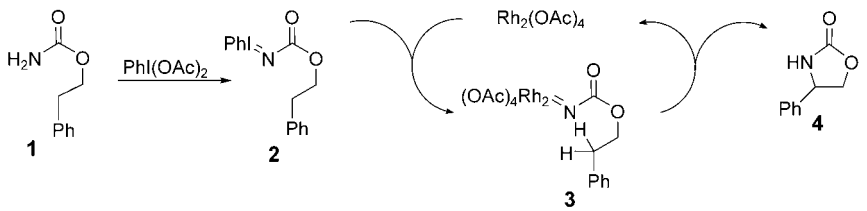

Scheme 1.

[*] Prof. Dr. H. M. L. Davies, Dr. M. S. Long
Department of Chemistry
University at Buffalo
The State University of New York
Buffalo, NY 14260-3000 (USA)
Fax: (+1) 716-645-6547
E-mail: hdavies@acsu.buffalo.edu

  DOI: 10.1002/anie.200500554

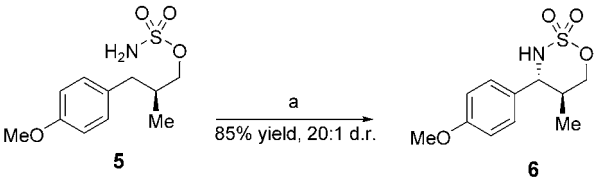

Scheme 3. a) $PhI(OAc)_2$, $Rh_2(OAc)_4$ (2 mol%), MgO, CH_2Cl_2, 40 °C.

with a suitable Lewis acid, the cyclic iminium ion formed can undergo attack from nucleophiles such as zinc acetylides, allyl silanes, and silyl enol ethers to form the elaborated 1,3-amino alcohols **11**–**14**. The nucleophilic additions appear to proceed through a well-ordered transition state, and the majority of examples presented exhibit good levels of diastereoselectivity (Scheme 4).[7,8]

Improved catalysts are required for further enhancement of C–H amination chemistry. Du Bois and co-workers originally used rhodium(II) acetate and rhodium triphenylacetate (tpa) as catalysts and found that regio- and diastereocontol was influenced by the catalysts, but neither was effective when low catalyst loadings were used. Inspired by the bridged dirhodium catalysts developed for carbenoid chemistry,[9] a second-generation catalyst $Rh_2(esp)_4$ (**15**, esp = α,α,α′,α′-tetramethyl-1,3-benzenedipropionate)[10] was designed which was capable of much higher turnover numbers (Scheme 5). Furthermore, this catalyst was effective in intermolecular reactions.

Che and co-workers have used manganese– and ruthenium–porphyrin catalysts for their amination reactions. In their original studies on intermolecular aminations with preformed iodinanes, catalyst turnover numbers as high as 2600 were reported.[2] More recently Che and co-workers have investigated intramolecular C–H insertion reactions of sulfamate esters using ruthenium–porphyrin complexes as catalysts. Interestingly five-membered-ring formation will take place in systems in which there is an activated C–H bond available for insertion, as exemplified by the formation of **19** from **18**. When a chiral porphyrin was employed, the insertions proceeded with impressive levels of enantioselectivity (Scheme 6).[11]

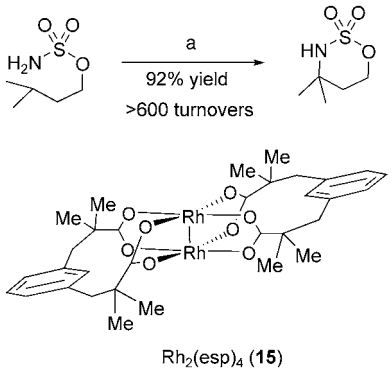

Scheme 5. a) $PhI(OAc)_2$, $Rh_2(esp)_4$ (0.15 mol%), MgO.

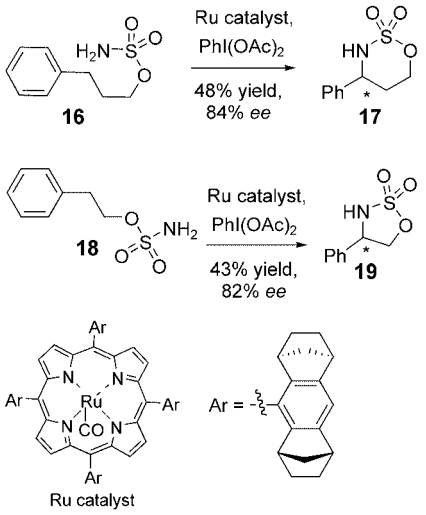

Scheme 6.

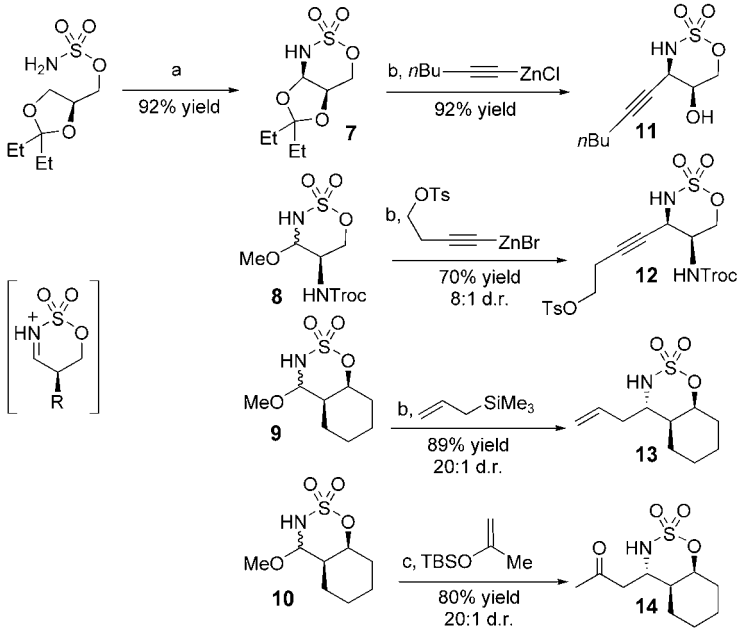

Scheme 4. a) $PhI(OAc)_2$, $Rh_2(OAc)_4$ (2–4 mol%), MgO; b) $BF_3{\cdot}OEt_2$, CH_2Cl_2, 40 °C; c) $Sc(OTf)_3$, CH_3CN. Ts = *p*-toluenesulfonyl, Troc = trichloroethyloxycarbonyl, TBS = *tert*-butyldimethylsilyl, OTf = trifluoromethylsulfonate.

The intramolecular insertion reactions of nitrenoids into C–H bonds as described above provide an attractive alternative to conventional methods of amine formation. Furthermore, the protocols are practical and tolerant of many different functional groups, therefore it is not surprising that they have been elegantly exploited in natural product synthesis. In their synthesis of tetrodotoxin in 2003, Hinman and Du Bois used the carbamate-based nitrenoid C–H insertion to form a pivotal C–N bond in **20** in a stereospecific fashion.[12] The sulfamate ester variant of this chemistry was showcased in the synthesis of the bromopyrrole alkaloids manzacidin A and C. A nitrenoid insertion was used early in the synthesis to stereospecifically set up the secondary amine in **21** which was subsequently converted into the cyclic amidine (Scheme 7).[6]

In conclusion, the advances made in performing and controlling nitrene-induced C–H amination reactions have provided a reliable and viable alterna-

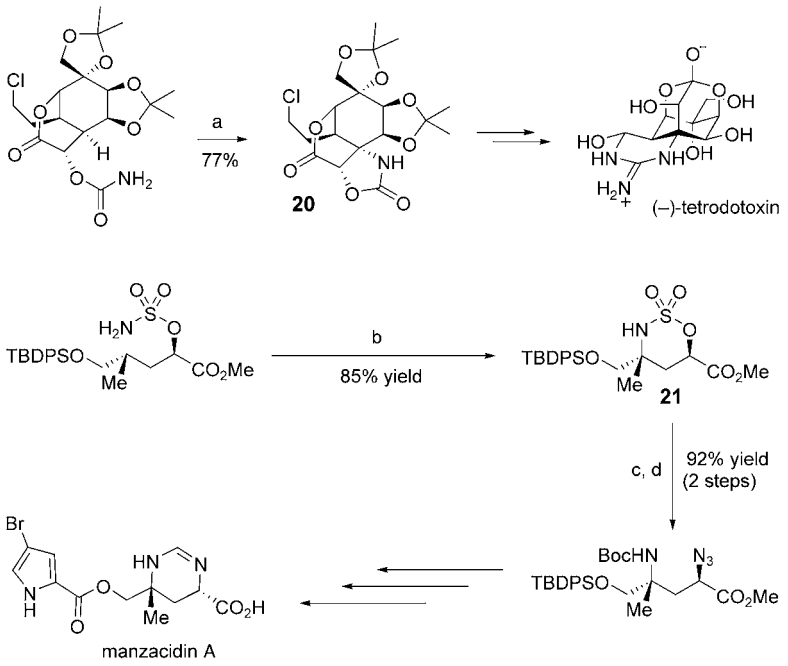

Scheme 7. a) $Rh_2(HNCOCF_3)_4$, $PhI(OAc)_2$, MgO, C_6H_6, 65 °C; b) $PhI(OAc)_2$, $Rh_2(OAc)_4$ (2 mol%), MgO, CH_2Cl_2; c) $(Boc)_2O$, pyridine; d) NaN_3, DMF. TBDPS = *tert*-butyldiphenylsilyl, Boc = *tert*-butyloxycarbonyl, DMF = *N*,*N*-dimethylformamide.

tive to classical methods of C–N bond formation. The processes are catalytic with transition metals, can be rendered enantioselective, and represent a powerful new synthetic tool ideally suited to the synthesis of complex target molecules.

Published online: May 11, 2005

[1] For a review on nitrene insertions into C–H bonds, see: P. Müller, C. Fruit, *Chem. Rev.* **2003**, *103*, 2905.
[2] R. Breslow, S. H. Gellman, *J. Am. Chem. Soc.* **1983**, *105*, 6728.
[3] X.-Q. Yu, J.-S. Huang, X.-G. Zhou, C.-M. Che, *Org. Lett.* **2000**, *2*, 2233.
[4] C. G. Espino, J. Du Bois, *Angew. Chem.* **2001**, *113*, 618; *Angew. Chem. Int. Ed.* **2001**, *40*, 598.
[5] P. M. Wehn, J. Du Bois, *J. Am. Chem. Soc.* **2002**, *124*, 12950.
[6] P. M. Wehn, J. Lee, J. Du Bois, *Org. Lett.* **2003**, *5*, 4823.
[7] J. J. Fleming, K. Williams Fiori, J. Du-Bois, *J. Am. Chem. Soc.* **2003**, *125*, 2028.
[8] K. Williams Fiori, J. J. Fleming, J. Du-Bois, *Angew. Chem.* **2004**, *116*, 4449; *Angew. Chem. Int. Ed.* **2004**, *43*, 4349.
[9] a) D. F. Taber, R. P. Meagley, J. P. Louey, A. L. Rheingold, *Inorg. Chim. Acta* **1995**, *239*, 25; b) H. M. L. Davies, *Eur. J. Org. Chem.* **1999**, 2459; c) H. M. L. Davies, C. Venkataramani, *Org. Lett.* **2003**, *5*, 1403.
[10] C. G. Espino, K. W. Fiori, M. Kim, J. Du Bois, *J. Am. Chem. Soc.* **2004**, *126*, 15378.
[11] J. L. Liang, S.-X. Yuan, J.-S. Huang, W.-Y. Yu, C.-M. Che, *Angew. Chem.* **2002**, *114*, 3615; *Angew. Chem. Int. Ed.* **2002**, *41*, 3465.
[12] A. Hinman, J. Du Bois, *J. Am. Chem. Soc.* **2003**, *125*, 11510.

Lab on a Chip

Microfluidics with Droplets**

*Detlev Belder**

Keywords:
analytical methods · high-throughput screening · lab on a chip · microfluidics · microreactors

In analogy to miniaturization in microelectronics, the integration of chemical processes on chips, where chemical reactions are performed in microchannels and -cavities, is currently the focus of significant research efforts. The ambitious aim is to shrink chemical laboratories to "lab-on-a-chip" systems. The development of technologies and miniaturized components like reactors and valves in order to realize such a handheld laboratory is currently a very active research area. In this context microfluidics is of particular importance as microfluidic channels play a major role as central elements of miniaturized labs in analogy to the conducting paths in microelectronics. Microfluidic channels are utilized for transport, mixing, and separation of reagents on the nanoliter scale. While tremendous progress has been made in the miniaturization of individual construction units of potential lab chips, interfacing such tiny devices to the macroscopic world is still a big challenge.

Zheng und Ismagilov[1] reported recently a straightforward and economic approach for handling and transfering a large number of samples on the nanoliter scale into basic microfluidic systems for subsequent screening assays. For this purpose aqueous samples several nanoliters in volume are introduced into a capillary using immiscible phases as spacers to form a sample array. While in classical flow injection analyses (FIA) air bubbles are used to separate a series of samples, Zheng and Ismagilov describe a three-phase liquid/liquid/gas system. An array of different aqueous samples is generated inside a capillary, while the sample plugs are surrounded by a fluorinated carrier fluid and additionally separated by gas bubbles (Figure 1).

Figure 1. An array of differently colored aqueous samples separated by air bubbles (dark segments) in a capillary filled with a fluorocarbon.

Zheng and Ismagilov report that such three-phase systems are much more robust than the classical two-phase gas/liquid[2] and liquid/liquid systems.[3] This reduces coalescence and carry-over of samples more efficiently. Preloaded capillaries are even suitable for long-term storage of samples on the nanoliter scale.

Such segmented flows, whereby aqueous sample droplets are floating in a hydrophobic liquid, are especially attractive in mircrofluidics, as reagents can be mixed within a droplet and simultaneously sample dispersion is minimized.[4] The mixing of compounds in microfluidic channels is challenging because of the low Reynolds numbers and the corresponding laminar flows. Significant research efforts have been devoted to solving this problem, for example, by the development of micromixers.[5]

By coupling a capillary to a microfluidic chip, Zheng and Ismagilov performed simple chemical reactions with the sample array. For this purpose the preformed samples are introduced into a microfluidic system with a T-junction, where they meet a reagent stream (Figure 2). In this type of microreactor, which has already been described in detail for two-phase systems,[6] the sample droplets merge with the reagent solution without distortion of the segmented flow. The reagent concentrations can be adjusted easily by regulating the flow rates.

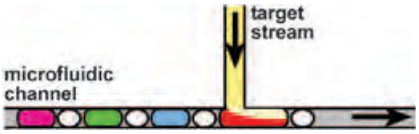

Figure 2. Schematic drawing of sample zones merging with a reagent solution in a microfluidic chip.

This technique was illustrated with two examples. In one case an assay was performed in which a set of enzymes was screened for phosphatase activity using fluorescein diphosphate as a fluorogenic substrate. An array of protein samples (≈15 nL), preloaded in a capillary as described above, was merged with the reagent solution at the T-junction. The presence of a phosphatase could be evident from the fluorescence of the hydrolyzed substrate (see Figure 3).

In a second example this approach was successfully utilized for screening a single protein against multiple crystal-

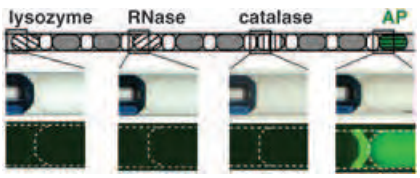

Figure 3. Schematic drawing and microscopic image of an enzyme assay for phosphatase activity using a fluorogenic substrate.

[*] Dr. D. Belder
Max-Planck-Institut für Kohlenforschung
Kaiser-Wilhelm-Platz 1
45470 Mülheim an der Ruhr (Germany)
Fax: (+49) 208-306-2275
E-mail: belder@mpi-muelheim.mpg.de

[**] The figures were obtained from ref. [1].

DOI: 10.1002/anie.200500620

lization agents. For this purpose an additional outlet capillary was coupled to the chip in order to collect the segmented crystallization solutions. Such glass capillaries are much better suited for time-consuming crystallization experiments than the solvent-permeable polydimethylsiloxane (PDMS) chips.[7]

Microfluidic chips prepared from PDMS appear to be well suited for coupling with capillaries and adapters owing to the elasticity of the material. It would be very attractive to extend this concept also to chips manufactured from glass or fused silica, which are considered the materials of choice for future chip laboratories because of their excellent chemical resistance and optical properties.

Segmented flow is not optimal for more complex chip laboratories since successive operations would require a homogeneous one-phase flow. In classical flow injection analyses, bubble gates are used for that purpose. Hibara et al.[8] have recently described a corresponding microfluidic system for the removal of air bubbles in aqueous flows that is based on channel segments with different hydrophobicity. In this approach, gas bubbles are removed utilizing hydrophobic channels, while the aqueous phase is guided into hydrophilic channels. The application of this approach to the system described by Zheng and Ismagilov could allow online coupling of succeeding analytical steps like electrophoresis. This would be a promising step toward the goal of a "lab on a chip".

Published online: May 13, 2005

[1] B. Zheng, R. F. Ismagilov, *Angew. Chem.* **2005**, *117*, 2576 – 2579; *Angew. Chem. Int. Ed.* **2005**, *44*, 2520 – 2523.
[2] V. L. Linder, S. K. Sia, G. M. Whitesides, *Anal. Chem.* **2005**, *77*, 64 – 71.
[3] H. Song, R. F. Ismagilov, *J. Am. Chem. Soc.* **2003**, *125*, 14613 – 14619.
[4] a) H. Song, J. D. Tice, R. F. Ismagilov, *Angew. Chem.* **2003**, *115*, 792 – 796; *Angew. Chem. Int. Ed.* **2003**, *42*, 768 – 772; b) A. Günther, S. A. Khan, M. Thalmann, F. Trachsel, K. F. Jensen, *Lab Chip* **2004**, 4, 278 – 286.
[5] J. M. Ottino, S. Wiggins, *Science* **2004**, *305*, 485 – 486.
[6] a) B. Zheng, J. D. Tice, R. F. Ismagilov, *Anal. Chem.* **2004**, *76*, 4977 – 4982; b) L. S. Roach, H. Song, R. F. Ismagilov, *Anal. Chem.* **2005**, *77*, 785 – 796; c) I. Shestopalov, J. D. Tice, R. F. Ismagilov, *Lab Chip* **2004**, 4, 316 – 321; d) B. Zheng, L. S. Roach, R. F. Ismagilov, *J. Am. Chem. Soc.* **2003**, *125*, 11170 – 11171.
[7] B. Zheng, J. D. Tice, L. S. Roach, R. F. Ismagilov, *Angew. Chem.* **2004**, *116*, 2562 – 2565.
[8] A. Hibara, S. Iwayama, S. Matsuoka, M. Ueno, Y. Kikutani, M. Tokeshi, T. Kitamori, *Anal. Chem.* **2005**, *77*, 943 – 947.

Membrane Junctions

Molecular Organization and Signal Transduction at Intermembrane Junctions

*Jay T. Groves**

Keywords:
membranes · nanostructures · signal transduction · surface chemistry · synapses

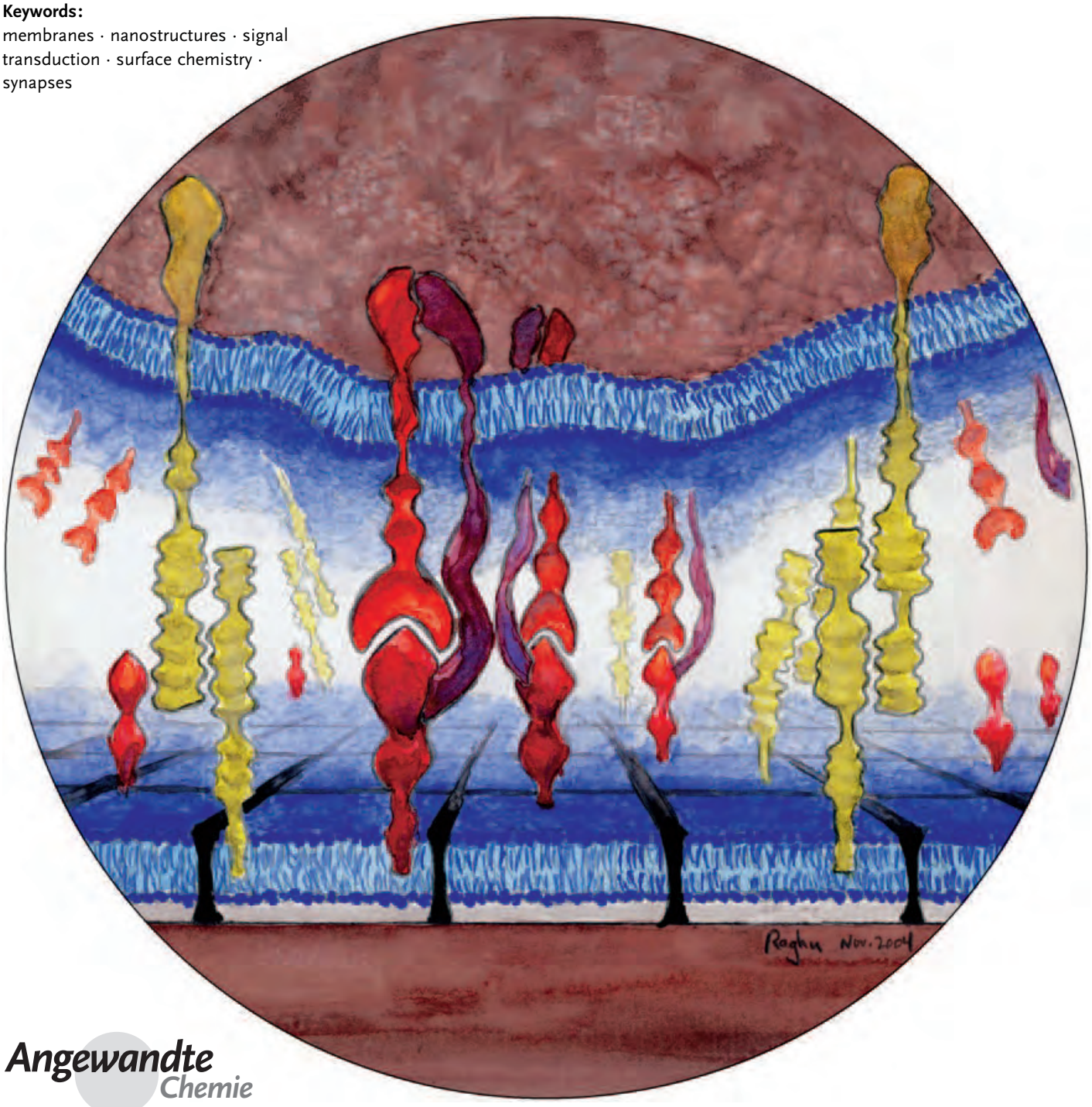

Angewandte Chemie

  DOI: 10.1002/anie.200461014

Surfaces create an environment in which multiple forces conspire together to yield a wealth of complex chemical processes. This is especially true of cell membranes, whose fluidity and flexibility enables responsive feedback with surface chemical interactions in ways not generally seen with inorganic materials. Spatial pattern formation of cell-surface proteins at intermembrane junctions provides many beautiful examples of these phenomena, and is also emerging as a functional aspect of intercellular signaling. Correspondingly, the study of interactions of cell-membrane surfaces is attracting significant attention from cell biologists and physical chemists alike. This convergence is fueled be recent, exquisite observations of protein pattern formation events within living immunological synapses along with parallel advances in membrane reconstitution, manipulation, and imaging technologies.

From the Contents

1. Introduction

The ability of cells to transmit signals to each other is an essential aspect of all multicellular life. Thousands of membrane-associated receptors and signaling molecules transduce signals between cells, and much attention has been directed toward understanding the chemical interactions between the receptors and ligands. However, in many cases, the properties of individual binding events have proven insufficient to account for the remarkable behavior exhibited by these proteins in living cells. Collective protein–protein interactions and the formation of molecular clusters have been widely implicated in signal transduction, and account for a first level of cooperativity.[1–6] More recently, coordinated rearrangement of cell-membrane receptors into distinctive patterns is emerging as a broadly significant theme of intercellular signaling. Hallmark examples are provided by the immunological synapses, which have been discovered over the last few years at junctions between a variety of immune cells and their respective target cells.[7–15] Spatial patterns of proteins within the junction develop as populations of receptors on one cell membrane interact with their cognate ligands on the apposed cell membrane. The emergent patterns can extend to several micrometers, thus transcending direct protein–protein contact interactions, and exhibit strong correlations with the ensuing intracellular signaling and effector functions.

Geometrical confinement on molecular length scales, which is inherent to intercellular junctions, has profound consequences on the biochemical reactions that take place in these spaces. In the case of the immunological synapses, protein patterns result from intimate cooperativity between both inter- and intramembrane protein binding, membrane mechanical constraints, and cytoskeletal rearrangements, which lead to lateral sorting of proteins within their respective fluid membranes.[16–18] A distinctive feature of the intermembrane junction environment is that driving forces for pattern assembly can arise without direct binding interactions among proteins. For example, bending constraints from the membrane impose an effectively repulsive interaction on receptor–ligand complexes with different preferred intermembrane spacing. Correspondingly, the effective kinetic rate for the formation of another receptor–ligand complex in the vicinity of one of similar size is enhanced by the pre-positioning of the membranes. This type of reaction feedback loop is capable of driving the formation of a rich array of patterns at intermembrane junctions.[19–23] Alternatively, preferential association with a particular membrane phase domain (raft[140]) can lead to colocalization. The generality of these types of forces suggests that tendencies towards spatial pattern formation are likely to have a wide-ranging influence within intercellular junctions.

Reaction-driven formation of spatial patterns is a widespread physical phenomenon with important implications outside of biological systems, such as in heterogeneous catalysis.[24–26] However, the complexity of pattern-forming reaction phenomena within living systems is unparalleled. Dramatic advances in unraveling the molecular aspects of cellular signaling systems, such as the immunological synapse, create distinct opportunities for highly quantitative experimental and computational investigations of the physical mechanisms underlying the elaborate signaling events that occur in live cell membranes.

In this Review recent developments in the study of physical mechanisms of signal transduction at intercellular junctions are summarized. The immunological synapses are emphasized as examples, which may reveal general themes of collective signaling interactions at intercellular junctions. These are discussed from a physical perspective and in the context of developing quantitative interpretations. Experimental model membrane systems and measurement techniques that address the hierarchical cooperativity of interactions among populations of signaling molecules at intermembrane junctions are highlighted.

[*] Dr. J. T. Groves
Department of Chemistry
University of California Berkeley
Fax: (+1) 510-642-8821
E-mail: JTGroves@lbl.gov

 DOI: 10.1002/anie.200461014

2. Spatial Patterns and Cell Signaling

2.1. Intercellular Synapses

A critical role of the immune system is to identify and destroy those cells that have become infected by a pathogen or have entered into some other form of aberrant life cycle. One class of immune cells that perform this surveillance are the T lymphocytes (T cells). These cells are the front-line of the adaptive immune system and their activation primarily occurs through interaction of T-cell receptors (TCRs) on the T cell with major histocompatibility complex proteins (MHC) that display peptide fragments on the surface of antigen-presenting cells (APCs). A variety of signals can be transduced depending on the nature of these interactions. For example, the recognition of peptide/MHC (pMHC) by TCRs on activated cytotoxic $CD8^+$ T cells induces killing of the target cell. In contrast, recognition of self-pMHC on APCs in the thymus by TCRs on thymocytes (immature T cells) results in destruction of the autoreactive thymocytes by apoptosis. Failure of this thymic selection process leads to autoimmune disease. Rheumatoid arthritis, multiple sclerosis, and psoriasis can all be traced to faulty signaling at T-cell synapses

T cells execute their recognition processes through formation of an immunological synapse with the target cell.[10,11,13–15,17,27–31] Numerous recent observations have revealed precisely organized and dynamic patterns of receptors and signaling molecules within the synapse[7–9,32–35] (Figure 1). Immunological synapses are not restricted to T cells: natural killer (NK) cells, which play a key role in the innate immune response, also form a rich collection of synaptic patterns during interactions with target cells. While the focus of this Review is restricted to T cells, many of the themes described have also been observed at NK cell synapses.[10]

In the case of the synapse of a mature T cell, the preferred geometry for sustained signaling consists of a central supramolecular activation cluster (c-SMAC), with dimensions of 1–3 μm, in which TCR–pMHC complexes accumulate. Other co-stimulatory molecules on the T-cell surface, including CD28 and cytotoxic T-lymphocyte antigen 4 (CTLA4), become enriched within the c-SMAC along with their shared cognate ligands, B7-1 and B7-2, on the APC surface. The c-SMAC is surrounded by a peripheral ring, which is populated by complexes between leukocyte function associated antigen 1 (LFA1) on the T cell and intercellular adhesion molecule 1 (ICAM1) on the APC (Figure 1 a). This structure, known as the periferal supramolecular activation cluster (p-SMAC), is also enriched with larger co-stimulatory molecules including CD2 and its ligand (CD48) on the T cell and APC, respectively. The size of the TCR–pMHC complexes fixes the intermembrane spacing within the c-SMAC at about 15 nm. The larger LFA1–ICAM1 complexes (ca. 40 nm) force the apposed membranes into a wider spacing within the peripheral ring of adhesion molecules. Ultimately, an elaborate interplay of co-stimulatory, adhesion, and signaling molecules[31,36–39] together with cytoskeletal attachments[18,40–42] and lipid rafts[43–46] becomes organized within immunological synapses.

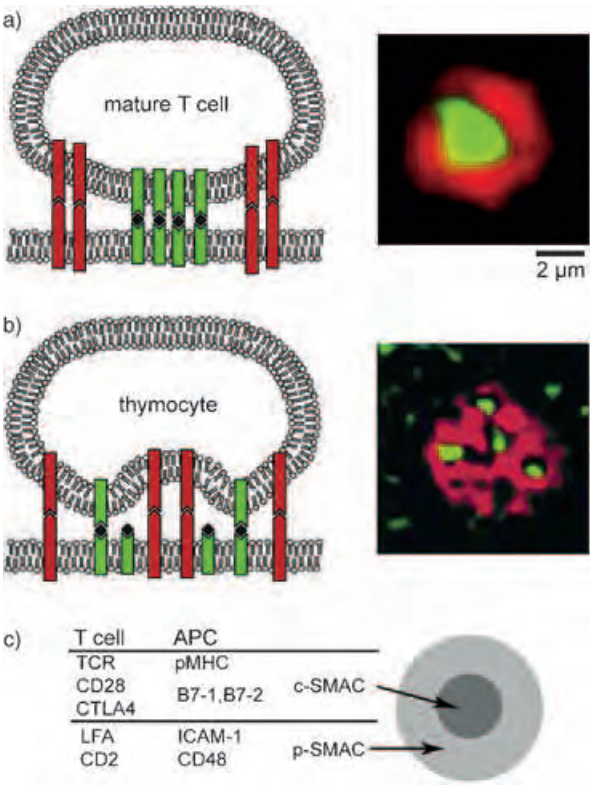

Figure 1. Synaptic patterns in different immune cell types: Schematic representations (left) and fluorescence images of live cells (right). a) Synapse of a mature T cell with TCR–peptide/MHC (green) in the center (c-SMAC) and LFA1–ICAM1 (red) at the periphery (p-SMAC). The fluorescence image is taken from ref. [8]. b) Schematic representation and fluorescence image of a thymocyte synapse (same color scheme as in (a)). The fluorescence image is taken from ref. [48]. c) Schematic representation of the molecular anatomy of a synapse of a mature T cell.

Thymocyte–APC interactions involve the same primary receptor–ligand pairs described above for the synapse of mature T cells, however their spatial organization is different. No c-SMAC forms at thymocyte–APC synapses. Instead, multifocal accumulations of TCR–pMHC condense and effervesce within a sea of LFA1–ICAM1 complexes[47,48] (Figure 1 b). A thermodynamic origin to the differing patterns, based on TCR expression levels, has been proposed[49] (see Section 2.2). However, the extent to which the differ-

Jay T. Groves received a BS in physics and chemistry from Tufts University (USA), followed by a PhD in biophysics from Stanford University. He then spent a year as a Visiting Scholar at Academia Sinica, in Taipei, Taiwan before returning to the USA to be the Division Director's Fellow at Lawrence Berkeley National Laboratory. In 2001 he joined the faculty of the Chemistry Department at the University of California, Berkeley. His research interests focus on the physical chemistry of lipid membranes, and the organizational principles these structures impose on living molecular systems.

ential patterns of proteins observed in mature T-cell and thymocyte synapses contribute to their differing cellular responses to TCR activation is not resolved.

Information regarding the structural organization of the immunological synapses described above was obtained through a variety of optical and electron imaging techniques. Protein patterns have been observed by imaging fluorescently labeled proteins in living cells[7,9,34,47] and in hybrid synapses formed from live cells and supported membranes.[8,48,50] Topographical patterns of intermembrane spacing within live immunological synapses have been imaged in hybrid synapses formed between live cells and supported membranes by using reflection interference contrast microscopy (RICM).[8] Measurements of intermembrane spacing in synapses between two living cells have also been obtained from electron microscopy images of two-dimensional slices made perpendicular to the synaptic interface.[51,52]

The immunological synapses are likely to have multiple functions that have varying degrees of importance for different cell–cell interactions. The synapse-forming process (see below) offers multiple possibilities for the inhibition and regulation of the assembly of a mature synaptic pattern. Once a synapse is formed, the increased concentration of TCR in the c-SMAC can increase the rate of TCR triggering, at least initially. Increased down-regulation of TCR in the c-SMAC can also occur, ultimately leading to reduced signaling. It has been proposed that the mature synaptic pattern serves as a mechanism to balance TCR signaling and degradation.[53] In addition to signaling, the structure of the immunological synapse may play a role in effector function by directing the secretion of cytokine or lytic granules towards the target cell.[54]

Immunological synapses can be corrupted by pathogens. Human immunodeficiency virus (HIV) and human T-cell lymphotropic virus type 1 (HTLV-1) have both been recently observed to take advantage of the concentration of targeted receptors and confined geometry of the synapse to facilitate cell to cell transmission.[55–57] Prion proteins also appear to spread from the immune to the nervous system at neuro-immunological synapses.[58,59]

Early stages of synaptogenesis and postsynaptic partner recognition in the central nervous system represent a similar task to that confronted by immune cells during surveillance. Recent results provide mounting evidence for common motifs between synapses in the nervous and immune systems.[12,51] For example, important proteins including MHC,[60] agrin,[61,62] and neuropilin-1[63,64] have recently been found to play functional roles in synapses from both systems.

2.2. Physical Driving Forces

Active transport by the cytoskeleton plays a key role in pattern formation at immunological synapses, and is one of the first activities triggered by signaling from the T-cell receptor.[18,40–42] The TCR starts to be transported towards the center of the forming synapse within moments of the first interaction with antigenic pMHC. Transport velocities ranging from 0.04–0.1 $\mu m s^{-1}$ have been measured by three dimensional fluorescence tracking microscopy.[65] The TCRs interact with the actin cytoskeleton directly through the TCRζ chain and the cytoskeletal regulator Vav.[66,67] Blocking active cytoskeletal transport, for example, with an actin polymerization inhibitor such as cytochalasin D, disrupts the formation of synapse in T cells.[8] As the TCRs accumulate in the c-SMAC, various adhesion and co-stimulatory molecules, including LFA1, are excluded from this central region and begin to form the encircling p-SMAC. It has been reported that the microtubule organization center (MTOC) is anchored to the membrane at the p-SMAC,[68] thus suggesting a mechanism in which this tubulin-based scaffold may be coordinated with the function of the actin cytoskeleton during formation of the synapse. Furthermore, treatment of cells with the potent microtubule inhibitor nocodazole interferes with TCR activation, thus providing additional support for a functional role of the MTOC in synapse signaling.[69]

In addition to providing various driving forces to create protein patterns within the immunological synapse, there is emerging evidence that the cytoskeleton plays multiple regulatory roles. For example, sustained accumulation of actin in the T-cell synapse depends both on the concentration of the agonist pMHC and engagement of co-stimulatory receptors CD28 or LFA1.[70] Signals from co-stimulatory molecules may thus regulate the formation of the large-scale protein pattern through their influence over the dynamics of the actin cytoskeleton. The cytoskeleton may also exert a regulatory role over synapse function mediated by the ezrin-radixin-moesin (ERM) proteins.[71] The ERM proteins act as general cross-linkers between the cortical actin filament network and the plasma membrane,[72] and are known to be involved in the T-cell immunological synapse.[73] Early stages of TCR signaling can trigger inactivation of the ERM proteins. This results in a partial disanchoring of the cortical actin cytoskeleton and seems to lead to more efficient formation of a T-cell/APC conjugate. How these multifarious roles for the cytoskeleton are integrated and what types of feedback mechanisms regulate these processes are currently open questions.

Membrane-governed self-assembly mechanisms have also been implicated in the formation of synapses. The size disparity between the various receptor–ligand complexes that form within T-cell synapses defines a specific topographical variation of the intermembrane spacing.[74] This has been observed directly in live T-cell synapses by electron microscopy[51,52] and RICM;[8] the membrane topography shown schematically on the left of Figure 1 is based on these observations. Once topographical structures begin to form at intermembrane junctions, other cell surface molecules can then be driven indirectly into spatial patterns by a size-exclusion effect. Evidence of a functional role for size-based sorting has been provided by a set of experiments in which genetic elongation of the extracellular domain of CD48 (a co-stimulatory ligand on the APC) was shown to disrupt its natural ability to augment antigen recognition by T cells.[75]

Mechanical constraints on the membrane provide the driving force for size-based protein sorting at intermembrane junctions. The interplay between protein organization and

membrane shape during the assembly of the synaptic pattern has been investigated using theoretical models for the collective interaction between populations of cell surface receptors and ligands in apposed membranes.[19–21,49,76,77] Receptor–ligand binding can be modeled as a reaction-diffusion process, which can be described mathematically by Smoluchowski equations. In this representation, receptor–ligand binding is characterized by the rates of association (on) and dissociation (off). The receptors and ligands are free to diffuse within the two-dimensional plane of their respective membranes. The effective local reaction rate between cognate receptor–ligand pairs depends on their local concentrations, the appropriate association rate, the local intermembrane spacing, and the size of the complex. A distinguishing feature of this modeling strategy is its incorporation of the evolving topography of the intermembrane junction. The energy content of the membrane shape is calculated by including contributions from membrane bending and stretching as well as contributions from distortions caused by formation of the receptor–ligand complex. The time evolution of the membrane shape is then coupled to the reaction-diffusion equations using a time-dependent Landau–Ginzburg equation. In this way, the intimate feedback between protein binding and membrane shape can be explored.

A notable feature of the immunological synapses is the characteristic transformation in the pattern that occurs as the synapse matures. The initial state of the helper T cell synapse consists of an outer ring of TCR–pMHC surrounding a central concentration of LFA1–ICAM1 complexes. The initial state of the cytotoxic T-cell synapse is less well organized. As signaling progresses, both types of T-cell synapse undergo a rearrangement process during which TCR and pMHC relocate to the c-SMAC while LFA1 and ICAM1 migrate to the periphery. Numerous other molecules on the cell surface are also sorted during this process. Calculations, based on measured values of protein binding kinetics, membrane bending rigidity and elasticity, and the size of the protein complexes, predict pattern reorganization with remarkable spatial and temporal resemblance to that observed in live T-cell synapses (Figure 2). The top two rows of images illustrate the sequential formation of a hybrid immunological synapse between a live cell and a supported membrane.[8] The top row contains RICM images, which reveal the changing topography of the junction. Brighter intensities in the RICM image correspond to regions where the intermembrane spacing is greater. The second row depicts a series of superimposed fluorescence images, which illustrate the distribution of MHC (green) and ICAM (red) in the junction. The lower three rows illustrate the topography, MHC, and ICAM profiles resulting from calculations according to the membrane-coupled reaction-diffusion modeling strategy mentioned above.[19] Although modeling studies suggest that membrane-mediated forces could drive pattern formation without directed transport by the cytoskeleton, it is important to note that mechanical properties of the cell membrane are significantly influenced by the cytoskeleton.[78] Thus, indirect influence from the cytoskeleton is inescapable. Furthermore, certain aspects of pattern formation may require a directed push by the cytoskeleton to occur.[21]

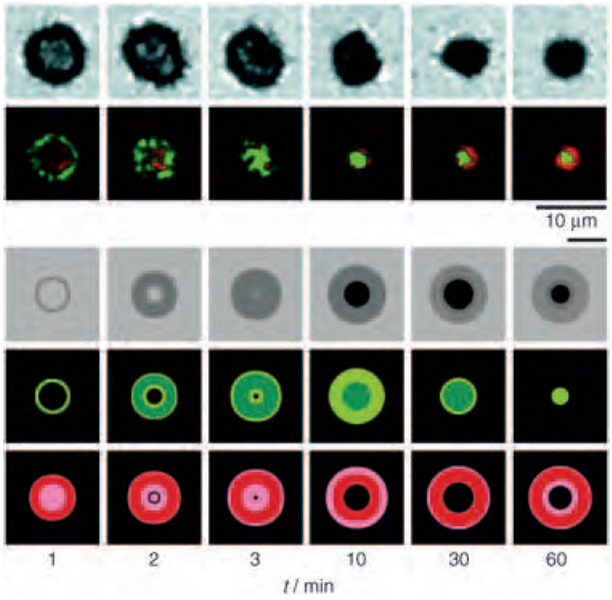

Figure 2. Time series of RICM images (top row) and superimposed fluorescence images (second row) tracking the formation of a synapse between an immunological T cell with a supported membrane displaying ICAM (red) and MHC (green). The data were taken from ref. [8]. The lower three rows illustrate the calculated topography and the MHC and ICAM patterns. For the calculated patterns of protein concentration illustrated in rows 4 and 5, regions with protein concentrations below the average are colored black, while protein-enriched regions are colored with progressively darker shades of green (MHC) or red (ICAM). Contrast optimization of the fluorescence data (row 2) produces a similar effect.

Irrespective of the role of the cytoskeleton, the membrane-governed tendencies to form patterns under non-equilibrium conditions constitute a set of forces that globally influence proteins on the cell surface. These membrane-mediated forces are similarly inescapable and will ultimately contribute to the overall organization of proteins within the synapse. For example, suppose that the actin cytoskeleton and the MTOC establish a pattern of membrane topography at an intercellular junction through a coordinated effort. This topography will then produce membrane-mediated driving forces that will influence the spatial organization of molecules not bound to the cytoskeleton. Cytoskeleton- and membrane-mediated mechanisms of spatial organization thus become inextricably coupled within an intercellular junction. The development of quantitative interpretations of the mechanisms of signal transduction between cells will likely require an inclusive treatment of both membrane and cytoskeletal effects.

Membrane-mediated forces exhibit an intrinsic sensitivity to the kinetics of protein binding. This results from the basic fact that the motion of a bound intermembrane protein complex is greatly hindered by the undulating topography of the junction. In order for a complex to move laterally within the membrane, the intermembrane spacing must comply. No corresponding hindrance affects unbound cell-surface proteins (Figure 3). The reaction-diffusion dynamics of protein organization can thus exhibit a greater sensitivity to reaction

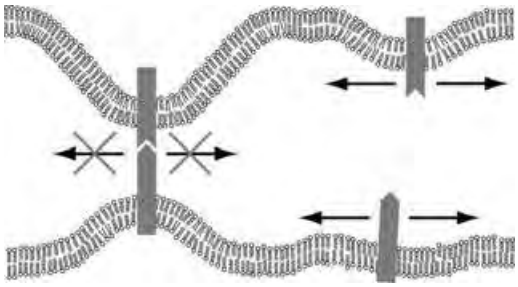

Figure 3. The lateral diffusion constraint experienced by intermembrane protein complexes. Topographical variations of the membrane hinder lateral motion unless the adjacent intermembrane spacing is comparable to the complex size. Uncomplexed proteins, in contrast, diffuse freely in their respective membranes.

kinetics than to diffusion kinetics. The extent to which the kinetics of protein binding influence pattern formation through membrane-mediated reaction-diffusion processes in the T-cell synapse is not clear. However, comprehensive analysis of biological data relating protein-binding kinetics to cell activation yields interesting correlations with calculated pattern-forming tendencies. Protein-binding kinetics that, according to the model, lead to formation of a mature synaptic pattern correlate strongly with activation of helper T cells. In contrast, no correlation is seen between pattern-forming tendencies and target cell lysis by cytotoxic T cells. This observation may reflect the multiple types of signals, and signaling mechanisms, that traverse the immunological synapse.[76] Modeling studies have also suggested that the dynamic multifocal synapses involved in thymocyte selection can result from low TCR expression and thermal fluctuations of the membrane. A possible mechanism by which TCR expression levels in thymocytes could be used to mediate differential signaling through the same molecules involved in T-cell activation is implied.[49] Interplay between the chemical kinetics of protein binding and membrane constraints at intercellular junctions produces a rich source of pattern-forming tendencies. These collective driving forces exhibit pronounced sensitivity to protein-binding kinetics and offer a mechanism for signal amplification.

The membrane-mediated forces described above result primarily from mechanical bending effects. Another class of forces originating from the membranes can result from lateral phase separation tendencies within the membrane.[79] These much-discussed raft structures are implicated in numerous signal-transduction processes,[80,81] including the T-cell synapse.[43,44,82,83] Whereas the physical chemistry of the separation of immiscible phases in lipid bilayer mixtures can be understood with a high degree of quantitative precision,[84,85] a similarly quantitative interpretation of phase-separation phenomena in living cell membranes remains elusive. With respect to the mechanical membrane bending effects discussed above, phase-separated membrane domains could exert substantial influences, and developing effective methods for considering these processes in the context of the topographical bending of the membrane and cytoskeletal interactions is important.

It is compelling to hypothesize that spatial patterns of molecules at intercellular junctions collectively convey information that supersedes the mere summation of individual signaling contributions. In addition to the immunological synapses, there exists substantive evidence of correlations between the spatial arrangement of receptor proteins and signaling activity in bacterial chemoreception,[5] intigrin signaling,[3] extra cellular matrix (ECM) cell adhesion,[4] and the ubiquitous cell-membrane raft domains.[80,86] However, the degree to which spatial patterns actually convey a supernumerary quantity of information remains an open question.

3. Experimental Model Systems

3.1. Hybrid Synapses Formed from Cells and Supported Membranes

A remarkable and fortuitous characteristic of lipid membranes is the tendency of lipid bilayer vesicles to spontaneously assemble into a single, continuous lipid membrane on an appropriate substrate (e.g., silicon oxide or various polymeric materials).[87,88] This vesicle fusion process is general. A vast collection of different membrane compositions, including charged phospholipids, glycolipids, membrane-linked proteins (e.g., by glycosylphosphatidylinositol (GPI) linkers), transmembrane proteins, and even phase-separated membrane rafts can be deposited under essentially identical conditions.[89] The orientation of the membranes is preserved during the fusion process.[90] Biological function can also be preserved, as beautifully illustrated by the observation of the formation of an active immunological synapse between supported membranes and living T cells. A schematic illustration of this hybrid synapse is illustrated in Figure 4. In fact,

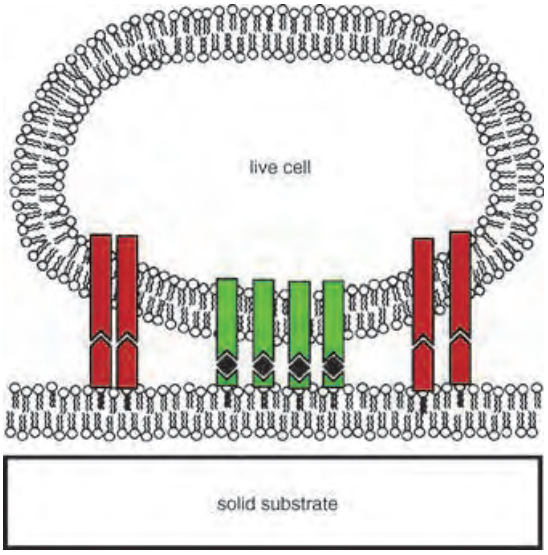

Figure 4. Schematic representation of a hybrid synapse formed from live cells and a supported membrane. In this example, the cognate ligands for receptors on the cell surface are displayed in the supported membrane in the GPI-linked form.

the highest resolution dynamic images of synapse formation in T cells have been obtained using supported membranes in place of live APCs.[8,50] The images in Figure 1a and 1b were both obtained from synapses with a supported membrane. In these examples, mature T cells (1a)[8] or thymocytes (1b)[48] form immunological synapses with supported membranes displaying membrane-linked forms of pMHC and ICAM1. A critical feature of supported membranes, which enables formation of a hybrid synapse, is the free lateral diffusivity of lipids and membrane-linked proteins. Supported bilayers are typically separated from the solid substrate by a film of water about 1 nm thick[91–93] and retain many of the properties of free membranes, including lateral fluidity. The fluidity acts over a long range, with mobile components of both leaflets of the bilayer diffusing freely over the entire surface of the substrate.[94]

A pivotal realization in the development of supported membrane technology was that barriers to lateral diffusion can be imposed on the supported membrane and used to partition it into corrals or other well-defined geometrically constrained configurations. Partitioning can be achieved by assembling membranes on prepatterned supports created by micro- or nanolithographic processes (e.g., photolithography, microcontact printing, or electron beam lithography).[95–101] In all cases, lipids and mobile proteins exhibit uninterrupted diffusion within the membrane, while at the same time there is no intermixing across barriers. The advantage of this general strategy of patterning membranes on surfaces is that it makes use of lithographic processing techniques, which have been developed extensively for the semiconductor industry, to achieve spatial control down to about 10 nm (the limit of state-of-the-art electron beam lithography). A fluorescence image of a supported membrane on a patterned substrate is depicted in Figure 5. This substrate was patterned with concentric hexagonal lines of chrome, 100 nm wide and spaced by 1 μm. Fluorescent probes in the membrane have been spot photobleached; the fluorescence recovery patterns illustrate the restricted diffusive connectivity within the supported membrane.

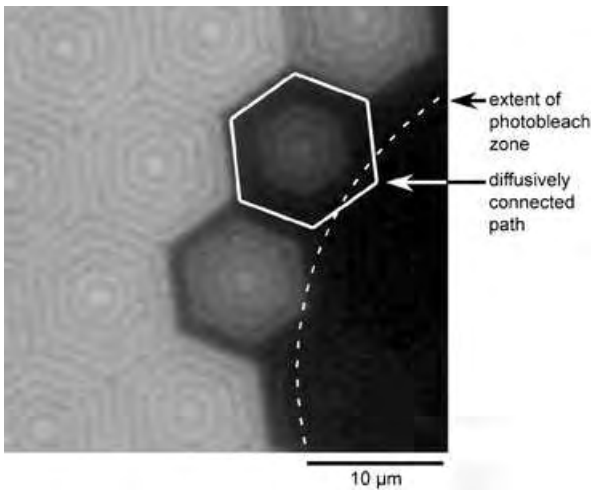

Figure 5. Fluorescence recovery after a photobleaching (FRAP) experiment on a substrate-partitioned supported membrane. The substrate is patterned by electron beam lithography. A diffracted image of the underlying chrome lines can be seen faintly in the fluorescence image. A supported membrane coats exposed regions of the underlying silica substrate and flows freely within diffusively connected regions, thus giving rise to the fluorescence recovery pattern seen here. This pattern is in diffusive equilibrium. (The image was supplied by K. Mossman.)

The formation of such hybrid synapses enables spatial restrictions of protein mobility and position to be imposed on living cell systems. An inherent requirement of this type of cellular dissection is the use of substrate patterns with subcellular (nanometer) length scales. New methods of membrane patterning that combine scanning probe lithography (SPL) with substrate diffusion barrier grids fabricated by electron beam lithography are extending fluid membrane patterning capabilities into the sub-micrometer range.[102]

Membranes can be deposited onto silica microbeads in much the same way that supported membranes are formed on monolithic substrates.[91,103,104] This format facilitates introduction of signaling molecules bound to the membrane surface to preexisting cell cultures. In one recent implementation, for example, a GPI-linked form of the postsynaptic cell-surface protein neuroligin-1 was displayed on membrane-coated microbeads. The functionalized beads were then introduced into a culture of primary hippocampal nerve cells. Through its interactions with β-neurexin on the neuronal cell surface, neuroligin-1 displayed on membrane-coated beads was able to induce preliminary stages of synaptogenesis in the neurons (Figure 6). The activity of the neuroligin-1 appeared to require display within a membrane environment, thus suggesting that surface rearrangements of this protein are required for its function.

3.2. Cell-Free Systems

There is significant interest in the development of entirely cell-free model systems to facilitate precise analysis of reaction processes at intermembrane junctions. Model intermembrane junctions, in which both membranes are reconstituted, have been created with supported membranes by several methods. Junctions can be formed by allowing intact giant unilamellar vesicles (GUVs) to interact with supported membranes. The use of RICM[105] to image the nanometer-scale topography of membrane junctions produced in this way has revealed a variety of phenomena, including coexistence of multiple adhesion states.[106–109] An alternative method of forming supported intermembrane junctions employs a combination of Langmuir–Blodgett and Langmuir–Schaeffer monolayer-transfer techniques. Two membranes are deposited onto a solid substrate by successive transfer of four monolayers from an air–water interface. This process has the advantage of uniformly coating a large surface area with a planar membrane, and has proven useful for neutron reflectivity studies.[110,111] Limitations of the Langmuir method include the difficulty of working with transmembrane proteins and an intrinsic requirement of intermembrane adhesion to achieve monolayer transfer; this precludes direct formation of weakly adhering junction states (described below). A third type of intermembrane junction can be formed by rupture of GUVs onto supported membranes. This technique produces

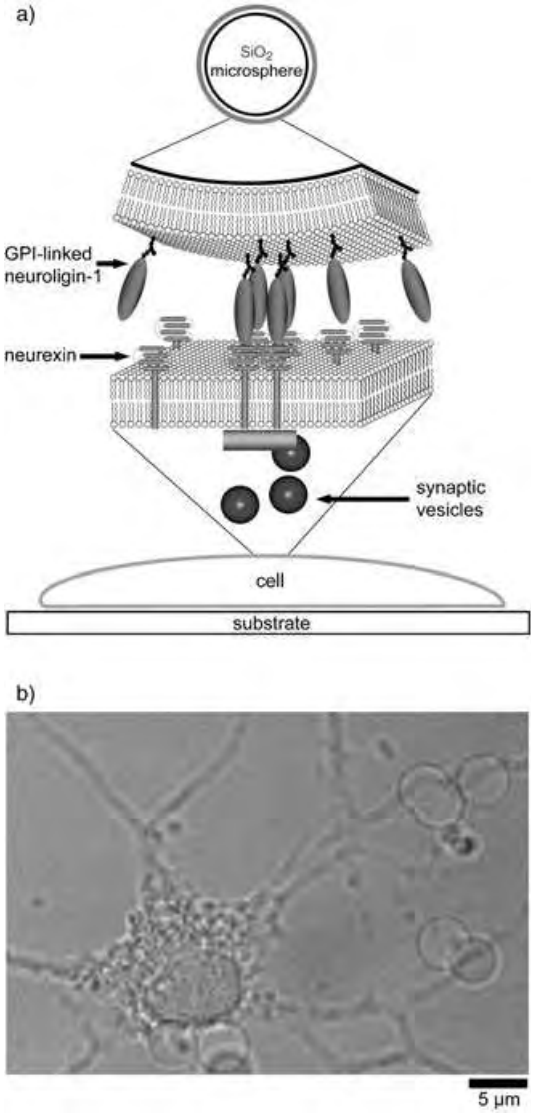

Figure 6. a) Schematic representation of a membrane-coated bead displaying a GPI-linked form of neuroligin-1. Neuroligin-1 binds its cognate receptor β-neurexin on the neuronal cell surface and triggers early stages of synaptogenesis. b) Bright field phase contrast image illustrating interactions between membrane-coated beads and primary neurons. (The image was supplied by M. Baksh and S. Pautot.)

planar junctions, with typical sizes of 10–50 μm, which exhibit multiple adhesion states and are well suited to optical and scanning probe imaging techniques.[112–115] This type of supported membrane junction has proven useful in the study of membrane-mediated reorganization of proteins into patterned states,[23] and is discussed further in Section 4.2 in the context of membrane topographical imaging.

Membrane–membrane interactions can also be characterized by examining the colloidal behavior of a population of membrane-coated beads.[116,117] The behavior of a colloidal system is driven by the potential for the interaction between pairs of particles. In the case of membrane-derivatized silica beads, this potential is dominated by membrane–membrane interactions. Hence, the phase behavior of the entire system is responsive to details of the interaction between the membranes. For example, the binding of a protein to a membrane-associated ligand at densities as low as 10^{-4} monolayer has been observed to trigger a phase transition. A typical colloidal phase transition triggered by protein binding to ligands on the membrane surface is depicted in Figure 7. The assay is

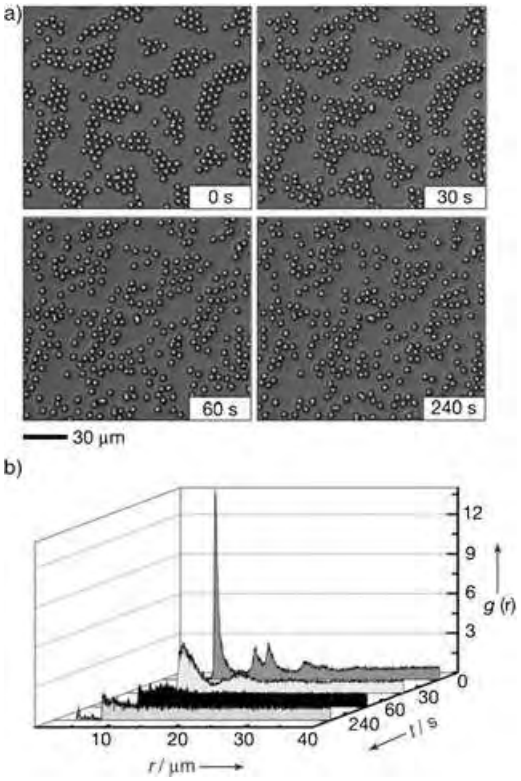

Figure 7. Colloidal phase transition of membrane-coated beads triggered by protein binding. a) Time sequence of images depicting the transition from a condensed to a dispersed colloidal phase, triggered by the addition of protein (5 $\mu g\,ml^{-1}$ final concentration IgG antibody specific to a membrane surface ligand). Transitions were triggered only when the appropriate ligand was also incorporated into the membrane. b) Corresponding plots of $g(r)$ for the time sequence in (a). Adapted from ref. [116].

performed by dispersing membrane-derivatized beads underwater, where they settle under gravity onto the underlying substrate and form a two-dimensional colloid. The beads exhibit free lateral diffusion and the system behaves as an ergodic fluid. For highly sensitive assays, the membrane composition is tuned so that the colloid weakly condenses (first picture in Figure 7a). The condensed distribution is dynamic, with individual beads continuously "evaporating" and recondensing into clusters. However, the overall structure is invariant. Quantitative analysis of the colloidal phases is performed by extracting the pair distribution function $g(r)$.

More than one type of membrane-coated bead can be mixed using fluorescent labels to enable them to be distinguished. In such a binary colloid format, interactions between membrane-associated proteins can be characterized by analysis of the colloid distribution. The distribution function for heterogeneous pairs, which counts the relative positions of beads of different type, can provide a measure of the

interaction strength between the different membrane compositions. This relatively high-throughput strategy of characterizing intermembrane protein-binding affinities could be of utility for the acquisition of large quantities of protein-binding data relevant to intercellular adhesion and signaling events.

4. Imaging Techniques

4.1. Dynamic Fluorescence Microscopy

Fluorescence microscopy is an extremely useful technique for resolving both static and dynamic aspects of molecular organization in membranes. Direct imaging of the fluorescence from probe molecules linked to membrane components of interest immediately offers lateral resolution of compositional variations to the diffraction limit. Quantitative analysis of fluorescence intensity changes within a three-dimensional volume has been used to monitor the flux of green fluorescent protein (GFP) labelled TCR into the c-SMAC during formation of the immunological synapse.[65] A similar type of strategy has been used in an elegant series of experiments to count, molecule by molecule, the amount of agonist pMHC in a T-cell synapse.[118] This information was then correlated with intracellular signaling activity to demonstrate that a single agonist pMHC ligand can trigger transient TCR signaling. Even more interestingly, blocking the co-stimulatory molecule CD4 substantially reduced the sensitivity of TCR signaling, thus suggesting a role for this molecule in signal amplification. These experiments demonstrate the enormous molecular detail with which aspects of signal transduction at immunological synapses can now be observed. Signaling was monitored by a conventional strategy using a calcium-sensitive fluorescent probe (fura-2AM), which was loaded into the T cell. Individual pMHC agonists were labeled with the phycobiliprotein phycoerythrin. Phycoerythrin is an approximately 240-kDa protein with about 34 fluorophores, which make it an extremely bright single molecule that can be tracked by confocal microscopy.

Single-molecule tracking is now being applied by a number of research groups to image molecular motions during formation of the synapse by using total internal reflection fluorescence (TIRF) microscopy. In the objective lens version of TIRF microscopy, a laser is focused off-center onto the back focal plane of an extremely high numerical aperture objective (e.g., NA = 1.45). The beam is then collimated by the objective lens and emerges at a glancing angle. As the beam meets the sample, it is totally internally reflected off of the coverslip/aqueous interface. Only an evanescent field penetrates the sample to excite fluorophores within a thin layer of 50–100 nm from the coverslip interface. This is an ideal configuration for imaging molecules in synapses formed with supported membranes. The extremely low fluorescence background provided by TIRF allows facile observation of single fluorophore probes, and is expected to greatly extend the applicability of single-molecule observations within hybrid synapses. An example of the set-up and representative diffusion tracks from single molecules in a supported membrane are illustrated in Figure 8a and 8b.

Another useful probe of molecular mobility is fluorescence correlation spectroscopy (FCS). Originally developed in the 1970s,[119] FCS has lately undergone a renaissance with the advent of fast hardware correlators, sensitive avalanche photodiodes (APDs), and extremely high NA objectives.[120–125] In applying FCS to membrane systems, a laser is typically focused to a diffraction-limited waist (< 0.5 μm) by a high aperture objective. The diffusion of fluorophores into and out of the excitation volume produces intensity fluctuations that are temporally correlated (Figure 8c and 8d). Analysis of the correlation data yields information about the diffusion of fluorophores within the excitation volume. Cross-correlations between signals from different color fluorophores can reveal specific molecular interactions. This type of observation can be particularly useful in resolving the specific sequences of molecular interactions occurring in the immunological synapses. Again, the simplified configuration provided by hybrid synapses formed from live cells and supported membranes is likely to be of high utility.

4.2. Topographical Imaging

The importance of geometrical constraints within the immunological synapse underscores the need for imaging methods capable of resolving nanometer-scale topography at intermembrane junctions. Two recent fluorescence imaging techniques enable real-time topographical imaging of intermembrane junctions with sub-nanometer precision. Intermembrane fluorescence resonance energy transfer (FRET) is exquisitely sensitive for membrane spacings up to 10 nm. Optical interferometry is most useful beyond this range. Reflection interference contrast microscopy (RICM) has been the dominant method of imaging topographical features of membranes near surfaces for over a decade[105–108,126–129] (for a recent review see ref. [109]). More recently, fluorescence interference contrast microscopy (FLIC) has emerged as a powerful alternative to RICM.[112,114,130,131] Applications of intermembrane FRET and FLIC imaging to resolve membrane topography are described below. A detailed review of the optics and implementation of these techniques is presented elsewhere.[132]

FRET occurs between membranes which have been doped with complementary fluorescent probes when the intermembrane spacing is comparable to the Förster distance for the probe pair (ca. 5 nm). Quantitative analysis of FRET efficiency provides measurement of intermembrane spacing with sub-nanometer precision.[112,113] A general schematic representation for interpretation of intermembrane FRET is depicted in Figure 9. The rate k_T of nonradiative energy transfer from a donor to a population of acceptors, which are distributed in an offset plane, is given by Equation (1).

$$k_T = \frac{\sigma\pi R_0^6}{2\tau_D z^4} \quad (1)$$

σ is the concentration of acceptor molecules, R_0 is the Förster distance (5 nm for the Texas Red/NBD pair[133]), τ_D is

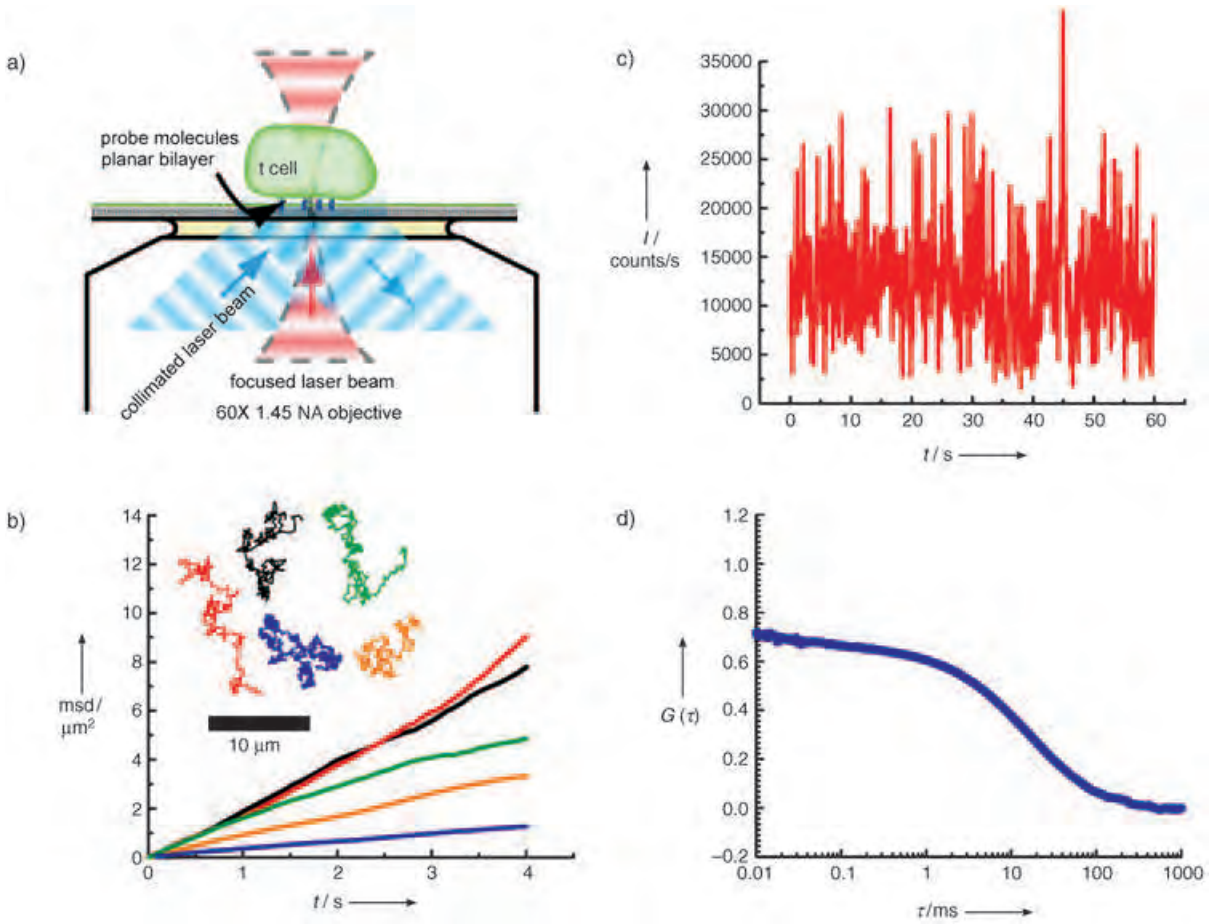

Figure 8. a) A combined system for TIRF and FCS microscopy. The collimated TIRF excitation (blue) emerges from the objective at a glancing angle and experiences total internal reflection at the coverslip/sample interface where it produces an evanescent field at the surface. The FCS excitation (red) is tightly focused on the sample interface. b) Characteristic diffusion tracks of a single molecule observed by TIRF microscopy, together with plots of the mean-square displacements (msd) of fluorescently labeled proteins bound to a supported membrane. c) Temporal fluorescence intensity fluctuations observed with focused excitation (FCS mode) reveal movements of fluorescently labeled antibodies bound to a supported membrane. Fluctuations are produced as the molecules diffuse into and out of the excitation spot. d) Autocorrelation of the intensity fluctuations can be used to quantify molecular motion. (The image was supplied by M. Forstner and A. Demond.)

the fluorescence lifetime of the donor in the absence of acceptors, and z is the distance between the donor and the plane of acceptors. Two leaflets of the bilayer membrane result in two planes of acceptors, separated from each other by about 4 nm. The NBD chromophore on the commonly used, tail-labeled NBDPC (1-palmitoyl-2-[12-[(7-nitro-2-1,3-benzoxadiazol-4-yl)amino]dodecanoyl]-*sn*-glycerol-3-phosphocholine) preferentially localizes in the glycerol/upper chain region of the membrane;[134] it can be taken to occupy a single plane for analysis. The total FRET efficiency E is obtained by summing up the different transfer pathways, denoted in Equation (2) with primes. Analysis of FRET efficiency using Equations (1) and (2) directly provides the distance between the planes of the probe molecules.

$$E = \frac{k'_T + k''_T}{k'_T + k''_T + 1/\tau_D} \qquad (2)$$

Quantitative measurements of FRET efficiency are fit to calculations, based on Equation (2), to determine the average intermembrane fluorophore spacing z. Calculated FRET efficiency curves are plotted against the measured efficiencies in Figure 9. These results indicate the average spacings to be 3.5, 4.6, and 6.7 nm for the PI, G_{M1}, and G_{M1}-cholera toxin junctions, respectively (PI = phosphatidylinositol, G_{M1} = Galβ1-3GalNAcβ1-4(NeuAcα2-3)Galβ1-4Glcβ1-1′-ceramide). An estimate of $R_0 = 5$ nm for the Texas Red/NBD pair is used[133] and an interleaflet probe separation distance of 4 nm was estimated for the Texas Red/DPPE bilayer. No adjustments were made for the two planes of the donor since there is evidence suggesting that negatively charged probes can be substantially enriched in the upper leaflet of supported membranes formed by fusion of small unilamellar vesicles.[135] The absolute values of these distance determinations are sensitive to the estimates of R_0 and, to a lesser extent, to interleaflet spacing. However, the relative distances obtained are accurate. For example, X-ray diffraction analysis of osmotically stressed multibilayers indicate that G_{M1} extends 1.2 nm above the surface of the phosphatidylcholine membrane;[136] we determine a difference of 1.1 nm in membrane

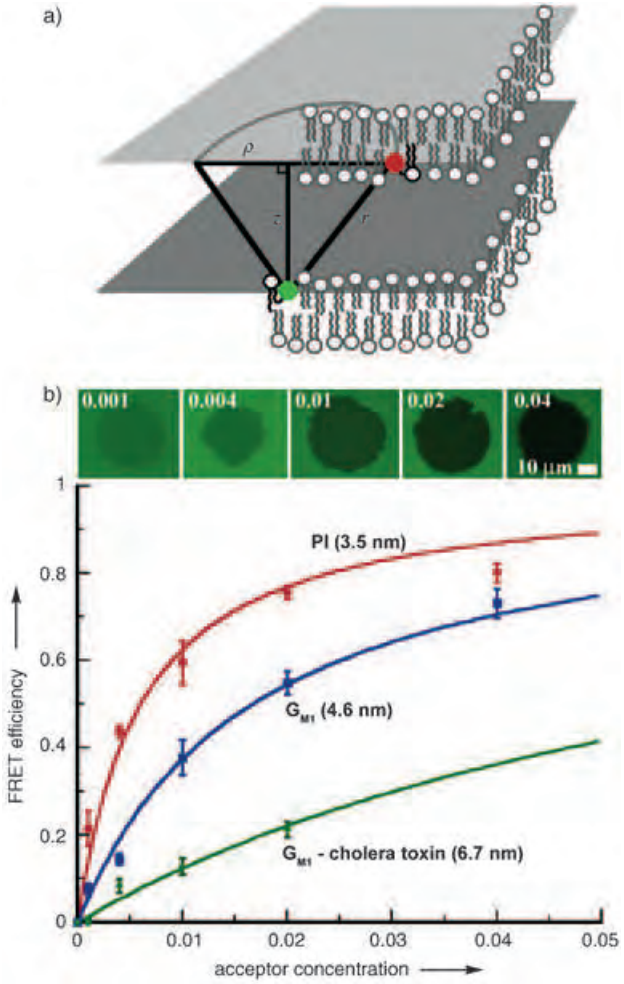

Figure 9. a) Schematic representation illustrating intermembrane FRET. A single probe molecule in one membrane can, in general, transfer resonance energy with one of multiple probes in the apposed membrane. This leads to a fourth power dependence of FRET efficiency on *z*, in contrast to the canonical sixth power dependence generally encountered for one-to-one molecular FRET between a donor and acceptor. b) FRET efficiency data for PI, G_{M1}, and G_{M1}-cholera toxin membrane junctions. The sequence of images depicts FRET data from PI junctions for each of the acceptor (Texas Red/DPPE, mole fraction σ; DPPE = *N*-(Texas Red sulfonyl)-1,2-dipalmitoyl-*sn*-glycero-3-phosphoethanolamine) concentration shown. Solid curves represent calculations based on Equation (2) with intermembrane separation distances (*z*) as labeled. Adapted from ref. [113].

spacing induced by G_{M1}, relative to the PI/DMPC membrane junctions (DMPC = dimyristoylphosphatidylcholine). The height of 3.2 nm determined from intermembrane FRET for the G_{M1}-cholera toxin complex is in direct agreement with structural information from X-ray crystallography data.[137] Although the highest resolution measurement of intermembrane spacing is achieved by quantifying FRET efficiency at a variety of acceptor concentrations, intermembrane FRET can be used in imaging mode with a single acceptor concentration. FRET is an intrinsically short range (10 nm) phenomenon, which cannot be used to resolve larger scale topographical features.

Measurements of intermembrane spacings beyond the range of FRET can be achieved using FLIC microscopy.[112,114,130,131] This technique exploits the spatial variation of the intensity within an optical standing wave to modulate the fluorescence intensity of probes as a function of their position along the optical axis, which is perpendicular to the interface in this configuration. A schematic representation of

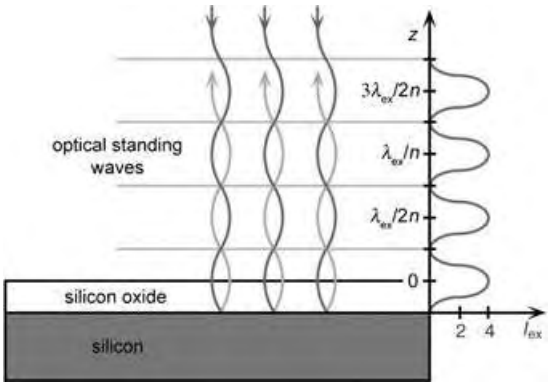

Figure 10. Schematic representation of a FLIC set-up using an oxidized silicon wafer as the substrate. Reflection off of the silicon/silicon oxide interface produces counter-propagating waves of the excitation light, which set up a standing wave of spatially varying optical intensity. The pattern of the excitation intensity exhibits a $\lambda/2$ spatial periodicity, and is plotted along the right vertical axis. Emitted fluorescence also experiences a photon self-interference effect (not shown) which is superimposed on the excitation pattern.

the set up on an oxidized silicon wafer is depicted in Figure 10. The primary optical reflection occurs at the interface between the silicon and silicon oxide. The oxide layer provides a controllable spacer, which allows the relevant features of the system to be positioned optimally with respect to the standing wave. A 60-nm thick oxide layer is useful for proteins at supported membrane interfaces. FLIC microscopy achieves nanometer resolution and can resolve topographical structures extending hundreds of nanometers from the primary plane. FLIC intensity images can be easily deconvolved into three-dimensional topography data using the simplified relation for fluorescence intensity I_F [Eq. (3)].

$$I_F \propto \left((1-r_f)^2 + 4\,r_f \sin^2\left(\frac{\phi_{ex}}{2}\right)\right)\left((1-r_f)^2 + 4\,r_f \sin^2\left(\frac{\phi_{em}}{2}\right)\right) \qquad (3)$$

This Equation is derived from basic optical principles.[138] ϕ_{ex} and ϕ_{em} are given by $(4\pi/\lambda_{ex})(n_w z + n_o z_o)$ and $(4\pi/\lambda_{em})(n_w z + n_o z_o)$, respectively. Indices of refraction for water (1.33) and silicon oxide (1.46) are represented by n_w and n_0, z is the height above the oxide surface, and z_o is the oxide thickness. The excitation and emission wavelengths λ_{ex} and λ_{em} are 560 and 645 nm when the Texas Red fluorophore is used. The reflection coefficient of the silicon/silicon oxide interface (0.46 at 645 nm) is represented by r_f. This approximation has a maximum error of about 2 nm over the distance range of typical experiments involving supported membrane junctions (5–75 nm); more involved calculations include the angular spread of incident and collected light as well as spectral bandwidth.[115,130–132]

Examples of the use of FLIC microscopy to resolve membrane topography at supported membrane junctions are illustrated in Figures 11 and 12. A notable feature of the upper membrane in a supported membrane junction is the existence of two distinctly different states of adhesion to the lower bilayer membrane. The first, referred to as type 1, is characterized by uniform intermembrane FRET, which indicates intermembrane distances of a few nanometers. In the second state (type 2), large intermembrane spacings (ca. 50 nm) are maintained by a balance between Helfrich (entropic) repulsion[139] and occasional adhesion sites that pin the two membranes together. No intermembrane FRET is visible in type 2 junctions; however, FLIC reveals large-scale thermal undulations. Schematic representations, FLIC images, and reconstructed surface topography maps for examples of the two junction types are illustrated in Figure 11. FLIC is easily performed in real time, thus allowing dynamic observations of membrane topographical fluctuations. The type 2 junction illustrated in Figure 11 exhibits fluctuations with amplitudes of approximately 4 nm root-mean-square, a lateral spatial correlation length of about 340 nm, and a correlation time of about 1 s. All values were determined by FLIC imaging.[114]

The combination of FLIC with conventional fluorescence imaging (and FRET) can be used to acquire highly detailed three-dimensional information about the organization of proteins and lipids at intermembrane junctions. Observations of an intermembrane junction, in which membrane-bound antibody proteins in the junction become organized into patterns as a result of adhesive interactions between the two membranes, are illustrated in Figure 12. A FLIC image of

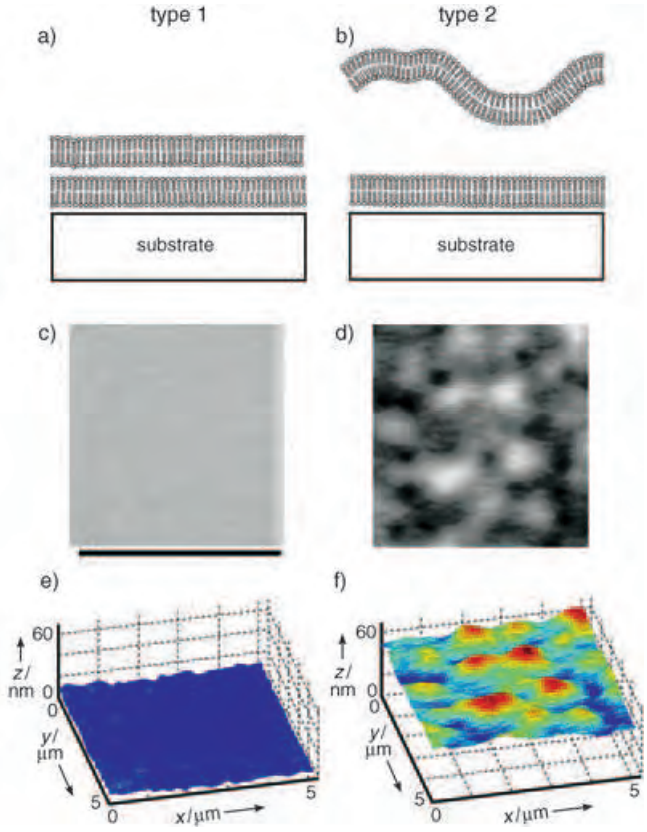

Figure 11. Type 1 (a) and type 2 (b) junctions. The corresponding FLIC images and topographical maps [computed from Eq. (3)]) are plotted in (c)–(f). The topography of type 2 junctions is dynamic, and fluctuates randomly with a characteristic temporal correlation time of about 1 s. (The image was supplied by Y. Kaizuka.)

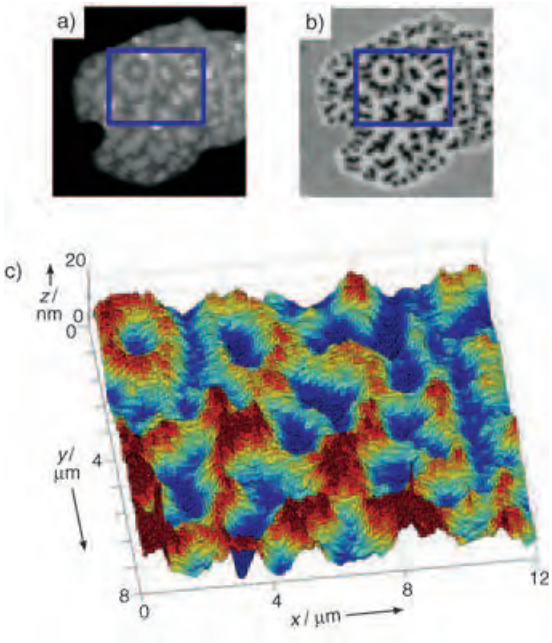

Figure 12. A supported intermembrane junction in which antibodies are bound to the lower membrane. A FLIC image of the upper membrane (a) reveals topographical features that reflect the distribution of fluorescently labeled antibodies (b) in the junction. c) Topographical map of the marked inset region of the junction. The topography of this protein intermembrane junction is static. (The image was supplied by R. Parthasarathy.)

probes in the upper membrane is depicted in Figure 12a, while direct fluorescence imaging of the antibodies is shown in Figure 12b. A topography map, computed from the FLIC data in Figure 12a, is plotted in Figure 12C. The membrane-bound antibodies diffuse freely on the membrane surface outside of the junction. The antibody is corralled into patterns in the junction, and loses much of its lateral mobility. Antibody mobility can be characterized by fluorescence recovery after photobleaching (FRAP), single-molecule tracking, or FCS. The topography map indicates that the hills and valleys of this junction have a height difference of about 12 nm, which is about the size of an antibody. The conformation of the membrane thus follows the topography of the interface, and therefore, this can be categorized as a type 1 junction. The topography of the protein intermembrane junction shown in Figure 12 is static in time, in contrast to the type 2 junction illustrated in Figure 11. FLIC imaging is instrumental in making these types of distinctions. Intermembrane FRET has been used to additionally confirm that valleys observed in the upper membrane of the protein intermembrane junction descend to within a few nanometers of the lower membrane.[115] The combined use of intermem-

brane FRET can increase the absolute resolution of FLIC by helping to break some of the degeneracy inherent to interference imaging techniques.

5. Conclusion and Outlook

The surfaces of cell membranes present a highly dynamic and responsive environment in which convergence of chemical and mechanical forces produces a rich collection of reaction processes. The natural fluidity and flexibility of membranes provides mechanisms for them to respond to chemical interactions in ways not generally seen with inorganic materials. Highly cooperative reaction processes, which combine chemical binding events with spatial pattern formation, are emerging as general themes among cell–cell interactions. The immunological synapses, discussed briefly here, represent the best resolved examples of such phenomena at the present time. As such, interactions between immune cells are attractive for highly quantitative investigations aimed at developing a physicochemical understanding of the underlying mechanisms that drive and regulate these events. Such studies of immunological synapses may further reveal mechanistic paradigms common to many intercellular signaling processes. Indeed, the physical characteristics of immune cell junctions are likely to be shared by intermembrane junctions in general. The parallel application of new imaging and manipulation techniques to reconstituted membrane systems and hybrid synapses represents a promising convergence of physical chemistry and cell biology. The blending of ideas and observations one can expect from this situation may well help to expose some of the secrets as to how molecules come to life.

I would like to thank the many students, postdoctoral fellows, and colleagues who have contributed to these projects. Financial support has been provided by the National Institutes of Health (NIH), the Department of Energy (DOE), the National Science Foundation (NSF), the Burroughs Wellcome Fund, The Searle Scholars Program, the Beckman Foundation, and the Hellman Family Faculty Fund. The watercolor art in this Review was created by Dr. Raghuveer Parthasarathy.

Received: June 19, 2004
Revised: October 15, 2004
Published online: April 21, 2005

[1] D. Bray, M. D. Levin, C. J. Morton-Firth, *Nature* **1998**, *393*, 85.
[2] M. Mammen, S.-K. Choi, G. M. Whitesides, *Angew. Chem.* **1998**, *110*, 2908; *Angew. Chem. Int. Ed.* **1998**, *37*, 2754.
[3] F. G. Giancotti, E. Rouslahti, *Science* **1999**, *285*, 1028.
[4] G. Maheshwari, G. Brown, D. A. Lauffenberger, A. Wells, L. G. Griffith, *J. Cell Sci.* **2000**, *113*, 1677.
[5] J. E. Gestwicki, L. L. Kiessling, *Nature* **2002**, *415*, 81.
[6] M. N. Teruel, T. Meyer, *Cell* **2000**, *103*, 181.
[7] C. R. F. Monks, B. A. Freidberg, H. Kupfer, N. Sciaky, A. Kupfer, *Nature* **1998**, *395*, 82.
[8] A. Grakoui, S. K. Bromley, C. Sumen, M. M. Davis, A. S. Shaw, P. M. Allen, M. L. Dustin, *Science* **1999**, *285*, 221.
[9] D. M. Davis, I. Chiu, M. Fasset, G. B. Cohen, O. Mandelboim, J. L. Strominger, *Proc. Natl. Acad. Sci. USA* **1999**, *96*, 15062.
[10] D. M. Davis, *TRENDS Immunol.* **2002**, *23*, 356.
[11] P. A. van der Merwe, S. J. Davis, *Science* **2002**, *295*, 1479.
[12] M. L. Dustin, D. R. Colman, *Science* **2002**, *298*, 785.
[13] M. M. Davis, M. Krogsgaard, J. B. Huppa, C. Sumen, M. A. Purbhoo, D. J. Irvine, L. C. Wu, L. Erlich, *Annu. Rev. Biochem.* **2003**, *72*, 717.
[14] J. B. Huppa, M. M. Davis, *Nat. Rev. Immunol.* **2003**, *3*, 973.
[15] D. M. Davis, M. L. Dustin, *TRENDS Immunol.* **2004**, *25*, 323.
[16] P. A. van der Merwe, *Curr. Opin. Immunol.* **2002**, *14*, 293.
[17] C. Wülfing, I. Tskvitaria-Fuller, N. Burroughs, M. D. Sjaastad, J. Klem, J. D. Schatzle, *Immunol. Rev.* **2002**, *189*, 64.
[18] C. L. Fuller, V. L. Braciale, L. E. Samelson, *Immunol. Rev.* **2003**, *191*, 220.
[19] S. Y. Qi, J. T. Groves, A. K. Chakraborty, *Proc. Natl. Acad. Sci. USA* **2001**, *98*, 6548.
[20] T. R. Weikl, J. T. Groves, R. Lipowsky, *Europhys. Lett.* **2002**, *59*, 916.
[21] N. J. Burroughs, C. Wülfing, *Biophys. J.* **2002**, *83*, 1784.
[22] A. K. Chakraborty, *AIChE J.* **2003**, *49*, 1614.
[23] R. Parthasarathy, J. T. Groves, *Proc. Natl. Acad. Sci. USA* **2004**, *101*, 12798.
[24] R. Imbihl, G. Ertl, *Chem. Rev.* **1995**, *95*, 697.
[25] M. Kim, M. Bertram, M. Pollmann, A. von Oertzen, A. S. Mikhailov, H. H. Rotermund, G. Ertl, *Science* **2001**, *292*, 1357.
[26] C. Sachs, M. Hildebrandt, S. Völkening, J. Wintterlin, G. Ertl, *Science* **2001**, *293*, 1635.
[27] S. K. Bromley, W. R. Burack, K. G. Johnson, K. Somersalo, C. Sumen, M. M. Davis, A. S. Shaw, P. M. Allen, M. L. Dustin, *Annu. Rev. Immunol.* **2001**, *19*, 375.
[28] M. L. Dustin, S. K. Bromley, M. M. Davis, C. Zhu, *Annu. Rev. Cell Dev. Biol.* **2001**, *17*, 133.
[29] M. F. Krummel, M. M. Davis, *Curr. Opin. Immunol.* **2002**, *14*, 66.
[30] F. E. McCann, K. Suhling, L. M. Carlin, K. Eleme, S. B. Taner, K. Yanagi, B. Vanherberghen, P. M. W. French, D. M. Davis, *Immunol. Rev.* **2002**, *189*, 179.
[31] Y. M. Vyas, H. Maniar, B. Dupont, *Immunol. Rev.* **2002**, *189*, 161.
[32] M. F. Krummel, M. D. Sjaastad, C. Wülfing, M. Davis, *Science* **2000**, *289*, 1349.
[33] K.-H. Lee, A. D. Holdorf, M. Dustin, A. Chan, P. M. Allen, A. S. Shaw, *Science* **2002**, *295*, 1539.
[34] S. Stoll, J. Delon, T. M. Brotz, R. N. Germain, *Science* **2002**, *296*, 1873.
[35] Y. M. Vyas, K. M. Mehta, M. Morgan, H. Maniar, L. Butros, S. Jung, J. K. Burkhardt, B. Dupont, *J. Immunol.* **2001**, *167*, 4358.
[36] S.-Y. Tseng, M. L. Dustin, *Curr. Opin. Cell Biol.* **2002**, *14*, 575.
[37] G. Werlen, E. Palmer, *Curr. Opin. Immunol.* **2002**, *14*, 299.
[38] T. N. Sims, M. L. Dustin, *Immunol. Rev.* **2002**, *186*, 101.
[39] C. W. Arendt, B. Albrecht, T. J. Soos, D. R. Littman, *Curr. Opin. Immunol.* **2002**, *14*, 323.
[40] C. Wülfing, M. M. Davis, *Science* **1998**, *282*, 2266.
[41] M. L. Dustin, J. A. Cooper, *Nat. Immunol.* **2000**, *1*, 23.
[42] V. Das, B. Nal, A. Roumier, V. Meas-Yedid, C. Zimmer, J.-C. Olivo-Marin, P. Roux, P. Ferrier, A. Dautry-Varsat, A. Alcover, *Immunol. Rev.* **2002**, *189*, 123.
[43] A. Viola, S. Schroeder, Y. Sakakibara, A. Lanzavecchia, *Science* **1999**, *283*, 680.
[44] M. L. Dustin, *J. Clin. Invest.* **2002**, *109*, 155.
[45] M. Dykstra, A. Cherukuri, H. W. Sohn, S. J. Tzeng, S. K. Pierce, *Annu. Rev. Immunol.* **2003**, *21*, 457.
[46] P. Pizzo, E. Giurisato, A. Bigsten, M. Tassi, R. Tavano, A. Shaw, A. Viola, *Immunol. Lett.* **2004**, *91*, 3.
[47] L. I. Richie, P. J. R. Ebert, L. C. Wu, M. F. Krummel, J. J. T. Owen, M. M. Davis, *Immunity* **2002**, *16*, 595.

[48] E. Hailman, W. R. Burack, A. S. Shaw, M. L. Dustin, P. M. Allen, *Immunity* **2002**, *16*, 839.
[49] S.-J. E. Lee, Y. Hori, A. K. Chakraborty, *Proc. Natl. Acad. Sci. USA* **2003**, *100*, 4383.
[50] J. T. Groves, M. L. Dustin, *J. Immunol. Methods* **2003**, *278*, 19.
[51] E. Donnadieu, P. Revy, A. Trautmann, *Immunology* **2001**, *103*, 417.
[52] F. E. McCann, B. Vanherberghen, K. Eleme, L. M. Carlin, R. J. Newsam, D. Goulding, D. M. Davis, *J. Immunol.* **2003**, *170*, 2862.
[53] K.-H. Lee, A. R. Dinner, C. Tu, G. Campi, S. Raychaudhuri, R. Varma, T. N. Sims, W. R. Burack, H. Wu, J. Wang, O. Kanagawa, M. Markiewicz, P. M. Allen, M. L. Dustin, A. K. Chakraborty, A. S. Shaw, *Science* **2003**, *302*, 1218.
[54] J. C. Stinchombe, G. Bossi, S. Booth, G. M. Griffiths, *Immunity* **2001**, *15*, 751.
[55] D. McDonald, L. Wu, S. M. Bohks, V. N. KewalRamani, D. Unutmaz, T. J. Hope, *Science* **2003**, *300*, 1295.
[56] D. Derse, G. Heidecker, *Science* **2003**, *299*, 1670.
[57] T. Igakura, J. C. Stinchcombe, P. K. C. Goon, G. P. Taylor, J. N. Weber, G. M. Griffiths, Y. Tanaka, M. Osame, C. R. M. Bangham, *Science* **2003**, *299*, 1713.
[58] J.-N. Tournier, A. Q. Hellmann, *TRENDS Immunol.* **2003**, *24*, 114.
[59] P. Aucouturier, R. I. Carp, C. Carnaud, T. Wisniewski, *Clin. Immunol.* **2000**, *96*, 79.
[60] G. S. Huh, L. M. Boulanger, H. Du, P. A. Riquelme, T. M. Brotz, C. J. Shatz, *Science* **2000**, *290*, 2155.
[61] A. A. Khan, C. Bose, L. S. Yam, M. J. Soloski, F. Rupp, *Science* **2001**, *292*, 1681.
[62] G. Bezakova, M. A. Ruegg, *Nat. Rev. Mol. Cell Biol.* **2003**, *4*, 295.
[63] R. Tordjman, Y. Lepelletier, V. Lemarchandel, M. Cambot, P. Gaulard, O. Hermine, P.-H. Roméo, *Nat. Immunol.* **2002**, *3*, 477.
[64] C. Wülfing, F. Rupp, *Nat. Immunol.* **2002**, *3*, 418.
[65] W. C. Moss, D. J. Irvine, M. M. Davis, M. F. Krummel, *Proc. Natl. Acad. Sci. USA* **2002**, *99*, 15024.
[66] C. Wülfing, A. Bauch, G. R. Crabtree, M. M. Davis, *Proc. Natl. Acad. Sci. USA* **2000**, *97*, 10150.
[67] S. Valensin, S. R. Paccani, C. Ulivieri, D. Mercati, S. Pacini, L. Patrussi, T. Hirst, P. Lupetti, C. T. Baldari, *Eur. J. Immunol.* **2002**, *33*, 435.
[68] J. R. Kuhn, M. Poenie, *Immunity* **2002**, *16*, 111.
[69] R. D. Huby, A. Weiss, S. C. Ley, *J. Biol. Chem.* **1998**, *273*, 12024.
[70] I. Tskvitaria-Fuller, A. L. Rozelle, H. L. Yin, C. Wülfing, *J. Immunol.* **2003**, *171*, 2287.
[71] S. Faure, L. I. Salazar-Fontana, M. Semichon, V. L. J. Tybulewicz, G. Bismuth, A. Trautmann, R. N. Germain, J. Delon, *Nat. Immunol.* **2004**, *5*, 272.
[72] A. Gautreau, D. Louvard, M. Arpin, *Curr. Opin. Cell Biol.* **2002**, *14*, 104.
[73] J. Delon, K. Kaibuchi, R. N. Germain, *Immunity* **2001**, *15*, 691.
[74] A. S. Shaw, M. L. Dustin, *Immunity* **1997**, *6*, 361.
[75] M. K. Wild, A. Cambiaggi, M. H. Brown, E. A. Davies, H. Ohno, T. Saito, P. A. van der Merwe, *J. Exp. Med.* **1999**, *190*, 31.
[76] S.-J. E. Lee, Y. Hori, J. T. Groves, M. L. Dustin, A. K. Chakraborty, *TRENDS Immunol.* **2002**, *23*, 492.
[77] S.-J. E. Lee, Y. Hori, J. T. Groves, M. L. Dustin, A. K. Chakraborty, *TRENDS Immunol.* **2002**, *23*, 500.
[78] R. Simson, E. Wallraff, J. Faix, J. Niewohner, G. Gerisch, E. Sackmann, *Biophys. J.* **1998**, *74*, 514.
[79] J. T. Groves, S. G. Boxer, H. M. McConnell, *Proc. Natl. Acad. Sci. USA* **1998**, *95*, 935.
[80] K. Simmons, E. Ikonen, *Nature* **1997**, *387*, 569.
[81] G. Vereb, J. Szöllösi, J. Matkó, P. Nagy, T. Farkas, L. Vígh, L. Mátyus, T. A. Waldmann, S. Damjanovich, *Proc. Natl. Acad. Sci. USA* **2003**, *100*, 8053.
[82] A. Viola, A. Lanzavecchia, *APMIS* **1999**, *107*, 615.
[83] M. Dykstra, A. Cherukuri, S. K. Pierce, *J. Leukocyte Biol.* **2001**, *70*, 699.
[84] S. L. Veatch, S. L. Keller, *Phys. Rev. Lett.* **2002**, *89*, 268101.
[85] H. M. McConnell, M. Vrljic, *Annu. Rev. Biophys. Biomol. Struct.* **2003**, *32*, 469.
[86] E. D. Sheets, D. Holowka, B. Baird, *Curr. Opin. Chem. Biol.* **1999**, *3*, 95.
[87] E. Sackmann, *Science* **1996**, *271*, 43.
[88] E. Sackmann, M. Tanaka, *TIBTECH* **2000**, *18*, 58.
[89] J. T. Groves, *Curr. Opin. Drug Discovery Dev.* **2002**, *5*, 606.
[90] J. Salafsky, J. T. Groves, S. G. Boxer, *Biochemistry* **1996**, *35*, 14773.
[91] T. M. Bayerl, M. Bloom, *Biophys. J.* **1990**, *58*, 357.
[92] S. J. Johnson, T. M. Bayerl, D. C. McDermott, G. W. Adam, A. R. Rennie, R. K. Thomas, E. Sackmann, *Biophys. J.* **1991**, *59*, 289.
[93] B. W. Koenig, S. Krueger, W. J. Orts, C. F. Majkrzak, N. F. Berk, J. V. Silverton, K. Gawrisch, *Langmuir* **1996**, *12*, 1343.
[94] J. T. Groves, C. Wülfing, S. G. Boxer, *Biophys. J.* **1996**, *71*, 2716.
[95] J. T. Groves, N. Ulman, S. G. Boxer, *Science* **1997**, *275*, 651.
[96] J. T. Groves, N. Ulman, P. S. Cremer, S. G. Boxer, *Langmuir* **1998**, *14*, 3347.
[97] A. van Oudenaarden, S. G. Boxer, *Science* **1999**, *285*, 1046.
[98] L. A. Kung, L. Kam, J. S. Hovis, S. G. Boxer, *Langmuir* **2000**, *16*, 6773.
[99] L. Kung, J. T. Groves, N. Ulman, S. G. Boxer, *Adv. Mater.* **2000**, *12*, 731.
[100] J. S. Hovis, S. G. Boxer, *Langmuir* **2001**, *17*, 3400.
[101] J. T. Groves, S. G. Boxer, *Acc. Chem. Res.* **2002**, *35*, 149.
[102] B. Jackson, J. T. Groves, *J. Am. Chem. Soc.* **2004**, 126, 13878.
[103] T. Buranda, J. Huang, G. V. Ramarao, L. K. Ista, R. S. Larson, T. L. Ward, L. A. Sklar, G. P. Lopez, *Langmuir* **2003**, *19*, 1654.
[104] A. R. Sapuri, M. M. Baksh, J. T. Groves, *Langmuir* **2003**, *19*, 1606.
[105] J. Rädler, E. Sackmann, *J. Phys. II* **1993**, *3*, 727.
[106] A. Albersdörfer, T. Feder, E. Sackmann, *Biophys. J.* **1997**, *73*, 245.
[107] A. Kloboucek, A. Behrisch, J. Faix, E. Sackmann, *Biophys. J.* **1999**, *77*, 2311.
[108] R. Bruinsma, A. Behrisch, E. Sackmann, *Phys. Rev. E* **2000**, *61*, 4253.
[109] E. Sackmann, R. Bruinsma, *ChemPhysChem* **2002**, *3*, 262.
[110] T. Charitat, E. Bellet-Amalric, G. Fragneto, F. Graner, *Eur. Phys. J. B* **1999**, *8*, 583.
[111] G. Fragneto, T. Charitat, F. Graner, K. Mecke, L. Perino-Gallice, E. Bellet-Amalric, *Europhys. Lett.* **2001**, *53*, 100.
[112] A. P. Wong, J. T. Groves, *J. Am. Chem. Soc.* **2001**, *123*, 12414.
[113] A. P. Wong, J. T. Groves, *Proc. Natl. Acad. Sci. USA* **2002**, *99*, 14147.
[114] Y. Kaizuka, J. T. Groves, *Biophys. J.* **2004**, *86*, 905.
[115] R. Parthasarathy, B. L. Jackson, T. J. Lowrey, A. P. Wong, J. T. Groves, *J. Phys. Chem. B* **2004**, *108*, 649.
[116] M. M. Baksh, M. Jaros, J. T. Groves, *Nature* **2004**, *427*, 139.
[117] T. M. Bayerl, *Nature* **2004**, *427*, 105.
[118] D. J. Irvine, M. A. Purbhoo, M. Krogsgaard, M. M. Davis, *Nature* **2002**, *419*, 845.
[119] D. Magde, E. Elson, W. W. Webb, *Phys. Rev. Lett.* **1972**, *29*, 705.
[120] P. Schwille, J. Korlach, W. W. Webb, *Cytometry* **1999**, *36*, 176.
[121] J. Korlach, P. Schwille, W. W. Webb, G. W. Feigenson, *Proc. Natl. Acad. Sci. USA* **1999**, *96*, 8461.
[122] S. T. Hess, S. Huang, A. A. Heikal, W. W. Webb, *Biochemistry* **2002**, *41*.
[123] N. Kahya, D. Scherfeld, K. Bacia, B. Poolman, P. Schwille, *J. Biol. Chem.* **2003**, *278*, 28109.
[124] K. Bacia, P. Schwille, *Methods* **2003**, *29*, 74.
[125] E. Haustein, P. Schwille, *Methods* **2003**, *29*, 153.

[126] J. O. Rädler, T. J. Feder, H. H. Strey, E. Sackmann, *Phys. Rev. E* **1995**, *51*, 4526.
[127] R. Hirn, T. M. Bayerl, J. O. Rädler, E. Sackmann, *Faraday Discuss.* **1998**, *111*, 17.
[128] Z. Guttenberg, A. R. Bausch, B. Hu, R. Bruinsma, L. Moroder, E. Sackmann, *Langmuir* **2000**, *16*, 8984.
[129] S. Marx, J. Schilling, E. Sackmann, R. Bruinsma, *Phys. Rev. Lett.* **2002**, *88*, 138102.
[130] A. Lambacher, P. Fromherz, *Appl. Phys. A* **1996**, *63*, 207.
[131] A. Lambacher, P. Fromherz, *J. Opt. Soc. Am. B* **2002**, *19*, 1435.
[132] R. Parthasarathy, J. T. Groves, *Cell Biochem. Biophys.* **2004**, *41*, 391.
[133] J. R. Lakowicz, *Principles of fluorescence spectroscopy*, *2nd ed.*, Kluwer Academic/Plenum, New York, **1999**.
[134] D. Huster, P. Müller, K. Arnold, A. Herrmann, *Biophys. J.* **2001**, *80*, 822.
[135] R. A. Provencal, J. D. Ruiz, A. N. Parikh, A. P. Shreve, *Biophys. J.* **2001**, *80*, 423A.
[136] T. McIntosh, S. A. Simon, *Biochemistry* **1994**, *33*, 10477.
[137] E. A. Merritt, S. Sarfaty, F. van den Akker, C. L'Hoir, J. A. Martial, W. G. J. Hol, *Protein Sci.* **1994**, *3*, 166.
[138] M. Born, E. Wolf, *Principles of Optics*, Cambridge University Press, Cambridge, **1999**.
[139] R. Lipowsky, E. Sackmann in *Handbook of Biological Physics*, *Vol. 1*, Elsevier Science, New York, **1995**.
[140] W. H. Binder, V. Barragan, F. M. Menger, Angew. *Chem.* **2003**, *115*, 5980; *Angew. Chem. Int. Ed.* **2003**, *42*, 5802

Communications

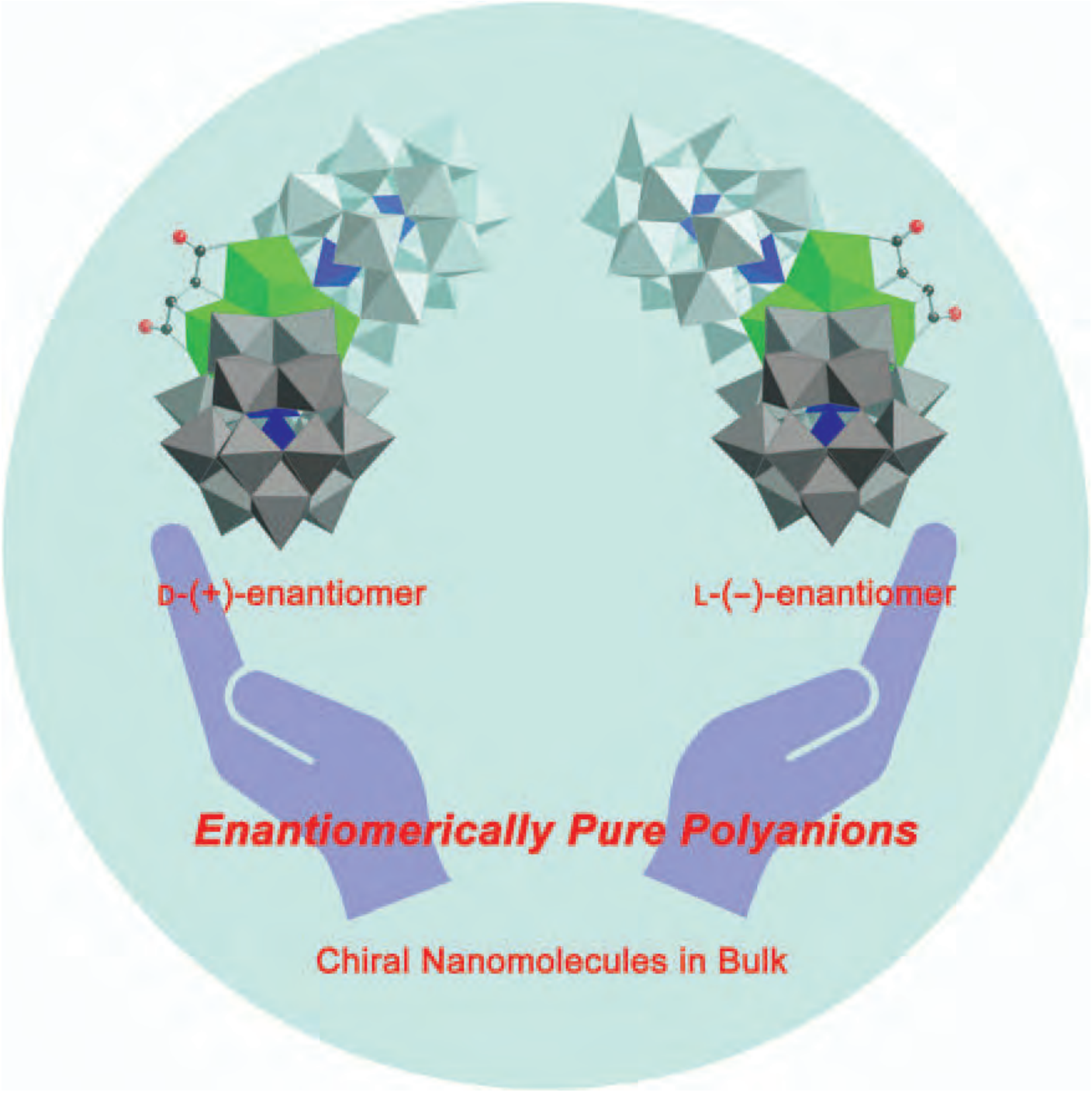

The amplification and transfer of chirality from a small organic natural product, tartrate, to a large multinanometer polytungstate is demonstrated. This strategy affords nonlabile, readily separable, and pure enantiomers of the polytungstates. For more information of this promising approach see the Communication by C. L. Hill and co-workers on the following pages.

  DOI: 10.1002/anie.200500415

Chirality Transfer

Enantiomerically Pure Polytungstates: Chirality Transfer through Zirconium Coordination Centers to Nanosized Inorganic Clusters**

*Xikui Fang, Travis M. Anderson, and Craig L. Hill**

Stable, nanometer-sized enantiomerically pure polyoxoanions could lead to useful chiral materials ranging from microporous solids and inorganic pharmaceuticals to catalysts for homogeneous asymmetric oxidation. However, chirality has been largely unexplored in polyoxometalate (POM) systems.[1] Most POMs with chiral structures undergo rapid racemization in solution, and racemic mixtures are usually seen in solution as well as in the solid state. Typically in crystals the two enantiomers coexist in the same unit cell, related to each other by a crystallographically imposed inversion center.[2] Although Pfeiffer effects have been demonstrated with a wide range of racemic POM systems, the chiral resolution of the enantiomers is frequently complicated by their solubility, lability, and structural similarity.[3,4] Three different synthetic routes to enantiopure POMs in the solid state have been reported. First, hydrothermal synthesis can produce solid inorganic materials with helical characters.[5] One example is the vanadium phosphate complex, $[(CH_3)_2NH_2]K_4[V_{10}O_{10}(H_2O)_2(OH)_4(PO_4)_7]\cdot 4H_2O$, with a chiral interpenetrating double helix of Zubieta and coworkers.[5a] Second, reactions of a few polymolybdates and chiral amino acids afford chiral POMs.[6] A recent study by Kortz et al. demonstrated that the bound amino acids are probably labile in solution, based on NMR spectroscopy and X-ray studies (weak bonding, approximately 2.3 Å, between the Mo and carboxylate O atoms).[6b] Therefore it is not surprising that the chirality of these complexes is largely localized on the amino acid moieties. Third, counterions can play a critical role in determining the solid-state structures of POMs, and, in some cases, cause achiral POMs to crystallize in chiral space groups.[7] Sometimes crystallization of racemic bulk solids can lead to chiral crystals.[8] However, there is no report of chiroptical activity in the solution-state for such enantiopure POM systems. Realization of an intrinsically chiral and configurationally stable POM should afford enantioselective catalytic properties and enhanced biological activities.[9] Furthermore, the control of chiral induction is an important component of the larger goal of effectively managing and utilizing chirogenic phenomena.

[*] X. Fang, Dr. T. M. Anderson, Prof. Dr. C. L. Hill
Department of Chemistry
Emory University
1515 Dickey Drive, Atlanta, GA 30322 (USA)
Fax: (+1) 404-727-6076
E-mail: chill@emory.edu

[**] We gratefully acknowledge the National Science Foundation (Grant CHE-0236686) for funding the research, and Grant CHE-9974864 for funding the D8 X-ray instrument.

Herein we report the synthesis and characterization of chiral, nonracemizing, enantiomerically pure polyoxotungstates, L-**1** and D-**1** prepared in bulk. Significantly, strong

$\{[\alpha\text{-}P_2W_{15}O_{55}(H_2O)]Zr_3(\mu_3\text{-}O)(H_2O)(\text{L-tartH})[\alpha\text{-}P_2W_{16}O_{59}]\}^{15-}$ L-**1**

$\{[\alpha\text{-}P_2W_{15}O_{55}(H_2O)]Zr_3(\mu_3\text{-}O)(H_2O)(\text{D-tartH})[\alpha\text{-}P_2W_{16}O_{59}]\}^{15-}$ D-**1**

chiroptical effects are manifested by the POM units as a result of chirality transfer from a far smaller enantiopure organic molecule, L- or D-tartaric acid ($HO_2CCH(OH)CH(OH)CO_2H$; L-tartH$_4$ or D-tartH$_4$). Both enantiomeric complexes have been characterized by elemental analysis, ^{31}P NMR, IR, and UV/Vis spectroscopy, in addition to the single-crystal X-ray structure analysis on the L enantiomer, and their solution chiroptical properties have been demonstrated by circular dichroism (CD) spectroscopy.

The synthetic approach involves recognition between an achiral host and chiral (nonracemic) guest molecule to produce a chiral microenvironment on the achiral host, a phenomenon revealed by induced circular dichroism (ICD).[10] This straightforward strategy, outlined in Figure 1,

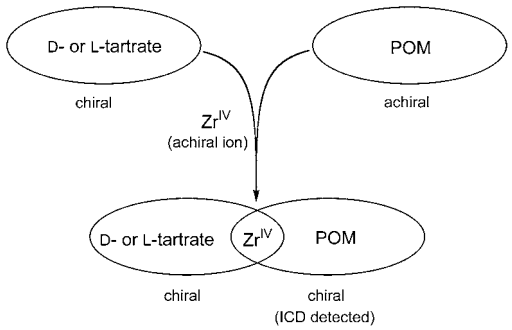

Figure 1. The interaction between D- or L-tartrate and the achiral POM unit through the coordinated Zr^{IV} ions.

relies on the "recognition" between α-$[P_2W_{15}O_{56}]^{12-}$ (**2**), an achiral lacunary Wells–Dawson POM unit of C_{3v} symmetry, and the simple C_2-symmetric D- or L-tartrate ligand.[11] Given the electrostatic repulsion between **2** and tartrate, a positively charged mediator is needed for chirality transfer. The Zr^{IV} ion, is well suited for this task because it has both high charge density and coordination flexibility.[12,13] In the systems reported herein, the Zr^{IV} ions transmit chirality from the chiral tartrate to the polytungstate units by binding strongly to both.

This approach facilitates the crystallization of L-**1** in the chiral orthorhombic space group $P2_12_12_1$, with only one enantiomer present in the unit cell ($Z = 4$). Crystallization in a chiral space group is a rare but ideal starting point for the generation of chiral materials. The structure of L-**1** consists of two units of **2** bridged by a central fragment containing three Zr^{IV} centers and one W^{VI} center (Figure 2a). All three zirconium atoms are nonequivalent and form a triangular unit sharing a coplanar μ_3-oxo oxygen atom. One of the zirconium atoms, Zr3, serves as a "hinge" between the two α-$[P_2W_{15}O_{56}]^{12-}$ units, while the other two zirconium ions (Zr1

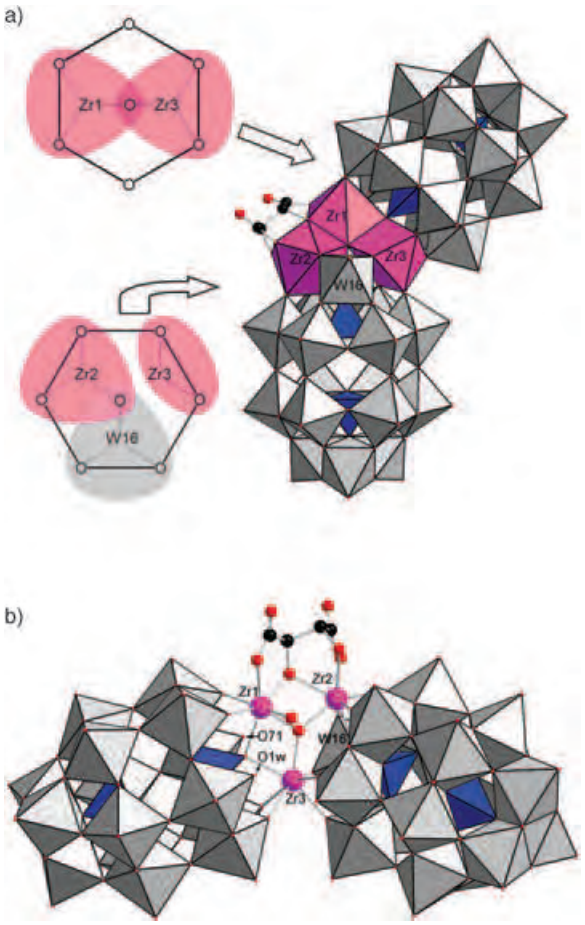

Figure 2. The structure of L-**1**. a) A combination ball-and-stick/polyhedral representation of L-**1** with the metal–oxide framework in polyhedral notation and the L-tart ligand in ball-and-stick notation; gray W, blue P, purple Zr, black C, red O. The hexagons illustrate the coordination between substituted Zr or W sites with the seven terminal oxygen atoms in the vacant positions of the polytungstate moieties. b) A side view of L-**1** showing the three Zr centers as well as the L-tart ligand in ball-and-stick representation.

and Zr2) are bridged by the L-tart unit, by chelation through both the hydroxy and carboxy groups in an unusual η^2:μ_1:μ_2:μ_1:μ_1 fashion (Scheme 1).[14] Bond valence sum calculations reveal that one of two "hydroxy" oxygen atoms on L-tart remains protonated while the other, which bridges the two Zr centers, does not. The asymmetric protonation reduces the local symmetry of the L-tart unit from C_2 to C_1. This mixed protonation state is very rarely observed in metal tartrate

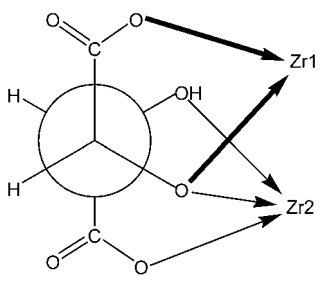

Scheme 1. The coordination environment of the L-tart ligand in L-**1**.

complexes,[14a] and is likely a key factor in providing the strong complexation between L-tart and the large metal–oxide framework. This complexation in turn dictates the configurational stability of L-**1**. In other words, the protonation state of the L-tart hydroxy groups adjusts in response to rearrangements in the coordination sphere of the zirconium ions caused by the ligation of **2**. Simultaneously the chelating L-tart maintains the enhanced complexation ability provided by the vicinal hydroxy oxygen atoms.

Two of the three vacant positions in the bottom α-$[P_2W_{15}O_{56}]^{12-}$ (**2**) unit shown in Figure 2a are occupied by zirconium ions, Zr2 and Zr3, and each bridges a pair of adjacent corner-sharing W octahedra in **2**. A tungsten atom (W16) is located in the third position, presumably from the decomposition of **2** in the acidic solution. In contrast, the top unit of **2** remains coordinatively unsaturated, which provides an energetically favorable coordination geometry about the zirconium ions (see the hexagonal schematics in Figure 2a). The top unit is rotated with respect to the bottom unit about the central rotation axis running through the two P atoms by about 60° such that only two vacant positions are occupied in a diagonal fashion by two zirconium ions, Zr1 and Zr3. This leaves two of the seven "ligating" oxygen atoms of **2** uncoordinated. Thus the entire framework of L-**1** exhibits no local symmetry in either the organic or inorganic moieties. The asymmetry of the L-tart ligand is extended to the POM structure by the zirconium ions, making L-**1** a topologically chiral species. It is also of note that the two uncoordinated terminal oxygen atoms in the top **2** unit mentioned above are also different from one another in L-**1** (Figure 2b). One of them is replaced by an aqua ligand O1w (W–OH_2 ca. 2.25 Å) while the other atom (O71) remains unprotonated (W=O ca. 1.76 Å).

The ^{31}P NMR (162 MHz, D_2O) spectrum of L-**1** shows four signals ($\delta = -6.29$, -6.62, -12.88, and -13.83 ppm) and the spectrum remains unchanged for several weeks, indicating that the C_1 symmetry exhibited by the solid-state structure (Figure 2) exists and persists in solution. These spectral data also preclude the presence of any diastereomers. The chirality of L-**1** is also demonstrated unambiguously by its solution-state optical properties. This optically active complex shows a negative optical rotation in contrast to the free L-(+)-tartaric acid precursor. As seen in Figure 3, the profile of the CD spectrum of L-(−)-**1** is totally different from that of its precursor, L-tartaric acid (Figure 3, inset), which only shows a single negative Cotton effect at 214 nm. In the long-wavelength spectral region where L-(−)-**1** is CD-active (above 240 nm; vertical dashed line in the inset), L-tartaric acid is almost CD silent. In contrast, L-(−)-**1** exhibits strong Cotton effects up to 350 nm, the spectral region where the characteristic oxygen-to-tungsten charge-transfer bands of both plenary and the lacunary Wells–Dawson polyanions occur.[15] These results clearly show the ICD in the metal–oxide cluster moiety. Recently, a systematic study of intrinsic circular dichroism in L-tartaric acid and its salts established that the magnitude ($\Delta\varepsilon$) of their CD spectra never exceeds 5 $dm^3 mol^{-1} cm^{-1}$ in the absorption region below 220 nm.[16] In contrast, the observed high ICD intensity for L-(−)-**1** suggests a moderately strong induced chirality. Thus the

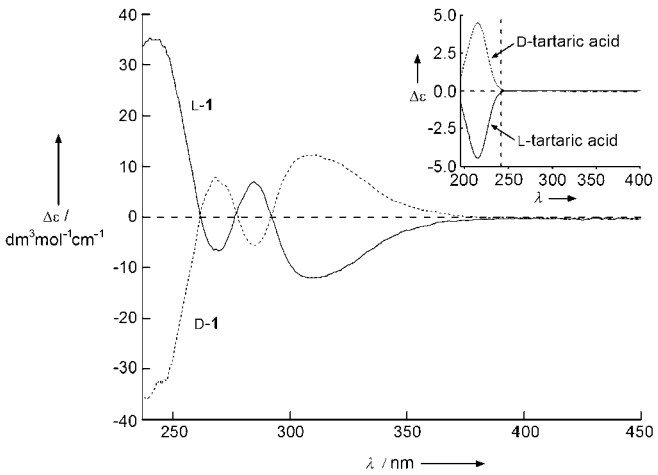

Figure 3. CD spectra of both the L-(−)- and D-(+)-enantiomers of **1** and their precursors, L-(+)- and D-(−)-tartaric acids (inset, the same scale units apply) as aqueous solutions. See text for details.

asymmetric arrangement of the zirconium ions in the substituted positions and the lowering of symmetry on the POM ligands facilitate transfer of chirality from L-tart to the POM, and the induced optical activity in **1** is quite pronounced. There is no detectable change in optical activity of L-(−)-**1** with time, again indicating no racemization of the enantiomeric complex in solution.

Significantly, the other enantiomer of the complex, D-**1**, can be prepared from the unnatural D-tartaric acid under synthetic conditions otherwise identical to those used in the preparation of L-**1**, and it exhibits the same physical and spectroscopic properties as L-**1** except for the chiroptical behavior. Although we were not able to obtain diffraction-quality crystals of D-**1**, the mirror-symmetrical CD spectra for L-(−)-**1** and D-(+)-**1** (Figure 3) confirm they are enantiomers of one another.

In conclusion, we have prepared and purified both enantiomers of a polytungstate. Chirality from a small organic ligand, tartrate, can be transferred to a much larger (ca. 2 × 1 × 1 nm) metal–oxide cluster through high-coordinate zirconium centers. The metal-substituted POM units in the two enantiomers show significant induced circular dichroism. The complexes are stable with respect to racemization, other rearrangements, and decomposition, a key point for applications in catalysis, material science, and applied biology.

Experimental Section

Preparation of $[(CH_3)_2NH_2]_{15}$(L-**1**)·25 H_2O: $ZrO(NO_3)_2$·6 H_2O (0.24 g, 0.7 mmol) was dissolved in H_2O (15 mL). L-Tartaric acid (0.105 g, 0.7 mmol) was then added to the stirred solution, resulting in a slurry. Solid $Na_{12}[\alpha\text{-}P_2W_{15}O_{56}]\cdot 18H_2O$[17] (1.00 g, 0.23 mmol) was added to the mixture in one portion with vigorous stirring. After 30 min at room temperature, a clear solution resulted to which dimethylamine hydrochloride (0.4 g, 5 mmol) was added. The solution was then heated to 70 °C for 15 min. Slow evaporation of the solution produced needle-like crystals after 24 h (yield 0.51 g, 49.5 %). Elemental analysis: calcd Zr 2.96, P 1.34, W 61.55; found Zr 3.08, P 1.40, W 63.38. $[(CH_3)_2NH_2]_{15}$(D-**1**)·29 H_2O was prepared in the same way except that D-tartaric acid was used instead of L-tartaric acid (yield 0.48 g, 46.4 %). Elemental analysis: calcd Zr 2.93, P 1.33, W 61.07; found Zr 3.01, P 1.42, W 60.25. The number of crystal water molecules was determined by thermogravimetric analysis (TGA).

X-ray analysis and crystal data for L-(−)-**1**, $[(CH_3)_2NH_2]_{15}\{[\alpha\text{-}P_2W_{15}O_{55}(H_2O)]Zr_3(\mu_3\text{-}O)(H_2O)(\text{L-tartH})[\alpha\text{-}P_2W_{16}O_{59}]\}\cdot 18H_2O$: colorless needles, crystal size $0.20\times0.04\times0.02$ mm^3, $C_{34}H_{161}N_{15}O_{141}P_4W_{31}Zr_3$, $M_r = 9133.27$, orthorhombic crystal system, space group $P2_12_12_1$ (No. 19), $a = 13.431(3)$, $b = 33.897(7)$, $c = 34.892(7)$ Å, $V = 15885(6)$ Å^3, $Z = 4$; $\rho_{calcd} = 3.674$ g cm^{-3}; $\mu(Mo_{K\alpha}) = 22.679$ mm^{-1}; $1.62 \le \theta \le 28.32°$. Data were collected with a Bruker SMART-APEX CCD sealed tube diffractometer with graphite monochromated $Mo_{K\alpha}$ ($\lambda = 0.71073$ Å) radiation. Data were measured using a series of combinations of ϕ and ω scans with 30 s frame exposures and 0.3° frames widths. The structure was solved by direct methods and refined by full-matrix least-squares against F^2 of all data using SHELXTL software. Hydrogen atoms, except for the water hydrogen atoms, were included in calculated positions and assigned isotropic thermal parameters, riding on their parent carbon, oxygen or nitrogen atoms. The refinement converges with $R_1 = 0.0941$ and $wR_2 = 0.2247$ for 8472 reflections with $I > 2\sigma(I)$. The Flack parameter = 0.06(2) indicates the correct absolute configuration. Max/min residual electron density 8.782/−3.863 e Å^{-3}. The highest residual peaks are all associated with W atoms. CCDC 257975 (L-(−)-**1**) contains the supplementary crystallographic data for this paper. These data can be obtained free of charge from the Cambridge Crystallographic Data Centre via www.ccdc.cam.ac.uk/data_request/cif.

1: ^{31}P NMR (162 MHz, D_2O): $\delta = -6.29$, -6.62, -12.88, -13.83 ppm; IR (KBr pellet, metal–oxygen stretching region): $\tilde{\nu} =$ 1086 (s), 1054 (sh), 1017 (m), 943 (s), 912 (s), 760 (s), 697 cm^{-1} (sh). The IR region for the tartrate ligand is not informative owing to its weak absorbance and overlap with that of the dimethyl ammonium countercations. L-(−)-**1**: $[\alpha]_D^{20} = -2.2$ ($c = 1.0$ in H_2O); $[M]_D = -200.9$; UV/Vis (H_2O, 2.2×10^{-6} M): λ_{max} (ε_{max}) = 196 (3.8×10^5), 280 nm (7.2×10^4, sh); CD (H_2O, $c = 2.2\times10^{-4}$ M, 0.1 cm cell): 241 ($\theta = 25.1$, $\Delta\varepsilon = 35.3$), 270 ($\theta = -4.8$, $\Delta\varepsilon = -6.7$), 285 ($\theta = 4.9$, $\Delta\varepsilon = 6.9$), 309 nm ($\theta = -8.6$, $\Delta\varepsilon = -12.0$). D-(+)-**1**: $[\alpha]_D^{20} = 2.0$ ($c = 1.0$ in H_2O); $[M]_D = 183.9$; UV/Vis (H_2O, 2.2×10^{-6} M): λ_{max} (ε_{max}) = 196 (4.1×10^5), 280 nm (7.8×10^4, sh); CD (H_2O, $c = 2.3\times10^{-4}$ M, 0.1 cm cell): 239 ($\theta = -27.0$, $\Delta\varepsilon = -36.0$), 268 ($\theta = 5.9$, $\Delta\varepsilon = 7.9$), 285 ($\theta = -4.2$, $\Delta\varepsilon = -5.7$), 312 nm ($\theta = 9.2$, $\Delta\varepsilon = 12.1$).

Circular dichroism spectra were measured using a JASCO J-715 spectropolarimeter with 1 mm path-length cells. Spectra were collected between 190 and 600 nm, with a step size of 0.5 nm and at a speed of 50 nm min^{-1}. Three spectra were recorded and averaged automatically by the instrument. Optical rotations were measured on a Perkin Elmer 341 digital polarimeter with a 10 cm path-length cell.

Received: February 3, 2005

Keywords: chirality · circular dichroism · polyoxometalate · tartaric acid · zirconium

[1] a) Topical issue on polyoxometalates (Guest Ed.: C. L. Hill), *Chem. Rev.* **1998**, *98*, 1; b) *Polyoxometalate Chemistry: From Topology via Self-Assembly to Applications* (Eds.: M. T. Pope, A. Müller), Kluwer, Dordrecht, **2001**; c) *Polyoxometalate Chemistry for Nano-Composite Design* (Eds.: T. Yamase, M. T. Pope), Kluwer, Dordrecht, **2002**; d) "Polyoxo Anions: Synthesis and Structure": M. T. Pope in *Comprehensive Coordination Chemistry II: Transition Metal Groups 3–6, Vol. 4* (Ed.: A. G. Wedd), Elsevier Science, New York, **2004**, chap. 4.10, pp. 635–678; e) "Polyoxometalates: Reactivity": C. L. Hill in *Comprehensive Coordination Chemistry II: Transition Metal Groups 3–6, Vol. 4* (Ed.: A. G. Wedd), Elsevier Science, New York, **2004**, chap. 4.10, pp. 679–759.

[2] a) R. Strandberg, *Acta Chem. Scand.* **1973**, *27*, 1004; b) M. T. Pope, *Inorg. Chem.* **1976**, *15*, 2008; c) A. Tézé, G. Hervé, *J. Inorg. Nucl. Chem.* **1977**, *39*, 999; d) R. Contant, J. P. Ciabrini, *J. Chem. Res. Miniprint* **1977**, 2601; e) R. Acerete, J. Server-Carrió, A. Vegas, M. Martínez-Ripoll, *J. Am. Chem. Soc.* **1990**, *112*, 9386; f) C. M. Tourné, G. F. Tourné, F. Zonnevijlle, *J. Chem. Soc. Dalton Trans.* **1991**, 143; g) F. Xin, M. T. Pope, *J. Am. Chem. Soc.* **1996**, *118*, 7731.

[3] The Pfeiffer effect refers to the observation of induced circular dichroism (CD) signals for a configurationally labile chirality when the equilibrium between the enantiomers is shifted in presence of a chiral ligand. See: P. Pfeiffer, K. Quehl, *Ber. Dtsch. Chem. Ges. A* **1931**, *64*, 2667; Pfeiffer effects in polyanion systems: a) J. F. Garvey, M. T. Pope, *Inorg. Chem.* **1978**, *17*, 1115; b) K. Nomiya, R. Kobayashi, M. Miwa, *Bull. Chem. Soc. Jpn.* **1983**, *56*, 3505. Since a Pfeiffer effect necessarily involves optical enrichment of polyanions under equilibrium conditions, this effect, alone, can not lead to isolation of bulk enantiomerically pure complexes, one goal and achievement of the present work.

[4] Optical resolution of one enantiomer of a chiral polyanion: T. Ama, J. Hidaka, Y. Shimura, *Bull. Chem. Soc. Jpn.* **1970**, *43*, 2654.

[5] a) V. Soghomonian, Q. Chen, R. C. Haushalter, J. Zubieta, C. J. O'Connor, *Science* **1993**, *259*, 1596; b) R. Kniep, H. G. Will, I. Boy, C. Röhr, *Angew. Chem.* **1997**, *109*, 1052; *Angew. Chem. Int. Ed. Engl.* **1997**, *36*, 1013; c) T. E. Gier, X. Bu, P. Feng, G. D. Stucky, *Nature* **1998**, *395*, 154; d) S. Neeraj, S. Natarajan, C. N. R. Rao, *Chem. Commun.* **1999**, 165; e) A. Yilmaz, X. Bu, M. Kizilyalli, G. D. Stucky, *Chem. Mater.* **2000**, *12*, 3243; f) J. Liang, Y. Wang, J. Yu, Y. Li, R. Xu, *Chem. Commun.* **2003**, 882; g) Y. Wang, J. Yu, M. Guo. R. Xu, *Angew. Chem.* **2003**, *115*, 4223; *Angew. Chem. Int. Ed.* **2003**, *42*, 4089.

[6] a) M. Inoue, T. Yamase, *Bull. Chem. Soc. Jpn.* **1995**, *68*, 3055; b) U. Kortz, M. G. Savelieff, F. Y. A. Ghali, L. M. Khalil, S. A. Maalouf, D. I. Sinno, *Angew. Chem.* **2002**, *114*, 4246; *Angew. Chem. Int. Ed.* **2002**, *41*, 4070.

[7] a) W. H. Knoth, R. L. Harlow, *J. Am. Chem. Soc.* **1981**, *103*, 1865; b) M. J. Manos, H. N. Miras, V. Tangoulis, J. D. Woollins, A. M. Z. Slawin, T. A. Kabanos, *Angew. Chem.* **2003**, *115*, 441; *Angew. Chem. Int. Ed.* **2003**, *42*, 425; c) L. S. Felices, P. Vitoria, J. M. Gutiérrez-Zorrilla, S. Reinoso, J. Etxebarria, L. Lezama, *Chem. Eur. J.* **2004**, *10*, 5138.

[8] Kortz and Matta have demonstrated interpolyanion chirality in the trimeric complex, $[(\beta_2\text{-}SiW_{11}MnO_{38}OH)_3]^{15-}$, which is present in an enantiomerically enriched (3:2) crystal. See U. Kortz, S. Matta, *Inorg. Chem.* **2001**, *40*, 815.

[9] POMs have a range of intriguing biological properties including potent antiviral activity: a) N. Fukuda, T. Yamase, *Biol. Pharm. Bull.* **1997**, *20*, 927; b) J. T. Rhule, C. L. Hill, D. A. Judd, R. F. Schinazi, *Chem. Rev.* **1998**, *98*, 327; c) J. T. Rhule, C. L. Hill, Z, Zheng, R. F. Schinazi, *Top. Biol. Inorg. Chem.* **1999**, *2*, 117; d) D. A. Judd, J. H. Nettles, N. Nevins, J. P. Snyder, D. C. Liotta, J. Tang, J. Ermolieff, R. F. Schinazi, C. L. Hill, *J. Am. Chem. Soc.* **2001**, *123*, 886; e) S. Shigeta, S. Mori, E. Kodama, J. Kodama, K. Takahashi, T. Yamase, *Antiviral Res.* **2003**, *58*, 265.

[10] ICD is realized when an achiral molecule(s) displays CD signals within their absorbing regions on association with a chiral inducer. For representative examples, see the recent review: S. Allenmark, *Chirality* **2003**, *15*, 409.

[11] A solid with one-dimensional helical strands constituted by L or D-tartrate, Mo_2O_4,and Gd has been reported. See a) C. Wu, C. Lu, X. Lin, D. Wu, S. Lu, H. Zhuang, J. Huang, *Chem. Commun.* **2003**, 1284; b) C. Wu, C. Lu, S. Lu, H. Zhuang, J. Huang, *Dalton Trans.* **2003**, 3192.

[12] D. T. Richens, *The Chemistry of Aqua Ions*, Wiley, Chichester, **1997**.

[13] Zirconium-containing polyanions are known: a) R. G. Finke, B. Rapko, T. J. R. Weakley, *Inorg. Chem.* **1989**, *28*, 1573; b) L. Meng, J. F. Liu, *Transition Met. Chem.* **1995**, *20*, 188; c) A. J. Gaunt, I. May, D. Collison, K. T. Holman, M. T. Pope, *J. Mol. Struct.* **2003**, *656*, 101.

[14] a) J. Gawroński, K. Gawrońska, *Tartaric and Malic Acids in Synthesis: A Source Book of Building Blocks, Ligands, Auxiliaries, and Resolving Agents*, Wiley-Interscience, New York, **1999**; b) S. F. Pedersen, J. C. Dewan, R. R. Eckman, B. K. Sharpless, *J. Am. Chem. Soc.* **1987**, *109*, 1279.

[15] The UV spectra of the plenary $[\alpha\text{-}P_2W_{18}O_{62}]^{6-}$ and lacunary $[\alpha_2\text{-}P_2W_{17}O_{61}]^{10-}$, $[\alpha\text{-}P_2W_{15}O_{56}]^{12-}$ (freshly prepared) Wells–Dawson POMs have similar absorption bands up to approximately 330 nm, all displaying distinct maxima at around 195 nm and a broad shoulder of moderate intensity at about 280 nm.

[16] J. Gawroński, J. Grajewski, *Org. Lett.* **2003**, *5*, 3301.

[17] The synthesis of $Na_{12}[\alpha\text{-}P_2W_{15}O_{56}]\cdot 18H_2O$ was by the literature method: R. Contant, *Inorg. Synth.* **1990**, *27*, 106.

DNA Cleavage

A Synthetic Block Copolymer Regulates S1 Nuclease Fragmentation of Supercoiled Plasmid DNA**

*Kensuke Osada, Yuichi Yamasaki, Satoshi Katayose, and Kazunori Kataoka**

The materials chemistry and physics of block copolymer supramolecular assembly continue to receive considerable attention in the construction of higher-ordered architectures with unique morphologies and functions.[1–10] Of particular

[*] Dr. K. Osada, Dr. Y. Yamasaki, Prof. Dr. K. Kataoka
Department of Materials Science and Engineering
Graduate School of Engineering, The University of Tokyo
Hongo 7-3-1, Bunkyo, Tokyo 113-8655 (Japan)
Fax: (+81) 3-5841-7139
E-mail: kataoka@bmw.t.u-tokyo.ac.jp
Dr. S. Katayose[+]
Department of Materials Science and Engineering
Tokyo University of Science
Yamazaki 2641, Noda, Chiba 278 (Japan)
[+] Present address:
Tsukuba Research Laboratories
JSR Corporation
25 Miyukigaoka, Tsukuba, Ibaraki 305-0841 (Japan)

[**] This work was supported by The Special Coordination Funds for Promoting Science and Technology, a Grant-in-Aid for Scientific Research on Priority Area A (Molecular Synchronization for Design of New Materials System) from the Ministry of Education, Culture, Sports, Science, and Technology (MEXT), and the Core Research Program for Evolutional Science and Technology (CREST) from the Japan Science and Technology Corporation (JST). The authors thank D. W. Grainger for critical reading of the manuscript.

Supporting Information for this article is available on the WWW under http://www.angewandte.org or from the author.

  DOI: 10.1002/anie.200500201

interest is the exploitation of the spatial order intrinsic to block copolymers for the amplification or modulation of molecular recognition processes by using integrated multisite interactions as well as a distinct spatial matching. Herein we report an unprecedented finding that DNA supramolecular assembly with the synthetic block copolymer poly(ethylene glycol)-*b*-poly(L-lysine) (PEG-PLL)[6,11–14] modulates supercoiled plasmid DNA into a particular structure. The incorporated DNA within the assembly is cleaved into seven distinct regular fragments by S1 nuclease, an enzyme known to cleave single-stranded DNA. The seven characteristic DNA fragments were of well-defined molecular sizes; in each case these were 10/12, 9/12, 8/12, 6/12, 4/12, 3/12, and 2/12 of the original plasmid length (Figure 1). It is notable that the cleaved sites

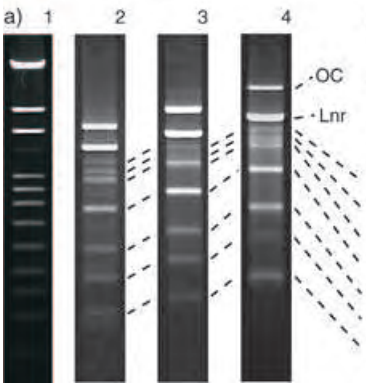

b)

Fragments

Length of the fragment [bp] / Size ratio to the native DNA [%]

no	pBR322 4363 bp	pGL3-Luc 5256 bp	ColE1 6646 bp	ratios in fraction
1	3690 / 84.6	4560 / 84.6	5630 / 84.8	10/12
2	3260 / 75.3	4100 / 76.1	5000 / 75.2	9/12
3	2940 / 67.4	3680 / 68.2	4490 / 67.6	8/12
4	2180 / 50.0	2740 / 50.8	3360 / 50.6	6/12
5	1460 / 33.5	1830 / 34.0	2240 / 33.7	4/12
6	1050 / 24.1	1340 / 24.9	1650 / 24.9	3/12
7	750 / 17.1	910 / 16.8	1090 / 16.4	2/12

Figure 1. Regulated fragmentation of plasmid DNAs complexed with PEG-PLL by the S1 nuclease: a) Gel electrophoresis results. Lane 1: marker DNA; lane 2: pBR322 (4363 bp); lane 3: pGL3-Luc (5256 bp); lane 4: ColE1 (6646 bp). OC = relaxed open circular DNA, Lnr = linearized DNA. b) Length of the obtained fragments and size ratio of them to the native DNA. The size ratio of each fragment from three plasmid DNAs is represented as a fraction in the right-hand column.

are located just outside of protein-coding regions, a fact which simultaneously indicates that the S1 nuclease cuts out genes from DNA.

The block copolymer used in this study comprises a cationic PLL segment, which is the plasmid-binding portion, and a nonionic PEG segment, which forms a hydrophilic and hydrated palisade surrounding the ion-paired complex between PLL and plasmid DNA (see the Supporting Information). This allows to obtain a water-soluble nanoscale assembly (100-nm size) without precipitation. The size-specific plasmid DNA cleavage by S1 nuclease was observed at an acidic pH value of 4.9 for the complex, particularly in a unit molar ratio (amino group/phosphate) of 1.0. As seen in lane 2 of Figure 1a, pBR322 DNA is cut into seven distinct fragments (as listed in Figure 1b). This regular fragmentation was not specific only for pBR322 but seems common for other plasmids. Surprisingly, the other plasmids, pGL3-Luc and ColE1, when complexed with PEG-PLL, were also cut into seven fragments of the same fractions when measured against each original plasmid (Figure 1a, lanes 3 and 4, and Figure 1b). The consistency of the fragmentation results clearly indicates the systematic cleavage of plasmid DNA at well-defined intervals. It should be noted that this regular cleavage of plasmid DNA complexed with PEG-PLL is only observed for the supercoiled DNA form. Relaxed open circular DNA, prepared by treatment with topoisomerase I, also formed stable complexes with PEG-PLL but exhibited no sensitivity to S1 nuclease (data not shown). Additionally, a complex with linear plasmid DNA, prepared by treatment with a restriction enzyme (EcoRI) having a unique recognition site on the plasmid, was smoothly degraded to oligo-DNA pieces in a nonspecific manner (data not shown). The observed differences in S1 nuclease sensitivity to plasmid isomer constructs suggest that topological features of the block copolymer–DNA supramolecular complex influence the enzymatic fragmentation process.

Polyion complex formation between DNA and cationic compounds is known to induce a coil–globule transition, thereby resulting in condensed complexes with ordered morphologies, mainly in toroidal or rod-like forms.[14–18] Consistent with this, charge-neutralizing DNA complexation with PEG-PLL produces a detectable transition from an expanded DNA superhelix into a compact state, as confirmed by static and dynamic light scattering[13] as well as by direct observation with fluorescence microscopy.[18] Although the structural details of the condensed plasmid in this complex have not yet been clarified, significant structural features are probably present in the supercoiled double-stranded DNA upon polyion-induced condensation. Constrained structural order (or regular disorder) in the double-stranded DNA structure might be regularly repeated in this polyion-induced condensation process. This would permit the DNA to adopt particular structures that compensate for the structural constraints accompanying conformation transitions during complexation. Consequently, these specific disordered sites in the condensed DNA strands may preferentially promote S1 nuclease attack, thereby resulting in the observed regular DNA fragmentation.

Supercoiled DNA associated with poly(L-lysine) homopolymer with degrees of polymerization (DP) of 19 and 260 exhibited only nonspecific S1 nuclease degradation without any ordered cleavage, as shown by a smeared electrophoresis gel stain (data not shown). This indicates that polyion complexation alone is not sufficient and that the PEG segment in the block copolymer plays a crucial role in regulating the nuclease sensitivity in addition to promoting the complex solution stability. Inter- or intramolecular steric repulsion of hydrated PEG segments may contribute to the modulated structure of plasmid DNA.

The sensitivity of single-strand-cleavage endonucleases like S1 nuclease against naked plasmid DNAs has been investigated since the 1980s.[19–22] The naked DNAs are first nicked and then linearized. The cleavage sites are cruciform loops, which are adopted by short inverted repeat (palindrome) sequences in the topologically stressed double helix.

Formation of the hairpin-loop structure relieves the topological strain in double-stranded circular DNA molecules. These inverted repeats, separated by nonrepetitious sections of DNA, are specifically cleaved by single-strand-specific nucleases at the center of each hairpin loop. Torsional stress of negative supercoiling of plasmid DNA occasionally induces a kink in the DNA strand with an acute angle. The high susceptibility of palindrome sequences to S1 nuclease digestion led us to assume that the regular fragmentation seen here in the system with the PEG-PLL/plasmid DNA (pDNA) complex might be a result of selective digestion at the cruciform loop regularly induced in the condensed DNA strands. To get an insight into this assumed mechanism, inverted repeats larger than five continuous sequences are picked up from three plasmids (pBR322, pGL3-Luc, and ColE1) by using computer analysis.[23] Neighboring smaller palindromes separated by one or two nonrepetitious sections of DNA were also taken into consideration. It is to be expected that hairpin stability will be directly proportional to stem length but inversely proportional to loop length. The inverted sequences were marked from four to one according to the hairpin stability, as summarized in Figure 2a as a function of base number. Obviously, there are quite a few palindrome sequences. Denaturation of the DNA double strand is necessary for transformation from the normal interstrand base pairing to the intrastrand base pairing of the cruciform structure. The binding energy of the A–T (adenine–thymine) pair is lower than that of the G–C (guanine–cytosine) pair, because two hydrogen bonds are contributing to the pairing between A and T while three contribute between G and C. Thus, the composition of A–T pairs within the palindrome sequences was also examined (Figure 2b). Refinement according to palindrome size and A–T composition allowed the extraction of several sites as candidates for S1 nuclease recognition; these are indicated as dotted lines in Figure 2a and b and as slashes in the pDNA maps (Figure 2d). By use of these refined sites, combinations satisfying the regular fragments were surveyed by consideration of fragment lengths, since two sites on the circular plasmid DNA must be cleaved (for example, 3/12+9/12 = 12/12). Consequently, combinations of cleavage sites yielding the seven DNA sizes were acquired for all three plasmid DNAs

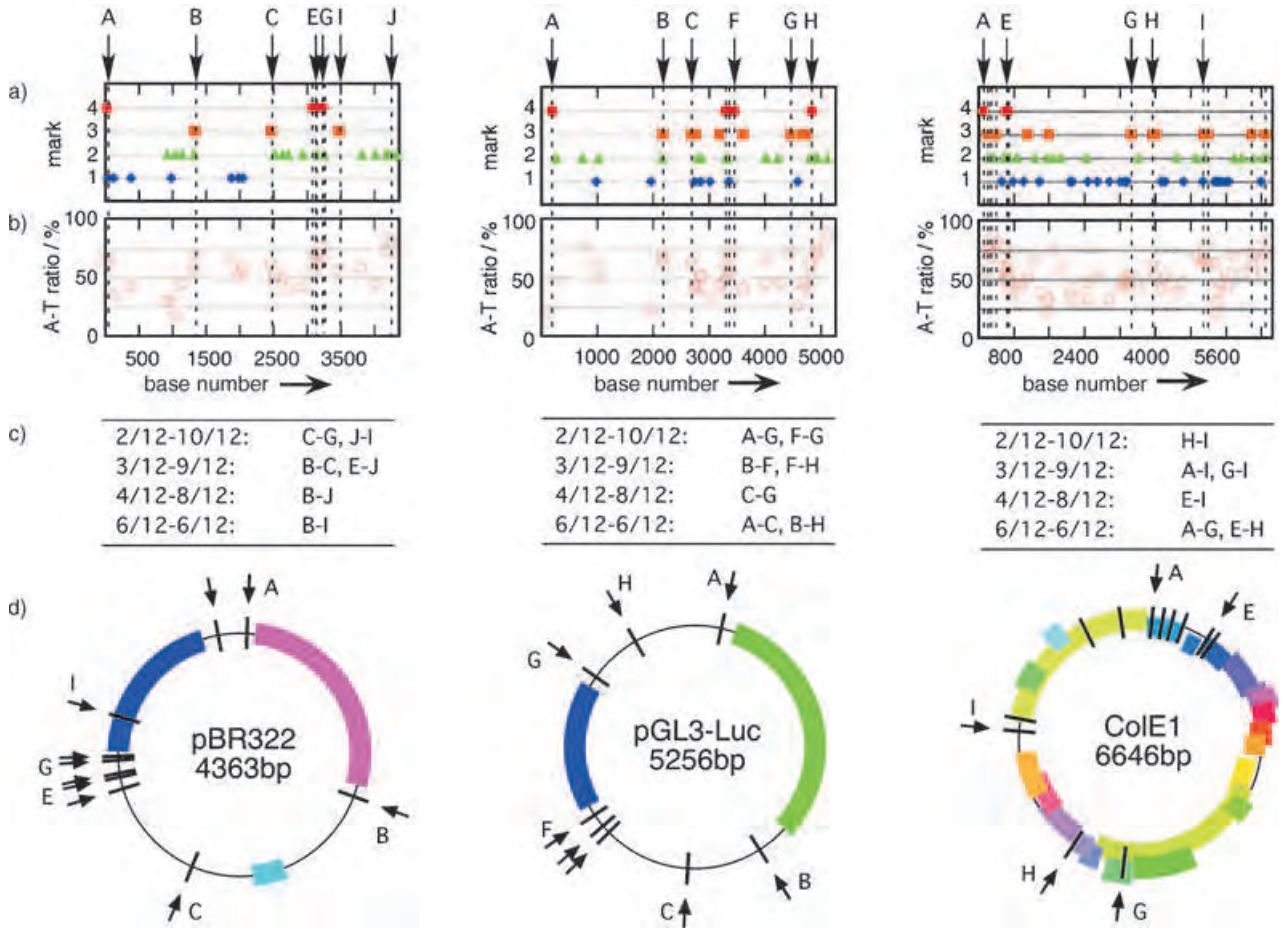

Figure 2. Palindrome maps and protein codes of the three plasmid DNAs pBR322 (left), pGL3-Luc (middle), and ColE1 (right). a) Cruciform stability by the size of inverted repeats. Higher mark numbers indicate higher cruciform stability. b) Percentage A–T composition in the considered palindrome sequences as a function of base number in the plasmid DNAs. Here, base 1 was defined as the recognition site of the EcoR1 restriction enzyme. The dotted lines in panels (a) and (b) indicate refined digestion sites as evaluated from the panels. The combinations of cleavage sites that satisfy the seven-piece fragmentation pattern are summarized in (c). Those evaluated cleavage sites are shown as arrows with capital letters in panels (a) and (d); in addition, correlation between the protein-coding regions and proposed cleavage sites is shown in (d).

(listed in Figure 2c) and those sites are indicated as arrows in Figure 2a and d. The regular fragmentation can be explained by assuming that the cruciform structures regularly induced in the DNA by complexation with the PEG-PLL block copolymer are digested by the single-strand-recognition endonuclease.

Obviously, development of the extruded cruciform structure requires definite stress. The cruciform formation in the naked pDNA is known to be driven by the torsional stress of negative supercoiling.[22] In the complex of pDNA with PEG-PLL, the stress of condensation by the polycation further amplified the torsional stress of the supercoiled conformation, so that the cruciform may be developed in multiple sites. It should be noted that the charge ratio of 1.0 is indeed a critical point in the pDNA transition from extended state to condensed state. The ethidium bromide exclusion assay showed an abrupt decrease in the relative fluorescence, which indicates condensation of DNA molecules, at a charge ratio range of around 1.0 (see the Supporting Information). Additionally, the transition of DNA shape is confirmed by direct observation with atomic force microscopy (Figure 3). Apparently, complex shapes at the charge ratio of 1.0 comprise preferentially condensed rod and toroid conformations.

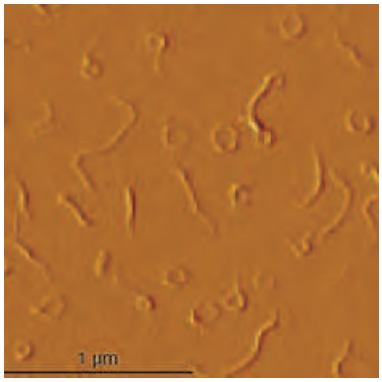

Figure 3. AFM image of plasmid DNA (pGL3-Luc) complexed with the PEG-PLL block copolymer at a charge ratio of 1.0. The image was taken in the amplitude mode for the complex after equilibration in solution for 24 hours. A scale bar is included in the figure.

Furthermore, the potential cleavage site (palindrome site) and protein-coding region have a very interesting correlation, in that the former is located just outside of the latter, as can be clearly seen in Figure 2d. It is worth mentioning that this is commonly observed among the three examined plasmids. This correlation is most distinctive in the ColE1 plasmid, which has various protein codes (Figure 2d). The fact that the selected inverted repeats are located just in the gap or at the terminus of various coding regions suggests that the cruciform structure may substantially contribute to the regulation of gene expression[21] and is most likely to be a landmark for DNA-binding proteins. It should be noted that hypersensitivity of structured DNA to S1 nuclease has been observed in regions of transcriptionally active genes in chromatin.[24] DNA breakage by S1 nuclease is observed in apoptotic cells[25] and also more in mitotic chromosomes than chromosomes in interphase cells.[26] This may be a reflection of the differences of stress under such circumstances. The cruciform structural motifs must be to regulate the binding of proteins, nucleases, promoters, or transcription factors; the full function remains to be determined. Yet, the potential for designing synthetic polymer constructs that reliably alter or mimic these supramolecular structures or for imparting new features of molecular recognition by using the materials of unconventional biopolymer complexes, as demonstrated here, is exciting.

In conclusion, we have demonstrated that the size-specific cleavage of plasmid DNA by S1 nuclease can be mediated by condensed complexes of plasmids with synthetic block copolymers without any sequence-specific binding. The recognition site is probably the cruciform structure induced by DNA complexation with the block copolymer. This means that DNA inherently retains sequences that can transform its secondary structure by certain stimuli and the synthetic polymer reveals the functional structure by complexation. The observed unique sensitivity of PEG-PLL/pDNA complexes to S1 nuclease should provide an insight into the mechanisms of endogenous protein-induced modification of DNA and into the design of artificial restriction enzymes and gene-exploring systems through supramolecular assembly of synthetic macromolecular materials.

Received: January 19, 2005
Published online: May 4, 2005

Keywords: block copolymers · DNA cleavage · hydrolases · molecular recognition · self-assembly

[1] J.-M. Lehn, *Science* **2002**, *295*, 2400 – 2403.
[2] G. M. Whitesides, B. Grzybowski, *Science* **2002**, *295*, 2418 – 2421.
[3] J. D. Hartgerink, E. Beniash, S. I. Stupp, *Science* **2001**, *294*, 1684 – 1688.
[4] D. E. Discher, A. Eisenberg, *Science* **2002**, *297*, 967 – 973.
[5] S. Jain, F. S. Bates, *Science* **2003**, *300*, 460 – 464.
[6] A. Harada, K. Kataoka, *Science* **1999**, *283*, 65 – 67.
[7] J. N. Cha, G. D. Stucky, D. E. Morse, T. J. Deming, *Nature* **2000**, *403*, 289 – 292.
[8] J. A. Hubbell, *Science* **2003**, *300*, 595 – 596.
[9] R. Savic, L. Luo, A. Eisenberg, D. Maysinger, *Science* **2003**, *300*, 615 – 618.
[10] A. V. Kabanov, V. A. Kabanov, *Adv. Drug Delivery Rev.* **1998**, *30*, 49.
[11] S. Katayose, K. Kataoka, *Bioconjugate Chem.* **1997**, *8*, 702 – 707.
[12] S. Katayose, K. Kataoka, *J. Pharm. Sci.* **1998**, *87*, 160 – 163.
[13] K. Itaka, K. Yamauchi, A. Harada, K. Nakamura, H. Kawaguchi, K. Kataoka, *Biomaterials* **2003**, *24*, 4495 – 4506.
[14] K. Miyata, Y. Kakizawa, N. Nishiyama, A. Harada, Y. Yamasaki, H. Koyama, K. Kataoka, *J. Am. Chem. Soc.* **2004**, *126*, 2355 – 2361.
[15] U. K. Laemmli, *Proc. Natl. Acad. Sci. USA* **1975**, *72*, 4288 – 4292.
[16] S. M. Mel'nikov, V. G. Sergeyev, K. Yoshikawa, *J. Am. Chem. Soc.* **1995**, *117*, 9951 – 9956.
[17] J. Rackstraw, A. L. Martin, S. Stolnik, C. J. Roberts, M. C. Garnett, M. C. Davies, S. J. B. Tendler, *Langmuir* **2001**, *17*, 3185 – 3193.
[18] Y. Yamasaki, S. Katayose, K. Kataoka, K. Yoshikawa, *Macromolecules* **2003**, *36*, 6276 – 6279.

[19] D. M. J. Lilley, *Nucleic Acids Res.* **1981**, *9*, 1271 – 1289.
[20] N. Panayotatos, R. D. Wells, *Nature* **1981**, *289*, 466 – 470.
[21] U. R. Mueller, W. M. Fitch, *Nature* **1982**, *298*, 582 – 585.
[22] M. Gellert, M. H. O'Dea, K. Mizuuchi, *Proc. Natl. Acad. Sci. USA* **1983**, *80*, 5545 – 5549.
[23] Palindrome sequence analyses were performed on a Macintosh iBook 400 MHz computer by using the FROG-Mac program (written by N. Miki at Osaka University and available from http://pharma1.med.osaka-u.ac.jp/freeware.html).
[24] A. Larsen, H. Weintraub, *Cell* **1982**, *29*, 609 – 622.
[25] M. C. Peitsch, C. Mueller, J. Tschopp, *Nucleic Acids Res.* **1993**, *21*, 4206 – 4209.
[26] G. Juan, W. Pan, Z. Darzynkiewicz, *Exp. Cell Res.* **1996**, *227*, 197 – 202.

Reaction Dynamics

Dynamic Effects on [3,3] and [1,3] Shifts of 6-Methylenebicyclo[3.2.0]hept-2-ene**

Christopher P. Suhrada, Cenk Selçuki, Maja Nendel, Carina Cannizzaro, K. N. Houk, Peter-Jürgen Rissing, Dirk Baumann, and Dieter Hasselmann**

Dedicated to Professor Wolfgang Kirmse on the occasion of his 75th birthday

The controversies over concerted versus stepwise diradical mechanisms of potentially pericyclic reactions have subsided with improvements in the understanding of stereoselectivity in thermal rearrangements that involve modestly stabilized diradical intermediates. The thermal rearrangements of vinylcyclopropanes[1] and vinylcyclobutanes,[2] including bicyclo[3.2.0]hept-2-ene,[3] involve diradical intermediates that lack a deep potential energy well, and their outcomes deviate from statistical predictions. The thermal rearrangement of 6-methylenebicyclo[3.2.0]hept-2-ene (**1**) to 5-methylenenorbornene (**3**) is more intriguing, as it yields a nonrandom distribution of products despite the stabilizing effect of the 6-methylene substituent on the intermediate **2**.

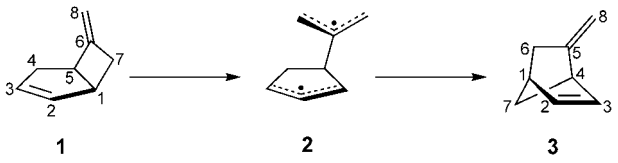

Dideuterio labeling has revealed a preference for [1,3] over [3,3] shifts,[4] and the stereochemistry observed with methyl labels has led to the hypothesis that diradical intermediates do not equilibrate rotationally before collapsing to form the bicyclic products.[5] New experimental studies of monodeuterated species currently show modest levels of both regio- and stereoselectivity (Table 1),[6] and DFT and ab initio calculations provide a theoretical framework for understanding these results.

Table 1: Deuterium label distribution in product **3** from the thermolysis of 7*x*-, 8*E*-, and 8*Z*-**1**, extrapolated to $t = 0$ min.

Educt	6*x*-**3**	6*n*-**3**	8*E*-**3**	8*Z*-**3**
7*x*-**1**	0.37	0.20	0.22	0.21
8*E*-**1**	0.13	0.23	0.64	–
8*Z*-**1**	0.24	0.14	–	0.62

UB3LYP and CASSCF calculations indicate that two modes of C1–C7 cleavage produce stereoisomeric diallyl intermediates **2** from **1** (Figure 1). The favored transition state, **TS-12n**, moves C7 toward C3 and places the 7*x* substituent in an *E* configuration. In contrast, **TS-12x** moves C7 away from C3 and puts the 7*x* substituent in the *Z* position. The preference (1.8 kcal mol^{-1}; CASPT2//UB3LYP) for **TS-12n** over **TS-12x** is analogous to torquoselectivity in electro-

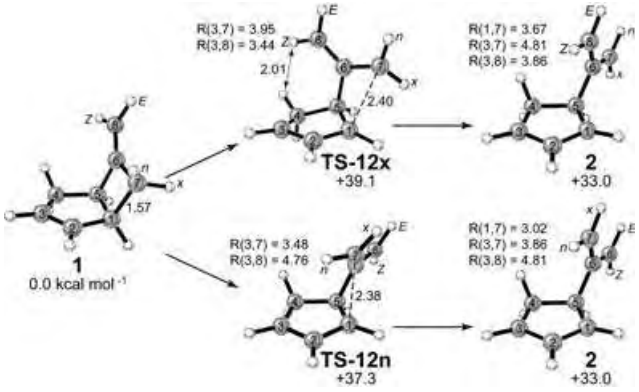

Figure 1. Two transition states for bond breaking lead to stereoisomeric diallyl intermediates **2**. Structures shown are (U)B3LYP-optimized with selected bond distances indicated in angstroms. Enthalpy values (CASPT2//UB3LYP), in kcal mol^{-1} relative to that of **1**, are listed below each structure label.

[*] C. P. Suhrada, Dr. C. Selçuki, Dr. M. Nendel, Dr. C. Cannizzaro, Prof. Dr. K. N. Houk
Department of Chemistry and Biochemistry
University of California, Los Angeles
Los Angeles, CA 90095-0569 (USA)
Fax: (+1) 310-206-8143
E-mail: houk@chem.ucla.edu
Dr. P.-J. Rissing, Dr. D. Baumann, Prof. Dr. D. Hasselmann
Fakultät für Chemie, Organische Chemie II
Ruhr-Universität Bochum
44780 Bochum (Germany)
Fax: (+49) 234-32-14109
E-mail: dieter.hasselmann@ruhr-uni-bochum.de

[**] Work at UCLA was supported by the National Science Foundation (research grant to K.N.H. and IGERT fellowship to C.P.S.) and TUBITAK (fellowship to C.S.). The Bochum group thanks the Deutsche Forschungsgemeinschaft and Fonds der Chemischen Industrie.

Supporting information for this article is available on the WWW under http://www.angewandte.org or from the author.

  DOI: 10.1002/anie.200500027

cyclic ring openings;[7] the favored structure minimizes closed-shell repulsion and maximizes hyperconjugation between the orbitals of the breaking C1–C7 σ bond and the C2–C3 π bond. Also, **TS-12x** brings the 8*Z* hydrogen atom into close proximity with the one in the 4-*cis* position.

The diradical **2** lies 4.3 kcal mol^{-1} below **TS-12n**. Once formed, **2** can isomerize by rotation about the C5–C6 bond with a calculated barrier of only 2.4 kcal mol^{-1} (**TS-22**, Figure 2). This motion exchanges the positions of C7 and C8. Allylic stabilization preserves the pseudo-*E*/*Z* configuration of C7 and C8 substituents during the lifetime of the intermediate; barriers for rotation about C6–C7 and C6–C8 are calculated to be ≈12–13 kcal mol^{-1} higher than those that separate **2** from the product **3**.

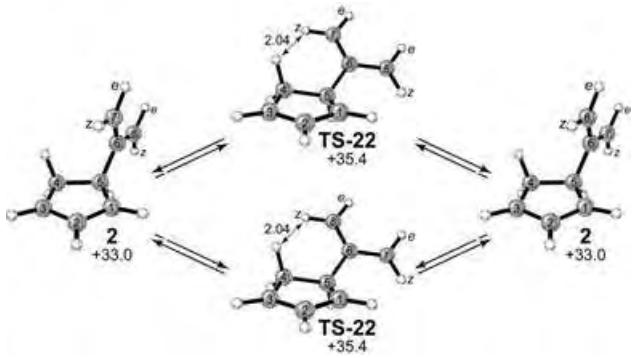

Figure 2. Rotation about C5–C6 exchanges the position of proximal and distal allyl termini, yet the pseudo-*E*/*Z* configuration of substituents is preserved. Structures shown are (U)B3LYP-optimized with selected bond distances indicated in angstroms. Enthalpy values (CASPT2//UB3LYP), in kcal mol^{-1} relative to that of **1**, are listed below each structure label.

In analogy to the bond-breaking step, the formation of a new bond at C3 can occur in two different stereochemical senses (Figure 3). Both transition states involve the formation of a bond between C3 and the proximal allyl terminus in **2**.[8] From a given intermediate **2**, the two products **3** that can be formed are thus epimers with respect to the substituents on that carbon. **TS-23n** is favored slightly and places the pseudo-*E* substituent in the 6*x* position in the product; **TS-23x** places the same substituent in the 6*n* position.

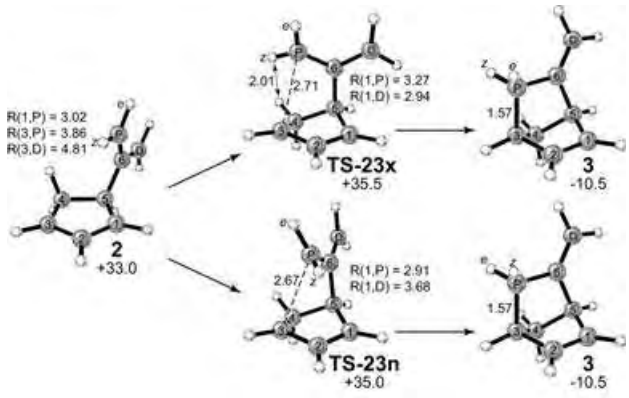

Figure 3. Two cyclization routes form epimeric products from a given intermediate **2**. Structures shown are (U)B3LYP-optimized with selected bond distances indicated in angstroms. Enthalpy values (CASPT2//UB3LYP), in kcal mol^{-1} relative to that of **1**, are listed below each structure label.

TS-23n and **TS-23x** lie only 2.0 and 2.5 kcal mol^{-1} above **2**, respectively. Compared with 2.4 kcal mol^{-1} for **TS-22**, this suggests that cyclization competes with conformational isomerization in the intermediate, and therefore a majority of products will come from an intermediate in the conformation in which it is initially formed.

These pathways imply the kinetic model outlined in Scheme 1 for a single-labeled system. For comparison with the experimental zero-time data, reversions from **2** to **1** may

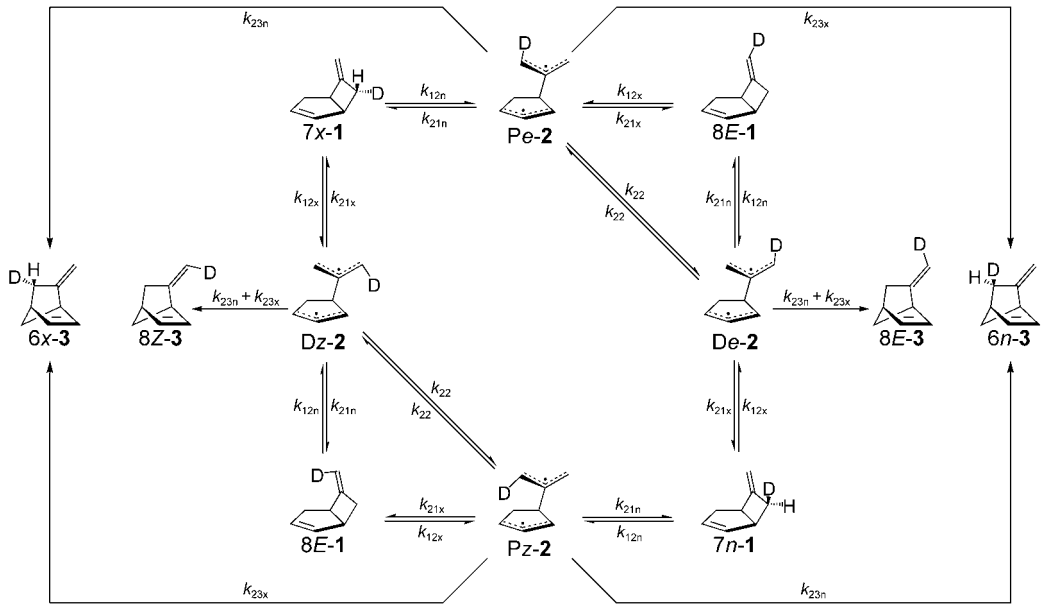

Scheme 1. Stepwise kinetic model for rearrangements of **1** bearing a single deuterium label on C7 or C8.

be ignored,[9] and the relative yield of products can be computed based on three independent parameters, related to k_{12n} versus k_{12x}, and k_{23n} versus k_{23x} versus k_{22} (Supporting Information).

With the model in Scheme 1 and the selectivity parameters from CASPT2//UB3LYP transition-state energies, calculations predict the product distribution listed in Table 2, Column 2. The major products of both experiments are correctly identified, although the minor product ratios deviate from experiment markedly.

Table 2: Product distributions from experiment, CASPT2//UB3LYP calculations, and least-squares fits of two theoretical models to the experimental data. Corresponding kinetic parameters and relative TS energies are listed along with predicted product distributions.[a]

	Experiment	CASPT2//UB3LYP (fully stepwise)	Least-squares fit (fully stepwise)	Least-squares fit (stepwise plus concerted [3s,3s])
7*x*-**1**→6*x*-**3**	0.37	0.39	0.33	0.39
7*x*-**1**→6*n*-**3**	0.20	0.25	0.28	0.22
7*x*-**1**→8*E*-**3**	0.22	0.26	0.20	0.20
7*x*-**1**→8*Z*-**3**	0.21	0.10	0.19	0.19
8*E*-**1**→8*E*-**3**[b]	0.63	0.64	0.62	0.61
8*E*-**1**→6*n*-**3**[b]	0.23	0.13	0.17	0.24
8*E*-**1**→6*x*-**3**[b]	0.14	0.23	0.21	0.15
R^2[c]	(1.000)	(0.251)	0.628	0.969
$k_{12n}/(k_{12n}+k_{12x})$	–	0.861	0.744	0.797
$k_{22}/(2k_{22}+k_{23n}+k_{23x})$	–	0.308	0.265	0.252
$k_{23n}/(k_{23n}+k_{23x})$	–	0.634	0.556	0.643
Fraction direct **TS-12x** to [3*s*,3*s*]-**3**	–	–	–	0.808
$\Delta\Delta G^{\ddagger}_{(\text{TS-12x}-\text{TS-12n})}$	–	+1.8	+1.0	+1.3
$\Delta\Delta G^{\ddagger}_{(\text{TS-22}-\text{TS-23n})}$	–	+0.4	+0.7	+0.9
$\Delta\Delta G^{\ddagger}_{(\text{TS-23x}-\text{TS-23n})}$	–	+0.5	+0.2	+0.6

[a] For CASPT2//UB3LYP, relative TS energies ($\Delta\Delta H^{\ddagger}$) give parameters that produce the product distribution. Least-squares fits produce both kinetic parameters and expected values for the product distribution; relative TS energies are calculated from the kinetic parameters thus obtained. [b] The 8*E*-**1** and 8*Z*-**1** experiments are redundant under all models considered, excluding isotope effects. For this reason, they have been averaged for comparison and fit to theory to simplify the analysis and not to assign the two 8-*d*-**1** experiments undue weight in comparison with the single 7-*d*-**1** experiment. For example, the entry for 8*E*-**1**→6*n*-**3** is actually the average of experimental proportion in which 8*E*-**1** forms 6*n*-**3**, and 8*Z*-**1** forms 6*x*-**3**. [c] $R^2=\Sigma(\gamma_{\text{predicted}}-\gamma_{\text{expt}})^2/\Sigma(\gamma_{\text{expt}}-\gamma_{\text{random}})^2$ in which γ_{random} represents the hypothetical nonselective product distribution: $\gamma_{\text{random}}=0.25$ for each product except the [1,3] product in the 8-*d*-**1** experiment, for which $\gamma_{\text{random}}=0.50$. Although the CASPT2//UB3LYP prediction does not involve a fit to experiment, the R^2 analysis is applied for comparison with the least-squares results.

We have also worked backward from the experimental result by means of a least-squares fit, to determine what combination of relative rates would lead to the observed outcome. Such a fit produces selectivity parameters and a corresponding expected product distribution, shown in Column 3 of Table 2. The fit parameters match the experimental outcome more closely, despite the fact that they differ only slightly from the CASPT2//UB3LYP predictions. However, closer inspection shows that the fit still does not reproduce the experimental result satisfactorily in all cases. For instance, the ratio among [3,3] products from 8-*d*-**1** (i.e., 8*E*-**1** and 8*Z*-**1**) is reversed, whereas the proportion of [1*r*,3*s*] products in the 7*x*-**1** experiment is higher than it should be.

The problem is solved by incorporating a concerted Cope pathway into the stepwise model. The addition of a corresponding fourth selectivity parameter, described below, improves the fit from $R^2=0.628$ to $R^2=0.969$ (Table 2, Column 4). The goodness of fit alone is evidence to support the presence of such a pathway, yet how can this be reconciled theoretically? Examination of the potential energy surface of the reaction gives clues to what may be happening.[10] Preliminary single-point energy calculations prompted us to suspect that a CASPT2//UB3LYP treatment[11] would give the most accurate representation of the PES shape (Figure 4a). At this level of theory, the **TS-12x** saddle point lies at a low value of R(3,8), and the transition vector has a component in the negative R(3,8) direction. At the same time, the flattening of the diradical potential energy well shifts **TS-23x** toward larger values of R(3,8), positioning it almost directly in front of **TS-12x**. Thus situated, one can easily envision how **TS-23x** might bifurcate the ensemble of trajectories passing over **TS-12x**, sending them either to intermediate **2** or to the product **3** (Figure 4b).[12]

According to this model, **TS-12x** is populated based on its relative free energy, as before. After the transition state, that population is divided into two portions according to a new parameter. One portion goes to **2** and a statistical distribution of products from there, and the other produces [3*s*,3*s*]-**3** directly. The relative TS energies corresponding to this fit are listed in Table 2 and agree reasonably well with CASPT2//UB3LYP values. As for the additional parameter, the fit suggests that $81\pm16\%$ of the **TS-12x** trajectories (16% of the total product distribution) go directly to **3**.

Having obtained an adequate quantitative fit between theory and experiment, we consider the fact that the experimental [1,3]/[3,3] ratio is subject to a large positional secondary isotope effect, outside of probable error limits: [1,3]/[3,3] = 58:42 from 7*x*-**1** but 63:37 from 8*E*-**1** or 8*Z*-**1** (see also Reference [4]). This remains puzzling: although our calculations predict reasonable isotope effects for the various rate constants in Scheme 1, their combined effect (60:40 from 7*x*-**1** versus 61:39 from 8-*d*-**1**) is much smaller than what is experimentally observed.

In summary, experiments and calculations reported herein establish how [1,3] versus [3,3] and [1*i*,3*s*] versus [1*r*,3*s*] preferences may arise in a strictly stepwise reaction as a result of stereoelectronic effects on the breakage and formation of bonds, along with incomplete conformational equilibration among intermediate diradicals. Whereas much of the observed selectivity can be explained by a fully stepwise, statistical model, we find that there is also a role for a formally concerted Cope pathway in the form of a nonstatistical post-

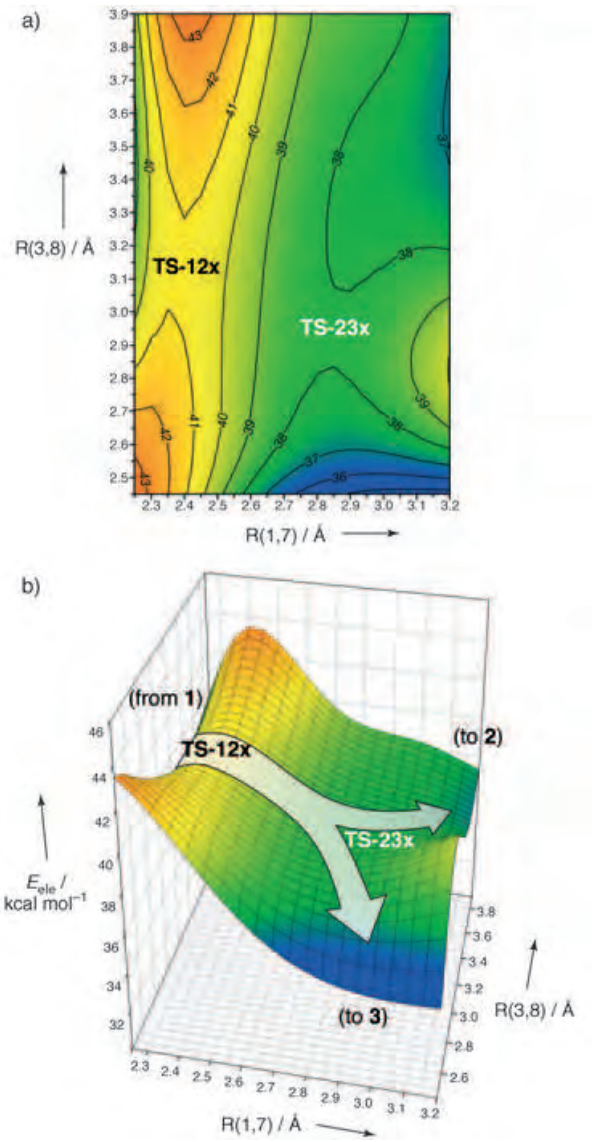

Figure 4. a) Two-dimensional projection of the potential energy surface for the rearrangement of **1** to **3**. The plot was mapped with CASPT2 single-point energy calculations on UB3LYP constrained-optimized structures at intervals of 0.05 Å in the coordinates R(1,7) and R(3,8), the bond-breakage and formation distances, respectively, for a [3,3] shift. Energy contours are marked in kcal mol^{-1}, relative to **1**. b) Three-dimensional representation of plot in part a) that schematically illustrates the concept of bifurcation of **TS-12x** reaction trajectories by **TS-23x**.

transition-state bifurcation. Dynamic simulations may yield additional insight into this process.

Experimental Section

The preparation of 7*x*-, 8*E*-, and 8*Z*-**1** is described in the Supporting Information. Thermolyses were carried out in the gas phase at 220 °C in a 20-L reaction flask at 1 to 3 mbar. *n*-Nonane served as an internal standard and *n*-hexane as collision partner. Samples were taken after approximately 20 %, 40 %, 60 %, and 80 % structural isomerization of starting material. Besides **3**, the only products observed were isotopomers of **1**. Ratios of individual isotopomers were determined by ^{2}H NMR spectroscopy (61.4 MHz) after separation of structural isomers by vapor-phase gas chromatography. Isotopomeric ratios were extrapolated to a thermolysis time $t = 0$ (Table 1).

Structures of **1** and **3**, as well as that of the intervening diradical **2** and associated transition species were optimized with both UB3LYP/6-31G(d) and (6,6)CASSCF/6-31G(d) in Gaussian 98.[13] (6,6)CASPT2/6-31G(d) single-point energies were calculated for both sets of stationary points in MOLCAS.[14] Kinetic isotope effects were calculated in the program Quiver[15] based on UB3LYP/6-31G(d) frequency data.

Received: January 4, 2005
Published online: April 28, 2005

Keywords: ab initio calculations · density functional calculations · diastereoselectivity · reaction mechanisms · sigmatropic rearrangement

[1] a) K. N. Houk, M. Nendel, O. Wiest, J. W. Storer, *J. Am. Chem. Soc.* **1997**, *119*, 10545; b) C. Doubleday, M. Nendel, K. N. Houk, D. Thweatt, M. Page, *J. Am. Chem. Soc.* **1999**, *121*, 4720; c) M. Nendel, D. Sperling, O. Wiest, K. N. Houk, *J. Org. Chem.* **2000**, *65*, 3259; d) C. Doubleday, *J. Phys. Chem. A* **2001**, *105*, 6333.
[2] P. A. Leber, J. E. Baldwin, *Acc. Chem. Res.* **2002**, *35*, 279.
[3] a) J. A. Berson, G. L. Nelson, *J. Am. Chem. Soc.* **1967**, *89*, 5503; b) J. A. Berson, G. L. Nelson, *J. Am. Chem. Soc.* **1970**, *92*, 1096; c) J. E. Baldwin, K. D. Belfield, *J. Am. Chem. Soc.* **1988**, *110*, 296; d) F.-G. Klärner, R. Drewes, D. Hasselmann, *J. Am. Chem. Soc.* **1988**, *110*, 297; e) B. K. Carpenter, *J. Am. Chem. Soc.* **1995**, *117*, 6336; f) B. K. Carpenter, *J. Am. Chem. Soc.* **1996**, *118*, 10329.
[4] a) D. Hasselmann, *Tetrahedron Lett.* **1972**, *13*, 3465; b) D. Hasselmann, *Tetrahedron Lett.* **1973**, *14*, 3739.
[5] D. Hasselmann, *Angew. Chem.* **1975**, *87*, 252; *Angew. Chem. Int. Ed. Engl.* **1975**, *14*, 257.
[6] a) P.-J. Rissing, PhD Dissertation, Ruhr University, Bochum (Germany), **1978**; b) D. Baumann, PhD Dissertation, Ruhr University, Bochum (Germany), **2001**.
[7] W. R. Dolbier, Jr., H. Koroniak, K. N. Houk, C. Sheu, *Acc. Chem. Res.* **1996**, *29*, 471.
[8] It is immediately evident that **TS-23n** forms a bond from C3 to the *proximal* allyl terminus. Although it appears feasible that **TS-23x** might involve rotation of the *distal* allyl carbon past C4 and into bonding distance with C3, IRC calculations show that this is not the case: the bond is formed to the proximal carbon in **TS-23x** as well as **TS-23n**.
[9] Although isotopomers of the educt **1** begin to accumulate with time, their effect on the distribution of labels in the product **3** vanishes upon extrapolation to $t = 0$. Examination of **1** at high levels of conversion shows a preponderance of the starting isotopomer, indicating that educt isomerization is slow in comparison with product formation. Regardless of its magnitude, the rate k_{21} is the same for all intermediates **2**, and therefore may be ignored in the computation of label distribution in product **3**.
[10] A transition state for a concerted [3*s*,3*s*] reaction, as well as one for a concerted [1*i*,3*s*] process, can be located with RB3LYP/6-31G(d) (Supporting Information), but these saddle points are only artifacts of the restricted formalism, and they disappear at the UB3LYP level.
[11] A CASPT2 single-point energy calculation was performed on each of the UB3LYP constrained-optimized structures used to construct the UB3LYP surface.
[12] A PES involving a post-TS bifurcation between a Cope pathway and formation of an allylic-stabilized diradical intermediate has been discussed in the case of an acyclic allenic triene: S. L.

Debbert, B. K. Carpenter, D. A. Hrovat, W. T. Borden, *J. Am. Chem. Soc.* **2002**, *124*, 7896.
[13] Gaussian 98 (Revision A.9), M. J. Frisch, G. W. Trucks, H. B. Schlegel, G. E. Scuseria, M. A. Robb, J. R. Cheeseman, V. G. Zakrzewski, J. A. Montgomery, R. E. Stratmann, J. C. Burant, S. Dapprich, J. M. Millam, A. D. Daniels, K. N. Kudin, M. C. Strain, O. Farkas, J. Tomasi, V. Barone, M. Cossi, R. Cammi, B. Mennucci, C. Pomelli, C. Adamo, S. Clifford, J. Ochterski, G. A. Petersson, P. Y. Ayala, Q. Cui, K. Morokuma, D. K. Malick, A. D. Rabuck, K. Raghavachari, J. B. Foresman, J. Cioslowski, J. V. Ortiz, B. B. Stefanov, G. Liu, A. Liashenko, P. Piskorz, I. Komaromi, R. Gomperts, R. L. Martin, D. J. Fox, T. Keith, M. A. Al-Laham, C. Y. Peng, A. Nanayakkara, M. Challacombe, P. M. W. Gill, B. G. Johnson, W. Chen, M. W. Wong, J. L. Andres, C. Gonzalez, M. Head-Gordon, E. S. Replogle, J. A. Pople, Gaussian, Inc., Pittsburgh, PA, **1998**.
[14] MOLCAS (Version 5.0), K. Andersson, M. Barysz, A. Bernhardsson, M. R. A. Blomberg, D. L. Cooper, T. Fleig, M. P. Fülscher, C. de Graaf, B. A. Hess, G. Karlström, R. Lindh, P.-Å. Malmqvist, P. Neogrády, J. Olsen, B. O. Roos, A. J. Sadlej, B. Schimmelpfennig, M. Schütz, L. Seijo, L. Serrano-Andrés, P. E. M. Siegbahn, J. Stålring, T. Thorsteinsson, V. Veryazov, P.-O. Widmark, Lund University, Sweden, **2001**.
[15] M. Saunders, K. E. Laidig, M. Wolfsberg, *J. Am. Chem. Soc.* **1989**, *111*, 8989.

Ion Exchange

$\{Sn[Zn_4Sn_4S_{17}]\}^{6-}$: A Robust Open Framework Based on Metal-Linked Penta-Supertetrahedral $[Zn_4Sn_4S_{17}]^{10-}$ Clusters with Ion-Exchange Properties**

*Manolis J. Manos, Ratnasabapathy G. Iyer, Eric Quarez, J. H. Liao, and Mercouri G. Kanatzidis**

The huge diversity in structure and pore size encountered in open-framework aluminosilicate zeolite materials is not yet reflected in sulfide and chalcogenide compounds. Interest in chalcogenides with open frameworks, however, is growing, and progress towards developing this important class of materials has been steady in the past decade.[1–3] Because of the wider chemical and bonding flexibility, in principle, chalcogenides can be even more diverse in composition and structure than zeolites. In addition, they can uniquely combine properties of zeolitic micropores—exploited in solid-acid, ion-exchange, and absorption materials—with properties of semiconductors that provide the basis of electronic, optical, and photonic applications.

Some chalcogenides with open frameworks are based on so-called supertetrahedral clusters, denoted as T*n* (*n* is the number of metal layers).[2c] Other frameworks are based on different units that range from simple tetrahedra to so-called penta-supertetrahedral clusters denoted as P*n*.[1a,2a,2b] Recently the family of compounds featuring $A_{10}[M_4M'_4S_{17}]$ ($A = K$, Cs; $M = Zn$, Cd, Fe, Co; $M' = Sn$, Ge)[4] and $A'[Sn_4M^{II}_4Se_{17}]$ ($A' = [K_{10}(H_2O)_{16}(CH_3OH)_{0.5}]$, $[K_{22}(H_2O)_7(CH_3OH)_{18}](SnSe_4)_3$; $[K_{36}Cl(H_2O)_{11}(CH_3OH)_{32}]$; $[K_6(H_2O)_3]$; $M^{II} = Co$, Zn, Mn, Cd, Hg)[5,6b] was shown to have discrete supertetrahedral clusters that belong to the penta-supertetrahedral series P*n*.[1a,2a,2b] This cluster type is an assembly of four $\{MQ_4\}$ (T1) and one $\{QM_4\}$ (anti-T1) structural units, in which M is the metal ion and Q is the chalcogen atom (see Figure 1a). The $[M_4M'_4S_{17}]^{10-}$ clusters have four terminal S atoms, which are potential binding sites to other clusters or metal centers, and can thus serve as building blocks for framework materials. However, to date no pertinent reports regarding such systems have appeared even though frameworks consisting of the partially destroyed P1 selenido clusters $[Cd_4Sn_3Se_{13}]^{6-}$ and $[Hg_4Sn_3Se_{13}]^{6-}$ were recently reported.[6]

Herein we describe $A_{5-x}K_{1+x}Sn[Zn_4Sn_4S_{17}]$ ($A = K^+$, Rb^+, Cs^+; $x = 0,4,5$), the first examples of compounds consisting of intact $[Zn_4Sn_4S_{17}]^{10-}$ clusters linked with Sn^{4+} centers. They feature a new type of open framework and have excellent chemical stability. Furthermore, we report the surprising finding that one-fifth of the K^+ ions play an important templating role in stabilizing the framework. The A^+ ions fill relatively large voids and exhibit remarkably facile ion-exchange properties similar to those of small-pore zeolites.

The synthesis of $K_6Sn[Zn_4Sn_4S_{17}]$[7] (**1**) was carried out by using the alkali polychalcogenide flux method,[8] with a K_2S/S ratio of 1:8–1:10 (that is, in a flux of relatively low basicity). For reasons that will become apparent below, we also succeeded in isolating the isostructural $CsK_5Sn[Zn_4Sn_4S_{17}]$ (**2**) and $RbK_5Sn[Zn_4Sn_4S_{17}]$ (**3**).[9]

Compound **1** crystallizes in the tetragonal acentric $I\bar{4}m2$ space group.[10] The noncentrosymmetric character of **1** is apparent when one looks at the (010) projection of the unit cell (Figure 1b). The critical building unit of **1** is the $[Zn_4Sn_4S_{17}]^{10-}$ cluster, which features a central tetrahedral $\{Zn_4S\}^{6+}$ core capped with four tridentate $\{SnS_4\}^{4-}$ fragments (see Figure 1a). To form the 3D framework, the cluster uses all four terminal S atoms to coordinate to four linking Sn atoms (Sn1), which in turn bind to four clusters (Figure 1c). This creates a full diamondlike framework with a zinc-blende (ZnS) topology (Figure 1d). Fourfold inversion rotation axes (-4) pass through the Sn1 atoms and the intracluster S1 atoms of the structure (Figure 1c).

The connection of tetrahedral chalcogenide clusters with metal linkers is a rational way to build open-framework compounds, yet it is still a relatively uncommon structural feature among the known crystalline examples. Generally in the latter compounds, the clusters tend to link by sharing terminal chalcogen atoms (μ_2-S or μ_2-Se). An exception to this is the $(Me_4N)_2[MGe_4Q_{10}]$ ($M = Mn$, Fe, Co, Zn, Cd) and

[*] Dr. M. J. Manos, Dr. R. G. Iyer, Dr. E. Quarez, Dr. J. H. Liao, Prof. M. G. Kanatzidis
Department of Chemistry, Michigan Sate University
East Lansing MI 48842-1793 (USA)
Fax: (+1) 517-355-1793
E-mail: kanatzid@cem.msu.edu

[**] Financial support from the National Science Foundation (DMR-0443785 and CHE-0211029 Chemistry Research Group) is gratefully acknowledged.

  DOI: 10.1002/anie.200500214

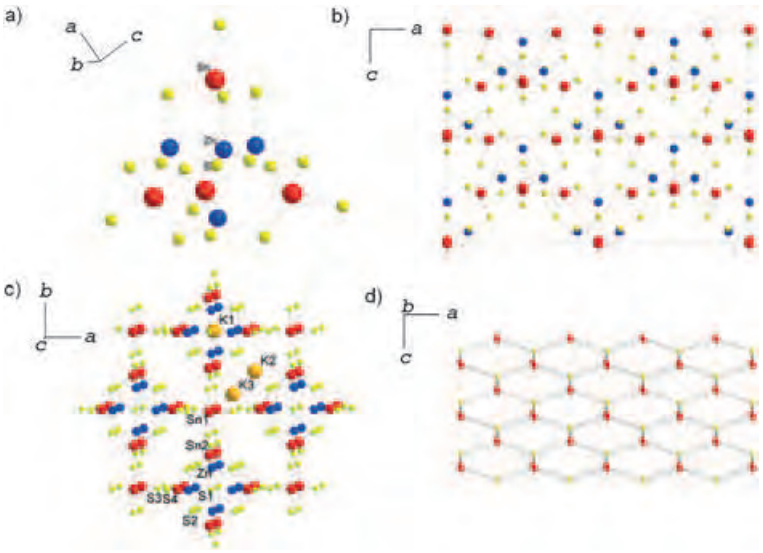

Figure 1. a) The $[Zn_4Sn_4S_{17}]^{10-}$ P1 cluster. b) A [010] projection showing the absence of a center of symmetry in the structure of compound **1**. Yellow, red, and blue balls represent S, Sn, and Zn atoms, respectively. K ions were removed for clarity. c) The $\{Sn[Zn_4Sn_4S_{17}]\}^{6-}$ framework viewed down the *c* axis. For clarity, K3 is shown in only one of the several subsites that are partially occupied by this ion. Selected distances [Å] and angles [°]: Sn1-S3 2.397(2), Sn2-S4 2.342, Sn-S2 2.3497(16), Sn2-S3 2.428(2), Zn-S1 2.3287(9), Zn-S2 2.3369(15), Zn-S4 2.353(2), K1-S2 3.4460(16), K2-S4 3.3637(15), K2-S2 3.145(2), K3-S3 3.791(3), K3-S4 3.253(5), Sn(1)-S(2)-Sn(2) 104.42(9). d) Skeletal version of the structure of $\{Sn[Zn_4Sn_4S_{17}]\}^{6-}$ depicting the topological relationship to diamond. The yellow balls are $[Zn_4Sn_4S_{17}]^{10-}$ clusters, and red balls are linking Sn atoms (Sn1).

$A_n[MGe_4Se_{10}]\cdot m\,H_2O$ (A = Rb, Cs; M = Ag: $n=3$, $m=2$; M = Mn: $n=2$, $m=3$) families, which feature adamantane clusters linked by tetrahedral M^{2+} centers.[11,12]

The most prominent aspect of the framework we describe here is the nature of the open space available in it. There are two types of large cavities: one that accommodates the K2 atoms and one that accommodates the K3 atoms. The K3 cavity is larger and both are indicated in Figure 2a, b. Out of the six K atoms in the formula, one atom is accommodated in site K1, one atom is in site K3, and four atoms are in site K2. K1 is in a tight eight-coordinate square-prismatic environment of S atoms. The K1–S2 bond length is 3.446(2) Å. Atoms K1, K2, and K3 occupy different environments in the tunnel network. K3 is in the largest cavity with a diameter of ≈9.7 Å and K2 is in the next largest cavity with a diameter of ≈6 Å. The atoms in the K3 site were modeled with several split subsites over the cavity.[14]

We can obtain a better understanding of the empty space in the $\{Sn[Zn_4Sn_4S_{17}]\}^{6-}$ framework if we plot the isosurface[13] that lies between the framework atoms and the voids (see Figure 2c, d). From this perspective, the relative size, shape, and interconnection of the cavities are revealed. It is apparent from these plots that the tunnel network in the structure is three-dimensional with a diamondlike topology similar to the topology of the filled space. Each cavity is not spherical but square and "pancake" in shape with the short dimension being parallel to the tetragonal *c* axis, Figure 2c, d. The two types of cavities (K2 and K3) communicate through narrow passages that are only ≈2 Å wide. This feature accounts for the observed selectivity in the ion-exchange properties observed for this framework (see below).

The K1 site seems to be an exact fit for this framework (see Figure 2c), and the role of this atom seems pivotal to the stability of the structure. This aspect was suggested by the results of experiments aimed at preparing analogues with larger alkali atoms such as $Rb_6Sn[Zn_4Sn_4S_{17}]$ and $Cs_6Sn[Zn_4Sn_4S_{17}]$; the experiments did not succeed. This lack of success implied that a K atom might be needed to occupy a K1 site to stabilize the framework. Conversely, the large cavities of K2 and K3 suggested that the K^+ ions are potentially very mobile and that it might be possible to replace them with larger Rb^+ or Cs^+ ions. Indeed compounds **2**, **3**, $Rb_5KSn[Zn_4Sn_4S_{17}]$ (**4**), and $(A_{5-x}K_x)KSn[Zn_4Sn_4S_{17}]$ (A = Rb, Cs) are all possible and can be prepared by high-temperature solid-state synthesis as well as topotactic ion-exchange reactions at room temperature.

A refinement of the crystal structures of **2** and **3** showed unequivocally that the K1 and K2 sites are occupied exclusively by K atoms. The largest site of K3 is occupied exclusively by Rb^+ and Cs^+ cations. However, refinement of the structure of the ion-exchanged material **4** showed that only K1

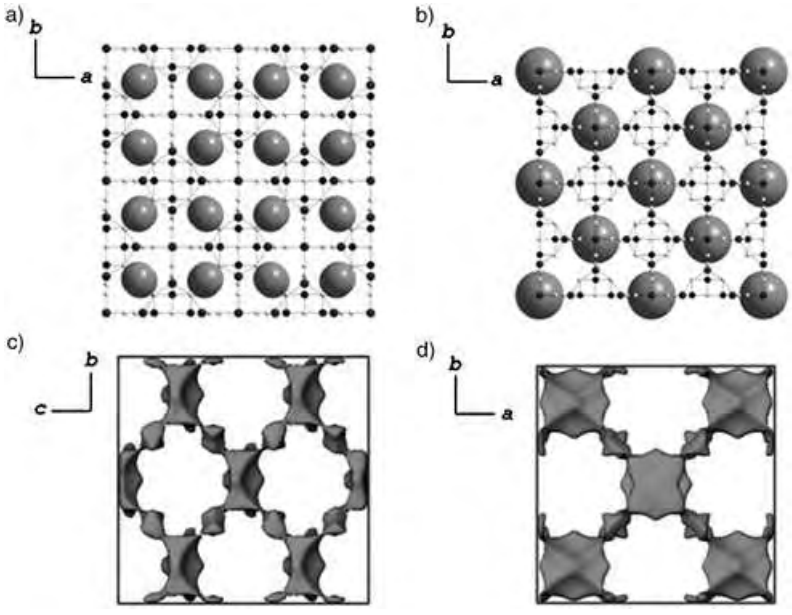

Figure 2. a) A [010] projection of the structure of **1** with the K2 sites represented by oversized spheres to show the available space around them. The diameter of the cavity hosting K2 is ≈6.0 Å. b) The same projection with the K3 sites now shown as oversized spheres. The diameter of the cavity hosting the K3 atoms is ≈9 Å. c) Depiction of the void space in $\{Sn[Zn_4Sn_4S_{17}]\}^{6-}$ viewed down the [100] direction of the isosurface representing the atom-free space in $\{KSn[Zn_4Sn_4S_{17}]\}^{5-}$ (2 Å from the van der Waals radius). d) The isosurface viewed down the [001] direction. The cavities containing the K3 atoms are square shaped "pancakes", whereas the cavities hosting the K2 atoms serve as connecting channels between the pancake-shaped cavities.

remains intact after ion-exchange (see below). Furthermore, analogues of **1** with larger metal ions, such as Hg^{2+} and Cd^{2+}, or with selenium analogues could not be isolated, possibly because they create larger K1 cavities thereby destabilizing the structure.[15] Because of these results, we are tempted to view the K1 site as a major reason for the stability of this structure type and likely to play the role of template. In this context and because it does not seem to be exchangeable, K1 must be considered as part of the framework whereas K2 and K3 are extraframework ions.

Since the extraframework K^+ ions are loosely bound, they are readily exchanged for other types of ions in solution. Complete ion exchange was achieved in a single-step reaction by stirring compound **1** in water for a few hours at room temperature with excess RbI and CsI.[16] The powder X-ray diffraction (XRD) patterns of compound **1** and those of the ion-exchanged material **4** are almost identical with the exception of a small shift of the diffraction peaks to lower 2θ angles (as expected) in the pattern of compound **4** (see Figure 3a, b). Energy-dispersive spectroscopy (EDS) analysis of the exchanged material was consistent with the formula of $Rb_5KSn_5Zn_4S_{17}$.

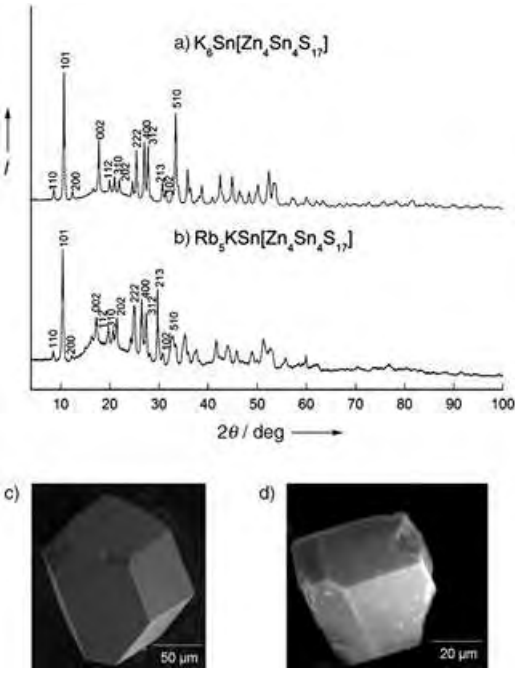

Figure 3. XRD ($Cu_{K\alpha}$ radiation) diagrams (with indexing of selected reflections) of: a) pristine $K_6Sn[Zn_4Sn_4S_{17}]$ and b) ion-exchanged $Rb_5KSn[Zn_4Sn_4S_{17}]$. c) SEM images of a single crystal of pristine $K_6Sn[Zn_4Sn_4S_{17}]$. d) A single crystal of ion-exchanged $Rb_5KSn[Zn_4Sn_4S_{17}]$.

Even whole single crystals of compound **1** can be ion-exchanged to give compound **4**,[17] which could be characterized by single-crystal X-ray diffraction. Figure 3c,d depicts typical well-formed crystals of pristine and ion-exchanged material. Crystallographic analysis on such a single crystal confirmed the replacement of only five of the K atoms (K2 and K3 from the large cavities),[18] whereas the K1 site remained totally unaffected. Again this result is consistent with the view that K1 may be necessary to form the $\{Sn[Zn_4Sn_4S_{17}]\}^{6-}$ framework.

The pale-yellow compound **1** and the analogues **2** and **3** show an optical energy gap of ≈ 2.87 eV, which indicates that they are semiconductors with wide band gaps. They also have high optical transparency to electromagnetic radiation, which begins from 2.87 eV and extends down to 0.30 eV as determined from combined IR–near-IR–UV/Vis spectroscopy. The high transparency and the noncentrosymmetric lattice of **1** prompted us to check for possible nonlinear optical (NLO) behavior. We note that the crystal structures of compounds **1**–**4** have the same topology and belong to the same point group $-42m$ as that of $AgGaS_2$. The latter has attained special interest for middle- and deep-IR applications due to its large NLO coefficients and high transmission in the IR region.[19] By using a pulsed Nd-YAG laser on polycrystalline samples of **1**, we observed the presence of a second harmonic generation (SHG) signal. More quantitative experiments are needed, however, to fully assess the NLO behavior of **1**–**4** materials.

In conclusion, $\{Sn[Zn_4Sn_4S_{17}]\}^{6-}$ is the first extended framework based on supertetrahedral $[M_4M'_4S_{17}]^{10-}$ clusters (P1) linked through metal ions. The compound is an ion-exchange material with properties reminiscent of those of small-pore zeolites. We are currently investigating the ion-exchange properties in more detail and the possibility of synthesizing mesostructured open frameworks by using discrete soluble P1 chalcogenide clusters and various metal linkers.[20]

Received: January 19, 2005
Published online: May 11, 2005

Keywords: cluster compounds · ion exchange · nonlinear optics · semiconductors · zeolites

[1] a) S. Dhingra, M. G. Kanatzidis, *Science* **1993**, *258*, 1769; b) T. J. McCarthy, T. A. Tanzer, M. G. Kanatzidis, *J. Am. Chem. Soc.* **1995**, *117*, 1294; c) G. A. Marking, M. G. Kanatzidis, *Chem. Mater.* **1995**, *7*, 1616; d) E. A. Axtel III, M. G. Kanatzidis, *Chem. Mater.* **1996**, *8*, 1350; e) J. A. Hanko, M. G. Kanatzidis, *Angew. Chem.* **1998**, *110*, 354; *Angew. Chem. Int. Ed. Engl.* **1998**, *37*, 342; f) E. A. Axtell III, Y. Park, K. Chondroudis, M. G. Kanatzidis, *J. Am. Chem. Soc.* **1998**, *120*, 124.

[2] a) X. Bu, N. Zheng, P. Feng, *Chem. Eur. J.* **2004**, *10*, 3356, and references therein; b) N. Zheng, X. Bu, P. Feng, *Angew. Chem.* **2004**, *116*, 4857; *Angew. Chem. Int. Ed.* **2004**, *43*, 4753; c) N. Zheng, X. Bu, P. Feng, *Nature* **2003**, *426*, 428; d) X. Bu, N. Zheng, Y. Li, P. Feng, *J. Am. Chem. Soc.* **2003**, *125*, 6024.

[3] a) P. Feng, X. Bu, N. Zheng, *Acc. Chem. Res.* **2005**, (ASAP article); b) H. Li, A. Laine, M. O'Keefe, O. M. Yaghi, *Science* **1999**, *283*, 1145; c) H. Li, J Kim, T. L. Groy, M. O'Keefe, O. M. Yaghi, *J. Am. Chem. Soc.* **2001**, *123*, 4867; d) H. Li, J. Kim, M. O'Keeffe, O. M. Yaghi, *Angew. Chem.* **2003**, *115*, 1863; *Angew. Chem. Int. Ed.* **2003**, *42*, 1819.

[4] a) O. Palchik, R. G. Iyer, J. H. Liao, M. G. Kanatzidis, *Inorg. Chem.* **2003**, *42*, 5052; b) O. Palchik, R. G. Iyer, J. H. Liao, M. G. Kanatzidis, *Z. Anorg. Allg. Chem.* **2004**, *630*, 2237.

[5] a) C. Zimmerman, M. Mellulis, S. Dehnen, *Angew. Chem.* **2002**, *114*, 4444; *Angew. Chem. Int. Ed.* **2002**, *41*, 4269; b) S. Dehnen, M. K. Brandmayer, *J. Am. Chem. Soc.* **2003**, *125*, 6618; c) M.

Mellulitis, C. Zimmerman, C. E. Anson, S. Dehnen, *Z. Anorg. Allg. Chem.* **2003**, *629*, 2325.

[6] a) N. Ding, D.-Y. Chung, M. G. Kanatzidis, *Chem. Commun.* **2004**, 1170; b) M. K. Brandmayer, R. Clérac, F. Weigend, S. Dehnen, *Chem. Eur. J.* **2004**, *10*, 5147.

[7] $K_6Sn[Zn_4Sn_4S_{17}]$ (**1**): A mixture of Sn (0.5 mmol), Zn (0.4 mmol), K_2S (1 mmol), and S (8 mmol) was sealed under vacuum ($\approx 10^{-4}$ torr) in a 9-mm silica tube, heated ($\approx 40\,^{\circ}C\,h^{-1}$) to 400 °C for 96 h, and then cooled to 25 °C at a rate of $6\,^{\circ}C\,h^{-1}$. The excess flux was removed with *N*,*N*-dimethylformamide (DMF) to reveal a mixture of pale yellow polyhedral crystals of **1** and orange crystals of $K_2Sn_2S_5$. In some preparations, the product contained a small quantity of S_8, which could be removed by washing with CS_2. Treating the mixture of **1** and $K_2Sn_2S_5$ with aqueous K_2CO_3 (pH 9–10) completely dissolved the ternary phase, and pure compound **1** was obtained (yield ≈30–60%). EDS analysis on several crystals of **1** gave an average composition of $K_{5.6}Sn_{5.2}Zn_4S_{17.2}$.

[8] M. G. Kanatzidis, A. Sutorik, *Prog. Inorg. Chem.* **1995**, *43*, 151.

[9] $K_5CsSn[Zn_4Sn_4S_{17}]$ (**2**) and $K_5RbSn[Zn_4Sn_4S_{17}]$ (**3**): A mixture of Sn (0.5 mmol), Zn (0.4 mmol), K_2S (0.9 mmol), Cs_2S or Rb_2S (0.1 mmol), and S (8 mmol) was sealed under vacuum ($\approx 10^{-4}$ torr) in a 9-mm silica tube, heated ($\approx 40\,^{\circ}C\,h^{-1}$) to 400 °C for 96 h, and then cooled to room temperature at a rate of $6\,^{\circ}C\,h^{-1}$. The excess flux was removed with DMF to reveal a mixture of pale yellow polyhedral crystals of **2** or **3** (yield 30–50% based on Sn) and orange crystals of $K_2Sn_2S_5$. The ternary phase was removed by washing with K_2CO_3. EDS analysis on several crystals of **2** and **3** gave compositions of $K_{5.1}CsSn_{5.1}Zn_{4.6}S_{17.6}$ and $K_{4.6}RbSn_5Zn_{4.7}S_{16.8}$, respectively.

[10] Crystal data: $K_6Sn_5Zn_4S_{17}$, space group $I\bar{4}m2$ (No. 119), $a = 13.7425(7)$, $c = 9.7272(5)$ Å, $V = 1837.04(16)$, $Z = 2$, $R1(F) = 0.0452$, $wR2(F^2) = 0.0878$; $K_5CsSn_5Zn_4S_{17}$, space group $I\bar{4}m2$, $a = 13.7684(11)$, $c = 9.5630(9)$ Å, $V = 1812.8(5)$, $Z = 2$, $R1(F) = 0.0669$, $wR2(F^2) = 0.1277$; $K_5RbSn_5Zn_4S_{17}$, space group $I\bar{4}m2$, $a = 13.7687(10)$, $c = 9.7767(6)$ Å, $V = 1853.4(2)$, $Z = 2$, $R1(F) = 0.0553$, $wR2(F^2) = 0.0762$. Further details on the investigation of the crystal structure may be obtained from the Fachinformationszentrum Karlsruhe, 76344 Eggenstein-Leopoldshafen, Germany (fax: (+49) 7247-808-666; e-mail: crysdata@fiz-karlsruhe.de), on quoting the depository numbers CSD-415015, CSD-415016, and CSD-415018 (for the compounds $K_6Sn_5Zn_4S_{17}$, $K_5CsSn_5Zn_4S_{17}$, and $K_5RbSn_5Zn_4S_{17}$, respectively).

[11] a) O. M. Yaghi, Z. Sun, D. A. Richardson, T. L. Groy, *J. Am. Chem. Soc.* **1994**, *116*, 807; b) J. Y. Pivan, Q. Achak, M. Louer, D. Louer, *Chem. Mater.* **1994**, *6*, 827.

[12] a) T. Jiang, A. Lough, G. A. Ozin, R. L. Bedard, R. Broach, *J. Mater. Chem.* **1998**, *8*, 721; b)A. Loose, D. S. Sheldrick, *Z. Naturforsch. B* **1997**, *52*, 687.

[13] T. F. Nagy, S. D. Mahanti, J. L. Dye, *Zeolites* **1997**, *19*, 57.

[14] The split-occupancy sites and possible rattling of these ions inside the cages explains the much higher thermal-displacement parameters of K3 and K2 relative to that of K1.

[15] Reactions aiming to form $K_6Sn[M_4Sn_4S_{17}]$ analogues ($M = Hg^{2+}$, Cd^{2+}, Co^{2+}, Fe^{2+}) or the Se analogue of **1** led to other quaternary and ternary phases. However, compounds with Sn atoms partially replaced by Ge, or Zn atoms partially replaced by other divalent atoms (such as Hg^{2+} or Cd^{2+}) have been isolated, and these results will be published elsewhere. Efforts to prepare $K_6Ge[Zn_4Ge_4S_{17}]$ resulted instead in $K_{10}Zn_4Ge_4S_{17}$.[4]

[16] Interestingly, the material exhibits selectivity against Li and Na ions. In water these have a strongly held hydration sphere that prevents the large hydrated ions from entering the structure. Preliminary ion-exchange experiments of compound **1** with CsCl at room temperature showed that only one K^+ ion can be exchanged by one Cs^+ ion. Crystallographic analysis of the exchanged material showed that only the K3 ions were exchanged with Cs ions.

[17] A typical ion-exchange experimental route for the preparation of compound **4** is as follows: An excess of solid RbI (0.2 mmol) was added to a suspension of compound **1** (0.01 mmol) in water (20 mL). The mixture was stirred for ≈12 h. Then, the yellowish-white crystalline material was isolated by filtration, washed several times with water, acetone, and ether (in this order), and dried in air.

[18] $Rb_5KSn_5Zn_4S_{17}$ (ion-exchanged), space group $I\bar{4}m2$, $a = 13.8354(10)$, $c = 9.8893(9)$ Å, $V = 1893.0(3)$, $Z = 2$, $R1(F) = 0.0793$, $wR2(F^2) = 0.1519$. Further details on the crystal structure investigations may be obtained from the Fachinformationszentrum Karlsruhe, 76344 Eggenstein-Leopoldshafen, Germany (fax: (+49) 7247-808-666; e-mail: crysdata@fiz-karlsruhe.de), on quoting the depository number CSD-415017.

[19] S. C. Abrahams, J. L. Bernstein, *J. Chem. Phys.* **1973**, *59*, 1625.

[20] T. Kerr, M. Armatas, P. N. Trikalitis, O. Palchik, M. G. Kanatzidis, unpublished results.

Nanostructures

Metallic Nanowires of Nb_3Te_4: A Nanostructured Chalcogenide**

Hannah K. Edwards, Pamela A. Salyer, Martin J. Roe, Gavin S. Walker, Paul D. Brown, and Duncan H. Gregory**

Since the discovery of carbon nanotubes,[1] there has been a sharp growth in the research of carbon nanostructures and, latterly, inorganic nanotubes and wires. The promise of a greater breadth of chemical and physical properties from inorganic nanostructures over their carbon counterparts has led to a proactive search for inorganic compounds with the capacity to be synthesized as nanowires or nanotubes. This evolving area of nanomaterials chemistry promises novel

[*] H. K. Edwards, Dr. P. A. Salyer, Dr. D. H. Gregory
School of Chemistry
University of Nottingham
University Park, Nottingham, NG72RD (UK)
Fax: (+44) 115-951-3563
E-mail: duncan.gregory@nottingham.ac.uk
H. K. Edwards, M. J. Roe, Dr. G. S. Walker, Dr. P. D. Brown
School of Mechanical, Materials and Manufacturing Engineering
University of Nottingham
University Park, Nottingham, NG72RD (UK)
Fax: (+44) 115-951-3800
E-mail: paul.brown@nottingham.ac.uk

[**] D.H.G. thanks the EPSRC for financial support of this work. D.H.G, P.D.B, and G.S.W thank the IDTC in Nanotechnology at the University of Nottingham for a studentship for H.K.E. The authors also acknowledge use of the EPSRC's Chemical Database (ICSD) service at the Daresbury Laboratory (UK).

Supporting information for this article is available on the WWW under http://www.angewandte.org or from the author.

 DOI: 10.1002/anie.200500157

properties through the transition from the bulk phase to the nanoscale and the introduction of additional design elements for materials, such as quantum confinement. The first inorganic nanotubes were synthesized by Tenne[2] and many new inorganic nanostructures have been produced since through a small number of increasingly understood synthetic methods.[3] By far the largest and most-studied family of these inorganic nanostructures is the transition-metal chalcogenides. This family is dominated by the dichalcogenides MX_2 (M = Group 4–6 metals, Re; X = S, Se, Te),[2–4] whose component layers of MX_6 polyhedra, which are separated by van der Waals interactions, are conducive to the rolling or scrolling required for the formation of nanotubes or wires (similar to the "dangling bonds" in graphene layers).[5] Only two nanostructured niobium chalcogenides are known, NbS_2[6] and $NbSe_2$.[7] Additionally, nanoscaled $NbSe_3$ has also been obtained after being physically cleaved from larger crystals.[8] Furthermore, and perhaps surprisingly, only one example of a metal telluride nanomaterial has been reported so far, the dichalcogenide $MoTe_2$.[9] Herein, we report the first example of a new class of inorganic nanowire, the telluride Nb_3Te_4. The niobium telluride is unique among the nanostructured chalcogenides in terms of its stoichiometry and, crucially, its structure. In contrast to the dichalcogenides, this 3:4 nanostructured compound is the first to be grown that is derived from a 1D bulk structure. The ensuing electronic properties of such nanowires can be inferred directly from the 1D crystal structure of the material.

Niobium telluride nanowires were synthesized at elevated temperature by direct chemical vapor transport (CVT) from the respective elemental powders in a sealed system (see the Experimental Section). The transition of the starting material from an intimate mixture of powders to nanostructured product was followed (ex situ) by powder X-ray diffraction (PXD; Figure 1). Elemental Nb and Te react after 1 h at 900 °C to form $NbTe_2$ (**1**; Figure 2a), which converts into Nb_3Te_4 (**2**) after 1 week. Both the Nb/Te phases are present at the intermediate times of 4 h, 1 day, and 3 days. Material held at 900 °C for 1 h and then annealed at 1160 °C for 2 days also converts from $NbTe_2$ into Nb_3Te_4 (**3**). Secondary electron (SE) images from scanning electron microscopy (SEM) show well-defined particles for **1** and **2**, as opposed to clusters of nanowires for **3**. Hexagonal lattice parameters of $a =$ 10.665(5) and $c = 3.643(2)$ Å were obtained for **3** from PXD data, which were in excellent agreement with previously reported single-crystal data.[10] The nanowires grow out from a central core as "sea-urchin-like" clusters (Figure 2b) with lengths of the order of 30 μm. Energy-dispersive X-ray spectroscopy (EDX) analysis yielded an Nb/Te atomic ratio of 43:57 (3:4), which is consistent with Nb_3Te_4 and in agreement with the PXD data. Furthermore, back-scattered electron (BSE) imaging indicated a lack of high contrast between the wires, thus suggesting the sample composition to be relatively constant throughout.

X-ray photoelectron spectroscopy (XPS) analysis of **3** yielded a Nb/Te elemental ratio of 0.762:1, again in close agreement with the expected ratio of 0.75:1 for Nb_3Te_4. Furthermore, high-resolution spectra gave binding energies (BEs) of 202.9 and 572.7 eV for the Nb and Te centers in **3**, concomitant with BEs in Nb_3Te_4 of 202.8 and 572.6 eV, respectively.[11] Additional oxide peaks at 206.8 and 576.3 eV were in excellent agreement with the ternary oxides

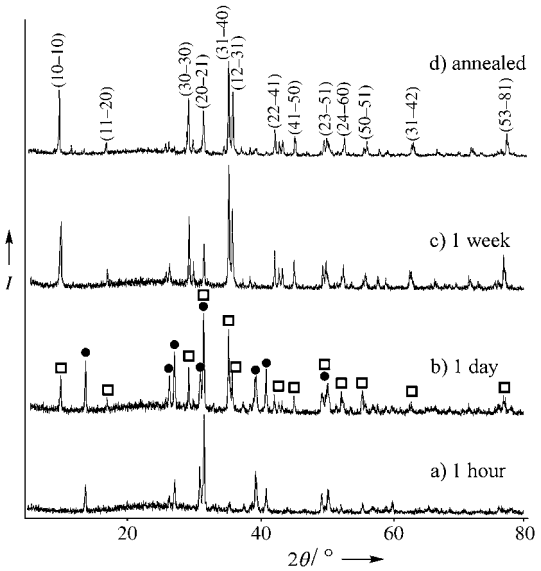

Figure 1. XRD patterns of samples sintered at 900 °C after a) 1 h (**1**), b) 24 h, and c) 1 week (**2**) showing the gradual transformation of **1** (solid circles) into **2** (open squares). These samples did not contain nanowires. d) XRD pattern of **1** sintered for 1 h at 900 °C followed by annealing at 1160 °C for 2 days. The resulting sample **3** was composed of clusters of nanowires. (Major peaks are indicated with indices.)

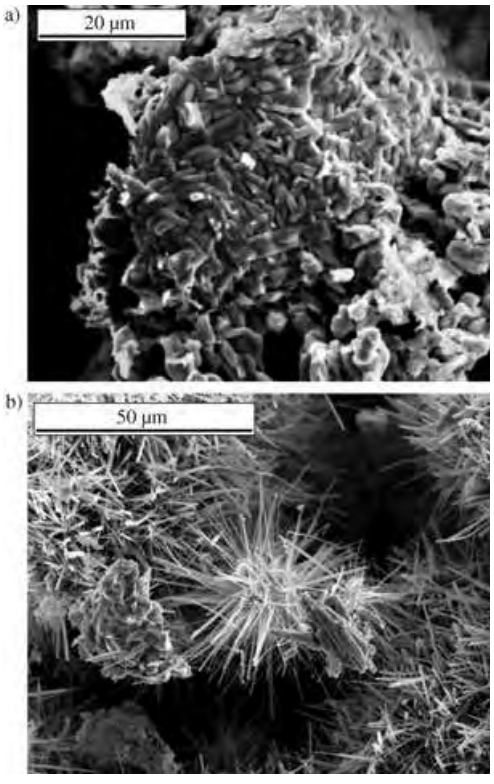

Figure 2. SEM micrographs of a) $NbTe_2$ particles after 1 h at 900 °C and b) a cluster of Nb_3Te_4 nanowires. The nanowires emanate from larger core particles of Nb_3Te_4.

$Nb_2Te_3O_{11}$ and $Nb_2Te_4O_{13}$ (where the BEs for the Nb and Te centers are 207.0 and 576.1 eV, respectively),[12] thus suggesting some surface oxidation of the telluride that probably occurred during postsynthetic handling. Similar oxide-layer phenomena are observed with nanotubes of NbS_2.[6b]

Transmission electron microscopy (TEM) analysis revealed the wires are straight with diameters of 50 nm–1 μm (Figure 3). The nanowires exhibit bundled structures, as

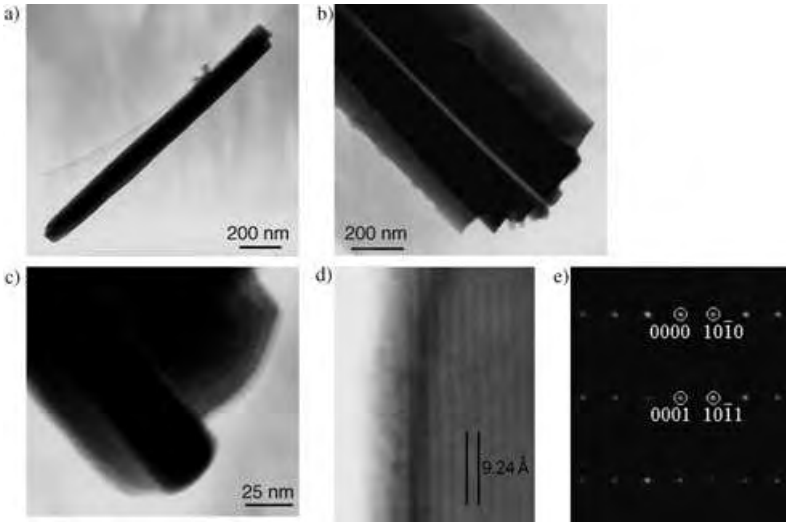

Figure 3. TEM images and SAED patterns of the Nb_3Te_4 nanowires. a) TEM image of a single nanowire. b) TEM image of bundled nanowires. c) High-magnification TEM image of rounded nanowire ends illustrating the amorphous surface layer found on some wires. (d, e) TEM image and corresponding [1−210] SAED pattern of the (10−10) lattice fringes of a Nb_3Te_4 nanowire.

if composed of many smaller filaments. Similar bundles are observed with NbS_2 and WS_2, for example,[6a,13] although for the telluride, selected-area electron diffraction (SAED) studies confirmed the presence of single crystalline wires, thus suggesting a cooperative growth mechanism. Many wires were found to have rounded ends. The indexing of the nanowire SAED patterns was consistent with the hexagonal $P6_3/m$ structure of Nb_3Te_4[10] and the indexing from PXD. TEM also showed the presence of a thin (< 5 nm) surface layer of amorphous material covering the ends and sides of some wires, which is consistent with the surface oxidation indicated by XPS. The combined PXD, XPS, and SAED results indicate that the wires have a Nb_3Te_4 core with a surface oxide layer of niobium(v) tellurate. High-resolution electron microscopy (HREM)/SAED revealed that Nb_3Te_4 wires grow with the [0001] direction parallel to the long axis of the wire. The orientation of the Nb_3Te_4 planes was also confirmed by measuring the lattice fringes (Figure 3d). The corresponding SAED pattern of projection [1−210] is shown in Figure 3e, where the plane spacings of 9.24 Å correspond to the (10−10) (i.e., 100) planes of Nb_3Te_4 (9.2414 Å).[10] This orientation leads to Nb−Nb chains and open channels running parallel to the long axis of the wire (Figure 4).

Separated wires from **3** display weak, temperature-independent magnetism between 1.8 and 300 K, which is characteristic of a Pauli paramagnet. The bulk material is reported to be a 1D metal and a superconductor (from electrical resistivity measurements) at approximately 2 K.[14] However, no anomaly in the specific heat was observed until 0.5 K and no Meissner effect is seen above 1.4 K.[15] Our results for Nb_3Te_4 nanowires concur with these earlier findings, thus suggesting that the wires are metallic but not superconducting above 1.8 K.

Although a precise growth mechanism has not yet been established, it is evident from investigating the heating regimes that the annealing process is fundamental to the growth of the nanowires. The elements first react to form $NbTe_2$ crystallites, which then transform to Nb_3Te_4 nanowires at 1160 °C. Elemental Te has a melting point of 449.5 °C,[16] and hence should be molten during the initial reaction step. It is considered that a CVT process subsequently occurs at elevated temperature to yield Nb_3Te_4 nanowires from the gas phase which then seed and nucleate outward from an initial core of material. This model is reinforced by SE images showing the characteristic sea-urchin-like form (Figure 2b). SE observations also indicate the formation of hollow-core particles which is consistent with mass transport from the inside to the outside. It is worth noting that transformation from $NbTe_2$ to Nb_3Te_4 should proceed through the loss of Te, but no Te-containing phases, other than Nb_3Te_4, were detected in the products by PXD. Indexing of the $NbTe_2$ phase reveals contraction along the *c* axis (i.e., between the Nb−Te layers) relative to the reported parameters,[17] thus suggesting that the initial telluride formed is $Nb_{1+x}Te_2$, by analogy to $Nb_{1+x}S_2$ and, for example, $V_{1+x}Te_2$.[18,19] This ditelluride phase is a subject of our further investigations.

The crystallographic orientation of the wires show that the growth direction is along the hexagonal *c* axis. Nb_3Te_4 has a large *a* value (10.671 Å) and small *c* value (3.647 Å). The growth direction of inorganic nanotubes and wires is commonly along that of the shortest lattice parameter. Nb_3Te_4 wires are consistent in this respect: they grow with their

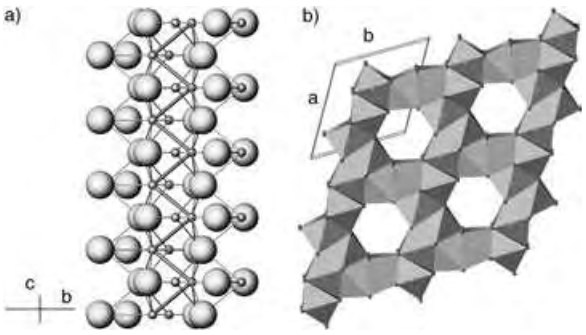

Figure 4. a) Crystal structure of Nb_3Te_4 to illustrate the Nb−Nb zigzag chains running parallel to the *c* axis (small spheres indicate Nb; larger spheres Te) and b) a polyhedral representation in the *a*–*b* plane, which shows the Nb-centred edge-sharing octahedra and open channels that also lie parallel to the *c* axis.

[00*l*] planes perpendicular to the long axis of the wire. Hence, this growth direction is distinct from chalcogenide nanowires that take a 2D structural basis (smaller *a* and larger *c* axis).[2,4] It is of key importance to the physical properties of the nanowires that the long axis of the wire is also in the same direction as the shortest Nb–Nb bond; infinite zigzag Nb chains run along the *c* axis. The intrachain Nb–Nb bond length is 2.973 Å, (Nb metal, Nb–Nb = 2.86 Å),[20] whereas the interchain Nb–Nb bond is much longer at 3.854 Å.[5] Anisotropic conduction along the *c* axis in large single crystals of Nb_3Te_4 was verified through resistivity and magnetoresistance experiments.[14b,21] Nb chains are able to carry charge linearly and are decoupled by the intervening Te atoms. This behavior should be mirrored at the nanoscale, thus inviting compositional and structural modification through substitution (of Te and/or Nb atoms) and intercalation ($M_xNb(Ta)_3X_4$); for example, the isostructural $Nb_3S(Se)_4$ and intercalates with M = In, Hg, Tl, and Cu, in which $0 < x \leq 1$[22] are known bulk materials. Hence, there is a real prospect of designing a new family of 1D-derived nanowires exhibiting metallic conduction, charge-density wave phenomena, superconductivity, or fast ionic transport. A systematic study of the growth and properties of such a family is currently underway.

In summary, we have synthesized metallic nanowires of Nb_3Te_4 for the first time by a high-temperature CVT process. This novel 1D system offers a promising basis for a new family of tailored nanostructured functional materials.

Experimental Section

Nb_3Te_4 nanowires were prepared from ground mixtures of niobium (99.9%, Aldrich) and tellurium powders (99.99%, Alfa; molar ratio = 3:4) in a nitrogen-filled recirculating glove box. The mixtures were initially heated in evacuated (approximately 10^{-3} mbar) 12-mm diameter sealed silica ampoules to 900 °C for between 1 h and 1 week. After quenching the ampoules in air, the ampoules were subsequently annealed at 1160 °C for 2 days. The resulting low-density black powder was characterized by PXD (Philips X'Pert θ-2θ diffractometer; $Cu_{K\alpha}$ radiation), SEM (JEOL 6400 SEM with an Oxford Instruments ISIS EDX system), XPS (VG Scientific Escalab Mark II spectrometer using $Al_{K\alpha}$ radiation at an anode potential of 10 kV and a filament emission current of 20 mA), and TEM (JEOL 2000fx TEM with an ISIS EDX system) for nanoscale imaging and SAED studies. Samples for analysis by SEM and XPS were prepared by depositing powder on to a carbon tab of sufficient thickness to prevent detection of the underlying carbon. Samples for TEM analysis were prepared by sonicating the powders in acetone for 3 min and then transfering drops of the suspension by pipette onto holey carbon-film Cu grids. Samples for SQUID (superconducting quantum interference device) analysis were prepared in similar a manner to separate the nanowires from any residual powder and were then loaded into gelatine capsules. Magnetic measurements were performed using a quantum design MPMS 5T SQUID susceptometer under a field of 1 Oe between 1.8 and 300 K.

Received: January 14, 2005
Published online: April 29, 2005

Keywords: chalcogenides · chemical vapor transport · nanostructures · niobium · tellurium

[1] S. Iijima, *Nature* **1991**, *354*, 56.
[2] R. Tenne, *Nature* **1992**, *360*, 444.
[3] a) C. N. R. Rao, F. L. Deepak, G. Gundiah, A. Govindaraj, *Prog. Solid State Chem.* **2003**, *31*, 5; b) M. Remškar, *Adv. Mater.* **2004**, *16*, 1497.
[4] For example: a) V. V. Ivanovskaya, G. Seifert, *Solid State Commun.* **2004**, *130*, 175; b) M. Nath, C. N. R. Rao, *Angew. Chem.* **2002**, *114*, 3601; *Angew. Chem. Int. Ed.* **2002**, *41*, 3451; c) M. Nath, C. N. R. Rao, *Pure Appl. Chem.* **2002**, *74*, 1545; d) Y. Feldman, *Science* **1995**, *267*, 222; e) R. Harpeness, A. Gedanken, A. M. Weiss, M. A. Slifkin, *J. Mater. Chem.* **2003**, *13*, 2603.
[5] a) R. Tenne, *Chem. Eur. J.* **2002**, *8*, 5297; C. N. R. Rao, M. Nath, *Dalton Trans.* **2003**, 1.
[6] a) X. Wu, Y. Tao, X. Ke, J. Zhu, J. Hong, *Mater. Res. Bull.* **2004**, *39*, 901; b) Y. Z. Jin, W. K. Hsu, Y. L. Chueh, L. J. Chou, Y. Q. Zhu, K. Brigatti, H. R. Kroto, D. R. M. , Walton, *Angew. Chem.* **2004**, *116*, 5788; *Angew. Chem. Int. Ed.* **2004**, *43*, 5670; c) C. Schuffenhauer, R. Popovitz-Biro, R. Tenne, *J. Mater. Chem.* **2002**, *12*, 1587; d) G. Seifert, H. Terrones, M. Terrones, T. Frauenheim, *Solid State Commun.* **2000**, *115*, 635; e) M. Remskar, A. Mrzel, A. Jesih, F. Levy, *Adv. Mater.* **2002**, *14*, 680.
[7] a) T. Tsuneta, T. Toshima, K. Inagaki, T. Shibayama, S. Tanda, S. Uji, M. Ahlskog, P. Hakonen, M. Paalanen, *Curr. Appl. Phys.* **2003**, *3*, 473; b) M. Nath, S. Kar, A. K. Raychaudhuri, C. N. R. Rao, *Chem. Phys. Lett.* **2003**, *368*, 690.
[8] E. Slot, M. A. Holst, H. S. J. van der Zant, S. V. Zaitsev-Zotov, *Phys. Rev. Lett.*, **2004**, *93*, 176602.
[9] L. H. Qiu, V. G. Pol, Y. Wei, A. Gedanken, *J. Mater. Chem.* **2003**, *13*, 2985.
[10] K. Selte, A. Kjekshus, *Acta Crystallogr.* **1964**, *17*, 1568.
[11] J. F. Moulder, W. F. Stickle, P. E. Sobol, K. D. Bomben, *Handbook of X-Ray Photoelectron Spectroscopy*, Physical Electronics, Minnesota, **1992**.
[12] F. Garbassi, J. C. J. Bart, G. Petrini, *J. Electron Spectrosc. Relat. Phenom.* **1981**, *22*, 95.
[13] M. Remškar, Z. Škraba, M. Regula, C. Ballif, R. Samjinés, F. Lévy, *Adv. Mater.* **1998**, *10*, 246.
[14] a) E. Amberger, K. Polborn, P. Grimm, M. Dietrich, B. Obst, *Solid State Commun.* **1978**, *26*, 943; b) Y. Ishihara, I. Nakada, *Solid State Commun.* **1983**, *45*, 129; c) Y. Ishihara, I. Nakada, *Jpn. J. Appl. Phys.* **1984**, *23*, 851.
[15] H. Okamoto, H. Taniguti, Y. Ishihara, *Phys. Rev. B* **1996**, *53*, 384.
[16] *Handbook of Chemistry and Physics*, 61st ed. (Ed.: R. C. Weast), CRC, Boca Raton, FL, **1980**, p. B154.
[17] B. E. Brown, *Acta Crystallogr.* **1966**, *20*, 264.
[18] a) F. Jellinek, G. Brauer, H. Mueller, *Nature* **1960**, *185*, 376; b) B. Morosin, *Acta Crystallogr. Sect. B* **1974**, *30*, 551; c) D. R. Powell, R. A. Jacobson, *J. Solid State Chem.* **1981**, *37*, 140.
[19] K. D. Bronsema, G. W. Bus, G. A. Wiegers, *J. Solid State Chem.* **1984**, *53*, 415.
[20] J. W. Edwards, R. Speiser, H. L. Johnston, *J. Appl. Phys.* **1951**, *22*, 424.
[21] Y. Ishihara, I. Nakada, *Jpn. J. Appl. Phys.* **1984**, *23*, 85.
[22] a) O. Hiroyuki, K. Takuya, G. Muramoto, I. Yoshiaka, S. Yuusuke, M. Iori, K. Hiroshi, I. Yuake, *Phys. B* **2003**, *329*, 1350; b) T. Ohtani, A. Tsubota, K. Ohshima, *Mater. Res. Bull.* **1999**, *34*, 1143; T. Ohtani, Y. Sano, Y. Yokota, *J. Solid State Chem.* **1993**, *103*, 504.

Molecular Targeting

Photo-Cross-Linked Small-Molecule Affinity Matrix for Facilitating Forward and Reverse Chemical Genetics**

*Naoki Kanoh, Kaori Honda, Siro Simizu, Makoto Muroi, and Hiroyuki Osada**

Affinity purification of small-molecule binding protein has been one of the most important techniques in forward chemical genetics (Figure 1a).[1,2] Once hit compound(s) which induce a specific phenotype in a cellular system are identified, the next step is to identify the molecular target. Thus, derivatization of the small molecules and structure–activity relationship studies are conducted to prepare tagged probes (for example, biotin conjugates) that can be used in a pull-down assay. Many targets of biologically important drugs have been discovered or identified by using this technique.[3–6] However, it remains challenging and time-consuming to derivatize small molecules without a loss in biological activity, and an easy-to-use, universal approach would be of great benefit in this context.

Affinity purification can also be used in reverse chemical genetics[7] for other purposes (Figure 1b). In vitro binding assays including small-molecule microarrays have been used to identify small-molecule ligands for proteins of interest. Although these techniques have led to the successful identification of ligand candidates, they do not provide information about the specificity of the ligand–protein interaction. If the ligand could be immobilized on an affinity matrix in a manner that was independent of the functional groups present, pull-down experiments and competitive binding assays using this matrix could be used to confirm whether or not an interaction is specific. We have looked for a rapid and general approach for the immobilization of small molecules on an affinity matrix to enhance the forward and reverse chemical genetics approaches described above.

Recently, we reported a coupling method that enables the introduction of a variety of small molecules onto glass slides through a photoaffinity reaction.[8] By using this method, aryl

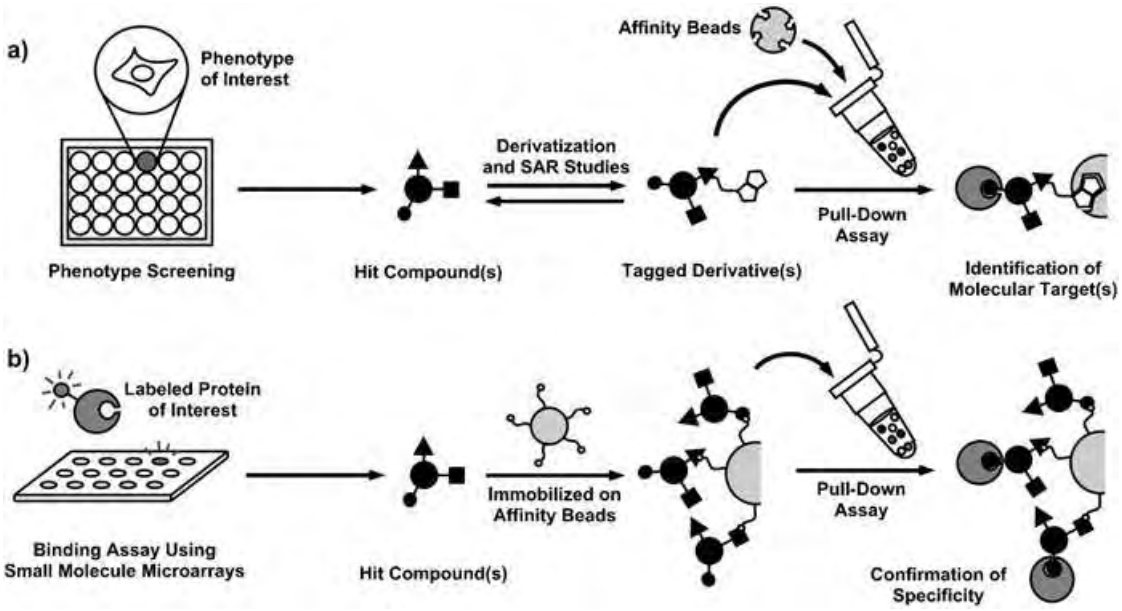

Figure 1. Affinity purification of small-molecule binding proteins in forward and reverse chemical genetics studies.

diazirine groups covalently attached to glass slides are transformed upon irradiation with UV light into highly reactive carbenes, which in turn bind to or insert irreversibly into a proximal small molecule in a manner that is independent of the functional groups.[9] This method, referred to as photo-cross-linking, has proven useful in the construction of small-molecule microarrays.[10] It is expected that a similar chemical approach could be used to introduce small molecules onto affinity gel, such as onto agarose beads. To test this hypothesis a photoaffinity linker **1** was introduced on agarose beads to prepare photoaffinity-linker-coated (PALC) agarose beads **3**, and the photo-cross-linking of complex small molecules onto **3** was demonstrated.

The preparation of **3** and the immobilization of small molecules on **3** were performed in a straightforward manner

[*] Dr. N. Kanoh, K. Honda, Dr. S. Simizu, Dr. M. Muroi, Dr. H. Osada
Antibiotics Laboratory
Discovery Research Institute
RIKEN
2-1 Hirosawa, Wako, Saitama 351-0198 (Japan)
Fax: (+81) 48-462-4669
E-mail: hisyo@riken.jp

[**] We would like to thank Fujisawa Pharmaceuticals (Osaka, Japan) for the generous gift of FK506, Rie Onose-Kanoh for technical assistance, and Dr. Takashi Nakamura and Dr. Hiroyuki Koshino for solid-state ^{17}F NMR measurements. This work was supported in part by the Chemical Biology Project (RIKEN) and grants from the Ministry of Education, Culture, Sports, Science, and Technology of Japan.

Supporting information for this article is available on the WWW under http://www.angewandte.org or from the author.

 DOI: 10.1002/anie.200462370

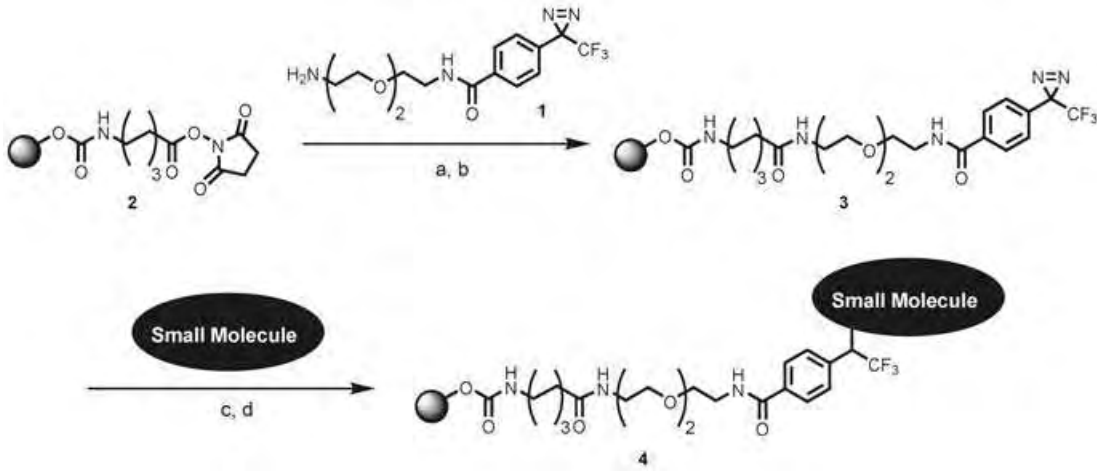

Scheme 1. Preparation of PALC agarose beads and photo-cross-linking of a small molecule. Reagents and conditions: a) **1**, $NaHCO_3$, NaCl, H_2O/dioxane (1:1), RT, 2 h; b) 1.0 M aq ethanolamine, RT, 1 h; c) 10 mM methanolic solution of small molecules, drying; d) irradiation at 365 nm, 4 J cm^{-2}; washing with organic solvent and water.

(Scheme 1). Activated CH sepharose 4B beads (Amersham Bioscience, Uppsala, Sweden; **2**) were first coupled with the photoaffinity linker **1**, and the beads were then blocked with 1.0 M aqueous ethanolamine, by using a solid-state coupling approach, to give **3**. Introduction of the photoaffinity linker **1** on the beads **2** was confirmed by high-resolution solid-state ^{19}F NMR measurements of **3** ($\delta = -65.9$ ppm, ArCF_3). To immobilize structurally diverse small molecules on **3** a methanolic solution of a small molecule was premixed with **3**, and then the mixture was concentrated and dried in vacuo. The dried beads were exposed to UV light (365 nm, 4 J cm^{-2}) from a UV cross-linker, and then washed thoroughly with methanol and water.

Figure 2 shows that the immobilization of the fluorescent rhodamine B depended on the photoaffinity linker **1** and irradiation with UV light: when agarose beads (sepharose CL-6B, Amersham Bioscience, Uppsala, Sweden) were irradiated in the presence of rhodamine B and then washed, no fluorescence was detected by fluorescence microscopy (Figure 2b). Fluorescence was observed only on PALC beads which had been irradiated in the presence of rhodamine B and then washed (Figure 2d). No fluorescence was observed on the beads in the absence of UV irradiation (Figure 2f). These results suggest that the photo-cross-linking strategy could be applied not only in studies using glass slides but also in assays with agarose beads.

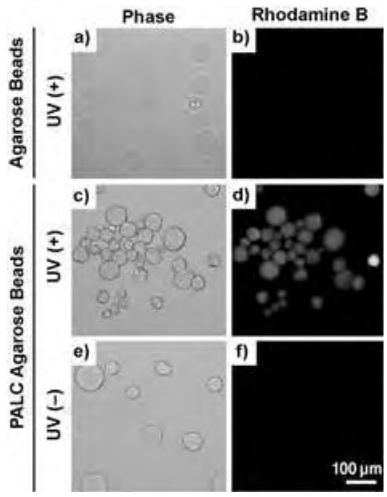

Figure 2. Observation of beads with immobilized rhodamine B by microscopy. Agarose beads and PALC agarose beads were mixed with rhodamine B and dried in vacuo. After incubation of the beads with or without irradiation, they were washed with methanol and water, and were observed under a microscope in the phase-contrast (a, c, e) or fluorescence mode (b, d, f).

To validate the binding ability of small molecules that had been photo-cross-linked on affinity beads with their target proteins we used the immunosuppressive drugs cyclosporin A (CsA) and FK506 (FK) as model ligands. CsA and FK are known to bind to the cellular targets cyclophilin A[11] and FKBP12,[3] respectively. In the specific case of CsA, photo-cross-linking with 4-benzoylbenzoic acid in solution[12] and a site-selective free-radical reaction on an appropriately protected CsA derivative[13] have been reported. Both molecules were photo-cross-linked on **3**, as shown in Scheme 1. The resulting CsA beads were incubated with the cell lysates of an *E. coli* BL21(DE3)pLysS strain over-expressing GST-cyclophilin A (GST-CypA), and the FK beads were incubated with the same *E. coli* strain, but which over-expressed $(His)_6$-FKBP12 (Figure 3a). First, we were able to identify a protein band of approximately 40 kDa that co-precipitated with the CsA beads (Lane 1). To determine the specificity of this interaction we examined whether or not CsA could compete for the binding of the CsA beads to the 40-kDa protein. The binding of CsA beads to the 40-kDa protein was found to be completely blocked by the addition of 10 and 100 μM CsA (Lanes 2 and 3), although no change in binding was observed in a control experiment using DMSO (Lane 4). The 40-kDa protein was reactive with an *anti*-GST antibody, thus indicating that the protein was GST-CypA (Figure 3b, left panel).

We were also able to identify a band of approximately 16 kDa (Figure 3a, Lane 6) that was reactive with an *anti*-$(His)_6$ antibody (Figure 3b, right panel); binding between the FK beads and the 16 kDa protein was blocked by a dose-

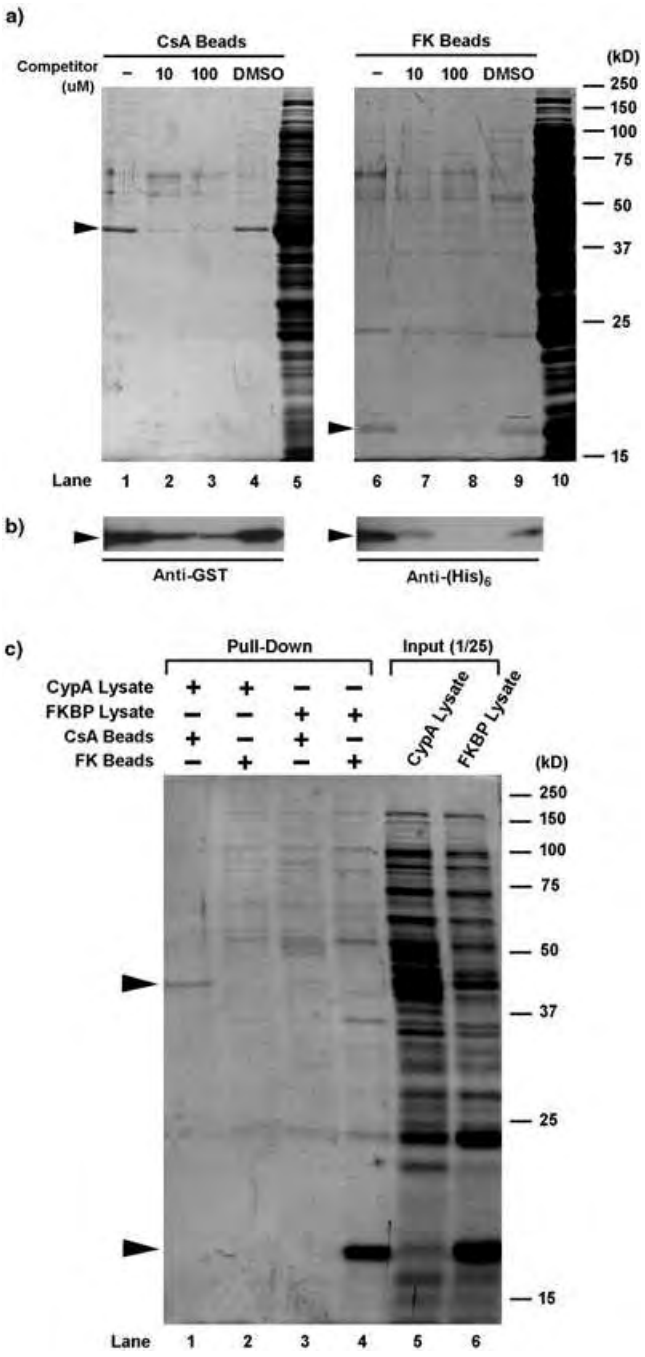

Figure 3. Detection of binding proteins for small-molecule-immobilized beads. Cell lysates of *E. coli* over-expressing GST-CypA or $(His)_6$-FKBP12 (namely, CypA lysate or FK lysate) were incubated with or without competitor. CsA beads or FK beads were then added to absorb the binding proteins. After the beads had been washed with the incubation buffer they were resuspended in SDS sample buffer, heated, and subjected to SDS-PAGE. The gels were visualized by CBB staining. a) Competition experiments. Lanes 1–4: CypA lysate plus CsA beads with CsA as a competitor; Lane 5: CypA lysate (loading control); Lanes 6–9: FK lysate plus FK beads with FK as a competitor; Lane 10: FK lysate (loading control). b) Western blot analysis. Protein bound specifically to the CsA beads was reactive to *anti*-GST antibody (left panel). Protein bound specifically to the FK beads was reactive with an *anti*-(His)6 antibody (right panel). c) Cross-experiments. Lane 1: CypA lysate plus CsA beads; Lane 2: CypA lysate plus FK beads; Lane 3: FK lysate plus CsA beads; Lane 4: FK lysate plus FK beads; Lane 5: CypA lysate (loading control); Lane 6: FK lysate (loading control).

dependent competition by the addition of FK506 (Figure 3a, Lanes 7 and 8). These results demonstrated that the protein was $(His)_6$-FKBP12 and also that the binding was specific.

The specificity of the interactions between a photo-cross-linked drug and immunophilin was further confirmed by cross-experiments (Figure 3c). Briefly, GST-CypA and $(His)_6$-FKBP12 did not co-precipitate with the FK and CsA beads, respectively (Lanes 2 and 3).

The next issue to be addressed was whether the photo-cross-linked affinity beads would be able to both purify the over-expressed proteins and also identify the cellular target(s) of the immobilized ligand. To address this question we incubated the CsA beads with Jurkat cell lysate, and the co-precipitated proteins were analyzed by sodium dodecyl sulfate polyacrylamide gel electrophoresis (SDS-PAGE, Figure 4a). This procedure led to the detection of a protein band of approximately 20 kDa by Coumassie Brilliant Blue (CBB)

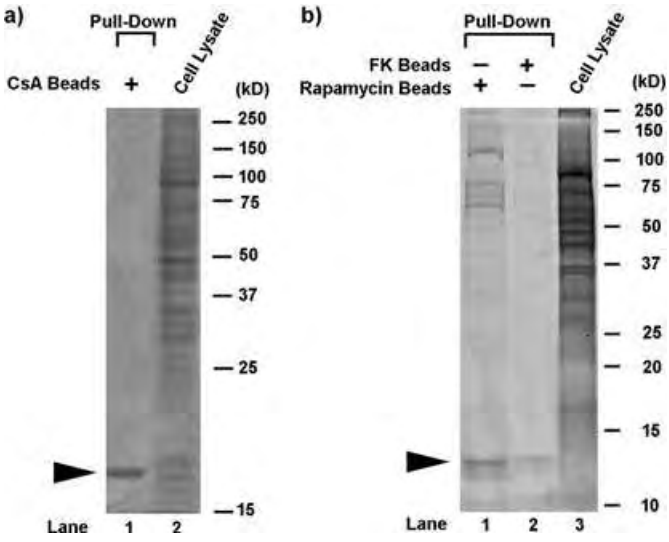

Figure 4. Detection of CsA-, FK-, and rapamycin-binding protein from the Jurkat cell lysate. The Jurkat cell lysate was first incubated with beads on which each of the small molecules were immobilized (CsA for Lane 1 of (a); rapamycin for Lane 1 of (b); FK for Lane 2 of (b)). The beads were then washed with lysis buffer containing 0.3% triton X-100, resuspended in SDS sample buffer, heated, and subjected to SDS-PAGE. The gels were visualized with CBB staining. The arrowheads indicate the bands which disappeared on addition of the respective small molecules (10 μM).

staining (Lane 1). To identify the protein the protein-containing region was excised and digested on SDS-polyacrylamide gel, and the resulting peptides were extracted and analyzed by MALDI-TOF MS (Supporting Information). The protein was identified from peptide mass fingerprinting (PMF) using the Mascot search program (Matrix science Inc., USA) and the Swiss-Prot database as human cyclophilin A with a protein score of 125—a score of greater than 52 is considered significant ($p < 0.05$). Besides being successful in the case of CsA beads, we also succeeded in purifying a human FKBP12 from Jurkat cell lysate by using both the FK beads and beads on which rapamycin was photo-cross-linked (Figure 4b).[14]

In summary, we have prepared PALC beads and demonstrated that photo-cross-linked small-molecule agarose beads can be used to identify and purify the binding protein. It was of note that complex small molecules such as FK506, rapamycin, and cyclosporin A could be introduced on the affinity matrix by using a uniform and straightforward procedure. Although the present procedure can not be applied to small molecules that degrade upon UV irradiation, technologies aimed at immobilizing ligands on an affinity matrix in a functional-group-independent manner are expected to facilitate the identification of molecular targets of small molecules in forward chemical genetics, and is also considered potentially useful for the confirmation of specificity between small molecules and proteins of interest in the field of reverse chemical genetics.

Received: October 20, 2004
Revised: March 18, 2005
Published online: May 4, 2005

Keywords: affinity purification · immobilization · molecular targeting · peptides · photochemistry

[1] S. M. Khersonsky, D.-W. Jung, T.-W. Kang, D. P. Walsh, H.-S. Moon, H. Jo, E. M. Jacobsen, V. Shetty, T. A. Neubert, Y.-T. Chang, *J. Am. Chem. Soc.* **2003**, *125*, 11804 – 11805.
[2] N. Shimizu, K. Sugimoto, J. Tang, T. Nishi, I. Sato, M. Hiramoto, S. Aizawa, M. Hatakeyama, R. Ohba, H. Hatori, T. Yoshikawa, F. Suzuki, A. Oomori, H. Tanaka, H. Kawaguchi, H. Watanabe, H. Handa, *Nat. Biotechnol.* **2000**, *18*, 877 – 881.
[3] M. W. Harding, A. Galat, D. E. Uehling, S. L. Schreiber, *Nature* **1989**, *341*, 758 – 760.
[4] L. Whitesell, E. G. Mimnaugh, B. De Costa, C. E. Myers, L. M. Neckers, *Proc. Natl. Acad. Sci. USA* **1994**, *91*, 8324 – 8328.
[5] N. Kudo, N. Matsumori, H. Taoka, D. Fujiwara, E. P. Schreiner, B. Wolff, M. Yoshida, S. Horinouchi, *Proc. Natl. Acad. Sci. USA* **1999**, *96*, 9112 – 9117.
[6] J. Taunton, J. L. Collins, S. L. Schreiber, *J. Am. Chem. Soc.* **1996**, *118*, 10412 – 10422.
[7] D. S. Tan, M. A. Foley, B. R. Stockwell, M. D. Shair, S. L. Schreiber, *J. Am. Chem. Soc.* **1999**, *121*, 9073 – 9087.
[8] N. Kanoh, S. Kumashiro, S. Simizu, H. Osada, Y. Kondoh, S. Hatakeyama, H. Tashiro, *Angew. Chem.* **2003**, *115*, 5742 – 5745; *Angew. Chem. Int. Ed.* **2003**, *42*, 5584 – 5587.
[9] Preliminary studies of the photochemical degradation of aryl diazirine in solution have been reported: a) J. Brunner, H. Senn, F. M. Richards, *J. Biol. Chem.* **1980**, *255*, 3313 – 3318; b) M. Nassal, *J. Am. Chem. Soc.* **1984**, *106*, 7540 – 7545; c) M. Platz, A. S. Admasu, S. Kwiatkowski, P. J. Crocker, N. Imai, D. S. Watt, *Bioconjugate Chem.* **1991**, *2*, 337 – 341.
[10] N. Kanoh, K. Honda, A. Asami, T. Amemiya, Y. Kondoh, S. Hatakeyama, H. Tashiro, H. Osada, unpublished results.
[11] R. E. Handschumacher, M. W. Harding, J. Rice, R. J. Druggge, D. W. Speicher, *Science* **1984**, *226*, 544 – 546.
[12] a) N. A. Cacalano, W. L. Cleveland, B. F. Erlanger, *J. Immunol. Methods* **1989**, *118*, 257 – 263; b) N. A. Cacalano, B.-X. Chen, W. L. Cleveland, B. F. Erlanger, *Proc. Natl. Acad. Sci. USA* **1992**, *89*, 4353 – 4357.
[13] a) M. K. Eberle, F. Nuninger, *J. Org. Chem.* **1992**, *57*, 2689 – 2691; b) P. J. Belshaw, D. M. Spener, G. R. Crabtree, S. L. Schreiber, *Chem. Biol.* **1996**, *3*, 731 – 738.
[14] a) S. L. Schreiber, *Science* **1991**, *251*, 283 – 287; b) S. L. Schreiber, *Cell* **1992**, *70*, 365 – 368.

Nanostructure Synthesis

Synthesis of Ultrathin Zinc Nanowires and Nanotubes by Vapor Transport**

*Xiaogang Wen, Yueping Fang, and Shihe Yang**

One of the most important challenges in the synthesis of nanowire materials is the control of size and morphology.[1,2] With regards to metallic nanowires, most studies have so far concentrated on gold and silver nanowires,[3–6] while less has been reported about their zinc counterparts. Ultrathin zinc wires are expected to display intriguing properties, such as metal–insulator transitions and 1D superconductivity. The magnetoresistance and thermopower of zinc-nanowire composites in insulating matrices were studied by Wu and coworkers,[7] who found that zinc nanowires with a diameter of 15 nm are metallic, whereas smaller nanowires show weak 1D localization with resistivity proportional to $T^{-1/2}$. The thermopower of zinc nanowires with a diameter of 4 nm was found to saturate at −130 μV/K. However, the structural details of the embedded zinc nanowires have not been investigated. Zinc nanowires may also be a good template to form 1D nanostructures of other important materials, such as ZnO, ZnS, and Cu.[8,9] Zinc nanowires and nanotubes with core/shell structures of Zn/ZnO and Zn/ZnS were usually prepared from ZnO[10–12] or ZnS[13–15] as precursors by a vapor–solid (VS) process. Recently, Peng et al. reported the synthesis of zinc nanofibers with diameters of 50–200 nm by evaporation of pure zinc powders.[16] Also, zinc nanowires have been prepared by electrochemical etching in HF solution.[17] Until now, however, the synthesis of discrete, ultrathin (< 10 nm) zinc nanowires and nanotubes had not been reported, although 6-nm-wide ZnO nanobelts have been described recently.[18] Herein, and to the best of our knowledge, we report the first synthesis of discrete zinc nanowires and nanotubes, with diameters of several nanometers, by a VS process using zinc foil as the precursor. The key to our success is the use of H_2O and NH_3 as molecular directing agents.

To synthesize zinc nanowires, the evaporation temperature was fixed at 900 °C, as lower temperatures (below 750 °C) failed to yield any zinc-based products. Figure 1 a shows an X-ray diffraction (XRD) pattern of as-prepared zinc nanowires. All of the observed signals for the sample match very well with those of hexagonal zinc ($a = 2.665$, $c = 4.947$ Å,

[*] X. Wen, Dr. Y. Fang, Prof. S. Yang
Department of Chemistry
Institute of NanoScience and Technology
The Hong Kong University of Science and Technology
Clear Water Bay, Kowloon, Hong Kong (China)
Fax: (+852) 2358-1594
E-mail: chsyang@ust.hk

[**] We are grateful to the Research Grant Council of Hong Kong and the Chemistry Department of the Hong Kong University of Science and Technology for supporting this research. S.Y. thanks the Hong Kong Young Scholar Cooperation Research Foundation of NSFC.

Supporting information for this article is available on the WWW under http://www.angewandte.org or from the author.

  DOI: 10.1002/anie.200500438

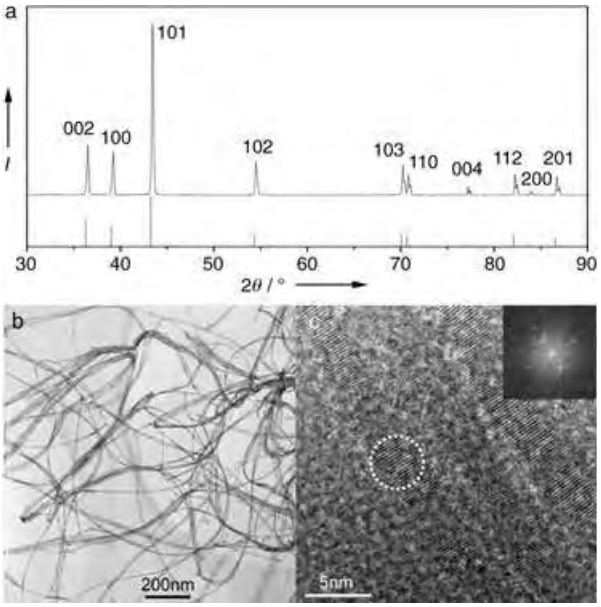

Figure 1. a) XRD pattern of the zinc nanowires prepared by the vapor-transport method, b) a typical TEM image of zinc nanowires prepared in an NH_3 atmosphere, and c) HRTEM image of three parallel zinc nanowires (the inset shows the corresponding FFT pattern of the sample indicated by the white dotted circle in the main panel). The zinc nanowires were deposited at 190–250 °C.

obtained from the JCPDS 04-0831 card), which indicates that the nanowires consist predominantly of pure zinc. Shown in Figure 1 b is a typical transmission electron microscopy (TEM) image of the zinc nanowires deposited over a temperature range of 190–250 °C, with a flow of N_2 of 20 sccm (standard cubic centimeters per minute) for carrying NH_3 (with a trace amount of residual water, $H_2O/NH_3 \approx 1{:}20$). The zinc nanowires have a uniform diameter of 3–8 nm (average diameter ≈ 5 nm) along its entire length, which is up to tens of micrometers. Some of the nanowires are bundled together. Figure 1 c shows a high-resolution TEM (HRTEM) image of three parallel zinc nanowires. The nanowires are 3–4 nm in diameter with excellent uniformity. Clear fringes perpendicular to the nanowire axis can be seen with an interplanar spacing of 0.25 nm in accordance with the distance between the (002) crystal planes, which suggests that the zinc nanowires grow along the [001] direction, that is, along the direction of the *c* axis of hexagonal zinc. This observation is also reflected in the fast Fourier transform (FFT) pattern (inset, Figure 1 c) of the area indicated by a white dotted circle in the main panel.

The products deposited in regions of different temperature of the furnace have different sizes and morphologies, as demonstrated by their TEM images (see the Supporting Information). The products formed in the 200 °C region are uniform, ultrathin nanowires with a diameter of 3–8 nm. In the 150 °C region, although thin nanowires of several nanometers in diameter can still be found, much thicker nanowires (50–70 nm) are found abundantly in a more twisted form. Finally, when the deposition temperature is 100 °C, the nanowires become even thicker (90–100 nm in diameter) and, moreover, these twisted nanowires are tangled together to form a network structure. Note that although the nanowires thicken as the deposition temperature decreases, they all have a pure hexagonal structure based on XRD and energy dispersive X-ray (EDX) analyses. Oxidized surface layers (ZnO) were not identified in these nanowires by HRTEM.

When the ammonia solution was replaced by pure water, ultrathin zinc nanotubes, rather than nanowires, were obtained as shown in Figure 2. In this experiment, the water

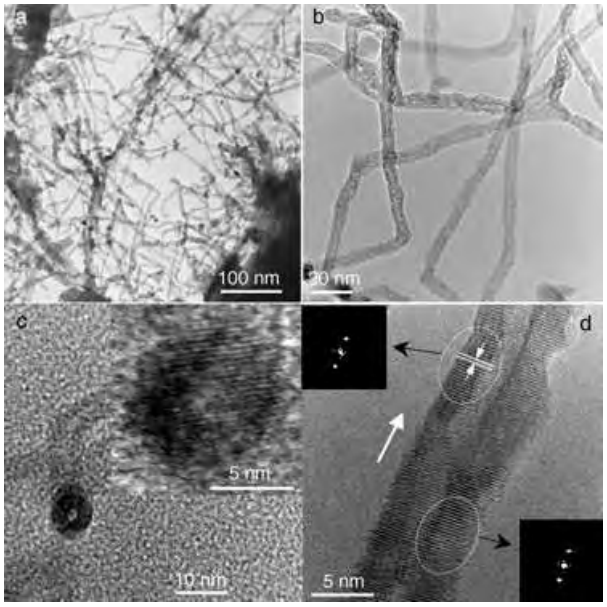

Figure 2. TEM images of zinc nanotubes synthesized in a water-vapor atmosphere. a) Low magnification, b) higher magnification, c) cross-sectional view of a tube end (the inset shows a HRTEM image), and d) HRTEM image of a single zinc nanotube (the insets show the FFT patterns from regions enclosed by the white dashed ellipsoids in the main panel).

vapor was transported into the reaction tube by N_2 through a sealed water bubble aeration setup. Figure 2 a is a low-magnification TEM image of the as-prepared zinc nanotubes, which have a uniform diameter (5–8 nm) along their length (several hundred nanometers to several micrometers) and are mostly open-ended. A higher magnification TEM image is shown in Figure 2 b and reveals the tubular structure more clearly. The inner diameters of the nanotubes are about 1–2 nm and the wall thicknesses are about 2–3 nm. The nanotubes are not very smooth on either the inner or outer surfaces. Although the 1D structure is generally tubelike, the zinc tubes are not completely continuous and the inner channels are often blocked. Figure 2 c highlights the end of a single nanotube so that the cross section can be seen directly. The nanotube appears to have a circular cross section; the diameter of the inner tube is 1.5 nm and the wall thickness is 3.0 nm. From the HRTEM image of the tip of the zinc nanotube in the inset of Figure 2 c, well-defined fringes with a spacing of approximately 0.27 nm can be seen and correspond to double the spacing between the (110) crystal planes ($d_{110} = 0.133$ nm). Consequently, the cross-sectional plane of the nanotube is the *ab* plane of hexagonal zinc, which suggests

that the growth direction of the nanotube is [001], similar to that for the zinc nanowires. Figure 2d shows a higher magnification HRTEM image of a single zinc nanotube. The tubelike structure is seen more clearly, and fringes spaced by approximately 0.25 nm are found to lie perpendicular to the tube axis, which confirms the [001] growth direction of the nanotube. As can be seen from the inset of Figure 2d, the FFTs of both side walls (enclosed by white dotted ellipsoids in the main panel) display the same spotted pattern and indicate the same crystal structure with the length of the nanotube extending along the [001] direction.

When only pure N_2 was used as the carrier gas, zinc nanowires could not be obtained. Instead, most of the products were well-defined polyhedral microparticles and XRD data indicate that the products are still pure zinc (see the Supporting Information). The microparticles deposited on an aluminum-foil substrate have a uniform size of 3–5 μm. Higher magnification scanning electron microscopy (SEM) images indicate that the particles have faceted morphologies that range from hexagonal columns (major) to polyhedra (minor; see the Supporting Information).

For comparison, the vapor–liquid–solid (VLS) approach was also explored to synthesize zinc nanowires. A small piece of lead foil (placed in the high-temperature region together with the zinc foils) was chosen as a catalyst as it has an appropriate melting point (325 °C). N_2/NH_3 was used as the carrier gas, while the other conditions were kept the same. Indeed, zinc nanowires could also be produced by the VLS process as shown in Figure 3. Most of the nanowires are

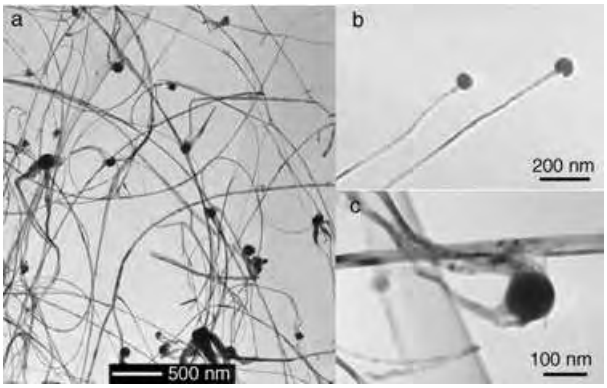

Figure 3. Zinc nanowires prepared by the VLS process. a) A typical TEM image, b) at higher magnification, and c) at even higher magnification to show that several zinc nanowires grow from one catalytic lead nanoparticle.

capped by a nanoparticle on their tips (see Figure 3a), as expected for the VLS process. The tips can be seen more clearly in Figure 3b. EDX analysis confirmed that the nanoparticles comprise lead and that the nanowires consist purely of zinc. Interestingly, the diameter of the zinc nanowires here (15–25 nm), although a little larger than the diameter of the nanowires prepared by the VS method, is much smaller than that of the lead nanoparticles (50–60 nm). The fact that thin zinc nanowires can also be formed on large lead nanodroplets by the VLS process is perhaps because of the confining effect of ammonia. In some cases, several zinc nanowires share a common, relatively large catalytic nanoparticle ($\approx$100 nm; Figure 3c), which suggests that this nanoparticle can provide nucleation sites for the growth of several nanowires simultaneously. The zinc nanowires prepared by the VLS method are obtained in a higher yield than those prepared without the lead catalyst, but they are less uniform and have a larger diameter probably as a result of the non-uniform and large sizes of the lead nanoparticles.

Presumably, the formation of the zinc nanowires in the absence of a catalyst is through a vapor–solid (VS) process. The zinc precursor was evaporated at high temperature (900 °C), and the vapor was transferred to the deposition region (200 °C) by carrier gas. On the basis of the data presented above, the size and morphology of the products are mainly controlled by the temperature of evaporation and deposition, and the composition of the carrier gas. A higher evaporation temperature ensures the formation of a sufficient density of zinc atoms or clusters for nucleation as well as a large temperature gradient favorable for the growth of zinc nanowires. At higher deposition temperatures the growth is relatively slow, whereas at lower temperatures the growth is faster. These temperature effects, when considered together with appropriate compositions of carrier gas, can be exploited so that ultrathin nanowires can be synthesized at high temperatures and thicker nanowires at low temperatures.

Here, the carrier gas appears to be the most important factor and is, in fact, essential to controlling the synthesis of the nanowires. The coordination of NH_3 and H_2O molecules to zinc atoms and clusters at the temperature region in which the nanowire deposition occurs plays a particularly important role. In this way, they act as capping agents to promote anisotropic growth of the nanowires. Specifically, the preferential adsorption of NH_3 and H_2O on the surfaces of the zinc nanowire, other than at the tips, has the effect of restraining the radial, but not the axial, growth so that 1D growth is facilitated. It is not surprising that such a molecularly directed growth yields nanowires that are much thinner than those from the VLS process. For the synthesis of zinc nanotubes in a water-vapor atmosphere, water clusters form much more easily through hydrogen-bonding interactions than ammonia clusters in the deposition region and so may act as templates for the nucleation of zinc. Such a zinc-shell structure that is supported by a core of water clusters may eventually evolve into a tubelike structure with open ends as a result of morphological developments of the water-cluster template (Scheme 1). The soft and dynamic nature of the water-cluster

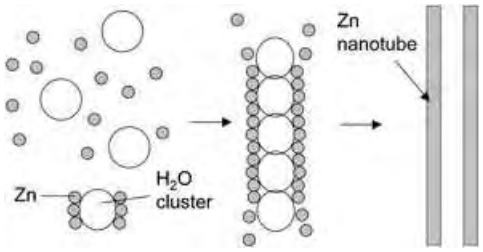

Scheme 1. A schematic representation of a possible mechanism for the formation of zinc nanotubes in the presence of water vapor.

template may explain the observed imperfect structure of the zinc nanotubes. A clearer understanding of the growth mechanisms of the nanowires and nanotubes requires more-detailed studies.

In summary, ultrathin zinc nanowires and nanotubes have been synthesized by both VS and VLS processes with pure zinc. The composition of the carrier gas is the key to controlling the size and morphology of the nanoproducts. Zinc nanowire crystals with diameters as small as 3 nm (average diameter ≈ 5 nm) could be synthesized in an ammonia atmosphere. Furthermore, when water vapor was used instead of ammonia, zinc nanotubes were obtained that are characterized by an inner diameter of 1–2 nm and a wall thickness of 2–3 nm. Our study highlights the essential role of small polar molecules, the adsorption of which modifies the kinetics of crystal growth and thus directs the 1D growth of zinc. Ultrathin metallic nanowires and nanotubes, with sizes that approach the Fermi wavelength, offer new opportunities to explore the effects of size on the transport and photonic properties of these materials and promise a wide range of applications in nanotechnology.

Experimental Section

The experimental setup consisted of a horizontal tube furnace (120 × 10 cm), a quartz tube (100 × 5 cm), and a gas-flow control system. Zinc foils (10 × 10 × 0.1 mm^3; 99.9% purity, Aldrich) were washed with absolute ethanol twice before loading onto a quartz substrate, which was positioned at the end of the quartz tube. A piece of aluminum foil or a quartz slide was positioned at the opening end of the quartz tube to serve as a product deposition substrate. The quartz tube was then mounted in the middle of the tube furnace. A flow of high-purity nitrogen (> 99.995%) was introduced into the quartz tube through a sealed container containing a diluted aqueous solution of ammonia (6.0 M) or pure water at a fast rate (about 200 sccm) for 40 min to remove air from the system. Afterwards, the N_2 flow was adjusted to 20 sccm and the tube furnace was heated to 900 °C at a rate of 30 °C min^{-1}. After heating at this temperature for 5 h, the system was allowed to cool unaided to room temperature and black products were obtained. XRD analyses were carried out on a Philips PW 1830 X-ray diffractometer with a 1.5405-Å $Cu_{K\alpha}$ rotating anode point source operated at 40 kV and 40 mA. Kβ radiation was eliminated with a nickel filter. TEM measurements were performed on Philips CM20 and JEOL 2010F transmission electron microscopes with an accelerating voltage of 200 kV. SEM images were observed with a JEOL 6300F microscope at an accelerating voltage of 15 kV.

Received: February 5, 2005
Published online: May 4, 2005

Keywords: high-temperature chemistry · nanostructures · synthesis design · zinc

[1] X. F. Duan, C. M. Lieber, *Adv. Mater.* **2000**, *12*, 298.
[2] Z. L. Wang, *Nanowires and Nanobelts: Materials, Properties, and Devices*, Kluwer Academic/Plenum Publishers, Boston, **2003**.
[3] Y. G. Sun, B. Gates, B. Mayers, Y. N. Xia, *Nano Lett.* **2003**, *3*, 955.
[4] X. Y. Zhang, L. D. Zhang, Y. Lei, L. X. Zhao, Y. Q. Mao, *J. Mater. Chem.* **2001**, *11*, 1732.
[5] J. K. N. Mbindyo, B. D. Reiss, B. R. Martin, C. D. Keating, M. J. Natan, T. E. Mallouk, *Adv. Mater.* **2001**, *13*, 249.
[6] B. H. Hong, S. C. Bae, C. W. Lee, S. Jeong, K. S. Kim, *Science* **2001**, *294*, 348.
[7] J. P. Heremans, C. M. Thrush, D. T. Morelli, M. C. Wu, *Phys. Rev. Lett.* **2003**, *91*, 076804.
[8] Q. Li, C. R. Wang, *Chem. Phys. Lett.* **2003**, *375*, 525.
[9] Q. Li, K. W. Kwong, D. Ozkaya, D. J. H. Cockayne, *Phys. Rev. Lett.* **2004**, *92*, 186102.
[10] Y. F. Yan, P. Liu, M. J. Romero, M. M. Al-Jassim, *J. Appl. Phys.* **2003**, *93*, 4807.
[11] X. Y. Kong, Y. Ding, Z. L. Wang, *J. Phys. Chem. B* **2004**, *108*, 570.
[12] J. Y. Li, X. L. Chen, *Solid State Commun.* **2004**, *131*, 769.
[13] Y. W. Wang, L. D. Zhang, G. W. Meng, C. H. Liang, G. Z. Wang, S. H. Sun, *Chem. Commun.* **2001**, 2632.
[14] Y. C. Zhu, Y. Bando, Y. Uemura, *Chem. Commun.* **2003**, 836.
[15] J. Q. Hu, Q. Li, X. M. Meng, C. S. Lee, S. T. Lee, *Chem. Mater.* **2003**, *15*, 305.
[16] X. S. Peng, L. D. Zhang, G. W. Meng, X. Y. Yuan, Y. Lin, Y. T. Tian, *J. Phys. D* **2003**, *36*, L35.
[17] S. S. Chang, S. O. Yoon, H. J. Park, A. Sakai, *Mater. Lett.* **2002**, *53*, 432.
[18] X. D. Wang, Y. Ding, C. J. Summers, Z. L. Wang, *J. Phys. Chem. B* **2004**, *108*, 8773.

Photocatalysis

Visible-Light-Induced H_2 Evolution from an Aqueous Solution Containing Sulfide and Sulfite over a ZnS–$CuInS_2$–$AgInS_2$ Solid-Solution Photocatalyst**

*Issei Tsuji, Hideki Kato, and Akihiko Kudo**

The photocatalytic splitting of water to generate H_2 and O_2 has attracted attention as a clean energy system. An important feature of this system is that it does not require complicated devices: the photocatalysts are simply placed in water, irradiated with sunlight, and then hydrogen is produced by a photocatalytic reaction. This water-splitting reaction does not depend on fossil fuels, and is therefore an ideal method to produce clean hydrogen fuel. The reaction is also attractive from the viewpoint of achieving an artificial

[*] I. Tsuji, H. Kato, Prof. A. Kudo
Department of Applied Chemistry
Faculty of Science
Tokyo University of Science
1-3 Kagurazaka, Shinjuku-ku, Tokyo 162-8601 (Japan)
Fax: (+81) 33235-2214
E-mail: a-kudo@rs.kagu.tus.ac.jp
Prof. A. Kudo
Core Research for Evolutional Science and Technology
Japan Science and Technology Agency (CREST, JST)
4-1-8 Honcho, Kawaguchi-shi, Saitama 332-001 (Japan)

[**] This work was supported by Core Research for Evolutional Science and Technology (CREST), a Grant-in-Aid for the Priority Area Research (No. 417) from the Ministry of Education, Culture, Science, and Technology, and the Tokyo Ohka Foundation for the Promotion of Science and Technology.

 DOI: 10.1002/anie.200500314

photosynthesis, which converts light into chemical energy. Many active photocatalysts for splitting water under UV irradiation have been reported. In particular, the NiO-loaded $NaTaO_3$:La photocatalyst showed extremely high activity, and the quantum yield amounted to 56% at 270 nm.[1] However, photocatalysts with wide band gaps (3 eV or above) do not absorb visible light, which is a large part of the solar spectrum. It is indispensable to develop highly active photocatalysts with a visible-light response.

A Pt-loaded CdS photocatalyst showed high activity for the evolution of hydrogen from aqueous solutions containing S^{2-} and SO_3^{2-} ions as sacrificial electron donors, under visible-light irradiation, even though most sulfide photocatalysts are unstable during the water-splitting reaction.[2–4] The sacrificial reagents make up half of the water-splitting reaction and they are routinely used as a test to make sure that the photocatalytic materials can reduce H_2O to H_2. Sacrificial electron donors that irreversibly consume photogenerated holes may promote hydrogen evolution. If the reaction could be turned into a practical application for the production of hydrogen gas from by-products such as hydrogen sulfide and sulfur dioxide, which are emitted in hydrogenation and flue-gas desulfurization processes at chemical plants, it would be especially interesting in light of current energy and environmental concerns.[5,6]

Photocatalysts driven by visible light that show high activity for hydrogen evolution, with the exception of the Pt-loaded CdS photocatalyst, have not been investigated until recently. We have succeeded in developing several photocatalysts that are driven by visible light by doping transition-metal ions such as Ni^{2+} and Cu^{2+}, as well as Pb^{2+} into ZnS, which is a highly active photocatalyst for hydrogen evolution under UV/Vis irradiation, even without the presence of a Pt co-catalyst.[7–11] Specifically, Ni- and Cu-doped ZnS photocatalysts showed a high activity for hydrogen evolution without the presence of any co-catalysts, and their apparent quantum yields were 1.3 and 3.7%, respectively, at 420 nm. We also developed solid-solution photocatalysts between ZnS (wide band gap) and $MInS_2$ (M = Cu, Ag; narrow band gap). The energy structures of the solid solutions were controllable by the change in their compositions. At 420 nm, the apparent quantum yields of Pt-loaded $(AgIn)_{0.22}Zn_{1.56}S_2$ (band gap 2.3 eV) and Pt-loaded $(CuIn)_{0.09}Zn_{1.82}S_2$ (band gap 2.3 eV) amounted to 20% and 13%, respectively.[12,13]

We have recently found that the $ZnS–CuInS_2–AgInS_2$ solid solution was a highly active photocatalyst that exhibited an absorption band over a wider wavelength range than $ZnS–AgInS_2$ and $ZnS–CuInS_2$ solid solutions. Herein, we report the evolution of hydrogen over a Ru-loaded $ZnS–CuInS_2–AgInS_2$ solid solution photocatalyst under visible-light irradiation. We also demonstrate hydrogen production under solar-light irradiation (air mass (AM) = 1.5).

Figure 1 shows X-ray diffraction patterns of the previously reported solid solution photocatalysts $(CuIn)_{0.09}Zn_{1.82}S_2$ (**1**) and $(AgIn)_{0.22}Zn_{1.56}S_2$ (**2**) and the solid solution $(CuAg)_{0.15}In_{0.3}Zn_{1.4}S_2$ (**3**). The crystal structure of the solid solution **1** between ZnS and $CuInS_2$ was a zinc-blende, low-temperature phase of ZnS (Figure 1a). The solid solution **2** between ZnS and $AgInS_2$ exhibited the wurtzite structure of a high-temperature phase of ZnS (Figure 1b). For **3**, which can be regarded as a solid solution of three sulfides ($ZnS–AgInS_2–CuInS_2$), diffraction patterns similar to those of both zinc-blende and wurtzite were obtained. The main peaks indicated the presence of zinc blende along with a negligible amount of unidentified impurities. The diffraction peaks of (111) and (222) planes were relatively intensive, thus indicating an anisotropic shape of the powder.

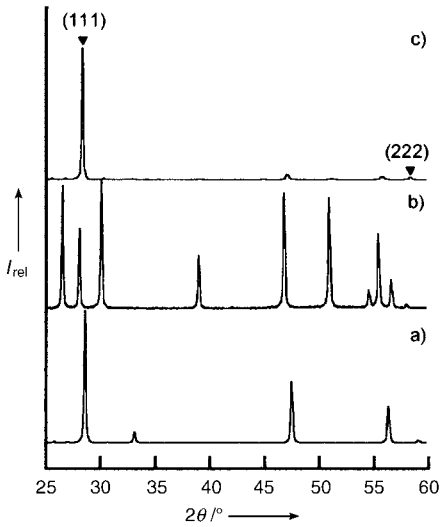

Figure 1. X-ray diffraction patterns (XRD) of the solid solution **1** (a), **2** (b), and **3** (c).

Figure 2 shows SEM images of the solid solution **3**. The small particles were about 200 nm in size (Figure 2a), and the average particle size of the solid solution was relatively small compared with those of the solid-solution photocatalysts **1** and **2** (several micrometers). Some of these small particles were platelike. Extremely large Plate-shaped particles, such as that shown in Figure 2b, were also observed in relatively large numbers. Therefore, we suggest that the anisotropy in

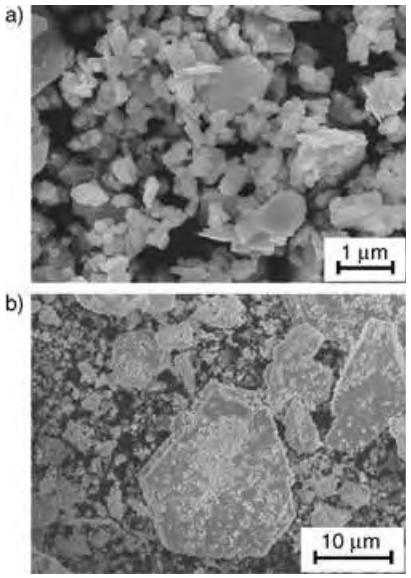

Figure 2. SEM images of solid solution **3**.

the XRD pattern is due to the presence of such particles. The surface area of the solid solution was 3.3 $m^2 g^{-1}$.

Figure 3 shows diffuse reflection spectra of the solid solutions and ZnS. The ZnS photocatalyst with a wide band gap (3.5 eV) had an UV absorption band. Unlike ZnS, the

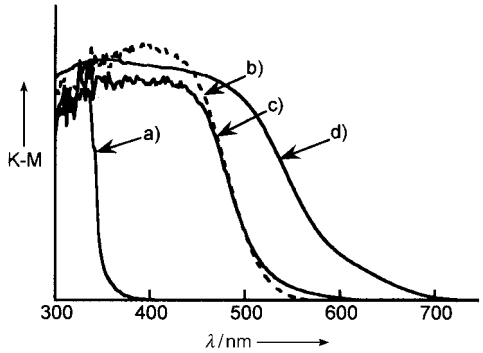

Figure 3. Diffuse reflection spectra of ZnS (a) and the solid solutions **1** (b), **2** (c), and **3** (d). K–M = diffuse reflection spectra converted into absorbance by the Kubelka–Munk method (arbitrary units).

solid solutions of ZnS and $MInS_2$ (M = Cu, Ag) had visible-light absorption bands; those bands with steep edges were due to band-gap transitions. The solid solutions **1** and **2** were able to use visible light up to 500 nm and thus the estimated band-gap energies are 2.4 eV. The absorption edge of the solid solution **3** was at a longer wavelength than those of other solid solutions. The color of the powder of **3** was dark orange. Taking into account the efficient use of visible light in a large part of the solar spectrum, we believe that this solid solution, with its long wavelength absorption band, is an attractive photocatalyst for hydrogen evolution.

When a Ru co-catalyst was loaded, the solid solution **3** effected hydrogen evolution under visible-light irradiation. The rate of hydrogen evolution was extremely high (2.3 mmol h^{-1}) under irradiation from a 300-W Xe lamp with a 420 nm cut-off filter. The optimized photocatalytic activities of the solid solutions **1** and **2** were 0.94 mmol h^{-1} and 1.16 mmol h^{-1}, respectively. The solid solution **3** produced hydrogen more efficiently than the solid solutions **1** and **2**. Vigorous evolution of hydrogen bubbles was observed over the photocatalyst particles irradiated with visible light.

Figure 4 shows H_2 evolution under simulated sunlight irradiation (AM 1.5) from an aqueous solution containing the sacrificial reagents SO_3^{2-} and S^{2-} over a Ru-loaded $(CuAg)_{0.15}In_{0.3}Zn_{1.4}S_2$ (**3**) solid-solution photocatalyst. Even under these conditions, the photocatalyst produced hydrogen gas efficiently. The initial rate of hydrogen evolution was 8.2 L $m^{-2} h^{-1}$, which was estimated from the irradiated area (33 cm^2). Although a slight deactivation was observed during the photocatalytic reaction, the activity remained comparatively stable over 20 h when the reaction solution was replaced periodically with fresh solution. As there were no significant changes in the XRD patterns of the catalyst before and after the reaction, we conclude that the slight deactivation was due to a change in the surface state and/or poisoning by products. The solid solution showed higher activity than

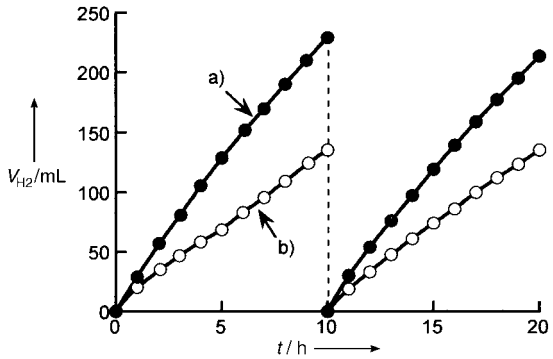

Figure 4. Photocatalytic H_2 evolution from an aqueous K_2SO_3 (0.25 mol L^{-1}) Na_2S (0.35 mol L^{-1}) solution (150 mL) under simulated sunlight irradiation over solid solution photocatalyst **3** loaded with 0.75 wt% Ru (a) and the Pt-black-loaded (2 wt%) CdS photocatalyst (b). Catalyst: 0.3 g; solar simulator: 300-W Xe short arc lamp with an AM-1.5 filter; reaction cell: top-window pyrex cell; irradiated area: 33 cm^2.

the well-known Pt-loaded CdS photocatalyst with wurtzite structure under the same reaction conditions (Figure 4). Its activity was also higher than that of the previously reported Pt-loaded $(AgIn)_{0.22}Zn_{1.56}S_2$ (**2**) solid solution photocatalyst (3.3 L $m^{-2} h^{-1}$).[12]

Figure 5 shows an action spectrum for hydrogen evolution from an aqueous solution containing K_2SO_3 and Na_2S over a Ru-loaded $(CuAg)_{0.15}In_{0.3}Zn_{1.4}S_2$ (**3**) photocatalyst. The onset

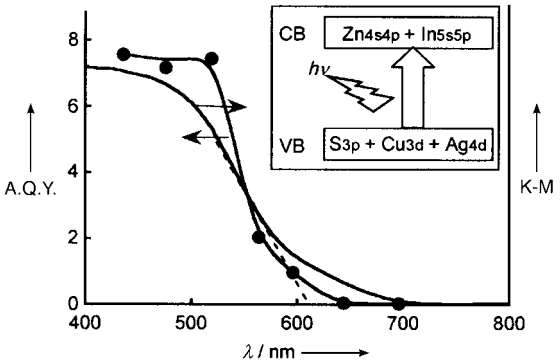

Figure 5. Action spectrum of H_2 evolution from an aqueous K_2SO_3 (0.25 mol L^{-1}) Na_2S (0.35 mol L^{-1}) solution (150 mL) over the solid solution **3** loaded with 0.75 wt% Ru. Catalyst: 0.3 g; light source: 300-W Xe lamp with cut-off and band-pass filters; reaction cell: top-window Pyrex cell. A.Q.Y. = apparent quantum yield. K–M = diffuse reflection spectra converted into absorbance by the Kubelka–Munk method (arbitrary units).

of the action spectrum "hydrogen evolution" agreed approximately with onset of the diffuse reflection spectrum. It was revealed that the visible-light response for hydrogen evolution was due to a band-gap transition between the valence and conduction bands; this band gap and thus the transition could be altered by making a solid solution. The visible-light response might be derived from the contribution of Cu 3d, Ag 4d, and S 3p orbitals to the valence band and that of In 5s5p and Zn 4s4p orbitals to the conduction band, respectively, as

in the cases of the $ZnS–AgInS_2$ and $ZnS–CuInS_2$ solid solutions. Hydrogen did not evolve through absorption of light in the region around 650–700 nm. This result indicates that a visible-light absorption band, which might be due to impurities and defects, was not responsible for the photocatalytic reaction. The comparatively high average quantum yield of 7.4% was obtained under monochromatic irradiation at 440, 480, and 520 nm.

In summary, we report that a $ZnS–CuInS_2–AgInS_2$ solid solution **3** is a highly active photocatalyst for the evolution of hydrogen under visible-light irradiation from an aqueous solution containing sulfide and sulfite. The activity of the solid solution that contained Cu and Ag atoms was higher than that of the previously reported $ZnS–MInS_2$ (M = Cu or Ag) solid solutions **1** and **2**. Although the quantum yield of the $ZnS–CuInS_2–AgInS_2$ solid solution was lower than that of the $ZnS–MInS_2$ (M = Cu or Ag) solid-solution photocatalysts, the former had higher activity when irradiated from a solar simulator. A sulfide photocatalyst that is able to produce hydrogen efficiently, even under solar-light irradiation would be an attractive functional material. Although it has not yet reached the level that it has a practical use, if quantum yields and activities can be further improved, this series of solid solutions could be used in photocatalytic hydrogen production.

Experimental Section

3: An aqueous solution of $Zn(NO_3)_2{\cdot}6H_2O$ (Wako Pure Chemicals; 99.0%), $AgNO_3$ (Tanaka Kikinzoku; 99.8%), and $In(NO_3)_3{\cdot}3.6H_2O$ (Kojundo Chemical; 99.9%) was purged with N_2 gas. An excess ($\approx$10%) of $In(NO_3)_3$, was added to the solution, followed by CuCl, freshly prepared by reduction of $CuCl_2{\cdot}2H_2O$ (Wako Pure Chemicals; 99.0%) with metallic Cu. Purging the reaction mixture with H_2S gas resulted in a grayish brown precipitate. The mixture was stirred for 15 h, washed with deionized water, and dried in air. The obtained powder was sealed in a quartz ampoule together with a small quantity of sulfur (about 1 wt%). The sealed ampoule was evacuated and heated over the course of 20 h to 600 °C and held at this temperature for 2 h. The phase of the product was confirmed by X-ray diffraction (Rigaku; MiniFlex). Surface areas were determined by BET (Brunauer–Emmett–Teller) measurement (Coulter; SA3100). Diffuse reflection spectra were obtained with a UV/Vis/NIR spectrometer (Jasco; Ubest U-570) and were converted from reflection to absorbance by the Kubelka–Munk method. Photocatalyst powders were observed by scanning electron microscopy (JEOL: JSM-6700F).

Photocatalytic reactions were conducted in a gas-closed circulation system. The photocatalyst powder (0.3 g) was dispersed by a magnetic stirrer in an aqueous solution (150 mL) containing K_2SO_3 and Na_2S as electron donors in a pyrex cell with a window on the top. The mixture was irradiated with visible light ($\lambda \geq 420$ nm) through a cut-off filter (HOYA; L42) from a 300-W Xe lamp (ILC technology; CERMAX LX-300). Ru co-catalyst was loaded by a photodeposition method in situ. An appropriate amount of $(NH_4)_2RuCl_6$ (Wako Pure Chemicals) was dissolved in an aqueous K_2SO_3 solution, the photocatalyst powder was added and the aqueous solution was irradiated under visible light for 20–30 min; subsequently, Na_2S was added into the solution. The optimum amount of the co-catalyst was about 0.7 wt%. Hydrogen production was measured by using on-line gas chromatography (Shimadzu; GC-8A, MS-5 A column, TCD, Ar carrier). The apparent quantum yields defined by Equation (1) were measured by using combined band-pass (Kenko) and cut-off (HOYA) filters, and a photodiode (OPHIRA: PD300-UV head and NOVA power monitor).

$$\text{A.Q.Y. } [\%] = \frac{\text{number of reacted electrons}}{\text{number of incident photons}} \times 100 = \frac{\text{number of evolved } H_2 \text{ molecules} \times 2}{\text{number of incident photons}} \times 100 \quad (1)$$

A solar simulator (YAMASHITA DENSO; YSS-80QA) was also used to test the photocatalytic reaction (AM 1.5). In this case, the amount of hydrogen gas evolved was determined by a volumetric measurement.

Received: January 27, 2005
Published online: May 6, 2005

Keywords: green chemistry · heterogeneous catalysis · hydrogen · photocatalysis

[1] H. Kato, K. Asakura, A. Kudo, *J. Am. Chem. Soc.* **2003**, *125*, 3082–3089.
[2] A. W.-H. Mau, C. B. Huang, N. Kakuta, A. J. Bard, *J. Am. Chem. Soc.* **1984**, *106*, 6537.
[3] M. Matsumura, S. Furukawa, Y. Saho, H. Tsubomura, *Phys. Chem.* **1985**, *89*, 1327.
[4] J. F. Reber, M. Rusek, *Phys. Chem.* **1986**, *90*, 824.
[5] S. C. March, L. Borrell, J. Gimenez, R. Simarro, J. M. Andujar, *Int. J. Hydrogen Energy* **1992**, *17*, 683.
[6] C. A. Linkous, T. E. Mingo, N. Z. Muradov, *Int. J. Hydrogen Energy* **1993**, *18*, 203.
[7] J. F. Reber, K. Meier, *J. Phys. Chem.* **1984**, *88*, 5903.
[8] H. Kisch, J. Bucheler, *Bull. Chem. Soc. Jpn.* **1990**, *63*, 2378.
[9] A. Kudo, M. Sekizawa, *Catal. Lett.* **1999**, *58*, 241.
[10] A. Kudo, M. Sekizawa, *Chem. Commun.* **2000**, 1371.
[11] I. Tsuji, A. Kudo, *J. Photochem. Photobiol. A* **2003**, *156*, 249.
[12] I. Tsuji, H. Kato, H. Kobayashi, A. Kudo, *J. Am. Chem. Soc.* **2004**, *126*, 13406.
[13] I. Tsuji, H. Kato, H. Kobayashi, A. Kudo, *J. Phys. Chem. B*, **2005**, *109*, 7323.

Self-Assembly

A Single-Crystal-to-Single-Crystal Transformation Mediated by Argentophilic Forces Converts a Finite Metal Complex into an Infinite Coordination Network**

*Qianli Chu, Dale C. Swenson, and Leonard R. MacGillivray**

Transition-metal ions play a prominent role in mediating chemical reactions, a central paradigm being catalysis.[1] The d orbitals of such ions are sources of directional bonding that organize substrates for stereocontrolled reactions that give molecular and polymeric products that cannot be obtained in the absence of the metal. Whereas a variety of transition-metal ions have been used to mediate chemical reactivity in the liquid phase,[1] such broad applicability to mediate reactivity in the organic solid state, particularly for the well-studied [2+2] photodimerization,[2] has not been realized.[3–8] In addition to forces that assemble molecules into strict geometries for stereocontrolled reactions, such ions can provide properties (e.g. color), and other components (e.g. counterions), that may be altered by the ensuing reaction that occurs within such solids.[4b,8]

Herein, we report the use of a transition-metal ion, in the form of Ag^I,[9] which mediates a [2+2] photodimerization in the solid state. Specifically, argentophilic forces, in the form of Ag···Ag interactions,[10] are used to guide stacking[11] of olefins in the dinuclear complex $[Ag_2(4\text{-stilbz})_4][CO_2CF_3]_2$ (**1**; where 4-stilbz = *trans*-1-(4-pyridyl)-2-(phenyl)ethylene) for a regiocontrolled head-to-head [2+2] photodimerization (Scheme 1). We show that the reaction occurs in 100% yield by a rare single-crystal-to-single-crystal (SCSC) transformation that, in addition to carbon–carbon single-bond making, involves breaking and formation of Ag···Ag and Ag···C interactions, respectively. Remarkably, the formation and breakage of the covalent and noncovalent bonds are accompanied by long-range movement of the Ag^I ions and rotation of the carboxylate ions,[12] which result in the finite dinuclear complex being converted into an infinite, one-dimensional (1D) coordination network. This study represents the first case in which a closed-shell d^{10} metal cation has been used to direct a reaction in the crystalline state.

Interactions between closed-shell d^{10} metal ions have been used to construct supramolecular assemblies[13] that exhibit host–guest, photophysical, and electrical properties.[14] For Ag^I, such Ag···Ag, or argentophilic, forces are evoked at separations < 3.4 Å, although separations up to 3.8 Å have been cited.[14] These separations fall within the distance criterion of Schmidt for a [2+2] a photodimerization in a solid.[2] Moreover, the ability of the Ag^I ion to engage in argentophilic forces, coupled with a tendency of the ion to exhibit linear coordination,[14] prompted us to investigate whether it would be possible to utilize Ag^I ions to guide the stacking of olefins in the solid state for a [2+2] photoreaction.[15]

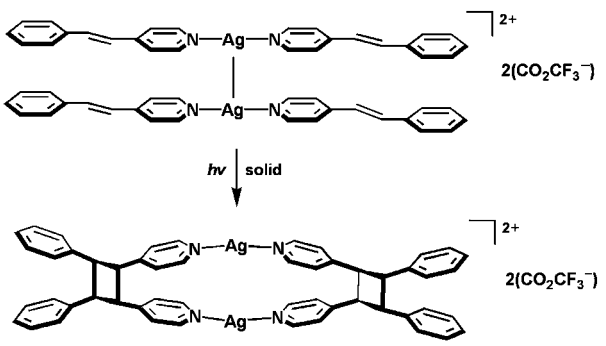

Scheme 1.

Reaction of a solution of $AgCO_2CF_3$ in acetonitrile with 4-stilbz afforded large colorless plates of **1** upon slow evaporation. The formulation of **1** was confirmed by ^{1}H NMR spectroscopy, as well as powder and single-crystal X-ray diffraction data.

Perspective views of **1** are shown in Figure 1. The metal and organic components have assembled to form a dinuclear complex sustained by an Ag···Ag force (Ag···Ag distance: 3.41 Å; Figure 1a).[16] The primary coordination sphere of the Ag^I ion is based on a T-shaped geometry that involves two *transoid* nitrogen atoms of two 4-pyridyl groups of two olefins and a single oxygen atom of a carboxylate ion (Figure 1a, inset). The olefins that span the Ag···Ag interaction lie approximately parallel, the pyridine units participating in offset, face-to-face π–π interactions (pyridine centroid–centroid distances 3.62 Å). The carboxylate group is twisted orthogonal to the stacked olefins such that each $-CF_3$ group points away from the metal complex. As a consequence of the assembly process, the C=C bonds, which are disordered (occupancies: site A 0.89(1); site B 0.11(1)) and adopt a criss-cross arrangement,[17] are separated by 3.82 Å. This distance satisfies the distance criterion for [2+2] photoreaction in a solid.[2] The complex self-assembles to form 1D quadruple π-stacked arrays (Figure 1b), which are canted at 60° (Figure 1c), with neighboring olefins offset and separated by 4.22 Å (C···C distances [Å]: C(21)···C(22)a 4.22, C(22)···C(21)a 4.22, C(21)···C(21)a 3.91, C(22)···C(22)a 4.87; a: $1.5-x$, $0.5-y$, $-z$).

To test whether the olefins are photoactive, either single crystals or a powdered crystalline sample of **1** was exposed to UV radiation (broadband Hg lamp) for 18 h. As shown in Figure 2, a ^{1}H NMR spectrum (solvent: [D$_6$]DMSO) of photoreacted **1** reveals that the olefins reacted to give *rctt*-

[*] Q. Chu, Dr. D. C. Swenson, Prof. L. R. MacGillivray
Department of Chemistry
University of Iowa
Iowa City, IA 52242-1294 (USA)
Fax: (+1) 319-335-1270
E-mail: len-macgillivray@uiowa.edu

[**] We are grateful to the National Science Foundation (CAREER Award, L.R.M., DMR-0133138) for funding. We also acknowledge Research Corporation (Research Innovation Award, L.R.M.) for partial support.

Supporting information for this article is available on the WWW under http://www.angewandte.org or from the author.

 DOI: 10.1002/anie.200500400

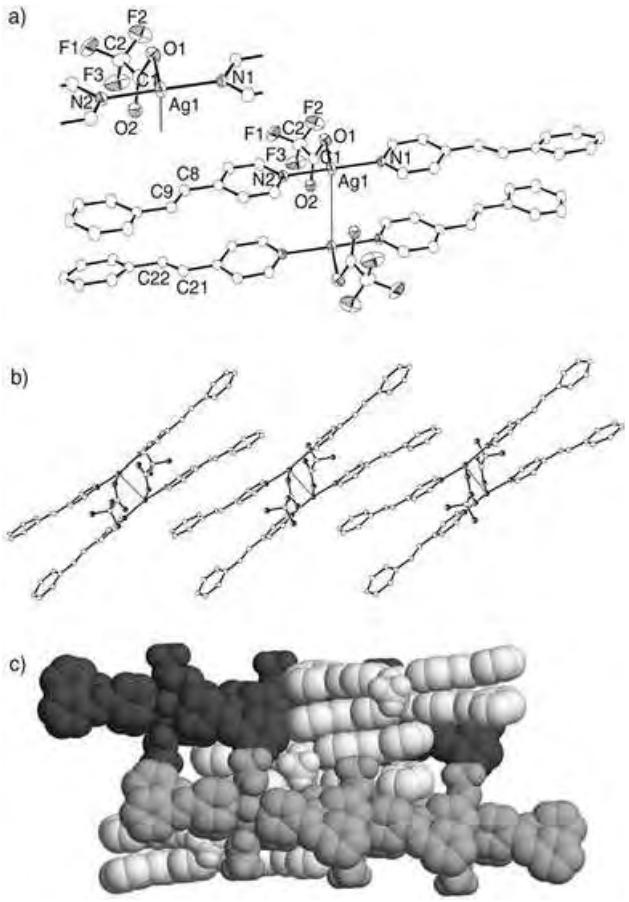

Figure 1. X-ray crystal structure of **1**: a) ORTEP view of the dinuclear assembly. Thermal ellipsoids set at 30 % probability. Inset: coordination environment of the Ag^{I} ion, b) 1D quadruple π-stacked arrays, c) space-filling view of adjacent 1D arrays (each strand is highlighted in different shade of gray). Selected interatomic distances [Å] and angles [°]: Ag1-N1 2.161(3), Ag1-N2 2.149(3), Ag1-O1 2.583(4), C8···C21 3.82, C8···C22 3.79, C9···C21 4.11, C9···C22 4.23; O1-Ag1-N1 94.7(1), N1-Ag1-N2 165.3(1), O1-Ag1-N2 98.1(1).

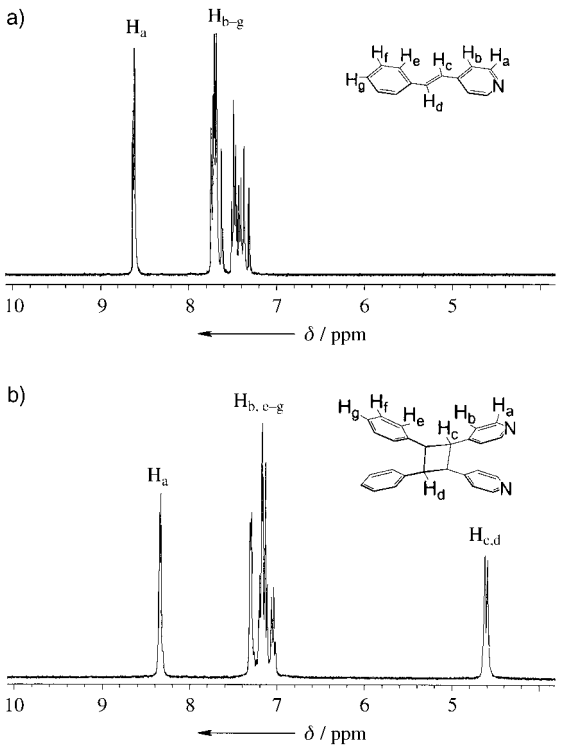

Figure 2. ^{1}H NMR spectra: a) **1** before photoreaction and b) **2** after photoreaction.

1,2-bis(4-pyridyl)-3,4-bis(phenyl)cyclobutane (4-pyr-ph-cb) in 100 % yield. The formation of the photoproduct is shown by the disappearance of the signals of the olefinic protons ($\delta = 7.50$ ppm) and the emergence of signals for the cyclobutane protons ($\delta = 4.60$ ppm). Optical microscopy revealed that the transparency and shape of the single crystals remained intact during the photoreaction, which suggested that the reaction occurred by a SCSC transformation.

An X-ray diffraction analysis of photoreacted **1** confirms that the reaction occurred by a SCSC transformation. As shown in Figure 3, the olefins of **1** reacted to give head-to-head 4-pyr-ph-cb in $[Ag_2(4\text{-pyr-ph-cb})_2][(CO_2CF_3)_2]$ (**2**) in quantitative yield (Figure 3a). The photoproduct adopts two orientations, with the cyclobutane ring of **2** exhibiting site occupancies different than that of the olefins of **1** (occupancies: site A 0.60; site B 0.40). These occupancies are consistent with the C=C bonds of the olefins undergoing a pedal-like motion in **1**[17] prior to the photoreaction.

The generation of 4-pyr-ph-cb is accompanied by major repositioning[12] of the Ag^{I} and carboxylate ions. Specifically, each Ag^{I} ion has moved approximately 1.16 Å (Ag···Ag distance in **2**: 5.73 Å) in a direction approximately parallel to the newly formed C–C bonds,[12a] while each carboxylate ion has undergone an approximate 90° rotation such that each $-CF_3$ group is oriented approximately perpendicular to the pyridyl groups (Figure 3b). Despite such long-range movement and rotation, the Ag–N and Ag–O bonds remain intact. In particular, the nitrogen and oxygen atoms form a trigonal planar coordination geometry around each Ag^{I} ion, with each metal atom lying approximately 0.37 Å out of the plane of the donor atoms.

An important consequence of the movement and rotation of the ions is that Ag···C interactions[18] (Ag···C(phenyl) distances: Ag(1)···C9C 2.63 Å) have formed between each repositioned Ag^{I} ion and a *para*-carbon atom of a phenyl group of a neighboring photoproduct (Figure 3c and inset). These forces link adjacent complexes of **2** to give a linear coordination polymer.[8] The Ag···C forces of the newly formed coordination polymer compare favorably to those networks with aromatics (e.g. cyclophanes) as donor ligands.[18] In the case of **2**, the photodimerization has, in effect, forced the Ag···Ag interactions[10] to break and the Ag···C interactions to form,[18] which, in turn, has resulted in the 1D geometry of the olefins of **1** being captured,[19] through coordination bonds, within the 1D polymer of **2**. To our knowledge, the photoconversion **1** into **2** represents the first case in which a finite metal complex has been transformed into an infinite coordination network in the solid state by a [2+2] photoreaction.[20,21]

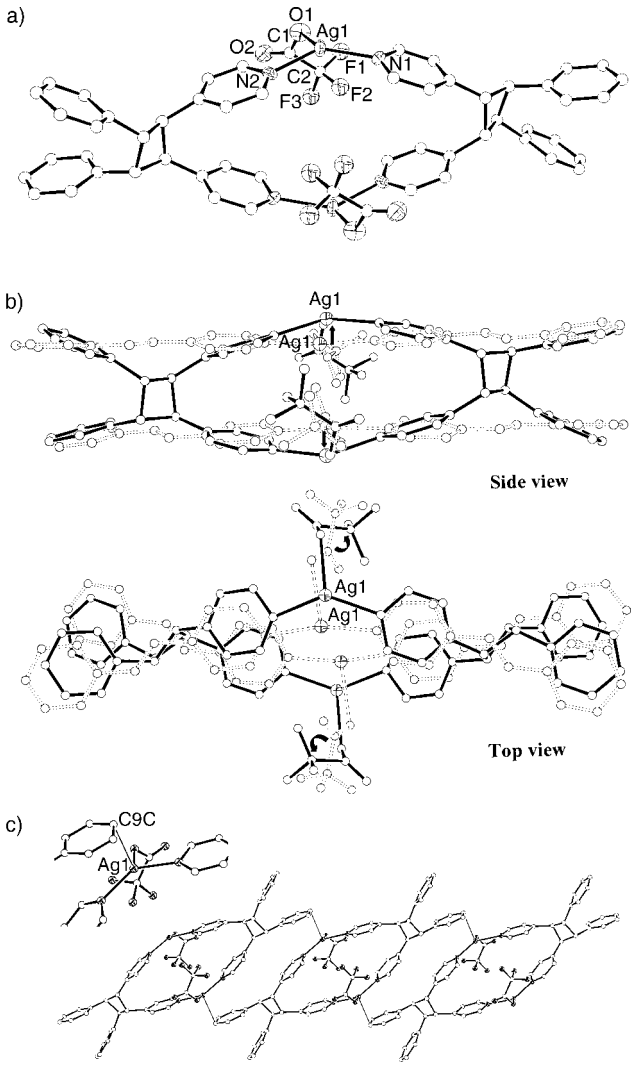

Figure 3. X-ray crystal structure of **2**: a) ORTEP view of the dinuclear assembly, thermal ellipsoids set at 30 % probability. b) overlay views of **2** (solid) and **1** (dashed) (arrows indicate movement of Ag^{I} atoms and carboxylate ions), c) newly formed 1D coordination polymer (inset: coordination environment of the Ag^{I} ion). Selected interatomic distances [Å] and angles [°]: Ag1-N1 2.22(1), Ag1-N2 2.27(1), Ag1-O1 2.44(2); N1-Ag1-N2 136(1), N1-Ag1-O1 112(2), N2-Ag1-O1 104(2).

Herein, we have revealed that argentophilic forces involving Ag^{I} ions can guide the stacking of olefins in the solid state for a regiospecific [2+2] photodimerization. The olefins assembled in a geometry that converts a finite metal complex into an 1D coordination network by a SCSC transformation.[8] Based these observations, we are now determining the reliability of using Ag···Ag interactions to direct reactivity in the solid state and plan to expand the reactants to olefins of increasing structural complexity.[11] That a finite complex can be converted into an infinite network by using a photodimerization and pyridyl units—chemical reactivity and ligands common to organic solid-state chemistry[2,22]—suggests this approach may also provide an entry to solids with properties that may be deliberately modified using photoresponsive building units.[25]

Experimental Section

Preparation of **1**: 4-stilbz was prepared according to a published procedure.[23] $AgCO_2CF_3$ was commercially available. Compound **1** was obtained by evaporation of a solution of 4-stilbz (0.100 g, 0.55 mmol) and $AgCO_2CF_3$ (0.061 g, 0.28 mmol) in acetonitrile (2.0 mL).

Solid-state photoreactions: UV irradiation of either single crystals or powdered crystalline **1** (500 W Hg lamp) over 18 h resulted in 100 % conversion of 4-stilbz to 4-pyr-ph-cb. The irradiation experiments were performed by placing either single crystals or finely ground samples of **1** between two pyrex plates and turning the sample in 9 h intervals to ensure uniform irradiation. ^{1}H NMR for **1** (300 MHz, [D$_6$]DMSO): $\delta = 8.62$ (dd, 4H), 7.50 (m, 18H); ^{1}H NMR for **2** (300 MHz, [D$_6$]DMSO): $\delta = 8.44$ (dd, 4H), 7.30 (m, 14H), 4.60 ppm (m, 4H).

X-ray crystallography: Crystal data for **1**: monoclinic, C2/c, $a =$ 22.048(2), $b = 13.156(2)$, $c = 17.9566(2)$ Å, $\beta = 98.44(1)°$, $V =$ 5152(1) Å^3, $Z = 4$, $\rho_{calcd} = 1.50$ g cm^{-3}, $R_1 = 0.051$ for 3965 reflections with $I > 2\sigma(I)$. Crystal data for **2**: monoclinic, *C*2/*c*, $a = 21.544(2)$, $b =$ 13.548(1), $c = 17.694(2)$ Å, $\beta = 99.00(1)°$, $V = 5101(1)$ Å^3, $Z = 4$, $\rho_{calcd} = 1.52$ g cm^{-3}, $R_1 = 0.096$ for 1977 reflections with $I > 2\sigma(I)$. All crystal data were measured on a Nonius KappaCCD single-crystal X-ray diffractometer. All non-hydrogen atoms of **1** were refined with anisotropic thermal parameters except the atoms of the low-occupancy site of the disordered olefin. These atoms were given isotropic thermal parameters that were restrained to be similar to the U_{iso} of the corresponding atom on the high-occupancy site of the disordered ligand. The conformation of the low-occupancy site was restrained to be the same as that of the high-occupancy site. The occupancies refined to 0.89(1) (A) and 0.11(1) (B). The carboxylate ion displayed highly anisotropic thermal motion and was modeled as disordered for the final cycles of refinement. The disordered sites were restrained to have the same conformation and corresponding atoms were given the same anisotropic thermal parameters (i.e. U(O1) = U(O1′), U(C1) = U(C1′)…). The occupancies refined to 0.59(1) (A) and 0.41(1) (B). Upon reaction, the single crystal of **2** fractured into several highly mosaic single-crystal domains. The data from one of these single-crystal domains were successfully indexed and integrated. An examination of zonal precession syntheses indicated minimal interference from other single-crystal domains. Owing to the high degree of mosaicity, data above 37.5° 2θ were excluded from the refinement as there were essentially no data above background levels in this shell. The reaction product was disordered (the cyclobutane can form in one of two orientations yielding two chemically equivalent complexes with partial occupancy) and the occupancies converged to and were fixed at 0.60 (A) to 0.40 (B). The limited data set limited the refinement model. The Ag and O atoms, as well as the N atoms, were refined with anisotropic thermal parameters while all other atoms were refined with isotropic thermal parameters. The pyridyl rings of the photoproduct were treated as rigid groups. The equivalent N atoms (N1A, N1B…) from each disordered site were found in close proximity and were given the same anisotropic thermal parameters. For the remaining atoms, chemically equivalent disorder atom sites (C1A, C1B; C2A, C2B…) were given the same isotropic thermal parameter. The carboxylate groups were disordered and were restrained to exhibit the same conformation. The thermal parameters for O1 were restrained by the rigid bond restraint to the thermal parameters of the Ag atom for the final cycles of refinement. The bond lengths and angles described above refer to the major occupied sites. All crystallographic calculations were conducted using SHELXL-97.[24] CCDC-261658 (**1**) and CCDC-261660 (**2**) contains the supplementary crystallographic data for this paper. These data can be obtained free of charge

from the Cambridge Crystallographic Data Centre via www.ccdc.cam.ac.uk/data_request/cif.

Received: February 2, 2005
Published online: May 4, 2005

Keywords: [2+2] photodimerization · self-assembly · silver · single-crystal reactions · topochemistry

[1] For recent reviews, see: a) A. Ajamian, J. L. Gleason, *Angew. Chem.* **2004**, *116*, 3842; *Angew. Chem. Int. Ed.* **2004**, *43*, 3754; b) P. G. Cozzi, *Chem. Soc. Rev.* **2004**, *33*, 410; c) B. C. G. Söderberg, *Coord. Chem. Rev.* **2004**, *248*, 1085; d) J. J. Becker, M. R. Gagne, *Acc. Chem. Res.* **2004**, *37*, 798.

[2] a) G. M. J. Schmidt, *Pure Appl. Chem.* **1971**, *27*, 647; b) V. Ramamurthy, K. Venkatesan, *Chem. Rev.* **1987**, *87*, 43.

[3] D. Braga, F. Grepioni, *Angew. Chem.* **2004**, *116*, 4092; *Angew. Chem. Int. Ed.* **2004**, *43*, 4002.

[4] [2+2] photodimerizations mediated by metals in the solid state, see: a) A. Michaelides, S. Skoulika, M. G. Siskos, *Chem. Commun.* **2004**, 2418; b) G. S. Papaefstathiou, Z. Zhong, L. Geng, L. R. MacGillivray, *J. Am. Chem. Soc.* **2004**, *126*, 9158; c) C. R. Theocharis, A. M. Clark, S. E. Hopkin, P. Jones, A. C. Perryman, F. Usanga, *Mol. Cryst. Liq. Cryst. Incorporating Nonlinear Opt.* **1988**, *156*, 85; d) F. D. Lewis, S. L. Quillen, P. D. Hale, J. D. Oxman, *J. Am. Chem. Soc.* **1988**, *110*, 1261; e) N. W. Alcock, P. de Meester, P. T. J. Kemp, *J. Chem. Soc. Perkin Trans. 2* **1979**, 921.

[5] γ-Ray-induced dimerization mediated by a metal in the solid state, see: T. H. Cho, B. Chaudhuri, B. B. Snider, B. M. Foxman, *Chem. Commun.* **1996**, 1337.

[6] γ-Ray-induced trimerization mediated by a metal in the solid state, see: G. C. D. de Delgado, K. A. Wheeler, B. B. Snider, B. M. Foxman, *Angew. Chem.* **1991**, *103*, 438; *Angew. Chem. Int. Ed. Engl.* **1991**, *30*, 420.

[7] Polymerizations of organic groups mediated by metals in the solid state, see: a) M. J. Vela, V. Buchholz, V. Enkelmann, B. B. Snider, B. M. Foxman, *Chem. Commun.* **2000**, 2225; b) M. J. Vela, B. B. Snider, B. M. Foxman, *Chem. Mater.* **1998**, *10*, 3167; c) M. J. Moloney, B. M. Foxman, *Inorg. Chim. Acta* **1995**, *229*, 323; d) C. B. Case, B. M. Foxman, *Inorg. Chim. Acta* **1994**, *222*, 339; e) J. S. Brodkin, B. M. Foxman, *J. Chem. Soc. Chem. Commun.* **1991**, 1073; f) G. Cao, T. E. Mallouk, *J. Solid State Chem.* **1991**, *94*, 59; g) B. Tieke, G. Wegner, *Makromol. Chem. Rapid Commun.* **1981**, *2*, 543; h) N. H. Agnew, M. E. Brown, *J. Polym. Sci. Part A.* **1971**, *9*, 2561.

[8] Thermal polymerization of a metal complex in the solid state that results in a 1D coordination network, see: K. Cheng, B. M. Foxman, *J. Am. Chem. Soc.* **1977**, *99*, 8102.

[9] Use of Ag^I to mediate organic transformations in solution, see: a) Y. Cui, C. He, *Angew. Chem.* **2004**, *116*, 4306; *Angew. Chem. Int. Ed.* **2004**, *43*, 4210; b) Y. Cui, C. He, *J. Am. Chem. Soc.* **2003**, *125*, 16202; c) N. S. Josephsohn, M. L. Snapper, A. H. Hoveyda, *J. Am. Chem. Soc.* **2003**, *125*, 4018; d) J. Cirakovi, T. G. Driver, K. A. Woerpel, *J. Am. Chem. Soc.* **2002**, *124*, 9370.

[10] P. Pyykkö, *Chem. Rev.* **1997**, *97*, 597.

[11] a) T. Caronna, R. Liantonio, T. A. Logothetis, P. Metrangolo, T. Pilati, G. Resnati, *J. Am. Chem. Soc.* **2004**, *126*, 4500; b) X. Gao, T. Friščić, L. R. MacGillivray, *Angew. Chem.* **2004**, *116*, 234; *Angew. Chem. Int. Ed.* **2004**, *43*, 232; c) N. Shan, W. Jones, *Tetrahedron Lett.* **2003**, *44*, 3687; d) D. G. Amirakis, M. A. Garcia-Garibay, S. J. Rowan, J. F. Stoddart, A. J. P. White, D. J. Williams, *Angew. Chem.* **2001**, *113*, 4386; *Angew. Chem. Int. Ed.* **2001**, *40*, 4256; e) L. R. MacGillivray, J. L. Reid, J. A. Ripmeester, *J. Am. Chem. Soc.* **2000**, *122*, 7817; f) Y. Ito, B. Borecka, J. Trotter, J. R. Scheffer, *Tetrahedron Lett.* **1995**, *36*, 6083.

[12] Recent studies on movement in molecular solids, see: a) K. Hanson, N. Calin, D. Burgaris, M. Scancella, S. C. Sevov, *J. Am. Chem. Soc.* **2004**, *126*, 10502; b) D. N. Dybtsev, H. Chun, K. Kim, *Angew. Chem.* **2004**, *116*, 5143; *Angew. Chem. Int. Ed.* **2004**, *43*, 5033; c) R. Matsuda, R. Kitaura, S. Kitagawa, Y. Kubota, T. C. Kobayashi, S. Horike, M. Takata, *J. Am. Chem. Soc.* **2004**, *126*, 14063; d) Z. Dominguez, T. A. V Khuong, D. H. Sanrame, M. A. Garcia-Garibay, *J. Am. Chem. Soc.* **2003**, *125*, 8827; e) J. L. Atwood, L. J. Barbour, A. Jerga, B. L. Schottel, *Science* **2002**, *298*, 1000; f) M. D. Hollingsworth, M. L. Peterson, K. L. Pate, B. D. Dinkelmeyer, M. E. Brown, *J. Am. Chem. Soc.* **2002**, *124*, 2094.

[13] M. Barboiu, G. Vaughan, N. Kyritsakas, J.-M. Lehn, *Chem. Eur. J.* **2003**, *9*, 763.

[14] a) O.-S. Jung, Y. J. Kim, Y.-A Lee, S. W. Kang, S. N. Choi, *Cryst. Growth Des.* **2004**, *4*, 23; b) M.-C. Brandys, R. J. Puddephatt, *Chem. Commun.* **2001**, 1508; c) M. Munakata, G. L. Ning, Y. Suenaga, T. Kuroda-Sowa, M. Maekawa, T. Ohta, *Angew. Chem.* **2000**, *112*, 4729; *Angew. Chem. Int. Ed.* **2000**, *39*, 4555; d) S. V. Lindeman, R. Rathore, J. K. Kochi, *Inorg. Chem.* **2000**, *39*, 5707; e) A. J. Blake, N. R. Champness, S. S. M. Chung, W.-S. Li, M. Schröder, *Chem. Commun.* **1997**, 1675.

[15] Earlier work of Schröder et al.[14e] and Puddephatt et al.[14b] suggest that the Ag^I ion can mediate a [2+2] photodimerization in solution.

[16] For a similar complex, see: H. Adams, N. A. Bailey, D. W. Bruce, S. C. Davis, D. A. Dunmur, P. D. Hempstead, S. A. Hudson, S. Thorpe, *J. Mater. Chem.* **1992**, *2*, 395.

[17] a) S. Ohba, H. Hosomi, Y. Ito, *J. Am. Chem. Soc.* **2001**, *123*, 6349; b) J. Harada, K. Ogawa, *J. Am. Chem. Soc.* **2001**, *123*, 10844.

[18] a) M. Munakata, L. P. Wu, G. L. Ning, *Coord. Chem. Rev.* **2000**, *198*, 171; b) A. N. Khlobystov, A. J. Blake, N. R. Champness, D. A. Lemenovskii, A. G. Majouga, N. V. Zyk, M. Schröder, *Coord. Chem. Rev.* **2001**, *222*, 155; c) A. P. Cote, G. K. H. Shimizu, *Inorg. Chem.* **2004**, *43*, 6663.

[19] a) J. D. Ranford, J. J. Vittal, D. Wu, *Angew. Chem.* **1998**, *110*, 1159; *Angew. Chem. Int. Ed.* **1998**, *37*, 114; b) Z. Xu, S. Lee, Y.-H. Kiang, A. B. Mallik, N. Tsomaia, K. T. Mueller, *Adv. Mater.* **2001**, *13*, 637; c) P. Brunet, E. Dewers, T. Maris, G. D. Enright, J. D. Wuest, *Angew. Chem.* **2003**, *115*, 5461; *Angew. Chem. Int. Ed.* **2003**, *42*, 5303.

[20] The reactivity of **1** can be regarded a photochemical equivalent of $NiBr_2[P(CH_2CH_2CN)_3]_2$ in which thermal polymerization results in a change in coordination geometry of the metal and formation of a 1D coordination polymer.[8]

[21] For photopolymerizations of organic solids involving olefins, see: M. Hasegawa, *Chem. Rev.* **1983**, *83*, 507.

[22] a) S. R. Seidel, P. J. Stang, *Acc. Chem. Res.* **2002**, *35*, 972; b) M. Fujita, K. Umemoto, M. Yoshizawa, N. Fujita, T. Kusukawa, K. Biradha, *Chem. Commun.* **2001**, 509; c) B. J. Holliday, C. A. Mirkin, *Angew. Chem.* **2001**, *113*, 2076; *Angew. Chem. Int. Ed.* **2001**, *40*, 202; d) D. L. Caulder, K. N. Raymond, *Acc. Chem. Res.* **1999**, *32*, 975.

[23] S. M. N. Efange, R. H. Michelson, R. P. Remmel, R. J. Boudreau, A. K. Dutta, A. Freshler, *J. Med. Chem.* **1990**, *33*, 3133.

[24] G. M. Sheldrick, SHELXL-97, Program for Refinement of Crystal Structure, University of Göttingen, Göttingen, Germany, **1997**.

[25] Note added in proof April 14, 2005: Since the submission of this manuscript a SCSC transformation mediated by Zn(ii) ions has been described, N. L. Toh, M. Nagarathinman, J. J. Vittal, *Angew. Chem.* **2005**, *117*, 2205; *Angew. Chem. Int. Ed.* **2005**, *44*, 2237.

Nanostructures

The Role of Precursor-Decomposition Kinetics in Silicon-Nanowire Synthesis in Organic Solvents**

*Doh C. Lee, Tobias Hanrath, and Brian A. Korgel**

The "bottom-up" chemical synthesis of semiconductor nanowires has been developed as an alternative strategy to conventional lithographic patterning for the preparation of functional nanostructures suitable for applications such as logic gates,[1] memory devices,[2] light-emitting devices,[3] sensors,[4] and photonic circuits.[5,6] Nanowire growth by the vapor–liquid–solid (VLS) mechanism has been very successful for a variety of different materials, including Group IV, Group II–VI, and Group III–V semiconductors,[7–12] and metal oxides.[13] These nanowires are in many ways like macromolecules, as they can be suspended in solvents and deposited on substrates or mixed with polymers as composites. Ideally, the aim is to synthesize nanowires by solution chemistry and move away from slow and expensive gas-phase chemical vapor deposition (CVD).

The colloidal synthesis of Si nanomaterials is extremely challenging and represents to some extent a "holy grail" in solution-based nanomaterials chemistry. In 2000, we showed that crystalline Si nanowires could be synthesized in solution by using Au nanocrystals as seeds to lower the crystallization barrier and promote crystalline nanowire growth.[14] By pressurizing the organic solvent, reaction temperatures exceeding the Au/Si eutectic temperature (363 °C) could be reached[15] and "VLS-like" nanowire growth could be promoted. We refer to this nanowire-growth mechanism as supercritical fluid–liquid–solid (SFLS) synthesis.[16]

In hindsight, we were very lucky to stumble across diphenylsilane as a suitable Si precursor for the synthesis. Very little is known about the chemistry of the relevant silanes (that is, aryl- and alkyl-substituted silanes and trisilane) in pressurized solvents at high temperature, and as we show herein, other potential precursors that would appear to be obvious choices fail completely. In fact, we have found that the SFLS process is very sensitive to the precursor-decomposition kinetics, and careful tuning of this process is required to optimize the nanowire quality and prevent unwanted homogeneous Si-particle nucleation. Herein, we report on the relationship between the silane decomposition chemistry and the quality of the Si nanowires produced by SFLS by using Au-nanocrystal seeds.

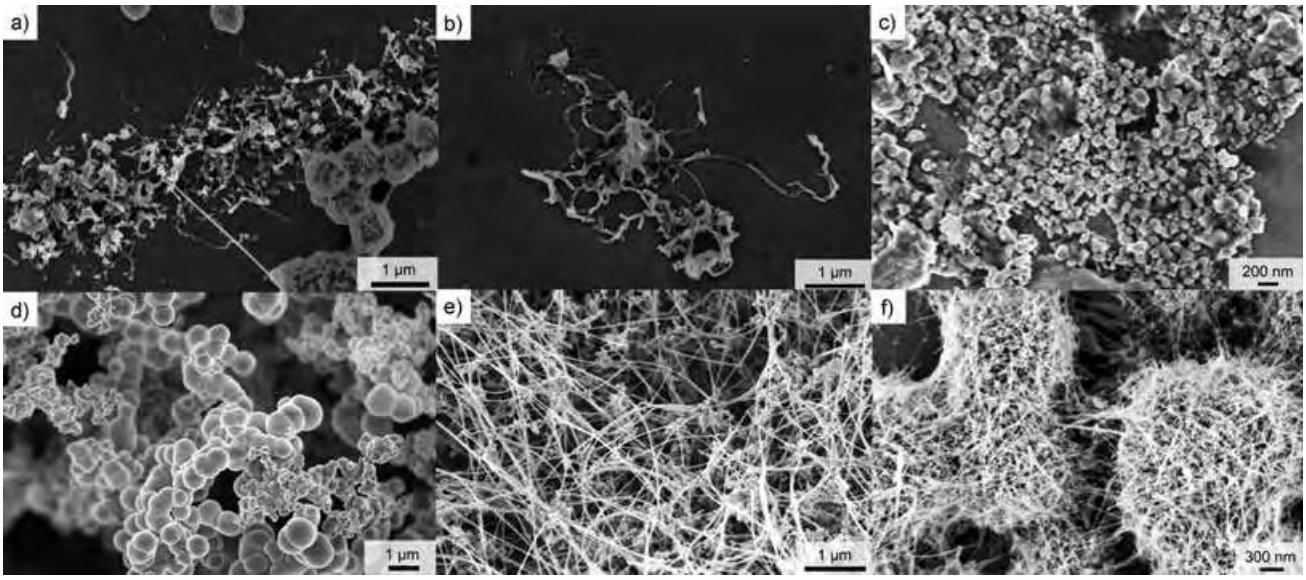

Figure 1. HRSEM images of the reaction products obtained from a) octylsilane, b) diethylsilane, c) tetraethylsilane, d) trisilane, e) phenylsilane, and f) diphenylsilane injected into hexane at 450 °C, approximately 7.2 MPa, and a concentration of 350 mM. The reactions were carried out for 5 min with a Au/Si molar ratio of 1:1000.

Figure 1 shows scanning electron microscopy (SEM) images of the solid product obtained from six different Si precursors injected into anhydrous hexane at 450 °C and 7.2 MPa with dodecanethiol-coated Au nanocrystals with an average diameter of approximately 4 nm. The silane concentration in each case was 350 mM with a Au/Si molar ratio of 1:1000, and the reactions were carried out for 5 min. The

[*] D. C. Lee, T. Hanrath, Prof. B. A. Korgel
Department of Chemical Engineering
Texas Materials Institute
Center for Nano- and Molecular Science and Technology
The University of Texas at Austin
Austin, TX 78712-1062 (USA)
Fax: (+1) 512-471-7060
E-mail: korgel@mail.che.utexas.edu

[**] This work was supported financially by the National Science Foundation, the Welch Foundation, and the Advanced Materials Research Center in collaboration with International SEMATECH. We acknowledge fruitful discussions with A. E. Saunders and thank J. P. Zhou for assistance with the high-resolution transmission electron microscopy.

 DOI: 10.1002/anie.200463001

images in Figure 1 show the products obtained from the alkyl silanes octylsilane, diethylsilane, and tetraethylsilane (Figure 1 a–c, respectively). In all cases, the nanowire was formed in extremely low yield or not at all. Only the monosubstituted alkyl silane, octylsilane, produced a measurable amount of crystalline Si nanowires, but in miniscule yield and with large amounts of oligomeric silicon- and carbon-containing impurities. The multisubstituted alkyl silanes, diethylsilane and tetraethylsilane, did not produce any crystalline nanowires, only curly amorphous wires in the case of diethylsilane and amorphous particulates in the case of tetraethylsilane. It appears that the Si–H bond is relatively reactive and labile, but homolytic cleavage of the alkyl Si–C bond is too slow to provide sufficient Si atoms for the Au-seed particles to sustain crystalline nanowire growth.

Trisilane is very reactive and decomposes rapidly at temperatures above 350 °C to produce silicon in nearly 100 % yield.[17] However, trisilane does not form Si nanowires in the presence of the Au nanocrystals. The reaction produces micrometer-sized amorphous Si colloids (Figure 1 d); surprisingly, the same product was obtained in the absence of Au nanocrystals.[18] Unlike the alkyl or aryl silane precursors, trisilane can undergo thermolysis through heterogeneous insertion at hydrogen-terminated sites on Si surfaces, which is a process that can lead to rapid particle formation once amorphous Si colloids have nucleated.[19] Furthermore, the Si–Si bonds in trisilane are very stable and do not dissociate at the typical SFLS reaction temperatures of approximately 450–500 °C. Therefore, dehydrogenation of trisilane at these reaction temperatures leaves a "bare" Si trimer, which appears not to dissolve in the Au-nanocrystal seeds. Trisilane can also be deposited on the sidewalls of any nanowires that have not fully formed to give rise to a thick amorphous coating. The alkyl silanes are not sufficiently reactive to produce high-quality crystalline nanowires by Au-seeded SFLS and trisilane is too reactive, which leads to the homogeneous particle formation of amorphous Si structures.

Aryl silanes exhibit suitable reactivity for the formation of high-quality nanowires. Figure 1 e,f shows the Si products obtained from phenylsilane and diphenylsilane: Both precursors yield large quantities of Si nanowires as the primary reaction product. As shown in Figure 2, the nanowires formed by using diphenylsilane as the precursor are crystalline with a diamond cubic structure and few defects. The alkyl- and aryl-substituted organosilanes exhibit qualitatively different reactivities at approximately 450 °C. The Si–C bonds in the alkyl-substituted silanes have lower dissociation enthalpies than those in the aryl-substituted silanes;[20,21] however, the aryl-substituted silanes can undergo disproportionation reactions of the type shown in Scheme 1, and therefore the aryl group is a more reactive substituent under the nanowire growth conditions.[22,23] Although the exact details of the disproportionation reactions have not been well-studied,[24] the mechanism appears to be associative and involves the exchange of a hydrogen atom and a phenyl group. The resonance effect of the benzene ring lowers the activation energy for the disproportionation reaction, whereas the alkyl group does not give rise to a resonance effect.[23] The alkyl-substituted silanes can only decompose by homolytic dissociation, which is very slow at these temperatures; however, the aryl silanes undergo a series

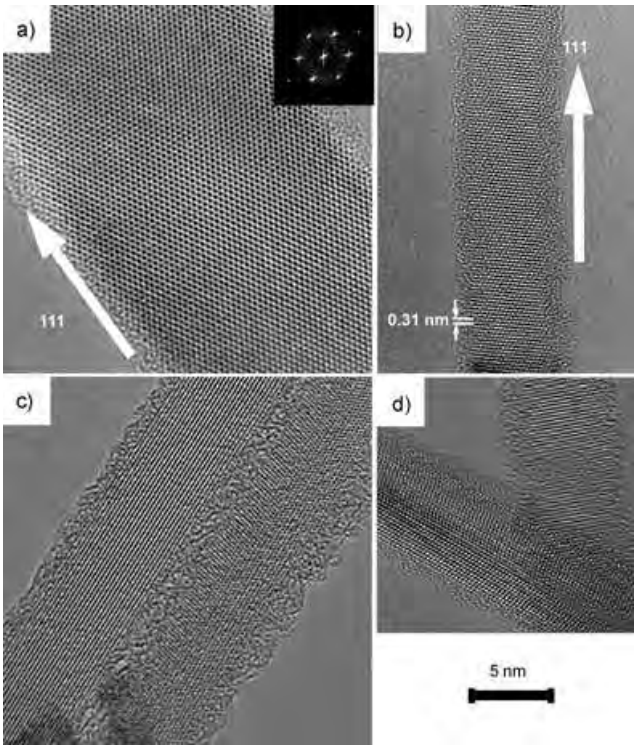

Figure 2. High-resolution TEM (HRTEM) images of Si nanowires produced by SFLS from Au nanocrystals and diphenylsilane at 450 °C. Under these conditions, SFLS yields predominantly ⟨111⟩-oriented nanowires, as shown in (a) and (b); however, limited numbers of ⟨110⟩- and ⟨211⟩-oriented nanowires are also found with diameters smaller than 10 nm (c, d). The fast Fourier transforms (FFTs) of the image in (a) are shown in the inset.

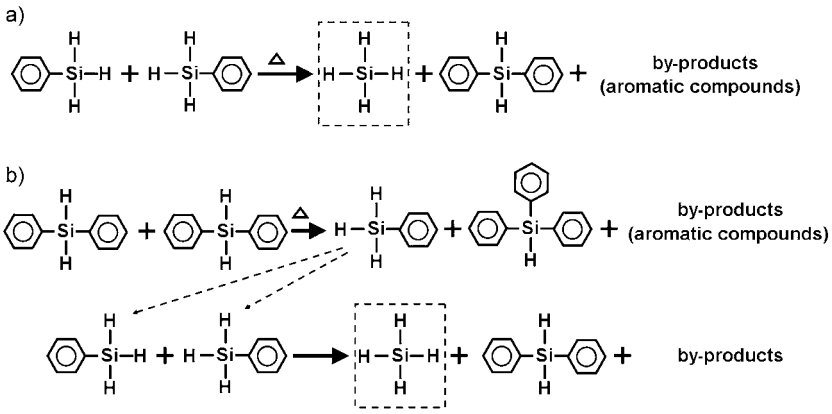

Scheme 1. Bimolecular disproportionation of a) phenylsilane and b) diphenylsilane. Silane decomposes at temperatures above approximately 350 °C to produce Si atoms.

of disproportionation reactions that yield silane and tetraphenylsilane as the final reaction products. Tetraphenylsilane is very stable and does not decompose below 500 °C,[24,25] and silane decomposes to silicon at approximately 350 °C.[26] On the basis of this proposed mechanism, silane generated in situ during the reaction promotes nanowire growth.

As expected from the proposed disproportionation mechanism for the decomposition of the aryl silanes, reactants with higher phenyl substitution give the product in lower yields. As shown in Scheme 1, phenylsilane requires only one disproportionation step to form silane, in contrast to diphenylsilane, which requires two consecutive reactions. Phenylsilane was found to lead to higher product yields than diphenylsilane. High-resolution SEM (HRSEM) analysis of the Si nanowires produced from diphenylsilane at 500 °C also showed that a significantly greater amount of carbonaceous by-products formed relative to those produced from phenylsilane. Perhaps because of its additional phenyl moiety, diphenylsilane exhibits an increased likelihood to form carbonaceous by-products as well as nanowires. For both diphenylsilane and phenylsilane, there appears to be a "threshold" concentration (approximately 120 mM for phenylsilane) below which little or no nanowire product is formed.

Figure 3 shows HRSEM images of the reaction products synthesized from phenylsilane (Figure 3a–c) and diphenylsilane (Figure 3d–e) at different reaction temperatures between 400 and 500 °C. When the synthesis was performed at 350 °C—just below the bulk-phase Si/Au eutectic temperature (363 °C)—from either phenylsilane or diphenylsilane, no significant quantities of solid product were yielded (the results are not shown). In the reactions carried out at just above the eutectic temperature (400 °C), nanowires did not form and only particulate materials that were poorly defined in structure, and so could not be clearly observed by HRSEM, were formed. This result is in stark contrast to the Au-nanocrystal-promoted SFLS synthesis of Ge nanowires, which are routinely grown at 385 °C in very high quality.[27] Since the Au/Ge system exhibits a similar eutectic temperature to that of the Au/Si system (361 °C),[27] similar results for the Si nanowires would be expected. The significantly lower growth temperature of the Ge nanowires appears to be directly related to the higher reactivity of the aryl germanes relative to the aryl silanes; therefore, the slow precursor-degradation kinetics appear to limit the Si-nanowire growth at temperatures just above the Au/Si eutectic temperature. The reaction temperature must reach approximately 450 °C

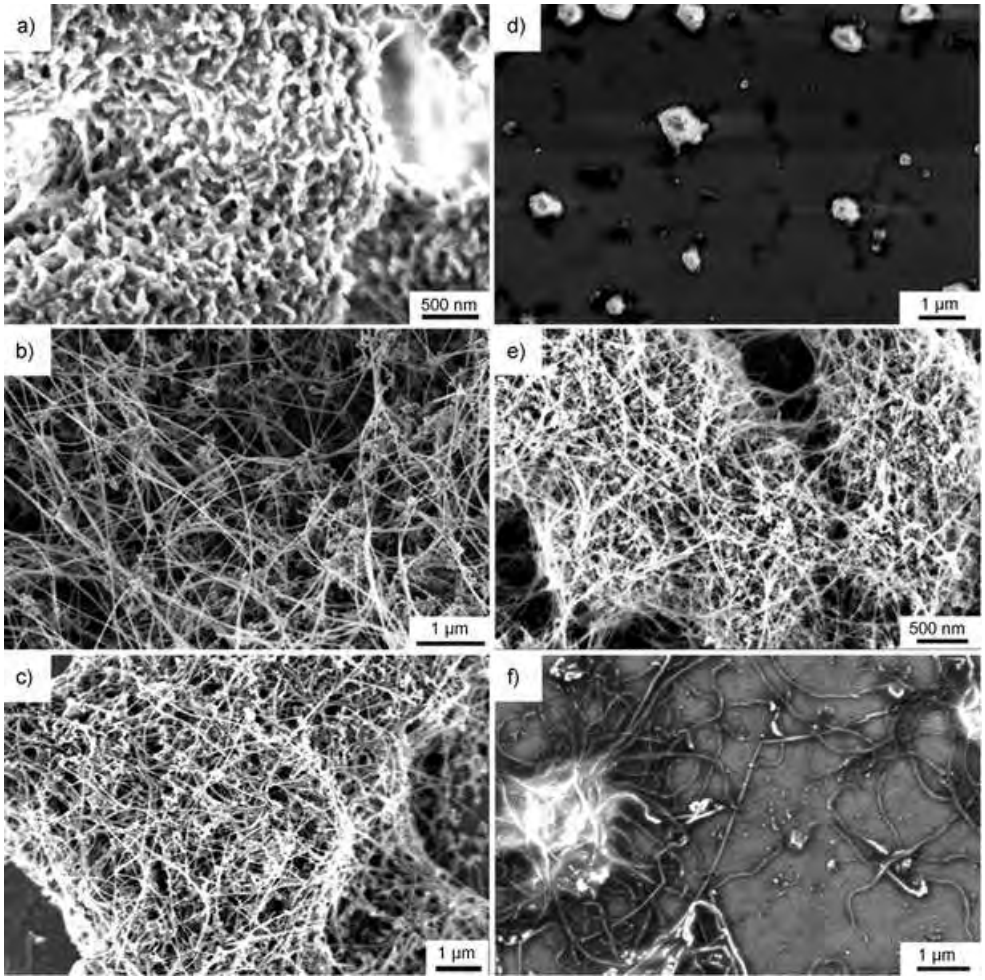

Figure 3. HRSEM images of the Si product obtained from phenylsilane (a–c) or diphenylsilane (d–f) in hexane at 400 °C (a, d), at 450 °C (b, e), and at 500 °C (c, f). For both precursors, reaction temperatures of at least 450 °C are required to form nanowires.

for high-quality crystalline Si nanowires to be produced. However, further increases in reaction temperature do not improve the nanowire growth: Phenylsilane produces nanowires at 500 °C but with a relatively high proportion of carbon-containing amorphous Si by-products, and reactions at temperatures higher than 500 °C result in significant pyrolysis of hexane.

As shown in Figures 2 and 4, ⟨111⟩ is the predominant growth direction for Si nanowires synthesized at 450 °C from

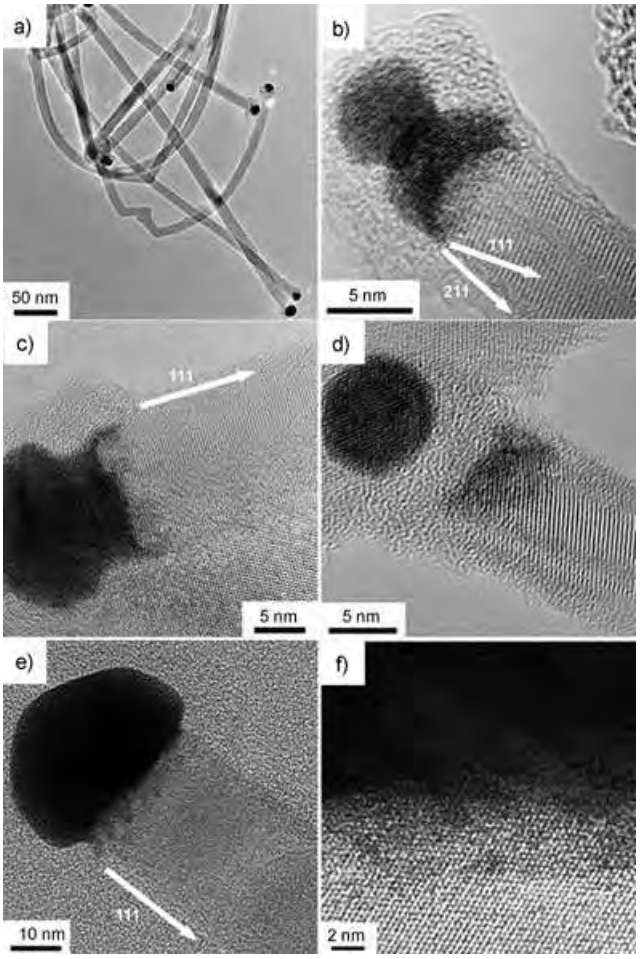

Figure 4. HRTEM images of Au-seed particles at Si-nanowire tips. a) HRTEM image of several nanowires with Au tips. b) The "curved" Au/Si interface of a ⟨211⟩-oriented nanowire. c) Au tip at the end of a ⟨111⟩-oriented Si nanowire. d) A nanowire that was exposed for two months to air that has oxidized at the Au/Si interface and the nanowire surface. e) Au tip at the end of a ⟨111⟩-oriented Si nanowire. f) The interface at the Au tip in (e) at a greater magnification of 1 000 000×.

Au nanocrystals and either phenylsilane or diphenylsilane. A few nanowires could be found with ⟨110⟩ or ⟨112⟩ growth directions. The preference for the ⟨111⟩ growth direction in the Si nanowires is consistent with Si whiskers grown in the gas phase by Au-seeded VLS at similar reaction temperatures.[28] Transmission electron microscopy (TEM) imaging of the Au/Si tip of the nanowires grown by SFLS reveals a flat, atomically abrupt interface with a Si (111) surface. Nanowires with ⟨112⟩ or ⟨110⟩ growth directions do not exhibit this flat cross-sectional interface (Figure 4b) but possess "curved" interfaces instead that appear to undergo reconstruction to form flat Si (111)/Au interfaces at the tip, as observed by Wu et al.[29] for Si nanowires grown by Au-seeded VLS with ⟨110⟩ orientation. The influence of the liquid–crystal interface and the fact that the Si (111)/Au interface exhibits the lowest free energy relative to other possible interfaces has been well-established from early work on Si whiskers.[28] The stability of the Si (111)/Au interface is further confirmed by our observations of a migrating Si/Au interface when it is exposed to the electron beam in TEM. Long exposure time of the Si/Au interface to the electron beam results in the generation of sufficient thermal energy for the Au interface to migrate approximately 14 nm into the nanowire (Figure 5). The

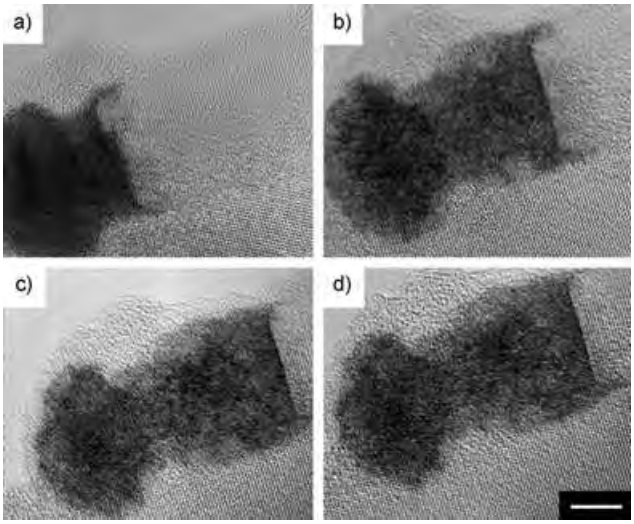

Figure 5. Au tip at the end of a Si nanowire exposed to a converged electron beam at 200 kV after a) 0, b) 1.5, c) 3, and d) 4.5 min. The Au interface migrates into the Si nanowire until it penetrates by approximately 14 nm. The nanowire maintains the sharp {111} interface at the Au/Si tip. Scale bar: 5 nm.

interface remains sharp and atomically smooth despite this progression. Compare this interfacial structure to the curved Au/SiO_2 interface that forms at the tip of a Si nanowire after two months of exposure to air (Figure 4d). The difference in the interfacial energy of the Au/SiO_2 interface relative to the Au/Si interface is reflected in the qualitatively different structures formed.

In summary, aryl silanes are effective precursors for the growth of crystalline Si nanowires by Au-nanocrystal-seeded SFLS, whereas alkyl silanes and trisilane are not. The quality of the Si product is related directly to the decomposition chemistry of the precursor: The precursor must be sufficiently reactive to saturate the Au-nanocrystal seeds with Si atoms and promote nanowire growth, but not so reactive that homogeneous particle nucleation and sidewall deposition overcome the metal-particle-directed crystallization. To put these findings into perspective, low-melting-point metals, such as In and Bi, have recently been used successfully as seeds to lower the metal/semiconductor eutectic temperature to below 300 °C and enable conventional solvents to be used

in the VLS method for the growth of nanowires composed of materials such as GaAs,[30] InN,[31] and CdSe.[32] For silicon nanowires, germanium nanowires, and carbon nanotubes,[33] however, the use of low-melting-point metals to lower the eutectic temperature is not a viable option because of the limited precursor reactivity for Group IV materials—even silane barely decomposes at approximately 350 °C.[21] Therefore, despite the technical challenges of high-pressure and high-temperature conditions, SFLS has an important role as a general synthetic technique for the synthesis of Group IV semiconductor nanowires.

Experimental Section

All silicon precursors (phenylsilane (Aldrich), diphenylsilane (Gelest), octylsilane (Gelest), diethylsilane (Aldrich), tetraethylsilane (Adlrich), and trisilane (Gelest)) were stored in an inert nitrogen atmosphere and were used without purification. The alkanethiol-capped Au nanocrystals were prepared according to established methods.[34] Stock solutions of the Si precursors and Au nanocrystals were prepared in anhydrous hexane in a nitrogen-filled glove box prior to injection into the reactor system.

Nanowire synthesis: The reactor system consisted of a 10-mL Ti grade-2 reaction cell, pressurized by using an HPLC pump and heated in a brass heating block.[27] The temperature was monitored with a thermocouple (Omega) that was placed on the wall of the heating block connected to a temperature controller. To help with sample collection after the reaction had been completed, an oxidized Si wafer placed inside the reactor was used as a deposition substrate (6.3 × 1.0 cm). The reactor cell was filled with anhydrous, oxygen-free hexane and sealed in a nitrogen-purged glove box. The reactor cell was connected to the high-pressure assembly and heated to the desired reaction temperature at a pressure of approximately 5.5 MPa before injection of the silane/Au nanocrystal mixture into the cell from a 500-μL HPLC injection loop. All the reactions were carried out for 5 min before careful immersion of the cell into an ice–water bath to quench the reaction. The cell was cooled to room temperature before opening. Care must be exercised when opening the reactor as it could still be under high pressure! The deposition substrate was carefully removed with sharp-edged tweezers, and the remaining product on the inner reactor walls was extracted with hexane and mild sonication. The reaction products were stored under nitrogen to minimize surface oxidation.

Characterization methods: HRSEM images were obtained on a field-emission LEO 1530 scanning electron microscope operated at an accelerating voltage of 2–3-kV. HRTEM was performed with a JEOL 2010F operated at an accelerating voltage of 200-kV. For TEM, the samples prepared by dispersion in chloroform with brief sonication followed by drop-casting on a lacey carbon grid (Electron Microscopy Sciences, LC200-Cu, Mesh 200). The nanowires were sufficiently long to stretch across the lacey carbon grid to provide a vacuum background for the HRTEM images. FFTs of the TEM images were obtained by using digital micrograph (Gatan) software.

Received: December 20, 2004
Published online: May 4, 2005

Keywords: nanowires · precursors · silicon · supercritical fluids · synthetic methods

[1] Y. Huang, X. F. Duan, Y. Cui, L. J. Lauhon, K. H. Kim, C. M. Lieber, *Science* **2001**, *294*, 1313.
[2] X. F. Duan, Y. Huang, C. M. Lieber, *Nano Lett.* **2002**, *2*, 487.
[3] M. S. Gudiksen, L. J. Lauhon, J. Wang, D. C. Smith, C. M. Lieber, *Nature* **2002**, *415*, 617.
[4] J. Hahm, C. M. Lieber, *Nano Lett.* **2004**, *4*, 51.
[5] C. J. Barrelet, A. B. Greytak, C. M. Lieber, *Nano Lett.* **2004**, *4*, 1981.
[6] F. Qian, Y. Li, S. Gradecak, D. L. Wang, C. J. Barrelet, C. M. Lieber, *Nano Lett.* **2004**, *4*, 1975.
[7] J. Westwater, D. P. Gosain, S. Tomiya, S. Usui, H. Ruda, *J. Vac. Sci. Technol. B* **1997**, *15*, 554.
[8] D. Wang, H. Dai, *Angew. Chem.* **2002**, *114*, 4977; *Angew. Chem. Int. Ed.* **2002**, *41*, 4783.
[9] T. I. Kamins, X. Li, R. S. Williams, *Nano Lett.* **2004**, *4*, 503.
[10] C. C. Chen, C. C. Yeh, C. H. Chen, M. Y. Yu, H. L. Liu, J. J. Wu, K. H. Chen, L. C. Chen, J. Y. Peng, Y. F. Chen, *J. Am. Chem. Soc.* **2001**, *123*, 2791.
[11] X. F. Duan, C. M. Lieber, *Adv. Mater.* **2000**, *12*, 298.
[12] E. A. Stach, P. J. Pauzauskie, T. Kuykendall, J. Goldberger, R. R. He, P. D. Yang, *Nano Lett.* **2003**, *3*, 867.
[13] M. H. Huang, Y. Y. Wu, H. Feick, N. Tran, E. Weber, P. D. Yang, *Adv. Mater.* **2001**, *13*, 113.
[14] J. D. Holmes, K. P. Johnston, R. C. Doty, B. A. Korgel, *Science* **2000**, *287*, 1471.
[15] C. L. Yaws, *Handbook of Thermodynamic Diagrams*, Gulf Publishing Company, Houston, Texas, **1996**.
[16] T. Hanrath, B. A. Korgel, *Adv. Mater.* **2003**, *15*, 437.
[17] A. J. Vanderwielen, M. A. Ring, H. E. Oneal, *J. Am. Chem. Soc.* **1975**, *97*, 993.
[18] L. E. Pell, A. D. Schricker, F. V. Mikulec, B. A. Korgel, *Langmuir* **2004**, *20*, 6546.
[19] M. T. Swihart, S. L. Girshick, *J. Phys. Chem. B* **1999**, *103*, 64.
[20] *Lange's Handbook of Chemistry* (Ed.: J. A. Dean), 15th ed., McGraw-Hill, New York, **1999**.
[21] L. M. Calle, A. S. Kana'an, *J. Chem. Thermodyn.* **1974**, *6*, 935.
[22] H. Gilman, D. H. Miles, *J. Org. Chem.* **1958**, *23*, 326.
[23] M. Itoh, K. Inoue, J.-I. Ishikawa, K. Iwata, *J. Organomet. Chem.* **2001**, *629*, 1.
[24] R. W. Coutant, A. Levy, *U.S. Clearinghouse Fed. Sci. Tech. Inform.*, **1969**.
[25] L. E. Nelson, N. C. Angelotti, D. R. Weyenberg, *J. Am. Chem. Soc.* **1963**, *85*, 2662.
[26] A. A. Onischuk, N. V. Panfilov, *Russ. Chem. Rev.* **2001**, *70*, 321.
[27] T. Hanrath, B. A. Korgel, *J. Am. Chem. Soc.* **2002**, *124*, 1424.
[28] A. P. Levitt in *Whisker Technology* (Ed.: A. P. Levitt), Wiley, New York, **1970**.
[29] Y. Wu, Y. Cui, L. Huynh, C. J. Barrelet, D. C. Bell, C. M. Lieber, *Nano Lett.* **2004**, *4*, 433.
[30] H. Yu, W. E. Buhro, *Adv. Mater.* **2003**, *15*, 416.
[31] S. D. Dingman, N. P. Rath, P. D. Markowitz, P. C. Gibbons, W. E. Buhro, *Angew. Chem.* **2000**, *112*, 1530; *Angew. Chem. Int. Ed.* **2000**, *39*, 1470.
[32] J. W. Grebinski, K. L. Richter, J. Zhang, T. H. Kosel, M. Kuno, *J. Phys. Chem. B* **2004**, *108*, 9745.
[33] D. C. Lee, F. V. Mikulec, B. A. Korgel, *J. Am. Chem. Soc.* **2004**, *126*, 4951.
[34] A. E. Saunders, M. B. Sigman, B. A. Korgel, *J. Phys. Chem. B* **2004**, *108*, 193.

Hydrogen Storage

Nanoscaffold Mediates Hydrogen Release and the Reactivity of Ammonia Borane**

*Anna Gutowska, Liyu Li, Yongsoon Shin, Chongmin M. Wang, Xiaohong S. Li, John C. Linehan, R. Scott Smith, Bruce D. Kay, Benjamin Schmid, Wendy Shaw, Maciej Gutowski, and Tom Autrey**

The increasing demand for clean energy sources that do not add more carbon dioxide and other pollutants to the environment has resulted in increased attention worldwide to the possibilities of a "hydrogen economy" as a long-term solution for a secure energy future based on potentially renewable resources.[1–3] Some of the greatest challenges are the discovery and development of new on-board hydrogen-storage materials and catalysts for fuel-cell-powered vehicles. New materials that store both high gravimetric ($\geq 90\ gm\,H_2\,kg^{-1}$) and high volumetric ($\geq 82\ gm\,H_2\,L^{-1}$) densities of hydrogen that can be delivered at temperatures between −20 and 85 °C are needed by the year 2015.[4] The volumetric constraints eliminate from consideration pressurized hydrogen systems and guide towards the development of solid storage materials.[5] There are several broad classes of solid hydrogen-storage materials that are currently being investigated as potential on-board storage materials: 1) metal materials, hydrides (e.g., MgH_2),[6] imides (e.g., $LiNH_2$),[7] and organic frameworks (e.g., Zn_4O(1,4-benezenedicarboxylate)),[8] 2) complex hydrides (e.g., $NaAlH_4$),[9] and 3) carbon materials (e.g., carbon nanofibers,[10] single-wall carbon nanotubes).[11] The most thoroughly studied complex hydride, $NaAlH_4$, has been shown to release hydrogen at 110 °C when doped with Ti;[12] however, the kinetics are very slow and hydrogen-storage densities are too low ($56\ gm\,H_2\,kg^{-1}$) to meet long-term targets. The temperatures for H_2 release from carbon materials are too low, and the reported storage densities are controversial.[13] The hydrolysis of metal hydrides is being explored, but the unfavorable thermodynamics for regeneration of the spent material prevents their widespread application. For example, the reaction $NaBH_4 + 4\,H_2O \rightarrow NaB(OH)_4 + 4\,H_2$ is exothermic by $-250\ kJ\,mol^{-1}$. Reaction enthalpy for hydrogen loss is an important property since near-thermoneutral thermodynamics will be critical for materials for reversible H_2 storage. To date, few of these materials meet the long-term gravimetric requirements and provide rapid hydrogen release at temperatures between −20 and 85 °C; thus, new materials and novel approaches are needed. Herein we show that the kinetics of hydrogen release are significantly enhanced at low temperatures for a new hybrid material, ammonia borane infused in nanoporous silica, and that the hydrogen purity is increased. These findings suggest that hydrogen-rich materials infused in nanoscaffolds offer a most promising approach to on-board hydrogen storage.

Chemical hydrogen-storage materials that release H_2 by thermolysis without generating CO_2 may offer an attractive alternative to other systems studied. For example, the NH_xBH_x family of compounds[14] should provide favorable gravimetric densities of 245, 196, 140, and 75 $gm\,H_2\,kg^{-1}$ for $x = 4$, 3, 2, and 1, respectively. As the NB unit is isoelectronic with CC, these materials are viewed as inorganic analogues of hydrocarbons. However, NH_xBH_x compounds are solids rather than gases at ambient temperature because of their greater polarity and stronger intermolecular interactions relative to organic analogues. The inherent polarity results from the different electronegativities of the B and N atoms: 2.0 and 3.0, respectively.[15] As solids, they provide far more favorable volumetric densities than do the corresponding gaseous hydrocarbons. The two hydrogen-rich materials ammonium borohydride (NH_4BH_4) and ammonia borane (NH_3BH_3) were first prepared in the mid-1950s as part of the US government's program to develop boron-based jet fuels. NH_4BH_4 evolves hydrogen slowly at temperatures above −40 °C and thus is too unstable for applications at room temperature.[16] On the other hand, ammonia borane (AB) is a stable solid at room temperature and requires external heating to release H_2. AB decomposes upon melting at 114 °C with the vigorous bubbling of H_2 gas, or alternatively the hydrogen from AB can be released from the solid material at temperatures below 100 °C, albeit at significantly lower rates.[17] The thermal decomposition of NH_3BH_3 at temperatures below 100 °C yields H_2 and a complex polyaminoborane-like material $-(NH_2BH_2)_n-$ (PAB).[18] At temperatures above 150 °C the PAB decomposes to yield a second equivalent of H_2, concurrent with the formation of a further oxidized polyiminoborane-like material $-(NHBH)_n-$ (PIB) and borazine (c-$(NHBH)_3$).[19] The latter is an inorganic analogue of benzene that is highly undesirable in the H_2 feed.

Recent computational results indicate that the NH_xBH_x molecules also display favorable thermodynamics: All four consecutive steps of hydrogen release from NH_xBH_x for $x =$ 4–1 are thermoneutral to within $40\ kJ\,mol^{-1}$.[14,20] These theoretical results are supported by experimental work that shows that the reaction enthalpy for H_2 loss from NH_3BH_3 is only moderately exothermic ($\Delta H_{rxn} = -21\ kJ\,mol^{-1}$).[21] The

[*] Dr. A. Gutowska, Dr. L. Li, Dr. Y. Shin, Dr. C. M. Wang, Dr. X. S. Li, Dr. J. C. Linehan, Dr. R. S. Smith, Dr. B. D. Kay, Dr. W. Shaw, Dr. M. Gutowski, Dr. T. Autrey
Pacific Northwest National Laboratory
Richland, WA 99352 (USA)
Fax: (+1) 509-375-6660
E-mail: tom.autrey@pnl.gov
B. Schmid
University of Oregon
Department of Chemistry
Eugene, OR (USA)

[**] This research was performed in part at the Interfacial and Nano Science Facility in the William R. Wiley Environmental Molecular Sciences Laboratory, a national scientific user facility sponsored by the Office of Biological and Environmental Research of the US Department of Energy and located at the Pacific Northwest National Laboratory (PNNL). Pacific Northwest is operated for the Department of Energy by Battelle. The authors wish to acknowledge support from the Laboratory Directed Research and Development Program at the PNNL and the Nano Science & Technology Initiative. T.A. thanks D. Thorn (LANL) and D. Schubert (US Borax) for helpful discussions.

  DOI: 10.1002/anie.200462602

low reaction exothermicity of AB thermolysis is in significant contrast to hydrolysis pathways of boron-based hydrogen-storage materials. Given the approximate thermoneutrality of thermolysis accompanied by relatively low temperatures for H_2 release, AB is a strong candidate for on-board hydrogen storage. However, although AB exceeds targets for volumetric and gravimetric density for a hydrogen-storage material, three additional physical obstacles must be overcome: 1) The rates of H_2 release at temperatures below 85 °C must be increased, 2) borazine formation must be prevented, and 3) reversibility must be demonstrated.

There are reports that nanophase metal hydrides show enhanced kinetics for reversible hydrogen storage relative to the bulk materials.[22–24] However, after a few hydriding/dehydriding cycles the kinetic enhancement is diminished for some materials, as they lose nanophase structure.[25] Herein we suggest that a nanophase scaffold loaded with a hydrogen-rich material may provide an attractive option to preserve the nanoscale dimensions through several hydriding/dehydriding cycles. To demonstrate the effect of a nanophase scaffold on hydrogen release we use a high-surface-area mesoporous silica material loaded with AB as a model system. Three notable observations are described in this work: 1) increased rates of H_2 release, 2) modifications of the nonvolatile polymeric products that lead to a change in the thermodynamics of hydrogen release, and 3) minimized formation of borazine.

Mesoporous silica materials have an extremely high surface area and a highly ordered pore structure, which give them the appearance of nanochanneled silica scaffolds.[26] The mesoporous silica material used in this work, SBA-15, which was prepared according to a literature procedure,[27] is shown in Figure 1. The SBA-15 was loaded with AB by dosing the silica scaffold with a saturated methanolic solution of AB. Because of the porous nature of the silica scaffold, the internal channels of SBA-15 were filled rapidly by a capillary action directly upon exposure. The sample was dried under vacuum to remove the methanol and produce the SBA-15 coated with AB (1:1 by weight). Attempts to observe AB coated on the pores of SBA-15 by transmission electron microscopy (TEM) in ultramicrotome cross-sectional slices of the sample were not successful as a result of the weak scattering of electrons by the light elements B and N; however, electron dispersive spectrometry (EDS) of the microtome samples showed the presence of both elements B and N. Further evidence for the embedded material was inferred from BET measurements that show that the SBA-15 surface area is reduced from 900 $m^2 gm^{-1}$ before coating to $< 50\ m^2 gm^{-1}$ after coating.

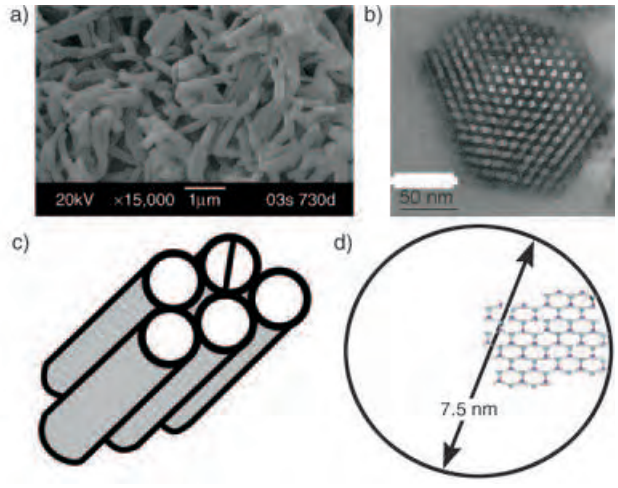

Figure 1. Schematic representation of AB in SBA-15, from the micro- to the nanoscale: a) SEM image of mesoporous silica; average particle size: 1 μm × 0.2 μm, surface area: ≈900 $m^2 gm^{-1}$, porous volume: 1.2 $mL g^{-1}$; b) TEM ultratome cross-sectional image of SBA-15 showing porous channels; c) schematic representation of parallel channels in SBA-15; pore diameter: 7.5 nm; d) schematic representation of a hydrogen-bonded AB network in the cross-section of a single pore.

Temperature-programmed desorption mass spectrometry (TPD/MS) was used to compare the temperature profiles of volatile products (H_2, borazine) released from neat AB and AB in the SBA-15 scaffold (Figure 2). Two peaks for neat AB

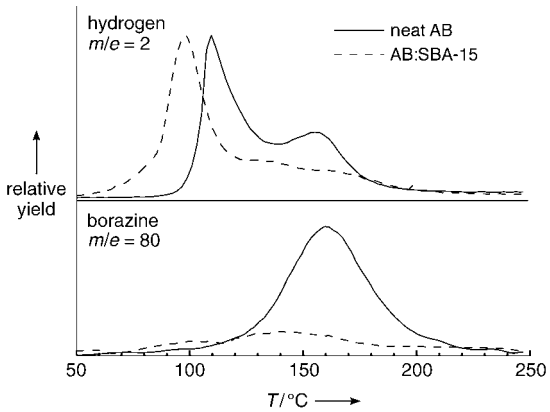

Figure 2. TPD/MS (1 °C min^{-1}) of volatile products generated by heating neat ammonia borane (solid line) and AB:SBA-15 (dashed line); $m/e = 2$ (H_2) and $m/e = 80$ (borazine, *c*-$(NHBH)_3$). The value $m/e = 2$ (H_2) is normalized to the area under the curve for neat ammonia borane (solid line). The corresponding scalar was used to normalize the $m/e = 80$ borazine data for AB:SBA-15.

at approximately 110 and 155 °C correspond to the release of the first equivalent of hydrogen with the formation of PAB, and the release of the second equivalent of hydrogen with the formation of PIB, respectively. There are two notable effects resulting from the nanostructure of AB in the SBA-15 scaffold: First, the temperature threshold for H_2 release ($m/e = 2$) is notably lower than the temperature threshold for neat AB, which is indicative of an enhanced rate of H_2 release. Second, the yield of the borazine side product ($m/e = 80$) is significantly lower than for neat AB. Solid-state ^{11}B NMR spectroscopy was used to analyze the nonvolatile products from neat AB and AB:SBA-15 to see if the borazine became entrapped within the mesoporous scaffold. However, no ^{11}B signal for borazine was observed, thus indicating that borazine is not likely to be trapped in the scaffold. Because borazine is not observed as a volatile product in the TPD/MS experiment and not detected by solid-state NMR spectroscopy, the mesoporous scaffold appears to affect the decomposition pathways of AB that lead to hydrogen formation.

Furthermore, if the PAB and PIB polymeric decomposition products formed in the SBA-15 scaffold do not form the more stabilized cyclization products, there may be a measurable difference between the reaction enthalpies for H_2 loss from AB:SBA-15 and neat AB.

Differential scanning calorimetry (DSC) experiments were used to quantify both the thermodynamics and kinetics for the release of the first equivalent of H_2 from neat AB and AB:SBA-15. Integration of the area under an isothermal DSC curve provides the enthalpy of reaction for H_2 release (ΔH_{rxn}). The enthalpy for H_2 loss from neat AB ($\Delta H_{rxn} = -21 \pm 1\ kJ\,mol^{-1}$) is in excellent agreement with the literature value for neat AB.[21] However, we find that the loss of H_2 from the AB in the scaffold is significantly less exothermic ($\Delta H_{rxn} = -1 \pm 1\ kJ\,mol^{-1}$). The difference in the observed ΔH_{rxn} for the release of H_2 from AB in the scaffold suggests that the nonvolatile products formed in the scaffold might be different from the nonvolatile products formed upon the release of H_2 from bulk AB. This hypothesis was confirmed by analysis of the ^{11}B NMR spectra of the nonvolatile products. After heating the 1:1 AB:SBA-15 mixture for 90 min at 85 °C only one resonance was observed (at $\delta = -23$ ppm), which we assign to PAB. On the other hand, after neat AB had been heated for 90 min at 85 °C three additional boron resonances were observed, as well as the PAB resonance.[28] The formation of the additional boron-containing products from neat AB must then contribute to the greater reaction exothermicity. The observation of a less exothermic enthalpy of reaction for H_2 loss from AB in the scaffold is important. As hydrogen loss becomes less exothermic, the reverse reaction, hydrogen uptake, becomes more favorable at a given pressure and temperature. The difference in the equilibrium between AB and PAB+H_2 in the neat material and the scaffold can be estimated from the van 't Hoff equation.[29] The experimental $\Delta\Delta H_{rxn}$ of 20 kJ mol^{-1} for H_2 loss from AB in the scaffold compared to H_2 loss from neat AB corresponds to a >4600-fold difference in pressure at room temperature!

The time dependence of H_2 release from neat AB at 80 °C and AB:SBA-15 at 50 °C is shown in Figure 3. The reaction exhibits sigmoidal kinetic behavior, and the extent of reaction (dashed curves) is indicative of an autocatalytic mechanism of hydrogen release.[30] The point ● on the integrated curve marks the half-life for hydrogen release. This analysis yields $t_{1/2} = 290$ min for the neat AB at 80 °C. The half-life for the 1:1 AB:SBA-15 sample at 80 °C could not be measured because the H_2 is released before the sample has reached this temperature ($t_{1/2} < 10$ min). However, if the temperature is decreased to 50 °C a baseline is observed for the AB:SBA-15 sample, and the kinetic analysis of the data results in a $t_{1/2}$ value of 85 min at 50 °C. Analysis of the integrated DSC data for various temperatures provides the half-life for hydrogen release as a function of temperature. Arrhenius treatment of this temperature-dependent rate data is shown in Figure 4. In both cases (neat AB and AB:SBA-15) a straight line is obtained; the gradient gives the apparent activation energy for hydrogen loss. These results suggest that the barrier for H_2 release from AB in the scaffold ($E_a \approx 67 \pm 5\ kJ\,mol^{-1}$) is significantly lower than the barrier for H_2 release from neat AB ($E_a \approx 184 \pm 5\ kJ\,mol^{-1}$). This large difference in activation energy manifests itself in a greater than 300-fold enhancement in the H_2-evolution rate at 70 °C. This result is important because one could potentially use the waste heat from a PEM (proton-exchange membrane) fuel cell (≈85 °C) to provide the heat to the hydrogen-storage media to drive hydrogen release.

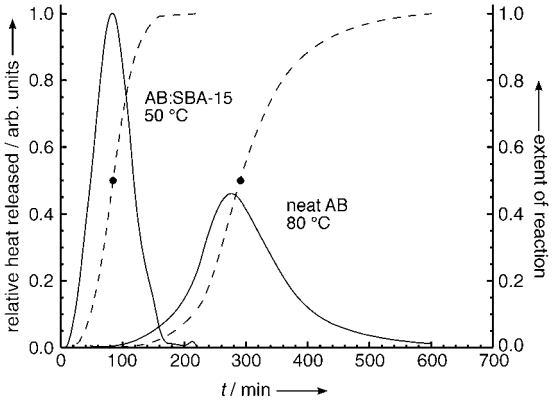

Figure 3. Scaled exotherms (solid lines) from isothermal DSC experiments that show the time-dependent release of H_2 from AB and AB:SBA-15 (1:1 wt/wt). The area under the curve for neat AB corresponds to $\Delta H_{rxn} = -21$ kJ mol^{-1}, and the area under the curve for AB:SBA-15 corresponds to $\Delta H_{rxn} = -1$ kJ mol^{-1}. The release of hydrogen from AB proceeds at a more rapid rate and at lower temperatures in SBA-15. The dashed line (——) is the integrated signal intensity; (●) is the point at which the reaction is 50% complete.

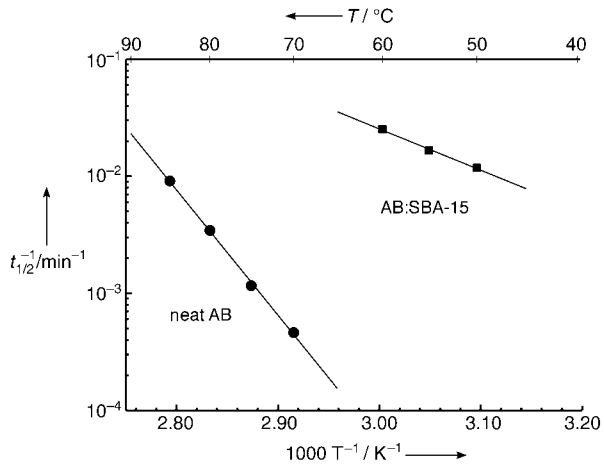

Figure 4. Arrhenius treatment of the temperature-dependent rate data yields a straight line with a gradient that is proportional to the apparent activation energy for hydrogen loss from neat AB (●; $E_a \approx$ 184 kJ mol^{-1}) or AB in the scaffold (■; $E_a \approx 67$ kJ mol^{-1}).

To our knowledge this is the first report of the use of an external agent (highly porous silica) to enhance the properties of a solid-state hydrogen-storage material. Coating the hydrogen-rich material AB within the mesoporus silica SBA-15 leads to: 1) suppression of borazine release, 2) modification of the enthalpy of the decomposition, and 3) lowering of the activation barrier for the loss of H_2. The enforced nanostructural geometry of the AB embedded in the scaffold may result in defect sites that initiate the dehydropolymeri-

zation reaction at lower temperatures. Alternatively, interfacial catalysis by the terminal SiO–H groups within the silica scaffold may result in the catalysis of the thermolysis of AB and control of the product distribution. These possibilities will be explored in forthcoming studies. The results for AB in the mesoporous silica are notable in themselves. We believe, however, that mesoporous materials may improve the kinetics and thermodynamics of hydrogen release from other materials, such as hydrogenated metal nitrides and imides or $LiBH_4$. For example, it has recently been reported that SiO_2 powder lowers the onset temperature for hydrogen release from $LiBH_4$.[31] The high surface area of SBA-15 would probably have very similar benefits and could enhance the kinetics for rehydriding, as the $LiBH_4$ would be confined to a nanophase structure.

Experimental Section

SBA-15 synthesis: Hexagonally ordered mesoporous silica (SBA-15) was prepared according to published procedures.[32] In a typical preparation of mesoporous silica with pores of 100 Å in diameter, pluronic P123 ($\bar{M}_W = 5800$; 12.0 g) was dissolved in 2 M HCl (360 mL) at 40 °C. Tetraethylorthosilicate (TEOS; 25.5 g) was added to the resulting milky solution, which was then stirred for 18 h at the same temperature. The mixture was transferred into a teflon-lined autoclave and heated at 100 °C for 24 h without stirring. The white precipitate was filtered, dried in air, and finally calcined at 550 °C for 6 h.

Preparation of AB:SBA-15: A solution of AB (50 mg) in methanol (300 μL) was added to a sample of SBA-15 (50 mg). The methanolic solution appeared to fill the internal channels of the mesoporous scaffold through a capillary action. The "wet" SBA-15 was dried under vacuum to produce a sample with an internal coating of ammonia borane (approximately 1:1 AB to SBA-15 by weight).

TEM: A thin section of the specimen was prepared for high-resolution TEM (HRTEM) by standard epoxy embedding followed by ultramicrotoming to a thickness of less than 50 nm. The HRTEM analysis was carried out with a Jeol JEM 2010 microscope with a specified point-to-point resolution of 0.194 nm. The operating voltage of the microscope was 200 keV. All images were recorded digitally with a slow-scan CCD camera (image size: 1024 × 1024 pixels), and image processing was carried out by using a digital micrograph (Gatan).

DSC/TPD/MS: DSC analyses were performed by using a Netzsch STA 409 TGA/DSC and a Pfeiffer QMS300 MS or a Setaram C80 calorimeter. The TPD/MS data for $m/e = 2$ (H_2) and $m/e = 80$ (borazine) were obtained by monitoring the off-gas with a heated fused (200 °C) silica capillary (a 1-m silanized fused silica capillary, 0.1 mm ID) attached to the top of the Netzsch instrument. The MS uses a standard electron impact ionization detector. The MS scanning rate was 12 s for a range of 1 to 100 amu. To obtain the relative yields of hydrogen and borazine, samples of AB (6.2 mg) and SBA-15:AB (1:1 wt/wt; 6.2 mg) were weighed into a Pt crucible for back-to-back experiments. The area under the SBA-15:AB curve was multiplied by a factor of two to provide a direct comparison for H_2 and borazine release from neat AB and AB embedded into the SBA-15 scaffold. A thermal ramp of 1 °C min^{-1} from room temperature to 200 °C with an argon flow of 20 $cm^3 min^{-1}$ were used in our analysis.

^{11}B NMR spectroscopy: Spectra of amino borane samples were recorded on a Varian Unity Inova spectrometer operating at a ^1H frequency of 800 MHz with a 4-mm 3-Ch Doty MAS probe. For the Bloch decay experiment a 200-kHz sweep width, a 5-μs 90°-pulse for ^{11}B (with and without ≈30 kHz decoupling), and a pulse delay of 5 s were used. Samples were spun at 15 kHz then cooled to 10–20 °C, and 128 scans were collected for each spectrum.

Received: November 13, 2004
Published online: May 4, 2005

Keywords: hydrogen storage · kinetics · mesoporous materials · nanostructures · thermochemistry

[1] P. Grant, *Nature* **2003**, *424*, 129–130.
[2] M. S. Dresselhaus, I. L. Thomas, *Nature* **2001**, *414*, 332–337.
[3] L. de Palacio, P. Busquin, Report from Europa Commission, "Hydrogen Energy and Fuels Cells: A Vision for Our Future", http://europa.eu.int/comm/research/energy/nn/nn_rt/nn_rt_hlg/article_1146_en.htm.
[4] Recent information can be found at: http://www.eere.energy.gov/hydrogenandfuelcells/pdfs/freedomcar_targets_explanations.pdf.
[5] W. Grochala, P. P. Edwards, *Chem. Rev.* **2004**, *104*, 1283–1316.
[6] J. Huot, J. F. Pelletier, G. Liang, M. Sutton, R. Schultz, *J. Alloys Compd.* **2002**, *330–332*, 727–731.
[7] P. Chen, Z. Xiong, J. Luo, J. Lin, K. L. Tan, *Nature* **2002**, *420*, 302–304.
[8] N. L. Rosi, J. Eckert, M. Eddaoudi, D. T. Vodak, J. Kim, M. O'Keeffe, O. M. Yaghi, *Science* **2003**, *300*, 1127–1129.
[9] L. Schlapbach, A. Zuttel, *Nature* **2001**, *414*, 353–358.
[10] D. J. Browning, M. L. Gerrard, J. B. Lakeman, I. M. Mellor, R. J. Mortimer, M. C. Turpin, *Nano Lett.* **2002**, *2*, 201–205.
[11] A. C. Dillon, K. M. Jones, T. A. Bekkedahl, C. H. Kiang, D. S. Bethune, M. J. Heben, *Nature* **1997**, *386*, 377–379.
[12] K. J. Gross, G. J. Thomas, C. M. Jensen, *J. Alloys Compd.* **2002**, *330*, 683–690.
[13] G. B. Tibbetts, G. P. Meisner, C. H. Olk, *Carbon* **2001**, *39*, 2291–2301.
[14] M. Gutowski, T. Autrey, J. Linehan, unpublished results.
[15] L. Pauling, *General Chemistry*, Dover Publications, New York, **1988**, p. 182.
[16] R. W. Parry, D. R. Schultz, P. R. Girardot, *J. Am. Chem. Soc.* **1958**, *80*, 1–3.
[17] J. Baumann, Dissertation, Physikalisch-chemische Untersuchungen zur Wasserstoffabgabe von BNH-Verbindungen, **2003**, TU-Bergakademie Freiberg, Germany. The research group in Freiberg has been investigating NH_3BH_3 as a hydrogen-storage material.
[18] F. Baitalow, J. Baumann, G. Wolf, K. Jaenicke-Rößbler, G. Leitner, *Thermochim. Acta* **2002**, *391*, 159–168.
[19] V. Sit, R. A. Geanangel, W. W. Wendlandt, *Thermochim. Acta* **1987**, *113*, 379–382.
[20] M. Gutowski, T. Autrey, *Prepr. Pap. Am. Chem. Soc. Div. Fuel Chem.* **2004**, *49*, 275–276.
[21] G. Wolf, J. Baumann, F. Baitalow, F. P. Hoffmann, *Thermochim. Acta* **2000**, *343*, 19–25.
[22] J. Liang, *Prepr. Pap. Am. Chem. Soc. Div. Fuel Chem.* **2003**, *48*, 281–283.
[23] H. Fujii, S. Orimo, *Phys. B* **2003**, *328*, 77–80.
[24] W. Oelerich, T. Klassen, N. Eigen, R. Bormann, *EUROMAT* **2000**, *13*, 141–145.
[25] Y. Suzuki, T. Haraki, H. Uchida, *J. Alloys Compd.* **2002**, *330–332*, 488–491.
[26] D. Zhao, J. Feng, Q. Huo, N. Melosh, G. H. Fredrickson, B. F. Chmelka, G. D. Stucky, *Science* **1998**, *279*, 548–552.
[27] Y. Shin, J. Liu, L.-Q. Wang, Z. Nie, W. D. Samuels, G. E. Fryxell, G. J. Exarhos, *Angew. Chem.* **2000**, *112*, 2814–2819; *Angew. Chem. Int. Ed.* **2000**, *39*, 2702–2707.
[28] The 800-MHz solid-state NMR spectrum is available as Supporting Information. Observed ^{11}B resonances: AB:SBA-15

(one signal, $\delta = -23$ ppm), neat AB (four signals, $\delta = -6$, -12, -23, -37 ppm).

[29] van 't Hoff equation: $\ln(p_{eq}/p^{o}_{eq}) = \Delta H/RT - \Delta S/R$. The difference in hydrogen overpressure can be calculated from $\Delta\Delta H$ of H_2 loss from AB bulk and AB in the scaffold. $\Delta\ln(p_{eq}/p^{o}_{eq}) = \Delta\Delta H/RT - \Delta\Delta S/R$. $\Delta\Delta S = 0$, $\Delta\Delta H = 20\ kJ\,mol^{-1}$, then $p_{eq}(AB)/p_{eq}(AB{:}SBA\text{-}15) = 4667$. As $\Delta H \approx 0$ in the scaffold, the pressure required for H_2 uptake by the spent AB is the pressure required to overcome the entropy of formation of the gaseous H_2. Reversibility processes will be addressed in a subsequent publication.

[30] For similar observations with $LiBH_4$ and triethanolamine, see: R. Custelcean, J. E. Jackson, *J. Am. Chem. Soc.* **2000**, *122*, 5251 – 5257.

[31] A. Zuttel, P. Wenger, P. Sudan, P. Mauron, C. Emmenegger, *J. Power Sources* **2003**, *118*, 1 – 7.

[32] D. Zhao, Q. Huo, J. Feng, B. F. Chmelka, G. D. Stucky, *J. Am. Chem. Soc.* **1998**, *120*, 6024 – 6036.

Nanoparticle Arrays

DNA-Encoded Self-Assembly of Gold Nanoparticles into One-Dimensional Arrays**

*Zhaoxiang Deng, Ye Tian, Seung-Hyun Lee, Alexander E. Ribbe, and Chengde Mao**

DNA-templated material assemblies usually fall into two categories: nonspecific electrostatic (or intercalative)[1] and sequence-specific assemblies.[2–5] The latter take advantage of the Watson–Crick base pairing and can assemble materials into well-defined structures by DNA-based molecular recognition. This approach is promising in controlling both the complexity and regularity of nanostructures. In previous work this approach was used to build small assemblies of gold nanoparticles (AuNPs).[3] The basic scheme is to hybridize mono-DNA-functionalized AuNPs with template-DNA strands to form the desired structures. It is conceivable to integrate this strategy with more extended and complicated DNA nanostructures[2,6] for nanoparticle assembly. One immediate challenge is to build large arrays by DNA-encoded self-assembly of AuNPs into well-extended micrometers-long one-dimensional (1D) arrays. The resulting linear structures could potentially link the nanometric properties of materials with the convenience of micrometric maneuverability.

Rolling-circle DNA polymerization is well-suited for the preparation of long, repetitive DNA single strands as templates for nanoparticle assembly. During the polymerization, a DNA polymerase uses a short (less than 100 bases long), circularized, single DNA strand as a template to synthesize long (more than 10000 bases), linear, tandemly repetitive single DNA strands under isothermal conditions.[7] This technique has found important applications in gene detection.[7c] Here, we use the products of rolling-circle polymerization to assemble AuNPs into extended 1D arrays up to 4 μm long.

Figure 1 illustrates our strategy to assemble micrometers-long AuNP arrays: 1) functionalization of 5-nm AuNPs with DNA 1 (with a 5′ thiol group) to form a 1:1 AuNP/DNA 1 conjugate (AuDNA 1); 2) rolling-circle polymerization[7] to synthesize template DNA ($\mathbf{T}_{long}$) with a large number of repeats complementary to DNA 1; and 3) hybridization of AuDNA 1 with $\mathbf{T}_{long}$ to form micrometers-long AuNP assemblies.

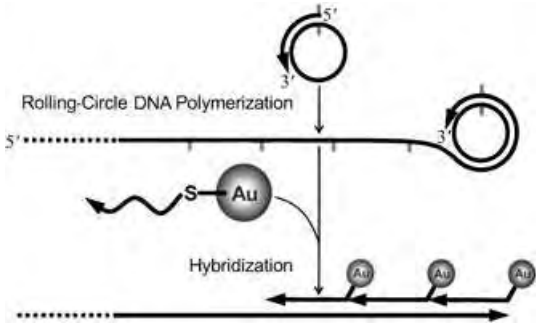

Figure 1. Synthesis of an extended gold nanoparticle array by combining DNA-encoded self-assembly and rolling-circle polymerization of DNA.

The reported methods[3] for synthesizing AuDNA 1 were adopted. The 53-base-long thiolated DNA 1 was first incubated with phosphine-capped 5-nm AuNPs in buffer 1 (see the Experimental Section) for over 3 h. Then, the AuDNA 1 conjugates were isolated by 3 % agarose gel electrophoresis in 10–20 % yields. Dark-red bands in the agarose gel corresponding to AuDNA 1 were easily determined (see the Supporting Information) by comparing the gel patterns to a pure AuNP band or by observing the evolution of the gel patterns while gradually increasing the amount of thiolated DNA 1 in the AuNP solution.

Before the assembly of micrometers-long AuNP arrays, we tested this scheme in the formation of smaller structures containing three to six AuNPs. Template-DNA strands ($\mathbf{T}_n$, $n = 3$–6, where n denotes the number of repeats in the template strands and each repeat is complementary to DNA 1) were prepared by ligation and purified by polyacrylamide gel electrophoresis (PAGE; 6 %, denaturing conditions). AuDNA 1 and the corresponding template strand were

[*] Z. Deng, Y. Tian, S.-H. Lee, A. E. Ribbe, Prof. C. Mao
Department of Chemistry
Purdue University
West Lafayette, IN 47907 (USA)
Fax: (+1) 765-494-0239
E-mail: mao@purdue.edu

[**] This work was supported by the NSF (EIA-0323452), the DARPA/DSO (MDA 972-03-1-0020), and Purdue University (a start-up fund). The AFM study was carried out in Purdue Laboratory for Chemical Nanotechnology (PLCN). We thank Prof. A. Ivanisevic for use of an AFM in some cases. EM imaging was conducted at Purdue electron microscopy consortium.

Supporting information for this article is available on the WWW under http://www.angewandte.org or from the author.

  DOI: 10.1002/anie.200463096

then mixed together in buffer 1 at different ratios, and an AuDNA 1/$\mathbf{T}_n$ molar ratio of 1:0.5 (in terms of the repeats) was finally chosen to produce the desired AuNP assemblies, since the excess of AuDNA 1 could compensate its slightly decreased hybridization ability. The AuNP assemblies were isolated by gel electrophoresis (3% agarose), eluted into buffer 2, and analyzed by transmission electron microscopy (TEM). The TEM images and statistical analyses in Figure 2 and Table 1 clearly show the formation of the desired structures in high yields.

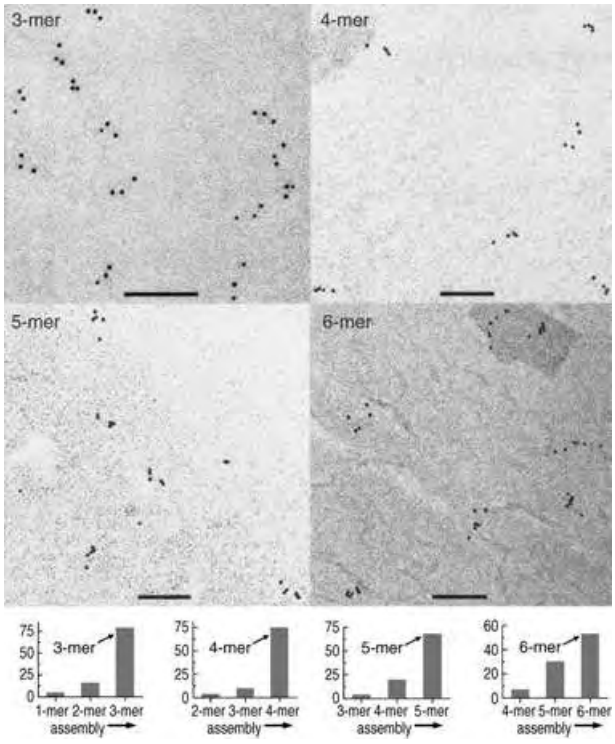

Figure 2. TEM images and statistical column charts showing the highly efficient assembly of gold nanoparticles into 3-, 4-, 5-, and 6-mers; all scale bars correspond to 100 nm.

Table 1: Typical yields for the AuNP assemblies from 3- to 6-mer obtained by TEM image analysis.[a]

	3-mer	4-mer	5-mer	6-mer
Counts of AuNPs [N_T]	619	345	466	660
Yield [%]	79	75	67.5	53

[a] N_T is the total number of observed AuNPs in the TEM images. The yield is defined as N_A/N_T, where N_A is the total number of AuNPs within the desired assembly. Particles located close to the edges of the TEM images were excluded.

The interparticle spacings of the AuNP assemblies were analyzed from the TEM images. To avoid the confusion in finding the correct particle pairs, only assemblies with easily distinguishable linear structures were chosen for the measurements. The results showed a center-to-center interparticle distance of (18.5 ± 6.9) nm (see the Supporting Information), consistent with the theoretical value of 18.0 nm for a 53-base-long DNA duplex. The observed interparticle distances had quite a wide distribution, which ranged from 6.1 to 33.9 nm. We attributed the spacing variation to the strong particle–particle and particle–substrate affinities, the bending, stretching, or partial unzipping of the DNA duplex during sample preparation, the flexibility of the linkage part between DNA and the AuNPs, and the 5-nm diameter of the AuNPs.[3b]

The synthesis of micrometers-long DNA template ($\mathbf{T}_{long}$) is key to the formation of extended AuNP arrays but is usually difficult. We solved this issue by rolling-circle DNA synthesis,[7] which used a circularized DNA 1 as the template, a 12-base-long DNA 2 as the primer, and a Phi29 DNA polymerase. The polymerization product ($\mathbf{T}_{long}$) contains many copies of the DNA 1 complement. $\mathbf{T}_{long}$ migrated very slowly in 1% agarose gel (Figure 3a) and is at least thousands

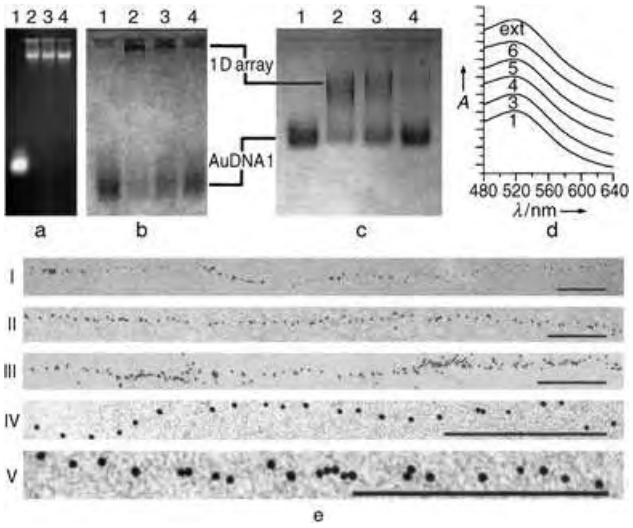

Figure 3. a) Agarose gel (1%) electrophoresis for the rolling-circle-synthesized products; lane 1: 53-base cDNA1, lanes 2–4: polymerized products obtained in different synthesis batches, which indicate good consistency. b, c) Agarose gel (b: 3%, c: 0.5%) electrophoresis of the extended 1D AuNP assembly; lane 1: AuDNA1, lanes 2–4: products obtained in 1:1, 1:0.5, and 1:0.25 ratios. d) Optical absorbance of the 1- (AuDNA1), 3-, 4-, 5-, and 6-mers and the extended (ext) 1D structure. e) TEM images of the extended 1D structures; (IV) and (V) are close-up views of part of the wires in (I) and (II); all scale bars are equivalent to 200 nm.

of bases long, with reference to a 100-base-pair DNA ladder (see the Supporting Information). The high-molecular-weight fraction was sliced from the gel, electrically eluted, precipitated from ethanol, and redispersed in doubly distilled H_2O (ddH_2O). The extended 1D arrays were prepared by combining AuDNA 1 and $\mathbf{T}_{long}$ at different ratios and annealing from 95 to 4 °C in buffer 1. The resulting aggregates were too large to migrate into a 3% agarose gel (Figure 3b), but they ran well in a 0.5% gel (Figure 3c). The aggregates at a ratio of 1:0.5 (AuDNA 1:repeat of $\mathbf{T}_{long}$) migrated slightly slower than those at a ratio of 1:1, which indicates that there were some unpaired segments on the template and thus an excess of

AuDNA 1 could improve the DNA hybridization. The aggregates at a ratio of 1:0.25 migrated the same as those at a ratio of 1:0.5, which implies that the template was saturated and thus incorporation of more particles was impossible. A ratio of 1:0.5 was chosen for the synthesis of the micrometers-long AuNP arrays.

Large-area atomic force microscopy (AFM), TEM, and field-emission scanning electron microscopy (FESEM) images showed 1D arrays of AuNPs up to 4 μm long aligned in a parallel fashion on TEM grids and silicon-wafer substrates (see the Supporting Information). The AuNP arrays could reach several micrometers in length, so it is reasonable to assume that the fluidic flow created during removal of the solution droplet could cause the long assemblies to be stretched and aligned. As shown in Figure 3e, the AuNPs were either well-separated within the appropriately stretched parts of the wires or entangled and coalesced on other parts. The visible absorbance spectra of the extended arrays and the 3- to 6-mers (Figure 3d) show no significant differences with that of AuDNA 1, in agreement with the large interparticle distances expected for a 53-base-pair DNA spacer.

In conclusion, we have successfully prepared extended 1D arrays of gold nanoparticles by combining rolling-circle polymerization and DNA-encoded self-assembly. The arrays obtained can dissolve in water and form a stable homogeneous solution, which enables subsequent modifications and easy manipulation. These results are an important step forward in obtaining extended nanoparticle arrays in a precise and controllable manner, which may help build structures with versatile functionalities. One of our further research goals is to design and fabricate more rigid and hierarchically complicated structures extending to one, two, or even three dimensions and to explore any potentially emerging physical properties.

Experimental Section

Buffer solutions: TBE buffer: tris(hydroxymethyl)aminomethane (Tris, 89 mM), ethylenediaminetetraacetate (EDTA, 2 mM), and boric acid (89 mM), pH 8.0. Buffer 1: 1:1 TBE + sodium chloride (0.2 M). Buffer 2: 1:1 TBE + sodium acetate (NaAc, 0.1 M). NEB Phi29 polymerase reaction buffer: Tris-HCl (50 mM), magnesium chloride (10 mM), ammonium sulfate (10 mM), and dithiothreitol (DTT, 4 mM).

Synthesis of $\mathbf{T}_n$ ($n = 3$–6): For the preparation of DNA templates $\mathbf{T}_n$, cDNA 1, a DNA strand complementary to DNA 1, was designed to leave four-base sticky ends at both sides of the duplex with DNA 1 that allow the formation of a ladder of duplexes. The corresponding templates were obtained by ligating cDNA 1 in the above product mixtures with a T4 DNA ligase (New England Biolabs, Inc., NEB). The 3- to 6-mers of cDNA 1 were then purified from a 6% denaturing polyacrylamide gel. DNA 1: 5′GAGTAGACCGTGCATCATGGACTAACCAGTGACCGCATCGGACAGCAGCCTGA3′; cDNA 1: 5′ACTCTCAGGCTGCTGTCCGATGCGGTCACTGGTTAGTCCATGATGCACGGTCT3′.

Rolling-circle synthesis of $\mathbf{T}_{long}$: Rolling-circle polymerization was conducted in solution (20 μL) at 37 °C for 90 min. The reaction was stopped by heating at 65 °C for 10 min. The reaction mixture contained 53-base-long circularized DNA 1 (0.1 μg), 12-base primer DNA 2 (5′CCATGATGCACG3′; 0.023 μg), Phi29 DNA polymerase (New England Biolabs, Inc., NEB; 5–10 units), NEB Phi29 polymerase reaction buffer, dNTP mix (1 mM), and BSA (0.1 mg mL^{-1}). The polymerization product was then dialyzed against ddH_2O for 16 h to remove salts and the dNTP monomers. The dialyzed sample was loaded onto 1% agarose gel containing ethidium bromide (0.5 μg mL^{-1}). For electrophoresis, the running buffer was half as concentrated as the TBE buffer and is designated 0.5 × TBE. The major band of the product (see the Supporting Information) was sliced and sealed into a dialysis membrane tube filled with 0.5 × TBE buffer. The product was electrically eluted from the gel block, extracted with butanol, precipitated with ethanol, and finally dispersed in ddH_2O (100 μL). The purified product was quantitated by measuring its UV absorbance at 260 nm. Typically, 3–5 μg of the $\mathbf{T}_{long}$ template was obtained.

Phosphine-capped gold nanoparticles (AuNPs): AuNPs (Ted Pella, Redding, CA; 5 nm) were stabilized by complexation with bis(*para*-sulfonatophenyl)phenylphosphine dihydrate dipotassium salt (salt 1, Strem Chemicals, Newburyport, MA). Typically, salt 1 (2 mg) was added to the AuNP solution (10 mL), and the mixture was shaken at 22 °C overnight. The AuNPs were then precipitated by adding solid sodium chloride until the color turned blue. After centrifugation, the supernatant was carefully removed with a pipette, and the AuNP precipitate was redispersed in ddH_2O to a concentration of 1–4 μmol, as estimated from the optical absorbance at 520 nm (1 OD equals 0.083 μmol for 5-nm AuNPs).

AuDNA 1: Thiolated DNA 1 and phosphine-protected AuNPs (1–4 μM) were mixed in buffer 1 at a molar ratio of 1:1 (estimated by optical absorbance). The mixture was incubated at 22 °C for over 3 h. The product containing AuNPs conjugated with different numbers of DNA 1 appeared as a series of dark-red bands in a 3% agarose gel with 0.5 × TBE as running buffer. The sample band corresponding to AuDNA 1 was sliced from the gel and sealed in a dialysis membrane tube prefilled with 0.5 × TBE buffer. AuDNA 1 was then electrically eluted into the dialysis tube, and the inner tubing buffer was carefully collected.

AuNP assemblies: Purified AuDNA 1 (0.3–0.8 μM based on the absorbance of AuNPs at 520 nm) was mixed with DNA templates at molar ratios (AuDNA 1:repeat of the template) of 1:1, 1:0.5, and 1:0.25. The mixtures were incubated in buffer 1: 95 °C (1 min), 65 °C (5 min), 50 °C (10 min), 37 °C (20 min), 22 °C (20 min), and 4 °C (20 min). The products were separated by electrophoresis on 3 or 0.5% agarose gel with buffer 2 as the running buffer. The ratios corresponding to the highest yields of the desired products were chosen, and the expected product bands were electrically eluted into buffer 2 and kept at 4 °C.

Microscopic analyses: 1) The TEM sample was prepared by dropping sample solution (5 μL) onto a carbon-coated TEM grid (400 mesh, EMS Inc.). After 1 min, the solution was wicked from the edge of the grid with a piece of paper. TEM images were taken with a Philips CM-10 transmission electron microscope operated at 80 kV in the bright-field mode. 2) The sample on a silicon wafer for AFM and FESEM imaging was prepared by spotting sample solution (5 μL) onto the silicon substrate. The drop was blown off after 1 min by compressed air and the surface of the wafer was washed once with aqueous magnesium acetate solution (2 mM, 30 μL). The sample was first checked with a Nanoscope IIIa multimode atomic force microscope operated in the tapping mode in air, and then subjected to imaging with a Hitachi S-4800 FESEM operated at 1 kV.

Received: December 29, 2004
Published online: May 4, 2005

Keywords:
DNA · gold · nanotechnology · polymerization · self-assembly

[1] a) H. Nakao, H. Shiigi, Y. Yamamoto, S. Tokonami, T. Nagaoka, S. Sugiyama, T. Ohtani, *Nano Lett.* **2003**, *3*, 1391–1394; b) M. G. Warner, J. E. Hutchison, *Nat. Mater.* **2003**, *2*, 272–277; c) G.

Wang, J. Zhang, R. W. Murray, *Anal. Chem.* **2002**, *74*, 4320 – 4327; d) F. Patolsky, Y. Weizmann, O. Lioubashevski, I. Willner, *Angew. Chem.* **2002**, *114*, 2429 – 2433; *Angew. Chem. Int. Ed.* **2002**, *41*, 2323 – 2327.

[2] N. C. Seeman, *Nature* **2003**, *421*, 427 – 431.

[3] a) A. P. Alivisatos, K. P. Johnsson, X. G. Peng, T. E. Wilson, C. J. Loweth, M. P. Bruchez, P. G. Schultz, *Nature* **1996**, *382*, 609 – 611; b) C. J. Loweth, W. B. Caldwell, X. G. Peng, A. P. Alivisatos, P. G. Schultz, *Angew. Chem.* **1999**, *111*, 1925 – 1929; *Angew. Chem. Int. Ed.* **1999**, *38*, 1808 – 1812; c) A. H. Fu, C. M. Micheel, J. Cha, H. Chang, H. Yang, A. P. Alivisatos, *J. Am. Chem. Soc.* **2004**, *126*, 10832 – 10833; d) D. Zanchet, C. M. Micheel, W. J. Parak, D. Gerion, A. P. Alivisatos, *Nano Lett.* **2001**, *1*, 32 – 35.

[4] a) C. A. Mirkin, R. L. Letsinger, R. C. Mucic, J. J. Storhoff, *Nature* **1996**, *382*, 607 – 609; b) T. A. Taton, C. A. Mirkin, R. L. Letsinger, *Science* **2000**, *289*, 1757 – 1760.

[5] a) J. D. Le, Y. Pinto, N. C. Seeman, K. Musier-Forsyth, T. A. Taton, R. A. Kiehl, *Nano Lett.* **2004**, *4*, 2343 – 2347; b) S. J. Xiao, F. R. Liu, A. E. Rosen, J. F. Hainfeld, N. C. Seeman, K. Musier-Forsyth, R. A. Kiehl, *J. Nanopart. Res.* **2002**, *4*, 313 – 317; c) H. Li, S. H. Park, J. H. Reif, T. H. LaBean, H. Yan, *J. Am. Chem. Soc.* **2004**, *126*, 418 – 419; d) C. M. Niemeyer, W. Bürger, J. Peplies, *Angew. Chem.* **1998**, *110*, 2391 – 2395; *Angew. Chem. Int. Ed.* **1998**, *37*, 2265 – 2268.

[6] a) C. D. Mao, W. Q. Sun, N. C. Seeman, *J. Am. Chem. Soc.* **1999**, *121*, 5437 – 5443; b) C. D. Mao, T. H. LaBean, J. H. Reif, N. C. Seeman, *Nature* **2000**, *407*, 493 – 496; c) D. G. Liu, M. S. Wang, Z. X. Deng, R. Walulu, C. D. Mao, *J. Am. Chem. Soc.* **2004**, *126*, 2324 – 2325; d) H. Yan, S. H. Park, G. Finkelstein, J. H. Reif, T. H. LaBean, *Science* **2003**, *301*, 1882 – 1884; e) B. Q. Ding, R. J. Sha, N. C. Seeman, *J. Am. Chem. Soc.* **2004**, *126*, 10230 – 10231; f) E. Winfree, F. R. Liu, L. A. Wenzler, N. C. Seeman, *Nature* **1998**, *394*, 539 – 544.

[7] a) A. Fire, S. Q. Xu, *Proc. Natl. Acad. Sci. USA* **1995**, *92*, 4641 – 4645; b) D. Y. Liu, S. L. Daubendiek, M. A. Zillman, K. Ryan, E. T. Kool, *J. Am. Chem. Soc.* **1996**, *118*, 1587 – 1594; c) P. M. Lizardi, X. Huang, Z. Zhu, P. Bray-Ward, D. C. Thomas, D. C. Ward, *Nat. Genet.* **1998**, *19*, 225 – 232.

C–H Activation

Copper-Mediated Selective Oxidation of a C–H Bond**

*Christophe Boldron, Patrick Gamez, Duncan M. Tooke, Anthony L. Spek, and Jan Reedijk**

Substituted hydroxybenzaldehydes are important feedstock materials for the pharmaceutical and perfume industries.[1,2] These compounds are commonly made by the selective oxidation of aromatic methyl groups. However, this chemical reaction is difficult and often proceeds to the carboxylic acid derivative. Thus, 4-hydroxy-3,5-dimethylbenzaldehyde (HDB) is a valuable intermediate, especially for the preparation of drugs.[3–5] A number of synthetic routes to HDB starting from 2,4,6-trimethylphenol (TMP) involving stoichiometric amounts or an excess of oxidant are known.[6–10] So far, the only catalytic oxidation of TMP to HDB was achieved by Takehira and co-workers.[11–14]

Copper-containing enzymes, such as vanillyl alcohol oxidase[15] or laccase[16] can selectively produce the aromatic aldehyde functional group from a methyl group. We report here a bioinspired Cu^{II}/neocuproine system to perform the selective *para*-formylation of mesitol [Eq. (1)]. The reaction

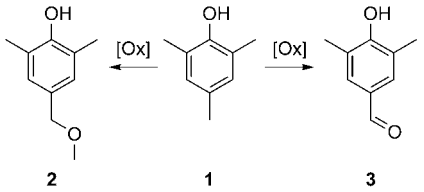

2 1 3 (1)

of TMP (**1**) with $[CuCl_2(neo)_x]$ (neo = neocuproine = 2,9-dimethylphenanthroline) and sodium methoxide as cocatalyst in methanol at room temperature leads to the formation of 4-(methoxymethyl)-2,6-dimethylphenol (**2**, MDP) and/or HDB (**3**), depending on the experimental conditions (Table 1).

Without neocuproine no oxidation products were observed (entry 1); neo is thus necessary for the reaction to proceed, most likely to increase the oxidation potential of the

[*] Dr. C. Boldron, Dr. P. Gamez, Prof. Dr. J. Reedijk
Leiden Institute of Chemistry
Gorlaeus Laboratories
Leiden University
PO Box 9502, 2300 RA Leiden (The Netherlands)
Fax: (+31) 71-527-4671
E-mail: reedijk@chem.leidenuniv.nl
Dr. D. M. Tooke, Prof. Dr. A. L. Spek
Department of Crystal and Structural Chemistry
Padualaan 8, 3584 CH University Utrecht (The Netherlands)

[**] Financial support from COST Action (D21/003/2001) and the Dutch National Research School Combination Catalysis (HRSMC and NIOK) is thankfully acknowledged.

Supporting information for this article is available on the WWW under http://www.angewandte.org or from the author.

 DOI: 10.1002/anie.200462946

Table 1: Results of the Cu^{II}/neocuproine-mediated oxidation of TMP (**1**) to MDP (**2**) and/or HDB (**3**) according to Equation (1).[a]

Entry	Reactant [equiv]				Product distribution [mol%][b]		
	TMP	$CuCl_2$	NaOMe	neo	TMP	MDP	HDB
1	1	2	2	0	100	–	–
2	4	2	2	4	71	29	–
3	2	2	2	4	49	51	–
4	1	2	2	4	–	60	20
5	0.5	2	2	4	–	–	100[c]
6	1	2	1.5	2	18	82[d]	–
7[e]	1	0.14	0.3	0.105	–	–	100[f]
8[e]	1	0.14	0.3	0.035	11	80[g]	9

[a] [Ox] = [$CuCl_2$(neo)$_x$] + NaOMe; see the Supporting Information for the experimental procedure. [b] The yields (±5%) were determined by ^{1}H NMR spectroscopy after a reaction time of 30 min. [c] No products of over-oxidation could be detected; HDB was isolated in 85% yield. [d] Isolated in 69% yield. [e] Optimized catalytic reactions performed at 65°C under argon with H_2O_2. The yields (±5%) were determined by ^{1}H NMR spectroscopy using 1,2,4,5-tetrabromobenzene as an internal standard. [f] After a reaction time of 6 h. [g] After a reaction time of 12 h.

Cu^{II}/Cu^{I} pair. The neo ligand is indeed a highly specific bidentate ligand for Cu^{I} species, while its affinity towards Cu^{II} species is known to be low.[17,18] The bis-neocuproine copper(I) complex $[Cu(neo)_2]^+$ is extremely stable due to the presence of *ortho*-methyl groups, which strongly stabilize the tetrahedral geometry of Cu^{I} ions, thereby preventing their reoxidation to Cu^{II}. The driving force of the reaction is thus the more facile reduction of copper(II) ions owing to the affinity of neo for copper(I) species (see the Supporting Information). This is confirmed when neo is replaced by the sterically far less crowded 2,2′-bipyridine, as the resulting copper complex is inactive.

The amount of TMP used in the reaction was then varied. When 2 or 1 equiv of TMP per Cu^{II}/neo were used, total conversion of the substrate could not be achieved (Table 1, entries 2 and 3). The oxidation reactions exclusively led to the formation of MDP in 29% and 51% yield, respectively. These results are in accordance with the fact that the formation of MDP is a two-electron process. If 0.5 equiv of TMP is allowed to react with 1 equiv of Cu^{II}/neo, both MDP and HDB are produced (entry 4). The quantitative formation of the benzaldehyde derivative HDB was achieved with a TMP/Cu ratio of 0.25 (four-electron oxidation; entry 5). A series of experiments was subsequently carried out to improve the selectivity towards the methoxymethyl derivative. This study showed that very good selectivities in MDP could only be reached when moderate amounts of the basic cocatalyst were used along with one equivalent of neo per copper ion. For instance, the *para*-methoxymethyl compound could be produced in 82% yield in the presence of 0.75 equiv of NaOMe instead of 1 equiv (entry 6).

Based on the active site found in enzymes containing the type-3 copper site, a dinuclear copper species bridged by a phenolate and a methoxide is proposed as the key intermediate of the reaction (Scheme 1). The *para*-benzylic proton is activated through the coordination of the phenolate to the metal ions. Deprotonated TMP reduces each Cu^{II} to Cu^{I}. This $2e^-$ transfer induces the polarization of the benzylic C–H bond, which results in a rearrangement of the aromatic ring to a quinone methide. The nucleophilic addition of methanol to the quinone methide leads to the formation of the *para*-methoxymethyl derivative MDP. A second step ($2e^-$ oxidation/MeOH) yields a ketal compound, which has been detected by ^{1}H NMR spectroscopy in the crude mixture after evaporation of the solvent. Hydrolysis during the work-up affords HDB. The same result was observed when argon was used in place of air, suggesting that molecular oxygen is not involved in the C–O bond formation.

To further study the reaction mechanism and detect the proposed active species, attempts were made to crystallize a key intermediate. Reaction of a DMF/MeOH (9:1) solution of sodium pentafluorophenoxide (1 equiv)—a phenolate that is inactive towards oxidation—and neo (2 equiv) with $CuCl_2$ (2 equiv), NaOMe (1.2 equiv), and acetonitrile yields diamond-shaped green crystals suitable for X-ray diffraction (see the Supporting Information). A PLATON[19] representation of the molecular structure of this compound is depicted in Figure 1. As previously postulated by several authors, [20] a dinuclear copper(II) species bridged by both a methoxide and a pentafluorophenoxide is obtained. To the best of our knowledge, this is the first crystallographic evidence of a self-assembled, mixed μ-methoxo-μ-phenoxo-bridged dinuclear copper complex with a mononucleating nonbridging ligand, namely, neocuproine. This structure is in total agreement with the proposed active species for the reaction described above.

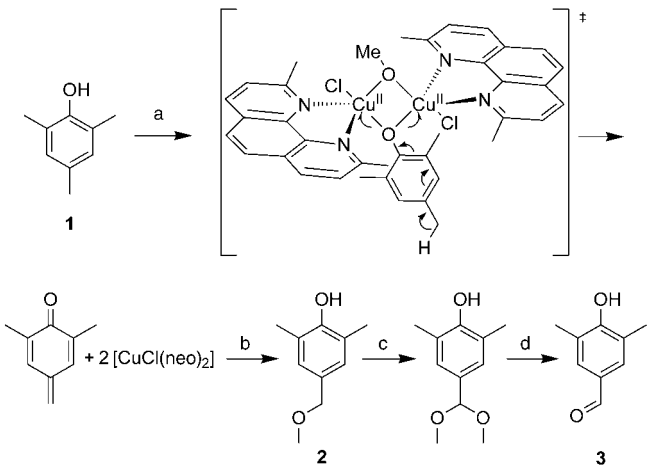

Scheme 1. Proposed reaction mechanism for the stoichiometric formation of MDP (**2**) and HDB (**3**) from TMP (**1**). a) NaOMe (2 equiv), $CuCl_2$ (2 equiv), neo (4 equiv), MeOH; b) MeOH; c) $2e^-$ oxidation: NaOMe (2 equiv), $CuCl_2$ (2 equiv), neo (4 equiv), MeOH; d) H_2O.

The investigation was then focused on performing this oxidation with catalytic amounts of the Cu^{II}/neo complex. This would provide an environmentally friendly and economically favorable system for industrial application. This mech-

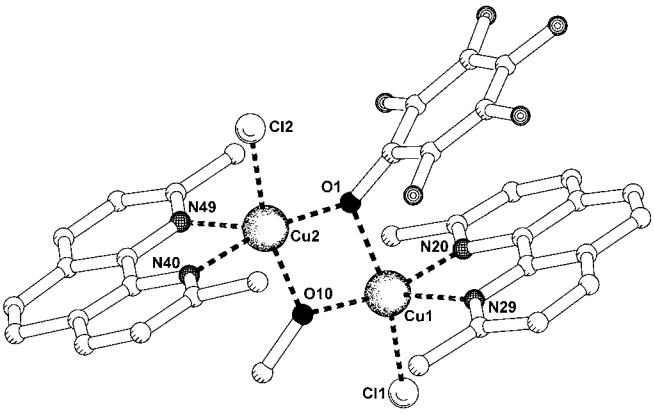

Figure 1. Molecular structure of $[Cu_2Cl_2(neo)_2(\mu\text{-}CH_3O)(\mu\text{-}C_6F_5O)]$. Selected bond lengths [Å] and angles [°]: Cu1–O1 2.066(7), Cu1–O10 1.950(6), Cu1–Cl1 2.276(3), Cu1–N20 2.025(8), Cu1–N29 2.270(9), Cu1–Cu2 3.137(8), Cu2–O1 1.947(6), Cu2–O10 1.966(7), Cu2–Cl2 2.265(3), Cu2–N40 2.043(8), Cu2–N49 2.256(8); Cu1-O1-Cu2 102.8(3), Cu1-O10-Cu2 106.4(3). See also the Supporting Information.

anism would imply the reoxidation of the Cu^{I} species, which a priori seems to be unlikely due to the very high stability of the $[Cu(neo)_2]^+$ cation. For this purpose, only 1 equiv of neo was used per Cu^{II} ion, as we anticipated a more facile reoxidation of the resulting Cu^{I} complex $[Cu(neo)]^+$. The first logical procedure was to perform the catalytic reaction in air, or in pure dioxygen, and heat the reaction mixture to promote the Cu^{I} oxidation. Only one catalytic cycle can be completed under these experimental conditions, suggesting that molecular oxygen is not strong enough to achieve the Cu^{I} reoxidation. To overcome this difficulty, hydrogen peroxide, an activated form of dioxygen, was successfully used as oxidant, and the experimental conditions were optimized. Thus, 0.14 equiv of $[CuCl_2(neo)]$, in the presence of 2 equiv of H_2O_2 and 0.3 equiv of NaOMe as basic cocatalyst, could catalyze the quantitative formylation of 1 equiv of TMP after 6 h (Table 1, entry 7). The selective oxidation was performed under argon and refluxing methanol. The controlled production of MDP could be carried out using a smaller amount of neo (0.035 equiv instead of 0.105 equiv; entries 7 and 8). Most likely, the presence of less ligand leads to the formation of different active species, allowing the isolation of the intermediate product **2**. No effective catalytic method for preparing MDP has yet been reported. Therefore, the synthetic procedure described here is the first effective catalytic preparation of MDP.

In conclusion, a new environmentally friendly, high-yielding procedure has been developed for the *para* C_{sp^3}-H oxidation of TMP. This compound can be selectively oxidized to form either MDP or HDB, two valuable industrial compounds. A key reaction intermediate, a self-assembled μ-methoxo-μ-phenoxo-bridged dinuclear copper complex involving a mononucleating ligand, was isolated and structurally characterized. This dicopper complex suggests the participation of bimetallic active species in the catalytic cycle as well as the nucleophilic attack of a methanolate anion to the bis-alkoxo-bridged complex. The substrate scope for this catalytic oxidation reaction is currently being investigated.

Received: December 15, 2004
Revised: March 9, 2005
Published online: May 4, 2005

Keywords: biomimetic synthesis · C–H activation · copper · homogeneous catalysis · oxidation

[1] F. Wang, G. Y. Yang, W. Zhang, W. H. Wu, J. Xu, *Adv. Synth. Catal.* **2004**, *346*, 633.
[2] L. Weisse, R. Neunteufel, H. Strutz (Hoechst AG), US Patent 5,395,978, **1995**.
[3] K. M. Youssef, M. A. El-Sherbeny, F. S. El-Shafie, H. A. Farag, S. A. A. Awadalla, *Arch. Pharm.* **2004**, *337*, 42.
[4] K. D. Turnbull (University of Arkansas), US Patent 6,657,052 B1, **2003**.
[5] H. Luebbers, R. A. Neunteufel (Hoechst AG), German Patent 27 32 227, **1979**.
[6] H. D. Becker, *J. Org. Chem.* **1965**, *30*, 982.
[7] W. E. Smith, *J. Org. Chem.* **1972**, *37*, 3972.
[8] S. L. Goldstein, E. McNelis, *J. Org. Chem.* **1984**, *49*, 1613.
[9] K. Omura, *J. Org. Chem.* **1984**, *49*, 3046.
[10] W. Baik, H. J. Lee, J. M. Jang, S. Koo, B. H. Kim, *J. Org. Chem.* **2000**, *65*, 108.
[11] K. Takehira, M. Shimizu, Y. Watanabe, H. Orita, T. Hayakawa, *Tetrahedron Lett.* **1990**, *31*, 2607.
[12] M. Shimizu, Y. Watanabe, H. Orita, T. Hayakawa, K. Takehira, *Tetrahedron Lett.* **1991**, *32*, 2053.
[13] M. Shimizu, Y. Watanabe, H. Orita, T. Hayakawa, K. Takehira, *Bull. Chem. Soc. Jpn.* **1993**, *66*, 251.
[14] K. Takaki, Y. Shimasaki, T. Shishido, K. Takehira, *Bull. Chem. Soc. Jpn.* **2002**, *75*, 311.
[15] R. H. H. van den Heuvel, M. W. Fraaije, M. Ferrer, A. Mattevi, W. J. H. van Berkel, *Proc. Natl. Acad. Sci. USA* **2000**, *97*, 9455.
[16] C. Crestini, D. S. Argyropoulos, *Bioorg. Med. Chem.* **1998**, *6*, 2161.
[17] B. R. James, R. J. Williams, *J. Chem. Soc.* **1961**, 2007.
[18] G. F. Smith, W. H. Mccurdy, *Anal. Chem.* **1952**, *24*, 371.
[19] A. L. Spek, *J. Appl. Crystallogr.* **2003**, *36*, 7.
[20] J. Gao, S. H. Zhong, R. A. Zingaro, *J. Mol. Catal. A: Chem.* **2004**, *207*, 15.

Selenenylation

Asymmetric Carboselenenylation Reaction of Alkenes with Aromatic Compounds**

Kazuki Okamoto, Yoshiaki Nishibayashi, Sakae Uemura, and Akio Toshimitsu**

Asymmetric functionalization of simple alkenes is one of the most attractive subjects in organic synthesis. A variety of asymmetric reactions such as epoxidation,[1] dihydroxylation,[2] aminohydroxylation,[3] hydroboration,[4] hydrosilylation,[5] cyclopropanation,[6] and carbonylation[7] have been reported for the introduction of new functional groups into alkene substrates to produce optically active compounds. The stereoselective addition of electrophilic reagents to simple alkenes is another versatile approach to provide synthetically useful compounds that bear various functionalized groups.[8,9] Recently, electrophilic selenium reagents with optically active moieties have been successfully employed in a number of stereoselective additions to simple alkenes.[10] Typically, the stereoselective selenenylation of simple alkenes with heteroatom-centered nucleophiles such as alcohols, nitriles, oximes, and azides gave the corresponding functionalized organoselenium compounds with high diastereoselectivity.[11,12] In all cases, the selenenylation proceeds via chiral episelenonium ions as key intermediates, which then undergo a ring-opening reaction by nucleophilic attack.

We recently reported the stereospecific reactions of chiral episelenonium ions generated from optically active (β-arylseleno)ethyl alcohols with carbon-centered nucleophiles such as alkenyl silyl ethers, trimethylsilyl cyanide, allyltrimethylsilane, and aromatic compounds.[13] This result prompted us to investigate the asymmetric carboselenenylation reaction of simple alkenes with carbon-centered nucleophiles. We describe herein the first example of the asymmetric carboselenenylation reaction of simple alkenes with aromatic compounds by using an optically active electrophilic selenium reagent.[14]

Treatment of an optically active areneselenenyl trifluoromethanesulfonate (triflate) **1a** (which is generated in situ from the reaction of a diaryl diselenide **2a** with bromine and silver triflate) with excess (*E*)-β-methylstyrene (**3a**) at −78 °C for 10 min in dichloromethane in the presence of molecular sieves (4 Å) and then with 2-methylfuran (**4a**) at −78 °C for 2 h gave 2-(1-phenyl-2-arylselenopropyl)-5-methylfuran (**5a**) in 73% yield with 91:9 d.r. (Scheme 1). Typical results are shown in Table 1. The presence of the 4-Å molecular sieves is essential to obtain **5a** in high yields (Table 1, entries 1–3). In fact, in the absence of the 4-Å molecular sieves, the yield of **5a** decreased, with an increase in the amount of 1-phenyl-2-aryleselenopropanol (**6**) (Table 1, entry 4). The compound **6** is considered to be formed by nucleophilic attack of adventitious water at the episelenonium ion intermediate. The use of a smaller amount of **3a** decreased the yield of **5a**

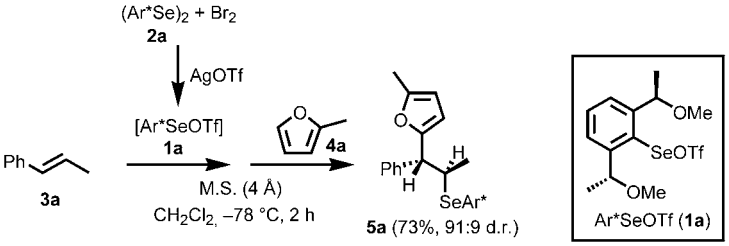

Scheme 1. Asymmetric carboselenenylation reaction of (*E*)-β-methylstyrene (**3a**) with 2-methylfuran (**4a**) by using an optically active electrophilic selenium reagent (**1a**). Tf = trifluoromethanesulfonyl.

Table 1: Asymmetric carboselenenylation reaction of (*E*)-β-methylstyrene (**3a**) with 2-methylfuran (**4a**) by using an optically active electrophilic selenium reagent (**1a**).[a]

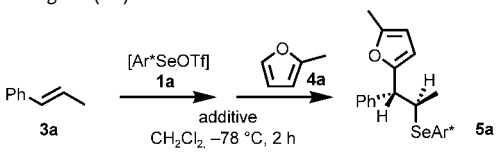

Entry	**3a** [equiv]	Additive	Yield [%][b]	d.r.[c]
1	10	M.S. (4 Å) (300 mg)	73	91:9
2	10	M.S. (4 Å) (100 mg)	57	91:9
3	10	M.S. (3 Å) (100 mg)	50	91:9
4	10	–	41[d]	91:9
5	2	–	25[e]	91:9

[a] All the reactions of **3a** (2.00 mmol) with **4a** (1.00 mmol) by using **1a** (0.20 mmol) were carried out at −78 °C for 2 h. [b] Yield of isolated product. [c] Determined by ^{1}H NMR. M.S. = molecular sieves. [d] 1-Phenyl-2-areneselenopropanol (**6**) was formed in 25% yield. [e] 1-Phenyl-2-areneselenopropanol (**6**) was formed in 35% yield.

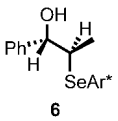

6

[*] K. Okamoto, Dr. Y. Nishibayashi,[+] Prof. Emeritus Dr. S. Uemura
Department of Energy and Hydrocarbon Chemistry
Graduate School of Engineering
Kyoto University
Katsura, Nishikyo-ku, Kyoto, 615-8510 (Japan)
Fax: (+81) 75-383-2517
E-mail: ynishiba@scl.kyoto-u.ac.jp
Prof. Dr. A. Toshimitsu
International Innovation Center
Kyoto University
Sakyo-ku, Kyoto, 606-8501 (Japan)
Fax: (+81) 75-753-9174
E-mail: akiot@iic.kyoto-u.ac.jp
[+] Current address:
Institute of Engineering Innovation
School of Engineering, The University of Tokyo
Yayoi, Bunkyo-ku, Tokyo, 113-8656 (Japan)
Fax: (+81) 35-841-1175

[**] This work was supported by a Grant-in-Aid for Scientific Research for Young Scientists (A) (No. 15685006) to Y.N. from the Ministry of Education, Culture, Sports, Science, and Technology, Japan.
Supporting information for this article is available on the WWW under http://www.angewandte.org or from the author.

  DOI: 10.1002/anie.200500573

(Table 1, entry 5). A high diastereoselectivity was only attained by the use of **1a**. When other C_2-symmetric areneselenenyl triflates bearing two ethoxy groups (**1b**)[15] and two benzyloxy groups (**1c**) were used instead of **1a**, a lower diastereoselectivity of the product and no formation of the product were observed, respectively. Although extremely high diastereoselectivities were reported in the selenenylation of **3a** with heteroatom-centered nucleophiles such as alcohols by using a variety of active areneselenenyl triflates (Scheme 2, **1d**–**1f**),[11,12h] these areneselenenyl triflates did not work effectively in this carboselenenylation reaction. Detailed results are given in the Supporting Information.

The asymmetric carboselenenylation reactions of **3a** with other furans **4b**–**4d** by using **1a** as an optically active electrophilic selenium reagent under similar reaction conditions gave the corresponding alkylated furans **5b**–**5d** in good yields with high diastereoselectivity (Table 2). In the reaction with furan (**4b**), the product **5b** was obtained in slightly lower yield (Table 2, entry 1). Other heterocyclic aromatic compounds such as 2-methylthiophene (**4e**) and *N*-methylpyrrole (**4f**) can be alkylated at the α position of the heterocyclic rings. In both cases, high diastereoselectivities (91:9 and 89:11 d.r., respectively) were attained (Table 2, entries 4 and 5). Unfortunately, no reaction occurred when *N*-methylindole was used as a heterocyclic aromatic compound. Not only heterocyclic aromatic compounds but also electron-rich benzene derivatives can be used in this asymmetric carboselenenylation reaction. The best diastereoselectivity was found in the reaction of **3a** with 1,3,5-trimethoxybenzene (**4i**), and the corresponding alkyl substituted derivative was formed with 95:5 d.r. (Table 2, entry 8). Recrystallization of the mixture from methanol gave only the major diastereoisomer in pure form. The molecular structure of the major diastereoisomer of **5i** was unambiguously determined by X-ray crystallographic analysis (see Supporting Information).[16] In contrast to the good reactivity of *N*,*N*-dimethylaniline (**4j**) and azulene (**4k**) (Table 2, entries 9 and 10), no reaction proceeded when anisole (**4g**) and 1,4-dimethoxybenzene (**4h**) were used as benzene derivatives (Table 2, entries 6 and 7).

Table 2: Asymmetric carboselenenylation reaction of (*E*)-β-methylstyrene (**3a**) with aromatic compound (**4**) by using **1a**.[a]

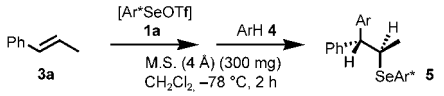

Entry	ArH (**4**)		Product (**5**)		Yield[%][b]	d.r.[c]
1		**4b**	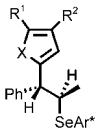 X = O; R^1 = H; R^2 = H	**5b**	36	91:9
2		**4c**	X = O; R^1 = Et; R^2 = H	**5c**	67	91:9
3		**4d**	X = O; R^1 = Me; R^2 = Me	**5d**	63	92:8
4		**4e**	X = S; R^1 = Me; R^2 = H	**5e**	52	91:9
5		**4f**	X = NMe; R^1 = H; R^2 = H	**5f**	48	89:11
6		**4g**			0	–
7	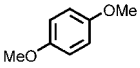	**4h**			0	–
8	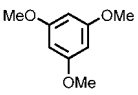	**4i**	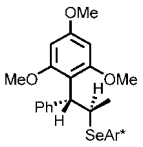	**5i**	77	95:5
9	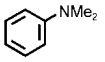	**4j**	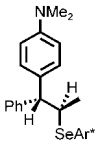	**5j**	51	90:10
10		**4k**	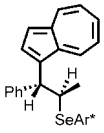	**5k**	34	91:9

[a] All the reactions of **3a** (2.00 mmol) with **4** (1.00 mmol) in the presence of **1a** (0.20 mmol) were carried out at −78 °C for 2 h. [b] Yield of isolated product. [c] Determined by ^{1}H NMR.

The asymmetric carboselenenylation reaction of other alkenes (**3**) was investigated next (Table 3). The introduction of a *p*-fluoro or *p*-phenyl substituent in the aromatic ring of β-methylstyrene slightly increased the diastereoselectivity (Table 3, entries 1 and 2). On the other hand, a slightly lower diastereoselectivity was attained in the reaction of *p*-methyl-(*E*)-β-methylstyrene (**3d**) (Table 3, entry 3). The introduction of a chloro substituent in the aromatic ring decreased the reactivity (Table 3, entries 4 and 5). Furthermore, the reaction of 2-((*E*)-1-propenyl)naphthalene (**3g**) proceeded smoothly to give the corresponding alkylated furan (**5q**) in good yield with 87:13 d.r. (Table 3, entry 6). Although the reason is not known, the presence of 4-Å molecular sieves decreased both the reactivity and the

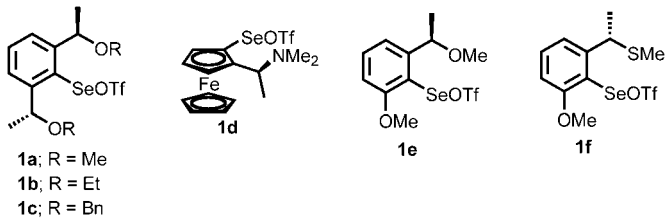

Scheme 2. Optically active electrophilic selenium reagents.

Table 3: Asymmetric carboselenenylation reaction of alkenes (**3**) with with 2-methylfuran (**4a**) by using **1a**.[a]

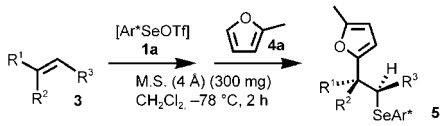

Entry	Alkene (**3**)	Product (**5**)	Yield[b]	d.r.[c]
	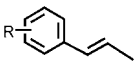	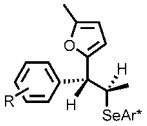		
1	R = *p*-F	**3b**	**5l**	55	93:7
2	R = *p*-Ph	**3c**	**5m**	55	94:6
3	R = *p*-Me	**3d**	**5n**	67	89:11
4	R = *p*-Cl	**3e**	**5o**	39	90:10
5	R = *m*-Cl	**3f**	**5p**	39	94:6
6	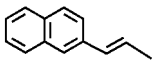	**3g**	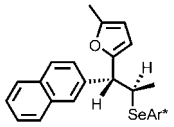	**5q**	70	87:13
7[d]		**3h**	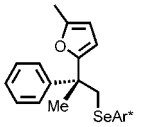	**5r**	40	90:10
8		**3i**	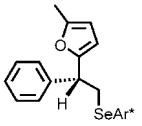	**5s**	45	78:22
9	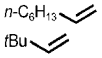	**3j**	**5t**	0	–
10		**3k**	**5u**	0	–

[a] All the reactions of **3** (2.00 mmol) with **4a** (1.00 mmol) in the presence of **1a** (0.20 mmol) were carried out at −78 °C for 2 h. [b] Yield of isolated product. [c] Determined by ^{1}H NMR. [d] In the absence of 4-Å molecular sieves.

diastereoselectivity of the reaction of α-methylstyrene (**3h**) (Table 3, entry 7). A lower diastereoselectivity was observed when styrene (**3i**) was used as an alkene (Table 3, entry 8). A similar trend of lower diastereoselectivity in the cases of **3h** and **3i** has been observed in the asymmetric oxyselenenylation with methanol by using **1b**.[15] Unfortunately, no reaction occurred in the reactions of aliphatic alkenes such as 1-octene (**3j**) and 3,3-dimethylbutene (**3k**).

The stereochemistry of the major diastereoisomer of **5i** (*R* configuration at the benzylic position) indicates that **3a** undergoes *Si*-face attack by the chiral areneselenium moiety (Figure 1). This stereoselective approach is supported by previous theoretical studies with density-functional calculations on the transition states by using **1a**.[17] Separately, we confirmed that the reductive cleavage of a chiral arylselenium moiety of **5j** (90:10 d.r.) with Bu_3SnH in the presence of a catalytic amount of AIBN in toluene at reflux for 6 h afforded optically active 1-(*N*,*N*-dimethylaminophenyl)-1-phenylpropane (**7**) in quantitative yield with 90:10 d.r. (HPLC) (Scheme 3). This result indicates that the removal of the arylselenium moiety in **5** proceeded without loss of optical purity at the benzylic position.

In summary, we have developed an asymmetric carboselenenylation reaction of simple alkenes with aromatic compounds by using a C_2-symmetric areneselenenyl triflate. The carbon–carbon bond-forming reaction proceeds with high diastereoselectivity. This reaction is a convenient procedure for the preparation of chiral hydrocarbons that bear an aryl moiety at the stereogenic carbon atom and can be considered as a new type of asymmetric Friedel–Crafts alkylation reaction of aromatic compounds with alkenes. Further work is aimed at the elucidation of the reaction mechanism in detail and broadening the scope of the asymmetric reaction.

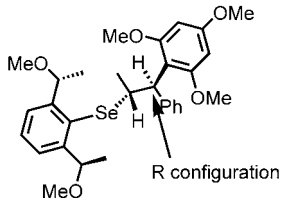

Figure 1. Stereochemistry of the major diastereoisomer of **5i**.

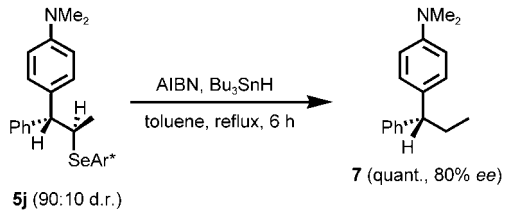

Scheme 3. Reductive cleavage of a chiral arylselenium moiety of **5j**. AIBN = azobisisobutyronitrile.

Experimental Section

5a: Molecular sieves (4 Å) (300 mg) and a solution of bromine (0.12 mmol) in CCl_4 (0.12 mL) were added to a solution of diselenide **2a** (54.4 mg, 0.10 mmol, > 99 % *ee*) in CH_2Cl_2 (4.0 mL) at −78 °C. After 30 min, silver triflate (61.7 mg, 0.24 mmol) was added. The resulting heterogeneous mixture was stirred at −78 °C for 30 min. *(E)*-β-Methylstyrene (**3a**) (236.4 mg, 2.00 mmol) was then added to the mixture at −78 °C followed by 2-methylfuran (**4a**) (81.2 mg, 1.00 mmol). The mixture was stirred for 2 h, quenched with saturated aqueous $NaHCO_3$ at −78 °C, and extracted with CH_2Cl_2. The combined organic layers were dried over $MgSO_4$ and concentrated. The residue was purified by silica-gel chromatography to give **5a** as a colorless oil (68.4 mg, 0.145 mmol, 73 % yield, 91:9 d.r.). The diastereoisomers could not be separated by flash chromatography. The diastereoselectivity does not change during the purification. The ratio of two diastereoisomers was determined by ^{1}H NMR and ^{77}Se NMR; ^{1}H NMR ($CDCl_3$, 400 MHz): major diastereoisomer: δ = 1.24 (d, J = 6.8 Hz, 3H), 1.39 (d, J = 6.4 Hz, 6H), 2.26 (s, 3H), 3.12 (s, 6H), 3.74 (dq, J = 10 and 6.8 Hz, 1H), 4.06 (d, J = 10 Hz, 1H), 5.13 (q,

$J = 6.4$ Hz, 2H), 5.86 (d, $J = 3.2$ Hz, 1H), 6.03 (d, $J = 3.2$ Hz, 1H), 7.27–7.46 ppm (m, 8H); minor diastereoisomer: $\delta = 3.83$ (dq, $J = 8.8$ and 6.4 Hz, 1H), 4.11 ppm (d, $J = 8.8$ Hz, 1H); $^{13}C\{^1H\}$ NMR ($CDCl_3$, 100 MHz): major diastereoisomer: $\delta = 13.7$, 20.6, 24.2, 44.3, 52.4, 56.3, 78.4, 105.9, 107.5, 125.2, 127.2, 128.1, 128.3, 128.5, 129.7, 140.6, 148.3, 151.2, 153.0 ppm; $^{77}Se\{^1H\}$ NMR ($CDCl_3$, 76 MHz): major diastereoisomer: $\delta = 236.9$ ppm (s); minor diastereoisomer: $\delta = 236.3$ ppm (s). Elemental analysis: calcd for $C_{26}H_{32}O_3Se$: C 66.23, H 6.84; found: C 66.31, H 6.92.

Received: February 16, 2005
Published online: May 4, 2005

Please note: Minor changes have been made to this manuscript since its publication in *Angewandte Chemie Early View*. The Editor.

Keywords: alkenes · asymmetric synthesis · diastereoselectivity · selenium · synthetic methods

[1] For a review, see: T. Katsuki, *Coord. Chem. Rev.* **1995**, *140*, 189, and references therein.
[2] For a review, see: H. C. Kolb, M. S. Van Nieuwenhze, K. B. Sharpless, *Chem. Rev.* **1994**, *94*, 2483, and references therein.
[3] a) G. Li, H.-T. Chang, K. B. Sharpless, *Angew. Chem.* **1996**, *108*, 449; *Angew. Chem. Int. Ed. Engl.* **1996**, *35*, 451; b) G. Li, H. H. Angert, K. B. Sharpless, *Angew. Chem.* **1996**, *108*, 2995; *Angew. Chem. Int. Ed. Engl.* **1996**, *35*, 2813.
[4] a) T. Hayashi, Y. Matsumoto, Y. Ito, *J. Am. Chem. Soc.* **1989**, *111*, 3426; b) K. Burgess, M. J. Ohlmeyer, *Chem. Rev.* **1991**, *91*, 1179, and references therein.
[5] a) Y. Uozumi, T. Hayashi, *J. Am. Chem. Soc.* **1991**, *113*, 9887; b) T. Hayashi, *Acc. Chem. Res.* **2000**, *33*, 354, and references therein.
[6] For a recent review, see: H. Lebel, J.-F. Marcoux, C. Molinaro, A. B. Charette, *Chem. Rev.* **2003**, *103*, 977, and references therein.
[7] For a review, see: F. Agbossou, J.-F. Carpentier, A. Mortreux, *Chem. Rev.* **1995**, *95*, 2485, and references therein.
[8] a) O. Kitagawa, T. Hanano, K. Tanabe, M. Shiro, T. Taguchi, *J. Chem. Soc. Chem. Commun.* **1992**, 1005; b) S. H. Kang, S. B. Lee, C. M. Park, *J. Am. Chem. Soc.* **2003**, *125*, 15748.
[9] a) S. H. Kang, M. Kim, *J. Am. Chem. Soc.* **2003**, *125*, 4684; b) S. H. Kang, M. Kim, S. Y. Kang, *Angew. Chem.* **2004**, *116*, 6303; *Angew. Chem. Int. Ed.* **2004**, *43*, 6177.
[10] For recent reviews, see: a) *Organoselenium Chemistry* (Ed.: T. G. Back), Oxford University Press, Oxford, **1999**; b) T. Wirth (Ed.), *Top. Curr. Chem.* **2000**, *208*; c) T. Wirth, *Angew. Chem.* **2000**, *112*, 3890; *Angew. Chem. Int. Ed.* **2000**, *39*, 3741.
[11] a) S. Fukuzawa, Y. Kasugahara, S. Uemura, *Tetrahedron Lett.* **1994**, *35*, 9403; b) Y. Nishibayashi, S. K. Srivastava, H. Takada, S. Fukuzawa, S. Uemura, *J. Chem. Soc. Chem. Commun.* **1995**, 2321; c) H. Takada, Y. Nishibayashi, S. Uemura, *J. Chem. Soc. Perkin Trans. 1* **1999**, 1511.
[12] a) S. Tomoda, M. Iwaoka, *Chem. Lett.* **1988**, 1895; b) T. Wirth, *Angew. Chem.* **1995**, *107*, 1872; *Angew. Chem. Int. Ed. Engl.* **1995**, *34*, 1726; c) S. Fukuzawa, K. Takahashi, H. Kato, H. Yamazaki, *J. Org. Chem.* **1997**, *62*, 7711; d) M. Tiecco, L. Testaferri, C. Santi, C. Tomassini, F. Marini, L. Bagnoli, A. Temperini, *Eur. J. Org. Chem.* **2000**, 3451; e) M. Tiecco, L. Testaferri, F. Marini, S. Sternativo, C. Santi, L. Bagnoli, A. Temperini, *Tetrahedron: Asymmetry* **2001**, *12*, 3053; f) M. Tiecco, L. Testaferri, L. Bagnoli, V. Purgatorio, A. Temperini, F. Marini, C. Santi, *Tetrahedron: Asymmetry* **2001**, *12*, 3297; g) T. G. Back, Z. Moussa, M. Parvez, *J. Org. Chem.* **2002**, *67*, 499; h) M. Tiecco, L. Testaferri, C. Santi, C. Tomassini, F. Marini, L. Bagnoli, A. Temperini, *Chem. Eur. J.* **2002**, *8*, 1118; i) L. Uehlin, G. Fragale, T. Wirth, *Chem. Eur. J.* **2002**, *8*, 1125; j) M. Tiecco, L. Testaferri, C. Santi, C. Tomassini, F. Marini, L. Bagnoli, A. Temperini, *Angew. Chem.* **2003**, *115*, 3239; *Angew. Chem. Int. Ed.* **2003**, *42*, 3131.
[13] a) A. Toshimitsu, K. Nakano, T. Mukai, K. Tamao, *J. Am. Chem. Soc.* **1996**, *118*, 2756; b) K. Okamoto, Y. Nishibayashi, S. Uemura, A. Toshimitsu, *Tetrahedron Lett.* **2004**, *45*, 6137.
[14] An asymmetric intramolecular cyclization of alkenes with aromatic compounds by using an optically active electrophilic selenium reagent was reported, but the reaction is not a direct carboselenenylation; the stepwise reaction first involves an oxyselenenylation and then a stereoselective intramolecular cyclization of an episelenonium ion with benzene derivatives to give the corresponding cyclic products with high diastereoselectivity: R. Déziel, E. Malenfant, C. Thibault, *Tetrahedron Lett.* **1998**, *39*, 5493.
[15] R. Déziel, S. Goulet, L. Grenier, J. Bordeleau, J. Bernier, *J. Org. Chem.* **1993**, *58*, 3619.
[16] The molecular structure of a major diastereoisomer of **5i** was unambiguously clarified by X-ray crystallographic analysis. CCDC-261554 contains the supplementary crystallographic data for this paper. These data can be obtained free of charge from the Cambridge Crystallographic Data Centre via www.ccdc.cam.ac.uk/data_request/cif.
[17] a) T. Wirth, G. Fragale, M. Spichty, *J. Am. Chem. Soc.* **1998**, *120*, 3376; b) X. Wang, K. N. Houk, M. Spichty, T. Wirth, *J. Am. Chem. Soc.* **1999**, *121*, 8567; c) M. Spichty, G. Fragale, T. Wirth, *J. Am. Chem. Soc.* **2000**, *122*, 10914.

Electron Transfer

Study of Anisotropic Interfacial Electron Transfer Across a Semiconductor/Solution Interface by Time-Resolved EPR Spectroscopy**

Kimio Akiyama, Shinji Hashimoto, Sachiko Tojo, Tadaaki Ikoma, Shozo Tero-Kubota, and Tetsuro Majima*

Interfacial electron transfer between molecular adsorbates and semiconductor nanoparticles has been investigated

[*] Prof. Dr. K. Akiyama, S. Hashimoto, Dr. T. Ikoma, Prof. Dr. S. Tero-Kubota
Institute of Multidisciplinary Research for Advanced Materials
Tohoku University
Sendai 980-8577 (Japan)
Fax: (+81) 22-217-5612
E-mail: akiyama@tagen.tohoku.ac.jp
Dr. S. Tojo, Prof. Dr. T. Majima
The Institute of Scientific and Industrial Research (SANKEN)
Osaka University Mihogaoka 8–1
Ibaraki, Osaka 567-0047 (Japan)

[**] This research was supported by a Grant-in-Aid for Scientific Research (No. 15350074) and a Priority Area (417) from the Ministry of Education, Science, Sports, and Culture, Japan. K.A. acknowledges support from CREST (Core Research for Evolutional Science and Technology) of the Japan Science and Technology Agency (JST).

 DOI: 10.1002/anie.200461681

intensively in recent years. The elementary reaction can be written as Equation (1):

$$S + h\nu \rightarrow S^* \rightarrow S^+ + e^-_{surf}(TiO_2) \rightarrow S^+ + e^-_{CB\ or\ trap}(TiO_2) \quad (1)$$

In this process the dye linked covalently to the TiO_2 through a carboxy group is excited from the ground state S to the excited state S*. The excited dye molecule then acts as an electron donor, and transfers an electron to the surface states and subsequently to the conduction band of colloidal TiO_2. A high quantum efficiency for the conversion of light energy into electricity in dye-sensitized solar cells requires the fast injection of electrons combined with a very slow back transfer of electrons.[1–11] Charge recombination associated with dye-sensitized TiO_2 systems has been rationalized in terms of the inverted Marcus region, where the recombination rate is slowed because of a highly exergonic reaction.[12–14]

The charge-separated state is one of the key intermediates in the photosensitization of electron transfer across the semiconductor/solution interface. The electron in the conduction band reverts to the ground state by recombination, or is trapped on an interior Ti^{3+} ion. The dye molecule remains as the radical cation, which is composed of the charge-separated state and the trapped electron within the TiO_2 particle. Time-resolved EPR (TREPR) spectroscopy has been applied successfully to obtain precise information on transient paramagnetic species. In nanocrystalline TiO_2 particles where bidentate ligands were used as electron donors, polarized EPR spectra originating from a limited distribution of geometries were interpreted by the fixed relative orientation of the magnetic tensor corresponding to the trapped electron and trapped hole.[15] Herein, we report the observation of charge-separated states of TiO_2 nanoparticles sensitized with xanthene dye. We determined the distances between the electron and the dye radical cation as well as their relative orientations by analysis of spin-polarized EPR spectra.

Colloidal TiO_2 particles were prepared by controlled hydrolysis of $TiCl_4$ at 2 °C and further dialysis of the sol.[16] The mean particle size was determined to be about 22 nm by dynamic light scattering studies. The two xanthene dyes (fluorescein (FL) and dichlorofluorescein (FL-Cl_2)) used in the experiments were obtained from Tokyo Kasei and were purified by recrystallization from ethanol before use. The output (coumarin 480, 485 nm) of a dye laser (Lumonics, HD300) pumped by an excimer laser (Lambda Physik COMPex 102) was used for excitation of FL and FL-Cl_2. The detection system for the TREPR signal has been described elsewhere.[17] A helium-flow cryostat (Oxford ESR900) was utilized for measurements at low temperatures.

Spin-polarized EPR spectra were observed after excitation with visible light of xanthene dyes adsorbed on colloidal TiO_2 (Figure 1). The polarization patterns (EAE), where A and E denote the enhanced absorption and emission of microwaves, respectively, were essentially identical for the two dye/TiO_2 systems. These results indicate that the precursor state responsible for injection of electrons into the TiO_2 nanoparticle has the same spin multiplicity in the two cases. Since the quantum yields of intersystem crossing in these dyes are very small, electron injection can be expected to occur from the excited singlet precursor state.[18] The polarized signals in each canonical magnetic field decayed with the same rate (approximately $1.0 \times 10^6\ s^{-1}$), with the phase of the polarization maintaining the EAE pattern during the decay.

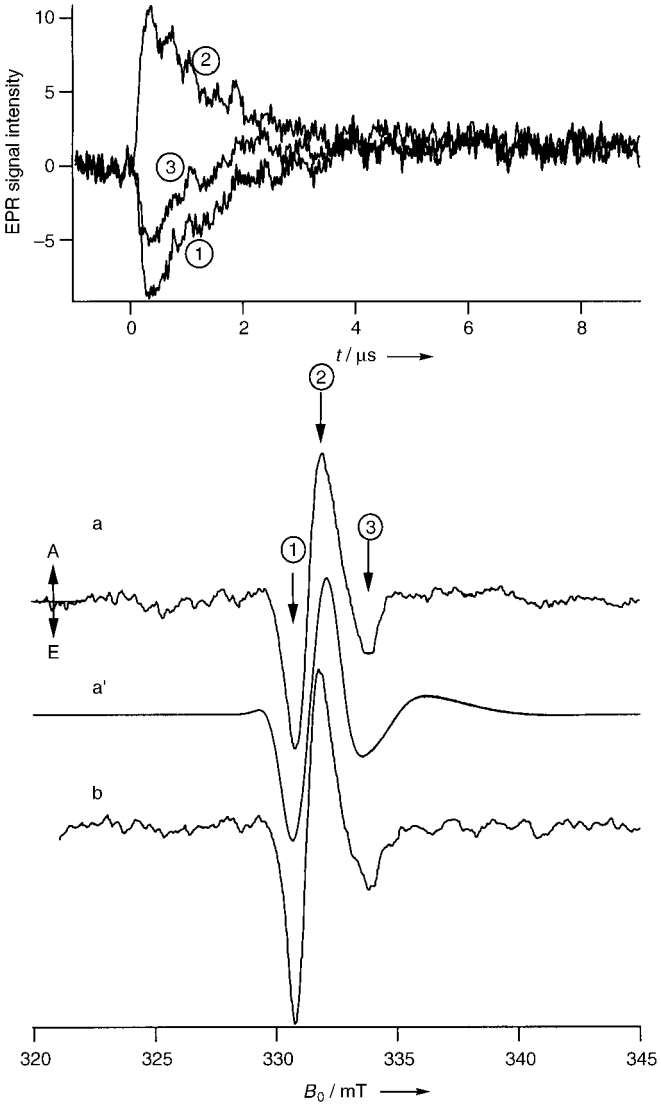

Figure 1. Top: temporal behavior of the polarization at different magnetic fields. Bottom: Time-resolved EPR spectra of FL (a) and FL-Cl_2 (b) adsorbed on colloidal TiO_2 nanoparticles observed at 500 ns after excitation with a laser pulse with a wavelength of 485 nm at 30 K, and the simulated spectrum (a').

The polarized spectra can be readily interpreted in terms of the polarization mechanism of the spin-correlated radical pair (SCRP), where coherent spin singlet/triplet mixing takes place within the radical pair.[19–22] For the calculation we assumed an axial symmetric **g** tensor ($g_\parallel = 1.958$ and $g_\perp = 1.988$) for the trapped electron on TiO_2 and isotropic g values for the dye radical cations.[23] From consideration of the contribution from unresolved hyperfine interactions, an anisotropy of the line widths, $\Delta H_\parallel = 0.8$ and $\Delta H_\perp = 0.3$ mT, was also assumed for the trapped electron. However, isotropic

line widths were used for the dye radical cations because of the expected significant delocalization of the unpaired electron. Exchange (J_{SS}) and dipolar (D_{SS}) interactions were the parameters used for simulation of the observed SCRP signals. D_{SS} is given by $D_{SS}R^3 = -2.786\ \mathrm{mT\,nm^3}$, in which R is the separation of the two unpaired electrons in the molecular center if a point dipole approximation is assumed. According to empirical estimates of the exchange coupling, the value of J_{SS} is negligible compared to the dipolar coupling for distances larger than 1.5 nm.[24–26]

We first calculated the spectrum under the assumption that the dye radical cation is distributed randomly on the surface of TiO_2. However, the observed spectral patterns could not be reproduced satisfactorily. As the local symmetry of the magnetic interactions of a trapped electron on a TiO_2 colloidal nanoparticle is highly anisotropic, the relative orientation between the **g** tensor of the trapped electron and the dipolar tensor of the electron–hole (dye radical cation) pair should be taken into account. In addition, the spin dynamics in the radical pair can also influence the polarization pattern. Unfortunately, the recombination rate of the radical pair at cryogenic temperatures has not been determined. We assumed for the calculation that the recombination rate of the singlet radical pair was of the same order as the polarization decay. The calculated SCRP spectra with different angles ϕ between the **g** tensor of the trapped electron and the dipolar tensor ($\mathbf{Z_d}$) are shown in Figure 2. The EAE polarization patterns were obtained when the angle was set between 90 and 100°. J_{SS} and D_{SS} values corresponding to a distance of 1.6 nm between two unpaired electrons were used for the calculation. The calculated results assuming positive values of J_{SS} are shown in Figure 2. The spectral widths were not significantly affected beyond a radical separation of 1.5 nm, because the small magnetic interaction between two unpaired electrons becomes almost equivalent to the line width. Thus, from the present analysis, we found the separation of the two unpaired electrons was greater than 1.5 nm. Since the size of the dye molecules is known, the trapped electron can be said to be localized at about 0.5 nm from the surface.

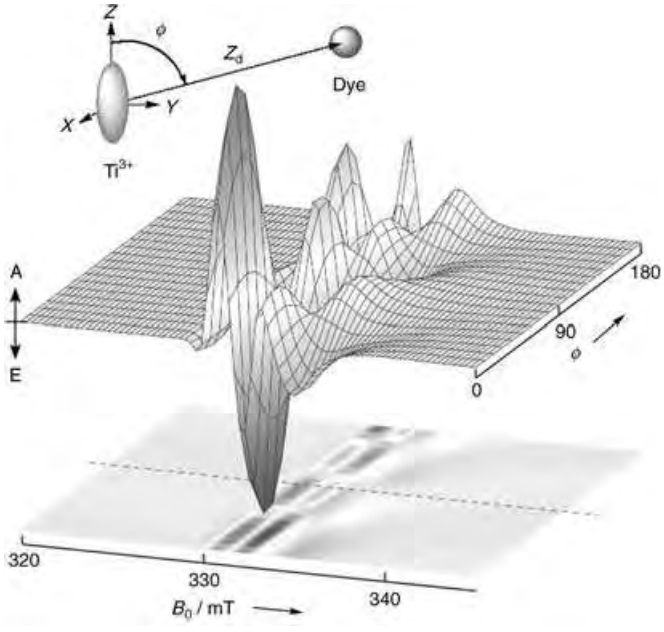

Figure 2. Calculated EPR spectra with different angles between the **g** tensor of the trapped electron and the dipolar tensor of the charge-separated state. The parameters used in the calculation are described in the text.

We obtained the simulated spectra of FL as shown in Figure 1a′ by using the same parameters (J_{SS}, D_{SS}, ϕ, and **g** tensor of the trapped electron). The spectrum observed in the FL-Cl_2/TiO_2 system was also reproduced by using essentially identical parameters. The deviation from the observed spectra can be ascribed to the distribution of dye molecules around ϕ on the TiO_2 colloidal semiconductor. To obtain the best fit of the observed EPR spectra we assumed a positive sign for the exchange interaction. As mentioned above, slow back electron transfer to the dye ground state occurs in the Marcus inverted region where recombination is slowed because of a large change in the free energy of the reaction. The sign of the exchange interaction between the radical pairs is determined by the charge-transfer interaction between the radical ion pair state and the nearby charge-recombined state.[27,28] The locally excited triplet state in the singlet precursor reaction systems effectively perturbs the radical ion pair states because of the small energy difference. The triplet radical ion pair state is selectively stabilized by perturbation from the locally excited triplet state through the electronic coupling, thus leading to positive J values.

The recombination rates for xanthene dye/TiO_2 systems were reported to range from several picoseconds up to microseconds and even milliseconds.[1–11] Colloidal TiO_2 particles had previously been shown to have a crystal structure corresponding to that of anatase.[29] The negatively charged dye molecule reacts with a positively charged Ti-hydroxy group and becomes bound to the Ti atom through formation of a bidentate surface complex. The electron injected from the excited dye molecule recombines through a geminate recombination pathway, but is also trapped in states (assigned to interior Ti^{3+} ions having D_{2d} symmetry) lying below the edge of the conduction band of the TiO_2 nanoparticle. A distribution of energetically different trap sites for the electron and its environments could be responsible for such recombination kinetics. The polarized EPR spectrum is observed at timescales of the order of a microsecond or shorter. In the analysis of the SCRP signal of the xanthene dye/TiO_2 system the relative orientations of the **g** tensor of the trapped electron and the vector of the dipole–dipole interaction between two unpaired electrons are fixed regardless of the expected uniform adsorption of the dye molecules on the surface of the TiO_2 nanoparticle. The observed polarized spectra were well-reproduced at an angle of around 90° between the **g** tensor of the electron and the dipolar tensor. This finding indicates that electron transfer across the semiconductor surface occurs with high orientational selectivity with respect to the radical stabilized on the xanthene dyes. As a result, an anisotropic orientation between the trapped electron and the hole is realized in the microsecond-scale interval after the injection of electrons. The relative orientation of trapped electrons versus cationic

dyes as reported here may correspond to a residual distribution that remains after most of the recombination events have already occurred on a much shorter time scale (femtoseconds to picoseconds) than corresponds to the time resolution of the present experiment.

In conclusion, we have observed polarized EPR spectra of xanthene dyes adsorbed on colloidal TiO_2 at low temperatures upon excitation with pulses of visible light. The SCRP polarization mechanism was adopted to analyze the polarization patterns and line shapes in detail. The positive sign of the exchange interaction of the radical pair was ascribed to charge recombination in the Marcus inverted region. The relative orientation of the magnetic tensor of the trapped electron and the dye radical cation is fixed, thus leading to orientational selectivity in electron transfer across the semiconductor nanoparticle.

Received: August 17, 2004
Revised: March 12, 2005
Published online: May 2, 2005

Keywords: electron transfer · EPR spectroscopy · nanoparticles · radical pair · semiconductors

[1] J. E. Moser, M. Grätzel, *J. Am. Chem. Soc.* **1984**, *106*, 6557–6564.
[2] J. E. Moser, M. Grätzel, *Chem. Phys.* **1993**, *176*, 493–500.
[3] *Surface Electron Transfer Process* (Eds.: R. D. Miller, G. L. McLendon, A. J. Nozik, W. Schmikler, F. Willig), VCH, New York, **1995**.
[4] S. Yan, J. T. Hupp, *J. Phys. Chem.* **1996**, *100*, 6867–6870.
[5] Y. Tachibana, J. E. Moser, M. Grätzel, D. R. Klug, J. R. Durrant, *J. Phys. Chem.* **1996**, *100*, 20056–20062.
[6] R. Argazzi, C. A. Bignozzi, T. A. Heimer, F. N. Castellano, G. J. Meyer, *J. Phys. Chem. B* **1997**, *101*, 2591–2597.
[7] D. Liu, R. W. Fessenden, G. L. Hug, P. V. Kamat, *J. Phys. Chem. B* **1997**, *101*, 2583–2590.
[8] T. Hannappel, B. Burfeindt, W. Storck, F. Willig, *J. Phys. Chem. B* **1997**, *101*, 6799–6802.
[9] M. Hilgendorff, V. Sundström, *J. Phys. Chem. B* **1998**, *102*, 10505–10514.
[10] S. Cherian, C. C. Wamser, *J. Phys. Chem. B* **2000**, *104*, 3624–3629.
[11] I. Martini, J. H. Hodak, G. V. Hartland, *J. Phys. Chem. B* **1998**, *102*, 607–614.
[12] H. Liu, J. N. Preiskorn, J. T. Hupp, *J. Am. Chem. Soc.* **1993**, *115*, 4927–4928.
[13] I. Martini, J. H. Hodak, G. V. Hartland, *J. Phys. Chem. B* **1998**, *102*, 9508–9517.
[14] X. Dang, J. T. Hupp, *J. Am. Chem. Soc.* **1999**, *121*, 8399–8400.
[15] A. A. Dubinski, G. D. Perekhodtsev, O. G. Poluektov, T. Rajh, M. C. Thurnauer, *J. Phys. Chem. B* **2002**, *106*, 938–944.
[16] S. Tojo, T. Tachikawa, M. Fujitsuka, T. Majima, *Chem. Phys. Lett.* **2004**, *384*, 312–316.
[17] Y. Kamata, K. Akiyama, S. Tero-Kubota *J. Phys. Chem. A* **1999**, *103*, 1714–1718.
[18] A. W.-H. Mau, O. Johansen, W. H. F. Sasse, *Photochem. Photobiol.* **1985**, *30*, 81.
[19] G. L. Closs, M. D. E. Forbes, J. R. Norris, *J. Phys. Chem.* **1987**, *91*, 3592–3599.
[20] P. J. Hore, D. A. Hunter, C. D. McKie, A. J. Hoff, *Chem. Phys. Lett.* **1987**, *137*, 495–500.
[21] P. J. Hore in *Advanced EPR in Biology and Biochemistry* (Ed.: A. J. Hoff), Elsevier, Amsterdam, **1989**.
[22] D. Stehlik, C. H. Bock, J. Petersenn, *J. Phys. Chem.* **1989**, *93*, 1612–1619.
[23] T. Rajh, J. M. Nedeljkovic, L. X. Chen, O. Poluektov, M. C. Thurnauer, *J. Phys. Chem. B* **1999**, *103*, 3515–3519.
[24] R. E. Coffmann, G. B. Buettner, *J. Phys. Chem.* **1979**, *83*, 2387–2392.
[25] M. D. E. Forbes, G. L. Closs, P. Calle, P. Gautam, *J. Phys. Chem.* **1993**, *97*, 3384–3389.
[26] G.-H. Goudsmit, H. Paul, A. I. Shushin, *J. Phys. Chem.* **1993**, *97*, 13243–13249.
[27] S. Sekiguchi, Y. Kobori, K. Akiyama, S. Tero-Kubota, *J. Am. Chem. Soc.* **1998**, *120*, 1325–1326.
[28] Y. Kobori, K. Akiyama, S. Tero-Kubota, *J. Chem. Phys.* **2000**, *113*, 465–468.
[29] C. Kormann, D. W. Bahnemann, M. R. Hoffmann, *J. Phys. Chem.* **1988**, *92*, 5196–5201.

Molecular Dynamics

The Importance of Molecular Vibrations: The Sign Change of the Optical Rotation of Methyloxirane**

Kenneth Ruud and Riccardo Zanasi*

Since the publication of the first measurement of the optical rotation of (*S*)-methyloxirane in the gas phase by Müller et al.[1] there has been much theoretical interest in the optical rotation of this molecule. To a large extent, this is because it has proven very difficult to obtain the correct sign of the optical rotation of this molecule at the experimental wavelength of 355 nm in theoretical calculations.[2–4] Several coupled-cluster investigations,[3,4] such as the highly correlated CC3 approach which includes triple excitation corrections, all predict a negative optical rotation for (*S*)-methyloxirane at the experimental wavelength of 355 nm. The geometry dependence of the property is important, but the

[*] Prof. Dr. K. Ruud
Department of Chemistry
University of Tromsø
9037 Tromsø (Norway)
Fax: (+47) 7764-4765
E-mail: ruud@chem.uit.no
Prof. Dr. R. Zanasi
Department of Chemistry
University of Salerno
via S. Allende, 84081 Baronissi (SA) (Italy)

[**] This project has benefited from a generous YFF grant to K.R. (Grant No. 162746/V00) as well as through a Strategic University Program in quantum chemistry (Grant No. 154011/420). Generous support from the University of Tromsø is also acknowledged. R.Z. would like to thank Prof. Rosini for helpful discussions.

  DOI: 10.1002/anie.200500642

use of different geometries[4] has not been sufficient to reproduce the experimental sign of the optical rotation at 355 nm.

DFT/B3LYP calculations provided a positive optical rotation at 355 nm, in agreement with experiment.[2,3] However, Tam et al.[3] argue that this result is a consequence of the incorrect prediction by the B3LYP functional of the energy for the excitation to the lowest Rydberg state, which is too low compared to experimental values because of the well-known limitations of common density functionals in reproducing the correct asymptotic limit for diffuse excited states.[5,6] The too low excitation energy leads to an unphysically strong dispersion of the optical rotation in the vicinity of electronic excitations, which occurs at too long wavelengths, and thus incorrectly increases and changes the sign of the optical rotation calculated at the DFT/B3LYP level of theory.

It was suggested in the coupled-cluster studies that the observed discrepancy between theory and experiment may be a result of vibrational effects. There has only been one study of zero-point vibrational effects on optical rotation in the literature,[7] which also included an examination of the zero-point vibrational corrections to (*S*)-methyloxirane. It was shown that zero-point vibrational corrections could be quite sizeable in comparison to the electronic contribution. However, at 589 nm and at the Hartree–Fock level of theory, the calculated zero-point vibrational correction was only 3.6 deg dm^{-1} g^{-1} mL, which was not enough to change the sign of the calculated CCSD or CC3 optical rotation.

Herein, we present calculations of the zero-point vibrational corrections of the optical rotation of (*S*)-methyloxirane at the DFT/B3LYP level of theory, with both 589 and 355 nm as the wavelength for the incident light. The zero-point vibrational corrections are calculated by using a computational method described previously.[7–9] The use of the B3LYP functional should give us some understanding of the importance of electron correlation effects,[10] although we keep in mind the potential problems of B3LYP calculations at 355 nm that result from the too low excitation energy. Our results were obtained using the aug-cc-pVDZ and aug-cc-pVTZ basis sets,[11,12] and are collected in Table 1.

Notably, the dispersion is also very strong for the zero-point vibrational corrections to the optical rotation, and these corrections are 18.6 (48.1) and 2.1 (10.7) at 355 and 589 nm, respectively, when calculated using the aug-cc-pVDZ (aug-cc-pVTZ) basis set. There is also a large difference in the zero-point vibrational correction calculated at the double- (DZ) and triple-zeta (TZ) levels of theory, which is primarily a result of the change in sign of the anharmonic contribution. In our approach, the anharmonic contribution arises from a shift in the molecular geometry, and is related to the cubic force field of the molecule.[8,9] When going from the DZ to the TZ basis set, the changes in the cubic force lead to a change of direction of the rotation of the methyl group, and thus to a change of the sign of the anharmonic term. The DFT/B3LYP results at the aug-cc-pVDZ level are in good agreement with our previous Hartree–Fock results at 589 nm (3.6).[7]

The vibrationally averaged optical rotation calculated at the B3LYP/aug-cc-pVTZ level of theory now appears quite meaningless, as it is much too large at 355 nm and has the wrong sign at 589 nm. However, if we combine our zero-point vibrational corrections (obtained with the aug-cc-pVTZ basis set) with the best correlated data for the optical rotation (the CC3 results of Kongsted et al.[4]), we find that their value for the equilibrium-geometry optical rotation of −23.2 at 355 nm leads to a vibrationally averaged optical rotation of 24.9, whereas at 589 nm their equilibrium-geometry optical rotation of −17.7 leads to a vibrationally averaged optical rotation of −7.0 when combined with our calculated zero-point vibrational correction (see Table 1). The experimental data at 589 nm were obtained in solution and were extrapolated to −26.9 in the innocuous solvent cyclohexane. Calculations show that the effects of a dielectric medium are to make the optical rotation more negative.[4]

Table 1: Calculated and experimental optical rotations of (*S*)-methyloxirane.[a]

λ [nm]	$[\alpha]_\lambda^e$	$[\alpha]_\lambda^{eff}-[\alpha]_\lambda^e$	$\langle[\alpha]_\lambda^{(2)}\rangle^{eff}$	$\langle[\alpha]_\lambda\rangle^{ZPV}$	$\langle[\alpha]_\lambda\rangle$	Exp.[1]
			aug-cc-pVDZ			
355	11.6	−24.0	42.6	18.6	30.1	10.2[b]
589.3	−14.9	−7.1	9.2	2.1	−12.8	−26.9[c]
			aug-cc-pVTZ			
355	27.5	20.0	28.1	48.1	75.6	10.2[b]
589.3	−7.7	5.5	5.2	10.7	3.0	−26.9[c]
			best theoretical estimates[d]			
355	−23.2			48.1	24.9	10.2[b]
589.3	−17.7			10.7	−7.0	−26.9[c]

[a] The optical rotation at the equilibrium geometry $[\alpha]_\lambda^e$, the anharmonic zero-point vibrational correction ($[\alpha]_\lambda^{eff}-[\alpha]_\lambda^e$), the harmonic vibrational correction $\langle[\alpha]_\lambda^{(2)}\rangle^{eff}$, the total zero-point vibrational correction $\langle[\alpha]_\lambda\rangle^{ZPV}$, and the vibrationally averaged optical rotation $\langle[\alpha]_\lambda\rangle$ were calculated at the B3LYP level of theory with two different basis sets. All results reported in units of deg dm^{-1} g^{-1} mL. [b] For the gas phase. [c] Cyclohexane solution. [d] Using the CC3 results[4] for the equilibrium-geometry optical rotation, and the B3LYP/aug-cc-pVTZ results reported herein for the vibrational correction.

The sensitivity of our calculated vibrational corrections to the quality of the basis (and in practice to the quality of the anharmonic force field), and the rather dramatic consequence this has for the vibrational corrections to the optical rotation of methyloxirane, highlights the inadequacy of a local-mode approximation to such a freely rotating methyl group. We might therefore expect that our anharmonic contribution may be too large. Furthermore, although there is no strict correlation between the dispersion dependence of the vibrational correction and the electronic contribution to the property, the dependence on dispersion may be exaggerated in our vibrational corrections by the too low B3LYP excitation energies. Still, even if our vibrational corrections are somewhat large, we believe an even more accurate calculation of the vibrational correction will leave our conclusion unchanged and lead to an improved agreement with experiment.

In conclusion, the observed change of sign of the optical rotation of (*S*)-methyloxirane when going from a wavelength of 589 to 355 nm is a result of the vibrational corrections to these properties. Our approach has inherent limitations because of the too low excitation energies predicted by the DFT/B3LYP level of theory, and the inadequacy of a local-

mode approximation in modeling the contributions to the optical rotation that result from the rotation of the methyl group. However, we believe that our results and conclusions will not be overturned by a more accurate calculation. The apparent success of DFT/B3LYP in obtaining the correct sign of the optical rotation at 355 nm[2,3] is shown to be fortuitous, in agreement with earlier observations.[3,4]

Received: February 21, 2005
Published online: April 29, 2005

Keywords: ab initio calculations · density functional calculations · methyloxirane · optical rotation · vibrational corrections

[1] T. Müller, K. B. Wiberg, P. H. Vaccaro, *J. Phys. Chem. A* **2000**, *104*, 5959.
[2] E. Giorgio, C. Rosini, R. G. Viglione, R. Zanasi, *Chem. Phys. Lett.* **2003**, *376*, 452.
[3] M. C. Tam, N. J. Russ, D. T. Crawford, *J. Chem. Phys.* **2004**, *121*, 3550.
[4] J. Kongsted, T. B. Pedersen, M. Strange, A. Osted, A. E. Hansen, K. V. Mikkelsen, F. Pawlowski, P. Jørgensen, C. Hättig, *Chem. Phys. Lett.* **2005**, *401*, 385.
[5] C. Diederich, S. Grimme, *J. Phys. Chem. A* **2003**, *107*, 2524.
[6] D. J. Tozer, N. C. Handy, *Phys. Chem. Chem. Phys.* **2000**, *2*, 2117.
[7] K. Ruud, P. R. Taylor, P.-O. Åstrand, *Chem. Phys. Lett.* **2001**, *337*, 215.
[8] P.-O. Åstrand, K. Ruud, P. R. Taylor, *J. Chem. Phys.* **2000**, *112*, 2655.
[9] K. Ruud, P.-O. Åstrand, P. R. Taylor, *J. Chem. Phys.* **2000**, *112*, 2668.
[10] P. J. Stephens, F. J. Devlin, J. R. Cheeseman, M. J. Frisch, *J. Phys. Chem. A* **2001**, *105*, 5356.
[11] T. H. Dunning, Jr., *J. Chem. Phys.* **1989**, *90*, 1007.
[12] R. A. Kendall, T. H. Dunning, Jr., R. J. Harrison, *J. Chem. Phys.* **1992**, *96*, 6796.

Self-Assembled Monolayers

Side-by-Side Patterning of Multiple Alkanethiolate Monolayers on Gold by Edge-Spreading Lithography**

*Matthias Geissler, Joseph M. McLellan, Jingyi Chen, and Younan Xia**

The ability to generate multicomponent patterns of high chemical and structural complexity is central to many scientific areas, including the fabrication of DNA arrays for monitoring gene expression,[1] the development of novel displays,[2] and the study of surface-related phenomena such as wetting, nucleation, and adhesion.[3] The methodology of patterning can vary depending on the type of materials involved and the resolution that needs to be achieved. Techniques such as photolithography,[1b] inkjet printing,[4] and microcontact printing,[5] as well as scanning probes,[6] can be used to introduce multiple functionalities at a surface with spatial control. Several of these techniques have reached high levels of maturity and sophistication, but the procedures often involve a number of lithographic steps, which necessitates alignment between them. This drawback has spurred the search for extended or alternative patterning methodologies. In a recent approach, Ryan et al. used a photomask that transmitted different wavelengths in different areas in combination with a monolayer of a photosensitive alkanethiol on gold.[7] Another approach suggested by Tien et al. involved the use of a multilevel polydimethylsiloxane (PDMS) stamp to fabricate aligned patterns of proteins on substrates.[8] For the same purpose, Delamarche and co-workers introduced a method called affinity contact printing, which employs the specific recognition between target proteins and their complementary binding partners on a PDMS stamp.[9] As recently demonstrated by Whitesides and co-workers,[10] the parallel patterning of multiple polymers, proteins, or cells with microfluidic systems might be straightforward, even though these methods are generally limited to the fabrication of simple and continuous patterns that result from constraints imposed by the channel geometries.

Herein, we describe an approach for patterning multiple self-assembled monolayers (SAMs) of alkanethiolates on

[*] Dr. M. Geissler, J. M. McLellan, J. Chen, Prof. Y. Xia
Department of Chemistry
University of Washington
Seattle, WA 98195-1700 (USA)
Fax: (+1) 206-685-8665
E-mail: xia@chem.washington.edu

[**] This work was supported in part by an AFOSR-MURI grant awarded to the University of Washington (UW), and a Fellowship from the David and Lucile Packard Foundation. J.M.M. and J.C. thank the Center for Nanotechnology at UW for an NSF-funded IGERT (DGE-9987620) Fellowship and a Nanotech Student Award, respectively. Y.X. is an Alfred P. Sloan Research Fellow (2000) and a Camille Dreyfus Teacher Scholar (2002). Measurements were conducted on instruments at the Nanotech User Facility, a member of the National Nanotechnology Infrastructure Network funded by NSF.

  DOI: 10.1002/anie.200500421

gold in a simple and convenient way without the need for alignment steps. We rely on the recently introduced technique of edge-spreading lithography (ESL).[11] The concept behind ESL is fairly simple: alkanethiol molecules are delivered from a PDMS stamp onto a coinage-metal substrate by the surface of a relief structure. Our previous studies only established the patterning of just one type of monolayer, but we now extend this technique to the side-by-side patterning of multiple SAMs by successive printing steps. We used monodispersed silica beads as the guides because: a) they are commercially available in a wide range of sizes; b) they can readily assemble into ordered two-dimensional (2D) arrays over relatively large areas; c) they are inert to most organic solvents and are mechanically more robust than most polymer beads of equivalent size; d) their hydrophilic surfaces support the spreading of thiols; and e) they can be easily removed from the substrate by sonication without leaving any notable residues on the surface. Figure 1 shows a schematic illustration of our approach in its simplest form, that is, the side-by-side patterning of two monolayers. A planar PDMS stamp was inked with an alkanethiol such as sulfanylhexadecanoic acid (SHA, $HS(CH_2)_{15}COOH$), and printed onto silica beads (1.6 μm diameter) deposited on a thin film of gold. Upon reaching the surface of the gold, the molecules formed a SAM around the circular footprint of each bead. As long as the supply of molecules was maintained through contact between the stamp and the array, the area of the SAM expanded radially by reactive spreading.[11,12] In a second step of ESL another thiol, such as eicosanethiol (ECT, $HS(CH_2)_{19}CH_3$), was printed in the same way to form a SAM that nucleated at the edges of the SHA monolayer rings. Once the stamp was removed and the beads were lifted off, a monolayer pattern of concentric rings was observed by lateral force microscopy (LFM).[13]

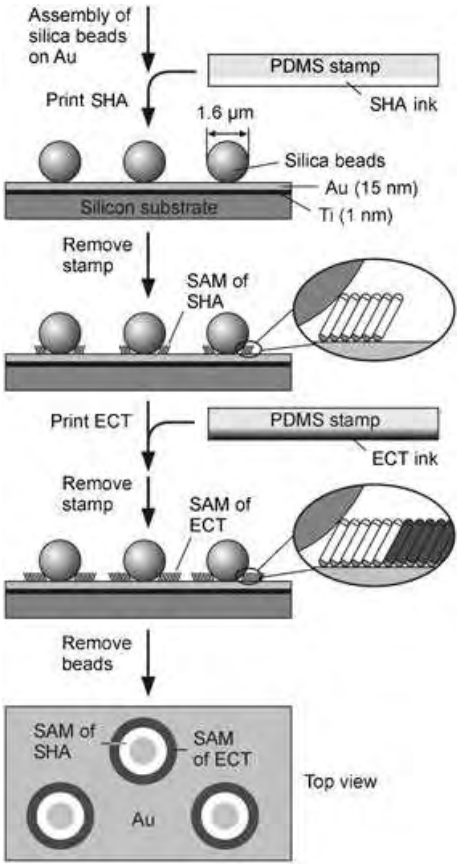

Figure 1. Schematic illustration of the ESL procedure used for side-by-side patterning of SHA and ECT monolayer rings on a gold substrate. The process involves two successive prints that are performed on a 2D array of silica beads supported on a thin film of gold. In the first step, SHA molecules (white) are guided from a planar stamp to the gold surface where they assemble into a monolayer, as directed by the circular footprint of each bead and lateral spreading. In the second step, ECT molecules (black) are applied in a similar fashion, thus forming a SAM that emerges from the edges of the SHA monolayer. Removal of the beads yields an array of concentric rings of SHA and ECT SAMs on the surface.

The functional groups involved in our experiments yield strong differences in contrast when imaged by LFM, as demonstrated by the control experiments shown in Figures 2a and b. The carboxy-terminated SAM appears bright as a result of the relatively strong adhesion forces between the COOH groups and the polar surface of the silicon nitride tip employed for our measurements.[14] Conversely, the methyl-terminated regions interact more weakly with the tip, which results in a darker appearance under LFM.[14] Figure 2c shows the result of a successive ESL experiment as described above. The resultant pattern was an array of concentric rings with an hexagonal arrangement in which the SHA and ECT portions were resolved clearly, both having a width on the order of

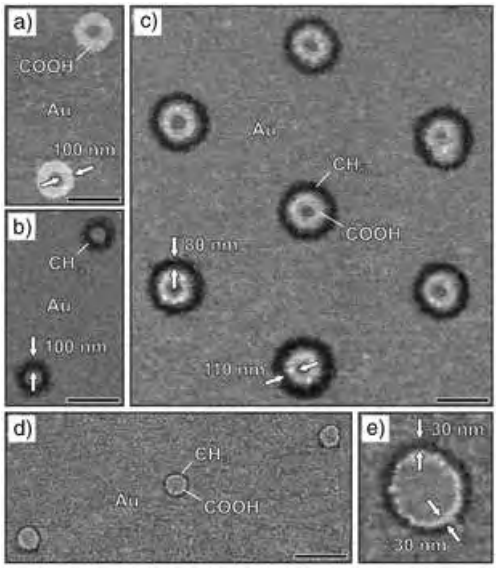

Figure 2. LFM images of carboxy- and methyl-terminated thiolate monolayer rings that were patterned on gold by ESL using SHA and ECT with 1.6-μm-diameter silica beads as guides. The COOH group appears bright, whereas the CH_3 group appears dark, as confirmed by reference measurements (a, b). These rings have a width of ≈100 nm, which was achieved with 1.0-mM ink solutions and a printing time of 1 min. c) Hexagonal array of concentric rings with well-resolved monolayer rings of 80- and 110-nm width. In this case, the printing times were 1 and 2.5 min for SHA and ECT, respectively. A decrease in the concentration of thiol in the ink to 0.1 mM along with contact times of 50 s and 2 min were key to confining the line width to 30 nm and below (d, e). All scale bars correspond to 500 nm.

100 nm. We used this approach to investigate the lower limits of resolution by decreasing the concentration of thiol molecules in the ink and the printing time. Figures 2d and e reveal striking results: the line widths were reduced to 30 nm and less without compromising the contrast or accuracy of the rings. It was difficult to elucidate the integrity of the SAMs on the molecular level, but if a close packing arrangement and a lattice constant of 0.501 nm[15] were assumed, the width of these rings corresponds to about 60 molecules. In principle, further reduction of the line width should be possible, although there may be several obstacles for both fabrication and analysis.

To demonstrate the versatility of our approach we added another alkanethiol, 12-hydroxydodecanethiol (HDDT, $HS(CH_2)_{12}OH$), and increased the number of successive prints from two to three (Figure 3). The use of HDDT proved advantageous since the resulting SAM appears gray in the LFM image, thus providing a sufficient contrast to both SHA and ECT monolayers. Insertion of the HDDT printing step inbetween those for SHA and ECT resulted in a concentric triple-ring system with high structural definition (Figure 3a). The width of each monolayer ring could be varied independently by tuning both the concentration of the ink and the printing time (Figure 3b). Furthermore, the SAMs could be arranged in any order (Figures 3c and d); switching of the printing order did not have any adverse effect on the appearance of the SAMs under LFM for the majority of samples. The monolayers shown in Figure 3 involve only three types of thiols and just a few of their possible combinations, but increasing the number of successive prints or adding more thiols to the process should be straightforward provided that suitable compounds are selected.[16]

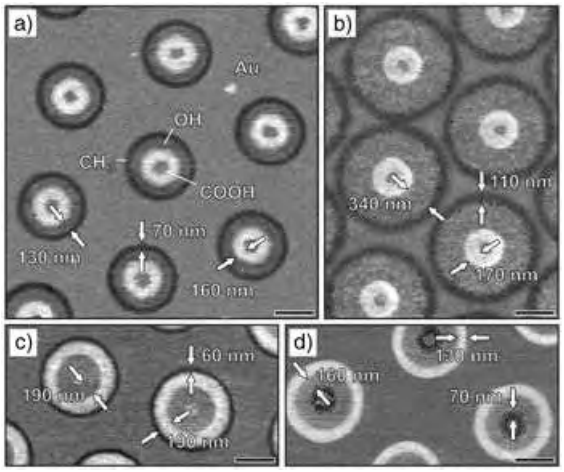

Figure 3. LFM images of concentric rings of carboxy- (bright), hydroxy- (gray), and methyl-terminated (dark) thiolate monolayers on gold. a) The rings were fabricated under the following conditions: 1 min for SHA, 1.5 min for HDDT, and 3 min for ECT. b) An increase in the printing times for HDDT and ECT to 3.5 and 4 min, respectively, resulted in wider rings for these two monolayers. c, d) The position of each monolayer in the concentric structure could be varied by changing the printing order. The pattern in (c) was generated by printing HDDT for 1.5 min, followed by printing of SHA and ECT for 3 min each. The sample shown in (d) was prepared by printing both ECT and HDDT for 1 min, and SHA for 2 min. All scale bars correspond to 500 nm.

To increase the versatility of our approach further, we explored the inclusion of non-thiol-based inks in the ESL experiments. Figure 4 illustrates one demonstration, in which 1-octadecylamine (ODA, $H_2N(CH_2)_{17}CH_3$) was selected as the non-thiol compound in conjunction with SHA and ECT. Amines can form monolayers on gold surfaces, but the stability of these layers is much lower than that of their thiol counterparts.[17] We deposited 2.3-μm silica beads on 30 nm of gold and made three successive prints (Figure 4a). After lift-off, the gold was etched in an aqueous solution containing both Fe^{3+} ions and thiourea.[18] Inspection of the etched sample by scanning electron microscopy (SEM) showed the presence of concentric gold rings on the substrate which were separated by a distinct, well-defined gap (Figure 4b). This

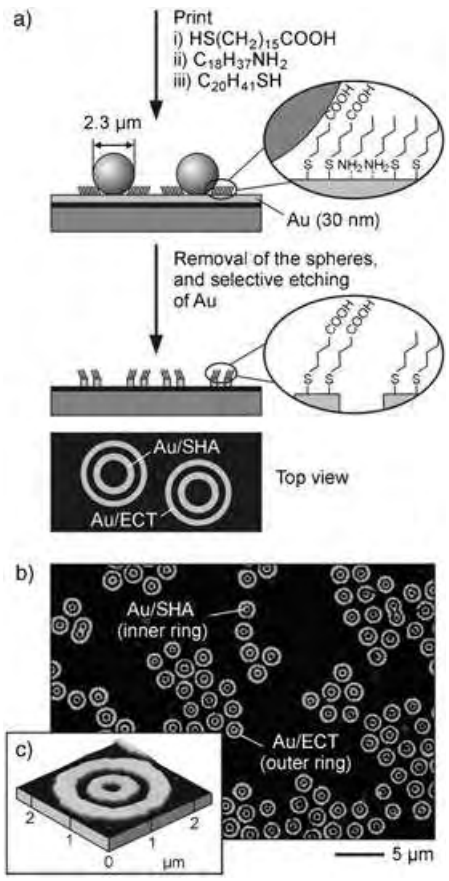

Figure 4. Fabrication of concentric gold rings by ESL and selective etching. The procedure depicted in (a) involves a 2D array of silica beads and an alkyl amine monolayer sandwiched between two concentric rings of thiolate SAMs. The amine monolayer has dual functions: it largely resists the adsorption of thiols while providing sufficient transparency during wet etching of the gold. b) SEM image showing an array of concentric gold rings that were fabricated with 2.3-μm-diameter silica beads and contact times of 1.5 min for SHA, 4 min for ODA, and 7 min for ECT. c) AFM image of the 3D topography of a pair of concentric gold rings. The gap between the two rings is 250 nm wide. The widths of the inner and outer rings are 260 and 340 nm, respectively.

finding reveals two characteristics of the ODA film: it was dense enough to resist the displacement by ECT molecules during ESL, but unlike the thiol monolayers, it was not sufficiently robust to protect the underlying gold from etching. Both the order and density of the array were low in this example, although the contrast and accuracy that could be achieved for individual rings were excellent as depicted by the atomic force microscopy (AFM) image in Figure 4c. Similar results were not obtained when ODA was replaced with either 1-octadecanol ($HO(CH_2)_{17}CH_3$) or *n*-octadecane (CH_3-$(CH_2)_{16}CH_3$). It is probable that in both these cases the interaction between the molecules and the gold surface was too weak, such that adequate monolayers were not formed. These findings highlight some of the possible limitations of this technique.

In summary, we have extended ESL from a novel microfabrication technique to a versatile tool capable of patterning multiple alkanethiolate SAMs on gold at the sub-100-nm scale without any need for alignment. Well-defined concentric rings of monolayers were achieved by using 2D arrays of silica beads as guides in successive printing steps with a planar PDMS stamp. While the width of the rings could be varied between 30 and 340 nm, the most attractive feature of this technique is its flexibility in the print order of the different alkanethiols—a finding that was quite surprising. When a non-thiol ink was incorporated, we demonstrated fabrication of concentric gold rings by a combination of successive prints and selective wet etching. The 2D arrays of silica beads served as a convenient model system for these initial demonstrations; however, the technique should be extendable to guides comprising other materials (for example, polymers, oxides, or metals) and with different geometries.[11a] Modification of the SAMs shown here, backfilling, or the use of other functional inks may also be helpful in further increasing the chemical complexity of the patterns.

Experimental Section

Gold substrates were prepared by e-beam evaporation (SEC 6000, CHA Industries) of 15 nm of gold (99.999%, Kurt J. Lesker Company) onto a silicon wafer (Montco Silicon Technologies) that had been primed with 1 nm of titanium (99.995%, Kurt J. Lesker Company) to promote adhesion between the gold film and the silicon substrate. The gold-coated wafer was then cut into smaller pieces ($\approx$1 cm^2), which were subjected to an air plasma treatment (Harrick Scientific Corp.) for 1 min to remove possible organic contaminants. Monodispersed silica beads were purchased from Duke Scientific (1.6 ± 0.06 μm) and from Bangs Laboratories (2.3 ± 0.1 μm). The commercial samples were diluted with deionized (DI) water to give suspensions containing $\approx$0.15 wt% of beads. A drop of the bead suspension was placed onto a freshly prepared gold substrate, and a 2D array was formed by capillary interaction while the water slowly evaporated.

Planar PDMS slabs were prepared from Sylgard 184 (Dow Corning) by curing the mixed prepolymers of PDMS on a flat polystyrene surface (Falcon 1001 petri dish, Becton Dickinson Labware) in an oven at 60°C for $\approx$20 h. The slabs were cut into pieces ($\approx$1 cm^2) which were used as stamps for inking and printing. Sulfanylhexadecanoic acid (Aldrich) was purified by recrystallization from toluene (Fisher Scientific). Eicosanethiol (Robinson Brothers Ltd.) was used as received. Hydroxydodecanethiol was kindly provided by Prof. G. M. Whitesides at Harvard University. Octadecylamine was from Aldrich; octadecanol and octadecane were both from Fluka, and used without further purification. In all examples, except for the high-resolution experiments, ethanolic solutions (1.0 mM) of these compounds provided the inks. Stamps were inked by covering one side entirely with the ink solution for 1 min, then dried with a stream of air, and placed by hand onto a colloidal array for various times. After each print, samples were allowed to rest for several minutes before further processing. Lift-off was accomplished by sonication in DI water for $\approx$1 min. Gold was etched in a solution of $Fe(NO_3)_3$ (20 mM, Fisher Scientific) and thiourea (30 mM, Acros Organics) in DI water at room temperature with gentle stirring. After removal from the etch bath, the samples were rinsed with DI water and dried in a stream of air.

AFM measurements were performed with a multimode Nanoscope III atomic force microscope (Veeco Instruments), operated under ambient conditions and in the contact mode to record both friction and height simultaneously. All measurements were conducted by using silicon nitride cantilevers (Veeco) with spring constants ranging from 0.06 to 0.58 $N\,m^{-1}$. SEM images were obtained with a Siron XL field-emission microscope (FEI Company) operated at an acceleration voltage of 5.0 kV. The width of the ring patterns was determined with an image analysis program (Image Tool 3.0, UTHSCSA).

Received: February 4, 2005
Published online: May 4, 2005

Keywords: lateral force microscopy · monolayers · nanolithography · self-assembly · thin films

[1] a) D. J. Lockhart, E. A. Winzeler, *Nature* **2000**, *405*, 827–836; b) R. J. Lipshutz, S. P. A. Fodor, T. R. Gingeras, D. J. Lockhart, *Nat. Genet.* **1999**, *21*, 20–24.
[2] a) S. R. Forrest, *Nature* **2004**, *428*, 911–918; b) J. A. Rogers, Z. Bao, K. Baldwin, A. Dodabalapur, B. Crone, V. R. Raju, V. Kuck, H. Katz, K. Amundson, J. Ewing, P. Drzaic, *Proc. Natl. Acad. Sci. USA* **2001**, *98*, 4835–4840.
[3] a) J. Aizenberg, A. J. Black, G. M. Whitesides, *Nature* **1999**, *398*, 495–498; b) M. Böltau, S. Walheim, J. Mlynek, G. Krausch, U. Steiner, *Nature* **1998**, *391*, 877–879; c) C. S. Chen, M. Mrksich, S. Huang, G. M. Whitesides, D. E. Ingber, *Science* **1997**, *276*, 1425–1428.
[4] *Inkjet Printing of Functional Materials* (Eds.: H. Sirringhaus, T. Shimoda), a special issue of *MRS Bull.* **2003**, *28*, 802–842.
[5] A. Bernard, J. P. Renault, B. Michel, H. R. Bosshard, E. Delamarche, *Adv. Mater.* **2000**, *12*, 1067–1070.
[6] a) L. M. Demers, D. S. Ginger, S.-J. Park, Z. Li, S.-W. Chung, C. A. Mirkin, *Science* **2002**, *296*, 1836–1838; b) G.-Y. Liu, N. A. Amro, *Proc. Natl. Acad. Sci. USA* **2002**, *99*, 5165–5170.
[7] D. Ryan, B. A. Parviz, V. Linder, V. Semetey, S. K. Sia, J. Su, M. Mrksich, G. M. Whitesides, *Langmuir* **2004**, *20*, 9080–9088.
[8] J. Tien, C. M. Nelson, C. S. Chen, *Proc. Natl. Acad. Sci. USA* **2002**, *99*, 1758–1762.
[9] J. P. Renault, A. Bernard, D. Juncker, B. Michel, H. R. Bosshard, E. Delamarche, *Angew. Chem.* **2002**, *114*, 2426–2429; *Angew. Chem. Int. Ed.* **2002**, *41*, 2320–2323.
[10] a) D. T. Chiu, N. L. Jeon, S. Huang, R. S. Kane, C. J. Wargo, I. S. Choi, D. E. Ingber, G. M. Whitesides, *Proc. Natl. Acad. Sci. USA* **2000**, *97*, 2408–2413; b) S. Takayama, J. C. McDonald, E. Ostuni, M. N. Liang, P. J. A. Kenis, R. Ismagilov, G. M. Whitesides, *Proc. Natl. Acad. Sci. USA* **1999**, *96*, 5545–5548.
[11] a) M. Geissler, J. M. McLellan, Y. Xia, *Nano Lett.* **2005**, *5*, 31–36; b) J. M. McLellan, M. Geissler, Y. Xia, *J. Am. Chem. Soc.* **2004**, *126*, 10830–10831.
[12] a) S. Rozhok, R. Piner, C. A. Mirkin, *J. Phys. Chem. B* **2003**, *107*, 751–757; b) M. Geissler, H. Schmid, A. Bietsch, B. Michel, E.

Delamarche, *Langmuir* **2002**, *18*, 2374 – 2377; c) E. Delamarche, H. Schmid, A. Bietsch, N. B. Larsen, H. Rothuizen, B. Michel, H. Biebuyck, *J. Phys. Chem. B* **1998**, *102*, 3324 – 3334; d) Y. Xia, G. M. Whitesides, *J. Am. Chem. Soc.* **1995**, *117*, 3274 – 3275.

[13] a) G. J. Leggett, *Anal. Chim. Acta* **2003**, *479*, 17 – 38; b) R. W. Carpick, M. Salmeron, *Chem. Rev.* **1997**, *97*, 1163 – 1194.

[14] C. D. Frisbie, L. F. Rozsnyai, A. Noy, M. S. Wrighton, C. M. Lieber, *Science* **1994**, *265*, 2071 – 2074.

[15] E. Delamarche, B. Michel, H. A. Biebuyck, C. Gerber, *Adv. Mater.* **1996**, *8*, 719 – 729.

[16] Suitable compounds should diffuse on the hydrophilic surface of silica beads, form a SAM on the gold that can extend by reactive spreading, have limited mass transport through the vapor phase, and show no cross-reactivity between functional groups.

[17] a) D. V. Leff, L. Brandt, J. R. Heath, *Langmuir* **1996**, *12*, 4723 – 4730; b) C. Xu, L. Sun, L. J. Kepley, R. M. Crooks, A. J. Ricco, *Anal. Chem.* **1993**, *65*, 2102 – 2107.

[18] M. Geissler, H. Wolf, R. Stutz, E. Delamarche, U.-W. Grummt, B. Michel, A. Bietsch, *Langmuir* **2003**, *19*, 6301 – 6311.

Multicomponent Reactions

Highly Enantioselective One-Pot, Three-Component Imino-Reformatsky Reaction**

Pier Giorgio Cozzi and Eleonora Rivalta*

The Reformatsky reaction,[1] discovered more than 115 years ago, is still widely used in synthesis.[2] High functional-group tolerance and the in situ preparation of the reagent have contributed to its success. The reagent is prepared by the activation of zinc metal through a variety of different methods.[3] Recently, renewed interest in the catalytic redox reaction[4] has positively influenced further studies in the field.[5] Honda and co-workers have developed a new, interesting variant of the Reformatsky reaction, which uses Et_2Zn and $[RhCl(PPh_3)_3]$ in catalytic amounts (Scheme 1).[6]

Imines are suitable substrates for the Reformatsky reaction, and the so-called imino-Reformatsky reaction was first described by Gilman 60 years ago.[7] Although the use of this reaction in synthesis has great potential, it can be problematic, as a mixture of β-aminoesters and β-lactams is generally obtained. Recently, this problem was solved by using imines derived from 2-methoxyaniline.[8] In view of the increasing importance of β-amino acids as valuable synthetic tools[9] we were attracted by the interesting work published by Adrian and co-workers,[8b] who presented an efficient, nickel-catalyzed Reformatsky-type three-component condensation that combines aldehyde, 2-methoxyaniline, and a bromocarbonyl reagent (esters, ketones, and amides) in a one-pot reaction. The method was successfully applied on the micro- and macroscale and to combinatorial synthesis. Herein, we present the first practical one-pot three-component enantioselective imino-Reformatsky reaction, which is based on the use of *N*-methylephedrine as a cheap and recoverable chiral ligand.[10]

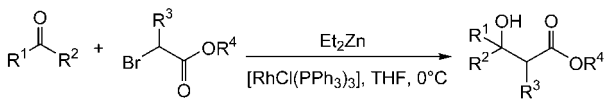

Scheme 1. Rhodium-catalyzed Reformatsky reaction developed by Honda and co-workers.

The efficient three-component Reformatsky reaction developed by Adrian and co-workers[8b] uses Me_2Zn in the presence of a catalytic amount of inexpensive $[NiCl_2(PPh_3)_2]$.[11] On the basis of detailed electrochemical study by Périchon, Sibille, and co-workers,[12] a reasonable mechanistic picture was presented by Adrian and co-workers. The mechanism involved the reduction of the Ni^{II} complex to a Ni^0 complex, oxidative addition of the bromoester to the Ni^0 complex, and a Ni^{II}/Zn^{II} exchange, which leads to an organozinc Reformatsky reagent. The proposed catalytic cycle (Scheme 2) was our starting point in developing an enantioselective variant. We reasoned that, contrary to other nickel-catalyzed[13] processes, a chiral ligand able to coordinate nickel was not crucial to transmit chiral information. Instead, we decided to surround the zinc enolate formed by transmetalation and the chelating imine with a chiral ligand able to coordinate zinc. Carreira and co-workers have developed a

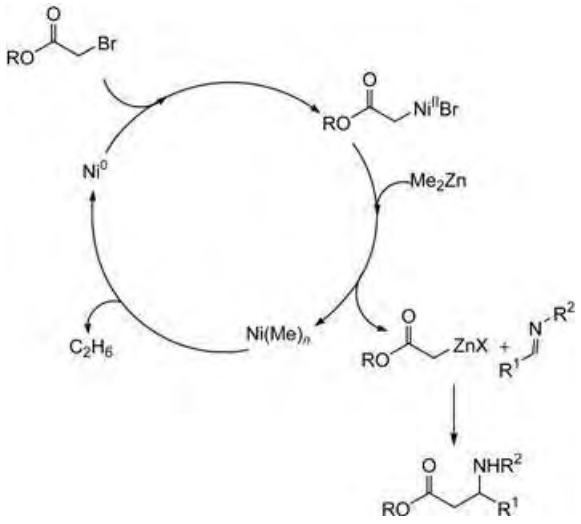

Scheme 2. Catalytic cycle for the imino-Reformatsky reaction mediated by nickel.

[*] Prof. Dr. P. G. Cozzi, Dr. E. Rivalta
Dipartimento di Chimica "G. Ciamician"
Università di Bologna
Via Selmi, 2, 40126 Bologna (Italy)
Fax: (+39) 051-2099-456
E-mail: piergiorgio.cozzi@unibo.it

[**] The European Commission through the project FP6-505267-1-(LIGBANK), the MIUR (Progetto Nazionale Stereoselezioni in Chimica Organica: Metodologie ed Applicazioni), and the FIRB (Progettazione, preparazione e valutazione biologica e farmacologica di nuove molecole organiche quali potenziali farmaci innovativi) are acknowledged for financial support for this research.

Supporting information for this article is available on the WWW under http://www.angewandte.org or from the author.

  DOI: 10.1002/anie.200462757

very efficient and simple method based on the use of *N*-methylephedrine for the addition of acetylides to aldehydes,[14] and Tan et al. have used *N*-alkylephedrine derivatives to add zinc acetylides to a ketone precursor of the anti-HIV drug efavirenz.[15] *N*-Methylephedrine can be considered as a privileged ligand[16] for zinc derivatives. For this reason we explored the Me_2Zn-mediated one-pot three-component imino-Reformatsky reaction with *N*-methylephedrine[17] as the chiral ligand. Me_2Zn plays several important roles in the reaction: a) Me_2Zn is the dehydrating agent responsible for the formation of the imine in situ; b) Me_2Zn can reduce the Ni^{II} salt to Ni^0; c) Me_2Zn reacts with the incipient nickel enolate to form the reactive zinc enolate; and, finally, d) Me_2Zn can coordinate *N*-methylephedrine, the amino alcohol used as a chiral ligand. We have chosen the imine obtained in situ from 2-methoxyaniline and *p*-chlorobenzaldehyde as a model substrate, in conjunction with different bromoacetates, Ni^{II} salts in catalytic amounts, and *N*-methylephedrine. We adjusted the protocol developed by Adrian and Snapper[8b] to investigate several experimental conditions of our process in detail (Table 1). In light of its multiple roles in this reaction, 4 equivalents of Me_2Zn was used. To ensure good enantiomeric excess, 1.5–1.6 equivalents of *N*-methylephedrine were employed in our process (Table 1, entries 2–5). *N*-methylephedrine can easily be separated from the adducts by acidic workup and recovered after extraction of the aqueous alkaline layer. The two solvents tested in the model reaction, CH_2Cl_2 and toluene, gave comparable results.[18] The crucial difference that determines the choice of solvent concerns the use of the nickel catalyst. $[NiCl_2(PPh_3)_2]$ is soluble in CH_2Cl_2 but is poorly soluble in toluene. We have also used $[Ni(acac)_2]$ hydrate, which is poorly soluble in both solvents. To compare results and guarantee reproducibility, we decided to add Ni^{II} salts as a solid to the reaction mixture containing Me_2Zn, imine, bromoester, and *N*-methylephedrine (see Supporting Information for details), at the indicated reaction temperature. The Ni^{II} salts are quickly dissolved in the reaction mixture and initiate the catalytic cycle. The $[RhCl(PPh_3)_3]$ complex also promotes the reaction, although the product was isolated with lower *ee* values than those obtained in the presence of nickel complexes (Table 1, entry 6). We also examined the enantiomeric excess attained in the model reaction with different bromoesters. Apart from the hindered *tert*-butyl bromoacetate (Table 1, entry 14), which gave a lower *ee* value than the others, similar enantiomeric excesses were attained with all type of esters examined.[19] Toluene was chosen as the solvent owing to the slightly better results obtained, and the scope of the reaction was investigated.

In Table 2 we report the results collected with different aldehydes. The reaction shows broad scope, since aromatic, aliphatic, unsaturated, and heterocyclic aldehydes are reactive and result in good to excellent enantioselectivites (up to 92% *ee*). Yields were generally only moderate, but no by-products were isolated. Better yield was obtained by increasing the reaction temperature, but at the expense of enantiomeric excess. We optimized the reaction temperature with all the different aldehydes so as to reach a compromise between yield and enantiomeric excess. Notably, α,β-unsaturated aldehydes are good reaction partners in this reaction and also lead to good enantiomeric excess.[20] The absolute configuration of the products obtained with (1*S*,2*R*)-*N*-methylephedrine as a chiral ligand was established in the case of aliphatic and aromatic aldehydes (isopropyl and phenyl), as shown in Scheme 3, following the general procedure of deprotection of 2-methoxyamines, developed by Josephsohn, Snapper, and Hoveyda (see Supporting Information for details).[21]

In conclusion, we have developed the first practical and highly efficient, enantioselective[22] one-pot three-component imino-Reformatsky reaction, which gives β-aminoesters in moderate to good

Table 1: Enantioselective one-pot imino-Reformatsky reaction of 4-chlorobenzaldehyde with 2-methoxyaniline and bromoacetates.[a]

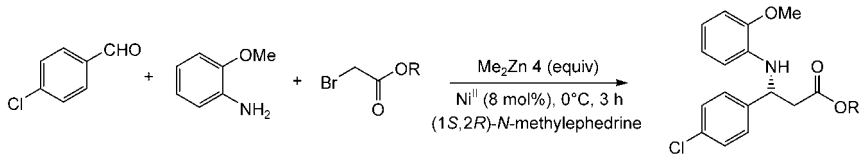

Entry	Ni^{II}	R	Solvent	Yield [%][b]	*ee* [%][c]
1[d,e]	$[NiCl_2(PPh_3)_2]$	Et	CH_2Cl_2	82	68
2[e]	$[NiCl_2(PPh_3)_2]$	Et	CH_2Cl_2	92	75
3[f]	$[NiCl_2(PPh_3)_2]$	Et	CH_2Cl_2	85	81
4[f,g]	$[NiCl_2(PPh_3)_2]$	Et	CH_2Cl_2	75	86
5[f,h]	$[NiCl_2(PPh_3)_2]$	Et	CH_2Cl_2	88	86
6[i]	$[RhCl(PPh_3)_3]$	Et	CH_2Cl_2	70	72
7[f]	$[NiCl_2(PPh_3)_2]$	Et	toluene	75	86
8[f]	$[Ni(acac)_2]$	Et	toluene	57	84
9[f]	$[Ni(acac)_2]$	Me	toluene	57	84
10[f]	$[NiCl_2(PPh_3)_2]$	Me	toluene	60	86
11[f]	$[NiCl_2(PPh_3)_2]$	*i*Pr	toluene	66	83
12[f]	$[Ni(acac)_2]$	Bn	toluene	70	82
13[f]	$[NiCl_2(PPh_3)_2]$	Bn	toluene	60	87
14[f]	$[NiCl_2(PPh_3)_2]$	*t*Bu	toluene	50	76
15[j]	$[NiCl_2(PPh_3)_2]$	Et	toluene	73	78

[a] All the reactions were carried out at 0°C for 3 h in the presence of *N*-methylephedrine (1.6 equiv) and the Ni^{II} salt (7.5–8 mol%). [b] Yield of isolated product after chromatographic purification. [c] Determined by HPLC analysis (see Supporting Information for details). [d] *N*-methylephedrine: 1 equiv. [e] $[NiCl_2(PPh_3)_2]$ was added as a solution in CH_2Cl_2 as reported by Adrian and co-workers.[8b] [f] The Ni^{II} salt was added as solid to the reaction mixture. [g] *N*-methylephedrine: 1.8 equiv. [h] *N*-methylephedrine: 2 equiv. [i] Wilkinson catalyst, $[RhCl(PPh_3)_3]$, (5 mol%) was used and added as a solution in CH_2Cl_2.[8b] The reaction was stirred for 13 h at 0°C. [j] Recycling experiment: *N*-methylephedrine, recovered from the reaction, was dried under high vacuum for 3 h. The crude *N*-methylephedrine containing 2-methoxyaniline (10%) (checked by NMR and ES-MS) was used in another model reaction without any purification. The reaction was performed at −10°C for 14 h with $[NiCl_2(PPh_3)_2]$ (8 mol%).

Table 2: Enantioselective imino-Reformatsky reaction with different aldehydes.

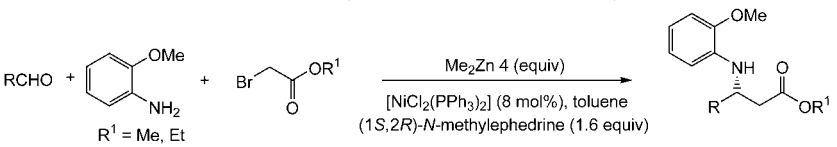

R^1 = Me, Et

Entry[a]	R	R^1	T [°C]	t [h]	Yield [%][b]	*ee* [%][c]
1	4-ClPh	Et	−25	3	62	90
2	4-ClPh	Me	−25	3	60	90
3	4-ClPh[d,e]	Et	−20	3	90	83
4	4-CF_3Ph	Et	−28	16	30	90
5	C_6F_5	Et	−28	6	41	90
6	PhCH=CH	Et	−20	48	60	85
7	Ph	Et	−30	48	63	83
8	Ph[d]	Et	−30	3	50	81
9	Ph[d,f]	Et	−20	4	85	57
10	*t*BuPh	Et	−30	24	40	82
11	*t*BuPh	Et	−30	48	76	74
12	2-thiophene	Et	−28	16	49	92
13	2-naphtyl	Et	−5	16	40	84
14	2-naphtyl	Et	25	1	72	74
15	4-MeOPh[d]	Et	−15	48	60	66
16	*i*Pr	Et	−10	48	57	64
17	*i*Pr	Et	−20	48	52	74
18	cyclohexyl[d]	Et	−20	3	67	80

[a] All the reactions were performed at the indicated temperature with *N*-methylephedrine (1.6 equiv) as a chiral ligand (see Supporting Information for experimental details).[b] Yield of isolated product after flash chromatography. [c] Determined by chiral HPLC analysis (Chiralcel OD column). [d] The reaction was slowly allowed to reach 0°C in 3–4 h before quenching. [e] A solution of Et_2Zn in toluene (1 M; 4 equiv) was used. GC–MS analysis performed on the crude reaction mixture after quenching revealed the presence of less than 5% of by-product derived from the attack of the ethyl on the imine. [f] The reaction was performed with the preformed purified imine in the presence of Me_2Zn (3 equiv) and *N*-methylephedrine (1 equiv) as chiral ligand.

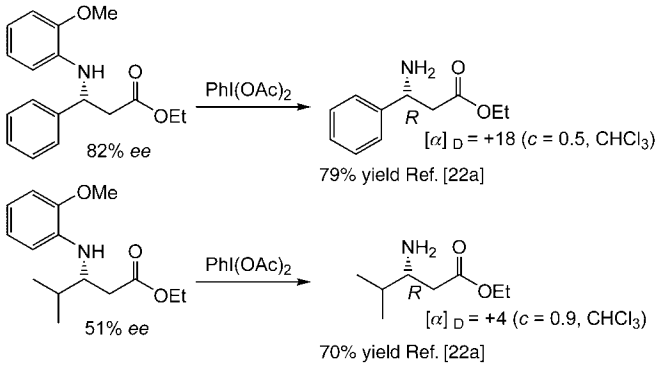

Scheme 3. Correlation of aromatic and aliphatic β-aminoesters with known compounds.

yields. The reaction uses an inexpensive nickel salt, bromoesters, and *N*-methylephedrine as a chiral ligand. The chiral auxiliary, *N*-methylephedrine, is completely recovered after workup of the reaction and could be recycled (Table 1, entry 15).[23] The imines are prepared in situ, in the same reaction flask, and Me_2Zn is used as a dehydrating agent. More importantly, the reaction shows broad scope, since aromatic, heterocyclic, aliphatic and unsaturated aldehydes are suitable substrates for the reaction. We believe that the enantioselectivity (64–92% *ee*) can be improved as many other inexpensive homochiral aminoalcohols are available.[24] Further studies of this reaction are in progress in our laboratory and will be reported in due course.

Received: November 30, 2004
Revised: February 25, 2005
Published online: May 6, 2005

Keywords: aminoesters · asymmetric synthesis · imines · multicomponent reactions · zinc

[1] S. Reformatsky, *Ber. Dtsch. Chem. Ges.* **1887**, *20*, 1210; for a review, see: R. Ocampo, W. R. Dolbier, Jr., *Tetrahedron* **2004**, *60*, 9325–9374.
[2] a) A. Fürstner, *Synthesis* **1989**, 571–590; b) A. Fürstner in *Organozinc Reagents* (Eds.: P. Knochel, P. Jones), Oxford University Press, New York, **1999**, pp. 287–305; c) J. A. Marshall, *Chemtracts* **2000**, *13*, 705–707; d) J. Podlech, T. C. Maier, *Synthesis* **2003**, 633–655; e) F. Orsini, G. Sello, *Curr. Org. Synt.* **2004**, *1*, 111–135; f) E. Nakamurai in *Organometallic in Synthesis, A Manual* (Ed.: M. Schlosser), Wiley, New York, **2002**, pp. 579–664.
[3] a) Rieke Zn: R. D. Rieke, S. J. Uhm, *Synthesis* **1975**, 452–453; b) Zn–Cu couple: E. Santaniello, A. Manzocchi, *Synthesis* **1977**, 698–699; Zn/Ag graphite: R. Csuk, A. Fürstner, H. J. Weidmann, Jr., *J. Chem. Soc. Chem. Commun.* **1986**, 775–776.
[4] A. Fürstner, *Chem. Eur. J.* **1998**, *4*, 567–570.
[5] For a variant with zinc and a catalytic amount of titanocene dichloride, see: a) Y. Ding, G. Zhao, *J. Chem. Soc. Chem. Commun.* **1992**, 941–942; b) L. Chen, G. Zhao, Y. Ding, *Tetrahedron Lett.* **2003**, *44*, 2611–2614; c) J. D. Parrish, D. R. Shelton, R. D. Little, *Org. Lett.* **2003**, *5*, 3615–3617.
[6] K. Kanai, H. Wakabayashi, T. Honda, *Org. Lett.* **2000**, *2*, 2549–2551.
[7] H. Gilman, M. Speeter, *J. Am. Chem. Soc.* **1943**, *65*, 2255–2256.
[8] a) J. C. Adrian, Jr., J. L. Barkin, L. Hassib, *Tetrahedron Lett.* **1999**, *40*, 2457–2460; b) J. C. Adrian, Jr., M. L. Snapper, *J. Org. Chem.* **2003**, *68*, 2143–2150; c) J. C. Adrian, Jr., J. L. Barkin, R. J. Fox, J. E. Chick, A. D. Hunter, R. A. Nicklow, *J. Org. Chem.* **2000**, *65*, 6264–6267.
[9] For comprehensive and authoritative reviews, see: a) L. Gerald, D. Seebach, *Biopolymers* **2004**, *76*, 206–243; b) D. Seebach, T. Kimmerlin, R. Sebesta, M. A. Campo, A. K. Beck, *Tetrahedron* **2004**, *60*, 7455–7506; see also: c) N. Sewald, *Angew. Chem.* **2003**, *115*, 5972–5973; *Angew. Chem. Int. Ed.* **2003**, *42*, 5794–5795; d) J.-A. Ma, *Angew. Chem.* **2003**, *115*, 4426–4435; *Angew. Chem. Int. Ed.* **2003**, *42*, 4290–4299; e) M. Liu, M. P. Sibi, *Tetrahedron*, **2002**, *58*, 7991–8035; f) S. Abele, D. Seebach, *J. Org. Chem.* **2000**, *65*, 1–15; g) G. Cardillo, C. Tomasini, *Chem. Rev.* ***1996***, *96*, 117–128.
[10] For asymmetric Mannich-type reactions with a chiral acetate or a chiral acetate equivalent, see: a) L. S. Liebeskind, M. E. Welker, R. W. Fengl, *J. Am. Chem. Soc.* **1986**, *108*, 6328–6343; b) C. Palomo, M. Oiarbide, A. Landa, M. C. Gonzàles-Rego, J. M. García, A. Gonzáles, J. M. Odriziola, M. Martin-Pastor, A. Linden, *J. Am. Chem. Soc.* **2002**, *124*, 8637–8643, and references therein; c) S. Saito, K. Hatanaka, H. Yamamoto, *Org. Lett.* **2000**,

2, 1891 – 1894; for enantioselective Mannich reactions, see: d) S. Kobayashi, H. Ishitani, *Chem. Rev.* **1999**, *99*, 1069 – 1094; e) A. Fujii, E. Hagiwara, M. Sodeoka, *J. Am. Chem. Soc.* **1999**, *121*, 5450 – 5458; f) D. Ferraris, B. Young, T. Dudding, T. Lectka, *J. Am. Chem. Soc.* **1998**, *120*, 4548 – 4549; g) S. Xue, S. Yu, Y. Deng, N. D. Wulff, *Angew. Chem.* **2001**, *113*, 2331 – 2334; *Angew. Chem. Int. Ed.* **2001**, *40*, 2271 – 2274; h) K. Juhl, N. Gathergood, K. A. Jørgensen, *Angew. Chem.* **2001**, *113*, 3083 – 3085; *Angew. Chem. Int. Ed.* **2001**, *40*, 2271 – 2274; i) A. G. Wenzel, E. N. Jacobsen, *J. Am. Chem. Soc.* **2002**, *124*, 12964 – 12965; j) T. Hamada, K. Manabe, S. Kobayashi, *J. Am. Chem. Soc.* **2004**, *126*, 7768 – 7769; k) D. Uraguchi, M. Terada, *J. Am. Chem. Soc.* **2004**, *126*, 5356 – 5357; l) T. Akiyama, J. Itoh, K. Yokota, K. Fuchibe, *Angew. Chem.* **2004**, *116*, 1592 – 1594; *Angew. Chem. Int. Ed.* **2004**, *43*, 1566 – 1568; m) B. M. Trost, L. R. Terrel, *J. Am. Chem. Soc.* **2003**, *125*, 338 – 339; n) S. Matsunaga, N. Kumagai, S. Harada, M. Shibasaki, *J. Am. Chem. Soc.* **2003**, *125*, 4712 – 4713; o) B. List, P. Pojarliev, W. T. Biller, H. J. Martin, *J. Am. Chem. Soc.* **2002**, *124*, 827 – 833; p) W. Notz, F. Tanaka, S.-i. Watanabe, N. S. Chowdari, J. M. Turner, R. Thayumanavan, C. S. Barbas, *J. Org. Chem.* **2003**, *68*, 9624 – 9634.

[11] An imino-Reformatsky reaction based on the use of Et_2Zn and a catalytic amount of $[RhCl(PPh_3)_3]$ has been developed: K. Kanai, H. Wakabayashi, T. Honda, *Heterocycles* **2002**, *58*, 47 – 51.

[12] a) S. Sibille, E. D. Incan, L. Leport, M.-C. Massebiau, J. Périchon, *Tetrahedron Lett.* **1987**, *28*, 55 – 58; b) S. Mcharek, S. Sibille, J.-Y. Nédélec, J. Périchon, *J. Organomet. Chem.* **1991**, *401*, 211 – 215; c) A. Conan, S. Sibille, J. Périchon, *J. Org. Chem.* **1991**, *56*, 2018 – 2024.

[13] J. Montgomery, *Angew. Chem.* ***2004***, *116*, 3980 – 3998; *Angew. Chem. Int. Ed.* **2004**, *43*, 3890 – 3908.

[14] a) N. K. Anand, E. M. Carreira, *J. Am. Chem. Soc.* **2001**, *123*, 9687 – 9688; b) D. E. Frantz, R. Fässler, E. M. Carreira, *J. Am. Chem. Soc.* **2000**, *122*, 1806 – 1807.

[15] L. Tan, C.-y. Chen, R. D. Tillyer, E. J. J. Grabowski, P. J. Reider, *Angew. Chem.* **1999**, *111*, 724 – 727; *Angew. Chem. Int. Ed.* **1999**, *38*, 711 – 713.

[16] T. P. Yoon, E. N. Jacobsen, *Science* **2003**, *299*, 1691 – 1693.

[17] Other chiral ligands were examined: binol, sparteine, chiral Schiff bases, tartramides gave racemic product; *N*-methylprolinol gave no reaction; cinchonine led to 57% *ee* but low conversion.

[18] The use of THF as reaction solvent gives an incomplete formation of imines compared with toluene and CH_2Cl_2.

[19] Bromoamides are reactive partners in our reaction but we have isolated racemic products by using several amides in the reaction with 4-chlorobenzaldehyde: P. G. Cozzi, E. Rivalta, unpublished results.

[20] Crotyl aldehyde afforded the corresponding β-aminoester adduct with 64% *ee* and in 60% yield; other unsaturated aldehydes are currently under investigation.

[21] For details, see: N. S. Josephsohn, M. L. Snapper, A. H. Hoveyda, *J. Am. Chem. Soc.* **2004**, *126*, 3734 – 3735.

[22] For a diastereoselective imino-Reformatsky reaction catalyzed by rhodium, see: a) T. Honda, H. Wakabayashi, K. Kanai, *Chem. Pharm. Bull.* **2002**, *50*, 307 – 308; b) A. Otaka, J. Watanabe, A. Yukimasa, Y. Sasaki, H. Watanabe, T. Kinoshita, S. Oishi, H. Tamamura, N. Fujii, *J. Org. Chem.* **2004**, *69*, 1634 – 1645.

[23] *N*-methylephedrine was completely recovered from the reaction (100% yield, >99% *ee*) contaminated with 10–16% of *o*-methoxyaniline (checked by integration of crude ^{1}H NMR spectra). We have performed a recycling experiment without purifying the *N*-methylephedrine recovered (Table 1, entry 15).

[24] Different asymmetric imino-Reformatsky reactions have been reported: a) Y. Ukaji, S. Takenaka, Y. Horita, K. Inomata, *Chem. Lett.* **2001**, 254 – 255; b) J. D. Clark, G. A. Weisenburger, D. K. Anderson, P.-J. Colson, A. D. Edney, D. J. Gallagher, H. P. Kleine, C. M. Knable, M. K. Lantz, C. M. V. Moore, J. B. Murphy, T. E. Rogers, P. G. Ruminski, A. S. Shah, N. Storer, B. E. Wise, *Org. Process Res. Dev.* **2004**, *8*, 51 – 61; c) A. Sorochinsky, N. Voloshin, A. Markovsky, M. Belik, N. Yasuda, H. Uekusa, T. Ono, D. O. Berbasov, V. A. Soloshonok, *J. Org. Chem.* **2003**, *68*, 7448 – 7454; for a chiral-ligand-controlled formation of β-amino acids, see: H. Doi, T. Sakai, M. Iguchi, K.-i Yamada, K. Tomioka, *J. Am. Chem. Soc.* **2003**, *125*, 2886 – 2887, and references therein.

C–H Activation

Coordinatively Unsaturated Cationic and Zwitterionic [Cp*Ru(κ^2-*P,N*)] Complexes: Ligand-Assisted Double-Geminal C–H Bond Activation and Reversible α-H Elimination at Ruthenium**

*Matthew A. Rankin, Robert McDonald, Michael J. Ferguson, and Mark Stradiotto**

The catalytic cleavage and functionalization of an otherwise unactivated C–H bond within the ligand sphere of a coordinatively unsaturated transition-metal complex is developing into a practical synthetic methodology, despite the inherent difficulty associated with breaking such robust σ bonds.[1] In contrast, the activation of multiple C–H bonds on a single substrate has proven to be a significantly greater challenge; stoichiometric transformations of this type are still uncommon and examples in which this reactivity has been incorporated into useful catalytic cycles are few.[1,2] Given the central role that multiple C–H bond activation processes could play in the functionalization of hydrocarbons and other relatively unreactive molecules, we are targeting new classes

[*] M. A. Rankin, Prof. Dr. M. Stradiotto
Department of Chemistry
Dalhousie University
Halifax, Nova Scotia B3H 4J3 (Canada)
Fax: (+1) 902-494-1310
E-mail: mark.stradiotto@dal.ca
Dr. R. McDonald, Dr. M. J. Ferguson
X-Ray Crystallography Laboratory
Department of Chemistry, University of Alberta
Edmonton, Alberta T6G 2G2 (Canada)

[**] Acknowledgment is made to the Natural Sciences and Engineering Research Council (NSERC) of Canada (including a Postgraduate Scholarship for M.A.R.), the Canada Foundation for Innovation, the Nova Scotia Research and Innovation Trust Fund, and Dalhousie University for their generous support of this work. We also thank Drs. B. Berno and M. Lumsden (Atlantic Region Magnetic Resonance Center, Dalhousie) for assistance in the acquisition of NMR spectroscopic data. Cp* = η^5-C_5Me_5.

Supporting information for this article is available on the WWW under http://www.angewandte.org or from the author.

 DOI: 10.1002/anie.200500528

of reactive transition-metal complexes that are designed to effect one or more C–H bond activation steps. On the basis of the propensity of late-transition-metal cations for C–H activation,[3] and the desirable reactivity characteristics commonly associated with P,N ligation,[4] one facet of our research targets coordinatively unsaturated cations supported by κ^2-*P,N*-ligated 1-P*i*Pr$_2$-2-NMe$_2$-indene (**1a**[H]) or 2-NMe$_2$-3-P*i*Pr$_2$-indene (**1b**[H]), as well as structurally related zwitterionic complexes that feature κ^2-*P,N*-ligated 2-NMe$_2$-3-P*i*Pr$_2$-indenide (**1**) in which the ten-π-electron indenide unit functions as a sequestered anionic charge reservoir.[5] We view these coordinatively unsaturated zwitterions as particularly attractive candidates for multiple C–H activation, since the anionic backbone in **1** is poised to accept a proton from a formally cationic metal center following an initial C–H bond activation step, thereby re-establishing coordinative unsaturation at the reactive metal center and enabling subsequent C–H activation processes. As part of this study, we identified the 16-electron cation [Cp*Ru(κ^2-*P,N*-**1b**[H])]$^+$ and the coordinatively unsaturated zwitterion [Cp*Ru(κ^2-*P,N*-**1**)] as important targets (Cp* = η^5-C$_5$Me$_5$); whereas 16-electron complexes of the type [Cp*RuL$_2$]$^+$X$^-$ (L = N- or P-donor fragments) have proven to be effective in the activation of C–H bonds, related P,N-ligated cations have yet to be isolated.[6,7] Herein, we report the preparation of a masked source of [Cp*Ru(κ^2-*P,N*-**1b**[H])]$^+$ that exhibits reversible C–H activation. We also report the facile isomerization of the putative zwitterion [Cp*Ru(κ^2-*P,N*-**1**)] to a [Cp*Ru(H)(κ^2-*P,C*)] hydridocarbene complex in an apparent double-geminal C–H bond activation process that is enabled by the proton-accepting ability of the indenide unit in **1**. Dynamic NMR spectroscopic and reactivity studies involving this hydridocarbene species provide compelling evidence for what appears to be the first documented interconversion of Ru(H)=CH and Ru–CH$_2$ fragments by reversible α-H elimination.

The addition of 0.25 equivalents of [(Cp*RuCl)$_4$] to **1a**[H] afforded **2a**, which was isolated in 92% yield (Scheme 1);[8] treatment of **2a** with NEt$_3$ resulted in a clean isomerization to **2b**. In the pursuit of the 16-electron cation [Cp*Ru(κ^2-*P,N*-**1b**[H])]$^+$ (**3**), complex **2b** was treated with Li(Et$_2$O)$_{2.5}$B(C$_6$F$_5$)$_4$. After 1.5 h, ^{31}P NMR spectroscopic analysis of the reaction mixture confirmed the consumption of **2b** ($\delta_{^{31}P}$ = 54.0 ppm) and the appearance of a single product ($\delta_{^{31}P}$ = 82.3 ppm), which was isolated in 83% yield as a pale-yellow solid. Elemental analysis data obtained from this solid were found to be consistent with **3**, but X-ray diffraction analysis allowed for the identification of this complex as the isomeric C–H activation product **4** (Figure 1),[8b,c] which exhibits

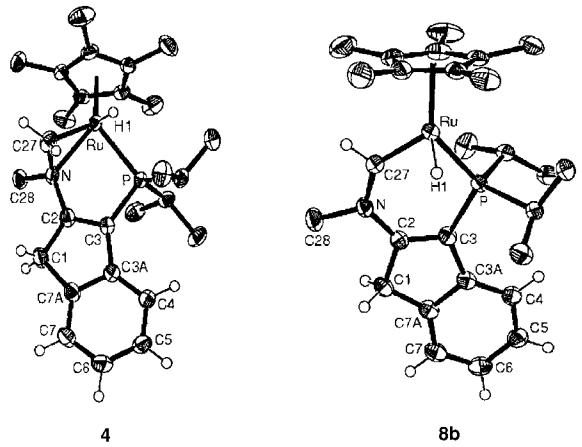

Figure 1. ORTEP diagrams for **4** and **8b** shown with 50% displacement ellipsoids; selected hydrogen atoms and the B(C$_6$F$_5$)$_4^-$ counteranion in **4** have been omitted for clarity. Selected bond lengths [Å] and angles [°]: **4**: Ru–P 2.3094(4), Ru–N 2.136(1), Ru–C27 2.071(2), P–C3 1.809(2), N–C2 1.441(2), N–C27 1.433(2), N–C28 1.484(2), C1–C2 1.503(2), C2–C3 1.336(2); P-Ru-N 82.26(4), Ru-P-C3 101.90(5), Ru-N-C27 67.67(9), Ru-N-C2 116.6(1), Ru-C27-N 72.55(9); **8b**: Ru–P 2.2374(7), Ru···N 3.05, Ru–C27 1.886(2), P–C3 1.812(2), N–C2 1.384(3), N–C27 1.374(3), N–C28 1.475(3), C1–C2 1.512(3), C2–C3 1.362(3); Ru-P-C3 112.74(9), C2-N-C27 123.5(2), C2-N-C28 117.1(2), C27-N-C28 119.4(2), N-C2-C3 129.3(2), P-C3-C2 122.7(2), Ru-C27-N 138.3(2).

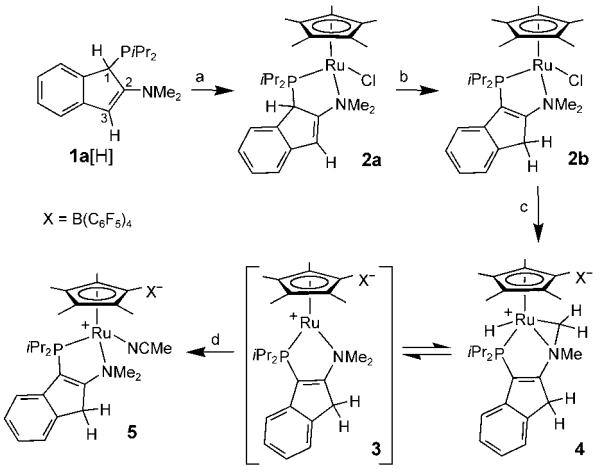

Scheme 1. Synthesis and reactivity of the masked [Cp*Ru(κ^2-*P,N*)]$^+$ complex **4**. Reagents: a) 0.25 [(Cp*RuCl)$_4$]; b) NEt$_3$; c) Li(Et$_2$O)$_{2.5}$B(C$_6$F$_5$)$_4$; d) MeCN.

interatomic distances in keeping with an aza-ruthenacyclopropane ring.[9] Notably, the ^{1}H and ^{13}C NMR spectra of **4** (300 K) in solution are not consistent with the rigid structure depicted in Figure 1.[8a] The effective mirror-plane symmetry, as well as the low-frequency and broadened ^{1}H NMR resonance of NMe$_2$ (δ = 0.95 ppm, $\Delta\nu_{1/2}$ = 20.3 Hz; cf. $\Delta\nu_{1/2}$ = 4.5 Hz for C$_5$Me$_5$ in **4**), suggest a reversible C–H oxidative addition process involving the NMe$_2$ unit of **4** in which the metalated and free N-C-H fragments exchange rapidly on the NMR timescale at 300 K.[10] On lowering the temperature from 300 to 178 K, the ^{1}H NMR spectra of **4** become increasingly complex and downfield signals attributable to non-metalated NMe groups emerge, thus suggesting a slowing of the aforementioned exchange process. However, neither low-frequency ^{1}H NMR signals attributable to Ru–H or agostic Ru-H-CH$_2$ units, nor new ^{31}P NMR resonances were detected over this temperature range. The apparent reversibility of the intramolecular C–H activation process leading to **4** suggests that this complex could serve as a masked source of

the coordinatively unsaturated target cation **3**. Indeed, treatment of **4** with CH_3CN cleanly yields **3**·CH_3CN (**5**),[11a] and as such we are currently assessing the intermolecular C–H bond activating abilities of **4**.

In an effort to prepare [Cp*Ru(κ^2-*P*,*N*-**1**)] (**7**), a zwitterionic analogue of **3**, compound **2b** was treated with $NaN(SiMe_3)_2$ in toluene at ambient temperature (Scheme 2);

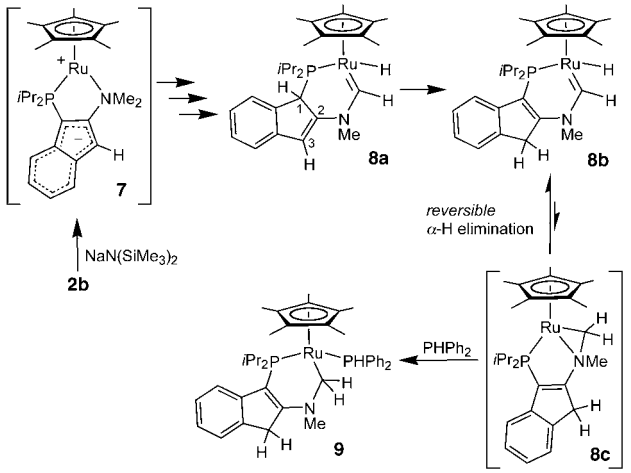

Scheme 2. Synthesis and reactivity of the hydridocarbene complex **8b**.

^{31}P NMR spectroscopic analysis of the reaction mixture after 24 hours indicated the clean conversion into a single product ($\delta_{^{31}P} = 78.2$ ppm), which was isolated as an orange powder in 84% yield. Elemental analysis data for this powder were in keeping with **7**, but further characterization revealed this material to be the isomeric double-geminal C–H bond activation product **8b**. The identification of **8b** as a hydridocarbene complex was based in part on the observation of ^1H NMR signals at $\delta = 12.1$ and -12.4 ppm, as well as a ^{13}C NMR resonance at $\delta = 244.1$ ppm; the structure of **8b** was subsequently confirmed by X-ray diffraction analysis (Figure 1).[8b,d] The contracted Ru–C27 (1.886(2) Å) and N–C27 (1.374(3) Å) distances in **8b** are comparable to some other N-stabilized Ru=C fragments.[12b–d] These interatomic distances, the short N–C2 distance (1.384(3) Å; cf. N–C28 1.475(3) Å), and the planarity of the nitrogen center are all indicative of significant π-bonding interactions in **8b** extending from the Ru=C fragment through to the indene backbone.

In monitoring the progress of the reaction, the consumption of **2b** was confirmed after 20 minutes, with the ^{31}P NMR spectrum displaying new signals at $\delta = 67.8$ (possibly corresponding to **7**) and 112.6 ppm (**8a**; ratio ≈ 1:8). After 1 hour, only the resonance at $\delta = 112.6$ ppm was detected, and the features observed in the ^1H NMR spectrum allowed for the tentative assignment of **8a** as the allylic isomer of **8b**.[11b] Over the ensuing 23 hours, **8a** evolved into **8b** in the absence of detectable intermediates. These observations are consistent with the mechanism outlined in Scheme 2,[11c] in which the transiently formed zwitterion **7** undergoes an intramolecular C–H activation process to yield a zwitterionic relative of **4**.[11d] Regioselective proton transfer from ruthenium to the indenide ligand backbone regenerates a coordinatively unsaturated alkylruthenium complex that undergoes a second C–H activation step (α-H elimination) to yield **8a**, which isomerizes to **8b**.[13] The facile rearrangement of **7** to **8b** is remarkable, since double-geminal C–H bond activation to give a Ru=C complex is rare and invariably requires extended heating and loss of a small molecule to facilitate the reaction.[12]

In exploring the reactivity of **8b**, we observed that treatment with $PHPh_2$ provided **9**, a product that can be viewed as an adduct of a 16-electron alkylruthenium species; perhaps the most striking feature in the crystal structure of **9** is the elongated Ru–CH_2 distance (2.124(2) Å) relative to the Ru=C unit in **8b**.[8b,e] The formation of **9** provided indirect evidence of the dynamic interconversion of Ru(H)=CH and Ru–CH_2 fragments (as in **8b** and **8c**[11e]) by reversible α-H elimination. In contrast to the well-established reversibility of β-H eliminations, reversible α-H elimination is rare,[14] and to the best of our knowledge the latter process involving ruthenium has not been documented previously.

Data from 1D- and 2D-exchange spectroscopic (EXSY) ^1H NMR experiments provide definitive spectroscopic evidence for the operation of reversible α-H eliminations involving **8b**.[8a] In the case of ^1H EXSY experiments, irradiation of either the Ru(*H*)=CH or the Ru(H)=C*H* signal in **8b** results in significant positively-phased enhancement of the other resonance, indicating that these two sites are undergoing chemical exchange. Similarly, the ^1H-^1H EXSY spectrum of **8b** exhibits positively-phased off-diagonal exchange cross-peaks that connect the two Ru(*H*)=C*H* environments. The observation of reversible α-H elimination involving ruthenium is significant, as the interconversion of Ru=C and Ru–alkyl species by this mechanism may play a role in the transmutation of olefin metathesis and hydrogenation catalysts in situ.[15]

In conclusion, we have prepared and isolated a masked variant of the first coordinatively unsaturated [Cp*Ru(κ^2-*P*,*N*)]$^+$ complex, which has proven to be capable of *single* C–H bond activation. By comparison, the putative zwitterion **7** exhibits much more aggressive reactivity with C–H bonds to yield a hydridocarbene by way of a remarkably facile *double* C–H activation process that is enabled by the proton-accepting ability of the ancillary ligand **1**; moreover, an NMR investigation of this hydridocarbene has revealed a reversible α-H elimination process previously undocumented for ruthenium. We are currently developing more cyclometalation-resistant analogues of **7**, with the aim of exploiting the proton-accepting function of **1** in the establishment of new and synthetically useful intermolecular multiple C–H bond activation processes.

Received: February 11, 2005
Published online: May 2, 2005

Keywords: carbene ligands · C–H activation · α-elimination · ruthenium · zwitterions

[1] a) R. H. Crabtree, *J. Organomet. Chem.* **2004**, *689*, 4083 – 4091; b) F. Kakiuchi, N. Chatani, *Adv. Synth. Catal.* **2003**, *345*, 1077 – 1101.

[2] For a recent example, see: D. B. Grotjahn, J. M. Hoerter, J. L. Hubbard, *J. Am. Chem. Soc.* **2004**, *126*, 8866 – 8867, and references cited therein.

[3] For a pioneering example involving a [Cp*ML$_n$] complex, see: a) H. F. Luecke, B. A. Arndtsen, P. Burger, R. G. Bergman, *J. Am. Chem. Soc.* **1996**, *118*, 2517 – 2518; b) B. A. Arndtsen, R. G. Bergman, *Science* **1995**, *270*, 1970 – 1973.

[4] K. N. Gavrilov, A. I. Polosukhin, *Russ. Chem. Rev.* **2000**, *69*, 661 – 682.

[5] For catalytic C–H/Si–H dehydrogenative cross-coupling mediated by [(η^4-cod)Rh(κ^2-*P*,*N*-**1b**[H])]$^+$ (cod = 1,5-cyclooctadiene) or the crystallographically characterized zwitterion [(η^4-cod)Rh-(κ^2-*P*,*N*-**1**)], see: M. Stradiotto, J. Cipot, R. McDonald, *J. Am. Chem. Soc.* **2003**, *125*, 5618 – 5619.

[6] M. Jiménez-Tenorio, M. C. Puerta, P. Valerga, *Eur. J. Inorg. Chem.* **2004**, 17 – 32, and references cited therein.

[7] While zwitterions featuring formally cationic Ru^{II} centers have been reported, none feature κ^2-*P*,*N* ligation and their reactivity properties have not been systematically explored; for a recent example, see: T. A. Betley, J. C. Peters, *Inorg. Chem.* **2003**, *42*, 5074 – 5084.

[8] a) The Supporting Information contains synthetic procedures and characterization data for all new compounds, NMR spectra for **4** at 300 K, EXSY NMR spectra for **8b**, and X-ray crystallographic details; b) CCDC-259456 (**4**), -259454 (**8b**), and -259455 (**9**·0.5 C_5H_{12}) contain the supplementary X-ray crystallographic data for this paper. These data can be obtained free of charge from The Cambridge Crystallographic Data Centre via www.ccdc.cam.ac.uk/data_request/cif; c) SG = space group, D/R/P = data/restraints/parameters; data for **4**: triclinic; SG = $P\bar{1}$; a = 10.1928(7), b = 15.617(1), c = 16.321(1) Å; α = 79.3438(9), β = 72.1948(9), γ = 88.2354(9)°; V = 2430.0(3) Å^3; Z = 2; D/R/P = 9913/0/686; R_1 = 0.0256; wR_2 = 0.0691; d) data for **8b**: monoclinic; SG = $P2_1/c$; a = 14.0492(5), b = 16.1616(6), c = 11.0248(4) Å; β = 95.5325(7)°; V = 2491.6(2) Å^3; Z = 4; D/R/P = 5088/0/288; R_1 = 0.0291; wR_2 = 0.0742; e) selected X-ray crystallographic data for **9**·0.5 C_5H_{12} are provided in the Supporting Information.

[9] K. Mauthner, C. Slugovc, K. Mereiter, R. Schmid, K. Kirchner, *Organometallics* **1997**, *16*, 1956 – 1961.

[10] We cannot conclusively rule out the involvement of agostic species in this dynamic process based on the available spectroscopic data; for comparison, the NMe_2 $^1J_{C,H}$ observed for **4** (129.5 Hz) is only modestly smaller than that of **5** (138.5 Hz and 139.0 Hz): M. Brookhart, M. L. H. Green, L.-L. Wong, *Prog. Inorg. Chem.* **1988**, *36*, 1 – 124.

[11] a) The identity of **5** was confirmed by comparison with the BF_4^- analogue (**6**), which was prepared from **2b** and $AgBF_4$ in CH_3CN (see the Supporting Information); b) diagnostic ^{1}H NMR resonances for **8a**: δ = 12.01 (br s, 1H; Ru=C-H), 5.83 (s, 1H; C3-H), 4.58 (d, $^2J_{P,H}$ = 13.7 Hz, 1H; C1-H), −11.80 (d, $^2J_{P,H}$ = 38.5 Hz, 1H; Ru-H); c) a detailed representation of this mechanistic proposal is provided in the Supporting Information; d) the viability of **7** as a reactive intermediate is supported by the observation that the related zwitterion [(η^4-cod)Rh(κ^2-*P*,*N*-**1**)][5] is an isolable species; e) the 18-electron intermediate **8c** is proposed by analogy with **4**; alternative 16-electron intermediates could also be invoked.

[12] a) V. M. Ho, L. A. Watson, J. C. Huffman, K. G. Caulton, *New J. Chem.* **2003**, *27*, 1446 – 1450, and references cited therein; b) G. Ferrando-Miguel, J. N. Coalter III, H. Gérard, J. C. Huffman, O. Eisenstein, K. G. Caulton, *New J. Chem.* **2002**, *26*, 687 – 700; c) V. F. Kuznetsov, A. J. Lough, D. G. Gusev, *Chem. Commun.* **2002**, 2432 – 2433; d) V. F. Kuznetsov, G. P. A. Yap, H. Alper, *Organometallics* **2001**, *20*, 1300 – 1309; e) J. N. Coalter III, J. C. Huffman, K. G. Caulton, *Chem. Commun.* **2001**, 1158 – 1159.

[13] The interconversion of allylic and vinylic indenylphosphine isomers is well established, see: M. Stradiotto, M. J. McGlinchey, *Coord. Chem. Rev.* **2001**, *219–221*, 311 – 378.

[14] E. Clot, J. Chen, D.-H. Lee, S. Y. Sung, L. N. Appelhans, J. W. Faller, R. H. Crabtree, O. Eisenstein, *J. Am. Chem. Soc.* **2004**, *126*, 8795 – 8804, and references cited therein.

[15] B. Schmidt, *Eur. J. Org. Chem.* **2004**, 1865 – 1880.

Sensors

Selective Electrochemical Detection of Hydrogen Fluoride by Ambiphilic Ferrocene Derivatives**

Christopher Bresner, Simon Aldridge, Ian A. Fallis,* Cameron Jones, and Li-Ling Ooi*

The selective detection of specific anions or whole acids/metal salts (HX or MX) in the presence of potentially competitive contaminants represents a fundamental chemical challenge for applications, for example, in sensor devices and in separation technologies.[1–4] In the former case, such a process typically involves recognition of both anionic and cationic components, accompanied by an appropriate reporter response.[2,3] Within this sphere, the detection of hydrogen fluoride represents a particularly timely goal, given its industrial use and its well-documented liberation in the hydrolysis of the fluorinated G-type chemical warfare agents (CWAs).[4–7] Given the low ambient levels of volatile fluorides, a potential sensor for airborne Sarin or Soman utilizes HF as the target analyte.

Selective binding of the fluoride anion by Lewis acid receptors based on boronic acid/ester has been reported by a number of groups.[4,8,9] Furthermore, significant electrochemical shifts have been shown to accompany the binding event for systems incorporating directly linked receptor and ferrocene components.[8a,b,d] Given the selective detection of fluoride demonstrated for these systems, we wondered whether incorporation of a suitable Lewis basic component within an appropriate molecular framework might facilitate selective HF recognition, either by binding of an intact HF

[*] C. Bresner, Dr. S. Aldridge, Dr. I. A. Fallis, Prof. C. Jones, Dr. L.-L. Ooi
Centre for Fundamental and Applied Main Group Chemistry
School of Chemistry, Cardiff University
Main Building, Park Place
Cardiff, CF10 3AT (UK)
Fax: (+44) 292-087-4030
E-mail: aldridges@cardiff.ac.uk

[**] We would like to thank the EPSRC for a studentship (C.B.), for financial aid (grant GR/S98771/01), and for access to the National Mass Spectrometry facility.

Supporting information for this article is available on the WWW under http://www.angewandte.org or from the author.

  DOI: 10.1002/anie.200500527

entity or distinct H^+ and F^- components. With this in mind, we set out to examine the response to hydrogen fluoride exposure of the mixed Lewis acid/Lewis base systems **1**–**3**.

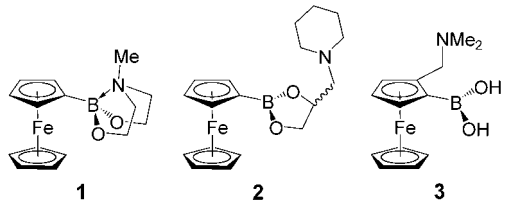

The compounds chosen sought to probe the stability of different molecular architectures to HF and to further examine the effect (if any) of the intramolecular N→B interaction in the H–F bond breaking process.

Compounds **1** and **2** can be synthesized by a one-pot process from $FcBBr_2$ [Fc = (η^5-C_5H_5)Fe(η^5-C_5H_4)][10] and one equivalent of the appropriate reagent, that is, $(Me_3SiOCH_2CH_2)_2NMe$ for **1** and *rac*-$(C_5H_{10}N)CH_2CH$-(OLi)CH(OLi) for **2**. The structure of **1** was corroborated by single-crystal X-ray diffraction (Figure 1), which also

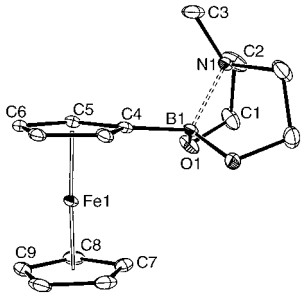

Figure 1. Molecular structure of $FcB(OCH_2CH_2)_2NMe$ (**1**) with ORTEP ellipsoids set at the 50% probability level; hydrogen atoms are omitted for clarity. Relevant bond lengths [Å] and angles [°]: Fe1-$Cp_{centroid}$ 1.649(2), Fe1-$C_5H_4BRR'_{centroid}$ 1.645(2), B1-N1 1.735(3), B1-O1 1.443(2), B1-C4 1.595(4); B1-C4-$C_5H_4BRR'_{centroid}$ 176.3(1).

confirmed the presence of an intramolecular N→B bond (1.735(3) Å).[11] Although suitable single crystals of **2** were not forthcoming, the three-coordinate nature of the boron center was implied by the ^{11}B NMR chemical shift ($\delta_B = 32.3$ ppm) and the ferrocene-based oxidation potential ($E_{1/2} = -0.5$ mV (96 mV)[12]), which are characteristic of this type of pendant boryl function [for comparison, $\delta_B = 34.1$ ppm, $E_{1/2} = +116.0$ mV (80 mV) for $FcBO_2C_2H_2Ph_2$ (three-coordinate boron)[13] and $\delta_B = 13.4$ ppm, $E_{1/2} = -190.5$ mV (85 mV) for **1** (four-coordinate boron)].

The NMR spectroscopic and electrochemical (CV) monitoring of the reactions of **1** and **2** with hydrogen fluoride (as the collidine complex 2,4,6-trimethylpyridine·$(HF)_{1.5}$) showed that the reaction requires three equivalents of HF to be driven to completion, and that a common ferrocene- and boron-containing product is formed in each case [quartet $\delta_B = 3.7$ ppm, $J_{BF} = 49.8$ Hz; $E_{1/2} = -320$ mV (75 mV)]. For the reaction with **1**, crystallographic investigation of the product revealed that this is the $[FcBF_3]^-$ anion,[14] isolated in this case as the $[(HOCH_2CH_2)_2N(H)Me]^+$ salt (**4**, Figure 2).

Given that **4** is formed by rupture of the boronic ester linkages in **1**, it is clear that the design of an ambiphilic

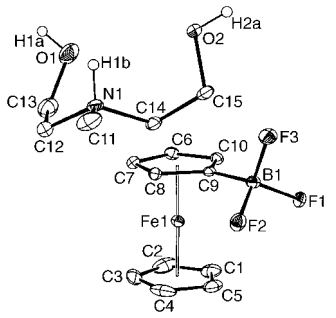

Figure 2. Molecular structure of $[(HOCH_2CH_2)_2N(H)Me][FcBF_3]$ (**4**) with ORTEP ellipsoids set at the 50% probability level; hydrogen atoms (except those attached to O1, O2, and N1) are omitted for clarity. Relevant bond lengths [Å] and angles [°]: Fe1-$Cp_{centroid}$ 1.648(3), Fe1-$C_5H_4BRR'_{centroid}$ 1.644(3), B1-F1 1.435(3), B1-F2 1.423(3), B1-F3 1.405(4), B1-C9 1.590(4); B1-C9-$C_5H_4BF_{3\,centroid}$ 179.6(2).

receptor system that survives exposure to HF necessitates the avoidance of structurally significant B–O bonds. Consequently, we have examined the whole acid sensing properties of 2-(*N*,*N*-dimethylaminomethyl)ferrocene boronic acid (**3**), a compound which was originally reported by Marr et al.,[15] and which has, for example, also been investigated by Shinkai and by Norrild and Søtofte as a carbohydrate sensor.[16] Tethering of the Lewis acidic and Lewis basic components to the cyclopentadienyl ring through B–C and N–C bonds allows isolation of an intact, charge-neutral HF host–guest complex.

In practice, the reaction of **3** with three equivalents of HF in acetonitrile leads to the isolation of the zwitterionic species [(η^5-C_5H_5)Fe{η^5-$C_5H_3(BF_3)(CH_2NMe_2H)$}] (**5**) in about 68% yield. The structure of **5** has been elucidated from spectroscopic and X-ray diffraction measurements and reveals—in addition to substitution of the two boronic acid OH groups by fluorine atoms[17]—the binding of a single equivalent of HF (Figure 3). The residual intramolecular H···F interaction is

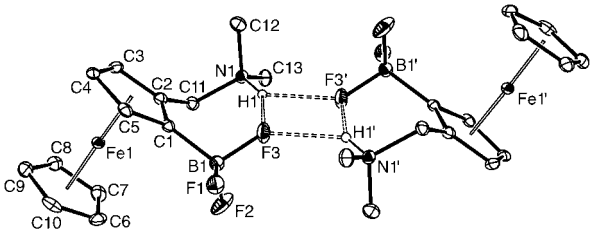

Figure 3. Hydrogen-bonded dimeric structure of [(η^5-C_5H_5)Fe{η^5-C_5H_3-$(BF_3)(CH_2NMe_2H)$}] (**5**) in the solid state with ORTEP ellipsoids set at the 50% probability level; hydrogen atoms (except that attached to N1 and N1′) are omitted for clarity. Relevant bond lengths [Å] and angles [°]: Fe1-$Cp_{centroid}$ 1.643(5), Fe1-$C_5H_3BF_{3\,centroid}$ 1.640(5), B1-C1 1.600(6), B1-F1 1.413(5), B1-F2 1.382(5), B1-F3 1.431(5), F3-H1 2.204, F3-H1′ 2.124, N1-H1 0.930, N1-F3 2.996(4), N1-F3′ 2.854(3); B1-C1-$C_5H_3CBF_{3\,centroid}$ 176.6(3), N1-H1-F3 142.5, N1-H1-F3′ 134.4.

relatively weak, as evidenced by a separation of 2.204 Å (0.92 Å for gaseous HF),[18] and is best viewed as an ionic hydrogen bond between the BF_3^- and NMe_2H^+ fragments.[19] In the solid state these hydrogen-bonded units are linked through additional intermolecular H···F interactions (2.124 Å) into centrosymmetric dimers.

The key feature of whole acid binding by **3** is its selectivity for HF over other acids. This can not only be demonstrated electrochemically, but also results in distinct *opposing* responses for HF and, for example, HCl. Thus, the voltammograms for **3** and **5** reveal a cathodic shift of −80 mV on HF binding [$E_{1/2} = +37.5$ mV (85 mV) for **3** and −43 mV (75 mV) for **5**; Figure 4, top]. The oxidation potential for **5** is markedly

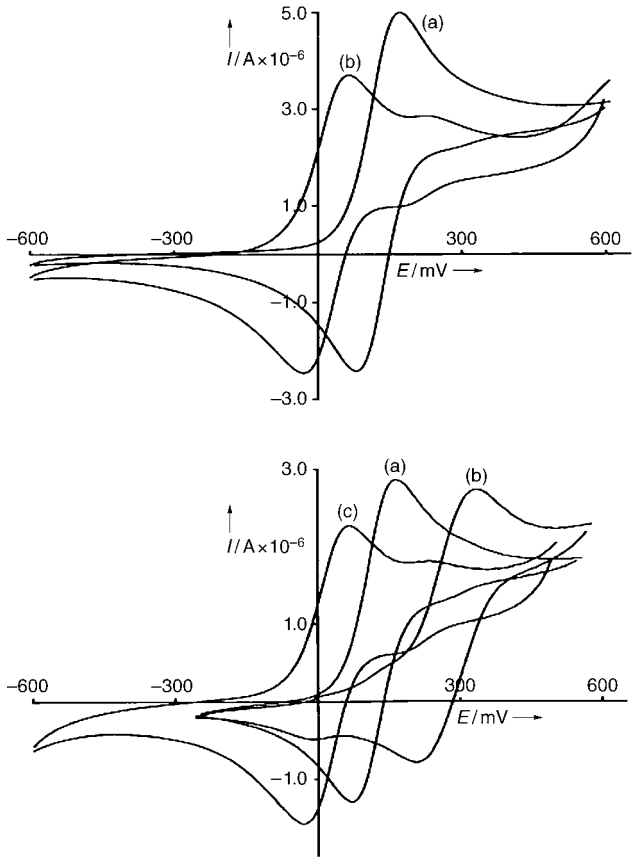

Figure 4. Top: Cyclic voltammograms of **3** (a) and of **5** (b). Bottom: Cyclic voltammograms of **3** (a), of **3** after addition of HCl (b), and of **3** after subsequent addition of nBu$_4$NF (c).

less negative than that for $[FcBF_3]^-$ [$E_{1/2} = -320$ mV (75 mV)], reflecting the overall charge neutrality of **5**. However, the net cathodic shift (with respect to **3**) is consistent with transformation of a three-coordinate electron-withdrawing boronic acid group into a net electron-donating four-coordinate boronate.[20] An entirely different electrochemical response is observed on addition of excess HCl to **3** (Figure 4, bottom). Here a significant anodic shift (+149.5 mV) is observed, and this (together with the lack of any discernable shift in the ^{11}B NMR spectrum of **3** on addition of HCl) is consistent with protonation of the amine functionality, but with no significant Lewis base coordination at the boron center. The identification of this species as cationic $[(\eta^5\text{-}C_5H_5)Fe\{\eta^5\text{-}C_5H_3[B(OH)_2](CH_2NMe_2H)\}]^+$ is given further credence by the addition of excess fluoride. This leads to an upfield shift in the ^{11}B NMR resonance (to $\delta_B = 3.0$ ppm) and to a CV trace that is essentially identical to that measured for an authentic sample of **5**. Thus it would appear that the opposing senses of the electrochemical shifts observed for **3** with HF and HCl[*] reflect the intrinsic selectivity of the boronic acid moiety for fluoride.[4,8]

In conclusion, it has been demonstrated that by avoiding structurally significant B–O bonds it is possible to construct robust organometallic receptor systems capable of selectively binding hydrogen fluoride. Such a system has been shown to be capable of differentiating between exposure to HF and exposure to related acids (such as HCl) by providing opposing electrochemical responses. This in turn can be related to the much stronger affinity of fluoride for boronic acid/ester receptors compared to other conjugate bases such as chloride.

Experimental Section

Details of the preparation and characterization of **1** and **2**, details of the reaction of **1** with HF, and characterizing data for **4** are included in the Supporting Information.

5: To **3** (24.4 mg, 0.085 mmol) in acetonitrile (ca. 20 cm^3) was added 2,4,6-trimethylpyridine·$(HF)_{1.5}$, (3 equiv of HF), and the reaction mixture was stirred for 20 min. Monitoring by ^{11}B NMR spectroscopy indicated complete conversion into a single product. Cannula filtration followed by cooling to −30 °C yielded **5** as a yellow-orange solid (yield: 18.0 mg, 68.4 %). ^{1}H NMR ([D$_3$]acetonitrile, 300 MHz, 20 °C): $\delta = 2.57$ (s, 3H, NCH_3), 2.83 (s, 3H, NCH_3), 3.75 (d $J = 13$ Hz, 1H, CH_2N), 4.08 (s, 5H, C_5H_5), 4.15 (m, 3H, C_5H_3), 4.55 (d $J = 13$ Hz, 1H, CH_2N), 6.98 ppm (v br s, 1H, NH). ^{13}C NMR ([D$_3$]acetonitrile, 76 MHz, 20 °C): $\delta = 40.7$ (br, NCH_3), 43.3 (br, NCH_3), 60.0 (NCH_2), 68.7 (CH of C_5H_5), 68.4, 70.6, 73.8 (CH of C_5H_3), 77.6 ppm (C-bound quaternary of C_5H_3), B-bound quaternary of C_5H_3 not observed. ^{11}B NMR ([D$_3$]acetonitrile, 96 MHz, 21 °C): $\delta =$ 3.0 ppm (q, $J_{B\text{-}F} = 49$ Hz). ^{19}F NMR ([D$_3$]acetonitrile, 283 MHz, 21 °C): $\delta = -133.9$ ppm (q, $J_{F\text{-}B} = 49$ Hz). IR (KBr disk): $\tilde{\nu} = 3174$ s (NH), 1489 w, 1473 w, 1448 w, 1388 m, 1297 w, 1248 w, 1187 m, 1165 w, 1139 m, 1102 s, 1035 s, 1009 s, 946 s, 921 s, 890 m, 853 m, 813 s, 757 w cm^{-1}. MS(EI): $[M-HF]^+ = 291$ (75 %), calcd 291.0683, found 291.0685; $[M-HF-NMe_2]^+ = 247$ (100 %), calcd 247.0185, found 247.0186.

For the crystal structure determinations of **1**, **4**, and **5** a suitable crystal was covered in predried mineral oil and mounted on an Enraf-Nonius Kappa CCD diffractometer at 150(2) K. Crystal data for **1** ($C_{15}H_{20}BFeNO_2$): orthorhombic, space group *Pnma*, $a = 12.522(3)$, $b = 10.602(2)$, $c = 10.421(2)$ Å, $V = 1383.5(5)$ Å^3, $Z = 4$, $\rho_{calcd} = 1.503$ g cm^{-3}, $\mu(Mo_{K\alpha}) = 1.089$ mm^{-1}; 8254 unique reflections were collected ($3.2 < \theta < 27.5°$); final R factor $R_1 = 0.034$. Crystal data for **4** ($C_{15}H_{23}BF_3FeNO_2$): monoclinic, space group $P2_1/n$, $a = 5.8490(1)$, $b =$

[*] That the response of **3** towards HCl is typical of other inorganic and organic acids (i.e., that there is little or no interaction of the conjugate anion with the boronate moiety) has been shown for related systems[8d] and can be demonstrated explicitly for **3** by cyclic voltammetry. Exposure of **3** to other sources of fluoride (e.g. KF/[18]crown-6) is accompanied by an electrochemical response (a cathodic shift of about 450 mV in MeCN) typical of fluoride coordination to the boron center[8d,13] but with no significant interaction of the tertiary amine function with the cation (K^+).

8.6140(2), $c = 32.1360(9)$ Å, $\beta = 92.210(1)°$, $V = 1617.9(1)$ Å^3, $Z = 4$, $\rho_{calcd} = 1.531$ g cm^{-3}, $\mu(Mo_{K\alpha}) = 0.970$ mm^{-1}; 3667 unique reflections were collected ($3.0 < \theta < 27.5°$); final R factor: $R_1 = 0.047$. Crystal data for **5** ($C_{13}H_{17}BF_3FeN$): monoclinic, space group $P2_1/a$, $a = 11.6268(5)$, $b = 7.3492(4)$, $c = 15.7888(7)$ Å, $\beta = 104.684(3)°$, $V = 1305.1(1)$ Å^3, $Z = 4$, $\rho_{calcd} = 1.583$ g cm^{-3}, $\mu(Mo_{K\alpha}) = 1.174$ mm^{-1}; 2982 unique reflections were collected ($3.1 < \theta < 27.5°$); final R factor: $R_1 = 0.056$. CCDC 263113 (**1**), CCDC 263114 (**4**), and CCDC 263115 (**5**) contain the supplementary crystallographic data for this paper. These data can be obtained free of charge from The Cambridge Crystallographic Data Centre via www.ccdc.cam.ac.uk/data_request/cif.

Received: February 11, 2005
Published online: May 17, 2005

Keywords:
molecular recognition · boron · electrochemistry · metallocenes · sensors

[1] For reviews on anion binding, see: a) A. P. de Silva, H. Q. N. Gunaratne, T. Gunnlaugsson, A. J. M. Huxley, C. P. McCoy, J. T. Rademacher, T. E. Rice, *Chem. Rev.* **1997**, *97*, 1515 – 1566; b) F. P. Schmidtchen, M. Berger, *Chem. Rev.* **1997**, *97*, 1609 – 1646; c) P. A. Gale, J. A. Sessler, V. Kral, *Chem. Commun.* **1998**, 1 – 8; d) P. D. Beer, P. A. Gale, *Angew. Chem.* **2001**, *113*, 502 – 532; *Angew. Chem. Int. Ed.* **2001**, *40*, 486 – 516; ; e) J. J. Lavigne, E. V. Anslyn, *Angew. Chem.* **2001**, *113*, 3212 – 3215; *Angew. Chem. Int. Ed.* **2001**, *40*, 3118 – 3130; ; f) P. A. Gale, *Coord. Chem. Rev.* **2003**, *213*, 191 – 221; g) R. Martínez-Máñez, F. Sancernón, *Chem. Rev.* **2003**, *103*, 4419 – 4476.

[2] For a recent example of whole metal salt (MX) binding, see: V. Gasperov, S. G. Galbraith, L. F. Lindoy, B. R. Rumbel, B. W. Skelton, P. A. Tasker, A. H. White, *Dalton Trans.* **2005**, 139 – 145.

[3] For an example of metal fluoride binding, see: M. T. Reetz, C. M. Niemeyer, K. Harms, *Angew. Chem.* **1991**, *103*, 1515 – 1517; *Angew. Chem. Int. Ed. Engl.* **1991**, *30*, 1472 – 1474.

[4] C. R. Cooper, N. Spencer, T. James, *Chem. Commun.* **1998**, 1365 – 1366.

[5] H. Sohn, S. Létant, M. J. Sailor, W. C. Trogler, *J. Am. Chem. Soc.* **2000**, *122*, 5399 – 5400.

[6] Y.-C. Yang, J. A. Baker, J. R. Ward, *Chem. Rev.* **1992**, *92*, 1729 – 1743.

[7] For a recent example of G-agent sensing, see: S.-W. Zhang, T. M. Swager, *J. Am. Chem. Soc.* **2003**, *125*, 3420 – 3421.

[8] a) C. Dusemund, K. R. A. S. Sandanayake, S. Shinkai, *J. Chem. Soc. Chem. Commun.* **1995**, 333 – 334; b) H. Yamamoto, A. Ori, K. Ueda, C. Dusemund, S. Shinkai, *Chem. Commun.* **1996**, 407; c) A. Yuchi, A. Tatebe, S. Kani, T. D. James, *Bull. Chem. Soc. Jpn.* **2001**, *74*, 509 – 510; d) S. Aldridge, C. Bresner, I. A. Fallis, S. J. Coles, M. B. Hursthouse, *Chem. Commun.* **2002**, 740 – 741; e) S. Arimori, M. G. Davidson, T. M. Fyles, T. G. Hibbert, T. D. James, G. I. Kociok-Kohn, *Chem. Commun.* **2004**, 1640 – 1641.

[9] For recent examples of fluoride binding by other three-coordinate boron-containing systems, see: a) S. Yamaguchi, S. Akiyama, K. Tamao, *J. Am. Chem. Soc.* **2001**, *123*, 11372 – 11375; b) Y. Kubo, M. Yamamoto, M. Ikeda, M. Takeuchi, S. Shinkai, K. Tamao, *Angew. Chem.* **2003**, *115*, 2082 – 2086; *Angew. Chem. Int. Ed.* **2003**, *42*, 2036 – 2040; ; c) S. Solé, F. P. Gabbaï, *Chem. Commun.* **2004**, 1284 – 1285; d) G. E. Herberich, U. Englert, A. Fischer, D. Wiebelhaus, *Eur. J. Inorg. Chem.* **2004**, 4011 – 4020.

[10] T. Renk, W. Ruff, W. Siebert, *J. Organomet. Chem.* **1976**, *120*, 1 – 25.

[11] For examples of intramolecular N→B bonds in closely related systems, see: a) A. A. Korlyukov, K. A. Lyssenko, M. Y. Antipin, V. N. Kirin, E. A. Chernyshev, S. P. Knyazev, *Inorg. Chem.* **2002**, *41*, 5043 – 5051; b) S. Aldridge, R. J. Calder, D. L. Coombs, C. Jones, J. W. Steed, S. J. Coles, M. B. Hursthouse, *New J. Chem.* **2002**, *26*, 677 – 686.

[12] Electrochemical data are reported for solutions in acetonitrile, referenced with respect to the ferrocene/ferrocenium couple. Peak-to-peak separations are given in parentheses.

[13] C. Bresner, PhD Thesis, Cardiff University, 2005.

[14] T. D. Quach, R. A. Batey, A. J. Lough, *Acta Crystallogr. Sect. E* **2001**, *57*, m320 – m321.

[15] G. Marr, R. E. Moore, B. W. Rockett, *J. Chem. Soc. C* **1968**, 24 – 27.

[16] a) A. Ori, S. Shinkai, *J. Chem. Soc. Chem. Commun.* **1995**, 1771 – 1772; b) J. C. Norrild, I. Søtofte, *J. Chem. Soc. Perkin Trans. 2* **2001**, 727 – 732.

[17] R. L. Giles, J. A. K. Howard, L. G. F. Patrick, M. R. Probert, G. E. Smith, A. Whiting, *J. Organomet. Chem.* **2003**, *680*, 257 – 262.

Biotransformations

Family Clustering of Baeyer–Villiger Monooxygenases Based on Protein Sequence and Stereopreference**

Marko D. Mihovilovic, Florian Rudroff, Birgit Grötzl, Peter Kapitan, Radka Snajdrova, Joanna Rydz, and Robert Mach*

Since its discovery by Adolf von Baeyer and Victor Villiger in 1899,[1] the oxidation process later named after the two scientists has become a powerful tool in synthesis to break carbon–carbon bonds in an oxygen-insertion process.[2] The regiochemistry of the reaction is governed by predictable

[*] Prof. Dr. M. D. Mihovilovic, Dipl.-Ing. F. Rudroff, Dipl.-Ing. B. Grötzl, Dipl.-Ing. P. Kapitan, MSc R. Snajdrova, MSc J. Rydz
Institute of Applied Synthetic Chemistry
Marie Curie Training Site GEMCAT
Vienna University of Technology
Getreidemarkt 9/163-OC, 1060 Wien (Austria)
Fax: (+43) 1-58801-15499
E-mail: mmihovil@pop.tuwien.ac.at

Prof. Dr. R. Mach
Institute of Chemical Engineering
Vienna University of Technology
Wien (Austria)

[**] Financial support by the European Commission under the Human Potential Program of FP-5 (contract no. HPMT-CT-2001-00243) and by the Austrian Science Fund (FWF; project no. P16373) is gratefully acknowledged. The authors thank Dr. Pierre E. Rouviere (E.I. DuPont Company) for supporting this project by the generous donation of six *Escherichia coli* expression systems for Baeyer–Villiger monooxygenases. Assistance by Dr. Erwin Rosenberg (Vienna University of Technology) during the determination of enantiomeric purity and by Dr. Christian Hametner (Vienna University of Technology) for NMR-based structure analysis is acknowledged.

Supporting Information for this article is available on the WWW under http://www.angewandte.org or from the author.

 DOI: 10.1002/anie.200462964

conformational, steric, and electronic effects,[3] and the rearrangement process of the tetrahedral peroxo Criegee intermediate proceeds with strict retention of configuration.[4] These factors are key prerequisites for performing the Baeyer–Villiger oxidation in an enantioselective manner.

The conversion of cyclic ketones into optically pure lactones (Scheme 1), in particular, allows access to highly

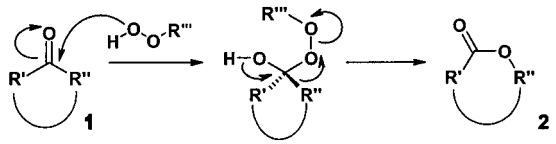

Scheme 1. Baeyer–Villiger oxidation of cyclic ketones **1** to form lactones **2**.

flexible compounds as platforms for the subsequent synthesis of bioactive compounds and natural products. Consequently, enantioselective Baeyer–Villiger oxidations have become a highly active field in asymmetric chemistry in recent years.[5] Currently, two major strategies are being developed with implementation of the "green-chemistry" concept aimed at sustainable, environmentally benign, and atom-efficient processes. Metal-based, de novo designed chiral catalysts have been continuously improved and are becoming promising candidates for industrial-scale applications.[6] By taking advantage of the vast catalytic repertoire of enzymes in nature, biocatalysis offers alternative entities for stereoselective oxidation processes with molecular oxygen utilized as the oxidant.[7] An increasing number of flavin-containing Baeyer–Villiger monooxygenases (BVMOs) have been identified during the past decade, and several such proteins display a remarkably broad acceptance profile for nonnatural substrates.[8]

Our approach to overcome some of the BVMO limitations, which have hampered the widespread utilization of oxidizing enzymes by synthetic chemists, utilizes living whole cells that are genetically engineered to express the required protein in high concentration.[9] This concept simplifies the problem of cofactor recycling, which arises because BVMOs require nicotinamide adenine dinucleotide (phosphate) in the reduced form (NAD(P)H) in the initial step of the catalytic cycle.[10] In addition, the tedious process of protein isolation is overcome and enzyme stability is not a limiting factor. As a result of the genetic modifications, the overexpressed BVMO becomes the major fraction in the organism's proteome, and side reactions by competing enzymes can be essentially avoided. This strategy was successfully optimized[11] and scaled up in pilot-plant industrial fermentation facilities[12] very recently.

The second major challenge in biocatalysis in general is the aspect of enantiodivergence. Artificial catalytic entities can be readily tailored to produce antipodal forms of the required products by inverting the chirality of the inducing ligand field. This strategy cannot be transferred to biotransformations, as there is no efficient process available to yield D-amino acid based proteins. Consequently, the identification and characterization of enzymes with overlapping substrate specificity that yield antipodal products is a key issue for the further implementation of biocatalytic methods in synthetic chemistry.

Recently, we and others have observed the formation of antipodal lactones by some representatives of the BVMO enzyme family.[13] This study compares the stereopreference, with respect to enantio- and regiodivergence, of cyclohexanone (CH) and cyclopentanone (CP) monooxygenases originating from *Acinetobacter* ($CHMO_{Acineto}$),[14] *Arthrobacter* ($CHMO_{Arthro}$),[15] *Brachymonas* ($CHMO_{Brachy}$),[16] *Brevibacterium* ($CHMO_{Brevi1}$, $CHMO_{Brevi2}$),[17] *Comamonas* ($CPMO_{Coma}$),[18] and *Rhodococcus* ($CHMO_{Rhodo1}$, $CHMO_{Rhodo2}$)[15] species in recombinant whole-cell-mediated Baeyer–Villiger oxidations with *Escherichia coli* as the host organism.

Initially, desymmetrization of prochiral ketones **1a–i** to the corresponding lactones **2a–i**, in part potential precursors in natural product synthesis, was investigated (Table 1). In a series of monocyclic ketones with prochiral substitution patterns, a significant clustering into two groups was observed: while the majority of BVMOs ("CHMO type") gave (−)-**2a–d** and (+)-**2e** lactones, $CPMO_{Coma}$ and $CHMO_{Brevi2}$ ("CPMO type") gave the antipodal products with moderate to excellent enantiomeric excess. This general trend is only violated by the enzyme $CHMO_{Brevi1}$, which displays the stereopreference of a CHMO-type BVMO but does not accept 4,4-disubstituted ketone **1c**. As observed previously for similar hydroxy compounds,[19] the oxidation of **1c** does not yield the expected seven-membered-ring lactone but rearranges under biotransformation conditions to give the more stable five-membered-ring system.

The enantiodivergent trend in biooxidation was also observed for fused bicycloketones **1f–h**. Generally, moderate to excellent stereoselectivity was obtained upon biooxidation with CHMO-type enzymes. CPMO-type BVMOs gave lactones with chirality consistent with the two-enzyme-groups hypothesis but with lower selectivity for **2f**.

Bridged bicyclo precursor **1i** is only oxidized by CPMO-type enzymes to form lactone **2i**. Together with previous studies of classical kinetic resolutions,[20] this is to some extent an exception of the hypothesis of stereodivergent biotransformations. However, the clearly differentiated substrate acceptance again supports the classification of the studied BVMOs into two groups.

Representatives of this enzyme library exhibited superior enantioselectivities for desymmetrizations with all ketones compared to those observed in previously reported bacterial BVMO oxidations. The potential of enantiodivergent biocatalysts with overlapping substrate acceptance for natural product synthesis is demonstrated by accessing various indole alkaloids such as alloyohimbane[21] from (−)-**2h** and antirhine[22] from the antipodal (+)-**2h**.

Intrigued by the significantly different behavior of the two BVMO clusters in the desymmetrization reactions, we investigated the regiodivergent transformation of fused ketones bearing a cyclobutanone structural motif (Scheme 2). This conversion is considered to be one of the "benchmark" reactions for asymmetric Baeyer–Villiger oxidations[23] and

Table 1: Enantiodivergent Baeyer–Villiger oxidation of prochiral ketones **1** by recombinant *E. coli* cells producing BVMOs of bacterial origin.[a]

Strain	Product								
	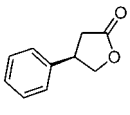 **2a**	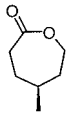 **2b**	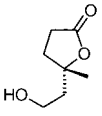 **2c**	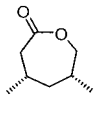 **2d**	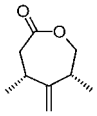 **2e**	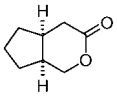 **2f**	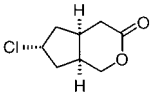 **2g**	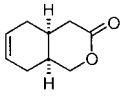 **2h**	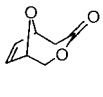 **2i**
$CHMO_{Acineto}$	53%	61%[9b]	59%	65%	54%	50%	78%	33%	n.c.[b]
	62% *ee* (−)	98% *ee* (−)	86% *ee* (−)	>99% *ee* (−)	92% *ee* (+)	89% *ee* (−)	>99% *ee* (−)	5% *ee* (−)	n.a.[c]
$CHMO_{Arthro}$	54%	50%	42%	35%	38%	66%	55%	46%	n.c.[b]
	87% *ee* (−)	>99% *ee* (−)	92% *ee* (−)	>99% *ee* (−)	96% *ee* (+)	82% *ee* (−)	>99% *ee* (−)	60% *ee* (−)	n.a.[c]
$CHMO_{Brachy}$	45%	69%	48%	40%	51%	71%	45%	56%	n.c.[b]
	93% *ee* (−)	>99% *ee* (−)	97% *ee* (−)	99% *ee* −)	94% *ee* (+)	91% *ee* (−)	>99% *ee* (−)	85% *ee* (−)	n.a.[c]
$CHMO_{Brevi1}$	73%	65%	n.c.[b]	61%	70%	21%	55%	10%	n.c.[b]
	98% *ee* (−)	>99% *ee* (−)	n.a.[c]	97% *ee* (−)	>99% *ee* (+)	65% *ee* (−)	95% *ee* (−)	71% *ee* (−)	n.a.[c]
$CHMO_{Brevi2}$	50%	59%	37%	56%	44%	42%	59%	92%	19%
	39% *ee* (+)	44% *ee* (+)	61% *ee* (+)	99% *ee* (+)	>99% *ee* (−)	0% *ee*	60% *ee* (+)	94% *ee* (+)	93% *ee* (+)
$CPMO_{Coma}$	66%	68%[13a]	54%	58%	63%	89%	92%	76%	53%
	37% *ee* (+)	46% *ee* (+)	76% *ee* (+)	*91*% *ee* (+)	99% *ee* (−)	9% *ee* (+)	*48*% *ee* (+)	>99% *ee* (+)	95% *ee* (+)
$CHMO_{Rhodo1}$	58%	72%	59%	59%	75%	62%	51%	47%	n.c.[b]
	52% *ee* (−)	>99% *ee* (−)	94% *ee* (−)	96% *ee* (−)	96% *ee* (+)	85% *ee* (−)	98% *ee* (−)	73% *ee* (−)	n.a.[c]
$CHMO_{Rhodo2}$	63%	67%	47%	64%	60%	75%	71%	51%	n.c.[b]
	50% *ee* (−)	95% *ee* (−)	94% *ee* (−)	90% *ee* (−)	96% *ee* (+)	75% *ee* (−)	95% *ee* (−)	73% *ee* (−)	n.a.[c]

[a] Yields are given for products isolated after flash column chromatography; *ee* values were determined by chiral-phase gas chromatography; the sign of specific rotation is given. [b] n.c. = no conversion. [c] n.a. = not applicable.

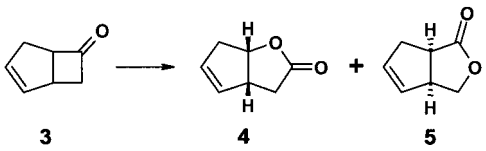

3 **4** **5**

Scheme 2. Regiodivergent Baeyer–Villiger oxidation of fused ketone **3** to "normal lactone" **4** and "abnormal lactone" **5**.

has been studied in detail with $CHMO_{Acineto}$.[24] Racemic compound **3** is transformed into two types of regioisomeric lactones in a resolution process: migration of the more-substituted carbon atom generates the expected "normal" lactone **4**, while "abnormal" lactone **5** is formed by migration of the less-substituted carbon atom.

Again, we observed a divergent trend for the two enzyme groups (Table 2).[25] CHMO-type proteins displayed a clean resolution that led to the formation of regioisomeric lactones **4** and **5** in approximately 1:1 ratio and with high optical purities. By contrast, $CPMO_{Coma}$ and $CHMO_{Brevi2}$ (CPMO-type enzymes) yielded predominantly "normal" lactone **4** in nearly racemic form. Trace amounts of "abnormal" product **5** were obtained in good enantiomeric excess.

To rationalize this significantly different biocatalytic activity, we compared the results from the biooxidations with sequence-analysis data for the genes and proteins of all eight BVMOs. While only minor correlation was observed on the DNA level of the structural genes, a significant trend in enzyme similarity was found at the amino acid level. Phylogenetic tree analysis of the representatives of the BVMO enzyme family vis-à-vis a remote reference sequence also resulted in clustering into two groups, which to a high degree reflected the reaction profiles of the biocatalysts (Figure 1). $CPMO_{Coma}$ and $CHMO_{Brevi2}$ form a distinctly different cluster while the other six enzymes form the

Table 2: Regiodivergent Baeyer–Villiger oxidation of racemic fused ketone **3** by recombinant *E. coli* cells producing BVMOs of bacterial origin.

	Yield **4**+**5**[a] [%]	Ratio **4**:**5**[b]	*ee* (1*S*,5*R*)-**4** [%]	*ee* (1*R*,5*S*)-**5** [%]
$CHMO_{Acineto}$	74	51:49	95	>99
$CHMO_{Arthro}$	86	53:47	88	>99
$CHMO_{Brachy}$	73	50:50	94	>99
$CHMO_{Brevi1}$	85	51:49	96	>99
$CHMO_{Brevi2}$	61	98:2	0	99
$CPMO_{Coma}$	61	97:3	0	>99
$CHMO_{Rhodo1}$	83	50:50	99	>99
$CHMO_{Rhodo2}$	81	50:50	97	>99

[a] Combined yields are given for the mixture of **4** and **5** after single flash column chromatography. [b] Ratio and *ee* values were determined by chiral-phase gas chromatography.

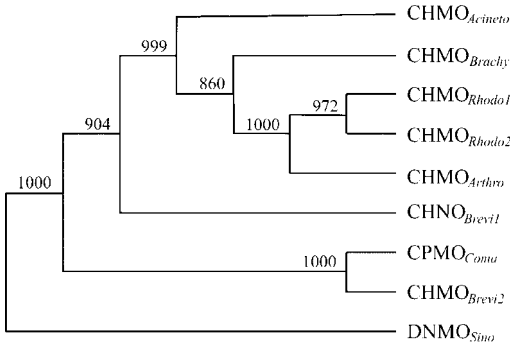

Figure 1. Phylogenetic tree of BVMOs originating from *Acinetobacter*, *Arthrobacter*, *Brachymonas*, *Brevibacterium*, *Comamonas*, and *Rhodococcus* species with the N^4-diaminopropane monooxygenase from *Sinorhizobium meliloti* (DNMO$_{Sino}$) as the outgroup (1000 bootstraps).

"CHMO-type" group. CHMO$_{Brevi1}$ is located at the borderline of the two clusters closer to the CHMO group, a fact which again agrees with its stereopreference and slightly modified substrate-acceptance profile.

A related phylogenetic tree analysis with biomolecular interpretation has been reported previously for a large general set of monooxygenases.[26] However, we consider our results to be the first connection of primary protein sequence with biocatalyst performance for BVMOs.

When the alignment of protein sequences of BVMOs included in this study is compared with the recently described point mutations in CHMO$_{Acineto}$,[27] two striking similarities can be identified. The Leu 143 Phe mutation exactly follows the separation in the two main enzyme groups. The CPMO type in both cases has a phenylalanine, whereas the CHMO type, with the exception of CHMO$_{Brevi1}$, has a leucine residue in this position, a fact again that reflects the borderline position of the latter enzyme. Phenylalanine is conserved in position 432 throughout the studied sequences with two exceptions: CHMO$_{Brevi1}$ and CHMO$_{Arthro}$. The Phe 432 Tyr mutation exactly mimics the amino acid composition of CHMO$_{Brevi1}$ at this position. This mutation has been indicated to significantly increase stereoselectivity and, interestingly, a similar trend was observed in this study.

Recently, the first X-ray structure for a moderately related BVMO from an extremophilic microorganism was solved.[28] This work gave valuable suggestions for the molecular mechanism of the enzymatic oxidation. However, the enzyme structure was determined in the absence of NADPH and no cocrystallization with a substrate is available, so far. As the authors suggest that the protein undergoes extensive conformational changes in the biocatalytic cycle, further conclusions for distant members of the BVMO family, such as those included in this study, seem rather speculative. However, when we consider the information together with recent results in modifying the enantioselectivity of CHMO$_{Acineto}$ by random mutagenesis,[27] we can begin to identify BVMO regions with major impact on biocatalytic behavior and stereopreference. Further structural and biotransformation studies on BVMOs more closely related to the two clusters outlined herein and on a larger set of ketones—currently being addressed in our laboratory—seem necessary for the development of a comprehensive and predictive model for this enzyme family to successfully expand the biocatalytic armament in the field of Baeyer–Villiger oxidations.

Received: December 16, 2004
Revised: March 1, 2005
Published online: April 29, 2005

Keywords: biocatalysis · bioorganic chemistry · monooxygenases · oxidation · phylogenetic analysis

[1] A. Baeyer, V. Villiger, *Chem. Ber.* **1899**, *32*, 3625 – 3633.
[2] G. R. Krow, *Org. React.* **1993**, *43*, 251 – 798; M. Renz, B. Meunier, *Eur. J. Org. Chem.* **1999**, 737 – 750.
[3] R. Noyori, T. Sato, H. Kobayashi, *Bull. Chem. Soc. Jpn.* **1983**, *56*, 2661 – 2679.
[4] K. Mislow, J. Brenner, *J. Am. Chem. Soc.* **1953**, *75*, 2318 – 2322.
[5] M. D. Mihovilovic, F. Rudroff, B. Grötzl, *Curr. Org. Chem.* **2004**, *8*, 1057 – 1069.
[6] C. Bolm in *Peroxide Chemistry* (Ed.: W. Adam), Wiley-VCH, Weinheim, **2000**, pp. 494 – 510; G. Strukul, *Angew. Chem.* **1998**, *110*, 1256 – 1267; *Angew. Chem. Int. Ed.* **1998**, *37*, 1198 – 1209.
[7] Z. Li, J. B. van Beilen, W. A. Duetz, A. Schmid, A. de Raadt, H. Griengl, B. Witholt, *Curr. Opin. Chem. Biol.* **2002**, *6*, 136 – 144; S. G. Burton, *Trends Biotechnol.* **2003**, *21*, 543 – 549.
[8] N. M. Kamerbeek, D. B. Janssen, W. J. H. van Berkel, M. W. Fraaije, *Adv. Synth. Catal.* **2003**, *345*, 667 – 678; M. D. Mihovilovic, B. Müller, P. Stanetty, *Eur. J. Org. Chem.* **2002**, 3711 – 3730; S. M. Roberts, P. W. H. Wan, *J. Mol. Catal. B* **1998**, *4*, 111 – 136.
[9] Expression systems for cyclohexanone monooxygenase from *Acinetobacter* (CHMO$_{Acineto}$): a) G. Chen, M. M. Kayser, M. D. Mihovilovic, M. E. Mrstik, C. A. Martinez, J. D. Stewart, *New J. Chem.* **1999**, *23*, 827 – 832; b) M. D. Mihovilovic, G. Chen, S. Wang, B. Kyte, R. Rochon, M. M. Kayser, J. D. Stewart, *J. Org. Chem.* **2001**, *66*, 733 – 738; c) for an alternative *Escherichia coli* based whole-cell biocatalyst, see: S. D. Doig, L. M. O'Sullivan, S. Patel, J. M. Ward, J. M. Woodley, *Enzyme Microb. Technol.* **2001**, *28*, 265 – 274; d) for a preceeding *Saccharomyces cerevisiae* expression system, see: J. D. Stewart, K. W. Reed, M. M. Kayser, *J. Chem. Soc. Perkin Trans. 1* **1996**, 755 – 757.
[10] For an isolated two-enzyme system, see: S. Rissom, U. Schwarz-Linek, M. Vogel, V. I. Tishkov, U. Kragl, *Tetrahedron: Asymmetry* **1997**, *8*, 2523 – 2526.
[11] H. D. Simpson, V. Alphand, R. Furstoss, *J. Mol. Catal. B* **2001**, *16*, 101 – 109; A. Z. Walton, J. D. Stewart, *Biotechnol. Prog.* **2002**, *18*, 262 – 268; S. D. Doig, P. J. Avenell, P. A. Bird, P. Gallati, K. S. Lander, G. J. Lye, T. Wohlgemuth, J. M. Woodley, *Biotechnol. Prog.* **2002**, *18*, 1039 – 1046.
[12] I. Hilker, V. Alphand, R. Wohlgemuth, R. Furstoss, *Adv. Synth. Catal.* **2004**, *346*, 203 – 214.
[13] a) H. Iwaki, Y. Hasegawa, P. C. K. Lau, S. Wang, M. M. Kayser, *Appl. Environ. Microbiol.* **2002**, *68*, 5681 – 5684; b) M. D. Mihovilovic, B. Müller, A. Schulze, P. Stanetty, M. M. Kayser, *Eur. J. Org. Chem.* **2003**, 2243 – 2249; c) M. D. Mihovilovic, F. Rudroff, B. Müller, P. Stanetty, *Bioorg. Med. Chem. Lett.* **2003**, *13*, 1479 – 1482; d) M. D. Mihovilovic, F. Rudroff, B. Grötzl, P. Stanetty, *Eur. J. Org. Chem.* **2005**, 809 – 816.
[14] N. A. Donoghue, D. B. Norris, P. W. Trudgill, *Eur. J. Biochem.* **1976**, *63*, 175 – 192.
[15] P. Brzostowicz, D. M. Walters, S. M. Thomas, V. Nagarajan, P. E. Rouviere, *Appl. Environ. Microbiol.* **2003**, *69*, 334 – 342.
[16] M. G. Bramucci, P. C. Brzostowicz, K. N. Kostichka, V. Nagarajan, P. E. Rouviere, S. M. Thomas (E. I. DuPont de Nemours &

Co., USA), WO 2003020890, **2003** [*Chem. Abstr.* **2003**, *138*, 233997].
[17] P. C. Brzostowicz, K. L. Gibson, S. M. Thomas, M. S. Blasko, P. E. Rouviere, *J. Bacteriol.* **2000**, *182*, 4241 – 4248.
[18] M. Griffin, P. W. Trudgill, *Eur. J. Biochem.* **1976**, *63*, 199 – 209.
[19] M. Taschner, D. J. Black, *J. Am. Chem. Soc.* **1988**, *110*, 6892 – 6893.
[20] B. G. Kyte, P. Rouviere, Q. Cheng, J. D. Stewart, *J. Org. Chem.* **2004**, *69*, 12 – 17.
[21] R. Riva, L. Banfi, B. Danieli, G. Guanti, G. Lesma, G. Palmisano, *J. Chem. Soc. Chem. Commun.* **1987**, 299 – 300.
[22] B. Danieli, G. Lesma, M. Mauro, G. Palmisano, D. Passerella, *Tetrahedron* **1994**, *50*, 8837 – 8852.
[23] V. Alphand, R. Furstoss, *J. Org. Chem.* **1992**, *57*, 1306 – 1309.
[24] D. R. Kelly, C. J. Knowles, J. G. Mahdi, I. N. Taylor, M. A. Wright, *J. Chem. Soc. Chem. Commun.* **1995**, 729 – 730.
[25] M. D. Mihovilovic, P. Kapitan, *Tetrahedron Lett.* **2004**, *45*, 2751 – 2754.
[26] M. W. Fraaije, N. M. Kamerbeek, W. J. H van Berkel, D. B. Janssen, *FEBS Lett.* **2002**, *518*, 43 – 47.
[27] M. T. Reetz, B. Brunner, T. Schneider, F. Schulz, C. M. Clouthier, M. M. Kayser, *Angew. Chem.* **2004**, *116*, 4167 – 4170; *Angew. Chem. Int. Ed.* **2004**, *43*, 4078 – 4081.
[28] E. Malito, A. Alfieri, M. W. Fraaije, A. Mattevi, *Proc. Natl. Acad. Sci. USA* **2004**, *101*, 13157 – 13162.

EPR Spectroscopy

Anisotropic Hyperfine Interaction in the Manganese(III) Hexaaqua Ion

Itana Krivokapič, Chris Noble, Søren Klitgaard, Philip Tregenna-Piggott, Høgni Weihe,* and Anne-Laure Barra*

The manganese(III) ion is ubiquitous among chemical systems that exhibit intriguing biological and physical properties, ranging from photosystem II and superoxide dismutase to the celebrated single-molecule magnet Mn_{12}. It is for this reason that complexes and clusters of the manganese(III) ion are widely recognized as the delicicae of high-field electron paramagnetic resonance (EPR) spectroscopists,[1] the fact that they invariably yield good-quality spectra being but a secondary consideration.[2–7]

Hitherto, the spatial property of the hyperfine interaction between the $S = 2$ electronic spin and the $I = 5/2$ nuclear spin in any chemically relevant manganese(III) compound has escaped observation. There are two fundamental reasons why knowledge of the hyperfine interaction energies is important. First, the magnitude and sign of the anisotropy relate directly to the manganese(III) coordination sphere. Secondly, the hyperfine interaction has been demonstrated to be instrumental in quantum tunneling of the magnetization in single-molecule magnets.[8,9]

In an EPR study of manganese(III) superoxide dismutase,[2] the hyperfine splittings were resolved and compared to those documented for a photo-oxidation product of manganese(III) in the high-affinity site of photosystem II. Consistency was found between the observed hyperfine splitting and the sign of the zero-field-splitting parameter in the two systems. However, these experiments were confined to X-band parallel-mode experiments, which can determine just one component of the hyperfine interaction matrix. Information concerning the spatial property of the hyperfine interaction matrix requires the use of higher frequencies, as shown in a study of manganese(III)-doped rutile.[12]

In this communication we report single-crystal and powder EPR spectra of the $[Mn(H_2O)_6]^{3+}$ ion at high fields and multiple frequencies. To minimize line broadening due to spin–spin dipolar interactions, the $[Mn(H_2O)_6]^{3+}$ ion was doped into the diamagnetic cesium gallium alum, $Cs[Ga(H_2O)_6](SO_4)_2 \cdot 6H_2O$, thus enabling the precise determination of the metal hyperfine interaction parameters.

Pale orange–red crystals of this sample were grown at 0 °C from a saturated 6 M sulfuric acid solution of the cesium gallium alum that contained 1 % cesium manganese alum. A trace of the corresponding chromium(III) alum was also added. The EPR lines of $[Cr(OH_2)_6]^{3+}$ were readily identified and were useful for crystal alignment.

The single-crystal EPR spectra exhibited several magnetically nonequivalent species, reflecting the space group of the host and the propensity of the $[Mn(OH_2)_6]^{3+}$ ion to distort along a Jahn–Teller active coordinate. There are four tervalent cations in the cubic unit cell, each occupying a site of S_6 symmetry on one of the four unique threefold axes of the unit cell. In addition, at low temperatures the $[Mn(OH_2)_6]^{3+}$ ion is expected to be locked into one of the three possible tetragonally elongated structures that results from the Jahn–Teller interaction. Such a distortion is clearly identified in the neat cesium manganese alum, which undergoes a phase transition from cubic to orthorhombic at 156 K. In the low-temperature phase, the metal ion is situated on a site with point symmetry C_i.[14] A total of twelve magnetically nonequivalent species is therefore anticipated for cesium gallium alum doped with manganese(III) ions, and the principal axes of the various interaction tensors are expected to be aligned close to the Mn–O bonds. Since the vectors of the Mn–O bonds are very closely aligned with the pseudo-crystallographic fourfold axes of the cubic unit cell, the

[*] I. Krivokapič, Dr. C. Noble, Priv.-Doz. Dr. P. Tregenna-Piggott
Laboratory for Neutron Scattering
ETH Zürich and Paul Scherrer Institute
5232 Villigen PSI (Switzerland)
Fax: (+41) 56-310-2939
E-mail: philip.tregenna@psi.ch
S. Klitgaard, Dr. H. Weihe
Department of Chemistry
University of Copenhagen
Universitetsparken 5, 2100 Copenhagen (Denmark)
E-mail: weihe@kiku.dk
Dr. A.-L. Barra
LCMI-CNRS B.P. 166
38042 Grenoble cedex 9 (France)

 DOI: 10.1002/anie.200463084

spectra are expected to simplify when the external magnetic field is aligned along one of these axes.

This expectation is, indeed, found to be the case. Figure 1 shows a 190-GHz spectrum taken between 0 and 6 T and obtained with the magnetic field parallel to a crystallographic

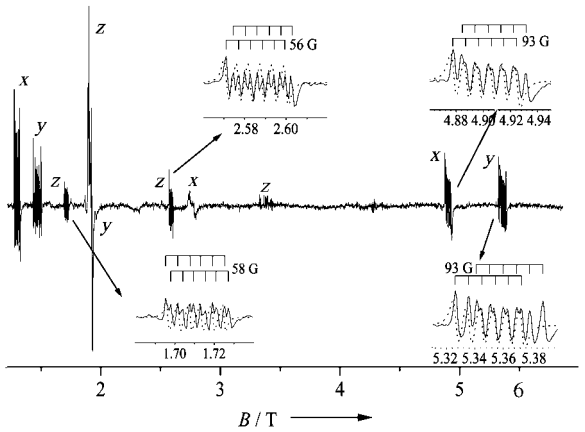

Figure 1. Single-crystal 190-GHz spectrum of the manganese(III) ion in cesium gallium alum obtained at 5 K with the magnetic field vector parallel to a crystallographic fourfold axis. Transitions corresponding to the magnetic field that is parallel to the molecular *x*, *y*, or *z* axis are designated accordingly. The inserts show the spacing between the hyperfine components of the least-complicated features in the spectrum. The simulated[10] spectra (dotted lines in the inserts) were calculated with the spin Hamiltonian parameters given in Equation (3).

fourfold axis. The spectrum exhibits several electronic transitions, each being split into a sextet due to the hyperfine interaction. Two types of sextets are identified in the spectrum: one in which the separation between neighboring lines is 92–93 Gauss; the other in which this splitting is 56–58 Gauss. Each electronic transition is doubled but this doubling is not found in the powder spectra, representative examples of which are shown in Figure 2. Therefore, the doubling must be due to either crystal twinning, a small misalignment when orienting the crystal, or a result of magnetically nonequivalent $[Mn(OH_2)_6]^{3+}$ ions that differ in terms of the orientation of the threefold axes for the sites on which they lie. Rotation of the magnetic field less than 10° away from the fourfold axis has the effect of rendering all sites magnetically nonequivalent, and the complexity of the spectrum increases enormously. The smaller hyperfine splitting of 57 Gauss appears again in the parallel-mode X-band spectra shown in Figure 3. The overlap of lines arising from magnetically nonequivalent species can be seen clearly, as the crystal is rotated in the {110} plane, away from the fourfold axis.

The hyperfine lines in the single-crystal spectra in Figures 1 and 3 were interpreted in terms of a spin Hamiltonian for $(S,I) = (2, 5/2)$.[11] In Equation (1), the five first terms describe the zero-field splittings, and the remaining lines describe the Zeeman energy and the hyperfine interaction.

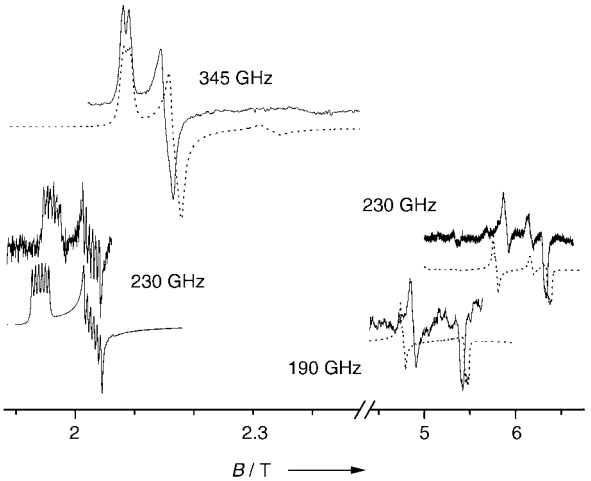

Figure 2. The strongest features (upper traces) in the EPR spectra of a powdered sample of the manganese(III) hexaaqua ion in cesium gallium alum. The frequencies used are designated. Only the field ranges 1.9–2.5 T and 4.5–6.7 T are shown. The separation between the hyperfine components of the low-field 230-GHz spectrum is 93 ± 1 Gauss. The simulated spectra (lower traces) are calculated with the parameters obtained from the single-crystal spectra [Eq. (3)]. All simulated spectra are obtained by using the same bandwidth (70 G) for each hyperfine line.

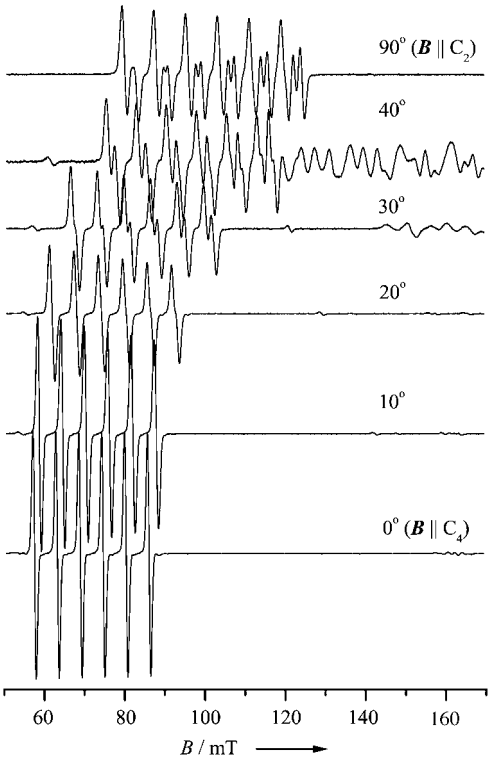

Figure 3. Single-crystal parallel-mode X-band spectra recorded with the magnetic field in the (110) crystallographic plane. The frequencies varied between 9.3107 and 9.3114 GHz. The angle indicated for each spectrum designates the angle between the crystallographic fourfold axis and the vector of the magnetic field. The separation between the hyperfine components in the low-field portion of the six spectra is 57, 58, 61, 66, 75, and 80 Gauss going from the bottom trace to the top.

$$\begin{aligned}\hat{\mathscr{H}} =& D(\hat{S}_z^2-2) + E(\hat{S}_x^2-\hat{S}_y^2)\\ &+B_4^4\frac{1}{2}[\hat{S}_+^4+\hat{S}_-^4] + B_0^4[35\hat{S}_z^4-155\hat{S}_z^2+72]\\ &+B_2^4\frac{1}{4}[(7\hat{S}_z^2\text{-}11)(\hat{S}_+^2+\hat{S}_-^2)+(\hat{S}_+^2+\hat{S}_-^2)(7\hat{S}_z^2-11)]\\ &+\mu_B(g_x B_x \hat{S}_x + g_y B_y \hat{S}_y + g_z B_z \hat{S}_z)\\ &+A_x \hat{S}_x \hat{I}_x + A_y \hat{S}_y \hat{I}_y + A_z \hat{S}_z \hat{I}_z\end{aligned} \quad (1)$$

The lines in the spectrum of Figure 1 as well as the low-angle lines in Figure 3 were assigned to specific transitions of this spin system, and the spin Hamiltonian parameters of Equation (1) were obtained by minimizing χ^2 in Equation (2). N is the number of observations; $B_{i,\mathrm{obs}}$ and $B_{i,\mathrm{calc}}$ are the observed and calculated ith resonance magnetic field, respectively. σ_i is an uncertainty associated with the ith observation and was set to a fraction of the bandwidth for most of the observations.

$$\chi^2 = \sum_{i=1}^{N} \frac{(B_{i,\mathrm{obs}}-B_{i,\mathrm{calc}})^2}{\sigma_i^2} \quad (2)$$

By using a total of 84 resonance magnetic fields in the fit and setting $g_x = g_y$ as well as $A_x = A_y$ as directly suggested by the experimental data (Figure 1), we were able to obtain the parameter values listed in Equation (3).

$$\begin{aligned}D &= -4.514(1)\ \mathrm{cm}^{-1}\\ E &= -0.161(5)\ \mathrm{cm}^{-1}\\ B_0^4 &= -0.0041(5)\ \mathrm{cm}^{-1}\\ B_2^4 &= -0.00014(5)\ \mathrm{cm}^{-1}\\ B_4^4 &= -0.00577(7)\ \mathrm{cm}^{-1}\\ g_x &= g_y = 2.000(1)\\ g_z &= 1.9844(6)\\ A_x &= A_y = -0.0087(2)\ \mathrm{cm}^{-1}\\ A_z &= -0.00531(5)\ \mathrm{cm}^{-1}\end{aligned} \quad (3)$$

These parameter values were then used to reproduce the powder spectra in Figure 2. The agreement is certainly acceptable. In reference [3] values for D and $|E|$ of $-4.491(7)\ \mathrm{cm}^{-1}$ and $0.248\ \mathrm{cm}^{-1}$, respectively, were derived from an EPR study of $Cs[Mn(OD_2)_6](SO_4)_2\cdot 6H_2O$, with a small but significant change in these parameters noted upon hydrogen-for-deuterium isotopic substitution. Note that the value of the orthorhombic zero-field splitting parameter E is slightly larger in magnitude than that determined for the diluted alum in the present study. The discrepancy is primarily a result of the large linewidths obtained for the undiluted alum, which made an inclusion of the fourth-order zero-field splitting parameters unwarranted. The parameters E and B_4^4 are somewhat negatively correlated, and a precise definition requires data from a range of frequencies, including X-band measurements, which are tractable only if the EPR linewidths are sufficiently narrow. The similar values of D suggests that the structure and bonding in the $[Mn(OD_2)_6]^{3+}$ is similar in the two systems.

With the choice of $E<0$ we see that the fourth-order spin Hamiltonian parameters B_0^4, B_2^4, and B_4^4 are all found to be negative, which was also found to be the case for $[Mn(cyclam)Br_2]Br$.[6] (cyclam = 1,4,8,11-tetraazacyclotetradecane). An analysis of this result, however, is not relevant in the present context and will not be discussed here.

The g values, with $g_x, g_y > g_z$, conform to what is expected for an elongated coordination sphere. According to a previous report, the relation $g_x - g_z = 2\zeta/3\Delta_{T_2}$ holds.[15] In this equation, ζ is the spin–orbit coupling parameter, and Δ_{T_2} is the energy separation between the ground-spin quintet and the $^5T_2$ (O notation) excited term. Using the experimentally determined $\Delta_{T_2} = 21\,400\ \mathrm{cm}^{-1}$[3] we find $\zeta = 223\ \mathrm{cm}^{-1}$, which corresponds to 63% of the free-ion value. In Equation (3), we have explicitly set the values of the hyperfine splitting constants as negative. The fit cannot discriminate between the possible sign combinations of these parameters. However, based on other arguments, presented below, we conclude that the parameters are negative.

The angular variation of the resonance magnetic fields as well as the angular variation of the separation between the hyperfine splitting components in Figure 3 is very well described by the effective spin Hamiltonian with $S=\frac{1}{2}$ for a non-Kramers doublet involving only the $+2$ and -2 M_S components in Equation (4), in which θ is the angle between the magnetic field vector and the elongation axis of the coordination sphere.

$$\hat{\mathscr{H}}_{\mathrm{approx}} = b\hat{S}_x + \mu_B g_z' \hat{S}_z B\cos\theta + A_z' \hat{S}_z \hat{I}_z \quad (4)$$

The parameters b, g_z', and A_z' of this effective Hamiltonian are related to those of Equation (1). It can be shown that to the second order in the perturbation theory, the zero-field splitting b of the two components is given by Equation (5).

$$b = 24B_4^4 + \frac{(\sqrt{6}E+\sqrt{54}B_2^4)^2}{2D-30B_0^4} \quad (5)$$

With the parameter values determined above, we see that the first and second term on the right-hand side of the equation have the same sign and are comparable in magnitude. The effective g_z' factor and the effective hyperfine splitting constant A_z' are related to g_z and A_z by Equations (6) and (7).

$$g_z' = 4g_z \quad (6)$$

$$A_z' = 4A_z \quad (7)$$

The effective Hamiltonian Equation (4) is applicable when the $|\pm 2\rangle$ components are well isolated from the remaining components of the spin quintet and when $h\nu > b$, ν being the spectrometer frequency, which is the case here. Using Equation (4) to interpret the spectra in Figure 3 only confirms Equations (6) and (7) and gives $|b| = 0.172\ \mathrm{cm}^{-1}$, which is in reasonable agreement with the value calculated from the formula for the second-order perturbation theory, Equation (5), $b = -0.156\ \mathrm{cm}^{-1}$. With the Hamiltonian Equation (4) the separation between neighboring hyperfine lines is,

to a good approximation, given by Equation (8).

$$B_r(M_I)-B_r(M_I-1) \approx \frac{A'_z}{g'_z \mu_B \cos\theta} \quad (8)$$

The experimental hyperfine line separations of the spectra in Figure 3 are reproduced within 1 Gauss by Equation (8).

For the tetragonally elongated coordination sphere, the relations in Equations (9) and (10) can be derived for the hyperfine coupling constants.[2,15]

$$A_z = P\left(\frac{1}{7}-\kappa-\frac{2\zeta}{\Delta_{T_2}}\right) = P\left(\frac{1}{7}-\kappa+(g_z-2.0023)\right) \quad (9)$$

$$A_x = A_y = P\left(-\frac{1}{14}-\kappa-\frac{\zeta}{2\Delta_{T_2}}\right) = P\left(-\frac{1}{14}-\kappa+(g_x-2.0023)\right) \quad (10)$$

The parameter κ for manganese(III) has been determined to be approximately 0.5.[12] Hence the term in parentheses becomes negative and we conclude that both hyperfine coupling constants are negative because the parameter P for ^{55}Mn is positive. Using Equations (9) and (10) together with the experimentally determined A values and the deviation of the g values from the free-electron g value, we obtain $P = 0.0170\ cm^{-1}$ and $\kappa = 0.43$. P depends on the expectation value $\langle r^{-3}\rangle$, as does the spin–orbit coupling parameter ζ; therefore, it can be expected to be related to the free-ion value in a similar way as the spin–orbit coupling parameter is related to the free-ion value. This is indeed the case; the free-ion value of P for manganese(III) has been calculated to $0.0212\ cm^{-1}$, and our value for the manganese(III) hexaaqua ion corresponds to 80% of this free-ion value, which is in good agreement with the spin–orbit coupling reduction (see above). In comparison, for rutile: Mn^{3+} $P = 0.0140\ cm^{-1}$. The average metal–oxygen bond length in rutile and $[Mn(H_2O)_6]^{3+}$ is 1.956 Å and 1.994 Å, respectively.[13,14] As shorter bond lengths are associated with stronger overlaps between metal- and oxygen-centered orbitals it is also expected that $P(\text{rutile}) < P([Mn(H_2O)_6]^{3+})$. By the same token, P is expected to be further reduced for a metal center that is surrounded by donors softer than oxygen.

In summary, we have presented the first observation and interpretation of the anisotropic hyperfine interaction in a chemically relevant monomeric complex that contains the manganese(III) ion. The hyperfine interaction parameters are related to more fundamental parameters such as the spin–orbit coupling parameter, as well as excited-state energies obtained from the absorption spectrum, which has been analyzed in detail. Basically, the analyses performed here are based on ligand–field theory, which offers a consistent description of the situation. A comprehensive treatment requires that Jahn–Teller coupling be considered explicitly, as dynamic effects can have profound effect on all the orbital electronic operators. This will be the topic of a paper currently in preparation.

Received: December 28, 2004
Published online: May 2, 2005

Keywords: EPR spectroscopy · hyperfine interactions · magnetic properties · manganese

[1] A.-L. Barra, D. Gatteschi, R. Sessoli, G. L. Abbati, A. Cornia, A. C. Fabretti, M. G. Uytterhoeven, *Angew. Chem.* **1997**, *109*, 2423 – 2426; *Angew. Chem. Int. Ed. Engl.* **1997**, *36*, 2329 – 2331.
[2] K. A. Campbell, D. A. Force, P. J. Nixon, F. Dole, B. A. Diner, D. R. Britt, *J. Am. Chem. Soc.* **2000**, *122*, 3754 – 3761.
[3] P. L. W. Tregenna-Piggott, H. Weihe, A.-L. Barra, *Inorg. Chem.* **2003**, *42*, 8504 – 8508.
[4] J. Krzystek, J. Telser, L. A. Pardi, D. P. Goldberg, B. M. Hoffman, L.-C. Brunel, *Inorg. Chem.* **1999**, *38*, 6121 – 6129.
[5] S. Mossin, H. Weihe, A.-L. Barra, *J. Am. Chem. Soc.* **2002**, *124*, 8764 – 8765.
[6] S. Mossin, M. Stefan, P. ter Heerdt, A. Bouwen, E. Goovaerts, H. Weihe, *Appl. Magn. Reson.* **2001**, *21*, 578 – 596.
[7] R. Basler, P. L. W. Tregenna-Piggott, H.-P. Andres, C. Dobe, H.-U. Güdel, S. Janssen, G. J. McIntyre, *J. Am. Chem. Soc.* **2001**, *123*, 3377 – 3378.
[8] W. Wernsdorfer, R. Sessoli, D. Gatteschi, *Europhys. Lett.* **1999**, *47*, 254 – 259.
[9] W. Wernsdorfer, A. Caneschi, R. Sessoli, D. Gatteschi, A. Cornia, V. Villar, C. Paulsen, *Phys. Rev. Lett.* **2000**, *84*, 2965 – 2968.
[10] J. Glerup, H. Weihe, *Acta Chem. Scand.* **1991**, *45*, 444 – 448; C. J. H. Jacobsen, E. Pedersen, J. Villadsen, *Inorg. Chem.* **1993**, *32*, 1216 – 1221.
[11] A. Abragam, B. Bleaney, *Electron Paramagnetic Resonance of Transition Ions*, Oxford University Press, Oxford, **1970**.
[12] H. J. Gerritsen, E. S. Sabisky, *Phys. Rev.* **1963**, *132*, 1507 – 1512.
[13] A. F. Wells, *Structural Inorganic Chemistry*, Clarendon, Oxford, **1984**.
[14] P. L. W. Tregenna-Piggott, H. P. Andres, G. J. McIntyre, S. P. Best, C. C. Wilson, J. A. Cowan, *Inorg. Chem.* **2003**, *42*, 1350 – 1365.
[15] J. S. Griffith, *The Theory of Transition Metal Ions*, Cambridge University Press, Cambridge, **1961**.

Bonding Analysis

Direct Estimate of the Conjugative and Hyperconjugative Stabilization in Diynes, Dienes, and Related Compounds**

*Daniel Cappel, Sandor Tüllmann, Andreas Krapp, and Gernot Frenking**

Compounds with conjugated double bonds such as 1,3-butadiene are energetically stabilized through π interactions. Kistiakowsky et al. suggested in 1936 that the energetic consequences can be assessed by stepwise hydrogenation first to 1-butene and then to butane [Eq. (1)].[1] The first step is

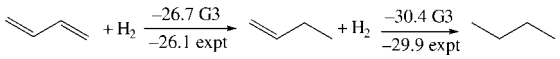

(1)

3.8 kcal mol^{-1} less exothermic (calculated value at G3 level 3.7 kcal mol^{-1})[2] than the second step, which according to Kistiakowsky et al. indicates the strength of the π conjugation in 1,3-butadiene. 1,3-Butadiyne has two pairs of conjugating double bonds and should have stronger conjugative stabilization than 1,3-butadiene, which has only one pair. A recent publication by Rogers et al. reported that the conjugation in the former compound is zero, because the stepwise hydrogenation of 1,3-butadiyne yields nearly equally exothermic values [Eq. (2)].[3]

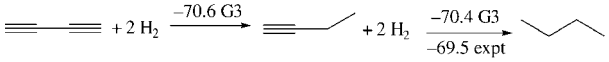

(2)

The results of Rogers et al.[3] have been confirmed in a recent publication of Jarowski et al.[4] But their divergent interpretation sparked renewed discussion.[5] Jarowski et al. pointed out that hyperconjugation plays an important role in the thermodynamics of the hydrogenation reactions, which was not considered by Rogers et al. Hyperconjugation has recently been suggested to be the driving force for the staggered equilibrium conformation of ethane, but the claim was not undisputed.[6] Jarowski et al.[4] estimated the strength of the hyperconjugation by comparing the calculated and experimental heats of hydrogenation of ethylene and 1-butene with the values for acetylene and 1-butyne. This shows that the hyperconjugative stabilization of acetylene by an ethyl group is 2.5–3.0 kcal mol^{-1} higher than the stabilization of ethylene by an ethyl substituent. A similar result was obtained using isodesmic reactions [Eqs. (3), (4)], which

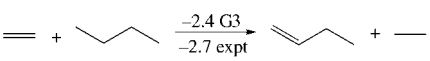

(3)

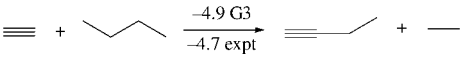

(4)

suggest that hyperconjugative stabilization of a triple bond is roughly twice as high as the stabilization of a double bond. The calculated energies for the reactions in Equations (5) and

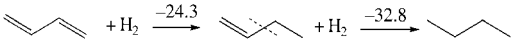

(5)

(6), which employ virtual intermediates in which hyperconjugation is eliminated, indicate that the conjugation in 1,3-butadiyne is now even slightly stronger (9.6 kcal mol^{-1})[7] than

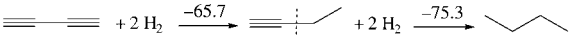

(6)

in 1,3-butadiene (8.5 kcal mol^{-1}). This is in agreement with previous theoretical investigations.[8,9]

The studies by Rogers et al.[3] and by Jarowski et al.[4] are based on the suggestion of Kistiakowsky[1] to correlate reaction energies with conjugative stabilization, and the latter work modified the original proposal by considering hyperconjugation. Jarowski et al.[4] pointed out that comparisons of heats of hydrogenation evaluate not only conjugative effects but also other structural and electronic differences between the conjugated molecule and its hydrogenated products. We note that the absolute values of the conjugative stabilization given by Equations (5) and (6) are very different from the data of Equations (1) and (2). It would be helpful if a direct estimate of the intrinsic conjugative stabilization in 1,3-butadiene and 1,3-butadiyne could be made based on a well-defined quantum chemical partitioning of the interaction energy. An attempt was published in 1979 by Kollmar, who calculated the resonance stabilization of 1,3-butadiyne (19 kcal mol^{-1}) to be nearly twice that of 1,3-butadiene (9.7 kcal mol^{-1}); this is in agreement with the chemical intuition that two conjugative π systems should be twice as strong as one system.[9] Kollmar's values come from calculations of the two molecules with hypothetical reference systems having nonresonating acetylene and ethylene units. It would be more useful if the actual $^{\cdot}C{\equiv}CH$ and $^{\cdot}HC{=}CH_2$ fragments would be used for an estimate of the conjugative stabilization.

Here we report on an energy decomposition analysis (EDA)[10] of the C–C interactions in 1,3-butadiene, 1,3-butadiyne, and related systems which allows a direct estimate of the intrinsic conjugative and hyperconjugative stabilization that arises from the mixing between the occupied and vacant orbitals of the conjugating fragments. EDA has proven to give important information about the nature of the bonding in main-group[11] and transition-metal compounds.[12] Since the method has been described in detail previously[10–12] we shall

[*] D. Cappel, S. Tüllmann, Dipl.-Chem. A. Krapp, Prof. Dr. G. Frenking
Fachbereich Chemie, Philipps-Universität Marburg
Hans-Meerwein-Strasse, 35043 Marburg (Germany)
Fax: (+49) 6421-282-5566
E-mail: frenking@chemie.uni-marburg.de

[**] This research was supported by the Deutsche Forschungsgemeinschaft.

 DOI: 10.1002/anie.200500452

describe the concept only briefly. In EDA, bond formation between the interacting fragments is divided into three steps, which can be interpreted in a plausible way. In the first step the fragments, which are calculated with the frozen geometry of the entire molecule, are superimposed without electronic relaxation; this yields the quasiclassical electrostatic attraction ΔE_{elstat}. In the second step the product wave function becomes antisymmetrized and renormalized, which gives the repulsive term ΔE_{Pauli}, termed Pauli repulsion. In the third step the molecular orbitals relax to their final form to yield the stabilizing orbital interaction ΔE_{orb}. The latter term can be divided into contributions of orbitals having different symmetry which is crucial for this study. The sum of the three terms $\Delta E_{elstat} + \Delta E_{Pauli} + \Delta E_{orb}$ gives the total interaction energy ΔE_{int}. Note that the latter is not the same as the bond dissociation energy, because the relaxation of the fragments is not considered in ΔE_{int}.

Table 1 gives the EDA results[13] of the calculated molecules. In all cases a central C–C single bond connects the interacting fragments, which are calculated in the electronic doublet state with the unpaired electron in a σ orbital. As expected, the C–C bond in 1,3-butadiyne has a much larger interaction energy ($\Delta E_{int} = -176.0$ kcal mol^{-1}) than in 1,3-butadiene ($\Delta E_{int} = -128.5$ kcal mol^{-1}). The electrostatic character[14] of the former bond is smaller (33.9%) than that of the latter (42.8%). The largest contribution to the C–C attraction in both molecules comes from the orbital term ΔE_{orb}. The partitioning of the C–C orbital interactions in σ and π bonding shows that σ bonding is stronger. We note that the strength of σ bonding in 1,3-butadiene ($\Delta E_{\sigma} = -207.5$ kcal mol^{-1}) is greater than in 1,3-butadiyne ($\Delta E_{\sigma} = -178.3$ kcal mol^{-1}). This is because σ bonding in 1,3-butadiyne involves only the C–C σ bond, while σ bonding in 1,3-butadiene has additional contributions from the hyperconjugative interactions of the C–H and terminal C–C bonds. Thus, σ bonding in 1,3-butadiyne comes from only the C–C mixing of the 2s and 2p(σ) atomic orbitals (AOs) of carbon, while the σ bonding in 1,3-butadiene comes not only from the 2s and 2p(σ) orbitals but also from the in-plane 2p(π_{II}) AO of carbon and the 1s AO of hydrogen. Consequently, the total value of the attractive orbital interactions in 1,3-butadiene is slightly larger ($\Delta E_{orb} = -227.0$ kcal mol^{-1}) than in 1,3-butadiyne ($\Delta E_{orb} = -223.3$ kcal mol^{-1}). The electrostatic attraction in 1,3-butadiene ($\Delta E_{elstat} = -169.9$ kcal mol^{-1}) is also larger than in 1,3-butadiyne ($\Delta E_{elstat} = -114.6$ kcal mol^{-1}), although the central C–C bond in the former is longer (1.453 Å) than in the latter (1.361 Å). This is because the unpaired electron in the $^{\bullet}HC{=}CH_2$ fragment is in a (formally) sp^2-hybridized orbital, which is more diffuse and thus has a higher density at the carbon nucleus of the other fragment than the unpaired electron in the more compact sp orbital of $^{\bullet}C{\equiv}CH$.

The most important results of our analysis are the calculated values for ΔE_{π}, which are a direct measure of the π conjugation in 1,3-butadiyne and 1,3-butadiene. Table 1 shows that the conjugative stabilization in the former molecule ($\Delta E_{\pi} = -45.0$ kcal mol^{-1}) is more than twice that calculated for the latter species ($\Delta E_{\pi} = -19.5$ kcal mol^{-1}). This is a reasonable result because the conjugation of the two π systems in 1,3-butadiyne takes place at a shorter C–C distance than in 1,3-butadiene.

How strong is the hyperconjugation in 1-butyne and 1-butene? The hyperconjugation of the multiple bonds in these molecules with the p(π) orbitals of the adjacent carbon atoms involve C–H and C–C bonds. To address the question whether C–H or C–C bonds are better hyperconjugative donors or acceptors, we first analyzed the C–C bonding

Table 1: Results of the energy decomposition analysis at the BP86/TZ2P level. Energy values in kcal mol^{-1}.

	HCC-CCH	H_2CCH-$CHCH_2$	HCC-CH_3	HCC-$C(CH_3)_3$	H_2CCH-CH_3	H_2CCH-$C(CH_3)_3$	HCC-$CHCH_2$	$(CH_3)_3C$-$C(CH_3)_3$	CH_3-CH_3
Symmetry	$D_{\infty h}$	C_{2h}	C_{3v}	C_{3v}	C_s	C_s	C_s	D_{3d}	D_{3d}
ΔE_{int}	−176.0	−128.5	−143.6	−133.1	−119.4	−108.8	−150.2	−93.2	−114.8
ΔE_{Pauli}	161.8	268.4	176.5	219.1	228.9	267.9	209.4	253.6	200.8
ΔE_{elstat}[a]	−114.6 (33.9%)	−169.9 (42.8%)	−125.5 (39.2%)	−151.8 (43.1%)	−147.5 (42.4%)	−171.8 (45.6%)	−143.1 (39.8%)	−163.5 (47.2%)	−131.3 (41.6%)
ΔE_{orb}[a]	−223.3 (66.1%)	−227.0 (57.2%)	−194.6 (60.8%)	−200.4 (56.9%)	−200.7 (57.6%)	−204.9 (54.4%)	−216.4 (60.2%)	−183.2 (52.8%)	−184.2 (58.4%)
ΔE_{σ}[b]	−178.3 (79.8%)	−207.5 (91.4%)	−174.6 (89.7%)	−179.8 (89.7%)	−191.5 (95.4%)	−195.4 (95.4%)	−195.9 (90.5%)	−171.0[d] (93.3%)	−174.3 (94.6%)
ΔE_{π}[b]	−45.0 (20.2%)	−19.5 (8.8%)	−20.1 (10.3%)	−20.6 (10.3%)	−9.3 (4.6%)	−9.5 (4.6%)	−20.5 (9.5%)	−11.6[d] (6.4%)	−10.0 (5.4%)
ΔE_{prep}	5.4	13.0	13.1	14.5	17.2	18.8	23.8	30.2	21.8
ΔE[c] ($=-D_e$)	−170.6	−115.5	−130.5	−118.6	−102.2	−90.0	−126.4	−63.0	−93.0
r(C-C) [Å]	1.361	1.453	1.456	1.469	1.500	1.516	1.419	1.591	1.532

[a] The percentages in parentheses give the contribution to the total attractive interactions $\Delta E_{elstat} + \Delta E_{orb}$. [b] The percentages in parentheses give the contribution to the orbital interactions ΔE_{orb}. [c] $\Delta E = \Delta E_{int} + \Delta E_{prep}$. [d] There is a small contribution of 0.6 kcal mol^{-1} from orbitals having δ symmetry.

situations in propyne $HC{\equiv}CCH_3$ and its trimethyl-substituted derivative 3,3-dimethyl-1-butyne $HC{\equiv}CCMe_3$. Table 1 shows that hyperconjugation of the C–H bonds in the former molecule is rather strong ($\Delta E_\pi = -20.1$ kcal mol^{-1}). The hyperconjugative stabilization in $HC{\equiv}CCMe_3$ is even slightly larger ($\Delta E_\pi = -20.6$ kcal mol^{-1}), although the C–C bond is a bit longer than in propyne. This means that C–C bonds stabilize multiple bonds through hyperconjugation better than C–H bonds. It is interesting to note that the hyperconjugative stabilization of the degenerate π systems in $HC{\equiv}CCH_3$ and $HC{\equiv}CCMe_3$ is even slightly stronger than the conjugative stabilization in 1,3-butadiene (−19.5 kcal mol^{-1}), which has nearly the same central C–C bond length (1.453 Å) as the former species (1.456 Å and 1.469 Å).

We also calculated the hyperconjugation in propene $H_2C{=}CHCH_3$ and its trimethyl-substituted derivative $H_2C{=}CHCMe_3$. The calculated ΔE_π values (Table 1) for the former molecule ($\Delta E_\pi = -9.3$ kcal mol^{-1}) and the latter species ($\Delta E_\pi = -9.5$ kcal mol^{-1}) suggest that the hyperconjugative stabilization of C–H and C–C bonds with olefinic double bonds is half as strong as that of C≡C triple bonds. This is reasonable because alkynes have two π components but alkenes have only one π component. The stabilization of the C–C bonds are again slightly larger than that of the C–H bonds.

Hyperconjugation involves donation from the occupied π orbitals of the multiple bonds into the vacant π* orbitals of the CH_3 or CMe_3 groups and backdonation from occupied π orbitals of CH_3 or CMe_3 into π* orbitals of the multiple bonds. Which of the two contributions is stronger? We estimated the strength of the π→π* donation and backdonation separately by carrying out EDA calculations on propene and propyne where the vacant π* orbitals of either fragment were deleted. The results show that both contributions are important for the hyperconjugation but that the backdonation from the π orbitals of CH_3 into the π* orbitals of the multiple bonds is stronger than the donation. In propene the calculated value for the π-orbital donation $\pi(H_2C{=}CH){\rightarrow}\pi^*(CH_3)$ becomes $\Delta E_\pi = -4.0$ kcal mol^{-1} when the virtual π orbitals in the $H_2C{=}CH^{\bullet}$ fragment are deleted, while the $\pi^*(H_2C{=}CH){\leftarrow}\pi(CH_3)$ π backdonation becomes $\Delta E_\pi = -6.0$ kcal mol^{-1} after deletion of the virtual π orbitals in the $CH_3^{\bullet}$ fragment. In the same fashion we found that the π-orbital donation $\pi(HC{\equiv}CH){\rightarrow}\pi^*(CH_3)$ becomes $\Delta E_\pi = -9.3$ kcal mol^{-1} after deletion of the π* orbitals of $HC{\equiv}CH^{\bullet}$, while the $\pi^*(HC{\equiv}CH){\leftarrow}\pi(CH_3)$ backdonation becomes $\Delta E_\pi = -12.8$ kcal mol^{-1} when the π* orbitals of $CH_3^{\bullet}$ are deleted.

We also calculated the conjugative stabilization between a triple and a double bond in but-1-en-3-yne $H_2C{=}CH{-}C{\equiv}CH$. Table 1 shows that the π-bonding contribution to the central C–C bonding ($\Delta E_\pi = -20.5$ kcal mol^{-1}), which involves only one π component of the triple bond, is slightly stronger than the π conjugation in 1,3-butadiene ($\Delta E_\pi = -19.5$ kcal mol^{-1}); this can be explained by the shorter C–C distance in the former compound. We finally calculated the strength of the hyperconjugation in ethane and 2,2,3,3-tetramethylbutane. The doubly degenerate C–C hyperconjugation in the latter compound ($\Delta E_\pi = -11.6$ kcal mol^{-1}) is slightly stronger than the degenerate C–H hyperconjugation in the former species ($\Delta E_\pi = -10.0$ kcal mol^{-1}).

In summary, EDA calculations show that the intrinsic conjugative stabilization arising from the π–π* interactions in 1,3-butadiyne is approximately twice as strong as that in 1,3-butadiene. Hyperconjugation of C–H and C–C bonds with multiple bonds is quite strong. The hyperconjugation is roughly half as strong as π conjugation between two multiple bonds. The hyperconjugation of C–C bonds is slightly stronger than hyperconjugation of C–H bonds.

Received: February 6, 2005
Published online: May 4, 2005

Keywords: bonding analysis · conjugation · density functional calculations · energy decomposition analysis · hyperconjugation

[1] a) G. B. Kistiakowsky, J. R. Ruhoff, H. A. Smith, W. E. Vaughan, *J. Am. Chem. Soc.* **1936**, *58*,146; b) J. B. Conant, G. B. Kistiakowsky, *Chem. Rev.* **1937**, *37*, 181; c) J. B. Conn, G. B. Kistiakowsky, E. A. Smith, *J. Am. Chem. Soc.* **1939**, *61*, 1868; Also see d) W. Fang, D. W. Rogers, *J. Org. Chem.* **1992**, *57*, 2294.

[2] The energy values shown in Equations (1)–(6) were taken from reference [4].

[3] a) D. W. Rogers, N. Matsunaga, A. A. Zavitsas, F. J. McLafferty, J. F. Liebman, *Org. Lett.* **2003**, *5*, 2373; b) D. W. Rogers, M. Matsunaga, F. J. McLafferty, A. A. Zavitsas, J. F. Liebman, *J. Org. Chem.* **2004**, *69*, 7143.

[4] P. D. Jarowski, M. D. Wodrich, C. S. Wannere, P. von R. Schleyer, K. N. Houk, *J. Am. Chem. Soc.* **2004**, *126*, 15036.

[5] E. K. Wilson, *Chem. Eng. News* **2004**, *82*(51), 48.

[6] a) V. Pophristic, L. Goodman, *Nature* **2001**, *411*, 565; b) P. R. Schreiner, *Angew. Chem.* **2002**, *114*, 3729; *Angew. Chem. Int. Ed.* **2002**, *41*, 3579; c) F. M. Bickelhaupt, E. J. Baerends, *Angew. Chem.* **2003**, *115*, 4315; *Angew. Chem. Int. Ed.* **2003**, *42*, 4183; d) F. Weinhold, *Angew. Chem.* **2003**, *115*, 4320; *Angew. Chem. Int. Ed.* **2003**, *42*, 4188; e) Y. Mo, W. Wu, L. Song, M. Lin, Q. Zhang, J. Gao, *Angew. Chem.* **2004**, *116*, 2020; *Angew. Chem. Int. Ed.* **2004**, *43*, 1986.

[7] The value of 9.8 kcal mol^{-1} in ref. [4] is a typographical error (P. von R. Schleyer, personal communication).

[8] a) L. C. Pauling, G. W. Wheland, *J. Chem. Phys.* **1933**, *1*, 362; b) L. C. Pauling, J. Sherman, *J. Chem. Phys.* **1933**, *1*, 679; c) L. Pauling, H. D. Springall, K. Palmer, *J. Am. Chem. Soc.* **1939**, *61*, 928; d) M. J. S. Dewar, G. J. Gleicher, *J. Am. Chem. Soc.* **1965**, *87*, 692; e) M. J. S. Dewar, H. N. Schmeising, *Tetrahedron* **1960**, 96; f) D. O. Highes, *Tetrahedron* **1968**, *24*, 6423; g) L. S. Bartell, *Tetrahedron* **1978**, *34*, 2891; h) L. S. Bartell, *J. Am. Chem. Soc.* **1959**, *81*, 3497; i) E. B. Wilson, Jr., *Tetrahedron*, **1962**, *17*, 191; j) K. Exner, P. von R. Schleyer, *J. Phys. Chem. A* **2001**, *105*, 3407.

[9] H. Kollmar, *J. Am. Chem. Soc.* **1979**, *101*, 4832.

[10] a) F. M. Bickelhaupt, E. J. Baerends, *Rev. Comput. Chem.* **2000**, *15*, 1; b) G. te Velde, F. M. Bickelhaupt, E. J. Baerends, S. J. A. van Gisbergen, C. Fonseca Guerra, J. G. Snijders, T. Ziegler, *J. Comput. Chem.* **2001**, *22*, 931; See also: c) T. Ziegler, A. Rauk, *Theor. Chim. Acta* **1977**, *46*, 1; d) K. Morokuma, *J. Chem. Phys.* **1971**, *55*, 1236.

[11] a) C. Esterhuysen, G. Frenking, *Theor. Chem. Acc.* **2004**, *111*, 381; b) A. Kovács, C. Esterhuysen, G. Frenking, *Chem. Eur. J.* **2005**, *11*, 1813.

[12] G. Frenking, K. Wichmann, N. Fröhlich, C. Loschen, M. Lein, J. Frunzke, V. M. Rayón, *Coord. Chem. Rev.* **2003**, *238–239*, 55.

[13] The EDA calculations were performed using the program package ADF: a) ref. [10a]; b) ref. [10b]; The calculations were carried out at the BP86 level: c) A. D. Becke, *Phys. Rev. A* **1988**, *38*, 3098; d) J. P. Perdew, *Phys. Rev. B* **1986**, *33*, 8822; The

basis sets used have TZ2P quality and uncontracted Slater-type orbitals (STOs) served as basis functions: e) J. G. Snijders, E. J. Baerends, P. Vernooijs, *At. Data Nucl. Data Tables* **1982**, *26*, 483; An auxiliary set of s, p, d, f and g STOs was used to fit the molecular densities and to represent the Coulomb and exchange potentials accurately in each SCF cycle: f) J. Krijn, E. J. Baerends, *Fit Functions in the HFS-Method*, Vrije Universiteit Amsterdam, The Netherlands, **1984**, Internal Report (in Dutch).

[14] By electrostatic character we mean the percentage contribution of the ΔE_{elstat} term to the total attractive interactions $\Delta E_{elstat} + \Delta E_{orb}$.

Metalloenzyme Inhibitors

Metal Ions as Cofactors for the Binding of Inhibitors to Methionine Aminopeptidase: A Critical View of the Relevance of In Vitro Metalloenzyme Assays**

*Rolf Schiffmann, Andreas Heine, Gerhard Klebe, and Christian D. P. Klein**

Methionine aminopeptidases (MetAPs) are highly conserved, ubiquitous metalloproteases that remove the N-terminal starter methionine residue from nascent polypeptide chains. Inhibitors of MetAPs can have numerous biological effects and are consequently under development for a variety of therapies, including anticancer,[1,2] anti-infective,[3] and anti-arthritis[4] drugs. Previous X-ray crystallographic analyses have resulted in a number of reported MetAP structures, including those of the human type II[5] and *Escherichia coli* enzymes.[6] All MetAPs share the "pita bread" folding motif. The active sites of the known MetAPs are very similar; all contain identical metal-chelating residues (2 × Asp, 2 × Glu, 1 × His) that coordinate two adjacent metal ions. These metal ions, in turn, activate a water molecule for nucleophilic attack on the N-terminal methionine amide bond of the peptide substrate. For experiments in vitro, cobalt(II) is most commonly used as the MetAP cofactor, as the resulting dicobalt enzyme has the highest catalytic activity.

We have conducted molecular dynamics studies[7,8] and virtual screening procedures with an emphasis on the MetAP from *E. coli* in pursuit of a rational design approach for MetAP inhibitors. A careful preparation of the active site with particular consideration of the water molecules bound to the two cobalt ions preceded the virtual screening runs. Among the most promising virtual screening hits, we identified thiabendazole (**1**), a frequently used antifungal and antiparasitic compound. The inhibitory activity of this compound against *E. coli* MetAP[6] was consequently tested with a published[9] in vitro assay method (Table 1). As is the case with all other known in vitro assay methods for MetAP, an excess of cobalt was present in the buffer to afford sufficient enzymatic activity.

We found thiabendazole (**1**) to be active in the upper nanomolar range, binding to *E. coli* MetAP with a K_i value of 0.4 μM. The subsequent use of **1** as the lead compound for structural modifications yielded more potent inhibitors based on the benzimidazole scaffold.[11] Because MetAP is an essential enzyme in all cells, we expected that **1** and particularly its more potent analogues would have an antibacterial effect against *E. coli*. However, all compounds were inactive against the growth of *E. coli* at concentrations up to 1 mM. This result, which was reminiscent of similar observations with a structurally distinct and even more potent class of MetAP inhibitors,[3] was initially attributed to insufficient compound uptake into the bacterial cell. To create a reliable basis for further rational drug design efforts, *E. coli* MetAP was crystallized with and without the inhibitor, and the resulting 3D structures were determined by X-ray diffraction at a resolution of 1.6 Å.

Table 1: Noncovalent inhibitors of MetAP.

	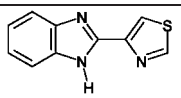 Thiabendazole (**1**)	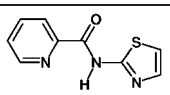 **2** (Luo et al.[3])	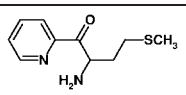 **3** (Douangamath et al.[10])
Structure of MetAP complex	This work (PDB code 1YVM)	This work[12]	Ref. [10]
Affinity towards MetAP	$K_i = 0.4$ μM (*E. coli*)	$IC_{50} = 5$ μM (*E. coli*)	$IC_{50} = 16$ μM (*S. aureus*)

Based on the virtual screening results, we assumed that thiabendazole (**1**) was localized in close proximity to the two cobalt ions deep in the active site of *E. coli* MetAP. Complexes between **1** and metal ions are known to form, and we expected the inhibitor to interact with the two metal cations of the active site. It therefore came as a complete surprise to find the inhibitor at the entrance of the active site, not bound to the "regular" cobalt ions at all, but rather to an additional cobalt ion, which is not present in the ligand-free structure. The binding mode is depicted in Figure 1. The

[*] R. Schiffmann, Dr. C. D. P. Klein
FR 8.2 Pharmazeutische und Medizinische Chemie
Saarland University
66041 Saarbrücken (Germany)
Fax: (+49) 681-302-4386
E-mail: cdpk@mx.uni-saarland.de
Dr. A. Heine, Prof. Dr. G. Klebe
Institut für Pharmazeutische Chemie
Marbacher Weg 6, 35032 Marburg (Germany)

[**] We thank Professor R. Hartmann for his continued support of our work. This project was supported by the Deutsche Forschungsgemeinschaft (KL1356) and the Fonds der Chemischen Industrie.

Supporting information for this article is available on the WWW under http://www.angewandte.org or from the author.

  DOI: 10.1002/anie.200500592

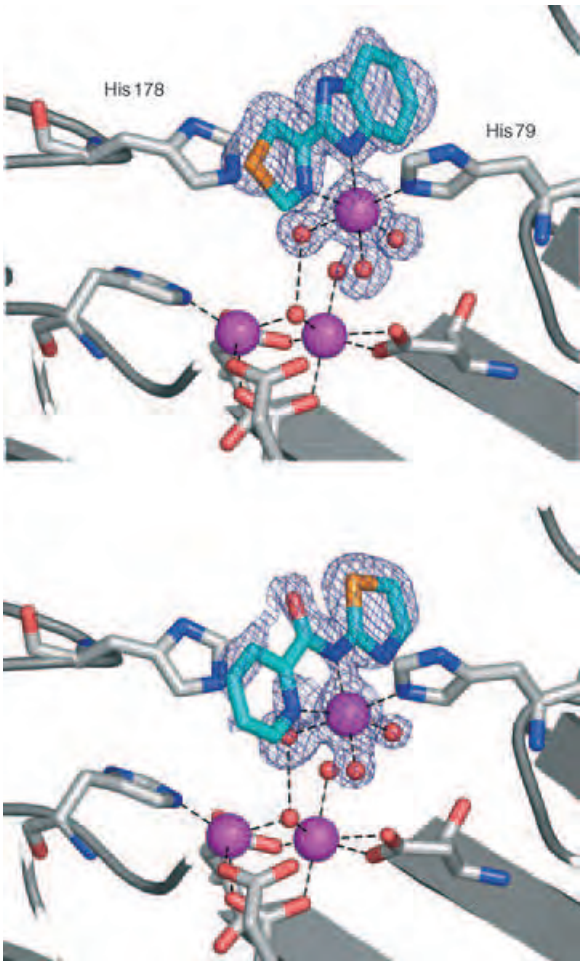

Figure 1. Electron density of thiabendazole (**1**, top) and compound **2** (bottom) near the active site of *E. coli* MetAP. The $2F_o-F_c$ electron density is contoured at 1 σ and shown within a radius of 1.5 Å around the inhibitor, the auxiliary cobalt ion, and the complexing water molecules. (C = turquoise, Co = magenta, N = blue, O = red, S = yellow.)

auxiliary cobalt ion is complexed in a nearly perfect octahedral geometry by two nitrogen atoms of thiabendazole, one histidine nitrogen atom (His79), and three water molecules.

Additionally, we determined the 3D structure of *E. coli* MetAP in complex with the lead compound **2**, which has been previously identified by Luo et al.[3] to a resolution of 1.6 Å. Through its pyridine and amide nitrogen atoms, this compound likewise binds an auxiliary cobalt ion that interacts with His79 and three water molecules at the entrance of the active site.[12] It is possible that the thiazole nitrogen atom, which is located 2.5 Å from the water molecule opposite the pyridine nitrogen atom and about 3 Å from the cobalt ion, also contributes to the stabilization of this complex.

The auxiliary cobalt ion at His79 is not present in enzyme preparations crystallized in the absence of ligand. This has been shown by the previous work of Lowther et al.,[6] and was confirmed by our determination of the structure of the ligand-free enzyme under otherwise identical conditions.

During the course of this work, Douangamath and co-workers[10] reported another MetAP inhibitor class, including **3**, and the binding modes of these compounds to *Staphylococcus aureus* MetAP. Remarkably, compound **3** and a close structural analogue also bind to an additional cobalt ion that is not present in the ligand-free active site. In contrast to the *E. coli* MetAP complexes with **1** and **2** reported herein, the auxiliary cobalt ion is not bound to His79, but rather to His178, and the inhibitors make additional interactions with the "regular" cobalt ions in the active site. Notably, the authors also described a potent inhibitor whose binding is not mediated by an auxiliary cobalt ion.

Three research groups have independently developed structurally distinct inhibitors of MetAPs (with considerable potency in vitro) which share the common feature of binding through auxiliary metal ions. The observation of ternary complexes that including additional cations must clearly be attributed to the high concentration of free metal ions in the in vitro assay; this certainly does not reflect the conditions in a living cell, as has already been pointed out by Douangamath and co-workers.[10] The inhibitors are therefore—most likely—not useful for therapeutic or other in-vivo use.

One may suggest that the problem could easily be solved by lowering the concentration of the metal cofactor in the assay buffer. This is not a viable solution, as MetAPs and many other therapeutically relevant metalloenzymes require high metal concentrations (usually in the range of 1 μM to 1 mM) to be active in vitro. However, the concentration of unbound transition metal ions in living cells is several orders of magnitude lower.[13]

Several conclusions can be drawn from these results. First, it is evident that structural information about the enzyme–inhibitor complex is of crucial importance for the understanding of in vitro assay results. Compounds **1**–**3** have been used as starting points for structure–activity studies, although it must now be assumed that they do not bind MetAP under physiological conditions. Their inactivity in vivo has been incorrectly attributed to insufficient pharmacokinetic properties.

Second, these findings call for more cautious interpretation of in vitro assay results, particularly in the field of metalloenzymes. It seems advisable to judge potential lead compounds not only with respect to pharmacokinetic properties ($\log P$, molecular weight, hydrogen bonding), but also under the perspective of their capacity for binding small inorganic ions. This would prevent the generation of meaningless in vitro assay results. It would also help to avoid investments in experimental substances that have unacceptable pharmacokinetic properties brought about by the binding of metals and other inorganic ions from foodstuffs and nutritional supplements in the gastrointestinal tract. A filtering algorithm that identifies adjacent heteroatoms that are prone to form complexes with inorganic cations should be straightforward to design. Such a tool may be easily implemented within the computer programs that are in current use for the handling of compound databases and for the selection of compounds to be used in virtual or experimental high-throughput screening.

In 1998, Katz et al.[14] proposed the deliberate use of auxiliary zinc ions to increase the binding affinity of serine protease inhibitors. To our knowledge, this group was the first

to describe ligand binding mediated by transition metal ions. The results presented herein may be interpreted similarly; analogous to Katz et al., we might suggest the design of transition metal cofactor-dependent compounds with increased affinity for the enzyme in vitro. However, recent findings on zinc homeostasis[13] indicate that the concentration of free zinc ions in the cell is too low to be used for this purpose, and it must be assumed that this is even more pertinent for other, less inert (redox active) cations such as cobalt. In contrast, it may be possible to use more abundant and inert cations such as calcium and magnesium as mediators for ligand binding. Notably, this would allow the coupling of ligand–receptor interactions to the intracellular concentration of these ions, which (especially calcium) play a major role in many signal-transduction processes. The design of specific high-affinity ligands that make ternary complexes with selected cations and biological target molecules, however, will be a challenging task.

Experimental Section

Crystallization and structure determination: Recombinant eMetAP (Arg175Gln to remove a secondary thrombin cleavage site within a surface loop) was overexpressed in *E. coli* strain BL21(DE3) and purified as previously reported.[2]

Crystals were grown with a slight modification in the conditions described before.[15] In brief, freshly prepared enzyme was kept in buffer containing HEPES (25 mM, pH 6.8), KCl (25 mM), NaCl (100 mM), $CoCl_2$ (1 mM), and methionine (15 mM). Crystals of the Co^{II}-containing enzyme were obtained overnight at 22 °C by vapor diffusion in 20-μL sitting drops after mixing the protein solution in buffer (13.5 mg mL^{-1}) to which *n*-octanoylsucrose (Calbiochem-Novabiochem Corp., La Jolla, CA) was added (final concentration = 48.8 mM), at a ratio of 1:1 with well solutions (500 μL) containing PEG 4000 (24–33 %), HEPES (0.1M, pH 7.1) and fresh $CoCl_2$ (2 mM).

Crystals of the thiabendazole complex were obtained by incubating the enzyme (13.5 mg mL^{-1}) in *n*-octanoylsucrose (49.8 mM) at room temperature for 5 min with a solution of the inhibitor dissolved in DMSO. The final inhibitor/enzyme ratio was 5:1 (DMSO, 1 %; *n*-octanoylsucrose, 48.8 mM) after mixing the preformed complex with well solution: PEG 4000 (24–33 %), HEPES (0.1M, pH 7.1) and $CoCl_2$ (2 mM).

The data set was collected on a Rigaku/MSC rotating anode generator (RU300) operated at 50 kV and 90 mA equipped with an R-axis 4++ imaging-plate detector. 360 frames with $\delta_\phi = 0.5°$ at a detector distance of 100 mm were collected at −170 °C with 18 % glycerol in mother liquor as cryoprotectant.

For compound **2**, the inhibitor/enzyme ratio was 2.5:1 and the well solution contained 4-mM $CoCl_2$. The data set was collected with an R-axis 4 imaging-plate detector under the conditions and parameters mentioned above and consisted of 240 frames.

Data were processed and scaled with the program HKL2000.[16] The MetAP structure published by Lowther and coworkers (PDB code 2MAT) was used without the cobalt atoms and water molecules as a starting model for molecular replacement in PHASER[17] followed by a rigid-body refinement in CNS.[18] Initial refinement was continued in CNS by using positional and slow-cooling protocols followed by restrained *B*-value refinement. Refinement was then continued with SHELXL97.[19] At least 20 cycles of conjugate gradient minimization with restraints on bond distances, angles, and *B* values were performed for each refinement step. In the final stages, hydrogen atoms were placed in calculated positions without the use of additional parameters. Intermittent cycles of model building were done with the program O.[20]

The coordinates have been deposited in the PDB (http://www.rcsb.org/pdb/) with access code 1YVM. All images were created with PYMOL.[21] 3D structures were checked and Ramachandran plots were generated with Procheck.[22]

Received: February 17, 2005
Published online: May 4, 2005

Keywords: drug design · inhibitors · metalloenzymes · methionine aminopeptidase · X-ray diffraction

[1] N. Sin, L. Meng, M. Q. W. Wang, J. J. Wen, W. G. Bornmann, C. M. Crews, *Proc. Natl. Acad. Sci. USA* **1997**, *94*, 6099.
[2] W. T. Lowther, D. A. McMillen, A. M. Orville, B. W. Matthews, *Proc. Natl. Acad. Sci. USA* **1998**, *95*, 12153.
[3] Q. Luo, J. Li, Z. Liu, L. Chen, J. Li, Z. Qian, Q. Shen, Y. Li, G. Lushington, Q. Ye, F. Nan, *J. Med. Chem.* **2003**, *46*, 2631.
[4] S. G. Bernier, D. D. Lazarus, E. Clark, B. Doyle, M. T. Labenski, C. D. Thompson, W. F. Westlin, G. Hannig, *Proc. Natl. Acad. Sci. USA* **2004**, *101*, 10768.
[5] S. Liu, J. Widom, C. W. Kemp, C. M. Crews, J. Clardy, *Science* **1998**, *282*, 1324.
[6] W. T. Lowther, A. M. Orville, D. T. Madden, S. Lim, D. H. Rich, B. W. Matthews, *Biochemistry* **1999**, *38*, 7678.
[7] C. Klein, G. Folkers, *Oncol. Res. Anti-Cancer Drug Des.* **2003**, *13*, 513.
[8] C. Klein, R. Schiffmann, G. Folkers, S. Piana, U. Röthlisberger, *J. Biol. Chem.* **2003**, *278*, 47862.
[9] G. Yang, R. B. Kirkpatrick, T. Ho, G. F. Zhang, P. H. Liang, K. O. Johanson, D. J. Casper, M. L. Doyle, J. P. Marino, S. K. Thompson, W. F. Chen, D. G. Tew, T. D. Meek, *Biochemistry* **2001**, *40*, 10645.
[10] A. Douangamath, G. E. Dale, A. D'Arcy, M. Almstetter, R. Eckl, A. Frutos-Hoener, B. Henkel, K. Illgen, S. Nerdinger, H. Schulz, A. MacSweeney, M. Thormann, A. Treml, S. Pierau, S. Wadman, C. Oefner, *J. Med. Chem.* **2004**, *47*, 1325.
[11] C. Klein, unpublished results.
[12] There was clear density for the auxiliary cobalt ion and the two water molecules in the same position as in the structure with thiabendazole. Additional density suggests the position of the planar ligand that could coordinate through its nitrogen atoms to the Co ion. However, multiple binding modes cannot be entirely ruled out, as the electron density is somewhat ambiguous and only clearly visible for a part of the ligand. The structure was therefore not deposited in the protein data bank.
[13] Y. Hitomi, C. E. Outten, T. V. O'Halloran, *J. Am. Chem. Soc.* **2001**, *123*, 8614.
[14] B. A. Katz, J. M. Clark, J. S. Finer-Moore, T. E. Jenkins, C. R. Johnson, M. J. Ross, C. Luong, W. R. Moore, R. M. Stroud, *Nature* **1998**, *391*, 608.
[15] W. T. Lowther, A. M. Orville, D. T. Madden, S. Lim, D. H. Rich, B. W. Matthews, *Biochemistry* **1999**, *38*, 7678.
[16] Z. Otwinowski, W. Minor, *Methods Enzymol.* **1997**, *276*, 307 (Macromolecular Crystallography, Part A).
[17] L. C. Storoni, A. J. McCoy, R. J. Read, *Acta Crystallogr. Sect. D* **2004**, *60*, 432.
[18] A. T. Brunger, P. D. Adams, G. M. Clore, W. L. DeLano, P. Gros, R. W. Grosse-Kunstleve, J. S. Jiang, J. Kuszewski, M. Nilges, N. S. Pannu, R. J. Read, L. M. Rice, T. Simonson, G. L. Warren, *Acta Crystallogr. Sect. D* **1998**, *54*, 905.
[19] G. M. Sheldrick, T. R. Schneider, *Methods Enzymol.* **1997**, 319.
[20] T. A. Jones, J. Y. Zou, S. W. Cowan, Kjeldgaard, *Acta Crystallogr. Sect. A* **1991**, *47*, 110.

[21] W. L. DeLano, *The PyMOL Molecular Graphics System* **2002**, DeLano Scientific LLC, San Carlos, CA, USA. http://www.pymol.org.
[22] R. A. Laskowski, M. W. MacArthur, D. S. Moss, J. M. Thornton, *J. Appl. Crystallogr.* **1993**, *26*, 283.

Chiral Molecules

Isotopic Chirality and Molecular Parity Violation**

Robert Berger, Guido Laubender, Martin Quack, Achim Sieben, Jürgen Stohner, and Martin Willeke*

Dedicated to Richard N. Zare on the occasion of his 65th birthday

Studies of isotope effects have a long tradition in providing fundamental insights into molecular spectroscopy and reaction dynamics,[1,2] usually dealt with theoretically on the basis of the electromagnetic interaction that is parity conserving, i.e. remains unchanged under space inversion at the origin.[3–5] Isotope effects are frequently caused by mass differences of the isotopes. There are also isotope effects due to the different nuclear spins of the isotopes,[6] and, in principle, isotope effects can arise independent of mass and spin because of symmetry restrictions on the molecular wavefunction leading to different symmetry selection rules for different isotopomers.[7] Here we report the first quantitative investigations of a new isotope effect, which leads to a ground-state energy difference $\Delta_{pv}E \approx \Delta_{pv}H_0^0/N_A$ for the enantiomers of molecules that are isotopically chiral, i.e. chiral only by isotopic substitution (Figure 1). This parity-violating isotope effect arises from the electroweak interaction between electrons and nucleons, mediated by the Z-boson, and thus depends upon nucleonic composition. Our calculations are of interest in relation to efforts of measuring $\Delta_{pv}E$ in enantiomers,[5,8] and they are also important for the fundamental understanding of isotope effects and molecular chirality. The present work opens a new avenue in this field by providing quantitative calculations on such chiral isotopomers in the framework of electroweak quantum chemistry[9] including the weak nuclear force. Since recent theoretical approaches predict absolute values of $\Delta_{pv}E$ that can be orders of magnitude larger[9–12] than anticipated on the basis of earlier calculations,[14,15] there is new hope that accurate measurements and calculations, particularly for molecules with light atoms, will provide additional insights into the standard model of high-energy physics.[5,16] We refer here to recent articles with extensive further references.[4,5,10,12]

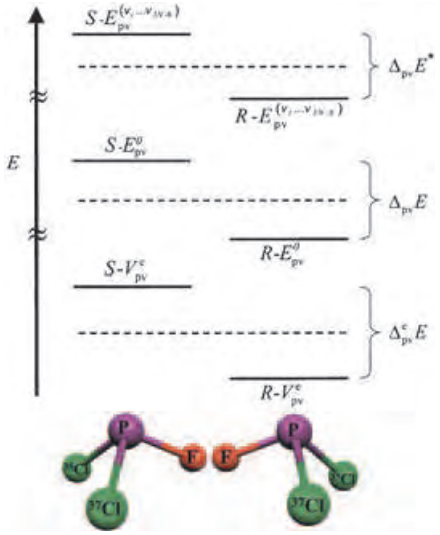

Figure 1. Scheme showing all quantities of interest as explained in the text. For the example $PF^{35}Cl^{37}Cl$ the relative magnitudes of the various $\Delta_{pv}E$ values are to scale, with $\Delta_{pv}E^*$ for the case $v_i=1$ for all i, but the comparison with much larger zero-point and vibrational excitation energies is, of course, not to scale. The magnitude of the reaction enthalpy for the stereomutation reaction $S=R$ is $|\Delta_{pv}H_0^0| \approx N_A|\Delta_{pv}E| = 3.3\times10^{-13}$ J mol^{-1} (at 0 K).

In this context we address and answer the following questions:

1. How large is $\Delta_{pv}E$ in isotopically chiral systems compared to "ordinary" enantiomers?
2. Is $\Delta_{pv}E$ dominated here by the parity-violating potential at the equilibrium geometry or by vibrationally averaging the parity-violating potential?
3. How does vibrational excitation change $\Delta_{pv}E$ (i.e. $\Delta_{pv}E^*$) in such systems compared to "ordinary" enantiomers where this question was addressed previously?[17]

The answers to these questions will help in planning future experiments possibly including isotopic enantiomers. We study the phosphane derivatives PHDX (X = F,^{35}Cl,^{37}Cl,^{79}Br,^{81}Br) and $P^{35}Cl^{37}ClY$ (Y = F,H,D) with these goals in mind. While isotopic chirality has been considered for some time,[3,18–20] as an isotope effect through variation of

[*] Prof. Dr. M. Quack, A. Sieben, Dr. M. Willeke
Laboratorium für Physikalische Chemie
Eidgenössische Technische Hochschule Zürich
8093 Zürich (Switzerland)
Fax: (+41) 1-632-1021
E-mail: martin@quack.ch
Dr. R. Berger, G. Laubender
Institut für Chemie
Technische Universität Berlin
Strasse des 17. Juni 135, 10623 Berlin (Germany)
Dr. J. Stohner
Zürcher Hochschule
Winterthur (ICB-ZHW)
8401 Winterthur (Switzerland)

[**] We thank Sieghard Albert and Michael Gottselig for help and discussions. Our work was supported financially by the ETH Zürich (including C4 and CSCS) and the Schweizerischer Nationalfonds. R.B. acknowledges financial support from the Volkswagen-Stiftung and computer time provided by the HLRN. G.L. thanks the Graduiertenkolleg 352 for a scholarship.

 DOI: 10.1002/anie.200462088

identity and mass of the isotopes, our work provides the first quantitative predictions of $\Delta_{pv}E$ resulting from the parity-violating isotope effect.

Figure 1 illustrates the quantities of interest. *R*-V^e_{pv} and *S*-V^e_{pv} refer to the parity-violating potentials at the Born–Oppenheimer (BO) equilibrium geometries of the *R* and *S* enantiomers. Because of the antisymmetry of the parity-violating potential with respect to space inversion,[5] the absolute magnitude of the difference $|\Delta^e_{pv}E|$ is just twice the absolute magnitude of each of the two potentials. Adding the zero-point vibrational energy and the average parity-violating potentials in the vibrational ground states to the BO parity-conserving potentials gives the ground state energy levels including parity violation for both enantiomers (*R*-E^0_{pv}, *S*-E^0_{pv}). Their difference corresponds to the in principle measurable ground state energy difference (if tunneling is negligible) or to the reaction enthalpy at 0 K $|R\text{-}E^0_{pv} - S\text{-}E^0_{pv}| = |\Delta_{pv}E| \approx |\Delta_r H^0_0/N_A|$ (the sign depends on the convention for the directed stereomutation reaction between *R* and *S*). Finally a similar definition applies to excited vibrational states $(v_1 \ldots v_{3N-6})$ of the chiral molecule, which occur as closely spaced doublets of levels for the two enantiomers with the parity-violating splitting $|\Delta_{pv}E^*(v_1 \ldots v_{3N-6})| = |R\text{-}E^{v_1 \ldots v_{3N-6}}_{pv} - S\text{-}E^{v_1 \ldots v_{3N-6}}_{pv}|$ provided that this splitting is much larger than the hypothetical tunneling splitting for the parity-conserving case but much smaller than the separation of vibrational levels.[3,8]

The parity-violating potentials were calculated within our multiconfiguration linear response (MC-LR) approach to electroweak quantum chemistry,[11] here within the random-phase approximation (RPA). The approximate parity-violating Hamiltonian in SI units is given in Equation (1).[10,11,17]

$$\hat{H}_{pv} = \frac{\pi G_F}{h m_e c\sqrt{2}} \sum_{A=1}^{N} Q_w(A) \sum_{i=1}^{n} [\hat{\vec{p}}_i \cdot \hat{\vec{s}}_i, \delta^3(\vec{r}_i - \vec{r}_A)]_+ \quad (1)$$

Here, G_F (Fermi constant) is $2.222527 \times 10^{-14}\, E_h a_0^3 = 1.43586 \times 10^{-62}\,\mathrm{J\,m^3}$ (Hartree energy E_h and Bohr radius a_0), m_e is the electron mass, h is Planck's constant, and c is the speed of light in vacuum. $\hat{\vec{p}}_i$ and $\hat{\vec{s}}_i$ are the linear momentum and spin operator of the electron i, and $\vec{r}_i$ denotes its position. $\vec{r}_A$ is the position vector of nucleus A. δ^3 represents the three-dimensional Dirac delta distribution and $[.,.]_+$ the anticommutator. The strength of the resulting effect is related to the numbers of protons Z_A and neutrons N_A in the nucleus A, which enter the Hamiltonian by means of the electroweak charge [Eq. (2)].

$$Q_w(A) = Z_A(1 - 4\sin^2\theta_w) - N_A \quad (2)$$

Here, θ_w is the Weinberg angle; we used $\sin^2\theta_w = 0.2319$ in our calculations. The electroweak charge Q_w differs for the various isotopes leading to the new parity-violating isotope effect discussed here. We first focus on the parity-violating potential energy at the equilibrium geometries of the electronic ground states V^e_{pv} (and $|\Delta^e_{pv}E| = |2V^e_{pv}|$). The results reported in Table 1 for V^e_{pv} correspond to the *R* configuration of the molecules **1**–**10**. A negative value of V^e_{pv} indicates a stabilization of the given structure, while the corresponding mirror image is destabilized by the same amount. The absolute values of V^e_{pv} of systems that are chiral due to substitution with different chlorine isotopes (**6**–**8**) are remarkably large, whereas the effect due to a deuteration (**1**–**5**) is two to three orders of magnitude smaller. This can be understood from the parity-violating operator $\hat{H}_{pv}$ given in Equation (1), which describes effectively a contact-like interaction between each electron and each nucleus, depending on the weak nuclear charge $Q_w(A)$ [Eq. (2)]. The parity-violating potential arises as a sum of contributions from the various nuclei, where typically the heavier nuclei dominate.[10] Therefore, simple deuteration results in an absolute value of V^e_{pv} that is small compared to systems that are chiral with different chlorine isotopes. We report in Table 1 also V^e_{pv} for the "ordinary" chiral systems $P^{79}Br^{35}ClF$ (**10**) and $PH^{35}ClF$ (**9**). For the isotopically chiral molecules $PH^{35}Cl^{37}Cl$ and $P^{35}Cl^{37}ClF$ the parity-violating potential is about one order of magnitude smaller than for the "ordinary" chiral molecule PHClF. This can be understood by the electroweak charges of ^{35}Cl and ^{37}Cl ($Q_w = -16.8$ vs -18.8) differing by about 10%. For the isotopically chiral systems one would thus expect a

Table 1: Equilibrium contribution and vibrationally averaged parity-violating energy of various ordinary *R* enantiomers and several isotopic *R* enantiomers.[a]

Compounds in *R* configuration	V^e_{pv} [$hc\,\mathrm{cm^{-1}}$]	E^0_{pv} [$hc\,\mathrm{cm^{-1}}$]	Basis set for geometry optimization and for 1D electronic potential calculations	Basis set for parity-violating energy calculations
PHDF (**1**)	-4.64×10^{-17}	-1.40×10^{-15}	6-311G(d,p)	6-311G(d,p)
	-5.73×10^{-17}	-1.11×10^{-15}	6-311G(d,p)	aug-cc-pVDZ
$PHD^{35}Cl$ (**2**)	-2.14×10^{-17}	-1.70×10^{-15}	6-311^{++}G(d,p)	6-311G(d,p)
$PHD^{37}Cl$ (**3**)	-2.14×10^{-17}	-1.66×10^{-15}	6-311^{++}G(d,p)	6-311G(d,p)
$PHD^{79}Br$ (**4**)	-4.09×10^{-17}	-1.60×10^{-14}	6-311^{++}G(d,p)	6-311G(d,p)
$PHD^{81}Br$ (**5**)	-4.09×10^{-17}	-1.63×10^{-14}	6-311^{++}G(d,p)	6-311G(d,p)
$PH^{35}Cl^{37}Cl$ (**6**)	8.44×10^{-15}	7.50×10^{-15}	6-311^{++}G(d,p)	aug-cc-pVDZ
$PD^{35}Cl^{37}Cl$ (**7**)	8.44×10^{-15}	8.97×10^{-15}	6-311^{++}G(d,p)	aug-cc-pVDZ
$P^{35}Cl^{37}ClF$ (**8**)	-1.53×10^{-14}	-1.38×10^{-14}	6-311^{++}G(d,p)	aug-cc-pVDZ
$PH^{35}ClF$ (**9**)	2.83×10^{-13}	2.88×10^{-13}	6-311G(d,p)	aug-cc-pVDZ
$P^{79}Br^{35}ClF$ (**10**)	-1.09×10^{-12}	-1.06×10^{-12}	6-311G(d,p)	6-311G(d,p)

[a] $V^e_{pv}/(hc)$ is the parity-violating potential calculated at the equilibrium geometry of the parity-conserving Born–Oppenheimer potential. All geometry optimizations and one-dimensional (1D) cuts through the parity-conserving potential energy hypersurface were carried out on the level of second order Møller–Plesset perturbation theory (MP2) within the frozen core approximation using Gaussian 98.[26] $E^0_{pv}/(hc)$ is the parity-violating potential averaged over the ground vibrational state as explained in the text. From the quantities given it is possible to calculate the parity-violating energy differences $|\Delta^e_{pv}E| = |2V^e_{pv}|$ and $|\Delta_{pv}E| = |2E^0_{pv}|$ (see text and refs. [11,17] for methods and basis sets). Parity-violating potentials were calculated with our modification[11] of the Dalton program.[27]

decrease of V_{pv}^{e} by an order of magnitude; one notes that for the symmetric equilibrium geometry of $PF^{35}Cl_2$ the atomic contributions to V_{pv}^{e} for the two ^{35}Cl nuclei are of exactly the same "normal" magnitude but cancel because of their different sign. In $PF^{35}Cl^{37}Cl$ a difference of about 10% remains with respect to exact cancellation. For a normal asymmetric molecule like PHFCl such a partial cancellation is not expected systematically and V_{pv}^{e} is an order of magnitude larger. H–D substitution leads to a large relative change of the electroweak charge but to little change in the parity-violating potentials simply because neither H nor D contribute much to V_{pv}^{e}. This explains the small parity-violating potentials with H/D isotopic chirality in Table 1. For isotopically chiral CHDTOH[20] we have discussed that those nuclei that lie in the C_s symmetry plane of the corresponding achiral isotopomers do not contribute to the parity-violating potential V_{pv}^{e}. Thus, the values of V_{pv}^{e} for $PHD^{35}Cl$ and $PHD^{37}Cl$ are identical (as also for the pairs $PH^{35}Cl^{37}Cl$(**6**)/$PD^{35}Cl^{37}Cl$(**7**) and $PHD^{79}Br$(**4**)/$PHD^{81}Br$(**5**)).

Isotopic substitution, however, does not only influence the parity-violating potential at the equilibrium structure, it also modifies the molecular motion and changes the average ground state geometry of a molecule.[17] It is, for instance, well known that the average X–D bond lengths are shorter than the average X–H bond lengths (see refs. [3,21] for a discussion of CH_4 including its potentially chiral isotopomers). To include this effect in the calculation of $\Delta_{pv}E$ we described the vibrational problem in the separable anharmonic adiabatic approximation (SAAA[17]). Our methods of calculation have been described in detail in refs. [11,17], and we have checked by test calculations that the nonseparable coupling in $V_{pv}(q_i)$ as a function of the reduced normal coordinates q_i is of minor importance.[17] We are allowed to talk of a measurable $\Delta_{pv}E$,[5,8] as it is much larger than the tunneling splitting. The latter was roughly estimated for **2** as 10^{-23} cm^{-1} to 10^{-20} cm^{-1} using a simple WKB method. For the other compounds[22] the tunneling splitting should be even smaller because of the higher inversion barrier or larger tunneling mass (see ref. [23] and references therein). With the parity-violating potential $V_{pv}(q_i)$ and the vibrational wavefunction $\Psi_i^{v_i}$ we calculated the expectation value $\langle E_{pv}\rangle_i^{v_i}$ of the parity-violating energy for the ith mode excited with v_i quanta [Eq. (3)].[17] Figure 2 illustrates this for (*R*)-PHDF.

$$\langle E_{pv}\rangle_i^{v_i} = \langle \Psi_i^{v_i} | V_{pv}(q_i) | \Psi_i^{v_i} \rangle \qquad (3)$$

Within the SAAA[17] we obtain the parity-violating energy $E_{pv}^{(v_1,\ldots,v_{3N-6})}$ for a vibrational state with vibrational quantum numbers v_i according to Equation (4).

$$E_{pv}^{(v_1,\ldots,v_{3N-6})} = \langle \prod_i^{3N-6} \Psi_i^{v_i} | V_{pv}^{e} + \sum_{i=1}^{3N-6} \Delta V_{pv}(q_i) | \prod_i^{3N-6} \Psi_i^{v_i} \rangle$$
$$= \sum_i^{3N-6} \langle E_{pv}\rangle_i^{v_i} - (3N-7)\, V_{pv}^{e} \qquad (4)$$

We use E_{pv}^{0} as the abbreviation for the ground state value with $v_i = 0$ for all i. The ground state parity-violating energy difference can be calculated as $|\Delta_{pv}E| = |2E_{pv}^{0}|$ or for excited states as $|\Delta_{pv}E^*| = |2E_{pv}^{(v_1,\ldots,v_{3N-6})}|$. We applied the procedure illustrated for (*R*)-PHDF to all compounds **1**–**10**. The results for E_{pv}^{0} are given in the third column of Table 1. For compounds **6**–**10** E_{pv}^{0} is similar to V_{pv}^{e}, whereas for **1**–**5**, which are chiral due to single deuteration, E_{pv}^{0} is up to three orders of magnitude larger than V_{pv}^{e}. The strong vibrational dependence for **1**–**5** opens up the possibility of increasing or decreasing the parity-violating energy by selected excitation of fundamentals.[17] For (*R*)-PHDF excitation with one quantum in ν_6 for instance leads to $E_{pv}^{(0,0,0,0,0,1)} = 9.90 \times 10^{-15}$ cm^{-1} (positive), whereas an excitation of ν_4 with one quantum results in $E_{pv}^{(0,0,0,1,0,0)} = -1.22 \times 10^{-14}$ cm^{-1} (negative). Simultaneous excitation of both modes leads to substantial compensation, with $E_{pv}^{(0,0,0,1,0,1)} = -8.57 \times 10^{-16}$ cm^{-1}. In (*R*)-$P^{35}Cl^{37}ClF$, however, the parity-violating energy is predicted to depend less upon vibrational excitation. At some stage the nonseparable, anharmonic effects will certainly become important and can be accounted for.[17]

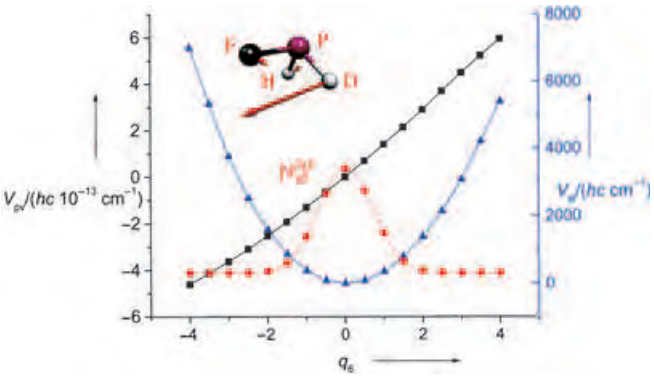

Figure 2. The one-dimensional cut through the parity-conserving potential energy hypersurface (MP2/6-311G(d,p)) of (*R*)-PHDF along the reduced normal coordinate q_6 (triangles, ordinate on the right). The displacement vectors of q_6 are indicated for the different atoms. We show no scale for the probability density $|\Psi_6^0|^2$ (circles), but the scale may be defined by its maximum value (0.28) of $|\Psi_6^0|^2$ in the figure. The squares (ordinate on the left) represent the parity-violating potential (RPA/6-311G(d,p)) along q_6.

We conclude that chirality caused by intermediate-mass isotopes can give rise to relatively large absolute values of the parity-violating energy difference $\Delta_{pv}E$. For **1**–**5**, which are chiral due to deuteration, the vibrational averaging is important for $\Delta_{pv}E$. The absolute value of the vibrationally averaged parity-violating ground state energy difference for **4**–**5** is more than two orders of magnitude larger than $\Delta_{pv}^{e}E$ at the equilibrium structure. For **6**–**10** $\Delta_{pv}^{e}E$ and $\Delta_{pv}E$ differ by less than 15%, and their absolute values are only about an order of magnitude smaller than those obtained for "ordinary" chiral molecules with similar elemental composition. These results suggest that compounds that are chiral by isotopic substitution are well-suited candidates for theoretical and experimental work on molecular parity violation. Whereas detection of parity-violating effects in the frequency domain[24] may not be feasible for a compound such as $P^{35}Cl^{37}ClF$, the time $t = h/(2\Delta_{pv}E)$ for a transition between parity eigenstates induced by the parity-violating energy difference $\Delta_{pv}E$ would correspond to about 600 s with an

initial time-dependent signal for the change of parity being perhaps realistic on a millisecond timescale (see ref. [8] for such experiments and ref. [25] for a preliminary conference account of spectroscopic work in relation to parity violation in isotopically chiral $P^{35}Cl^{37}ClF$).

Received: September 23, 2004
Revised: December 8, 2004
Published online: May 6, 2005

Keywords: ab initio calculations · chirality · electroweak quantum chemistry · isotope effects · parity violation

[1] F. Fernández-Alonso, B. D. Bean, J. D. Ayers, A. E. Pomerantz, R. N. Zare, L. Bañares, J. Aoiz, *Angew. Chem.* **2000**, *112*, 2860 – 2864; *Angew. Chem. Int. Ed.* **2000**, *39*, 2748 – 2752.
[2] B. D. Bean, F. Fernández-Alonso, R. N. Zare, *J. Phys. Chem. A* **2001**, *105*, 2228 – 2233; J. D. Ayers, A. E. Pommerantz, F. Fernández-Alonso, F. Ausfelder, B. D. Bean, R. N. Zare, *J. Chem. Phys.* **2003**, *119*, 4662 – 4670.
[3] M. Quack, *Angew. Chem.* **1989**, *101*, 588 – 604; *Angew. Chem. Int. Ed. Engl.* **1989**, *28*, 571 – 586.
[4] M. Quack, *Nova Acta Leopold.* **1999**, *81*, 137 – 173.
[5] M. Quack, *Angew. Chem.* **2002**, *114*, 4812 – 4825; *Angew. Chem. Int. Ed.* **2002**, *41*, 4618 – 4630.
[6] R. R. Ernst, *Angew. Chem.* **1992**, *104*, 817 – 835; *Angew. Chem. Int. Ed. Engl.* **1992**, *31*, 805 – 823.
[7] M. Quack, *Mol. Phys.* **1977**, *34*, 477 – 504.
[8] M. Quack, *Chem. Phys. Lett.* **1986**, *132*, 147 – 153.
[9] A. Bakasov, T. K. Ha, M. Quack in *Proc. of the 4th Trieste Conference (1995), Chemical Evolution: Physics of the Origin and Evolution of Life* (Eds.: J. Chela-Flores, F. Raulin), Kluwer, Dordrecht, **1996**, pp. 287 – 296.
[10] A. Bakasov, T. K. Ha, M. Quack, *J. Chem. Phys.* **1998**, *109*, 7263 – 7285; Erratum: A. Bakasov, T. K. Ha, M. Quack, *J. Chem. Phys.* **1999**, *110*, 6081.
[11] R. Berger, M. Quack, *J. Chem. Phys.* **2000**, *112*, 3148 – 3158.
[12] R. Berger in *Relativistic Electronic Structure Theory, Part II—Applications* (Ed.: P. Schwerdtfeger), Elsevier, Dordrecht, **2004**, pp. 188 – 288.
[13] G. Laubender, R. Berger, *ChemPhysChem* **2003**, *4*, 395 – 399.
[14] R. A. Hegstrom, D. W. Rein, P. G. H. Sandars, *J. Chem. Phys.* **1980**, *73*, 2329 – 2341.
[15] S. F. Mason, G. E. Tranter, *Mol. Phys.* **1984**, *53*, 1091 – 1111.
[16] L. Hoddeson, L. Brown, M. Riordan, M. Dresden, *The Rise of the Standard Model*, Cambridge University Press, Cambridge, **1997**.
[17] M. Quack, J. Stohner, *Phys. Rev. Lett.* **2000**, *84*, 3807 – 3810. M. Quack, J. Stohner, *Z. Phys. Chem. (Oldenbourg)* **2000**, *214*, 675 – 703; M. Quack, J. Stohner, *J. Chem. Phys.* **2003**, *119*, 11228 – 11240; M. Quack, J. Stohner, *Chirality* **2001**, *13*, 745 – 753.
[18] J. Lüthy, J. Retey, D. Arigoni, *Nature* **1969**, *221*, 1213 – 1215.
[19] R. Harris, L. Stodolsky, *Phys. Lett. B* **1978**, *78*, 313 – 317.
[20] R. Berger, M. Quack, A. Sieben, M. Willeke, *Helv. Chim. Acta* **2003**, *86*, 4048 – 4060.
[21] R. Marquardt, M. Quack, *J. Phys. Chem. A* **2004**, *108*, 3166 – 3181.
[22] S. Creve, M. T. Nguyen, *J. Phys. Chem. A* **1989**, *102*, 6549 – 6557.
[23] R. Berger, M. Gottselig, M. Quack, M. Willeke, *Angew. Chem.* **2001**, *113*, 4342 – 4345; *Angew. Chem. Int. Ed.* **2001**, *40*, 4195 – 4198.
[24] C. Daussy, T. Marrel, A. Amy-Klein, C. T. Nguyen, C. Bordé, C. Chardonnet, *Phys. Rev. Lett.* **1999**, *83*, 1554 – 1557.
[25] A. Sieben, R. Berger, M. Quack, M. Willeke in *18th Colloquium on High Resolution Spectroscopy (2003)*, Dijon, France, **2003**, p. 161.
[26] Gaussian 98 (Revision A.11.1), M. J. Frisch, G. W. Trucks, H. B. Schlegel, G. E. Scuseria, M. A. Robb, J. Cheeseman, R. V. G. Zakrzewski, J. A. Montgomery, Jr., R. E. Stratmann, J. C. Burant, S. Dapprich, J. M. Millam, A. D. Daniels, K. N. Kudin, M. C. Strain, O. Farkas, J. Tomasi, V. Barone, M. Cossi, R. Cammi, B. Mennucci, C. Pomelli, C. Adamo, S. Clifford, J. Ochterski, G. A. Petersson, P. Y. Ayala, Q. Cui, K. Morokuma, P. Salvador, J. J. Dannenberg, D. K. Malick, A. D. Rabuck, K. Raghavachari, J. B. Foresman, J. Cioslowski, J. V. Ortiz, A. G. Baboul, B. B. Stefanov, G. Liu, A. Liashenko, P. Piskorz, I. Komaromi, R. Gomperts, R. L. Martin, D. J. Fox, T. Keith, M. A. Al-Laham, C. Y. Peng, A. Nanayakkara, M. Challacombe, P. M. W. Gill, B. Johnson, W. Chen, M. W. Wong, J. L. Andres, C. Gonzalez, M. Head-Gordon, E. S. Replogle, J. A. Pople, Gaussian, Inc., Pittsburgh, PA, **1998**.
[27] T. Helgaker, H. Jensen, J. P. Jørgensen, J. Olsen, K. Ruud, H. Ågren, T. Andersen, K. L. Bak, V. Bakken, O. Christiansen, P. Dahle, E. K. Dalskov, T. Enevoldsen, B. Fernandez, H. Heiberg, H. Hettema, D. Jonsson, S. Kirpekar, R. Kobayashi, H. Koch, K. V. Mikkelsen, P. Norman, M. J. Packer, T. Saue, P. R. Taylor, O. Vahtras, *Dalton: An Electronic Structure Program*, Release 1.2.1 ed., **1997**.

Cover Picture

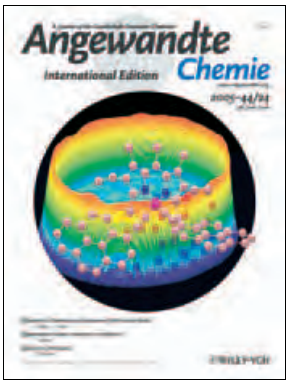

Gilles Ulrich,* Christine Goze, Massimo Guardigli, Aldo Roda, and Raymond Ziessel*

An energy-cascade device is created by linking ethynylpyrene fragments to boron centers. The cover picture shows such a Bodipyrene dye in which irradiation of the pyrene moiety gives a virtual Stokes shift of 10000 cm^{-1}. The background shows a 3D plot of a fluorescence well containing femtomolar amounts of labeled biomaterial. In their Communication on page 3694 ff., G. Ulrich, R. Ziessel, and co-workers describe how biomolecules can be labeled with these dyes, which are very promising for fluorescence imaging.

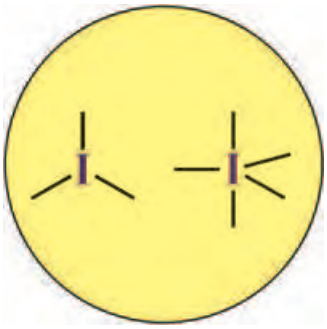

Hypervalent Iodine Compounds
In his Minireview on page 3656 ff., T. Wirth describes recent advances and trends in hypervalent iodine chemistry. The stability and versatility of these compounds has opened the route to new applications in organic synthesis.

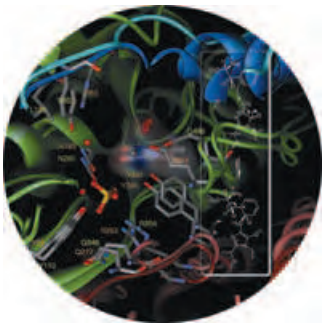

Enzyme Mechanisms
Lyases catalyze the removal of the nonacidic β protons of histidine and phenylalanine with the release of ammonia. In their Review on page 3668 ff., J. Rétey and L. Poppe summarize the latest findings that have led to revision of the long-accepted reaction mechanism.

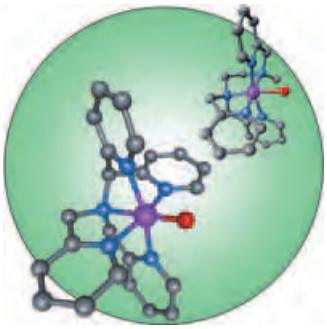

Oxoiron(IV) Complexes
Structural insight obtained through a combination of X-ray crystallography, NMR spectroscopy, and DFT calculations of novel oxoiron(IV) complexes with pentadentate aza ligands is discussed by L. Que, Jr., C. J. Cramer, and co-workers in their Communication on page 3690 ff.

Contents

VIP ***The following Communications have been judged by at least two referees to be "very important papers" and will be published online at www.angewandte.org soon:***

Web Sites

Books

Highlights

Supramolecular Chemistry

Welcome to the superbowl! The coupling of five resorcinarene-based compounds affords the covalent bowl-shaped analogues of hydrogen-bonded hexameric capsular assemblies (see picture). Such molecules offer stability, solubility, and functionality beyond those of their non-covalent cousins, and provide interesting insight into intracavity reactions, molecular transport, and complexation processes.

Minireviews

I^{III} and I^{V} Reagents

New reagents and reactions show the potential of hypervalent iodine compounds in organic synthesis: The understanding of the structures and reactivities of iodine(III) and iodine(V) compounds forms the basis for novel synthetic strategies and their application in the synthesis of complex natural products.

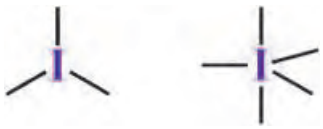

Reviews

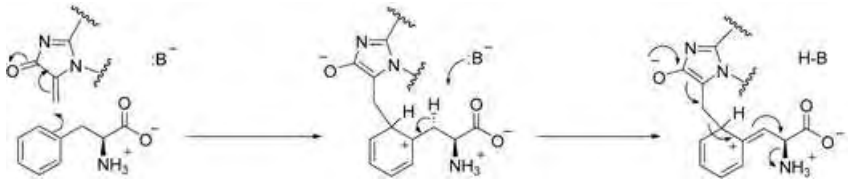

In the enzymatic superelectrophile 5-methylene-3,4-dihydroimidazol-4-one (MIO), delocalization of the lone pair of electrons on the nitrogen atom into the Michael system is prohibited for stereoelectronic reasons, and nucleophilic attack at the exocyclic double bond makes the ring aromatic. The MIO group in histidine and phenylalanine ammonia-lyases activates a β hydrogen atom of the corresponding amino acid and facilitates the elimination of ammonia (see scheme).

Enzyme Mechanisms

Communications

Stabilizing the oxoiron(IV) unit: From a combination of X-ray crystallography, NMR spectroscopy, and DFT calculations, the relative thermal stabilities of two oxoiron(IV) complexes with pentaaza ligands, such as that shown in the picture, can be ascribed to the number of pyridine rings that are oriented parallel to the Fe=O bond. (Fe pink, N blue, O red, C black.)

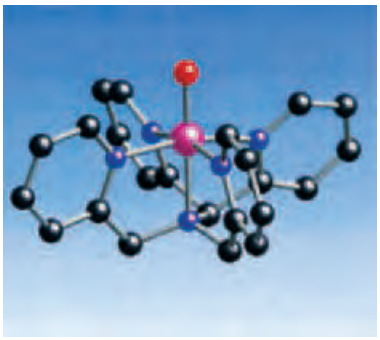

Oxoiron(IV) Complexes

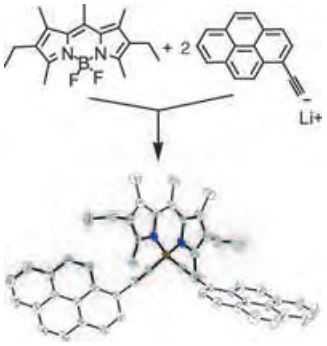

All aglow: A new class of highly luminescent dyes is built by the attachment of a pyrene fragment to the boron center of a boradiazaindacene moiety through an ethynyl unit (see scheme). Very efficient energy transfer from the pyrene to the indacene center produces virtual large Stokes shifts, which are maintained, along with strong luminescence ($\Phi = 32$–$45\,\%$) when the dyes are attached to proteins such as bovine serum albumin.

Fluorescence Imaging

For the USA and Canada:
ANGEWANDTE CHEMIE International Edition (ISSN 1433-7851) is published weekly by Wiley-VCH PO Box 191161, D 69451 Weinheim, Germany. Air freight and mailing in the USA by Publications Expediting Inc. 200 Meacham Ave., Elmont, NY 11003. Periodicals postage paid at Jamaica NY 11431. US POSTMASTER: send address changes to *Angewandte Chemie*, Wiley-VCH, 111 River Street, Hoboken, NJ 07030. Annual subscription price for institutions: US$ 4948.00/4498.00 (valid for print and electronic / print or electronic delivery); for individuals who are personal members of a national chemical society, or whose institution already subscribes, or who are retired or self-employed consultants, print only: US$ 394.00. Postage and handling charges included. All Wiley-VCH prices are exclusive VAT.

The best in chemistry –

for more than a hundred years

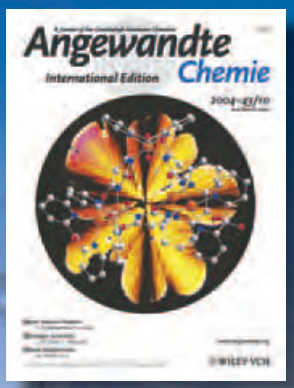

A Journal of the Gesellschaft Deutscher Chemiker

Angewandte International Edition **Chemie**

www.angewandte.org

1888: ***The beginning of a success story***

Constant Innovations

- **1962:** *First issue of the International Edition*
- **1976:** *Graphical abstracts*
- **1979:** *Cover pictures*
- **1988:** *Centenary of Angewandte*
- **1989:** *Routine use of color*
- **1991:** *New section: Highlights*
- **1992:** *Computerized editorial tracking system*
- **1995:** *Internet service for readers*
- **1998:** *Regular press service; full-text online*
- **2000:** *New section: Essays; EarlyView: Communications available online ahead of the printed version*
- **2001:** *New section: Minireviews*
- **2002:** *Online submission of manuscripts*
- **2003:** *Weekly publication; new section: News; new layout*
- **2004:** *Backfiles (1962-1997); ManuscriptXpress: Online system for authors and referees*

Angewandte's advisors...

Frans C. De Schryver
Katholieke Universiteit Leuven

*» Over the years **Angewandte Chemie** has been a beacon for sound, exciting, and novel chemistry and has built its well-deserved reputation on nonsubjective, thorough, but constructive refereeing and a highly professional layout. I am sure that the new initiatives will further strengthen its leadership with the help of scientists and the outstanding staff. «*

Angewandte Chemie International Edition *is a journal of the German Chemical Society (GDCh)*

GDCh

WILEY InterScience® DISCOVER SOMETHING GREAT

WILEY-VCH

16131412_gu

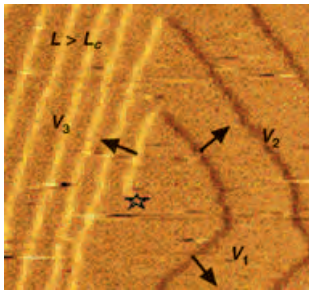

The critical length and density of the steps, rather than step morphology and velocity of deposition, are useful for understanding the effectiveness of the additive molecules in modifying the crystallization kinetics in biomineralization. This biological control stems from a change in solid–solution interfacial energies, which delays the formation of active steps on the growing crystal face (see picture).

Crystal Growth

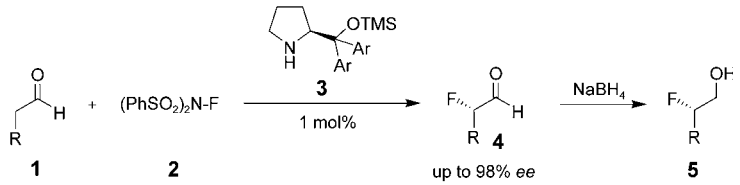

An easy protocol has been developed for the formation of stereogenic carbon–fluorine centers by the organocatalytic asymmetric α-fluorination of aldehydes **1**. The 2-fluoroaldehydes **4** are formed with **2** as the fluorinating agent and only 1 mol% of a sterically demanding silylated prolinol **3** as catalyst. The 2-fluoroaldehydes are subsequently reduced to the corresponding alcohols **5** without loss of enantiomeric excess.

Enantioselective Fluorination

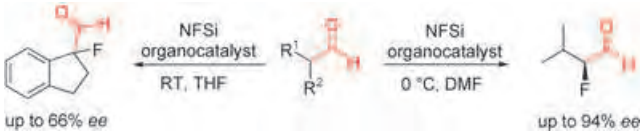

Linear and branched aldehydes are asymmetrically α-fluorinated with L-proline- and pyrrolidine-based organocatalysts (see scheme; NFSi: *N*-fluorobenzenesulfonamide). In the first case, yields and enantioselectivities were high; in the second, the yields remained high and the enantioselectivities were moderate. Significantly, linear aldehydes were only monofluorinated.

Enantioselective Fluorination

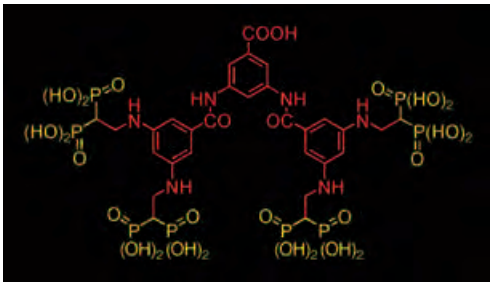

Close to the bone: A dendritic molecule that contains four bone-seeking bisphosphonic acid groups (see picture) has been prepared for targeting proteins to bone tissue. The tetra(bisphosphonic acid) molecule provides a high density of bisphosphonic acid groups per attachment site at the protein and will aid the design of bone-seeking proteins with minimal modification.

Bioorganic Chemistry

Contents

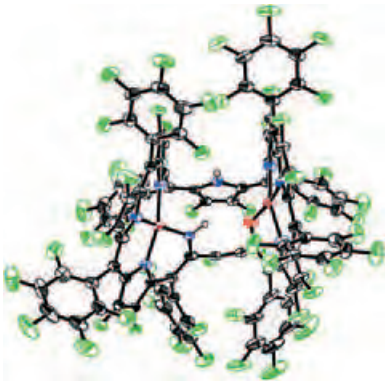

Metallooctaphyrin complexes: Dimetalation of perfluorinated [36]octaphyrin with copper(II) results in the hydrolytic ring opening of one of the pyrrole rings (see structure), whereas with silver ions perfluorinated [36]octaphyrin and *meso*-pentafluorophenyl-substituted [36]octaphyrin gave disilver(I) complexes of [34]octaphyrin.

Metalloporphyrinoids

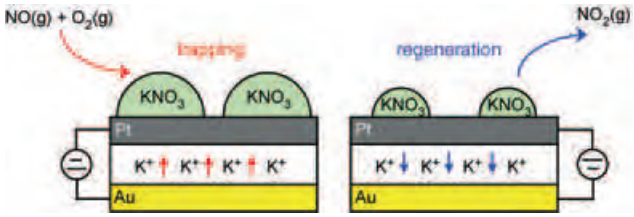

Fort NOx: The principle of an NO_x trap based on the use of solid alkali-metal-ion conductors is demonstrated. The trap efficiently stores NO_x and subsequently releases mainly NO_2 under isothermal conditions (see scheme); this is relevant to the abatement of nitrogen oxides in the exhaust gases of fuel-efficient automotive engines.

Chemical Traps

An unprecedented skeletal reorganization initially hindered a concise route based on a tandem [4+2]/[3+2] nitroalkene cycloaddition for the synthesis of the strained title compound. Conditions to suppress the observed dyotropic rearrangement were developed, and X-ray crystallographic analysis of the BF_3 derivative (see picture) of the azafenestrane revealed significant planarization around the central carbon atom.

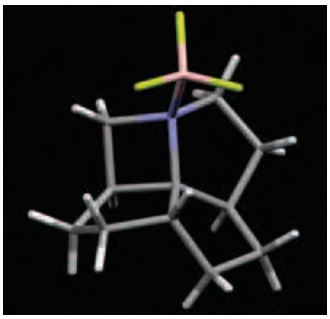

Strained Polycycles

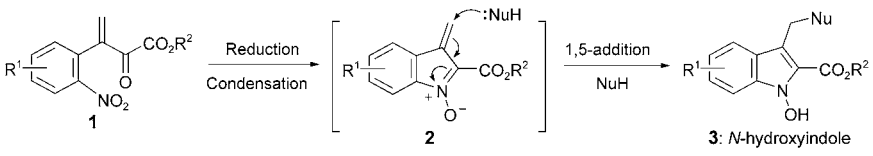

Generation (1→2) and trapping (2→3) of the fleeting α,β-unsaturated nitrone system **2** leads to the rare, biologically important *N*-hydroxyindole **3** in synthetically useful yields. This structural motif is found within the molecule of the antibiotic nocathiacin I.

Indole Synthesis

Contents

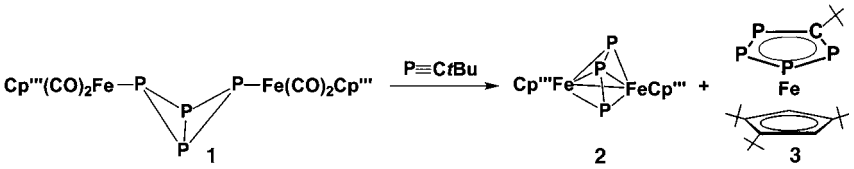

Different faces of phosphorus chemistry: The reaction of the bicyclotetraphosphine complex **1** with *t*BuC≡P leads to the first 1,2,3,4-tetraphosphaferrocene complex **2** and an allylic P_3-bridged complex **3**. $Cp''' = \eta^5\text{-}C_5H_2tBu_3$.

Polyphosphorus Ligands

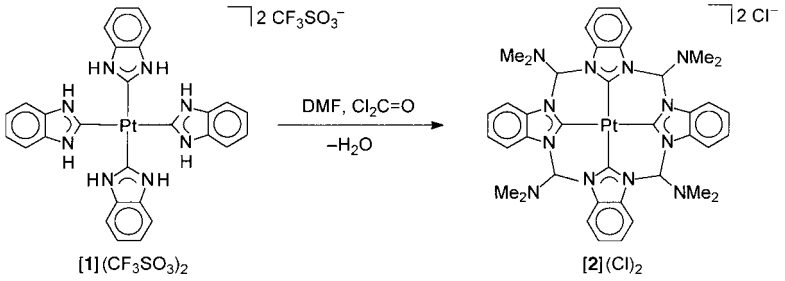

A template-controlled reaction cascade starting from $[Pt(PMe_3)_4](CF_3SO_3)_2$ and 2-azidophenyl isocyanide yields the tetracarbene complex $[\mathbf{1}](CF_3SO_3)_2$. The four NH,NH-stabilized carbene ligands in $[\mathbf{1}]^{2+}$ can be bridged at the metal template by reaction with *N*,*N*-dimethylformamide (DMF) and diphosgene to give the coordinated cyclic tetracarbene ligand with crown ether topology in complex $[\mathbf{2}](Cl)_2$.

Carbene Complexes

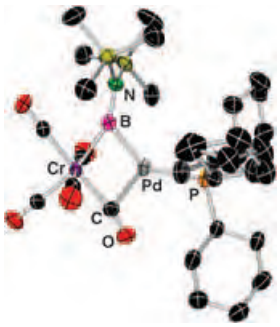

The heat is on: In the first instance of thermal reactivity of the terminal borylenes $[(OC)_5M{=}B{=}N(SiMe_3)_2]$ (M = Cr, W), the new heterodinuclear complexes $[(OC)_4M(\mu\text{-}CO)\{\mu\text{-}BN(SiMe_3)_2\}Pd(PCy_3)]$ (see structure; M = Cr) are synthesized. The compounds feature a semibridging borylene ligand and, by virtue of the dative Pd—B bonding interaction, represent the only examples of terminal borylene species stabilized by a transition-metal base.

Borylene Complexes

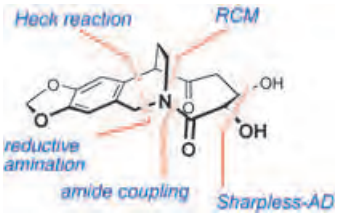

The unusual [5.3.2]bicyclic structure of the insecticidal *Amaryllidaceae* alkaloids cripowellins A and B has been synthesized for the first time by a sequence of Sharpless dihydroxylation, ring-closing metathesis (RCM), and intramolecular Heck reaction (see scheme). The asymmetric synthesis of the 1-*epi* aglycon proceeds with virtually complete diastereo- and enantioselectivity (≥ 98 % *de*, ≥ 98 % *ee*) in 13 steps and an overall yield of 5.6 %.

Natural Product Synthesis

Contents

Service

Supramolecular Chemistry

Very Large Container Molecules

*Kari Rissanen**

Keywords:
calixarenes · cavitands · host–guest chemistry · resorcinarenes

Vase- or bowl-shaped molecules, which are synthetically challenging targets as well as objects with aesthetic structural symmetry, attract the attention of both synthetic and structural chemists alike. Many vase- or bowl-shaped molecules have been reported, but it was not until the discovery and utilization of calixarenes and resorcinarenes that these molecular objects were recognized as intriguing synthetic targets or structurally elegant compounds. With the birth of calixarene (derived from the Latin word *calix* for vase) and resorcinarene chemistry these vase-shaped molecules were brought to the front row in modern chemistry. Seminal work by Gutsche[1] on calixarenes and by Cram[2] on cyclophanes and resorcinares (Figure 1) gave new insight into functional vase- and bowl-shaped molecules which, in turn, was one of the seeds to the birth of supramolecular chemistry and chemistry "beyond the molecule".[3]

Calixarenes, with their four phenolic OH groups, are the more flexible of the two families of compounds, yet they remain easy to functionalize on either the upper or lower rim, or on both.[1] The octaphenolic resorcinares allow intramolecular rigidification by attachment of a bridge, typically through bis-*O*-alkylation, between adjacent aromatic rings to give rigid bowl-shaped cavitands.[2] When properly functionalized, the rigid cavitand is a unique structural building block on the way to larger dimeric capsulelike molecules, namely carcerends.[2] The synthesis of carcerands requires a suitable guest molecule that remains incarcerated inside the dimeric covalent molecule. By suitable modulation of the synthesis sequence, one or two of the cavitand-connecting bridges can be omitted to lead to hemicarcerands from which the incarcerated guest can be released. The resorcinarene-based cavitands, carcerands, and hemicarcerands have a very limited bowl size which is dictated by the size and conformation of the inner 16-membered cyclophane ring.

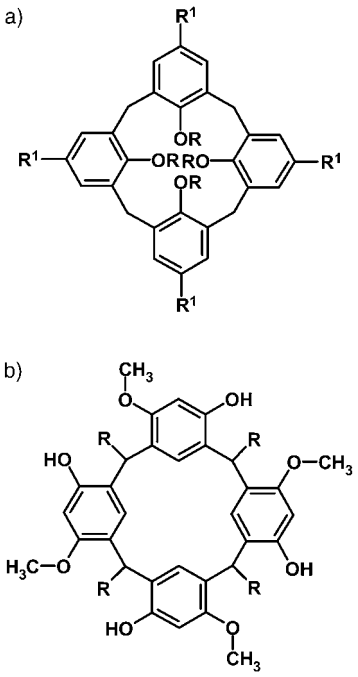

Figure 1. The structures of a) calixarene and b) resorcinarene.

In the latter half of the 1990s, two different approaches to increase the volume of the bowl or container were developed. As the extension of the carcerend "wall" was not synthetically rewarding, Harrison[4] and Dalcanale[5] and their respective co-workers used self-organization and metal coordination to bridge two cavitand halves into dimeric capsular structures to form so-called coordination cages. This approach resulted in much larger container molecules constructed from two cavitand halves. The second approach, which was synthetically more simplistic, was reported by MacGillivray and Atwood in 1997 with the crystal structure of a very large self-assembling hydrogen-bonded hexameric assembly (Figure 2a) that consisted of six core resorcinarene units and eight water molecules.[6] The pyrogallarene analogue of the hexameric assembly, prepared from pyrogallol (1,2,3-trihydroxybenzene) instead of resorcinol (1,3-dihydroxybenzene), was later reported by Mattay and co-workers.[7]

These extraordinary noncovalent spherical assemblies have volumes of about 1400 Å^3, which is truly a very large intracavity volume. Their noncovalent synthesis, which utilizes self-assembly, offers unsurpassed ease of preparation. However, what is gained in the synthesis is lost in the stability of the assembly. As the assembly is typically constructed from multiple weak hydrogen-bonding interactions, its stability is often very weak in competing hydrogen-bonding solvents (e.g. water, dimethylsulfoxide, *N*,*N*-dimethylformamide) while its solubility in organic solvents is often limited. These features prevent the use of these assemblies in further applications, however, their relative insolubility in organic media often enhances recrystallization of the assemblies and makes possible the determination of their crystal structures. The formation, guest-exchange properties, and stabilities of these large self-assembling hydro-

[*] Prof. Dr. K. Rissanen
Nanoscience Center
Department of Chemistry
University of Jyväskylä
40014 Jyväskylä (Finland)
Fax: (+358) 14-260-2652
E-mail: kari.rissanen@jyu.fi

  DOI: 10.1002/anie.200500714

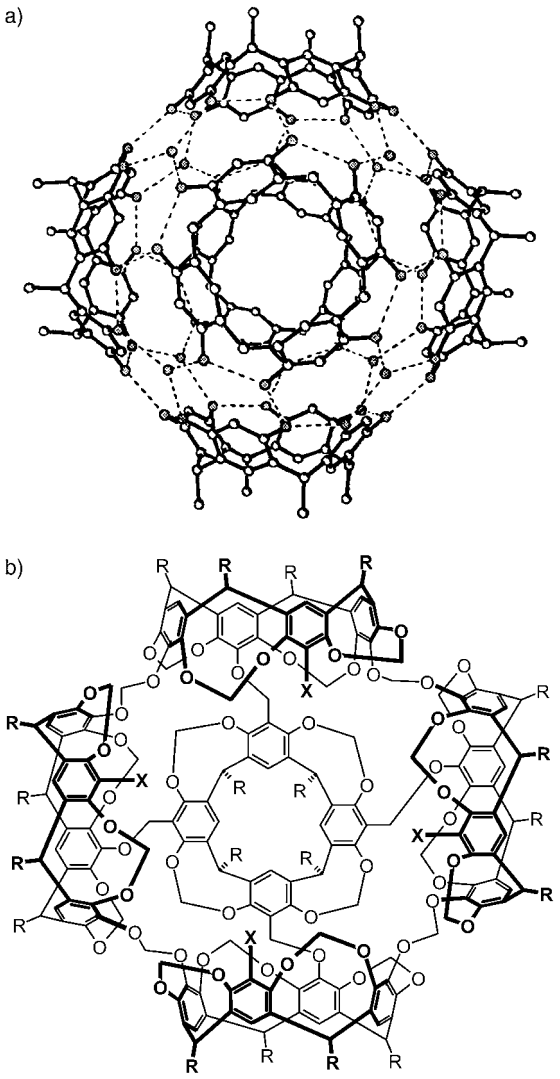

Figure 2. a) The hexameric hydrogen-bonded resorcinarene assembly by MacGillivray and Atwood[6] (oxygen atoms are shaded), and b) the covalent resorcinarene pentamer by Sherburn and co-workers[12] (R = pentyl, X = H, Br).

gen-bonded dimeric, tetrameric, and hexameric assemblies have been studied and reported extensively by the groups of Rebek,[8] Atwood,[9] Cohen,[10] and Kaifer.[11]

Covalent cousins of the very large hydrogen-bonded capsular assemblies described above were recently reported by Sherburn and co-workers,[12] and, indeed, their studies on "superbowls" have opened a new chapter on very large container molecules. They used a multistep regioselective protection/deprotection strategy to combine five resorcinare molecules into one very large covalent container molecule: a superbowl. One unique resorcinare acts as the platform on which four other equivalent resorcinares are covalently attached as "walls" (Figure 2).

Their work started with a retrosynthetic analysis of the target pentaresorcinarene molecule. A multitude of covalent connections between the five components were required, and careful inspection of the various target molecule models led Sherburn and co-workers to employ classical carcerand linkers, $-OCH_2O-$, between the walls and $-CH_2O-$ linkers between the platform and the walls. This combination allowed the necessary flexibility to form the interbowl bonds, while preventing holes in the superbowl structure that were large enough for the entry and exit of all but the smallest of guest molecules.

The multistep synthetic route[12] to the pentaresorcinarene started from an *n*-pentyl-footed tetrabromocavitand, which upon chemo- and regioselective double lithium–bromine exchange with *n*BuLi gave the A,C-dibromodiol. Protection of the dibromodiol as the bis-methoxymethyl (MOM) ether $(MOM)_2$-A,C-$(Br)_2$, followed by selective single lithium–bromine exchange, boronate ester formation, and oxidative hydrolysis gave the required unsymmetrically functionalized diprotected bromoalcohol cavitand $(MOM)_2$-(Br)-(OH), which yielded the corresponding bis-methoxymethyl phenol $(MOM)_2$-(H)-(OH) upon reductive debromination. Combination of four molar equivalents of the $(MOM)_2$-(Br)-(OH) cavitand (or its debrominated analogue $(MOM)_2$-(H)-(OH)) with a tetrabromomethyl cavitand, which acts as the platform of the pentaresorcinarene, resulted in the multiply MOM-protected tetrabromopentamer (or its debrominated analogue, respectively). Subsequent hydrolysis of the eight MOM ether groups of the pentamers led to the respective octaol. The final "wall-closure" step was performed by using a standard resorcinarene-to-cavitand method.[12]

The X-ray crystal structure of Sherburn's covalent tetrabrominated pentamer[12] is strikingly similar to that of MacGillivray and Atwood's hydrogen-bonded hexamer[6] (Figure 3). However, this is not surprising as both structures comprise resorcinarenes with similar spatial orientations.

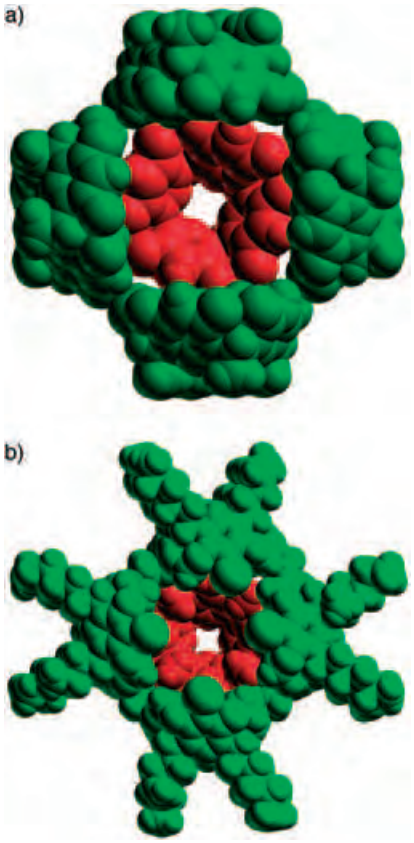

Figure 3. X-ray crystal structures of a) the hydrogen-bonded hexameric assembly[6] with one of the resorcinarene units removed, and b) the covalent tetrabrominated pentamer.[12] (Solvent molecules are omitted from both structures; green wall, red platform).

The hexamer described by MacGillivray and Atwood has a slightly larger intracavity volume (ca. 1375 Å^3) relative to that of the covalent pentamer (ca. 1050 Å^3). If we take into account the different constitutions of the structures, that is, a hexamer versus a pentamer, the intracavity volumes are essentially the same (1375 Å^3/6 = 229 Å^3 per monomer; 1050 Å^3/5 = 210 Å^3 per mono-

mer). The X-ray crystal structure of the pentamer with the bromine substituents shows a slightly unsymmetrical cavity aperture of approximately 10 Å, whereas in the hydrogenated analogue the aperture is slightly bigger. The hydrogenated analogue binds tetra-*n*-hexylammonium ions with a complexation constant of approximately $460\,\text{M}^{-1}$ for the 1:1 host–guest association, but under similar conditions the brominated pentamer did not show any binding of tetraalkylammonium ions. Thus the size of the cavity aperture, as well as the presence of large bromine substituents on the rim, appear to be crucial for the association process.

Despite its weak complexation ability, the covalent resorcinare pentamer provides an entry to very large container molecules. The covalent approach developed by Sherburn and co-workers offers molecules that display considerably greater stability, structural variation, functional group tolerance, and solubility in organic solvents. This example of how to construct very large covalent container molecules can and will lead to more robust nanosized objects for intracavity reactions (however, product inhibition has to be solved first), catalysis, and transport. In particular, encapsulation of drugs and their delivery is a stimulating possibility: On the basis of this seminal work by Sherburn and co-workers[12] it is easy to visualize very large covalent but hydrolyzable container molecules that can be decomposed under specific conditions to release the drug into a specific target organ or cell. Also a nonhydrolyzable covalent pentamer with a removable cap (attached to the pentamer through a combination of hydrogen bonds and one covalent bond, or with hydrolyzable bonds) offers intriguing possibilities for the controlled release of the guest. These features are not offered by solely hydrogen-bonded systems.

Published online: May 11, 2005

[1] C. D. Gutsche, *Calixarenes Revisited*, Royal Society of Chemistry, Hertfordshire, **1998**.

[2] D. J. Cram, J. M. Cram, *Container Molecules and Their Guests*, Royal Society of Chemistry, Hertfordshire, **1997**.

[3] a) F. Vögtle, *Supramolecular Chemistry*, Wiley, Chichester, **1991**; b) J.-M. Lehn, *Supramolecular Chemistry*, VCH, Weinheim, **1995**; c) J. W. Steed, J. L. Atwood, *Supramolecular Chemistry*, Wiley, Chichester, **2000**.

[4] O. D. Fox, N. K. Dalley, R. G. Harrison, *J. Am. Chem. Soc.* **1998**, *120*, 7111.

[5] a) P. Jacopozzi, E. Dalcanale, *Angew. Chem.* **1997**, *109*, 665; *Angew. Chem. Int. Ed. Engl.* **1997**, *36*, 613; b) R. Pinalli, V. Cristini, V. Sottili, S. Geremia, M. Campagnolo, A. Caneschi, E. Dalcanale, *J. Am. Chem. Soc.* **2004**, *126*, 6516.

[6] L. R. MacGillivray, J. L. Atwood, *Nature* **1997**, *389*, 469.

[7] T. Gerkensmeier, W. Iwanek, C. Agena, R. Fröhlich, S. Kotila, C. Näther, J. Mattay, *Eur. J. Org. Chem.* **1999**, 2257.

[8] a) A. Shivanyuk, J. Rebek, *Chem. Commun.* **2001**, 2424; b) A. Shivanyuk, J. Rebek, *Proc. Natl. Acad. Sci. USA* **2001**, *98*, 7662; c) A. Shivanyuk, J. Rebek, *J. Am. Chem. Soc.* **2003**, *125*, 3432; d) M. Yamanaka, A. Shivanyuk, J. Rebek, *J. Am. Chem. Soc.* **2004**, *126*, 2939.

[9] a) J. L. Atwood, L. J. Barbour, A. Jerga, *Chem. Commun.* **2001**, 2376; b) L. R. MacGillivray, K. T. Holman, J. L. Atwood, *J. Supramol. Chem.* **2001**, *1*, 125.

[10] a) L. Avram, Y. Cohen, *Org. Lett.* **2002**, *4*, 4365; b) L. Avram, Y. Cohen, *J. Am. Chem. Soc.* **2002**, *124*, 15148; c) L. Avram, Y. Cohen, *Org. Lett.* **2003**, *5*, 1099; d) L. Avram, Y. Cohen, *Org. Lett.* **2003**, *5*, 3329; L. Avram, Y. Cohen, *J. Am. Chem. Soc.* **2003**, *125*, 16180.

[11] I. E. Philip, A. E. Kaifer, *J. Am. Chem. Soc.* **2002**, *124*, 12678.

[12] E. S. Barrett, J. L. Irwin, A. J. Edwards, M. S. Sherburn, *J. Am. Chem. Soc.* **2004**, *126*, 16747.

I^{III} and I^{V} Reagents

Hypervalent Iodine Chemistry in Synthesis: Scope and New Directions

*Thomas Wirth**

Keywords:
hypervalent compounds · iodine · oxidations · rearrangements · total synthesis

The impressive development of hypervalent iodine chemistry in recent years is reflected by the number of publications in this area. Although the synthesis of the first hypervalent iodine compound dates back more than 100 years, the investigation of the reactivities of these compounds and their efficient use as metal-free reagents in organic synthesis is still ongoing. This contribution summarizes recent achievements and highlights key findings and developments that will influence future research and lead to novel applications of hypervalent iodine reagents in synthesis.

1. Introduction

Organic molecules bearing hypervalent iodine moieties have been transformed from laboratory curiosities to useful and routinely employed reagents in organic synthesis. Several reagents in which the oxidation state of the iodine atom is not −1 are now routinely accessible and, not surprisingly, several aspects of their chemistry have been reviewed recently.[1] It is therefore not the purpose of this article to summarize all efforts in this area comprehensively; instead, a rather select number of important developments during the last couple of years are emphasized, and their significance for synthetic chemistry is highlighted.

2. Oxidations

The facile oxidation of alcohols to the corresponding carbonyl compounds is one of the prominent features of hypervalent iodine compounds appreciated by many synthetic chemists.[2] Iodine(v) compounds such as the Dess–Martin periodinane (DMP; **1**) and *ortho*-iodoxybenzoic acid (IBX; **2**) are known to be explosive reagents, but the simple one-step oxidation of 2-iodobenzoic acid to IBX with oxone[3] has made it a quite popular reagent,[4] despite its low solubility in most organic solvents. Reactions must usually be carried out in DMSO at slightly elevated temperatures. IBX (**2**) can be used in DMSO at room temperature to synthesize α-aminoaldehydes from the corresponding amino-alcohols without racemization,[5] but a survey of other solvents and reaction conditions looks promising.[6] The perceived disadvantage of **2** being an almost insoluble reagent in ethyl acetate or dichloromethane is turned into an advantage as the reagent and by-products can be completely removed simply by filtration.

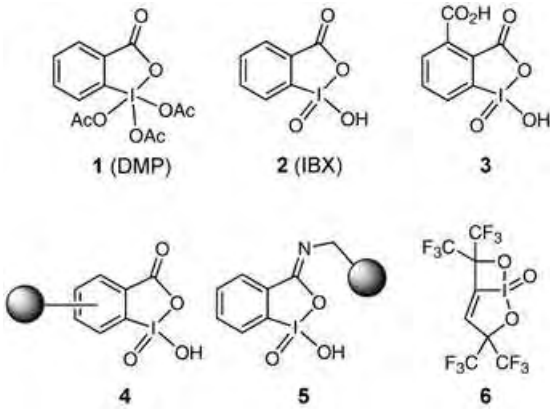

The use of IBX (**2**) in ethyl acetate led to a high-yielding procedure for the oxidation of 1,2-dihydronaphthols to the corresponding naphthols.[7] But other protocols and reagents have also been developed to overcome some initial preparative limitations. More-soluble derivatives such as **3**[8] and completely insoluble polymer-bound IBX reagents **4**[9] have been prepared. Whereas first attempts focused on the syn-

[*] Prof. Dr. T. Wirth
Cardiff School of Chemistry
Cardiff University
Park Place, Main Building, Cardiff, CF10 3AT (UK)
Fax: (+44) 29-2087-6968
E-mail: wirth@cf.ac.uk

  DOI: 10.1002/anie.200500115

thesis of reagents **4** with a polymer linkage to the aromatic core of the IBX reagent, recent developments exploit the oxidative properties of the IBX amides **5** introduced by Zhdankin and co-workers.[10,11] The synthesis of polymer-bound IBX amides **5** is much shorter and can lead to reagents with similar efficiency.[12]

The replacement of DMSO as the common solvent for oxidations with IBX (**2**) with ionic liquids such as $[bmim]^+X^-$ (bmim = 1-butyl-3-methylimidazolium; $X^- = Cl^-$, Br^-, PF_6^-)[13] have dramatically improved the applicability of this reagent. Although the soluble derivative **3** and polymer-bound reagents **4** and **5** seem to be limited to the oxidation of alcohols to their carbonyl counterparts, the replacement of DMSO with an ionic liquid was found to allow the introduction of an α,β-unsaturation in carbonyl compounds, as initially reported by Nicolaou.[14] Although the synthesis of the tetracoordinate 1,2-iodoxetane-1-oxide **6** is quite elaborate, the compound has been successfully used as an oxidant for alcohols.[15] This recent example elegantly demonstrates that even hypervalent iodine compounds with aliphatic substituents can be prepared and that further developments along these lines can be expected. The dehydrogenation of carbonyl compounds can also be efficiently used for the synthesis of quinones, and even the IBX-mediated aromatization of polycyclic compounds **7** to form **8** proceeds in good yields (Scheme 1).[16]

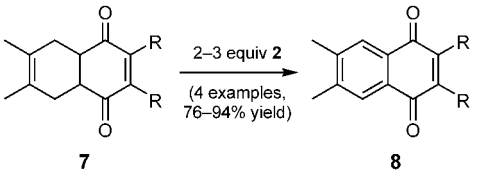

Scheme 1. Aromatization of polycyclic compounds.

The area of carbon–heteroatom bond oxidation is still dominated by the iodine(v) reagents mentioned above, but iodine(III) reagents continue to increase in importance as non-explosive and readily available reagents for such oxidations. Several of these reagents can now be synthesized under solvent-free conditions, and even some subsequent transformations have been performed as solid-state reactions with high efficiency.[17] It is difficult to oxidize aliphatic alcohols with reagents such as (diacetoxyiodo)benzene, but catalytic amounts of TEMPO (2,2,6,6-tetramethyl-1-piperidinyloxyl)[18] facilitate such reactions. Depending on the reaction conditions, primary alcohols can be oxidized to the corresponding aldehydes[18] or to carboxylic acids[19] without affecting neighboring stereogenic centers. The racemization-free preparation of epoxyaldehydes or amino acid derivatives was achieved, and this method has already found its way into several natural product syntheses.[20]

Oxidations in the presence of metal complexes are possible:[21] Chiral Mn(salen) complexes with (diacetoxyiodo)benzene as cooxidant have been used for efficient racemic resolutions of secondary alcohols.[22] Several of these reactions use water as the partial or sole solvent, and hence the hydrolysis of (diacetoxyiodo)benzene to iodosylbenzene, which is known to occur under alkaline conditions, cannot be excluded. Kita and co-workers developed conditions to oxidize alcohols in water[23] with iodosylbenzene together with KBr, and exclusive oxidation of alcohols to carboxylic acids was observed.[24] The mild reaction conditions and the broad functional-group tolerance of hypervalent iodine reagents have led to the development of sequential transformations involving an oxidation step. There is no need to isolate and purify potentially unstable intermediates; this is especially useful when stereogenic centers are present in the α position to the newly generated carbonyl group.

Oxidations with iodosylbenzene and KBr in aqueous methanol instead of water leads to the formation of the corresponding methyl esters **9**.[25] In a similar process, IBX-mediated oxidations of alcohols (or aldehydes) were carried out in the presence of *N*-hydroxysuccinimide and the corresponding *N*-hydroxysuccinimide esters **10** were obtained in good yields.[26] The oxidation of propargylic alcohols with IBX (**2**) to the corresponding unstable aldehydes can be performed in the presence of acetamidine, and pyrimidines are obtained directly in a one-pot process.[27] Intramolecular reactions are also possible, for example, oxidative cyclizations to highly functionalized cyclopentanols **11** (Scheme 2).[28]

Hypervalent iodine reagents have also proven to be mild oxidants for phenolic substrates. Spirocyclizations of various compounds have been studied extensively.[29] Domino oxidation/Diels–Alder reactions are also versatile sequences,[30] as

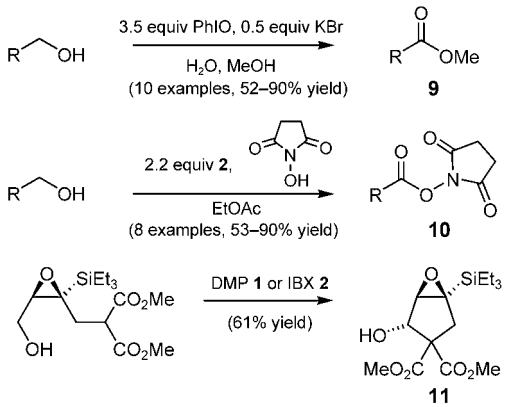

Scheme 2. Oxidations with hypervalent iodine compounds followed by subsequent transformations in the one-pot synthesis of esters or carbocycles.

Thomas Wirth received his Diplom from the University of Bonn in 1989 and his PhD from the Technical University of Berlin (S. Blechert, 1992). After a postdoctoral stay with K. Fuji at Kyoto University as a JSPS fellow 1992/93, he started his independent research on stereoselective oxidation reactions (University of Basel, B. Giese) and obtained his habilitation in 1999. He was a visiting professor at the University of Toronto (1999), Chuo University in Tokyo (2000), and Osaka University (2004). He was awarded the Werner Prize from the New Swiss Chemical Society in 2000.

shown in studies towards the synthesis of tashironin[31] or in oxidations followed by radical cyclization reactions to generate bicyclic compounds.[32]

In all these oxidations stoichiometric amounts of an iodoarene are generated as a by-product. To facilitate the purification of the product and to achieve an easy separation from the iodoarene, polystyrene-bound versions[33] of (diacetoxy)iodobenzene have been prepared and used with similar efficiency in the reactions mentioned above.[24,25,34] The synthesis of fluorous hypervalent iodine compounds such as **12** also allows easy recovery and recycling of the reduced

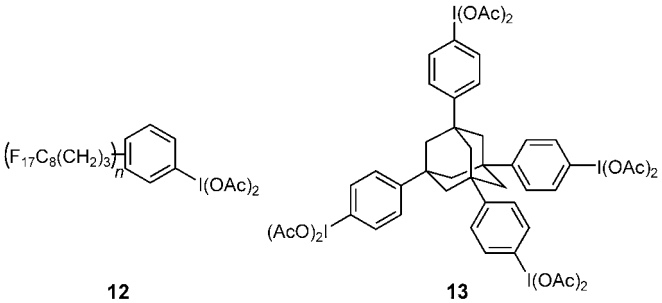

12 **13**

reagent through extraction into a fluorous organic phase.[35] Similar ease of separation was reported in reactions with the adamantane derivative **13**, in which case the reduced compound can be easily recovered and reoxidized.[36]

Analogously to the oxidation of a carbon–oxygen single bond, secondary amines can be oxidized with IBX (**2**). A series of amines **14** were oxidized to the corresponding imines **15** efficiently.[37] Other hypervalent iodine reagents such as the alkylperoxy-λ^3-iodane **16** are also suitable for this transformation.[38] Mechanistic investigations indicate that both **2** and **16** serve as single-electron-transfer reagents in this reaction. Under certain reaction conditions, compounds containing a carbon–nitrogen double bond (e.g. aldoximes **17**) have been oxidized to the corresponding nitrile oxides **18**, which are trapped in a 1,3-dipolar cycloaddition to form isoxazolines **19** (Scheme 3).[39]

The synthesis of diazo compounds by oxidation of hydrazone derivatives **20** was reported recently.[37,40] Silyl-protected hydrazones **20** are oxidized with (difluoroiodo)-benzene in situ to the corresponding diazo compounds **21**, which then react with carboxylic acids to form the corresponding esters **22**.[40] The main advantage of this elaborate esterification is the wide applicability to a range of labile substrates. The oxidation of the nitrogen–nitrogen bonds in 2-pyridylhydrazones led to the formation of the corresponding triazolopyridines, compounds with remarkably high antibacterial activities.[41] The oxidation of hydrazones to diazo compounds of type **21** in the presence of thioketones results in the high-yielding formation of thioepoxides, which are precursors for sterically hindered tetrasubstituted alkenes.[42]

3. Formation of Carbon–Carbon Bonds

Reactions leading to the formation of carbon–carbon bonds are important applications of hypervalent iodine reagents. These reactions proceed either through reactive intermediates such as radicals or carbocations, or they are ligand-coupling reactions mediated by trivalent iodine derivatives. The oxidative coupling of appropriately substituted phenol derivatives has been developed into a powerful tool for the synthesis of polycyclic compounds. Kita and coworkers recently showed that this reaction can be used successfully as a key step in the synthesis of complex natural products. They found that intermediate **23** could only be cyclized with R = CH_2OTBS (but not with R = CO_2Me) in the presence of [bis(trifluoroacetoxy)iodo]benzene and MK10 as a solid acid additive. After optimization of the diastereoselectivity of the spirocyclization to **24** by a variation of the protecting groups, this reaction was key to the first diastereoselective synthesis of discorhabdin A (Scheme 4).[43]

A combination of [bis(trifluoroacetoxy)iodo]benzene and heteropoly acids (e.g. $H_3[PW_{12}O_{40}]$) were recently used as efficient reagent combinations for intramolecular oxidative coupling reactions in the synthesis of spirodienone alkaloids such as morphinandienone and neospirinedienone.[44] The

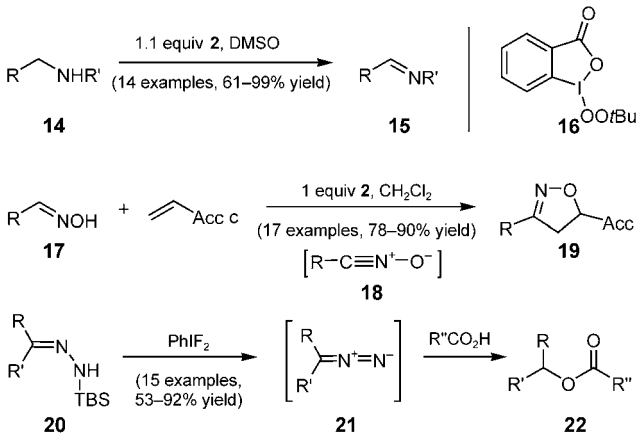

14 **15** **16** **17** **18** **19** **20** **21** **22**

Scheme 3. Oxidation of carbon–heteroatom and heteroatom–heteroatom bonds with hypervalent iodine reagents. Acc = acceptor substituent, TBS = *tert*-butyldimethylsilyl.

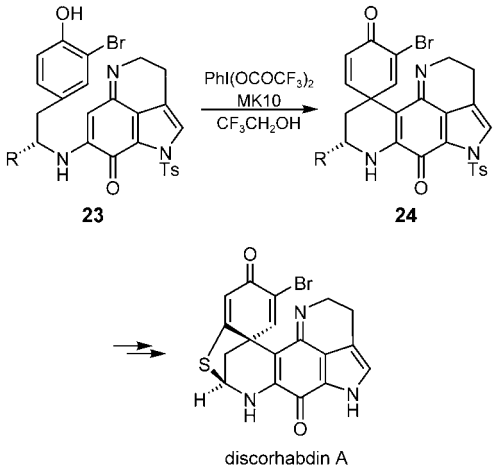

23 **24**

Scheme 4. Hypervalent iodine mediated spirocyclization in the total synthesis of discorhabdin A.

established combination of [bis(trifluoroacetoxy)iodo]benzene and boron trifluoro etherate proved to be efficient in the synthesis of aporphine alkaloids such as glaucine.[45] These reactions are believed to be initiated by a SET (single-electron transfer) to the electron-rich aromatic moiety. This concept has now been extended to couple 3-alkylthiophenes to give the corresponding 2,2′-bithiophene derivatives in moderate yields.[46] Whereas the oxidative coupling reactions initiated by a SET lead to radical cations as intermediates, mechanistic investigations revealed that radicals are not involved in aryl transfer in ligand-coupling reactions of trivalent iodine derivatives.[47]

Although the generation of iodonium ylides as carbene precursors in cyclopropanation reactions is known, more-efficient routes for the cyclopropanation of alkenes involve carbene precursors with two acceptor substituents. Malonic acid derivatives can be employed to synthesize cyclopropanes **25**,[48] and α-nitro carbonyl compounds have been successfully added under rhodium catalysis to generate compounds **26** as versatile precursors for cyclopropane amino acids.[49] Iodonium ylides derived from bis(phenylsulfonyl)methane can also be used for insertion reactions into the C–H bonds of alkenes. This reaction has been used to functionalize pyrroles[50] and flavones.[51] Reactions of unfunctionalized alkenes can lead to subsequent extrusion of sulfur dioxide and to the formation of functionalized indanes such as **27** (Scheme 5).[52]

The generation of benzynes by using silylated hypervalent iodine compounds such as **28a** is known and was recently

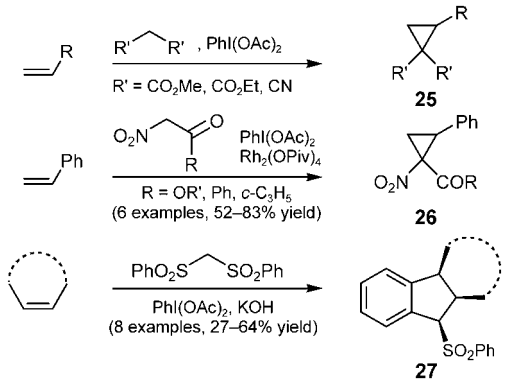

Scheme 5. Synthesis of cyclopropane and indane derivatives with hypervalent iodine reagents. Ts = *p*-toluenesulfonyl.

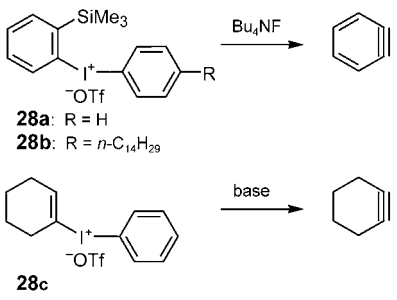

Scheme 6. Generation of benzyne and cyclohexyne from suitable hypervalent iodine precursors. Piv = pivaloyl.

optimized by the introduction of more-soluble compounds **28b** (Scheme 6), which led to a better performance in subsequent Diels–Alder reactions.[53] Similar precursors such as **28c** were recently used for the generation of cyclohexyne intermediates, and the elimination/addition mechanism was established by kinetic deuterium isotope studies.[54]

4. Formation of Carbon–Heteroatom Bonds and Heteroatom–Heteroatom Bonds

The use of hypervalent iodine reagents for the formation of carbon–heteroatom and heteroatom–heteroatom bonds is well established, and a wide range of substrates have been used in these transformations. The functionalization of carbonyl compounds at the α position is still under intensive investigation. Different types of halogenations have been reported with (difluoroiodo)arene and (dichloroiodo)arene derivatives as very powerful reagents. Advances in the preparation of organofluorine compounds by using hypervalent iodine reagents were extensively reviewed recently.[55] The selective introduction of fluorine atoms is possible under mild and neutral conditions in the presence of *p*-(difluoroiodo)toluene (**30**) as a stable and safe reagent. Various improved methods for the synthesis of **30** were reported recently,[56,57] but new hypervalent difluoroiodo derivatives have also been synthesized.[58] The fluorination of sulfur-substituted esters or amides **29** (E = S) has been investigated intensively, and the reaction proceeds through a sulfur-Pummerer-reaction to yield **31**.[59] Depending on the reaction conditions, difluorination or oxidation to the sulfoxides occurs, whereas the corresponding selenium substrates **29** (E = Se) only yield monofluorinated products **31** (Scheme 7).[57]

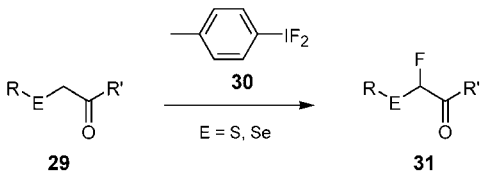

Scheme 7. Fluorination of sulfur- or selenium-substituted esters or amides.

p-(Difluoroiodo)toluene (**30**) can also be used to fluorinate β-dicarbonyl compounds. Hara et al. showed that the addition of a hazardous HF–amine complex, as described earlier,[60] is not necessary.[61] The combination of pyridinium polyhydrogen fluoride (Olah reagent) with either (diacetoxyiodo)benzene or [bis(trifluoroacetoxy)iodo]benzene is, however, necessary for an efficient *ipso*-fluorination of *para*-substituted phenols.[62] A similar reagent combination is necessary for the fluorinative ring expansion of cyclic iodo ethers (**69**→**70**; see Scheme 19 in Section 5).[63]

Catalytic asymmetric halogenation reactions are still rare. *p*-(Dichloroiodo)toluene (**32**) was recently used in combination with a titanium–taddol catalyst **33** for stereoselective chlorinations of 1,3-diketone derivatives and led to products

such as **34** with up to 70% *ee* Scheme 8.[64] This enantioselectivity is slightly lower than that attained when using *N*-chlorosuccinimide as the chlorinating agent in similar reactions.[65] The recently reported biphenyl derivative **35** might

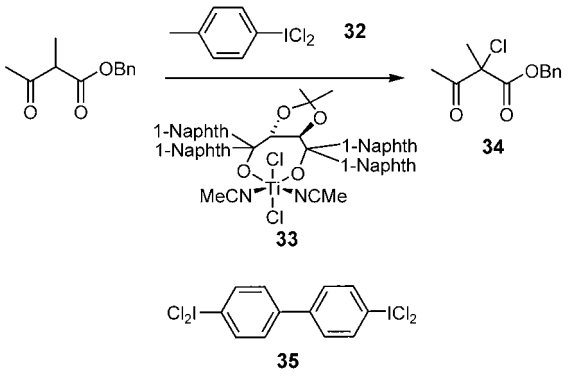

Scheme 8. Catalytic approach to stereoselective chlorination with hypervalent dichloroiodo derivatives. Naphth = naphthyl.

be advantageous in such reactions.[66] Although the stereoselectivities are only moderate, the transfer of ligands X from the great number of known compounds of the type $ArIX_2$ to enolizable substrates by using a stereoselective catalytic protocol is very promising. The main challenge in the development of such transformations will be the efficient suppression of the uncatalyzed background reaction between the hypervalent iodine reagent and the substrate. A two-step approach for the halogenation of enolizable substrates has been reported as well. Microwave-induced α tosylation with [hydroxy(tosyloxy)iodo]benzene followed by treatment with magnesium halides led to an efficient synthesis of the corresponding α-halocarbonyl compounds.[67]

The direct reaction of hypervalent iodine reagents with enolizable substrates has been the focus of a series of other publications. The introduction of oxygen functionalities α to carbonyl groups is well established and is being used advantageously in natural product synthesis.[68] The activation of the 2-position of tetrahydrofurans with hypervalent iodine compounds has been investigated, and processes for the protection of alcohols as tetrahydrofuranyl ethers **36** have been developed by using peroxyiodane **16** in combination with carbon tetrachloride in a radical process[69] or with (diacetoxyiodo)benzene through an ionic mechanism Scheme 9.[70] A similar reaction has also been observed with alkenyl or alkynyl iodanes to oxidize tetrahydrofuran.[71] Also tetrahydrothiophene derivatives can be employed in a similar process for the synthesis of thionucleosides.[72]

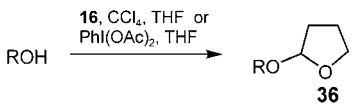

Scheme 9. Protection of alcohols as THF acetals with hypervalent iodine compounds.

The synthesis of polymer-bound hypervalent iodine reagents[33c] such as **37** is already well established, and many reports indicate an efficiency almost similar to that of their soluble counterparts. The reactions of the novel polymer-bound compounds **38** with enolizable substrates yield polymer-bound products **39** (Scheme 10), which can be used in

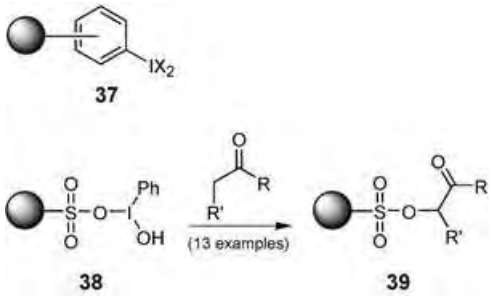

Scheme 10. Novel polymer-supported hypervalent iodine reagents in synthesis.

various subsequent reactions, from simple substitutions to the elaborate syntheses of heterocyclic compounds.[73] For example, reactions of **39** with thioamides led to the formation of thiazoles in good yields.[74]

Polymer-bound reagents **40** were developed by Kirschning and co-workers (Scheme 11).[78,79] The diazide **40a** is a safe

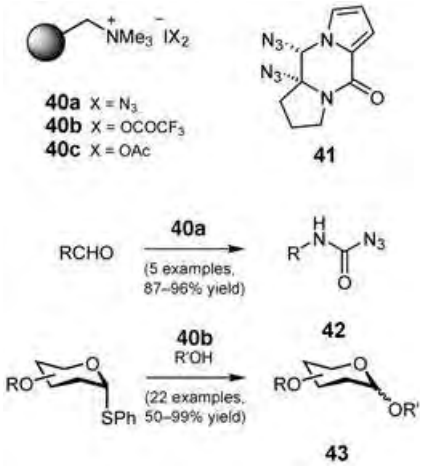

Scheme 11. Azidations and related reactions with polymer-supported hypervalent iodine reagents **40a–c**.

reagent for reactions with azide anions or azidyl radicals. The *syn* diazidation of a double bond with **40a** was used as a key step in the preparation of **41** in the synthesis of (±)-dibromophakellstatin.[75] The reaction of **40a** with aldehydes allowed the synthesis of carbamoyl azides **42** via the corresponding acyl azides in good yields.[76] The polymer-supported azide **40a** have also been used for the azidonation of benzyl ethers and are a safe alternative to IN_3. Furthermore, the diazide based on **37** ($X = N_3$) was used successfully in the synthesis of organotellurophosphanes.[77] Reagent **40b** was used for the activation of thioglycosides in the synthesis

of 2-desoxyglycoconjugates **43**,[78] and **40c** can be employed in iodoacylation reactions.[79]

The introduction of nitrogen functions into organic molecules with hypervalent iodine compounds is carried out with iminoiodanes **44** rather than with azide-based reagents. Many processes such as metal-catalyzed aziridinations of alkenes rely on the capability of these reagents to serve as useful nitrene precursors.[80] Unfortunately, these reagents **44** are sometimes difficult to prepare owing to their thermal sensitivity, and some have even been claimed to be explosive.[81] Recently, one-pot procedures were developed starting from easily accessible hypervalent iodine compounds and appropriate nitrogen sources. A mixture of (diacetoxyiodo)-benzene and sulfonamides were used in manganese or ruthenium porphyrin catalyzed aziridations of alkenes or amidations of the benzylic position of hydrocarbons such as indane (**45**) as shown in the reaction to give **46** Scheme 12.[82]

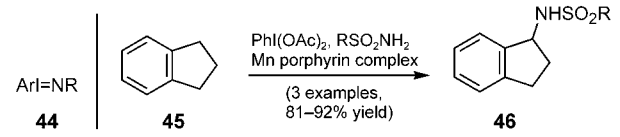

Scheme 12. Activation of C–H bonds in hypervalent iodine mediated aminations.

Similar combinations of iodosylbenzene (PhI=O) and sulfonamides or sulfonimidamides can be used for the generation of iminoiodanes in situ and have been applied to copper-catalyzed aziridinations of alkenes.[48b,83] Other nucleophiles such as sulfur trioxide can be used together with iodosylbenzene for the direct formation of cyclic sulfates from alkenes.[84]

Although rhodium catalysts are known to be efficient in C–H insertion reactions, they have rarely been used together with hypervalent iodine compounds. Du Bois and co-workers have developed procedures for aminations through selective C–H bond oxidation. Carbamates[85] and sulfamate esters **47**[86] can be efficiently cyclized to products **48** under rhodium catalysis (Scheme 13). Because (diacetoxyiodo)benzene is

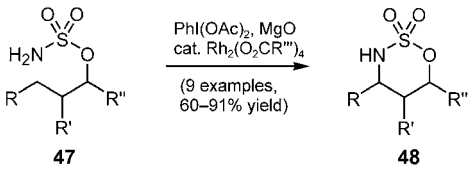

Scheme 13. Activation of C–H bonds in rhodium-catalyzed cyclization reactions.

used as oxidant, a base such as magnesium oxide is necessary to scavenge the generated acetic acid. New catalysts[87] are now allowing intermolecular C–H insertions, and combinations with subsequent transformations[88] have expanded the scope of this transformation.

Similar reaction conditions have been employed in aziridinations of alkenes in inter- and intramolecular reactions. The proposed mechanism involves the formation of an iminoiodane followed by rhodium-catalyzed C–H insertion or aziridination, which can be followed by nucleophilic ring-opening. Recent stereochemical results indicate that the addition of the metallonitrene might also proceed in a stepwise fashion without the formation of an aziridine intermediate, and in some cases the reaction even proceeds without the rhodium catalyst.[89]

Under different reaction conditions, the aziridinations of alkenes with a combination of (diacetoxyiodo)benzene and *N*-aminophthalimide can also proceed without metal catalysts.[90] The direct formation of carbon–heteroatom bonds by replacing C–H bonds of aromatic compounds has been used for the synthesis of various target molecules. The reactions of electron-rich arenes might proceed through a SET mechanism, but others have been shown to involve an ionic pathway. Various functional groups in combination with various hypervalent iodine reagents have been used to effect aromatic substitution. Depending on the reaction conditions and on the substitution pattern of the aromatic moiety, spiro compounds can be obtained by *ipso* cyclization, especially with 4-methoxy or 4-halo substitutents on the aromatic moiety.[91] This principle has also been applied to the synthesis of a muscarinic M_1 receptor antagonist.[92] Products of such initial spirocyclizations are likely to be intermediates in the reaction to products **50**, **52**, and **54** (Scheme 14). Sulfonamides **49**

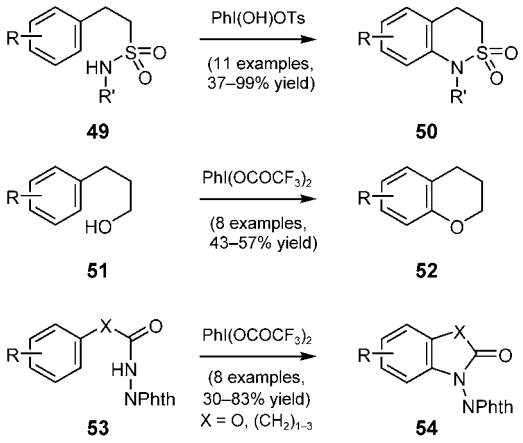

Scheme 14. Cyclizations of aromatic compounds in heterocycle synthesis. NPhth = phthalimidoyl.

undergo cyclization to form the corresponding 2,1-benzothiazine compounds **50** and the highest yields are attained with [hydroxy(tosyloxy)iodo]benzene as reagent.[93] However, polymer-supported reagents have been investigated as well.[94] Alcohols **51** are direct precursors for the chroman derivatives **52**,[95] whereas the acylimino phthalimides **53** can be cyclized to give a variety of different substituted lactams **54**.[96]

The chemistry of alkynyl(aryl)iodonium compounds is manifold, and their preparation usually involves a ligand-exchange reaction of the corresponding alkynyl stannane. Several new approaches for their synthesis have been developed, including ligand exchange of silylated alkynes[97] or from alkynyl boronates[98] as precursors; polymer-supported reagents[99] have also been synthesized. They are powerful

and versatile carbene precursors in natural product synthesis[100] which was recently demonstrated in the preparation of **55** as a key intermediate in the synthesis of halichlorine Scheme 15.[101] Alkynyl(aryl)iodonium compounds are frequently used for insertion reactions into heteroatom–hydrogen bonds for heterocycle synthesis.[102] These reagents were recently used in the alkynylation of metal complexes. The reaction with diorganoplatinum(II) complexes provides a general route for the synthesis of alkynylplatinum(IV) complexes **56**[103] as well as iridium(III)–σ-alkynyl complexes in high yields (Scheme 15).[104]

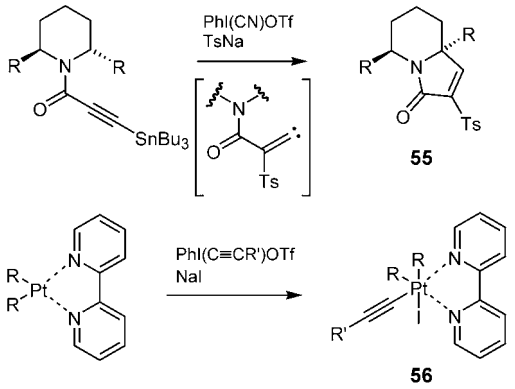

Scheme 15. Alkynyl iodo compounds in cyclizations via carbene intermediates (top) and in the synthesis of metal complexes (bottom). Tf = trifluoromethanesulfonyl.

The stabilization of hypervalent iodine moieties by intramolecular coordination has led to the development of chiral reagents such as **57**;[105] recently IBX esters **58** were reported

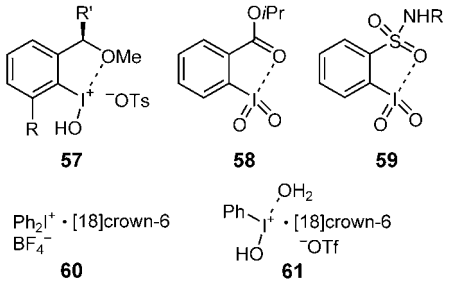

as reagents for the selective oxidation of sulfides to sulfoxides.[106] Several sulfamide derivatives **59** have also been prepared and evaluated in oxidation reactions.[107] Recent work by Ochiai et al. has shown that intermolecular stabilization of the hypervalent iodine moiety using [18]crown-6 can be used to form complexes **60**[108] or **61**,[109] which show interesting reactivities as they can be used for reactions in aqueous solvents.

5. Fragmentations and Rearrangements

The use of hypervalent iodine reagents in the fragmentation of tertiary cyclopropanol systems is already established and was reviewed recently.[110] The oxidative fragmentation of hemiacetals has been applied to the synthesis of functionalized medium-sized ring systems by using a combination of (diacetoxyiodo)benzene and iodine. This reaction is believed to proceed through a radical pathway by β scission of the corresponding alkoxy radicals. Medium-sized lactones **62**[111] or, with photochemical assistance, cycloheptane or cyclooctane derivatives **63** have been obtained (Scheme 16).[112]

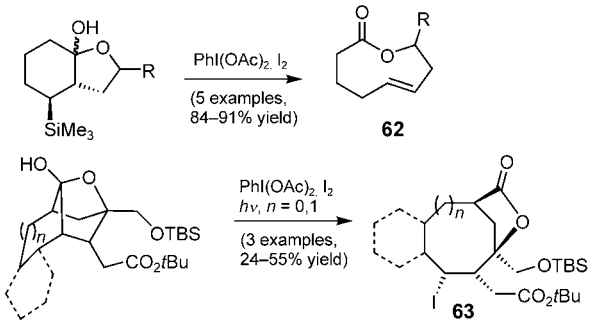

Scheme 16. Oxidative fragmentations in the synthesis of medium-sized ring systems.

The property of hypervalent iodine compounds to react as electrophilic reagents followed by the exploitation of their excellent leaving-group character has been used in various rearrangements for the synthesis of functionalized molecules. Their use in Hofmann-type rearrangements is well established, and the intermediate isocyanate has been used for the synthesis of heterocycles.[113] This reaction has now been extended to peptide chemistry in water, thus allowing the efficient rearrangement of *N*-protected glutamine to diaminobutyric acid derivatives, which have been used successfully for the synthesis of polymyxin B heptapeptide.[114] Treatment of aryl-substituted alkenes with hypervalent iodine compounds can lead to the formation of intermediates that can be stabilized by the aryl substituent via phenonium ions such as **64**; a rearrangement might occur. Internal nucleophiles lead to cyclized products **65**,[115] and external nucleophiles such as methanol/water result in the corresponding ketones **66** (Scheme 17).[116]

Similar intermediates might be involved in the rearrangement of chalcones. This reaction was used recently for the efficient synthesis of isoflavones **67** in a one-pot reaction (Scheme 18).[117]

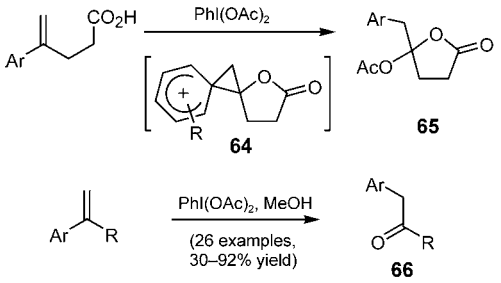

Scheme 17. Rearrangements of aryl alkenes via phenonium ion intermediates.

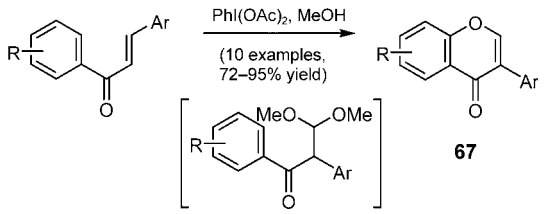

Scheme 18. Rearrangement–cyclization sequence for isoflavone synthesis.

The generation of a hypervalent iodine moiety as a leaving group has been explored with various substrates. Iodolactone **68**[118] can be oxidized to the diacetoxyiodo derivative, which then rearranges via phenonium ion **64** to compound **65**.[115] Iodoethers **69** are readily obtained from the corresponding unsaturated alcohols by an iodocyclization reaction.[119] Treatment of **69** with (difluoroiodo)toluene (**30**) leads to difluorination of the iodine atom and finally to rearranged ring-expanded cyclic ethers **70** in good yield (Scheme 19).[120]

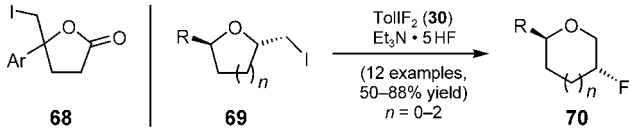

Scheme 19. Oxidative ring expansion with fluorination.

An oxidative rearrangement of allylic tertiary alcohols **71** has only precedence in organochromium chemistry. Iwabuchi and co-workers showed that IBX (**2**) in DMSO can be used for efficient rearrangement to the α,β-unsaturated carbonyl compounds **72** (Scheme 20); this process is compatible with a variety of protecting groups.[121]

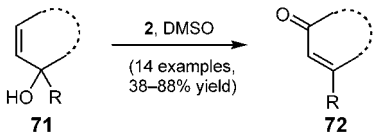

Scheme 20. IBX-controlled oxidative rearrangement of allylic alcohols.

6. Summary and Outlook

The great advantages of hypervalent iodine compounds, for example, their low toxicity compared with heavy-metal reagents, mild reaction conditions, fast accessibility of a large variety of reagents, and easy handling have led to their increased use in synthesis. This Mini-review will hopefully stimulate the application of hypervalent iodine reagents in synthesis, and the discovery of new transformations with these compounds will surely be the basis for different and improved synthetic strategies and concepts.

I thank my co-workers for their excellent contributions, Professor H. Sasai for his hospitality during my stay at Osaka University in autumn 2004 where parts of this review were written, and Dr. B. Linclau, Southampton University, for a preprint.

Received: January 12, 2005
Published online: April 12, 2005

[1] V. V. Zhdankin, P. J. Stang, *Chem. Rev.* **2002**, *102*, 2523–2584.
[2] a) H. Thoma, Y. Kita, *Adv. Synth. Catal.* **2004**, *346*, 111–124; b) H. Thoma, Y. Kita, *Yuki Gosei Kagaku Kyokaishi* **2004**, *62*, 116–127.
[3] M. Frigerio, M. Santagostino, S. Sputore, *J. Org. Chem.* **1999**, *64*, 4537–4538.
[4] a) T. Wirth, *Angew. Chem.* **2001**, *113*, 2893–2895; *Angew. Chem. Int. Ed.* **2001**, *40*, 2812–2814; b) T. Wirth in *Organic Synthesis Highlights V* (Eds.: H.-G. Schmalz, T. Wirth), Wiley-VCH, Weinheim, **2003**, pp. 144–150.
[5] D. E. N. Jacquot, H. Hoffmann, K. Polborn, T. Lindel, *Tetrahedron Lett.* **2002**, *43*, 3699–3702.
[6] J. D. More, N. S. Finney, *Org. Lett.* **2002**, *4*, 3001–3003.
[7] C. Chen, S. F. Martin, *Org. Lett.* **2004**, *6*, 3581–3584.
[8] A. P. Thottumkara, T. K. Vinod, *Tetrahedron Lett.* **2002**, *43*, 569–572.
[9] a) M. Mülbaier, A. Giannis, *Angew. Chem.* **2001**, *113*, 4530–4532; *Angew. Chem. Int. Ed.* **2001**, *40*, 4393–4394; b) G. Sorg, A. Mengel, G. Jung, J. Rademann, *Angew. Chem.* **2001**, *113*, 4532–4535; *Angew. Chem. Int. Ed.* **2001**, *40*, 4395–4397; c) N. N. Reed, M. Delgado, K. Hereford, B. Clapham, K. D. Janda, *Bioorg. Med. Chem. Lett.* **2002**, *12*, 2047–2049; d) Z. Lei, C. Denecker, S. Jegasothy, D. C. Sherrington, N. K. H. Slater, A. J. Sutherland, *Tetrahedron Lett.* **2003**, *44*, 1635–1637.
[10] V. V. Zhdankin, A. Y. Koposov, B. C. Netzel, N. V. Yashin, B. P. Rempel, M. J. Ferguson, R. R. Tykwinski, *Angew. Chem.* **2003**, *115*, 2244–2246; *Angew. Chem. Int. Ed.* **2003**, *42*, 2194–2196.
[11] V. V. Zhdankin, A. Y. Koposov, L. Su, V. V. Boyarskikh, B. C. Netzel, V. C. Young, *Org. Lett.* **2003**, *5*, 1583–1586.
[12] a) W. J. Chung, D. K. Kim, Y. S. Lee, *Tetrahedron Lett.* **2003**, *44*, 9251–9254; b) P. Lecarpentier, S. Crosignani, B. Linclau, *Mol. Diversity* **2005**, *9*, in press.
[13] a) Z. Liu, Z. Chen, Q. Zheng, *Org. Lett.* **2003**, *5*, 3321–3323; b) G. Karthikeyan, P. T. Perumal, *Synlett* **2003**, 2249–2251; c) J. S. Yadav, B. V. S. Reddy, A. K. Basak, A. V. Narsaiah, *Tetrahedron* **2004**, *60*, 2131–3135; d) B. S. Chhikara, R. Chandra, V. Tandon, *Tetrahedron Lett.* **2004**, *45*, 7585–7588.
[14] a) K. C. Nicolaou, Y. L. Zong, P. S. Baran, *J. Am. Chem. Soc.* **2000**, *122*, 7596–7597; b) K. C. Nicolaou, T. Montagnon, P. S. Baran, Y. L. Zong, *J. Am. Chem. Soc.* **2002**, *124*, 2245–2258.
[15] a) T. Kawashima, K. Hoshiba, N. Kano, *J. Am. Chem. Soc.* **2001**, *123*, 1507–1508; b) N. Kano, M. Ohashi, K. Hoshiba, T. Kawashima, *Tetrahedron Lett.* **2004**, *45*, 8173–8175.
[16] S. Kotha, S. Banerjee, K. Mandal, *Synlett* **2004**, 2043–2045.
[17] M. S. Yusubov, T. Wirth, *Org. Lett.* **2005**, *7*, 519–521.
[18] A. De Mico, R. Margarita, L. Parlanti, A. Vescovi, G. Piancatelli, *J. Org. Chem.* **1997**, *62*, 6974–6977.
[19] A. Dondoni, A. Massi, E. Minghini, S. Sabbatini, V. Bertolasi, *J. Org. Chem.* **2003**, *68*, 6172–6183.
[20] a) G.-D. Kang, P. W. Howard, D. E. Thurston, *Chem. Commun.* **2003**, 1688–1689; b) I. Paterson, O. Delgado, G. J. Florence, I. Lyothier, J. P. Scott, N. Sereinig, *Org. Lett.* **2003**, *5*, 35–38; c) I. Paterson, M. Tudge, *Angew. Chem.* **2003**, *115*, 357–361; *Angew. Chem. Int. Ed.* **2003**, *42*, 343–347.
[21] R. S. Varma, R. Dahiya, R. K. Saini, *Tetrahedron Lett.* **1997**, *38*, 7029–7032.
[22] W. Sun, H. Wang, C. Xia, J. Li, P. Zhao, *Angew. Chem.* **2003**, *115*, 1072–1074; *Angew. Chem. Int. Ed.* **2003**, *42*, 1042–1044.

[23] H. Tohma, Y. Kita, *Yuki Gosei Kagaku Kyokaishi* **2004**, *62*, 116 – 127.
[24] a) H. Tohma, S. Takizawa, T. Maegawa, Y. Kita, *Angew. Chem.* **2000**, *112*, 1362 – 1364; *Angew. Chem. Int. Ed.* **2000**, *39*, 1306 – 1308; b) H. Tohma, T. Maegawa, S. Takizawa, Y. Kita, *Adv. Synth. Catal.* **2002**, *344*, 328 – 337.
[25] H. Tohma, T. Maegawa, Y. Kita, *Synlett* **2003**, 723 – 725.
[26] A. Schulze, A. Giannis, *Adv. Synth. Catal.* **2004**, *346*, 252 – 256.
[27] M. C. Bagley, D. D. Hughes, H. M. Sabo, P. H. Taylor, X. Xiong, *Synlett* **2003**, 1443 – 1446.
[28] S. Thorimbert, C. Taillier, S. Bareyt, D. Humilière, M. Malacria, *Tetrahedron Lett.* **2004**, *45*, 9123 – 9126.
[29] S. Rodríguez, P. Wipf, *Synthesis* **2004**, 2767 – 2783.
[30] D. Gabrilidis, C. Kalogiros, L. P. Hadjiarapoglou, *Synlett* **2004**, 2566 – 2569.
[31] S. P. Cook, C. Gaul, S. J. Danishefsky, *Tetrahedron Lett.* **2005**, *46*, 843 – 847.
[32] S. P. Fletcher, D. L. J. Clive, J. Peng, D. A. Wingert, *Org. Lett.* **2005**, *7*, 23 – 26.
[33] a) M. Okawara, K. Mizuta, *Kogyo Kagaku Zasshi* **1961**, *64*, 232 – 235; b) Y. Yamada, M. Okawara, *Makromol. Chem.* **1972**, *152*, 153 – 162; c) H. Togo, K. Sakuratani, *Synlett* **2002**, 1966 – 1975.
[34] K. Sakuratani, H. Togo, *Synthesis* **2003**, 21 – 23.
[35] C. Rocaboy, J. A. Gladysz, *Chem. Eur. J.* **2003**, *9*, 88 – 95.
[36] H. Tohma, A. Maruyama, A. Maeda, T. Maegawa, T. Dohi, M. Shiro, T. Morita, Y. Kita, *Angew. Chem.* **2004**, *116*, 3679 – 3682; *Angew. Chem. Int. Ed.* **2004**, *43*, 3595 – 3598.
[37] K. C. Nicolaou, C. J. N. Mathison, T. Montagnon, *J. Am. Chem. Soc.* **2004**, *126*, 5192 – 5201.
[38] T. Sueda, D. Kajishima, S. Goto, *J. Org. Chem.* **2003**, *68*, 3307 – 3310.
[39] B. Das, H. Holla, G. Mahender, J. Banerjee, M. R. Reddy, *Tetrahedron Lett.* **2004**, *45*, 7347 – 7350.
[40] M. E. Furrow, A. G. Myers, *J. Am. Chem. Soc.* **2004**, *126*, 12222 – 12223.
[41] A. K. Sadana, Y. Mirza, K. R. Aneja, O. Prakash, *Eur. J. Med. Chem.* **2003**, *38*, 533 – 536.
[42] M. K. J. ter Wiel, J. Vicario, S. G. Davey, A. Meetsma, B. L. Feringa, *Org. Biomol. Chem.* **2005**, *3*, 28 – 30.
[43] H. Tohma, Y. Harayama, M. Hashizume, M. Iwata, Y. Kiyono, M. Egi, Y. Kita, *J. Am. Chem. Soc.* **2003**, *125*, 11235 – 11240.
[44] a) H. Hamamoto, Y. Shiozaki, H. Nambu, K. Hata, H. Tohma, Y. Kita, *Chem. Eur. J.* **2004**, *10*, 4977 – 4982; b) H. Hamamoto, Y. Shiozaki, K. Hata, H. Tohma, Y. Kita, *Chem. Pharm. Bull.* **2004**, *52*, 1231 – 1234.
[45] a) W.-J. Huang, O. V. Singh, C.-H. Chen, S.-S. Lee, *Helv. Chim. Acta* **2004**, *87*, 167 – 174; b) E. Anakabe, L. Carrillo, D. Badía, J. L. Vicario, M. Villegas, *Synthesis* **2004**, 1093 – 1101.
[46] H. Tohma, M. Iwata, T. Maegawa, Y. Kiyono, A. Maruyama, Y. Kita, *Org. Biomol. Chem.* **2003**, *1*, 1647 – 1649.
[47] M. Ochiai, Y. Kitagawa, M. Toyonari, *ARKIVOC* **2003**, *6*, 43 – 48.
[48] a) M. B. Camacho, A. E. Clark, T. A. Liebrecht, J. P. DeLuca, *J. Am. Chem. Soc.* **2000**, *122*, 5210 – 5211; b) P. Dauban, L. Sanière, A. Tarrade, R. H. Dodd, *J. Am. Chem. Soc.* **2001**, *123*, 7707 – 7708; c) A. S. Biland, S. Altermann, T. Wirth, *ARKIVOC* **2003**, *6*, 164 – 169.
[49] R. P. Wurz, A. B. Charette, *Org. Lett.* **2003**, *5*, 2327 – 2329.
[50] C. Batsila, E. P. Gogonas, G. Kostakis, L. P. Hadjiarapoglou, *Org. Lett.* **2003**, *5*, 1511 – 1514.
[51] W. Adam, E. P. Gogonas, L. P. Hadjiarapoglou, *Tetrahedron* **2003**, *59*, 7929 – 7934.
[52] a) W. Adam, E. P. Gogonas, L. P. Hadjiarapoglou, *Eur. J. Org. Chem.* **2003**, 1064 – 1068; b) W. Adam, E. P. Gogonas, L. P. Hadjiarapoglou, *Synlett* **2003**, 1165 – 1169; c) W. Adam, E. P. Gogonas, L. P. Hadjiarapoglou, *J. Org. Chem.* **2003**, *68*, 9155 – 9158.
[53] a) T. Kitamura, T. Abe, Y. Fujiwara, T. Yamaji, *Synthesis* **2003**, 213 – 216; b) T. Abe, T. Yamaji, T. Kitamura, *Bull. Chem. Soc. Jpn.* **2003**, *76*, 2175 – 2178.
[54] M. Fujita, W. H. Kim, Y. Sakanishi, K. Fujiwara, S. Hirayama, T. Okuyama, Y. Ohki, K. Tatsumi, Y. Yoshioka, *J. Am. Chem. Soc.* **2004**, *126*, 7548 – 7558.
[55] N. Yoneda, *J. Fluorine Chem.* **2004**, *125*, 7 – 17.
[56] M. Sawaguchi, S. Ayuba, S. Hara, *Synthesis* **2002**, 1802 – 1803.
[57] M. A. Arrica, T. Wirth, *Eur. J. Org. Chem.* **2005**, 395 – 403.
[58] A. B. Sheremetev, D. E. Dmitriev, S. M. Konkina, *Russ. Chem. Bull. Int. Ed.* **2004**, *53*, 1130 – 1132.
[59] a) M. F. Greaney, W. B. Motherwell, D. A. Tocher, *Tetrahedron Lett.* **2001**, *42*, 8523 – 8526; b) W. B. Motherwell, M. F. Greaney, D. A. Tocher, *J. Chem. Soc. Perkin Trans. 1* **2002**, 2809 – 2815; c) W. B. Motherwell, M. F. Greaney, D. A. Tocher, *J. Chem. Soc. Perkin Trans. 1* **2002**, 2816 – 2826.
[60] S. Hara, M. Sekiguchi, A. Ohmori, T. Fukuhara, N. Yoneda, *Chem. Commun.* **1996**, 1899 – 1900.
[61] M. Yoshida, K. Fujikawa, S. Sato, S. Hara, *ARKIVOC* **2003**, *6*, 36 – 42.
[62] O. Karam, A. Martin-Mingot, M.-P. Jouannetaud, J.-C. Jacquesy, A. Cousson, *Tetrahedron* **2004**, *60*, 6629 – 6638.
[63] T. Inagaki, Y. Nakamura, M. Sawaguchi, N. Yoneda, S. Ayuba, S. Hara, *Tetrahedron Lett.* **2003**, *44*, 4117 – 4119.
[64] H. Ibrahim, F. Kleinbeck, A. Togni, *Helv. Chim. Acta* **2004**, *87*, 605 – 610.
[65] L. Hintermann, A. Togni, *Helv. Chim. Acta* **2000**, *83*, 2425 – 2435.
[66] M. S. Yusubov, L. A. Drygunova, V. V. Zhdankin, *Synthesis* **2004**, 2289 – 2292.
[67] J. C. Lee, J. Y. Park, S. Y. Yoon, Y. H. Bae, S. J. Lee, *Tetrahedron Lett.* **2004**, *45*, 191 – 193.
[68] D. M. Hodgson, J.-M. Galano, M. Christlieb, *Tetrahedron* **2003**, *59*, 9719 – 9728.
[69] M. Ochiai, T. Sueda, *Tetrahedron Lett.* **2004**, *45*, 3557 – 3559.
[70] A. N. French, J. Cole, T. Wirth, *Synlett* **2004**, 2291 – 2294.
[71] M. Ochiai, Y. Tsuchimoto, T. Hayashi, *Tetrahedron Lett.* **2003**, *44*, 5381 – 5384.
[72] N. Nishizono, R. Baba, C. Nakamura, K. Oda, M. Machida, *Org. Biomol. Chem.* **2003**, *1*, 3692 – 3697.
[73] K. C. Nicolaou, T. Montagnon, T. Ulven, P. S. Baran, Y.-L. Zhong, F. Sarabia, *J. Am. Chem. Soc.* **2002**, *124*, 5718 – 5728.
[74] M. Ueno, H. Togo, *Synthesis* **2004**, 4673 – 4677.
[75] R. Chung, E. Yu, C. D. Incarvito, D. J. Austin, *Org. Lett.* **2004**, *6*, 3881 – 3884.
[76] L. G. Marinescu, C. M. Pedersen, M. Bols, *Tetrahedron* **2005**, *61*, 123 – 127.
[77] J.-M. Chen, X.-J. Lin, X. Huang, *J. Chem. Res. Synop.* **2004**, 43 – 44.
[78] J. Jaunzems, E. Hofer, M. Jesberger, G. Sourkouni-Argirusi, A. Kirschning, *Angew. Chem.* **2003**, *115*, 1198 – 1202; *Angew. Chem. Int. Ed.* **2003**, *42*, 1166 – 1170.
[79] A. Kirschning, E. Kunst, M. Ries, L. Rose, A. Schönberger, R. Wartchow, *ARKIVOC* **2003**, *6*, 145 – 163.
[80] P. Dauban, R. H. Dodd, *Synlett* **2003**, 1571 – 1586.
[81] P. J. Stang, V. V. Zhdankin, *Chem. Rev.* **1996**, *96*, 1123 – 1178.
[82] J.-L. Liang, J.-S. Huang, X.-Q. Yu, N. Zhu, C.-M. Che, *Chem. Eur. J.* **2002**, *8*, 1563 – 1572.
[83] P. H. Di Chenna, F. Robert-Peillard, P. Duban, R. H. Dodd, *Org. Lett.* **2004**, *6*, 4503 – 4505.
[84] R. I. Robinson, S. Woodward, *Tetrahedron Lett.* **2003**, *44*, 1655 – 1657.
[85] C. G. Espino, J. Du Bois, *Angew. Chem.* **2001**, *113*, 618 – 620; *Angew. Chem. Int. Ed.* **2001**, *40*, 598 – 600.

[86] C. G. Espino, P. M. Wehn, J. Chow, J. Du Bois, *J. Am. Chem. Soc.* **2001**, *123*, 6935 – 6936.
[87] C. G. Espino, K. W. Fiori, M. Kim, J. Du Bois, *J. Am. Chem. Soc.* **2004**, *126*, 15378 – 15379.
[88] K. W. Fiori, J. J. Fleming, J. Du Bois, *Angew. Chem.* **2004**, *116*, 4449 – 4452; *Angew. Chem. Int. Ed.* **2004**, *43*, 4349 – 4352.
[89] A. Padwa, T. Stengel, *Org. Lett.* **2002**, *4*, 2137 – 2139.
[90] L. B. Krasnova, R. M. Hili, O. V. Chernoloz, A. K. Yudin, *ARKIVOC* **2005**, *4*, 26 – 38.
[91] E. Miyazawa, T. Sakamoto, Y. Kikugawa, *J. Org. Chem.* **2003**, *68*, 5429 – 5432.
[92] H. Mizutani, J. Takayama, Y. Soeda, T. Honda, *Heterocycles* **2004**, *62*, 343 – 355.
[93] Y. Misu, H. Togo, *Org. Biomol. Chem.* **2003**, *1*, 1342 – 1346.
[94] K. Sakuratani, H. Togo, *ARKIVOC* **2003**, *6*, 11 – 20.
[95] H. Hamamoto, K. Hata, H. Nambu, Y. Shiozaki, H. Tohma, Y. Kita, *Tetrahedron Lett.* **2004**, *45*, 2293 – 2295.
[96] Y. Kikugawa, A. Nagashima, T. Sakamoto, E. Miyazawa, M. Shiiya, *J. Org. Chem.* **2003**, *68*, 6739 – 6744.
[97] T. Kitamura, M. Kotani, Y. Fujiwara, *Synthesis* **1998**, 1416 – 1418.
[98] V. V. Zhdankin, P. J. Persichini, R. Cui, Y. Jin, *Synlett* **2000**, 719 – 721.
[99] A. B. Sheremetev, E. V. Mantseva, *Tetrahedron Lett.* **2001**, *42*, 5759 – 5761.
[100] K. S. Feldman, *ARKIVOC* **2003**, *6*, 179 – 190.
[101] K. S. Feldman, A. L. Perkins, K. M. Masters, *J. Org. Chem.* **2004**, *69*, 7928 – 7932.
[102] Z. Liu, Z.-C. Chen, Q.-G. Zheng, *J. Chem. Res. Synop.* **2003**, 715 – 717.
[103] A. J. Canty, T. Rodemann, *Inorg. Chem. Commun.* **2003**, *6*, 1382 – 1384.
[104] D. Bykowski, R. McDonald, R. R. Tykwinski, *ARKIVOC* **2003**, *6*, 21 – 29.
[105] U. H. Hirt, M. F. H. Schuster, A. N. French, O. G. Wiest, T. Wirth, *Eur. J. Org. Chem.* **2001**, 1569 – 1579.
[106] A. Y. Koposov, V. V. Zhdankin, *Synthesis* **2005**, 22 – 24.
[107] a) A. Y. Koposov, D. N. Litvinov, V. V. Zhdankin, *Tetrahedron Lett.* **2004**, *45*, 2719 – 2721; b) V. V. Zhdankin, R. N. Goncharenko, D. N. Litvinov, A. Y. Koposov, *ARKIVOC* **2005**, *4*, 8 – 18.
[108] M. Ochiai, T. Suefuji, K. Miyamoto, N. Tada, S. Goto, M. Shiro, S. Sakamoto, K. Yamaguchi, *J. Am. Chem. Soc.* **2003**, *125*, 769 – 773.
[109] M. Ochiai, K. Miyamoto, Y. Yokota, T. Suefuji, M. Shiro, *Angew. Chem.* **2005**, *117*, 77 – 80; *Angew. Chem. Int. Ed.* **2005**, *44*, 75 – 78.
[110] M. Kirihara, H. Kakuda, *Yuki Gosei Kagaku Kyokaishi* **2004**, *62*, 919 – 928.
[111] M. A. Hatcher, K. Borstnik, G. H. Posner, *Tetrahedron Lett.* **2003**, *44*, 5407 – 5409.
[112] N. G. Ramesh, A. Hassner, *Synlett* **2004**, 975 – 978.
[113] O. Prakash, H. Batra, H. Kaur, P. K. Sharma, V. Sharma, S. P. Singh, R. M. Moriarty, *Synthesis* **2001**, 541 – 543.
[114] K. Yamada, H. Urakawa, H. Oku, R. Katakai, *J. Pept. Res.* **2004**, *64*, 43 – 50.
[115] A. C. Boye, D. Meyer, C. K. Ingison, A. N. French, T. Wirth, *Org. Lett.* **2003**, *5*, 2157 – 2159.
[116] M. W. Justik, G. F. Koser, *Tetrahedron Lett.* **2004**, *45*, 6159 – 6163.
[117] a) Y. Kawamura, M. Maruyama, T. Tokuoka, M. Tsukayama, *Synthesis* **2002**, 2490 – 2496; b) Y. Kawamura, M. Maruyama, K. Yamashita, M. Tsukayama, *Int. J. Mod. Phys. B* **2003**, *17*, 1482 – 1486.
[118] J. Hass, S. Piguel, T. Wirth, *Org. Lett.* **2002**, *4*, 297 – 300.
[119] A. N. French, S. Bissmire, T. Wirth, *Chem. Soc. Rev.* **2004**, *33*, 354 – 362.
[120] T. Inagaki, Y. Nakamura, M. Sawaguchi, N. Yoneda, S. Ayuba, S. Hara, *Tetrahedron Lett.* **2003**, *44*, 4417 – 4419.
[121] M. Shibuya, S. Ito, M. Takahashi, Y. Iwabuchi, *Org. Lett.* **2004**, *6*, 4303 – 4306.

Enzyme Mechanisms

Friedel–Crafts-Type Mechanism for the Enzymatic Elimination of Ammonia from Histidine and Phenylalanine

*László Poppe and János Rétey**

Keywords:
ammonia-lyases · biocatalysis · enzymes · histidine · phenylalanine

Dedicated to Professor George Olah

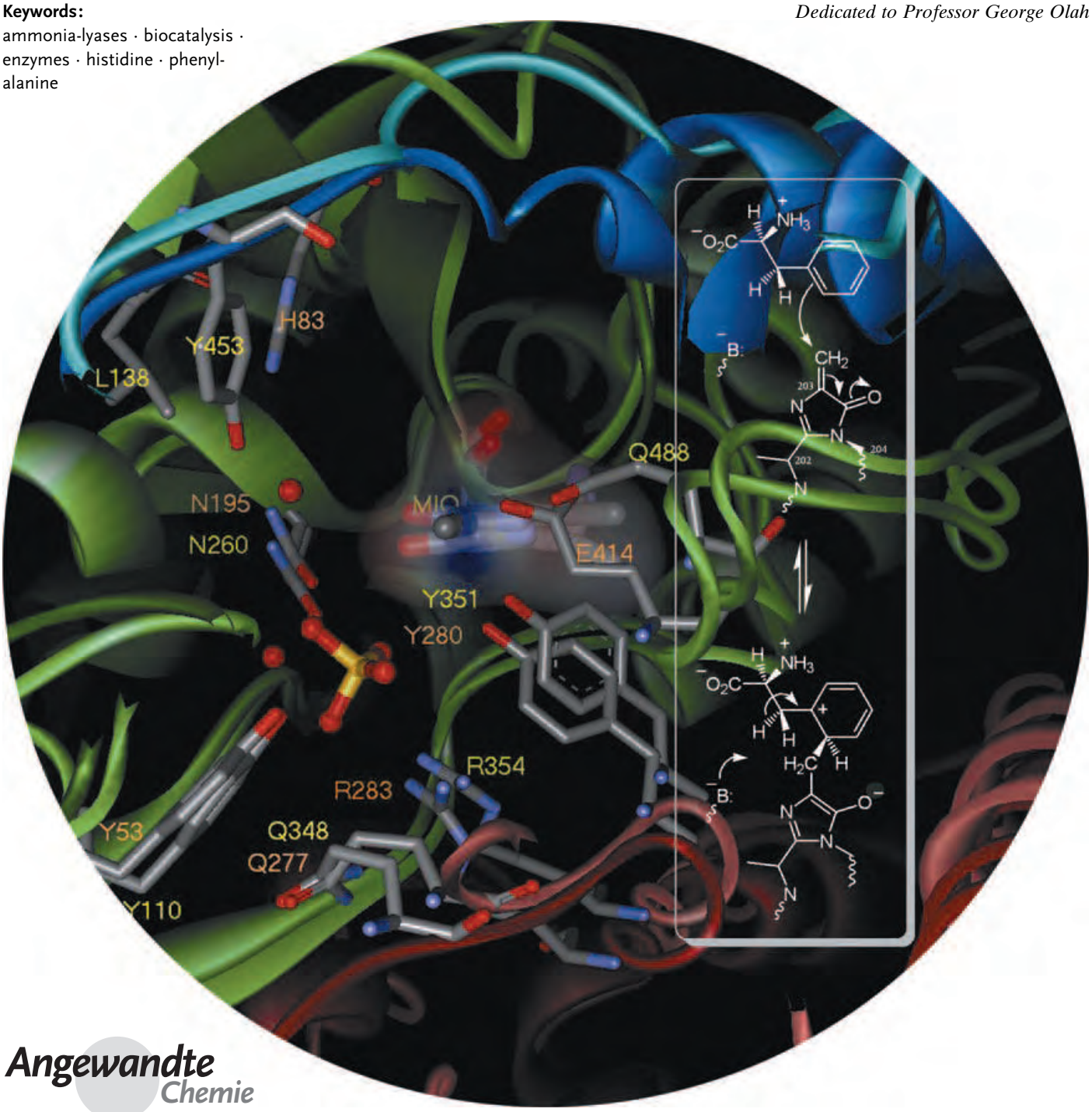

DOI: 10.1002/anie.200461377

The surprisingly high catalytic activity and selectivity of enzymes stem from their ability to both accelerate the target reaction and suppress competitive reaction pathways that may even be dominant in the absence of enzymes. For example, histidine and phenylalanine ammonia-lyases (HAL and PAL) trigger the abstraction of the nonacidic β protons of these amino acids while leaving the much more acidic ammonium hydrogen atoms untouched. Both ammonia-lyases have a catalytically important electrophilic group, which was believed to be dehydroalanine for 30 years but has now been revealed by X-ray crystallography and UV spectroscopy to be a highly electrophilic 5-methylene-3,5-dihydroimidazol-4-one (MIO) group. Experiments suggest that the reaction is initiated by the electrophilic attack of MIO on the aromatic ring of the substrate. This incomplete Friedel–Crafts-type reaction leads to the activation of a β proton and its stereospecific abstraction, followed by the elimination of ammonia and regeneration of the MIO group. The plausibility of such a mechanism is supported by a synthetic model. The application of the PAL reaction in the biocatalytic synthesis of enantiomerically pure α-amino β-aryl propionates from aryl acrylates is also discussed.

From the Contents

1. Introduction

Almost all biochemical processes are catalyzed by enzymes. Reactions for which nonenzymatic analogues exist can be accelerated by a factor of up to 10^{20} by these biocatalysts. Even more challenging for the biochemist are enzyme-mediated transformations that would never occur in the absence of the enzyme, because either the corresponding substrates are completely stable under most conditions or alternative reactions are much faster. It has been proposed that enzymes not only catalyze certain transformations but also suppress alternative, competing reactions. This activity is especially important in cases in which highly reactive intermediates are involved, but is a general property of enzymes which leads to a high reaction selectivity. For this ability of enzymes to suppress competing reactions the term "negative catalysis" has been coined.[1] Some proteins function exclusively as negative catalysts. For example, hemoglobin and myoglobin bind dioxygen reversibly at their heme iron (Fe^{II}) center and prevent its oxidation to Fe^{III}, which occurs spontaneously in free heme.

To generate highly reactive intermediates, the activation of relatively stable substrates is required; examples are reactions that involve radical intermediates. Radical initiators include adenosylcobalamin[1–3] (coenzyme B_{12}) and S-adenosylmethionine (SAM) in combination with iron–sulfur clusters.[4] Both are protected forms of the 5′-deoxyadenosyl radical, which can be generated by the corresponding enzymes.

Another method of substrate activation involves the action of electrophiles. As the side chains of all proteinogenic amino acids contain only nucleophilic groups, cofactors or post-translationally modified side chains are required for electrophilic catalysis. The role of the electrophilic cofactor pyridoxal phosphate in amino acid metabolism has been known for a long time.[5] More recently, a number of post-translational modifications were discovered that transform nucleophilic groups into electrophilic groups (Table 1).

Serine, whose OH group is an important nucleophile in many enzymatic reactions, can be transformed into a pyruvyl group.[6] The pyruvyl enzymes catalyze similar reactions to those in which pyridoxal phosphate is used. As they only occur in certain bacteria, one can speculate that the pyruvyl group was the evolutionary precursor of pyridoxal phosphate. Another modification involves the internal tripeptide Ala-Ser-Gly and leads to the very strong electrophile 5-methylene-3,5-dihydroimidazol-4-one (MIO). The corresponding enzymes are the topic of this Review. Another recently discovered modification of serine or cysteine side chains leads to formylglycine, which occurs in prokaryotic and eukaryotic aryl sulfatases.[7] Further modifications affect the aromatic

[*] Prof. Dr. J. Rétey
Institut für Organische Chemie
Universität Karlsruhe
Fritz-Haber-Weg 6, 76128 Karlsruhe (Germany)
Fax: (+49) 721-608-4823
E-mail: janos.retey@ioc.uka.de
Prof. Dr. L. Poppe
Institute of Organic Chemistry
Research Group for Alkaloid Chemistry
Budapest University of Technology and Economics
1111 Budapest, Gellért tér 4 (Hungary)

 DOI: 10.1002/anie.200461377

Table 1: Conversion of nucleophilic amino acid side chains into electrophiles by post-translational modifications.

Precursor	Electrophilic prosthetic group	Enzyme
serine	pyruvate	histidine decarboxylase, SAM decarboxylase
serine or cysteine	MIO	histidine ammonia-lyase (HAL), phenylalanine ammonia-lyase (PAL)
serine or cysteine	formylglycine	prokaryotic or eukaryotic aryl sulfatases
tyrosine	dopaquinone	

amino acids tyrosine and tryptophan, which are oxidized to quinones. The mechanism of action of quinoenzymes is attracting a great deal of attention.[8]

Finally, the modification of lysine to pyrrolysine was discovered recently.[9] It was first proposed that a specific lysyl-tRNA is modified at the 6-amino group through the formation of an amide with 4*R*,5*R* 4-substituted pyrroline-5-carboxylic acid.[10] A more recent report stated that pyrrolysine is formed before the binding to tRNA occurs.[11] The codon of the resulting pyrrolysyl-tRNA is the stop codon UAG. Precedence for such a pretranslational modification is the formation of selenocysteinyl-tRNA from a specific seryl-tRNA.[12]

2. HAL in Histidine Metabolism

Whereas the catabolism of most amino acids starts with transamination to the corresponding 2-keto acid, histidine is degraded in a different way. The first step of histidine metabolism consists of the elimination of ammonia catalyzed by histidine ammonia-lyase (HAL; Scheme 1). The product, (*E*)-urocanate, is further processed to imidazolonepropionate, a transformation catalyzed by urocanase (urocanate hydratase, imidazolonepropionate hydrolase).

Each subunit of this enzyme contains a tightly bound NAD^+ molecule, which functions as an electrophile and forms a covalent adduct with the imidazole ring of the substrate.[13]

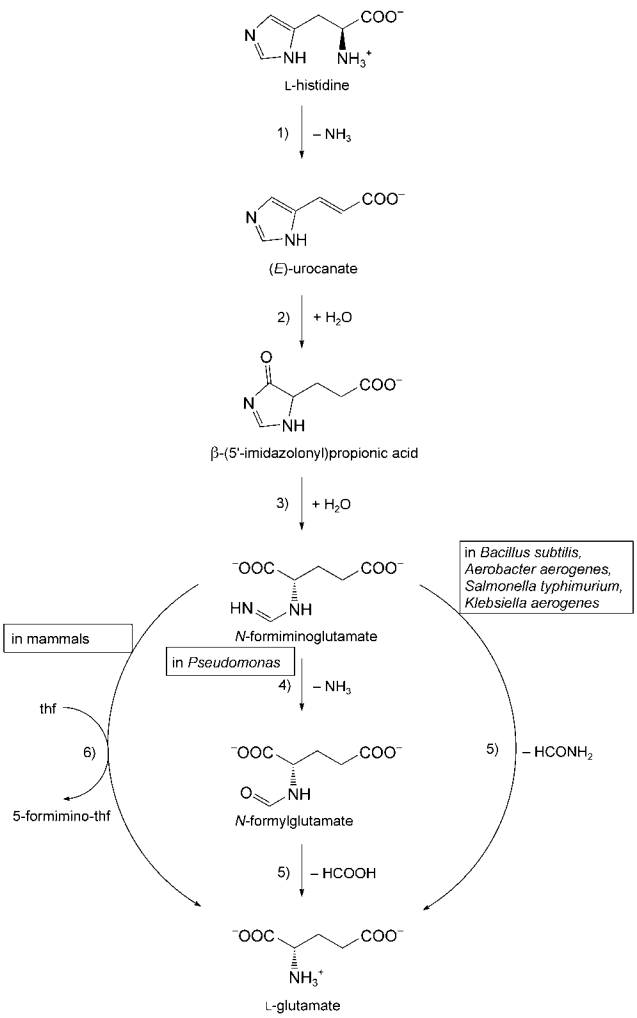

Scheme 1. Degradation pathway of histidine in various organisms; enzymes involved: 1) histidine ammonia-lyase, 2) urocanase, 3) imidazolonepropionate hydrolase, 4) formiminoglutamate hydrolase, 5) *N*-formylglutamate aminohydrolase, 6) glutamate formiminotransferase. thf = tetrahydrofolate.

The result is an "umpolung", which is followed by the addition of water to form 4-hydroxyimidazolylpropionate.[13] This compound tautomerizes spontaneously to racemic imidazolonepropionate. The next step is catalyzed by imidazo-

László Poppe graduated as a chemical engineer from Budapest University of Technology and Economics (BUTE) and completed his PhD in 1987 with L. Novák on pheromone synthesis and biocatalysis. He was a research fellow at the Central Research Institute for Chemistry of the Hungarian Academy of Sciences before becoming a research professor at BUTE in 2001. He also spent over a year (1991–1992) as an Alexander von Humboldt Fellow with J. Rétey at the Universität Karlsruhe. His areas of interest are the stereoselective synthesis of biologically active compounds, biocatalysis, and enzyme mechanisms.

János Rétey studied chemistry at the ETH Zürich and completed his PhD on the stereospecificity of oxidoreductases in 1963 with V. Prelog. After postdoctoral periods with F. Lynen (München) and D. Arigoni (ETH Zürich) he became a lecturer at the ETH Zürich. In 1972 he moved as Professor of Biochemistry to the Universität Karlsruhe. His research interests include the mechanisms and stereospecificity of enzyme reactions, synthetic enzyme models, bioorganic and bioinorganic chemistry, and the investigation of enzyme structures by molecular biological methods.

lonepropionate hydrolase, which is enantioselective for the *S* substrate. As imidazolonepropionate racemizes spontaneously, the result is a kinetic resolution that leads quantitatively to (*S*)-formiminoglutamate. The formimino group may be removed in one or two steps, depending on the organism. In mammals it is transferred to tetrahydrofolate by glutamate formiminotransferase. In certain bacteria, such as *Bacillus subtilis*,[14] *Klebsiella aerogenes*,[15] and *Salmonella typhimurium*,[16] hydrolysis to formamide occurs; in *Pseudomonas* spp.,[17] hydrolysis first to formylglutamate then, in a second step, to formate and glutamate takes place. Histidinaemia, a rare but usually lethal disease in humans, is caused by a defect in HAL.[18]

Urocanate is a component of human sweat and protects the skin from UV radiation. When exposed to UV radiation, the *E* form of urocanate is converted into the *Z* form, which can initiate an immunosuppressive process.[19] Urocanase deficiency in the liver is believed to be a cause of mental retardation.[20] The recently elucidated structure of urocanase is consistent with the previously proposed mechanism.[21]

The genes of *Pseudomonas putida* that code for HAL (*hutH*) and urocanase (*hutU*) have been cloned and sequenced.[22] The HAL sequences from human, rat, and murine tissues are also described in the literature.[23]

In certain bacteria the structural and regulatory genes that code for the enzymes of the histidine utilization pathways are clustered in the *hut* operon (Figure 1).[24] For example, in

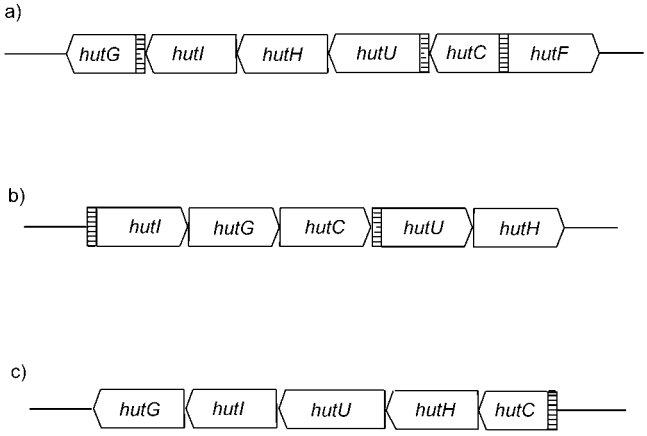

Figure 1. Structure and regulation of histidine utilization (*hut*) operons in a) *P. putida*, b) *Klebsiella aerogenes* and *Salmonella typhimurium*, c) *Bacillus subtilis*. Promotors are marked as shaded boxes; the gene boxes indicate the direction of transcription.

P. putida the *hut* operon has six open reading frames and four regions whose transcription is regulated by three promotors. The three structural genes, *hutU*, *hutH*, and *hutI*, are negatively regulated by a promoter–repressor system. The expression of all three genes is induced by urocanate, not by histidine. Therefore, a basal expression of HAL is necessary. Interestingly, transcription by *hutF* occurs in the opposite direction to transcription by the other genes. The organization of the *hut* operon in other bacteria is different from that in *P. putida*.[24] Only *P. putida* possesses *hutF*, which codes for formylglutamate amidohydrolase.[14,24a,b]

3. PAL in Plant and Fungal Metabolism

Phenylalanine can be degraded in two different ways, depending on the organism. Whereas in animals and most bacteria transformation to the corresponding 2-keto acid is the initial step, in plants,[25] fungi,[26] and at least one bacterium[27] the initial step is the elimination of ammonia catalyzed by phenylalanine ammonia-lyase (PAL).[28] The product of the elimination reaction is (*E*)-cinnamate, which is the precursor of a large number of plant metabolites, including lignin, coumarins, and flavonoids.[25] Lignin is the major constituent of wood; the flavonoids are the colorful components of many flowers (Figure 2). By genetic modification it was possible to alter lignin or flavonoid levels and thus flower color.[29] PAL lies at the branching point between the primary and secondary metabolism of plants, which makes it a target for herbicides.[30,31]

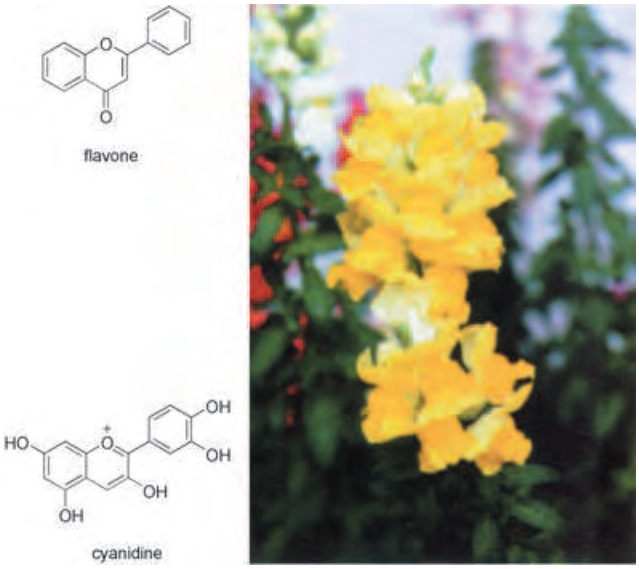

Figure 2. Colors of the plant world: anthocyanins (flavonoid pigments).

The metabolism of phenylalanine in plants is shown in Scheme 2. The biosynthesis of phenylalanine follows the well-known shikimate pathway.[31a] Hydroxylation at the *para* position leads to tyrosine, another essential amino acid. Rearrangement through the action of a 2,3-aminomutase affords β-phenylalanine, which is a precursor of taxol, an important anticancer agent.[32] The hydroxylation of (*E*)-cinnamic acid, the immediate product of the PAL reaction, can take place at either the *ortho* or the *para* position and leads to coumarins or 4-hydroxybenzoic acid, respectively. The latter is a building block of ubiquinone.[33,34]

In some plants, substituted coumaric acids can be converted into the corresponding coenzyme A esters. Feruloyl-CoA, for example, is transformed by hydroxycinnamoyl-CoA hydratase/lyase.[34] This mechanistically interesting reaction consists of the addition of water to the Michael system, followed by a retroaldol cleavage to give vanillin, an

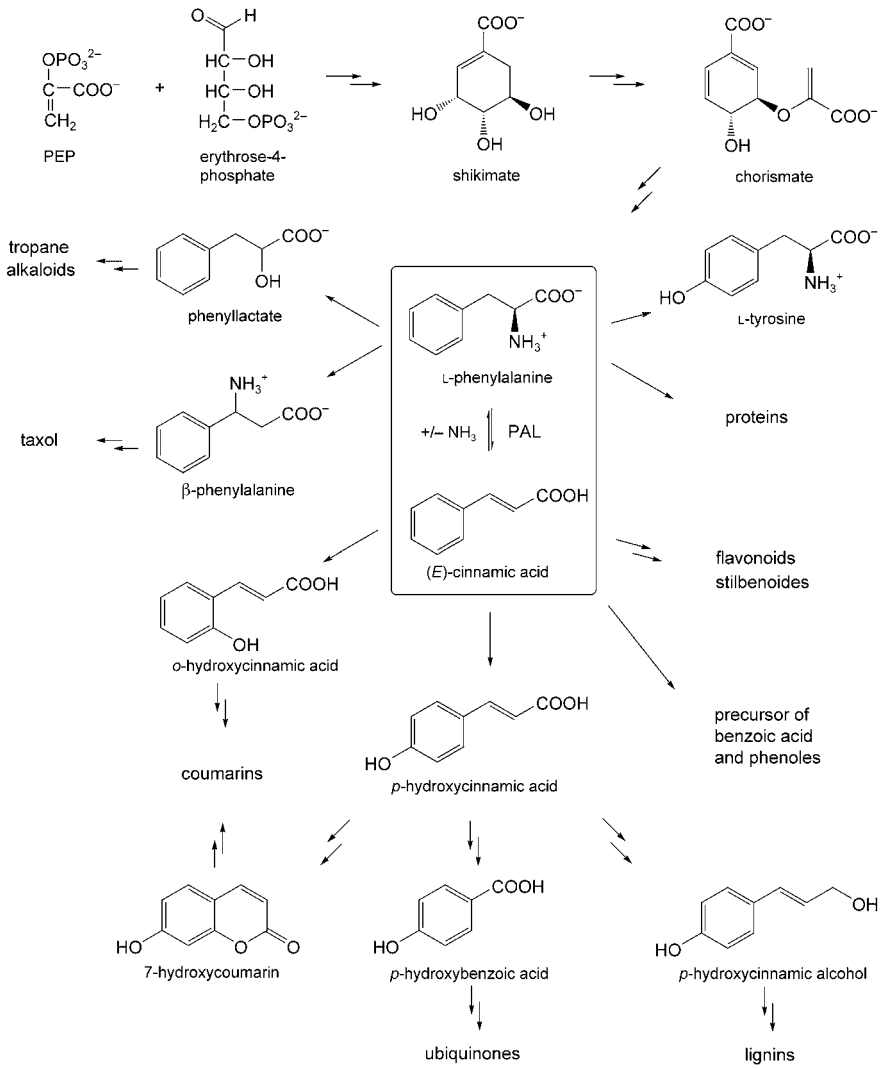

Scheme 2. Metabolism of L-phenylalanine.

important flavor substance, which is eventually oxidized to vanillic acid.

A partially purified PAL from *Rhodotorula glutinis* (also known as *Rhodosporidium toruloides*) is commercially available.[35] It is the most thoroughly investigated fungal PAL enzyme.[26] Recently, the isolation and properties of PAL from *Streptomyces maritimus* were also described.[27] This is the only bacterial PAL known to date. It is involved in the biosynthesis of the antibiotic enterocin via (*E*)-cinnamate and benzoyl-CoA. The rarity of PAL in bacteria may be explained by the absence of phenylpropanoids in these species. On the other hand, (*E*)-cinnamate may be the precursor of some specific bacterial products. A similar case is the discovery of tyrosine ammonia-lyase (TAL) in *Rhodobacter capsulatus*.[36] The recombinant enzyme reacts 150 times faster with tyrosine than with phenylalanine and corresponds to an alternative pathway to *p*-coumaryl-CoA. It is involved in the biosynthesis of the photoactive yellow protein chromophore of this bacterium.

4. Mechanism of the HAL and PAL Reactions

4.1 Early Mechanistic Proposals for HAL and PAL: Discovery of a Catalytically Important Electrophilic Group

After the elucidation of the structure of urocanic acid by Hunter in 1912,[37] its intermediacy in the histidine degradation pathway was proposed. Cell-free systems from various organisms were able to transform histidine into glutamate. Edlbacher named such systems "histidases".[38] Later the name histidase was restricted to one of the component enzymes, which catalyzes the conversion of histidine into urocanic acid and ammonia. Tabor and Mehler described the purification of the enzyme from *P. putida* in 1954;[17a] the partial characterization of the enzyme was described by Peterkofsky.[39]

A mechanism for the HAL reaction was first proposed in 1967 by Abeles and coworkers,[40] who found that histidase contains a catalytically essential electrophilic group. Evidence for the presence of this group was the inhibition of HAL by strong nucleophiles, such as KCN, CH_3NO_2, and $NaBH_4$. When the radioactively labeled inhibitors $[^{14}C]CN^-$[41] and $[^3H]NaBH_4$[42] were used, total hydrolysis of the inhibited protein afforded [^{14}C]aspartate and [^{3}H]alanine, respectively. From these results it was concluded that the prosthetic electrophile is dehydroalanine, which behaves as a Michael acceptor. It was suggested that the amino group of the substrate reacts with the dehydroalanine residue, whereby the leaving ability of the now positively charged ammonium group would be enhanced.[40] In the following this mechanism is referred to as the E_1cB mechanism.

Although the E_1cB mechanism via the EC^- state (see Scheme 3) does not explain how the nonacidic β proton of histidine can be abstracted by an enzymatic base, it has been accepted by most enzymologists for almost 30 years. Moreover, the same mechanism was also assumed for the PAL reaction,[28,43] in which the existence of dehydroalanine had been indicated by similar experiments to those described for HAL.[40]

The E_1cB mechanism for the PAL reaction is illustrated in Scheme 3. In the first step the α ammonium group of phenylalanine must be deprotonated, which enables a nucleophilic addition to the prosthetic electrophile to occur. In this way a secondary ammonium group is formed. From this point three pathways are possible.[43] By the E_1cB mechanism, H_{Si} abstraction would lead to a benzylic carbanion (EC^-), whereas by an E_1 mechanism cleavage of the N–C^α bond would result in an α carbocation (EC^+). However, the occurrence of both intermediates is unlikely because the

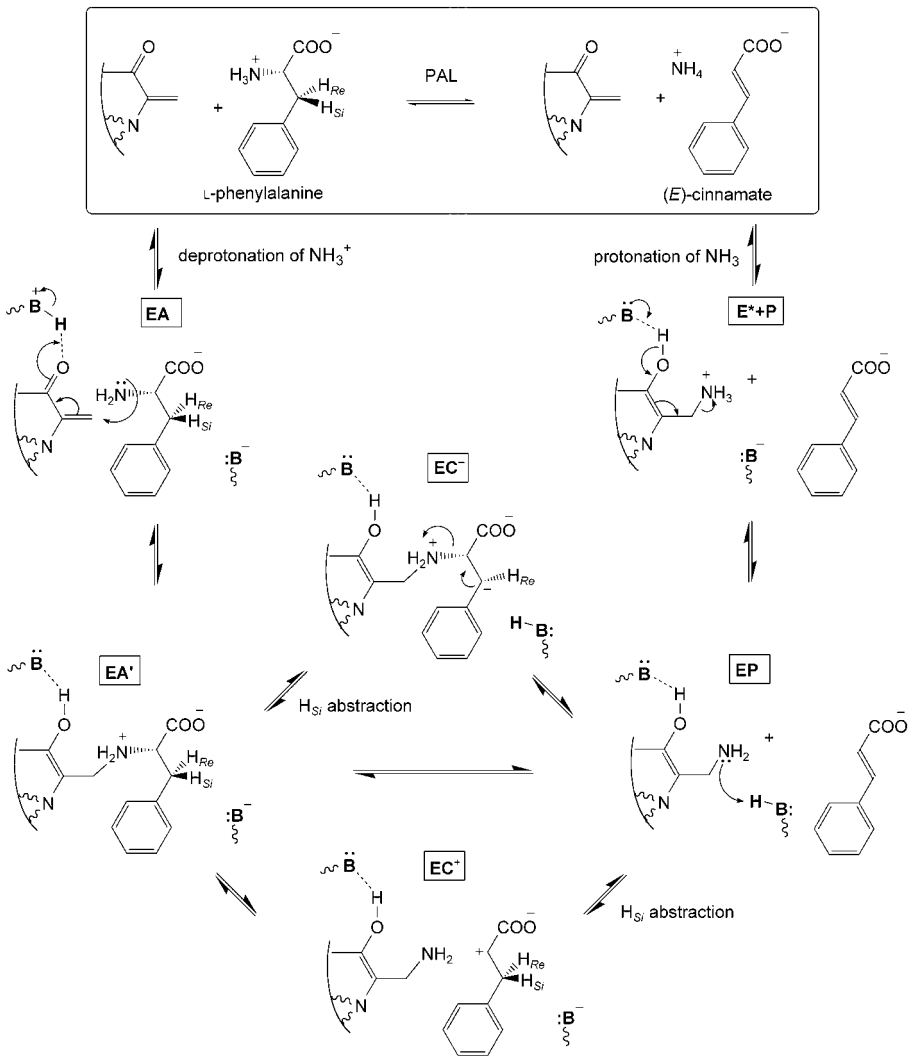

Scheme 3. Mechanism of the PAL reaction, as proposed by Hanson and Havir (1970)[28] and modified by Hermes et al. (1985).[43] The states EA, EA′, EC^-, EC^+, EP, and E*+P are depicted according to the proposal of Hermes et al.

pK_a value for the abstraction of a benzylic proton is more than 40, and the carbocation α to the carboxy group is also too high in energy. Although the following steps would be chemically plausible, both reaction pathways are improbable because of the high-energy intermediates involved. As a third alternative, a concerted reaction (E_2 mechanism) that leads directly from the EA′ state to the EP state was also considered.[43]

In a thorough kinetic analysis of the PAL reaction, Hermes et al. measured kinetic isotope effects for [^{15}N]- and [3-$^2H_2$]phenylalanine and concluded that the mechanism is not concerted.[43] (For further details of the studies with isotope-labeled substrates, see Section 6.2). The difficulty in abstracting the nonacidic β proton is also discussed by Hermes et al.,[43] but no solution to this chemical challenge is offered. Nevertheless, the kinetic ^{15}N-isotope effect of ≈1% is interpreted in favor of the addition of the amino group to the prosthetic dehydroalanine residue.

A further mechanistically relevant observation was interpreted in the same sense. In 1962, Peterkofsky reported that in the presence of radiolabeled urocanate a substantial portion of the radioactivity was found in histidine, whereas [^{15}N]ammonia was not incorporated.[39] This observation indicated the involvement of a relatively stable amino enzyme intermediate, which could revert to histidine in the presence of [^{14}C]urocanate. These results seemed to support the formerly accepted E_1cB mechanism, as it was believed that the amino group was covalently bound to the enzymatic electrophile.[40,43] A convincing alternative explanation for Peterkofsky's results is presented in Section 4.2.

Although according to Hermes et al.[43] both the concerted (E_2) and the carbonium-ion (E_1) mechanisms are ruled out on the basis of double-kinetic-isotope-effect measurements, we also considered this possibility. A positively charged ammonium ion is known to enhance the acidity of the neighboring hydrogen atoms.[44] Such an effect may be significant in the enzymatic elimination of ammonia from aspartate and 3-methylaspartate. However, in these substrates the β hydrogen atom is activated additionally by the neighboring carboxy group. It is therefore not surprising that the corresponding enzymes aspartase and methylaspartase do not have a prosthetic electrophile, as revealed by the determination of their crystal structures.[45–48] Moreover, these two ammonia-lyases belong to the enolase superfamily, as concluded on the basis of their sequence similarity and structure, which suggests that in a first step a proton is removed from position 3. Thus, the reaction is not concerted as was originally believed.

In the last 10 years, no results that support the E_1cB mechanism have been published. Although the E_1cB mechanism is favored on the basis of modeling studies in a recent publication that describes the first X-ray crystal structure of PAL,[49a] a more recently published X-ray crystal structure of higher resolution[49b] supports another mechanism, which is discussed in Section 4.2.

4.2. An Alternative Mechanistic Proposal: Friedel–Crafts Attack by the Prosthetic Electrophile

As discussed in the previous section, the main problem with the "old" E_1cB mechanism for ammonia-lyase-catalyzed

reactions is that it does not explain the abstraction of the nonacidic β protons by the enzymatic base. The pK_a value for the abstraction of the benzylic protons is above 40,[50] so that an extremely strong base would be required to abstract them under harsh conditions, for example, at high temperature. At the same time, the much more acidic ammonium hydrogen atoms should remain untouched, as the positive charge is required for the ammonium group to retain its leaving ability. In the so-called Hofmann degradation of the second type, the trimethylammonium group cannot lose its positive charge even under harsh basic conditions.

The experimental basis for the postulation of an alternative mechanism emerged in an indirect way. It originated in the search for the precursor of the prosthetic dehydroalanine residue. It was known that dehydroalanine can be formed by the dehydration of serine either in vitro or during the biosynthesis of the lantibiotics.[51] After some controversy[22a,52] the question was solved by specific mutations of serine residues that are conserved in a number of HAL and PAL sequences.[53] The mutation of Ser143 in HAL from *P. putida*[54] and Ser202[*] in PAL from parsley (*Petroselinum crispum*)[55] to alanine led to a decrease in the activity of the enzyme by a factor of more than 1000 (Table 2).[55] The

Table 2: Comparison of the kinetic constants of HALs isolated from *Pseudomonas* ATCC 11299b and *P. putida*, and mutant enzymes expressed in *E. coli* BL21(DE3).[54]

HAL-derivative source	K_m [mM]	V_{max} [U mg^{-1}]
wild-type *Pseudomonas* ATCC 11299b	4.0	28
wild-type *Pseudomonas putida*	5.3	25
recombinant wild-type *E. coli*	3.6	25
recombinant mutant S112A	4.9	26
recombinant mutant S143A	7.5	0.021
recombinant mutant S393A	3.6	20
recombinant mutant S418A	3.5	22

mutation of other conserved serine residues had little or no effect on the activity. This result identified the two serine residues mentioned as the precursors of the catalytically essential dehydroalanine residue. Interestingly, the mutation of the essential serine residue to cysteine led to fully active wild-type enzyme.[56] It can be concluded that the post-translational modification can remove either water or SH_2, but in a site-specific manner.[56]

After obtaining these results, we turned to the question of the role of dehydroalanine in the reaction mechanism. A literature search helped to solve the problem. Klee et al.[57] found that 5-nitrohistidine is also a substrate of HAL. Moreover, whereas β-dideuterated histidine showed a kinetic isotope effect of 1.5–2.0, no such effect was observed for β-dideuterated 5-nitrohistidine.[57] The explanation for this difference is illustrated in Scheme 4: The presence of the nitro group leads to a decrease in the electron density of the imidazole ring and thus to an increase in the acidity of the

[*] This residue is Ser203 in the sequence of PAL from *P. crispum* (P24481) in the SWISS-PROT database.

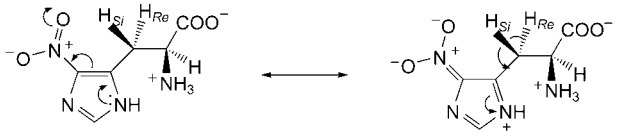

Scheme 4. Activation of the β hydrogen atoms by the nitro group of 5-nitro-L-histidine, a substrate of HAL.

β hydrogen atoms. As a consequence, the abstraction of the β proton is no longer the rate-determining step, and no kinetic isotope effect is observed.

This result suggested that the function of the prosthetic dehydroalanine residue may be similar to that of the nitro group, namely, the acidification of the β hydrogen atom. To test this idea, the activity of 5-nitrohistidine was measured both with wild-type HAL and with HAL derivatives mutated at Ser143 or inactivated by treatment with $NaBH_4$.[58] The reaction rate is practically independent of the HAL derivative used. In other words, the presence of the nitro group makes the prosthetic electrophile unnecessary. A further conclusion is that the nitro group and the prosthetic electrophile do in fact have the same function, namely, the acidification of the β hydrogen atom.

This conclusion and the precedent for electrophilic attack at the imidazole ring in the urocanase reaction[13] led to the proposal of an alternative mechanism, which is depicted in Scheme 5.[58] Attack at the imidazole ring of histidine by the prosthetic electrophile creates a similar situation to the presence of the nitro substituent and facilitates the abstraction of H_{Re}[59] by the enzymatic base. The ammonium group is then cleaved as ammonia, and, in a final step, the fragmentation of the adduct gives urocanate and regenerates the prosthetic group.[58]

Such a mechanism is less plausible for the PAL reaction, as the phenyl ring is not as electron rich as the imidazole ring. Through the attack by the prosthetic electrophile, the aromaticity would be lost at least transiently, which is unfavorable energetically. This would be the first biological Friedel–Crafts reaction.[60] However, a number of experiments supported such a mechanism for the PAL reaction.[61] In analogous experiments to those described for HAL, the PAL mutants Ser202Ala and Ser202Thr reacted much faster with 4-nitrophenylalanine than with the unsubstituted substrate ($k_{cat} < 20$).[61]

PALs from various sources also accept tyrosine as a substrate, but react with it at a much lower rate ($k_{cat} < 50$). If the Friedel–Crafts-type attack plays a role in the mechanism, then *m*-tyrosine should be a much better substrate, as is indeed the case. Recombinant PAL from parsley even reacts with *m*-tyrosine 10–20% faster than with L-phenylalanine. The proposed mechanism is illustrated in Scheme 6.[61]

More recently, the chemical feasibility of the electrophile-assisted elimination of ammonia was demonstrated with a chemical model.[62] One portion of the model compound mimicked the essential parts of the substrate (phenylalanine), and another portion mimicked the electrophilic Michael acceptor (MIO) in a sterically appropriate position (Scheme 7).

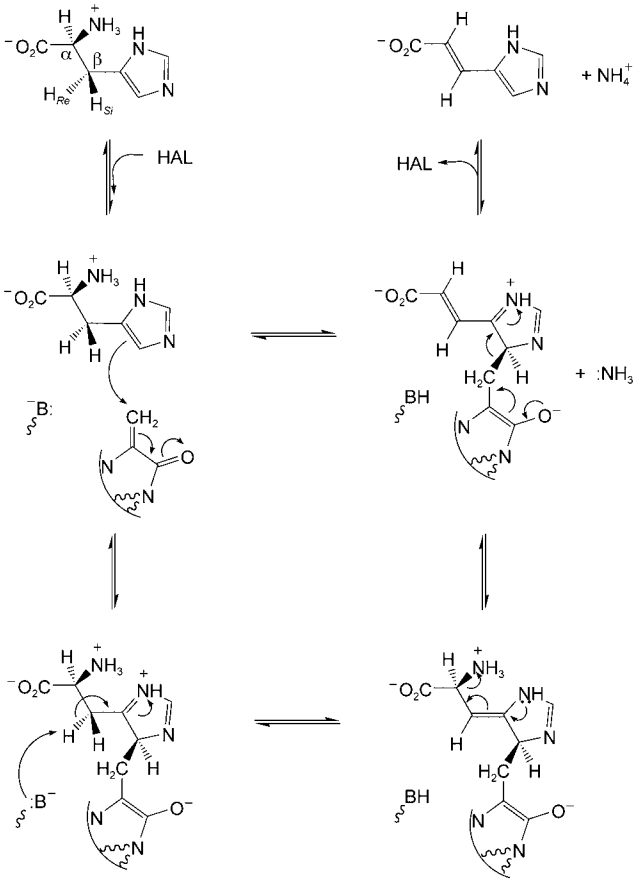

Scheme 5. Alternative mechanism for the HAl reaction.[58]

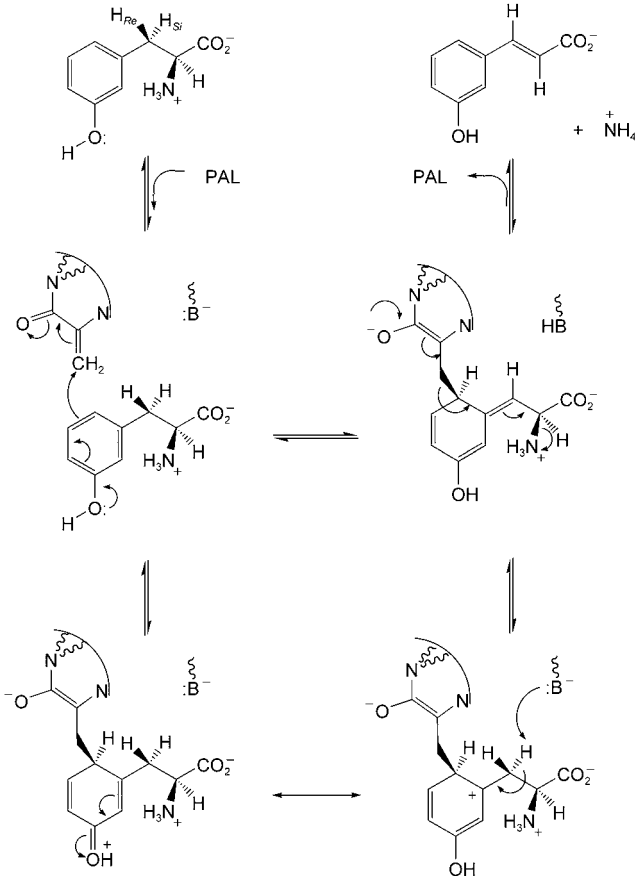

Scheme 6. Mechanism of the PAL reaction with *m*-tyrosine as the substrate, assuming a Friedel–Crafts-like attack.

The following measures were taken to facilitate the reaction: a) The reaction was carried out in an intramolecular fashion, b) a methoxy group was introduced to enhance the nucleophilicity of the phenyl ring at the position of attack, and c) the electrophilicity of the Michael acceptor was enhanced by using an α,β-unsaturated aldehyde instead of the corresponding amide. Under Friedel–Crafts conditions ($BF_3{\cdot}Et_2O$ or $AlCl_3$) two diastereomeric tricyclic compounds were isolated in excellent yields, but no trace of the product that would arise from the elimination of dimethylamine was detected. Evidently, the competing abstraction of a proton from the ring, accompanied by rearomatization and completion of the substitution, suppressed the abstraction of the benzylic proton. PAL prevents the abstraction of a ring proton by excluding bases from the hydrophobic pocket which the phenyl group occupies. Therefore, we had to take a further measure to mimic this "negative catalysis". When we substituted the hydrogen atoms on the phenyl ring for methyl groups (Scheme 7) the completion of the Friedel–Crafts substitution was prevented, and we could isolate the desired elimination product.[62]

Evidence for the active role of the phenyl ring in the process was provided by deactivating the phenyl ring, either by removing the methoxy group or by exchanging it for a nitro group. In these cases no elimination products were detected.[62]

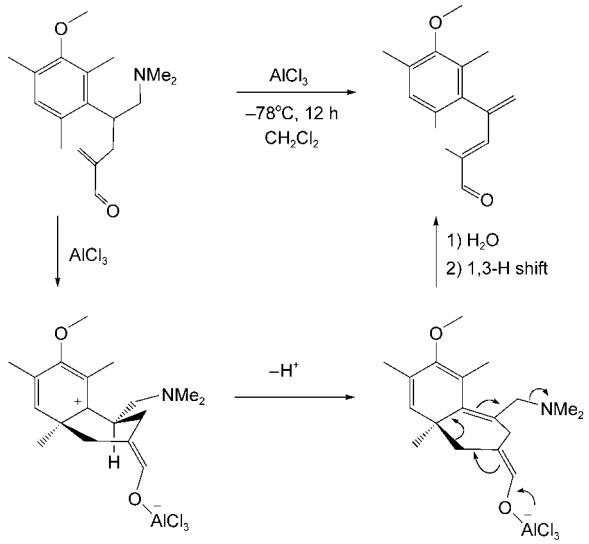

Scheme 7. Synthetic model system for modeling the PAL reaction.

4.3. Discovery of 5-Methylene-3,5-dihydroimidazol-4-one (MIO) as the Prosthetic Electrophile of HAL and PAL

The prerequisite for site-directed mutation in HAL and PAL was the cloning and heterologous expression of both enzymes. Success was first achieved with HAL. The expres-

sion of its gene from *P. putida* in *E. coli* by using the pT7-7 expression vector yielded about 100 mg of the pure enzyme from 1 L of overnight culture of the recombinant bacteria. The access to gram quantities of pure HAL facilitated its crystallization.[58] However, the crystal structure could only be solved after the mutation of a solvent-exposed cysteine residue to alanine.[63b]

HAL from *P. putida* had been characterized previously by biochemical methods.[52] The X-ray structure at a resolution of 2.1 Å confirmed that it is a homotetramer and also led to an unexpected result, namely, that the prosthetic electrophile is not dehydroalanine but MIO.[64] MIO can be regarded as a modified dehydroalanine residue and is formed post-translationally by cyclization followed by the elimination of two water molecules from the inner tripeptide Ala142-Ser143-Gly144 (Scheme 8).

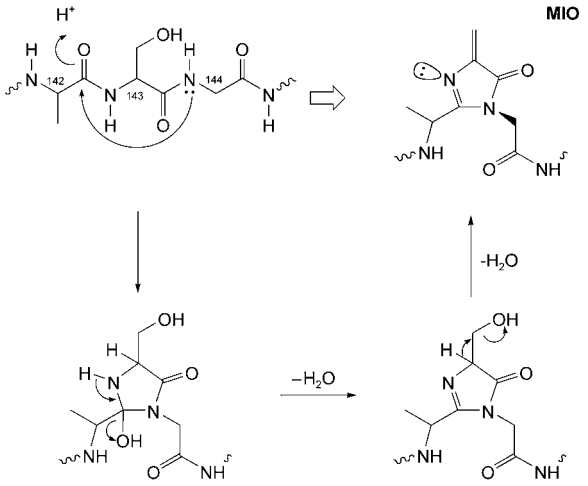

Scheme 8. Formation of the MIO group in HAL by post-translational modification.

MIO is the only catalytically important protein-derived cofactor with such a heterocyclic structure. An example of a noncatalytic species is the fluorophore of the green fluorescent protein. This fluorophore also has an MIO structure, but the exocyclic methylene group has a *p*-hydroxyphenyl substituent.[65]

As catalytically active HAL is also formed in an in vitro translation system, the information for the biosynthesis of MIO must be in the amino acid sequence and hence in the folding of the polypeptide chain.[66] The homotetramer exhibits D_2 symmetry and consists mainly of α helices (Figure 3). Each subunit can be subdivided into two domains. The N-terminal domain is globular with eight helices and four short β strands; the C-terminal domain consists of five long, nearly parallel α helices surrounded by six other helices.[64]

In each active center (identified by the presence of the MIO groups) there are amino acid residues from three subunits (Figure 4). The importance of these active-site amino acids for catalysis is supported by mutational analysis. The much higher electrophilicity of MIO relative to dehydroalanine makes the Friedel–Crafts attack at the aromatic ring feasible.[52]

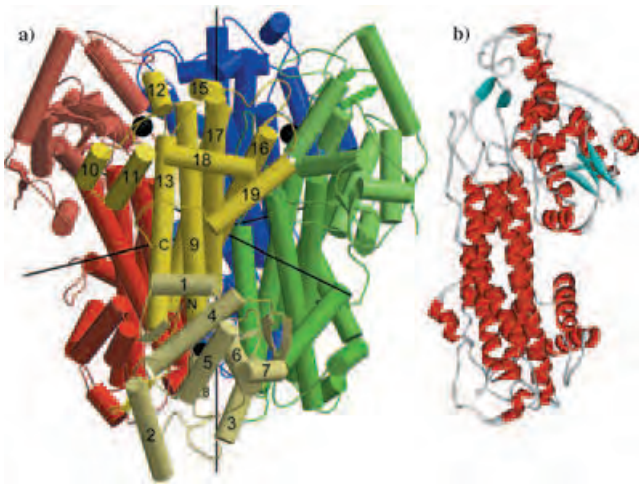

Figure 3. X-ray crystal structure of the homotetramer of HAL (a) and one subunit (b).[64]

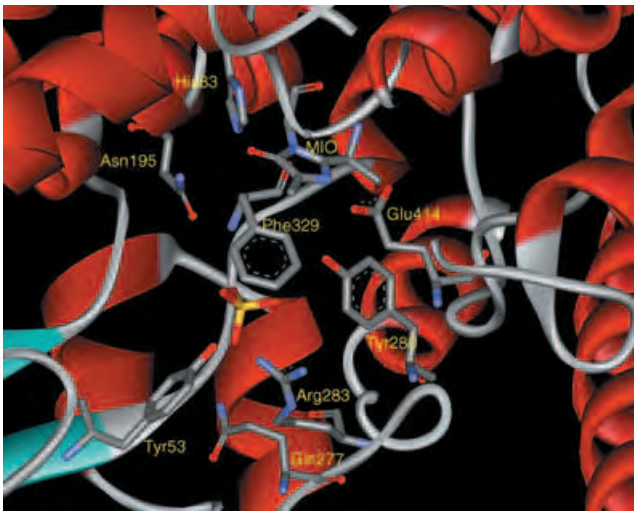

Figure 4. Substrate-free active site of HAL.

In MIO, the delocalization of the lone pairs of electrons on the nitrogen atoms into the Michael system is prevented. In the case of the sp^2-hybridized nitrogen atom the orbital of the lone pair of electrons is orthogonal to the π orbitals of the α,β-unsaturated carbonyl system, and in the case of the sp^3-hybridized nitrogen atom the $sp^3 \rightarrow sp^2$ transition is prevented by the fold of the polypeptide chain. However, the barrier to this transition is not excessively high.[67] Moreover, the attack of a nucleophile at the exocyclic double bond renders the imidazole ring aromatic, which compensates for the transient loss of aromaticity of the imidazolyl or phenyl group of the substrate.

The mechanism of the PAL reaction initiated by a Friedel–Crafts attack is shown in Scheme 9. An example of a lone pair of electrons on a nitrogen atom that is prevented from undergoing delocalization into an adjacent carbonyl group is provided by quinuclidone (Scheme 10), which does not behave as a lactam, but as a ketoamine.

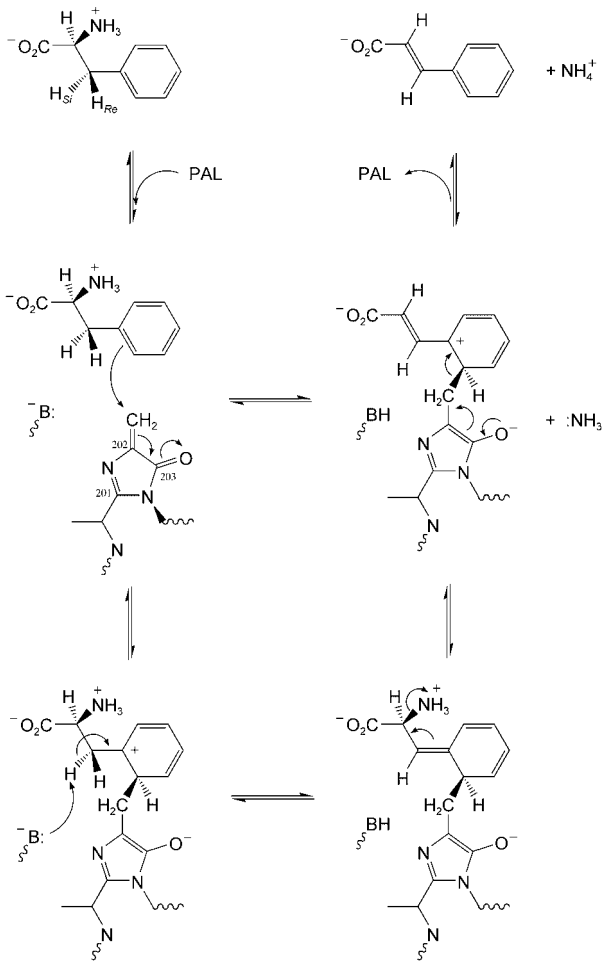

Scheme 9. Mechanism of the PAL reaction involving a Friedel–Crafts-type attack of the MIO group on the phenyl moiety of L-phenylalanine.

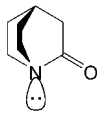

Scheme 10. Structure of quinuclidone.

In 1970, Klee reported a shoulder at about 315 nm in the UV spectrum of HAL, but no explanation for its occurrence could be offered at that time.[68] The idea emerged that the cross-conjugated system of MIO could be responsible for the shoulder. We recorded UV difference spectra of HAL and PAL mutants that do not contain the MIO group and the corresponding wild-type enzymes. In both cases a distinct absorption maximum (λ_{max}) was observed at 308 nm (Figure 5).[69] This method has also been used by others to show the presence of MIO.[70]

The very recently published X-ray crystal structures of PAL from *Rhodosporidium toruloides*[49a] and parsley[49b] further confirm the presence of MIO.

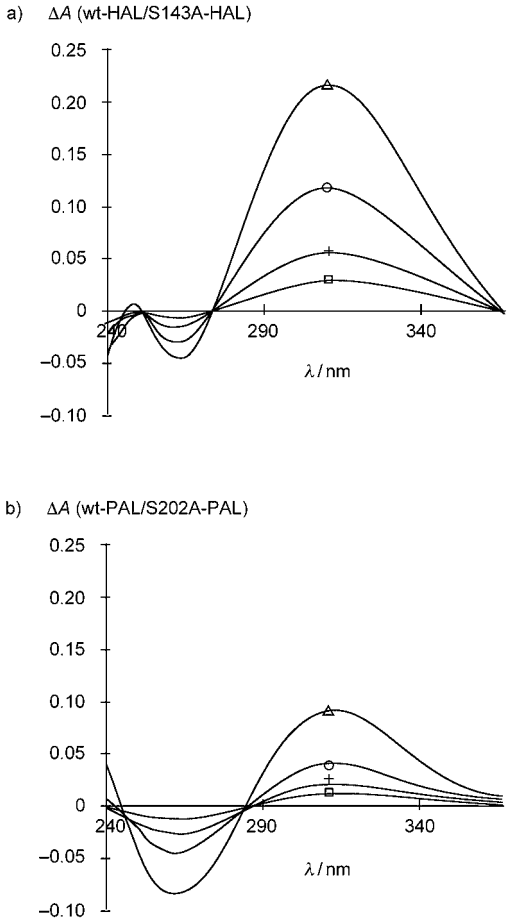

Figure 5. UV difference spectra of a) wild-type HAL and the mutant Ser143Ala-HAL, and b) wild-type PAL and the mutant Ser202Ala-PAL. Concentrations in mg mL^{-1}: △ 1.6, ○ 0.8, + 0.4, □ 0.2; wt = wild-type.

5. The Active Sites of HAL and PAL

5.1 Identification of Active-Site Amino Acids by Site-Directed Mutagenesis

The amino acids in the active site of HAL were identified by X-ray crystal-structure analysis.[64,71] In Scheme 11 the relative positions of these amino acids are shown, together with the substrate modeled into the active site.[72] All mutations were carried out on the Cys273Ala mutant, which had been used for the X-ray crystal-structure analysis. The k_{cat} value of this mutant was about 5 times lower than that of wild-type HAL, whereas its K_m value was 4.5 times higher. The kinetic constants of several mutants are listed in Table 3.[72] The importance of Glu414 was highlighted by the decrease in the k_{cat} value for the Glu414Ala mutant by a factor of 21000. The likely function of this residue is the abstraction of the H_{Re} proton from the substrate as the enzymatic base. As can be seen from Scheme 11, Glu414 is assisted in the abstraction of H_{Re} by Tyr280 on a neighboring subunit. On the basis of the structure of cysteine-inhibited HAL, Baedeker and Schulz postulated a different mechanism, by which Tyr280 abstracts H_{Re} with assistance from Glu414.[67] There are arguments in

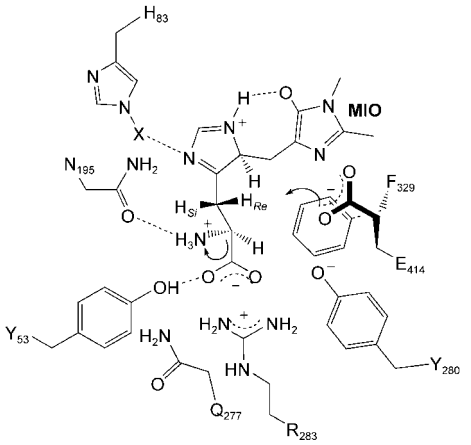

Scheme 11. Model of the active site of HAL with the substrate arranged according to the Friedel–Crafts-like mechanism.[74]

Table 3: Kinetic constants of active-site mutants of C273A HAL.[72]

Mutation in C273A HAL	K_m [mM]	k_{cat} [s^{-1}]	$k_{cat,C273A}/k_{cat,mut}$
–	18 ± 3	18 ± 1	1[a]
R283K	4.1 ± 0.7	0.79 ± 0.03	20
Y280F	8 ± 1	0.32 ± 0.01	55
F329A	4.4 ± 0.7	0.18 ± 0.01	100
Q277A	7 ± 2	0.14 ± 0.01	125
E414Q	1.7 ± 0.9	0.053 ± 0.0025	339
N195A	3 ± 1	0.018 ± 0.001	1000
R283I	18.0 ± 4	0.011 ± 0.001	1640
Y53F	8 ± 1	0.0068 ± 0.0004	2650
H83L	1.2 ± 0.4	0.001 ± 0.0002	18000
E414A	6.1 ± 0.7	0.00086 ± 0.00007	20930

[a] $k_{cat,C273A}/k_{cat,wt} = 0.21$.

favor of both suggestions. The fact that the HAL mutant Glu144Ala shows a greater loss of activity than Tyr280Phe relative to the wild-type enzyme would support the former view,[64,72] whereas the observation that Gln488 occupies a position in PAL analogous to Glu144 in HAL, but that Tyr351 is conserved, speaks for the second view.

A large decrease in k_{cat} was also observed for the mutant His83Leu. His83 is most likely involved in the binding of the imidazole ring of the substrate. The distance (4.15 Å) suggests that the binding occurs through a water molecule or a hydronium ion. Although in the X-ray crystal structure no metal ion is observed, it has been found that Zn^{2+}, Mn^{2+}, and similar metal ions increase the activity of HAL.[73] We suggest that the species represented with an "X" in Scheme 11 could be either a hydronium or a metal ion. The guanidino group of Arg283 is the counter ion of the carboxylate group of the histidine substrate and can be substituted for Lys with a relatively small loss of activity. However, its substitution by Ile, a neutral amino acid, leads to a large decrease in the k_{cat} value. An even larger loss of activity is observed for the mutation Tyr53→Phe. Tyr53 interacts with the carboxylate group of the substrate and may play a role in the abstraction and binding of the α amino group. Tyr53 may also be responsible for the stability of the amino enzyme intermediate,[39] possibly with the assistance of Asn195, whose substitution for Ala causes a 1000-fold decrease in k_{cat}. Somewhat controversial is the effect of the mutation Phe329→Ala. One research group[72] found a 100-fold decrease in activity, whereas another[67] found a 2500-fold decrease. Phe329 is conserved in all members of the HAL/PAL family and in the second model[67] interacts with the imidazolyl group of the substrate. It is postulated that the phenyl group of Phe329 is required to induce MIO formation by steric compression. The mutant Phe329Gly leads to an inactive HAL protein which does not contain MIO,[71] whereas the mutant Phe329Ala formed the MIO group but showed very low activity.

To elucidate the role of the active-site amino acids of PAL it was necessary to resort to its high sequence homology with HAL, which allowed modeling of the active site of PAL (see also Section 5.2). On the basis of this model and the kinetic constants of a number of PAL mutants (Table 4), functions of the active-site residues could be proposed.[74] All except two amino acids are found to occupy almost identical positions. His83 and Glu414 in HAL are exchanged for Leu138 and Gln488, respectively, in PAL.

In an attempt to transform PAL into HAL, the PAL mutants Leu138His and Gln488Glu were prepared, as well as the double mutant Leu138His/Gln488Glu.[74,75] Whereas for the single mutants the k_{cat} values decreased only slightly, the double mutant was 145 times less active than wild-type PAL (Table 4). More dramatic was the change in the K_m values for

Table 4: Kinetic constants of active-site mutants of PAL.[74]

Mutation in wt-PAL	K_m [mM]	k_{cat} [s^{-1}]	$k_{cat,wt}/k_{cat,mut}$
wt	0.12 ± 0.004	13.5 ± 0.1	1
Q488E	0.057 ± 0.006	2.1 ± 0.04	6
L138H	13.5 ± 0.6	0.99 ± 0.02	14
R354A	0.057 ± 0.003	0.104 ± 0.005	130
L138H/Q488E	55 ± 4.9	0.093 ± 0.004	145
Y351F	0.024 ± 0.004	0.057 ± 0.001	235
F400A	0.027 ± 0.005	0.039 ± 0.001	345
S203A	0.019 ± 0.001	0.031 ± 0.0001	435
Q488A	0.033 ± 0.002	0.022 ± 0.002	615
Q348A	0.03 ± 0.01	0.0057 ± 0.0004	2370
N260A	0.033 ± 0.003	0.005 ± 0.001	2700
Y110F		0.00018	75000

the Leu138His mutants. These values are more than 100 times higher than that for the wild-type enzyme, thus supporting the view that Leu138 is part of the hydrophobic binding pocket that harbors the phenyl group of the substrate. Because of the relatively strong adhesion of the phenyl group to this hydrophobic environment, the rate-limiting step in the PAL reaction is the release of the product, (*E*)-cinnamate. Therefore, in contrast to the HAL reaction, no primary kinetic deuterium-isotope effect is observed in the PAL reaction.[43] Recently, it was shown that with the mutant Leu138His the release of the product is faster and a kinetic deuterium-isotope effect ($k_H/k_D = 2.3$) is observed.[75] The assumption that the PAL double mutant Leu138His/Gln488Glu would

behave like HAL was only partially endorsed. Whereas the K_m value for histidine was similar to that with HAL, the k_{cat} value was 8000 times lower. It seems that amino acid residues other than those in the active site also affect the reaction rate.

The largest loss of activity was found with the PAL mutant Tyr110Phe. Tyr110 in PAL is thought to have the same function as Tyr53 in HAL, but it seems to be even more important. Similarly, Asn260 and Tyr348 in PAL correspond to Asn195 and Tyr280 in HAL and probably have the same important functions. In this case the phenolate form of Tyr348 is definitely the enzymatic base that abstracts the β H_{Si} proton of the substrate.[76] Arg354 and Phe400 in PAL correspond to Arg283 and Phe329 in HAL, and their mutations affect the kinetic constants of the two enzymes to a similar extent.[74]

Another interesting difference between HAL and PAL is found with the mutants Ser143Thr and Ser203Thr. Although practically inactive, the HAL mutant Ser143Thr shows a maximum at 305 nm in the UV difference spectrum versus the MIO-free mutant Ser143Ala, whereas no such absorption maximum is observed in a similar experiment with the Ser203Thr mutant of PAL. These results indicate that the HAL mutant Ser143Thr still forms the MIO structure but that the corresponding PAL mutant does not. The exchange of the two other amino acid residues directly involved in MIO formation to give HAL mutants Ala142Ser and Gly144Val led to decreased V_{max} values (by a factor of 6 and 44, respectively), but these effects are less dramatic.[77] Other mutations at the same positions (Ala142Gly, Ala142Asp, and Gly144Ala) resulted in moderate loss of activity. No activity at all was reported for the HAL mutant Asp145Ala.[67]

5.2. Modeling the Active Sites of HAL and PAL

Molecular modeling was applied as a complementary tool for the interpretation of the enzyme kinetic data from reactions with HAL and PAL mutants modified at active-site residues. Thus, a histidine molecule was modeled into the X-ray crystal structure of HAL[64] with its amino group at binding distance from the exocyclic methylene carbon atom of MIO and its carboxylate near the guanidino group of Arg283′.[67] Inspection of this arrangement revealed that there is no strong base near the β hydrogen atom of the substrate and no specific binding site for the imidazole ring of histidine, thus suggesting that direct ammonia abstraction is not compatible with the experimental structure.

However, the experimental HAL structure[64] was found to be compatible with a Friedel–Crafts attack of the MIO group at the aromatic ring of the substrate.[58,61,64] Two slightly different substrate-binding models have been described for HAL.[64,71,72] In the first model,[64,72] the imidazole ring of histidine is positioned close to Leu146 and thus "below" the MIO group. In the second, later, proposal[67] the imidazole ring is positioned "above" MIO and interacts with Phe329. Both models are consistent with the functions of the amino acid residues at the active site as concluded from mutational experiments, and both rationalize the experimental finding that urocanate is released before ammonia.[39]

The electronic spectra of a truncated MIO model were calculated at the PM3 level of theory and used to estimate the degree of polarization of the MIO moiety in the substrate-free state of HAL (Scheme 12).[72] The calculated absorption

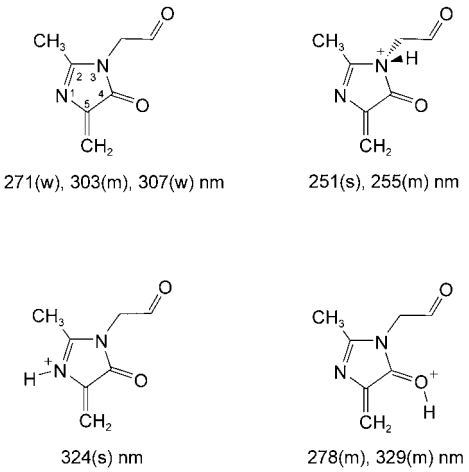

Scheme 12. A model compound for nonprotonated MIO and its singly protonated forms; the calculated UV absorption maxima are given.

maxima at $\lambda = 303$ and 307 nm for the nonprotonated MIO model were in good agreement with the experimentally determined maximum at about $\lambda = 308$ nm in the UV difference spectrum of HAL. Calculated UV spectra for MIO structures fully protonated at the carbonyl oxygen atom, at N1, or at N3 were significantly different, thus indicating that MIO is not polarized significantly in substrate-free HAL.

To investigate the functions of the active-site residues of PAL, the X-ray structure of HAL was used as a template for homology modeling of the PAL structure (Figure 6).[74] In agreement with biochemical data, PAL was modeled as homotetramer (Figure 6, right). The model revealed that catalytically important residues are located at highly isosteric positions within two distinct regions of the protein chains in both HAL and PAL.

In the region of the active site, the PAL model closely resembles the X-ray crystal structure of HAL (Figure 7). All the active-site residues in the PAL model occupy positions that would be expected on the basis of comparison with the HAL sequence and structure. Moreover, the model constructed for the PAL from *Petroselinum crispum*[86] (*Pc*-PAL; Figure 6, right) shows excellent similarity with the recently published X-ray crystal structures of the PAL from *Rhodosporidium toruloides*[49a] (*Rt*-PAL; Figure 6, middle column; PDB codes for *Rt*-PAL: 1T6J and 1T6P) and *Pc*-PAL.[49b]

Interestingly, the residues His137 and Gln138 at the active site of *Rt*-PAL are replaced by Phe140 and Leu141 in the *Pc*-PAL model. This difference stems from differences in the sequences of the two PALs in this region rather than errors in the modeling of *Pc*-PAL. Moreover, the loop 105–123, which contains the catalytically important Tyr110 residue, is not present in the *Rt*-PAL structure.[49a] The absence of this loop can lead to the ambiguous arrangement of the substrate when modeling within this structure.

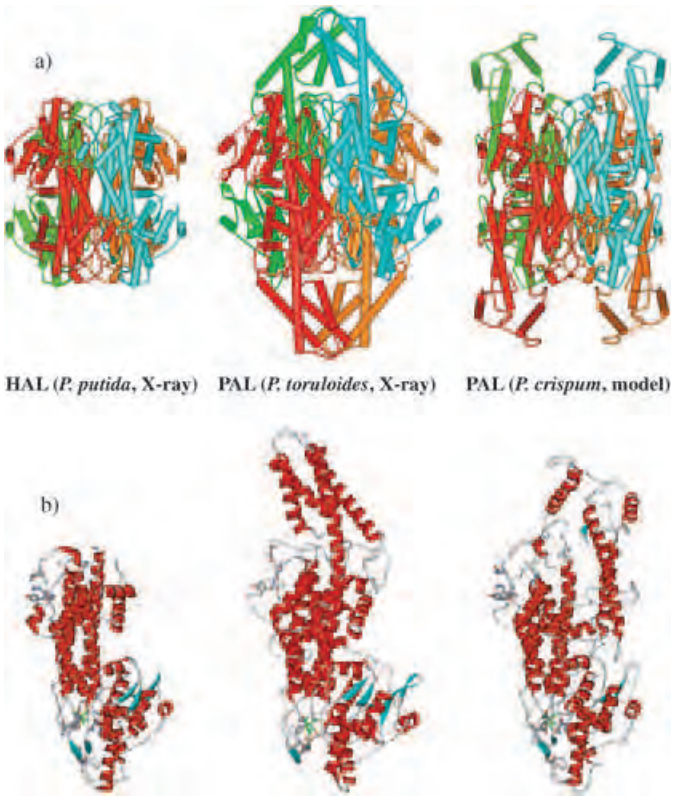

Figure 6. Comparison of the X-ray crystal structures of HAL (from *Pseudomonas putida*)[64] and PAL (from *Rhodosporidium toruloides*)[49a] with the homology model of PAL (from *Petroselinum crispum*):[86] a) tetrameric structures; b) single subunits (the catalytically important residues are shown as stick models; moieties containing MIO prosthetic groups are colored green).

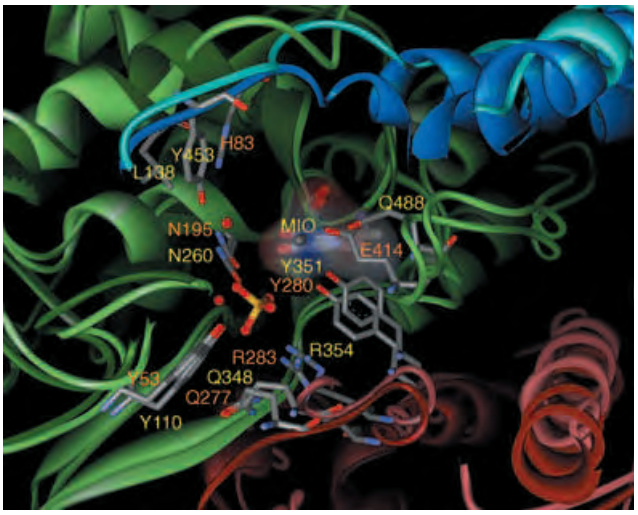

Figure 7. Model of the substrate-free active site of PAL (from *P. crispum*)[86] superimposed on the active site of HAL (from *P. putida*)[64] The lighter colors (yellow labels; light-blue, light-green, and light-red ribbons) indicate the PAL model; the darker colors (orange labels, blue, green, and red ribbons) indicate the HAL structure.

The modeling of a σ-complex-like intermediate (Figure 8a) and the product-binding state with (*E*)-cinnamate

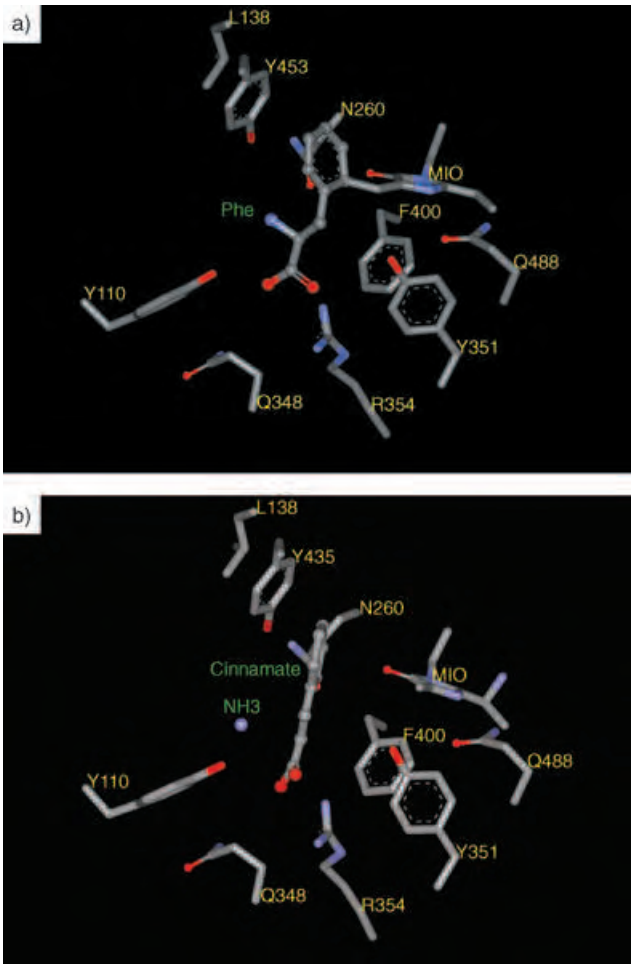

Figure 8. Models of the cationic intermediate (a) and product-binding states (b) at the PAL active site according to the Friedel–Crafts-like mechanism.

plus ammonia (Figure 8b) at the active site of *Pc*-PAL provided more information about the catalytic functions of the amino acid residues (Scheme 13).

A common feature of the tetrameric HAL and PAL structures is that a tyrosine residue (Tyr53 in HAL and

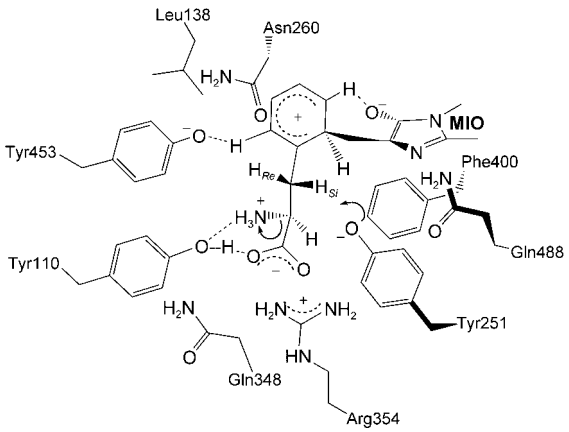

Scheme 13. Proposed catalytic roles of the active-site residues on the basis of the model of PAL.[86]

Tyr110 in PAL) is located at the edge of the channel through which the substrate can enter or the product be released from the active site. Mutations of Tyr to Phe at these positions lead to a dramatic decrease in catalytic activity (Scheme 14).[74] The existence of this narrow channel may account for the experimental finding[39,74] that after the elimination the product (*E*)-cinnamate is released first (Scheme 14e), followed by the ammonia in the form of an ammonium ion (Scheme 14f).

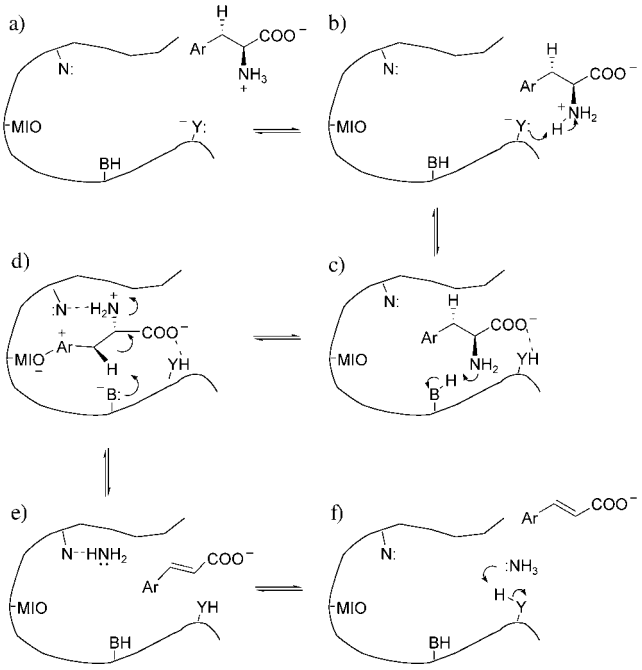

Scheme 14. Proposed mode of substrate binding (a–c), elimination (d), and release of the product (e, f) in HAL and PAL, assuming a Friedel–Crafts-like mechanism.

6. HAL and PAL Inhibitors and Alternative Substrates

6.1. Inhibition of HAL by Cysteine

Among the inhibitors of HAL, L-cysteine is the most interesting, because its behavior provided clues as to the reaction mechanism.[58] Inhibition by cysteine is reversible at neutral pH and under anaerobic conditions, but irreversible above pH 10.5 and in the presence of oxygen. An absorption occurs at about $\lambda = 340$ nm, the intensity of which is proportional to the degree of inhibition.[68b]

The first proposals for the structure of the chromophore generated had been made before MIO was discovered as the prosthetic group of HAL.[78] Soon after the discovery of the MIO group[64] two research groups described the structure and proposed mechanisms for its formation.[79] In both cases it was assumed that the thiolate group of cysteine reacts as a nucleophile with MIO, which is consistent with our previous proposal.[58,78b] The follwing arguments favor the attack of the thiolate group: 1) L-Cysteine and L-homocysteine but no other nonaromatic amino acids act as inhibitors, and 2) the thiol groups of the two inhibitors are positioned at the correct distance to attack MIO (relative to the 5-position of the imidazole ring of histidine).

To isolate the chromophore that absorbs at $\lambda = 335$–340 nm, the inhibited HAL protein was denatured and partially digested with pronases. After separation of the peptides produced, those that contained the chromophore were identified and characterized spectroscopically. Although the oligopeptides described in the two reports differed in length, they both contained the same chromophore structure (**1** and **2** in Scheme 15).[79] Viewed superficially, this finding

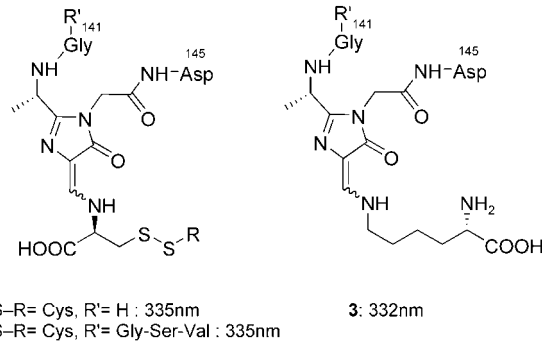

1: S–R= Cys, R'= H : 335nm
2: S–R= Cys, R'= Gly-Ser-Val : 335nm
3: 332nm

Scheme 15. Chromophore groups in the isolated oligopeptides after treatment of the HAL protein with L-cysteine or after reaction with L-lysine followed by proteolytic digestion.

supports the previously favored mechanism, in which the α amino group of histidine is the nucleophile that reacts with MIO.[28,41–43] However, both research groups believe that the isolated chromophore is the product of a rearrangement, as illustrated in Scheme 16.[79] The initial addition of the thiolate group of cysteine to MIO affords a highly nucleophilic enolate, which, like in the photorespiration by the enzyme ribulose-1,5-bisphosphate carboxylase (rubisco),[80] reacts with dioxygen to give a peroxide anion. A vinylogous thioester formed in an electrocyclic reaction coupled with a 1,3-H shift from a C atom to an O atom then undergoes intramolecular aminolysis followed by disulfide formation with a further cysteine molecule.

The postulated rearrangement was supported by the observation of other proteolysis products. Merkel isolated the adduct from lysine and MIO as the main product (**3** in Scheme 15).[79a,c] Evidently the initially formed vinylogous thioester had undergone an intermolecular aminolysis with the ε amino group of lysine molecules present in the lysate as the products of extensive proteolysis. This explanation is consistent with the observation that the inhibited but intact protein shows an absorption maximum at $\lambda = 338$ nm, whereas for the isolated cysteine adduct $\lambda_{max} = 335$ nm was found, and for the lysine adduct $\lambda_{max} = 332$ nm.[79a,c]

The isolated pure peptide containing the chromophore that absorbs at $\lambda = 335$ nm was slightly unstable to chromatography on a reversed-phase column under acidic conditions, as manifested by a smaller extra peak in the elution diagram. This degradation product was also isolated and characterized spectroscopically. From the spectral data (UV, NMR, MS) its

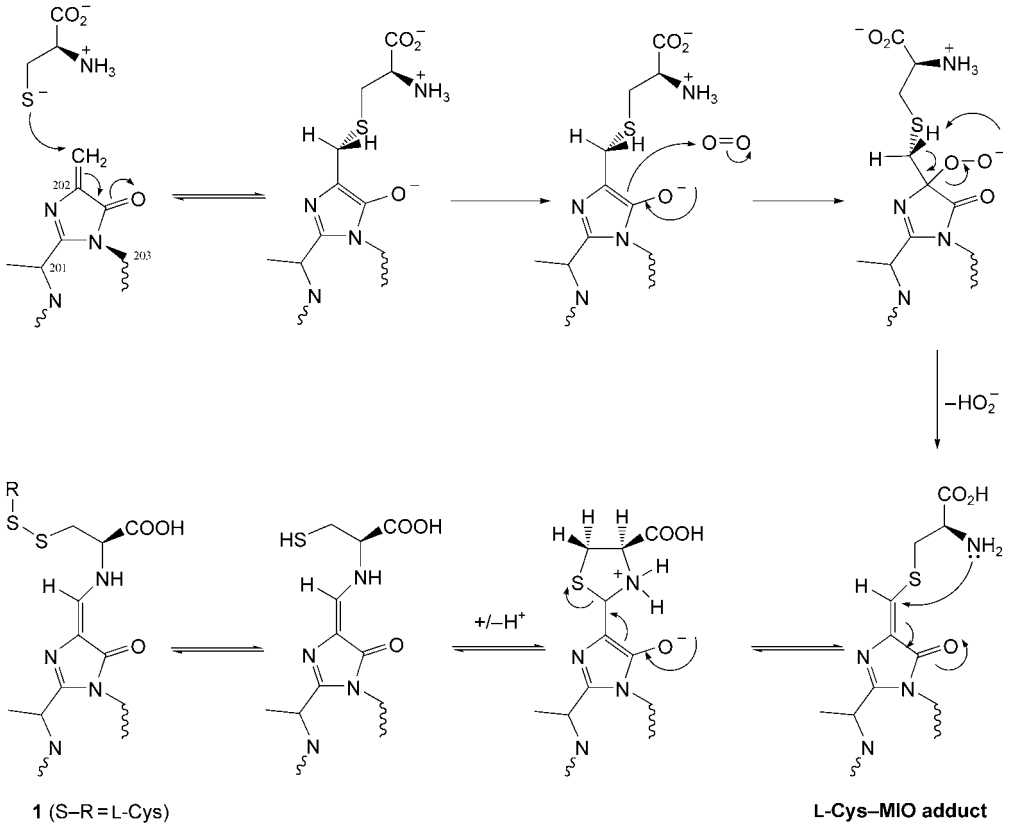

Scheme 16. Proposed mode of addition of L-cysteine to MIO followed by oxidation and rearrangement.

chromophore was identified as an MIO group with a hydroxy substituent on the exocyclic methylene group. The compound forms two tautomers and is reductone-like, like vitamin C. Its absorption maximum occurs at 310 nm, very close to that of MIO ($\lambda_{max} = 308$ nm). A possible mechanism for the formation of this degradation product involves a further rearrangement followed by ester hydrolysis (Scheme 17).[79a,c]

When L-[^{35}S]cysteine was used as an inhibitor of HAL, it was incorporated into the peptide containing the chromophore that absorbs at $\lambda = 335$ nm.[79a,c] This finding seems to contradict previous results.[68b,78a] A plausible explanation for this deviation could be that in the earlier studies the initially formed chromophore had already been converted into products devoid of cysteine. Recently, the X-ray crystal structure of the cysteine-inhibited HAL was determined, but the cysteine moiety was not observed despite very high resolution.[67] As the crystals had been prepared several months before they were submitted to X-ray crystallographic examination, rearrangement of the chromophore might have occurred, so that it was no longer possible to localize the cysteine unit.

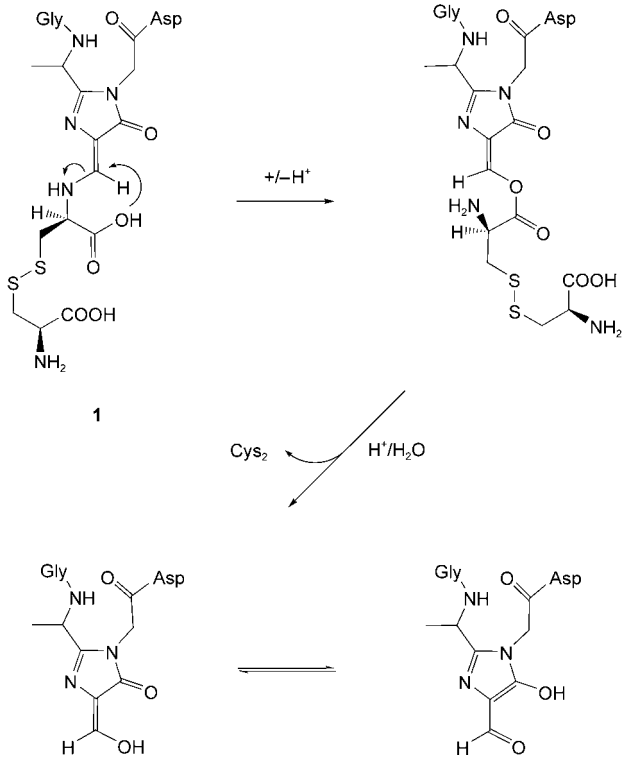

Scheme 17. Degradation of the chromophore **1** upon hydrolysis.

6.2. The Behavior of Substrate Analogues and Kinetic Isotope Effects in the PAL Reaction

In recent years a number of research groups have examined the above issues and interpreted the results in

favor of the Friedel–Crafts-type mechanism.[81–83,94] However, before the new mechanism was proposed some relevant publications had appeared,[43,84] in which 2,5-dihydrophenylalanine (**4**, Scheme 18) was identified as a moderately good

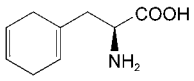

2,5-dihydrophenylalanine, **4**

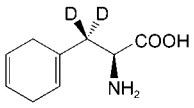

β-$^2H_2$-2,5-dihydrophenylalanine, **5**

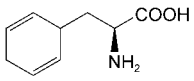

1,4-dihydrophenylalanine, **6**

Scheme 18. Partially hydrogenated phenylalanine derivatives for the kinetic investigation of the PAL reaction.

substrate of PAL. In contrast to phenylalanine, the 3,3′-dideutero derivative **5** exhibited a primary kinetic isotope effect of about 2, thus indicating that the deprotonation is partially rate limiting.[43] It seems that the activation of the βH_{Si} hydrogen atom is less efficient in this substrate analogue, but still possible through the electrophilic attack of MIO at the double bond next to the side chain. No activation of the β hydrogen atoms is expected, however, in 1,4-dihydrophenylalanine (**6**). It was discovered that the Birch reduction of L-phenylalanine affords, beside 2,5-dihydrophenylalanine as the main product, some 1,4-dihydro-L-phenylalanine.[81] As expected, this compound was not a substrate for PAL but showed weak inhibitory properties.

On the assumption that the most difficult step in the PAL reaction is the Friedel–Crafts-type attack with concomitant dearomatization of the phenyl ring, it was anticipated that the substitution of the phenyl group for the nonaromatic cyclooctatetraenyl group could facilitate the reaction. Racemic cyclooctatetraenylalanine, however, showed a very low V_{max} value (0.6% of the value for L-phenylalanine).[85] A possible explanation for the low reactivity of this compound is that the different size and nonplanar geometry of the cyclooctatetraene ring may make the electrophilic attack by MIO more difficult.

Another interesting aspect is the synergistic inhibition of PAL by various phenols with glycine. Although glycine alone does not inhibit PAL at all and the phenols are only very weak inhibitors, together in 1:1 ratio they act as strong inhibitors.[83,94] For example, the combination *m*-cresol/glycine could be seen to correspond to *m*-tyrosine, which is an excellent substrate of PAL. *m*-Cresol and glycine together inhibit PAL competitively with a K_i value of 0.89 mM, which is more than twenty times lower than that observed for glycine or *m*-cresol alone.[94] Alunni et al.[83] analyzed this synergistic inhibition systematically and found that the pair phenol/glycine showed the strongest inhibition ($K_i = 0.014$ mM), whereas the pair *p*-cresol/glycine hardly inhibited PAL at all. Except for the pair *m*-cresol/glycine, all other pairs showed mixed inhibition.

The kinetic isotope effect was also studied with phenylalanine labeled with deuterium or tritium on the phenyl ring. Gloge et al. found a conventional secondary kinetic isotope effect of 1.09 ± 0.01 on the overall reaction rate with [$^2H_5$]phenylalanine.[94] Since a deuterated carbon atom changes its hybridization from sp^2 to sp^3 in the first putative chemical step, an inverse secondary isotope effect should be expected. However, this effect may be overcompensated by the influence of the four other deuterium atoms on the phenyl ring.

Lewandowicz et al. confirmed the normal secondary kinetic isotope effect with [$^2H_5$]phenylalanine through competitive methods, i.e. determination of the enrichment of the deuterated material in the unconverted substrate.[82] The obtained k_H/k_D value of 1.13 ± 0.02 was similar to that described by Gloge et al. (1.09 ± 0.01).[94] Lewandowicz et al. also measured secondary kinetic tritium-isotope effects with phenylalanine labeled with tritium at the *ortho* position of the phenyl group.[82] The isotope effect showed a strong dependence on the reaction progress. For the first 5% conversion the k_H/k_T value was 0.85; it then reached the normal value and was about 1.15 at 20% conversion. The authors interpreted these results in favor of the Friedel–Crafts-type mechanism. Simple semiempirical calculations supported this interpretation. It was concluded that with [$^2H_5$]phenylalanine both the Hanson/Havir and the Friedel–Crafts-type mechanism should give a conventional secondary kinetic deuterium-isotope effect, but that the k_H/k_T value should be higher for the latter.

6.3. *N*-Methylated L-Phenylalanines in the PAL Reaction

N-Methyl-L-phenylalanine, *N*-methyl-4-nitro-L-phenylalanine, and *N*,*N*-dimethyl-4-nitro-L-phenylalanine were investigated as substrates or inhibitors of PAL from *Petroselinum crispum*.[86] Although *N*-methyl-L-phenylalanine was a moderate substrate ($K_m = 6.6$ mM, $k_{cat} = 0.22\ s^{-1}$), no reverse reaction was observed with methylamine and (*E*)-cinnamate. The K_m value for ammonia in the reverse reaction with (*E*)-cinnamate was determined to be 4.4 M at pH 8.8 and 2.6 M at pH 10. *N*-Methyl-4-nitro-L-phenylalanine and *N*,*N*-dimethyl-4-nitro-L-phenylalanine did not act as substrates but instead showed strong inhibitory effects ($K_i = 130$ and 8 nM, respectively).[86] This finding can be better interpreted in terms of the Friedel–Crafts-type mechanism than with the Hanson/Havir mechanism.[28]

Molecular modeling of *N*-methyl- and *N*,*N*-dimethyl-4-nitro-L-phenylalanine in the orientation that corresponds to the Friedel–Crafts-type mechanism[86] into the active site of PAL[74] demonstrated that the nitrated aromatic rings fit well into the apolar binding pocket. On the other hand, the increased gas-phase proton affinities of *N*-methyl- and *N*,*N*-dimethyl-L-phenylalanine relative to that of L-phenylalanine[87] indicate that the *N*-methylamino and *N*,*N*-dimethylamino moieties might be more strongly bound than the nonmethylated groups. Moreover, if the 4-nitro moiety on the

aromatic ring hinders the addition to MIO, the *N*-methylated group will remain anchored to Tyr100, thus keeping the β H_{Si} hydrogen atom[76] far from the enzymatic base Tyr348. These effects may together account for the strong inhibition.

In contrast, if one considers that 4-nitro-L-phenylalanine reacts with both wild-type PAL and the MIO-free mutant Ser202Ala,[61] and that *N*-methyl-L-phenylalanine is a moderate substrate for wild-type PAL,[86] a faster reaction would be expected by the E_1cB route for 4-nitro-*N*-methyl-L-phenylalanine. An electron-withdrawing group at 4-position of the phenyl ring would facilitate the deprotonation from the EA′ state (Scheme 3) and also stabilize the developing carbanion in the EC state.

7. Use of the Reverse HAL and PAL Reactions in Biocatalysis

The synthesis of enantiomerically pure natural amino acids and their non-natural derivatives and analogues is an important goal in synthetic chemistry. For example, the pharmacophores of protease inhibitors, an extremely important class of pharmaceuticals against HIV, influenza, and human cytomegalovirus, have a phenylalanine-like architecture.

As the ammonia-lyase reactions proceed by the stereodestructive elimination of ammonia from L-amino acids, the D-amino acids could in principal be produced by the enantioselective removal of the corresponding L-amino acids from the racemate. However, the stereoconstructive nature of the reverse reaction (the enantioselective addition of ammonia to α,β-unsaturated acids) made this approach more attractive for the preparation of amino acids by biotransformations.[88]

The reversibility of the HAL reaction was recognized about four decades ago.[89] Under extreme reaction conditions (4M NH_4OH, pH 10) HAL can catalyze the reverse (amination) reaction in vitro.[90] The synthetic utility of HAL is quite restricted, because it reacts with only a limited number of analogues, such as 5-nitrohistidine and 5- or 2-fluorohistidines.[57,91] However, it was recently reported that HAL can be used for the production of a wider selection of aromatic L-amino acids from the corresponding acrylic acid derivatives.[92]

More than 20 years ago it was recognized that PAL also catalyzes the enantioselective addition of ammonia to aryl acrylic acids when the ammonia concentration is increased to 5M.[93] Furthermore, L-phenylalanine ammonia-lyase tolerates a broader, more structurally diverse range of substrates than HAL, while strictly maintaining the enantioselectivity of the ammonia addition. This broader substrate tolerance—in addition to the demand for structures derived from phenylalanine in protease inhibitors—makes PAL a valuable tool for the preparation of enantiomerically pure amino acids from achiral acrylate precursors. Methods for PAL-catalyzed biotransformations have been elaborated for the enantioselective synthesis of all pyridinylalanine isomers,[94] 5-pyrimidinylalanine and several fluoro- and chlorophenylalanines,[85,95] and other substituted aryl alanines[85] (Table 5). Various aryl alanines were prepared in enantiomerically pure form (>99% *ee*) by PAL catalysis in moderate to almost quantitative yields.

Table 5: Synthesis of enantiomerically pure L-phenylalanine analogues by PAL catalysis.

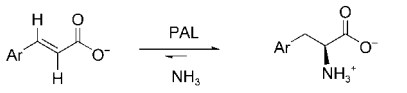

Entry	Ar	Ref.	Entry	Ar	Ref.	Entry	Ar	Ref.
1		[93]	9		[85]	17		[95]
2		[94]	10		[85]	18		[95]
3		[94,95]	11		[85,95]	19		[95]
4		[94]	12		[85,95]	20		[95]
5		[94]	13		[85,95]	21		[95]
6		[85]	14		[85]	22		[95]
7		[85,95]	15		[95]	23		[95]
8		[85,95]	16		[95]	24		[95]

With the whole cells of *Rhodotorula graminis* as the PAL source, no reaction was observed when 4-chloro-, 3,4-dichloro-, 2,4,6-trichloro-, 4-bromo-, 4-methyl-, 4-formyl-, 4-amino-, 4-nitro-, or 2-hydroxyphenylacrylate, naphth-2-ylacrylate, or furan-3-ylacrylate were tested as substrates.[95] However, when the differences between *Pc*-PAL and *Rt*-PAL in the active site region are considered (see Section 5.2), it seems reasonable that there may be slight differences in the substrate tolerance of yeast and plant PAL enzymes.

More recently, a PAL enzyme of plant origin was found to be a useful reagent for the asymmetric synthesis of non-natural amino acids.[96] PAL can also be catalytically active in organic solvents, such as *n*-octanol.[97]

Enzymes can not only be used for synthetic processes as single biocatalysts. Combinatorial biosynthetic approaches can also be designed for the synthesis of natural products and for the construction of libraries of non-natural analogues of natural products. The usefulness of this strategy was demonstrated with synthesis of the chalcones naringenin and pinocembrin from L-tyrosine and L-phenylalanine, respectively, by recombinant *E. coli* with an artificial gene cluster assembled from the PAL gene of the yeast *Rhodotorula rubra* and the genes that code for chalcone isomerase and chalcone synthase of other organisms.[98]

8. Tyrosine 2,3-aminomutase: Another MIO Enzyme

A number of ammonia-lyases[88] and aminomutases use different cofactors and mechanisms. Ethanolamine ammonia-lyase, for example, is dependent on coenzyme B_{12}, as is β-lysine 5,6-aminomutase.[3] Both enzymes have radical intermediates. α-Lysine 2,3-aminomutase is a radical SAM (S-adenosyl-L-methionine) enzyme;[4] aspartate and methylaspartate ammonia-lyases do not require a cofactor.

Until recently HAL and PAL were the only enzymes known to contain the MIO group. Christenson et al. discovered another enzyme, tyrosine 2,3-aminomutase,[70] which contains the MIO group and uses a similar mechanism to that of HAL and PAL. The enzyme is produced by *Streptomyces globisporus*, and its product, (*S*)-β-tyrosine, is believed to be a precursor of the antibiotic C-1027, which shows potent anticancer and antimicrobial activity.[99] One portion of C-1027 is (*S*)-3-chloro-4,5-dihydroxy-β-phenylalanine, which is most likely formed from (*S*)-β-tyrosine, as 3,4-dihydroxyphenylalanine and 3-chlorophenylalanine are poor substrates of the isolated mutase.[70] The gene that codes for the mutase was isolated from *S. globisporus*, overexpressed in *E. coli*, and shown to have a high sequence homology with the HAL/PAL enzyme family.

Evidence for the presence of an MIO group in tyrosine 2,3-aminomutase has been provided in several ways: 1) The mutation of serine to alanine in the inner-peptide sequence Ala152Ser153Gly154 reduces the k_{cat}/K_m value by a factor of 640; 2) the UV difference spectrum between the wild-type enzyme and its Ser153Ala mutant shows an absorption maximum at ~310 nm; 3) nucleophiles such as $NaBH_4$ or KCN inhibit the mutase, but preincubation with L-tyrosine or 4-hydroxycinnamate protect the enzyme from inhibition; 4) the optimum pH value for the mutase reaction is about 8.8, similar to those for the HAL and PAL reactions.

Further mechanistic studies revealed that 4-hydroxycinnamate is an intermediate in the mutase reaction and that it is released slowly as a by-product of the reaction. In other words, tyrosine 2,3-aminomutase also displays ammonia-lyase activity. Normally, the mutase does not release the ammonia formed at the active site, but adds it to the intermediate 4-hydroxycinnamate at the β position. This second step is a Michael addition to a α,β-unsaturated acid derivative, and therefore the easier part of the overall reaction.[70] Interestingly, the mutase also exhibits β-tyrosine racemase activity, but α-tyrosine is not racemized. Thus, the readdition of ammonia to the Michael system is reversible and not enantiospecific. A mechanism for the L-tyrosine 2,3-aminomutase reaction is illustrated in Scheme 19.

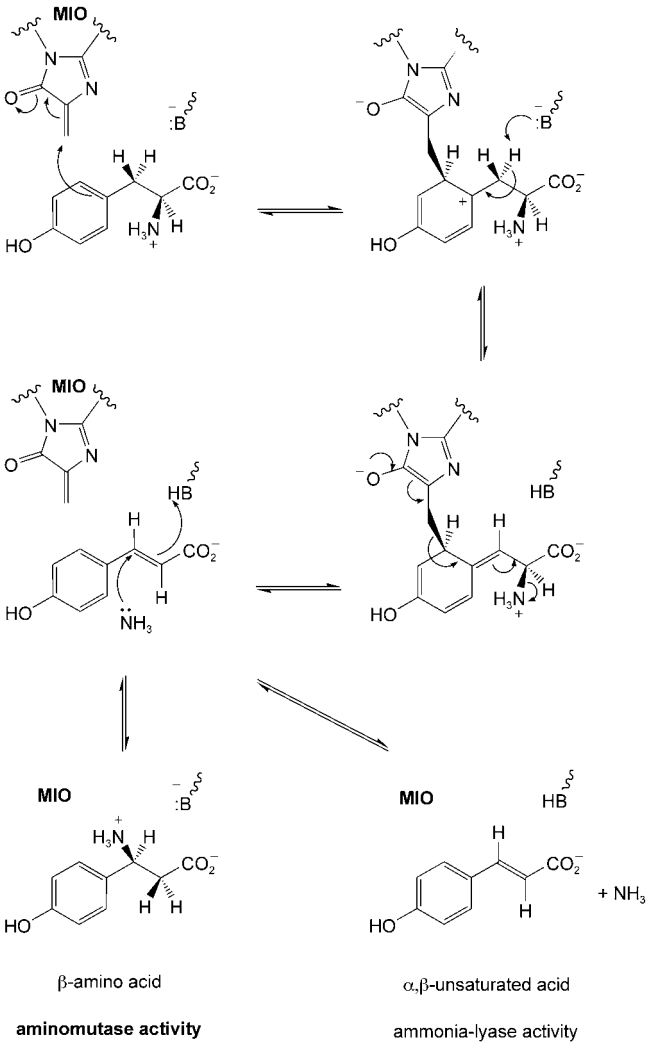

Scheme 19. Proposed mechanism of action of L-tyrosine 2,3-aminomutase.[70]

The question arises as to whether there are still undiscovered MIO enzymes. Several mechanistic devices exist for the activation of the inert β position of carboxylic acids. Highly reactive radical species, such as 5′-deoxyadenosyl and glycyl radicals, can abstract protons from inert positions to form an activated substrate radical which can react further under enzymatic control.[1] Electrophilic activation is an alternative in all cases in which there is an aromatic ring at the adjacent position. There are a few examples for which it has still not been established definitively whether a radical or an electrophilic activation mechanism operates.

9. Conclusions and Outlook

Herein we have reviewed the elucidation of the mechanism by which the chemically difficult elimination of ammonia from histidine and phenylalanine is catalyzed by the corresponding ammonia-lyases HAL and PAL. These enzymes use the recently discovered superelectrophilic prosthetic group 5-methylene-3,5-dihydroimidazol-4-one to activate the nonacidic β hydrogen atoms of their substrates by a Friedel–Crafts-type attack at the aromatic ring. In the σ-complex generated, proton abstraction from the ring is prevented by excluding any bases in the binding pocket of the enzyme. Instead, the exocyclic proton is abstracted by an appropriately positioned enzymatic base. The exocyclic double bond formed in this way is the prerequisite for a concomitant process that involves the elimination of ammonia, rearomatization, and fragmentation. The MIO group is thereby regenerated, and the product, (*E*)-urocanate or (*E*)-cinnamate, is formed.

The above mechanism is supported by the results of several biochemical studies, as well as by the X-ray crystal structures of HAL and PAL, and modeling studies. Before these discoveries it was believed for thirty years that the prosthetic electrophile was dehydroalanine and that the α-NH_2 group of the substrate added to this Michael acceptor. This "old" mechanism was unsatisfactory for several reasons. It did not explain how the nonacidic β proton ($pK_a > 40$) could be abstracted by an enzymatic base, or why most amino acids do not inhibit HAL, but L-cysteine and L-homocysteine do. Finally, dehydroalanine itself is not a good Michael receptor, because the delocalization of the lone pair of electrons on the nitrogen atom decreases its electrophilicity.

Since the publication of the "new" mechanism and in particular of the X-ray crystal structure of HAL, a number of research groups have reported results that support the Friedel–Crafts-type mechanism, and no arguments against it have been published.

Recently, a new bacterial MIO enzyme with tyrosine 2,3-amino-mutase activity was discovered. We look forward to the discovery of further MIO enzymes.

We thank Dr. Csaba Paizs for his help with the preparation of the manuscript. J.R. thanks his former students for their enthusiastic involvement in the MIO project: Dr. Andreas Gloge, Dr. Birgid Langer (formerly Schuster), Dr. Martin Langer, Dr. Dietrich Merkel, Dr. Gaby Morlock, Dr. Andrea Pauling, Dr. Gunhild Reck, Dr. Dagmar Röther, Dr. Alexander Skolaut, Dr. Sandra Viergutz, and Dr. Karl-Heinz Weber. J.R. also thanks Professor Georg E. Schulz, Dr. Torsten F. Schwede, and Dr. Mathias Baedeker for the fruitful collaboration on the X-ray crystal structure of HAL and for a plasmid of the modified PAL gene.

We are grateful to Professor Nicholas Amrhein and Professor Klaus Hahlbrock, who gave us the antibody against PAL and the PAL gene from parsley, respectively. The excellent technical assistance of Ingrid Merkler and Stefanie Vollmer is also greatfully acknowledged.

The research at Karlsruhe was supported by the Deutsche Forschungsgemeinschaft, the Fonds der Chemischen Industrie, and the Land Baden-Württemberg. L.P. thanks the Alexander von Humboldt Foundation for a fellowship and OTKA (T-048854) for financial support.

Received: July 21, 2004
Revised: October 29, 2004
Published online: May 20, 2005

[1] J. Rétey, *Angew. Chem.* **1990**, *102*, 373–379; *Angew. Chem. Int. Ed. Engl.* **1990**, *29*, 355–361.
[2] a) P. A. Frey, M. K. Essenberg, R. H. Abeles, *J. Biol. Chem.* **1967**, *242*, 5369–5377; b) T. H. Finlay, J. Valinsky, K. Sato, R. H. Abeles, *J. Biol. Chem.* **1972**, *247*, 4197–4207; c) Y. Zhao, P. Such, J. Rétey, *Angew. Chem.* **1992**, *104*, 212–213; *Angew. Chem. Int. Ed. Engl.* **1992**, *31*, 215–216; d) Y. Zhao, A. Abend, M. Kunz, P. Such, J. Rétey, *Eur. J. Biochem.* **1994**, *225*, 891–896.
[3] For selected reviews, see: a) W. Buckel, B. T. Golding, *Chem. Soc. Rev.* **1996**, *25*, 329–337; b) E. N. G. Marsh, C. L. Drennan, *Curr. Opin. Chem. Biol.* **2001**, *5*, 499–505; c) R. Banerjee, *Chem. Rev.* **2003**, *103*, 2083–2094; d) T. Toraya, *Chem. Rev.* **2003**, *103*, 2095–2127.
[4] P. A. Frey, O. T. Magnusson, *Chem. Rev.* **2003**, *103*, 2129–2148.
[5] P. Christen, P. K. Mehta, *Chem. Rec.* **2001**, *1*, 436–447.
[6] E. E. Snell, *Methods Enzymol.* **1986**, *122*, 128–135.
[7] G. Lukatela, N. Krauss, K. Theis, T. Selmer, V. Gieselmann, K. von Figura, W. Saenger, *Biochemistry* **1998**, *37*, 3654–3664.
[8] a) J. E. Dove, J. P. Klinman, *Adv. Protein Chem.* **2001**, *58*, 141–174; b) S. J. Firbank, M. S. Rogers, C. M. Wilmot, D. M. Dooley, M. A. Halcrow, P. F. Knowles, M. J. McPherson, S. E. Phillips, *Proc. Natl. Acad. Sci. USA* **2001**, *98*, 12932–12937.
[9] G. Srinivasan, C. M. James, J. A. Krzycki, *Science* **2002**, *296*, 1459–1462.
[10] B. Hao, W. Gong, T. K. Ferguson, C. M. James, J. A. Krzycki, M. K. Chan, *Science* **2002**, *296*, 1462–1466.
[11] S. K. Blight, R. C. Larue, A. Mahapatra, D. G. Longstaff, E. Chang, G. Zhao, P. T. Kang, K. B. Green-Church, M. K. Chan, J. A. Krzycki, *Nature* **2004**, *431*, 333–335.
[12] M. Thanbichler, A. Böck, *Methods Enzymol.* **2002**, *347*, 3–16.
[13] J. Klepp, A. Fallert-Müller, K. Grimm, W. E. Hull, J. Rétey, *Eur. J. Biochem.* **1990**, *192*, 669–676.
[14] L. A. Chasin, B. Magasanik, *J. Biol. Chem.* **1968**, *243*, 5165–5178.
[15] P. Lund, B. Magasanik, *J. Biol. Chem.* **1965**, *240*, 4316–4319.
[16] H. K. Meiss, W. J. Brill, B. Magasanik, *J. Biol. Chem.* **1969**, *244*, 5382–5391.
[17] a) H. Tabor, A. H. Mehler, *J. Biol. Chem.* **1954**, *210*, 559–568; b) T. G. Lessie, F. C. Neidhard, *J. Bacteriol.* **1967**, *149*, 1800–1810; c) B. E. Uhlim, A. J. Clark, *J. Bacteriol.* **1981**, *163*, 386–390.
[18] R. G. Taylor, H. L. Levy, R. R. McInnes, *Mol. Biol. Med.* **1991**, *8*, 101–116.
[19] a) D. H. Hug, J. K. Hunter, *J. Bacteriol.* **1970**, *152*, 874–876; b) A. R. Young, *Phys. Med. Biol.* **1997**, *42*, 789–802.
[20] a) T. Yoshida, K. Tada, Y. Honda, T. Arakawa, J. Tohoku, *J. Exp. Med.* **1971**, *104*, 305–312; b) Z. Kalatatic, K. Lipovac, Z. Jereniac, D. Juretic, M. Dumic, B. Zurga, L. Res, *Metabolism* **1980**, *29*, 1013–1019.
[21] D. Kessler, J. Rétey, G. E. Schulz, *J. Mol. Biol.* **2004**, *342*, 183–194.
[22] a) M. W. Consevage, A. T. Phillips, *Biochemistry* **1985**, *24*, 301–308; b) M. Fessenmaier, R. Frank, C. Schubert, J. Rétey, *FEBS Lett.* **1991**, *286*, 55–57.
[23] a) R. G. Taylor, J. Garcia-Heras, S. J. Sadler, R. G. Lafreniere, H. F. Willrad, D. H. Ledbetter, R. R. McInnes, *Cytogenet. Cell Genet.* **1991**, *56*, 178–181; b) R. G. Taylor, D. Grieco, G. A. Clarke, R. R. McInnes, B. A. Taylor, *Genomics* **1993**, *16*, 231–

240; c) R. G. Taylor, R. R. McInnes, *J. Biol. Chem.* **1994**, *269*, 27473 – 27477.
[24] a) "Regulation in the *hut* System": B. Magasanik in *The Operon* (Eds.: J. H. Miller, W. S. Reznikoff), Cold Spring Harbor Laboratory Press, Cold Spring Harbor, **1987**, pp. 373 – 387; b) L. Hu, S. L. Allison, A. T. Phillips, *J. Bacteriol.* **1989**, *171*, 1489 – 1495; c) S. A. Boylan, L. J. Eades, *Mol. Gen. Genet.* **1984**, *193*, 92 – 97; d) A. J. Nieuwkoop, S. A. Baldauf, M. E. S. Hudspeth, R. A. Bender, *J. Bacteriol.* **1988**, *170*, 2240 – 2246; e) M. Oda, A. Sugishita, K. Furukawa, *J. Bacteriol.* **1988**, *170*, 3199 – 3205.
[25] a) K. Hahlbrock, D. Scheel, *Annu. Rev. Plant Phys. Plant Mol. Biol.* **1989**, *40*, 347 – 369; b) C. Appert, E. Logemann, K. Hahlbrock, J. Schmid, N. Amrhein, *Eur. J. Biochem.* **1994**, *225*, 491 – 499.
[26] J. G. Anson, H. J. Gilbert, J. D. Oram, N. P. Minton, *Gene* **1987**, *58*, 189 – 199.
[27] L. Xiang, B. S. Moore, *J. Biol. Chem.* **2002**, *277*, 32505 – 32509.
[28] K. R. Hanson, E. A. Havir, *Arch. Biochem. Biophys.* **1970**, *141*, 1 – 17.
[29] a) B. V. Charlwood, M. Pletsch, *J. Herbs Spices Med. Plants* **2002**, *9*, 139 – 151; b) T. Kusumi, *Bio Ind.* **1999**, *16*, 31 – 39; c) K. M. Davies, S. J. Bloor, G. B. Spiller, *Plant J.* **1998**, *13*, 259 – 266.
[30] J. Zoń, N. Amrhein, *Liebigs Ann. Chem.* **1992**, 625 – 628.
[31] a) G. M. Kishore, D. M. Shah, *Annu. Rev. Biochem.* **1988**, *57*, 627 – 663; b) E. Haslam, *Shikimic Acid: Metabolism and Metabolites*, Wiley, New York, **1993**.
[32] a) P. E. Flemming, U. Mocek, H. G. Floss, *J. Am. Chem. Soc.* **1993**, *115*, 805 – 807; b) K. Walker, H. G. Floss, *J. Am. Chem. Soc.* **1998**, *120*, 5333 – 5334.
[33] W. W. Poon, B. N. Marbois, K. F. Faull, C. F. Clarke, *Arch. Biochem. Biophys.* **1995**, *320*, 305 – 314.
[34] A. Mitra, Y. Kitamura, M. J. Gasson, A. Narbad, A. J. Parr, J. Payne, M. J. C. Rhodes, C. Sewter, N. J. Walton, *Arch. Biochem. Biophys.* **1999**, *365*, 10 – 16.
[35] PAL from *Rhodotorula glutinis*, Sigma Biochemicals and Reagents, Cat. No. P1016.
[36] J. A. Kyndt, T. E. Meyer, M. A. Cusanovich, J. J. Van Beumen, *FEBS Lett.* **2002**, *512*, 240 – 244.
[37] A. Hunter, *J. Biol. Chem.* **1912**, *11*, 537 – 545.
[38] S. Edlbacher, *Hoppe-Seyler's Z. Physiol. Chem.* **1926**, *157*, 106.
[39] A. Peterkofsky, *J. Biol. Chem.* **1962**, *237*, 787 – 795.
[40] T. A. Smith, F. H. Cordelle, R. H. Abeles, *Arch. Biochem. Biophys.* **1967**, *120*, 724 – 725.
[41] a) D. Hodgins, R. H. Abeles, *J. Biol. Chem.* **1967**, *242*, 5158 – 5159; b) D. Hodgins, *J. Biol. Chem.* **1971**, *246*, 2977 – 2985.
[42] R. B. Wickner, *J. Biol. Chem.* **1969**, *244*, 6550 – 6552.
[43] J. D. Hermes, P. M. Weiss, W. W. Cleland, *Biochemistry* **1985**, *24*, 2959 – 2967.
[44] a) M. Varma, C. J. M. Stirling, *J. Chem. Soc. Chem. Commun.* **1981**, 553 – 554; b) M. B. Smith, J. March, *Advanced Organic Chemistry*, Wiley-VCH, Weinheim, **2001**, p. 1321.
[45] W. Shi, J. Dunbar, M. M. K. Jayasekera, R. E. Viola, G. K. Farber, *Biochemistry* **1997**, *36*, 9136 – 9144.
[46] M. M. K. Jayasekera, W. Shi, G. K. Farber, R. E. Viola, *Biochemistry* **1997**, *36*, 9145 – 9150.
[47] a) C. V. Levy, P. A. Sedelnikova, Y. Kato, Y. Asano, D. W. Rice, P. J. Baker, *Struct. Fold. Des.* **2002**, *10*, 105 – 113; b) Y. Asano, Y. Kato, C. Levy, P. Baker, D. Rice, *Biocatal. Biotransform.* **2004**, *22*, 131 – 138.
[48] M. Asuncion, W. Blankenfeldt, J. N. Barlow, D. Gani, J. H. Naismith, *J. Biol. Chem.* **2002**, *277*, 8306 – 8311.
[49] a) J. C. Calabrese, D. B. Jordan, A. Boodhoo, S. Sariaslani, T. Vannelli, *Biochemistry* **2004**, *43*, 11403 – 11416; b) H. Ritter, G. E. Schulz, *Plant Cell* **2004**, *16*, 3426 – 3436.
[50] F. G. Bordwell, Y. Zhao, *J. Org. Chem.* **1995**, *60*, 3932 – 3933.
[51] H. G. Sahl, R. W. Jack, G. Bierbaum, *Eur. J. Biochem.* **1995**, *230*, 827 – 853.
[52] J. Rétey, *Biochim. Biophys. Acta* **2003**, *1647*, 179 – 184.
[53] "Novel Cofactors": B. Langer, M. Langer, J. Rétey, *Adv. Protein Chem.* **2002**, *55*, 175 – 214.
[54] M. Langer, G. Reck, J. Reed, J. Rétey, *Biochemistry* **1994**, *33*, 6462 – 6467.
[55] B. Schuster, J. Rétey, *FEBS Lett.* **1994**, *349*, 252 – 254.
[56] a) B. Langer, A. Lieber, J. Rétey, *Biochemistry* **1994**, *33*, 14034 – 14039; b) B. Langer, D. Röther, J. Rétey, *Biochemistry* **1997**, *36*, 10867 – 10871.
[57] C. B. Klee, K. L. Kirk, L. A. Cohen, *Biochem. Biophys. Res. Commun.* **1979**, *87*, 343 – 348.
[58] M. Langer, A. Pauling, J. Rétey, *Angew. Chem.* **1995**, *107*, 1585 – 1587; *Angew. Chem. Int. Ed. Engl. Angew. Chem. Int. Ed.* **1995**, *34*, 1464 – 1465.
[59] J. Rétey, H. Fierz, W. P. Zeylemaker, *FEBS Lett.* **1970**, *6*, 203 – 204.
[60] J. Rétey, *Naturwissenschaften* **1996**, *83*, 439 – 447.
[61] B. Schuster, J. Rétey, *Proc. Natl. Acad. Sci. USA* **1995**, *92*, 8433 – 8437.
[62] M. Rettig, A. Sigrist, J. Rétey, *Helv. Chim. Acta* **2000**, *83*, 2246 – 2265.
[63] a) D. Hernandez, J. G. Stroh, A. T. Phillips, *Arch. Biochem. Biophys.* **1993**, *307*, 126 – 132; b) T. F. Schwede, M. Bädeker, M. Langer, J. Rétey, G. E. Schulz, *Protein Eng.* **1999**, *12*, 151 – 153.
[64] T. F. Schwede, J. Rétey, G. E. Schulz, *Biochemistry* **1999**, *38*, 5355 – 5361.
[65] M. Ormö, A. B. Cubitt, K. Kallio, L. A. Gross, R. Y. Tsien, S. J. Remington, *Science* **1996**, *273*, 1392 – 1395.
[66] D. Merkel, J. Rétey, unpublished results.
[67] M. Baedeker, G. E. Schulz, *Eur. J. Biochem.* **2002**, *269*, 1790 – 1797.
[68] a) C. B. Klee, *J. Biol. Chem.* **1970**, *245*, 3143 – 3152; b) C. B. Klee, *Biochemistry* **1974**, *22*, 4501 – 4507.
[69] D. Röther, D. Merkel, J. Rétey, *Angew. Chem.* **2000**, *112*, 2592 – 2594; *Angew. Chem. Int. Ed.* **2000**, *39*, 2462 – 2464.
[70] a) S. D. Christenson, W. Liu, M. D. Toney, B. Shen, *J. Am. Chem. Soc.* **2003**, *125*, 6062 – 6063; b) S. D. Christenson, W. Wu, M. A. Spies, B. Shen, M. D. Toney, *Biochemistry* **2003**, *42*, 12708 – 12718.
[71] M. Baedeker, G. E. Schulz, *Structure* **2002**, *10*, 61 – 67.
[72] D. Röther, L. Poppe, S. Viergutz, B. Langer, J. Rétey, *Eur. J. Biochem.* **2001**, *268*, 6011 – 6019.
[73] C. B. Klee, *J. Biol. Chem.* **1972**, *247*, 1398 – 1406.
[74] D. Röther, L. Poppe, G. Morlock, S. Viergutz, J. Rétey, *Eur. J. Biochem.* **2002**, *269*, 3065 – 3075.
[75] S. Viergutz, J. Rétey, *Chem. Biodiversity* **2004**, *1*, 296 – 302.
[76] a) K. R. Hanson, R. H. Wightman, J. Staunton, A. R. Battersby, *J. Chem. Soc. Chem. Commun.* **1971**, 185 – 186; b) G. W. Kirby, J. Michael, *J. Chem. Soc. Chem. Commun.* **1971**, 187.
[77] S. Viergutz, J. Rétey, unpublished results.
[78] a) D. Hernandez, J. G. Stroh, A. T. Phillips, *Arch. Biochem. Biophys.* **1993**, *307*, 126 – 132; b) K. Weber, J. Rétey, *Bioorg. Med. Chem.* **1996**, *4*, 1001 – 1006.
[79] a) D. Merkel, PhD thesis, Universität Karlsruhe, **1999**; b) D. Galpin, B. E. Ellis, M. E. Tanner, *J. Am. Chem. Soc.* **1999**, *121*, 10840 – 10841; c) D. Merkel, J. Rétey, *Helv. Chim. Acta* **2000**, *83*, 1151 – 1160.
[80] T. Andrews, G. Lorimer, N. Tolbert, *Biochemistry* **1973**, *12*, 11 – 18.
[81] A. Skolaut, J. Rétey, *Arch. Biochem. Biophys.* **2001**, *393*, 187 – 190.
[82] A. Lewandowicz, J. Jemielity, M. Kańska, J. Zoń, P. Paneth, *Arch. Biochem. Biophys.* **1999**, *370*, 216 – 221.
[83] S. Alunni, A. Cipiciani, G. Fioroni, L. Ottavi, *Arch. Biochem. Biophys.* **2003**, *412*, 170 – 175.

[84] K. R. Hanson, E. A. Harry, C. Ressler, *Biochemistry* **1979**, *18*, 1431 – 1439.
[85] A. Gloge, J. Zoń, Á. Kövári, L. Poppe, J. Rétey, *Chem. Eur. J.* **2000**, *6*, 3386 – 3390.
[86] S. Viergutz, L. Poppe, A. Tomin, J. Rétey, *Helv. Chim. Acta* **2003**, *86*, 3601 – 3612.
[87] S. Campbel1, E. M. Marzluff, M. T. Rodgers, J. L. Beauchamp, M. E. Rempe, K. F. Schwinck, D. L. Lichtenberger, *J. Am. Chem. Soc.* **1994**, *116*, 5251 – 5264.
[88] a) L. Poppe, J. Rétey, *Curr. Org. Chem.* **2003**, *7*, 1297 – 1315; b) H. Kamachi, H. Aoki, *Bio Ind.* **2003**, *20*, 12 – 20.
[89] V. R. Williams, J. M. Hiroms, *Biochim. Biophys. Acta* **1967**, *139*, 214 – 216.
[90] R. L. Fuchs, J. F. Kane, *J. Bacteriol.* **1985**, *167*, 98 – 101.
[91] C. B. Klee, K. L. Kirk, L. A. Cohen, P. McPhie, *J. Biol. Chem.* **1975**, *250*, 5033 – 5040.
[92] H. Aoki, H. Kamachi (Showa Denko K. K., Japan), Jpn. Kokai Tokkyo Koho (2004), JP 2004041107 A2 [*Chem. Abstr.* **2004**, *140*, 117363].
[93] a) S. Yamada, K. Nabe, N. Izuo, K. Nakamichi, I. Chibata, *Appl. Environ. Microbiol.* **1981**, *42*, 773 – 778; b) C. T. Evans, K. Hanna, C. Payne, D. Conrad, M. Misawa, *Enzyme Microb. Technol.* **1987**, *9*, 417 – 421; c) M. Yanaka, D. Ura, A. Takahashi, N. Fukuhara (Mitsui Toatsu Chemicals), JP 06,113,870 (1994) [*Chem. Abstr.* **1994**, *121*, 155941y].
[94] A. Gloge, B. Langer, L. Poppe, J. Rétey, *Arch. Biochem. Biophys.* **1998**, *359*, 1 – 7.
[95] W. Liu, (Great Lakes Chemical Co.) USP 5,981,239 (1999) [*Chem. Abstr.* **1999**, *131*, 321632].
[96] H. Aoki, H. Kamachi (Showa Denko K.K., Japan), PCT Int. Appl. (2003), WO 2003000915 A1 [*Chem. Abstr.* **2003**, *138*, 54648].
[97] D. G. Rees, D. H. Jones, *Biochim. Biophys. Acta* **1997**, *1338*, 121 – 126.
[98] K. Masafumi, H. E. Il, O. Yasuo, H. Sueharu, *J. Ind. Microbiol. Biotechnol.* **2003**, *30*, 456 – 461.
[99] J. L. Hu, Y. C. Xie, M. Y. Xie, R. Zhang, T. Otani, Y. Mihami, Y. Yamada, T. Marunaka, *J. Antibiot.* **1988**, *41*, 1575 – 1579.

Communications

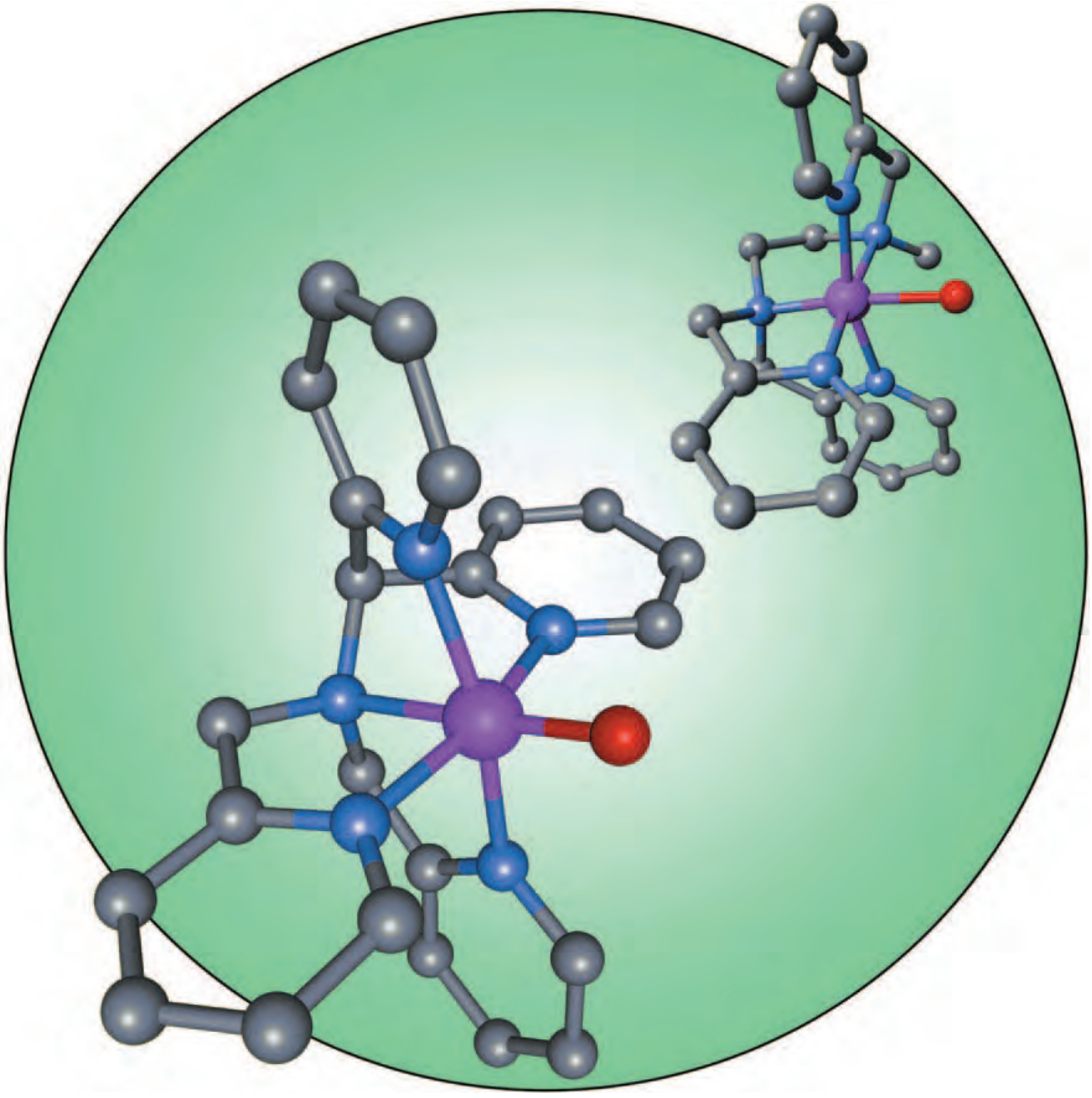

The structures of recently discovered non-heme oxoiron(IV) complexes of two pentadentate ligands have been deduced, one by X-ray crystallography and the other by ^{1}H NMR spectroscopy. Detailed experimental and theoretical studies are described by L. Que, Jr., C. J. Cramer et al. on the following pages.

  DOI: 10.1002/anie.200500485

Oxoiron(IV) Complexes

Structures of Nonheme Oxoiron(IV) Complexes from X-ray Crystallography, NMR Spectroscopy, and DFT Calculations**

Eric J. Klinker, József Kaizer, William W. Brennessel, Nathaniel L. Woodrum, Christopher J. Cramer, and Lawrence Que, Jr.**

Oxoiron(IV) species are frequently invoked as reactive intermediates in the oxygen-activation mechanisms of mononuclear nonheme iron enzymes.[1] In 2003, the trapping of the first nonheme oxoiron(IV) intermediate in the reaction of O_2 with the 2-oxoglutarate-dependent enzyme TauD, which was complexed with 2-oxoglutarate and its substrate taurine, was reported.[2–5] Contemporaneously, the first examples of well-characterized synthetic oxoiron(IV) complexes with nonheme ligand environments were also described.[6,7] The presumably reactive oxoiron(IV) units could be stabilized sufficiently by tetraaza ligands such as macrocyclic tetramethylcyclam (TMC) and tripodal tris(2-pyridylmethyl)amine (TPA) to allow their spectroscopic characterization at low temperature. In the case of the TMC complex, its considerable stability allowed it to be crystallized and its structure to be determined by X-ray crystallography. These results represented the first high-resolution structural data for any oxoiron(IV) complex, heme or nonheme. Subsequently it was found that the oxoiron(IV) unit could also be generated from precursor iron(II) complexes of pentadentate pentaaza ligands such as *N*,*N*-bis(2-pyridylmethyl)-*N*-bis(2-pyridyl)methylamine (N4Py) and *N*-benzyl-*N*,*N*′,*N*′-tris(2-pyridylmethyl)-1,2-diaminoethane (Bn-TPEN) by treatment with a peracid or PhIO. In fact, $[Fe^{IV}(O)(N4Py)]^{2+}$ (**1**) and $[Fe^{IV}(O)(Bn\text{-}TPEN)]^{2+}$ (**2**) could be produced in high yields at room temperature by reaction with excess solid iodosylbenzene in CH_3CN to afford solutions with significant thermal stability.[8] Herein, we report insight into the structures of **1** and **2** obtained from a combination of X-ray crystallography, NMR spectroscopy, and DFT (density functional theory) calculations, and their relative thermal stabilities.

Complexes **1** and **2** exhibit half-lives of approximately 60 and 6 h, respectively, at room temperature. The greater thermal stability of **1** allowed the isolation of single crystals for X-ray crystal structural analysis (Figure 1) to provide only the second high-resolution structure of an oxoiron(IV) complex. The X-ray crystal structure of **1** shows an Fe–O bond length of 1.639(5) Å, a value that is essentially identical to the length of 1.646(3) Å reported for the analogous bond in $[Fe(O)(TMC)(NCCH_3)](SO_3CF_3)_2$ (**3**).[6] Trans to the oxo ligand in **1** is the amine nitrogen atom that holds the pentadentate ligand together, with an Fe–N1 bond length of 2.033(8) Å, the longest metal–ligand bond in the molecule. The O1, Fe, and N1 atoms are nearly colinear with an O1-Fe-N1 angle of 178.6(3)°. Coordinated in the equatorial plane are the four pyridine nitrogen atoms, whose rings are aligned parallel to the Fe–O axis, and the iron atom lies 0.252 Å above the plane subtended by these four pyridyl nitrogen atoms towards the oxo ligand. Interestingly, the equatorial Fe–N bond lengths are on average 1.957(5) Å; these bonds are shorter than the corresponding equatorial bonds in **3** by 0.1 Å and reflect the stronger bonding ability of a pyridine moiety relative to a tertiary amine.

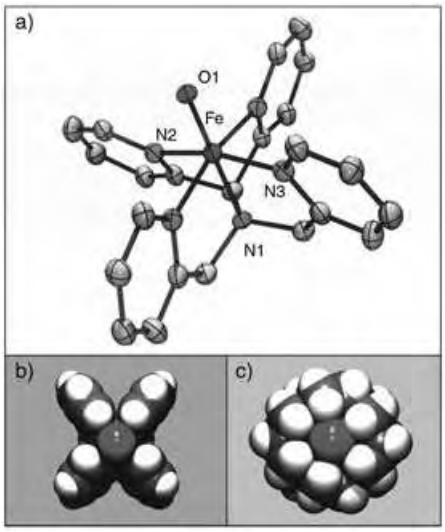

Figure 1. Molecular structure of **1** (a) and top views of space-filling models of **1** (b) and **3** (c). Metal–ligand bond lengths [Å] for **1**: Fe–O 1.639(5), Fe–N1 2.033(8), Fe–N2 1.964(5), Fe–N3 1.949(5).

Figures 1b and c compare the top views of space-filling models of **1** and **3** and reveal a large difference in the accessibility of the oxoiron unit in the two complexes. Whereas the hydrogen atoms of the TMC macrocycle nestle nicely around the oxo atom in **3** and restrict access,[6] the oxo group in **1** is much more exposed not only from the top of the molecule but also along channels that form between adjacent pyridine rings. This difference may rationalize the relative reactivities of the two complexes. While **3** is quite inert toward hydrocarbon substrates, at room temperature **1** can attack C–H bonds as strong as those in cyclohexane.[6,8]

[*] N. L. Woodrum, Prof. Dr. C. J. Cramer
Department of Chemistry and
Supercomputer Institute
University of Minnesota
207 Pleasant Street SE, Minneapolis, MN 55455 (USA)
Fax: (+1) 612-624-2006
E-mail: cramer@chem.umn.edu
E. J. Klinker, Dr. J. Kaizer, W. W. Brennessel, Prof. Dr. L. Que, Jr.
Department of Chemistry and
Center for Metals in Biocatalysis
University of Minnesota
207 Pleasant Street SE, Minneapolis, MN 55455 (USA)
Fax: (+1) 612-624-7029
E-mail: que@chem.umn.edu

[**] This work was supported by grants from the National Institutes of Health (GM-33162 to L.Q.) and the National Science Foundation (CHE-0203346 to C.J.C.).

Supporting information for this article is available on the WWW under http://www.angewandte.org or from the author.

Single crystals of **2** have not yet been isolated, so its structure must be deduced by alternative means. A recent EXAFS (extended X-ray absorption fine spectrum) study[9] revealed the presence of a short Fe–O bond of 1.67 Å and Fe–N bond lengths that average 2.00 Å, as expected, but no insight was gained into how the pentadentate ligand wraps around the metal center. The flexibility of the ligand requires three conformational isomers, if we neglect enantiomers, to be considered (Figure 2). Isomer **A** contains two pyridine rings that eclipse the Fe–O axis and a third that is perpendicular to it, as found in the structure of the iron(II) precursor.[9] In isomer **B** one ring eclipses the Fe–O axis and two are perpendicular to it, whereas in isomer **C** two rings are perpendicular to the Fe–O axis and the other is coordinated trans to the oxygen atom.

We found ^{1}H NMR spectroscopy to be a very useful technique to probe the structures of the nonheme oxoiron(IV) complexes, and the spectra of **1** and **2** are shown in Figure 3. The $S = 1$ iron(IV) centers of **1** and **2** have favorable electronic relaxation properties that give rise to relatively sharp and well-resolved, paramagnetically shifted proton resonances that span 200 ppm. The number of signals observed for **1** is consistent with the presence of mirror symmetry, as established from the solid-state structure. Two sets of pyridine resonances (β, β′, and γ) can be readily identified by a COSY experiment (see Supporting Information). The shift pattern for the protons of the pyridine rings is unique for the low-spin iron(IV) center, with one β proton shifted downfield and the β′ proton shifted upfield. In iron(II) and iron(III) pyridine complexes, both β protons are typically shifted downfield with comparable paramagnetic shifts.[10,11]

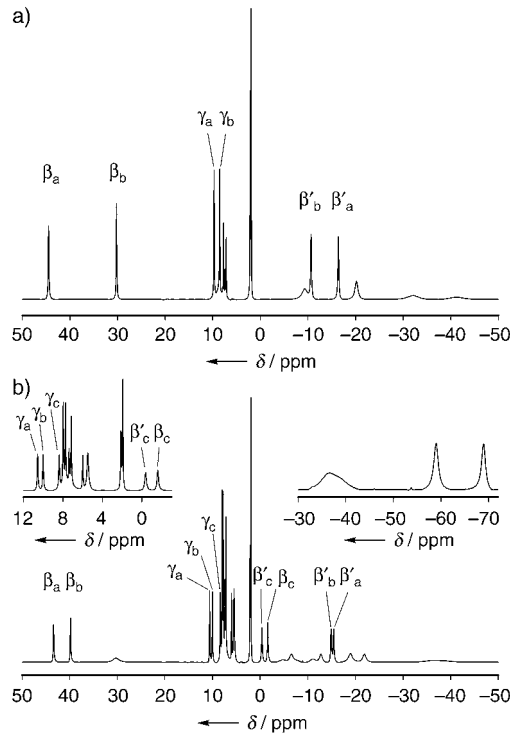

Figure 3. ^{1}H NMR spectra of **1** (a) and **2** (b, and insets) in CD_3CN. Peaks from pyridine ring protons are assigned based on cross peaks identified in COSY spectra. The left inset shows the expanded region near $\delta = 0$ ppm (0.5×) for **2** and reveals the third set of pyridine ring protons, while the right inset shows the $-30 > \delta > -75$ ppm region (10×) of **2**.

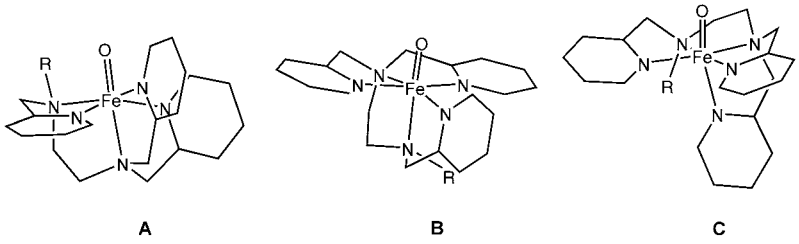

Figure 2. The three possible isomers (**A**–**C**) of $[Fe^{IV}(O)(R\text{-TPEN})]^{2+}$ complexes. R = Bn or Me.

Not surprisingly, the ^{1}H NMR spectrum of **2** is more complex as a result of the lower symmetry of this complex. Two sets of pyridine β, γ, and β′ protons are readily identified from their COSY cross peaks (see Supporting Information) and found at chemical shifts that are comparable to those found for **1**. Their integrations indicate that these peaks account for only two of the three pyridine rings in the complex. Examination of a second COSY spectrum with a narrower spectral width (see Supporting Information) reveals the β, γ, and β′ protons of the third pyridine. These protons exhibit smaller paramagnetic shifts and have a distinct shift pattern in which both β and β′ peaks are shifted upfield and the peak for the γ proton is shifted downfield. The spectrum of the corresponding 5-Me-Bn-TPEN complex **4** shows the disappearance of the β'_c proton, thereby leading us to assign the c set of pyridine protons to the unique pyridine on the Bn-TPEN ligand.

The presence of a pyridine ring with a unique shift pattern in **2** suggests that the Bn-TPEN ligand adopts a wrapping mode that corresponds to isomer **A** (Figure 2). The two pyridines that display similar shift patterns to those found in **1** would correspond to the two that are parallel to the Fe–O axis, while the pyridine that lies perpendicular to the Fe–O axis would give rise to the unusual shift pattern. The difference in their paramagnetic shifts can be easily rationalized by the fact that these pyridines must interact differently with iron d orbitals that have differing amounts of unpaired spin density.

To provide a theoretical foundation upon which to interpret our observations, DFT calculations were carried out to assess the relative energies of the three possible isomers of **2** (Figure 2). Of several models examined, the pure density functional BPW91 model provided an optimized structure for **1** that agreed well with crystallographic data (0.0957 Å root-mean-square deviation over all heavy atoms; see Supporting Information for results using all functionals). Primarily on this basis, BPW91 was chosen for the study of **2**. Table 1 provides Fe–O bond lengths and relative energies for all optimized structures and spin states. The triplet state is

Table 1: Relative BPW91 energies (E [kcal mol^{-1}]) for **2A**–**C** and Fe–ligand bond lengths (Å; for $S=1$ isomers only).[a]

	1[b]	**2A**	**2B**	**2C**
E ($S=1$)[c]		0.0	5.3	12.5
E ($S=2$)[c]		16.6	19.0	
Fe-O	1.639	1.640	1.643	1.645
Fe-N1	2.082 (amine, ax)	2.078 (amine)	2.010 (amine)	2.051 (amine)
Fe-N2	1.976 (py $\parallel$)	2.022 (py $\perp$)	2.040 (py $\perp$)	2.058 (py $\perp$)
Fe-N3	1.983 (py $\parallel$)	1.976 (py $\parallel$)	1.976 (py $\parallel$)	2.042 (py $\perp$)
Fe-N4		1.990 (py $\parallel$)	2.002 (py $\perp$)	2.104 (py, ax)
Fe-N5		2.132 (amine, ax)	2.191 (amine, ax)	2.004 (amine)
Fe-N_{av}	2.000	2.040	2.044	2.052

[a] See Supporting Information for Cartesian coordinates of the geometry-optimized structures of the three isomers **2A**–**C**. [b] Crystallographic bond lengths for **1** included for comparison. [c] Energy for the $S=1$ state of isomer **2A** set to zero. py = pyridine, ax = axial.

favored over the pentet state in each of the two lower-energy isomers (the pentet was not converged for isomer **C**), and all further discussion refers only to triplet states.

Of the three isomers of **2**, **A** is predicted to be lowest in energy, with isomers **B** and **C** lying 5.3 and 12.5 kcal mol^{-1} higher in energy, respectively.[12] When the iron atom is removed and the relative energies of the frozen ligands are computed at the same level of theory, the relative energies of **A**, **B**, and **C** are found to be 1.0, 0.0, and 2.4 kcal mol^{-1}, respectively. Thus, the relative energies of the iron complexes do not derive from differences in steric energy in the supporting ligand but rather from interactions of the ligand with the Fe=O moiety.

Examination of the data in Table 1 suggests that the metal–ligand bond lengths rationalize the relative stabilities of the three isomers of **2**. Equatorial pyridine ligands aligned parallel to the Fe=O axis always have shorter Fe–N bonds than those aligned perpendicular to the Fe=O axis. This shorter distance contributes to the ability of parallel pyridines to stabilize the high-valent iron center through electron donation better than perpendicular pyridines, as judged by second-order perturbation theory in the natural bond orbital (NBO) basis. [13,14] The difference in Fe–N bond lengths is easily explained by the greater steric demand of the α hydrogen atoms of the pyridines that lie perpendicular to the Fe=O axis. Thus, among the three isomers of **2**, the most stable isomer **A** has one pyridine ring perpendicular and two rings parallel to the Fe=O axis to give rise to an average bond length of 2.040 Å over all Fe–N bonds. The less-stable isomers, by contrast, both contain *two* perpendicular equatorial pyridines, with the remaining ring either parallel (**B**) or trans to the oxo atom (**C**). These differences give rise to average Fe–N bond lengths of 2.044 and 2.052 Å, respectively. For comparison, all four of the pyridine rings in the N4Py complex **1** are oriented parallel to the Fe=O axis with an average Fe–N bond length of 2.00 Å and thereby it achieves maximum stabilization among the four structures. Not surprisingly, the half-life of **1** is an order of magnitude greater than that of **2**.

In summary, we have gained structural insight into novel oxoiron(IV) complexes with pentadentate pentaaza ligands by a combination of X-ray crystallography, NMR spectroscopy, and DFT calculations. The X-ray structure of **1** establishes the metrical parameters for this complex and shows the expected ligand topology in which all four pyridines are oriented approximately parallel to the Fe=O axis. In the absence of a crystal structure for **2**, NMR spectral data and DFT calculations clearly favor **2A** as the most stable isomer. We thus conclude that pyridine rings aligned parallel to the Fe=O bond contribute significantly to the stability of the oxoiron(IV) unit and allow such complexes to be observed at room temperature.

Experimental Section

Complexes **1** and **2** were generated from their respective iron(II) precursors following reported procedures,[8] while the generation of **4** followed a similar protocol. The synthesis for the precursor to **4**, [(5-Me-Bn-TPEN)Fe^{II}(OSO_2CF_3)](SO_3CF_3), is described in the Supporting Information.

^{1}H NMR spectra were recorded on a Varian Inova VI-500 spectrometer at ambient temperature, with reported ^{1}H NMR chemical shifts (δ [ppm]) referenced to residual solvent peaks. The COSY spectrum for **1** was collected using 256 points in t_1 with a spectral width of 54.3 kHz and a delay of 30 ms. The COSY spectra for **2** were collected using 256 points in t_1 with spectral widths of 47.8 and 19.7 kHz and a delay of 30 ms.

X-ray crystal structure data for **1**: Blue needles were isolated upon layering pentane on a solution of **1** in acetonitrile: $C_{27}H_{27}Cl_2FeN_7O_9$, monoclinic, space group Cm, $a=11.955(4)$, $b=17.954(5)$, $c=7.084(2)$ Å, $\beta=93.708(5)°$, $V=1517.3(8)$ Å^3, $Z=2$, $\rho_{calcd}=1.577$ g cm^{-3}, crystal dimensions: $0.32\times0.12\times0.04$ mm^3; Bruker CCD diffractometer; $Mo_{K\alpha}$ radiation, 173(2) K; $2\theta_{max}=50.1°$, 5606 reflections, 2669 independent ($R_{int}=0.0454$), direct methods; multiscan absorption correction ($\mu=0.739$ mm^{-1}); refinement (on F^2) with SHELXTL-Plus (version 5.10), 301 parameters, 126 restraints, $R_1=0.0499$ ($I>2\sigma$) and wR_2 (all data) = 0.1178, GOF = 1.046, max/min residual electron density: 0.435/−0.211 e Å^{-3}. CCDC 261401 (**1**) contains the supplementary crystallographic data for this paper. These data can be obtained free of charge from the Cambridge Crystallographic Data Centre via www.ccdc.cam.ac.uk/data_request/cif. See Supporting Information for additional experimental details.

Computational Methods: The molecular geometry of [Fe(O)(N4Py)]$^{2+}$ ($S=1$) was optimized at the unrestricted BLYP,[15,16] BPW91,[16,17] BP86,[15,18,19] BP86-VWN5,[15,19,20] B3LYP,[15,16,19] B3PW91,[15,17] B3P86,[15,19,20] and BHANDH[15] levels using the LACVP*[21–23] effective core potential on iron and the 6-31G**[24–29] basis set on all other atoms. The BPW91 model was found to provide good agreement with the known crystal structure and was chosen on this basis for modeling Fe(Me-TPEN) (in Me-TPEN, the benzyl group of Bn-TPEN is replaced by a methyl group). Three conformers of Fe(Me-TPEN) were optimized at this level for the $S=1$ spin state, and in the two lowest energy cases for the $S=2$ spin state. All structures were verified as minima by computation of analytical vibrational frequencies. Calculations were performed using Jaguar 5.0[30] and Jaguar NBO Version 5.0.[31]

Received: February 8, 2005
Revised: March 3, 2005
Published online: May 25, 2005

Keywords: bioinorganic chemistry · density functional calculations · iron · nitrogen heterocycles · NMR spectroscopy

[1] M. Costas, M. P. Mehn, M. P. Jensen, L. Que, Jr., *Chem. Rev.* **2004**, *104*, 939.
[2] J. C. Price, E. W. Barr, B. Tirupati, J. M. Bollinger, Jr., C. Krebs, *Biochemistry* **2003**, *42*, 7497.
[3] J. C. Price, E. W. Barr, T. E. Glass, C. Krebs, J. M. Bollinger, Jr., *J. Am. Chem. Soc.* **2003**, *125*, 13008.
[4] D. A. Proshlyakov, T. F. Henshaw, G. R. Monterosso, M. J. Ryle, R. P. Hausinger, *J. Am. Chem. Soc.* **2004**, *126*, 1022.
[5] P. J. Riggs-Gelasco, J. C. Price, R. B. Guyer, J. H. Brehm, E. W. Barr, J. M. Bollinger, Jr., C. Krebs, *J. Am. Chem. Soc.* **2004**, *126*, 8108.
[6] J.-U. Rohde, J.-H. In, M. H. Lim, W. W. Brennessel, M. R. Bukowski, A. Stubna, E. Münck, W. Nam, L. Que, Jr., *Science* **2003**, *229*, 1037.
[7] M. H. Lim, J.-U. Rohde, A. Stubna, M. R. Bukowski, M. Costas, R. Y. N. Ho, E. Münck, W. Nam, L. Que, Jr., *Proc. Natl. Acad. Sci. USA* **2003**, *100*, 3665.
[8] J. Kaizer, E. J. Klinker, N. Y. Oh, J.-U. Rohde, W. J. Song, A. Stubna, J. Kim, E. Münck, W. Nam, L. Que, Jr., *J. Am. Chem. Soc.* **2004**, *126*, 472.
[9] J.-U. Rohde, S. Torelli, X. Shan, M. H. Lim, E. J. Klinker, J. Kaizer, K. Chen, W. Nam, L. Que, Jr., *J. Am. Chem. Soc.* **2004**, *126*, 16750.
[10] Y. Zang, J. Kim, Y. Dong, E. C. Wilkinson, E. H. Appelman, L. Que, Jr., *J. Am. Chem. Soc.* **1997**, *119*, 4197.
[11] L.-J. Ming, in *Physical Methods in Bioinorganic Chemistry: Spectroscopy and Magnetism* (Ed.: L. Que, Jr.), University Science Books, Sausalito, CA, **2000**, pp. 375.
[12] When the B3LYP functional is used in place of the BPW91 functional, the relative energies are found to be 0.0, 4.8, and 12.2 kcal mol^{-1}, respectively (see Supporting Information).
[13] A. E. Reed, L. A. Curtiss, F. Weinhold, *Chem. Rev.* **1988**, *88*, 899.
[14] C. J. Cramer, *J. Mol. Struct. (Theochem)* **1996**, *370*, 135.
[15] A. D. Becke, *Phys. Rev. A* **1988**, *38*, 3098.
[16] C. Lee, W. Yang, R. G. Parr, *Phys. Rev. B* **1988**, *37*, 785.
[17] J. P. Perdew, J. A. Chevary, S. H. Vosko, K. A. Jackson, M. R. Pederson, D. J. Singh, C. Fiolhais, *Phys. Rev. B* **1992**, *46*, 6671.
[18] J. P. Perdew, A. Zunger, *Phys. Rev. B* **1981**, *23*, 5048.
[19] J. P. Perdew, *Phys. Rev. B* **1986**, *33*, 8822.
[20] S. H. Vosko, L. Wilk, M. Nusair, *Can. J. Phys.* **1980**, *58*, 1200.
[21] P. J. Hay, W. R. Wadt, *J. Chem. Phys.* **1985**, *82*, 299.
[22] P. J. Hay, W. R. Wadt, *J. Chem. Phys.* **1985**, *82*, 270.
[23] W. R. Wadt, P. J. Hay, *J. Chem. Phys.* **1985**, *82*, 284.
[24] R. C. Binning, Jr., L. A. Curtiss, *J. Comput. Chem.* **1990**, *11*, 1206.
[25] M. S. Gordon, *Chem. Phys. Lett.* **1980**, *76*, 163.
[26] R. Ditchfield, W. J. Hehre, J. A. Pople, *J. Chem. Phys.* **1971**, *54*, 724.
[27] P. C. Hariharan, J. A. Pople, *Mol. Phys.* **1974**, *27*, 209.
[28] P. C. Hariharan, J. A. Pople, *Theor. Chim. Acta* **1973**, *28*, 213.
[29] W. J. Hehre, R. Ditchfield, J. A. Pople, *J. Chem. Phys.* **1972**, *56*, 2257.
[30] Jaguar 5.0, Schrodinger, LLC, Portland, Oregon, **2002**.
[31] Jaguar NBO Version 5.0, E. D. Glendening, J. K. Badenhoop, A. E. Reed, J. E. Carpenter, J. A. Bohmann, C. M. Morales, F. Weinhold, (Theoretical Chemistry Institute, University of Wisconsin, Madison, WI, **2001**); http://www.chem.wisc.edu/~nbo5.

Fluorescence Imaging

Pyrromethene Dialkynyl Borane Complexes for "Cascatelle" Energy Transfer and Protein Labeling**

Gilles Ulrich, Christine Goze, Massimo Guardigli, Aldo Roda, and Raymond Ziessel**

The design of strongly luminescent probes is a thriving subject which finds applications in electroluminescent devices and fluorescence technology.[1,2] Fluorescent labels and probes have found widespread uses in biomedicine, polymer science, and sensor chemistry.[3,4] One of the most promising classes of dyes is that of cyanines stabilized with BF_2 fragments, such as 4,4-difluoro-4-bora-3a,4a-diaza-s-indacene (Bodipy) derivatives.[5] These non-ionic, stable molecules have exceptional optical and luminescence properties,[6] and a wide range of dyes have been engineered by modification of the pyrrole substituents.[7] To date, chemical modification of the BF_2 fragment with ethynylaryl modules has rarely been attempted.[8]

Frequently encountered deficiencies in the use of Bodipy derivatives are the small Stokes shifts ($\Delta\lambda \approx 600\ cm^{-1}$) between the lowest energy absorption band and the emission band, and the quenching of their fluorescence on conjugation to proteins.[5] Larger Stokes shifts would be advantageous in simplifying simultaneous excitation and emission detection, since background interferences are reduced and wide-band excitation and emission filters may be used, thus increasing the intensity of the fluorescence signal. Also desirable is the enhancement of this signal intensity by incorporation of a chromophore active in the region 350–370 nm where Bodipy species do not absorb, pyrene is an example of such a chromophore.[9]

Herein, we describe an elegant method for increasing the Stokes shift of Bodipy derivatives and minimizing fluorescence quenching after bioconjugation. This approach involves functionalization of the Bodipy core by binding ethynylpyrene entities directly to the boron center. Irradiation of the pyrene chromophore results in exclusive emission from the Bodipy core as a result of efficient intramolecular energy

[*] Dr. G. Ulrich, C. Goze, Dr. R. Ziessel
Laboratoire de Chimie Moléculaire, ECPM
25 rue Becquerel, 67087 Strasbourg Cedex 02 (France)
Fax: (+33) 3-9024-2689
E-mail: gulrich@chimie.u-strasbg.fr
ziessel@chimie.u-strasbg.fr
Prof. M. Guardigli, Prof. A. Roda
Department of Pharmaceutical Sciences
University of Bologna
Via Belmeloro 6, 40126 Bologna (Italy)

[**] This work was supported by the Centre National de la Recherche Scientifique, and the Ministère de la Recherche et des Nouvelles Technologies. "Cascatelle" is a French word meaning "a very small cascade".

Supporting information for this article is available on the WWW under http://www.angewandte.org or from the author.

  DOI: 10.1002/anie.200500808

transfer, so that these new dyes function as a small cascade device or "cascatelle". Further functionalization enables ready attachment of the dyes to biopolymers such as proteins.

While trigonal alkynylboranes are well-known,[10] tetrahedral species are rare[11] and herein we describe the first such compounds in which two ethynyl units are bound to the boron center of a bora-indacene (Figure 1). The syntheses of **1** and **2** involve the displacement of fluoride from boron by 4-lithioethynyltoluene and 1-lithioethynylpyrene, respectively. Both compounds are obtained in satisfactory yield (**1** 62%, **2** 30%), and have been characterized by chemical analyses, full spectroscopic measurements, and crystal structure determinations.

The structure determinations (Figure 1) show an almost exact tetrahedral geometry for the sterically congested boron atoms. In both, the N-B-N angle is 106°, while the C-B-C angle for **1** is 115° and for **2** is 111°. The B–C and C≡C bonds fall in the ranges 1.58–1.60 Å and 1.18–1.20 Å, respectively. The B–C distances are longer than those of trigonal tris(3,3-dimethyl-1-butynyl)borane but similar to those in its tetrahedral pyridine adduct.[12]

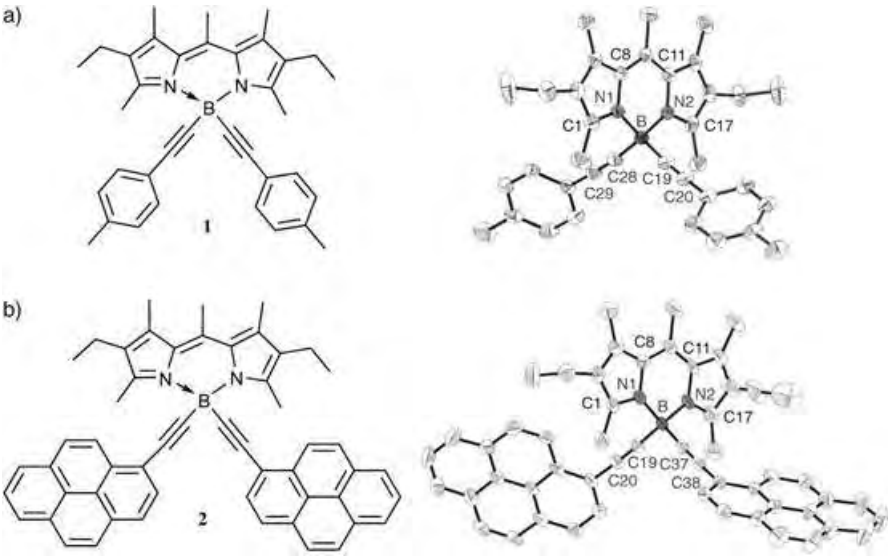

Figure 1. Structures of **1** (a) and **2** (b). Selected bond lengths [Å] and angles [°]: for **1** B-C28 1.589, B-C19 1.595, B-N1 1.562, B-N2 1.557, C28-C29 1.206, C19-C20 1.204, N1-C1 1.350, N1-C8 1.403, N2-C17 1.351, N2-C11 1.401; C28-B-C19 114.76, C28-B-N2 108.67, N1-B-N2 106.05, N2-B-C19 109.62. For **2** B-C19 1.603, B-C37 1.585, B-N1 1.563, B-N2 1.565, C20-C19 1.187, C37-C38 1.194, N1-C1 1.352, N1-C8 1.402, N2-C17 1.344, N2-C11 1.403; C19-B-C37 111.61, C19-B-N1 108.18, N1-B-N2 105.89, N2-B-C37 109.64, N2-B-C19 110.99.

The electronic absorption spectra of **1** and **2** reflect the presence of the separate Bodipy and ethynylaryl units (Figure 2). A strong band at 516 nm is attributed to the $S_0 \rightarrow S_1$ Bodipy transition, while a second weaker and broader band at 371 nm (clearly seen in Figure 2a) is typical of the $S_0 \rightarrow S_2$ transition.[13,14] Peaks observed at higher energies may be confidently assigned to the spin-allowed π–π* transitions of the ethynyl ($\lambda \approx 320$ nm) and toluyl ($\lambda \approx 265$ nm) groups (Figure 2). For **2**, a strong absorption at 330–370 nm, partially overlapping the $S_0 \rightarrow S_2$ Bodipy transition, is assigned to the ethynylpyrene unit.[9] The spectroscopic data are summarized in Table 1.

When excited at 516 nm, both **1** and **2** emit strongly, with high fluorescence quantum yields, in the region 535–540 nm. The radiative rate constants have values close to 1.5×10^8 s^{-1}. For **2**, excitation in the pyrene absorption band did not lead to pyrene emission but instead to emission characteristic of the indacene core. The fluorescence excitation spectrum matches the absorption spectrum, indicating that there is an efficient energy transfer from the pyrene to the Bodipy moiety. The quantum yield measurements are consistent with an efficiency close to 100% for this transfer. The result is that there are virtual Stokes shifts of approximately 10^4 cm^{-1}.

To devise a means of grafting these highly fluorescent units onto biopolymers, we synthesized an indacene derivative bearing an iodophenyl substituent on the *meso* position. Substitution of the iodine by a carboxybutylethynyl unit ultimately led to the activated ester **3d** (Scheme 1), which was expected to be reactive towards protein amino acid side-chain nucleophiles such as the terminal amino group of lysine (Scheme 1).[16]

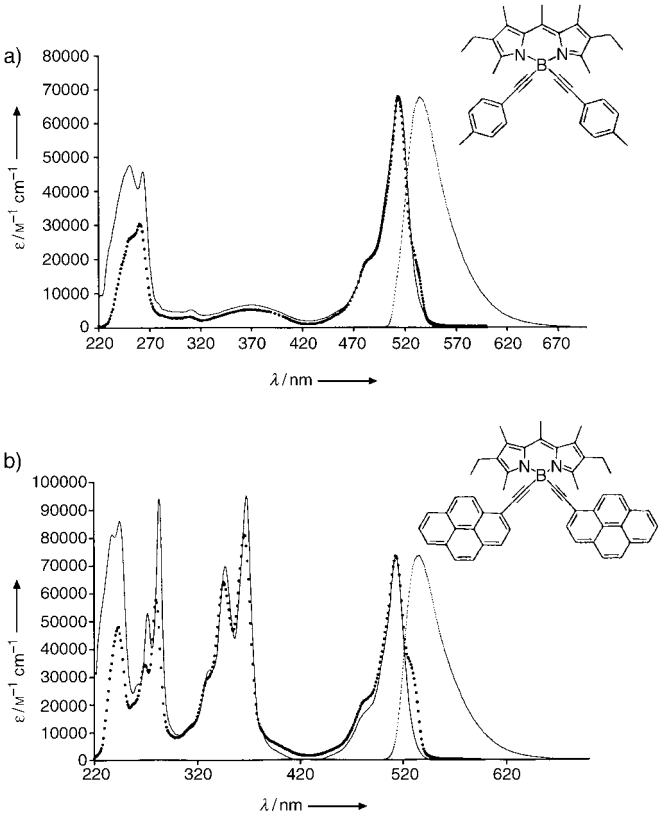

Figure 2. Absorption (——), emission (-----), and fluorescence excitation spectra (•••••) for compounds **1** (a) and **2** (b) in dichloromethane solution. Emission spectra were obtained upon excitation in the ethynyltoluyl moiety absorption (252 nm) for **1** and in the ethynylpyrene moiety absorption (371 nm) for **2**, while fluorescence excitation spectra were measured upon emission at 535 nm.

Table 1: Spectroscopic[a] data at 298 K for the new compounds.

Compound	λ_{abs} [nm]	ε_{max} [$M^{-1}cm^{-1}$]	λ_F [nm]	τ_F [ns]	ϕ_F [b] [%]	η [c] [%]	k_r [$10^8 s^{-1}$]	k_{nr} [$10^6 s^{-1}$]
1	516	67100	537	9.0	95		1.1	5.6
2	516	73000	535	6.2	94		1.5	9.7
	371	95000	535		90	96		
3b	523	50000	539	6.2	90		1.5	16.1
	370	61500	539		85	94		
3e	522	61000	538	5.0	82		1.6	36.0
	370	88000	538		55	67		

[a] Determined in aerated dichloromethane solution. [b] Determined using rhodamine 6G ($\phi_F = 0.76$ in water[15]) as reference. All ϕ_F were corrected for changes in refractive index. [c] Efficiency energy transfer from ethynylpyrene to the indacene moiety, calculated by dividing the quantum yield found by excitation in the chromophores by those found by excitation in the indacene moiety.

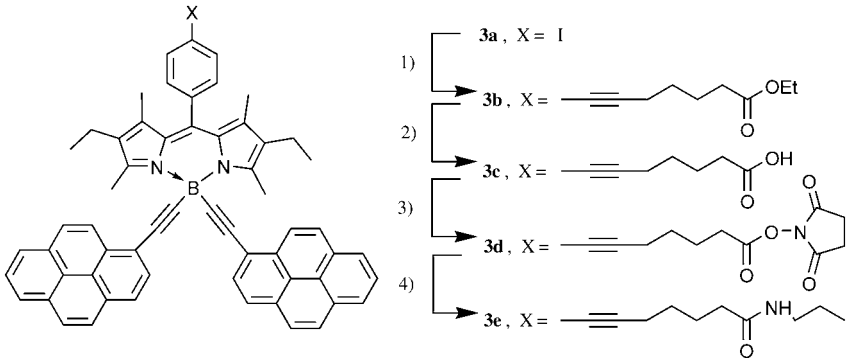

Scheme 1. 1) HC≡C$(CH_2)_4$COOEt (1 equiv), [$PdCl_2(PPh_3)_2$] (6% mol), CuI (10% mol), RT, 16 h, 91%. 2) NaOH (10 equiv), ethanol/THF (1:1), 60°C, 12 h, 87%. 3) DMAP (2 equiv), EDCI (2 equiv), *N*-hydroxysuccinimide (2 equiv), RT, 1 h, 54%. 4) *n*-propylamine, RT, 1 h, 74%. DMAP = dimethylaminopyridine, EDIC = 1-ethyl-3-(3-dimethylaminopropyl)carbodiimide.

succimimide (NHS) esters.[17] Indeed, it proved possible to attach multiple fluorescent tags to BSA using **3d** in various label/protein ratios (ranging from 2:1 to 10:1), in a 1:1 (v/v) water/DMSO solution. Characterization of the conjugates in terms of label/protein molar ratio was performed by means of UV/Vis absorption spectroscopy, under the assumption that the absorption spectra of the conjugates are the sum of the absorption spectra of BSA and the Bodipy dye and that these spectra coincide with those of the free BSA and **3e**, respectively (Figure 3).

The experimentally determined label/protein molar ratios of the conjugates were in good agreement with the label/protein molar ratio used in the conjugation reaction (Table 2), indicating a high reaction yield. These BSA conjugates essentially maintain the spectroscopic characteristics of the model compound **3e** (Scheme 1 and Table 1). The fluorescence emission of aqueous solutions of the conjugates shows maximum intensity at 544 nm (Figure 4), being slightly red-shifted in comparison to that of compound **3e** in dichloromethane. All the protein conjugates remain strongly fluorescent, with an efficiency of energy transfer from the ethynylpyrene chromophore to the indacene moiety similar to that found for **3e** (see Figure 3). The efficiency of the energy transfer from the pyrene to the indacene moiety drops for **3e** and the labeled BSA conjugates when compared to that of **3b**, which has an ester function. This drop is likely to be due to the presence of the amide function in **3e** and the labeled conjugates which provides a non-radiative channel for the deactivation process.[18]

The fluorescence quantum yield decreases slightly with the increase in the degree of labeling of the conjugates,

The demonstration of the suitability of derivative **3d** for protein labeling and the evaluation of the spectroscopic properties of its protein conjugates were performed using bovine serum albumin (BSA) as a model protein which has 59 lysine residues that can potentially react with *N*-hydroxy-

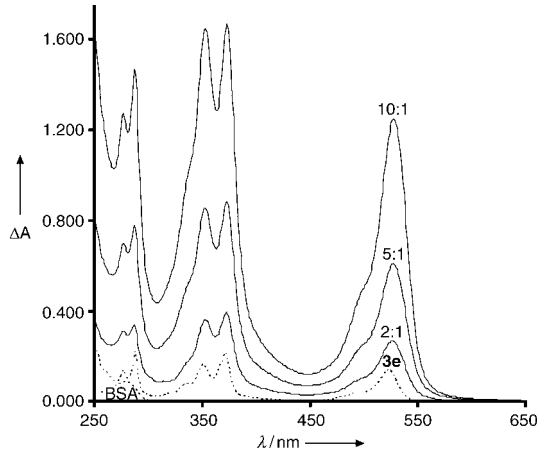

Figure 3. UV/Vis absorption spectra of the BSA conjugates of **3d** in water at a concentration of about 2.3×10^{-6} M and the BSA:**3d** ratios indicated; for comparison, the absorption spectra of BSA in water and of **3e** in dichloromethane at the same concentration are also shown (•••••).

Table 2: Label/protein molar ratios evaluated by UV/Vis spectroscopy and fluorescence properties of the BSA conjugates of **3d** in aqueous solution.

Conjugate	Label/protein molar ratio[a]	ϕ_F [b] [%]	η [c] [%]
2:1	1.9–1.8:1	75[d], 45[e]	61
5:1	4.3–5.2:1	63[d], 38[e]	61
10:1	8.9–9.9:1	49[d], 32[e]	67

[a] The values are the label/protein molar ratios of the conjugates evaluated from the absorption at 528 nm and from the comparison of the absorption of the conjugate at 280 nm with those of free BSA and **3d**. [b] Determined using rhodamine 6G ($\phi_F = 0.76$ in water[15]) as reference. [c] Efficiency of the energy transfer from the ethynyltoluyl or ethynylpyrene chromophore to the indacene moiety, calculated by dividing the quantum yield found by excitation in the chromophores by those found by excitation in the indacene moiety. [d] Upon excitation in the indacene moiety absorption at 528 nm. [e] Upon excitation in the ethynylpyrene chromophore absorption at 370 nm.

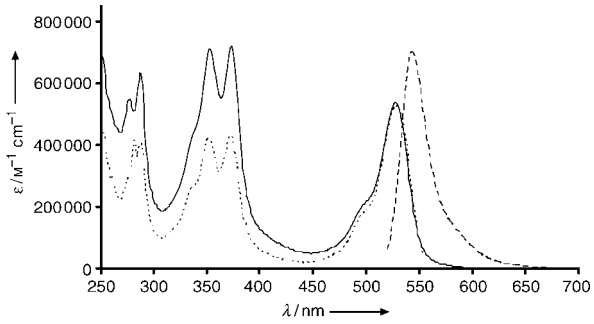

Figure 4. Absorption (——) and emission (-----) spectra of the 10:1 BSA conjugate of **3d** in water solution recorded upon excitation in the ethynylpyrene moiety absorption at 370 nm, and the fluorescence excitation spectra (••••) measured upon emission at 544 nm.

indicating a slight degree of self-quenching. However, the overall fluorescence intensity of the conjugates, as evaluated on the basis of their molar extinction coefficients and fluorescence quantum yields, still increases with the degree of labeling (Figure 5 and Table 2).

To compare the performance of the new Bodipy derivative with that of conventional fluorescent labels, fluorescence-imaging experiments were conducted. Figure 5 shows fluorescence images of spots containing the same amount of the BSA conjugates of **3d** or a fluorescein-labeled rabbit immunoglobulin G (IgG) with a 2.3:1 fluorescein/antibody labeling ratio (the fluorescein-labeled IgG and the 2:1 conjugate spots thus contain comparable amounts of fluorescent label molecules). The comparison of the fluorescence intensities of the spots indicates that, upon excitation in the UV spectral region, the BSA conjugates of **3d** are more efficient emitters than the fluorescein-labeled immunoglobulin (Figure 5a). The fluorescence emission of the BSA conjugates is stronger than that of the fluorescein-labeled IgG even when the latter is measured using fluorescein-specific excitation and emission filters (Figure 5b); the BSA conjugates are only weakly fluorescent using fluorescein filters because such filters do not match the absorption and emission bands of **3d**). This observation demonstrates that the peculiar absorption and emission properties of **3d** could be successfully exploited also using the conventional excitation sources used in fluorescence microscopy, such as mercury arc lamps. Indeed, their most intense emission line of such lamps (365–366 nm) is close to the maximum of the absorption band of the ethynylpyrene chromophore, whereas fluorescein has only a weak absorption at this wavelength.

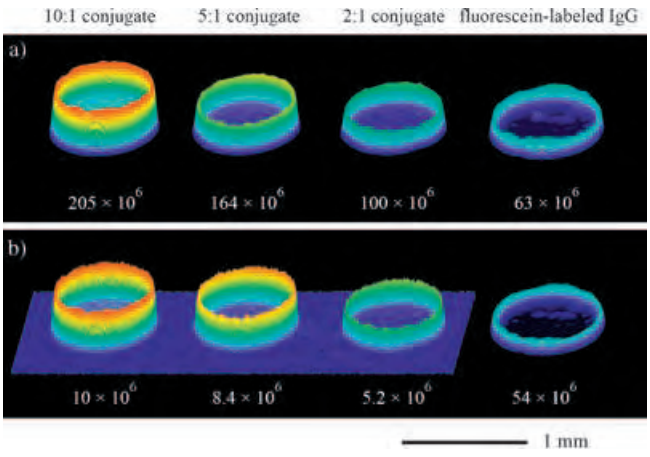

Figure 5. Pseudocolored 3D plots of fluorescence images of spots (diameter ≈ 800 μm) containing approximately 5×10^{-15} mol of the BSA conjugates of **3d** or a fluorescein-labeled rabbit immunoglobulin G. Spots were obtained using a manual microarrayer device, which employs an array of pins to transfer small volumes (ca. 3 nL) of solution onto microscope glass slides. Images were acquired with a standard epifluorescence microscope using either a) a wide-band UV excitation filter and a visible light emission filter or b) fluorescein-specific excitation and emission filters (because of their relatively low intensity, the images of BSA conjugate spots in (b) are shown using a different intensity scale). The images represent the actual fluorescence intensity of each spot, evaluated by integrating the signal over the whole spot area and expressed in arbitrary units.

The key feature of the present molecular design is the introduction of a supplementary chromophore linked by an ethynyl bridge to a tetrahedral boron atom. Such "Bodipyrene" dyes have three outstanding features: 1) relative ease of synthesis; 2) very large Stokes shifts resulting from an efficient, spin-allowed energy transfer from the excited pyrene subunit to the emitting state of the indacene center (a "cascatelle" process); 3) convenient functionalization to introduce an activated ester group suitable for grafting the dye to biopolymers. Very importantly, attachment of the dyes to a protein appears to produce only minor quenching effects and the singular other properties of the dyes are maintained. Fluorescence-imaging microscopy shows that these new labels are considerably superior to conventional fluorophores. The notion of a cascatelle process, clearly substantiated by the present work, is open to many avenues of development, leading to possibilities such as the multichromatic patterning of biomaterials using a single excitation source.

Received: March 4, 2005

Keywords: boron · fluorescence imaging · luminescence · protein labeling · Stokes shift

[1] S. R. Forest, P. E. Burrows, M. E. Thompson in *Organic Electroluminescent Materials and Devices* (Eds.: S. Miyata, H. S. Nalwa), Gordon and Breach, Langhorne, PA, **1996**.
[2] B. Valeur in *Molecular Fluorescence: Principles and Applications*, Wiley-VCH, Weiheim, **2002**, 351–378.
[3] *Fluorescence Spectroscopy in Biology: Advanced Methods and their Applications to Membranes, Proteins, DNA, and Cells* (Eds.: H. Martin, H. Rudolf, F. Vlastimil) Springer, Heidelberg, **2005**.
[4] "Probe Design and Chemical Sensing": J. R. Lakowicz in *Topics in Fluorescence Spectroscopy, Vol. 4* (Ed.: J. R. Lakowicz), Plenum, New York, **1994**.
[5] R. P. Haugland, *Handbook of Molecular Probes and Research Products, 9th ed.*, Molecular Probes, Eugene, **2002**.
[6] G. Sathyamoorthi, L. T. Wolford, A. M. Haag, J. H. Boyer, *Heteroat. Chem.* **1994**, *5*, 245; A. Burghart, H. Kim, M. B. Wech, L. H. Thorensen, J. Reibenspies, K. Burgess, *J. Org. Chem.* **1999**, *64*, 7813; K. Rurack, M. Kollmannsberger, J. Daub, *Angew. Chem.* **2001**, *113*, 396; *Angew. Chem. Int. Ed.* **2001**, *40*, 385.
[7] R. P. Haugland, H. C. Kang, US Patent US 4,774,339, **1998**.

[8] S. Murase, T. Tominaga, A. Kohama, European Patent EP 1253151 A1, **2002**.
[9] M. Hissler, A. Harriman, A. Khatyr, R. Ziessel, *Chemistry Eur. J.* **1999**, *5*, 3366.
[10] S. Yamaguchi, S. Akiyama, K. Tamao, *J. Am. Chem. Soc.* **2000**, *122*, 6335; W.-L. Jia, D. Saong, S. Wang, *J. Org. Chem.* **2003**, *68*, 701; Y. Kubo, M. Yamamoto, M. Ikeda, M. Takeuchi, S. Shinkai, S. Yamaguchi, K. Tamao, *Angew. Chem.* **2003**, *115*, 2082; *Angew. Chem. Int. Ed.* **2003**, *42*, 2036.
[11] B. Qian, S. W. Baek, M. R. Smith III, *Polyhedron* **1999**, *18*, 2405; L. Ding, K. Ma, G. Dürner, M. Bolte, F. Fabrizi de Biani, P. Zanello, M. Wagner, *J. Chem. Soc. Dalton Trans.* **2002**, 1566.
[12] M. J. Bayer, H. Pritzkow, W. Siebert, *Eur. J. Inorg. Chem.* **2002**, 2069.
[13] J. Karolin, L. B.-A. Johansson, L. Strandberg, T. Ny, *J. Am. Chem. Soc.* **1994**, *116*, 7801.
[14] G. Ulrich, R. Ziessel, *J. Org. Chem.* **2004**, *69*, 2070.
[15] J. Olmsted III, *J. Phys. Chem.* **1979**, *83*, 2581.
[16] G. T. Hermanson, *Bioconjugate Techniques*, Academic Press, San Diego, **1996**.
[17] C. C. Goodno, H. E. Swaisgood, G. L. Catignani *Anal. Biochem.* **1981**, *115*, 203.
[18] G. P. Der-Balian, N. Kameda, G. L. Rowley, *Anal. Biochem.* **1988**, *173*, 59.

Crystal Growth

Control of Biomineralization Dynamics by Interfacial Energies**

*Ruikang Tang, Molly Darragh, Christine A. Orme, Xiangying Guan, John R. Hoyer, and George H. Nancollas**

The constructive interaction of an inorganic crystal phase with an organic matrix results in the formation of composite biomaterials that have an exceptional appearance and remarkable physical properties.[1–4] During this process, living organisms may make use of peptides and proteins to deterministically modify nucleation, growth kinetics, surface morphology, and facet stability.[5–7] This control can range from the most specific binding of protein or macromolecular functional groups, to a nonspecific control, in which the species in solution change the thermodynamic driving force of crystallization.[6–8] It is generally agreed that proteins which are most active in the mediation of biologically directed mineral growth contain acidic amino acid residues, specifically, regions rich in carboxylates that interact with mineral surfaces to influence both the crystal morphologies and rates of formation.[7,9–11]

The mechanisms of biomineralization have been the subject of extensive discussion. A widely accepted view is that the organic matrix or the other molecules control the crystal structure by epitaxial matching.[6,8] Another suggestion is that the adsorption of additives does not occur on crystal faces but rather on dislocation lines for crystal growth or dissolution, which influences their morphology and rates of movement.[11,12] In this step-control model, the altered crystal shape is the result of dynamic processes, and the resulting crystal geometries are based on these modified surface steps. Herein, we report on a new mechanism based on modifications that result from a change of solid–solution interfacial energies. In this third mechanism, the adsorption of structure-controlling molecules may not influence the step dynamics.

A constant composition (CC) method sensitive to changes at the nanomolar level provides reliable rates of crystal growth,[13] and the development of in situ fluid atomic force microscopy (AFM) enables the visualization of these processes in real time. Brushite (dicalcium phosphate dihydrate, $CaHPO_4{\cdot}2H_2O$) is one of the more important mineral phases that has frequently been invoked as a precursor phase in the biological formation of apatite.[14] It is readily crystallized from aqueous solutions and has been found in developing bone, immature dentins, and even in renal stones.[15] It is also a good model system for biominerals as it is very stable with respect to structural rearrangements and the crystals are large enough to be employed as substrates for dynamic AFM examination. Citric acid, $HOOC(CH_2)_2CH(COOH)(CH_2)_2COOH$, a carboxylate-rich molecule, is often considered as a model system for more complicated naturally occurring proteins.[11] Deficiencies of urinary citrate predispose one to renal stone formation.[16] We expect that the general trends found for this model brushite–citrate system will also hold for the other crystallizing biominerals.

Figure 1 shows typical CC curves for brushite growth in the absence and presence of citrate. The normalized brushite-growth rate R in the absence of an additive is almost unchanged at citrate concentrations below 1.0×10^{-6} M ($R = 4.20\pm0.15\times10^{-5}\,\mathrm{mol\,m^{-2}\,min^{-1}}$). However, the rate is reduced by about 50% ($R = 2.08\pm0.05\times10^{-5}\,\mathrm{mol\,m^{-2}\,min^{-1}}$) in the presence of 2.1×10^{-6} M citrate, and the degree of inhibition increases with increasing citrate concentration to $0.22\pm0.01\times10^{-5}\,\mathrm{mol\,m^{-2}\,min^{-1}}$ or 95% inhibition at a citrate concentration of 1.0×10^{-5} M. A further increase in citrate concentration does not change the CC growth curves, which suggests that the maximum degree of inhibition by citrate is about 95%. It is important to note that as the ratios of calcium

[*] R. Tang, X. Guan, Prof. G. H. Nancollas
Department of Chemistry, University at Buffalo
The State University of New York
Buffalo, NY 14260 (USA)
Fax: (+1) 716-645-6947
E-mail: ghn@buffalo.edu
R. Tang
Department of Chemistry, Zhejiang University
Hangzhou, Zhejiang 310027 (China)
M. Darragh, C. A. Orme
Department of Chemistry and Materials Science
Lawrence Livermore National Laboratory
Livermore, CA 94551 (USA)
J. R. Hoyer
The Children's Hospital of Philadelphia
University of Pennsylvania, School of Medicine
Philadelphia, PA 19104 (USA)

[**] This work was supported by the National Institutes of Health (NIDCR grant number DE03223).

  DOI: 10.1002/anie.200500153

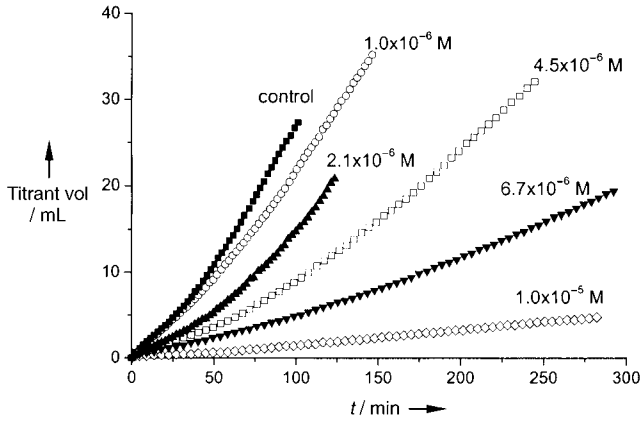

Figure 1. CC growth curves of brushite in the presence of citrate. The relative supersaturation with respect to brushite (σ) was 0.250; the pH value and ionic strength were 5.60 and 0.15 M, respectively; the curves have been normalized to the same seed mass of 10.0 mg. The growth rates are calculated from the gradient of these CC curves.

to citrate in the reaction solutions are always greater than 800, changes in the calcium concentration as a result of the formation of calcium citrate complexes can be ruled out. Thus, citrate effectively retards the growth of brushite crystals.

Typical platelike brushite crystals with smooth (010) surfaces served as suitable substrates for AFM (the Miller indices (*hkl*) denote a single plane and [*uvw*] specify a unique vector direction). In common with observations of other solution-based crystals growing near equilibrium,[11,12,17–19] parallel in situ AFM experiments, made under the same conditions as those for the CC experiments, show that brushite crystals in pure solutions grow on atomic steps generated at complex dislocation hillocks (Figure 2). These are triangular in shape with crystallographically distinct steps along the [101], [201], and [001] directions (Figure 2). In pure supersaturated solution, they have anisotropic spreading velocities in the order $[101] \approx [001] > [201]$, which is also reflected by the different terrace spacings between the growing steps.[11]

Qiu et al. and Orme et al. have proposed that the modification of biological mineralization (step control) is a result of additive binding at step edges to change the step velocities and morphologies.[11,12] However, in the present study of brushite biomineralization, neither the step morphology (Figure 2) nor the kinetics are affected by the presence of citrate even though it has been recognized as an effective inhibitor. At each of the citrate concentrations examined, neither defect nor the loss of defined direction for any of the three steps is observed in the AFM investigations performed in situ. Furthermore, the velocities of all three steps are not significantly changed in the presence of citrate (Figure 3). It is interesting that such a decrease in the crystal growth rate and change of crystal habit would be attributed conventionally to a decrease in step-spreading speed,[11,12] thus emphasizing that the pinned defects on the steps are consequences of the specific binding/adsorption of additives with resulting growth modification. Although the measured step velocities are not perfectly constant, the maximum variation is only about 10%. Nevertheless, in the parallel CC experiments, the bulk inhibition reaches more than 50%, so the conventional understanding of growth inhibition in terms of reduced step velocity does not apply.

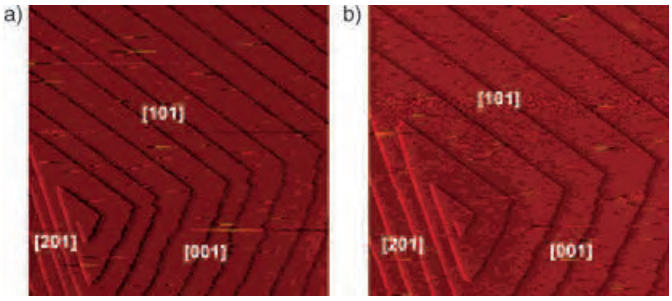

Figure 2. AFM frames of a growing (010)-brushite face: a) in the absence of citrate; b) in the presence of citrate. Introduction of citrate molecules reduces the brushite growth rate by changing the terrace spacing between the growth steps rather than the morphology or velocity of the steps, which results in a marked decrease of the step density on the growing surface.

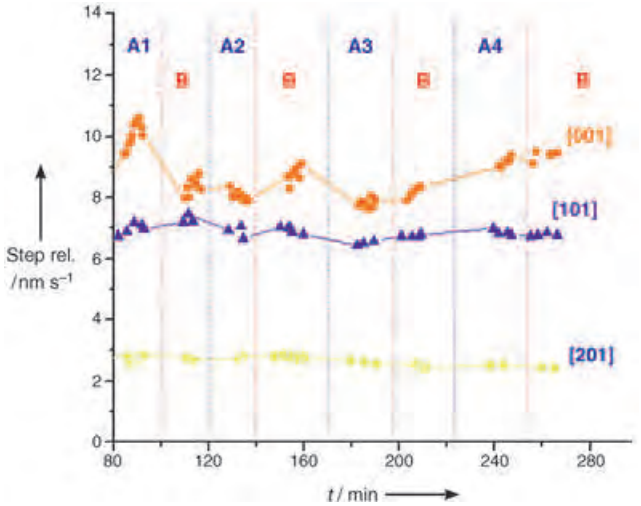

Figure 3. Evolution of the velocities of all three steps for crystals grown in solutions with and without citrate. All experimental conditions were kept constant, and there was no change in the spreading rates of steps in the absence and presence of citrate. The vertical red dotted lines indicate the time at which the crystals were exposed to a pure growth solution supersaturated with calcium phosphate (marked as B areas), while the blue dotted lines indicate the times at which the growth solutions contained citrate. In areas A1, A2, A3, and A4, the citrate concentrations were 1.0×10^{-6}, 5.0×10^{-6}, 1.0×10^{-5}, and 2.0×10^{-5} M, respectively.

It is noteworthy that citrate dramatically decreases the step density, especially for the [101] and [001] steps (Figure 2). It is well-known that the bulk growth rate R depends not only upon the step velocity but also upon the step density.[17–19] R is dominated by the two fastest growth steps ([101] and [001] steps), and the decrease in step density accounts for the observed inhibition in the bulk CC seeded growth experiments. Thus, the retardant effect is attributed to a decrease of step velocity. However, these modifications in step density are

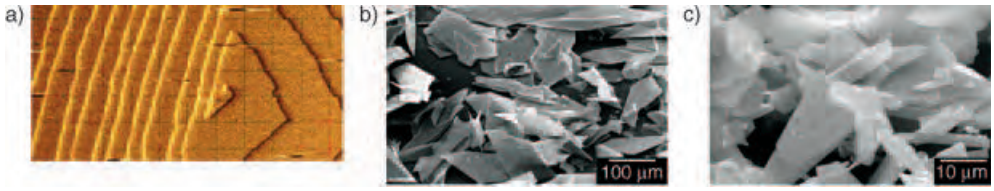

Figure 4. a) AFM image shows that inhibition effects (decreasing step density) are anisotropic; increasing citrate concentration (5.0×10^{-5} M) results in density reductions of fast growth steps [101] and [001], which are much more significant than that of the slow growth step [201]. In bulk crystallization experiments, the morphologies of grown brushite crystallites change from typical platelike (b) to rodlike (c) at high citrate concentrations (1.0×10^{-5} M) as a result of this anisotropic modification.

anisotropic; the ratio of [101] or [001] step spacings to those of [201] increases with increasing citrate (Figure 4a), which implies that the inhibition order is $[101]\approx[001]>[201]$. It follows that although [201] steps have the lowest growth rate in the control experiments, they are much less influenced by the presence of citrate than the [101] and [100] steps. With increasing citrate concentration and greater inhibition on [001] and [101] steps, the growth of [201] steps eventually dominates. At higher concentrations of citrate (1.0×10^{-5} M), the effective growth in the [001] and [101] directions decreases markedly and, as expected, the typical platelike brushite crystallites become rodlike (Figure 4b,c). The much lower inhibitory influence on the [201] steps also explains why citrate cannot fully inhibit brushite CC growth rates. Our results are in general agreement with the essential role of step modification in biomineralization. However, there is one important new feature: the results clearly show that biological systems may use step density rather than step velocity to change mineralization rates by modifying step energies while the velocity and morphology are virtually unchanged.

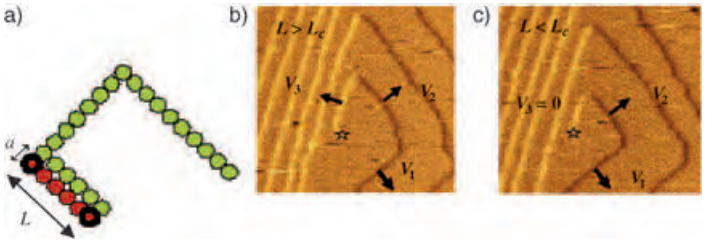

Figure 5. a) Enlargement of a dislocation source; the green represents the original step while the orange represents the new growth. The images in b) and c) show that the critical length is the minimum length at which the step will begin growing outward and the following step will begin growing. Adding biological additives such as citrate, and thus altering the energetics of the crystal formation, can in turn alter the shape of the crystal. The dislocation source on brushite surface is marked with a star.

Crystal growth in solution occurs at surface dislocations, which provide constant sources of steps.[17] Two terms that determine whether a step will grow or dissolve are related to the solution supersaturation S and the free energy of the step edge. The total change in free energy of the system is given by Equation (1). Here, n is the number of growth units adsorbing

$$\Delta G = -n\,\Delta\mu + 2a\gamma_{step} \qquad (1)$$

to the surface and $\Delta\mu$ is the change in chemical potential per growth unit during this phase transformation ($\Delta\mu \propto \ln S$). The second term relates the free energy of the step edge γ_{step} and the diameter a of the newly added growth units. The diagram (Figure 5a) shows the relationship between n and the step length such that $n = L/a$. The addition of molecules to a step becomes favorable at the point at which $\Delta G \leq 0$. Solving for L gives the critical length L_C, the length at which the step will begin growing outward and the following step will develop (Figure 5b,c). The spontaneous step growth does not occur until L_C is reached; rather, it will remain stationary or dissolve with no contribution to the growth rate. In this way, the mass of a brushite crystal increases as calcium and phosphate ions are deposited along steps on the crystal surfaces. These steps grow by spiraling outward from the dislocation sources on the surface. The relationship between terrace widths for the steps and the critical length L_C has been discussed.[18,19] Figure 2b suggests that citrate increases L_C, and in turn increases the period of time that it takes for a dislocation to create new step edges (this conclusion is supported by the nucleation study described below). As the step velocity is not inhibited by citrate, the terrace widths become larger and the step density is decreased on the growing (010) brushite surfaces. In Equation (1), when the supersaturation is kept constant, the only variable that can influence the value of L_C is the step energy, γ_{step}. It follows that γ_{step} is modified by the presence of citrate in the solution.

To further test this model, we have measured the interfacial tensions of brushite surfaces in the solutions by using a thin-layer wicking (TLW) method.[20] As predicted, the results, which are summarized in Table 1, show that the adsorption of citrate increases the interfacial energy γ_{SL} of brushite. In terms of an isotropic model γ_{step}, the mean value for all crystal-plane-step energies can be considered to be a

Table 1: Influence of citrate on brushite interfacial tension γ_{SL}. The increasing surface tension values and induction times (τ) in supersaturated brushite solutions with increasing citrate concentration are in agreement with Equation (3).

	γ_{SL} [mJ m^{-2}]	$\tau_\sigma = 0.450$ [min]
Control	4.53	≈400
2.0×10^{-6} M citrate	5.96	≈560
5.0×10^{-6} M citrate	7.06	≈760
1.0×10^{-5} M citrate	8.87	≈1100

function of γ_{SL}. In an analogous relationship between γ_{step} and L_C for steps at the microscopic level, the Kelvin–Gibbs equation [Eq. (2)] expresses the dependence, on a macro-

$$r^* = \frac{2\gamma_{SL}\,\Omega}{kT\ln S} \tag{2}$$

scopic scale, of the energy of formation of nucleated droplets of minimum radius r^* (assuming spherical shape) and surface tension γ_{SL}. In Equation (2), Ω is the volume occupied by each growth unit. It implies that spontaneous crystallization does not occur in bulk until critical conditions are reached, or the driving force (supersaturation) is sufficiently high. Rather, a metastable equilibrium condition persists during an "induction period" τ prior to crystal formation. If the simplifying assumption is made that τ is essentially concerned with classical nucleation, we can use Equation (3), in which, C_1 and

$$\ln\tau \propto \left[C_1 + C_2\frac{\gamma_{SL}^3}{k^3\,T^3\,(\ln S)^2}\right] \tag{3}$$

C_2 are independent constants. Equation (3) shows that the increase of the interfacial tension γ_{SL} following the introduction of citrate results in the inhibition of brushite growth and increase of the induction time.

Mann et al. suggested that the interaction of carboxyl groups with Ca^{2+} ions may increase the local concentration of a carboxylated additive in the vicinity of these cations, thereby lowering the energy barrier for nucleation and inducing the precipitation of calcium salts, such as calcium oxalate and calcite, in the "modified" supersaturated solutions.[1,6,8] In contrast, the CC nucleation results in the present study show that citrate dramatically increases the induction times and nucleation is retarded (Figure 6). The data in Table 1 further confirm the relationship between the induction time and surface tension as a function of citrate concentration. The data support the suggestion that citrate

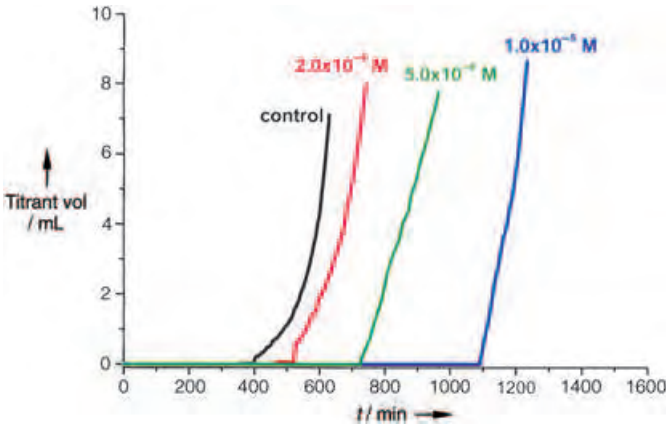

Figure 6. CC nucleation studies of brushite at different citrate concentrations. Although the carboxylate-rich molecules may bind to calcium ions in the solution to result in higher local concentrations near these molecules, the nucleation of brushite is not promoted by the mechanism of epitaxial control as suggested by Mann et al.[6,8] Instead, the longer nucleation induction times in the presence of citrate indicate that this carboxylate-rich compound is a nucleation inhibitor.

delays the formation of active step sources and increases the time for the formation of critical one-dimensional steps. In this process, interfacial energetic control plays the most important role as it can modify the critical conditions directly, as described by Equations (2) and (3). It is also well known that solution properties, such as surface tension, can be changed by the adsorption of additives. Although additives such as simple inorganic ions are unable to bind to the precipitated solid surfaces by an "epitaxial fit" or incorporate into the crystal lattice, the crystallization and morphology of the resulting crystals can be altered by these foreign additives. However, the interfacial energetic control can provide an interesting explanation of these modified crystallizations.

Our results suggest that the addition of biological growth modifiers alters mineral surface energies, thus changing the critical step length and delaying the formation of active steps for crystal growth. In bulk crystallization, these effects are manifested by longer induction times and delayed nucleation. We also conclude that the alteration of crystal habit may be because of the anisotropic modification of step densities in different growth directions and consequently changes of crystal geometry. These conclusions emphasize the importance of interfacial energies in biomineralization and their effect on critical step length. Approaches involving surface–step adsorption, for example by using a Langmuir model, may be misleading. This finding will be important for improving our understanding of the mechanisms of biomineralization.

Experimental Section

Constant composition for bulk-crystallization studies: This method can mimic in vivo biologically stabilized conditions for crystallization. Titrant solutions are added to maintain constant concentrations of the reaction solution during the experiments, and the kinetic growth results can be calculated from the addition rates of the titrant. Crystallization experiments were performed in double-walled Pyrex vessels with magnetic stirring (450 rpm). The supersaturated reaction solutions (200 mL) were prepared by mixing calcium chloride and potassium dihydrogen phosphate with sodium chloride to maintain the physiological ionic strength, $I = 0.15\ \mathrm{mol\,L^{-1}}$. The pH value was adjusted to 5.60 ± 0.01 with 0.1 M KOH solution. For experiments in the presence of additive, citrate solutions (1.00×10^{-4} or 1.00×10^{-3} M) were added prior to pH adjustment. Nitrogen presaturated with water vapor at 37 °C was passed through the reaction solutions to exclude carbon dioxide. The growth reactions were initiated by the introduction of brushite seed crystallites (10.0 mg); no seed was used for the CC nucleation experiments. Titrant addition was potentiometrically controlled using glass (Orion 91–01) and Ag/AgCl reference electrodes (Orion 900100). During crystallization, the electrode potential was constantly compared with a preset value, and the difference, or error signal, activated two motor-driven titrant burettes to maintain a constant thermodynamic driving force. Concentrations of the titrant solutions which were used to compensate reaction solutions for growth are given by Equations (4a) and (4b) for titrant burette no. 1 and Equations (5a) and (5b) for titrant burette no. 2. Here, W and T

$$T_{CaCl_2} = 2\,W_{CaCl_2} + C_{eff} \tag{4a}$$

$$T_{NaCl} = 2\,W_{NaCl} - 2\,C_{eff} \tag{4b}$$

$$T_{KH_2PO_4} = 2\,W_{KH_2PO_4} + C_{eff} \tag{5a}$$

$$T_{KOH} = 2\,W_{KOH} + 2\,W_{KOH} \tag{5b}$$

are the total concentrations in the reaction solutions and titrants, respectively, and C_{eff} is the effective titrant concentration with respect to brushite. During the reactions, slurry samples were periodically withdrawn and filtered, and the solutions were analyzed for calcium and phosphate. The total concentrations of calcium and phosphate remained constant to within $\pm 1.5\,\%$ during the experiments.

The growth flux rate R is calculated by using Equation (6), in

$$R = \frac{C_{eff}}{A_T}\frac{dV}{dt} \tag{6}$$

which C_{eff}, the effective titrant concentration with respect to brushite, indicates the molar amount of growth per liter of added titrants, dV/dt is the gradient of the CC titrant curves, and A_T is the surface area. The initial value of A_T was calculated from the specific surface area of the seed crystals, which was determined by Brunauer–Emmett–Teller (BET) nitrogen adsorption, and subsequent values were estimated from the growth model for brushite. Growth rates were calculated from the first 20 minutes of the reaction.

For the nucleation tests, the induction time τ was determined directly from the beginning of a steady and continuous addition of titrant solutions by CC.

Solution speciation and supersaturation: The supersaturation S and relative supersaturation σ are given by Equation (7), in which IP

$$\sigma = S - 1 = \left[\frac{IP}{K_s}\right]^{1/2} - 1 \tag{7}$$

is the ionic activity product, and the solubility activity product of brushite K_s is 2.36×10^{-5}. Solution speciation calculations were made by using the extended Debye–Hückel equation proposed by Davies[21] from mass balance expressions for total calcium and total phosphate with appropriate equilibrium constants by successive approximation for the ionic strength.

In situ atomic force microscopy: AFM images were collected in contact mode with a Digital Instruments Nanoscope III instrument. All images were acquired in height and deflection modes by using the lowest tip force possible to reduce the tip–surface interaction. The brushite seed crystal was anchored inside the fluid cell, and supersaturated solutions (identical to the CC reaction solutions) were passed through it while the images were taken.

Scanning electron microscopy (SEM): Samples under vacuum were sputter-coated with a thin carbon deposit to provide conductivity and then examined with a field-emission SEM (Hitachi S-4000), typically at 20 or 30 KeV.

Received: January 14, 2005
Published online: May 6, 2005

Keywords: biomineralization · crystal growth · interfaces · materials science · surface chemistry

[1] S. Mann, D. D. Archibald, J. M. Didymus, T. Douglas, B. R. Heywood, F. C. Meldrum, N. J. Reeves, *Science* **1993**, *261*, 1286–1292.
[2] S. Weiner, H. D. Wagner, *Annu. Rev. Mater. Sci.* **1998**, *28*, 271–298.
[3] A. P. Alivisatos, *Science* **2000**, *289*, 736–737.
[4] A. Berman, J. Hanson, L. Leiserowitz, T. F. Koetzle, S. Weiner, L. Addadi, *Science* **1993**, *259*, 776–779.
[5] L. Addadi, L. J. Moradian, E. Shay, N. G. Maroudas, S. Weiner, *Proc. Natl. Acad. Sci. USA* **1987**, *84*, 2732–2736.
[6] S. Mann, J. M. Didymus, N. P. Sanderson, B. R. Heywood, E. J. A. Samper, *J. Chem. Soc. Faraday Trans.* **1990**, *86*, 1873–1880.
[7] A. Berman, L. Addadi, S. Weiner, *Nature* **1988**, *331*, 546–548.
[8] S. Mann, B. R. Heywood, S. Rajam, J. D. Birchall, *Nature* **1998**, *394*, 692.
[9] C. S. Sikes, M. L. Yeung, A. P. Wheeler, in *Surface Reactive Peptides and Polymers: Discovery and Commercialization*, ACS Symposium Series XIII (Eds.: C. S. Sikes, A. P.Wheeler), ACS Books, Washington DC, **1991**, p. 444.
[10] A. George, L. Bannon, B. Sabsay, J. W. Dillon, J. Malone, A. Veis, N. A. Jenkins, D. J. Gilbert, N. G. Copeland, *J. Biol. Chem.* **1996**, *271*, 32869–32871.
[11] S. R. Qiu, A. Wierzbicki, C. A. Orme, A. M. Cody, J. R. Hoyer, G. H. Nancollas, S. Zepeda, J. J. De Yoreo, *Proc. Natl. Acad. Sci. USA* **2004**, *101*, 1811–1815.
[12] C. A. Orme, A. Noy, A. Wierzbicki, M. T. McBride, M. Grantham, H. H. Teng, P. M. Dove, J. J. DeYoreo, *Nature* **2001**, *411*,775–779.
[13] M. B. Tomson, G. H. Nancollas, *Science* **1978**, *200*, 1059–1060.
[14] S. V. Dorozhkin, M. Epple, *Angew. Chem.* **2002**, *114*, 3260–3277; *Angew. Chem. Int. Ed.* **2002**, *41*, 3130–3146.
[15] R. Z. LeGeros, *Calcium Phosphates in Oral Biology and Medicine*, Karger, Basel, **1991**.
[16] C. Y. C. Pak, *Miner. Electrolyte Metab.* **1994**, *20*, 371–377.
[17] W. K. Burton, N. Cabrera, F. C. Frank, *Philos. Trans. R. Soc. London Ser. A* **1951**, *243*, 299–358.
[18] C. J. Cramer, D. G. Truhlar, *Science* **1992**, *256*, 213–217.
[19] H. H. Teng, P. M. Dove, C. A. Orme, J. J. De Yoreo, *Science* **1998**, *282*, 724–727.
[20] C. J. Van Oss, R. F. Giese, Z. Li, K. Murphy, J. Norris, M. K. Chaudhury, R. J. Good, *J. Adhes. Sci. Technol.* **1992**, *6*, 413–428. The values of γ_{SL}, determined by TLW methods, are always lower than those obtained by other surface-tension measurements as the double-layer effects are also included; see W. Wu, G. H. Nancollas, *Adv. Colloid Interface Sci.* **1999**, *79*, 229–279; however, all the determination methods reach the same conclusion that the brushite–solution interfacial energy is increased by citrate.
[21] C. W. Davies, *Ion Association*, Butterworth, London, **1962**.

Enantioselective Fluorination

Enantioselective Formation of Stereogenic Carbon–Fluorine Centers by a Simple Catalytic Method**

*Mauro Marigo, Doris Fielenbach, Alan Braunton, Anne Kjærsgaard, and Karl Anker Jørgensen**

The unique properties of fluorinated molecules have led to the wide interest in these compounds in organic syntheses, medicinal and agricultural chemistry, as well as materials sciences.[1] This interest has been manifested in the enormous number of publications relating to organofluorine compounds.[2] In this context, structures in which the fluorine atom is attached to a chiral center are gaining increasing importance. Despite this great interest, there is still no simple and direct catalytic method to obtain optically active fluorinated compounds.[3] The development of stable electrophilic fluorine sources such as Selectfluor, 1-fluoropyridinium salts, and *N*-fluorodibenzenesulfonimide (NFSI) has marked an important milestone for the realization of these reaction types.[4] As a consequence, the first examples of catalytic enantioselective fluorinations of β-keto esters that apply both metal- and organocatalytic approaches were reported.[5,6] Recently, these methods were also applied toward the synthesis of chiral fluorinated β-keto phosphonates.[7]

To our knowledge, no enantioselective catalytic method for the direct α-fluorination of aldehydes has been described. Recently, asymmetric carbon–heteroatom bond formation reactions that proceed via enamine intermediates were reported in which chiral secondary amines are used as catalysts.[8–11] These procedures also showed promise for application toward fluorination reactions. So far, the only access to α-fluorinated aldehydes uses a chiral auxiliary strategy that involves a multistep process.[12] The authors state that the resulting α-fluorinated products decompose rapidly on silica and as a result, they must be derivatized directly from the crude mixture.

Herein we present a new and easy access to stereogenic carbon–fluorine centers through the direct enantioselective α-fluorination of aldehydes with an organocatalytic approach. The general reaction is shown below, including the functionalization of α-fluorinated aldehydes in situ to optically active α-fluoroalcohols, which are important organic compounds[1] and which have found direct use in liquid crystal compositions.[13]

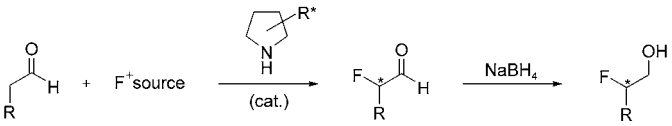

As fluorine is the most electronegative element, the reaction conditions must be chosen carefully under the following terms: 1) *N*-fluorination of the catalyst is likely; therefore, the α-fluorination reaction must be faster than this process. 2) Undesired racemization and difluorination events must be rigorously avoided. Taking these considerations into account, we started our screening experiments with catalysts that had been previously applied with success in asymmetric C–Cl[10b,c] and C–S[11] bond formation reactions. The results of the screening in which 3-phenylpropanal (**1a**) was used as substrate with the commercially available NFSI (**2**) as the fluorinating reagent are presented in Table 1.

The use of L-proline (**4a**), L-prolinamide (**4b**), and the C_2-symmetric catalyst **5** gave low yields and moderate enantioselectivities (Table 1, entries 1–3). This behavior was not a surprise, as the chemical and physical properties of fluorine amplify some of the problems that are encountered in the related chlorination reaction. Because of the high electronegativity of fluorine, the catalyst easily forms enamine

Table 1: Screening of catalysts and reaction conditions for the α-fluorination of 3-phenylpropanal (**1a**) with NFSI (**2**) as F^+ ion source.[a]

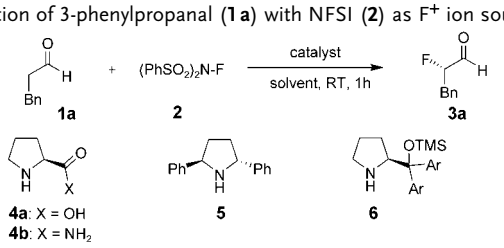

Entry	**1a** [equiv]	**2** [equiv]	Cat. [mol%]	Solvent	Conv. [%][b]	*ee* [%][c]
1	1	1.2	**4a** (20)	CH_2Cl_2	<10	30
2	1	1.2	**4b** (20)	CH_2Cl_2	24	40
3	1	1.2	**5** (20)	CH_2Cl_2	17	48[d]
4	1	1.2	**6** (20)	CH_2Cl_2	40	87
5	1	1.2	**6** (20)	MeCN	61	93
6	1	1.2	**6** (20)	MTBE	53	93
7	1	1.2	**6** (10)	MTBE	62	93
8	1	1.2	**6** (5)	MTBE	74	93
9	1.5	1	**6** (5)	MTBE	88	93
10[e]	1.5	1	**6** (1)	MTBE	>90	93
11[f]	1.5	1	**6** (0.25)	MTBE	90	93

[a] The catalyst and the aldehyde were mixed in the solvent at room temperature for 15 min before addition of NFSI (0.2 mmol); Ar = Ph-3,5-$(CF_3)_2$; Bn = benzyl. [b] Conversion determined by GC after 1 h; entries 1–5: incomplete consumption of NFSI; entries 6–10: full consumption of NFSI (the difference to 100% conversion refers to the difluorinated product). [c] Percent *ee* values were determined by GC on a chiral-phase column (Astec G-TA) and verified by HPLC (Chiralcel OJ column) after reduction of **1a** to the alcohol and acetylation; for details, see Supporting Information. [d] 23% *ee* after 3 h. [e] Conversion and % *ee* were determined by GC after 2 h. [f] 10 mmol NFSI, 8 h.

[*] M. Marigo, Dr. D. Fielenbach, Dr. A. Braunton, A. Kjærsgaard, Prof. Dr. K. A. Jørgensen
The Danish National Research Foundation: Center for Catalysis
Department of Chemistry, Aarhus University
DK-8000 Aarhus C (Denmark)
Fax: (45) 8919-6199
E-mail: kaj@chem.au.dk

[**] This work was made possible by a grant from The Danish National Research Foundation. M.M. thanks EU: HMPT-CT-2001-00317 for financial support.

Supporting information for this article is available on the WWW under http://www.angewandte.org or from the author.

 DOI: 10.1002/anie.200500395

species with both the starting material and the fluorinated product. The enhanced acidity of the α proton in the fluorinated product even favors its enamine formation, as discussed below. Furthermore, in contrast to the chlorination reaction, the small fluorine atom does not contribute to an added steric shielding that would disfavor the enamine equilibrium. This second enamine formation causes either difluorination or racemization.

Use of the silylated prolinol derivative **6** as a catalyst significantly improved the conversion and enantioselectivity of the reaction (Table 1, entry 4). NMR spectroscopy studies revealed that the catalyst is slowly desilylated upon mixing with NFSI. The desilylated **6** shows very low catalytic activity (10% conversion after 20 h and 61% *ee*). Therefore, the low conversion was caused by inactivation of the catalyst. We rationalized that the solvent could influence the reaction rate and deprotection of the catalyst. Acetonitrile still did not lead to full conversion, because of catalyst degradation (entry 5). However, an improvement was observed with methyl-*tert*-butyl ether (MTBE); all reactions performed in this solvent showed complete consumption of NFSI, but a significant amount of the difluorinated product was formed as well. Lowering the amount of catalyst to 5 mol% decreased the difluorination problem. Finally, the use of only 1 mol% of catalyst **6** and an excess of the aldehyde **1a** resulted in more than 90% yield of the monofluorinated product within 2 h (entry 10). Performing the reaction on a larger scale (10 mmol) allowed us to further decrease the catalyst loading to only 0.25 mmol%. Furthermore, 90% conversion was obtained, maintaining the enantioselectivity of 93% *ee* after 8 h reaction time (entry 11). Other commercially available F^+ ion sources such as Selectfluor turned out to be unsuitable for the reaction, as the silylated catalyst **6** is immediately deprotected in the presence of the BF_4^- counterion.

With these optimized conditions in hand, the general scope of the reaction was probed by application to a series of aldehydes. As mentioned above, α-fluorinated aldehydes easily decompose on silica gel.[12] Notably, α-fluoroaldehydes are more volatile than the starting compounds. The formation of α-fluorinated aldehydes was confirmed by GC–MS and NMR spectroscopic analysis of the crude reaction mixtures. The α-fluoroaldehydes **3a**, **3d–f**, and **3h** were reduced directly to the resulting β-fluoroalcohols without loss of enantiomeric excess, and the isolated yields given in Table 2 confirm the high conversion in the organocatalytic enantioselective fluorination step. For the volatile substrates **1b**, **1c** and **1g**, yields were calculated according to GC analysis of the crude reaction mixtures before reduction to the β-fluoroalcohols. The results are presented in Table 2.

For all examples in which a variety of different R substituents were evaluated, excellent enantioselectivities of more than 91% *ee* were obtained, and the enantioenriched products were formed in good yields with only 1 mol% of catalyst **6** (Table 2). In the case of substrate **1a** in reaction with 20 mol% of the catalyst, more than 90% of the catalyst could be recovered after flash chromatography.

The absolute configuration of the β-fluoroalcohols was determined to be *S* by comparison of their optical rotation values with those reported in the literature.[14] The stereochemical outcome of the reaction can be explained by the formation of an *E*-configured enamine, where the sterically demanding substituent of the pyrrolidine ring shields the *Re* face of the enamine.

Table 2: Organocatalytic enantioselective α-fluorination of aldehydes by NFSI, catalyzed by **6** (1 mol%).[a]

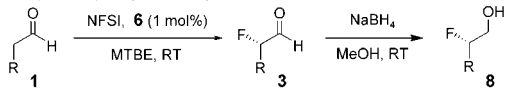

Entry	Aldehyde	R	*t* [h]	Yield [%]	*ee* [%][b]
1[c]	**1b**	Pr	6	**3b** >95	96
2[c]	**1c**	Bu	28	**3c** >90	91
3[d,e]	**1d**	Hex	4	**8d** 55	96
4[d]	**1e**	$BnO(CH_2)_3$	2	**8f** 64	91
5[d]	**1a**	Bn	2	**8a** 74	93
6[d]	**1f**	Cy	5	**8g** 69	96
7[c]	**1g**	*t*Bu	2	**3e** >90	97
8[d]	**1h**	1-Ad	2	**8h** 75	96

[a] Compound **2** (0.25 mmol) was added to a mixture of **1** (0.38 mmol) and **6** (0.0025 mmol) in MTBE (0.5 mL) at room temperature for the stated period of time; Ad = adamantyl; Bn = benzyl; Cy = cyclohexyl. [b] Percent *ee* values were determined by GC or HPLC on a chiral phase; see Supporting Information for separation conditions. [c] Yields were based on GC analysis of the crude mixtures before reduction owing to the volatility of the products. [d] Isolated yields of the alcohol after reduction with $NaBH_4$. [e] 1.1 equiv NFSI; 1 equiv aldehyde.

This hypothesis is confirmed by a model based on DFT calculations of the optimized enamine intermediate at the B3LYP/6-31G(d) level of theory.[15] The lowest-energy structure of the enamine intermediate is presented in Figure 1. The

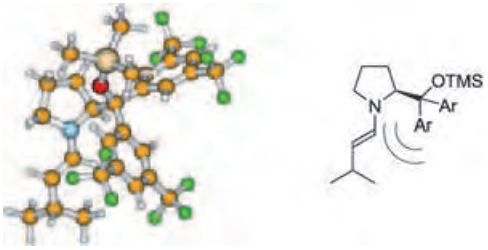

Figure 1. DFT-calculated model of the optimized structure of the enamine formed by isovaleraldehyde and catalyst **6**; Ar = Ph-3,5-$(CF_3)_2$.

intermediate structure shows that one of the 3,5-di(trifluoromethyl)phenyl groups covers the *Re* face of the enamine. As a consequence, the electrophilic F^+ ion attack occurs from the *Si* face, providing excellent enantioselectivities. This model is in agreement with our experimental observations.

The high configurative stability of the α-fluorinated products observed under the reaction conditions is a surprising phenomenon, especially as difluorination is also observed under certain reaction conditions. Figure 2 illustrates our theory to explain such stability of the optically active products. As shown in Figure 1, one of the 3,5-di(trifluoromethyl)phenyl groups points towards the reactive center of the enamine **A**. In the preferably formed (*S*,*S*)-**B** imminium ion, the remaining hydrogen atom is situated in between the

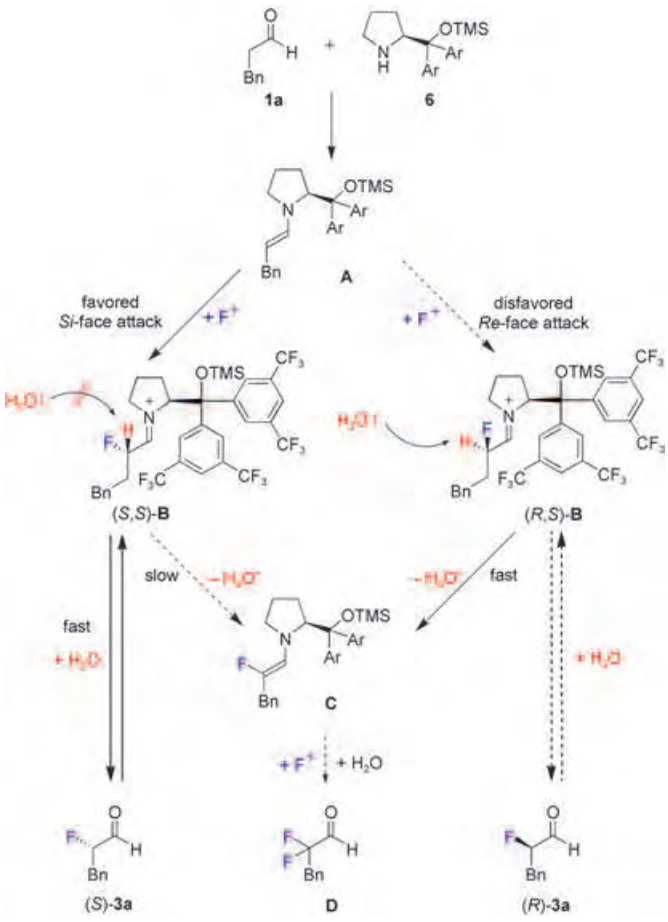

Figure 2. Explanation of the observed configurative stability of the α-fluorinated aldehydes under the reaction conditions in accordance with kinetic resolution experiments; Ar = Ph-3,5-$(CF_3)_2$.

fluorine atom and the shielding substituent of the catalyst. This hydrogen atom is thus placed in a sort of hydrophobic pocket, which prevents its abstraction as a proton from nucleophilic attack by a water molecule. On the other hand, in the disfavored (*R*,*S*)-**B** intermediate, the hydrogen atom is placed on the open *Si* face and can be easily abstracted to form enamine intermediate **C**. We envisaged that a kinetic resolution experiment could support this hypothesis: a racemic mixture of α-fluoroaldehyde **3a** was slowly converted (20% in 4 h) to the difluorinated product **D** in the presence of 0.5 equiv NFSI (**2**) and 1 mol% of the catalyst **6**. This experiment clearly revealed that (*R*)-**3a** was consumed faster than (*S*)-**3a** and was supported by an enantiomeric excess of the latter of 20% *ee*. This observation supports our proposal of an embedded proton in the favored (*S*,*S*)-**B** intermediate in the enantiomeric reaction.

We have extended the scope of the reaction to the formation of quaternary stereocenters. A modified protocol was developed for the branched aldehyde **1i**. The sterically encumbered substrate required a sterically less-demanding catalyst and higher temperatures to keep the reaction rate high. With 5 mol% of catalyst **7** in a reaction performed at 60 °C, the β-fluoroalcohol product **8i** was generated in 78% yield with 48% *ee*.

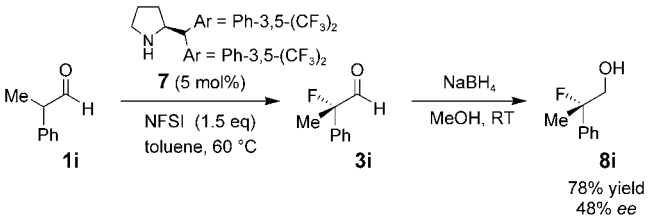

Besides the in-situ reduction to alcohols, other direct transformations that proceed without epimerization, for example, the HWE olefination, are described in the literature.[8]

In summary, a simple method for the formation of stereogenic carbon–fluorine bonds through a direct, catalytic α-fluorination of aldehydes has been developed. A range of aldehydes can be directly fluorinated in the α position in good yields and with excellent enantioselectivities. The use of NFSI as a stable, easily handled, and commercially available electrophilic fluorine source in combination with the advantages of organocatalysis affords this simple protocol. Moreover, 1 mol% of a sterically encumbered chiral pyrrolidine derivative that is easily accessible in four steps from L-proline was sufficient for obtaining good to high yields and high enantioselectivities. It should be pointed out that optically active α-fluorinated aldehydes are unstable on silica gel and are more volatile than the starting compounds. Thus, the optically active α-fluorinated aldehydes were directly reduced to the corresponding α-fluorinated alcohols, without loss of enantioselectivity. We believe that this procedure represents an important new organocatalytic reaction and a significant improvement of existing methods, and that it will find intensive use in the synthesis and application of optically active fluorine compounds. [16]

Received: February 2, 2005
Published online: April 28, 2005

Keywords: aldehydes · asymmetric catalysis · electrophilic substitution · enantioselectivity · organocatalysis

[1] a) B. E. Smart, *J. Fluorine Chem.* **2001**, *109*, 3; b) K. Mikami, Y. Itoh, Y. M. Yamamaka, *Chem. Rev.* **2004**, *104*, 1; c) T. Hiyama, K. Kanie, T. Kosumoto, Y. Morizawa, M. Shimizu, *Organofluorine Compounds*, Springer, Berlin, **2000**; d) *Organofluorine Chemistry: Principles and Commercial Applications* (Eds.: R. E. Banks, B. E. Smart, J. C. Tatlow), Plenum, New York, **1994**; e) V. A. Soloshonok, *Enantiocontrolled Synthesis of Fluoro-organic Compounds*, Wiley, Chichester, **1999**; f) P. Ramachandran, *ACS Symp. Ser.* **2000**, *746*.
[2] H. Schofield, *J. Fluorine Chem.* **1999**, *100*, 7.
[3] a) J.-A. Ma, D. Cahard, *Chem. Rev.* **2004**, *104*, 6119; b) H. Ibrahim, A. Togni, *Chem. Commun.* **2004**, 1147; c) K. Muñiz, *Angew. Chem.* **2001**, *113*, 1701; *Angew. Chem. Int. Ed.* **2001**, *40*, 1653; d) S. France, A. Weatherwax, T. Lectka, *Eur. J. Org. Chem.* **2005**, 475.
[4] a) S. D. Taylor, C. C. Kotoris, G. Hum, *Tetrahedron* **1999**, *55*, 12431; b) P. T. Nyffeler, S. Gonalez Durón, H. D. Burkhart, S. P. Vincent, C.-H. Wong, *Angew. Chem.* **2004**, *117*, 196; *Angew. Chem. Int. Ed.* **2005**, *44*, 192.

[5] For metal-catalyzed approaches, see: a) L. Hintermann, A. Togni, *Angew. Chem.* **2000**, *112*, 4530; *Angew. Chem. Int. Ed.* **2000**, *39*, 4359; b) Y. Hamoshima, K. Yagi, H. Takano, L. Tamás, M. Sodeoka, *J. Am. Chem. Soc.* **2002**, *124*, 14530; c) J.-A. Ma, D. Cahard, *Tetrahedron: Asymmetry* **2004**, *15*, 1007.

[6] For an organocatalyzed approach, see: D. Y. Kim, E. J. Park, *Org. Lett.* **2002**, *4*, 545.

[7] a) L. Bernardi, K. A. Jørgensen, *Chem. Commun.* **2005**, 1324; b) Y. Hamashima, T. Suzuki, Y. Shimura, T. Shimizu, N. Umebayashi, T. Tamura, N. Sasamoto, M. Sodeoka, *Tetrahedron Lett.* **2005**, *46*, 1447.

[8] For examples of C–N bond formation, see: a) A. Bøgevig, K. Juhl, N. Kumaragurubaran, W. Zhuang, K. A. Jørgensen, *Angew. Chem.* **2002**, *114*, 1868; *Angew. Chem. Int. Ed.* **2002**, *41*, 1790; b) B. List, *J. Am. Chem. Soc.* **2002**, *124*, 5656; c) H. Vogt, S. Vanderheiden, S. Bräse, *Chem. Commun.* **2003**, 2448; d) N. Kumaragurubaran, K. Juhl, W. Zhuang, A. Bøgevig, K. A. Jørgensen, *J. Am. Chem. Soc.* **2002**, *124*, 6254.

[9] For examples of C–O bond formation, see: a) G. Zhong, *Angew. Chem.* **2003**, *115*, 4379; *Angew. Chem. Int. Ed.* **2003**, *42*, 4247; b) S. P. Brown, M. P. Brochu, C. J. Sinz, D. W. C. MacMillan, *J. Am. Chem. Soc.* **2003**, *125*, 10808; c) Y. Hayashi, J. Yamaguchi, K. Hibino, M. Shoji, *Tetrahedron Lett.* **2003**, *44*, 8293; d) A. Córdova, M. Enquist, I. Ibrahem, J. Casas, *J. Am. Chem. Soc.* **2004**, *126*, 8914; e) N. Momiyama, H. Torii, S. Saito, H. Yamamoto, *Proc. Natl. Acad. Sci. USA* **2004**, *101*, 5374; f) W. Wang, J. Wang, H. Lia, L. Liao, *Tetrahedron Lett.* **2004**, *45*, 7235; g) A. Bøgevig, H. Sundén, A. Córdova, *Angew. Chem.* **2004**, *116*, 1129; *Angew. Chem. Int. Ed.* **2004**, *43*, 1109; h) Y. Hayashi, J. Yamaguchi, T. Sumaiya, M. Shoji, *Angew. Chem.* **2004**, *116*, 1132; *Angew. Chem. Int. Ed.* **2004**, *43*, 1112; i) Y. Hayashi, J. Yamaguchi, T. Sumiya, K. Hibino, M Shoji, *J. Org. Chem.* **2004**, *69*, 5966; j) A. Córdova, H. Sundén, A. Bøgevig, M. Johansson, F. Himo, *Chem. Eur. J.* **2004**, *10*, 3673.

[10] For C–Cl bond formation, see: a) M. P. Brochu, S. P. Brown, D. W. C. MacMillan, *J. Am. Chem. Soc.* **2004**, *126*, 4108; b) N. Halland, A. Braunton, S. Bachmann, M. Marigo, K. A. Jørgensen, *J. Am. Chem. Soc.* **2004**, *126*, 4790; c) M. Marigo, S. Bachmann, N. Halland, A. Braunton, K. A. Jørgensen, *Angew. Chem.* **2004**, *116*, 5623; *Angew. Chem. Int. Ed.* **2004**, *43*, 5507; d) N. Halland, M. A. Lie, A. Kjærsgaard, M. Marigo, B. Schiøtt, K. A. Jørgensen, *submitted*.

[11] For C–S bond formation, see: M. Marigo, T. C. Wabnitz, D. Fielenbach, K. A. Jørgensen, *Angew. Chem.* **2005**, *117*, 804; *Angew. Chem. Int. Ed.* **2005**, *44*, 794, .

[12] F. A. Davis, P. V. N. Kasu, G. Sundarababu, H. Qi, *J. Org. Chem.* **1997**, *62*, 7546.

[13] For a representative patent, see: H. Nohira, M. Kamei, S. Nakamura, K. Yoshinaga, M. Kai, JP 62093248, JP 04024556, US 4798680, US 4873018, **1989**.

[14] a) Y. Takeuchi, K. Nagata, T. Koizumi, *J. Org. Chem.* **1989**, *54*, 5453; b) F. A. Davis, W. Han, *Tetrahedron Lett.* **1992**, *33*, 1153.

[15] Gaussian 98 (Revision A.7), M. J. Frisch, G. W. Trucks, H. B. Schlegel, G. E. Scuseria, M. A. Robb, J. R. Cheeseman, V. G. Zakrzewski, J. A. Montgomery, Jr., R. E. Stratmann, J. C. Burant, S. Dapprich, J. M. Millam, A. D. Daniels, K. N. Kudin, M. C. Strain, O. Farkas, J. Tomasi, V. Barone, M. Cossi, R. Cammi, B. Mennucci, C. Pomelli, C. Adamo, S. Clifford, J. Ochterski, G. A. Petersson, P. Y. Ayala, Q. Cui, K. Morokuma, D. K. Malick, A. D. Rabuck, K. Raghavachari, J. B. Foresman, J. Cioslowski, J. V. Ortiz, A. Baboul, B. B. Stefanov, G. Liu, A. Liashenko, P. Piskorz, I. Komaromi, R. Gomperts, R. L. Martin, D. J. Fox, T. Keith, M. A. Al-Laham, C. Y. Peng, A. Nanayakkara, C. Gonzalez, M. Challacombe, P. M. W. Gill, B. Johnson, W. Chen, M. W. Wong, J. L. Andres, C. Gonzalez, M. Head-Gordon, E. S. Replogle, J. A. Pople, Gaussian, Inc., Pittsburgh, PA, **1998**.

[16] Note added in proof (April 26, 2005): After the submission of this paper, Enders and Hüttl published the fluorination of carbonyl compounds catalyzed by chiral amines with Selectfluor as the fluorine source. The highest enantioselectivity was obtained for cyclohexanone (36% *ee*): D. Enders, M. R. M. Hüttl, *Synlett* **2005**, 991.

Enantioselective Fluorination

Direct Asymmetric α-Fluorination of Aldehydes**

*Derek D. Steiner, Nobuyuki Mase, and Carlos F. Barbas, III**

Organic molecules containing fluorine have attracted much attention because they show distinctive characteristics in comparison with their parent compounds owing to the unique C–F bond.[1] Substitution of hydrogen by fluorine is often considered isosteric and the high C–F bond strength generally protects fluorine from metabolic transformations. In addition, as fluorine has the ability to function as a hydrogen bond acceptor, fluorine-substituted bioactive compounds are useful analogues and probes of hydrogen bonding characteristics. The selective formation of carbon-fluorine bonds under mild conditions is thus a highly desirable methodology, especially in medicinal chemistry.[2] Previous approaches toward asymmetric fluorination relied on stoichiometric amounts of chiral fluorinating reagents[3] or chiral auxiliaries.[4] More recently, the catalytic asymmetric fluorination of β-keto esters with titanium and palladium as Lewis acids was reported.[5]

α-Fluoro aldehydes have been characterized as unstable compounds that generally decompose upon purification. As a result, their syntheses have been very limited. Synthesis of α-fluoro aldehydes was first reported by Middleton and Bingham, who treated silyl enol ethers with trifluoromethyl hypofluorite (CF_3OF).[6] Subsequently, enolate methodologies that use commercially available electrophilic fluorinating reagents such as NFSi (*N*-fluorobenzenesulfonamide; **5**) and Selectfluor (F-TEDA-BF_4 or 1-chloromethyl-4-fluoro-1,4-diazoniabicyclo[2.2.2]octane bis(tetrafluoroborate); **3**) have

[*] D. D. Steiner, Prof. Dr. N. Mase,[+] Prof. Dr. C. F. Barbas, III
The Skaggs Institute for Chemical Biology and
the Departments of Chemistry and Molecular Biology
The Scripps Research Institute
10550 North Torrey Pines Road, La Jolla, CA 92037 (USA)
Fax: (+1) 858-784-2583
E-mail: carlos@scripps.edu

[+] Present address:
Department of Molecular Science, Faculty of Engineering
Shizuoka University
3-5-1 Johoku, Hamamatsu 432-8561 (Japan)

[**] This study was supported by the NIH (CA27489).

Supporting information for this article is available on the WWW under http://www.angewandte.org or from the author.

  DOI: 10.1002/anie.200500571

been employed to produce α-fluoro carbonyls.[7] Although there is an extensive body of research on the α-fluorination of carbonyls, there are no examples of direct asymmetric fluorinations of aldehydes. Herein, we report the first examples of direct α-fluorinations with asymmetric induction.

Proline and its analogues have been found to be excellent catalysts in asymmetric aldol,[8] Mannich,[9] and α-chlorination[10] reactions of carbonyls. Our early work in fluorine chemistry focused on the use of α-fluoro carbonyl compounds as nucleophiles in reactions catalyzed by enzymes,[11] catalytic antibodies,[12] and organocatalysts[13] in asymmetric aldol reactions and, in one case, the Mannich reaction.[14] The asymmetric α-fluorination of aldehydes is based on the same principles of organocatalysis that we used in our first Michael, aldol, and Mannich catalytic asymmetric aldehyde addition reactions.[15]Initial screening of electrophilic fluorinating reagents was done with L-proline and 2-phenylpropionaldehyde (**1a**) in acetonitrile at room temperature (Table 1).

Table 1: Comparison of N–F reagents for direct α-fluorination of aldehydes.[a]

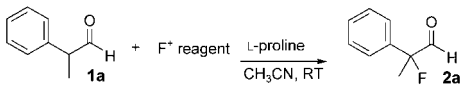

Entry	N–F Reagent		*t*	Yield [%][b]	*ee* [%][c]
1	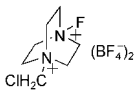	**3**	24 h	87	4
2	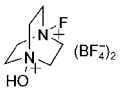	**4**	24 h	90	0
3	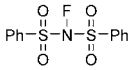	**5**	24 h	87	25
4		**6**	5 d	NR	–
5	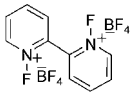	**7**	5 d	7	12

[a] N–F reagent (1.2 equiv) was added to a mixture of aldehyde and catalyst at ambient temperature. [b] All isolated yields determined after aqueous workup. [c] Enantiomeric excess determined by chiral GLC analysis (Bodman γ-TA).

2-Phenylpropionaldehyde was chosen for screening because of its excellent reactivity and because the product is unable to racemize, as it has no proton alpha to the aldehyde. It was found that NFSi (**5**) was the only fluorinating reagent to provide any enantioselectivity in a reasonable time period. Commercially available fluorinating reagents Selectfluor (**3**) and Accufluor (**4**) were employed, but afforded 4 and 0% *ee* respectively. The pyridinium fluoride reagents **6** and **7** were minimally reactive, and thus gave very low yields. Therefore, NFSi (**5**) was used for subsequent reactions.

Following this selection of an electrophilic fluorinating reagent, a solvent screen was undertaken. Acetonitrile is a standard reaction solvent used in electrophilic fluorination. Acetonitrile (Table 2, entry 1, 87% conversion, 25% *ee*) was adequate, but tetrahydrofuran, dimethylformamide (DMF), 1,4-dioxane, and methanol all provided the product in higher yield. Interestingly, THF afforded both the best selectivity and highest chemical yield (Table 2, entry 4, 94% conversion, 28% *ee*). DMSO has a mildly exothermic reaction with NFSi, possibly explaining the poor aldehyde fluorination in this medium.

Table 2: Effect of solvent on organocatalyzed α-fluorination.

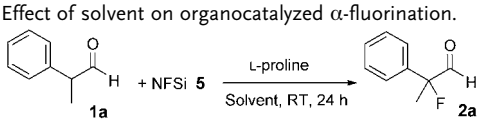

Entry	Solvent	Conversion [%][a]	*ee* [%][b]
1	CH_3CN	87	25
2	DMF	92	20
3	DMSO	30	22
4	THF	94	28
5	1,4-dioxane	93	25
6	CH_2Cl_2	32	18
7	NMP[c]	87	19
8	Et_2O	10	20
9	toluene	9	15
10	MeOH	93	5
11	EtOH	76	15
12	C_6H_{14}	8	17
13	H_2O	NR	NR
14	[bmim]PF_6[d]	39	26
15	[bmim]BF_4[d]	56	19

[a] Conversion measured by ^{1}H NMR spectroscopy of the crude reaction mixture and correlated to GC, owing to high volatility of products. [b] Enantiomeric excess determined by chiral GLC analysis (Bodman γ-TA). [c] NMP = *N*-methylpyrrolidinone. [d] BMIM = 1-butyl-3-methylimidizolium.

It is important to note that α-fluorinated aldehydes are generally not stable under column purification or distillation conditions, and that the addition of an α-fluorine significantly increases the volatility relative to that of the starting aldehyde.[16] These characteristics of α-fluorinated aldehydes make them difficult substrates to manipulate. To optimize the fluorination reaction with branched aldehydes, **1a** was subjected to a catalyst screen with NFSi as the electrophilic fluorinating reagent and THF as a standard solvent (Table 3). The silylated L-prolinol derivative **9c**, with the sterically demanding triisopropylsilyl (TIPS) group, provided the highest enantioselectivity (44% *ee*, 90% yield), although the reaction yield was much improved with the proline-derived tetrazole catalyst **11** (38% *ee*, 98% yield).

We next examined the organocatalytic asymmetric fluorination of straight-chain aldehydes. These aldehydes are prone to self-react under organocatalysis to yield self-aldol products. Decyl aldehyde (**1b**), which is slow to form the self-aldol product and which has a high boiling point, was chosen as a general aldehyde for reaction optimization (Table 4). The initial fluorination reactions of decyl aldehyde were monitored by ^{1}H NMR and ^{19}F NMR spectroscopy in $CDCl_3$, CD_3CN and [D_7]DMF. All reactions reached completion after approximately 30 minutes. Also, after initial α-fluoro decyl

Table 3: Screening of catalysts for direct enantioselective α-fluorination of 2-phenylpropionaldehyde.

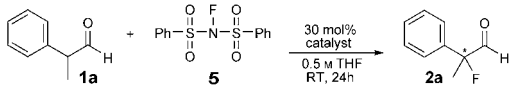

1a + **5** → **2a**

Entry	Catalyst	Yield [%][a]	*ee* [%][b]
1	**8a** R = OH	94	28
	8b R = O*t*Bu	90[c]	13
	8c R = morpholine	63	8
	8d R = OBn	75	28
2	**9a** R = H	70	24
	9b R = Me	83	24
	9c R = TIPS	90	44
3	**10a** R^1,R^2 = H	99	12
	10b R^1 = H, R^2 = *n*Bu	30	12
	10c R^1,R^2 = pyrrolidine	84	12
	10d R^1,R^2 = pyrrolidine, TFA	85	16
	10e R^1,R^2 = morpholine	66	16
	10f R^1 = H, R^2 = Ph	88	0
4	**11**	98	38
5	**12a** R = H	70	0
	12c R = CH_3	75	28
6	**13a** R = OH	93	22
	13b R = O*t*Bu	65	27
7	**14a**	77	16
8	**15**	34[c]	24
9	**16a** R = CH_3	19[c]	18
	16b R = CH_2OCH_3	42[c]	14
10	pyrrolidine	84	0
11	no catalyst	0[c]	0

[a] Yield measured by ^{1}H NMR spectroscopy of the crude reaction mixture and correlated to GC, owing to high volatility of products. [b] Enantiomeric excess determined by chiral GLC analysis (Bodman γ-TA). [c] Reactions continued for 48 h before workup and analysis.

Table 4: Catalyst screening for direct enantioselective α-fluorination of linear aldehydes.

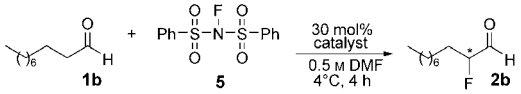

1b + **5** → **2b**

Entry	Catalyst	Conversion [%][a]	*ee* [%][b]
1	**8a** R = OH	29	29
	8e R = NH_2	50	22
2	**9b** R = Me	30	32
	9c R = TIPS	30	37
3	**11**	32	30
4	**13b** R = CH_3	trace	–
5	**14a** R^1 = H, R^2 = *t*Bu	65	76
	14b R^1,R^2 = CH_3	30	88
6	**15**	9	50
7	**16b** R = CH_2OCH_3	21	46[c]
8	pyrrolidine	71[d]	0
9	no catalyst	0	0

[a] Yield measured by ^{1}H NMR spectroscopy of the crude reaction mixture and correlated to GC, owing to high volatility of products. [b] Enantiomeric excess determined by chiral GLC analysis (Bodman γ-TA). [c] Opposite enantiomer from that obtained with other catalysts. [d] Stoichiometric amount of pyrrolidine.

aldehyde formation (^{19}F NMR (CD_3CN): $\delta = -200.2$ ppm) the $CDCl_3$ and CD_3CN reactions showed steady formation of α,α-difluoro product (^{19}F NMR (CD_3CN): $\delta = -115.2$ ppm).[17] Subsequent reactions with THF also gave the α,α-difluoro product. Therefore, DMF, which inhibited formation of the α,α-difluoro product, was employed throughout the catalyst screening with linear aldehydes.

Interestingly, imidazolidinone catalysts **14a** and **14b** (Table 4, entry 5) provided the desired product with the highest enantioselectivities. Catalyst **14a** was used in a sub-stoichiometric amount, yet in repeated reactions would not progress beyond 65% completion. The highest optical purity was obtained with catalyst **14b** (30% conversion, 88% *ee*). Use of the hydrochloric, trifluoroacetic or 5-methyltetrazole salts of **14a** and **14b** resulted in diminished enantioselectivity and no enhancement in turnover. Lowering the reaction temperature to −20°C inhibited the reactivity greatly, without increasing the enantioselectivity. Conversely, raising the temperature to room temperature resulted in an increased formation of side products, presumably self-aldol products.

To determine the scope of the reaction, we subjected a series of aldehydes to the optimized conditions (Table 5). Generally, **14b** catalyzed the direct asymmetric α-fluorination of linear aldehydes with good to excellent yields (Table 5, entries 1–6) and with enantioselectivities ranging from 86% for 2-fluoro-1-octanal (**2e**) (Table 5, entry 4) to 96% for 2-fluoro-isovaleraldehyde (**2c**) (Table 5, entry 1). Linear aldehydes were transformed with the highest enantioselectivity when reacted with equimolar imidazolidinone **14b** as a chiral promoter at 4°C in DMF. The absolute stereochemistry was confirmed for several compounds: **2e** was reduced to 2-fluoro-1-octanol with sodium borohydride,[18] 2-fluoro-2-phenylpropionaldehyde (**2a**) was oxidized to the corresponding carboxylic acid,[19] and (*S*)-(−)-2-fluoro-isovaleraldehyde (**2c**) is known in the literature.[20] In each case, the optical rotation of the compounds prepared compared favorably with the literature values reported. These results are all consistent with the assignment of an *S* configuration to the fluorinated aldehydes and are in agreement with a *Si*-face approach of the electrophile. The *Re* face of the enamine is shielded by the sterically demanding benzyl and 2,2-dimethyl substituents of

Table 5: Direct organocatalytic enantioselective α-fluorination of aldehydes.[a]

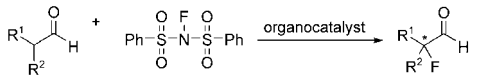

Entry	Aldehyde		Catalyst	*t* [h]	Yield [%][b]	*ee* [%][c]
1		**2c**	**14b**	2	74[d]	96
2		**2b**	**14b**	3	90	88
3		**2d**	**14b**	3	59	93
4		**2e**	**14b**	3	94	86
5		**2f**	**14b**	3	40[d]	92
6		**2g**	**14b**	2	97	88
7	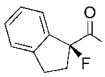	**2h**	**9c**	6	98	66
			11	2	98	55
			8a	24	93	44
8	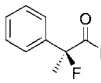	**2a**	**9c**	6	92	40
			11	2	99	45
			8a	24	93	28

[a] Reaction conditions for linear aldehydes (entries 1–6): 4 °C in DMF with stoichiometric amounts of chiral promoter **14b**; branched aldehydes (entries 7 and 8): room temperature in THF with 30 mol% catalyst. [b] Yield measured by ^{1}H NMR spectroscopy of the crude reaction mixture and correlated to GC, owing to high volatility of products. [c] Enantiomeric excess determined by chiral GLC analysis (Bodman γ-TA). [d] Yield and enantiomeric excess determined by chiral HPLC of the corresponding hydrazone derivative with Daicel CHIRALCEL OD-R.

the catalysts. Similar models have been proposed with sterically demanding enamine catalysts.[21]

Our methodology was extended to branched aldehydes **2h** and **2a** (Table 5, entries 7 and 8) to show the broad scope of this reaction. With L-proline (**8a**), silylated prolinol derivative **9c**, and proline-derived tetrazole **11** as catalysts for the formation of chiral quaternary α-fluoro aldehydes, excellent yields of up to 98% were attained, albeit with moderate enantioselectivities of up to 66%. Reactions of branched aldehydes were carried out at room temperature in THF with 30 mol% catalyst. The reaction rate was greatly enhanced when **11** was used with branched aldehyde substrates, although **9c** provided products with higher enantioselectivity. Catalyst **8a** gave excellent yields, but had diminished enantioselectivity and slow reaction times.

In summary, we have developed an organocatalytic α-fluorination reaction for branched aldehydes that delivers optically active quaternary α-fluoroaldehydes in high yield and with moderate enantioselectivity. In conjunction, we have developed a highly enantioselective direct mono α-fluorination reaction of linear aldehydes employing imidazolidinones as chiral promoters. The chiral α-fluoroaldehydes that can now be readily prepared are versatile synthons and should find considerable utility. This new methodology complements our previous studies in fluorine chemistry that used fluorine-containing ketones as nucleophiles in enamine-based addition reactions, and extends the chemistry of aldehydes in a significant way.[22]

Received: February 16, 2005
Published online: May 13, 2005

Keywords: aldehydes · asymmetric catalysis · electrophilic substitution · enantioselectivity · organocatalysis

[1] K. Mikami, Y. Itoh, M. Yamanaka, *Chem. Rev.* **2004**, *104*, 1–16.
[2] a) *Organofluorine Compounds in Medicinal Chemistry and Biomedical Applications* (Eds.: R. Filler, Y. Kobayashi, L. M. Yagupolski), Elsevier Science, Amsterdam, **1993**; b) *Organofluorine Compounds; Chemistry and Application*s (Ed.: T. Hiyama), Springer, New York, **2000**.
[3] a) E. Differding, R. W. Lang, *Tetrahedron Lett.* **1988**, *29*, 6087–6090; b) N. Shibata, E. Suzuki, T. Asahi, M. Shiro, *J. Am. Chem. Soc.* **2001**, *123*, 7001–7009; c) F. A. Davis, H. Qi, G. Sundarababu, *Enantiocontrolled Synthesis of Fluoro-Organic Compounds* (Eds.: V. A. Soloshonok), Wiley, Chichester, **1999**, pp. 1–32; d) D. Cahard, C. Audouard, J. C. Plaquevent, N. Roques, *Org. Lett.* **2000**, *2*, 3699–3701.
[4] a) D. Enders, M. Potthoff, G. Raabe, J. Runsink, *Angew. Chem.* **1997**, *109*, 2454–2456; *Angew. Chem. Int. Ed. Engl.* **1997**, *36*, 2362–2364; b) F. A. Davis, P. V. N. Kasu, *Tetrahedron Lett.* **1998**, *39*, 6135–6138.
[5] a) L. Hintermann, A. Togni, *Angew. Chem.* **2000**, *112*, 4530–4533; *Angew. Chem. Int. Ed.* **2000**, *39*, 4359–4362; b) Y. Hamashima, K. Yagi, H. Tanako, L. Tamas, M. Sodeoka, *J. Am. Chem. Soc.* **2002**, *124*, 14530–14531.
[6] W. J. Middleton, E. M. Bingham, *J. Am. Chem. Soc.* **1980**, *102*, 4845–4846.
[7] a) R. E. Banks, *J. Fluorine Chem.* **1998**, *87*, 1–17; b) E. Differding, H. Ofner, *Synlett* **1991**, 187–189.
[8] a) B. List, R. A. Lerner, C. F. Barbas III, *J. Am. Chem. Soc.* **2000**, *122*, 2395–2396; b) K. Sakthivel, W. Notz, T. Bui, C. F. Barbas, *J. Am. Chem. Soc.* **2001**, *123*, 5260–5267; c) A. B. Northrup, D. W. C. MacMillan, *J. Am. Chem. Soc.* **2002**, *124*, 6798–6799; d) C. Pidathala, L. Hoang, N. Vignola, B. List, *Angew. Chem.* **2003**, *115*, 2891–2894; *Angew. Chem. Int. Ed.* **2003**, *42*, 2785–2788; e) H. Torii, M. Nakadai, K. Ishihara, S. Saito, H. Yamamoto, *Angew. Chem.* **2004**, *116*, 2017–2020; *Angew. Chem. Int. Ed.* **2004**, *43*, 1983–1986; f) N. Mase, F. Tanaka, C. F. Barbas III, *Angew. Chem.* **2004**, *116*, 2474–2477; *Angew. Chem. Int. Ed.* **2004**, *43*, 2420–2423; g) D. E. Ward, V. Jheengut, O. T. Akinnusi, *Org. Lett.* **2005**, *7*, 1181–1184; h) J. T. Suri, D. B. Ramachary, C. F. Barbas III, *Org. Lett.* **2005**, *7*, 1383–1385; i) R. Thayumanavan, F. Tanaka, C. F. Barbas III, *Org. Lett.* **2004**, *6*, 3541–3544.
[9] a) A. Cordova, S. Watanabe, F. Tanaka, W. Notz, C. F. Barbas, *J. Am. Chem. Soc.* **2002**, *124*, 1866–1867; b) Y. Hayashi, W. Tsuboi, I. Ashimine, T. Urushima, M. Shoji, K. Sakai, *Angew. Chem.* **2003**, *115*, 3805–3808; *Angew. Chem. Int. Ed.* **2003**, *42*, 3677–3680; c) B. List, P. Pojarliev, W. T. Biller, H. J. Martin, *J. Am. Chem. Soc.* **2002**, *124*, 827–833; d) N. S. Chowdari, J. T. Suri, C. F. Barbas III, *Org. Lett.* **2004**, *6*, 2507–2510; e) W. Notz, F. Tanaka, S. Watanabe, N. S. Chowdari, J. M. Turner, R. Thayumanavan, C. F. Barbas III, *J. Org. Chem.* **2003**, *68*, 9624–9634;

f) W. Notz, K. Sakthivel, T. Bui, G. Zhong, C. F. Barbas III, *Tetrahedron Lett.* **2002**, *43*, 199 – 201; g) W. Notz, S.-i. Watanabe, N. S. Chowdari, G. Zhong, J. M. Betancort, F. Tanaka, C. F. Barbas III, *Adv. Synth. Catal.* **2004**, *346*, 1131 – 1140.

[10] a) M. P. Brochu, S. P. Brown, D. W. C. MacMillan, *J. Am. Chem. Soc.* **2004**, *126*, 4108 – 4109; b) N. Halland, A. Braunton, S. Bachmann, M. Marigo, K. A. Jorgensen, *J. Am. Chem. Soc.* **2004**, *126*, 4790 – 4791.

[11] C. F. Barbas III, Y.-F. Wang, C.-H. Wong, *J. Am. Chem. Soc.* **1990**, *112*, 2013 – 2014.

[12] J. Hoffmann, G. Zhong, B. List, D. Shabat, J. Anderson, S. Gramatikova, R. A. Lerner, C. F. Barbas III, *J. Am. Chem. Soc.* **1998**, *120*, 2768 – 2779.

[13] G. Zhong, J. Fan, C. F. Barbas III, *Tetrahedron Lett.* **2004**, *45*, 5681 – 5684.

[14] A. Cordova, W. Notz, G. Zhong, J. M. Betancort, C. F. Barbas III, *J. Am. Chem. Soc.* **2002**, *124*, 1842 – 1843.

[15] a) W. Notz, F. Tanaka, C. F. Barbas III, *Acc. Chem. Res.* **2004**, *37*, 580 – 591; b) P. I. Dalko, L. Moisan, *Angew. Chem.* **2004**, *116*, 5138 – 5175; *Angew. Chem. Int. Ed.* **2004**, *43*, 5248 – 5286; c) J. M. Betancort, C. F. Barbas III, *Org. Lett.* **2001**, *3*, 3737 – 3740.

[16] S. T. Purrington, N. V. Lazaridis, C. L. Bumgardner, *Tetrahedron Lett.* **1986**, *27*, 2715 – 2716.

[17] H. Suga, M. Schlosser, *Tetrahedron* **1990**, *46*, 4261 – 4264.

[18] S. Hara, T. Hoshio, M. Kameoka, M. Sawaguchi, T. Fukuhara, N. Yoneda, *Tetrahedron* **1999**, *55*, 4947 – 4954.

[19] O. Gov, A. Burchardt, G. Haufe, *Tetrahedron: Asymmetry* **1997**, *8*, 399 – 408.

[20] F. A. Davis, V. Srirajan, D. D. Titus, *J. Org. Chem.* **1999**, *64*, 6931 – 6934.

[21] M. Marigo, T. C. Wabnitz, D. Fielenbach, K. A. Jørgensen, *Angew. Chem.* **2005**, *117*, 804 – 807; *Angew. Chem. Int. Ed.* **2005**, *44*, 794 – 797.

[22] Note added in proof (April 26, 2005): Since our submission of this study, Enders and Hüttl reported results concerning L-proline/Selectfluor transformations related to our results (Table 1, entry 1); see: D. Enders, M. R. M. Hüttl, *Synlett* **2005**, 991 – 993.

Bioorganic Chemistry

A Dendritic Tetra(bisphosphonic acid) for Improved Targeting of Proteins to Bone**

*Geeti Bansal, Jennifer E. I. Wright, Cezary Kucharski, and Hasan Uludağ**

Protein-based therapeutic agents are being actively pursued for the treatment of skeletal diseases.[1] As endogenous regulators of cellular activity, proteins have the potential to modulate cellular activity at skeletal sites to obtain a desired tissue response. For example, protein-based cytokines that can stimulate the formation of new bone or inhibit the cell activity that is responsible for bone loss will be beneficial for the treatment of diseases such as osteoporosis and arthritis. Despite the demonstrated efficacy of several proteins in preclinical disease models,[2] the clinical entry of most proteins has been hampered as a result of undesired side effects at extraskeletal sites. As systemically administered proteins are not naturally targeted to skeletal tissue, the desired efficacy is achieved only at exuberant doses of the protein by nonspecific deposition at skeletal tissues. In this case, pharmacological activity at extraskeletal sites becomes unacceptable. If proteins could be engineered to exhibit a strong affinity for bone, then systemic administration would allow delivery of the proteins selectively to the skeletal sites.

Bone affinity can be imparted to a molecule by chemical modification with bisphosphonic acids (BPs), a class of compounds with exceptionally high affinity for the bone mineral hydroxyapatite (HA). Bisphosphonic acids are chemical analogues of endogenous pyrophosphate in which the central, hydrolytically labile P-O-P linkage has been replaced by the hydrolysis-resistant P-C-P bond. Intravenous administration of molecules that contain bisphosphonic acid groups results in significant deposition (20–50% of injected dose) of the molecules at bone tissue.[3,4] The exceptional affinity of bisphosphonic acid derivatives for minerals has been utilized to deliver radiopharmaceutical and imaging agents to skeletal tissue.[5,6] To target proteins to bone, we devised conjugation schemes by which 1-amino-1,1-diphosphonic acid (aminoBP)[7] and 2-(3-mercapto-propylsulfanyl)-ethyl-1,1-bisphosphonic acid (SH-BP)[8] were conjugated to proteins

[*] Dr. G. Bansal, J. E. I. Wright, C. Kucharski, Dr. H. Uludağ[+]
Chemical & Materials Engineering Department
526, Chemical & Materials Engineering Building
University of Alberta
Edmonton, Alberta T6G 2G6 (Canada)
Fax: (+1) 780-492-2881
E-mail: hasan.uludag@ualberta.ca

[+] Other addresses:
Department of Biomedical Engineering, Faculty of Medicine
and
Faculty of Pharmacy & Pharmaceutical Sciences
University of Alberta
Edmonton, Alberta T6G 2G6 (Canada)

[**] Financial support was provided by the Canadian Institutes of Health Research (CIHR) and the Whitaker Foundation.

  DOI: 10.1002/anie.200500350

with heterofunctional linkers in aqueous medium.[9–14] The affinity of proteins for hydroxyapatite in vitro was shown to be proportional to the extent of conjugation of the bisphosphonic acid groups.[9,12,14] Intraosseous injection of the aminoBP conjugates confirmed the high affinity in vivo of the conjugates for bone[10] as well as their capability to "seek" bone tissue after systemic injection in rats.[11] The length of the tether between the bisphosphonic acid derivative and the protein was found to be an important factor for the affinity of the conjugates to minerals: conjugates with shorter tethers displayed a higher mineral affinity than those with longer tethers.[13] A higher density of the bisphosphonic acid ligand at the vicinity of proteins was postulated for the beneficial effect of shorter tethers. On the basis of these observations, the ideal approach to target bone would rely on creating a high density of bisphosphonic acids on proteins through short tethers. To this end, we have prepared a new dendritic molecule composed of four bisphosphonic acid moieties linked through a benzene ring (**8**, COOH-4BP; Scheme 1). This compound should provide a higher density of bisphosphonic acid groups on the proteins as four BP units are attached per protein site, unlike the conventional approach that relies on one-to-one linkage (Scheme 2). A carboxylic acid moiety was also incorporated into **8** to allow its conjugation to proteins through a short (zero carbon atom) tether using carbodiimide chemistry (Scheme 2).

The synthesis of COOH-4BP (**8**) is outlined in Scheme 1. Tetraethyl methylenebisphosphonate (**1**; 4 mmol) was converted into tetraethyl ethylidenebisphosphonate (**3**) by reaction, first, with formaldehyde (20 mmol) in diethylamine (0.42 mL) according to the method of Degenhardt and Burdsell to give the intermediate tetraethyl 2-methoxyethylene-bisphosphonate (**2**).[15] Methanol was removed from **2** by adding a catalytic amount of *p*-toluenesulfonic acid monohydrate to a solution of **2** in toluene and then heating the mixture at reflux with a Soxhlet apparatus (CaH_2) to give **3**, which was purified by chromatography on silica gel (60–270 mesh; 4:1 $CHCl_3$/hexane as eluent). Meanwhile, 3,5-bis(3,5-dinitrobenzoylamino)benzoic acid (**6**) was prepared from a mixture of 3,5-diaminobenzoic acid (**4**; 19.7 mmol) and 3,5-dinitrobenzoyl chloride (**5**; 43.4 mmol) in *N*,*N*-dimethylacetamide and was then reduced to 3,5-bis(3,5-diaminobenzoylamino)benzoic acid (**7**) with H_2 and 10% Pd/C.[16] Then compound **3** (1.6 mmol) was coupled to the amine moieties of **7** (0.4 mmol) by an anti-Markovnikov reaction in THF (15 mL) at 60 °C for 5 hours to give 3,5-bis[3,5-di(ethylamino-2,2-tetraethylbisphosphonate)benzoylamino]benzoic acid. After removal of the solvent, the residue was dissolved in CH_2Cl_2 and the phosphonate esters were hydrolyzed with bromotrimethylsilane ($BrSi(CH_3)_3$)[15] for 48 hours to afford the dendritic tetra(bisphosphonic acid) **8** (Scheme 1).[17]

Bovine serum albumin (BSA) served as the model protein for conjugation of the bisphosphonic acid derivative. Acid **8** was activated by treating equimolar concentrations (0–20 mM) of NHS and EDC in MES (morpholinoethanesulfonic acid) buffer (0.1M, pH 4.5) for 45 minutes. The activated acid **8** (0.15–1.25 mM) was then incubated with BSA (5 mg mL^{-1}) in MES buffer for 3 hours, after which time the unreacted components were removed by dialysis against 0.2 M carbonate buffer (pH 10; ×4) and deionized water (×2). The dialyzed samples were further purified by gel permeation chromatography (Bio-Rad P2 gel-fine; 18 × 1.2 cm^2 column) with deionized water as eluent. Samples of BSA mixed with **8** in the absence of EDC/NHS as well as BSA conjugated to SH-BP[14] served as controls. These control samples were purified by dialysis only. All conjugates were analyzed for an average

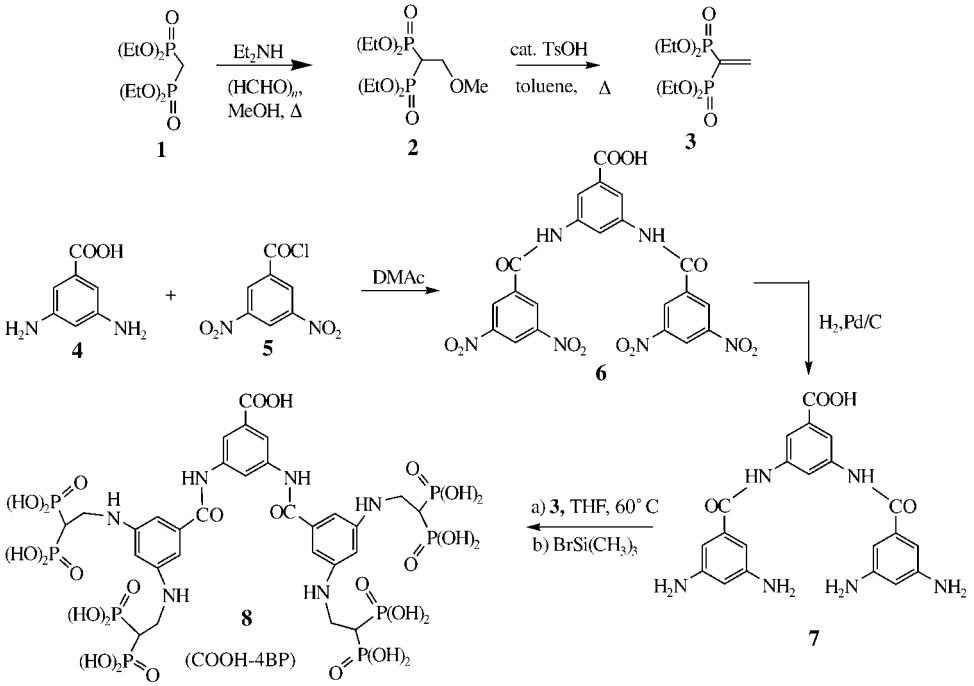

Scheme 1. Synthesis of tetra(bisphosphonic acid) **8**. TsOH = *p*-toluenesulfonic acid, DMAc = *N*,*N*-dimethylacetamide.

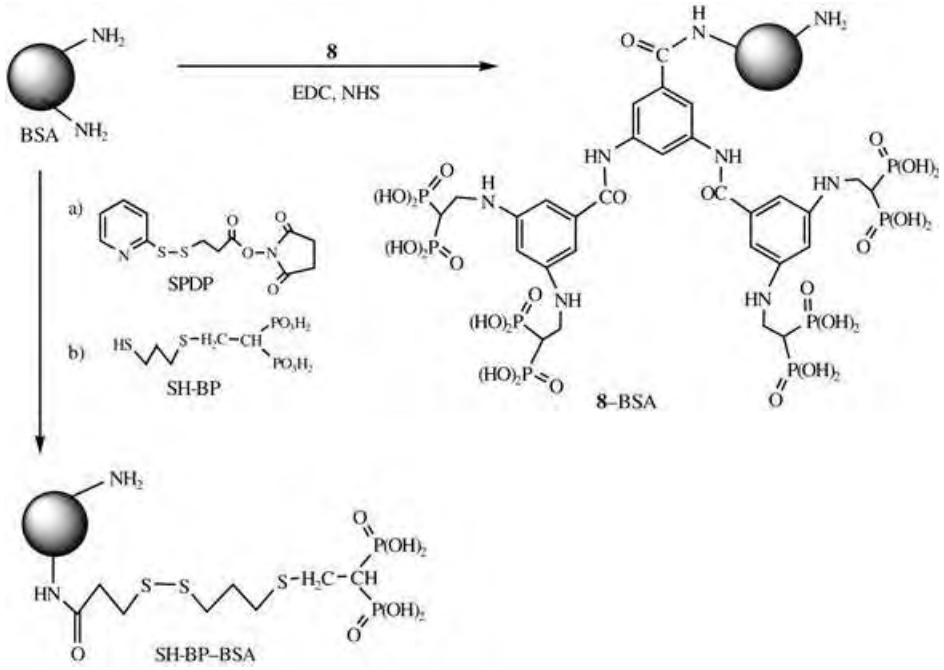

Scheme 2. Conjugation of **8** (COOH-4BP) and SH-BP to model protein BSA. EDC = 1-ethyl-3-(3-dimethylaminopropyl)carbodiimide, NHS = *N*-hydroxysuccinimide, SPDP = *N*-succinimidyl 3-(2-pyridyldithio)propionate.

number of bisphosphonic acid substituents (i.e. the number of BP groups attached per BSA) by using the Bradford assay for protein concentrations[18] and the Ames assay[19] for phosphate concentrations.

SDS-PAGE (sodium dodecylsulfate–polyacrylamide-gel electrophoresis) analysis of the obtained proteins indicated the migration of protein as single bands, which confirmed a lack of protein–protein linking during the conjugation reactions (data not shown). The number of bisphosphonic acid substituents for a representative set of **8**–BSA conjugates ([EDC] = [NHS] = 0–20 mM; [**8**] = 1.25 mM) are summarized in Figure 1 a. The control sample of BSA ([EDC] = [NHS] = 0 mM) revealed 0.8 molecules of **8** per BSA protein which presumably represents the extent of free COOH-4BP (**8**) not removed by dialysis (or gel chromatography). The conjugates

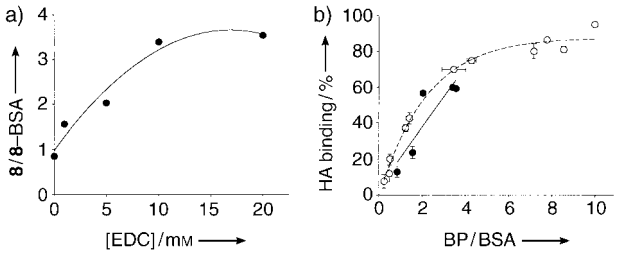

Figure 1. a) Number of tetra(bisphosphonic acid) substituents **8** per BSA conjugate upon coupling **8** (1.25 mM) to BSA in the presence of equimolar quantities of EDC and NHS ([EDC] = [NHS] = 0–20 mM). b) Correlation between the number of bisphosphonic acid (BP) substituents per BSA protein conjugate (mean ± SD) and the percentage binding to hydroxyapatite (HA; mean ± SD) in phosphate buffer (100 mM). Note the linear increase in the percentage binding of the conjugates at low numbers of BP groups for both SH-BP–BSA (○) and **8**–BSA (●). See Ref. [9] for details about the methods.

8–BSA showed an increasing efficiency of conjugation (up to 3.6 molecules of **8** per BSA) as the concentration of EDC and NHS was increased (Figure 1 a). The binding of the conjugates to hydroxyapatite was assessed in phosphate buffer (100 mM, pH 7.4), which was previously optimized for investigating such protein–HA binding.[7] Figure 1 b summarizes the relationship between the binding of the conjugates to hydroxyapatite and the conjugation efficiency (that is, the number of bisphosphonic acid groups per BSA) for SH-BP–BSA and **8**–BSA. Both conjugates exhibited an increased level of binding to hydroxyapatite as a function of conjugation efficiency. Whereas a plateau in the percentage binding to hydroxyapatite was evident with SH-BP–BSA, no such plateau was seen for **8**–BSA, partly as a result of our inability to obtain more than 3.6 bisphosphonic acid groups per BSA (two other independent reactions did not yield higher numbers of bisphosphonic acid substituents). This excellent correlation between the conjugation efficiency and the affinity for hydroxyapatite was in accord with the results obtained previously for aminoBP and SH-BP conjugations with hydroxyapatite.[9,14]

The conjugates were then analyzed for binding to hydroxyapatite and bone in the presence of serum proteins. Fresh bone matrix was obtained from Sprague–Dawley rats,[9] and the serum proteins originated from tissue-culture grade adult bovine serum. The use of bone matrix and serum proteins in the binding medium provides more stringent conditions for an assessment of binding and better represents the situation in vivo. The BSA conjugates for this analysis had similar levels of substitution by bisphosphonic acids: 3.4 and 3.6 for SH-BP–BSA and **8**–BSA, respectively. Owing to the presence of serum, ^{125}I-labeled conjugates were used for this analysis and were added to unlabeled (cold) proteins to give

approximately 10^6 cpm (counts per minute) at a concentration of 0.1 mg mL^{-1} protein (hot/cold = 1:100).[9] In 30 and 60% serum media, both conjugates exhibited a higher level of binding to hydroxyapatite than unmodified BSA (Figure 2a).

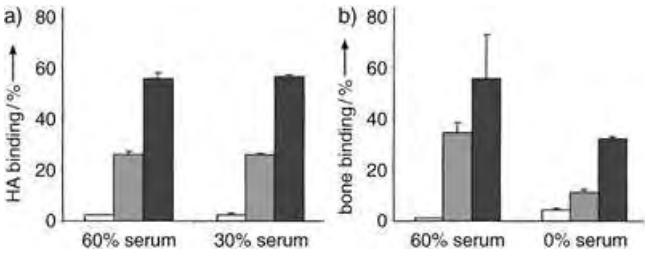

Figure 2. Percentage binding of BSA protein (□) and its conjugates (SH-BP–BSA ■, **8**–BSA ■) to a) HA and b) bone in serum-containing media (200 mM phosphate buffer). For both binding matrices, **8**–BSA gave the highest extent of binding, followed by SH-BP—BSA, while only a low level of binding was observed with the control (BSA protein) under all conditions. See Ref. [9] for details about the methods.

Conjugates prepared with **8** exhibited a higher level of binding to hydroxyapatite relative to SH-BP–BSA, despite the same number of bisphosphonic acid substituents. A similar result was obtained when hydroxyapatite was replaced by bone as the binding matrix (Figure 2b), with the **8**–BSA conjugate exhibiting superior levels of binding than the SH-BP–BSA conjugate.

Finally, the ability of these two conjugates to target bone was evaluated in rats. The ^{125}I-labeled conjugates (as above) were injected intravenously through the tail vein and bone (femora and tibiae), and deposition of the proteins was assessed by explanting the bones and determining the counts in these tissues. The depositions of the control BSA and the SH-BP–BSA conjugate at the bone were similar at both femora and tibia, which indicates a lack of targeting by the SH-BP–BSA conjugate (Figure 3). The presence of approximately 3.4 bisphosphonic acid substituents per BSA protein was not expected to impart a strong affinity to bone, as our previous studies required around 10 bisphosphonic acid groups per BSA for successful bone-targeting.[11] However,

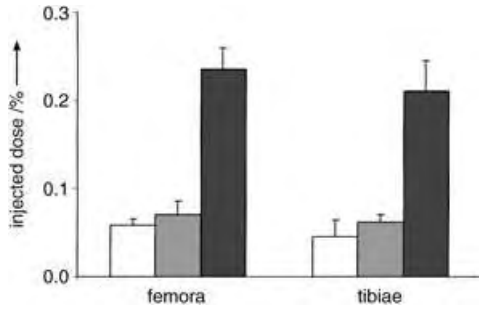

Figure 3. Delivery of BSA (control; □), SH-BP–BSA (■), and **8**–BSA (■) to femora and tibiae after intravenous injection in Sprague–Dawley rats ($n = 3$ per group). Bone-targeting was assessed one day after injection. Note the lack of bone-targeting by the SH-BP–BSA conjugate (i.e. similar to BSA) and the significantly improved bone-targeting by **8**–BSA. See Ref. [11] for details about the methods.

conjugate **8**–BSA, with a similar extent of bisphosphonic acid substituents, gave 4.1- and 4.7-fold higher delivery (relative to control BSA) at the femora and tibiae, respectively (Figure 3). A similar result was obtained in a repeat study in which the control BSA and **8**–BSA were injected subcutaneously: delivery increased by 3.7- (femora) and 3.4-fold (tibiae) as a result of conjugation of **8** (data not shown).

In conclusion, we have reported the synthesis of a novel, dendritic tetra(bisphosphonic acid) **8**. The synthesized molecule is introduced through a minimal tether length at the attachment site and provides a high density of bisphosphonic acid groups per protein site modified. Dendritic **8** gave higher numbers of total bisphosphonic acid groups attached per protein relative to SH-BP conjugates and exhibited its intended effect, namely bone-targeting, at a lower extent of protein modification which is an important consideration for maintaining the pharmacological activity of proteins when they are derivatized with bone-seeking ligands. The studies reported here should further stimulate the efforts to design "bone-seeking" proteins with minimal degree of modification.

Received: January 29, 2005
Published online: May 6, 2005

Keywords: bioorganic chemistry · bone-targeting · drug delivery · protein engineering

[1] D. Puleo, *BioDrugs* **2003**, *17*, 301–314.
[2] S. A. Gittens, H. Uludağ, *J. Drug Targeting* **2001**, *6*, 407–429.
[3] A. G. Porras, S. D. Holland, B. J. Gertz, *Clin. Pharm.* **1999**, *36*, 315–328.
[4] G. M. Blake, S. J. Park-Holohan, G. J. Cook, I. Fogelman, *Semin. Nucl. Med.* **2001**, *31*, 28–49.
[5] C. L. De Ligny, W. J. Gelsema, T. G. Tji, Y. M. Huigen, H. A. Vink, *Nucl. Med. Biol.* **1990**, *17*, 161–179.
[6] H. Uludağ, *Current Pharm. Design.* **2002**, *8*, 1929–1944.
[7] D. Kontaci, J. K. Denike, W. J. Wechter, *Synth. Commun.* **1996**, *26*, 2037–2043.
[8] I. S. Alferiev, N. R. Vyavahare, C. V. Song, R. J. Levy, *J. Polym. Sci. Part A* **2001**, *39*, 105–116.
[9] H. Uludağ, N. Kousinioris, T. Gao, D. Kantoci, *Biotechnol. Prog.* **2000**, *16*, 258–267.
[10] H. Uludağ, T. Gao, G. R. Wohl, D. Kantoci, R. F. Zernicke, *Biotechnol. Prog.* **2000**, *16*, 1115–1118.
[11] H. Uludağ, J. Yang, *Biotechnol. Prog.* **2002**, *18*, 604–611.
[12] S. A. Gittens, J. R. Matyas, R. F. Zernicke, H. Uludağ, *Pharm. Res.* **2003**, *20*, 978–987.
[13] S. A. Gittens, P. I. Kitov, J. R. Matyas, R. Löbenberg, H. Uludağ, *Pharm. Res.* **2004**, *21*, 608–616.
[14] G. Bansal, J. E. I. Wright, S. Zhang, R. F. Zernicke, H. Uludağ, *J. Biomed. Mater. Res.* **2005**, in press.
[15] C. R. Degenhardt, D. C. Burdsall, *J. Org. Chem.* **1986**, *51*, 3488–3490.
[16] Y. Ishida, M. Jikei, M. Kakimoto, *Macromolecules* **2000**, *33*, 3202–3211.
[17] **2**: ^{1}H NMR ($CDCl_3$, J [Hz]): $\delta = 4.19$ (m, 8H), 3.90 (td, 2H, $J =$ 5.4, 16.2), 3.36 (s, 3H), 2.68 (tt, 1H, $J = 10.8$, 24), 1.31 ppm (t, 12H, $J = 9.3$); The hydrogen atom on the carbon atom in P-C_A-P resonates as a triplet of triplets, through coupling to two phosphorus and to two hydrogen atoms on the adjacent C_B atom, whereas the two hydrogen atoms on C_B couple with two

phosphorus nuclei to give a triplet that splits into a doublet by the hydrogen atom on C_A. **3**: ^{1}H NMR ($CDCl_3$, J [Hz]): $\delta = 7.00$ (dd, 2H, $J = 34.2, 33.9$), 4.15 (m, 8H), 1.32 ppm (t, 12H, $J = 6.9$); ^{13}C NMR ($CDCl_3$): $\delta = 149.01$, 132.03, 63.12, 16.2 ppm.[15] **6**: ^{1}H NMR (DMSO): $\delta = 11.08$ (s, 2H), 9.23 (s, 4H), 9.02 (s, 2H), 8.76 (s, 1H), 8.19 ppm (s, 2H); MS: $m/z = 539$ $[M-H]^-$. **7**: ^{1}H NMR (DMSO): $\delta = 10.11$ (s, 2H), 8.42 (s, 1H), 8.04 (s, 2H), 6.31 (s, 4H), 5.99 ppm (s, 2H), in agreement with those reported.[17] The addition of four ethylidenebisphosphonic acid groups to the four amine (NH_2) groups of **7** was confirmed by ^{1}H NMR spectroscopy and mass spectrometry. **8**: ^{1}H NMR (D_2O and NaOD, J [Hz]): $\delta = 7.94$ (m, 1H), 7.81 (m, 2H), 6.74 (m, 4H), 6.52 (m, 2H), 3.45 (m, 8H), 2.05 ppm (tt, 4H, $J = 3.3, 7.5$); ^{13}C NMR: $\delta = 147.52$, 138.96, 121.31, 88.44, 47.66, 40.51 ppm; ^{31}P NMR: $\delta = 18.1$ ppm; MS: $m/z = 1171$ $[M-H]^-$, 1173 $[M+H]^+$; IR: $\tilde{\nu} = 1202$ cm^{-1} (P=O).

[18] M. M. Bradford, *Anal. Biochem.* **1976**, *72*, 248–254.

[19] B. N. Ames, *Methods Enzymol.* **1966**, *8*, 115–117.

Natural Product Synthesis

A Remarkable Ring Contraction En Route to the Chartelline Alkaloids**

Phil S. Baran, Ryan A. Shenvi, and Christos A. Mitsos*

Marine fauna continually produce molecules endowed with potent bioactivities and extraordinary structures.[1] The securines (**1**, **2**), securamines (**3**, **4**), chartellines (**5**–**7**), and chartellamides (**8**, **9**; Scheme 1) are members of a structurally unique class of natural products that were isolated by Christophersen and co-workers from the bryozoa *Chartella papyracea* and *Securiflustra securifrons*.[2] They contain an interesting arrangement of various heterocyclic entities that are wound around a prenyl unit and adorned with halogen atoms. With such a dense array of sensitive and exotic functionalities, such as spiro-β-lactam, indolenine, chloroenamide, and 2-bromoimidazole units, it is understandable why no member of this family has yet succumbed to total synthesis since their isolation over two decades ago.[3]

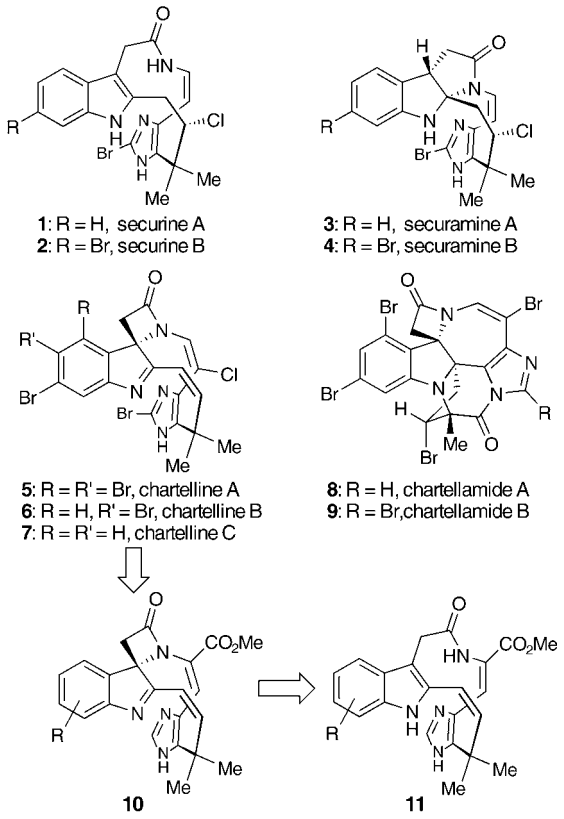

Scheme 1. Structures of the chartellines, chartellamides, securines, and securamines, and the retrosynthetic analysis of the carbocyclic skeleton.

The belief that macrocyclic constructs such as **10** and **11** would behave differently than their individual heterocyclic subunits was central to our synthetic plan. Specifically, late-stage chemo- and regioselective halogenations and a bromine-induced rearrangement of **11** to **10** were planned. The presence of extensive halogen substitution in these natural products perhaps suggests that many of the biotransformations that create such complex polycyclic structures are indeed accomplished with electrophilic sources of bromine and chlorine; it is this hypothesis that inspired the current approach. However, there are no examples for such a ring contraction of a pyrroloindoline unit and ample precedent that suggests its failure (Scheme 2).[4] Pyrroloindoline intermediates of type **A** have not been known to undergo ring contraction to strained spiro systems of type **B** (see Scheme 2). Furthermore, an indolenine, such as **C**, can be rapidly hydrated (**D**) and undergo a 1,2-shift to an oxindole (**E**).[5] Notwithstanding this bleak outlook, we hypothesized that π stacking and conformational effects in the macrocycle **11** would provide sufficient driving force for a bromine-induced ring contraction to yield **10** (via an intermediate of type **A**). Herein, we present the successful execution of this approach, which resulted in a short and practical route to the

[*] Prof. Dr. P. S. Baran, R. A. Shenvi, Dr. C. A. Mitsos
Department of Chemistry
The Scripps Research Institute
10650 North Torrey Pines Road
La Jolla, CA 92037 (USA)
Fax: (+1) 858-784-7375
E-mail: pbaran@scripps.edu

[**] Steven Nguyen is gratefully acknowledged for his technical contributions. We thank Dr. D. H. Huang and Dr. L. Pasternak for assistance with the NMR spectroscopic analysis, and Dr. G. Suizdak and Dr. R. Chadha for assistance with the mass-spectrometric and X-ray crystallographic analysis, respectively. We are grateful to Biotage for their generous donation of the microwave process vials used extensively during these studies. Financial support for this work was provided by The Scripps Research Institute, the Department of Defense (predoctoral fellowship to R. A. S.), Eli Lilly & Co, GlaxoSmithKline, and the Searle Scholarship Fund.

Supporting information for this article is available on the WWW under http://www.angewandte.org or from the author.

  DOI: 10.1002/anie.200500522

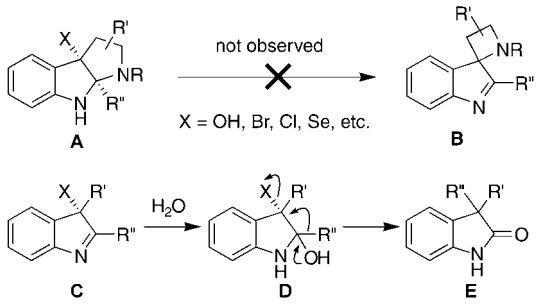

Scheme 2. The known reactivity profile of oxidized indoles suggests that the proposed rearrangement (**11**→**10**) is unlikely to occur.

carbocyclic skeleton of the chartelline, securine, and securamine alkaloid families.

The synthetic pathway to **10** is outlined in Scheme 3. Thus, treatment of the readily available serine-derivative **12** with prenylmagnesium bromide furnished α-amino ketone **13** which could be easily transformed into imidazole **14** in 84% yield via an imidazoline-2-thione intermediate.[6] The corresponding primary alcohol of **14** has been previously synthesized in nine steps[7] and was used in the total synthesis of the anticancer agents phenylahistin and aurantiamine and libraries that were based upon these compounds.[7,8] In preparation for linking the imidazole and indole subunits, it was necessary to convert the vinyl group of **14** into an alkynyl group. This conversion was carried out by the Johnson–Lemieux oxidation of **14** to the corresponding aldehyde followed by treatment with reagent **15**, developed by Ohira and Bestmann and co-workers,[9] to furnish alkyne **16** in 63% yield. The coupling of **16** and 2-bromoindole **17**[10] was accomplished by employing the method of Sonogashira et al. for a copper-accelerated[11] Heck alkyne synthesis[12] to afford **18** in 71% yield. Subsequent hydrogenation to the *cis* olefin,[13] removal of the TBS protecting group, and MnO_2-mediated oxidation of the resulting alcohol led to the crystalline aldehyde **19** (m.p. 50–55 °C, CH_2Cl_2/hexanes), whose markedly folded structure was discerned through X-ray crystallography (see Scheme 3 for the ORTEP representation). After a number of abortive attempts, the reliable Horner–Wadsworth–Emmons reaction finally emerged as an effective means to mediate the macro-

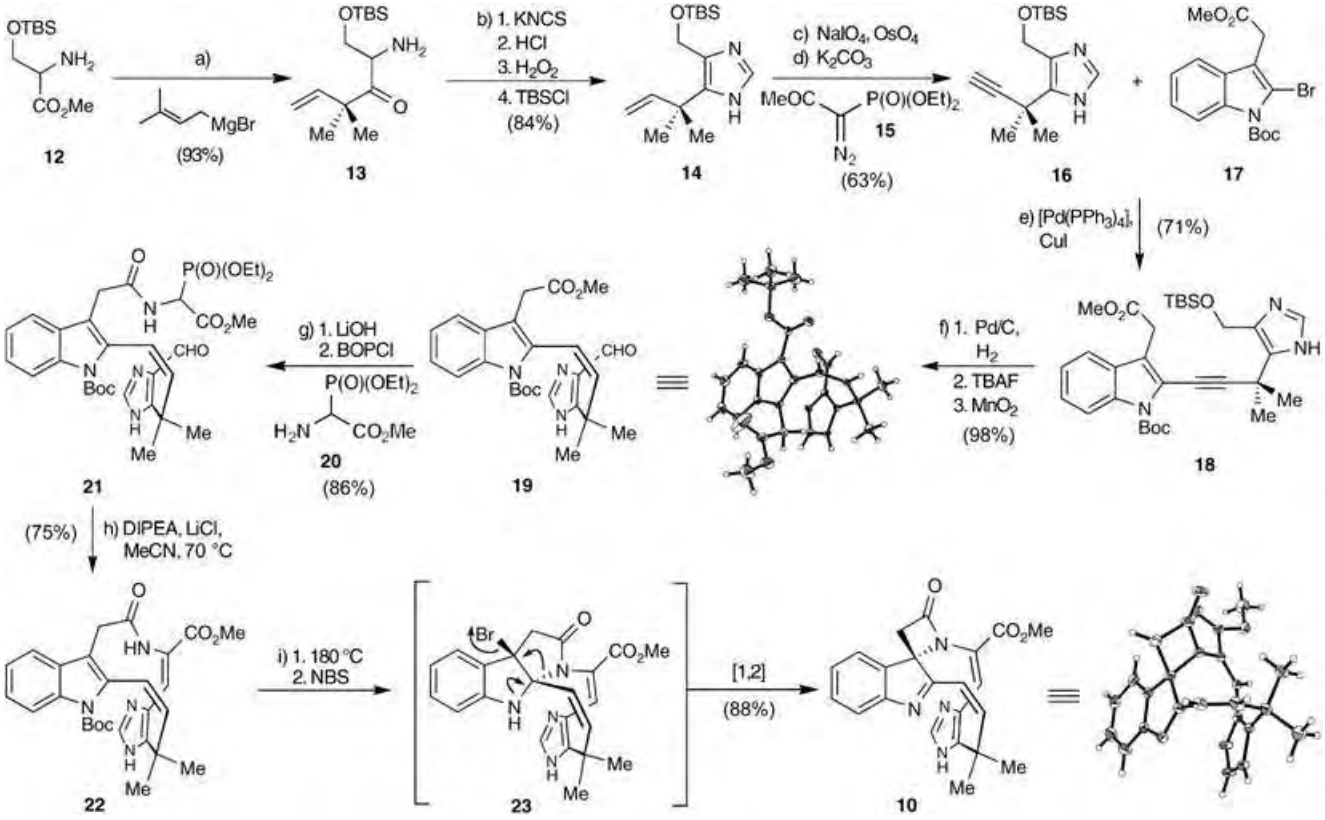

Scheme 3. Construction of the complete chartelline, securine, and securamine carbocyclic skeletons. Reagents and conditions: a) prenylmagnesium bromide, THF, −78 °C, 93%; b) 1. KNCS (20 equiv), NH_4Cl (20 equiv), toluene 105–110 °C, 4 h; 2. 6 N HCl, 25 °C, 20 min; 3. i. H_2O_2 (11 equiv), THF, 25 °C, 6 h; ii. 2 M NaOH/saturated aq $NaHCO_3$ (4:1), 25 °C, 1 h; 4. TBSCl (1.0 equiv), Et_3N (1.0 equiv), CH_2Cl_2, 25 °C, 84% from **13**; c) $NaIO_4$ (3.0 equiv), OsO_4 (0.03 equiv), THF/H_2O (2:1), 25 °C, 18 h; d) **15** (1 equiv), K_2CO_3 (1.5 equiv), MeOH, 25 °C, 6 h, 63% from **14**; e) $[Pd(PPh_3)_4]$ (0.3 equiv), CuI (0.7 equiv), *i*$PrNH_2$ (10 equiv), DME, 70 °C, 30 min, 71%; f) 1. H_2, 10% Pd/C (0.1 equiv), $MgSO_4$ (2 equiv), EtOH, 25 °C, 4 h; 2. TBAF (1.1 equiv), THF, 0→25 °C, 3 h; 3. MnO_2 (20 equiv), CH_2Cl_2, 25 °C, 8 h, 98% from **18**; g) 1. LiOH (3 equiv), THF/H_2O (4:1), 25 °C, 5 h; 2. **20** (2.6 equiv), BOPCl (1.5 equiv), DIPEA (2.0 equiv), 0 °C, 2 h, 86% from **19**; h) LiCl (9.0 equiv), DIPEA (20 equiv), CH_3CN, 70 °C, 4 h, 75%; i) 1. 180 °C, 8 min; 2. NBS (1.0 equiv), $KHCO_3$ (20 equiv), THF/H_2O, 35 min, 88% from **22**. TBS = *tert*-butyldimethylsilyl , KNCS = potassium thiocyanate, Boc = *tert*-butoxycarbonyl, DME = 1,2-dimethoxyethane, TBAF = tetra butylammonium fluoride, BOPCl = bis(2-oxo-3-oxazolidinyl)phosphinic chloride, DIPEA = diisopropylethylamine, NBS = *N*-bromosuccinimide.

cyclization.[14] Aldehyde **19** was primed for this reaction through saponification with LiOH and coupling with amine **20**[15] in the presence of BOPCl to furnish phosphonate **21** in 86% yield. Macrocyclization under the conditions developed by Masamune, Roush, and co-workers[16] produced macrocycle **22** in 75% yield and set the stage for the critical rearrangement.

Macrocycle **22** was converted into the chartelline skeleton **10** in 88% yield and in a single operation by simple thermolytic removal of the Boc protecting group in **22** (180 °C, no solvent)[17] followed by treatment of the resulting free indole (**11**, Scheme 1) with NBS and aqueous $KHCO_3$. The structure of this crystalline substance (m.p. 190–220 °C (decomp; CH_3CN)) was verified by X-ray crystallographic analysis (see Scheme 3 for the ORTEP representation). Although we speculate that the reaction proceeds through intermediate **23**, several degenerate pathways to **10** could also be envisaged.

As alluded to above, a number of unanticipated roadblocks were encountered during our efforts to accomplish macrocyclization. Some of these experiences are briefly summarized in Scheme 4, with the resistance of **24** to undergo ring-closing metathesis, the failure of a seemingly simple macrolactamization (**25**), and the refusal of **26** to take part in a Heck-type[18] ring closure.

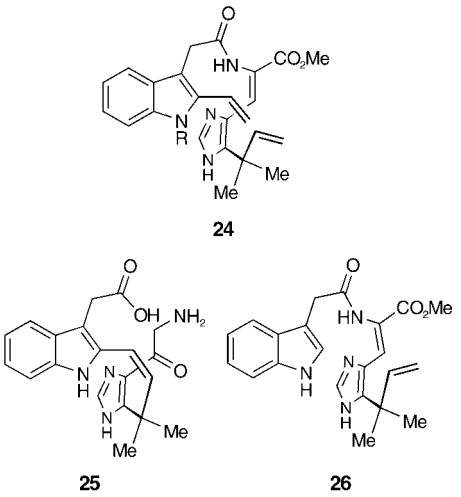

Scheme 4. Selected dead-end routes to the chartelline, securamine, and securine carbocyclic skeletons.

Notable aspects of the approach described herein include synthetic efficacy (approximately 19% overall yield and 10 steps); rapid access to the carbocyclic skeletons of the chartelline, securine, and securamine alkaloids; and a remarkable ring contraction (**22**→**10**) that proceeds in high yield, despite the inherent ring strain of the β-lactam unit and an abundance of discouraging literature precedent (Scheme 2). The distinctive architecture of the chartelline alkaloids inspired this approach, and it is possible that a similar strategy is employed in nature to forge the intriguing spiro-β-lactam ring in the chartellines from securine-like structures. Completion of the total synthesis of the chartellines and related alkaloids will be reported shortly.[19]

Received: February 11, 2005
Published online: May 18, 2005

Keywords: cascade reactions · chartellines · natural products · securamines · total synthesis

[1] Marine natural products have a proven track record for improving human health; for a review of those that are in current medical use, see: D. J. Newman, G. M. Cragg, *Curr. Med. Chem.* **2004**, *11*, 1693–1713; for some early pioneering efforts in this field, see: W. Fenical, *Chem. Rev.* **1993**, *93*, 1673–1683.

[2] a) L. Chevolot, A.-M. Chevolot, M. Gajhede, C. Larsen, U. Anthoni, C. Christophersen, *J. Am. Chem. Soc.* **1985**, *107*, 4542–4543; b) U. Anthoni, L. Chevolot, C. Larsen, P. H. Nielsen, C. Christophersen, *J. Org. Chem.* **1987**, *52*, 4709–4712; c) U. Anthoni, K. Bock, L. Chevolot, C. Larsen, P. H. Nielsen, C. Christophersen, *J. Org. Chem.* **1987**, *52*, 5638–5639; d) L. Rahbaek, U. Anthoni, C. Christophersen, P. H. Nielsen, B. O. Petersen, *J. Org. Chem.* **1996**, *61*, 887–889; e) L. Rahback, C. Christophersen, *J. Nat. Prod.* **1997**, *60*, 175–177.

[3] a) X. Lin, S. M. Weinreb, *Tetrahedron Lett.* **2001**, *42*, 2631–2633; b) S. C. Chaffee, PhD Thesis, Yale University, **2001**; c) X. Lin, PhD Thesis, Pennsylvania State University, **2002**; d) J. L. Pinder, S. M. Weinreb, *Tetrahedron Lett.* **2003**, *44*, 4141–4143; e) P. Korakas, PhD Thesis, Yale University, **2003**; f) T. Nishikawa, S. Kajii, M. Isobe, *Chem. Lett.* **2004**, *33*, 440–441; g) P. Korakas, S. Chaffee, J. B. Shotwell, P. Duque, J. L. Wood, *Proc. Natl. Acad. Sci. USA* **2004**, *101*, 12054–12057; h) T. Nishikawa, S. Kajii, M. Isobe, *Synlett* **2004**, 2025–2027.

[4] See Ref. [3] and J. A. Joule, K. Mills, *Heterocyclic Chemistry*, Blackwell, Oxford, **2000**, p. 589; R. J. Sundberg, *Indoles*, Academic Press, San Diego, **1996**, p. 175.

[5] For example, see: H. Wang, A. J. Ganesan, *J. Org. Chem.* **2000**, *65*, 4685–4693; ring contractions of six-membered rings to form indolenines are also known, see: P. L. Feldman, H. Rapoport, *J. Am. Chem. Soc.* **1987**, *109*, 1603–1604; M. Node, H. Nagasawa, K. Fuji, *J. Org. Chem.* **1990**, *55*, 517–521.

[6] a) S. Grivas, E. Ronne, *Acta Chem. Scand.* **1995**, *49*, 225–229; b) J. G. Schantl, I. M. Lagoja, *Heterocycles* **1998**, *48*, 929–938.

[7] Y. Hayashi, S. Orikasa, K. Tanaka, K. Kanoh, Y. Kiso, *J. Org. Chem.* **2000**, *65*, 8402–8405.

[8] K. Kanoh, S. Kohno, J. Katada, J. Takahashi, I. Uno, Y. Hayashi, *Bioorg. Med. Chem. Lett.* **1999**, *7*, 1451–1457; E. A. Couladouros, A. D. Magkos, personal communication.

[9] S. Müller, B. Liepold, G. J. Roth, H. J. Bestmann, *Synlett* **1996**, 521–522; S. Ohira, *Synth. Commun.* **1989**, *19*, 561–564.

[10] Prepared from methyl-3-indoleacetate by bromination with NBS followed by protection with a Boc group using Boc_2O and catalytic dimethylaminopyridine.

[11] K. Sonogashira, Y. Tohda, N. Hagihara, *Tetrahedron Lett.* **1975**, 4467–4470.

[12] H. A. Dieck, R. F. Heck, *J. Organomet. Chem.* **1975**, *93*, 259–263.

[13] S. Shinjiro, K. Matsumoto, H. Tokuyama, T. Fukuyama, *Org. Lett.* **2003**, *5*, 1891–1893.

[14] K. C. Nicolaou, M. W. Härter, J. L. Gunzner, A. Nadin, *Liebigs Ann.* **1997**, 1283–1301.

[15] U. Schmidt, A. Lieberknecht, J. Wild, *Synthesis* **1984**, 53–60; see also: B. M. Schiavi, D. J. Richard, M. M. Joullié, *J. Org. Chem.* **2002**, *67*, 620–624.

[16] M. A. Blanchette, W. Choy, J. T. Davis, A. P. Essenfeld, S. Masamune, W. Roush, T. Sakai, *Tetrahedron Lett.* **1984**, *25*, 2183 – 2186.
[17] P. S. Baran, C. A. Guerrero, N. B. Ambhaikar, B. D. Hafensteiner, *Angew. Chem.* **2005**, *117*, 612 – 615; *Angew. Chem. Int. Ed.* **2005**, *44*, 606 – 609; for the first report of this deprotection method, see: V. H. Rawal, M. P. Cava, *Tetrahedron Lett.* **1985**, *26*, 6141 – 6142.
[18] P. S. Baran, E. J. Corey, *J. Am. Chem. Soc.* **2002**, *124*, 7904 – 7905.
[19] Detailed experimental procedures, copies of all spectral data, and full characterization are contained in the Supporting Information. CCDC-263124 (**19**) and -263125 (**10**) contain the supplementary crystallographic data for this paper. These data can be obtained free of charge from the Cambridge Crystallographic Data Centre via www.ccdc.cam.ac.uk/data_request/cif.

Main Group Chemistry

Telluradistibirane and Telluradibismirane: Three-Membered Heterocycles of Heavier Main Group Elements**

*Takahiro Sasamori, Eiko Mieda, Nobuhiro Takeda, and Norihiro Tokitoh**

The chemistry of three-membered heterocycles has been widely explored in organic chemistry from the viewpoint of their unique structures and properties, which are attributed to their strained skeletons.[1,2] Although numerous papers have been published on the theory, preparation, and applications of three-membered heterocycles containing one heteroatom such as nitrogen, oxygen, or sulfur, only very few examples of three-membered ring compounds containing heavier chalcogen atoms such as selenium or tellurium have appeared to date.[3] In addition, three-membered ring systems composed of three heavier heteroatoms are also scarce, most likely owing to the instability of these systems. To synthesize such three-membered heterocycles that incorporate selenium or tellurium together with other heavier heteroatoms in their skeletons, one effective method should be the chalcogenation of highly reactive heavier double-bond compounds by formal [2+1] cycloaddition reactions. In the case of heavier Group 14 elements, selenadimetalliranes and telluradimetalliranes (Ch-M-M three-membered ring compounds; Ch = Se, Te, M = Si, Sn) have been successfully synthesized by chalcogenation reactions of the corresponding kinetically stabilized dimetallenes (M=M double-bond compounds) using elemental chalcogens.[4] There has also been much interest in doubly bonded compounds between heavier Group 15 elements, that is, heavier congeners of azo compounds. We synthesized a series of kinetically stabilized distibene (ArSb=SbAr)[5,6] and dibismuthene (ArBi=BiAr)[5,7] compounds by using 2,4,6-tris[bis(trimethylsilyl)methyl]phenyl (Tbt) and 2,6-bis[bis(trimethylsilyl)methyl]-4-[tris(trimethylsilyl)methyl]phenyl (Bbt) groups as effective steric protection groups. However, whereas no tellurirane containing two heavier Group 15 elements was obtained from the tellurization reaction of BbtP=PBbt using elemental Te or (nBu)$_3$P=Te,[8] selenadiphosphiranes[8,9] and a selenadistibirane[10] were synthesized by the selenization reaction of the corresponding diphosphene (Mes*P=PMes* (Mes* = 2,4,6-tri-*tert*-butylphenyl), BbtP=PBbt, etc.) and distibene (BbtSb=SbBbt), respectively. Herein, we report the tellurization reaction of the kinetically stabilized distibene BbtSb=SbBbt (**1**) and dibismuthene BbtBi=BiBbt (**2**), which led to the formation of novel three-membered heterocycles, that is, the first stable telluradistibirane and telluradibismirane, respectively.

The reaction of BbtBi=BiBbt (**2**, 30 mg, 0.02 mmol), which was readily prepared by reductive coupling of BbtBiBr$_2$ with Mg in almost quantitative yield,[5] with an excess amount of elemental tellurium (26 mg, 10 equiv) in [D$_6$]benzene solution was performed in the hope of generating a telluradibismirane derivative. After heating the mixture at 60 °C for 72 h, then at 80 °C for 72 h, and finally at 100 °C for 72 h, **2** disappeared completely as judged by the ^{1}H NMR spectra. However, not the desired telluradibismirane but only the ditelluride **3** (Bbt-Te-Te-Bbt) was obtained (12 mg, 42 %) as green crystals after purification by GPLC. The structure of **3** was determined by spectroscopic data (^{1}H, ^{13}C, ^{125}Te NMR, FAB-MS) and X-ray crystallographic analysis.[11] Although mechanism for the formation of **3** is not clear at present, **3** was most likely generated by over-tellurization of **2** under severe conditions such as heating at 60–100 °C, which would be required to dissolving elemental tellurium in benzene.

Since nBu$_3$P=Te has been known to function as a tellurization reagent under mild conditions,[12] we selected nBu$_3$P=Te as an alternative tellurium source for the tellurization of **1** and **2**. When a solution of **2** (49 mg, 0.03 mmol) in benzene (2.0 mL) was mixed with two equivalents of nBu$_3$P=Te (23 mg, 0.06 mmol) at room temperature, telluradibismirane **5**, in the form of an insoluble brown powder, precipitated from the reaction mixture (Scheme 1). After the suspension

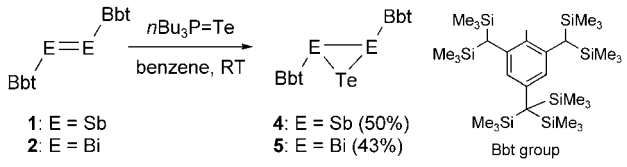

1: E = Sb
2: E = Bi

4: E = Sb (50%)
5: E = Bi (43%)

Scheme 1. Synthesis of telluradipnictiranes.

[*] Dr. T. Sasamori, E. Mieda, Dr. N. Takeda, Prof. Dr. N. Tokitoh
Institute for Chemical Research, Kyoto University
Gokasho, Uji, Kyoto 611-0011 (Japan)
Fax: (+81) 774-38-3209
E-mail: tokitoh@boc.kuicr.kyoto-u.ac.jp

[**] This work was supported by Grants-in-Aid for Scientific Research (Nos. 14078213 and 16750033), COE Research on "Elements Science" (No. 12CE2005), and 21st Century COE of Kyoto University Alliance for Chemistry from the Ministry of Education, Culture, Sports, Science and Technology, Japan. This manuscript was written at TU Braunschweig during the tenure of a von Humboldt Senior Research Award of one of the authors (N. Tokitoh), who is grateful to the von Humboldt Stiftung for their generosity and to Prof. Reinhard Schmutzler and Prof. Wolf-Walther du Mont for their warm hospitality.

 DOI: 10.1002/anie.200462122

was left to stand for 2 h, **5** was isolated as a pure material by filtration followed by washing with hexane (23.3 mg, 0.013 mmol, 43%). In this case, the tellurization reaction of **2** occurred at room temperature probably due to the fact that nBu$_3$P=Te is more soluble than elemental tellurium. In addition, no ditelluride **3** was observed in the ^{1}H NMR spectrum of the crude mixture. Distibene **1** was also tellurized by this method, giving the corresponding telluradistibirane **4**. Treatment of **1** with nBu$_3$P=Te under conditions similar to those applied to **2** afforded **4** as an orange powder in 50% yield. Three-membered ring compounds were obtained by the tellurization reaction of **1** and **2**, in contrast to the case of sulfurization reactions of **1**, which resulted in the formation of corresponding four-, five-, and six-membered ring compounds.[13] The formation of **4** and **5** is worthy of note not only as the synthesis of new members of three-membered heterocycles, but also as a new finding on the reactivity of distibenes and dibismuthenes toward the tellurization reaction.

The telluradistibirane **4** was found to be thermally stable in [D$_6$]benzene solution up to 140°C, and showed satisfactory ^{1}H and ^{13}C NMR spectral data. In addition, no change was observed in [D$_6$]benzene solution at 60°C under photoirradiation with a 100-W high-pressure Hg lamp. Although the telluradibismirane **5** was stable under ambient conditions, heating a solution of **5** in [D$_6$]benzene at 80°C for 1 h afforded a trace amount of ditelluride **3**. After the solution was heated at 100°C for 1 h, **5**, **2**, and **3** were observed in the ratio of 1:0.2:0.1. Additional heating of the solution at 110°C for 1 h gave an unidentified compound (**X**) together with **2** and **3** as the final products in a ratio of **X**:**2**:**3** = 1:2:2 as judged by ^{1}H NMR spectroscopy. Unfortunately, the reaction mechanism and the structure of the final product for the decomposition process of **5** are still unclear owing to the instability of compound **X** during the purification procedure. On the other hand, ^{125}Te NMR spectra of **4** measured in [D$_8$]toluene show a signal at $\delta = -622.3$ ppm within an upfield region, which is characteristic of such three-membered ring compounds. For example, some telluradisilirane ($\delta_{Te} = -784$ ppm)[4a] and telluradistannirane ($\delta_{Te} = -903$ ppm)[4b] derivatives were reported to show their ^{125}Te NMR signals in an up-field region, similar to the case of **4**. In addition, the ^{125}Te NMR chemical shift of dimesityltelluradistibirane (**6**), a model compound for **4**, was computed as $\delta = -700$ ppm by a GIAO calculation, which supports the experimentally observed chemical shift of **4**. Unfortunately, no signal was observed in the ^{125}Te NMR spectrum of **5** probably due to considerable peak broadening caused by the adjacent two bismuth atoms having nuclear spins of 9/2.

The molecular structures of **4** and **5** were determined by X-ray crystallographic analysis.[14] The structure of telluradibismirane **5** is shown in Figure 1 as a representative. The selected bond lengths and angles of **4** and **5** are depicted in Figure 2 together with the optimized structural parameters of model compounds, dimesityltelluradistibirane (**6**) and dimesityltelluradibismirane (**7**).[15] In both **4** and **5**, the two Bbt groups are oriented *trans* with regard to the central three-membered rings. The tellurirane skeletons of **4** and **5** are almost isosceles triangles with bond lengths (**4**: Sb–Sb

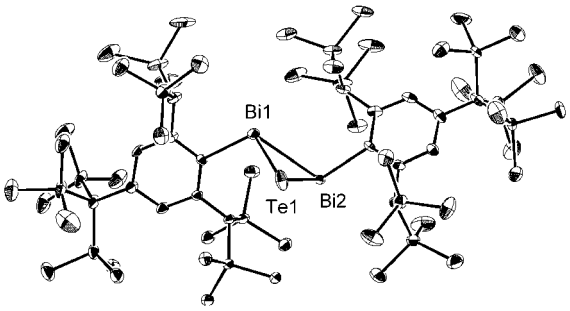

Figure 1. Molecular structure of **5** (ORTEP drawing; thermal ellipsoid plot (50% probability)).

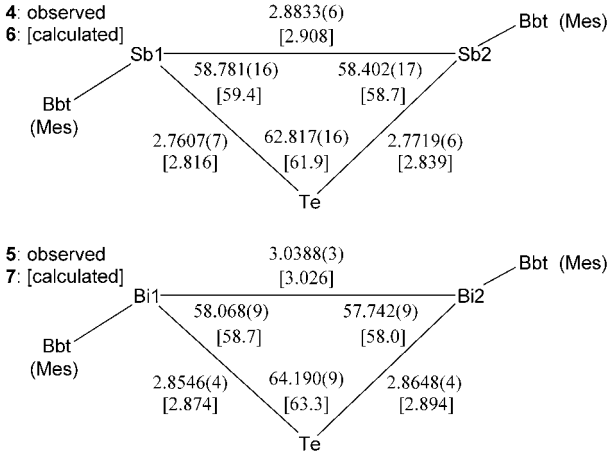

Figure 2. Selected bond lengths [Å] and bond angles [°] of **4** and **5**. Values in braces are calculated structural parameters for Mes-substituted model compounds **6** and **7**.

2.8833(6), Sb–Te 2.7607(7), 2.7719(6); **5**: Bi–Bi 3.0388(3), Bi–Te 2.8546(4), 2.8648(4) Å) that are comparable with previously reported values for the respective single bonds.[16] In addition, calculated structural parameters obtained by structural optimization (B3LYP) for the model compounds **6** and **7** supported the experimentally observed values obtained for the central three-membered-ring skeletons of **4** and **5**. These experimental and theoretical studies on the structures of **4** and **5** indicate that the telluradistibirane and telluradibismirane feature three-membered-ring character (**A**) rather than the π-complex character (**B**) as shown in Scheme 2. Interestingly, the telluradisilirane **8**, which is reported to be obtained by the reaction of Mes$_2$Si=SiMes$_2$ with elemental tellurium, features π-complex character (**B**) rather than the three-membered-ring character (**A**).[4a] It should be noted

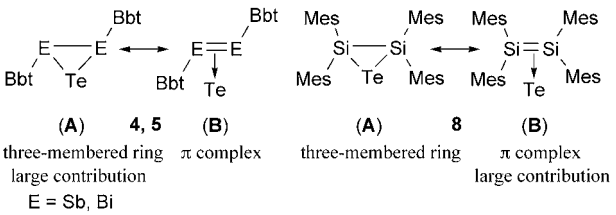

Scheme 2. Structures of telluriranes.

that the structural features of the corresponding tellurirane derivatives of heavier Group 15 elements differ from those of heavier group 14 elements.

In summary, we have synthesized the first stable telluradistibirane, **4**, and telluradibismirane, **5**, by a tellurization reaction of the reactive double-bond systems, BbtSb=SbBbt and BbtBi=BiBbt, by using $(n\mathrm{Bu})_3\mathrm{P}{=}\mathrm{Te}$ as a tellurization reagent. We have demonstrated here that telluradistibirane and telluradibismirane derivatives, which are three-membered ring compounds composed of much heavier elements, Sb, Bi, and Te, can be isolated without any oligomerization by using an appropriate steric protecting group and synthetic method. Further investigation of the physical and chemical properties of the newly obtained three-membered ring systems **4** and **5** is currently in progress.

Experimental Section

4: Addition of $n\mathrm{Bu}_3\mathrm{P}{=}\mathrm{Te}$ (33 mg, 0.10 mmol) to a solution of **1** (70.4 mg, 0.05 mmol) in benzene (2 mL) at room temperature, led to the immediate precipitation of an orange powder. After the reaction mixture had been left to stand for 2 h, telluradistibirane **4** was separated by filtration, and then further purified by GPLC (40 mg, 0.025 mmol, 50 %). **4**: orange crystals, m.p. 161 °C (decomp); ^{1}H NMR (300 MHz, [D$_6$]benzene): $\delta = 0.33$ (s, 54 H), 0.36 (s, 36 H), 0.37 (s, 36 H), 2.87 (s, 4 H), 6.96 ppm (s, 4 H); ^{13}C NMR (75 MHz, [D$_6$]benzene): $\delta = 2.09$ (q), 2.28 (q), 5.65 (q), 22.21 (s), 37.69 (d), 126.90 (d), 138.33 (s), 145.83 (s), 150.88 ppm (s); ^{125}Te NMR (94 MHz, [D$_8$]toluene): $\delta = -622.3$ ppm; UV/Vis (hexane): λ_{max} (ε) = 458 (680), 390 (3100), 346 nm (8500); HRMS (FAB): m/z: 1619.4440([M+H]$^+$), calcd for $C_{60}H_{135}{}^{121}Sb_2Si_{14}{}^{130}Te$ ([M+H]$^+$): 1619.4472; elemental analysis calcd (%) for $C_{60}H_{134}Sb_2Si_{14}Te$: C 44.48, H 8.34; found: C 44.23, H 8.23.

5: $n\mathrm{Bu}_3\mathrm{P}{=}\mathrm{Te}$ (23 mg, 0.06 mmol) was added to a solution of **2** (49.0 mg, 0.03 mmol) in benzene (2 mL) at room temperature. The color of the reaction mixture immediately changed to dark brown. After the resulting suspension had been stirred for 2 h, the reaction mixture was filtered, and the residue was washed with hexane (20 mL) to afford brown crystals of telluradibismirane **5** (23.3 mg, 0.013 mmol, 43 %). **5**: brown crystals, m.p. 156 °C (decomp); ^{1}H NMR (400 MHz, [D$_6$]benzene): $\delta = 0.33$ (s, 36 H), 0.34 (s, 54 H), 0.36 (s, 36 H), 2.29 (s, 4 H), 7.20 ppm (s, 4 H); ^{13}C NMR (100 MHz, [D$_6$]benzene): $\delta = 2.31$ (q), 2.41 (q), 5.65 (q), 22.10 (s), 43.15 (d), 126.54 (d), 145.08 (s), 151.68 (s), 161.38 ppm (s); UV/Vis (hexane): λ_{max} (ε) = 521 (2100), 450 (3200), 338 nm (18700); HRMS (FAB): m/z: 1795.6004 ([M+H]$^+$), calcd for $C_{60}H_{135}Bi_2Si_{14}{}^{130}Te$ ([M+H]$^+$): 1795.6004; elemental analysis calcd (%) for $C_{60}H_{134}Bi_2Si_{14}$ Te: C 40.16, H 7.53; found: C 40.12, H 7.48.

Received: September 27, 2004
Revised: December 12, 2004
Published online: May 20, 2005

Keywords: chalcogenides · heterocycles · multiple bonds · strained molecules · X-ray diffraction

[1] For a review of three-membered heterocycles, see: *Comprehensive Heterocyclic Chemistry II* (Eds.: A. R. Katritzky, C. W. Rees, E. F. Scriven), *Vol. 1A* (Ed.: A. Padwa), Pergamon, Oxford, **1996**.

[2] We have recently reported the synthesis and structures of the heavier analogues of a cyclopropabenzene, sila- and germa cyclopropabenzenes and bis(silacyclopropa)benzenes, unprecedented heavier congeners of cycloproparene derivatives, see: a) K. Hatano, N. Tokitoh, N. Takagi, S. Nagase, *J. Am. Chem. Soc.* **2000**, *122*, 4829; b) N. Tokitoh, K. Hatano, T. Sasaki, T. Sasamori, N. Takeda, N. Takagi, S. Nagase, *Organometallics* **2002**, *21*, 4309; c) T. Tajima, K. Hatano, T. Sasaki, T. Sasamori, N. Takeda, N. Tokitoh, *Chem. Lett.* **2003**, *32*, 220; d) T. Tajima, K. Hatano, T. Sasaki, T. Sasamori, N. Takeda, N. Tokitoh, N. Takagi, S. Nagase, *J. Organomet. Chem.* **2003**, *686*, 118. In addition, unique three-membered ring systems of heavier Group 14 elements have been reported as a review, see: A. Sekiguchi, V. Y. Lee, *Chem. Rev.* **2003**, *103*, 1429.

[3] For a review of selenirenes and tellurirenes, see: N. Tokitoh, W. Ando, N. Choi in *Comprehensive Heterocyclic Chemistry II* (Eds.: A. R. Katritzky, C. W. Rees, E. F. Scriven), *Vol. 1A* (Ed.: A. Padwa), Pergamon, Oxford, **1996**, pp. 173–240; N. Tokitoh, W. Ando in *Science of Synthesis, Houben-Weyl Methods of Molecular Transformations*, *Vol. 9* (Eds.: D. Belllus, S. V. Ley, R. Noyori, M. Regitz, E. Schaumann, I. Shinkai, E. J. Thomas, B. M. Trost, M. Regitz, G. Maas), Thieme, Stuttgart, **2001**, pp. 61–65.

[4] a) R. P. K. Tan, G. R. Gillette, D. R. Powell, R. West, *Organometallics* **1991**, *10*, 546; b) A. Schäfer, M. Weidenbruch, W. Saak, S. Pohl, H. Marsmann, *Angew. Chem. Int.* **1991**, *103*, 873; *Angew. Chem. Int. Ed. Engl.* **1991**, *30*, 834; c) A. Schäfer, M. Weidenbruch, W. Saak, S. Pohl, H. Marsmann, *Angew. Chem.* **1991**, *103*, 978; *Angew. Chem. Int. Ed. Engl.* **1991**, *30*, 962.

[5] T. Sasamori, Y. Arai, N. Takeda, R. Okazaki, Y. Furukawa, M. Kimura, S. Nagase, N. Tokitoh, *Bull. Chem. Soc. Jpn.* **2002**, *75*, 661.

[6] N. Tokitoh, Y. Arai, T. Sasamori, R. Okazaki, S. Nagase, H. Uekusa, Y. Ohashi, *J. Am. Chem. Soc.* **1998**, *120*, 433.

[7] N. Tokitoh, Y. Arai, R. Okazaki, S. Nagase, *Science* **1997**, *277*, 78.

[8] T. Sasamori, N. Takeda, N. Tokitoh, *J. Phys. Org. Chem.* **2003**, *16*, 450.

[9] M. Yoshifuji, K. Shibayama, N. Inamoto, *Chem. Lett.* **1984**, 603.

[10] N. Tokitoh, T. Sasamori, R. Okazaki, *Chem. Lett.* **1998**, 725.

[11] **3**: dark-green crystals, m.p. 238.6–240.0 °C (decomp); ^{1}H NMR (300 MHz, [D$_6$]benzene): $\delta = 0.34$ (s, 72 H), 0.35 (s, 54 H), 3.05 (s, 4 H), 7.05 ppm (s, 4 H); ^{125}Te NMR (94 MHz, [D$_6$]benzene): δ = 328.7 ppm; HRMS (FAB): m/z: 1505.5448 ([M+H]$^+$), calcd for $C_{60}H_{135}Si_{14}{}^{128}Te^{130}Te$ 1505.5443; elemental analysis calcd (%) for $C_{60}H_{134}Si_{14}Te_2$: C 47.91, H 8.98; found: C 48.20, H 9.05; the X-ray crystallographic analysis of **3** will be described elsewhere.

[12] For example, the synthesis of an alkylidenetelluragermirane derivative with tributylphosphine telluride has been reported; see: K. Kishikawa, N. Tokitoh, R. Okazaki, *Organometallics* **1997**, *16*, 5127.

[13] Treatment of **1** with S_8 in benzene afforded the corresponding 1,3,2,4-dithiadistibolane, 1,2,4,3,5-trithiadistibolane, and 1,2,3,5,4,6-tetrathiadistibinane derivatives; see: T. Sasamori, E. Mieda, N. Takeda, N. Tokitoh, *Chem. Lett.* **2004**, *33*, 104.

[14] Crystal data for **4** ($C_{60}H_{134}Sb_2Si_{14}Te$): $M_r = 1620.03$, $T = 103(2)$ K, monoclinic, $C2/c$ (no. 15), $a = 38.348(3)$, $b = 9.2753(5)$, $c = 47.689(3)$ Å, $\beta = 92.732(3)°$, $V = 16943.2(18)$ Å^3, $Z = 8$, $\rho_{calcd} = 1.270$ g cm^{-3}, $\mu = 1.205$ mm^{-1}, $\lambda = 0.71070$ Å, $2\theta_{max} = 50.0$, 51832 measured reflections, 13961 independent reflections, 793 refined parameters, GOF = 1.159, $R_1 = 0.0658$ and w$R_2 = 0.1420$ [$I > 2\sigma(I)$], $R_1 = 0.0757$ and w$R_2 = 0.1480$ (for all data), largest difference peak and hole 3.312 and −2.129 e Å^{-3}, respectively, (around Sb and Te atoms); crystal data for **5** ($C_{60}H_{134}Bi_2Si_{14}Te$): $M_r = 1794.49$, $T = 103(2)$ K, monoclinic, $C2/c$ (no. 15), $a = 39.199(2)$, $b = 9.2798(3)$, $c = 47.120(2)$ Å, $\beta = 92.517(2)°$, $V = 17123.9(13)$ Å^3, $Z = 8$, $\rho_{calcd} = 1.392$ g cm^{-3}, $\mu = 4.666$ mm^{-1}, $\lambda = 0.71070$ Å, $2\theta_{max} = 51.0$, 69668 measured reflections, 15682 independent reflections, 819 refined parameters, GOF = 1.121, $R_1 = 0.0381$ and w$R_2 = 0.0717$ [$I > 2\sigma(I)$], $R_1 = 0.0433$ and w$R_2 = 0.0736$ (for all data), largest difference peak and hole 2.230 and −1.456 e Å^{-3}, respectively, (around Bi and Te atoms). CCDC-

249239 (**4**) and -249238 (**5**) contains the supplementary crystallographic data for this paper. These data can be obtained free of charge from the Cambridge Crystallographic Data Centre via www.ccdc.cam.ac.uk/data_request/cif. The intensity data were collected on a Rigaku/MSC Mercury CCD diffractometer. The structure was solved by direct methods (SHELXS-97) and refined by full-matrix least-squares procedures on F^2 for all reflections (SHELXL-97).

[15] Structural optimization for **6** and **7** was carried out by using the Gaussian 98 program with density functional theory at the B3LYP level. The triple zeta basis sets ([3s3p]) for Sb and Bi, and double zeta basis sets ([2s2p]) for Te were used with effective core potentials; the 6-31G* basis set was used for C and H.

[16] Sb–Sb and Bi–Bi bond lengths are reported as 2.837 and 2.990 Å, respectively, in $Ph_2E–EPh_2$, see: H. Bürger, R. Eujen, G. Becker, O. Mundt, M. Westerhausen, C. Witthauer, *J. Mol. Struct.* **1983**, *98*, 265; F. Calderazzo, R. Poli, G. Pelizzi, *J. Chem. Soc. Dalton Trans.* **1984**, *11*, 2365; a few examples of compounds containing an E–Te bond (E = Sb, Bi) have been reported to date; Sb–Te bond lengths observed in a cluster compound are in the range of 2.75 – 72.78 Å, see: S. S. Dhingra, R. C. Haushalter, *J. Am. Chem. Soc.* **1994**, *116*, 3651; Bi–Te bond lengths observed in $(Dis_2Bi)_2Te$ ($Dis = CH(SiMe_3)_2$) are 2.872 and 2.889 Å, see: H. J. Breunig, I. Ghesner, E. Lork, *J. Organomet. Chem.* **2002**, *664*, 130.

Nanoparticles

Radical Mechanism of a Place-Exchange Reaction of Au Nanoparticles**

*Petre Ionita, Bruce C. Gilbert, and Victor Chechik**

The exchange reaction shown in Equation (1) is a convenient method to prepare functionalized metal nanoparticles, and its

(1)

mechanism has been studied by several research groups.[1–3] Murray and co-workers carried out detailed kinetic studies on the exchange of thiol-protecting groups on Au particles with other thiols.[4,5] The exchange was shown to be an associative (bimolecular) process, with both the incoming ligand and Au nanoparticles participating in the rate-determining step. As well as by evidence from kinetic studies, this mechanism is supported by the sensitivity of the place-exchange reaction to the electronic effects of the incoming ligand. The fact that the reaction is facilitated under oxidizing conditions, for example, in an electrochemical cell or in the presence of oxygen, is particularly intriguing.[6] To explain the apparent catalytic effect of oxidizing reagents, it was tentatively proposed that Au^{I} thiolates could act as reaction intermediates.

Recently, we applied a spin-labeling method to study an exchange reaction with disulfides.[7] We found with EPR spectroscopy that Au nanoparticles protected with weakly bound ligands (for example, phosphines or amines) undergo a rapid place-exchange reaction with disulfides. The S–S bond in the disulfide is broken during the reaction, and the two branches of the disulfide molecule do not adsorb adjacent to each other on the Au surface.[7,8]

We noticed, however, that although spin-labeled disulfides are very stable under exchange-reaction conditions, the EPR signal of the parent (spin-labeled) thiol decays rapidly during the reaction. The apparent destruction of the spin label (a nitroxide group) is most likely brought about by a redox reaction that involves either Au ions or organic free radicals. To detect the possible formation of free radicals during the exchange reaction of triphenylphosphane-protected Au nanoparticles with alkanethiols, we performed a series of EPR spin-trapping experiments.

The spin-trapping technique used in this study relies on the fast addition (trapping) of short-lived radicals to the diamagnetic spin trap DMPO (5,5-dimethyl-4,5-dihydro-3*H*-pyrrole-*N*-oxide). The product of such an addition is a persistent free radical, with a lifetime that is long enough that it can be detected by direct EPR measurements (Scheme 1).[9]

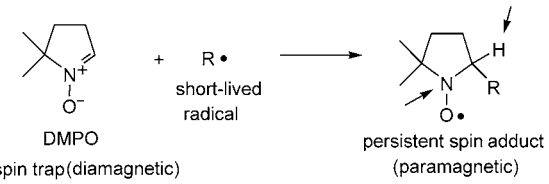

Scheme 1. Spin trapping of short-lived radicals by DMPO.

An important feature of the DMPO spin adducts is the sensitivity of the hyperfine coupling constants of the unpaired electron in the adduct with the hydrogen and nitrogen atoms (shown by arrows in Scheme 1) to the chemical composition of the short-lived radical. The EPR spectra of the spin adducts, therefore, provide useful information about the structure of the original radical.

In a typical spin-trapping experiment, a solution of *n*-butanethiol (2.5×10^{-3} M) in toluene/CH_2Cl_2 (4:1, *v*/*v*) was added to a mixture of triphenylphosphane-protected Au nanoparticles ($1.25–10 \times 10^{-4}$ M) and DMPO ($1.25–5 \times 10^{-2}$ M) in the same solvent mixture. The formation of spin adducts in the reaction mixture was monitored by EPR spectroscopic analysis.

A strong EPR signal was observed immediately after mixing (Figure 1a). Analysis of the hyperfine splitting allowed us to assign its structure to the spin adduct of DMPO and butanethiol radical $C_4H_9S^{\bullet}$ (Table 1). The spectrum was also identical to that of an authentic spin adduct

[*] Dr. P. Ionita, Prof. B. C. Gilbert, Dr. V. Chechik
Department of Chemistry
University of York
Heslington, York YO105DD (UK)
Fax: (+44) 1904-432-516
E-mail: vc4@york.ac.uk

[**] This work was supported financially by the EPSRC.

  DOI: 10.1002/anie.200500518

Figure 1. EPR spectra of DMPO–SC_4H_9 spin adducts a) trapped during the exchange reaction of triphenylphosphane-protected Au nanoparticles with butanethiol and b) prepared by the oxidation of butanethiol with PbO_2 in the presence of DMPO.

Table 1: EPR hyperfine coupling constants (G) of the DMPO spin adducts in toluene/CH_2Cl_2 (4:1, *v*/*v*).

	a_N [G]	$a_{H(1)}$ [G]	$a_{H(2)}$ [G]
DMPO–SC_4H_9	13.69[a] (13.73)[b]	11.69[a] (11.71)[b]	–
DMPO–OOC_4H_9	12.85[a] (12.72)[c]	9.31[a] (9.36)[c]	1.53[a] (1.44)[c]
DMPO–H	14.88[a] (14.83)[b]	19.32[a] (19.27)[b]	19.32[a] (19.27)[b]

[a] Observed during exchange reaction. [b] Observed on oxidation with PbO_2. [c] Previously reported values (toluene).[9]

DMPO–SC_4H_9 prepared by the oxidation of butanethiol with lead dioxide (Figure 1, Table 1). The exact amount of the spin adduct formed varied, but double integration of the EPR spectra revealed that the amount of the spin adduct accounted for 3–12 % of the amount of butanethiol used in the reaction. Importantly, no EPR signal was observed if the reaction was carried out in the absence of oxygen (for example, in an argon atmosphere).

As well as by the trapping of free radicals, the spin adducts can sometimes form by two alternative reactions,[10,11] namely, the Forrester–Hepburn mechanism (nucleophilic addition followed by oxidation) and the Eberson mechanism (inverse spin-trapping; Equations (2) and (3), respectively).

$$\mathrm{DMPO} + \mathrm{Nu}^- \rightarrow \mathrm{DMPO{-}Nu}^- \xrightarrow{\mathrm{ox}} \mathrm{DMPO{-}Nu}^{\cdot} \quad (2)$$

$$\mathrm{DMPO} \xrightarrow{\mathrm{ox}} \mathrm{DMPO}^{+\cdot} \xrightarrow{\mathrm{Nu}^-} \mathrm{DMPO{-}Nu}^{\cdot} \quad (3)$$

To test if the spin adducts are formed by the reaction given in Equation (2), we studied the nucleophilic addition of butanethiol to the DMPO spin trap under exchange-reaction conditions. NMR spectroscopic experiments showed the absence of a Michael addition on the reaction timescale. The Eberson mechanism can also be ruled out, as we observed no EPR signal with a control reaction mixture of the DMPO spin trap with Au nanoparticles in the presence of oxygen. This lack of a signal implies that the spin trap can not be oxidized under the reaction conditions.

We conclude, therefore, that the observed spin adducts are formed by trapping of the parent short-lived radicals formed during the exchange reaction. As the relative amount of the observed spin adduct was quite high (up to 12 % of the added alkanethiol, see above), the radical pathway must play a key role in the mechanism of the exchange reaction.

A likely route to RS$^{\cdot}$ radicals is the Au-nanoparticle-catalyzed oxidation of RSH with molecular oxygen. This mechanism is consistent with the fact that no radicals are formed when the exchange reaction is carried out in an inert atmosphere, and with reports that exchange reactions are significantly slower in the absence of air (confirmed by our own control experiments with alkanethiols and triphenylphosphane-protected Au nanoparticles). The oxidation of thiols is further supported by the formation of alkane disulfides (as observed by NMR spectroscopic analysis) when the exchange reaction is carried out in the absence of the spin trap.

To test the feasibility of such a mechanism, we set out to explore whether Au nanoparticles can catalyze the air oxidation of organic compounds. Indeed, the addition of *tert*-butyl hydroperoxide or sodium borohydride to a mixture of phosphine-protected Au nanoparticles and DMPO in air led to intense EPR spectra of the corresponding spin adducts of DMPO with *t*BuOO$^{\cdot}$ and H$^{\cdot}$ radicals (Figure 2). The structure

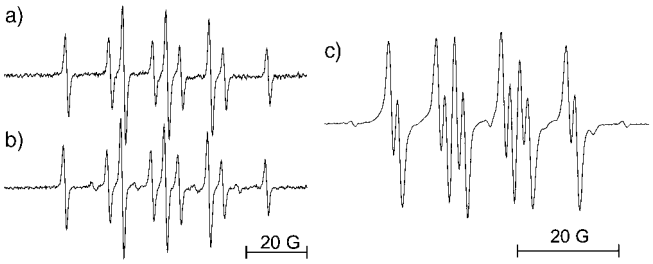

Figure 2. EPR spectra of the spin adducts DMPO–H produced by a) Au-nanoparticle-catalyzed oxidation of BH_4^- with air and b) oxidation of BH_4^- with PbO_2. c) EPR spectrum of DMPO–OO*t*Bu produced by nanoparticle-catalyzed oxidation of *t*BuOOH with air.

of the H$^{\cdot}$ adduct was confirmed by comparison with an authentic radical generated by the oxidation of $NaBH_4$ with PbO_2 (Figure 2, Table 1). The peroxide adduct was identified by comparison with previously reported data (Table 1).[9] No radicals were detected in the absence of Au nanoparticles or air. These experiments confirmed the oxidizing power of the mixture of Au nanoparticles and air.

On the basis of our findings, we propose a mechanism for the exchange reaction (Scheme 2). The reaction starts with the adsorption of oxygen on the phosphine-protected nanoparticle surface to form an active catalyst. This superoxide-type species then abstracts a hydrogen atom from the incoming ligand (alkanethiol) to form a sulfur-centred radical, which is then successfully trapped with DMPO. We speculate that in the absence of the spin traps, the sulfur-centred

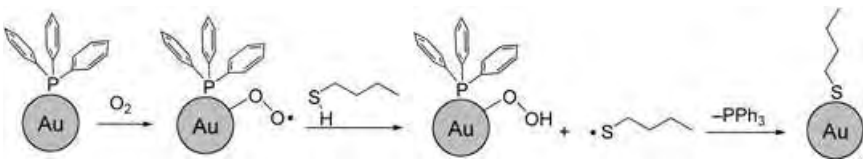

Scheme 2. Proposed mechanism of radical formation.

radicals rapidly replace the outgoing ligands (triphenylphosphane) from the Au surface.

This mechanism is consistent with several features of previously reported exchange reactions.[12,13] Meisel and co-workers described the oxidation of 4-amino-2,2,6,6-tetramethylpiperidine-1-oxyl (4-amino-tempo) to 4-oxo-2,2,6,6-tetramethylpiperidine-1-oxyl (4-oxo-tempo) with Au nanoparticles in the presence of oxygen.[14] The authors proposed that this reaction included Au nanoparticle mediated electron transfer from the NH_2 group to oxygen (to form a hydroperoxide radical), in a similar process to the mechanism given in Scheme 2. The electrocatalytic reduction of oxygen on Au nanoparticles was also reported by Murray and co-workers.[15]

Interestingly, we were unable to trap free radicals when the exchange reaction was carried out with thiol-protected Au nanoparticles. This failure to trap radicals could result from a number of factors, including the relatively slow kinetics of exchange reactions that involve thiol-protected nanoparticles, or the reduction of radicals by the outgoing ligand. There is, however, some indirect evidence for the involvement of free radicals in the reactions of thiol-protected Au nanoparticles, for example, the suppression of the exchange reaction in the absence of oxygen, the destruction of the nitroxide spin labels during the exchange of thiols with Au nanoparticles, and the oxidation of 4-amino-tempo (see above). It is, therefore, likely that at least some features of the proposed mechanism are quite general and not restricted to the phosphine-protected nanoparticles.

In conclusion, we have shown that the exchange reaction of phosphine-protected Au nanoparticles with alkanethiols in air proceeds by a free-radical pathway. Oxidation of the alkanethiols by molecular oxygen adsorbed on the nanoparticles is proposed as the key step in these reactions. The feasibility of such a reaction is demonstrated by the Au-nanoparticle-catalyzed oxidation of BH_4^- and *t*BuOOH with air.

Received: February 10, 2005
Published online: May 4, 2005

Keywords: EPR spectroscopy · gold · ligand exchange · nanostructures · spin trapping

[1] M. Hasan, D. Bethell, M. Brust, *J. Am. Chem. Soc.* **2002**, *124*, 1132.
[2] R. L. Donkers, Y. Song, R. W. Murray, *Langmuir* **2004**, *20*, 4703.
[3] V. Chechik, H. J. Wellsted, A. Korte, B. C. Gilbert, H. Caldararu, P. Ionita, A. Caragheorgheopol, *Faraday Discuss.* **2004**, *125*, 279.
[4] Y. Song, R. W. Murray, *J. Am. Chem. Soc.* **2002**, *124*, 7096.
[5] Y. Song, T. Huang, R. W. Murray, *J. Am. Chem. Soc.* **2003**, *125*, 11694.
[6] M. S. El-Deab, T. Ohsaka, *Electrochem. Commun.* **2002**, *4*, 288.
[7] P. Ionita, A. Caragheorgheopol, B. C. Gilbert, V. Chechik, *J. Am. Chem. Soc.* **2002**, *124*, 9048.
[8] V. Chechik, *J. Am. Chem. Soc.* **2004**, *126*, 7780.
[9] G. R. Buettner, *Free Radical Biol. Med.* **1987**, *3*, 259.
[10] P. Ionita, B. C. Gilbert, A. C. Whitwood, *Perkin Trans. 2* **2000**, 2436.
[11] P. Ionita, B. C. Gilbert, A. C. Whitwood, *Lett. Org. Chem.* **2004**, *1*, 70.
[12] J. H. Chen, T. Jiang, G. Wei, A. A. Mohamed, C. Homrighausen, J. A. K. Bauer, A. E. Bruce, M. R. M. Bruce, *J. Am. Chem. Soc.* **1999**, *121*, 9225.
[13] M. J. Hostetler, A. C. Templeton, R. W. Murray, *Langmuir* **1999**, *15*, 3782.
[14] Z. Y. Zhang, A. Berg, H. Levanon, R. W. Fessenden, D. Meisel, *J. Am. Chem. Soc.* **2003**, *125*, 7959.
[15] J. E. Hutchison, T. A. Postlethwaite, R. W. Murray, *Langmuir* **1993**, *9*, 3277.

Aqueous Foams

Aqueous Foams Stabilized Solely by Silica Nanoparticles**

Bernard P. Binks and Tommy S. Horozov*

Foams occur as end products or during the processing of products in a wide range of areas including the detergent, food, and cosmetic industries. They are mixtures of immiscible fluids in which a vapor phase is dispersed as millimeter-sized bubbles in the continuous phase of a liquid.[1] To prevent collapse of the foam, surfactants or proteins are usually added whose molecules cover the liquid/vapor interfaces. Small solid particles exhibit some similarities with such molecules by adsorbing at interfaces and acting as excellent emulsifiers of oil and water.[2] However, the use of small solid particles in stabilizing aqueous foams in air–water–particle systems in the absence of any other surface-active substance has not been demonstrated previously. Here we describe the preparation and stability of aqueous foams stabilized solely by nanoparticles of silica that exhibit different extents of hydrophobicity. By using a novel dispersion method, suitably hydrophobic particles can be dispersed in water and very stable foams can be formed in which aggregates of particles adsorb at the surfaces of micrometer-sized bubbles.

Certain small solid particles have been used in conjunction with surfactant molecules, which they adsorb at fluid/fluid interfaces, to either stabilize or destabilize drops in emulsions and bubbles in foams.[2] It is only recently, however, that their precise role is being elucidated in surfactant-free systems. Unlike surfactant molecules, most colloidal particles, although surface-active, are not amphiphilic. The exceptions

[*] Prof. B. P. Binks, Dr. T. S. Horozov
Surfactant & Colloid Group
Department of Chemistry
University of Hull
Hull HU6 7RX (UK)
Fax: (+44) 1482-466-410
E-mail: b.p.binks@hull.ac.uk

[**] We thank Wacker-Chemie, Burghausen, for donating the silica particles.

  DOI: 10.1002/anie.200462470

are so-called Janus particles, in which two separated regions of different wettability exist on the surface of a given particle. Such particles are both surface-active and amphiphilic.[2] The particles used in this work are not amphiphilic, but are homogeneously coated. In contrast to surfactant molecules, adsorption of solid particles to fluid/liquid interfaces does not change the interfacial tension.[3] A key parameter that affects adsorption appears to be the contact angle, θ (measured through water), that particles exhibit at the interface. The angle θ increases with the hydrophobicity of the particle. If θ is large enough, particles prefer to stay in air (or oil) rather than in water. However, if adsorbed, they are strongly held at the fluid interface. The energy ΔG required to remove a small spherical particle of radius r from an air/water surface is at a maximum at $\theta = 90°$.[2] It can be shown that for the particles used here for which $r \approx 10^{-7}$ m and $\theta = 90°$, ΔG is several orders of magnitude greater than the thermal energy. Hence, the particles are practically irreversibly adsorbed, in marked contrast to surfactant molecules that adsorb and desorb reversibly.

The well-documented flotation method relies on the attachment of mineral particles to air bubbles by adding to the slurry surface-active molecules as frothing agents and collectors.[4] Only two examples have been reported in which particles are employed as foam stabilizers in water-containing systems. Wilson[5] utilized relatively large, charged polystyrene latex particles (several μm) and varied the pH and the concentrations of salt and added surfactant to optimize foaming. These results indicate that θ approaches 90° for systems that display high foamability and stability. Sun and Gao[6] used particles (diameter $d \geq 1$ μm) of either teflon, polyethylene, or polyvinylchloride, but needed to add 20–40 wt% of ethanol to the aqueous dispersions to obtain a foam in sufficient quantity and of reasonable stability. Similarly, air-in-liquid metal (e.g. Al) foams are thought to be stabilized by ceramic particles such as SiC, but the underlying physics is not understood and surface-active impurities are commonly present.[7]

We show here the effect of the inherent hydrophobicity of silica nanoparticles on their ability to stabilize aqueous foams. Particles of intermediate hydrophobicity act as emulsifiers of oil and water by the formation of close-packed adsorbed layers at interfaces, which prevents coalescence of droplets.[8] They also adsorb around air bubbles and drastically slow down or halt completely the transfer of gas between them.[9] Hydrophilic silica particles contain surface silanol groups that react with silanizing agents to impart hydrophobicity. The latter is quantified in terms of the residual content of SiOH, which varies here from 100 to 14%. On the basis of a simple theory for predicting the contact angle that a particle exhibits at an air/water surface when the surface-energy components of the solid are known,[10] we calculate that $\theta = 13°$ for the most hydrophilic silica particles and $\theta = 84°$ for the most hydrophobic ones used here (see inset in Figure 1). In acknowledgement of the fact that more hydrophobic particles are required to adsorb for foam stabilization, we prepare foams either with particles initially in air or by dispersing them in water with the aid of ethanol, which is deliberately removed *before* the foaming tests.

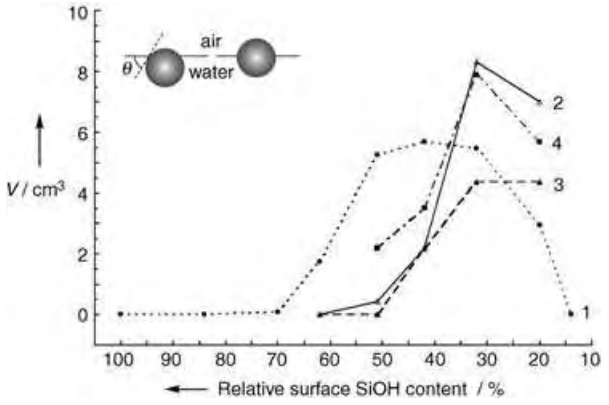

Figure 1. Volume of foam (V) produced at room temperature from 7 cm³ of water in the presence of fumed silica nanoparticles of different hydrophobicity (given as the percentage of SiOH on their surfaces) at 3 wt/v% (hand-shaken, 1) and 0.86 wt/v% (homogenized, 2–4). The conditions and time delays after the formation of the foam are 1) no salt, 0 and 1 h (----), 2) no salt, 10 s (——), 3) no salt, 27 h (– – –), and 4) 8.5 mM NaCl, 13.5 h (–•–•). The inset shows schematically the position of a particle at an air–water surface if hydrophilic (high % SiOH, left) or more hydrophobic (low % SiOH, right).

Figure 1 shows the volume of foam produced as a function of the hydrophobicity of the nanoparticles under different conditions. In the absence of salt and for hand-shaken systems (3 wt/v% particles initially in air, curve 1) no foam is formed for hydrophilic (≥ 70% SiOH) or very hydrophobic particles (14% SiOH, dry powder remained on water surface), but the foamability increases progressively for particles of intermediate hydrophobicity. These foams contain approximately 30% water when formed and are subsequently very stable to collapse. An alternative method is to disperse the particles in a solution of water/ethanol, which allows the more hydrophobic particles to become wetted, then to remove the ethanol by repeated sedimentation–redispersion cycles in pure water, and aerate the dispersion by using an Ultra Turrax homogenizer. The initial volume of foam in this case (0.86 wt/v% particles, curve 2) shows a more pronounced maximum with respect to the hydrophobicity of the particles, with the most effective being those that contain 32% SiOH.

The foams obtained with 32 and 20% SiOH are wet and even after a long time contain around 60% water. They are very stable to collapse. The decrease in their volume is a result of water drainage and bubble compaction, but not to loss of air (Figure 1, curve 3, 27 h). This is also evident in Figure 2 in which photographs of the vessels for particles of different hydrophobicities (% SiOH, given) are shown at 10 minutes (upper) and 13.5 hours (lower) after homogenization. For particles with a surface content of SiOH of greater than 42%, it can be seen that they reside mainly in the water phase (cloudy) with little foam, whereas for particles with 32 and 20% SiOH they are located entirely within the white, creamy foam that envelopes the air bubbles. The size of the bubbles decreases progressively with an increase in hydrophobicity of the particles.

The stability of the foam prepared with particles that contain 32% SiOH was measured by using the Dispersion Stability Analyzer 24 (DiStA 24)[11] and compared to that of

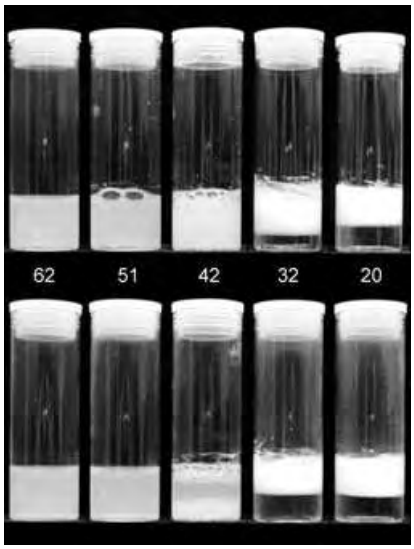

Figure 2. Appearance of vessels at room temperature at 10 minutes (upper) and 13.5 h (lower) after homogenization of aqueous dispersions containing 0.86 wt/v% silica particles (of different hydrophobicities, given as the percentage of SiOH (62, 51, 42, 32, and 20%) on their surfaces) in pure water.

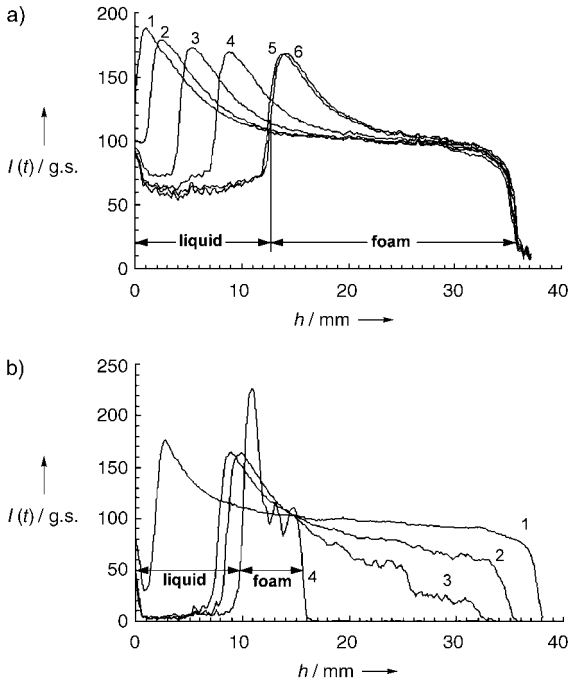

Figure 3. Vertical profiles (versus height, *h*) of scattered light in gray-scale (g.s.) units measured using DiStA 24 at 25 °C at different times after generation of the foam by homogenization: a) with 1 wt/v% silica particles in pure water containing 32% SiOH on their surfaces: 1) 30 s, 2) 10.5 min, 3) 31 min, 4) 1 h, 5) 24 h, and 6) 62 h; b) with 5.8 wt% aqueous SDS: 1) 36 s, 2) 10.6 min, 3) 31 min, and 4) 18 h.

foams made with the popular surfactant sodium dodecyl sulphate (SDS). This analyzer uses a scanner to take side images of the foam at preset time intervals. The images are automatically analyzed, and the vertical profile of light scattered from the sample is obtained. The destructive processes that occur in the foam can be detected and monitored well before it is possible to observe them with the naked eye.

The vertical profiles of the scattered light intensity are shown in Figure 3 for the silica-stabilized foam (part a) and that stabilized by the surfactant (part b) at different times after formation of the foam. In both cases the intensity of the light close to the bottom of the sample decreases with time, while the maximum light intensity shifts upwards. These changes are a result of the drainage of water from between the bubbles in the foam, with a clear serum appearing at the bottom in contact with a concentrated foam at the top (see Figure 2). In the case of the particle-stabilized foam, this drainage takes place relatively slowly and is over after several hours. By contrast, the fast drainage of water out of the foam in the surfactant-stabilized case (few minutes) leads to a significant shift upwards of the intensity maximum and a drastic decrease in the intensity in the upper part of the profile. The collapse of the foam is accompanied by the appearance of local maxima and minima. Such changes in the light intensity are a direct consequence of coarsening of the foam as a result of both bubble coalescence and disproportionation. Adsorbed particles clearly prevent the occurrence of both of these phenomena.

Optical microscope images of bubbles in foams stabilized by particles with 32% SiOH, in the presence and absence of salt, are given in Figure 4a–c. Distinct nonspherical bubbles, with diameters of 5–50 μm, are a feature of these systems. Their surfaces are rough as a result of ripples. Similar ripples have been observed in the case of a planar air/water monolayer of silica nanoparticles after compression (Figure 4d) which suggests that the bubbles are covered with dense particle layers compressed to a high surface pressure that is close to the surface tension of water (71.9 $mN\,m^{-1}$).[12]

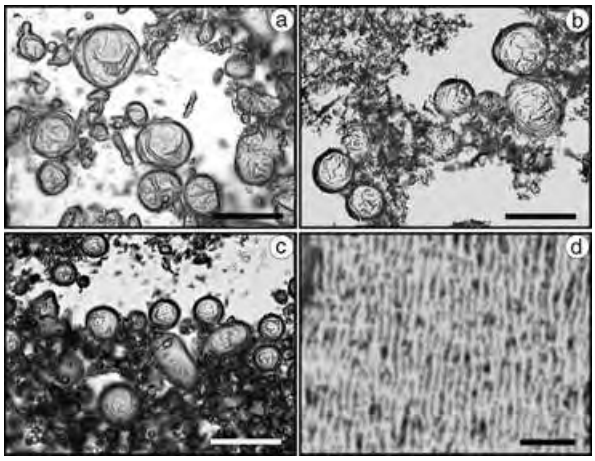

Figure 4. Optical microscopy images of aqueous foams stabilized by silica nanoparticles that contain 32% SiOH on their surfaces. Conditions and time after formation by homogenization: a) no salt, 3 wt/v% particles, 40 h, b) 8.5 mM NaCl, 0.86 wt/v% particles, 5 min, and c) 1 M NaCl, 0.37 wt/v% particles, 5 min. Also shown in d) is the image of a planar monolayer of silica nanoparticles (with 50% SiOH) at the air–water surface after compression to a surface pressure of 70 $mN\,m^{-1}$. The corrugations are parallel to the trough barriers. All scale bars: 50 μm.

Stable bubbles are probably formed by coalescence between smaller bubbles that are covered with dilute particle layers during homogenization.[13] As the bubble area decreases, excess particles cannot be released as they are irreversibly adsorbed and so the surface corrugates to increase in area. As silica particles in water and bare air–water surfaces are negatively charged, it is anticipated that addition of salt to water should enhance the transfer of particles to the surface by reducing the energy barrier to adsorption.[14] It may also increase their contact angle as hydrophobicity increases, with both of these factors leading to improved stabilization of the foam. Indeed, this is the case as seen in Figure 1 (curve 4) and in Figure 5, in which even a small amount of electrolyte

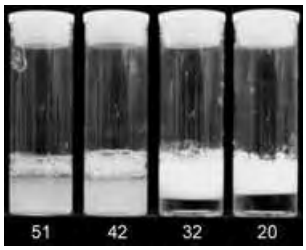

Figure 5. Appearance of vessels at room temperature in systems containing 0.86 wt/v% silica nanoparticles of different hydrophobicity (given as the percentage SiOH) in 8.5 mM NaCl at $t = 13.5$ h after formation of the foam by homogenization. Note that particles reside mainly in water for SiOH contents of 51 and 42%, but are entirely within the foam for SiOH contents of 32 and 20%.

(8.5 mM) improves both the foamability and foam stability. Particles that are initially relatively hydrophilic (42 and 51% SiOH) can now stabilize foams to a higher extent than in the absence of salt (compare with Figure 2).

Nanoparticles are effective foaming agents of air and water, and by controlling their hydrophobicity, foams that are completely stable to collapse, coalescence, and disproportionation can be prepared. We plan to investigate further the influence of pH and the concentration of salt in these systems. Manipulation of the behavior of particles adsorbed at fluid interfaces in this way enables the development of a novel range of foams for use in food, detergent, and cosmetic formulations.[15]

Experimental Section

Methods: Fumed silica particles of primary diameter 20–50 nm and surface area 200 $m^2 g^{-1}$ were supplied by Wacker-Chemie. During preparation, some particles fuse irreversibly to form aggregates (few hundred nm) of particles. The different hydrophobic grades were obtained after silanization of hydrophilic silica with dichlorodimethylsilane.[8] Their surface content of silanol varied from 100 to 14%. Water was passed through a reverse osmosis unit and then a Milli-Q reagent system—its pH value was 5.6 owing to dissolved CO_2. The salt used was NaCl (99.9% pure) from Prolabo. Foams were prepared in sample tubes (inner diameter:2.5 cm, height:7.5 cm) either by shaking by hand the system of powdered particles resting on 7 cm^3 of water (20 s, frequency:5 Hz) or by aerating the same volume of an aqueous dispersion of particles by using an Ultra Turrax homogeniser (Janke & Kunkel) with a 1.8-cm-diameter head operating at 11000 rpm for 3 minutes (6 × 30 s with 30 s rest periods). In the latter, the powders were wet with ethanol, then mixed with water to give a suspension that contained < 2 wt% ethanol. The ethanol was removed by repeated sedimentation–redispersion cycles in pure water to attain less than 10^{-4} wt% residual ethanol. Photographs of the vessels were taken with a Kodak DX4330 digital camera. The surfactant-stabilized foam was formed by homogenizing 5 cm^3 of an aqueous solution of SDS (Lancaster, 99%) at 8000 rpm for 1 minute. The stability of the foams was measured with the automated Dispersion Stability Analyser 24 developed recently.[11] An optical microscope (Nikon Optiphot-2) was used to observe the structure around and between the bubbles in the foams. A planar monolayer at the air–water surface was formed by the spreading of a dispersion of silica particles in chloroform and compressing in a Langmuir trough. The images were captured by the same microscope in reflected light.

Received: October 29, 2004
Revised: March 22, 2005
Published online: May 11, 2005

Keywords: foams · interfaces · nanostructures · silica · surface chemistry

[1] D. Exerowa, P. M. Kruglyakov, *Foams and Foam Films*, Elsevier, Amsterdam, **1997**.
[2] B. P. Binks, *Curr. Opin. Colloid Interface Sci.* **2002**, *7*, 21–41.
[3] E. Vignati, R. Piazza, T. P. Lockhart, *Langmuir* **2003**, *19*, 6650–6656.
[4] *Colloidal Science of Flotation* (Eds.: A. V. Nguyen, H-J. Schulze), Marcel Dekker, New York, **2003** *Surfactant Science Series*, *Vol. 118*.
[5] J. C. Wilson, Ph.D. thesis, University of Bristol, UK, **1980**.
[6] Y. Q. Sun, T. Gao, *Metall. Mater. Trans. A* **2002**, *33 A*, 3285–3292.
[7] *Cellular Metals: Manufacture, Properties, Applications* (Eds.: J. Banhart, N. A. Fleck, A. Mortensen), MIT-Verlag, Berlin, **2003**.
[8] B. P. Binks, S. O. Lumsdon, *Langmuir* **2000**, *16*, 8622–8631.
[9] a) Z. Du, M. P. Bilbao-Montoya, B. P. Binks, E. Dickinson, R. Ettelaie, B. S. Murray, *Langmuir* **2003**, *19*, 3106–3108; b) E. Dickinson, R. Ettelaie, T. Kostakis, B. S. Murray, *Langmuir* **2004**, *20*, 8517–8525.
[10] B. P. Binks, J. H. Clint, *Langmuir* **2002**, *18*, 1270–1273.
[11] T. S. Horozov, B. P. Binks, *Langmuir* **2004**, *20*, 9007–9013.
[12] R. Aveyard, J. H. Clint, D. Nees, V. N. Paunov, *Langmuir* **2000**, *16*, 1969–1979.
[13] We anticipate that the fumed silica particles will aggregate in bulk and that the extent of aggregation may depend on the hydrophobicity of the particle and the concentration of the electrolyte. Whether discrete primary particles or aggregates of particles, or both, adsorb around air bubbles is not known, but work to determine this is in progress. One consequence of particle aggregation is the increased viscosity of the aqueous phase (gelling) which results in slower drainage of foam films and increased stability of the foam.
[14] V. N. Paunov, B. P. Binks, N. P. Ashby, *Langmuir* **2002**, *18*, 6946–6955.
[15] Note added in proof: Since the submission of this article, a paper by Alargova et al. appeared which describes the stabilization of aqueous foams by micron-long polymer rod particles: R. G. Alargova, D. S. Warhadpande, V. N. Paunov, O. D. Velev, *Langmuir* **2004**, *20*, 10371–10374.

Metalloporphyrinoids

Dicopper and Disilver Complexes of Octaphyrin(1.1.1.1.1.1.1.1): Reversible Hydrolytic Cleavage of the Pyrrolic Ring to a Keto–Imine**

*Soji Shimizu, Yasuo Tanaka, Katsuyuki Youfu, and Atsuhiro Osuka**

Of the various expanded porphyrins developed in recent years,[1] octaphyrins hold a unique position in view of their dynamic figure-of-eight conformations as well as their ability to coordinate two metal ions,[2] while some octaphyrins are known to be planar and aromatic.[3] Curiously, the metalation of figure-of-eight octaphyrins is often accompanied by rather unexpected skeletal rearrangements.[4] Vogel et al. revealed an interesting equilibrium of the dipalladium complex of octaphyrin(1.1.1.0.1.1.1.0) and its bis-spiro derivative, and isolated the dinickel complex of a spirodicorrole upon metalation of dioxooctaphyrin(1.1.1.0.1.1.1.0).[5] Both processes involved large skeletal rearrangements. We also reported that complexation of [36]octaphyrin(1.1.1.1.1.1.1.1) **1** with copper provided the dicopper(II) complex **2**, which underwent a quantitative thermal splitting reaction into two copper(II) porphyrins, **3**, through an unprecedented metathesis that involved the scission and formation of at least two carbon–carbon bonds.[6] This reaction is thought to be driven by severe distortion of the complex **2**. Herein, we report the dimetalation of perfluorinated [36]octaphyrin(1.1.1.1.1.1.1.1) **4**[7] with copper(II) ions which leads to unusual hydrolytic ring opening of one pyrrole ring to give the keto–imine form. We also report facile dimetalations of **1** and **4** with silver ions to quantitatively provide figure-of-eight disilver complexes.

A solution of **4** in CH_2Cl_2 was stirred with $Cu(OAc)_2$ (50 equiv) and NaOAc for 6 hours at room temperature to provide two dicopper complexes, **5** and **6**, in respective yields of 58 and 14%. The parent-ion peak in the ESI-TOF (electrospray ionization/time of flight) mass spectrum for complex **5** was observed at $m/z = 2375$ ($[M-H]^-$), which is 16 mass units larger than the expected mass of a dicopper complex (see Table 1). The absorption spectrum of **5** comprises a broad band at 396 nm and a less intense band at 699 nm and is significantly different from that of **4** (Figure 1). The crystal structure of **5** was determined by single crystal X-ray diffraction analysis and is shown in Figure 2.[8] The complex exhibits a bent U-shaped ellipsoidal conformation, in which one pyrrole ring is hydrolytically cleaved to give a keto–imine. One of the two copper ions (Cu1) is bound to the keto-carbonyl oxygen atom (O1) and the nitrogen atoms of the nearby tripyrrolic subunit, while Cu2 is bound to the imine nitrogen atom (N5) and the nearby second tripyyrolic subunit. The coordination-bond lengths are in the range of 1.92–2.02 Å, and the distance between the two Cu ions is 5.41 Å.

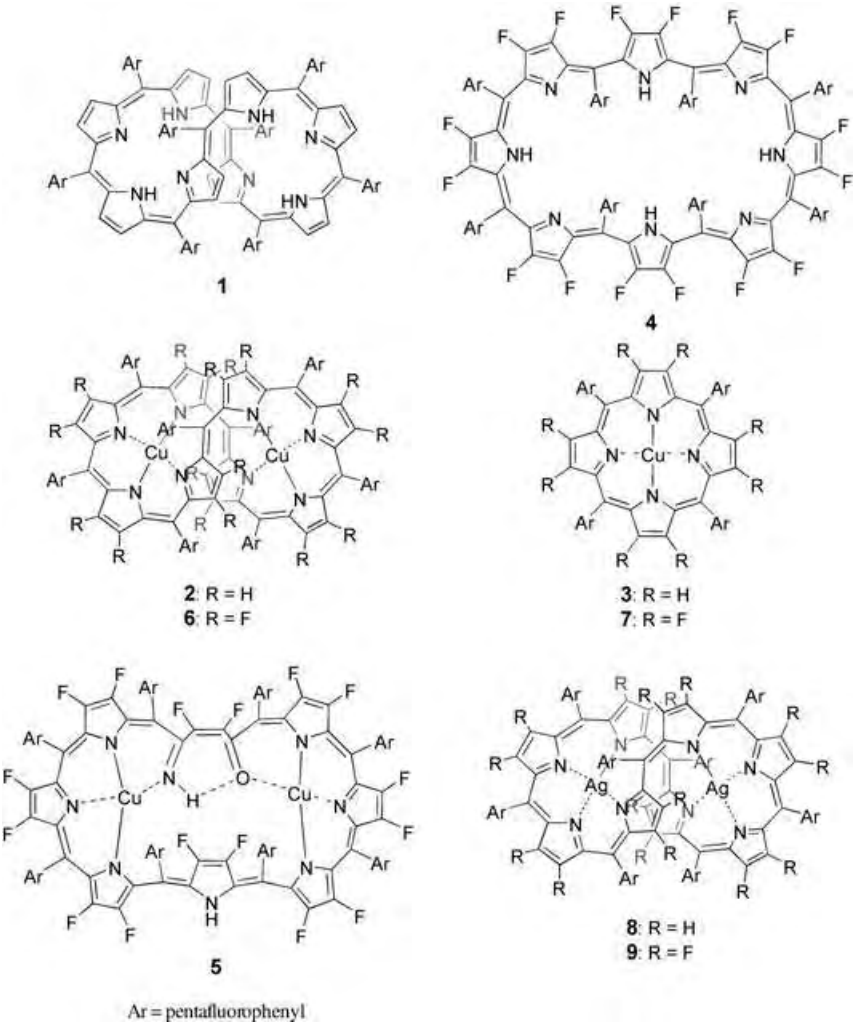

[*] S. Shimizu, Y. Tanaka, K. Youfu, Prof. A. Osuka
Department of Chemistry, Graduate School of Science
Kyoto University, and
Core Research for Evolutional Science and Technology (CREST) (Japan)
Science and Technology Agency, Sakyo-ku, Kyoto 606-8502 (Japan)
Fax: (+81) 75-753-3970
E-mail: osuka@kuchem.kyoto-u.ac.jp

[**] This work was partly supported by a grant-in-aid (B; No. 15350022) from the Ministry of Education, Culture, Sports, Science, and Technology (Japan). We thank Dr. Ko Furukawa at the Institute for Molecular Science for SQUID and ESR measurements. S.S. and K.Y. thank the JSPS for Research Fellowships for Young Scientists.

Supporting information for this article is available on the WWW under http://www.angewandte.org or from the author.

  DOI: 10.1002/anie.200500676

Table 1: Selected physical data for **5**, **8**, and **9**.

5: UV/Vis (CH_2Cl_2): λ_{max} (ε): 396 (6.25), 699 nm (2.16×10^{-4} $M^{-1}cm^{-1}$); HRMS (ESI-TOF): *m/z* calcd for $C_{88}N_8F_{56}OCu_2H$: 2374.7966; found: 2374.7966 (100%) $[M-H]^-$.

8: ^1H NMR (600.17 MHz, $CDCl_3$, 298 K): $\delta=7.98$ (d, $J=5.0$ Hz, 2H), 6.82 (d, $J=4.1$ Hz, 2H), 6.81 (d, $J=4.1$ Hz, 2H), 6.58 (d, $J=5.0$ Hz, 2H), 6.57 (d, $J=4.6$ Hz, 2H), 6.51 (d, $J=5.0$ Hz, 2H), 6.26 (d, $J=4.6$ Hz, 2H), 5.64 ppm (dd, $J_1=3.9$ Hz, $J_2=4.1$ Hz, 2H); ^{19}F NMR (564.73 MHz, $CDCl_3$, 298 K, C_6F_6): $\delta=-131.14$ (d, $J=22.5$ Hz, 2F; *o*-F), -136.28 (d, $J=22.5$ Hz, 2F; *o*-F), -136.86 (d, $J=19.1$ Hz, 2F; *o*-F), -138.10 (br d, $J=82.4$ Hz, 2F; *o*-F), -138.72 (m, 4F; *o*-F), -139.61 (d, $J=15.6$ Hz, 2F; *o*-F), -142.86 (s, 2F; *o*-F), -151.31 (t, $J=19.1$ Hz, 2F; *p*-F), -152.39 (t, $J=20.8$ Hz, 2F; *p*-F), -152.57 (t, $J=20.8$ Hz, 2F; *p*-F), -152.73 (br s, 2F; *p*-F), -160.30 (m, 2F; *m*-F), -161.32 (m, 2F; *m*-F), -161.53 (m, 4F; *m*-F), -161.77 (m, 2F; *m*-F), -162.37 (br s, 2F; *m*-F), -163.26 (m, 2F; *m*-F), -166.23 ppm (br d $J=93.2$ Hz, 2F; *m*-F); UV/Vis (CH_2Cl_2): λ_{max} (ε): 408 (0.57), 780 (0.88), 1151 nm (0.08×10^{-5} $M^{-1}cm^{-1}$); HRMS (ESI-TOF): *m/z* calcd for $C_{88}H_{16}N_8F_{40}Ag_2$: 2157.8967; found: 2157.8963 (100%) $[M]^-$.

9: ^{19}F NMR (564.73 MHz, $CDCl_3$, 298 K, C_6F_6): $\delta=-131.01$ (d, $J=22.4$ Hz, 2F; *o*-F), -136.68 (s, 2F; β-F), -137.94 (d, $J=22.5$ Hz, 2F; *o*-F), -138.85 (d, $J=100.1$ Hz, 2F; β-F), -139.35 (d, $J=19.0$ Hz, 2F; *o*-F), -139.72–-139.99 (m, 6F; *o*-F), -141.40 (dd, $J_1=15.5$ Hz, $J_2=88.8$ Hz, 2F; *o*-F), -141.43 (s, 2F; β-F), -143.19 (s, 2F; β-F), -143.35 (d, $J=20.7$ Hz, 2F; *o*-F), -143.80 (s, 2F; β-F), -144.19 (s, 2F; β-F), -144.91 (s, 2F; β-F), -147.86 (s, 2F; β-F), -148.66 (t, $J=17.3$ Hz, 2F; *p*-F), -149.47–-149.66 (m, 6F; *p*-F), -160.15 (m, 2F; *m*-F), -160.95 (m, 4F; *m*-F), -161.20 (m, 2F; *m*-F), -161.38 (m, 2F; *m*-F), -161.63 (m, 2F; *m*-F), -161.87 (br d, $J=82.9$ Hz, 2F; *m*-F), -163.42 ppm (br s, 2F; *m*-F); UV/Vis (CH_2Cl_2): λ_{max} (ε): 328 (0.47), 422 (0.73), 791 nm (1.24×10^{-5} $M^{-1}cm^{-1}$); HRMS (ESI-TOF): *m/z* calcd for $C_{88}N_8F_{56}Ag_2$: 1222.8721; found: 1222.8714 (100%) $[M]^{2-}$.

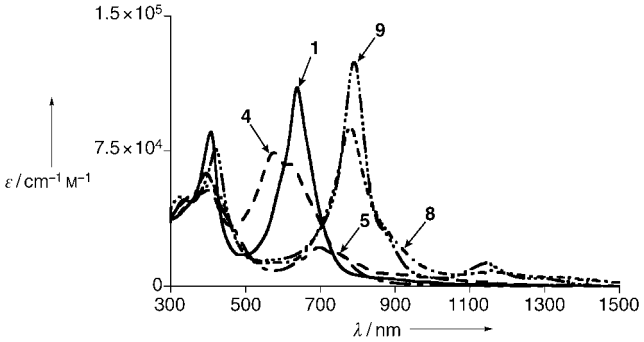

Figure 1. UV/Vis absorption spectra of **1** and **4**, and complexes **5**, **8**, and **9** in CH_2Cl_2.

Coordination features of the two copper ions in **5** are likely closer to a square-planar geometry than the highly distorted structure of **2**. The mean planes defined by Cu1, N2, N3, and N4, and by Cu2, N6, N7, and N8, are relatively flat and almost parallel to each other. The ligating carbonyl oxygen atom O1 and imine nitrogen atom N5 are somewhat deviated from these planes (O1 by 0.8 Å; N5 by 1.2 Å). Interestingly, **5** was quantitatively demetalated to give **4** upon treatment with trifluoroacetic acid and H_2SO_4 with concomitant recyclization of the keto–imine unit to the pyrrole ring. Measurement of the magnetic susceptibility (χ) by SQUID revealed that the copper ions in **5** were both present as paramagnetic d^9 forms

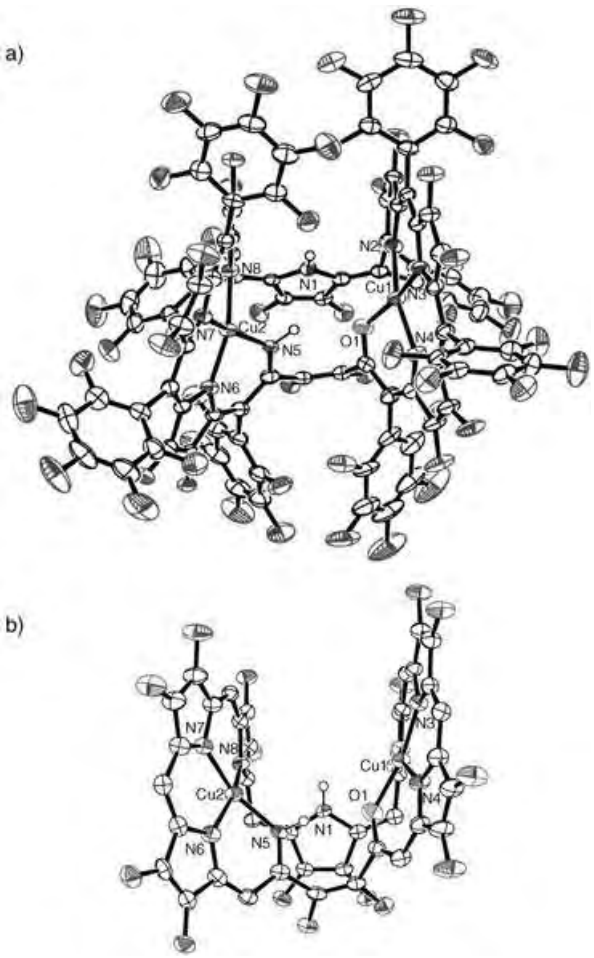

Figure 2. X-ray crystal structure of **5**: a) top view and b) side view. The thermal ellipsoids are scaled to the 50% probability level. Solvent molecules are omitted in the top view while *meso*-pentafluorophenyl substituents are also omitted in the side view for clarity.

of Cu^{II} ($\chi_p T=0.81$ emu K mol^{-1} at room temperature), in accord with the crystal structure.[9]

The minor product **6** exhibits an absorption spectrum that is quite similar to that of **2** (see Supporting Information), and its high-resolution ESI-MS spectrum showed a peak for the molecular ion at $m/z=2357.7978$ (calcd for $C_{88}N_8F_{56}Cu_2=2357.7938$) with the expected isotopic peak pattern. Although efforts to obtain suitable crystals of **6** for X-ray analysis were unsuccessful, these data suggest that **6** is a dicopper complex that adopts a figure-of-eight structure, similar to **2**. Upon heating complex **6** in solution, it underwent hydrolysis to give **5** with concomitant decomposition, whereas, interestingly, thermolysis of **6** in the solid state led to its splitting into perfluorinated Cu^{II} porphyrin **7**.[10] One possible route to **5** may be through initial formation of **6** followed by subsequent hydrolytic ring opening of one pyrrole ring, facilitated by the strongly electron-deficient nature of the perfluorinated macrocycle in **6**.

Among the transition-metal salts tested, we found that complexation of **1** and **4** with salts of silver(I), a heavier congener of copper, proceeded smoothly without any rearrangement of the macrocyclic ring, in sharp contrast to

dimetalation with copper, to provide disilver(I) complexes. A solution of **1** in a mixture of $CHCl_3$ and methanol (3:1) was heated at reflux in the presence of AgOAc (10 equiv) for 15 minutes. Disilver complex **8** was obtained as a blue solid in 98% yield. The parent-ion peak for this complex appeared at $m/z = 2158$ (M^-; calcd for $C_{88}H_{16}N_8F_{40}Ag_2 = 2158$) in the ESI-TOF mass spectrum (see Table 1). The structure of **8** was revealed by single-crystal X-ray diffraction analysis (Figure 3)

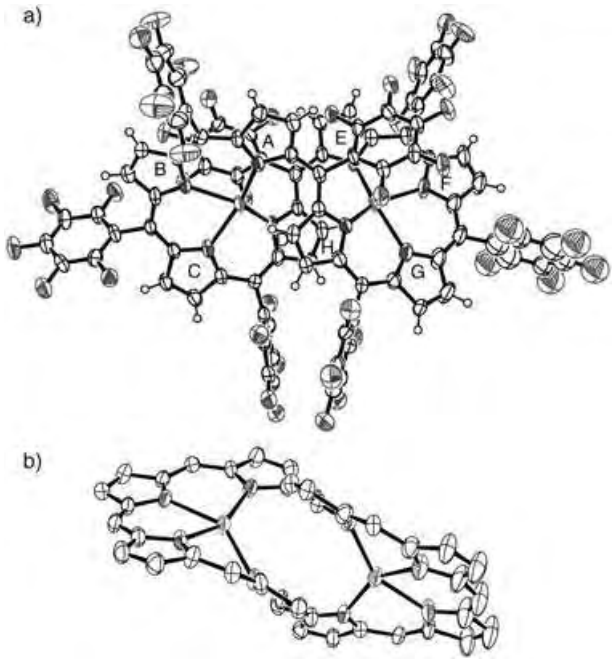

Figure 3. X-ray crystal structure of **8**: a) top view and b) side view. The thermal ellipsoids are scaled to the 50% probability level. Solvent molecules are omitted in the top view while *meso*-pentafluorophenyl substituents and β-hydrogen atoms are also omitted in the side view for clarity.

to adopt a near-C_2-symmetric figure-of-eight conformation, in which two silver ions are each bound within porphyrin-like hemicyclic cavities with Ag–N bond distances in the range of 2.27–2.37 Å.[11] Tripyrrolic units consisting of pyrroles A, B, and C, and E, F, and G are relatively flat, while pyrroles D and H are tilted by 33 and 43°, respectively, from these planes. As a consequence, the structure of **8** is rather distorted from square-planar geometry, but the extent of this distortion is modest relative to **2**. Interestingly, pentafluorophenyl substituents at the crossing *meso* position lie just over the silver atoms in parallel with the tripyrrolic units, with an interplanar distance of approximately 3.2 Å, while pyrroles D and H are placed below silver ions with Ag–βC distances of 2.89 and 2.87 Å, respectively. Relative to the structures of silver complexes of porphyrins and porphyrinoids,[12] relatively long Ag–N distances lead to the assignment of **8** as a disilver(I) complex of [34]octaphyrin(1.1.1.1.1.1.1.1).

In accord with this assignment, the ^{1}H NMR spectrum of **8** revealed eight sharp signals for the peripheral β protons of which seven signals were observed as doublets in the range of $\delta = 7.98$–6.26 ppm and one signal was observed at $\delta =$ 5.64 ppm as a double-doublet. The observed double-doublet signal cannot be explained by considering only proton–proton coupling, but can be accounted for in terms of additional through-space coupling with the proximal Ag^I ion as the Ag^I ion ($I = 1/2$) is placed close to the β-CH protons of pyrroles D and H (see Supporting Information). In the ^{19}F NMR spectrum of **8**, the peaks from the *ortho* and *meta* fluorine atoms that are close to the Ag^I ions are split similarly.[13] While the absorption spectrum of **1** displayed a broad Soret-like band at 638 nm, the spectrum of **8** displayed Soret-like bands at 408 and 780 nm and a Q-like band at 1151 nm, probably reflecting the 34-π-electron system of the macrocycle. As an excess of AgOAc was needed for complete metalation, the initial step may be silver(I)-promoted oxidation of [36]octaphyrin to [34]octaphyrin, which then may bind two Ag^I ions inside the porphyrin-like hemi-macrocycles.

In an analogous manner, treatment of **4** with CF_3COOAg (10 equiv) in a mixture of CH_2Cl_2 and methanol (10:1) for 40 minutes at room temperature provided almost quantitatively the disilver complex **9** as a dark green solid. Complex **9** displayed its parent-ion peak at $m/z = 2445$ [M^-] in the ESI-TOF mass spectrum and its ^{19}F NMR spectrum revealed sharp signals, which indicate its diamagnetic nature and a C_2-symmetric structure in solution (see Table 1). The absorption spectrum of **9** displayed bands at 422 and 791 nm and Q-band-like bands at 1143 and 1287 nm (Figure 1). The final structural confirmation of **9** was provided by single-crystal X-ray analysis.[14] As shown in Figure 4, complex **9** has a figure-of-eight conformation in the solid state which is quite similar to that of **8**. Pyrrole rings D and H are located below the silver

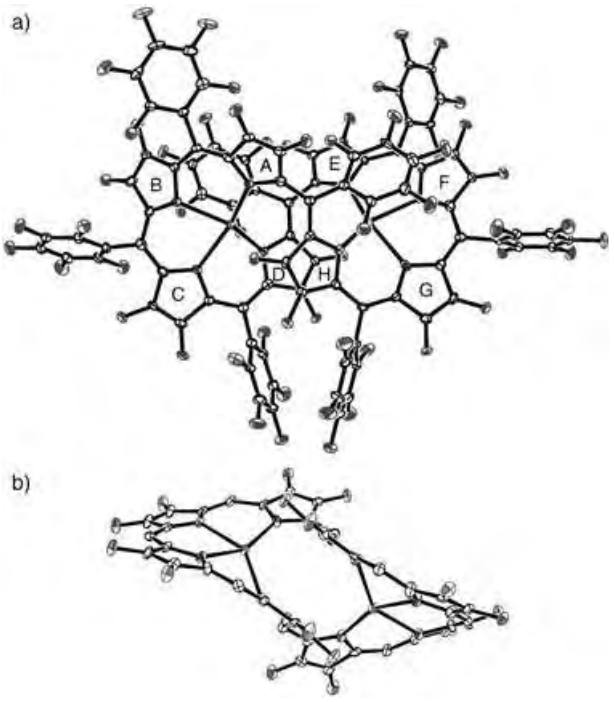

Figure 4. X-ray crystal structure of **9**: a) top view and b) side view. The thermal ellipsoids are scaled to the 50% probability level. Solvent molecules are omitted in the top view while *meso*-pentafluorophenyl substituents are also omitted in the side view for clarity.

ions on the opposite hemi-macrocycle with their pyrrolic β-fluorine atoms close to the silver ion, while the pentafluorophenyl substituents at the *meso* positions between pyrroles D and E and between pyrroles A and H also lie close to the silver ions. These structural features lead to through-space coupling of the related fluorine atoms with silver ions.[15] The Ag–N bond distances are in the range of 2.27–2.40 Å. We thus assigned complex **9** as a disilver(I) complex of perfluorinated [34]octaphyrin.

Despite the figure-of-eight structures that are similar to that of **2**, both disilver complexes **8** and **9** are thermally stable and do not exhibit any splitting reactivity, as observed for **2**. A major reason for the absence of thermal splitting reactivity may be the 34-π-electron systems of **8** and **9** which rationally preclude splitting into two 18-π-electron porphyrins. We thus attempted the reduction of **8** and **9** with $NaBH_4$ which caused spontaneous demetalation of the complexes to provide the respective free-base [38]octaphyrins.

In summary, metalation of the perfluorinated octaphyrin **4** with copper resulted in the formation of the dicopper complex **5** with an unprecedented concomitant hydrolytic ring opening of one of the pyrrole units. The octaphyrin framework was restored by demetalation with TFA and H_2SO_4. In contrast, metalation of both octaphyrin **1** and **4** with silver proceeded with initial two-electron oxidation of the ligands to give twisted figure-of-eight disilver(I) complexes of [34]octaphyrins that are thermally very stable. The structures and properties of dimetal complexes of octaphyrins are diverse and depend on the individual properties of the metal ion and the ligand, and they hail great potential for expanded porphyrins, which are actively pursued in our laboratory.

Received: February 23, 2005
Revised: March 22, 2005
Published online: May 11, 2005

Keywords: copper · macrocycles · porphyrinoids · silver

[1] a) A. Jasat, D. Dolphin, *Chem. Rev.* **1997**, *97*, 2267; b) T. D. Lash, *Angew. Chem.* **2000**, *112*, 1833; *Angew. Chem. Int. Ed.* **2000**, *39*, 1763; c) H. Furuta, H. Maeda, A. Osuka, *Chem. Commun.* **2002**, 1795; d) J. L. Sessler, D. Seidel, *Angew. Chem.* **2003**, *115*, 5292; *Angew. Chem. Int. Ed.* **2003**, *42*, 5134; e) T. K. Chandrashekar, S. Venkatraman, *Acc. Chem. Res.* **2003**, *36*, 676; f) A. Ghosh, *Angew. Chem.* **2004**, *116*, 1952; *Angew. Chem. Int. Ed.* **2004**, *43*, 1918; g) J.-Y. Shin, H. Furuta, K. Yoza, S. Igarashi, A. Osuka, *J. Am. Chem. Soc.* **2001**, *123*, 7190.

[2] a) A. Werner, M. Michels, L. Zander, J. Lex, E. Vogel, *Angew. Chem.* **1999**, *111*, 3866; *Angew. Chem. Int. Ed.* **1999**, *38*, 3650; b) J. Setsune, Y. Katakami, N. Iizuna, *J. Am. Chem. Soc.* **1999**, *121*, 8957; c) N. Sprutta, L. Latos-Grażyński, *Chem. Eur. J.* **2001**, *7*, 5099.

[3] a) V. G. Anand, S. K. Pushpan, S. Venkatraman, A. Dey, T. K. Chandrashekar, B. S. Joshi, R. Roy, W. Teng, K. Ruhlandt-Senge, *J. Am. Chem. Soc.* **2001**, *123*, 8620; b) D. Seidel, V. Lynch, J. L. Sessler, *Angew. Chem.* **2002**, *114*, 1480; *Angew. Chem. Int. Ed.* **2002**, *41*, 1422.

[4] L. Latos-Grażyński, *Angew. Chem.* **2004**, *116*, 5234; *Angew. Chem. Int. Ed.* **2004**, *43*, 5124.

[5] E. Vogel, M. Michels, L. Zander, J. Lex, N. S. Tuzum, K. N. Houk, *Angew. Chem.* **2003**, *115*, 2964; *Angew. Chem. Int. Ed.* **2003**, *42*, 2857.

[6] Y. Tanaka, W. Hoshino, S. Shimizu, K. Youfu, N. Aratani, N. Maruyama, S. Fujita, A. Osuka, *J. Am. Chem. Soc.* **2004**, *126*, 3046.

[7] S. Shimizu, J.-Y. Shin, H. Furuta, R. Ismael, A. Osuka, *Angew. Chem.* **2003**, *115*, 82; *Angew. Chem. Int. Ed.* **2003**, *42*, 78.

[8] Crystal data for **5**: $C_{88}H_4F_{56}N_8O_3Cu_2$, $M_W = 2412.07$, monoclinic, space group $P2_1/n$ (no. 14), $a = 17.7961(14)$, $b = 23.5392(18)$, $c = 22.4783(17)$ Å, $\beta = 92.598(2)°$, $V = 9406.6(13)$ Å^3, $Z = 4$, $\rho_{calcd} = 1.703\ g\,cm^{-3}$, $T = -153\,°C$. $R = 0.0648$, $R_w = 0.1731$ (all data), GOF = 0.972 ($I > 2\sigma(I)$).

[9] In the temperature range 20–2 K, the susceptibility value slightly decreased ($\chi_p T = 0.70\ emu\,K\,mol^{-1}$ at 2 K), which can be accounted for in terms of weak antiferromagnetic coupling of the two copper(II) ions ($J = -0.306\ cm^{-1}$, $g = 2.110$) despite the long separation (5.41 Å). See Supporting Information.

[10] Differential scanning calorimetry (DSC) measurement on **6** revealed sharp exothermic responses around 170–200 °C (see Supporting Information).

[11] Crystal data for **8**: $C_{114}H_{28}F_{50}N_{10}Ag_2O_7$, $M_W = 2815.19$, triclinic, space group $P\bar{1}$ (no. 2), $a = 15.908(8)$, $b = 15.978(7)$, $c = 21.28(1)$ Å, $\alpha = 99.02(4)$, $\beta = 94.61(4)$, $\gamma = 106.71(4)°$, $V = 5071(4)$ Å^3, $Z = 2$, $\rho_{calcd} = 1.843\ g\,cm^{-3}$, $T = -150\,°C$. $R = 0.092$, $R_w = 0.253$ (all data), GOF = 1.298 ($I > 2\sigma(I)$).

[12] a) W. R. Scheidt, J. U. Mondal, C. W. Eigenbrot, A. Adler, L. J. Radonovich, J. L. Hoard, *Inorg. Chem.* **1986**, *25*, 795; b) H. Furuta, T. Ogawa, Y. Uwatoko, K. Araki, *Inorg. Chem.* **1999**, *38*, 2676; c) C. Brücker, C. A. Barta, R. P. Brinas, J. A. Krause Bauer, *Inorg. Chem.* **2003**, *42*, 1673.

[13] Similar through-space coupling of the protons of a *p*-phenylene moiety with cadmium(II) ions was reported, see: a) M. Stępień, L. Latos-Grażyński, *J. Am. Chem. Soc.* **2002**, *124*, 3838; b) M. Stępień, L. Latos-Grażyński, *Acc. Chem. Res.* **2005**, *38*, 88.

[14] Crystal data for **9**: $C_{90}H_2F_{56}N_8Cl_2Ag_2O_3$, $M_W = 2593.61$, triclinic, space group $P\bar{1}$ (no. 2), $a = 14.820(2)$, $b = 17.797(2)$, $c = 19.159(3)$ Å, $\alpha = 67.010(2)$, $\beta = 87.229(2)$, $\gamma = 66.519(2)°$, $V = 4232.2(10)$ Å^3, $Z = 2$, $\rho_{calcd} = 2.035\ g\,cm^{-3}$, $T = -183\,°C$. $R = 0.061$, $R_w = 0.117$ ($I > 3\sigma(I)$), GOF = 0.945. CCDC-264267 (**5**), 264268 (**9**), and 264302 (**8**) contain the supplementary crystallographic data for this paper. These data can be obtained free of charge from the Cambridge Crystallographic Data Centre via www.ccdc.cam.ac.uk/data_request/cif.

[15] Selected signals of the β-, *o*-, and *m*-fluorine atoms were coupled with Ag^I ions probably as a result of through-space interactions (see Supporting Information).

Chemical Traps

An Electrochemically Driven and Electrochemically Regenerated NO_x Trap**

*Norman MacLeod, Federico J. Williams, Mintcho S. Tikhov, and Richard M. Lambert**

Absorption traps are used in a wide variety of different applications to prevent potentially harmful chemicals from entering the environment and/or from coming into contact with sensitive downstream equipment. Many of the materials in use cannot be regenerated so that concerns relating to sustainable usage and environmentally acceptable disposal are important; in other cases, regeneration can only be accomplished with relative difficulty. Herein we describe a new principle that can be used to address both these issues.

A key application where chemical traps have found widespread use is in the control of NO_x emissions generated by fuel-efficient automotive engines which, by reducing the atmospheric CO_2 burden, can significantly mitigate the impact of road transport on global warming. Unfortunately, such engines produce much higher concentrations of nitrogen oxides (NO_x) than conventional gasoline engines[1] with attendant adverse impact on human health and the environment.[2] As a consequence, conventional "three-way" catalytic converters are inadequate and a post-converter NO_x trap is required. These traps consist of an alkaline-earth component (usually barium) that is able to store NO_x species as various nitrates and nitrites under the oxygen-rich conditions typical of "lean" engine operation. Precious metals, usually platinum, are also used as they aid in the uptake of NO_x by providing sites for the adsorption and catalytic oxidation of NO to NO_2. To restore the trap the engine is momentarily switched to "rich operation", generating a large concentration of reducing species that cause reduction of the adsorbed nitrate/nitrite species to nitrogen thus regenerating the active $BaO/BaCO_3$ component. A disadvantage of this procedure is that relatively high temperatures (≈ 900 K) are required for complete regeneration. Although the current generation of NO_x traps is very effective when run under these conditions, a number of significant problems remain, especially the need for regular high-temperature excursions, the requirement of periodic rich engine operation (which partially defeats the object of lean operation), and susceptibility to poisoning by sulfur compounds present in the fuel.

Herein we report a novel electrochemically driven NO_x trap that can operate effectively over a range of temperatures and can be regenerated as required in a controlled manner, without the requirement for temperature excursions or changes in gas-phase composition. Although NO_x trapping is used herein to illustrate the technique, the general method employed could be applicable in a wide variety of different applications, including, for example, removal oxides of carbon and sulfur. The trap consists of a thin porous layer of a precious metal (Pt, Pd, or Rh) deposited onto the surface of a solid electrolyte wafer that is biased to deliver the active species to the metal surface where it encounters the adsorbed NO_x. We used sodium and potassium ionic conductors although a variety of other solid electrolytes could be used, depending on the application.

NO_x-trapping and trap-regeneration measurements were performed in a well-mixed microreactor operated at atmospheric pressure and described in detail elsewhere.[3] X-ray photoelectron spectroscopy (XPS) measurements were carried out with a VG ADES 400 spectrometer system[4] and in situ infrared spectroscopy measurements were performed with a Perkin Elmer GX2000 spectrometer utilizing a Harrick Refractor Reactor specular reflection accessory.

The performance of the trap is illustrated in Figure 1 which shows the effects of 1) electrochemically trapping NO_x

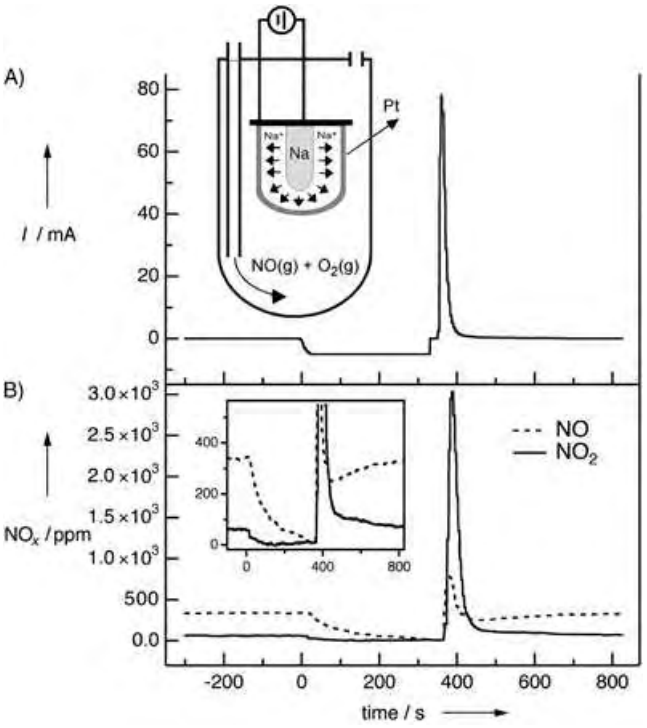

Figure 1. Trapping and regeneration carried out with a Pt|Na–β″alumina|Na electrochemical cell as shown in the inset of (A). A) Variations in the galvanic current passed through the trap and B) the composition of the exit gas. The counter electrode (metallic sodium) is not in contact with the gas atmosphere. Gas feed was 400 ppm NO_x + 5% O_2 at 150 mL min^{-1} at 573 K. Initial reactant feed at open circuit, negative current imposed at $t = 0$ (A) resulting in electrochemical pumping of sodium towards the Pt electrode and NO_x trapping from the gas phase (B). Inset in (B) shows gas-phase composition over 0–800 s interval in more detail. Reversing the current decomposes the trapped nitroxy species resulting in the desorption of mainly NO_2.

[*] Dr. N. MacLeod, Dr. F. J. Williams, Dr. M. S. Tikhov, Professor R. M. Lambert
Department of Chemistry
University of Cambridge
Cambridge CB2 1EW (UK)
Fax: (+44) 1223-336-362
E-mail: rml1@cam.ac.uk

[**] F.J.W. acknowledges partial financial support from the Leverhulme Trust.

  DOI: 10.1002/anie.200500393

and subsequent 2) trap regeneration with release of (mainly) NO_2. Initially, under open circuit conditions with trap at 573 K, the exit gas composition (identical to the inlet gas composition) was 340 ppm NO, 60 ppm NO_2 and 5% O_2. These concentrations are representative of lean-burn engine exhaust. At $t=0$ a constant current of -5 mA (4.2×10^{-4} A cm^{-2}, ca. 10 V) was applied between the counter and working electrodes, by means of a galvanostat, driving sodium ions to the surface of the porous platinum film where they were discharged at the three-phase boundary ($Na^+ + e^- \rightarrow$ Na) the sodium then reacted with ambient gas, trapping NO_x. Within approximately 10 s of current application the exit concentration of NO_x from the reactor declined reaching a value of 15 ppm after 300 s of current flow which corresponds to 95.5% removal of NO_x and essentially 100% suppression of NO_2. (Note that in our experiment the apparent time dependence of NO_x uptake is entirely determined by the mean residence time of gas molecules in the trap (ca. 60 s) and not by the intrinsic rate of trapping). The trap was then switched to open circuit for 15 s after which it was polarized in the opposite sense. This resulted in a current spike of approximately $+80$ mA (6.7×10^{-3} A cm^{-2}) which correlated with a very large release of NO_x which consisted principally of NO_2 accompanied by a small quantity of NO. This feature is important because NO_2 is much more reactive than NO towards the reductant species present in engine exhaust (CO, H_2, hydrocarbons).[5] Its production during trap regeneration is therefore an additional advantage because it implies much more efficient conversion of stored NO_x into N_2, hence cleaner operation, under practical conditions. Integration of the current/time curves in Figure 1 showed that the amounts of sodium pumped to/from the trap during the trapping/regeneration cycle were equal—that is, there is no loss of Na during operation. The nitrogen balance obtained by integrating the NO_x curves (N trapped during NO_x uptake versus N desorbed during regeneration) closed within 4%. This behavior was reproducible and repeated in a number of separate experiments.

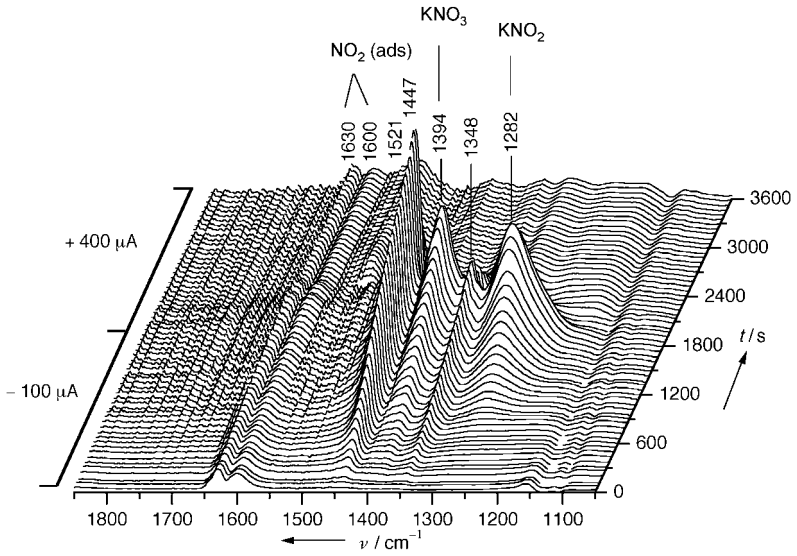

Figure 2. In situ reflectance infrared spectroscopy measurements determine the nature of the nitroxy species resulting from NO_x trapping. Experiments were performed using a Pd | K–β″alumina | Au cell with 400 ppm NO_x + 5% O_2, 150 mL min^{-1}, at 423 K. A negative current traps NO_x; a positive current decomposes the surface compounds, restoring the initial condition.

To investigate the nature of the species generated by NO_x uptake a separate set of experiments was performed under very similar conditions using an in situ reflectance infrared spectroscopy cell. The data presented in Figure 2 were obtained with a palladium metal film deposited onto a K–β″Al_2O_3 electrolyte wafer, spectra were recorded every 60 s with currents of -100 μA and $+400$ μA being used to drive K^+ ions to and from the metal surface, respectively. Prior to current application (spectrum at $t=0$ in Figure 2), bands were observed at 1630 and 1600 cm^{-1}, which are characteristic of adsorbed NO_2 on palladium sites.[6] Following current application, two bands developed ($t=180$ s) at 1447 cm^{-1} and 1348 cm^{-1}. The ratio of their intensities was constant indicating that they were due to the same chemical species. On the basis of the observed frequencies these bands are assigned to the symmetric and asymmetric stretches of a highly dispersed potassium nitrite species.[6] Subsequently, a band appeared at 1394 cm^{-1} which may be confidently assigned to bulk-like KNO_3,[6] indicating the onset of three-dimensional growth of nitrate crystallites on the palladium surface. Finally, ($t=$ 900 s) a band appeared at 1282 cm^{-1} which may be assigned to bulk-like KNO_2.[6]

After 1800 s the current direction was reversed ($I=$ 400 μA), thus pumping potassium ions away from the surface. This change resulted in a rapid decline in the intensity of all the bands between 1200 and 1500 cm^{-1}, directly demonstrating the electrochemically induced decomposition of the various nitrate/nitrite species. Clearly, the evolution of surface species with amount of charge passed is in very good accord with variations in gas composition at the trap exit. (The small remaining feature at 1521 cm^{-1} is assigned to residual nitrate on the palladium surface.)

Further confirmation of the electrochemically induced formation and destruction of NO_x-storing surface species and of their chemical identity was obtained by ex situ XPS (Figure 3). The pumping of Na to and from the Pt surface and the concomitant accumulation and destruction, respectively, of alkali metal nitrate and nitrite are clearly apparent.[7] Thus the XPS findings are in complete agreement with the trapping/regeneration behavior and the in situ IR results. Note that the spectroscopic measurements called for compact samples and as a result truly reversible alkali metal counter electrodes were impractical. Although irreversible in the strict sense, the Au electrodes employed behaved reversibly over many cycles because in any given experiment the extent of alkali depletion of the bulk electrolyte was negligible and was restored when the current was reversed.

Optimization of trap design, for example to improve gas throughput and active trapping surface area, are important practical issues that remain to be addressed—however these are beyond the aim of this report. Our object was to demonstrate a novel concept: a solid-state electrochemical device that operates at modest temperatures, stores NO_x very

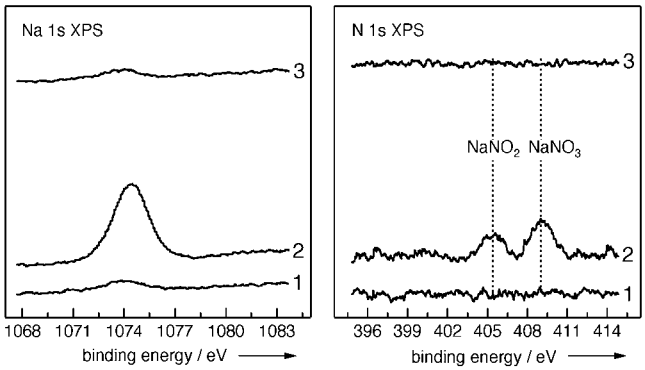

Figure 3. Na 1s (left) and N 1s (right) XP spectra obtained using a Pt | Na–β″alumina | Au cell after exposing the Pt electrode to a reactive gas atmosphere (0.1% NO + 5% O_2 at 473 K) under open circuit conditions (spectra 1), after pumping Na to the Pt electrode (spectra 2), and after pumping Na away from the Pt electrode (spectra 3).

effectively, and can be efficiently regenerated isothermally. In terms of practical application, the stability of an electrochemical trap device against long-term degradation by water vapor in the gas stream represents a materials issue that would have to be solved. In this regard K–β″aluminas are significantly more stable in the presence of water vapor than Na–β″aluminas. For example, they survive long periods at 900 K/15% humidity/atmospheric-pressure conditions that are more severe than those that would be encountered in the application envisaged here.[8] Moreover, NASICON-type alkali metal ion conducting ceramics, an alternative class of materials that could be used, exhibit transport properties that are independent of water vapor pressure and can have good stability in wet atmospheres.[9]

Conventional NO_x traps have a storage capacity of approximately 1 g NO/litre of trap volume before regeneration is necessary. Our trap had an effective volume of 3×10^{-3} litre and the data presented in Figure 1 correspond to storage of 0.13 g NO/litre of trap volume over the course of this experiment. A $NaNO_3$ film of 60 nm thickness (readily attainable with our system) equates to a maximum theoretical trapping capacity of 1 g NO/litre so that the achievable trapping capacity should be at least as good as that with conventional traps.

Received: February 1, 2005
Revised: March 2, 2005
Published online: May 11, 2005

Keywords: absorption · chemical traps · electrochemistry · fuel-efficient engines · nitrogen oxides

[1] N. Takahashi H. Shinjoh, T. Ijima, T. Suzuki, K. Yamazaki, K. Yokota, H. Suzuki, N. Miyoshi, S. Matsumoto, T. Tanizawa, T. Tanaka, S. Tateishi, K. Kasahara *Catal. Today* **1996**, *27*, 63–69.
[2] M. Z. Jacobson, J. H. Seinfeld, G. R. Carmichael, D. G. Streets, *Geophys. Res. Lett.* **2004**, *31*, L02116.
[3] F. J. Williams, N. Macleod, M. S. Tikhov, R. M. Lambert, *Electrochim. Acta* **2002**, *47*, 1259–1265.
[4] F. J. Williams, A. Palermo, M. S. Tikhov, R. M. Lambert, *J. Phys. Chem. B* **2000**, *104*, 615–621.
[5] R. Burch, J. A. Sullivan, T. C. Watling, *Catal. Today* **1998**, *42*, 13–23.
[6] K. I. Hadjiivanov, *Catal. Rev. Sci. Eng.* **2000**, *42*, 71–144.
[7] I. V. Yentekakis, A. Palermo, N. C. Filkin, M. S. Tikhov, R. M. Lambert, *J. Phys. Chem. B* **1997**, *101*, 3759–3768.
[8] S. Heavens, W. Jones, Ionotec Ltd., personal communication.
[9] O. A. Smirnova, R. O. Fuentes, F. Figueiredo, V. V. Kharton, F. M. B. Marques, *J. Electroceram.* **2003**, *11*, 179–189.

Strained Polycycles

Synthesis of *cis*,*cis*,*cis*,*cis*-[5.5.5.4]-1-Azafenestrane with Discovery of an Unexpected Dyotropic Rearrangement**

Scott E. Denmark and Justin I. Montgomery*

Fenestranes[1] [*fenestra* (Lat.), window] are a unique family of compounds with four fused carbocycles that share a central quaternary carbon atom which exhibits planarizing distortion (for example, **1**, Scheme 1).[2] By changing ring sizes and ring-

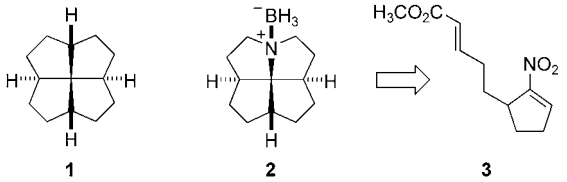

1 **2** **3**

Scheme 1. *cis*,*cis*,*cis*,*cis*-[5.5.5.5]-Fenestrane (**1**) and *cis*,*cis*,*cis*,*cis*-[5.5.5.5]-1-azafenestrane·BH_3 (**2**).

fusion configurations, variable planarization of the central carbon atom results, thus giving chemists a tool with which to probe one of the cornerstone theories of organic chemistry.[3] Unfortunately, unsubstituted fenestranes are low-molecular-weight hydrocarbons, and therefore crystallization for single-crystal analysis and quantification of the distortions to the central carbon atom is difficult.[4] By substituting a nitrogen

[*] Prof. S. E. Denmark, J. I. Montgomery
Department of Chemistry
University of Illinois
Urbana, IL 61801 (USA)
Fax: (+1) 217-333-3984
E-mail: denmark@scs.uiuc.edu

[**] We are grateful to the National Institutes of Health for generous financial support (GM30938). J.I.M. thanks the Procter & Gamble Company, Abbott Laboratories, and Johnson & Johnson for graduate fellowships. We thank Scott R. Wilson and Teresa Prussak-Wieckowska of the UIUC George L. Clark X-Ray Facility for collection and interpretation of X-ray data.

Supporting information for this article is available on the WWW under http://www.angewandte.org or from the author.

  DOI: 10.1002/anie.200500367

atom for one of the external bridgehead carbons, new opportunities for X-ray crystallographic analysis exist.

We recently reported the first synthesis of a 1-azafenestrane, *cis*,*cis*,*cis*,*cis*-[5.5.5.5]-1-azafenestrane·BH_3 (**2**),[5] which featured the tandem [4+2]/[3+2] cycloaddition[6] of nitrocyclopentene **3** as the key step. Although the tandem cycloaddition allows for rapid and stereoselective formation of the required skeleton, problematic steps in the synthesis of nitroalkene **3** led to a poor overall yield of azafenestrane **2** (18 steps, 0.02% overall yield). Furthermore, azafenestrane **2** displayed only modest planarizing distortions to the central carbon atom.[7] Therefore, an efficient route to an even more strained azafenestrane was sought, and the successful realization of that goal is described herein.

Contraction of one of the pyrrolizidine five-membered rings in azafenestrane **2** should lead to increased planarization of the central carbon atom.[8] Retrosynthetic analysis for *cis*,*cis*,*cis*,*cis*-[5.5.5.4]-1-azafenestrane (**4**) is presented in Scheme 2. The azetidine ring in **4** should be formed through

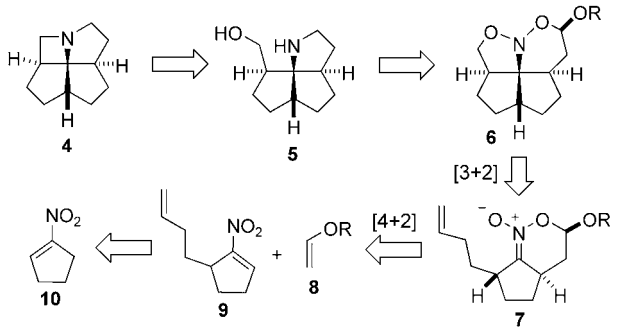

Scheme 2. Retrosynthetic analysis for *cis*,*cis*,*cis*,*cis*-[5.5.5.4]-1-azafenestrane (**4**).

an irreversible intramolecular displacement of an activated alcohol **5**, which is derived from nitroso acetal **6** through hydrogenolysis. This reduction involves two N–O-bond cleavages and a reductive amination to form the pyrrolidine ring in a single operation. Nitroso acetal **6** is the direct product of tandem inter-/intramolecular [4+2]/[3+2] cycloaddition of nitroalkene **9** and a suitable vinyl ether. Presumably, vinyl ether **8** would approach from the less hindered side of the nitroalkene (opposite the tethered olefin) to give an *anti* relationship between the hydrogen atoms at the ring-fusion sites in nitronate **7**. An *exo*-fold, [3+2] cycloaddition[9] with the unactivated dipolarophile[10] would then set the remaining two stereogenic centers (final ring fusion and central carbon atom) in the required sense for the all-*cis* azafenestrane skeleton. The required 5-butenyl-1-nitrocyclopentene **9** would be available from 1-nitrocyclopentene (**10**) through 1,4-addition followed by regeneration of the nitroalkene.

A route analogous to that reported for nitroalkene **3** involving nitroallylation[11] was first investigated for the synthesis of **9**. Although the desired target was obtained, a very poor overall yield for the sequence prompted the development of a more efficient synthesis (Scheme 3). Treatment of 1-nitrocyclopentene (**10**)[12] with 3-butenylcyanozinc cuprate **11**,[13] followed by trapping of the resulting nitronate[14] with phenylselenyl bromide, provided a mixture of nitroselenides. Upon oxidation, *syn* selenoxide elimination gave the desired nitroalkene **9**, along with its double-bond isomer **12** (**9**/**12**, 2:1) in 78% combined yield from 1-nitrocyclopentene. All attempts at chromatographic separation of the two nitroalkenes were unsuccessful. Ultimately, the most efficient way to separate the two nitroalkenes was simply to carry out the next step of the azafenestrane synthesis with the mixture of compounds. Trimethylaluminum-promoted [4+2] cycloaddition of trisubstituted nitroalkene **9** with various vinyl ethers takes place in less than one hour at −78 °C and leaves tetrasubstituted nitroalkene **12** unreacted.

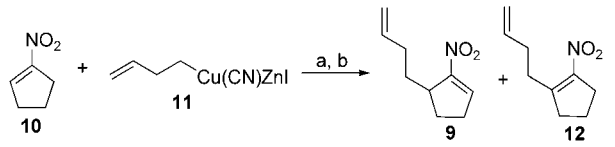

Scheme 3. a) THF, 0 °C, 1 h, then PhSeBr, 0 °C→RT, 1 h; b) H_2O_2, THF, 0 °C→RT, 30 min (78% from **10**; **9**/**12** 2:1).

Treatment of nitroalkene **9** (Scheme 4) with *n*-butyl vinyl ether in the presence of trimethylaluminum was expected to provide nitroso acetal **6** (Scheme 2, R = *n*-butyl), the product

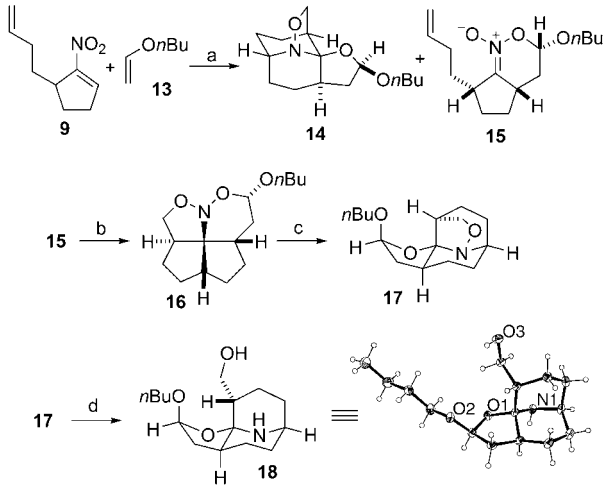

Scheme 4. a) $AlMe_3$, CH_2Cl_2, −78 °C, 30 min (48% **14**, 36% **15**); b) K_2CO_3, toluene, reflux, 2 h; c) SiO_2, room temperature; d) H_2 (26 atm), Raney Ni, MeOH, 14 h (46% from **15**). ORTEP-3 plot of **18** (30% thermal ellipsoids).

of tandem [4+2]/[3+2] cycloaddition. However, the major product of the reaction was compound **14**, which contains an azabicyclononane ring system and two five-membered rings! The minor [4+2] cycloadduct **15** derived from *endo* approach of *n*-butyl vinyl ether from the same face as the tethered dipolarophile was also isolated. The structure of aminal **14** was established from studies carried out with the minor cycloadduct **15**: Thermal intramolecular [3+2] cycloaddition of nitronate **15** with its tethered dipolarophile in refluxing toluene gave nitroso acetal **16**. However, upon purification with silica gel, a new product, **17**, which is a diastereomer of aminal **14**, was formed. The structure of **17**, and by analogy

that of its diastereomer **14**, was confirmed by X-ray crystallographic analysis[15] of hydrogenation product **18**, in which the only N–O bond has been cleaved.

This novel rearrangement that converts nitroso acetal **16** into aminal **17** involves breaking both an N–O bond and a C–C bond with formation of a C–O bond and a C–N bond (Scheme 5). Analysis of the 3D structure of nitroso acetal **16** clearly shows the two breaking bonds in near-perfect antiperiplanar alignment. The ensuing transposition, known as a dyotropic rearrangement,[16] can take place readily to give the rearranged product **17**.[17]

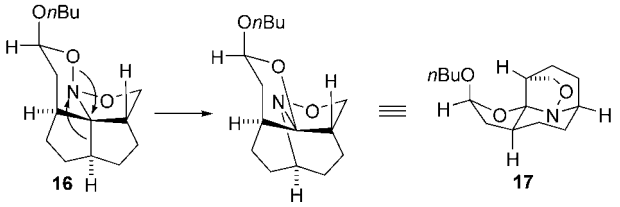

Scheme 5. Dyotropic rearrangement of nitroso acetal **16**.

Although this unexpected dyotropic rearrangement is mechanistically intriguing and potentially useful synthetically, its occurrence in the formation of the major product under the conditions employed for the tandem cycloaddition reaction precludes formation of the desired amino alcohol **5**. However, from conformational analysis of nitroso acetal **19** (the product of tandem [4+2]/[3+2] cycloaddition with approach of the dienophile from the opposite side to that occupied by the tethered dipolarophile, and the precursor to aminal **14**), a means to prevent the rearrangement became apparent (Scheme 6). The 1,2-oxazine ring in nitroso acetal **19-*ax*** adopts a chair conformation, which places the butyloxy group in an (anomerically stabilized) axial orientation. This conformation exhibits the required stereoelectronic alignment of the two migrating bonds (bold); thus the rearrangement takes place readily to give aminal **14**. However, in a second low-energy conformation, depicted in structure **19-*eq***, a chair flip has occurred, and the migrating bonds (bold) are no longer in alignment. By favoring this conformation, the rearrangement should be suppressed, and hydrogenolysis might provide the desired tricyclic amino alcohol **5**. Calculations[18] suggest that the two conformers are very close in energy. A nitroso acetal derived from a bulkier vinyl ether might favor the equatorial conformer and consequently deter or prevent the undesired dyotropic rearrangement.

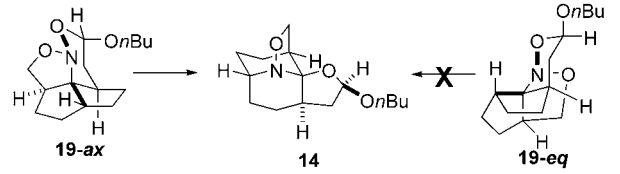

Scheme 6. Conformations of nitroso acetal **19**.

In the event, tandem cycloaddition of *tert*-butyl vinyl ether with nitroalkene **9** promoted by trimethylaluminum (Scheme 7) led to formation of nitroso acetal **21** with no rearrangement under the reaction conditions, thus providing support for the proposed hypothesis. The crude reaction mixture contained, in a 2:1 ratio, nitroso acetal **21** (*endo* approach of the dienophile from the side opposite the tethered dipolarophile) and the minor nitronate (*endo* approach of the dienophile from the same side as the dipolarophile), which does not undergo spontaneous [3+2] cycloaddition. Purification of nitroso acetal **21** on silica gel did lead to partial rearrangement to aminal **23**; however, chromatography on basic alumina provided **21** in 67% yield.

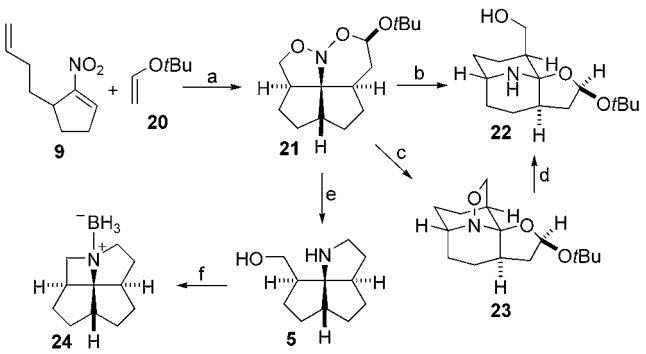

Scheme 7. a) $AlMe_3$, CH_2Cl_2, −78 °C, 1 h, purification on Al_2O_3 (67%); b) H_2 (1 atm), Raney Ni, MeOH, (94%); c) MeOH, 3 h, room temperature, (70%); d) H_2 (26 atm), Raney Ni, MeOH, room temperature, 15 h, (98%); e) H_2 (26 atm), Raney Ni, 10% H_2O-saturated EtOAc in EtOAc (0.25 M), 20 h, (85%); f) PPh_3, diisopropyl azodicarboxylate (DIAD), CH_2Cl_2, 0 °C, 40 min, then BH_3·THF, −78 °C→RT, 1 h (87%).

With nitroso acetal **21** in hand, we were poised to complete the synthesis in short order. Unfortunately, standard hydrogenolysis conditions (H_2, Raney Ni, MeOH) provided the reduced, rearranged product **22**, with no sign of the desired amino alcohol. An investigation of reaction conditions uncovered the fact that protic solvents induced the dyotropic rearrangement. In fact, simply stirring nitroso acetal **21** in methanol at room temperature provided aminal **23** in good yield. Consequently, new hydrogenation conditions had to be developed that would allow reduction of nitroso acetal **21** without promoting the rearrangement. Attempts to carry out the hydrogenation in nonprotic, dry solvents were unsuccessful; however, rearrangement did not take place under these conditions. In the end, it was discovered that by adding a controlled amount of water in the form of water-saturated ethyl acetate (10% in dry ethyl acetate) to the reaction mixture, the desired hydrogenolysis took place to give amino alcohol **5** while still suppressing the rearrangement.

At the outset of the synthesis, the formation of the azetidine ring from amino alcohol **5** was believed to be the most challenging step of the proposed route. However, simple treatment of **5** under Mitsunobu[19] coupling conditions led to formation of the desired azafenestrane, which was efficiently isolated as its borane complex *cis*,*cis*,*cis*,*cis*-[5.5.5.4]-1-azafenestrane·BH_3 (**24**) in 87% yield.[20] The availability of **24** from 5-butenyl-1-nitrocyclopentene **9** in only three steps and 50% overall yield demonstrates the power of the tandem

nitroalkene cycloaddition reaction for rapidly building molecular complexity.

To quantify the planarizing distortions at the central carbon atom in **24**, X-ray crystallographic analysis is required. Although the azafenestrane–borane adduct is a crystalline solid, crystals suitable for X-ray diffraction could not be obtained.[21] Fortunately, simple treatment of **24** with boron trifluoride etherate promoted an exchange to give the crystalline BF_3 adduct **25** (Scheme 8). Cooling of a warm, saturated solution of **25** in hexane to room temperature gave crystals of a quality suitable for X-ray crystallographic

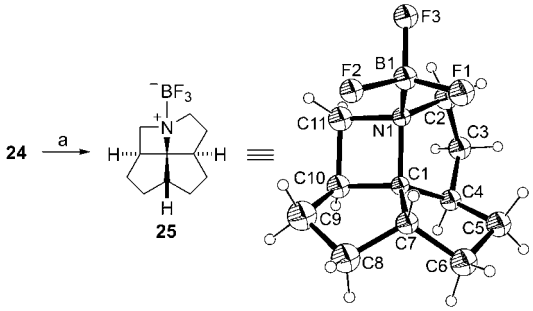

Scheme 8. a) $BF_3{\cdot}OEt_2$, room temperature. ORTEP-3 plot of **25** (form 1, 30% thermal spheres).

analysis that formed in an unambiguous[22] space group $P2_1/n$.[23] The two most populated crystal forms in the disordered model exhibit similar planarization as defined by the angles around the central carbon atom; form 1: N1-C1-C7 119.8(7)° and C4-C1-C10 120.7(8)°, form 2: N1-C1-C7 119.2(8)° and C4-C1-C10 121.2(10)°. The degree of distortion agrees well with calculated values for the corresponding parent hydrocarbon.[2] Ab initio DFT calculations predict that the strain energy of azafenestrane **4** is 17.8-kcal mol^{-1} higher than that of the previously synthesized *cis*,*cis*,*cis*,*cis*-[5.5.5.5]-1-azafenestrane.[24]

In conclusion, the synthesis of *cis*,*cis*,*cis*,*cis*-[5.5.5.4]-1-azafenestrane·BH_3 (**24**) was completed efficiently in five steps and 26% overall yield from 1-nitrocyclopentene by using a tandem [4+2]/[3+2] cycloaddition of a nitroalkene as the key step. Along the way, an unprecedented dyotropic rearrangement was discovered that converts nitroso acetals into tetracyclic aminals. The rearrangement is controlled by the conformation of the six-membered ring in the nitroso acetal precursors. By utilizing a bulky vinyl ether and developing new hydrogenation conditions, the rearrangement was suppressed, thus allowing the synthesis of the desired azafenestrane. The [5.5.5.4]-1-azafenestrane was analyzed by X-ray crystallography as its BF_3 adduct to quantify the planarizing distortion around the central carbon atom. Efforts toward even more strained azafenestranes, as well as investigations into the reported dyotropic rearrangement and its use in synthesis, are currently underway.

Received: January 31, 2005
Published online: May 11, 2005

Keywords: cycloaddition · dyotropic rearrangement · fenestranes · nitroalkenes · strained molecules

[1] V. Georgian, M. Saltzman, *Tetrahedron Lett.* **1972**, *13*, 4315.
[2] M. Thommen, R. Keese, *Synlett* **1997**, 231.
[3] a) H. van 't Hoff, *Arch. Neerl. Sci. Exactes Nat.* **1874**, *9*, 445; b) Le Bel, *Bull. Soc. Chim. Fr.* **1874**, *22*, 337.
[4] Low-temperature crystallization could possibly be employed; see: J. Benet-Buchholz, T. Haumann, R. Boese, *Chem. Commun.* **1998**, 2003.
[5] S. E. Denmark, L. A. Kramps, J. I. Montgomery, *Angew. Chem.* **2002**, *114*, 4296; *Angew. Chem. Int. Ed.* **2002**, *41*, 4122.
[6] a) S. E. Denmark, A. Thorarensen, *Chem. Rev.* **1996**, *96*, 137; b) S. E. Denmark, J. J. Cottell in *The Chemistry of Heterocyclic Compounds: Synthetic Applications of 1,3-Dipolar Cycloaddition Chemistry Toward Heterocycles and Natural Products* (Eds.: A. Padwa, W. H. Pearson), Wiley-Interscience, New York, **2002**, pp. 83–167.
[7] Central angles in **2**: N-C-C 116.1°, C-C-C 116.6°.
[8] Calculated central angles for **4**: N-C-C 117.9°, C-C-C 123.6° (DFT B88-LYP). All calculations were performed with CAChe WorkSystem Pro Version 6.1.10, Fujitsu Limited.
[9] S. E. Denmark, D. S. Middleton, *J. Org. Chem.* **1998**, *63*, 1604.
[10] S. E. Denmark, C. B. W. Senanayake, *Tetrahedron* **1996**, *52*, 11579.
[11] D. Seebach, G. Calderari, P. Knochel, *Tetrahedron* **1985**, *41*, 4861.
[12] E. J. Corey, H. Estreicher, *J. Am. Chem. Soc.* **1978**, *100*, 6294.
[13] P. Knochel, M. C. P. Yeh, S. C. Berk, J. Talbert, *J. Org. Chem.* **1988**, *53*, 2390.
[14] S. E. Denmark, L. R. Marcin, *J. Org. Chem.* **1993**, *58*, 3850.
[15] Monoclinic, $P2_1/c$, crystal ($0.64\times0.56\times0.10$ mm^3) from hexane: $a=11.087(4)$ Å, $b=14.064(5)$ Å, $c=9.473(4)$ Å, $\beta=96.733(7)°$, $V=1466.9(10)$ Å^3, $\rho=1.220$ Mg m^{-3}. Bruker SMART CCD data $2\theta_{max}=50.74°$, Mo radiation, $\lambda=0.71073$ Å, ω-scan profiles, 193(2) K, reflections (11547 measured, 2691 independent, $2020>2\sigma(I)$), limits ($-13\le h\le13$, $-16\le k\le16$, $-11\le l\le11$), corrected for L-p effects and absorption (integration, $\mu=0.084$ mm^{-1}, transmission $0.992>0.941$). Direct-methods solution (Bruker SHELXTL) and full-matrix least-squares refinement on F^2 (Bruker SHELXTL) by using 179 parameters against 2691 data points, observed $R1=0.040$, $wR2=0.094$, residual range 0.18 to -0.18 e Å^{-3}. CCDC 262117 contains the supplementary crystallographic data for this paper. These data can be obtained free of charge from the Cambridge Crystallographic Data Centre via www.ccdc.cam.ac.uk/data_request/cif.
[16] M. T. Reetz, *Adv. Organomet. Chem.* **1977**, *16*, 33.
[17] The role of silica in promoting the dyotropic rearrangement remains obscure.
[18] Local minima for **19-*ax*** and **19-*eq*** (both pseudo chairs in minimized form) are within 1 kcal mol^{-1} (PM3).
[19] a) O. Mitsunobu, *Synthesis* **1981**, 1; b) P. G. Sammes, S. Smith, *J. Chem. Soc. Chem. Commun.* **1983**, 682.
[20] Full experimental details for **24** and all other compounds are available as Supporting Information.
[21] Adduct **24** was soluble in many organic solvents. Thin needles could be obtained from hexane at low temperature, but multiple attempts to collect X-ray diffraction data were unsuccessful. Crystals could be obtained from other nonpolar solvents (e.g. tetraalkyl silanes, fluorocarbons) at ambient temperature, but again, only weak diffraction patterns were observed.
[22] A detailed analysis of the unusual X-ray crystal structure of **25** is available in the Supporting Information.
[23] Monoclinic, $P2_1/n$, crystal ($0.60\times0.20\times0.04$ mm^3) from hexane: $a=6.257(3)$ Å, $b=14.424(6)$ Å, $c=12.596(5)$ Å, $\beta=91.932(8)°$, $V=1136.0(9)$ Å^3, $\rho=1.351$ Mg m^{-3}. Bruker SMART CCD data $2\theta_{max}=50.60°$, Mo radiation, $\lambda=0.71073$ Å, ω-scan profiles,

193(2) K, reflections (12439 measured, 2055 independent, 676 > $2\sigma(I)$), limits ($-7 \le h \le 7$, $-17 \le k \le 17$, $-15 \le l \le 15$), corrected for L-p effects and absorption (integration, $\mu = 0.112\ mm^{-1}$, transmission 0.995 > 0.946). Direct-methods solution (Bruker SHELXTL) and full-matrix least-squares refinement on F^2 (Bruker SHELXTL) by using 196 parameters and 237 restraints against 2050 data points, observed $R1 = 0.076$, $wR2 = 0.240$, residual range 0.28 to $-0.26\ e\ Å^{-3}$. CCDC 262116 contains the supplementary crystallographic data for this paper. These data can be obtained free of charge from the Cambridge Crystallographic Data Centre via www.ccdc.cam.ac.uk/data_request/cif.

[24] This value represents the total energy difference between **4** and *cis*,*cis*,*cis*,*cis*-[5.5.5.5]-1-azafenestrane (B88-LYP) with an adjustment for removal of a CH_2 group in **4** (energy of unstrained CH_2 determined by the average difference in total energy upon minimization of ethane, propane, and butane); see: a) T. Dudev, C. Lim, *J. Am. Chem. Soc.* **1998**, *120*, 4450; b) R. D. Bach, O. Dmitrenko, *J. Org. Chem.* **2002**, *67*, 3884.

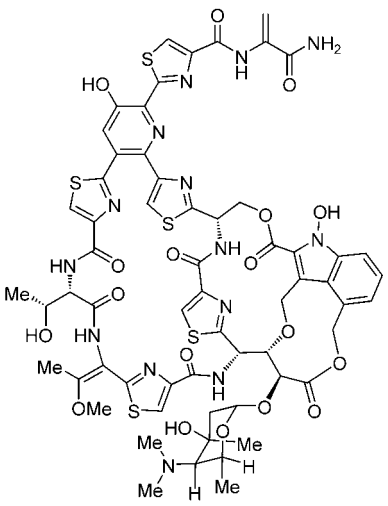

Indole Synthesis

Construction of Substituted *N*-Hydroxyindoles: Synthesis of a Nocathiacin I Model System**

K. C. Nicolaou, Sang Hyup Lee, Anthony A. Estrada, and Mark Zak*

Rare as they appear to be in nature, *N*-hydroxyindoles are intriguing chemical entities as they may play important biological roles and serve as useful synthetic building blocks.[1,2] One of the most impressive naturally-occurring molecules that features this unit is the recently discovered nocathiacin I (**1**), an antibiotic isolated from *Nocardia sp.* (ATCC-202099)[3] and the fungus *Amicolaptosis sp.*[4] Compound **1** exhibits strikingly potent activity in vitro and in vivo against Gram-positive bacteria.[3a,4] Given the complex structure of this antibiotic and the prominent position of a highly substituted *N*-hydroxyindole motif within its structure, as well as the lack of general methods for the construction of such systems, we deemed the development of suitable synthetic methodologies in this area as an important goal. Herein we report a new synthetic technology for the construction of substituted *N*-hydroxyindoles **2** from simple aromatic precursors and its application to the synthesis of a nocathiacin I model system **3**, which contains this unusual molecular framework.

Scheme 1 depicts the general concept for the construction of *N*-hydroxyindoles formulated on the basis of relevant precedents.[2] Thus, selective reduction of nitro ketoester **I**

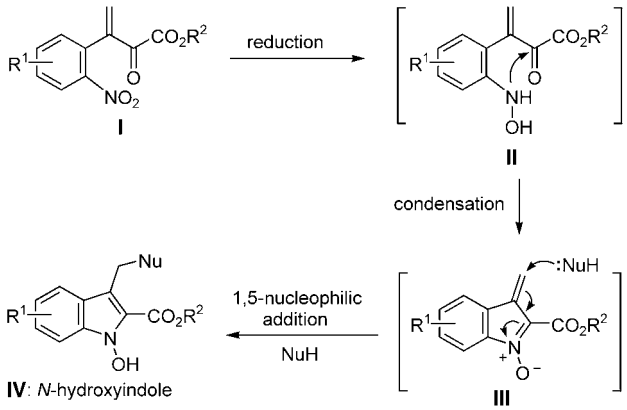

Scheme 1. General scheme for the construction of substituted *N*-hydroxyindoles **IV**.

under appropriate conditions to hydroxylamine **II** was expected to initiate an intramolecular condensation with the carbonyl group, leading to the α,β-unsaturated nitrone system **III**, whose capture with nucleophiles would deliver the desired substituted *N*-hydroxyindoles **IV**.

The required starting material for these studies, nitro ketoester **6**, was readily prepared by standard chemistry[2c,5,6] in two steps from aromatic compound **4** via intermediate **5** (Scheme 2). Schemes 3 and 4 summarize the initial results of this study and demonstrate the feasibility of this plan under two different sets of experimental conditions. Thus, addition

[*] Prof. Dr. K. C. Nicolaou, Dr. S. H. Lee, A. A. Estrada, M. Zak
Department of Chemistry and
The Skaggs Institute for Chemical Biology
The Scripps Research Institute
10550 North Torrey Pines Road, La Jolla, CA 92037 (USA)
and
Department of Chemistry and Biochemistry
University of California, San Diego
9500 Gilman Drive, La Jolla, CA 92093 (USA)
Fax: (+1) 858-784-2469
E-mail: kcn@scripps.edu

[**] We thank Dr. D. H. Huang, Dr. G. Siuzdak, and Dr. R. Chadha for NMR spectroscopic, mass spectrometric, and X-ray crystallographic assistance, respectively. Financial support for this work was provided by grants from the National Institutes of Health (USA) and the Skaggs Institute for Chemical Biology, and fellowships from the National Institutes of Health (USA) (to A.A.E.), The Skaggs Institute for Research (to M.Z.), and Eli Lilly & Company (to M.Z.).

  DOI: 10.1002/anie.200500724

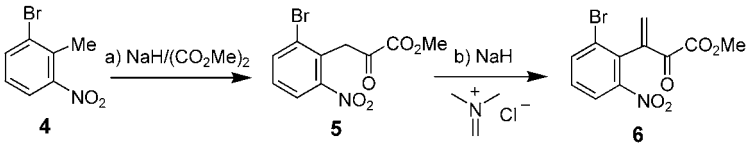

Scheme 2. Synthesis of nitro ketoester **6**. Reagents and conditions: a) NaH (4.0 equiv), $(CO_2Me)_2$ (5.0 equiv), DMF, 0 °C, 1 h; then 25 °C, 18 h, 60%; b) NaH (1.1 equiv), $CH_2{=}N^+Me_2Cl^-$ (3.0 equiv), THF, 0 °C, 1 h; then 25 °C, 12 h, 80%. DMF = *N*,*N*-dimethylformamide.

of activated zinc [Zn][2b] (prepared from zinc dust, 1,2-dibromoethane, and TMSCl) in THF to a solution of **6** and NH_4Cl in THF at 25 °C (Scheme 3) resulted in the formation of *N*-hydroxyindoline derivative **8** (56%; Table 2) along with small amounts of hydroxylactam **13** (10%) whose structure was proven beyond doubt through X-ray crystallographic analysis[7] (see ORTEP drawing, Scheme 3). These observations can be explained by invoking ring closure of the initially formed hydroxylamine **7**, leading to *N*-hydroxy tertiary alcohol **8** (path A; Scheme 3), and 1,4-addition of NH_3 to unreduced starting material **6** followed by lactamization and enolization of the initially formed amino ester **12** to form **13** (path B; Scheme 3). The *N*-hydroxy tertiary alcohol **8** was found to be rather labile, losing a molecule of water to generate nitrone **9** whose isolation remains elusive, although its presence can be surmised by TLC and NMR spectroscopy as well as through trapping by a variety of nucleophiles. Indeed, **8** reacted with benzyl alcohol or phenylmethanethiol in DME at 40 °C in the presence of *p*TsOH to afford *N*-hydroxyindoles **10** (55%; Table 2) and **11** (90%), respectively. These *N*-hydroxyindole-forming reactions are assumed to proceed either directly from *N*-hydroxy tertiary alcohol **8** by S_N2'-type displacement or by 1,5-addition to the initially formed nitrone **9**, or through both mechanistic pathways. These results are in contrast to those of Myers and Herzon[2b] in which the products obtained by 1,5-addition to a sterically congested α,β-unsaturated nitrone proved unstable to isolation, readily reverting back to the starting material.

In an effort to find a more direct access to the desired *N*-hydroxyindoles, a second protocol involving $SnCl_2$ as a reducing agent[2c,e] was explored. According to this method, **6** was treated with $SnCl_2{\cdot}2H_2O$ (2.2 equiv) and benzyl alcohol or phenylmethanethiol (benzyl mercaptan, 5.0 equiv) in DME in the presence of 4-Å molecular sieves at 40 °C for 1–1.5 h, circumstances that led, through path A_1, directly to the formation of adducts **10** (60%, see ORTEP drawing[7]) or **11** (55%), respectively (Scheme 4). These conditions were arrived at after a systematic investigation in which benzyl alcohol was used as the nucleophile, whereby the effects of solvent, temperature, time, amount of water, and stoichiometry were examined. The absence of the *N*-hydroxy tertiary alcohol **8** from the reaction mixture under these conditions is presumably due to its fleeting nature under the reaction

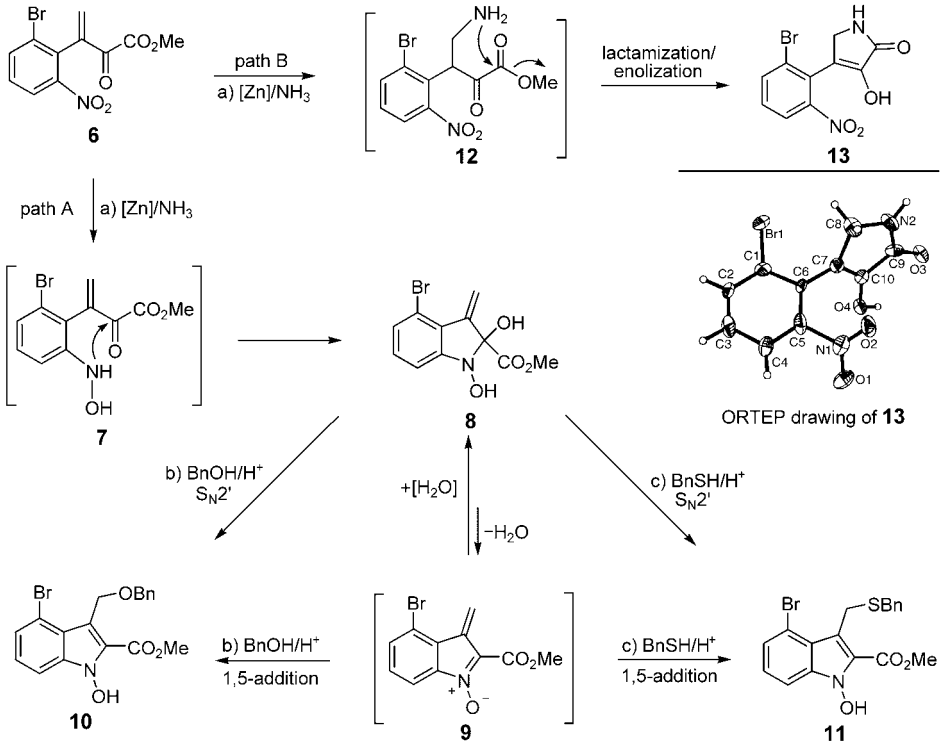

Scheme 3. Zn/NH_4Cl-induced generation and trapping of α,β-unsaturated nitrone **9** to form *N*-hydroxyindoles. Reagents and conditions: a) Zn dust (4.9 equiv), $BrCH_2CH_2Br$ (0.33 equiv), THF, reflux, 1 h; then cool to 25 °C; then TMSCl (0.2 equiv); and then a mixture of aqueous NH_4Cl (1.0 N; 2.2 equiv) and **6** (1.0 equiv), 25 °C, 15 min, **8** (56%), **13** (10%); b) **8** (1.0 equiv), *p*TsOH (3.0 equiv), molecular sieves (4 Å; 20 wt%), BnOH (5.0 equiv), DME, 40 °C, 3 h, **10** (55%); c) **8** (1.0 equiv), *p*TsOH (3.0 equiv), molecular sieves (4 Å; 20 wt%), BnSH (5.0 equiv), DME, 40 °C, 1 h, **11** (90%). TMS = trimethylsilyl; *p*TsOH = *p*-toluenesulfonic acid; Bn = benzyl; DME = 1,2-dimethoxyethane. ORTEP drawing of **13** drawn at the 50% probability level.

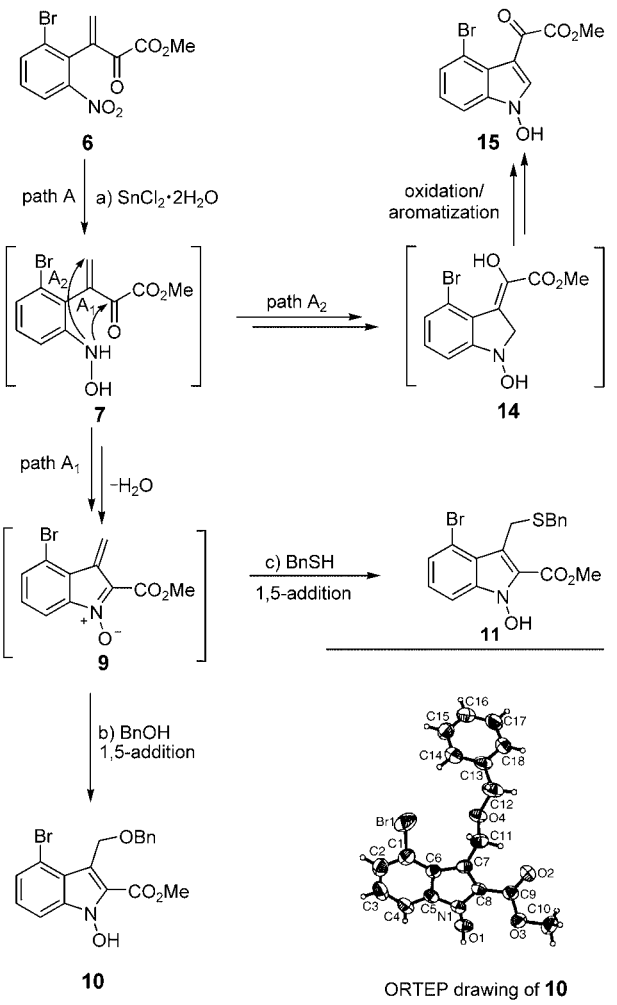

Scheme 4. $SnCl_2 \cdot 2H_2O$-induced generation and trapping of α,β-unsaturated nitrone **9** to form *N*-hydroxyindoles. Reagents and conditions: a, b) $SnCl_2 \cdot 2H_2O$ (2.2 equiv), molecular sieves (4 Å; 20 wt%), BnOH (5.0 equiv), **6** (1.0 equiv), DME, 40°C, 1.5 h, **10** (60%), **15** (17%); a, c) $SnCl_2 \cdot 2H_2O$ (2.2 equiv), molecular sieves (4 Å; 20 wt%), BnSH (5.0 equiv), **6** (1.0 equiv), DME, 40°C, 1 h, **11** (55%), **15** (15%). ORTEP drawing of **10** drawn at the 50% probability level.

conditions (acidic), which promote its conversion into nitrone **9** and/or its trapping by the nucleophile. The $SnCl_2$-promoted reaction, however, also yields ketoester *N*-hydroxyindole **15** in small amounts (15–17%). This byproduct presumably arises from the initially generated hydroxylamine **7** through path A_2, which involves intramolecular 1,4-addition followed by oxidation/aromatization of the resulting enolic species **14** (Scheme 4). An alternative mechanism for the generation of **15** may involve the nitroso intermediate (formed by partial reduction of **6**) or its hydrated counterpart, which could undergo, through its nitrogen atom, intramolecular addition to the neighboring Michael acceptor; this event may then be followed by rearrangement (or elimination of H_2O) to the observed compound **15**.

To explore the generality and scope of the developed reaction, a number of nucleophiles were employed to capture the labile nitrone (**9** or its hydrated form **8**) under the direct $SnCl_2 \cdot 2H_2O$ conditions. The results are shown in Table 1. Thus, both primary and secondary alcohols enter the reaction smoothly, affording good yields of the expected substituted *N*-hydroxyindoles (compounds **10** and **16–18**; Table 1, entries 1–4). The somewhat modest yields in these and the other reactions listed in Table 1 are presumably a consequence of a competing pathway through which the *N*-hydroxy group of one molecule of **8** or **7** reacts as a nucleophile to trap another of these species, thus leading to oligomeric materials. In fact, a dimer of **8** was detected by mass spectrometry. Besides hydroxy-bearing nucleophiles, thiols (Table 1, entries 5–8) and amines (Table 1, entries 9 and

Table 1: Preparation of *N*-hydroxyindoles from nitro ketoester **6**.[a]

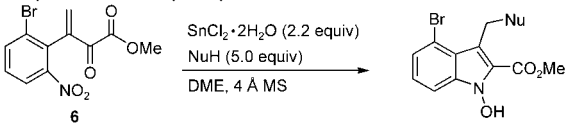

Entry	NuH	*T* [°C]	*t* [h]	Product	Yield [%][b]
1	$PhCH_2OH$	40	1.5	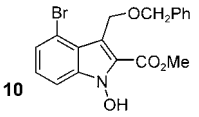 **10**	60
2	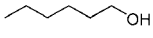	40	2.0	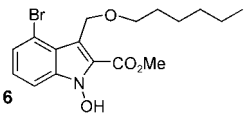 **16**	54
3	EtOH	40	1.3	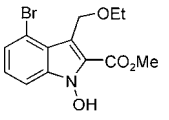 **17**	47
4[c]	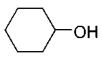	40	3.0	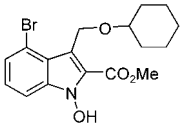 **18**	41
5	$PhCH_2SH$	40	1.0	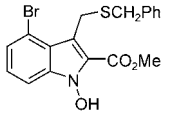 **11**	55
6	PhSH	40	0.7	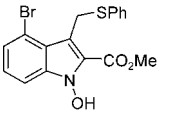 **19**	68
7	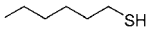	40	2.0	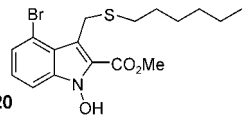 **20**	75
8	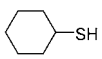	40	2.5	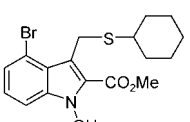 **21**	73

Table 1: (Continued)

Entry	NuH	T [°C]	t [h]	Product	Yield [%][b]
9		40	6.0	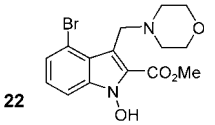 **22**	27
10	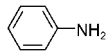	40	3.0	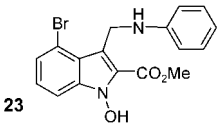 **23**	18
11	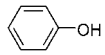	40	22	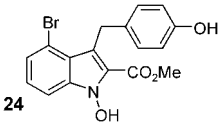 **24**	40
12	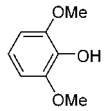	50	3.0	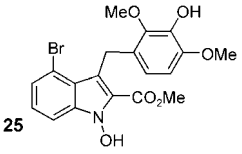 **25**	31

[a] Reactions were carried out on a 0.06–0.10-mmol scale in anhydrous DME (concentration: 0.12–0.16 M) and the products were purified by PTLC (silica gel). [b] Yields of isolated products. [c] $SnCl_2 \cdot 2H_2O$ (3 equiv).

10) also participated in this reaction to furnish *S*-substituted *N*-hydroxyindoles **11** and **19–21** and *N*′-substituted *N*-hydroxyindoles **22** and **23**, respectively. Interestingly, phenols react as carbon nucleophiles in this process and form carbon–carbon rather than carbon–oxygen bonds to give compounds **24** and **25** (Table 1, entries 11 and 12). Compound **25** (Table 2) was recrystallized from acetonitrile and its structure was confirmed by X-ray crystallographic analysis[7] (Figure 1).

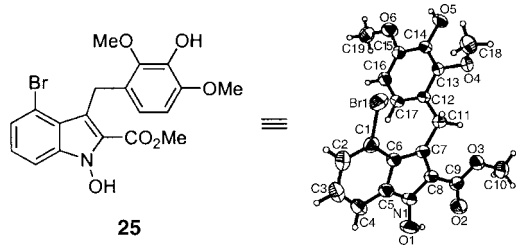

25

Figure 1. ORTEP drawing of compound **25** drawn at the 50% probability level.

Despite the presently unknown origins of this rather special and exclusive reactivity of phenolic nucleophiles towards these reactive species (i.e. **8** and/or **9**), its potential in delivering novel molecular diversity remains considerable and warrants further exploration.

Having developed this technology, we then proceeded to apply it to the synthesis of the nocathiacin I model system **3**, which contains the *N*-hydroxyindole structural motif and one of the thiazole rings of the natural product. Scheme 5 outlines the successful execution of this explorative study. Thus, the

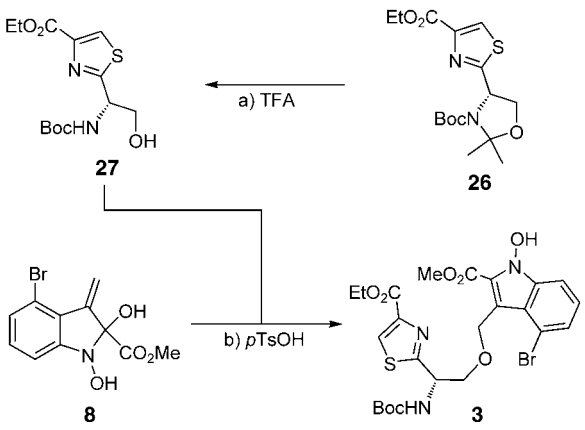

Scheme 5. Construction of *N*-hydroxyindole nocathiacin I model system **3**. Reagents and conditions: a) TFA/MeOH/CH_2Cl_2 (3:1:2), 25 °C, 30 min, 68%; b) *p*TsOH (3.0 equiv), molecular sieves (4 Å; 20 wt%), **27** (4.0 equiv), **8** (1.0 equiv), DME, 25 °C, 10 min; then 40 °C, 2 h, 44%. Boc = *tert*-butoxycarbonyl; TFA = trifluoroacetic acid.

Table 2: Selected physical properties for compounds **3**, **8**, **10**, and **25**.

3: $R_f = 0.43$ (silica gel, EtOAc/hexanes 7:3); $[\alpha]_D^{32} = -3.0$ ($c = 0.5$, $CHCl_3$); IR (film) $\tilde{\nu}_{max} = 3354, 2978, 2919, 1707, 1490, 1460, 1437, 1390, 1360, 1255, 1231, 1161, 1119, 1090, 1025, 879, 773, 743\ cm^{-1}$; ^1H NMR (600 MHz, CD_3CN, 66 °C): $\delta = 9.22$ (s, 1H), 8.06 (s, 1H), 7.50 (d, $J = 7.7$ Hz, 1H), 7.36 (d, $J = 7.7$ Hz, 1H), 7.22 (t, $J = 7.7$ Hz, 1H), 5.81 (br s, 1H), 5.17 ($^1/_2$ABq, $J = 11.4$ Hz, 1H), 5.14 ($^1/_2$ABq, $J = 11.4$ Hz, 1H), 5.04 (dt, $J = 7.4$, 4.8 Hz, 1H), 4.33 (q, $J = 7.0$ Hz, 2H), 3.97 (s, 3H), 3.96 (dd, $J = 10.0$, 4.8 Hz, 1H), 3.93 (dd, $J = 10.0$, 4.8 Hz, 1H), 1.39 (s, 9H), 1.35 ppm (t, $J = 7.0$ Hz, 3H); ^{13}C NMR (150 MHz, CD_3CN): $\delta = 174.0$, 162.2, 162.0, 156.2, 147.7, 137.2, 128.9, 127.2, 127.0, 126.9, 120.9, 115.9, 115.2, 110.2, 80.4, 71.2, 62.1, 61.9, 54.2, 53.1, 28.4, 14.5 ppm; HRMS (ESI) (%): calcd for $C_{24}H_{28}BrN_3O_8SNa$ [M+Na^+]: 620.0673; found: 620.0674

8: $R_f = 0.53$ (silica gel, EtOAc/hexanes 6:4); IR (film) $\tilde{\nu}_{max} = 3389, 2954, 2849, 1737, 1596, 1566, 1460, 1431, 1290, 1255, 1231, 1184, 1155, 1096, 1026, 885, 802, 749\ cm^{-1}$; ^1H NMR (600 MHz, CD_3CN): $\delta = 7.64$ (s, 1H), 7.14 (t, $J = 7.9$ Hz, 1H), 7.11 (dd, $J = 7.9$, 1.3 Hz, 1H), 6.85 (dd, $J = 7.9$, 1.3 Hz, 1H), 6.32 (s, 1H), 5.40 (s, 1H), 5.08 (br s, 1H), 3.61 ppm (s, 3H); ^{13}C NMR (150 MHz, CD_3CN): $\delta = 170.3$, 154.8, 144.3, 132.1, 127.3, 123.4, 117.9, 111.8, 111.7, 98.9, 53.6 ppm; HRMS (ESI) (%): calcd for $C_{11}H_{10}BrNO_4Na$ [M+Na^+]: 321.9685; found: 321.9684.

10: $R_f = 0.58$ (silica gel, EtOAc/hexanes 6:4); IR (film) $\tilde{\nu}_{max} = 3194, 2952, 2848, 1710, 1525, 1433, 1353, 1312, 1255, 1226, 1185, 1122, 1047, 1024, 909, 874, 771, 730, 690\ cm^{-1}$; ^1H NMR (400 MHz, CD_3CN): $\delta = 9.49$ (br s, 1H), 7.45 (d, $J = 8.1$ Hz, 1H), 7.39–7.23 (m, 6H), 7.18 (t, $J = 8.1$ Hz, 1H), 5.10 (s, 2H), 4.61 (s, 2H), 3.88 ppm (s, 3H); ^{13}C NMR (150 MHz, CD_3CN): $\delta = 162.2$, 139.9, 137.2, 129.2, 128.9, 128.3, 127.1, 126.9, 126.8, 121.0, 116.0, 115.9, 110.2, 72.7, 61.8, 52.9 ppm; HRMS (ESI) (%): calcd for $C_{18}H_{16}BrNO_4Na$ [M+Na^+]: 412.0155; found: 412.0155

25: $R_f = 0.42$ (silica gel, EtOAc/hexanes 6:4); IR (film) $\tilde{\nu}_{max} = 3414, 2934, 2835, 1708, 1675, 1615, 1489, 1440, 1396, 1347, 1287, 1249, 1085, 1030, 894, 746\ cm^{-1}$; ^1H NMR (600 MHz, CD_3CN): $\delta = 9.21$ (s, 1H), 7.51 (d, $J = 7.9$ Hz, 1H), 7.28 (d, $J = 7.9$ Hz, 1H), 7.21 (t, $J = 7.9$ Hz, 1H), 6.46 (d, $J = 8.6$ Hz, 1H), 6.38 (s, 1H), 5.92 (d, $J = 8.6$ Hz, 1H), 4.62 (s, 2H), 3.86 (s, 3H), 3.82 (s, 3H), 3.74 ppm (s, 3H); ^{13}C NMR (150 MHz, CD_3CN): $\delta = 162.5$, 147.5, 146.0, 139.7, 138.0, 128.6, 127.3, 126.5, 126.4, 121.2, 119.2, 118.6, 116.3, 110.4, 107.5, 60.4, 56.7, 52.6, 24.7 ppm; HRMS (ESI) (%): calcd for $C_{19}H_{18}BrNO_6Na$ [M+Na^+]: 458.0210; found: 458.0200

previously synthesized thiazole derivative **26**[8] was partially deprotected by controlled exposure to TFA in $MeOH/CH_2Cl_2$ at 25 °C to afford hydroxy Boc-protected amine **27** in 68 % yield. Coupling of the latter compound with **8** in the presence of *p*TsOH in DME at 40 °C then resulted in the formation of *N*-hydroxyindole model system **3** (Table 2) in 44 % yield (unoptimized).[9]

Besides possibly facilitating the total synthesis of nocathiacin I (**1**), the described new synthetic technology may find numerous applications in synthetic endeavors directed towards polyfunctional *N*-hydroxyindoles and other biologically interesting molecules.

Received: February 25, 2005
Published online: May 13, 2005

Keywords: indoles · natural products · nitrones · nucleophilic addition · synthetic methods

[1] For selected reviews on *N*-hydroxyindoles and their derivatives, see: a) M. Somei, *Adv. Heterocycl. Chem.* **2002**, *82*, 101 – 155; b) M. Somei, *Heterocycles* **1999**, *50*, 1157 – 1211; c) R. M. Acheson, *Adv. Heterocycl. Chem.* **1990**, *51*, 105 – 175.

[2] a) A. Wong, J. T. Kuethe, I. W. Davies, *J. Org. Chem.* **2003**, *68*, 9865 – 9866; b) A. G. Myers, S. B. Herzon, *J. Am. Chem. Soc.* **2003**, *125*, 12080 – 12081; c) S. Katayama, N. Ae, R. Nagata, *J. Org. Chem.* **2001**, *66*, 3474 – 3483; d) Z. Wróbel, M. Makosza, *Tetrahedron* **1997**, *53*, 5501 – 5514; e) A. Reissert, H. Heller, *Ber. Dtsch. Chem. Ges.* **1904**, *37*, 4364 – 4379.

[3] a) W. Li, J. E. Leet, H. A. Ax, D. R. Gustavson, D. M. Brown, L. Turner, K. Brown, J. Clark, H. Yang, J. Fung-Tomc, K. S. Lam, *J. Antibiot.* **2003**, *56*, 226 – 231; b) J. E. Leet, W. Li, H. A. Ax, J. A. Matson, S. Huang, R. Huang, J. L. Cantone, D. Drexler, R. A. Dalterio, K. S. Lam, *J. Antibiot.* **2003**, *56*, 232 – 242; c) K. L. Constantine, L. Mueller, S. Huang, S. Abid, K. S. Lam, W. Li, J. E. Leet, *J. Am. Chem. Soc.* **2002**, *124*, 7284 – 7285; d) nocathiacin antibiotics: J. E. Leet, H. A. Ax, D. R. Gustavson, D. M. Brown, L. Turner, K. Brown, W. Li, K. S. Lam, WO 2000003722 A1, **2000** [*Chem. Abstr.* **2000**, 132, 121531].

[4] T. Sasaki, T. Otani, H. Matsumoto, N. Unemi, M. Hamada, T. Takeuchi, M. Hori, *J. Antibiot.* **1998**, *8*, 715 – 721.

[5] For an example of this type of α-methylenation, see: J. Ezquerra, C. Pedregal, *Tetrahedron: Asymmetry* **1994**, *5*, 921 – 926.

[6] For α-functionalization of a substituted toluene, see: C.-g. Shin, Y. Yamada, K. Hayashi, Y. Yonezawa, K. Umemura, T. Tanji, J. Yoshimura, *Heterocycles* **1996**, *43*, 891 – 898.

[7] CCDC-264685 (**13**), -264686 (**10**), and -264687 (**25**) contain the supplementary crystallographic data for this paper. These data can be obtained free of charge from the Cambridge Crystallographic Data Centre via www.ccdc.cam.ac.uk/data_request/cif.

[8] a) C.-g. Shin, A. Okabe, A. Ito, A. Ito, Y. Yonezawa, *Bull. Chem. Soc. Jpn.* **2002**, *75*, 1583 – 1596; b) For the thio derivative, see: K. C. Nicolaou, M. Nevalainen, B. S. Safina, M. Zak, S. Bulat, *Angew. Chem.* **2002**, *114*, 2021 – 2025; *Angew. Chem. Int. Ed.* **2002**, *41*, 1941 – 1945.

[9] We have also recently synthesized a more advanced model system containing the 15-membered lactone–ether ring of nocathiacin I through both intermolecular and intramolecular versions of this *N*-hydroxyindole method. More details will be published in due course.

DNA Structures

Drastic Effect of a Single Base Difference between Human and *Tetrahymena* Telomere Sequences on Their Structures under Molecular Crowding Conditions**

*Daisuke Miyoshi, Hisae Karimata, and Naoki Sugimoto**

G-rich sequences, which are abundant throughout the genomes of most organisms, can fold into G-quadruplexes. There is little direct evidence for the formation of G-quadruplexes in vivo,[1] but there is growing interest in their potential roles in many biological systems.[2] In addition, various functional molecules can form G-quadruplex structures in vitro.[3] G-rich sequences have extraordinary structural polymorphism that depends on the sequence and the environmental conditions.[4] Importantly, the polymorphic nature of the G-quadruplexes makes them a promising nanomolecular material, because a regulated structural transition between different types of G-quadruplexes can provide the basis for switchable molecular devices.[5] Moreover, the G-rich sequences are attracting interest as functional elements in molecular electronics.[6] Therefore, regulation of the polymorphic nature of the G-quadruplex presents a novel methodology for both developing molecular devices in vitro and controlling biological phenomena in vivo.

Changes in the environmental conditions can result in various structural changes of nucleic acids,[7] especially G-quadruplexes. For example, we reported that structural transitions between antiparallel and parallel G-quadruplexes, and between duplex and quadruplex, are induced by molecular crowding,[8] which is a critical environmental factor affecting the structure of biomacromolecules.[9] The effect of molecular crowding on the structures and functions of biomacromolecules has been examined because living cells are inherently molecularly crowded environments that contain a wide variety of biomolecules. For example, the total biomolecule concentration in *Escherichia coli* is in the range of 300 to 400 $g L^{-1}$.[9] This value is different from the typical biomolecule concentrations ($< 1 g L^{-1}$) generally used for

[*] Prof. Dr. N. Sugimoto
Frontier Institute for Biomolecular Engineering Research (FIBER) and Department of Chemistry
Faculty of Science and Engineering, Konan University
8-9-1 Okamoto, Higashinada-ku, Kobe 658-8501 (Japan)
Fax: (+81) 78-435-2766
E-mail: sugimoto@konan-u.ac.jp
Dr. D. Miyoshi
FIBER, Konan University (Japan)
H. Karimata
Department of Chemistry, Faculty of Science and Engineering
Konan University (Japan)

[**] This work was supported in part by Grants-in-Aid from the Ministry of Education, Science, Sports, and Culture, Japan.

Supporting information for this article is available on the WWW under http://www.angewandte.org or from the author.

  DOI: 10.1002/anie.200462667

in vitro experiments. However, only a few systematic experimental studies of G-quadruplex structures under molecular crowding conditions have been reported.[8] Herein we present evidence that molecular crowding induces drastically different structures in the G-quadruplexes formed by *Tetrahymena* (Tet) and human (Hum) telomere sequences. These sequence motifs differ by only one base, which indicates that the single mutation in the telomere sequence is crucial for the regulation of its polymorphic nature and, therefore, its potential biological functions and material properties.

Figure 1 shows the circular dichroism (CD) spectra of samples (50 μmol L^{-1}) of four telomere DNA sequences (sites where Tet and Hum differ are underlined): intermolecular

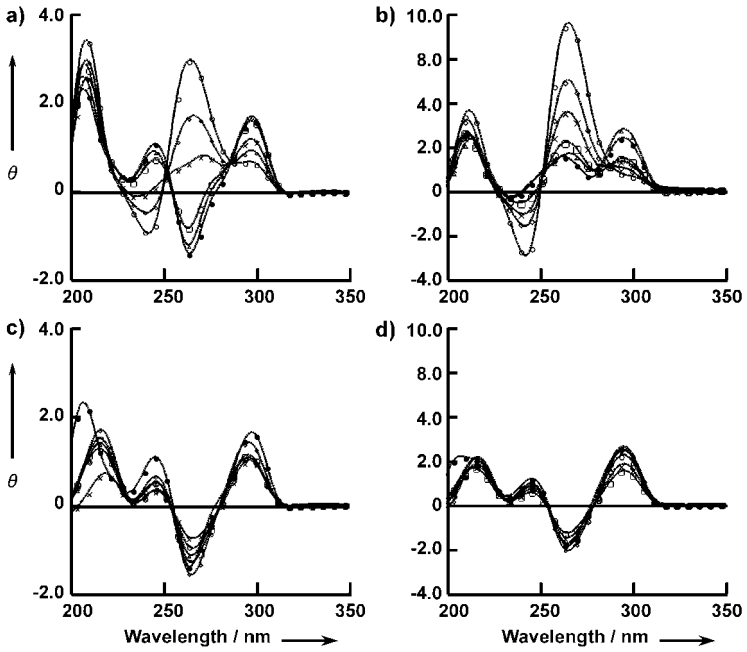

Figure 1. CD spectra (θ in 10^5 deg cm^2 $dmol^{-1}$) of samples of inter-Tet (a), intra-Tet (b), inter-Hum (c), and intra-Hum (d) at 4 °C without (●) and with 40 wt% cosolute. Cosolutes include ethylene glycol (△), diethylene glycol (□), triethylene glycol (×), PEG 200 (◇), and PEG 2000 (○).

Tetrahymena (inter-Tet; d[$TGG_3T_2\underline{G}G_3T$]; Figure 1a), intramolecular *Tetrahymena* (intra-Tet; d[$T_2G(G_3T_2\underline{G})_3G$]; Figure 1b), intermolecular human (inter-Hum; d[$TAG_3T_2\underline{A}G_3T$]; Figure 1c), and intramolecular human (intra-Hum; d[$(G_3T_2\underline{A})_3G_3$]; Figure 1d). CD measurements were carried out with and without a cosolute.[10] Polyethylene glycol (PEG) and its related small molecules are commonly used as cosolutes in aqueous solution to mimic molecular crowding conditions, because they do not react with nucleotides and a variety of molecular weights are available.[8–10] Except for intra-Tet, the CD spectra of the telomere sequences in the absence of cosolute have positive and negative peaks at 295 and 265 nm, respectively, which indicates that these telomere sequences fold into antiparallel G-quadruplexes.[8,11] Intermolecular *Oxytricha* (inter-Oxy; d[$G_4T_4G_4$]) and intramolecular *Oxytricha* (intra-Oxy; d[$(G_4T_4)_3G_4$)]) telomere sequences also show an antiparallel structure in the absence of the cosolute (see the Supporting Information). However, the CD spectrum of intra-Tet has positive peaks at 295 and 260 nm in the absence of cosolute, thus indicating a mixture of parallel and antiparallel G-quadruplexes.[8,11] These results are consistent with those of previous reports that describe the structure of these telomere sequences.[12]

Surprisingly, the CD spectra in the presence of cosolutes with various molecular weights reveal that, under crowding conditions, a single G-to-A replacement in the loops affects the entire telomere structure. Specifically, the CD spectra of inter-Tet and intra-Tet in the presence of higher-molecular-weight cosolutes have a positive peak at approximately 260 nm and a shoulder near 295 nm. In contrast, the CD spectra of inter-Hum and intra-Hum do not change under these conditions. This finding indicates that the *Tetrahymena* but not the human telomere DNA undergoes a structural transition from an antiparallel to a parallel G-quadruplex in the presence of higher-molecular-weight cosolutes such as PEG 2000. Furthermore, the CD spectra of inter-Oxy, intra-Oxy, d[$(T_3G_4)_4$], d[$(G_3T_3)_3G_3$], d[$(G_4T_2)_3G_4$], and d[$(T_2AG_3)_4$] in the presence and absence of the cosolute demonstrated that these telomere sequences, except d[$(T_2AG_3)_4$], undergo the structural transition by adding the cosolute (see the Supporting Information). These telomere sequences have different molecularities (intermolecular or intramolecular), sequence lengths, and numbers of G-quartets (guanine plane), nucleotides in the loop, and extra nucleotides at the termini, which indicates that these factors are not important participants in the transition. Therefore, the single base difference between human and *Tetrahymena* telomere sequences critically affects the entire structure of the telomere DNA. However, the CD spectra suggest that the cosolutes cause a more dramatic shift to a parallel G-quadruplex for inter-Tet (Figure 1a) than for intra-Tet (Figure 1b).

Phan et al.[12a,b] reported the solution structure of inter-Tet in the presence of Na^+ ions and of inter-Hum in the presence of K^+ ions. Inter-Tet forms two antiparallel dimeric G-quadruplexes with different positions of the loops. Inter-Hum also has two different structures: a dimeric parallel G-quadruplex with loops located in the grooves (propeller structure) and a dimeric antiparallel G-quadruplex with loops located on the G-tetrad planes. Wang and Patel[12c,d] reported that intra-Tet and intra-Hum form intramolecular antiparallel G-quadruplexes with Na^+ ions. Parkinson et al.[13] used X-ray crystallography to show that the inter-Hum and intra-Hum form dimeric and monomeric propeller-type parallel G-quadruplex structures in the presence of K^+ ions, although the human telomere sequences used in their study were slightly different from those used here. On the basis of these structural studies, one can conclude that inter-Tet and intra-Tet fold into antiparallel G-quadruplexes in the presence of Na^+ ions. Inter-Hum and intra-Hum can fold into dimeric and monomeric antiparallel G-quadruplexes, respectively, in the presence of Na^+ ions and

can potentially fold into propeller-type parallel G-quadruplexes as a monomer and dimer, respectively.

The excluded volume, one of the factors of molecular crowding,[9] can induce the association of monomers into multimeric complexes.[9,14] For example, monomeric and dimeric antiparallel G-quadruplexes can associate into multistranded G-wires.[8] Inter-Tet and intra-Tet likely underwent this structural transition because their parallel structure must be either four- or multistranded, such as in a G-wire structure (Figure 2). Inter-Hum and intra-Hum, however, could not

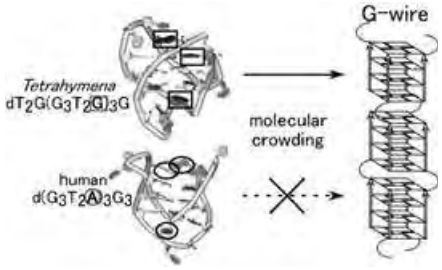

Figure 2. Schematic illustration of the structures of intra-Tet and intra-Hum in dilute and molecular crowding conditions. G (□) and A (○) correspond to the single-mutation sites.

undergo the antiparallel-to-parallel transition under conditions of molecular crowding because the parallel structures form propeller-type G-quadruplexes, which may have excluded volumes larger than that of the antiparallel G-quadruplex.[12,13] In addition, the thermodynamic properties of intra-Tet and intra-Hum in the presence and absence of 40 wt% PEG200 were examined by using UV melting curves monitored at 295 nm. The melting temperatures (T_m) of intra-Tet were 70.4 and 62.0 °C, respectively, whereas these T_m values for intra-Hum were 65.0 and 60.8 °C, respectively. Therefore, a larger stabilization of intra-Tet by the cosolutes may induce the structural transition.

To further verify the formation of the G-wire structure, we performed native gel electrophoresis on a 10% polyacrylamide gel.[15] Figure 3a shows the migration of intra-Tet and intra-Hum in the presence of 0 to 40 wt% PEG2000. The migration pattern of intra-Tet is typical for a G-wire (indicated by asterisks).[16] Furthermore, the ratio of intra-Tet migrating at the top of the gel increased as the concentration of PEG2000 was increased (indicated by arrows). In denaturing gel electrophoresis, the band at the top of the gel with intra-Tet samples disappeared, and another moderately migrating band appeared (arrow in Figure 3b). All of these results indicate that the band observed at the top of the native gel for intra-Tet samples corresponds to a highly ordered G-wire complex, whereas intra-Hum remains as a compact intramolecular G-quadruplex structure even in the presence of 40 wt% PEG2000. This concept is further confirmed by the CD spectra, which show that titration with PEG2000 causes a structural transition from an antiparallel G-quadruplex to a parallel-oriented G-quadruplex of intra-Tet but

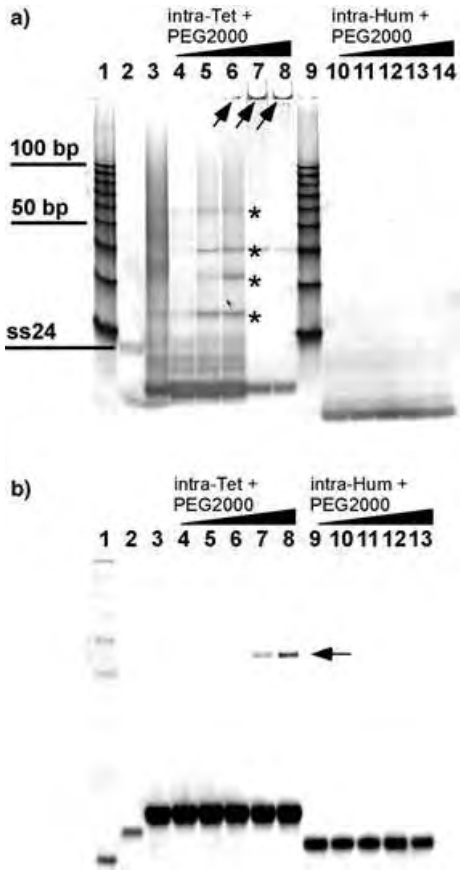

Figure 3. a) Native gel electrophoresis of intra-Tet and intra-Hum in the absence and presence of PEG2000. See the Experimental Section for details. Lanes 1 and 9: 10-bp DNA ladder; lane 2: single-stranded 24-mer DNA; lane 3: inter-Tet with Mg^{2+} and spermidine; lanes 4–8: intra-Tet in the presence of 0, 10, 20, 30, and 40 wt% PEG2000, respectively; lanes 10–14: intra-Hum in the presence of 0, 10, 20, 30, and 40 wt% PEG2000, respectively. b) Denaturing gel electrophoresis of intra-Tet and intra-Hum in the absence and presence of PEG2000. See the Experimental Section for details. Lane 1: 10-base DNA ladder; lane 2: single-stranded 24-mer DNA; lane 3: inter-Tet with Mg^{2+} and spermidine; lanes 4–8: intra-Tet in the presence of 0, 10, 20, 30, and 40 wt% PEG2000, respectively; lanes 9–13: intra-Hum in the presence of 0, 10, 20, 30, and 40 wt% PEG2000, respectively.

not intra-Hum (Figure 4). The CD spectrum of intra-Tet in the presence of 40 wt% PEG2000 (○) in Figure 4a) has a

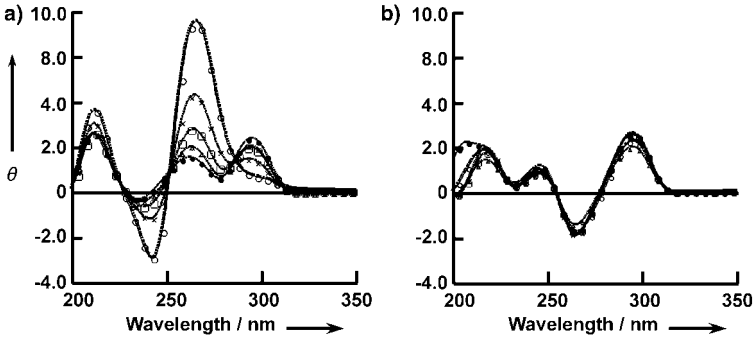

Figure 4. CD spectra of samples of intra-Tet (a) and intra-Hum (b) at 4 °C without (●) or with 10 (△), 20 (□), 30 (×), or 40 wt% (○) PEG2000.

small shoulder around 295 nm, which indicates that the antiparallel G-quadruplex still remains in this condition. This shoulder may correspond to the remaining band present in the antiparallel G-quadruplex of intra-Tet (Figure 3a). In addition, the migration of inter-Tet in the presence of Mg^{2+} ions and spermidine (lane 3 in Figure 3a), where there is a high potential for the formation of G-wires,[16] shows a very diffuse band, and lanes 4 to 8 provide some evidence of discrete retarded complexes. Therefore, the migration of intra-Tet in the presence of PEG 2000 shows a higher-ordered and, thus, a longer G-wire structure. Finally, although it is difficult to prepare homogeneous G-wires, they can be obtained by cutting out the band in the denaturing gel.

In summary, we have demonstrated that a single G-to-A substitution in the loops of telomere sequences leads to drastically different structures. Under molecular crowding conditions, *Tetrahymena* telomere sequences fold into very long, highly ordered G-wires, whereas human telomere sequences fold into antiparallel G-quadruplexes. Further studies are required, such as on the effect of monovalent cations on the structure of the telomere sequences under molecular crowding conditions. However, the results reported here indicate that a single mutation in the telomere sequence is a critical factor affecting the polymorphic nature of the G-quadruplex and, therefore, of telomere function in cell-like conditions.

Apart from the biological aspects, there is growing interest in G-rich sequences as functional elements in molecular electronics.[6,17] A theoretical study suggested that the G-wire structure is promising for nanoscale biomolecular electronics because of its highly order structure.[18] However, its electrical properties have not yet been described because of the difficulty in creating and controlling the G-wire structure. Herein, we have described the control of the G-wire structure by a single mutation and by adjusting the solution conditions. These findings make it possible to measure electrical transport through G-wires.

Experimental Section

All cosolutes were purchased from Wako Pure Chemical Co. Ltd. (Japan) and used without further purification. Oligonucleotides were synthesized, purified, and confirmed as described elsewhere.[19] The DNA samples were heated to 80 °C, gently cooled at a rate of 2.0 K min^{-1}, and incubated overnight at 4 °C.

CD spectra of DNA samples (50 μmol L^{-1} total strand concentration) were obtained by using a J-820 spectropolarimeter (JASCO Co. Ltd., Japan) with a 0.1-cm-path-length quartz cell. CD measurements were carried out in a buffer containing NaCl (100 mmol L^{-1}), Na_2HPO_4 (10 mmol L^{-1}), and ethylenediaminetetraacetic acid disodium salt (Na_2EDTA, 1 mmol L^{-1}, pH 7.0) with or without cosolutes at the desired temperature. It was possible to induce the formation of G-wires by inter-Tet and intra-Tet by adding a cosolute and without heating. In this study, however, to ensure that the structures reached equilibrium, CD spectra were recorded after heating and slow cooling to 4 °C followed by an overnight incubation.

UV melting curves for DNA samples (50 μmol L^{-1} total strand concentration) were recorded at 295 nm[20] by using a Shimadzu UV-1700 instrument (Shimadzu Co. Ltd., Japan) with a 0.1-cm-path-length quartz cell. The measurements were carried out at 4 °C in a buffer containing NaCl (100 mmol L^{-1}), Na_2HPO_4 (10 mmol L^{-1}), and Na_2EDTA (1 mmol L^{-1}, pH 7.0) with or without cosolutes. Before measurements were made, the DNA samples were heated, cooled, and incubated to allow them to equilibrate, as described above. The samples were heated at 0.5 K min^{-1} to obtain the melting curves.

Native gel electrophoresis was carried out at 4 °C and 5 V cm^{-1} on a 10 % nondenaturing polyacrylamide gel in a buffer containing NaCl (100 mmol L^{-1}), Na_2HPO_4 (10 mmol L^{-1}), and Na_2EDTA (1 mmol L^{-1}, pH 7.0). Ice-cold loading buffer (2 μL, 40 % glycerol and 1 % blue dextran) was mixed with the DNA sample (2 μL, 25 μmol L^{-1}). Before measurements were made, the DNA samples were heated, cooled, and incubated to allow them to equilibrate, as described above. Denaturing gel electrophoresis was carried out using the same procedure as that for native gel electrophoresis, except that the loading buffer contained 50 % formamide and electrophoresis was performed at room temperature. Gels were stained with GelStar nucleic acid gel stain (Cambrex, ME, USA) and imaged using FLS-5100 film (Fuji Photo Film Co. Ltd., Japan).

Received: November 19, 2004
Published online: April 29, 2005

Keywords: DNA structures · molecular devices · nanostructures · oligonucleotides · self-assembly

[1] a) C. Schaffitzel, I. Berger, J. Postberg, J. Hanes, H. J. Lipps, A. Plückthun, *Proc. Natl. Acad. Sci. USA* **2001**, *98*, 8572 – 8577; b) A. Siddiqui-Jain, C. L. Grand, D. J. Bearss, L. H. Hurley, *Proc. Natl. Acad. Sci. USA* **2002**, *99*, 11593 – 11598; c) M. L. Duquette, P. Handa, J. A. Vincent, A. F. Taylor, N. Maizels, *Genes Dev.* **2004**, *18*, 1618 – 1629.

[2] a) S. Neidle, M. A. Read, *Biopolymers* **2001**, *56*, 195 – 208; b) R. H. Shafer, I. Smirnov, *Biopolymers* **2001**, *56*, 209 – 227; c) J.-L. Mergny, C. Helene, *Nat. Med.* **1998**, *4*, 1366 – 1367; d) S. Neidle, G. Parkinson, *Nat. Rev. Drug Discovery* **2002**, *1*, 383 – 393.

[3] a) R. F. Macaya, P. Schultze, F. W. Smith, J. A. Roe, J. Feigon, *Proc. Natl. Acad. Sci. USA* **1993**, *90*, 3745 – 3749; b) N. Jing, M. E. Hogan, *J. Biol. Chem.* **1998**, *273*, 34992 – 34999; c) N. Sugimoto, T. Toda, T. Ohmichi, *Chem. Commun.* **1998**, 1533 – 1534; d) A. M. Whitney, S. Ladame, S. Balasubramanian, *Angew. Chem.* **2004**, *116*, 1163 – 1166; *Angew. Chem. Int. Ed.* **2004**, *43*, 1143 – 1146.

[4] a) D. Sen, W. Gilbert, *Nature* **1990**, *344*, 410 – 414; b) D. Sen, W. Gilbert, *Biochemistry* **1993**, *31*, 65 – 70; c) M. A. Keniry, *Biopolymers* **2001**, *56*, 123 – 146; d) F. M. Chen, *Biochemistry* **1992**, *31*, 3769 – 3776.

[5] a) C. Mao, W. Sun, Z. Shen, N. C. Seeman, *Nature* **1999**, *397*, 144 – 146; b) P. Alberti, J.-L. Mergny, *Proc. Natl. Acad. Sci. USA* **2003**, *100*, 1569 – 1573; c) J. T. Davis, *Angew. Chem.* **2004**, *116*, 684 – 716; *Angew. Chem. Int. Ed.* **2004**, *43*, 668 – 698.

[6] V. A. Szalai, H. H. Thorp, *J. Am. Chem. Soc.* **2000**, *122*, 4524 – 4525.

[7] Y. Fang, T. S. Spisz, J. H. Hoh, *Nucleic Acids Res.* **1999**, *27*, 1943 – 1949.

[8] a) D. Miyoshi, A. Nakao, N. Sugimoto, *Biochemistry* **2002**, *41*, 15017 – 15024; b) D. Miyoshi, S. Matsumura, S. Nakano, N. Sugimoto, *J. Am. Chem. Soc.* **2004**, *126*, 165 – 169.

[9] a) S. B. Zimmerman, A. P. Minton, *Annu. Rev. Biophys. Biomol. Struct.* **1993**, *22*, 27 – 65; b) J. R. Wenner, V. A. Bloomfield, *Biophys. J.* **1999**, *77*, 3234 – 3241; c) P. R. Davis-Searles, A. J. Saunders, D. A. Erie, D. J. Winzor, G. J. Pielak, *Annu. Rev. Biophys. Biomol. Struct.* **2001**, *30*, 271 – 306; d) A. P. Minton, *J. Biol. Chem.* **2001**, *276*, 10577 – 10580.

[10] The molecular weights of the cosolutes used, ethylene glycol, diethylene glycol, triethylene glycol, PEG 200, and PEG 2000, are 62, 106, 150, 200 (average), and 2000 (average), respectively:

S. Nakano, H. Karimata, T. Ohmichi, J. Kawakami, N. Sugimoto, *J. Am. Chem. Soc.* **2004**, *126*, 14330 – 14331.
[11] a) M. Lu, Q. Guo, N. R. Kallenback, *Biochemistry* **1992**, *31*, 2455 – 2459; b) P. Balagurumoorthy, S. K. Brahmachari, *J. Biol. Chem.* **1994**, *269*, 21858 – 21869; c) A. Risitano, K. R. Fox, *Nucleic Acids Res.* **2004**, *32*, 2598 – 2606.
[12] a) A. T. Phan, Y. S. Modi, D. J. Patel, *J. Mol. Biol.* **2004**, *338*, 93 – 102; b) A. T. Phan, D. J. Patel, *J. Am. Chem. Soc.* **2003**, *125*, 15021 – 15027; c) Y. Wang, D. J. Patel, *Structure* **1994**, *2*, 1141 – 1156; d) Y. Wang, D. J. Patel, *Structure* **1993**, *1*, 263 – 282.
[13] G. N. Parkinson, M. P. H. Lee, S. Neidle, *Nature* **2002**, *417*, 876 – 880.
[14] A. P. Minton, *Biopolymers* **1981**, *20*, 2093 – 2120.
[15] V. Dapic, V. Abdomerovic, R. Marrington, J. Peberdy, A. Rodger, J. O. Trent, P. J. Bates, *Nucleic Acids Res.* **2003**, *31*, 2097 – 2107.
[16] a) D. Sen, W. Gilbert, *Biochemistry* **1992**, *31*, 65 – 70; b) T. C. Marsh, J. Vesenka, E. Henderson, *Nucleic Acids Res.* **1995**, *23*, 696 – 700.
[17] a) S. Delaney, J. K. Barton, *Biochemistry* **2003**, *42*, 14159 – 14165; b) D. Porath, A. Bezryadin, S. de Vries, C. Dekker, *Nature* **2000**, *403*, 635 – 637; c) G. B. Schuster, *Acc. Chem. Res.* **2000**, *33*, 253 – 260.
[18] A. Calzolari, R. D. Felice, E. Molinari, *Appl. Phys. Lett.* **2002**, *80*, 3331 – 3333.
[19] a) T. Ohmichi, S. Nakano, D. Miyoshi, N. Sugimoto, *J. Am. Chem. Soc.* **2002**, *124*, 10367 – 10372; b) S. Nakano, T. Kanzaki, N. Sugimoto, *J. Am. Chem. Soc.* **2004**, *126*, 1088 – 1095.
[20] J. L. Mergny, A. T. Phan, L. Lacroix, *FEBS Lett.* **1998**, *435*, 74 – 78.

Host–Guest Systems

Size-Selective and Reversible Encapsulation of Single Small Hydrocarbon Molecules by a Cavitand–Porphyrin Species**

*Jun Nakazawa, Jun Hagiwara, Maki Mizuki, Yuichi Shimazaki, Fumito Tani, and Yoshinori Naruta**

Small hydrocarbon molecules are subject to processes of biological isolation, sequestration, and selective reactions that are mediated by biomolecular recognition events.[1] One particularly noteworthy biological process of hydrocarbons is the enzymatic monooxygenation of methane and related small hydrocarbons.[2,3] The mechanisms through which these chemical transformations occur are of particular interest in light of their potential applicability for the development of catalysts for large-scale industrial chemical transformations.[4]

One of the major shortcomings of artificial hydrocarbon-recognition model systems is the absence of the requisite strong interactions between the host and the guest molecules. This feature of hydrocarbons makes the selective recognition processes less efficient. One of the most effective natural mechanisms for the recognition of hydrocarbons is an encapsulation process mediated by capsulelike molecules that have a hydrophobic cavity with a given shape and volume.[5] Various guest-encapsulating carcerands and related molecules have been reported.[6] These compounds typically have rigid enclosed structures and are not suitable for release or exchange of encapsulated guest molecules. For further reaction of the encapsulated guest molecules, the host requires an active site with a flexible portal for guest exchange.

Other researchers have reported host compounds with cup-shaped calix[4]arenes,[7] cavitands,[8] cyclodextrin, etc.[9] that have cavities suitable to accommodate small organic molecules in combination with a flat porphyrin, which acts both as a lid for the cavity and as a ligand for metal ions. These compounds have been demonstrated to encapsulate pyridines, imidazoles, adamantanes, etc.

In work described herein, we have designed a new cavitand–porphyrin **1** as a host compound for smaller hydrocarbons such as methane and ethane. To accommodate small guest molecules and to retain suitable flexibility of the portal, the cavitand and the porphyrin are connected by two ether linkages. With use of **1** as a host, we have successfully demonstrated size-selective and reversible encapsulation of small hydrocarbons within the host cavity.

Williamson-type coupling between A,B-type bis(chloromethyl)cavitand **3**[10] and *meso*-bis(2-hydroxyphenyl)diphenylporphyrin (**4**) (used as a mixture of four regio- and atropisomers: 5,10; 5,15; α,α; and α,β)[11] gave *syn* (**1**, 46% yield based on **3**) and *anti* (**2**, 14% yield) cavitand–porphyrin species (Supporting Information).

The structures of the two isomers were determined by ^{1}H NMR spectra as follows: The ^{1}H NMR signals of all bridged -OCH_2O- protons of the *syn* isomer **1** showed large upfield shifts relative to those of the starting cavitand **3** (H_{ao}, H_{ai}, H_{bo}, and H_{bi}: $\Delta\delta = -3.41$, -5.65, -0.52, and -2.42 ppm, respectively) owing to the large anisotropic effect of the porphyrin ring current (Supporting Information). This observation suggests that the cavitand and porphyrin moieties of **1** adopt a fully overlapping geometry and that the portal is very narrow.

We examined the encapsulation of various small hydrocarbon molecules in **1** (Figure 1). Upon exposure of CH_4 gas to a solution of **1** in $CDCl_3$, a new proton signal appeared at $\delta = -7.19$ ppm (Figure 1b), which disappeared when Ar was bubbled into the solution.[12] The large upfield shift ($\Delta\delta = -7.34$ ppm) from the signal of free methane ($\delta = 0.15$ ppm) is rationalized by anisotropic effects arising from both the cavitand and porphyrin aromatic ring systems which are

[*] J. Nakazawa, J. Hagiwara, M. Mizuki, Dr. Y. Shimazaki, Dr. F. Tani, Prof. Dr. Y. Naruta
Institute for Materials Chemistry and Engineering
Kyushu University
Higashi-ku, Fukuoka 812–8581 (Japan)
Fax: (+81) 92-642-2715
E-mail: naruta@ms.ifoc.kyushu-u.ac.jp

[**] This work was supported by Grants-in-Aid for Scientific Research on Priority Areas (no. 15036254) from MEXT and for Scientific Research (A) (no. 14204073) and for Exploratory Research (no. 16655039) from the JSPS as well as by a grant from The Asahi Glass Foundation.

Supporting information for this article is available on the WWW under http://www.angewandte.org or from the author.

  DOI: 10.1002/anie.200500732

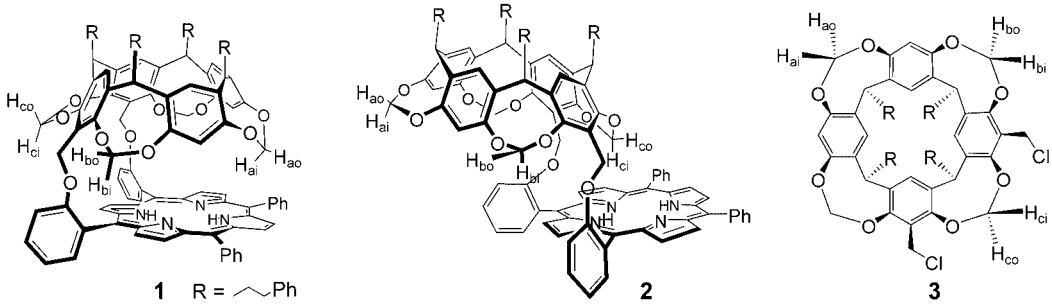

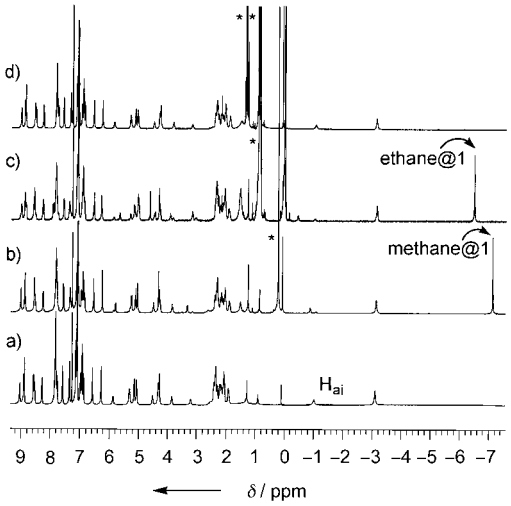

Figure 1. ^{1}H NMR spectra of **1** with hydrocarbons in $CDCl_3$ under atmospheric pressure at 25 °C. a) **1**, b) **1** with methane, c) **1** with ethane, d) **1** with propane. *Signals of the free hydrocarbons.

estimated to contribute to the upfield shift of the signal for the encapsulated molecule by $\delta = -3$–-4[5b,c,13] and $\delta = -4$–-5 ppm,[14] respectively. Thus, the signal at $\delta = -7.19$ ppm is assigned to the protons of the encapsulated methane molecule. Only one CH_4 molecule was trapped in the cavity, as confirmed by the integration ratio of the ^{1}H NMR signals. Furthermore, the solvent $CDCl_3$ is not trapped in the cavity, as confirmed by ^{13}C NMR spectroscopy.

The perfect separation of the signals corresponding to free and encapsulated methane protons indicates that the guest-exchange rate in **1** with the bulk solvent phase is slower than the ^{1}H NMR timescale. The fact that CH_4 is trapped in and purged from the cavity when CH_4 or Ar, respectively, are bubbled into the solution suggests that the portal of the cavity has enough flexibility to exchange the encapsulated guest.

Encapsulation of other small hydrocarbons in **1** was also observed, as indicated by the ^{1}H NMR chemical shifts of various encapsulated small hydrocarbons in **1** (Table 1). Ethane, ethylene, acetylene, and cyclopropane encapsulated by **1** give rise to signals upfield to those for the protons of the free hydrocarbons. However, addition of either propane or CH_2Cl_2 to the solution of **1** does not cause an upfield shift of the proton signals, indicating that **1** cannot encapsulate hydrocarbons larger than cyclopropane.

Each proton signal of the encapsulated hydrocarbon appears as a sharp singlet, thus indicating that the encapsulated hydrocarbons in the cavity of **1** are capable of free rotation.

Table 1: ^{1}H NMR chemical shifts[a] and binding constants K_{11}[b] of hydrocarbons in **1**.

Guest	δ_{free} [ppm]	$\delta_{@1}$ [ppm]	$\Delta\delta$ [ppm]	K_{11} [M^{-1}]
methane	0.15	−7.19	−7.34	81 ± 18
acetylene	1.91	−5.37	−7.28	130 ± 20
ethylene	5.39	−2.07	−7.46	49 ± 5
ethane	0.85	−6.49	−7.34	9.4 ± 1.4
cyclopropane	0.23	−6.95	−7.18	9.6 ± 2.3
propane	1.31, 0.88		–[c]	

[a] Chemical shifts relative to TMS in $CDCl_3$. [b] Conditions: [**1**] = 5 mM in $CDCl_3$ at 25 °C, 1 atm. [c] Not encapsulated.

Upon the encapsulation of hydrocarbons, the ^{1}H NMR signals of the peripheral protons of the cavitand moiety of **1** undergo a downfield shift. In particular, a remarkable downfield shift is observed for H_{ai} for the cavitand -OCH_2O- segment (Figure 1),[15] that is located closest to the porphyrin plane and which acts as a sensitive marker of the portal shape. The magnitude of this shift shows a positive correlation with guest volumes[16] (Figure 2). This is attributed to a process in which the cavitand is forced to move away from the porphyrin plane upon complexation with a guest molecule. A concomitant decrease in the porphyrin anisotropic effect accompanies this movement.

To evaluate the affinity and selectivity of guest binding of **1**, we determined the 1:1 binding constant K_{11} of the

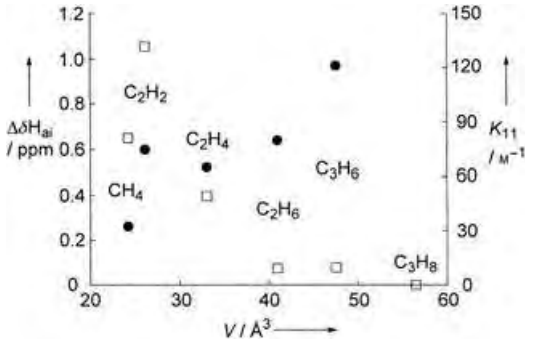

Figure 2. ^{1}H NMR chemical shift difference $\Delta\delta H_{ai}$ (●) and binding constant K_{11} (□) versus guest molecular volume *V*. $\Delta\delta H_{ai} = \delta(H_{ai}$ of hydrocarbon@**1**$) - \delta(H_{ai}$ of **1**$)$. Guest volumes (Connolly solvent-excluded volumes) were estimated according to the method described in reference [16].

hydrocarbon encapsulation. The K_{11} values are shown in Table 1. Acetylene exhibits the greatest affinity of encapsulation in the cavity, and the binding constants decrease in the following order: acetylene $\gg$ methane $>$ ethylene $\gg$ cyclopropane $\approx$ ethane. Among the saturated hydrocarbons examined in this work, large differences in K_{11} values were observed (methane/ethane/propane = 8.6:1.0:$\approx$0). The selectivity of encapsulation appears to be related to the volume and shape of the guest molecules. Figure 2 shows the plot of K_{11} versus molecular volumes[16] for various hydrocarbons. An inverse correlation is observed between K_{11} and guest volumes for most of the small hydrocarbons examined. However, the remarkable large binding constant of acetylene cannot be explained only in terms of molecular volume. Since the acetylene protons favor stronger CH/π interactions with electron-rich aromatic π systems that act as electron donors,[17] the high affinity of acetylene may be due to this attractive effect induced by the aromatic walls of the host molecule.

Prior to this work, the cavitand compound with the smallest cavity observed was the benzene-capped cavitand reported by Paek et al.[5b] This compound encapsulates a wide range of guest sizes, from methanol to tetrahydrofuran to *n*-propanol (K_{11} = 238, 14, and 3 M^{-1}, respectively, measured at −40 °C). However, **1** has an even smaller cavity and narrower portal, and shows higher selectivity for small guest molecules.

In summary, we have synthesized a new capsule-shaped host **1**, which can selectively and reversibly bind a single hydrocarbon molecule of sizes ranging from methane to cyclopropane. The binding constants are inversely correlated with the molecular volumes of the guest hydrocarbons with the exception of acetylene. Compound **1** has the smallest cavity among known cavitand compounds and the high size selectivity for small hydrocarbons reported thus far. The syntheses of metal complexes of this cavitand–porphyrin and investigations of their guest-encapsulation properties and reactivity are in progress in our laboratory.

Experimental Section

Determination of binding constants: Hydrocarbon gas was bubbled directly into the solution of **1** in $CDCl_3$ (5 mM, 0.6 mL) in an NMR tube with a gas-tight screw cap. ^{1}H NMR spectra were measured at various hydrocarbon concentrations (5–50 mM) at 25 °C. The amount of free and encapsulated hydrocarbons were determined by the integration of their proton signals relative to the host signals at δ = 7.13–6.84 ppm (20 protons). The [$\mathbf{1}_{free}$] values were estimated from the amount of trapped hydrocarbon. The 1:1 binding constants were calculated by using Equation (1).

$$K_{11} = \frac{[\text{hydrocarbon}_{@\mathbf{1}}]}{[\mathbf{1}_{free}][\text{hydrocarbon}_{free}]} \quad (1)$$

The average value and standard deviation of K_{11} were determined by ten independent measurements.

Received: February 26, 2005
Published online: May 4, 2005

Keywords: cage compounds · cavitands · host–guest systems · hydrocarbons · porphyrinoids

[1] a) J.-M. Lehn, *Supramolecular Chemistry. Concepts and Perspectives*, VCH, Weinheim, **1995**; b) D. M. Rudkevich, *Angew. Chem.* **2004**, *116*, 568; *Angew. Chem. Int. Ed.* **2004**, *43*, 558, and references therein.
[2] M.-H. Baik, M. Newcomb, R. A. Friesner, S. J. Lippard, *Chem. Rev.* **2003**, *103*, 2385, and references therein.
[3] T. L. Poulos, B. C. Finzel, A. J. Howard, *Biochemistry* **1986**, *25*, 5314.
[4] A. E. Shilov, A. A. Shteinman, *Acc. Chem. Res.* **1999**, *32*, 763; D. E. De Vos. M. Dams, B. F. Sels, P. A. Jacobs, *Chem. Rev.* **2002**, *102*, 3615, and references therein.
[5] a) N. Branda, R. Wyler, J. Rebek, Jr., *Science* **1994**, *263*, 1267; b) K. Paek, C. Ihm, H. Ihm, *Tetrahedron Lett.* **1999**, *40*, 4697; c) K. Paek, J. Cho, *Tetrahedron Lett.* **2001**, *42*, 1927; d) A. Shivanyuk, A. Scarso, J. Rebek, Jr., *Chem. Commun.* **2003**, 1230.
[6] A. Jasat, J. C. Sherman, *Chem. Rev.* **1999**, *99*, 931.
[7] a) T. Nagasaki, H. Fujishima, M. Takeuchi, S. Shinkai, *J. Chem. Soc. Perkin Trans. 1* **1995**, 1883; b) D. M. Rudkevich, W. Verboom, D. N. Reinhoudt, *J. Org. Chem.* **1995**, *60*, 6585; c) H. Ohkawa, S. Arai, S. Takeoka, T. Shibue, H. Nishide, *Chem. Lett.* **2003**, *32*, 1052.
[8] a) O. Middel, W. Verboom, D. N. Reinhoudt, *J. Org. Chem.* **2001**, *66*, 3998; b) S. D. Starnes, D. M. Rudkevich, J. Rebek, Jr., *J. Am. Chem Soc.* **2001**, *123*, 4659.
[9] a) Y. Kuroda, T. Hiroshige, T. Sera, Y. Shiroiwa, H. Tanaka, H. Ogoshi, *J. Am. Chem. Soc.* **1989**, *111*, 1912; b) J. A. A. W. Elemans, M. B. Claase, P. P. M. Aarts, A. E. Rowan, A. P. H. J. Schenning, R. J. M. Nolte, *J. Org. Chem.* **1999**, *64*, 7009.
[10] P. Timmerman, H. Boerrigter, W. Verboom, G. J. VanHummel, S. Harkema, D. N. Reinhoudt, *J. Inclusion Phenom. Mol. Recognit. Chem.* **1994**, *19*, 167.
[11] The mixture of porphyrins **4** was synthesized analogously to *meso*-tetrakis(2,6-dihydroxyphenyl)porphyrin: a) F. Tani, M. Matsu-ura, S. Nakayama, M. Ichimura, N. Nakamura, U. Naruta, *J. Am. Chem. Soc.* **2001**, *123*, 1133; b) E. Tsuchida, E. Hasegawa, T. Komatsu, T. Nakata, H. Nishide, *Chem. Lett.* **1990**, *19*, 389.
[12] When CD_4 gas was bubbled into a solution of *syn*-**1** and when CH_4 gas was bubbled into a solution of *anti*-**2** in $CDCl_3$, no signals were observed from $\delta = -4$ to -8 ppm.
[13] a) D. J. Cram, M. E. Tanner, C. B. Knobler, *J. Am. Chem. Soc.* **1991**, *113*, 7717; b) C. Ihm, M. Kim, H, Ihm, K. Paek, *J. Chem. Soc. Perkin Trans. 2* **1999**, 1569.
[14] C. J. Medforth in *The Porphyrin Handbook*, *Vol. 5* (Eds.: K. M. Kadish, K. M. Smith, R. Guilard), Academic, San Diego, **2000**, pp. 5–7.
[15] Although porphyrin N-H function is closest to the encapsulated guest, the ^{1}H NMR signal shift for N-H is small.
[16] The volumes were calculated by using ChemPropStd command in Cambridge Soft Chem3D Pro.(Connolly solvent-excluded volume, prove radius 1.4 Å); M. L. Connolly, *J. Mol. Graphics* **1993**, *11*, 139.
[17] a) S. L. Price, A. J. Stone, *J. Chem. Phys.* **1987**, *86*, 2859; b) M. Nishino, M. Hirota, Y. Umezawa in *The CH/π Interaction*, Wiley-VCH, New York, **1998**, pp. 52–54.

Protein Trapping

Trapping of Proteins under Physiological Conditions in a Nanopipette**

Richard W. Clarke, Samuel S. White, Dejian Zhou, Liming Ying, and David Klenerman**

Dielectrophoresis (DEP) uses the directed motion of particles caused by polarization effects in a nonuniform electric field,[1] and it has proved to be a powerful tool in performing sample sorting,[2–6] trapping,[6–8] and manipulation[6,9–11] on micrometer- and submicrometer-sized particles to date. These experiments have been largely performed in low-conductance solutions by using metal electrodes—conditions that are nonphysiological and in which damage by electrolysis is also possible. Herein, we use a nanopipette for electrodeless dielectrophoresis and show clear evidence, by using wide-field fluorescence imaging, for the reversible trapping of Alexa-488-labeled proteins (protein G and immunoglobulin G (IgG)) and also of the fluorophore alone. Our results show a dielectrophoretic concentration enhancement for these fluorophore-labeled proteins of at least a factor of 300. This concentration enhancement was shown to take place in less than a second and to be within about a factor of two of that observed with DNA. This finding opens up new possibilities for miniaturized bioanalysis.

Previous applications of DEP have focused on the separation of micrometer- and submicrometer-scale objects, such as cells,[9] viruses,[10] and colloidal particles,[12] and the manipulation and trapping of long DNA molecules.[7] More recently, DEP has been applied as a bottom-up approach to assemble functional structures by using nanosized building blocks[13–16] and submicrometer-diameter fibrils from single-wall carbon nanotubes.[17] DEP has also been utilized in separating metallic carbon nanotubes from semiconducting carbon nanotubes,[18] and evidence for the trapping of bovine serum albumin has been presented.[19] All of these studies have used metallic microelectrodes for their DEP traps. These have the advantage of flexible designs for the electrodes and a relatively low voltage being required to generate a high-field gradient on the microscale. However, there are limitations in the application of trapping by metallic DEP. Firstly, it is not compatible with biological samples, as the low-ionic-strength solutions that are used will lead to unfolding of DNA and proteins. Secondly, proteins will be easily drawn to the metal surface of the electrodes where they will become denatured. Thirdly, complex electrochemical reactions such as electrolysis may occur at the microelectrodes. These reactions not only generate gas bubbles that interfere with trapping but they may also damage the trapped molecules and degrade the electrodes. This is a particular problem at the predicted high electric fields required to trap proteins.[20] To address this problem, Chou and co-workers developed DEP traps by patterning geometrical constrictions in an insulating quartz substrate instead of the traditional metallic microelectrodes.[21] The constrictions in a microfluidic channel are used to create a high-field gradient with a local maximum; DNA was successfully trapped in this high-field region under ionic buffer conditions. Recently, we used a laser-pulled glass nanopipette filled with ionic buffer to generate a high-field gradient near the pipette tip.[22] We have shown that DNA and proteins maintain their functionality after passing through this high electric field in the pipette tip.[23] We have also probed the motion of fluorophore-labeled double- and single-stranded 40-mer DNA, a one kilobase single-stranded DNA, and a single nucleotide triphosphate (deoxycytidine 5′-triphosphate, dCTP) just inside and outside the pipette tip at different frequencies and amplitudes of applied voltages.[22] A strong trapping effect was observed during the negative half cycle for all DNA samples and also for dCTP. DNA might have been a special case for the trapping of molecules by DEP since it is a highly charged polyelectrolyte because of its phosphate backbone. Herein, we present unequivocal evidence of the reversible trapping of proteins in the nonuniform electric field generated in the tip of a nanopipette, by using fluorescence microscopy with wide-field illumination.

A schematic representation of the experimental setup is shown in Figure 1. The borosilicate glass pipettes have a 3–6° half-cone angle and an inner diameter of 100–150 nm. The pipette and bath solution contain 100–150 mM sodium chlo-

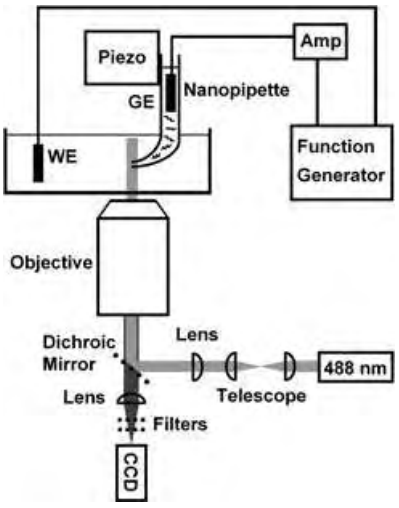

Figure 1. Schematic of the experimental setup used. Amp = current and voltage amplifier ($\times 10^8$), Piezo = piezoelectric nanopositioning stage, WE = working electrode, GE = ground electrode, CCD = charge-coupled device.

[*] R. W. Clarke,[+] S. S. White,[+] Dr. D. Zhou, Dr. L. Ying, Dr. D. Klenerman
Department of Chemistry
University of Cambridge
Lensfield Road, Cambridge (UK)
Fax: (+44) 1223-336-362
E-mail: ly206@cam.ac.uk
dk10012@cam.ac.uk

[+] These authors contributed equally to this work.

[**] This work was funded by the Biotechnology and Biological Sciences Research Council (BBSRC), UK. We thank Universal Imaging Corporation, UK, for the loan of the Photometrics CCD camera and MetaMorph software.

Supporting Information for this article is available on the WWW under http://www.angewandte.org or from the author.

 DOI: 10.1002/anie.200500196

ride. An electric field is generated in the tip of the pipette on application of a voltage between the electrodes in the pipette (GE) and bath (WE). In these experiments, the pipette electrode was earthed and a voltage was applied to the bath electrode. Application of 1 V results in a maximum electric field of about $10^6\ V\,m^{-1}$ in the pipette tip.[22] We used wide-field illumination of the pipette by using an expanded 488-nm laser beam and detected the fluorescence with a CCD camera. This enabled the spatial distribution of fluorophore-labeled biomolecules in the pipette on application of different voltages to be examined.

We studied protein G and IgG labeled with multiple Alexa-488 fluorophores, and as a comparison we also studied a single-stranded 20-mer DNA labeled with a Rhodamine Green fluorophore. When certain potential differences were applied between the two electrodes, we observed fluorescence in an area close to the tip; this fluorescence is proportional to the concentration of molecules, a fact allowing us to confirm that the molecules must be trapped in this tip region. Qualitatively, all these samples showed the same trapping behavior: Figure 2 A–D shows representative wide-field images obtained at −5, −1, +1, and +5 V, respectively, with protein G in the pipette. There is weak localization at +1 V, but a clear, confined build-up of protein G occurs upon application of −5 V. Once the electric field is removed, the trapped protein molecules quickly disperse away by simple diffusion in less than a second. Figure 2 E shows a line scan along the nanopipette at −5 V: protein G is clearly localized very close to the pipette tip in a region with a full width at half maximum of (990 ± 80) nm. The observed trap is also completely reversible: when a sine wave is applied (0.5 Hz) at either 1 or 5 V, cycles of "trapping" followed by "release" are seen. Videos of this time-dependent behavior of the pipette upon application of a sine wave at 0.1 Hz with an amplitude of 1 V (Movie 1) and 5 V (Movie 2) are shown in the Supporting Information.

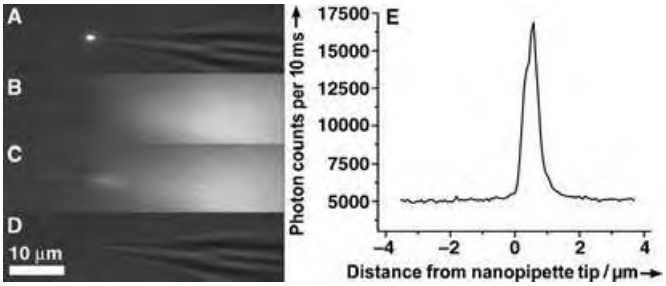

Figure 2. A)–D) Representative wide-field fluorescence images showing the dependence of protein G concentration in the nanopipette on applied voltage: A) −5, B) −1, C) +1, D) +5 V. The nanopipette was wide-field illuminated by a 7-mW laser beam at 488 nm and contained 100 nM Alexa-488-labeled protein G in PBS buffer, the same buffer solution as in the bath. Images (A) and (D) were recorded with very low background illumination to simultaneously record the pipette position and fluorescence (exposure time 10 ms). Images (B) and (C) were recorded without background illumination (exposure time 100 ms). E) Line scan along the axis of a wide-field illuminated nanopipette filled with the same solution as used for (A)–(D) and with the bath electrode at −5 V.

A representative graph of the dependence of the fluorescence intensity of the trapped protein G with applied voltage is shown in Figure 3. It is clear from the Figure that the protein G concentrates at the tip of the pipette below a voltage of −5 V. There is also a far smaller population build-up at approximately +2 V. Comparison of the fluorescence intensity at zero-applied voltage with the highest integrated fluorescence intensity allows us to estimate the concentration enhancement in the pipette tip. This value varied between pipettes, because of variation in size and taper angle, but was always in the range of 300–3000. IgG gave similar concentration enhancements.

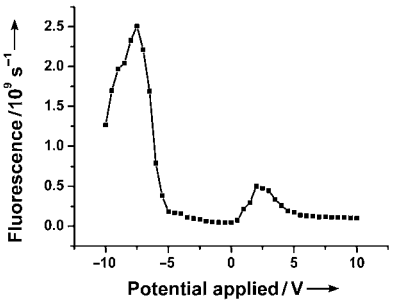

Figure 3. Integrated fluorescence response of the protein G solution in a nanopipette to applied voltage. The nanopipette tip was wide-field illuminated at 488 nm and contained 100 nM Alexa-488-labeled protein G. The intensity of the fluorescence was integrated in the same small trap region. All experiments were performed in PBS buffer, the same buffer solution as in the bath. Fluorescence data were derived from images of 1-ms time resolution and were acquired 2 s after the bath electrode changed polarity to the value indicated.

We compared the enhancement in protein G concentration with that for single-stranded 20-mer DNA in the pipette under the same experimental conditions. The DNA gave a concentration enhancement approximately two times larger than protein G (600–6000) and also showed the onset of trapping at about half the applied voltage. A video of the DNA trapping in the pipette is shown in the Supporting Information (Movie 3). Similar concentration enhancements were observed when using a DC voltage rather than an AC voltage. The number of trapped molecules did not increase significantly with time, since there is a very low rate of flow of molecules to the tip once a negative voltage has been applied to the bath electrode. To test whether the trapping was dye dependant, Alexa-647-labeled IgG was investigated. Exactly the same trapping phenomenon as with Alexa-488-labeled IgG and protein G was observed, a result indicating that the trapping of the protein is not dye specific.

We also studied the free Alexa-488 dye to determine how much the dye contributed to the observed trapping. The onset of strong trapping occurred at approximately −1.1 V—a lower amplitude of voltage than that observed with the DNA and the proteins. Another key difference is that the trap was much larger than that with either the proteins or the DNA, as shown in Figure 4. The dye trap is approximately 8 μm in length. These observations indicate that not only the dye but also the protein or DNA has an effect on the trapping voltage and the size of the trap region.

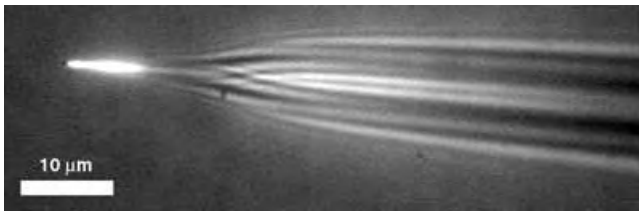

Figure 4. Fluorescence image recorded by using wide-field illumination (5.2 mW) of a nanopipette filled with 100 nM Alexa-488 dye in PBS buffer, the same buffer solution as in the bath. At −2 V there is a large dielectrophoretic concentration of dye confined to the first 8 μm of the nanopipette tip. This image was acquired with an exposure time of 1 s.

The net electric-field-induced force acting on the biomolecules in the nanopipette is a result of the combination of three components: electroosmosis, electrophoresis, and dielectrophoresis. The direction and magnitude of these forces depend on the applied voltage and the position of the molecules in the pipette. In particular, the dielectrophoretic force is proportional to the square of the electric field and will be largest at the pipette tip.[22] Here, we have applied higher voltages (up to 10 V) than we have used previously for controlled delivery (up to 400 mV) to increase the magnitude of the dielectrophoretic effect. Protein G is negatively charged under the conditions of this experiment and the contribution of electroosmotic flow is small,[22] so at a positive applied voltage the electrophoretic force and dielectrophoretic force act in the same direction to pull protein G out of the pipette tip. It appears that there is a range of voltages (1.5–3.5 V) at which some build-up of protein occurs in the tip but the protein is still able to flow out of the pipette. By contrast, on the application of a negative voltage the dielectrophoretic force opposes the electrophoretic force. Hence, close to the tip the two forces balance, and trapping can occur in a small, localized region inside the tip without any flow either to the bath solution or to the capillary electrode.

This work has demonstrated that, under the same experimental conditions, proteins can be trapped with an increase in concentration that is within a factor of two of that observed with DNA. There seems to be no theoretical basis for this observation and it was not expected. While there is clearly a contribution from the dye, there also appears to be a significant contribution from the protein as well. The observed trapping by DEP at DC or low-frequency AC voltages may reflect the contribution of the structured water molecules and counterions around the biological molecule to the dipole induced under these high electric fields, rather than the structure of the biomolecule itself. This will need further experimental and theoretical investigation.

In summary, we have shown that we can trap nanometer-sized proteins, as well as DNA, in physiological buffer. This results in concentration enhancements of at least a factor of 300, with this enhancement obtained in less than a second. Extension of this methodology to the single-molecule limit should be possible with optimization of the trap geometry, thereby allowing prolonged solution studies of individual molecules. Practically, this is a new and potentially powerful method to trap, concentrate, and manipulate both DNA and proteins. It could be used as the basis of ultrasensitive and highly miniaturized bioassays, particularly when performed in parallel in two-dimensional nanofabricated devices.

Experimental Section

The protocol in the Alexa Fluor 488 (Alexa-488) protein-labeling kit provided by Molecular Probes (USA) was employed to label rabbit IgG. Briefly, 1M freshly prepared sodium bicarbonate solution (50 μL) was added to rabbit IgG (0.5 mL, 2 mg mL^{-1}) in phosphate-buffered saline (PBS) buffer to adjust the pH value of the solution to about 8.3. The combined solution was then transferred to a vial of Alexa-488 reactive dye, and the mixture was gently stirred for 1 h at room temperature. The reaction mixture was then loaded on a purification resin column supplied with the kit, to separate the protein from the unreacted dye, and washed once with eluting buffer to give a purity of $>99\,\%$. The labeled rabbit IgG was in the first fluorescent band. The degree of labeling was determined by measuring the UV absorbance at 280 and 494 nm, by using the equations provided by Molecular Probes (USA). The average labeling was 7 Alexa-488 fluorophores per IgG molecule. HPLC-purified 20-base oligonucleotide 5′-CTATGCAGCCATTGTAGTCC-3′ (IBA, Germany) was labeled at the 3′ terminus with the fluorophore Rhodamine Green. Protein G was purchased from Molecular Probes (USA). The average labeling was 2.3 Alexa-488 fluorophores per protein G molecule.

The nanopipettes, with inner radii of around 50 nm, were made by using a laser-based pipette puller (Model P-2000, Sutter Instrument Co., USA), and a two-line program was used to pull borosilicate glass capillaries (inner diameter = 0.58, outer diameter = 1 mm), with the following parameters: Heat = 350, Fil = 3, Vel = 30, Del = 220, Pull and Heat = 330, Fil = 2, Vel = 27, Del = 180, Pull = 250.

For the pipette experiments, a 100 nM DNA, 100 nM protein, or 100 nM Alexa-488 dye solution was backfilled to the bent nanopipette by a microfiller (Microfil 34, World Precision Instruments, USA). A coverglass-bottomed dish (Willco Wells GWST-1000, Netherlands) containing buffer (2–3 mL) was used as the bath. A home-built nanomanipulation system consisting of a piezoelectric translational stage (Tritor 38, Piezosystem Jena, Germany) was used to position the nanopipette. The pipette tip was placed 5–10 μm above the dish surface. A voltage was applied to the nanopipette through two Ag/AgCl electrodes, one in the bath and the other inside the pipette, which served as the working and ground electrodes, respectively. The ion-current flow through the pipette was amplified by a high-impedance amplifier and monitored by an oscilloscope. The ion current flowing through the pipette was the same in the presence and absence of DNA or protein since the ion current is dominated by the flow of sodium and chloride ions. In addition, no ion-current reduction because of partial blocking could be detected with DNA, protein, or antibody in the pipette. Identical buffers were used both in the pipette and in the bath. For the DNA experiments, buffer (10 mM tris(hydroxymethyl)aminomethane hydrochloride (Tris-HCl), 1 mM ethylenediaminetetraacetate (EDTA), and 100 mM NaCl at pH 7.4) was used with EDTA added to remove multivalent cations in the solution. For the protein and dye experiments, a different buffer (10 mM phosphate, 150 mM NaCl, 2 mM NaN_3 at pH 7.2) was used.

A home-built wide-field fluorescence microscope was used to record images of the trapping of dye-labeled biomolecules in the nanopipette. Laser beams (488 nm, Argon ion, model 35LAP321–230, Melles Griot, USA) were spatially filtered and collimated before being sent to the microscope. A home-built fluorescence microscopy attachment was mounted to the rear port of a TE2000U optical microscope (Nikon, USA). The laser beam was focused to the back focal point of an oil immersion objective (Apochromat 60×, NA 1.45, Nikon, USA) after passing through a dichroic mirror (FITC/CY5, AHF Analysentechnik AG, Germany). Fluorescence was collected by

the same objective, filtered by a bandpass filter (535 AF45, Omega Optical, USA) and imaged onto a CCD camera (see Figure 1). The potential waveforms applied to the electrodes were created by using a function generator (Model DS345, Stanford Research Systems, USA).

All experimental data (except for Figure 4) were acquired by using a Photometrics Cascade 512B High Speed CCD camera (Roper Scientific, USA) and a PICOLO Pro 2 video capture card (Euresys Inc., USA). The data for Figure 4 were acquired by using a Watec WAT-902H CCD camera (Watec, Japan). The conversion of the raw video format into AVI format was performed by using the VirtualDub 1.4.10 program (Build 13870).

Received: January 18, 2005
Published online: May 10, 2005

Keywords: biomolecule trapping · DNA · electrophoresis · nanotechnology · proteins

[1] H. A. Pohl, *Dielectrophoresis*, Cambridge University Press, Cambridge, **1978**.
[2] M. Washizu, S. Suzuki, O. Kurosawa, T. Nishizaka, T. Shinohara, *IEEE Trans. Ind. Appl.* **1994**, *30*, 835.
[3] B. H. Lapizco-Encinas, B. A. Simmons, E. B. Cummings, Y. Fintschenko, *Anal. Chem.* **2004**, *76*, 1571.
[4] H. Morgan, M. P. Hughes, N. G. Green, *Biophys. J.* **1999**, *77*, 516.
[5] N. G. Green, H. Morgan, *J. Phys. D* **1997**, *30*, L41.
[6] M. P. Hughes, *Nanotechnology* **2000**, *11*, 124.
[7] C. L. Asbury, A. H. Diercks, G. van den Engh, *Electrophoresis* **2002**, *23*, 2658.
[8] C. L. Asbury, G. van den Engh, *Biophys. J.* **1998**, *74*, 1024.
[9] T. Schnelle, T. Müller, R. Hagedorn, A. Voigt, G. Fuhr, *Biochim. Biophys. Acta* **1999**, *1428*, 99.
[10] M. P. Hughes, H. Morgan, F. J. Rixon, J. P. H. Burt, R. Pethig, *Biochim. Biophys. Acta* **1998**, *1425*, 119.
[11] Y. Huang, K. L. Ewalt, M. Tirado, T. R. Haigis, A. Forster, D. Ackley, M. J. Heller, J. P. O'Connell, M. Krihak, *Anal. Chem.* **2001**, *73*, 1549.
[12] R. Pethig, Y. Huang, X. B. Wang, J. P. H. Burt, *J. Phys. D* **1992**, *25*, 881.
[13] R. Krupke, F. Hennrich, H. B. Weber, M. M. Kappes, H. von Lohneysen, *Nano Lett.* **2003**, *3*, 1019.
[14] X. Q. Chen, T. Saito, H. Yamada, K. Matsushige, *Appl. Phys. Lett.* **2001**, *78*, 3714.
[15] K. D. Hermanson, S. O. Lumsdon, J. P. Williams, E. W. Kaler, O. D. Velev, *Science* **2001**, *294*, 1082.
[16] X. F. Duan, Y. Huang, Y. Cui, J. F. Wang, C. M. Lieber, *Nature* **2001**, *409*, 66.
[17] J. Tang, B. Gao, H. Z. Geng, O. D. Velev, L. C. Qin, O. Zhou, *Adv. Mater.* **2003**, *15*, 1352.
[18] R. Krupke, F. Hennrich, H. von Lohneysen, M. M. Kappes, *Science* **2003**, *301*, 344.
[19] L. Zheng, J. P. Brody, P. J. Burke, *Biosens. Bioelectron.* **2004**, *20*, 606.
[20] L. Zheng, S. Li, P. J. Burke, J. P. Brody, *Proc. Third IEEE Conf. Nanotech.* **2003**, p. 437.
[21] C. F. Chou, J. O. Tegenfeldt, O. Bakajin, S. S. Chan, E. C. Cox, N. Darnton, T. Duke, R. H. Austin, *Biophys. J.* **2002**, *83*, 2170.
[22] L. M. Ying, S. S. White, A. Bruckbauer, L. Meadows, Y. E. Korchev, D. Klenerman, *Biophys. J.* **2004**, *86*, 1018.
[23] A. Bruckbauer, D. J. Zhou, L. M. Ying, Y. E. Korchev, C. Abell, D. Klenerman, *J. Am. Chem. Soc.* **2003**, *125*, 9834.

Inclusion Complexes

Ultrastable Rhodamine with Cucurbituril**

*Jyotirmayee Mohanty and Werner M. Nau**

Rhodamines are arguably the most important fluorescent dyes as shown by their classical and contemporary applications,[1–8] for example, in dye lasers, as quantum counters, as photosensitizers, for spectral calibration in fluorometers, in single-molecule detection, as imaging agents for biomolecules, for scanning confocal microscopy, in fluorescence correlation spectroscopy (FCS), and in high-throughput screening assays. The various applications are made possible through the combination of their water solubility, close-to-unity quantum yields, high extinction coefficients, and very high photostability. Rhodamine 6G (Rh6G) is the most prominent derivative and has become a prototype for many reasons,[3,4] including its photostability: the first continuous-wave dye laser, for example, was based on an aqueous solution of Rh6G containing 1.5% triton X as surfactant.[9] Efforts have been made to improve the fluorescence and lasing characteristics of rhodamines, in particular in regard to their stability towards adsorption, aggregation, and photochemical decomposition, by derivatization or use of additives.[3,7] These approaches have frequently had limited success and often sacrifice other advantageous features of the chromophore.

We now describe the development of an ultrastable rhodamine derivative through the complexation of Rh6G by cucurbit[7]uril (CB7).[10,11] The additive leads to an unprecedented long fluorescence lifetime and an exceptional supramolecular stabilization, including the suppression of undesirable aggregation, the prevention of surface adsorption, and a

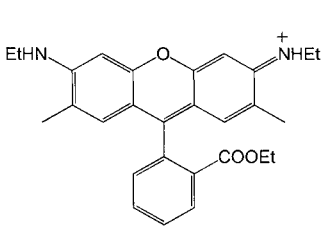

rhodamine 6G (Rh6G)

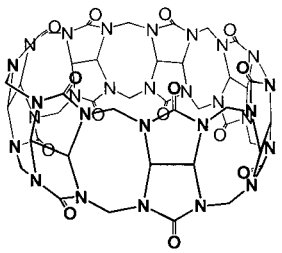

cucurbit[7]uril (CB7)

[*] Dr. J. Mohanty,[+] Prof. Dr. W. M. Nau
School of Engineering and Science
International University Bremen
Campus Ring 1, 28759 Bremen (Germany)
Fax: (+49) 421-200-3229
E-mail: w.nau@iu-bremen.de

[+] Permanent address:
Radiation Chemistry & Chemical Dynamics Division
Bhabha Atomic Research Centre, Mumbai (India)

[**] This work was supported by the International University Bremen.

  DOI: 10.1002/anie.200500502

substantial decrease in the quantum yield of photobleaching. These features enable the applicability of this water-soluble dye to be expanded.

Cucurbiturils are macrocyclic host molecules which can form inclusion complexes with organic guests, with the strongest complexes formed with positively charged guests.[12–14] Although their supramolecular chemistry has recently been intensively investigated, relatively few investigations have dealt with photochemical investigations such as their effect on fluorophores,[11,15–21] and their complexation behavior with classical fluorescent dyes has not yet been addressed. The addition of CB7 to solutions of Rh6G in water results in the immediate formation of a 1:1 host–guest complex (as established by Job's plots) with a high binding constant ($>50000\,\text{M}^{-1}$, by UV/Vis titration). Low concentrations of CB7 (1 mM) are therefore sufficient to ensure a virtually quantitative complexation of the fluorescent dye at the most relevant nano- to micromolar concentrations of the dye. The formation of the complex is also reflected in a decrease in the diffusion coefficient of the dye from $2.80\times10^{-6}\,\text{cm}^2\,\text{s}^{-1}$[22] to $(1.27\pm0.05)\times10^{-6}\,\text{cm}^2\,\text{s}^{-1}$, as determined by FCS. The characteristic upfield ^{1}H NMR shifts on complexation,[12,14,23] and in particular the marked change in the photophysical properties (see below), provide further evidence for the formation of an inclusion complex in which Rh6G experiences a drastically altered microenvironment. The addition of 2,3-diazabicyclo[2.2.2]oct-2-ene, which is known to form a strong inclusion complex with CB7,[11,20] leads to dissociation of the Rh6G complex through competitive binding. This result provides further experimental support that the Rh6G complex with CB7 is of the inclusion type; the size of Rh6G, however, prevents the dye from being completely immersed.

Complexation of Rh6G by CB7 (1 mM) causes a sharpening and a bathochromic shift of the absorption band (Figure 1). The latter effect is characteristic for the immersion of the guest in a less polar environment, and is similar to that observed in *n*-octanol ($\varepsilon=10.3$).[24] The shift in the fluorescence (Figure 1) is less pronounced, and the resulting smaller Stokes shift suggests that relaxation of the dye through geometrical and solvent effects is smaller, as expected for inclusion in a less polar and more-confined environment.[25] Importantly, the fluorescence quantum yield remains unchanged and close to unity (0.89 ± 0.02).[24]

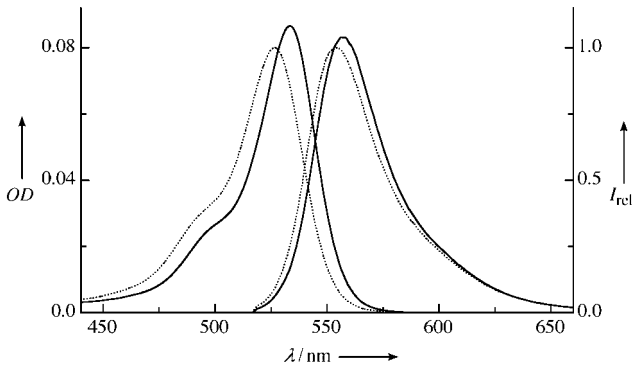

Figure 1. Absorption and fluorescence spectra of Rh6G (1 μM) in water in the absence (dotted lines) and presence (solid lines) of 1 mM CB7.

Strikingly, the fluorescence lifetime of Rh6G increases from 4.08 ± 0.03 ns in water to 4.76 ± 0.04 ns inside CB7. The latter value is the longest lifetime hitherto reported for this dye. The effect on the lifetime of Rh6G is opposite to that observed on its immersion in organic, less polar solvents, and the absolute increase is also more pronounced.[24] This special effect is related to the very low polarizability/refractive index (close to the gas phase) which a guest molecule experiences inside the CB7 cavity. We recently interpolated this low polarizability from solvatochromic effects experienced by an azo chromophore,[20,21] and the present result represents the first practically relevant example of what we have recently described as the supramolecular approach to radiative decay engineering.[21] According to the Strickler–Berg Equation,[26] the rate constant for the radiative decay of a chromophore (the ratio of the fluorescence quantum yields divided by the fluorescence lifetime) increases with the square of the refractive index, such that low environmental polarizabilities result in slower radiative decay rates and expectedly longer fluorescence lifetimes. Indeed, the rate of radiative decay decreases from $(2.18\pm0.02)\times10^8\,\text{s}^{-1}$ to $(1.87\pm0.06)\times10^8\,\text{s}^{-1}$ upon complexation of Rh6G by CB7, an observation which is in keeping with the lower polarizability inside the CB7 cavity.[20] In addition, the rate of the radiationless decay (obtained as the difference between the observed rate of fluorescence decay and the rate of radiative decay) decreases from $(2.7\pm0.1)\times10^7\,\text{s}^{-1}$ to $(2.3\pm0.1)\times10^7\,\text{s}^{-1}$ upon complexation by CB7. The slower radiationless decay of Rh6G in the CB7 complex ensures a constant fluorescence quantum yield regardless of the slower rate of radiative decay. The reduced rate of the radiationless decay can be related, among other things, to a partial protection from the bulk water, which is known to quench Rh6G fluorescence[8]—as evident by its longer fluorescence lifetime in D_2O (4.36 ns).[24,27]

The enhancement of the fluorescence lifetime of Rh6G by an additive is unique and could be of interest, for example, for assays based on fluorescence lifetimes,[28] as well as fluorescence lifetime imaging microscopy.[29] However, the addition of CB7 has benefits which go far beyond this photophysical peculiarity and are of more immediate relevance for practical use. First, CB7 reduces the photobleaching of Rh6G, a phenomenon which describes the tendency of fluorescent dyes to permanently lose their ability to fluoresce as a consequence of photon-induced chemical damage. Increasing the photostability of rhodamines either with additives or by structural modifications has remained an active field of dye research[3–5] since the photostability of a fluorescent dye is a key parameter, along with its brightness, for practical applications. This has been reinforced[3,4] in recent years by the development of single-molecule detection and scanning confocal microscopic techniques, for which chromophore stability is quintessential. Numerous additives for rhodamines have been tested to date which have in common that their photostabilizing properties are limited, that they operate either by preventing secondary photolytic steps, for example, as antioxidants to prevent oxidation, or by quenching undesired reactive triplet states, and that they have to be applied in high concentrations, which in turn may lead to undesirable fluorescence quenching effects.[3] If the use of

organic solvents or surfactants are disregarded, none of the previously recommended techniques actually involves a discrete complexation of the dye and modification of the intrinsic rate constants for the primary elementary photoprocesses like CB7 does, thus establishing the current approach as a novel strategy for photostabilization in water.[3]

The photostabilization of Rh6G by CB7 is already sizable (a factor of ca. 1.5) at low levels of irradiation ($< 1\ kW\,cm^{-2}$, photoreactor with lamps emitting visible light), but it becomes remarkably high at high levels of irradiation (ca. $10\ MW\,cm^{-2}$, 10 Hz pulsed 2nd harmonic 532 nm Nd-YAG laser excitation, ca. 0.1 J pulse energy, pulse width ca. 10 ns), where two-step two-photon decomposition dominates.[4] As is apparent from Figure 2, there is a dramatic

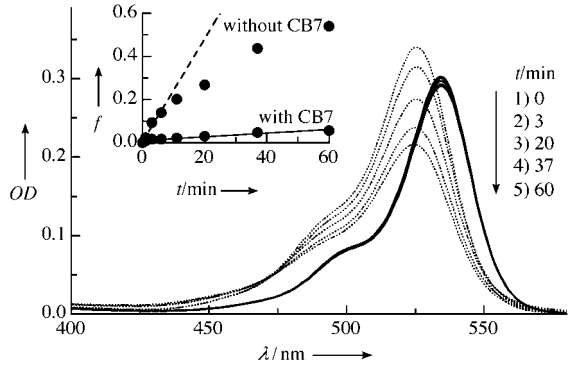

Figure 2. Photobleaching of Rh6G (ca. 4 μM) in aerated water in the absence (dotted lines) and presence (solid lines) of 1 mM CB7 followed through the decrease of the visible absorption with increasing time of pulsed 532-nm Nd-YAG laser irradiation. The inset shows the graph and correlation lines for the characteristic function $f = \log([10^{A_0}-1]/[10^{A}-1])$ versus irradiation time for the determination of the relative quantum yield of photobleaching (see Experimental Section). For the unstabilized solution, the correlation line refers to the initial 10-min time period because of the formation of absorbing photoproducts at longer times.

increase (factor of 30 ± 3) in the photostability upon addition of CB7, as quantified through absorbance-based quantum yields of photobleaching during the initial pulsed-laser photolysis period (at longer times absorbing photoproducts are formed,[25] which cause the graph to become nonlinear). The high levels of irradiation described in Figure 2 are most relevant for dye lasers, but also in scanning confocal microscopy, where irradiances of $1\ MW\,cm^{-2}$ can be reached.[4] Apparently, CB7 selectively prevents the two-step two-photon photolysis, and it does not have the common drawbacks, namely, it does not act as a quencher, does not absorb in the visible region, and consequently displays no autofluorescence. These combined properties distinguish CB7 from other stabilizing additives.[3]

The higher photostability of Rh6G is presumably caused by a combination of factors. Cucurbiturils generally provide an extremely inert reaction medium; for example, it is very resistant to oxidation and even withstands ozonolysis.[30] In addition, the fluorescent dye is quite efficiently protected from water,[11] which may further reduce intermolecular follow-up (photo)chemistry,[25] including photoionization from higher excited states relevant in the two-step two-photon decomposition.[4]

There is another benefit of using CB7 as an additive to Rh6G solutions. It improves the stability of the emission by greatly increasing the thermal stability of the dye solution by preventing unspecific adsorption to glass and plastic surfaces. This was a previously documented problem for xanthene dyes.[4] The addition of CB7 to an aqueous solution of Rh6G prevents this adsorption virtually completely, such that the dye depletion can be conveniently quantified with reference to a CB7-stabilized solution. Figure 3 shows the temporal

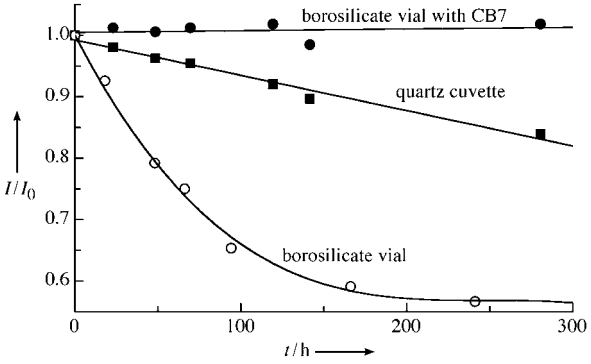

Figure 3. Temporal evolution of the fluorescence intensity of Rh6G (1 μM) in aerated water under ambient light in different sample containers.

evolution of the steady-state fluorescence intensity of aqueous Rh6G solutions stored in different sample containers under ambient conditions and daylight. The CB7-stabilized Rh6G solution (1 μM) stored in a standard sample vial showed no significant loss of fluorescence intensity over a period of several weeks. In contrast, an unstabilized solution with the same concentration of Rh6G in the same vial showed a dramatic reduction in the fluorescence intensity. Some improvement (a factor of ca. 3 after 10 days) could be achieved by using quartz cuvettes instead of borosilicate vials, but the CB7-stabilized sample excelled (Figure 3). The stabilization factor can only be estimated in these cases ($>$ 100), since the fluorescence behavior of the CB7 solution implied indefinite stability after two weeks storage, thus providing a gold standard. Additional experiments using polypropylene showed that this material was the poorest choice for handling and storage of Rh6G, unless CB7 was present; the tendency of Rh6G to adsorb to surfaces follows the order: polypropylene $\gg$ borosilicate glass $>$ quartz glass. The depletion of the dye as a result of surface adsorption was, as expected, found to be most pronounced at very relevant low concentrations of the dye since at higher concentrations a surface-area-dependent adsorption–desorption equilibrium can be attained.[4] Clearly, the addition of CB7 greatly simplifies sample handling and eliminates a number of uncertainties related to the actual dye concentration studied, irrespective of the materials used. More importantly, the increased thermal (as well as photochemical) stability of CB7-containing Rh6G solutions allows the storage of aqueous Rh6G dye solutions, in particular of very dilute (nM)

solutions, for an extended period of time. This, therefore, allows the use of water as the solvent but eliminates the need to prepare the respective aqueous solutions freshly before each experiment, for example, for spectral calibration or as a diffusion coefficient reference in FCS. The addition of high concentrations of surfactants, which are similarly known to reduce unspecific adsorption but afford microheterogeneous solutions,[4] is also avoided.

In fact, we found that the prevention of unspecific adsorption becomes indispensable in confocal microscopy experiments (FCS mode). A routine sample preparation cycle (see Experimental Section) reduced the initial fluorescence intensity, assessed through the count rate, by nearly one order of magnitude compared to an identically handled CB7-stabilized Rh6G solution—from 96 to 13 KHz (Figure 4, $t = 0$)—although the extinction coefficient of the uncomplexed

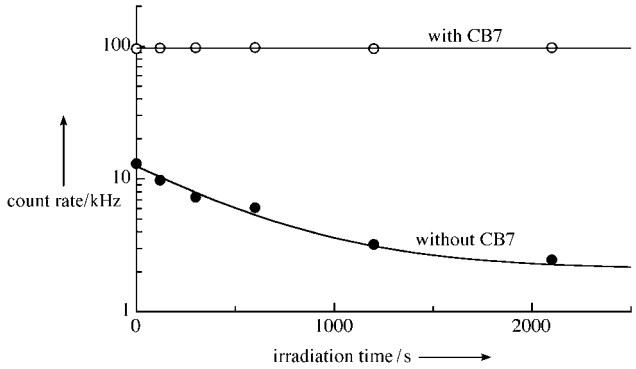

Figure 4. Dependence of the registered count rate of a Rh6G solution (10 nM) in the time course of an extended FCS measurement in a Lab-Tek 8-chambered borosilicate cover glass.

Rh6G at the employed Ar/2 laser wavelength (514 nm) is about 50% higher (Figure 1). In addition, the average number of molecules in the focal volume afforded directly by the FCS experiment decreased by a factor of 12 when CB7 was absent (from 5.6 to 0.46), thus suggesting that more than 90% of the Rh6G molecules were actually already lost during sample preparation by adsorption to the plastic and glass walls in the absence of the stabilizer. Moreover, the count rate of the unstabilized Rh6G solution continued to deplete during the course of the on-going FCS measurements, while that of the CB7-stabilized solution remained quite stable with prolonged irradiation (Figure 4, note the logarithmic scale). The count rate after 35 minutes was nearly 50 times higher with CB7, which illustrates the importance of appropriately stabilized dye solutions for long-time FCS measurements.

Finally, the formation of the supramolecular complex not only prevents surface adsorption, but also reduces adverse effects arising from aggregation of the dye, a phenomenon which comes into play at higher concentrations of dye that are relevant, for example, for dye lasers.[7,8] The addition of CB7 results ultimately in a stronger fluorescence of concentrated Rh6G solutions ($>10\,\mu M$), which in the absence of CB7 display a weaker fluorescence (and absorbance) than is extrapolated from lower concentrations as a consequence of Rh6G dimerization.[4] Addition of CB7 appears to suppress dye aggregation by selective formation of complexes containing only a single dye molecule. CB7 therefore plays an important role in breaking up fluorescent dye aggregates, thus providing an attractive alternative to the use of organic solvents or micellar solutions, the use of which is discouraged, for example, for dye lasers because of reduced dye photostability, poorer thermooptic performance, and economic as well as environmental considerations.[7,8,25] It should be noted that the photostabilization, adsorption, and FCS experiments (see above) were performed at low concentrations of the dye, where the deaggregating effect of CB7 is less important.

The concept of using a macrocyclic host to improve the solubility of Rh6G, enhance its photostability, and modify its photophysical characteristics is as simple as it is appealing. That the currently described supramolecular effects on the fluorescent properties of Rh6G are nevertheless nontrivial and critically dependent on the choice of CB7 as a unique host is readily seen by comparison with the effects of cyclodextrins as classical water-soluble hosts, which do not show the combination of desirable photophysical and photochemical effects. For example, their binding constants with Rh6G are very low, approximately only $200\,M^{-1}$,[31] such that a significant fraction of dye remains uncomplexed even in solutions saturated with host.

In summary, the addition of CB7 to aqueous solutions of Rh6G has exposed a synergistic interplay of several advantageous effects, which include high brightness, increased fluorescence lifetimes, spectral shifts, increased photostability at low and in particular high levels of irradiation, and the prevention of unspecific adsorption and dye aggregation. These factors are of interest for multiple practical applications: for dye lasers, for storing dilute Rh6G solutions, in confocal microscopy, for biomolecule labeling (note that complexation of a fluorophore by CB7 in a labeled peptide has recently been reported),[11] for high-throughput screening assays, and in PCR with fluorescence read-out. Several of these applications are currently under detailed evaluation.

Experimental Section

Rh6G was obtained from Molecular Probes and CB7 was synthesized as reported.[10,11] All measurements were made in water under air. The photolysis of Rh6G solutions with and without CB7 at high levels of irradiation were carried out by using the 2nd harmonic (532 nm) output of an Nd-YAG laser (Continuum Surelite III 10 model, 0.1 J pulse energy). The absorbance of Rh6G was monitored on a Varian Cary 4000 UV/Vis spectrophotometer parallel to an optically matched unstabilized solution. For quantification of the relative photobleaching quantum yield, the decrease in the absorbance at 532 nm (A) at different irradiation times was plotted according to the pertinent function $\log([10^{A_0}-1]/[10^{A}-1])$, and the ratio of the slopes of the plots were corrected for different extinction coefficients at the irradiation wavelength to afford the relative photobleaching quantum yields.[32] The low-irradiance photolysis was performed with 1 μM solutions in a Luzchem LZC-4V photoreactor equipped with 14 cool white fluorescent tubes, and the relative quantum yield for photobleaching in the presence of CB7 was determined accordingly, but no corrections for differential absorbance were made as a consequence of the broad-band irradiation.

The long-term storage experiments under ambient conditions were performed by monitoring the decrease in the integrated steady-state fluorescence intensity (measured on a Varian Cary Eclipse fluorometer) of the stabilized and unstabilized Rh6G solutions (1 μM) in different sample containers. For the FCS experiments on a confocal microscope (Carl Zeiss LSM 510 Meta, Confocor 2), 10 nM Rh6G solutions were obtained by diluting a freshly prepared 1 μM dye solution with water or with a 1 mM solution of CB7 in an Eppendorf polypropylene standard reaction vial, and immediately transferring a 400 μL sample volume with an Eppendorf pipette/polypropylene tip into a Lab-Tek 8-chambered borosilicate cover glass (chamber walls are polystyrene). The count rate obtained in the course of prolonged 514 nm Ar/2 laser excitation (irradiance estimated as ca. 0.1 $MW\,cm^{-2}$) was then followed over time. A control experiment demonstrated that the addition of 1 mM CB7 did not significantly enhance the background count rate in the FCS mode.

The fluorescence lifetimes of 200 nM Rh6G solutions in the presence and absence of CB7 were measured by time-correlated single-photon counting on an FLS-920 fluorometer (Edinburgh Instruments) using a H_2-flash lamp ($\lambda_{ex} = 527$ nm, $\lambda_{mon} = 552$ nm) for excitation by reconvolution of the fluorescence decay with the instrument response function. The fluorescence quantum yield of the CB7-stabilized dye was determined from integrated corrected fluorescence spectra with reference to Rh6G in water ($\Phi_f = 0.89$).[24]

Received: February 9, 2005
Published online: May 11, 2005

Keywords: dyes/pigments · fluorescence · inclusion compounds · photostability · single-molecule detection

[1] K. H. Drexhage, T. W. Hansch, E. P. Ippen, F. P. Schäfer, C. V. Shank, B. B. Snavely, *Dye Lasers*, Springer, Berlin, **1973**.
[2] O. Valdes-Aguilera, D. C. Neckers, *Acc. Chem. Res.* **1989**, *22*, 171 – 177.
[3] C. Eggeling, J. Widengren, R. Rigler, C. A. M. Seidel, in *Applied Fluorescence in Chemistry, Biology and Medicine* (Eds.: W. Rettig, B. Strehmel, S. Schrader, H. Seifert), Springer, Heidelberg, **1999**, pp. 193 – 240.
[4] C. Eggeling, J. Widengren, R. Rigler, C. A. M. Seidel, *Anal. Chem.* **1998**, *70*, 2651 – 2659.
[5] P. S. Dittrich, P. Schwille, *Appl. Phys. B* **2001**, *73*, 829 – 837.
[6] J. Slavik, *Fluorescent probes in cellular and molecular biology*, CRC, Boca Raton, FL, **1994**.
[7] J. C. Mialocq, M. Meyer, P. Hébert, X. Armand, D. Lambert, *Opt. Commun.* **1990**, *77*, 185 – 191.
[8] S. Sinha, A. K. Ray, S. Kundu, S. Sasikumar, K. Dasgupta, *Appl. Phys. B* **2002**, *75*, 85 – 90.
[9] O. G. Peterson, S. A. Tuccio, B. B. Snavely, *Appl. Phys. Lett.* **1970**, *17*, 245 – 247.
[10] J. Kim, I.-S. Jung, S.-Y. Kim, E. Lee, J.-K. Kang, S. Sakamoto, K. Yamaguchi, K. Kim, *J. Am. Chem. Soc.* **2000**, *122*, 540 – 541.
[11] C. Marquez, F. Huang, W. M. Nau, *IEEE Trans. Nanobiosci.* **2004**, *3*, 39 – 45.
[12] W. L. Mock in *Comprehensive Supramolecular Chemistry*, *Vol. 2* (Ed.: F. Vögtle), Elsevier, New York, **1996**, pp. 477 – 493.
[13] J. W. Lee, S. Samal, N. Selvapalam, H.-J. Kim, K. Kim, *Acc. Chem. Res.* **2003**, *36*, 621 – 630.
[14] C. Marquez, R. R. Hudgins, W. M. Nau, *J. Am. Chem. Soc.* **2004**, *126*, 5806 – 5816.
[15] B. D. Wagner in *Handbook of Photochemistry and Photobiology*, *Vol. 3* (Ed.: H. S. Nalwa), American Scientific Publishers, Stevenson Ranch, CA, **2003**, pp. 1 – 57.
[16] H.-J. Buschmann, T. Wolff, *J. Photochem. Photobiol. A* **1999**, *121*, 99 – 103.
[17] B. D. Wagner, A. I. MacRae, *J. Phys. Chem. B* **1999**, *103*, 10114 – 10119.
[18] B. D. Wagner, S. J. Fitzpatrick, M. A. Gill, A. I. MacRae, N. Stojanovic, *Can. J. Chem.* **2001**, *79*, 1101 – 1104.
[19] S. Y. Jon, N. Selvapalam, D. H. Oh, J.-K. Kang, S.-Y. Kim, Y. J. Jeon, J. W. Lee, K. Kim, *J. Am. Chem. Soc.* **2003**, *125*, 10186 – 10187.
[20] C. Marquez, W. M. Nau, *Angew. Chem.* **2001**, *113*, 4515 – 4518; *Angew. Chem. Int. Ed.* **2001**, *40*, 4387 – 4390.
[21] J. Mohanty, W. M. Nau, *Photochem. Photobiol. Sci.* **2004**, *3*, 1026 – 1031.
[22] R. Rigler, U. Mets, J. Widengren, P. Kask, *Eur. Biophys. J.* **1993**, *22*, 169 – 175.
[23] The upfield ^1H NMR shifts in a 1 mM Rh6G solution, for example, amount up to 0.1 ppm upon addition of 1 mM CB7, but they are observed for all protons, thus suggesting an "unselective" complexation.
[24] D. Magde, R. Wong, P. G. Seybold, *Photochem. Photobiol.* **2002**, *75*, 327 – 334.
[25] J. C. Mialocq, P. Hébert, X. Armand, R. Bonneau, J. P. Morand, *J. Photochem. Photobiol. A* **1991**, *56*, 323 – 338.
[26] S. J. Strickler, R. A. Berg, *J. Chem. Phys.* **1962**, *37*, 814 – 822.
[27] The fact that the lifetime of the Rh6G·CB7 complex increases also slightly when assembled in D_2O compared to H_2O (4.88 ± 0.05 versus 4.76 ± 0.04 ns) demonstrates directly that quenching by water is reduced by the supramolecular host, but not completely eliminated, presumably because the dye is too large to be fully included.
[28] J. A. Smith, R. M. West, M. Allen, *J. Fluoresc.* **2004**, *14*, 151 – 171.
[29] K. Suhling, P. M. W. French, D. Phillips, *Photochem. Photobiol. Sci.* **2005**, *4*, 13 – 22.
[30] H. J. Buschmann, *Vom Wasser* **1995**, *84*, 263 – 269.
[31] S. Hamai, K. Sasaki, *J. Inclusion Phenom. Mol. Recognit. Chem.* **2003**, *45*, 19 – 25.
[32] W. Adam, G. Fragale, D. Klapstein, W. M. Nau, J. Wirz, *J. Am. Chem. Soc.* **1995**, *117*, 12578 – 12592.

Polyphosphorus Ligands

Tetraphosphacyclopentadienyl and Triphosphaallyl Ligands in Iron Complexes**

Manfred Scheer, Shining Deng, Otto J. Scherer, and Marek Sierka*

Dedicated to Professor Gerd Becker on the occasion of his 65th birthday

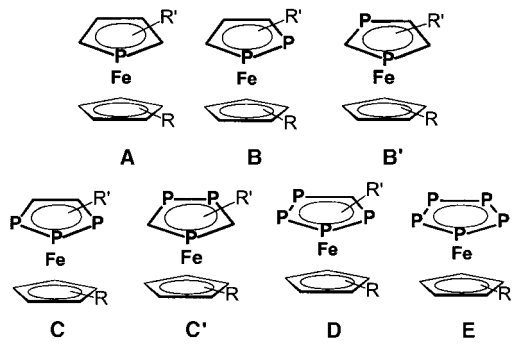

Since the first synthesis of $[Ti(\eta^5\text{-}P_5)_2]^{2-}$ by Ellis et al.[1] the search for decaphosphaferrocene has been a challenge in the field of phosphorus-containing complexes.[2] In addition, the lower phosphorus-containing complexes with $[(RC)_nP_{5-n}]^-$ ligands ($n = 1$–3) are of particular interest since η^5-phospholyl complexes show activity in various homogeneous catalysis applications.[3] Among the series of ferrocene complexes with $[(RC)_nP_{5-n}]^-$ ligands ($n = 0$–5) the syntheses of **A**[4] and **E**[5] have been benchmarks in the development of polyphospholyl complex chemistry.[6]

Whereas the ferrocenes of type **B**[7] as well as **B′** and **C′**[8] were synthesized later using phosphaalkyne as starting material for **B′** and **C′**, the missing 1,2,3-triphosphaferrocene **C** was only recently synthesized by Scherer et al. by the reaction of the tetraphosphabicyclobutadiene complex **1** with diphenylacetylene.[9] In the series shown, the hitherto missing complex **D** is of interest for us, since our general goal lies in the use of P_n ligand complexes as linking units for the formation of soluble supramolecular aggregates[10] as well as 1D and 2D polymers and networks.[11] Thus, we developed a synthesis for the first completely characterized 1,2,3,4-tetraphosphaferrocene complex **D** by a method using *t*BuC≡P as starting material, the results of which are reported herein.

The reaction of **1** with *t*BuC≡P leads to the desired complex in a mixture of products which have been separated by chromatography [Eq. (1); $Cp''' = \eta^5\text{-}C_5H_2tBu_3$]. In each of these thermolysis reactions a very broad signal appears at $\delta = 92$ ppm ($\omega_{1/2} = 300$ Hz) in the ^{31}P NMR spectrum, which probably represents a polymeric product. The main products isolated are complexes **4** and **3**, whereas **6** and the known *cyclo*-P_5 complex **5**[12] could only be obtained in small amounts.[13] The structure of the main products gives evidence for a P_3/P_1 fragmentation[14] of the bicyclo-tetraphosphine complex **1**, with subsequent further reaction with one or two equivalents of phosphaalkyne to give the products **3** and **4**,

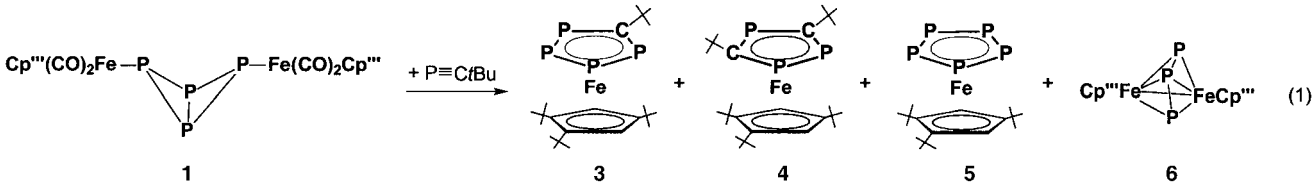

1 3 4 5 6 (1)

respectively. Similar observations were made for an indanyl-substituted derivative of **1** and 1-methylcyclohexylphosphaalkyne by Scherer et al.[15]

The crystals of complexes **3** and **6** are green and those of **4** are red. The compounds are readily soluble in toluene and CH_2Cl_2 and slightly soluble in nonpolar solvents, such as *n*-pentane. The mass spectrum of each compound shows the appropriate molecular ion peak. The $^{31}P\{^1H\}$ NMR spectrum of the major product **4** shows two groups of signals of an AM_2 spin system, which is very similar to the values found in complexes of type **C′**.[8] Furthermore, the molecular structure of **4**[16] (see Supporting Information) is similar to those of other type **C′** derivatives[8] and reveals the staggered conformation of the *t*Bu groups of the five-membered rings to minimize steric repulsion. The rings are tilted by only 0.7°.

The ^{31}P NMR spectrum of the target complex **3** reveals an AA′MM′ spin system at $\delta = 122.8$ ppm for the P_M and $P_{M'}$ atoms, and at $\delta = 80.4$ ppm for the P_A and $P_{A'}$ atoms.

Complex **3** crystallizes in the monoclinic space group $P2_1/n$ with two independent molecules in the unit cell.[16] In

[*] Prof. Dr. M. Scheer, Dipl.-Chem. S. Deng
Institut für Anorganische Chemie
Universität Regensburg
93040 Regensburg (Germany)
Fax: (+49) 941-943-4441
E-mail: mascheer@chemie.uni-regensburg.de
Dr. M. Sierka
Institut für Chemie
Humboldt-Universität zu Berlin
Unter den Linden 6, 10099 Berlin (Germany)
Prof. Dr. O. J. Scherer
Fachbereich Chemie
Universität Kaiserslautern
Erwin-Schrödinger-Strasse, 67663 Kaiserslautern (Germany)

[**] This work was comprehensively supported by the Deutsche Forschungsgemeinschaft and the Fonds der Chemischen Industrie. The authors thank Prof. Dr. H. Sitzmann for helpful discussions about the synthesis of the starting material and Dr. E Matern for the simulation of the ^{31}P NMR spectra.

Supporting information for this article is available on the WWW under http://www.angewandte.org or from the author.

 DOI: 10.1002/anie.200500194

Figure 1 the top view of both molecules is shown, revealing that in the solid state both enantiomers are present, these become equivalent in solution owing to the free rotation of the five-membered rings.

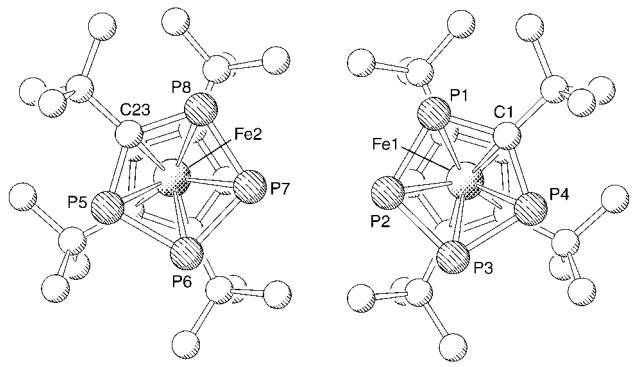

Figure 1. Top-view of the two independent molecules of **3** in the crystal structure. Hydrogen atoms are omitted for clarity. Selected bond lengths [Å] and angles [°]: P1-C1 1.759(3), P1-P2 2.115(1), P2-P3 2.115(1), P3-P4 2.116(1), P4-C1 1.769(3), P5-C23 1.766(3), P8-C23 1.759(3), P5-P6 2.1167(13), P6-P7 2.1190(13), P7-P8 2.1152(12); P1-C1-P4 124.67(18), P1-P2-P3 104.02(5), P2-P3-P4 103.59(5), C1-P1-P2 103.75(11), C1-P4-P3 103.85(11), P5-C23-P8 125.05(17), P5-P6-P7 103.53(7), P6-P7-P8 104.03(5), C23-P5-P6 103.73(11), C23-P8-P7 103.58(11).

In the sandwich complex **3** both five-membered rings are nearly parallel (Figure 2). The tilting angles between the five-membered rings are 4.93(2)° (molecule A) and 5.24(2)° (molecule B). Since the structural data of both molecules are similar only molecule A is considered hereafter. The averaged P–C and P–P bond lengths of the tetraphospholyl ring are 1.763(3) and 2.115(1) Å, respectively, and are therefore shorter than corresponding single bonds. The P–P bonds in **3** are slightly longer than the averaged bond lengths in the *cyclo*-P_5 rings of [Cp‴Fe(η^5-P_5)] (2.079(8) Å)[12] and [Cp^{x}Fe(η^5-P_5)] (Cp^x = η^5-C_5Me_4Et) (2.096(3) Å)[17] and thus more comparable to those of the *cyclo*-P_3C_2-ring in [Cp‴Fe(η^5-$P_5C_3Ph_2$)] (av. P–C 1.775(4) Å, av. P–P 2.124(2) Å).[9] Since each of the angles in the tetraphospholyl ring of **3** deviate from 120° (av. P-P-P 102.8°, P(1)-C(1)-P(4) 127.1(19)°) the five-fold symmetry of the ring is distorted, which is similar to the situation in the P_3C_2 ring of [Cp‴Fe(η^5-$P_3C_2Ph_2$)].[9]

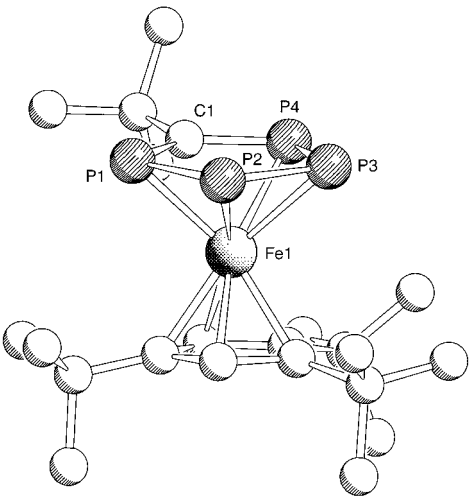

Figure 2. Molecular structure of **3** (molecule A). Hydrogen atoms are omitted for clarity. Selected bond lengths [Å] and angles [°] [molecule B]: P1-C1 1.759(3) [1.766(3)], P1-P2 2.115(1) [2.117(1)], P2-P3 2.115(1) [2.119(1)], P3-P4 2.116(1) [2.115(1)], P4-C1 1.769(3) [1.759(3)]; P4-Fe1-P3 53.36(3) [53.33(3)], C1-Fe1-P1 45.16(8) [45.48(8)], P3-Fe1-P1 89.86(3) [89.99(4)], P4-Fe1-P2 89.96(4) [89.86(3)], P3-Fe1-P2 52.94(3) [53.02(3)], C2-C1-Fe1 138.3(2) [138.2(2)].

Complex **6** contains the first triphosphaallyl unit in a binuclear complex. To date only *cyclo*-P_3 ligands[18] and organoallylic EtE_3 units (E = P, As)[19] are the only known phosphorus or allylic groups to bridge two metal centers. The molecular structure of **6**[16] (Figure 3) reveals a *cis*-orientation

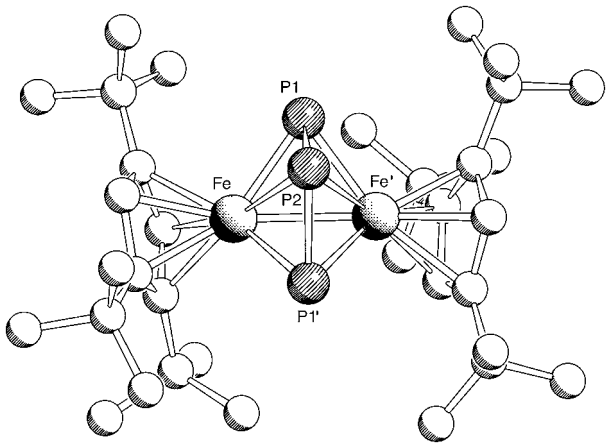

Figure 3. Molecular structure of **6**. Hydrogen atoms are omitted for clarity. Selected bond lengths [Å] and angles [°]: Fe-Fe 2.589(1), P1(1′)-P2 2.148(1), Fe-P1 2.225(1), Fe-P2 2.446(1); P1-P2-P1′ 100.71(7), Fe-P1-Fe′ 71.51(4), Fe-P2-Fe′ 63.92(4).

of the Cp‴ groups, whereas the allylic P_3 unit is directed away from the Fe–Fe axis. The P–P bond length of the allylic P_3 moiety is 2.148(1) Å and thus shorter than a single bond and slightly longer than the P–P double bond of the EtP_3 unit in [{(tripod)Co}$_2$(μ,η^3-EtP_3)] (2.110 Å; tripod = CH_3C-$(CH_2PPh_2)_3$).[19] The distance between the Fe atoms (2.589(1) Å) is in the same range as those of the various [{Cp′Fe(CO)$_2$}$_2$] complexes.[20]

Since the electronic structure of **6** was not clear upon initial inspection, we decided to carry out density functional theory (DFT) calculations. Theoretical methods have proven to be a useful tool in analyzing the structure and properties of phosphorus-containing transition-metal complexes.[1,2,21] Calculations are performed on the original complex **6** and, additionally, to analyze the steric influence of the bulky *t*Bu groups, on a model compound **6a** in which the *t*Bu groups are replaced by H atoms.

Structure optimizations of **6** and **6a** yield close lying low-spin doublet states (Table 1) with an unpaired electron delocalized over the d orbitals of both Fe atoms (see Supporting Information). Comparison of the results obtained

Table 1: Comparison of relative energies of different electronic states ΔE [kJ mol^{-1}] and selected structural parameters ([Å], [°]) for the central Fe_2P_3 unit of compounds **6a** and **6** (BP86 calculations).

	6a (C_{2v})[a]		**6** (C_2)[a]		Exp
	$^2A_2$	$^2B_1$	^2A	^2B	
ΔE	−3.2	0.0	9.1	0.0	
Fe-Fe′	2.483	2.741	2.640	2.832	2.589
Fe-P1	2.215	2.192	2.219	2.202	2.225
Fe-P1′	2.215	2.192	2.215	2.196	2.206
Fe-P2	2.488	2.361	2.481	2.365	2.446
Fe-C	2.114–2.126	2.093–2.120	2.090–2.166	2.080–2.157	2.102–2.158
P2-P1(1′)	2.189	2.272	2.191	2.263	2.148
P1-P2-P1′	99.89	94.46	97.99	93.40	100.71
Fe-P1-Fe′	68.18	77.40	73.07	80.19	71.51
Fe-P2-Fe′	59.86	70.95	64.28	73.57	63.92

[a] Symmetry point group.

for **6** and **6a** indicates that the steric repulsion between *t*Bu groups has an important influence on the electronic structure. For **6a** calculations yield two almost degenerate $^2A_2$ and $^2B_1$ states with the latter one being slightly less stable. These two states differ by the occupancy of the a_2 and b_1 orbitals which are composed of d_{xz} and d_{xy} orbitals of the Fe and Fe′ atoms (with both Fe atoms located on the *y* axis). The $(b_1)^2(a_2)^1$ configuration of the $^2A_2$ state facilitates a weak Fe–Fe′ bonding interaction. Promoting one electron from the b_1 to a_2 orbital results in the $^2B_1$ state ($(b_1)^1(a_2)^2$), which weakens the Fe···Fe′ interaction and facilitates the $P_3 \rightarrow$ Fe π donation. In **6** the stability of the ^2A and ^2B states, which correspond to the $^2A_2$ and $^2B_1$ states of **6a**, respectively, is reversed. The ^2A state is now less stable as a result of the stronger Fe–Fe′ interaction which results in a higher repulsion between bulky Cp‴ ligands.

To rationalize the differences between different states of **6** and **6a** we performed an atoms-in-molecules (AIM)[22] topological analysis of the electronic charge density for both systems (Figure 4; see Supporting Information). The bonding of the ^2B state of **6** is similar to the $^2B_1$ state of **6a**. However, the ^2A and $^2A_2$ states differ because of the absence of the Fe–Fe′ bond in **6** which is a result of the repulsion between bulky *t*Bu groups.

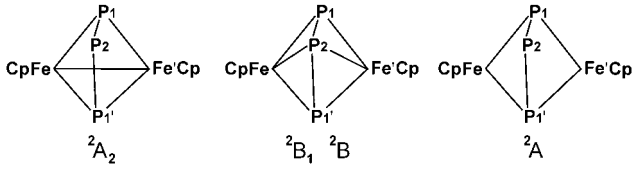

Figure 4. Bonding schemes of the compounds **6a** ($^2A_2$ and $^2B_1$ states) and **6** (^2A and ^2B states) from the AIM analysis of electronic charge densities (Cp denotes η^5-C_5H_5 in **6a** and η^5-$C_5H_2tBu_3$ in **6**).

The structure parameters calculated for the slightly less stable ^2A state of **6** are in better agreement with experimental data than those calculated for the ^2B state. Thus, the $\mu,\eta^2{:}\eta^2$-coordination of the allylic P_3 ligand is the most probable one. Results obtained for **6** and **6a** show that the weak attractive Fe···Fe′ interaction and repulsion between the bulky *t*Bu groups are two competing effects. The DFT method may not be accurate enough to properly describe the balance of the two interactions, and the energy difference between the two states is certainly within its margin for error. The delocalization of the unpaired electron over both Fe atoms is the reason that signals for an AA′X spin system are observed in the ^{31}P NMR spectrum of **6**. However, the paramagnetism might cause the large chemical shift differences in both signals, which is especially pronounced for the P1 and P1′ atoms.

In conclusion, the results have shown that the bicyclotetraphosphine complex **1** is an excellent starting material for the synthesis of novel polyphosphorus-ligand-containing metallocenes. With the synthesis of the 1,2,3,4-tetraphosphaferrocene the path has been cleared for its application in the formation of well-defined aggregates by intermolecular assembly.

Experimental Section

All manipulations were performed under an atmosphere of dry nitrogen using a glovebox and Schlenk technique. Solvents were purified and degassed by standard procedures.

*t*BuC≡P (0.223 g, 2.23 mmol) was added to a solution of **1** (1.82 g, 2.23 mmol) in toluene (150 mL) at room temperature. The reaction mixture was heated under reflux for 36 h. After removal of all volatile material in vacuum, the residue was dissolved in dichloromethane (10 mL) and transferred onto silica gel. Chromatographic work-up on a silica gel column (40 × 2.5 cm) eluting with hexane/dichloromethane (10:1) gave first a red fraction of **6**, then a green fraction of **5**, an orange-red fraction of **4**, and finally an olive-green fraction of **3**. Each product was recrystallized from *n*-hexane. A fifth band (green) contained the proposed polymeric compound mentioned in the main text. If, as in some cases, the separation was not complete after column chromatography, the separation was completed in a glovebox by thin layer chromatography (TLC) using a hexane/dichloromethane (10:1) solvent mixture.

3: Yield: 60 mg (11%); ^{1}H NMR (250 MHz, C_6D_6): $\delta = 1.62$ (s, 9H), 1.20 (s, 9H), 1.35 (s, 18H), 4.22 ppm (s, 2H); ^{31}P NMR (250 MHz, C_6D_6, AA′MM′ spin system): $\delta(P_A) = \delta(P_{A'}) = 81.6$ (m, 2P), $\delta(P_M) = \delta(P_{M'}) = 122.8$ ppm (m, 2P), $^1J(P_AP_M) = -431.2$ Hz, $^2J(P_AP_{M'}) = 9.4$ Hz, $^3J(P_AP_{A'}) = -54.7$ Hz, $^1J(P_MP_{M'}) = -425.2$ Hz (simulated values); EI-MS (100°C) *m*/*z* (%): 482 [M^+] (100), 382 [M^+–PC*t*Bu] (71), 121 [$C_5H_4tBu]^+$ (23.8).

4: Yield: 110 mg (20%); ^{1}H NMR (250 MHz, C_6D_6): $\delta = 1.25$ (s, 9H), 1.24 (s, 18H), 1.36 (s, 18H), 4.58 ppm (s, 2H); ^{31}P NMR (250 MHz, C_6D_6): $\delta = 52.6$ (t, 1P), 42.7 ppm (d, 2P), ^2J(P,P) = 43.9 Hz; EI-MS (60°C) *m*/*z* (%) 520 [M^+] (4), 432 [M^+–P*t*Bu] (71.5), 295 $[(C_5H_3tBu_2)FeP_2]^+$, (100), 233 ($[Cp‴]^+$ (28).

5: Yield: 4 mg (2%); ^{1}H NMR (250 MHz, C_6D_6): $\delta = 1.08$ (s, 9H), 1.21 (s, 18H), 3.9 ppm (s, 2H); ^{31}P NMR (250 MHz, C_6D_6): $\delta =$ 165.4 ppm (s, 5P).

6: Yield: 5 mg (2%); ^{1}H NMR (250 MHz, C_6D_6): $\delta = 1.22$ (s, 9H), 1.30 (s, 18H), 4.16 ppm (s, 2H); ^{31}P NMR (250 MHz, C_6D_6): $\delta(P_A) = \delta(P_{A'}) = 677.8$ (dd, 1P), $\delta(P_X) = -380.9$ ppm (t, 2P), $J(P_AP_X) =$ 390.2 Hz, $J(P_{A'}P_X) = 32.6$ Hz; EI-MS (90°C) *m*/*z* 671 (%) [M^+]

(5.7), 614 [M^+–*t*Bu] (8.4), 382 [M^+–Cp‴Fe], (27.8). Fifth fraction: ^{31}P NMR (250 MHz, C_6D_6): $\delta = 92$ ppm, $\omega_{1/2} = 300$ Hz.

All theoretical calculations were performed using the TURBOMOLE program package.[23] We employ the triple zeta plus polarization (TZVP) basis set on all atoms.[24] We considered BP86[25] and B3LYP[26] exchange-correlation functionals. Comparison of structural parameters calculated for **6** using both functionals (see Table 1 for BP86 and the Supporting Information for B3LYP results) shows that the BP86 provides a more reliable description. To speed up calculations with BP86 functional the Coulomb part was evaluated using the MARI-J method.[27] To confirm that a calculated structure and density are not the result of symmetry restrictions, the calculations are performed both by using symmetry and without symmetry. The most stable spin states have been found employing the pseudo Fermi smearing technique.[28] All nuclear coordinates have been fully optimized. Convergence criteria were set to 10^{-3} a.u. for the norm of the gradients and 10^{-5} a.u. for energy change. The AIM analysis was performed with the AIMPAC program.[29]

Received: January 18, 2005
Published online: May 11, 2005

Keywords: density functional calculations · iron · metallocenes · phosphorus · polyphosphorus ligands

[1] E. Urnezius, W. W. Brennessel, C. J. Cramer, J. E. Ellis, P. v. R. Schleyer, *Science* **2002**, *295*, 832.
[2] J. Frunzke, M. Lein, G. Frenking, *Organometallics* **2002**, *21*, 3351.
[3] F. Mathey in *Phosphorus-Carbon Heterocyclic Chemistry: The Rise of a New Domain* (Ed.: F. Mathey), Pergamon, Oxford, **2001**, pp. 767; *Homogeneous Catalysis with Organometallic Compounds*, *Vol. 1* and *2* (Eds.: B. Cornils, W. A. Herrmann), VCH, Weinheim, **1996**; K. B. Dillon, F. Mathey, J. F. Nixon in *Phosphorus: The Carbon Copy*, Wiley, New York, **1998**; F. Mathey, *Angew. Chem.* **2003**, *115*, 1616–1643; *Angew. Chem. Int. Ed.* **2003**, *42*, 1578–1604.
[4] F. Mathey, *Tetrahedron Lett.* **1976**, 4155–4158.
[5] O. J. Scherer, T. Brück, *Angew. Chem.* **1987**, *99*, 59; *Angew. Chem. Int. Ed. Engl.* **1987**, *26*, 59.
[6] F. Mathey, *Coord. Chem. Rev.* **1994**, *137*, 1–52.
[7] N. Maigrot, N. Avarvari, C. Charrier, F. Mathey, *Angew. Chem.* **1995**, *107*, 623–625; *Angew. Chem. Int. Ed. Engl.* **1995**, *34*, 590–592.
[8] a) C. Müller, R. Bartsch, A. Fischer, P. G. Jones, R. Schmutzler, *J. Organomet. Chem.* **1996**, *512*, 141–148; b) R. Bartsch, P. B. Hitchcock, J. F. Nixon, *J. Organomet. Chem.* **1988**, *340*, C37–C39; c) R. Bartsch, P. B. Hichcock, J. F. Nixon, *J. Chem. Soc. Chem. Commun.* **1987**, 1146–1148; d) C. Müller, R. Bartsch, A. Fischer, P. G. Jones, *J. Organomet. Chem.* **1993**, *453*, C16–C18.
[9] O. J. Scherer, T. Hilt, G. Wolmershäuser, *Angew. Chem.* **2000**, *112*, 1484–1485; *Angew. Chem. Int. Ed.* **2000**, *39*, 1425–1427.
[10] B. Junfeng, A. Virovets, M. Scheer, *Science* **2003**, *300*, 781–782.
[11] B. Junfeng, A. Virovets, M. Scheer, *Angew. Chem.* **2002**, *114*, 1808–1811; *Angew. Chem. Int. Ed.* **2002**, *41*, 1737–1740.
[12] O. J. Scherer, T. Hilt, G. Wolmershäuser, *Organometallics* **1998**, *17*, 4110–4112.
[13] S. Deng, Diplom thesis, Karlsruhe **2002**.
[14] For P_3/P_1 fragmentation of P_4 phosphorus see M. Scheer, K. Schuster, U. Becker, *Phosphorus Sulfur and Silicon* **1996**, *109–110*, 114–141; M. Scheer, U. Becker, *Chem. Ber.* **1996**, *129*, 1307–1310; M. Scheer, U. Becker, J. Magull, *Polyhedron* **1998**, *17*, 1983–1989.
[15] C. Eichhorn, PhD thesis, Kaiserslautern, **2003**.
[16] Crystal structure analyses of **3**, **4** and **6** were performed on a STOE IPDS diffractometer with $Mo_{K\alpha}$ radiation ($\lambda = 0.71073$ Å) for **3** and **6** and $Ag_{K\alpha}$ radiation ($\lambda = 0.56087$ Å) for **4**. The structures were solved by direct methods with the program SHELXS-97,[30a] and full matrix least-squares refinement on F^2 in SHELXL-97[30b] was performed with anisotropic displacements for non-hydrogen atoms. Hydrogen atoms were located in idealized positions and refined isotropically according to the riding model. In compound **4** the C atoms of all CH_3 groups are disordered; a merohedral twin could not be ruled out. **3**: $C_{22}H_{38}FeP_4$, $M_r = 482.25$, crystal dimensions $0.30 \times 0.15 \times 0.05$ mm^3, monoclinic, space group $P2_1/n$ (No. 14), $a = 8.679(1)$, $b = 15.985(1)$ Å, $c = 35.579(2)$ Å, $\beta = 96.14(1)°$, $T = 150(1)$ K, $Z = 8$, $V = 4907.7(6)$ Å^3, $\rho_{calcd} = 1.305$ Mg m^{-3}, $\mu(Mo_{K\alpha}) = 0.881$ mm^{-1}, 9640 independent reflexes ($R_{int} = 0.0549$, $2\theta_{max} = 53.18°$), 6244 observed with $F_o = 4\sigma(F_o)$, 511 parameters, $R_1 = 0.0400$, $wR_2 = 0.0971$. **4**: $C_{27}H_{45}FeP_3$, $M_r = 518.39$, crystal dimensions $0.30 \times 0.20 \times 0.05$ mm^3, orthorhombic, space group *Pnma* (No. 62), $a = 16.361(3)$ $b = 16.933(3)$ Å, $c = 10.102(2)$ Å, $T = 203(2)$ K, $Z = 4$, $V = 2798.7(10)$ Å^3, $\rho_{calcd} = 1.230$ Mg m^{-3}, $\mu(Mo_{K\alpha}) = 0.378$ mm^{-1}, 2963 independent reflexes ($R_{int} = 0.0988$, $2\theta_{max} = 41.72°$), 2387 observed with $F_o = 4\sigma(F_o)$, 226 parameters, $R_1 = 0.0704$, $wR_2 = 0.1913$. **6**: $C_{34}H_{58}Fe_2P_3$, $M_r = 671.41$, crystal dimensions $0.16 \times 0.10 \times 0.02$ mm^3, monoclinic, space group $C2/c$ (No. 15); $a = 10.207(2)$, $b = 15.635(3)$, $c = 22.210(4)$ Å, $\beta = 94.63(3)°$, $T = 100(1)$ K, $Z = 4$, $V = 3532.8(12)$ Å^3, $\rho_{calcd} = 1.262$ Mg m^{-3}, $\mu(Ag_{K\alpha}) = 0.978$ mm^{-1}, 3174 independent reflexes ($R_{int} = 0.0591$, $2\theta_{max} = 50.72°$), 2247 observed with $F_o = 4\sigma(F_o)$; 186 parameters, $R_1 = 0.0448$, $wR_2 = 0.1039$. CCDC-258064 (**3**), CCDC-258065 (**4**), and CCDC-258066 (**6**) contain the supplementary crystallographic data for this paper. These data can be obtained free of charge from the Cambridge Crystallographic Data Centre via www.ccdc.cam.ac.uk/data_request/cif.
[17] O. J. Scherer, T. Brück, G. Wolmershäuser, *Chem. Ber.* **1988**, *121*, 935.
[18] O. J. Scherer, *Acc. Chem. Res.* **1999**, *32*, 751–762; K. H. Whitmire, *Adv. Organomet. Chem.* **1998**, *42*, 1–145.
[19] A. Barth, G. Huttner, M. Fritz, L. Zsolnai, *Angew. Chem.* **1990**, *102*, 956–958; *Angew. Chem. Int. Ed. Engl.* **1990**, *29*, 929–931.
[20] M. Scheer, K. Schuster, U. Becker, A. Krug, H. Hartung, *J. Organomet. Chem.* **1993**, *460*, 105–110.
[21] M. Lein, J. Frunzke, G. Frenking, *Inorg. Chem.* **2003**, *42*, 2504–2511.
[22] R. F. W. Bader, *Chem. Rev.* **1991**, *91*, 893–928.
[23] a) R. Ahlrichs, M. Bär, M. Häser, H. Horn, C. Kölmel, *Chem. Phys. Lett.* **1989**, *162*, 165–169; b) O. Treutler, R. Ahlrichs, *J. Chem. Phys.* **1995**, *102*, 346–354.
[24] a) A. Schäfer, H. Horn, R. Ahlrichs, *J. Chem. Phys.* **1992**, *97*, 2571–2577; b) A. Schäfer, C. Huber, R. Ahlrichs, *J. Chem. Phys.* **1994**, *100*, 5829–5835; c) K. Eichkorn, F. Weigend, O. Treutler, R. Ahlrichs, *Theor. Chem. Acc.* **1997**, *97*, 119–124.
[25] a) A. D. Becke, *Phys. Rev. A* **1988**, *38*, 3098–3100; b) S. H. Vosko, L. Wilk, M. Nusair, *Can. J. Phys.* **1980**, *58*, 1200–1211; c) J. P. Perdew, *Phys. Rev. B* **1986**, *33*, 8822–8824; Erratum: J. P. Perdew, *Phys. Rev. B* **1986**, *34*, 7406.
[26] a) A. D. Becke, *J. Chem. Phys.* **1993**, *98*, 5648–5652; b) C. Lee, W. Yang, R. G. Parr, *Phys. Rev. B* **1988**, *37*, 785–789.
[27] a) K. Eichkorn, O. Treutler, H. Öhm, M. Häser, R. Ahlrichs, *Chem. Phys. Lett.* **1995**, *242*, 652; b) M. Sierka, A. Hogekamp, R. Ahlrichs, *J. Chem. Phys.* **2003**, *118*, 9136–9148.
[28] P. Nava, M. Sierka, R. Ahlrichs, *Phys. Chem. Chem. Phys.* **2003**, *5*, 3372–3381.
[29] F. W. Biegler-König, R. F. W. Bader, T. H. Tang, *J. Comput. Chem.* **1982**, *3*, 317–328.
[30] a) G. M. Sheldrick, SHELXS-96, Universität Göttingen, **1996**; b) G. M. Sheldrick, SHELXL-97, Universität Göttingen, **1997**.

Carbene Complexes

Template Synthesis of a Coordinated Tetracarbene Ligand with Crown Ether Topology**

F. Ekkehardt Hahn, Volker Langenhahn, Thomas Lügger, Tania Pape, and Duc Le Van*

Nucleophilic attack at the carbon atom of a coordinated isocyanide is one of the oldest methods for the preparation of carbene complexes.[1] Particularly protic nucleophiles like alcohols and primary amines have been useful in this reaction. They give in good yield carbene complexes in which the carbene ligand has a H substituent at the N-position.[2] The use of functionalized isocyanides like 2-hydroxyethyl isocyanide containing both the isocyanide function and the nucleophile in the same molecule leads, when the isocyanide is coordinated to a metal center in a high oxidation state, to complexes with a heterocyclic NH,O-stabilized carbene ligand.[3]

We reported on the template-controlled cyclization of 2-hydroxyphenyl isocyanide, which was obtained from complexes containing 2-(trimethylsiloxy)phenyl isocyanide[4] by cleavage of the O–Si bond[5] (Scheme 1). The synthesis of complexes containing benzannulated NH,NH-stabilized N-heterocyclic carbene ligands was also achieved in a template synthesis.[6] In this reaction 2-azidophenyl isocyanide was used as a synthon for the unstable 2-aminophenyl isocyanide. 2-Azidophenyl isocyanide, when coordinated to a transition metal, can be activated at the azido function by a Staudinger reaction.[7] Hydrolysis of the initially obtained iminophosphorane leads to immediate cyclization and formation of the NH,NH-stabilized carbene ligand. Both the NH,O- (in **A**) and the NH,NH-stabilized carbene ligand (in **C**) are easily alkylated at the N-position to form the carbene complexes **B** and **D** (Scheme 1). The carbene ligands in complexes **A**–**C** are not stable when removed from the metal center. The template-controlled synthesis of **D** offers an alternative to the direct reaction of stable benzannulated carbene ligands[8,9] and benzimidazolium salts[10] with transition-metal complexes for the preparation of carbene complexes. Here we report on a modified cyclization reaction of coordinated 2-azidophenyl isocyanide for the synthesis of the tetracarbene complex $[\mathbf{5}](CF_3SO_3)_2$ (Scheme 2) and on a method to bridge the four NH,NH-stabilized carbene ligands in $[\mathbf{5}]^{2+}$ to give complex $[\mathbf{8}]^{2+}$, which contains a cyclic tetracarbene ligand with crown ether topology (Scheme 3).

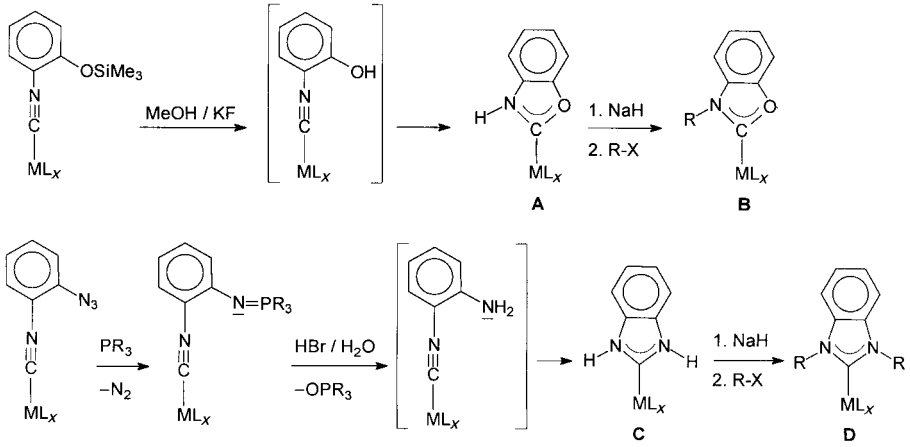

Scheme 1. Template-controlled cyclization of β-functionalized phenyl isocyanides to give N-heterocyclic carbene ligands. $ML_x = W(CO)_5$, $Mo(CO)_5$, $Cr(CO)_5$.

The preparation of a cationic tetracarbene complex of type $[\mathbf{5}]^{2+}$ (Scheme 2) starting from a cationic square-planar tetrakis(2-azidophenyl isocyanide)metal(II) complex by a fourfold Staudinger reaction, hydrolysis, and cyclization in analogy to the preparation of **C** (Scheme 1) appears initially unproblematic. Homoleptic tetrakis(phenyl isocyanide) complexes of Pd^{II} and Pt^{II} have been described,[11] while Ni^{II} is known to polymerize isocyanides.[12] However, the preparation of complexes of type $[M(C{\equiv}N\text{-}Ar)_4]^{2+}$ starting from PdX_2 or PtX_2 (X = Cl, I) requires a tenfold excess of aryl isocyanide and yields, particularly upon stoichiometric application of the aryl isocyanide, often only the diisocyanide complexes[13] of type $[MX_2(C{\equiv}N\text{-}Ar)_2]^{2+}$. Similar results were obtained in the reaction of 2-azidophenyl isocyanide **2** with PtX_2. Contrary to this, the more nucleophilic alkyl isocyanides readily form homoleptic complexes[3e,14] with Pt^{II} and Pd^{II}.

To avoid the problems associated with the preparation of tetrakis(2-phenyl isocyanide) complexes we developed the template-controlled reaction cascade depicted in Scheme 2. First tetrakis(trimethylphosphane)platinum(II) bis(trifluoromethanesulfonate) $[\mathbf{1}](CF_3SO_3)_2$ was treated with four equivalents of ligand **2**. At first only one of the phosphine ligands is replaced by an isocyanide ligand in the formation of complex $[\mathbf{3}]^{2+}$. No further substitution takes place at this stage. The liberated phosphine ligand can attack the metal center in $[\mathbf{3}]^{2+}$ to regenerate $[\mathbf{1}]^{2+}$. An alternative reaction path is the Staudinger reaction of the liberated phosphine with the

[*] Prof. Dr. F. E. Hahn, Dr. V. Langenhahn, Dr. T. Lügger, T. Pape, Dr. D. Le Van[+]
Institut für Anorganische und Analytische Chemie
Westfälische Wilhelms-Universität Münster
Wilhelm Klemm-Strasse 8, 48149 Münster (Germany)
Fax: (+49) 251-833-3108
E-mail: fehahn@uni-muenster.de

[+] Deceased September 22, 2004

[**] This work was supported financially by the Deutsche Forschungsgemeinschaft (SFB 424) and the International Graduate College "Template Directed Chemical Synthesis" (GRK 673).

Supporting information for this article is available on the WWW under http://www.angewandte.org or from the author.

 DOI: 10.1002/anie.200462690

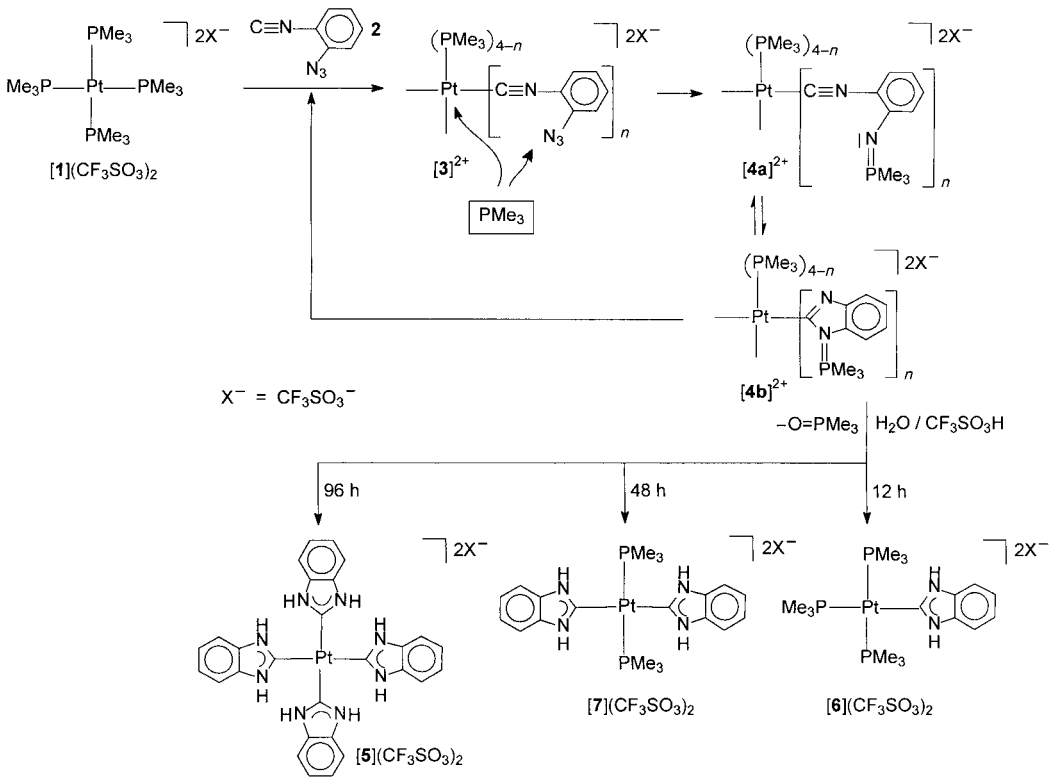

Scheme 2. Synthesis of Pt^{II} carbene complexes $[\mathbf{5}](CF_3SO_3)_2$, $[\mathbf{6}](CF_3SO_3)_2$, and $[\mathbf{7}](CF_3SO_3)_2$.

azido function of the coordinated 2-azidophenyl isocyanide. If the Staudinger reaction proceeds faster than the backreaction to $[\mathbf{1}]^{2+}$, the competitor for a coordination site at platinum (PMe_3) is consumed and irreversible liberation of N_2 gives the iminophosphorane complex $[\mathbf{4a}]^{2+}$. This reaction is indeed observed.

For electron-rich transition metals, the chemical equilibrium between the complexes with the open and cyclized forms of the iminophosphorane ligand ($[\mathbf{4a}]^{2+}/[\mathbf{4b}]^{2+}$) resides mainly on the side of the noncyclized ligand (type $[\mathbf{4a}]^{2+}$), which has been confirmed crystallographically for the $W(CO)_5$ complex (Scheme 1).[6a,15] However, the Pt^{II}-coordinated isocyanide carbon atom in $[\mathbf{4a}]^{2+}$ is much more strongly activated for the nucleophilic attack of the iminophosphorane nitrogen atom. We therefore postulate that the iminophosphorane ligand in $[\mathbf{4a}]^{2+}$ cyclizes in an intramolecular fashion to give complex $[\mathbf{4b}]^{2+}$ as the main product.[16] This would also explain the subsequent reactions. The formation of an ylide-type heterocycle in $[\mathbf{4b}]^{2+}$ leads to a strong *trans* effect. The PMe_3 ligand in *trans* position to the ylide in $[\mathbf{4b}]^{2+}$ is more labile than a PMe_3 ligand *trans* to the phenyl isocyanide in $[\mathbf{4a}]^{2+}$. Consequently, complex $[\mathbf{4b}]^{2+}$ reacts by substitution of the *trans* phosphine ligand for an isocyanide ligand **2**, which then again undergoes Staudinger reaction and cyclization. The reaction sequence substitution of a phosphine, Staudinger reaction, and cyclization proceeds a total of four times. The four cyclized iminophosphorane ligands were hydrolyzed after a total reaction time of 96 h with H_2O/CF_3SO_3H giving the tetracarbene complex $[\mathbf{5}](CF_3SO_3)_2$ in 57% yield (Scheme 2).

Complex $[\mathbf{5}](CF_3SO_3)_2$ was characterized by NMR spectroscopy and X-ray diffraction. The ^1H NMR spectrum exhibits the expected low-field resonance[6] for the amine protons at $\delta = 12.77$ ppm. The protons of the symmetrically substituted aromatic ring give rise to two multiplets at $\delta =$ 7.56 ppm and $\delta = 7.38$ ppm. The signal for the carbene carbon atom was observed in the ^{13}C NMR spectrum at $\delta =$ 168.6 ppm with pronounced platinum–carbon coupling ($^1J_{Pt\text{-}C}$=920.7 Hz), which is indicative of carbene coordination to the platinum atom.

Single crystals of $[\mathbf{5}](CF_3SO_3)_2 \cdot 4\,THF$ for a diffraction study (Figure 1)[17] were obtained by recrystallization from THF. The structure analysis shows a platinum atom on a crystallographic inversion center with almost perfect square-planar coordination of four carbene ligands. The Pt–C bond lengths (2.025(3) Å and 2.020(3) Å) fall in the range reported for Pt^{II} complexes with acyclic NH,NH-stabilized carbene ligands (2.043(9) Å and 2.041(8) Å).[14c] They are significantly shorter than those reported for the Pt^{II} complex with a six-membered N-heterocyclic NH,NH-stabilized carbene ligand.[16] One of the two unique carbene ligands in the asymmetric unit is rotated about the Pt–C bond out of the PtC_4 plane and is oriented almost perpendicular to this plane (angle between the PtC_4 plane and plane C2/N21/C21C22/N22 85.30°). The second carbene ligand is almost coplanar with the PtC_4 plane (angle between PtC_4 plane and plane C1/N11/C11C12/N12 0.73°). A similar rotation of the carbene planes relative to the ML_4 plane (83.06° and 79.84°) has been described for Pd^{II} complexes with benzannulated N-heterocyclic carbenes.[10]

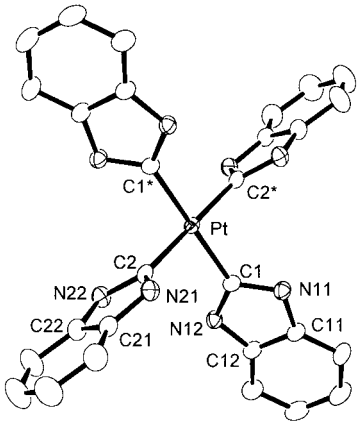

Figure 1. Molecular structure of the dication $[\mathbf{5}]^{2+}$ in crystalline $[\mathbf{5}](CF_3SO_3)_2 \cdot 4\,C_4H_8O$. The asymmetric unit contains one-half of the dication; the platinum atom resides on a crystallographic inversion center. Selected bond lengths [Å] and bond angles [°]: Pt–C1 2.025(3), Pt–C2 2.020(3), N11–C1 1.345(3), N11–C11 1.396(3), N12–C1 1.350(3), N12–C12 1.393(3); C1-Pt-C2 88.12(10), C1-Pt-C2* 91.88(10), C1-Pt-C1* 180.0, N11-C1-N12 106.0(2), N21-C2-N22 105.2(2).

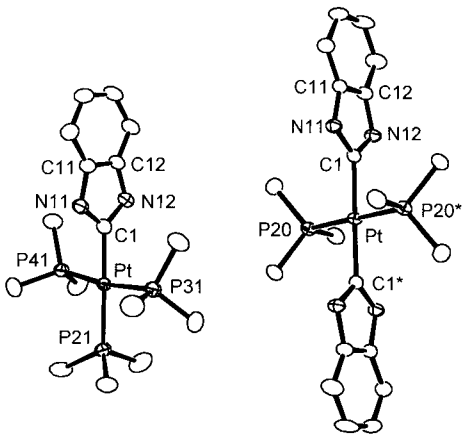

Figure 2. Molecular structures of the dications $[\mathbf{6}]^{2+}$ (left) in crystalline $[\mathbf{6}](CF_3SO_3)_2$ and $[\mathbf{7}]^{2+}$ (right) in crystalline $[\mathbf{7}](CF_3SO_3)_2 \cdot 2\,CH_3OH$. The platinum atom in dication $[\mathbf{7}]^{2+}$ resides on a crystallographic inversion center. Selected bond lengths [Å] and bond angles [°] for $[\mathbf{6}]^{2+}$: Pt–C1 2.018(4), Pt–P21 2.3309(11), Pt–P31 2.3260(10), Pt–P41 2.3262(10), N11–C1 1.346(6), N11–C11 1.395(5), N12–C1 1.344(5), N12–C12 1.397(5); C1-Pt-P21 178.79(12), C1-Pt-C31 86.11(10), C1-Pt-C41 85.89(10), P21-Pt-P31 93.46(4), P21-Pt-P41 94.58(4), P31-Pt-P41 171.63(4), N11-C1-N12 107.1(4). Selected bond lengths [Å] and bond angles [°] for $[\mathbf{7}]^{2+}$: Pt–C1 2.025(2), Pt–P20 2.3012(6), N11–C1 1.339(3), N11–C11 1.385(3), N12–C1 1.354(3), N12–C12 1.396(3); C1-Pt-C1* 180.0, P20-Pt-P20* 180.0, C1-Pt-P20 89.73(7), N11-C1-N12 106.1(2).

The complex dication $[\mathbf{5}]^{2+}$ is formed in a domino reaction in which each of the trimethylphosphane ligands in $[\mathbf{1}]^{2+}$ is replaced in a stepwise manner by an isocyanide ligand, which subsequently reacts with the liberated phosphine to form a cyclic iminophosphorane ligand, thereby generating the conditions for the next phosphine substitution. Because of the sensitivity of the iminophosphorane ligand towards acid, the reaction can be terminated after each cycle by addition of an acid, even before all four iminophosphorane ligands have been formed. This method was used for the preparation of the monocarbene complex $[\mathbf{6}]^{2+}$ and the *trans*-dicarbene complex $[\mathbf{7}]^{2+}$ (Scheme 2), which were isolated after hydrolysis of the reaction mixture with CF_3SO_3H/H_2O after reaction times of 12 h and 48 h, respectively. However, compounds $[\mathbf{6}](CF_3SO_3)_2$ and $[\mathbf{7}](CF_3SO_3)_2$ obtained this way were contaminated with large amounts of unreacted ligand **2** and were difficult to purify. To obtain X-ray quality crystals, we prepared complexes $[\mathbf{6}](CF_3SO_3)_2$ and $[\mathbf{7}](CF_3SO_3)_2$ again from $[\mathbf{1}](CF_3SO_3)_2$ and stoichiometric amounts of **2**.

The ^{13}C NMR spectrum of the monocarbene complex $[\mathbf{6}]^{2+}$ exhibits a resonance for the carbene carbon atom at $\delta = 167.2$ ppm, which is comparable to that observed for the carbene carbons in $[\mathbf{5}]^{2+}$. In contrast to the resonance in $[\mathbf{5}]^{2+}$ the carbene signal for $[\mathbf{6}]^{2+}$ shows $^2J_{P\text{-}C}$ coupling to the phosporous atoms in *cis* (13.4 Hz) and *trans* (115.6 Hz) positions. Two resonances for the phosphorous atoms at $\delta = -15.2$ ppm (d, Pt satellites, $^2J_{P\text{-}P} = 27.8$ Hz, $^1J_{Pt\text{-}P} = 2143.8$ Hz, 2P *cis* to carbene) and $\delta = -25.2$ (t, Pt satellites, $^2J_{P\text{-}P} = 27.8$ Hz, $^1J_{Pt\text{-}P} = 2143.4$ Hz, P *trans* to carbene) were observed in the $^{31}P\{^1H\}$ NMR spectrum. Similar observations were made for the *trans*-dicarbene complex $[\mathbf{7}]^{2+}$, where the resonance for the carbene carbon atoms appears at $\delta = 168.4$ ppm (t, Pt satellites, $^2J_{P\text{-}C} = 12.1$ Hz, $^1J_{Pt\text{-}C} = 854.5$ Hz) in the ^{13}C NMR spectrum.

Single crystals suitable for X-ray diffraction analyses of $[\mathbf{6}](CF_3SO_3)_2$ and $[\mathbf{7}](CF_3SO_3)_2 \cdot 2\,CH_3OH$ (Figure 2)[17] were obtained by recrystallization from methanol. The structure analysis of $[\mathbf{6}](CF_3SO_3)_2$ confirms that the formation of just one NH,NH-stabilized carbene ligand, i.e. the cyclic iminophosphorane precursor, is completed before a second phosphine ligand is substituted. The molecular structure of $[\mathbf{7}](CF_3SO_3)_2 \cdot 2\,CH_3OH$ shows that the second isocyanide ligand enters and cyclizes in *trans* position to the first carbene ligand.

The bonding parameters in the dications $[\mathbf{6}]^{2+}$ and $[\mathbf{7}]^{2+}$ are only marginally different from the equivalent parameters in $[\mathbf{5}]^{2+}$. Particularly the Pt–C bond lengths are independent of the type of ligand in *trans* position. Both dications are coordinated in a slightly distorted square-planar geometry; the distortions observed in $[\mathbf{6}]^{2+}$ are larger than those in $[\mathbf{7}]^{2+}$. The carbene planes in both complex cations are oriented almost perpendicular to the PtL_4 plane (angle between planes 87.35° for $[\mathbf{6}]^{2+}$ and 75.92° for $[\mathbf{7}]^{2+}$).

Attempts to connect the four NH,NH-stabilized carbene ligands in $[\mathbf{5}]^{2+}$ by deprotonation and bridging alkylation with dibromomethane or 1,2-dibromoethane to give a cyclic tetracarbene ligand were initially unsuccessful. The removal of eight NH protons from $[\mathbf{5}]^{2+}$ using NaH generates a sixfold negatively charged anion that is insoluble and unreactive in all common solvents. Highly charged intermediates are avoided in the reaction of $[\mathbf{5}]^{2+}$ with DMF, which also serves also as the solvent for the reaction. Diphosgene is also added to trap the water formed. By this method four $Me_2N\text{-}CH$ bridges are introduced between the carbene ligands, and complex $[\mathbf{8}](Cl)_2$ is formed in over 60% yield. Complex cation $[\mathbf{8}]^{2+}$ contains a cyclic tetracarbene ligand with a crown ether topology (Scheme 3).

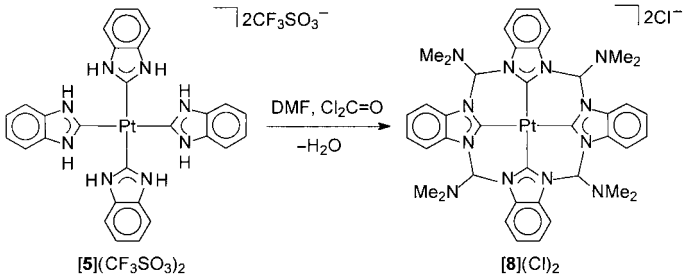

Scheme 3. Template synthesis of $[\mathbf{8}]^{2+}$ from $[\mathbf{5}]^{2+}$.

The ^{13}C NMR spectrum of $[\mathbf{8}](Cl)_2$ (in $[D_6]$DMSO) differs only slightly from that of $[\mathbf{5}](CF_3SO_3)_2$. The bridging alkylation of the N1 and N3 positions at the carbene ligands has little effect on the chemical shift of the atoms within the heterocycle.[6] Two new resonances were observed for the carbon atoms of the bridging CH-N$(CH_3)_2$ groups.

The X-ray diffraction study (Figure 3)[17] shows complex $[\mathbf{8}]^{2+}$ to contain a platinum atom surrounded in an almost perfect square-planar fashion by four carbene carbon atoms. The Pt–C bond lengths are about 0.05 Å shorter than those in dication $[\mathbf{5}]^{2+}$. The bridges between the carbene ligands force in $[\mathbf{8}]^{2+}$, in contrast to $[\mathbf{5}]^{2+}$, the carbene planes to be almost coplanar with the PtC_4 plane (maximum angle between carbene planes and PtC_4 plane 15.6°).

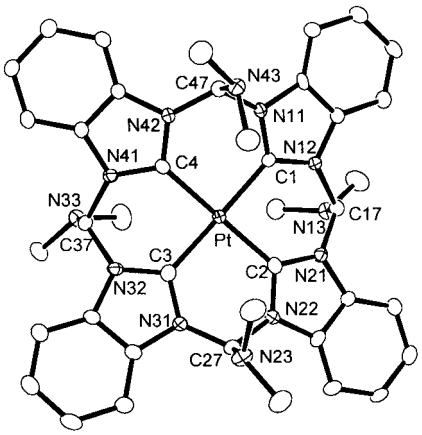

Figure 3. Molecular structure of the dication $[\mathbf{8}]^{2+}$ in crystalline $[\mathbf{8}](Cl)_2 \cdot 4\,CH_3OH$. Selected bond lengths [Å] and bond angles [°]: Pt–C1 1.980(4), Pt–C2 1.969(4), Pt–C3 1.973(4), Pt–C4 1.978(4); C1-Pt-C2 89.89(14), C1-Pt-C3 179.03(15), C1-Pt-C4 90.19(14), C2-Pt-C3 90.54(15), C2-Pt-C4 178.77(15), C3-Pt-C4 89.40(14).

We have demonstrated that the homoleptic Pt^{II} tetracarbene complex $[\mathbf{5}]^{2+}$ can be prepared from the tetrakis(trimethylphosphane)platinum(II) dication $[\mathbf{1}]^{2+}$ and 2-azidophenyl isocyanide (**2**) in a template-controlled reaction cascade. Mono- and dicarbene intermediates in this multistep reaction were also isolated. The connection of the four NH,NH-stabilized carbene ligands in $[\mathbf{5}]^{2+}$ using the sp^3 carbon atom of a CH-NMe_2 group as a bridge to yield a coordinated cyclic tetracarbene ligand was achieved by reaction of $[\mathbf{5}]^{2+}$ with DMF in the presence of diphosgene. Attempts to introduce an sp^2-hybridized bridging atom between the carbene ligands and to remove the platinum atom from the macrocycle are currently underway.

Received: November 22, 2004
Published online: May 11, 2005

Keywords: carbene complexes · platinum · structure determination · template synthesis

[1] a) L. Tschugajeff, M. J. Skanawy-Grigorjewa, A. Posnjak, *Z. Anorg. Allg. Chem.* **1925**, *148*, 37–42; b) A. Burke, A. L. Balch, J. H. Enemark, *J. Am. Chem. Soc.* **1970**, *92*, 2555–2557; c) W. M. Butler, J. H. Enemark, *Inorg. Chem.* **1971**, *10*, 2416–2419; d) W. M. Butler, J. H. Enemark, J. Parks, A. L. Balch, *Inorg. Chem.* **1973**, *12*, 451–457.
[2] a) K. H. Dötz, H. Fischer, P. Hofmann, F. R. Kreissl, U. Schubert, K. Weiss, *Transition Metal Carbene Complexes*, Verlag Chemie, Weinheim, **1983**; b) B. Crociani in *Reactions of Coordinated Ligands*, *Vol. 1* (Ed.: P. S. Braterman), Plenum, New York, **1986**, p. 553.
[3] a) W. P. Fehlhammer, H. Hoffmeister, H. Stolzenberg, B. Boyadjiev, *Z. Naturforsch. B* **1989**, *44*, 419–428; b) W. P. Fehlhammer, H. Hoffmeister, B. Boyadjiev, T. Kolrep, *Z. Naturforsch. B* **1989**, *44*, 917–922; c) U. Kernbach, W. P. Fehlhammer, *Inorg. Chim. Acta* **1995**, *235*, 299–305; d) W. P. Fehlhammer, K. Bartel, B. Weinberger, U. Plaia, *Chem. Ber.* **1985**, *118*, 2220–2234; e) W. P. Fehlhammer, K. Bartel, U. Plaia, A. Völkl, A. T. Liu, *Chem. Ber.* **1985**, *118*, 2235–2254; f) U. Plaia, H. Stolzenberg, W. P. Fehlhammer, *J. Am. Chem. Soc.* **1985**, *107*, 2171–2172.
[4] P. Jutzi, U. Gilge, *J. Organomet. Chem.* **1983**, *246*, 159–162.
[5] Reviews: a) F. E. Hahn, *Angew. Chem.* **1993**, *105*, 681–696; *Angew. Chem. Int. Ed. Engl.* **1993**, *32*, 650–665; b) M. Tamm, F. E. Hahn, *Coord. Chem. Rev.* **1999**, *182*, 175–209; c) F. E. Hahn, M. Tamm, *J. Chem. Soc. Chem. Commun.* **1993**, 842–843; d) F. E. Hahn, M. Tamm, *J. Organomet. Chem.* **1993**, *456*, C11-C14; e) F. E. Hahn, M. Tamm, *J. Chem. Soc. Chem. Commun.* **1995**, 569–570; f) M. Tamm, T. Lügger, F. E. Hahn, *Organometallics* **1996**, *15*, 1251–1256; g) U. Kernbach, T. Lügger, F. E. Hahn, W. P. Fehlhammer, *J. Organomet. Chem.* **1997**, *541*, 51–55; h) F. E. Hahn, L. Imhof, *Organometallics* **1997**, *16*, 763–769.
[6] F. E. Hahn, V. Langenhahn, N. Meier, T. Lügger, W. P. Fehlhammer, *Chem. Eur. J.* **2003**, *9*, 704–712; F. E. Hahn, C. García Plumed, M. Münder, T. Lügger, T. Pape, *Chem. Eur. J.* **2004**, *10*, 6285–6293.
[7] H. Staudinger, J. Meyer, *Helv. Chim. Acta* **1919**, *2*, 635–646.
[8] F. E. Hahn, L. Wittenbecher, R. Boese, D. Bläser, *Chem. Eur. J.* **1999**, *5*, 1931–1935.
[9] F. E. Hahn, L. Wittenbecher, D. Le Van, R. Fröhlich, *Angew. Chem.* **2000**, *112*, 551–554; *Angew. Chem. Int. Ed.* **2000**, *39*, 541–544.
[10] F. E. Hahn, M. Foth, *J. Organomet. Chem.* **1999**, *585*, 241–245.
[11] H. J. Keller, R. Lorentz, *J. Organomet. Chem.* **1975**, *102*, 119–122.
[12] W. Drenth, R. J. M. Nolte, *Acc. Chem. Res.* **1979**, *12*, 30–35.
[13] a) F. E. Hahn, T. Lügger, *J. Organomet. Chem.* **1994**, *481*, 189–193; b) F. E. Hahn, T. Lügger, M. Beinhoff, *Z. Naturforsch. B* **2004**, *59*, 196–201.
[14] a) J. S. Miller, A. L. Balch, *Inorg. Chem.* **1972**, *11*, 2069–2074; b) J. G. Crossley, A. G. Orpen, *Acta. Crstallogr.* **1995**, *C51*, 1102–1105; c) W. P. Fehlhammer, T. Bliß, W. Sperber, J. Fuchs, *Z. Naturforsch. B* **1994**, *49*, 494–500.
[15] M. Basato, G. Facchin, R. A. Michelin, M. Mozzon, S. Pugliese, P. Sgarbossa, A. Tassan, *Inorg. Chim. Acta* **2003**, *356*, 349–356.

[16] a) M. Basato, F. Benetollo, G. Facchin, R. A. Michelin, M. Mozzon, S. Pugliese, P. Sgarbossa, S. M. Sbovata, A. Tassan, *J. Organomet. Chem.* **2004**, *689*, 454–462; b) R. A. Michelin, A. J. L. Pombeiro, M. F. C. G. da Silva, *Coord. Chem. Rev.* **2001**, *218*, 75–112.

[17] X-ray structure determinations: [**5**]$(CF_3SO_3)_2\cdot 4\,C_4H_8O$ ($C_{46}H_{56}N_8F_6O_{10}PtS_2$): $M_w = 1254.20$, colorless crystal, $0.36\times 0.28\times 0.25$ mm, $a = 9.641(4)$, $b = 10.440(4)$, $c = 14.224(5)$ Å, $\alpha = 108.280(12)$, $\beta = 104.839(12)$, $\gamma = 90.715(13)°$, $V = 1307.3(8)$ Å^3, $\rho_{calcd} = 1.593$ g cm^{-3}, $\mu = 2.847$ mm^{-1}, ω- and φ-scans, 14742 measured intensities ($3.1° \le 2\theta \le 60.0°$), $\lambda = 0.71073$ Å, $T = 153(2)$ K, semiempirical absorption correction ($0.472 \le T \le 0.536$), 7367 independent ($R_{int} = 0.0337$) and 7348 observed ($I \ge 2\sigma(I)$) intensities, $P\bar{1}$, $Z = 1$, $R = 0.0315$, $wR = 0.0705$, refinement of 379 parameters against $|F^2|$ with H atoms at calculated positions, the asymmetric unit contains 1/2 molecule of the complex and two molecules of THF. [**6**]$(CF_3SO_3)_2$ ($C_{18}H_{33}N_2F_6O_6P_3PtS_2$): $M_w = 839.58$, yellow crystal, $0.20\times 0.20\times 0.20$ mm, $a = 12.1131(5)$, $b = 13.2949(5)$, $c = 20.3941(8)$ Å, $\beta = 90.5830(10)°$, $V = 3284.1(2)$ Å^3, $\rho_{calcd} = 1.763$ g cm^{-3}, $\mu = 4.617$ mm^{-1}, ω- and φ-scans, 37128 measured intensities ($4.0° \le 2\theta \le 60.0°$), $\lambda = 0.71073$ Å, $T = 153(2)$ K, semiempirical absorption correction ($0.459 \le T \le 0.459$), 9527 independent ($R_{int} = 0.0343$) and 8001 observed ($I \ge 2\sigma(I)$) intensities, $P2_1/c$, $Z = 4$, $R = 0.0355$, $wR = 0.0903$, refinement of 368 parameters against $|F^2|$ with H atoms at calculated positions, the asymmetric unit contains one molecule of the complex, one of the triflate anions is disordered. [**7**]$(CF_3SO_3)_2\cdot 2\,CH_3OH$ ($C_{24}H_{38}N_4F_6O_8P_2PtS_2$): $M_w = 945.73$, colorless crystal, $0.45\times 0.19\times 0.10$ mm, $a = 9.1125(4)$, $b = 18.1914(7)$, $c = 10.9333(4)$ Å, $\beta = 103.4470(10)°$, $V = 1762.72(12)$ Å^3, $\rho_{calcd} = 1.782$ g cm^{-3}, $\mu = 4.270$ mm^{-1}, ω- and φ-scans, 13913 measured intensities ($4.4° \le 2\theta \le 50.0°$), $\lambda = 0.71073$ Å, $T = 153(2)$ K, semiempirical absorption correction ($0.250 \le T \le 0.675$), 3100 independent ($R_{int} = 0.0279$) and 2764 observed ($I \ge 2\sigma(I)$) intensities, $P2_1/n$, $Z = 2$, $R = 0.0175$, $wR = 0.0385$, refinement against of 290 parameters against $|F^2|$ with H atoms at calculated positions, the asymmetric unit contains 1/2 molecule of the complex and one molecule of methanol. [**8**]$Cl\cdot 4\,CH_3OH$ ($C_{44}H_{60}N_{12}Cl_2O_4Pt$): $M_w = 1087.03$, colorless crystal, $0.35\times 0.06\times 0.04$ mm, $a = 16.434(3)$, $b = 14.397(3)$, $c = 19.529(4)$ Å, $\beta = 91.148(4)°$, $V = 4619.8(16)$ Å^3, $\rho_{calcd} = 1.563$ g cm^{-3}, $\mu = 3.209$ mm^{-1}, ω- and φ-scans, 52223 measured intensities ($3.2° \le 2\theta \le 60.0°$), $\lambda = 0.71073$ Å, $T = 153(2)$ K, semiempirical absorption correction ($0.399 \le T \le 0.882$), 13421 independent ($R_{int} = 0.0684$) and 8268 observed ($I \ge 2\sigma(I)$) intensities, $P2_1/n$, $Z = 4$, $R = 0.0363$, $wR = 0.0710$, refinement of 592 parameters against $|F^2|$ with H atoms at calculated positions, the asymmetric unit contains one molecule of the complex and four molecules methanol. CCDC-237759 ([**5**](CF3SO$_3$)$_2\cdot 4\,C_4H_8O$), CCDC-237760 ([**6**]$(CF_3SO_3)_2$), CCDC-237761 ([**7**]-$(CF3SO_3)_2\cdot 2\,CH_3OH$), and CCDC-256449 ([**8**]$Cl_2\cdot 4\,CH_3OH$) contain the supplementary crystallographic data for this paper. These data can be obtained free of charge from the Cambridge Crystallographic Data Centre via www.ccdc.cam.ac.uk/data_-request/cif.

Borylene Complexes

Terminal Borylene Complexes Stabilized by a Transition-Metal Base**

Holger Braunschweig, Daniela Rais, and Katharina Uttinger*

Transition-metal carbonyl complexes constitute one of the most prominent classes of organometallic compounds, displaying a wealth of structural complexity and chemical reactivity. Carbonyl complexes are found widely in organometallic chemistry[1a] and homogeneous catalysis,[1b] for reasons that relate to the experimental accessibility of CO and its efficient, synergic binding to transition metals. In the quest for molecules that display similar properties borylenes, B–R, have been identified as excellent candidates.[2] However, the instability and consequent high reactivity of borylene as a free molecule[3] mean that transition-metal borylene complexes are challenging targets for synthetic chemists.[4]

A variety of bonding modes is available to the carbonyl ligand, ranging from terminal to different types of bridging coordination, including semi-bridging and triply bridging (μ_3).[1] Of these modes, only the terminal and symmetrical bridging modes had thus far been realized for the borylene group. Bridged borylenes, for example, $[\{(\eta^5\text{-}C_5H_5)Mn(CO)_2\}_2(\mu\text{-}BNMe_2)]$[5a] (**1**) or $[\{(\eta^5\text{-}C_5H_4Me)Fe(CO)\}_2(\mu\text{-}CO)\{\mu\text{-}BN(SiMe_3)_2\}]$[5d] (**2**), represent the most numerous and well-studied class of borylene compounds (Scheme 1).[5] Appropriate synthetic routes to their terminal borylene counterparts were developed more recently.[6] Investigation of the chemical reactivity of compounds such as $[(OC)_5M{=}B{=}N(SiMe_3)_2]$ (M = Cr, W),[6a] revealed their remarkable stability. To date, for reactivity to be observed, photochemical activation was required, which leads to an unprecedented intermetallic borylene transfer.[6d,f]

Herein we present the first instance of thermal reactivity of the terminal borylene complexes $[(OC)_5M{=}B{=}N(SiMe_3)_2]$

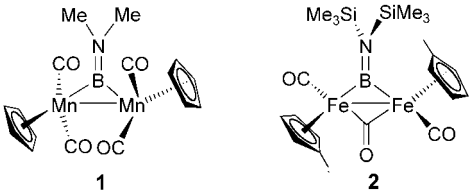

1 **2**

Scheme 1. Homodinuclear bridged borylene complexes.

[*] Prof. H. Braunschweig, Dr. D. Rais, K. Uttinger
Institut für Anorganische Chemie
Bayerische Julius-Maximilians-Universität Würzburg
Am Hubland, 97074 Würzburg (Germany)
Fax: (+49) 931-888-4623
E-mail: h.braunschweig@mail.uni-wuerzburg.de

[**] This work was supported by the DFG and the EPSRC. D.R. thanks the Alexander von Humboldt Foundation for a postdoctoral fellowship. The authors thank Dr. D. Scheschkewitz for performing the X-ray diffraction study of compound **6**.

 DOI: 10.1002/anie.200500302

(M = Cr **3**, M = W **4**; Scheme 2).[6a] These species, upon reaction with $[Pd(PCy_3)_2]$ (**5**),[7] generate the heterodinuclear systems $[(OC)_4M(\mu\text{-}CO)\{\mu\text{-}BN(SiMe_3)_2\}Pd(PCy_3)]$ (M = Cr **6**, M = W **7**), featuring an unprecedented semi-bridging borylene ligand.

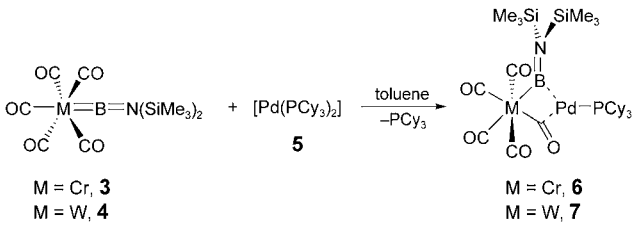

Scheme 2. Synthesis of bridged borylene complexes **6** and **7**.

All transition-metal borylenes feature carbon monoxide as an ancillary ligand.[4–6] In an attempt to expand the scope of the photochemically promoted borylene transfer as a synthetic route to electronically more diverse systems, we focused our attention on the transfer of the borylene unit to carbonyl-free complexes of the late transition metals. We chose $[Pd(PCy_3)_2]$ (**5**) because of the electron-rich but highly unsaturated nature of the palladium center, which suggested potentially high reactivity of this species in borylene transfer reactions. Indeed, when **5** was added to an equimolar amount of **3** or **4** in C_6D_6, multinuclear NMR spectroscopy revealed immediate consumption of the starting materials, prior to irradiation, and formation of new compounds, **6** or **7**, respectively, with concomitant liberation of tricyclohexylphosphine (Scheme 2).

The $^{11}B\{^1H\}$ NMR spectrum of the reaction mixture featured a broad downfield-shifted resonance signal at $\delta =$ 100 ppm for **6** and $\delta = 97$ ppm for **7** [cf. for **3**, $\delta = 92$ ppm; for **4**, $\delta = 87$ ppm],[6a] suggesting formation of bridged borylene species. A sharp singlet at $\delta = 9.8$ ppm in the $^{31}P\{^1H\}$ NMR spectra indicated the presence of noncoordinated tricyclohexylphosphine. Accordingly, we inferred that the singlets at $\delta = 34.2$ ppm (**6**) and at $\delta = 41.9$ ppm (**7**), which are the only other signals in the $^{31}P\{^1H\}$ NMR spectra, arise from a palladium complex with only one PCy_3 ligand.

The atom connectivity within the compounds was conclusively determined by performing a single-crystal X-ray diffraction study of **6** (Figure 1).[8] Pale yellow crystals were obtained upon cooling a saturated solution of the complex in toluene to −30 °C.

Compound **6** is a semi-bridging borylene complex, which also contains a semi-bridging carbonyl ligand linking the $\{(OC)_4Cr\}$ and $\{Pd(PCy_3)\}$ fragments. The Cr1–B1 bond (2.0842(18) Å) is considerably longer than that in the terminal borylene precursor **3** (1.996(6) Å)[6d] and consistent with the increased coordination number at boron, while the Pd1–B1 bond (2.0425(18) Å) is in the range (2.006(9) to 2.077(6) Å), of those reported for compounds with bonds between palladium and three-coordinate boron centers.[9]

The most intriguing structural feature of **6** relates to the almost orthogonal orientation of the bis(trimethylsilyl)amino substituent at boron with respect to the plane containing the two transition metal centers and boron (Si1-N1-B1-Pd1 91.12(15)°). Such a disposition differs significantly from that observed in other bridged borylene complexes, such as **1**[5a] and **2**[5d], for which the structural parameters are in agreement with the presence of a formally sp^2-hybridized boron atom (Scheme 1). Accordingly, assuming a formally sp^2-hybridized boron atom in **6**, the orthogonal disposition of the amino substituent would preclude any effective N–B π donation, and should result in considerable elongation of the N–B bond. However, despite the increased coordination number at boron, the B1–N1 bond (1.377(2) Å) is negligibly longer than that in terminal borylene **3** (1.353(6) Å),[6d] thus indicating a significant double bond character of the B–N linkage. These structural features suggest that the bonding mode of the borylene ligand in **6** differs significantly from that adopted in other complexes.

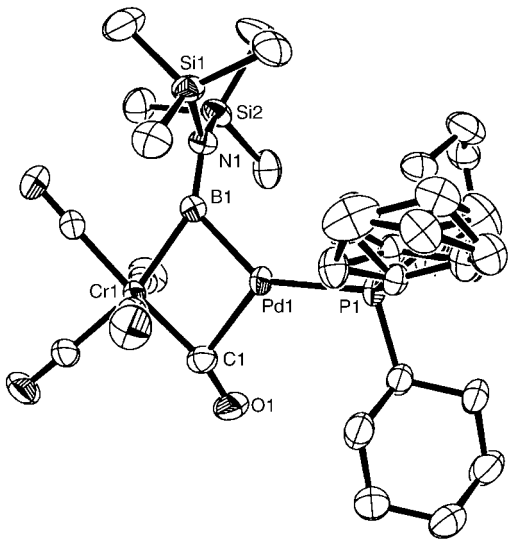

Figure 1. Molecular structure of **6**. Bond lengths [Å] and angles [°]: Pd1-B1 2.0425(18), Cr1-B1 2.0842(18), B1-N1 1.377(2), Pd1-P1 2.3470(10); N1-B1-Cr1 152.33(13), N1-B1-Pd1 128.74(12), Cr1-C1-O1 165.49(16), Pd1-C1-O1 115.20(14).

The bonding interactions that characterize **6** can be rationalized on the basis of the theoretically predicted analogy between borylene and carbon monoxide.[10] Thus, the electronically saturated chromium borylene **3** behaves as a π-acceptor ligand, while the Lewis basic palladium fragment $\{Pd(PCy_3)\}$ donates electron density into the π* orbitals of CO and the empty π orbitals of the borylene. Partial rehybridization of the carbon and boron atoms is necessary, this results in a more efficient π-acceptor capability and in CO and $B{=}N(SiMe_3)_2$ forming a pair of non-compensating semi-bridging ligands. Relevant angles for the CO moiety (Pd1-Cr1-C1(O1) 54.2°; Cr1-C1-O1 165.5°) are in accord with the classification scheme for semi-bridging carbonyl ligands developed by Crabtree.[11] The analogous values for the borylene ligand (Pd1-Cr1-B1 49.8°, Cr1-B1-N1 152.3°) have no literature precedent but are clearly intermediate between those typical of a symmetrically bridging and a terminal arrangement.

Furthermore, by virtue of the aforementioned Pd–B dative interaction, **6** is the only example of a terminal

borylene complex which is stabilized by a transition-metal center acting as a Lewis base. Only a handful of related compounds, featuring amines[6b,e] or a phosphine[5e] as stabilizing bases, are reported, none of which, however, was obtained by addition of the base to a pre-formed terminal borylene complex. Such reactivity suggests that residual Lewis acidity is unexpectedly retained by the boron atom in **3** and **4** despite the presence of the amino substituent, and testifies for the thermodynamic and kinetic stability of the Cr–B linkage in the complexes. This situation differs markedly from that, for instance, of the cationic iron species $[(\eta^5\text{-}C_5Me_5)(OC)_2Fe{=}BMes][BAr^f{}_4]$ (Mes = 2,4,6-$C_6H_2Me_3$; Ar^f = 3,5-$C_6H_3(CF_3)_2$), the chemistry of which is dominated by borylene displacement.[12]

In conclusion, we have described the first instance of thermal reactivity of a terminal borylene complex $[(OC)_5M{=}B{=}N(SiMe_3)_2]$. Upon reaction with the electron-rich $[Pd(PCy_3)_2]$ system, heterodinuclear complexes are formed in which the borylene ligand adopts a semi-bridging bonding mode, providing further empirical confirmation of its close relationship to CO.

Experimental Section

All manipulations were conducted either under an atmosphere of dry argon or in vacuo using standard Schlenk line or glove-box techniques.

6: A pale yellow solution of **5** (0.276 g, 0.413 mmol) in toluene (4 mL) was added to solid **3** (0.150 g, 0.413 mmol). Yellow crystals formed from the bright yellow solution at room temperature. The mixture was then stored at −35 °C yielding yellow crystals of **6** (0.249 g, 81 %). ^{1}H NMR (400 MHz, C_6D_6, 25 °C, TMS): δ = 1.94–1.13 (m, 33 H, Cy), 0.42 ppm (s, 18 H, $SiMe_3$); $^{13}C\{^1H\}$ NMR (101 MHz, C_6D_6, 25 °C): δ = 223.5 (d, $J_{C\text{-}P}$ = 2 Hz, CO), 223.0 (d, $J_{C\text{-}P}$ = 3 Hz, CO), 33.7 (d, $^1J_{C\text{-}P}$ = 14 Hz, C_1, Cy), 31.4 (d, $^3J_{C\text{-}P}$ = 6 Hz, $C_{3,5}$, Cy), 27.7 (d, $^2J_{C\text{-}P}$ = 11 Hz, $C_{2,6}$, Cy), 26.4 (s, C_4, Cy), 3.7 ppm (s, $SiMe_3$); $^{31}P\{^1H\}$ NMR (162 MHz, C_6D_6, 25 °C): δ = 34.2 ppm (s); $^{11}B\{^1H\}$ (64 MHz, C_6D_6, 25 °C): δ = 100 ppm (s, $\omega_{1/2}$ = 752 Hz). IR (toluene): $\tilde{\nu}$ = 2030, 1957, 1932, 1858 cm^{-1}, (C=O). Elemental Analysis (%) calcd for $C_{29}H_{51}NBCrO_5PPdSi_2$: C 46.44, H 6.85, N 1.87; found: C 46.43, H 6.80, N 1.86.

7: A pale yellow solution of **5** (0.135 g, 0.202 mmol) in toluene (4 mL) was added to solid **4** (0.100 g, 0.202 mmol). After 24 h the volume of the red solution was reduced to approximately half and the mixture was cooled to −80 °C. An orange microcrystalline solid of **7** deposited after several days. This solid was isolated and dried in vacuo (0.120 g, 67 %). ^{1}H NMR (300 MHz, C_6D_6, 25 °C, TMS): δ = 1.96–1.13 (m, 33 H, Cy), 0.42 ppm (s, 18 H, $SiMe_3$); $^{13}C\{^1H\}$ NMR (75 MHz, C_6D_6, 25 °C): δ = 203.1 (d, $^1J_{C\text{-}W}$ = 121 Hz, $J_{C\text{-}P}$ = 2 Hz, CO), 200.5 (d, $J_{C\text{-}P}$ = 3 Hz, CO), 34.0 (d, $^1J_{C\text{-}P}$ = 12 Hz, C_1, Cy), 31.4 (d, $^3J_{C\text{-}P}$ = 5 Hz, $C_{3,5}$, Cy), 27.8 (d, $^2J_{C\text{-}P}$ = 11 Hz, $C_{2,6}$, Cy), 26.4 (s, $^4J_{C\text{-}P}$ = 1 Hz, C_4, Cy), 3.9 ppm (s, $SiMe_3$); $^{31}P\{^1H\}$ NMR (121 MHz, C_6D_6, 25 °C): δ = 41.9 ppm (s); $^{11}B\{^1H\}$ (96 MHz, C_6D_6, 25 °C): δ = 97 ppm (s, $\omega_{1/2}$ = 884 Hz). IR (toluene): $\tilde{\nu}$ = 2043, 1955, 1932, 1873 cm^{-1}, (C=O). Elemental Analyses: (%) calcd for $C_{29}H_{51}NBO_5PPdSi_2W$: C 39.49, H 5.83, N 1.59; found: C 39.48, H 5.75, N 1.65.

Received: January 26, 2005
Published online: May 11, 2005

Keywords: boron · borylene complexes · bridging ligands · carbonyl ligands · palladium

[1] a) F. A. Cotton, G. Wilkinson, *Advanced Inorganic Chemistry*, 5th ed., Wiley, New York, **1988**; b) J. P. Collman, L. S. Hegedus, J. R. Norton, R. G. Finke, *Principles and Applications of Organotransition Metal Chemistry*, University Science Books, Mill Valley, **1987**.

[2] a) A. W. Ehlers, E. J. Baerends, F. M. Bickelhaupt, U. Radius, *Chem. Eur. J.* **1998**, *4*, 210–221; b) U. Radius, F. M. Bickelhaupt, A. W. Ehlers, N. Goldberg, R. Hoffmann, *Inorg. Chem.* **1998**, *37*, 1080–1090; c) C. Boehme, J. Uddin, G. Frenking, *Coord. Chem. Rev.* **2000**, *197*, 249–276.

[3] a) P. L. Timms, *J. Am. Chem. Soc.* **1967**, *89*, 1629–1632; b) P. L. Timms, *Acc. Chem. Res.* **1973**, *6*, 118–123.

[4] a) H. Braunschweig, *Angew. Chem.* **1998**, *110*, 1882–1898; *Angew. Chem. Int. Ed.* **1998**, *37*, 1786–1801; b) H. Braunschweig, M. Colling, *Coord. Chem. Rev.* **2001**, *223*, 1–51; c) H. Braunschweig, *Adv. Organomet. Chem.* **2004**, *51*, 163–192.

[5] a) H. Braunschweig, T. Wagner, *Angew. Chem.* **1995**, *107*, 904–905; *Angew. Chem. Int. Ed. Engl.* **1995**, *34*, 825–826; b) H. Braunschweig, B. Ganter, *J. Organomet. Chem.* **1997**, *545–546*, 163–167; c) H. Braunschweig, M. Müller, *Chem. Ber.* **1997**, *130*, 1295–1298; d) H. Braunschweig, C. Kollann, U. Englert, *Eur. J. Inorg. Chem.* **1998**, 465–468; e) M. Shimoi, S. Ikubo, Y. Kawano, K. Yasuro, K. Katoh, H. Ogino, *J. Am. Chem. Soc.* **1998**, *120*, 4222–4223; f) H. Braunschweig, C. Kollann, W. Klinkhammer, *Eur. J. Inorg. Chem.* **1999**, 1523–1529; g) S. Aldridge, D. L. Coombs, C. Jones, *Chem. Commun.* **2002**, 856–857; h) D. L. Coombs, S. Aldridge, S. J. Coles, M. B. Hursthouse, *Organometallics* **2003**, *22*, 4213–4217; i) H. Braunschweig, K. Radacki, D. Rais, F. Seeler, K. Uttinger, *J. Am. Chem. Soc.* **2005**, *127*, 1386–1387.

[6] a) H. Braunschweig, C. Kollann, U. Englert, *Angew. Chem.* **1998**, *110*, 3355–3357; *Angew. Chem. Int. Ed.* **1998**, *37*, 3179–3180; b) G. J. Irvine, C. E. F. Rickard, W. R. Roper, A. Williamson, L. G. Wright, *Angew. Chem.* **2000**, *112*, 978–980; *Angew. Chem. Int. Ed.* **2000**, *39*, 948–950; c) H. Braunschweig, C. Kollann, U. Englert, *Angew. Chem.* **2001**, *113*, 4327–4329; *Angew. Chem. Int. Ed.* **2001**, *40*, 4198–4200; d) H. Braunschweig, M. Colling, C. Kollann, H. G. Stammler, B. Neumann, *Angew. Chem.* **2001**, *113*, 2359–2361; *Angew. Chem. Int. Ed.* **2001**, *40*, 2298–2300; e) C. E. F. Rickard, W. R. Roper, A. Williamson, J. L. Wright, *Organometallics* **2002**, *21*, 4862–4872; f) H. Braunschweig, M. Colling, C. Hu, K. Radacki, *Angew. Chem.* **2003**, *115*, 215–218; *Angew. Chem. Int. Ed.* **2003**, *42*, 205–208; g) D. L. Coombs, S. Aldridge, C. Jones, D. J. Willock, *J. Am. Chem. Soc.* **2003**, *125*, 6356–6357.

[7] W. Kuran, A. Musco, *Inorg. Chim. Acta* **1975**, *12*, 187–193.

[8] Crystal data for **6**: $C_{29}H_{51}BCrNO_5PPdSi_2$, M_r = 750.07, yellow blocks, 0.15 × 0.25 × 0.30 mm, monoclinic, space group $P2(1)/n$, a = 10.293(4), b = 16.264(7), c = 21.535(9) Å, α = 90.00, β = 90.285(8), γ = 90.00°, V = 3605(3) Å^3, Z = 4, ρ_{calcd} = 1.382 g cm^{-3}, T = 193(2) K; Bruker-Apex platform with CCD detector, graphite-monochromated $Mo_{K\alpha}$ radiation, $2\theta_{max}$ = 56.56; 36867 reflections, 8944 independent (R_{int} = 0.0240), absorption correction SADABS (μ = 9.46 cm^{-1}) The structure was solved using direct methods, refined against full matrix (F_o^2) with the SHELX software package (425 parameters/0 restraints). All non-hydrogen atoms were refined anisotropically. C24 to C29 were assigned split positions. Hydrogen atoms were refined on idealized positions. R_1 = 0.0260 ($I > 2\sigma$), W_R = 0.0662 (all data), GooF = 1.040, max/min residual electron density: 0.875/−0.293 × 10^{30} em^{-3}. CCDC-258168 contains the supplementary crystallographic data for this paper. These data can be obtained free of charge from The Cambridge Crystallographic Data Centre via www.ccdc.cam.ac.uk/data_request/cif.

[9] a) S.-Y. Onozawa, Y. Hatanaka, T. Sakakura, S. Shimada, M. Tanaka, *Organometallics* **1996**, *15*, 5450 – 5452; b) S.-Y. Onozawa, M. Tanaka, *Organometallics* **2001**, *20*, 2956 – 2958.
[10] R. D. Barr, T. B. Marder, A. G. Orpen, I. D. Williams, *J. Chem. Soc. Chem. Commun.* **1984**, 112 – 114, and references therein.
[11] R. H. Crabtree, M. Lavin, *Inorg. Chem.* **1986**, *25*, 805 – 812.
[12] D. L. Coombs, S. Aldridge, A. Rossin, C. Jones, D. J. Willock, *Organometallics* **2004**, *23*, 2911 – 2926.

Natural Product Synthesis

Asymmetric Synthesis of the 1-*epi* Aglycon of the Cripowellins A and B**

Dieter Enders, Achim Lenzen, and Gerhard Raabe*

In 1997 researchers at Bayer AG reported on two new *Amaryllidaceae* alkaloids,[1] cripowellins A (**1**) and B (**2**), which had been isolated from the bulbs and roots of *Crinum powellii*, a popular ornamental plant in Europe.[2,3] The two compounds differ only in their glycosidic parts. The assumption that both of these sugar moieties are derived biogenically from β-D-glucose accounts for the depicted absolute stereochemistry. Their common aglycon comprises a [5.3.2]bicyclic core, a structural motif unique among the *Amaryllidaceae* alkaloids. One of both bridgehead atoms is a trisubstituted amide N atom and therefore not a stereogenic center.

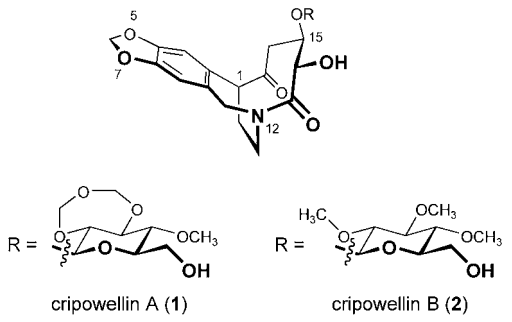

In addition to their unusual structure, which contains five-, six-, seven-, nine-, and ten-membered rings, both alkaloids exhibit extraordinary biological properties. Their insecticidal activity compares well to that of natural pyrethroids—not only with regard to their strength but also their broad activity. It is important to note that mainly the aglycon seems to be responsible for their biological activity because it alone shows the same activity as the two glycosides.[2] However, practically nothing is known about the mode of action.[4] In order to clarify that and to determine structure–activity relationships, the synthesis of stereoisomers and derivatives of the cripowellins will be necessary.

Because of their unique structures and their high biological activity, Bayer AG has patented both cripowellins and some of their derivatives.[2] Their exceptional position was also recognized by experts at the Irseer conference on natural products in 1997, where cripowellin A (**1**) was voted the second most interesting new natural product.[5] Despite all this attention, a synthesis of the cripowellins, their aglycon, or one of their stereoisomers has not been described so far. This seems to be highly desirable in the light of the small quantities obtainable from natural sources.[3]

We now report on the first asymmetric synthesis of the skeleton of the cripowellins A and B in the form of their 1-*epi* aglycon **15**. Our remarkably short synthesis started with the asymmetric dihydroxylation[6] of the benzoylated allyl alcohol **3**[7,8] to give the diol **4** (Scheme 1); the 72% yield of this reaction is quite efficient when one considers the obvious problem of regioselectivity. In addition, the asymmetric induction was virtually complete (≥98% *ee*).[9] Acetonide formation and saponification of the ester functionality yielded the primary alcohol **5** in nearly quantitative yield. This alcohol was oxidized to the corresponding acid **6** in two steps, and **6** was subsequently coupled with the amine **10** (available from the reductive amination of bromopiperonal (**9**) with 3-butene-1-amine) to give the amide **7**.

According to our synthetic route a ring-closing metathesis (RCM)[10] of this amide to give the azacyclononene lactam derivative **8** was proposed to follow. The structure of the RCM precursor **7** had to be designed carefully taking into account the "problem of medium sized rings". It had to be restricted conformationally in a way which would favour the metathesis. Both the dioxolane ring[11] and the tertiary amide[12] were assumed to operate synergistically thus favoring the formation of the nine-membered ring.[13] Our assumptions were confirmed by the successful RCM. By employing Grubbs' second-generation catalyst and by performing the reaction under high dilution (1 mM), we were able to obtain **8** in a very good yield of 77%.

After that the [5.3.2]bicyclic core was supposed to be built up by means of a Heck reaction of the piperonyl moiety to the double bond.[14] After extensive studies, we finally succeeded in the selective synthesis of the two Heck products **11** and **12** (Scheme 2). Under neutral reaction conditions, we observed exclusively the formation of product **11**, which has a disubstituted *Z*-configurated double bond. Under cationic conditions, on the other hand, the reaction yielded selectively the trisubstituted olefin **12**.[15] The formation of this anti-Bredt alkene is worth mentioning because the additional ring strain in this bicyclic compound cannot be compensated by stability from the conjugation with the aromatic moiety (both are nearly perpendicular to each other). The double bond of this anti-Bredt alkene is not configurationally stable under the

[*] Prof. Dr. D. Enders, Dipl.-Chem. A. Lenzen, Prof. Dr. G. Raabe
Institut für Organische Chemie, RWTH Aachen
Landoltweg 1, 52074 Aachen (Germany)
Fax: (+49) 241-809-2127
E-mail: enders@rwth-aachen.de

[**] This work was supported by the Deutsche Forschungsgemeinschaft (SFB 380) and the Fonds der Chemischen Industrie. We thank Prof. Rosenkranz, Prof. Stetter, Dr. Lieb, and their co-workers, Bayer AG, for valuable discussions at the beginning of this project.

  DOI: 10.1002/anie.200500556

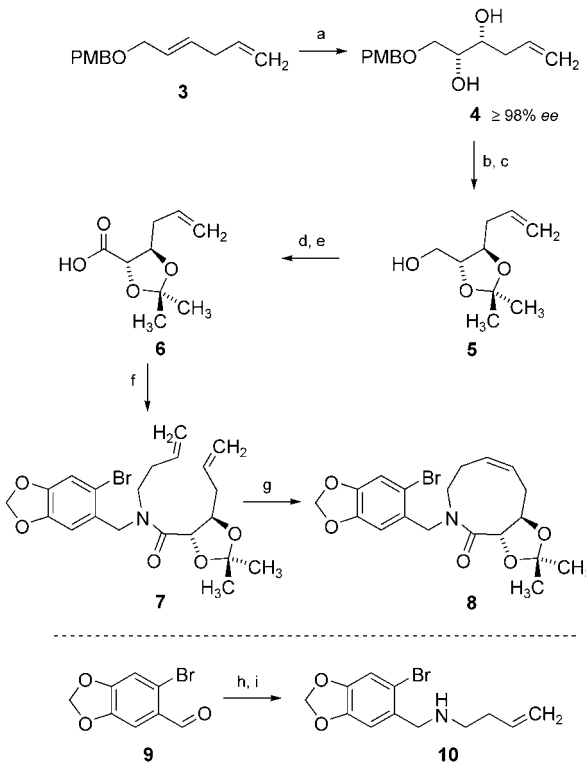

Scheme 1. Synthesis of the nine-membered-ring lactam intermediate **8**. a) AD-mix β, $K_2OsO_4 \cdot 2H_2O$ (0.006 equiv), $MeSO_2NH_2$ (1.0 equiv), *t*BuOH/H_2O (1:1), 0 °C, 2.25 h, 72%; b) 2,2-DMP, PTSA (0.05 equiv), 25 °C, 1 h; c) K_2CO_3 (1.5 equiv), MeOH, 25 °C, 2 h, 97% (two steps); d) CO_2Cl_2 (1.1 equiv), DMSO (2.3 equiv), Et_3N (5.0 equiv), CH_2Cl_2, −78→25 °C; e) $NaClO_2$ (80%, 2.5 equiv), $NaH_2PO_4 \cdot 2H_2O$ (2.0 equiv), 2-methyl-2-butene (18 equiv), acetone/H_2O (1:1), 0→25 °C, 0.5 h; f) FEP (1.2 equiv), amine **10** (1.1 equiv), Et*i*Pr_2N (3.2 equiv), CH_2Cl_2, 0→25 °C, 12 h, 66% (three steps); g) Grubbs' 2nd generation catalyst (0.1 equiv, addition in portions), CH_2Cl_2, reflux, 2.5 h, then DMSO (5.0 equiv), 25 °C, 12 h, 77%; h) 3-butene-1-amine (1.2 equiv), MS 4 Å, CH_2Cl_2, 25 °C, 12 h; i) $NaBH_4$ (1.0 equiv), MeOH, 25 °C, 2 h, 94% (two steps). 2,2-DMP = 2,2-dimethoxypropane, DMSO = dimethyl sulfoxide, FEP = 2-fluoro-1-ethyl pyridinium tetrafluoroborate, MS = molecular sieves, PMB = *p*-methoxybenzoyl, PTSA = *p*-toluenesulfonic acid.

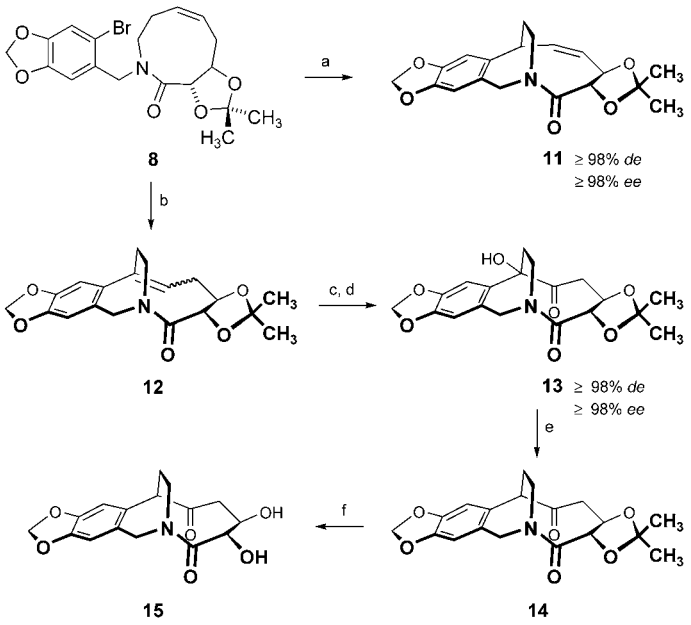

Scheme 2. Completion of the synthesis of the 1-*epi* aglycon **15** of the cripowellins A (**1**) and B (**2**). a) $Pd(OAc)_2$ (0.2 equiv), PPh_3 (0.6 equiv), Et_3N (3.5 equiv), DMF, 110 °C, 6 h, 59%; b) $Pd(OAc)_2$ (0.15 equiv), dppp (0.2 equiv), Ag_2CO_3 (3.0 equiv), toluene, 124 °C, 4 h, 59%; c) $K_2OsO_4 \cdot 2H_2O$ (0.05 equiv), NMO (97%, 3.1 equiv), acetone/H_2O (10:7), 25 °C, 3 h, then Na_2SO_3 (2.3 equiv); d) CO_2Cl_2 (2.5 equiv), DMSO (5.3 equiv), Et_3N (10.0 equiv), CH_2Cl_2, −78→25 °C, 55% (two steps); e) SmI_2 (excess, ca. 7.2 equiv), *t*BuOH (3.0 equiv), THF, 25 °C, 12 h, 99%; f) Dowex-50, H_2O, 25 °C, 4.25 h, 56%. DMF = dimethyl formamide, dppp = 1,3-bis(diphenylphosphanyl)propane, NMO = *N*-methylmorpholine *N*-oxide, THF = tetrahydrofuran.

reaction conditions employed since the *E*/*Z* ratio was observed to be time dependent.[16] To our surprise, both Heck reactions were completely diastereoselective with regard to the orientation of the ethylene bridge; we were able to isolate only compounds **11** and **12**, in which this bridge is on the upper face of the molecule.[17] To the best of our knowledge, this is the first example of a (highly diastereoselective) intramolecular Heck reaction of a highly functionalized (aza)cyclonene derivative.[18]

Olefin **11** proved to be extremely difficult to functionalize. We therefore decided to continue with the *E*/*Z* mixture of olefins **12**, which seemed to be more reasonable to us anyway because a differentiation between the olefinic C atoms was assumed to be easier (singly vs. doubly substituted). Both olefins **12** were first transformed into the α-hydroxy ketone **13** in a two-step sequence consisting of dihydroxylation and Swern oxidation. Deoxygenation of **13** with SmI_2 in the presence of *t*BuOH proceeded smoothly to give **14**.[19] The high yield of 99% in this reaction was astonishing because α-hydroxy ketones are normally not very good substrates for SmI_2-induced defunctionalizations.[20] Likewise, the stability of the acetonide-protected 1,2-diol unit is worth mentioning. In the case of carboxylates, the reductive cleavage of the α-C–O bond is commonly observed.[21] The cleavage of the acetonide protecting group in the presence of Dowex-50 finally yielded the 1-*epi* aglycon **15** of the cripowellins A (**1**) and B (**2**).

At this point we were very much interested in the spatial structure of this compound—especially with regard to the known structure of the bisacetate of cripowellin A and the biological activity of the cripowellins.[2,3] In the search for derivatives of the 1-*epi* aglycon **15** suitable for an X-ray structure analysis, we were finally rewarded by its bisacetate, **16** (Scheme 3).[22] A comparison of its crystal structure with the one obtained from the bisacetate of cripowellin A clearly shows the same spatial orientation of the keto and the lactam carbonyl groups: both are *syn* to each other and in spatial proximity. This substructure had been identified as the probable pharmacophor by researchers at Bayer AG after extensive investigations on structure–activity relationships.[4] Therefore it seems reasonable to expect the 1-*epi* aglycon **15** to be biologically active, too. Yet, this still needs to be proven by biological tests.

In summary, we report the first access to this unique [5.3.2]bicyclic skeleton of the cripowellins A (**1**) and B (**2**). Key steps in our synthesis are a highly enantioselective

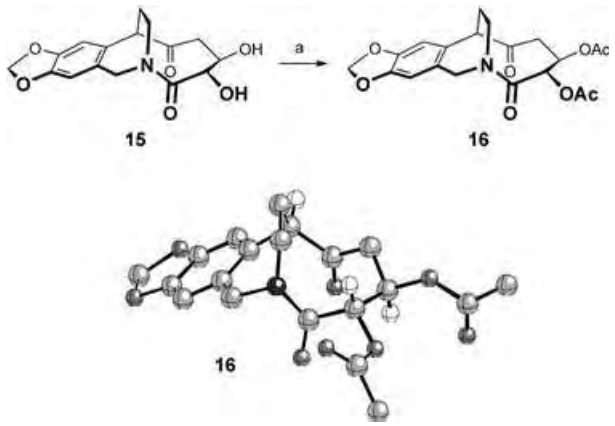

Scheme 3. Synthesis and crystal structure of the bisacetylated 1-*epi* aglycon **16**. a) $Sc(OTf)_3$ (0.3 equiv), Ac_2O/CH_3CN (1:1), 25 °C, 2 h, 65 %. Tf = trifluoromethanesulfonyl.[22]

Sharpless dihydroxylation, a properly designed ring-closing metathesis, and a highly diastereoselective intramolecular Heck reaction. Considering the complexity of the target molecule, this synthesis is very short (13 steps in the longest linear sequence, 15 steps altogether; 5.6 % overall yield). In addition, the diastereo- and enantioselectivity are virtually complete ($\geq$ 98 % *de*, $\geq$ 98 % *ee*). The crystal structure of the bisacetate of the 1-*epi* aglycon **16** reveals the same spatial orientation of the ketone and the lactam carbonyl groups as in the cripowellins. Therefore one may be curious whether the 1-*epi* derivatives exhibit the same biological activity as the cripowellins and their aglycon. The 1-*epi* aglycon **15** might at least help to further clarify their hitherto unknown mode of action.[23]

Received: February 12, 2005
Published online: May 13, 2005

Keywords: alkaloids · asymmetric syntheses · Heck reactions · insecticides · ring-closing metatheses

[1] Representative reviews about the *Amaryllidaceae* alkaloids: a) O. Hoshino in *The Alkaloids*, *Vol. 51* (Ed.: G. A. Cordell), Academic Press, New York, **1998**, pp. 324 – 424; b) S. F. Martin in *The Alkaloids*, *Vol. 30* (Ed.: A. Brossi), Academic Press, New York, **1987**, pp. 251 – 376; c) C. Fuganti in *The Alkaloids*, *Vol. 15* (Ed.: R. H. F. Manske), Academic Press, London, **1975**, pp. 83 – 164.

[2] M. Gehling, A. Göhrt, D. Gondol, J. Lenz, O. Lockhoff, H.-F. Moeschler, R. Velten, D. Wendisch, W. Andersch, C. Erdelen, A. Harder, N. Mencke, A. Turberg, U. Wachendorff-Neumann (Bayer AG), DE 196 10 279A1, **1997** [*Chem. Abstr.* **1997**, *127*, 278406].

[3] R. Velten, C. Erdelen, M. Gehling, A. Göhrt, D. Gondol, J. Lenz, O. Lockhoff, U. Wachendorff, D. Wendisch, *Tetrahedron Lett.* **1998**, *39*, 1737 – 1740.

[4] Researchers at Bayer AG have determined that cripowellins A and B are neither acetylcholin esterase inhibitors nor PP1 inhibitors (personal communication).

[5] T. Lindel, *Nachr. Chem. Tech. Lab.* **1997**, *45*, 775 – 779.

[6] Review: H. C. Kolb, M. S. VanNieuwenhze, K. B. Sharpless, *Chem. Rev.* **1994**, *94*, 2483 – 2547.

[7] Prepared by esterification of the known alcohol with *para*-methoxybenzoic acid chloride (87 % yield): J. A. Rao, M. P. Cava, *J. Org. Chem.* **1989**, *54*, 2751 – 2753.

[8] The asymmetric dihydroxylation of allylic alcohols normally proceeds with only moderate enantioselectivity, in contrast to the reaction of the corresponding *para*-methoxybenzoic acid esters: E. J. Corey, A. Guzman-Perez, M. C. Noe, *J. Am. Chem. Soc.* **1995**, *117*, 10805 – 10816.

[9] The enantiomeric excess was determined by HPLC on a chiral stationary phase. For this, *ent*-**4** was prepared analogously to **4** but using AD-mix α instead.

[10] Representative reviews on ring-closing metathesis: a) A. Deiters, S. F. Martin, *Chem. Rev.* **2004**, *104*, 2199 – 2238; b) R. R. Schrock, A. H. Hoveyda, *Angew. Chem.* **2003**, *115*, 4740 – 4782; *Angew. Chem. Int. Ed.* **2003**, *42*, 4592 – 4633; c) A. Fürstner, *Angew. Chem.* **2000**, *112*, 3140 – 3172; *Angew. Chem. Int. Ed.* **2000**, *39*, 3012 – 3043; d) M. E. Maier, *Angew. Chem.* **2000**, *112*, 2153 – 2157; *Angew. Chem. Int. Ed.* **2000**, *39*, 2073 – 2077; e) S. Blechert, *Pure Appl. Chem.* **1999**, *71*, 1393 – 1399; f) A. Fürstner, *Top. Organomet. Chem.* **1998**, *1*, 37 – 72; g) R. H. Grubbs, S. Chang, *Tetrahedron* **1998**, *54*, 4413 – 4450; h) M. Schuster, S. Blechert, *Angew. Chem.* **1997**, *109*, 2124 – 2145; *Angew. Chem. Int. Ed. Engl.* **1997**, *36*, 2036 – 2055; i) H.-G. Schmalz, *Angew. Chem.* **1995**, *107*, 1981 – 1984; *Angew. Chem. Int. Ed. Engl.* **1995**, *34*, 1833 – 1836; j) F.-X. Felpin, J. Lebreton, *Eur. J. Org. Chem.* **2003**, 3693 – 3712.

[11] For the synthesis of nine-membered rings with similar conformational constraints similar to those of the dioxolane ring by metathesis, see: a) P. W. R. Harris, M. A. Brimble, P. D. Gluckman, *Org. Lett.* **2003**, *5*, 1847 – 1850; b) J. S. Clark, F. Marlin, B. Nay, C. Wilson, *Org. Lett.* **2003**, *5*, 89 – 92; c) K. P. Kaliappan, N. Kumar, *Tetrahedron Lett.* **2003**, *44*, 379 – 381; d) M. Hirama, T. Oishi, H. Uehara, M. Inoue, M. Maruyama, H. Oguri, M. Satake, *Science* **2001**, *294*, 1904 – 1907; e) J. S. Clark, O. Hamelin, *Angew. Chem.* **2000**, *112*, 380 – 382; *Angew. Chem. Int. Ed.* **2000**, *39*, 372 – 374; f) S. J. Bamford, K. Goubitz, H. L. van Lingen, T. Luker, H. Schenk, H. Hiemstra, *J. Chem. Soc. Perkin Trans. 1* **2000**, 345 – 351; g) T. Oishi, Y. Nagumo, M. Hirama, *Chem. Commun.* **1998**, 1041 – 1042; h) M. Delgado, J. D. Martín, *Tetrahedron Lett.* **1997**, *38*, 6299 – 6300.

[12] For secondary and tertiary amides in ring-closing metatheses, see: a) A. J. Brouwer, R. M. J. Liskamp, *J. Org. Chem.* **2004**, *69*, 3662 – 3668; b) L. Banfi, A. Basso, G. Guanti, R. Riva, *Tetrahedron Lett.* **2003**, *44*, 7655 – 7658.

[13] There are only very few examples for the synthesis of nine-membered rings by methathesis without conformational constraints. They are limited almost exclusively to nine-membered cyclic ethers for which the *gauche* effect can be exploited: a) M. T. Crimmins, M. T. Powell, *J. Am. Chem. Soc.* **2003**, *125*, 7592 – 7595; b) M. T. Crimmins, K. A. Emmitte, A. L. Choy, *Tetrahedron* **2002**, *58*, 1817 – 1834; c) Y. Baba, G. Saha, S. Nakao, C. Iwata, T. Tanaka, T. Ibuka, H. Ohishi, Y. Takemoto, *J. Org. Chem.* **2001**, *66*, 81 – 88; d) M. T. Crimmins, A. L. Choy, *J. Org. Chem.* **1997**, *62*, 7548 – 7549.

[14] Representative reviews on the Heck reaction: a) S. Bräse, A. de Meijere in *Metal-Catalyzed Cross-Coupling Reactions*, 2nd ed. (Eds.: A. de Meijere, F. Diederich), Wiley-VCH, Weinheim, **2004**, pp. 217 – 315; b) J. T. Link, L. E. Overman in *Metal-Catalyzed Cross-Coupling Reactions* (Eds.: F. Diederich, P. J. Stang), Wiley-VCH, Weinheim, **1998**, pp. 231 – 269; c) A. B. Dounay, L. E. Overman, *Chem. Rev.* **2003**, *103*, 2945 – 2963; d) J. T. Link in *Organic Reactions*, *Vol. 60* (Eds.: L. E. Overman), Wiley, New York, **2002**, pp. 157 – 534; e) A. de Meijere, F. E. Meyer, *Angew. Chem.* **1994**, *106*, 2473 – 2506; *Angew. Chem. Int. Ed. Engl.* **1994**, *33*, 2379 – 2411.

[15] Apart from **12**, minor amounts of **11** could also be isolated when the Heck reaction was performed under cationic conditions (in

the crude product the ratio **12**/**11** was determined to be 8.2:1 by means of gas chromatography). However, **11** could be easily separated from **12** by column chromatography on silica gel because of its higher polarity.
[16] After 4 h (complete conversion): $E/Z = 1{:}1.7$; after 24 h: $E/Z = 1{:}1$ (determined by gas chromatography).
[17] The relative configurations were determined by NOE measurements.
[18] For the synthesis of bicyclic systems by a sequence of RCM and Heck reactions, see: a) M. Lautens, V. Zunic, *Can. J. Chem.* **2004**, *82*, 399–407; b) R. Grigg, M. York, *Tetrahedron Lett.* **2000**, *41*, 7255–7258; c) R. Grigg, V. Sridharan, M. York, *Tetrahedron Lett.* **1998**, *39*, 4139–4142.
[19] J. D. White, T. C. Somers, *J. Am. Chem. Soc.* **1994**, *116*, 9912–9920.
[20] G. A. Molander, G. Hahn, *J. Org. Chem.* **1986**, *51*, 1135–1138.
[21] G. A. Molander in *Organic Reactions*, *Vol. 46* (Ed.: L. A. Paquette), Wiley, New York, **1994**, pp. 211–367.
[22] CCDC 263133 (**16**) contains the supplementary crystallographic data for this paper. These data can be obtained free of charge from the Cambridge Crystallographic Data Centre via www.ccdc.cam.ac.uk/data_request/cif.
[23] We will report separately on our alternative synthetic approaches to the cripowellins in detail: K. Catlin, RWTH Aachen, unpublished results; C. Janeck, Ph.D. Thesis, RWTH Aachen, **2000**; M. Backes, Ph.D. Thesis, RWTH Aachen, **2004**.

Theoretical Chemistry

Exploring Polymorphism: The Case of Benzene**

Paolo Raiteri, Roman Martoňák, and Michele Parrinello*

The prediction of crystal structures from the molecular structure is of great importance for the chemical and pharmaceutical industries as well as for fundamental science, and it represents a great challenge for theoretical chemists and physicists.[1–7] An even harder task is the computational exploration of all possible polymorphs of a given compound. Crystalline benzene is a case in point: its phase diagram has been investigated for almost 40 years, but its structures have been only partially elucidated.

A small and simple molecule, benzene, has provided a challenging testing ground for many theorists in spite of its limited significance in chemical practice. Only three of the experimentally observed phases have been correctly reproduced by computer simulations.[8–13] Here, by using a novel theoretical algorithm[14] we describe that at finite temperature there are at least seven possible stable phases. Our results help to answer a number of pending questions and identify six of the experimental structures. For the seventh, with limited experimental data, we are able to propose a complete structure.

A tentative phase diagram showing all the benzene phases identified in the literature is shown in Figure 1. At room temperature X-ray and Raman scattering[15,16] have determined the existence of five phases, I, II, III, III′, and IV, but a good agreement between theory and experiment has been obtained only for the first three,[8–13] while phases III′ and IV are more controversial. It has in fact been argued that benzene III′ may be only a distortion of benzene III,[15] while benzene IV has been hypothesized as being a polymer-like compound, where new chemical bonds have been formed due to the very high pressure.[16] However, more recent far-infrared spectroscopic data support the existence of both phases as true benzene crystals.[17] Less detailed evidence is available for the remaining phases I′ and V. The former has been identified only on the basis of a discontinuity in the lattice constants as a function of temperature, and it has been suggested that the transformation benzene I→benzene I′ is a second order transition.[15] Finally, in the high-temperature region only Raman data can be called on to support of the existence of another phase, here called benzene V.[16]

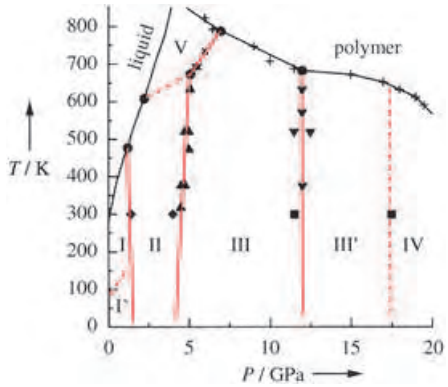

Figure 1. Proposed phase diagram of solid benzene. For phases I, II, III, III′, and IV we follow the nomenclature of ref. [15]. As a consequence phase IV of ref. [16] becomes here phase V. The liquid–solid boundary and all the points reported in the picture are taken from refs. [15,16]. Hypothetical phase boundaries are represented with dashed lines.

The practical relevance of crystal structure prediction has stimulated the development of many computational protocols,[1–7] among which the most common approach is to generate large numbers of structures and select the one with the lowest enthalpy by means of different minimization

[*] Dr. P. Raiteri, Dr. R. Martoňák,[+] Prof. M. Parrinello
Computational Science
Departement für Chemie und Angewandte Biowissenschaften
ETHZ, USI Campus
Via Buffi 13, 6900 Lugano (Switzerland)
Fax: (+41) 919-138-817
E-mail: paolo.raiteri@phys.chem.ethz.ch

[+] Permanent address:
Department of Physics
Faculty of Electrical Engineering and Information Technology
Slovak University of Technology
Ilkovičova 3, 812 19 Bratislava (Slovakia)

[**] We thank A. Laio for many interesting discussions, J. D. Dunitz for his critical remarks, and A. Gavezzotti for many helpful suggestions for improving the manuscript.

 DOI: 10.1002/anie.200462760

techniques. Entropy is usually neglected or evaluated in the harmonic lattice approximation. Here we take a different approach and apply a new general method, called metadynamics,[14] where the search for stable polymorphs is guided by the Gibbs free energy, taking fully into account the role of temperature and pressure. In its application to solid–solid phase transitions, metadynamics[18] shares the basic idea of the Parrinello–Rahman technique,[19,20] where the simulation box edges act as an order parameter to favor a structural transition. The technique allows a fast and accurate exploration of the Gibbs free energy surface as a function of this order parameter. Early applications of this method to inorganic crystals have been very encouraging.[18,21]

The problem of determining all the possible polymorphs of a given compound, consisting of a search for stable or metastable crystal structures at a given temperature T and pressure P, can be formulated as a search for minima of the Gibbs free energy $G(\mathbf{h})$ in the space of a suitable order parameter, $\mathbf{h}$. In the simulation of crystals, periodic boundary conditions are commonly used, and if no defects are present, the simulation box defined by its edges a, b, and c has to be commensurate with the crystalline unit cell. Therefore, the simulation box vectors, arranged in a 3×3 matrix, $\mathbf{h}=(a,b,c)$, can be used as an order parameter that discriminates between different crystal structures in the same way as in the Parrinello–Rahman technique.[19,20] It is convenient to take the box matrix $\mathbf{h}$ as upper triangular, which effectively freezes the rotations of the box and reduces the dimensionality of the order parameter to 6. This can be easily achieved by a rotation of the simulation cell so that the a vector is aligned with the x Cartesian axis and the b vector lies in the xy Cartesian plane.

Metadynamics explores the Gibbs free energy $G(\mathbf{h})$ in the subspace of the order parameter $\mathbf{h}$ in a stepwise fashion by means of a steepest-descent-like dynamics [Eq. (1)], where δh

$$\mathbf{h}^{t+1}=\mathbf{h}^{t}+\delta h\left(\frac{\phi^{t}}{|\phi^{t}|}\right) \tag{1}$$

is the maximum allowed variation of the box dimensions. The driving force, $\phi^{t}=-\partial G^{t}/\partial\mathbf{h}$, is a gradient of the Gibbs free energy plus a time-dependent potential that discourages the system from going into previously visited configurations. This potential is obtained as a sum of Gaussians placed on all previously visited points in the space of the order parameter $\mathbf{h}$ [Eq. (2)].

$$G^{t}(\mathbf{h},t)=G(\mathbf{h})+\sum_{t'<t} W\exp\left[\frac{-(\mathbf{h}-\mathbf{h}^{t'})^{2}}{2\,\delta h^{2}}\right] \tag{2}$$

The parameters W and δh determine the resolution in energy and order parameter and can be chosen following the empirical guidelines provided in ref. [18]. The derivative of the Gibbs free energy can be calculated using Equation (3),

$$\frac{\partial G}{\partial h_{ij}}=-V[\mathbf{h}^{-1}(\mathbf{p}-P]_{ji} \tag{3}$$

where P is the external pressure and $\mathbf{p}$ is the averaged pressure tensor. The latter can easily be evaluated from molecular dynamics runs at constant $\mathbf{h}$ and temperature. Entropy is thus automatically accounted for through its volume–pressure dependence. As the dynamics proceeds, the added Gaussians modify the free energy landscape by filling the potential energy well relative to the initial crystal structure so that eventually the system must escape to a new basin of attraction, corresponding to a new crystal structure.

Each metadynamics step consists of: a) the equilibration of the system at the desired $\mathbf{h}$ and temperature, b) the calculation of the average pressure tensor $\mathbf{p}$, and c) the evolution of $\mathbf{h}$ according to Equation (1) followed by the rescaling of the atomic coordinates. Each of steps a and b consists of a 1-ps molecular dynamics run at constant temperature (300 K) and $\mathbf{h}$. The external pressure, P, is fixed at 2 GPa.

Many force fields have been developed for studying organic crystals (see, for example, refs. [22–24]). Because it is known that force fields optimized on static crystal structures may perform poorly in dynamic calculations, here we adopted the GROMOS96 force field.[25] The molecules are fully flexible and hydrogen atoms are explicitly considered. The partial atomic charges were obtained by the standard RESP[26] method and are $-0.11\,e$ for the carbon atoms and $0.11\,e$ for the hydrogen atoms. The long-range electrostatic interactions are computed with the Particle Mesh Ewald (PME) summation. The simulation supercell is replicated in space by means of the periodic boundary conditions. All the molecules in the simulation box are free to move and to find a suitable periodic arrangement without any restriction on the number of molecules in the unit cell. For the time-dependent potential we chose the Gaussian width, δh, between 2 and 3 Å and the Gaussian height, W, between 500 and 2500 kJ mol^{-1}, while the $W/\delta h^{2}$ ratio fulfills the guidelines given in ref. [18].

This method offers a number of competitive advantages over standard approaches to crystal structure prediction. At finite temperature the Gibbs free energy is much smoother than the potential energy surface at $T=0$. This eliminates most of the shallow minima, leaving only the relevant ones. Another consequence of explicitly considering a finite temperature is that we can discover phases that are stabilized by entropy. In our application to benzene, only a limited number of thermodynamically stable phases are found, some of which (benzene I and V) are unstable at $T=0$ and $P=0$. A further advantage of this method is that it can be implemented on modest computer equipment like standard PCs. In our case, a whole metadynamics run took a couple of hours on a 2-GHz Pentium IV workstation. Clearly, however, the cost of the method depends mainly on the intermolecular potential used for the MD simulations.

We tackled the problem of determining all the polymorphs of benzene assuming only the knowledge of its molecular structure. As an initial step in our procedure, we generated a periodic lattice with two molecules in the unit cell, where lattice vectors and molecular orientations were taken at random. Then we performed a pure steepest descent relaxation of the box and of the atomic coordinates using a simulation cell that contained no more than eight molecules. Once the system relaxed to an energy basin, the temperature

was raised to room temperature and a short conventional constant-pressure molecular dynamics simulation was performed. If the system so generated is unstable, the procedure was started again.

We used tens of randomly generated crystal structures as starting points for the metadynamics. Most of them have no symmetry and are highly metastable, and a few metadynamics steps were often sufficient to escape from the shallow energy basin and obtain a more stable structure, which most of the time is similar to benzene I or III. This structure was then used as a building block for larger simulation cells used in subsequent metadynamics runs. In a series of trial runs it was observed that if we chose a MD simulation cell that was too small, no structural transition was observed. On the other hand, in large MD cells stacking faults were created at low energy cost, thus preempting the crystal-to-crystal phase transition. With a cell of 192 independent molecules it was possible to observe smooth crystal-to-crystal transformations.

The structure factor F_{hkl} provides a means to monitor the occurrence of a phase transition [Eq. (4)].[18] When a pronounced change in a selected reflection of F_{hkl} was observed, the dynamics was stopped and the new structure was optimized with respect to the box edges and the internal coordinates, both at $T=0$ and at the experimental condi-

$$F_{hkl} = \sum_j e^{-i \vec{G}_{hkl} \vec{r}_j} \quad (4)$$

Table 1: Comparison of experimental[15] and theoretical data of the seven benzene polymorphs.[a]

		Lattice paramenters		Space group	
		Theory	Expt	Theory	Expt
I	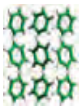	*a* 7.42 *b* 9.74 *c* 7.27 β 90.0 V_m 131.4	7.49 9.71 7.07 90.0 128.5	*Pbca* *Z*=4	*Pbca* Z=4
I′	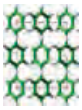	*a* 7.48 *b* 9.47 *c* 7.14 β 90.0 V_m 126.4	– – – – –	*Cmca* *Z*=4	– – – – –
II	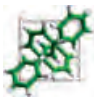	*a* 5.72 *b* 5.72 *c* 14.6 β 90.0 V_m 119.4	5.54 5.54 15.3 90.0 117.4	$P4_32_12$ Z=4	$P4_32_12$ *Z*=4
III	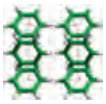	*a* 7.51 *b* 5.50 *c* 5.50 β 110.0 V_m 106.7	7.44 5.20 5.31 109.4 96.88	$P2_1/c$ *Z*=2	$P2_1/c$ *Z*=2
III′	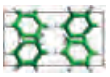	*a* 9.01 *b* 5.90 *c* 7.90 β 109.0 V_m 99.3	5.15 4.96 7.23 110.9 86.3	*C*2/*c* *Z*=4	$P2_1/c$ *Z*=2
IV	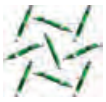	*a* 9.27 *b* 5.87 *c* 6.40 β 90.0 V_m 87.1	9.13 4.96 6.46 101.8 71.6	*Pbam* *Z*=4	*Pbam* *Z*=4
V		*a* 5.60 *b* 4.04 *c* 9.52 β 95.0 V_m 107.3	– – – – –	$P2_1$ *Z*=2	– – – – –

[a] The cell lengths (*a*, *b* and *c*) are in Å, the angle β is in degrees, and the molecular volume (V_m) is in Å^3. All the crystalline phases have $\alpha=\gamma=90$. The theoretical data are computed at room temperature and experimental pressure,[15] except for benzene I′ and V, which are computed at $T=0$ K and $P=0$ GPa and $T=600$ K and $P=5$ GPa, respectively. The experimental data relative to benzene II are from ref. [11], and the experimental crystallographic assignments of benzene III′ and IV are rather tentative.[15]

tions.[15] This was the key step in the identification of the new stable structures. The space group and the number of molecules in the unit cell for the equilibrium structure were determined by the program PLATON.[27] Then we simulated the powder diffraction spectra $S(2\theta)$ for all the equilibrated structures. Comparison of the structural information and of $S(2\theta)$ with the available experimental data allowed the matching of theoretical and experimental phases. In particular, the difference in the interplanar distances is quite low ($\approx 6\,\%$), and there is a good correspondence in the relative peak heights of the $S(2\theta)$. We label the structures found by the metadynamics with the names of the experimental phases to which they correspond. A most noticeable result is that Table 1 exhausts the list of all the minima that are found by metadynamics; it is not a selection of those structures that better fit the experimental data.

Benzene I is found to be stable at room temperature, but it converts into a different structure, benzene I′, upon relaxation at 0 K. This supports the hypothesis of the existence of a such a phase suggested in ref. [15], and benzene I is an example of a phase stabilized at room temperature by an entropic contribution. The two other well-characterized phases, benzene II and III,[10,11] are also found correctly by the metadynamics. It is interesting to note that benzene II, which is stable between 2 and 5 GPa,[15] has the same packing as its inorganic analogue, borazine, at ambient pressure.[28]

Moving to the high-pressure side of the phase diagram, the metadynamics is able to answer some open questions. Benzene III′ indeed exists, and it is not a modification of benzene III as proposed in ref. [15] but a new monoclinic phase in the space group $C2/c$, which may better match the experimental data when one cell parameter and the number of molecules in the unit cell are halved. At even higher pressure, benzene IV comes into play, and we are able to determine that it belongs to the *Pbam* space group. Finally, we assign the seventh structure discovered, whose space group is $P2_1$, to benzene V. Owing to the lack of structural information the last assignment is tentative and should be confirmed by experiment; moreover, this structure appears to be unstable at pressures lower than 5 GPa. The quantitative agreement between theory and experiment decreases with increasing pressure. This is not surprising since the potential has been modeled on low-pressure data.

In view of the very delicate balance between the different energy contributions we find our results remarkably good. The accuracy of our predictions, the absence of spurious minima, and a comparison between the lattice energies computed with the GROMOS96 and with the W99 force fields (Table 2) give an a posteriori validation of the capability of the force field used. It is worth noting that the GROMOS96[25] force field was not optimized for studying crystal structures. We were able to fill the experimental gaps in the understanding of the phase diagram of benzene by determining all the stable crystal structures. This success demonstrates that our methodology is a new and powerful tool for the fast and accurate determination of the relevant polymorphs of an organic molecular crystal, and that it may help solve the problem of crystal structure prediction. The most promising aspect of our work is that it provides a workable new paradigm in which the Gibbs free energy and not the potential energy surface plays the determining role. Since in most practical applications the relevant structures are those which are stable at ambient conditions, this appears to us a major step forward. This is especially true for substances like most organic molecules for which $T = 300$ K is very close to the melting temperature. Once the thermodynamically relevant phases are found, the calculations can be further refined with the use of more accurate potentials and thus the relative enthalpy of the different phases can be determined.[11,21] By using methods of statistical mechanics it is also possible to draw a full phase diagram.[29] These extensions are, however, outside the scope of the present work.

Table 2: Lattice energies in kJ mol^{-1} for all the benzene phases that are stable at $T = 0$ and $P = 0$ computed with both the GROMOS96[25] and the W99[22] force fields.[a]

	GROMOS96	W99
II	0.00	0.00
III	0.25	0.43
III′	1.25	0.84
IV	2.07	0.37

[a] For both force fields we considered the molecules as rigid units and we minimized the energy with respect to the lattice vectors and molecular orientations. We observed that upon cooling benzene I converts into I′ for the GROMOS96 force field, while the opposite occurs for the W99 force field. The reference structure is benzene II. The atomic charges are those used for the molecular dynamics simulations.

Received: November 30, 2004
Published online: May 11, 2005

Keywords: crystal structure prediction · molecular dynamics · phase transitions · polymorphism

[1] J. P. M. Lommerse, W. D. S. Motherwell, H. L. Ammon, J. D. Dunitz, A. Gavezzotti, D. W. M. Hofmann, F. J. J. Leusen, W. T. M. Mooij, S. L. Price, B. Schweizer, M. U. Schmidt, B. P. van Eijck, P. Verwer, D. E. Williams, *Acta Crystallogr. Sect. B* **2000**, *56*, 697 – 713.
[2] W. D. S. Motherwell, H. L. Ammon, J. D. Dunitz, A. Dzyabchenko, P. Erk, A. Gavezzotti, D. W. M. Hofmann, F. J. J. Leusen, W. T. M. Mooij, S. L. Price, H. Scheraga, B. Schweizer, M. U. Schmidt, B. P. van Eijck, P. Verwer, D. E. Williams, *Acta Crystallogr. Sect. B* **2002**, *58* 647 – 661.
[3] S. L. Price, *Adv. Drug Delivery Rev.* **2004**, *56*, 301 – 319.
[4] S. Datta, D. J. W. Grant, *Nat. Rev. Drug Discovery* **2004**, *3*, 42 – 57.
[5] R. J. Wawak, J. Pillardy, A. Liwo, K. D. Gibson, H. A. Scheraga, *J. Phys. Chem. A* **1998**, *102*, 2904 – 2918.
[6] Y. Yonetani, K. Yokoi, *Mol. Phys.* **2001**, *99*, 1743 – 1750.
[7] J. Pillardy, Y. A. Aranautova, C. Czaplewski, K. D. Gibson, H. A. Scheraga, *Proc. Natl. Acad. Sci. USA* **2001**, *98*, 12351 – 12356.
[8] T. Shoda, K. Yamahara, K. Okazaki, D. E. Williams, *THEOCHEM* **1994**, *313*, 321 – 334.
[9] T. Shoda, K. Yamahara, K. Okazaki, D. E. Williams, *THEOCHEM* **1995**, *333*, 267 – 274.
[10] M. M. Thiéry, C. Rérat, *J. Chem. Phys.* **1996**, *104*, 9079 – 9089.

[11] B. P. van Eijck, A. L. Spek, W. T. M. Mooij, J. Kroon, *Acta Crystallogr. Sect. B* **1998**, *54*, 291 – 299.
[12] V. E. Bazterra, M. B. Ferraro, J. C. Facelli, *J. Chem. Phys.* **2002**, *116*, 5984 – 5991 and V. E. Bazterra, M. B. Ferraro, J. C. Facelli, *J. Chem. Phys.* **2002**, *116*, 5992 – 5995.
[13] Y. Yonetani, K. Yokoi, *Mol. Phys.* **2002**, *100*, 3915 – 3919.
[14] A. Laio, M. Parrinello, *Proc. Natl. Acad. Sci. USA* **2002**, *99*, 12562 – 12567.
[15] M. M. Thiéry, J. M. Léger, *J. Chem. Phys.* **1988**, *89*, 4255 – 4271.
[16] F. Cansell, D. Fabre, J.-P. Petitet, *J. Chem. Phys.* **1993**, *99*, 7300 – 7304.
[17] L. Ciabini, M. Santoro, R. Bini, V. Schettino, *J. Chem. Phys.* **2001**, *115*, 3742 – 3749.
[18] R. Martoňák, A. Laio, M. Parrinello, *Phys. Rev. Lett.* **2002**, *90*, 75503.
[19] M. Parrinello, A. Rahman, *Phys. Rev. Lett.* **1980**, *45*, 1196 – 1199.
[20] M. Parrinello, A. Rahman, *J. Appl. Phys.* **1981**, *52*, 7182 – 7190.
[21] C. Ceriani, A. Laio, E. Fois, A. Gamba, R. Martoňák, M. Parrinello, *Phys. Rev. B* **2004**, *70*, 113403.
[22] D. E. Williams, *J. Comput. Chem.* **2000**, *21*, 1154 – 1166.
[23] Y. A. Aranautova, A. Jagielska, J. Pillardy, H. A. Scheraga, *J. Phys. Chem. B* **2003**, *107*, 7143 – 7154.
[24] J. Wang, R. M. Wolf, J. W. Caldwell, P. A. Kollman, D. A. Case, *J. Comput. Chem.* **2004**, *25*, 1157 – 1174.
[25] D. van der Spoel, A. R. Buuren, D. P. Tieleman, H. J. C. Berendsen, *J. Biomol. NMR* **1996**, *8*, 229 – 238.
[26] C. Bayly, P. Cieplak, W. Cornell, P. A. Kollman, *J. Phys. Chem.* **1993**, *97*, 10269 – 10280.
[27] A. L. Spek, *J. Appl. Crystallogr.* **2003**, *36*, 7 – 13.
[28] G. Raabe, *Z. Naturforsch.* **2004**, *59*, 609 – 614.
[29] E. Sanz, C. Vega, J. L. F. Abascal, L. G. MacDowell, *Phys. Rev. Lett.* **2004**, *92*, 255701.

Polyoxometalates

The Ball-Shaped Heteropolytungstates $[\{Sn(CH_3)_2(H_2O)\}_{24}\{Sn(CH_3)_2\}_{12}(A\text{-}XW_9O_{34})_{12}]^{36-}$ **

Ulrich Kortz, Firasat Hussain, and Markus Reicke*

Polyoxometalates can be considered as soluble metal-oxide fragments with an enormous structural variety and a multitude of interesting properties.[1–6] The first polyanions were reported almost two centuries ago.[7,8] Nevertheless, interest in this class of compounds is larger than ever before. The search for novel polyanions is predominantly driven by the catalytic properties of many transition-metal-substituted polyoxotungstates,[9] and by potential applications in bio- and nanotechnology.

Besides being useful, the symmetry and molecular nature of polyoxometalates are highly attractive features. Until recently, the isopolyanion $[Mo_{36}O_{112}(H_2O)_{18}]^{8-}$,[10] the heteropolyanions $[As_4W_{40}O_{140}]^{28-}$[11] and $[H_7P_8W_{48}O_{148}]^{33-}$[12] were the largest polyoxometalates reported. However, in the last couple of years we have witnessed the discovery of several polyoxometalates with truly spectacular sizes. Especially Müller et al. reported on gigantic mixed-valence polyoxomolybdate rings and spheres containing up to 368 molybdenum atoms.[13] Pope et al. reported on a polyoxotungstate with 148 tungsten atoms, $[As_{12}Ce_{16}(H_2O)_{36}W_{148}O_{524}]^{76-}$.[14] Sécheresse et al. have treated the cationic oxo-thio linker $[Mo_2O_2S_2(OH_2)_6]^{2+}$ with many different lacunary polyoxotungstates resulting in large polyanion assemblies.[15] Our group has reported a large tungstoarsenate(III) with 65 tungsten atoms which was prepared by self-condensation of the dilacunary polyanion precursor $[As_2W_{19}O_{67}(H_2O)]^{14-}$.[16] Recently we also reported on large polyoxotungstates based on titanium(IV).[17]

It is important to realize that the mechanism of formation of polyoxometalates is still not well understood and commonly described as self-assembly. Therefore it is usually not possible to design a multi-step sequence for the synthesis of a novel polyoxometalate. As a result the design of novel polyoxometalates remains a challenge.

In our search for a cationic linker which is hydrolytically stable and allows for covalent attachment of organic functional groups we identified the diorganotin group (R_2Sn^{2+}, $R = CH_3$, C_6H_5 etc.) as an interesting candidate. We have already demonstrated that this electrophile can be incorporated in lone-pair-containing polyanion precursors.[18] Furthermore, we have discovered that the two organic groups are always *trans* to each other, which allows the construction of large polyanions with unexpected geometries. Herein we report the reactivity of dimethyltindichloride with the trilacunary Keggin precursors $[A\text{-}XW_9O_{34}]^{9-}$ (X = P, As).

Interaction of $(CH_3)_2SnCl_2$ with $Na_9[A\text{-}PW_9O_{34}]$ in the ratio 3:1 in aqueous medium (pH 4) resulted in the dodecameric, ball-shaped anion $[\{Sn(CH_3)_2(H_2O)\}_{24}\{Sn(CH_3)_2\}_{12}(A\text{-}PW_9O_{34})_{12}]^{36-}$ (**1**; Figure 1 and Figure 2). We were also able to prepare the isostructural arsenic analogue $[\{Sn(CH_3)_2(H_2O)\}_{24}\{Sn(CH_3)_2\}_{12}(A\text{-}AsW_9O_{34})_{12}]^{36-}$ (**2**) by an identical procedure. Both compounds crystallized as mixed cesium–sodium salts and are in fact isomorphous.[19] Owing to the high symmetry of the solid state arrangement (space group $Im\bar{3}$), the asymmetric unit of **1** and **2** is very small and includes only five tungsten and two tin atoms (Figure 1). The spherical structure of **1** and **2** is spectacular in terms of geometry and size (diameter of ≈ 30 Å) and is unprecedented in polyoxotungstate chemistry (Figure 2 and Figure 3). This supermolecular assembly is composed of 12 trilacunary $[A\text{-}XW_9O_{34}]^{9-}$ (X = P, As) Keggin fragments which are linked by a total of 36 dimethyltin groups (12 inner $(CH_3)_2Sn^{2+}$ and 24 outer $(CH_3)_2(H_2O)Sn^{2+}$ groups) resulting in a polyanion with T_h symmetry. Note that **1** and **2** have almost 1000 atoms and a

[*] Prof. U. Kortz, F. Hussain, M. Reicke
International University Bremen
School of Engineering and Science
P.O. Box 750 561, 28725 Bremen (Germany)
Fax: (+49) 421-200-3229
E-mail: u.kortz@iu-bremen.de

[**] U.K. thanks the International University Bremen for research support, the Florida State University Chemistry Department (USA) for unlimited access to the single-crystal X-ray diffractometer, and Prof. A. Müller, Dr. H. Bögge (both Bielefeld University), and Dr. M. H. Dickman (IUB) for helpful discussions. Figure 1–7 were generated by Diamond Version 3 (copyright Crystal Impact GbR). Figure 8 is courtesy of Dr. Bögge. X = P, As.

 DOI: 10.1002/anie.200500548

Figure 1. Ball-and-stick representation of the asymmetric unit of **1**; green C, red O. This Figure is also representative of the As-analogue **2**, as both structures are isomorphous.

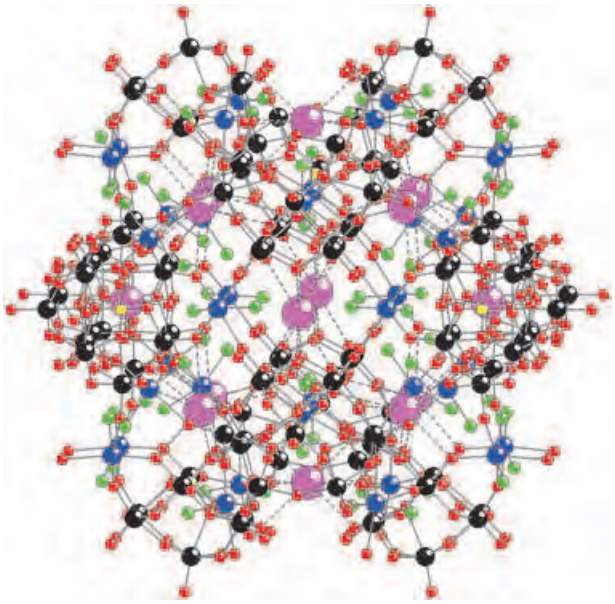

Figure 2. Ball-and-stick representation of **1** and **2** including the 14 cesium counterions. black W, blue Sn, yellow P/As, red O, green C, and purple Cs. For clarity no hydrogen atoms are shown.

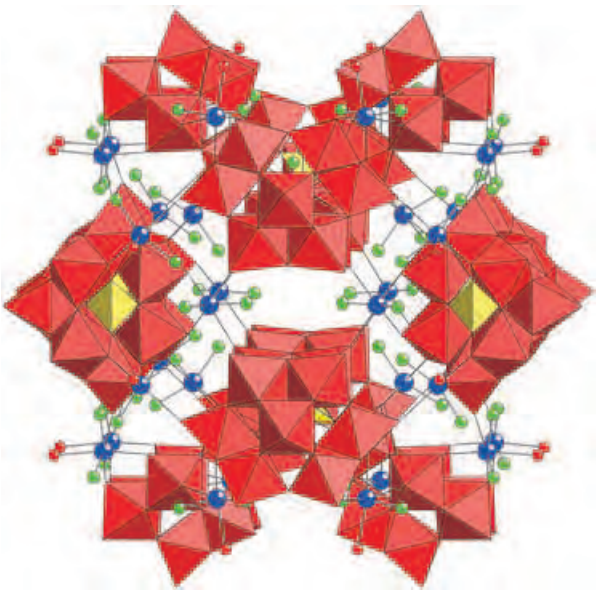

Figure 3. Polyhedral representation of **1** and **2**. The WO_6 octahedra are red and the XO_4 tetrahedra (X = P, As) are yellow, otherwise, the color scheme is the same as in Figure 2. For clarity no hydrogen or cesium atoms are shown.

molar mass of around 33 000 g mol^{-1}. In addition, 14 cesium ions are closely associated with **1** and **2** in the solid state. They are located in hydrophilic surface pockets of the spherical clusters, thereby stabilizing the assembly further (Figure 2).

Polyanions **1** and **2** are the second largest, discrete polyoxotungstates reported.[14] Furthermore, the overall shape of **1** and **2** resembles Müller's Keplerates which are highly symmetrical polyoxomolybdates.[20] This class of compounds is characterized by spherical clusters with icosahedral symmetry of the type $(pentagon)_{12}(linker)_{30}$ where the centers of the 12 pentagons describe an icosahedron and the centers of the 30 linkers an icosidodecahedron. Close inspection of the structure of **1** and **2** indicates that it is best described as a "pseudo Keplerate". Although the 12 hetero atoms (P in **1** and As in **2**) describe an almost perfect icosahedron (Figure 4), the 12 inner tin atoms do not (Figure 5). Of note is that the 24 outer tin atoms also form a highly symmetrical

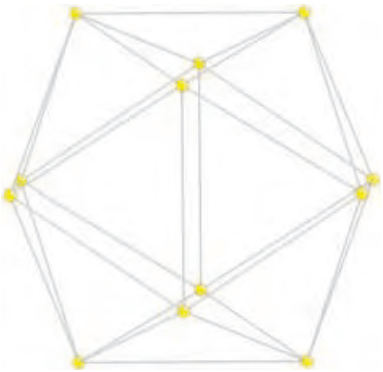

Figure 4. Representation of the icosahedron described by the hetero atoms of **1** (P) and **2** (As).

arrangement (Figure 6) as do the 14 cesium ions which describe a hexacapped cube (Figure 7). Therefore polyanions **1** and **2** exhibit some analogies with a Russian doll, but are in fact more complex as the shells have varying size, symmetry, and chemical composition. The multishell nature of **1** and **2** is nicely visible in Figure 8 (cesium ions not included for clarity).

Bond valence sum calculations (BVS) of **1** and **2** indicate that the terminal oxygen atoms attached to the 24 outer tin atoms belong to water molecules. There are no other protonation sites on **1** and **2** and therefore the charge must be −36.[21] This is fully consistent with elemental analysis, which indicated the presence of 14 cesium and 22 sodium ions. The cesium ions could be identified by X-ray diffraction, but not sodium ions which is probably a result of disorder.

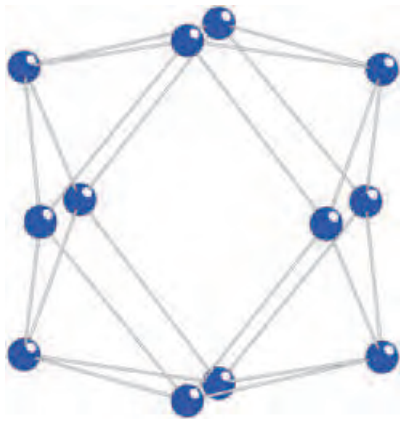

Figure 5. Representation of the polyhedron described by the 12 inner tin atoms of **1** and **2**.

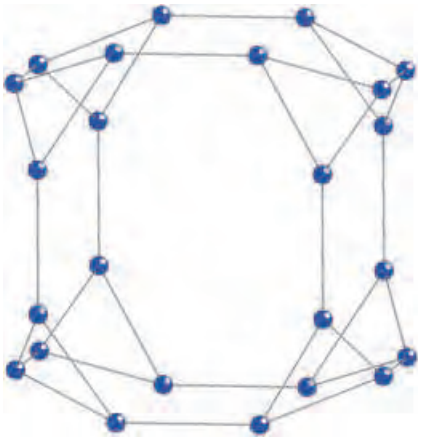

Figure 6. Representation of the polyhedron described by the 24 outer tin atoms of **1** and **2**.

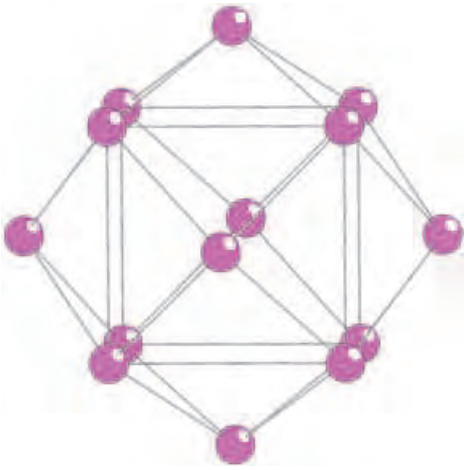

Figure 7. Representation of the hexacapped cube described by the 14 cesium ions of **1** and **2**.

The central cavity of the ball-shaped **1** and **2** has a diameter of around 8 Å and it does not contain any water molecules or ions. The pocket is actually hydrophobic because it is lined by 12 methyl groups. This hydrophobicity probably explains why polyanions **1** and **2**, which were synthesized in aqueous medium, do not contain any guests. Nevertheless, we believe that in principle small guest molecules with appropriate size and polarity can be encapsulated during formation of **1** and **2**. Furthermore, we identified hydrophobic channels (lined by methyl groups) passing through the entire structure of **1** and **2**, which could allow for loading and discharging of guest molecules even after the polyanions have been formed. In addition, the surface of **1** and **2** has 14 hydrophilic pockets, which are all occupied by cesium ions (Figure 2).

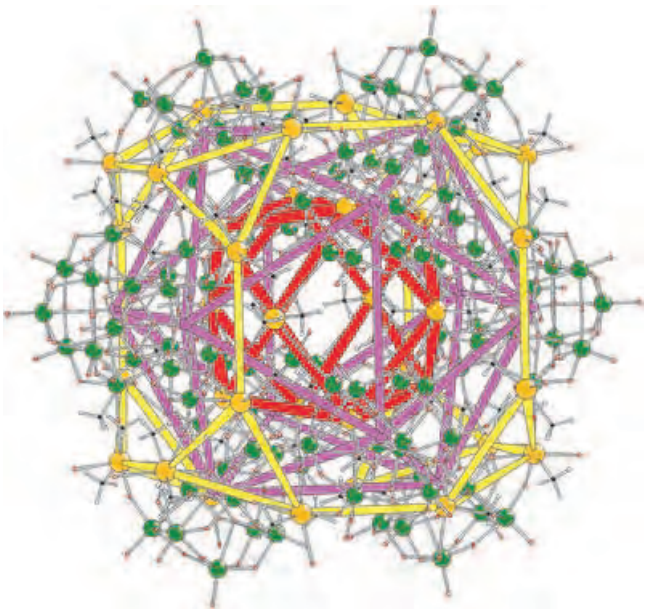

Figure 8. Ball-and-stick representation of **1** and **2** highlighting the different polyhedral shells; red 12 inner Sn atoms, purple 12 hetero atoms, yellow 24 outer Sn atoms (green spheres tungsten).

We also investigated the solution properties of **1** by multinuclear solution NMR (^{183}W, ^{119}Sn, ^{31}P, ^{13}C, ^{1}H) spectroscopy at room temperature in D_2O (400 MHz JEOL ECX instrument). The ^{183}W NMR spectrum of **1** shows two singlets at $\delta = -134.0$ and -157.9 ppm, with an intensity ratio 1:2. The ^{31}P NMR spectrum of **1** has a singlet at $\delta = -13.1$ ppm and the ^{119}Sn NMR spectrum has a singlet at $\delta = -170.8$ ppm. The ^{13}C NMR spectrum shows two signals at $\delta = 22.1$ and 8.4 ppm, with an intensity ratio 1:2 and the ^{1}H NMR spectrum shows two signals at $\delta = 1.9$ and 0.8 ppm, also with an intensity ratio 1:2. Thus for solutions of **1** we identified two types of tungsten, carbon, and hydrogen environments and, one type of phosphorus environment. The ^{183}W NMR results indicate that all 12 Keggin units are magnetically equivalent and the six belt tungsten atoms ($\delta = -157.9$ ppm) can be distinguished from the three capping tungsten atoms ($\delta = -134.0$ ppm). As expected, all 12 phosphorus atoms are fully equivalent. The NMR spectroscopy results of **2** are in good agreement with those of **1** (relative intensities in parenthesis): ^{183}W NMR: $\delta = -131.4$ (1), -139.1 ppm (2); ^{119}Sn NMR: $\delta = -228.4$ ppm; ^{13}C NMR: $\delta = 20.8$ (1), 10.3 ppm (2); ^{1}H NMR: $\delta = 2.0$ (1), 0.9 ppm (2). We do not have a good explanation why solution NMR spectroscopy does not enable the two types of tin atoms

in **1** and **2** to be distinguished which we identify in the crystal structure (Figures 1–3, 5, 6).

In summary, we have synthesized the supermolecular, spherical polyoxotungstate assemblies **1** and **2** using a simple one-pot procedure in aqueous medium. The structures of these compounds are unprecedented and allow for a multitude of studies including host–guest chemistry, ion exchange, gas storage, and use in catalysis and medicine. We have demonstrated that the dimethlytin group is a highly reactive electrophile which allows lacunary polyanion fragments to be linked in an unprecedented fashion. The resulting compounds are diamagnetic which allows multinuclear solution NMR studies to be performed, which is of major importance for medicinal applications. The fact that all tungsten centers are in the fully oxidized +VI state also allows for unequivocal determination of the charges of the product polyanions. In addition to the results we have already published (see ref. [18]) and the structure presented herein, we have several other discrete and also polymeric polyanion structures with completely unprecedented geometries. These results will be published elsewhere.

Experimental Section

$Cs_{14}Na_{22}$**1**·149 H_2O: A sample of $Na_9[A\text{-}PW_9O_{34}]$ (1.46 g, 0.600 mmol; synthesized according to ref. [22]) was added to a stirred solution of $(CH_3)_2SnCl_2$ (0.435 g, 1.98 mmol) in H_2O (20 mL). The pH value was adjusted to 4 by addition of 4 M HCl. This solution was heated to 80 °C for 1 h and then cooled to room temperature and filtered. Addition of 1.0 M CsCl solution (0.5 mL) to the colorless filtrate and slow evaporation at room temperature led to a white crystalline product after about one week. Yield: 1.3 g (69 %). IR: $\tilde{\nu}$ = 1084(s), 1070(s), 1019(m), 977(sh), 961(sh), 945(s), 928(s), 882(m), 833(s), 774(vs), 719(vs), 668(m), 640(sh), 596(w), 574(w), 520(m), 495(sh), 478(w), 465(w) cm^{-1}. Elemental analysis (%) calcd for $Cs_{14}Na_{22}$**1**·149 H_2O: Cs 5.0, Na 1.4, W 52.8, Sn 11.4, P 1.0, C 2.3, H 1.5; Found: Cs 4.6, Na 1.2, W 53.6, Sn 11.9, P 1.2, C 2.5, H 1.2.

$Cs_{14}Na_{22}$**2**·149 H_2O: The synthesis of this compound was analogous to $Cs_{14}Na_{22}$**1**·149 H_2O, but instead of $Na_9[A\text{-}PW_9O_{34}]$ we used $Na_8H[A\text{-}AsW_9O_{34}]$ (1.59 g, 0.600 mmol; synthesized according to ref. [23]) and the pH value was adjusted to 3. Yield: 1.2 g (63 %). IR: $\tilde{\nu}$ = 1015(sh), 983(sh), 951(s), 901(sh), 863(s), 840(sh), 773(s), 715(s), 658(s), 578(sh), 520(w), 484(w), 471(w), 411(m) cm^{-1}. Elemental analysis (%) calcd for $Cs_{14}Na_{22}$**2**·149 H_2O: Cs 4.9, Na 1.3, W 52.1, Sn 11.2, As 2.4, C 2.3, H 1.5; found: Cs 4.5, Na 1.2, W 53.1, Sn 11.6, As 2.6, C 2.4, H 1.6.

Elemental analyses were performed by Kanti Labs Ltd. in Mississauga, Canada.

Received: February 14, 2005
Published online: May 11, 2005

Keywords: organic–inorganic hybrid composites · polyoxometalates · supramolecular chemistry · tin · tungsten

[1] M. T. Pope, *Heteropoly and Isopoly Oxometalates*, Springer, Berlin, **1983**.
[2] M. T. Pope, A. Müller, *Angew. Chem.* **1991**, *103*, 56 – 70; *Angew. Chem. Int. Ed. Engl.* **1991**, *30*, 34 – 48.
[3] *Polyoxometalates: from Platonic Solids to Anti Retroviral Activity* (Eds.: M. T. Pope, A. Müller), Kluwer, Dordrecht, **1994**.
[4] *Chem. Rev.* **1998**, *98*, 1 – 389 (Special Thematic Issue on Polyoxometalates).
[5] *Polyoxometalate Chemistry: From Topology via Self-Assembly to Applications* (Eds.: M. T. Pope, A. Müller), Kluwer, Dordrecht, **2001**.
[6] *Polyoxometalate Chemistry for Nano-Composite Design* (Eds.: T. Yamase, M. T. Pope), Kluwer, Dordrecht, **2002**.
[7] J. Berzelius, *Poggendorff's Ann. Phys.* **1826**, *6*, 369.
[8] a) J. F. Keggin, *Nature* **1933**, *131*, 908 – 909; b) J. F. Keggin, *Proc. R. Soc. London Ser. A* **1934**, *144*, 75 – 77.
[9] C. L. Hill, C. M. Prosser-McCartha, *Coord. Chem. Rev.* **1995**, *143*, 407 – 455.
[10] B. Krebs, I. Paulat-Böschen, *Acta Crystallogr. Sect. B* **1982**, *38*, 1710 – 1718.
[11] M. Leyrie, G. Hervé, *Nouv. J. Chim.* **1978**, *2*, 233 – 237.
[12] R. Contant, A. Tézé, *Inorg. Chem.* **1985**, *24*, 4610 – 4614; R. Contant, *Inorg. Synth.* **1990**, *27*, 104 – 111.
[13] a) A. Müller, B. Botar, S. K. Das, H. Bögge, M. Schmidtmann, A. Merca, *Polyhedron* **2004**, *23*, 2381 – 2385; b) A. Müller, S. Q. N. Shah, H. Bögge, M. Schmidtmann, *Nature* **1999**, *397*, 48 – 50.
[14] K. Wassermann, M. H. Dickman, M. T. Pope, *Angew. Chem.* **1997**, *109*, 1513 – 1516; *Angew. Chem. Int. Ed. Engl.* **1997**, *36*, 1445 – 1448.
[15] E. Cadot, M. A. Pilette, J. Marrot; F. Sécheresse, *Angew. Chem.* **2003**, *115*, 2223 – 2226; *Angew. Chem. Int. Ed.* **2003**, *42*, 2173 – 2176, and references therein.
[16] U. Kortz, M. G. Savelieff, B. S. Bassil, M. H. Dickman, *Angew. Chem.* **2001**, *113*, 3488 – 3491, *Angew. Chem. Int. Ed.* **2001**, *40*, 3384 – 3386.
[17] a) F. Hussain, B. S. Bassil, L.-H. Bi, M. Reicke, U. Kortz, *Angew. Chem.* **2004**, *116*, 3567 – 3571; *Angew. Chem. Int. Ed.* **2004**, *43*, 3485 – 3488; b) U. Kortz, S. S. Hamzeh, N. A. Nasser, *Chem. Eur. J.* **2003**, *9*, 2945 – 2952.
[18] a) F. Hussain, U. Kortz, *Chem. Commun.* **2005**, 1191-1193; b) F. Hussain, M. Reicke, U. Kortz *Eur. J. Inorg. Chem.* **2004**, 2733 – 2738.
[19] Crystal data for $Cs_{14}Na_{22}$**1**·149 H_2O: A colorless block of for $Cs_{14}Na_{22}$**1**·149 H_2O with dimensions 0.10 × 0.09 × 0.05 mm^3 was mounted on a glass fiber for indexing and intensity data collection at 173 K on a Bruker D8 SMART APEX CCD single-crystal diffractometer using $Mo_{K\alpha}$ radiation (λ = 0.71073 Å). Of the 7655 unique reflections ($2\theta_{max}$ = 56.60°), 6604 reflections (R_{int} = 0.150) were considered observed ($I > 2\sigma(I)$). Direct methods were used to solve the structure and to locate the tungsten and tin atoms (SHELXS-97). Then the remaining atoms were found from successive difference maps (SHELXL-97). The final cycle of refinement, including the atomic coordinates, anisotropic thermal parameters (W, Sn, P, and Cs atoms), and isotropic thermal parameters (O atoms) converged at R = 0.064 and R_w = 0.148 ($I > 2\sigma(I)$). In the final difference map the deepest hole was −2.488 e $Å^{-3}$ and the highest peak 2.839 e $Å^{-3}$. Routine Lorentz and polarization corrections were applied and an absorption correction was performed using the SADABS program (G. M. Sheldrick, Siemens Analytical X-ray Instrument Division, Madison, WI, **1995**). Crystal data for $Cs_{14}Na_{22}$**2**·149 H_2O: A colorless block of for $Cs_{14}Na_{22}$**2**·149 H_2O with dimensions 0.10 × 0.10 × 0.05 mm^3 was mounted on a glass fiber. Indexing and intensity data collection, and structure solution and refinement was as for for $Cs_{14}Na_{22}$**1**·149 H_2O. Of the 7714 unique reflections ($2\theta_{max}$ = 56.56°), 6356 reflections (R_{int} = 0.138) were considered observed ($I > 2\sigma(I)$). R = 0.056 and R_w = 0.133 ($I > 2\sigma(I)$). In the final difference map the deepest hole was −2.539 e $Å^{-3}$ and the highest peak 3.597 e $Å^{-3}$. CCDC-263197 and CCDC-263198 contain the supplementary crystallographic data for this paper. These data can be obtained free of charge from the Cambridge

Crystallographic Data Centre via www.ccdc.cam.ac.uk/data_-request/cif.
[20] A. Müller, P. Kögerler, A. W. M. Dress, *Coord. Chem. Rev.* **2001**, *222*, 193 – 218.
[21] I. D. Brown, D. Altermatt, *Acta Crystallogr. Sect. B* **1985**, *41*, 244 – 247.
[22] P. J. Domaille, *Inorg. Synth.* **1990**, *27*, 100.
[23] L.-H. Bi, R.-D. Huang, J. Peng, E.-B. Wang, Y.-H. Wang, C.-W. Hu, *Dalton Trans.* **2001**, 121 – 129.

Polyoxometalates

The Wheel-Shaped Cu_{20} Tungstophosphate $[Cu_{20}Cl(OH)_{24}(H_2O)_{12}(P_8W_{48}O_{184})]^{25-}$ Ion**

*Sib Sankar Mal and Ulrich Kortz**

Polyoxometalates are a unique class of metal-oxide clusters. This family of compounds was discovered by Berzelius many years ago, but only recently the full potential of these species has been realized.[1–2] The search for novel polyanion structures is predominantly driven by the manifold applications of these compounds in areas as diverse as catalysis, bio- and nanotechnology, medicine, and materials science.[3–9]

The structural beauty of polyoxometalates is an additional feature that has contributed to this class attracting so much attention. Especially the work of Müller et al. has resulted in discrete molecular species with spectacular sizes and symmetries. For example, they reported gigantic mixed-valence polyoxomolybdate rings and spheres containing up to 368 molybdenum atoms.[10] Pope et al. reported a polyoxotungstate with 148 tungsten atoms, $[As_{12}Ce_{16}(H_2O)_{36}W_{148}O_{524}]^{76-}$.[11]

Interestingly all of the above species were synthesized without using any polyanion precursor. It must be realized that formation of polyanions is a self-assembly process, which depends more on the reaction conditions (e.g. pH value, concentration and ratio of reagents, ionic strengths) than on the type of polyanion precursors used.

We have been interested for some time in transition-metal-substituted polyoxotungstates, especially with respect to their magnetic and electrochemical properties.[12] There is interest in the synthesis of molecular species with high spin ground states. Lately Christou et al. reported the largest molecular magnet known to date composed of 84 manganese atoms.[13] Until then the so called "Mn_{12} acetate" had probably been the most attractive species in the area of single-molecule magnets.[14] Also polyoxometalate chemistry plays a major role in this field, as it allows for a bottom-up synthesis of paramagnetic multimetal-oxo-hydroxo clusters which are encapsulated and stabilized by diamagnetic polyanion fragments.[5–8,15] The magnetic and EPR properties of such discrete clusters can be analyzed in great detail, as usually intermolecular interactions are negligibly small.[12] Nevertheless, it must be realized that routinely polyoxotungstates with only three or four transition-metal ions have been synthesized, and only a handful of systems containing five or more paramagnetic centers.[12a,b,16]

In our search for highly lacunary polyanion ligands that might be an appropriate template for significantly larger paramagnetic clusters we have focused our attention on the established crown heteropolyanion $[H_7P_8W_{48}O_{184}]^{33-}$.[17] This species is composed of four $[H_2P_2W_{12}0_{48}]^{12-}$ fragments which are linked by capping tungsten atoms resulting in a cyclic arrangement. The stability of $[H_7P_8W_{48}O_{184}]^{33-}$ in aqueous solution over an unusually large pH range (1–8) and its large central cavity (diameter of around 10 Å) are highly attractive features. We can consider $[H_7P_8W_{48}O_{184}]^{33-}$ as a superlacunary polyanion, but surprisingly this species has been largely neglected as a precursor.[18] This situation is probably because Tézé and Contant concluded in 1985 that $[H_7P_8W_{48}O_{184}]^{33-}$ "does not give complexes with divalent or trivalent transition-metal ions".[17a] Nevertheless, we decided to investigate in detail the reactivity of paramagnetic 3d metal ions with $[H_7P_8W_{48}O_{184}]^{33-}$ in aqueous medium.

Interaction of $CuCl_2$ with $K_{28}Li_5[H_7P_8W_{48}O_{184}]$ in the ratio 24:1 in aqueous medium (pH 6) resulted in the large, wheel-shaped anion $[Cu_{20}Cl(OH)_{24}(H_2O)_{12}(P_8W_{48}O_{184})]^{25-}$ (**1**; Figures 1–3. Polyanion **1** crystallized as a mixed potassium-

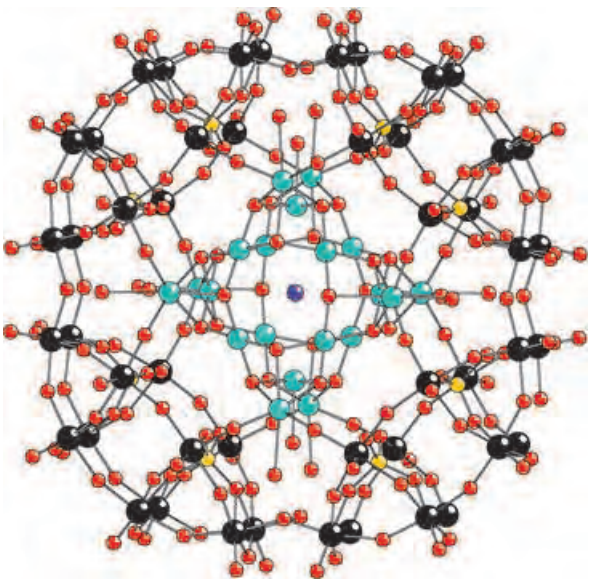

Figure 1. Ball-and stick-representation of $[Cu_{20}Cl(OH)_{24}(H_2O)_{12}(P_8W_{48}O_{184})]^{25-}$ (**1**). Black W, turquoise Cu, yellow P, violet Cl, red O.

[*] S. S. Mal, Prof. U. Kortz
International University Bremen
School of Engineering and Science
P.O. Box 750 561, 28725 Bremen (Germany)
Fax: (+49) 421-200-3229
E-mail: u.kortz@iu-bremen.de

[**] U.K. thanks the International University Bremen and the DFG (grant KO 2288/3-1) for research support. U.K. also highly appreciates that Prof. J. Kopf at Hamburg University allowed him access to the single-crystal X-ray diffractometer. Figure 1–Figure 5 were generated by Diamond Version 3 (copyright Crystal Impact GbR).

 DOI: 10.1002/anie.200500682

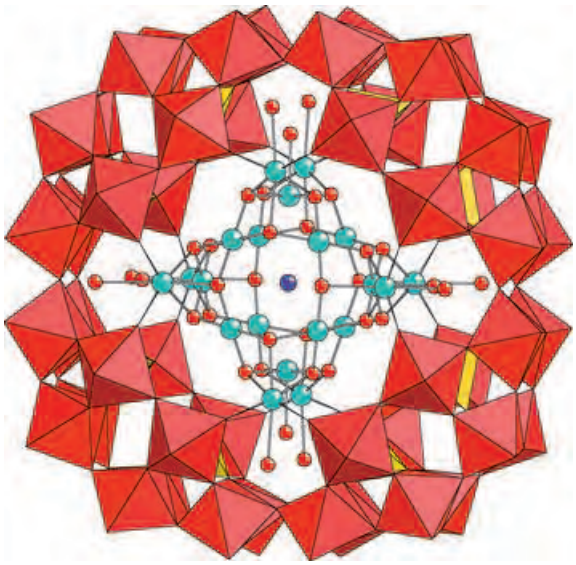

Figure 2. Combined polyhedral/ball-and-stick representation of **1**. The WO_6 octahedra are red and the PO_4 tetrahedra are yellow. Otherwise, the labeling scheme is the same as that in Figure 1.

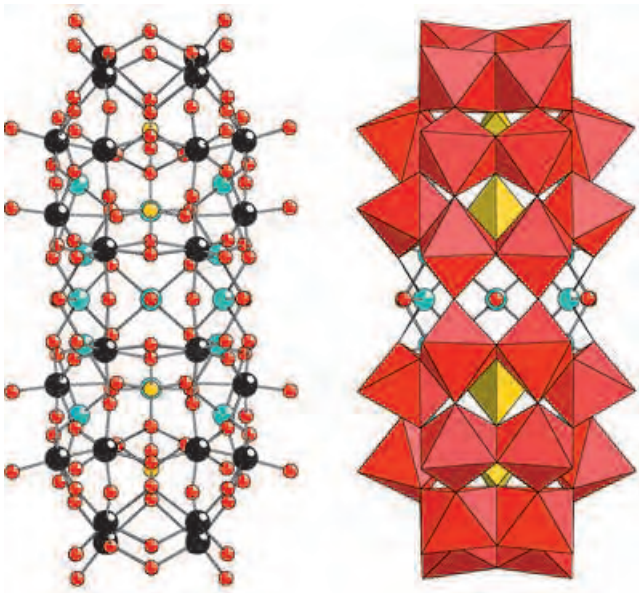

Figure 3. Side view of **1** showing ball-and-stick (left) and combined polyhedral/ball-and-stick (right) representations.

lithium salt in the tetragonal system (space group $I4/m$).[19] As a result, the asymmetric unit of **1** includes only six tungsten and three copper atoms (Figure 4).

The polyanion **1** is unprecedented in structure, size, and composition. This molecule is the first transition-metal-substituted derivative of $[H_7P_8W_{48}O_{184}]^{33-}$ and it incorporates more paramagnetic 3d metal ions than any other polyoxotungstate to date.[12a,b,16] The structure of the wheel-shaped $[H_7P_8W_{48}O_{184}]^{33-}$ precursor is maintained in **1** and the cavity is filled with a highly symmetrical copper-hydroxo cluster (Figure 1, Figure 2, and Figure 5). This structure emphasizes that the template effect plays an important role during

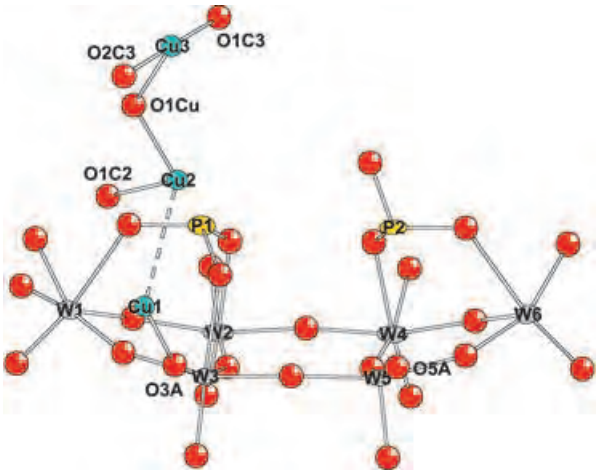

Figure 4. Ball-and-stick representation of the asymmetric unit of **1**, thermal ellipsoids shown are set at 50% probability.

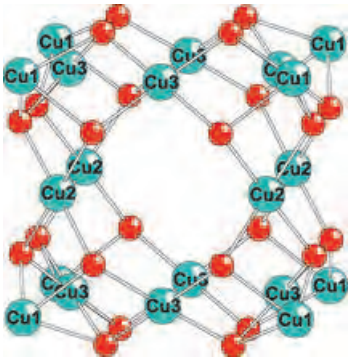

Figure 5. Ball and stick representation of the copper-hydroxo cluster in **1** showing all structurally equivalent copper atoms with the same label. Only the oxo-ligands bridging neighboring copper ions are shown.

formation of **1**. We have shown that the oxo-groups in the cavity of the tungstophosphate precursor $[H_7P_8W_{48}O_{184}]^{33-}$ do actually interact with transition-metal ions in aqueous medium, but some heating is required (see Experimental Section). Therefore, $[H_7P_8W_{48}O_{184}]^{33-}$ can indeed be considered as a superlacunary polyanion precursor and we expect that other transition-metal ions besides copper(II) can also be incorporated.

The Cu_{20} cluster in **1** is composed of only three structurally unique types of copper(II) ions (eight Cu1, four Cu2, and eight Cu3; see Figure 5). All 20 copper centers are bridged to neighboring copper ions by μ_3-oxo ligands to give a highly symmetrical, cage-like assembly. Based on bond valence sum calculations all 24 bridging oxygen atoms are monoprotonated.[20] The center of the cavity (which has a diameter of around 7 Å) is occupied by a chloride ion (Figure 1 and Figure 2). The coordination numbers and geometries of Cu1, Cu2, and Cu3 are different from each other. Cu1 is coordinated in a strongly distorted octahedral fashion and exhibits Jahn–Teller distortion with axial elongation. The equatorial plane is composed of Cu1–O3A (1.922(14) Å), Cu1–O5A (1.926(15) Å), Cu1–O2C3 (1.980(14) Å), and Cu1–O1Cu (1.986(14) Å) bonds. The two axial bonds are

Cu1–O1C3 (2.358(16) Å) and a very long bond Cu1–O5W (2.504(17) Å) to a terminal water molecule.[20] This very long bond Cu1–O5W is not shown in Figure 4 as the bond order is almost negligibly small (around 0.1), nevertheless, this bond is shown in Figures 1–3. The angle O1C3-Cu1-O5W is only 145° which reflects steric hindrance of the water ligand. Cu2 has square-pyramidal coordination geometry with two Cu2–O2C3 (1.922(14) Å) and two Cu2–O1Cu (1.925(14) Å) bonds in the equatorial plane and a long bond to a terminal water ligand, Cu2–O1C2 (2.29(3) Å).[20] Finally, Cu3 has a square-planar coordination geometry which is composed of Cu3–O1C3 (1.905(16) Å), Cu3–O1Cu (1.933(14) Å), Cu3–O1C3′ (1.947(16) Å), and Cu3–O2C3 (1.948(14) Å) bonds. The copper–copper distances in **1** are: Cu1···Cu2 2.812(3) Å, Cu1···Cu3 3.045(4) Å, and Cu1···Cu3′ 3.052(4) Å.

We also investigated the solution properties of **1** by ^{31}P NMR spectroscopy at room temperature in D_2O (400 MHz; JEOL ECX instrument). We observed a singlet at $\delta = -29.3$ ppm indicating that all eight phosphorus atoms in **1** are equivalent, which is in complete agreement with the solid-state structure (Figure 1 and Figure 2). We have not yet obtained a good ^{183}W NMR spectrum for **1** (expected are three signals of equal intensity), probably due to solubility problems.

In summary, we have synthesized a large, wheel-shaped, Cu_{20} containing polyanion by direct reaction of copper(II) ions with $[H_7P_8W_{48}O_{184}]^{33-}$. The polyanion **1** contains more paramagnetic 3d transition-metal centers than any other polyoxotungstate reported to date. Furthermore, it is stable in solution, as shown by ^{31}P NMR spectroscopy. Contrary to prior reports, we have shown that the wheel-shaped $[H_7P_8W_{48}O_{184}]^{33-}$ 1) actually does react with transition-metal ions in aqueous medium using simple, one-pot procedures, 2) is to be considered as a superlacunary polyanion precursor, 3) acts as a template which allows the construction of large transition-metal-oxo clusters, and 4) is probably also reactive towards many other electrophiles (e.g. rare earths and organotin species). We consider $[H_7P_8W_{48}O_{184}]^{33-}$ as a ligand of choice in our search for paramagnetic polyanions with high spin ground states. Currently we are investigating the magnetic, EPR, and electrochemical properties of **1** and these results will be reported elsewhere. We are also interested to see of derivatives of **1** incorporating other transition-metals besides copper(II) and other guests besides Cl^- can be isolated. In fact, we have already prepared a cobalt(II)-containing derivative with a structure different from **1**. Furthermore, the cage-like structure of **1** allows studies in host–guest chemistry, ion exchange, gas storage, catalysis and medicine to be envisaged.

Experimental Section

Preparation $K_{12}Li_{13}$**1**$\cdot 22H_2O$: A sample of $CuCl_2\cdot 2H_2O$ (0.10 g, 0.60 mmol) was dissolved in a 1M $LiCH_3COO$ buffer solution (20 mL) at pH 6.0, then $K_{28}Li_5[H_7P_8W_{48}O_{184}]\cdot 92H_2O$ (0.37 g 0.025 mmol) (synthesized according to ref [17b]) was added. This solution was heated to 80 °C for 1 h and after cooling to room temperature it was filtered. The filtrate was allowed to evaporate in an open beaker at room temperature. After 1–2 days a blue crystalline product started to appear. Evaporation was allowed to continue until the solution level had approached the solid product, which was then collected by filtration and air-dried. Yield: 0.11 g (30%). IR: $\tilde{\nu} = 1137$(sh), 1121(s), 1080(s), 1017(m), 979(sh), 951(sh), 932(s), 913(sh), 832(sh), 753(s), 681(s), 570(sh), 523(w), 470 cm^{-1}(w). Elemental analysis (%) calcd for $K_{12}Li_{13}$**1**$\cdot 22H_2O$: K 3.2, Li 0.6, W 59.2, Cu 8.5, P 1.7; found: K 3.4, Li 0.8, W 58.8, Cu 8.6, P 1.6.

Elemental analysis was performed by Kanti Labs Ltd. in Mississauga, Canada.

Received: February 23, 2005
Published online: May 11, 2005

Keywords: copper · polyoxometalates · supramolecular chemistry · template synthesis · tungsten

[1] J. Berzelius, *Poggendorff's Ann. Phys.* **1826**, *6*, 369.
[2] a) J. F. Keggin, *Nature* **1933**, *131*, 908–909; b) J. F. Keggin, *Proc. R. Soc. London Ser. A* **1934**, *144*, 75–77.
[3] M. T. Pope, *Heteropoly and Isopoly Oxometalates*, Springer, Berlin, **1983**.
[4] M. T. Pope, A. Müller, *Angew. Chem.* **1991**, *103*, 56–70; *Angew. Chem. Int. Ed. Engl.* **1991**, *30*, 34–48.
[5] *Polyoxometalates: from Platonic Solids to Anti Retroviral Activity* (Eds.: M. T. Pope, A. Müller), Kluwer, Dordrecht, **1994**.
[6] *Chem. Rev.* **1998**, *98*, 1–389 (Special Thematic Issue on Polyoxometalates).
[7] *Polyoxometalate Chemistry: From Topology via Self-Assembly to Applications* (Eds.: M. T. Pope, A. Müller), Kluwer, Dordrecht, **2001**.
[8] *Polyoxometalate Chemistry for Nano-Composite Design* (Eds.: T. Yamase, M. T. Pope), Kluwer, Dordrecht, **2002**.
[9] C. L. Hill, C. M. Prosser-McCartha, *Coord. Chem. Rev.* **1995**, *143*, 407–455.
[10] a) A. Müller, B. Botar, S. K. Das, H. Bögge, M. Schmidtmann, A. Merca, *Polyhedron* **2004**, *23*, 2381–2385; b) A. Müller, S. Q. N. Shah, H. Bögge, M. Schmidtmann, *Nature* **1999**, *397*, 48–50.
[11] K. Wassermann, M. H. Dickman, M. T. Pope, *Angew. Chem.* **1997**, *109*, 1513–1516; *Angew. Chem. Int. Ed. Engl.* **1997**, *36*, 1445–1448.
[12] Examples of recent work include: a) B. S. Bassil, S. Nellutla, U. Kortz, A. C. Stowe, J. van Tol, N. S. Dalal, B. Keita, L. Nadjo, *Inorg. Chem.* **2005**, *44*, 2659–2665; b) L.-H. Bi, U. Kortz, S. Nellutla, A. C. Stowe, N. S. Dalal, B. Keita, L. Nadjo, *Inorg. Chem.* **2005**, *44*, 896–903; c) A. C. Stowe, S. Nellutla, N. S. Dalal, U. Kortz, *Eur. J. Inorg. Chem.* **2004**, 3792–3797; d) D. Jabbour, B. Keita, I. M. Mbomekalle, L. Nadjo, U. Kortz, *Eur. J. Inorg. Chem.* **2004**, 2036–2044; e) U. Kortz, S. Nellutla, A. C. Stowe, N. S. Dalal, U. Rauwald, W. Danquah, D. Ravot, *Inorg. Chem.* **2004**, *43*, 2308–2317; f) U. Kortz, S. Nellutla, A. C. Stowe, N. S. Dalal, J. van Tol, B. S. Bassil, *Inorg. Chem.* **2004**, *43*, 144–154.
[13] A. J. Tasiopoulos, A. Vinslava, W. Wernsdorfer, K. A. Abboud, G. Christou, *Angew. Chem.* **2004**, *116*, 2169–2173; *Angew. Chem. Int. Ed.* **2004**, *43*, 2117–2121.
[14] a) R. Sessoli, D. Gatteschi, A. Caneschi, M. A. Novak, *Nature* **1993**, *365*, 141–143; b) T. Lis, *Acta Crystallogr. Sect. B* **1980**, *36*, 2042–2046.
[15] J. M. Clemente-Juan, E. Coronado, *Coord. Chem. Rev.* **1999**, *193–195*, 361–394.
[16] a) L.-H. Bi, U. Kortz, *Inorg. Chem.* **2004**, *43*, 7961–7962; b) T. M. Anderson, W. A. Neiwert, K. I. Hardcastle, C. L. Hill, *Inorg. Chem.* **2004**, *43*, 7353–7358; c) P. Mialane, A. Dolbecq, J. Marrot, E. Rivière, F. Sécheresse, *Angew. Chem.* **2003**, *115*, 3647–3650; *Angew. Chem. Int. Ed.* **2003**, *42*, 3523–3526; d) J. M. Clemente-Juan, E. Coronado, J. R. Galán-Mascarós, C. J. Gómez-García, *Inorg. Chem.* **1999**, *38*, 55–63; e) K. Wassermann, R. Palm, H.-J. Lunk, J. Fuchs, N. Steinfeldt, R. Stösser,

Inorg. Chem. **1995**, *34*, 5029 – 5036; f) T. J. R. Weakley, *J. Chem. Soc. Chem. Commun.* **1984**, 1406 – 1407.

[17] a) R. Contant, A. Tézé, *Inorg. Chem.* **1985**, *24*, 4610 – 4614; b) R. Contant, *Inorg. Synth.* **1990**, *27*, 110.

[18] A cerium-containing derivative of $[H_7P_8W_{48}O_{184}]^{33-}$ with the formula $[(K)Ce_6P_8W_{56}O_{208}]^{21-}$ was recently presented at a conference. M. T. Pope, *International Symposium on Nanostructures and Physicochemical Properties of Polyoxometalate Superclusters and Related Colloid Particles*, Shonan Village Center, Kanagawa, Japan, 21.-25. November 2004.

[19] Crystal data for $K_{12}Li_{13}$**1**$\cdot 22\,H_2O$: A blue block with dimensions $0.09 \times 0.07 \times 0.06\ mm^3$ was mounted on a glass fiber for indexing and intensity data collection at 153 K on a Bruker D8 SMART APEX CCD single-crystal diffractometer using $Mo_{K\alpha}$ radiation ($\lambda = 0.71073$ Å). Of the 9102 unique reflections ($2\theta_{max} = 56.12°$), 5826 reflections ($R_{int} = 0.083$) were considered observed ($I > 2\sigma(I)$). Direct methods were used to solve the structure and to locate the tungsten and copper atoms (SHELXS-97). Then the remaining atoms were found from successive difference maps (SHELXL-97). The final cycle of refinement, including the atomic coordinates, anisotropic thermal parameters (W, Cu, P, K and Cl atoms), and isotropic thermal parameters (O atoms) converged at $R = 0.068$ and $R_w = 0.179$ ($I > 2\sigma(I)$). No lithium ions could be located crystallographically. In the final difference map the deepest hole was $-3.054\ e\,Å^{-3}$ and the highest peak $4.663\ e\,Å^{-3}$. Routine Lorentz and polarization corrections were applied and an absorption correction was performed using the SADABS program (G. M. Sheldrick, Siemens Analytical X-ray Instrument Division, Madison, WI, **1995**). Further details on the crystal structure investigations may be obtained from the Fachinformationszentrum Karlsruhe, 76344 Eggenstein-Leopoldshafen, Germany (fax: (+49) 7247-808-666; e-mail: crysdata@fiz-karlsruhe.de), on quoting the depository number CSD-415126.

[20] I. D. Brown, D. Altermatt, *Acta Crystallogr. Sect. B* **1985**, *41*, 244 – 247.

